

# Batteries

2023 Annual Progress Report

Vehicle Technologies Office

(This page intentionally left blank)

## Disclaimer

This report was prepared as an account of work sponsored by an agency of the United States government. Neither the United States government nor any agency thereof, nor any of their employees, makes any warranty, express or implied, or assumes any legal liability or responsibility for the accuracy, completeness, or usefulness of any information, apparatus, product, or process disclosed or represents that its use would not infringe privately owned rights. Reference herein to any specific commercial product, process, or service by trade name, trademark, manufacturer, or otherwise does not necessarily constitute or imply its endorsement, recommendation, or favoring by the United States government or any agency thereof. The views and opinions of authors expressed herein do not necessarily state or reflect those of the United States government or any agency thereof.

## Acknowledgements

The projects reported in this report were supported through various contracts funded by the U.S. Department of Energy, Vehicle Technologies Office. A list of contributing authors appears in the sections for specific projects in this report.

## Acronyms

ABL	Active buffer layer
ABMR	Advanced Battery Materials Research
AC	Alternating current
ACPA	4,4'-Azobis(4-cyanopentanoic acid)
ACS	American Chemical Society
AEM	Advanced Electrolyte Model
AER	All-electric range
AFLB	"Anode-free" lithium battery
AFM	Atomic force microscopy
AFSE	Fluorinated saturated electrolyte (FSE) with 0.1% wt additive
AI	Artificial Intelligence
AIMD	Ab initio molecular dynamics
AIR	Areal interfacial resistance
ALD	Atomic layer deposition
ALS	Advanced Light Source
AMD	Applied Materials Division (at ANL)
AMO	Advanced Manufacturing Office
AMR	Annual Merit Review
ANL	Argonne National Laboratory
AOM	Amphiphathic organic molecules
APL	Applied Physics Laboratory
APR	Annual progress report
APS	Advanced Photon Source (laboratory)
AQ	Anthraquinone
AQC	Anthraquinone-2-carboxylic acid
AQT	Soluble-type 1,5-bis(2-(2-(2-methoxyethoxy) ethoxy) ethoxy) anthra-9,10-quinon
ARL	Army Research Laboratory
ASI	Area-specific impedance
ASLSB	All solid lithium-sulfur battery
ASR	Area-specific resistance
ASSB	All solid-state battery
ASSLB	All solid-state Li metal batteries
ASSLMB	All-solid-state Li metal battery
ATIR	Attenuated total reflectance (spectroscopy)
B500	Battery500 (Consortium)
BAM	Battery active materials
BCC	Body-centered cubic
BET	Brunauer, Emmett, and Teller (surface area analysis)
BEV	Battery electric vehicle
BIL	Bipartisan Infrastructure Law
BLI	Beyond Lithium-ion
BM	Black mass

BMF	Battery manufacturing facility
BMP	Black mass purification (at NREL)
BMR	(Advanced) Battery Materials Research (program)
BMS	Battery management system
BNL	Brookhaven National Laboratory
BOL	Beginning of life
BOM	Bill of materials
BTC	Battery Technology Center
BTFE	Bis(2,2,2-trifluoroethyl) ether
BTMS	Behind-the-Meter-Storage
CAD	Computer-aided design
CAFE	Corporate Average Fuel Economy
CAM	Cathode active materials
CAMP	Cell analysis, modeling, and prototyping (facility)
CB	Carbon black
CBD	Conductive binder domain
CBSE	Cluster-based solid electrolytes
CCA	Carbon conductive additive
CCC	Cell cooling coefficient
CC-CV	Constant current constant voltage (charging protocol)
CCD	Critical current density
CD	Current density
CE	Coulombic efficiency
CEI	Cathode electrolyte interfaces
CFM	Carbon-based framework materials
CLP	Cycle life projection
CM	Co-melting (synthesis method)
CMC	Carboxymethyl cellulose
CNEB	Climbing image nudged elastic band
CNM	Center for Nanoscale Materials (at ANL)
CNS	Carbon nano structures
CNT	Carbon nano-tubes
COA	Certificates of analysis
CP	Co-precipitation
CPE	Constant phase element
CPI	Composite polymer introduction (layer)
CSM	Continuous symmetry measure
CSTR	Continuous stirred tank reactor
CV	Cyclic voltammetry
CY	Calendar year
DAC	Dry aerosol calcination
DBU	Diazabicycloundecane
DCIR	Direct current inner resistance
DCM	Dichloromethane (solvent)
DCR	Direct current resistance

DCT	Diffraction contrast tomography
DEB	Double-end binding (sites)
DEGDME	Diethylene glycol dimethyl ether
DEMS	Differential electrochemical mass spectrometry
DEPP	Diethyl phenylphosphonite
DFEC	Bis(trifluoroethyl) carbonate (DFEC)
DFOB	(Lithium) difluoro(oxalate)borate
DFT	Density function theory
DL	Deep-learning (algorithm)
DLE	Direct lithium extraction
DLP	Double-layer pouch (cell)
DMC	Dimethyl carbonate
DME	Dimethyl ether
DMF	Dimethylformamide
DMSO	Dimethylsulfoxide
DOD	Depth-of-discharge
DOE	Department of Energy
DOL	Dioxolane
DOS	Density of state
DPA	Destructive physical analysis
DPDMS	Diphenyldimethoxysilane
DRS	Disordered rock-salt
DRT	Distribution of relaxation times (analysis)
DRX	Disordered (rocksalt) transition metal oxides
DS	Double-sided
DSC	Differential scanning calorimetry
DST	Dynamic stress test
DTG	Derivative Thermo-Gravimetric (technique)
EADL	Electrochemical Analysis and Diagnostic Laboratory (at ANL)
EB	Electron beam
EBS	Electron back-scattering diffraction
EBS/EDS	Electron backscatter diffraction - energy dispersive X-ray spectrometry
EC	Ethylene carbonate
EC/DEC	Ethylene carbonate/diethyl carbonate (electrolyte)
EC/DMC	Ethylene carbonate/dimethyl carbonate (electrolyte)
EC/EMC/DEC	Ethylene carbonate/ethyl methyl carbonate/diethyl carbonate (electrolyte)
EC-AFM	Electrochemical atomic force microscopy
EC-EMC	Ethylene carbonate –ethyl methyl carbonate electrolytes
ECMF	Electrocatalyst modified framework material
ECS	Electrochemical Society
EDS	Energy dispersive spectroscopy
EDTA	Electric Drive Transportation Association
EDV	Electric Drive Vehicle
EDX	Energy-dispersive x-ray (spectroscopy)
EEL	Electron Energy Loss (Spectroscopy)

EELS	Electron energy loss spectroscopy
EERE	Energy Efficiency and Renewable Energy (DOE Office)
EIA	Energy Information Administration
EIS	Electrochemical impedance spectroscopy
EMC	Ethylmethyl carbonate
EMN	Energy Materials Network
EMS	Energy management system
EMT	Effective medium theory (calculation)
EO	Ethylene oxide
EODV	Voltage at the end of discharge
EOL	End of life
EPA	Environmental Protection agency
EPD	Electrophoretic deposition
EPR	Electron Paramagnetic Resonance
ESS	Energy storage system
EV	Electric vehicle
EXAFS	Extended X-ray absorption fine structure
FAMU	Florida A&M University
FASP	Flame-assisted spray pyrolysis synthesis
FC	Fast-charge
FCC	Face-centered cubic (structure)
FCG	Full concentration-gradient
FDES	Fluorinated deep eutectic solvent
FEC	Fluoro ethylene carbonate
FEMC	Fluoroethyl methyl carbonate
FFT	Fast Fourier-transform
FIB	Focused ion beam
FMMB	Mono-methyl-2,2,3,3-tetrafluorobutandiol
FOA	Federal opportunity announcement
FRS	Filtered Rayleigh Scattering
FSE	Fluorinated saturated electrolyte
FSI	(Lithium) bis(trifluoromethanesulfonyl)imide
FSP	Flame spray pyrolysis
FSP-DP	Flame spray pyrolysis - droplet-to-particle mode
FSP-GP	Flame spray pyrolysis - gas-to-particle mode
FTC	Freeze tape casting (technique)
FTIR	Fourier transform infrared spectroscopy
FWHM	Full width at half maximum
FY	Fiscal year
GC	“generation/collection” (mode)
GCMA	Glycerol carbonate methacrylate
GDL	(Carbon paper) gas diffusion layer
GDOES	Glow discharge optical emission spectrometry
GED	Gravimetric energy density
GEIS	Galvanostatic electrochemical impedance spectroscopy



GEMT	(McLachlan) generalized effective medium theory
GGA	Generalized gradient approximation
GHG	Green-house gases
GITT	Galvanostatic intermittent titration
GIXRD	Grazing incidence X-ray diffraction
GMU	George Mason University
GN	Glutaronitrile
GOS	Grain orientation spread
GPA	Geometric phase analysis
GPC	Gel permeation chromatography
GREET	Greenhouse gas regulated energy and emissions and transpiration
GROD	Grain reference orientation deviation
GSAS	General structure analysis systems
GSE	Glassy solid electrolyte
HAADF	High-angle annular dark-field
HATN	Hexaazatrinaphthylene
HAWCS	Hybrid Alternative Wet-Chemical Synthesis
HAXPES	High energy x-ray photoelectron spectroscopy
HBL	Homogeneous baseline (coating design)
HEV	Hybrid electric vehicle
HEXRD	High-energy XRD
HF	Hydrofluoric acid
HFB	Hexafluorobenzene
HFE	Hydrocarbon vs. fluoroether
HFTO	Hydrogen and Fuel Cell Technologies Office
HG	Hand-grinding (mixing strategy)
HOMO	Highest occupied molecular orbital (energy level)
HOMO/LUMO	Highest occupied molecular orbital/lowest unoccupied molecular orbital (energy level)
HP	Hot-pressed (sample)
HPC	Highly porous carbon
HPLC	High-performance liquid chromatography
HPPC	Hybrid pulse power characterization
HRTEM	High-resolution transmission electron microscopy
HV	High viscosity (slurry)
HVM	High volume manufacturing
IC	Incremental capacity
ICE	Internal combustion engine
ICP	Inductively coupled plasma
IEA	International Energy Agency
INL	Idaho National Laboratory
IOFM	Inorganic-organic framework materials
IPA	Isopropanol
IPF	Inverse pole figure
IR	Infra-red
IRCL	Irreversible capacity loss

IZ	Isoxazole
KIC	Plane strain fracture toughness
KMC	Kinetic Monte Carlo (simulations)
KPFM	Kelvin Probe Force Microscopy
LAADF	Low-angle annular dark-field
LAGP	$\text{Li}_{1.5}\text{Al}_{0.5}\text{Ge}_{1.5}(\text{PO}_4)_3$
LAM	Loss of active materials
LAMMPS	Large-scale atomic/molecular massively parallel simulator
LAMNE	Loss of active materials at the negative electrode
LAMPE	Loss of active materials at the positive electrode
LANL	Los Alamos National Laboratory
LATP	$\text{Li}_{1.17}\text{Al}_{0.17}\text{Ti}_{1.83}(\text{PO}_4)_3$
LBNL	Lawrence Berkeley National Laboratory
LBS	Lithium thioborates
LCA	Life cycle analysis
LCE	Lithium-carbonate equivalent
LCFC	Low-cost fast charge (battery)
LCI	Life-cycle inventory
LCO	Lithium cobalt oxide
LCOE	Levelized cost of electricity
LCRC	Laboratory Computing Resource Center (at ANL)
LDV	Light-duty vehicles
LE	Liquid electrolyte
LEDC	Lithium ethylene dicarbonate
LFP	Li-iron phosphate
LGPS	$\text{Li}_{10}\text{GeP}_2\text{S}_{12}$
LHCE	Localized high concentration electrolyte
LHS	Left hand-side
LIBRA	Lithium Ion Battery Recycling Analysis
LIC	Lithium-ion conducting
LLI	Loss of lithium inventory
LLNL	Lawrence Livermore National Laboratory
LLS	Layered-layered spinel
LLZ	$\text{Li}_7\text{La}_3\text{Zr}_2\text{O}_{12}$
LLZO	Lithium lanthanum zirconate
LLZTO	$\text{Li}_{6.75}\text{La}_3\text{Zr}_{1.75}\text{Ta}_{0.25}\text{O}_{12}$
LMA	Lithium metal anode
LMB	Lithium metal battery
LMNOF	Li-Mn-Nb-O-F
LMO	Lithium manganese oxide
LMR	Lithium manganese rich (cathode)
LMSSB	Li metal solid-state battery
LMTO	$\text{Li}_{1.2}\text{Mn}_{0.4}\text{Ti}_{0.4}\text{O}_2$ (cathode)
LMTOF	Li-Mn-Ti-O-F
LNMO	$\text{LiNi}_{0.5}\text{Mn}_{0.5}\text{O}_2$

LNMTO	$\text{LiNi}_{0.5}\text{Mn}_{1.2}\text{TiO}_{0.3}\text{O}_4$
LNO	Lithium-nickel oxide
LNTMOF	$\text{Li}_{1.15}\text{Ni}_{0.45}\text{Ti}_{0.3}\text{Mo}_{0.1}\text{O}_{1.85}\text{F}_{0.15}$
LPBSI	$\text{Li}_7\text{P}_2\text{S}_8\text{Br}_{0.5}\text{I}_{0.5}$
LPC	Large particle cathodes
LPF	$\text{Li}/\text{LiFePO}_4$ (half-cell)
LPO	$\text{Li}_3\text{PO}_4$
LPS	$\text{Li}_3\text{PS}_4$
LPSBI	$\text{Li}_7\text{P}_2\text{S}_8\text{Br}_{0.5}\text{I}_{0.5}$
LPSIB	$\text{Li}_7\text{P}_2\text{S}_8\text{I}_{0.5}\text{Br}_{0.5}$
LPSX	$\text{Li}_7\text{-yPS}_6\text{-yX}_y$
LSCE	Locally-superconcentrated electrolyte
LSE	Localized saturated electrolyte
LSV	Linear scanning voltammetry
LT	Low-temperature
LTAP	$\text{Li}_{1.3}\text{Al}_{0.3}\text{Ti}_{1.7}(\text{PO}_4)_3$
LTMO	$\text{Li}_{1.2}\text{Mn}_{0.4}\text{Ti}_{0.4}\text{O}_2$
LTO	Lithium titanate, $\text{Li}_4\text{Ti}_5\text{O}_{12}$
LUMO	Lowest unoccupied molecular orbital (energy level)
LV	Low viscosity
LYB	$\text{Li}_3\text{YBr}_6$
LYC	$\text{Li}_3\text{YCl}_6$
MAS	Magic angle spinning
MC	Monte Carlo (method)
MCA	Multicomponent alloy
MCF	Methyl chloroformate
MERF	Materials Engineering Research Facility
MFA	Material flow analysis
MGF	Mixed glass former (glassy film)
MIC	Molecular ionic composites
ML	Machine learning
MLFF	Machine learning-based force field
MLMD	Machine learning-based molecular dynamic (simulation)
MLPC	Multi-layer pouch cell
MMB	Monomethyl butanediol
MOF	Metal Organic Framework
MOSN	Mixed oxy-sulfide-nitride (glass)
MP	Methyl propionate
MPFPC	Methyl (pentafluoropropyl)carbonate
MRS	Materials Research Society
MS	Mass spectroscopy
MSD	Mean square displacements
MSR	Material-stress reduction (protocol)
MTFPC	Methyl (tetrafluoropropyl)carbonate
NASICON	(Na) Super Ionic CONductor

NATM	Naturally abundant material
NBR	Nitrile butadiene rubber
NCA	$\text{LiNi}_{0.8}\text{Co}_{0.15}\text{Al}_{0.05}\text{O}_2$
NCM	$\text{Li}_{1+w}[\text{Ni}_x\text{Co}_y\text{Mn}_z]_{1-w}\text{O}_2$
NEB	Nudged elastic band (method)
NETL	National Energy Technology Laboratory
NEXAFS	Near-edge X-ray absorption fine structure (measurements)
NF	Nanoflakes
NG	Natural graphite (anode)
NHTSA	National Highway Transportation Safety Administration
NIB	Sodium (Na)-ion battery
NIR	Near-infrared (emission)
NKB	Nitrogen doped integrated Ketjen Black (particles)
NMA	$\text{LiNi}_{0.9}\text{Mn}_{0.05}\text{Al}_{0.05}\text{O}_2$
NMC	Nickel manganese cobalt (oxide)
NMCA	Nickel-manganese-cobalt-aluminium oxide (cathode)
NMFCN	$\text{NaMnFeCoNiO}_2$
NMP	N-methylpyrrolidone
NMR	Nuclear magnetic resonance
NP	Nanoparticles
NPDF	Neutron PDF
NR	Neutron reflectometry
NREL	National Renewable Energy Laboratory
NTO	(Lithium manganese) nickel titanium oxide
NVP	$\text{Na}  \text{Na}_3\text{V}_2(\text{PO}_4)_3$ (cathode)
NVT	Canonical ensemble (N, V, T conditions)
OCV	Open circuit voltage
OEM	Original equipment manufacturer
OER	Oxygen evolution reactions
OES	Optical Emission Spectroscopy
OMSH	Ordered macroporous sulfur host
OPLS	Optimized potentials for liquid simulations
ORNL	Oak Ridge National Laboratory
ORR	Oxygen reduction reaction
OSE	Optical spectroscopic ellipsometry
OSU	Oregon State University
P&E	Processing Science & Engineering
P&ID	Piping and instrumentation diagram
PAA	Polyacrylic Acid
PAD	Polymer Assisted Deposition
PAN	Polyacrylonitrile
PAQ	9,10-phenanthrenequinone
PAW	Projected augmented wave
PBDT	Poly-2,2'-disulfonyl-4,4'-benzidine ter-ephthalamide
PBE	Perdew, Burke, and Ernzerhof (parameters)

PBLM	Parallel brick layer model
PC	Propylene carbonate
PCC	Project completion cell
PDF	Pair density function
PE	Polyethylene
PECVD	Plasma-enhanced chemical vapor deposition
PEEK	Polyetheretherketone
PEGDA	Poly(ethylene glycol) diacrylate
PEGDGE	Poly(ethylene glycol) diglycidyl ether
PEGDMA	Polyethylene glycol dimethacrylate
PEI	Polyethylenimine
PEM	Poly(ethylene malonate)
PEO	Polyethyleneoxide
PES	Prop-1-ene-1,3-sultone
PET	Polyethylene terephthalate
PEV	Plug-in electric vehicle
PEY	Partial electron yield
PFE	Pentafluoroethane
PFIB-SEM	Plasma focused ion beam scanning electron microscopy
PFM	Poly (9,9-dioctylfluorene-co-fluorenone-comethylbenzoic ester)
PFPE	Perfluoropolyether
PFY	Partial fluorescence yield
PHEV	Plug-in hybrid electric vehicle
PHM	Poly(hexylene malonate)
PI	Principal investigator
PITT	Potentiostatic intermittent titration technique
PL	Photoluminescence
PLD	Pulsed laser deposition
PLIF	Planar Laser Induced Fluorescence
PMF	Poly(melamine-co-formaldehyde) methylated
PMS	Power management system
PMTH	Dipentamethylenethiuram hexasulfide
PNCM	Phosphate-affected NCM cathode
PNNL	Pacific Northwest National Laboratory
PPM	Poly(pentylene malonate)
PPO	Polyphenylene oxide
PSD	Particle size distribution
PSU	Pennsylvania State University
PTF	Post-Test Facility
PTFE	Poly(tetrafluoroethylene) (cathode)
PTM	Poly(trimethylene malonate)
PTO	Pyrene-4,5,9,10-tetraone
PTSI	p-toluenesulfonyl isocyanate
PVDF	Poly(vinylidene fluoride)
PVP	Poly(vinylpyrrolidone)

PXRD	Powder X-ray diffraction
QC	Quantum chemistry
R&D	Research and Development
RAFT	Reversible addition fragmentation chain-transfer
RAM	Resonant acoustic mixer
RCT	Rate capability test
RE	Reference electrode
RHS	Right hand-side
RIM	Reflection interference microscope
RIXS	Resonant inelastic x-ray scattering
RM	Redox mediator
RMD	Reactive molecular dynamics
RME	Relative molal enthalpy
RNGC	Realizing Next Generation Cathodes
RNMC	Reaction network-based Monte Carlo
ROI	Return on investment
RPM	Revolutions per minute
RPT	Reference performance test
RR	Reduced-repulsion (channel)
RRDE	Rotating ring disk electrode
RST	Reactive Spray Technology
RT	Room temperature
RTMS	Reciprocal ternary molten salts
SAED	Selected area electrode diffraction
SAXS	Small angle X-Ray scattering
SBC	Soluble base content
SBIR	Small Business Innovation Research
SCA	Supply chain analysis
SCN	Li <sub>6</sub> PS <sub>5</sub>
SCP	Sulfur containing polymer
SDS	Safety data sheet
SE	Solid electrolyte
SECM	Scanning electrochemical microscope
SEI	Solid electrolyte interphase
SEM	Scanning electron microscopy
SLAC	Stanford acceleration laboratory
SNL	Sandia National Laboratories
SOA	State of the art
SOC	State of charge
SOW	Statement of work
SPAN	Sulfurized Polyacrylonitrile
SPC	Small particle cathodes
SPE	Solid polymer electrolyte
SPLE	Single-particle-layer electrode
SPM	Scanning probe microscopy

SRL	Synchrotron Radiation Lightsource
SRO	Short-range order
SSB	Solid-state battery
SSE	Solid-state electrolyte
SSE-A	Anode-side solid secondary electrolytes
SSLMB	Solid-state Li-metal battery
SSR	Supersaturation ratio
SSRL	Stanford Synchrotron Radiation Lightsource
SSS	Stainless steel spacers
STEM	Scanning transmission electron microscopy
STEM-	Scanning transmission electron microscopy- high-angle annular dark-field
STTR	Small Business Technology Transfer Program
SXRD	Surface X-ray diffraction
TAC	Technical Advisory Committee
TARDEC	(U.S. Army) Tank Automotive Research, Development and Engineering Center
TCP	Technology Collaboration Program
TEA	Technoeconomic analysis
TEGDME	Tetraethyleneglycoldimethyl
TEM	Transmission electron microscopy
TES	Tender-energy x-ray absorption spectroscopy
TEY	Total electron yield
TFE	Trifluoroethanol
TFP	Tris(2,2,2-trifluoroethyl) phosphate
TFSI	Bistriflimide (anion)
TGA	Thermal gravimetric analysis
TGC	Titration gas chromatography
THF	Tetrahydrofuran
TMA	Trimethylaluminum
TMB	Trimethylboroxine
TMDC	Transition metal dichalcogenide
TMO	Transition metal oxide
TMP	Trimethyl phosphate
TMPMA	Trimethylolpropane methacrylate
TOF-SIMS	Time-of-flight secondary ion mass spectrometry
TPP	Triphenylphosphate
TRL	Technology Readiness Level
TR-XAS	TR-XRD and absorption
TR-XRD	Time-resolved x-ray diffraction
TTE	Tetrafluoropropyl ether
TTT	Time-temperature-transition
TVR	Taylor Vortex Reactor
TXM	Transmission X-ray microscopy
UAH	University of Alabama at Huntsville
UCB	University of Valifornia, Berkeley
UCI	University of California, Irvine

UCSD	University of California, San Diego
UCV	Upper cutoff voltage
UF	Ultra-Fine (concentrator)
UHE	Ultra-high energy (cathode)
UHV	Ultrahigh vacuum (system)
UIC	University of Illinois at Chicago
UM	University of Michigan
UMD	University of Maryland
UNC	University of North Carolina
UNCC	University of North Carolina-Charlotte
URI	University of Rhode Island
USABC	United States Advanced Battery Consortium
USCAR	United States Council for Automotive Research
USDRIIVE	U.S. Driving Research and Innovation for Vehicle efficiency and Energy sustainability
USGS	United States Geological Survey
VC	Vinylene carbonate
VCU	Virginia Commonwealth University
VED	Volumetric energy density
VNCM	Virgin NCM cathode
VOC	Volatile organic compounds
VR	Voltage ramp
VSP	Voucher Service Provider
VTO	Vehicle Technologies Office
WAXS	Wide-angle X-ray scattering
WT-EXAFS	Wavelet-transformed EXAFS
XANES	X-ray absorption near edge structure
XAS	X-ray absorption spectroscopy
XCEL	EXtreme Fast Charge Cell Evaluation of Lithium-ion Batteries
XFC	Extreme fast charging
XPB	X-ray powder diffraction
XPEEM	X-ray photoemission electron microscopy
XPS	X-ray photoelectron spectroscopy
XRD	X-ray diffraction
XRF	X-ray fluorescence (microscopy)
XRR	X-ray reflectivity
XRS	X-ray Raman Spectroscopy
XSEDE	Extreme Science and Engineering Discovery Environment



# Executive Summary

## Introduction

The U.S. Department of Energy's (DOE) Vehicle Technologies Office (VTO) funds research, development, demonstration, and deployment of new, efficient, and clean mobility options that are affordable for all Americans. Technologies supported by VTO include electric drive components such as advanced energy storage devices (primarily batteries); power electronics and electric drive motors; advanced structural materials; energy efficient mobility systems; innovative powertrains to reduce greenhouse gas and criteria emissions from hard-to-decarbonize off-road, maritime, rail, and aviation sectors; and fuels. One of the major VTO objectives is to enable U.S. innovators to rapidly develop the next generation of technologies that achieve the cost, range, and charging infrastructure necessary for the widespread adoption of plug-in electric vehicles (PEVs). An important prerequisite for the electrification of the nation's light duty transportation sector is development of more cost-effective, longer lasting, and more abuse-tolerant PEV batteries. One of the ultimate goals of this research, consistent with the current vehicle electrification trend, is an EV which can provide the full driving performance, convenience, and price of an internal combustion engine (ICE) vehicle. To achieve this, VTO has established the following overarching goal (Source: FY2023 Congressional Budget Request<sup>1</sup>):

*... reducing electric vehicle (EV) battery cell cost by 50 percent to \$60/kWh by 2030 to achieve EV cost parity with internal combustion engine vehicles; eliminating dependence on critical materials such as cobalt, nickel, and graphite, reducing battery supply chain vulnerabilities by 2030; and establishing a lithium battery recycling ecosystem to recover 90 percent of spent lithium batteries and re-introducing 90 percent of key materials into the battery supply chain by 2030.*

VTO works with key U.S. automakers through the United States Council for Automotive Research (USCAR) – an umbrella organization for collaborative research consisting of Stellantis N.V., the Ford Motor Company, and General Motors. Collaboration with automakers through the partnership known as U.S. Driving Research and Innovation for Vehicle Efficiency and Energy Sustainability (U.S. DRIVE) attempts to enhance the relevance and the success potential of its research portfolio. VTO competitively selects projects for funding through funding opportunity announcements (FOAs). Directly funded work at the national laboratories are awarded competitively through a lab-call process. Stakeholders for VTO R&D include universities, national laboratories, other government agencies and industry (including automakers, battery manufacturers, material suppliers, component developers, private research firms, and small businesses).

This document summarizes the progress of VTO battery R&D projects supported during the fiscal year 2023 (FY 2023). In FY 2023, the DOE VTO battery R&D funding was approximately \$141 million. Its R&D focus was on the development of high-energy batteries for PEVs. The electrochemical energy storage roadmap (which can be found at the EERE Roadmap web page<sup>2</sup>) describes ongoing and planned efforts to develop electrochemical storage technologies for EVs. To advance battery technology, which can in turn improve market penetration of PEVs, the program investigates various battery chemistries to overcome specific technical barriers, e.g., battery cost, performance, life (both the calendar life and the cycle life), its tolerance to abusive conditions, and its recyclability/sustainability. VTO R&D has had considerable success, lowering the cost of EV battery packs to \$130/kWh in 2022, based on useable energy (representing a nearly 90% reduction since 2008) yet even further cost reduction is necessary for EVs to achieve head-to-head cost competitiveness with internal combustion engines (without Federal subsidies). In addition, today's batteries also need improvements in such areas as their ability to accept charging at a high rate, referred to as extreme fast charging (XFC) (15-minute charge) – to provide a “refueling” convenience similar to ICEs, and the ability to operate adequately at low

<sup>1</sup> <https://www.energy.gov/sites/default/files/2022-04/doe-fy2023-budget-volume-4-eere-v2.pdf>, FY 2023 Congressional Budget Request, Volume 4, Part 1, Page 5.

<sup>2</sup> <http://energy.gov/eere/vehicles/downloads/us-drive-electrochemical-energy-storage-technical-team-roadmap>.

temperatures. Research into “next-gen lithium-ion” batteries which would provide such functionalities is one of the R&D focus areas. VTO is funding research on both “next gen” chemistries (which employ an alloy anode and/or a high voltage cathode) and beyond lithium-ion (BLI) chemistries (which can, for example, employ a lithium metal anode). Current cycle and calendar lives of next gen and BLI chemistries are well short of goals set for EVs. To quantify the improvements needed to accelerate large-scale adoption of PEVs and HEVs, certain performance and cost targets have been established. Some sample performance and cost targets for EV batteries, both at cell level and at system (pack) level, are shown in Table ES- 1.

**Table ES- 1: Subset of EV Requirements for Batteries and Cells**

Energy Storage Goals (by characteristic)	Pack Level	Cell Level
Cost @ 100k units/year (kWh = useable energy)	\$100/kWh*	\$75/kWh*
Peak specific discharge power (30s)	470 W/kg	700 W/kg
Peak specific regen power (10s)	200 W/kg	300 W/kg
Useable specific energy (C/3)	235 Wh/kg*	350 Wh/kg*
Calendar life	15 years	15 years
Deep discharge cycle life	1000 cycles	1000 cycles
Low temperature performance	>70% useable energy @C/3 discharge at -20°C	>70% useable energy @C/3 discharge at -20°C
	*Current commercial cells and packs not meeting the goal	

The batteries R&D effort includes multiple activities, ranging from focused fundamental materials research to prototype battery cell development and testing. It includes, as mentioned above, R&D on “next-gen” and BLI materials and cell components, as well as on synthesis and design, recycling, and cost reduction. Those activities are organized into mainly two program elements:

- Advanced Battery and Cell R&D
- Advanced Materials R&D.

A short overview of each of those program elements is given below.

#### **Advanced Battery and Cell R&D**

The *Advanced Battery and Cell R&D* activity focuses on the development of robust battery cells and modules to significantly reduce battery cost, increase life, and improve performance. This work mainly spans the following general areas:

- United States Advanced Battery Consortium (USABC)-supported battery development & materials R&D (12 projects)
- Processing science and engineering (15 projects)
- Recycling and sustainability (three projects)
- Extreme fast charging (multiple projects organized into three “thrust areas”)
- Testing, Analysis, High-Performance Computing, Lab-I4 (eight projects)
- Small business innovative research (SBIR) (multiple Phase I and Phase II projects).

Chapters I through VI of this report describe projects under the *Advanced Battery and Cell R&D* activity. This effort involves close partnership with the automotive industry, through a USABC cooperative agreement. In FY 2023, VTO supported 12 USABC cost-shared contracts with developers to further the development of advanced automotive batteries and battery components. The estimated DOE share of those USABC contracts

(over the life of the contracts) is approximately \$39M. These include low-cost, high safety fast charge automotive cells (Microvast, Inc.), high energy and power density lithium-ion battery based on neocarbonix™ polymer binder-free electrode technology for EV applications (Nanoramic), evaluation of advanced Li-ion cell architectures for extreme fast charging (XFC) batteries for EVs (EnPower, Inc.), solvent-free electrode manufacturing for low cost/fast charging batteries (Worcester Polytechnic Institute), low-cost, fast-charge EV system -Ni-rich NCM cathode, coated anode, fluorinated solvents (Farasis), pre-lithiation of silicon-containing anodes for EV batteries (Applied Materials, Inc.), development of a self-sustaining model for the recycling of large-format lithium-ion Batteries (American Battery Technology Company), silicon-based EV cells (Ionblox, Inc.), low-cost and fast charge semi-solid Li-LFP cells for EVs, low-cost, fast-charging silicon nanowire cell technology (Amprius), lithium electrode based cell and manufacturing (Farasis Energy USA), and a closed loop recycling process for end-of-life EV lithium-ion batteries (Worcester Polytechnic Institute).

In addition to the USABC projects listed above, VTO also supports fifteen *processing science and engineering* projects at the national labs and two in industry. Most strategies for increasing the performance (and reducing cost) of lithium-ion batteries focus on novel battery chemistries, material loading modifications, and increasing electrode thickness. The latter approach is generally considered useful for increasing energy density (and in turn, the overall cell capacity). However, practical thicknesses are constrained by ionic transport limitations (which limit cell power) and processing issues. Project participants in this area include ANL, BNL, LBNL, and ORNL, Applied Materials, Inc., and Albermarle Corporation. The estimated value of those advanced processing projects (over project lifetime) is approximately \$35M.

The *Recycling and Sustainability* activity involves studies of the full life-cycle impacts and costs of lithium-ion battery production/use; cost assessments and impacts of various recycling technologies; and the available material and cost impacts of recycling and secondary use. Current participants include ANL and NREL and the associated budget is approximately \$10M.

To become truly competitive with the internal combustion engine vehicle (ICEV) refueling experience, EV charging times must also be significantly shorter than at present. A research project to understand/enable extreme fast charging (XFC) in enhanced lithium-ion systems – charging an EV at power rates of up to 400 kW, began back in FY 2017. Projects on three “thrust areas”: anode & electrolyte thrust, electrode and cell design thrust, and electrochemical and thermal performance thrust. Team members include LBNL, INL, ANL, and SLAC. Earlier, a “behind the meter” storage project was started by a team which includes NREL, and SNL. This area focuses on novel battery technologies to facilitate the integration of high-rate EV charging, solar power generation technologies, and energy-efficient buildings while minimizing both cost and grid impacts. Starting with FY 2023, those projects have been moved from the Batteries R&D program to the the Electrification R&D program in VTO – and are no more reported in the Batteries Annual Progress Report.

The *battery testing, analysis, and high-performance computing* activity develops requirements and test procedures for batteries (to evaluate battery performance, battery life and abuse tolerance). Battery technologies are evaluated according to USABC-stipulated battery test procedures. The *battery testing* activity includes performance, life and safety testing, and thermal analysis and characterization. It currently includes four projects based at ANL, INL, SNL, and NREL. The testing activity also supports cell analysis, modeling, and prototyping (CAMP) projects at ANL, which include benchmarking and post-test analysis of lithium-ion battery materials at three labs (ANL, ORNL, and SNL). Projects include testing (for performance, life, and abuse tolerance) of cells (for contract cells, laboratory-developed cells, and university-developed cells), and benchmarking systems from industry; thermal analysis, thermal testing, and modeling; cost modeling; and other battery use and life studies. *Cost assessments and requirements analysis* includes an ANL project on developing the performance and cost model BatPaC. This rigorously peer-reviewed model developed at ANL is used to design automotive lithium-ion batteries to meet the specifications for a given vehicle and estimate its cost of manufacture.

VTO also supports several *small business innovation research* (SBIR) contracts. These SBIR projects focus on development of new battery materials and components and provide a source of new ideas and concepts. The section on SBIR projects includes a short list of recent Phase I and Phase II projects awarded during FY 2023.

### Advanced Materials R&D

The *Advanced materials research & development* activity (covered in Chapters VIII to Chapter XX of this report) addresses fundamental issues of materials and electrochemical interactions associated with rechargeable automotive batteries. It develops new/promising materials and makes use of advanced material models to discover them, utilizing scientific diagnostic tools and techniques to gain insight into their failure modes and processes. It is conducted by various national labs, universities, and industry partners. The work is divided into two general areas –“next gen” chemistries (which can, for example, employ an alloy anode and/or a high voltage cathode) and beyond lithium-ion (BLI) chemistries (which can, for example, employ a lithium metal anode). The projects are distributed as follows:

- Next generation (next-gen) lithium-ion battery technologies (24 projects)
  - Advanced anodes (17 projects)
  - Advanced cathodes (six projects)
  - Frontier science at interfaces (five projects)
  - No-cobalt/Low-cobalt cathodes (six projects)
  - Diagnostics (four projects)
  - Modeling of advanced material (four projects)
  - Low temperature electrolytes (three projects).
- Beyond lithium-ion battery technologies
  - Metallic lithium (four projects)
  - Solid-state batteries (32 projects)
  - Lithium sulfur (eight projects)
  - Lithium-air Batteries (three projects)
  - Sodium-ion batteries (four projects)
  - Battery500 Consortium (several keystone and seedling projects).

The *next generation lithium-ion battery* R&D area’s goal is to advance material performances, designs, and processes to significantly improve performance and reduce the cost of lithium-ion batteries using an alloy or intermetallic anode and/or high voltage cathode. Specific areas of investigation include high-energy anodes (e.g., those containing silicon or tin), high voltage cathodes, high voltage and non-flammable electrolytes, novel processing technologies, high-energy and low-cost electrode designs, and certain other areas. This work spans a range of U.S. DRIVE activities.

- Advanced anodes R&D includes 10 multi-lab collaborative projects – based in national laboratory consortiums (NREL, PNNL, ANL, ORNL, and LBNL), in industry (Applied Materials, Enovix, Group-14 Technology, Sila Nano, and Solid Power), and at universities (Stonybrook University, University of Delaware, and University of Maryland).
- Advanced cathodes R&D projects have been assigned to three consortia: the consortium for earth-abundant cathode active materials (EaCAM), the consortium for cation disordered rocksalt materials DRX+, and the cathode electrolyte interface (CEI). This work is conducted by ANL, PNNL, LBNL, SLAC, ORNL, NREL, INL, SNL, LLNL, and the University of Chicago.
- Diagnostics R&D includes five projects ranging from interfacial processes to *in situ* diagnostic techniques and advanced microscopy, thermal diagnostics, and synthesis and characterization. The various researchers for these projects are based at LBNL, BNL, PNNL, and SLAC.

- There are four modeling projects: electrode materials design and failure prediction (ANL), model-system synthesis and advanced characterization (LBNL), design of high-energy, high-voltage lithium batteries through first-principles modeling (LBNL), and characterization and modeling of Li-metal batteries: modeling and design of amorphous solid-state Li conductors (LBNL).
- There are six low-temperature electrolyte projects: ethylene carbonate-lean electrolytes for low temperature, Li-ion batteries (LBNL), fluorinated solvent-based electrolytes for low temperature Li-ion battery (ANL), synthesis, screening and characterization of novel low temperature electrolyte for lithium-ion batteries (BNL), Li-Ion Batteries with new fluorinated electrolytes, fluorinated ester local high concentration electrolytes for operation of Li-ion batteries under extreme conditions, and novel organosulfur-based electrolytes for high voltage Li-ion Batteries.

R&D on *beyond lithium-ion battery technologies* includes solid-state technology, lithium metal systems, lithium sulfur, lithium air, and sodium-ion. The main areas of focus include new methods to understand/stabilize lithium metal anodes; lithium polysulfides to enable the use of sulfur cathodes; and developing electrolytes for lithium air and lithium sulfur cells. These systems offer further increases in energy and potentially reduced cost compared to the next-gen lithium-ion batteries. However, they also require additional breakthroughs in materials (often at a fundamental level) before commercial use. VTO is investigating the issues and potential solutions associated with cycling metal anodes. The main research topics include: coatings, novel oxide and sulfide-based glassy electrolytes, and *in situ* diagnostics approaches to characterize and understand Li metal behavior during electrochemical cycling.

- Metallic lithium R&D includes four projects based at three national laboratories (LLNL, PNNL, and SLAC).
- Solid state batteries R&D includes 27 projects. These are based at multiple national laboratories (ANL, PNNL, LBNL, NREL, LLNL, ORNL, BNL, SLAC), universities (University of California, University of Maryland, College Park, Iowa State University of Science and Technology, Virginia Polytechnic Institute and State University, Penn State University Park, University of Wisconsin-Milwaukee, University of Houston, Virginia Commonwealth University, and University of Louisville), and an industry member (General Motors LLC).
- Lithium sulfur R&D includes eleven projects – four of them based at national laboratories (ANL, BNL, LBNL, and PNNL), five at universities (the University of Wisconsin Milwaukee, University of California, San Diego, University of Pittsburgh, and Penn State University), and the remaining two in industry (Navitas Systems and Giner, Incorporated).
- Additional beyond lithium-ion projects include three projects on Lithium-air batteries (two at ANL and one at the University of Illinois) and four projects on sodium-ion batteries (based at ANL, BNL, LBNL, and PNNL).

The *Battery500 Innovation Center* is a combined effort by a team of four national labs (PNNL, BNL, INL, and SLAC) and five universities (University of Texas-Austin, Stanford University, Binghamton University, University of Washington, and University of California, San Diego) with the goal to develop commercially viable lithium battery technologies with a cell level specific energy of 500 Wh/kg while simultaneously achieving 1,000 deep-discharge cycles. The consortium keystone projects focus on innovative electrode and cell designs that enable maximizing the capacity from advanced electrode materials. The consortium works closely with the R&D community, battery/materials manufacturers, and end-users/OEMs to ensure that these technologies align well with industry needs and can be transitioned to production.

### Recent Highlights

Development of New High-Energy Cathodes Containing 60% Manganese (ANL)

In 2021, the Materials Research Group at ANL reported the development of novel Co-free  $\text{Li}_2\text{MnNiO}_4$  cathodes based on lithiated-spinel structures<sup>3</sup>. These Li-excess spinels (LxS) surpass conventional spinels such

<sup>3</sup> Chem. Comm. (2021), doi.org/10.1039/D1CC04334J

as  $\text{LiMn}_2\text{O}_4$  and  $\text{LiMn}_{1.5}\text{Ni}_{0.5}\text{O}_4$  by doubling the Li concentration in their pristine states, while maintaining cubic symmetry.  $\text{Li}/\text{LxS-L}_2\text{MnNiO}_4$  cells exhibit remarkable energy densities, delivering  $\sim 225$  mAh/g capacity between 2.5 – 5.0 V.

Increasing the Mn content is a promising approach for sustainability of the Li-ion battery supply chain. A newly developed series of Mn-rich LxS cathodes, referred to as  $\text{LxS-Li}_2\text{Mn}_{1+x}\text{Ni}_{1-x}\text{O}_4$  ( $0 < x < 0.5$ ), exhibits an impressive specific capacity of up to 250 mAh/g when cycled between 2 – 5.0 V vs. Li. Figure ES- 1(a) shows a representative XRD pattern of  $\text{Li}_2\text{Mn}_{1.2}\text{Ni}_{0.8}\text{O}_4$  with the previously reported  $\text{LxS-Li}_2\text{MnNiO}_4$ . Refinement analysis indicates a lower disordering ratio for  $\text{LxS-Li}_2\text{Mn}_{1.2}\text{Ni}_{0.8}\text{O}_4$  (11%) vs  $\text{LxS-Li}_2\text{MnNiO}_4$  (18%). Consequently, the initial discharge capacity of  $\text{LxS-Li}_2\text{Mn}_{1.2}\text{Ni}_{0.8}\text{O}_4$  improved from 225 to 250 mAh/g, increasing the energy density from 800 to 920 Wh/kg, while maintaining similar cycling as the  $\text{LxS-Li}_2\text{MnNiO}_4$ , Figure ES- 1 (b) and (c). Also,  $\text{LxS-Li}_2\text{Mn}_{1.2}\text{Ni}_{0.8}\text{O}_4$  exhibits enhanced rate performance, Figure ES- 1 (d), attributed to its more well-established 3D Li-ion diffusion channels.

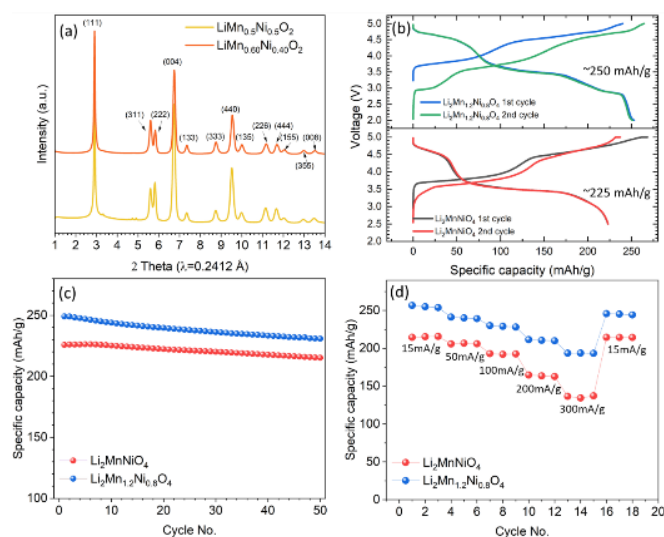


**Figure ES- 1. Structural and electrochemical properties of  $\text{LxS-Li}_2\text{MnNiO}_4$  and  $\text{LxS-Li}_2\text{Mn}_{1.2}\text{Ni}_{0.8}\text{O}_4$ : (a) X-ray diffraction patterns, (b) 1<sup>st</sup> and 2<sup>nd</sup> cycle voltage profiles, (c) cycle performance, and (d) rate capability.**

#### An Inorganic-Rich Interphase for Li Metal Batteries with Improved Cycle Life (BNL)

$\text{CsNO}_3$  was identified as a dual-functional additive to form good interphases on both the NMC cathode and Li metal anode to enable a Li metal battery with long cycle life and faster charge capability. Using 1,2-dimethoxyethane (DME)-LiFSI based electrolyte containing an  $\text{CsNO}_3$  additive, the  $\text{LiNi}_{0.8}\text{Mn}_{0.1}\text{Co}_{0.1}\text{O}_2\|\text{Li}$  cell retained more than 80% of initial capacity after 200 1C cycles, even with a high cathode loading of  $5\text{mAh}/\text{cm}^2$ . In contrast, the cell using the baseline electrolyte experienced a loss of capacity within 20 cycles, duplicate cells displayed similar behavior. The resulting interphase is dominated by the inorganic species  $\text{CsFSI}$  and is free of  $\text{LiF}$ , which is the component often believed to be necessary for a good interphase. These results indicate that both cathode and anode must have been well protected during the cycling, validating the dual protection strategy proposed. (Figure ES- 2)

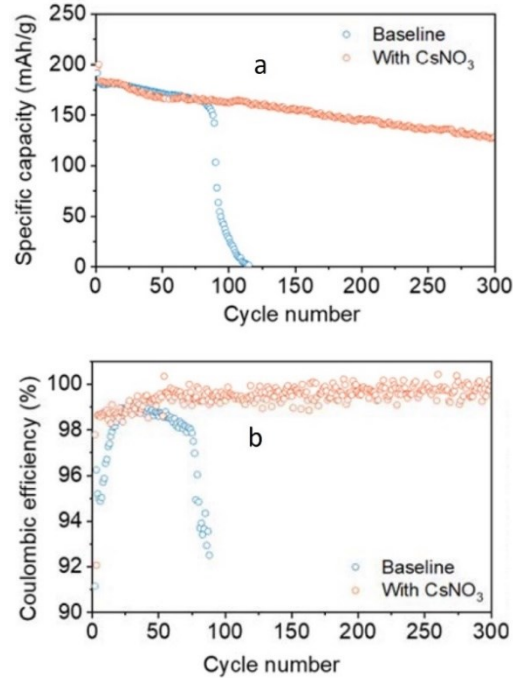


**Figure ES- 2. (a) Cycling stability of baseline electrolyte and electrolyte containing 3 wt% CsNO<sub>3</sub> additive. (b) Coulombic efficiency of the cell in (a).**

Fast Diagnosis of Li-ion Battery Health from High-Rate Data using Artificial Intelligence (NREL and LBNL) NREL and INL are developing methods to rapidly diagnose Li-ion battery SOH during high-rate cycling, specially 10-minute fast charge and two-hour discharge. The goal is to quickly determine the severity of battery aging modes (e.g., loss of active material [LAM], loss of Li inventory [LLI]) without taking the battery out of commission for a standard slow-rate evaluation, which can take up to 40 hrs. To develop online SOH diagnostics, NREL's battery physics models are combined with INL's machine-learning tools. Figure ES- 3 illustrates the overall workflow. First, an electrochemical battery model is developed that can predict high-rate battery performance of aged cells. Second, features, such as the incremental capacity during charge, are extracted from the synthetic data generated by the electrochemical model. Third, the synthetic data is used to train a machine-learning algorithm to associate how the high-rate voltage response should change under different aging conditions. Fourth, after training the machine-learning model on synthetic data, the model is tested on real cells. Compared to the standard 40-hour full-capacity diagnostic, the new method provides a 10x speedup in quantifying failure modes and enables earlier life projections using less data. Importantly, the new method can analyze the cell SOH each time the battery is used and can use high rate and rest information for failure mode identification, quantification, and projection.

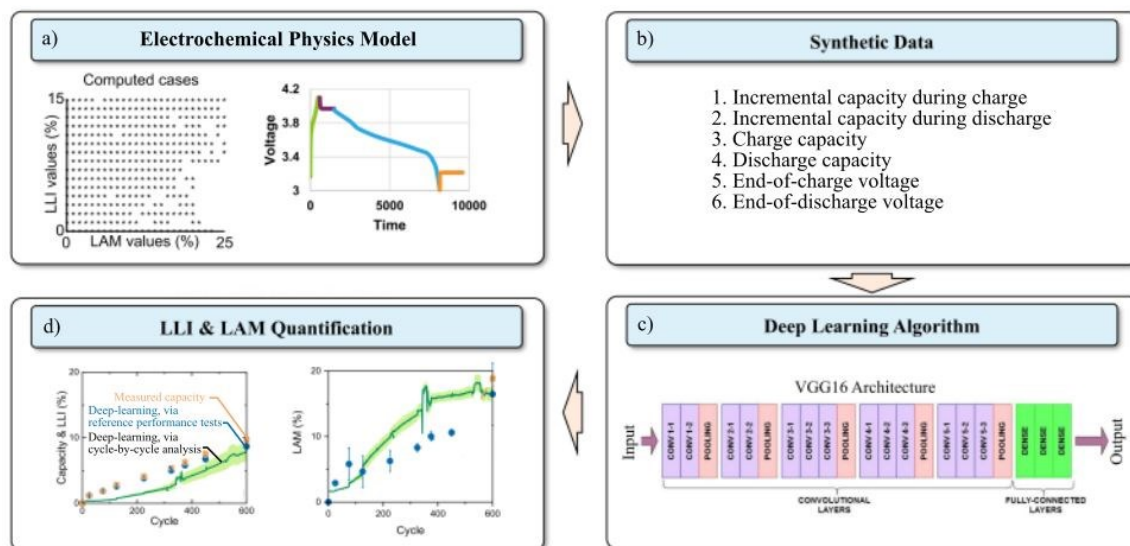


**Figure ES-3. Process to develop an online battery state-of-health monitor by using electrochemical models and machine learning. Validation data is from single-layer pouch cells aged under 10-minute fast-charge and 2-hour discharge cycling protocol.**

Advancing All-Solid-State Li-Sulfur Battery through Materials and Interfacial Innovations (PNNL)

A PNNL team has developed an integrated approach that improves the performance of all-solid-state Li-S batteries (Figure ES- 4). They have developed a Li compatible solid-state electrolyte (SSE) with high ionic conductivity ( $>5$  mS/cm at room temperature) and integrated it with engineered carbon materials to host the sulfur. Through rational design of the sulfur-carbon-SSE triple-phase, near-theoretical sulfur capacity ( $\sim 1600$  mAh/g) in Li-S batteries, with a high sulfur mass loading ( $>10$  mg/cm<sup>2</sup>) (Figure ES- 4c) has been achieved. This lays a solid foundation for the further fabrication and manufacturing of high-capacity electrodes (up to 16 mAh/cm<sup>2</sup>) and high-energy batteries.

Moreover, the sulfur cathodes deliver superior power performance. Figure ES- 4c shows the cell capacities as a function of current densities, demonstrating both high-rate capability and electrode robustness. Based on the team's preliminary results, the engineered cathodes ( $\sim 1500$  mAh/g at 5 mg/cm<sup>2</sup>) have a great potential to meet a cell-level energy of a 500Wh/kg in a 5Ah Li-S pouch cell using a 30  $\mu$ m SSE separator, and 37.5  $\mu$ m thick Li (Figure ES- 4b). The improved stability of the developed SSE towards Li metal also allows for stable cycling of all-solid-state Li-S cells. At 2 mAh/cm<sup>2</sup> capacity, the all-solid-state Li-S coin cells have demonstrated over 250 cycles without capacity decay or failure (Figure ES- 4f). The team is now working on enhancing the cycle life of all-solid-state Li-S batteries of further increased S loading to achieve high energy goals in prototype pouch cells.



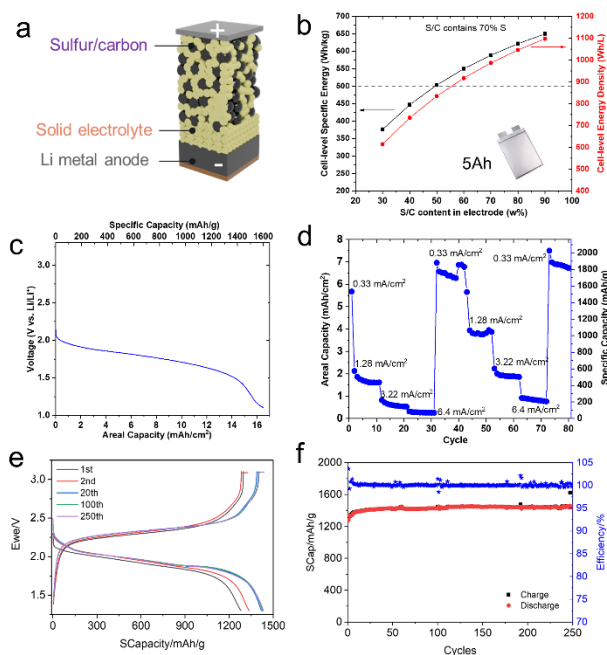


**Figure ES- 4.** (a, b) Schematic and cell energy estimation based on experimental inputs, (c, d) Discharge profile (10 mg S/cm<sup>2</sup>) and rate capability of cell (3.7 mg S/cm<sup>2</sup>), and (e, f) Charge/discharge profiles and cycling of all-solid-state Li-S coin cell (1.5 mg S/cm<sup>2</sup>), all cells were tested at 20°C.

### Collaborative Activities

In addition to the above, VTO has in place extensive and comprehensive ongoing coordination efforts in energy storage R&D across all of DOE and with other government agencies. It coordinates efforts on energy storage R&D with both the Office of Science and the Office of Electricity. Coordination and collaboration efforts also include program reviews and technical meetings sponsored by other government agencies and inviting participation of representatives from other government agencies to contract and program reviews of DOE-sponsored efforts. DOE coordinates such activities with the Army's Advanced Vehicle Power Technology Alliance, the Department of Transportation/National Highway Traffic Safety Administration (DOT/NHTSA), the Environmental Protection Agency (EPA), and the United Nations Working Group on Battery Shipment Requirements. Additional international collaboration occurs through the International Energy Agency's (IEA's) Hybrid Electric Vehicles Technology Collaboration Program (HEV TCP); and bilateral agreements between the U.S. and China.

### Organization of this Report

This report covers all the FY 2023 projects which are part of the advanced battery R&D program in VTO. We are pleased with the progress made during the year and look forward to continued cooperation with our industrial, government, and scientific partners to overcome the remaining challenges to delivering advanced energy storage systems for vehicle applications.



Brian Cunningham, Program  
Manager, Batteries  
Vehicle Technologies Office



Tien Q. Duong, Vehicle  
Technologies Office



Haiyan Croft, Vehicle  
Technologies Office



Simon Thompson, Vehicle  
Technologies Office



Nicolas Eidson, Vehicle  
Technologies Office



Tina Chen, Vehicle  
Technologies Office



Thomas Do, Vehicle  
Technologies Office



Jake Herb, Vehicle Technologies  
Office

# Table of Contents

<b>Vehicle Technologies Office Overview .....</b>	<b>1</b>
Annual Progress Report .....	1
Organization Chart.....	2
<b>Batteries Program Overview.....</b>	<b>3</b>
Introduction.....	3
Goals	3
<b>I USABC Battery Development &amp; Materials R&amp;D.....</b>	<b>20</b>
I.1 Low-cost, High-safety Fast-charge Automotive Cells (Microvast, Inc.).....	22
I.2 Low-Cost and Fast-charging Lithium-ion Battery based on Neocarbonix™ NMP/PVDF-binder Free Electrode Processing for EV Applications (Nanoramic).....	26
I.3 Advanced Li-ion Cell Architectures for Extreme Fast Charging (XFC) Batteries for Electric Vehicles (EnPower, Inc.).....	36
I.4 Solvent-free Electrode Manufacturing for Low Cost/Fast Charging Batteries (Worcester Polytechnic Institute).....	38
I.5 Development of Advanced Low-Cost/Fast-Charge (LC/FC) Batteries for EV Applications (Farasis Energy USA).....	54
I.6 Pre-lithiation of Silicon-containing Anodes for High-Performance EV Batteries (Applied Materials, Inc.).....	62
I.7 Strategic Collaboration for the Development of a Self-Sustaining Model for the Recycling of Large-Format Lithium-Ion Batteries (American Battery Technology Company).....	73
I.8 Silicon-based EV Cells Meeting Cost, Calendar Life and Power Requirements (Ionblox, Inc.) .....	78
I.9 Low-Cost and Fast Charge Semi-Solid Li-LFP Cell for EV Applications (24M).....	86
I.10 Low-cost, Fast-charging Silicon Nanowire Cell Technology (Amprius).....	91
I.11 Development of Lithium Electrode Based Cell and Manufacturing for Automotive Traction Applications (Farasis Energy) .....	99
I.12 A Closed Loop Recycling Process for End-of-Life Electric Vehicle Li-ion Batteries-Phase III (Worcester Polytechnic Institute) .....	106
<b>II Processing Science &amp; Engineering .....</b>	<b>117</b>
II.1 Processing Next Generation Li-ion Battery Cathode Materials (ANL).....	119
II.2 Novel Processing Approaches for LLZO (ANL) .....	127
II.3 Supercritical Fluid Processing of Battery Cathode Materials (ANL).....	133
II.4 Process R&D and Scale-up of Critical Battery Materials (ANL).....	141

II.5	Structure-Activity Relationships in the Optimizing Electrode Processing Streams for LiBs (LBNL).....	149
II.6	Higher Energy Density <i>via</i> Inactive Components and Processing Conditions (LBNL).....	155
II.7	Minimizing Side Reactions in Next-Generation Lithium Ion Battery Cathodes Through Structure-Morphology Optimization (ANL) .....	162
II.8	<i>In Situ</i> Spectroscopies of Processing Next-Generation Cathode Materials (ANL, BNL) .....	173
II.9	Towards Solventless Processing of Thick Electron-Beam (EB) Cured LIB Cathodes (ORNL) .....	182
II.10	Performance Effects of Electrode Processing for High-Energy Lithium-Ion Batteries (ORNL) .....	188
II.11	Advanced Anode Manufacturing through Ultra-Thin Li Deposition (Applied Materials, Inc.) .....	193
II.12	Thin-film lithium metal manufacture by room temperature electrodeposition (Albemarle Corporation) .....	205
II.13	GMC CRADA: Multilayer Composite Solid State Lithium Batteries for EV Battery Applications (ANL).....	211
II.14	Cabot CRADA: Spray Synthesis of Additive Battery Particles (ANL) .....	219
II.15	Solid Power CRADA: Interface-Engineered, High-Energy Oxide Cathodes for All-Solid-State Lithium Batteries (ANL) .....	223
<b>III</b>	<b>Recycling and Sustainability .....</b>	<b>232</b>
III.1	Battery and Critical Materials Life Cycle Analysis (ANL).....	233
III.2	Lithium-ion Battery Recycling Prize Support (NREL).....	244
III.3	Battery ReCell Center (ANL, NREL, ORNL, INL, Michigan Tech U, UC San Diego, Worcester Polytechnic Institute, Tennessee State U) .....	252
<b>IV</b>	<b>Extreme Fast Charging (XFC) .....</b>	<b>333</b>
IV.1	Extreme Fast Charge Cell Evaluation (XCEL) Thrust-1: Electrolytes for fast charging .....	335
IV.2	XCEL Thrust-2: Electrode & Cell Design for Fast Charging.....	343
IV.3	XCEL Thrust 3: Electrochemical and Thermal Performance.....	354
<b>V</b>	<b>Testing, Analysis, High-Performance Computing, Lab-I4.....</b>	<b>360</b>
V.1	BatPaC Model Development (ANL) .....	361
V.2	Battery Performance and Life Testing (ANL).....	369
V.3	Battery Abuse Testing (SNL).....	372
V.4	Battery Thermal Analysis and Characterization Activities (NREL) .....	375
V.5	Cell Analysis, Modeling, and Prototyping (CAMP) Facility Research Activities (ANL).....	383

V.6	Materials Benchmarking Activities for CAMP Facility (ANL) .....	388
V.7	Electrochemical Performance Testing (INL).....	396
V.8	Machine Learning for Accelerated Life Prediction and Cell Design (INL, NREL).....	400
<b>VI</b>	<b>Small Business Innovation Research (SBIR).....</b>	<b>409</b>
<b>VII</b>	<b>Next Generation Lithium-Ion Materials: Advanced Anodes R&amp;D.....</b>	<b>412</b>
VII.1	Silicon Consortium Project (NREL, ANL, PNNL, SNL, ORNL, LBNL) .....	413
VII.2	Si-Based Li Ion Batteries with Long Cycle Life and Calendar Life (PNNL).....	419
VII.3	Integrated Modeling and Machine Learning of Solid-Electrolyte Interface Reactions of the Si Anode (LBNL) .....	427
VII.4	Rationally Designed Lithium-Ion Batteries Towards Displacing Internal Combustion Engines (Group14 Technologies).....	449
VII.5	Ultra-Low Volume Change Silicon-Dominant Nanocomposite Anodes for Long Calendar Life and Cycle Life (Sila Nanotechnologies) .....	453
VII.6	Solid State Li Ion Batteries Using Si Composite Anodes (Solid Power Inc.).....	456
VII.7	Fully Fluorinated Local High Concentration Electrolytes Enabling High Energy Density Si Anodes (Stony Brook University) .....	459
VII.8	Devising mechanically compliant and chemically stable synthetic solid-electrolyte interphases on silicon using ex situ electropolymerization for long cycling Si anodes (University of Delaware) .....	470
VII.9	Rational Electrolyte Design for Li-ion Batteries with Micro-sized Si Anodes (University of Maryland, College Park).....	477
VII.10	Free-Energy Driven Approaches to Self-Forming and Self-Terminating SEIs on Si Anodes (LBNL).....	492
<b>VIII</b>	<b>Next-Gen Lithium-Ion: Advanced Cathodes R&amp;D.....</b>	<b>499</b>
VIII.1	Earth-Abundant Cathode Active Materials (EaCAM) Consortium (ANL, ORNL, NREL, LBNL, PNNL, SLAC).....	500
VIII.2	Cation Disordered Rocksalt Materials DRX <sup>+</sup> Consortium (LBNL, ORNL, PNNL, ANL, SLAC, UC Santa Barbara).....	549
VIII.3	Cathode-Electrolyte Interphase (CEI) Consortium (PNNL).....	589
<b>IX</b>	<b>Next Generation Lithium-Ion Materials: Diagnostics .....</b>	<b>617</b>
IX.1	Interfacial Processes (LBNL) .....	618
IX.2	Advanced <i>in situ</i> Diagnostic Techniques for Battery Materials (BNL).....	624
IX.3	Microscopy Investigation on the Fading Mechanism of Electrode Materials (PNNL) .....	633
IX.4	In-Operando Thermal Diagnostics of Electrochemical Cells (LBNL) .....	641

IX.5	Pre-Lithiation of Silicon Anode for High Energy Li-Ion Batteries (Stanford U).....	647
<b>X</b>	<b>Next-Gen Lithium-Ion: Modeling Advanced Materials .....</b>	<b>653</b>
X.1	Electrode Materials Design and Failure Prediction (ANL) .....	654
X.2	Characterization and Modeling of Li-Metal Batteries: Model-system Synthesis and Advanced Characterization (LBNL).....	661
X.3	Design of High-Energy, High-Voltage Lithium Batteries through First-Principles Modeling (LBNL).....	670
X.4	Modeling of Solid-State Conductors (LBNL).....	677
<b>XI</b>	<b>Next-Gen Li-ion: Low Temperature Electrolytes .....</b>	<b>687</b>
XI.1	Ethylene Carbonate-Lean Electrolytes for Low Temperature, Safe Li-ion batteries (LBNL) .....	688
XI.2	Fluorinated Solvent-Based Electrolytes for Low Temperature Li-ion Battery (ANL).....	693
XI.3	Synthesis, Screening and Characterization of Novel Low-temperature Electrolyte for Lithium-ion Batteries (BNL) .....	698
XI.4	Extending the Operating Range and Safety of Li-Ion Batteries with New Fluorinated Electrolytes (Koura) .....	709
XI.5	Fluorinated Ester Local High Concentration Electrolytes for Operation of Li-Ion Batteries under Extreme Conditions(Stony Brook Univ) .....	722
XI.6	Novel Organosulfur-Based Electrolytes for Safe Operation of High Voltage Li-Ion Batteries Over a Wide Operating Temperature (GM) .....	735
<b>XII</b>	<b>Beyond Li-ion R&amp;D: Metallic Lithium .....</b>	<b>757</b>
XII.1	Lithium Dendrite Prevention for Lithium Batteries (PNNL) .....	758
XII.2	Integrated Multiscale Model for Design of Robust 3-D Solid-state Lithium Batteries (LLNL) .....	766
XII.3	Advanced Polymer Materials for Li-ion (SLAC).....	774
XII.4	Anode-Free Lithium Batteries (PNNL).....	782
<b>XIII</b>	<b>Beyond Li-ion R&amp;D: Solid-State Batteries .....</b>	<b>789</b>
XIII.1	Lithium Dendrite-Free Solid Electrolytes for High Energy Lithium Batteries (University of Maryland, College Park).....	791
XIII.2	Development of Thin, Robust, Lithium-Impenetrable, High-Conductivity, Electrochemically Stable, Scalable, and Low-Cost Glassy Solid Electrolytes for Solid-State Lithium Batteries (Iowa State University).....	799
XIII.3	Molecular Ionic Composites: A New Class of Polymer Electrolytes to Enable All Solid-State and High Voltage Lithium Batteries (Virginia Polytechnic Institute and State University)..	803

XIII.4	Hot Pressing of Reinforced All-solid-state Batteries with Sulfide Glass Electrolyte (General Motors LLC).....	811
XIII.5	Developing Materials for High-Energy-Density Solid State Lithium-Sulfur Batteries (Penn State University, University Park).....	827
XIII.6	Fundamental Understanding of Interfacial Phenomena in Solid-State Batteries (General Motors).....	834
XIII.7	Multidimensional Diagnostics of the Interface Evolutions in Solid-State Lithium Batteries (University of Houston).....	842
XIII.8	First-Principles Modeling of Cluster-Based Solid Electrolytes (Virginia Commonwealth University).....	847
XIII.9	Predictive Engineering of Interfaces and Cathodes for High-Performance All Solid-State Lithium-Sulfur Batteries (University of Louisville).....	855
XIII.10	Enabling Continuous Production of Defect-free, Ultrathin Sulfide Glass Electrolytes for Next Generation Solid-state Lithium Metal Batteries (ANL).....	864
XIII.11	Stable Solid-State Electrolyte and Interface for High-Energy All-Solid-State Lithium-Sulfur Battery (PNNL).....	870
XIII.12	Scale-Up of Novel Li-Conducting Halide Solid State Battery Electrolyte (LBNL).....	879
XIII.13	Low-Pressure All Solid State Cells (NREL).....	884
XIII.14	3D Printing of All-Solid-State Lithium Batteries (LLNL).....	888
XIII.15	Substituted Argyrodite Solid Electrolytes and High-Capacity Conversion Cathodes for All-Solid-State Batteries (Oak Ridge National Laboratory).....	895
XIII.16	Multifunctional Gradient Coatings for Scalable, High-Energy-Density Sulfide-Based Solid-State Batteries (ANL).....	905
XIII.17	Thick Selenium-Sulfur Cathode Supported Ultra-thin Sulfide Electrolytes for High-energy All-solid-state Lithium Metal Batteries (ANL).....	915
XIII.18	Synthesis of Composite Electrolytes with Integrated Interface Design (ANL).....	924
XIII.19	Polymer Electrolytes for Stable Low Impedance Solid State Battery Interfaces (ORNL)....	935
XIII.20	Inorganic-Polymer-Composite Electrolyte with Architecture Design for Lithium Metal Solid State Batteries (BNL).....	946
XIII.21	Ion-Conductive High Li <sup>+</sup> Transference Number Polymer Composites for Solid-State Batteries (LBNL).....	954
XIII.22	Precision Control of the Li Surface for Solid-state Batteries (Oak Ridge National Laboratory)	962
XIII.23	Lithium Halide-Based Superionic Solid Electrolytes and High-Voltage Cathode Interfaces (ANL).....	969

XIII.24	Polyester-Based Block Copolymer Electrolytes for Lithium-Metal Batteries (University of California, Berkeley) .....	978
XIII.25	Development of All Solid-State Battery using Anti-Perovskite Electrolytes (ANL) .....	986
XIII.26	High-Conductivity and Electrochemically Stable Lithium Thioborate Solid-State Electrolytes for Practical All-Solid-State Batteries (SLAC/Stanford University).....	994
XIII.27	Solid state batteries with long cycle life and high energy density through materials design and integration (LBNL).....	1002
<b>XIV</b>	<b>Beyond Li-Ion R&amp;D: Lithium Sulfur Batteries .....</b>	<b>1019</b>
XIV.1	A Novel Chemistry: Lithium-Selenium and Selenium-Sulfur Couple (ANL) .....	1020
XIV.2	Development of High Energy Lithium-Sulfur Batteries (PNNL).....	1030
XIV.3	Mechanistic Investigation for the Rechargeable Li-Sulfur Batteries (BNL, U of Wisconsin Milwaukee).....	1040
XIV.4	New electrolyte binder for Lithium sulfur battery (LBNL).....	1050
XIV.5	Strategies to Enable Lean Electrolytes for High Loading and Stable Lithium-Sulfur Batteries (UCSD).....	1065
XIV.6	New Engineering Concepts for High Energy Density Li-S Batteries (UPitt).....	1082
XIV.7	Development of Li-S Battery Cells with High Energy Density and Long Cycling Life (PSU) 1098	
XIV.8	Nanostructured Design of Sulfur Cathodes for High Energy Lithium-Sulfur Batteries (Stanford University).....	1104
XIV.9	Fluorinated Glyme Solvents to Extend Lithium-Sulfur Battery Life Fluorinated Glyme Solvents to Extend Lithium-Sulfur Battery Life (Navitas Advanced Solutions Group) .....	1109
XIV.10	Liquid Electrolytes for Lithium-Sulfur Batteries with Enhanced Cycle Life and Energy Density Performance (Giner).....	1121
XIV.11	Development of Functional Electrolytes for Li-S Battery Cells (PSU).....	1133
<b>XV</b>	<b>Beyond Li-ion R&amp;D: Lithium-Air Batteries .....</b>	<b>1138</b>
XV.1	Lithium-Air Batteries (ANL).....	1139
XV.2	Lithium Oxygen Battery Design and Predictions (ANL) .....	1146
XV.3	Development of a High-Rate Lithium-Air Battery Using a Gaseous CO <sub>2</sub> Reactant (UIC). 1153	
<b>XVI</b>	<b>Beyond Li-ion R&amp;D: Sodium-Ion Batteries .....</b>	<b>1164</b>
XVI.1	An Exploratory Study of Novel Sodium-Ion Battery Systems (BNL) .....	1165
XVI.2	Development of Advanced High-energy and Long-life Sodium-ion Battery (ANL).....	1173
XVI.3	Tailoring High Capacity, Reversible Anodes for Sodium-Ion Batteries (LBNL) .....	1183
XVI.4	Electrolytes and Interfaces for Stable High-Energy Sodium-ion Batteries (PNNL) .....	1190



**XVII Beyond Li-ion R&D: Battery500..... 1203**  
XVII.1 Battery 500 phase 2: B500 Innovation Center (PNNL)..... 1204

## List of Figures

Figure ES- 1. Structural and electrochemical properties of $\text{LxS-Li}_2\text{MnNiO}_4$ and $\text{LxS-Li}_2\text{Mn}_{1.2}\text{Ni}_{0.8}\text{O}_4$ : (a) X-ray diffraction patterns, (b) 1 <sup>st</sup> and 2 <sup>nd</sup> cycle voltage profiles, (c) cycle performance, and (d) rate capability...	xx
Figure ES- 2. (a) Cycling stability of baseline electrolyte and electrolyte containing 3 wt% $\text{CsNO}_3$ additive. (b) Coulombic efficiency of the cell in (a).....	xxi
Figure ES- 3. Process to develop an online battery state-of-health monitor by using electrochemical models and machine learning. Validation data is from single-layer pouch cells aged under 10-minute fast-charge and 2-hour discharge cycling protocol. ....	xxii
Figure ES- 4. (a, b) Schematic and cell energy estimation based on experimental inputs, (c, d) Discharge profile (10 mg S/cm <sup>2</sup> ) and rate capability of cell (3.7 mg S/cm <sup>2</sup> ), and (e, f) Charge/discharge profiles and cycling of all-solid-state Li-S coin cell (1.5 mg S/cm <sup>2</sup> ), all cells were tested at 20°C.....	xxiii
Figure 1. Chemistry classes, status, and R&D needs.....	4
Figure 2. Battery R&D Program Structure .....	6
Figure 3. Structural and electrochemical properties of $\text{LxS-Li}_2\text{MnNiO}_4$ and $\text{LxS-Li}_2\text{Mn}_{1.2}\text{Ni}_{0.8}\text{O}_4$ : (a) X-ray diffraction patterns, (b) 1 <sup>st</sup> and 2 <sup>nd</sup> cycle voltage profiles, (c) cycle performance, and (d) rate capability.....	8
Figure 4. Two possible reaction pathways to the formation of $\text{Li}_2\text{O}$ from reaction of $\text{O}_2$ , $\text{Li}^+$ , and $e^-$ . The reaction highlighted by yellow is the one occurring in the solid-state Li-air battery.....	8
Figure 5. Solid-state Li-air battery cell performance at a limited capacity of 1000 mAh/g showing galvanostatic cycling over 1000 cycles and a small polarization gap.....	9
Figure 6. (a) Composition-property correlation in the Li-Ni-Mn-(Co) space; inset: Li/Ni mixing due to the reduced energy barrier ( $\Delta E$ ) for Ni migration in the absence of Co. (b) Morphological tuning via Li stoichiometry control. ....	9
Figure 7. (a) Particle size variation of the NM9505 as a function of Li over transition metal ratio, Li/TM. Inset: simulated particle microstructure for Li/TM= 0.95 and 1.05. Scale bars: 100 nm. (b, c) Capacity retention and voltage profiles of NM9505 with 0.95Li (red) and 1.05Li (black).....	10
Figure 8. (a) Cycling stability of baseline electrolyte and electrolyte containing 3 wt% $\text{CsNO}_3$ additive. (b) Coulombic efficiency of the cell in (a).....	11
Figure 9. Process to develop an online battery state-of-health monitor by using electrochemical models and machine learning. Validation data is from single-layer pouch cells aged under 10-minute fast-charge and 2-hour discharge cycling protocol.....	12
Figure 10. a) Comparison of incremental capacity obtained on different cathodes. Inset: an SEM image of the samples. b) Comparison of cathode energy density and retention of various fluorinated cathodes. ....	13
Figure 11. Schematic illustration of battery fabrication and recycling using the Quick-Release Binder. The Li iron phosphate (LFP) cathode material and graphite (Gr) anode material are fabricated into cathode and anode sheets, which are then cut to assemble cells for cycling test. Upon recycling, the cells are disassembled, and the LFP cathodes and graphite anodes are individually treated with high pH aqueous solution to separate the electrode materials from the current collector foils. The LFP and graphite electrode materials are retrieved from their aqueous suspensions. ....	14
Figure 12. Images of Si NPs (a) before and (b) after applying a molecular coating and processing into an electrode.....	14
Figure 13. The cycle life of batteries containing a Si NP-based anode and an NMC811 cathode achieves U.S. DRIVE goals of cycle life >1000 with an anode available specific capacity >2000 mAh/g at a nominal voltage of 0.01 V vs $\text{Li/Li}^+$ .....	15

Figure 14. Empirical voltage threshold for Li plating as function of SOC determined using validated electrochemical model ..... 15

Figure 15. (a) First cycle voltage profiles and (b) cycling stability of  $\text{Li}_{1.2}\text{Mn}_{0.5}\text{Ti}_{0.3}\text{O}_{1.9}\text{F}_{0.1}$  DRX cathodes cycled at 10-20 mA  $\text{g}^{-1}$ . (c) Schematic showing agglomeration of carbon black vs. conformal graphite coatings on DRX particle surfaces. .... 16

Figure 16. (a, b) Schematic and cell energy estimation based on experimental inputs, (c, d) Discharge profile (10 mg  $\text{S}/\text{cm}^2$ ) and rate capability of cell (3.7 mg  $\text{S}/\text{cm}^2$ ), and (e, f) Charge/discharge profiles and cycling of all-solid-state Li-S coin cell (1.5 mg  $\text{S}/\text{cm}^2$ ), all cells were tested at 20°C..... 17

Figure 17. (a) Scheme of a regulating  $\text{SP}^2$  polymer coating at the Li anode that blocks solvents while transports salts. (b) Compared to the bare ones, Li metals with  $\text{SP}^2$  coating exhibit improved Li cycling efficiency when using different electrolytes. Tests of full cells with  $\text{SP}^2$ -coated Li anodes indicated improved cyclability using (c) carbonate and (d) fluorinated ether electrolytes. .... 18

Figure 18. Short-circuiting mechanism in garnet solid-state battery driven by mechanical defects. Reproduced from McConohy et al. Nature Energy 8, 241 (2023). .... 18

Figure 19. (a) Schematic showing that increasing molecular diversity increases the solvation entropy of the electrolyte. (b) Illustration showing that HEE has smaller ion clusters and superior ion transport. (c) Ionic conductivity doubles for the HEE compared to conventional electrolytes. (d) HEE enables stable cycling at fast charging conditions..... 19

Figure I.1.1 Energy density versus cycle life of the C/3 reference performance cycle during 25% and 100% fast charge (FC) for the year 1 and year 2 cells. The cells cycled from 2.7-4.25V, room temperature, using a 15-min fast charge + C/3 CCCV charge and dynamic stress test (DST) discharge. .... 23

Figure I.1.2 The capacity retention (left) and capacity (right) for identical electrode designs but with baseline thickness copper & aluminum foils (baseline), 2um thinner Cu foil (Cu), and 2um thinner copper + aluminum foil (Cu+Al). Cells tested from 2.7-4.25V, 30°C, 1CCCV ..... 24

Figure I.1.3 Capacity retention versus cycle life (left) and capacity versus cycle life (right) for an electrolyte formulation study. The cells were cycled from 2.7-4.25V, 30°C, at 1CCCV..... 24

Figure I.1.4 25%FC reference capacity for a 335 Wh/kg cell. Tested from 2.7-4.25V, 30°C, 15-min fast charge cycle and C/3 CCCV other charging, DST discharge..... 25

Figure I.2.1 NX electrode process technology steps..... 28

Figure I.2.2 R2R NX cathode & anode electrode rolls without using PFAS based polymers..... 29

Figure I.2.3 NX >10Ah battery pouch cell parameters and pictures of the pouch cells ..... 30

Figure I.2.4 NX >10Ah battery pouch cell design and initial capacity check performance summary ..... 30

Figure I.2.5 NX >10Ah battery pouch cell design energy density comparison ..... 31

Figure I.2.6 NX >10Ah battery pouch cell design BOL HPPC data based on USABC test protocols..... 31

Figure I.2.7 NX >10Ah battery pouch cell Power Density vs. Energy Density Discharged ..... 31

Figure I.2.8 NX >10Ah battery pouch cell using NCM83 as cathode initial capacity check. .... 32

Figure I.2.9 NX >10Ah battery pouch cell using NCM83 as cathode initial energy density performance. .... 32

Figure I.2.10 NX >10Ah battery pouch cell using NCM83 as cathode initial 15mins-Fast-charging. .... 33

Figure I.2.11 NX >10Ah battery pouch cell using NCM83 as cathode initial C-Rate discharge. .... 33

Figure I.2.12 NX >10Ah battery pouch cell using NCM83 as cathode C/3 cycling performance. .... 34

Figure I.2.13 NX >10Ah battery pouch cell using NCMA (Ni88) as cathode 1C1C cycling performance. .... 34

Figure I.4.1 Calculated 4C CC and CCCV charging capacities of 2-layer dry NMC/Graphite cell using EC:EMC:MA and EC:DMC:MA = 30:(70-x):x electrolytes with different MA fraction $x$ .	40
Figure I.4.2 a, c) Schematics of the trench and cylindrical hole designs, respectively. b, d) Normalized 4C capacity of NMC half-cell with $L_{cat} = 150 \mu\text{m}$ vs cathode layer width $W_{cat}$ and channel width $W_{ch}$ in the trench and cylindrical hole design, respectively.	41
Figure I.4.3 a) Schematic of using graded particle size configurations to improve fast charging while mitigating side reactions. b) 4C constant current charging capacity of NMC/graphite full cells with different particle size arrangements. An electrode configuration is denoted as $\{R_{c1}   R_{c2}    R_{a2}   R_{a1}\}$ : $R_{c1}$ ( $R_{a1}$ ) and $R_{c2}$ ( $R_{a2}$ ) are the cathode (anode) particle size ( $\mu\text{m}$ ) in the layer next to current collector and separator, respectively.	42
Figure I.4.4 Spatial distributions of salt concentration (a) and liquid potential (b) across the cathode in NMC/graphite full cell with the $\{8 1    3 3\}$ (orange) and $\{2 1    3 3\}$ (blue) configurations upon galvanostatic charging at 4C. c) Comparison of SOC distribution of NMC particles in the $\{8 1    3 3\}$ and $\{2 1    3 3\}$ configurations upon 4C charging.	42
Figure I.4.5 a, b) Effect of cathode and anode electronic conductivities on 4C charging (a) and discharging (b) capacities of NMC/graphite cell with $30 \text{ mg/cm}^2$ of NMC and $15 \text{ mg/cm}^2$ of graphite. c) Effect of cathode and anode electronic conductivities on 4C charging capacity of NMC/graphite cell with $20 \text{ mg/cm}^2$ of NMC and $10 \text{ mg/cm}^2$ of graphite. d) Schematic of the dependence of charge transfer ( $R_{ct}$ ), electronic ( $R_{elec}$ ) and ionic ( $R_{ion}$ ) conductivities on electrode thickness.	43
Figure I.4.6 Manufactured 2-sided cathode (a) and anode (b) for 1.5Ah cells.	44
Figure I.4.7 Overcome defects in cathode calendaring step. (a) Defect observed towards the end of the electrode. (b) Defect-free cathode after process/pressure optimization. (c) Schematic of the calender to illustrate the non-uniform pressure in nip zone.	45
Figure I.4.8 Summary of the solvent-free manufacturing system developed. (a) The R2R system with multiple calendaring steps. (b) Electrode used to characterize the electrode non-uniformity. (c) The lowest non-uniformity achieved is $\pm 3.5\%$ .	46
Figure I.4.9 The calendaring models developed to predict the stress/pressure during calendaring dry powder on current collector. (a) Analytical model, (b) Numerical finite element model.	47
Figure I.4.10 Visual appearance of received large double-sided dry-printed (a) cathode electrode, (f) anode electrode. SEM characterization on (b) cathode front surface, (c) cathode back surface; (g) anode front surface, (h) anode back surface; (d), (e) cathode cross-section; (i), (j) anode cross-section.	47
Figure I.4.11 Impedance Spectra of the (a) cathode tortuosity measurement, (b) anode tortuosity measurement.	48
Figure I.4.12 (a) Charge rate performance of DP cathode. (b) CC charge ratio of DP cathode in the charge rate test. (c) Charge rate performance of DP and SC anode electrodes. (d) CC charge ratio of DP anode in the charge rate test.	49
Figure I.4.13 SEM images of (a) prepared dry-printed NMC811 cathode electrodes. (b) slurry-cast NMC811 cathode electrodes. (c) dry-printed graphite anode. (d) slurry-cast graphite anode electrodes.	50
Figure I.4.14 (a) Tortuosity of SC and DP electrodes. (b) Nyquist impedance plots of the SC and DP electrodes symmetrical cells.	50
Figure I.4.15 (a) Charge-rate tests of DP and SC pouch cells. (b) The 0.33C cycle performance of DP and SC pouch cell.	51
Figure I.4.16 Manufacturing cost of slurry manufacturing and the proposed solvent-free manufacturing.	51
Figure I.4.17 Capacity and retention plots for cells made of wet coat electrodes (W) vs cells made from dry coat electrodes (D) undergoing identical DST cycles with C/3 charge conditions.	52
Figure I.4.18 /3 grading plots for multilayer pouch cells using solvent based and solvent free electrodes.	52

Figure I.5.1 Electrolyte Optimization for Improving Cycling Stability of DLP Cells with Pure C5 Cathodes: (a) Capacity Retention, (b) Average Discharge Voltage, (c) Cathode Energy density, and (d) DCR..... 57

Figure I.5.2 Effects of Activation Conditions and Active Cathode Materials Composition on Cycling Stability of DLP Cells with C5C2 Blended Cathodes: (a) Capacity Retention, (b) Average Discharge Voltage, (c) Cathode Energy density, and (d) DCR. .... 58

Figure I.5.3 Electrolyte Optimization for Improving Cycling Stability of DLP Cells with C5C2-Blend 1 Cathodes: (a) Capacity Retention, (b) Average Discharge Voltage, (c) Cathode Energy density, and (d) DCR. .... 60

Figure I.5.4 Fast Charge Cycling Stability of DLP cells: (a) with C5C2-Blend 1 Cathodes and Filled with E6 Electrolytes; and (b) C5C2-Blend 2 Cathodes and Filled with E5 Electrolytes. .... 60

Figure I.6.1 Example Image a) SiOx Anode rolls for 29 Ah cell build b) 3000 meters of Lithium deposited on plastic substrate on R2R c) Thickness for run: 5.3 um +/- 0.02 um < 1 % non-uniformity..... 67

Figure I.6.2 Comparison of discharge capacity vs cycle number for SIDT prelithiation and the corresponding capacity fade plot (C/5 charge CV hold to C/20 and C/3 Dis)..... 68

Figure I.6.3 Photographs of pre-lithiated SiOx anode sheets (6 μm Li) before shipment to Farasis (left and middle) and 2 Ah pouch cell built by Farasis (right). .... 69

Figure I.6.4 Comparison of cell voltage vs. capacity for SIDT and the corresponding baseline during the formation cycle. Note: F3 is the control sample, F1 indicate 6 um pre-Li and F2 8 um pre-Li. .... 70

Figure I.6.5 Plot on the left indicate retained capacity vs. cycle number for the pre-Li anode (F1&F2) vs. baseline (F3) at 25 °C and 1C charge-1C discharge cycling conditions. The figure on the right show capacity (Ah) vs. cycle number (F1&F2) vs. baseline (F3). F3 is the control sample, F1 indicate 6 um pre-Li and F2 8 um pre-Li. .... 70

Figure I.6.6 Plot on the left indicate retained capacity vs. cycle number for the pre-Li anode (F1&F2) vs. baseline (F3) at 45 °C and 1C charge-1C discharge cycling conditions. The figure on the right show capacity (Ah) vs. cycle number (F1&F2) vs. baseline (F3). F3 is the control sample, F1 indicate 6 um pre-Li and F2 8 um pre-Li. .... 70

Figure I.6.7 Idaho National Lab gap chart summary of cell performance indicating the EV cell targets vs. interim cell delivered by SpectraPower. .... 72

Figure I.7.1 Demonstration of closed-loop North American lithium-ion battery supply chain ..... 75

Figure I.8.1 Ionblox approach to reach the USABC calendar life and cell cost targets..... 79

Figure I.8.2 Electrolyte study progress and next steps..... 81

Figure I.8.3 Capacity retention comparison of nine cathodes studied by Ionblox..... 82

Figure I.8.4 Summary of surface passivation approaches..... 82

Figure I.8.5 Comparison of ALD Oxide1 vs baseline on the calendar life performance. Right: capacity retention; Left: resistance growth. .... 83

Figure I.8.6 Comparison of ALD Oxide2 vs baseline on the calendar life performance. Right: capacity retention; Left: resistance growth. .... 83

Figure I.8.7 Comparison of ALD Oxide2 vs baseline on the calendar life performance. Right: capacity retention; Left: resistance growth. .... 84

Figure I.8.8 The rate performance of lithium doped anode with Polymer 4 passivation at three different thickness (T3>T2>T1)..... 84

Figure I.8.9 Summary of cells, form factor, and the planned tests that were shipped to national labs as Mid-Program cell build and delivery..... 85

Figure I.9.1 Fast charge (0-80% SOC) voltage vs. time data is shown for three cells with > 6 mAh/cm <sup>2</sup> areal capacity .....	88
Figure I.9.2 Ionic conductivity, measured at ambient temperature, for selected electrolyte formulations that were tested during Phase 1. Some formulations, boxed in red, exhibited superior performance and are the focus of development during Phase 2 .....	89
Figure I.9.3 Voltage vs. capacity curves for 1st cycle charge and discharge of a selected large-format cell assembled on 24M's automated pilot line. Areal capacity is ~6 mAh/cm <sup>2</sup> . Inset: Box-and-whisker plot of cell capacities, in Ah, showing range and quartiles. ....	90
Figure I.10.1 Cycling data of cells to test effect of dopant gas 2 on anode life, grouped by cathode and scaled dopant flow. ....	94
Figure I.10.2 Peak specific discharge power and minimum voltage during DST cycling in 3.7Ah Si/NCMA cells with improved electrolyte formulations. Formulation #1045 is the baseline formulation at the start of the program. ....	95
Figure I.10.3 C/3 capacity, energy, and nominal voltage retention during calendar life test for baseline cell chemistry .....	96
Figure I.10.4 Interim cell chemistry DST cycle life with 275Wh/kg net energy and peak power density of 700 W/kg. ....	97
Figure I.10.5 Interim cell CAD, picture, and DST cycling .....	98
Figure I.11.1 (a) Capacity and Coulombic efficiency vs. cycle number and (b) Capacity retention for 0.15 Ah Li metal (A1) pouch cells with C2 cathode and E1 electrolyte (C/5 charge and C/1.5 discharge).....	101
Figure I.11.2 (a) Capacity and Coulombic efficiency vs. cycle number and (b) Capacity retention for 0.3 Ah Li metal (A3) pouch cells with C2 cathode and E1 electrolyte (C/5 charge and C/1.5 discharge). ....	101
Figure I.11.3 Li Coulombic efficiency at C/3 in Li Cu coin cells as a function of cycle number in different electrolyte (E1 vs. E3) .....	102
Figure I.11.4 (a) Capacity and Coulombic efficiency vs. cycle number and (b) Capacity retention for 0.15 Ah Li metal (A1) pouch cells with C2 cathode and E3 electrolyte (C/5 charge and C/1.5 discharge).....	102
Figure I.11.5 (a) Capacity and Coulombic efficiency vs. cycle number and (b) Capacity retention for 0.2 Ah Li metal (A1) pouch cells with C1 cathode and E1 electrolyte (C/10 charge and C/3 discharge). ....	103
Figure I.11.6 Pictures of (a) Aged Li anode and (b) Aged cathode with the separator after disassembling of Cell #2 in Figure I.11.5.....	103
Figure I.11.7 (a) Discharge curves of coin cells with the aged Li anode vs Cu foil and (b) Discharge curves of coin cells with the aged cathode vs Li chip comparing with the pouch cell discharge curve at C/10 @342 cycles of Cell #2 in Figure I.11.5.....	104
Figure I.11.8 Discharge capacity @C/10 and @C/3, OCV @50%SOC of sixteen delivery 0.4 Ah Li metal (A3) pouch cells with C2 cathode and E1 electrolyte. ....	104
Figure I.12.1 a) SEM images for 021123-PCAM081222-C-Al; b) XRD pattern for 021123-PCAM081222-C-Al; c) rate performance comparison for 021123-PCAM081222-C-Al and control NMC622 .....	108
Figure I.12.2 a) SEM images, b) XRD pattern, c) electrochemical performance, and d) cyclic performance for recycled cathode samples with different doping/coating strategies. ....	109
Figure I.12.3 a) SEM images for 072523-PCAM081222-D-0.1Zr-C-Al; b) XRD pattern; c) rate performance comparison; d-e) cyclic performance comparison for 072523-PCAM081222-D-0.1Zr-C-Al with control NMC622 sample. ....	110
Figure I.12.4 a) SEM images; b) the XRD pattern; c) electrochemical performance; d) cyclic performance for cathode powder with different Zr/B doping/coating .....	111

Figure I.12.5 a) SEM images; b) XRD patter; c) first cycle discharge capacity for cathode powder with different doping/coating strategy .....	111
Figure I.12.6 SEM images for recycled 83Ni precursors.....	112
Figure I.12.7 a) electrochemical performance for 051723-PCAM4-5%-D-Sr/Mg/Zr-W(1+DI)-C-B (450.7) and Farasis control; b) capacity retention for 051723-PCAM4-5%-D-Sr/Mg/Zr-W(1+DI)-C-B (450.7) and Farasis control .....	113
Figure I.12.8 a) SEM images; b) XRD patterns; c) comparison for primary particle size for cathode sintered at AE and WPI; d) rate performance comparison; e) cycle performance comparison for 071523-PCAM4-5%-D-Sr/Mg/Zr-W(1:2, 300, 30)-C-B (450.7) with Farasis control. ....	114
Figure I.12.9 The cross-section results for Farasis control and 071523-PCAM4-5%-D-Sr/Mg/Zr-W(1:2, 300, 30)-C-B (450.7). ....	115
Figure I.12.10 SEM images for precursors with different reaction time. ....	115
Figure II.1.1 preCAM particle formation with varying the pH of the co-precipitation reactions at fast reactions (top row). Spherical particle formation is strongly dependent on the applied pH, regardless of the residence time. Particle density is improved with longer residence time. Optimal pH (pH = 10.5) and longer residence time (4h) are interacting parameters for improved particle properties (bottom row). ....	121
Figure II.1.2 Voltage profiles of CAMs with different tap densities and morphologies. Top row, left to right; a. Hexagon shaped loosely aggregated primaries with 0.9 g/cc tap density, b. Nodular secondary particles with 1.3 g/cc tap density, c. Spherical secondary particle with 1.6 g/cc tap density (Electrode information: AM:C:Binder = 84:8:8. The average mass of loading ~8-10 mg/cm <sup>2</sup> . Coin half-cell cycling protocol: First formation cycle at C/20 (1C = 175 mA/g) between 2.0 V – 4.7 V at 30°C).....	121
Figure II.1.3 Discharge/Charge ASI profiles of CAMs with different tap densities and morphologies. Top row, a1-a2. Hexagon shaped loosely aggregated primaries with 0.9 g/cc tap density, b1-b2. Nodular secondary particles with 1.3 g/cc tap density, c1-c2. Spherical secondary particle with 1.6 g/cc tap density (Electrode information: AM:C:Binder = 84:8:8. The average mass of loading ~8-10 mg/cm <sup>2</sup> . Coin half-cell HPPC protocol: 3C 10s Discharge/2.25C 10s Charge (1C = 175 mA/g). ....	122
Figure II.1.4 Morphology of preCAMs synthesized using carboxylic acid groups as chelating and precipitating agents; a. Fast reaction, 15 min (Batch, 1L), b. Long reaction, 24 h (Batch, 1L) c. Fast reaction, 30 min residence time (Continuous, 1L).....	123
Figure II.1.5 Morphology of preCAMs with lamellar cracks at 300 and 500°C (SEMs on the left). TG/DSC profile of the preCAM shows two distinct mass losses. XRD profiles display one phase for 300°C (cubic) and a mixture of two phases (cubic + hexagonal) for 500°C pretreatments. ....	124
Figure II.1.6 Morphology of CAMs calcined under flowing oxygen at 750 °C (left) and 850°C (right). Lamellar cracks are more apparent at lower temperature. ....	124
Figure II.2.1 Particle Production with Dry Aerosol Calcination Concept .....	129
Figure II.2.2 DAC trials using NCA green powder .....	130
Figure II.2.3 SP synthesis of AL- and Mg-doped LNO .....	130
Figure II.2.4 FSP configuration for 500 g/hour production.....	131
Figure II.3.1 (Preparation of polycrystalline hydroxide precursor and monocrystalline NMC811).....	134
Figure II.3.2 (Rate performances of polycrystalline and monocrystalline NMC811) .....	135
Figure II.3.3 (C/10 cycling results of polycrystalline and monocrystalline NMC811) .....	135
Figure II.3.4 (Preparation of monocrystalline oxide precursor and monocrystalline NMC96-2-2) .....	136
Figure II.3.5 (Preparation of lithiated single crystal precursor and single crystal cg-LFP CAM).....	137

Figure II.3.6 (Preparation of lithiated single crystal precursor and single crystal cg-LFP CAM) .....	137
Figure II.3.7 (Capacity and rate capability results of cg-LFP).....	138
Figure II.3.8 (Synthesis of nano-sized carbon-layered single-crystal LFP cathode) .....	138
Figure II.3.9 (Bragg coherent X-ray diffraction imaging of CAMs from 3 synthesis processes).....	139
Figure II.3.10 (XPS results of CAMs from 3 synthesis processes).....	139
Figure II.4.1 Flow Reactor for K-TCl. ....	143
Figure II.4.2 Synthesis routes to F-DCI.....	143
Figure II.4.3 <sup>19</sup> F NMR and structure of LiBHFiP .....	144
Figure II.4.4 FDMB-based materials for Lithium-metal cells. ....	144
Figure II.4.5 NMR spectra for FMBMC.....	145
Figure II.4.6 Anode-free cycling of FDMB-based electrolyte.....	145
Figure II.4.7 Synthesis of F4DEE and F5DEE. ....	146
Figure II.4.8 Corrosion current vs applied voltage in Li-FSI cells. ....	146
Figure II.4.9 Corrosion current graph vs. applied voltage in fluorinated electrolytes. ....	147
Figure II.5.1 Electronic conductivity of pellets of LFP mixed with carbon black at low levels of carbon.....	150
Figure II.5.2 Electronic conductivity of pellets of NMC mixed with carbon black at low levels of carbon. ...	150
Figure II.5.3 SEM of 45x magnification of the surface of an LFP electrode of 3 mAh/cm <sup>2</sup> with 5% Denka Black and 7% PVdF1. Fine cracks are observed on the surface. ....	151
Figure II.5.4 SEM of 100x magnification of the surface of an LFP electrode of 3 mAh/cm <sup>2</sup> with 5% CNT and 5% PVdF1. No cracks are observed on the surface but there is the scar of a bubble. ....	151
Figure II.5.5 SEM of 100x magnification of the surface of an LFP electrode of 3 mAh/cm <sup>2</sup> with 5% CNT and 5% PVdF2. The surface is fairly rough, similar to the other electrode with CNTs, and showed cracks like the first electrode. ....	152
Figure II.5.6 <i>Left</i> , SEM of 10000x magnification of the surface of an LFP powder of primary particles. <i>Right</i> , the D <sub>50</sub> particle size is 0.69 microns. ....	152
Figure II.5.7 <i>Left</i> , SEM of 10000x magnification of the surface of an LFP powder of secondary particles. <i>Right</i> , the D <sub>50</sub> particle size is 8.5 microns.....	153
Figure II.5.8 Electronic conductivity of secondary particles of LFP mixed with different fractions of CNT or Denka Black and pressed into pellets. ....	153
Figure II.5.9 SEM of 100x magnification of the surface of an LFP electrode of 4 mAh/cm <sup>2</sup> with 5% Denka Black and 5% PVdF1. Fine cracks are observed on the surface.....	154
Figure II.6.1 Carbon nanofiber and NMP slurry sample after 5 minutes of mixing (LBNL).....	157
Figure II.6.2 Carbon nanofiber and NMP slurry sample after 15 minutes of mixing (LBNL).....	157
Figure II.6.3 Carbon nanofiber and NMP slurry sample after 25 minutes of mixing (LBNL).....	158
Figure II.6.4 <i>Left</i> , High shear homogenizer; <i>Middle</i> , Thinky; <i>Right</i> , planetary ball mill. ....	158
Figure II.6.5 <i>Denka black powder prior to mixing</i> . ....	159
Figure II.6.6 <i>Denka black and binder after 4 minutes in the Thinky</i> . ....	159
Figure II.6.7 <i>Denka black and binder after 60 minutes in the homogenizer</i> . ....	159



- Figure II.6.8 Denka black and binder after 6 hours of ball milling..... 160
- Figure II.6.9 Denka black and binder after 4 minutes in the ball mill. .... 160
- Figure II.7.1 Two dimensional waterfall plot of the evolution of different phases obtained using X-ray diffraction at the Advanced Photon Source (APS, ANL) during the in situ calcination of NMC111-hydroxides with different lithium salts. The evolution of the (003) peak is highlighted that indicates the formation of the layered phase. (a) Calcination of NMC111(OH)<sub>2</sub> with LiOH. (b) Calcination of NMC111(OH)<sub>2</sub> with Li<sub>2</sub>CO<sub>3</sub>. Earlier formation of the (003) layered phase is observed during the calcination with LiOH. .... 165
- Figure II.7.2 Atomistic simulations of the lithiation reaction of the transition metals (denoted as “M”). (a) Reaction between spinel type transition metal oxide (M<sub>2</sub>O<sub>4</sub>) and LiOH. Rapid lithiation of the spinel phase is observed in the ab initio molecular dynamic (AIMD) simulations conducted at 750K. (b) AIMD simulation of the lithiation of the transition metal hydroxide (M(OH)<sub>2</sub>) precursors with hydrated LiOH. Lithiation of the metals is highly dependent on the removal of water that forms during the reaction. The final configuration is the formation of the lithiated disordered rocksalt phase. Achieving the layered oxide phase from the AIMD simulations is a challenge. .... 166
- Figure II.7.3 Comparison between the experimentally observed (dashed line) and computationally predicted (solid lines) evolution of the different phases during the calcination of NMC111-hydroxide with lithium salts. The transition metal hydroxide (NMC111(OH)<sub>2</sub>) phase is denoted by the blue lines, the intermediate oxide phase is depicted by red, and the layered phase is shown in black. (a) Evolution of different phases during the calcination of NMC111(OH)<sub>2</sub> with LiOH. (a) Formation of phases during the calcination of NMC111(OH)<sub>2</sub> with Li<sub>2</sub>CO<sub>3</sub>. The possible chemical reactions are shown on top of the main figures, and the melting points of the individual lithium salts are pointed out..... 167
- Figure II.7.4 Comparison between the precipitation of NMC111-carbonate in a batch and a continuous reactor. Total concentration of the transition metals (TMs) is maintained at 45 mM, and the ratio of [NH<sub>3</sub>]:[TM<sup>2+</sup>] is kept at 15:1 during the entire reaction process. (a) Schematic diagram of a batch reactor. (b) Time dependent evolution of the supersaturation ratio (SSR) within the batch reactor for NiCO<sub>3</sub> (black line), MnCO<sub>3</sub> (red line) and CoCO<sub>3</sub> (blue line). Due to continuous precipitation, the SSR of various precipitates decreases with time. (c) Schematic representation of a continuous reactor, where the inflow and outflow of reactants and products are denoted clearly. (d) Time dependent supersaturation ratio (SSR) of NiCO<sub>3</sub>, MnCO<sub>3</sub> and CoCO<sub>3</sub>, in the continuous reactor, is denoted by the black, red, and blue lines, respectively. All the SSR initially increases with time, which eventually saturates at a particular limit. (e) Comparison between the time dependent relative fraction of TM precipitates as obtained from the batch (dashed) and continuous (solid) reactors. In the batch mode, fraction of Ni increases with time, which indicates Ni-rich surface of the precipitate carbonate particles. However, the fraction of TMs in the continuous reactor reaches a steady state value after some initial transient. .... 168
- Figure II.7.5 Performance estimation of Ni-rich NMC811 cathode particles using mesoscale level computations. (a) Increasing capacity with increasing specific area of the cathode particles observed at different C-rates. The experimentally observed capacities at 0.1C is also clearly denoted, which is adopted from Youngho Shin from MERF at ANL. (b-c) Normalized lithium concentration profile observed at 1C in a secondary particle with very low (b) and very high (c) specific surface area. The final capacity for these two particular microstructures are denoted by “A” and “B” in Figure II.7.5(a). (d-e) Distribution of diffusion lengths in the two particle microstructures shown in Figures II.7.5(b) and (c). The probability of experiencing smaller diffusion lengths is much larger in the particle microstructure shown in Figure II.7.5(c), which demonstrates larger specific surface area..... 169
- Figure II.7.6 Computational simulation of the calcination of MnCO<sub>3</sub> with Li<sub>2</sub>CO<sub>3</sub> at elevated temperatures. (a) Initial microstructure of the MnCO<sub>3</sub> particles with average size around 30 nm. (b) Particle microstructure after calcining for 15 hours. The temperature is increased from room temperature at a rate of 1°C/min. Sintering induced grain growth is well captured by the developed methodology. (c) Evolution of different phases during calcination is predicted by the computational model (solid line) and compared with the experimental results (dashed), which is adopted from Kan et al., JPS 266 (2014) 341 – 346. Removal of the TMCO<sub>3</sub> is shown by the blue line, the oxide intermediate is denoted by the red lines, and the formation of the layered phase is

depicted by the black one. The most probable chemical reaction is shown at the top. Note that the formation of the spinel phase is not captured here..... 171

Figure II.8.1 Li stoichiometry as a tuning handle for the structure and morphology of Ni/Mn-based Co-free cathodes. (a) Composition-property correlation in the Li-Ni-Mn-(Co) space, highlighting the performance needs in terms of capacity, cycling stability and safety and the unavoidable consequence of Li/Ni mixing. (b) Morphological tuning via Li stoichiometry, demonstrated by the abrupt difference in particle size and shape of  $\text{Li}_x\text{Ni}_{0.95}\text{Mn}_{0.05}\text{O}_2$  at  $x = 0.95$  (left) and  $x = 1.05$  (right) calcined from the same hydroxide precursor (middle). (c, d) High-angle annual dark field (HAADF)-scanning transmission electron microscopy (STEM) image and the corresponding atomic arrangement of the intergrown RS/layered (L) phases within the composite NM9505, wherein the two phases share the same *ccp* oxygen framework. (e) 3D-TXM mapping of the Ni valence distribution in NM9505-0.95Li (green represents  $\text{Ni}^{3+}$  and red represents  $\text{Ni}^{2+}$ , while the uniform yellowish color shows a mixture of both  $\text{Ni}^{3+}$  and  $\text{Ni}^{2+}$ ). (f) Specific and normalized capacity of NM9505-0.95Li and 1.05Li at 0.5C between 2.7-4.4 V against Li. .... 176

Figure II.8.2 Strong dependence of structure and morphology on Li-stoichiometry in NM9505. (a) SEM images of the NM9505 calcined from the precursors with Li stoichiometry of 0.90, 0.95, 1.00, 1.025, 1.05, up to 1.10 (from left to right), showing the strong dependence of the morphology of the primary particles on Li stoichiometry. Scale bar: 500 nm. (b) Particle size distribution of NM9505, showing the small size (below 100 nm) and narrow size distribution of the calcined NM9505 with Li stoichiometry below 1.00 (Li deficient, as shadowed), in contrast to the large size and wide size distribution of the samples with near stoichiometry and Li excess. (c) Synchrotron XRD patterns of NM9505, showing the evolution of the structure ordering with the increases of Li stoichiometry ( $\lambda = 0.6199 \text{ \AA}$ ). (d) The calculated phase fraction and domain size of the layered phase. (e) First-cycle CE (average of six cells) and the capacity retention of NM9505 with different Li stoichiometry after 100 cycles at 0.5C, showing higher values in the Li-deficient ones (0.9Li and 0.95Li), compared to those with Li excess (1.05Li and 1.10Li)..... 177

Figure II.8.3 Impact of Li stoichiometry on phase progression and crystallization during calcination of NM9505. (a) Heating profile of the in situ XRD experiment. (b-d) Contour plots of the time-resolved in situ XRD patterns during calcination of NM9505-0.95Li. (e) Calculated RS phase fraction as a function of time during calcination of NM9505-0.95Li (red circles) and NM9505-1.05Li (green circles), respectively. Inset: structure evolution from RS phase (purple shading) dominated to layered phase (green shading) dominated structure during calcination. f, Crystal growth of the layered phase as a function of time for NM9505-0.95Li (red circles) and NM9505-1.05Li (green circles), respectively. Inset: SEM images of NM9505-1.05Li at 600°C and 720°C, showing the particle growth during calcination..... 178

Figure II.8.4 Rational design of high-Ni NMC cathodes with local stoichiometry control (LSC) for high-voltage and safe operation. (a) Schematics of making hetero-structured particles via the LSC route, alternative to the traditional way of employing uniform or core-shell composition, to meet the multifaceted performance requirements (e.g., high energy density, high cycling and thermal stabilities). (b) Multimodal synchrotron X-ray characterization for disentangling the interplay between local stoichiometry and electrochemical redox in stabilizing high-Ni cathodes. (c) Thermal release profiles of the electrodes charged to 4.4 V, produced by differential scanning calorimetry (DSC, showing greatly improved thermal stability of LSC-NMC9055 (orange) compared to homo-NMC9055 (black). The DSC profile from NMC333 (blue) is also provided for reference. (d) Cycling performance of LSC-NMC9055 (orange), in comparison to that of homo-NMC9055 (black) and NMC333 (blue), between 2.7 and 4.4 V at a rate of C/2. (e, f) Discharge capacity and voltages measured from LSC-NMC9055 (green) between 3.0 and 4.3 V at a rate of C/3 Charge, C/2 Discharge. Data taken under the same conditions from the baseline NMC811 (blue) and core-shell NMC811 (red) were provided for comparison to NMC9055..... 179

Figure II.8.5 (a) In situ XRD/DSC on calcination of  $\text{LiNiO}_2$  from  $\text{Ni}(\text{OH})_2$ , showing the heat flow (top) and the correlated contour plot of the in situ XRD (bottom) as a function of temperature. (b) DSC from  $\text{Ni}(\text{OH})_2$  with and without LiOH, showing the different behaviors..... 180

Figure II.9.1 XPS of  $\text{LiFePO}_4$  cathode materials before and after EB process..... 184

Figure II.9.2 (a, b) neutron diffraction patterns of LFP before and after EB radiation. (c) SEM image of LFP electrode after EB processing, and (d) EDX mapping of O, C and P of the electrode. ....	185
Figure II.9.3 (a) voltage curves and (b) cycling performance of single unit pouch cells with EB cured LFP cathode and matching graphite electrodes. ....	186
Figure II.9.4 SEM images of (a) CB-LFP electrode (5wt% carbon black), (b) CNT-CB-LFP electrode (2 wt% carbon black + 0.5 wt% CNT). (c) Cell discharge voltage curves at different C rates with electrodes shown in (a) and (b). (d) capacity retention of different electrodes at different discharge C rates. ....	186
Figure II.9.5 (a) FTIR spectra of radiation cured polymer electrolytes. (b) cycling performance of Li/LFP cells with thick Li (in coin cell) and thin Li (in pouch cell). (c) 1 <sup>st</sup> and 48 <sup>th</sup> cycle voltage curve of Li/LFP cells with thick Li in coin cell. ....	187
Figure II.10.1 The setup that was used for the fabrication of the FTC cathodes. ....	189
Figure II.10.2 X-ray tomography image of the top structured power layer. The scale bar is 200 $\mu$ m. The porosity of this configuration is approximately 70%. ....	189
Figure II.10.3 SEM images of dense structured cathodes for Li-ion batteries. (a) top view, (b,c) view at an angle, (d) FIB image showing the porosity gradient in the bulk structure. ....	190
Figure II.10.4 (a) Rate performance and (b) long term cycling of several Li-ion half cells based on the structured cathodes shown in Figure 3. The active material loadings are indicated on the plot. ....	191
Figure II.10.5 SEM images of flexible LATP scaffolds prepared by freeze drying techniques. ....	191
Figure II.11.1 Cell manufacturing steps including pre-lithiation for silicon anodes. ....	198
Figure II.11.2 1C/1C rate CCCV cycling performance of 11.3Ah capacity pouch cell (Cell build was done by Ionblox).....	198
Figure II.11.3 Ionblox Summary of electrochemical data from formation process for the BP3 Final deliverable cells with Applied Materials Pre-Li. Summary of cell parameters are shown with Energy density reaching 337 Wh/kg and 800 Wh/L. ....	199
Figure II.11.4 SAFT America summary of cells with ~ 20 $\mu$ m Li per side: (A) Images of 7Ah pouch cells (B) Pouch cell in testing fixture (C) discharge capacity vs. Cycle life for 7Ah pouch cells for different Applied Materials Li samples (81166-01&02 transfer vs. 81166-03&04 Type B surface protected). ....	200
Figure II.11.5 Comparison of the cycling performance of cells with NMC622 cathode and different sources of Lithium from different manufactures.....	201
Figure II.11.6 Progress Summary for Lithium protection layer selection (PNNL) ....	201
Figure II.11.7 Progress Summary BatPaC Cost Model (Argonne National Laboratory): BatPaC 5.0 was used for the Li metal study (whereas 4.0 was used for the Si studies in BP2). ....	202
Figure II.11.8 Progress Summary ( <b>Idaho National Laboratory</b> ): Applied Materials/SAFT America Li metal NMC interim cells. Pouch Cell data: 20 $\mu$ m Lithium anode/NMC 811 Cathode and M47(1.0M LiFSI/DME+TTE electrolyte. (a) shows the capacity vs. cycle number during the discharge at C/3 rate (b) the corresponding energy in watt hours for discharging at C/3 rate. ....	203
Figure II.11.9 Applied Materials Technical roll to roll (Li Deposition) using SmartWeb™ platform. Images of Li on plastic substrate after coating, Li on Cu anode and pre-Li anodes are shown.....	203
Figure II.12.1 Single compartment electrodeposition cell setup with batch produced Li anode on Cu. Cross-sectional & front view of Li anode provided ....	206
Figure II.12.2 Cell testing comparison of single compartment electrodeposited Li anodes against commercial anode.....	207
Figure II.12.3 Spray chamber to fabricate robust Gen 3B membrane ....	207

Figure II.12.4 Dual compartment electrodeposition cell setup with batch produced Li anode on Cu.....	208
Figure II.12.5 Cell testing comparison of single & dual compartment electrodeposited Li anodes against commercial anode.....	208
Figure II.12.6 Projected Li anode cost in \$/m <sup>2</sup> vs. Li anode thickness in μm.....	209
Figure II.13.1 Transition from benchtop coating to roll-to-roll pilot-scale coating at ANL.....	213
Figure II.13.2 Viscosity versus shear rate for all the prepared LLZO inks at 25 °C.....	214
Figure II.13.3 Photographs of dry LLZO-PEO films prepared with different mixing conditions.....	214
Figure II.13.4 Plan-view SEM images of LLZO-PEO coatings made from different inks: a.) 10 min, 2000rpm; b.) 10 min, 3500rpm; c.) 30 min, 2000rpm; d.) 30 min, 3500rpm; e.) 2 min, 60 G; f.) 2 min, 80 G; g.) 2 min, 100 G; h.) 10 min, 100 G. The coating speed is included in the image numbers, e.g., *.1 represents 0.1 m/min speed and *.2 represents 0.5 m/min speed.....	215
Figure II.13.5 Cross section SEM images of LLZO-PEO coatings made from different inks: a.) 10 min, 2000rpm; b.) 10 min, 3500rpm; c.) 30 min, 2000rpm; d.) 30 min, 3500rpm; e.) 2 min, 60G; f.) 2 min, 80 G; g.) 2 min, 100 G; h.) 10 min, 100 G. The coating speed is included in the image numbers, e.g., *.1 represents 0.1 m/min speed and *.2 represents 0.5 m/min speed.....	216
Figure II.13.6 Photographs of (a) PVDF-LLZO-LiTFSI inks; and (b) coatings; as well as plan-view (c, d, e) and cross-section (f, g) SEM images of the coated films.....	217
Figure II.13.7 EIS measurements of the Li PVDF-LLZO-LiTFSI Cu cell at RT, 40 °C, and 60 °C.....	217
Figure II.14.1 Electron microscopy of the Li-Al series samples. HR-TEM performed on a JEOL3010.....	221
Figure II.14.2 Electron microscopy of the Li-Al series samples. HR-TEM performed on a JEOL3010.....	221
Figure II.14.3 SEM/EBSD image of Ni <sub>83</sub> CAM.....	222
Figure II.15.1 SEM images of A and B) Ni <sub>0.8</sub> Mn <sub>0.1</sub> Co <sub>0.1</sub> (OH) <sub>2</sub> precursor; C and D) LiNi <sub>0.8</sub> Mn <sub>0.1</sub> Co <sub>0.1</sub> O <sub>2</sub> calcined at 750 °C for 12h under oxygen.....	225
Figure II.15.2 Charge-discharge (left) and dQ/dV profiles (middle) of NMC811 at 4.2V and 4.5V cut-off voltages. The graph on the right compares the discharge values with error bars calculated using data from 2 cells.....	225
Figure II.15.3 (top left) Coulombic efficiencies of the NMC811 samples in the 1 <sup>st</sup> cycle. (top & bottom right) Effects on capacities achieved during a 20h hold at 2.5V and a 60h hold at 4.5V. (bottom right) residual currents measured (e.g., surface stability) from each sample at the end of the 60h hold at 4.5V.....	226
Figure II.15.4 Areal impedance of the samples during chg-dchg using upper cutoff voltages of 4.2V and 4.5V.....	226
Figure II.15.5 (top) Rate performance of NMC811 cathode-electrodes stepwise from C/10, C/5, C/2, 1C and C/10 using an upper cutoff voltage of 4.2V (cycles 1-15) and 4.5V (cycles 15-30). .....	227
Figure II.15.6 ALD Al <sub>2</sub> O <sub>3</sub> Thickness on the Si wafer during heat treatment (0 cycle number) and 1, 3 and 5 ALO ALD cycles on NMC811.....	228
Figure II.15.7 XPS spectra of NMC811 before and after LNO ALD.....	228
Figure II.15.8 XPS spectra of NMC811 before and after Al <sub>2</sub> O <sub>3</sub> ALD.....	229
Figure II.15.9 Capacity testing (left) and resistance (right) of NMC811 coated with ALD Al <sub>2</sub> O <sub>3</sub> and LNO...230	230
Figure II.15.10 Resistance (left), Coulombic efficiency (center), and capacity (right) of uncoiated NMC811 and NMC811 coated with ALD Al <sub>2</sub> O <sub>3</sub> . .....	230

Figure III.1.1 Supply chain mix for Ni production from different resource types for: (a) Mining and beneficiation from sulfide ores; (b) Mining and beneficiation for laterite ores; and (c) Class I Ni production. .... 236

Figure III.1.2 Cradle-to-gate impacts of Ni production from sulfide (with ores of different Ni grades) and laterite ores..... 236

Figure III.1.3 Location of investigated sedimentary- and brine-based lithium projects within the US. .... 237

Figure III.1.4 Preliminary LCA results for Li-chemical production from different sources. .... 237

Figure III.1.5 Illustrative figure showing the type of data that can be viewed in the battery module. Here, a graph shows the GHG per kWh of a battery based on the battery parameters selected..... 240

Figure III.1.6 Comparison of the different emissions values for selected battery chemistry along with their respective constituents in terms of percentage..... 240

Figure III.1.7 Final side-by-side comparison of the impacts/emissions of the eight selected battery choices within the Battery Module with an option to change the displayed “selected metric” and “selected unit.” The green box on the right side displays the variables selected by the user for all eight battery types. .... 241

Figure III.2.1 The Lithium-Ion Battery Recycling Prize is a key pillar of VTO’s critical materials strategy for batteries, which addresses critical materials issues for Li-ion batteries and recovery of materials for re-introduction into the supply chain..... 245

Figure III.2.2 An illustration of the Lithium-Ion Battery Recycling Prize and continuation phases. .... 247

Figure III.2.3 Informational flyers shared at the NAATBatt Lithium Battery Recycling workshop. .... 249

Figure III.2.4 An informational advertisement included in the NAATBatt bi-weekly e-newsletter. .... 250

Figure III.3.1 Basic processing steps associated with direct recycling..... 253

Figure III.3.2 Pilot-scale system designed and purchased for ReCell ..... 254

Figure III.3.3 Electrochemical discharge capacity of an NMC 111 versus graphite cell using the recycled electrolyte versus a standard gen 2 electrolyte at C/3 except for 4 C/10 formation cycles and a C/20 cycle with HPPC study every 50 cycles. .... 255

Figure III.3.4 a) water content of diethyl carbonates (DEC) from Karl Fischer titration. b) Electrochemical discharge capacity of an NMC 111 versus graphite cell with various recycled electrolytes using different solvents for the washing process..... 255

Figure III.3.5 (a) Mn<sup>2+</sup> calibration curve for quantification of transition metal dissolution in the aged electrolyte; (b) IC profile of Mn<sup>2+</sup> in thermal aged electrolyte; (c) IC profile for the harvested electrolyte from the cycled NMC622/graphite coin cells showing the presence of high amount Mn<sup>2+</sup>, Ni<sup>2+</sup>, and Cu<sup>2+</sup>; (d) synthesis of “spent” electrolyte by heating at 55°C of Gen 2 electrolyte mixed with NMC622 and graphite powders; (e) 31P-NMR of pristine and the aged electrolyte; (f) vacuum distillation apparatus used for EMC recycling; (g) 1H-NMR spectra of recycled EMC compared with pristine EMC; and (h) 13C-NMR spectra of recycled EMC compared with those of pristine EMC. .... 257

Figure III.3.6 Photograph of the HFIH delamination system (left) and zoom-in shot of the hot zone with anode shreds in an alumina boat being processed (right). .... 258

Figure III.3.7 Photograph of materials recovered from HFIH processing. Left: high purity copper foil current collector, and right: delaminated anode flakes..... 259

Figure III.3.8 SEM micro images of graphite powder from anode materials recovered by HFIH process. .... 259

Figure III.3.9 Photograph of materials recovered from a large batch (~ 20 g) HFIH processing run. High purity copper foil (left) and active anode (right) were separated using a sieve after delamination..... 260

Figure III.3.10 Photos showing the slurry formed from recovered anode films using (a) KOH/EG and (b) LiOH/EG; (c) photo of ~1.5 kg recovered anode films; (d) charge/discharge profiles for the reprocessed anode in comparison with baseline anode. ....	261
Figure III.3.11 Separation equipment: (a) RE Roll and (b) optical sorter .....	263
Figure III.3.12 Magnetic susceptibility of cathode materials using a SQUID magnetometer at Argonne National Laboratory .....	264
Figure III.3.13 a) flotation recovery of individual cathode active materials after various surface treatment, b) morphology of cathode active materials after the pre-treatment.....	265
Figure III.3.14 a) HAADF image of both delaminated cathode active materials and recycled cathode active materials after a thermal pyrolysis treatment at 600°C; electron energy loss spectrum (EELS) of b) Ni L-edge and c) Co L-edge obtained on various recycled cathode active materials after various pre-treatment processes. ....	265
Figure III.3.15 TGA curves of commercial black mass V1B and separated products in air.....	266
Figure III.3.16 A schematics of a centrifugal ultrafine (UF) gravity separation concentrator.....	267
Figure III.3.17 SEM images of (a) 0.2SiNCM, (b) 1SiNCM, and (c) 5SiNCM cathode. (Inset: images at higher magnification).....	268
Figure III.3.18 (a) XPS Ni 2p spectra of as-prepared cathode surfaces, (b) CV scan of 1SiNCM, and (c) Initial charge-discharge profile of cells at formation cycle. ....	268
Figure III.3.19 Completed installation of 1L black mass purification reactor (Nutsche filter-dryer).....	271
Figure III.3.20 Summary of rational pH baselining tests for representative matrix solutions, verifying redox stability of reactor components while simultaneously obtaining an empirical pH/temperature background of the specific solution composition used in BMP treatment.....	272
Figure III.3.21 (a) Technoeconomic sensitivity analysis to evaluate the cost impact of varying several adjustable post-treatment rinse parameters, using the EverBatt model revised this FY; (b) Structural (XRD) analysis of NMC-622 materials following BMP treatment and rinsing with a series of solvents. ....	273
Figure III.3.22 a) Breakdown cost of the direct recycling process in RTMS; b) The 40 <sup>th</sup> charge capacities of EoL-NMC, P-NMC, and Re-NMC-x in half-cell tests; Cathode regeneration cost (c) and cell manufacturing cost (d) through different processes. Virgin = virgin production process; Pyro = pyrometallurgy recycling process; Hydro = hydrometallurgy recycling process; Direct = direct recycling process in RTMS.....	275
Figure III.3.23 XPS analysis of EoL NMC 622 at each stage of the relithiation process.....	275
Figure III.3.24 Charge and discharge curves of third cycle at C/10 in half cells of EoL NMC 622 at each stage of the relithiation process.....	276
Figure III.3.25 Pouch cell performance of 50 g-scale upcycling products tested by CAMP_ANL.....	278
Figure III.3.26 (left) Cross-sectional slices showing relative Ni (green) and Co (red) content sampled from 3D TXM from a single particle after coprecipitation upcycling and relithiation at four different temperatures. (right) Plots indicating mean 3D Ni and Co ratios as a function of distance from the secondary particle and primary particle surfaces.....	280
Figure III.3.27 Selected non-impedance-based electrochemical metrics that may presumably reflect anode upcycling quality.....	283
Figure III.3.28 Selected correlation analysis: Selected electrochemical performance metrics vs treatment solvent properties.....	284
Figure III.3.29 (a) SEM of SC-83Ni-15h; (b) XRD of SC-83Ni-15h; (a) SEM of SC-83Ni-15h; (c) SEM of SC-83Ni-25h; (d) XRD of SC-83Ni-15h; (e) rate performance comparison between single-crystal cathodes and control samples; (f) cycle performance comparison between single-crystal cathodes and control samples.....	285

Figure III.3.30 Bulk powder compaction setup and results .....	286
Figure III.3.31 Nano-CT images of different NMC 622 particles .....	286
Figure III.3.32 Results from two stages of optical sorting to get a copper and aluminum fraction.....	287
Figure III.3.33 Weight percent of NMC 622 digested by MAE determined by ICP OES analysis.....	287
Figure III.3.34 Energy consumed by MAE reactions along with weight percent digested of NMC 622 during the reaction.....	288
Figure III.3.35 Schematic illustration of membrane-based separation of Li/Co/Ni separation. (a) separation of Co and Ni from Li ions using membrane 1 (IL-based membrane with Cyanex 301 extractant; (b) separation of Co from Ni ions using membrane 2 ( IL-based membrane with P66614Cl as extractant). .....	289
Figure III.3.36 (a) Change in concentration of Li <sup>+</sup> , Co <sup>+</sup> , and Ni <sup>+</sup> ions during transport experiment with membrane 1; (b) Bar graph showing the percentage of separated metal ions; and (c) % metal ion separation during successive 3 transport cycles. ....	290
Figure III.3.37 (a) Change in concentration of Co <sup>+</sup> , and Ni <sup>+</sup> ions during transport experiment with membrane 2; (b) Bar graph showing the percentage of separated metal ions; and (c) % metal ion separation during successive 3 transport cycles. ....	290
Figure III.3.38 Schematic illustration of membrane-based sequential separation of Li/Co/Ni separation using membrane 1 and 2 together.....	290
Figure III.3.39 (a) Change in concentration of Li <sup>+</sup> , Co <sup>+</sup> , and Ni <sup>+</sup> ions during first transport experiment with membrane 1; (b) Change in concentration of Co <sup>+</sup> , and Ni <sup>+</sup> ions during second transport experiment with membrane 2; and (c) Bar graph showing the percentage of separated metal ions. ....	291
Figure III.3.40 Electrodialysis results for recovering lithium from an anode wash water sample and converting it to lithium hydroxide (LiOH) .....	292
Figure III.3.41 The schematic of the circular economy model developed using Al(OH) <sub>3</sub> sorbents. ....	293
Figure III.3.42 (Solvent-membrane separation for the purification of Ni, Co, Li rich leached liquor, a]. effect of flowrate (O:A-ml/min), b]. extraction efficiency per membrane at O:A-1:1 flowrate (ml/min) and 10 %v/v D2EPHA, c]. extraction efficiency per membrane at O:A-1:2 flowrate (ml/min) and 10 % v/v D2EPHA, d]. extraction efficiency per membrane at O:A-1:1 flowrate (ml/min) and 20 % v/v D2EPHA, e]. Selective stripping in stages at O:A-1:1 flowrate (ml/min) with 20 % v/v D2EPHA, f]. Re-used of 20% v/v D2EPHA, mixed metals solution [(Ni-1.2, Co-0.90, Mn-0.61, Li-0.30, Cu-0.101, Al-0.075, and Fe-0.055 g/L)]. .....	294
Figure III.3.43 (a) Synthesis route for the photosensitive monomer Spiropyran; (b) 1H-NMR spectrum of the synthesized photo-sensitive monomer for structure identification and purity check; (c) photo-responsive isomerization of the synthesized monomer examined and characterized by UV-Vis spectroscopy; (d) UV-Vis spectra of the closed and open isomers when subject to UV irradiation (black curve: close structure monomer, blue curve: open structure monomer). ....	295
Figure III.3.44 Images of flow sheet demonstrating the process for LCO and NMC111 .....	296
Figure III.3.45 (Staubli Male (left) and female (right) configurable interconnect for secondary use battery application/Jonathan Harter).....	298
Figure III.3.46 (Secondary Use Energy Storage System Line Diagram for Residential Application/Jonathan Harter).....	299
Figure III.3.47 (Secondary Use Energy Storage System Schematic Jonathan Harter) .....	299
Figure III.3.48 ICP OES analysis of contaminants in ball milled silicon .....	300
Figure III.3.49 Charge and discharge curves of C/20 cycling in half cells of ball milled silicon electrodes from a) non-doped silicon boules, b) boron-doped silicon boules and c) boron-doped EoL PV silicon.....	300

Figure III.3.50 Example voltage response from the electrochemical characterization procedure. ....	304
Figure III.3.51 Measurement of performance metrics. (Left) Rate capability. (Middle) Charge-depleting drive cycle. (Right) Charge-sustaining application cycle. ....	304
Figure III.3.52 Rapid diagnostic pulses recorded across the voltage window. Examples are just from the charge direction, pulses were also performed in the discharge direction. ‘Dynamic’ PsRP measurements, overlaid on the C/2 and 1 C charges and discharge, are summarized at right, showing that the average voltage throughout the pulse is increasing, as the average current during the pulse sequence is unchanged. In total, the current data set has about 13,000 independent pulse measurements. ....	305
Figure III.3.53 Performance of various diagnostic pulses at predicting the measured performance metrics. ..	306
Figure III.3.54 Estimation of state-of-charge using various rapid diagnostic pulses.....	306
Figure III.3.55 (Elastic custom ordered 80Nm high speed nutrunner with axial compensation connected on benchtop prior to robotic integration/Jonathan Harter).....	308
Figure III.3.56 (EIS data from 6 cells and cells 1&2, 3&4, 5&6 in series/Jonathan Harter).....	309
Figure III.3.57 Left.) Schematic of electrochemical model with multiple active materials per electrode Right) Electrochemical model parameters: solid-state diffusivity and exchange current density for NMC 111.....	310
Figure III.3.58 Stage Composition Diagrams for a run with 10% (v/v) Cyanex 272. (Distribution correlations derived from Guimares, Hydrometallurgy, 150 (2014) 173-177).....	311
Figure III.3.59 Impacts of cut-off of cobalt supply from DRC.....	313
Figure III.3.60 US and global maximum production capacity.....	313
Figure III.3.61 Solid state NMR data comparison of different recycled and relithiated samples. a) <sup>6</sup> Li NMR of upcycled NMC 111 with hydrothermal synthesis. b) <sup>7</sup> Li NMR data comparison of redox relithiated samples at different stages. c) <sup>19</sup> F NMR data of NMC 111 samples after washing and relithiation with redox chemistry. ....	314
Figure III.3.62 The effect of washing and acid etching on upcycled NMC 111. a) <sup>2</sup> H MAS NMR on samples after acid etching b) Electrochemical performance comparison of the etched NMC111 after upcycling to NMC 622 with different heat treatments .....	315
Figure III.3.63 (a) Example of upcycling to NMC811 using a Ni sulfate-based precursor under standard heating conditions (5C/min ramp to 900C, 1 hr. hold, and cool). (b) Example of temperature step studies for understanding kinetics for upcycling processes.....	316
Figure III.3.64 Map of collection centers and agents (placed at centroids of census tracts) in the state of New York. ....	317
Figure III.3.65 Comparing battery collection with and without collection events.....	318
Figure III.3.66 LIBRA model top level modular structure .....	319
Figure III.3.67 Projected availability of end-of-life batteries for recycling from different sources.....	320
Figure III.3.68 differential capacity of a M35A (NCA/graphite) 18650 charging before and after heat treatment b) EIS of a MJ1 (NMC811/graphite + silicon) 18650 before and after heat treatment c) external short circuit results of M325A and MJ1 cells before heat treatment, at both 25 and 50mOhm short resistance .....	327
Figure IV.1 Energy delivered during a 15-minute fast charge and improvements seen with the incorporation of an improved binder, an improved separator, and an improved electrolyte. ....	334
Figure IV.1.1 Charge acceptance during a CCCV (4.2V cutoff, time cutoff equivalent to given C-rate) charge of graphite  NMC811 pouch cells employing two highly concentrated electrolytes: HCE-18B (a) and HCE-21 (b).....	337



Figure IV.1.2 Ligand-wise desolvation energies, and b. cation solvation number for highly concentrated electrolyte HCE-18B at 30 °C as a function of total salt concentration as calculated using the advanced electrolyte model.....	337
Figure IV.1.3 Ligand-wise binding energies for Gen2 electrolyte and a highly concentrated electrolyte, HCE13. ....	337
Figure IV.1.4 a. Ionic conductivities of HPE electrolyte and Gen2 electrolyte at different temperatures. b. Voltage and current versus charging time for cells charged at the 6C with a time cutoff of 10 min and discharged at the 1C rate. c. Long-term cycling performance of 2-Ah pouch cells filled with different electrolytes cycled at C/3 standard rate and XFC protocols. d. Optical and (e, f and g) SEM images of graphite electrode from Gen2 cell after 1500 XFC cycles (① is area without Li plating, and ② is area with Li plating). h. Optical and i. SEM images of graphite electrode from HPE cell. ....	338
Figure IV.1.5 A comparison of Gen2 + 3wt% FEC (BL) and a cell with 20% of the EMC replaced with AN (20AN) at 30 °C. a. Overpotential measurements collected at 40% SOC after CC charging at various C-rates with relaxed upper cutoff voltage. b. Charging time of batteries with different electrolytes at varying C-rate with CC-CV protocol to 80% SOC between 3-4.2 V. ....	339
Figure IV.1.6 A novel detailed experimental workflow to estimate the desolvation energy of the electrolyte. ....	340
Figure IV.1.7 a) Long-term relaxation profiles for the restricted diffusion measure of Gen-2. The short-term relaxation behavior exhibits the expected linear concentration profile when plotted vs the square root of time (b). A table of the various diffusion coefficients (c).....	341
Figure IV.2.1 Electrochemical model predictions for a.) cell voltage and b.) lithium plating onset at 6C for different cell designs. ....	345
Figure IV.2.2 Scoping study of effect of capacity loading for mono-layer graphite anodes versus high-nickel NMC (NMC811 and NMC90-5-5 (red curves)) with 96% active material in cathode, Celgard 2500 separator and Gen2 + 2wt% FEC electrolyte. ....	345
Figure IV.2.3 Data from a reference electrode cell with NMC811 positive electrode (Pos), Graphite negative electrode (Neg), Celgard 2500 separator and Gen2 electrolyte. The left and right panels show data from cycle 120 and cycle 260, respectively. ....	347
Figure IV.2.4 $\mu$ -XRF maps corresponding to Ni, Co, and Mn ( <b>a</b> ) of cell with a voltage cutoff of 4.1 V and 6C charging and ( <b>b</b> ) of cell with a voltage cutoff of 4.15 V and the MSR charging protocol after 600 XFC cycles. Regions of higher fluorescence signal correspond to more NMC material in the cathode thickness. All scale bars in the figure are 10 mm. ....	348
Figure IV.2.5 Comparison of discharge capacity (a, b) and capacity retention (d, e) at 1C (a, d) and 6C (b, e) cycling of NMC811 samples in the voltage window of 3-4.3V, c, f) comparison of charge and discharge rate capability, respectively. ....	349
Figure IV.2.6 Quantification of Lithium Plating and Lithiation during and after a 4C Fast Charge. Plot of lithiation based on state-of-charge analysis (blue) and lithium plating (pink) during (circle) and after (triangle) a 4C fast charge. Scans taken during charge were obtained using rapid-scan tomography. The total current passed (purple) represents ideal behavior. Recovered capacity was determined after discharging the cell at C/5. ....	350
Figure IV.2.7 Distribution of lithium plating during and after a 4C charge. Top-down view of segmented lithium plating (purple) on a graphite electrode (gray) for (a) the final charge scan, (b) the first rest scan, and (c) the final rest scan. ....	350
Figure IV.2.8 Comparison of $LixC$ content in the baseline sample (top) vs. laser ablated (bottom). Li in graphite at multiple depths is shown as lines (left) or contour plots (right).....	351
Figure IV.3.1 Impedance and transportation polarization for cells incorporating different fast charge solutions. ....	355

Figure IV.3.2 Comparison of SEI components for cells cycled at different fast charging rates. ....	356
Figure IV.3.3 Electrochemical/thermal/aging model of XCEL Gr/NMC811 Round 2 cell. ....	357
Figure IV.3.4 Empirical voltage threshold for lithium plating as function of SOC determined using electrochemical modeling. ....	358
Figure V.1 Estimated costs of cells in automotive battery packs with different combination of electrodes. The packs are rated for 100 kWh <sub>Total</sub> (85 kWh <sub>Useable</sub> ), 300 kW, 315 V, 168 cells, and produced at a plant volume of 100K packs/year .....	360
Figure V.1.1 Waterfall plot detailing the changes in costs between BatPaC v4.0 and v5.1. Results are for a 94 kWh, 200 kW, NMC811-G pack manufactured at 100,000 packs per year.....	363
Figure V.1.2 Correlation plots showing the relative importance of parameters to achieving selected specific energy (Wh/kg), specific power (W/kg), and cost (\$/kWh) targets. Solid darker colors indicate the variable has a high degree of positive correlation, where higher values are necessary to achieve the goal. Hatched darker colors indicate strong negative correlation, where lower values are needed to meet the target. Light colors indicate the variable has minimal or no correlation, and its value has a limited impact on achieving the target. ....	364
Figure V.1.3 Distribution of energy consumption in three lithium-ion gigafactories, each making NMC-G pouch cells at production volumes of 5, 25, and 50 GWh per year, respectively. ....	365
Figure V.1.4 Simulated swelling of a single Silicon particle, (a) – (d). Comparison of simulated (blue) and experimentally measured (red) electrode thickness (e) and voltage (f) for the current profile for a ~C/20 charge as highlighted by the gray shaded region in inset (e).....	366
Figure V.1.5 Study of cooling plates performance for cooling cylindrical lithium-ion battery cells in a module. (a) different designs of cooling plates, (b) validation of a developed simple mathematical model with a computational fluid dynamics (CFD) study, (c) prediction of cells' maximum temperature as a function of number of flow channels, $N_{ch}$ in the cooling plate (left axis) and number of cell rows, $N_{row}$ per module (right axis). In this study, 10 cells per row were assumed, giving 800 cells in the module, (d) prediction of the pressure drop across the cooling plate as a function of $N_{ch}$ and $N_{row}$ .....	367
Figure V.2.1 Representative data collected at the EADL on advanced batteries. The capacity change normalized to the beginning of life (BOL) is plotted against the normalized calendar aging time, from BOL to end of testing (EOT). The dash curve represents a typical lifetime degradation model as a frame of reference. ....	371
Figure V.4.1 Efficiency summary of cells tested in NREL's calorimeters. Caption Credits/Source: NREL-Andrew Schiek.....	377
Figure V.4.2 Superior Graphite/Toda 120P/NMC-111, 532, 622, and 811 heat generation curves for a 2C full discharge (2a-top) and 2C full charge (2b – bottom) Caption Credits/Source: NREL-Josh Major .....	378
Figure V.4.3 BOL and EOL heat efficiency of 1520P/NMC cells under various discharge currents over an SOC range from 100% to 0%. Caption Credits/Source: NREL-Josh Major .....	379
Figure V.4.4 BOL and EOL heat efficiency of 1520P/NMC cells under various charge currents over an SOC range from 100% to 0%. Caption Credits/Source: NREL-Josh Major .....	379
Figure V.4.5 BOL and EOL heat efficiency of a 1520P/NMC111 cell under a 3C full charge. Caption Credits/Source: NREL-Josh Major .....	380
Figure V.4.6 BOL and EOL heat efficiency of a 1520P/NMC811 cell under a 3C full discharge. Caption Credits/Source: NREL-Josh Major .....	381
Figure V.4.7 Infrared image of lithium battery cell at the end of a fast charge, 3.2C. Caption Credits/Source: NREL- Aron Saxon .....	382
Figure V.5.1 Images of the multifunctional coater installed in the CAMP Facility's dry room.....	385

Figure V.5.2 Electrochemical behavior of electrodes containing SWCNTs cycled vs. Li-metal in the 3.4 – 5.0 V range at 30 °C. (a) shows profiles of cycle 1 and 2 and (b) shows profile of cycle 100. (c) Discharge capacity and (d) Columbic efficiency as a function of cycle number. The g refers to grams of SWCNTs in the electrode.....	386
Figure V.6.1 Schematic diagram (left) and standalone polymer film (right) of solid polymer electrolyte.....	390
Figure V.6.2 Rate (left) and cycling (right) performance of Li/SP/LiFePO <sub>4</sub> cell. ....	391
Figure V.6.3 Schematic diagram of wet-impregnation coating (top) and SEM images of pristine (bottom a-b) and Al <sub>2</sub> O <sub>3</sub> coated (bottom c-d) NCM523 particles. ....	392
Figure V.6.4 Rate and cycling performance Li/NCM523 half cells w/ and w/o Al <sub>2</sub> O <sub>3</sub> coating. ....	393
Figure V.6.5 (a) SEM image and (b–d) TEM images of pristine and heat treated SiO samples. ....	393
Figure V.6.6 (left) First lithiation voltage profile and (right) Cycle tests of SiO-pristine and SiO heat-treated at different temperatures. ....	394
Figure V.8.1 Decision tree framework for the classification and quantification of failure modes in Li-ion batteries. The framework was demonstrated for both Graphite/NMC532 and graphite/NMC811 cells. (Chen 2023).....	402
Figure V.8.2 (Gering 2023) RPT (C/20) and cycle by cycle data that show differences due to polarization effects. Pink curves represent the trendlines for CBC data just following the RPTs, effectively removing polarization hysteresis effects between RPT conditions. (A) Cell 4 which was charged at a 6C rate and had undergone lithium plating, while panel (B) shows cell 16 which was charged at a 4C rate with no signs of lithium plating.....	403
Figure V.8.3 (Weddle, Kim, Chen, et al. <i>J. Power Sources</i> , 2023) [Battery aging modes determined using C/20 fits and the high-rate modeling tool. Age mode diagnostics of LLI and LAMPE are shown for the R1 XCEL cells (termed “Low Loading”) for cells cycled at 1C, 4C, 6C, and 9C.] .....	404
Figure V.8.4 Spatiotemporal contours (x-axis is the longitudinal direction, and y-axis is the temporal direction from top to bottom) of primary and secondary variables from P2D models. Top: results from PDE integration. Middle: PINN predictions. Bottom: Absolute error between the PDE and PINN solutions. Columns from left to right are for: electrolyte Li-ion concentration, electrolyte potential, solid-phase anode potential, solid-phase cathode potential, anode particle surface concentrations, cathode particle surface concentrations, electrolyte-phase current, anode Faradaic current, and cathode Faradaic current. ....	405
Figure V.8.5 Gaps and areas where sharing of data can aid the development process for new or modified battery technologies. (Ward, 2022).....	406
Figure V.8.6 DOE Vehicle Technologies Office Datahub, batterydata.energy.gov, supporting battery R&D.	407
Figure VII.1.1 Single layer pouch cell fixtures and a temperature-controlled chamber enables calendar aging studies for various Si materials under controlled conditions. ....	415
Figure VII.1.2 Capacity fade associated with calendar aging for various Si materials paired with NMC cathodes (left) and LFP cathodes (right) with GenF3 electrolyte. ....	415
Figure VII.1.3 Deconvolution of capacity fade due to calendar aging and cycling.....	416
Figure VII.1.4 SRE-based regression of Si-containing cells at three different aging temperatures. Across the different anonymized cells analysis was limited to those with at least 15% Si content in the negative electrode. ....	417
Figure VII.2.1 (a) Ionic conductivity of E-baseline electrolyte before and after 55 °C storage for eight-days. (b) 1 <sup>st</sup> cycle voltage profiles and (c) cycling performance of Li  NMC622 coin-cells in fresh and stored E-baseline electrolyte tested at room temperature.....	421
Figure VII.2.2 Experiment design to check the crosstalk during the calendar aging.....	421

Figure VII.2.3 Impedance growth of (a) Si Si and (b) NMC622 NMC622 symmetric cells with FEC-containing E-baseline electrolyte during storage at 55°C. The electrodes were retrieved from pre-conditioned half-cell or full-cells. (c) X-ray spectra of pre-conditioned NMC622 cathodes before and after storage at 55°C. ....	422
Figure VII.2.4 Impedance growth of a) Si Si and b) NMC622 NMC622 symmetric cells with FEC-free E-10 electrolyte during storage at 55°C with electrodes retrieved from pre-conditioned half-cell or full cell. c) X-ray spectra of NMC622 cathodes before and after storage at 55°C. ....	423
Figure VII.2.5 Calendar life test protocol .....	424
Figure VII.2.6 (a) Impedance evolution of SLP cells with FEC-containing electrolyte (E-baseline) during the calendar life test at various temperatures. (b) Impedance growth of SLP cells with FEC-free electrolyte (E-10) during the calendar life test at various temperatures, (c) Discharge capacity and voltage profiles of the SLP cells with E-10 electrolyte on the 180th day of calendar aging at various temperatures. The initial voltage profile during the formation cycle at 25°C was also plotted as a reference. ....	425
Figure VII.3.1 a) Schematic of a constrained network block with inputs of orbital coefficients $C$ , atomic numbers $v$ , and atomic positions $R$ . b) Schematic of the architecture of CoeffNet; $C$ , $v$ , and $R$ for both reactants and products are passed through a constrained network block shown in a). $C'$ , which is the output of the network, and $R$ and linearly interpolated through $p$ and are used as node features of the interpolated transition-state graph. Outputs of the last network are interpreted either as coefficients of the molecular orbital or are averaged after subtraction with the outputs of the constrained network block of the reactants to get the activation barrier. ....	429
Figure VII.3.2 a) Illustration of change in molecular dynamics force-field when a chemical reaction happens based on precomputed templates of the reactants and products. b) Schematic representation of MD algorithm combining “coarse grain” (rigid molecules) MD with reactions now possible with LAMMPS.....	430
Figure VII.3.3 Continuum-level model domain with representative physics, electrochemical/chemical reactions, independent coordinates, and select boundary conditions.....	432
Figure VII.3.4 Example potentiostatic-hold protocol for Si-LFP cell with formation cycles, voltage hold portion and reference performance test (RPT) cycles highlighted.....	433
Figure VII.3.5 Gibbs free energy change ( $\Delta G$ ) for electrochemical oxidation of EC based on DFT calculations, accounting for the effect of applied potential and the relative concentration of $EC^+$ . ....	434
Figure VII.3.6 Energy diagrams for reactions between EC and $^1O_2$ , based on mechanisms reported in the literature. Both pathways considered suffer from high barriers and are therefore implausible under ambient or near-ambient conditions.....	435
Figure VII.3.7 Energy diagrams for reactions between EC and superoxide. A hydrogen/proton abstraction mechanism (gray) is energetically unfavorable, while nucleophilic substitution (green) has a moderate barrier and is thermodynamically favored.....	436
Figure VII.3.8 Energy diagrams for reactions between EC and peroxide. All three reactions shown – proton abstraction, nucleophilic substitution, and addition – can occur rapidly under ambient conditions.....	437
Figure VII.3.9 Comparison of predicted and DFT-computed reaction energy barriers on the test set for a) a minimal basis representation (i.e. only s and p basis functions) and b) a full basis (using the def2-SVP basis set).....	438
Figure VII.3.10 Residual between the $C$ from DFT and from CoeffNet predictions for a) a minimal basis set and c) a full basis. Comparison of predicted and DFT values of the HOMO of the transition-state sampled on a 4x4x4 grid for a bounding box of 1.25 Å away from the farthest atom of each molecule in each direction for b) minimal-basis representation and d) the full basis representation. ....	439
Figure VII.3.11 Quaternion-based representation of two interacting molecules. A scheme to reduce this representation to the minimal six degrees of freedom has been developed to be used to build a Machine Learning interatomic potential. ....	440

Figure VII.3.12 Representation of the new Li-Si phase emerging from Li diffusion when embedding a seed of $\text{Li}_{13}\text{Si}_{14}$ inside a matrix made of $\text{Li}_{15}\text{Si}_{14}$ . Color scheme: Si: yellow, Li: pink.....	440
Figure VII.3.13 Energy barrier for $\text{PF}_6 + \text{Li}^+ \rightarrow \text{PF}_5 + \text{LiF}$ reaction using a continuum solvation model (with three different dielectric constants) compared to First-Principles MD. The reaction coordinate is the difference in distances between P-F and Li-F. Energies are in eV and reaction coordinates in Angstrom. ....	441
Figure VII.3.14 (a) Predicted SEI thickness dynamics for at each voltage during the 180 h hold. (b) Measured irreversible leakage current and model predicted responses at several voltage-holds of Si half-cells.....	442
Figure VII.3.15 (a) Normalized capacity, (b) normalized current during 400 hr voltage-hold on Si-LFP cells with five different electrolytes (data: symbols, lines: model fit). (c) Total, reversible (lithiation) and irreversible (SEI) capacities during the hold.....	444
Figure VII.3.16 Comparison of (a) calendar life, and (b) reference performance test cycle capacities for the electrolytes investigated.....	445
Figure VII.4.1 Interim build battery performance (Farasis cycling data) improvement over baseline.....	451
Figure VII.4.2 Calendar life update for interim & baseline batteries comprising Group14 Si-C. ....	451
Figure VII.5.1 Expected cycle life of Final Cells .....	454
Figure VII.5.2 Improvement in normalized recoverable capacity of cells after 1 month of storage at 100% SOC and 60°C via electrolyte modification through cocktails of commercial additives. ....	455
Figure VII.6.1 Continuous Si anode coating.....	457
Figure VII.6.2 Cycle life of the baseline and ultra-high energy (UHE) Si anodes in Li half cells (3 mAh/cm <sup>2</sup> loading, C/5 – C/5, 0.05 – 1.0V): (left) Si anode capacity vs. cycle; (right) capacity improvement achievement under the project. ....	457
Figure VII.6.3 Cycle life of a Si-NMC full pouch cell (3 mAh/cm <sup>2</sup> loading, C/5–C/5, 2.5–4.1 V, 45°C). The cell retains 80% of initial capacity after 1100 cycles.....	458
Figure VII.6.4 Calendar life of a Si-NMC full pouch cell. The cell is charged to 4.1V at C/10 and stored at 50°C. After various storage periods, the cell discharge energy is checked at C/10 and 2.5 – 4.1V. The cell recovers 93% of initial energy after 256 days.....	458
Figure VII.7.1 Electrochemical cycling of Si-graphite/NMC622 full cells cycled using either LHCE or control electrolyte (1M $\text{LiPF}_6$ 3/7 EC/DMC + 10% FEC). (a) Gravimetric capacity vs. cycle number; (b, c) Voltage profiles of (b) cycle 1 and (c) cycle 100. ....	460
Figure VII.7.2 Secondary electron SEM images of (a,b) pristine Si-graphite electrode, and electrode after cycling 100x in (b, e) LHCE, (c,f) 1M $\text{LiPF}_6$ EC/DMC + 10% FEC. Images are shown at magnifications of (a-c) 5000x and (d-f) 10,000x.....	460
Figure VII.7.3 Energy dispersive spectroscopy (EDS) images of Si-graphite electrodes after cycling 100x in (a) LHCE or (b) 1M $\text{LiPF}_6$ EC/DMC + 10% FEC.....	461
Figure VII.7.4 Cryo high-resolution (HR)TEM images of cycled Si electrodes in (a-b) 1M $\text{LiPF}_6$ in EC/DMC + 10%FEC and (c-d) LHCE.....	462
Figure VII.7.5 Cryo STEM image, Li EELS maps and spectra of SEI formed in (a-c) 1M $\text{LiPF}_6$ in EC/DMC + 10%FEC and (d-f) F-LHCE.....	462
Figure VII.7.6 HAXPES spectra of C 1s, O 1s, F 1s, P 2p, and Li 1s acquired at 2500 eV and 6000 eV measuring SEI formed on anodes cycled in (a) control electrolyte and (b) LHCE after 100 cycles. Atomic concentrations of each element in the electrodes cycled in the two electrolytes obtained at (c) 2500 eV and (d) 6000 eV.....	463

Figure VII.7.7 HAXPES spectra of C 1s, O 1s, F 1s, and Li 1s and the corresponding atomic concentrations of each element acquired at 6000 eV measuring CEI formed on cathodes cycled in control electrolyte and LHCE after 100 cycles. ....	464
Figure VII.7.8 Discharge capacity of Si-graphite/LiFePO <sub>4</sub> coin cells galvanostatically cycled inside isothermal microcalorimeter at a C/5 rate between 2.5 – 3.8 V for 50 cycles. ....	466
Figure VII.7.9 Voltage profiles and corresponding heat flow profiles during (a, c) cycle 2 and (b, d) cycle 50 for Si-graphite/LiFePO <sub>4</sub> coin cells with (a,b) 1M LiPF <sub>6</sub> 30:70 EC:DMC + 10% wt. FEC electrolyte or (c, d) LHCE electrolyte. ....	466
Figure VII.7.10 Comparison of IMC measured total heat flow (black) and the sum of polarization and entropy contributions to heat flow (red) during (a, c) cycle 2 and (b, d) cycle 50 for Si-graphite/LiFePO <sub>4</sub> coin cells with (a, b) 1M LiPF <sub>6</sub> 30:70 EC:DMC + 10% wt. FEC electrolyte and (c, d) LHCE electrolyte. ....	467
Figure VII.7.11 Summary of parasitic heat evolved during cycle 2 and cycle 50 for Si-graphite/LiFePO <sub>4</sub> coin cells with (a, b) 1M LiPF <sub>6</sub> 30:70 EC:DMC + 10% wt. FEC electrolyte or (c, d) LHCE electrolyte. ....	468
Figure VII.7.12 Flammability testing of electrolytes (a) 1M LiPF <sub>6</sub> 3/7 EC/DMC +10% FEC, (b) LHCE. Flammability measurements were collected by placing 500 $\mu$ L of electrolyte in a stainless-steel container and placing the flame from a butane lighter over the electrolyte for 2 seconds. Photos are shown after flame removal. ....	468
Figure VII.8.1 Schematic description of the principles of electropolymerization and electrophoretic deposition .....	472
Figure VII.8.2 Samples FTIRs of successful electrodepositions using electropolymerization and electrophoretic depositions. Electropolymerization in LiTFSI/THF precursors: (a) isoprene (IP) $\rightarrow$ polyisoprene (PIP), (b) Methyl methacrylate (MMA) $\rightarrow$ PMMA. Electrophoretic deposition of cationic polymers from aqueous precursors: (c) Chitosan, (d) Dextran-HCl.....	473
Figure VII.8.3 Sample C/3 cycling of electrodepositions using electropolymerization and electrophoretic depositions and their corresponding coulombic efficiencies. Electropolymerization coating of porous electrodes in LiTFSI/THF precursors: (a) isoprene (IP) $\rightarrow$ polyisoprene (PIP) on LiPAA-bound electrodes, (b) Methyl methacrylate (MMA) $\rightarrow$ PMMA on p84-bound electrodes. (c) Electrophoretic deposition coating of cationic polymers Dextran-HCl on Si thin film. All cycling shown are in half-cells. ....	474
Figure VII.8.4 Sample calendar life evaluations in porous electrodes. (a) SEI generated in situ from Fluoroethylene carbonate (FEC) additive to Gen2 electrolyte and using p84-bound electrodes (b) polyisoprene (PIP) synthetic SEI in cells with LiPAA-bound electrodes and Gen2 electrolytes.....	475
Figure VII.9.1 Electrolytes solvation of 1.0 M LiPF <sub>6</sub> /EC-EMC (EE), 1.0 M LiPF <sub>6</sub> in FEC-FEMC-TTE (FFT), and 1.0 M LiPF <sub>6</sub> in FEC-SL-TTE (FST). A, Raman spectra in the range of 800-650 cm <sup>-1</sup> . B-C, in-situ multi-nuclear NMR spectrum, all data were collected at r.t. NMR tuning and shimming was using external reference deuterated solvent of D <sub>2</sub> O in a co-axis NMR tube. B, <sup>7</sup> Li-NMR. C, <sup>19</sup> F-NMR.....	479
Figure VII.9.2 Solvation structure of FST electrolyte. a, distribution of the Li <sup>+</sup> solvates of FSI electrolyte from MD simulations, showing a percent for a specific solvate Li+(PF <sub>6</sub> , SL, FEC), only the solvates with more than 1% are shown for clarity. b, X-ray weighted structure factor for TTE, FEC, SL solvents and FST electrolytes from both MD simulations and experiments at room temperature with exception of SL (30 °C). c, a snapshot of MD simulation cell at 25 °C with solvent shown as a wireframe and TTE diluent highlighted using blue iso-surface.....	480
Figure VII.9.3 Binding energies of Li <sup>+</sup> to solvents from wB97XD/6-31+G(d,p) DFT calculations with all solvates immersed in implicit solvent modeled using PCM(ether) model.....	480
Figure VII.9.4 Radial distribution functions g(r) for FST electrolyte from MD simulations at 25 °C. Despite a slight magnitude of the higher peak for Li-Oc(FEC) g(r) compared to Li-O(SL), a significantly higher Li-O(SL) coordination number of 2.9 was observed vs. 0.8 Oc(FEC) coordination number. It is due to the higher	

number density of SL vs. FEC (630 SL vs. 280 FEC in the MD simulation box) and two oxygens being present in the -SO <sub>2</sub> group of SL vs. only one carbonyl Oc present in FEC.....	481
Figure VII.9.5 Reduction potentials FEC from wB97XD/6-31+G(d,p) DFT calculations with all solvates immersed in implicit solvent modeled using PCM(ether) model. The initial configurations of the representative solvates were extracted from MD simulations.....	481
Figure VII.9.6 Reduction potentials from QC calculations using G4MP2 composite methodology TTE immersed in implicit solvent modeled using SMD( $\epsilon=20$ ) model. ....	482
Figure VII.9.7 Effect of LiF/Li <sub>2</sub> O/Li <sub>2</sub> CO <sub>3</sub> SEI on the Li <sub>x</sub> Si alloy anode. A, Work of separation for LiF Li <sub>x</sub> Si, Li <sub>2</sub> O Li <sub>x</sub> Si, and Li <sub>2</sub> CO <sub>3</sub>  Li <sub>x</sub> Si interfaces. B-D, Electron localized function and $E_{int}$ between the Li <sub>x</sub> Si (Li <sub>15</sub> Si <sub>4</sub> , Li <sub>12</sub> Si <sub>7</sub> , and LiSi) alloys and major SEI components (LiF, Li <sub>2</sub> O and Li <sub>2</sub> CO <sub>3</sub> ). B, LiF. C, Li <sub>2</sub> O. D, Li <sub>2</sub> CO <sub>3</sub> . ....	482
Figure VII.9.8 (A) Cartoon demonstration of the simplified model where the topological distribution of the LiF and Li <sub>2</sub> O phases was set to be parallel so that the Li <sup>+</sup> conduction path could penetrate along the SEI. (B) Formation energy v.s Fermi level (referenced to the VBM) for the most favorable native defects in LiF and Li <sub>2</sub> O under lithium-rich ( $\mu_{Li} = 0$ ) chemical potential conditions. Transitions are marked with stars. (C) The formation energy of Schottky defects was $E_f[\text{SchottkyLiF0}] = E_f[\text{vacLi}] + E_f[\text{vacF}]$ and its evolution with Fermi energy was plotted by a dashed orange line. Based on defect formation energy calculation, the dominant point defects of LiF and Li <sub>2</sub> O in equilibrium with the Li anode are Schottky defects and Li <sup>+</sup> interstitial defects, respectively.....	483
Figure VII.9.9 A, The normalized concentration profile of interstitial Li <sup>+</sup> and mobile electron Li <sub>2</sub> O within Li <sub>2</sub> O/LiF space charge region. The inserted scheme shows the configuration of the Li <sub>2</sub> O/LiF space charge model. B, The total ionic conductivity of the Li <sub>2</sub> O/LiF composite SEI as a function of the volume fraction of LiF when the grain size of Li <sub>2</sub> O is equal to 15 nm and 1 nm, respectively. ....	483
Figure VII.9.10 Morphology of Si particles and electrode thickness after cycling. (A-D), Focused ion beam (FIB) cross-section SEM images of the SiMP electrodes after 50 cycles of operation in different electrolytes: (A), pristine; (B), FST; (C), FFT; (D), EE.....	484
Figure VII.9.11 (A) The SEM images of the pristine 1-5 $\mu$ Si electrodes, show the electrode thickness of pristine 4.1 mAh cm <sup>-2</sup> $\mu$ Si electrode about 18 $\mu$ m. (B-D), the electrode thickness evolution under different cycled numbers (1st, 20th, 50th, and 200th) with EE (B), FFT (C), and FST (D) electrolytes. (E), the histogram of thickness evolution in the three electrolytes, and the SiMPs expansion trend. The dashed line here is only for the guidance of the eye. The $\mu$ Si  Li cells are cycled to a specific cycle, then stopped at the discharge state to make these ex-situ measurements. ....	485
Figure VII.9.12 Li <sub>2</sub> O and LiF distribution on $\mu$ Si anode in the FST (A-B) and FFT (C-D) electrolytes. A, C, HR-TEM images, the colored dots represent the area of corresponding EELS spectral images in b and d. B, D, typical EEL spectra near the surface of the $\mu$ Si particles with the marked four areas in A, C (from surface to inner layer).....	486
Figure VII.9.13 Characterizations of Cycled NCA Electrodes in FFT and FST electrolytes. A-F, typical HR-TEM images of cycled NCA electrodes recovered from $\mu$ Si  NCA full cells after 50 cycles with FFT (A) and FST (B) electrolyte; the atomic distribution of CEI element on the surface of the NCA electrodes cycled in different electrolytes, FFT (C), FST (D); the XPS F1s (E) and O1s (F) surface spectra for NCA cathodes with FFT (upper) and FST (below) electrolytes. ....	487
Figure VII.9.14 (A) Leakage current of the cell using different electrolytes, including LiFSI-based electrolytes (4.0 M LiFSI DME, 1.0 M LiFSI DME/TTE,), as well as LiPF <sub>6</sub> -based electrolytes (LiPF <sub>6</sub> THF/MTHF, 1.0 M LiPF <sub>6</sub> EC/DEC/FEC). (B) The capacity leakage during voltage hold is integrated by the leakage current. (C) The CE and the leakage current @180h of Li  Si and Li  graphite cells in a variety of electrolytes. ....	488
Figure VII.9.15 (A) The relatively molecular ratio of LiF, Li <sub>2</sub> O, Li <sub>4</sub> SiO <sub>4</sub> and Li <sub>2</sub> CO <sub>3</sub> and ROLi/ROCO <sub>2</sub> Li in SEI of 2M LiPF <sub>6</sub> THF/MTHF, 1M LiPF <sub>6</sub> EC/DEC/FEC, 1M LiFSI DME/TTE, and 4M LiFSI DME. (B) The calculated LUMO energy and band gap of variety SEI compositions. ....	489

Figure VII.9.16 TEM and EDS analysis of nano silicon particles in 2M LiPF <sub>6</sub> THF/MTHF after calendar aging. (A) TEM image. (B) EDS Si map. (C) EDS C map. (D) EDS O map. (E) EDS F map. ....	490
Figure VII.10.1 Electrolyte Downselect for Year 3. High-entropy mixed-anion locally superconcentrated electrolyte (HE-LSCE) consisting of two lithium salts of LiFSI and LiClO <sub>4</sub> , DME solvent, and TTE diluent as a downselected electrolyte for Year 3. LSCE with single LiFSI salt as a positive control electrolyte and GenF3 carbonate-based electrolyte as a negative control. ....	494
Figure VII.10.2 Evaluation of Si-LFP Cells and Degradation of Si Anodes. (a-c) Galvanostatic cycling profile of Si-LFP cells cycled by (a) HE-LSCE, (b) LSCE, and (c) GenF3. All cells were cycled with 3 formation cycles with C/10 followed by repeated charge and discharge with C/3. (d) Evolution of area specific resistance (ASR) during Si-LFP cycling. (e) Capacity retention of Si-LFP cells. (f-h) FIB-SEM cross-sectional images of Si anodes after 1 <sup>st</sup> lithiation. ....	495
Figure VII.10.3 Analysis of SEI on Si Anode by XPS. (a) atomic content in SEI on Si anode. (b) C1s XPS spectra from SEI on Si anode. (c) F1s XPS spectra from SEI on Si anode. (d) Atomic content assigned to inorganic SEI components determined by spectra deconvolution. ....	496
Figure VII.10.4 Stability of Electrolytes with NMC811 cathode and Testing of Si-NMC811 cells. (a) Leakage current evolution test during cycling of Li-NMC811 cells. (b-d) galvanostatic cycling profile of Si-NMC811 cells with (b) HE-LSCE, (c) LSCE, and (d) GenF3. (e) Capacity retention of Si-NMC811 cells (f) Columbic efficiency of Si-NMC811 cells. All cells were cycled with 3 formation cycles with C/10 followed by repeated charge and discharge with C/3. ....	497
Figure VIII.1.1 Diagnostic tests are conducted at various stages of the oxide development process. ....	504
Figure VIII.1.2 (a) BatPaC techno-economic evaluation (Wh/kg <sub>cell</sub> ) of the initial LMR-NM <i>EaCAM</i> baseline as a function of power-to-energy ratio (P:E) and minimum rated SOC. (b) Anticipated performance of LMR-NM through improvements in metrics identified in the analysis. ....	504
Figure VIII.1.3 (a) Electrochemical modeling of discharge capacity at 1C for LMR-NM as a function of primary size and agglomeration within secondary particles. (b) Discharge capacity of LMR-NM as a function of C-rate only considering primary particle size. ....	505
Figure VIII.1.4 (a) High-angle annular dark-field (HAADF) image of a hydroxide-based secondary particle. (b) High-resolution TEM image of a corresponding primary particle. (c) HAADF image of a carbonate-based secondary particle. (d) HRTEM image of a corresponding primary particle. ....	506
Figure VIII.1.5 (a) Discharge rate data from a series of electrodes with various loadings and thicknesses as described in the text. The electrodes underwent a first-cycle activation between 4.6-2.0V (vs. Li/Li <sup>+</sup> ) followed by rate tests carried out between 4.5-2.5V. Charge cycle rates were constant at 20mA/g while discharge rates were increased from 20-400mA/g as listed in the figure. The electrolyte was 1.2 M LiPF <sub>6</sub> in a 3:7 wt. mixture of EC and EMC with 0.5 wt.% lithium difluoro(oxalate) borate (LiDFOB). All tests were conducted at 30°C. (b) Similar rate tests, as in (a), performed on electrodes with a fixed loading (9.2mg/cm <sup>2</sup> ) but calendered to different porosities/thicknesses. ....	507
Figure VIII.1.6 In-situ laminography imaging of an LMR-NM cathode-electrode in a pouch cell. (a) schematic of the pouch cell configuration and the laminography scan geometry. (b) a representative slice through the LMR-NM cathode-electrode in the reconstructed 3D volume of the imaged pouch cell. ....	508
Figure VIII.1.7 EXAFS fittings for the parent compound (a-c) Li <sub>2</sub> Mn <sub>1-x</sub> Sn <sub>x</sub> O <sub>3</sub> and (d-f) Li[Mn <sub>1-x</sub> Sn <sub>x</sub> ] <sub>0.5</sub> Ni <sub>0.5</sub> O <sub>2</sub> and cathode material (g-i) 0.3Li <sub>2</sub> [Mn <sub>1-x</sub> Sn <sub>x</sub> ] <sub>0.5</sub> Ni <sub>0.5</sub> O <sub>2</sub> at a Sn content of x = 0.01 (top panel: a, c, e) and x = 0.05 (bottom panel: b, d, f). Solid and hollow circles refer to  χ(R)  and Re{χ(R)} of the dataset, respectively. Similarly, the solid and dotted lines refer to the fitted  χ(R)  and Re{χ(R)} curve, respectively. The vertical dash line is the range of fit. A factor of k <sup>3</sup> has been applied to these FT spectra. (c, f, i) Summarized coordination numbers and bond distances for the first and second Sn shells. Last digit error is given in the parentheses. ....	509



Figure VIII.1.8 ${}^6\text{Li}$ MAS NMR data comparison of $\text{Li}_2\text{Mn}_{1-x}\text{Sn}_x\text{O}_3$ and $0.3\text{Li}_2\text{Sn}_x\text{Mn}_{1-x}\text{O}_3 \cdot 0.7\text{LiMn}_{0.5}\text{Ni}_{0.5}\text{O}_2$ , each with $x = 0$ and $0.02$ .....	510
Figure VIII.1.9 (a) $dQ/dV$ plots of $0.3\text{Li}_2\text{Sn}_x\text{Mn}_{1-x}\text{O}_3 \cdot 0.7\text{LiNi}_{0.5}\text{Mn}_{0.5}\text{O}_2$ ( $x= 0, 0.01, 0.02, 0.05$ ). All electrodes were activated with a first-cycle charge between 4.7-2.0V at $\sim C/20$ and subsequently cycled between 4.4-2.5V (Li metal anodes, 30C, $\sim C/3$ ). (b) ASI comparison obtained by hybrid pulse power characterization (HPPC). (c) and (d) Transmission electron microscopy imaging revealing the difference in grain size between the baseline $x = 0$ sample (c) and the $x = 0.01$ sample (d). (e) Comparison of the crystallite size parameter ( $L_{\text{vol}}$ ) of the cathode materials as obtained from the analysis of high-resolution X-ray diffraction data. (f) Elemental map of Sn and Ni in the Sn = 0.01 sample.....	511
Figure VIII.1.10 (a) Synchrotron X-ray diffraction patterns of pristine 400~900°C LMNO powders. (b) The enlarged view of the diffraction peaks of (311), (222) for LMNO400-600 and (101), (006), (102) for LMNO700-900 and (c) The enlarged view of the diffraction peaks of (440) for LMNO400-600 and (108), (110) for LMNO700-900. (e) Calculated $c/a$ ratio for LMNO400-900. (f) The evolution of disorder level of LMNO as a function of temperature from 400°C to 900°C.....	512
Figure VIII.1.11 (a) Comparison of electrochemical performance for LMNO400-900 samples: (a) 2nd cycle charge (top panel) and discharge (bottom panel) voltage profiles (b) 2nd cycle charge and discharge $dQ/dV$ plot (d) Capacity evolution of 2nd cycle charge/discharge capacity. (d) Rate performance @ 200mA/g.....	513
Figure VIII.1.12 (a) Number of Li-M and M-M (M=Ni,Mn) pairs in the TM layer for each configuration. (b) $\text{LiMn}_x$ ( $x=6,5,4,3,2,1$ ) clusters in the TM layer for each configuration. All configurations are sorted by total energy and referred to the lowest energy (Energy = 0).....	514
Figure VIII.1.13 Side view of the 60%- $\text{LiMn}_{0.5}\text{Ni}_{0.5}$ /40%- $\text{Li}_2\text{MnO}_3$ model (a) ribbon model and (b) staggered model. Transition metal sites are represented by purple and silver polyhedrons for Mn and Ni respectively. Li ions are represented by green spheres. Oxygen outside the oxygen sub-lattice structure is represented by red spheres and red sticks represent O-O bonds. ....	515
Figure VIII.1.14 Mean square displacement (MSD) time evolution for (a) ribbon model (b) staggered ribbon model. Colored lines represent the evolution of the MSD for each Li ion in the simulation cell. The black line represents the ensemble average of the MSD. The red dashed line represents the linear regression used to compute the slope used to determine the jump diffusivity using the Einstein relationship. In the Inset schematics blue represent $\text{Li}_2\text{MnO}_3$ layers and green represent $\text{LiMn}_{0.5}\text{Ni}_{0.5}$ regions.....	516
Figure VIII.1.15 Number of oxygen dimers formed during Ab-Initio Molecular Dynamics simulations at 900K (a) comparison of ribbon vs staggered ribbon model (b) ribbon model at two states of charge. ....	516
Figure VIII.1.16 Number of oxygen dimers formed during Ab-Initio Molecular Dynamics simulations at 900K (a) Ribbon model at 86% SOC (b) staggered ribbon model at 86%SOC. ....	517
Figure VIII.1.17 NMR spectrum of LMR-NM material (a) experimental data in blue represents the material with 10h high temperature holds and the red line the 96h high temperature hold during calcination. (b) Theoretically predicted shifts for all the possible configurations of the material at different temperatures. ....	517
Figure VIII.1.18 Li-Mn-O phase diagram containing stoichiometric rock salt, stoichiometric spinel, and defect spinel phases. Reproduced from Thackeray et al. [8]. ....	518
Figure VIII.1.19 Electronic total energies of tetragonal spinel and monoclinic layered $\text{LiMnO}_2$ phases relative to orthorhombic $\text{LiMnO}_2$ , computed with a) ferromagnetic (FM) and b) antiferromagnetic (AFM) spin polarization. The density functionals assessed are PBE-sol+U, $r^2\text{SCAN}$ , and $r^2\text{SCAN}+U$ .....	519
Figure VIII.1.20 a) Mn 2p and b) Mn3s XPS spectra of the single-crystal samples. Mn L-edge soft XAS profiles of the samples collected in c) TEY and d) FY mode. e) $\text{Mn}^{3+}$ contents estimated from the various characterization techniques.....	520
Figure VIII.1.21 STEM-HAADF and Mn L2/L3-edge STEM-EELS spectra collected on a LNMO-F5 crystal probed: a) in the (102) surface region of 1 to 31 nm at a step size of 6 nm and b) in the bulk region from 120 to 820 nm at a step size of 50 nm.....	521

Figure VIII.1.22 (a) XRD patterns of LNMO, LNMO_Fe, LNMO_Mg and LNMO_Zn single-crystal samples, b) a typical SEM image showing particle morphology of the samples, (c, d) XPS spectra of Mn 2p, Zn 2p, Mg 2p and Fe 2p, (e, f) Mn and Ni L-edge soft XAS spectra collected in the TEY mode. ....	522
Figure VIII.1.23 SEM images of Fe-doped LNMO in various morphologies: a) polyhedron, b) octahedron and c) rod. ....	522
Figure VIII.1.24 (a) SAED pattern and HRTEM images collected on a rod-shaped LNMO single crystal doped with Fe. Crystal facets were determined based on SAED and FFT of the TEM images collected on the corresponding edge. (b) STEM-EDX elemental mapping of Mn (orange), Ni (purple), Fe (cyan) and O (red) at the single-particle level. Ni enrichment is seen on the (102) facet. ....	523
Figure VIII.1.25 Chemical structures, names and acronyms for the additives tested in this study. ....	524
Figure VIII.1.26 Cycling performance of the LMR-NM//graphite cells containing the baseline Gen2, and Gen2 with different a) singular additives (the legends show the wt% and name of each additive) and b) dual additives. ....	525
Figure VIII.1.27 FOME vs. FOMP for all single additives, dual additives, and Gen2 baseline. (The green region presents the high-power density region, and the gold region presents the high energy density region.) .....	525
Figure VIII.1.28 Area specific impedance (ASI) for LMR-NM//Gr cells with electrolytes containing additive(s) as shown compared to the Gen2 baseline. (The pink and brown numbers are initial and final ASI (in the unit of $\Omega \text{ cm}^2$ ) for each additive(s) containing cell. The initial and final ASI for Gen2 baseline is 28.56 and 119.73 $\Omega \text{ cm}^2$ , respectively, as shown in black numbers. The impedance rise percentages for each sample and baseline are present in percentiles). ....	526
Figure VIII.1.29 a) Cycling performance of the LMR-NM//graphite cells containing Gen2 electrolyte with different amounts of TMSPi. Area specific impedance (ASI) for LMR-NM//Gr cells with electrolytes containing additives of (b) 0.5wt% TMSPi, (c) 1wt% TMSPi, (d) 2wt% TMSPi, and (e) 3wt% TMSPi compared to the Gen2 baseline. (The pink and brown numbers are initial and final ASI (in the unit of $\Omega \text{ cm}^2$ ) for each additives containing cell. The initial and final ASI for Gen2 baseline is 28.56 and 119.73 $\Omega \text{ cm}^2$ , respectively, as shown in black numbers. The impedance rise percentages for each sample and baseline are present as denoted). ....	527
Figure VIII.1.30 Cycling performance of the LMR-NM//graphite cells containing LDF + LiDFOB + tVCBO compared to the Gen2 baseline, LDF + LiDFOB and LDF + tVCBO. ....	527
Figure VIII.1.31 Specific discharge capacity and coulombic efficiency of Gen2 and fluorinated carbonate electrolytes. (Testing protocol: 3 wetting cycles of constant current (CC) charge/discharge at 0.1 C from 2.5 – 4.3V, followed by 2 activation cycles of CC charge/ CCCV discharge at 0.05 C from 2.5 – 4.6 V, and 5 HPPC tests with 0.3C aging cycles.) ....	528
Figure VIII.1.32 Charging and discharging ASI. ....	528
Figure VIII.1.33 Voltage profile and dQdV of HPPC prep cycle (2.5-4.4V, 0.04 C). ....	529
Figure VIII.1.34 IC results of electrolyte after cycling. ....	530
Figure VIII.1.35 IC quantification of Mn and Ni in electrolyte after cycling. ....	530
Figure VIII.1.36 ICP-MS quantification of Mn and Ni in Gr anode after cycling. ....	531
Figure VIII.1.37 Capacity fade (a) and impedance rise (b) of cells with LMR-NM cathodes and graphite anodes. The inset in (b) is an enlarged view of the data in the 3.4-4.2 V range ....	532
Figure VIII.1.38 Capacity fade (a) and impedance rise (b) of cells with LMR-NM cathodes and LTO anodes. ....	533
Figure VIII.1.39 Capacity-voltage (a) and differential capacity (b) profiles from cells with LMR-NM cathodes and LTO anodes cycled in the 1.2-2.93 V range. Note that these profiles are of the C/25-rate cycles. ....	533

Figure VIII.1.40 Cycling protocol (a), capacity retention (b) and ASI plots (c) of LMR-Gr cells with and without the voltage hold at 4.4V.....	534
Figure VIII.1.41 (a) Capacity retention of LMR/graphite cells at 30°C and 50°C. (b) The current response measured during the voltage hold at 30°C and 50°C (c) voltage profiles of LMR/graphite cells. Dashed lines indicate the voltage profiles of the cell at the end of cycle as shown in Figure 2a. Solid lines indicate that the voltage profiles of the re-assembled cells with the fresh electrolyte. ....	535
Figure VIII.1.42 <sup>6</sup> Li solid state NMR data for pristine powder (left panel) and mass normalized comparison of pristine electrode and cycled samples (right panel). ....	536
Figure VIII.1.43 Voltage vs. time profile showing locations at which LMR-NM samples were collected for DSC.....	536
Figure VIII.1.44 DSC profiles of delithiated LMR-NM during thermal ramping from 50°C to 385°C at a scan rate of 5°C/min when charged to 4.4V (a) and 4.7V (b) before and after activation. Data from two samples are shown in each plot. ....	537
Figure VIII.1.45 DSC profiles of delithiated LMR-NM during thermal ramping from 50°C to 385°C at a scan rate of 5°C/min when charged to 4.4V (a) and 4.7V (b) before and after activation with addition of fresh electrolyte. ....	538
Figure VIII.1.46 Three major structural degradations, namely, transgranular cracking, secondary phase formation and void formation, are identified in the cycled LNMO cathodes. High magnification STEM-HAADF images show different parts of a transgranular crack, (a) primary particle surface where the crack ends, (b) middle part of the crack and (c) crack tip. The spinel structure in (b) and (c) is oriented in the same direction as the zone axis indicated in (a). The STEM-HAADF image intensities plotted in the right-most column, are measured along arrows in the respective images. The structural models in the middle panels are orientated in the same direction as the images to illustrate the actual atomic arrangements. ....	540
Figure VIII.1.47 (a) BoL morphological quantification for LNO electrodes sintered under varying concentrations of oxygen (20%, 60%, 100%) showing a consistent bi-modal size distribution. (b) CT reconstructions of multiple stacked samples of LMR-NM electrodes awaiting further image-based quantification. (c) High-voltage LNMO electrode showing slight irreversible expansion of particles following initial formation. ....	541
Figure VIII.1.48 (a) Ion polished pristine LMR-NM electrode cross-section in scanning electron microscope. (b) EBSD of cross-sectioned particle shows two grains of similar orientation that can be mapped for strain along the grain boundary; a transmission electron microscopy sample was lifted out from this grain boundary. ....	542
Figure VIII.1.49 (a) Voltage profiles of anode, cathode, and total cell voltages during the first 5 cycles using the custom ATR-FTIR spectro-electrochemical cell. (b) dq/dV and FTIR absorption intensities for EC-Li (coord.) and EC (free) during cycles 4 and 5. ....	543
Figure VIII.1.50 (a) FTIR spectra of Gen 2 electrolyte (black) and of Gen 2 + 1 wt% Mn(PF <sub>6</sub> ) <sub>2</sub> (blue).....	544
Figure VIII.2.1 (a) XRD of ball-milled precursors, (b) as-prepared and ball-milled DRX cathode material, (c) particle size distribution and (d) SEM of ball-milled DRX cathode material.....	551
Figure VIII.2.2 (a) SEM images of as-prepared DRX cathode material calcined at 0.5h, 4.0h, and 12.0h as both loose powder and pellet. (b, c) <sup>19</sup> F-NMR of as-prepared DRX calcined as pellets and loose powder.....	552
Figure VIII.2.3 (a) XRD patterns and (c) SEM image of DRX material synthesized through solid-state method. (b) <sup>19</sup> F-NMR and (d) PSA of previous and current DRX scale-up batches.....	553
Figure VIII.2.4 Waterfall plots showing the in-situ powder diffraction data for the solid state synthesis of LMTF-2532 (left), LMTF-2622 (middle), and LMTF-1811 (right) DRX materials. The different compositions were annealed to different temperatures, so the temperature profile at the right shows the temperature plateaus in colors matching the plot labels and the point at which the hold temperature was reached is indicated by the	

- black line on the waterfall plots. The formation of several short lived intermediates can be seen. The overall phase progression appears to be similar between different compositions..... 554
- Figure VIII.2.5 Normalized Total electron Yield (TEY) soft X-ray Absorption spectra (sXAS) of LMTF2531 (a), LMTF2622 (b) and LMTF1811 (c) along with the spectra of their respective precursors, as indicated. Left (right) y-axis corresponds to the normalized intensity of the synthesized sample (precursor)..... 555
- Figure VIII.2.6 (a) XRD and (b) SEM images of coprecipitated DRX precursor and calcined DRX cathode material. .... 556
- Figure VIII.2.7 (a) XRD patterns and (b) SEM images of DRX precursor and samples calcined at 700 °C, 800 °C, and 900 °C. (c) SEM/EDS analysis of DRX materials calcined at 900°C. .... 556
- Figure VIII.2.8 (a) XRD patterns of scaled up DRX compounds using a large size tube furnace (Inset: photo of the large tube furnace, inner diameter: 2.6 inch) and (b) connection of moisture and O<sub>2</sub> traps to the large tube furnace. .... 557
- Figure VIII.2.9 Powder XRD data and corresponding Rietveld plots obtained for DRX powders (Mn/Ti =5/3) prepared through a combustion synthesis route. Results are shown for (a) metal oxide and (b-c) metal oxyfluoride compositions. All samples were heat-treated under flowing Ar using the conditions indicated. Data were collected on a lab diffractometer using a Mo radiation source with a 2 : 1 mixture of K $\alpha$ 1 : K $\alpha$ 2 ( $\lambda$ 1 = 0.70930 Å;  $\lambda$ 2 = 0.71359 Å)..... 558
- Figure VIII.2.10 XRD data and corresponding Rietveld plots obtained for Mn-rich DRX powders (Mn/Ti =7/1) prepared through a combustion synthesis route. Results are shown for (a) metal oxide and (b-c) metal oxyfluoride compositions heated for 1 h at 1,000 °C under flowing Ar. Data were collected on a lab diffractometer using a Mo radiation source with a 2 : 1 mixture of K $\alpha$ 1 : K $\alpha$ 2 ( $\lambda$ 1 = 0.70930 Å;  $\lambda$ 2 = 0.71359 Å)..... 559
- Figure VIII.2.11 Surface plots of the in-situ XRD patterns obtained for the Li<sub>1.25</sub>Mn<sub>0.5</sub>Ti<sub>0.3</sub>O<sub>1.95</sub>F<sub>0.05</sub> powder. Data were acquired on a lab diffractometer using a Cu radiation source with 2 : 1 K $\alpha$ 1 : K $\alpha$ 2 ( $\lambda$ 1 = 1.54056 Å;  $\lambda$ 2 = 1.54439 Å). Scans were collected at room temperature and 100 – 800 °C with a total scan time of 10 minutes at each temperature..... 560
- Figure VIII.2.12 Galvanostatic cycling performance of DRX cathodes prepared through a combustion synthesis route. The nominal cathode powder composition is Li<sub>1.35</sub>Mn<sub>0.7</sub>Ti<sub>0.1</sub>O<sub>1.85</sub>F<sub>0.15</sub>. (a) Voltage profiles for various cycles and (b) charge/discharge capacity over 30 cycles. All cells were cycled between 2.0 V and 4.8 V at a specific current of 10 mA g<sup>-1</sup> for the first 5 cycles and 20 mA g<sup>-1</sup> for subsequent cycles..... 560
- Figure VIII.2.13 SEM images of M80 (a) and NMC811 (b) particles. Scale bars are 10  $\mu$ m, (c) operando DEMS results collected during the 1<sup>st</sup> charge of M80 cathode to 4.8 V. The dQ/dV curve (grey) as well as gas evolution profiles of O<sub>2</sub> (olive) and CO<sub>2</sub> (pink) are plotted as a function of voltage. (d) Mn L-edge XANES profiles collected on the pristine and recovered M80 electrode at 4.8 V..... 562
- Figure VIII.2.14 (a) The 1<sup>st</sup> charge voltage profiles of M80 and NMC811 cathodes at a current density of 10 mA/g, (b) DSC profiles collected on M80 cathodes recovered at OCV, 4.4, 4.6, 5.0 V, respectively, and (c) DSC profiles collected on M80 and NMC811 cathodes recovered at 4.4 V..... 563
- Figure VIII.2.15 (a) Voltage profiles for the 1<sup>st</sup> formation cycle at 10 mA/g. (b) Cycling performance of Li||DRX cells at 20 mA/g charging and discharging, after four formation cycles at 10 mA/g. The voltage range is 2.0 – 4.8 V (vs Li/Li<sup>+</sup>). .... 564
- Figure VIII.2.16 Performance of DRX half-cells with ED01 and ED04 electrolytes: (a) voltage profiles at selected cycle numbers, (b) cycling performance at 20 mA/g charging and discharging after four formation cycles at 10 mA/g, and (c) discharge rate capability with 20 mA/g charging current after three formation cycles at 10 mA/g. .... 564
- Figure VIII.2.17 (a) <sup>7</sup>Li spin echo solid-state NMR spectra collected at 100 MHz and under 60 kHz MAS and (b) C K-edge sXAS-TEY spectra of pristine electrodes and DRX electrodes cycled in ED01 and ED04 electrolytes..... 565

- Figure VIII.2.18 (a-c) STEM images and (d-f) EELS results of (a,d) pristine DRX, (b,e) DRX cycled in ED01 (after 100 cycles) and (c,f) DRX cycled in ED04 (after 100 cycles). ..... 566
- Figure VIII.2.19 (a) Long-term cycling performance of Li||DRX cells with ED01 and ED04 at 20 mA/g charging and discharging, after four formation cycles at 10 mA/g (1st batch Argonne DRX). (b) Voltage profiles for the 1st formation cycle at 10 mA/g and (c) cycling performance at 20 mA/g charging and discharging of Li||DRX cells with new LHCEs in comparison with ED01 and ED04, after four formation cycles at 10 mA/g (2nd batch of Argonne DRX). ..... 567
- Figure VIII.2.20 (a) DEMS results depicting CO<sub>2</sub> evolution during cycling of LMTO in half cell, and (b) Nyquist plot depicting growth in impedance over long-term cycling of LMTO in a full cell. Impedance measurements were taken after each charge listed. For both experiments, the cells were charged at a constant rate of 0.1 Li hr<sup>-1</sup> (32.9 mA g<sup>-1</sup>) in a voltage window of 4.8 – 1.5 V vs. Li/Li<sup>+</sup> and the electrolyte was 1M LiPF<sub>6</sub> in 3:7 EC:EMC. The EIS scan employed an amplitude of 5 mV and a frequency range of 20 MHz to 100 kHz. .... 568
- Figure VIII.2.21 (a) Cumulative CO<sub>2</sub> evolution from a DRX material prepared using <sup>13</sup>C labelled Li<sub>2</sub>CO<sub>3</sub> (<sup>13</sup>CBN) and Super P carbon (<sup>12</sup>CBK). (b) Cumulative CO<sub>2</sub> evolution from a <sup>13</sup>CBN DRX and <sup>13</sup>C labelled carbon black (<sup>13</sup>CBK) cathode. (c) Cumulative CO<sub>2</sub> evolution from a <sup>12</sup>CBN DRX and a <sup>13</sup>CBK cathode. (a-c) are all normalized to the weight loading of the DRX material (LMTO). Horizontal dotted lines mark the initial amounts of solid native carbonate in LMTO. (d-f) are the same cumulative CO<sub>2</sub> evolution profiles as (a-c), but instead normalized to the carbon black surface area. In each case, the electrolyte-originating CO<sub>2</sub> is nearly identical when normalized to the carbon black surface area rather than the LMTO loading, implying that the carbon black governs electrolyte stability. .... 569
- Figure VIII.2.22 Outgassing from a Li||DRX (LMTF2622) cell employing EC-lean electrolytes with three different additives. .... 570
- Figure VIII.2.23 Activation barriers (in red) for the decomposition of EC with singlet oxygen. .... 571
- Figure VIII.2.24 energy diagrams for reactions between ethylene carbonate (EC) and a) singlet oxygen <sup>1</sup>O<sub>2</sub>; or b) superoxide (O<sub>2</sub><sup>-1</sup>). .... 572
- Figure VIII.2.25 Morphology and chemical state of graphite coated DRX cathodes (a) HAADF-STEM image and energy dispersive spectroscopy (EDS) map of graphite coated cathodes. (b) HAADF image showing the position where EELS signals were taken (c) EELS taken from marked regions in (b). .... 573
- Figure VIII.2.26 Effect of ball milling with and without carbon on DRX morphology. (a) SEM image of the particle milled with carbon, (b) SEM image of the particle milled without carbon, (c) HAADF image and corresponding EDS elemental map showing the carbon distribution on the DRX particle milled with carbon, (d) HAADF image and EDS elemental map showing the particle agglomeration on the particle milled without carbon (the carbon map in d indicates the carbon film on TEM grid). .... 574
- Figure VIII.2.27 A comparison of chemical nature of cations for DRX particles milled with and without carbon. (a) HAADF image indicating the position and direction of EELS acquisition, (b) EELS acquired at Ti-L, O-K and Mn-L edges for the particle milled with carbon. (c) HAADF image indicating the position and direction of EELS acquisition for the particle milled without carbon, (d) EELS acquired at Ti-L, O-K and Mn-L edges for the particle milled without carbon. .... 575
- Figure VIII.2.28 Spatial distribution of different carbon species on DRX particle surface; (a) Gr (10%) coated DRX, showing a coating layer thickness of 5-10 nm with residual graphite, (b) Gr (5%) coated DRX, showing a coating layer thickness of 5-10 nm at some regions, while some regions are uncoated. (c) 5%(Gr)+5%(C-65) coated DRX; Gr coating ranges from 5-20 nm and C-65 coating ~25 nm; some residual chunks of graphite are evident. .... 576
- Figure VIII.2.29 (a) SEM image of DRX particles wrapped by reduced graphene oxide and (b) XRD of DRX particles wrapped by reduced graphene oxide compared with DRX. .... 577

Figure VIII.2.30 (a)(b) SEM images of PEI coated DRX particles wrapped by reduced graphene oxide and (c) XRD of PEI-DRX particles wrapped by reduced graphene oxide compared with DRX and PEI coated DRX. ....	577
Figure VIII.2.31 ICP-MS signal of $\text{Li}_{1.2}\text{Mn}_{0.6}\text{Ti}_{0.2}\text{O}_{1.8}\text{F}_{0.2}$ particles dispersed in various solvents at (a) 1 h and (b) 24 h.....	578
Figure VIII.2.32 The electrochemical performance of the electrodes with different ratios of DB to CNT: discharge capacity, coulombic efficiency and electrochemical impedance spectroscopy from left to right.....	578
Figure VIII.2.33 The electrochemical performance of the electrodes with different amounts of CNT.....	579
Figure VIII.2.34 (Left) the active-area specific-capacity and coulombic efficiency versus cycle number, (Center) the discharge voltage curves versus specific capacity at a discharge rate of 20 mAh/g, and (Right) Nyquist plot of electrochemical impedance spectroscopy data taken over the first 50 cycles.....	580
Figure VIII.2.35 sgc MC-simulated voltage curves of spinel $\text{Li}_x\text{Mn}_2\text{O}_4$ with varying disorder from $d = 0.0$ (ordered spinel, dark blue) to $d = 0.5$ (fully disordered spinel, dark red). ....	580
Figure VIII.2.36 Averaged concentrations of $\text{Li}_x\text{Mn}_2\text{O}_4$ tet (green triangles) and oct (red circles) coordination at $d = 0.0$ (a) and $d = 0.1$ (b); and averaged concentrations of tet Li categorized by the species in their face-sharing nearest neighbor oct sites, including isolated with no face-sharing (black triangles), face-sharing with Li (blue), face-sharing with Mn (purple), and face-sharing with both Li and Mn (orange) at $d=0$ (c) and $d=0.1$ (d). Insets show local Li environments, including isolated tet Li inserted during the green regime and the fully lithiated spinel's oct Li in panel c, and oct Li and face-sharing tet Li inserted during the red regime in panel d. ....	581
Figure VIII.2.37 A comparison of experimentally captured and simulated ionic channeling pattern (CP) associated with different atomic species along (110) direction for $\text{Li}_{1.2}\text{Mn}_{0.7}\text{Ti}_{0.1}\text{O}_{1.7}\text{F}_{0.3}$ DRX. (a) Schematic to illustrate the electron rocking beam technique and recording of electron channeling pattern (ECP) with high angle annular dark field (HAADF) detector, while the ICP associated with each atomic species is recorded with characteristic x-ray energy dispersive spectroscopy (XEDS) technique. (b) ECP image recorded by HAADF and ICP images for F, O, Mn and Ti detected by XEDS. (c) Atomic model viewing along the [110] zone axis and correspondingly the simulated ICP images. ....	582
Figure VIII.2.38 Electrochemical voltage profile of the $\delta$ phase cycled between 1.5 and 4.8 V for the first 20 cycles. ....	582
Figure VIII.2.39 Rietveld refinement of synchrotron XRD discharged to 3.5 V at the 20 <sup>th</sup> cycle. ....	583
Figure VIII.2.40 Capacity retention over 100 cycles when cycled in different voltage windows at 20 mA/g. ....	583
Figure VIII.2.41 Migration barrier of different TM species. The energy profile of (a) $\text{Mn}^{2+}$ , (b) $\text{Mn}^{3+}$ , (c) $\text{Mn}^{4+}$ and (d) $\text{Ti}^{4+}$ when migrating from one octahedral site to another.....	584
Figure VIII.2.42 Thermodynamic driving force evaluations of DRX-to- $\delta$ phase transformation. (a) Calculated thermodynamic driving force ( $E_S - E_\gamma$ ) at $\text{LiMnO}_2$ - $\text{Li}_2\text{TiO}_3$ composition tie line. (b) Calculated thermodynamic driving force ( $E_S - E_\gamma$ ) of composition with $\text{Li}_{1.208/\text{f.u.}}$ and two different $F=0/\text{f.u.}$ and $F=0.25/\text{f.u.}$ ....	584
Figure VIII.2.43 In-situ heating diffraction experiments conducted on a) chemically-delithiated $\text{Li}_{0.57}\text{Ti}_{0.7}\text{Mn}_{0.2}\text{O}_2$ and b) pristine $\text{Li}_{1.1}\text{Ti}_{0.7}\text{Mn}_{0.2}\text{O}_2$ under Ar. ....	585
Figure VIII.2.44 Analysis of thermally-relaxed, chemically-delithiated $\text{Li}_{0.57}\text{Mn}_{0.7}\text{Ti}_{0.2}\text{O}_2$ . a) TEM image and selected area electron diffraction, b) Voltage profile (1.5-4.8 V, 20 mA/g), and c) Synchrotron XRD pattern and Rietveld refinement fit. d) Illustration of the local structure transformation from Mn-rich delithiated DRX to spinel -like phase. ....	586
Figure VIII.2.45 Illustration of the intercalation calculation of DRX structures. (a) Calculated (circle) and experimental (solid line) voltage profiles of $\text{Li}_{1.3-x}\text{Mn}_{0.4}\text{Nb}_{0.3}\text{O}_{1.6}\text{F}_{0.4}$ . (b) Calculated content of $\text{Mn}^{2+}$ , $\text{Mn}^{3+}$ , $\text{Mn}^{4+}$ , and O <sup>-</sup> per formula unit (f.u.) as a function of Li content (x). ....	587

Figure VIII.3.1 The CEI Consortium has three focused groups working on Model Cathode Materials (left), Electrolytes (middle) and Characterization & Modeling (right).....	590
Figure VIII.3.2 Baseline performances of commercial polycrystal NMC811 and graphite (Gr) cycled between (a) 2.6 and 4.2 V, and (b) 2.6 and 4.3 V. All the rest testing conditions are similar to those listed in the table below.....	591
Figure VIII.3.3 Atomic Force Microscope (AFM) images of NMC811 stored in different environments after various days. (a1-a3) are NMC811 stored in ambient environment for 1, 5 and 10 days, respectively. (b1-b3) are those stored in dry air (with 0.1% RH) for 1, 5 and 10 days, respectively. (c1-c3) are NMC811 stored in N <sub>2</sub> for 1, 5 and 10 days, respectively. ....	593
Figure VIII.3.4 The first charge-discharge curves of NMC811 stored in (a) N <sub>2</sub> , (b) dry air and (c) ambient environment for different days. For each sample after storage, 60°C overnight drying in vacuum is conducted before slurry coating process. ....	594
Figure VIII.3.5 (a) SEM image of NMC811 stored in ambient environment for 30 days, (b) SEM image of the stored NMC811 after certain treatment, (c) The first charge-discharge curves of NMC811 stored in ambient environment for different days. Stored NMC811 are tested in half coin cells between 2.7-4.4 V. Relatively low mass loading of ca.5 mg/cm <sup>2</sup> of NMC811 is used since the goal is to only to check the usable capacity after storage.....	594
Figure VIII.3.6 Cycling performances of (a) Li/NMC811 (bare vs. coated) and (b) graphite/NMC811 (bare vs. coated) coin cells. Testing conditions for half cells in (a): 2.8 V-4.4 V vs. Li/Li <sup>+</sup> ; C/10 for charge and C/3 for discharge. Mass loading for bare NMC811: 9.69mg/cm <sup>2</sup> ; mass loading of NMC811 coated by 2 nm CeO <sub>2</sub> : 10.56 mg/cm <sup>2</sup> . Testing conditions for full cells in (b): 2.7 V-4.3 V vs. graphite, C/3 for both charge and discharge. The active material mass loading of bare NMC811, NMC811 coated by 2 nm CeO <sub>2</sub> , and NMC811 coated with 4 nm CeO <sub>2</sub> are 9.40 mg/cm <sup>2</sup> , 10.97 mg/cm <sup>2</sup> , and 9.21 mg/cm <sup>2</sup> , respectively. N/P ratio in the full coin cell: 1.8. The initial testing conditions for materials understanding are not exactly the same as the Consortium's coin cell protocol and will be repeated later when more knowledge is gathered.....	595
Figure VIII.3.7 Rate performances of graphite/NMC811 (bare vs. coated) coin cells. Testing conditions for half cells in 2.7 V-4.3 V vs. graphite, C/5, C/5, C/3, C/2, C/1, C/2, C/3 for both charge and discharge.....	596
Figure VIII.3.8 Evolution of (a) a- and b-lattice parameters, (b) c-lattice parameter, (c) unit-cell volume, and (d) Li-O and Ni-O bond distances for the different Li <sub>x</sub> NiO <sub>2</sub> phases with a comparison between calculations with and without vdW-correction. ....	598
Figure VIII.3.9 (a) Metal acetate precursor powders; (b) Spontaneous solid to molten transition of the mixed powder at above 80 °C; (c) SEM and (d) TEM image and (e) XRD of the NMC622 single crystals synthesized by eutectic method with a temperature-swing annealing. (f) Half-cell cycling data using SC-NMC622 synthesized by eutectic method. ....	598
Figure VIII.3.10 (a) SEM image of NMC622-coated NMC9055 SC particles synthesized by eutectic method; (b) Half-cell performance of the pristine NMC9055 and NMC622-coated NMC9055 SC particles synthesized by eutectic method. ....	599
Figure VIII.3.11 (a, b) Voltage profiles showing the two types of cathode aging protocols in graphite//NMC622 full cells. Protocol #1: charge cells to 4.4 V followed by a >450 h potentiostatic hold at 4.4 V. Protocol #2: cycle the full cell between 3 V-4.4 V. At the end of each charge, constant voltage is held at 4.4 V for 50 h. (c, d) Impedance spectra of full cells cycled using protocols #1, and #2, respectively, measured at UCV at various increments. (e, f) SEM/EDX spectra of the charged graphite anodes (rinsed) extracted from cells that underwent the protocol #1, and #2, respectively. Different map numbers represent different spots on the anode.....	600
Figure VIII.3.12 Evolution of the <sup>13</sup> C NMR of solutions of LiClO <sub>4</sub> /EC solutions after electrolysis at high potential. The measurements tracked (a) the appearance and growth of VC simultaneous to (b) the evolution of a complex set of intermediates from EC oxidation, which (c) could be quantified as a function of time. ....	601

- Figure VIII.3.13 Impact of Li-borate salt additives on high-loading NMC811 capacity retention measured after 50 cycles at C/3 rate using a 4.6 V upper voltage cutoff. Error bars represent the standard deviation of three cells in each case. (SNL Unpublished data)..... 601
- Figure VIII.3.14 High voltage cycling of high loading NMC 811 cathode in half cells using Li metal as the counter electrode. C/3 charge-discharge curves using the electrolytes (A) Gen2 + VC, 0.9M LiTFSI-C3mpyrTFSI-FM (B) w/o LiBOB additive (C) with LiBOB additive. (D) Li/NMC811 performance curves of electrolyte (A), (B), and (C). All tests are in half cells between 2.8 V and 4.4 V. The active mass loading of the cathodes with electrolyte (A)-(C) are 16.95 mg/cm<sup>2</sup>, 14.6 mg/cm<sup>2</sup>, 14 mg/cm<sup>2</sup>, respectively. (Univ. Chicago unpublished data)..... 602
- Figure VIII.3.15 Cycling stability of Li|NMC 532-coin cells using Li as the anode cycled between 2.8 and 4.3 V vs. Li/Li<sup>+</sup> at C/3 charge and discharge rate. a) short ALD Li-precursor exposure and b) long ALD Li-precursor exposure. Mass loading of NMC532: 12.1mg/cm<sup>2</sup> (~1.88mAh/cm<sup>2</sup>)..... 603
- Figure VIII.3.16 Comparison of parasitic heat resulting during cycling of Li/NMC811 cells cycled in two voltage ranges (3.0 V–4.1 V and 3.0 V–4.3 V). ..... 604
- Figure VIII.3.17 Entropic heat flow determination of Li/NMC811 coin cells. Entropic heat flow vs. x (Li<sub>x</sub>Ni<sub>0.8</sub>Mn<sub>0.1</sub>Co<sub>0.1</sub>O<sub>2</sub>) for (a) the 1st cycle from 3.0 V to 4.1 V, (b) the 1st cycle from 3.0 V to 4.3 V, (c) the 3rd cycle from 3.0 V to 4.1 V, and (d) the 3rd cycle from 3.0 V to 4.3 V..... 604
- Figure VIII.3.18 HAXPES Characterization of Interfaces Post Formation from NMC811 cathodes recovered from Li/NMC811 cells after three formation cycles between 3.0 V-4.1 V or 3.0 V-4.3 V at C/10 rate, with measurements collected in both the discharged and charged states (3.0 V-4.1 V and 3.0 V-4.3 V). ..... 605
- Figure VIII.3.19 HAXPES measurements collected on post NMC811 cathodes recovered from Li/NMC811 cells after 100x cycles at C/2 rate (a) O 1s data, (b) C 1s data, (c) F 1s data..... 606
- Figure VIII.3.20 Voltage-dependent potential energy profiles showing degradation of ethylene carbonate towards vinylene carbonate on Pt (111) surface. .... 607
- Figure VIII.3.21 (a) and (b) Predicted stress distribution at pre-existing crack tips; (c) Post-mortem TEM image highlighting the formation of steplike cracks in cycled NMC76 single crystals (PNNL unpublished results); (d) Predicted local stress as a function of distance between two pre-existing cracks. .... 608
- Figure VIII.3.22 Calculated XAS spectrum of crystalline (red inset) and highly disordered phases (green inset) of Li<sub>2</sub>CO<sub>3</sub> (left) and Li<sub>2</sub>O (right). In the structure representation, Li, O and C are shown as green, red and brown spheres, respectively..... 608
- Figure VIII.3.23 Median nickel fluorescence intensity as a function of time and voltage during charging of a half-cell containing LiNi<sub>0.9</sub>Mn<sub>0.05</sub>Co<sub>0.05</sub>O<sub>2</sub> and 1M LiTFSI in 3:7 volume % EC:TEGDME..... 609
- Figure VIII.3.24 Redeposition behavior of cobalt (left), manganese (center), and nickel (right) as a function of initial pixel intensity. The median intensity of the initial redeposition frame is shown as a vertical line. Peaks falling to the left of the line represent redeposition at low intensity regions. Peaks falling to the right of the line represent redeposition at high intensity regions. “Any redeposition” refers to the behavior of all pixels experiencing TM redeposition. “Top 15%” and “Top 1% Redeposition” refer to initial intensities of the pixels with the most aggressive (top 15% and 1%) increases in fluorescence intensity. .... 610
- Figure VIII.3.25 Schematic showing relevant interfacial processes to be studied and planned evaluation methods. Interfacial/ surface and near-surface analysis techniques will be paired with modeling to deconvolute CEI formation mechanisms..... 610
- Figure VIII.3.26 (a) Cyclic Voltammetry of PAD-LMO in LP58 model electrolytes (1.2M LiPF<sub>6</sub> in EC:EMC=3:7), (b) Mn L-edge NEXAFS of Cycled PAD-LMO in TEY mode and (c) Comparison of the Oxidation States of PAD-LMO in Charged/Discharged State..... 611
- Figure VIII.3.27 Schematic showing a typical scanning electrochemical microscope..... 612



Figure VIII.3.28 (a) cyclic voltammetry (CV) for oxidation of LP58 at a 2 mm Pt disk. (b) CV for LP58 at a 3 mm GC electrode. (c) linear sweep voltammetry (LSV) collected at a 2 mm Pt disk electrode for oxidation of LP58 (d) Generation/collection SECM (GC-SECM) tip current collected for a 10 mm Pt tip electrode near the 2 mm Pt disk substrate. Tip voltage was varied from 3.3 V to 2.6 V (e) LSV for a LMO model cathode material in LP58 (f) GC-SECM tip current collected for a 10 mm Pt disk tip electrode near a LMO substrate undergoing voltage sweep.....	613
Figure IX.1.1 ATR-FTIR spectra of Li metal after exposure to GEN2 electrolyte. The residual electrolyte was removed by drying (black), kimwipe (red), rinsing with 30 uL EMC (green). ATR spectrum of GEN2 electrolyte dried on Cu (grey) is included for reference. ....	619
Figure IX.1.2 Characterization of a Li surface after reaction with GEN2 electrolyte: effect of vacuum drying a) ATR-FTIR spectra of Li sample after 30 min and 48 hrs of drying under vacuum b) optical image of the Li surface after drying electrolyte with Kimwipe and drying for 48hr under vacuum c) AFM topography image of the Li surface after exposure to GEN2 d) white light (WL) image corresponding to c) and e) nano-FTIR spectra from 7 different locations on the sample. ....	620
Figure IX.1.3 a) ATR-FTIR spectra of Li metal surface after reaction with GEN2 electrolyte immediately after exposure (green), after 24hr exposure (orange); b) close up plot of C=O deformation vibrations generated from species on Li surface and in electrolyte after reaction with Li metal (purple).....	621
Figure IX.1.4 Atomic force microscopy: topography (top) and tapping amplitude (bottom) of a silicon nitride window capped with two layers of graphene. The right column are zoom-ins on the black boxes in the left column of the figure.....	621
Figure IX.1.5 ATR and nano-FTIR of dried GEN2 electrolyte (blue), suspended graphene (black) and graphene/GEN2 interface (red).....	622
Figure IX.1.6 Illustration of the tip-sample region in which the near-field-induced dipole moment, $p$ , is visualized as both a net dipole and a sum of two dipoles (top). Equations relating the real and imaginary parts of the complex valued nano-FTIR spectrum to the local dielectric properties of the sample material (bottom left) and an algebraic expression for the local extinction coefficient as a function of the real and imaginary parts of the nano-FTIR spectrum (bottom right).....	622
Figure IX.2.1 Left panel, measured PDF data of SEIs on Cu foil and on Li foil in Cu  Li cells. Middle panel, PDF data of SEI on Li foil in Li  NMC cells. Right panel, PDF data of SEI on Cu foil in Cu  NMC cells. Calculated PDF patterns of possible SEI components are also shown for data analysis. ....	626
Figure IX.2.2 (a) Cyclabilities of the NMC811  Li coin cells using three kinds of electrolytes: 1.2 M LiFSI in F5; 1.2 M LiFSI in F4 with DFOB additive; 1.2 M LiFSI in FDMB. The molecular structures of involved solvents and additives are shown in the top panel. (b) Sulfur x-ray fluorescence mapping on lithium metal anode. Due to the relatively high concentration of sulfur species, quantification of absolute sulfur amount cannot be obtained. Instead, only relative sulfur amount can be known as shown in the color scale bar. (c) Sulfur K-edge XAS of NMC cathode for CEI study using 1.2 M LiFSI in F5 electrolyte.....	628
Figure IX.2.3 (a) Schematic diagram of an in-situ coin cell used in this study. (b) Bubble formation in the in situ NMC  Li coin cells upon exposure to X-ray beam at 8.4 keV energy. (c) 2D-XANES maps at Ni K-edge collected from the in-situ coin cells upon charging (top) and the corresponding energy histogram (bottom) of the 2D XANES maps. (d) Particle movement caused by extensive beam damage during in-situ experiments. (e) Artifacts generated from data analysis due to particle movement on the 2D-XANES map (left) and the corresponding energy histograms generated from the 2D XANES maps (right).....	630
Figure IX.2.4 (a) illustration of the single-layer pouch cell configuration. (b) the <i>in situ</i> TXM experiment setup. (c) 2D Ni K-edge XANES mapping of Li/Mn-rich NMC during charge-discharge. The top panel, distribution of white line energies in the file of view. The bottom panel, the histogram of the white line energies. ....	631
Figure IX.3.1 In situ bias TEM measurement of electrical properties of solid electrolyte interphase. a, Schematic of experiment setup. b-d, TEM images showing W wire with sharp tip and Cu wire with SEI layer	

on the surface. e, Typical I-V curves showing the critical voltage. Scale bars, 50  $\mu\text{m}$  in **c** and 100 nm in **b** and **d**..... 634

Figure IX.3.2 I-V curves and  $dI/dV$ -V curves taken from SEI layers formed on Cu and Li. a-c, I-V curves measured from SEI on Cu formed in the different electrolytes under electron beam off condition with bias range from (a) 0-2.5 V, (b) 0-5 V and (c) 0-10 V. d-f, Corresponding differential conductance derived from the above I-V curves (a-c). g-i, I-V curves measured from SEI on Li formed in the different electrolytes under electron beam off condition with bias range from (g) 0-2.5 V, (h) 0-5 V and (i) 0-10 V. j-l, Corresponding differential conductance derived from the above I-V curves (g-i). Insets of (e-f) and (k-l): critical voltage. .. 635

Figure IX.3.3 Dependence of microstructure of Li deposits on rate of differential conductance. a, Low magnification cryo-scanning transmission electron microscopy-high angle annular dark field (STEM-HAADF) images of Li deposits formed in low concentration electrolyte (LCE), pseudo-localized high concentration electrolyte (PLHCE), high concentration electrolyte (HCE), and localized high concentration electrolyte (LHCE) electrolytes; gray and blue bar indicates the area fraction of Li and solid electrolyte interphase (SEI). b, SEI layer configuration maps derived from the STEM-HAADF images, the inset at each image is the high-resolution TEM images of Li deposits; c, 3D reconstruction of Li deposits. d,  $dI/dV$ -V curves of SEI on Li formed in those four electrolytes, where the slope of  $dI/dV$  as a function of V is termed as rate of differential conductance. .... 637

Figure IX.3.4 Electrochemical cell performances. a, Coulombic efficiency (CE) of Li||Cu cells. b, Long-term cycling stability of Li||NMC811 cells in low concentration electrolyte (LCE), pseudo-localized high concentration electrolyte (PLHCE), high concentration electrolyte (HCE), and localized high concentration electrolyte (LHCE) electrolytes. Inset numbers: initial CE and average CEs from 10 cycles..... 638

Figure IX.4.1 (a) Schematic of the model cell with electrodeposited and foil lithium electrodes. The METS sensor is deposited on the dielectric film with a thin film copper current collector on which 15  $\mu\text{m}$  lithium is electrodeposited. (b) EIS spectra of the cell measured after cell assembly (pre-SEI, blue) and after cycling to allow SEI growth (post-SEI, red). Two semi-circles are visible on both spectra but attributing each semi-circle to particular electrodes is ambiguous because of the lack of spatial information with EIS..... 642

Figure IX.4.2 METS Spectrum and the best-fit lines (purple) at different current magnitudes for pre-SEI growth (a, top) and post-SEI growth (b, bottom) cases. From the frequency dependence of the thermal penetration depth, the spatial resolution i.e. resolution of the contribution of each electrode is achieved. From the non-linear dependence of electrode kinetics on the current, the resolution of transport (SEI resistance) and the kinetic overpotential is achieved..... 643

Figure IX.4.3 Schematics of the LAGP symmetric cell (a) Base Case, (b) Thicker Thermal Insulation Layer, (c) Double Layer and (e), (f), (g) their corresponding temperature rise in 2 mins at different current frequencies. (d) Schematic illustration shows the simulated temperature distribution of the SSBs at cross section using COMSOL. (h) Temperature evolution for the above different configurations showing both experiments and simulation results. (i) Experiments setup for the alternating current heating of LAGP symmetric cell and the images of the cell. .... 644

Figure IX.4.4 (a) Battery configurations for different capacities (small to large): single layer to cylindrical/pouch cell and module and pack level. (b) Alternating Current heating power as a function of frequency at various temperatures. For a 5 Ah cell configuration, (c) Time required to reach 40  $^{\circ}\text{C}$  temperature rise under different solid-state electrolyte thickness and ionic conductivity. (d) Time required to reach 40 $^{\circ}\text{C}$  temperature rise as a function of ionic conductivity if electrolyte thickness in 25  $\mu\text{m}$ ..... 645

Figure IX.5.1 a, Schematic of preparing lithium-containing Cu current collector by annealing. b, Digital photos of the Li on Cu foil before (left) and after (right) prelithiation by annealing. c, XRD analysis results of bare Cu foil and prelithiated current collector. New peaks observed from Li-containing current collector are marked with yellow symbols. .... 649

Figure IX.5.2 a) XRD analysis of lithium containing Cu current collectors with different time of annealing (0, 0.5, 1, 2, and 3 hours) and b) enlarged plot of XRD results for  $2\theta = 40 - 55^{\circ}\text{C}$ ) Li 1s XPS on Cu side of

samples before and after annealing. d) Corresponding schematic diagram showing the progress of prelithiation from Li on Cu foil..... 649

Figure IX.5.3 a) SEM analysis of lithium containing Cu current collectors after annealing at various temperatures (scale bar = 50  $\mu\text{m}$ ) and b) schematic diagram of the possible diffusion mechanism of Li into Cu, respectively (orange : Cu, silver : Li). ..... 650

Figure IX.5.4 a) Initial coulombic efficiency of graphite anodes with lithiated current collectors. Time of annealing describes the degree of lithiation. b) A schematic of coin cell setup with lithiated current collectors and c) extraction of Li during cycling..... 651

Figure X.1.1 Computationally predicted voltage vs. time curves for lithium alloying and plating phenomena. Time evolution of the domain containing lithium metal alloy (red) and deposited lithium (magenta) is shown in the left. The electrolyte on top is also denoted in blue. The applied current density is 100  $\mu\text{A}/\text{cm}^2$ ..... 655

Figure X.1.2 Computation predicted voltage vs. capacity curves obtained during plating and stripping of lithium with alloying metal anodes. (a) Thinner alloying anode layer is used with thickness around 50 nm, which experiences both alloying and plating reactions. During stripping, the plated lithium strips first and the dealloying process starts later. (b) With 2  $\mu\text{m}$  thick metal foil, all the deposited lithium ends up alloying with the metal. No plating of lithium is observed. During stripping only dealloying is observed..... 656

Figure X.1.3 (a) Experimentally observed interdiffusion of ions at the LCO cathode and LPS solid-electrolyte interface (adopted from Sakuda et al., Chem. Mater. 2010 949 – 956). (b) Initial distribution of Co (blue), P (green), and S (red) atoms near the interface used in the computational model. (c) Distribution of Co, P, and S at the interface after simulating the interdiffusion of ions for 2.7 hours. Similar distributions of atoms as observed in experiments are also predicted by the computational models. .... 657

Figure X.1.4 Model predicted evolution of the interphase region with time is reported here. (a) The initial interphase layer is denoted by the dotted line. The interphase after interdiffusion for 2.7 hours is shown by the solid line. (b) Computational model predicted increase in interphase layer thickness with time is denoted by the black line along the left axis. Shift of the LCO/LPS interface into the cathode with time is shown by the red line. .... 657

Figure X.1.5 Impact of adhesion strength on the Li deposition near void domains. (a) Initial mesh of a porous Li|SE interface. (b) Li deposit at the contact points for weak adhesion between the electrode and electrolyte. (c) For well adhered Li|SE interface, majority of the initial deposition happens at the pore domain. (d) Output voltage response for strong and weak adhesion between the anode and electrolyte, where strong adhesion leads to higher overpotential. .... 658

Figure X.1.6 Under the assumption that Li can deposit inside the pores adjacent to solid electrolytes, without direct contact with the metal electrode, it is possible to demonstrate the formation and evolution of internal voids within the lithium electrode from the interfacial pores. (a – e) Evolution of lithium deposits at the interface after plating for 100s, 500s, 1000s, 2500s, and 5000s, respectively, at a current density of 1  $\text{mA}/\text{cm}^2$ . .... 658

Figure X.1.7 (a) Computational mesh used for simulating the stripping of lithium from the Li/CNT composite electrode. The LLZO solid electrolyte is located on top and shown in blue, the CNT is shown in black, and the Li metal is denoted in red. (b) Increase in voltage with time during the stripping process. Without any CNT, the voltage response is shown in red. The black curve shows the voltage response with CNT, but Li transport from metal to CNT is not considered. Blue to green lines indicate voltage response under different magnitudes of the reaction rate constant ( $k_{\text{reac}}$ ). .... 659

Figure X.1.8 Lithium concentration profile within the Li/CNT composite at different times. (a) At around 10 mins majority of the stripping happens from the Li metal anode, without any depletion from the CNTs. (b) After 40 mins, the Li metal surface is almost completely depleted, and the CNT experiences delithiation. Li moves from metal to the CNT. (c) Li concentration profile after 70 mins when both the metal and CNT are depleted..... 660

Figure X.2.1 (a) Voltage profiles of Li | LYC | Li and Li-In | LYC | Li-In symmetrical cells when cycled at a constant current density of 0.2 mA/cm<sup>2</sup>. (b) SEM image collected from the recovered AEI region of the cycled Li | LYC | Li cell. (c) XRD patterns collected on various samples as indicated. (d) EIS data collected at the OCV of the Li-In | LYC | Li-In cell after various cycles, in the frequency range between 1 MHz – 100 mHz. (e) Cross-sectional SEM image collected from the recovered AEI region of the cycled Li-In | LYC | Li-In cell. 662

Figure X.2.2 (a) SEM images collected at the LYC/Li-In anode interface before and after cycling to various cycle numbers and b) XRF mapping of In distribution at the LYC/Li-In anode interface before and after 1000 cycles. .... 663

Figure X.2.3 K-edge XANES spectra of Y (a) and In (b) collected on various reference compounds and recovered Li-In anode after 1000 cycles. (c) XRF elemental maps of Cl, In and Y collected from the cross-section of the NMC811-LYC|LYC|Li-In ASSB cell after 1000 cycles. The expanded view of the cross section is shown on the right. (d) Cl K-edge  $\mu$ XAS spectra collected from the p1-p6 locations as indicated in the expanded view in c), and (e) comparison of Cl K-edge  $\mu$ XAS spectra of p2 and reference compounds. .... 664

Figure X.2.4 (a) XRD patterns and (b) Nyquist plots of the Li<sub>3</sub>YCl<sub>6-x</sub>I<sub>x</sub> (x = 0, 0.5, 1.0 and 1.5) solid electrolytes synthesized using the high-energy ball-milling method. .... 665

Figure X.2.5 Charge/discharge voltage profiles of the ASSB cells during the 1<sup>st</sup> and 2<sup>nd</sup> cycles: a) LYC as the SE and b) LYCI-1.0 as the SE. c) Comparison of the 1<sup>st</sup> charge voltage profile of the cells. .... 665

Figure X.2.6 (a) The phase diagram of Li-Ga, (b) galvanostatic cycling data obtained on a Li<sub>3</sub>Ga<sub>7</sub> | LYC | Li<sub>3</sub>Ga<sub>7</sub> symmetric cell, (c) schematic of the ASSB cell with a NMC811 composite cathode, a LYC SE separator and a Li<sub>3</sub>Ga<sub>7</sub> composite anode, and (d, e, f) rate capability, voltage profiles and capacity retention at 0.5C of the ASSB cell shown in (c). .... 667

Figure X.2.7 (a, d) Voltage profiles of the SC-NMC811 ASSB cells cycled at 0.2 C. (b, e) Discharge capacity retention and coulomb efficiency of the ASSB cycled at 0.2 C. (c, f) Nyquist plots collected at the discharged state after various cycles as indicated. (a, b, c) are obtained from the cell with a Si anode material whereas (d, e, f) are obtained from the cell with a pre-synthesized Li-Si alloy anode. .... 668

Figure X.3.1 The distribution of *D*<sub>rLi</sub> and *D*<sub>rO</sub> of 20 selected compounds. .... 671

Figure X.3.2 (a) Calculated overpotentials ( $\Delta V$ ) for a current density of 0.044 mA cm<sup>-2</sup> across room temperature cathode coatings of *l*<sub>c</sub> = 1 and 10 nm. The dashed line represents  $\Delta V = 0.1$  V. (b) Calculated O<sup>2-</sup> diffusion time *t* in the selected compounds assuming an *r* = 1  $\mu$ m primary particle and an *l*<sub>s</sub> = 2 nm surface rocksalt phase. The dashed line represents *t* = 1 h. The green regions represent favorable  $\Delta V$  and *t*. .... 672

Figure X.3.3 High-throughput computational screening procedure to select cathode coatings for Li-ion battery. .... 673

Figure X.3.4 Comparison of model predicted and DFT (red) HOMO of the transition state and (b) orbital density along the reaction axis of three representative SN2 reactions. .... 675

Figure X.4.1 (a) A schematic of tetrahedral-octahedral face-sharing Li configuration. (b) A metal compatibility heatmap extracted from high-throughput DFT calculations. .... 678

Figure X.4.2 (A) General structure of argyrodite with different sulfur (S) sites (4a – red, 4c – green, 16e – yellow). (B) Energy above the hull with different substitutions. .... 679

Figure X.4.3 Arrhenius plots of Li<sub>5.91</sub>PS<sub>4.91</sub>(BH<sub>4</sub>)<sub>1.09</sub>, Li<sub>6</sub>PS<sub>5</sub>Cl, and Li<sub>6</sub>PS<sub>5</sub>Br from electrochemical impedance spectroscopy (EIS) measurements. .... 680

Figure X.4.4 Structure of  $\beta$ -Li<sub>3</sub>PS<sub>4</sub>. (i) The unit cell from ND refinement, (ii) splitting of Li1' (8d) site, and (iii) splitting of Li2' (4b). .... 681

Figure X.4.5 Distributions of NRMS atomic displacements for each DFT-relaxed structure from refined XRD and ND sites. .... 681

Figure X.4.6 Li fractional occupancies as a function of temperature for the a) XRD structure and b) ND structure of $\beta$ -Li <sub>3</sub> PS <sub>4</sub> .....	682
Figure X.4.7 Phase diagram of the Li <sub>2</sub> S-P <sub>2</sub> S <sub>5</sub> system at 0, 700, and 1000 K. Solid lines denote the convex hull. Stable phases are marked with green squares and unstable phases with gold stars.....	683
Figure X.4.8 Free energy above the hull ( $E_{\text{hull}}$ ) for all phases from 0 to 1000 K.....	683
Figure XI.1.1 (a) C/3 Charge and Discharge Capacities (2.8-4.2 V operating window) at 30 °C and -20 °C respectively, for different electrolyte compositions. (b) Capacity Retention (on the basis of Discharge Capacities) at -20 °C for different electrolyte compositions, given as a percentage of 30 °C capacity.....	689
Figure XI.1.2 (a) Total resistance of cells with ACN-containing electrolyte and baseline electrolyte at 20°C and -20 °C, deconvoluted into (b) SEI Resistance and (c) Charge Transfer Resistance.....	690
Figure XI.1.3 (a) dQ/dV for ACN-based electrolytes, peaks for all of which correspond to FEC reduction. (b) dQdV for Baseline vs ACN-based electrolyte. The ratios in the legend correspond to ACN1 (1:2:7), ACN2 (2:1:7), and ACN3 (3:0:7). .....	691
Figure XI.1.4 Ethylene (C <sub>2</sub> H <sub>4</sub> ) and Carbon dioxide (CO <sub>2</sub> ) evolution during the first formation cycle for ACN-based and Baseline electrolyte. ....	691
Figure XI.2.1 (a) Scheme of solvent design transition from carbonates to fluorinated esters. (b) Atomic charge analysis of carbonyl groups in EA, EA-f, f-EA, and f-EA-f. (c) Physical properties of electrolyte solvents used in this study.....	694
Figure XI.2.2 Representative solvation structures from MD simulations. (a) 1 M LiPF <sub>6</sub> in EA/FEC (9/1); (b) 1 M LiPF <sub>6</sub> in EA-f/FEC (9/1); (c) 1 M LiPF <sub>6</sub> in f-EA/FEC (9/1); and (d) 1 M LiPF <sub>6</sub> in f-EA-f/FEC (9/1).....	694
Figure XI.2.3 (a) Coordination number of fluorinated ester EA-f, f-EA and f-EA-f and FEC from MD simulations; (b) quantification of contact ion pairs (CIP) and solvent separated ion pairs (SSIP) for 1 M LiPF <sub>6</sub> in EA/FEC (9/1), 1 M LiPF <sub>6</sub> in EA-f/FEC (9/1), 1 M LiPF <sub>6</sub> in f-EA/FEC (9/1) and 1 M LiPF <sub>6</sub> in f-EA-f/FEC (9/1) electrolyte; (c) indicative structure of CIP and SSIP. ....	695
Figure XI.2.4 (a) Arrhenius plots of electrolytes with different fluorinated solvents and Gen 2 and (b) lithium salt solubility test for 1M LiPF <sub>6</sub> in EA-f/FEC (9/1) (left), 1M LiPF <sub>6</sub> in f-EA/FEC (9/1) (center), and 1M LiPF <sub>6</sub> f-EA-f/FEC (9/1) (right) electrolytes at -20°C and -40°C.....	695
Figure XI.2.5 (a) dQ/dV profiles of graphite NMC622 cells with different electrolytes during the 1 <sup>st</sup> charging; (b) C-rate capability with different electrolytes at -20°C. Normalized voltage profiles at various C-rates with (c) Gen 2, (d) 1 M LiPF <sub>6</sub> in EA/FEC (9/1), (e) 1 M LiPF <sub>6</sub> in EA-f/FEC (9/1), and (f) 0.9 M LiPF <sub>6</sub> + 0.1 M LiDFOB in EA-f/FEC (9/1) electrolyte. ....	696
Figure XI.3.1 The graphic Abstract of a review paper to be published on <i>Electrochemical Energy Reviews</i> ..	700
Figure XI.3.2 Ionic conductivities of the three salts in the MA–FEC solvent system and the STD electrolyte measured at different electrolytes. ....	701
Figure XI.3.3 Charge–discharge cycling performance of NCM 622    graphite cells with 3 salts in the MA–FEC solvent system and the STD electrolyte at (a) -20 °C and (b) 25 °C.....	701
Figure XI.3.4 Charge–discharge cycling performance of NCM 622    graphite cells with STD; LiBF <sub>4</sub> -MA (base); and electrolytes with 1% LiBOB, 1% LiF <sub>2</sub> PO <sub>2</sub> , and 1% LiTMSP additives at (a) -20 °C and (b) 25 °C LiF <sub>2</sub> PO <sub>2</sub> , and 1% LiTMSP electrolyte formulations at (a) -20 and (b) 25 °C. ....	702
Figure XI.3.5 F 1s (left), P 2p (center), and B 1s (right) XPS spectra of the graphite anodes after 5 formation cycles at 25 °C with different electrolyte formulations. ....	703
Figure XI.3.6 F 1s (left), P 2p (center), and B 1s (right) XPS spectra of the graphite anodes after 50 cycles at 25 °C with different electrolytes formulations.....	704

Figure XI.3.7 Cycling performance of Li  Gr half cell with 20% extra lithium plating on the graphite anode at -20 °C with (a) baseline electrolyte (8), (b) designed electrolyte (861) at 0.1 C charge/0.2 C discharge condition .....	705
Figure XI.3.8 Cycling performance of NMC811  Gr cell at (a) room temperature (b) -20 °C with baseline electrolyte and designed electrolyte (861) at 0.2 C discharge/0.2 C charge condition. ....	706
Figure XI.3.9 The TEM images of the (a) pristine graphite; (b) graphite cycled with baseline electrolyte (BE) and (c) graphite cycled with designed electrolyte (DE).....	707
Figure XI.3.10 The graphic Abstract of a review paper that is ready to be submitted to a scientific journal for publication. ....	707
Figure XI.4.1 Wide operating temperature characterization of electrolytes in 230 mAh pouch cells with artificial graphite anode and NMC811 single crystal cathode. a) initial cycling at 30°C, followed by rate characterization at 0 °C, and continued 30 °C cycling followed by b) 45°C high temperature cycling. Electrolyte compositions tested: control (black traces, EC/DEC/EMC 1/1/1 v/v + 1v% VC + 1M LiPF <sub>6</sub> ), 20v% KDC-713 (pink traces), 20v% KDC-502 (green traces), 20v% KDC-403 (blue traces), and 20v% KDC-301 (red traces) electrolytes. The fluorinated electrolytes were added at 20 v% to the control electrolyte. The salt was 1M LiPF <sub>6</sub> and VC was at 1% in all electrolytes. Operating voltage range: 4.3V – 2.75V. ....	712
Figure XI.4.2 XPS with sputtering for depth profile of graphite anodes after wide operating temperature test a) overlaid representative carbon C1s spectra from each level of sputtering and b) percent total anode composition of C-Li (lithiated graphite) peak throughout sputtering for 20% 403 and control anodes .....	713
Figure XI.4.3 Fast charge cycling test in 230 mAh single crystal NMC811/artificial graphite pouch cells, with a cathode capacity loading of ~ 2.2 mAh/cm <sup>2</sup> a) discharge capacity measured during 4C charge (CCCV) and 1C discharge and b) impedance for cells with control (black traces, EC/DEC/EMC 1/1/1 v/v + 1v% VC + 1M LiPF <sub>6</sub> ), 20v% KDC-713 (pink traces), 20v% KDC-502 (green traces), 20v% KDC-403 (blue traces), and 20v% KDC-301 (red traces) electrolytes .....	714
Figure XI.4.4 Graphite anodes (7.78 mg/cm <sup>2</sup> ) after fast charge cycling test in 230 mAh single crystal NMC811/artificial graphite pouch cells with either control (EC/DEC/EMC 1/1/1 v/v + 1v% VC + 1M LiPF <sub>6</sub> ) or 20% KDC-403 electrolytes.....	714
Figure XI.4.5 Connection between interfacial vs bulk transport property measurements and discharge capacity of 230 mAh NMC811/Gr multilayer pouch cells with control, 20% methyl acetate, 20% methyl propionate, 20% methyl butyrate, or 20% 403 electrolytes with a) pouch cell impedance from 0 °C to -20 °C, b) electrolyte conductivity from 30 °C to -10 °C, c) electrolyte viscosity from 30 °C to -10 °C, and pouch cell discharge capacities during rate tests at 0 °C to 20°C with d) C/2 discharge rate, e) 1C discharge rate, and f) 2C discharge rate where regions shaded in blue are where benefits from improved interfacial transport appear to dominate discharge capacity and regions shaded in gold are where benefits from improved bulk electrolyte transport appear to dominate discharge capacity. ....	715
Figure XI.4.6 0°C cycling test in 230 mAh single crystal NMC811/artificial graphite pouch cells with a) control (black), 20v% KDC-403 (bright blue), 20v% KDC-403 (steel blue), and 20v% KDC-403 (sky blue) electrolytes ; b) control (black), 20v% KDC-403 (bright blue), 20v% methyl propionate (green), and 20v% KDC-403+20v% methyl propionate (teal) electrolytes; . The control electrolyte is EC/DEC/EMC 1/1/1 v/v + 1v% VC + 1M LiPF <sub>6</sub> . ....	716
Figure XI.4.7 Coulombic efficiency and rate performance of Li/NMC811 with various loadings in half cells with Silatronix baseline electrolyte.....	717
Figure XI.4.8 Coulombic efficiency and rate performance of Li/Graphite with various loadings in half cells with Silatronix baseline electrolyte.....	718
Figure XI.4.9 Coulombic efficiency and rate performance of Li/NMC811 with various loadings in half cells with Silatronix baseline electrolyte.....	718

Figure XI.4.10 Coulombic efficiency and rate performance of Li/Graphite with various loadings in half cells with Silatronix baseline electrolyte.....	719
Figure XI.4.11 Coulombic efficiency and rate cycle performance of Graphite (LN3024-141-5) /NMC811 (LN3174-179-4) full cell with Silatronix baseline and Gen 2 (G2) electrolytes. ....	719
Figure XI.4.12 Rate performance of MAGE3/NMC811 coin cells with Gen 2 and Silatronix baseline electrolytes.....	719
Figure XI.4.13 ASI plots at 50% SOC of Graphite (LN3024-141-5) /NMC811 (LN3174-179-4) full cell with baseline (grey) and Gen 2 (orange).....	720
Figure XI.5.1 (a, b) Conductivity and (c, d) viscosity measurements of Gen2 LHCEs over a temperature range of 20-50°C. (b, d) show Arrhenius plots.....	723
Figure XI.5.2 Voltage stability of Gen2 LHCEs where the limiting current density was defined as $1 \times 10^{-4}$ A/cm <sup>2</sup> . A lower voltage cutoff of 0.05 V vs. Li/Li <sup>+</sup> was used. ....	724
Figure XI.5.3 Flammability testing of the electrolytes: (a) 1M LiPF <sub>6</sub> in 3:7 EC:DMC, (b-i) Gen2 LHCEs....	724
Figure XI.5.4 XPS (a, e) C 1s (b, f) F 1s and (c, g) Li 1s spectra of recovered (a-c) NMC811 cathodes and (e-g) graphite anodes after 200x cycles under 1C/1C CCCV cycling condition with either LiPF <sub>6</sub> EC:DMC or LHCE F. (d, h) Elemental composition of interphases formed on (d) cathodes and (h) anodes. ....	725
Figure XI.5.5 SEM images of NMC811 cathodes post cycling 200x under the 1C/1C CCCV condition in either (a-c) LiPF <sub>6</sub> EC:DMC electrolyte or (d-f) LHCE F electrolyte), at (a, d) 1000X, (b, e) 2000X, and (c, f) 5000X magnification. ....	726
Figure XI.5.6 Baseline cycling of NMC811/graphite pouch cells with Gen2 electrolyte and a control electrolyte 1M LiPF <sub>6</sub> 3:7 EC:DMC. (a) LHCEs A - D (b) LHCEs E - H.....	727
Figure XI.5.7 High voltage cycling of NMC811/graphite pouch cells with Gen2 electrolyte and a control electrolyte 1M LiPF <sub>6</sub> 3:7 EC:DMC. (a) LHCEs A - D (b) LHCEs E - H.....	728
Figure XI.5.8 High temperature cycling of NMC811/graphite pouch cells with Gen2 electrolyte and a control electrolyte 1M LiPF <sub>6</sub> 3:7 EC:DMC. (a) LHCEs A - D (b) LHCEs E - H.....	729
Figure XI.5.9 Low temperature cycling of NMC811/graphite pouch cells: discharge capacity vs. cycle number over 100 cycles at -20 ° C.....	729
Figure XI.5.10 Fast charge cycling of NMC811/graphite with Gen2 electrolyte and a control electrolyte 1M LiPF <sub>6</sub> 3:7 EC:DMC. (a) LHCEs A - D (b) LHCEs E - H. ....	730
Figure XI.5.11 Ternary phase diagram of salt, solvent II, and diluent V. ....	731
Figure XI.5.12 Ternary phase diagram of salt, solvent II, and diluent VI. ....	732
Figure XI.5.13 Calculated and experimentally determined conductivity at 25°C as a function of salt concentration for electrolyte formulations with Salt : Solvent II : diluent molar ratios of 1 : 3.2 : x (x = 0, 1.6, 3.2, 6.4).....	733
Figure XI.6.1 The capacity retention of full cells using the as-fabricated cathodes and NEI graphite anode under 4.2V upper cutoff voltage. ....	736
Figure XI.6.2 Capacity retention using AG or NG as anode and NCM1 as cathode under different upper cutoff voltages. a) artificial graphite; b) natural graphite.....	737
Figure XI.6.3 Coulombic efficiency using AG or NG as anode and NCM1 as cathode under different upper cutoff voltages. a) artificial graphite; b) natural graphite .....	737
Figure XI.6.4 SEM images of the as-fabricated cathode for 4.2V design (a). Top view and (b). cross section view.....	738

Figure XI.6.5 SEM images of the as-fabricated graphite anode for all upper cutoff voltage design (a). Top view and (b). cross section view.....	738
Figure XI.6.6 Discharge capacity versus cycle number throughout the variable temperature and cycling rate test for upper cutoff voltage conditions of (A) 4.2V, (B) 4.3V, (C) 4.4V, and (D) 4.5V. The control cell (pink markers) is discharged at C/3 and 25°C throughout the entire test while the sister test cells (blue and red markers) were discharged at C/10 for three cycles, then at a C/3 rate for 25 cycles under varying temperature conditions, as specified for each column of designated cycle numbers.....	740
Figure XI.6.7 Coulombic efficiency data versus cycle number throughout the variable temperature and cycling rate test for upper cutoff voltage conditions of (A) 4.2V, (B) 4.3V, (C) 4.4V, and (D) 4.5V. The control cell (green markers) is discharged at C/10 and 25°C throughout the entire test while the sister test cells (red and black markers) were discharged at varying rates under varying temperature conditions, as specified for each column of designated cycle numbers.....	741
Figure XI.6.8 Initial voltage versus capacity curves after formation for specified upper voltage cutoff conditions at (A) 25°C, (B) -5, and (C) -20°C with a charge/discharge rate of 10/C.....	742
Figure XI.6.9 Discharge capacity versus cycle number of three sister coin cells with a charge/discharge rate of C/10 for formation and C/3 for cycling and an upper cutoff voltage of (A) 4.2V, (B) 4.3V, (C) 4.4V, and (D) 4.5V. (E) Averaged discharge capacity versus cycle number for each set of three cells at each upper cutoff voltage. Average capacity retention at 600 cycles is also specified in the legend for each upper cutoff voltage. ....	743
Figure XI.6.10 (A) X-ray diffraction patterns of the cathode measured immediately after formation and a 2 hr hold at the specified applied voltage. (B) Magnified view of the (003) Bragg peak. (C) Magnified view of the (101), (006), and (102) Bragg peaks. (D) Magnified view of the (108) and (110) Bragg peaks. ....	744
Figure XI.6.11 A. Our designed pouch cell, with labeled compartments. B. Our designed testing fixture. C. Example initial pressure data of a pouch cell. ....	744
Figure XI.6.12 (A) Capacity, (B) coulombic efficiency, and (C) capacity retention of pouch cells tested at 25°C and a discharge rate of C/3 with specified upper cutoff voltage conditions over 275 cycles. Each voltage condition was tested with two sister cells, cell 1 and 2, as shown in (A) and (C). Capacity retention after 275 cycles is calculated for cell 1 at each voltage condition and is specified in the legend of (C). ....	745
Figure XI.6.13 Pressure maps of pouch cells before (as prepared, after formation under 3.0V) and after 275 cycles at each specified upper voltage cutoff condition at 25°C. Corresponding pressure map legend is shown to the right.....	746
Figure XI.6.14 Free energy cycle of the oxidation reaction ( $A \rightarrow A^{+} + e^{-}$ ). Here $A(g)$ and $A(sol)$ denote molecule A in gas phase and solvated phase, respectively. $A^{+}$ denotes the oxidized cation of A. ....	747
Figure XI.6.15 Oxidation potentials of eight carbonate based solvent molecules calculated from DFT simulations. Benchmarking calculations done with B3LYP functional and 6-31g* and 6-31+g* basis sets successfully reproduced the oxidation potentials previously reported by He et al.2 .....	748
Figure XI.6.16 Molecular (a) HOMO and (b) LUMO orbitals of neutral DMC molecule. The yellow and blue regions show the positive and negative isosurfaces. The iso value is 0.02 au. ....	748
Figure XI.6.17 Long-term capacity retention (a) and Coulombic efficiency (b) of AA002  AC019 full cells using conventional electrolyte cycling at different cutoff voltages. ....	749
Figure XI.6.18 Long-term capacity retention (a) and Coulombic efficiency (b) of AA002  AC019 full cells using sulfone electrolytes cycling at different cutoff voltages.....	750
<b>1st CE</b> .....	750
Figure XI.6.19 Long-term capacity retention of AA002  AC019 full cells using EMS electrolytes with additives (a) VC, LiDFOB, ANL $\delta$ , FEC; and (b) VC, ANL $\chi$ , ANL $\delta$ cycled at 4.5V. ....	751



Figure XI.6.20 Capacity retention (a) and Coulombic efficiency (b) of AA002  AC019 full cells using Gen2 and sulfone electrolytes with additives cycling at different cutoff voltages cycled at 4.5V. ....	752
1st CE.....	752
Figure XI.6.21 Chemical structures of LiPF <sub>6</sub> , LiFSI, EMS, TMS, EC, EMC, LiDFOB, VC and FEC.....	753
Figure XI.6.22 The differential capacity profiles of Li  Graphite half cells using 1.2M LiFSI EMS electrolytes with (a) 2 wt.% VC, FEC, ANL $\delta$ and ANL $\chi$ ; and (b) ANL $\chi$ and both ANL $\chi$ and VC.....	754
Figure XI.6.23 Linear sweep voltammograms (LSVs) of various EMS based electrolytes without additive or with 2 wt.% VC or TFDTD, scan rate 0.2 mV/s, aluminum as the working electrode and lithium metal as both the reference and counter electrodes.....	754
Figure XI.6.24 (a) 5th cycle and (b) 500th cycle voltage profiles of AA002  AC019 full cells using 1.2M LiFSI EMS electrolyte with VC, ANL $\chi$ and VC + ANL $\chi$ additives. ....	755
Figure XII.1.1 a) SEM images and (b) electronic conductivities of pristine and heat-treated Cu@PI. (c, d) SEM and EDS mapping images for the backside and cross-sectional SEM images of Li deposited for 4 mAh cm <sup>-2</sup> on (c) pristine Cu@PI and (d) heat-treated Cu@PI at a current density of 0.4 mA cm <sup>-2</sup> . ....	759
Figure XII.1.2 Cycling performance of EDLi  NMC622 coin cells with EDLi on Bare Cu, Pristine Cu@PI, and Heat-treated Cu@PI.....	760
Figure XII.1.3 a) Comparison of areal mass of EDLi (5 mAh cm <sup>-2</sup> ) on bare Cu and Cu@PI. B) Cycling performance of EDLi  NMC622 cells based on specific energy density (Wh kg <sup>-1</sup> ) for bare Cu and Cu@PI... 760	760
Figure XII.1.4 a,b) SEM images and c,d) XPS Ni 3p spectra of the EDLi surfaces after 180 cycles in EDLi  NMC622 cells with a,c) Bare Cu and b,d) Cu@PI.....	761
Figure XII.1.5 SEM images (top and cross-sectional views) of deposited Li (at C/2 for 4 mAh cm <sup>-2</sup> ) on (a,c) bare Cu and (b,d) TL@CBL@Cu.....	762
Figure XII.1.6 a) Cycling performance of Li  NMC811 cells at C/2 for charging and discharging, b) Charge/discharge voltage profiles at 200 <sup>th</sup> cycle. c) Charging rate capability at various charge rates (x) with a constant discharge current rate of C/10. The cells were first conducted in two formation cycles at C/10, where 1C = 4.8 mA cm <sup>-2</sup> . The voltage range was from 2.8 to 4.4 V (vs. Li/Li <sup>+</sup> ).....	762
Figure XII.1.7 Cycling performance of Li  NMC622 cells at (a) C/10 for charging and C/3 for discharging, (b) C/5 for charging and discharging, (c) various charge current densities (x) with a constant discharge current density (C/10). The cells were first conducted two formation cycles at C/10, where 1C = 4.0 mA cm <sup>-2</sup> . The voltage range is from 2.8 to 4.4 V (vs. Li/Li <sup>+</sup> ).....	763
Figure XII.1.8 (a-e) In situ bias TEM measurement of electrical properties of SEI. (a) Schematic of experiment setup. (b-d) TEM images showing W wire with sharp tip and Cu wire with SEI layer on the surface. (e) Typical I-V curves showing the critical voltage. Scale bars, 50 $\mu$ m in (c) and 100 nm in (b) and (d). (f) Correlation between SEI structure and its electrical property. Atomic structure of SEI layers on the Li deposits formed in LCE, PLHCE, HCE, and LHCE.....	764
Figure XII.2.1 Crack tip propagation behavior in cubic LLZO. (a) Schematic illustration of LLZO sample preparation and crack generation. (b) Crack propagation within bulk LLZO along the {100} plane. (c) Crack propagation from the surface of the {100} plane. (d) Crack introduced along the {110} plane and its propagation within the bulk (left) and from the surface (right). (e) Local Li redistribution during crack propagation. (f) Phase evolution of LLZO in the vicinity of the crack.....	768
Figure XII.2.2 LLZO(001)  LCO(104) interface after 10 ns of large-scale molecular dynamic simulation at 1500 K using the developed machine-learning force field. The atomic model shows two interfacial regions with different initial chemical compositions (Li-rich on the left side; Li-deficient on the right side). Li is blue, La is green, Zr is magenta, O is red, and Co is yellow. The concentration profiles of each species are also presented as a function of position normal to the interface. ....	769

Figure XII.2.3 (a) (Left) positional probability density of Co-ions in cubic LLZO showing diffusion pathways with yellow isosurface (red spheres represent O ions, and green and magenta polyhedra are  $\text{LaO}_8$  and  $\text{ZrO}_6$ , respectively), (middle) histogram for volume of sites where Co ions resided in LLZO with a colormap showing average residence time at each histogram bin (two distinct volume ranges correspond to tetrahedral and octahedral Li sites in LLZO, respectively), and (right) Arrhenius plots for Co diffusivities with various Co contents. (b) Atomic structure of LLZO  $\Sigma 7$  GB with (213) GB plane and [111] axis after 10 ns, showing Co segregation at GB areas. Co concentration as a function of time is also shown below the atomic structure. (c) The number of Co clusters in an amorphous LLZO as a function of time with the structures before and after the MD simulation. .... 770

Figure XII.2.4 Assessing the variability and statistical behavior of the computed effective transport properties arising from microstructural configuration and local property variation. (a) Input local diffusivity ( $D$ ) at 300K as calculated using MLFF for the bulk and grain boundaries (GBs) of LCO, LLZO, and their interfaces. UB and LB stand for upper-bound and lower-bound, respectively. (b) Generation of 600 2D microstructures with varied configurations for the LCO-LLZO composite. The volume fractions are approximately 50%:50%, and the presence of GBs and interfaces are considered. (c) A list of models with different assumptions for the local diffusivities at the GBs and interfaces. (d) The calculated effective diffusivities ( $D_{\text{eff}}$ ) of all 600 microstructures by assuming different models listed in (c). Each dataset of  $D_{\text{eff}}$  is plotted with the corresponding histograms aside. (e) Performance of a random forest ML model (22 descriptors) in predicting the  $D_{\text{eff}}$ . .... 771

Figure XII.2.5 Mesoscale modeling of Li transport and mechanical stress distribution in LLZO-cathode composite during lithiation. (a) Model setup. The inset schematically shows the volume expansion of a unit cell of the cathode active material after Li insertion. (b) Depth of discharge (DOD) as a function of normalized simulation time. (c,d) Distributions of normalized Li concentration ( $c_{\text{Li}}$ ) at DOD=45% (c) without and (d) without considering the stress effect on Li transport. (e,f) The corresponding distributions of von Mises stress ( $\sigma_{\text{VM}}$ ) at DOD=45% (e) without and (f) with considering the stress effect on Li transport. .... 772

Figure XII.3.1 Chemical structure of  $\text{SP}^2_{\text{perF}}$  ..... 775

Figure XII.3.2 (a-c) The O1s spectra of SEI from 1 M LiTFSI DOL/DME with 1wt%  $\text{LiNO}_3$  electrolyte. (a) bare Cu, sputtered for 2 min; (b)  $\text{SP}^2_{\text{perF}}$  coated Cu after 2 min of sputtering; (c)  $\text{SP}^2_{\text{perF}}$  coated Cu after 3 min of sputtering. (d) The S/C elemental ratio of SEI from 1 M LiTFSI DOL/DME electrolyte at different sputtering time. (e) The F/C elemental ratio of SEI from 1 M  $\text{LiPF}_6$  EC/DEC electrolyte at different sputtering time. The Li||Cu cells were cycled at 0.5 mA  $\text{cm}^{-2}$ , 1 mAh  $\text{cm}^{-2}$  for 10 cycles. The samples were rinsed with 200  $\mu\text{L}$  DME. The sputtering power was 2 kV  $\mu\text{A}$ . .... 776

Figure XII.3.3 (a) Experimental setup for optical cell. Images were taken from the top-down view on the Cu electrode as Li was deposited on it. (b-c) Optical microscope images of Li deposited on Cu at 0.2 mA  $\text{cm}^{-2}$  current density: (b)  $\text{SP}^2_{\text{perF}}$  coated Cu; (c) bare Cu. Scale bar: 25  $\mu\text{m}$ . (d) Steady-state viscosity of  $\text{SP}^2_{\text{perF}}$  soaked in ether (1 M LiTFSI DOL/DME with 1wt%  $\text{LiNO}_3$ ) and carbonate (1 M  $\text{LiPF}_6$  EC/DEC with 10% FEC) electrolytes at room temperature, as well as 1 M LiTFSI in DME (labeled as Electrolyte). .... 777

Figure XII.3.4 Electrochemical characterizations of  $\text{SP}^2_{\text{perF}}$  with different electrolytes. (a) CE measured on coated Cu in Li||Cu cells with 40  $\mu\text{L}$  of ether (1 M LiTFSI DOL/DME 1wt%  $\text{LiNO}_3$ ), carbonate (1 M  $\text{LiPF}_6$  EC/DEC 10% FEC), or FDMB (1 M LiFSI FDMB) electrolyte. (b) Electrochemical impedance spectroscopy (EIS) measurement overtime with coated Li||Li symmetric cell in electrolytes. (c) Calculated impedance increase (%) over 100 hours of resting procedure in an open circuit. .... 777

Figure XII.3.5 (a) Rate-capability of Li||NMC811 cells at high cathode loading of 5 mAh  $\text{cm}^{-2}$ . (b-d) Cycling performance of Li||NMC811 coin cells in lean electrolyte condition (3 g  $\text{Ah}^{-1}$ ) with and without  $\text{SP}^2_{\text{perF}}$  coating. Three repetitions are shown. .... 778

Figure XII.3.6 Cycling of  $\text{SP}^2_{\text{perF}}$ -coated Li in Li||NMC811 cells with 1 M LiFSI FDMB electrolyte. (a) Rate capabilities. (b) Long-term cycling with 2.5 mAh  $\text{cm}^{-2}$  positive electrodes. (c) Charging voltage curve at 100<sup>th</sup> cycle at C/5 charging rate. (d) Long-term cycling with 5 mAh  $\text{cm}^{-2}$  electrodes. (e) Cycle life (80% capacity retention) plotted against excess lithium amount. The  $\text{SP}^2_{\text{perF}}$  coating is compared with other coatings or

- electrolyte strategies. The x axis locations of Point 4, 5, 7, 11, and 12 are  $10 \text{ mAh cm}^{-2}$ , and they are offset slightly for visualization. .... 778
- Figure XII.4.1 (a) Schematic illustration for the internal pressure effect on density and uniformity of the lithium layer deposited on copper (Cu) electrode in 2032 coin-cells. Corresponding SEM images (b) for the top (c) and cross-sectional views of the Cu electrodes after the 1<sup>st</sup> Li deposition to 4.5V and EDS mappings for SEIs (d) all elements and (e) Cu element and (f) S element after 1<sup>st</sup> cycle Li deposition and stripping. (g) Cycling performance of NMC811||Cu cells with different internal pressures cycled between 3.5V – 4.4V. (h) Quantified elements distribution in SEIs formed at different internal pressures. .... 784
- Figure XII.4.2 (a) Schematic illustration of the SEI formation depending on the different morphologies of the initial metallic Li deposited on the Cu current collectors under the different internal pressures, digital photographs, and SEM images of Li/SEI layers on Cu substrates formed after 1st cycle. (b) XPS mappings of peak components (Li<sub>2</sub>O and Li<sub>2</sub>CO<sub>3</sub>), fitted XPS Li 1s spectra of the SEI layers formed on the Li depositions on the Cu substrate collected from Cu||NMC811 cells (c: AFC-1t and d: AFC-2t) and depth profiles of the elements (e: AFC-1t and f: AFC-2t, solid: after charge and empty: after discharge) in the SEI layers formed after the 1st formation cycle (at C/10, 3.5-4.5V). .... 785
- Figure XII.4.3 Cycling performance, (a) capacity and (b) Coulombic efficiency of the 250 mAh Cu||NMC532 pouch cells with E1 electrolyte cycled between 3.5V – 4.4V at C/10 charge and C/3 discharge after 2 formation cycles at C/10. The insert in (b) shows the image of the cell after cycling. .... 786
- Figure XII.4.4 Nail penetration of the 250 mAh Cu||NMC532 cells at full charged state after 146 cycles for E1-1 and 149 cycles for E1-2, (a, e) charge voltage profile before nail penetration, snapshots of the infrared images for the cells (b, f) before nail penetration and (c, g) after nail penetration when the maximum temperatures were reached. (d, h) photos of the cells after nail penetration. .... 786
- Figure XII.4.5 (a) Schematic illustration of the floatable protective layer (FPL) coated on Cu current collector for the uniform Li deposition and stable SEI layer under high internal pressures, digital photographs of (b1) FPL coated Cu, (b2) after 1<sup>st</sup> Li deposition and (b3) the pressure domain on the pressure indicating film, and SEM images of (c1) the surface of FPL layer, (c2) cross-sectional images of detachable FPL from Cu current collector, after Li deposition under (c3) high and (c4) low internal pressures, respectively. (d) Cycling stabilities of Cu||NMC811 cells with pristine Cu under different pressures (1t and 2t), and FCL coated Cu (2t) and their (e) Coulombic efficiency at C/10 in the cut-off voltage range of 3.5-4.4V after two formation cycles in 3.5-4.5V. .... 787
- Figure XIII.1.1 Phase field simulations of Li penetration into interlayer with different lithiophobicity. Li growth on a simplified conical shape surface flaw of the (a) lithiophobic interlayer and (b) lithiophilic interlayer. (c) Nucleation rate as a function of overpotential at electrolyte with different contact angle against Li. The inserted figure shows the simulated Li nucleation rate distribution in the corresponding interlayer. (d) Li striping from porous interlayer at 0, 1.5 and 3 s. .... 792
- Figure XIII.1.2 (a) XRD of LNI-25%Mg powder. (b) SEM, (c) EDS mapping and (d) Mg element line scan of activated Li/LNI/Mg interface in Li/LNI-Mg/LPSC/Li cells. The thickness of the LNI-Mg interlayer is 18.5  $\mu\text{m}$ . The Mg element line scan in (d) is captured along the yellow line of Figure (b). (e) Galvanostatic cycling of Li/LPSC/Li cells sandwiched with LNI-25% Mg composite at constant current densities/capacity of  $4 \text{ mA cm}^{-2} / 4 \text{ mAh cm}^{-2}$  at 25 oC. .... 793
- Figure XIII.1.3 (a) The predicted upper limit of CCD (orange line) and reported CCDs (orange scatters) as a function of capacity. The red target on the top right represents a target of high rate and high energy density ASSLMB. (b) Molecular dynamics-calculated diffusion coefficients of bulk and differently oriented surfaces for Li metal and LiMg alloy at room temperature. The inset scheme illustrates different diffusion mechanisms. (c) SEM showing the grain distributions and sizes of the LiMgLa and LiMg alloys. .... 794
- Figure XIII.1.4 (a) Digital pictures of the wettability of molten Li-Mg-La against LLZTO pellets. (b) Scanning electronic microscope (SEM) images for the cross-section of the LiMgLa|LLZTO interface before cycling at different scales, showing decent contact. (c) Electrochemical impedance spectra of anode/LLZO/anode symmetric cells with LiMgLa, LiLa, and LiMg anodes from 1 MHz to 0.1 without an external pressure at room

- temperature. (d) Delivered maximum capacity of LiMgLa LiLa and LiMg anodes during stripping at a current density of  $1.0 \text{ mA}\cdot\text{cm}^{-2}$  with a voltage cut-off of 5.0 V. (e) VSC of LiMgLa anodes with different compositions during stripping at a current density of  $1.0 \text{ mA}\cdot\text{cm}^{-2}$ . (g, h) Galvanostatic cycling of the LiMgLa|LLZTO|LiMgLa symmetric cell at various current densities at room temperature. .... 796
- Figure XIII.1.5 Cycle performance of the all-solid-state Li metal cells with (a) Small ( $\sim 5 \text{ }\mu\text{m}$ ) and (b) large ( $10\sim 15 \text{ }\mu\text{m}$ ) NMC811 particles. Inset are SEM images with corresponding NMC811 particles. (c) Cycling curves of the Li symmetric cell using thin film electrolyte. Inset is the cross-sectional image of the interface between Li and SE. (d) Charge and discharge curve of the SSB with thin film electrolyte at 0.1 C and (e) corresponding cycling performance. .... 797
- Figure XIII.2.1 Pseudo-ternary phase diagram detailing some of the new glass compositions synthesized in the  $\text{Li}_2\text{S} - \text{SiS}_2 - \text{Li}_{3.48}\text{SiO}_{3.74}$  system. .... 800
- Figure XIII.2.2 Preform #3 with a small section of drawn thin film of around  $300 \text{ }\mu\text{m}$  after drawing. .... 801
- Figure XIII.2.3 A.C. Conductivity results from cathode composites with mass ratios of S:ISU-6:VGCF of 3:6:1 when charged. (A) From  $\text{Li}_2\text{S}$  starting material. (B) From sulfur starting material. .... 802
- Figure XIII.3.1 Schematic representation of the combined XRF and XAS experiments, which allow us to identify the local concentration and chemical structure of the interested element at the cross-section. .... 804
- Figure XIII.3.2 Rate capability of Li/Li and Li/LiFePO<sub>4</sub> cells using the new formulation for the solid-state rigid polymer electrolyte at  $22 \text{ }^\circ\text{C}$ . (a) Voltage profile of a Li/Li cell cycled at various current densities. Both charging and discharging time are 2 hours for each cycle and the current density increases from  $0.025$  to  $0.3 \text{ mA cm}^{-2}$  with 5 cycles for each step. (b) Typical voltage profiles of the Li/LiFePO<sub>4</sub> cell cycled at different current densities. (c) Specific charge and discharge capacities of LiFePO<sub>4</sub> when cycled at various current densities. The thickness of the rigid polymer electrolyte used in this study is  $130 \pm 20 \text{ }\mu\text{m}$ , and the LiFePO<sub>4</sub> mass loading in the cathode is  $3.6 \pm 0.4 \text{ mg cm}^{-2}$ . Li/Li and Li/LiFePO<sub>4</sub> cycling tests reveal a limiting current density of about  $0.3 \text{ mA cm}^{-2}$  and stable long-term cycling at  $0.1 \text{ mA cm}^{-2}$  of the rigid polymer electrolyte at  $22 \text{ }^\circ\text{C}$ . .... 805
- Figure XIII.3.3 Lithium-ion hopping in MD simulations of salt-in-glycerol electrolytes. (a) Radial distribution functions (rdfs) of the O atoms of glycerol and TfO<sup>-</sup> to Li<sup>+</sup> at  $50 \text{ }^\circ\text{C}$  in glycerol/LiTfO = 2. Dashed lines represent the cumulative coordination number and shaded bars highlight rdf plateaus at  $\approx 1$ , and 3 O-Li coordination numbers. (b) Internuclear distances between a Li<sup>+</sup> and representative O atoms in the inner solvation shell, highlighting the ligand exchange of Li<sup>+</sup> in a 2 to 4 Å and  $\sim 1 \text{ ps}$  duration hop between donor (red trace) and acceptor (cyan) molecules. A spectator Li<sup>+</sup>-O distance is shown for reference (green trace). (c and d) Snapshots of the inner solvation shell of the Li<sup>+</sup> before and after a hopping event. .... 806
- Figure XIII.3.4 Hydro/solvogels formed from PBDT charged double helix polymer, ionic liquid (IL) and water and/or DMF. Gel properties vary widely based on solvent content (water + DMF) and IL type. Much stiffer gels result from  $\sim 1:1$  DMF-H<sub>2</sub>O casting solvent. More milky gels appear to be more strongly liquid crystalline (rods aligned) and more mechanically robust. *Left to right:* BmimTFSI in 1:1 water-DMF, BmimDCA in water, EmimTfO in 2:1 water-DMF, BmimTfO in water, and EmimTfO in water. These gels carry critical implications for final mechanical properties of fully dried MIC battery electrolyte films. .... 807
- Figure XIII.3.5 Morphology of PBDT-PEG membranes. (a) Molecular structures of PBDT with Na<sup>+</sup> or Li<sup>+</sup> counterions and PEG400. (b) Image of a single-ion-conducting solid polymer electrolyte film containing 24.5 wt% LiPBDT with a thickness of  $80 \pm 10 \text{ }\mu\text{m}$ . (c) Atomic force microscopy (AFM) tapping mode images of the PBDT-PEG membranes over a  $1 \text{ }\mu\text{m}^2$  area. Increasing the PBDT concentration in the membranes leads to the formation of a single-bundle phase. (d) Conceptual  $\sim 100 \text{ nm}$  scale model of the biphasic internal network of PBDT-PEG membranes (Li<sup>+</sup> or Na<sup>+</sup> form) where PBDT-rich bundles (orange lines) interact with PEG (blue lines). (e) Conceptual nanometer-scale model of the ionic interactions within a PBDT bundle. At a rod-rod distance of  $\sim 2 \text{ nm}$ , the counterions interact with both the sulfonate anion from the PBDT double helix and low molecular weight PEG. This proposed model gives a framework to discuss mechanical and conductivity results. .... 808

Figure XIII.3.6 Mechanical robustness of the PBDT-PEG membranes. Uniaxial stress-strain curves for the PBDT-PEG membranes with (a)  $\text{Na}^+$  counterions and (b)  $\text{Li}^+$  counterions at a force ramp rate of  $1 \text{ N min}^{-1}$  at  $30^\circ\text{C}$ . All membranes were repeated by cutting three test samples from each PBDT-PEG membrane. The slope of the stress-strain curves at  $< 0.5\%$  strain yields the Young's modulus ( $E$ ), with values of  $E$  and the toughness ( $U_T$ ) with standard deviations. In general, the Li-based membranes have higher modulus and lower strain at break than the Na-based membranes and are comparable to or better than our IL-based MIC materials. The Na-based membranes show 3-10X higher conductivity than comparable Li-based membranes..... 809

Figure XIII.3.7 Relationship between ionic conductivity ( $\sigma_0$ ) and modulus (either  $G'$  or  $E/3$ ) for PBDT-PEG membranes and various polymeric single-ion conducting electrolytes at  $30^\circ\text{C}$ . Filled symbols represent materials with recorded shear moduli ( $G'$ ) and open symbols materials with recorded tensile moduli ( $E$ ). The PBDT-PEG membranes (pink open triangles) consistently show higher moduli and/or  $\sigma_0$  when compared to other single-ion polymeric electrolytes. Experimental errors are smaller than symbol sizes. The published article reported below lists the external references involved in this plot. .... 809

Figure XIII.4.1 Pictures of reinforced LiPSiS glass SSE separators, which are translucent, bendable, and  $135 - 180 \mu\text{m}$  thick. The dark brown crosshatch pattern is attributed to the underlying non-woven fiberglass reinforcement. Figures reproduced from [1]..... 812

Figure XIII.4.2 Schematics and pictures of the semi-solid Li/S cell designs developed for this project. a) Schematic of a semi-solid coin cell design. b) Top-down picture of a semi-solid coin cell with sulfur cathode sealed using an annular Kapton tape disc and a reinforced LiPSiS glass film separator. c) Schematic of a single layer semi-solid pouch cell design. The pouch cell casing is not included in the schematic. d) Top-down picture of a single layer semi-solid pouch cell core and a side-view picture of the same with the reinforced LiPSiS glass film separator indicated by a red arrow. Figures reproduced from [1]. .... 813

Figure XIII.4.3 Cycling data for semi-solid Li/S coin and pouch cells with 1:1 (v/v) DME:DOL + 1M LiTFSI liquid electrolyte. a) Initial cycling behavior of coin cells without  $\text{LiNO}_3$  co-salt. The semi-solid cell cycles normally while the control cell does not complete its first charge due to the parasitic polysulfide shuttle. b) Cycling data for a semi-solid pouch cell without  $\text{LiNO}_3$  co-salt. c) Cycling data for control and semi-solid pouch cells with  $\text{LiNO}_3$  co-salt. The LiPSiS SSE separator improves both cell cycle life and coulombic efficiency. Figures reproduced from [1]. .... 814

Figure XIII.4.4 a) DSC scan for LiPSiS glass SSE with glass transition,  $T_g$ , and crystallization onset,  $T_c$ , indicated with arrows. b) A picture of the fiberglass non-woven (NW) paper used to reinforced the SSE separator. c) Picture of the green SSE/NW/SSE stack prior to hot pressing. d) Picture of the finished reinforced SSE separator after hot pressing. e) A SEM micrograph of a green SSE separator surface shows considerable porosity. f) A SEM micrograph of a hot-pressed SSE separator surface shows that the pores are largely eliminated. Figures reproduced from [1]. .... 815

Figure XIII.4.5 a) Solubility times series for  $(\text{Li}_2\text{S})_{60}(\text{SiS}_2)_x(\text{P}_2\text{S}_5)_{40-x}$  ( $x = 0, 4, 20, 28, 40$ ) glasses soaked in DME:DOL. After 2 weeks the  $x = 0, 4$  and  $20$  sample solutions showed signs of discoloration, which is attributed to dissolution of the glass. The  $x = 28$  and  $40$  sample solutions remain clear over the course of the experiment. b) Raman spectra of pristine DOL:DME solvent and solutions obtained by soaking  $(\text{Li}_2\text{S})_{60}(\text{SiS}_2)_x(\text{P}_2\text{S}_5)_{40-x}$  ( $x = 0, 4, 20, 28, 40$ ) glasses in DME:DOL. The location of structural unit vibrational modes are indicated with colored bars from left to right; namely,  $\text{P}_2\text{S}_7^{4-}$  (pink),  $\text{P}_2\text{S}_6^{4-}$  (blue),  $\text{PS}_4^{3-}$  (green), and  $\text{S}_8$  (orange). Two vibrational modes of DME:DOL are also indicated (brown). c) Summary of dissolved species as a function of glass composition. Figures reproduced from [2]. .... 816

Figure XIII.4.6 CCDs of symmetric Li/SSE/Li test cells with or without a liquid electrolyte interlayer and a different stack pressures at  $25^\circ\text{C}$ . The SSE separators are  $(\text{Li}_2\text{S})_{60}(\text{SiS}_2)_{28}(\text{P}_2\text{S}_5)_{12}$  glass wafers of approximately  $600 \mu\text{m}$  thickness. a) An all-solid-state test cell with direct Li/SSE contact and  $3 \text{ MPa}$  stack pressure experiences shorting failure at a CCD of  $1.8 \text{ mA cm}^{-2}$ . b) A semi-solid test cell with liquid electrolyte Li/SSE interlayer and a  $0.1 \text{ MPa}$  stack pressure experiences shorting failure at a CCD of  $3.0 \text{ mA cm}^{-2}$ . Note: the test was paused for two days at 20 hours due to a planned facility power outage. Figures reproduced from [2]..... 816

Figure XIII.4.7 Both LiPS and LiPSiS glass SSEs exhibit poor thermal stability and devitrify when hot-pressed. Devitrification during hot pressing increases the viscosity of the glass in the supercooled liquid state. As a result, much higher pressures are required to consolidate the glasses. a) pXRD spectrum of LiPS glass SSE after hot pressing. b) pXRD spectrum of LiPSiS glass after hot pressing. Figures reproduced from [1, 14].

..... 817

Figure XIII.4.8 a) A picture of the experimental setup used to expose sulfide SSE powders to a dry room environment. The setup includes a 300L volume tabletop glovebox, a cartridge-based desiccant system, a microcontroller system to control the moisture setpoint, a personal H<sub>2</sub>S detector, and a fan to continuously mix the glovebox air. b) Diagram of the experimental setup's control system to maintain moisture setpoints. c) H<sub>2</sub>S generation of different SSEs in a -40°C dewpoint dry room as a function of time. d) Reduction in ionic conductivity versus maximum H<sub>2</sub>S reading for different sulfide SSEs. e) Ionic conductivity of LPSI sulfide SSE after exposure as a dry powder to different dry room environments for 30 min. The star marks the ionic conductivity of LPSI sulfide SSE after exposure to a -40°C dewpoint dry room for 30 min while immersed in anhydrous dodecane. Figures were reproduced from [3].

..... 819

Figure XIII.4.9 a) pXRD of LPS, 70:30 samples after hot-pressing using various protocols. b) pXRD of LPSO, 70:25:5 samples after hot-pressing using various protocols c) DSC crystallization completion of LPS, 70:30 vs. LPSO, 70:25:5 at 230°C. Bottom right inset graphic illustrates the crystallization process of crystallite nucleation and growth. The poor thermal stability of the LiPS glass leads to extensive devitrification, whereas the thermally stable LiPSO glass remains largely vitreous.

..... 820

Figure XIII.4.10 a) Picture of LPS, 70:30 and LPSO, 70:25:5 reinforced pellets after hot pressing using various protocols. In general, the LPSO, 70:25:5 samples are much more deformable than the LPS, 70:30 samples. b) Picture of a hot-pressed standalone, reinforced LPSO, 70:25:5 SSE separator film. The film is flexible and translucent. c) Close up picture of the same film after being cut into a disc. The crosshatch pattern is attributed to the underlying non-woven fiber reinforcement.

..... 821

Figure XIII.4.11 a) First cycle voltage profiles for cold-pressed (blue) and hot-pressed (red) cathode composites with NCM622 active material, β-Li<sub>3</sub>PS<sub>4</sub> SSE, and carbon black conductive additive. b) Cyclic capacities for the same. Though the hot-pressed cell initially delivers lower capacity, it goes on to retain its capacity better than the cold-pressed cell. Figures reproduced from [4].

..... 821

Figure XIII.4.12 a) First cycle voltage profiles for NCM622 composites with either glassy Li<sub>3</sub>PS<sub>4</sub> (solid), β-Li<sub>3</sub>PS<sub>4</sub> (dash), or glassy Li<sub>7</sub>P<sub>3</sub>S<sub>11</sub> (dot) SSEs and 2 wt.% carbon black additive. b) Processed SEM image of a hot-pressed NCM85105/βLi<sub>3</sub>PS<sub>4</sub> cathode composite. c) Processed SEM image of a hot-pressed NCM622/β-Li<sub>3</sub>PS<sub>4</sub> cathode composite. The color scheme for the processed images is as follows: white = SSE particle, black = pore, blue = intact NCM particle, and red = damaged NCM particle. Figures reproduced from [4].

..... 822

Figure XIII.4.13 SEM images of cathode composite composed of a low voltage active material (AM) and LPSO glass SSE a) before and b) after hot pressing. c) Porosity of cathode composites before and after hot pressing. d) DSC scans of NCM622 and low voltage AM cathode composites. The NCM622 cathode composites exhibit large exothermic reactions indicative a reaction between the NCM622 and the LPS SSE. On the other hand, the low voltage AM cathode composite exhibit no exothermic reactions in the same temperature range. Small exothermic signals around 250°C are attributed to the devitrification of the glassy SSEs.

..... 823

Figure XIII.4.14 Cyclic capacity of cells with cathode composites composed of low voltage active material (AM) and highly processable LPSO glassy SSE cycled at 60°C. Hot pressing (HP) improves the utilization of AM by nearly 70% compared to cold pressing (CP).

..... 823

Figure XIII.4.15 Pictures of a solvate ionic liquid (SIL) electrolyte and a DME:DOL + 1M LiTFSI electrolyte under an exposed flame. The DME:DOL electrolyte readily ignites whereas the SIL does not.

..... 823

Figure XIII.4.16 a) Picture of (oxy)sulfide glass SSE samples soaked in SIL and dilute SIL. b) Mass loss of (oxy)sulfide glass SSE samples after soaking in a variety of SIL for 7 days. Reduced mass loss is associated with increased SSE oxygen content. c) UV-Vis spectra of (oxy)sulfide SSE samples after soaking in SIL for 7

days. d) UV-Vis spectra for (oxy)sulfide SSE samples after soaking in dilute SIL for 7 days. Reduced absorbance is associated with increased SSE oxygen content. ....	824
Figure XIII.5.1 (a) GITT and open circuit voltage (OCV) curves of S-C-SSE and S-C-LPS cathodes at the third cycle. Current pulses of 0.03 C for 30 mins were employed, followed by 4-hour resting. (b) Overpotential profiles of S-C-SSE and S-C-LPS cathodes from the GITT measurement. ....	828
Figure XIII.5.2 Rate performance of all-solid-state Li-In  S batteries with different additives in sulfur cathodes. The areal sulfur loading of sulfur cathodes is controlled between 2-3 mg <sub>sulfur</sub> cm <sup>-2</sup> . The cells were tested at 60 °C. ....	829
Figure XIII.5.3 (a) XPS survey spectra of lithiated S-C-LPS. (b) Distribution of lithium to sulfur atomic ratios in the active material at different sites on S-C-LPS and developed new electrode surfaces. (c) High-resolution S 2 <i>p</i> spectra of two sites on S-C-LPS cathode surfaces. ....	829
Figure XIII.5.4 Rate performance of sulfur cathodes using different cathode additives at 60 °C with an areal sulfur loading of 2-3 mg cm <sup>-2</sup> . ....	830
Figure XIII.5.5 Raman spectral mapping images (10×10 μm) of the sulfur electrode surface after first discharge at 0.1 C and 60 °C showing the distribution of sulfur/carbon ratio (based on intensity) (a) and LPS SSE (b). (c) Raman spectra of the sulfur cathode surface at two different sites. ....	830
Figure XIII.5.6 (a) Cycling performance and (b) corresponding galvanostatic charge-discharge profiles of sulfur cathodes using the new SSE we developed at room temperature. ....	831
Figure XIII.5.7 Cycling performance of the Li-S ASSBs with alloy anodes. The cells were tested at 0.1C under 60 °C, and the specific capacity is based on the weight of sulfur. ....	831
Figure XIII.5.8 (a) Cycling performance of the high loading cell with 5.45 mg cm <sup>-2</sup> sulfur cathode using the lithium alloy anode under 0.1C, (b) cycling performance of the cell with 2.5 mg cm <sup>-2</sup> sulfur loading tested under 1C rate for over 1000 cycles. ....	832
Figure XIII.6.1 SEM surface image of a) Commercial LLZO, b) Hot pressed LLZO. Fracture image of c) Commercial LLZO, d) Hot pressed LLZO. e) Nyquist plots obtained from EIS. f) Grain size distribution. ....	836
Figure XIII.6.2 The schematics of estimated equilibrium contact area fractions (filled markers) for the LiF, Li <sub>2</sub> O and LLZO at high (a,c,e, 10 <sup>3</sup> A/cm <sup>2</sup> ) and low (b,d,f, 1 mA/cm <sup>2</sup> ) current densities with different <i>P</i> <sub>hold</sub> / <i>Y</i> <sub>0</sub> ratios. The dashed arrows start from the contact area fraction in FEM towards the contact area fraction in KMC (unfilled markers). Triangles: LiF, Circles: Li <sub>2</sub> O, Squares: LLZO. ....	838
Figure XIII.6.3 The schematics of estimated equilibrium contact area fractions for the LiF, Li <sub>2</sub> O and LLZO at 10 mA/cm <sup>2</sup> with different <i>P</i> <sub>hold</sub> / <i>Y</i> <sub>0</sub> ratios. ....	839
Figure XIII.6.4 Optical ellipsometry spectra of the new LLZO pellet after exposure to air. This spectral change is explained by the formation of the surface layer as shown on the right. ....	840
Figure XIII.7.1 Illustration of the in situ ToF-SIMS and in-SIM AFM measurements. a, schematic illustration of ToF-SIMS analysis on Ag-C/Li <sub>6</sub> PS <sub>5</sub> Cl interface. b, schematic illustration of AFM measurement on selected Ag-C region. ....	843
Figure XIII.7.2 Stiffness measurements of selected Ag-C region. a, schematic illustration of single point stiffness measurement. b, force-distance curve on Ag-C layer. c, line scan of stiffness measurements on Ag-C layer. d, stiffness plot along the scan line displays in c, with 100 nm interval for each test. e-f, force-distance curve on pristine and lithiated Ag-C layers. ....	844
Figure XIII.7.3 Stiffness measurements of selected Ag-C/Li <sub>6</sub> PS <sub>5</sub> Cl interface. a, Optical image of selected region for AFM characterization. b, AFM topography of the identical area as shown in optical image. c, stiffness mapping of boxed region in red, with 1000 nm interval for each test. ....	845
Figure XIII.8.1 (A) Schematics show the channel spaces around each Li ion (LiVol) and between the neighboring Li ions (LiLiVol). It also shows the simple spring model capturing the Li-anion interaction in the	

system. (B) The calculated total void space (VoidVol), channel space surrounding each Li-ion (LiVol), channel space between neighboring Li ions (LiLiVol), deviation of Li ion from its equilibrium against  $\text{BH}_4^-$  (Li-H), deviation of Li ion from its equilibrium against  $\text{Cl}^-$  (Li-Cl), and deviation of the neighboring Li-Li distance from equilibrium. (C) Strong correlation between the channel space LiVol and the ionic conductivity/activation energy of the SSE. (D) Deviations of Li ion from its equilibrium against  $\text{Cl}^-$  (solid lines),  $\text{BH}_4^-$  (dotted lines), and neighboring Li (dashed lines) with elevated temperature at two Cl concentrations  $x = 0.875$  and  $x = 0.125$ . [Use EERE\_Figure\_Caption] ..... 851

Figure XIII.8.2 (A) Explicit interface models of  $\text{Li}_6\text{PS}_5(\text{BH}_4)$ -Li with three different terminating species in close contact with Li metal surface. (B) Bond analyses for the interface models based on molecular dynamics simulations up to 200 ps. The  $\text{BH}_4^-$  clusters are stable throughout the simulation, while some  $\text{PS}_4^{3-}$  units are breaking up due to the reduction of P by the Li metal. (C) Radial distribution function analyses at the interface showing the formation of  $\text{LiBH}_4$  with the characteristic peaks around 3-4.5 Å. [Use EERE\_Figure\_Caption] ..... 852

Figure XIII.8.3 Direct showing of charge (electron) transfer from Li metal to P in the solid electrolytes. The bottom position (e.g., at 22 Å in the case of  $\text{Li}_6\text{PS}_5\text{Cl}$ ) corresponds to the top of the Li metal surface of each case. The color bar corresponds to the amount of charge transfer from Li metal to P. [Use EERE\_Figure\_Caption] ..... 852

Figure XIII.8.4 Change of atomic distribution across the interface measured by the calculated change of atomic deviation ( $\sigma$ ). [Use EERE\_Figure\_Caption] ..... 853

Figure XIII.9.1 Scalable synthesis of F/I hybrid doped argyrodite electrolytes. (a) XRD patterns and (b) Raman spectra of solvent-synthesized  $\text{Li}_6\text{PS}_5\text{I}$  and  $\text{Li}_6\text{PS}_5\text{F}_x\text{I}_{1-x}$  ( $x = 0.25, 0.5, 0.75$ ) argyrodites. SEM images and EDS mapping of (c)  $\text{Li}_6\text{PS}_5\text{I}$  and (d)  $\text{Li}_6\text{PS}_5\text{F}_{0.75}\text{I}_{0.25}$ . It is noted that the  $x$  value only refers to the amount of F from the precursor and does not reflect the accurate F-doping content in argyrodites. .... 856

Figure XIII.9.2 Anion-disorder in dual-doped argyrodite SEs and its impact on Li-ion conduction. (a) Arrhenius plots (30-90 °C) of  $\text{Li}_6\text{PS}_5\text{I}$  and hybrid-doped  $\text{Li}_6\text{PS}_5\text{F}_x\text{I}_{1-x}$  ( $x = 0.25, 0.5, 0.75$ ) argyrodites; (b) Nyquist plots and (c) composition dependent ionic conductivity of  $\text{Li}_6\text{PS}_5\text{I}$  and hybrid-doped  $\text{Li}_6\text{PS}_5\text{F}_x\text{I}_{1-x}$  argyrodites at RT; Atomic-scale structures of (d)  $\text{Li}_6\text{PS}_5\text{I}$ , and (e)  $\text{Li}_6\text{PS}_5\text{F}_{0.25}\text{I}_{0.75}$  optimized by density functional theory (DFT) calculations. In each panel, the energy change associated with swapping a S atom at 4d site (cage-center) with a halogen (I in panel (a), and F in panel (b)) are indicated. The Li, P, S, F and I atoms are depicted as blue, purple, yellow, red, and green spheres, respectively. .... 858

Figure XIII.9.3 Electrochemical stability of F/I hybrid-doped argyrodites against lithium metal. (a) Cycling performance of Li symmetric cells with  $\text{Li}_6\text{PS}_5\text{I}$ , and hybrid-doped  $\text{Li}_6\text{PS}_5\text{F}_x\text{I}_{1-x}$  ( $x = 0.25, 0.75$ ) argyrodites as SEs under current density of  $0.05 \text{ mA cm}^{-2}$ . (b) Nyquist plots of  $\text{Li}_6\text{PS}_5\text{F}_{0.75}\text{I}_{0.25}$ -based symmetric cell before and after cycling for 100 cycles. (c) Voltage profiles of  $\text{Li}_6\text{PS}_5\text{F}_{0.75}\text{I}_{0.25}$ -based symmetric cell cycling up to 1100 h (current density of  $0.05 \text{ mA cm}^{-2}$ ) and XPS spectra of cycled symmetric cell with  $\text{Li}_6\text{PS}_5\text{F}_{0.75}\text{I}_{0.25}$  SE: (d) I 3d, (e) S 2p, and (f) Li 1s. In the XPS, the doublet peaks for I 3d at 619.4 and 630.5 eV (panel (d)) originate from Li-I bonding, while the peak at 56.2 eV for Li 1s (panel (f)) can be attributed to Li-F bonding. This clearly indicates presence of LiI and LiF. .... 859

Figure XIII.9.4 Performance of F/I hybrid-doped argyrodites in solid-state lithium battery. (a) Charge-discharge voltage profiles and (b) cycling performance of Li metal batteries with  $\text{Li}_6\text{PS}_5\text{F}_{0.75}\text{I}_{0.25}$  as the SE and LTO as the active cathode cycled at 0.1 C rate (current density of  $0.02 \text{ mA cm}^{-2}$ ) at room temperature. .... 860

Figure XIII.9.5 Electrochemical cycling performance of batteries consisting of Li anode, SP-S cathode with 4.0 mg/cm<sup>2</sup> loading pressed with 25% SE,  $\text{Li}_6\text{PS}_5\text{F}_{0.5}\text{Cl}_2$  SE with 5 μL of ionic liquid (LiTFSI in PYR:DOL(1:3) at 3M) at the cathode-SSE interface. (a) Capacity variation, and Coulombic efficiency as a function of cycles at 60 °C at C/20, (b) Discharge profiles at selected cycles. .... 861

Figure XIII.10.1 Schematic of multimodal synchrotron analysis of sulfide glass samples. .... 865

Figure XIII.10.2 Schematic of the processing steps for developing ultrathin glass. .... 865



Figure XIII.10.3 K-means clustering phase analysis of a Li-B-S glass with both phase heterogeneity due glass thickness and noncrystalline impurities. ....	866
Figure XIII.10.4 Comparison of impurity concentration of the core and after the core is pressed to the desired thickness (preforming). Impurity concentration increase with preforming. ....	866
Figure XIII.10.5 Optimization of processing conditions significantly reduced the concentration of crystalline inclusions. Post-processing treatments can further decrease the impurity concentration. ....	867
Figure XIII.10.6 Comparison impurity concentration of contaminated LPS and LBS glass disks.....	868
Figure XIII.10.7 A PXRD waterfall plot for the in situ diffraction experiment for LBS (right). Selected PXRD indicating the crystalline impurities (left). ....	868
Figure XIII.11.1 Li/Li <sub>7</sub> P <sub>2</sub> S <sub>8</sub> Br <sub>1-x</sub> I <sub>x</sub> /Cu (x=0, 0.5, and 1) cross-sectional SEM images and corresponding elemental mappings after Li plating: (a) Li/Li <sub>7</sub> P <sub>2</sub> S <sub>8</sub> Br/Cu, (b) Li/Li <sub>7</sub> P <sub>2</sub> S <sub>8</sub> Br <sub>0.5</sub> I <sub>0.5</sub> /Cu, and (c) Li/Li <sub>7</sub> P <sub>2</sub> S <sub>8</sub> I/Cu. ....	872
Figure XIII.11.2 (a) Cycling performance and (b) voltage profiles of the cell S/Li <sub>7</sub> P <sub>2</sub> S <sub>8</sub> Br <sub>0.5</sub> I <sub>0.5</sub> /Li under 0.1 C (1 C = 1600 mA g <sup>-1</sup> ) at 2 mAh cm <sup>-2</sup> and 20 °C.....	872
Figure XIII.11.3 Photo image and thickness measurement of the processed (a) dry SSE film and (b) dry sulfur cathode. (c) Photo image of all-solid-state pouch cell and (d) typical charge/discharge curves at 60°C.....	873
Figure XIII.11.4 Electrical field and current path in Li <sub>6.7</sub> P <sub>2</sub> S <sub>8</sub> Br <sub>0.5</sub> I <sub>0.2</sub> -0.3LiI pellet under constant current and different pressure: (a) no pressure, (b) 54 MPa, (c) 245 MPa, and (d) 575 MPa. (e) Effective ionic conductivity and porosity of Li <sub>6.7</sub> P <sub>2</sub> S <sub>8</sub> Br <sub>0.5</sub> I <sub>0.2</sub> -0.3LiI pellet as a function of pressure. (f) Elastic modulus and effective ionic conductivity of Li <sub>6.7</sub> P <sub>2</sub> S <sub>8</sub> Br <sub>0.5</sub> I <sub>0.2</sub> -0.3LiX (X = I, Br, Cl, F). ....	874
Figure XIII.11.5 a) Photo image of the Ag coated Cu current collector, b) SEM image of the Ag coated Cu, c-e) EDS of Ag coated Cu, and f) Initial plating/stripping profiles of Li/SSE/Cu cells using Cu with/without Ag coating.....	875
Figure XIII.11.6 Impact of pressure on Li stripping/plating: a, b) Cycling of Li/SSE/Li cells with SSE pellets fabricated at different pressures (cell testing is performed at a constant stack pressure of 5M Pa and room temperature, 0.5h for each step of plating or stripping at a current 0.5 mAcm <sup>-2</sup> ). c,d) Cycling of Li/SSE/Li cells at different stack pressures (SSE pellets were fabricated at constant pressure of 700 MPa). ....	876
Figure XIII.11.7 Morphological changes of Li plating with presence of C-M interlayer. (a) Voltage profiles during 0.5 mA cm <sup>-2</sup> discharging (Li plating) of Li/SSE/C-M/Cu cell (Inset: cross-section SEM images C-M before and after Li plating). (b-e) Top-view SEM images of the C-M interlayer when (b) pristine, (c) 2 mAh cm <sup>-2</sup> , (d) 4 mAh cm <sup>-2</sup> , and (e) 10 mAh cm <sup>-2</sup> . ....	877
Figure XIII.12.1 Impact of binder loading for MSB1-13. Ionic conductivity vs. MSB1-13 content. ....	881
Figure XIII.12.2 (Left) The retention of a pellet cell with LIC catholyte and cathode interlayer in ~40 cycles at 0.1 C. Cell structure: Li-In(150μm)/Gen2.2(300μm)/LIC(300μm)/NMC-LIC-C(100μm). (Right) Charge/discharge curves of a tape cast cell with cell structure: Li-In(150μm)/Gen2.2-MSB(40μm)/LIC-MSB(40μm)/NMC-LIC-C-MSB(100μm). ....	881
Figure XIII.12.3 Li-In(150μm)/Gen2.2-MSB(40μm)/LIC-MSB(40μm)/NMC-LIC-C-MSB(30μm) cell structure. Retention of a tape-cast large area (5.7 cm <sup>2</sup> ) cell with a stack pressure of <2 MPa. ....	882
Figure XIII.13.1 Voltage profiles for all-solid-state Si/hi nickel cathode cell cycled at RT .....	885
Figure XIII.13.2 VE-XPS reduction results on Li <sub>2.8</sub> Sc <sub>0.8</sub> Zr <sub>0.2</sub> Cl <sub>6</sub> showing formation of a passivating SEI followed by plating of metallic lithium. ....	886
Figure XIII.13.3 VE-XPS oxidation results on Li <sub>2.8</sub> Sc <sub>0.8</sub> Zr <sub>0.2</sub> Cl <sub>6</sub> . Throughout the experiment, the lithium signal decreases as it migrates away from the surface. The resulting decomposition products, ScCl <sub>3</sub> and ZrCl <sub>4</sub> , form as expected. Over the course of the experiment, the net Cl 2p signal decreases, suggesting the formation of fugitive Cl <sub>2</sub> gas, also as expected.....	887

- Figure XIII.14.1 Composite polymer electrolytes. (a) Tape casted CPE films with (bottom) and without (top) FEC additive. (b) Young's modulus ( $E$ ) and ionic conductivity as functions of LLZTO weight percentage in PEGDA/PEGMEA/PEO-LiTFSI polymer electrolytes. (c) The Li plating/stripping cycling stability test with  $0.1 \text{ mA/cm}^2$  current density and 1h plating/stripping period. .... 890
- Figure XIII.14.2 Four LFP-Li cells with different integration methods showing the improvement of charge/discharge capacity at C/10 rate..... 891
- Figure XIII.14.3 (a) Pictures of sintered LLZTO pellets coated with a layer of LCO before and after co-sintering at  $900 \text{ }^\circ\text{C}$  for 2h in Ar. (b) ICP-OES (all elements except for oxygen) and IGA analysis (oxygen) of LLZTO pellets after co-sintering with LCO. The LCO layer was removed before analysis. (c) XRD comparison of pristine LLZTO powder and Co-doped LLZTO pellets (prepared by removing the LCO layer after co-sintering with LCO at  $900 \text{ }^\circ\text{C}$  for 2h in Ar)..... 892
- Figure XIII.14.4 (a) EIS plots and (b) DC polarization curves of pristine and Co-doped LLZTO pellets with Au as ion blocking electrodes..... 893
- Figure XIII.15.1 Solvent-treated LPSCl powders were electrochemically characterized by (a) room temperature ionic conductivity, (b) temperature-dependent ionic conductivity, and (c) stability against lithium metal at  $100 \text{ } \mu\text{A/cm}^2$ ,  $150 \text{ } \mu\text{A/cm}^2$ , and  $200 \text{ } \mu\text{A/cm}^2$ ..... 896
- Figure XIII.15.2 Raman mapping based on the K-means clustering analysis respectively for (a) Li/neat LPSCl interface and (b) Li/ LPSCl-TOL interface. (c-d) The corresponding centroid spectra of the clusters shown in (a). Each color stands for a chemistry or structure, with red in (a) and green in (b) representing bulk LPSCl. 897
- Figure XIII.15.3 Process schematic depicting PIB-LPSCl composite film fabrication. .... 898
- Figure XIII.15.4 (a) Nyquist plots showing decreased interfacial resistance after cold pressing of a C@Al|5 wt% PIB-LPSCl|C@Al cell. (b) Comparison of the ionic conductivity of various LPSCl separators. The control sample is a cold-pressed pellet with a thickness of  $490 \text{ } \mu\text{m}$ . Sample 5c stands for calendered LPSCl thin film separator with 5wt% PIB binder (average thickness =  $64 \text{ } \mu\text{m}$ ). Sample 5cp stands for 5wt% PIB LPSCl thin film separator after cold pressing (average thickness =  $48 \text{ } \mu\text{m}$ )..... 898
- Figure XIII.15.5 (a) Initial galvanostatic cycling profiles of the In|LPSCl|NMC cells at 5 and 30 MPa stack pressures. (b) Initial galvanostatic cycling profiles of the In|LPSCl|LIC|NMC cells at 5, 15, and 30 MPa stack pressures. .... 899
- Figure XIII.15.6 The cross-sectional optical microscopic images of the (a) LIC|LPSCl interface and (b) NMC|LPSCl interface. The green box represents the mapping region. Raman imaging (following K-means clustering analysis) of the (c) LIC|LPSCl interface and (d) NMC|LPSCl interface is also displayed. The black arrow indicates the interface for each Raman mapping. Each color-coded zone represents a region with similar structure and chemistry, and the corresponding centroid spectra, following the same color-coding, are shown in (e) and (f), respectively. Dash lines mark peaks different from those in bulk LPSCl, stemming from the LPSCl oxidation decomposition..... 900
- Figure XIII.15.7 X-ray absorption studies to reveal the capacity loss mechanism in NMC811 cathodes using argyrodite solid electrolytes. (a) Schematic of the basic components of a XAS measurement setup. (b) Experimental setup of the XAS instrument and the part of the sample holder containing NMC811 cathode samples (pristine, charged and charged-discharged). (c) Ni K-edge spectrum of Pristine (green), Charged (blue), and Charged-discharged (red) Ni-rich NMC811 cathodes that were in contact with an argyrodite sulfide solid state electrolyte..... 901
- Figure XIII.15.8 Transmission X-ray Microscope (TXM) to visualize the morphological change of NMC-811 cathodes change at different cycling conditions. (a) Experimental setup of the TXM instrument. (b) The sample holder containing Charged NMC-811 sample that have been cycled using argyrodite solid electrolytes. TXM images of NMC-811 (c) charged sample, (d) charged-discharged sample. .... 902
- Figure XIII.16.1 Weight gain of uncoated  $\text{Li}_6\text{PS}_5\text{Cl}$  powders and  $\text{Li}_6\text{PS}_5\text{Cl}$  powders after 1 and 10 ALD  $\text{Al}_2\text{O}_3$  cycles during exposure to (a) pure  $\text{O}_2$  and (b) humidified  $\text{O}_2$ . .... 907

Figure XIII.16.2 Weight gain of uncoated $\text{Li}_6\text{PS}_5\text{Cl}$ powders and $\text{Li}_6\text{PS}_5\text{Cl}$ powders after 1, 10, and 100 ALD $\text{Al}_2\text{O}_3$ cycles, 10 ALD ZnS cycles, and 10 ALD ZnS cycles during exposure to humidified $\text{O}_2$ .	907
Figure XIII.16.3 (a) Arrhenius plots, (b) ionic conductivity at $25^\circ\text{C}$ , (c) current-time curves (DC polarization at 200 mV, $25^\circ\text{C}$ ) and (d) electronic conductivity at $25^\circ\text{C}$ for $\text{Li}_6\text{PS}_5\text{Cl}$ pellets pressed from powders coated by 1, 10, and 100 ALD alumina cycles in comparison to pellets pressed from uncoated powders.	908
Figure XIII.16.4 Li  Li Symmetric cell cycling performance at an applied current density of $0.5 \text{ mA/cm}^2$ at $25^\circ\text{C}$ and 6 MPa stack pressure of (a) uncoated $\text{Li}_6\text{PS}_5\text{Cl}$ and (b) $\text{Li}_6\text{PS}_5\text{Cl}$ after 10 cycles of ALD $\text{Al}_2\text{O}_3$ . Total Li thickness is $20 \mu\text{m}$ .	909
Figure XIII.16.5 Full cell cycling data comparing performance of LPSCl coated with 10 cycles ALD $\text{Al}_2\text{O}_3$ (blue) with cells assembled from uncoated material (green).	910
Figure XIII.16.6 Total cell impedance as a function of cycle number for full cells assembled from uncoated (green) and 10x ALD $\text{Al}_2\text{O}_3$ -coated LPSCl, corresponding to the cycling data in Figure XIV.21.5.	911
Figure XIII.16.7 Interfaces modeled in this work. The left image shows the all-solid-state battery containing $\text{Li}_6\text{PS}_5\text{Cl}$ electrolyte powders coating with ALD-grown oxides. The three smaller schematics on the right are the magnified representation of the Li-anode    Coating and $\text{Li}_6\text{PS}_5\text{Cl}$    Coating and $\text{LiCoO}_2$ -cathode    Coating interfaces.	912
Figure XIII.17.1 Synchrotron XRD patterns of (a) $\text{Li}_{5.5}\text{PS}_{4.5}\text{Br}_{1.5}$ synthesized at $500^\circ\text{C}$ for 12h, $\text{Li}_{5.5}\text{PS}_{4.4}\text{O}_{0.1}\text{Br}_{1.5}$ synthesized at (b) $500^\circ\text{C}$ for 12h and (c) $600^\circ\text{C}$ for 12h. SEM images of (c) $\text{Li}_{5.5}\text{PS}_{4.5}\text{Br}_{1.5}$ synthesized at $500^\circ\text{C}$ for 12h, $\text{Li}_{5.5}\text{PS}_{4.4}\text{O}_{0.1}\text{Br}_{1.5}$ synthesized at (d) $500^\circ\text{C}$ for 12h and (e) $600^\circ\text{C}$ for 12h. Insets in (d-f) shows the corresponding high magnification SEM images.	917
Figure XIII.17.2 (a) Room temperature ionic conductivity measurement of $\text{Li}_{5.5}\text{PS}_{4.5}\text{Br}_{1.5}$ synthesized at $500^\circ\text{C}$ for 12h, $\text{Li}_{5.5}\text{PS}_{4.4}\text{O}_{0.1}\text{Br}_{1.5}$ synthesized at $500^\circ\text{C}$ for 12h and $600^\circ\text{C}$ for 12h. (b) Room temperature ionic conductivity measurement of commercial $\text{Li}_6\text{PS}_5\text{Cl}$ from vendor. Lithium stripping/plating behavior of symmetrical cells using solid electrolytes of $\text{Li}_{5.5}\text{PS}_{4.5}\text{Br}_{1.5}$ synthesized at $500^\circ\text{C}$ for 12h (c) and commercial $\text{Li}_6\text{PS}_5\text{Cl}$ (d). The current densities were increased gradually from $0.1 \text{ mA/cm}^2$ to $1.4 \text{ mA/cm}^2$ .	917
Figure XIII.17.3 Image for the in situ synchrotron XRD set up for the measurement of moisture stability of solid state electrolytes.	918
Figure XIII.17.4 Synchrotron XRD patterns of the synthesized $\text{Li}_{5.5}\text{PS}_{4.4}\text{O}_{0.1}\text{Br}_{1.5}$ and $\text{Li}_{5.5}\text{PS}_{4.4}\text{O}_{0.1}\text{Br}_{1.5}$ electrolyte under 20% humidity. The time interval of XRD patterns was 1 minute.	919
Figure XIII.17.5 (a) In situ Se K-edge X-ray absorption near edge spectroscopy (XANES) of composite Se cathode during charge/discharge of all-solid-state Li-Se cells using Li metal anode and $\text{Li}_6\text{PS}_5\text{Cl}$ sulfide solid electrolytes at C/10 ( $1\text{C}=675 \text{ mA g}^{-1}$ ). Selected Se XANES of composite Se cathode during (b) discharge and (c) charge process.	920
Figure XIII.17.6 SEM images of Spandex prepared by electrospinning at a feeding rate of (a) $0.21 \text{ ml/h}$ and (b) $0.42 \text{ ml/h}$ .	921
Figure XIII.17.7 SEM images of Spandex by electrospinning with a feeding rate of $0.42 \text{ ml/h}$ using different solvents: (a) NMP; (b) DMF. The concentration of solution is 10 wt.%.	921
Figure XIII.17.8 SEM images of Spandex nanofibers by electrospinning with a feeding rate of $0.42 \text{ ml/h}$ using THF cosolvent: (a) DMF/THF=3:2, v/v; (b) DMF/THF=8:2, v/v; (c) DMF/THF=9:1, v/v. The concentration of solution is 10 wt.%.	922
Figure XIII.18.1 a) Schematic of the mesoscale model used for modeling lithium plating through soft and heterogenous SEI vs. strong and uniform SEI. b) Computed dendrite velocity as a function of relative bulk electrolyte modulus for the weak and strong SEIs. c) A phase map demonstrating the competition between conductivity and elastic modulus of the SEI layer in determining the stability of lithium deposition process.	925
Figure XIII.18.2 a) Schematic of slot-die coating salt-rich SEI precursor layers and generating SEI under controlled conditions on copper electrodes. b) Applying potentials of $0.05 \text{ V}$ and $1.0 \text{ V}$ for 2 hours at $25^\circ\text{C}$	

with lithium bis(fluorosulfonyl)imide (LiFSI)-rich interlayers shows that lower potentials generate better cell characteristics. c) Varying the thickness of LiTFSI-rich interlayers shows that thicker 600 nm layers have better performance. d) Incorporating LLZO nanofibers in a coated trilayer structure can decrease the effective interface resistance by >85% compared to typical cells assembled with freestanding membranes..... 926

Figure XIII.18.3 a) Schematics of metal oxide ALD coatings on copper electrodes during the initial formation and lithium plating steps. b) Charge loss in a Cu||Li half-cell with PEO-LiTFSI solid polymer electrolyte cell before the onset of lithium plating. c) Current density at which different cells shorted. d) Coulombic efficiency of lithium plating and stripping..... 927

Figure XIII.18.4 (a) Calibration curve of Li content in Al-LLZO nanofiber synthesis. (b) STEM-EDS images of Al-LLZO with 25% excess Li. (c) X-ray diffraction patterns of Al-LLZO with varied contents of excess Li. .... 928

Figure XIII.18.5 (a) Scanning electron micrograph of the cross-section of the 83% dense pellet made with Al-doped LLZO nanofibers. (b) Impedance spectrum of the pellet (photo inset) with sputtered Au blocking electrodes. (c) Arrhenius plots of two different densified Al-doped LLZO nanofiber pellets..... 929

Figure XIII.18.6 (a) Photograph of reflux surface modification set-up. (b) Raman spectra of bare LLZO and silane-modified LLZO over time. (c) Comparison of the Zr-O peak shift with bare LLZO and silane-modified LLZO nanofibers after exposure to air. (d) FT-IR spectrum of LLZO nanoparticles and APTES-modified LLZO nanoparticles showing surface functional groups. .... 930

Figure XIII.18.7 Ionic conductivity of (a) 10 wt % and (b) 50 wt% LLZO nanoparticle composite electrolytes with different surface modifications compared to the baseline PEO-LiTFSI polymer electrolyte. (c) Estimated transference number of the electrolytes vs. LLZO loading. Small dots represent single measurements; large dots and error bars represent the average and standard deviation of three cells. .... 931

Figure XIII.18.8 (a) Schematic of crosslinked xTJ composite membrane chemistry, where PEO oligomers with acrylate end-groups (T) covalently bond to the amines on APTES@LLZO and the end-groups of other PEO oligomers (J). (b) Arrhenius plots of this crosslinked membrane with no LLZO (xTJ-LiTFSI) and with 10 and 50 wt % APTES@LLZO nanoparticles. (c) Arrhenius plots of linear PEO (600 kDa) and LiTFSI with 0, 10, and 50 wt % APTES@LLZO nanoparticles to compare the effects of crosslinking. .... 932

Figure XIII.18.9 (a) Schematics of the computational model used to model conductivity in composites, using multiple interphases that enhance or disrupt Li<sup>+</sup> transport. (b) Fit of experimental data with unmodified LLZO NPs in PEO-LiTFSI to the model, showing that improvement in PEO conductivity from small LLZO contents is outweighed by more resistive interphases at higher LLZO contents. (c) Further heat treatment of LLZO nanofibers (left) can ensure fiber-to-fiber contact and build a percolation network with sintered scaffolds (right). .... 933

Figure XIII.19.1 Ion transport characteristics of SIC polymer and the resulting 3D composite. (a) Ionic conductivity of 60VEC-SIC, 70 VEC-SIC, 80VEC-SIC, and 60EC-SIC as a function of inverse temperature. Inset, a digital photograph of 60VEC-SIC membrane. (b) Ionic conductivity of 70 VEC-SIC, 3D composite with 70VEC-SIC, and Dense LATP plate trilayer with 70VEC-SIC, as a function of inverse temperature. (c) and (d) Li<sup>+</sup> transference number ( $t_+$ ) measurement results of 60VEC-SIC, 70VEC-SIC, and 3D composite with 70VEC-SIC at 70 °C. (c) Chronoamperometry with an applied potential of 10 mV. Current is normalized to initial current. (d) The impedance spectra before and after the applied potential. (e) Impedance spectra at 20 °C of Dense LATP trilayer w/ 70VEC-SIC, and Dense LATP trilayer w/linear PEO-LiTFSI..... 937

Figure XIII.19.2 Rate performance in SIC polymer and Gen2 3D composite. (a, c) Li/Li stripping/plating test of 70VEC-SIC and 3D composite electrolyte at increasing currents while keeping the capacity cycled per cycle constant at 0.5 mAh/cm<sup>2</sup>. (b, d) Evolution of the impedance spectra before and after cycling (shown in a, c) at various currents. (e) Linear sweep voltammetry (LSV) of 70 VEC-SIC, 70VEC-SIC filled LATP scaffold, at 0.05 mV/s and 70 °C. (f) Bar chart comparing the normalized limiting current ( $i \times L$ ) of xPEO-LiTFSI, 3D composite with xPEO-LiTFSI, 70 VEC-SIC, and 3D composite with 70VEC-SIC, measured via LSV at 0.05 mV/s and 70 °C. .... 938

Figure XIII.19.3 Failure mechanisms in SIC polymer and Gen2 3D composite. (a, c) Li//Li symmetric cell cycling of cells made with 70VEC-SIC and the 3D composite with 70VEC-SIC, respectively. Cycling is done at 1 mA/cm<sup>2</sup> and 70 °C with each half cycle being 0.5 h long. (b, d), Proposed failure mechanisms in a and c, respectively. .... 939

Figure XIII.19.4 Normalized lithium concentration in PE at steady state current under 10 mV applied potential: a) fully PE domain; b) 15 vol% LAMP particles; c) 30 vol% LAMP particles; d) 50 vol% particles; e) 50 vol% particles connected via partial sintering; f) fully dense LAMP block. The line plots represent normalized concentration along the line passing through the center of the domain. .... 940

Figure XIII.19.5 Full cell cycling results using xPEO-LiTFSI and two lithium anode sources at current density of 50 μA/cm<sup>2</sup> at 70 °C. (a) Cell configurations; (b) Voltage profiles; (c) Average charge and discharge capacity as a function of cycle number; averaged over 6 cells for each type of lithium; (d) Normalized average charge and discharge capacity, normalized to the discharge capacity of the first cycle. (e) Anode interface impedance evolution as a function of cycle number; open symbols, after plating (charge to 4.2V); solid symbols, after stripping (discharge to 2.8 V) (f) Cathode interface impedance evolution as a function of cycle number. Symbols follow the same rule as Panel e. .... 942

Figure XIII.19.6 SEM images of Li anode morphology at different cycling stages. Row (a) – Row (g): Pristine (a), conditioned (b), after first plating (charge to 4.2 V) (c), after first stripping (discharge to 2.8 V) (d), after 5<sup>th</sup> plating (e), after 5<sup>th</sup> stripping (f), and after cell capacity faded to < 10% (g). Column (i, ii), morphology of Li chip at two different magnifications; Column (iii, iv), morphology of Li foil at two different magnifications. The scale bar at the top of the columns applies to all the images in the same column. .... 943

Figure XIII.20.1 (a) Fabrication of PVDF/LiTFSI polymer electrolyte using NMP based solvent casting method. (b) Cyclabilities of NMC811||Li, LiFePO<sub>4</sub>||Li, LiMn<sub>2</sub>O<sub>4</sub>||Li and LiCoO<sub>2</sub>||Li cells using the fabricated PVDF polymer electrolyte. (c) Degradation mechanism probed by the soft x-ray absorption spectroscopy (XAS) both at nitrogen and carbon K-edges. The fluorescence mode, which has a probing depth of around 100nm, is used. (d) left, degradation mechanism probed by soft XAS at oxygen K-edge; right, the reactivity between NMP and lithium metal anode indicated by the solution which turned from transparent to yellowish after putting lithium disk in NMP solvent after 12 hours. The vial was placed in the Ar-filled glove box. .... 948

Figure XIII.20.2 (a) Schematic of the *in situ* solid-state cell design. (b) The *in situ* solid-state cell using argyrodite as the SSE. (c) The first cycle charging curve of the *in situ* solid-state cell mentioned in (b). (d) The *in situ* Ni K-edge XANES data collected from position 1 in the *in situ* cell. (e) The *in situ* Ni K-edge XANES data collected from position 2 in the *in situ* cell. (f) The *in situ* solid-state cell using Li<sub>3</sub>YCl<sub>6</sub> as the SSE. (g) Y K-edge XANES data of the pristine catholyte measured in the cell. (h) Y K-edge ft-EXAFS data of the pristine catholyte measured in the cell. .... 949

Figure XIII.20.3 (a) Photograph of 20-μm-thick SIC-SPE; (b) Critical current density of SIC-SPE measured at 50 °C; (c) EIS plot of a Li<sup>0</sup>/SIC-SPE/Li<sup>0</sup> cell showing the charge transfer resistance; (d,e) Limiting current density of MIC-SPE (d) and SIC-SPE (e) measured at 50 °C; (f) Selected charge-discharge curves of Li-LiFePO<sub>4</sub> cell. The cathode loading is 2.2 mg/cm<sup>2</sup>; (g) Long-term cycling performance of SIC-SPE tested under Li<sup>0</sup>-Li<sup>0</sup> symmetric cell configuration; (h) Cycling stability of Li-LiFePO<sub>4</sub> cell at 50 °C and 0.2C. .... 951

Figure XIII.20.4 Charge and discharge curves for Electrolyte A with NMC-Electrolyte-Lithium structure. Electrolyte in (a) is Electrolyte A and in (b) is hierarchical ceramic electrolytes denoted as ABA. Both batteries are with >8 mg/cm<sup>2</sup> loading and cycled at 0.5C. .... 952

Figure XIII.20.5 Specific capacity of three batteries at different C-rates at >8 mg/cm<sup>2</sup> cathode loading. .... 952

Figure XIII.21.1 Nyquist plots of a concentrated liquid electrolyte, LiTFSI dissolved in EC in a 1:2 molar ratio, and two mixtures of this liquid electrolyte with LAMP. LAMP-MSE has a particle size of 600 nm, and the LAMP-Toshiba has a particle size of 5~15 μm. The impedance spectra were measured using a cell with two copper wire electrodes separated by 22 mm with a calibrated cell constant of 19.5 cm<sup>-1</sup>. .... 955

Figure XIII.21.2 Impedance study of the effect of LAMP to a concentrated liquid electrolyte EC/LiTFSI=2/1. (a) Nyquist plots of the concentrated electrolyte at different LAMP content at 25 °C. The inset shows the

equivalent circuit used to fit the data when LATP is added to the liquid electrolyte. The pure liquid electrolyte is fitted using a simple R/C circuit. (b) The evolution of R1 as a function of LATP volume fraction and temperature. (c) Arrhenius plot of 1/R2 shows that R2 is related to a physical process with an activation energy of 76 ~ 81 kJ/mol.....	956
Figure XIII.21.3 (a) Nyquist plots of EC/LiFSI=2/1 with 0 and 30 wt% LATP at 0 °C. (b) Nyquist plot of EC/LiTFSI=2/1 with 20 wt% LPSCI at 20 °C.....	957
Figure XIII.21.4 Voltage profiles of a Li/LiFePO <sub>4</sub> cell with a PVDF/LATP-based composite polymer electrolyte cycled at ambient temperature at 0.1, 0.2, and 0.3 mA/cm <sup>2</sup> .....	960
Figure XIII.22.1 (a) Cu/Li/Li <sub>6</sub> PS <sub>3</sub> Cl/Li/Cu cells tested with 3 different types of Li. First from a commercial source dubbed #3 in prior quarterly reports on Cu and evaporated Li of 2 different thicknesses (10 and 30 μm). (b) Two cells tested at 5 MPa and 17 MPa, both with the 10 μm thick Li metal.....	963
Figure XIII.22.2 (a) Schematics of adhesion measurements using AFM; (b) An average withdraw curve of a Li-coated probe from LiPON surface; (c) Adhesion forces of Li to glass and Li to LiPON; SEM images of (d) an as-received AFM probe, (e) an as-coated probe, and (f) a post F-D measurement probe.....	964
Figure XIII.22.3 a-d) pictures of four Li metal films with a) untreated, b) Ar/O <sub>2</sub> etched, c) Cu coated, and d) LiPO coated. e-h) SEM images of the same four Li metal films with e) untreated, f) Ar/O <sub>2</sub> etched, g) Cu coated, and h) LiPO coated.....	965
Figure XIII.22.4 IR data for the four Li films shown in Figure 1 from 400-1500 cm <sup>-1</sup> as measured by attenuated total internal reflection (ATIR).....	966
Figure XIII.22.5 Nyquist plots and Li//Li cycling data with a dry crosslinked PEO-LiTFSI polymer electrolyte with pristine Li metal (a-b), O <sub>2</sub> etched Li (c-d), and LiPON coated Li (e-f). .....	967
Figure XIII.23.1 <i>In situ</i> Neutron diffraction contour plots of the direct water synthesis pathway: (top) heating from RT to 500 °C and (bottom) cooling from 500 °C to RT.....	970
Figure XIII.23.2 <i>In situ</i> Neutron diffraction contour plots of the ammonium-assisted synthesis pathway: (top) heating from RT to 500 °C and (bottom) cooling from 500 °C to RT. (top) depicts the presence of YCl <sub>3</sub> precursors along with the early formation of (ND <sub>4</sub> Cl) <sub>3</sub> [YCl <sub>6</sub> ] intermediate at ~100 °C. ....	971
Figure XIII.23.3 Arrhenius plot comparison for the Li <sub>3</sub> YCl <sub>6</sub> M, PMA, and AC samples.....	972
Figure XIII.23.4 Initial charge-discharge comparison for NMC811/Li <sub>3</sub> YCl <sub>6</sub> /Li-In cells. ....	973
Figure XIII.23.5 Tape-casted LIC membrane and characterization. a) Optical image and dimensions. b) Cross-section of LIC membrane reinforced by non-woven fabric. c) FT-IR spectrum of LIC membrane showing complete removal of solvent. O-H bond comes from air exposure during FTIR characterization. d) XRD pattern of LIC powder and LIC membrane showing the identical phase.....	974
Figure XIII.23.6 Nyquist plot of LPSC/LIC bilayer membrane at room temperature between two carbon coated aluminum current collectors. Data collected by Anna Mills and Guang Yang from FSU and ORNL, respectively. ....	975
Figure XIII.23.7 Electrochemical profile of solid-state batteries with halide electrolyte. a-c) Cell architecture and corresponding charge and discharge voltage profiles. d-f) Capacity retention. g-i) Impedance profiles measured at charge state. All cells were tested at 60 °C, under 50 MPa stacking pressure and at 10 mg/cm <sup>2</sup> cathode loading. ....	976
Figure XIII.24.1 Voltage ( <i>V</i> ) behavior as a function of time ( <i>t</i> ) for various applied current densities at 90°C for PES/LiTFSI electrolytes with salt concentrations of a) <i>r</i> = 0.02, and b) <i>r</i> = 0.04.....	979
Figure XIII.24.2 Normalized limiting current, <i>i<sub>L</sub></i> of PES/LiTFSI and PEO/LiTFSI electrolytes as a function of salt concentration, <i>r</i> . The dashed lines are linear fits of the data with the intercept constrained at zero. The red data represents PES/LiTFSI electrolytes, and the black data represents PEO/LiTFSI electrolytes. All data was collected at 90°C.....	980

Figure XIII.24.3 a) Ionic conductivity ( $\kappa$ ), b) current fraction, ( $\rho_+$ ), and c) restricted diffusion coefficient ( $D$ ) as a function of salt concentration ( $0.005 \leq r \leq 0.15$ (where $r = [\text{Li}^+]/[\text{O}^-]$ ) for two molecular weights of PES at $90^\circ\text{C}$ . Three data points at each salt concentration represents reproducibility of the data. The low molecular weight ( $14 \text{ kg mol}^{-1}$ ) is shown in blue circles, while the high molecular weight is shown in pink squares ( $22 \text{ kg mol}^{-1}$ ).....	980
Figure XIII.24.4 Efficacy ( $\kappa\rho_+$ ) as a function of salt concentration for two molecular weights of PES at $90^\circ\text{C}$ . The low molecular weight ( $14 \text{ kg mol}^{-1}$ ) is shown in blue circles, while the high molecular weight is shown in pink squares ( $22 \text{ kg mol}^{-1}$ ). .....	981
Figure XIII.24.5 (a) Atom transfer radical polymerization reaction scheme and (b) reversible addition fragmentation chain transfer polymerization scheme for synthesizing PS-PES-PS block copolymers. ....	981
Figure XIII.24.6 $^1\text{H}$ NMR of a polyester homopolymer synthesized using a condensation reaction. The molecular weight of the homopolymer was approximately $13 \text{ kg mol}^{-1}$ . The peak shifts are correlated with the corresponding hydrogens on the molecular structure except for peak B which is correlated to the methyl terminated end-group. ....	982
Figure XIII.24.7 $^1\text{H}$ NMR of a PS-PES-PS block copolymer synthesized with ATRP. The molecular weight of the polyester block and the styrene block was approximately $13 \text{ kg mol}^{-1}$ and $15 \text{ kg mol}^{-1}$ , respectively. The peak shifts are correlated with the corresponding hydrogens on the molecular structure. ....	983
Figure XIII.24.8 Final reaction product obtained after reaction of PES with TTI in 1-methyl 2-pyrrolidone at $120^\circ\text{C}$ . ....	983
Figure XIII.24.9 a) Storage modulus ( $G'$ ) and b) loss modulus ( $G''$ ) as a function of frequency for PES ( $26 \text{ kg mol}^{-1}$ )/10 wt% TTI, PEO ( $20 \text{ kg mol}^{-1}$ ), and PEO ( $50 \text{ kg mol}^{-1}$ ) at $90^\circ\text{C}$ . The measurements were taken in the absence of salt. PES/TTI is shown in blue circles, PEO-20 is shown in open red triangles, and PEO-50 is shown in yellow triangles. ....	984
Figure XIII.24.10 a) Ionic conductivity ( $\kappa$ ), b) current fraction, ( $\rho_+$ ), and c) restricted diffusion coefficient ( $D$ ) of PES electrolyte as a function of TTI weight percent at $90^\circ\text{C}$ . The salt concentration ( $r = [\text{Li}^+]/[\text{O}^-]$ ) was fixed to 0.08. Two data points at each weight percent represent reproducibility of the data. ....	984
Figure XIII.25.1 Temperature dependent lithium-ion conductivity measured for different electrolyte formulations. AP-5 has the best lithium-ion conductivity. ....	987
Figure XIII.25.2 Voltage profile of symmetrical cells using $\text{Li}_2\text{HOCl}_{0.75}\text{Br}_{0.25}$ (AP)/ $\text{Li}_{6.4}\text{La}_3\text{Zr}_{1.4}\text{Ta}_{0.6}\text{O}_{12}$ (LLZTO) composite electrolyte. ....	988
Figure XIII.25.3 Steady leakage current measured as a function of working potential to show the potential reaction between the Al foil with the electrolyte. ....	989
Figure XIII.25.4 Transmission X-ray microscopy (TXM) image of a $\text{LiNi}_{0.6}\text{Mn}_{0.2}\text{Co}_{0.2}\text{O}_2$ (NMC622) after being charged to 4.2 V. The color in the 3D map is the white line energy of Ni absorption edge. A red color means a higher oxidation state on Ni. ....	990
Figure XIII.25.5 Comparison of accelerating rate calorimeter (ARC) profiles for delithiated $\text{LiNi}_{0.8}\text{Mn}_{0.1}\text{Co}_{0.1}\text{O}_2$ (4.2V) mixed with conventional carbonate-based liquid electrolyte, and $\text{Li}_2\text{HOCl}_{0.75}\text{Br}_{0.25}$ (AP)/ $\text{Li}_{6.4}\text{La}_3\text{Zr}_{1.4}\text{Ta}_{0.6}\text{O}_{12}$ (LLZTO) composite electrolyte.....	990
Figure XIII.25.6 .....	991
Figure XIII.25.7 SEM image of an electrolyte film after thermal annealing at $250^\circ\text{C}$ . ....	992
Figure XIII.25.8 Measurement of electric resistance as a function of the stacking pressure (a) and temperature (b).....	992
Figure XIII.26.1 Lithium thioborate-lithium halide electrochemical evaluation. (a) EIS of SS- $\text{Li}_{10}\text{B}_{10}\text{S}_{19}\text{X}_2$ -SS ( $\text{X}=\text{Cl}, \text{Br}, \text{and I}$ ) and SS- $\text{Li}_{10}\text{B}_{10}\text{S}_{20}$ -SS cells at 360 MPa, room temperature. (b) EIS of SS- $\text{Li}_{10}\text{B}_{10}\text{S}_{20-y}\text{I}_y$ -SS	

cells, $y=1, 2, 4,$ and $6$ at $360$ MPa, room temperature. (c) Ionic conductivity of each lithium thioborate at $360$ MPa, room temperature. ....	995
Figure XIII.26.2 (a) SEM image of pressed LBS-LiI pellet (top row) and polycrystal in pellet (bottom row) with EDS mapping of sulfur and iodine. (b) TEM image with EELS (high-loss) and corresponding EDS mapping of sulfur, boron, lithium, and iodine. ....	995
Figure XIII.26.3 LiI-lithium thioborate electrochemical evaluation. (a) Symmetric cell cycling at $0.25$ mA cm <sup>-2</sup> of Li-Li <sub>10</sub> B <sub>10</sub> S <sub>20</sub> -YLi-Li ( $Y=1, 2, 4, 6$ ) at $10$ MPa, room temperature. (b) Symmetric cell cycling of LBS-LiI at $0.1$ mA cm <sup>-2</sup> , $10$ MPa, room temperature. ....	996
Figure XIII.26.4 Electrochemical performance and anode analysis of Li-LBS-LiI-Li symmetric cells. (a) Critical current density testing of cell in steps of $0.2$ mA cm <sup>-2</sup> at room temperature, $10$ MPa. (b) EIS of symmetric cell before and after cycling. (c) SEM image of the Li interface with the LBS-LiI pellet after cycling. Inset: a high-resolution image of the porous Li interface, showing small particles. (d) XPS of the same Li interface after cycling. ....	997
Figure XIII.26.5 Schematic representation of the six cell types tested in this study. ....	998
Figure XIII.26.6 Top: Charge and discharge capacity and CE (%) of full cells with $0.25$ mAh NMC cathode as designated (with and without C65 carbon). All cells had $450$ -micron LBS-LiI SSE, Li anode, and were cycled at C/20 rate, room temperature, and $70$ MPa pressure. Bottom: Optimization of four ratios of NMC:LBS-LiI in cathode: $60:40, 70:30, 80:20,$ and $90:10$ . Cells were cycled at $0.05C, 70$ MPa pressure, room temperature. ...	998
Figure XIII.26.7 a. Room-temperature EIS of LiZrCl. b. SEM of NMC with LiZrCl in a $70:30$ ratio. NMC particles are highlighted in yellow. ....	999
Figure XIII.26.8 Full cell cycling of cells with NMC cathodes and LBS-LiI SSE. (a) Current-voltage plot of LBS-LiI and LiZrCl in Li-SSE-SSE/C65 composite pressed pellet. Sweep rate: $1$ mV/s. (b) Discharge capacity vs. cycle of $6$ cell types with $70:30$ NMC:SSE ratio in cathode. (c) First cycle discharge capacity (mAh) and 15 <sup>th</sup> / 1 <sup>st</sup> cycle discharge capacity (%) for all cells with LiZrCl catholyte. (d) $200$ cycles of full cell with NMC:LiZrCl $70:30$ ratio cathode, LBS-LiI pellet SSE, and In anode. ....	1000
Figure XIII.27.1 (a) Free energy of the BCC (red), FCC (green) and $\gamma$ (blue) phases as a function of Li content ( $xLi$ ) at $T=300K$ . (b) Free energy functions in (a), enlarged in the range $xLi = 0.6\sim 0.9$ . (c) The relationship between BCC and $\gamma$ structures. The structure of $\gamma$ is obtained from removing one corner atom and one center atom in the $3*3*3$ super-cell of BCC structure and relax neighboring atoms around the vacancies. (d) The equilibrium and over electrochemical potential of Li in the Ag-Li system as functions of $y$ in formula AgLi <sub>y</sub> . ....	1004
Figure XIII.27.2 (a) schematic of the continuum simulation model. (b) Simulated electrochemical potential of Ag particle (black dashes) and equilibrium bulk potential (solid blue) as functions of lithiation time. (c)-(d) Ratio of Li current flowing into Ag particle, depositing on BL/CC and BL/SE interfaces as functions of lithiation time, assuming (c) equal ASR on both interfaces and (d) lower ASR on BL/CC interface. ....	1005
Figure XIII.27.3 (a) Volume percentage of Ag-Li alloy in the BL as a function of lithiation time. (b) Mechanism for interface separation between the BL/CC and BL/SE. (c) Calculated internal stress as a function of lithiation time in an anode-free setup. (d) Calculated evolution of deposited Li thickness as a function of lithiation time on BL/CC and BL/SE interfaces combining electrochemical and mechanical effects. ....	1006
Figure XIII.27.4 SEM images of (a) Ag, (b) Sn, and (c) Si nanoparticles as received from vendors. SEM images of (d) Ag-C, (e) Sn-C and (f) Si-C composites after rolling to ABL thin film. ....	1007
Figure XIII.27.5 Voltage curves during galvanostatic discharge/charge cycles in half cells with (a) No ABL, (b) first 3, and (c) last 15 discharge-charge cycles of Ag-C ABL, (d) first 3, and (e) last 15 cycles of Sn-C ABL and (f) Si-C ABL, at current density of $1$ mA cm <sup>-2</sup> after precycling at $0.5$ mA cm <sup>-2</sup> . ....	1008
Figure XIII.27.6 (a-b) SEM images of NMC811/rGO composites by (a) hybridization method and (b) mechanical ball-mill mixing. (c) Charge-discharge profiles of various cathode composite (carbon contents: $\sim 2$ wt%). ....	1009



- Figure XIII.27.7 (a) XRD patterns of LYC and n-LYC prepared by mechanochemical synthesis, (b) Room-temperature ionic conductivity and activation energy of LYC and n-LYC, and (c) LSV profiles collected on the SE+ $C|SE|Li-In$  cells (SE = LYC or n-LYC). The sweep rate is  $0.02 \text{ mV s}^{-1}$ . ..... 1010
- Figure XIII.27.8 (a) A schematic of the  $Li-In|SS-nLYC|NMC811$  ASSB cell configuration, (b, c) charge–discharge profiles of the ASSB cell during the first two cycles at 0.1 C and the subsequent cycles at 0.2, 0.5 C and 1 C, respectively. Cycling was performed at room temperature in the voltage window of 3.0–4.3 V vs.  $Li^+/Li$ . ..... 1011
- Figure XIII.27.9 (a) An amorphous  $Li-Cl-Ga-F$  structure constructed for theoretical modelling. (b) The evolution of the applied external shear stress ( $\sigma_{xz}$ ) and  $xz$ -tilt distance of the amorphous structure as a function of time in the classical MD simulation. The  $xz$ -tilt distance is a representative of shear strain. A maximum of 10 and 50 MPa of external periodic stress was applied to the amorphous structure to study its mechanical response. (c) A snapshot of the amorphous structure at an external shear strain  $\gamma_{xz} = 0.15$ . The grey-scale color (white-low and black-high) represents value of non-affine displacement, at an interval of  $\Delta\gamma_{xz} = 0.05$ . The shear transformation zone (STZ) formed is circled in red. .... 1012
- Figure XIII.27.10 (a) Fracture strengths of LLZO (Black) and LLZO-MgO (Red). (b) SEM image of the LLZO electrolyte. Green arrows point to abnormally grown grains. .... 1013
- Figure XIII.27.11 Prepared thin (80  $\mu\text{m}$ ) LLZO electrolytes with area of (a)  $1 \text{ cm}^2$ , (b)  $4.8 \text{ cm}^2$  and (c)  $8.4 \text{ cm}^2$ . (d) Stress/strain curve for the small and large area LLZOs. .... 1014
- Figure XIII.27.12 Ionic conductivity and oxidation stability test. (a) Nyquist plots of SN+Li salts mixtures. (b) Linear Sweep Voltammetry (LSV) of the SN+Li salts mixtures in the range of 3.0 ~ 5.5 V vs.  $Li/Li^+$ . ..... 1014
- Figure XIII.27.13 (a) Cell configuration for the solid state cells with SN-based catholytes. Charge and discharge curve of the (b) SN+LiTFSI and (c) SN+LiTFSI+LiBOB. .... 1015
- Figure XIII.27.14 (a) SEM image of commercial as-received LPSCl particles. (b) SEM image of lab ball-milled processed LPSCl particles. (c) EIS measurement of the two LPSCl materials with blocking electrodes. (d) EIS measurement of the two TEGDMA/LPSCl composites with block electrodes. (e) Details of the measurement conditions and calculated results. .... 1016
- Figure XIII.27.15 (a) Charge and discharge (CD) plots of the as–prepared electrolyte solutions based on the coated NMC811//SE// $Li-In$  cell at 0.1C rate. (b) Specific discharge capacity plots of the cells as a function of the CD cycles at 0.1C (c) Coulombic efficiency of the cells with as–prepared SEs as a function of the CD cycles. .... 1017
- Figure XIV.1.1 Practical application validation for the combination of OMSH-Se/S cathode with HFE-based electrolyte. Cycling performance of OMSH-Se/S cathode in HFE-based electrolyte under a)  $0^\circ \text{C}$  condition, b)  $55^\circ \text{C}$  condition. c) Schematic graph of  $Li-Se/S$  pouch cell configuration. d) Cycling performance of  $Li-Se/S$  pouch cell with thick  $Li$  metal anode (200  $\mu\text{m}$ ). e) Charge/discharge voltage profiles of various cycles of  $Li-Se/S$  pouch cell with 200  $\mu\text{m}$   $Li$  metal anode. f) Cycling performance of  $Li-Se/S$  pouch cell with thin  $Li$  metal anode (40  $\mu\text{m}$ ). g) Charge/discharge profiles of various cycles of  $Li-Se/S$  pouch cell with 40  $\mu\text{m}$   $Li$  metal anode. .... 1022
- Figure XIV.1.2 In situ phase transformation analysis of cathode material. a) Charge and discharge curve of OMSH-Se/S cathode at 0.15 C in HFE-based electrolyte and the corresponding in situ HEXRD patterns. b) Discharge curve of OMSH-Se/S cathode at 0.1 C in HFE-based electrolyte and the corresponding in situ XANES spectra. c) The standard Se and  $Li_2Se$  XANES spectra. d) First derivatives of in situ XANES spectra. .... 1023
- Figure XIV.1.3 Interphase and morphology characterizations of cycled electrodes. ToF-SIMS chemical mappings (S- and Se-) and 3D element reconstructions (Se-) of cycled OMSH-Se/S cathode in a) DME- and b) HFE-based electrolytes. c) Depth profile (Se-) of cycled OMSH-Se/S cathode in both DME- and HFE-based electrolytes. d) SEM image of cycled  $Li$  metal anode in  $Li-Se/S$  cell with DME-based electrolyte. e) ToF-SIMS chemical mappings (Se-, N-, and F-) of cycled  $Li$  metal anode in  $Li-Se/S$  cell with DME-based

electrolyte. f) SEM image of cycled Li metal anode in Li-Se/S cell with HFE-based electrolyte. g) ToF-SIMS chemical mappings (Se-, N-, and F-) of cycled Li metal anode in Li-Se/S cell with HFE-based electrolyte. 1025

Figure XIV.1.4 TEM image of cycled OMSH-Se/S cathode in HFE-based electrolyte. b, c) TEM image and corresponding EDS elements mappings (C, N, Zn, Co, S, Se) of cycled OMSH-Se/S cathode in HFE-based electrolyte. .... 1025

Figure XIV.1.5 (a) Schematic of working principles of CoZn-YSIL in regulating the Li deposition behavior and preventing the Li side reaction with cathode dissolving species. (b) SEM image of CoZn-YSs. (c) TEM image and corresponding EDS element mappings of CoZn-YSs (interesting elements are C, N, Co, and Zn). (d) Top-view SEM image of CoZn-YSIL (inset: digital photograph of CoZn-YSIL). (e) Cross section-view SEM image of CoZn-YSIL (inset: digital photograph of folded CoZn-YSIL). (f) High-resolution Zn 2p and N 1s XPS spectra of CoZn-YSIL..... 1026

Figure XIV.1.6 Cycling performance of high-loading Li/S cells with and without CoZn-YSIL at the cathode side under the current of 0.1 C. (f) Charge and discharge voltage profiles of various cycles of high-loading Li/S cell with CoZn-YSIL under the current of 0.1 C. .... 1027

Figure XIV.2.1 (a) Schematic illustration of PSC preparation. (b) Digital photograph of the PSC, Scanning Electron Microscope (SEM), and surface profilometric images of PSC (c and d) and BSC (e and f). The color from blue to red represents the height from low to high. (g) X line-scan profiles of PSC and BSC. (h) Discharge and charge profiles of the PSC and BSC upon cycling at an E/S of 4 mL g<sup>-1</sup>. The grey bar highlights the early occurrence of ISC in PSC. .... 1032

Figure XIV.2.2 Optical profilometric images of CSC at S loading of 6 mg cm<sup>-2</sup> (a) and 4 mg cm<sup>-2</sup> (c). Discharge and charge profiles of the BSC and CSC at S loading of 6 mg cm<sup>-2</sup> (b) and 4 mg cm<sup>-2</sup> (d) in E/S = 4 mL g<sup>-1</sup>..... 1033

Figure XIV.2.3 Digital photographs (a-c) and SEM images (d-i) of the pristine Li anode (a and d), the Li anode after assembly but before cycling (b and e), and the Li anode after cycling with PSC (c, f-i). (g) Cross-section of (f). Higher-resolution images of PR (h) and VR (i) of (f). .... 1034

Figure XIV.2.4 Simulation (a-d) and schematic illustration (e-f) of the *llocal* distribution and Li anode evolution in the Li-S cell with a rough cathode. (a) Geometry of the model. (b) *llocal, cathode* distribution. (c) *llocal, anode* distribution in the first discharge (t=5 h) and charge (t=15 h). t=0-10 h is the first charge. t=10-20 h is the first discharge. (d) The moving boundary of Li anode at the beginning (t=0 h) and the end of first cycle (t=20 h). (e) The rough cathode, separator, and Li metal anode before they are assembled in a cell. (f) The rough cathode imprints its pattern on the soft Li metal anode. (g) During cycling, Li islands form in the PR protruding from Li metal anode. (h) Sharp Li metal dendrites penetrate through the separator causing an ISC. .... 1035

Figure XIV.2.5 Strategy for multiscale model development for a Li-S battery..... 1036

Figure XIV.2.6 (a) Comparison of the Li-S discharge curves between experimental data and the multiscale model for the 20 μm and 90 μm electrodes at 0.1C. (b) The polysulfides concentration profiles during the discharge for both LPC (up) and SPC (down). .... 1036

Figure XIV.2.7 Micro-CT characterization: sulfur electrodes without additive (a) before and (b) after rinsed in electrolyte; sulfur electrodes with additive (c) before and (b) after rinsed in electrolyte. (e) Cycling performance of 30% porosity sulfur electrode with additive and comparison with baseline electrodes without additive at 50% and 70% porosities, E/S=10 mLg<sup>-1</sup> S..... 1038

Figure XIV.3.1 The performance of PMTH|Li6PS5Cl|Li cell under A) moderate active mass loading condition; B) high active mass loading condition; C) Charge/discharge profiles of PMTH|Li6PS5Cl|LiIn cell at different current densities at 25 °C; D) Energy density comparison of the state-of-the-art organic cathodes reported in Li-organic ASSBs; E) Proposed reaction mechanism for PMTH cathode during battery operation. .... 1042

Figure XIV.3.2 a) GITT profile and b) polarization plots of PMTH|Li6PS5Cl|LiIn cell upon one discharge/recharge cycle at 0.07C. c) EIS evolution at different SOC states upon one charge/discharge cycle.

d) A schematic cell setup for in-situ stack pressure measurement. e) The variation of cell stack pressure upon two consecutive cycles. f) Schematic illustration of volumetric change within the cell upon one discharge/recharge cycle.....	1043
Figure XIV.3.3 Schematic illustration of the preparation of NC/S.....	1044
Figure XIV.3.4 FESEM images of (a) NC750, (b) NC800, (c) NC900, and (d) NC950. Nitrogen adsorption/desorption isotherm of NC800; (b) Corresponding pore size distribution curves of NC750, NC800, NC900, and NC950.....	1046
Figure XIV.3.5 (a) Cycling performance and Coulombic Efficiency at 0.5 C, and (b) Rate capability cathodes at different C-rate of S/NC750, S/NC800, S/NC900, and S/NC950 composite; FESEM images of the discharged electrodes with (c) NC750, (d) NC800, (e) NC900, and (f) NC950. All the carbons were tested in coin cells. ....	1047
Figure XIV.3.6 (a) Cycling performance of S/NC800 pouch cell with sulfur loading of 1.2 mg cm <sup>-2</sup> and E/S ratio of 10 uL mg <sup>-1</sup> ; (b) corresponding discharge/charge profile; (c) HPLC chromatograms of S/NC800 and S/Ketjenblack pouch cells after 3 cycles; (d) Cycling performance of S/NC800 pouch cell with sulfur loading of 5 mg cm <sup>-2</sup> and E/S ratio of 10 uL mg <sup>-1</sup> ; (e) Corresponding discharge/charge profile.....	1048
Figure XIV.4.1 <b>Scheme 1.</b> Schematic diagram of the role of micelle-structured additive and imide salt.....	1052
Figure XIV.4.2 <b>Scheme 2.</b> The synthesis route of 1,1,1,2,2,3,3,4,4-nonafluoro-6-(2-methoxyethoxy)hexane (F <sub>4</sub> EO <sub>2</sub> ). ....	1053
Figure XIV.4.3 CV curves of the (a) TDLiTFSI, (b) T5FDLiTFSI, (c) T10FDLiTFSI, (d) T20FDLiTFSI, (e) T5FDLiTFSI-FSI, and (f) T5FDLiFSI electrolyte solutions with the Li//electrolyte//S/C cell configuration at 0.1mV/s.....	1055
Figure XIV.4.4 CD plots of the as-prepared electrolyte solutions based S/C//electrolyte//Li half-cell at 0.1 C rate, (a) at first cycle and (b) after 20 cycles. (c) Specific discharge capacity plots of the cells as a function of CD cycles at 0.1 C. (d) Coulombic efficiency of the LSBs with as-prepared electrolyte solutions as a function of CD cycles. ....	1057
Figure XIV.4.5 FE-SEM images of the (a) bare Li-anode and cycled Li-anode with (b) TDLiTFSI (c) T5FDLiTFSI, (d) T10FDLiTFSI, (e) T20FDLiTFSI, (f) T5FDLiTFSI-FSI, and (g) T5FDLiFSI electrolytes solutions. (Photographic images of the Li-anodes are shown as inset in the SEM images). ....	1058
Figure XIV.4.6 FE-SEM images of the (a) bare S/C composite cathode and cycled S/C cathodes with (b) TDLiTFSI (c) T5FDLiTFSI, (d) T10FDLiTFSI, (e) T20FDLiTFSI, (f) T5FDLiTFSI-FSI, and (g) T5FDLiFSI electrolyte solutions. ....	1059
Figure XIV.4.7 XPS survey spectra of cycled Li-anode with (a) TDLiTFSI (b) T5FDLiTFSI, (c) T10FDLiTFSI, (d) T20FDLiTFSI, (e) T5FDLiTFSI-FSI, and (f) T5FDLiFSI electrolyte solutions.....	1060
Figure XIV.4.8 High-resolution XPS spectra of (a) F 1s and (b) S 2p for cycled Li-anode with as-prepared electrolyte solutions. ....	1060
Figure XIV.5.1 (a) The photos showing the Li foil immersed into 0.5 M Li <sub>2</sub> S <sub>6</sub> before and after 1 week; (b) Photos of 100 μm Li foils inside the new electrolyte with 0.5 M Li <sub>2</sub> S <sub>6</sub> for 1 month (86.43% Li inventory retention) and the bare new electrolyte for 4 weeks (being shining); The voltage profiles of the HATN/CNT-S cathode with 5.30 mg <sub>sulfur</sub> cm <sup>-2</sup> with a low E/S ratio of 6 μl mg <sub>sulfur</sub> <sup>-1</sup> in the baseline electrolyte of 1 M LiTFSI in DOL/DME (1:1, vol), 2 wt.% LiNO <sub>3</sub> (c) and the new electrolyte (d) at 0.05 C, 1 C = 1000 mA g <sup>-1</sup> .....	1068
Figure XIV.5.2 (a) The photo of the cycled Li anodes in the baseline and new electrolytes (Q2, 2023); (b) The photo of the TGC solutions in the two electrolytes with the table of the correlated TGC results; The large-area cryo-SEM images of the cycled Li anodes (top-view) and the corresponding accumulated Energy-dispersive X-ray (EDX) spectra in (c & d) the baseline and (e & f) new electrolytes. ....	1069
Figure XIV.5.3 (a) The schematic of the HPLC-UV methodology used to investigate the LiNO <sub>3</sub> amount; (b) The HPLC-UV spectra of LiNO <sub>3</sub> solutions ranging from 0.5 mM to 1 mM and (c) The corresponding standard	

curve of  $\text{LiNO}_3$ ; (d) The HPLC-UV spectra of the NPL solutions ranging from 0.1 mM to 4 mM and (e) The corresponding standard curve of the NPL additive in the new electrolyte. .... 1070

Figure XIV.5.4 (a) The Cryo-FIB image of the cross-section view of the HATN/CNT-S cathode with a high S loading of  $\sim 9.56 \text{ mg cm}^{-2}$ . (b) The demonstration of segmentation of cathode components, including micron-sized sulfur (magenta), Voids (dark blue), and HATN/CNT + super P + binder (red) of the first slice of 40 milling slices by Cryo-FIB (slice interval of 100 nm). (c) The 3-D reconstruction of 40 Cryo-FIB slices in total using Avizo3D software, giving the distributions sulfur (yellow) and the void volume (cyan, 7.5%). (d) The 3-D segmentation of the HATN/CNT-S cathode for 3-D tortuosity ( $\tau$ ) calculation using a MatLab application of TauFactor. .... 1071

Figure XIV.5.5 (a and b) A summarized overview of Ampcera's overall work plan. The synthesis of the HATN monomer and polymer. (c) The project schedule of industrial production of the materials. (d) The H-NMR spectrum of the scaled HATN monomer. .... 1073

Figure XIV.5.6 Digital images of the HATN monomer synthesis at 50-g scale (a = initial & b = final). The digital image in (c) is the HATN monomer product with a ruler for reference. (d) The image of the polymerization setup. (e) a zoomed-in view of the HATN/CNT polymer composite product. .... 1074

Figure XIV.5.7 Digital images of the HATNCNT-S cathode based on the HATN/CNT composite from Ampcera. (a) Batch C and (b) Batch A that followed the same polymerization process. .... 1075

Figure XIV.5.8 (a) The cycling behavior of the GM C-S cathode with a sulfur loading of  $3.4 \text{ mg cm}^{-2}$  and an E/S ratio of  $8 \mu\text{l mg}_{\text{sulfur}}^{-1}$  in the baseline electrolyte using  $100 \mu\text{m}$  Li anode. (b) The related voltage profiles. (c) The cycling behavior of the GM C-S cathode in the new electrolyte under the same conditions as the baseline. (d) The corresponding voltage profiles. The TGC results are inserted. .... 1076

Figure XIV.5.9 (a) The large-area cryo-SEM images of the cycled Li anode (cross-section view). (b) the Energy-dispersive X-ray (EDX) element mapping of the selected area. (c) the corresponding accumulated EDX spectra of the Li anode cycled in the baseline electrolyte. (d) The cryo-FIB cross-section image of the cycled Li anode. (e) the Energy-dispersive X-ray (EDX) element mapping of the selected area. (f) the corresponding accumulated EDX spectra of the Li anode cycled in the baseline electrolyte. .... 1077

Figure XIV.5.10 (a) The voltage profiles and cycling behavior of the HATN/CNT-S cathode with  $\sim 6.5 \text{ mg}_{\text{sulfur}} \text{ cm}^{-2}$  with a low E/S ratio of  $6 \mu\text{l mg}_{\text{sulfur}}^{-1}$  in the baseline electrolyte (a and b) and the new electrolyte (c and d) at 0.05 C, 1 C =  $1000 \text{ mA g}^{-1}$ . .... 1078

Figure XIV.5.11 (a) Voltage profiles of the HATN/CNT-S cathode with  $\sim 6.4 \text{ mg}_{\text{sulfur}} \text{ cm}^{-2}$  with a low E/S ratio of  $6 \mu\text{l mg}_{\text{sulfur}}^{-1}$  or a calculated E/C ratio of  $4.64 \text{ g Ah}^{-1}$  from 0.05 C to 0.2 C, 1 C is  $1000 \text{ mA g}^{-1}$ . The cells were assembled by pairing against  $100 \mu\text{m}$  Li anodes in the new electrolyte. (b) the cycling behavior of the HATN/CNT-S cathode in the new electrolyte. .... 1079

Figure XIV.5.12 (a) Photos of the synthesized UCSD C-S and HATN/CNT-S (b) cathode sheets ( $5 \times 5 \text{ cm}^2$ ). (c) The schematic of pouch-cell assembly details at GM. Photos of single-layer dry pouch cells produced at GM. (d) GM C-S, (e) UCSD C-S and HATNCNT-S. (f) The vacuum sealing station was set up at UCSD. .... 1080

Figure XIV.6.1 Cycling performance of baseline electrode with modified electrolyte (1 wt.% of CA) as an additive at low and high sulfur loadings. .... 1084

Figure XIV.6.2 Li cycling performance with modified electrolyte (1 wt.% CA additive) at 1 mA current for 1 h for 103 cycles. .... 1085

Figure XIV.6.3 Electrochemical cycling performance of MCA3 electrode along with areal capacities cycled at 2.5 mA current for 4 h for alloying and de-alloying, respectively from 150 to 250 cycles after rate capability test. .... 1086

Figure XIV.6.4 Cyclic performance and Coulombic efficiency of 10% PTA coated CFM-S electrode cycled between 1.8-2.8V at C/20 and 1.7-2.8V at C/10 using standard electrolyte. .... 1087

Figure XIV.6.5 Cyclic performance of 10% PTA coated CFM-S electrode cycled between 1.8-2.8V at C/20 and 1.7-2.8V at C/10 with modified electrolyte with 1wt. % of the chemical additive (CA).....	1087
Figure XIV.6.6 Cyclic performance of MCA3 electrode along with areal capacities cycled at 3 mA current for 4 h for alloying and de-alloying, respectively from 325 to 500 cycles after cycling at various currents for different time periods described in the text.....	1088
Figure XIV.6.7 Electrochemical cycling performance of 10% PTA coated CFM-S electrode cycled between 1.8-2.8V at C/20 and 1.7-2.8V at C/10 using standard electrolyte and with 1 wt.% additives EA1, EA2. ....	1089
Figure XIV.6.8 Electrochemical cycling performance of MCA3 electrodes cycled at 3 mA for 5 h with a stable areal capacity of 11.9 m Ah cm <sup>-2</sup> for cycles after cycling at various currents for different periods described in the text. ....	1090
Figure XIV.6.9 Electrochemical cycling performance of CFM-S electrode cycled between 1.8-2.8V at C/20 and 1.7-2.8V at C/10 and C/5 using standard electrolyte. ....	1091
Figure XIV.6.10 Electrochemical cycling performance of PMCA3 as current collector cycled at 1 mA cm <sup>-2</sup> current density with 5 mAh cm <sup>-2</sup> areal capacity showcasing the potential of MCA alloys for current collectors in Li-based batteries. Digital image of MCA3 pellet in the inset. ....	1092
Figure XIV.7.1 (a) and (b), N <sub>2</sub> adsorption/desorption isotherms (a) and (b) pore size distribution of optimized SPC. (c) and (d), N <sub>2</sub> adsorption/desorption isotherms (c) and (d) pore size distribution of conventional SPAN. ....	1099
Figure XIV.7.2 (a) The galvanostatic charge and discharge curves of cells based on optimized SPC-1 cathodes at 200 mA g <sup>-1</sup> . (b) Evolution of charge-discharge capacity and Coulombic efficiency (CE) <i>versus</i> cycle number at 200 mA g <sup>-1</sup> .....	1100
Figure XIV.7.3 Discharge profiles of the Li-S cells based on optimized SPC-1 cathodes in carbonate electrolytes at increasing current densities from 0.1 to 5.0 A g <sup>-1</sup> based on SPC-1 composite.....	1100
Figure XIV.7.4 (a) and (b), SEM images of Li anodes disassembled form the cycled SPC-1 cathode-based Li-S batteries in the carbonate-based electrolyte. (c) and (d), SEM images of Li anodes disassembled form the cycled SPC cathode-based Li-S batteries in the ether-based electrolyte. ....	1101
Figure XIV.7.5 (a) and (b), Cycling performances of the SPC-1-based Li-S batteries at 200 mA g <sup>-1</sup> in previous electrolyte (a) and in new electrolyte (b). ....	1101
Figure XIV.7.6 Cycling performances of optimized SPC cathodes fabricated with different binders tested at low E/S ratio of 5 $\mu$ L mg <sup>-1</sup> and excessive Li metal. Compared with previously used binders (binder 1), upon the construction of high areal capacity SPC cathodes, the optimized binder 2 delivered improved cycling stability and the optimized binder 3 could afford higher areal capacity in Li-S batteries.....	1102
Figure XIV.7.7 (a) Galvanostatic charge and discharge curves of SPC-2-based cells at 200 mA g <sup>-1</sup> cathode material in carbonate-based electrolyte. (b) Corresponding evolution of discharge capacity and Coulombic efficiency (CE) <i>versus</i> cycle number in (a). ....	1102
Figure XIV.8.1 Single atoms by GAUSS for ASSLSBs. (a) Schematic of GAUSS for cobalt (Co) single atoms. Precursors are firstly dissolved in ethanol and soaked on HGDY aerogel. Solvated HGDY aerogel is dried and placed on the hotplate set at a temperature of 450 °C. Immediately, sparking reaction happens and spreads quickly through the entire aerogel, achieving an ultra-high temperature up to 1640 K within 40 milliseconds. (b-d) Characterizations of single atoms by GAUSS. b, STEM image of Co single atoms on HGDY. Wavelet transforms for d, Co/HGDY. and e, Co foil reference. ....	1105
Figure XIV.8.2 Ultrafast single atom synthesis for all-solid-state lithium-sulfur batteries (ASSLSBs). (a) Schematic of Co single atoms enabled ultra-fast Li-S conversion in ASSLSBs. (b) Charge/discharge curves of ASSLSBs using bare sulfur cathodes, S@HGDY cathodes, and S@Co/HGDY cathodes at 60 °C at 0.05 C. (c) Cyclic voltammetry profiles of ASSLSBs using bare sulfur cathodes, and S@Co/HGDY cathodes at 60 °C. ....	1106

Figure XIV.8.3 Density functional theory calculations of sulfur reduction reaction. Energy profiles for the reduction of bare sulfur and sulfur@Co/HGDY. The optimized structures of the intermediates are shown in the inset.....	1107
Figure XIV.8.4 Rate and cycling performance of ASSLSBs using bare sulfur cathodes, S@HGDY cathodes and S@Co/HGDY cathodes at 60 °C.....	1107
Figure XIV.9.1 Navitas and ANL propose to develop electrolytes for Li-S batteries based on new fluorinated co-solvents (PFG). Incorporating PFG will surpass state of art DOL/DME electrolytes by reducing polysulfide solubility and protecting electrodes to improve the capacity and cycle life for EV applications. ....	1110
Figure XIV.9.2 Structure of novel partially fluorinated glymes (PFG) to be synthesized by ANL for evaluation in Li-S batteries. The color shading highlights where the fluorination occurs. ....	1111
Figure XIV.9.3 Structures of the other partially fluorinated ether and glymes (PFGs) with varying fluorination degrees. ....	1111
Figure XIV.9.4 30000-0 Setaflash Series 3 Closed Cup Flash Point Tester.....	1112
Figure XIV.9.5 Specific capacity (Left) and Coulombic efficiency (Right) variations with cycling for coin cells with thiourea additive. CR2032, 1.0 mg S/cm <sup>2</sup> loading, 1.6-2.6V, C/10, room T. The synergetic effect of thiourea and PFG-1 appeared to be decreasing with cycling. ....	1113
Figure XIV.9.6 The electrochemical performance of coin cells with electrolyte PFG-2 as co-solvent and LiNO <sub>3</sub> as additive. (PVDF binder, 80AM/14CB/6PVDF, uncalendared. CR2032, C/10, room T. E/S ratio = 6.5-7; loading ≈ 3.5 mg S/ cm <sup>2</sup> ). ....	1114
Figure XIV.9.7 The Coulombic efficiency (CE) of coin cells with electrolyte PFG-2 as co-solvent and LiNO <sub>3</sub> as additive. PVDF binder, 80AM/14CB/6PVDF, uncalendared. CR2032, C/10, room T. E/S ratio = 6.5-7; loading ≈ 3.5 mg S/ cm <sup>2</sup> .....	1115
Figure XIV.9.8 The Coulombic efficiency of coin cells from ANL.....	1116
Figure XIV.9.9 (a) Li Cu cell (0.2 mA/cm <sup>2</sup> , 3.0 mAh/cm <sup>2</sup> ), SEM images of Li anode surface after charge-discharge of Li/Cu half-cell in electrolyte (b,c) Without PFG-1, and (d,e) with PFG-1. ....	1116
Figure XIV.9.10 Double-Layer Pouch (DLP, 55x105mm “BB2590” cell format) cell assembly process. (A) assembled cathode-anode-cathode, (B) cell is taped inside pouch before sealing and filling, (C) The pilot coated single sided cathode before assembly.....	1117
Figure XIV.9.11 The sulfur specific capacity ( <i>Left</i> ) and Coulombic efficiency ( <i>Right</i> ) of DLP cells with baseline electrolyte with 3% LiNO <sub>3</sub> as additive. HSV 1800 PVDF binder, 80AM/14CB/6PVDF, uncalendared. C/10, room T. E/S ratio = 5; Sulfur loading ≈ 3.6 mg S/cm <sup>2</sup> .....	1118
Figure XIV.9.12 Capacity of DLP cells with baseline electrolyte with 3% LiNO <sub>3</sub> as additive. HSV 1800 PVDF binder, 80AM/14CB/6PVDF, uncalendared. C/10, room T. E/S ratio = 5; Sulfur loading ≈ 3.6 mg S/cm <sup>2</sup> . .	1118
Figure XIV.9.13 The electrochemical performance of DLP cells with baseline electrolyte + 3% LiNO <sub>3</sub> and PFG-2 electrolyte {Baseline + 3% LiNO <sub>3</sub> /PFG-2 (4:1 ratio)}. PVDF (HSV 1800) binder, 80AM/14CB/6PVDF, uncalendared; DLP's are C-A-C in BB2590 format, C/10, room T; E/S ratio = 5; Sulfur loading ≈ 3.6 mg S/ cm <sup>2</sup> .....	1119
Figure XIV.10.1 Ionic conductivity of the two series of electrolytes with varying content of fluorinated co-solvents: (a) ionic conductivity of LiTFSI-based electrolytes and (b) ionic conductivity of LiFSI-based electrolytes. ....	1123
Figure XIV.10.2 Electrochemical performance of Li-S cells with electrolyte composition containing HFMP fluorinated co-solvents with both series of electrolytes: a) discharge capacity, b) coulombic efficiency (LiFSI-series), c) discharge capacity, d) coulombic efficiency (LiTFSI-series).....	1124
Figure XIV.10.3 Cycling performance of Li-S cells with LiFSI-baseline and with 3% HFMP fluorinated co-solvent electrolytes: a) discharge capacity, b) coulombic efficiency.....	1125

Figure XIV.10.4 (a) Linear Sweep Voltammetry curves and (b) Li plating/stripping performance of symmetrical cells containing baseline and fluorinated co-solvent based electrolyte.....	1125
Figure XIV.10.5 In Panel (a), voltage profiles are depicted with five representative positions on the voltage curves for the baseline electrolyte, HFMP, and TFEM-containing systems during the initial discharge cycle at a 0.05 C rate. Panels (b-d) present Raman spectra corresponding to each electrolyte at the five characteristic locations indicated in Panel (a).....	1127
Figure XIV.10.6 (a), the <i>operando</i> Raman spectra of the HFMP-containing electrolyte are illustrated during the initial discharge at a 0.05 C rate. The X-axis and spectra were labeled with three characteristic Raman peaks, with elementary sulfur highlighted in black, long-chain polysulfides in red and intermediate polysulfides in blue. Panel (b) presents the corresponding normalized heatmap of intensity from (a), enhancing the visibility of changes in Raman peaks.....	1127
Figure XIV.10.7 Normalized XRF mapping image of anodes and cathodes. For each electrolyte, two distinct sets of cells are featured, one having undergone 1 cycle, and the other 20 or more cycles.....	1128
Figure XIV.10.8 Normalized X-ray Absorption Near Edge Spectra (XANES) of the standard reference including elemental sulfur, Li <sub>2</sub> S and various polysulfides.....	1129
Figure XIV.10.9 Normalized X-ray Absorption Near Edge Spectra (XANES) for the anodes and cathodes. The XANES were acquired from locations marked as number 1 (brighter, higher intensity) and number 2 (darker, lower intensity) on the electrodes, selected based on XRF mapping.....	1130
Figure XIV.10.10 (a) Schematic of the polysulfide adsorption test carried out in DME/DOL (1:1; v/v) solvent, with the inset showing the adsorption of polysulfides on the MXene flake surface. (b) Visual assessment of Li <sub>2</sub> S <sub>6</sub> solution color change after soaking candidate materials in Li <sub>2</sub> S <sub>6</sub> solution for 72 h. (c) UV-Vis absorption spectra of residual Li <sub>2</sub> S <sub>6</sub> solution and (d) calculated LiPS adsorption capability of candidate materials after 72 h in Li <sub>2</sub> S <sub>6</sub> solution. Lithium polysulfide adsorption characteristics of Ti-outer layered MXenes, (e) Adsorption isotherms of Li <sub>2</sub> S <sub>6</sub> in DME/DOL and (f) adsorption on Ti <sub>2</sub> CT <sub>x</sub> , Ti <sub>3</sub> CNT <sub>x</sub> and Ti <sub>3</sub> C <sub>2</sub> T <sub>x</sub> modeled using pseudo-first-order (yellow) and pseudo-second-order kinetic models (green). Experimental data points are connected by a dotted line.....	1131
Figure XIV.11.1 (a) Voltage profiles for the Li-S coin cells at different cycles in electrolyte A; (b) Cycling performance of Li-S coin cell in electrolyte A. ....	1134
Figure XIV.11.2 Cycling performance of Li-S coin cells in baseline electrolyte 1M LiTFSI in DEE/DOL + 2 wt.% LiNO <sub>3</sub> and the newly developed electrolyte A. charge/discharge at 0.05C for the first 2 cycles for formation, then the coin cells was cycled at 0.1C for charge/discharge. 1C= 1000mAh/g; S mass loading: 4.0 mg S/cm <sup>2</sup> .....	1134
Figure XIV.11.3 (a) Comparison of cycling profiles between the baseline (1M LiTFSI in DME/DOL 1:1 v/v + 2 wt.% LiNO <sub>3</sub> ) and the new electrolytes LS38, LS54; Cycling profiles of LS38 combined with different additives at (b) 1 wt.% A1-A4 (LS40-LS43) and (c) 5 wt.% A1-A4 (LS50-LS53), respectively. ....	1135
Figure XIV.11.4 Comparison of cycling profiles between the baseline (1M LiTFSI in DME/DOL 1:1 v/v + 2 wt.% LiNO <sub>3</sub> ) and the new electrolytes LS38 to LS88 (a); Voltage profiles between baseline and the new electrolytes after 1 <sup>st</sup> cycle (b); and after 5 <sup>th</sup> cycle (c).....	1135
Figure XIV.11.5 Comparison of cyclic voltammetry profiles between a) the baseline (1M LiTFSI in DME/DOL 1:1 v/v + 2 wt.% LiNO <sub>3</sub> ) and the new electrolytes b) LS87, c) LS88.....	1136
Figure XIV.11.6 Comparison of impedance profiles between a) the baseline (1M LiTFSI in DME/DOL 1:1 v/v + 2 wt.% LiNO <sub>3</sub> ) and the new electrolytes b) LS87, c) LS88.....	1136
Figure XIV.11.7 (a) Galvanostatic charge/discharge potential profile of the KB/S cathode in a functional electrolyte with/without redox mediator (first cycle at 0.05 C). (b) Cycling performance of the KB/S cathode in different electrolytes (cycle at 0.1 C).....	1137

Figure XV.1.1 (A) Two working electrode cell design that was implemented in a Swagelok cell. The addition of an additional working electrode (i.e. carbon paper) in the electrolyte and separated from the cathode, allows for the detection of electrochemical active species generated from the cathode. Note: RM is short for redox mediator. B) Voltage profile during the intermittent galvanostatic charging executed between the cathode electrode and the lithium metal anode (reference and counter electrode). C) Cyclic voltammograms observed at different SOCs sampled between the carbon paper electrode coated with Co Single atom catalyst (SAC) and the lithium metal anode..... 1140

Figure XV.1.2 Li-O<sub>2</sub> battery cycling performance: (A,B) voltage-capacity profiles of LiAl/rGO with Ionic Liquid at 500 and 1000 mAh/g<sub>Cat</sub> of capacity, (C) Galvano-static discharge/charge profiles of LiAl/rGO with Ionic Liquid (EMIM-BF<sub>4</sub>) (Red), LiAl/rGO (Green), and rGO with Ionic Liquid (EMIM-BF<sub>4</sub>) (Black)..... 1142

Figure XV.1.3 Synchrotron-based High-Energy X-ray diffraction pattern (HE-XRD) of several samples ... 1142

Figure XV.1.4 (A) A series of triaryl methyl cation redox mediators were synthesized and investigated as ORR redox mediator (RM) for Li-O<sub>2</sub> battery. Various function groups were substituted to examine their effect on the discharge capacity and redox potential. (B) Discharge capacity using a commercial carbon paper with various redox mediators at their solubility limit. (C) Relationship between RM potential and reaction rate (derived from CV)..... 1144

Figure XV.1.5 Cycling results for the solid-state Li-air battery. .... 1144

Figure XV.2.1 (A) SEM images taken from as-synthesized SnIrS<sub>3</sub> nanorods. (B) Atomic resolution scanning transmission electron microscopic high-angle annular dark field (STEM HAADF) image and STEM-EDS spectrum image that shows the distribution of S, Sn, and Ir elements. (C) Atomic resolution STEM image was taken along the [111] direction. (D) A comparison plot between simulated and observed PXRD patterns. (E) The 3D atomic structure determined from three-dimensional electron diffraction (3DED) datasets viewed along the b axis. The six coordinated metal atoms are highlighted as square bipyramids in the structure. (F) A magnified image shows a five-coordinated metal atom in the structure, showing the triangular bipyramid shape view along the a, b, and c axis. .... 1148

Figure XV.2.2 Galvanostatic cycling results of Li-air cell with SnIrS<sub>3</sub> cathodes and redox mediator of SnI<sub>2</sub> at the current density of (A) 0.5 mA.cm<sup>-2</sup> and (B) 1 mA.cm<sup>-2</sup> at a limited capacity of 0.5mAh.cm<sup>-2</sup> (C) Galvanostatic cycling results of Li-air cell at the current density and capacity of 1 mA.cm<sup>-2</sup> and 1 mAh.cm<sup>-2</sup>, respectively..... 1149

Figure XV.2.3 (A) The surface energies of different facets with different terminations. The blue arrow points to the most stable Sn terminated (100) surface. The side views of (B) Sn terminated, (C) Ir terminated, (D) bottom of Sn terminated, (E) bottom of Ir terminated (100) surfaces. The Ir, Sn, and S atoms are in blue, light purple, and yellow, respectively. The black lines represent the periodic boundaries. The red arrows point to possible O<sub>2</sub> adsorption sites to be investigated. .... 1150

Figure XV.2.4 The most favorable adsorption structure of (A) O<sub>2</sub>, (B) LiO<sub>2</sub>, and (C) Li<sub>2</sub>O<sub>2</sub> on the Ir terminated IrSnS<sub>3.6</sub>(100) surface. Close-up structure of O<sub>2</sub> in (A) on the di-iridium sulfur bridge site is shown in (D). Close-up structure of LiO<sub>2</sub> in (B) on this same is shown in (E) from a different perspective. (f) Reaction free energies plot for LiO<sub>2</sub> formation and Li<sub>2</sub>O<sub>2</sub> formation on the Ir terminated IrSnS<sub>3.6</sub>(100) surface. (G) Schematic illustrating the involvement of the di-iridium sulfur bridge site in the LiO<sub>2</sub> reaction. The Ir, Sn, S, O, and Li atoms are in blue, light purple, yellow, red, and green, respectively. Black lines in (A)–(C) are the periodic boundaries. The blue line in (f) represent the LiO<sub>2</sub> disproportionation reaction pathway, while the red line show a (Li<sup>+</sup> + e<sup>-</sup>) transfer to LiO<sub>2</sub> to form Li<sub>2</sub>O<sub>2</sub>. .... 1151

Figure XV.3.1 (A-B) Linear sweep voltammetry results of Te and S based catalysts during: (A) CO<sub>2</sub>RR and (B) CO<sub>2</sub>ER. (C-D) EIS measurements for both catalysts at two different overpotentials during: (C) CO<sub>2</sub>RR and (D) CO<sub>2</sub>ER..... 1155

Figure XV.3.2 (A-B) Linear sweep voltammetry results of Te and S based catalysts at three different IL:DMSO ratios during: (A) CO<sub>2</sub>RR and (B) CO<sub>2</sub>ER. (C-D) EIS measurements fat three different IL/DMSO ratios for both catalysts at two different overpotentials during: (C) CO<sub>2</sub>RR and (D) CO<sub>2</sub>ER..... 1156



Figure XV.3.3 Cycling results for Te based catalyst at different DMSO:IL ratios. ....	1156
Figure XV.3.4 Band gaps determined from density of state calculations (A) SbBiTe <sub>3</sub> (B) SbBiS <sub>3</sub> .....	1157
Figure XV.3.5 24 surface energies with different terminations (including 001, 010, 015, 100, 101, 102, 110, 111 facets).....	1157
Figure XV.3.6 A plot of the elementary reactions for the discharge mechanism of Li <sub>2</sub> CO <sub>3</sub> and C.....	1158
Figure XV.3.7 (A-B) Low- and high-resolution TEM images of discharged cathode showing Li <sub>2</sub> CO <sub>3</sub> , and C deposited on a Sb <sub>0.67</sub> Bi <sub>1.33</sub> Te <sub>3</sub> cathode. (C) EELS spectra of Li <sub>2</sub> CO <sub>3</sub> and C on the cathode surface after its 5 <sup>th</sup> discharge cycle; (i) Li K-edge, (ii) O K-edge, (iii) C K-edge, and (iv) A-C K-edge. (D) SEM image of cathode after 5 <sup>th</sup> discharge cycle. (E) CO <sub>2</sub> evolution results of a cell charged at current density of 1 mA/cm <sup>2</sup> using DEMS. (F) Stability of the Sb <sub>0.67</sub> Bi <sub>1.33</sub> Te <sub>3</sub> catalyst after 100 cycles.....	1159
Figure XV.3.8 AIMD results for CO <sub>2</sub> in EMIM-BF <sub>4</sub> /DMSO/1M LiTFSI electrolyte with: (left) 6:4 and (right) 9:1 volume ratios of DMSO/EMIM-BF <sub>4</sub> . ....	1159
Figure XV.3.9 (A-B) Nearest neighbor radial distribution describing interionic interactions between H <sup>2</sup> site of EMIM <sup>+</sup> (A) and Li <sup>+</sup> (B) and the most electronegative atoms of BF <sub>4</sub> <sup>-</sup> and TFSI <sup>-</sup> and ion-molecular interactions involving O atom of DMSO. (C-D) Mean-square displacement of the center-of-mass of electrolyte constituents in 6:4 (C) and 9:1 (D) DMSO/EMIM-BF <sub>4</sub> mixture compositions. ....	1160
Figure XV.3.10 (A-B) CV and LSV results. (C-E) Galvanostatic cycling at different current densities and capacities. (F) Stability of the catalyst through a continuous series of varying current densities.....	1161
Figure XV.3.11 (A-B) XRD and Raman characterization of the charge and discharge products. (C) Discharge product characterization under Ar atmosphere. (D) DEMS analysis of the gaseous products during charge. (E-F) Electrolyte stability using NMR and LSV methods. ....	1162
Figure XV.3.12 (A-C) XPS characterization of the SEI layer. (D) Charge transfer resistance at different cycles measured with EIS. ....	1163
Figure XVI.1.1 XRD data and Rietveld refinement of P3 Na <sub>0.75</sub> Li <sub>0.08</sub> Cu <sub>0.25</sub> Mn <sub>0.66</sub> O <sub>2</sub> with the inset graph showing the solved crystal structure. (b) Selected charge-discharge profiles of Na <sub>0.75</sub> Li <sub>0.08</sub> Cu <sub>0.25</sub> Mn <sub>0.66</sub> O <sub>2</sub> from the first 15 cycles. (c) Selected charge-discharge profiles of Na <sub>0.66</sub> Cu <sub>0.33</sub> Mn <sub>0.66</sub> O <sub>2</sub> from the first 15 cycles..	1167
Figure XVI.1.2 Selected (a) Mn K-edge XANES spectra and (b) Cu K-edge XANES spectra from the <i>in operando</i> XAS experiments for P3 type Na <sub>0.75</sub> Li <sub>0.08</sub> Cu <sub>0.25</sub> Mn <sub>0.66</sub> O <sub>2</sub> . (c) Summarized charge compensation mechanism of P3 type Na <sub>0.75</sub> Li <sub>0.08</sub> Cu <sub>0.25</sub> Mn <sub>0.66</sub> O <sub>2</sub> based on the XAS study. ....	1168
Figure XVI.1.3 (a) In situ XRD patterns of P3-Na <sub>0.75</sub> Li <sub>0.08</sub> Cu <sub>0.25</sub> Mn <sub>0.66</sub> O <sub>2</sub> at C/5 rate. (b) Charge-discharge curve of in situ battery cycling and the states of charge where the XRD patterns were taken in (a).....	1169
Figure XVI.1.4 (a) Oxygen K-edge TEY. The arrow indicates the peak from Na <sub>2</sub> CO <sub>3</sub> . (b) Oxygen K-edge PFY. The arrow indicates the peak from oxidized lattice oxygen. (c) Mn L-edge TEY (d) Cu L-edge TEY. The arrow indicates the peak from reduce Mn. (e) Cu L-edge PFY data of P3-Na <sub>0.75</sub> Li <sub>0.08</sub> Cu <sub>0.25</sub> Mn <sub>0.66</sub> O <sub>2</sub> at different states .....	1170
Figure XVI.1.5 (a) hard XAS of charged P3-Na <sub>0.75</sub> Li <sub>0.08</sub> Cu <sub>0.25</sub> Mn <sub>0.66</sub> O <sub>2</sub> electrode. (b) soft XAS in TFY mode of charged P3-Na <sub>0.75</sub> Li <sub>0.08</sub> Cu <sub>0.25</sub> Mn <sub>0.66</sub> O <sub>2</sub> electrode. The arrow indicates the region with enhanced fluorescence yield. (c) mRIXS of charged P3-Na <sub>0.75</sub> Li <sub>0.08</sub> Cu <sub>0.25</sub> Mn <sub>0.66</sub> O <sub>2</sub> electrodes. (d) Integrated energy-dependent photon emission spectra of charged P3-Na <sub>0.75</sub> Li <sub>0.08</sub> Cu <sub>0.25</sub> Mn <sub>0.66</sub> O <sub>2</sub> electrodes. The excitation energies used for emission spectra are 530.9, 531.1 and 531.3 eV. (e) summarized redox couple mechanism of P3-Na <sub>0.75</sub> Li <sub>0.08</sub> Cu <sub>0.25</sub> Mn <sub>0.66</sub> O <sub>2</sub> during charging. ....	1171
Figure XVI.2.1 (a) SEM and the corresponding EDX mapping; (b) XRD pattern; and (c) cycling performance of the developed O3 FCG NaNi <sub>0.8</sub> Co <sub>0.1</sub> Mn <sub>0.1</sub> O <sub>2</sub> cathode. ....	1175

- Figure XVI.2.2 (a) Charge-discharge voltage profiles, (b, c) area specific impedance (ASI) analysis, (d) capacity retention, and (e) coulombic efficiency of NFM and NFMA cathodes cycled between 1.5 – 4.5 V vs. Na. (f) Rate performance at current density from 10 mA/g to 500 mA/g..... 1176
- Figure XVI.2.3 Ex-situ XRD analysis collected at various charged and discharged states marked in (a) for the (b) NFM and (c) NFMA electrodes. .... 1177
- Figure XVI.2.4 XRD patterns of (a) NFM and (b) NFMMT. SEM images of (c) NFM and (d) NFMMT... 1178
- Figure XVI.2.5 Electrochemical performance of NFM and NFMMT. (a, b) Charge and discharge profiles of NFM (a) and NFMMT (b) at 20 mA g<sup>-1</sup> in the voltage range of 1.5-4.5 V. (c) Long-cycle performance of NFM and NFMMT at 200 mA g<sup>-1</sup> between 1.5 and 4.5 V. .... 1178
- Figure XVI.2.6 (a-c) Voltage profiles and (d) capacity retention of the bare and ALD-AlF<sub>3</sub> coated NFM cathodes; voltage ranges of 2.0 – 4.3 V vs. Na; current density of 15 mA/g for (a-c) and 100 mA/g for (d). .... 1179
- Figure XVI.2.7 (a) The 1<sup>st</sup> voltage curve, cycling performance and rate capability of Sb<sub>7</sub>-RP<sub>63</sub>/C<sub>30</sub> anode during charge/discharge in LHCE electrolytes. .... 1180
- Figure XVI.2.8 (a) P 2p XPS spectra of the Sb<sub>7</sub>-RP<sub>63</sub>/C<sub>30</sub> anode during charge/discharge in the LHCE electrolytes. Depth profile XPS (b) C 1s and (c) F 1s of discharged Sb<sub>7</sub>-RP<sub>63</sub>/C<sub>30</sub> anode in the LHCE electrolytes. .... 1181
- Figure XVI.2.9 (a) Charge/discharge curves in the carbonate electrolytes and (b) cycling performance in the LHCE electrolytes of Sb<sub>7</sub>-RP<sub>63</sub>/C<sub>30</sub> anode with an areal Sb<sub>7</sub>-RP<sub>63</sub> loading of 2.12 mg cm<sup>-2</sup> at C/3; Stripping/plating of Na metal in the (c) carbonate and (d) LHCE electrolytes using Na/Na symmetric cell with a high areal capacity loading of 4.0 mAh cm<sup>-2</sup> at a current density of 1.0 mA cm<sup>-2</sup>..... 1181
- Figure XVI.3.1 a) SEM image of NTO powder after heating to 60°C. Inset shows optical image of white powder, b) SEM image of NTO powder after dry ball milling with acetylene black. Inset shows optical image of powder, now colored black, c) 1<sup>st</sup> and 2<sup>nd</sup> cycles of sodium half cells containing NTO powder heated to 60°C, carbon-coated NTO, and carbon coated NTO with carbon nanotubes added, d) capacity as a function of cycle number for the three types of cells. . All the cells were cycled at 8 mA g<sup>-1</sup> using an electrolyte of 0.5 M sodium tetrphenylborate (NaBPh<sub>4</sub>) in diethylene glycol dimethyl ether (DEGDME). .... 1185
- Figure XVI.3.2 (a, b) capacity retention and (c) first-cycle Coulombic efficiency of sodium half-cells containing 500°C-heated NTO with and without 20 wt.% carbon additive and carbon-coated 500 °C-heated NTO without and with 20 wt.% carbon additives (d) rate capability of selected cells. All the cells were cycled at 8 mA g<sup>-1</sup> between 0.05 and 2.0 V. The capacity was normalized only based on the mass of 500 °C-heated NTO. All the cells were cycled at 8 mA g<sup>-1</sup> using an electrolyte of 0.5 M sodium tetrphenylborate (NaBPh<sub>4</sub>) in diethylene glycol dimethyl ether (DEGDME). .... 1186
- Figure XVI.3.3 (a, b) The cycling profiles of sodium vanadium phosphate (NVP)/500 °C-heated NTO full-cells cycled in 1 M sodium bis(trifluoromethanesulfonyl)imide (NaTFSI)-ethylene carbonate (EC)/diethyl carbonate (DEC) electrolyte. All the cells were cycled at a current rate of C/10 calculated based on NVP and capacity is normalized based on NVP. The N/P ratio is ~1.1 - 1.5. .... 1186
- Figure XVI.3.4 Synchrotron XRD patterns of NTO (bottom, in gold) and Mg<sub>0.37</sub>Ti<sub>1.815</sub>O<sub>4</sub> (top, in blue). An asterisk marks the swollen phase of the latter. This peak disappears after the material is dried. .... 1187
- Figure XVI.3.5 (left) Discharge/charge capacity retentions (discharge-open squares and triangles, charge closed symbols) and coulombic efficiencies (filled circles) of cells containing Mg<sub>0.37</sub>Ti<sub>1.815</sub>O<sub>4</sub> (in blue) and Na<sub>0.74</sub>Ti<sub>1.815</sub>O<sub>4</sub> (in gold) electrodes. (Middle and right) 2<sup>nd</sup> and 10<sup>th</sup> cycle dQ/dV plots of these cells. All the cells were cycled in 0.5 M NaPh<sub>4</sub>B/DEGDME electrolyte at a current rate of 8 mA g<sup>-1</sup>. .... 1187
- Figure XVI.3.6 (a, b) Ti K-edge spectra in the XANES region for Mg<sub>0.74</sub>Ti<sub>1.815</sub>O<sub>4</sub> electrodes at the end of the 1<sup>st</sup> discharge and charge, and an expanded view, (c) Ti L-edge spectra in the fluorescence yield (FY) mode, and (d) *ex-situ* synchrotron XRD patterns of Mg<sub>0.74</sub>Ti<sub>1.815</sub>O<sub>4</sub> electrodes at end of the 1<sup>st</sup> discharge and charge. .... 1188

Figure XVI.3.7 (left) Second cycles of two sodium half-cells containing NNT heated to either 500°C or 700°C in argon, showing slight differences, (middle) dQ/dV plot of the same data, and (right) expanded dQ/dV plot showing details. Both cells were cycled in 0.5 M NaPh<sub>4</sub>B/DEGDME electrolyte at a current rate of 10 mA g<sup>-1</sup>.

..... 1189

Figure XVI.4.1 Charge – discharge profile of PB cathodes in half-cell with sodium metal, 85 % active material loading capacity: 1.5 – 2.0 mAh/cm<sup>2</sup>; (a) baseline 1M NaClO<sub>4</sub>/EC-DMC (1:1 in vol) + 5 %wt. FEC; (b) NaFSI/DME/PEO (1/2/0.6 molar ratio) + 5 %wt. NaPF<sub>6</sub>; (c) 1.0 M NaPF<sub>6</sub>/TMP-FEC (3:7 in vol.); (d) 1.0 M NaPF<sub>6</sub>/DEGDME; (e) 1.0 M NaBF<sub>4</sub>/TEGDME; (f) 1.2 M NaPF<sub>6</sub> in TEGDME 5%wt. TTE; (g) Cycling performance of PB cathodes in different electrolytes. .... 1192

Figure XVI.4.2 Charge–discharge profile of PB cathodes in half-cell with sodium metal at different percentages of active mass: (a) 85 % active material, calendaring electrode; (b) 90 % active material, calendaring electrode; (c) 90 % active material, non-calendaring electrode, the electrolyte of 1.2 M NaPF<sub>6</sub> in TEGDME 5%wt. TTE; (g) Cycling performance of different PB cathodes, loading capacity: 1.5 – 2.0 mAh/cm<sup>2</sup>. .... 1193

Figure XVI.4.3 Flammability test and self-extinguish of different electrolytes. .... 1194

Figure XVI.4.4 Ionic conductivity of three electrolytes ..... 1194

Figure XVI.4.5 Redox stability of three electrolytes ..... 1195

Figure XVI.4.6 Cycling performance of C@Al||NVP cell at the voltage of 2.5 – 3.8 V using pristine NVP or pre-cycled NVP cathode in LPH03 electrolyte (condition: formation 1 cycle at C/10, 9 cycles at C/20 and long cycling at C/3)..... 1197

Figure XVI.4.7 Cycling performance of Cu||NVP cell at the voltage of 2.5 – 3.7 V with and without constant voltage step at 3.7 V in LCHE electrolyte (condition: formation 1 cycle at C/10, 9 cycles at C/20 and long cycling at C/3)..... 1197

Figure XVI.4.8 Cycling performance of C@Al||NVP cell at the voltage of 2.5 – 3.8 V using pristine NVP and electrolytes LPH03-LPH-05 (condition: formation 1 cycle at C/10, 9 cycles at C/20 and long cycling at C/3, resting time at 3.8 V in 10 minutes)..... 1198

Figure XVI.4.9 Cryo-PFIB-SEM of sodium morphology after an initial plating at 1.0 mA/cm<sup>2</sup> on different current collectors: Cu; C@Cu and C@Al (from left to right) at the magnification of 2 μm and 50 nm in ether-based electrolyte LPH-03 (NaPF<sub>6</sub> salt concentration >1 M). .... 1199

Figure XVI.4.10 In-situ TEM to observe the sodium growth on different current collectors: Cu, C@Cu, Al, C@Al at very low current and at 2.5 V. The apparition of sodium chunk can be seen by the orange dotted line at time different depending on the kind of substrates. .... 1200

Figure XVI.4.11 The growth rate of sodium represented by the time area curve with contact area normalization based the data of Figure XVII.4.10..... 1200

Figure XVI.4.12 Ex-situ TEM and energy dispersive spectroscopy (EDS) mapping of pre-cycled Na<sub>3</sub>V<sub>2</sub>(PO<sub>4</sub>)<sub>3</sub> (NVP) cathode in Na||NVP half-cell at C/5 and the NVP cathode in AFSBs C@Al||NVP after one cycle. .. 1201

Figure XVII.1.1 (a) SEM images of different commercial NMC 811 cathodes. (b) 1<sup>st</sup> cycles, (c) Cycling performances, and (d) Coulombic efficiencies of different commercial NMC 811 cathodes cycled between 2.8 ~ 4.4 V with the charge current of C/10 and discharge current of C/3 vs. Li metal anode tested inside coin cells with 50 uL LP30 electrolyte. (e) Heat evolved for three different NMC 811s (EcoPro vs. Targray vs. Targray + B) with the M47 electrolyte using the aluminum protected Hohsen coin cells during the charging to 4.8 V at 60 °C. .... 1206

Figure XVII.1.2 (a) Linear sweep voltammetry of Li|Al cells with LP57 electrolyte and LSE; the inset shows the components within the test cell. (b) Cycling performances of Li|LiNiO<sub>2</sub> cells at room temperature with the listed cycling parameters. (c) Charge curves at different C-rates after 400 cycles and (d) the corresponding capacity retention compared to the maximum charge capacity during the formation cycle. (e,f) HAADF-STEM

images of cycled  $\text{LiNiO}_2$  electrode with the (e) LP57 electrolyte and (f) LSE. Surface degraded phases are identified and labeled. The diamonds represent the different atomic arrangements in each material based on the intensity profiles for those areas. Anything not indicated with a diamond has the standard layered oxide structure of  $\text{Li}_{1-x}\text{NiO}_2$ . (g) Semi-quantitative densities of the various atomic arrangements found in each sample. (h,i) Cross-section SEM images of cycled  $\text{LiNiO}_2$  cathodes with the (h) LP57 electrolyte and the (i) LSE. Green arrows and red arrows are used, respectively, to highlight small cracks (smaller than the radius of the particle) and large cracks (larger than the radius of the particle) within each secondary particle. .... 1208

Figure XVII.1.3 (a) Electrochemical performance of the  $\text{Li}||\text{NMC811}$  full cell tested in different electrolytes; (b) Electrochemical performance of the  $\text{Li}||\text{NMC811}$  full cell in AFSE at high loading cathode; (c) Rate capacity of the  $\text{NMC811}||\text{Li}$  coin cells tested in different electrolytes; (d)  $\text{NMC811}||\text{Li}$  pouch cell. .... 1209

Figure XVII.1.4 Electrochemical Performance of 2.0 M LiFSI-D1 electrolyte. (a,b) Electrochemical window compared with 2.0 M LiFSI-DME electrolyte tested with  $\text{Al}||\text{Li}$  cell (a), and  $\text{Cu}||\text{Li}$  cell, the scan rate is 0.5 mV/s; (c,d) Li stripping and plating CE under full plating/stripping conditions (c) and with 5 mAh Li reservoir (d), the cycle current is  $0.5 \text{ mA cm}^{-2}$  and capacity loading is  $1 \text{ mAh cm}^{-2}$ ; (e,f) full cell  $\text{NCA}||\text{Li}$  performance with N/P ratio of 2, areal capacity of  $2.0 \text{ mAh cm}^{-2}$ . (g,h) 100 mAh homemade pouch cell performance with NCA areal loading of  $4.0 \text{ mAh cm}^{-2}$ . .... 1210

Figure XVII.1.5 SEM images of Li plating morphology on  $50 \mu\text{m}$  Li electrode at various current densities and areal capacities in DEE-FDEB electrolyte. The rSEI was formed by 10 cycles at either  $4 \text{ mA cm}^{-2}$  plating and stripping (high-current formation) or  $0.4 \text{ mA cm}^{-2}$  plating and  $4 \text{ mA cm}^{-2}$  stripping (low-current formation) for  $4 \text{ mAh cm}^{-2}$ . In the final step, 0.2, 0.5 or  $1 \text{ mAh cm}^{-2}$  capacity was plated at  $4 \text{ mA cm}^{-2}$  (high-current plating) or  $0.4 \text{ mA cm}^{-2}$  (low-current plating). The applied current profiles for rSEI formation and final Li plating are shown on the left. The capacities of final Li plating are labeled by columns on the top. Yellow and green arrows indicate Li and rSEI respectively. The scale bars are  $40 \mu\text{m}$ . The schematics on the right illustrate the top surface morphology of Li and rSEI. .... 1212

Figure XVII.1.6 Electrochemical performance of  $\text{Li}||\text{NMC811}$  cells with different LHCE electrolytes. (a) Li plating/stripping curves in  $\text{Li}||\text{Cu}$  cells, (b) LSV curves with scan rate  $0.05 \text{ mV s}^{-1}$  from OCV ( $\sim 2.9 \text{ V}$ ) to 5.0 V, (c) first cycle charge/discharge profiles at C/10, (d) cycling performance of the cells with charging at C/10 and discharging at C/3. Li metal ( $50 \mu\text{m}$  thick) on Cu foil and 75  $\mu\text{L}$  electrolyte were used for coin cells. ... 1213

Figure XVII.1.7 (a) Cycling performance of Co, Al and Nb modified 90% Ni NMC tested with the M47 electrolyte (PNNL) using the aluminum protected Hohsen coin cells in the voltage range of 2.8 to 4.4 V with C/10 charge and C/3 discharge current at  $30 \text{ }^\circ\text{C}$ . The charge and discharge curves of (b) Co, (c) Al and (d) Nb modified samples at cycle 10, 50, 100 and 150. .... 1214

Figure XVII.1.8 (a) Surface residual Li contents of pristine and aged (stored in ambient air for 1–3 months) LNO, NC, NM, and NA cathodes, showing the accumulation of residual Li species as a function of storage period and dopant. (b) Cycling performance of fresh and aged (3 months) LNO, NC, NM, and NA cathodes. The cells were cycled between 2.8 and 4.4 V at a C/3 rate for 100 cycles after three formation cycles at a C/10 rate. After 100 cycles, the cells were cycled for another two cycles at a C/10 rate for capacity check. (c) Rate performance test of the fresh and aged (3 months) LNO, NC, NM, and NA cathodes. The fresh cathodes are termed as LNO-F, NC-F, NM-F, NA-F, while the aged cathodes are termed as LNO-A, NC-A, NM-A, and NA-A. .... 1216

Figure XVII.1.9 (a) Electrochemical performances; (b) Voltage profiles of Lithium sulfur batteries with different electrolytes. .... 1217

Figure XVII.1.10 Electrochemical performance of  $\text{NMC811}||\text{Li}$  cells in M1 electrolyte. (a) Cycle performance of ( $4.5 \text{ mAh cm}^{-2}$ )  $\text{NMC811}||\text{Li}$  ( $20 \mu\text{m}$ ) cell in the voltage range of 2.8 V to 4.4 V at 0.3C, the voltage profile is shown on the right; (b) Cycle performance of ( $4.5 \text{ mAh cm}^{-2}$ )  $\text{NMC811}||\text{Li}$  ( $20 \mu\text{m}$ ) cell in the voltage range of 2.8 V to 4.7 V at 0.3C, the voltage profile is shown on the right. .... 1218

- Figure XVII.1.11 Stacked (a)<sup>1</sup>H and (b)<sup>19</sup>F NMR spectra of FDMB (in CDCl<sub>3</sub>) and its possible synthetic intermediates MFB (in CDCl<sub>3</sub>) and FB (in DMSO-d<sub>6</sub>). The spectra of FDMB have been zoomed in vertically for easy comparison with the other compounds..... 1219
- Figure XVII.1.12 Electrochemical performance of Li||S cells with Baseline and DMFN series of electrolytes. (a) Li plating/stripping curves in Li||Cu cells, (b) Ionic conductivity plots from -20°C to 60 °C, (c) Charge rate capability test of Li||S full cell tested in different electrolytes (d) First cycle charge/discharge voltage profiles at C/20 (1.8 – 2.8 V), cycling performance of full cell at (e) C/10 and (f) C/5 charge and discharge rates (1.7 – 2.8 V). Li metal (250 μm thick) and an E/S ratio of 8 μL/mg-S were used in the L||S full cells..... 1220
- Figure XVII.1.13 (a) Cycling performance of Co, Al and Nb modified 90% Ni NMC tested with the M47 electrolyte (PNNL) using the aluminum protected Hohen coin cells in the voltage range of 2.8 to 4.4 V with C/10 charge and C/3 discharge current at 45 °C. dQ/dV vs. V curves at cycle 10, 50, 100, 150 and 200 of (b) Co, (c) Al and (d) Nb modified 90% Ni NMC tested with the M47 electrolyte (PNNL) using the aluminum protected Hohen coin cells in the voltage range of 2.8 to 4.4 V with C/10 charge and C/3 discharge current at 45 °C. .... 1221
- Figure XVII.1.14 (a) Evolution of the DSC peaks with LNO, NC, NM, NA, and NMg cathodes as a function of SOC state. (b) 2D contour plots of the evolution of DSC peaks. (c) Evolution of the DSC peak temperature and heat release from the cathodes as a function of SOC state. Cathodes with different SOC states were obtained by charging the cathode to different capacities. .... 1222
- Figure XVII.1.15 SEM images of Li deposition on the (a and b) bare Cu foil and (c and d) polymer PN2 coated on Cu foil at a high current density of 6.0 mA cm<sup>-2</sup> and 25 °C. The time for deposition is 1 min, so the Li deposition amounts are 0.1 mAh cm<sup>-2</sup>. The electrolyte used in the Li-Cu cells: 1 M LiPF<sub>6</sub> in EC/DEC (wt% 1:1) + 15wt.% FEC + 1wt.% LiDFOB. .... 1223
- Figure XVII.1.16 The long cycle performance of 90 mAh Li||NMC811 pouch cell in LiFSI/M1 electrolytes. The 4 cm x 5 cm homemade pouch cell is fabricated and assembled in a glovebox with the NMC811 cathode areal loading of 4.5 mAh cm<sup>-2</sup> and lithium thickness of 20 μm. The electrolytes are controlled to 4 g Ah<sup>-1</sup>. The cell is cycled between 2.8V and 4.4V with the first formation cycle at 0.1C, then a long cycle at 0.3C for both charge and discharge. The carton on the left side shows the actual pouch cell. .... 1224
- Figure XVII.1.17 Top part: Chemical structures of fluorinated 1,2-diethoxyethane solvent molecules. a) Capacity and CE retention of F1F0, F1F1 and F1F2 electrolytes over cycling number. The data of F5DEE was adapted from previous results. The charge/discharge curves of b) F1F0, c) F1F1 and d) F1F2 at various cycles. .... 1225
- Figure XVII.1.18 (a), (b) Projected density of states (PDOS) of LHCEs with diluent of (a) TTE, (b) ND. (c), (d) Thickness of the 4 mAh cm<sup>-2</sup> Li deposited on Cu electrode using LHCEs with diluent of (c) TTE, (d) ND ..... 1226
- Figure XVII.1.19 (a) Molecular structures of the diluents. (b) C–O–C stretching modes of DME in the FT-IR of the solvents and electrolytes. (c) LSV of the electrolytes in Li || Carbon cells. (d) Voltage profiles of the Li || Cu cell employed for CE testing. Q<sub>T</sub> is the capacity of Li deposited as a Li reservoir. Q<sub>C</sub> is the capacity of Li plated and stripped during the cycling process. Q<sub>S</sub> is the capacity of Li that can be stripped after the cycling process. (e) Discharge specific capacities of Li || LNO cells. (f) EIS data of the Li || LNO cells after 200 cycles tested at 3.8 V. (g) Rate performances of Li || LNO cells. (h) Cycling performances of anode-free Cu || LNO cells. .... 1229
- Figure XVII.1.20 Long-term cycling performance of Li||NMC811 full cells with baseline (M47) and DB-based electrolytes..... 1230
- Figure XVII.1.21 Molecular design of F2DEM. .... 1231
- Figure XVII.1.22 (a) The CE measurements of the three electrolytes based on the modified Aurbach method. (b) Li||Cu CE of all three electrolytes. The cells were cycled at 0.5 mA cm<sup>-2</sup> for 1 mAh cm<sup>-2</sup> and stripped to 1 V at 0.5 mA cm<sup>-2</sup>. (c) Li||Cu CE over 250 cycles under a fast plating (1 mA cm<sup>-2</sup>) and slow stripping (0.4 mA cm<sup>-2</sup>)

- <sup>2</sup>) condition. (d) LSV in Li||Pt cells. The leakage currents of the three electrolytes were measured by sweeping up to 7 V at 1 mV s<sup>-1</sup>..... 1232
- Figure XVII.1.23 Performance of Cu||LFP pouch cell cycling between 2.5 V and 3.65 V. (a, b) C/2 charge and 2C discharge capacity (1C = 200 mA or 2 mA cm<sup>-2</sup>) and CE profile over 80 cycles. (c, d) C/2 charge and C/5 discharge capacity and CE profile over 150 cycles. (e, f) C/2 charge and C/2 discharge capacity and CE profile over 100 cycles. .... 1233
- Figure XVII.1.24 (a) The long cycle performance of the 10 mAh cm<sup>-2</sup> NMC811||Li (N/P = 1) coin cell in LiFSI/M1 electrolytes. The electrolytes are controlled to ~5 g Ah<sup>-1</sup>. The cell is cycled between 2.8V and 4.4V with the first formation cycle at 0.1C, then a long cycle at 0.3C for both charge and discharge. The areal capacity was shown on the right axis beside the specific capacity. (b) Selected charge/discharge voltage profiles at 1<sup>st</sup>, 5<sup>th</sup>, 100<sup>th</sup>, and 200<sup>th</sup> cycle. .... 1234
- Figure XVII.1.25 The Li||NCM811 full cell study of the representative electrolyte. (a). The full cell with medium loading cycling between 2.5 V and 4.7 V and the voltage profiles (d). The anode-free (b, e) and Li||NCM811 (c, f) full cell with practical cell configuration cycling between 2.5 and 4.5 V..... 1234
- Figure XVII.1.26 Electrochemical performance of Li||NCM811 coin cell in 1 M LiPF<sub>6</sub> in EC/DEC (v/v = 1:1) with 15 wt % FEC and 1 wt % LiDFOB, or the novel carbonate-based electrolyte, between 2.8 V to 4.4 V when charging at C/3 and discharging at C/3. A constant-current–constant-voltage protocol was used for cycling: the cell was charged to 4.4 V and then held at that voltage until the current dropped below C/20. 2 formation cycles at 0.1C for charge/discharge between 2.8 V to 4.4 V. 1 C = 4.3 mA/cm<sup>2</sup>. .... 1235
- Figure XVII.1.27 Electrochemical performance of Li||S cells with Baseline and DMFN series of electrolytes. (a) Li plating/stripping curves in Li||Cu cells. (b) Charge rate capability test of Li||S full cell tested in different electrolytes. (c) Discharge rate capability test of Li||S full cell tested in different electrolytes. (d) First cycle charge/discharge voltage profiles at C/20 (1.8 – 2.8 V). (e,f) Cycling performance of full cell at (e) C/10 and (f) C/5 charge and discharge rates (1.7 – 2.8 V). Li metal (250 μm thick) and an E/S ratio of 8 μL/mg-S were used in the L||S full cells. .... 1236
- Figure XVII.1.28 SEM-EDS of Li anodes in a) Baseline electrolyte and b) LS76. .... 1237
- Figure XVII.1.29 XPS of a) Li anodes and b) sulfur cathodes in the baseline and LS76 after 1<sup>st</sup> cycle. .... 1237
- Figure XVII.1.30 Electrochemical performance of modified LHCE compared to TTE-based LHCE in (a) Li||Cu half-cells and (b) Li||SPAN full-cells at lean electrolyte condition of 5 g (Ah)<sup>-1</sup>..... 1238
- Figure XVII.1.31 Post-mortem analysis performed on Li-SPAN full-cells following 50 cycles in TTE-based *versus* modified LHCE: (a) SEM images of Li anodes; (b) XPS results showing interphase chemistry on both Li anode and SPAN cathode; (c) Electrolyte consumption calculated from <sup>1</sup>H-NMR analysis. .... 1239
- Figure XVII.1.32 Data of LFP cathodes of various thicknesses show no significant impact of thickness on specific capacity, as was observed for high-Ni NMC cathodes..... 1240
- Figure XVII.1.33 High-capacity SPAN composite (CS SPAN). (a) battery curve and (b) cycling performance for CS SPAN composite with LDME electrolyte at 0.2C..... 1240
- Figure XVII.1.34 Morphology of deposited Li layer on different substrate. (a) SEM images of top-view Li crystalline seed deposited on the Fe/LiF substrate; (b) 1 mAh cm<sup>-2</sup> Li plated on the Fe/LiF nanocomposite and Cu substrate, under 0.5, 3, 5 mA cm<sup>-2</sup>. (c) Cryo-FIB-SEM images of 1 mAh cm<sup>-2</sup> Li deposited on the Fe/LiF nanocomposite and Cu substrate under 3 mA cm<sup>-2</sup>..... 1241
- Figure XVII.1.35 Potential energy profiles for Reaction 2 (Li<sub>2</sub>S<sub>2</sub> → Li<sub>2</sub>S + S\*) for the two different types of functional electrocatalysts considered. .... 1243
- Figure XVII.1.36 (a) Solvation structure, (b) free energy profile, (c) electronic Laplacian revealing the type of bonding, and (d) electron density isosurfaces. The key geometries obtained from AIMD frames revealed two types of pathways as shown in (b). The grey curve stands for the geometry-induced pathway which includes

charge variation throughout the reaction, and the blue one indicates the pathway where electron uptake happens prior to the S-S cleavage. This event series takes place when Li:S = 1:2.....	1244
Figure XVII.1.37 (a) The schematic of the processes involved in the methodology to quantify the standard sample of $\text{CH}_3\text{S}_3\text{CH}_3$ by ICP-MS, and (b) the longer chain polysulfides by combining semi-preparative HPLC-UV with ICP-MS .....	1245
Figure XVII.1.38 After 7 days resting period: Electrolyte collected in (a) baseline and (b) SS electrolyte; Cross-section images of Lithium in (c) baseline electrolyte and in (d) SS electrolyte; (e) $\text{Li}^+$ detected by ICP-MS in different electrolytes; (f) $\text{Li}^0$ detected in anode by TGC. Green dotted line indicates $\text{Li}^0$ amount in pristine foil.....	1246
Figure XVII.1.39 (a) the discharge/charge profiles for SPAN before and after post-thermal treatment at 0.2C ( $1\text{C}=600\text{ mAh g}_{\text{SPAN}}^{-1}$ ); (b) TGA-Mass Spectrometry (TGA-MS) results for mass traces at $m/z=34$ ( $\text{H}_2\text{S}$ ) and 64 ( $\text{S}_2$ ); (c) the proposed structural change for SPAN before and after post-thermal treatment.....	1247
Figure XVII.1.40 (a) CV profiles of NiMoP, MoP, $\text{Ni}_2\text{P}$ , and carbon symmetric cells at a scan rate of $0.1\text{ mV s}^{-1}$ . (b) Rate performance of $\text{Li}_2\text{S}$ mechanically mixed with NiMoP, MoP, $\text{Ni}_2\text{P}$ , and carbon at the rates ranging from C/10 to 1 C. (c) UV-vis spectra recorded after immersing NiMoP, MoP, $\text{Ni}_2\text{P}$ , and C in $\text{Li}_2\text{S}_6$ solution for 2 h. Inset: digital images for $\text{Li}_2\text{S}_6$ adsorption. (d) XRD patterns and (e) SEM image of the synthesized $\text{Li}_2\text{S} @ \text{Ni}_x\text{Mo}_y\text{P}_z @ \text{C}$ composite with a one-step carbothermal reduction. (f) Long-term cycling performance of anode-free Ni    $\text{Li}_2\text{S} @ \text{Ni}_x\text{Mo}_y\text{P}_z @ \text{C}$ and Ni    $\text{Li}_2\text{S} @ \text{C}$ cells.....	1248
Figure XVII.1.41 Potential energy profiles for Reaction 2 ( $\text{Li}_2\text{S}_2 \rightarrow \text{Li}_2\text{S} + \text{S}^*$ ) for various multicomponent functional electrocatalysts systems considered in this study .....	1250
Figure XVII.1.42 The discharge current at which the discharge capacity reached 70% of the discharge capacity at C/10 was identified (a), plotted vs cathode thickness (b), and fitted with a power law relationship. The determined exponent k is indicative of the limiting factor of the discharge capacity.....	1251
Figure XVII.1.43 Electrochemical performance of CS SPAN with/without conductive additives. Cycling performance of CS SPAN (a)without super-p; (b) with 3% super-p; charge/discharge curves for CS SPAN with/without carbon additive at (c) 25 <sup>th</sup> cycle; and (d) 250 <sup>th</sup> cycle. Electrolyte: 2M LiFSI in DME-BTTFE solvent, LDME. Rate C/5 ( $1\text{C} = 600\text{ mAh g}^{-1}$ , CCCV to 0.05C at 3.3V).....	1252
Figure XVII.1.44 (a) Symmetric cells cycled in an electrolyte with 0.2 M $\text{Li}_2\text{S}_6$ added. (b) Comparison of high-sulfur loading ( $4\text{ mg cm}^{-2}$ ) cycling performances of cells with and without the $\text{TiP}_2$ catalyst. (c) Galvanostatic charge-discharge voltage profiles over the 15th cycle for cells with and without $\text{TiP}_2$ catalyst. (d) Long-term cycling performances of cells with different catalysts integrated into $\text{Li}_2\text{S}$ cathodes: NiMoP (Blue), $\text{Ni}_2\text{P}$ (Green), MoP (Red). High-resolution XPS data of NiMoP particles before and after adsorbing $\text{Li}_2\text{S}_6$ : (e) Ni 2p and (f) Mo 3d. (g) SEM image of $\text{Li}_2\text{S}$ nucleation morphology on NiMoP, $\text{Ni}_2\text{P}$ , MoP, and C. (h) TEM image of $\text{Li}_2\text{S} @ \text{Ni}_x\text{Mo}_y\text{P}_z @ \text{C}$ . (i) Cycling performances of anode-free pouch cells at C/20 rate. ....	1253
Figure XVII.1.45 (Potential energy profiles for Reaction 2 ( $\text{Li}_2\text{S}_2 \rightarrow \text{Li}_2\text{S} + \text{S}^*$ ) for the various multicomponent functional electrocatalysts systems considered in this research study. ....	1254
Figure XVII.1.46 Plot of measured discharge capacity for various cathode thicknesses as a function of increasing C-Rate. Plot of the b) critical current density, and c) critical C-rate for each cathode thickness. .	1255
Figure XVII.1.47 CS SPAN with optimized additive. (a) Charge/discharge curves; (b) Cycling performance. Cathode: 90% CS SPAN, 2% super-p, 6% PAA, and 2% CNT. Active material areal loading is $> 3\text{ mg cm}^{-2}$ . Electrolyte: 2M LiFSI in DME-BTTFE solvent, LDME. Rate C/2 ( $1\text{C} = 600\text{ mAh g}^{-1}$ , CCCV to 0.05C at 3.3V) .....	1256
Figure XVII.1.48 XPS S 2p spectra for CS SPAN cathodes. (a) S 2p spectra of different cycles; (b) the charged CS SPAN depth-profile S 2p spectra, which results collected from the cathode/electrolyte and cathode/current collector interfaces. ....	1256

- Figure XVII.1.49 (a) Schematic of dry electrode fabrication procedure. Surface SEM images of the (b) dry-processed electrode and (c) slurry-processed electrode. Cross-sectional SEM images of (d) dry-processed electrode and (e) slurry-processed electrode. The sulfur loading is  $8 \text{ mg cm}^{-2}$ ..... 1258
- Figure XVII.1.50 (a) Cycling performances of slurry-processed and dry-processed electrodes. SEM images of (b) dry-processed and (c) slurry-processed electrodes after 10 cycles. The sulfur loading is  $8 \text{ mg cm}^{-2}$ . (d) Nyquist plots of dry-processed, slurry-processed & calendared, and slurry-processed electrodes. (e) Cycling performances of dry-processed and slurry-processed & calendared electrodes..... 1260
- Figure XVII.1.51 Potential energy profiles of  $\text{Li}_2\text{S}_2 \rightarrow \text{Li}_2\text{S} + \text{S}^*$  reaction for the various multicomponent functional electrocatalysts systems considered in this research study ..... 1261
- Figure XVII.1.52 Left: Snapshot from AIMD simulations illustrating interfacial effects of SPAN with electrolyte molecules. Center: Graphs show percent of sulfur fragments dissolved in the electrolyte phase during discharge for DMC (blue) and DME (orange) solutions. Right: Electron density map depict molecular interactions among SPAN, LiFSI and solvent molecules. Dotted lines indicate bond cleavage. At the bottom, the free energy evolution is shown during two simulations: one where charge transport drives reactivity (blue solid line), and another where the system reactivity follows molecular restructuring (dashed line). Color code for atoms: Li purple; O: red; S: yellow; N: blue; C; gray; H: white; F light blue..... 1262
- Figure XVII.1.53 Comparison of CE values of lithium half cells with one of four electrolyte (LHCE, LiTFSI, F4, or F5) and one of two current collector architectures (foil in fold or foam in purple). Bars indicate the average CE of 3 cells tested for each condition while the error bars mark the extreme values of the cells measured. No trend is observed in CE for either structure across electrolyte..... 1263
- Figure XVII.1.54 Electrochemical impedance spectra collected at four points of the cycling protocol for cells with a) copper foil substrate and LHCE electrolyte; b) copper foam substrate and LHCE electrolyte; c) copper foil substrate and LiTFSI electrolyte; and d) copper foam substrate and LiTFSI electrolyte. .... 1264
- Figure XVII.1.55 Electrochemical performance of a single cathode batch (loading:  $4.05 \text{ mgS/cm}^2$ ) calendared from 65% to 64, 62, and 60 %, with  $8 \mu\text{L/mg}$  electrolyte amount control. 1st cycle is cycled at 0.05 C rate, rest of the cycles, cycled at 0.1 C ..... 1265
- Figure XVII.1.56 Electrochemical performance of coin cell assembly with low and high pressure (loading:  $3.82 \text{ mgS/cm}^2$ ). Low and high pressure cells differ only by the use of a 0.5 mm spacer and a 1.0 mm spacer, respectively ..... 1266
- Figure XVII.1.57 Three pressure fixture designs used in pouch cells to apply external pressures. The electrochemical performances of Li-NMC811 SLPCs were studied based on the three pressure fixture designs. In Li-NMC811 SLPCs,  $50 \mu\text{m}$ -thickness Li metal foil, NMC811 electrode with the areal capacity of  $4.2 \text{ mAh/cm}^2$ , LiFSI-DME-TTE (molar ratio: 1:1.2:3) were used as the anode, cathode, and electrolyte, respectively. .... 1267
- Figure XVII.1.58 The cycling performances (a) and charge/discharge overpotentials over cycling (b) of the Li-NMC811 SLPCs based on three pressure fixture designs. .... 1268
- Figure XVII.1.59 The DSC curves of (a) Li-Gr, (b) Li-Si, (c) Li metal plated in Carbonate and (d) Li metal plated in LHCE. Graphite and Si anodes are lithiated to the desired capacity in half cell setup with the rate of C/20. Li metal is plated in Li||Cu coin cell to the desired capacity at a current density of  $0.5 \text{ mA/cm}^2$ . .... 1269
- Figure XVII.1.60 Electrochemical performance of Li-S coin cells with electrode formulations using different binders: (a,b) CMC, (c,d) CMC/SBR, and (e,f) PAA-co-acrylamide. Average areal loadings of corresponding electrodes are: 3.9, 3.5, and  $3.5 \text{ mg-S/cm}^2$ . The standard DOL/DME electrolyte at electrolyte-to-sulfur ratio (E/S ratio) of 8:1 ( $\mu\text{L/mg}$ ) was used. 1st and 2nd cycles are cycled at 0.05 C rate, rest of the cycles, cycled at 0.1 C..... 1271
- Figure XVII.1.61 Electrochemical performance Li-S SLP cell and ultrasonic mapping characterization at the EOL. Electrode areal loading is  $4.4 \text{ mg-S/cm}^2$ . The standard DOL/DME electrolyte at electrolyte-to-sulfur ratio (E/S ratio) of 8:1 ( $\mu\text{L/mg}$ ) was used. 1st and 2nd cycles were cycled at 0.05 C rate, rest of the cycles were



cycled at 0.1 C. In the ultrasonic mapping of the cell at the EOL in the lower right panel, the blue color area indicates the less electrolyte while red color indicates more electrolyte. .... 1272

Figure XVII.1.62 Electrochemical performance Li-S SLP cell and ultrasonic mapping characterization after 4 month shelf-life. Electrode areal loading is 4.8 mg-S/cm<sup>2</sup>. The standard DOL/DME electrolyte at electrolyte-to-sulfur ratio (E/S ratio) of 8:1 (μl/mg) was used. 1st and 2nd cycles were cycled at 0.05 C rate, rest of the cycles were cycled at 0.1 C..... 1273

Figure XVII.1.63 The morphologies of Li metal anode of Li-NMC811 single-layer pouch cell after fully charged under 10 psi in the three pressure fixture designs: “constant thickness,” “constant thickness + forms,” and “constant pressure.” ..... 1274

Figure XVII.1.64 *Ex-situ* synchrotron XRD mapping of NMC811 cathodes from Li-NMC811 single-layer pouch cells under 10 psi at BOL and EOL in the “constant thickness and “constant thickness + foams” designs ..... 1275

Figure XVII.1.65 Cycling performances of Li-S coin cells with electrode formulations using different binders: (a,b) CMC/SBR, and (c) PAA-co-acrylamide. Average areal loading of corresponding electrodes between 3.5-3.8 mg-S/cm<sup>2</sup>. The standard DOL/DME electrolyte at electrolyte-to-sulfur ratio (E/S ratio) of 8:1 (μl/mg) was used. All the cells were cycled at 0.05 C rate for the first two cycles and at 0.1 C for the rest of the cycles. 1276

Figure XVII.1.66 Voltage profile and cycling performances of Li-S coin cells with (a,b) *ex-situ* gel polymer electrolyte and CMC/SBR sulfur electrode formulation and (c,d) *in-situ* semi-solid electrolyte and PAA-co-acrylamide sulfur electrode formulation. The average areal loading of electrodes for (a,b) and (c,d) are 3.5 mg-S/cm<sup>2</sup> and 4.2 mg-S/cm<sup>2</sup>, respectively. The standard DOL/DME electrolyte at electrolyte-to-sulfur ratio (E/S ratio) of 8:1 (μl/mg) was used. All the cells were cycled at 0.05 C rate for the first two cycles and at 0.1 C for the rest of the cycles..... 1277

Figure XVII.1.67 SLPC baseline testing protocols and results of (a) Li-NMC811 and (b) Li-SPAN..... 1278

Figure XVII.1.68 Coin cell results for cathodes C01-C12 showing (a-d) specific discharge capacity versus cycle number and (e-h) median discharge voltage versus cycle number for the first 15 cycles. For every cell, there were two formation cycles at 0.05C charge and discharge followed by cycling at 0.1C for charge and discharge. Electrochemical results are divided four ways: (a,b,e,f) densely cathodes with a reduction in dry cathode thickness of 20%, (c,d-g,h) porous cathodes with a reduction in dry cathode thickness of 5%, (a, c, e, g) E/S = 10 μL mg<sup>-1</sup> S, and (b, d, f, h) E/S = 4 μL mg<sup>-1</sup> S. Hollow and solid markers were used to distinguish between cathode blocks more easily. .... 1280

Figure XVII.1.69 Voltage profiles and cycle life performance of Li-S coin cells with Li-PAA binder formulation Average areal loading of 3.5 mg-S/cm<sup>2</sup>. The standard DOL/DME electrolyte at electrolyte-to-sulfur ratio (E/S ratio) of 8:1 (μl/mg) was used. 1st and 2nd cycles are cycled at 0.05 C rate, rest of the cycles, cycled at 0.1 C ..... 1280

Figure XVII.1.70 Voltage profiles and cycle life performance of Li-S pouch cells (0.7 Ah) with electrode formulations using CMC/SBR. Average areal loading of electrodes is 3.5 mg-S/cm<sup>2</sup>. The standard DOL/DME electrolyte at electrolyte-to-sulfur ratio (E/S ratio) of 5:1 (μl/mg) was used. 1st and 2nd cycles are cycled at 0.05 C rate, rest of the cycles, cycled at 0.1 C. (a) cell 1, (b) cell 2, and (c) cell3. Pressure mapping of pouch cells 1 and 2 (e) and cell 3 (f) at the end of cycling. .... 1281

Figure XVII.1.71 Voltage profiles and cycle life performance of Li-S pouch cells (1 Ah) with electrode formulations using CMC/SBR. Average areal loading of electrodes is 3.6 mg-S/cm<sup>2</sup> (a and b) and 2.5 mg-S/cm<sup>2</sup> (c and d). The standard DOL/DME electrolyte at electrolyte-to-sulfur ratio (E/S ratio) of 5:1 (μl/mg) was used. 1st and 2nd cycles are cycled at 0.05 C rate, rest of the cycles, cycled at 0.1 C. .... 1282

Figure XVII.1.72 Performance of Li||NMC811 pouch cells experiencing different calendar aging condition including variations in SOC and temperature (a) OCV and 10 psi, (b) CV and 10 psi, and (c) pressure 50 vs 10 psi. Capacity fade is based on a C/3 discharge followed by C/10 charge during reference performance tests which occurred every 28 days..... 1282

- Figure XVII.1.73 High energy lateral XRD maps showing differences in cathode utilization for (a) Test 100-OCV-25-10, which was aged at open circuit, exhibiting expected homogeneity and from (b) Test 100-CV-25-10 exhibiting marked inhomogeneity due to aging while held at constant voltage. The increased inhomogeneity in Test 100-CV-25-10 is attributed to gas generation which blocks access to part of the electrode creating non-uniform utilization of the NMC. .... 1283
- Figure XVII.1.74 (a) Molecule structures of the solvents and additives used in the Stanford electrolytes. (b) Cycling data of coin cells using Stanford electrolytes in different voltage windows. The Battery500 coin cell test protocol is followed..... 1284
- Figure XVII.1.75 (a) The absolute amount of TM deposition quantified from X-ray fluorescence mapping. (b) The normalized amount (normalized by TM stoichiometry in NMC811) of TM deposition quantified from X-ray fluorescence mapping. .... 1285
- Figure XVII.1.76 Nanoscale Young's modulus measurement performed on SEI formed on Li metal in 1M LiPF<sub>6</sub> in EC:DEC (left) and in 1.2M LiFSI in DME:TTE electrolyte (right). .... 1286
- Figure XVII.1.77 AIMD simulation showing interfacial structural evolution for a Li metal surface covered with SEI formed with Li<sub>2</sub>O and LiOH, in contact with a 1:2 EC:DMC electrolyte. a) Initial structure, b) initial structure color coded showing Li<sub>2</sub>O and LiOH regions on the Li metal surface, c) final structure after ~11 ps (AIMD at 300 K) showing EC molecules reacting preferentially on the Li<sub>2</sub>O surface, and d) close-up of structure shown in c. The red arrow highlights reduced EC molecules and the green arrow shows the motion of the Li metal atoms towards the SEI surface..... 1287
- Figure XVII.1.78 (a) Voltage profiles obtained from a GITT experiment using an EcoPro NMC 811 cathode by the Univ. Binghamton team (Cell ID: E-C #3\_4.4) and the pseudo-OCV profile obtained from a RPT 0 test using a Targray NMC 811 cathode by INL (Cell ID: T-C\_4.4). (b) Voltage profiles presented in normalized capacity as SOC..... 1288
- Figure XVII.1.79 (a) Coulombic efficiency and capacity retention of NMC811||Li cells using Stanford F5DEE electrolyte. (b) Synchrotron XRD data of SEI samples from different cycles. The wavelength used is 0.1818 Å. (c) The zoomed in regions in (b)..... 1289
- Figure XVII.1.80 a) PDF data of SEI samples from various cycles. The reference data at the bottom are calculated from model compounds. (b) Selected zoomed-in regions in (a). The reference data at the bottom are measured. .... 1290
- Figure XVII.1.81 (a) The XRD patterns of SEI samples collected from both charged and discharge states. The top panel is for the 100<sup>th</sup> cycle and the bottom for the 30<sup>th</sup> cycle. (b) Sulfur K-edge X-ray absorption spectroscopy of SEI samples at charged and discharged states (both from 30<sup>th</sup> cycle). (c) Schematic illustration of the SEI reduction and dissolution process during charge-discharge. .... 1291
- Figure XVII.1.82 Comparison of indentation deformation curves via atomic force microscope for SEI on lithium metal for LP40 baseline electrolyte and LHCE electrolyte ..... 1291
- Figure XVII.1.83 The DSC curves of (a) Li-Gr, (d) Li-Si, (g) Li plated in LHCE, and (j) Li plated in Carbonate after 10 cycles. The SEM images of anode morphology after 1 cycle and after 10 cycles: (b-c) graphite, (e-f) Si, (h-i) Li plated in LHCE, and (k-l) Li plated in Carbonated electrolyte. Inserts: the digital images of Li plated on the Cu after 10 cycles. The amount of heat released from the oxidation peak of each DSC curve is labeled in the corresponding figures. Graphite and Si anodes are cycled in half-cell configuration at a rate of C/20, and Li metal anodes are cycled in Li||Cu cells at a rate of 0.5mA/cm<sup>2</sup>..... 1293
- Figure XVII.1.84 (a) SEI computed for LP30 electrolyte. It is an amorphous structure composed by nuclei of Li<sub>x</sub>O, Li<sub>x</sub>F, and hybrid structures as Li<sub>x</sub>O-CH<sub>3</sub>. Organic fragments are attached to the inorganic nuclei surface. (b) SEI thermal decomposition induced by a temperature ramp of 30 K/ps (blue line). At each temperature, the free energy F of the sample is evaluated (red curve). The first minimum in F corresponds to the thermal decomposition at about 400K of the organic fragments located in the open spaces of the porous SEI. The second minimum in F (~550 K) reveals decomposition of the organic fragments on the surface of the inorganic

nuclei. At higher temperatures other minima reveal melting of the surface inorganic nanoparticles, and the overall system becomes highly unstable.....	1294
Figure XVII.1.85 The schematic of the semi-preparative HPLC-UV chromatograms of five different concentrations of derivatized polysulfide mixtures .....	1295
Figure XVII.1.86 (a) Quantification of Lithium after, when no electrochemical operation is performed (b) Lithium inventory after resting .....	1296
Figure XVII.1.87 Lithium metal morphology after resting in moderately (a, b, c, d) and Weakly solvating electrolyte (e, f, g, h). Here, images are from fresh lithium (a, e), 24 hours rest (b, f), 7 days rest (c, g); and 30 days (d, h) .....	1296
Figure XVII.1.88 Li <sup>+</sup> -coordinated polysulfide-solvent interactions have strong dependence on solvation environments. Left: Free energy of Li <sub>2</sub> S <sub>x</sub> interaction with DMC, DOL, and DME. Right: Electronic Laplacian isosurfaces (iso-value = 0.09) of the corresponding structures (only showing x = 3 cases) illustrate the solvent effect on the type of bonding .....	1297
Figure XVII.1.89 Electrochemical cycling results of (a) Li  Cu and (b) NMC  Cu cells. XRD Rietveld refinement results of SEI collected on Cu foil of (c) Li  Cu and (d) NMC  Cu cells after 50 cycles. ....	1298
Figure XVII.1.90 (a-b) Schematic pictures of the SEI compositions and structures based on XRD results. (c) F1s XPS spectra on the surface of Li metal anodes after three cycles of cyclic voltammetry using Li  NMC811 and Li  Carbon cells in the voltage range of 2.8-4.2 V. (d) F1s spectra of the cycled NMC811 in Li  NMC811 cycles. ....	1299
Figure XVII.1.91 Comparison of the amount of Ni- present in the SEIs of the anodes cycled in LP57 and LSE. (a) Absolute intensities versus sputtering depth (nm) for the Ni- secondary ion fragments. (b) 3-D rendered volumes displaying the distribution of Ni- throughout the bulk of the SEI. The color of the pixels in the 3-D renders correspond to the intensity that is denoted with the color bar. Data were collected on lithium-metal anodes obtained from Li   LiNi <sub>0.7</sub> Mn <sub>0.25</sub> Al <sub>0.05</sub> O <sub>2</sub> cells cycled for 500 cycles at 2.8 – 4.6 V vs. Li/Li <sup>+</sup> .....	1300
Figure XVII.1.92 Nanomechanical properties of SEI on lithium metal formed on several electrolytes. ....	1301
Figure XVII.1.93 (a) $\mu$ -XRF maps corresponding to Ni, Co, and Mn at the first electrode cycled 600 times at 4.15 V. (b) $\mu$ -XRF maps corresponding to Ni, Co, and Mn at the second electrode cycled 600 times at 4.1 V with the 100 $\mu$ m focusing optics.....	1302
Figure XVII.1.94 Electrochemical cycling performance of Li metal batteries in baseline electrolyte and with CsNO <sub>3</sub> additive. (a) Coulombic efficiency measurement in a Li  Cu cell. (b) Cycling stability of Li metal cell with NMC811 cathode and Li metal anode with baseline electrolyte and electrolyte containing 3 wt% CsNO <sub>3</sub> additive. NMC811 loading is 9 mg/cm <sup>2</sup> and Li metal anode used is 250 $\mu$ m thick. Cycling is performed at C/2 rate. (c) Ionic conductivity of baseline electrolyte, CsNO <sub>3</sub> -containing electrolyte and commercial electrolyte using 1M LiPF <sub>6</sub> in EC/EMC (volume ratio 3:7). (d) Cycling stability of Li metal cell using NMC811 cathode with 21 mg/cm <sup>2</sup> loading and 50 $\mu$ m thick Li metal anode in the electrolyte containing 3 wt% CsNO <sub>3</sub> additive. The cells go through two formation cycles at a rate of C/10 and five cycles at C/5 rate before being cycled at 1C rate and 2C for later cycles. (e) Selected charge-discharge profiles of Li  NMC811 cell cycled at under conditions specified in (d) using CsNO <sub>3</sub> -containing electrolyte.....	1304
Figure XVII.1.95 Crystalline and amorphous components in lithium metal anode interphase. (a) Crystalline components of the anode interphase revealed by synchrotron XRD and Rietveld refinement. The red is the fit and the blue is the XRD pattern for individual phases calculated from Rietveld refinement. (b) Amorphous components of the anode interphase revealed by PDF studies. The scattered plot is the measured PDF data, and the red is the PDF pattern calculated from the possible individual components of the SEI. SEI species were characterized after 50 cycles in the baseline electrolyte and after 200 cycles in the electrolyte containing the CsNO <sub>3</sub> additive. The cycling was performed at C/2 rate. The color code for the atoms is the same in all subfigures: red: oxygen; blue: nitrogen; cyan: fluorine; brown: carbon; white: hydrogen; gold: lithium; dark yellow: cesium, light yellow: sulfur.....	1306

- Figure XVII.1.96 Spatial distributions of Ni<sup>-</sup> to other electrolyte decomposition fragments detected in the anode SEI formed in LP57 and relative quantifications of the various secondary-ion fragments detected within the SEI of cycled lithium-metal anodes. (a) A series of X-Y views at various sputtering depths of the sputtered volume in the depth profiles of the Ni<sup>-</sup>, PO<sub>2</sub><sup>-</sup>, C<sub>2</sub>HO<sup>-</sup>, and LiF<sub>2</sub><sup>-</sup> secondary ion fragments from the SEI formed with LP57. (b) Total yield maps of the Ni<sup>-</sup> to Li<sub>2</sub><sup>-</sup> secondary-ion fragments from the SEI formed with LP57. (c) Absolute secondary-ion yields versus sputtering depth (nm) for the Ni<sup>-</sup> secondary ion fragment measured for LP57 and HVE. (d) Net integrated yields for all fragments of interest that were integrated between the crossing depths at 0.6 of its maximum from the SI yield profile for LP57 and HVE. The analyzed volume for LP57 corresponds to a 100 μm x 100 μm analysis area by 650 nm in depth. The analyzed volume for HVE corresponds to a 100 μm x 100 μm analysis area by 300 nm in depth. The color of the pixels in the TOF-SIMS renders correspond to yields that are denoted with the color bar. Data were collected on lithium-metal anodes from NMA-70 half-cells with LP57 (Figures 1a-d) or HVE (Figures 1c,d) electrolyte that were cycled for 500 cycles at a voltage window of 2.8 – 4.6 V vs Li/Li<sup>+</sup> ..... 1308
- Figure XVII.1.97 Square deviation matrices presenting the net squared deviations between two secondary-ion fragment maps (F<sub>1</sub> and F<sub>2</sub>) for (a) LP57 and (b) HVE. The boxes are color-coded based on the magnitude of the net squared deviation. Larger values (yellow) indicate a lower similarity between the spatial distributions of two secondary-ion fragments. Data were collected on lithium-metal anodes from NMA-70 half-cells with LP57 or HVE electrolyte that were cycled for 500 cycles at a voltage window of 2.8 – 4.6 V vs Li/Li<sup>+</sup> ..... 1309
- Figure XVII.1.98 Computational setting for the analysis and evaluation of electrical conductance in the SEI. (a) Simulation cell with different E/A ratio. (b) Final states of the SEI formed by reaction between electrolyte and Li metal with different E/A ratio and simulation time via AIMD and ReaxFF method. (c) Schematic of I–V curve calculation set-up of simulated SEI via ab initio DFT with a Green’s function approach. ε, voltage ..... 1310
- Figure XVII.1.99 Illustration of reactions over Li metal during cycling as captured by the kMC approach. 1311
- Figure XVII.1.100 TXM images above Ni K-edge (8350 eV) of the LiNiO<sub>2</sub> cathodes at (a) pristine state, (b) 73% SOC, and (c) 87% SOC. The blue arrows point to some cracks in the LiNiO<sub>2</sub> particles. .... 1311
- Figure XVII.1.101 Variation of the energy edge position map for the LiNiO<sub>2</sub> cathode in (a) its pristine state, (b) at 73% SOC, and (c) at 87% SOC. (d) Shows the summed XANES spectra corresponding to (a), (b) and (c). .... 1312
- Figure XVII.1.102 (a) Schematic of *in-situ* cell use for AFM experiments with labeled parts. (b) SEM images of lithium metal deposited on a copper substrate under same conditions as used in AFM experiments (c) *In-situ* tapping mode images of lithium metal deposited in coin cells and transferred to *in-situ* cell (d). Higher resolution tapping mode images showing the SEI morphology and associated roughness measurements..... 1314
- Figure XVII.1.103 Example force vs. time and indentation vs. time curves, including the hold segment (a). The same force curves plotted as a traditional force-indentation force curve (b). 2D image of modulus measurements of representative 2 x 2 μm sample regions (c). Histograms of all modulus measurements on a log scale, with associated geometric mean (d). .... 1316
- Figure XVII.1.104 (a) Charge discharge curves of first (Red) and second (Blue) cycle and points a, b, and c at which the cells were stopped and (b) HPLC-UV data of derivatized polysulfide solution after 1<sup>st</sup> discharge (Red), 1<sup>st</sup> charge (Blue) and two formation cycles (Green). .... 1317
- Figure XVII.1.105 HPLC-UV data of derivatized polysulfide solution after 1<sup>st</sup> discharge in SPAN (Blue) and DME solvent background (Red) ..... 1318
- Figure XVII.1.106 Potential Li-S Batteries' SEI components (a) LiOH (b) Li<sub>2</sub>CO<sub>3</sub> (c) LiF (d) Li<sub>2</sub>S (e) Li<sub>2</sub>SO<sub>4</sub> (f) Li<sub>2</sub>O. before filtering (left) and after filtering (right). .... 1320

## List of Tables

Table 1: Subset of Requirements for Advanced High-Performance EV Batteries and Cells (Cost and Low Temperature Performance are Critical Requirements) .....	3
Table I.4.1 Comparison of Our Technology to Current Slurry Casting Technology.....	39
Table I.4.2 The Parameters of the 4 Batches of Cathode and Anode to Optimize the Design for the Final Deliverable.....	45
Table I.4.3 Average Porosity and Tortuosity of the High-loading Dry Printed and MV Slurry Cast Electrodes. ....	48
Table I.5.1 A Comparison in First Cycle Efficiency, C/20 and C/3 Capacities, DCR and Discharge Rate Performance among DLP Cells with Pure C5 Cathodes Filled with Two Different Electrolytes .....	56
Table I.5.2 A Comparison in C/20 and C/3 Capacities, DCR and Discharge Rate Performance among DLP Cells with Different Cathodes Filled with E5 Electrolytes .....	58
Table I.5.3 A Comparison in First Cycle Efficiency, C/20 and C/3 Capacities, DCR, Discharge Rate Performance and Fast Charge Capability among DLP Cells with C5C2-Blend 1 Cathodes Filled with Different Electrolytes .....	59
Table I.6.1 Budget Period 1 and 2 Summary and Status Updates of Key Performance Deliverables. ....	63
Table I.6.2 Proposed Milestones and Current Status Updates .....	64
Table I.6.3 Cells Level Attributes and their Details for the 2 Ah Cell Build.....	67
Table I.6.4 Comparison of Different pre-Li Samples vs. Baseline. ....	69
Table I.6.5 2 Ah Cell Attributes for Farasis Cell Builds.....	69
Table I.8.1 Summary of Electrolytes and their Impact on Calendar Life and Cycle Life.....	80
Table I.8.2 List of cathode active materials and their properties. ....	81
Table I.9.1 USABC Targets for the 24M Project .....	87
Table I.10.1 End of Program Cell Performance Objectives.....	92
Table I.10.2 Baseline Cell Technology Gap Analysis Table .....	95
Table I.11.1 Average Li Coulombic Efficiency at C/3 in Li Cu Coin Cells with Different Electrolyte (E1 vs. E3).....	102
Table I.12.1 The SBC Results for 072523-PCAM081222-D-0.1Zr-C-Al and 6kg Recycled NMC622 Cathode Powder. ....	110
Table I.12.2 The SBC Results for 071523-PCAM4-5%-D-Sr/Mg/Zr-W(1:2, 300, 30)-C-B (450.7).....	114
Table I.12.3 The ICP-OES Results for Impurities in the Recovered Lithium Carbonate.....	116
Table II.4.1 Protecting Group Summary.....	143
Table II.11.1 Li Deposition System Manufacturing Target Performance.....	194
Table II.11.2 Cell Performance Data Summary for Pre-lithiated Anodes. ....	194
Table II.11.3 Cell Performance Data Summary for Lithium Metal Anodes.....	195
Table II.11.4 Proposed Milestones and Corresponding Status Updates. ....	197
Table II.11.5 BP3 Final Deliverable Task: Detailed Cell Information of Samples Shipped to INL from SAFT America for Testing and Characterization. ....	200

Table II.11.6 Progress Summary (Idaho National Laboratory): Gap chart for the Applied Materials/Ionblox pre-Li SiO <sub>x</sub> interim cells. ....	202
Table II.13.1 LLZO-PEO Ink Mixing Conditions. ....	213
Table II.13.2 <b>Ionic Conductivity of the LLZO-PVDF-LiTFSI Composite SE Films.</b> .....	217
Table II.14.1 Synthesis Data for Coating Particle Candidate Set1. ....	220
Table II.15.1 Summary of Performance Metrics for LMR Coated Cells.....	230
Table II.15.2 Summary of Performance Metrics for LMR coated cells. ....	231
Table III.1.1 Major Clay-based Li-reserves in North America (U.S.).....	238
Table III.1.2 Major Brine-based Li-reserves in North America (U.S.).....	239
Table III.2.1 Breakthrough Scoring Criteria.....	248
Table III.3.1 Summary of Delamination of Small Batched of Anode Shreds by HFIH .....	260
Table III.3.2 Rietveld Refinement Data of the Prepared NCM622 Cathodes.....	268
Table III.3.3 Metal Content in the Stripped Solution Using 0.5 M [H <sub>2</sub> SO <sub>4</sub> ]. ....	294
Table III.3.4 Joining Type Rating Table.....	308
Table IV.2.1 Single-layer Pouch Cell Deliverables Fabricated at the CAMP Facility in FY23.....	346
Table V.2.1 Status of Cell Testing Deliverables in FY2023.....	370
Table V.4.1 CAMP Cells to be Used for Thermal Characterization—Cathode Material was Supplied by Toda and Anode material was Supplied by Superior Graphite .....	377
Table V.4.2 Percentage of Capacity Remaining After Aging the CAMP Cells for EOL Thermal Characterization—Cathode Material was Supplied by Toda and Anode Material was Supplied by Superior Graphite. ....	378
Table V.5.1 Summary of Electrode Library Distributions.....	387
Table V.7.1 Articles Tested for USABC .....	398
Table V.7.2 Articles Tested for Benchmark .....	398
Table V.7.3 Articles Tested for Low Cobalt.....	399
Table VII.2.1 Intensity Ratios of I(003)/I(104) from NMC622 Cathode Tested in E-baseline Electrolyte. ....	422
Table VII.2.2 Intensity Ratios of I(003)/I(104) from NMC622 Cathode Tested in E-10 Electrolyte.....	423
Table VII.2.3 Preparation Parameter of Single Layer Pouch Cells and their Testing Procedures.....	424
Table VII.2.4 Discharge Capacities during Calendar Life Test at Various Temperatures.....	426
Table VII.4.1 Electrochemical Objectives for DoE Project – EE0009187.....	449
Table VII.5.1 Cell Performance Targets.....	453
Table VII.6.1 Capacity and Cycle Life of the Si Anodes .....	457
Table VII.8.1 Summary of Program Objectives .....	471
Table VIII.1.1 Heat Generated during Temperature Ramping between 120°C to 350°C.....	538
Table VIII.1.2 Table Showing the Changes in Mean Porosity, Particle Diameter, and Particle Volume for LNO Electrodes Sintered under 20%, 60%, and 100% Oxygen. ....	542
Table VIII.2.1 Electrolyte Formulations for ED01-ED04. ....	563

Table VIII.3.1 Key Parameters from the Full Coin Cell Protocol .....	592
Table VIII.3.2 The Unit Cell Parameters and Normalized Stabilization Energies (Relative to the <i>R3m</i> Cell).597	
Table IX.4.1 Summary of Impedances Related to Kinetic and Transport Overpotentials at the Interface Measured using METS and EIS for the Cell Pre-SEI Growth.....	643
Table IX.4.2 Summary of Impedances Related to Kinetic and Transport Overpotentials at the Interface Measured using METS and EIS for the Cell Post-SEI Growth. ....	643
Table XI.1.1 Solvent Compositions(ACN:EC:EMC wt ratio) that were tested for low temperature performance .....	689
Table XI.4.1 Summary Of Electrodes Tested By Argonne. ....	717
Table XI.6.1 Electrode Roll Loading Information for Pouch Cell Design. ....	738
Table XI.6.2 Discharge Capacity Values at Specified Discharge Rates, Temperatures, and Upper Cutoff Voltage Conditions. ....	741
Table XI.6.3 Discharge Capacity, Reversibility, and Retention Values of Cells at Specified Discharge Rates and Upper Cutoff Voltage Conditions. ....	743
Table XI.6.4 Data Associated with Two Figures for AA002  AC019 Full Cells Various Electrolytes: 1st-Cycle Coulombic Efficiency (1st CE), 1st-cycle Discharge Capacity (1st DC), Capacity Retention after 500 Cycles (CR-500), Average 500-Cycle Discharge Capacity (AC-500) and Average CE of 500 Cycles (ACE). ....	750
Table XI.6.5 Data Associated with Two Earlier Figures for AA002  AC019 Full Cells Various Electrolytes: 1st-cycle Coulombic efficiency (1st CE), 1st-cycle Discharge Capacity (1st DC), Capacity Retention after 500 Cycles (CR-500), Average 500-Cycle Discharge Capacity (AC-500) and Average CE of 500 Cycles (ACE). ....	752
Table XIII.4.1 Densities and Porosities of Cold-pressed and Hot-pressed NCM Cathode Composites. ....	821
Table XIII.4.2 Summary of Electrochemical Characterization of Cells with Cathode Composites Composed of Low Voltage Active Material (AM) and Highly Processable LPSO Glassy SSE. ....	822
Table XIII.12.1 Ionic Conductivity of LYB Tapes with Binders, Cast from Toluene Slurries. ....	880
Table XIII.16.1 Summary of Relevant Performance Metrics for Full Cells Assembled Using Coated and Uncoated LPSCI. ....	910
Table XIII.16.2 The Three Most Stable LPSCI    Oxide Interfaces, with the Lowest Driving Forces for Interface Reactions. ....	912
Table XIII.16.3 Reaction Thermodynamics at Li    Oxide Interfaces, with a Specific Focus on Oxide Chemistries in an Adjacent Table. ....	913
Table XIII.16.4 Reaction Thermodynamics at LiCoO <sub>2</sub>    Oxide Interfaces, with a Specific Focus on Oxide Chemistries in a Previous Table. ....	913
Table XIII.19.1 Comparison between Gen2 and Gen1 3D Composite Electrolytes.....	940
Table XIII.21.1 Acidic Washing Impact on LLZO (All Acid Concentrations are 0.1 M).....	958
Table XIII.21.2 Basic Washing Solution Impact on LLZO. ....	959
Table XIV.3.1 Nitrogen Content and Porosity of Different Samples. ....	1046
Table XIV.4.1 Compositions of the Prepared Electrolyte Solutions. ....	1054
Table XIV.6.1 Calculated Free Energies of Solvation in DME Solvent (Values Given in kcal/mol) .....	1093
Table XIV.6.2 Calculated Free Energies of Solvation in DOL Solvent (Values Given in kcal/mol).....	1093
Table XIV.6.3 Calculated Free Energies of Solvation in DME Solvent (Values Given in kcal/mol) .....	1094

Table XIV.6.4 Calculated Free Energies of Solvation in DOL Solvent (Values Given in kcal/mol).....	1094
Table XIV.9.1 Flash Points of the Most Widely Used LIB Electrolytes [4] and PFG Electrolyte for Li-S Batteries. ....	1112
Table XIV.10.1 List of Fluorinated Solvents and Li Salts Used in the Electrolyte Formulations. ....	1123
Table XVI.4.1 Reversibility of Sodium Stripping/plating Process Evaluated Through CE Values In Varying The Current Collector And Electrolyte Composition. ....	1196
Table XVII.1.1 The Highest Occupied Molecular Orbital (HOMO) and the Lowest Unoccupied Molecular Orbital (LUMO) Energy for the Diluents. ....	1226
Table XVII.1.2 Combination of Conductive Additives and Binders Examined to Develop Gen 1 Modified Sulfur Cathodes.....	1270
Table XVII.1.3 The Highest Occupied Molecular Orbital (HOMO) and the Lowest Unoccupied Molecular Orbital (LUMO) Energy for the Diluents. ....	1319



## Vehicle Technologies Office Overview

Vehicles move our national economy. Each year in the United States, vehicles transport 18 billion tons of freight—about \$55 billion worth of goods each day<sup>4</sup>—and move people more than 3 trillion vehicle-miles.<sup>5</sup> Growing our economy requires transportation, and transportation requires energy. The transportation sector accounts for approximately 27% of total U.S. energy needs<sup>6</sup> and the average U.S. household spends over 15% of its total family expenditures on transportation,<sup>7</sup> making it, as a percentage of spending, the most costly personal expenditure after housing. Transportation is critical to the overall economy, from the movement of goods to providing access to jobs, education, and healthcare.

The transportation sector has historically relied heavily on petroleum, which supports over 90% of the sector's energy needs today,<sup>8</sup> and, as a result, surpassed electricity generation to become the largest source of CO<sub>2</sub> emissions in the country.<sup>9</sup> The Vehicle Technologies Office (VTO) will play a leading role in decarbonizing the transportation sector and address the climate crisis by driving innovation and deploying clean transportation technologies, all while maintaining transportation service quality and safety.

VTO funds research, development, demonstration, and deployment (RDD&D) of new, efficient, and clean mobility options that are affordable for all Americans. VTO leverages the unique capabilities and world-class expertise of the National Laboratory system to develop new innovations in vehicle technologies, including: advanced battery technologies; advanced materials for lighter-weight vehicle structures and better powertrains; energy-efficient mobility technologies (including automated and connected vehicles as well as innovations in efficiency-enhancing connected infrastructure); innovative powertrains to reduce greenhouse gas (GHG) and criteria emissions from hard to decarbonize off-road, maritime, rail, and aviation sectors; and technology integration that helps demonstrate and deploy new technology at the community level. Across these technology areas and in partnership with industry, VTO has established aggressive technology targets to focus RDD&D efforts and ensure there are pathways for technology transfer of federally supported innovations into commercial applications.

VTO is uniquely positioned to accelerate sustainable transportation technologies due to strategic public-private research partnerships with industry (e.g., U.S. DRIVE, 21<sup>st</sup> Century Truck Partnership) that leverage relevant expertise. These partnerships prevent duplication of effort, focus DOE research on critical RDD&D barriers, and accelerate progress. Working closely and in collaboration with the Office of Energy Efficiency and Renewable Energy's Bioenergy Technologies and Hydrogen and Fuel Cell Technologies Offices, VTO advances technologies that assure affordable, reliable mobility solutions for people and goods across all economic and social groups; enable and support competitiveness for industry and the economy/workforce; and address local air quality and use of water, land, and domestic resources.

## Annual Progress Report

As shown in the organization chart (below), VTO is organized by technology area: Batteries R&D; Electrification R&D; Materials Technology R&D; Decarbonization of Off-Road, Rail, Marine, and Aviation; Energy Efficient Mobility Systems; Technology Integration; and Analysis. Each year, VTO's technology areas prepare an Annual Progress Report (APR) that details progress and accomplishments during the fiscal year. VTO is pleased to submit this APR for Fiscal Year (FY) 2023. The APR presents descriptions of each active project in FY 2023, including funding, objectives, approach, results, and conclusions.

---

<sup>4</sup> Bureau of Transportation Statistics, DOT, Transportation Statistics Annual Report 2020, Table 4-1, <https://www.bts.gov/tsar>.

<sup>5</sup> Davis, Stacy C, and Robert G Boundy. Transportation Energy Data Book: Edition 40. Oak Ridge, TN: Oak Ridge National Laboratory 2022. <https://doi.org/10.2172/1878695>. . Table 3.09 Shares of Highway Vehicle-Miles Traveled by Vehicle Type, 1970-2019.

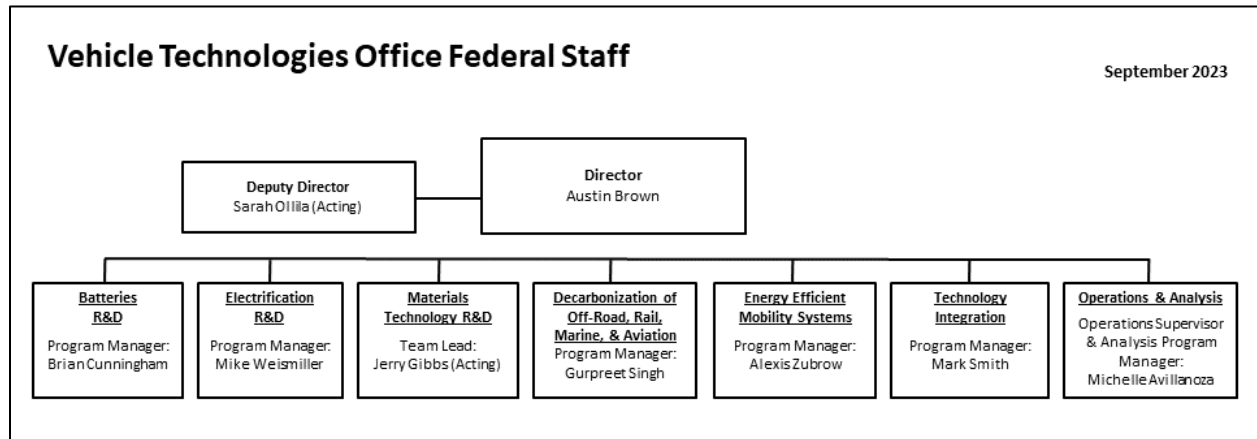
<sup>6</sup> [Ibid. Table 2.02 U.S. Consumption of Total Energy by End-use Sector, 1950-2021.](#)

<sup>7</sup> [Ibid. Table 11.1 Average Annual Expenditures of Households by Income, 2020.](#)

<sup>8</sup> [Ibid. Table 2.03 Distribution of Energy Consumption by Source and Sector, 1973 and 2021.](#)

<sup>9</sup> Environmental Protection Agency, Draft U.S. Inventory of Greenhouse Gas Emissions and Sinks, 1990-2019, Table 2-11. Electric Power-Related Greenhouse Gas Emissions and Table 2-13. Transportation-Related Greenhouse Gas Emissions.

## Organization Chart



# Batteries Program Overview

## Introduction

During the fiscal year 2023 (FY 2023), the Vehicle Technologies Office (VTO) battery program continued research and development (R&D) support of battery technologies for plug-in electric vehicles (PEVs), e.g., plug-in hybrids, extended range electric vehicles, and all-electric vehicles. One objective of this support is to enable U.S. innovators to rapidly develop next generation of technologies that achieve the cost, range, and charging infrastructure necessary for the widespread adoption of PEVs. Stakeholders involved in VTO R&D activities include universities, national laboratories, other government agencies and industry partners – including automakers, battery manufacturers, material suppliers, component developers, private research firms, and small businesses. VTO works with key U.S. automakers through the United States Council for Automotive Research (USCAR) – an umbrella organization for collaborative research consisting of Stellantis N.V., the Ford Motor Company, and the General Motors Company. Collaboration with automakers through the U.S. DRIVE (Driving Research and Innovation for Vehicle Efficiency and Energy Sustainability) partnership enhances the relevance and the success potential of the research platform. An important prerequisite for the electrification of the nation’s light duty transportation sector is the development of more cost-effective, longer lasting, and more abuse tolerant PEV batteries and accordingly, VTO battery R&D is focused on the development of high-energy batteries for PEVs.

## Goals

The goal of this research is to address barriers to EVs reaching the full driving performance, convenience, and price of an internal combustion engine (ICE) vehicle. EVs have the advantage of a very high efficiency compared to other vehicle types, a simplified drivetrain, and a flexible primary energy source (i.e., the electricity needed to charge an EV can come from coal, natural gas, wind turbines, hydroelectric, solar energy, nuclear, or any other resource). Another current focus is the 12V start/stop (S/S) micro-hybrid architecture, in which the engine is shut down whenever a vehicle stops. Vehicles with the S/S functionality are being deployed worldwide. Table 1 shows a subset of the targets for high-performance EVs set by U.S. DRIVE<sup>10</sup>.

**Table 1: Subset of Requirements for Advanced High-Performance EV Batteries and Cells (Cost and Low Temperature Performance are Critical Requirements).**

Energy Storage Goals (by characteristic)	System Level	Cell Level
Cost @ 100k units/year (kWh = useable energy)	\$125/kWh*	\$100/kWh
Peak specific discharge power (30s)	470 W/kg	700 W/kg
Peak specific regen power (10s)	200 W/kg	300 W/kg
Useable specific energy (C/3)	235 Wh/kg*	350 Wh/kg
Calendar life	15 years	15 years
Deep discharge cycle life	1000 cycles	1000 cycles
Low temperature performance	>70% useable energy @C/3 discharge at -20 °C	>70% useable energy @C/3 discharge at -20 °C

## State of the Art

Battery R&D attempts to advance battery technology to help improve the market penetration of PEVs by overcoming the current barriers. To accomplish this, it focuses on: (1) a significantly reduced battery cost, (2)

<sup>10</sup> <https://uscar.org/download/246/energy-storage-system-goals/12837/goals-for-advanced-high-performance-batteries-for-electric-vehicle-ev-applications.pdf>

increased battery performance, e.g., extreme fast charge (XFC) and low temperature performance for enhanced lithium-ion, (3) improved life advanced chemistry cells, (4) increased tolerance to abusive conditions; and (5) more cost-effective recycling and sustainability.

The status of the broad battery chemistry types (current lithium-ion, next gen, and BLI) is summarized in Figure 1. Battery R&D spans mainly three areas:

- Current technology (enhanced lithium-ion): including cells with current materials (graphite anode/transition metal oxide cathode) and features like XFC compatibility, low temperature performance and improved abuse tolerance.
- Next-gen lithium-ion: Cells containing an alloy anode, usually silicon-based, and/or a high voltage (>4.5 V) cathode.
- Beyond lithium-ion (BLI): Cells containing Li metal anodes.

Over the past 13 years, PEVs have become more commercially viable, with battery costs dropping almost 90% since 2010. Further cost reductions in high-energy batteries for PEVs are always desirable. In addition, although today’s batteries approach very attractive cost numbers, they still need the ability to accept extreme fast charging (XFC) and to perform better in low-temperature operations to compete with ICEs in all-weather performance and “refueling” convenience. Research into “enhanced lithium-ion” batteries (which would providing these functionalities) is one of the R&D focus areas. For further gains in energy density and cost reduction, research is needed in both “next gen” chemistries (which employ an alloy anode and/or a high voltage cathode) and BLI chemistries (see Figure 1). Cycle and calendar lives of next-gen and BLI chemistries fall well short of EV goals. Most cells employing a significant amount of silicon provide around 1,000 deep-discharge cycles but with less than five years of calendar life; BLI cells typically provide much less of a cycle life (400 cycles or less). In addition, the requisite low temperature performance and extreme fast charge capability are lacking in all chemistries.

Current Technology Lithium-ion (Graphite/NMC)		Next Generation Lithium-ion (Silicon Composite/High -voltage NMC)		Longer-term Battery Technology (Lithium Metal)	
<b>Battery Pack Cost</b>		<b>Battery Pack Cost</b>		<b>Battery Pack Cost</b>	
<ul style="list-style-type: none"> <li>▪ Current: \$235/kWh</li> <li>▪ Potential: \$100-\$160/kWh</li> </ul>		<ul style="list-style-type: none"> <li>▪ Current: \$256/kWh</li> <li>▪ Potential: \$90-\$125/kWh</li> </ul>		<ul style="list-style-type: none"> <li>▪ Current: ~\$320/kWh</li> <li>▪ Potential: \$70-\$120/kWh</li> </ul>	
Large-format EV cells	20-60 Ah	Large-format EV cells	20-60 Ah	Large-format EV cells	TBD (Today)
Current cycle life	1,000 -5,000	Current cycle life	500 -700	Current cycle life	400
Calendar life	10-15 years	Calendar life	Low	Calendar life	TBD
Mature manufacturing		Mature manufacturing		Mature manufacturing	
Fast-charge		Fast-charge		Fast-charge	
<b>R&amp;D Needs</b>		<b>R&amp;D Needs</b>		<b>R&amp;D Needs</b>	
<ul style="list-style-type: none"> <li>▪ High-voltage cathode/electrolyte</li> <li>▪ Lower-cost electrode processing</li> <li>▪ Extreme fast-charging</li> </ul>		<ul style="list-style-type: none"> <li>▪ High-voltage cathode/electrolyte</li> <li>▪ Lower-cost electrode processing</li> <li>▪ Durable silicon anode with increased silicon content</li> </ul>		<ul style="list-style-type: none"> <li>▪ High-voltage cathode</li> <li>▪ Lithium protection</li> <li>▪ Highly-conductive solid electrolyte</li> </ul>	

Figure 1. Chemistry classes, status, and R&D needs.

Because of the large variation in different battery technologies, battery research also includes multiple activities focused to address remaining high-cost areas within the entire battery supply chain.

## Battery Technology Barriers

The major remaining challenges to commercializing batteries for PEVs are as follows:

**A. Cost.** The current cost of high-energy lithium-ion batteries is approximately \$150 – \$200/kWh (on usable energy basis), a factor of two-three times too high from where it needs to be. The main cost drivers are the high cost of raw materials, costs associated with materials processing, the cell and module packaging, and manufacturing.

**B. Performance.** Historically, a higher energy density was needed to reduce the weight and volume of PEV batteries, but those weight and volume issues have been to a large degree addressed. The use of higher energy materials is still an effective way to reduce costs further and extend driving range, but cell chemistries that provide higher energy have life and performance issues. Also, existing chemistries (e.g., graphite anodes paired with transition metal oxide cathodes) need improvement in XFC and low temperature performance to compete favorably with gas-powered vehicles in the areas of performance and customer convenience.

**C. Life.** The life issue for mature lithium-ion technologies has mainly been mostly addressed. However, both next-gen and BLI cell technologies still suffer major cycle and calendar life issues.

**D. Abuse Tolerance.** Many lithium-ion batteries are not intrinsically tolerant to abusive conditions; however, full packs have been engineered by automotive OEMs to mitigate much of the risk. The reactivity of high nickel cathodes and flammability of current lithium-ion electrolytes are areas for possible improvement. The characteristics of next-gen and BLI chemistries to abusive conditions are not well-understood. However, silicon anode cells show very high temperatures during thermal runaway and lithium metal-based batteries have a long history of problematic dendrite growth which can lead to internal shorts and thermal runaway. Thus, research into enhanced abuse tolerance strategies will continue.

**E. Recycling and Sustainability.** Currently, automotive OEMs pay a relatively large cost (5-15% of the battery cost) to recycle end of life PEV batteries. The various chemistries used in lithium-ion cells results in variable backend value. Alternatively, unless they get recycled, lithium-ion batteries could lead to a shortage of key materials (lithium, cobalt, and nickel) vital to the technology. Finding ways to decrease the cost of recycling could thus significantly reduce the life cycle cost of PEV batteries, avoid material shortages, lessen the environmental impact of new material production, and potentially provide low-cost active materials for new PEV battery manufacturing.

## Program Organization Matrix

VTO's energy storage effort includes multiple activities, ranging from focused fundamental materials research to prototype battery cell development and testing. The R&D activities can involve either shorter-term pre-competitive research by commercial developers or exploratory materials research generally spearheaded by national laboratories and universities. The program elements are organized as shown in Figure 2. Battery R&D activities are organized into the following program elements: Advanced Batteries and Cells R&D, Battery Materials R&D, and the current focus.

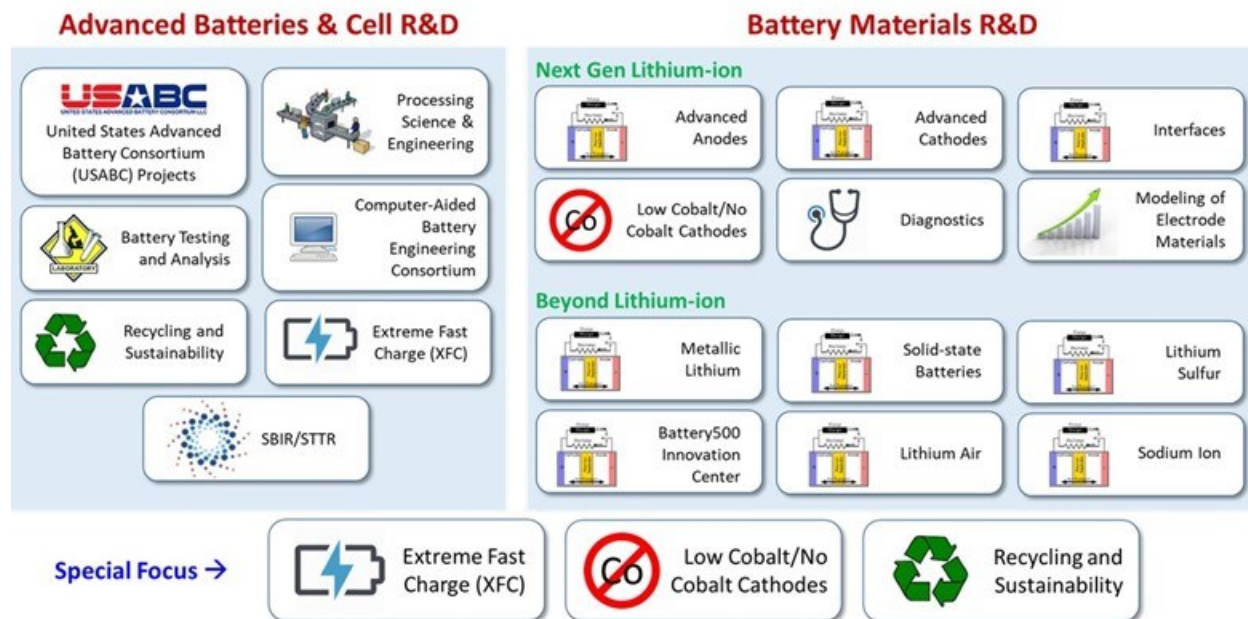


Figure 2. Battery R&D Program Structure.

Advanced Cell and Battery Research and Development activity. This activity focuses on the development of robust battery cells to significantly reduce battery cost, increase life, and improve performance. Part of this effort takes place in close partnership with the automotive industry, through a cooperative agreement with the *United States Advanced Battery Consortium (USABC)*. In FY 2023, the USABC supported twelve cost-shared contracts with developers to further the development of batteries and battery components for PEVs. In addition to the USABC projects, DOE supports battery and material suppliers via contracts administered by the National Energy Technology Laboratory (NETL). Other projects in this area include performance, life and abuse testing of contract deliverables, laboratory- and university-developed cells, and benchmarking new technologies from industry; thermal analysis, thermal testing, and modeling; cost modeling; secondary usage and life studies; and recycling studies for core materials. The *processing science & engineering* activity supports the development and scale-up of manufacturing technologies needed to enable market entry of next-generation battery materials and cell components – emphasizing disruptive materials and electrode production technologies that could significantly reduce cost and environmental impact while increasing yield and process control relative to existing production technologies. Several *small business innovation research (SBIR)* projects, also supported by VTO, are focused on the development of new battery materials/components and are the source of new ideas and concepts and are covered in that chapter.

Advanced Materials Research activity. This activity addresses fundamental issues of materials and electrochemical interactions associated with rechargeable automotive batteries. It develops new/promising materials and uses advanced material models to discover them and their failure modes, as well as scientific diagnostic tools and techniques to gain insight into why they fail. This work is carried out by researchers at national labs, at universities, and at commercial facilities. It includes the *next generation lithium-ion* research activity focused on the optimization of next generation, high-energy lithium-ion electro-chemistries that incorporate new battery materials. It emphasizes identifying, diagnosing, and mitigating issues that impact the performance and lifetime of cells constituted of advanced materials. Research continues in the six areas of advanced anodes, advanced cathodes, advanced electrolytes, electrode issues, interfaces, diagnostics, and modeling. The *beyond lithium-ion (BLI)* Technology activity addresses fundamental issues associated with lithium metal batteries, develops new/promising materials, and uses advanced material models to discover such materials using scientific diagnostic tools/techniques. It includes solid-state battery technologies, lithium metal, lithium sulfur, lithium air, and sodium-ion systems. The VTO *Battery500* projects are also managed in conjunction with this program element.

Special Focus. The current focus targets three areas of battery research. The first area is concerned with enabling *extreme fast charging* (XFC) in enhanced lithium-ion systems. It started with a 2017 research project to understand XFC, followed by a set of XFC awards (listed in the last year's report). In the second area, recognizing the issues of price volatility and supply reliability with cobalt, DOE started several projects to develop and optimize low cobalt cathode materials. The third area consists of a set of *recycling and sustainability* projects, which involve studies of full life-cycle impacts and costs of battery production and use; cost assessments and impacts of various battery recycling technologies; and the material availability for recycling and secondary usage and their cost impacts.

As further resource, the Electrochemical Energy Storage Roadmap describes ongoing and planned efforts to develop battery technologies for PEVs and can be found at the EERE Roadmap page <http://energy.gov/eere/vehicles/downloads/us-drive-electrochemical-energy-storage-technical-team-roadmap>. VTO also has extensive ongoing *collaboration* efforts in batteries R&D across the DOE and with other government agencies. It coordinates efforts on energy storage with the DOE Office of Science, and the DOE Office of Electricity. Coordination and collaboration efforts include membership and participation in program reviews and technical meetings by other government agencies, and the participation of representatives from other government agencies in the contract and program reviews of DOE-sponsored efforts. DOE also coordinates with the Department of Army's Advanced Vehicle Power Technology Alliance, the Department of Transportation/National Highway Traffic Safety Administration (DOT/NHTSA), the Environmental Protection Agency (EPA), and the United Nations Working Group on Battery Shipment Requirements. Additional international collaboration occurs through a variety of programs and initiatives. These include: the International Energy Agency's (IEA's) Hybrid Electric Vehicles Technology Collaboration Program (HEV TCP); and the G8 Energy Ministerial's Electric Vehicle Initiative (EVI); as well as bilateral agreements between the U.S. and China.

## Battery Highlights from FY 2023

The following are some of the highlights associated with battery R&D funded by VTO (including highlights related to market developments, R&D breakthroughs, and commercial applications).

### **Development of New High-Energy Cathodes Containing 60% Manganese (ANL)**

In 2021, the Materials Research Group at ANL reported the development of novel Co-free  $\text{Li}_2\text{MnNiO}_4$  cathodes based on lithiated-spinel structures<sup>11</sup>. These Li-excess spinels (LxS) surpass conventional spinels such as  $\text{LiMn}_2\text{O}_4$  and  $\text{LiMn}_{1.5}\text{Ni}_{0.5}\text{O}_4$  by doubling the Li concentration in their pristine states, while maintaining cubic symmetry. Li/LxS- $\text{Li}_2\text{MnNiO}_4$  cells exhibit remarkable energy densities, delivering ~225 mAh/g capacity between 2.5 – 5.0 V.

Increasing the Mn content is a promising approach for sustainability of the Li-ion battery supply chain. A newly developed series of Mn-rich LxS cathodes, referred to as  $\text{LxS-Li}_2\text{Mn}_{1+x}\text{Ni}_{1-x}\text{O}_4$  ( $0 < x < 0.5$ ), exhibits an impressive specific capacity of up to 250 mAh/g when cycled between 2 – 5.0 V vs. Li. Figure 3(a) shows a representative XRD pattern of  $\text{Li}_2\text{Mn}_{1.2}\text{Ni}_{0.8}\text{O}_4$  with the previously reported LxS- $\text{Li}_2\text{MnNiO}_4$ . Refinement analysis indicates a lower disordering ratio for LxS- $\text{Li}_2\text{Mn}_{1.2}\text{Ni}_{0.8}\text{O}_4$  (11%) vs LxS- $\text{Li}_2\text{MnNiO}_4$  (18%). Consequently, the initial discharge capacity of LxS- $\text{Li}_2\text{Mn}_{1.2}\text{Ni}_{0.8}\text{O}_4$  improved from 225 to 250 mAh/g, increasing the energy density from 800 to 920 Wh/kg, while maintaining similar cycling as the LxS- $\text{Li}_2\text{MnNiO}_4$ , Figure 3 (b) and (c). Also, LxS- $\text{Li}_2\text{Mn}_{1.2}\text{Ni}_{0.8}\text{O}_4$  exhibits enhanced rate performance, Figure 3 (d), attributed to its more well-established 3D Li-ion diffusion channels.

---

<sup>11</sup> Chem. Comm. (2021), doi.org/10.1039/D1CC04334J

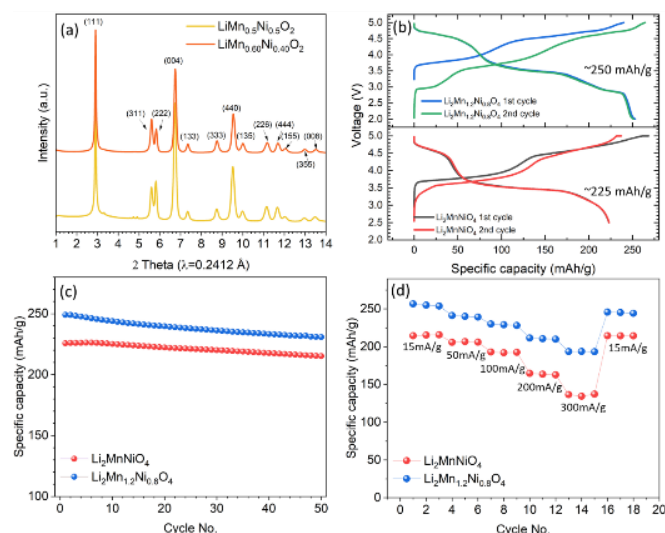


**Figure 3. Structural and electrochemical properties of LxS-Li<sub>2</sub>MnNiO<sub>4</sub> and LxS-Li<sub>2</sub>Mn<sub>1.2</sub>Ni<sub>0.8</sub>O<sub>4</sub>: (a) X-ray diffraction patterns, (b) 1<sup>st</sup> and 2<sup>nd</sup> cycle voltage profiles, (c) cycle performance, and (d) rate capability.**

### Room Temperature Rechargeable Solid-State Li-Air Battery (Illinois Institute of Technology and ANL)

There is interest in developing new battery chemistries to replace current Li-ion batteries. One area of research has been Li-oxygen (Li-O<sub>2</sub>) batteries based on the formation and decomposition of Li peroxide (Li<sub>2</sub>O<sub>2</sub>). This product results from the two-electron reaction between Li<sup>+</sup> and O<sub>2</sub> by either of the two pathways shown in **Figure 4**. This chemistry potentially has several times the energy density of currently used Li-ion cells. A Li-O<sub>2</sub> battery cell based on Li oxide (Li<sub>2</sub>O) formation and decomposition potentially has an even higher energy density than one based on Li<sub>2</sub>O<sub>2</sub>. This is because it is based on a four-electron reaction as shown in **Figure 4**. The four-electron reaction can deliver an energy density about four times that of a Li-ion battery. However, the four-electron reaction is much more difficult to achieve.

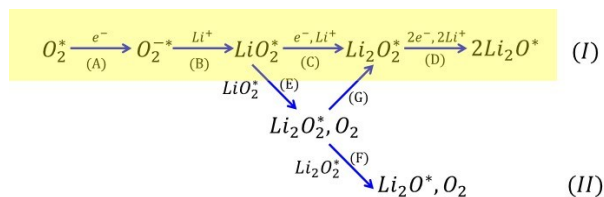


**Figure 4. Two possible reaction pathways to the formation of Li<sub>2</sub>O from reaction of O<sub>2</sub>, Li<sup>+</sup>, and e<sup>-</sup>. The reaction highlighted by yellow is the one occurring in the solid-state Li-air battery.**

In this work, teams from Illinois Institute of Technology and ANL have found that by using a solid-state electrolyte in a Li-O<sub>2</sub> battery the product formed on the cathode is Li<sub>2</sub>O and not Li<sub>2</sub>O<sub>2</sub>. The solid-state electrolyte is a composite polymer electrolyte of Li<sub>10</sub>GeP<sub>2</sub>S<sub>12</sub> nanoparticles embedded in a modified polyethylene oxide polymer. In lab testing, the battery is rechargeable at 1000mAh/g for 1,000 cycles with a low polarization gap at room temperature as shown in **Figure 5**. The battery can run in an air atmosphere and is thus referred to as Li-air battery. Further work is planned to investigate large cell performance.



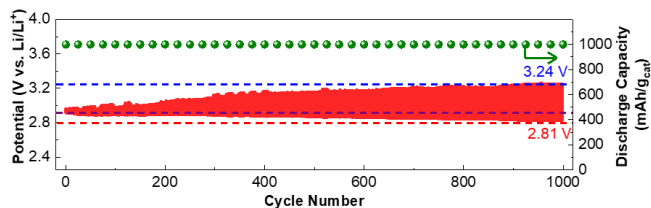


Figure 5. Solid-state Li-air battery cell performance at a limited capacity of 1000 mAh/g showing galvanostatic cycling over 1000 cycles and a small polarization gap.

### Stabilizing Cobalt-Free Cathodes with Li Stoichiometry Control (ANL and BNL)

Li-ion batteries' heavy reliance on high-cost and scarce cobalt in many of their cathodes raises supply-chain and sustainability concerns. Eliminating Co from cathodes, while maintaining high energy, remains elusive, as doing so detrimentally affects their layering and cycling stability. Researchers from ANL and BNL have recently designed a Li-stoichiometry control approach to synthesize Co-free cathodes, specifically  $\text{Li}_x\text{Ni}_{0.95}\text{Mn}_{0.05}\text{O}_2$  (NM9505). Structural and morphological control was achieved by tuning Li stoichiometry, resulting in a transition from large-sized particles (100s of nm) with a single layered phase to small layered-rocksalt composites (10s of nm) with decreasing Li Content (Figure 6).

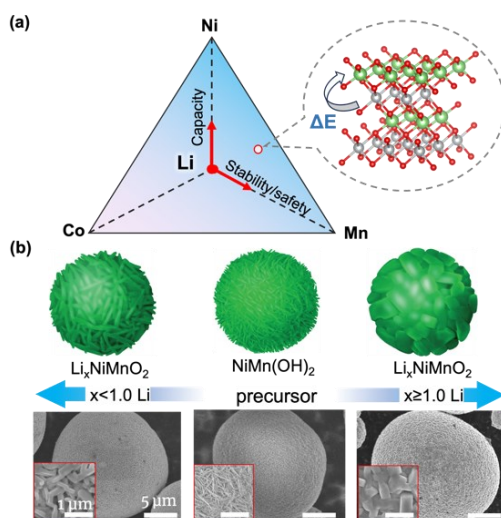
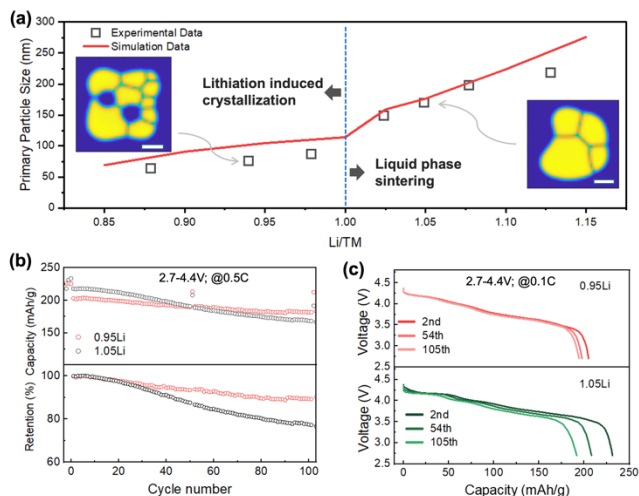


Figure 6. (a) Composition-property correlation in the Li-Ni-Mn-Co space; inset: Li/Ni mixing due to the reduced energy barrier ( $\Delta E$ ) for Ni migration in the absence of Co. (b) Morphological tuning via Li stoichiometry control.

Experimental characterization with computational modeling of the calcination process revealed the crucial role of Li stoichiometry in controlling the rocksalt-to-layered phase transformation and crystal growth (Figure 7 a). These insights were used to synthesize Li-deficient composite-structured NM9505. This material does not require surface washing to remove Li residue, promising potentially lower cost. Due to its low anisotropic lattice expansion and contraction during cycling, Li-deficient NM9505 exhibited 90% capacity retention and *close-to-zero* voltage fade (a common issue with Li and Mn excess cathodes) for 100 deep cycles. (Figure 7 bc).



**Figure 7. (a)** Particle size variation of the NM9505 as a function of Li over transition metal ratio, Li/TM. Inset: simulated particle microstructure for Li/TM= 0.95 and 1.05. Scale bars: 100 nm. **(b, c)** Capacity retention and voltage profiles of NM9505 with 0.95Li (red) and 1.05Li (black).

#### ***An Inorganic-Rich Interphase for Li Metal Batteries with Improved Cycle Life (BNL)***

CsNO<sub>3</sub> was identified as a dual-functional additive to form good interphases on both the NMC cathode and Li metal anode to enable a Li metal battery with long cycle life and faster charge capability. Using 1,2-dimethoxyethane (DME)-LiFSI based electrolyte containing an CsNO<sub>3</sub> additive, the LiNi<sub>0.8</sub>Mn<sub>0.1</sub>Co<sub>0.1</sub>O<sub>2</sub>||Li cell retained more than 80% of initial capacity after 200 1C cycles, even with a high cathode loading of 5mAh/cm<sup>2</sup>. In contrast, the cell using the baseline electrolyte experienced a loss of capacity within 20 cycles, duplicate cells displayed similar behavior. The resulting interphase is dominated by the inorganic species CsFSI and is free of LiF, which is the component often believed to be necessary for a good interphase. These results indicate that both cathode and anode must have been well protected during the cycling, validating the dual protection strategy proposed. (Figure 8)

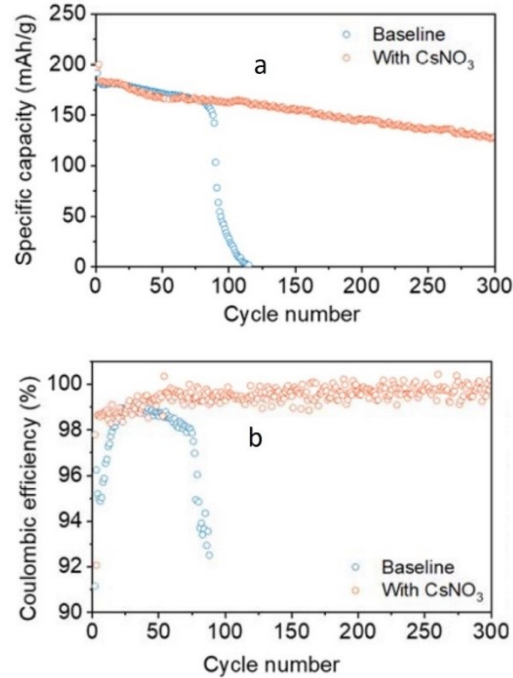


**Figure 8. (a) Cycling stability of baseline electrolyte and electrolyte containing 3 wt% CsNO<sub>3</sub> additive. (b) Coulombic efficiency of the cell in (a).**

#### ***Fast Diagnosis of Li-ion Battery Health from High-Rate Data using Artificial Intelligence (NREL and LBNL)***

NREL and INL are developing methods to rapidly diagnose Li-ion battery SOH during high-rate cycling, specially 10-minute fast charge and two-hour discharge. The goal is to quickly determine the severity of battery aging modes (e.g., loss of active material [LAM], loss of Li inventory [LLI]) without taking the battery out of commission for a standard slow-rate evaluation, which can take up to 40 hrs. To develop online SOH diagnostics, NREL's battery physics models are combined with INL's machine-learning tools. Figure 9 illustrates the overall workflow. First, an electrochemical battery model is developed that can predict high-rate battery performance of aged cells. Second, features, such as the incremental capacity during charge, are extracted from the synthetic data generated by the electrochemical model. Third, the synthetic data is used to train a machine-learning algorithm to associate how the high-rate voltage response should change under different aging conditions. Fourth, after training the machine-learning model on synthetic data, the model is tested on real cells. Compared to the standard 40-hour full-capacity diagnostic, the new method provides a 10x speedup in quantifying failure modes and enables earlier life projections using less data. Importantly, the new method can analyze the cell SOH each time the battery is used and can use high rate and rest information for failure mode identification, quantification, and projection.

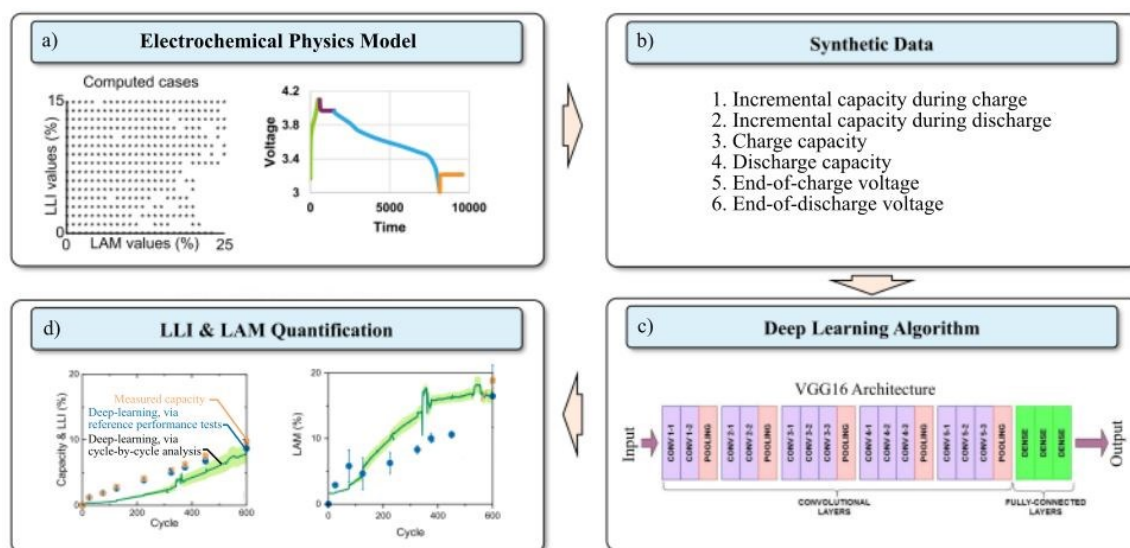


**Figure 9.** Process to develop an online battery state-of-health monitor by using electrochemical models and machine learning. Validation data is from single-layer pouch cells aged under 10-minute fast-charge and 2-hour discharge cycling protocol.

### Enhanced Energy and Improved Cyclability of Earth-Abundant Cathodes (LBNL)

Li and manganese rich (LMR) layered oxides are leading materials in the earth abundant cathode category. However, performance issues, such as capacity decay, voltage fade, and impedance rise, remain as roadblocks. Here we show that a new fluorination approach can address some of these challenges. We have developed a molten-salt approach where we use fluoride salt mixtures with a low fluoroacidity to improve fluorination efficacy and reduce impurities in the final product. The treated cathodes show improved performance, particularly reduced oxygen gas evolution, decreased side reactions, higher energy density and energy retention. **Figure 10** shows the results using fluorinated Co-free LMR,  $\text{Li}_{1.2}\text{Ni}_{0.2}\text{Mn}_{0.6}\text{O}_2$  (referred to as LNMO). We used large micron-sized single-crystal samples (Figure 10b inset) to demonstrate the effect of *in situ* fluorination. Using the optimized F precursor, we obtained phase-pure fluorinated LNMO samples, including LNMO-F1, LNMO-F2.5 and LNMO-F5 with a fluorination level of 0.5%, 0.125%, and 2.5% (Figure 10a). In Figure 10b, fluorinated LNMO shows additional redox processes at  $\sim 2.7$ , 4.7 and 4.75 V, indicating the involvement of a high-voltage spinel-type ( $\text{LiNi}_x\text{Mn}_{2-x}\text{O}_4$ ) component. These features lead to increased energy density and better energy retention. The initial discharge energies were  $\sim 705$ , 725, 715, and 730 Wh/kg for LNMO, LNMO-F1, LNMO-F2.5, and LNMO-F5 cathodes. After 50 cycles, the specific energies were  $\sim 695$ , 650, 725 and 775 Wh/kg (Figure 10d). *Operando* diagnostics revealed decreased oxygen activities in fluorinated LMR and reduced side reactions at high voltages. Future work will investigate the cost impact of this technology (including the ability to recover and re-use the molten salt).

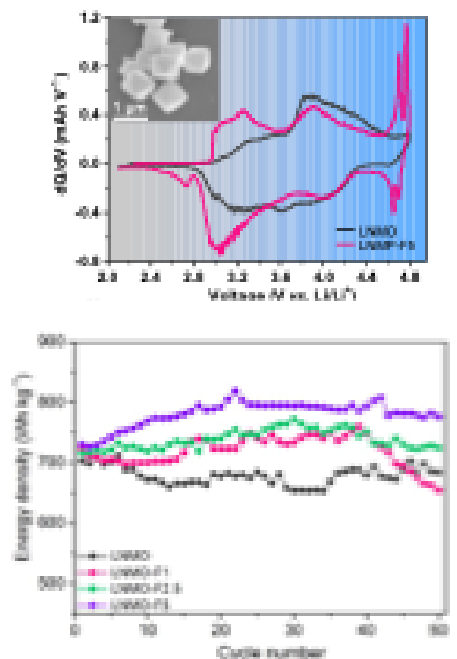
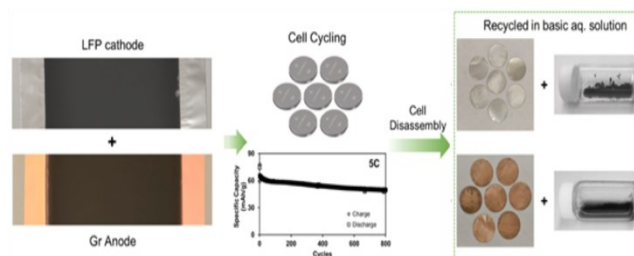


Figure 10. a) Comparison of incremental capacity obtained on different cathodes. Inset: an SEM image of the samples. b) Comparison of cathode energy density and retention of various fluorinated cathodes.

#### ***Binder Design for Recyclable Batteries (LBNL)***

A circular economy requires batteries to be designed so that at their constituents can be recovered end of life and either reused or repurposed. However, current electrode binders require expensive processes such as shredding, grinding, pyrolysis, or organic solvents to recover materials, which can release toxic gases that need to be recovered. Our team has developed a dissolvable ionic crosslinked polymer (DCIP, or *Quick-Release Binder*) that meets this challenge. This binder, which is a drop-in replacement for current binders, can be used to bind electrode (anode or cathode) materials and provides comparable performance at one-tenth of the cost of current commercial binders. The crosslinking is readily dissociated in basic condition (i.e., an aqueous sodium hydroxide solution), thus providing a plausible approach to recycle materials such as  $\text{LiFePO}_4$  cathode and graphite anode through a simple washing method using water. The three-dimensional network structure of DICP enhances the mechanical integrity of the electrodes. Therefore, with the application of this robust binder, the Li-ion batteries achieve excellent performance. Figure 11 shows the fabrication of a graphite/LFP battery with the Quick-Release binder, as well as a process demonstration. The recycled cathode, anode, and binder components can be re-fabricated into new cells that exhibit capacity comparable to fresh materials. The solvent employed in both the electrode preparation and the recycling processes is merely low-cost distilled water. Future work will test this new binder in larger pouch cells to investigate any scale up issues and potentially the use of other, less corrosive, bases in the processing with this binder. (Figure 11)



**Figure 11.** Schematic illustration of battery fabrication and recycling using the Quick-Release Binder. The Li iron phosphate (LFP) cathode material and graphite (Gr) anode material are fabricated into cathode and anode sheets, which are then cut to assemble cells for cycling test. Upon recycling, the cells are disassembled, and the LFP cathodes and graphite anodes are individually treated with high pH aqueous solution to separate the electrode materials from the current collector foils. The LFP and graphite electrode materials are retrieved from their aqueous suspensions.

### ***Silicon Anode Technology for Next-Generation Li-Ion Batteries. (NREL)***

NREL has developed a novel processing technology for Si that could disrupt current Li-ion battery (LIB) technology. NREL's silicon nanoparticle (Si NPs) production process is like a process used in the semiconductor chip and solar cell manufacturing industries. The Si NPs are then coated with molecules that transform them into a form compatible with conventional battery electrode manufacturing. Many years of work have contributed to our understanding of failure processes in silicon-based LIBs. These studies resulted in strategies to engineer silicon that led to the development of NREL's patented Si NP molecular coating technology, which can be seen in images of the Si NPs with and without the coating (**Figure 12**). Recent studies<sup>12</sup> have shown this processing methodology:

- Stabilizes the Si NP active material against degradation during handling in air, potentially simplifying manufacturing.
- Enables full access to all the Si NP active material in the electrode during the first lithiation cycle, enhancing the available specific capacity.
- Encapsulates the Si NP active material in an organic matrix material, mitigating cycle and calendar life performance declines.

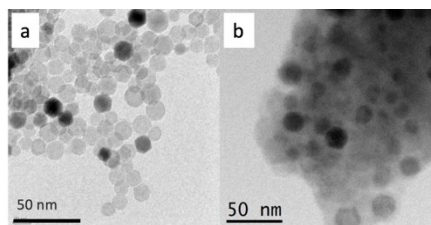


**Figure 12.** Images of Si NPs (a) before and (b) after applying a molecular coating and processing into an electrode.

Research-scale coin cells (3mAh capacity) achieve impressive cycling life (nearly 1000 cycles) and capacity (over 2000mAh/g) metrics, **Figure 13**. Preliminary cost modeling finds that a scaled PECVD production process would approach the \$5–\$15/kg DOE target for active material costs.

Calendar life is the major performance metric limiting commercial adoption of silicon-based LIBs – is under active investigation. In addition, the team plans to test performance of these NP-Si based is full single layer pouch cells.

<sup>12</sup> <https://doi.org/10.1039/D2TA08935A> and <https://doi.org/10.1002/aenm.202203921>

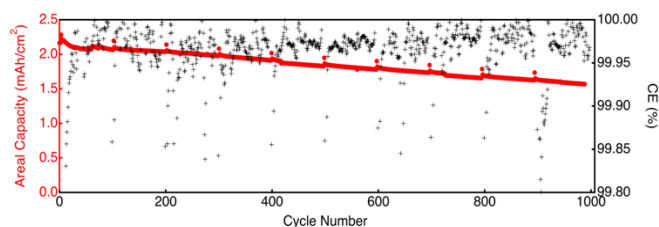


**Figure 13.** The cycle life of batteries containing a Si NP-based anode and an NMC811 cathode achieves U.S. DRIVE goals of cycle life >1000 with an anode available specific capacity >2000 mAh/g at a nominal voltage of 0.01 V vs Li/Li<sup>+</sup>.

#### ***Voltage Boundaries to Prevent Li-Plating During Fast Charge Cycling (LBNL and NREL)***

A reliable method for preventing Li plating is needed to enable extreme fast charging. The task is complicated by significant variations in charging conditions. These factors include, but are not limited to climate, battery age, and charge rate. Fast charging is often accomplished with complex protocols involving several steps to maximize charge acceptance while preventing Li plating. How these advanced protocols need to be optimized with aging is not well understood. To address these issues, researchers at NREL and LBNL jointly investigated strategies to avoid Li plating during extreme fast charging using well-validated models<sup>13</sup>. The team combined pseudo-2D electrochemical modeling with data visualization methods to reveal relationships between the cell voltage and Li-plating onset criteria. The cell investigated was a graphite/NMC532 cell using Gen2 electrolyte, 1.2 M LiPF<sub>6</sub> in (EC:EMC) (3:7 by weight), with a loading of 2.5 mAh/cm<sup>2</sup>. A wide range of operating conditions were investigated including advanced charging protocols and various thermal conditions.

Through several thousand electrochemical simulations, the team determined simple voltage limits as a function of SOC that can be used to avoid Li plating. The voltage threshold plotted in **Figure 14** is the lowest voltage at which Li plating is predicted at a given SOC. We envision this threshold could be used to stop fast charging or determine when to move to the next step in an advanced protocol. On average, Li plating occurs within 5% SOC after crossing the voltage threshold. The voltage threshold does change significantly with SOC. The team then used models to investigate how the plating onset voltage changed with aging. Aging was approximated by modifying several different model parameters to represent a wide variety of aging mechanisms. The Li plating onset becomes more variable with increased aging and the threshold for plating can be significantly reduced with cell aging/capacity fade.

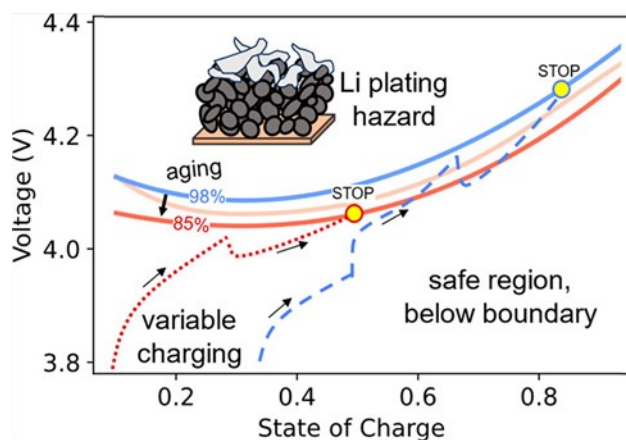


**Figure 14.** Empirical voltage threshold for Li plating as function of SOC determined using validated electrochemical model.

<sup>13</sup> <https://doi.org/10.1021/acenergylett.3c01591>

### Carbon Coatings Improve the Cycling Performance of Disordered Rocksalt Cathodes (ORNL)

Li-excess disordered rocksalt (DRX) oxides and oxyfluorides are a promising class of next-gen Li-ion cathodes due to their high specific energy ( $\geq 800$  Wh/kg) and compositional flexibility. Despite their promise, DRX cathodes typically require large amounts of conductive carbon (20-30%) to obtain high capacity and stable cycling. This approach compromises the electrode-level energy density and exacerbates electrolyte breakdown. To address these issues, researchers have developed a mechanical milling process to apply conformal graphite coatings to DRX cathodes. Figure 15 a-b compare cycling performance of Co/Ni-free DRX cathodes ( $\text{Li}_{1.2}\text{Mn}_{0.5}\text{Ti}_{0.3}\text{O}_{1.9}\text{F}_{0.1}$ ) containing either a graphite coating or one of two carbon blacks. At a moderate carbon loading (10%,  $\sim 20$ -micron thick conformal coating), the carbon black-based electrodes exhibit high initial capacity (ca. 250-300 mAh/g, compared to 200mAh/g for current commercial cathodes) but rapidly fade over 50 cycles. On the other hand, the graphite coated DRX shows superior cycling stability with 85% capacity retention after 45 cycles (vs. 56-58% retention for cells with carbon black).

Diagnostics results show that carbon blacks agglomerate on the DRX surface which yields precarious electrical contacts throughout the electrode (see Figure 15c). On the other hand, the graphite coating provides two key advantages by: (i) protecting the DRX surface from parasitic reactions (e.g., electrolyte oxidation) and (iii) providing a robust conductive network that can withstand repeated volume changes during cycling. Ongoing work is focused on optimizing the graphite coating, reducing the carbon content to  $\leq 5\%$ , and investigating scale up issues.

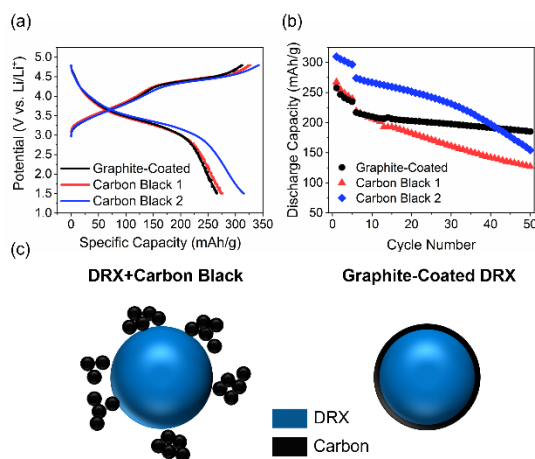


**Figure 15.** (a) First cycle voltage profiles and (b) cycling stability of  $\text{Li}_{1.2}\text{Mn}_{0.5}\text{Ti}_{0.3}\text{O}_{1.9}\text{F}_{0.1}$  DRX cathodes cycled at  $10\text{-}20$  mA  $\text{g}^{-1}$ . (c) Schematic showing agglomeration of carbon black vs. conformal graphite coatings on DRX particle surfaces.

### Advancing All-Solid-State Li-Sulfur Battery through Materials and Interfacial Innovations (PNNL)

A PNNL team has developed an integrated approach that improves the performance of all-solid-state Li-S batteries (Figure 16). They have developed a Li compatible solid-state electrolyte (SSE) with high ionic conductivity ( $>5$  mS/cm at room temperature) and integrated it with engineered carbon materials to host the sulfur. Through rational design of the sulfur-carbon-SSE triple-phase, near-theoretical sulfur capacity ( $\sim 1600$  mAh/g) in Li-S batteries, with a high sulfur mass loading ( $>10$  mg/cm<sup>2</sup>) (Figure 16c) has been achieved. This lays a solid foundation for the further fabrication and manufacturing of high-capacity electrodes (up to 16 mAh/cm<sup>2</sup>) and high-energy batteries.

Moreover, the sulfur cathodes deliver superior power performance. Figure 16c shows the cell capacities as a function of current densities, demonstrating both high-rate capability and electrode robustness. Based on the team's preliminary results, the engineered cathodes ( $\sim 1500$  mAh/g at 5 mg/cm<sup>2</sup>) have a great potential to meet a cell-level energy of a 500Wh/kg in a 5Ah Li-S pouch cell using a 30  $\mu\text{m}$  SSE separator, and 37.5  $\mu\text{m}$  thick Li



(Figure 16b). The improved stability of the developed SSE towards Li metal also allows for stable cycling of all-solid-state Li-S cells. At 2 mAh/cm<sup>2</sup> capacity, the all-solid-state Li-S coin cells have demonstrated over 250 cycles without capacity decay or failure (Figure 16f). The team is now working on enhancing the cycle life of all-solid-state Li-S batteries of further increased S loading to achieve high energy goals in prototype pouch cells.

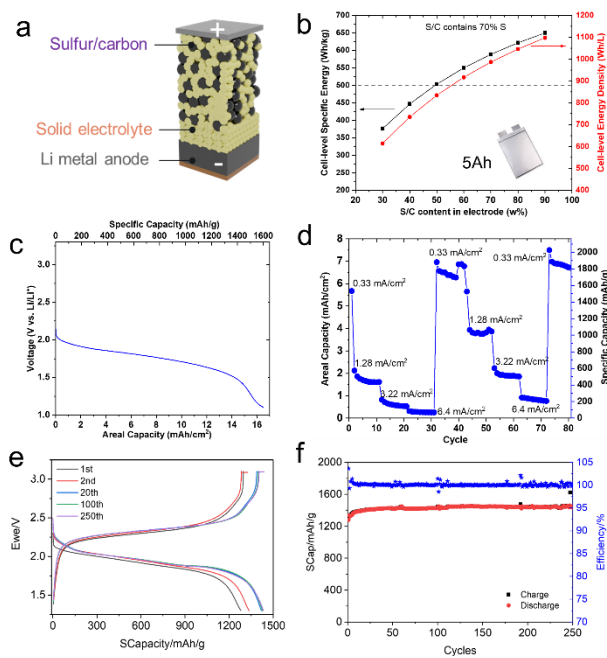


**Figure 16.** (a, b) Schematic and cell energy estimation based on experimental inputs, (c, d) Discharge profile (10 mg S/cm<sup>2</sup>) and rate capability of cell (3.7 mg S/cm<sup>2</sup>), and (e, f) Charge/discharge profiles and cycling of all-solid-state Li-S coin cell (1.5 mg S/cm<sup>2</sup>), all cells were tested at 20°C.

### ***Transport-Regulating Polymer Coating to Improve the Cyclability of Li Metal Batteries (Stanford)***

Li metal batteries are promising candidates for next gen energy storage devices, however, the inefficiencies in Li metal plating and stripping has been one of the main obstacles impeding commercialization. Researchers at Stanford have invented a polymer coating for the Li anode that improves the battery cyclability by > two-fold. The dual-function polymer coating, denoted as SP<sup>2</sup>, is engineered to selectively block solvents while facilitating the transfer of salt molecules, resulting in formation of a salt-derived SEI layer (Figure 17a). Several common electrolytes, including ether, carbonate, and fluorinated carbonate-based electrolytes demonstrated improved Li cycling efficiency when using the polymer coating (Figure 17b). Further, employing the SP<sup>2</sup> polymer coated Li anode in full battery with either carbonate or fluorinated ether electrolytes exhibits enhanced cyclability by a factor of greater than two (Figure 17c and d). The concept of introducing a regulating polymer coating at the Li anode presents an opportunity for researchers to harness the potential of polymer chemistry to enhance battery cyclability.

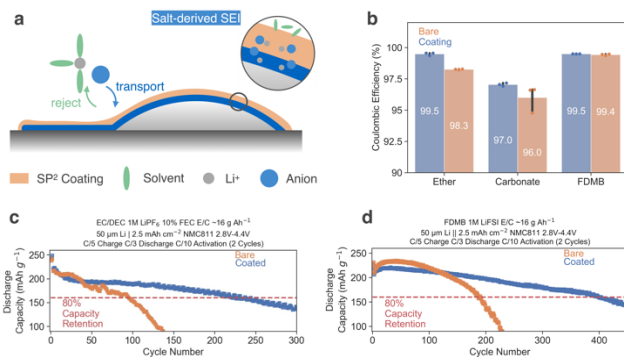


**Figure 17. (a) Scheme of a regulating SP<sup>2</sup> polymer coating at the Li anode that blocks solvents while transports salts. (b) Compared to the bare ones, Li metals with SP<sup>2</sup> coating exhibit improved Li cycling efficiency when using different electrolytes. Tests of full cells with SP<sup>2</sup>-coated Li anodes indicated improved cyclability using (c) carbonate and (d) fluorinated ether electrolytes.**

### Enabling Fast-Charging in Solid-State Batteries (SLAC and Stanford)

Garnet solid electrolyte is chemically compatible with Li metal and thus may enable a safer and energy-dense Li-metal based battery. One major challenge for garnet solid-state battery is fast charging. Short-circuiting resulting from Li intrusion into the solid electrolyte is a failure mechanism that makes fast charging challenging with this system. SLAC and Stanford have developed a mechanistic understanding of short-circuiting in garnet solid-state batteries. By using *in-situ* SEM combined with an electrical microprobe, we have investigated the probability of short-circuiting at the nanoscale level. We discovered that, in the absence of mechanical defects, extraordinary current density, on the order of 10,000 mA/cm<sup>2</sup>, can be achieved without short circuiting. When local mechanical defects are present (e.g., dents, scratches, etc.), the critical current density at which short-circuiting occurs decreases substantially. Specifically, the average local critical current density decreases from 5 A/cm<sup>2</sup> to 1 A/cm<sup>2</sup>. Our work highlights the importance of reducing mechanical defects at the solid electrolyte surface. We have also developed ultrathin coatings to improve the surface mechanical properties to make solid electrolytes more resistant towards mechanical failure. Specifically, ultrathin Ag doping increases the mechanical toughness and increases the critical current density. (Figure 18)

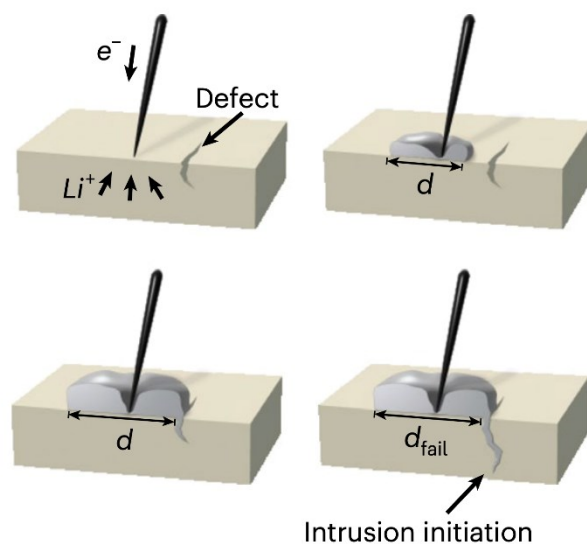


**Figure 18. Short-circuiting mechanism in garnet solid-state battery driven by mechanical defects. Reproduced from McConohy et al. Nature Energy 8, 241 (2023).**

### High-Entropy Electrolytes for Li Metal Batteries (Stanford and SLAC)

Recent advances in electrolyte engineering have greatly improved cyclability of Li metal batteries by enhancing electrochemical stability at the electrode interfaces. Improving cycling stability, however, seems to compromise ionic conductivity that directly hampers fast-charging capabilities, and concurrently achieving stability and conductivity has been challenging.

Scientists this year designed a novel class of electrolytes called high-entropy electrolytes (HEEs) that improves ionic conductivity without sacrificing cycling stability. By utilizing up to five different solvents the solvation entropy of the electrolyte was observed to increase (Figure 19a). Solvation entropy was shown to play a critical role in modulating the ion clustering behavior within the electrolyte. HEEs have smaller ion clusters that allows for faster ion transport (Figure 19b). It was observed that HEEs possess more than 100% improvements in ionic conductivity compared to the conventional low entropy counterparts (Figure 19c). Improved ion transport allows for a more uniform  $\text{Li}^+$  concentration profile and Li deposition morphology (Figure 19b). In addition, the superior ionic conductivity enabled cycling at fast charging conditions of up to 2C (full charging in 30 minutes).

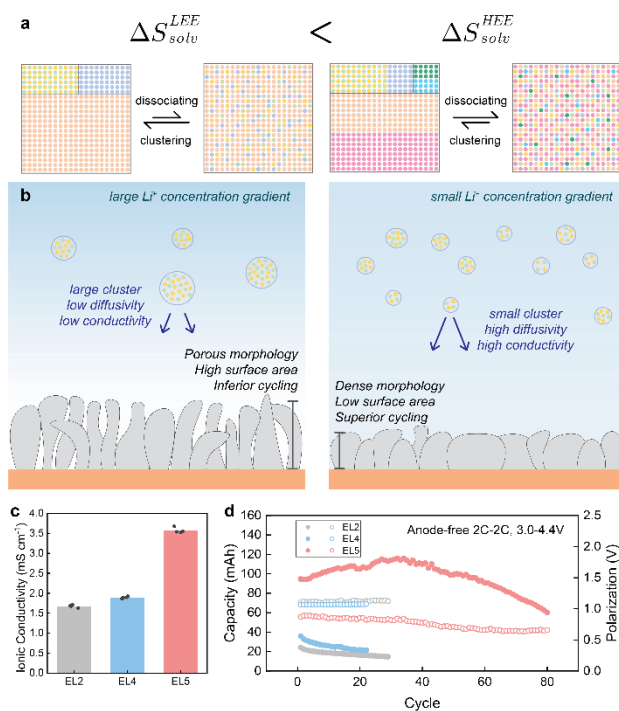


**Figure 19.** (a) Schematic showing that increasing molecular diversity increases the solvation entropy of the electrolyte. (b) Illustration showing that HEE has smaller ion clusters and superior ion transport. (c) Ionic conductivity doubles for the HEE compared to conventional electrolytes. (d) HEE enables stable cycling at fast charging conditions.

## I USABC Battery Development & Materials R&D

The United States Advanced Battery Consortium (USABC) is a subsidiary of USCAR and a cooperative agreement with the DOE. The USABC mission is to develop electrochemical energy storage technologies that advance commercialization of next generation EV applications through funding precompetitive development contracts. The consortium, comprised of General Motors, Ford, and Stellantis, competitively awards battery and material development contracts, for which the recipient contributes a 50% cost share. USABC issues requests for proposal information, evaluates submitted proposals, and manages the resulting development contracts. The USABC working structure consists of a technical advisory committee (TAC) which makes technical recommendations to the USABC management committee (MC).

USABC has developed mid- and long-term battery goals for EV applications, plug-in hybrid vehicle applications, separators, 12V start-stop batteries, and other vehicular applications. In addition, it developed standard test procedures to evaluate performance of batteries and progress towards goals. The goals and test procedures can be found at <https://uscar.org/usabc/>. Table I.1 and Table I.2 show some of the goals.

In 2022, the USABC continued to fund and manage multiple contracts in the areas of low cost and fast charge EV batteries, beyond Li-ion batteries (i.e. cells using a Li metal anode), high voltage electrolytes, novel recycling technology, and prelithiation technology.

**Table I.1 USABC Goals for low-cost/fast-charge advanced batteries for EVs (CY 2023).**

End of Life Parameter	Units	Value
Peak Discharge Power Density, 30 s	W/l	1400
Peak Specific Discharge Power, 30 s	W/kg	700
Usable Energy Density	Wh/l	550
Specific Usable Energy (defined at power target)	Wh/lg	275
Calendar Life	Years	10
Cycle Life (25% FC)	Cycles	1000
Cost (@ 250k annual volume)	\$/kWh	75
Normal Recharge Time	Hours	<7
Fast Rate Charge Minutes 8	Minutes	80% UE in 15 minutes

**Table I.2 USABC Goals for non fast-charge batteries for EVs (CY 2023)**

End of Life Parameter	Units	Value
Peak Discharge Power Density, 30 s	W/l	1500
Peak Specific Discharge Power, 30 s	W/kg	700
Usable Energy Density	Wh/l	750
Specific Usable Energy (defined at power target)	Wh/lg	350
Calendar Life	Years	15
Cycle Life (25% FC)	Cycles	1000
Cost (@ 250k annual volume)	\$/kWh	100
Normal Recharge Time	Hours	<7

The rest of this chapter contains detailed reports on the status of the following individual projects.

- Low-cost, High-safety Fast-charge Automotive Cells (Microvast, Inc.)
- Low-Cost and Fast-charging Lithium-ion Battery based on Neocarbonix™ NMP/PVDF-binder Free Electrode Processing for EV Applications (Nanoramic)
- Advanced Li-ion Cell Architectures for Extreme Fast Charging (XFC) Batteries for Electric Vehicles (EnPower, Inc.)
- Solvent-free Electrode Manufacturing for Low Cost/Fast Charging Batteries (Worcester Polytechnic Institute)
- Development of Advanced Low-Cost/Fast-Charge (LC/FC) Batteries for EV Applications (Farasis Energy USA)
- Pre-lithiation of Silicon-containing Anodes for High-Performance EV Batteries (Applied Materials, Inc.)
- Strategic Collaboration for the Development of a Self-Sustaining Model for the Recycling of Large-Format Lithium-Ion Batteries (American Battery Technology Company)
- Silicon-based EV Cells Meeting Cost, Calendar Life and Power Requirements (Ionblox, Inc.)
- Low-Cost and Fast Charge Semi-Solid Li-LFP Cell for EV Applications (24M)
- Low-cost, Fast-charging Silicon Nanowire Cell Technology (Amprius)
- Development of Lithium Electrode Based Cell and Manufacturing for Automotive Traction Applications (Farasis Energy USA)
- A Closed Loop Recycling Process for End-of-Life Electric Vehicle Li-ion Batteries-Phase III (Worcester Polytechnic Institute).

## I.1 Low-cost, High-safety Fast-charge Automotive Cells (Microvast, Inc.)

### Wenjuan Mattis, PhD, Principal Investigator

Microvast, Inc.  
3259 Progress Dr. #121  
Orlando, FL 32826  
E-mail: [wenjuanmattis@microvast.com](mailto:wenjuanmattis@microvast.com)

### Nicolas Eidson, DOE Technology Development Manager

U.S. Department of Energy  
E-mail: [Nicolas.Eidson@ee.doe.gov](mailto:Nicolas.Eidson@ee.doe.gov)

Start Date: January 15, 2020	End Date: March 31, 2024	
Project Funding: \$5,700,000	DOE share: \$2,850,000	Non-DOE share: \$2,850,000

### Project Introduction

Automakers worldwide have announced plans to begin transitioning from gasoline powered vehicles to ones driven via electricity. To make these bold adoption plans a reality the lithium-ion battery must continue to improve so electric drive trains can become competitive in cost and convenience to a traditional gasoline powered vehicle.

Making the battery cost less is quite challenging, specifically for higher energy or higher power cells, as raw materials make up a significant portion of the batteries cost; meaning the most significant cost benefits must arise from lowering the material prices. Metals such as Li, Cu, Co, Ni, and Al are heavily used in today's battery cells with cobalt being the most expensive and least sustainable, historically. Therefore, one of the most immediate challenges facing the Li-ion battery community today is how to eliminate the use of cobalt and other expensive materials while still having a high-performance, especially if cost parity to internal combustion engine vehicles is to be achieved.

Fast charge creates additional technical complications that must be overcome, mostly in high energy cells. It is well-documented that Li plating and dendrite formation can occur, potentially leading to performance or safety issues as the cells continue to age. This project aims to tackle these challenges thru demonstration of a working fast charge, high energy battery cell.

### Objectives

This project was originally conceived to develop low-cost (i.e., approaching 75 \$/kWh when manufactured at significant scale), high energy (> 310 Wh/kg), fast charge (< 15-minutes) Li-ion battery cells for use in electric vehicles. In addition the project now has added efforts toward utilizing higher Si/C contents in the anode and pushing the cell energy density higher towards 350 Wh/kg while still delivering 15min fast charging. These three terms (cost, energy density, fast charge) have historically not been possible in one cell system, so careful engineering is necessary to prepare a cell capable of meeting the power, energy and cost goals. In addition, the designed cell must consider effects from temperature (hot and cold conditions), as well as safety, for the technologies under development to be practically applied in a mainstream product.

### Approach

In order to develop a high energy, low-cost, fast charging, and safe battery cell for automotive applications, every aspect of the cell's components must be considered. A Li-ion cell is a complex system, and, as such, each component within the cell can influence the cell's eventual specifications.

To address cost, energy density, and safety part of the projects effort was in developing a new full concentration gradient (FCG) cathode material. The cobalt was reduced to provide cost savings while the Ni content was increased to help boost the energy density. Since the FCG technology allows variation of cathode composition along the particles diameter it is possible to locate more stable phases at the cathode, electrolyte interface – boosting cycle life and increasing cell safety.

Another unique material approach being explored in this project is the use of a fast charge electrolyte additive that provides dual passivation to the SEI and CEI. A stable interface is important to slow resistance growth; however, it hinders fast charge. The project developed a new synthesis process for this compound which is intended to lower the cost of production.

The project cell will also integrate a graphite/silicon composite based anode blend to help provide energy density for the cell. In addition, it will incorporate Microvast’s unique aramid separator that aids in cell safety, as it is significantly more stable thermally than traditional polymer or polymer ceramic coated materials used in automotive cells today. Through the combination of these advanced materials, the project goals for a low-cost, fast charge cell can become attainable.

**Results**

To evaluate the fast charge (FC) performance U.S.A.B.C. requires 100% FC cycle testing and 25% FC cycle testing. In both cases after the 15min charging period defined in the testing protocol completes the cell is charged at 0.33CCCV and then discharged using a dynamic stress test (DST) profile to the specified useable energy thruput. In Figure I.1.1 the gravimetric energy density versus cycle number is presented for the reference performance test (RPT) 0.33C check cycles. The Year 1 deliverable cell was a 38 Ah, 260 Wh/kg cell using an artificial graphite anode. The Year 2 deliverable cell was 53 Ah, > 300 Wh/kg cell based on high Ni, low Co cathode and a SiOx/graphite blend anode. As expected, the cycle life was impacted by increased energy density of the cell; but it should be noted that well over 1,000 25%FC cycles was shown to be possible. 1,000 25%FC cycles is the sought target of U.S.A.B.C., which our year 2 project cell appears well capable of delivering (see Figure I.1.1).

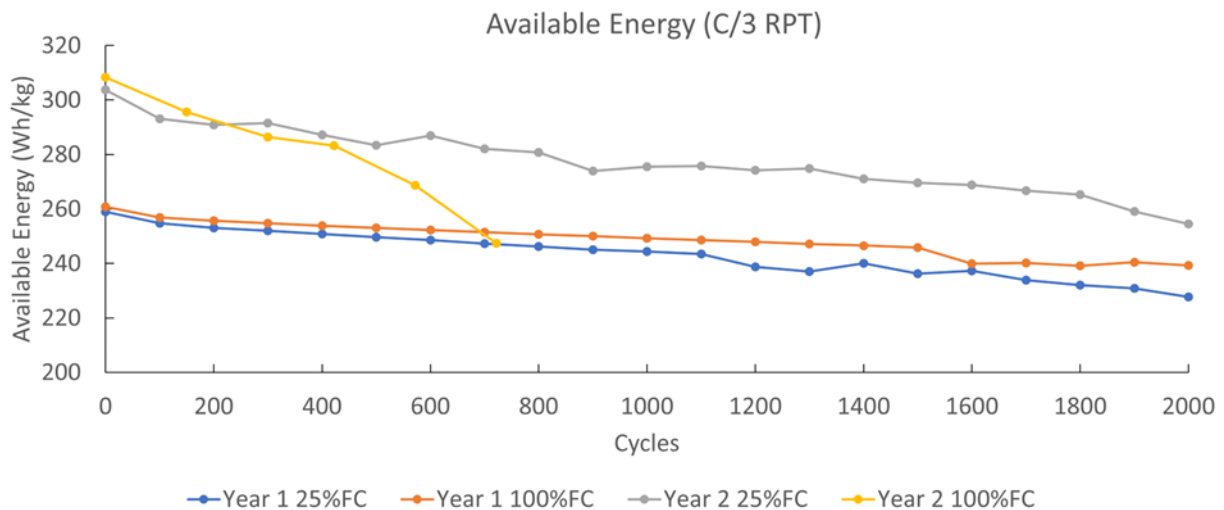


**Figure I.1.1 Energy density versus cycle life of the C/3 reference performance cycle during 25% and 100% fast charge (FC) for the year 1 and year 2 cells. The cells cycled from 2.7-4.25V, room temperature, using a 15-min fast charge + C/3 CCCV charge and dynamic stress test (DST) discharge.**

Since the year 2 cell the major focus has been on implementing thinner electrode foils to boost energy density (and conceivably reduce the metal consumption/cost of the cell long term), refinement of the electrolyte, and

the utilization of our polyaramid separator into the cell construction. In Figure I.1.2 an example of the foil trials is shown, with the comparison of cell performance when copper, or copper and aluminum foils each were reduced by 2um in thickness.

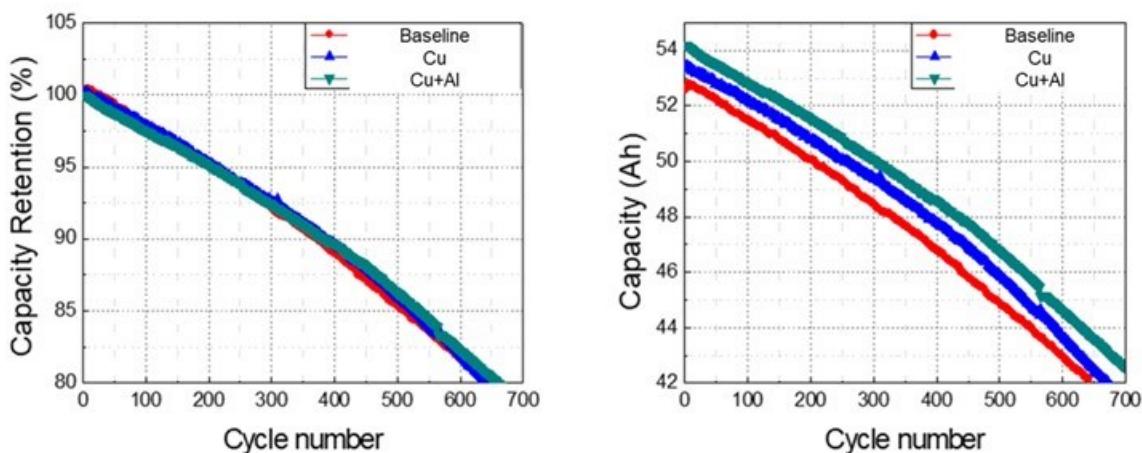


Figure I.1.2 The capacity retention (left) and capacity (right) for identical electrode designs but with baseline thickness copper & aluminum foils (baseline), 2um thinner Cu foil (Cu), and 2um thinner copper + aluminum foil (Cu+Al). Cells tested from 2.7-4.25V, 30°C, 1CCCV.

Regarding the electrolyte, it plays a key role in the cycle life and fast charge performance of the cell. A good fast charge electrolyte needs to form stable surface electrolyte interfaces (SEI) while also keeping low internal resistance. In Figure I.1.3 an example of one experiment round testing different electrolyte formulations is shown. Every cycle result is made from the same cell batch, so the variation in lifetimes is based solely on the electrolyte formulation. One observation we noted during our studies was performance at room temperature and higher temperature is not always similar. Since the project is primarily focused on 30°C cycle temperatures we selected the systems with better performance at that condition in most cases. This could need further examination in the future, as cells do experience heating during fast charging; although our thermocouples typically only record  $< 5^{\circ}\text{C}$  temperature change in most cases for project cells.

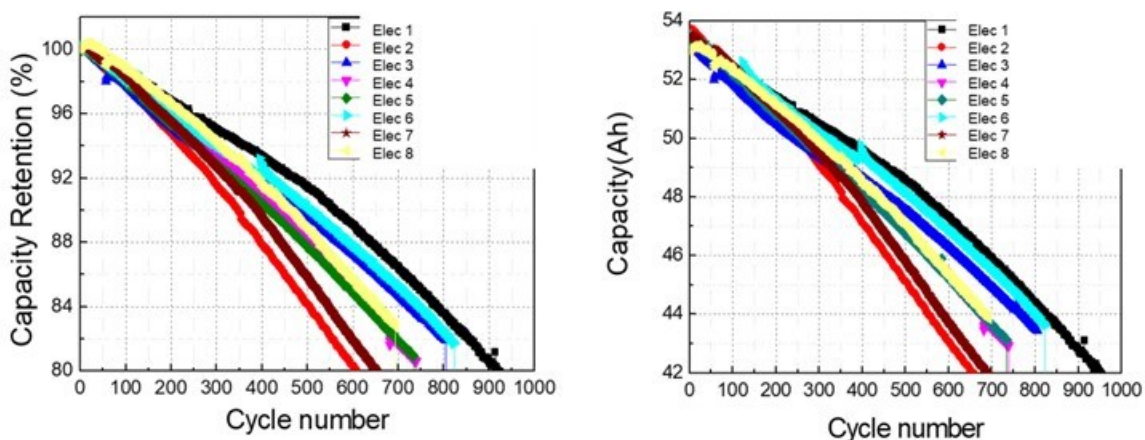
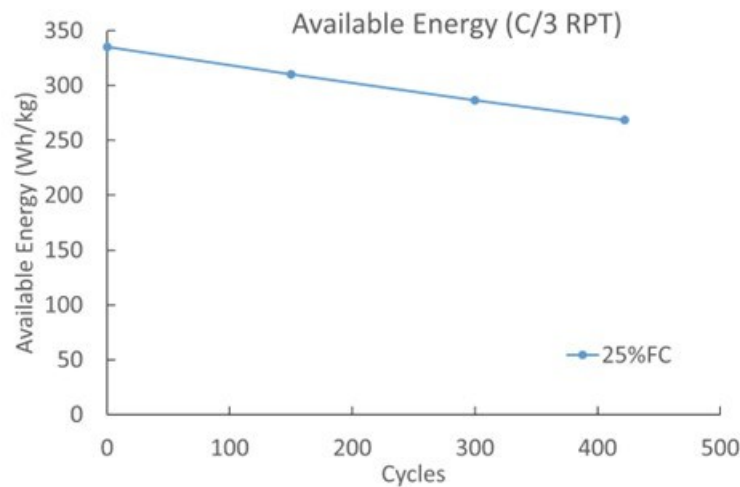


Figure I.1.3 Capacity retention versus cycle life (left) and capacity versus cycle life (right) for an electrolyte formulation study. The cells were cycled from 2.7-4.25V, 30°C, at 1CCCV.





**Figure I.1.4 25%FC reference capacity for a 335 Wh/kg cell. Tested from 2.7-4.25V, 30°C, 15-min fast charge cycle and C/3 CCCV other charging, DST discharge.**

Finally, work in the past year has begun to explore the impacts of increasing the cell energy density further from 310 Wh/kg. To do this a Si/C company joined the project as material supplier and are providing their advanced Si/C material for use in the cell. As the cell energy density is increased we have observed that the cell resistance is increasing and the difference between available energy and useable energy in the cell has widened. With that in mind, there may become a point where fast charge and energy density is optimized, and further pursuit to higher energy cells results in lower Wh utilization. Currently the project team is able to achieve about 450 cycles when doing 25% FC testing on a 335 Wh/kg cell (Figure I.1.4); something that we are still trying to improve thru improved cell pressure, refined cell design, and further adjustment of the system electrolyte.

### Conclusions

The project is on track to produce a high energy density fast charge battery with more than 1,000 25%FC cycles, a key objective. In order to control the costs materials selected must be carefully considered to avoid high price components (such as cobalt) within the cell. Thru our tests its been shown that reduction of the copper and aluminum foil thickness does not drastically change the cycle performance of the cell. Its also been observed that the electrolyte selection plays a key role in the eventual outcome of the cell performance. As the cell is pushed to higher energy density the design increases cell resistance and makes maintaining power at low states of charge more challenging; to the point that continuing to increase the energy density for fast charge cells may not make the most practical sense when considering a final vehicle pack. Overall, the project is making good progress toward high energy, low cost fast charging battery technology.

### Acknowledgements

Microvast would like to thank Vijay Saharan, our USABC program manager, and the rest of the work group for their advice and direction during the project. Also thanks to Rick Costantino and Marshall McNally for their feedback.

## I.2 Low-Cost and Fast-charging Lithium-ion Battery based on Neocarbonix™ NMP/PVDF-binder Free Electrode Processing for EV Applications (Nanoramic)

### Ben Cao, PhD, Principal Investigator

Nanoramic Laboratories  
7 Audubon Rd Suite 100  
Wakefield, MA 01880  
E-mail: [ben.cao@nanoramic.com](mailto:ben.cao@nanoramic.com)

### Ji Chen, PhD, Principal Investigator

Nanoramic Laboratories  
7 Audubon Rd Suite 100  
Wakefield, MA 01880  
E-mail: [ji.chen@nanoramic.com](mailto:ji.chen@nanoramic.com)

### Brian Cunningham, DOE Technology Development Manager

U.S. Department of Energy  
E-mail: [Brian.Cunningham@ee.doe.gov](mailto:Brian.Cunningham@ee.doe.gov)

Start Date: December 6, 2021	End Date: June 30, 2024	
Project Funding: \$3,600,000	DOE share: \$1,800,000	Non-DOE share: \$1,800,000

### Project Introduction

Nanoramic has re-invented the way electrodes are manufactured by completely removing high molecular weight PFAS-polymers such as PVDF and PTFE and the toxic NMP solvent from the active material layer. This dramatically improves Li-ion battery (LiB) performance while decreasing the cost of manufacturing and the capital expenditures related to mixing, coating and drying, NMP solvent recovery, and calendaring. In the Neocarbonix™ (NX) electrodes, a 3D nanoscopic carbon matrix works as a mechanical scaffold for the electrode active material and mimics the polymer chain entanglement. Chemical bonds are also present between the surface of the carbon, the active materials, and the current collector promoting adhesion and cohesion. As opposed to polymers, however, the 3D nanoscopic carbon matrix is very electrically conductive, which enables very high power (high C-rates). This scaffold structure is also more suitable for producing thick electrode active material, which is a powerful way to increase the energy density of LiB cells.

### Objectives

Nanoramic aims to advance the Li-ion battery energy storage devices ("pouch cells") by combining Ni-rich NMC/NCMA (or other new types) Neocarbonix cathodes and Si-dominant (Si element weight%  $\geq 50\%$ ) Neocarbonix anodes.

The R&D objectives of this LCFC EV battery project include:

- LCFC-EV battery cell capacity  $\geq 9\text{-}10$  Ah at BOL (with some 65 Ah large cells).
- LCFC-EV battery energy density:  $\geq 330$  Wh/kg,  $\geq 850$  Wh/L at BOL.
- LCFC-EV battery fast-charging: 80%SOC in 15 mins.
- LCFC-EV battery DST cycle life with C/3 charge at 30 °C: 1000 cycles with C/3 capacity retention  $\geq 80\%$ .
- LCFC-EV battery DST cycle life with  $\geq 3.5C$  15 mins fast-charge (25%FC) at 30 °C: 1000 cycles with C/3 capacity retention  $\geq 80\%$ .
- LCFC-EV battery cost  $\leq \$79/\text{kWh}$  at BOL

## Approach

Neocarbonix (NX) Lithium-ion batteries leverage proprietary American-made innovations at the electrode level. NX is a platform for manufacturing electrodes for advanced energy storage. Initially designed for ultracapacitor electrodes in diverse applications, then this approach extended to LIB cathodes and anodes electrodes, maintaining the nanocarbon binding structure while altering the active material to graphite/Silicon for the anode and NMC/NCMA for the cathode electrodes.

NX electrodes achieve three main goals:

1. Reduction in cost of manufacturing and in the \$/kWh of LIBs
2. Increase in energy density by combining cathodes and anodes with high loading electrodes.
3. Sustainability benefits: safer, PFAS-free, and NMP-free, reduced energy consumption and CO<sub>2</sub> emissions with lower boiling point solvents, simplified recycling

Today, these batteries are produced using outsourced partners and in-house manufacturing, including large-scale equipment at Kodak in Rochester, NY. This technology aims to consolidate domestic manufacturing, enhancing U.S. competitiveness and supply chain security.

NX was born as a scalable technology to improve power density in energy storage, by removing conventional polymer binders from the active material coatings. Conventional electrodes for LIBs are fabricated by mixing an active material, conductive additives, and a polymer binder in a slurry. Conventional cathodes are manufactured using NMP-based slurries and PVDF polymer binders. Those binders have very high molecular weight and promote cohesion of active material particles and adhesion to the current collector foil via two main mechanisms: 1) the entanglement promoted by long polymer chains, and 2) hydrogen bonds between the polymer, the active material, and the current collector. However, the polymer binder-based method presents significant drawbacks in performance: power density, energy density, and cost to manufacture.

NX electrodes do not have PVDF binders in cathodes and use reduced amounts of PFAS-free polymers in Graphite or Silicon-Graphite anodes. Instead, a 3D carbon matrix replaces binders, forming a cohesive layer during slurry preparation and in an R2R coating and drying step, strongly attaching to the metallic current collector. This technology is advantageous due to scalability and its "drop-in" nature, aligning with conventional electrode manufacturing processes.

The NX electrode process technology includes the four steps shown in

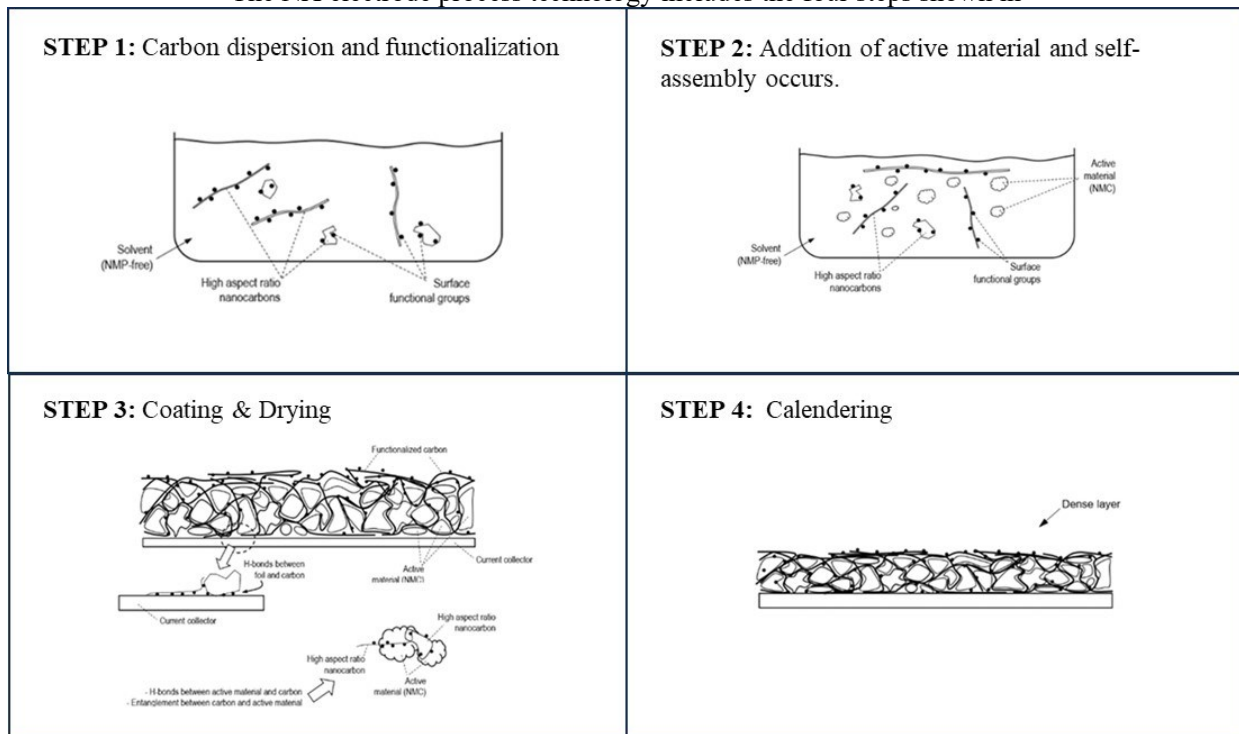


Figure I.2.1.

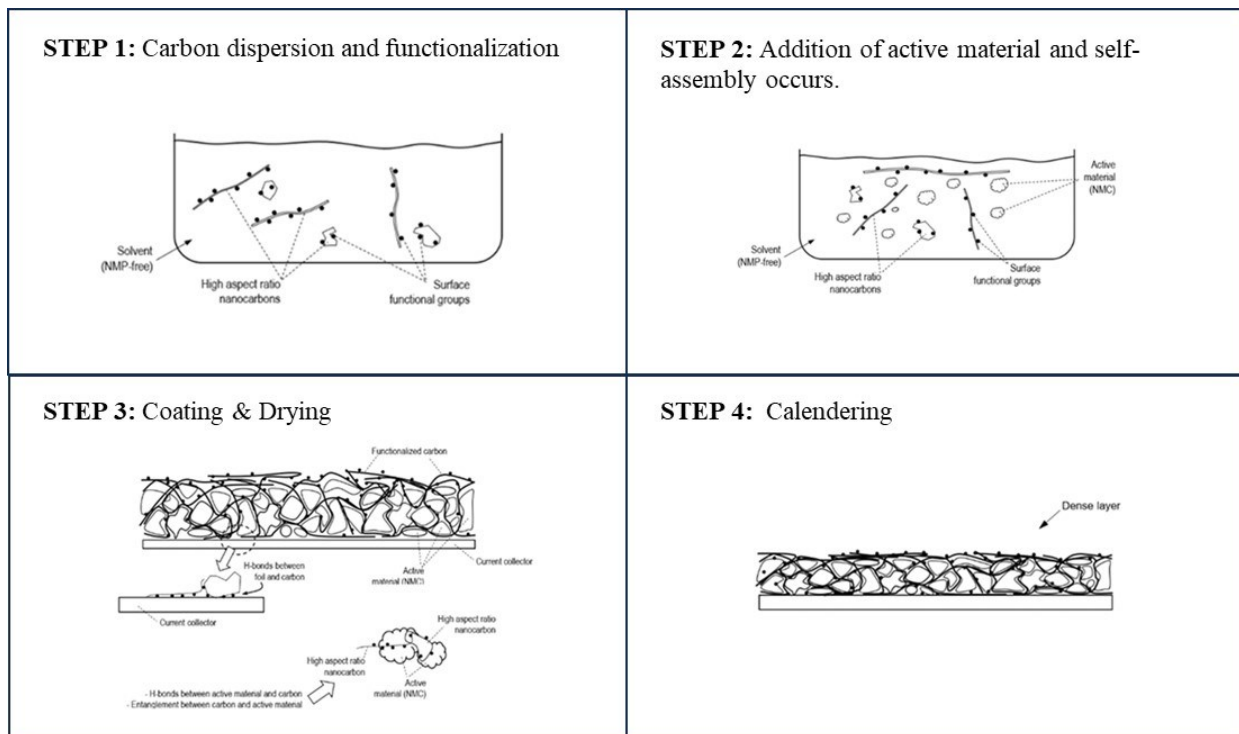


Figure I.2.1 NX electrode process technology steps.

The 3D carbon matrix is formed during a proprietary slurry preparation: high aspect ratio 1D and 2D carbon materials disperse and chemically functionalize through a 2-step process. This functionalization aims to create

an organized self-assembled structure on active material particle surfaces. The slurry, often water-based for non-moisture sensitive cathodes like LFP or LMFP and for all anodes, easily evaporates; alcohols are used for high Ni-based cathodes. Electrostatic interactions facilitate the self-organized structure, and after drying, bonding between the carbon matrix, active material particles, and the current collector occurs through surface functional groups and strong entanglement. Post-coating, electrodes undergo calendaring to control press density and porosity of the active layer, which can be optimized based on mass loading and LIB cell requirements.

This technology allows thick electrode coatings (150um per side of current collector) by using solvents with a strong 3D carbon matrix. The combination is designed for thick wet coatings without cracking during drying due to low surface tension. Thick cathodes, coupled with high-capacity anodes, drive a significant increase in energy density and cost reduction.

NX technology reduces the cell impedance by having highly electrically conductive electrodes, and highly electrically conductive cathode electrodes. Neocarbonix™ electrodes feature a 3D nanoscopic carbon matrix acting as a mechanical scaffold for the active material, mimicking polymer chain entanglement.

## Results

Cathode and Anode R2R coating first batch complete. Pictured below are rolls completed with coating partners. (Figure I.2.2)

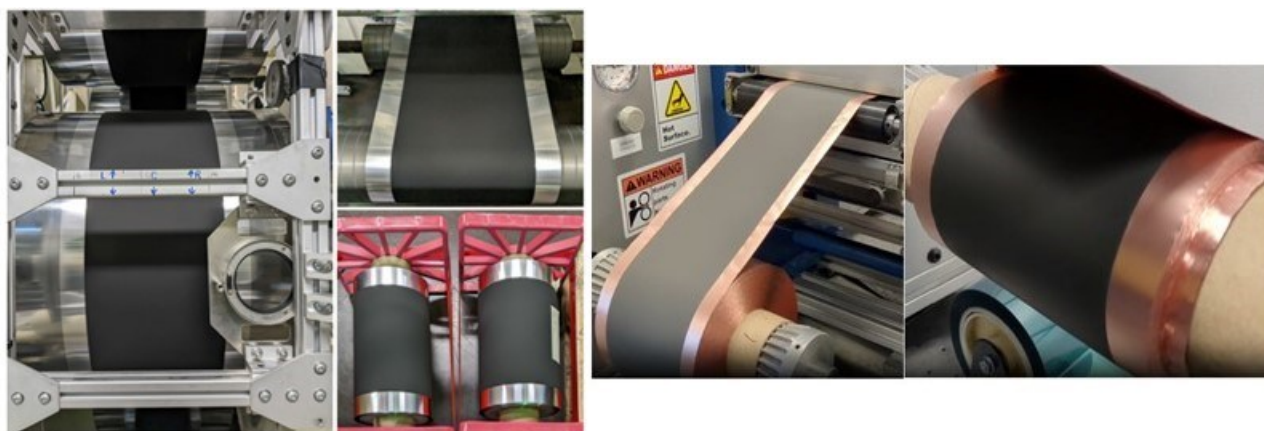


Figure I.2.2 R2R NX cathode & anode electrode rolls without using PFAS based polymers.

50 of NX  $\geq 10$  Ah cells were constructed and tested in 2023 with the following parameters: (Figure I.2.3)

Cell Specifications (30 °C)	NX ≥10 Ah NCMA #3    Si-C #8
NX Electrode Loading (mAh/cm <sup>2</sup> )	5.5
Core D (mm)	85
Core C (mm)	95
Thickness T1 [mm]	~7.9
Core Volume (mL)	~63.5
Measured Weight (g)	~171
Voltage range (V)	4.2 - 2.5
C/10 Core Energy Density (Wh/L)	941
C/10 Total Specific Energy (Wh/kg)	350
C/3 Core Energy Density (Wh/L)	922
C/3 Total Specific Energy (Wh/kg)	343

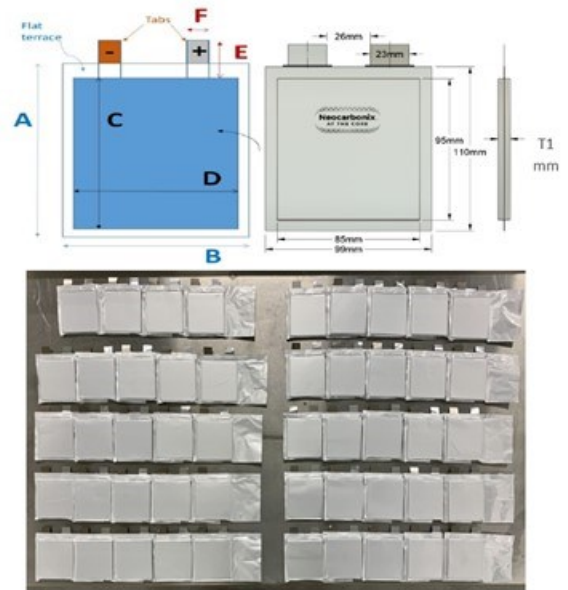


Figure I.2.3 NX >10Ah battery pouch cell parameters and pictures of the pouch cells.

NCMA Cell Design #1 in NX ≥10Ah shows has the best BOL capacity and energy. (See the figures, from Figure I.2.4 to Figure I.2.13.)

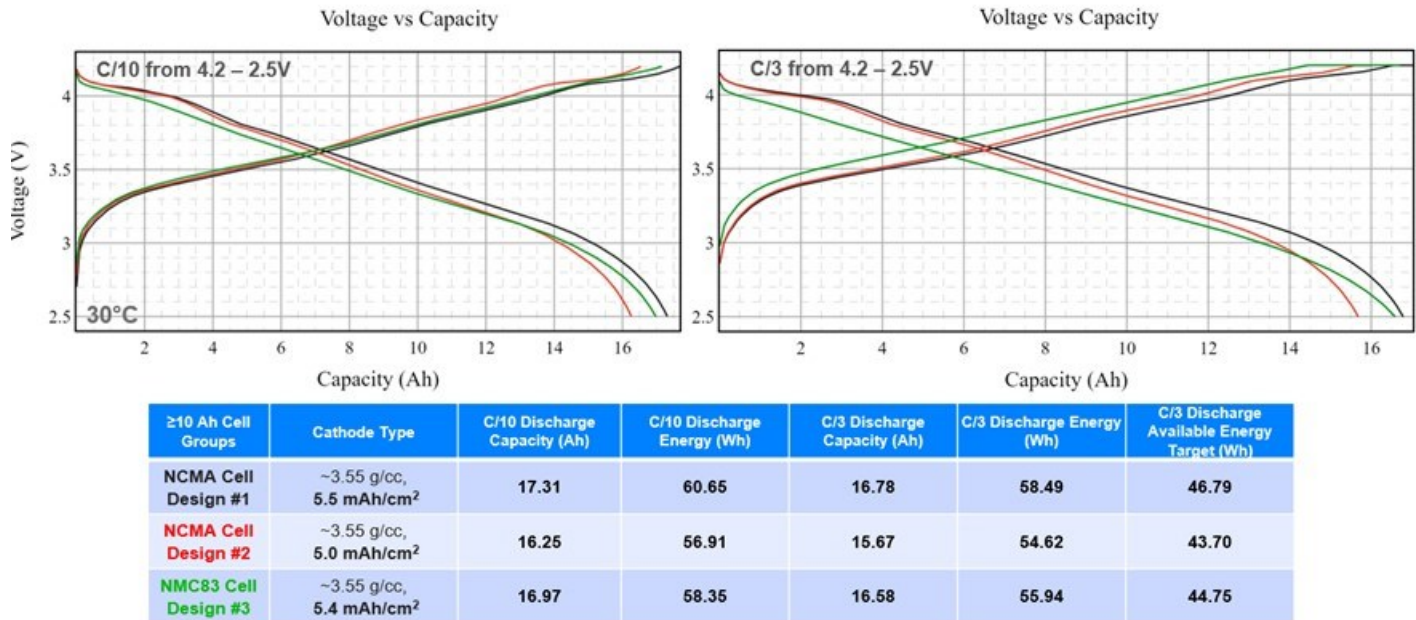


Figure I.2.4 NX >10Ah battery pouch cell design and initial capacity check performance summary.

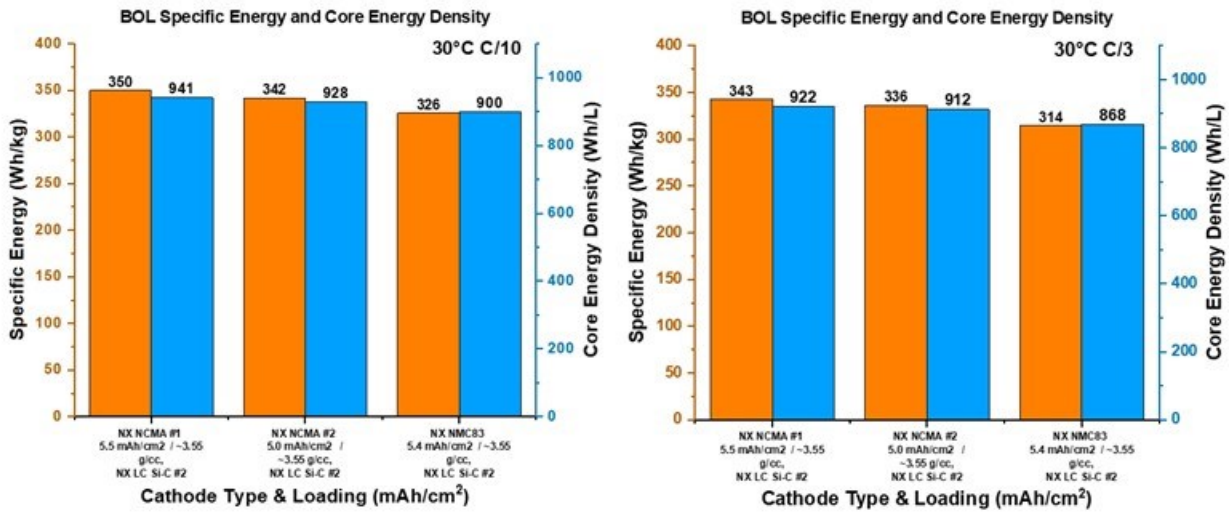


Figure I.2.5 NX >10Ah battery pouch cell design energy density comparison.

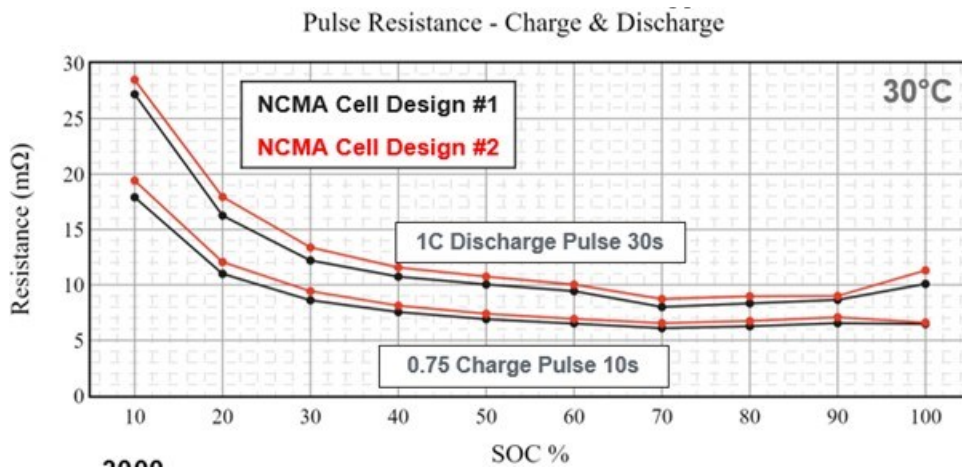


Figure I.2.6 NX >10Ah battery pouch cell design BOL HPPC data based on USABC test protocols.

From Section 4.4 of USABC EV Test Manual Rev 3, using a full range HPPC and OCV vs SOC curve, the Power Capabilities can be calculated:

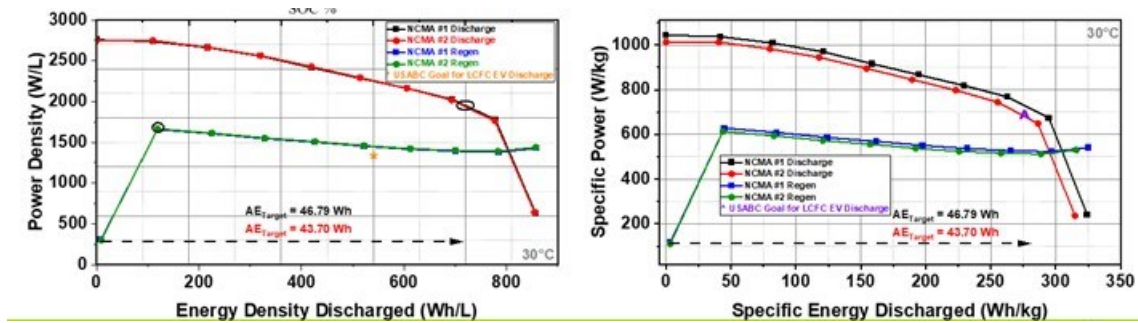
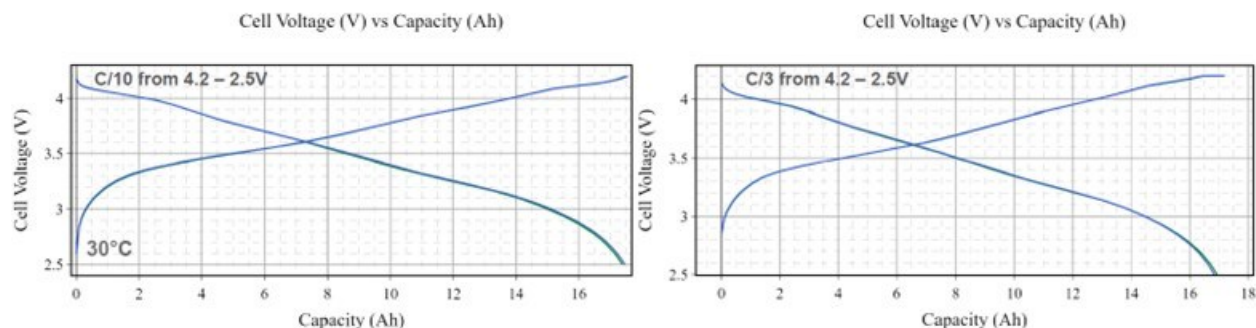


Figure I.2.7 NX >10Ah battery pouch cell Power Density vs. Energy Density Discharged.

NX Ni-Rich NMC83||SiGr ≥10 Ah BATTERY PROTOTYPE DELIVERY

For Recipient Use Only  
Protected Information



≥10 Ah Cell Groups	Cathode Type	C/10 Discharge Capacity (Ah)	C/10 Discharge Energy (Wh)	C/3 Discharge Capacity (Ah)	C/3 Discharge Energy (Wh)	C/3 Discharge Available Energy Target (Wh)
NMC83 Cell Design #3 - Batch 1	~3.5 g/cc, ~5.5 mAh/cm <sup>2</sup>	16.93	58.88	16.33	56.37	45.10
NMC83 Cell Design #3 - Batch 2	~3.5 g/cc, ~5.5 mAh/cm <sup>2</sup>	17.00	59.15	16.42	56.74	45.39

□ AE<sub>Target</sub> = 80% BOL C/3 Energy

Figure I.2.8 NX >10Ah battery pouch cell using NCM83 as cathode initial capacity check.

NX Ni-Rich NMC83||SiGr ≥10 Ah BATTERY PROTOTYPE DELIVERY

For Recipient Use Only  
Protected Information

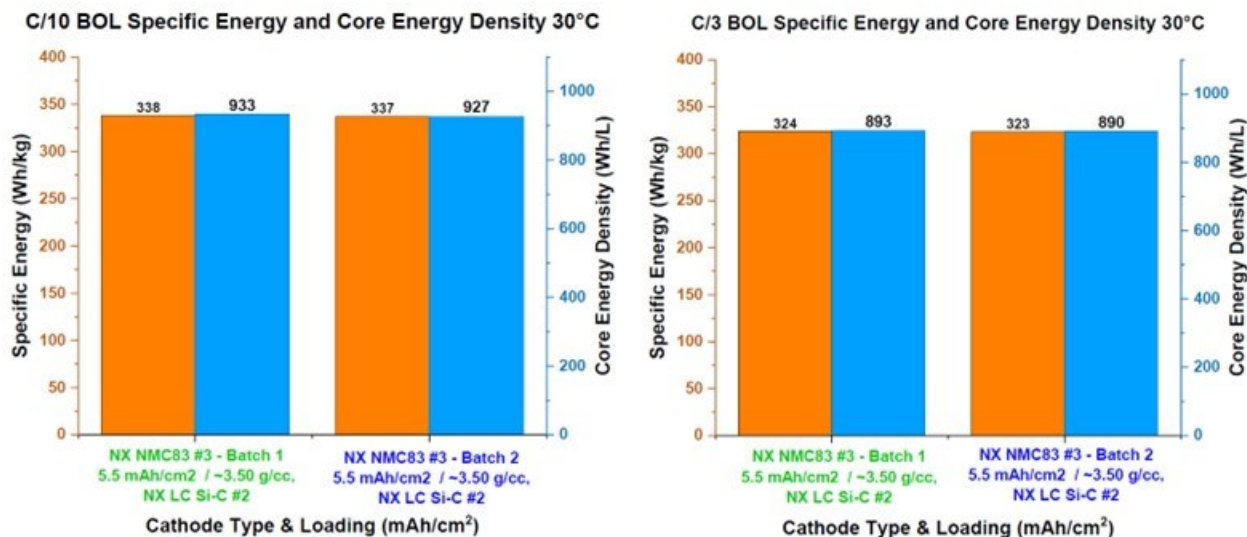
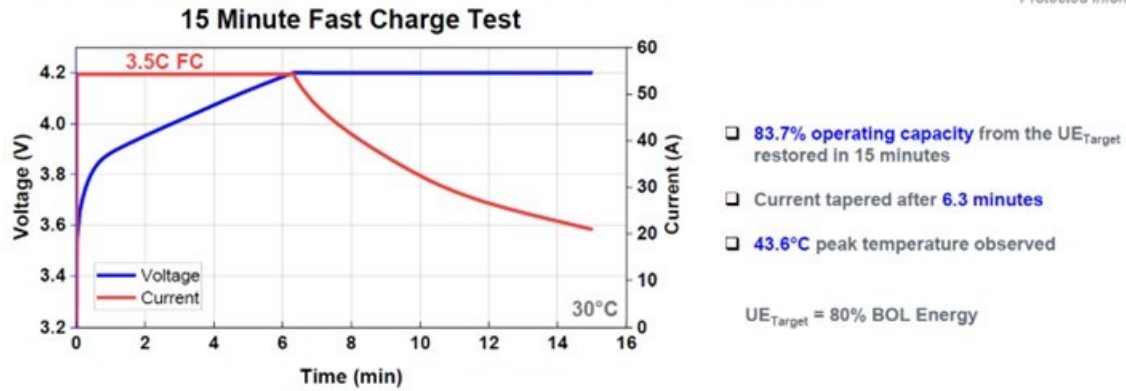


Figure I.2.9 NX >10Ah battery pouch cell using NCM83 as cathode initial energy density performance.



### NX Ni-Rich NMC83||SiGr ≥10 Ah BATTERY PROTOTYPE

For Recipient Use Only  
Protected Information

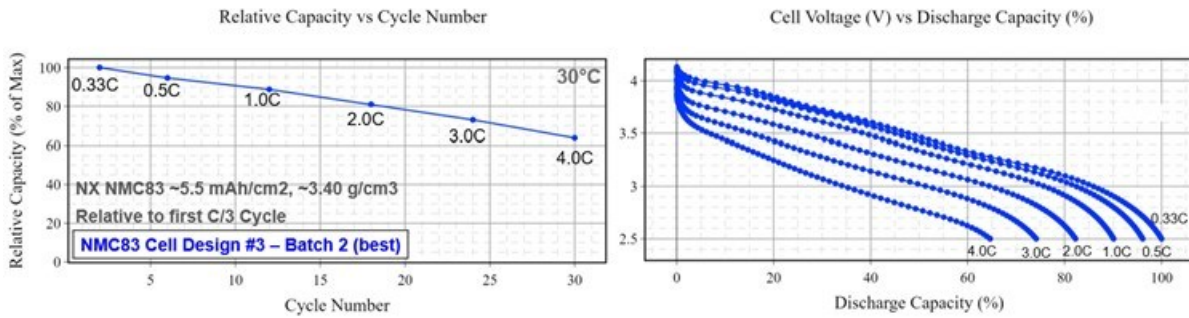


≥10 Ah Cell Groups	Cell IDs	Rated C/3 Capacity (Ah)	Operating Capacity of UE Target Discharge C/3 (Ah)	15-Min Charge (Ah)	% Operating Capacity Restored	Peak Temperature (°C)
NMC83 Cell Design #3 Batch 2	B02C05K00150	15.09	11.53	9.45	81.96	41.96
	B02C07K00150	14.56	11.12	9.23	83.00	43.40
	B02C17K00150	14.93	11.40	9.46	82.98	44.46
	B02C27K00150	15.63	11.97	10.40	86.88	44.53
Average		15.05	11.51	9.64	83.71	43.59

Figure I.2.10 NX >10Ah battery pouch cell using NCM83 as cathode initial 15mins-Fast-charging.

### NX Ni-Rich NMC83||SiGr ≥10 Ah BATTERY PROTOTYPE

For Recipient Use Only  
Protected Information



- NMC83 Design #3 shows 64% capacity retention at 4C compared to first C/3 capacity with 4C peak temperature of ~45 °C

Figure I.2.11 NX >10Ah battery pouch cell using NCM83 as cathode initial C-Rate discharge.

## NX Ni-Rich NMC83||SiGr ≥10 Ah BATTERY PROTOTYPE

For Recipient Use Only  
Protected Information

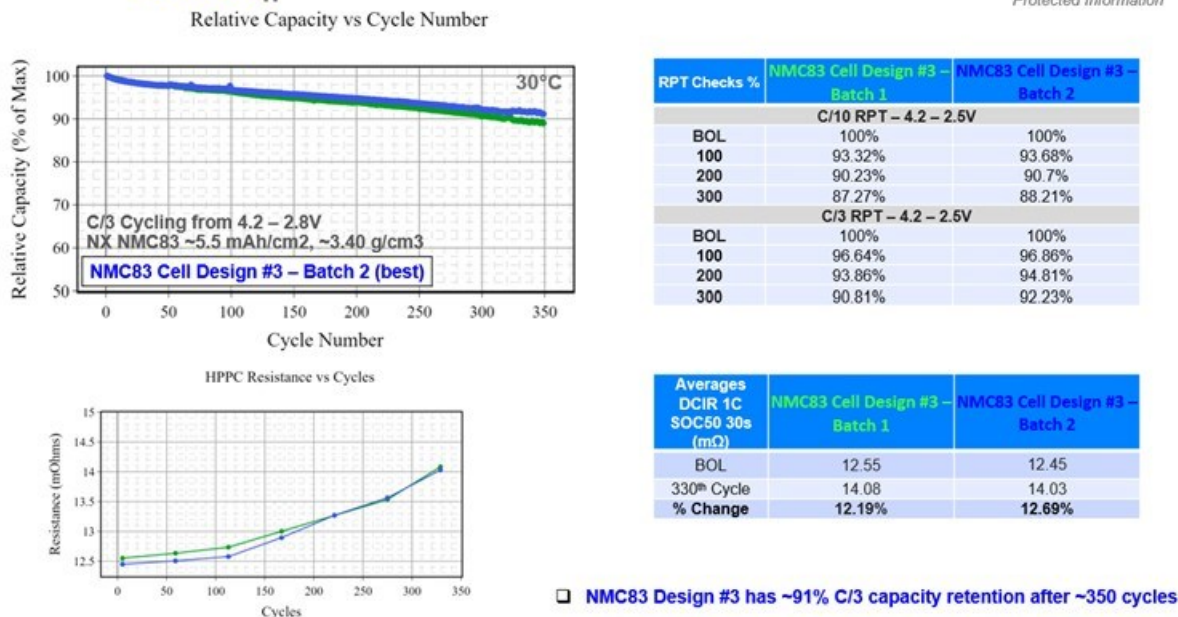


Figure I.2.12 NX >10Ah battery pouch cell using NCM83 as cathode C/3 cycling performance.

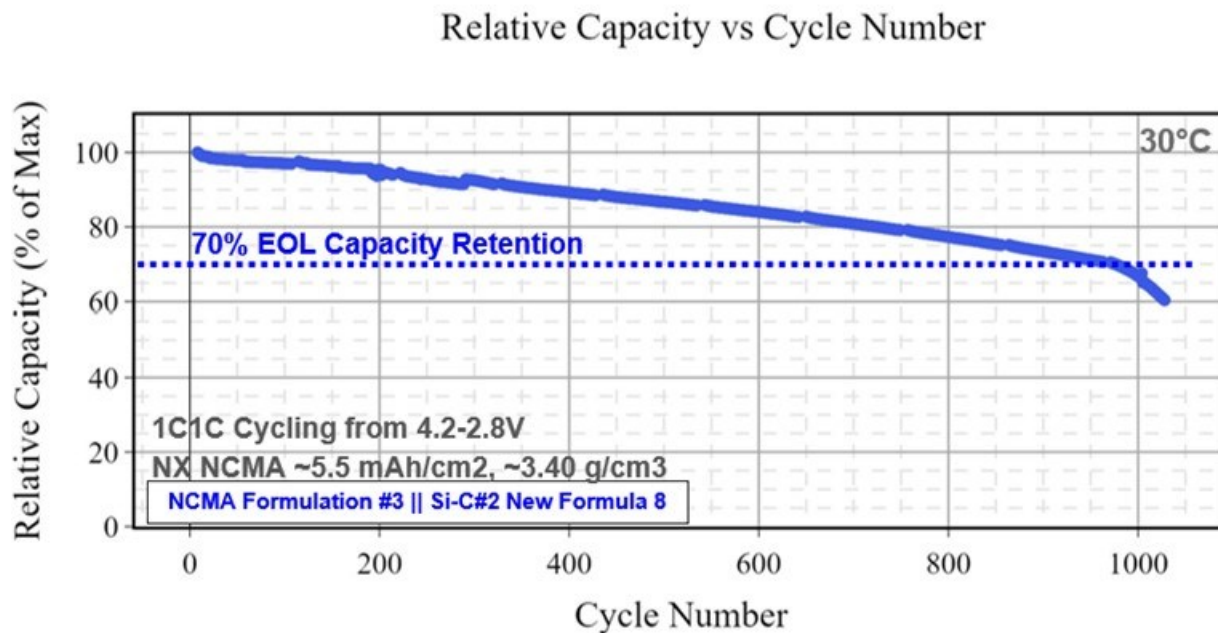


Figure I.2.13 NX >10Ah battery pouch cell using NCMA (Ni88) as cathode 1C1C cycling performance.

### Conclusions

The following are the conclusions for the Neocarbonix (NX) Ni-Rich NCM83/NCMA||Si-Gr ≥10 Ah Battery Prototype Cell Development:

1. NX Cathode and Anode R2R electrode coating without using PFAS polymers and without using NMP-solvent successfully completed.

2.  $\geq 10$  Ah cell design complete: using NCMA and NCM83 both cathodes combined with Si-Gr anode electrodes.
3. Energy density between 320-350 Wh/kg and 850-900 Wh/L have been achieved during 2023 project progress.
4. Initial 15 mins fast-charging performance: pass the 83-84% operating capacity ( $AE_{\text{target}}$  discharged) restored in 15 mins.
5. At 4C-Rate discharge, the  $>10$ Ah NX pouch cell prototype can achieve  $\geq 64\%$  capacity retention compared to C/3 discharge capacity.
6. 1C1C acceleration cycling performance shows: 1000 cycles with  $\sim 70\%$  capacity retention.
7. C/3 cycling performance shows that after  $\sim 350$  cycles, the cell capacity retention is  $\geq 90\%$ .
8. Intermediate NX 14-15Ah cell delivery has been finished and delivered to INL and internal Nanoramic test results have been updated in 2023.

### **Acknowledgements**

Nanoramic would like to thank Dr. Minghong Liu (FORD), our USABC program manager, and Dr. Meng Jiang (GM) for all the support and great communication during the current on-going USABC R&D project; Nanoramic would like to also thank all the members of the USABC work group for their advice and support during the project.

## I.3 Advanced Li-ion Cell Architectures for Extreme Fast Charging (XFC) Batteries for Electric Vehicles (EnPower, Inc.)

### Donald Pile, Principal Investigator

EnPower, Inc.  
8740 Hague Rd  
Indianapolis IN 46256  
E-mail: [donald@enpowerinc.com](mailto:donald@enpowerinc.com)

### Nicolas Eidson, DOE Technology Development Manager

U.S. Department of Energy  
E-mail: [Nicolas.Eidson@ee.doe.gov](mailto:Nicolas.Eidson@ee.doe.gov)

Start Date: July 18, 2022

End Date: August 30, 2024

Project Funding: \$2,009,374

DOE share: \$1,004,687

Non-DOE share: \$1,004,687

### Project Introduction

As Battery Electric Vehicle (BEV) adoption increases to serve the needs of mainstream consumers, it is ever more critical for battery cell technology to be low-cost with fast-charging (LCFC) capability, all while maintaining a minimum required vehicular range to be practical. However, an inherent tradeoff between energy (range) and power (fast-charge) exists for all Li-ion cells, and current battery cell technology is unable to satisfy both requirements. EnPower addresses this fundamental energy-power tradeoff with its unique and proprietary multilayer electrode architectures that increase the rate capability of thick, high-energy density electrodes. By using simultaneous multilayer slot-die coating, EnPower is also able to keep costs low with no detriment to throughput and yield. In this Development Program, EnPower will (i) iterate through multiple designs of multilayer graphite anodes and multilayer NMC811 cathodes, (ii) investigate electrolyte formulations for optimized performance, and (iii) scale up to a large format pouch cell size to arrive at a final deliverable cell build meeting key LCFC objectives.

### Objectives

The objective of the proposed program is to improve the NMC811/Graphite pouch cell system to meet the energy, power, and cycle life requirements defined by USABC for low-cost, fast-charge (LC/FC) cells. This will be accomplished over a performance period of 24 months, with final cell deliverables shipped to Idaho National Laboratory (INL) and Sandia National Laboratories. The following performance targets are key objectives:

- Fast Charging: 80% Usable Energy (U.E.) in <15 min.
- $\geq 309$  Wh/kg,  $\geq 734$  Wh/L @ BOL
- ~35 Ah pouch cells
- NMC811/Graphite(only)

### Approach

The general approach of this project is to design electrode pairs using EnPower's multilayer coating architecture and relatively high mass loadings that can obtain the  $\geq 309$  Wh/kg usable specific energy (@ BOL) when scaled up to a large format pouch cell. These electrodes will be developed during the first task. The second task will be an ~4 Ah interim deliverable cell build for testing at INL of cells based on the Task 1 developments. Electrolyte development and optimization will be conducted during the third task, followed by large format integration during the fourth task. The final deliverable, ~35 Ah large format pouch cells, comprises the fifth (last) task.

The higher energy density will be achieved through a combination of higher nickel content lithium nickel manganese cobalt oxide (NMC) along with higher upper voltage limit (approaching 4.3 V). The achievement of high charging rate will be gained through the multilayer coating technology, which enables more uniform lithiation distribution throughout the thickness of the coating, coupled with an optimized electrolyte formulation that will stabilize the electrode surfaces and maintain a high solution conductivity. Additional gains in energy density will be realized through the “economy of scale” of the larger cell size whereby there is lesser percentage of inactive packaging as more electrode active material is packed inside.

## Results

Results to date include developing an improved multilayer anode (MLA) coating formulation and an improved multilayer cathode (MLC) coating formulation, compared to those developed during the Technology Assessment Program (TAP) project. These improvements were realized by employing some new active materials in the coatings based on new availability and learnings of key materials properties. The cathode electrode employs a higher nickel-content lithium nickel manganese cobalt oxide (NMC) powder that enables achieving more capacity and energy by charging to greater than 4.2 V upper voltage limit. The top layer in the anode coating employs a higher rate-capable graphite. While more fully explored during the later Task 3, a higher voltage-capable electrolyte solution was qualified over the generic electrolyte formulation employed for routine electrode development. Additionally, a fast charge protocol was developed from reviewing several different charging schemes. This interim deliverable fast charge protocol utilizes a three-phase, step-down in power for fixed percentages of the 15-minute fast charge time period, though further improvement is expected for the final deliverable.

The Task 2, interim deliverable cell build is incorporating these first-year developments. The interim deliverable cell energy density targets at beginning of life are 692 Wh/L and 280 Wh/kg. At the electrode stack level, the present values are 668 Wh/L and 294 Wh/kg, slightly lower than and slightly better than the targets, before accounting for decreases from the small ~4Ahr prototype-scale cell packaging. Idaho National Laboratory will test this cell build according to typical USABC test protocols. More development work will be done during the second project year to increase the energy densities while maintaining fast charge capability.

## Conclusions

Progress to date has realized gains based on materials selections in the multilayer coating formulations. These improvements will be tested in the interim cell build that is based on a small pouch cell that is not optimized for energy densities. Remaining work entails (i) optimizing the coating densities and loadings (including electrode balancing), (ii) optimizing the electrolyte formulation for the stability of active materials at high charging rates and higher cathode potentials, and (iii) developing a large format pouch cell (approximately ten-times greater capacity) to realize size-scaling benefits to achieve greater energy densities.

## Acknowledgements

EnPower thanks the United States Advanced Battery Consortium (USABC), a subsidiary of the United States Council for Automotive research (USCAR), for support on this project.

## I.4 Solvent-free Electrode Manufacturing for Low Cost/Fast Charging Batteries (Worcester Polytechnic Institute)

### Yan Wang, Principal Investigator

Worcester Polytechnic Institute  
100 Institute Road  
Worcester, MA 01609  
E-mail: [yanwang@wpi.edu](mailto:yanwang@wpi.edu)

### Nicolas Eidson, DOE Technology Development Manager

U.S. Department of Energy  
E-mail: [Nicolas.Eidson@ee.doe.gov](mailto:Nicolas.Eidson@ee.doe.gov)

Start Date: November 19, 2019

End Date: September 15, 2023

Project Funding : \$548,351

DOE share: \$222,673

Non-DOE share: \$325,678

### Project Introduction

In conventional lithium-ion batteries, a slurry made of active materials, conductive additive and polymeric binder is cast onto the current collector. The coated electrodes are subsequently dried and calendared. In the slurry casting method, organic solvent (NMP) is used to make the slurry, which contributes significantly to the total cost of lithium-ion battery manufacturing (the solvent itself, solvent drying and recovery). In efforts to lower the battery cost associated with the NMP solvent, different approaches have been investigated. Finding a less expensive solvent to replace NMP has been the subject of much research. Water based approaches have been studied and found to compare favorably to organic solvent-based approaches [1-3]. This approach has achieved significant success on the anode side of Li-ion batteries, and aqueous slurries using Styrene Butadiene Rubber (SBR) as the binder have already been commercialized for graphitic anodes. However, the costly time-consuming and energy-intensive drying step following coating remains part of the fabrication process. In addition, NMP is still being used to dissolve PVDF binder on the cathode side, since binders dissolved in aqueous systems are not chemically or electrochemically stable at the high voltages seen at the positive electrode.

Complete elimination of the solvent is a promising approach to lower both the cost and manufacturing time of Li-ion batteries. Michael Wixom (previously at A123 Systems) at Navitas Systems, who collaborate with Maxwell Technologies, has proposed and developed a solvent-free electrode manufacturing process [4]. Telsa acquired Maxwell to commercialize the technology in 2019. In the manufacturing process, the active material, conductive carbon, and Polytetrafluoroethylene (PTFE) binder were pressed onto current collector directly to fabricate the electrode, as a viable approach to fabricate supercapacitors. However, to make Li-ion battery electrodes, the following additional challenges have been identified: (1) PTFE is not electrochemically stable in a lithium battery anode; (2) it is difficult to fabricate thin electrodes, which are essential to provide sufficient power for Li-ion batteries; (3) the electrode is stiff, which complicates or precludes winding for cylindrical cells/prismatic wound cell formats.

Structured electrodes have been demonstrated to improve battery charging rates. For example, experiments [5, 6] reveal that electrolytic transport becomes a major source of cell polarization at conditions of high current and/or large electrode thicknesses, both of which are the case for high rate charging of EV batteries. To enable fast charge, different structured electrodes have been developed [7, 8]. However, previous methods often utilize complex manufacturing processes and are difficult to scale up.

### Objectives

The project's objective is to develop low-cost batteries capable of fast charging for EV applications according to the USABC targets. In order to achieve the goal, the team will further develop a solvent-free manufacturing

method for hetero-structured electrodes in order to achieve fast charging capability and low-cost batteries. The hetero-structure enables fast charging and solvent-free manufacturing allows low cost. It is inherently challenging to fabricate hetero-structured electrodes using the traditional slurry casting method due to the complicated solvent drying process. In this project, the team will fabricate advanced electrodes with NMC622 and graphite as the cathode and anode materials, respectively.

### Approach

Our proposed solvent-free manufacturing could potentially achieve low cost and fast charge concurrently. In this project, solvent-free manufacturing is used to fabricate electrodes with layered structures, whereby layers have varying porosities strategically tuned to enable fast charge batteries. During electrode fabrication, dry mixed powder is directly sprayed onto the current collector. Subsequent hot rolling results in melting of the binder and formation of a strong bond between particles and current collector. In order to enable high rate, electrodes with a multi-porosity hetero-structure will be fabricated. Compared to other methods, such as co-extrusion, to fabricate multi-porosity hetero-structured electrodes, the proposed method does not involve any solvent or complicated hardware and can be easily scaled up. Due to the elimination of solvent, the solvent-free manufactured layered electrodes allow for fast charge (structured electrode), low cost (no solvent and drying), and fast production (no drying step) when compared to the conventional wet processed electrodes. Table I.4.1 is a comparison of our technology to current slurry casting technology to fabricate battery electrodes.

**Table I.4.1 Comparison of Our Technology to Current Slurry Casting Technology**

	Current technology	Our proposed technology
Material mixing	Wet mixing with solvent	Dry mixing without solvent
Coating	Slurry coating	Dry printing
Dry	Dry step needs	No drying
Solvent recovery	Organic solvent needs to be recovered	No recovery step
Electrode	Uniform porosity electrode	Porosity graded electrode

### Results

#### Modeling

The following modeling tasks were performed in the past annual period.

#### Electrolyte selection for dry-printed electrodes

We evaluated the effect of employing alternative electrolytes on improving the charging performance of dry-printed electrodes. In previous study, our modeling suggests that replacing the EC:EMC electrolyte with EC:DMC in the high loading NMC cells (NMC loading: 30 mg/cm<sup>2</sup>) could increase the 4C charging capacity by more than 10%. This prediction was confirmed by electrochemical testing. Literature search showed that adding esters as co-solvents to carbonate solvent has the benefit of lowering freezing points, reducing viscosity and increasing ionic conductivity. Further literature search shows that Dahn's group reported that addition of methyl acetate (MA) could significantly increase the ionic conductivity of EC:EMC and EC:DMC electrolytes. The effect of adding MA to EC:EMC and EC:DMC on the dry-printed NMC cells was accessed based on the reported electrolyte properties. In the calculations, the ionic diffusivity of the electrolyte is assumed to increase with MA addition in the same proportion as conductivity. Figure I.4.1 shows that the 4C/15-min CCCV (4C charging to 4.2 V + CV with a total charging time of 15 minutes) capacity of the 2-layer dry NMC/Graphite cell increases roughly linearly with MA fraction. 30 wt% MA gives 16% and 7% higher capacity than the EC:EMC and EC:DMC baselines, respectively. The reason that EC:EMC sees a bigger increase in capacity than EC:DMC is that MA induces a larger increase in conductivity in the former. As shown in Figure I.4.1, the enhancement is larger due to the extension of the CC step in the charging process. We believe that the predicted improvement is significant enough to be experimentally tested.

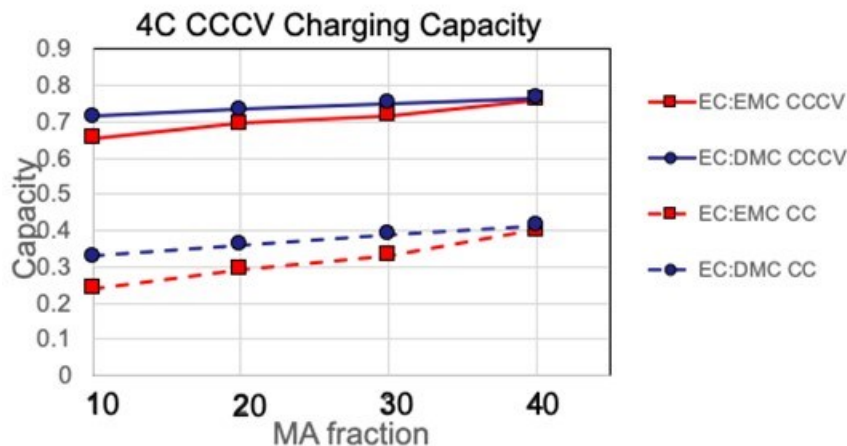
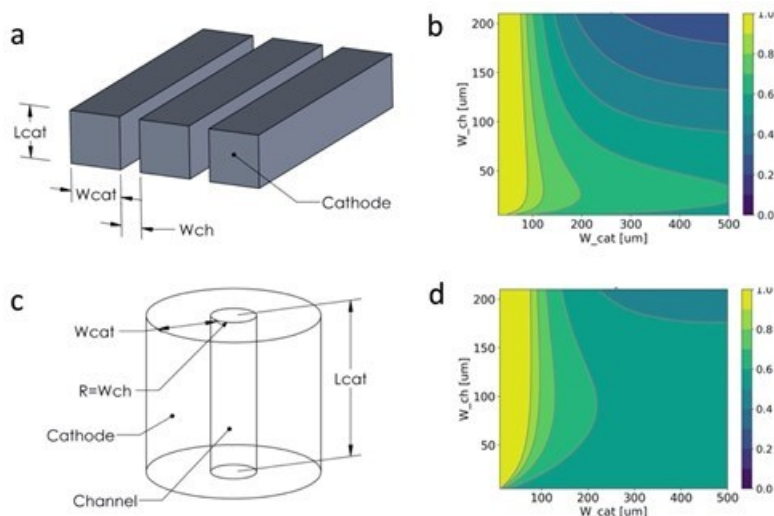


Figure I.4.1 Calculated 4C CC and CCCV charging capacities of 2-layer dry NMC/Graphite cell using EC:EMC:MA and EC:DMC:MA = 30:(70-x):x electrolytes with different MA fraction  $x$ .

### Design of 3D structured electrodes

Looking beyond the current dry-printed electrode manufacturing process, we evaluated the effect of introducing 3D texture into the electrode on improving its rate performance in addition to the 2-layer design. We recently developed a highly efficient analytical model for predicting battery rate performance in 3D as an alternative to the P2D model, which are very computation costly to implement in 3D. The model applies the uniform reaction and quasi-steady-state approximations to greatly simplify the modeling of electrolyte transport and combines with the single particle model to predict the state of charge distribution in the solid phase. The computation time of the analytical model is several orders of magnitude lower than P2D simulations and could complete a scan of the electrode parameter space to identify the optimal parameter values within reasonable amount of time. We considered 3D texture in NMC cathode with either a trench geometry (Figure I.4.2a) or cylindrical hole geometry (Figure I.4.2c). Three important parameters in both designs are the cathode thickness  $L_{cat}$ , cathode layer width  $W_{cat}$  and electrolyte channel width  $W_{ch}$ . Figure I.4.2 b,d shows the 4C capacity as a function of  $W_{cat}$  and  $W_{ch}$  for both designs at a fixed  $L_{cat} = 150 \mu\text{m}$ . They show that there exists a critical  $W_{cat}$  below which full capacity utilization could be achieved at sufficiently large  $W_{ch}$ . An interesting feature is that an optimal  $W_{ch}$  exists to maximize the capacity above the critical  $W_{cat}$ . Below the critical  $W_{cat}$ , however, increasing  $W_{ch}$  above  $\sim 50 \mu\text{m}$  has almost no effect on the rate capability. While the critical  $W_{cat}$  values for both designs are comparable, the cylindrical hole design corresponds to a larger volume fraction of the active materials and thus offers high energy density. It is important to note that the predicted critical  $W_{cat}$  is around  $100 \mu\text{m}$ . From a manufacturing perspective, the dry-printing technique is more viable for creating texture with a feature of size above  $100 \mu\text{m}$ .





**Figure I.4.2 a, c) Schematics of the trench and cylindrical hole designs, respectively. b, d) Normalized 4C capacity of NMC half-cell with  $L_{cat} = 150 \mu\text{m}$  vs cathode layer width  $W_{cat}$  and channel width  $W_{ch}$  in the trench and cylindrical hole design, respectively.**

#### **Electrode design with graded particle size distribution**

For the 2-layer graphite anode configurations, we explored another design by using different particle sizes in each layer. Typical NMC and graphite particles used in commercial batteries have particle diameters around  $10 \mu\text{m}$ . Reducing particle size could benefit fast charging by accelerating lithium solid diffusion but has the downside of increasing the surface area – volume ratio and inducing faster capacity fade due to exacerbated side reactions. To mitigate the negative effect, we consider a 2-layer electrode configuration (Figure I.4.3a) where only cathode and anode particles in the layer close to the separator have reduced particle size. The configuration is denoted as  $\{R_{c1} | R_{c2} || R_{a2} | R_{a1}\}$ , where  $R_{c1}$  ( $R_{a1}$ ) and  $R_{c2}$  ( $R_{a2}$ ) are the cathode (anode) particle size ( $\mu\text{m}$ ) in the layer next to current collector and separator, respectively. Compared to the baseline line  $\{5 | 5 || 5 | 5\}$  (uniform large particle size), the constant current charging capacity of the two-layer structure at 4C is higher by 43%. Interestingly, the two-layer structure even outperforms electrodes with uniform small particle size ( $R = 1 \mu\text{m}$ ). The green curve in Figure I.4.3b shows that the 4C constant current charging capacity gradually increases when particle size  $x$  in configuration  $\{x | 1 || 1 | x\}$  is varied from 1 to  $10 \mu\text{m}$ . We hypothesize that this somewhat surprising result originates from the ability of graded particle size to improve the uniformity in reaction distribution across the electrodes. On the other hand, placing small particles in the layer next to the current collector leads to inferior charging performance. This is illustrated by the orange curve in Figure I.4.3b, which shows that the continuous decay of 4C constant charging current capacity in the  $\{1 | x || 1 | 1\}$  configuration when  $x$  increases from 1 to  $10 \mu\text{m}$ .

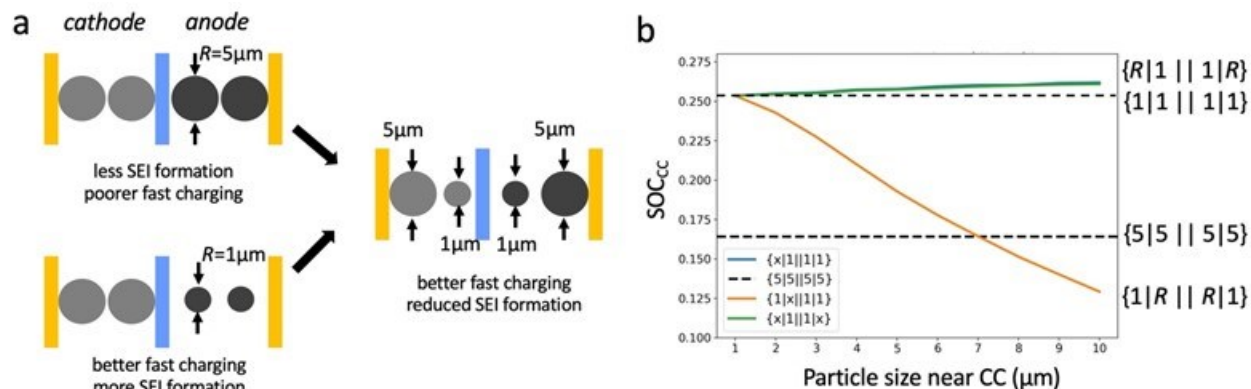


**Figure I.4.3** a) Schematic of using graded particle size configurations to improve fast charging while mitigating side reactions. b) 4C constant current charging capacity of NMC/graphite full cells with different particle size arrangements. An electrode configuration is denoted as  $\{R_{c1} | R_{c2} || R_{a1} | R_{a2}\}$ ;  $R_{c1}$  ( $R_{a1}$ ) and  $R_{c2}$  ( $R_{a2}$ ) are the cathode (anode) particle size ( $\mu\text{m}$ ) in the layer next to current collector and separator, respectively.

To further shed light on how graded particle size improves charging rate capability, we examine the spatial distributions of salt concentration and liquid potential across the cathode in the two-layer structure. As shown in Figure I.4.4, increasing the cathode particle size difference between the two layers from  $2\mu\text{m}$  vs  $1\mu\text{m}$  to  $8\mu\text{m}$  vs  $1\mu\text{m}$  decreases the gradient in these quantities, which helps reduce cell polarization and extends the charging time before the cutoff voltage is reached. In addition, the particles in the layer close the separator has a smaller SOC gradient and higher utilization of the active material in the  $\{8|1 || 3|3\}$  configuration when compared to  $\{2|1 || 3|3\}$  at the same charging time. This leads to a higher average SOC in the cathode when constant current charging is terminated at the 4.2V cutoff voltage.

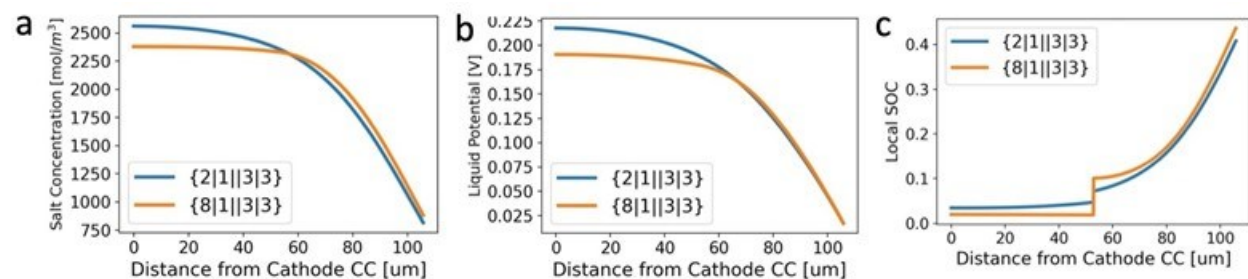


**Figure I.4.4** Spatial distributions of salt concentration (a) and liquid potential (b) across the cathode in NMC/graphite full cell with the  $\{8|1 || 3|3\}$  (orange) and  $\{2|1 || 3|3\}$  (blue) configurations upon galvanostatic charging at 4C. c) Comparison of SOC distribution of NMC particles in the  $\{8|1 || 3|3\}$  and  $\{2|1 || 3|3\}$  configurations upon 4C charging.

#### Effect of electrical conductivity on fast charging performance

Because the conductive additive amount in NMC and graphite electrodes is reduced to 2 wt% in the new electrode design with a high NMC loading of  $30 \text{ mg/cm}^2$ , we evaluated the impact of this change by modeling the effect of electronic conductivity on the fast-charging performance of the NMC/graphite cells. Using the battery model calibrated for the dry-printed NMC/graphite cell, we examined the dependence of the 4C charging and discharging capacities on the electronic conductivities of cathode and anode, respectively. As shown in Figure I.4.5a, increasing the cathode conductivity  $\sigma_{cat}$  from 0.1 to 1 S/m increases the 4C charging capacity by almost 100% from  $\sim 0.12$  to  $\sim 0.25$ . On the other hand, varying the anode conductivity  $\sigma_{an}$  between 1 and 100 S/m does not significantly influence the capacity. We note that the graphite anode has higher intrinsic conductivity than NMC, which is why we chose larger conductivity values for investigation on the anode side.  $\sigma_{cat}$  is found to have a lesser effect on the 4C discharging capacity, which increases from 0.245 to

0.28 upon raising  $\sigma_{cat}$  from 0.1 to 1 S/m, see Figure I.4.5b. The effect of  $\sigma_{cat}$  is also less pronounced in the low-loading NMC/graphite cell with 20 mg/cm<sup>2</sup> of NMC, see Figure I.4.5c. Such thickness dependence by considering the contributions of different types of resistances in the electrodes. The total electrode resistance could be expressed as  $R = R_{ct} + R_{elec} + R_{ion}$ , where  $R_{ct}$  is the charge transfer resistance associated with the charge transfer process at the electrode/electrolyte interface,  $R_{elec}$  is the electronic resistance and  $R_{ion}$  is the ionic resistance. As illustrated in Figure I.4.5d, these resistances have different thickness dependence:  $R_{ct} \propto L^{-1}$ , and  $R_{elec}, R_{ion} \propto L$ . As such, the electrode resistance is dominated by  $R_{ct}$  when electrode is thin and  $R_{elec} / R_{ion}$  for thick electrode, which explains the observed effect of  $\sigma_{cat}$  in thick vs thin electrodes. The criteria for determining the optimal amount of conductive additive are thus given by:  $R_{elec} < R_{ct}$  and  $R_{elec} \approx R_{ion}$ .

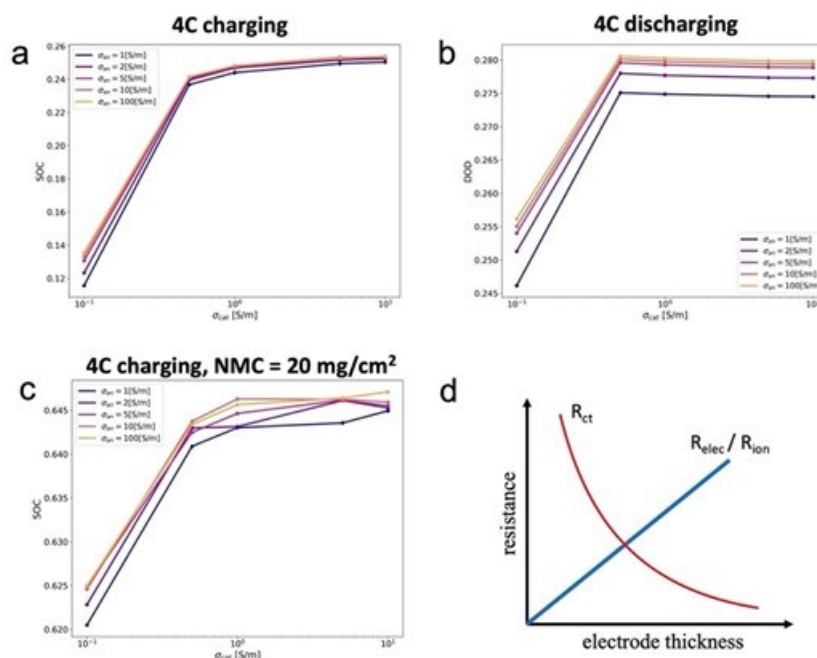
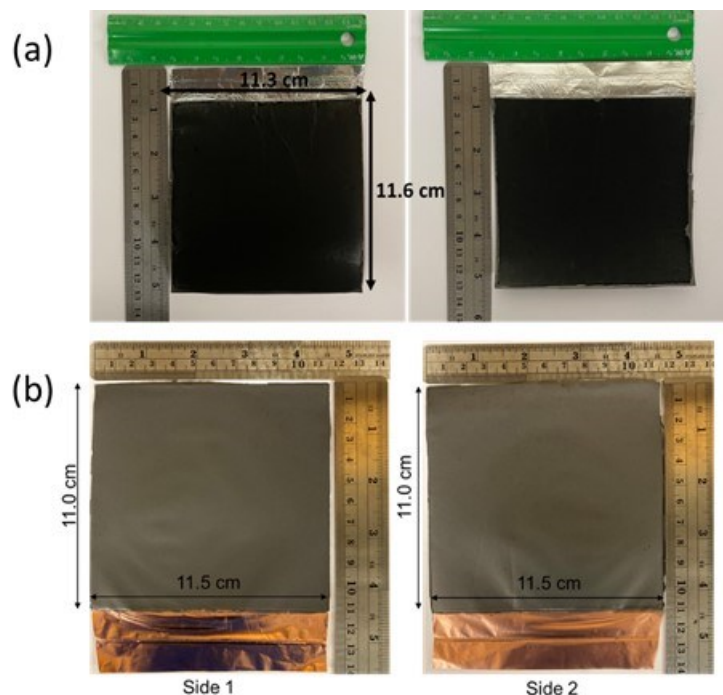


Figure I.4.5 a, b) Effect of cathode and anode electronic conductivities on 4C charging (a) and discharging (b) capacities of NMC/graphite cell with 30 mg/cm<sup>2</sup> of NMC and 15 mg/cm<sup>2</sup> of graphite. c) Effect of cathode and anode electronic conductivities on 4C charging capacity of NMC/graphite cell with 20 mg/cm<sup>2</sup> of NMC and 10 mg/cm<sup>2</sup> of graphite. d) Schematic of the dependence of charge transfer ( $R_{ct}$ ), electronic ( $R_{elec}$ ) and ionic ( $R_{ion}$ ) conductivities on electrode thickness.

#### Electrode fabrication and manufacturing process development

First, the process was successfully developed to fabricate large-scale (~100mm x 100mm) and two-side coated electrodes. For cathode manufacturing, firstly, NMC, PVDF and C65 with a 95:3:2 composition similar to the recipe used for latest pouch deliverables. The mixed powder was sprayed on 1<sup>st</sup> side of the current collector (carbon coated Al foil) to achieve an average area loading of ~29.6 mg/cm<sup>2</sup>. Followed by a hot plate heating in air for ~1hr, the sample was pressed down to ~43% porosity using room temperature rolling. After the rolling, the sides of the current collector were flipped (2<sup>nd</sup> side now facing the sprayer gun while 1<sup>st</sup> facing the substrate) for 2<sup>nd</sup> side coating. Same mixed powder was sprayed on 2<sup>nd</sup> side to achieve similar loading. Followed by similar hot plate heating step as for 1<sup>st</sup> side, the sample was pressed down to overall sample porosity of ~36%. The sample after final pressing bends along the pressing direction. A planarization step (hot plate heating at 140°C for 5mins and sandwiching the sample between two large glass slides) was used to make the sample flat (Figure I.4.6a). Finally, the sample was vacuum sealed and shipped for punching into coin cells and further electrochemical testing.



**Figure I.4.6 Manufactured 2-sided cathode (a) and anode (b) for 1.5Ah cells.**

For anode manufacturing, graphite and PVDF were mixed with a ratio of 96:4, which is same as the latest deliverables. The PVDF was sprayed on the 1<sup>st</sup> side of the Cu foil current collector to enhance the bonding, the loading for the PVDF was controlled to be  $\sim 0.05 \text{ mg/cm}^2$ , then the PVDF coated current collector was heated at  $200 \text{ }^\circ\text{C}$  for 30 minutes to melt the PVDF, after that, the mixed graphite/PVDF was sprayed on the current collector to a loading of  $\sim 15 \text{ mg/cm}^2$ . Followed by a hot plate heating in glovebox for  $\sim 1 \text{ hr}$  at  $250 \text{ }^\circ\text{C}$ , the sample was pressed down to  $\sim 40\%$  porosity using room temperature rolling. After the 1<sup>st</sup> roller pressing, the sample bends along the roller pressing feeding direction, a planarization step (hot plate heating at  $150^\circ\text{C}$  for 25mins and sandwiching the sample between two large glass slides) was used to make the sample flat before performing the 2<sup>nd</sup> side spraying. The current collector was flipped for 2<sup>nd</sup> side coating, PVDF was sprayed and heated, then the mixed graphite/PVDF was sprayed to 2<sup>nd</sup> side at a loading of  $\sim 15.0 \text{ mg/cm}^2$ , followed by the heating in the glove box ( $250^\circ\text{C}$  for 1 hour). The final pressing was used to press down to overall sample porosity of  $\sim 32\%$  (Figure I.4.6b).

After developing the manufacturing process, four batches of two-layer anodes were fabricated to optimize the design for final deliverables. The main parameter that needs to be optimized is the carbon contents in the top layer and bottom layer. The parameters are summarized in Table I.4.2. Carbon content varies from 0% to 1% for the bottom layer. For top layer, carbon content was chosen to be relatively lower, ranging from 0% to 0.5%, in order to main acceptable bonding strength for the top layer which is more porous. The rest of the parameters, including porosity and loading, are maintained at the same level for all the batches. In addition, cathode mixing recipe was also changed to evaluate the impact of mixing sequence. After the optimization, the parameters of Batch 3 in Table I.4.2 were selected for final deliverables.

**Table I.4.2 The Parameters of the 4 Batches of Cathode and Anode to Optimize the Design for the Final Deliverable.**

		Batch 1	Batch 2	Batch 3	Batch 5
Anode	Bottom layer porosity	30%	30%	30%	30%
	Bottom layer composition (Gr:PVDF:C)	96%:4%:0%	96%:3%:1%	96%:3%:1%	96%:4%:0%
	Top layer porosity	42%	42%	42%	42%
	Top layer composition (Gr:PVDF:C)	96%:4%:0%	96%:4%:0%	96%:3.5%:0.5%	96%:4%:0%
Cathode	Composition (NMC:PVDF:C)	95%:3%:2%	95%:3%:2%	95%:3%:2%	95%:3%:2%
	Mixing recipe	Sequential	Sequential	Sequential	All-mixed

A total of 110 two-side coated cathodes and 51 two-side coated two-layer anodes were fabricated with parameters chosen above and all the electrodes for deliverables have been delivered to Microvast. The parameters are summarized as follows: Anode, bottom layer: porosity 30%, composition (Gr:PVDF:C) 96%:3%:1%; top layer: porosity 42%, composition (Gr:PVDF:C) 96%:3.5%:0.5%. Cathode, composition (NMC:PVDF:C) 95%:3%:2%, porosity 35-37%.

During the fabrication of these electrodes, it is found the process optimization is needed to overcome defects in cathode and increase yield. During the final few gradual compression steps, defects can be observed towards the end of electrodes which reduces the manufacturing yield. These defects include foil/electrode wrinkling and electrode peel-off or detachment (Figure I.4.7a). It was previously found that gradual pressing can effectively reduce wrinkling defects. However, gradual pressing alone was not able to completely eliminate the defects. It is then hypothesized that uneven pressure in the nip zone is the main cause of the defects (Figure I.4.7c). To verify this hypothesis and seek a solution, uniform nip pressure is ensured by adjusting the gap across the electrode width before the few final presses. By adopting this approach, the defects can be effectively eliminated (Figure I.4.7b). As compared with cathode, the fabrication of anode is less challenging, and no such defects were observed.

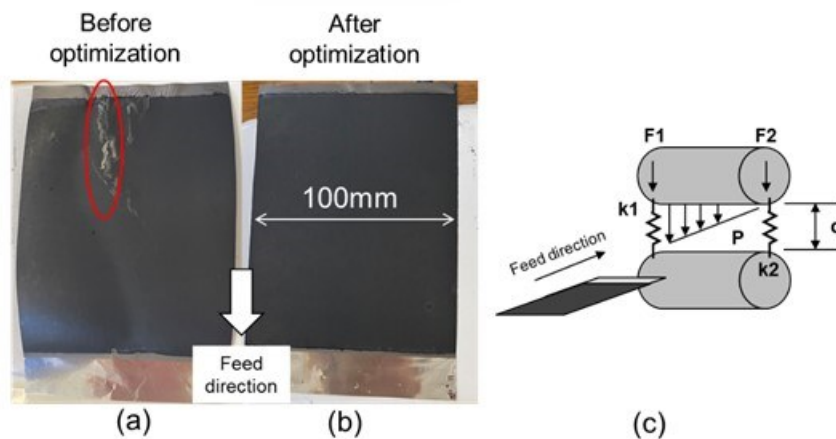


**Figure I.4.7 Overcome defects in cathode calendering step. (a) Defect observed towards the end of the electrode. (b) Defect-free cathode after process/pressure optimization. (c) Schematic of the calender to illustrate the non-uniform pressure in nip zone.**

The R2R manufacturing system integrated with spraying and multiple calendaring steps developed during this project is shown in Figure I.4.8a. The system is capable of fabricating 100mm wide electrodes for pouch cell evaluation. The calender chosen for fabricating 100mm wide cathode is 15-ton mechanical calender and that chosen for anode is 3-ton mechanical calender. The selection of calender is based on the modeling the pressure of the calendaring process, as will be discussed later. The achieved lowest non-uniformity on 100mm x 100mm area is  $\pm 3.5\%$ .

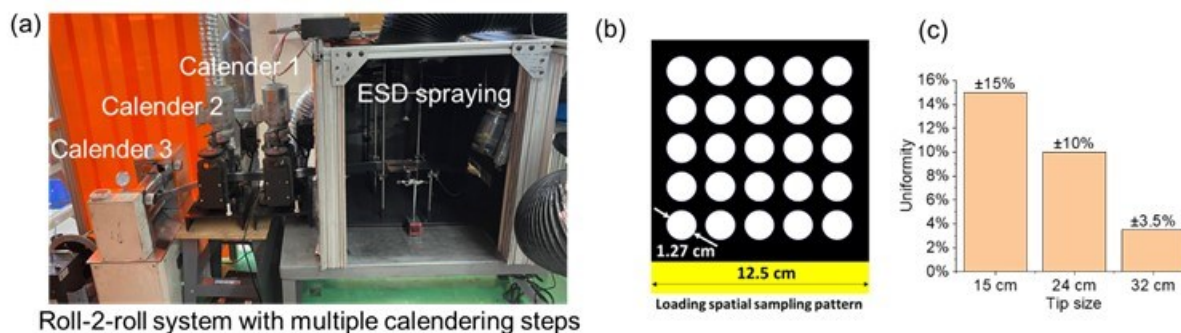


**Figure I.4.8 Summary of the solvent-free manufacturing system developed. (a) The R2R system with multiple calendaring steps. (b) Electrode used to characterize the electrode non-uniformity. (c) The lowest non-uniformity achieved is  $\pm 3.5\%$ .**

During the development of the manufacturing process, an analytical calendaring model (Figure I.4.9a) has been developed to predict pressure/stress which considers powder friction, roller/foil friction, powder compressibility, roller geometry, compression ratio, etc. In order to obtain the parameters needed for the stress model, powder compressibility was measured for cathode and anode powders. Cathode powder (NMC:C:P=90:5:5) was loaded in a pressing die and compressed by hydraulic press. The applied pressure and volume change were recorded, and the pressure-volume relationship was fitted by  $P/P_0 \sim (V_0/V)^K$ , wherein  $K$  is used to characterize the compressibility of powder mixture. The same experiment was performed for anode powder mixture (Gr:C:P=90:5:5). It was found  $K \sim 4.8$  for anode and for cathode powder mixing,  $K \sim 10.8$ . High value of  $K$  in cathode powder suggests it requires higher pressure to compress the cathode powder. In addition, powder rheology of cathode powder has been measured. Friction coefficient changes slightly with composition changes (NMC = 0.437; NMC:C:PVDF = 0.445; NMC:C = 0.482.) at 80kPa loading. Preliminary calendaring modeling result shows  $>10X$  higher pressure when calendaring cathode as compared with anode. Based on the model predicted pressure, it is found to press 100mm wide cathode,  $\sim 5.6$  tons force is needed, while to press 100mm wide anode,  $< 1$  ton is needed. Therefore, roller with 100mm diameter (3 tons) was selected for anode, and roller with 150mm diameter (15 tons) was selected for cathode for final deliverables. A finite element model (Figure I.4.9b) has also been developed to model the powder calendaring process for process optimization and compared with analytical model.

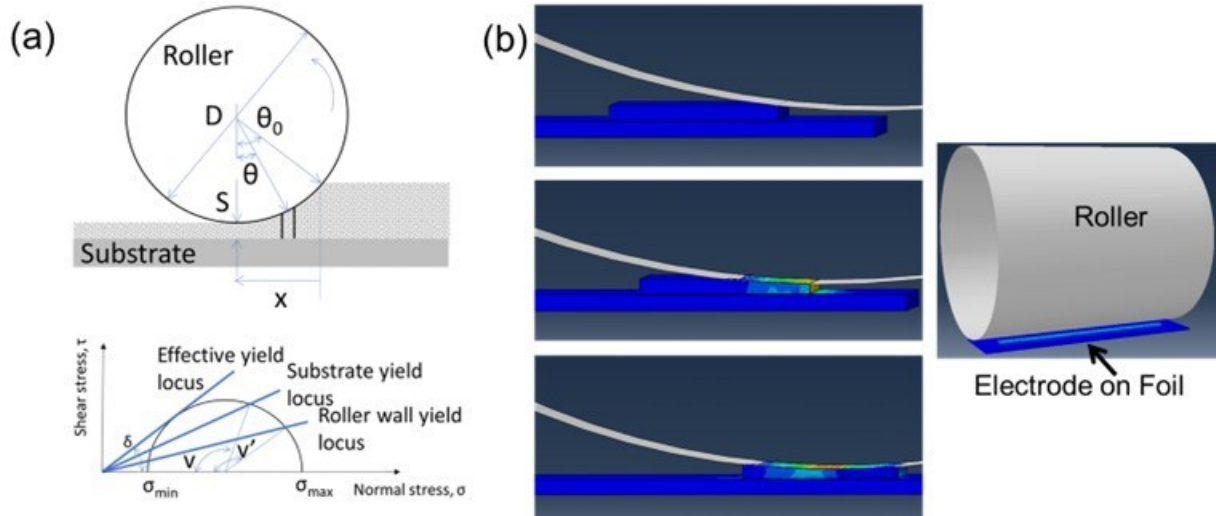


Figure I.4.9 The calendering models developed to predict the stress/pressure during calendering dry powder on current collector. (a) Analytical model, (b) Numerical finite element model.

**Electrode Properties Characteristics**

**Electrodes physical examination**

The electrode's recipe has been modified since Jan 2023 by increasing the active material to 96%(2% C65, 2% PVDF) from 90% (5% C65, 5% PVDF), resulting in higher loading capacities for both the cathode and anode. The electrodes were also double-coated to further increase its energy density, but issues of weak bonding led to a subsequent adjustment of the cathode active material ratio to 95%(2% C65, 3% PVDF). For anode, the active material ratio was kept as 96%, but C65 and PVDF were adjusted to 0.5% and 3.5% respectively. Upon inspection of the received double-sided electrodes in Apr 2023, only the anode showed minor texturing due to the calender roller, which doesn't affect its function. SEM analysis shown in Figure I.4.10 confirmed uniform material distribution and revealed open pores in the electrodes, hinting at decreased tortuosity. For further evaluations, 12mm single-sided electrodes were produced from the larger electrodes.

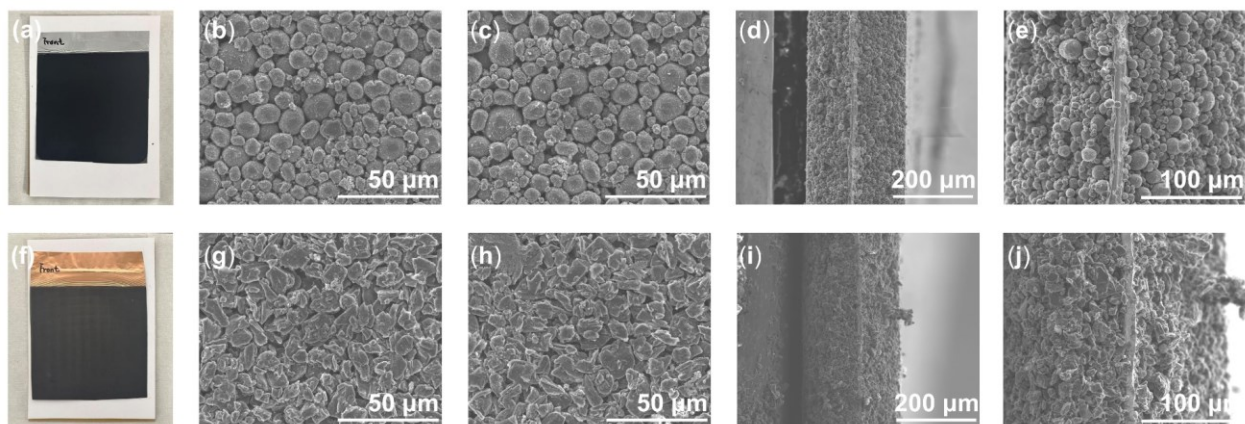


Figure I.4.10 Visual appearance of received large double-sided dry-printed (a) cathode electrode, (f) anode electrode. SEM characterization on (b) cathode front surface, (c) cathode back surface; (g) anode front surface, (h) anode back surface; (d), (e) cathode cross-section; (i), (j) anode cross-section.

The tortuosity of received cathode and anode were measured with the prepared 12mm single-sided electrodes. The impedance spectra are shown in Figure I.4.11 and the corresponding obtained tortuosity value are

presented in Table I.4.3. Both the dry-printed cathode and anode exhibited significantly lower tortuosity than the slurry control electrodes provided by MV.

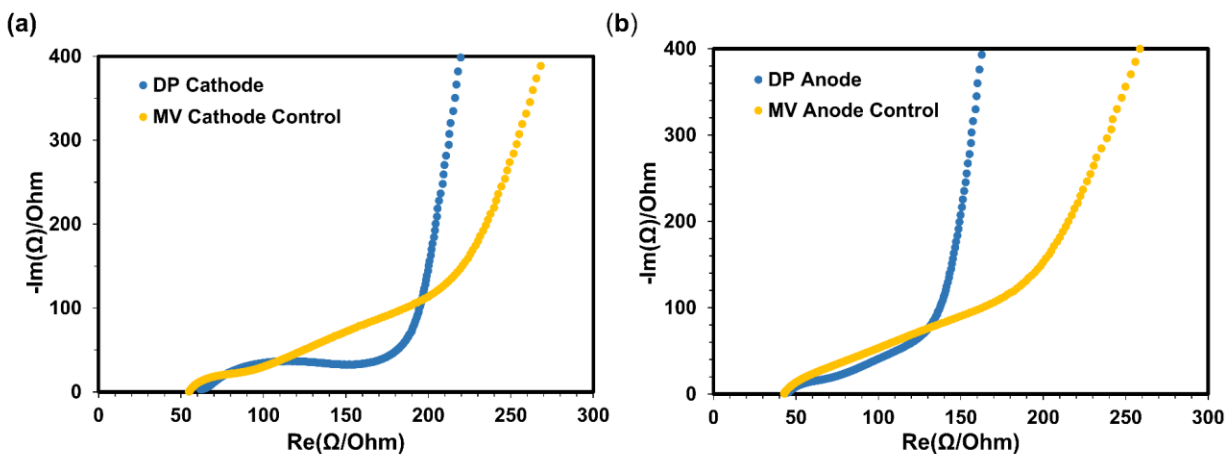


Figure I.4.11 Impedance Spectra of the (a) cathode tortuosity measurement, (b) anode tortuosity measurement.

Table I.4.3 Average Porosity and Tortuosity of the High-loading Dry Printed and MV Slurry Cast Electrodes.

Cathode	Dry Printed Electrode	Slurry Cast Electrode
Average Porosity	38.18%	33.88%
$\tau$	1.3	3.36
Anode	Dry Printed Electrode	Slurry Cast Electrode
Average Porosity	38.40%	38.04%
$\tau$	1.45	2.8

#### Cell fabrication and tests

Charge rate performance tests were conducted on 12mm cathode and anode electrodes using 2032-coin cells, paired with a 15mm lithium disk. Results from Figure I.4.12(a) and (c) indicate no capacity loss from high loading, with the cathode achieving 88.3% efficiency and the anode 95.47%. Yet, a significant decrease in the CC charging ratio was noted at 2C, attributable to the coin cell's high resistance. Thus, while the high loading electrode functions well, it's not optimal for coin cell testing due to resistance issues.



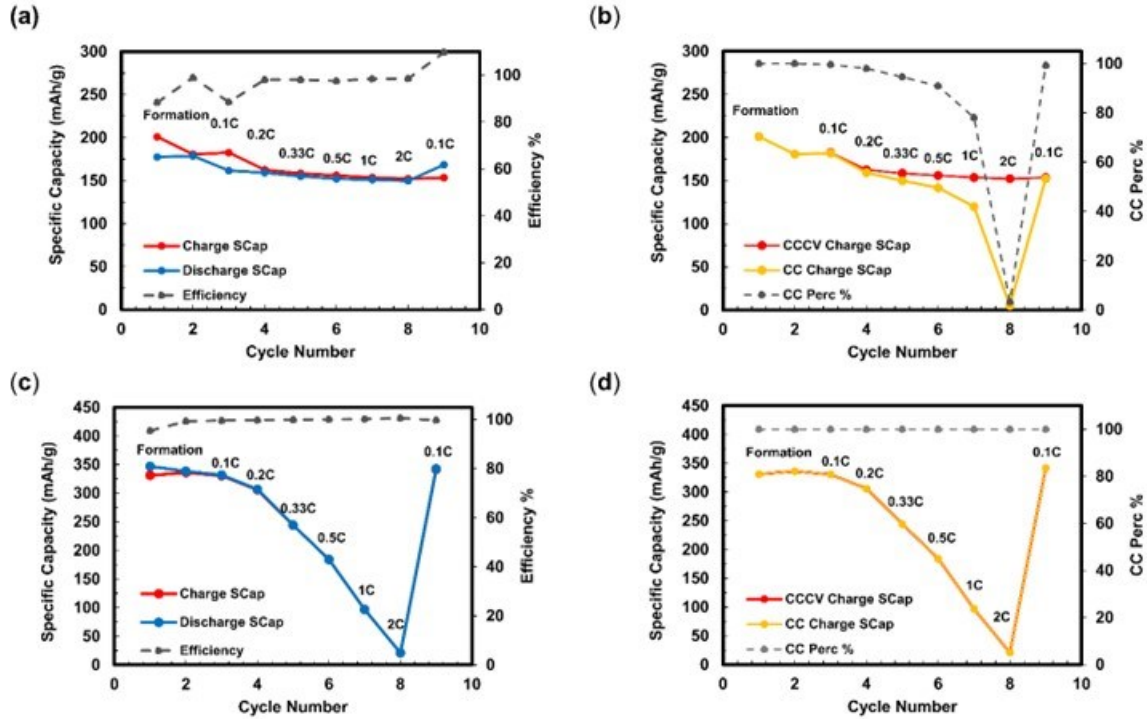


Figure I.4.12 (a) Charge rate performance of DP cathode. (b) CC charge ratio of DP cathode in the charge rate test. (c) Charge rate performance of DP and SC anode electrodes. (d) CC charge ratio of DP anode in the charge rate test.

**Technology feasibility verification on NMC811**

Some dry-printed NMC811 electrode was also prepared to further explore the feasibility of solvent-free electrode manufacturing technology on NMC811 active material. Displayed in Figure I.4.13, the dry-printed NMC811 electrodes were examined with SEM, revealing a uniform carbon and PVDF binder distribution mainly on AM particle surface. Unlike slurry-casted electrodes, the dry-printed electrodes had more open pores, which is able to improve electrolyte wettability and enhancing Li<sup>+</sup> exchange.

The tortuosity factor represents the actual Li-ion diffusion path in a porous electrode and significantly affects the rate performance of LIBs. Figure I.4.13(a) showcases tortuosity results derived from EIS measurements in Figure I.4.14(b). DP electrodes have notably lower tortuosity than SC electrodes (2.21 vs. 2.63 for cathode, and 2.87 vs. 3.53 for anode). This finding aligns with SEM images, showing more open pores in DP electrodes.

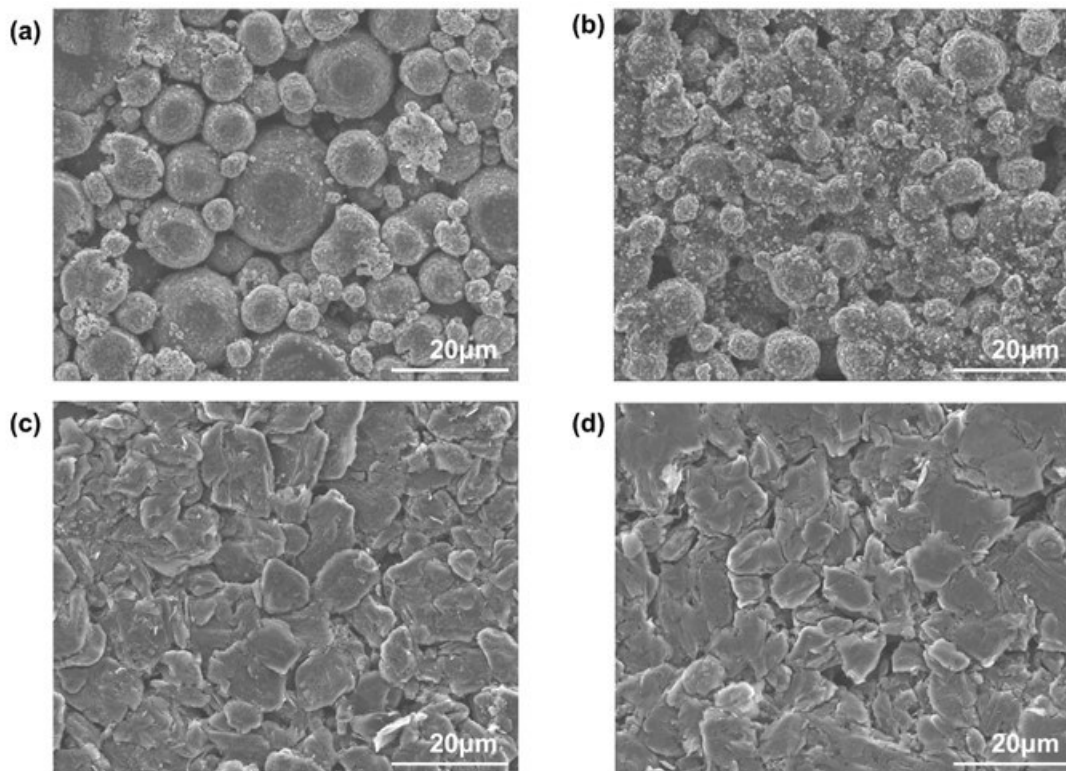


Figure I.4.13 SEM images of (a) prepared dry-printed NMC811 cathode electrodes. (b) slurry-cast NMC811 cathode electrodes. (c) dry-printed graphite anode. (d) slurry-cast graphite anode electrodes.

Then the electrodes were fabricated into single-layer pouch cells to evaluate their charge-rate performance and cycle performance. As presented in Figure I.4.15, the DP NMC811 cells delivered better charge-rate and long cycle performance. The efficiency drop after 2C on DP cells was due to the unmatched rate performance of graphite anode.

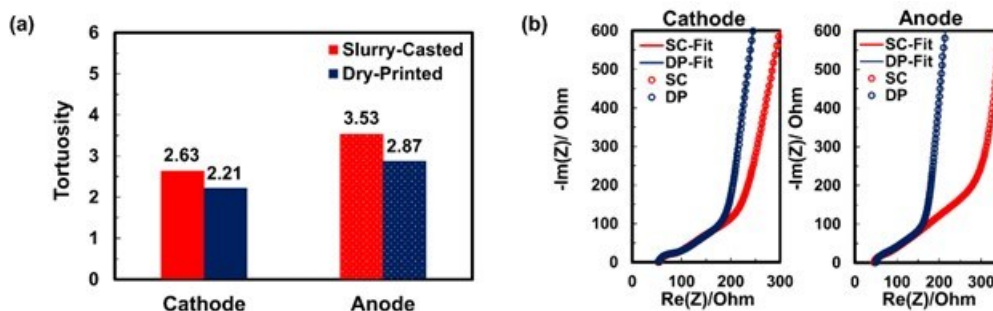


Figure I.4.14 (a) Tortuosity of SC and DP electrodes. (b) Nyquist impedance plots of the SC and DP electrodes symmetrical cells.

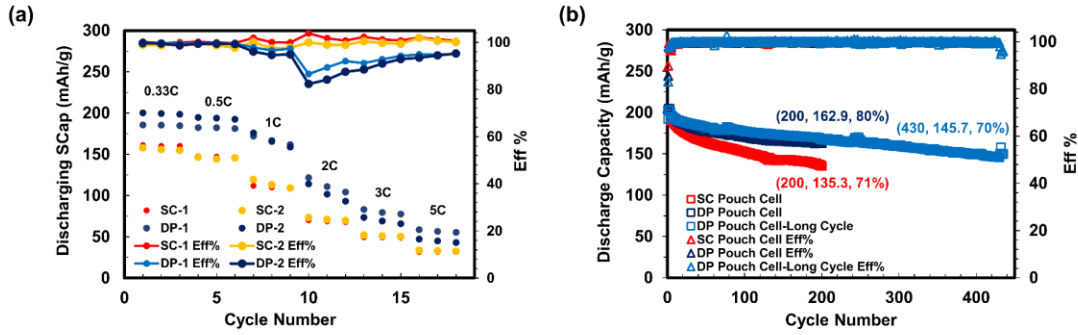


Figure I.4.15 (a) Charge-rate tests of DP and SC pouch cells. (b) The 0.33C cycle performance of DP and SC pouch cell.

**Cost modeling and analysis**

The other task that this work embarked on was the cost analysis on solvent-free electrode manufacturing process to explore its prospective cost advantages on a 50GWh/year manufacturing scale. The analysis was performed with BatPaC version 5.0, a calculation method based on Microsoft® Office Excel spreadsheets, developed at Argonne National Lab for estimating the performance and manufacturing cost of lithium-ion batteries.

The cost analysis covered preparation (storage, mixing, and transport), casting (include drying), and NMP recovery. The costs of solvent-free manufacturing were derived by excluding solvent-related expenses from the slurry model.

The modeling results, shown in Figure I.4.16, reveal dry manufacturing costs just \$276.9M, or 45.8% of the \$605.2M for slurry manufacturing. This method offers a 95.6% energy saving in electrode production. The total savings of \$328.3M represents a potential manufacturing saving of \$6.6/kWh, leading to a 6.4% cost reduction at the battery cell level.

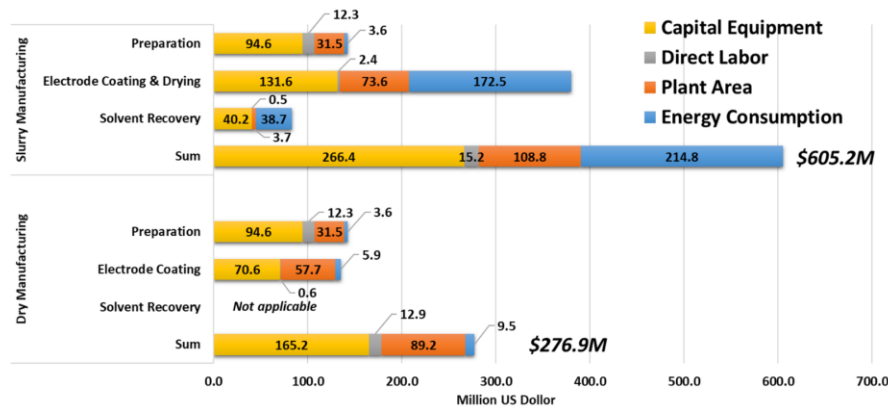
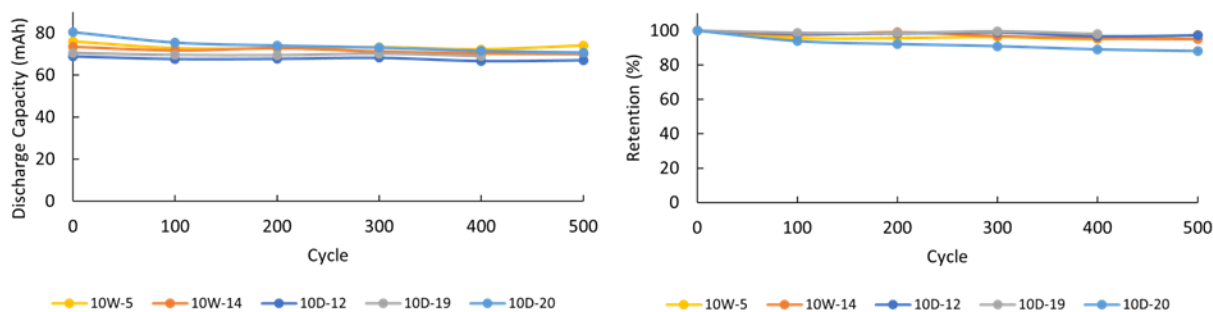


Figure I.4.16 Manufacturing cost of slurry manufacturing and the proposed solvent-free manufacturing.

- \* Direct labor rate was set on \$25/hour
- \*\*The Plant Area cost was calculated based on \$3,000/m<sup>2</sup> per year (includes rent, utility, and management)
- \*\*\*Energy Cost is \$0.165/kWh (United States Bureau of Labor Statistics, May 2023)
- \*\*\*\* Provided by Argonne National Lab, the battery cell price was set to \$104/kWh

### 1.6Ah Pouch Cell Tests at Microvast

In order to compare the dry casting vs wet casting electrode single layer pouch cells were used to compare the performance. In Figure I.4.17 the performance comparison of solvent based wet electrodes vs solvent free dry electrodes is compared in a single layer pouch cell. The wet electrodes were fabricated on a single transfer coating line typically used to make Ah size batteries, so it is very encouraging that the dry electrode system, which avoids costs from solvent, its recovery, and slurry drying, is highly comparable in cycle performance under identical dynamic stress test testing conditions.



**Figure I.4.17 Capacity and retention plots for cells made of wet coat electrodes (W) vs cells made from dry coat electrodes (D) undergoing identical DST cycles with C/3 charge conditions.**

Since the solvent free dry cast electrodes were able to show comparable cycle performance in Figure I.4.17 the scale of the test cells was advanced into multilayer cells of ~1.6 Ah capacity. In Figure I.4.18, the graded capacity at C/3 for the traditional solvent made and solvent free electrodes are shown. The dry electrode electrodes are very comparable, though the deviation is a bit larger. That is not surprising given the dry electrode manufacturing is still a developing technique, and with more time the consistency is expected to further improve. The cells have just begun to cycle under various DST procedures and charging conditions.

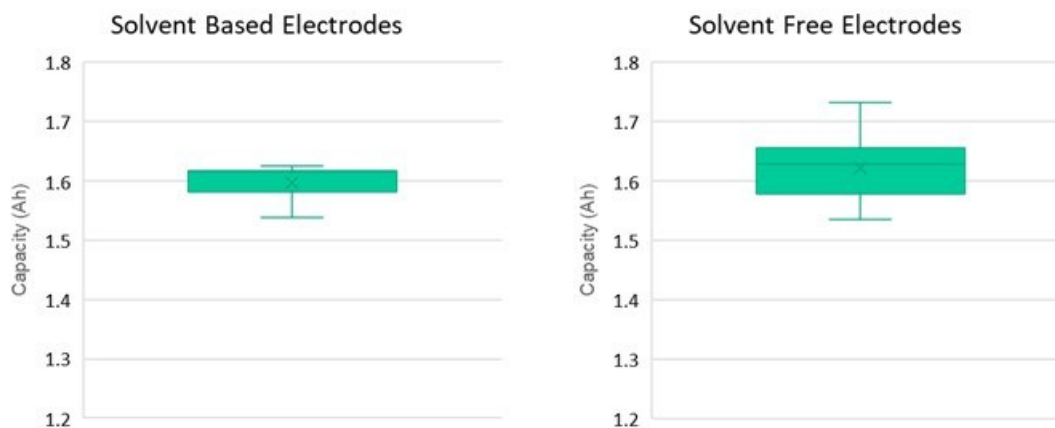


**Figure I.4.18 /3 grading plots for multilayer pouch cells using solvent based and solvent free electrodes.**

### Conclusions

In the realm of modeling, various designs for electrolytes and electrode structures have been explored to enhance the fast-charging capabilities of the electrode. From the manufacturing aspect, 100mm\*100mm large thick electrodes with double sides coated have been designed and fabricated. Special attention was given to the calendaring step during the fabrication process to optimize the quality of the electrode. Tests performed at WPI revealed that these electrodes are of superior quality, both in terms of physical attributes and electrochemical

performance. Further investigations confirmed that the same manufacturing techniques are equally effective for NMC811 cathodes, resulting in reduced electrode tortuosity and improved charge rate performance. Additionally, pouch cells are undergoing tests at Microvast. While the 1.6Ah multi-layer pouch cells might require further refinement, the single-layer pouch cells have already showcased promising results suggesting that the dry electrode system can potentially offer comparable cycle performance when subjected to identical dynamic stress test conditions.

### Key Publications

1. Yangtao Liu, Xiangtao Gong, Chinmoy Podder, Fan Wang, Zeyuan Li, Jianzhao Liu, Jinzhao Fu, Xiaotu Ma, Panawan Vanaphuti, Rui Wang, Andrew Hitt, Yavuz Savsatli, Zhenzhen Yang, Mingyuan Ge, Wah-Keat Lee, Bryan Yonemoto, Ming Tang, Heng Pan, Yan Wang\*, Roll-to-roll solvent-free manufactured electrodes for fast-charging batteries (2023), *Joule*, DOI:10.1016/j.joule.2023.04.006

### References

1. Bitsch, B., J. Dittmann, M. Schmitt, P. Schaffer, W. Schabel, and N. Willenbacher. 2014. "A novel slurry concept for the fabrication of lithium-ion battery electrodes with beneficial properties." *Journal of Power Sources* no. 265:81-90. doi: 10.1016/j.jpowsour.2014.04.115.
2. Ruffo, R., C. Wessells, R. A. Huggins, and Y. Cui. 2009. "Electrochemical behavior of LiCoO<sub>2</sub> as aqueous lithium-ion battery electrodes." *Electrochemistry Communications* no. 11 (2):247-249. doi: 10.1016/j.elecom.2008.11.015.
3. Doberdo, I., N. Löffler, N. Laszczynski, D. Cericola, N. Penazzi, S. Bodoardo, G. T. Kim, and S. Passerini. 2014. "Enabling aqueous binders for lithium battery cathodes - Carbon coating of aluminum current collector." *Journal of Power Sources* no. 248:1000-1006. doi: 10.1016/j.jpowsour.2013.10.039.
4. Wixom, Michael. 2013. *Dry Process Electrode Fabrication* 2013 [cited 13 May 2013]. Available from [http://energy.gov/sites/prod/files/2014/03/f13/es134\\_wixom\\_2013\\_p.pdf](http://energy.gov/sites/prod/files/2014/03/f13/es134_wixom_2013_p.pdf).
5. Zheng, Honghe, Jing Li, Xiangyun Song, Gao Liu, and Vincent S. Battaglia. 2012. "A comprehensive understanding of electrode thickness effects on the electrochemical performances of Li-ion battery cathodes." *Electrochimica Acta* no. 71:258-265. doi: 10.1016/j.electacta.2012.03.161.
6. Gallagher, K. G., S. E. Trask, C. Bauer, T. Woehrle, S. F. Lux, M. Tschech, P. Lamp, B. J. Polzin, S. Ha, B. Long, Q. L. Wu, W. Q. Lu, D. W. Dees, and A. N. Jansen. 2016. "Optimizing Areal Capacities through Understanding the Limitations of Lithium-Ion Electrodes." *Journal of the Electrochemical Society* no. 163 (2):A138-A149.
7. Bae, C. J., C. K. Erdonmez, J. W. Halloran, and Y. M. Chiang. 2013. "Design of battery electrodes with dual-scale porosity to minimize tortuosity and maximize performance." *Advanced Materials* no. 25 (9):1254-8. doi: 10.1002/adma.201204055.
8. Sander, J. S., R. M. Erb, L. Li, A. Gurijala, and Y. M. Chiang. 2016. "High-performance battery electrodes via magnetic templating." *Nature Energy* no. 1.

### Acknowledgements

The development team (WPI/TAMU/Rice/Microvast) would like to thank the following for all of the help, advice, support and suggestions: USABC program manager Lamuel David (Stellantis) and USABC work group members Zoe Zhou (Ford), Meng Jiang (GM), Nico Eidson and Bryant Polzin (DOE), and Brian Ingram (ANL).

## I.5 Development of Advanced Low-Cost/Fast-Charge (LC/FC) Batteries for EV Applications (Farasis Energy USA)

### **Madhuri Thakur, Principal Investigator**

Farasis Energy USA  
21363 Cabot Blvd  
Hayward, CA 94545  
E-mail: [mthakur@farasis.com](mailto:mthakur@farasis.com)

### **Tina Chen, DOE Technology Development Manager**

U.S. Department of Energy  
E-mail: [Tina.Chen@ee.doe.gov](mailto:Tina.Chen@ee.doe.gov)

Start Date: February 1, 2021

End Date: February 28, 2024

Project Funding: \$4,060,000

DOE share: \$2,030,000

Non-DOE share: \$2,030,000

### **Project Introduction**

The goal of this project is to develop a low cost/ fast charge lithium-ion cell technology that meets the USABC goals for Advanced Low-Cost/Fast-Charge (LC/FC) Batteries for EV's applications. Farasis headed the development effort which will bring together technical contributions from many leaders in the Li-ion technology industry including Umicore, BASF, Talga, Imerys, Celgard, Zeon and Solvay, etc. The 36-month development effort will be iterative, with an intermediate Go/No Go Milestone based on cell performance goals and progress tracked against the USABC goals for Advanced Low-Cost/Fast-Charge (LC/FC) Batteries. The major objective of this project is to develop cell technology capable of providing 275 Wh/kg after 1000 cycles at a cost target of \$75/kWh and with having charge time of 15 min. for 80 % of the capacity. Key technologies that are developed and integrated into cells include a low-cost cathode, high surface area anode, and electrolyte additives, etc. As a large volume battery manufacturer, a major goal of the project will be to help accelerate production and enable the commercialization of several novel cell component technologies (including low cobalt NCM, Mn-rich NCM, electrolytes, coated graphite as well as high surface area natural graphite) by supporting scale-up and providing a commercialization path. Deliverables will include large pouch cells produced at our manufacturing facility in China/Europe/US with parallel performance and safety testing done at Farasis, cost models associated with the deliverable technology, and a production roadmap to commercialization comprising all components of the cell. The project's total budget will be ~ \$4.06 M with Farasis covering 50 % of the cost.

The key barriers for this project include fast charging without Li plating, low cost, and energy density. Fast charging is a crucial enabler of the mainstream adoption of electric vehicles (EVs) to make them competitive with the internal combustion engine cars. None of today's EVs can withstand fast charging due to the risk of lithium plating. Efforts to enable fast charging hampered by the trade-off nature of a lithium-ion battery. The implementation of the fast charge can lead to sacrificing cell durability. A compromise is required between fast charge capability and cell durability, especially for energy-dense cells. To achieve the target of energy density of the cells, high-voltage and high-capacity cathodes are desired. However, the selection of such cathodes will be limited by the cost target.

### **Objectives**

- Develop an EV cell technology of providing 275 Wh/kg after 1000 cycles at a cost target of \$0.075/Wh.
- Develop a fast charge cell having a charge time of 15 min. for 80 % of the capacity.
- Develop low-cost, high-capacity cathodes such as Mn-rich, Ni-rich cathodes or their blended composite cathode.
- Develop high surface area graphite anodes with fast charge capability.

- Develop and optimize electrolytes and conductive additives to stabilize Mn-rich / Ni-rich cathodes and improve safety.
- Optimize the negative/positive electrode formulation for maximum energy density and cycle life, and fast charging capability.

### Approach

- Phase I of the project, which lasted for approximately 15 months, has been focused on the development and characterization of materials and the development of negative/positive electrode technology. Initial sets of single-layer pouch (SLP) or double-layer pouch (DLP) cells (ca. 0.1-0.5 Ah) were used to evaluate different positive/negative electrode composites and material combinations in an iterative manner. The specific plan includes: (1) to evaluate the capacity and first-cycle efficiency of different low-cost cathode materials using coin cell builds, (2) to identify a graphite candidate with excellent fast charge capability as the anode material, and (3) to down-select low-cost, high-capacity cathodes while having good cycling stability. Several types of graphite materials with different sizes, surface area and morphology were evaluated using SLP or DLP cell builds. Three criteria including cell resistance, discharge rate capability and fast charge capability were used for the screening of graphite anode materials. The cathode materials were down-selected using SLP or DLP cell builds among a wide range of materials including Ni-rich NCM, stabilized Mn-rich cathode materials, zero-Co cathode materials, and their blended composites. Three criteria including cell resistance, discharge rate capability and cycling stability were also used for the screening of low-cost high-capacity cathode materials. A second iteration leads to narrowing down the range of electrode designs and introducing materials improvements. The electrolyte development effort was conducted in parallel with the cell optimization work. The electrolyte work has focused on evaluating and optimizing electrolyte formulas with additives to meet the requirement of the graphite anodes and the down-selected low-cost, high-capacity cathodes. A combination of device level testing and fundamental electrochemical measurements will be used to guide the development of large form factor cells for Phase II of the project. In the middle of Phase I, baseline cells with a capacity of ca. 73 Ah using Farasis “next generation” cell chemistry have been built and delivered to national labs for evaluation and testing.
- Phase II of the project, which lasted for approximately 17 months, has been shifted to manufacturing and testing of larger format pouch cells using a refined subset of cell chemistries developed in Phase I. Some chemistry developments have been continued at Phase II to address specific issues identified in Phase I builds and to pursue further optimization of cell level performance. To achieve the targeted energy density of 300 Wh/kg, we have evaluated the Mn-rich, Ni rich and their blended cathodes with a capacity of > 200 mAh/g. Other cell components such as foil, separators, electrolyte, conductive additives, and pouch materials have also been evaluated for fast charge cell development. This will occur in two iterations starting with ca. 75 Ah form factor cells (Gen 1 cells) for the intermediate evaluation and progressing to the final deliverable cells (Gen 2 cells) based on a large pouch cell form factor, which will be ca. 66 Ah using the optimized high-energy cell chemistry with achieving a cost target of 75 Wh/kg and a charge time of 15 min. for the 80 % of the capacity. Phase II of the program will also include testing to guide system development in future applications; these tests will characterize cells in small groups to efficiently evaluate their behavior on a large scale where thermal management, cycling-induced gradients, and failure isolation become important.

### Results

Farasis has built several sets of single-layer pouch (SLP) or double-layer pouch (DLP) cells with seven different cathodes and evaluated their initial performance and cycling stability during the past two years. The evaluated cathodes include 2 types of Mn-rich (C2 and C4), 2 Ni-rich (C1 and C3), 1 HV-NCM (C5) and 1 zero-Co (C6) and C5C2 blended materials. Later, Farasis down selected C2 Mn-rich, C5 HV-NCM and their blended composite (C5C2-blend 1 and C5C2 blend 2) cathodes for further development and optimization including coating technique, slurry formula and activation conditions. Due to some unsolved issues including severe voltage fade and significant increase in direct current resistance (DCR) with cycling, Farasis believes

that it is hard to use pure Mn-rich (C2 or C4) cathodes for the development of fast charge cells at the current stage. Based on compromising the C/3 capacity, cost, regular C-rate cycling stability, DCR change with cycling, and fast charge cycling stability, Farasis has down selected either pure C5 HV-NCM or C5C2 blend composite cathodes as the cathode chemistry for final deliverable cell builds. In 2023, Farasis further developed C5C2 blended composite cathodes, and optimized electrolyte formulas with additives for cells with pure C5 and C5C2 blended cathodes, respectively. Farasis also continued to develop fast charge cells based on C5C2 blended cathodes and filled with optimal electrolytes this year.

#### **Electrolyte development for pure C5 HV-NCM cathodes:**

A set of DLP cells have been built with lab-coated (L-coated) A1 graphite anodes and pilot-line coated (P-coated) pure C5 cathodes. Pouch cells were divided into two groups and filled with E1 and E5 high-voltage (HV) electrolytes for each group separately. The initial performance and cycling stability of the cells have been evaluated. Table I.5.1 shows a comparison in first cycle efficiency, C/20 and C/3 capacities, DCR, and discharge rate performance among DLP cells filled with two different electrolytes. The cells filled with E5 electrolytes show higher first cycle efficiency, higher C/20 and C/3 capacities, lower DCR and better discharge rate performance than those filled with E1 electrolytes. Figure I.5.1 shows a comparison in cycling stability of pouch cells at a regular C-rate (C/2) charge/discharge between filled with E1 and E5 electrolytes. The cells filled with E5 show a lower decay rate in capacity than those filled with E1. The cells filled with E5 can achieve a cycle life of > 825-945 cycles at a capacity retention of 80 %. Moreover, the cells filled with E5 show higher (>700 Wh/kg) initial cathode-specific energy density as well as lower decay rate in cathode-specific energy density than those filled with E1. Regarding DCR change with cycling, the cells filled with E5 show a similar rate in the growth of DCR with cycling to those filled with E1; however, the cells filled with E5 show much lower DCR for either fresh or aged cells than those filled with E1, which is beneficial to fast charge capability and fast charge cycling stability of the cells. In conclusion, E5 is a better electrolyte than E1 for pouch cells with pure C5 cathodes.

**Table I.5.1 A Comparison in First Cycle Efficiency, C/20 and C/3 Capacities, DCR and Discharge Rate Performance among DLP Cells with Pure C5 Cathodes Filled with Two Different Electrolytes**

Electrolyte	First-cycle efficiency (%)	C/20 capacity @ 1 <sup>st</sup> cycle (%)	C/3 capacity @ 4.4 V (mAh/g)	DCR @ 50% DoD (ohm)	Rate_discharge* (2.5C vs. C/5)
E1	85.0	184	169	0.330	28.9-30.3 %
E5	89.2	196-197	190	0.186-0.188	78.8-81.5 %

\* Discharge rate performance is evaluated by the ratio of 3C to C/5 discharge capacity.

#### **Positive electrode development:**

Several sets of DLP cells have been built and evaluated with fixed L-coated A1 graphite anodes and different P-coated cathodes. The cathodes include pure C5, C5C2-blend 1 and C5C2-blend 2 cathodes. All the cells were filled with E5 electrolytes. Two different activation conditions (activation at either a charge cut-off voltage (Vmax) of 4.5 or 4.4 V) were applied for C5C2-blend 1 and C5C2-blend 2 cathodes during the first formation cycle. Several key criteria were used to narrow the cathodes for future cell builds including C/3 capacity, DCR, discharge rate performance, cycling stability and cost. Table I.5.2 shows a comparison in C/20 and C/3 capacities, DCR, and discharge rate performance among DLP cells with different cathodes. When the cells with C5C2 blended cathode were activated at 4.5 V, the cells with C5C2-blend 1 and C5C2-blend 2 cathodes can achieve a C/3 capacity of 192 and 195 mAh/g, respectively, which are higher than those with pure C5 cathode activated at 4.4 V. However, when the cells with C5C2 blended cathode were activated at 4.4 V, the cells with C5C2-blend 1 and 2 cathodes can achieve a C/3 capacity of only 180 and 179 mAh/g, respectively, which are much lower than those with pure C5 cathode activated at 4.4 V.



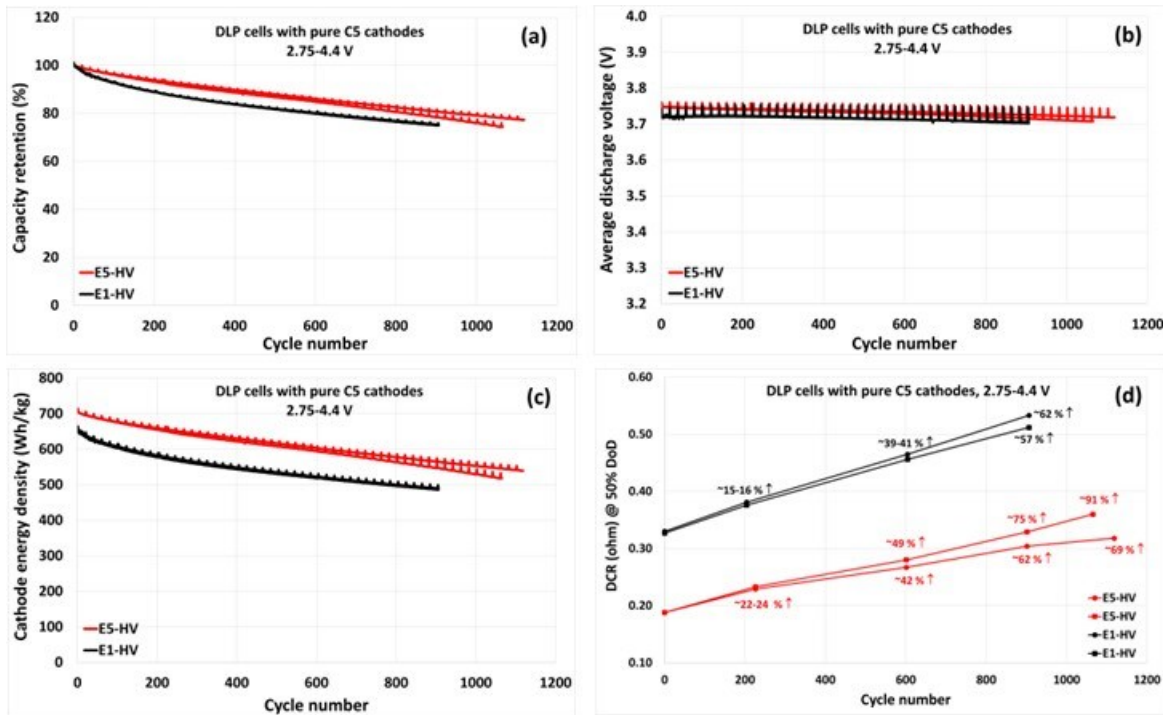


Figure I.5.1 Electrolyte Optimization for Improving Cycling Stability of DLP Cells with Pure C5 Cathodes: (a) Capacity Retention, (b) Average Discharge Voltage, (c) Cathode Energy density, and (d) DCR.

The cells with **C5C2 blended** cathodes show higher DCR than those with pure **C5** cathodes due to lower electronic conductivity of **C5C2 blended** composites. However, all the cells with **C5C2 blended** cathodes still show excellent discharge rate performance, especially for the case of activation at 4.4 V. Figure I.5.2 shows the effects of activation conditions and active materials composition on the cycling stability of DLP cells with **C5C2 blended** cathodes. Cells with **C5C2 blended** cathodes show higher decay rate in capacity than those with pure **C5** cathodes. The cycling stability of the cells decreases in the following order: pure **C5** cathodes activated at 4.4 V > **C5C2-blend 1** cathodes activated at 4.4 V > **C5C2-blend 1** cathodes activated at 4.5 V > **C5C2-blend 2** cathodes activated at 4.4 V > **C5C2-blend 2** cathodes activated at 4.5 V. This indicates that higher activation  $V_{max}$  and higher the amount of **C2** in the **C5C2 blended** composites (the amount of **C2** in **C5C2-blend 2** is higher than that in **C5C2-blend 1**) are harmful to the cycling stability of the cells. Moreover, cells with **C5C2 blended** cathodes show higher voltage fade than those with pure **C5** cathodes. The average cell discharge voltage of the cells decreases in the following order: pure **C5** cathodes activated at 4.4 V > **C5C2-blend 1** cathodes activated at 4.4 V  $\cong$  **C5C2-blend 1** cathodes activated at 4.5 V  $\cong$  **C5C2-blend 2** cathodes activated at 4.4 V > **C5C2-blend 2** cathodes activated at 4.5 V. Higher activation  $V_{max}$  and higher the amount of **C2** in the **C5C2 blended** composites lead to faster drop in average cell discharge voltage with cycling. In addition, a significant increase in DCR with cycling was observed for the cells with **C5C2 blended** cathodes, especially for the case of activation at high  $V_{max}$ . A significant increase in DCR with cycling will deteriorate the fast charge capability of aged cells and thus decrease fast charge cycling stability of the cells with **C5C2 blended** cathodes. Although the cells with **C5C2 blended** cathodes can achieve high C/3 capacity and show low cost, the poor cycling stability in capacity, severe voltage fade and significant increase in DCR with cycling are still major obstacles for using them as candidate cathodes for large-format fast charge cell development. Farasis intends to use more stable **C5** cathodes with relatively high cost for the build of final deliverable large-format cells to meet the project target in the cost, energy density, fast charge time and cycling stability.

**Table I.5.2 A Comparison in C/20 and C/3 Capacities, DCR and Discharge Rate Performance among DLP Cells with Different Cathodes Filled with E5 Electrolytes**

Cathode	C/20 capacity (mAh/g)	C/3 Capacity (mAh/g)	DCR @ 50% DoD (ohm)	Rate_discharge* (3C vs. C/5)
Pure C5 activated @ 4.4 V	196	190	0.188	N/A
C5C2-blend 1 activated @ 4.4 V	184	180	0.203	87.5 %
C5C2-blend 1 activated at 4.5 V	201	192	0.197	84.8 %
C5C2-blend 2 activated at 4.4 V	183	179	0.213	88.3 %
C5C2-blend 2 activated at 4.5 V	203	195	0.196	84.8 %

- The cells were activated either in the voltage window of 2.75-4.5 V or 2.75-4.4 V only during the first formation cycle. After the activation, all the cells were operated in the same voltage window of 2.75-4.4 V for the measurement of initial performance.

\* Discharge rate performance is evaluated by the ratio of 3C to C/5 discharge capacity.

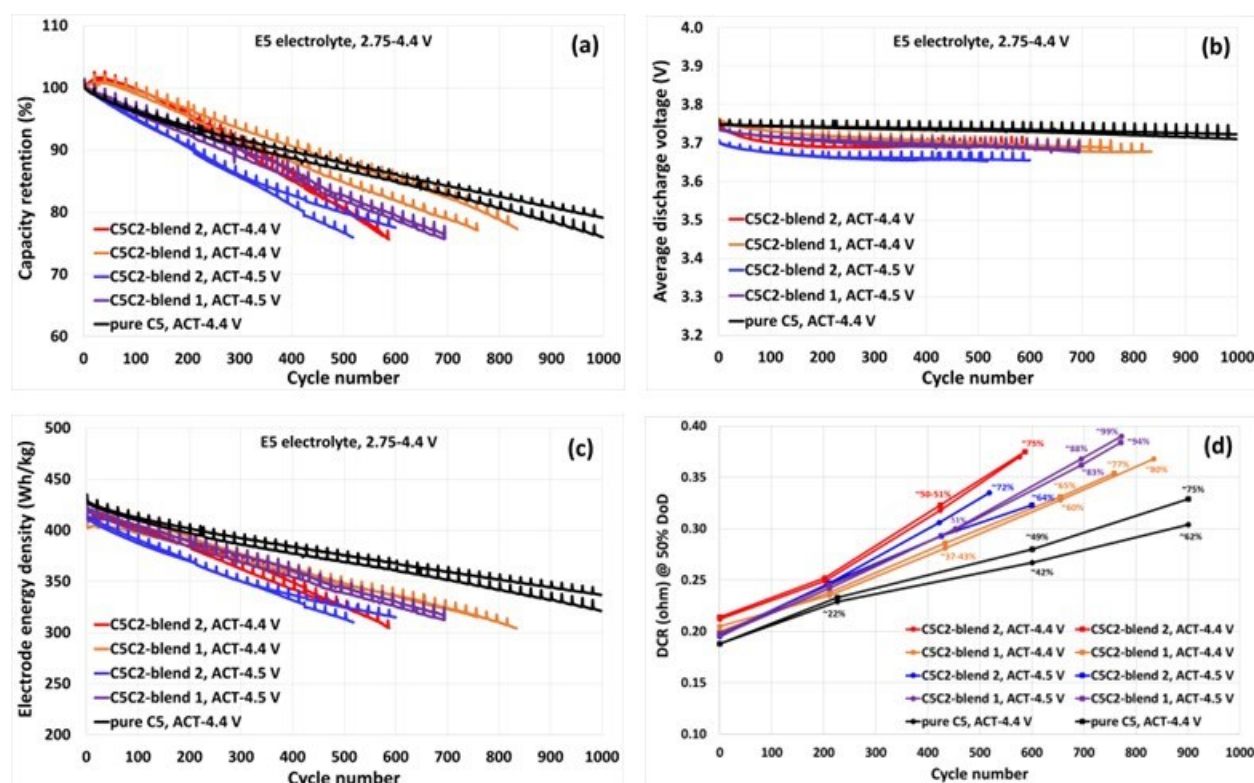


**Figure I.5.2 Effects of Activation Conditions and Active Cathode Materials Composition on Cycling Stability of DLP Cells with C5C2 Blended Cathodes: (a) Capacity Retention, (b) Average Discharge Voltage, (c) Cathode Energy density, and (d) DCR.**

#### **Electrolyte development for pouch cells with C5C2-blend 1 cathodes:**

A set of double-layer pouch (DLP) cells have been built with L-coated A1 graphite anodes and P-coated C5C2-blend 1 cathodes. The cells were filled with four types of electrolytes: E5 (high voltage electrolyte), E6 (high voltage, fast charge electrolyte), E7 (electrolyte designed for Mn-rich cathode materials) and E8 (E6

with an electrolyte additive), respectively. Several criteria were used to narrow the electrolytes for future cell builds including C/3 capacity, DCR, discharge rate performance, fast charge capability and cycling stability. Table I.5.3 shows a comparison in first cycle efficiency, C/20 and C/3 capacities, DCR, discharge rate performance and fast charge capability. The cells filled with **E5** and **E6** show similar first-cycle efficiency, C/20 and C/3 capacities. However, the cells filled with **E6** show lower DCR, better discharge rate performance and better fast charge capability than those filled with **E5**. The cells filled with **E8** show slightly lower first cycle efficiency, lower C/20 and C/3 capacities, slightly higher DCR than, while similar discharge-rate performance and fast charge capability to those filled with **E6**. This indicates that the electrolyte additive in **E8** may improve the cathode stability without sacrificing the discharge rate performance and fast charge capability of the cells. The worse electrolyte is **E7**. The cells filled with **E7** show not only lowest first-cycle efficiency, C/20 and C/3 capacities; but also, highest DCR, worst discharge rate performance and fast charge capability. Figure I.5.3 shows the effect of electrolyte formula on the cycling stability of DLP Cells with **C5C2-blend 1** cathodes. The cells filled with **E6** show slightly lower decay rate in capacity retention than, similar rate in the increase of DCR with cycling to; but higher voltage fade (as indicated by a quicker decrease in average discharge voltage with cycling) than those filled with **E5**. The cells filled with **E7** show worse cycling stability and faster increase in DCR with cycling compared with those filled with **E5** and **E6** electrolytes. From a comparison in the cycling test data within initial ~120 cycles, the cells filled with **E8** may show even better cycling stability and lower voltage fade than those filled with **E6**, indicating that the electrolyte additive may be effective to improving the stability of **C5C2-blend 1** cathodes and thus pouch cells.

**Table I.5.3 A Comparison in First Cycle Efficiency, C/20 and C/3 Capacities, DCR, Discharge Rate Performance and Fast Charge Capability among DLP Cells with C5C2-Blend 1 Cathodes Filled with Different Electrolytes**

Electrolyte	First cycle efficiency @ 4.5 V (%)	C/20 capacity @ 4.4 V (mAh/g)	C/3 Capacity @ 4.4 V (mAh/g)	DCR @ 50% DoD (ohm)	Rate_discharge* (3C vs. C/5)	Fast Charge Capability (Max SoC <sup>+</sup> ) (%)
<b>E5</b>	87.4	201	192	0.197	84.8 %	N/A
<b>E6</b>	87.3	200/202	192/194	0.183	85.7 %	≥ 79.0
<b>E7</b>	85.8	193/196	181/184	0.229-0.246	72.4 %	≥ 73.2
<b>E8</b>	86.6	199	191	0.190-0.194	85.9 %	≥ 79.1

All pouch cells were activated in the voltage window of 2.75-4.5 V during the first formation cycle.

\* Discharge rate performance is evaluated by the ratio of 3C to C/5 discharge capacity.

+ Fast charge capacity is evaluated by the measurement of maximum SoC which there is no Li plating occurring after the cells are charged to at 3C rate.

#### **Fast charge cell development:**

Figure I.5.4 shows a comparison in cycling stability between regular C-rate (C/2) and fast (15 min. charge to 80 % SoC) charge of two types of DLP cells: (a) with **A1** graphite anodes and **C5C2-blend 1** cathodes and filled with **E6** electrolytes; and (b) with **A1** graphite anodes and **C5C2-blend 2** cathodes and filled with **E5** electrolytes. For each type of cell, four cells were selected for the cycling test: two cells for fast charge cycling, while another two cells for regular C-rate (such as C/2) charge cycling. For the cells with fast charge cycling, the cycling test was interrupted every several tens of cycles for RPT (reference performance testing) to obtain C/3 capacity of aged cells. Please note that 80 % SoC charge limit for aged cells is based on their actual C/3 capacity after aging. Therefore, we adjusted the fast charge current and charge capacity limit accordingly so that we still charge the cells to 80 % SoC within 15 min. The cells with **C5C2-blend 1** cathodes and filled with **E6** electrolytes show better cycling stability in the case of 15 min. fast charge than that in the case of regular C-rate charge, indicating that there is no Li plating occurring during fast charge cycling. In addition, the operating SoC range in the case of fast charge is 0-80 % SoC, narrower than that in the case of regular C-rate charge (0-100 % SoC), which also improves the cycling stability in the case of fast charge. Similarly, the

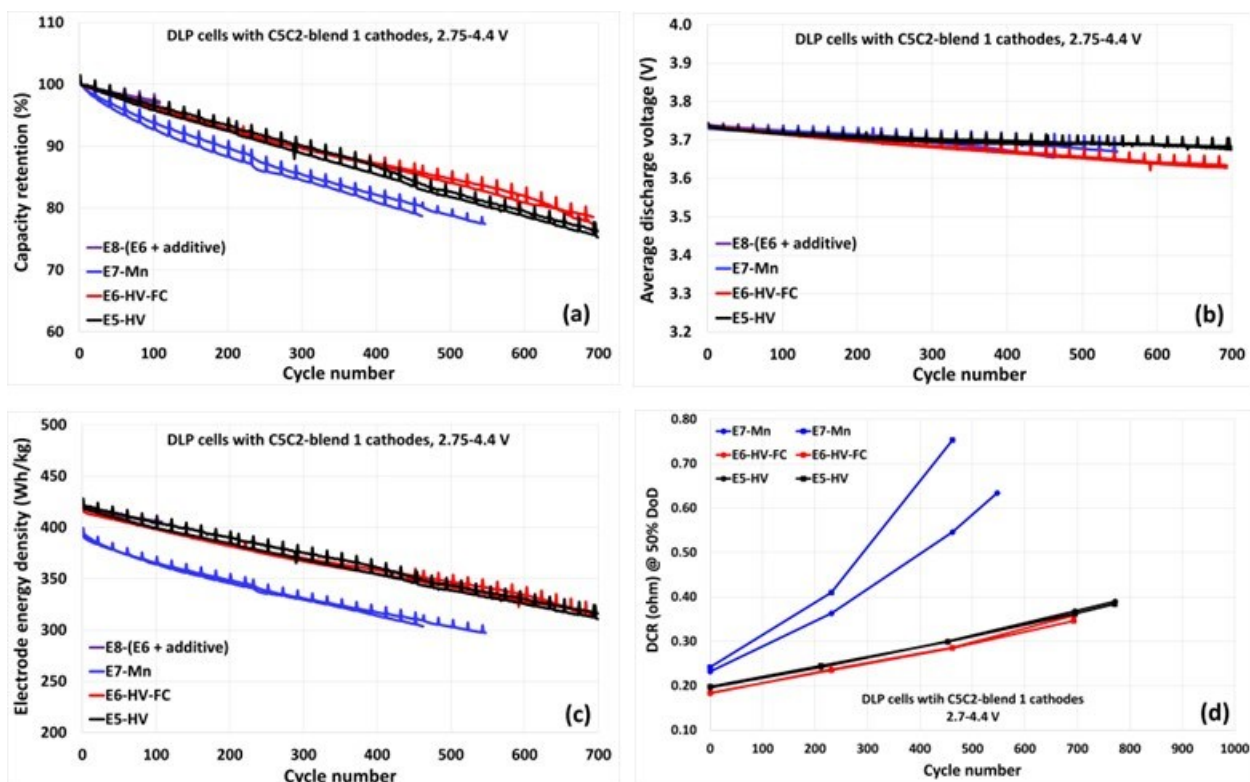


Figure I.5.3 Electrolyte Optimization for Improving Cycling Stability of DLP Cells with C5C2-Blend 1 Cathodes: (a) Capacity Retention, (b) Average Discharge Voltage, (c) Cathode Energy density, and (d) DCR.

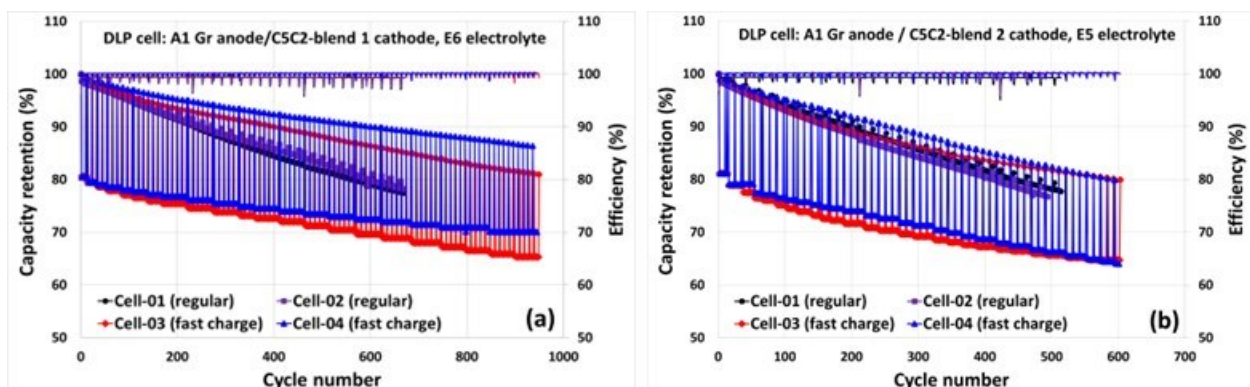


Figure I.5.4 Fast Charge Cycling Stability of DLP cells: (a) with C5C2-Blend 1 Cathodes and Filled with E6 Electrolytes; and (b) C5C2-Blend 2 Cathodes and Filled with E5 Electrolytes.

cells with and C5C2-blend 2 cathodes and filled with E5 electrolytes show slightly better cycling stability in the case of 15 min. fast charge than that in the case of regular C-rate charge. Moreover, the cells with C5C2-blend 1 and C5C2-blend 2 cathodes can achieve > 1000-1200 and > 580 fast charge cycles, respectively. Based on a compromise between cell cost and fast charge cycling stability, Farasis will select C5C2-blend 1 cathode as an optimal cathode and E8 as an optimal electrolyte to build multi-layer pouch cells with a cell capacity of ~ 2 Ah, and then further verify their excellent fast charge cycling stability in ~2 Ah cell level.

Some of the 2 Ah cells will be delivered to national labs for further evaluation together with final deliverable large-format (66 Ah) cells.

### Conclusions

Farasis has shown > 825-945 cycles in double-layer pouch (DLP) cell with a lab-coated graphite anode and a pilot-line coated pure **C5** cathode before reaching 80 % capacity retention when the cell filled with an **E5** electrolyte. Farasis has also shown > 635 cycles in DLP cell with a lab-coated graphite anode and a pilot-line coated **C5C2-blend 1** cathode before reaching 80 % capacity retention when the cell is filled with an **E6** electrolyte and activated at 4.5 V. Moreover, Farasis has demonstrated a cycle life of > 1000 and > 600 fast (15 min. charge to 80 % SoC) cycles in DLP cell with **C5C2-blend 1** and **C5C2-blend 2** cathodes before reaching 80 % capacity retention, respectively. Finally, Farasis has identified an optimal cathode with relatively low cost, relatively high capacity and excellent cycling stability, an optimal graphite anode with fast charge capability, and an optimal electrolyte with high voltage stability as chemistries for final deliverable **Gen 2** pouch cells. Farasis is building **Gen 2** cells based on these optimal cell components. The **Gen 2** cells will be delivered to national labs for evaluation.

## I.6 Pre-lithiation of Silicon-containing Anodes for High-Performance EV Batteries (Applied Materials, Inc.)

### **Subra Herle, Ph.D., Principal Investigator**

Applied Materials, Inc.  
3225 Oakmead Village Dr  
Santa Clara, CA 95054  
E-mail: [Subra\\_Herle@amat.com](mailto:Subra_Herle@amat.com)

### **Haiyan Croft, DOE Technology Development Manager**

U.S. Department of Energy  
E-mail: [haiyan.croft@ee.goe.gov](mailto:haiyan.croft@ee.goe.gov)

Start Date: April 5, 2021

End Date: July 31, 2022

Project Funding: \$2,922,239

DOE share: \$1,426,053

Non-DOE share: \$1,496,186

### **Project Introduction**

The increasing energy density (Wh/kg and Wh/L) of the Li-ion cell is needed to improve EV cell performance and decrease the cost (\$/kWh). In the last decade, significant attention has been focused on enabling high-capacity cathode materials and thinner, better separators to increase cell capacity from the cathode side. More recently, Cell Manufacturers are also exploring improved anode performance with the use of silicon-blended graphite anodes. Si/SiO<sub>x</sub> blended with graphite can significantly improve the anode capacity and enables fast-charge EV cells. These gains, however, are offset by a first-cycle irreversible loss of lithium which can degrade performance by 30% or more. Additionally, only some of the lithium that enters the Si/SiO<sub>x</sub>-Gr anode is active. Some of the lithium is consumed during the solid electrolyte interface (SEI) cell formation cycle. The continual buildup of SEI layers upon subsequent cell cycling further decreases energy density causing gradual cell degradation. Cell manufacturers are “pre-lithiating” the Si/SiO<sub>x</sub>-Gr anode to counter the first-cycle irreversible lithium loss. Pre-lithiation provides additional lithium to the anode to compensate for the loss during the first cycle and SEI formation, and therefore, increases energy density by >10-30% over equivalent graphite-based cells. Applied Materials high volume manufacturing (HVM) tools and technology innovation can provide benefits that none of the existing approaches for prelithiation can meet, including ease of integration with existing Li-ion battery process flows, uniform, defect-free lithium films, scalable thickness, and to industry-standard widths, all at low cost/performance, in a safe environment.

### **Objectives**

The objective of this program is to develop and validate a prelithiation process for high volume manufacturing (HVM) specifically targeted for the requirements of an EV battery and battery manufacturing and demonstrate that silicon-graphite anode-based cells can meet USABC’s EV CY2020 goals for specific energy and other performance, cost targets. Table I.6.1 captures key aspects of the performance deliverables.

Table I.6.1 Budget Period 1 and 2 Summary and Status Updates of Key Performance Deliverables.

Program Cell Performance Goals		
Parameter	Pouch Cells (Pre-lithiated Silicon Anodes), 2Ah Year-1	Pouch Cells (Pre-lithiated Silicon Anodes), >29 Ah Year-2 (End of Program)
Gravimetric Energy Density	≥200 Wh/kg	≥349 Wh/kg
Cycle Life (DST)	500 Cycles	≥1000 Cycles
Calendar Life	N/A	≥ 3 Years (Est.)
Peak Power Performance	N/A	>Current Li-ion Baseline
Fast Charge	>Current Li-ion Baseline	>Current Li-ion Baseline
Status update	<p><b>Completed BP1 deliverables:</b>                      Prelithiation Process Baseline                      Cathode &amp; SiOx-Graphite composition/loadings.                      Selection of the pre-lithiation thickness.                      Selection of Electrolyte comp.                      Post-Treatment for passivation                      SLP pouch cell learnings.                      Demonstrated performance of 2Ah cells by SpectraPower.                      Independent testing at INL for BP1, 2 Ah cells completed.</p>	<p>Ongoing: Applied Materials and Farasis BP2 activities and engagement.                      2Ah Cell build by Farasis Pre-Li anode show FCE increased by 11%, capacity increased by 11%, and gravimetric energy density increased by 9.5 % (Wh/kg) vs. control.                      Data in good agreement with SpectraPower 2 Ah data (Milestone 5).                      Farasis completed coating of 1250 meters of 25 wt% SiOx anodes.                      R2R prelithiation of anodes: In progress                      Alignment and Follow-ups with Farasis team for the 29 Ah cell builds for Final Deliverables in progress.</p>

**Approach**

With funding support from USABC and working closely with partners, we continue to use a production-proven platform combined with a PVD deposition source to pre-lithiated Si/SiOx graphite anode and specifically address 1st cycle irreversible loss of such anodes. Si-based anodes are necessary to increase cell energy density and fast charge capability to meet USABC goals. Cells made with varying weight fractions of silicon/silicon suboxide with graphite blended in the anode formulation and different thicknesses of lithium deposited on the silicon anodes to bridge the 1st cycle irreversible loss were optimized.

In **Budget Period-1 (BP-1)**, Applied Materials engaged with SpectraPower (subcontractor) and Farasis Energy USA (manufacturing partner) extensively to review and provide guidance in alignment with the project scope of work (SoW) to provide pre-lithiated anode samples and testing in R&D type coin, single layer, and finally high capacity 2 Ah pouch cells during the first phase of the program. The tasks' details, milestones, and status updates are summarized in Table I.6.1. *All tasks associated with BP1 are now completed.*

In **Budget Period-2 (BP-2)**, Applied Materials continued to work with SpectraPower, Idaho National Laboratory, and Farasis Energy USA to determine the performance of the high capacity 2 Ah cells prepared by the SIDT pre-lithiation approach and compare with the corresponding non-prelithiated control (SiOx-Graphite anodes). Farasis Energy USA and Idaho National Laboratory results aligned with the results obtained from BP1 (SpectraPower). This completes milestone 5 for BP2 and further guided the planning and preparation of the final deliverables for BP2 end-of-program goals (milestones/status updates are captured in Table I.6.2). BP2 section *tasks associated with BP2 are currently in progress.* Table I.6.2 Below captures all the proposed milestone and corresponding status updates All Budget Period-1 milestones were completed and preparations started towards meeting Budget Period-2 objectives, as summarized below:

Table I.6.2 Proposed Milestones and Current Status Updates

M.S.	Milestone Description Budget Period - 1	Status as of 12/14/2023 Completed
1	<p>Confirm Cell Baseline Cathode Loading NCM 523 and 811 cathode loading analysis report containing.</p> <p>A) Performance of coin and pouch cells B) The selection of cathode loading to properly balance the cells meeting target performance</p>	<p>Month 3→6 (PQ2): Completed</p> <p>NMC 811 chosen over NMC 523</p>
2	<p>Anode Loading and Lithium Thickness Anode loading and Lithium Thickness analysis report containing.</p> <p>A) Performance of coin and pouch cells B) The selection of the appropriate lithium thickness for a given anode silicon content and total loading, meeting target performance</p>	<p>Month 6→9 (PQ3): Completed</p> <p>Optimum Pre-Li loading studies: Completed BTR Silicon Oxide chosen over Targray um-sized silicon powder based on the results from both pre-lithiated and non SLP and non-pre-lithiated MLP cell results. Pre-Li thickness of 6 um was down selected for Si and SiO<sub>x</sub>- Gr anode</p>
3	<p>Pre-treatment and post-treatment (Passivation) CO<sub>2</sub> passivation analysis report containing</p> <p>A) Performance of coin and pouch B) The selection of a pre-treatment and post-treatment passivation process for subsequent steps</p>	<p>Month 9 (PQ3): Completed</p> <p>Pretreatment: Optimized drying conditions -Completed Particle removal- Not required for S2S. Post treatment: Optimized CO<sub>2</sub> surface passivation- Completed.</p> <p>Packaging &amp; Shipping Pre-Li Anode Protocol- Completed</p>
4	<p>2Ah Cell Performance Verification 2Ah Cell Performance analysis report containing.</p> <p>A) Performance of 2Ah pouch with complete USABC test protocol B) Demonstrated performance of 2Ah cells to USABC goals.</p> <p>Go/No-Go condition: 2Ah pre-lithiated cells do not show improvement over current non-pre-lithiated baseline.</p>	<p>Month 12 (PQ4→PQ5): Completed</p> <p>Demonstrated 2 Ah cell with prelithiation →10 % improvement in capacity vs. baseline cells. Baseline SLP built completed in Feb 2022, Initial testing in full cell paired with NMC: SLP Pre-Li (Si &amp; SiO<sub>x</sub>) Q5 2022→Completed. MLP Baseline cells with Si, SiO<sub>x</sub>, Graphite matched with NMC 523 and 811 cathode built</p>
4	<p>Delivery of 2Ah Cell to INL for Verification Delivery of 17 prelithiated cells along with 8 baseline cells</p> <p>Relevant parties will work together for Phase 2 (BP-2) of the USABC program continuation after GO decision has been made.</p>	<p>BP-2 In Progress - (PQ5/PQ6)</p> <p>Data package for Go/No go decision à End of July → Completed.</p> <p>2 Ah Cell Deliverable for Idaho National Lab All the 2 Ah cells delivered met the specifications needed for testing and characterization. Specific energy 207Wh/kg, energy Density of 380 Wh/L for the Pre-Li cells.</p>



	Budget Period - 2	In Progress
5	<p><b>R2R System Baseline</b> Targeted Goal: Complete 2Ah cell tests using R2R pre-lithiated anode that meets cell energy density goals and compare the results from 2Ah baseline cells made using S2S pre-lithiation.</p> <p>2Ah Cell Performance analysis report containing: Performance of 2Ah pouch cells Comparison of 2Ah S2S cells (Milestone 4) to results from R2R system (Milestone 5).</p>	<p>Budget Period-2 work was formally approved by USABC in October (10/14/2022) 18 (PQ6) (1.5 year) <b>PQ (6-10) → Completed</b> <b>Idaho National Lab:</b> Current data comparing to baseline (No pre-Li), the cells with pre-Li anode show higher capacity, lower capacity fade, higher available energy vs. baseline. <b>Farasis team 2 Ah cell builds</b>→ cells with pre-Li anode show FCE increased by 11%, capacity increased by 11%, and gravimetric energy density increased by 9.5 % vs. non-Pre Li control→ Results in alignment with BP1 SpectraPower data.</p>
6	<p><b>Final Deliverables updates Anode rolls for 29 Ah cell builds.</b> <b>Production Cells First Round</b> Targeted Goal: Complete &gt;29 Ah EV cells using &gt;25 wt% SiOx and 4.5 mAh/cm<sup>2</sup> anode loading and NMC811 cathode, complete cell testing as per USABC protocol (Wh/kg, Wh/L, BOL fast charging). - Production Cell Performance analysis report containing: - Performance of production cells with agreed USABC test protocol Demonstrated performance of large capacity cells in comparison to USABC goals.</p>	<p>Month 27 (PQ10→12) (with NCE) <b>PQ10→29Ah Cell – Anode roll for 29 Ah cell build.</b> Farasis completed 1400 meters of coating SiOx-Gr on anode rolls → Shipment [June 12,2023]. Ran into challenges with first batch of this anode→ Next batch of anode coatings initiated by Farasis. Edge quality of incoming rolls were damaged (<b>telescoping/tears</b>). Timeline affected for Dec 2023 completion.</p> <p>Farasis completed second round of coating of 1250 meters of 25 wt% SiOx anodes→ Rolls shipped to Applied Materials [Nov 06, 2023]→ Task Completed. The anodes tested for quality, web tear, edge alignment, thickness uniformity and moisture content by KF titration→ In progress. Installation and engineering upgrades of the 400 mm R2R tool→ This tool was used for Li transfer. 400mm transfer tool was able to validate proof-of-concept for effective R2R transfer. <b>However, we need advanced R2R tool capability for processing longer coating length of 1200 meters of final deliverable rolls.</b> Timeline for processing of the anodes → March 2023.</p>
7	<p><b>Production Cells Second Round</b> Targeted goal: Complete 2<sup>nd</sup> round of &gt;29 Ah EV cells and complete cell performance meeting USABC specifications (Wh/kg, Wh/L, BOL fast charging). - Production Cell Performance analysis report containing: - Performance of production cells with agreed USABC test protocol Meet USABC End of Program Goals on large capacity cells.</p>	<p>Month 30 (PQ10→12): <b>Production cells tasks milestone's 6 &amp; 7 scheduled in parallel depending on Farasis manufacturing line availability.</b></p>

8	USABC Cost Modeling	Month 33 (PQ11)
	Target goal: End of program cost target estimated at 6 GWh scale with 5 $\mu\text{m}$ thick Li-pre-lithiation is ~ \$4.90/kWh. - BatPaC Cost analysis report containing - Updated cost model for pre-lithiated Si/SiO <sub>x</sub> cells based on results from this program	Initial Cost model update Discussed in PQ6 review. Further updates refer. The cost model will be updated with data from Farasis 29 Ah cell build (~ Feb 2023).

## Results

Budget Period-2 is currently extended till June 30, 2024. Delays were a result of supply chain logistics issues caused by Covid pandemic. The cascading effect of the shift in timeline was discussed and aligned with USABC. We continue to work with Farasis Energy USA to meet the program deliverables. We thank the USABC team for the approval and continued guidance.

**Task A.1.** Applied Materials: Pre-Lithiation - Anode Characterization & Optimization S2S Test Stand-Completed.

**Task A.2.** Applied Materials: Pre-Lithiation Year 2- Anode Characterization & Alternate Approach for Pre-Lithiation - Substrate Independent Deposition and Transfer (SIDT)- Pre-Treatment and Post-Treatment; Completed: BP2 Final Deliverable tasks; work in progress.

### Key highlights:

- Applied Materials deposited ~ 3000 meters of R2R-Li coating @ 5.0  $\mu\text{m}$  → Task *Completed*.
- We used the 400 mm R2R R&D transfer tool for learnings of the SIDT process development.
- SIDT transfer of 5.0  $\mu\text{m}$  of Li from polymer substrate to Farasis anode substrate. *Initial process learnings completed*.
- Electrochemical testing and transfer validation with Farasis anode samples → *Completed*.
- 400mm transfer tool was able to validate proof-of-concept for effective R2R transfer. However, we need advanced R2R tool capability for processing longer coating length of 1200 meters of final deliverable rolls.

### Next Steps:

- 800mm production quality R2R transfer tool will be used for the final cell deliverables. We are aggressively accelerating the installation activities to accommodate the timeline for the installation of the tool.
- Shipping of the pre-Li anodes back to Farasis → March 2024
- Continue alignment and follow-ups with Farasis team for the 29 Ah cell builds. (Figure I.6.1)

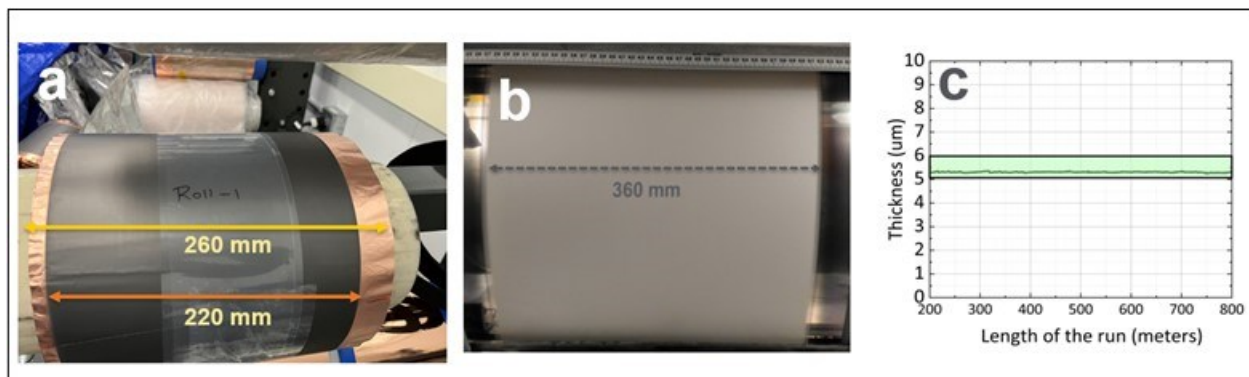


**Figure I.6.1 Example Image a) SiOx Anode rolls for 29 Ah cell build b) 3000 meters of Lithium deposited on plastic substrate on R2R c) Thickness for run: 5.3 um +/- 0.02 um < 1 % non-uniformity.**

**Task S.2.** Build and Test Pouch cells with Si/SiOx Blended Anode, Pre-lithiation and Protective layer (SpectraPower): SpectraPower Updates: Year 2

Cell Testing and performance demonstration of 2Ah pouch cells by SIDT approach: Table I.6.3 shows the cells level attributes and their details for the 2 Ah cell build with SIDT pre-lithiation approach and their respective values. Table I.6.3 also compares of the value with pre-Li and non-pre-Li for reference. (Figure I.6.2)

**Table I.6.3 Cells Level Attributes and their Details for the 2 Ah Cell Build.**

Attributes	Unit	Value (non-Pre-Li)	Value (pre-Li)
Cathode	NA	NMC 811	
Anode	NA	25 wt.% SiOx - Graphite	
Electrolyte		1.1 M LiPF6 EC: EMC 3:7 10 wt.% FEC	
Separator	um	Celgard 2320 (20 um)	
Cell Capacity	Ah	2.445	2.557
N/P with pre-Li	Ratio	1.19	1.22
Cycling Temp	°C	RT	RT
Cathode Loading	mg/cm <sup>2</sup>	26.06	26.24
Anode Loading	mg/cm <sup>2</sup>	10.08	11.19
Arial loading (Cathode)	mAh/cm <sup>2</sup>	4.85	4.88
Arial loading (Anode)	mAh/cm <sup>2</sup>	5.83	6.04
Chr/Dis rate	mA	500	500
Voltage Range (with CV~C/20)	V	4.2-2.8	4.2-2.8
Retained Cap @ 400 Cycles	%	79.0	88.0

### Comparison of 2 Ah SIDT Pre-lithiated SiOx Cells vs. Non Prelithiated Control:

Figure I.6.2 shows the comparison of SIDT pre-Li anodes vs. control samples. Results show slower capacity fade from SIDT pre-Li samples vs. non-pre-Li samples. The 2 Ah pre-Li cells built by SIDT show > 88 % retention at 400 cycles, better performance compared to non-Pre Li control cells (~77%).

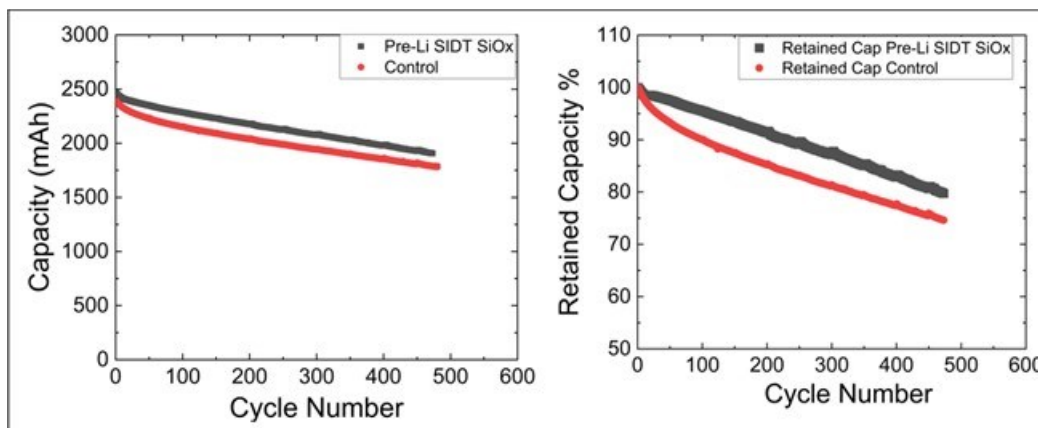


Figure I.6.2 Comparison of discharge capacity vs cycle number for SIDT prelithiation and the corresponding capacity fade plot (C/5 charge CV hold to C/20 and C/3 Dis).

#### Summary:

- 2 Ah Cell built with SIDT has > 88 % retention @ 400 cycles (C/4).
- Capacity fade from SIDT samples vs. non-pre-Li samples indicate slower degradation for SIDT.
- **The Spectra Power part of the tasks for the program deliverables completed.**

**Task F.2.** Build and Test Large Pouch cells (EV) with Si/SiOx Blended Anode, Pre-lithiation and Protective layer (Farasis): Year 2

Demonstration of 2Ah pouch cells (Milestone 5): **Objective:** To establish the R2R baseline by comparing the 2Ah cells pre-lithiated in the R2R system to the performance of 2Ah cells pre-lithiated in the S2S system (Milestone 4). **Summary of the testing:** Cell Fabrication Status at Farasis: 2 Ah Pouch cells with non-Prelithiated (control) and Prelithiated Silicon/Graphite Composite Anode and NMC 811 as cathode were assembled by Farasis in factory production environment. (Figure I.6.3)

- Cell Type: Multilayer Pouch Cells, 2 Ah
- Anode: Prelithiated Farasis single-sided SiOx/graphite anode (Specific capacity: 650 mAh/g)
- Pre-Li Layer Thickness: (1) 6  $\mu\text{m}$ , (2) 8  $\mu\text{m}$
- Cathode: NMC 811

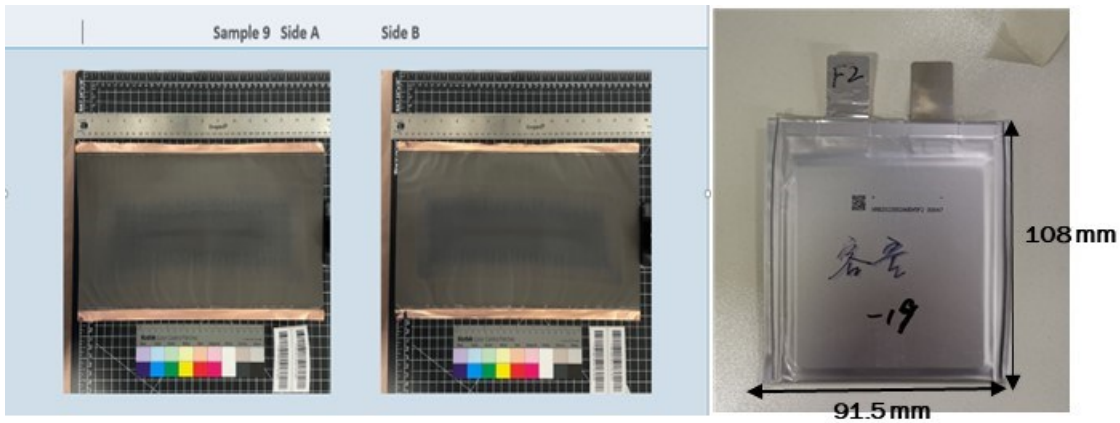


Figure I.6.3 Photographs of pre-lithiated SiOx anode sheets (6 μm Li) before shipment to Farasis (left and middle) and 2 Ah pouch cell built by Farasis (right).

The data are summarized in Table I.6.4, Table I.6.5, and Figure I.6.4, Figure I.6.5, and Figure I.6.6:

Table I.6.4 Comparison of Different pre-Li Samples vs. Baseline.

No.		Charge Capacity /mAh	Discharge Capacity /mAh	ICE	DCR-1C 10S /mΩ
F1	6μm Pre-Li	2912.8	2452.0	84.2%	34.85
F2	8μm pre-Li	2885.7	2469.2	85.6%	32.72
F3	No pre-Li	2984.3	2224.6	74.5%	49.48

Table I.6.5 2 Ah Cell Attributes for Farasis Cell Builds.

Attributes	Unit	Value (non-Pre-Li)	Value (pre-Li)
Cathode	NA	Ni Rich	
Anode	NA	650 mAh/g SiO/Gr	
Cell Capacity	Ah	2.2	2.4
N/P with pre-Li	Ratio	1.2	1.1
Cycling Temp	°C	25	25
Chr/Dis rate	mA	1C/1C	1C/1C
Voltage Range (with CV~C/20)	V	4.2-2.5	4.2-2.5
Retained Cap @ 400 Cycles	%	85	80

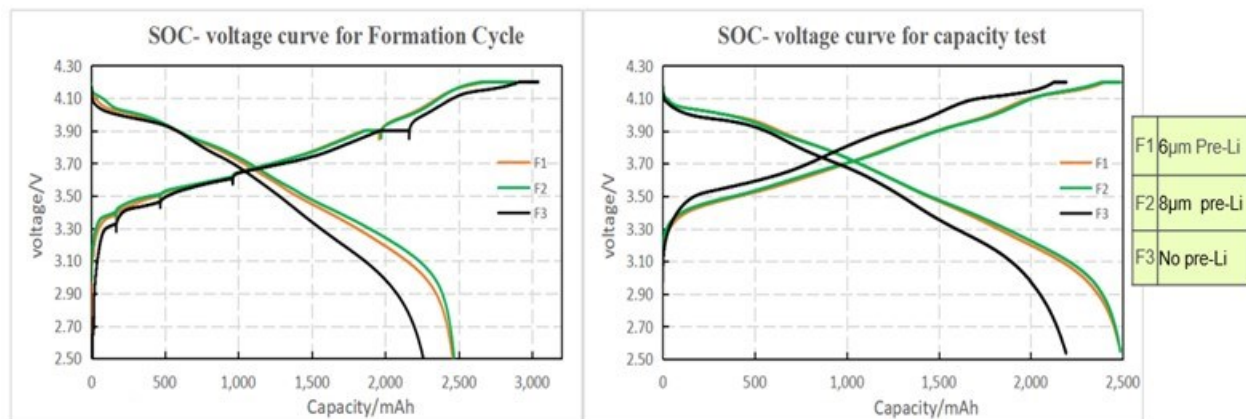


Figure I.6.4 Comparison of cell voltage vs. capacity for SIDT and the corresponding baseline during the formation cycle. Note: F3 is the control sample, F1 indicate 6 μm pre-Li and F2 8 μm pre-Li.

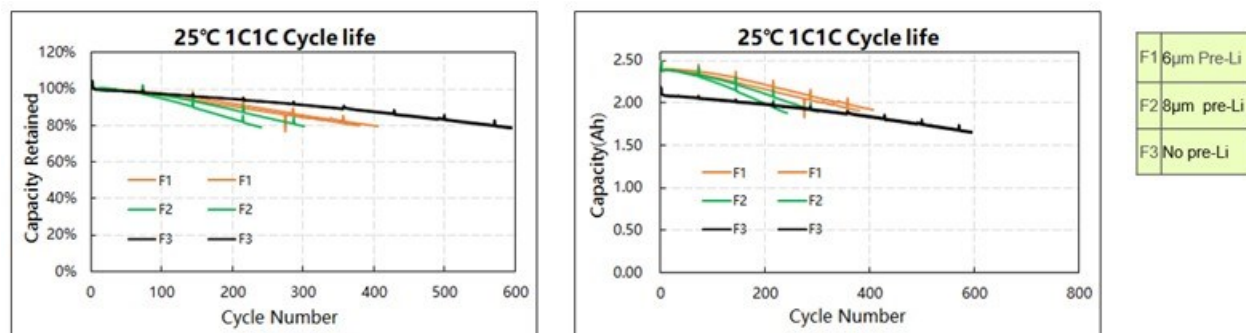


Figure I.6.5 Plot on the left indicate retained capacity vs. cycle number for the pre-Li anode (F1&F2) vs. baseline (F3) at 25 °C and 1C charge-1C discharge cycling conditions. The figure on the right show capacity (Ah) vs. cycle number (F1&F2) vs. baseline (F3). F3 is the control sample, F1 indicate 6 μm pre-Li and F2 8 μm pre-Li.

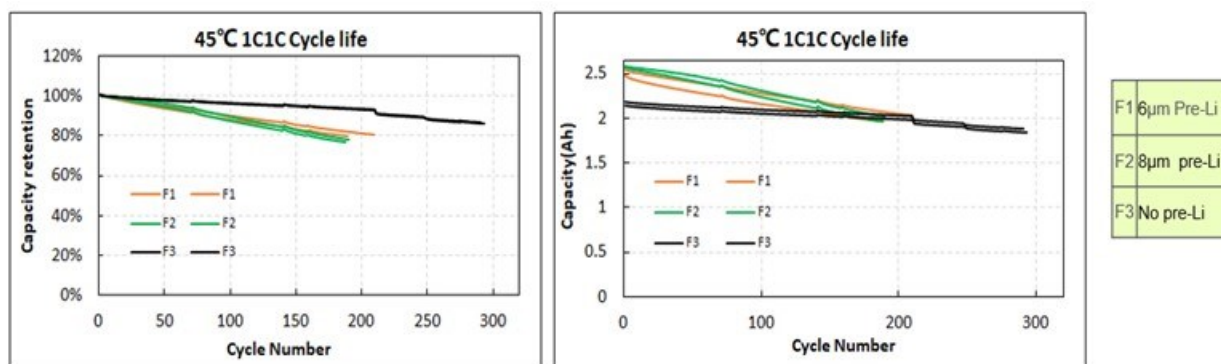


Figure I.6.6 Plot on the left indicate retained capacity vs. cycle number for the pre-Li anode (F1&F2) vs. baseline (F3) at 45 °C and 1C charge-1C discharge cycling conditions. The figure on the right show capacity (Ah) vs. cycle number (F1&F2) vs. baseline (F3). F3 is the control sample, F1 indicate 6 μm pre-Li and F2 8 μm pre-Li.

**Summary of the Farasis Study:**

Based on the results obtained from this study

- Based on current available data, comparing to baseline (No pre-Li), the cells with pre-Li anode show FCE increased by 11%, capacity increased by 11%, and gravimetric energy density increased by ~9.5 % (Wh/kg).
- 2 Ah Cell built by SIDT: At 25° C and 1C/1C cycling Pre-Li (6μ) 2 Ah Cell reached 400 cycles at 80 % retention, with cell capacity higher than that of non-pre-Li cell.
- Capacity fade of pre-Li cells higher than control (~ 5% at 400 cycles).
- 2 Ah Cell built by SIDT: At 45° C and 1C/1C cycling Pre-Li (6μ) 2 Ah Cell reached 210 cycles at 80 % retention, with cell capacity higher than that of non-pre-Li cell.
- Capacity fade of pre-Li cells at higher temperature cycling seems accelerated (~ 10% at 200 cycles).
- Based on available data, Farasis recommended 5.0 um Pre-Li for further ~29 Ah cells build.

**Task F2 and Task A2:** Farasis & Applied Materials (Milestone 6): 29Ah Cell – Anode roll for 29 Ah status.

- Farasis completed coating of 1250 meters of 25 wt% SiOx anodes → Rolls shipped to Applied Materials [Oct 16, 2023] → Task Completed.
- Applied Materials received anode rolls (1250 meters of SiOx anodes) from Farasis [Nov 06, 2023].
- We tested for quality check/ web tear, edge alignment, thickness uniformity etc., Task completed
- Reviewed and aligned data with Farasis.
- As received anode roll was tested for moisture using KF titration and the moisture was >500 ppm. We are optimizing the process conditions to dry the anode in a R2R setting to meet the moisture threshold for prelithiation. We were able to decrease the moisture to <200 ppm (Farasis recommended target < 350ppm).
- Tentative timeline for processing of the anodes (Early March 2024).
- Applied Materials completed 3000 meters of R2R Lithium metal coating @ 5.0 um on PET substrate for final cell deliverables and stored in Al vacuum pouch.

Idaho National Laboratory (INL) provided the status updates for Interim Cells as a part of deliverables. 2 Ah pre-Lithiated Cells (17) and 2 Ah non- prelithiated control cells (8) shipped to INL from SpectraPower. Results are summarized below in the Gap chart Figure I.6.7.

During the PQ8 quarterly meeting, the USABC team, in alignment with program partners and Applied Materials, suggested INL to continue cycling of both baseline control cells and pre-lithiated cells at C/3 charge/discharge conditions. The key points are summarized below.

- All the 2 Ah cells delivered met the initial specifications needed for further testing and characterization. The approximate beginning of life (BOL) Specific Energy 207Wh/kg, energy Density of 380 Wh/L for the Pre-Li cells, were observed.
- **For calendar life testing** cells at 30 °C, a 33.2 % fade was observed for baseline control cells vs. a 21.5% fade for Pre-Li at RPT5, in comparison at RPT1, a 13.4% fade was observed for baseline control cells vs. a 2.5 % fade for Pre-Li.

Applied Materials Interim EV Cell							
EV Cell Targets	Units	USABC EOL Cell	Program EOL (Base/Pre-Li)	Cell 10(CalLT Base)		Cell 8(CalLT Pre-Li)	
				RPT0	RPT2	RPT0	RPT5
Peak Discharge Power Density (30 sec)*	W/L	1400	413.4/538.4	800	421	540	148
Peak Specific Discharge Power (30 sec)*	W/kg	700	231.5/301.5	448	236	302	83
Peak Specific Regen Power (10 sec)	W/kg	300	37.6/19.0	45	55	22	34
Available Energy Density	Wh/L	550 (590)	206.7/291.5	306	246	356	296
Specific Available Energy	Wh/kg	275 (240)	115.8/155.8	171	138	199	166
Calendar Life (Yrs)	Years	10			0.18		0.44
DST Cycle Life	Cycles	1000					
Operating Environment**	°C	-30 to +52					
Normal Recharge Time	Hours	<7 Hours, J1772					
High Rate Charge	Minutes	80% UE <sub>Target</sub> in 15 min					
Maximum Operating Voltage	V	N/A					
Minimum Operating Voltage	V	>0.55*V <sub>max,op</sub>					
Survival Temperature Range, 24 hr	°C	-40 to +66					
Maximum Self Discharge	%/Month	<1					
INL ID Number				570		570	
Hardware Level				Cell		Cell	
Ampere Hour Capacity				1.6		2	

Figure I.6.7 Idaho National Lab gap chart summary of cell performance indicating the EV cell targets vs. interim cell delivered by SpectraPower.

### Program (schedule)-Update

Budget Period-2 is currently extended till June 30, 2024. Delays were a result of supply chain logistics issues caused by Covid pandemic. The cascading effect of the shift in timeline was discussed and aligned with USABC. We continue to work with Farasis Energy USA to meet the program deliverables. We thank the USABC team for the approval and continued guidance.

### Conclusions

In 2023, the Applied Materials-led team consisting of SpectraPower and Farasis completed all Year-1 milestones and started work towards Year-2 objectives. We are currently in the final phase of the program to deliver SiOx anode rolls to Farasis for 29 Ah cell builds.

### Acknowledgements

The Applied Materials-led team would like to sincerely thank our partners (SpectraPower and Farasis Energy USA) for their contributions and consistent efforts in supporting us to enable this technology and Dr. Lee Walker at INL for the cell testing results (Baseline Cells). Dr. Brian Ingram from ANL performed postmortem analysis of the cycled cells and provided us feedback.

We would also like to thank USABC, DOE program managers and reviewers for their constant encouragement and providing guidance throughout. We also acknowledge significant contributions from our Applied Materials engineering and process team for their support.



## I.7 Strategic Collaboration for the Development of a Self-Sustaining Model for the Recycling of Large-Format Lithium-Ion Batteries (American Battery Technology Company)

### **Ryan M Melsert, Principal Investigator**

American Battery Technology Company  
100 Washington St, Suite 100  
Reno, NV, 89503  
E-mail: [RMelsert@batterymetals.com](mailto:RMelsert@batterymetals.com)

### **Brian Cunningham, DOE Technology Development Manager**

U.S. Department of Energy  
E-mail: [Brian.Cunningham@ee.goe.gov](mailto:Brian.Cunningham@ee.goe.gov)

Start Date: October 1, 2021

End Date: March 31, 2024

Project Funding: \$2,000,000

DOE share: \$500,000

Non-DOE share: \$1,500,000

### **Project Introduction**

As vehicle-related research and development in advanced battery technology continues to progress, the market competitiveness and penetration of EVs, PHEVs, and HEVs have been steadily increasing. However, the total life cycle costs of the associated large format batteries still present an obstacle to further adoption, and a major potential avenue to decrease these costs is to increase the residual value of these batteries at their end of lives. Unfortunately, many currently available operations for the recycling of large format lithium-ion batteries require a tipping-fee to be paid in order for these batteries to be processed, actually further increasing their life cycle costs. This recycling business model is unsustainable, as it prohibitively adds life cycle costs and discourages end users from returning their batteries to the market at end-of-life.

This project team has developed an integrated processing train for the recycling of large format lithium-ion batteries that substantially reduces both upfront capital and operating costs, while refining the battery metals to the specialty chemical specifications defined by leading cathode manufacturers in order to extract additional revenue and establish a true closed-loop circular economy. Through these enhancements, this integrated process is able to operate economically while providing high residual value to end-of-life material owners, which provides an economic incentive for current holders and stockpilers of feedstock to return their materials to the market to enable the closed-loop supply chain to operate.

### **Objectives**

The objective of this project is to demonstrate that the existing business model of the lithium-ion battery recycling industry can be challenged, and that a sustainable recycling system can be operated that can result in the manufacturing of cells from recycled battery metals that have equal performance to otherwise identical cells from virgin-sourced material, while also being produced at lower cost, with lower environmental footprint, and from domestic US based resources.

The primary USABC targets addressed in this program are those of cell cost, maximum percentage of active cathode manufactured from recycled materials, and the percentage of battery metals that are sourced from the domestic US. In addition to these metrics, it is critical to demonstrate that both active cathode powders and full multi-layer test cells that are manufactured from these recycled metals can achieve the same performance as otherwise identical components that are manufactured from virgin metals. As a result, the performance metrics of standalone active cathode powder and of full multilayer pouch test cells need to be achieved in order for the above USABC performance targets to be validated. The active cathode powder and cell level test procedures for this project will follow the guidelines set forth in the “United States Advanced Battery Consortium Battery Test Manual for Electric Vehicles” as detailed by the US DOE VTO.

## Approach

In order to validate the commercial performance of these recycled battery metal products, an approach has been established that consists of three major tasks spread across two budget periods.

- Budget Period 1 (10/1/21 - 9/30/22):
  - **Task 1**
    - Bench scale recovery and purification of battery metals from recycled sources, analytical characterization of recycled metals to ensure all product specifications are being achieved
    - Synthesizing of high-energy density active cathode material from control group virgin-sourced battery metals, in order to prepare material for test cell development
    - Cell development and balancing of half-cell, single-layer pouch cells, and multi-layer pouch cells using control group virgin-sourced battery metals
    - Performance testing of multi-layer pouch cells from control group virgin-sourced active cathode material to establish benchmarks
- Budget Period 2 (10/1/22 - 3/31/24):
  - **Task 2**
    - Large scale recycling of large format automotive cells, recovery and purification of battery metals, and analytical characterization of products
    - Synthesis of high energy density active cathode material from various blends of recycled and virgin sourced battery metals
    - Fabrication of multi-layer pouch cells from each blend of recycled and virgin sourced battery metals active cathode material
    - Performance testing of test cells, and comparison of cell performance against control group cells
  - **Task 3**
    - Analysis of life cycle operations with cost, performance, and environmental impact metrics

In order to ensure that industry relevant high energy density active cathode materials are utilized in this evaluation, ABTC has formed a strategic collaboration for this project team with BASF, one the largest manufacturers of high-energy density automotive cathode material in North America. Through this strategic collaboration, during this project BASF is receiving recycled battery cathode grade metal feedstocks (Nickel, Cobalt, and Manganese Sulfates, as well as Lithium Hydroxide) from ABTC's battery recycling processes, and is using these metal feedstocks to synthesize its high energy density active cathode material. Multiple batches of this active cathode material are being manufactured using various blends of virgin-sourced and recycled-sourced battery metal feedstocks, and BASF is characterizing the performance of these active cathode material batches in order to quantify the impact on performance of virgin versus recycled battery metal feedstocks.

In addition to synthesizing active cathode material from recycled battery metals, this project is taken a step further and an additional strategic collaboration has been formed with C4V. C4V is a battery R&D and manufacturing company that operates out of the Northeast Center for Chemical Energy Storage (NECCES), a US DOE Center of Excellence Energy Frontier Research Center, at Binghamton University. This center has world class facilities for the fabrication and testing of all types of form factors and chemistries of high energy density lithium-ion batteries. During this project, C4V is receiving the batches of virgin-sourced and recycled-sourced active cathode material from BASF and is fabricating large format automotive test cells in order to quantify the performance of these various batches of active cathode material at the cell level. These cells will be tested through individual characterizations, cycle life, and calendar life procedures and the impact on virgin vs recycled battery metal feedstocks for each batch will be quantified.

These strategic collaborations between battery recyclers, cathode manufacturers, and cell manufacturers in North America will enable the demonstration of the full closed-loop circular manufacturing supply chain of

large format lithium-ion battery cells. The program includes battery module and cell recycling, battery metal recovery and purification, active cathode synthesis, large format cell manufacturing, and rigorous testing of these cells side-by-side with otherwise identical cells manufactured from virgin sourced battery metals. (Figure I.7.1)

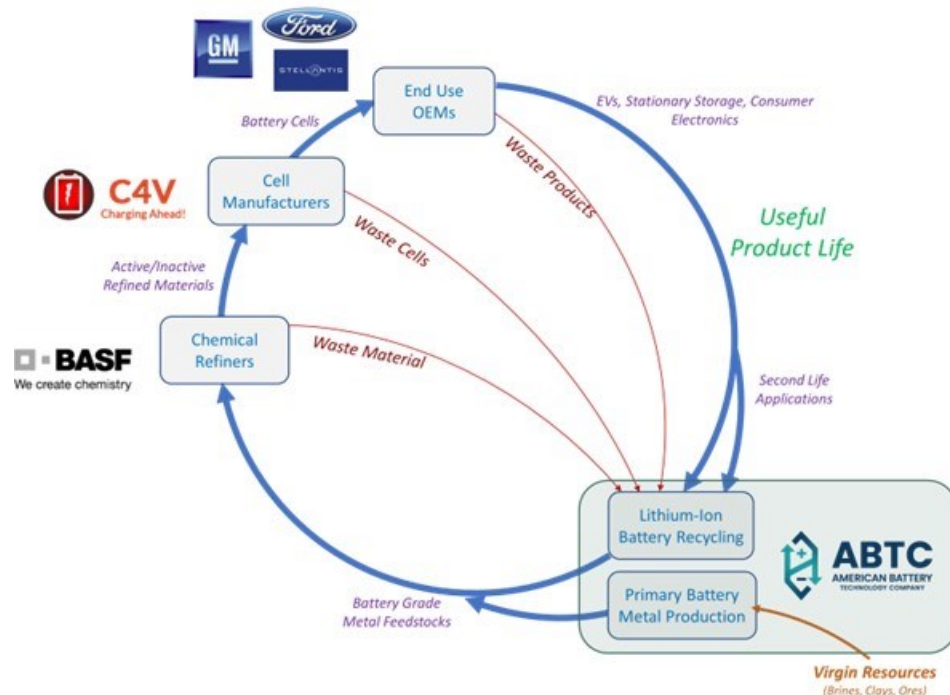


Figure I.7.1 Demonstration of closed-loop North American lithium-ion battery supply chain.

## Results

The project team has completed all activities within Budget Period 1, including the generation of bench scale samples of recycled lithium hydroxide and transition metal sulfates, the characterization of these products by both ABTC and BASF to confirm they meet all required product specifications, the synthesis of control group active cathode material from virgin sourced metals, the cell development and fabrication of cells from this control group active cathode material, and the performance testing of these control group cells.

The testing and performance benchmarking of the control group cells were performed throughout Q3 and Q4 2022, and the initial results were presented to the USABC team. The data to date demonstrates that the performance of the tested cells is aligned with industry metrics, and that these control group cells will serve as successful baselines for the sensitivity studies to be performed during the second budget period of this project.

Within this current Budget Period 2, the ABTC and BASF teams have collaborated to develop packaging and shipment specifications, as well as the delivery schedule, for kg-level batches of recycled products. ABTC, BASF, and C4V have further worked with the USABC team to develop an optimized approach to the delivery of blended virgin/recycled cathode metal ratios that will allow the team to more efficiently complete Task 2 and move into Task 3. With this information in hand, the ABTC team has commenced the production of LiOH and Ni/Co/Mn sulfates at battery cathode specification from end of life and scrap batteries. The teams have aligned on the schedule for the shipments and processing of each of these batches of material to enable the pCAM/CAM synthesis to occur from Q3 2023 through Q1 2024.

Further details around results are outlined below;

1. All 4 bench scale battery metal samples (nickel sulfate, cobalt sulfate, manganese sulfate, and crystallized lithium hydroxide monohydrate powders) have been generated, and have undergone analytical characterization and have had certificates of analysis (COA) issued by ABTC
2. The purities of these battery metal samples were evaluated by BASF, and were confirmed to achieve all required specifications to be manufactured into high energy density cathode precursor and active cathode material
3. The initial production batch of cathode precursor material was synthesized and converted into active cathode material by BASF, and delivered to the C4V team for initial cell development
4. All non-cathode materials have been procured for fabrication of control group pouch cells by C4V
5. Initial coin cells were fabricated from control group active cathode material for initial cell development
6. Single and multi-layer control group cells have been fabricated and tested, and final cell balancing was performed to finalize the cell-level design specifications
7. Multi-layer pouch cells were fabricated and have undergone initial performance testing to set baseline metrics for subsequent sensitivity studies
8. The batches of recycled metals are being prepared and shipped to BASF for synthesis into active cathode material
9. C4V is finalizing the cell build details, and C4V and INL are aligning on the updated testing procedures and electrolyte formulations for both the control cells and the subsequent test cells

The project team is continuing the process of recycling batches of large format automotive lithium-ion batteries, recovering and purifying the elemental battery metals, and generating large batches of battery metal products in order to enable to the large-scale synthesis of blended batches of active cathode materials.

## Conclusions

In conclusion, the industry for the recycling of large-format automotive lithium-ion batteries is still nascent, with ABTC operating one of only a handful of commercial scale operations within North America. For the most part, these early facilities generally function in a manner that allows for end-of-life batteries to be processed into non-hazardous materials, however the current paradigm, aside from at ABTC's facility, does not allow for extracted battery metals to be manufactured at significantly lower costs or environmental impact than comparable virgin-sourced battery metals from mining operations. Furthermore, these recycled battery metals are generally blended with virgin-sourced battery metals in the manufacturing of new large-format automotive battery cells, and the industry requests the demonstration and validation that cells made from a substantial quantity of recycled metals can achieve the same performance as cells made from virgin-sourced battery metals.

In order to demonstrate this wide breadth of operations within the battery manufacturing supply chain, this strategic collaboration has been formed to bring together each of the necessary skillsets and facilities to address this scope of work. Through this combined effort, an integrated recycling system is being demonstrated that processes commercial quantities of battery feedstock, the constituent battery metals are being extracted and purified to battery grade specifications, active cathode material is being manufactured from these recycled battery metals, large-format battery cells are being fabricated from these recycled materials, and then these automotive cells will be tested against otherwise identical cells manufactured with virgin-sourced battery metals.

At the end of this demonstration process, the recorded operational data will be used to calculate the total cost of production of these recycled battery metals versus comparable virgin-sourced battery metals, the relative environmental impact of these operations compared to baseline processes, and the performance of these battery cells versus stated USABC project goals.

**Acknowledgements**

ABTC would like to acknowledge the diligence and hard work performed by its collaborators, BASF and C4V, throughout the undertaking of this program. Without their efforts, this project development and demonstration of a self-sustaining business model for the recycling of large format lithium-ion batteries within North America wouldn't have been possible.

ABTC would also like to thank the USABC team for providing an opportunity to showcase an integrated network for closing the domestic battery manufacturing supply chain. We are grateful for the group's dedication to decarbonizing transportation and look forward to continuing to build long-lasting and mutually beneficial collaborations.

## I.8 Silicon-based EV Cells Meeting Cost, Calendar Life and Power Requirements (Ionblox, Inc.)

### **Masoud Rahman, Principal Investigator**

Ionblox, Inc.  
3390 Gateway Blvd.  
Fremont, CA 94538  
E-mail: [Masoud@ionblox.com](mailto:Masoud@ionblox.com)

### **Brian Cunningham, DOE Technology Development Manager**

U.S. Department of Energy  
E-mail: [Brian.Cunningham@ee.goe.gov](mailto:Brian.Cunningham@ee.goe.gov)

Start Date: April 5, 2022	End Date: June 30, 2024	
Project Funding: \$1,730,378	DOE share: \$865,189	Non-DOE share: \$865,189

### **Project Introduction**

It is well known that silicon-based anodes suffer from continuous growth of the solid electrolyte interphase (SEI) which increases the cell resistance, consumes lithium, and decreases the capacity, power, and energy of the cell. The continuous growth of the SEI is driven by the large volume expansion of the silicon anodes combined with an unstable SEI that promotes electrolyte decomposition.

Ionblox has been able to achieve several USABC cell targets such as power, energy, fast charge, and cycle life. This project will continue the research and development that started during the first USABC LC/FC1 project and focuses on meeting the calendar life, resistance, and cell cost targets. This program will focus on electrolyte and active material development to properly passivate and form stable protective layers on the anode (SEI) and cathode (cathode electrolyte interphase - CEI) surfaces.

### **Objectives**

The key goals of this project are: 1) reaching the USABC calendar life and resistance cell targets via surface passivation, anode and cathode material development and electrolyte engineering; and 2) meeting the USABC cell cost target by optimizing the lithiation process of the silicon anode.

### **Approach**

A unique aspect of the current LC/FC2 program is that it will continue building on the success of the previous LC/FC1 program. The LC/FC2 program will start on solid footing with cells already performing well with respect to cycle life, energy, fast charge, rate capability, and safety. Ionblox understands the last remaining challenges needing development to qualify and commercialize the technology and therefore will primarily focus on improving the calendar life, reducing resistance growth (as a function of storage and cycling) and meeting the cell cost targets. Additional cell specifications with respect to fast charging, high energy, high power, low temperature performance, safety and manufacturability will also be met during this program.

The proposed program will focus on electrolyte and active material development to properly passivate and form stable protective layers known as solid electrolyte interface (SEI) on the active anode (SEI) and cathode (CEI) surfaces. Novel electrolyte formulations will minimize unwanted surface electrolyte reactions, while maintaining low temperature performance, high-rate capability, long cycle life, low cost, and ability to pass the safety requirements for EVs. Active material development will focus on surface passivation to minimize unwanted side reactions and improve calendar life. Regarding the USABC cost target, the Ionblox key approach will be based on Li-doped SiO<sub>x</sub> material/process development to reduce cost and improve the overall performance of the cells. Tradeoffs in cell cost and performance between pre-lithiation of the anode and Li-doped SiO<sub>x</sub> will be made. The summary of Ionblox approach in this program is shown in Figure I.8.1.

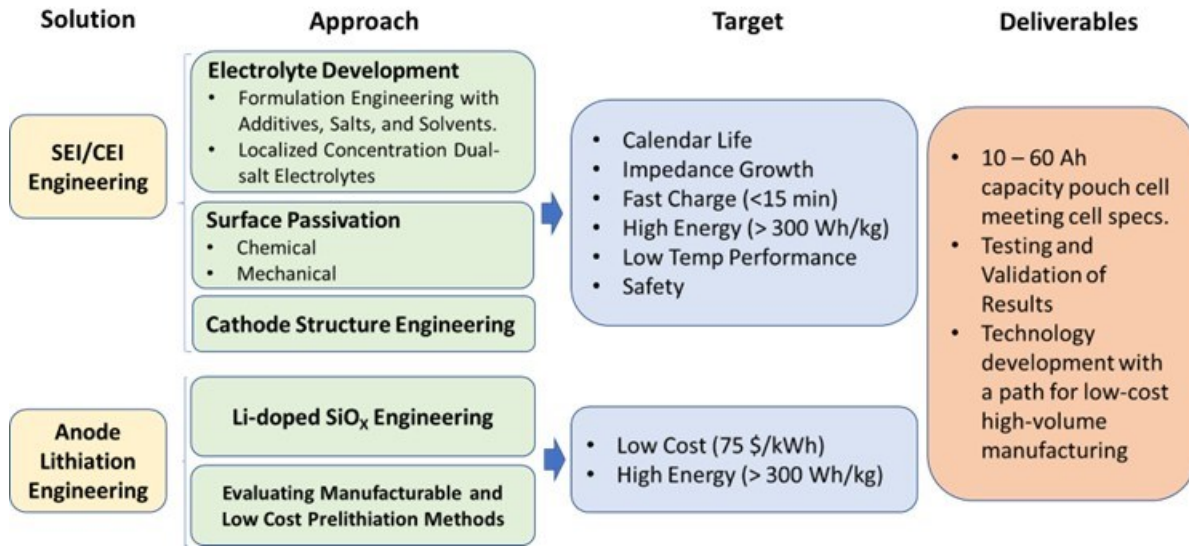


Figure I.8.1 Ionblox approach to reach the USABC calendar life and cell cost targets.

**Results**

In this section the progress on key approaches that were employed to improve the calendar life and reduce the impedance growth are presented.

**Electrolyte Development**

During 2023, Ionblox finished the coin cell study of 14 electrolytes. In order to achieve a complete investigation of electrolyte parameters, the impact of solvent, salt, additives, and concentration were considered in the design of experiment for the electrolyte study. The summary of electrolytes and their impact on cycle life as well as calendar life is presented in Table I.8.1.

The electrolytes were designed with the objectives of SEI/CEI stabilization, anti-gassing, thermal stability, and HF-scavenging. The evaluations started on coin cells with identical anodes and cathodes. The impact of each electrolyte on the calendar life and cycle life was compared against the baseline electrolyte (E0). Among the electrolytes, E1 showed improvement on calendar life, therefore, it was down selected for the Mid-Program cell build and delivery to National Labs. Among all the electrolytes that were studied the Localized High Concentration Electrolyte (LHCE) demonstrated the least promising performance and therefore, they are no longer being considered as promising approach to continue.

**Table I.8.1 Summary of Electrolytes and their Impact on Calendar Life and Cycle Life**

Description	Type	Cycle Life vs E0	Calendar Life vs E0	Evaluation
<b>E0</b>	Baseline	~800 cycles to 80% SOH	4-5 RPTs till 80% SOH	
<b>E1</b>	Additive	100 cycle loss	<1 RPT gain	Beneficial
<b>E10*</b>	Additive	150 cycle loss	<1 RPT gain	Neutral
<b>E8</b>	Additive	50 cycle loss	N/A	Neutral
<b>E9</b>	Additive	N/A	<1 RPT loss	Neutral
<b>E3</b>	Solvent	200 cycle loss	N/A	Detrimental
<b>E2</b>	Solvent	No change	<1 RPT loss	Neutral
<b>E7</b>	Solvent	No change	<1 RPT loss	Neutral
<b>E4*</b>	Salt	No change	No change	Neutral
<b>E5</b>	Salt	100 cycle loss	N/A	Neutral
<b>E6</b>	Salt	200 cycle loss	N/A	Detrimental
<b>E11*</b>	Salt	600 cycle loss	<3 RPT loss	Detrimental
<b>L1</b>	LHCE	800 cycle loss	N/A	Detrimental
<b>L2</b>	LHCE	800 cycle loss	N/A	Detrimental

Based on the results from Table I.8.1 E1 was down selected for the Mid-Program cell build. Additionally, the internal data from another study at Ionblox showed that E12 could be a potential candidate for prelithiated cells with Lithium film. Therefore, both E1 and E12 were selected for Mid-Program cell build. The cells have been delivered to NREL, INL, and SNL during quarters 5 and 6.

The summary of electrolyte study and next steps is shown in Figure I.8.2. As the next step, E1 has been selected for Li-doped SiO<sub>x</sub> design. The cycle life studies have reached around 300 cycles and the calendar life studies have finished RPT1. The initial data indicates that E1 has improved capacity retention during calendar life studies and reduced the resistance growth. The complete dataset will be presented in the next report.



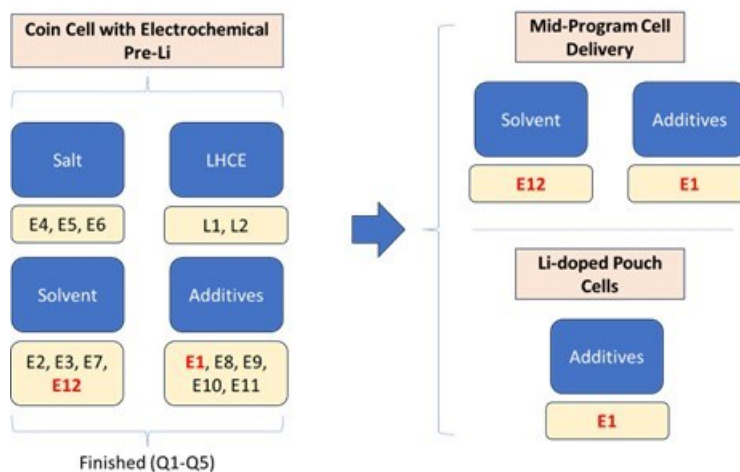


Figure I.8.2 Electrolyte study progress and next steps.

**Cathode Structure Engineering**

The chemistry, crystallinity, morphology, and surface properties of cathode active material can affect the stability of the CEI and SEI layers. Ionblox selected nine commercial cathode active materials which are listed in Table I.8.2. Cathode 6 is a mix of Cathode 3 & 4 and Cathode 9 is a mix of Cathode 3 & 5. The coin cell study of all the nine cathodes was completed in 2023. The calendar life (CL) measurements up to RPT6 (90 days) showed that Cathode #9 has a smaller resistance growth compared to Cathode #1 while demonstrating similar capacity retention.

Due to better CL performance, Cathode #9 which is a mixture of single crystalline (SC) and polycrystalline (PC) NMC 811 (both from the same supplier) was down selected for Mid-Program cell build.

Table I.8.2 List of cathode active materials and their properties.

Cathode#	Crystallinity	NCM	Voltage Range (V)
1 (Baseline)	SC	811	2.5 – 4.2
2	PC	811	2.5 – 4.2
3	PC	811	2.5 – 4.2
4	SC	811	2.5 – 4.2
5	SC	811	2.5 – 4.2
6	PC + SC	811	2.5 – 4.2
7	SC	622	2.5 – 4.2
8	PC	90505	2.5 – 4.2
9*	PC + SC	811	2.5 – 4.2

The comparison of the capacity retention of all the nine cathodes that were studied by Ionblox is shown in Figure I.8.3. The calendar life study performed at an accelerated condition of 50 °C and 100% state of charge (SOC). Each RPT (reference performance test) is equivalent to 15 days.

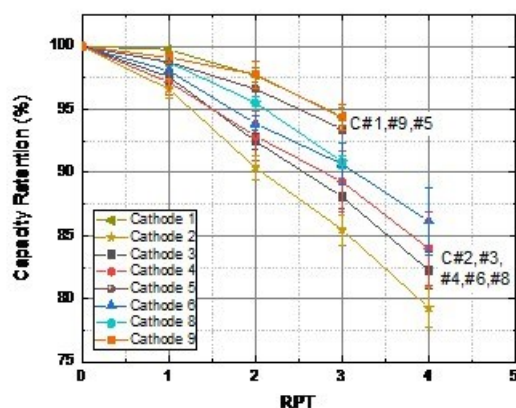


Figure I.8.3 Capacity retention comparison of nine cathodes studied by Ionblox.

### Surface Passivation

One of the key approaches to increase the calendar life and control the resistance growth is surface passivation. Ionblox studied the effect of surface passivation on both anode and cathode. During 2023, Ionblox completed the evaluation of cathode passivation via Polymer #1, #2, #3, and Polymer #4. Among the four polymers that were considered for surface passivation, only Polymer #4 showed improvement on calendar life. Therefore, Polymer #4 was selected as a candidate for surface passivation of Li-doped SiO<sub>x</sub> anodes. The study of surface passivation of Li-doped SiO<sub>x</sub> at three coating thicknesses started in 2023.

In addition to surface passivation via polymers, anode active material powder was sent to a leading Atomic Layer Deposition (ALD) company in the U.S. Samples were coated with two different oxides (Oxide1 and Oxide2) at three different thicknesses. The summary of surface passivation approaches is shown in Figure I.8.4.

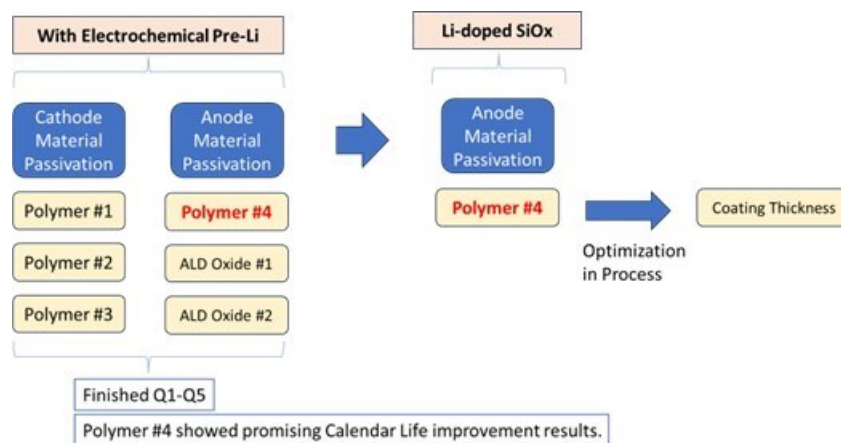


Figure I.8.4 Summary of surface passivation approaches.

The study of surface passivation via ALD Oxide1 and Oxide 2 at three different thicknesses ( $T_3 > T_2 > T_1$ ) was completed at Q5. The resistance growth and capacity retention data are presented in Figure I.8.5 and Figure I.8.6. The calendar life study was performed on coin cells at accelerated condition (temperature of 50 °C). Each RPT is equal to 15 days. The data indicates that ALD Oxide 1 and Oxide 2 did not result in significant changes in calendar life performance.

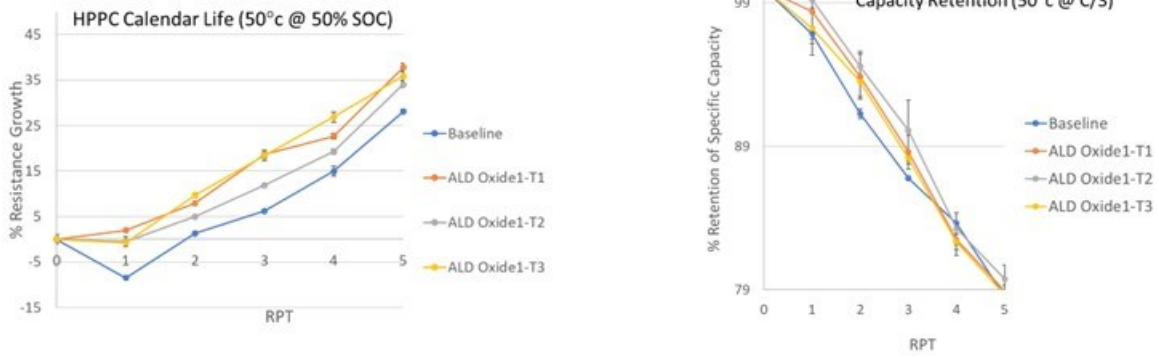


Figure I.8.5 Comparison of ALD Oxide1 vs baseline on the calendar life performance. Right: capacity retention; Left: resistance growth.

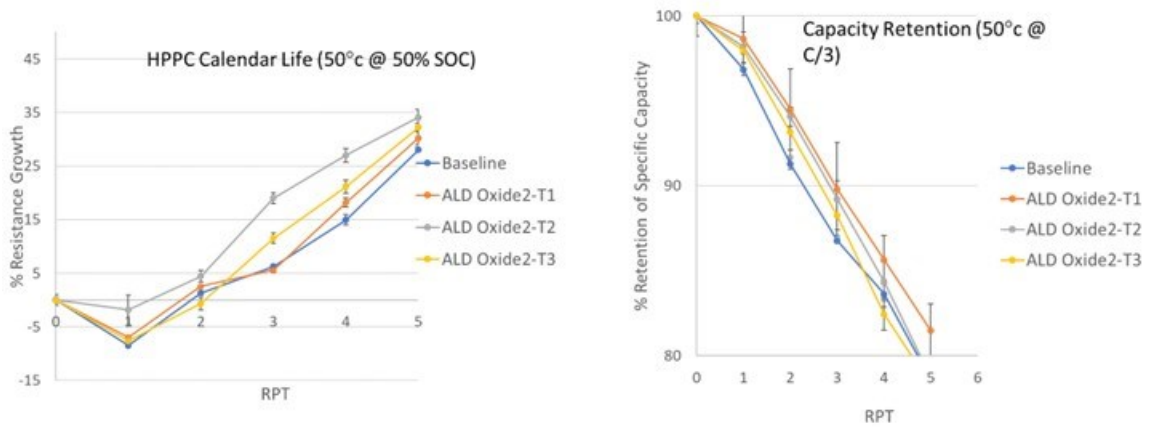


Figure I.8.6 Comparison of ALD Oxide2 vs baseline on the calendar life performance. Right: capacity retention; Left: resistance growth.

The cycling performance of both ALD Oxide 1 and Oxide 2-coin cells (measured at 1C:1C at room temperature) are compared against the baseline in Figure I.8.7. The data indicates that there is no significant changes in the cycling behavior of passivated cells.



Figure I.8.7 Comparison of ALD Oxide2 vs baseline on the calendar life performance. Right: capacity retention; Left: resistance growth.

The fast charge rate study of Polymer#4 on Li-doped SiOx anode in coin cells at three different thicknesses (T3>T2>T1) is presented in Figure I.8.8. The initial data indicates that at the optimized thickness of T2 the fast charge capability is not affected.

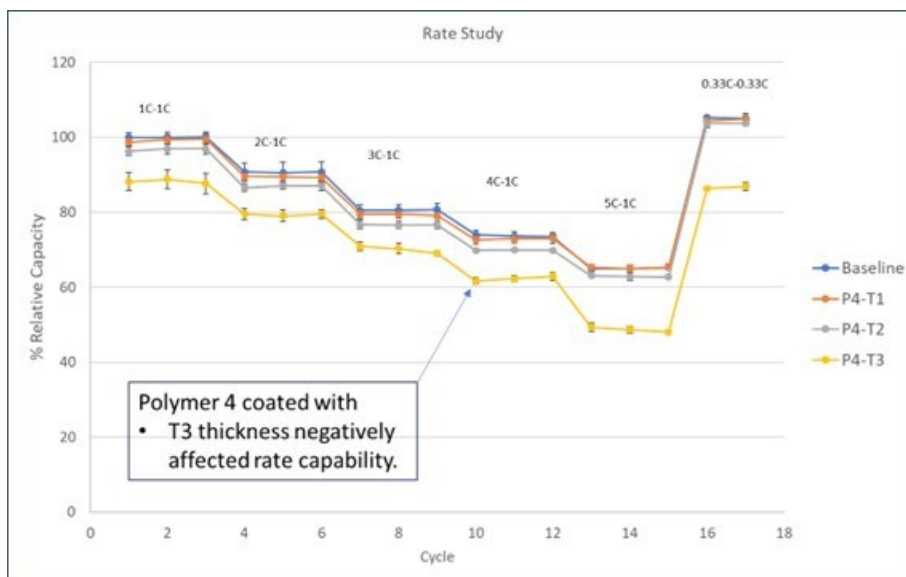


Figure I.8.8 The rate performance of lithium doped anode with Polymer 4 passivation at three different thickness (T3>T2>T1).

Cycling studies on passivated Li-doped SiOx with Polymer#4 on coin cells have started in 2023. During the first 300 cycle minor deviations are noticed against the non-passivated sample. This study will be finished in early 2024 and the data will be presented in the next report.

**Mid-Program Pouch Cell Build**

For Mid-Program cell build and delivery the following materials were down selected:

- Electrolyte: E1 and E12
- Cathode: Cathode #9 and Cathode #10

- Pre-lithiation: Lithium powder and Lithium on Polymer (Li/Polymer)

Based on the above materials two splits were built and shipped to INL, NREL, and SNL.

- Split #2: Cathode #9, E0, Lithium powder.
- Split #4: Cathode #4, E12, Li/Polymer.

Split #4 was built in two different form factors and the larger form-factor were sent to NREL and SNL in order to determine the thermal performance and safety of Ionblox cells in the higher capacity form factor. The summary of cells and form factors as well as the planned tests at each national lab is summarized in the Figure I.8.9.

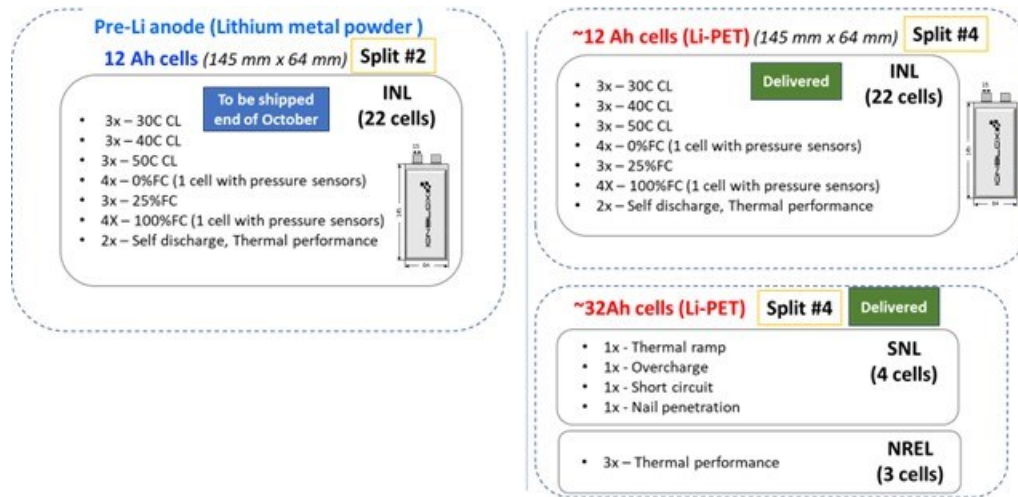


Figure I.8.9 Summary of cells, form factor, and the planned tests that were shipped to national labs as Mid-Program cell build and delivery.

### Conclusions

During 2023 the Mid-Program cells were built and delivered to national labs. Currently, the baseline cells as well as the Mid-Program cells are being tested and evaluated by Ionblox as well as the national labs. Ionblox compared the calendar life performance of nine cathodes and the best performing cathodes were down selected for the Mid-Program cell build. Additionally, Ionblox designed various electrolytes in order to study the impact of various electrolyte components such as salt, solvent, additives, and localized high concentration electrolytes. Finally, Ionblox completed the study of surface passivation via atomic layer deposition as well as polymers on both anode and cathode. Learnings from electrolyte, cathode, and surface passivation has been passed to lithium-doped silicon oxide design which currently is moving forward.

### Acknowledgements

This work is being performed under the guidance and support from the USABC technical work group: Lamuel David (program manager), Meng Jiang, Brian Robert, Jack Deppe, Brian Cunningham, Lee Walker, Andrew Schiek and Loraine Torres-Castro. Ionblox would like to acknowledge the support and technical feedback from the USABC technical work group (Stellantis, Ford, GM), Department of Energy, Idaho National Lab, Sandia National Lab, and National Renewable Energy Lab.

## I.9 Low-Cost and Fast Charge Semi-Solid Li-LFP Cell for EV Applications (24M)

### Junzheng Chen, Principal Investigator

Organization: 24M Technologies, Inc

Address: 130 Brookline St.

Cambridge, MA 02139

E-mail: [jchen@24-m.com](mailto:jchen@24-m.com)

### Thomas Do, DOE Technology Development Manager

U.S. Department of Energy

E-mail: [thomas.do@ee.goe.gov](mailto:thomas.do@ee.goe.gov)

Start Date: October 5, 2022

End Date: September 30, 2024

Project Funding: \$3,778,896

DOE share: \$1,889,448

Non-DOE share: \$1,889,448

### Project Introduction

24M Technologies has developed a breakthrough manufacturing process that leverages proven and emerging chemistries to deliver lithium-ion batteries with low cost and inactive materials content. In this program, 24M will develop large-format, automotive-capable lithium metal/LFP cells with both high energy density and fast charge capability. 24M's unique electrode and cell architectures are inherently capable of accommodating large volume-change active materials, and 24M's cells exhibit unprecedented levels of abuse tolerance. The manufacturing process requires less than one half the number of unit operations of conventional lithium-ion technology and has been demonstrated in automated pilot and commercial production.

24M's proprietary flowable (semi-solid) electrode technology enables unique cell architectures with several advantages compared to conventional Li-ion batteries. For automotive applications, a key advantage is the novel manufacturing method, which dramatically reduces manufacturing complexity and cost. Additionally, it is readily scalable according to market demand. The small footprint for equipment and comparatively low capital equipment investment needed further reduce the manufacturing risk.

24M's unique electrode and cell architectures significantly lower the materials cost in each cell. 24M believes that its cell design has lower materials cost per energy (\$/kWh) than any Li-ion cell of comparable energy and power in the market or under development. Cells based on semi-solid electrodes have a higher ratio of active materials to inactive materials than conventional cells, providing an inherent, sustainable advantage in the cell bill of materials.

Finally, unlike most development approaches in advanced batteries, 24M's core technologies are platforms for electrode and cell design and manufacturing that are not limited to any particular set of active materials. Therefore, 24M's cells can leverage all of the active materials available today and those developed in the future.

As a platform player, 24M maintains the flexibility to drop-in next generation active material as lithium-ion chemistries evolve and as alternative chemistries (such as Na-ion or Mg-ion) emerge.

### Objectives

24M will demonstrate that its novel electrode, cell and manufacturing approach can be applied to high-energy density lithium metal/LFP chemistry to enable mass production of automotive-capable cells with dramatically lower cost. The approach outlined below has been planned to develop high energy density semi-solid electrode formulations, and to demonstrate the manufacturing of prototype cells based on those formulations that meet or exceed the USABC targets outlined in Table I.9.1 for each phase of the program.

**Table I.9.1 USABC Targets for the 24M Project**

	Phase 1	Phase 2
Cell Footprint (cm <sup>2</sup> )	300	300
Cell Capacity (Ah)	2	20
Energy Density (Wh/L)	500	550
Specific Energy (Wh/kg)	250	275
Number of Cells	18	33
Charge time to 80% Energy (min)	30	15

## Approach

24M has planned activities designed to achieve the objectives identified in the preceding section. For each activity, the task-specific objectives and approaches are described below.

### 1. Materials Evaluation and Selection

Developing high energy density cells with fast charge capability involves the optimization of several cell components, including the cathode, electrolyte, separator, and anode, as well as the integration of these components. Ultimately, active and inactive materials and electrode formulations will be selected that optimally balance the tradeoffs of power performance, safety, processability, and life (cycle and calendar) in a 24M automotive cell.

In this program, LFP and LMFP active materials from commercial sources are characterized for physical characteristics, such as tap density, particle size, and surface area. These characteristics influence the mechanical and electrical properties of SemiSolid slurries made using the active materials, and hence their ability to be made into electrodes using 24M's process. Electrodes of various formulations and designs will be electrochemically tested in Li/LFP and Li/LFMP cells to optimize the volumetric loading, conductive additive concentration, and electrode thickness for energy density and charge rate.

Electrolyte formulations will be developed and screened, with the goals of high ionic conductivity, good Coulombic efficiency, and high charge rate capability. Ionic conductivity is critically important for fast charge and discharge capability, due to the high thickness of 24M electrodes compared to conventional ones. Lithium plating/stripping efficiency will be tested in Li/Cu cells to determine the stability of the electrolyte against lithium metal, as well as the rate at which lithium is lost due to side reactions. Higher efficiency reduces the amount of excess lithium required in the cell, and hence the energy density. Lithium/Lithium symmetric cell testing will be performed to determine the capability of these electrolytes to prevent dendrite formation. Electrolytes will also be selected with consideration to their performance at low temperatures. Finally, supply chain analysis will be performed, to ensure that the electrolytes can be obtained at low cost.

Separators will be chosen and developed for the ability to prevent and/or block lithium dendrites. Functional coatings may be applied to polymeric or other separators to improve these characteristics. Candidate separators will be used in Li/Li symmetric cells and Li/LFP full cells to test their dendrite blocking performance..

### 2. Cell Safety Testing

24M will work with USABC and national lab partners to perform safety testing on cells from this program. Safety testing will include external short circuit, nail penetration, overcharge, and thermal ramp testing. Performance of the cells during safety testing will be considered in future rounds of development to improve safety.

### 3. Commercial-Ready Cell Manufacturing

In this program, 24M will adapt its existing pilot line in Cambridge, MA to assemble lithium metal/LFP cells of a commercially relevant size. The pilot line produces cells using standard lithium-ion chemistry, with an electrode footprint area of 300 cm<sup>2</sup>. 24M's current electrode forming process is based on automated dispensing and shaping of both anode and cathode semi-solid suspensions, using conventional foil current collectors. As part of this program, the pilot line is modified to handle lithium metal foil anodes and to assemble the same into full cells. Cells built on the line will be tested internally, as well as at National Laboratory partner facilities.

#### Results

24M has achieved notable progress along numerous development pathways, some of the most notable being in the following categories:

##### **Selection of SemiSolid LFP and LMFP cathode active materials:**

24M has evaluated several LFP active materials for Phase 1 and 2 cells and several LMFP materials for use in Phase 2. Physical properties such as tap density, oil absorption, and particle size, were measured to determine the materials' suitability for use in high volume loading SemiSolid slurry electrodes. One blend of two materials was downselected for its ability to form high volume loading slurry. Optimization of electrode thickness and volume loading was performed to select a design capable of high energy density while meeting the requirements for fast charge capability. LMFP materials were also evaluated for the same physical properties, and they are currently undergoing long term testing in graphite-LMFP cells to evaluate their cycling stability. Some of the LMFP materials under evaluation are expected to have sufficient cycle stability to meet Phase 2 targets.

##### **SemiSolid cathode design:**

24M has developed a cathode formulation and design, based on an initial electrolyte formulation, with an areal capacity of approximately 6 mAh/cm<sup>2</sup>. The thickness and active materials loading were chosen to achieve sufficient energy density while maintaining the ability to fast charge at a rate consistent with the Phase 1 target. In Phase 2, 24M will work on optimizing formulations and mixing processes to improve volumetric loading of LFP and LMFP slurries and increase energy density further. In Phase 1, we have demonstrated fast charging in small-scale pouch cells from 0 to 80% SOC in 25-30 minutes (Figure I.9.1).

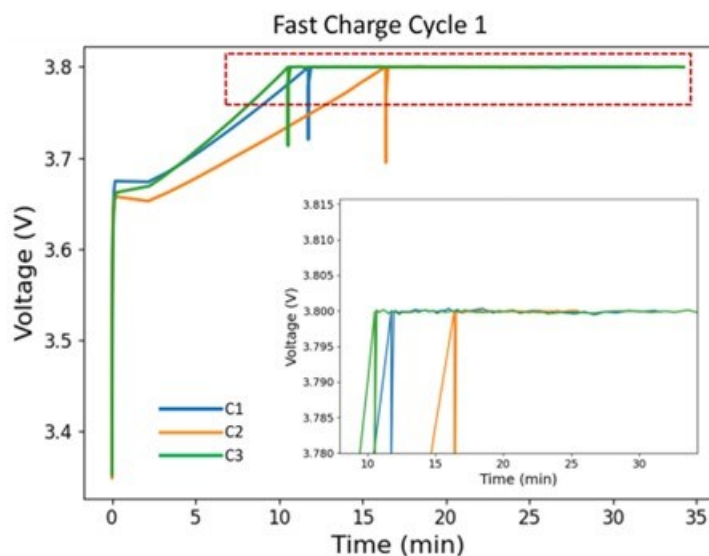
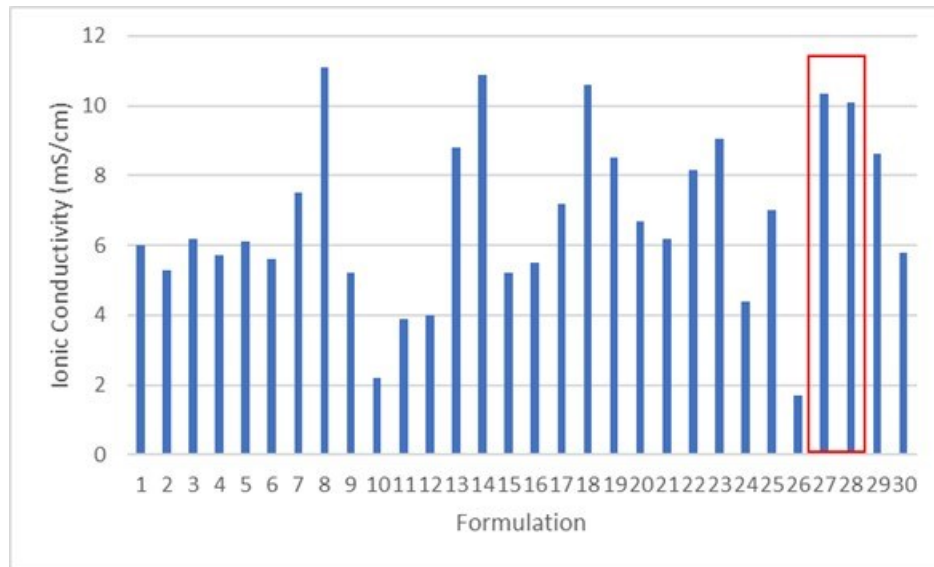


Figure I.9.1 Fast charge (0-80% SOC) voltage vs. time data is shown for three cells with > 6 mAh/cm<sup>2</sup> areal capacity.



**Development of high performance electrolyte for superior fast charge performance:**

24M has evaluated dozens of candidate electrolyte formulations for suitability in lithium metal-LFP cells, with an emphasis on high ionic conductivity, good lithium cycling Coulombic efficiency, and good fast charge performance. Ionic conductivity for selected compositions is shown in Figure I.9.2. In Phase 2, we will focus on one solvent system, where some formulations exhibited  $>10$  mS/cm ionic conductivity (boxed in red in Figure 1), as well as excellent Coulombic efficiency in Li-Cu cells. Moreover, these formulations maintain excellent ionic conductivity at temperatures as low as  $-20^{\circ}\text{C}$ . 24M has filed a provisional patent application for this family of electrolytes. This family of electrolytes was not developed in time to be integrated into cell builds for Phase 1 deliverables; however, it will be the focus of investigation and cell builds in Phase 2.



**Figure I.9.2** Ionic conductivity, measured at ambient temperature, for selected electrolyte formulations that were tested during Phase 1. Some formulations, boxed in red, exhibited superior performance and are the focus of development during Phase 2.

**Successful construction of large footprint lithium metal/LFP cells on 24M's automated pilot plant**

24M assembled 31 large-area ( $300\text{ cm}^2$ ) Li-LFP cells for the Phase 1 deliverable for the program. The cells use SemiSolid LFP electrodes with an average capacity of  $1.78\text{ Ah}$  ( $\sim 6\text{ mAh/cm}^2$  areal capacity) and a standard deviation of  $0.063\text{ Ah}$ . Cells have been delivered to Sandia National Laboratories and Idaho National Laboratory for safety and performance testing, respectively. An example of formation (first cycle data for one cell is shown in Figure I.9.3).

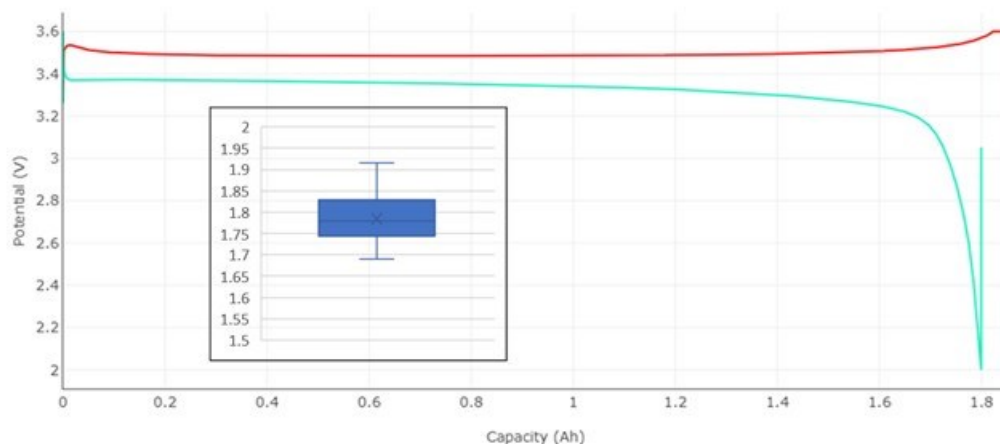


**Figure I.9.3** Voltage vs. capacity curves for 1st cycle charge and discharge of a selected large-format cell assembled on 24M's automated pilot line. Areal capacity is  $\sim 6$  mAh/cm<sup>2</sup>. Inset: Box-and-whisker plot of cell capacities, in Ah, showing range and quartiles.

### Conclusions

In this program to date, 24M has successfully demonstrated that its unique manufacturing method and electrode format for lithium-ion battery cells can be applied to Li metal/LFP cells. 24M has successfully demonstrated that the thick SemiSolid electrodes could meet the 80% in 30min fast charge target go/no-go milestone in the Q2. Project Phase 1 deliverable cells were produced and delivered to USABC, and testing of these cells is ongoing. In addition, the 24M team has made significant progress to select active and electrolyte materials for Phase 2 development as cell energy density and electrolyte performance requirements increase.

### Key Publications

1. "Enabling Current and Future Energy Needs with 24M's Exceptional SemiSolid™ and Unit Cell Platform," Naoki Ota, Junzheng Chen, AABA 14, 2023
2. Song, Junhua, et al. High Performance Electrolyte for Electrochemical Energy Storage Devices, and Methods of Producing the Same, U.S. Provisional Application No. 63545692, filed 25 October 2023.

### Acknowledgements

Jing Gao (GM) served as the USABC program manager for this project.

## I.10 Low-cost, Fast-charging Silicon Nanowire Cell Technology (Amprius)

### Ionel Stefan, Principal Investigator

Amprius, Inc.  
1180 Page Ave.,  
Fremont, CA 94538  
E-mail: [ionel@amprius.com](mailto:ionel@amprius.com)

### Tina Chen, DOE Technology Development Manager

U.S. Department of Energy  
E-mail: [tina.chen@ee.goe.gov](mailto:tina.chen@ee.goe.gov)

Start Date: March 1, 2022

End Date: August 31, 2024

Project Funding: \$2,999,319

DOE share: \$1,499,659

Non-DOE share: \$1,499,660

### Project Introduction

Amprius' differentiating technology – an anode made of silicon nanowires – is potentially capable of meeting the USABC performance and commercialization criteria. Silicon offers significantly higher energy capacity than graphite but expands during lithiation. As a result, conventional approaches to silicon anodes have not enabled the long cycle life required for electric vehicle applications. Amprius grows pure silicon nanowires directly on the current collector, without binders or conductive additives. Nanowires do not rely on particle-to-particle contact and thus enable longer cycle life than particle-based approaches as well as higher rate and power.

In a previous USABC contract that ended in 2018, Amprius cells with silicon nanowire anode and NMC721 cathode met or exceeded most USABC 2020 goals for EV applications and has reduced the gap in Cycle and Calendar Life. Silicon anodes have much lower thickness than graphite anodes and a voltage that is at least 100 mV higher, which enables fast charging and prevents lithium plating. Amprius cells can charge to 80% SOC in 15 minutes. Test results were confirmed by tests at Idaho National Laboratory in both 3 Ah and 10 Ah cell form factors.

The main gaps remaining toward commercialization are the cost of production for the silicon nanowire anode, as well as cycle and calendar life performance. The silicon nanowire anode is a direct replacement for graphite anode, and the rest of the cell components and assembly process are largely similar or identical to those used in graphite cells. Due to the importance of scale-up and cost reduction direction for Amprius' business, activities related to scale-up have already started with Amprius funding and will not be sought here. However, a description of these activities and timely updates of the results and cost model will be proposed instead. Most of the work in the current project addresses the other two main remaining gaps, cycle and calendar life, with additional tasks on cell development for EV applications.

Amprius proposed a program with a 2.5 years duration, to develop and demonstrate EV cell technology that, at the minimum, meets all UASBC goals for fast charge cells. Silicon composition and surface modifications, based on latest insights into material changes during cycling, coupled with electrolyte development, should close the performance gap in cycle and calendar life. Cell design activities for larger form factors will seek to preserve and enhance the intrinsic fast charge capabilities of smaller cells with size silicon nanowire anodes. At program's end, Amprius will deliver cells with energy densities greater than 1,000 Wh/L and specific energy of 400 Wh/kg, capable to reach at least 80% SOC during 15 minutes of fast charging.

### Objectives

The objective of the two and a half-year program is to develop a material structure and composition for the silicon nanowire anode which, based on preliminary results, will significantly strengthen the material and,

thereby, extend cycle life and calendar life. The material change relies on dopants introduced in the silicon structure during fabrication, which reduce silicon domain sizes and, thus, stress induced cracking. Coupled with electrolyte development, material changes should reduce and eliminate the performance gap in cycle and calendar life. A parallel effort will include a plasma deposition technology development that targets increases in silane utilization during anode fabrication, a key performance parameter for reducing the cost of the fabricated anode, to meet USABC targets. At the end of the program, Amprius expects to meet all end of life requirements in the EV Gap Chart, while exceeding the requirements by more than 20% at the beginning of life for most parameters (see Table I.10.1).

**Table I.10.1 End of Program Cell Performance Objectives.**

End of Life Characteristics at 30 °C	Units	Cell Level Goals	Amprius Targets for program at BOL, 30 °C
Peak Discharge Power Density, 30 s Pulse	W/L	1400	3000
Peak Specific Discharge Power, 30 s Pulse	W/kg	700	1200
Peak Specific Regen Power, 10 s Pulse	W/kg	300	400
Usable Energy Density	Wh/L	550	1000
Specific Usable Energy (defined at power target)	Wh/kg	275	400
Calendar Life	Years	10	>10
Cycle Life (25% FC)	Cycles	1000	>1000
Cost (@ 250k annual value)	\$/kWh	75	<75
Normal Recharge Time	Hours	< 7 Hours, J1772	<7
Fast Rate Charge	Minutes	80% U.E. Target in 15 min	>80% U.E. in 10 min
Minimum Operating Voltage	V	>0.55 Vmax	>0.55 Vmax
Unassisted Operating Temperature Range	Wh/kg	70% Specific Useable Energy at -20 °C	70% Specific Useable Energy at -20 °C
Survival Temperature Range, 24 h	°C	-40 to +66	-40 to +66
Maximum Self-discharge	%/month	<1	<0.5

### Approach

Amprius' silicon nanowire anode cells already meet most of the criteria, as discussed in the previous section. The most significant performance gaps are in cycle life and calendar life, and cost is a major gap related to the scale-up of the technology toward large volume manufacturing. Calendar life was significantly improved in the previous USABC project by electrolyte development by improving SEI and CEI formation, and the work proposed here will continue and build upon that experience. The cycle life gap mitigation is the major focus of the project and preliminary experiments suggest that the material modification direction is the most constructive toward that goal.

The project tasks have objectives that target the USABC goals. In particular, the silicon material and electrolyte properties will be optimized toward the USABC goals. A short list of the main objectives is described below:

1. Find Si doping or alloying compositions that improve targeted metrics
2. Find material density and electrode loading levels that improve targeted metrics
3. Optimize electrolyte composition to improve targeted metrics
4. Optimize cell design and anode/electrolyte/cathode matching to improve targeted metrics
5. Deliver cells for external evaluation and verification of progress

The main tasks cover four main work directions, with relatively independent task objectives, although targeting the same goals.

The first three tasks cover the bulk of the research and, although they mainly address the same barriers (cycle life and calendar life barriers), they do it by relatively independent approaches. The first task addresses the intrinsic problem of silicon surface cracking by modifications in silicon density and composition (doping and alloying), in the nanowire volume and at the surface. This task is scheduled to last 18 months, and will test at least three dopant elements (nitrogen, oxygen and carbon).

The second task addresses the same barriers by changes to the electrolyte composition development. This task is scheduled to last 24 months, developing electrolyte formulation for different anode compositions, as well as for different cathode types (Ni-content, coatings).

The third task includes the development of a larger form factor cell for EV applications and improves performance by optimization to cycling parameters (voltage, N/P ratio), which directly affect or interact with the anode material. Results from this task use optimized anode and electrolyte materials from Tasks 1 and 2 and give feedback to the respective development by evaluating the cells in USABC matrix of tests. This task is scheduled to last for 27 months, with three rounds of cell evaluation starting at 9 months intervals.

The last two tasks have testing, verification and reporting as objectives. Three sets of 30 cells are scheduled to be delivered, including the baseline cell (~3Ah, 4.5x50x56mm small form factor) at 6 months into the program, interim cell (~10Ah, 9x54x66mm) at 18 months, and the optimized cell (target 80Ah, 8x99x300mm) at the end of the project.

## Results

### *Dopants reduce impedance increase during cycling, with small overall effect on cycle life*

In FY2023, Amprius evaluated the second and third dopant elements of the three proposed for evaluation during the project. The dopants were introduced in the silicon material during the silicon deposition process by mixing dopant gas with the silane precursor gas. Single and multi-layer cells were assembled with the anodes produced for evaluation of the electrochemical properties, and on cycle life in particular. Although a strong effect on stabilizing the impedance increase was observed, the increase in cycle life was relatively modest. A comparison of cycling data is shown in Figure I.10.1. for different cathode loadings and dopant 2 levels.

Dopant 3 based materials had a negligible effect on the performance of the silicon anode material. Further experimentation has been restricted due to hardware issues on the testing platform assigned to dopant gas testing.

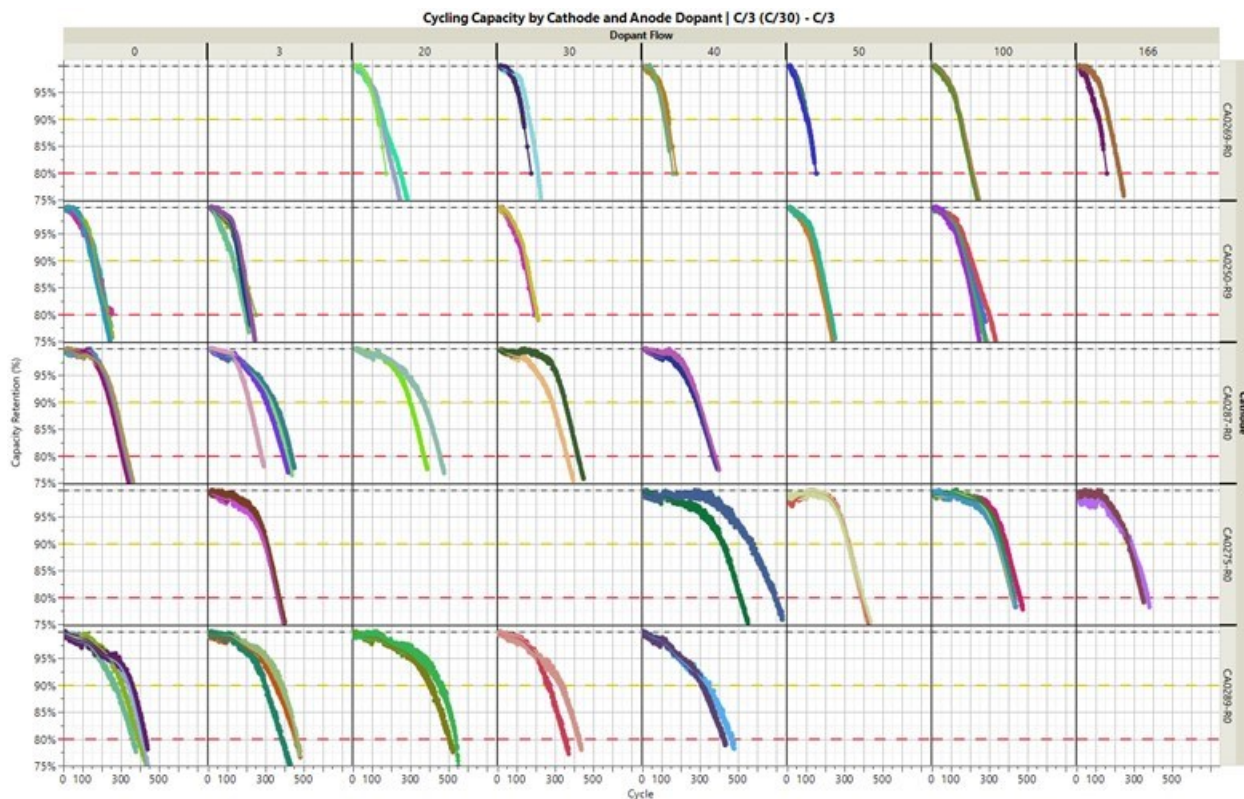


Figure I.10.1 Cycling data of cells to test effect of dopant gas 2 on anode life, grouped by cathode and scaled dopant flow.

***Amprius reduced the main gap in performance, cycle life, by identifying electrolyte additives that improve Solid Electrolyte Interphase (SEI) stability.***

The electrolyte solution formulation was optimized with new solvents, additives, and salts, as well as with new formulation strategies, such as super-concentrated electrolytes, localized high concentration electrolytes, and gel electrolyte forming additives. The formulation development used materials compatible with pure silicon anodes that were available at the start of the project.

Both new solvents and additive sets have resulted in improved calendar life, the most consequential result expected from electrolyte development. For example, in Figure I.10.2., the a new electrolyte formulation optimization results in no power degradation after 3 months of storage at 45°C for some combinations. Power degradation is usually the most deleterious effect observed at high temperature and the first few month results are very promising. These formulations also significantly expand the cycle life compared to the baseline chemistry tested in FY22 (~200 cycles). Tests are continuing in FY2024.

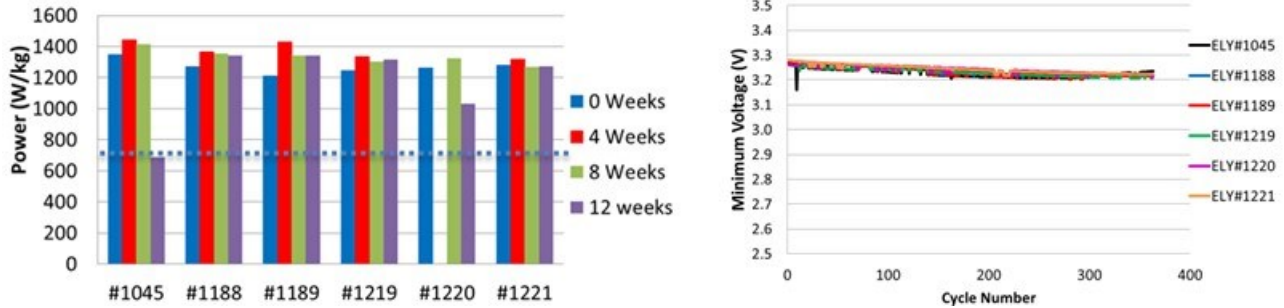


Figure I.10.2 Peak specific discharge power and minimum voltage during DST cycling in 3.7Ah Si/NCMA cells with improved electrolyte formulations. Formulation #1045 is the baseline formulation at the start of the program.

***Amprion performed the baseline evaluation of the silicon nanowire technology at the start of the program***

The initial round of testing on baseline battery cells was completed. The cells meet the targets for capacity, available energy, power, and thermal performance.

Below are the cell and test parameters used during the preliminary round of testing:

- Target cell’s capacity at beginning of life = 3.7 Ah
- Target cell’s energy at beginning of life = 13.0 Wh
- Available energy at end of life = 10.4 Wh
- $V_{max,100} = V_{maxop} = 4.25$  V
- $V_{min,0} = 2.50$  V
- $V_{min,op} = 3.2$  V
- $V_{min,pulse} = 2.25$  V
- $V_{max,pulse} = 4.35$  V
- $IMAX = 2C$

The baseline test results are summarized in Table I.10.2. The calendar life tests are continuing in FY2024.

**Table I.10.2 Baseline Cell Technology Gap Analysis Table**

End of Life Characteristics at 30°C	Units	Cell Level Goals	Baseline Q3
Peak Discharge Power Density, 30 s Pulse	W/L	1400	>2800
Peak Specific Discharge Power, 30 s Pulse	W/kg	700	>1300
Peak Specific Regen Power, 10 s Pulse	W/kg	300	>810
Usable Energy Density	Wh/L	550	>900
Specific Usable Energy (defined at power target)	Wh/kg	275	>400
Calendar Life	Years	10	>1 year
Cycle Life (25% FC)	Cycles	1000	~200
Cost (@ 250k annual value)	\$/kWh	75	TBD
Normal Recharge Time	Hours	< 7 Hours, J1772	<7

Fast Rate Charge	Minutes	80% U.E. Target in 15mins	~90%
Minimum Operating Voltage	V	>0.55 Vmax	0.59 Vmax
Unassisted Operating Temperature Range	Wh/kg	70% Specific Useable Energy at -20°C	82% Specific Useable Energy at -20°C
Survival Temperature Range, 24 Hr	°C	-40 to +66	-40 to +66
Maximum Self-discharge	%/month	<1	<0.5

The Si/NMC811 baseline cells exceed power and energy goals by more than 50%, as expected based on the performance at the start of the program. The rest of the performance metrics, measured for the first time for this chemistry, also indicated very good performance. Highlights of the baseline performance evaluation include a fast charge of 90% of usable energy in 15 minutes, a loss of less than 20% of usable energy at -20°C, and a self-discharge rate of <0.5% per month. Calendar life performed well relative to previous results, exceeding the 12 months mark at 50°C. At the latest reference performance check, the capacity and energy retentions of the tested cells remain above 90%. (Figure I.10.3)



Figure I.10.3 C/3 capacity, energy, and nominal voltage retention during calendar life test for baseline cell chemistry.

#### ***Amprius improved cycle life by cell design optimization***

Two directions were selected for improving DST cycle life by cell design optimization:

1. High energy cells with large energy margin for 700/275 Power/Energy ratio
  - 400 – 450 Wh/kg cell designs
  - High anode and cathode loadings, narrow voltage range
  - Power exceeds 700 Wh/kg, but with lower margin



2. High power cells with lower energy margin for 700/275 Power/Energy ratio
  - 350 – 400 Wh/kg cell designs
  - Moderate anode and low cathode loadings, wide voltage range
  - Power significantly exceeds 700 Wh/kg, but energy has lower margin.

The first direction was tested early in the project, and it was found that power capability degrades faster than capacity, i.e., impedance growth is faster than lithium inventory loss. Thus, the second option (higher initial power capability) was selected for further cycle life optimization. For the second direction, Amprius is also testing new chemistry cathode NCMA with very low mass loading targeting 350 Wh/kg for DST cycling. As seen in Figure I.10.3., cells are cycling well at 500 cycles with constant energy density of 275Wh/kg with peak power density of 700 W/kg. This chemistry was selected for the Interim cell delivery.

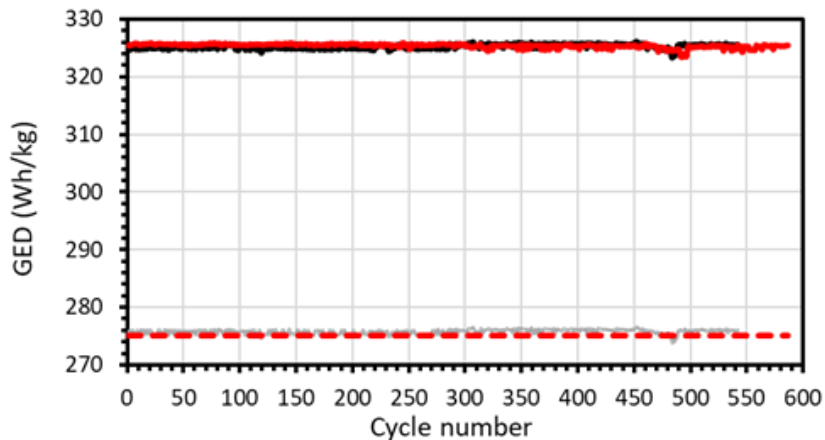


Figure I.10.4 Interim cell chemistry DST cycle life with 275Wh/kg net energy and peak power density of 700 W/kg.

**Amprius developed a new form factor for Interim cell deliveries, with a target capacity of 10Ah**

Amprius developed the Interim form factor of pouch cell with at least 10Ah capacity. To achieve this and serve as precursor to the final form factor with a capacity of 80Ah and tabs on opposite sides, the 10 Ah form factor was selected to be a double-length cell with the same width and thickness as the baseline cell form factor, the 54x65mm footprint. Doubling the length resulted in about 130mm length and, for a thickness of 5mm, in a capacity of about 10.5 Ah with the Si/NMC811 chemistry. Thickness and number of electrodes were adjusted for the Interim Si/NCMA chemistry.(Figure I.10.4)

The CAD drawing and real picture are shown in Figure I.10.5. and the cell with the Interim chemistry has the following specifications:

- Target cell's capacity at beginning of life = 10 Ah
- Target cell's energy at beginning of life = 34 Wh
- Usable energy target (UE) = 25Wh
- $V_{max,100} = V_{max,op} = 4.05$  V
- $V_{min,0} = 2.50$  V
- $V_{min,op} = 3.2$  V
- $V_{min,pulse} = 2.25$  V
- $V_{max,pulse} = 4.25$  V
- $IMAX = 4C$

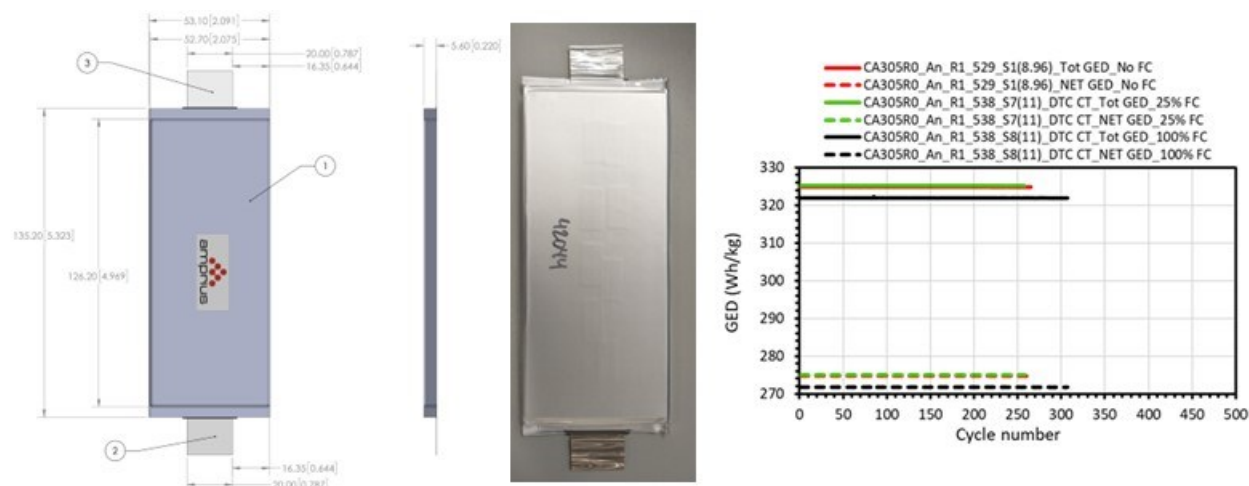


Figure I.10.5 Interim cell CAD, picture, and DST cycling.

Amprius has built 21 cells with nominal capacity of 10 Ah to be shipped to INL for DST tests. 11 additional 10 Ah cells were built to be shipped to SNL for safety tests.

### Conclusions

During the project's second year, Amprius continued the task work to reduce the gaps in cycle life and calendar life. These tasks included silicon nanowire anode material structure, loading, and composition optimization, electrolyte development, and cell parameters optimization. Silicon doping showed relatively small effects with the first dopant element, but anode structure and loading, as well as cycling parameters increased cycle life more than 500 cycles in cells with the optimized Interim Chemistry and design.

The baseline cell chemistry (Si/NMC811) was evaluated using USABC test protocols. The 3.7Ah cells exceed energy and power goal targets by at least 50%, and the chemistry showed very good low temperature performance, power density and storage loss. Calendar and cycle life tests continued in FY2023, with calendar life demonstrating over 1 year of storage at high temperature. During FY2023, Amprius built and delivered 21 Interim cells with a capacity of 10Ah to Idaho National Laboratory for Interim performance evaluation, and 11 cells to Sandia National Laboratory for safety evaluation.

During FY2024, Amprius will continue to increase cycle life and calendar by optimizing anode structure and exploring advanced components, extend cell cycle life by tuning anode structure and testing new electrolyte formulations, and finish the design and assembly of the final cells with capacities  $\geq 80$  Ah.

### Acknowledgements

Amprius and the program PI are thankful to the USABC program manager Ion Halalay, who retired recently, and who's experience and expertise have been instrumental in shaping the program direction. We appreciate all that you have done for us and wish you a happy retirement.

## I.11 Development of Lithium Electrode Based Cell and Manufacturing for Automotive Traction Applications (Farasis Energy USA)

### Madhuri Thakur, Principal Investigator

Farasis Energy USA, Inc.  
21363 Cabot Blvd  
Hayward, CA 94545  
E-mail: [mthakur@farasis.com](mailto:mthakur@farasis.com)

### Tina Chen, DOE Technology Development Manager

U.S. Department of Energy  
E-mail: [Tina.Chen@ee.doe.gov](mailto:Tina.Chen@ee.doe.gov)

Start Date: March 1, 2022  
Project Funding: \$2,610,000

End Date: August 31, 2024  
DOE share: \$1,305,000

Non-DOE share: \$1,305,000

### Project Introduction

This project is to develop lithium (Li) electrode-based cell and manufacturing for automotive traction applications. To increase the energy density of the lithium-ion battery beyond 350 Wh/Kg and 850 Wh/L we need to use high energy density cathode material with pre-lithiated silicon anode or Li metal anode. Li metal is an ideal electrode for rechargeable batteries due to its extremely high theoretical specific capacity  $\sim 3860 \text{ mAh g}^{-1}$ , low density ( $0.534 \text{ g cm}^{-3}$ ) and the lowest negative electrochemical potential ( $-3.040 \text{ V}$  vs. the standard hydrogen electrode). Unfortunately, uncontrollable dendritic Li growth and limited Coulombic efficiency during Li plating/stripping inherent in these batteries have prevented their practical applications over the past 40 years. With the emergence of post-Li-ion batteries, safe and efficient operation of Li metal anodes has become an enabling technology which may determine the fate of several promising candidates for the next generation energy storage systems, including rechargeable Li-air batteries, Li-S/Se batteries, and Li metal batteries which utilize intercalation compounds as cathodes. To implement the Li metal batteries in the electric vehicles (EVs) application needs to see the scalability of these technologies. Farasis will work on all the cell components of the Li metal batteries such as cathode materials (Ni rich, high voltage NCM or Mn-rich), separator, electrolyte, and Li anode (pure Li foil, Li alloy foils, Li-X composite and surface coating). Farasis will optimize the cell design and manufacturing as well as selection of the materials. The 24-months of development effort will be iterative, with an intermediate Milestone based on cell performance goals and progress tracked against the USABC goals for lithium electrode-based cell and manufacturing for the automotive application. Key technologies that are developed and integrated into cells include a cathode material (NCM), Li metal anode in a liquid, salt-concentrated electrolyte with different additives as well as a coated separator. As a large volume battery manufacturer, a major goal of the project will be to accelerate production and enable the commercialization of several novel cell component technologies (including Li metal anode) by supporting scale-up and providing a commercialization path. Deliverables will include small single- or double-layer or multi-layer pouch cells to validate the production capability of this electrode. The project's total budget will be  $\sim \$2.61 \text{ M}$  with Farasis covering 50% of the cost.

### Objectives

- Develop a Li metal cell technology of providing Beginning-of-Life (BOL) energy density of  $\sim 400\text{-}450 \text{ Wh/kg}$ , End-of-Life (EOL) energy density of  $375 \text{ Wh/kg}$  after 500 cycles at a cost target of  $\sim \$50\text{-}60/\text{kWh}$  based on the Li metal price.
- Develop Lithium anode with Li metal foils, Li alloy foils, Li-X composite and surface coating.
- Develop electrolyte technology using new solvent, salt components and additives to improve Li Coulombic efficiency and SEI formation on the Li metal surface.

- Develop coated separators to suppress Li dendrite formation/growth and internal shorting.
- Optimize cell design and manufacturing with integration of advanced Li anode, electrolyte, separator and high energy density cathode. Deliver 0.4 Ah (Phase 1) and 2 Ah (Phase 2) Li metal pouch cells to the national labs for performance evaluation tests.

### Approach

- Phase I of the project lasts ~12 months, and the focus is development and characterization of different Li anodes with high energy density cathode materials and down-selection of the materials targeting the energy density of ~375 Wh/kg in the big cells. Initial evaluation is done on the coin cells for different Li metal anodes, cathodes, electrolyte and separator studies. We use different thickness Li foils/Li alloy foils coated on Cu foils as the anodes, and Ni-rich NCM electrodes. The electrolyte used is diluted salt-concentrated electrolytes with some additives to stabilize Li metal anodes and NCM cathodes. Based on the technology demonstrated by coin cells, the large-format pouch cells are expected to achieve an energy density of ~350 Wh/kg and a cycle life of 200-250 cycles. At the end of month 12 we deliver 0.4 Ah pouch cells to the national labs for performance evaluation tests.
- Phase II of the project is scheduled for 12 months, where the focus will be to achieve high energy density with good cycle life. We will focus on the optimization of electrolyte and separator and see the impact of different N/P ratios on the cycle life. We will also optimize the cell design and manufacturing of pouch cells. The final deliverable will be 2 Ah pouch cells with target energy density of ~400-450 Wh/kg and a cycle life of 500 cycles.

### Results

#### *Li metal electrode technology development:*

Different Li metal anodes were developed for Li metal cell technology. Li metal anodes A1 and A3 were compared in pouch cells with the same cathode (C2), separator (S2) and electrolyte (E1). The pouch cells with A1 anode used 1 layer of double-sided C2 cathode (~3.3 mAh/cm<sup>2</sup>) and the cell capacity was ~0.15Ah. The pouch cells with A3 anode used 2 layers of double-sided C2 cathode (~3.3 mAh/cm<sup>2</sup>) and the cell capacity was ~0.3Ah. All the cells were charged at C/5 and discharged at C/1.5. Capacity check with charge and discharge rate of C/10 was executed every 50 cycles. Figure I.11.1 (a) and (b) show cell capacity, Coulombic efficiency and capacity retention vs. cycle number for 0.15 Ah pouch cells with A1 anode. The cell capacity decreases with cycling and the capacity retention decreases to 80% after 228 cycles (Cell #1) and 231 cycles (Cell #2), respectively. Their Coulombic efficiency is stable at ~100% except some fluctuations around 70 cycles for Cell #1. Figure I.11.2 (a) and (b) display cell capacity, Coulombic efficiency and capacity retention vs. cycle number for 0.3 Ah pouch cells with A3 anode. The capacity retention decreases to 79.8% for both cells after 228 cycles (Cell #1) and 235 cycles (Cell #2). The Coulombic efficiency for Cell #1 is stable at ~100% while for Cell #2 exhibits some fluctuations between 93% and 100%. Comparing Figure I.11.1 with A1 anode and Figure I.11.2 with A3 anode, their capacity retention follows similar trend with cycling. Li metal anodes A1 and A3 demonstrate the similar cycle life (~230 cycles at C/5 charge and C/1.5 discharge till 80% capacity retention) of pouch cells with C2 cathode and E1 electrolyte.

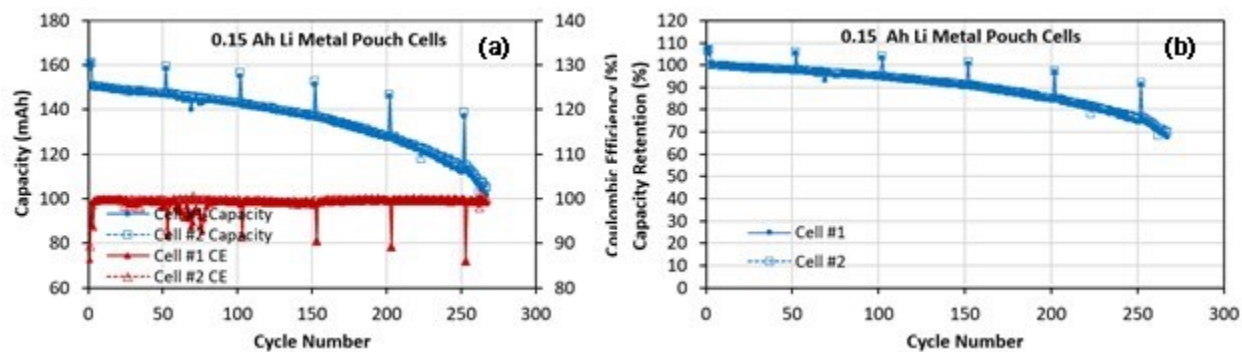


Figure I.11.1 (a) Capacity and Coulombic efficiency vs. cycle number and (b) Capacity retention for 0.15 Ah Li metal (A1) pouch cells with C2 cathode and E1 electrolyte (C/5 charge and C/1.5 discharge).

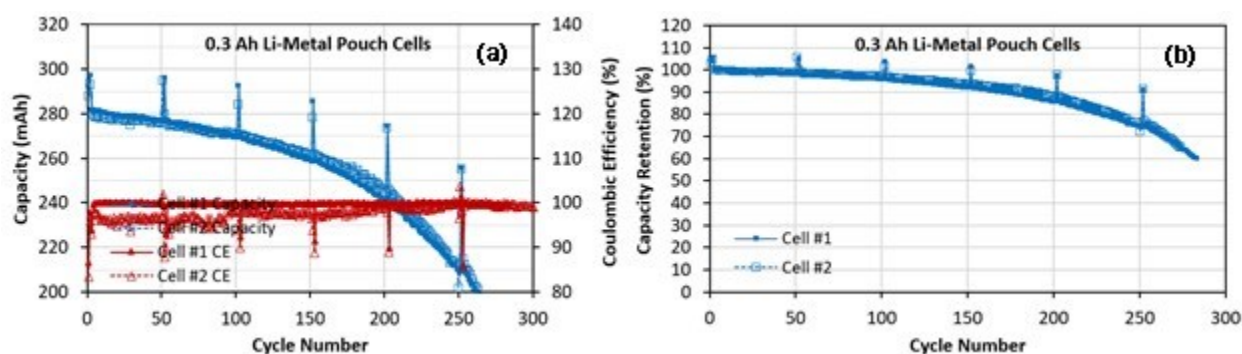


Figure I.11.2 (a) Capacity and Coulombic efficiency vs. cycle number and (b) Capacity retention for 0.3 Ah Li metal (A3) pouch cells with C2 cathode and E1 electrolyte (C/5 charge and C/1.5 discharge).

#### Electrolyte technology development:

Li Coulombic efficiency was tested in Li/Cu coin cells to evaluate the stability of electrolyte with Li metal anode. Different electrolytes, E1 and E3, were compared. Figure I.11.3 shows their Li Coulombic efficiency at C/3 in Li/Cu coin cells as a function of cycle number. Li Coulombic efficiency in E1 electrolyte fluctuates slightly (<2% spread), suggesting stable Li metal surface with E1 electrolyte. Li Coulombic efficiency in E3 electrolyte exhibits some fluctuations of mostly <4% spread, bigger fluctuation than that in E1 electrolyte. As shown in Table I.11.1, the average Li Coulombic efficiency in E1 electrolyte is 98.99% for cycles 6 to 50 and increases to 99.40% for cycles 51 to 300, whereas in E3 electrolyte is 98.89% for cycles 6 to 50 and 99.36% for cycles 51 to 300. Accordingly, E1 electrolyte performs slightly better than E3 electrolyte in terms of 0.04%-0.1% higher average Li Coulombic efficiency with less fluctuations.

Also, 0.15 Ah pouch cells with A1 anode, C2 cathode and E1 electrolyte performs better than those with E3 electrolyte in terms of the cycle life at C/5 charge and C/1.5 discharge. Figure I.11.4 (a) and (b) show capacity retention of 79.7% (Cell #1) and 80.1% (Cell #2) after 160 and 157 cycles. Their Coulombic efficiency is stable at ~100% within 150 cycles but decreases to 98.0% (Cell #1) and 99.0% (Cell #2) at the 160th and 157th cycle, respectively. The pouch cells in Figure I.11.1 and Figure I.11.4 can be compared with the only difference on the electrolyte. The former used E1 electrolyte and the latter used E3 electrolyte. Comparison of Figure I.11.1 with Figure I.11.4 reveals that E1 electrolyte performs longer cycle life than E3 electrolyte (~230 cycles vs. ~160 cycles at C/5 charge and C/1.5 discharge till 80% capacity retention) in pouch cells with A1 anode and C2 cathode.

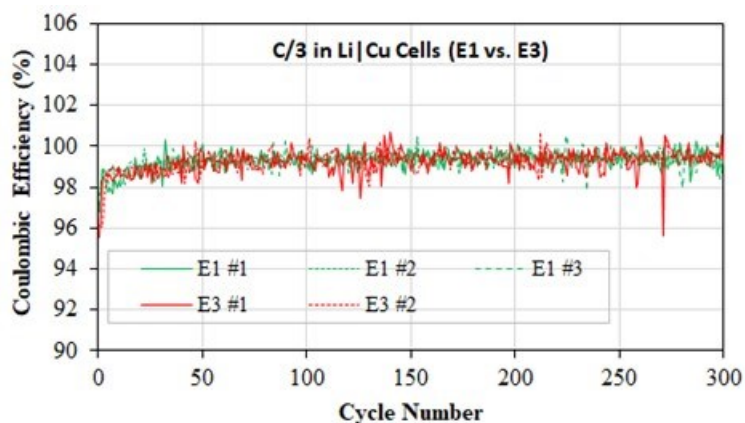


Figure I.11.3 Li Coulombic efficiency at C/3 in Li|Cu coin cells as a function of cycle number in different electrolyte (E1 vs. E3).

Table I.11.1 Average Li Coulombic Efficiency at C/3 in Li|Cu Coin Cells with Different Electrolyte (E1 vs. E3)

Cell#	E1 Electrolyte		E3 Electrolyte	
	Cycles 6-50	Cycles 51-300	Cycles 6-50	Cycles 51-300
1	98.91%	99.42%	98.83%	99.34%
2	99.14%	99.37%	98.94%	99.38%
3	98.92%	99.40%		
Average	98.99%	99.40%	98.89%	99.36%

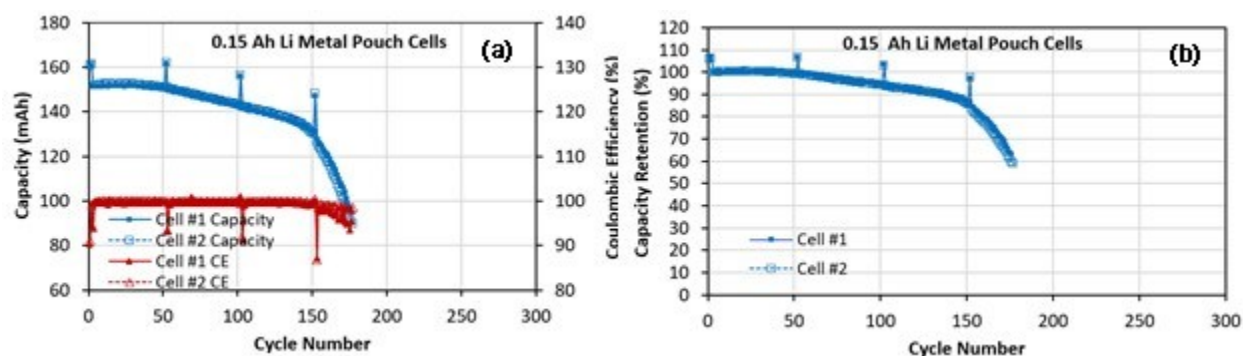


Figure I.11.4 (a) Capacity and Coulombic efficiency vs. cycle number and (b) Capacity retention for 0.15 Ah Li metal (A1) pouch cells with C2 cathode and E3 electrolyte (C/5 charge and C/1.5 discharge).

#### Li metal cell development:

0.2 Ah Li metal pouch cells (A1, C1 and E1) used a double-sided C1 cathode ( $\sim 4 \text{ mAh/cm}^2$ ), two single-sided A1 anodes, and S2 separator in E1 electrolyte. Two pouch cells (#1 and #2) were cycled at C/10 charge and C/3 discharge between 2.75 and 4.3 V. Capacity check @C/10 charge and discharge was executed every 20 cycles. As shown in Figure I.11.5, for Cell #1, the capacity retention is 79.9% after 378 cycles and 73.0% after 509 cycles. The Coulombic efficiency (CE) is stable at  $\sim 102\%$  @C/10 charge and C/3 discharge but is  $\sim 100\%$  for capacity check @C/10 charge and discharge. The capacity retention of Cell #2 is 79.9% after 343 cycles and decreases to 77.7% after 349 cycles. Its CE is stable at  $\sim 102\%$  till 338 cycles and subsequently decreases to  $\sim 80\%$  and even further to 65% at cycle 349. As usually defined cycle life at 80% capacity retention, these

two cells have the cycle life of 378 cycles and 343 cycles, respectively. Cell #2 after cycling was fully discharged before disassembling in the glove box. There is a thick layer (~80  $\mu\text{m}$  thick) on the aged Li anode and somewhere the surface layer partially sticks to the separator upon the separation of the anode from the separator. Whereas, the separator touching the aged cathode is clean (Figure I.11.6). Some discs that were used to make coin cells were punched from the aged Li anode and the aged cathode after soaking in the electrolyte solvent to dissolve out the electrolyte salt in the electrode coating. The aged Li anode vs Cu foil in coin cells were discharged at C/3 until -0.6 V and their discharge capacity is 2.295, 2.372, 2.216 and 2.333 mAh/cm<sup>2</sup>, respectively (Figure I.11.7 (a)). Their average capacity is 2.304 mAh/cm<sup>2</sup> (equivalent to Li foil thickness of 11.2  $\mu\text{m}$ ). The result suggests that the aged Li anode still remain 62% of original Li metal thickness (i.e., 11.2/18=62%) after 349 cycles of the pouch cell. Accordingly, the Li metal was consumed at average 19.5 nm thick per cycle or average 0.11% thickness loss each cycle. As estimated from such Li consumption rate, Li metal anode can run about 900 cycles prior to its depletion. The aged cathode vs Li chip in coin cells were fully charged and then discharged at C/10 until 2.75 V. Their discharge capacity is 161.4 and 169.2 mAh/g for two coin cells, respectively. As a comparison, the pouch cell capacity at cycle 342 @C/10 is 179.6 mAh/g (Figure I.11.7 (b)), 6-11% higher than the discharge capacity of the aged cathode in coin cells because the mass used to calculate the specific capacity of the aged cathode in coin cells includes some residue mass from coating SEI layer, electrolyte salt not completely dissolved out of coating and cleaning of back-side coating (from double-sided coating in the pouch cells to single-sided coating in the coin cells). Therefore the pouch cell capacity fade is mainly from the aged cathode since the aged Li anode still has excess Li metal (equivalent to 11.2  $\mu\text{m}$  thick Li foil).

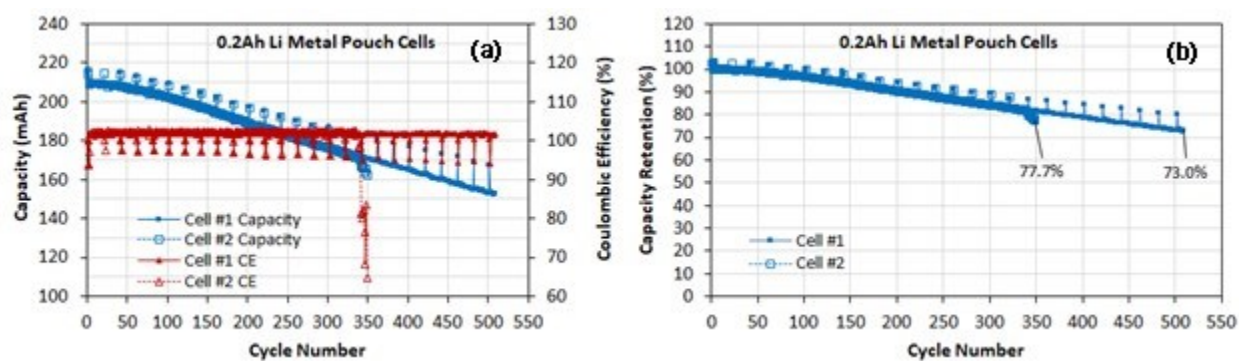


Figure I.11.5 (a) Capacity and Coulombic efficiency vs. cycle number and (b) Capacity retention for 0.2 Ah Li metal (A1) pouch cells with C1 cathode and E1 electrolyte (C/10 charge and C/3 discharge).

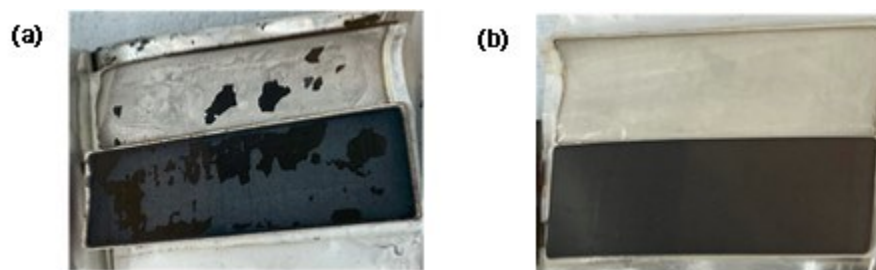


Figure I.11.6 Pictures of (a) Aged Li anode and (b) Aged cathode with the separator after disassembling of Cell #2 in Figure I.11.5.

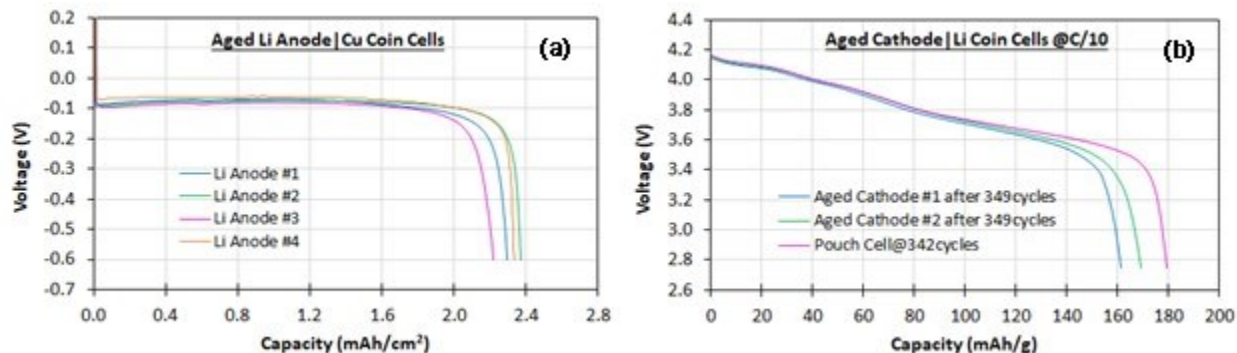


Figure I.11.7 (a) Discharge curves of coin cells with the aged Li anode vs Cu foil and (b) Discharge curves of coin cells with the aged cathode vs Li chip comparing with the pouch cell discharge curve at C/10 @342 cycles of Cell #2 in Figure I.11.5.

#### Phase I Deliverable Cell Fabrication and Testing:

Sixteen 0.4 Ah pouch cells in pressure jigs were delivered to a national lab for performance evaluation tests including thermal performance, cycle life and calendar life. The pouch cells used 3 layers of double-sided C2 cathode ( $\sim 3.3$  mAh/cm<sup>2</sup>), A3 Li anode, S2 separator and E1 electrolyte. Discharge capacity @C/10 and C/3, OCV @50%SOC of sixteen delivery cells were tested before delivery and are shown in Figure I.11.8. The discharge capacity @C/10 is 443 – 463 mAh. The discharge capacity @C/3 is 432 – 446 mAh. The OCV @50%SOC is 3.825 – 3.834V. The sixteen pouch cells have good consistency with <5% spread.

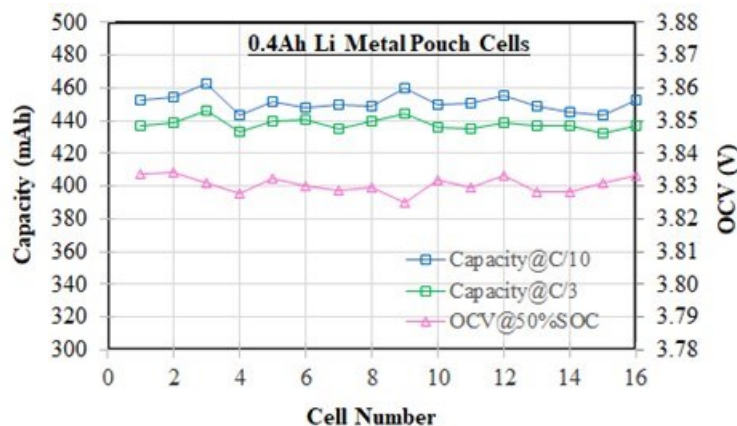


Figure I.11.8 Discharge capacity @C/10 and @C/3, OCV @50%SOC of sixteen delivery 0.4 Ah Li metal (A3) pouch cells with C2 cathode and E1 electrolyte.

#### Conclusions

Farasis has tested the cycle life of pouch cells with different Li anode, cathode and electrolyte. Two 0.15 Ah pouch cells with A1 anode, C2 cathode and E1 electrolyte show the cycle life of 228 cycles and 231 cycles, respectively, till 80% capacity retention. Two 0.3 Ah pouch cells with A3 anode, C2 cathode and E1 electrolyte have the cycle life of 228 cycles and 235 cycles, respectively. Accordingly, Li metal anodes A1 and A3 demonstrate the similar cycle life ( $\sim 230$  cycles) at C/5 charge and C/1.5 discharge till 80% capacity retention of pouch cells with C2 cathode and E1 electrolyte. E1 electrolyte performs better than E3 electrolyte in terms of the cycle life of pouch cells with A1 anode and C2 cathode ( $\sim 230$  cycles vs.  $\sim 160$  cycles at C/5 charge and C/1.5 discharge till 80% capacity retention). Also, in terms of Li Coulombic efficiency at C/3 in Li/Cu coin cells, E1 electrolyte performs slightly better than E3 electrolyte with 0.04%-0.1% higher average Li Coulombic efficiency (98.99% vs. 98.89 for cycles 6 to 50 and 99.40% vs. 99.36% for cycles 51-300).



Two 0.2 Ah pouch cells with A1 anode, C1 cathode and E1 electrolyte have the cycle life of 378 cycles and 343 cycles at  $C/10$  charge and  $C/3$  discharge till 80% capacity retention. Post-mortem analysis of one pouch cell demonstrates the pouch cell capacity fade is mainly from the aged cathode since the aged Li anode still has excess Li metal. Sixteen 0.4 Ah pouch cells (A3 anode, C2 cathode and E1 electrolyte) in pressure jigs have been delivered to a national lab for performance evaluation tests including thermal performance, cycle life and calendar life. Farasis will further optimize Li metal anode, cathode, separator, electrolyte and pouch cell manufacturing process so as to enhance the energy density and cycle life of Li metal pouch cells. Farasis will build 2 Ah Phase II pouch cells and deliver to the national labs for performance evaluation tests.

## I.12 A Closed Loop Recycling Process for End-of-Life Electric Vehicle Li-ion Batteries-Phase III (Worcester Polytechnic Institute)

### **Yan Wang, Principal Investigator**

Worcester Polytechnic Institute  
100 Institute Road  
Worcester, MA 01609  
E-mail: [yanwan@wpi.edu](mailto:yanwan@wpi.edu)

### **Tina Chen, DOE Technology Development Manager**

U.S. Department of Energy  
E-mail: [tina.chen@ee.goe.gov](mailto:tina.chen@ee.goe.gov)

Start Date: March 10, 2021  
Project Funding: \$831,318

End Date: March 9, 2024  
DOE share: \$466,198

Non-DOE share: \$365,120

### **Project Introduction**

The U.S. Department of Energy (DOE) has established aggressive goals to lower the cost of lithium-ion batteries (LIBs) for EVs. Therefore, in the Phase III program, the team will target lowering the cathode cost by 30% (relative to commercial equivalent) by significantly increasing the amount of recycled materials (>80%) in the synthesized cathode materials. In the WPI/BRs recycling process, virgin materials (CoSO<sub>4</sub>, NiSO<sub>4</sub> and MnSO<sub>4</sub>) must be added to the leaching solution in order to reach the target ratio of Ni, Mn and Co. Earlier generation spent EV batteries use mostly NMC111 or mixed NMC111 and LMO or NMC622 as the cathode materials, and the leaching solution has more Mn than Co and Ni. However, in order to increase the energy density and lower the cost, high nickel cathode materials (for example NMC622 or above) are preferred by the EV industry. Therefore, in order to transform the Mn-rich leaching solution into a Ni-rich metal sulfate solution, supplemental virgin materials CoSO<sub>4</sub> and NiSO<sub>4</sub> are needed. In the Ascend Elements' (AE, was named as Battery Resources) cost model, the virgin materials currently account for 45% of the bill of materials (BOM) cost, since 0.36 kg of virgin materials are added to the leaching solution per kg of NMC622 cathode output. Therefore, in order to further reduce the cathode cost by 30%, which will help reach the DOE cost target (less than \$100/kWh, ultimately \$80/kWh) [1], the team will increase the use of recycled materials to >80%.

In addition, the LIB industry is a dynamic field with ongoing innovations and continually evolving materials delivering ever improving performance. It is critical that recycling technologies keep pace with state-of-the-art LIB technologies. Li<sub>Nix</sub>MnyCozAlaO<sub>2</sub> (x<sup>3</sup>0.8) has the potential to be used in the next generation of LIBs [2]. The specific capacity of Li<sub>Nix</sub>MnyCozAlaO<sub>2</sub> is >200mAh/g. Al can be introduced as dopant and/or coating to stabilize the materials. Therefore, it is critical to be able to synthesize such high nickel cathode materials from spent LIBs in order to remain competitive in the cathode supplier space.

Finally, the team will further improve the performance of recovered NMC622 from spent LIBs. Compared to A123 control NMC622, the recycled materials have inferior cycle performance and elevated gas generation. The reduced cycle life is likely because the stabilizing alumina coating developed rapidly in Phase II cannot fully protect the NMC622. The gas generation is likely because the soluble base content on the recovered NMC622 is higher than that of control powder. It is expected that the process improvement from this task will equally benefit the higher nickel work streams.

During this 3 year program, >300 coin cells, 90 2Ah cells will be produced from recycled automotive lithium ion batteries and 60 2Ah cells format cells from control materials will be produced. 60 2Ah cells will be delivered to Argonne National Laboratory for testing using EV application USABC test methods. The original

cost of the proposed program is \$1,996,180, which includes a 50% cost share by WPI, Farasis Energy USA and Ascend Elements. Due to the added work, the new cost is \$2,328,184. At the end of program, the team expects to be able to lower the cathode cost by 30%, produce high quality NMCA or Ni-rich cathode with different coating or doping strategies and solve the cycle life and gas generation issues observed with the recycled NMC622. Achieving these targets is challenging, but necessary in order to offer a product with low cost, high quality, and high energy, and to remain aligned with market trends.

### Objectives

The overall objective of phase III program is: 1) to lower the cathode cost by >30% relative to commercial equivalent material through increasing the recycled content of the metal sulfate solution to >80% (<20% virgin materials); 2) to develop  $\text{LiNi}_x\text{Mn}_y\text{Co}_z\text{Al}_a\text{O}_2$  ( $x^3.0.8$ ) and other possible doping or coating strategies for Ni-rich cathode materials from the spent EV batteries; 3) to improve the performance of the recovered NMC622 (solve the gas generation and improve the cycle life) in order to be comparable with commercial material.

### Approach

High-quality NMC111&NMC622 have been successfully synthesized using WPI's closed loop recycling process for end-of-life xEV LIBs. Although much knowledge has been gained from this experience, technical challenges remain in obtaining additional Ni and Mn from other recycling streams in order to further lower the cathode cost, synthesizing NMCA precursor and cathode powder by co-precipitation and solid-state reaction. In addition, the recovered NMC622 has worse cycle life and gas generation compared to control powder, which also need to be addressed.

Recovering Ni from Ni/MH will be studied in order to reduce the amount of the virgin metal sulfate and lower the cost of the recovered cathode materials. In typical Ni/MH batteries, Ni accounts for 17.9wt% [3]. According to Inside EVs [4], ~60,000 tons Ni/MH batteries (Toyota Prius HEVs) were sold in 2013. Assuming that HEVs with Ni/MH batteries have 8~10 years life, there are 60,000 tons of spent Ni/MH batteries in U.S, which have over 10,000 tons of Nickel. In Ni/MH batteries, the cathode is  $\text{Ni}(\text{OH})_2$  coated on Nickel foam. The anode is hydrogen absorbing alloys coated on steel. Although there is a high content of Ni in Ni/MH batteries, obtaining high concentration of pure Ni solution can be challenging. Impurities will significantly degrade the performance of recovered cathode materials. If the concentration of obtained solution is not high enough, a high amount of virgin chemicals will still need to be added in order to reach target concentrations. In addition to Ni/MH batteries, the team will also investigate other recycling streams for Ni that can be readily incorporated into the existing process.

High Nickel  $\text{LiNi}_x\text{Mn}_y\text{Co}_z\text{Al}_a\text{O}_2$  ( $x^3.0.8$ ) has the advantages of high capacity and safety and is considered a promising next generation cathode material for LIBs which could enable a driving range of 300 miles. However, the ultra-high nickel amount will also increase issues related to capacity fade. Therefore, we would expect technical challenges related to the precursor synthesis and cathode sintering steps. Although our previous research on NMC111 and NMC622 should provide good guidance, the optimum synthesis conditions for NMCA precursor need to be determined. It will thus be necessary to thoroughly investigate the effects of various factors on the key properties (eg. morphology, tap density etc.) of resultant precursor, and experimentally determine the ideal combination of pH, temperature, reactant concentrations and flowrates, residence time, stirring speed, etc.

The high Ni content also has implications on the preparation of NMCA by high temperature calcination of precursor and the Li source. For good electrochemical performances of NMCA, the calcination needs to occur in an oxygen environment, unlike static (closed reactor) air atmosphere for NMC111, and flowing air for NMC622. This seems to be attributed to the difficulty of oxidizing  $\text{Ni}^{2+}$ . Therefore, it is essential to examine effects of oxygen partial pressure on resultant cathode properties. Moreover, compared to the calcination temperature and calcination time required for NMC111 and NMC622, the temperature and calcination time for NMCA are expected to be lower and shorter in order to minimize undesired cation mixing. It is thus critical to

optimize the calcination temperature and furnace residence time in order to produce high quality NMCA cathode powder.

Aluminum incorporation in the NMCA needs to be carefully studied. There are the following three possible ways to add Al in NMCA. We will study these different approaches separately and a combination of these approaches to determine how to improve the cycle life.

- (1) During precursor synthesis.  $\text{Al}_2(\text{SO}_4)_3$  can be added into metal sulfate solution. Then  $\text{Al}^{3+}$  will be co-precipitated with  $\text{Ni}^{2+}$ ,  $\text{Mn}^{2+}$  and  $\text{Co}^{2+}$  as  $\text{NiMnCoAl}(\text{OH})_2$  precursor.
- (2) During sintering.  $\text{Al}(\text{OH})_3$  is mixed with  $\text{NiMnCo}(\text{OH})_2$  precursor and Li source (LiOH) for sintering.
- (3) After sintering.  $\text{Al}_2\text{O}_3$  can be coated onto  $\text{LiNiMnCoO}_2$  surface by dry or wet methods.

Therefore, a detailed study needs to be conducted to determine the best way to dope or coat Al. In addition, the amount of Al doping or coating needs to be determined.

Another technical challenge is to improve the cycle life and reduce the gas generation of recovered NMC622 developed in the Phase II program. It is expected that improvement strategies found to be effective for this will also enhance and inform results for Phase III chemistry.

## Results

### NMC622

Last year, WPI delivered 100g of recycled NMC622 cathode powder (021123-PCAM081222-C-Al) to Farasis for the fabrication of single layer pouch cells (SLPs). The morphology and layered structure of 021123-PCAM081222-C-Al were analyzed and depicted in Figure I.12.1 a, b. The content of transition metals, lithium, and aluminum in the recycled materials was tested by ICP-OES and found to be consistent with the design. The electrochemical performance of 021123-PCAM081222-C-Al was demonstrated in Figure I.12.1 c. The 021123-PCAM081222-C-Al delivered comparable rate performance as control NMC622 sample at low rates, it has an improvement at 1C, which is 9.7% better than NMC622 at 1C. However, based on Farasis's SLP test results, the 021123-PCAM081222-C-Al shows slightly worse cycle performance than the control NMC622 sample.

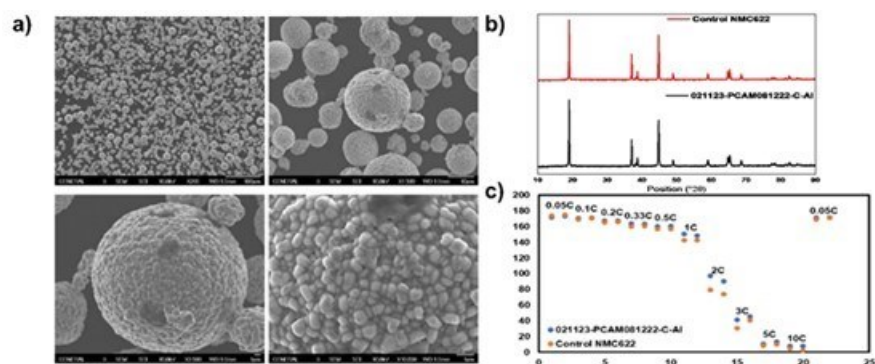
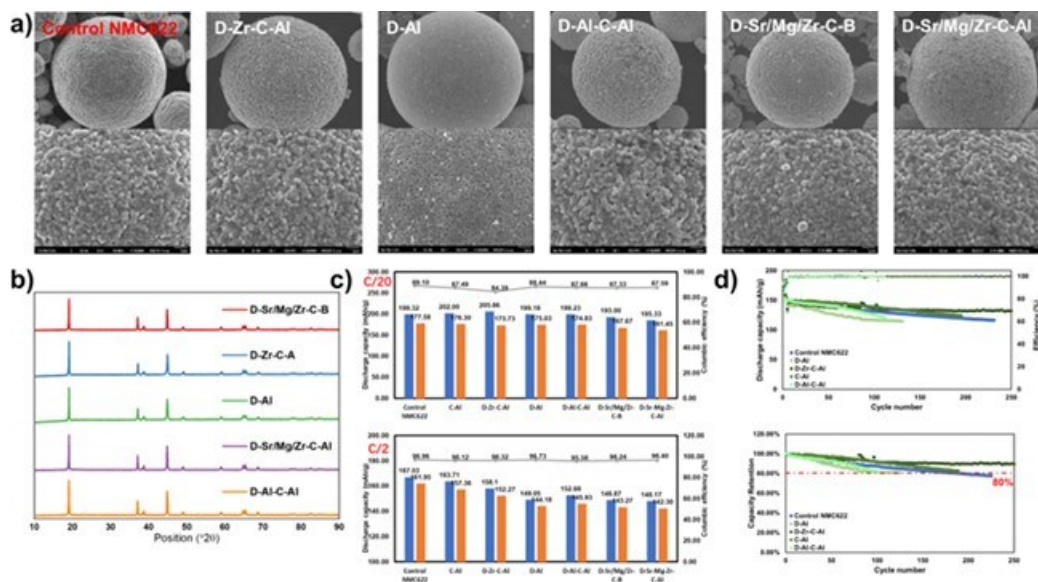


Figure I.12.1 a) SEM images for 021123-PCAM081222-C-Al; b) XRD pattern for 021123-PCAM081222-C-Al; c) rate performance comparison for 021123-PCAM081222-C-Al and control NMC622.

To further improve the cyclic performance of recycled MC622, various doping and coating strategies were employed to enhance the cycle performance. These strategies included  $\text{Al}_2\text{O}_3$  doping;  $\text{ZrO}_2$  doping,  $\text{Al}_2\text{O}_3$  coating; and combinations of  $\text{Al}_2\text{O}_3$  doping and  $\text{Al}_2\text{O}_3$  coating. Additionally, based on the optimized doping/coating strategy for recycled  $^{83}\text{Ni}$ , two batches of recycled NMC622 cathode powder were synthesized using SrO/MgO/ $\text{ZrO}_2$  doping,  $\text{Al}_2\text{O}_3$  coating, and SrO/MgO/ $\text{ZrO}_2$  doping,  $\text{B}_2\text{O}_3$  coating. As shown in Figure I.1.2 a, b, the SEM images and XRD pattern analysis confirm that the treatment did not affect the spherical shape and good layer structure of the recycled cathode powder. Additionally, Figure I.12.2c illustrates the

electrochemical performance of the recycled NMC622 with modified materials. The introducing of the MgO and SrO will decrease the discharge capacity at C/20, and the other recycled cathode powder with different doping/coating materials delivered comparable discharge capacity at C/20. Among all recycled cathode powder with the different doping/coating strategies, the C-Al, and D-Zr-C-Al sample delivered the highest discharge capacity at C/2, which is comparable as the control NMC622 cathode powder, and other recycled cathode powder delivered lower discharge capacity as the control NMC622 cathode powder. Additionally, SLPs were fabricated to test the cyclic performance. In Figure I.12.2 d, the D-Zr-C-Al sample showed the best cyclic performance, slightly better than the control sample.



**Figure I.12.2 a) SEM images, b) XRD pattern, c) electrochemical performance, and d) cyclic performance for recycled cathode samples with different doping/coating strategies.**

Based on the promising cycle performance mentioned above, the WPI team conducted a scale-up sintering experiment at AE, and successfully obtained approximately 150g of the 072523-PCAM081222-D-0.1Zr-C-Al cathode powder. As shown in Figure I.12.3 a, b, the 072523-PCAM081222-D-0.1Zr-C-Al cathode powder exhibits a spherical shape and maintains a good layer structure with no impurity peaks compared to the control NMC622 powder. Furthermore, the content of transition metals, lithium, zirconium, and aluminum, as analyzed by ICP-OES, aligns with our design expectations. Following this, the 072523-PCAM081222-D-0.1Zr-C-Al and the 072523-PCAM081222-C-Al are sintered together in the same batch. Based on the results of the WPI tests, it is evident that the various coating and doping stages do not have any discernible impact on the SBC number. Therefore, to meet the requirements for supplying 072523-PCAM081222-D-0.1Zr-C-Al to Farasis, the SBC number of 072523-PCAM081222-C-Al is taken as the representative value. Table I.12.1 illustrates that the SBC of 072523-PCAM081222-C-Al is closely aligned with the control, with 0.132wt% of free lithium content. The electrochemical performance is tested with coin cells and single layer pouch cells. As shown in Figure I.12.3.c, the coin cell test results show that the 072523-PCAM081222-D-0.1Zr-C-Al delivered comparable discharge capacity with control NMC622 cathode powder. As depicted in Figure I.12.3 d, the discharge capacity and initial columbic efficiency of 072523-PCAM081222-D-0.1Zr-C-Al at C/20, tested by SLP, closely matched those of the Farasis control sample. As shown in Figure I.12.3 e, after 250 cycles, the capacity retention for 072523-PCAM081222-D-0.1Zr-C-Al is 98.07%, which is slightly higher than that of control NCM622 cathode powder (94.77% and 96.87%).

Since the test results at WPI show that the 072523-PCAM081222-D-0.1Zr-C-Al cathode powder delivered slightly better electrochemical performance than the control NMC622 cathode powder, WPI delivered ~150g of 072523-PCAM081222-D-0.1Zr-C-Al cathode powder to Farasis for double layer pouch cell testing.

Meanwhile, WPI also sent 6kg of recycled NMC622 precursor to AE for synthesizing recycled cathode power. As shown in Table I.12.1, the SBC number for 6kg of recycled NMC622 (0.133wt%) is comparable with the pervious batch (0.132wt%) and control NMC622 cathode (0.123wt%). The 6kg recycled NMC622 cathode powder is sent to Farasis for the fabrication of 2Ah cell.

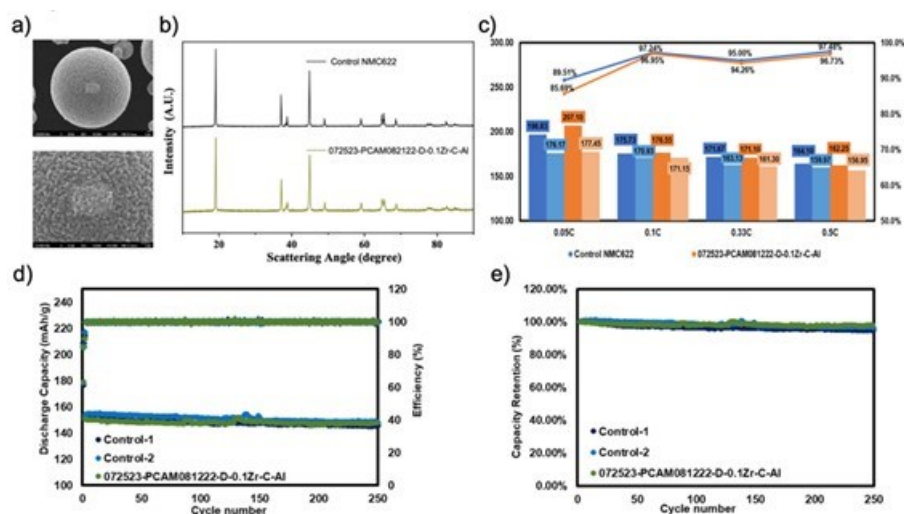


Figure I.12.3 a) SEM images for 072523-PCAM081222-D-0.1Zr-C-Al; b) XRD pattern; c) rate performance comparison; d-e) cyclic performance comparison for 072523-PCAM081222-D-0.1Zr-C-Al with control NMC622 sample.

Table I.12.1 The SBC Results for 072523-PCAM081222-D-0.1Zr-C-Al and 6kg Recycled NMC622 Cathode Powder.

Recycled experiment-Sample Name	Residual Lithium			Free Li (ppm)	Free Li (wt.%)
	Li <sub>2</sub> CO <sub>3</sub> (ppm)	LiOH (ppm)*	Total (ppm)		
Control (Test by WPI)	3284.04	2128.89	5414.93	1233.78	0.123
072523-PCAM081222-C-Al	1313.61	3698.94	5012.56	1318.6	0.132
092723-PCAM081222-D-Zr-C-Al (6kg)	2435.667	3007.056	5442.722	1328.881	0.133

### High Nickel NMC (83% Ni)

Based on our findings, we sintered a batch of recycled cathode powder using various Zr and B coating/doping approaches to assess its SBC number and electrochemical performance. Figure I.12.4 a reveals that the recycled cathode powders retained their spherical shape, and the introduction of dopants or coatings did not alter their morphology. The XRD pattern, as depicted in Figure I.12.4 b, confirms that these powders preserved a well-defined layered structure. From the data presented in Figure I.12.4 c, the C-Zr/B variant showcased the highest discharge capacity of 216.54mAh/g, coupled with an average initial columbic efficiency of 91.13%. This performance is on par with the Farasis control sample. However, as highlighted in Figure I.12.4 d, the C-Zr/B's retention dropped to 80% after a mere 54 cycles, in contrast to the Farasis control sample which maintained this retention rate up to 86 cycles. It is noteworthy that the D-Zr-C-B sample exhibited a cycle retention similar to the Farasis control, achieving 80% capacity retention after 87 cycles.

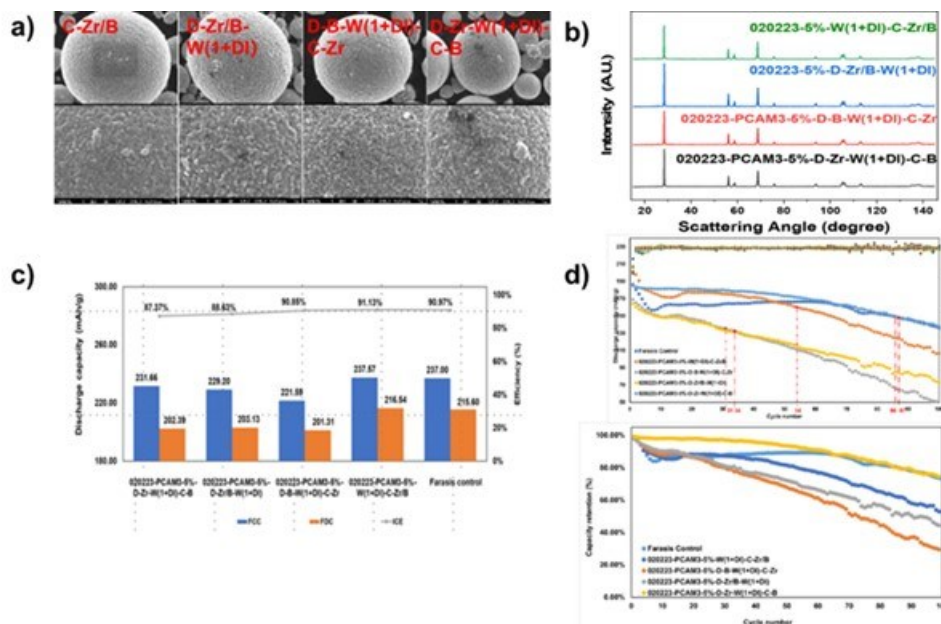


Figure I.12.4 a) SEM images; b) the XRD pattern; c) electrochemical performance; d) cyclic performance for cathode powder with different Zr/B doping/coating.

To match the doping/coating strategy of the Farasis control sample, Sr and Mg were added as dopants based on Zr doping with B coating, and Zr/B co-coating samples. As shown in Figure I.12.5 a, the SEM images of the recycled cathode powders showed that the Sr/Mg did not affect their morphology, and XRD patterns (Figure I.12.5 b) indicated that the recycled cathode powders maintained good layer structure. The ICP results indicated that the concentration of transition metals, lithium, dopant, and coating materials matched the design. However, the electrochemical performance (Figure I.12.5 c) The D-Sr/Mg/Zr-W-C-B delivered the highest discharge capacity as the Farasis control.

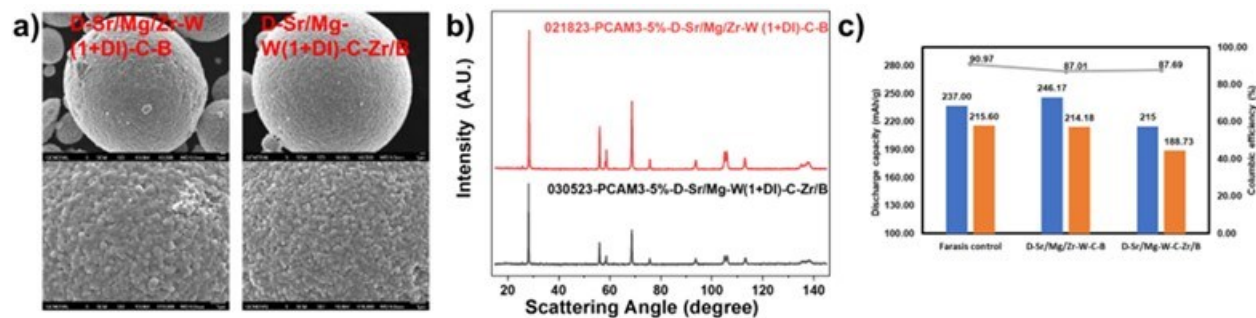


Figure I.12.5 a) SEM images; b) XRD pattern; c) first cycle discharge capacity for cathode powder with different doping/coating strategy.

In order to further advance towards Phase III objectives, we prepared the 4th batch of co-precipitation reactions, utilizing a higher proportion of recycled materials in a metal sulfate solution (MS solution). The average concentrations of Ni, Mn, and Co in the initial MS solution obtained, which were determined to be 0.853 mol/L, 0.171 mol/L, and 0.210 mol/L, respectively. To meet the target Mn concentration of 0.09 mol/L, the solution was appropriately diluted based on the concentration of Mn. Recycled NiSO<sub>4</sub> and virgin CoSO<sub>4</sub> were subsequently introduced into the MS solution. Following these adjustments, the concentrations of Ni, Mn, and Co matched the desired targets of 1.245 mol/L, 0.09 mol/L, and 0.165 mol/L, respectively. In order to increase the mole ratio of recycled materials, the recycled NiSO<sub>4</sub> is introduced to replace the virgin NiSO<sub>4</sub> powder. The concentration of impurity in the recycled NiSO<sub>4</sub> powder is acceptable for MS solution.

preparation. Through calculations, it was determined that the final MS solution contained a mole ratio of recycled materials of 95%, including the original NiSO<sub>4</sub>, MnSO<sub>4</sub>, and CoSO<sub>4</sub> present in the MS solution, as well as the recycled NiSO<sub>4</sub> powder. A three-day reaction was carried out using the aforementioned MS solution. (Figure I.12.6) illustrates the synthesized batch 4 recycled 83Ni precursor collected at different days. The particles exhibited increased size and density over time, while retaining a spherical shape. The measured tap density of the precursor collected at different time points corresponded well with these observations.

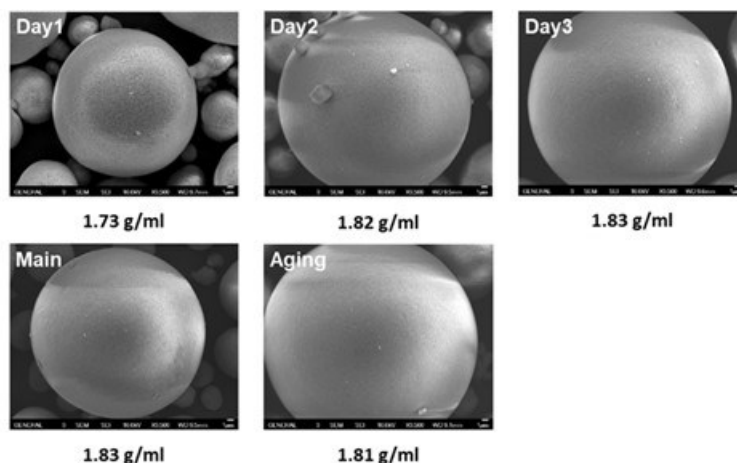
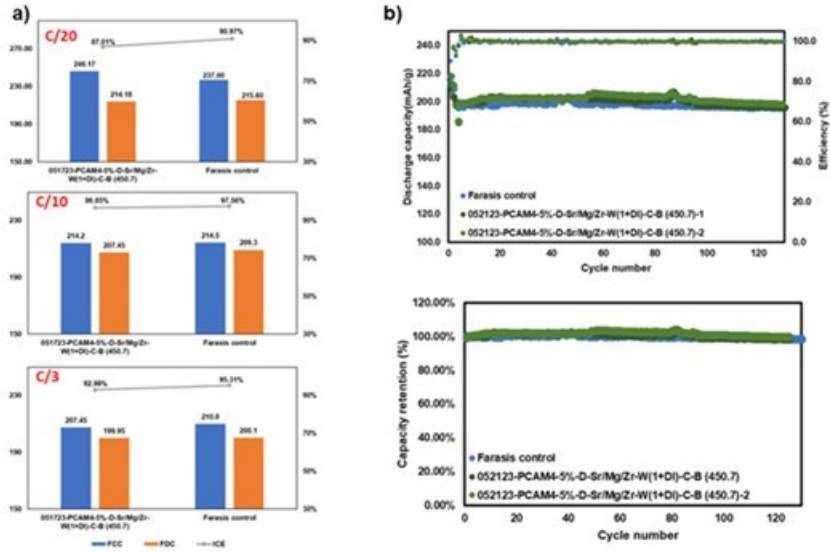


Figure I.12.6 SEM images for recycled 83Ni precursors.

Subsequently, the day 3 precursor was employed to produce recycled 83Ni cathode powder through sintering with LiOH and the dopant SrO/MgO/ZrO<sub>2</sub>. Following washing with a 1M LiOH solution, the cathode powder underwent vacuum drying and was mixed with B<sub>2</sub>O<sub>3</sub> coating material. Electrochemical performance was evaluated and compared to that of the Farasis control sample. As depicted in Figure I.12.7, the discharge capacities for the 051723-PCAM4-5%-D-Sr/Mg/Zr-W(1+DI)-C-B (450.7) sample were measured as 214.18 mAh/g, 207.45 mAh/g, and 199.95 mAh/g at C/20, C/10, and C/3, respectively, demonstrating comparability to the Farasis control sample. Furthermore, the SLP was fabricated to assess cyclic performance. After 130 cycles, the recycled 83Ni sample exhibited capacity retentions of 99.80% and 98.54%, while the Farasis control sample displayed a capacity retention of 98.64%, further demonstrating their similarity in performance.





**Figure I.12.7 a) electrochemical performance for 051723-PCAM4-5%-D-Sr/Mg/Zr-W(1+DI)-C-B (450.7) and Farasis control; b) capacity retention for 051723-PCAM4-5%-D-Sr/Mg/Zr-W(1+DI)-C-B (450.7) and Farasis control.**

Afterwards, WPI team conducted a scale-up sintering experiment at AE, yielding approximately 150g of recycled 83Ni cathode powder (070523-PCAM4-5%-D-Sr/Mg/Zr-W(1:2, 300, 30)-C-B (450.7)). As shown in Figure I.12.8 a and b, this new batch of recycled 83Ni cathode powder exhibited a spherical shape and maintained a good layer structure. As displayed in Figure I.12.8 c, the primary particle size of recycled 83Ni cathode powder was larger than that sintered at WPI. The tap density of the recycled 83Ni cathode powder (2.73g/cc) is comparable to that sintered at WPI (2.78g/cc). The concentration of Li, transition metals, dopants, and coating material, as analyzed by ICP-OES, matched our design expectations. As shown in Table I.12.2, the SBC number for recycled 83Ni cathode powder (0.129wt%) was lower than the samples sintered at WPI (0.162wt%), but comparable to Farasis control sample (0.118wt%). As displayed in Figure I.12.8 d, the recycled 83Ni cathode powder delivered comparable rate performance as Farasis control sample tested by coin cells. Meanwhile, Figure I.12.8 e showed that the discharge capacity of recycled 83Ni cathode powder and Farasis control sample was comparable, as tested by SLPs. However, after 210 cycles, the capacity retention for recycled 83Ni cathode powder was ~7% lower than that of the Farasis control sample.

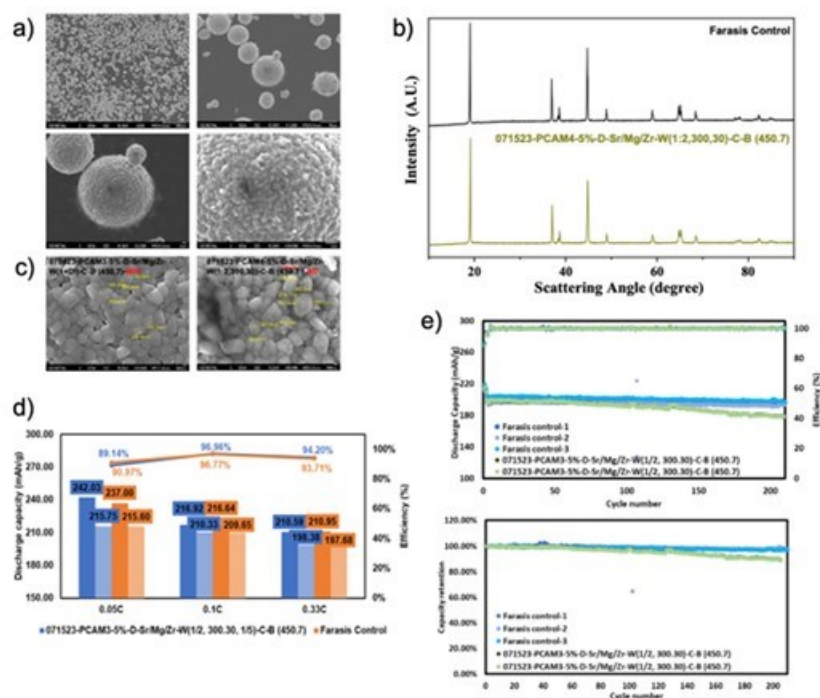


Figure I.12.8 a) SEM images; b) XRD patterns; c) comparison for primary particle size for cathode sintered at AE and WPI; d) rate performance comparison; e) cycle performance comparison for 071523-PCAM4-5%-D-Sr/Mg/Zr-W(1:2, 300, 30)-C-B (450.7) with Farasis control.

Table I.12.2 The SBC Results for 071523-PCAM4-5%-D-Sr/Mg/Zr-W(1:2, 300, 30)-C-B (450.7).

Recycled experiment-Sample Name	Residual Lithium			Free Li (ppm)	Free Li (wt.%)
	Li <sub>2</sub> CO <sub>3</sub> (ppm)	LiOH (ppm)*	Total (ppm)		
Farasis Control	4515.561	1157.583	5673.144	1183.656	0.118
071523-PCAM4-5%-D-Sr/Mg/Zr-W(1/2; 300,30)-C-B (450.7)	2339.882	2940.528	5280.409	1291.611	0.129

To explore the potential reasons for the poor cyclic performance of recycled 83Ni cathode powder, cross-section and BET tests were conducted to assess the porosity of the cathode powder. As shown in Figure I.12.9, the recycled 83Ni cathode powder exhibited more pores and larger pore sizes compared to the Farasis control powder. This observation was corroborated by the BET results, which indicated that the BET value for the recycled 83Ni cathode powder (0.6165 m<sup>2</sup>/g) was higher than that of the Farasis control powder (0.2747m<sup>2</sup>/g), implying that the recycled powder had a larger surface area.

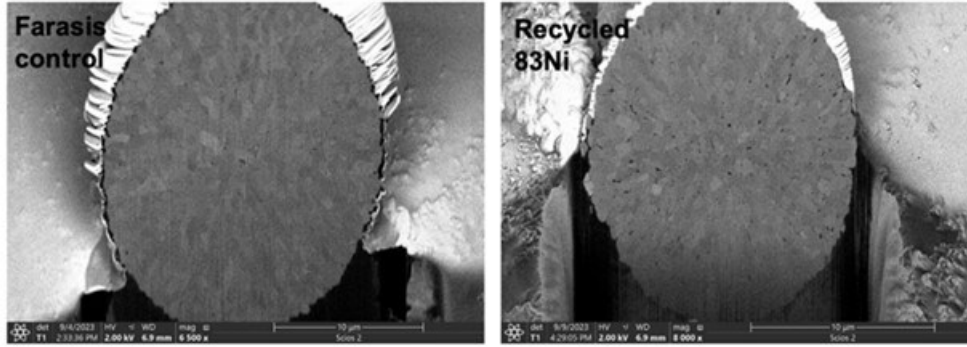


Figure I.12.9 The cross-section results for Farasis control and 071523-PCAM4-5%-D-Sr/Mg/Zr-W(1:2, 300, 30)-C-B (450.7).

To obtain the denser cathode powder, WPI team performed the 5th batch of co-precipitation reactions, utilizing a higher concentration of metal sulfate solution (MS solution). After appropriately diluting and adding virgin NiSO<sub>4</sub> and CoSO<sub>4</sub> into the MS solution, the concentration of Ni, Mn, and Co reached the desired targets, and the concentration of impurities including Cu, Fe, Al, Na, Mg, and Li is acceptable.

In response to the higher concentration of MS solution, the residence time was increased, and the flow rates of the MS solution and ammonia solution were reduced, while maintaining the reaction temperature and pH number. As depicted in Figure I.12.10, as the reaction processing, the flakes began to diminish in size, and the precursor became denser. With the progression of the co-precipitation reaction, the tap density steadily increased and stabilized after 72 hours. Additionally, the Batch 5 precursor exhibited a higher tap density than the Batch 3 precursor, indicating that it was denser. The team collected the precursor from Day 3 afterwards and ultimately obtained approximately 2.5kg of precursor for further study.

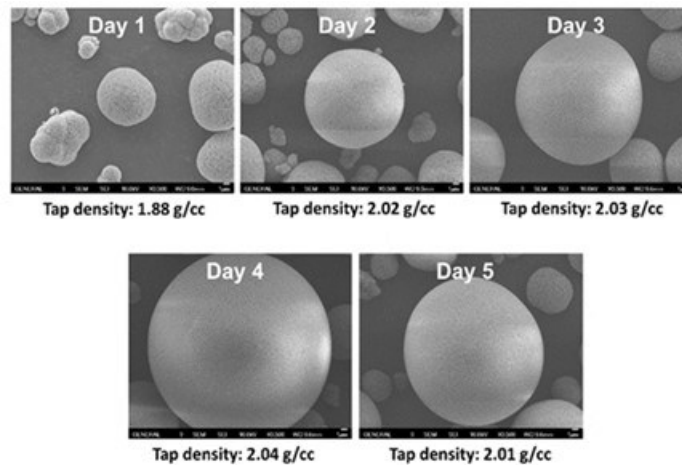


Figure I.12.10 SEM images for precursors with different reaction time.

### ***Lithium recovery***

This year, WPI launched a project focused on lithium recovery. In the conventional approach, the cathode powder from the black mass is fully dissolved in acid. Once valuable transition metals are extracted, the remaining lithium salt solution is concentrated to enhance the lithium content. This is followed by a recrystallization and purification process to yield battery-grade lithium carbonate. On the other hand, the innovative selective leaching method prioritizes the extraction of lithium in its initial phase. After undergoing recovery and purification procedures, battery-grade lithium carbonate is then recrystallized. Impressively, this approach allows for a selective recovery rate of 99.8% lithium, boasting a purity of 99.99%. For the successful large-scale application of the selective leaching technique, it's crucial to optimize the solid-to-liquid (S/L) ratio

used in the leaching process. Concurrently, factors such as temperature and stirring speed should be fine-tuned in harmony with the S/L ratio. A detailed purity assessment of the recovered lithium carbonate is conducted using ICP-OES. As presented in Table I.12.3, it is observed that the most dominant impurity, nickel, is less than 5ppm. Concentrations of other transition metals are found to be below 2ppm, with copper, iron, aluminum, and magnesium all registering less than 0.5ppm. In conclusion, the reclaimed lithium carbonate boasts a purity surpassing 99.99%, thus fulfilling the standards for battery-grade lithium carbonate.

**Table I.12.3 The ICP-OES Results for Impurities in the Recovered Lithium Carbonate.**

Impurity Concentration						
Ni	Mn	Co	Cu	Fe	Al	Mg
<5ppm	<2ppm	<2ppm	<0.5ppm	<0.5ppm	<0.5ppm	<0.5ppm

### Conclusions

In this USABC Phase III project, the team has successfully improved the cyclic performance of the recycled NMC622 by utilizing different doping and coating strategies. In addition, different washing methods, amount of excess Li, doping/coating elements, and sintering conditions have been employed to optimize the electrochemical performance of the recycled 83Ni cathode. Then, denser precursors have been prepared using a higher concentration of metal sulfate solution. Finally, selective lithium leaching has been investigated to recover lithium from spent batteries.

### Key Publications

Xiaotu Ma, Mengyuan Chen, Zhangfeng Zheng, Dennis Bullen, Jun Wang, Chloe Harrison, Eric Gratz, Yulin Lin, Zhenzhen Yang, Youtian Zhang, Fan Wang, David Robertson, Seoung-Bum Son, Ira Bloom, Jianguo Wen, Mingyuan Ge, Xianghui Xiao, Wah-Keat Lee, Ming Tang, Qiang Wang, Jinzhao Fu, Yubin Zhang, Bryer C. Sousa, Renata Arsenault, Peter Karlson, Nakia Simon, Yan Wang,\* (2021), [Recycled Cathode Materials Enabled Superior Performance for Lithium-Ion Batteries](#), Joule, DOI:10.1016/j.joule.2021.09.005

### References

1. Offices, E. g. <https://www.energy.gov/eere/vehicles/batteries>.
2. Kim, U.-H.; Kuo, L.-Y.; Kaghazchi, P.; Yoon, C. S.; Sun, Y.-K., Quaternary Layered Ni-Rich NCMA Cathode for Lithium-Ion Batteries. *ACS Energy Letters* 2019, 4 (2), 576-582.
3. Lin, S.-L.; Huang, K.-L.; Wang, I.-C.; Chou, I.-C.; Kuo, Y.-M.; Hung, C.-H.; Lin, C., Characterization of spent nickel–metal hydride batteries and a preliminary economic evaluation of the recovery processes. *Journal of the Air & Waste Management Association* 2016, 66 (3), 296-306.
4. insideevs <https://insideevs.com>.

### Acknowledgements

The development team (WPI/AE/Farasis) would like to thank the following for all of the help, advice, support and suggestions: USABC program manager Renata Arsenault (Ford) and USABC work group members Nakia Simon (Stellantis), Kely Markley (GM), Nicolas Eidson (DOE), Bryant Polzin (DOE), and Brian Ingram (ANL).

## II Processing Science & Engineering

The processing science & engineering activity supports the development and scale-up of manufacturing technologies needed to enable market entry of next-generation battery materials and cell components that could significantly reduce cost and environmental impact while increasing yield and process control relative to existing production technologies. The research portfolio spans material discovery, scale-scale up, slurry formulation, electrode engineering, and cell prototyping.

Material discovery scale-up address several related barriers to manufacturing cost and material performance for novel battery materials. These seek to develop new advanced manufacturing processes that reduce cost and provide advanced new materials for evaluation. The industry-relevant continuous processes are developed for scalable production of cathode materials, precursors and electrolytes, such as continuous flow, co-precipitation, supercritical fluid synthesis and flame spray pyrolysis. In situ experimentation and multiscale modeling are applied to designing new processes for improving battery performance and reducing processing cost.

### *Slurry formulation*

LBNL investigated the effect of the ratio between carbon black and binder on slurry properties (i.e., viscosity) and electrode properties (i.e., adhesion and cohesion strength). There appears to be an ideal solvent content with regard to mixing and casting that correlates linearly with the surface area of carbon additives. LBNL also built and tested early iterations of a miniature automated coating/drying line, which can observe electrode coating production process.

### *Material screening and prototyping*

ANL screened two electrolytes, free-standing polymer electrolyte and sulfide based (Li<sub>6</sub>PS<sub>5</sub>Cl) electrolyte, for all solid-state batteries. Promising results have been demonstrated. Particularly, the sulfide based all-solid-state batteries with NMC811 and silicon electrodes demonstrated 70% capacity retention after 1000 cycles. Additionally, ANL installed a multifunctional coater which provides many new capabilities to the CAMP Facility including interchangeable coating heads, corona treatment and an IR drying zone. Volume evolution during lithium plating and stripping was also evaluated using operando energy dispersive X-ray diffraction (EDXRD).

### *Electrode engineering and prototyping*

ORNL has developed a two-layer electrode architecture with a denser energy layer at bottom and a more porous power layer on top, which showed improved capacity with high areal capacity (6 mAh/cm<sup>2</sup>) compared to the conventional structure and can be applied for fast charging application. In addition, Li<sup>+</sup> dynamics in hybrid polymer electrolytes based on PEO electrolyte, Al-LLZO filler and LiTFSI or LiFSI salt were evaluated via experiment and simulation. ORNL also continues developing an electron beam curing process for electrode manufacturing, which could enable solventless processing high throughput (i.e., >300 m/min line speed) and significant processing energy saving. A new green radiation curable resin from domestic supplier was evaluated and is compatible with both NMC and graphite and graphite/silicon materials. This technology was licensed to Ateios Systems and won an R&D 100 Award and a 2022 FLC Technology Transfer Award in 2022.

The rest of this chapter contains detailed reports on the status of the following individual projects.

- Processing Next Generation Li-ion Battery Cathode Materials (ANL)
- Novel Processing Approaches for LLZO (ANL)
- Supercritical Fluid Processing of Battery Cathode Materials (ANL)
- Process R&D and Scale-up of Critical Battery Materials (ANL)
- Structure-Activity Relationships in the Optimizing Electrode Processing Streams for LiBs (LBNL)
- Higher Energy Density via Inactive Components and Processing Conditions (LBNL)

- Minimizing Side Reactions in Next-Generation Lithium Ion Battery Cathodes Through Structure-Morphology Optimization (ANL)
- In Situ Spectroscopies of Processing Next-Generation Cathode Materials (ANL, BNL)
- Towards Solventless Processing of Thick Electron-Beam (EB) Cured LIB Cathodes (ORNL)
- Performance Effects of Electrode Processing for High-Energy Lithium-Ion Batteries (ORNL)
- Advanced Anode Manufacturing through Ultra-Thin Li Deposition (Applied Materials, Inc.)
- Thin-film lithium metal manufacture by room temperature electrodeposition (Albemarle Corporation)
- GMC CRADA: Multilayer Composite Solid State Lithium Batteries for EV Battery Applications (ANL)
- Cabot CRADA: Spray Synthesis of Additive Battery Particles (ANL)
- Solid Power CRADA: Interface-Engineered, High-Energy Oxide Cathodes for All-Solid-State Lithium Batteries (ANL).

## II.1 Processing Next Generation Li-ion Battery Cathode Materials (ANL)

### **Ozge Kahvecioglu, Principal Investigator**

Argonne National Laboratory  
9700 South Cass Avenue  
Lemont, IL 60439  
E-mail: [okahvecioglu@anl.gov](mailto:okahvecioglu@anl.gov)

### **Haiyan Croft, DOE Technology Development Manager**

U.S. Department of Energy  
E-mail: [Haiyan.Croft@ee.doe.gov](mailto:Haiyan.Croft@ee.doe.gov)

Start Date: October 1, 2022	End Date: September 30, 2023	
Project Funding (FY23): \$1,475,000	DOE share: \$1,475,000	Non-DOE share: \$0

### **Project Introduction**

Emerging synthesis technologies that can significantly reduce the manufacturing costs for battery materials, are critical for US competitiveness in the advancements of energy security, especially when new chemistries are invented. Deployment of such, could provide affordable mobility and can address reduction of CO<sub>2</sub> emissions through the electrification of vehicles. The state-of-the-art Li-ion batteries (LIBs) for electric vehicles (EVs) consist of transition metal oxides as the cathode active materials, which is the most expensive part of the battery cell, due to its manufacturing costs and scarcity of each component. Addressing the manufacturing costs and mitigating the dependencies to other countries requires the invention of new chemistries that can leverage earth-abundant elements as active materials. However, it takes over a decade to transition a newly invented material from bench-scale synthesis to mass production. Because it requires extensive performance validation test to be made at actual format cells, which requires a minimum of a kilogram quantity of the material with consistent quality. There are no reliable sources of such materials available to the research community. The availability of hard-to-make, on-demand materials is critical to battery research community to explore and progress toward developing advanced LIBs chemistry. In a close collaboration with other partners in the program, the Process R&D and Scale Up Group at Materials Engineering Research Facility (MERF) at Argonne National Laboratory is utilizing non-traditional, advanced co-precipitation synthesis methods, such as the Taylor Vortex Reactor (TVR), to produce large quantities of uniformly high quality materials. Samples of the materials are distributed to collaborating research groups for investigation and performance evaluation. By evaluating new precipitation technologies, the Process R&D and Scale-up of Advanced Active Materials for Li-ion Batteries project establishes new platforms for scalable and economically feasible manufacturing processes of next generation cathode materials. The results presented in this report demonstrate that the MERF's developed TVR technology can produce high-quality materials with the desired composition and morphology at scale for ultimate deployment in full-scale manufacturing. The development and employment of the TVR platform by the project makes advances in new materials synthesis and deployment faster than ever before.

### **Objectives**

The multifaceted objective of the program is to provide the research community with materials that they design and want to investigate and, therefore, ascertain the key missing link between the discovery of advanced active battery materials, evaluation of these materials, and ultimately, high-volume manufacturing of the selected targets to reduce the risk associated with their commercialization. We perform systematic process and material engineering research to develop cost-effective, customized synthesis and to produce sufficient quantities of high-quality target materials by optimizing process parameters tailored to specific material compositions, evaluating material purity profiles, and applying emerging manufacturing technologies to address challenges

associated with manufacturing advanced materials. The technical targets of this program are developing customized synthesis processes for each material selected, scaling up to multi-kilogram quantities with reproducibility under rigorous quality control, and evaluating emerging manufacturing technologies to assist fundamental research and reduce the commercialization risk of newly invented active battery materials.

## Approach

Over the past five years, the advantages of utilizing an emerging synthesis technology, the Taylor Vortex Reactor (TVR), were demonstrated for producing of cathode precursors for lithium-ion batteries. This innovative reactor has a cylindrical rotor and tremendous Taylor vortices in the annulus. It produces homogenous micro-mixing with high mass and heat transfer, enabling a high degree of uniform supersaturation thus eliminating local concentration and temperature gradient. This results in faster kinetics and denser particles with minimal optimization. The TVR continuously produces spherical precursor particles with a narrow particle size distribution, which is critical to achieve high-quality battery materials, and is now the preferred platform for rapid production of new chemistries that are not commercially available. Advances in battery technologies has created a need on dense, spherical cathode active materials (CAMs) with relatively smaller secondary particles (e.g.; less than 10  $\mu\text{m}$ , preferably between 3 to 6  $\mu\text{m}$ ) when the concern is improving fast charging features of the battery or else increasing rate-capability of the batteries. The demand is increasing each year as new technologies are being developed. However, there is no commercial source of smaller CAMs for the compositions that have not been validated for large-scale manufacturing. TVR offers to address these demands due to its unique feature capable of producing smaller, dense and spherical particles by changing its rotation speed without compromising the intrinsic electrochemical features of the end product. Within the project's scope, TVR technology has been used for custom-size precursors (preCAMs) synthesis per our collaborators' project's needs. The project team continued supporting the researchers across the Nation by providing a wide range of different, commercially non-available chemistries, morphologies and/or particle sizes.

## Results

### *Optimization of Cobalt Free Mn-rich Hydroxide Precursors: pH and Residence Time*

In FY23, our activities were concentrated around optimizing the co-precipitation conditions through a systematic approach. Last year, we monitored the particle formation as a function of varying pH (pH = 11.6  $\rightarrow$  11.0), through a hydroxide based continuous co-precipitation route to synthesize  $\text{Mn}_{0.65}\text{Ni}_{0.35}(\text{OH})_2$ , in TVRs at a substantially lower residence time ( $\tau = 1\text{h}$ ). In FY23, we further decreased the pH of the reaction: first, to improve the morphology (e.g. spherical) and second, to improve the particle density. The outcome of this systematic approach delivered spherical particle formation at an optimal reaction pH of 10.5. Reducing the pH value beyond pH = 10.5, altered the spherical morphology to a nodular structure, as well as decreased the particle density by  $\sim 25\%$ . Overall, the spherical particles had still low densities ( $\sim 0.9\text{ g/cc}$ ) due to the fast nature of the co-precipitation reaction using 1h as the residence time. It is known that the longer residence times in co-precipitation reactions, in general, delivers higher densities with the slow construction of secondary particles due to residing in the reaction media longer. Thus, using the optimal pH value from the fast reactions, we applied longer residence time of 4 hours to improve the particle densities without compromising the spherical morphologies. It is crucial to note here that the residence time of 4 hours in a TVR, is, in fact, three times faster than that of time in conventional continuous stirred tank reactors (CSTRs). These conditions delivered 1.62 g/cc tap density for the preCAMs. Further, we investigated slightly higher pH condition to screen the upper & lower limits of pH values for Mn-rich hydroxide preCAM synthesis, where both morphology and tap density were observed to decay. The resulting particle morphologies and tap densities from these systematic studies are displayed in Figure II.1.1. The preliminary conclusion pointed out that the pH of the reaction was the most affective parameter for obtaining spherical particles which also contributes to the density of the material, whereas the residence time was the most important parameter to improve particle density. Note that, the transition metal to ammonia mol ratios, rotation speed and temperature of all co-precipitation reactions were kept constant. Further investigation is needed to increase the densities close to 2.0 g/cc while maintaining the spherical morphologies.



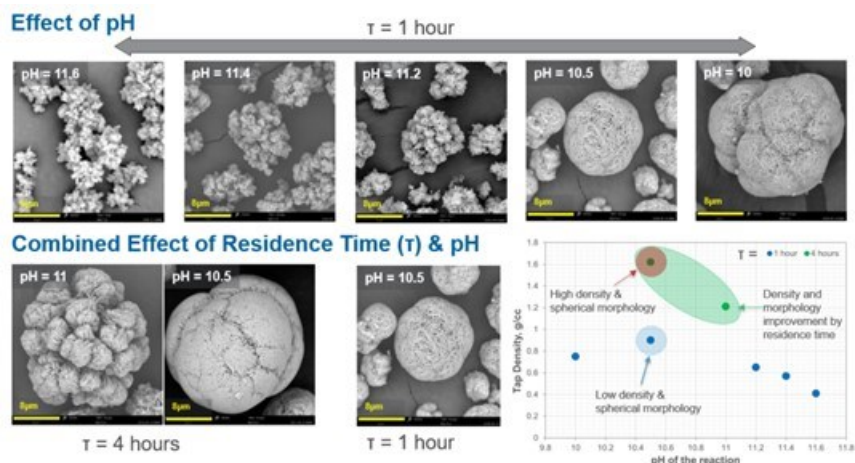


**Figure II.1.1** preCAM particle formation with varying the pH of the co-precipitation reactions at fast reactions (top row). Spherical particle formation is strongly dependent on the applied pH, regardless of the residence time. Particle density is improved with longer residence time. Optimal pH (pH = 10.5) and longer residence time (4h) are interacting parameters for improved particle properties (bottom row).

The preCAMs are mixed with excess LiOH.H<sub>2</sub>O and were calcined at 900°C under flowing oxygen for 12 hours in a box furnace. The tap density was achieved as high as 2.1 g/cc for the CAM synthesized using the spherical and denser preCAM which was obtained at optimal pH (10.5) and residence time (4 h). This material is under calcination optimization for future electrochemical validation tests. The first cycle voltage profiles of previously reported low density materials (Figure II.1.2a) and new and higher density materials were compared in Figure II.1.2. The material density was shown to have minimal impact on discharge capacities at the first formation cycle, where 56% increase in the density resulted in 1.2% loss in discharge capacity.

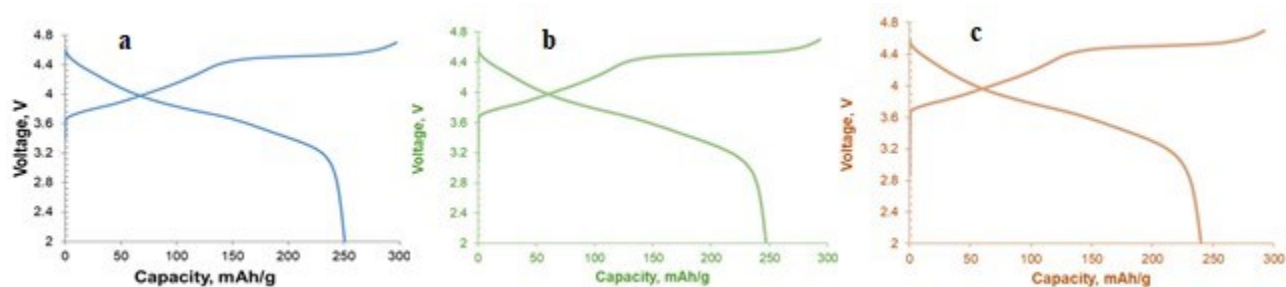


**Figure II.1.2** Voltage profiles of CAMs with different tap densities and morphologies. Top row, left to right; a. Hexagon shaped loosely aggregated primaries with 0.9 g/cc tap density, b. Nodular secondary particles with 1.3 g/cc tap density, c. Spherical secondary particle with 1.6 g/cc tap density (Electrode information: AM:C:Binder = 84:8:8. The average mass of loading ~8-10 mg/cm<sup>2</sup>. Coin half-cell cycling protocol: First formation cycle at C/20 (1C = 175 mA/g) between 2.0 V - 4.7 V at 30 °C).

The discharge capacities were comparable to an optimal CAM processed from carbonate precursors, however the most pronounced influence of the increased particle density was found in the impedance profiles of the materials (Figure II.1.3), where there was a clear trend of impedance rise as the material's density was increased. Fundamental studies to understand the underlying mechanism of this occurrence will be collaboratively studied with the EaCAM partners.

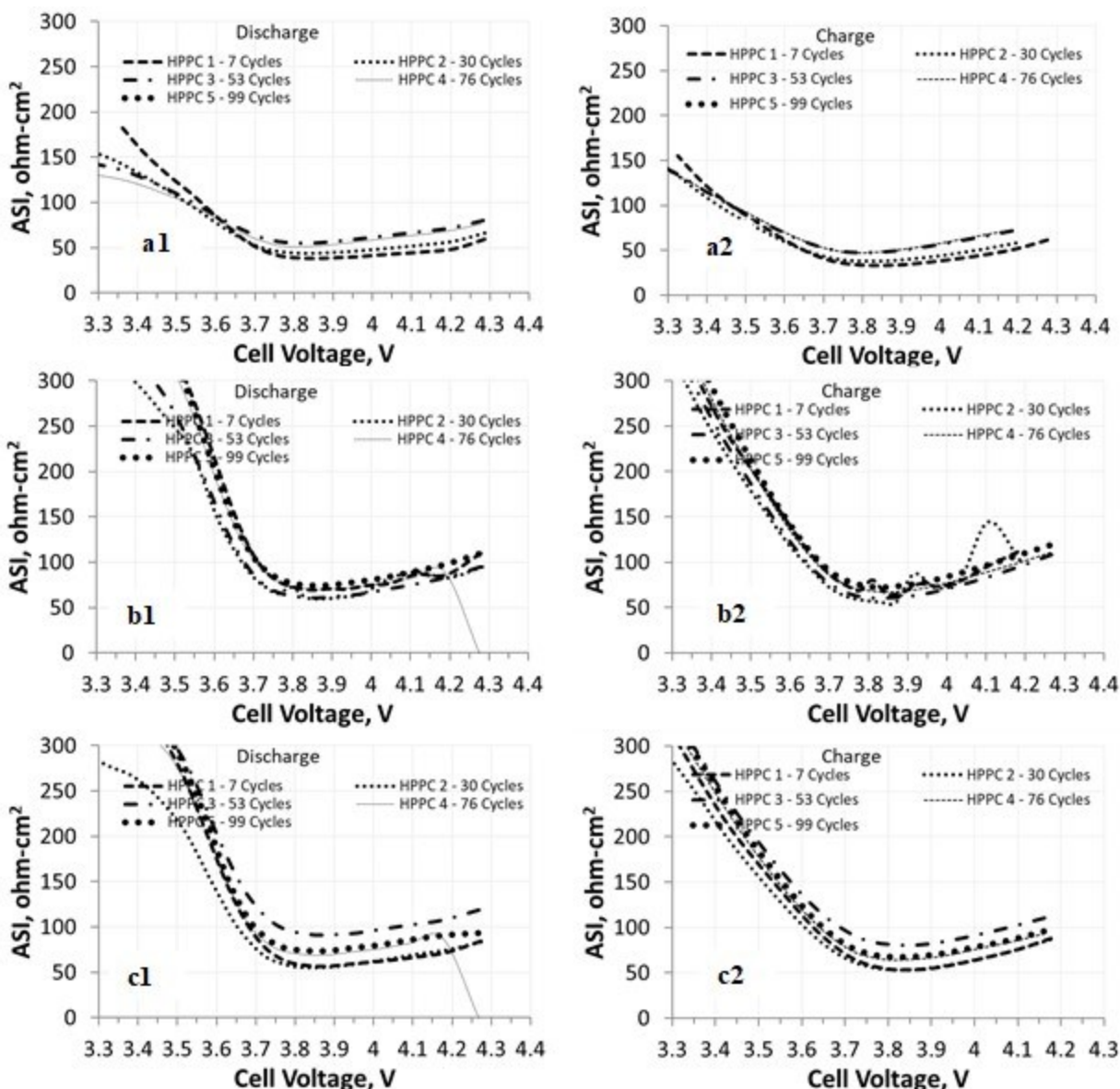
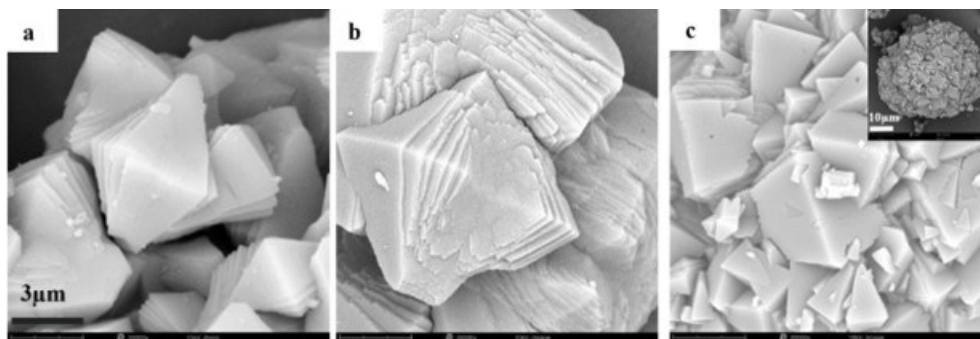


Figure II.1.3 Discharge/Charge ASI profiles of CAMs with different tap densities and morphologies. Top row, a1-a2. Hexagon shaped loosely aggregated primaries with 0.9 g/cc tap density, b1-b2. Nodular secondary particles with 1.3 g/cc tap density, c1-c2. Spherical secondary particle with 1.6 g/cc tap density (Electrode information: AM:C:Binder = 84:8:8. The average mass of loading  $\sim$ 8-10 mg/cm<sup>2</sup>. Coin half-cell HPPC protocol: 3C 10s Discharge/2.25C 10s Charge (1C = 175 mA/g).

#### **Preliminary Co-precipitation Studies with Low/No Ammonia for the Cobalt Free preCAMs**

Challenges in producing the preCAMs of manganese-rich materials are known. The preferred co-precipitation route for these materials is the carbonate route which typically delivers low density and highly porous precursor particles. This route has been studied for decades, yet the procedures for continuous operation concerning to limit the particle overgrowth, are still being optimized. Hydroxide co-precipitation route, on the other hand, brings in several challenges, such as, forming multiple oxidation states of manganese species, and compositional heterogeneity, and air sensitivity, etc. This year, we started looking into different co-precipitation routes to eliminate the problems with those common synthesis routes and seek opportunities for a greener process to reduce, if not, to eliminate ammonia in the co-precipitation step through using different chelating and precipitating agents.

Initially, we studied batch operations to observe the co-precipitation reactions, using different chelating and precipitating agents from the carboxylic acid groups. First, we investigated the molarities of each reactant solution and the transition metal to chelating agent mol ratios. This was followed by monitoring the mixing time, pH and temperature of the reaction. Our preliminary batch operations resulted in single crystal-like preCAM formation (Figure II.1.4) and these preCAMs showed excellent air stability under ambient conditions. After preliminary batch operations, the findings were transferred to a fast and continuous operation in 1L TVR. Preliminary findings showed that the batch reactions promotes isolation of the octahedron shaped crystals while continuous operations at TVR displays aggregated octa/polyhedrons at different primary particle sizes built in a spherical morphology with rough surfaces (Figure II.1.4.c inset). The strong agglomeration was expected due to the micro-mixing efficiency of the TVRs, promoting agglomeration of primaries.



**Figure II.1.4** Morphology of preCAMs synthesized using carboxylic acid groups as chelating and precipitating agents; a. Fast reaction, 15 min (Batch, 1L), b. Long reaction, 24 h (Batch, 1L) c. Fast reaction, 30 min residence time (Continuous, 1L).

#### ***Pretreatment and Calcination of PreCAMs***

The calcination of Mn-based cathodes are typically done at air or oxygen atmospheres at elevated temperatures ( $T \geq 900^\circ\text{C}$ ) for long duration holds. Several publications in literature also suggest an intermediate hold at relatively lower temperatures is required (e.g.  $500$  or  $600^\circ\text{C}$ ) to ensure complete removal of evolving gasses (e.g.;  $\text{H}_2\text{O}$ ,  $\text{CO}_2$ ) and in parallel, to initiate phase homogenization and prelithiation of the materials. The intermediate hold at lower temperature is known in industrial applications when the scale is larger and when the depth of powder loading is thicker. With all this in mind, we have investigated the pretreatment of the Mn-based preCAMs obtained through co-precipitation with carboxylic acid groups. These materials have significant amount of carboxylic moieties, as well as crystal water ( $\geq 1.5$  mol  $\text{H}_2\text{O}$  by TGA) and could significantly affect the calcination atmosphere as they decompose to generate  $\text{CO}_2$  gas. Figure II.1.5 displays the morphologies and XRD profiles of pretreated preCAMs. Prior to pretreatment experiments we conducted TG/DSC analysis for the precursors. There is two distinct mass losses observed in the TG profile where the complete removal of  $\text{H}_2\text{O}$  was finalized around  $220^\circ\text{C}$ . The first endothermic peak associated with the removal of  $\text{H}_2\text{O}$  was found at  $\sim 211^\circ\text{C}$ . Second mass loss, starts  $\sim 220^\circ\text{C}$  and finishes at  $\sim 313^\circ\text{C}$ . A strong exothermic peak occurs at  $273^\circ\text{C}$  which is associated with the decomposition of carboxylic groups. The XRD profiles at two pretreatment temperatures also showed distinct phases: single cubic phase at  $300^\circ\text{C}$ , matching with  $\text{NiMn}_2\text{O}_4$ , and a mixture of both cubic (e.g.;  $\text{Mn}_2\text{O}_3$ ) and hexagonal (e.g.;  $\text{NiMnO}_3$ ) phases at  $500^\circ\text{C}$ . The morphology of the pretreated preCAMs showed lamellar cracks, however maintained their overall octahedral secondary morphology up to  $500^\circ\text{C}$ .

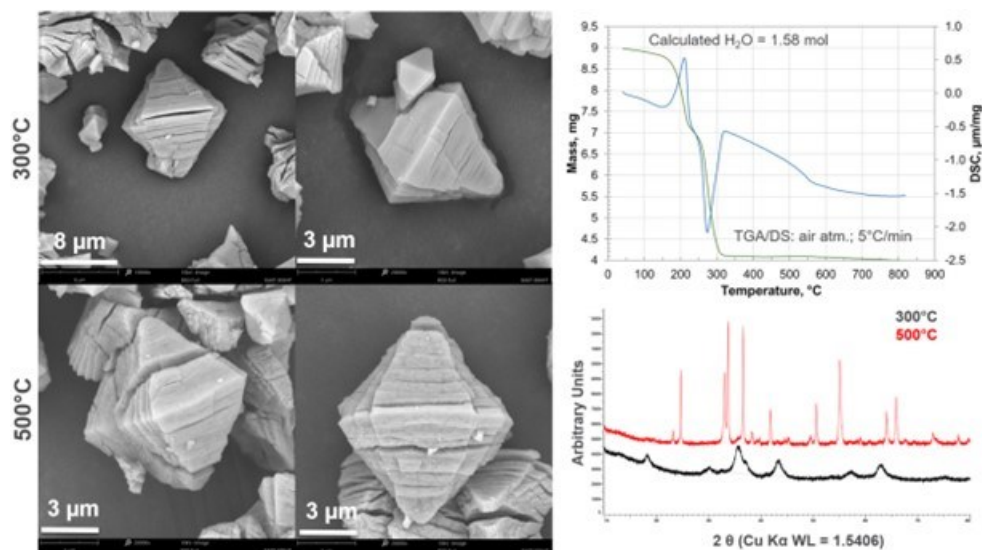


**Figure II.1.5** Morphology of preCAMs with lamellar cracks at 300 and 500 °C (SEMs on the left). TG/DSC profile of the preCAM shows two distinct mass losses. XRD profiles display one phase for 300 °C (cubic) and a mixture of two phases (cubic + hexagonal) for 500 °C pretreatments.

Preliminary calcinations of these preCAMs were done using a similar calcination conditions with the carbonate-based and hydroxide-based preCAMs, except we applied lower maximum temperatures of 750 and 850 °C, to observe the particle morphology. Due to the lamellar cracking pattern at the absence of lithium (pretreatment conditions, refer to Figure II.1.5 SEMs), it was expected that the higher temperatures could induce cracking. However, the lamellar cracking was as similar as those without lithium when calcined at 750 °C, showing stacked plate-like morphology (Figure II.1.6, left). On the other hand, calcination done at 850 °C displayed more intact particle structure, preserving the overall octahedron morphology, and the cracks were disappeared through the lithiation leaving a porous structure (Figure II.1.6, right). Future studies will be investigating the structural evolution of phases under different calcination regimes through *ex situ* and *in situ* XRD studies.

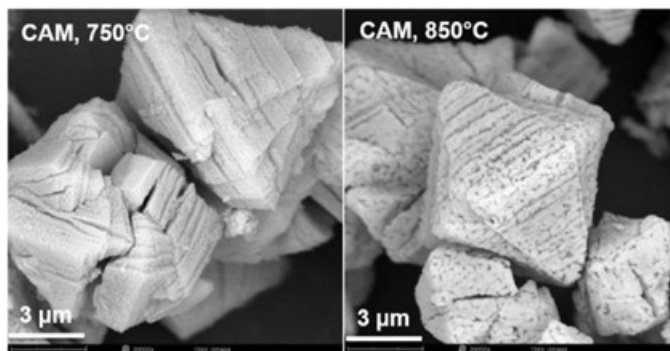


**Figure II.1.6** Morphology of CAMs calcined under flowing oxygen at 750 °C (left) and 850 °C (right). Lamellar cracks are more apparent at lower temperature.

#### **Custom Size preCAM and CAM Production in Support of US Battery Community**

One of the objective of this program is to support basic R&D and domestic US battery community, with the materials that are not commercially available. Over the past year, we have supported University of Washington (UW) (AMMTO project, DE-EE00009112) with custom size NMC622 CAMs. The UW's developed technology, if successful, is targeting 10% improvement in volumetric and gravimetric energy density over conventional Lithium-ion battery pouch cells. The size-specific NMC622 materials synthesized at MERF were

used in acoustic additive processing of thick patterned, with fine featured 3D electrode manufacturing. The preliminary results by UW team indicated a 30-40% improvement in manufacturing efficiency and reliability. MERF have continued collaborating with DOE-VTO funded project named, Process Science and Engineering Program focusing on “synthesis by design” (BAT183). MERF also continued providing Ni(OH)<sub>2</sub> materials for the ReCell program participants for upcycling the spent battery cathode materials.

### Conclusions

MERF's experimental active cathode materials process R&D and scale-up program assists the battery research community, allows for a comprehensive evaluation of new materials by industrial laboratories, and supports basic research. In fiscal year 2023 the program provided several new and/or reproduced, not commercially available materials. Samples of uniform, high-quality materials were distributed for further evaluation and research. Different cathode active material compositions have been synthesized using 1L TVR, and some of the material with higher quantity demand were scaled up in 10L TVR. Scalability of TVR technology was also studied for faster reaction with substantially reduced residence time. All the materials produced at MERF were shared with the collaborators either in the form of precursor or active cathode material, ranging from 100 to 1,000 g per sample.

### Key Publications

1. Jihyeon Gim, Jinhyup Han, Ozgenur Kahvecioglu, Peng Zuo, Liafeng, Zou, Fulya Dogan, Anil Mani, et.al. “Performance Optimization of High Ni (>90%) Cathode Materials: Synthesis & Modification.” Presentation, 242nd Electrochemical Society Meeting, October 9-13, 2022.
2. Gregory Krumdick, Kris Pupek, Ozgenur Kahvecioglu, Trevor Dzwiniel, Youngho Shin, and Joseph Libera, “Accelerating Complex Battery Materials to Market: Leveraging Science to De-risk Technology Scale-up and Accelerate Commercialization.” Poster Presentation, 13th International Conference on Advanced Lithium Batteries for Automobile Applications, Ben Guerir, Morocco, October 17, 2022.
3. Feng Wang, Pallab Barai, Ozge Kahvecioglu, Krzysztof Z. Pupek, Jianming Bai, and Venkat Srinivasan, “Process Design for Calcination of Nickel-Based Cathode Materials by In Situ Characterization and Multiscale Modelling”, *Journal of Materials Research* 37, October 14, 2022: 3197-3215
4. Seoung-Bum Son, Zhengcheng Zhang, Jihyeon Gim, Christopher S. Johnson, Yifen Tsai, Michael Kalensky, Susan Lopykinski, Ozgenur Kahvecioglu, Zhenzhen Yang, Anthony T. Montoya, Ira Bloom, “Transition Metal Dissolution in Lithium-ion Cells: A Piece of the Puzzle.” *Journal of Physical Chemistry C*, 127 (4). January 19, 2023: 1767-1775.
5. Bingning Wang, Jihyeon Gim, Seoung-Bum Son, Ilya A Shkrob, Daniel P Abraham, Stephen E Trask, Yang Qin, Ozge Kahvecioglu, Andrew N Jansen, Chen Liao, “Electrolyte Study for High Nickel LiNi<sub>0.9</sub>Mn<sub>0.05</sub>Co<sub>0.05</sub>O<sub>2</sub> Cathodes.” *Journal of the Electrochemical Society*, 170 (2) February 2, 2023: 020505.
6. Feng Wang, Pallab Barai, Ozge Kahvecioglu, Krzysztof Z. Pupek, Jianming Bai, and Venkat Srinivasan, “Tackle Engineering Challenges in Battery Manufacturing by Multiscale-correlated Experimentation and Modelling.” Poster Presentation, International Battery Association Conference, March 5-10, 2023.
7. Norman S Luu, Patricia E Meza, Andre M Tayamen, Ozgenur Kahvecioglu, Sonal V Rangnekar, Janan Hui, Julia R Downing, Mark C Hersam, “Enabling Ambient Stability of LiNiO<sub>2</sub> Lithium-ion Battery Cathode Materials via Graphene-Cellulose Composite Coatings.” *Chemistry of Materials*, 35 (13) June 22, 2023: 5150-5159.
8. Ozgenur Kahvecioglu, “Emerging Technology for Producing High Energy Density Cathode Active Materials.” Invited Presentation, The Center for Research in Extreme Batteries 14th Bi-annual Meeting, June 23, 2023.

## **Acknowledgements**

Continuous support from Haiyan Croft of the U.S. Department of Energy's Office of Vehicle Technologies is gratefully acknowledged. Dr. Carrie Siu, Dr. Mateusz Zuba, Francis Kim, Gerald Jeka, Andrew Turczynski, and Dr. Kris Puppek are greatly acknowledged for their assistance in the synthesis and characterization studies. Participants of previous Low/No Cobalt Deep-Dive program and current EaCAM and DRX + Consortiums and all our collaborators funded by VTO and AMMTO that are using MERF-made materials are acknowledged for their continuous feedback on the TVR-made materials.

## II.2 Novel Processing Approaches for LLZO (ANL)

### Joseph Libera, Principal Investigator

Argonne National Laboratory  
9700 South Cass Avenue  
Lemont, IL 60439  
E-mail: [jlibera@anl.gov](mailto:jlibera@anl.gov)

### Haiyan Croft, DOE Technology Development Manager

U.S. Department of Energy  
E-mail: [Haiyan.Croft@ee.doe.gov](mailto:Haiyan.Croft@ee.doe.gov)

Start Date: October 1, 2022	End Date: September 30, 2023	
Project Funding (FY23): \$400,000	DOE share: \$400,000	Non-DOE share: \$0

### Project Introduction

Aerosol manufacturing technology holds the potential of commodity scale production of energy storage materials in powder form. Reduced liquid chemical waste and suitability for continuous operation are advantages of aerosol processing has competing liquid based synthesis. Aerosol synthesis of powders falls broadly into several categories: (a) spray drying, (b) spray pyrolysis, (c) flame spray pyrolysis and (d) gas combustion synthesis where (a)-(c) are droplet based and (d) is gas phase entirely. At the Argonne's MERF aerosol synthesis facility modalities (a)-(c) are pursued for materials research into energy storage materials.

Flame spray pyrolysis (FSP) is a materials synthesis technique that uses solutions of organic and/or inorganic metal salts in flammable liquids. In the gas-to-particle mode (FSP-GP), the liquid solution is atomized using oxygen and combusted to atomic species from which particles condense and are collected in the exhaust filters. If the available combustion enthalpy is insufficient, particle formation follows the droplet-to-particle modality (FSP-DP) and the produced solids retain some history of the spray droplets.

Spray pyrolysis (SP) starts as in FSP by producing liquid droplets of metal salt solutions but not using combustible solvents. Droplet solvent is removed by evaporation in a tube furnace followed by solid-state reaction of the dried particle to produce the desired solid materials. Optional addition of enthalpic components such as ethylene glycol or organic acids allows for exothermic support of the solid-state reactions.

In Spray Drying (SD) the drying of the droplets and subsequent solid-state reactions that characterize Spray Pyrolysis are decoupled and only the dried particles are collected to be separately solid state reacted in calcination furnaces. This technique allows for the exclusion of the spray solvent and/or combustion gases in the calcination step and enable controlled atmosphere calcination such as inert gas or pure oxygen.

At Argonne's MERF facility, we use these three modalities synergistically to produce the same target material and thus gain greater understanding of the material apart from the process. In, general FSP-GP produces nano-sized powder, while FSP-DP produces micron-sized agglomerates of nano-sized primary particles. SP produces micron sized secondary particles consisting of sub-micron primary particles. SD produces micron particles of the constituent metal salts which following a separate calcination retain their particle characteristics. For the FSP and SP techniques, we seek to optimize the process to produce ready to use particles in the proper phase purity. However, the gaseous environment in the processing reactors requiring separate calcination and or powder refinement can thermodynamically prohibit this. In the industrial setting even these additional steps are amenable to continuous processing following continuous aerosol powder production.

## Objectives

Develop Aerosol Manufacturing Technology as a manufacturing option for Li-ion battery active cathode phase and for solid electrolyte powder for use in conventional and solid state Li-ion batteries for the automotive sector. Obtain economically competitive protocols and recipes using the lowest cost precursor and solvent options. Produce optimized LLZO for separator and catholyte applications. Leverage the advantages of the atomically mixed nano-powder produced by FSP to access otherwise difficult to produce materials.

## Approach

Solid-state electrolyte (a) garnets such as aluminum doped lithium lanthanum zirconium oxide Al-LLZO and energy storage materials (b) high Ni cathode active phases are the focus of development using multiple aerosol technologies. Aerosol synthesis is co-optimized with downstream calcination, powder refinement, and validation in battery test cells. The research focuses on the lowest cost precursors available in commodity scales, typically nitrates salts of the metals. Advanced concepts are explored that utilize unique powder morphology and phases accessible only by aerosol processing.

The ANL MERF FSP reactor has features that allow for convenient and high throughput sample production. A glovebox design filter box allows for collection of nanomaterials and restoration of the filter media within 15 minutes of a run completion allowing for up to 6 generated and collected samples per workday. Material that deposits on the walls of the reactor does not significantly cross-contaminate from sample to sample. On a day to day basis, a clean-in-place brushing fixture allows for the combustion tube to be cleaned of wall deposits for changeover to new material systems further assuring no cross contamination between runs. This year, a scale up by 10x was facilitated by the addition of a baghouse to enable a nominal production rate of 500 g/hour.

The ANL FSP facility has been designed to produce powder materials in an industrially relevant way using liquid spray (droplet) combustion, which can produce materials at the highest possible rate compared to ultrasonic atomization or gas-fed precursor introduction. In order to best navigate the complexities of spray combustion, the ANL FSP facility has a suite of in-situ advanced diagnostics. These include (a) laser diagnostic system for Filtered Rayleigh Scattering (FRS) and Planar Laser Induced Fluorescence (PLIF) imaging of temperature and species distribution respectively, (b) Optical Emission Spectroscopy (OES) of the flame zone, (c) In-situ Raman spectroscopy and (d) particle size analysis using Scanning Mobility Particle Sizing (SMPS). Ex-situ diagnostics are also applied including (a) XRD and temperature programmed XRD, (b) BET-SA, (c) DSC-IR/MS, (d) electrochemical testing and electron microscopy (SEM and TEM).

Several years of research at ANL has exposed two major challenges in producing some Li-containing metal oxides directly in one-step. (a) While the obtained green powders can be successfully calcined into the target layered phase, as the formulations tend toward high-Ni, sintering behavior becomes predominant and complete loss of green powder particle morphology occurs necessitating post-processing, erasing much of the advantage of aerosol synthesis. (b) Direct conversion to the target phase is in competition with the impurity phases  $\text{Li}_2\text{CO}_3$  and  $\text{LiOH}$ , which readily occur in SP or FSP, but become greater challenges in high-Ni target formulations. In order overcome these challenges, a new overall processing scheme is proposed where some or all of the calcination is performed in the aerosol phase while retaining the principle advantages of continuous processing and short overall processing time. The scheme is shown schematically in Figure II.2.1. Baghouse separation is an inexpensive and in mature industrial technology. In the first baghouse, we are essentially performing a gas/solid separation where the solid is fed continuously to the next step of dry aerosol calcination with a new gas stream more amenable to the target phase formation. This process of gas/solid separation can be repeated gain if necessary depending on the sensitivity of the phase formation to the activities of the outgas products such as  $\text{H}_2\text{O}$  and/or  $\text{CO}_2$ .



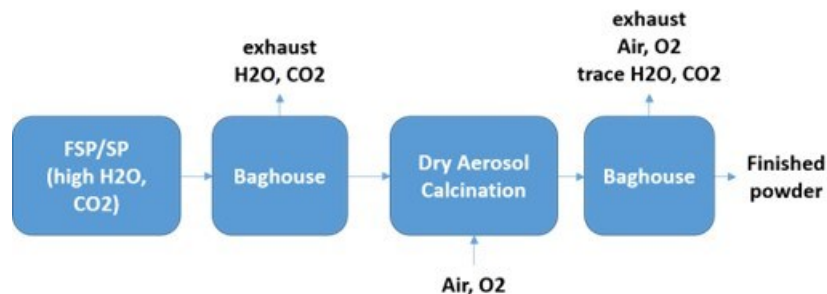


Figure II.2.1 Particle Production with Dry Aerosol Calcination Concept.

## Results

### Identifying the need for DAC

There appears to be direct relationship between the lithium ion conductivity of a target Li-metal oxide and the sensitivity to hydroxide/carbonate competition with the target phase. Thus, the materials LLZO and NCM9055 are not obtained in a single step using either SP or FSP given the high H<sub>2</sub>O or CO<sub>2</sub> in the synthesis environment. However, both of these materials readily form the target phases in post-calcination operations where the activity of H<sub>2</sub>O and CO<sub>2</sub> are kept low in the calcination environment. However, both of these materials also exhibit extensive sintering that seems to be related the fluxing by unreacted lithium carbonate when T>700 deg C. This sintering necessitates milling and sieving to produce powders meeting application specifications. With both LLZO and NCM9055, milling operations produce a large fraction of undesirable fines and an overall surface area >2 m<sup>2</sup>/g. For both of these materials, their very high moisture sensitivity makes this very problematic. However, for NCM9055, we found that very long calcination times including a slow ramp from 525 to 725 deg. C avoided sintering altogether and preserved the starting particle morphology. It is worth noting that the reason for needing very high temperature for NCM9055 is the relatively high amount of rock salt structure in green powders formed in SP and FSP processing. Conversion of rock salt to layered-phase is kinetically difficult so higher temperatures or longer time is required. So in order to avoid long calcination times it is important to react the majority of carbonate in a contact-less sintering environment such as provided by dry aerosol calcination.

### Dry Aerosol Calcination:

Dry aerosol calcination (DAC) requires powder to be entrained/fluidized in a carrier gas and transported through a calcination furnace. While many technologies exist at large scale, a convenient research unit in the form a venturi-type entrainment aerosolizer was deployed in the ANL FSP system. The TOPAS SAG410 unit was adapted to the FSP by substituting for the burner assembly and otherwise maintaining the closed system gas control and furnace arrangement. The unit is capable processing 2-325 g powder/m<sup>3</sup> of gas. In general, DAC is able to process ~10x more powder mass/unit gas volume than either the SP or FSP synthesis steps so that the calcination DAC equipment required in a production setting will be able to service multiple synthesis units. For evaluating the feasibility, DAC at the ANL facility is performed by batch-wise processing of previously generated powder by SP or FSP. An example of DAC performance is shown in Figure II.2.2. Green powder with an NCA target composition generated in the SP system was used to compare DAC with typical muffle furnace calcination protocol. The muffle furnace calcination consisted of 12 hours calcination at 650 deg C. Surface area measurements were performed to reveal the degree of sintering where the green powder surface area was SA=6.3m<sup>2</sup>/g. From Figure II.2.2 we see that one pass of the powder using DAC at 850 or 950 deg C reduced the surface area of the powder to less than 12 hours at 650 deg. C in the muffle furnace. This example demonstrates the equivalence of very short time DAC calcination with long duration muffle furnace treatment. Importantly, the green powder particle morphology is preserved using DAC even at 950 deg C whereas in the muffle furnace, heavy sintering occurs for T>700 C.

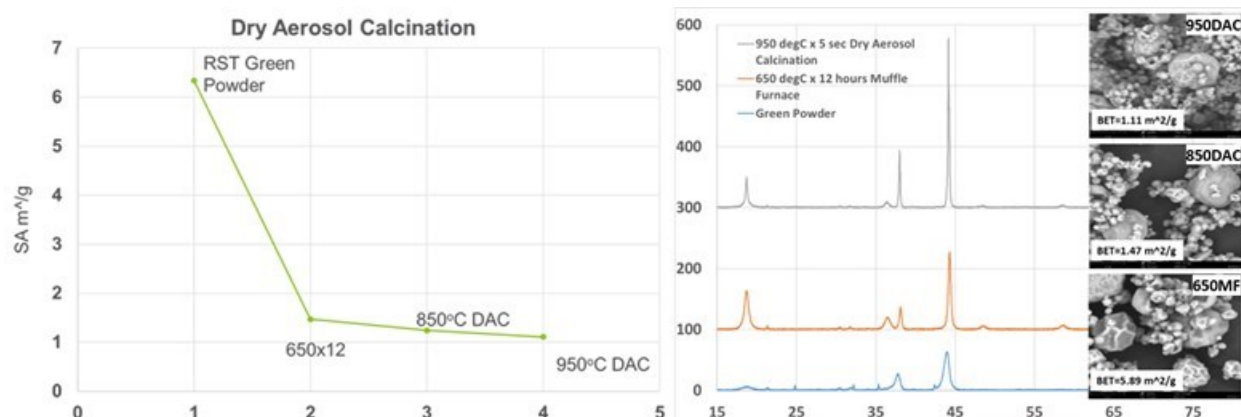


Figure II.2.2 DAC trials using NCA green powder.

### LNO Synthesis using Spray Pyrolysis

Mg- and AL-doped LNO was synthesized by SP using aqueous nitrate solutions. All atoms Li, Al or Mg and Ni were present in the starting spray solution so that the green powder was obtained in one simple step. Calcination followed the protocol described above for NCM9055, which preserves the starting particle morphology. The quality of the layered phase was evaluated using the ratio of the [003] and [104] XRD reflections. This ratio was optimized at 730 deg C calcination temperature. Samples of Al- and Mg-doped LNO calcined at 700 or 730 deg C were used to make half-cells for electrochemical evaluation. Although the 730 samples provided a better ratio, the 700 deg C samples showed better initial capacity and retention than the 730 deg C samples. (Figure II.2.3)

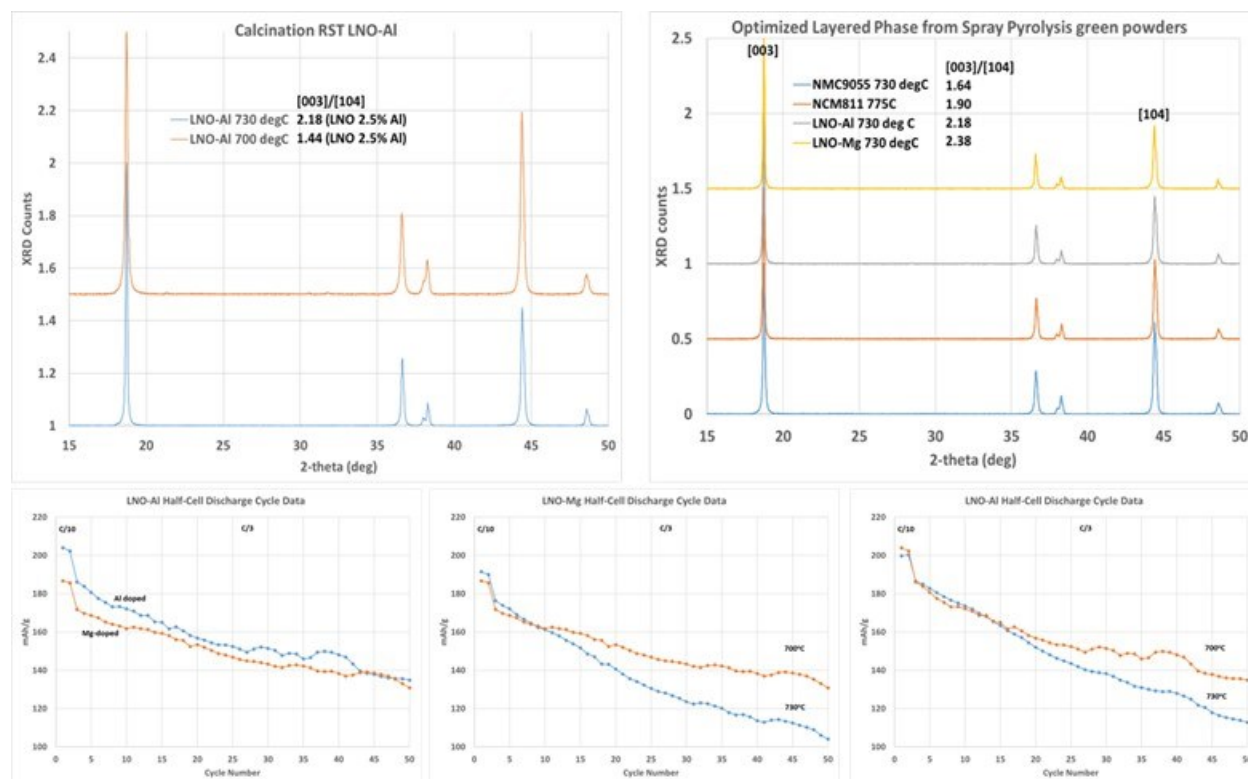


Figure II.2.3 SP synthesis of AL- and Mg-doped LNO.

### Scale-Up of Flame Spray Pyrolysis

The original design of the ANL FSP unit was for a 1x production rate of nominally 50g/hour which is limited by the collection rate capability and exhaust handling blower. However, the current burner can accommodate a 10x production rate and collection at 10x can be accomplished by the addition of a baghouse. A unit was purchased and installed into a support frame that includes engineering control enclosures for the maintenance of the unit and collection of the generated nanopowders. It was desired to maintain the lower 1x original production rate while allowing for configurability to accommodate 10x production for short periods when larger samples are requested and to test the sensitivity of material properties to production rate. In order to allow for both scenarios, a rework of the exhaust handling strategies for the two configurations was made that allows for switching between the two in 1-2 days. Figure II.2.4 shows the configuration for 10x production.



Figure II.2.4 FSP configuration for 500 g/hour production.

### COVID-19 Impact:

Impact of the covid-19 pandemic was limited to delivery of the baghouse unit which was delayed by 6 months by backorders following emergence from covid-19 restrictions by the manufacturer. Commissioning of the scaled FSP system was planned for FY22 but has been delayed to FY23.

### Conclusions

A limitation of Spray Pyrolysis and Flame Spray Pyrolysis that prevents direct synthesis of certain important Li-containing phases was identified. A potential solution to this limitation is Dry Aerosol Calcination that can be used as a continuous post-synthesis processing step, which preserves the important feature of continuous production in aerosol technology. A aerosolizer unit was purchased and retrofitted to the existing FSP processing unit that allows for the evaluation of the DAC concept for materials produced in either the SP or FSP synthesis units. These evaluation data will determine the feasibility of continuous powder production with the desired target phase properties. The concept was demonstrated for NCA and showed that despite the very short residence time, an equivalent outcome to that of long duration muffle furnace calcination is possible. Mg- and Al-doped Lithium nickel oxide cathode was synthesized by Spray Pyrolysis. FSP production at 500 g/hour was enabled by the addition of a baghouse to the ANL FSP facility.

### Key Publications

1. Formation of lithium-metal-oxygen layer and removal of lithium carbonate on solid state electrolytes, K Donghyeon, JW Elam, JA Libera, Y Liang, KIM HackSung, AU Mane, US Patent App. 17/207,445.
2. Solvent-free processing of lithium lanthanum zirconium oxide coated-cathodes, JL Durham, JA Libera, AL Lipson, Y Liang, US Patent App. 16/938,037.
3. Cathode materials for use in lithium cells and batteries, MM Thackeray, E Lee, JA Libera, KU Kyojin, US Patent App. 17/351,944
4. Understanding the constant-voltage fast-charging process using a high-rate Ni-rich cathode material for lithium-ion batteries, K Ku, SB Son, J Gim, J Park, Y Liang, A Stark, E Lee, J Libera, Journal of Materials Chemistry A 10 (1), 288-295.

5. Investigating the Calcination and Sintering of  $\text{Li}_7\text{La}_3\text{Zr}_2\text{O}_{12}$  (LLZO) Solid Electrolytes Using Operando Synchrotron X-ray Characterization and Mesoscale Modeling, P Barai, T Fister, Y Liang, J Libera, M Wolfman, X Wang, J Garcia, Hakim Iddir, and Venkat Srinivasan, Chemistry of Materials 33 (12), 4337-4352.

### **Acknowledgements**

We greatly acknowledge the long-term support and vision provided by Peter Faguy. The authors greatly acknowledge the continuing collaboration and advice from Toivo Kodas and Cabot Corporation. We also acknowledge the contributions to this research by E.J. Lee. We greatly acknowledge the expertise of Hack-Sung Kim in the development of the custom Raman spectrometer. We also acknowledge the Manufacturing Science and Engineering Initiative at ANL for providing support for the advanced diagnostics for the FSP unit.

## II.3 Supercritical Fluid Processing of Battery Cathode Materials (ANL)

### Youngho Shin, Principal Investigator

Argonne National Laboratory  
9700 South Cass Avenue  
Lemont, IL 60439  
E-mail: [yshin@anl.gov](mailto:yshin@anl.gov)

### Haiyan Croft, DOE Technology Development Manager

U.S. Department of Energy  
E-mail: [Haiyan.Croft@ee.doe.gov](mailto:Haiyan.Croft@ee.doe.gov)

Start Date: October 1, 2022

End Date: September 30, 2023

Project Funding (FY23): \$775,000

DOE share: \$775,000

Non-DOE share: \$0

### Project Introduction

The development of advanced, rapid, reproducible manufacturing processes for cathode materials is essential for improving performance, increasing lifespan, ensuring safety, and reducing the prices of lithium-ion batteries. Polycrystalline cathode particles currently used in lithium-ion batteries, produced via conventional co-precipitation process, are intrinsically vulnerable to grain-boundary fracture (by the anisotropic volume change during lithium extraction/insertion) inside particles that lead to rapid impedance growth and capacity decay. The development of innovative manufacturing processes to overcome the inherent limitations of these polycrystalline cathode particles is required. An emerging supercritical fluids technology, under process development and scale-up as one of the main goals of this program, can provide advanced cathode materials with high electrode density due to a robust single-crystal particle structure without internal void fraction, improved rate capability due to submicron particle size, cycling stability due to suppressed particle crack and resistance layer, and facet-controlled particle morphology, thus enabling consequent mass production of high-performance battery cathode materials. These material properties result from a higher degree of supersaturation and the instant formation of single-crystal oxide particles because of the dramatically reduced solubility of metal ions under supercritical hydrothermal reaction conditions. The supercritical hydrothermal reaction is a practical and scalable synthesis process for producing single-crystal cathode materials mitigating the intrinsic structural problems of conventional polycrystalline cathode materials.

### Objectives

The aim of the project is to establish a flexible R&D capability of supercritical fluid reaction as an emerging manufacturing process for active battery materials. This process is one of the emerging manufacturing technologies with the goal of reducing the risks associated with the discovery of advanced active battery materials, market evaluation of these materials, and their commercialization with mass production. The production and delivery of advanced single-crystal battery materials with the desired particle size, composition distribution, and shape are also essential roles of this program to support fundamental research groups. We perform systematic engineering research to develop a cost-effective supercritical fluids process and to produce sufficient quantities of target materials with high quality by optimizing the synthesis parameters and material composition. These advanced battery materials, which are not yet commercially available and not achievable by traditional co-precipitation techniques, are produced and distributed to research groups and industrial partners to get their feedback to further optimize the synthesis process. Our effort deepens fundamental understandings of the structure-property relationship of battery cathode materials and ultimately can contribute to selecting the customized material composition before the material would be deemed suitable and desirable for large-scale manufacturing.

## Approach

Single-crystal cathode particles mitigating rapid impedance growth and capacity decay (these are typical drawbacks of current polycrystalline cathode particles due to the intergranular fracture during cycling) are developed and produced. The morphology of single-crystal cathode particles can be customized by changing reactants, solvents, reaction pressure, and reaction temperature of the hydrothermal process. The advanced single-crystal active battery materials with tunable particle size, morphology, and composition distribution are synthesized by the installed batch supercritical hydrothermal reaction system. To move toward mass production of single-crystal materials, a pre-pilot scale continuous supercritical hydrothermal system is installed enabling process commercialization. The synthesis condition is optimized and then customized material is produced in quantities suitable for distribution for a comprehensive investigation. The mechanical and electrochemical characterization of the produced cathode materials is carried out in collaboration with research groups and industrial partners. The battery cathode materials selected for FY23 are single-crystal nickel-rich NMC and LFP cathode materials. In collaboration with various research groups, material characterization and electrochemical performance of the synthesized single-crystal cathode materials are performed to improve the synthesis process based on feedback.

## Results

The synthesis of single-crystal cathode materials is attracting a lot of attention to overcome the intrinsic particle crack issue during the cycling of polycrystalline cathode materials, which are currently used in most lithium-ion batteries. Three synthesis processes were set up and compared to produce single-crystal cathode materials. We used and compared (1) a conventional co-precipitation CSTR process, (2) a subcritical hydrothermal batch process, and (3) a supercritical hydrothermal continuous process. Figure II.3.1 shows the synthesis of monocrystalline NMC811 using the first (1) conventional co-precipitation CSTR process.

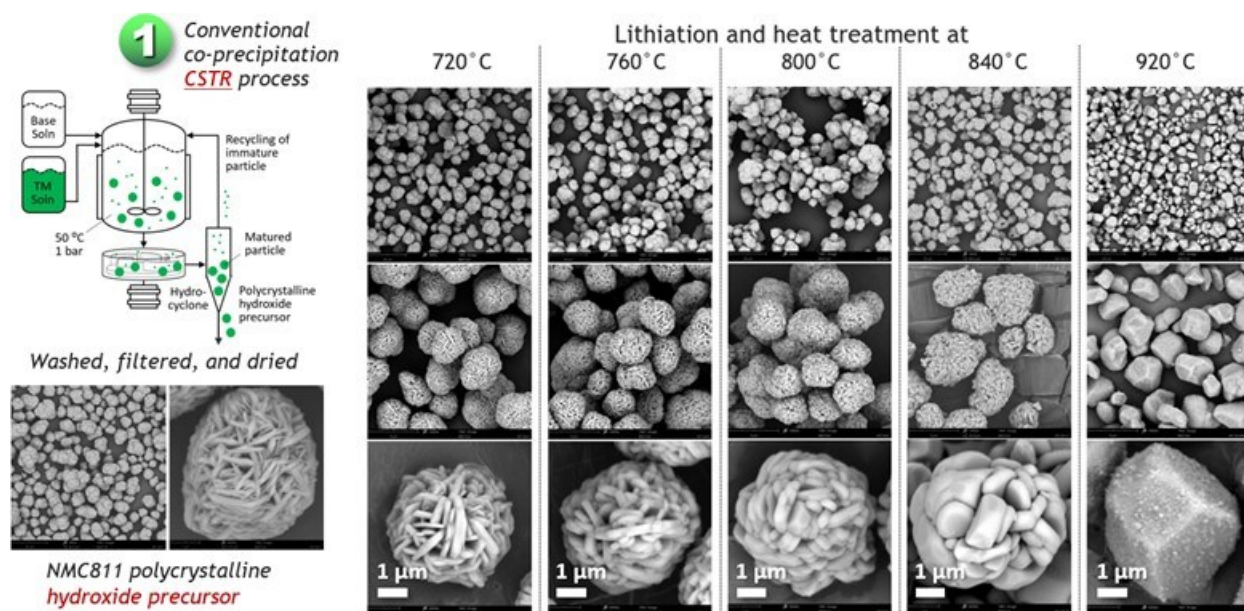


**Figure II.3.1 (Preparation of polycrystalline hydroxide precursor and monocrystalline NMC811).**

We obtained NMC811 polycrystalline hydroxide precursor, then mixed with a lithium source and heat treated at 720, 760, 800, 840, and 920 °C. As the heat treatment temperature increases, the primary particles of hydroxide precursor gradually grow and eventually convert to a monocrystalline particle at 920 °C.

We carried out a rate performance evaluation of the prepared NMC811 materials. The graph on the right of Figure II.3.2 shows that the 760 °C polycrystalline sample B has the best initial discharge capacity. However,

the normalized capacity graph on the left of Figure II.3.2 shows that the 920 °C monocrystalline sample E has a relatively better rate capability.

1 Via conventional co-precipitation CSTR process

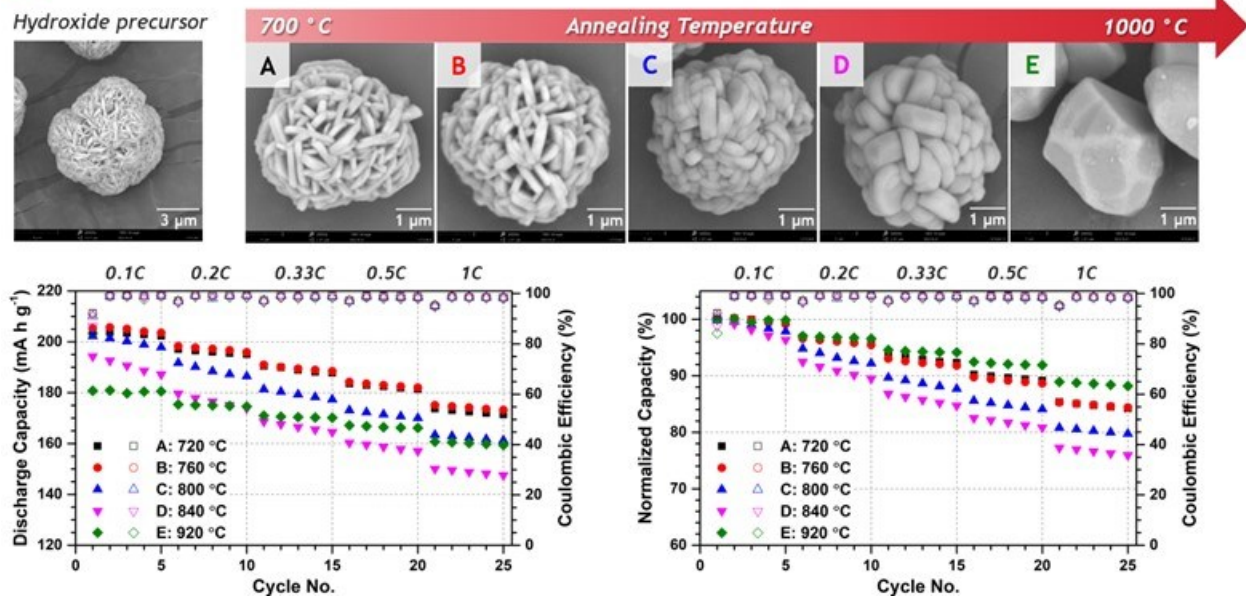


Figure II.3.2 (Rate performances of polycrystalline and monocrystalline NMC811).

1 Via conventional co-precipitation CSTR process

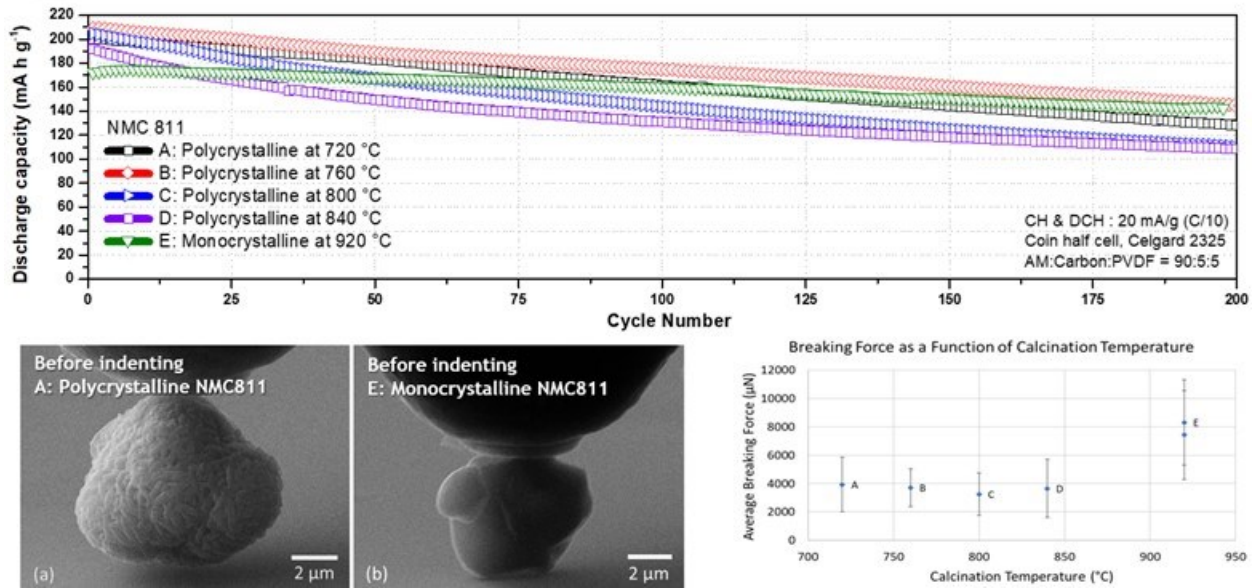


Figure II.3.3 (C/10 cycling results of polycrystalline and monocrystalline NMC811).

Figure II.3.3 is the result of the C/10 charge-discharge cycling of each sample. The 760 °C polycrystalline sample B in red has the highest initial discharge capacity of 210 mAh/g. The 920 °C monocrystalline sample E in green has the lowest initial discharge capacity of 175 mAh/g, but it has the best capacity retention and the best discharge capacity after 200 cycles. The figure below shows the nano-indentation test to measure the particle-breaking force of the prepared polycrystalline and monocrystalline NMC811 samples. Monocrystalline

particles have over twice the particle strength of polycrystalline particle. This robustness of monocrystalline material is one of the reasons that lead to better capacity retention. So, by this first (1) conventional co-precipitation CSTR process approach, we produced monocrystalline NMC811. While the capacity retention of this material is significantly improved, it suffers from excessive heat treatment costs, serious lithium loss, and deteriorated initial discharge capacity. For these reasons, we set out to develop a new synthesis process that can produce superior single-crystal materials with scalability and economic feasibility.

The second approach, shown in Figure II.3.4, uses (2) a subcritical hydrothermal batch process to make monocrystalline oxide precursors, followed by lithiation and heat treatment at 760 °C, which is a relatively low calcination temperature. The installed subcritical hydrothermal batch reactor is 4-liter in size and produces 25 to 50 grams per batch. We used this system and the prepared NMC96-2-2 oxide precursor and its cathode particle are about 3 microns in size and have a monocrystalline morphology before and after heat treatment.

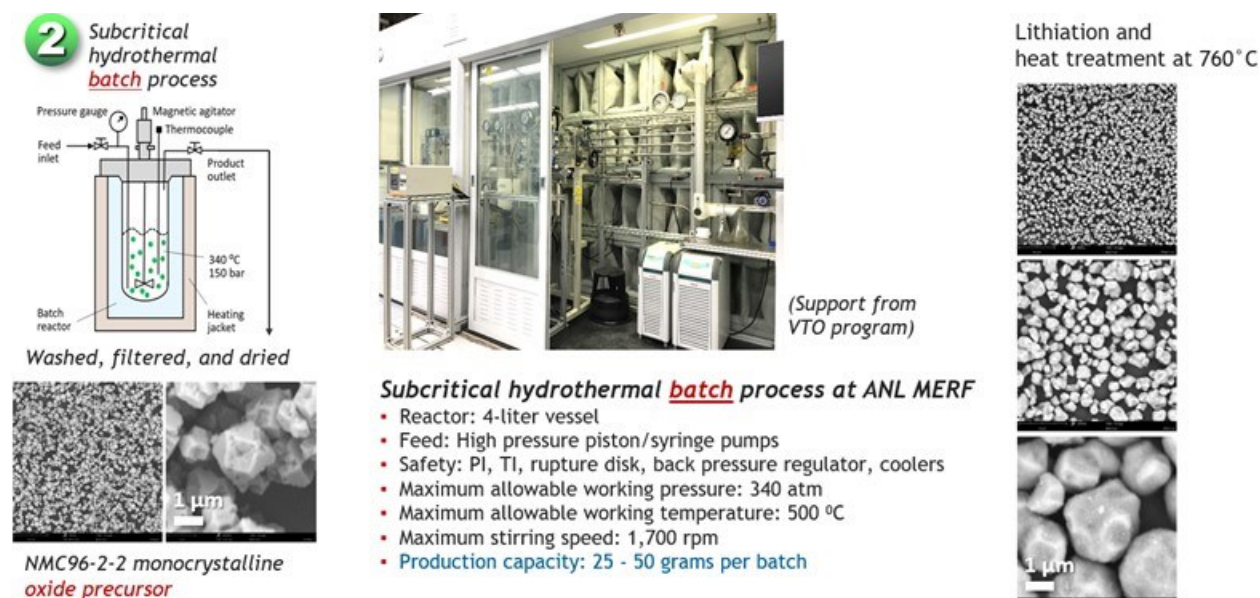
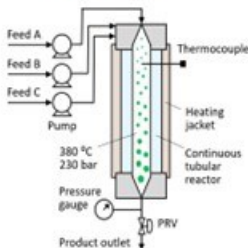


Figure II.3.4 (Preparation of monocrystalline oxide precursor and monocrystalline NMC96-2-2).

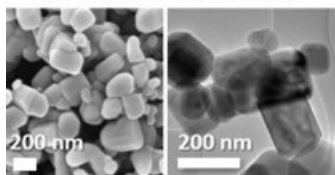
The third approach is the production of lithiated single-crystal particles using (3) a supercritical hydrothermal continuous process. This innovative process enables simultaneous single-crystal formation and lithiation under supercritical water conditions in less than 10 minutes. During this 10-minute processing, we can also have a carbon coating on the surface of the lithiated single-crystal particles. This is a rapid and economical process that eliminates several steps in the currently used cathode manufacturing process, such as grinding lithium, mixing it with precursors, and particle surface coating. And, as shown in Figure II.3.5, the installed pre-pilot-scale supercritical hydrothermal continuous system can produce 200 grams of carbon-coated lithiated single-crystal material per hour. As shown in Figure II.3.6, using the preliminarily produced carbon-coated lithiated single-crystal LFP material, we conducted heat treatment at various temperatures. Since the lithiation is completed with the single-crystal formation within 10 minutes, we applied only 1-hour heat treatment instead of the conventional 10 to 20 hours heat treatment. And, in collaboration, we are analyzing the formation of Fe<sub>2</sub>O<sub>3</sub> impurity as a function of heat treatment temperature by in-situ XRD.



**3** *Supercritical hydrothermal continuous process*



Washed, filtered, and dried



Single crystal lithiated cg-LFP precursor



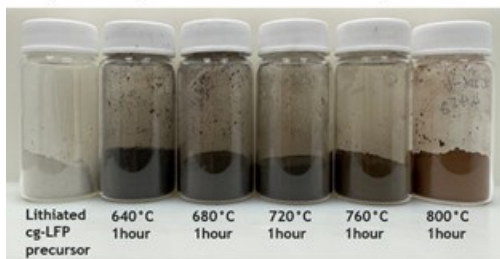
(Support from VTO and AMMTO programs)

**Pre-pilot supercritical hydrothermal continuous process at ANL MERF**

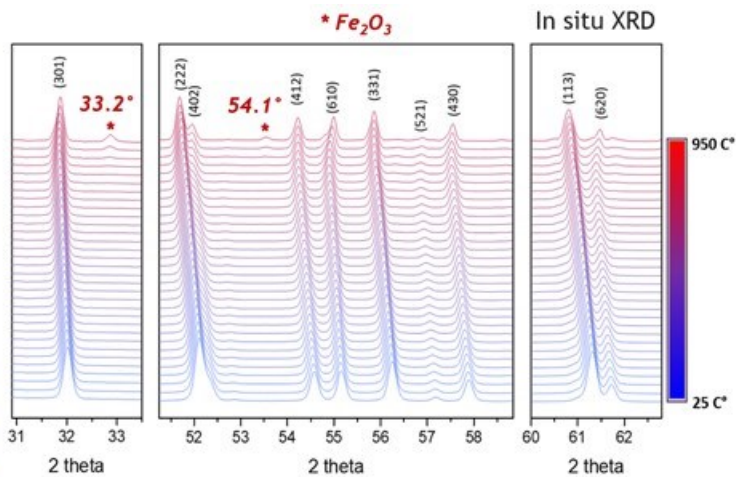
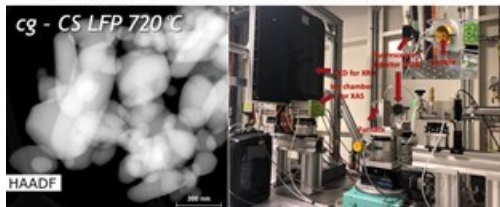
- Reactor: Tubular type
- Feed: High pressure piston pumps
- Safety: PI, TI, rupture disk, back pressure regulator, coolers
- Maximum allowable working pressure: 340 atm
- Maximum allowable working temperature: 500 °C
- Production capacity: 200 grams SC CAM per hour (2-MT/year)

Figure II.3.5 (Preparation of lithiated single crystal precursor and single crystal cg-LFP CAM).

Prepared cg-LFPs at various temperatures



Correlated in situ XRD/XAS: correlation of Fe valence states to the phase evolution during the heating



- As the annealing temperature increased, Fe<sub>2</sub>O<sub>3</sub> peaks are observed.

Figure II.3.6 (Preparation of lithiated single crystal precursor and single crystal cg-LFP CAM).

Figure II.3.7 is the result of an electrochemical performance evaluation of carbon-coated single-crystal LFP samples prepared at various temperatures. And, the carbon-coated LFP annealed at 720 °C for 1 hour shows the best initial discharge capacity of 160 mAh/g and improved rate capability. We analyzed the crystallinity and surface carbon coating of this single-crystal LFP. As shown in the EDS mapping of Figure II.3.8, the surfaces of every single-crystal LFP particle are coated with carbon. The line scan result shows a significant increase in carbon content near the surface of the particle. In the HRTEM image on the left below, it is demonstrated how uniform and dense this carbon coating is.

This carbon layer can be controlled from 1 nanometer to tens of nanometers in thickness, and it completely covers the surface of each particle. And we confirmed that there are nanoscale distorted graphene fragments distributed in the amorphous carbon layer. We named this carbon graphene coated LFP (cg-LFP). This new carbon coating technology, which co-occurs with the formation of lithiated single-crystal particles, reduces carbon content for practical cathode electrode, increases electronic conductivity, and protects cathode particle surface.

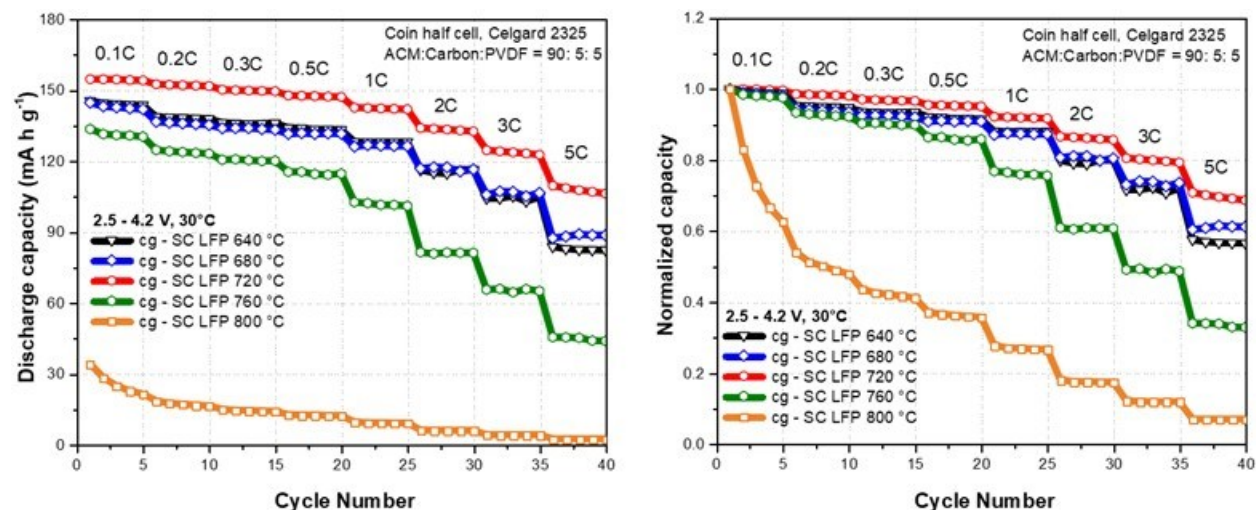
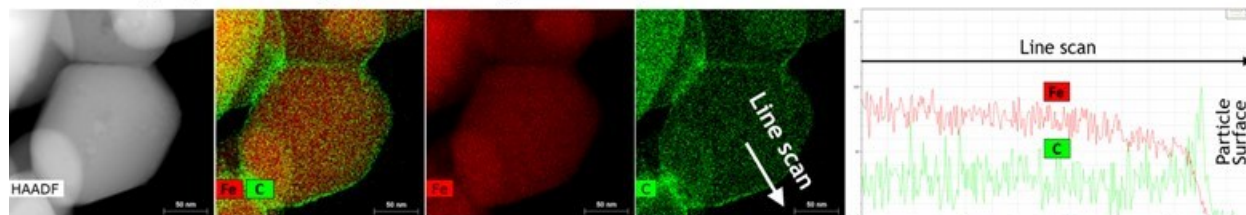


Figure II.3.7 (Capacity and rate capability results of cg-LFP).

#### EDS mapping of carbon-graphene coating on LiFePO<sub>4</sub>



#### HRTEM of carbon-graphene coating on LiFePO<sub>4</sub>

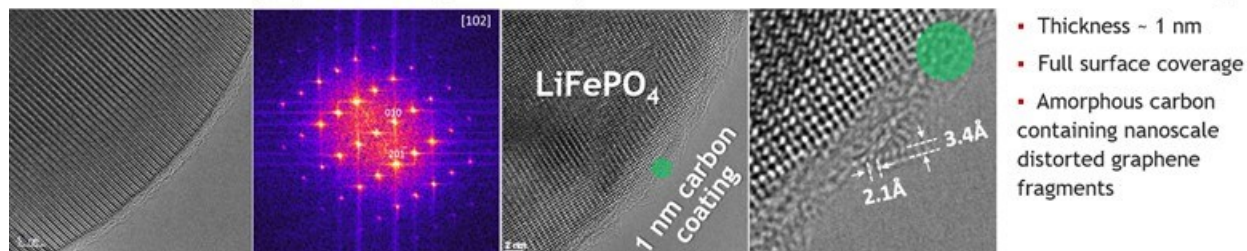


Figure II.3.8 (Synthesis of nano-sized carbon-layered single-crystal LFP cathode).

We have synthesized so-called single-crystal particles using three different synthesis processes. NMC811 by (1) conventional co-precipitation CSTR process, NMC96-2-2 by (2) subcritical hydrothermal batch process, and cg-LFP by (3) supercritical hydrothermal continuous process. To investigate whether these materials are truly single-crystals, we performed BCDI analysis as shown in Figure II.3.9. This BCDI analysis images the internal structure of crystalline material. It reveals defects, dislocations, and vacancies in particles. Therefore, the particles with the nasty structure produced by the first and second processes appear to be monocrystalline

particle rather than single-crystal particle. On the other hand, cg-LFP, produced by the supercritical hydrothermal continuous process, is close to a perfect single-crystal particle.

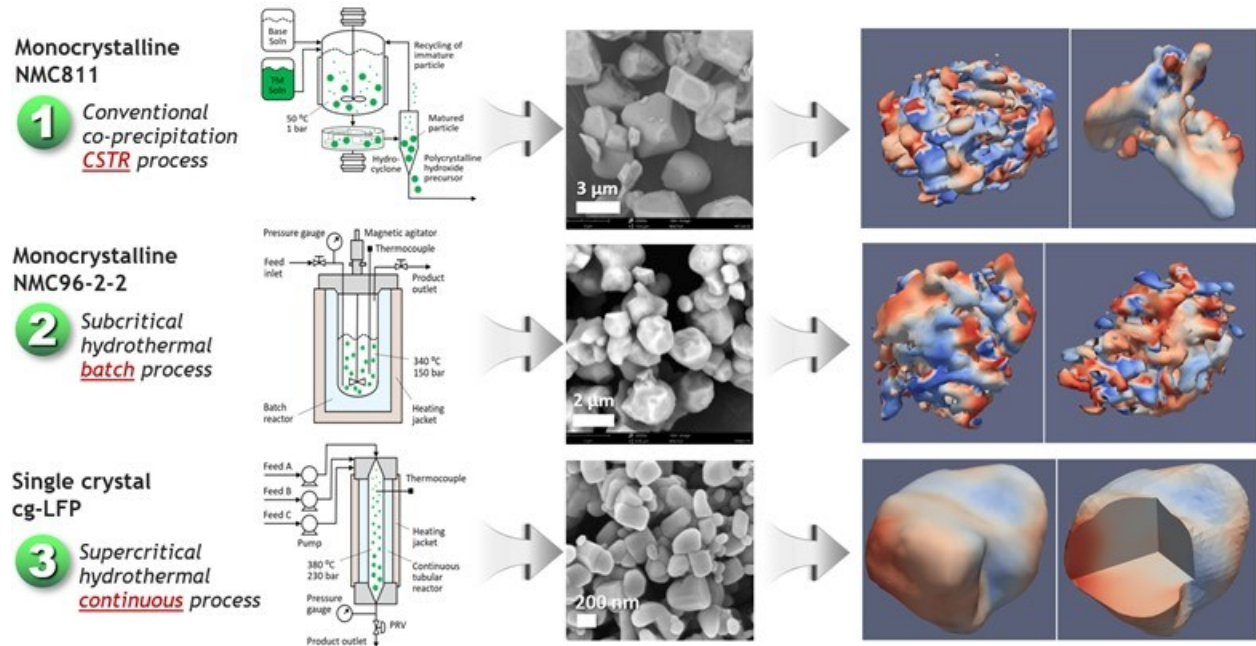


Figure II.3.9 (Bragg coherent X-ray diffraction imaging of CAMs from 3 synthesis processes).

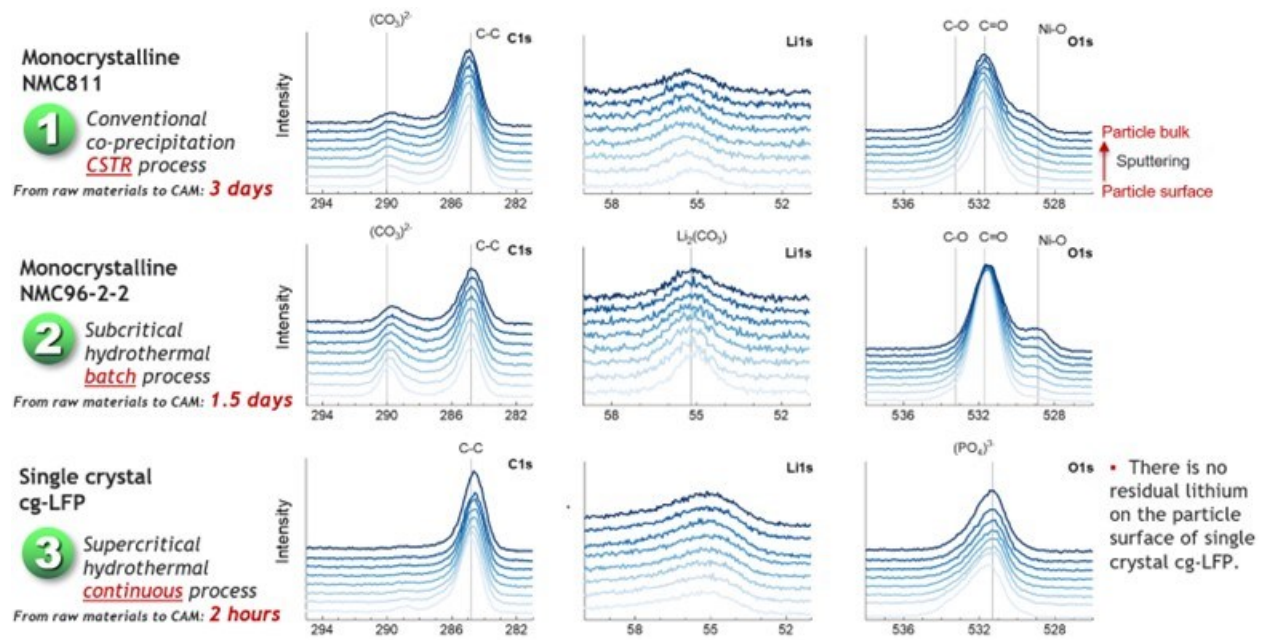


Figure II.3.10 (XPS results of CAMs from 3 synthesis processes).

The first conventional co-precipitation process takes 3 days from feed chemicals to the final cathode particles, while the second subcritical hydrothermal batch process takes a day and a half. On the other hand, the developed supercritical hydrothermal continuous process takes just two hours from feed chemicals to the final single-crystal cathode material. And this advanced synthesis process has one more unique material feature

which is no residual lithium on the particle surface. To check the residual lithium on the particle surface, XPS analysis was performed on the three samples while sputtering (Figure II.3.10). In the three graphs in the first column, both the first and second synthesis processes leave lithium carbonate on the surface of the final cathode particles. However, there is no residual lithium on the particle surface of single crystal LFP, which mitigates side reactions with electrolytes and enables a longer cycle life of batteries. During this third synthesis process, the residual lithium on the particle surface is automatically removed by contact with the cooled reaction media water. Therefore, we do not need the cathode washing step and 2nd heat treatment of the conventional NMC synthesis process.

## Conclusions

A pre-pilot-scale continuous-flow supercritical hydrothermal platform process was developed and installed with partial support from this program. This process enables the production of true single-crystal battery materials, with robust structures withstanding particle cracks, a significant increase of surface coating effect due to the non-porous particle structure, and no residual lithium on the cathode particle surface. In terms of process innovation, this process has one-step formation of single-crystal particles with carbon-graphene nano surface coating, simultaneous/uniform lithiation during the formation of single-crystal particles, short heat treatment, no troublesome lithium grinding/mixing, no cathode washing, and no re-calcination process. This innovative process enables rapid manufacturing from feed chemicals to final single-crystal cathode materials within 2 hours. This continuous supercritical hydrothermal process is a material synthesis platform that is able to produce single-crystal cathode materials with a solid structure and unique mechanical/electrochemical properties. We will continue the maturation of this advanced continuous supercritical hydrothermal process, process scale-up, and production of high-performance single-crystal battery materials to support fundamental research groups and industry partners.

## Key Publications

1. 3D Quantification of Elemental Gradients within Heterostructured Particles of Battery Cathodes, E. Allen, Y. Shin, W. Judge, M. Wolfman, V.D. Andrade, S.M. Cologna, J. Cabana, ACS Energy Lett., 8, 3, 1371–1378 (2023)
2. Synthesis of Platinum Nanoparticles on Strontium Titanate Nanocuboids via Surface Organometallic Grafting for the Catalytic Hydrogenolysis of Plastic Waste, K.E. McCullough, I.L. Peczak, R. Kennedy, Y.-Y. Wang, J. Lin, X. Wu, A.L. Paterson, F. Perras, J. Hall, A.J. Kropf, R.A. Hackler, Y. Shin, J. Niklas, O.G. Poluektov, J. Wen, W. Huang, A. Sadow, K.R. Poeppelmeier, M. Delferro, M.S. Ferrandon, J. Mater. Chem. A, 11, 1216-1231 (2023)
3. Resolution-enhanced X-ray Fluorescence Microscopy via Deep Residual Networks, L. Wu, S. Bak, Y. Shin, Y.S. Chu, S. Yoo, I.K. Robinson, X. Huang, npj Computational Materials 43 (2023)

## Patent and Invention Disclosures

1. Patent filed - Invention disclosure ANL-IN-22-043: METHOD FOR CARBON-LAYERED GRAIN-FREE SINGLE-CRYSTAL CATHODE PARTICLE AND PARTICLE PREPARED BY THE SAME

## Acknowledgements

We gratefully acknowledge the collaboration with Dr. Seoung-Bum Son (Argonne Post-Test Facility), Dr. Feng Wang (Argonne AMD), Dr. Donghyeon Kang (Argonne AMD), and Dr. Wonsuk Cha (Argonne APS) and Prof. Sangkee Min (University of Wisconsin-Madison).

## II.4 Process R&D and Scale-up of Critical Battery Materials (ANL)

### **Trevor Dzwiniel, Principal Investigator**

Argonne National Laboratory  
9700 South Cass Avenue  
Lemont, IL 60439  
E-mail: [tdzwiniel@anl.gov](mailto:tdzwiniel@anl.gov)

### **Haiyan Croft, DOE Technology Development Manager**

U.S. Department of Energy  
E-mail: [Haiyan.Croft@ee.doe.gov](mailto:Haiyan.Croft@ee.doe.gov)

Start Date: October 1, 2022	End Date: September 30, 2022	
Project Funding (FY23): \$1,200,000	DOE share: \$1,200,000	Non-DOE share: \$0

### **Project Introduction**

New experimental materials are constantly invented to improve the safety, energy density, cycle life, and calendar life of lithium ion batteries for EV. These materials are typically synthesized in discovery laboratories in small batches providing amounts sufficient only for limited basic evaluation but not in quantities required for full scale validation and prototyping. In addition, bench-scale processes are often un-optimized, not validated, and generate materials with inconsistent purity and yield. This project aims to assist the advanced battery research community by enabling access to larger quantities of high-quality innovative materials.

New electrolyte formulations and new electrolyte materials will be required for recently emphasized cathode materials based on earth abundant elements (Mn-rich layered oxides and disordered rock salts). We are using continuous flow reaction technology to speed up process optimization and lower production cost that allows for faster production and easier scale up.

### **Objectives**

The objective of this project is to conduct research toward scaling up production of advanced materials for Li-ion batteries originally created in small quantities by discovery scientists at various research organizations. Scaling up the original route used by discovery scientists often requires an extensive modification of the bench-scale chemistry and systematic, science-based process research and development to allow for 1) safe and cost effective production, 2) development of an engineering flow diagram, 3) design of a mini-scale system layout, 4) construction of the experimental system, and 5) validation of the optimized process, all of which are needed for full industrial implementation. The experimental system will be assembled, and the materials will be manufactured in quantities sufficient for full scale industrial evaluation and to support further research. The materials produced by the program will be fully characterized to confirm chemical identity and purity. Analytical methods will be developed for quality control. The electrochemical performance of the materials will be validated to confirm that these properties match the original data generated by the discovery scientist. Sample of the materials produced by the project will be available to the advanced lithium-ion battery research community to support basic development and large scale performance validation.

### **Approach**

New materials for experimental electrolyte formulations often have complex molecular structure that translates frequently into increased synthesis difficulties and cost. Argonne's Applied Materials Division's Process R&D group, operated in the newly expanded Materials Engineering Research Facility (MERF) is evaluating emerging production technologies to address the challenges. A comprehensive, systematic approach to scale-up of advanced battery materials has been defined. This approach starts with analyzing of the original route the new material was first made in the discovery lab and initial electrochemical evaluation. This determines if the

material is to be added to the inventory database, ranked, prioritized and selected for scale up. The Applied Materials Division's Process R&D group at Argonne consults with the DOE technology manager to prioritize new materials based on level of interest, validated performance and scale up feasibility. The new candidate materials for scale up are discussed with DOE for final approval. The Process R&D group evaluates several approaches, including non-standard manufacturing technologies, to determine the best route to scale up of each particular material. One such technology is a Continuous Flow Chemical Reactor that enables the continuous synthesis of materials from discovery through process development and production scale. Continuous flow reactor technology can be used for rapid screening of reaction conditions to better understand the fundamentals of process kinetics and thermodynamics. The technology offers a cost-effective and safer alternative to traditional batch processes by improving material and energy usage and minimizing the environmental impact of the manufacturing operation. At this point, the scale-up process begins with a feasibility study, followed by proof of concept testing, first stage scale-up and, as needed, further scale-up cycles. Several Go/No Go decisions are made after feasibility determination and electrochemical validation testing. For each material, we will develop a scalable manufacturing process, analytical methods and quality control procedures. We also prepare a "technology transfer package" which includes detailed procedures of the revised process for material synthesis, materials balance, analytical methods and results (Specification Sheet) and the SDS for the material. The detailed process description allows for preliminary estimates of production cost, an important factor for decision making in industry. We apply the newly developed process to manufacture kilogram quantities of the material. We fully chemically characterize each material and make samples available for industrial evaluation and to the research community. We also provide feedback to discovery chemists helping to guide future research.

## Results

We reported over the last several years the flow synthesis of lithium tricyanoimidazolid (Li-TCI). This is now complete using a customized flow reactor (Figure II.4.1). This reactor uses three feed lines, one for the diazotization solution, one for the substrate, and one for the cyanide quench step. The first two react in a coiled tube to produce a diazonium intermediate at 35-40°C, for approximately 10 minutes. This solution is then quenched immediately into a large diameter tube to allow the nitrogen gas to separate and not interfere with subsequent reaction times by building up additional pressure. The effluent is collected and the product-containing organic layer is separated using a membrane separator. The organic solution is concentrated to yield the potassium salt of tricyanoimidazole (K-TCI). The K-TCI is then converted to the protonated form using hydrochloric acid and extracting with MTBE. Final conversion to the lithium salt is done using lithium hydroxide or lithium carbonate in acetonitrile. The salt is then dried.

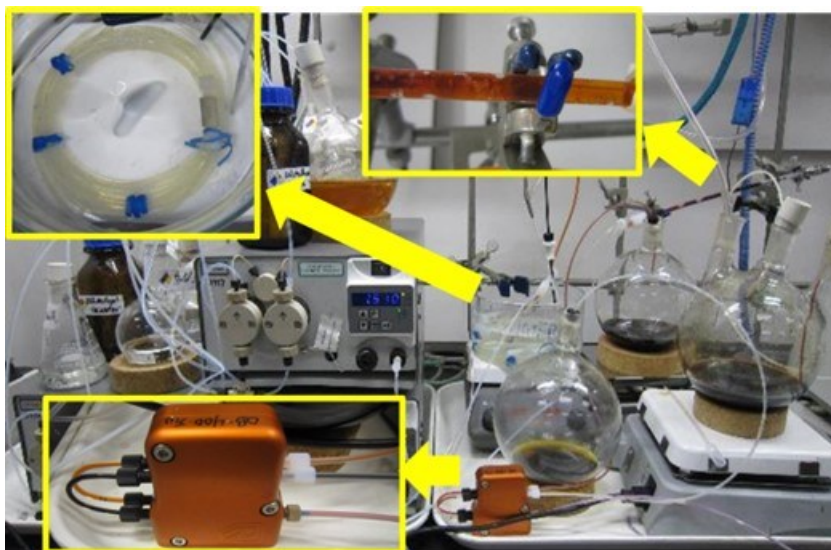


Figure II.4.1 Flow Reactor for K-TCl.

A similar structure was also explored several years ago- 2-fluoro-4,5-dicyanoimidazole (F-DCI). This material proved difficult to synthesize. The original route used p-methoxybenzyl bromide as a protecting group reagent.<sup>1,2</sup> This was both expensive and inefficient, requiring multiple chromatographic purifications. This year, we investigated alternative protecting groups in an effort to simplify the process (Figure II.4.2).

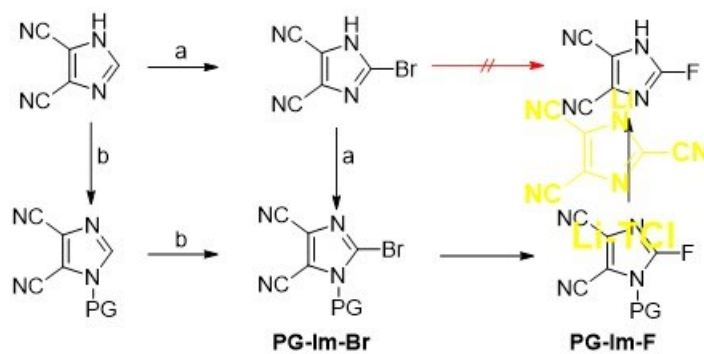


Figure II.4.2 Synthesis routes to F-DCI.

Several protecting groups failed to make even intermediate compounds, whilst others successfully fluorinated. However, no successful synthesis of F-DCI resulted from the new protecting groups, using both routes a and b in Figure II.4.2. Common protecting groups such as Boc, OAc, and OTs were all unstable or had non-reproducible behavior. Iso-butyl formed only extremely slowly and never fully converted, while the -CO<sub>2</sub>-i-Bu protecting group formed but was not stable to fluorination conditions. Benzyl (Bn), benzoyl (Bz) trichloroethyl (Troc), isobutyl (i-Bu), *etc.* were examined, but did not cleanly react or form a product from the imidazole. Only Bn, Bz, and Me were stable to fluorination conditions, and none cleanly deprotected. (Table II.4.1)

Table II.4.1 Protecting Group Summary

Protecting Group	PG-Im-Br	PG-Im-F	Im-F
PMB	Yes	Yes	Yes
Troc	Yes	No	N/A
Bn, Bz	Yes	Yes	No
i-Bu	No	N/A	N/A

Protecting Group	PG-Im-Br	PG-Im-F	Im-F
CO <sub>2</sub> -i-Bu	Yes	No	N/A
Me	Yes	Yes	No
Boc, OAc, OTs	No	N/A	N/A

We continue to look for other materials that are expected to have use as additives to LiFSI-based batteries, allowing higher voltage use. One of these is lithium tetrakis(hexafluoroisopropyl)borate (LiBHFip).<sup>3</sup> This was synthesized on a 15g scale using a modified process that is scalable. The <sup>19</sup>F NMR of this material shows high purity and matches the literature data. (Figure II.4.3)

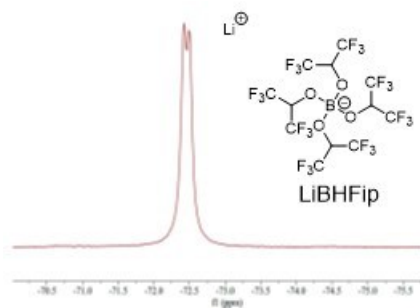


Figure II.4.3 <sup>19</sup>F NMR and structure of LiBHFip.

Other materials expected to enable high voltage use are based off a paper describing a new structural motif-2,2,3,3-tetrafluorobutanediol, dimethyl ether.<sup>4</sup> We have scaled this material up to the 100g level as part of a collaboration with Zhenan Bao at Stanford University, who is part of the Batt500 program. We are also exploring multiple new structures based off this motif for use in lithium metal, silicon anode, and anode-free cells. This later work is in collaboration with Daniel Abraham at Argonne. Several of these structures are depicted in Figure II.4.4.

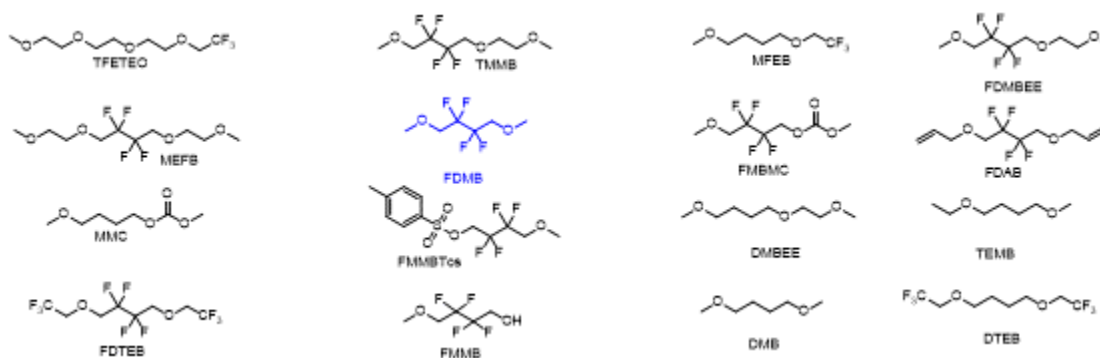


Figure II.4.4 FDMB-based materials for Lithium-metal cells.

These materials are all fully characterized by spectroscopic methods such as NMR and GC/MS. In a typical example, FMBMC was prepared from tetrafluorobutanediol, monomethyl ether using methyl chloroformate and base. The material was purified by distillation and analyzed by GC/MS (>99%) and both <sup>1</sup>H and <sup>19</sup>F NMR spectroscopy (Figure II.4.5).



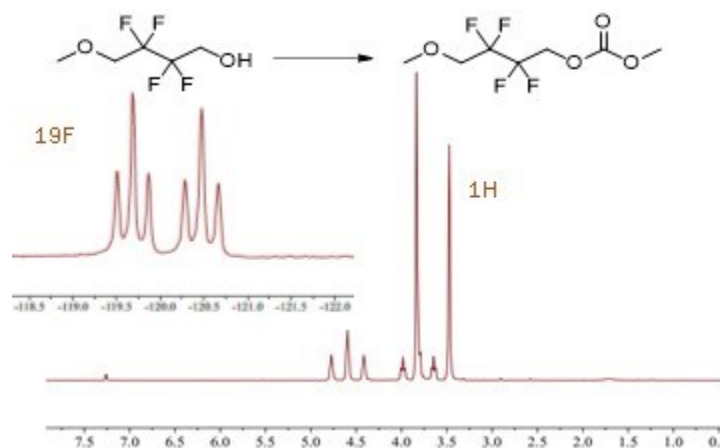


Figure II.4.5 NMR spectra for FMBMC.

We continue to examine these materials for use in anode-free cells. FDMB- based electrolytes have shown some promise, with up to 50 cycles achieved in coin cells before reaching 80% capacity (Figure II.4.6).

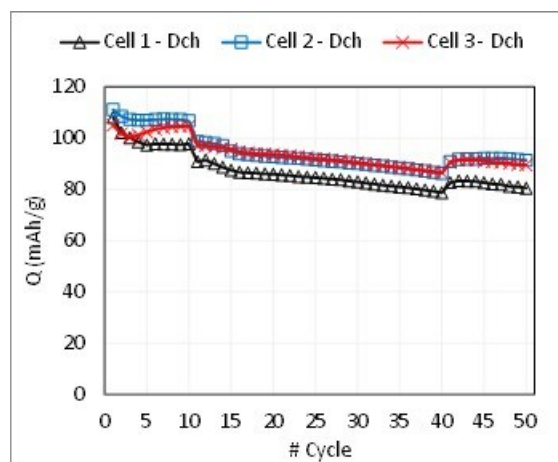


Figure II.4.6 Anode-free cycling of FDMB-based electrolyte.

One of the more interesting problems is the synthesis of non-symmetric versions of these materials, requiring first a mono-alkyl material. Mono-alkylation is a relatively difficult task and here proved more challenging than usual, as the mono-methyl and di-methyl materials have nearly identical boiling points, making separation highly challenging. Here, we developed flow chemistry conditions that minimized the formation of the dimethyl material. Conditions were developed on the Syrris flow reactor system to increase the reaction selectivity from only 77% in the best of batch conditions to >99% if the flow reactor. However, this was not able to be duplicated on larger systems in spite of additional study into reaction time, workup and other variables not directly examined in the initial study. Optimization of larger scale runs eventually obtained >98% selectivity, providing sufficient material for the ongoing synthetic studies.

Related to the FDMB chemistry, we are developing synthetic technology and scaling up other new fluorinated materials in collaboration with Zhenan Bao at Stanford.<sup>5</sup> These “F<sub>x</sub>DEE” materials (Figure II.4.7) are fluorinated ethers where the fluorogroups are at the ends of the molecule rather than in the center as seen in FDMB. Some improvements to the synthesis were discovered, such as reducing the amount of catalyst in the first reaction and optimizing the molar ratios of materials in the second reaction. Both materials are currently planned to be scaled to the 1kg level in early FY24.

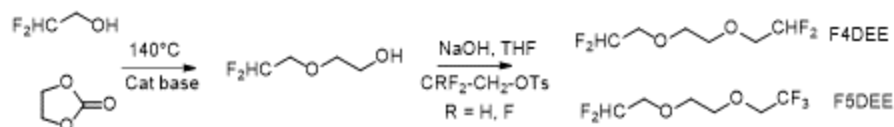


Figure II.4.7 Synthesis of F4DEE and F5DEE.

Corrosion studies on high-voltage Li-FSI cells are still ongoing as we investigate additional materials for aluminum current collector passivation, although thus far, few materials show substantial improvements (Figure II.4.8). “Cathode free” CR2032 coin cells using aluminum-clad stainless steel coin cell casings were assembled as follows: Al-clad cap – Al foil – separator – separator – Li metal – spacer – spacer – spring – s. s. cap. These cells were charged from 3.5 V to 5.0V in 0.05 V steps and held 1h at each step. The electrolyte composition is 0.8M Li-FSI + 0.2M Li-additive salt in 3:7 EC:EMC, and the cycling tests were run at 55°C in a temperature-controlled chamber. The aluminum clad coin cell case is essential to prevent stainless steel corrosion by Li-FSI containing electrolyte. Passivation failure of the additive is clearly observed by rapid rise of the current. A low baseline indicates passivation of the aluminum.

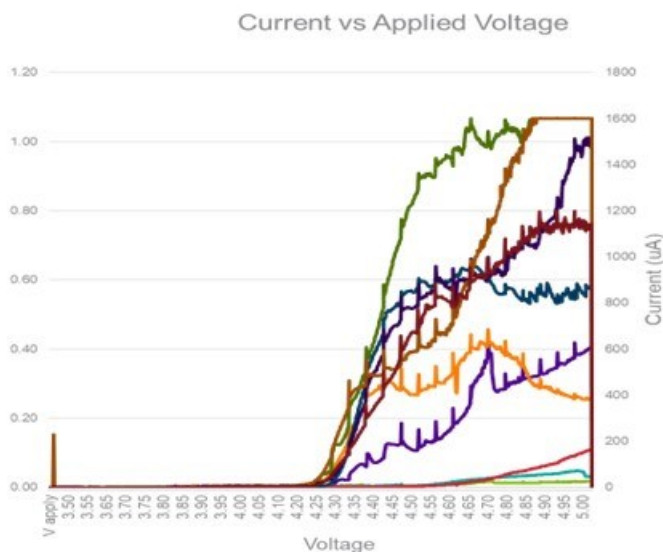
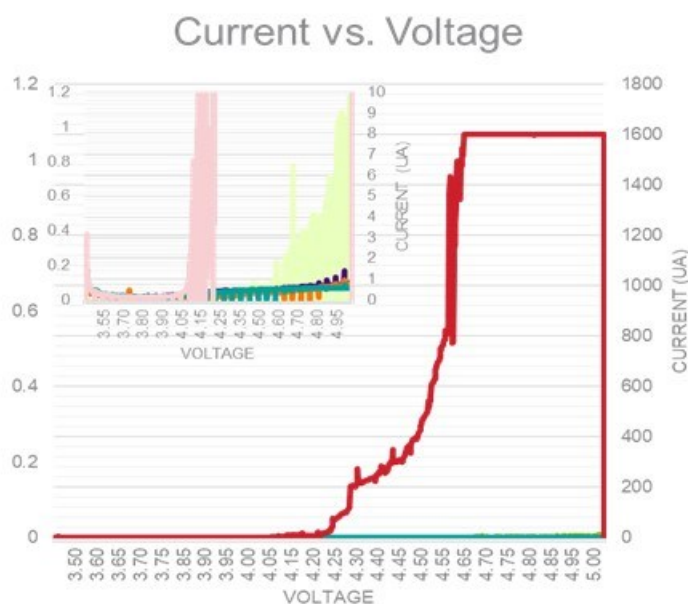


Figure II.4.8 Corrosion current vs applied voltage in Li-FSI cells.

We have found that several of the new fluorinated materials appear to act to suppress current collector corrosion, at least using this coin cell protocol. Shown in Figure II.4.9 are several electrolyte compositions—one clearly fails, whilst the remaining electrolytes appear to prevent corrosion current. The insert shows the very low measured current in the newly formulated electrolytes, now measured in single-digit microamps as opposed to the hundreds of microamps in other studies.



**Figure II.4.9 Corrosion current graph vs. applied voltage in fluorinated electrolytes.**

The project is still affected by the COVID-19 pandemic, mostly expressed as delays in procurement of lab supplies, chemicals and equipment. In particular, component parts for existing equipment has taken a long time to procure. Certain vendors have either gone out of business or offer limited supplier- this has delayed the coin cell testing whilst we find and evaluate new vendors for aluminum-clad coin cell components needed for the corrosion testing. Common stainless steel parts cannot be used in this test.

## Conclusions

The Process group's experimental materials scale-up program assists the battery research community and allows for a comprehensive evaluation of new materials by industrial laboratories as well as supports basic research. In FY23 the program provided several new, not commercially available materials. Samples of high, uniform quality materials were distributed for further evaluation and research. Over 250 samples, ranging from grams to hundreds of grams of experimental battery materials have been provided to researchers since the program inception.

Evaluation of emerging manufacturing technologies such as continuous flow reactors, microwave assisted reactions, acoustic mixing or reactive distillations to improve product quality while lowering manufacturing costs are all under consideration. We utilize our recently acquired, customized Syrris ASIA320 and Corning Advanced-Flow™ continuous flow chemical reactors to develop expedient manufacturing processes for new electrolyte solvents, salts and additives by improving safety, minimize waste stream and lower material and energy costs.

The large emphasis placed on new cathode materials, especially disordered rock salts and manganese-rich layered oxides, will eventually require new electrolytes to fully meet the potential of these novel materials. New classes of electrolyte solvents (fluorinated butandiol ethers) have started to be developed. New materials have been synthesized and have been investigated for aluminum passivation for use in high voltage LiFSI-based cells. Flow chemistry and flow reactions have proven invaluable in these projects- -there is no other practical route to manufacture these materials.

New materials are initially available only in small amounts, if at all. Because manufacturers minimally require kilo amounts for validation and advanced development, this drastically slows the development of the

technology. This program is uniquely positioned to deliver experimental materials in sufficient quantity to enable thorough investigation and validation by the broad, independent research community

## Key Publications

### Patents and Patent Applications

1. Zhengcheng Zhang, Qian Liu, Krzysztof Pupek, Trevor L. Dzwiniel, “Non-Flammable Electrolytes.” U. S. Patent Appl. US 2023/0100910 A1 Mar. 30, 2023.
2. Chen Liao, Trevor L. Dzwiniel, Kewel Liu, “Borate Salts, Polymers and Composites.” U. S. Patent 11,649,358 B2 May 16, 2023.
3. Trevor L. Dzwiniel, Krzysztof Pupek, “Continuous Method for Preparing Carbonate Esters” U. S. Patent 11,708, 345 B2, July 25, 2023.

### Papers:

1. Qian Liu, Wei Jiang, Jiayi Xu, Yaobin Xu, Zhenzhen Yang, Dong-Joo Yoo, Krzysztof Z. Pupek, Chongmin Wang, Cong Liu, Kang Xu & Zhengcheng Zhang, “A fluorinated cation introduces new interphasial chemistries to enable high-voltage lithium metal batteries.” *Nat Commun.* **2023**, *14*, 3678.
2. Gary P. Wiederrecht, Renaud Bachelot, Hui Xiong, Konstantinos Termentzidis, Alexandre Nominé, Jier Huang, Prashant V. Kamat, Elena A. Rozhkova, Anirudha Sumant, Michele Ostraat, Prashant K. Jain, Chris Heckle, Jie Li, and Krzysztof Z. Pupek, “Nanomaterials and Sustainability.” *ACS Energy Lett.* **2023**, *8*(8), 3443–3449.

## References

1. Paul G. Apen and Paul G. Rasmussen "Nucleophilic aromatic substitution in 4,5-Dicyanoimidazoles," *Heterocycles*, **1989**, *29* (7), 1325.
2. Crystal G. Gensmore and Paul G. Rasmussen “New Acetylenic Momoers and Polyers from 4,5-Dicyanoimidazole.” *Macromolecules* **2004**, *37*, 5900.
3. Binayak Roy, Pavel Cherepanov, Cuong Nguyen, Craig Forsyth, Urbi Pal, Tiago Correia Mendes, Patrick Howlett, Maria Forsyth, Douglas MacFarlane, Mega Kar “Lithium Borate Ester Salts for Electrolyte Application in Next-Generation High Voltage Lithium Batteries” *Adv. Energy Mater.* **2021**, *11*, 2101422.
4. Zhiao Yu, Hansen Wang, Xian Kong, William Huang, Yuchi Tsao, David G. Mackanic, Kecheng Wang, Xinchang Wang, Wenxiao Huang, Snehashis Choudhury, Yu Zheng, Chibueze V. Amanchukwu, Samantha T. Hung, Yuting Ma, Eder G. Lomeli, Jian Qin, Yi Cui & Zhenan Bao. “Molecular design for electrolyte solvents enabling energy-dense and long-cycling lithium metal batteries.” *Nature Energy*, **2020**, *5*, 526.
5. Zhiao Yu, Paul E. Rudnicki, Zewen Zhang, Zhuojun Huang, Hasan Celik, Solomon T. Oyakhire, Yuelang Chen, Xian Kong, Sang Cheol Kim, Xin Xiao, Hansen Wang, Yu Zheng, Gaurav A. Kamat, Mun Sek Kim, Stacey F. Bent, Jian Qin, Yi Cui, and Zhenan Bao, “Rational solvent molecule tuning for highperformance lithium metal battery electrolytes.” *Nature Energy*, **2022**, *7*, 94.

## Acknowledgements

Continuous support from Brian Cunningham, and Haiyan Croft of the U.S. Department of Energy’s Office of Vehicle Technologies is gratefully acknowledged. MERF Critical Battery Materials Team included: Trevor Dzwiniel, Kris Pupek, Amber Tabaka. Argonne’s Collaborators included: John Zhang, Daniel Abraham, Qian Liu, Wenquan Lu, Bryant Polzin, Steven Trask.

## II.5 Structure-Activity Relationships in the Optimizing Electrode Processing Streams for LiBs (LBNL)

### Vince Battaglia, Principal Investigator

Lawrence Berkeley National Laboratory  
1 Cyclotron Road, MS 70R0108B  
Berkeley, CA 94720  
E-mail: [vsbattaglia@lbl.gov](mailto:vsbattaglia@lbl.gov)

### Haiyan Croft, DOE Technology Development Manager

U.S. Department of Energy  
E-mail: [Haiyan.Croft@ee.doe.gov](mailto:Haiyan.Croft@ee.doe.gov)

Start Date: October 1, 2019

End Date: September 30, 2025

Project Funding (FY23): \$500,000

DOE share: \$500,000

Non-DOE share: \$0

### Project Introduction

The broad problem we face is the need to go through an entire empirical study to determine how much and what type of carbon and binder is needed to make a highly functioning electrode of high loading everytime we change the basic chemistry of a proposed, new, active material. This problem can be broken down into two parts: 1) a lack of a proven methodology to minimize the level of inactive components to maximize energy density and minimize cost while maintaining cycleability of active materials of a wide variety of size and electrochemical properties; and 2) a lack of fundamental understanding in the properties required of a slurry to cast thick electrodes that dry to form a uniform coating of carbon, binder and active material that adheres to the substrate, is absent of cracks, and does not fracture or delaminate during electrode punching or slicing.

### Objectives

Our objective *this year* was to broadly assess the ability to make thick electrodes of LFP, which is reported to be a difficult process to perform by most battery manufacturers. Most of our research to date has been on NMC-type materials. We will investigate LFP electrode production by looking at the impact of using various carbon additives and binders added to a commercial LFP material on the final electrode appearance and performance. We will also use our experience with NMC to compare directly with the measurements we make using the primary particles of LFP and then investigate the impact of making thick electrodes of LFP by switching to an LFP material that consists of secondary particles. This will allow us to assess whether the challenge to making LFP electrodes is due to surface chemistry or particle size.

### Approach

Our approach is a combination of empirical research, advanced diagnostics, and multi-variable statistics to arrive at correlations that start from rheological properties and follow all the way through to electrochemical properties in a half-cell pouch-cell. We will investigate pair wise combinations of different binders and different carbons to determine the band of ratios that promote good electronic conductivity, cohesion, adhesion, and open porosity. We will measure the electronic conductivity of different ratios of carbon and active material that lead to enough conductivity. We will prepare laminates of combinations of binder and active material to establish a minimum amount binder necessary to provide minimum levels of adhesion and cohesion. We will measure the rheological properties of slurries of different ratios of components in different levels of solvent to establish how the components impact rheology and the rheological properties that lead to thick electrodes with no cracks. We will measure the physical properties of electrodes such as adhesion, cohesion, surface roughness and cracks, and correlate to the rheological properties. We will test the electrochemical performance and cycleability of electrodes in cells and correlate to physical properties of the

electrodes. Through this approach, we should be able to explain how changes in the slurry composition and mixing procedures can affect electrode performance and provide direction for improvements.

## Results

As presented in the AMR in June 2023, we have a very good idea of how to make electrodes from typical NMC materials, which usually have decent electronic conductivity and typically arrives as secondary particles with an average particle size of 10 microns. It is fairly well known that it is difficult to make electrodes of lithium iron phosphate (LFP) that is usually in the form of primary particles of 700 nm size. Our overall goal is to understand why processing conditions for making thick electrodes of NMC do not translate to LFP. (Just so the reader is aware, this is not unique to LFP. We have discovered that different process conditions and component fractions are required for DRX, Si, and most solid-state battery chemistries.) It is fairly well known that LFP has a poorer inherent conductivity than NMC. As such, LFP typically arrives with a conductive carbon coating that is formed during the synthesis of the material by using carbonates of the metals' as precursors. From our work with NMC, we demonstrated that we can produce cycleable electrodes with as low as 0.8 % carbon black (Denka Black). (Less carbon results in poor electrode performance.) This low level of carbon (0.8%) was used with a low level of binder of 1.2%. It is our contention that NMC has good enough electronic conductivity that carbon is not needed for the purpose of improving the conductivity of NMC itself. However, since binder is located between NMC particles, we believe the carbon is needed to make the binder conductive to allow for good electronic conductivity between particles. 0.8 % carbon is needed because 1.2% binder is needed to hold the NMC particles together. To assess this aspect for LFP, we mixed carbon powder with the LFP powder, produced a condensed pellet and then measured the electronic conductivity of the pellet. The results of that work are provided in Figure II.5.1.

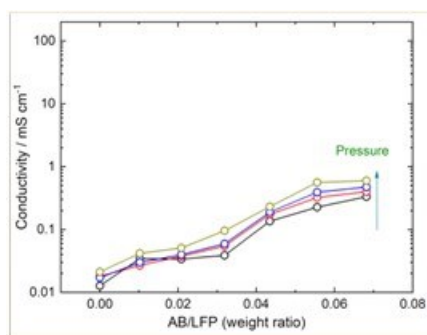


Figure II.5.1 Electronic conductivity of pellets of LFP mixed with carbon black at low levels of carbon.

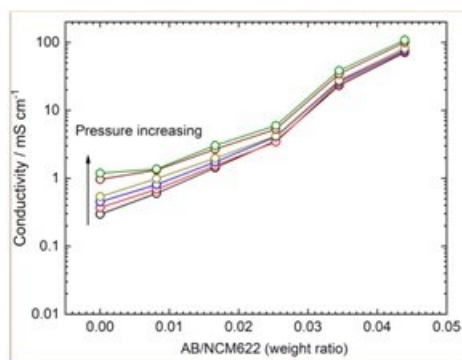
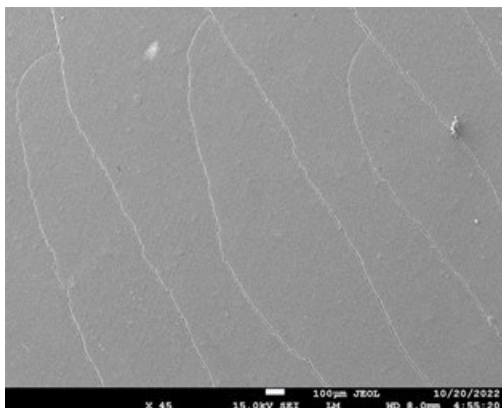


Figure II.5.2 Electronic conductivity of pellets of NMC mixed with carbon black at low levels of carbon.

For comparison, the conductivity of pellets of NMC and carbon is shown in Figure II.5.2. One sees that the conductivity of the NMC starts about two orders of magnitude higher than the conductivity of LFP. What we

are interested in seeing is if ca. 1 % carbon is good enough for LFP, as it was for NMC, or does one need to add some additional amount of carbon to get the conductivity up to that of NMC with no carbon.

In our first pass at making thick electrodes of LFP, we took a small step and tried to make electrodes of 3 mAh/cm<sup>2</sup> using two different carbon additives (Denka Black and carbon nanotubes (CNTs)) and two different solubilized PVdF binders (PVdF1: KF9300 from Kureha and PVdF2: HSV1810 from Arkema). We adjusted the NMP content to roughly match the slurry consistency that worked well for NMC electrodes. The SEM of LFP electrodes with 5% Denka Black and KF9300 is given in Figure II.5.3. One sees that there are fine cracks on the surface of this electrode, otherwise, the surface is rather smooth from a magnification of x45. Cracks such as these can lead to fracture during the punching or slitting process.



**Figure II.5.3 SEM of 45x magnification of the surface of an LFP electrode of 3 mAh/cm<sup>2</sup> with 5% Denka Black and 7% PVdF1. Fine cracks are observed on the surface.**

A second electrode was formulated with 5% CNTs and 5% PVdF1. Under SEM, that electrode at 100x magnification looks fairly rough, indicative of less homogeneity as found with the Denka Black electrode. The image also shows where a bubble had formed and popped on the surface. (Figure II.5.4)

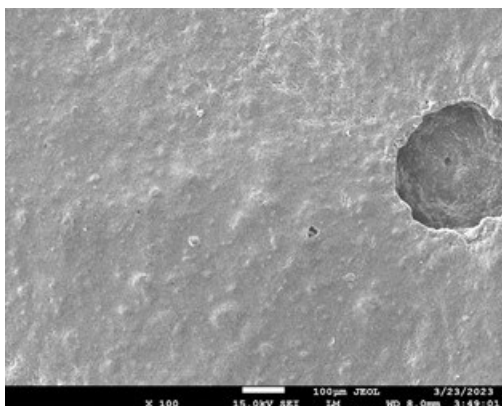


**Figure II.5.4 SEM of 100x magnification of the surface of an LFP electrode of 3 mAh/cm<sup>2</sup> with 5% CNT and 5% PVdF1. No cracks are observed on the surface but there is the scar of a bubble.**

A third electrode was prepared with 5% CNT and 5% of PVdF2. This electrode surface appeared rough under 100x magnification like the second laminate and showed cracks like the first, as seen in Figure II.5.5.

Attempts to cycle these electrodes failed as portions of the laminates flaked off the substrate as a result of punching out disks for coin cell testing.

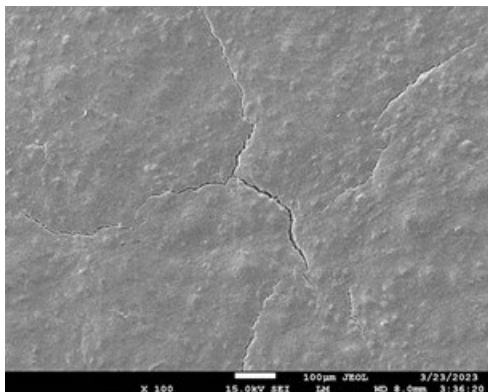
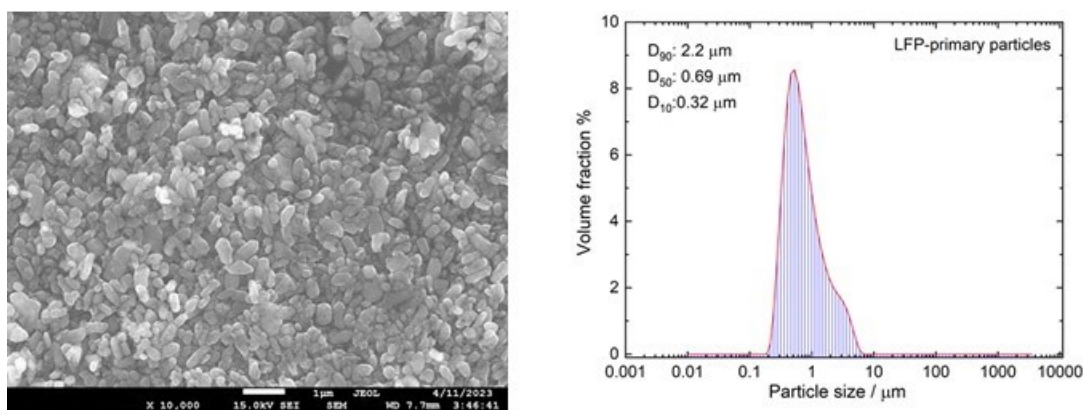


**Figure II.5.5** SEM of 100x magnification of the surface of an LFP electrode of 3 mAh/cm<sup>2</sup> with 5% CNT and 5% PVdF2. The surface is fairly rough, similar to the other electrode with CNTs, and showed cracks like the first electrode.

At this point, we were not able to produce electrodes of LFP primary particles greater than or equal to 3 mAh/cm<sup>2</sup> that cycled well even though we easily do this for NMC. To further understand this, we obtained another source of LFP from a start-up that produces secondary particles. This material's secondary particles are around 8.5 microns in diameter, which mimics what we typically see in NMC. Now we have a powder with the density, inherent conductivity, and surface chemistry of LFP but with the macro-structure of NMC and we can test to see which of these properties may be of more importance.

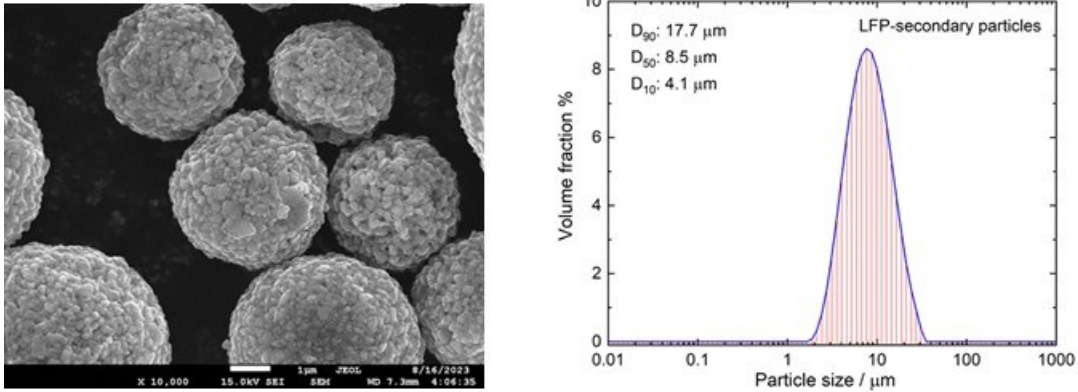
Figure II.5.6 is the SEM of the LFP powder of primary particles in the work presented above. Next to the image is the particle size distribution of the particles. One sees that the average size is around 0.69 microns.

Figure II.5.7 shows the structure of new material that is aggregated into secondary particles. The particle size of the aggregated secondary particles is 8.5 microns. We also measured the BET surface area of the two materials and found they were nearly identical at 13.9 for the material in primary particles and 14.1 m<sup>2</sup>/g for the material in secondary particles. This suggests that the particles are loosely aggregated in the secondary particles and their interior particles may be accessible by electrolyte.



**Figure II.5.6** Left, SEM of 10000x magnification of the surface of an LFP powder of primary particles. Right, the D<sub>50</sub> particle size is 0.69 microns.





**Figure II.5.7** Left, SEM of 10000x magnification of the surface of an LFP powder of secondary particles. Right, the D<sub>50</sub> particle size is 8.5 microns.

Like we did with the primary particles, we measured the conductivity of pellets of the secondary particles made by mixing Denka Black and mixing CNTs with the secondary particles at different weight ratios of carbon to LFP. That data is presented in Figure II.5.8. for the secondary particles. We see here that the LFP powder mixed with CNT leads to pellet of higher conductivity than the powder mixed with Denka Black. We saw a similar result for NMC. One explanation is that the carbon nanotubes consist of continuous pathways of highly graphitic carbon which provides long-range conductivity whereas the Denka Black consists of a number of small particles (around 50 nm) that must make electrical connection by jumping from particle to particle. Comparison of the conductivity of secondary particles from this vendor when there is no carbon additive is similar to the conductivity of the primary particles of 1 mS/cm (Figure II.5.1).

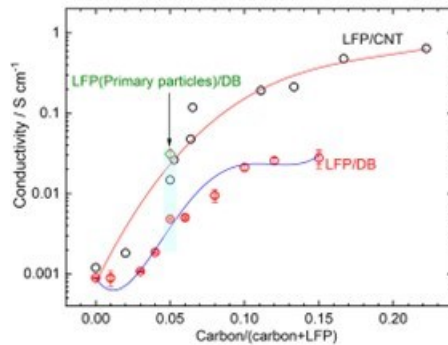


**Figure II.5.8** Electronic conductivity of secondary particles of LFP mixed with different fractions of CNT or Denka Black and pressed into pellets.

Electrodes were made of the secondary particles of LFP using 5% Denka Black and either 5% PVdF1: KF9700 from Kureha or PVdF2: HSV1810 from Arkema. However, this time we found we could make electrodes up to and greater than 4 mAh/cm<sup>2</sup> without cracks at a magnification of 100x, as seen in Figure II.5.9.

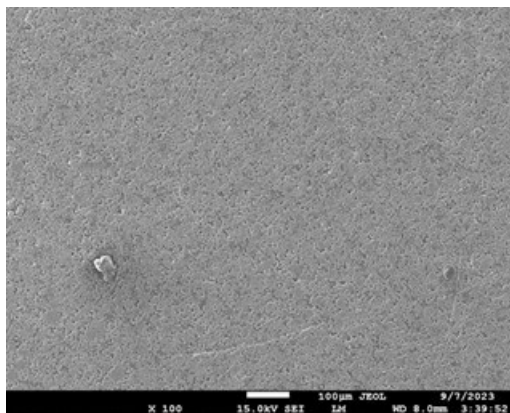


**Figure II.5.9 SEM of 100x magnification of the surface of an LFP electrode of 4 mAh/cm<sup>2</sup> with 5% Denka Black and 5% PVdF1. Fine cracks are observed on the surface.**

Electrodes of the different binders, carbons, and loadings are presently under test. We should know shortly which has a definitive impact on cycle life. Now that this initial survey is nearly complete, we expect to go back and perform more detailed analysis of the binder / carbon ratios and the binder active material ratios. We will also investigate the impact of solvent content on material mixing, casting and drying, and investigate combinations of carbons. Once we have a reasonable understanding of how best to combine these materials and the ratios, we will push to minimize the inactive component fractions to discern what minimum fraction can be achieved while still demonstrating excellent cycleability. This will be especially important for the medium energy LFP if it is to have an acceptable energy density in a cell. This research will ultimately further enhance our understanding of material properties and how best to handle active materials of different densities, electronic conductivities, size, and shape to make excellent performing electrodes without significant trial and error.

### Conclusions

This year we initiated a study on the impact of changing the active material in an electrode formulation from NMC to LFP where the LFP is available separately as a primary particle and as a secondary particle. At the same time, we also started to investigate different sources of binder and different forms of carbon additive. At this point, without completing the adhesion and cohesion testing and the cycleability testing, what we can say is that we can produce much thicker electrodes of LFP if it comes as secondary particles. Our present hypothesis is that the particle size greatly impacts the rheology of the slurry and solvent content which in turn affects film height and cracking. Further investigation of binary interactions and ternary interactions will provide additional insight into how these materials perform with each other and whether the performance is additive or something more complicated. We intend to complement the material presented here with more electrochemical analysis, physical analysis, and rheological analysis in future reports.

### Acknowledgements

LBNL staff members Yanbao Fu, Kenny Higa, and Daniel Collins-Wildman performed the work presented.

## II.6 Higher Energy Density *via* Inactive Components and Processing Conditions (LBNL)

### Vincent Battaglia, Principal Investigator

Lawrence Berkeley National Laboratory  
1 Cyclotron Rd  
Berkeley, CA 94720  
E-mail: [vsbattaglia@lbl.gov](mailto:vsbattaglia@lbl.gov)

### Kenny Higa, Principal Investigator

Lawrence Berkeley National Laboratory  
1 Cyclotron Road, MS 70R0108B  
Berkeley, CA 94720-8168  
E-mail: [khiga@lbl.gov](mailto:khiga@lbl.gov)

### Haiyan Croft, DOE Technology Development Manager

U.S. Department of Energy  
E-mail: [Haiyan.Croft@ee.doe.gov](mailto:Haiyan.Croft@ee.doe.gov)

Start Date: April 1, 2023	End Date: September 30, 2028	
Project Funding (FY23): \$500,000	DOE share: \$500,000	Non-DOE share: \$0

### Project Introduction

The performance of an electrode is influenced by its structure—the spatial arrangements of components making up the electrode. These arrangements are determined by the electrode fabrication process. As in most manufacturing processes, process design for electrode fabrication involves a large number of choices, through which manufacturers can use to optimize electrode performance. Unfortunately, the relationships among process decisions, structure, and performance are difficult to predict and expensive to explore at the scales needed for industrial equipment. This project will explore these relationships in the context of laboratory-scale fabrication and introduce approaches to simulate production steps on larger scales.

### Objectives

The objectives of this project are to;

- Develop procedures, based on techniques that are relatively accessible to manufacturers, for obtaining information about component arrangements in slurries and electrodes.
- Develop techniques that can be easily adopted by manufacturers to quantitatively analyze this information and rapidly obtain insights that can be useful in process development and in guiding adjustments in live processes.
- Develop methods of establishing relationships among process variables, component arrangements and electrode structure, and performance that can be adopted by manufacturers for their specific formulations.

### Approach

In the near-term, our approach will focus on using imaging techniques and rheometry. Broadly speaking, our approach to achieving the objectives above, incorporating automation when practical, and developing tools as needed, is to use well-controlled, consistent procedures for the following sequence of steps:

1. produce slurries
2. extract slurry samples
3. prepare and obtain images of slurry samples

4. quantitatively characterize slurry images
5. obtain rheological data for slurry samples
6. produce coatings from slurries
7. obtain images of coatings
8. quantitatively characterize coating images
9. perform electrochemical testing

Information obtained through this approach will be used to establish relationships among process variables, component arrangements and electrode structure, and performance.

## Results

Funding for this project arrived roughly halfway through the fiscal year, so our work has focused on establishing capabilities and trialing techniques that will be needed later in this project.

We have identified slurry production by roller mills as a technique that is likely to translate in a relatively straightforward way from the laboratory scale to the industrial scale. To enable slurry production on roller mills as well as consistent rheological measurements of slurry samples, both in a controlled atmosphere, we have refurbished a large glovebox and a coating table, and procured a rheometer, compact roller mills, and a Thinky mixer. We have installed these, along with an existing computer-controllable rotor-stator mixer and an Ethernet connection, in the refurbished glovebox. This arrangement allows for preparation, rheological characterization, and casting of conventional battery electrode slurries with minimal transport time and without air exposure, which would otherwise have the potential to affect sample quality and measured values.

In parallel, we have trialed a procedure for producing slurries containing carbon nanofibers and N-methyl-2-pyrrolidone (NMP) with a Thinky mixer and extracting slurry samples for imaging by confocal microscopy. Sample extraction and preparation is presently a manual process, so we employ a semi-automated process for image collection, with the intent of obtaining a representative set of images. The figures below, Figure II.6.1, Figure II.6.2 and Figure II.6.3 show selected images of samples extracted at different times in the mixing process. Even under the lowest available magnification, some individual fibers are visible, and it appears that there is a visually detectable trend of homogenization as mixing progresses. From this vantage point, one sees small aggregates growing with mixing time to the 25<sup>th</sup> minute of mixing where carbon appears as a single porous media. This provides some confidence that mixing progression can be quantitatively characterized through image analysis / machine learning.

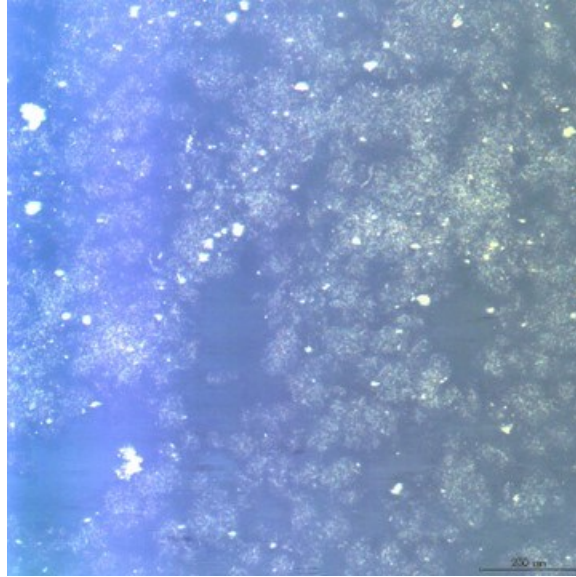


**Figure II.6.1 Carbon nanofiber and NMP slurry sample after 5 minutes of mixing (LBNL)**

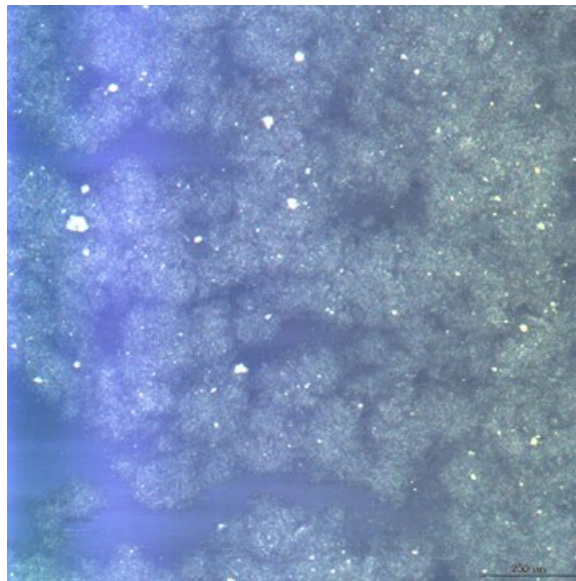


**Figure II.6.2 Carbon nanofiber and NMP slurry sample after 15 minutes of mixing (LBNL)**

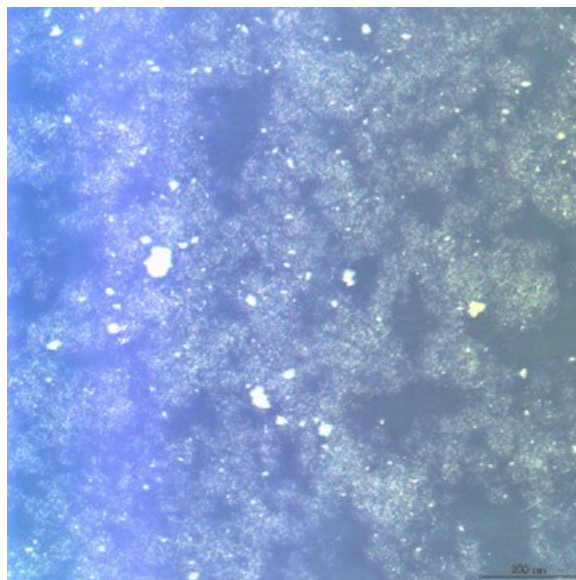


**Figure II.6.3 Carbon nanofiber and NMP slurry sample after 25 minutes of mixing (LBNL)**

We also investigated different mixers and a few combinations of mixers. The three most common used in a lab setting are the high shear homogenizer, the Thinky mixer, and a planetary ball mill (which incorporates a mixing media of hard spheres) as seen in Figure II.6.4.



**Figure II.6.4 Left, High shear homogenizer; Middle, Thinky; Right, planetary ball mill.**

In the following set of experiments, we used a formulation that we found worked well for making electrodes with NMC active material, except here, the NMC was excluded so that we could see the impact of mixing on the Denka Black morphology: Denka Black = 0.12 g; PVdF = 0.147 g; and NMP = 3.91 g. If the NMC were present, it would be difficult to see effects on structure and aggregation on such a low fraction of carbon. Figure II.6.5 is an SEM of the pre-mixed Denka Black at a magnification of 10,000x. One can see that the powder consists of several small particles of high surface area that are sparsely aggregated. This is basically how we want the carbon to setup except we need to do this while trying to mix in binder and active material. So, to some extent, we are looking to mix the materials with minimal impact on the carbon.

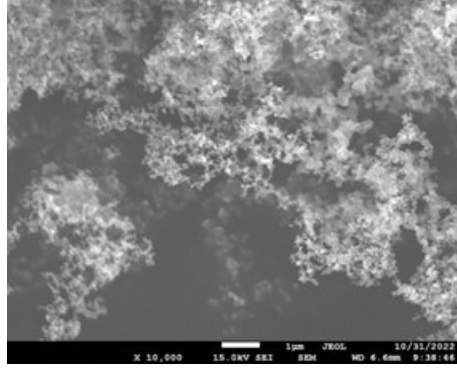


**Figure II.6.5 Denka black powder prior to mixing.**

The first mixer used was the Thinky. This machine works by spinning and stretching material and relying on plenary motion and centripetal force to mix materials together. The material was mixed for 4 minutes. In Figure II.6.6, the SEM shows at 10000x that the carbon still looks a lot like the fresh powder but with an overall structure that is slightly more compact.

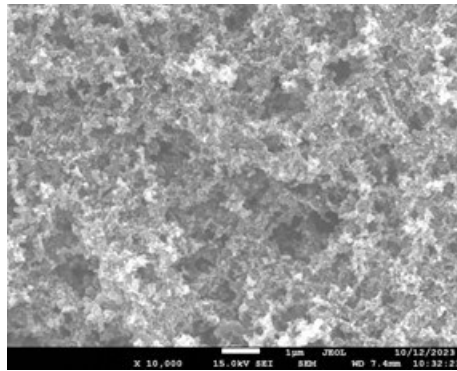


**Figure II.6.6 Denka black and binder after 4 minutes in the Thinky.**

The next mixer tested was the high shear homogenizer. The homogenizer primary function is to breakup agglomerates by bringing materials together through a narrow gap that shears and smashes materials through narrow gaps. We used this to mix the carbon and binder together for 60 minutes. Figure II.6.7 shows the SEM of the material at 10000x when mixed with binder. The carbon looks similar to fresh powder, perhaps slightly more aggregated with less open space than the Thinky.

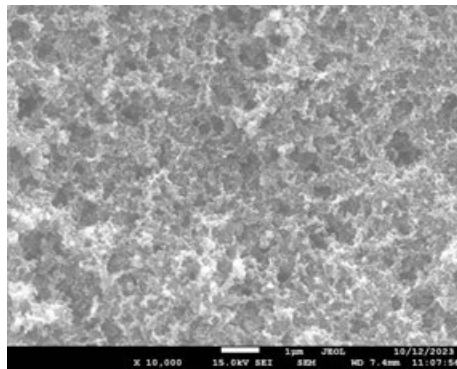


**Figure II.6.7 Denka black and binder after 60 minutes in the homogenizer.**

The third mixer used was the planetary ball mill. The equipment works by using hard material to breakup less hard material against the wall of the jar using planetary action. We first dry ball-milled 0.5 g of Denka black

with 28 g of ZrO<sub>2</sub> balls (3 to 5 mm) at 500 rpm for 6 hours. This made the most significant change to the carbon, as seen in SEM of 10000x provided in Figure II.6.8. We see the Denka black particles appear agglomerated with less surface area.

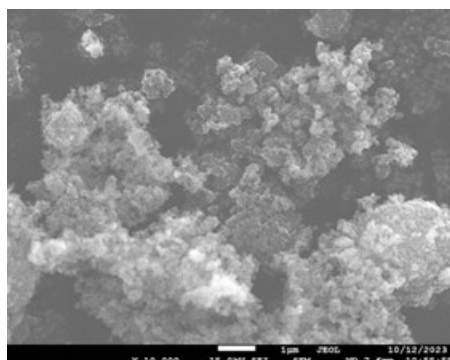


**Figure II.6.8 Denka black and binder after 6 hours of ball milling.**

After the carbon was ball milled, it was added to a Thinky mixer with PVdF and NMP in the same ratio as the other mixtures. This demonstrated a significantly different material than what we saw using the other mixtures. (Figure II.6.9)

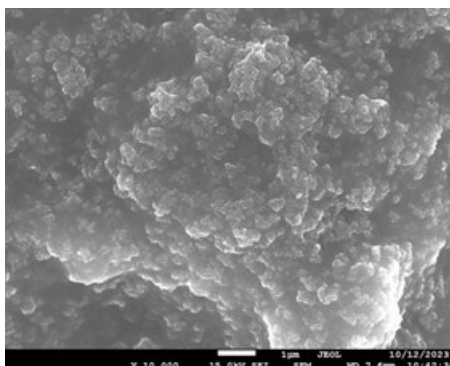


**Figure II.6.9 Denka black and binder after 4 minutes in the ball mill.**

Here, the carbon particles are compacted together into tight, roundish agglomerates which are further combined into a more compact structure that found with the other mixers.

The next thing to do will be to apply these slurries as films onto aluminum substrates, observe the drying of the films and measure the adhesion and cohesion and ability to form porous structures. We'll also want to make full electrodes from combining these materials with NMC using different mixers, monitor for cracks or delamination and then test the electrodes in cells.

## Conclusions

Since this project began halfway through the fiscal year, our efforts have focused on establishing experimental capabilities that will be used to perform project tasks in subsequent years. We have refurbished a large glovebox so that within a single controlled atmosphere, we can perform slurry mixing with any of three different methods, take rheological measurements, and fabricate coatings. We have also developed preliminary procedures for collection of confocal images of slurry samples, which we will refine into techniques for image collection for quantitative processing by image analysis / machine learning techniques for rapid determination of mixing progress. We also now have some sense of what each potential mixer has on the inactive components and are looking forward to seeing how the mixing impacts physical film properties and electrochemical properties.



## **Acknowledgements**

LBL staff members Kenny Higa, Yanbao Fu, and Daniel Collins-Wildman, along with UC Berkeley student Saniya Shrotiya have contributed to this project.

## II.7 Minimizing Side Reactions in Next-Generation Lithium Ion Battery Cathodes Through Structure-Morphology Optimization (ANL)

### Venkat Srinivasan, Principal Investigator

Argonne National Laboratory  
9700 South Cass Avenue  
Lemont, IL 60439  
E-mail: [vsrinivasan@anl.gov](mailto:vsrinivasan@anl.gov)

### Haiyan Croft, DOE Technology Development Manager

U.S. Department of Energy  
E-mail: [haiyan.croft@hq.doe.gov](mailto:haiyan.croft@hq.doe.gov)

Start Date: October 1, 2022

End Date: September 30, 2023

Project Funding (FY23): \$500,000

DOE share: \$500,000

Non-DOE share: \$0

### Project Introduction

Due to their widespread application in automotive and grid storage devices, lithium ion batteries are presently being manufactured at large scale, which is expected to increase substantially in the next decade. The most expensive component of a lithium ion battery is its cathode, and cheaper synthesis of these components can potentially help to lower the cost of the commercially available lithium ion cells. Accordingly, it is necessary to study the “science behind the synthesis” of conventional, as well as novel, cathode materials with application in lithium ion batteries to devise synthesis routes that are easily scalable. Commercially the cathode particles are synthesized using a two-step process, namely, coprecipitation and calcination. The hydroxide or carbonate based transition metal precursors ( $\text{TM}(\text{OH})_2$  or  $\text{TMCO}_3$ ) are firstly coprecipitated in water based reactors. These cathode precursors are later calcined with lithium salt at elevated temperatures in the presence of oxygen to oxidize and lithiate them, which finally leads to the layered oxide cathodes ( $\text{LiTMO}_2$ ). Doping and surface coatings are included to stabilize the cathode structure under high states of charge (SOC), which is necessary to minimize undesired reactivity and maximize the cycle life of the cells.

Formation of the cathode precursors using the coprecipitation process can be conducted in either batch mode or in a continuous mode (continuous stirred tank reactors (CSTR), Taylor vortex reactor (TVR), etc.). While the former may be beneficial for screening purposes, the latter is usually adopted by the industries for the large scale and continuous synthesis of the cathode precursors. Due to the differences in reactivity of the different transition metals (for example, propensity of formation of the transition metal ammonia complex), and variability of their solubility product ( $K_{sp}$ ), the precipitated cathode precursor may not contain the desired amount of the transition metal being fed into the reactor. The differences in chemical composition in the cathode precursors obtained from the batch and the continuous processes have not been investigated yet in details. Similarly, adaptability of synthesis techniques optimized using the batch mode reactors to the continuous processes needs to be investigated further.

Calcination of the cathode precursors is a very important step because the oxidation, lithiation, and layering of the cathode particles occur during this high temperature process. The type of lithium salt being used in the calcination step can influence the lithiation and subsequent layering of the cathode particles. Lithium hydroxide ( $\text{LiOH}$ ) demonstrates a lower melting point (around  $465^\circ\text{C}$ ) than lithium carbonates ( $\text{Li}_2\text{CO}_3$ ) that melts at around  $725^\circ\text{C}$ . But  $\text{LiOH}$  is substantially more expensive than the carbonate based salts because of their different synthesis procedures. Even though more expensive, calcination of Ni-rich cathode precursors needs to be conducted with  $\text{LiOH}$  for complete lithiation and layering of the cathode particles. Limitations experienced during calcination with the carbonate based lithium salts needs to be investigated thoroughly using both *in situ* experimental and computational techniques. Evolution of different phases, for example, removal of

water, formation of oxide intermediate, and the layering process needs to be investigated to properly understand the science behind the calcination of cathode precursors. If the cathode precursors are rich in manganese, and excess lithium is also used during the calcination process, lithium-manganese-rich (LMR) phases can form, which effectively helps to enhance the capacity of the cells after the activation of the oxygen redox process. Formation of the lithium and manganese rich phases within the layered cathode particles should be studied thoroughly to decipher the mechanism behind their successful synthesis.

The desired final outcome from the cathode particles is enhanced performance and cycle life. Hence, it is very important to investigate the voltage vs. capacity curves obtained from the synthesized cathode particles, which is accomplished by using the mesoscale level computational techniques. Performance of the cathode particles can depend on the diffusion coefficient of lithium, diffusion length, and electrochemically active surface area, all of which are taken into consideration within the developed methodology. Different cathode materials experience different magnitudes of lithium diffusivity, such as, Ni-rich NMC and LMR-NMC type cathodes demonstrate diffusion coefficients around  $10^{-14}$  m<sup>2</sup>/s and  $10^{-18}$  m<sup>2</sup>/s, respectively. As a result, to obtain similar performance from these two types of cathodes, the diffusion length of the LMR-NMC cathode particles needs to be much smaller than the diffusion length observed in Ni-rich NMC particles. Since the diffusion length is substantially affected by the sintering of cathode primary particles during the calcination process, the calcination protocol of LMR-NMC and Ni-rich NMC cathodes can significantly impact their overall performance.

### Objectives

This year's project activities have four major objectives: i) Deciphering the difference in NMC111 calcination mechanism while using LiOH and Li<sub>2</sub>CO<sub>3</sub> as the lithium salt. ii) Understanding the difference in metal composition in transition metal carbonate (TMCO<sub>3</sub>) precipitates obtained using batch and continuous reactors. iii) Understanding the impact of calcination temperature, or primary particle size, on the achievable capacity at different rates. (iv) Understanding the reaction mechanisms during the calcination of TMCO<sub>3</sub> cathode precursors. Overall aim of this year's activities is to develop a better understanding of the different phases that evolve during the calcination of transition metal hydroxide as well as transition metal carbonate type cathode precursors. On the coprecipitation of precursors, the possibility of formation of transition metal gradients within batch and continuous reactors will be investigated. Finally, the performance of different Ni-rich cathodes with varying primary particle size will be estimated. The concept of diffusion length will be used to justify the observed variation in capacity of the NMC811 cathode particles.

### Approach

An in situ X-ray diffraction based characterization technique and multiscale mathematical modeling scheme is developed for the extraction of different reaction mechanisms occurring during the calcination of cathode active particles at elevated temperatures. To understand the difference in calcination with different types of lithium salt (LiOH vs. Li<sub>2</sub>CO<sub>3</sub>), equal amount of nickel (Ni), manganese (Mn) and cobalt (Co) based hydroxide (NMC111(OH)<sub>2</sub>) precursors are heated separately with LiOH and Li<sub>2</sub>CO<sub>3</sub> and the evolution of different phases are visualized using the X-ray diffraction analysis at the Advanced Photon Source (APS, ANL). A constant temperature ramp of 2°C/min is used in all in-situ heating experiments where the temperature is increased from room temperature to 900°C. Stability of the intermediate phase and the formation of the final layered phase depends strongly on the type of lithium salt being used (LiOH or Li<sub>2</sub>CO<sub>3</sub>). On the computational side, density functional theory (DFT) and ab-initio molecular dynamics (AIMD) based calculations are conducted using the Vienna Ab Initio Simulation Package (VASP) to understand the variation in lattice structure occurring at the atomic scale during the calcination of the cathode precursors. The exchange-correlation potentials are treated by the generalized gradient approximation (GGA) and the interaction between valence electrons and ion cores is described by the projected augmented wave (PAW) method. Moreover, the GGA+U scheme is used for applying the on-site correlation effects among 3d electrons of the transition metal. At the mesoscale level, a phase field based methodology is developed for understanding the calcination of NMC cathodes, which involves the chemical reactions and mass transport processes associated with the removal of water, incorporation of oxygen within the lattice structure, addition of lithium within the cathode through reaction

with lithium salt, formation of the layered phase, and surface diffusion mediated sintering of the cathode primary particles. Interplay between the different reaction mechanisms observed while calcining the hydroxide and carbonate cathode precursors with various lithium salts will be explored in the subsequent sections.

To simulate the coprecipitation within the batch and the continuous reactors, fundamental mass balance relations are satisfied to determine the equilibrium concentration of different cations and anions within the batch reactor. Various equilibrium relations available in the literature are adopted to conduct the analysis. Adoption of charge neutrality and autoionization of water ( $[H^+] \cdot [OH^-] = 10^{-14}$ ) provides two extra equations needed for estimation of the pH of the reacting solution. Standard mass inflow and outflow relations are used for capturing the behavior observed in the continuous processes.

Finally, the computational estimation of the performance of the cathode particles involves two parts, where the first is the generation and characterization of the computational microstructure, and the second one is electrochemical modeling to solve for concentration and potential fields in electrode and electrolyte domains. The cathode microstructures are generated by digitizing the SEM images of various cathode particles calcined at different temperatures, which led to the formation of various cathode microstructures with different primary particle sizes as well as different internal porosities. However, majority of the internal pores are trapped inside the cathode, and electrolytes are unable to flow into it. Presence of conductive additives on the surface of the cathode particles are taken into consideration for enabling the flow of electrons, which leads to a decrease in the electrochemically active surface area. To obtain the diffusion characteristics, the distribution of length of line segments inside the solid electrode (the origin and termination of line segments is the electrode/electrolyte interface) is generated. The histogram of all the estimated diffusion lengths can be divided into three segments, the smaller ones correspond to the primary particles, the intermediate ones indicate the secondary particles, and the largest diffusion lengths are associated with the presence of current collecting conductive additives. For estimating the performance of these cathode active particles with different primary particle size and specific surface area, various partial differential equations for mass and charge conservation in electrode and electrolyte is solved using finite volume method in MATLAB. The electrochemical reaction at the interface is modeled using Butler-Volmer kinetics.

## Results

Results obtained from the various research activities adopted this year will be discussed below. All the experiments for characterizing the calcination of NMC111-hydroxide precursors, and estimation of cell level voltage vs. capacity performance of NMC811 cathode particles, are conducted at ANL. The experimental results for the calcination of  $TMCO_3$  cathode precursors are obtained from the existing literature.

### ***Deciphering the reaction kinetics of NMC111 hydroxide cathode precursors with lithium salt at elevated temperatures during the calcination process.***

Transition metal hydroxide ( $NMC111(OH)_2$ ) cathode precursors are mixed with stoichiometric amount of lithium hydroxide ( $LiOH$ ) or lithium carbonate ( $Li_2CO_3$ ) salt, and calcined at elevated temperatures. Evolution of the different phases during the calcination process are visualized using the *in situ* XRD at the APS (ANL). The waterfall plot demonstrating the formation and destruction of the hydroxide, spinel and layered phases are shown in Figure II.7.1, where the calcination with  $LiOH$  and  $Li_2CO_3$  is shown in (a) and (b), respectively. Location of the (003) peak, which is considered to be the most prominent signature of the layered phase, is highlighted by the red box in Figure II.7.1. Due to the similarity of the  $NMC111(OH)_2$  based initial reactants and  $LiNMC111O_2$  based final layered oxide cathode as the final products, the initial and final XRD signatures are very similar. Note that some initial differences are observed due to the difference in adopted lithium salt, such as, the peak at two theta  $6^\circ$  which corresponds to  $Li_2CO_3$  that is only observed in Figure II.7.1(b), and not present in the  $LiOH$  case.

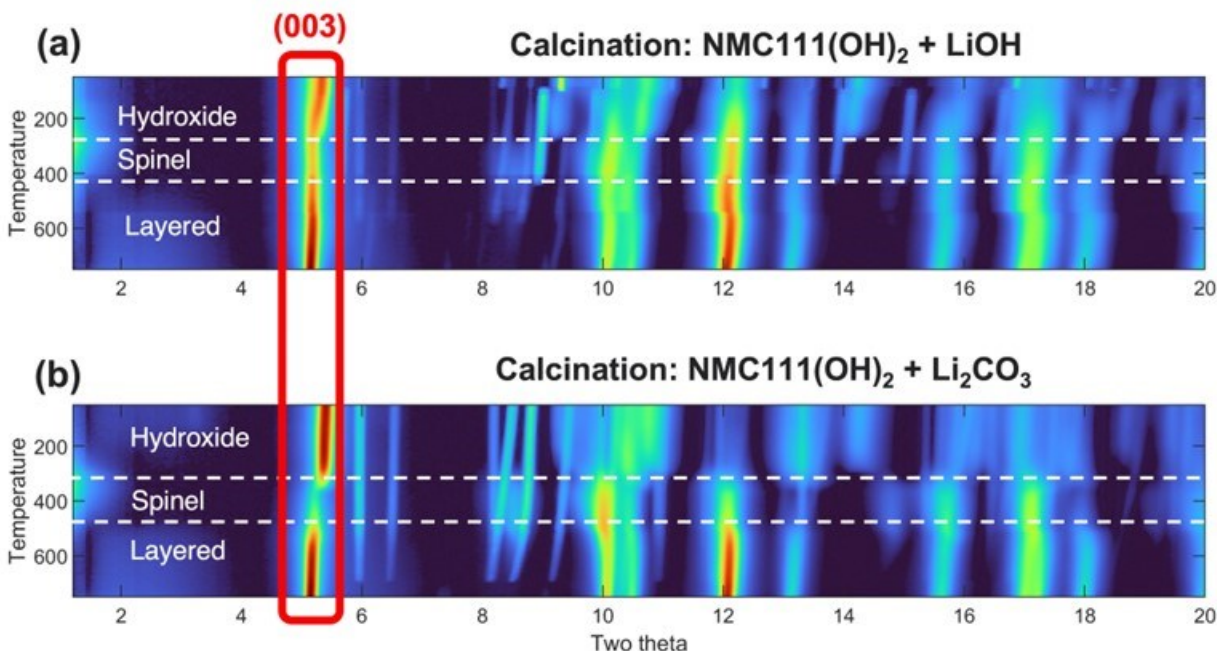


**Figure II.7.1** Two dimensional waterfall plot of the evolution of different phases obtained using X-ray diffraction at the Advanced Photon Source (APS, ANL) during the in situ calcination of NMC111-hydroxides with different lithium salts. The evolution of the (003) peak is highlighted that indicates the formation of the layered phase. (a) Calcination of NMC111(OH)<sub>2</sub> with LiOH. (b) Calcination of NMC111(OH)<sub>2</sub> with Li<sub>2</sub>CO<sub>3</sub>. Earlier formation of the (003) layered phase is observed during the calcination with LiOH.

In both the calcination protocols with LiOH and Li<sub>2</sub>CO<sub>3</sub>, initially the NMC111(OH)<sub>2</sub> decomposes at around 250°C to 300°C, and forms the spinel type transition metal oxide along with the release of water. The major difference in the two calcination procedures appear in the stability of the intermediate phase, which is substantially influenced by the difference in melting temperature of LiOH and Li<sub>2</sub>CO<sub>3</sub>. Note LiOH melts at around 465°C, which is much lower than the melting point of Li<sub>2</sub>CO<sub>3</sub> (around 725°C). The intermediate spinel is much short-lived for LiOH as compared to Li<sub>2</sub>CO<sub>3</sub>. Interestingly, in Figure II.7.1(a), lithiation/layering of the NMC111 precursors occurs at around 400°C, which is much earlier than the melting of LiOH. Similarly, in Figure II.7.1 (b), during the calcination of NMC111 with Li<sub>2</sub>CO<sub>3</sub>, formation of the lithiated layered phase is observed at around 500°C, which is again much before the melting of Li<sub>2</sub>CO<sub>3</sub> at 725°C. Hence, some form of solid state reaction is evident between the cathode precursor and the lithium salt, which leads to the early lithiation and layering of the transition metal oxides. Note that the oxidation of the transition metals occurs either during the formation of the spinel intermediates or at the time of the lithiation process.

In order to decipher the mechanism of lithiation during the calcination of NMC111-hydroxide precursors, AIMD based atomistic simulations of the reaction between the spinel type oxidized transition metal intermediate (M<sub>2</sub>O<sub>4</sub>) and LiOH is conducted, and the results are depicted in Figure II.7.2(a). Rapid lithiation of the oxidized transition metals, and formation of a lithiated disordered rocksalt phase, are observed during the simulation conducted at 750K. On the contrary, if the AIMD simulations are initiated from the NMC111(OH)<sub>2</sub> phase, the reaction with LiOH slows down significantly, which is clearly shown in Figure II.7.2 (b). Removal of the lattice water molecules must be conducted before successful lithiation of the cathode particles. After removing the water molecules from the computational domain, formation of the lithiated disordered rocksalt phase is observed even when the initial transition metal is NMC111(OH)<sub>2</sub>, but the total amount of time required for the lithiation process depends strongly on the rate of the water removal process. Note that during the *in situ* calcination, complete removal of the water containing hydroxide phase is observed before the initiation of the lithiation/layering process. Due to the presence of oxygen, the transition metals (TMs) get oxidized almost simultaneously with the removal of water, which occurs within the temperature of 300°C and

converts into the spinel phase (occurs for both the LiOH and Li<sub>2</sub>CO<sub>3</sub> salts). Lithiation of these oxidized spinel type TM-intermediate is observed during the in situ calcination of NMC111-hydroxides. This dictates that the scenario presented in Figure II.7.2 (a), where lithiation of the spinel intermediate is simulated, should correlate better with the experimental observations.

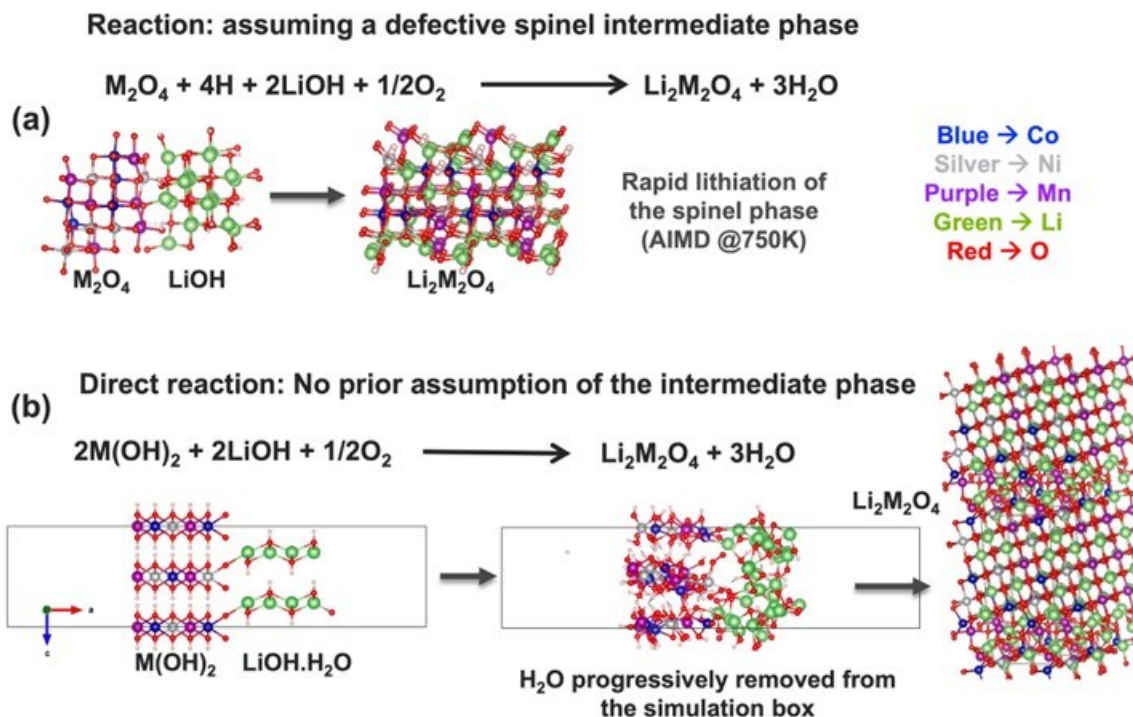


**Figure II.7.2** Atomistic simulations of the lithiation reaction of the transition metals (denoted as “M”). (a) Reaction between spinel type transition metal oxide (M<sub>2</sub>O<sub>4</sub>) and LiOH. Rapid lithiation of the spinel phase is observed in the ab initio molecular dynamic (AIMD) simulations conducted at 750K. (b) AIMD simulation of the lithiation of the transition metal hydroxide (M(OH)<sub>2</sub>) precursors with hydrated LiOH. Lithiation of the metals is highly dependent on the removal of water that forms during the reaction. The final configuration is the formation of the lithiated disordered rocksalt phase. Achieving the layered oxide phase from the AIMD simulations is a challenge.

Being guided by the *in situ* XRD observations and atomistic mechanisms, a mesoscale level computational framework is developed for capturing the evolution of different phases and sintering induced changes in particle size during the calcination of NMC111-hydroxide cathode precursors with both LiOH and Li<sub>2</sub>CO<sub>3</sub>. The various chemical reactions taken into account are as follows: removal of water (from the hydroxides), oxidation of the TMs, lithiation, and layering. Surface, grain-boundary, and bulk diffusion mediated grain growth of the primary particle is also taken into account, where the activation energy barrier for sintering the layered phase is assumed to be much smaller than that of the lithiated disordered rocksalt phase. Accordingly, significant grain growth is simulated after the formation of the layered phase. Note that major sintering of the primary particles can also occur after the removal of water and before the oxidation of the TMs, but is never observed because of the limited stability of the desired intermediate phase. Oxidation of the TMs, or surface coverage by the oxygen ions, can significantly slow down the grain growth phenomena.

Figure II.7.3(a) and Figure II.7.3 (b) demonstrate the evolution of different phases with temperature as observed during the calcination of NMC111-hydroxides with LiOH and Li<sub>2</sub>CO<sub>3</sub>. The blue, red, and black lines indicate the water containing hydroxides, intermediate, and layered phases, respectively. The experimentally observed evolution of different phases are denoted by the dashed lines, whereas model predictions are shown by the solid ones. The possible calcination reaction is shown on top of the Figure II.7.3 (a) and Figure II.7.3

(b), where formation of  $\text{CO}_2$  is only observed while calcining with  $\text{Li}_2\text{CO}_3$ . Due to the difference in the melting temperature of  $\text{LiOH}$  and  $\text{Li}_2\text{CO}_3$ , evolution of the lithiated layered phase within the TM-precursors occur at different temperatures (also alluded to while describing Figure II.7.1). The developed mesoscale level computational methodology assumes a factor of five (5x) larger magnitudes of reaction rate constant associated with the lithiation process for the  $\text{LiOH}$  salt as compared to  $\text{Li}_2\text{CO}_3$ , to capture the difference in their melting temperatures. Reaction rate constants for other physical phenomena, such as, dehydration and oxidation of TMs, are kept constant during the calcination with both the lithium salts. Evolution of the layered phase (denoted by the black line) is captured relatively well by the developed mesoscale level computational methodology for the calcination of both  $\text{LiOH}$  and  $\text{Li}_2\text{CO}_3$ . In Figure II.7.3(a), the sudden decrease in the rate of evolution of the layered phase at around  $500^\circ\text{C}$  is observed in both experiments and theoretical models. This is attributed to the early lithiation and layering of the surface of the cathode primary particles during calcination with  $\text{LiOH}$ . But the propagation of the layered phase into the center of the primary particle is limited by diffusion of lithium, which is a slow process, and effectively slows down the propagation of the layered phase. A similar decrease in rate of layering is also observed in Figure II.7.3(b) while calcining TM-precursors with  $\text{Li}_2\text{CO}_3$ , but the extent of the decrease in rate of layering is much less during the transition, which occurs at around  $600^\circ\text{C}$ .

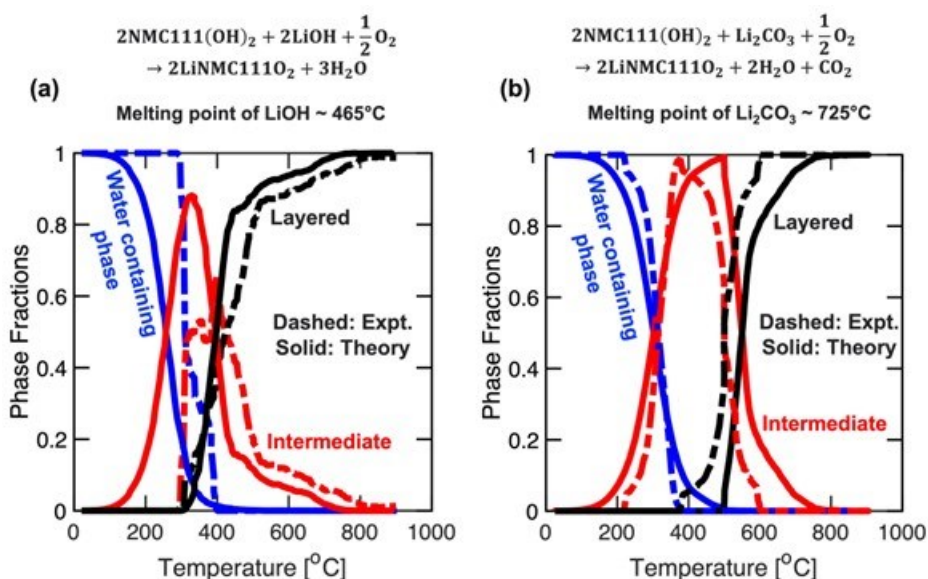


Figure II.7.3 Comparison between the experimentally observed (dashed line) and computationally predicted (solid lines) evolution of the different phases during the calcination of NMC111-hydroxide with lithium salts.

The transition metal hydroxide ( $\text{NMC111}(\text{OH})_2$ ) phase is denoted by the blue lines, the intermediate oxide phase is depicted by red, and the layered phase is shown in black. (a) Evolution of different phases during the calcination of  $\text{NMC111}(\text{OH})_2$  with  $\text{LiOH}$ . (a) Formation of phases during the calcination of  $\text{NMC111}(\text{OH})_2$  with  $\text{Li}_2\text{CO}_3$ . The possible chemical reactions are shown on top of the main figures, and the melting points of the individual lithium salts are pointed out.

#### **Competition between the precipitation of transition metal carbonates within batch and continuous processes.**

Coprecipitation of transition metal carbonates are computationally simulated in batch and continuous mode reactors by solving chemical equilibrium and mass balance relations. Impact of fluid flow on the overall coprecipitation process is not investigated in this study. The turbulence and mixing within the fluid medium are assumed to maintain uniform distribution of reactants and products within both reactors. Schematic representation of a batch and a continuous reactor are shown in Figure II.7.4(a) and Figure II.7.4 (c), respectively, where the inflow and outflow of reactants and products are clearly depicted within the schematic of the continuous reactor. Precipitation of transition metal carbonate ( $\text{TMCO}_3$ ) is assumed to occur within the reactors, where equal amount of  $\text{NiSO}_4$ ,  $\text{MnSO}_4$  and  $\text{CoSO}_4$  are used as the source of TMs, and ammonium

bicarbonate ( $\text{NH}_4\text{HCO}_3$ ) is used as the source of both the carbonate ( $\text{CO}_3^{2-}$ ) anions as well as the ammonia ( $\text{NH}_3$ ) based chelating agents. Due to the very low solubility of the  $\text{TMCO}_3$  in water, their precipitation becomes evident as the concentration of  $\text{TM}^{2+}$  cations and  $\text{CO}_3^{2-}$  anions increase within the reacting solution, and their supersaturation ratio (SSR) exceeds unity. SSR of the  $\text{NiCO}_3$ ,  $\text{MnCO}_3$ , and  $\text{CoCO}_3$ , as observed in the batch and the continuous reactors, are shown by the black, red, and blue lines, in Figure II.7.4 (b) and Figure II.7.4 (d), respectively. Due to the continuous precipitation of the  $\text{TMCO}_3$  products, SSR of the individual metals decrease with time (see Figure II.7.4 (b)). However, the concentration of TMs within the continuous reactors keeps on increasing due to the inflow of metals and carbonates, and as the SSR exceeds unity, precipitation of the products also occurs. After an initial transition period, the SSR of  $\text{NiCO}_3$ ,  $\text{MnCO}_3$ , and  $\text{CoCO}_3$  reach a steady state within the continuous reactors, which is clearly shown in Figure II.7.4 (d).

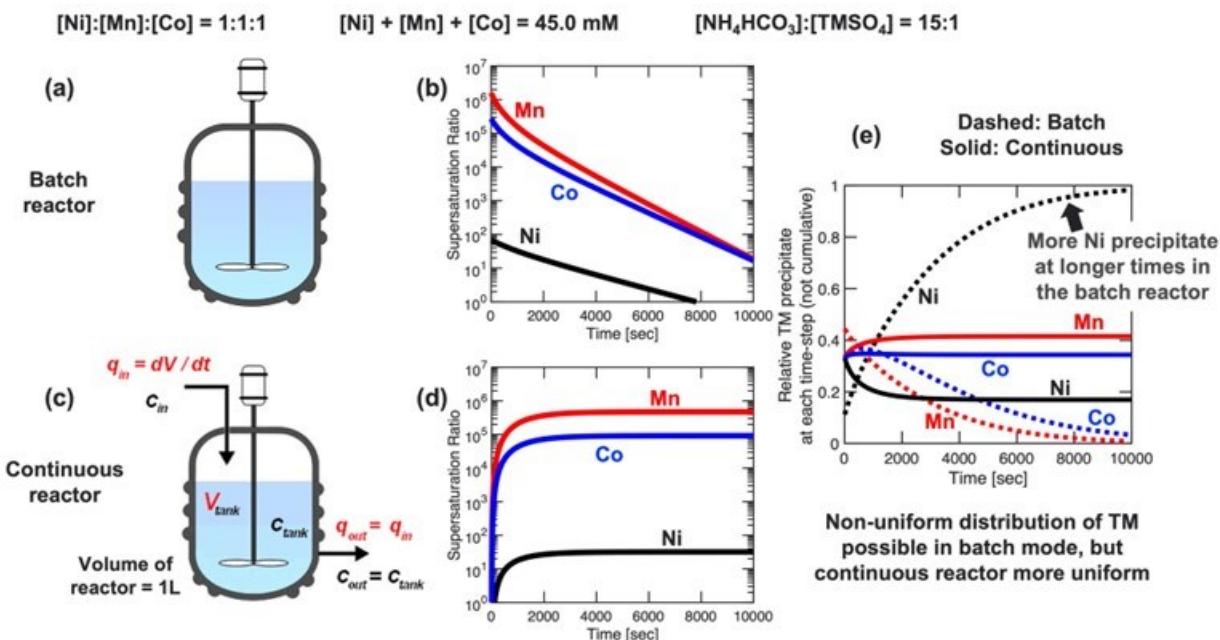


Figure II.7.4 Comparison between the precipitation of NMC111-carbonate in a batch and a continuous reactor. Total concentration of the transition metals (TMs) is maintained at 45 mM, and the ratio of  $[\text{NH}_3]:[\text{TM}^{2+}]$  is kept at 15:1 during the entire reaction process. (a) Schematic diagram of a batch reactor. (b) Time dependent evolution of the supersaturation ratio (SSR) within the batch reactor for  $\text{NiCO}_3$  (black line),  $\text{MnCO}_3$  (red line) and  $\text{CoCO}_3$  (blue line). Due to continuous precipitation, the SSR of various precipitates decreases with time. (c) Schematic representation of a continuous reactor, where the inflow and outflow of reactants and products are denoted clearly. (d) Time dependent supersaturation ratio (SSR) of  $\text{NiCO}_3$ ,  $\text{MnCO}_3$  and  $\text{CoCO}_3$ , in the continuous reactor, is denoted by the black, red, and blue lines, respectively. All the SSR initially increases with time, which eventually saturates at a particular limit. (e) Comparison between the time dependent relative fraction of TM precipitates as obtained from the batch (dashed) and continuous (solid) reactors. In the batch mode, fraction of Ni increases with time, which indicates Ni-rich surface of the precipitate carbonate particles. However, the fraction of TMs in the continuous reactor reaches a steady state value after some initial transient.

The main aim of this study is to decipher the time dependent precipitation of the different TMs in the batch and the continuous reactors. Accordingly, the relative TM precipitate at each time step is plotted in Figure II.7.4 (e) for both the batch and continuous reactors by the dashed and solid lines, respectively. Note that the fraction TM precipitate is not cumulative, and indicates the fractional magnitude at that particular instant. Due to their lower solubility products, initially enhanced amount of  $\text{MnCO}_3$  and  $\text{CoCO}_3$  gets precipitated in the batch reactor. With increasing time, precipitation induced removal of Mn and Co ions from the solution leads to less precipitation of the  $\text{MnCO}_3$  and  $\text{CoCO}_3$  at longer times. Accordingly, enhanced precipitation of  $\text{NiCO}_3$  is observed within the batch reactor at longer residence times. Hence,  $\text{TMCO}_3$  particles obtained from the batch



reactor is expected to be rich in Mn and Co close to the center, rich in Ni on the surface. On the contrary, precipitation of transition metals in the continuous reactor reaches a steady fraction after an initial transient. This is consistent with the trend observed in Figure II.7.4 (d), where the SSR of different  $\text{TMCO}_3$  reaches a steady magnitude with time. Note that, in the continuous reactor, at steady state the precipitation of Ni is substantially less than the precipitation of Mn and Co. This can be attributed to two factors:

- Higher solubility product of  $\text{NiCO}_3$  as compared to Mn and Co-carbonates.
- Higher stability of the Ni-ammonia complex that leads to a decrease in the concentration of free  $\text{Ni}^{2+}$  cations that can precipitate by reacting with the  $\text{CO}_3^{2-}$  anions.

Accordingly, the  $\text{TMCO}_3$  particles precipitated in a continuous reactor demonstrates Ni-deficient composition, but the chemical composition remains uniform throughout the radius of the entire particle.

### Exploring the impact of particle structure and morphology in determining the final performance of Ni-rich NMC cathode materials.

Ni-rich NMC cathodes are of significant interest due to their higher capacity within the conventional voltage limit of 4.2V. However, in order to minimize the side reactions experienced by the Ni-rich cathodes, and effectively maximize their cycle life, efforts have been initiated to increase the size of the primary particles by sintering out the grain boundary regions. Experimental efforts at the MERF (ANL) have attempted to increase the sintering temperature during the calcination of NMC811 cathodes, which leads to larger primary particles and smaller surface area. However, increasing the size of the primary particles leads to an enhancement in their diffusion length, which can lead to increase in mass transfer resistance and smaller magnitudes of achievable capacity, which is investigated as part of the present project using computational means.

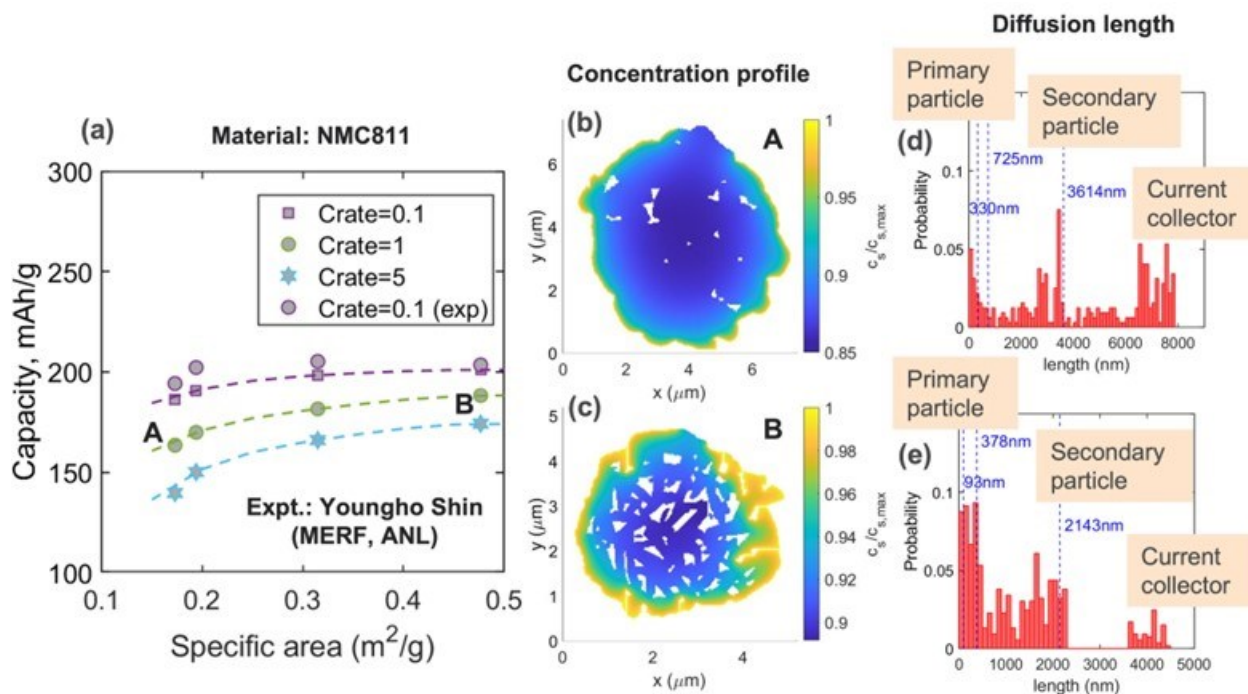


Figure II.7.5 Performance estimation of Ni-rich NMC811 cathode particles using mesoscale level computations. (a) Increasing capacity with increasing specific area of the cathode particles observed at different C-rates. The experimentally observed capacities at 0.1C is also clearly denoted, which is adopted from Youngho Shin from MERF at ANL. (b-c) Normalized lithium concentration profile observed at 1C in a secondary particle with very low (b) and very high (c) specific surface area. The final capacity for these two particular microstructures are denoted by “A” and “B” in Figure II.7.5(a). (d-e) Distribution of diffusion lengths in the two particle microstructures shown in Figures II.7.5(b) and (c). The probability of experiencing smaller diffusion lengths is much larger in the particle microstructure shown in Figure II.7.5(c), which demonstrates larger specific surface area.

Experimentally several cathode particles were generated by Youngho Shin (MERF, ANL) by changing the temperature of calcination, which led to cathodes with different primary particle size and different surface area (measured using the BET technique). The specific capacity of those cathodes obtained at 0.1C are shown in Figure II.7.5(a) by the purple circles. Data point on the left of the Figure II.7.5 (a) are obtained from particles with smaller specific surface area and larger primary particle size, which were calcined at higher temperatures. On the contrary, the data points on the right corresponds to the cathode particles with higher surface area and smaller primary particles, which are obtained by calcining at lower temperatures. Computationally generated cathode microstructures with large and small primary particles are shown in Figure II.7.5 (b) and Figure II.7.5 (c), respectively. The simulated distribution of the normalized lithium concentration is also shown in Figures (b) and Figure II.7.5(c), where larger concentration gradients are evident in the cathodes with bigger primary particles. The distribution of diffusion lengths as observed in cathode particles with lower and higher specific surface area is shown in Figure II.7.5 (d) and Figure II.7.5 (e). The diffusion lengths are much longer for cathode microstructures with larger primary particles. It is evident that smaller specific surface area and larger primary particle size leads to higher mass transfer resistance and effectively lower observable specific capacity, even at 0.1C rate, which is clearly shown in Figure II.7.5 (a). The computational model is also able to capture the mass transport limitations with increasing diffusion lengths even at very low C-rates, which is only possible through the incorporation of the decrease in diffusion coefficients with increasing lithium concentration in the cathode particles. Increasing the rate of operation to 1C and 5C leads to a further enhancement in mass transport limitations and subsequent decrease in achievable specific capacity, which is well captured by the simulations in Figure II.7.5 (a). Since the cathode particle microstructure is altered by changing the calcination temperature, a possible pathway to connect the cathode synthesis to its performance is elaborated in this study.

#### **Computationally investigate the calcination of LMR-NMC cathodes.**

Due to the heavy commercialization of the Ni-rich cathodes and the higher price associated with the extraction of Ni, substantial focus has shifted on the fabrication of cathode materials with earth abundant minerals. A well investigated candidate is the Li-Mn-rich NMC layered oxide cathodes, which has been studied extensively for the last couple of decades for enabling higher capacity and increasing its cycle life. However, less effort has been invested in deciphering and modeling the synthesis of these Li and Mn-rich (LMR) cathode particles, specifically their calcination procedures. In the present project, the detailed computational procedure developed to understand the calcination of Ni-rich layered oxide cathodes, is adapted to decipher the calcination mechanism of the LMR-NMC cathode particles. The required knowledgebase and possible chemical reactions are extracted from the detailed *in situ* calcination of Mn-carbonate with lithium-carbonate salt reported in the existing literature, which is also provided on top of Figure II.7.6 (see Kan et al., *Journal of Power Sources* 266 (2014) 341 – 346). The experimentally observed elimination of the  $\text{TMCO}_3$  phase, evolution of the oxidized intermediate phase, and formation of the layered phase is shown by the blue, red, and black dashed lines, respectively, in Figure II.7.6(c).

In order to capture the evolution of different phases and sintering of particles during the calcination process, the phase field based methodology developed for the calcination of NMC111 cathodes have been modified to predict the following reactions: (i) Removal of carbon di-oxide, (ii) Oxidation of TMs by reacting with oxygen from environment, and (iii) Lithiation and layering of the cathode particles through the reaction with the lithium salt. The initial  $\text{TMCO}_3$  precursor particle microstructure adopted in the computational analysis is shown in Figure II.7.6 (a). The precursor particles are heated at a rate of  $1^\circ\text{C}/\text{min}$ , which is consistent with the experiments reported in the literature. The  $\text{Li}_2\text{CO}_3$  salt particles are not simulated in the present analysis. All the chemical reactions, such as, removal of  $\text{CO}_2$ , oxidation, and lithiation are assumed to occur at the free surface. The final particle microstructure after calcining for 15 hours (and  $925^\circ\text{C}$  temperature) is shown in Figure II.7.6 (b), where significant amount of grain growth is observed due to the sintering of the primary particles. Finally, in Figure II.7.6 (c), the model predicted evolution of the TM-carbonates, oxidized intermediates, and layered phases are shown by the solid blue, red, and black lines, respectively. Change in particle size due to the variation in species concentration within the cathodes, as well as the high temperature sintering processes, are modeled in the computational framework. Since majority of the sintering induced

particle growth occurs within the layered phase, larger diffusion length induced decrease in the rate of oxidation or lithiation is not observed in the present simulations. Good correlation between the experimentally observed and computationally predicted evolution of different phases are shown in the Figure II.7.6 (c). Note that specific to the LMR-NMC materials, formation of the  $\text{Li}_2\text{MnO}_3$  spinel phase occurs only after the complete layering of the cathode particles. The present computational methodology is not capable of capturing the formation of the spinel phase, which we plan to incorporate within the modeling framework as part of our future activity.

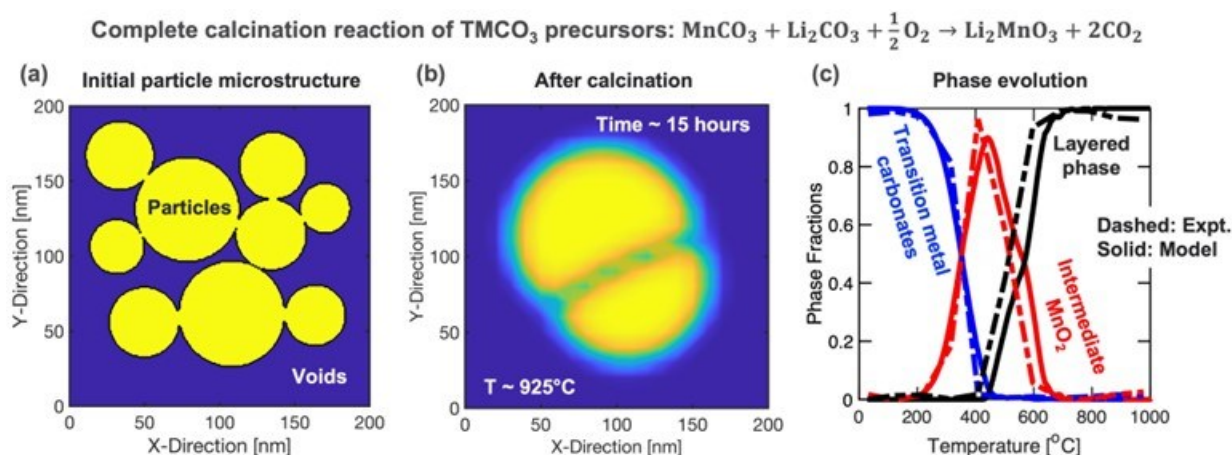


**Figure II.7.6** Computational simulation of the calcination of  $\text{MnCO}_3$  with  $\text{Li}_2\text{CO}_3$  at elevated temperatures. (a) Initial microstructure of the  $\text{MnCO}_3$  particles with average size around 30 nm. (b) Particle microstructure after calcining for 15 hours. The temperature is increased from room temperature at a rate of  $1^\circ\text{C}/\text{min}$ . Sintering induced grain growth is well captured by the developed methodology. (c) Evolution of different phases during calcination is predicted by the computational model (solid line) and compared with the experimental results (dashed), which is adopted from Kan et al., *JPS* 266 (2014) 341 – 346. Removal of the  $\text{TMCO}_3$  is shown by the blue line, the oxide intermediate is denoted by the red lines, and the formation of the layered phase is depicted by the black one. The most probable chemical reaction is shown at the top. Note that the formation of the spinel phase is not captured here.

## Conclusions

Detailed investigation of the calcination of NMC cathodes are conducted using in situ characterization and computational modeling techniques. Irrespective of the type of the cathode precursors (hydroxide or carbonate), they are converted to their oxides by removal of water or carbon di-oxide, prior to the lithiation and layering process. According to in situ experiments, early lithiation is observed if lithium hydroxide ( $\text{LiOH}$ ) is used as the sources of the lithium salt as compared to lithium carbonate ( $\text{Li}_2\text{CO}_3$ ) due to the difference in their melting temperatures. Lithiation of the transition metals (TMs) start well before the melting of the lithium salts, which can be attributed to some form of solid state reaction or the formation of a low temperature eutectic when the lithium salts are mixed with the TM-oxides. Atomistic simulations indicate that the layered structure of the TM-hydroxides is completely destroyed before the reaction with lithium salt and final layering process, which is in contrast to the topotactic transition of the cathode particles hypothesized in several existing literature. The mesoscale level models are capable of capturing the removal of the hydroxides and carbonate phases, evolution of the oxidized intermediate phase, and finally can successfully predict the formation of the layered phase. The reaction rate constant associated with the lithiation process is a factor of five (5x) larger for  $\text{LiOH}$  based lithium salt as compared to lithium carbonate.

During the coprecipitation process, by comparing the distribution of transition metals within the simulated cathode precursors, it is observed that gradient in the TM composition is possible if the precursors are precipitated in a batch reactor (such as, enhanced Mn at the center and more Ni close to the surface). These unintended gradients evolve due to the difference in the solubility products for the different TM compounds (for example, the solubility of  $\text{MnCO}_3$  is less than the solubility of  $\text{NiCO}_3$  in water). However, the possibility

of forming the concentration gradients can diminish if the particles are precipitated in a continuous mode. Due to the difference in their solubility products, or because of their tendency of forming metal-ammonia complex, the TM composition within the precipitate can be far from the desired value in the continuous reactors, but their distribution should be uniform throughout the radius of the precipitated precursors.

Finally, dependence of the cell performance on the calcination temperature is studied using the developed computational technique. The larger primary particles obtained by calcining the cathode particles at higher temperatures can be helpful for minimizing the side reactions, but introduces mass transport limitations within the cathode active particles that demonstrate larger diffusion lengths. The study also revealed that the decrease in lithium diffusivity with increasing lithium concentration within the Ni-rich cathode active particles is significant, such that the mass transport limitations associated with larger primary particles are observed even at very low rates of C/10.

### Key Presentations

1. Pallab Barai, Mark Wolfman, Xiaoping Wang, Jiajun Chen, Arturo Gutierrez, Juan Garcia, Jianguo Wen, Tim Fister, Hakim Iddir, and Venkat Srinivasan. [Morphology of Transition Metal Carbonate Cathode Precursors](#). In: *The Electrochemical Society Fall Meeting* October 2022.
2. D. Tewari, A. Gutierrez, J. R. Croy, and V. Srinivasan. Designing Cathode Morphology for Materials with Solid Transport Limitation. In: *The Electrochemical Society Fall Meeting* October 2022.
3. Pallab Barai, Juan Garcia, Tiffany Kinnibrugh, Ke Chen, Mark Wolfman, Xiaoping Wang, Tim Fister, Feng Wang, Hakim Iddir, and Venkat Srinivasan. [Deciphering the Interplay between Thermodynamics and Kinetics during Cathode Calcination](#). In: *The Electrochemical Society Spring Meeting* June 2023.

### Acknowledgements

This research is supported by the Vehicle Technologies Office (VTO), Department of Energy (DOE), USA. Argonne National Laboratory is operated for DOE Office of Science by UChicago Argonne, LLC under the contract number DE-AC02-06CH11357. The authors also acknowledge the computing resources provided by the Laboratory Computing Resource Center (LCRC) at Argonne National Laboratory. Portions of this work were performed at GeoSoilEnviroCARS (The University of Chicago, Sector 13), Advanced Photon Source (APS), Argonne National Laboratory. GeoSoilEnviroCARS is supported by the National Science Foundation – Earth Sciences (EAR – 1634415) and Department of Energy - GeoSciences (DE-FG02-94ER14466). This research used resources of the Advanced Photon Source, a U.S. Department of Energy (DOE) Office of Science User Facility operated for the DOE Office of Science by Argonne National Laboratory under Contract No. DE-AC02-06CH11357. Regarding the computational and experimental research, the atomistic computations were conducted by Juan Garcia and Hakim Iddir, and the mesoscale level computational modeling and subsequent analysis was carried out by Pallab Barai and Venkat Srinivasan. All the experimental research was conducted by Timothy Fister, Tiffany Kinnibrugh, Mark Wolfman, and Xiaoping Wang. The electrochemical modeling, analysis, and simulations, for estimating the performance of the cathode particles, was conducted by Deepti Tewari. Also, Venkat Srinivasan managed the entire project, and made sure that the project follows the correct direction without deviating much from its primary goal.

## II.8 *In Situ* Spectroscopies of Processing Next-Generation Cathode Materials (ANL, BNL)

### **Feng Wang, Principal Investigator**

Argonne National Laboratory  
Applied Materials Division  
9700 S. Cass Avenue  
Lemont, IL 60439  
E-mail: [fengwang@anl.gov](mailto:fengwang@anl.gov)

### **Jianming Bai, Co-Principal Investigator**

Brookhaven National Laboratory  
National Synchrotron Light Source II  
Upton, NY 11973  
E-mail: [jmbai@bnl.gov](mailto:jmbai@bnl.gov)

### **Haiyan Croft, DOE Technology Development Manager**

U.S. Department of Energy  
E-mail: [Haiyan.Croft@ee.doe.gov](mailto:Haiyan.Croft@ee.doe.gov)

Start Date: October 1, 2019	End Date: September 30, 2024	
Project Funding (FY23): \$500,000	DOE share: \$500,000	Non-DOE share: \$0

### **Project Introduction**

Lithium-ion battery (LIB) technology provides critical energy-storage needs for society, ranging from everyday electronics to electrified transportation and power grids. The demand for lighter devices and longer-duration storage continues to fuel the need for energy-denser batteries. This need, in turn, requires designing new battery materials, understanding how they function and, ultimately, making them through scalable synthesis and processing – namely, manufacturing at scale. Technical advances in characterization and computation in the past decade have greatly facilitated the discovery and design of battery materials, but how to make them with the required capacity, power, lifespan, and safety is another layer of complexity, becoming the real hurdle to their practical use – very often we know what we want, but don't know how to make them. The difficulty largely lies in the knowledge gap in understanding the processes of materials synthesis and processing, wherein reactions often proceed via kinetic pathways under non-equilibrium conditions, so making it hard to be predicted by theories or computations. As there are a variety of processing parameters (precursor concentration, reaction time, temperature, pressure, pH value, ...), optimization of materials synthesis and processing mostly relies on trial and error.

Under this project, *in situ* spectroscopic techniques are developed deliberately to study the synthesis and processing of next-generation commercially viable cathode active materials (CAMs). Over the years, unique *in situ* capabilities and sample environments have been developed under the Vehicle Technology Office (VTO)-funded projects, allowing measurements at scales varying from the bulk phases to a single particle, as well as interfaces [1]. This allows access to the details of the processes, elucidating how synthesis parameters affect the kinetic reaction pathways and, consequently, the target material phases and their properties. This project is part of the *Processing Science & Engineering* (P&E) program, involving collaboration between Argonne National Laboratory (ANL), Brookhaven National Lab (BNL), and other national laboratories, universities and industries. A long-term synergistic collaboration has been established to develop processing science and technologies by leveraging the unique capabilities and expertise in different institutes, particularly in *in situ* characterization, precursor development, multiscale modeling and scale-up. The tools and techniques developed under this project are also used to support other projects funded under the P&E and other programs

by the VTO, such as Battery 500 program in collaboration with Binghamton University and deep-dive cathode programs in collaboration with Lawrence Berkeley National Lab (LBNL).

The materials focus of this project is on nickel-manganese-cobalt (NMC) oxide cathodes, with high Ni and low Co (without Co), to boost the energy density while reducing cost. As the electric vehicle market is expected to grow exponentially in the next decade, the reliance on Co as a key component in cathodes poses significant sustainability concerns due to its high cost and scarce supply chain. However, it is believed that Co is critical for the thermodynamic stability of the layered structure, and it may persist in cathodes over time [2]. To enable the commercial application of high-Ni NMC cathodes, strategies are needed to manage the competing factors of high Ni loading. High output capacity requires high Ni content; but as Ni content increases, Ni sitting at octahedra tends to go to Li sites in the crystal lattice, resulting in reduced electrochemical activity. In addition, cathodes are generally charged to high voltages (above 4.2 V) to achieve high energy density, meanwhile introducing a number of mechanical issues such as cracking due to lattice collapse, gas release, structural reconstruction (or surface densification). Such undesired phenomena may happen concomitantly and, consequently, lead to poor cyclability and voltage decay, which has been a main obstacle to the realization of high-Ni CAMs with true commercial potential. Several approaches, such as coating/doping strategies [3], high-entropy cathode design [4], have been developed, but the fundamental challenge remains, including structural disordering and the resulted cycling instability in the layer-structured cathodes [5]. Eventually, addressing such issues relies on synthesis and processing, in obtaining the materials with controlled structure morphology and surface properties.

### Objectives

This project is part of the P&E program, aiming to develop processing science and technologies for scalable production of CAMs, to fill the gap from materials discovery to manufacturing, focusing on next-generation commercially viable CAMs for EVs. Specifically:

- Developing a fundamental understanding of the process and involved reactions during the synthesis and processing of Ni/Mn based cathode materials.
- Designing processes for scalable production of high-performance Ni/Mn-based cathodes.

### Approach

A science-based data-driven approach is taken in this project to enable *synthesis and processing by design* [1]. Specifically, synchrotron X-ray based in situ techniques are developed for real-time probing of the intermediate phases and their structural evolution during synthesis/processing by utilizing the world-leading facilities at ANL, BNL and other national laboratories. This allows access to the details of the processes, elucidating how the processing parameters affect the kinetic reaction pathways and, consequently, the target material phases and their properties. Such studies, with insights into the reaction process and the involved intermediates under real conditions, provide a basis for materials synthesis/processing by design – rationally selecting synthesis/processing parameters to improve performance and reduce cost.

Since most battery materials are in the polycrystalline form, powder diffraction is commonly employed for monitoring the structural evolution during synthesis/processing. Among various scattering and spectroscopy techniques, X-ray diffraction (XRD) is arguably the most powerful tool for in situ characterization of synthesis and processing reactions. Advanced synchrotron facilities provide powerful powder diffraction capability that allows following the reactions and processes with high precision and in short time. Over the years, various in situ techniques have been developed for studying synthesis/processing reactions. With the special design of sample configuration and environment, the samples may be loaded into different beamlines/facilities for complementary characterization using multiple in situ techniques, such as x-ray fluorescence imaging, X-ray absorption spectroscopy (XAS), XRD, and X-ray total scattering coupled with pair distribution function (PDF) analysis. This capability enables both bulk measurements with a large volume of materials being sampled and local probing of structural/chemical evolution in heterogeneous materials and at surfaces/interfaces. By coupling with electrochemical characterization of the final products, such studies shed light on the process-

structure-property relationship, thereby providing a science basis for designing scalable processes suited to the commercial production of next-generation cathode materials.

## Results

### 1. Stabilizing Cobalt-Free Cathodes with Lithium-Stoichiometry Control

This study addresses the critical challenge of eliminating Co from high energy density LIBs. Instead of making the traditional layer-structured cathodes [2-5], we tackled the challenge with a novel approach, namely producing Co-free cathodes ( $\text{Li}_{1-x}\text{Ni}_{0.95}\text{Mn}_{0.05}\text{O}_2$ ; NM9505) with a composite structure and refined small primary particle size, resulting in exceptional performance, including a 90% first-cycle Coulombic efficiency, 90% capacity retention, and *close-to-zero* voltage fade for 100 cycles. By using high-brightness synchrotron sources and multiple X-ray probing tools, we revealed the intergrown structure of the composite cathodes, leading to suppressed anisotropic lattice expansion and contraction during cycling. *In situ* XRD during high-temperature synthesis revealed the evolution of the structure and the role of Li-deficiency in hindering crystallization.

#### 1.1 Li-stoichiometry Control during Synthesis

As illustrated in Figure II.8.1 a, Ni/Mn-based Co-free cathodes are attractive for their high capacity, high thermal stability and safety. However, they suffer from Li/Ni disordering and cycling instability mainly because of the introduction of  $\text{Ni}^{2+}$  to balance charge neutrality. Growing evidence shows that Li/Ni mixing is hardly avoidable in the Ni/Mn-based CAMs and becomes worse as Mn content increases, resulting from interplane super-exchange and intraplane magnetic frustration among the magnetic  $\text{Ni}^{2+}$ ,  $\text{Ni}^{3+}$ , and  $\text{Mn}^{4+}$  ions [6]. Consequently, the structural instability and associated capacity decay and voltage fade have been the major challenges for the practical use of Co-free layered CAMs, despite numerous efforts over the past decade. Herein, by following the common practice of adding extra Li during the calcination, we added 5% extra Li in making to compensate for Li loss during calcination. As expected, a highly ordered hexagonal layered structure with low Li/Ni mixing (2.6%) was obtained in the synthesized NM9505-1.05Li (not shown here). By reducing the amount of Li source to  $\text{Li}/\text{TM} = 0.95$ , we obtained the NM9505-0.95Li with a composite structure consisting of a major layered phase and a minor Li-containing rocksalt (RS) phase of about 19.6 mol%, determined by Rietveld refinement of the synchrotron XRD data. The composites consist of the major layered phase and minor RS-structured phase intergrown within the same cubic-closest packed (*ccp*) oxygen framework, by multiscale characterization using synchrotron XRD, transmission electron and X-ray microscopy (TEM and TXM) as shown in Figure II.8.1c-e. The composite NM9505-0.95Li maintains high-capacity retention of 90% (versus 75% in NM9505-1.05Li) for 100 deep cycles up to 4.4 V (Figure II.8.1 f), indicating the structural robustness of the composite structure during the high-voltage operation.

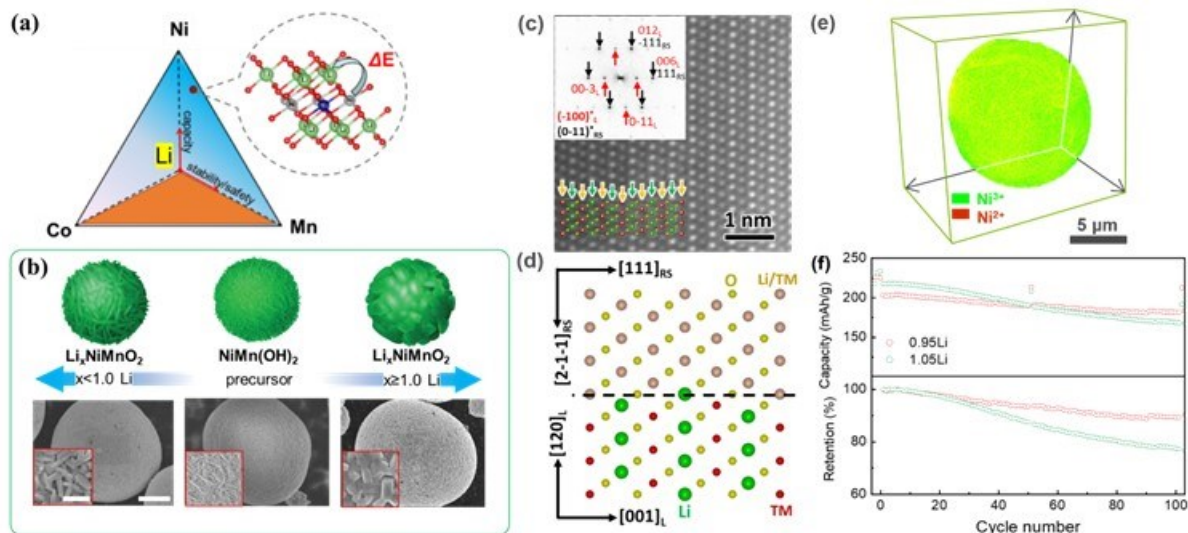


**Figure II.8.1** Li stoichiometry as a tuning handle for the structure and morphology of Ni/Mn-based Co-free cathodes. (a) Composition-property correlation in the Li-Ni-Mn-(Co) space, highlighting the performance needs in terms of capacity, cycling stability and safety and the unavoidable consequence of Li/Ni mixing. (b) Morphological tuning via Li stoichiometry, demonstrated by the abrupt difference in particle size and shape of  $\text{Li}_x\text{Ni}_{0.95}\text{Mn}_{0.05}\text{O}_2$  at  $x = 0.95$  (left) and  $x = 1.05$  (right) calcined from the same hydroxide precursor (middle). (c, d) High-angle annual dark field (HAADF)-scanning transmission electron microscopy (STEM) image and the corresponding atomic arrangement of the intergrown RS/layered (L) phases within the composite NM9505, wherein the two phases share the same ccp oxygen framework. (e) 3D-TXM mapping of the Ni valence distribution in NM9505-0.95Li (green represents  $\text{Ni}^{3+}$  and red represents  $\text{Ni}^{2+}$ , while the uniform yellowish color shows a mixture of both  $\text{Ni}^{3+}$  and  $\text{Ni}^{2+}$ ). (f) Specific and normalized capacity of NM9505-0.95Li and 1.05Li at 0.5C between 2.7-4.4 V against Li.

### 1.2 Structural and Morphological Tuning by Li Stoichiometry

The impact of the Li stoichiometry on the particle morphology, structure, and electrochemical performance was systematically studied using a series of samples prepared in Li-deficient (0.90 and 0.95Li), near-stoichiometry (1.0 and 1.025Li), and Li-excess (1.05 and 1.1Li) conditions, with the main results shown in Figure II.8.2. In the presence of deficient Li, small-sized layered-RS composites form and due to their low anisotropic lattice expansion and contraction during charging/discharging, they exhibit excellent structural stability, offering high first-cycle Coulombic efficiency, *close-to-zero* voltage fade, and high capacity retention.



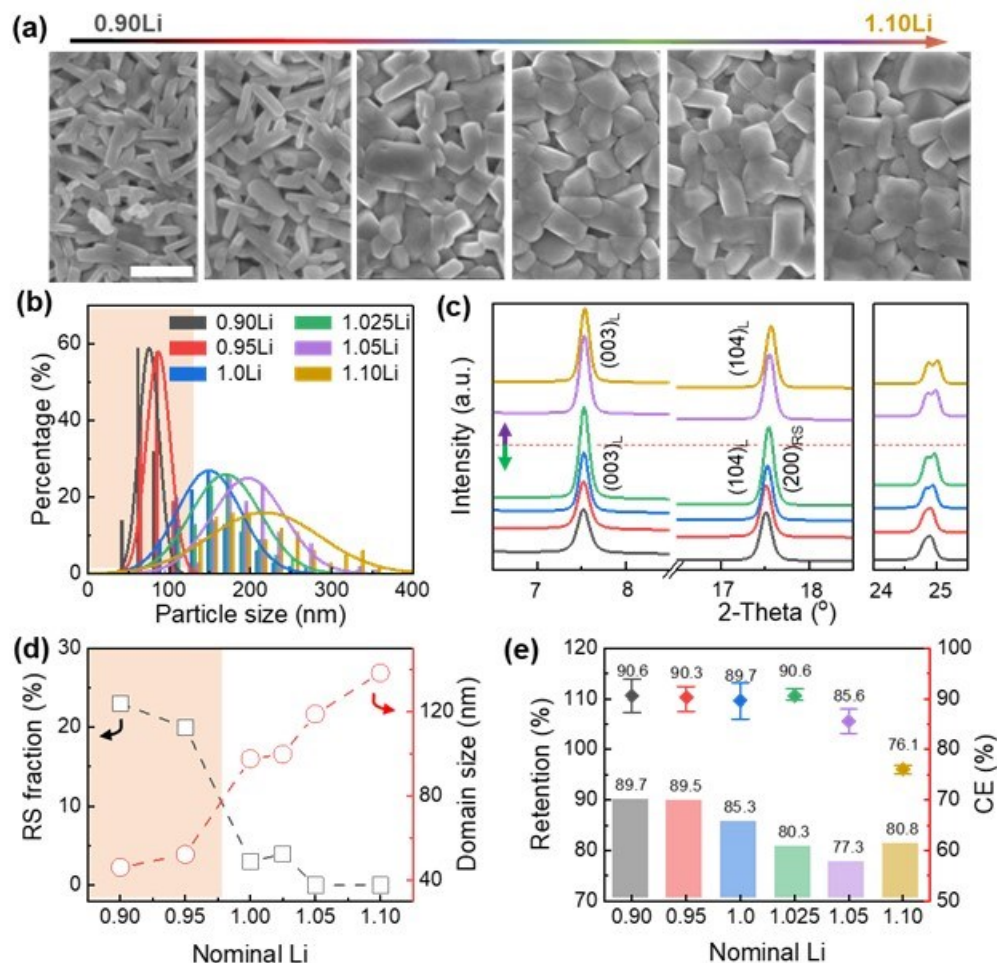
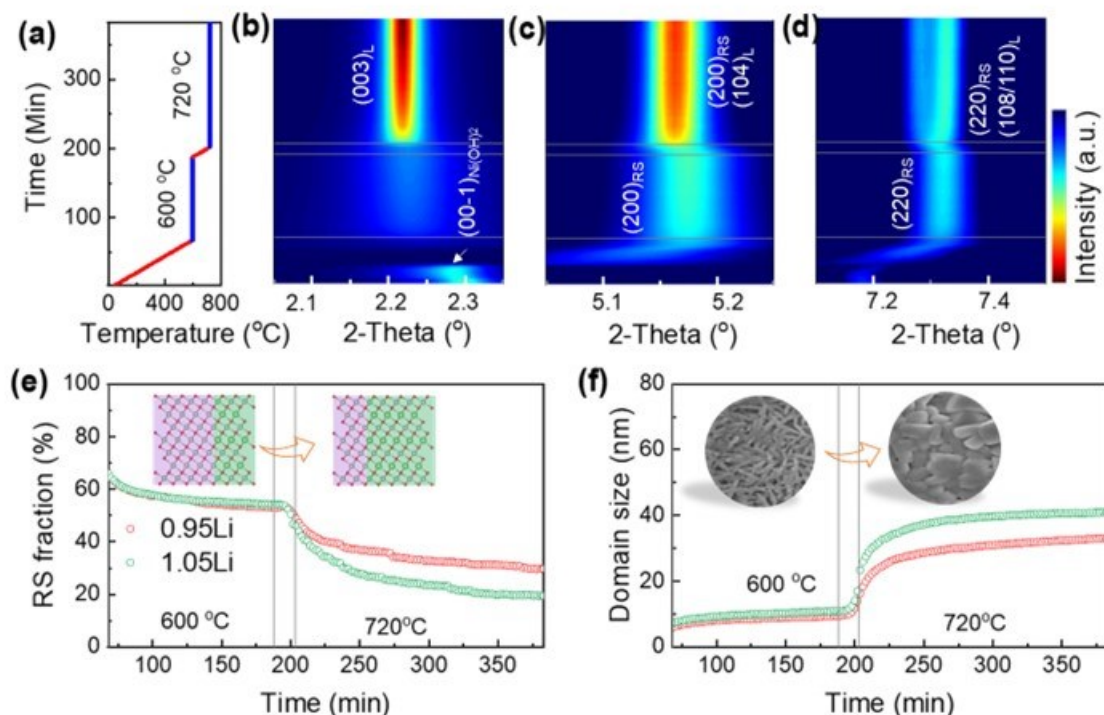


Figure II.8.2 Strong dependence of structure and morphology on Li-stoichiometry in NM9505. (a) SEM images of the NM9505 calcined from the precursors with Li stoichiometry of 0.90, 0.95, 1.00, 1.025, 1.05, up to 1.10 (from left to right), showing the strong dependence of the morphology of the primary particles on Li stoichiometry. Scale bar: 500 nm. (b) Particle size distribution of NM9505, showing the small size (below 100 nm) and narrow size distribution of the calcined NM9505 with Li stoichiometry below 1.00 (Li deficient, as shadowed), in contrast to the large size and wide size distribution of the samples with near stoichiometry and Li excess. (c) Synchrotron XRD patterns of NM9505, showing the evolution of the structure ordering with the increases of Li stoichiometry ( $\lambda = 0.6199 \text{ \AA}$ ). (d) The calculated phase fraction and domain size of the layered phase. (e) First-cycle CE (average of six cells) and the capacity retention of NM9505 with different Li stoichiometry after 100 cycles at 0.5C, showing higher values in the Li-deficient ones (0.9Li and 0.95Li), compared to those with Li excess (1.05Li and 1.10Li).

### 1.3 Impact of Li-stoichiometry on the Crystallization Dynamics

Further analysis of the calcination process was made using *in situ* synchrotron XRD, to reveal the lithiation-driven structural ordering and crystal growth. The main results were given in Figure II.8.3, showing that the overall process between NM9505-0.95Li and NM9505-1.05Li is similar, via various physico-chemical processes including (a) removal of water from the TM hydroxides, (b) oxidation and lithiation of the cathode precursors by reaction with O and Li salts, and (c) diffusion of mass (including all species, such as TM, Li, and O) resulting in sintering of the particles. The structure of the NM9505 forms the intermediate Li-containing RS and then transforms into the layered phase. At the low temperature range (up to 600°C), a high RS content is maintained. The layered domain size remains small for both cases, due to the sluggish kinetics of crystallization at low temperatures. As the temperature increased, the RS proportion dropped quickly. This process is thermally driven and, with further oxidation of Ni, more Li was incorporated into the structure and,

consequently, turning RS into layered phases. During the same period, the layered domain size grew abruptly, which indicates that the role of lithiation is critical in driving crystal growth (besides structural ordering). At high temperatures, the kinetics of structural ordering and crystal growth were strongly dependent on the Li/TM ratios. A lower RS fraction was observed in NM9505-1.05Li compared to that of 0.95Li and, correspondingly, the transformation rate from RS to layered phase was much faster in the former. As a result, a higher RS content was obtained in the final NM9505-0.95Li after holding it at 720°C for 3 hours.



**Figure II.8.3** Impact of Li stoichiometry on phase progression and crystallization during calcination of NM9505. (a) Heating profile of the in situ XRD experiment. (b-d) Contour plots of the time-resolved in situ XRD patterns during calcination of NM9505-0.95Li. (e) Calculated RS phase fraction as a function of time during calcination of NM9505-0.95Li (red circles) and NM9505-1.05Li (green circles), respectively. Inset: structure evolution from RS phase (purple shading) dominated to layered phase (green shading) dominated structure during calcination. f, Crystal growth of the layered phase as a function of time for NM9505-0.95Li (red circles) and NM9505-1.05Li (green circles), respectively. Inset: SEM images of NM9505-1.05Li at 600°C and 720°C, showing the particle growth during calcination.

Li stoichiometry played a predominant role in governing crystal growth. Li-excess NM9505 displayed faster crystal growth, through a different pathway than the Li-deficient one. Multiscale computational modeling showed that the primary particle growth was mainly mediated by mass transfer, which was predominantly determined by two mechanisms: lithiation-induced crystallization and liquid phase sintering. With Li-deficiency, the primary particle size can be maintained small. Those small primary particles consisting of intergrown RS and layered phases are formed in Li-deficient CAMs and due to the small anisotropic lattice expansion and contraction during cycling, they exhibit high structural stability. These findings demonstrate an efficient route to structural and morphological tuning via Li stoichiometry for stabilizing Co-free cathodes, with the desired cost-efficiency by eliminating the extra coating/doping steps. By offering a promising and cost-effective alternative to Co-reliant cathodes, our study addresses the critical need for the development of sustainable LIBs.

## 2. Hetero-structured Cathodes with Local Stoichiometry Control for High-Voltage Operation

The growing demand for LIBs to power electric vehicles and other energy-dense devices continues to fuel the need for cathodes of increasingly higher nickel content. The relentless pursuit of high Ni content, however, raises concerns on compromising cell lifetime and safety, especially under high-voltage operation. Alternative to the traditional design of uniform or core-shell composition, we report a rational control of local stoichiometry in high-Ni cathodes, enabling their high thermal and cycling stabilities – up to 258 °C at the fully charged state and 91.4% capacity retention for 100 cycles between 2.7 and 4.4 V (Figure II.8.4). Multimodal synchrotron X-ray characterization unveils the heterostructure of secondary particles, featuring a high-Ni core ( $\text{LiNi}_{0.90}\text{Mn}_{0.05}\text{Co}_{0.05}\text{O}_2$ ) covered by a thin Ni-gradient layer that remains stable over prolonged cycling due to suppressed oxygen release and structural deterioration. This work underlines, the intricate interplay between local stoichiometry and redox reactions in stabilizing high-Ni cathodes for high-voltage operation while ensuring safety. With the demonstrated practical solution to the long-standing issues preventing high-voltage operation of high-Ni cathodes, this work constitutes an important step towards the deployment of these cathodes in next-generation LIBs.

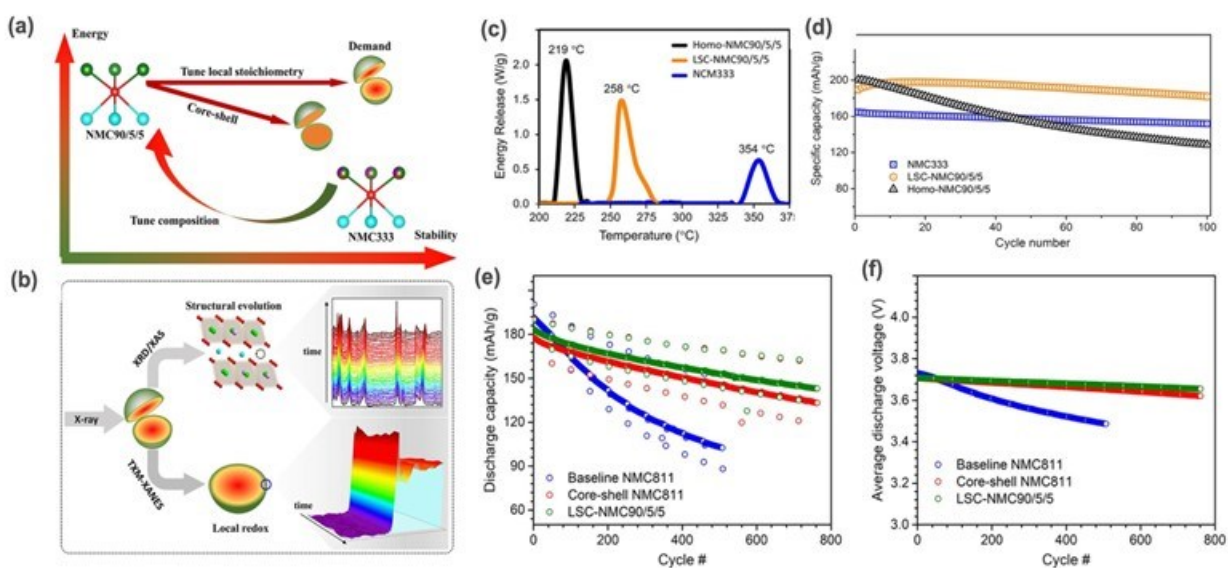


**Figure II.8.4** Rational design of high-Ni NMC cathodes with local stoichiometry control (LSC) for high-voltage and safe operation. (a) Schematics of making hetero-structured particles via the LSC route, alternative to the traditional way of employing uniform or core-shell composition, to meet the multifaceted performance requirements (e.g., high energy density, high cycling and thermal stabilities). (b) Multimodal synchrotron X-ray characterization for disentangling the interplay between local stoichiometry and electrochemical redox in stabilizing high-Ni cathodes. (c) Thermal release profiles of the electrodes charged to 4.4 V, produced by differential scanning calorimetry (DSC), showing greatly improved thermal stability of LSC-NMC9055 (orange) compared to homo-NMC9055 (black). The DSC profile from NMC333 (blue) is also provided for reference. (d) Cycling performance of LSC-NMC9055 (orange), in comparison to that of homo-NMC9055 (black) and NMC3333 (blue), between 2.7 and 4.4 V at a rate of C/2. (e, f) Discharge capacity and voltages measured from LSC-NMC9055 (green) between 3.0 and 4.3 V at a rate of C/3 Charge, C/2 Discharge. Data taken under the same conditions from the baseline NMC811 (blue) and core-shell NMC811 (red) were provided for comparison to NMC9055.

## 3. Correlative in situ XRD/Differential Scanning Calorimetry (DSC) on Calcination of $\text{LiNiO}_2$

Correlated in situ XRD/DSC were developed for taking data simultaneously to obtain information on crystallographic and thermal changes during calcination. An example on studying the calcination of LNO from  $\text{Ni}(\text{OH})_2$  is given in Figure II.8.5 (a). The heat release during dehydration and lithiation be learned from DSC (top) and correspondingly, the structural change can be learned from in situ XRD. Such measurements were performed on two different samples, S1 (without Li source) and S2 (with Li source) under the same conditions,

as shown in (Figure II.8.5(b)). In the S1 sample, there is only one peak at around 333.8 °C due to the thermal release during the decomposition of Ni(OH)<sub>2</sub>. In contrast, there are 3 peaks at 101.7, 300.7 and 439.8 °C in S2, which can be assigned to the thermal release arising from the dehydration of LiOH·H<sub>2</sub>O, decomposition of Ni(OH)<sub>2</sub> and melting of the LiOH, respectively. And interestingly, the decomposition of the Ni(OH)<sub>2</sub> in S2 is about 30 °C lower than that in S1, which is consistent with the in situ XRD measurements (Figure II.8.5 (a)) due to the early Li-intercalation that facilitated the decomposition. Such in situ XRD/DSC studies were further correlated to in situ XRD/XAS measurements under the same conditions (not shown here), to obtain comprehensive information regarding structural and chemical evolution and their correlation with the involved intermediates. The results have been submitted for publication and will be reported in the future.

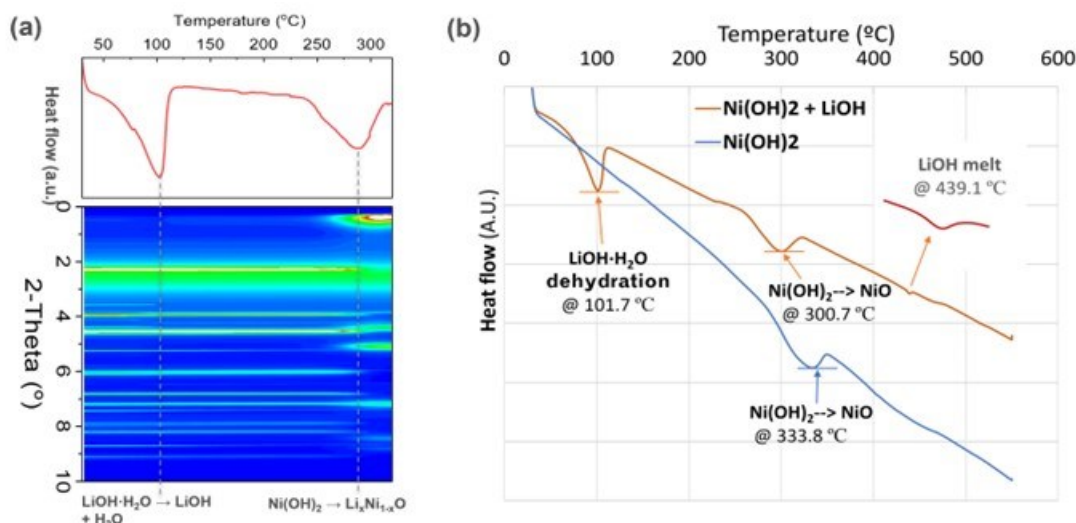


**Figure II.8.5** (a) In situ XRD/DSC on calcination of LiNiO<sub>2</sub> from Ni(OH)<sub>2</sub>, showing the heat flow (top) and the correlated contour plot of the in situ XRD (bottom) as a function of temperature. (b) DSC from Ni(OH)<sub>2</sub> with and without LiOH, showing the different behaviors.

## Conclusions

In FY23, unique spectroscopic techniques were developed for studies of the synthesis and processing of Ni/Mn-based CAMs, including i) correlated *in situ* XRD/DSC on crystallographic and thermal changes during calcination; ii) correlated *in situ* XRD/XAS for correlation between structural and chemical evolution during calcination of CAMs, iii) synchrotron X-ray spectromicroscopy for probing lithiation-driven structural ordering. Through *in situ* spectroscopy studies using those unique techniques, new insights into the processes and reaction during calcination of Ni/Mn-based CAMs were obtained, such as kinetic pathways in calcination of LNO from Ni(OH)<sub>2</sub>, impact of the size secondary particles to the lithiation process, correlated structural and chemical evolution during calcination. Those insights were further applied to developing new protocols, including the lithium stoichiometry control for making composite-structured cathodes and the control of the local stoichiometry to make hetero-structured cathodes, enabling high cycling stability during high-voltage operation.

New research activities were initiated, including i) studies on the impact of Nb coating on the structure and morphology of Ni/Mn-based CAMs; ii) surface conditioning of Ni/Mn-based CAMs; iii) investigation of the heat treatment to LiFePO<sub>4</sub> cathodes through in situ X-ray and electron microscopy/spectroscopy studies.

## Key Publications

1. Tayal, P. Bara, H. Zhong, O. Kahvecioglu, K. Pupek, L. Ma, S. Ehrlich, V. Srinivasan, X. Qu, J. Bai, F. Wang, In Situ Insights into Cathode Calcination: Lithiation-limited Crystallization of LiNiO<sub>2</sub> from Hydroxides (*submitted*).

2. K. Chen, P. Barai, O. Kahvecioglu, L. Wu, K. Z. Pupek, M. Ge, L. Ma, S. N. Ehrlich, H. Zhong, Y. Zhu, V. Srinivasan, J. Bai, F. Wang, Stabilizing Cobalt-Free Cathodes with Lithium-Stoichiometry Control for Sustainable Lithium-ion Batteries, *Nature Communications* (accepted; DOI: <https://doi.org/10.21203/rs.3.rs-2748325/v1>).
3. Yin, M. Ge, Y. Chung, J. Bai, W-K. Lee, K. Kisslinger, S. N Ehrlich, X. Xiao, B. Qiu, S. E Trask, A. R Dunlop, A. N Jansen, Z. Liu, Y. Shin, F. Wang, *Small Structures* (online: <https://doi.org/10.1002/ssstr.202300236>)
4. F. Wang, Probing Lithium-ion in Battery Materials Using Transmission Electron Microscopy-Electron Energy-Loss Spectroscopy, [International Workshop on the Characterisation and Quantification of Lithium, from the Micro- to the Nano-Scale, from Mining to Energy](#), Paris, June 26-27, Invited talk.
5. F. Wang, P. Barai, O. Kahvecioglu, J. Bai, and V. Srinivasan, “Rational Design of Calcination of Nickel-based Cathode Materials by in situ Characterization and Multiscale Modeling”, *J. Mater. Res.* 37, 3197–3215, 2022.
6. J. Yao, J. Qi, Q. Dong, Y. Shen, L. Chen, S. Liu, Y. Wang, L. Li, Q. Mao, S. Yang, L. Gao, K. Zhang, K. Xu, F. Wang, J. Zhao, J. Bai, “A New Lithium Nickel Oxide Cathode Material with a Composite Structure for High-Performance Li-ion Batteries”, Online: DOI: 10.21203/rs.3.rs-1450650/v1.

## References

1. F. Wang, J. Bai, “Synthesis and Processing of High-Nickel Cathode Materials by Design”, *Batteries & Supercaps*, 5, e202100174, 2022.
2. Gent, William E., Grace M. Busse, and Kurt Z. House. "The predicted persistence of cobalt in lithium-ion batteries." *Nature Energy* 7 (2022): 1132-1143.
3. Park, Geon-Tae, et al. "Introducing high-valence elements into cobalt-free layered cathodes for practical lithium-ion batteries." *Nature Energy* 7 (2022): 946-954.
4. Zhang, Rui, et al. "Compositionally complex doping for zero-strain zero-cobalt layered cathodes." *Nature* 610 (2022) 67-73.
5. K. Chen, P. Barai, O. Kahvecioglu, K. Z. Pupek, M. Ge, L. Ma, S. N. Ehrlich, H. Zhong, V. Srinivasan, J. Bai, F. Wang, Stabilizing Cobalt-Free Cathodes with Lithium-Stoichiometry Control for Sustainable Lithium-ion Batteries, submitted (DOI: <https://doi.org/10.21203/rs.3.rs-2748325/v1>)
6. D. Wang, et al. "Intrinsic role of cationic substitution in tuning Li/Ni mixing in high-Ni layered oxides." *Chemistry of Materials* 31 (2019) 2731-2740.

## Acknowledgements

The work was supported by the Energy Efficiency and Renewable Energy, Office of Vehicle Technologies of the U.S. Department of Energy. We thank the contribution by our team members, Ke Chen, Yusuf Celebi and by collaborators, Lijun Wu, Yimei Zhu, Lu Ma, Steve Ehrlich, Mingyuan Ge, Andy Kiss, Wah-Keat Lee, Juergen Thieme (BNL), Pallab Barai, Ozge Kahvecioglu, Krzysztof Pupek, YoungHo Shin, Venkat Srinivasan, Steve Trask, Alison Dunlop, Andrew Jansen (ANL), Fengxia Xin, Hui Zhou, Stanley Whittingham (Binghamton University).

## II.9 Towards Solventless Processing of Thick Electron-Beam (EB) Cured LIB Cathodes (ORNL)

### Zhijia Du, Principal Investigator

Oak Ridge National Laboratory  
One Bethel Valley Rd  
Oak Ridge, TN 37831  
E-mail: [duz1@ornl.gov](mailto:duz1@ornl.gov)

### Haiyan Croft, DOE Technology Development Manager

U.S. Department of Energy  
E-mail: [Haiyan.Croft@ee.doe.gov](mailto:Haiyan.Croft@ee.doe.gov)

Start Date: October 1, 2018

End Date: September 30, 2024

Project Funding (FY23): \$350,000

DOE share: \$350,000

Non-DOE share: \$0

### Project Introduction

There are a variety of technical attributes to electron beam (EB) curing of LIB binders. EB curing uses solvent-free compositions that have low emissions (VOCs, etc.) and are recognized by federal, state and local governments as being a more desirable technology. Solvent or water-based processing requires high drying energy and results in significant CO<sub>2</sub> emissions. EB curing offers significant process energy savings, is ultra-high speed, and utilizes much more compact equipment than conventional drying ovens (much less plant floor space required). Furthermore, it is compatible with heat-sensitive substrates. Conventional thermal drying of LIB electrodes is typically conducted using multiple temperature stages; however, EB can be conducted in a single step. Solvent-free electrode compositions are rated as non-flammable, which translates into lower insurance costs, less stringent storage requirements and, a reduction in handling hazards.

EB treatment is a fast, robust materials processing technology that commonly delivers low cost and excellent performance for high-volume materials production. Based on decades of development and commercial deployment, self-shielded machines routinely operate with high reliability and low maintenance in industrial roll-to-roll production environments. ORNL is developing, demonstrating, and transitioning technology for high-speed roll-to-roll EB processing of LIB electrodes (i.e. coating formation and binder curing). Further specific advantages of this processing route for LIBs are:

**Unmatched throughput** – We estimate  $\geq 600$  m<sup>2</sup>/min throughput can be achieved based on  $\geq 300$  m/min line speed for roll widths up to 2 m (\$1.5-2.0M installed with machine footprint  $\sim 10$  m<sup>2</sup>).

**Thicker electrodes** (synergy with Task 1) – Up to 150 microns can be achieved at the throughput rate mentioned above. Coatings of several hundred microns could be processed at higher capital cost per unit throughput, modest reduction in energy efficiency, and larger equipment footprint.

**Excellent energy efficiency** – Electrical efficiencies  $\geq 60\%$  are possible, including voltage transformer losses (i.e.,  $\geq 60\%$  of electrical line energy is converted to productive EB energy).

**Environmentally friendly** – EB processing requires no solvent and no initiator and has low emissions.

### Objectives

- Significant process energy savings
- Ultra-high electrode processing speed
- Utilize much more compact equipment than conventional drying ovens.

## Approach

ORNL is working on a multiphase approach to develop, demonstrate, and transition EB processing of roll-to-roll battery materials.

- Phase 1 – Demonstrate the technology’s key differentiating attributes of high throughput and thick layer processing.
- Phase 2 – Address the key challenges of EB curing parameters and resulting material performance; develop ultra-thick (38 mg/cm<sup>2</sup> NMC 622) coating methods requiring little or no solvent.
- Phase 3 – Demonstrate ultra-thick cathode coatings and optimized curing system in conjunction with a high-speed coating line together with a key equipment partner and battery manufacturer.
- Phase 4 – Installation, commissioning, and operation of a custom roll-to-roll EB curing line at BMF.
- Phase 5 – Optimize EB process with low-cost electrode materials and demonstrate solid-state battery cathode and electrolyte application.

## Results

The electron beam processing technology was used to evaluate its compatibility with LFP cathode. Figure II.9.1 shows the high-resolution X-ray photoelectron spectroscopy (XPS) spectra of the Li 1s, Fe 3p, P 2p, O 1s and C 1s core levels to observe the changes in the oxidation states of the elements before and after electron beam radiation. The P 2p shows a peak at 132.9 eV, revealing that the valence state of P is 5+. The peak at 56.5 eV corresponds to Li 1s, which is superposed by the iron peak of Fe 3p. The O 1s shows a peak at 531.0 eV, confirming that the valence state of O in the LiFePO<sub>4</sub>/C composite is divalent. The two shoulder peaks at 531.9 and 533.0 eV are attributed to the C–O and C=O bands arising from functional groups of impurities absorbed on the sample surface. The C 1s shows peaks at 284.0 and 284.4 eV, which correspond to the short-order sp<sup>2</sup>-coordinated and sp<sup>3</sup>-coordinated carbon atoms. The additional peak at 288.2 eV is the C=O band arising from functional groups of impurities absorbed on the sample surface. After EB radiation, the peaks assigned to C=O band in both C 1s and O 1s disappeared, which indicates EB process can clean the LFP cathode materials.

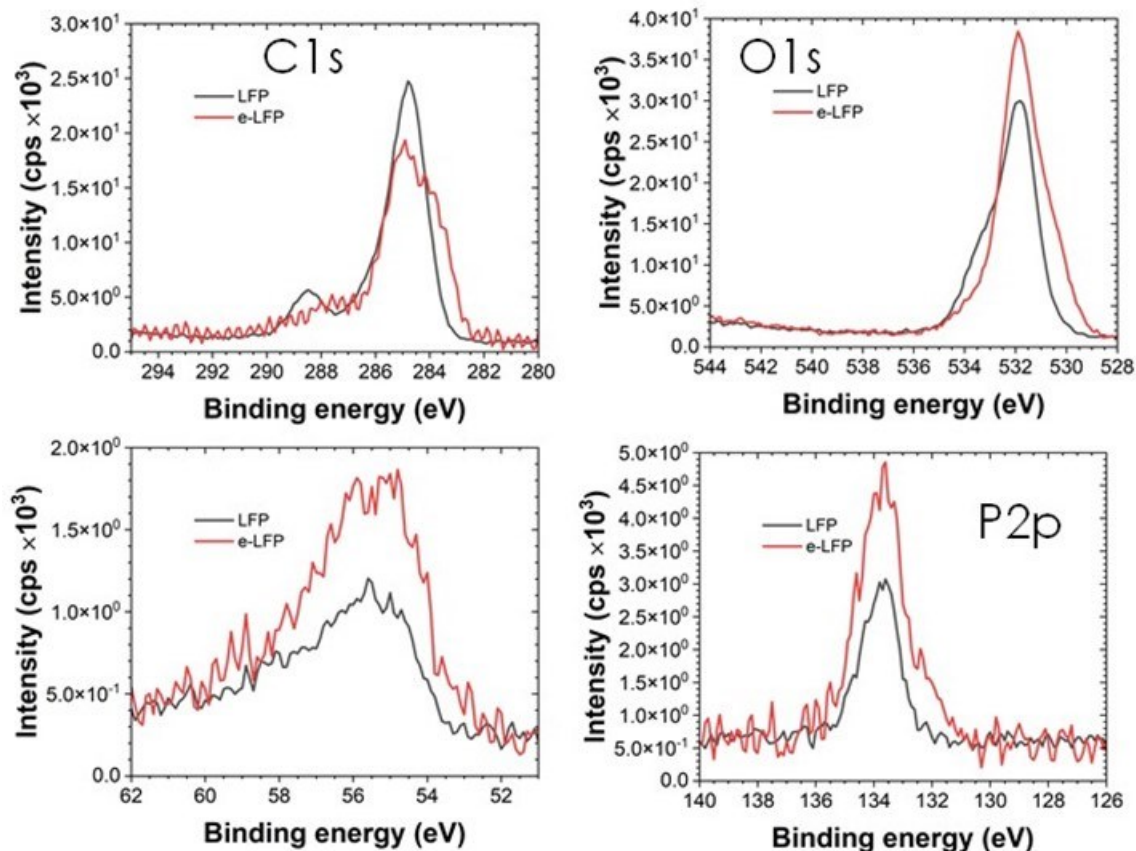


Figure II.9.1 XPS of  $\text{LiFePO}_4$  cathode materials before and after EB process.

To better understand if the ebeam irradiation has effect on the microstructures of materials, neutron diffraction was conducted on LFP and graphite powders before and after EB radiation as shown in Figure II.9.2. To clearly see the changes in LFP, only neat active materials powders were placed under EB curing excluding carbon black and binder in electrode setting. Neutron powder diffraction (NPD) experiments were carried out at the SNS's NOMAD beamline on LFP powder before and after EB. TOPAS Academic V6 suite was utilized to perform the Rietveld refinements on both diffraction patterns. The NPD results shows no changes in LFP crystal lattice parameters. Therefore, EB curing process can be used without interfering the microstructure of active materials.

A similar binder resin was used as previous FYs. Figure II.9.1c show the morphology of the electrodes after EB curing process. LFP particles used in this study were composed of tiny primary particles (0.2–1  $\mu\text{m}$ ) agglomerated into larger secondary particles (3–8  $\mu\text{m}$ ). The LFP particles and carbon black are uniformly dispersed in the electrode without any appreciable defects such as agglomeration or cracks. EDX in Figure II.9.1d shows the distribution of elements across the electrode with C from carbon black and P/O from LFP. The LFP particles are well distributed throughout the carbon network.



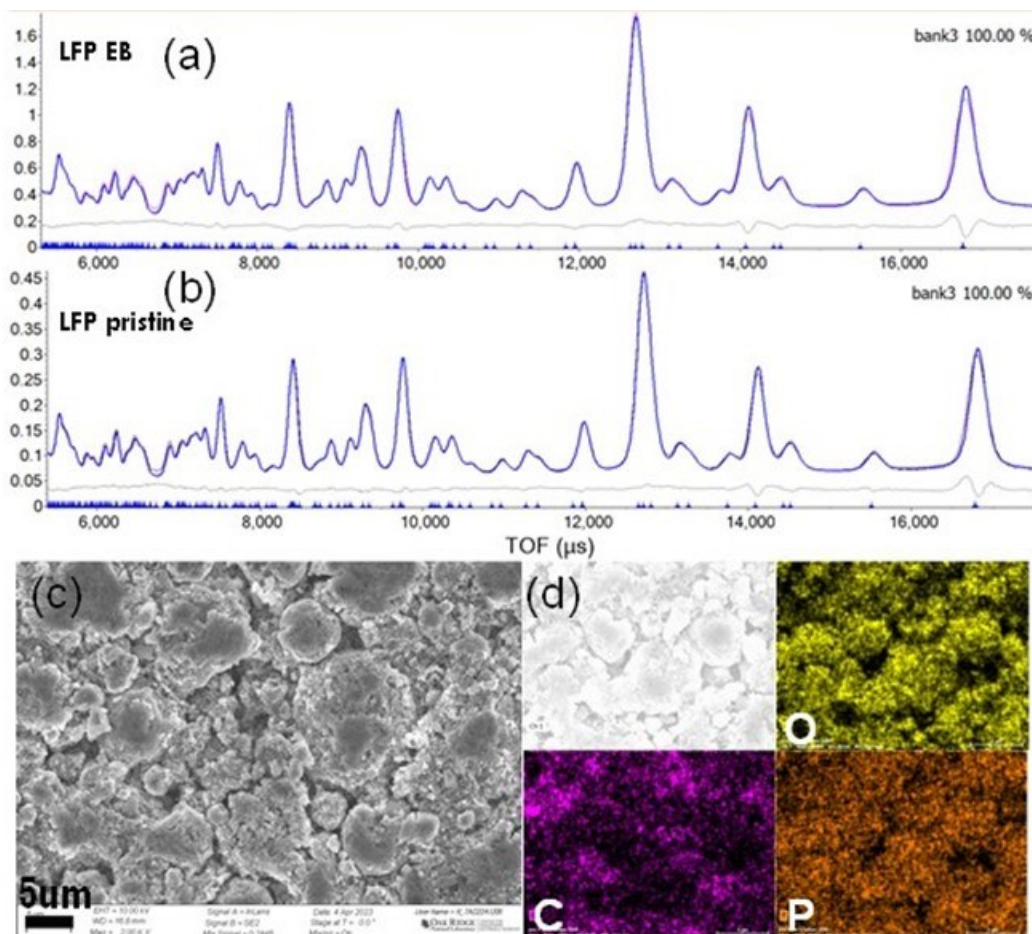


Figure II.9.2 (a, b) neutron diffraction patterns of LFP before and after EB radiation. (c) SEM image of LFP electrode after EB processing, and (d) EDX mapping of O, C and P of the electrode.

Figure II.9.3a shows the voltage profiles of LFP electrodes using an EB-cured acrylate binder in Li-ion full cells with matching graphite electrodes. The voltage curves show plateaus reflecting the graphite intercalation stages. The electrode can deliver ~160 mAh/g capacity, which is typical for LFP materials. Figure II.9.3b shows the cycling performance of the discharge capacity for EB cured LFP electrodes paired with graphite electrodes in full cells. The ratio of the negative electrode to the positive electrode is set to be around 1.2. The use of full cell, instead of half-cell, can provide more accurate cycling performance. The cell demonstrated excellent cycling performance with minimum capacity fading after more than 300 cycles.

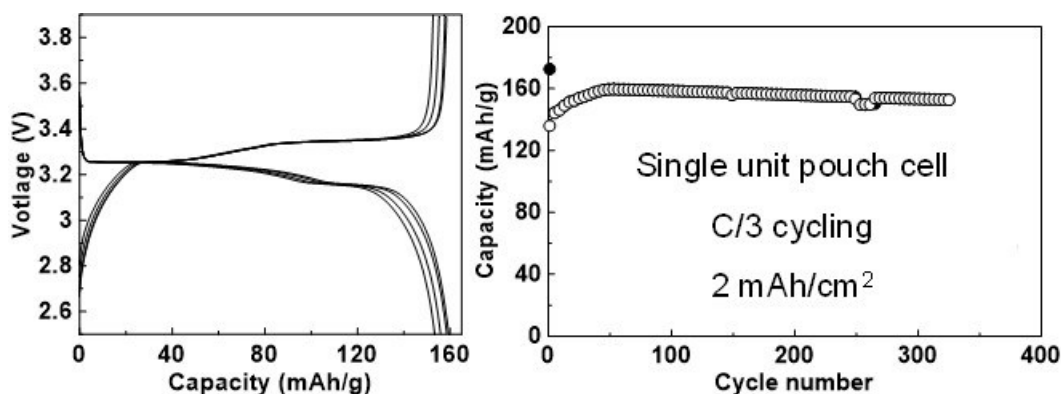


Figure II.9.3 (a) voltage curves and (b) cycling performance of single unit pouch cells with EB cured LFP cathode and matching graphite electrodes.

Figure II.9.4 shows the SEM images of LFP composite electrodes using both carbon black and carbon nanotubes. For the carbon black only (5wt% carbon black) based cathodes, individual carbon black aggregates from even larger aggregates in the interstitial regions among LFP particles. Being 0D in nature, the electronic paths formed by the carbon black agglomerates are not effective. The electrons associated with the charge-transfer reaction have a long transport pathway through several LFP primary particles to the carbon black conductive network. For CNT electrode (2 wt% carbon black + 0.5 wt% CNT), CNTs are well dispersed across the electrode. CNTs are uniformly spread over the entire electrodes, forming a 3D CNT network and thus highly efficient electron conducting pathways.

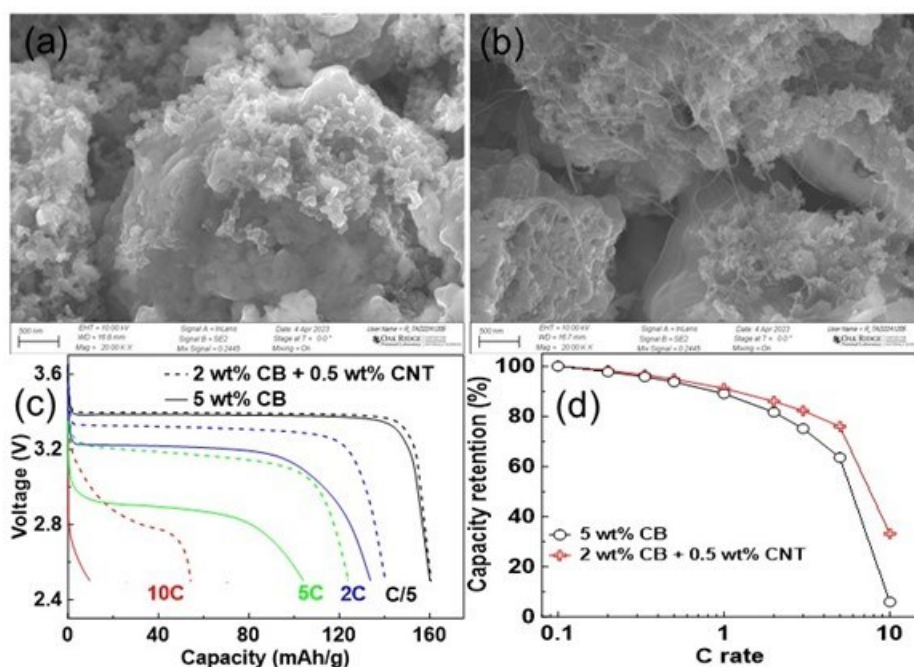


Figure II.9.4 SEM images of (a) CB-LFP electrode (5wt% carbon black), (b) CNT-CB-LFP electrode (2 wt% carbon black + 0.5 wt% CNT). (c) Cell discharge voltage curves at different C rates with electrodes shown in (a) and (b). (d) capacity retention of different electrodes at different discharge C rates.

Figure II.9.4c shows the cell voltage curves under different discharge C rates from C/5 to 8C. All electrodes demonstrate similar specific capacity ( $\sim 160$  mA h/g) at C/5. For the CB electrode, the capacity decreased gradually with increasing C rate up to 5C and was not able to deliver any appreciable capacity at 10 C rate. The polarization also increased rapidly from 1C to 5C due to insufficient conductivity provided by the carbon

black matrix. For the LFP electrodes with CNT, excellent capacity retention was observed up to 5C. The polarization increases from C/5 to 5C is insignificant, which can be ascribed to the effective 3D electronic pathways in the CNT network.

EB processing technology has been continued to study its application in solid state Li metal batteries. The Li ion conducting polymer precursor is formulated with acrylated polymer and LiTFSI as the salt. FTIR transmittance spectra are shown in Figure II.9.5a to verify the cross-linking of acrylate groups in PEGDA. The region with  $810\text{ cm}^{-1}$  peak is from the bending vibration of the  $\text{CH}_2=\text{CH}$  bond in acrylate groups. The unsaturated carbon-carbon bond peaks disappeared after radiation curing, proving the completion of cross-linking of PEGDA. After radiation curing, the liquid precursors completely crosslinked and formed a network with good flexibility feature and free-standing capability. Then full cells were assembled with composite LFP cathode, polymer electrolyte membrane and Li metal electrode. Figure II.9.5b shows the cycling performance of the cells with both thick Li electrode and thin Li electrode. Both have good cycling performance up to 50 and 30 cycles. Fig. 5c shows the voltage curve of the 1<sup>st</sup> cycle and 48<sup>th</sup> cycle. The exact failure mechanism with this voltage curve is not clear yet.

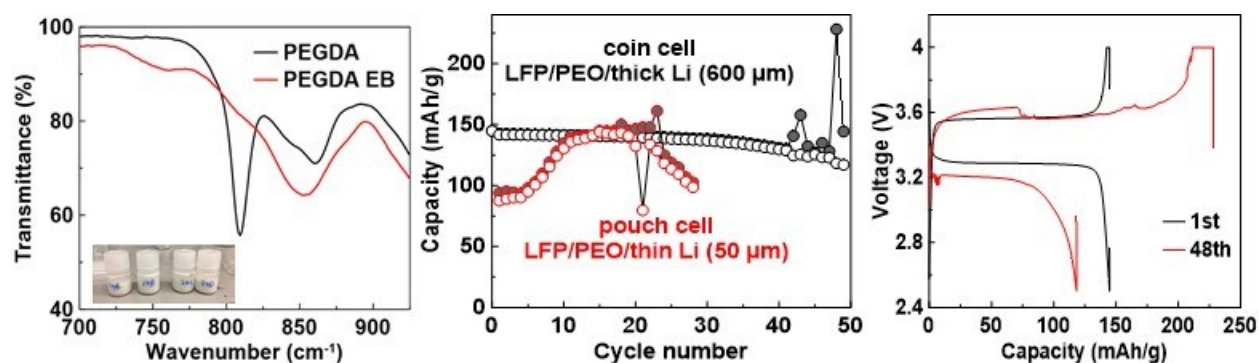


Figure II.9.5 (a) FTIR spectra of radiation cured polymer electrolytes. (b) cycling performance of Li/LFP cells with thick Li (in coin cell) and thin Li (in pouch cell). (c) 1<sup>st</sup> and 48<sup>th</sup> cycle voltage curve of Li/LFP cells with thick Li in coin cell.

### Conclusions

- EB radiation can clean the surface of LFP cathode materials and has no effect on LFP microstructures as evidenced by XPS and neutron powder diffraction.
- EB curing process is compatible with LFP electrode. Adding CNT can result in better rate performance for LFP electrode.
- EB process and application in Li metal polymer cells were carried out in LFP electrode.

### Key Publications

Toward Solventless Processing of Thick Electron-Beam (EB) Cured Lithium-Ion Battery Cathodes, Zhijia Du, Jianlin Li, VTO AMR 2023.

### Acknowledgements

We would like to acknowledge the collaboration from Prof Guangsheng Zhang at UAH and Dr Jue Liu at SNS at ORNL.

## II.10 Performance Effects of Electrode Processing for High-Energy Lithium-Ion Batteries (ORNL)

### Zhijia Du, Principal Investigator

Oak Ridge National Laboratory  
One Bethel Valley Rd,  
Oak Ridge, TN 37831  
E-mail: [duz1@ornl.gov](mailto:duz1@ornl.gov)

### Georgios Polyzos, Co-Principal Investigator

Oak Ridge National Laboratory  
One Bethel Valley Rd,  
Oak Ridge, TN 37831  
Email: [polyzosg@ornl.gov](mailto:polyzosg@ornl.gov)

### Haiyan Croft, DOE Technology Development Manager

U.S. Department of Energy  
E-mail: [Haiyan.Croft@ee.doe.gov](mailto:Haiyan.Croft@ee.doe.gov)

Start Date: October 1, 2018

End Date: September 30, 2024

Project Funding (FY23): \$450,000

DOE share: \$450,000

Non-DOE share: \$0

### Project Introduction

This project at the DOE Battery Manufacturing R&D Facility (BMF) at ORNL builds on past research successes in the areas of battery electrode process development and optimization, cost reduction, cell energy density improvements, and manufacturability advancements, which support the Vehicle Technologies Office (VTO) and Electrochemical Energy Storage Tech Team ultimate targets of \$60/kWh system cost, 500 Wh/kg cell energy density, 800 W/kg cell power density, and 10-15 min extreme fast charging times. Our goal is to perform the science needed to reduce high-risk, high-payoff technologies to lower risk levels, such that U.S. industry will consider their integration in future products. Once a new material, process, or concept has demonstrated feasibility for integration and scaling, the BMF will work to make it a viable processing methodology (preferably with industry partners) with validated performance in a full pouch cell design. While doing so, the BMF will leverage a large array of complimentary projects and sponsors that will provide additional experience and a fast, efficient methodology for solving problems faced by the domestic lithium-ion battery (LIB) industry.

### Objectives

To improve cell energy and power density and reduce battery pack cost by manufacturing thick electrodes with tailored electrode architecture via advanced processing and high-energy, high-voltage cathode materials:

- Fabricate thick (6-8 mAh/cm<sup>2</sup>) and crack-free cathodes via aqueous processing
- Evaluate compatibility of high Ni-NMC with aqueous processing
- Develop bilayer electrodes via freeze tape casting for improved rate performance
- Develop polymer electrolyte for solid-state batteries
- Understand the conduction mechanism in polymer electrolyte and optimize the formulation
- Demonstrate a solid-state battery with an energy density  $\geq 300$  Wh/kg (cell level)

### Approach

- Fabricate crack-free NMC622 cathodes with high areal loading (4-8 mAh/cm<sup>2</sup>) via aqueous processing.
- Develop bilayer electrode architecture via freeze tape casting
- Develop composite polymer electrolyte
- Characterize the electrochemical performance of the composite electrolytes

- Investigate the electrolyte-cathode interface
- Evaluate rate performance and long term cyclability

## Results

### 1. Develop tailored electrode architecture via freeze tape cast.

Structured cathode electrodes were fabricated using a roll-to-roll fully automated freeze tape casting (FTC) configuration shown in Figure II.10.1. The two-zone areas of the freeze bed can be varied from room temperature to  $-50\text{ }^{\circ}\text{C}$ . Ni-rich layer oxides (NMC 622), carbon black (CB) and cellulose binder (90, 5, 5 wt%, respectively) were used for the aqueous slurry formulations. The ice templating was achieved by the solidification of the applied aqueous slurry (at  $-9\text{ }^{\circ}\text{C}$ ) and a followed sublimation process to remove the ice crystals and structure the electrodes. To mitigate the current collector corrosion the pH of the slurry was lowered by adding phosphoric acid (1.5 wt% with respect to the solid content) [1]. A double layer configuration based on a bottom dense and a top porous layer was used to utilize the energy and power density of the electrodes. Details on the architecture of the ice templated electrodes can be found elsewhere [2]. The porosity of the top structured electrode was controlled by tailoring the water to solid content of the slurry.



Figure II.10.1 The setup that was used for the fabrication of the FTC cathodes.

A representative X-ray tomography image of the top structured layer is shown in Figure II.10.2. The vertically aligned and almost single NMC particle thick layers can be infiltrated with solid state electrolytes and significant improvements in the capacity and energy density of the measured cells were obtained [2].

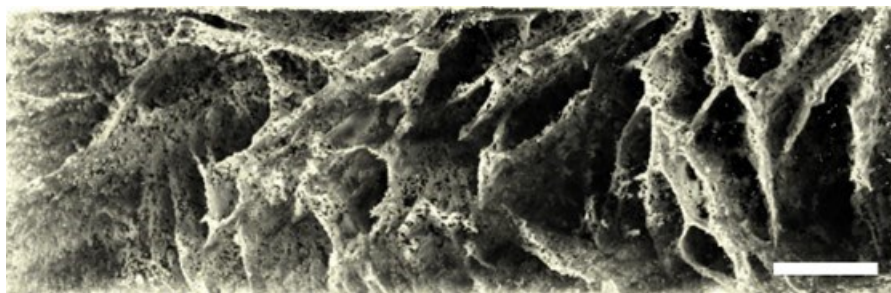


Figure II.10.2 X-ray tomography image of the top structured power layer. The scale bar is  $200\text{ }\mu\text{m}$ . The porosity of this configuration is approximately 70%.

Reducing the porosity while maintaining the aligned pore structure can reduce the electrolyte amount and improve the gravimetric and volumetric energy density. Scanning electron microscopy (SEM) and focused ion beam (FIB) images of dense cathode structures for Li-ion batteries are shown in Figure II.10.3. The porous channels enhance the diffusion of the  $\text{Li}^+$  ions and improve the mass-transport limitations in thick electrodes.

SEM-FIB imaging was performed to characterize the porosity through the entire bulk structure of the cathodes. FIB technique was utilized to etch the cathode structure. In Figure II.10.3d it is shown that the porous structures are not restricted to the surface but are evident in the bulk phase as well. A gradient in the porosity is clearly shown with the bottom part of the electrode being denser.

Impedance measurements were performed on Li-ion half cells based on two layer structured and single layer non-structured cathodes with active material loading  $4 \text{ mAh cm}^{-2}$ . The  $\text{Li}^+$  diffusion coefficients ( $D_{\text{Li}^+}$ ) were calculated from the fitting analysis results. The  $D_{\text{Li}^+}$  for the structured and non-structured electrodes were  $1.4 \times 10^{-16}$  and  $5.1 \times 10^{-17} \text{ cm}^2 \text{ s}^{-1}$ , respectively [3]. The 2.7-fold increase in the diffusion coefficient improved the rate and long-cycling performance of the cells. The results are summarized in Figure II.10.4. NMC 622 half cells were cycled from 3 to 4.3 V. The two-layer NMC622 cathode exhibited much higher performance at higher C-rate ( $\geq C/2$ ) and much improved cycle life (>10% and 100% improvement at 1C and 2C discharge rate, respectively).

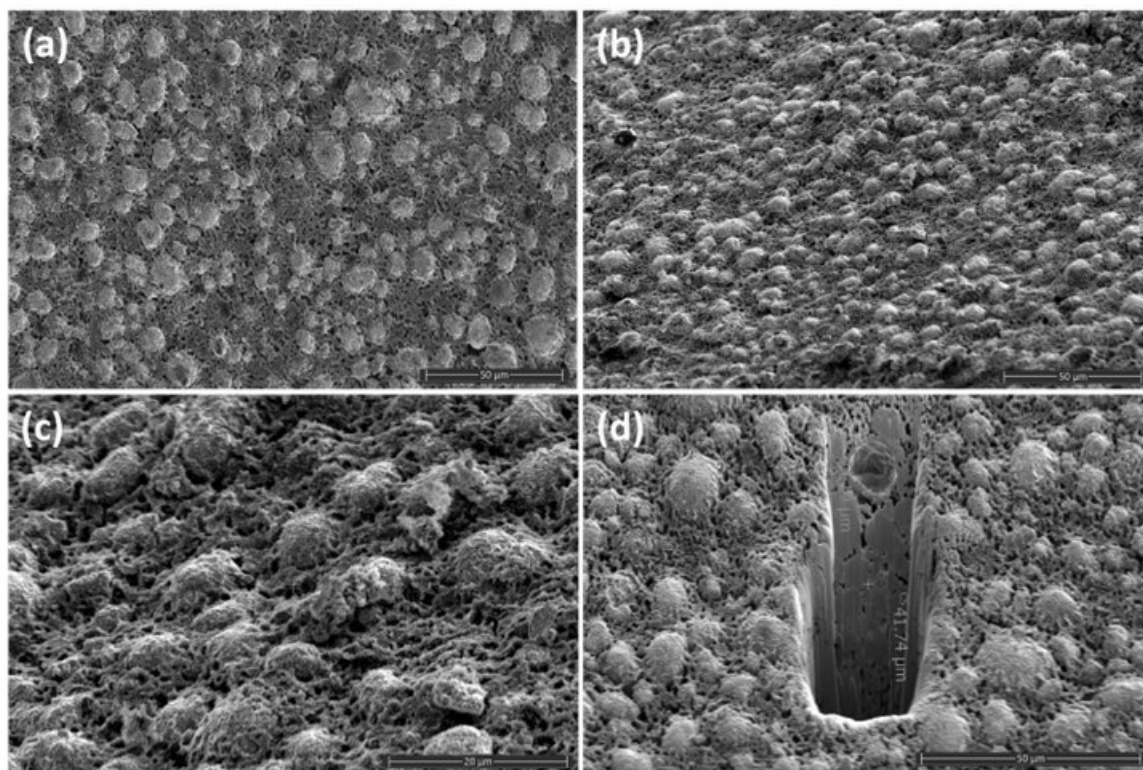


Figure II.10.3 SEM images of dense structured cathodes for Li-ion batteries. (a) top view, (b,c) view at an angle, (d) FIB image showing the porosity gradient in the bulk structure.

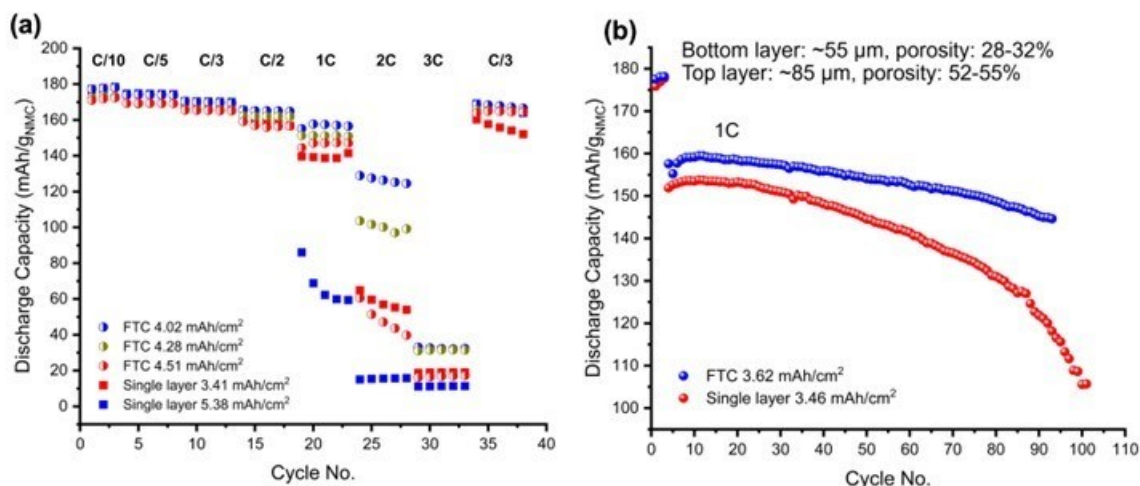


Figure II.10.4 (a) Rate performance and (b) long term cycling of several Li-ion half cells based on the structured cathodes shown in Figure 3. The active material loadings are indicated on the plot.

## 2. Development of polymer electrolytes for FTC cathodes

Solid state electrolyte scaffolds based on NASICON lithium aluminum titanium phosphate  $\text{Li}_{1.3}\text{Al}_{0.3}\text{Ti}_{1.7}(\text{PO}_4)_3$  (LATP) were developed. LATP particles were moldified and binded in an aqueous solution. Freeze drying of the solution resulted in flexible scaffold structures that are shown in the SEM images in Figure II.10.5. Hybrid composite polymer-in-ceramic electrolytes were fabricated by infiltrating the structures in Figure II.10.5 with a polymer electrolyte with lithium bis(trifluoromethanesulfonyl)imide (LiTFSI) salt. This configuration utilized the high conductivity and dendrite resistance of the interconnected lithium ceramic phase with the flexibility and good interfacial properties of the polymer phase [4]. These scaffold electrolyte separators were combined with in-situ polymerized catholytes. The work is ongoing.

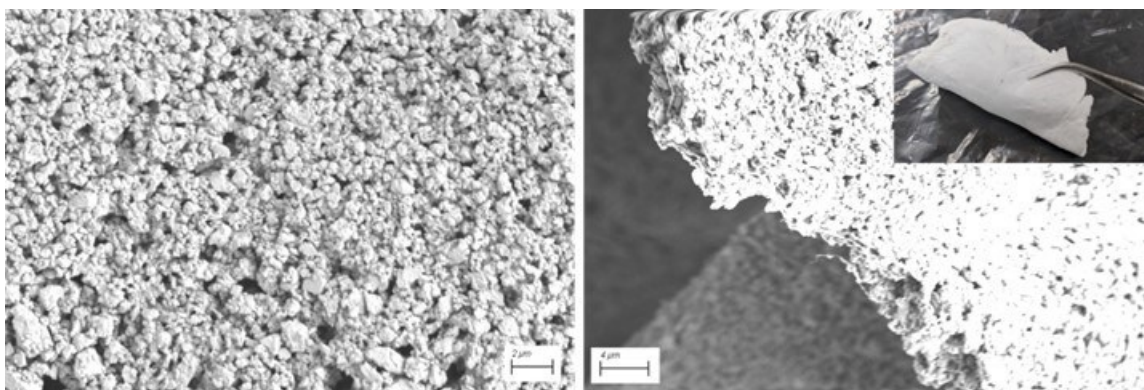


Figure II.10.5 SEM images of flexible LATP scaffolds prepared by freeze drying techniques.

## Conclusions

This project aims to advanced manufacturing science and develop tailored electrode architectures to improve energy density while reducing manufacturing cost. In terms of technical achievements, it fabricated thick, crack-free NMC622 cathodes ( $4\text{--}8\text{ mAh/cm}^2$ ); demonstrated improved rate performance of thick NMC622 cathode via 2-layer architecture; correlated conductivity with nano cluster domain of composite polymer electrolyte; Demonstrated a working solid-state battery at room temperature with  $> 100$  cycles. Electrolyte crosslinking with flexible LATP scaffolds resulted in 5- to 6-fold improvement in the overpotential values.

**Key Publications**

1. G. Polizos, S. Kalnaus, X.C. Chen, M. Dixit, M. Balasubramanian, J. Sharma, R. Tao, J. Li. Two-layer cathode architecture for high-energy density and high-power density solid state batteries. *Mater. Today Chem.* 33, 101704 (2023)
2. G Polizos, M. Goswami, J.K. Keum, L. He, C.J. Jafta, J. Sharma, Y. Wang, L.T. Kearney, R. Tao, J. Li. Nanoscale ion transport enhances conductivity in solid polymer-ceramic lithium electrolytes. *ACS Nano* (revised manuscript submitted)
3. R. Tao, G. Polizos, M. Dixit, J. Sharma, J. Li. Freeze Tape Casting Electrode with Bi-Layered Architecture for High-Performance Lithium-Ion Batteries. *ACS Appl. Energy Mater* (under review)
4. G. Polizos, R. Tao, J. Li. “Structured cathodes enabled by freeze tape casting for high energy density/high power Li-ion batteries. Oral Presentation, 242<sup>nd</sup> ECS Meeting, Atlanta 10/10/2022

**References**

1. A. Kukay, R. Sahore, A. Parejiya, W. Blake Hawley, J. Li, D. L. Wood. Aqueous Ni-rich-cathode dispersions processed with phosphoric acid for lithium-ion batteries with ultra-thick electrodes, *J. Colloid Interface Sci.* 581 (2021) 635–643.
2. G. Polizos, S. Kalnaus, X.C. Chen, M. Dixit, M. Balasubramanian, J. Sharma, R. Tao, J. Li. Two-layer cathode architecture for high-energy density and high-power density solid state batteries. *Mater. Today Chem.* 33, 101704 (2023)
3. Tao, G. Polizos, M. Dixit, J. Sharma, J. Li. Freeze Tape Casting Electrode with Bi-Layered Architecture for High-Performance Lithium-Ion Batteries. *ACS Appl. Energy Mater* (under review)
4. G Polizos, M. Goswami, J.K. Keum, L. He, C.J. Jafta, J. Sharma, Y. Wang, L.T. Kearney, R. Tao, J. Li. Nanoscale ion transport enhances conductivity in solid polymer-ceramic lithium electrolytes. *ACS Nano* (revised manuscript submitted)

**Acknowledgements**

We are grateful to ORNL team members and external collaborators Congrui Jin, Alejandro Franco and Abbas Shodiev for contributing on electrolyte wetting investigation. We also thank Dr. Ozge Kahvecioglu at the Materials Engineering Research Facility (MERF), Argonne National Laboratory, for providing the NMC811 powder.



## II.11 Advanced Anode Manufacturing through Ultra-Thin Li Deposition (Applied Materials, Inc.)

### **Subra Herle, Ph.D., Principal Investigator**

Applied Materials, Inc.  
3225 Oakmead Village Dr  
Santa Clara, CA 95054  
E-mail: [Subra\\_Herle@amat.com](mailto:Subra_Herle@amat.com)

### **Haiyan Croft, DOE Technology Development Manager**

U.S. Department of Energy  
E-mail: [Haiyan.Croft@ee.doe.gov](mailto:Haiyan.Croft@ee.doe.gov)

Start Date: May 25, 2022

End Date: October 31, 2023

Project Funding: \$6,528,338

DOE share: \$2,820,373

Non-DOE share: \$3,707,965

### **Project Introduction**

Much of the doubling in Li-ion battery energy density over the past 30 years has been achieved through cathode material improvements. Anode energy density have languished, partly due to integration and manufacturing challenges, including the lack of an effective, scalable manufacturing solution for incorporating minimal amounts of lithium for pre-lithiation of Si/SiO<sub>x</sub>-C and producing ultra-thin lithium metal anodes (1-20µm) cost-effectively at high volume.

None of the existing approaches meet high volume manufacturing (HVM) requirements for lithiation and prelithiation. In this direction, Applied Materials' current strategy is unique, considering and including ease of integration with existing Li-ion battery process flows and production of defect-free lithium films scalable in thickness and to industry-standard widths, at a low cost, in a safe environment.

### **Objectives**

The project aims to develop and validate a cost-effective ultra-thin Li deposition system for advanced anode high-volume manufacturing (HVM) and demonstrate the following. (Table II.11.1, Table II.11.2, and Table II.11.3)

- Objective 1: Advanced batteries with pre-lithiated SiO<sub>x</sub>-C anodes with energy density >337Wh/kg from TRL 5 to TRL 7
- Objective 2: Advanced batteries with Li-metal anode with energy density >375Wh/kg from TRL 4 to TRL 6
- Objective 3: Develop a Li deposition system to meet high volume mfg. (HVM) requirements TRL 4 to TRL 8.

**Table II.11.1 Li Deposition System Manufacturing Target Performance.**

Li Deposition System Manufacturing Target Performance (Measured with respect to established Baseline)		
Parameter	Measure (Minimum Manufacturing Goals)	End of Program Performance Goals (10 µm Li deposition)
Mechanical System Throughput, Web Speed Increase	≥100%	>20m/min → Goal Demonstrated
Substrate Width Increase	≥100%	800 mm → Goal Demonstrated
Uniformity Increase	≥50%	+/- 7.5% → Goal Demonstrated (< 3.0%)
Uptime Increase	≥50%	Uptime > 50% → Goal Demonstrated
Status	Line speed & uniformity requirements met for 400- and 800-mm wide substrate	

Samples generated from Applied Materials ultra-thin Li deposition system are validated for Pre-Lithiation and Lithium metal anode: Current updates on cell performance data are summarised below (see Status).

**Table II.11.2 Cell Performance Data Summary for Pre-lithiated Anodes.**

Partners: ZenLabs & Applied Materials	Cell Performance for Pre-lithiated Anodes (Minimum Manufacturing Goals)		
	Pouch Cells (Pre-lithiated Si-Anodes) (>2 Ah) BP-1	Pouch Cells (Pre-lithiated Si-Anodes) (>10 Ah) BP-2	Pouch Cells (Pre-lithiated Si-Anodes) (>10 Ah) BP-3
Energy Density	≥300 Wh/kg	≥319 Wh/kg	≥337 Wh/kg
Cycle Life	600 Cycles	1000 Cycles	1100 Cycles
Fast Charge	N/A	80% in ≤15 minutes	80% in ≤15 minutes
Status	Completed (305 Wh/Kg & 700 cycles)	Completed ( <b>333 Wh/Kg &amp; 1000 cycles</b> 1C1C CC-CV cycles)  DST cycling at INL achieved >1000 DST cycles.	Final cell deliverables shipped to INL for validation.

**Table II.11.3 Cell Performance Data Summary for Lithium Metal Anodes.**

Partners: SAFT America, PNNL & Applied Materials	Cell Performance for Lithium Metal Anodes (Minimum Manufacturing Goals)		
	Parameter	Pouch Cells (Lithium Metal Anodes) (5-10 Ah) BP-1	Pouch Cells (Li Metal Anodes) (~10 Ah) BP-2
Energy Density	≥300 Wh/kg	≥337 Wh/kg	≥375 Wh/kg
Cycle Life	200 Cycles	300 Cycles	500 Cycles
Fast Charge	N/A	N/A	N/A
Status	Completed (300 Wh/kg & 200 cycles PNNL)	Completed (315 Wh/kg & 500 cycles 0.1C-0.3D cycles). Cycling at INL completedà achieved target goals for Li metal cell cycling	Final cell deliverables are built and shipped to INL for testing.

**Approach**

With funding support from DoE and working closely with the leading U.S. cell makers Ionblox (formerly Zenlabs Energy: pre-lithiated SiO<sub>x</sub>-C anode) and Saft America (Li metal anode) and leveraging advanced battery research capabilities of key National Laboratories (PNNL, LBNL, ANL), Applied Materials proposes accelerating the time to market of a high productivity lithiation solution based on physical vapor deposition for both SiO<sub>x</sub>-C anodes and Li-metal anodes. Applied Materials will accelerate the development of its current R&D roll-to-roll (R2R) lithium deposition system based on Applied's production-proven SmartWeb™ platform. Li-coated anodes will be fabricated and shared with project partners for integration into cells and characterization. As validated by the project collaborators, the deposition equipment and processes will be optimized to achieve volume manufacturing performance targets while meeting the battery performance and cost targets. Zenlabs was focused on high silicon content SiO<sub>x</sub>-C based batteries and Saft & Pacific Northwest National Lab (PNNL) on high energy density Li-metal batteries. Lawrence Berkeley National Laboratory (LBNL) was responsible for investigating prelithiated SiO<sub>x</sub>-C and lithium metal surface and interface properties, stabilization, and providing metrology services for the program. The partners closely worked with Argonne National Laboratory (ANL) to update the techno-economic BatPaC model to incorporate battery architectures that use prelithiated Si/SiO<sub>x</sub>-C and Li metal anode-based batteries.

**Budget Period 1 (BP-1): Hardware and Process Baseline and Pathfinding (Completed)**

In Budget Period 1 of the project, the team performed design, procure and operationalize hardware for Li deposition and surface protection. Hardware and Process baseline was established and deposited samples generated for pathfinding and initial cell testing.

**Budget Period 2 (BP-2): Roll-to-Roll (R2R) HVM Test Preparations (Completed)**

In Budget Period 2, the team completed scale up design for the Li deposition and protection equipment, procure and operationalized scaled up components and further optimized the hardware and process. Cell testing was moved to large format cells to meet or exceed interim performance goals towards high volume manufacturing (HVM).

**Budget Period 3 (BP-3): R2R HVM Validation (In Progress with NCE)**

In Budget Period 3, the team was on validating the Li deposition and protection hardware and process to meet the equipment and cell performance goals for high volume manufacturing (HVM) readiness level. The team also established a cell and pack level techno-economic model incorporating these advanced anodes.

## Results

1. All program deliverables were completed and met target performance.
2. Final cells are shipped to INL for validation.
3. No cost extension due to slow down with COVID-19 pandemic was approved with the project end date of Dec 31, 2023.

The project now has reached the end of budget period 3 (BP3). In BP3, we are in the process of planning and executing final cell deliverables to Idaho National Laboratory (INL), interim and final deliverables cells were built by SAFT America, Pacific Northwest National Laboratory (PNNL) and Ionblox (formerly Zenlabs). The key deliverables for BP2 involved delivering six 11 Ah multilayer Pre-Li SiOx pouch cells made by Ionblox, and twenty-three 7 Ah multilayer Lithium metal pouch cells made by SAFT America to INL.

INL updates (Applied Materials- Ionblox **Pre-Li SiOx**) pouch cells: Ionblox pre-Li cells are in the testing phase: Gap chart results are updated in this report (

*Interim Pre-Li SiOx cells performance achieved BP-2 goals for static capacity, HPPC, and HPPC available energy.*

### **SAFT Li metal Pouch Cells:**

Completed 500 charge/discharge cycles for the Li metal pouch cells. Ultra-thin Li/Cu with CO<sub>2</sub> surface protection was provided by Applied Materials. Cell data with initial discharge capacity around 6.8 Ah (C/10 Chr. C/3 Discharge) with ~ 80 % capacity retention after 500 cycles was validated (Table II.11.4). *Interim Li metal cells performance achieved BP-2 target goal > 70 % capacity retention.*

We continue to significantly scale up efforts to enhance the performance and optimize hardware and process for the R2R deposition tool. New deposition hardware was installed which led to further improvements in deposition rate. *Our best-known method (BKM) processes improved Li utilization rate and cross web thickness width and uniformity.*

Ultra-thin vacuum deposited Li on plastic rolls & inline passivated by CO<sub>2</sub> were handled in the dry room for transfer process onto either copper current collector or customer's anode. Transfer equipment developments were made using two new roll-roll (R2R) transfer tools in the dry-room.

Novel stack design and additional new chemistries investigated for Li surface protection as a part of the program using S2S tools and the samples were shipped to partners for evaluation. All tasks related to the planning and execution of samples for the final cell deliverables have now been completed. These samples were shipped to Saft America and Ionblox for final cell builds. Testing plans for these cells discussed and aligned with partners and DOE.

**Table II.11.4 Proposed Milestones and Corresponding Status Updates.**

Milestone	Type	Status as of 11/30/2023
Complete Gen. 3 source testing on test stand.	Technical	Gen 2-version was upgraded to Gen 3 on the R2R tool & characterized → Baseline process established. Further testing and process development will continue → Completed.
Addition of Second Process Chamber	Technical	Second process chamber was installed on a R2R platform → Completed.
Protection layer material for scale up to R2R processing Selected	Technical	Upgraded CO <sub>2</sub> passivation module on Li deposition tool for In-situ R2R CO <sub>2</sub> passivation → Completed.
HVM runs with protection layer.	Technical	Installation and final tool hardware upgrade → Completed. Process optimization Completed → Materials shipped to partners for final cell fabrication.
Cell performance verified. (At INL)	Technical	Li Metal based cells (SAFT) Idaho National Lab BP-3 deliverables Completed. Pre-Li SiO <sub>x</sub> -C anode and Li coating for the final cell deliverables → completed.
End of Project		Final Cell Fabrication, Formation completed and Delivery: Dec 2023

All Budget Period-1 and 2 milestones were completed, and preparations started towards meeting Budget Period-3 objectives, as summarized above.

**In the following section,** we capture the program's key highlights and learnings, including data from Applied Materials and our partners. Figure II.11.1 shows schematics relating to the cell manufacturing steps with Applied Materials prelithiation process envisioned to be integrated with the existing battery manufacturing line.

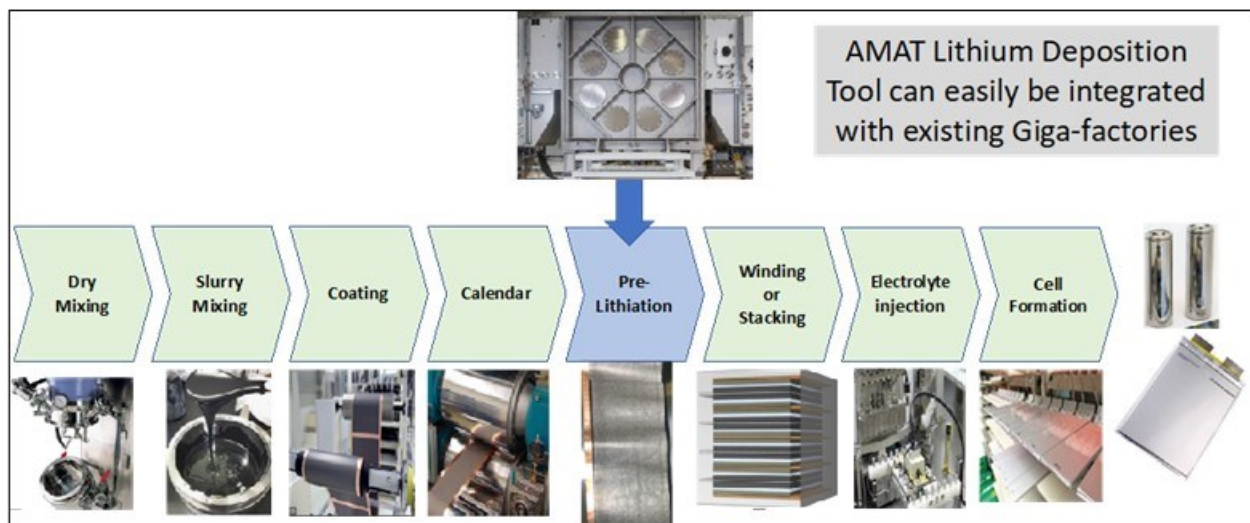


Figure II.11.1 Cell manufacturing steps including pre-lithiation for silicon anodes.

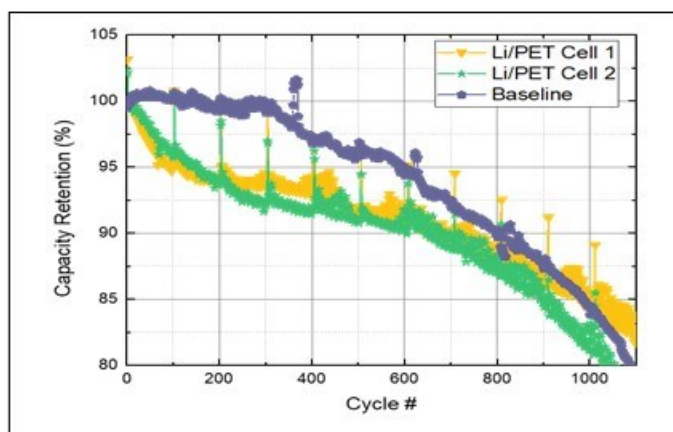


Figure II.11.2 1C/1C rate CCCV cycling performance of 11.3Ah capacity pouch cell (Cell build was done by Ionblox).

Ionblox cycled 12 Ah capacity (pouch cells) integrating pre-lithiated silicon anode using the transfer rolls consisting of lithium deposited directly on PET Li from AMAT and the high-capacity nickel-rich 811 NCM cathode from the same lot delivered to INL. Figure II.11.2 shows the 1C/1C rate CC-CV cycling performance from a baseline pouch cell and data from two transfer cells under a voltage of 4.2V to 2.5V. Cycling from the transfer Li/PET Pre-Li cells show impressive performance with comparable cycling to the baseline cell with >1000 cycles completed while retaining 80% of their initial capacity.

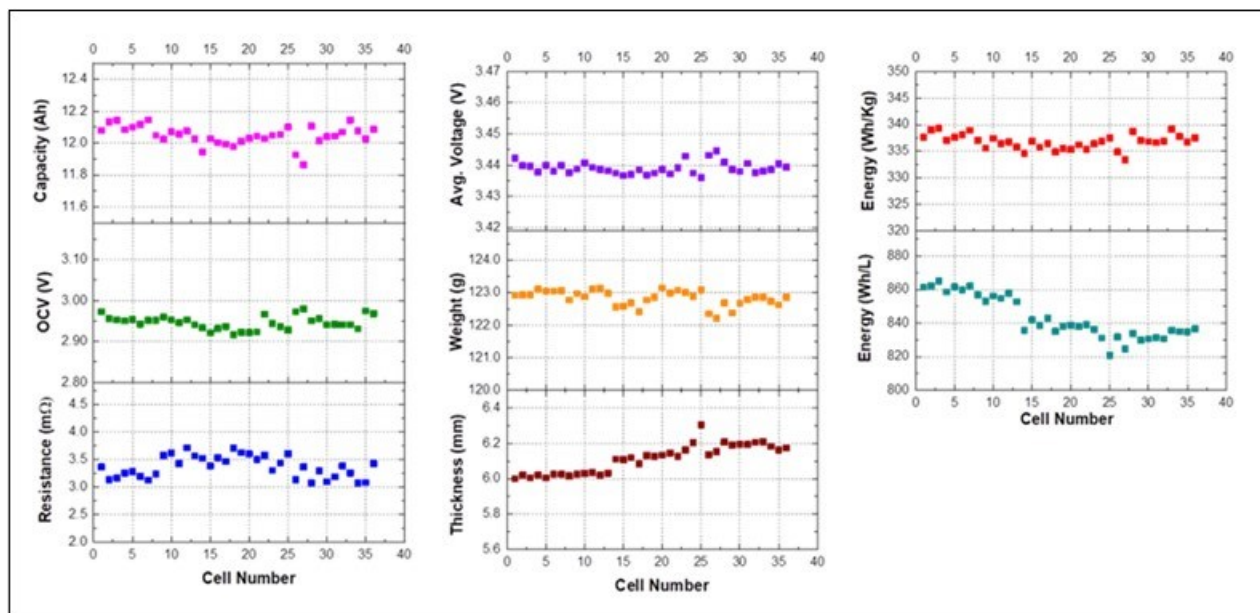


Figure II.11.3 Ionblox Summary of electrochemical data from formation process for the BP3 Final deliverable cells with Applied Materials Pre-Li. Summary of cell parameters are shown with Energy density reaching 337 Wh/kg and 800 Wh/L.

The pouch cells have a cell footprint of 64 x 145 x 6.0 mm with a specific energy of **337 Wh/kg** meeting the final program cell deliverable target. The assembled pouch cells have completed the formation process and the cells have an average capacity of 12.0 Ah and a specific energy of 337 Wh/kg at a C/3 rate and 25°C. The electrochemical data such as capacity, open circuit voltage (OCV), resistance, average voltage, weight, thickness, specific energy (Wh/Kg), and energy density (Wh/L) obtained from the formation process for the multiple pouch cells are summarized in Figure II.11.3. The data shows good consistency and reproducibility among the cells assembled using the transfer process.

For all groups shown in Figure II.11.4, the performance of cells in each group is very consistent, indicating little variation from cell manufacturing. After 250 cycles, both cells using SDIT Li foil show small capacity loss (<2%) at C/3, while both cells using Type B surface protected Li foil have about 5% capacity loss at C/3. Both groups deliver excellent cycling stability and are likely to have more than 80% capacity retention after 300 cycles. Table II.11.5 summarizes key parameters of the final deliverable's cells to INL for testing. The energy density reaches 407Wh/kg at stack level.

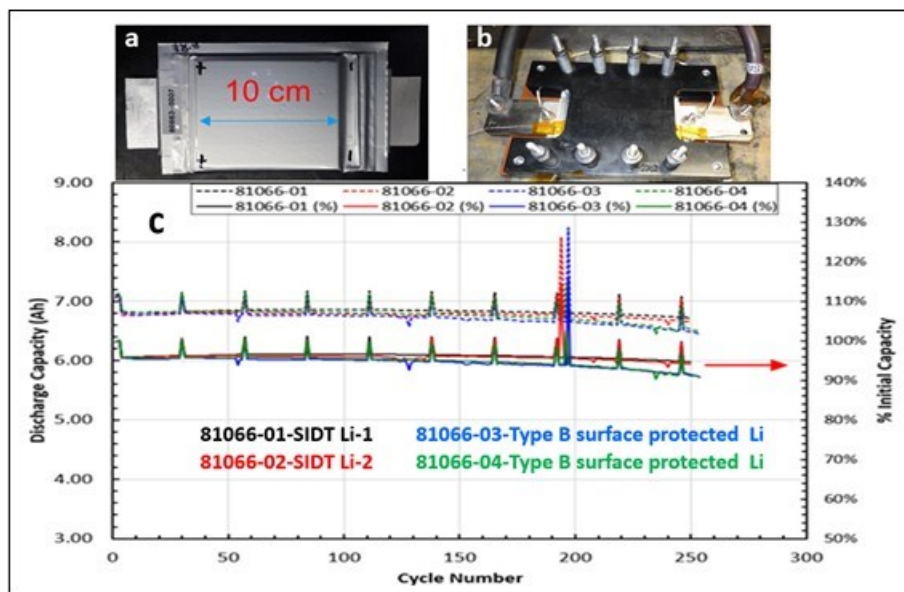


Figure II.11.4 SAFT America summary of cells with ~ 20  $\mu\text{m}$  Li per side: (A) Images of 7Ah pouch cells (B) Pouch cell in testing fixture (C) discharge capacity vs. Cycle life for 7Ah pouch cells for different Applied Materials Li samples (81166-01&02 transfer vs. 81166-03&04 Type B surface protected).

Table II.11.5 BP3 Final Deliverable Task: Detailed Cell Information of Samples Shipped to INL from SAFT America for Testing and Characterization.

Serial Number	ACI (mOhm)	OCV (V)	Thickness (mm)	Weight (g)	Wet Weight (g)	Volume (cm <sup>3</sup> )	C2 (Ah)	D2 (Ah)	Capacity at C/3 (Ah)
81299-01	7.961	3.60469	6.2650	113.90	63.21	50.69	9.686	9.689	9.302
81299-02	8.208	3.60453	6.2470	113.16	63.20	49.96	9.568	9.575	9.192
81299-03	7.751	3.60702	6.1685	113.15	63.32	49.83	9.537	9.538	9.157
81299-04	8.056	3.60440	6.2850	112.70	62.22	50.48	9.585	9.589	9.205
81299-05	8.388	3.60444	6.2635	114.06	63.26	50.80	9.644	9.650	9.264
81299-06	8.325	3.60487	6.2555	114.11	63.66	50.45	9.644	9.648	9.262
81299-07	8.122	3.60492	6.1795	114.01	63.16	50.85	9.703	9.648	9.262
81299-09	8.557	3.60816	6.0800	113.42	63.15	50.27	9.461	9.449	9.071



Data provided by work done by PNNL. transfer samples from Applied Materials have the best performance after 400 cycles as shown in Figure II.11.5.

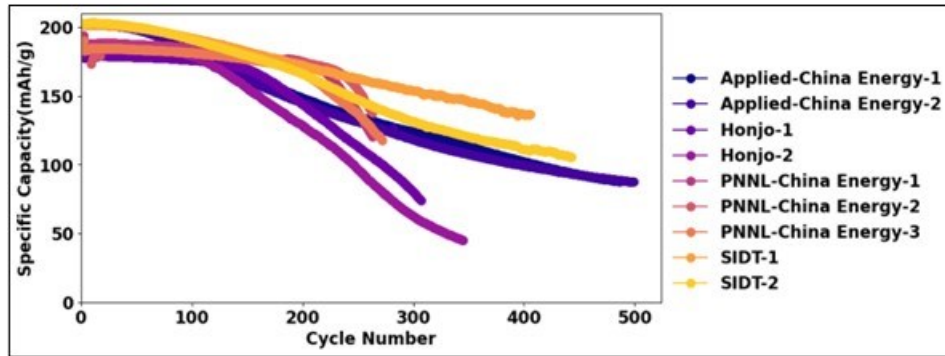


Figure II.11.5 Comparison of the cycling performance of cells with NMC622 cathode and different sources of Lithium from different manufacturers.

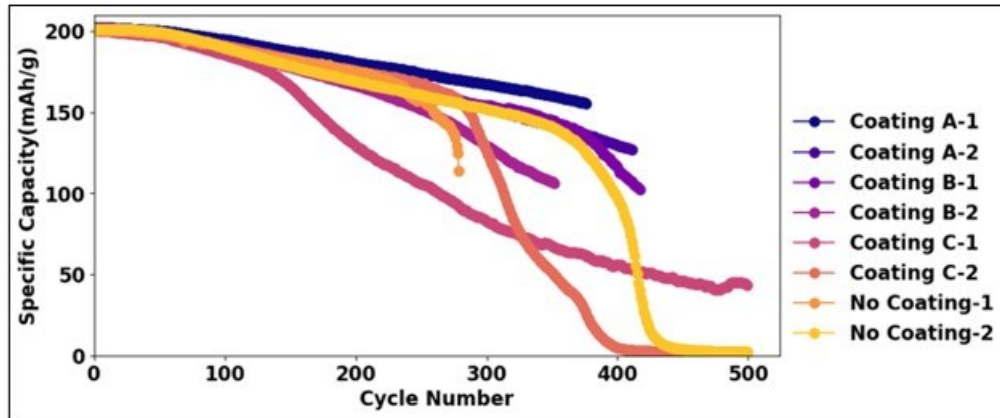


Figure II.11.6 Progress Summary for Lithium protection layer selection (PNNL)

PNNL fabricated and evaluated different protection layer samples (Figure II.11.6) of Li metal provided by Applied Materials and demonstrated after 400 charge-discharge cycles, Coating A shows the best performance delivering ~ 176 mAh/g capacity and cycling which is significant improvement from baseline with no coating in coin cell study.

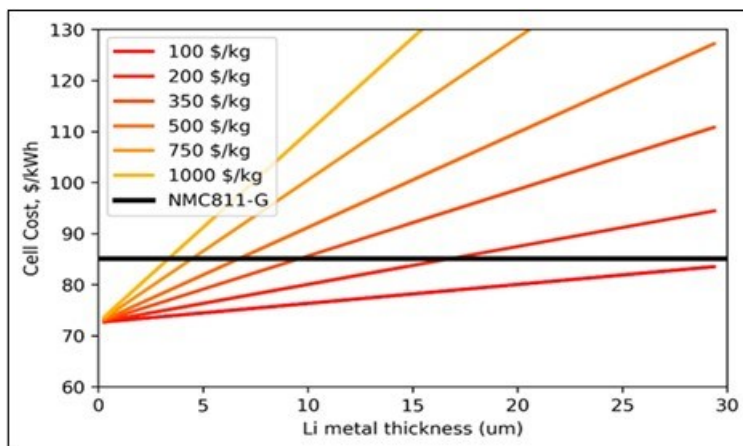


Figure II.11.7 Progress Summary BatPaC Cost Model (Argonne National Laboratory): BatPaC 5.0 was used for the Li metal study (whereas 4.0 was used for the Si studies in BP2).

Expanding on work ANL examined a wider range of lithium metal costs and single-sided that would be of the utmost interest for Applied Materials. Cell cost rises with the coating thickness as shown in the Figure II.11.7, the cell cost as a function of Li coating thickness and Li metal cost. The black line represents the break-even point for the corresponding NMC811-graphite cell; being below that line would indicate that even using a Li metal anode, the cell cost can be lower than the current technology depending on the cost and needed thickness of Li. We note that even if Li metal is 1000\$/kg, coating a ~5-micron layer of lithium metal will still be comparable in price.

Table II.11.6 Progress Summary (Idaho National Laboratory): Gap chart for the Applied Materials/Ionblox pre-Li SiOx interim cells.

AppMat/Ionblox Interim EERE Cell								
EV Cell Targets	Units	USABC EOL Cell	Cell 1(0% FC)		Cell 4(100% FC)		Cell 6(30C CaLT)	
			RPT0	RPT8	RPT0	RPT5	RPT0	RPT7
Peak Discharge Power Density (30 sec)*	W/L	1400	3325	2454	3335	1503	3292	1659
Peak Specific Discharge Power (30 sec)*	W/kg	700	1541	1137	1545	696	1525	769
Peak Specific Regen Power (10 sec)	W/kg	300	1919	1488	1921	1360	1872	1266
Useable Energy Density	Wh/L	550 (552)	658	600	662	527	659	540
Useable Specific Energy	Wh/kg	275 (244)	305	278	307	244	305	250
Calendar Life (Yrs)	Years	10						0.61
DST Cycle Life	Cycles	1000		1064		665		
Operating Environment**	°C	-30 to +52						
Normal Recharge Time	Hours	<7 Hours, J1772						
High Rate Charge	Minutes	80% UETarget in 15 min	Fast charge testing was not performed for these cells*					
Maximum Operating Voltage	V	N/A						
Minimum Operating Voltage	V	>0.55*Vmax <sub>op</sub>						
Survival Temperature Range, 24 hr	°C	-40 to +66						
Maximum Self Discharge	%/Month	<1						
INL ID Number				578		578		578
Hardware Level				Cell		Cell		Cell
Ampere Hour Capacity				12		12		12

Table II.11.6 highlights updates of Cell 1, which completed **1064 DST cycle life** at 0% fast charge, satisfying the USABC EOL life goal. **100 % fast charge cells** completed 665 cycles.

Figure II.11.8 Highlights < 20 % Capacity fade at 500 cycles for the Li metal samples provided by Applied Materials in BP2.

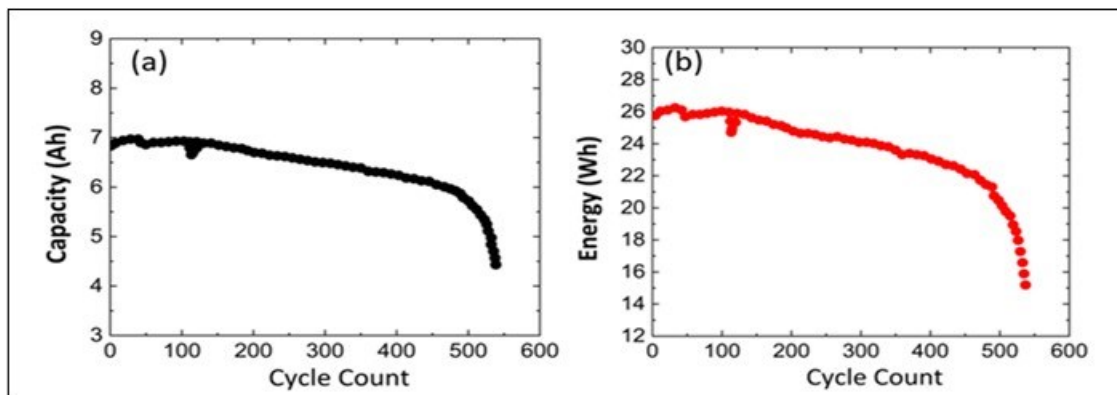


Figure II.11.8 Progress Summary (Idaho National Laboratory): Applied Materials/SAFT America Li metal NMC interim cells. Pouch Cell data: 20  $\mu\text{m}$  Lithium anode/NMC 811 Cathode and M47(1.0M LiFSI)/DME+TTE electrolyte. (a) shows the capacity vs. cycle number during the discharge at C/3 rate (b) the corresponding energy in watt hours for discharging at C/3 rate.

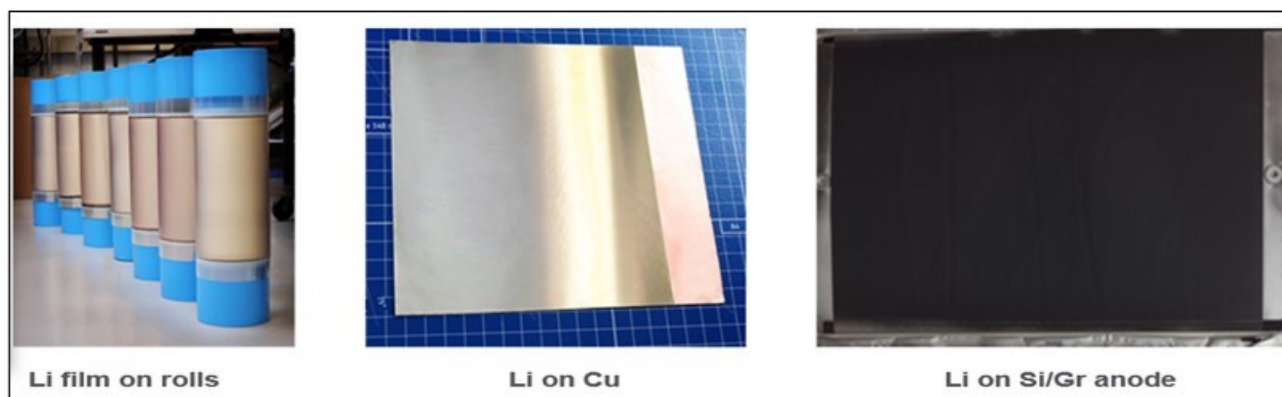


Figure II.11.9 Applied Materials Technical roll to toll (Li Deposition) using SmartWeb™ platform. Images of Li on plastic substrate after coating, Li on Cu anode and pre-Li anodes are shown.

The salient features include 1. high quality (>99.9%) pure ultra-thin lithium films deposited onto anode substrates of choice 2. Deposited Lithium thickness can be controlled between 1-20  $\mu\text{m}$  (<3%, $\sigma$ 1 non uniformity) 3. New process of baseline Substrate Independent Deposition and Transfer (transfer) process was established 4. A second new R2R tool was commissioned for Li processing 5. Additionally, Deposition tools was installed and commissioned in Auxiliary Dry Room Facility for Li surface protection layer development resulting in the generation of five different surface protection materials for Lithium metal being screened. One candidate was chosen for further testing. Figure II.11.9 show samples of Ultra-thin lithium films and Pre-Li anodes samples delivered to partners for evaluation. Post-treatment after deposition helps maintains pristine Li surface.

### Conclusions

In 2023, the Applied Materials-led team consisting of Ionblox (formerly Zenlabs Energy), Saft America, LBNL and PNNL and ANL completed all Year-3 milestones and deliverables.

### Key Publications

Year-3 results were presented by Dr. Subra Herle at the 2023 EERE VTO Annual Merit Review in June. Project ID: Bat 592

## **Acknowledgments**

Ajey M. Joshi served as the program director for this project. The Applied Materials team would like to sincerely acknowledge our key partners (Ionblox - formerly Zenlabs, Saft America, LBNL, PNNL, and ANL) for their expert contributions and consistent efforts in supporting us to enable this technology. We also acknowledge significant contributions from our Applied Materials engineering and process team, who have worked tirelessly to make significant progress towards the overall program goals.

We take this opportunity to thank DOE program management team and reviewers for their critical comments, constant encouragement, and guidance. Finally, this project was made possible in part by EERE funding for which we are grateful.

## II.12 Thin-film lithium metal manufacture by room temperature electrodeposition (Albemarle Corporation)

### Marjanul Manjum, Principal Investigator

Albemarle Corporation  
4250 Congress Street, Suite 900  
Charlotte, NC, 28209  
E-mail: [marjanul.manjum@albemarle.com](mailto:marjanul.manjum@albemarle.com)

### Haiyan Croft, DOE Technology Development Manager

U.S. Department of Energy  
E-mail: [Haiyan.Croft@ee.doe.gov](mailto:Haiyan.Croft@ee.doe.gov)

Start Date: May 12, 2020	End Date: April 11, 2024	
Project Funding: \$5,391,760	DOE share: \$4,310,960	Non-DOE share: \$1,080,800

### Project Introduction

Albemarle Corporation with its partners, Argonne National Laboratory and Solid Power, will develop and prototype pilot-scale production of room-temperature electrodeposited lithium metal films to accelerate the adoption of next generation re-chargeable lithium metal batteries. The proposed electrodeposition technology has the potential to significantly improve the efficiency and cost of manufacturing ultra-thin lithium metal anodes thereby opening a new pathway to cost-effective lithium metal batteries. This program will demonstrate that electrodeposition can be a commercially viable path to low-cost lithium metal anodes. Success will motivate further scale-up of U.S.-based lithium metal anode production and encourage the growth of a domestic battery industry based on this enabling technology.

### Objectives

The objective of the project is to research, develop, and establish an economically feasible roll-to-roll electrodeposition method to produce ultra-thin ( $\leq 20 \mu\text{m}$ ) high-quality lithium metal anodes from low-cost aqueous lithium salts at room temperature.

### Approach

The approach for the project is as follows:

1. Optimization of single compartment cell (May 2020 – February 2022)  
This includes selection of the electrolyte (catholyte) chemistry, batch production of lithium anodes at high deposition rates ( $\geq 1 \mu\text{m}/\text{min}$ ), and validation of produced lithium anodes through coin & pouch cell testing.
2. Optimization of dual compartment cell (May 2020 – February 2022)  
This includes development of water impermeable lithium-ion conductive membrane, development of engineering controls to mitigate water crossover, batch production of lithium anodes at high deposition rates ( $\geq 1 \mu\text{m}/\text{min}$ ), and validation of lithium anodes through coin and pouch cell testing.
3. Process scale up and validation in prototype system (August 2020 – July 2024)
4. Development of electrodeposition cost model (November 2020 – July 2024)

## Results

### 3. Deposited high-quality lithium (Li) metal from proprietary electrolyte in single compartment cell

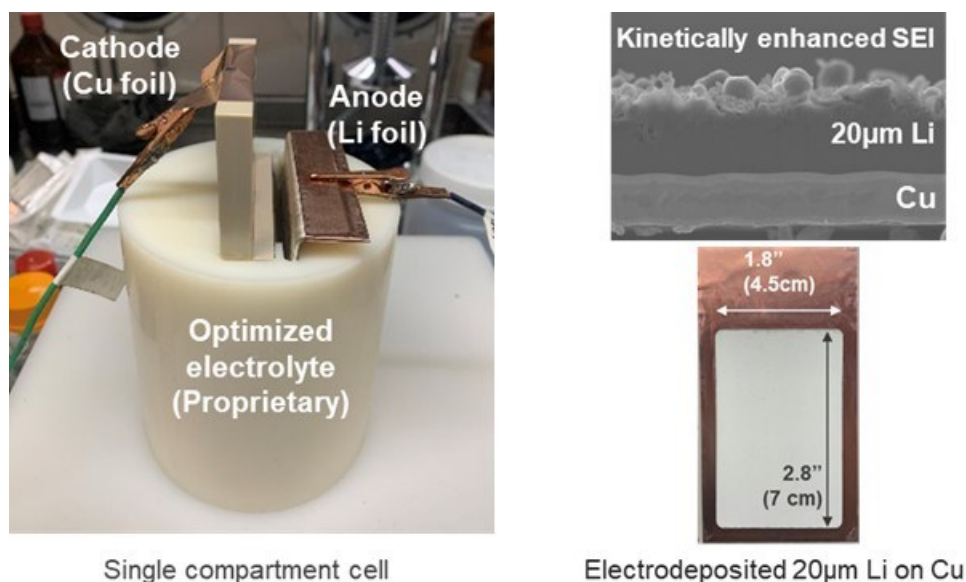


**Figure II.12.1** Single compartment electrodeposition cell setup with batch produced Li anode on Cu. Cross-sectional & front view of Li anode provided

We fabricated a single compartment cell that consists of a lithium electrolyte chamber with platinum (Pt) anode and copper (Cu) cathode. We performed multiple electrodepositions runs to down select the electrolyte (catholyte) chemistry that enables uniform Li deposits at high current densities. Having selected the best electrolyte (catholyte) chemistry, we batch produced 20 µm Li anodes on Cu of size 4.5 cm x 7 cm. Cross-sectional imaging of the anodes shows a kinetically enhanced SEI that is known to promote faster charge transfer of lithium ions at the anode interface, thereby stabilizing lithium deposition. (Figure II.12.1)

Independent cell testing performed at Argonne National Lab Cell Analysis, Modeling, and Prototyping (CAMP) Facility shows that single compartment electrodeposited Li anode achieves 2 times longer cycle life than the commercial anode of same thickness (Figure II.12.2). We attribute this longer cycle life to kinetically enhanced SEI of the electrodeposited anode.

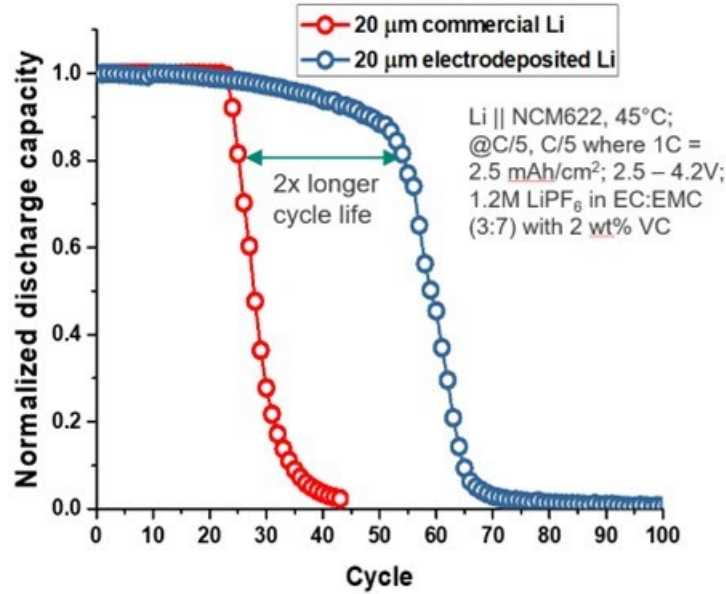


Figure II.12.2 Cell testing comparison of single compartment electrodeposited Li anodes against commercial anode

4. *Developed new Li-ion selective membrane with proprietary engineering controls to enable dual compartment electrodeposition.*

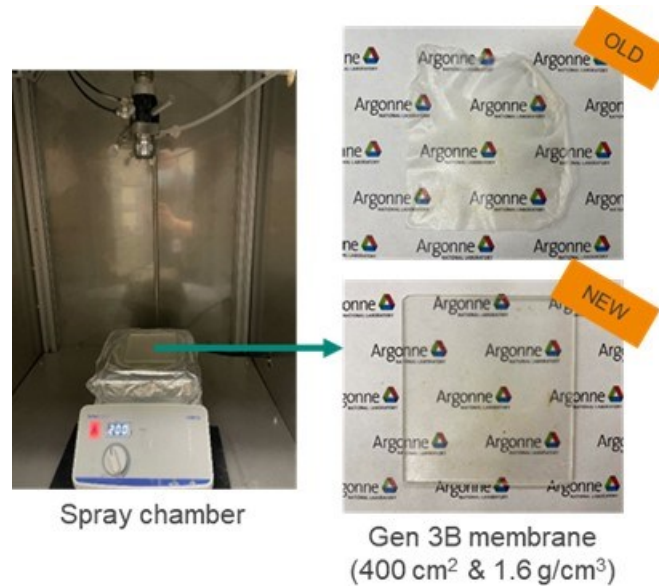


Figure II.12.3 Spray chamber to fabricate robust Gen 3B membrane

We developed three different generations of membrane chemistries & architectures to reduce water crossover into catholyte. The third generation (3B) membrane of 300 μm thickness shows nearly fifteen-fold reduction in water crossover compared to earlier generations (Figure II.12.3). We also developed proprietary engineering controls that can eliminate crossover water. We were able to limit water crossover to below 300 ppm by combining the action of the Gen 3B membrane with engineering controls. This water crossover limit enables high-quality deposition of Li metal.

### 5. Deposited high-quality Li metal from aqueous salt in dual compartment cell

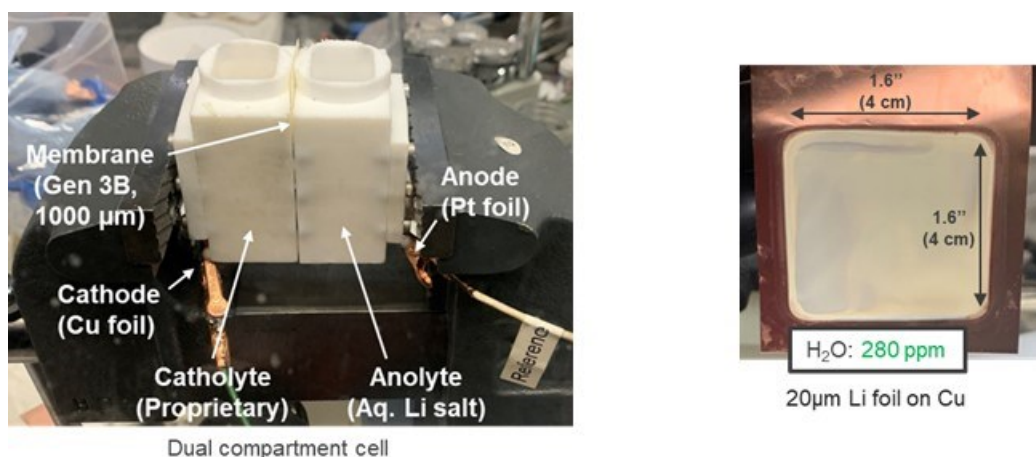


Figure II.12.4 Dual compartment electrodeposition cell setup with batch produced Li anode on Cu

We fabricated a dual compartment cell that consists of an anolyte chamber with Pt anode, a Gen 3B membrane, & catholyte chamber with Cu cathode. Proprietary engineering controls were added to the cell to mitigate water crossover. Next, we deposited 20 μm Li anode on Cu of size 4 cm x 4 cm with water crossover below 300 ppm (Figure II.12.4).

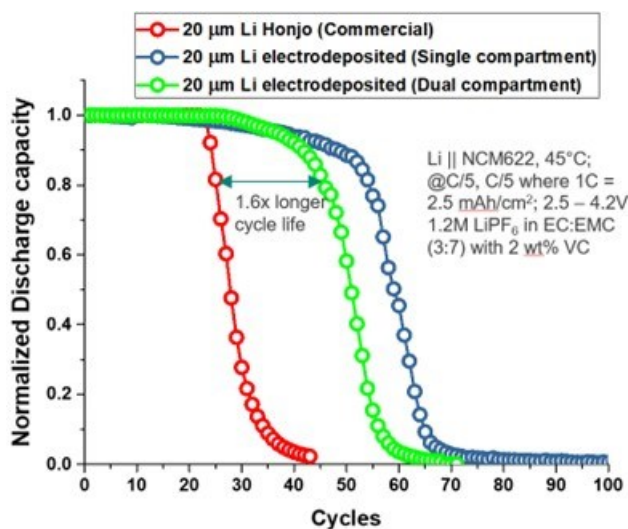


Figure II.12.5 Cell testing comparison of single & dual compartment electrodeposited Li anodes against commercial anode.

Independent cell testing performed at the Argonne National Lab CAMP facility shows that dual compartment electrodeposited Li anode achieves 1.6 times longer cycle life than the commercial anode of same thickness (Figure II.12.5).

### 6. Ongoing fabrication of prototype unit to demonstrate roll-to-roll manufacturing of electrodeposited Li

We evaluated 5 electrodeposition equipment manufacturers and selected a vendor among them for the design and construction of the Li prototype unit. Working with our external and internal safety experts, the team performed preliminary process, mechanical, and electrical design of the unit, including a detailed hazard identification and mitigation study. We addressed the recommendations and finalized the design of the unit. Construction of the unit has progressed throughout the year with weekly updates given by the vendor. The



installation at Argonne National Laboratory is estimated by January 2024 and validation is expected to run through July 2024. The unit will be housed in the Manufacturing Engineering Research Facility at Argonne, with significant room modifications already made in anticipation of the installation.

**7. Techno-economic analysis shows electrodeposition route of manufacturing Li anodes has potential to be cost effective at GWh scale for thicknesses < 8  $\mu\text{m}$**

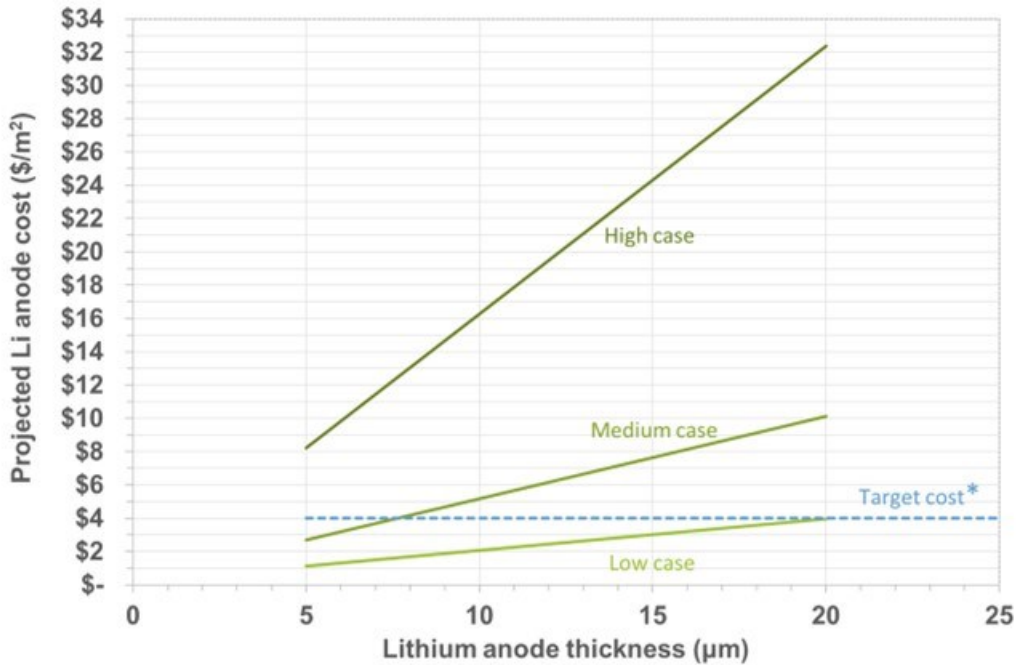


**Figure II.12.6 Projected Li anode cost in \$/m<sup>2</sup> vs. Li anode thickness in  $\mu\text{m}$**

A preliminary techno-economic analysis (TEA) was performed by considering that the Li anodes produced will supply a 25 GWh cell facility producing 18650 cells. The TEA accounts for process, engineering, material, and labor costs (Figure II.12.6). The target cost was set from the work of Albertus et al.<sup>1</sup>

Note: The techno-economic model is not final and will be revised as we demonstrate roll-to-roll manufacturing of electrodeposited Li on the prototype unit.

### Conclusions

In conclusion, we deposited high-quality Li metal from an aqueous Li salt in a dual compartment cell. We achieved this through the development of proprietary electrolyte (catholyte) that enables uniform deposition of Li metal and a new generation Li-ion conductive membrane with engineering controls that mitigate water crossover. We also made significant progress in fabrication of the prototype unit that will enable us to demonstrate roll-to-roll manufacturing of electrodeposited lithium in FY2024. Finally, we performed techno-economic analysis to estimate that electrodeposition route of manufacturing Li anodes has potential to be cost effective at GWh scale for thicknesses < 8  $\mu\text{m}$ .

### Key Publications

1. A poster summarizing key achievements was presented at the 2023 EERE VTO Annual Merit Review in June 2023, 2023 Vehicle Technologies Annual Merit Review (Project ID: Bat 522).

### References

1. Albertus, et al. "Status and challenges in enabling the lithium metal electrode for high-energy and low-cost rechargeable batteries." *Nature Energy* 3.1 (2018): 16-21.

## **Acknowledgements**

This work is supported by the U.S. Department of Energy's Office of Energy Efficiency and Renewable Energy (EERE) Award Number DE-EE0009094. We would like to thank: (1) VTO: Haiyan Croft, Ahmad Pesaran, Jack Deppe for providing technical guidance and valuable insights during the monthly review meetings; (2) NETL: Aaron Yocum and Jennifer Burbage for helping navigate the contracting aspects; (3) Argonne National Laboratory: John Hryn, Edward Barry, Donghyeon Kang, Zachary Hood, Matthew Earlam, & Michael Dziekan for lab scale research work and process scale-up activities. CAMP facility for cell testing, (4) Solid Power Operating, Inc: Brian Francisco and Adam Jansons for cell testing; and (5) Albemarle Corporation: Marjanul Manjum, Kristina Butler, Subramanian Venkatachalam, & Job Rijssenbeek for project oversight.

## II.13 GMC CRADA: Multilayer Composite Solid State Lithium Batteries for EV Battery Applications (ANL)

### Yuepeng Zhang, Principal Investigator

Argonne National Laboratory  
9700 S Cass Ave  
Lemont, IL, 60439  
E-mail: [yuepeng@anl.gov](mailto:yuepeng@anl.gov)

### Shaomao Xu, Principal Investigator

General Motors, LLC  
30470 Harley Earl Blvd  
Warren, MI, 48092  
E-mail: [shaomao.xu@gm.com](mailto:shaomao.xu@gm.com)

### Haiyan Croft, DOE Technology Development Manager

U.S. Department of Energy  
E-mail: [Haiyan.Croft@ee.doe.gov](mailto:Haiyan.Croft@ee.doe.gov)

Start Date: October 1, 2022

End Date: September 30, 2023

Project Funding (FY23): \$700,000

DOE share: \$350,000

Non-DOE share: \$350,000

### Project Introduction

Argonne National Laboratory teams with General Motors, LLC to develop manufacturing solutions to fabricate high-energy-density and low-cost all-solid-state lithium batteries (ASSBs) to support domestic EV battery production. ASSBs have several advantages over lithium-ion batteries (LIBs). Due to higher safety thresholds associated with solid electrolytes (SEs), ASSBs show the possibility of using lithium metal or silicon anodes, and thus the potential for obtaining comparatively higher energy and power density. The SE can also prevent chemical interactions with dissolved active materials and thus solve the issue of long-term instability of LIBs. However, there are also challenges associated with ASSBs, such as local stress and contact-loss between SE and active materials in cathodes due to active material “breath”, poor contact and high ionic resistance at the SE-cathode interface, difficulty in fabricating thin SEs, and the absence of scalable and cost-effective manufacturing processes [1]. In this project, the team will perform a feasibility study which examines the fabrication of ASSBs through direct coating of SEs on cathodes and replacement of conventional component stacking processes to address some of the above challenges.

### Objectives

Our ultimate goal is to develop manufacturing solutions to fabricate ASSBs with superior electrochemical and cycling performance as compared to current state-of-the-art lithium-ion batteries (LIBs). The team is targeting two major deliverables: (1) demonstration of direct coating of SE on cathode and its economic and performance feasibility; and (2) material and process knowledge for scalable coating of high-quality polymer-ceramic SEs and high-nickel content cathodes for ASSBs.

### Approach

Co-development and co-optimization of electrolyte and electrode ink materials and coating processes will be conducted to achieve highly compatible SEs and cathodes. The team will use polymer-Li<sub>7</sub>La<sub>3</sub>Zr<sub>2</sub>O<sub>12</sub> (LLZO) composite electrolytes and LLZO-LiNi<sub>0.8</sub>Mn<sub>0.1</sub>Co<sub>0.1</sub>O<sub>2</sub> (NMC811)-based cathodes as model systems. Ink compositions, synthesis methods, and rheological properties, as well as coating and drying parameters will be optimized to achieve high solid concentration cathode with >80 wt.% active materials and desirable lithium-ion transport within SE, cathode, and across SE-cathode interfaces. The coating process will first be optimized

using lab-scale coating equipment and then transferred to roll-to-roll coating systems for scalability demonstration.

## Results

### *Optimization of Mixing Conditions for SE Fabrication*

The first step of electrode and SE coating is slurry mixing. The mixing process is often overlooked, but an in-depth investigation is required for better understanding of the relationship between ink properties and electrode properties for SSE fabrication [2]. For instance, particle size distribution, slurry uniformity, and compositions are critical parameters to determine the quality of electrodes, which varies depending on the mixing process. For different material systems, the optimal mixing process can also be different, depending on: (1) particle size, shape, and loading; (2) binder polymer structure, molecular weight, and concentration; and (3) solvent type and ratio, dielectric property, and evaporation rate. In addition, the interactions between particle and polymer (e.g., binding/adsorption behavior), polymer and solvent (e.g., pH and conductivity), and other factors (e.g., Zeta potential, rheological behavior) also play a role. Therefore, our first study concerns the effects of different mixing methods on SE fabrication.

There are a variety of mixing methods, including magnetic stirring, high shear mixing, wet ball milling, ultrasonic mixing etc. [3]. In this study, we report two high-speed mixing methods, i.e., off-axis dual asymmetric centrifugal mixing (off-axis hereafter) and acoustic mixing. Both methods are more energy efficient for industrial use than slow mixing processes like magnetic stirring or ultrasonication. The mixing principle of the off-axis mixer relies on a dual axis of rotation, where the mixing container rotates around its own axis, while the high-speed mixing arm revolves in a circular motion in the opposite direction. The combination of rotation and revolution motions thus mixes samples in the container by whirling in the direction of the circumference and also moving upward and downward along the rotation shaft [4]. On the other hand, acoustic mixers translate mechanical system resonances to the mixing media as a longitudinal acoustic pressure wave with a short amplitude and high frequency [5]. The total mixing energy ( $E_{mix}$ ) from an acoustic mixer can be calculated as follows:

$$E_{mix} = \frac{P_{mix} \cdot t_{mix}}{mass}$$

where  $P_{mix}$  is the total power (G-force),  $t_{mix}$  is the total mixing time.

To compare the two mixing methods, we tested different mixing parameters for each, e.g., the rotation speed (rpm) and time for the off-axis mixer, and G-force and time for the acoustic mixer. Ink viscosity and coatability was used as criteria to assess the effectiveness of the mixing conditions. A benchtop slot-die coater (*FOM Technologies VectorSC*) was used first. With the eventual goal of industrial scale coating, optimization of mixing conditions followed by coating parameters at the benchtop scale will enable a systematic transition to the larger pilot-scale coating in the following study (Figure II.13.1).

Ink preparation was conducted in two-steps: (1) a 6 wt.% polyethylene oxide (PEO) (molecular weight (Mw): 600,000 Da) in acetonitrile (ACN) solution was prepared, to which LLZO nanoparticles (from *MSE Supplies*) were added in a 1:1 mass ratio of PEO to LLZO, resulting in a final solution of 11.3 wt.% total solid concentration; (2) the solution was then processed by either off-axis mixing (*FlackTek SpeedMixer*) or acoustic mixing (*ResodynAcoustic® LabRAM II™*), as shown in Table II.13.1. Relatively high Mw PEO was used to be compatible with the Mw of those commonly used for >4 V cell voltage, e.g., polyvinylidene fluoride (PVDF). A 50  $\mu\text{m}$  dry film thickness was the target while the wet film and coating gap were held constant at 1028  $\mu\text{m}$  and 1100  $\mu\text{m}$ , respectively. The ink was coated onto a thin foil of copper. Zirconia balls were added to the off-axis mixing to accelerate PEO dissolution in ACN and LLZO particle dispersion. For each ink, two coatings were made with 0.1 m/min and 0.5 m/min speed to improve statistics.



Figure II.13.1 Transition from benchtop coating to roll-to-roll pilot-scale coating at ANL.

Table II.13.1 LLZO-PEO Ink Mixing Conditions.

Mixing Tool	Mixing rpm / g-force	Mixing Time (min)	5 mm Zirconia Balls	Coating Speed (m/min)		Pump Rate at 0.1 m/min ( $\mu\text{L}/\text{min}$ )	Pump Rate at 0.5 m/min ( $\mu\text{L}/\text{min}$ )	Coating Distance (mm)	Particle Buildup in Die Head
Off-Axis Mixer	2000 rpm	10	Yes	0.1	0.5	2570	12850	50	No
Off-Axis Mixer	2000 rpm	30	Yes	0.1	0.5	2570	12850	50	No
Off-Axis Mixer	3500 rpm	10	No	0.1	0.5	2570	12850	100	Yes
Off-Axis Mixer	3500 rpm	30	Yes	0.1	0.5	2570	12850	50	No
Acoustic Mixer	60 G	2	No	0.1	0.5	2570	12850	50	Yes
Acoustic Mixer	80 G	2	No	0.1	0.5	2570	12850	50	Yes
Acoustic Mixer	100 G	2	No	0.1	0.5	2570	12850	50	Yes
Acoustic Mixer	100 G	10	No	0.1	-	2570	-	50	Yes

Shear rate versus viscosity measurements were carried over for all inks and the results are plotted in Figure II.13.2. All the inks showed a typical shear thinning behavior in the range of 0.1 1/s - 5000 1/s and a similar viscosity at high shear rates (e.g., >1000 1/s). However, different mixing conditions led to different ink viscosity at low shear rates, where the acoustic 60 G-2 min ink showed the largest viscosity, and the off-axis 2000 rpm-30 min and 3500 rpm-30min inks had the lowest viscosities. It is also apparent that for both off-axis and acoustic mixing, ink viscosity decreased with a longer mixing time. These results indicate that an extended mixing time facilitates ink flow and processibility.

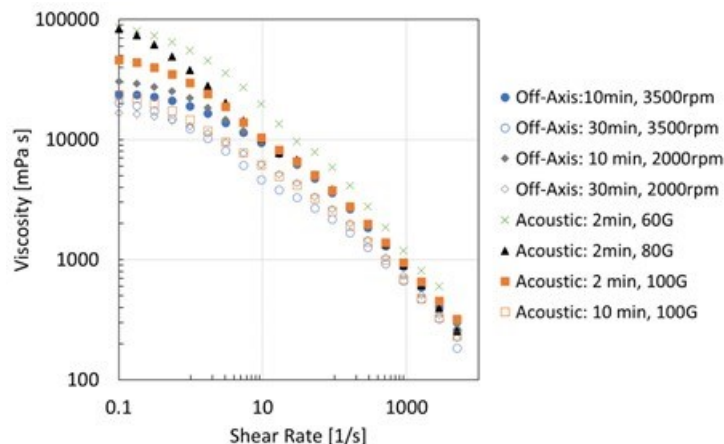


Figure II.13.2 Viscosity versus shear rate for all the prepared LLZO inks at 25 °C.

After coating, the films were dried in air for one hour at room temperature (RT) and then characterized by scanning electron microscopy (SEM). Figure II.13.3 shows the optical photographs of all the dry films, which shows varying degrees of spotty contrast on certain samples, indicating microstructure non-uniformity of these samples. The samples that had fewer spotty features were those prepared by off-axis mixers for 30 min (e.g., Samples c, d, g, and h in Figure II.13.3). With a closer look by plan-view SEM (Figure II.13.4), it was found that the spots shown in the optical images were large LLZO particle agglomerates with a typical size of a 10  $\mu\text{m}$  - 20  $\mu\text{m}$ . These agglomerates were observed for all the acoustic mixing samples but were observed less in the 30 min off-axis samples. Among acoustic mixing samples, it can be stated that as the mixing energy increased, the number of large agglomerates decreased, indicating that higher mixing energy improved LLZO dispersion. However, when the 2-min and 10-min 100 G acoustic samples (Figure II.13.4 g, h) were compared, there was not an observable difference, suggesting that mixing time is less effective than mixing power (G-force) for particle dispersion for very high energy mixing. On the other hand, in comparison with the 10-minute off-axis samples (Figure II.13.4 a, b), low power acoustic mixing samples showed a better particle dispersion, indicating a higher energy was generated by the acoustic mixing which is still beneficial.

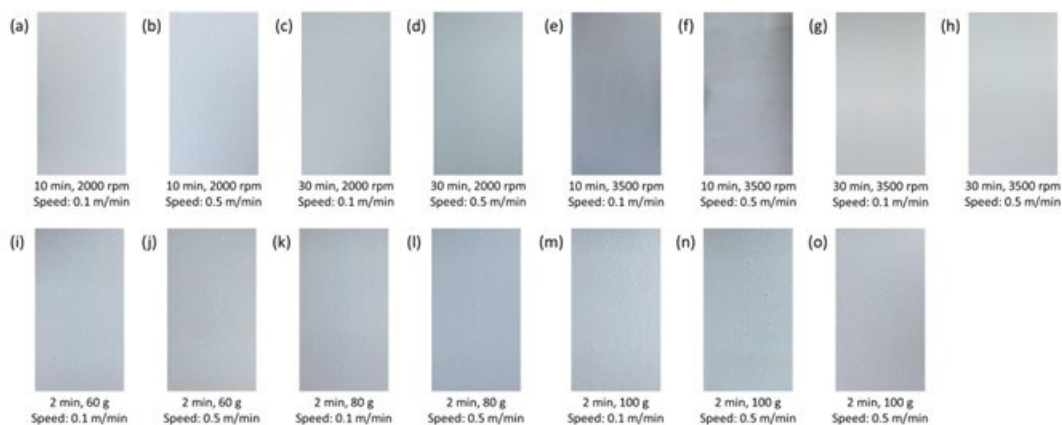
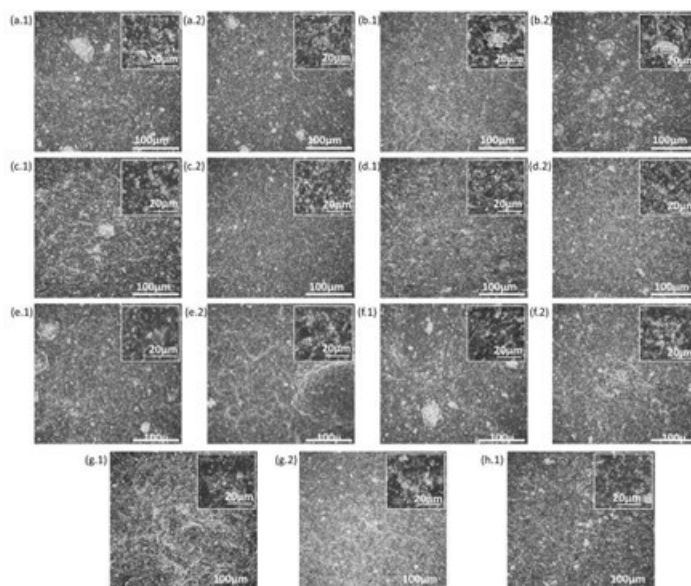


Figure II.13.3 Photographs of dry LLZO-PEO films prepared with different mixing conditions.



**Figure II.13.4** Plan-view SEM images of LLZO-PEO coatings made from different inks: a.) 10 min, 2000rpm; b.) 10 min, 3500rpm; c.) 30 min, 2000rpm; d.) 30 min, 3500rpm; e.) 2 min, 60 G; f.) 2 min, 80 G; g.) 2 min, 100 G; h.) 10 min, 100 G. The coating speed is included in the image numbers, e.g., \*.1 represents 0.1 m/min speed and \*.2 represents 0.5 m/min speed.

In addition to plan-view SEM, cross-section SEM analysis was also carried out to view LLZO particle distribution in film's thickness direction. As shown in Figure II.13.5, the 30 min off-axis mixing samples showed the best thickness uniformity and a thickness close to the target dry film thickness of 50  $\mu\text{m}$  (Figure II.13.5c, d). No obvious large-size agglomerates were observed for these two samples, which are consistent with the plan-view SEM and optical observation. All other samples showed uneven thicknesses and large bumps, caused by LLZO agglomeration and sedimentation. Comparing acoustic and off-axis mixing samples, the off-axis mixing samples showed less bumps overall. Among the acoustic mixing samples, the ones that were prepared with higher mixing power showed better thickness uniformity. However, increasing mixing time from 2 min to 10 min in 100 G conditions barely changed the LLZO particle dispersion (LLZO agglomeration was observed; Figure II.13.5 g, h). On the other hand, when off-axis mixing samples are compared, increasing mixing speed from 2000 rpm to 3500 rpm with 10 min identical mixing time reduced thickness variation, but LLZO agglomeration and sedimentation was still observed (Figure II.13.5 a, b). Only by increasing the mixing time from 10 min to 30 min were these defective features significantly removed (Figure II.13.5 a-d). These results indicate that mixing time is a dominant factor for coating uniformity control for off-axis mixing. Finally, it should be noted that although acoustic mixing showed less effective LLZO dispersion compared to the off-axis mixing, the mixing time used for acoustic mixing may not be sufficient yet to fully homogenize LLZO particles in the inks. A slight increase of acoustic mixing time may result in the same uniformity inks as 30 min off-axis mixing. In fact, the viscosity measurements have indicated that the 100 G 10 min acoustic mixing sample already showed a similar viscosity range to the 30 min off-axis mixing samples.

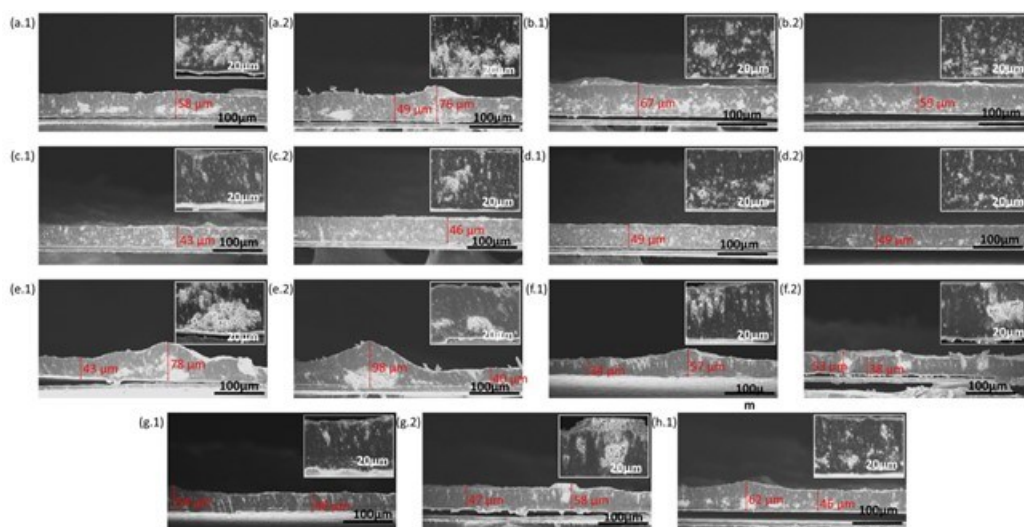


Figure II.13.5 Cross section SEM images of LLZO-PEO coatings made from different inks: a.) 10 min, 2000rpm; b.) 10 min, 3500rpm; c.) 30 min, 2000rpm; d.) 30 min, 3500rpm; e.) 2 min, 60G; f.) 2 min, 80 G; g.) 2 min, 100 G; h.) 10 min, 100 G. The coating speed is included in the image numbers, e.g., \*.1 represents 0.1 m/min speed and \*.2 represents 0.5 m/min speed.

#### **Preliminary Electrochemical Performance Evaluation of SE Films**

With the knowledge of the optimal mixing conditions, LLZO-PVDF films with the same LLZO particle loading (e.g., LLZO:PVDF=1:1) and mixing conditions (2000 rpm off-axis, *Thinky* mixer) were prepared. Lithium bis(trifluoromethane)sulfonimide (LiTFSI) was added in the mixing step to enable Li<sup>+</sup> conductivity in PVDF. The PVDF and LiTFSI mass ratio of 1:1 was used. After mixing, a homogeneous slurry was obtained with no sign of sedimentation or gelation (Figure II.13.6a). Additionally, a uniform SE film was coated on a Cu foil by blade coating (Figure II.13.6b). The microstructure observed using plan-view SEM indicates that the LLZO particles were uniformly distributed in the PVDF matrix (Figure II.13.6c) and most of the particles were well separated from one another despite a small amount of minor agglomeration (Figure II.13.6d, e). The cross-section SEM images show relatively uniform film thickness of ~30 μm and a uniform distribution of LLZO particles (Figure II.13.6f, g). This observation is consistent with our 2000 rpm off-axis mixing LLZO-PEO samples, indicating the transferability of the gained knowledge. The preliminary electrochemical performance of the fabricated LLZO-PVDF-LiTFSI film was analyzed by electrochemical impedance spectroscopy (EIS) measurement in a Swagelok cell using Li metal and Cu foil as the two electrodes (Figure II.13.7). A relatively low ionic conductivity of 10<sup>-6</sup> S/cm was calculated between RT and 60 °C based on the measured interfacial resistance (Figure II.13.7 and Table II.13.2), indicating that LLZO nanoparticles were not activated in this sample. This is likely because the LLZO particles were isolated and did not form an interconnected transport network. Optimization of SE composition and microstructure such as LLZO loading, LiTFSI concentration, and LLZO distribution within PVDF will be performed in our next step to improve Li<sup>+</sup> transport.



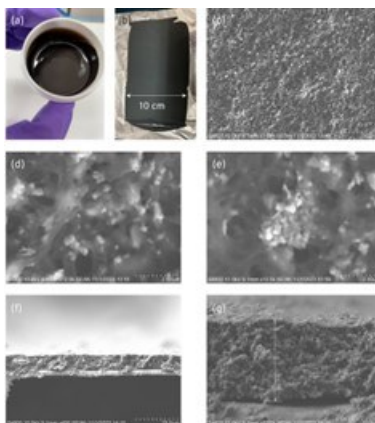


Figure II.13.6 Photographs of (a) PVDF-LLZO-LiTFSI inks; and (b) coatings; as well as plan-view (c, d, e) and cross-section (f, g) SEM images of the coated films.

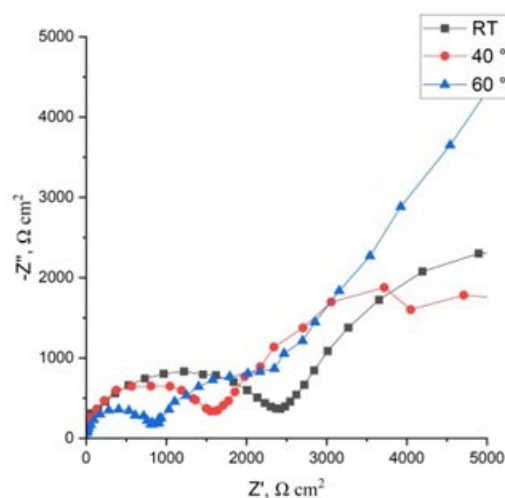


Figure II.13.7 EIS measurements of the Li|PVDF-LLZO-LiTFSI|Cu cell at RT, 40 °C, and 60 °C.

Table II.13.2 Ionic Conductivity of the LLZO-PVDF-LiTFSI Composite SE Films.

Temperature, °C	25	40	60
Ionic conductivity, S/cm	$1.2 \times 10^{-6}$	$1.9 \times 10^{-6}$	$3.8 \times 10^{-6}$

## Conclusions

Our experiments showed a clear influence of mixing conditions on ink rheology, along with a correlation between ink rheology and coating quality. Specifically, off-axis mixing with a moderate rotational speed and extended mixing time (e.g., in this case 2000 rpm and 30 min) facilitates ink flow and LLZO nanoparticle dispersion in a viscous polymer solution, thus creating a high probability of more uniform coating. Compared with off-axis mixing, acoustic mixing with the studied setting (e.g., 60 G to 100 G, 2 min to 10 min) showed less effectiveness for our nanoparticle SE inks. However, this mixing method is still promising from a manufacturing perspective since it requires significantly shorter mixing time. Even for a 2 min mixing time, the 100 G mixing power has already shown the capability of improving ink flow at low shear rates.

In addition, our coating trials on PVDF-LLZO films indicate the feasibility of fabricating uniform polymer-ceramic composite SE using the proposed manufacturing process. Further optimization of ink formulation is needed to enable high ionic conductivity of the composite SE, which is our next R&D focus.

## References

1. Jurgen Janek and Wolfgang G Zeier. “Challenges in speeding up solid-state battery development.” *Nature Energy* 8 (2023): 230-240.
2. Leire Fernandez-Diaz, Julen Castillo, Elene Sasieta-Barrutia, Maria Arnaiz, Marta Cabello, Xabier Judez, Alexandre Terry, Laida Otaegui, Maria C. Morant-Miñana, Aitor Villaverde. “Mixing methods for solid state electrodes: Techniques, fundamentals, recent advances, and perspectives.” *Chemical Engineering Journal* 464 (2023): 142469.
3. Alexander Kraytsberg, Yair Ein-Eli. “Conveying advanced Li-ion battery materials into practice the impact of electrode slurry preparation skills” *Advanced Energy Materials* 6 (2016): 1600655.
4. Naoki Adachi, Osamu Sakurada, Minoru Hashiba. “Rheological properties of zirconia slurries prepared using a new planetary mixer.” *Journal of the Ceramic Society of Japan* 112 (2004): S196-S198.
5. Aileen Vandenberg and Kay Wille. “Evaluation of resonance acoustic mixing technology using ultra high performance concrete.” *Construction and Building Materials* 164 (2018): 716-730.

## Acknowledgements

The PIs are thankful to the significant contributions from our team members, Jungkuk Lee and Sam Miller at Argonne National Laboratory and Yubin Zhang, Mengyuan Chen, and Chuanlong Wang at General Motors, LLC. We are also grateful for the help and constructive discussions with Ozge Kahvecioglu, Andrew Jansen, and Steve Trask, and the support of our DOE manager, Haiyan Croft.

## II.14 Cabot CRADA: Spray Synthesis of Additive Battery Particles (ANL)

### Joseph Libera, Principal Investigator

Argonne National Laboratory  
9700 South Cass Avenue  
Lemont, IL 60439  
E-mail: [jlibera@anl.gov](mailto:jlibera@anl.gov)

### Haiyan Croft, DOE Technology Development Manager

U.S. Department of Energy  
E-mail: [Haiyan.Croft@ee.doe.gov](mailto:Haiyan.Croft@ee.doe.gov)

Start Date: October 1, 2022	End Date: September 30, 2023	
Project Funding (FY23): \$300,000	DOE share: \$300,000	Non-DOE share: \$0

### Project Introduction

High energy cathode materials for next-generation Li-ion batteries such as nickel-rich lithium nickel cobalt manganese oxides (NCMs) usually suffer from major cycle and calendar life issues. The implementation of these high-Ni NCM materials relies heavily on particle surface coating to overcome their instability issue under charge-discharge conditions.

So far, only the aqueous wet-coating process has been commercially adopted. However, wet coating techniques require relatively high energy cost and pose potential emissions of volatile organic compounds. Other under development technologies, such as chemical vapor deposition (CVD) and atomic layer deposition (ALD), have multiple disadvantages in terms of limited compositions, low throughput, and expensive running costs. In contrast, dry particle coating provides more viable and versatile feasibility for surface modification of CAMs and the relevant reported results have shown potential advantages of such dry processes.

### Objectives

To support the advancement of dry coating technology, different simple and mixed-metal oxides have been successfully demonstrated for surface modification of Ni-rich NCMs. However, the cell performance of coated CAMs demonstrated in the relevant research is far from satisfactory for commercial implementation. Therefore, more complex, and effective surface coating materials, especially nanoscale lithium metal oxides, are urgently needed and required advanced synthesis processes.

### Approach

#### *Flame spray pyrolysis (FSP) at ANL:*

FSP is a flexible aerosol manufacturing platform capable of producing lithium metal oxides with various compositions. In FSP, combustible solutions containing organic and/or inorganic metal salts are combusted in spray flames to yield combustion gas and solid products where the solid products are the targeted synthesized material. A principal advantage of FSP is the flexibility in defining product chemistry by combining all component elements in a single solution with a high likelihood that all the components will be homogeneously mixed in the product particles which makes FSP an extremely useful technique for probing candidate particles composition. The size of particles made by FSP spans the range of 20 nm to several microns, making these materials excellent candidate for dry particle coating applications.

#### *Dry particle coating at Cabot:*

During a dry coating process, larger (micron-sized) CAM particles are coated directly with fine submicron-sized particles by mechanical forces without using any solvents or binders. As the size of the coating material

particles is very small, van der Waals or electrostatic interactions and the mechanical forces applied by the coating process keep them attached to the larger core CAM particles. In some cases, to enable strong coating adhesion and optimal protection, the coated CAM particles are optionally heat treated so the coating particle sinter with CAM core particle.

#### **CAM life extension using dry particle coatings:**

Dry coating and subsequent heat treatment will be evaluated by electrochemical testing in half- and full-coin cells. ANL will focus on the investigation of coating the pCAM while Cabot will focus on the coating of CAMs. Both investigations will use both the ANL FSP particles as well as the Cabot fumed oxide particles.

### **Results**

#### **Synthesis of coating particle candidate Set1 :**

Flame Spray Pyrolysis was used to synthesize nanosized metal oxide particles in the Li-Al, Li-Ti, and Li-Nb systems. In each series, well known compounds in the series as well as the pure oxides were synthesized as well as a lightly or partially lithiated composition. The goal of varying the Li for 0 to stoichiometric ratios for various compounds was to simulate what might otherwise occur during the heat treatment of the coating particles and the cathode and where Li is contributed by CAM Li, either creating a deficit, neutral or excess of Li in the CAM near surface region. Thus the series are intended to elucidate the impact on CAM Li resulting from the coating particle treatment. Table II.14.1 shows the composition of all the samples made in candidate Set1.

**Table II.14.1 Synthesis Data for Coating Particle Candidate Set1.**

System	Target	Observed Phases
Li-Al	Al <sub>2</sub> O <sub>3</sub>	Al <sub>2</sub> O <sub>3</sub> : I
	Li <sub>0.1</sub> Al <sub>0.9</sub> O <sub>x</sub>	Al <sub>2</sub> O <sub>3</sub> : P-4m2, Fd-3m
	LiAlO <sub>2</sub>	LiAlO <sub>2</sub> : P4212, R-3m; Al <sub>2</sub> O <sub>3</sub> : Fd-3M
Li-Ti	TiO <sub>2</sub>	TiO <sub>2</sub> : I41/amd, P42/mnm
	Li <sub>0.1</sub> Ti <sub>0.9</sub> O <sub>x</sub>	TiO <sub>2</sub> : I41/amd, P42/mnm; Li <sub>4</sub> Ti <sub>5</sub> O <sub>12</sub> : Fd-3m; Ti <sub>3</sub> O <sub>5</sub> : C2/m
	Li <sub>2</sub> TiO <sub>3</sub>	Li <sub>2</sub> TiO <sub>3</sub> : Fd-3m, C2/c; Li <sub>2</sub> Ti <sub>3</sub> O <sub>7</sub> : Pbnm
	Li <sub>4</sub> Ti <sub>5</sub> O <sub>12</sub>	Li <sub>4</sub> Ti <sub>5</sub> O <sub>12</sub> : Fd-3m; TiO <sub>2</sub> : I41/amd, P42/mnm
Li-Nb	Nb <sub>2</sub> O <sub>5</sub>	Nb <sub>2</sub> O <sub>5</sub> : R-3m
	LiNbO <sub>3</sub>	LiNbO <sub>3</sub> : R3c; Nb <sub>2</sub> O <sub>5</sub> : R-3m

In the Li-Al series, the FSP samples produced pure Al<sub>2</sub>O<sub>3</sub> and LiAlO<sub>2</sub> as targeted by the input solution whereas the Li<sub>0.1</sub>Al<sub>0.9</sub>O<sub>x</sub> sample produced alumina phases slightly different than the pure alumina case with no Li phase detected. Electron microscopy of the Li-Al series is shown in Figure II.14.1 and Figure II.14.2 and reveals that the particle size is very small for the pure alumina case (~10 nm) compared to the LiAlO<sub>2</sub> sample (~30 nm). This difference in particle sizes is likely to have profound effects on CAM particle coating outcomes but not in predictable ways. In the Li-Ti series, a mixture of rutile and anatase was obtained for the no-Li sample while the targeted Li-Ti compounds were synthesized with minor rutile anatase impurity.

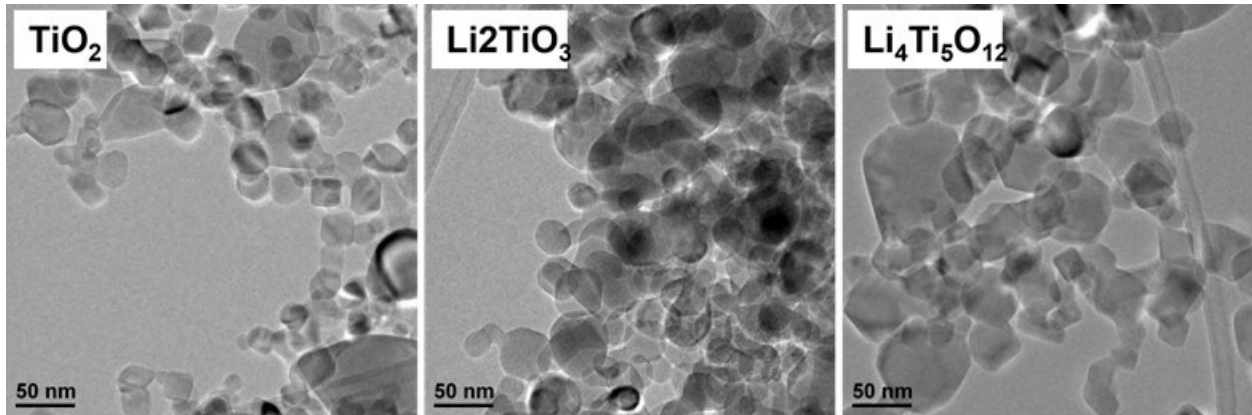


Figure II.14.1 Electron microscopy of the Li-Al series samples. HR-TEM performed on a JEOL3010

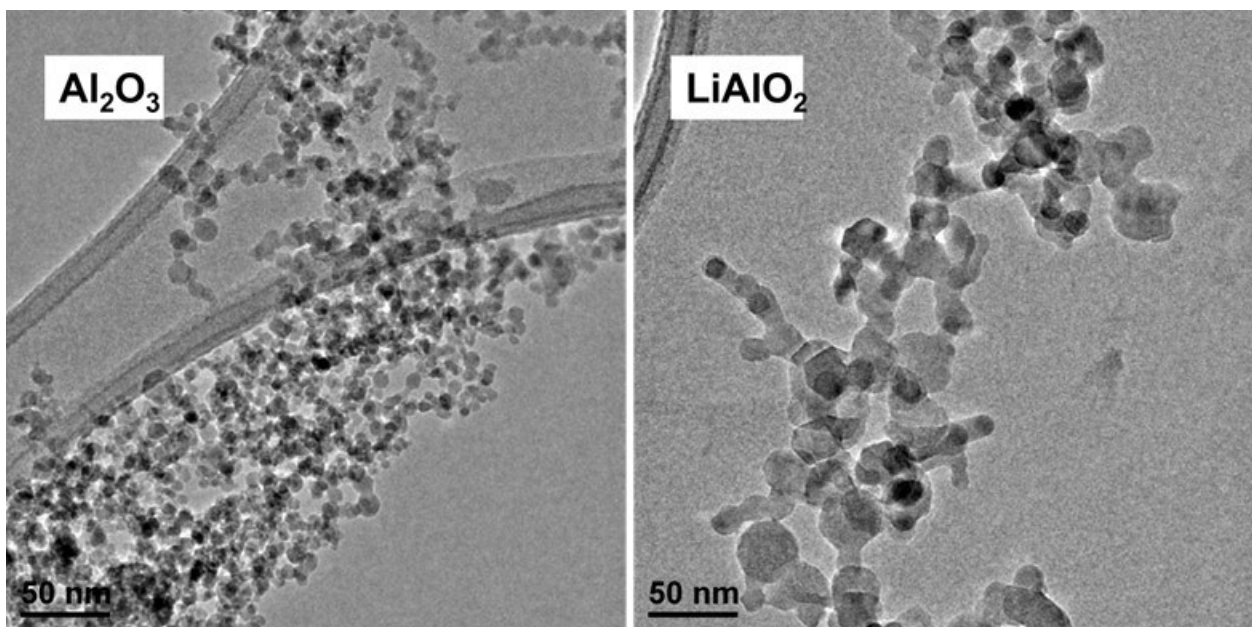


Figure II.14.2 Electron microscopy of the Li-Al series samples. HR-TEM performed on a JEOL3010

#### ***Selection of Test Material for this Study:***

Our industrial collaborator Cabot Corporation employs a workflow that requires 100g batches of CAM material for their pilot scale dry coating process. This requires a large source of CAM material. In addition, it is important to obtain a CM that does not already have a surface coating or other life extension aspect to its manufacture. For this purpose we sourced 30 kg of Ni83 pCAM. Part of the ANL effort on this project is to investigate the effect of using the additive particles prior to formation, ie, mixing them with the pCAM prior to calcination. Otherwise large quantities need to be prepared for Cabot Corp. It is advantageous then to use the Ni83 pCAM for both purposes. An alternative substrate has also been identified and purchased. Ronbay single crystal S8303 was obtained. This untreated CAM provides a contrasting substrate of very similar chemical composition to the Ni83 CAM but in single crystal form as opposed to the polycrystal Ni83 pCAM.

#### ***Diagnostic for Coated CAM/pCAM materials:***

In order to understand the mechanisms involved in treating CAMs or pCAMs with the FSP and/or fumed metal oxide nanoparticles, surface and bulk morphology of the final CAM particles needs to be investigated. For this purpose we have established SEM/EBSD (electron backscatter diffraction) to identify differences in treated and untreated CAMs by observing the effects on the grain morphology. An example of EBSD for the Ni83

being used in this study is shown in Figure II.14.3. In addition, in-situ calcination of coated pCAM are performed at ANL/APS and BNL/NSLS to elucidated the destiny of the coating particles during any heat treatment protocols attempted for the coated CAM particles.

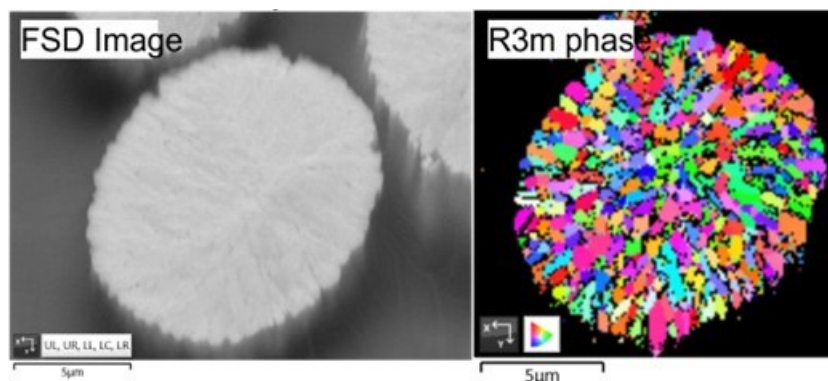


Figure II.14.3 SEM/EBSD image of Ni83 CAM

### Conclusions

A study was commenced to investigate dry nanoparticle coating of high-Ni CAM and pCAM materials in order to extend their cycle life. FSP was used to synthesize a starting set of metal oxide nanoparticles, targeting a gradient of Li content within each Li-metal series. All target phases were obtained using FSP. Suitable untreated CAM and pCAM materials were identified and purchased for this study that provide a contrast in morphology as well as a pCAM for performing coating of both pCAM and CAM versions of the process. Suitable specialized diagnostics were identified and tested for the material in this project.

### Acknowledgements

We greatly acknowledge the support provided by Haiyan Croft. The authors greatly acknowledge the continuing collaboration of Cabot Corporation. We also acknowledge the contributions to this research by Feng Wang.

## II.15 Solid Power CRADA: Interface-Engineered, High-Energy Oxide Cathodes for All-Solid-State Lithium Batteries (ANL)

### Jeffrey Elam, Principal Investigator

Argonne National Laboratory  
9700 South Cass Avenue  
Lemont, IL 60439  
E-mail: [jelam@anl.gov](mailto:jelam@anl.gov)

### Jason Croy, Principal Investigator

Argonne National Laboratory  
9700 South Cass Avenue  
Lemont, IL 60439  
E-mail: [croy@anl.gov](mailto:croy@anl.gov)

### Haiyan Croft, DOE Technology Development Manager

U.S. Department of Energy  
E-mail: [Haiyan.Croft@ee.doe.gov](mailto:Haiyan.Croft@ee.doe.gov)

Start Date: October 1, 2022	End Date: September 30, 2023	
Project Funding (FY23): \$1,000,000	DOE share: \$500,000	Non-DOE share: \$500,000

### Project Introduction

The performance of solid-state batteries utilizing sulfide solid state electrolytes is limited by the poor chemical/electrochemical stability of the cathode-electrolyte interface. These problems are particularly severe for Ni-rich nickel-manganese-cobalt (NMC) cathodes and lead to low cycle life. Ultrathin, conformal protective coatings on these cathode surfaces can improve the cycle life of solid-state batteries. Solid Power (Louisville, CO) is an industry-leading developer of next-generation all-solid-state batteries (ASSB) and has a MWh-scale roll-to-roll pilot manufacturing line. Argonne has extensive experience in cathode development including atomic layer deposition (ALD) thin film coating methods to engineer cathode surfaces for improved performance and lifetime. This CRADA project will evaluate ALD protective coatings on two cathode materials, a commercial high-nickel cathode material (NMC811), and a lithium-manganese-rich cathode material (LMR) developed at Argonne.

### Objectives

The objective of this project is to identify, optimize, and scale up ALD protective coatings on NMC811 and LMR cathode powders that enhance the storage capacity and cycle life of ASSB using sulfide-based solid state electrolytes.

### Approach

This project will evaluate four ALD coating chemistries on two cathode materials (NMC811 and LMR). The cathode powders will be synthesized at Argonne. Initial baseline performance will be measured in ASSB die cells at Solid Power and Argonne using uncoated cathode materials and conventionally coated cathode materials. The ALD coatings will be developed at Argonne for both cathode materials and characterized to determine the composition, thickness, and uniformity on the cathode powders. The coating performance will be evaluated in ASSB die cells at Solid Power and Argonne to measure performance parameters including capacity, lifetime, and resistance. The highest performing coatings will be optimized and scaled up for evaluation in Solid Power pilot-scale manufacturing.

## Results

### **NMC811- Synthesis and Electrochemical Performance Verification**

NMC-811, high-nickel cathode materials have been chosen as a benchmark to establishing baseline performance of uncoated cathode-oxides and evaluation of coated analogues in solid-state cells for this project. We have successfully synthesized a high-quality, NMC811 hydroxide precursor and subsequently lithiated to create a final cathode active material product. The electrochemical performance of cathode-electrodes, fabricated from the NMC811 product, has been validated through various electrochemical tests.

The  $\text{Ni}_{0.8}\text{Mn}_{0.1}\text{Co}_{0.1}(\text{OH})_2$  precursor was prepared through a co-precipitation process utilizing a 4-liter continuous stirred tank reactor (CSTR). During the CSTR synthesis, a metal sulfate solution containing  $\text{NiSO}_4$ ,  $\text{MnSO}_4$ , and  $\text{CoSO}_4$  was slowly pumped into a vessel and vigorously mixed with sodium hydroxide and  $\text{NH}_4\text{OH}$  to generate  $\text{M}(\text{OH})_2$  precipitates. The reaction was conducted at a pH of 11.3 and a temperature of 50 °C under a nitrogen atmosphere to achieve a narrow size distribution of spherical particles, and to prevent the oxidation of  $\text{Mn}^{2+}$ . The flow rate of the metal sulfate solution remained constant, whereas the flow rate of the sodium hydroxide solution was regulated based on the reaction's pH. The precipitate was thoroughly rinsed with water until the conductivity of the wash solution fell below 10  $\mu\text{s}/\text{cm}^2$ . Subsequently, the precursor was dried at 110 °C under a nitrogen flow for 12 hours in an oven and stored in a nitrogen-filled container before utilization.

NMC811-cathodes were synthesized by blending the  $\text{Ni}_{0.8}\text{Mn}_{0.1}\text{Co}_{0.1}(\text{OH})_2$  precursor with  $\text{LiOH}\cdot\text{H}_2\text{O}$  through ultrasonic mixing, followed by calcination at 750 °C under a flow of oxygen for 12 hours. Two batches of materials were calcined under this protocol; 1) a small, 10g batch was synthesized to assess the quality of the precursor and final cathode product; and 2) a larger, 200g batch was prepared, after validation of the small batch, for future coating studies. Figure II.15.1 shows the SEM images of the NMC811 hydroxide precursor (A and B), and the lithiated cathode (C and D) from the large batch, both of which are composed of dense, spherical particles.

The electrochemical performance of the NMC811 cathode-oxide was investigated using CR2032 coin-cells with lithium metal anodes. The positive electrodes were prepared by coating slurries of the active material (84 wt.%), carbon black (8.0 wt%), and poly(vinylidene difluoride) (PVDF, 8.0 wt.%) in N-methyl-2pyrrolidinone (NMP) onto an Al foil current collector. The coated electrodes were dried initially in an oven at 75 °C for 4 hours in air, followed by further drying in a vacuum oven at 110 °C overnight. Cell assembly was carried out in an argon-filled glove box, utilizing an NMC811 cathode-electrode punches (14 mm), lithium metal anodes, and 1.2M  $\text{LiPF}_6$  in EC:EMC 3:7 wt% as the electrolyte. Figure II.15.2 compares the charge-discharge and  $dQ/dV$  profiles of both the small- and large-batch NMC811 samples, cycled between 2.5V-4.2V and 2.5V-4.5V. Both sets of samples exhibited high capacities ranging from 177 to 185 mAh/g at 4.2V and 213 to 218 mAh/g at 4.5V, which are comparable to those of commercial NMC811, with the large batch giving slightly better performance.



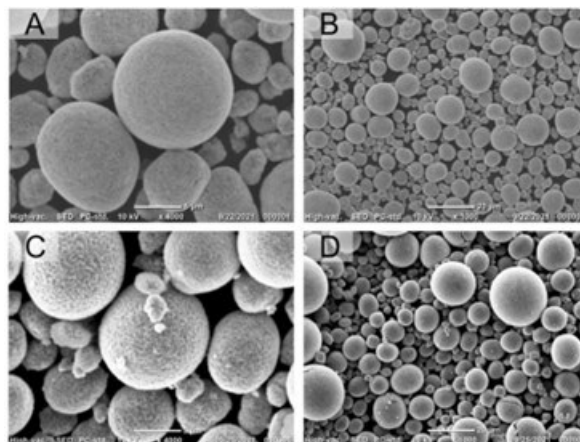


Figure II.15.1 SEM images of A and B) Ni<sub>0.8</sub>Mn<sub>0.1</sub>Co<sub>0.1</sub>(OH)<sub>2</sub> precursor; C and D) LiNi<sub>0.8</sub>Mn<sub>0.1</sub>Co<sub>0.1</sub>O<sub>2</sub> calcined at 750 °C for 12h under oxygen.

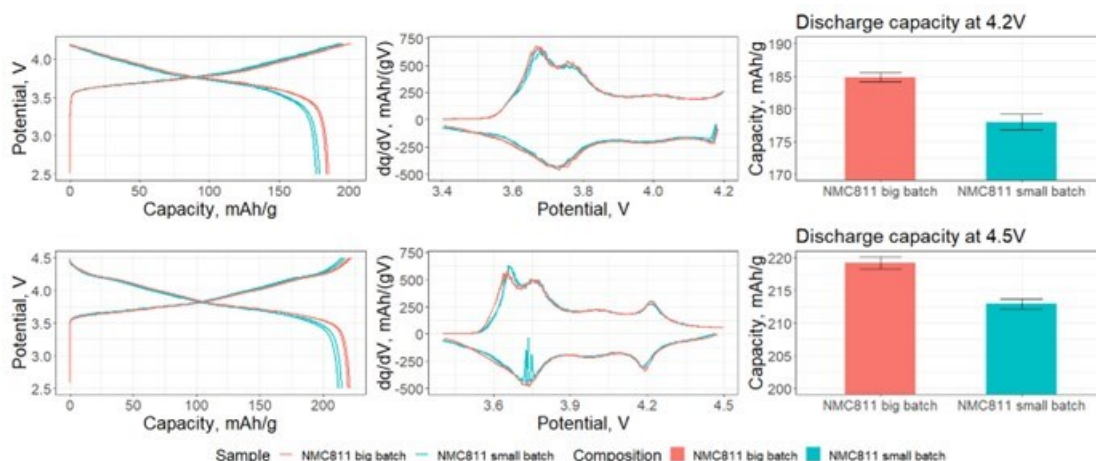
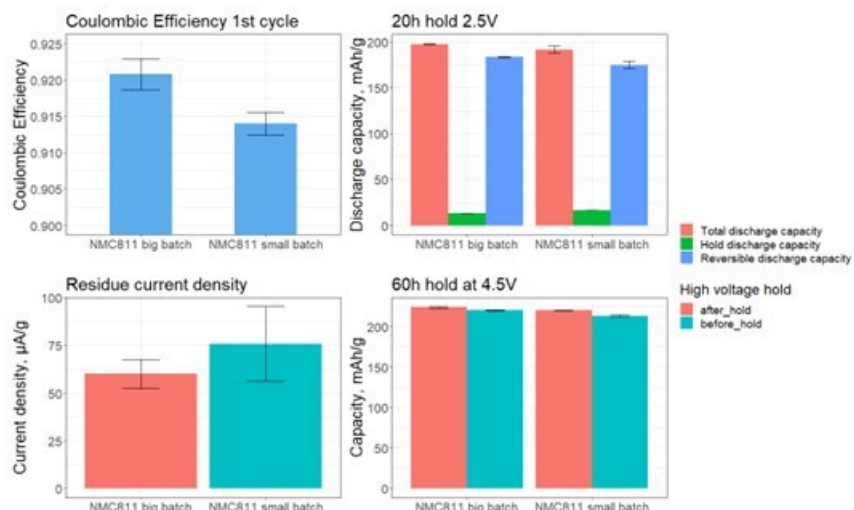


Figure II.15.2 Charge-discharge (left) and dQ/dV profiles (middle) of NMC811 at 4.2V and 4.5V cut-off voltages. The graph on the right compares the discharge values with error bars calculated using data from 2 cells.

To assess the kinetic properties of NMC811, a 20-hour hold at 2.5V was introduced during the first discharge step. A greater capacity during the hold step indicates slower kinetics at the end of discharge and can be indicative of defects such as Li<sup>+</sup>/Ni<sup>+</sup> mixing in high-Ni NMCs (or other phenomena), but in general, can also be used to gauge the quality of the oxide where higher efficiencies are desired. The small batch NMC811 exhibited a slightly lower first-cycle coulombic efficiency and a higher capacity gain during the 20-hour hold at 2.5V compared to the large batch NMC811.

A 60-hour hold at 4.5V was introduced during the charging process to evaluate the cathode's stability at high voltage. A higher current at the end of the 60-hour hold from the small batch sample suggests more side reactions are occurring at high voltage revealing a less stable cathode surface. In contrast, the big batch NMC811 exhibited a smaller residual current than the small batch, indicating a more stable cathode (Figure II.15.3).



**Figure II.15.3** (top left) Coulombic efficiencies of the NMC811 samples in the 1<sup>st</sup> cycle. (top & bottom right) Effects on capacities achieved during a 20h hold at 2.5V and a 60h hold at 4.5V. (bottom right) residual currents measured (e.g., surface stability) from each sample at the end of the 60h hold at 4.5V.

The cell impedance was examined multiple times at various state-of-charge/state-of-discharge (SOC) by incorporating multiple rest periods and measuring voltage drops during these intervals. In Figure II.15.4, the impedance profiles of the two samples are presented for the voltage ranges of 2.5–4.2V and 2.5–4.5V. Notably, the ‘big-batch’ NMC811 consistently exhibited lower impedance in all cases compared to the small-batch NMC811.

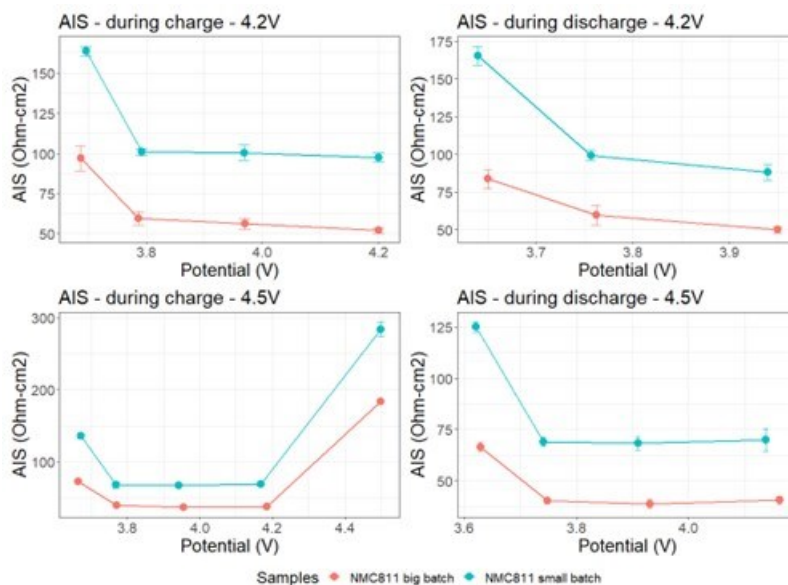


**Figure II.15.4** Areal impedance of the samples during chg-dchg using upper cutoff voltages of 4.2V and 4.5V.

NMC811 samples were cycled at various rates, including  $C/10$ ,  $C/5$ ,  $C/2$ , and  $1C$ , within the voltage ranges of 2.5V–4.3V and 2.5V–4.5V to evaluate their rate performance (see Figure II.15.5). Both the big batch and the small batch NMC811 demonstrated comparable performance, delivering around 195mAh/g at  $C/10$  and 170mAh/g at  $1C$  rate with a 4.3V upper cut-off voltage. The big batch exhibited slightly better rate

performance at 4.5V than those of the small batch. Furthermore, the cyclability of both sample sets (not shown) was very similar and comparable to that of commercial NMC811 cathodes.

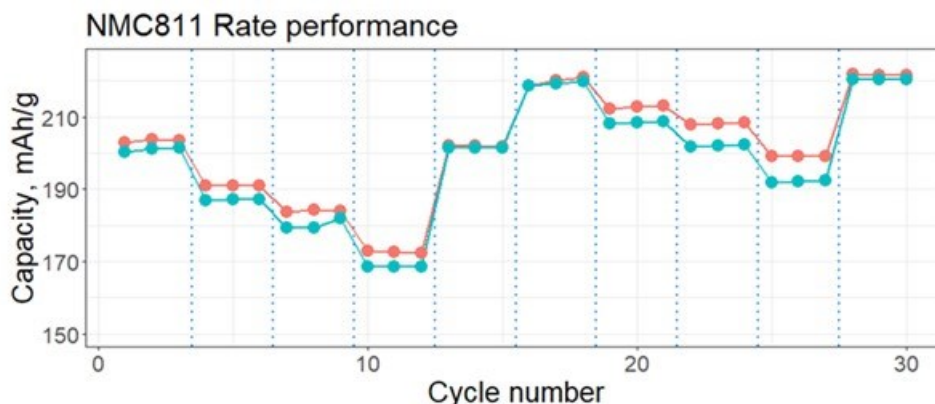


Figure II.15.5 (top) Rate performance of NMC811 cathode-electrodes stepwise from C/10, C/5, C/2, 1C and C/10 using an upper cutoff voltage of 4.2V (cycles 1-15) and 4.5V (cycles 15-30).

In summary, we have completed an optimization study of the synthesis of NMC811 cathode oxides and thoroughly evaluated their electrochemical performance through a series of tests. The large batch of material described herein is shown to be of high quality and performs on par with commercial NMC811 materials. This cathode active material is being employed in our ongoing coating studies both at Argonne National Laboratory and at Solid Power.

#### ALD Coatings on Cathode Powders

In this project, we selected four ALD coatings for evaluation: aluminum oxide ( $\text{Al}_2\text{O}_3$ ), lithium niobate ( $\text{LiNbO}_3$ , LNO), magnesium oxide ( $\text{MgO}$ ), and a metal fluoride composite (TW). In this report, we describe the ALD  $\text{Al}_2\text{O}_3$  and LNO coatings. We first performed the  $\text{Al}_2\text{O}_3$ ALD on the NMC811 and lithium manganese-rich  $0.3\text{Li}_2\text{MnO}_3$   $0.7\text{LiMn}_{0.5}\text{Ni}_{0.5}\text{O}_2$  (LMR) cathodes. Prior to coating the cathodes, we performed a qualification test of  $\text{Al}_2\text{O}_3$  on Si coupons and measured a growth per cycle value of  $1.2 \text{ \AA/cycle}$  as expected. To prepare a control sample for the ALD-coated cathodes, we subjected the cathode powder to the same heat and low pressure treatment used for the ALD but did not perform any coating. Next, we coated the cathode materials using 1, 3 and 5  $\text{Al}_2\text{O}_3$  ALD cycles. While coating the cathode powders, we coated Si witness coupon to monitor the thickness of  $\text{Al}_2\text{O}_3$  deposited. The thickness of deposited  $\text{Al}_2\text{O}_3$  film monitored during these ALD conditions on NMC811 is shown in Figure II.15.6. The zero cycle ALD received no coating but just the heat treatment.

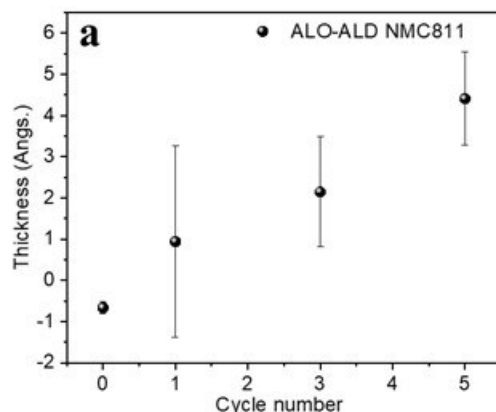


Figure II.15.6 ALD Al<sub>2</sub>O<sub>3</sub> Thickness on the Si wafer during heat treatment (0 cycle number) and 1, 3 and 5 ALO ALD cycles on NMC811.

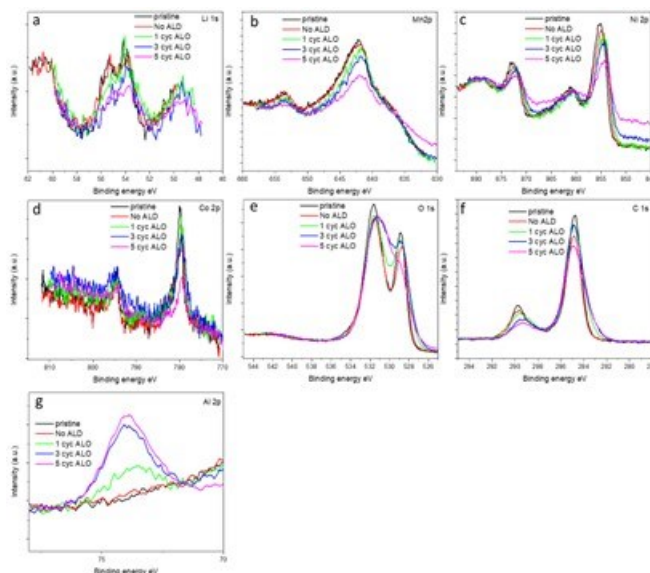
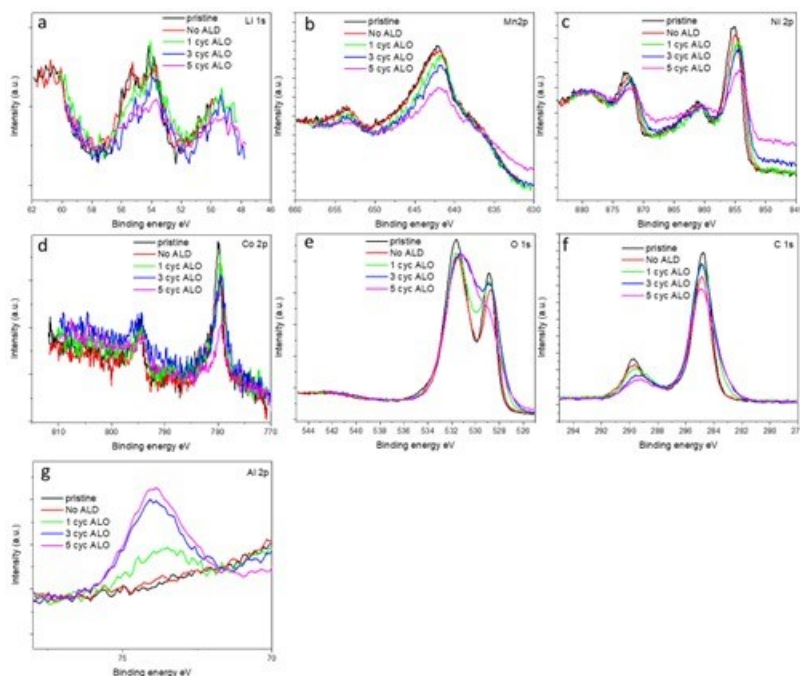


Figure II.15.7 XPS spectra of NMC811 before and after LNO ALD.

Figure II.15.7 shows X-ray photoelectron spectroscopy (XPS) measurements of NMC811 following 0, 1, 3, and 5 ALD Al<sub>2</sub>O<sub>3</sub> cycles. The increase in the Al 2p signal (Figure II.15.7 g) along with the decrease in the intensity of the transitional metal peak (Figure II.15.7 b-d) are consistent with the layer-by-layer Al<sub>2</sub>O<sub>3</sub> ALD on the NMC811 surface. In addition, the reduction of C 1s peak at ~ 290 eV (Figure II.15.7 f), indicates that carbonate is removed and the amount increases with ALD cycles. Similar XPS results were obtained for the Al<sub>2</sub>O<sub>3</sub> ALD on the LMR cathode surfaces.

Next, we perform the lithium niobate (LNO) ALD on the NMC811 and LMR cathode materials. To coat the same thickness as 5 cycles of ALO-ALD, we perform 3 cycles of LNO. After the qualification test, the average growth per cycle for LNO was 2 Å/cycle. Figure II.15.8 shows the XPS measurements of the NMC811 cathode powder following 0, and 3 ALD LNO cycles. Figure II.15.8 shows that the transition metal signals decrease, while the Nb 3d peak increases following the LNO ALD.



**Figure II.15.8 XPS spectra of NMC811 before and after  $\text{Al}_2\text{O}_3$  ALD**

Four samples of cathode powders (10 grams each) coated with 5 cycles of  $\text{Al}_2\text{O}_3$  and 3 cycles of LNO on both NMC811 and LMR were shipped to Solid Power for testing.

### **Electrochemical Testing**

All solid state battery cells were fabricated and tested at Solid Power using the following conditions:

- Cell format: pelletized separator with a Lithium metal anode and a sprinkled cathode composite.
- Cathode composite contains active material provided by ANL, Solid Power's solid-state electrolyte, and carbon.
- Cycling conditions for NMC materials:
  - Cells were cycled from 2.5-4.2 V at 45 °C and symmetrical charge/discharge rate of C/10 for 6 cycles and increased to C/3 for additional cycles.
- Cycling conditions for LMR materials:
  - Cells were cycled from 2.5-4.7 V at C/10 for 3 cycles. Then they were cycled from 2.5-4.5 at C/10 for additional cycles. Cells were kept at 45 °C for the entire test.
- Materials Tested
  - NMC811 3x LNO
  - NMC811 5x ALO
  - Uncoated NMC811
  - LMR 3x LNO
  - LMR 5x ALO
  - Uncoated LMR

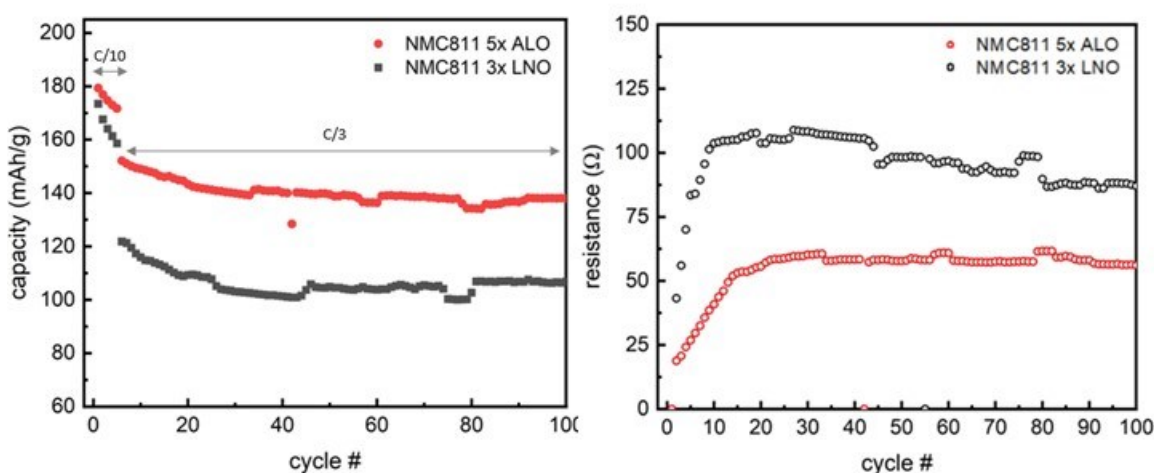
The LMR material showed poor cycling performance from the first cycle onward and rapid capacity fade during the 4.7 V upper limit cycles. Both ALO and LNO coated materials' capacity leveled off during the 4.5 V upper limit cycles. The performance is summarized in Table II.15.1. This performance was similar to the uncoated LMR materials when tested in solid state batteries. We are currently investigating the origin of this low performance of the LMR cathodes.

Table II.15.1 Summary of Performance Metrics for LMR Coated Cells.

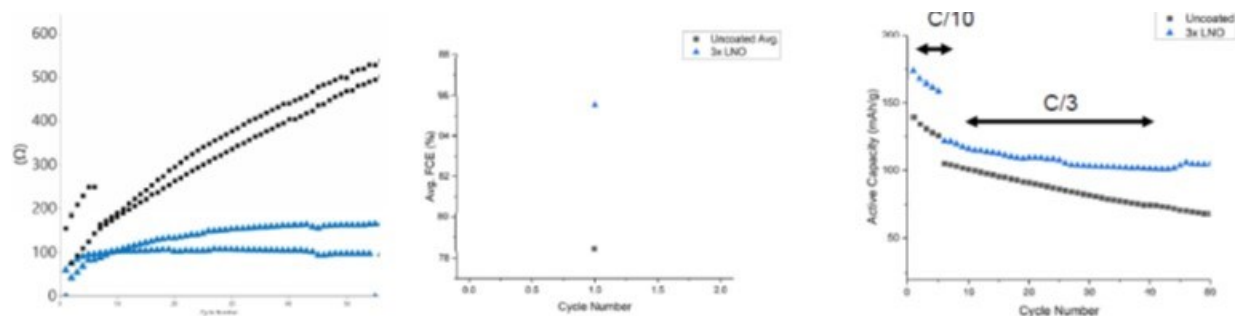
CAM	4.7 V, 1st Dis (mAh/g active)	FCE	4.5 V, 1st Dis (mAh/g active)
LMR 3x LNO	3.009	8.853	0.348
LMR 5x ALO	8.831	17.225	3.943*

\*There is a capacity drop seen for cycles 4 and 5 in the ALO coated material, but the capacity recovered and was consistent at  $\sim 3.9$  mAh/g active material. This dip could be due to an electrochemical process in the cell or possibly testing conditions were briefly interrupted, e.g. power interruption.

The NMC811 coated with ALD  $\text{Al}_2\text{O}_3$  (ALO) showed less capacity fade during the C/10 cycling regime and significantly higher capacity in the C/3 cycling regime compared to the LNO coated material. The NMC811 ALO coated material showed significantly lower resistance compared to LNO coated material. Both materials exhibit a rapid rise in resistance until  $\sim 15$  cycles whereafter they level off (Figure II.15.9).

Figure II.15.9 Capacity testing (left) and resistance (right) of NMC811 coated with ALD  $\text{Al}_2\text{O}_3$  and LNO.

Compared to the uncoated NMC811 material, the  $\text{Al}_2\text{O}_3$ -coated material showed a significantly lower resistance, higher Coulombic efficiency, and higher active capacity as shown in Figure II.15.10. Similarly, the NMC811 material coated with ALD LNO outperformed the uncoated NMC811 cathode material.

Figure II.15.10 Resistance (left), Coulombic efficiency (center), and capacity (right) of uncoated NMC811 and NMC811 coated with ALD  $\text{Al}_2\text{O}_3$ .

The performance for the coated NMC811 material is summarized in Table II.15.2.

Table II.15.2 Summary of Performance Metrics for LMR coated cells.

CAM	0.1C, 1st Dis (mAh/g active)	FCE	0.33C, 1st Dis (mAh/g active)
NMC811 3x LNO	173.414	85.542	121.798
NMC811 5x ALO	179.279	86.737	152.067

### Concluions

We have synthesized the NMC811 and LMR cathode materials, coated with ALD Al<sub>2</sub>O<sub>3</sub> and LiNbO<sub>3</sub>, and tested these materials in solid state batteries. The performance of the LMR in the solid state batteries is poor and the origin of this behavior is under investigation. The cycling behavior of the NMC811 is improved significantly by the ALD Al<sub>2</sub>O<sub>3</sub> and LiNbO<sub>3</sub> coatings.

### Acknowledgements

The PIs are grateful to Dr. Zachary Hood at Argonne for helpful discussions.

### III Recycling and Sustainability

Lithium-ion batteries are used for a range of applications – from smartphones and laptops to electric vehicles and other applications. Recycling techniques for these batteries exist, but it is necessary to ensure their cost effectiveness before large-scale adoption. Improving this cost-effectiveness will help users turn them in for recycling instead of discarding them. This will lead to lower raw material costs and make batteries more affordable. In addition, it will also reduce the consumption of substantial amounts of critical materials (e.g., cobalt) which are both expensive and often dependent on foreign sources.

To address the currently limited infrastructure for collection, storing, and transporting discarded lithium ion batteries for eventual recycling, a Battery Recycling Prize was established by the Vehicle Technologies Office (VTO) to be directed and administered by the National Renewable Energy Laboratory (NREL). This effort complements early-stage laboratory, university, and industry research to develop low-cobalt (or no cobalt) active cathode materials for next-generation Li-ion batteries and the Lithium Battery R&D Recycling Center with the aim of developing closed-loop cost-effective recycling processes to recover critical lithium battery materials. Researchers are using less energy-intensive processing methods and capturing more valuable forms of materials for “direct recycling”— the recovery, regeneration, and reuse of battery components directly without breaking down the chemical structure. ReCell is a collaboration between Argonne National Laboratory, the National Renewable Energy Laboratory, Oak Ridge National Laboratory, Idaho National Laboratory, Michigan Technological University, the University of California at San Diego, Worcester Polytechnic Institute, and Tennessee State University, with Argonne National Lab as the lead of the consortium.

The rest of this chapter contains detailed reports on the status of the following individual projects.

- Battery and Critical Materials Life Cycle Analysis (ANL)
- Lithium-ion Battery Recycling Prize Support (NREL)
- Battery ReCell Center (ANL).



## III.1 Battery and Critical Materials Life Cycle Analysis (ANL)

### Jarod Kelly, Principal Investigator

Argonne National Laboratory  
9700 South Cass Avenue  
Lemont, IL 60439  
E-mail: [jkelly@anl.gov](mailto:jkelly@anl.gov)

### Linda Gaines, Co-Principal Investigator

Argonne National Laboratory  
9700 South Cass Avenue  
Lemont, IL 60439  
E-mail: [lgaines@anl.gov](mailto:lgaines@anl.gov)

### Michael Wang, Co-Principal Investigator

Argonne National Laboratory  
9700 South Cass Avenue  
Lemont, IL 60439  
E-mail: [mqwang@anl.gov](mailto:mqwang@anl.gov)

### Jake Herb, DOE Technology Development Manager

U.S. Department of Energy  
E-mail: [Jake.Herb@ee.doe.gov](mailto:Jake.Herb@ee.doe.gov)

### Tina Chen, DOE Technology Development Manager

U.S. Department of Energy  
E-mail: [Tina.Chen@ee.doe.gov](mailto:Tina.Chen@ee.doe.gov)

Start Date: October 1, 2022

End Date: September 30, 2023

Project Funding (FY23): \$400,000

DOE share: \$400,000

Non-DOE share: \$0

### Project Introduction

This project examines automotive batteries and the critical materials used in them, spanning raw material extraction, their processing into usable chemical forms and/or battery components, their subsequent assembly into batteries, and end-of-life. This is accomplished using multiple analytical techniques, including life-cycle analysis (LCA), material flow analysis (MFA), and supply chain analysis (SCA). These techniques enable the identification of hot spots along the supply chains of critical materials and batteries for energy use, greenhouse gas (GHG) emissions, and other environmental burdens. We consider battery materials produced for current and near future batteries, along with battery assembly and use in battery electric vehicles (BEVs).

Understanding material production using LCA is essential to determine the energy and environmental burdens of battery production, as embodied emissions of battery materials comprise a significant share of their life-cycle burdens. Additionally, regional aspects of material extraction and processing can influence the environmental effects of battery production. The growing need to secure a robust supply of battery materials has led to an increased push for their recycling, especially for cathodes, which can further alter the battery's environmental performance. We study multiple battery materials for their energy and environmental burdens based on their respective supply chain in the U.S. battery mix. We also characterize the batteries' bill-of-materials for present-day and future vehicles to update their environmental impacts.

The project updated Argonne's Greenhouse gases, Regulated Emissions and Energy use in Technologies (GREET®) model with: (a) Important material and energy input data (life-cycle inventory or LCI data) and

supply chain mix for nickel production from laterite ores; and (b) Material composition and energy/power density of automotive batteries (lithium-ion batteries or LIBs) for light-, medium-, and heavy-duty vehicles across hybrid, plug-in hybrid, electric, and fuel-cell powertrains. We also investigated the ongoing initiatives for commercial-scale domestic production of battery-grade lithium (Li) chemicals (lithium carbonate/Li<sub>2</sub>CO<sub>3</sub> and lithium hydroxide/LiOH) from both sedimentary clays and low Li-content brines (geothermal, chemical, and oil-based), and their likely environmental burdens via a preliminary LCA. Additionally, we incorporated the environmental impacts of battery recycling from Argonne's EverBatt model into GREET to account for battery production pathways from virgin and recycled material cathode inputs. These updates serve as vital resources to the LCA community and to researchers interested in understanding the environmental burdens of current supply chains and resource types and comparing them with the burdens of alternative supply chain routes and resource types. We also developed a battery module for a comprehensive analysis of the energy and environmental burdens of LIBs on a per-kWh basis. This project also facilitates engagement within the International Energy Agency's (IEA) HEV Task 46 project, associated with electrifying two-wheelers and medium-duty and heavy-duty vehicles, and Task 48 investigating issues related to automotive battery swapping.

### Objectives

- Battery Life Cycle Analysis with Expanded GREET Model
  - Battery LCA Expansion and Update
    - Characterize, update, and release bill-of-material (BOM) and energy/power density of the lithium-ion batteries (LIB) for vehicle applications in Argonne's GREET LCA model to provide up-to-date information for computing LIB energy and environmental burdens
    - Characterize, update, and release state-of-knowledge on nickel (Ni) production from laterite ores within the GREET model
  - Continue to investigate domestic production of battery-grade Li-chemicals from brines and sedimentary clays and extend both for LCA into GREET
  - Incorporate recycled material results from Argonne's EverBatt model into GREET to provide pathways for recycled cathode material inputs
  - Develop a battery module that will allow users to determine individual battery impacts and compare several battery types at once
  - IEA HEV TCP Task 46 support for the study of medium- and heavy-duty HEV and BEV LCA
- Battery Critical Materials Assessment
  - Study the supply chain for domestically-produced phosphorus cathodes
  - Determine how variations in cathode supply chain will impact the LCA of both the materials and the resultant batteries
  - Investigate how limited battery material resources can be used to decrease total environmental impacts across vehicle electrification
  - IEA HEV TCP Task 40 and 48 support for the study of critical materials and battery swapping

### Approach

Argonne has developed and updated the GREET LCA module for battery materials and batteries based on industrial insights, relevant supply chains (for U.S. battery use), and market changes. In FY23, we made research efforts to collect LCI data related to batteries and critical materials. Argonne updated the LCI for nickel (Ni) production, accounting for its corresponding supply chain (for global nickel sulfate or NiSO<sub>4</sub> production). For Ni, we disaggregated its combined LCI (material and energy inputs) for laterite ores (provided in GREET 2022) by different production stages. Argonne also investigated the current efforts aimed at the domestic production of battery-grade Li-chemicals from sedimentary clays and low Li-content brines (the work on brines updates our prior understanding of these efforts in FY22). We also provided a preliminary LCI

for domestic Li-chemical production from these resources based on publicly available data from commercial entities in this domain. Further, we developed a stand-alone beta version of a battery module to facilitate a user-friendly comparison of the inventory and the environmental impacts and emissions of select battery chemistries available in GREET. Argonne also incorporated the environmental impact results for LIB recycling from the EverBatt model into GREET to compare battery production impacts from virgin and recycled materials/material precursors. Additionally, Argonne updated the bill-of-materials (BOM) and energy/power density of LIBs for light-, medium-, and heavy-duty vehicles in the GREET model across hybrid, plug-in hybrid, electric, and fuel-cell powertrains.

We have maintained close interactions with stakeholders for technological developments associated with LIB production and performance, and to maintain Argonne's position as the world's leader in battery and critical materials LCA. During FY23, Argonne staff: 1) gave invited talks and presentations to government, industry, and academia; 2) interacted with international groups such as the IEA to coordinate research; 3) improved the understanding of environmental impacts of battery materials production; and 4) responded to numerous requests for information.

## Results

### ***Battery Life Cycle Analysis with Expanded GREET Model***

In FY23, Argonne updated its life-cycle inventory (LCI) within GREET for nickel production from laterite ores and the BOM and power/energy density of LIBs for all vehicles spanning different powertrains. For Ni, we disaggregated the previous single-step pathway for Class I Ni metal production from laterite ores into different production steps along with their corresponding supply chain stages. We also updated the supply chain mix of Ni production from sulfide and laterite ores to account for the global supply chain of Class I Ni metal and nickel sulfate (NiSO<sub>4</sub>) production and nickel sulfate's subsequent use in LIBs meant for the United States. Further, we used the latest version of Argonne's Battery Performance and Cost (BatPaC) model (BatPaC 5.1) to update the LIB BOM and energy/power density of LIBs for light-duty, medium-duty, and heavy-duty vehicles with hybrid, plug-in hybrid, electric, and fuel-cell powertrains. Also, we have investigated the ongoing commercial initiatives for domestic Li-chemical production from sedimentary clays and low Li-content brines (geothermal, chemical, and crude oil) within the U.S. and North America. From this, we provided a preliminary LCI of such production based on public data associated with these initiatives. Additionally, we have incorporated the recycled material results from Argonne's EverBatt model for recycled cathodes and batteries within GREET. We created a battery module that evaluates the LIB's environmental burdens for different cathodes. All these efforts are documented in publicly available technical reports.

Nickel (Ni), a vital constituent of key LIB cathode chemistries like NMC and NCA, is produced from sulfide and laterite ores in different countries that show a wide variation in ore grade. The continued mining of Ni from sulfidic Ni ores – the dominant Ni source – has caused a major decline in its ore grade over time and also led to increasing Ni production from laterite ores to meet Ni demand. Argonne disaggregated its single LCI for Ni production (averaged across different locations, ore types, and ore grades) into separate, independent Ni production pathways and corresponding LCIs for sulfidic and lateritic Ni. While the LCI for sulfidic Ni enabled an estimation of variation in its production impacts with ore grade, that for lateritic Ni considered a single ore grade (1.6%) and a single production step due to the lack of data. Further, we updated the supply chain mix for Ni production from both ore types to account for their supply to the United States. We document the details of our work in a technical memo [1].

In FY23, Argonne disaggregated the production pathway and associated LCI for lateritic Ni into step-by-step production, considering the same ore grade, based on new literature [2]. While the overall material and energy inputs and the resultant environmental burdens across all production steps remain the same as in FY22 (based on [3]), this disaggregation provides deeper insights into major contributors to these burdens. Additionally, we updated the supply chain mix for Class I Ni production from sulfide and laterite ores to account for the share of different sources (countries and ore types) to global Class I Ni metal production (Figure III.1.1), as this Ni forms the input for the subsequent NiSO<sub>4</sub> precursor used to produce LIB cathodes for the U.S. market.

Lateritic Ni impacts are predominated by natural gas use during the high-pressure acid leaching (HPAL) and other associated processes (labeled as “primary metal extraction” in Figure III.1.2), while the updates to the supply chain mix provide a more present-day picture of impacts for sulfidic Ni across different ore grades (Figure III.1.2). We also revised the process SO<sub>x</sub> emissions for sulfidic Ni production during the primary extraction (pyrometallurgical processing) step, accounting for scrubbers that help avoid 95% of these emissions generated during this processing, based on feedback from other researchers. Our findings reinforce the need for alternative technologies for lateritic Ni production that avoid/minimize fossil fuel usage, judicious management of sulfidic Ni reserves to prolong their lifetime, and large-scale adoption of technologies for Ni recycling.

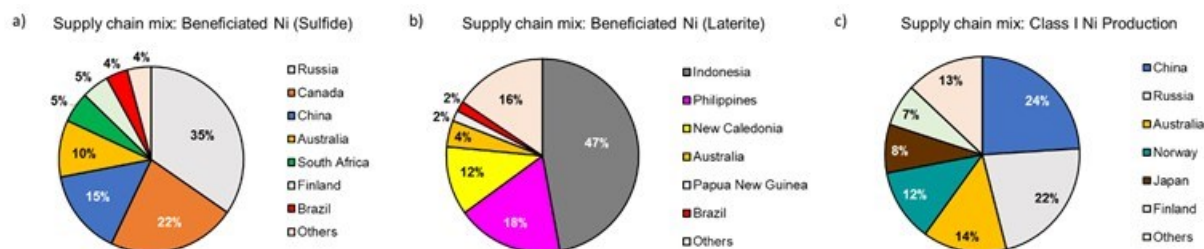


Figure III.1.1 Supply chain mix for Ni production from different resource types for: (a) Mining and beneficiation from sulfide ores; (b) Mining and beneficiation for laterite ores; and (c) Class I Ni production.

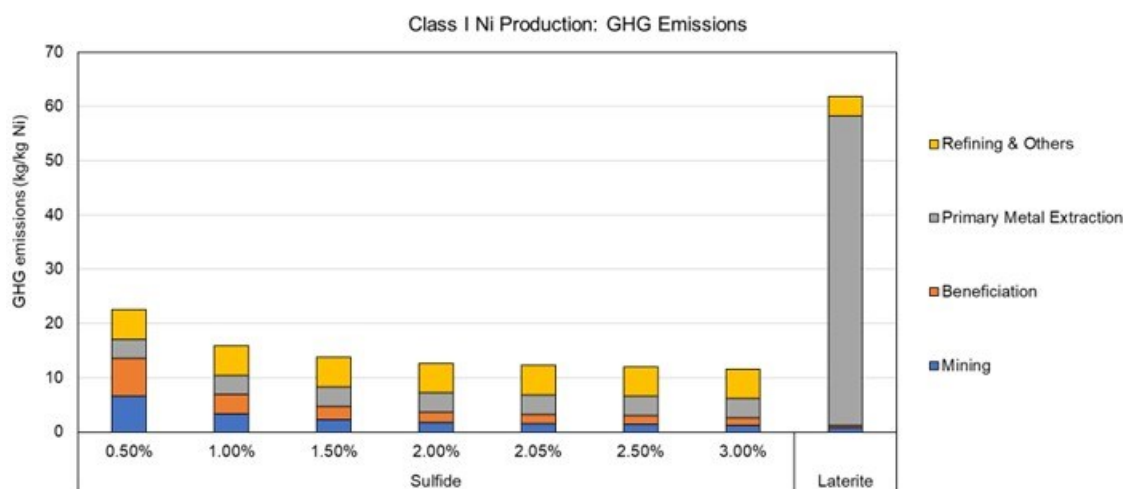


Figure III.1.2 Cradle-to-gate impacts of Ni production from sulfide (with ores of different Ni grades) and laterite ores.

Salar brines (Chile and Argentina) and Australia’s spodumene lithium reserves – each with significant processing in China – dominate the battery-grade global Li-chemical production (Li<sub>2</sub>CO<sub>3</sub> and LiOH) supply, making the U.S. import-dependent for these chemicals. The federal government has sought to address this gap by incentivizing efforts to commercialize domestic Li-chemical production from low Li-content brines (geothermal, chemical, and crude oil-based) and sedimentary clays. In FY23, we investigated the ongoing initiatives for Li-chemical production from both clays and brines (the brine-related work is an extension of our prior effort in FY22, documented in a technical report [4]). Our findings are reported in a technical report [5] detailing the major projects based on these resources, their location, resource potential, annual production, and other aspects (Table III.1.1 and Table III.1.2). Figure III.1.3 presents these locations visually. The successful completion of all projects in these tables can help the U.S. achieve self-sufficiency in meeting its Li-needs. Both clays and brines are touted to be more environment-friendly Li-chemical sources than existing sources

(high Li-content brines and spodumene ores) due to their use of (a) zero-carbon steam from sulfuric acid plants for energy needs for clays and (b) direct lithium extraction (DLE) for brines, which requires less land, co-produces brines with other materials or energy, and transfers the residual brine to the reserve, thus avoiding issues associated with brine evaporation in Salar brines. Since these claims merit a comparison of environmental burdens of Li-chemical production from these sources with that reported for existing reserves, we provide preliminary LCIs based on publicly available data from commercial entities engaged in this domain for seven projects. These LCIs are also documented in our report [5], and the brine-based LCI builds upon the previous LCI provided in FY22 [4] based on existing literature [6]. Our preliminary GHG results, indicate lower GHG burdens for DLE- and clay-based production of  $\text{Li}_2\text{CO}_3$  over all other sources, barring the Chilean Salar brines (GHG impacts for U.S. projects are averaged across their respective projects; Figure III.1.4). More work is needed to account for process  $\text{CO}_2$  emissions for clay-based  $\text{Li}_2\text{CO}_3$  production and understand the corresponding environmental burdens for Li-chemical production for comparison with existing pathways.

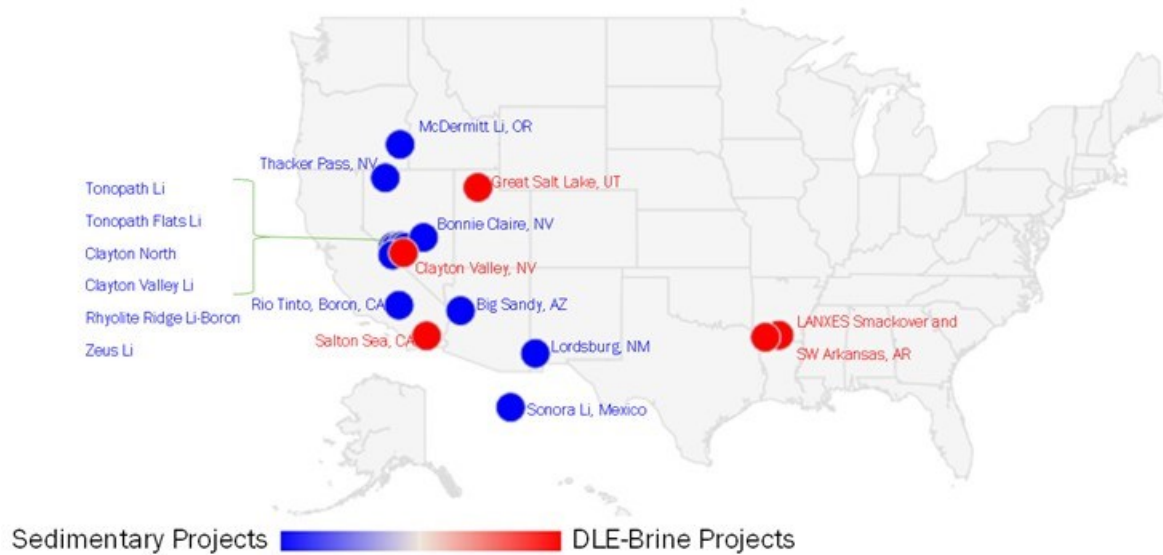


Figure III.1.3 Location of investigated sedimentary- and brine-based lithium projects within the US.

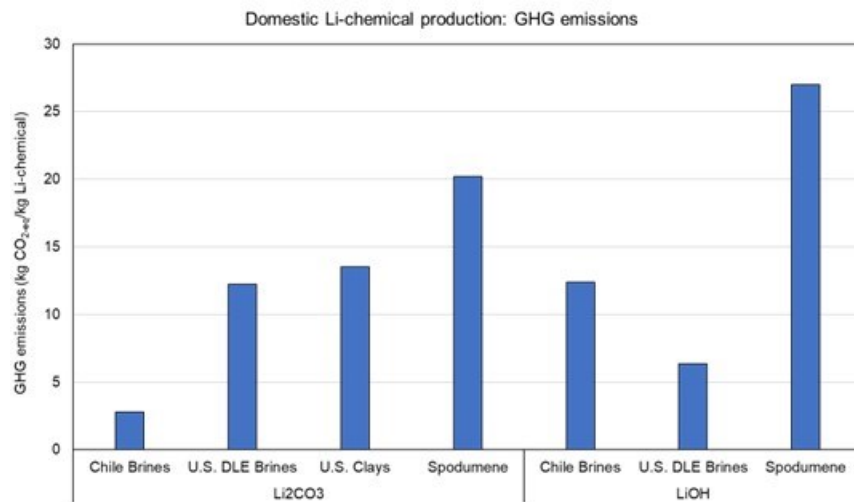


Figure III.1.4 Preliminary LCA results for Li-chemical production from different sources.

Table III.1.1 Major Clay-based Li-reserves in North America (U.S.)

Owner/ Resource Developer	Project	Resource Estimate MMT LCE			Li Chemical Produced/To Be Produced	Annual Production MT/Year
		Measured	Indicated	Inferred		
Jindalee Resources Limited	McDermitt Lithium		11.1 @ 1,340 ppm Li	10.4 @ 1,340 ppm Li		
	Clayton North					
Lithium Americas	Thacker Pass	7 @ 2,450 ppm Li	9.1 @ 1,850 ppm Li	3 @ 1,870 ppm Li	Li <sub>2</sub> CO <sub>3</sub>	66,783
Century Lithium	Clayton Valley Lithium		6.28 @ 905 ppm Li		Li <sub>2</sub> CO <sub>3</sub>	27,400
Ioneer USA	Rhyolite Ridge Lithium-Boron	0.36 @ 1,700 ppm Li	0.73 @ 1,550 ppm Li	0.17 @ 1,600 ppm Li	LiOH and Li <sub>2</sub> CO <sub>3</sub>	20,558 Li <sub>2</sub> CO <sub>3</sub> 22,000 LiOH
Noram Ventures	Zeus Lithium	0.532 @ 860 ppm Li	4.643 @ 951 ppm Li	1.090 @ 871 ppm Li	Unclear	5,971
American Lithium Corporation	Tonopah Lithium	4.2 @ 924 ppm Li	4.63 @ 727 ppm Li	1.86 @ 713 ppm Li	Unclear	24,000 Years 1-6 48,000 Year 7+
Arizona Lithium	Big Sandy		0.151 @ 1,940 ppm Li	0.170 @ 1,780 ppm Li	Unclear	
	Lordsburg					
Rio Tinto	Boron					10 current; 5,000 future
Bacanora Lithium	Sonora Lithium	1.91 @ 3,480 ppm Li	3.13 @ 3,120 ppm Li	3.80 @ 2,650 ppm Li	Li <sub>2</sub> CO <sub>3</sub>	17,500 Years 1-4 35,000 Year 5+
American Battery Technology Company	Tonopah Flats			15.80 @ 561 ppm Li	LiOH	5,000 Initial 30,000 Future
Nevada Lithium Resources	Bonnie Claire			18.37 @ 1,013 ppm Li	Li <sub>2</sub> CO <sub>3</sub>	32,300

Table III.1.2 Major Brine-based Li-reserves in North America (U.S.)

Owner/ Resource Developer	Project	Resource Estimate MMT LCE		Proj ect Life Yea rs	Li Chemical Produced/ To Be Produced	Annual Production MT/Year
		Indicated	Inferred			
Compass Minerals	Ogden: East	2.36 @	0.045 @	35	Li <sub>2</sub> CO <sub>3</sub>	10,791
	Ogden: West	256 mg/L	256 mg/L	34	LiOH	27,712
Controlled Thermal Resources	Hell's Kitchen				LiOH	25,000 in 2024 300,000 Future
Standard Lithium	LANXESS - Standard Lithium	3.14 @ 168 mg/L		>25	Li <sub>2</sub> CO <sub>3</sub>	20,900
	Southwest Arkansas		1.195 @ 255 mg/L	20	LiOH	30,000
Pure Energy Minerals	Clayton Valley Brine		0.247 @ 123 mg/L		LiOH	11,500

Embodied emissions from battery materials significantly influence the environmental burdens of batteries. This use is a function of the battery's material composition (or bill-of-materials/BOM) and energy/power density. In FY23, Argonne updated these parameters for LIBs used in various powertrains (hybrid, plug-in hybrid, electric, and fuel-cell) of all vehicles (light/medium/heavy-duty) in the GREET model, based on Argonne's Battery Performance and Cost (BatPaC 5.1) model [7,8]. Note that the battery sizing for these vehicle-powertrain combinations is based on the latest version of Argonne's Autonomie model (Autonomie 2023) [9]. Autonomie is a simulation tool that computes vehicle characteristics like fuel economies, battery sizing, and component weights based on various performance characteristics determined in consultation with automotive companies and/or auto component manufacturers. The prominent change in LIBs vis-à-vis previous GREET versions results from differing battery configurations that achieve the desired LIB voltage and capacity of different powertrain-vehicle combinations. The BatPaC 5.1 model also fine-tunes the operational parameters of LIBs to reflect their actual performance for different vehicles, further modifying their respective energy/power densities for the concerned automotive application. These changes are also considered in computing energy and environmental burdens of LIBs for different vehicles and powertrains in the GREET model. More details are provided in our technical memo [10].

Recycling of batteries has become important in the present-day context for both avoiding/reducing the impacts associated with battery production and ensuring a secure supply of critical battery materials less vulnerable to supply chain disruptions. While the energy use and environmental burdens of battery production from virgin materials are provided within the GREET model, another Argonne model – EverBatt [11,12] – provides the impacts of LIB recycling. EverBatt primarily focuses on recycling LIB cathodes (via direct cathode recycling route) and cathode precursors (via pyrometallurgical and hydrometallurgical routes, with the precursors used subsequently to produce the cathode). In FY23, we have incorporated the impacts of cathodes/cathode precursor recycling from EverBatt in GREET to provide pathways for LIB production from virgin and recycled materials. The pathways allow users to define the virgin and recycled content shares of cathode/cathode precursors. This reflects the real-life time lag in shifting LIB production from entirely virgin materials (~100% share) to entirely recycled content (~100%), with a substantial interim duration involving the use of virgin and recycled materials in varying ratios. In a technical memo, we document our work for incorporating the EverBatt model's findings into GREET [13].

In FY23, Argonne developed a GREET battery module as a tool based on the GREET battery inventory. This module is an important step towards making the battery LCA information contained within GREET more accessible, intuitive, and interactive for the benefit of the battery industry and researchers. The user can

interact with detailed inventory and impacts associated with a single battery by making appropriate selections in each battery parameter field regarding its capacity, chemistry, and vehicle all-electric driving range. With eight battery chemistries and four possible EV ranges, the battery module can be used to compare 32 different battery types. The results from each battery selection are displayed as descriptive graphs that can help the user identify the key emission/impact contributors for a particular battery chemistry, as shown in Figure III.1.5, which shows how each material or major process stage impacts the metric of interest and how that leads to the cumulative burden for the LIB.

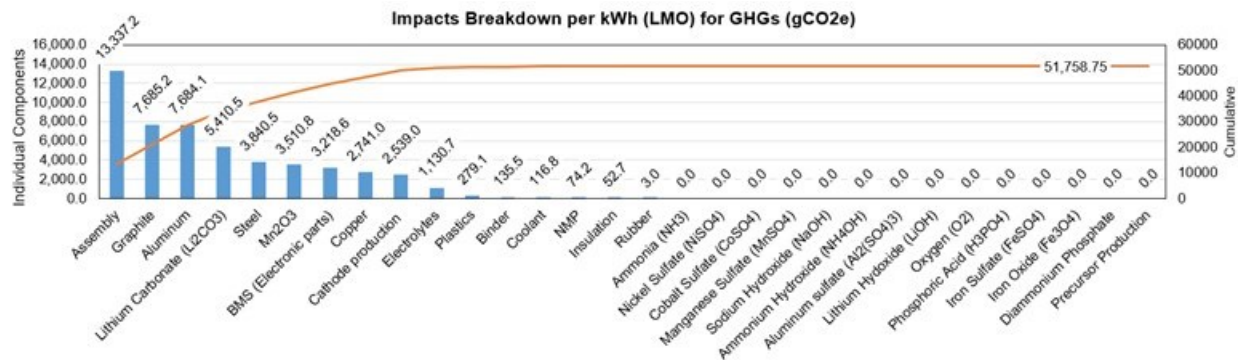


Figure III.1.5 Illustrative figure showing the type of data that can be viewed in the battery module. Here, a graph shows the GHG per kWh of a battery based on the battery parameters selected.

Additionally, a detailed breakdown of the top contributors to each type of emissions/impact e.g., total energy, SOx, NOx, can be displayed by the user as shown in Figure III.1.6. This allows the user to more easily identify the hotspots associated with that specific battery’s production stages across multiple metrics at one time. Finally, users have the option of a side-by-side comparison of a selected emissions/impacts category of their choice for the eight different battery selections made in each of the battery fields, as shown in Figure III.1.7. In doing this, the user can more easily evaluate impacts of numerous parametric selections concurrently.

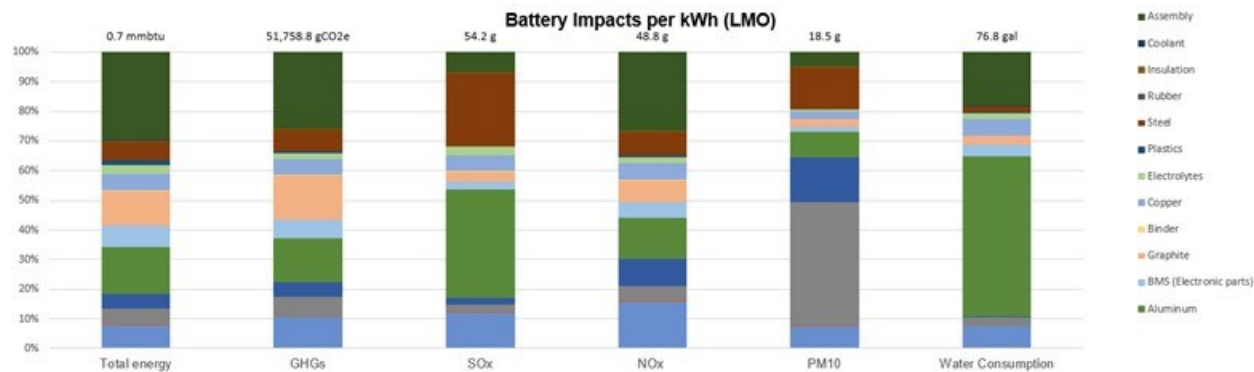


Figure III.1.6 Comparison of the different emissions values for selected battery chemistry along with their respective constituents in terms of percentage.



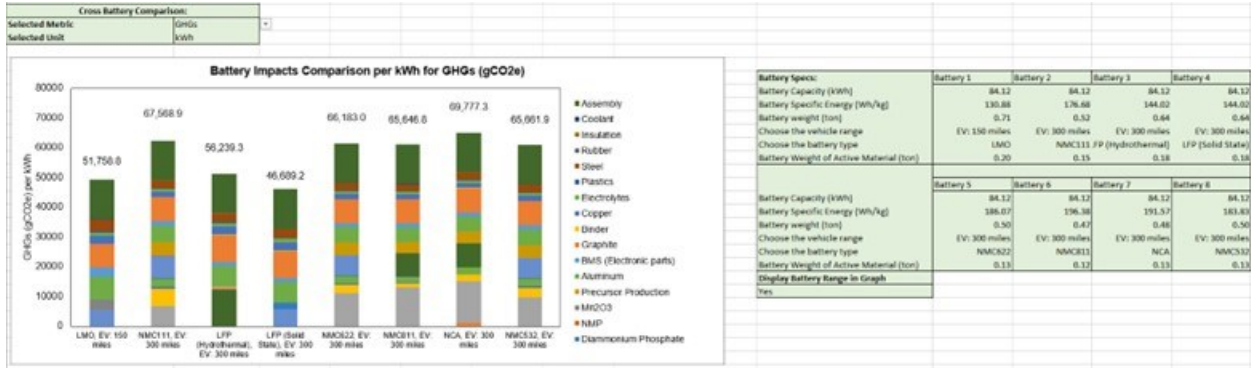


Figure III.1.7 Final side-by-side comparison of the impacts/emissions of the eight selected battery choices within the Battery Module with an option to change the displayed “selected metric” and “selected unit.” The green box on the right side displays the variables selected by the user for all eight battery types.

**Battery Critical Materials Assessment**

There has been a rapid rise in the use of lithium iron phosphate (LFP) cathode material due both to the perceived impending shortfall in the supplies of cobalt and nickel and also to the improved safety, lower cost, and longer lifetime of batteries with LFP cathodes. Numerous OEMs have announced that they will produce both passenger cars and commercial vehicles, including school buses, using LFP cathode material. Concurrently, there have been developments in North America all along the material supply chain for producing the material. Phosphorus can be recovered from either igneous or sedimentary rock, which differ in chemical composition and properties that influence the process chain from material in-the-ground through purification steps. Recycling of LFP cathode material directly, without breaking down the crystalline structure, has been demonstrated, and is expected to be commercialized soon with DOE’s help. In addition, it may be possible to recover some phosphate chemicals from agricultural runoff. There are some possible environmental justice implications that would arise from such a scheme. All of these factors combined lead us to conclude that a complete LCA of LFP is warranted.

LCA looks at one unit of a given product (the functional unit) and tracks the inputs and outputs of its production, use, and final disposition. It does not integrate all of the impacts from the entire population of such products. Nor does it examine the material flows—the total quantities of materials that are required to produce this population of products, and where the unit operations occur. It does recognize that impacts may increase or decrease as raw materials change (lower ore grade, alternative material). We have recognized the importance of various questions that must be asked in order to most effectively apply the LCA results to real-world problems.

An example concerns how best to use a limited quantity of battery material. With a given fixed capacity of battery material, how can use phase emissions minimize from a fleet of vehicles that must travel a set number of total miles? Analysis confirms that battery-powered vehicles maximize emission benefits if they are driven long distances, and that small batteries can achieve greater benefit per kWh of material than larger batteries. This illustrates a need to go beyond theoretical product-focused LCA and consider variants in real-world usage patterns and these LCA results can scale to fleets and populations to minimize emissions.

Other important topics addressed within the critical materials thrust this year include issues related to the circular economy, in particular discussions with ARPA-E and a presentation of the keynote address at their workshop in June. It is currently impossible for batteries to be completely “circular” because of the rapid growth in the LIB market which necessitates new material extraction. Thus, design for recycling is another important area of consideration that could improve circulatory issues, yet this topic does not currently receive sufficient attention; we presented the benefits of design for recycling in the context of a circular economy at the NAATBatt Recycling Workshop in August.

Finally, related to IEA activities, the IEA HEV Task 46 for medium- and heavy-duty vehicle LCA continued in FY23 with several organizational meetings and completion of specific work tasks. Members of Task 46 have collected data and begun to conduct LCAs for several medium- and heavy-duty vehicles subject to specific global conditions with harmonization of components to the extent that they are representative of the operating vehicles in those locales. Additionally, planning for an expert workshop has been conducted, but some delays have occurred due to task lead's difficulties. We have also joined IEA Task 48 on Battery Swapping. There has been one meeting (remote and delayed) in Asia, with a focus on small batteries. It is unclear what the implications are in terms of efficiency of utilization of battery materials. There is probably a more rapid material turnover rate, but a better return in emission reductions per kWh. There are clear economic cases to be made for swapping of batteries for bikes and scooters and for large, standardized batteries in buses, but the case for passenger cars is extremely problematic. Staff also performed numerous reviews of journal articles and proposals and are active in committees such as the NAATBatt Recycling and Second Life committees.

### Conclusions

Argonne continues to examine the energy and environmental burdens associated with battery technologies and continued expansion of its associated supply chain. In FY23, Argonne continued to improve its modeling capabilities for both batteries and battery-related critical materials. To do this, we have engaged with industry, investigated literature, conducted engineering modeling, and developed tools for user engagement. Argonne conducted a first of its kind LCA of potential for domestic Li production from clay and brine mineral assets and compared that against existing literature of world-wide lithium production. Argonne continued to update the material composition and performance characteristics of automotive LIBs to ensure that they represent the current state of knowledge. Argonne's battery life-cycle inventory data in GREET is exhaustive and is increasingly relevant to the industry. Thus, the GREET battery module development was an effort towards making battery LCA and comparisons more user-friendly and useful for the battery industry and the research community.

### Key Publications

1. Rakesh K. Iyer, and Jarod C. Kelly, *Lithium Production in North America: A Review (No. ANL/ESIA-23/8)*. Argonne, IL (United States), 2023. <https://doi.org/10.2172/2202264>
2. Linda Gaines, Jingyi Zhang, Xin He, Jessey Bouchard, and Hans Eric Melin. "Tracking Flows of End-of-Life Battery Materials and Manufacturing Scrap", *Batteries* 2023, 9, 360. <https://doi.org/10.3390/batteries9070360>
3. Gavin E. Collis, Qiang Dai, Joanne S. C. Loh, Albert Lipson, Linda Gaines, Yanyan Zhao, and Jeffrey Spangenberg. "Closing the Loop on LIB Waste: A Comparison of the Current Challenges and Opportunities for the U.S. and Australia towards a Sustainable Energy Future", *Recycling* 2023, 8, 78. <https://doi.org/10.3390/recycling8050078>
4. Rakesh K. Iyer, Qiang Dai, and Jarod C. Kelly, *Nickel Life Cycle Analysis: Updates and Additions in the GREET Model (Rev. 1)*, Argonne National Laboratory, 2023.
5. Rakesh K. Iyer, and Jarod C. Kelly, *Updates to Lithium-Ion Battery Material Composition for Vehicles*, Argonne National Laboratory, Argonne, IL, 2023.
6. Rakesh K. Iyer, and Jarod C. Kelly, *Linkage of EverBatt with GREET*, Argonne National Laboratory, Argonne, IL, 2023.
7. Rakesh K. Iyer, Siddharth, Shukla, and Jarod C. Kelly, *Nickel Updates in GREET 2023*, Argonne, IL, 2023.

### Select Presentations

1. Rakesh K. Iyer, and Jarod C. Kelly, "Lithium-Ion Batteries: Influence of Supply Chain Factors on Environmental Impacts", *40th Annual International Battery Seminar & Exhibit*, Orlando, FL.
2. Gaines, Linda. Recycling and Flows of Critical Battery Materials, CRC Meeting, Golden, CO, December 2022.
3. Gaines, Linda. More Battery Materials of Possible Interest, NAATBatt Annual Meeting, Litchfield Park, AZ, February 2023.

4. Gaines, Linda. Tracking Flows of End-of-Life Battery Materials and Manufacturing Scrap, International Battery Seminar, Orlando, FL, March 2023.
5. Gaines, Linda. How Can We Supply Our Li-Ion Battery Materials?, MIT Future Energy Systems Center, Cambridge, MA, May 2023.
6. Gaines, Linda. Lithium-Ion Battery Material Considerations, Green Drives, Naperville, IL, May 2023.
7. Gaines, Linda. Lithium-Ion Supply Chain Considerations, ARPA-E Workshop, Chicago, IL, June 2023.
8. How Can We Supply Our Battery Materials?, Chemistry World (Royal Society), virtual, June 2023.
9. Design for Recycling, NAATBatt Recycling Workshop, Indianapolis, IN, August 2023.
10. Material Considerations for Vehicle Electrification, COMVEC, Schaumburg, IL, September 2023.

## References

1. Iyer RK, Shukla S, Kelly JC. Nickel Updates in GREET 2023. Argonne, IL: 2023.
2. Northey SA, Haque N. Life cycle based water footprint of selected metal production Assessing production processes of copper, gold and nickel. 2013.
3. Northey SA, Haque N, Lovel R, Cooksey MA. Evaluating the application of water footprint methods to primary metal production systems. *Miner Eng* 2014;69:65–80. <https://doi.org/10.1016/J.MINENG.2014.07.006>.
4. Iyer RK, Kelly JC. Lithium Production from North American Brines. Argonne, IL (United States): 2022. <https://doi.org/10.2172/1891626>.
5. Iyer RK, Kelly JC. Lithium Production in North America: A Review. Argonne, IL (United States): 2023. <https://doi.org/10.2172/2202264>.
6. Huang TY, Pérez-Cardona JR, Zhao F, Sutherland JW, Paranthaman MP. Life Cycle Assessment and Techno-Economic Assessment of Lithium Recovery from Geothermal Brine. *ACS Sustain Chem Eng* 2021;9:6551–60. <https://doi.org/10.1021/ACSSUSCHEMENG.0C08733>.
7. Argonne. BatPaC: A Lithium-Ion Battery Performance and Cost Model for Electric-Drive Vehicles (version 5.0) 2022. <http://www.cse.anl.gov/batpac> (accessed June 17, 2022).
8. Knehr KW, Kubal JJ, Nelson PA, Ahmed S. Battery Performance and Cost Modeling for Electric-Drive Vehicles (A Manual for BatPaC v5.0). Argonne, IL (United States): 2022. <https://doi.org/10.2172/1877590>.
9. Islam ES, Nieto Prada D, Vijayagopal R, Rousseau A. Detailed Simulation Study to Evaluate Future Transportation Decarbonization Potential. Lemont: 2023.
10. Iyer RK, Kelly JC. Updates to Lithium-Ion Battery Material Composition for Vehicles. Lemont: 2023.
11. Argonne National Laboratory. EverBatt 2023. <https://www.anl.gov/amd/everbatt> (accessed August 16, 2023).
12. Dai Q, Spangenberg J, Ahmed S, Gaines L, Kelly JC, Wang M. EverBatt: A Closed-loop Battery Recycling Cost and Environmental Impacts Model. Lemont: 2019.
13. Iyer RK, Kelly JC. Linkage of EverBatt with GREET. Argonne, IL: 2023.

## III.2 Lithium-ion Battery Recycling Prize Support (NREL)

### **Lauren Lynch, Principal Investigator**

National Renewable Energy Laboratory  
15013 Denver West Pkwy  
Golden, CO 80401  
E-mail: [lauren.lynch@nrel.gov](mailto:lauren.lynch@nrel.gov)

### **Sandra Loi, Co-Principal Investigator**

National Renewable Energy Laboratory  
15013 Denver West Pkwy  
Golden, CO 80401  
E-mail: [sandra.loi@nrel.gov](mailto:sandra.loi@nrel.gov)

### **Jake Herb, DOE Technology Development Manager**

U.S. Department of Energy  
E-mail: [Jake.Herb@ee.doe.gov](mailto:Jake.Herb@ee.doe.gov)

Start Date: October 1, 2017  
Project Funding: \$9,805,223

End Date: September 30, 2023  
DOE share: \$9,805,223

Non-DOE share: \$0

### **Project Introduction**

Lithium-ion batteries (LIBs) are the primary choice for portable electronics (smartphones, tablets, and laptops), power tools, and electric vehicles (EV) for personal, commercial, industrial, and military applications. While lithium-ion battery costs have fallen more than 90% since 2008, energy density and performance have rapidly increased, paving the way for an accelerated transition to clean transportation. With the global lithium-ion battery market projected to experience continued growth over the next decade, the Department of Energy (DOE) is working with industry to build a robust and sustainable U.S. battery supply chain that will support increased market demand.

On November 15, 2021, President Joseph R. Biden, Jr. signed the Infrastructure Investment and Jobs Act, also commonly known as the Bipartisan Infrastructure Law (BIL).<sup>14</sup> The BIL is a once-in-a-generation investment in infrastructure, designed to modernize and upgrade American infrastructure to enhance U.S. competitiveness, driving the creation of good-paying union jobs, tackling the climate crisis, and ensure stronger access to economic, environmental, and other benefits for disadvantaged communities.

As part of this effort, the BIL authorizes appropriations of \$200 million for the research, development, and deployment of technologies to collect, transport, sort, and process (recycle) end-of-life LIBs and for the potential use of LIBs in second use application. There is an additional \$135M appropriated covering multiple battery end-of-life (EOL) areas to accelerate and increase battery recycling rates. By developing these technologies, the aim is to:

- Ensure that the United States has a viable battery materials processing industry to supply the North American battery supply chain.
- Expand the capabilities of the United States in advanced battery manufacturing.
- Enhance national security by reducing the reliance of the United States on foreign competitors for critical materials and technologies.

<sup>14</sup> <https://www.energy.gov/articles/biden-administration-announces-316-billion-bipartisan-infrastructure-law-boost-domestic>

- Enhance the domestic processing capacity of minerals necessary for battery materials and advanced batteries.
- Ensure that the United States has a viable domestic manufacturing and recycling capability to support and sustain a North American battery supply chain.

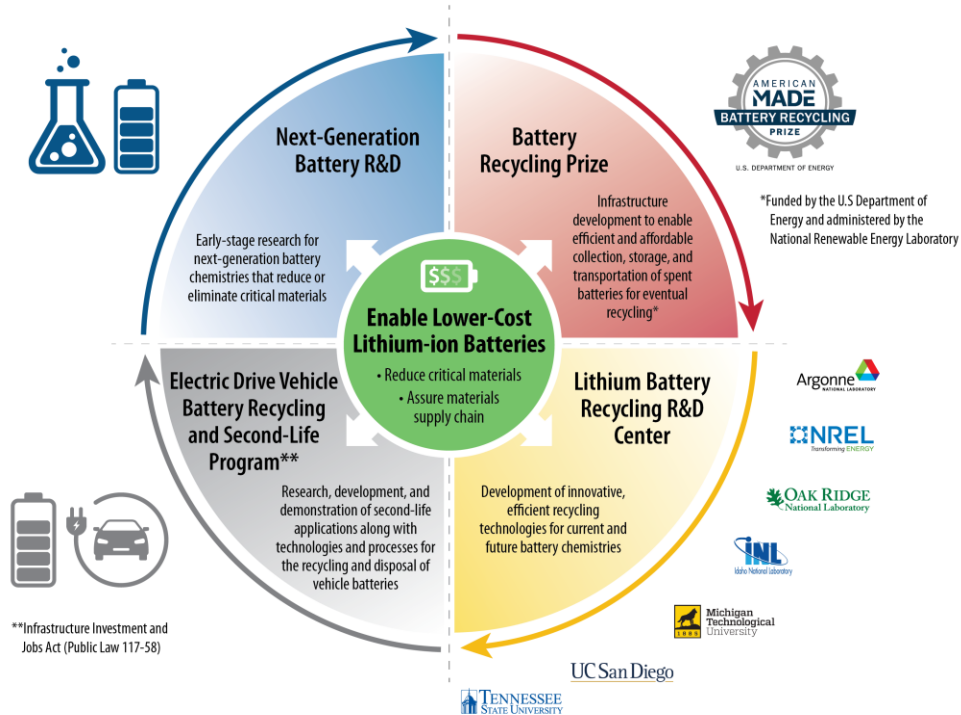


**Figure III.2.1 The Lithium-Ion Battery Recycling Prize is a key pillar of VTO’s critical materials strategy for batteries, which addresses critical materials issues for Li-ion batteries and recovery of materials for re-introduction into the supply chain.**

Section 40207(e) of the BIL titled Lithium-Ion Battery Recycling Prize called for the continuation of the Lithium-Ion Battery Recycling Prize for additional rounds after completion of Phase III.<sup>15</sup> The prize, first launched in January 2019, is designed to incentivize American entrepreneurs to develop and demonstrate processes that, when scaled, have the potential to capture and recycle 90% of lithium-based battery technologies in the United States, covering consumer electronics, stationary, and transportation applications. (Figure III.2.1) This continuation of the Lithium-Ion Battery Recycling Prize aims to further the goal of contributing to the recovery target through innovative solutions to current challenges in collecting, sorting, storing, and transporting discarded lithium-ion batteries (LIBs). The continuation of the Lithium-Ion Battery Recycling Prize will award a total of \$7.4 million in cash prizes and voucher support to participants in two phases over approximately 3 years.

**Background**

The U.S. Energy Information Administration (EIA) projects that U.S. light-duty battery EV sales will reach 1.3 million by 2025, and others project even higher sales growth. Global EV sales are expected to reach 30 million by 2030, up from 1.1 million in 2017. This growth in EV sales and increased demand for consumer and stationary uses are expected to double the demand for Li-ion batteries by 2025 and quadruple the demand by

<sup>15</sup> <https://eere-exchange.energy.gov/Default.aspx#FoaId1b505245-04d8-4b2a-bfab-46c5c8ad2de9>

2030. Demand for the global production of battery materials, such as lithium, cobalt, manganese, nickel, and graphite, will grow at similar rates depending on the future changes in the composition. Analysis has shown that recycled material could potentially provide one-third of United States cathode material needs for Li-ion batteries by 2030. The current recycling supply chain for collecting, sorting, safe storing, and transporting Li-ion batteries and recovering valuable materials is limited, particularly for larger batteries used in EVs and industrial applications. Preventing the Li-ion batteries from ending up at landfills, particularly consumer electronics (as some have caused fires), is important not for the recovery of key materials but for the economy and the environment.

In response, the DOE Vehicle Technologies Office (VTO), within the Office of Energy Efficiency and Renewable Energy (EERE), developed a Research Plan to Reduce, Recycle, and Recover Critical Materials in Li-ion Batteries. The Lithium-Ion Battery Recycling Prize was launched as part of this initiative to incentivize American entrepreneurs to find innovative solutions to solve current challenges associated with collecting, sorting, storing, and transporting discarded Li-ion batteries safely and economically for the eventual recovery of valuable materials for re-introduction to the battery production supply chain. This prize was first introduced as a \$5.5-million collaboration between VTO and DOE's Advanced Manufacturing Office (AMO) with \$4.5M funding support from VTO and \$1M from AMO.

Over three progressive phases, each team conceived a solution to collect, sort, store and transport spent lithium batteries to recyclers; developed a prototype; and then demonstrated its viability. Phase III: Pilot Validation challenged teams to implement pilot validation of the end-to-end solution and gather data to support the solution's projected impact. Fifteen winners were selected at the end of Phase I, with each team receiving a \$67,000 cash prize. Seven winners were selected at the end of Phase II, with each team receiving a \$357,000 cash prize and an up to \$100,000 noncash voucher to support validation and demonstration of their pilot-scale solution. Finally, four winners were selected at the end of Phase III to receive a \$500,000 cash prize.

- **Li Industries** of Blacksburg, Virginia, developed a machine learning-based, automated Smart Battery Sorting System capable of accurately and efficiently sorting and separating batteries by several characteristics, including chemical composition, size, weight, and packaging type.
- **Renewance** of Chicago, Illinois, designed a digital platform that tracks and manages batteries throughout their full life cycle by utilizing existing infrastructure for decommissioning, collection, warehousing, sorting, transportation, and recycling services.
- **Smartville** of San Diego, California, demonstrated heterogeneous unifying battery facilities to reduce costs and create value in the reverse logistics supply chain.
- **Titan Advanced Energy Solutions**, of Salem, Massachusetts, created a battery market intelligence platform called Battago to generate, aggregate, and connect battery data to create a transparent marketplace and bridge the gap between battery owners, integrators, and end of life recyclers.

## Objectives

The purpose of the Lithium-Ion Battery Recycling Prize is to incentivize American entrepreneurs to develop and demonstrate processes that, when scaled, have the potential to capture 90% of ALL spent or discarded lithium-based battery technologies in the U.S.— including consumer electronics, stationary, and transportation applications— for eventual recycling and materials recovery. This 90% recycling rate of lithium-based batteries would be a significant achievement compared to the 5% recycling rate demonstrated at the beginning of the prize. It is the goal of this prize to find innovative solutions to current challenges in safe and economic collecting, sorting, storing, and transporting discarded (or end-of-life) Li-ion batteries.

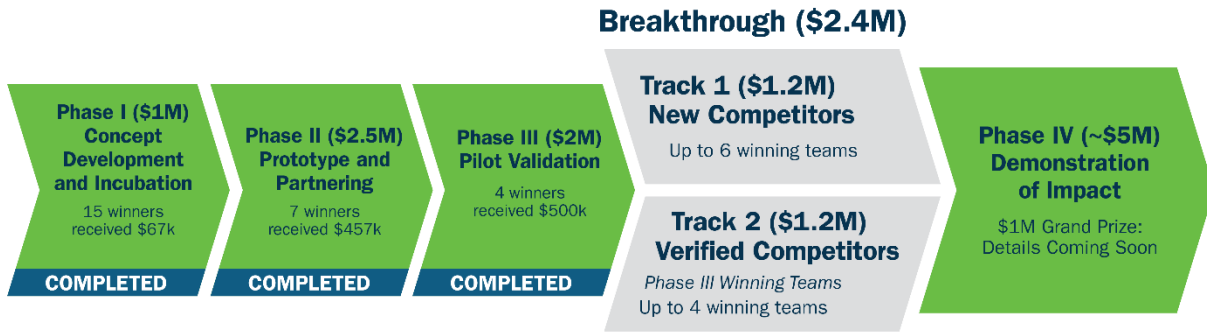


**Figure III.2.2** An illustration of the Lithium-Ion Battery Recycling Prize and continuation phases.

This continuation of the prize began in 2023 with a 1-year public Lithium-Ion Battery Recycling Prize Breakthrough (Breakthrough) contest to incentivize new submissions from battery industry entrepreneurs that demonstrate innovative solutions that meet the goal of the prize (Figure III.2.2). Breakthrough winners will be invited to participate in the Lithium-Ion Battery Recycling Prize Phase IV: Demonstration of Impact to demonstrate the efficacy of their solutions to establish an infrastructure to move spent or discarded LIBs from consumers to recyclers across all commercial uses. This continuation aims to guide participants as they progress the market implementation of their proposed solution and contribute to the recovery of spent or discarded LIBs.

The National Renewable Energy Laboratory (NREL) continues to administer the Lithium-Ion Battery Recycling Prize on behalf of DOE utilizing the established framework within the American-Made Challenges program.

**Approach**

Before announcing the Lithium-Ion Battery Recycling Prize Continuation, prize administrators guided the development of an updated prize framework while adapting to the new priorities of the evolving LIB recycling landscape. As part of this continuation, NREL emphasized the importance of a “Breakthrough” sub-phase to open the prize to new participants while providing continued support for the Phase III winning teams. The resulting Breakthrough contest includes two competition tracks—Track 1: New Competitors and Track 2: Verified Competitors—lasting approximately one year.

Track 1 encourages legal business entities based in the United States to participate in Breakthrough as new competitors with single process ideas, partial solutions or full concept solutions that enable or meet the prize goal. Track 1 is open to new participants and previous competitors of the Lithium-Ion Battery Recycling Prize. Running simultaneously, Track 2 invites Phase III winners to compete in Breakthrough as verified competitors with unique goals designed to nurture further development of the existing winning concept solutions. Track 2 participants are eligible to receive additional \$100,000 noncash vouchers to support the continued validation and demonstration of their Phase III pilot-scale solutions. The provided vouchers allow participating teams to access tools, equipment, and expertise at national labs and approved facilities and organizations within the American-Made Network.

Breakthrough winners will be invited to participate in the Lithium-Ion Battery Recycling Prize Phase IV: Demonstration of Impact to demonstrate the efficacy of their solutions to establish an infrastructure to move spent or discarded LIBs from consumers to recyclers across all commercial uses. Phase IV of the prize will begin with the Breakthrough winner announcement and last approximately 1.5 years.

**Introducing Evaluation Entities**

To support Phase IV of the prize, prize administrators developed a new opportunity for LIB recyclers and testing organizations to play a key role in the validation and evaluation of concept solutions as Evaluation

Entities. These Evaluation Entities must be identified in the Breakthrough submission package and pre-approved by DOE and the prize administration team. To become an Evaluation Entity for Phase IV, qualified recyclers must be equipped to handle the assessment of LIB material incoming from teams they intend to work with. For second-use applications, teams can refer to approved testing organizations. All Evaluation Entities must follow the documented process to become voucher service providers within the American-Made Network.

### **Developing Breakthrough Contest Rules**

Once the prize framework was in place, prize administrators worked closely with DOE to draft the Breakthrough contest official rules, including a thorough explanation of the prize continuation, competitor tracks, and expectations for evaluation entities. Both competitor tracks will be required to submit a 20-page maximum written narrative and 90-second maximum video with a detailed explanation of their proposal or concept progression. In addition, participants must provide a 30-minute virtual presentation to DOE representatives that includes a robust overview of their solution.

The submission outlines are tailored specifically to the unique objectives of each track and will be scored accordingly based on the metrics below (Table III.2.1).

**Table III.2.1 Breakthrough Scoring Criteria**

Track 1	Track 2
<p><b>Innovativeness (30%):</b></p> <ul style="list-style-type: none"> <li>• Represents a unique, innovative approach to meeting prize goals or significantly advances an existing idea, process, or technology.</li> <li>• Submission includes documented understanding of current state of the art and demonstrates how the concept furthers LIB recovery rates as a process improvement or end-to-end solution.</li> </ul>	<p><b>Impact (40%):</b></p> <ul style="list-style-type: none"> <li>• The estimated annual recovery capacity at full scale is supported by pilot validation results, as well as credible calculations and assumptions via techno-economic analysis or life cycle analysis modeling.</li> <li>• The pilot validation results demonstrate a high level of functionality and feasibility for the solution at full scale and will significantly contribute to LIB recovery rates.</li> </ul>
<p><b>Feasibility (45%):</b></p> <ul style="list-style-type: none"> <li>• Proposed annual recovery capacity is supported by credible calculations and assumptions via techno-economic analysis or life cycle analysis modeling.</li> <li>• Likelihood of making a substantial contribution toward the recovery rate for LIBs and degree to which scale-up plan is credible.</li> <li>• As appropriate, address reviewer comments from Phase III submissions.</li> </ul>	<p><b>Expansion of Concept (35%):</b></p> <ul style="list-style-type: none"> <li>• Provide proof of progression of concept that supports the estimated recovery rate of the LIB commercial use at full scale.</li> <li>• The market transformation plan demonstrates a high level of functionality and feasibility to successfully bring the concept to full scale.</li> <li>• As appropriate, address reviewer comments from Phase III submissions.</li> </ul>
<p><b>Evaluation Entity (25%):</b></p> <ul style="list-style-type: none"> <li>• Team has identified and confirmed proposed validation plan with a VSP Evaluation Entity with the appropriate process and capabilities to evaluate the concept impact and contribution to LIB recovery rates.</li> <li>• Submission outlines an evaluation plan to conduct the validation and provide required feedback documentation in Phase IV, as applicable.</li> </ul>	<p><b>Evaluation Entity (25%):</b></p> <ul style="list-style-type: none"> <li>• Team has identified and confirmed proposed validation plan with a VSP Evaluation Entity with the appropriate process and capabilities to evaluate the concept impact and contribution to LIB recovery rates.</li> <li>• Submission outlines an evaluation plan to conduct the validation and provide required feedback documentation in Phase IV, as applicable.</li> </ul>



**Results**

With the prize continuation framework and rules in place, prize administrators successfully launched the Breakthrough contest.

**Continuation Announcement and Breakthrough Contest Launch**

Prize administrators developed a promotion plan to publicly announce the prize continuation and Breakthrough contest. The winner announcement included a joint press release and e-blast from VTO and the Office of Manufacturing and Energy Supply Chains, an update on the HeroX website, and social media. The prize administrators developed all content, graphic design, and social media promotion for the announcement, which took place on June 12, 2023.

After the prize announcement, administrators coordinated information webinars for individuals interested in either of the Breakthrough contest participation tracks. These webinars were recorded and made available on the HeroX website. In addition, NREL continued to provide updates and social media to spread awareness of the competition.

**Industry Collaboration Event**

To spread awareness for the prize continuation, prize administrators hosted a networking reception at the NAATBatt Lithium Battery Recycling workshop on August 8, 2023 (Figure III.2.3). The reception presented an opportunity for prize participants, industry stakeholders, voucher service providers, and potential Evaluation Entities to network and learn more about opportunities to participate in the competition. Prize administrators developed a presentation for the NAATBatt event and designed flyers to spread awareness about the prize. The flyers have been shared at additional outreach events (Figure III.2.4).



Figure III.2.3 Informational flyers shared at the NAATBatt Lithium Battery Recycling workshop.

After the reception, prize administrators NAATBatt bi-weekly newsletter to inform others within the industry about participation opportunities.

**AMERICAN MADE BATTERY RECYCLING PRIZE**  
U.S. DEPARTMENT OF ENERGY

## Breakthrough Contest Now Open to Submissions!

**Track 1 (\$1.2M) New Competitors**  
Up to 6 winning teams

**Track 2 (\$1.2M) Verified Competitors**  
Phase III Winning Teams  
Up to 4 winning teams

**Phase IV (~\$5M) Demonstration of Impact**  
\$1M Grand Prize: Details Coming Soon

*Lithium-ion battery recyclers and testing organizations are encouraged to join the prize as **Evaluation Entities**.*

Learn More:  
[batteryrecyclingprize.org](https://batteryrecyclingprize.org)

Figure III.2.4 An informational advertisement included in the NAATBatt bi-weekly e-newsletter.

### **Breakthrough Contest Voucher Support**

As part of the Breakthrough contest, Phase III winning teams were invited to participate as “verified competitors” and receive \$100,000 in voucher funding to support the continued development of their concept solutions alongside organizations and national labs within the American-Made Network. Prize administrators provided support throughout the voucher process, from updating the existing voucher guidelines, reviewing statements of work, and initiating collaborations. Updates to the voucher guidelines included considerations for Phase IV of the prize and Evaluation Entities.

### **Key Publications**

1. “Biden-Harris Administration Announces \$192 Million to Advance Battery Recycling Technology.” Energy.gov. June 12, 2023. <https://www.energy.gov/articles/biden-harris-administration-announces-192-million-advance-battery-recycling-technology>

### **Resulting Outreach:**

1. “DOE announces \$192 million in new funding for EV battery R&D and recycling.” EV Engineering News. August 18, 2023. <https://chargedevs.com/newswire/doe-announces-192-million-in-new-funding-for-ev-battery-rd-and-recycling/>
2. “Plugged-in: EV revolution fuels Battery Belt emergence from the Midwest to the South.” Bakertilly. July 26, 2023. <https://www.bakertilly.com/insights/ev-revolution-fuels-battery-belt-emergence-midwest-south>
3. “US Announces \$192 Million in IRA Battery Recycling Funding.” Happy Eco News. July 19, 2023. <https://happyeconews.com/us-ira-battery-recycling-funding/>
4. “US \$192m boost for lithium R&D, battery recycling, innovation.” Batteries International. June 23, 2023. <https://www.batteriesinternational.com/2023/06/23/us-192m-boost-for-lithium-rd-battery-recycling-innovation/>

5. “\$192 Million In Funding For Recycling & Advanced Battery Development.” Bylt.news. June 19, 2023. <https://bylt.news/battery-construction-research-development/>
6. “White House Announces Funding for Battery Recycling Technology.” SMACNA.org. June 14, 2023. <https://www.smacna.org/stay-informed/news-and-publications/member-update/biden-administration-announces-new-funding-for-domestic-market-battery-recycling-technology>
7. “Smartville Wins Inaugural Battery Recycling Prize with Its Scalable Second Life Battery Solution.” Smartville. May 2, 2023. <https://smartville.io/second-life-batteries/>
8. “Building a robust battery recycling industry, one company at a time.” Argonne National Laboratory. November 16, 2022. <https://www.anl.gov/article/building-a-robust-battery-recycling-industry-one-company-at-a-time>
9. “DOE earmarks more funding to recycle batteries.” Resource Recycling. June 20, 2023. <https://resource-recycling.com/recycling/2023/06/20/doe-earmarks-more-funding-to-recycle-batteries/>
10. “DOE funding targeted toward battery recycling.” Recycling Today. June 13, 2023. <https://www.recyclingtoday.com/news/us-doe-battery-recycling-evs-household-funding/>
11. “DOE announces over \$192 million for battery recycling.” PV Magazine. June 27, 2023. <https://pv-magazine-usa.com/2023/06/27/doe-announces-over-192-million-for-battery-recycling/>
12. “US supercharges lithium battery recycling with \$192m funding.” Innovation News Network. June 14, 2023. <https://www.innovationnewsnetwork.com/us-supercharges-lithium-battery-recycling-with-192m-funding/33878/>
13. “\$192 Million to Advance Battery Recycling Technology from Joe Biden Administration.” CleanTechnica. June 13, 2023. <https://cleantechnica.com/2023/06/13/192-million-to-advance-battery-recycling-technology-from-joe-biden-administration/>
14. “DOE Invests \$192M in 3 Programs Advocating Battery Recycling.” ExecutiveGov. June 13, 2023. <https://executivegov.com/2023/06/doe-invests-192m-in-3-programs-advocating-battery-recycling/>
15. “DOE Allocates \$192 Million to Battery Recycling Tech, Consortium.” Bloomberg Law. June 12, 2023. <https://news.bloomberglaw.com/energy/doe-allocates-192-million-to-battery-recycling-tech-consortium>
16. “The Need For Better Batteries Is Clear.” CleanTechnica. August 8, 2023. <https://cleantechnica.com/2023/08/08/the-need-for-better-batteries-is-clear/>
17. “Biden Administration Pledges \$192mn for Battery Recycling Initiatives.” SupplyChainBrain. June 13, 2023. <https://www.supplychainbrain.com/articles/37470-biden-administration-pledges-192mn-for-battery-recycling-technology>

### Acknowledgements

DOE Battery Recycling Prize Team includes Jake Herb and Bryant Polzin. The NREL Battery Recycling Prize Team Nicholas Langle, Lauren Lynch, Sandra Loi, and Rebecca Martineau.

### III.3 Battery ReCell Center (ANL, NREL, ORNL, INL, Michigan Tech U, UC San Diego, Worcester Polytechnic Institute, Tennessee State U)

#### **Jeff Spangenberg, Principal Investigator**

Argonne National Laboratory  
9700 South Cass Avenue  
Lemont, IL 60439  
E-mail: [jspangenberg@anl.gov](mailto:jspangenberg@anl.gov)

#### **Jake Herb, DOE Technology Development Manager**

U.S. Department of Energy  
E-mail: [Jake.Herb@ee.doe.gov](mailto:Jake.Herb@ee.doe.gov)

Start Date: October 1, 2022	End Date: September 30, 2023	
Project Funding (FY23): \$10,000,000	DOE share: \$10,000,000	Non-DOE share: \$0

#### **Project Introduction**

The use of lithium-ion batteries has steeply risen in recent years, starting with electronics and expanding into many applications, including the growing electric vehicle (EV) and grid storage industries. But the technologies to optimize recycling of these batteries have not kept pace.

The ReCell Center, U.S. Department of Energy's (DOE) first advanced battery recycling center, will help the United States grow a globally-competitive recycling industry and reduce our reliance on foreign sources of battery materials.

#### **Objectives**

DOE sees an opportunity to economically recycle lithium-ion and future batteries and accelerate the growth of a profitable recycling market for spent EV, electronics, and stationary storage batteries. This can be done by developing novel recycling techniques to make lithium-ion recycling cost-effective by using less energy-intensive processing methods and capturing more metals and other high-value materials in forms that make reuse easier.

A profit-driven battery recycling infrastructure will help meet the Vehicle Technology Office's goal of lowering the cost of new batteries and increasing the use of domestic recycled battery materials.

#### **Approach**

ReCell is a collaboration of researchers from academia and national laboratories that are working together with industry to develop new recycling processes and battery designs that will enable greater material recovery at end of life. The most promising processes and designs are demonstrated at pilot scale at the ReCell laboratory facilities based at Argonne. Validated processes and designs will be licensed to industry for commercialization.

Direct recycling has been a major focus area for ReCell with the hope that enough barriers are removed or better understood through the team's work that industry would start looking closer at it and eventually start to take the lead in further development and ultimately commercialization. We are happy to learn the industry has really stepped up their interest in the technology and similarly, more companies both start-up and established are working in their own capacity to explore this technology. There are now currently three known companies that base their technologies on direct recycling. This is a rewarding feeling for the ReCell team and hope to help continue the momentum.

New space is being prepared at Argonne that will greatly increase the footprint of highbay lab area. This new space will house a pilot plant scale research system. The system will be able to generate kg quantities of materials for research and demonstration. The system will be flexible so that new pilot plant unit operations or system of operations can be swapped in and out of the process for testing. The space is expected to be complete in FY24 Q2. Equipment has already be ordered and will be installed once the space is available.

FY23 welcomed the center's second Industry Collaboration Meeting. With 191 Registrants from 80 organizations the 3-day event, held at Argonne, gave stakeholders the opportunity to hear what ReCell was up to. More time was made available to hear directly from industry through presentation and panels. ReCell plans to continue this event in the future to help ensure its goals are met.

As we enter FY24 the expanded scope continues from FY23. Figure III.3.1 shows the focus areas and listed below are their description.

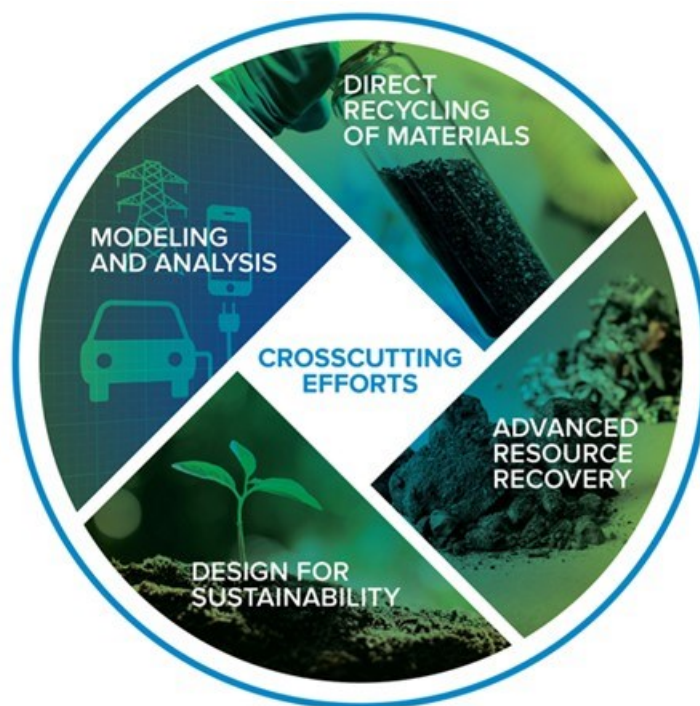


Figure III.3.1 Basic processing steps associated with direct recycling

- Direct Recycling of Materials: Recycling materials back to their original purpose without destroying their chemical structure
- Advanced Resource Recovery: Recapturing materials for reuse in batteries or other applications through chemical conversion
- Design for Sustainability: Working toward more sustainable batteries by improving material choice, battery design, and second life opportunities
- Modeling and Analysis: Developing tools to provide a deep materials/process understanding, and evaluate economic and environmental impacts

The results of the various projects within ReCell are in the following section. They are broken down by focus area and categories are used whenever possible. Following the results section is a conclusions section which provides individual conclusions made for each of the projects.

## Results

### Direct Recycling Projects (Preprocessing)

#### Cell Preprocessing

Pre-processing cells is a critical step in ReCell's direct recycling model. The configuration of battery packs, modules, and cells varies between different electric vehicle models and presents significant challenges for disassembly and material liberation. As a consequence, current commercial methods for battery size reduction used by recyclers have been determined to create a large amount of contamination. This type of contamination is an issue of great importance when direct recycling is the preferred route of recycling. A clean black mass needs to be generated for recycling to be economically and technically viable. In addition, pre-processing techniques must not adversely affect separation processes further down the line (e.g., we may not want to shred with water because it will cause problems for the recovery of electrolyte salts).

A pilot-scale system was designed with two equipment manufacturers to shred, wash, and dry material. The system was purchased this fiscal year and is expected to arrive in early 2024. This system will enable continuous shredding and washing of material for recycling. The shredding-washing system is connected to a dryer so that the output material is washed and dried shreds that can be used as the feedstock for various recycling processes in ReCell (Figure III.3.2). The entire system will have the ability to be operated under inert atmosphere for improved safety depending on the type and state of charge of batteries being shredded for recycling. The pilot system will be installed in the new pilot scale facility that is under construction at Argonne National Laboratory and expected to be completed in late spring 2024.



Figure III.3.2 Pilot-scale system designed and purchased for ReCell

During this fiscal year, the team processed over 50 kg of material to be used in other ReCell projects. The material that was generated underwent one or more of the following processes depending on which project was requesting material: shredding, electrolyte removal, drying, materials separation, and thermal binder removal. Preparing materials for other groups allowed us to test and put together a number of different recycling processes that have been developed in ReCell over the years.

In the previous fiscal year, end-of-life and manufacturing scrap pouch cells were the main input into the shredder because ReCell received a large quantity from an industry partner. The shredder at Argonne, our existing smaller scale system, was tested with different types of material such as cylindrical cells, consumer electronics, and laptop batteries. A thermal imaging camera and GoPro was used to take video of cylindrical cells shredded at various states of charge under inert atmosphere. The data collected was analyzed to determine the degree of thermal behavior observed as a function of state of charge. Significant energy release was observed for cells at 100% state of charge. We determined that freezing batteries above 0% state of charge in liquid nitrogen then immediately shredding them was an effective way to eliminate thermal events within the shredder.

#### Electrolyte Components Removal and Recovery

Electrolyte needs to be removed during a Li-ion battery recycling process, because it will create problems in downstream processes due to the fluorine and its flammability. The removal can occur in water, but this makes it difficult to separate the  $\text{LiPF}_6$  for recovery and will create methanol or ethanol from the carbonate solvents. Alternatively, a carbonate solvent based washing system can recover the all of the electrolyte components. This wash liquid then can be distilled to create solvent for reuse and an electrolyte concentrate that can be

reformulated and reused. In past years, we have demonstrated that this process can create a workable recovery process. This year was focused on solving some of the remaining issues in scaling this process up and reusing the solvent.

We have performed further cycling on the recovered and reconstituted electrolyte using a scalable distillation process. The results are shown in Figure III.3.3. The recycled electrolyte in this case slightly outperforms the baseline electrolyte all the way out to 300 cycles. This indicates that the electrolyte quality is good enough to be reused using this scaled up process.

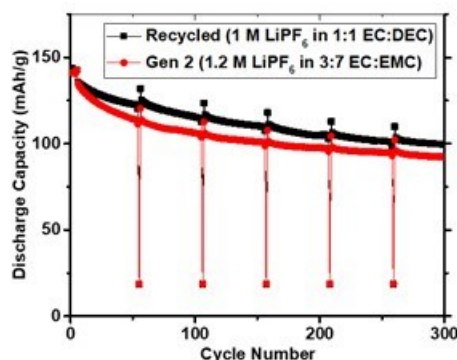


**Figure III.3.3** Electrochemical discharge capacity of an NMC 111 versus graphite cell using the recycled electrolyte versus a standard gen 2 electrolyte at C/3 except for 4 C/10 formation cycles and a C/20 cycle with HPPC study every 50 cycles.

One of the other factors that significantly affects the economics of the washing process is the ability to reuse the washing solvent. Past experiments have shown some reduction in performance by reusing the solvent. One possible hypothesis was that the water content of reused solvents is higher than that of pristine anhydrous solvent. We tested the water content by using a Karl Fischer titrator, and the results are in Figure III.3.4. The water content of the recovered solvent is about ten times that of pristine solvent. This can be removed via molecular sieves to achieve a low water content. However, the cycling data from the different solvents did not differ substantially. The recovered solvent without drying actually slightly outperformed the drier electrolytes. The variability in performance between batches of recovered electrolyte needs to be addressed as we scale this process further.

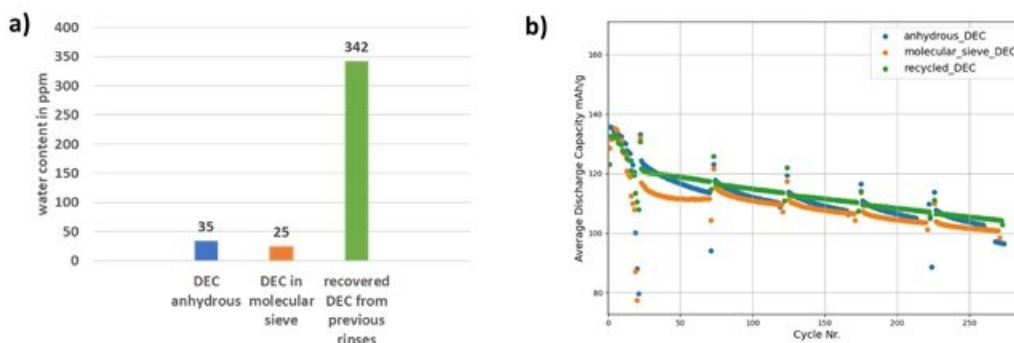


**Figure III.3.4 a)** water content of diethyl carbonates (DEC) from Karl Fischer titration. **b)** Electrochemical discharge capacity of an NMC 111 versus graphite cell with various recycled electrolytes using different solvents for the washing process.

**Recycling Electrolytes by Precipitation and Distillation**

In lithium-ion battery, the electrolyte acts as a media to support redox reactions at electrodes by transferring  $\text{Li}^+$  ions. During the battery recycling process, electrolyte needs to be removed from the materials to allow for further processing to recover other materials. The spent electrolyte is hazardous and will pollute the environment if no appropriate action is taken to dispose of it. To save cost and maintain sustainability, it is crucial to recover the spent electrolyte from the used batteries. Nevertheless, the spent electrolyte contains numerous impurities such as transition metal ions, including  $\text{Ni}^{2+}$ ,  $\text{Mn}^{2+}$ ,  $\text{Co}^{2+}$  and  $\text{Cu}^{2+}$  and  $\text{Al}^{3+}$  from corrosion reaction of current collectors, and the oxidized and reduced products of electrolyte. Therefore, recycling the recovered electrolyte from the used cells by the approach of rejuvenating the spent electrolyte is not sufficient due to the contamination. In this project, we propose a new approach based on organic chemistry separation method to recycle electrolyte solvent and salt by vacuum distillation process for electrolyte solvents and precipitation process for lithium salt. The recycled solvents and lithium salt can be formulated into high purity electrolyte solutions for new cell fabrication. This approach can be easily applied by using the available infrastructure in the chemical industry and can be easily scaled up for large-scale electrolyte recycling.

In FY23, the focus of this project was on recycling the low-boiling point electrolyte solvents from the spent electrolyte using vacuum distillation process. In particular, we have generated 100 g of aged Gen 2 electrolyte [1.2 M  $\text{LiPF}_6$  EC/EMC (3/7 w/w)] by thermal treatment ( $55^\circ\text{C}$  for 60 hours) in the presence of anode powder (Superior Graphite 1520P) and cathode powder (NMC622 Targray). This aged electrolyte is a replica of the spent electrolyte and used for the initial recycling study. After a high-speed centrifuge (7,000 rpm) process, the active electrode powders were precipitated, and the upper liquid electrolyte layer was collected. Multi-NMR ( $^1\text{H}$ ,  $^{13}\text{C}$ ,  $^{31}\text{P}$ ,  $^{19}\text{F}$  and  $^{31}\text{P}$ ) were measured for the upper liquid electrolyte and compared to the pristine Gen 2 to determine the structure change and electrolyte decomposition under this aged condition. Ion chromatography (IC) was employed to detect and quantify the transition metal ( $\text{Mn}^{2+}$ ,  $\text{Ni}^{2+}$ ,  $\text{Co}^{2+}$ ,  $\text{Cu}^{2+}$ ) dissolution in the aged electrolyte. The aged liquid electrolyte was then subject to Rotovap at slightly reduced pressure and the low-boiling point EMC solvent was collected in the receiving bottle.  $^1\text{H}$ - and  $^{13}\text{C}$ -NMR spectrum of the recycled EMC solvent are identical to those of the pristine solvent confirming the high feasibility of this process. Low boiling-point EMC solvents was successful recycled from the spent electrolyte by reduced pressure distillation.(Figure III.3.5)



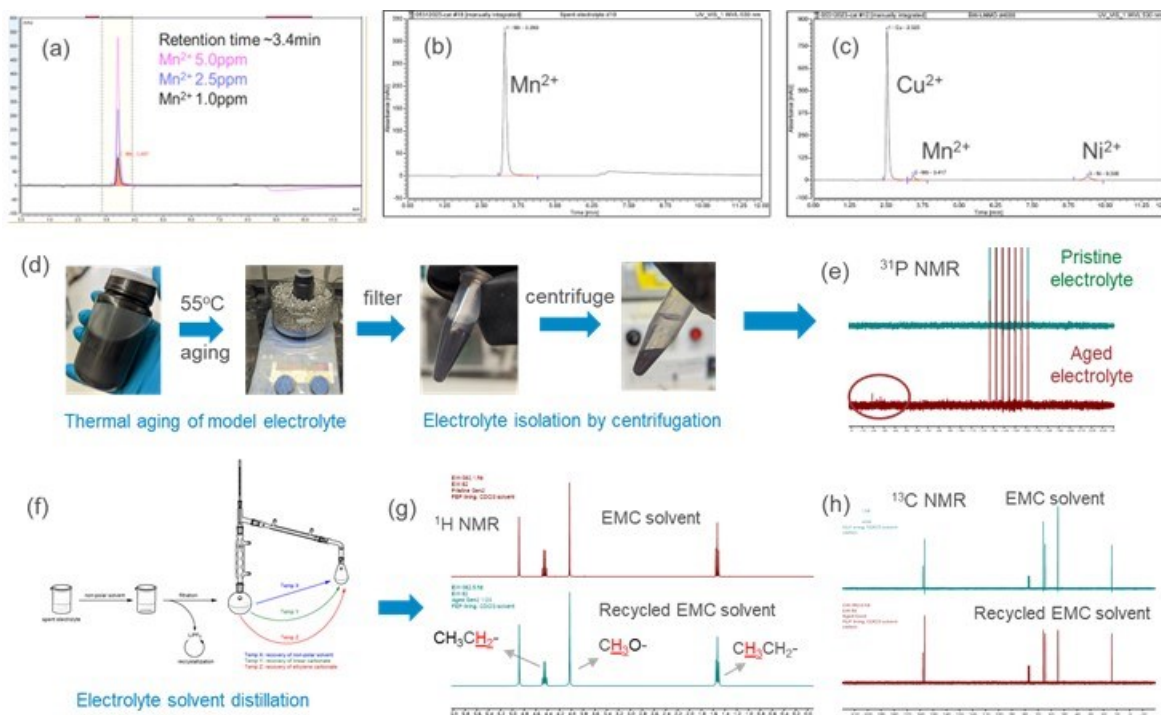


**Figure III.3.5** (a)  $Mn^{2+}$  calibration curve for quantification of transition metal dissolution in the aged electrolyte; (b) IC profile of  $Mn^{2+}$  in thermal aged electrolyte; (c) IC profile for the harvested electrolyte from the cycled NMC622/graphite coin cells showing the presence of high amount  $Mn^{2+}$ ,  $Ni^{2+}$ , and  $Cu^{2+}$ ; (d) synthesis of “spent” electrolyte by heating at  $55^{\circ}C$  of Gen 2 electrolyte mixed with NMC622 and graphite powders; (e)  $^{31}P$ -NMR of pristine and the aged electrolyte; (f) vacuum distillation apparatus used for EMC recycling; (g)  $^1H$ -NMR spectra of recycled EMC compared with pristine EMC; and (h)  $^{13}C$ -NMR spectra of recycled EMC compared with those of pristine EMC.

At the end of FY23, our research has been extended to the recycling of the high boiling-point (bp) cyclic carbonate – ethylene carbonate (EC) from the model “spent” electrolyte. The spent electrolyte solution was first subject to a Rotovap or short-pass distillation at slightly reduced pressure to completely remove the low boiling-point linear carbonate EMC. The remaining mixture of EC/ $LiPF_6$  was treated by a sublimation process. At room temperature under vacuum, EC can be sublimed and condensed on the surface of the cold finger of the asparagus with decent yield. This research will be expanded in next year.

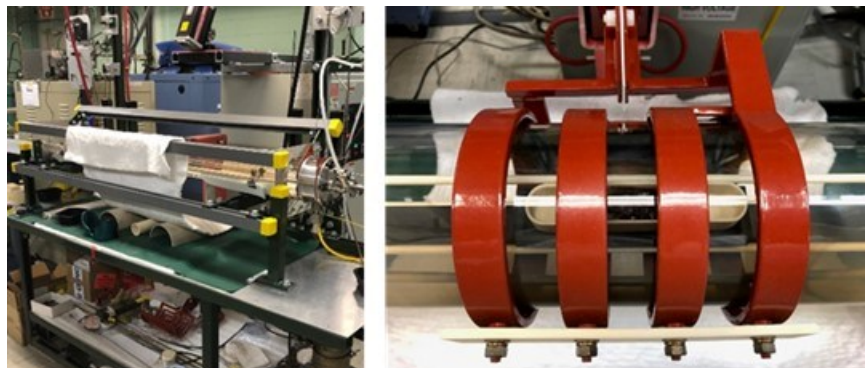
### Recycling through Spot Heat Treatment

The objective of this project is to develop and demonstrate a delamination and separation process for recycling and upcycling of electrode (cathode and anode) active materials by high-frequency induction heating. This process utilizes high-frequency induction heating for delamination and recovery of active electrode materials from current collector metal foils. This process is capable of delivery of heat/energy for processing right at the spots where it needs the most for processing and heat treatment, consumes the least amount of energy (electrical powder), requires no fluids of any type. Therefore, the developed process exhibits the highest level of sustainability and the least amount of  $CO_2$  generation.

During FY2023, we developed a low energy consumption and environment friendly processing method for delamination of shredded anodes by high-frequency induction heating (HFIH) process. The HFIH recovery demonstrated that high levels of recovery yields can be achieved, and high purity of materials can be recovered through the HFIH delamination process. We applied the process for delamination and separation of larger batches (~20 g) of anode shreds and observed similar levels of recovery yields and materials purity. Recovered anode materials were used for electrochemical cell testing and observed similar levels of charging/discharging performance when compared to these cells constructed using pristine anode materials.

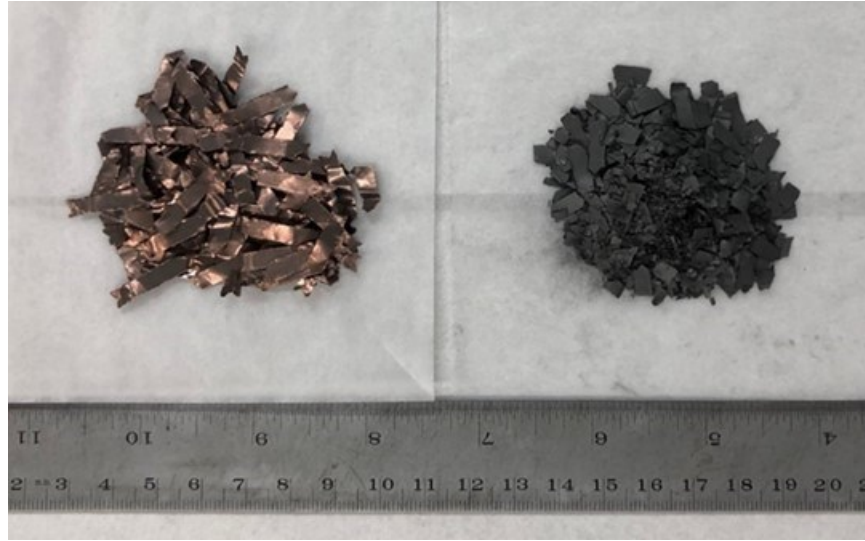
In this fiscal year, we initially explored delamination of small batches of shredded anodes by induction heating in air. Results indicate that high levels of yields can be achieved through high-frequency induction heating (HFIH) process, but the copper foils got oxidized by oxygen in air. We modified our delamination process by flowing protective inert gas through the HFIH processing chamber during the delamination process. Such a modification allows recovery of high purity copper foils without oxidation, shifting the process towards better profitability when adapting for production/manufacturing. Following the success, we applied the developed process to delamination and separation of larger batches of anode shreds. Similar levels of high recovery yields of greater than 97% were demonstrated. Recovered anode materials were put inside electrochemical cells for testing and demonstrated comparable performance as the cells made of pristine anode materials.

Figure III.3.6 shows the high-frequency induction heating (HFIH) processing system that were developed at Argonne National Laboratory (left photo) and a zoom-in shot of the anode materials contained in an alumina boat for processing within the hot zone of the HFIH system (right photo). The HFIH delamination system consists of air-tight quartz tube housing that allows flowing controlled gas atmosphere through the system. Inert gas is being flow through the system during delamination to prevent copper foils from oxidation and to protect the recovered anode materials from cuprite contamination.



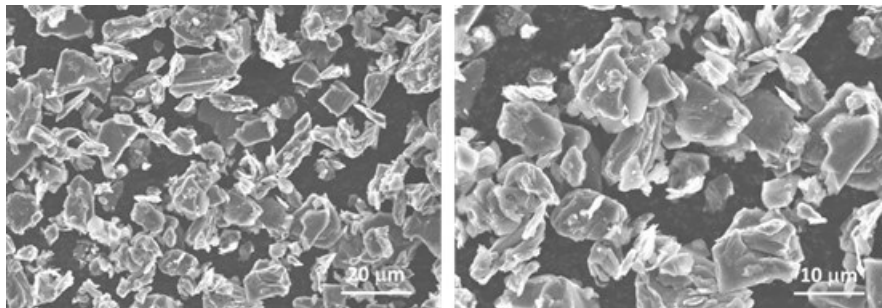
**Figure III.3.6 Photograph of the HFIH delamination system (left) and zoom-in shot of the hot zone with anode shreds in an alumina boat being processed (right).**

Figure III.3.8 shows a photograph of recovered copper foils (left) and flakes of anode material (right). With inert gas flowing through the processing system, the recovered copper foils exhibited shiny surfaces – indicating no oxidation to copper foils during the high temperature delamination process. Avoiding oxidation of copper foils not only can increase the value of recovered copper foils as scrap metal but also can increase the purity and value of recovered graphite materials (averting cuprite contamination).



**Figure III.3.7** Photograph of materials recovered from HFIH processing. Left: high purity copper foil current collector, and right: delaminated anode flakes.

Figure III.3.8 shows scanning electron microscopy (SEM) images of ground powder from the delaminated anode materials by HFIH process. SEM energy dispersive X-ray spectroscopy elemental analysis indicates no copper contamination. As we can see from these images, graphite particles in the resulting powder are evenly distributed with a particle size of  $\sim 10\ \mu\text{m}$ .



**Figure III.3.8** SEM micro images of graphite powder from anode materials recovered by HFIH process.

We conducted HFIH delamination experiments with small batches of samples of approximately 3.0 grams starting anode shreds. Table III.3.1 summarizes the amounts of recovered materials from seven different runs and their corresponding recovery ratios and graphite fractions. We have achieved an average recovery ratio of 97% with graphite content of nearly 70% of the total weight of recovered materials. Our results demonstrated the effectiveness of HFIH delamination process for recycling of anode materials. HFIH delamination process requires only minimal amount of electrical energy which could come from a renewable source with no need for any other type of resources, such as water or chemical solvent.

Table III.3.1 Summary of Delamination of Small Batched of Anode Shreds by HFIH

Sample ID	Initial Weight (g)	Weight after processing (g)	Recovery Ratio (%)	Weight of Black Mass (g)	Weight of Cu Foil (g)	Graphite Fraction (%)
104	3.03	2.94	97.0	2.014	0.892	69.3
106	3.06	2.97	97.1	2.047	0.909	69.2
108	3.03	2.94	97.0	2.007	0.897	69.1
110	3.09	2.99	96.8	2.068	0.898	69.7
112	3.08	3.00	97.4	2.069	0.888	70.0
114	3.05	2.97	97.4	2.029	0.934	68.5
116	3.04	2.94	96.7	2.014	0.912	68.8
Average			97.1			69.2

A large batch anode delamination run was conducted with ~20 g anode shreds contained inside a graphite boat. Inert gas was flowing through the HFIH delamination system to prevent oxidation of copper foil and possible cuprite contamination to the delaminated anode (graphite) materials. Figure III.3.9 shows the materials recovered from this delamination. Our results indicate that both alumina and graphite containers are suitable for HFIH anode delamination with inert gas flowing through the system during processing. Multiple anode delamination experiments were conducted with ~20 g starting anode shreds by HFIH process with inert gas flowing. We consistently observed recovery ratio of greater than 97% and graphite fraction of ~70% by weight in the recovered materials.

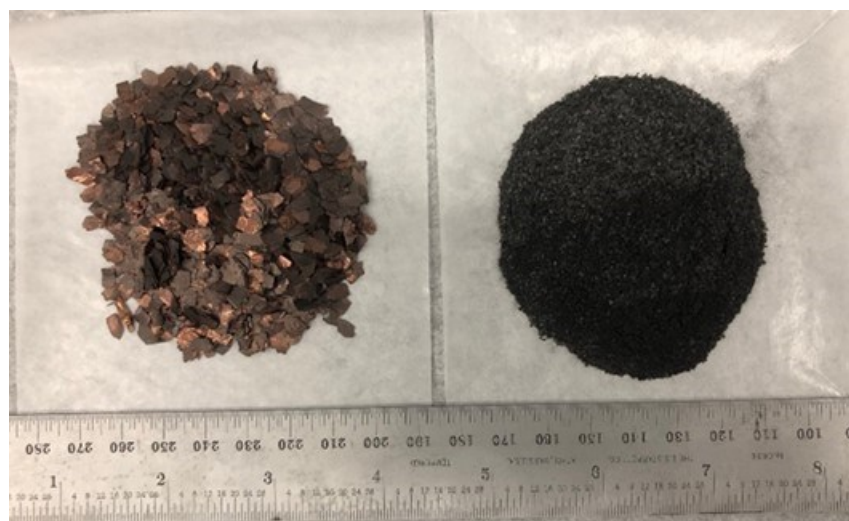


Figure III.3.9 Photograph of materials recovered from a large batch (~ 20 g) HFIH processing run. High purity copper foil (left) and active anode (right) were separated using a sieve after delamination.

#### **Solvent-based Electrode Recovery**

Both hydrometallurgical and direct recycling methods require the separation of active electrode material from metal foil, which is an enabling yet challenging task in the pre-processing step. The goal of this project is to develop efficient separation processes to recover electrode materials and metal foils. In contrast to the conventional separation processes that involve the use of highly toxic solvents like NMP and DMF, this project utilizes green solvents to recover both electrode materials and metal foils from spent electrodes as well as from manufacturing scraps. Three types of green solvents-based separation processes have been developed, including SolveX (ethylene glycol, EG), SolveY (triethyl phosphate), and SolveZ (water) processes. Those green solvents are inexpensive, nontoxic and do not cause water and/or air pollution, and do not incur a penalty

in terms of damages to active materials and current collectors. All three processes have been demonstrated for the direct recycling and remanufacturing of electrode scraps, including both cathode and anode scraps.

In FY 23, we modified the SolveX process to recycle industrial anode scraps. The SolveX process was improved by adding alkali hydroxides into ethylene glycol, which could accelerate the delamination process. It is found that reprocessing or remanufacturing the recovered anode films into new electrode was greatly affected by the type of alkali hydroxides, where anode films from both KOH and NaOH formed agglomerated slurry while the one from LiOH led to slurry with similar rheology property as the baseline, as shown in Figure III.3.10 a) and b). The recovered anode films were characterized and analyzed to attribute the differences to the defluorination reaction. Additionally, we scaled up the process to deliver ~1.5kg recovered anode films for industry collaborator (Figure III.3.10 c). The anode films recovered from the LiOH/EG solution were reprocessed into new coating and tested in half cell to compare with the baseline anode. A reversible capacity of ~320 mAh/g was obtained for both baseline and recovered anodes (see Figure III.3.10 d).



**Figure III.3.10** Photos showing the slurry formed from recovered anode films using (a) KOH/EG and (b) LiOH/EG; (c) photo of ~1.5 kg recovered anode films; (d) charge/discharge profiles for the reprocessed anode in comparison with baseline anode.

In addition to the modification and optimization of SolveX process, SolveZ process was finalized and published. Cost for the SolveZ process was evaluated by EverBatt, which showed \$0.81 to process 1 kg anode scrap, most of which arises from capital investments, and the operating cost. SolveZ process not only exhibited great profitability but also help reduce the GHG emissions from graphite by 87% and lead to a reduction of 99% SOx emissions from virgin Cu production.

### **Direct Recycling Projects (Separations)**

#### **Aqueous Sequential Separation**

In a typical recycling process, the spent cells are discharged and shredded, followed by electrolyte recovery and component separation to remove/reclaim components like plastics, pouch material, and steel casing. As a result, a feedstock of anode and cathode on their current collectors is generated. This feedstock contains the most valuable components in a lithium-ion cell, including black mass (e.g., active cathode materials and graphite), Cu foils, and Al foils. To reclaim active cathode materials with high purity for direct regeneration, separation of electrode materials and their current collector as well as of anodes and cathodes is required. Current techniques require a complex set of separation processes to produce clean streams of material, resulting in lower recovery rates and higher costs. The objective of this project is to develop an aqueous separation process to sequentially separate anode/cathode and electrode/current collectors to recover cathode films, anode films and metal foils. This process utilizes a buffer solution to first peel off anode films from copper foils, followed by adding a surfactant to facilitate the delamination of cathode films. The designed water solution does not damage the active cathode materials nor corrode the metal foils. In addition, this process enables room temperature separation in a low-priced water solution, reducing energy consumption and processing costs.

In FY23, we explored the aqueous sequential separation process for recovering materials from commercial spent electrodes. The separation of commercial cathode was performed using LFP cathode from a commercial cylindrical cell. It is found that using the non-ionic surfactant could not delaminate the commercial cathode. Changing the non-ionic surfactant to an anionic surfactant like sodium dodecyl sulfate (SDS) can accelerate the delamination process together with increasing the reaction temperature to 80 °C. The separated anode films from the sequential process were further treated using the SolveY protocol to remove the PVDF binder. SolveY recovered graphite was recoated as new anode and evaluated in half cells. The recovered graphite showed a reversible capacity of ~335 mAh/g with stable cycle performance. In addition to water-based sequential recovery process, we expanded the concept of sequential separation to ethylene glycol (EG) based process, especially for the recovery of commercial electrodes that exhibit tighter adhesion between electrode coating and current collector. It took <1 min to fully delaminate industrial spent anode in EG at 120 °C, while it took ~10 min to peel off industrial cathode films in EG with LiOH. Time difference of delamination allows using EG for sequential separation.

### ***Solvent-based Dual Process***

Within the loop of Direct Recycling, separation and subsequent direct regeneration of active cathode materials are of great importance as cathode represents one of the most valuable components in a lithium-ion cell. Cathode materials are tightly bonded to Al foil through the organic PVDF binder, making them challenge to be separated. In addition, the separated cathode materials are lithium deficient, further requiring a relithiation process to convert those delithiated cathode particles to a stoichiometric material. Current strategy involves several isolated separation and regeneration processes that make recycling complicated and expensive. It is thus desirable to develop a process with dual functionality that can separate and simultaneously restore lithium in the same solvent system. In this project, the team will develop a solvent-based dual process to separate as well as regenerate the cathode active materials. The objective of this project is to accomplish both separation and regeneration of cathode materials through a one-pot solvent-based dual process. This process utilizes a greener solvent that will not only delaminate the spent cathode films from aluminum foils but also restore the lithium back to stoichiometry. This process avoids complicated processes, making recycling scalable and more profitable. Furthermore, the process is completed in a greener solvent at a relatively low temperature and ambient pressure, which will both reduce energy consumption and alleviate environmental impact.

In FY23, we optimized the relithiation process to reduce process cost with the assistance of EverBatt modeling. Nearly 60% of processing cost for relithiation is from materials including the solvent ethylene glycol (EG) and the lithium precursor LiOH. We thus reduced the usage of both solvent and LiOH by introducing LiOH/EG suspension (2 M), comparing to previously used LiOH/EG solution with low LiOH concentration (e.g., 0.5 M), so that the NMC solid to EG solvent ratio could be greatly increased. Physical characterizations and electrochemical test in half cells confirmed the successful regeneration of delithiated NMC111. Reducing the usage of LiOH and EG reduced ~30% of total processing cost, or ~40% of material cost. In addition to process optimization for cost reduction, we found that the PVDF binder in the delaminated films greatly affect the direct regeneration of cathode. The defluorination reaction between LiOH and PVDF produced LiF that would deposit on the cathode particles. Mitigation methods such as washing with copious water and adding KOH to the LiOH/EG solution have been tested, which requires further studies.

### ***Anode/Cathode Separation and Purification***

After battery shredding, electrolyte recovery, and component separation (i.e. plastics, cell casing, magnetic ferrous-based metals) we are left with electrode fragments that include anode/copper foil and cathode/aluminum foil. Separation of the anode and cathode is a critical step in the direct recycling process to purify black mass. Being able to efficiently produce multiple clean streams of material (cathode, anode, and Al/Cu foil) will make direct battery recycling more profitable. The separation of anode, cathode, and metals can be achieved in a couple different ways. First, delamination and binder removal (i.e., via thermal binder removal or a solvent-based delamination and binder removal process) must be performed on the anode/cathode mixture to yield two product streams consisting of mixed Al/Cu foils sieved from combined anode/cathode powders. The mixed anode/cathode powders and metals would each have to undergo separation processes. The

second method will produce more clean streams of product by separating the electrode laminates while attached to foils prior to delamination and binder removal. At this point, you would have one batch that contains cathode and Al foil while the other is anode and Cu foil. Binder removal would be performed on the two batches to produce separate streams of Al foil, Cu foil, anode powder, and cathode powder. The presence of four separate product streams after a simple anode/cathode separation would reduce black mass complexity and significantly streamline subsequent steps in the direct recycling process.

Two new separation systems were purchased, installed, and safety approved at Argonne National Laboratory. One was a large-scale Rare Earth (RE) Roll separator and the other was a lab-scale optical sorter (Figure III.3.11). The large-scale RE Roll separator was custom-designed with 3 separate magnetic rolls to conduct a multi-pass separation within a single piece of equipment. Conditions for the feed hopper to the system and belt speed, splitter position, and splitter angle of each of the 3 magnetic rolls were optimized using shredded manufacturing scrap pouch cells. High speed videos were recorded at minimum and maximum speed range to give visual clue for best belt speed and splitter angles for separation. Using the high speed video, a process was optimized to give greater than 90% separation efficiency. To give insight into how impurities will affect the electrochemical performance of recycled materials, pristine commercial anode and cathode powders were mixed and tested electrochemically. Mixtures of NMC/graphite, graphite/NMC, LMO/graphite, graphite/LMO, LFP/graphite, and graphite/LFP were tested where the impurity was 0.5, 1, and 2%. Higher percentages of impurity material decreased electrochemical performance while lower percentages had little to no effect. The color sorter was used to separate graphite electrodes from bare copper foil (up to 71% purity after a few brief experiments) and the non-magnetic fraction from RE Roll separation experiments which contained mostly anode with some plastics and a small amount of cathode (up to 97% copper achieved).

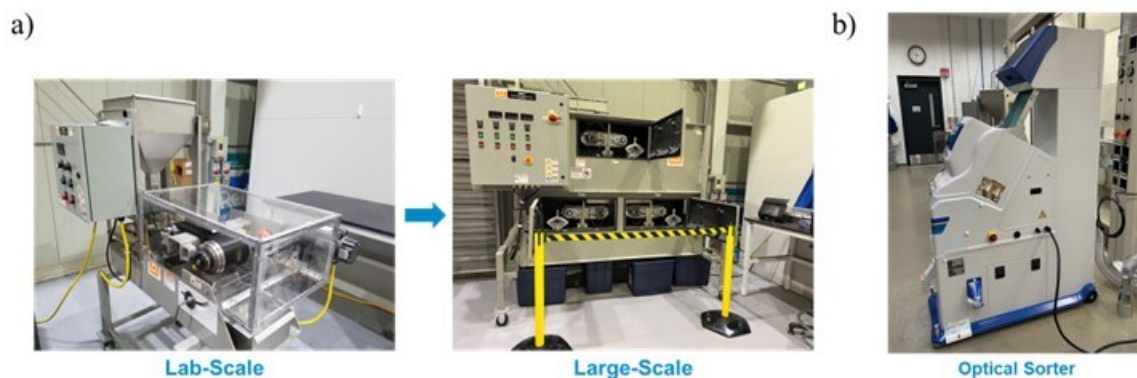


Figure III.3.11 Separation equipment: (a) RE Roll and (b) optical sorter

### ***Cathode/Cathode Separation***

Most direct recycle operations will involve the collection of “black mass” which is a mixture of anode and cathode powders recovered from size reduced cells. Even if cells are presorted before processing, it is still highly likely that some mismatch of battery types, and ultimately cathode materials, will occur. Additionally some manufacturers utilize a mixture of different chemistries for the cathode, such as lithium manganese oxide (LMO) and lithium nickel manganese cobalt oxide (NMC). While the LMO is less likely to be reused, the NMC could be used in a modern cell. Direct recycling of lithium-ion batteries will require the ability to effectively separate different cathode chemistries. Recovering and separating complex mixtures of cycled cathode powders will make recycled material more usable in the battery market. This work focuses on scale-up of proven techniques as well as the separation and recovery of complex mixtures of cycled cathode powders.

A lab-scale Rare Earth (RE) Roll magnetic separator was used this fiscal year to continue to optimize the separation of mixtures of cathode electrodes. In order to better understand the magnetic differences between different cathode materials, magnetic susceptibility was conducted on LFP, LMO, various NMC compositions, NCA, and LCO using a SQUID magnetometer at Argonne’s Center for Nanoscale Materials. Measured

magnetic susceptibility of pristine cathode powders was observed in the order of LFP > LMO > NMC > NCA > LCO (Figure III.3.12). Mixtures of pristine LFP and NMC111, NCA and LCO, LMO and NMC111, and LFP/LMO/NMC111 were fed through the RE Roll and conditions were optimized to improve cathode purity in magnetic and non-magnetic fractions. Depending on the mixture, 2 or 3 passes through the RE Roll system were required to achieve purities greater than 80 or 90% and recoveries between 60-90%. To give insight into how impurities will affect the electrochemical performance of recycled materials, pristine commercial anode and cathode powders were mixed and tested electrochemically. Mixtures of LMO/NMC111, LFP/NMC111, LMO/NMC111, LFP/LMO, LFP/NMC111, and LMO/LFP were tested where the impurity was 0.5, 1, and 2%. Higher percentages of impurity material decreased electrochemical performance while lower percentages had little to no effect.

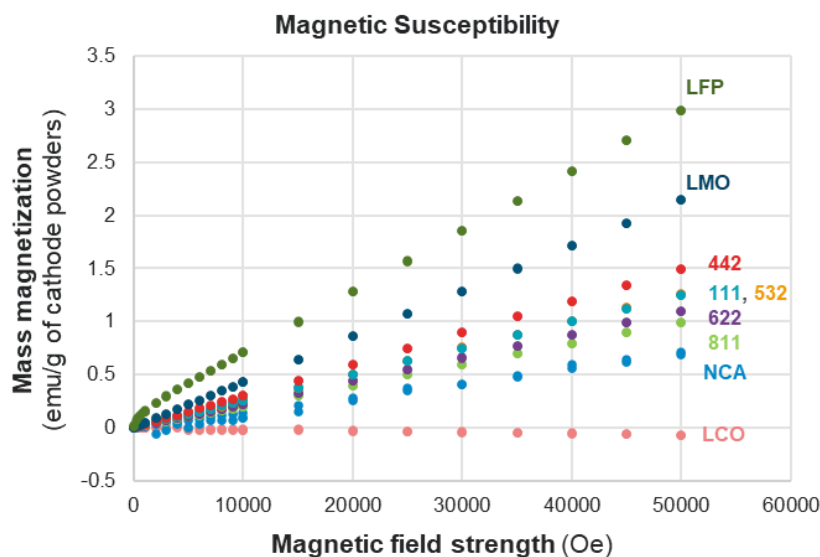


Figure III.3.12 Magnetic susceptibility of cathode materials using a SQUID magnetometer at Argonne National Laboratory

#### ***Cathode/Cathode Separation via Froth Flotation***

The objective is to separate mixed cathode compositions using the froth flotation method. The aim for this year is to separate recycled spent cathode active materials using the froth flotation method. It has been previously found that pretreatment processes have a significant impact on both surface and bulk properties of the recycled cathode materials. The objective is to study the impact of various cathode recycling processes on both bulk and surface chemistry of the recycled cathode materials.

Laboratory froth flotation trials were performed using 1-L Denver flotation cell. The feed materials were mixed with DI water to prepare a 1-10% solid slurry. Collector chemical was initially added to the slurry and conditioned for 3 minutes. Frother chemical was then added to the slurry and conditioned for 1 minutes. The slurry was then aerated, and froth was recovered every 1-3 minutes until no materials floated anymore. The composition of both floated materials and sink product was determined by ICP. In addition, the impact of various pretreatment processes on both the bulk and surface properties of recycled cathode active materials were evaluated. The bulk properties of recycled cathode active materials were evaluated by XRD, SEM and ICP, while the surface properties of recycled cathode active materials were examined using S-TEM and XPS.

Figure III.3.13a) shows the flotation recovery of NMC materials obtained from recycled lithium-ion batteries. With an addition of flotation collector, the floatability of the pristine cathode active materials should be 95% or higher. The result shows that the floatability of the recycled cathode active materials was deteriorated significantly after the recycled cathode active materials were heat treated. Figure III.3.13 b) shows the



morphology of individual cathode active material from spent lithium-ion batteries after various pre-treatment methods. The delaminated cathode (DC) contained polyvinylidene fluoride (PVDF) polymers. Both mechanical separation and thermal pyrolysis methods removed and/or decomposed PVDF binders, and it is challenging to distinguish the difference in morphology of recycled cathode active materials after various surface treatment.

Figure III.3.14 a) shows high-angle annular dark-field imaging (HAADF) image of recycled cathode active materials. Two recycled cathode active materials were compared including cathode materials manually delaminated from foils and cathode materials after a thermal pyrolysis at 600 °C followed by an anode/cathode froth flotation separation. The result showed that the layered structure of the recycled cathode active materials (CAM) was preserved in the delaminated cathode active materials. After a thermal pyrolysis at 600 °C, the recycled cathode active materials exhibited a structural change associated with a loss of lithium (Li) from two transitional metal layers. Figure III.3.14 b) and c) shows the electron energy loss spectra (EELS) of both Ni L-edge and Co L-edge. A peak shift was found in both Ni L-edge and Co L-edge with the recycled cathode materials after a pyrolysis treatment at 600 °C compared to the delaminated cathode materials. This result indicates that both Ni and Co atoms within the cathode structure were shifted to a higher valency, due to a loss of lithium (Li) on the surface.

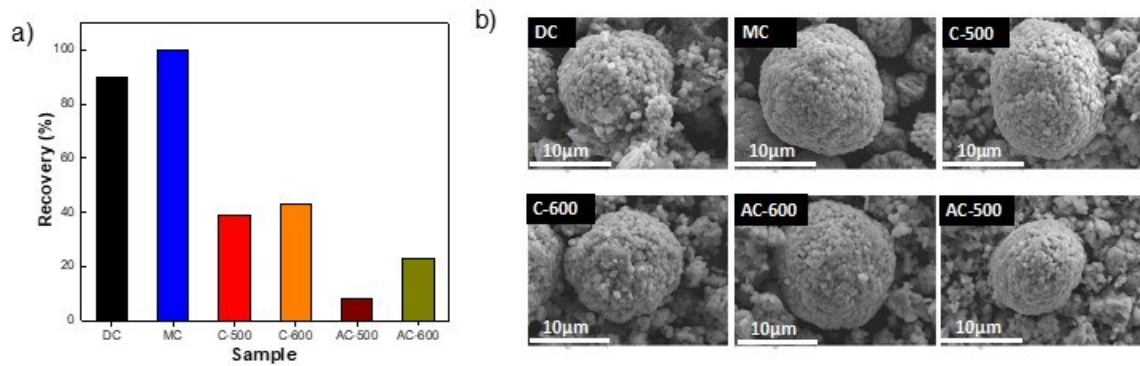


Figure III.3.13 a) flotation recovery of individual cathode active materials after various surface treatment, b) morphology of cathode active materials after the pre-treatment.

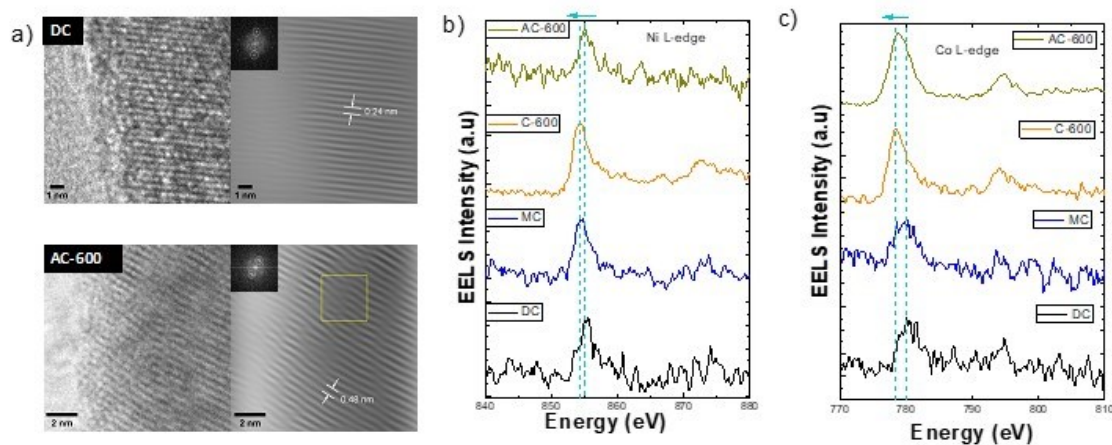


Figure III.3.14 a) HAADF image of both delaminated cathode active materials and recycled cathode active materials after a thermal pyrolysis treatment at 600°C; electron energy loss spectrum (EELS) of b) Ni L-edge and c) Co L-edge obtained on various recycled cathode active materials after various pre-treatment processes.

### **Molten-Salt Assisted Flotation for Separation of Electrode Materials**

This project is to develop an efficient molten-salt assisted flotation methodology to separate anode particles from cathode particles through a cost-effective molten-salt system. This research will capitalize on the large density difference between cathodes (e.g., NMC, LCO) and anodes (graphite). A multicomponent, low-temperature melting system with a controlled density will be developed for this purpose.

Two binary molten salts (MSs) featuring densities between graphite (2.3 g/cc) and NMC 622 (4.7 g/cc) have been used for separation of Graphite/NMC 622 mixture. In MS with a melting point of 300 °C, a gap between top and bottom layer formed after cooling down. Graphite enriched layer was floated on the top part while NMC enriched layer sunk to the bottom of molten salts. According to XRD results, top layer contains 61 wt% of graphite while bottom layer contains 90 wt% of NMC 622.

Room temperature MS—ionic liquid (IL) with a density of 2.7 g/cm<sup>3</sup> have formulated for room-temperature separation of Graphite/NMC 622 mixture. A gap between top and bottom layer formed in IL after low-speed centrifuge at 3000 rpm. According to TGA results, top layer contains 97.8 wt% of graphite while bottom layer contains 93.2 wt% of NMC 622.

Commercial black mass V1B has been investigated in the separation process. The separation has been scaled up from 2 to 10 g by using separation funnel. A gap between top and bottom layer formed in IL after stay still overnight. According to TGA results, top layer contains 99.3 wt% of graphite while bottom layer contains 88.9 wt% of NMC 622. (Figure III.3.15)

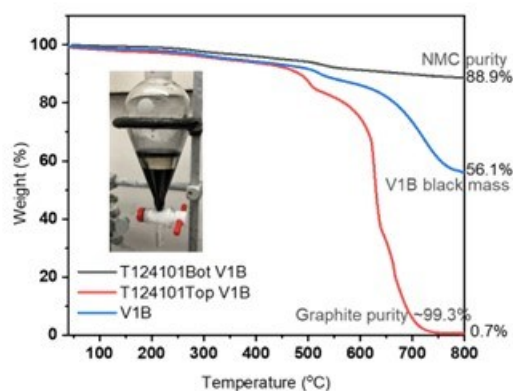


Figure III.3.15 TGA curves of commercial black mass V1B and separated products in air.

### **Solvent-based Gravity Separations**

A separation between recycled anode and cathode materials from spent lithium-ion batteries is essential for the direct recycling applications. Froth flotation is commonly used for the separation between graphite and lithium metal oxides based on the difference in their surface hydrophobicity. Water is the liquid medium used in the froth flotation process. The presence of carbon additives and PVDF binders in cathode composite materials complicates the separation efficiency. In addition, the use of water as the liquid medium tends to change both surface and bulk properties of recycled cathode active materials.

The objective of this project is to develop an alternative anode/cathode separation technology that can be coupled with the delamination process. A gravity separation technology is developed based on the difference in the specific gravity between the recycled anode and cathode materials. The objective in the previous year was to optimize the separation efficacy between the pristine anode materials and pristine cathode materials. Graphite was used the pristine anode materials, and lithium nickel-cobalt-manganese oxide was used as pristine cathode material. The objective for this FY is to recycle and separate anode and cathode materials from spent lithium-ion batteries.

Figure III.3.16 shows a schematic drawing of the UF concentrator. The feed materials were mixed with DI water or organic liquid medium to prepare a slurry. In each trial, the slurry was slowly fed into a central tube of the Falcon L40 concentrator at a flow rate of approximately 2 L/min. The concentrator bowl rotated at a speed of 1,000 – 3,000 RPM, at which particles in the slurry within the rotating bowl were subject to a centrifugal force of up to 50-300 G. The lighter particles were flushed with the overflow stream to the overflow product. Particle beds within the concentrator bowl are collected manually as the concentrate product.

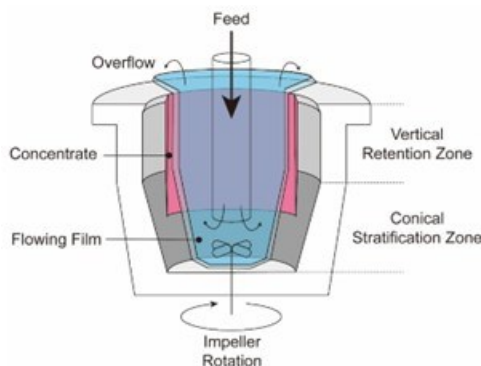


Figure III.3.16 A schematics of a centrifugal ultrafine (UF) gravity separation concentrator.

### **Direct Recycling Projects (Contamination)**

#### **Role of Impurities in Recycled Cathodes**

In the hydrometallurgy recovery process, a variety of impurities introduced from different sources can potentially enter the leachate. The presence of impurity during the co-precipitation reaction is an important factor which could have unintended impacts on the properties of the final cathode products. It is crucial to maintain a stable and high-quality recovered product from recycling industry. Therefore, this project objective is to determine the impacts of impurity on the synthesized NCM622 materials via hydrometallurgical method, as part of the efforts to understand and optimize the recycling process. In the year of 2023, we studied the silicon impurity (Si nano particles) under this project. Silicon, because of its high specific capacity, is intensively pursued as one of the most promising anode material for next-generation LIBs.<sup>2</sup> Clearly, they may have an impact on the recovery of the cathodes.

Metal sulfate solution (Ni:Co:Mn = 6:2:2) was used in co-precipitation reaction to synthesize transition metal hydroxide, followed by sintering with  $\text{Li}_2\text{CO}_3$  to obtain NCM622 cathode material. To introduce impurity, Si nanoparticles were added into metal sulfate solution prior to the co-precipitation step, with three amount levels of 0.2, 1, and 5 at% (relative atomic percent of the total transition metals). The obtained materials are denoted as 0.2SiNCM, 1SiNCM, and 5SiNCM, respectively. A control group of virgin material with no extra impurity is denoted as VNCM. Next, the obtained materials will undergo a series of characterization and testing.

Metal sulfate solution (Ni:Co:Mn = 6:2:2) was used in co-precipitation reaction to synthesize transition metal hydroxide, followed by sintering with  $\text{Li}_2\text{CO}_3$  to obtain NCM622 cathode material. To introduce impurity, Si nanoparticles were added into metal sulfate solution prior to the co-precipitation step, with three amount levels of 0.2, 1, and 5 at% (relative atomic percent of the total transition metals). The obtained materials are denoted as 0.2SiNCM, 1SiNCM, and 5SiNCM, respectively. A control group of virgin material with no extra impurity is denoted as VNCM. Next, the obtained materials will undergo a series of characterization and testing.

As revealed by the SEM in Figure III.3.17, it is found that the Si impurity has almost no impact on particle morphology. Even at 5 at% high concentration level, the as-prepared secondary particles still show a regular size and spherical appearance which is close to the virgin control group.

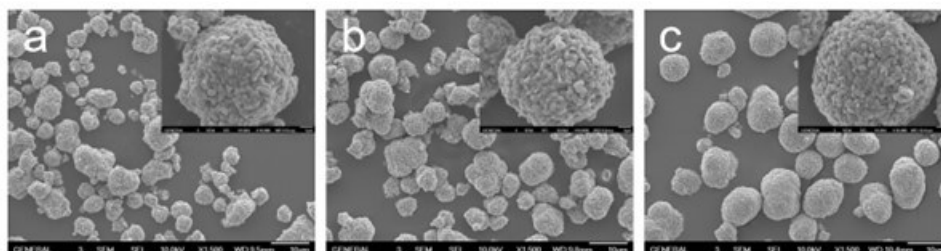


Figure III.3.17 SEM images of (a) 0.2SiNCM, (b) 1SiNCM, and (c) 5SiNCM cathode. (Inset: images at higher magnification).

In addition, the tap density of synthesized 12 h precursor powders stay at a consistent high level around 1.80 g/ml for all samples, regardless of the impurity added. XRD results prove that the crystal structures of materials are not affected by the addition of silicon. And there is no evidence of secondary phase in as-prepared materials. Interestingly, both EDS and XRD do not confirm any Si-related substances in materials. (Table III.3.2)

Table III.3.2 Rietveld Refinement Data of the Prepared NCM622 Cathodes.

Sample	a (Å)	c (Å)	V (Å <sup>3</sup> )	Ni <sub>Li</sub> (%)	Chi <sup>2</sup>
VNCM	2.868	14.225	101.43	3.9	2.99
0.2SiNCM	2.867	14.227	101.36	4.1	2.54
1SiNCM	2.867	14.227	101.33	3.7	2.62
5SiNCM	2.868	14.228	101.41	4.3	2.92

In a simulation test where the solution environment is set as the co-precipitation condition, it is found that the silicon nanoparticles could gradually dissolve in the ammonia within 3 hours. This provides a good explanation for the presence of hollow in some cathode particles and the absence of the SiO<sub>2</sub> phase in cathodes. It has been clear that Si nanoparticles dissolve during co-precipitation to form silicates that remain on the surface of each grains. The SiO<sub>3</sub><sup>2-</sup> XPS signal at about 102 eV in precursors further validates this conclusion. According to Figure III.3.18 a), consistency in XPS spectra across all samples suggests that there has been no alteration in the oxidation states of Ni ions. The CV scan shows a slight shift of oxidation peak from 3.89 V of VNCM to 3.94 V of 1SiNCM, as well as the rise of  $\Delta E$  to above 0.1 V. In Figure III.3.18 c), SiNCM discharge capacities are a bit lower (~10 mAh/g) than virgin standard, due to the degradation in kinetics. In specific, 5SiNCM has the worst discharge capacity of 171 mAh/g, compared to VNCM which has 180 mAh/g, the best of all.

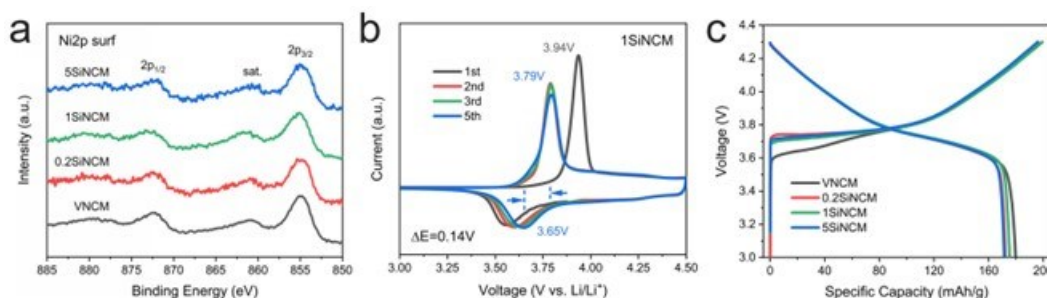


Figure III.3.18 (a) XPS Ni 2p spectra of as-prepared cathode surfaces, (b) CV scan of 1SiNCM, and (c) Initial charge-discharge profile of cells at formation cycle.

### **Purification of Black Mass**

Successful implementation of direct recycling at scale is contingent on the ability to produce high-purity material outputs. The presence of metallic impurities within recycled cathode materials both reduces purity metrics – a critical factor to industrial acceptance of the recycled product – and adversely impacts cell performance. In particular, mechanical shredding (the predominant preprocessing technique utilized in direct recycling) introduces trace levels of Al and Cu from the electrode current collector. These contaminants are particularly challenging to remove from the fine shredded fraction, where the contaminants are on the same order of size magnitude as the target cathode particles and traditional separation approaches (optical sorting, magnetic separation, froth floatation, etc.) are unviable. Without appropriate purification, this fine fraction cannot be directly recycled.

To date, few strategies exist to selectively remove metallic impurities from mixtures of shredded end-of-life material (black mass; BM) while concurrently achieving the target goal of direct recycling: i.e., recovering the active material in maximally intact form. Hydrometallurgical purification strategies typically employ conditions under which all metals (including target cathode active materials such as Li, Ni, Co, and Mn) are converted to ionic form via chemical leaching. These leaching techniques – typically acidic solution-based processes – are highly effective to ionize impurity metals, but also promote the breakdown of the cathode's physicochemical structure. Thus, existing hydrometallurgical approaches are problematic in the context of direct recycling, and new methods are warranted to enable the selective ionization of contaminants while retaining the active material intact. Alkaline aqueous conditions are reported to be nondestructive to metal oxides, and also enable effective ionization of Al<sub>2</sub>O<sub>3</sub> and CuO. However, matrix and process parameters must be optimized to enable rapid and complete ionization of these metals without inducing damage to the cathode active material.

Thus, in the present work, we are optimizing an aqueous dissolution process to ionize solid Al and Cu so that the target cathode active material can be recovered in the solid phase via physical filtration. This “black mass purification” (BMP) approach will ultimately operate in conjunction with a reversible and tunable adsorbent filter to recover ionized metals from solution. The BMP process enables effective purification of trace-level contaminants from shredded BM, and improves the circularity of the overall process line by (1) enabling direct recycling of an otherwise-unusable BM feedstock; (2) enhancing overall component recovery by enabling the selective recapture of metallic contaminants in purified form.

The primary objectives for this task in FY23 were (1) to scale up the contaminant dissolution process optimized in FY21 and FY22 to process  $\geq 50$  g batches of BM; (2) to continue to develop and demonstrate post-treatment rinse procedures to obtain optimal surface properties of the treated cathode material; and (3) to demonstrate integration of BMP process with upstream and downstream ReCell methods.

Efforts towards scale-up were initiated in FY22 with the purchase of a custom-designed 1L reactor (Pope Inc.) and a preliminary set of associated balance-of-plant supplies. As reported in the FY22 annual report, this unit was initially scheduled for delivery by the end of Q1 FY23. However, substantial delays were encountered by the vendor and the reactor was not received until the end of Q2 FY23. In Q2 and Q3, our project team worked closely with NREL's ESH&Q team to spec, design, build, and install local infrastructure to support the safe and effective operation of the reactor and auxiliary equipment. Q3 and Q4 efforts centered around validation of reactor performance, re-developing our work flow at scale, and re-evaluating treatment parameter optima. Reactor validation tests have been conducted on a variety of pristine NMC materials with varying stoichiometries, with the goal of simultaneously obtaining scientifically useful information, e.g., verifying that treatment conditions do not adversely impact the NMC; further exploring the impact of post-treatment solvent rinses on NMC surface chemistry; and baselining pH drift in the absence of contaminant reaction.

Further, the techno-economic analysis (TEA) framework developed in FY22 was expanded in FY23 through collaboration with the EverBatt team at Argonne National Laboratory (Argonne). We have further refined the model for use as a tool to guide our selection of post-treatment rinse conditions. Specifically, tunable

parameters were added to the model to represent several key post-rinse parameters, including the number of rinses, the time per rinse, the pH of the rinse solution, and solvent identity. Adjustments to the cost model allowed us to separately test how changes to these parameters would affect cost outcomes, thereby facilitating a form of sensitivity analysis by which post-treatment conditions can be rationally improved.

This FY, continued effort was also made to further increase visibility of this research. This included a presentation at the US/UK Workshop Series in Electrochemical Energy Storage Research (Golden, CO, July 2023) and publishing a manuscript highlighting the accomplishments of the project to date.

Substantial work in FY23 was centered around the installation and commissioning of a Nutsche Filter Dryer custom 1 L batch reactor (ordered in Q2 FY22; received Q2 FY23). In addition to simply scaling up the prototype bench-scale system developed in FY21 and FY22, the Nutsche reactor introduces a baffling design that will facilitate improved homogeneity of mixing, relative to our previous process. Our previous findings (see Key Publication 1) suggest that this will increase reaction kinetics and shorten overall reaction time, so repeated validation of certain operating parameters such as required run time will be necessary at the 1 L scale. To support the reactor unit, associated local infrastructure and auxiliary equipment also needed to be spec'd, designed, and installed. Selected highlights of the setup and installation work completed in FY23 included:

- (1) Design and installation of a custom-designed caustic-resistant containment environment, including chemically compatible containers and splash guards;
- (2) Design and installation of an internal racking system that enables weight-assisted raising and lowering of the reactor body for material introduction/removal and provides multiple mounting points for reactor stability;
- (3) Design and installation of a vacuum filtration line for more rapid draining of the supernatant following reaction, which included sourcing, electrically modifying, and installing a caustic and high-temperature-resistant diaphragm pump;
- (4) Developing a custom Python program to simultaneously record temperature and pH output signals from measurement probes;
- (5) Extensive discussions with multiple members of ESH&Q team, culminating in a successful Readiness Verification and full ESH&Q and administrative approvals.

The above efforts were nontrivial, given that all components must be materially appropriate for caustic environments and must also be able to withstand the 60 °C reaction temperature. A photo of the completed setup is shown in Figure III.3.19.



**Figure III.3.19 Completed installation of 1L black mass purification reactor (Nutsche filter-dryer).**

A new hire was brought onto the NREL ReCell team in Q2 FY23 to aid with this setup and take over primary operator responsibilities for the scaled-up experimental setup.

Following successful commissioning and safety review of the 1 L Nutsche filter-dryer reactor, preliminary baseline testing was completed as an initial step towards scale-up objectives. Baseline testing included two primary thrusts:

- (1) Baselining pH behavior for the solution matrix at the reaction temperature; and
- (2) Baselining representative pristine samples with varying Ni content.

Experimental testing for the first of these thrusts was designed to both validate proper performance of the reactor (i.e., ensure no adverse reactivity between the alkaline solution matrix and reactor components) and to obtain an empirical temperature/pH baseline for the treatment solution, both with and without the presence of chelating agent (Figure III.3.20). The temperature dependence of pH response is highly solution-specific – and while temperature effects associated with physical changes in the pH probe can be compensated for using the Automatic Temperature Compensation (ATC) methods built into the probe software, the variation of pH electrode potential ( $E$ ) with temperature depends on a solution-specific equilibrium constant  $K_{eq}$  (Eq. 1):

$$E = E^0 - \frac{RT}{nF} \ln K_{eq} \quad (1)$$

For non-ideal multi-component solutions, it is most convenient to determine pH/temperature relationships empirically rather than attempting to calculate via first-principles theory.

Thus, our team conducted a series of baseline tests, where individual parameters were varied rationally to probe specific behaviors. The pH of system with KOH only at room temperature was tested both outside of the reactor and inside the reactor, to ensure that the reactor did not contain any form of reactive contamination that would introduce additional redox activity; the pH was then monitored in the reactor at elevated temperature, to ensure that higher-temperature operation would not induce parasitic redox reactions and to empirically determine the pH of the “background” KOH solution absent chelating agent; and finally, the pH of the full

matrix solution of KOH + chelating agent at the operating temperature was evaluated to provide a robust baseline. The results of these tests are shown in Figure III.3.21 a). It should be noted that obtaining a proper baseline is critical to tie observed pH changes during black mass purification treatment to the progress of the Al corrosion reaction, as discussed in Key Publication 1.

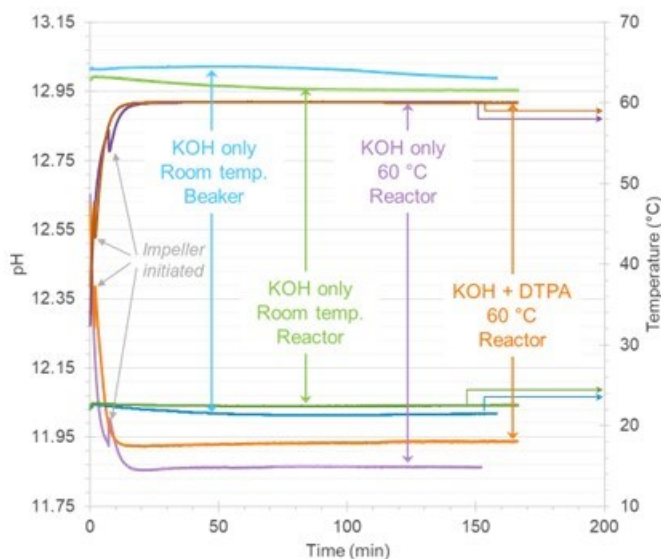


**Figure III.3.20 Summary of rational pH baselining tests for representative matrix solutions, verifying redox stability of reactor components while simultaneously obtaining an empirical pH/temperature background of the specific solution composition used in BMP treatment.**

The second set of baseline tests included a combination of experimental and TEA inputs. Experimentally, a series of commercial pristine NMC powders were processed in the 1 L reactor in 50 g batches. Impeller speed was selected to maximize homogeneity of mixing and minimize “dead zones”, according to qualitative sand-in-water particle distribution tests conducted during reactor commissioning. Following treatment, the NMC was vacuum-filter-dried and recovered. While the primary goal of such testing was to evaluate the impacts – ideally none – on the NMC and to further validate the reactor performance, a secondary benefit was the production of substantial quantities of treated material that could then be utilized in support of our second objective (continued optimization of post-treatment rinse conditions). Thus, following treatment and solids recovery, portions of the treated solids were subjected to a series of rinses with varying solvent compositions. The solvents were selected based on both performance-based chemical rationale and on the results of TEA-informed sensitivity analysis, with the goal being removal of the treatment solvent while avoiding adverse effects such as Li leaching, deposition of undesired residues, or surface-structural damage – all at a minimal process cost. Technoeconomic sensitivity analysis conducted in collaboration with Argonne led us to several important conclusions:

1. Reducing the pH of the rinse solution from 13 (i.e., BMP matrix conditions) to 12 reduces the cost of the overall process by \$0.71/kg-BM, but reducing the pH further (to 11 or 10) only marginally improves cost outcomes, all other factors held constant;
2. Using a 3-step rinse sequence that uses a cheaper solvent for the first two rinses, followed by a more expensive (but materially necessary) solvent for the third rinse reduces the cost of the overall process by \$1.16/kg-BM relative to using the more expensive solvent for all three rinses, all other factors held constant;
3. The number of rinse steps has a substantially greater impact on cost than the time per rinse, all other factors held constant.



A graphical depiction of conclusions based on TEA sensitivity analysis is provided in Figure III.3.21 a), with stars indicating the “baseline” conditions held constant as parameters within a certain category are varied. Further, our refined analysis suggests that even under the most expensive combinations of treatment and post-rinse conditions, the BMP process provides substantial revenue (\$3.4 – \$5.35/kg-BM) by enabling the direct recycling of the fine fraction of shredded material, vs sending this material to a standard hydrometallurgical recycling line.

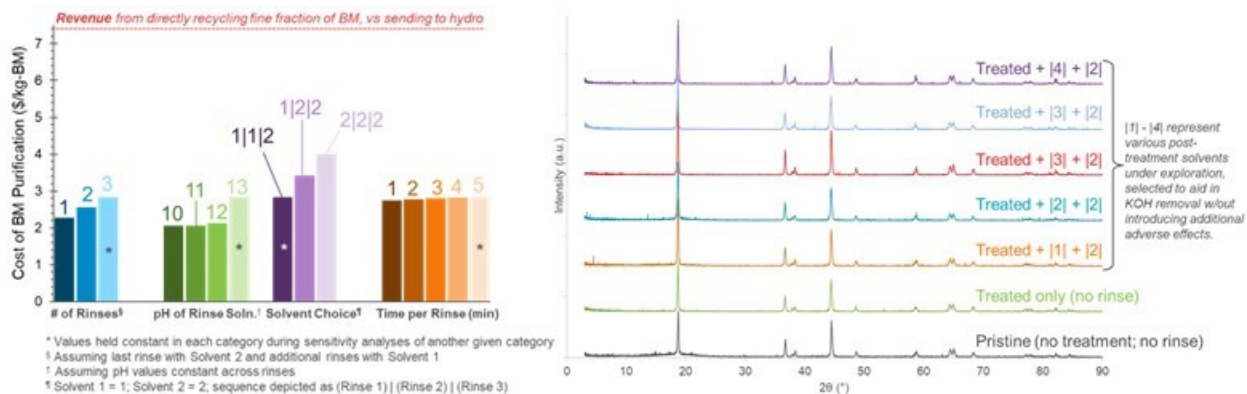


**Figure III.3.21 (a) Technoeconomic sensitivity analysis to evaluate the cost impact of varying several adjustable post-treatment rinse parameters, using the EverBatt model revised this FY; (b) Structural (XRD) analysis of NMC-622 materials following BMP treatment and rinsing with a series of solvents.**

Experimentally, a subset of the combinations shown in Figure III.3.21 was applied to the portions of the 50 g test batches of baseline pristine NMC material. Structural characterization of treated + rinsed NMC-622 is shown in Figure III.3.21 b). It is evident that there is no substantial structural impact of either the treatment process alone or the supplemental rinsing procedure. Additional characterization – including electrochemical full-cell tests and detailed chemical analysis – are underway to further probe the performance distinctions between rinsing treatments and identify optima.

Finally, in FY23 we continued to collaborate with the Cell Preprocessing team at Argonne to source relevant “upstream” material for use in the 1L BMP reactor. Towards the end of Q4 we received cathode-rich fines from manufacturing scrap, both before and after thermal binder removal. The use of manufacturing scrap – rather than end-of-life material – for initial testing will allow us to fine-tune the new reactor with a relatively simple, but still practically relevant, system. Further, the acquisition of material both before and after thermal binder removal enables a systematic evaluation of the impacts of residual binder on process efficacy and the viability of use in subsequent downstream processes. The acquisition of this material represents initial work towards our third objective (integration of BMP process with upstream and downstream ReCell methods), and in particular, reflects integration of the BMP process with cell preprocessing, RE roll separation, and thermal binder removal methods. Following completion of these initial manufacturing scrap tests, we will expand our testing matrix to include additional upstream materials (e.g., solvent-treated material) to determine how the BMP process may best be incorporated into a recycling process line. In FY24, we also plan to coordinate with downstream methods (e.g., relithiation and upcycling) to identify any challenges of incorporating BMP-processed material into their respective techniques. The larger scale (1 L solution / 50 g batches) enabled by the Nutsche reactor will be critical to achieve our FY24 milestones.

### **Direct Recycling Projects (Relithiation)**

#### **Hydrothermal Relithiation**

The direct regeneration method based on hydrothermal relithiation with a subsequent short annealing step developed by UCSD team can successfully resolve the compositional and structural defects of chemically delithiated NCM111 (D-NCM111). It also recovers the electrochemical performance to the same level as the

pristine Toda NCM111 (T-NCM111)<sup>1,2</sup>. The process parameters involved in the hydrothermal and annealing steps, such as temperature, time and the Li-bearing precursor composition, have been extensively explored and optimized<sup>3,4</sup>. Life cycle analysis has revealed that this optimized method substantially outperforms the conventional pyrometallurgical and hydrometallurgical recycling routes in reducing operation costs, greenhouse gas emissions, and energy consumption.

Currently, the team is focusing on refining this method to make it efficient and cost-effective for scaling. Based on this target, the team has successfully scaled up the hydrothermal relithiation process to relithiate 50g cycled NCM622 and 100g delithiated NCM111 in single batches. In this FY, the process parameters are further investigated to develop the hydrothermal relithiation process protocol of NCM111 that supports large-scale regeneration under various practical conditions. The feasibility and scalability of hydrothermal relithiation for delithiated NCM111, spent NCM111, and spent NCM622 will be evaluated through extensive characterization and electrochemical testing. These efforts are crucial for advancing towards the goal of efficient, large-scale battery material regeneration.

In the past four quarters, we investigated the solid-liquid ratio impact on the hydrothermal relithiation process at 100 °C. We successfully demonstrated that the hydrothermal relithiation process could be successfully scaled up to relithiate D-NCM111 in 4M LiOH solution with increased solid/liquid ratio of 1:1 at 100 °C. In a parallel study, we increased the solid/liquid ratio of 0.5:1 at 220 °C for spent NCM 111. We also systematically evaluated washing conditions post-hydrothermal process of both D-NCM111 and spent NCM111, reducing water use by 20x. Excess Li was measured on the surface of the particles, and we validated the effectiveness of using Li residue on the NCM surface from the hydrothermal treatment as the Li source during the annealing step. This way, no Li additives are needed in this step. In addition, we investigated the space occupancy impact of reactants (LiOH solution and black mass) in the hydrothermal reactor during hydrothermal relithiation at 100 °C. We will continue the investigation regarding space occupancy impact in the following FY.

### ***Ionothermal Relithiation***

The objective of this project is to develop a cost-effective ionothermal lithiation process that entails ionic liquids (ILs) or reciprocal ternary molten salts (RTMS) to relithiate and/or upgrade spent cathodes at ambient pressure and low temperature. The unique solvation environment of these ILs and RTMS including negligible vapor pressures, negligible flammability, wide liquidus ranges, good thermal stability provides new reaction or reactive flux media for controlling the formation of solid-state materials with a minimum perturbation of morphologies. During first 3 years of this project, ionothermal relithiation of chemically delithiated NMC111(D-NMC111) was extensively investigated under different reaction conditions. In FY23, the ionothermal relithiation of end-of-life (EoL) NMC622 (SolveY\_ORNL) in RTMS has been investigated at different experiment conditions to lower the overall cost and improve the tolerance to impurities. The techno-economic analysis has been performed using EverBatt model.

A high-temperature flux relithiation method based on RTMS fluxes to relithiate spent NMC622 has been optimized. After optimization of heating processes, the yield of molten salt is up to 90%. By reusing 90% of RTMS for once, the cathode regeneration cost decreases from \$19.21/kg to \$14.88/kg, which is much lower than those of conventional recycling technologies (e.g. \$25.22/kg by conventional hydro recycling technologies, \$30.11/kg by hydro recycling technologies, and \$29.25/kg of virgin powder). (Figure III.3.22)

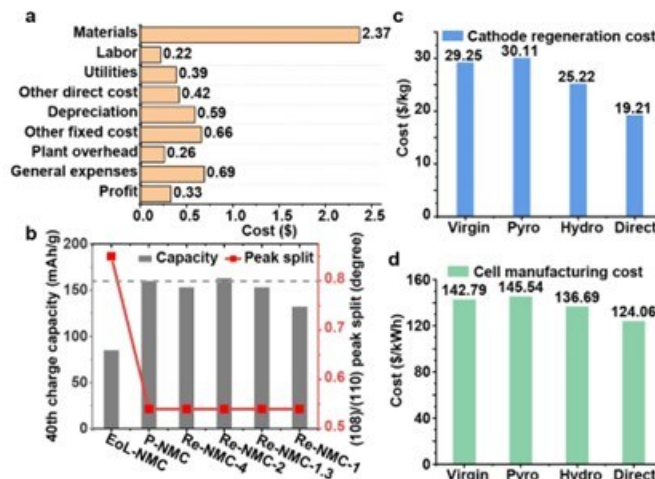


Figure III.3.22 a) Breakdown cost of the direct recycling process in RTMS; b) The 40<sup>th</sup> charge capacities of EoL-NMC, P-NMC, and Re-NMC-x in half-cell tests; Cathode regeneration cost (c) and cell manufacturing cost (d) through different processes. Virgin = virgin production process; Pyro = pyrometallurgy recycling process; Hydro = hydrometallurgy recycling process; Direct = direct recycling process in RTMS.

The influence of impurities in EoL-NMC on the ionothermal relithiation process has been investigated by collaborating with Argonne teams. The removal of P/F-related impurities during ionothermal relithiation process has been validated by the XPS, TGA, NMR, and EDS results.

### Relithiation via Redox Chemistry

The scope of this project is to develop a direct cathode recycling method that utilizes redox mediator chemistry for End-of-Life (EoL) battery cathodes. One of the main characteristics of the EoL cathode is Li deficiencies due to the formation of the irreversible anode SEI layer. We have demonstrated a room-temperature relithiation process using redox mediators. The redox mediators reversibly shuttle charges in an electrochemical cell which deliver lithium ions and electrons from the anode (e.g. Li metal) to the cathode materials with Li deficiencies. The reaction is simple, efficient and fast to relithiate EoL cathode powders.

In FY23, we added a pre-relithiation washing step to remove residual PVDF and LiF from cycled EoL cathode material. We tested several basic solutions to prevent lithium from leaching since acidic solutions are known to leach lithium from EoL cathode material during washing steps. Confirmation of the removal of LiF species after this washing step and the evolution of leftover PVDF byproducts during the relithiation process is shown in the XPS analysis in Figure III.3.23.

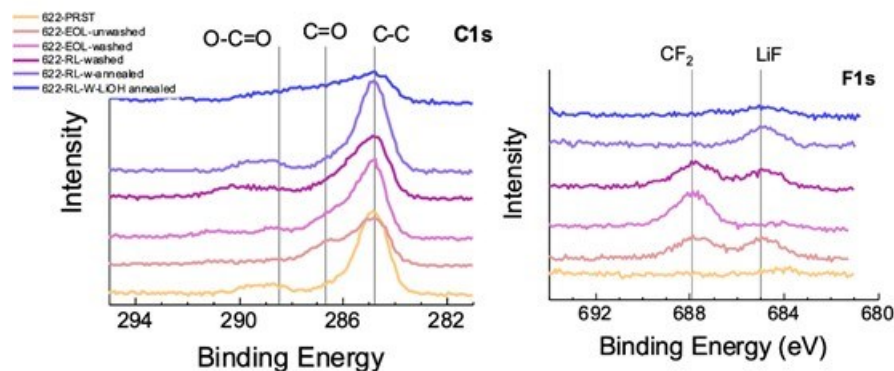


Figure III.3.23 XPS analysis of EoL NMC 622 at each stage of the relithiation process

We also introduced sieving and grinding of the initial EoL cathode material to remove agglomerated particles. The beneficial effect of these mitigation techniques on the reversible C/10 cycling performance of the relithiated material is shown Figure III.3.24.

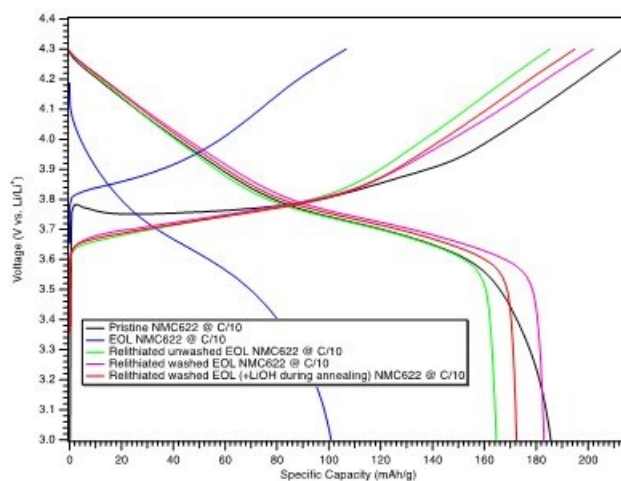


Figure III.3.24 Charge and discharge curves of third cycle at C/10 in half cells of EoL NMC 622 at each stage of the relithiation process

### Chemical Relithiation

Among the first steps of a recycling effort focused on end-of-life lithium-ion cells is the need to ascertain the lithium content of the recovered materials and develop the process to restore that active lithium content. This loss of lithium over time, seen as gradual cycle-to-cycle loss of active lithium is caused by the trapping lithium cations outside the circuit in a variety of irreversible processes (SEI formation, corrosion, and electronic isolation of particles). At approximately 20% loss, various issues including electrode cell balancing, voltage drift, and impedance changes, make the cathodes performance more difficult to predict and the user observes loss of performance. The recovered material's structure is a lithium-deficient version of the starting materials, with further observable structural changes related to the temperature of operation, initial stoichiometry, or processing conditions. Typical structural changes include site mixing of lithium and nickel, surface oxygen loss, and surface structure degradation (crossover, metal dissolution). The relithiation section focuses on a variety of methods to achieve and evaluate relithiation including performance, ease of use, costs, and waste generated to achieve a stoichiometric material.

For the solid-state methods, we have focused this past year on reducing costs and waste materials by going to a significantly decreasing the amount of carrier solvent (to solvent-free) method in association with calculations completed by the EverBatt team led by Qiang Dai (Argonne). In FY22 we showed that the lowest cost method uses a dry coating of the lithium hydroxide (finely ground) followed by a short duration RAM mixing to homogenize the sample. A two-tier anneal stage that allowed the lithium precursor to (1) decompose to active lithia at 350 °C, and (2) and a higher temperature anneal that homogenizes the lithium cation content in the samples. Further studies by CAMP identified a second washing step was needed as there was evidence (electrochemical / analytical) that the sample had an (easily removed by a DMC wash) film coating from the final processing stage.

Similar issues were associated with samples provided initially by ORNLs solvent Y process. The effort is being finalized and set for review publication led by NREL. An initial review publication based on these cross-lab processes has been developing, while a review of the RAM-based materials study has been started in association with the EverBatt team.

## ***Direct Recycling Projects (Upcycling and Cathode Studies)***

### ***Hydrothermal Upcycling***

This project aims to enhance cathode materials by increasing their nickel (Ni) content. It begins by chemically delithiating NCM111, the starting material. However, recycling NCM111 into high-Ni NCM-based materials presents challenges, including unstable surface structures and rapid degradation. To address this, the project focuses on transforming polycrystalline particles into single crystalline particles with higher Ni content and customizable shapes, improving particle structural stability for better performance, implementing hydrothermal processes for eco-friendly recycling, and exploring methods for various cathode states of health (SOHs). These efforts aim to advance high-performance cathode materials, overcoming limitations of low-Ni compositions.

Over the past four quarters, our research has made substantial progress in the transformation of cathode materials. Using a direct sintering process, we successfully converted polycrystalline, delithiated NCM111 (referred to as D-NCM111) into single crystalline materials, including NCM433, NCM622, and NCM811. Notably, we've also achieved a significant milestone by scaling up this process, increasing production from 1 gram to 50 grams. This scalability enhances the applicability of our approach for larger industrial applications.

Our method demonstrates remarkable adaptability, accommodating a diverse range of spent NCM111 feedstock with varying States of Health (SOHs) due to the self-saturation advantage from the hydrothermal reaction. We've validated its effectiveness with spent NCM111 feedstock having different levels of D-NCM111, prepared through chemical delithiation in an  $\text{NO}_2\text{BF}_4$  solution. Additionally, we extended our research to include real spent EV batteries, assessing the potential impact of impurities from battery scraps and electrolytes. This real-world focus addresses practical challenges. To deepen our insights, we conducted comprehensive analyses of the sintering process, including valence and structural changes. Techniques such as X-ray photoelectron spectroscopy (XPS), transmission X-ray microscopy (TXM), solid-state nuclear magnetic resonance (NMR), and in-situ X-ray diffraction (XRD) were employed.

Our ongoing work focuses on understanding differences in surface and bulk properties among the scaled-up samples. This research contributes to the development of advanced cathode materials with enhanced performance and quality, making it a significant step in advancing the field of materials science.

### ***Ionothermal Upcycling***

Beyond the direct recycling, the direct upcycling is to upcycle spent cathodes to the next-generation cathodes, which is of great significance to maximize the value of spent materials and to sustain the fast development of LIBs.<sup>[1]</sup> The key process of upcycling technology is to heal the compositional and structural defects of degraded Li-deficient cathode particles, which can retain the highly added value of cathode particles to the maximum extent. Reciprocal ternary molten salts (RTMS) are those molten salts containing two cation species and two anion species that offer many advantages, such as negligible vapor pressures, negligible flammability, wide liquidus ranges, good thermal stability, and much synthesis flexibility. The objective of this project is to develop a cost-effective ionothermal process to upcycle chemically delithiated NMC111(D-NMC111) to Ni-rich NMCs in RTMS at ambient pressure.

A high-temperature flux method based on RTMS fluxes for upcycling D-NMC 111 to NMC 622 (Up-NMC 622) has been scaled up to 50 g. Up-NMC 622 from ionothermal process exhibited the best performance among different upcycling processes in pouch cell tests at CAMP\_ANL (Figure III.3.25). For the upcycling NMC 111 to 811, the upcycling temperature and heating time have been optimized to be 800 °C and 5 h, respectively to achieve the best rate performance. Different molten salts have been used to control the morphology and surface composition of products. Without surface modification, the first charging capacity of upcycled NMC 811 was close to the pristine NMC 811, but the first cycle columbic efficiency was relatively low (71%). Thus, the surface modification was used to stabilize NMC 811 surface. Now the first cycle columbic efficiency of upcycled NMC 811 has been increased to 77%.

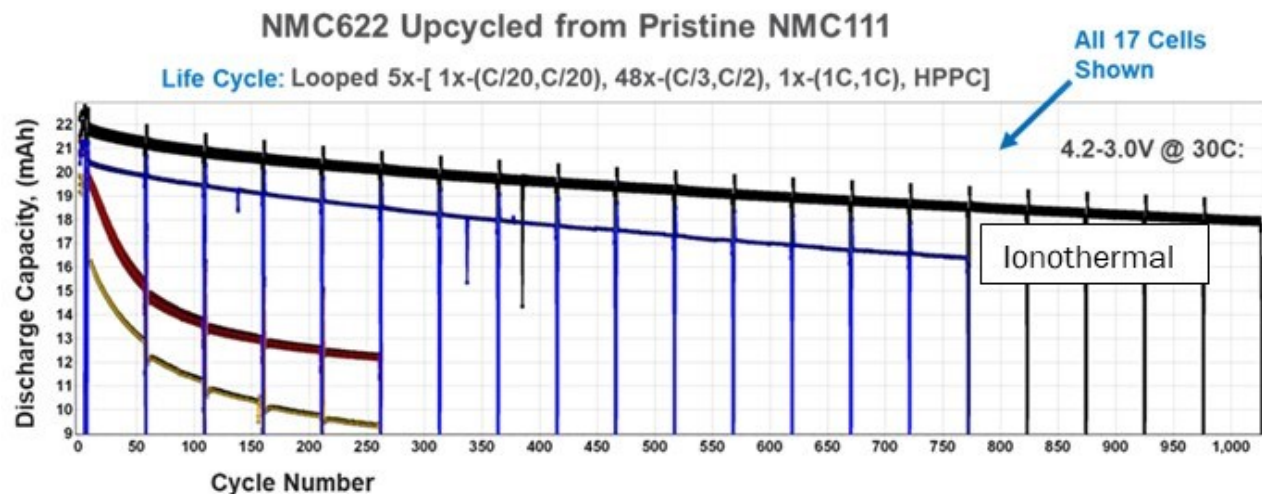


Figure III.3.25 Pouch cell performance of 50 g-scale upcycling products tested by CAMP\_ANL.

The tolerance of ionothermal upcycling method has been investigated by using mixed NMCs as raw material. Two different mass ratios of D-NMC 111 to SolveY-NMC 622 (1:1 and 4:1) were used as raw materials to obtain upcycled NMC 622. Increasing the content of D-NMC 111 in raw materials from 50% to 80% results in the increased first charge capacity of upcycled products from 180 to 200 mAh/g. In addition, the mixture of D-NMC 111 and SolveY-NMC 622 were used as raw materials to obtain upcycled NMC 811. The upcycled NMC 811 exhibited bad rate performance of 75 mAh/g at 1C. After surface modification, the capacity of upcycled NMC 811 increased from 75 to 125 mAh/g at 1C. The effect of SolveY-NMC 622 on the ionothermal upcycling process will be further investigated.

### Solid State Upcycling

Battery upcycling is a process under development that utilizes recovered older generation materials (i.e. NMC333) as a precursor to create current marketable energy storage materials (i.e. NMC622) at a lower overall cost compared to the cost of generating a material from pristine resources (from EverBatt). In addition to the materials available from automotive sources, materials from non-transportation sectors may also play a role in adding anomalous materials to the waste stream, for instance LiCoO<sub>2</sub> from consumer electronics. We are designing and evaluating methods to upcycle the metal ratios of recovered cathode materials to convert them to more current cathode formulations that are more relevant to the marketplace. Our FY23 focus is upcycling our baseline cathode NMC333 (LiNi<sub>0.33</sub>Mn<sub>0.33</sub>Co<sub>0.33</sub>O<sub>2</sub>) system to NMC622 and NMC811. For upcycling, additional details related to the NMC811 cation diffusion and oxide stability will be investigated as NMC811 is less stable (to oxygen loss and surface reduction) than other lower nickel content NMC materials. We are working with cross-cutting teams led by Fulya Dogan (CSE) and Tim Fister (CSE) to employ additional characterization methods that probe the structural changes in the upcycled material.

In FY22 we focused our efforts on establishing the role of (1) defining and controlling the particle growth that results from the upcycling process, and (2) understanding the role of nickel precursor salt in determining the temperature needed to equilibrate the sample and identification of amorphous salt impurities from the associated salt anion. In FY23 we extended our materials collaboration with the Fister group to better understand how the (1) salt anion is carried thru the process and (2) what thermal processes occur at specific temperatures to determine the optimum annealing time and temperature.

For the salt anion study, we were able to identify that the process used, initially focused on acetate and sulfate salts, was an important variable. The nickel acetate salts were found to decompose to carbon dioxide and nano-NiO (near ~280 °C), while the sulfate salt was found to last until ~650 °C with assumed release of sulfur oxides. However, we have noted, from XRD data, the sulfate salts appear to persist as amorphous lithium

sulfates on the electrode surface upon cooling. In a similar surface contamination study last year, this contamination was noted by Alison Dunlop at CAMP as one of the reasons for a slight underperformance of our earlier relithiation samples. A post anneal wash was found to clean the sample surfaces with restoration of capacity.

For the annealing study, we supplied precursor and coated samples to the Fister Group and they were able to identify, at APS, the temperatures of precursor decomposition, the formation of a critical intermediate phase (later identified at a disordered rock salt-like (LiNi)O), and the temperature needed for homogeneity. At this time, we have found that our previous 900 °C /3 h annealing routine gave homogeneous samples with good XRD properties but could be shortened to 1h with maintenance of the desired cation ordering on cooling. Electrochemical studies indicated improved performance, but samples have not achieved the needed NMC622 (or NMC811) capacities. Initial studies indicate that this may be due to a subtle surface re-arrangement caused by the intermediate phase or loss of lithium at the internal interfaces

### **Upcycling via Co-Precipitation Process**

Cathode materials directly recovered from vehicles are about 10-15 years old when they reach their end-of-life (EOL) and are likely to have lower energy density than cathode materials being manufactured today. To increase the profit from a directly recycled cathode, processes need to be developed to increase the capacity to meet modern energy storage needs. Currently, the goal of cathode upcycling is tailored to convert cathodes of lower nickel composition,  $\text{LiNi}_{0.33}\text{Co}_{0.33}\text{Mn}_{0.33}\text{O}_2$  (NMC111), into higher nickel contents, NMC622 and NMC811, to achieve greater capacities. An upcycling approach based on a rapid coprecipitation method first developed by Lipson et al. (ACS Appl. Energy Mater. 2021, 4, 2, 1972–1977) is proposed to accomplish this goal. The NMC111 particles are coated with a  $\text{Ni}(\text{OH})_2$  phase using coprecipitation. The coating reaction is performed in a 4L continuous stirred tank reactor (CSTR) where NMC111 material is placed in the reactor body. A  $\text{Ni}(\text{SO}_4)$  solution is pumped into the reactor, and the drop in the pH of the reaction solution is monitored. Cation migration into the bulk structure is induced during relithiation and conversion of  $\text{Ni}(\text{OH})_2$  to  $\text{LiNiO}_2$  at temperatures above 800°C. The coprecipitation process uses a similar path to the original cathode manufacturing process, which takes advantage of established infrastructure and reduces capital cost due to minimal equipment, short processing time, and low chemical cost. Additionally, the reaction produces highly conformal coatings, which improves the retention of the original spherical morphology during upcycling. During relithiation, the method results in deeper diffusion of the Ni-rich phase, a more uniform composition, and better structural adhesion to prevent spalling during cycling.

In FY23, TODA NMC111 material was used as a baseline to upcycle into NMC622. From initial optimization, we found that NaOH needed to be added to the CSTR alongside  $\text{Ni}(\text{SO}_4)$  to reduce the rate of the pH drop to improve compositional control and achieve higher Ni addition. From these conditions, a bulk composition of  $\text{Ni}_{0.64}\text{Co}_{0.18}\text{Mn}_{0.18}(\text{OH})_2$  was achieved, measured by ICP-OES. EverBatt modeling has been initiated to evaluate the process and determine the input parameters needed. Electrochemical tests of the NMC622 upcycled material, relithiated at 900°C, showed improved capacity ( $163.9 \pm 0.5$  mAh/g) over the baseline NMC111 material ( $154.6 \pm 0.1$  mAh/g) at C/10, 2.0 to 4.3 V vs. Li/Li<sup>+</sup>. Still, capacity retention was significantly reduced, from  $97.302 \pm 0.001\%$  to  $66.55 \pm 0.03\%$  at 50 cycles at C/3.

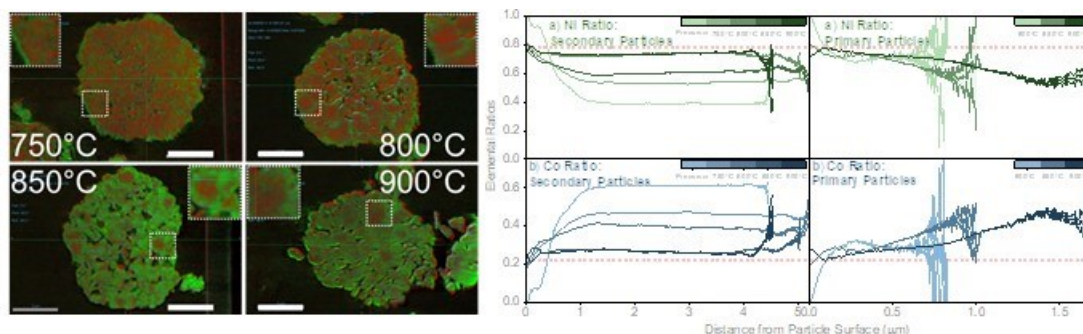


**Figure III.3.26 (left) Cross-sectional slices showing relative Ni (green) and Co (red) content sampled from 3D TXM from a single particle after coprecipitation upcycling and relithiation at four different temperatures. (right) Plots indicating mean 3D Ni and Co ratios as a function of distance from the secondary particle and primary particle surfaces.**

While SEM-EDS did not indicate spatial heterogeneity of Ni content in the secondary particles after relithiation, diffusion limitations of the Ni-rich phase were suspected of contributing to decreased capacity retention and lower capacity compared to commercial NMC622. Pinpointing the diffusion limitations motivated the pursuit of higher-resolution imaging and characterization methods. Tomographic transmission X-ray microscopy (TXM), a non-destructive 3D technique at  $\sim 20\text{-}30$  nm/pixel resolution, was collected at APS. The results are shown in Figure III.3.26. For our study, relative Ni and Co energies were collected from the upcycled NMC622 materials relithiated from 750 to 900°C after the coprecipitation reaction. Using TXM, we quantified significant elemental gradients in 3D, with 99% confidence intervals, comprised of a Ni-rich phase that was distinctly present on the surface of the secondary particles from precursor and 750-800°C. At higher temperatures of 850-900°C, the Ni-rich phase diffused into the secondary particles, but Ni-rich phases remained on the grain boundaries of the primary particles.

#### **Anode Upcycling via Tailored Solvent Treatment**

This project aims to develop a novel approach to “upcycling” spent graphite by using tailored chemical treatment to remove adverse (i.e., highly resistive and/or poorly passivating) species present in the solid-electrolyte interphase (SEI) at end of life while retaining beneficially passivating components of the SEI. When successfully applied, this approach offers several distinct benefits to cell manufacturers. Such benefits include reducing lithiation requirements at the cathode (since  $\sim 10\text{-}15\%$  of the cyclable Li in a virgin cell is irreversibly consumed during formation<sup>1</sup> and reducing or eliminating the cell formation process, which by some reports accounts for nearly 1/3 of the total cost of virgin battery manufacturing.<sup>2</sup> To achieve this outcome, we are exploring various classes of solvent chemistries to alter the identity of the SEI present on as-received end-of-life graphite. A primary aim is *tunability*, i.e., having the ability to draw structure-property-performance relationships between applied solvent(s), removed and remaining SEI species, and electrochemical response of the resulting graphite product.

A critical consideration underlying this effort is identifying which end-of-life SEI products are “good” vs “bad” in terms of their net influence on graphite performance. While the composition and functional purpose of the graphite SEI has been a predominant field of study within the battery community for decades,<sup>3</sup> there is still debate regarding the precise role – whether beneficial or deleterious – of each of the hundreds of potential species, given the difficulty of robustly deconvoluting each species’ contribution to overall SEI stability from confounding factors such as SEI structure, density, thickness, etc. Further, defining success in this task is complex, given that the desire is not to recover pristine graphite performance, but rather to produce an “upcycled” product that offers a distinct benefit over virgin graphite. Thus, in addition to developing a technical chemistry approach to achieve selective SEI removal, the scope of this task also includes developing correlative metrics for graphite performance relative to (tuned) SEI composition, and identifying performance metrics which can be used to evaluate the quality of the upcycled material in a practically relevant context.



The primary objectives for this task in FY23 (its first funded year) included (1) development of an experimentally informed model framework to incorporate and downselect electrochemical validation techniques, i.e., to identify which measured electrochemical properties meaningfully correlate with “good” vs “bad” SEI in aged/upcycled samples; and (2) demonstration of the selective removal of adverse SEI species using tailored solvent treatment. For the second objective, a target of achieving 75% reduction in charge transfer resistance over end-of-life graphite was set before any formal work on the project had commenced. During the course of our research, it became apparent that this target was both not practically measurable and also did not accurately reflect the quality of the upcycling treatment from a performance perspective. Thus, our second objective was expanded to include the development of more realistic and meaningful metrics with which to evaluate the upcycled material.

To achieve our objectives, we divided our efforts into three primary sub-tasks: (1) Experimental treatment of spent anodes; (2) Characterization, including both electrochemical and physico-chemical; (3) Electrochemical modeling using both a refined physics-based pseudo-2D (P2D) single-particle model and equivalent circuit fitting. Task (1) was conducted on a commercial end-of-life anode (cycled 200+ times, to ~80% SOH); tasks (2) and (3) were conducted on a rational material set of pristine and 200+-cycled anodes of a consistent graphite chemistry, all obtained from a single industrial vendor, as well as on the upcycled products. The inclusion of baseline materials (pristine and 200-cycled graphite) under the characterization and modeling efforts provides benchmarks for material performance under the anticipated “endpost” performance conditions, i.e., a theoretical “best case” and “worst case”.

Efforts towards our first objective (experimental treatment of spent anodes) involved developing a robust, reproducible experimental procedure for solvent-based anode treatment. We have presumed that the end-of-life graphite material to be treated will be obtained in a powdered form, and thus the minimum required processing would be the re-casting of this material onto a fresh current collector – which necessitates exposure to a coating solvent. In this case, the impact would be to redistribute all components – including graphite, SEI species, and binder – within the re-cast electrode. To obtain a representative control system involving the minimum degree of treatment, we mechanically liberated the as-received graphite, suspended the liberated material in a coating solvent, and attempted to recast. For this experiment, both heavily cycled (200+-cycled) and materially identical pristine graphite were evaluated. The delaminated/re-cast pristine graphite was readily resuspended into slurry and printed smoothly onto Cu foil; however, the heavily cycled material gelled and produced a chunky slurry that could not effectively be printed onto Cu. Alternative solvents suitable to dissolve for the binder chemistry in the as-received graphite system were also evaluated with the heavily cycled material, producing similar results. This strongly indicates that the “no-treatment” condition of pure resuspension/recasting is not, in fact, viable; and that some degree of selective treatment is required even to obtain a workable electrode for subsequent analysis.

Using structure-property chemical rationale and previous experimental insights, we identified an initial set of target solvents for the removal of hypothetically undesired SEI components. Given that solvent properties strongly influence the nature of the species solubilized, we rationally targeted solvents with a range of properties and anticipated solvation behaviors to evaluate the resulting impact on SEI removal/retention. Throughout FY24, we screened six solvents spanning a range of polarity, proticity, and molecular size. The efficacy of each solvent was evaluated firstly by reprocessibility (i.e., the ability to generate a printable slurry); secondly by electrochemical performance in symmetric-cell configuration; and thirdly by a complementary suite of advanced characterization tools. As mentioned above, the first of these evaluation criteria is nontrivial, and two solvents were discounted from continued analysis due to the inability to recast the treated material. A summary of our electrochemical and physicochemical methods of analysis are briefly described below.

For electrochemical characterization, we developed a symmetric cell protocol to comprehensively probe the anode’s electrochemical behavior while minimizing artificial disruptions to the SEI, e.g., through the presence of an infinite Li source in a traditional half cell. The symmetric cell format also enables us to isolate anode

response from cathode response, as compared to a full-cell configuration where the cathode typically dominates the cell's voltage signal and cross-talk may interfere with SEI evolution. The goal of our electrochemical analysis is to identify electrochemical signals tied to SEI stability/resistance, which may be used to parameterize and validate the electrochemical model and facilitate rapid screening of experimental upcycling treatment conditions. During FY23, the baseline material set (pristine and 200-cycled graphite) as well as all solvent-treated graphite samples were electrochemically analyzed using this symmetric cell approach. In each case, a disc of the target graphite material was assembled into a half cell (vs  $\text{Li}^0$ ) for one cycle of lithiation, and was then disassembled and paired with an analogous aged sample that had not been lithiated. The symmetric cell protocol we developed includes several C/10 “break-in” cycles, impedance analysis, and a series of rate performance tests (C/20 to 3C).

The electrochemical data obtained from the baseline material set, along with select physical material properties obtained through SEM (e.g., particle size and electrode thickness) was then used for initial development and parameterization of a single-particle performance model. The goal of this physics-based electrochemical model is to quantify the penalty of a “good” vs “bad” SEI on kinetic (Butler-Volmer) and transport behavior within an aged graphite particle, and to determine which electrochemical signals are strong indicators of SEI quality in order to facilitate a pared-down test matrix for experimental samples. In particular, the Butler-Volmer kinetic description of overpotential has been adjusted to include an adjustable term to capture the resistance introduced by the SEI, as indicated in Eq. 1-2:

$$i = i_0 \left[ \exp\left(\frac{\alpha_a F}{RT} \eta\right) - \exp\left(-\frac{\alpha_c F}{RT} \eta\right) \right] \quad (1)$$

$$\eta = \phi_s - \phi_e - U(\theta_s, T) - i R_{\text{film}} \quad (2)$$

In FY23, the P2D model framework was established. Preliminary parameter adjustment using the aged graphite samples produced reasonable fits to the experimental data at selected rates; further optimization is underway to fully capture sample performance across all rates and to accurately reflect rate performance data of the upcycled anode samples. We have found that the accessible capacity in the heavily aged samples is substantially reduced relative to the nominal capacity of the graphite; we are continuing to explore the extent to which this capacity reduction can be attributed to SEI obstruction vs physical material loss, e.g. through sample flaking during handling and subsequent cycling. The film resistance ( $R_{\text{film}}$ ) was believed to be a critical parameter reflecting the quality of the SEI, and so substantial effort was directed towards determining an appropriate measure of cell resistance. Resistance can be quantified through the P2D model fits of symmetric cell rate performance data, and can also be validated through equivalent circuit deconvolution of impedance data. Thus, in addition to the P2D model, our team has refined an equivalent circuit model (ECM) that provides a physically meaningful representation of the symmetric cell system and that has been used to extract resistance metrics (e.g., SEI resistance and charge transfer resistance) for the baseline and upcycled graphite materials. Additionally, we have identified a set of “beyond-impedance” metrics that may reasonably reflect upcycling quality. A subset of these metrics is shown in Figure III.3.27 for a set of graphite materials treated with a chemically rational solvent series.

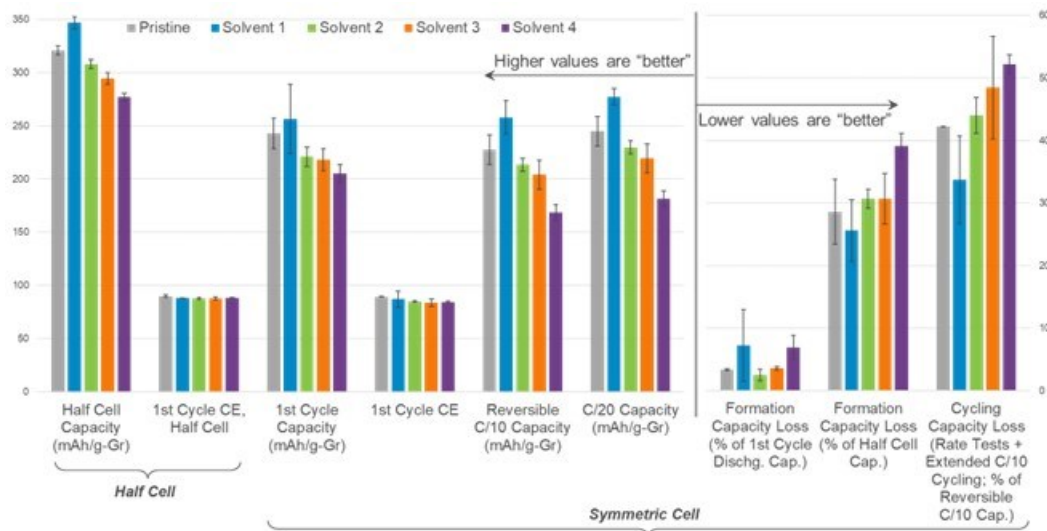


**Figure III.3.27 Selected non-impedance-based electrochemical metrics that may presumably reflect anode upcycling quality.**

Multi-phase characterization is critical to evaluating the impact of the various treatment solvents on the chemistry, structure, and morphology of the upcycled anode material. This FY, we collaborated closely with the Post-Test Facility at Argonne to comprehensively characterize both the baseline material set (pristine, 25-cycled, and 200+-cycled anodes from a single industrial source) and a set of upcycled materials treated with a chemically rational series of solvents. Analyses conducted by the Post-Test Facility included SEM, FT-IR, Raman, XPS, XRD, and GD-OES. These methods were complemented by several additional characterization techniques conducted in-house, including Raman distribution mapping, TGA, and DSC. Further, we devoted substantial effort this FY to improving quantification in our characterization data, e.g., through peak fitting/deconvolution, to extract physically meaningful and materially representative values. We have begun to apply both standard and customized data analysis tools to further probe and quantify XRD, Raman, and XPS data signals. Taken together, this characterization approach offers a holistic view of the physico-chemical state of the anode materials both before and after solvent treatment. This information is crucial to determining precisely how the solvent treatment conditions impact the end-of-life graphite, and how this in turn impacts the materials' electrochemical performance. Through this broad characterization and data analysis effort, we were able to define and extract quantified characterization signals that, when compared to electrochemical performance data, indicate a stable and well-performing SEI – i.e., upcycling success.

This FY, our overarching project goal has been to rationally inform the target properties and performance of the upcycled anode product and concurrently streamline the selection of treatment solvents by identifying which signals (electrochemical and/or physico-chemical) track these target metrics. We have demonstrated substantial progress towards drawing these ties in a quantified manner. In particular, we have conducted broad correlation analysis with all data collected on graphite treated with a rational solvent series according to sub-task 1 (see Approach), drawing on quantified materials characterization metrics developed under sub-task 2 and the quantified electrochemical metrics associated with sub-task (3). We have drawn correlations between (1) solvent properties and materials characterization signals; (2) solvent properties and electrochemical signals; and (3) materials characterization and electrochemical signals. We have identified patterns of strong, moderate, and weak correlation and have emphasized analysis of those properties/metrics showing the strongest correlations. One such sample correlation set is shown in Figure III.3.28.

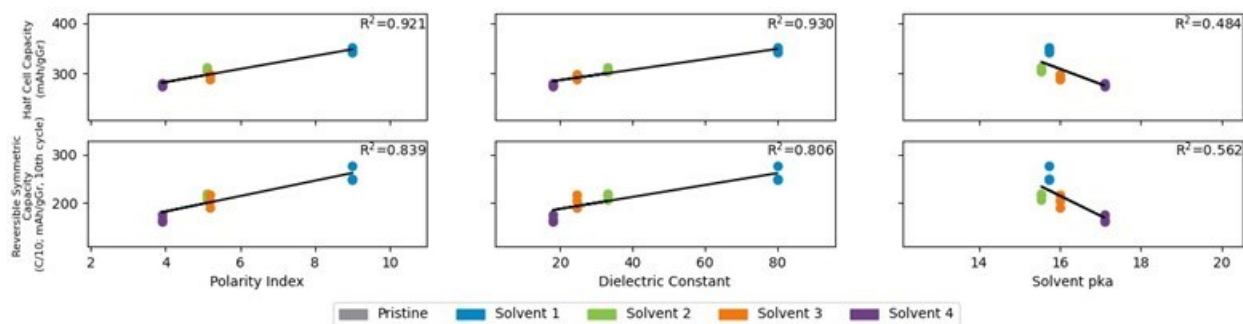


**Figure III.3.28 Selected correlation analysis: Selected electrochemical performance metrics vs treatment solvent properties.**

As evidenced above, we have developed a broad series of metrics that demonstrate both tunability of SEI species removal based on solvent choice and substantial progress towards recovering and, by certain metrics, exceeding pristine material performance. In particular, upcycled material treated with Solvent 1 shows improvements in reversible symmetric cell capacity relative to the pristine material and shows lower capacity loss over the course of extended rate test + C/10 cycling. Additionally, Solvent 2 shows improvements in the percent of capacity lost during initial symmetric cell formation, indicating that less Li is irreversibly consumed to form the SEI – a key goal of this effort. It should also be highlighted that without any form of treatment, the EoL cycled material is not re-castable, so the ability to achieve or exceed pristine material performance through a tailored solvent washing approach represents substantial progress in the first year of this task.

### Single Crystal Cathode Production

Lithium-ion batteries, especially cathode materials, are very dynamic. The cathode materials in spent lithium-ion batteries may not find a market even if high quality materials can be recovered. For example, NMC111 is one of the common cathode materials for EV batteries, however, the industry is moving to high-nickel NMC to increase the energy density and lower the cost. Single-crystal cathode materials hold the promise of better performance in terms of cycle life and rate performance. Conventional cathode materials are secondary particles that include numerous primary particles, which can be potential single-crystal particles. In this project, the team will develop methods to upgrade NMC polycrystal materials to single crystal NMC particles.

We have successfully upcycled polycrystalline  $\text{LiNi}_{1/3}\text{Mn}_{1/3}\text{Co}_{1/3}\text{O}_2$  (NMC111) and  $\text{LiNi}_{0.6}\text{Mn}_{0.2}\text{Co}_{0.2}\text{O}_2$  (NMC622) into single crystal structure on a bench scale. Both upcycled single crystal NMC111 and NMC622 (SC-NMC111, SC-NMC622) showed comparable or better rate and cycle performance than polycrystalline NMC111 and NMC622. Especially, we have successfully scaled up this process for NMC111 with impressive performance. Therefore, in FY23, we will apply this etching process to 83Ni and understand the mechanism of Mn self-coating in the etching process.

In FY23, we synthesized a batch of polycrystal 83Ni cathode by coprecipitation reaction, and applied the etching method to this polycrystal 83Ni, which can avoid the effects of coating or doping elements and increase the Ni content in the final product. The morphology, structure, composition, and electrochemical performance were evaluated by SEM, XRD, ICP-OES, and coin cells.

The polycrystal 83Ni cathode has been converted to single-crystalline 83Ni cathode after 15 hours and 25 hours etching process (Figure III.3.29 a) and c). And Figure III.3.28 b) and d) show that both of them have a layered structure. With the optimized etching and sintering process, the SC-83Ni-25h shows best rate and cycle performance (Figure III.3.29 e) and f). The rate performance of SC-83Ni-25h is the highest compared to pristine-83Ni, commercial 83Ni and commercial 811. And the cycling performance of SC-83Ni-25h exhibits an extremely stability compared to control samples, even though the commercial materials have coating and doping. These results show that the Mn coating layer can effectively suppress structural degradation and side reactions of the enhanced performance of Ni-rich cathode materials.

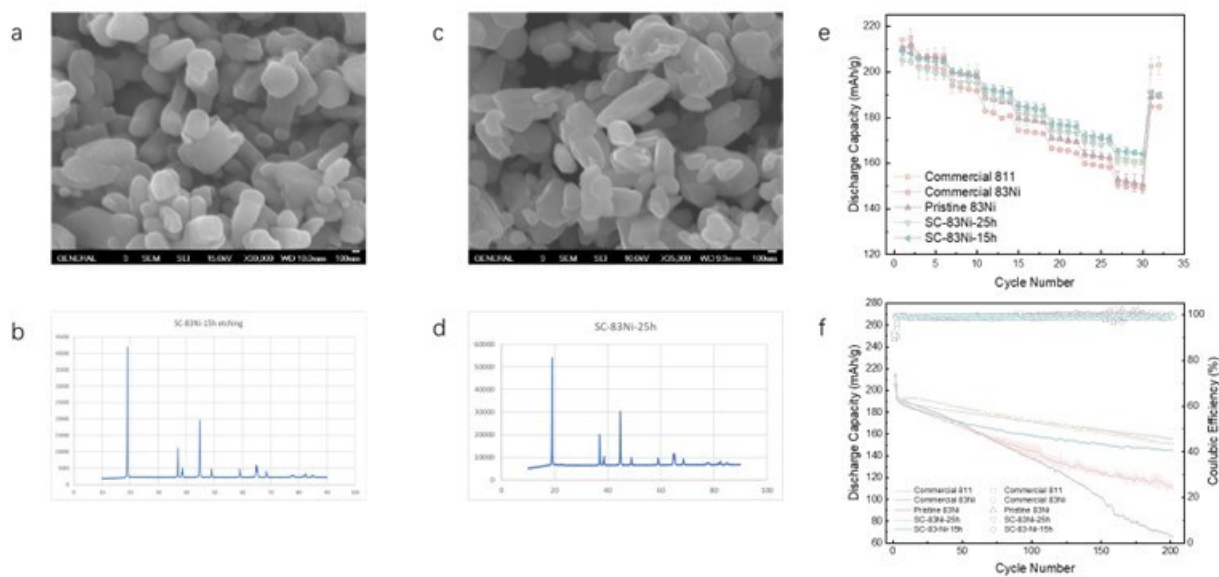


**Figure III.3.29** (a) SEM of SC-83Ni-15h; (b) XRD of SC-83Ni-15h; (c) SEM of SC-83Ni-25h; (d) XRD of SC-83Ni-25h; (e) rate performance comparison between single-crystal cathodes and control samples; (f) cycle performance comparison between single-crystal cathodes and control samples.

#### ***Mechanical Method of Damage Mitigation***

In cathode materials, there is a correlation between electrochemistry and mechanical properties. Cathode particle degradation typically involves particle cracking and lithium inventory loss, both of which affect the mechanical properties of the material. However, even pristine cathode particles have cracks, indicating not all end-of-life cracks need to be repaired to replicate pristine performance. This project focuses on characterizing the correlation between mechanics and electrochemistry in order to optimize the high-temperature annealing step such that it minimizes cost while still restoring recycled cathode particles to pristine condition. The goal is to compare the mechanical properties of pristine versus end-of-life (EoL) versus recycled cathode material and develop characterization methods to easily compare the quality between cathode particles. The project has developed several characterization methods to quantify mechanical properties of cathode particles, including a bulk compression method that measures the average particle properties, and nanoscale computed tomography imaging that shows particle cracking.

Using an Instron and a powder die press, bulk properties such as average particle strength and Young's modulus can be measured. This technique is meant to provide a fast method of characterizing the average properties of different powders and can measure the instantaneous modulus and the creep response of the powder at different stresses. Clear differences between pristine, EoL, and recycled NMC 622 powder were measured, suggesting that this is a useful way to characterize the quality of NMC powders. (Figure III.3.30)

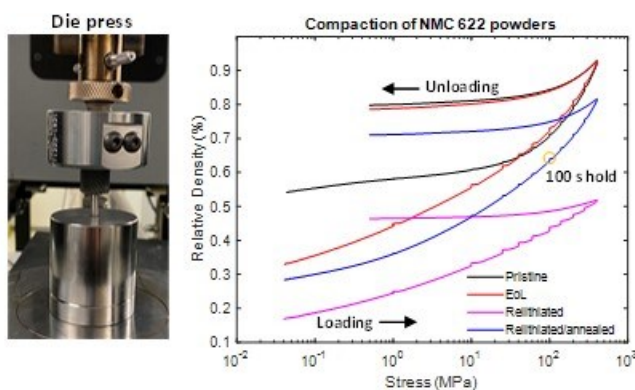


Figure III.3.30 Bulk powder compaction setup and results

Nanoscale CT images of individual particles were taken to see if the annealing step fully fixes the cracking during the recycling process. While these images are not representative of the powder on average, it would seem like there is still some cracking in the fully recycled particle. (Figure III.3.31)

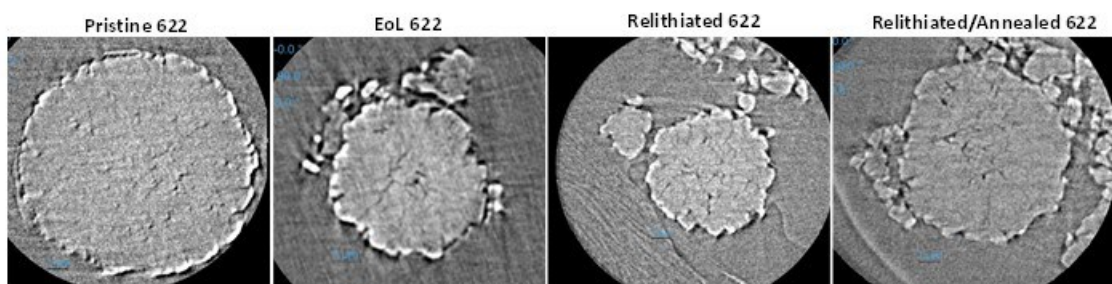


Figure III.3.31 Nano-CT images of different NMC 622 particles

### Advanced Resource Recovery

#### Graphite to Graphene

Recycled graphite from spent Li-ion batteries has a low value as it is typically sold as carbon for steel making. There is an opportunity to increase the value of the graphite by turning it into graphene. Graphene can be used in a myriad of applications including additives to composites for strength and electrical conductivity, coating material for carbon fibers, printed electronics, and lubricants. This project aims to scale-up a process for making graphene from spent Li-ion battery graphite, and then prove that it can be used in various applications.


We have successfully scaled the process up to 500 g of graphite in a batch, which produces about 50 g of graphene. Yield and the characterization of the graphene was similar to that produced in the smaller batch. This graphene has then been processed by the University of Virginia into composite materials. However, the results have shown a lot of variability. Further investigation revealed that there were bubbles in the test bars that were controlling the properties of the material. This is currently being rectified via vacuum processing and should give more reliable mechanical property measurements.

In addition to work on graphene itself, this project also looked at the other materials that would be produced when you separate out the graphite in our direct recycling process. This includes looking at separation methodologies. We utilized optical sorting to separate copper from aluminum to get a clean copper fraction. Two stages are needed to get high sorting efficiency largely due to the shape and size of the battery shreds, which makes them occasionally fly to the wrong side of the sorter. Overall, the copper fraction has greater than 98% purity when melted (combustibles burned). The aluminum or reject fraction still has a mixture of

materials primarily because they are attached in clumps, although there is a small amount of copper. The middling fraction would typically be recycled to the start of the sorting process and at 15% this is a reasonable approach. (Figure III.3.32)

Sample	Copper (%)	Al containing (%)	Combustible (%)	Clumps	% of total
Accepts	97.4	1.4	1.2	0	50.9
Rejects	4.3	42.6	4.1	49.1	32.5
Middling	64.2	18.9	8.1	8.9	14.7

**Rejects**



**Accepts**




Figure III.3.32 Results from two stages of optical sorting to get a copper and aluminum fraction.

**Microwave Assisted Extraction**

The goal of this project is to use microwave assisted extraction (MAE) as a process intensification technique for hydrometallurgical battery material recycling. MAE has the potential to require reduced amounts of solvents and lower acid concentrations which would directly address the main drawbacks of hydrometallurgical processes. The optimization of this process will include experimenting with acid concentration, composition, temperature applied and reaction time. The end goal of this optimization is to incorporate the finding into EverBatt to calculate extraction cost predictions and collaborate with other ReCell recovery efforts.

In FY23, batch tests were conducted with citric acid at a low concentration of 0.5M to optimize temperature and hold time during the microwave reaction for full digestion of NMC 622. The leachate from the microwave reaction was filtered directly after the heat treatment to remove undigested solids and the recovered solution was evaluated with ICP OES to determine the weight percent digested. The results of this ICP OES analysis are shown in Figure III.3.33.

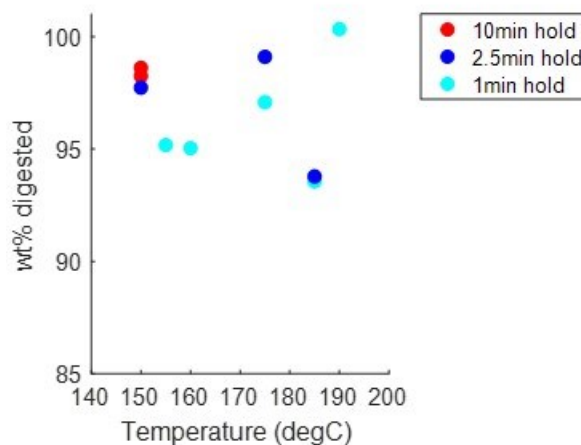


Figure III.3.33 Weight percent of NMC 622 digested by MAE determined by ICP OES analysis

There is a clear trend that temperatures above 150 °C lead to greater weight percent digestion with successful digestion in hold times as low as 1 minute. Another important factor to track for MAE parameter optimization is the energy consumed by the microwave based on the applied power which is shown in Figure III.3.34. The total energy consumed during each reaction is higher for longer reaction times at lower temperatures which is indicative that the optimal reaction protocol should include higher temperature for shorter hold times.

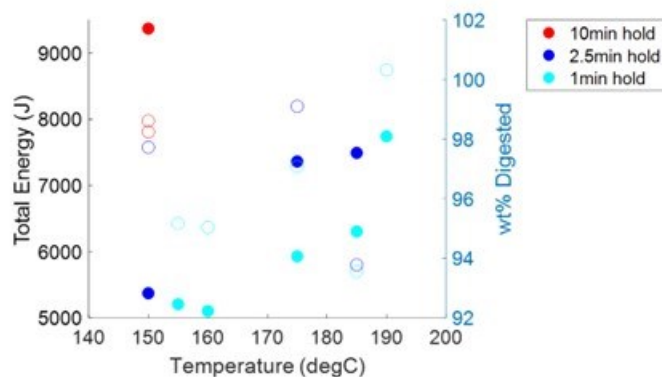


Figure III.3.34 Energy consumed by MAE reactions along with weight percent digested of NMC 622 during the reaction

### ***Electrometallurgical Extraction and Recycling Using Molten Hydroxide Salts***

Recycling critical metals from Li-ion batteries is necessary to improve battery production sustainability and support a domestic battery supply chain. Pyrometallurgical processes produce Co and Ni alloys from used cathodes at elevated temperatures (> 1000 °C) using coke as a reductant and producing CO<sub>2</sub>. Decreasing the process temperatures and using chemistries that do not produce CO<sub>2</sub> to extract critical materials from Li-ion batteries would improve sustainability of Li-ion battery recycling while providing a domestic source of critical metals.

The overall objective of this project is to develop a recycling route that uses low melting-temperature molten hydroxide salts to electrochemically recover transition metals from Li-ion cathode materials. This method uses a two-step process to recover transition metals. In step one, cathode material is immersed in the salt and electrochemically reduced to dissolve the transition metal ions into the salt. In step two, the dissolved transition metals are electroplated onto a separate cathode. This is a new project with an initial objective to demonstrate feasibility of this recovery process with fresh NMC 622 powders and black mass materials.

The work performed in FY23 focused on identifying process parameters needed to extract Ni and Co from NMC materials in molten hydroxide salts, including the hydroxide salt composition and treatment conditions necessary to achieve extraction of the transition metals. Scoping tests were performed using fresh NMC 622 and 111. Additionally, recovering transition metals from black mass was investigated.

Salt solutions of LiOH-KOH and NaOH-KOH were tested to determine the effect of salt composition on transition metal recovery. Tests performed in LiOH-KOH were successful, recovering transition metal alloys from NMC. Tests performed in NaOH-KOH did not result in metal recovery. Additionally, the moisture content of the LiOH-KOH salt significantly impacted the process chemistry and metal recovery. Tests in hydrated salt resulted in direct oxide reduction of the NMC to a mixed alloy, preventing recovery of individual transition metals. Tests in dry salt resulted in reduction of NMC to a soluble form and dissolved transition metals into the salt. The transition metals could then be electrodeposited and recovered from the molten salt.

Cyclic voltammetry (CV) was used to monitor the chemistry of the molten hydroxide salt during testing. The electrochemical window of the salt increased significantly after drying the salt. After reduction of NMC to soluble species (first process step) was performed, multiple electrochemical peaks were observed in the CVs of the salt. In the second process step, electrodeposition at different voltages resulted in recovery of different alloy compositions, indicating that the composition of the recovered metal alloy can be controlled. Further investigation of the electrodeposition of the individual metals is necessary to refine processing conditions for selective separation.

A test with black mass material demonstrated similar behavior to NMC in the process and only metallic components were collected at the deposition cathode. Some Al and Cu contamination was observed in the



deposition product from this test. Further testing to define the electrochemical behavior of Cu and Al in the molten hydroxides is necessary to define appropriate processing conditions that prevent Cu and Al contamination in the Ni and Co product.

#### ***Ionic liquid based supported membranes for Li/Co/Mn separation***

Critical metal recovery from spent lithium-ion batteries (LIBs) is crucial for ensuring metal sustainability and environmental safety.<sup>1, 2</sup> Lithium, cobalt and nickel, major components of LIB cathodes, face increasing demand due to the rapid growth of portable electronics and electric vehicles, posing challenges to their supply chains and environmental impact. Solvent extraction, adsorption, ion exchange, and electrowinning are the technologies used to recover and recycle these metal ions. These separation methods have disadvantages, such as toxic waste generation, expensive, energy-intensive, and required high volumes of extractants. To address these challenges, it is essential to develop a cost-effective, efficient separation method that does not require a high volume of extractant, making the process ecofriendly by reducing the carbon footprint. An ion-exchange polymer inclusion membrane (IEPIM) is designed to separate lithium, cobalt, and nickel ions from lithium ions in aqueous solutions. This IEPIM is composed of a polymer host (PVDF-HFP), an extractant, and a plasticizer. The separation strategy is based on proton pumping, which is driven by the pH gradient between the feed and stripping solutions and facilitates the metal ion transport through the membrane. This process is based on the ion exchange principle, where protons are exchanged for cobalt and nickel ions at the membrane interface, enabling their selective separation from lithium ions. The IEPIM effectively separates cobalt and nickel from lithium ions in aqueous media, achieving a remarkable transport efficiency exceeding 90%. The objective of this project is to develop easily scalable low-cost smart membrane-based separation of electrode materials (Li, Co, & Ni) from spent LIBs.

An IEPIM containing extractant (Cyanex 301) and ionic liquid ( $[[C_8mim][NTf_2]]$ ) (membrane 1) were synthesized for simultaneous separation of Co and Ni from Li ions and second IEPIM containing P<sub>66614</sub>Cl as extractant and a plasticizer (membrane 2) were synthesized to separate Co from Ni (as shown in Figure III.3.35).

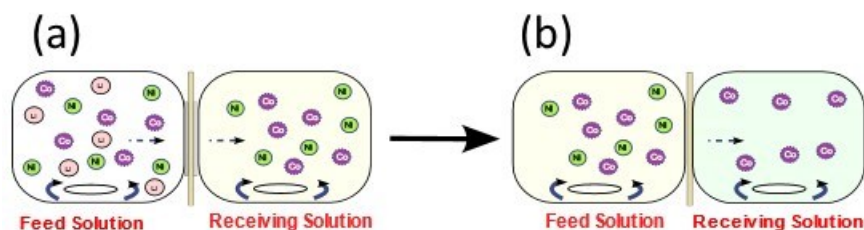


**Figure III.3.35 Schematic illustration of membrane-based separation of Li/Co/Ni separation. (a) separation of Co and Ni from Li ions using membrane 1 (IL-based membrane with Cyanex 301 extractant; (b) separation of Co from Ni ions using membrane 2 ( IL-based membrane with P66614Cl as extractant).**

~ 90 % Co<sup>2+</sup>, & Ni<sup>2+</sup> ions were simultaneously separated from Li<sup>+</sup> ion from 0.1 mM aqueous solution of Li<sup>+</sup>, Ni<sup>2+</sup>, and Co<sup>2+</sup> using Membrane 1 (see Figure III.3.36 a) and b). This membrane demonstrated good stability over 3 successive transport cycles for 16 days of continuous use (see Figure III.3.36c). Then Co<sup>2+</sup> & Ni<sup>2+</sup> ions solution was separated with purity ~ 90 % using membrane 2 (see Figure III.3.37 a) and b) with robust membrane stability over 3 successive transport cycles for 16 days of continuous use (see Figure III.3.37c). Overall, this process resulted in the separation of Li<sup>+</sup>, Co<sup>2+</sup>, and Ni<sup>2+</sup> ions from the aqueous solution with an overall purity of ~ 90%.

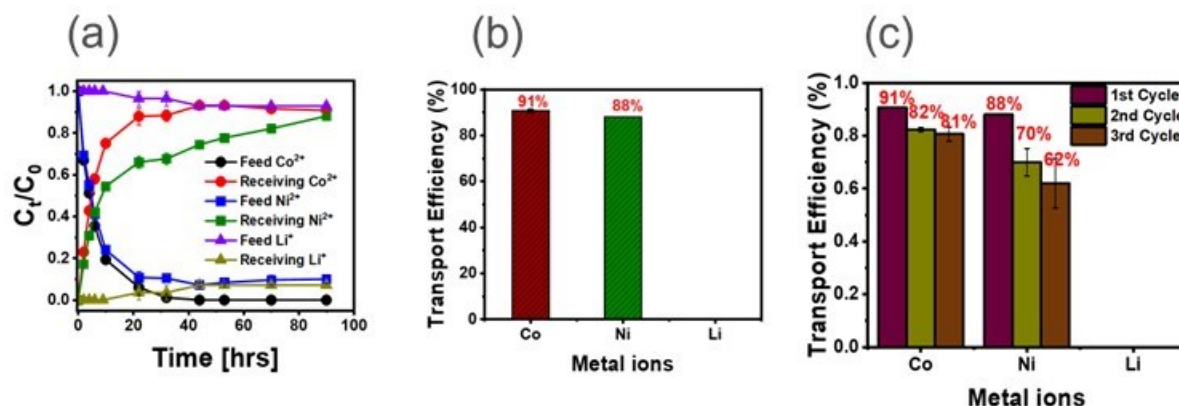


Figure III.3.36 (a) Change in concentration of  $\text{Li}^+$ ,  $\text{Co}^{2+}$ , and  $\text{Ni}^{2+}$  ions during transport experiment with membrane 1; (b) Bar graph showing the percentage of separated metal ions; and (c) % metal ion separation during successive 3 transport cycles.

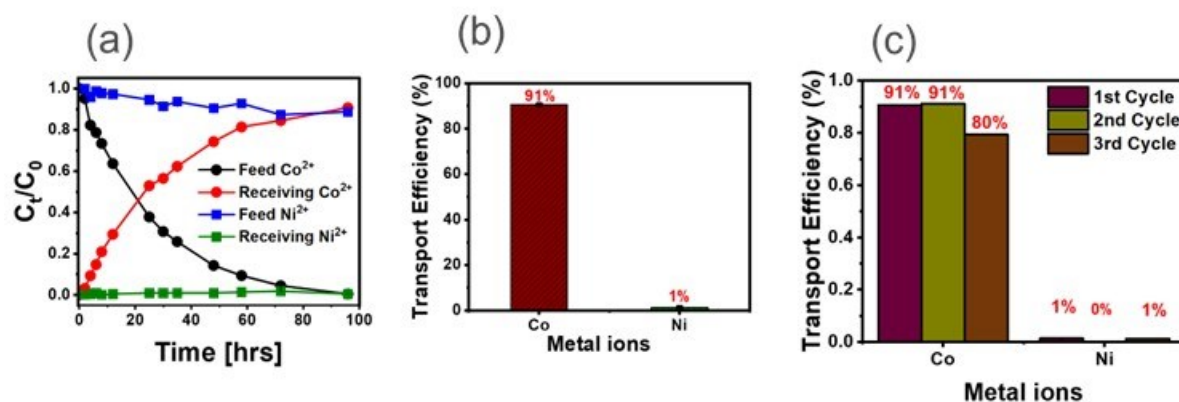


Figure III.3.37 (a) Change in concentration of  $\text{Co}^{2+}$  and  $\text{Ni}^{2+}$  ions during transport experiment with membrane 2; (b) Bar graph showing the percentage of separated metal ions; and (c) % metal ion separation during successive 3 transport cycles.

To shorten the process, we designed the transport apparatus for sequential separation of  $\text{Li}^+$ / $\text{Co}^{2+}$ / $\text{Ni}^{2+}$  ions simultaneously (see Figure III.3.38) using membrane 1 and 2.

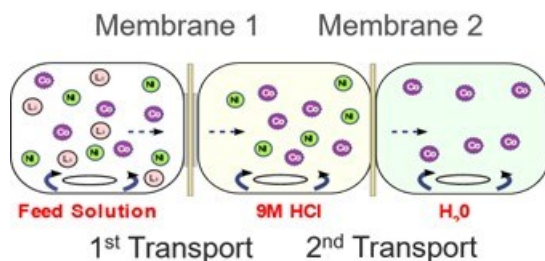


Figure III.3.38 Schematic illustration of membrane-based sequential separation of  $\text{Li}^+$ / $\text{Co}^{2+}$ / $\text{Ni}^{2+}$  ions using membrane 1 and 2 together.

Overall, 85% of  $\text{Co}^{2+}$ , & 62% of  $\text{Ni}^{2+}$  were separated sequentially while 87% of  $\text{Li}^+$  remained in the feed solution (see Figure III.3.39). This process saves times and allows the separation of the ions in a single process. However, the process needs to be optimized to get a better transport efficiency.

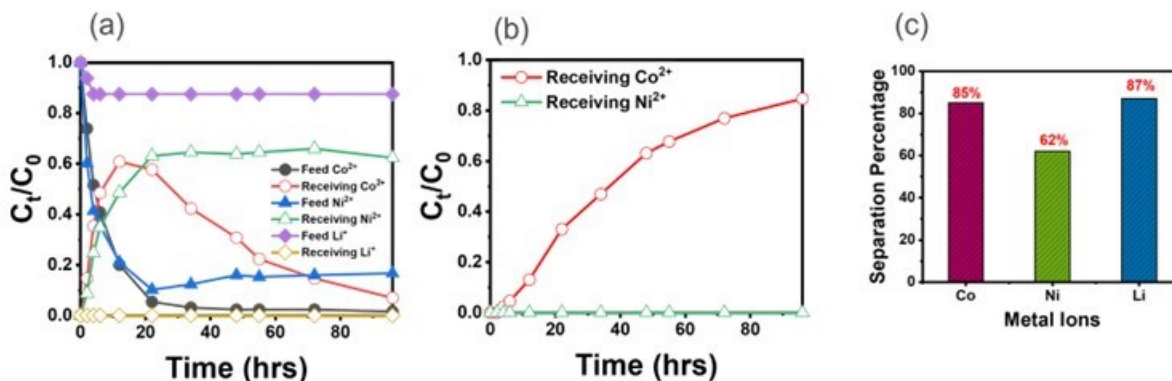


Figure III.3.39 (a) Change in concentration of  $Li^+$ ,  $Co^+$ , and  $Ni^+$  ions during first transport experiment with membrane 1; (b) Change in concentration of  $Co^+$ , and  $Ni^+$  ions during second transport experiment with membrane 2; and (c) Bar graph showing the percentage of separated metal ions.

#### **Separation and Recovery of Cathode Active Materials from End-of-life LIBs using Membrane Solvent Extraction**

The overarching goal of this project is to demonstrate the scalability, reliability, and cost-effectiveness of advanced recycling technologies such as membrane solvent extraction (MSX) technology to separate and recover critical materials from EOL electric vehicle (EV) LIBs in order to meet the growing demand and to establish a domestic source for these critical materials. It will provide end-to-end processing of EOL EV battery materials from black mass to remanufacturing of new EV cells.

The main research milestone of FY23 was to produce 100g quantities of high purity cathode active materials (Co, Li, Ni) using an energy efficient cost-effective, and environmentally friendly membrane-based technology from EOL EV batteries. This was via membrane solvent extraction (MSX), a single step continuous process can be linearly scaled up while requiring low chemical usage, energy consumption, and cost, while generating low amounts of overall waste. Successful completion of the milestone dictates that the recovery of these cathode active materials be  $>90\%$ , with  $>99.5\%$  component purity.

FY23 began with assembly of an 8 m<sup>2</sup> surface area polypropylene membrane-based MSX system with an automated pH control system for individual element extraction. This larger surface area ensured the ability to separate adequate amounts of cathode active materials while also demonstrating scalability of the MSX process. EOL LIB black mass is dissolved in 2M H<sub>2</sub>SO<sub>4</sub> to make the feed solution for the MSX process. Impurities (non-cathode active materials often found in LIBs such as Fe, B, Al, Cu) were removed from the feed solution using MSX with DEHPA as an extractant. This impurity removal increased feed solution purity from  $\sim 55$  wt.% cathode active materials to  $>99.5$  wt.%. Separation of individual cathode critical elements is done via MSX, using Cyanex 272 as an extractant and controlling pH for selective precipitation of critical elements from solution in their oxalate form using oxalic acid. Cobalt is the first to be extracted from the mixed material solution via selective precipitation from solution, then Lithium and Nickel are separated afterward by precipitating Nickel with an additional pH shift in the same extractant solution.

Some process modifications were made to include a pH controller which provided the ability to precipitate individual LIB cathode materials. Stage 1 using DEHPA extractant successfully removed undesired impurities, yielding a combined purity of cathode active materials of over 99.5%. 117 g of CoSO<sub>4</sub> and 102 g of NiSO<sub>4</sub> were recovered from 20L of this purified feed solution after 78 hours of total system runtime. Cobalt was recovered from the blend of cathode active materials at  $>90\%$  recovery with  $>99.5$  wt.% purity in the second MSX stage using Cyanex 272.

### Electrodialysis to Extract Lithium from Recycling Process Streams

During lithium-ion battery recycling, lithium can end up in solution (e.g., water, ionic liquid, ethanol, etc.) from a recycling process for a variety of reasons. For example, the lithium may come from the electrolyte, lithium could be leached from electrodes especially in water, and lithium can be added to a solution as part of the process. With the limited supply of lithium available in the United States, it will be critical to recover this lithium from rather than disposing of it as waste. In this project we have focused on collecting and analyzing waste streams from various ReCell lithium-ion battery recycling processes (e.g., electrode washing and solvent-based relithiation) to determine how much lithium, and potentially other critical materials or impurities, are present in solution and can be recovered to add value to a recycling process. As part of the recovery process, we also investigated methods to convert lithium to a product (i.e., lithium hydroxide) that could be reintroduced into the lithium-ion battery supply chain.

For this project, we purchased and installed bench-scale electro dialysis and reverse osmosis systems at Argonne National Laboratory. Water samples from anode washing and relithiation experiments were collected during this fiscal year and analysis showed that lithium contents ranged from ~200-3500 ppm. For most samples, other impurities (i.e., Al, Co, Cu, K, Mn, Na, Ni) were measured in solution below 30 ppm. Depending on the sample, the main salt components detected in anode wash water were lithium carbonate ( $\text{Li}_2\text{CO}_3$ ) and lithium fluoride ( $\text{LiF}$ ). Experiments were conducted using electro dialysis and reverse osmosis to determine operating parameters for recovering lithium from process water and converting it to lithium hydroxide. During the project,  $\text{Li}_2\text{CO}_3$  was successfully concentrated from solution using a benchtop standard electro dialysis (SED) system and converted to  $\text{LiOH}$  using a benchtop bipolar membrane electro dialysis (BPED) system (Figure III.3.40).

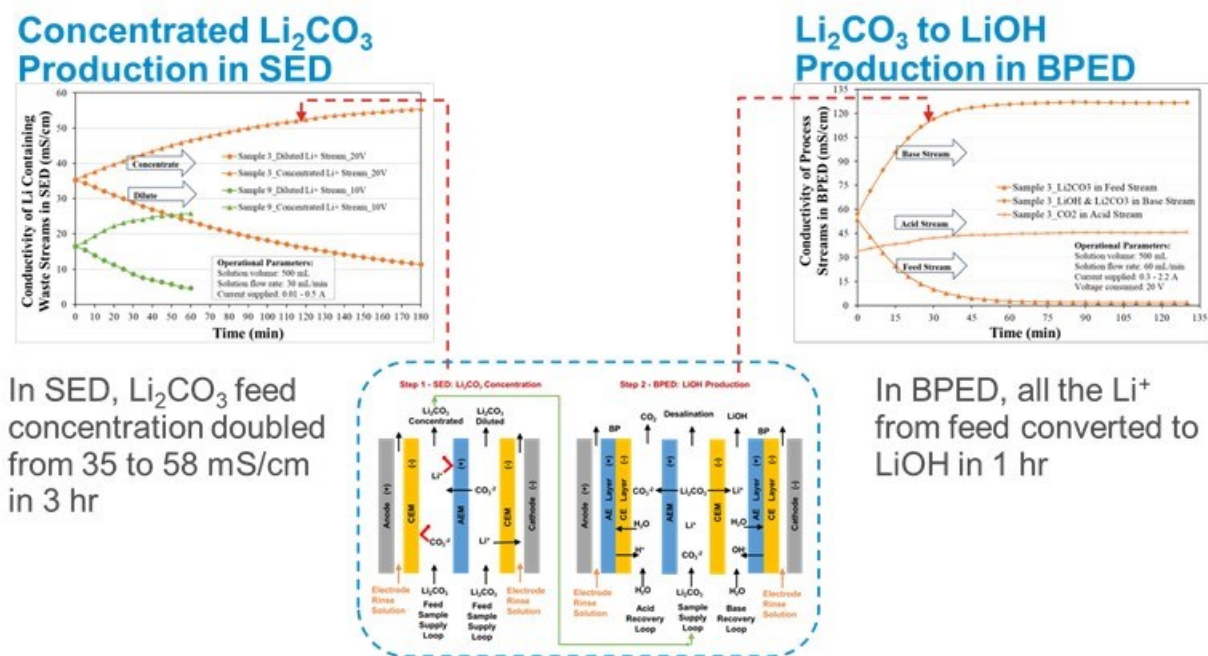


Figure III.3.40 Electro dialysis results for recovering lithium from an anode wash water sample and converting it to lithium hydroxide ( $\text{LiOH}$ )

### Using Sorbents to Recover Critical Materials from Leachate Solution

Lithium-ion batteries plays an essential role in the electrification of the transportation sector, and battery demand for lithium compounds will see a significant increase in the upcoming decades. This has raised concerns on the supply of lithium and as a result, technologies are being developed to process unconventional lithium sources. Lithium, Cobalt, Nickel and Graphite have been identified as the critical elements and is essential for US energy security. To improve domestic supply chain and reduce the import of critical minerals,

team is well poised to address the technology opportunities to increase critical mineral supply. The knowledge gained from the earlier work on sorbents can be used to selectively extract lithium from the end of life LIBs. The main goal is to develop processes to produce battery grade precursor materials and work with potential industry partners and teams and enable a pre-commercial critical mineral recovery plant in the United States. The objective of this project is to develop a cost-effective sorbent to recover lithium from the leachate solution.

Aluminum hydroxide,  $\text{Al}(\text{OH})_3$  has been developed as a novel sorbent to selectively extract lithium from the leachate solution. Aluminum hydroxide, an abundant mineral found in nature, exists in four polymorphs: gibbsite, bayerite, nordstrandite, and doyleite. From the high-temperature oxide melt solution calorimetry studies, the enthalpic stability order was measured to be gibbsite > bayerite > amorphous  $\text{Al}(\text{OH})_3$ . The least stable form, amorphous  $\text{Al}(\text{OH})_3$ , undergoes a reaction with lithium, resulting in the formation of a stable layered double hydroxide phase. Consequently, amorphous  $\text{Al}(\text{OH})_3$  shows promise as a sorbent material for selectively extracting lithium from the downstream leachate solution from the black mass. The schematic of the circular economy developed for the  $\text{Al}(\text{OH})_3$  sorbent is shown in Figure III.3.41. About 3.6 g of  $\text{Al}(\text{OH})_3$  was hydrothermally treated in a Teflon-lined autoclave (50% filling) with 20 mL of leachate solution

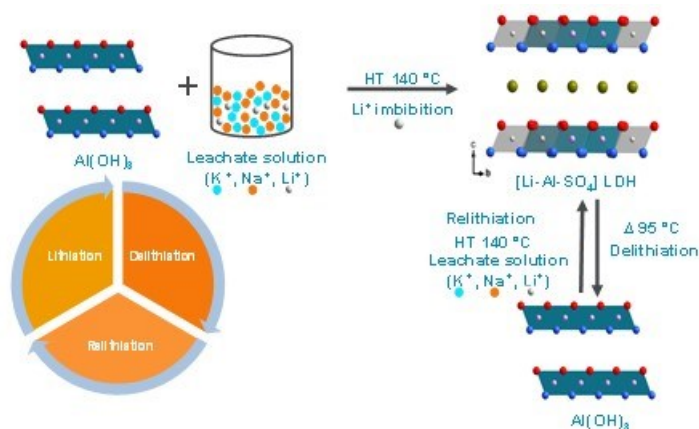


**Figure III.3.41** The schematic of the circular economy model developed using  $\text{Al}(\text{OH})_3$  sorbents.

(containing  $\sim 8,000$  ppm of Li and 17,000 ppm of Na) at  $140^\circ\text{C}$  for 18h. The resulting  $[\text{Li-Al-SO}_4]$ LDH  $[\text{Li}_{0.89}\text{Al}_2(\text{OH})_6(\text{SO}_4)_{0.45} \cdot 1.8\text{H}_2\text{O}]$  solid particles were separated by centrifugation followed by repeated washing with distilled water and air drying. The ICP OES results indicate the recovery of lithium almost 90% in a single step. About 0.5 g of  $[\text{Li-Al-SO}_4]$ LDH along with 50 mL of distilled water were taken in a round bottom flask, and the mixture was stirred continuously at  $95^\circ\text{C}$  for 24 has described elsewhere. The round bottom flask was attached to a condenser to minimize vaporization. Further steps of delithiation with distilled water were carried out from the air dried partially delithiated sample from the previous step, until all the lithium was removed from the LDH structure in four consecutive steps. About 0.25 g of completely delithiated LDH was hydrothermally treated in a Teflon-lined autoclave with 65 mL of simulant solution at  $140^\circ\text{C}$  for 18 h. The washing and drying steps were followed as mentioned above for the lithiation. We observed the relithiation of the sorbent. Hence, we demonstrated that the reuse of  $\text{Al}(\text{OH})_3$  sorbent to recover lithium from the leachate solution.

### **Continuous Extraction - Hydro Process**

This project will deliver a faster and less complicated separation and purification process for nickel sulfate, which is the standard material used for cathode material synthesis. Membrane systems mimic counter-current extraction but increase the separation efficiency and use less solvent for a greener sustainable process. Standard mixer/settlers need significant time for layer separation. Membrane technology speeds up processing since it does not require waiting for gravity separation and can readily separate emulsions. The elemental composition of the black mass will be determined using ICP-OES. Simulated solution that mimics the metals in the black mass will be prepared using analytical grade metal salts. Extraction of Mn, Co will be harnessed

while Impurities (Fe, Cu, Al) will be selectively removed D2EPHA/ CYANEX 272 via continuous flow and membrane separation technology. Selective stripping of metals from loaded extractant will be performed and the extractant will be regenerated and reused severally. The purified nickel solution will be concentrated and crystallized to provide ultra-high purity nickel sulfate.

Results are shown in Figure III.3.42. We have demonstrated that Fe, Mn, Al, and Cu are easily extracted, leaving a raffinate rich in Co, Ni, and Li. Mn is readily stripped from Mn and Al, and the extractant can be purified and re-used multiple times without degradation in performance. The Mn stripped solution is relatively high purity (97%) with some Co and Ni co-extracting (Table III.3.3).

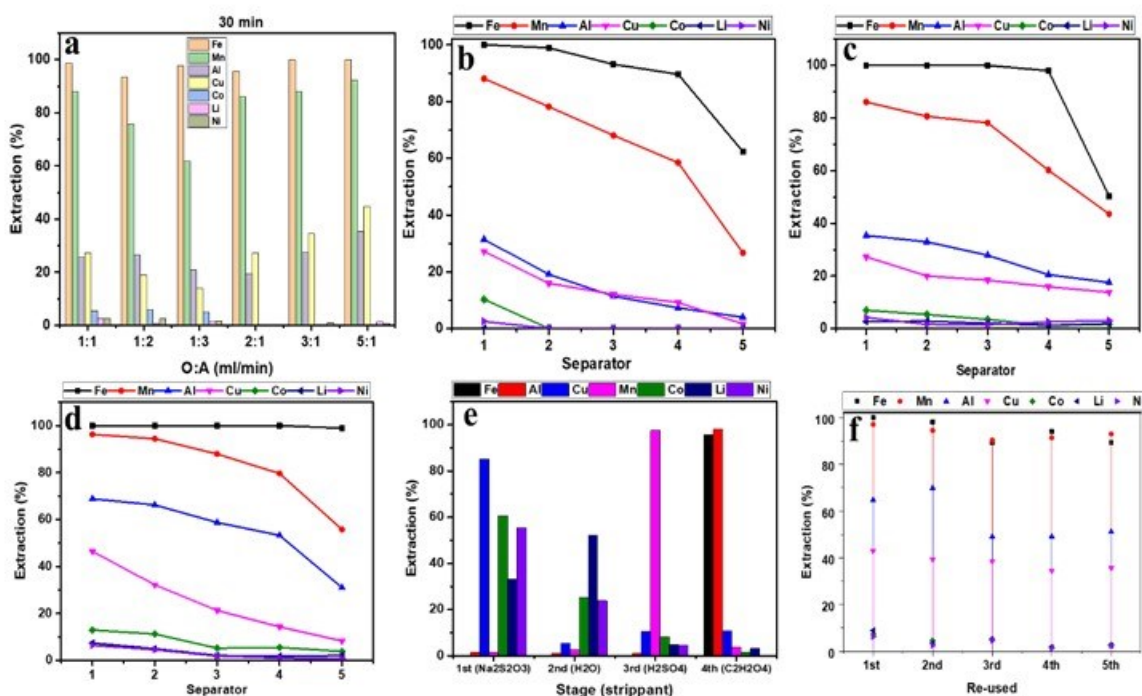


Figure III.3.42 (Solvent-membrane separation for the purification of Ni, Co, Li rich leached liquor, a]. effect of flowrate (O:A-ml/min), b]. extraction efficiency per membrane at O:A-1:1 flowrate (ml/min) and 10 %v/v D2EPHA, c]. extraction efficiency per membrane at O:A-1:2 flowrate (ml/min) and 10 % v/v D2EPHA, d]. extraction efficiency per membrane at O:A-1:1 flowrate (ml/min) and 20 % v/v D2EPHA, e]. Selective stripping in stages at O:A-1:1 flowrate (ml/min) with 20 % v/v D2EPHA, f]. Re-used of 20% v/v D2EPHA, mixed metals solution [(Ni-1.2, Co-0.90, Mn-0.61, Li-0.30, Cu-0.101, Al-0.075, and Fe-0.055 g/L)].

Table III.3.3 Metal Content in the Stripped Solution Using 0.5 M [H<sub>2</sub>SO<sub>4</sub>].

Metal	Mn	Fe	Al	Cu	Co	Li	Ni
Conc. (ppm)	1978	1.66	2.2	9.1	25.0	3.86	21.6

### Photo-Controlled Recovery of Nickel Cobalt Manganese for Sustainable Recycling of Batteries

In this project, we propose an alternative approach by using photo-controlled copolymers to efficiently abstract transition metal ions from the spent cathode solution. Instead of using corrosive acids, environmentally benign polymer materials will be designed and synthesized. When subject to photo irradiation, the isomerization of

polymer shows strong chelating effect with transition metal ions which preferably separates the transition metals from the cathode solution. This method involves an environmentally benign process with high recycling efficiencies.

In FY23, the focus of this project was the design and synthesis of photo-responsive monomers and polymers that could reversibly capture and release Ni, Mn, and Co ions from an aqueous cathode waste stream. An optimal photo-switch monomer 2-(3',3'-dimethyl-6-nitrospiro[chromene-2,2'-indolin]-1'-yl)ethyl methacrylate (Spiropyran) was identified and has been synthesized *via* a multiple-step reaction. <sup>1</sup>H-NMR characterization and purity check of the synthesized monomer was conducted. Since the monomer contains photo-switch group, its response with photo irradiation was validated. The photo-responsive isomerization of the synthesized monomer was examined and characterized by UV-Vis spectrometry. (Figure III.3.43)

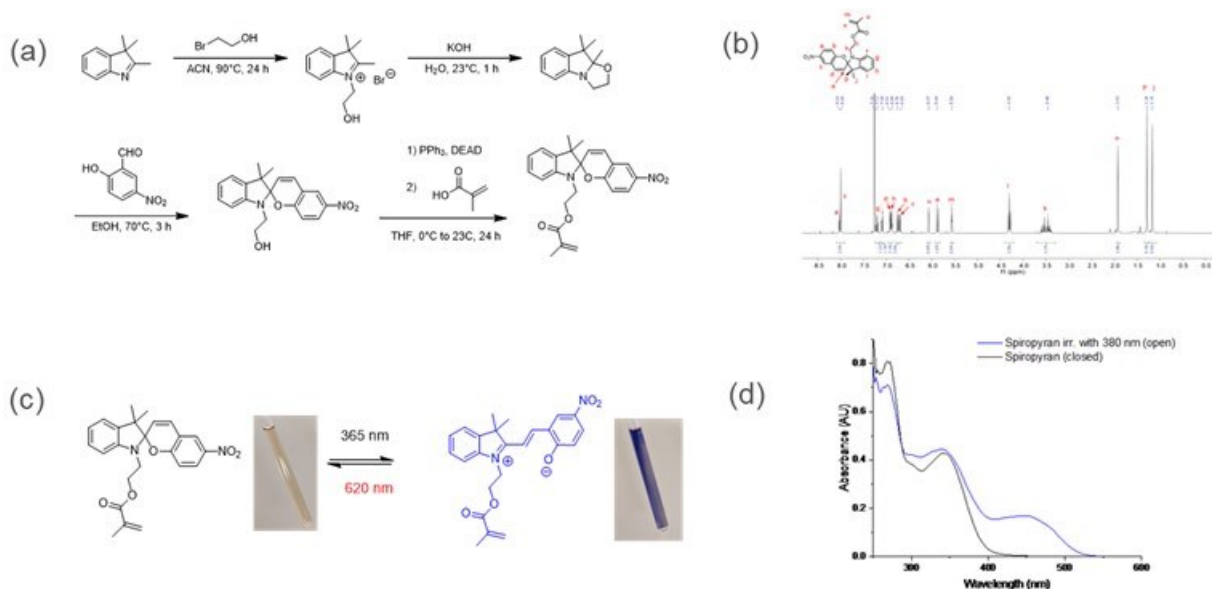


**Figure III.3.43** (a) Synthesis route for the photosensitive monomer Spiropyran; (b) <sup>1</sup>H-NMR spectrum of the synthesized photo-sensitive monomer for structure identification and purity check; (c) photo-responsive isomerization of the synthesized monomer examined and characterized by UV-Vis spectroscopy; (d) UV-Vis spectra of the closed and open isomers when subject to UV irradiation (black curve: close structure monomer, blue curve: open structure monomer).

At the end of FY23, our research has been extended to the synthesis of Spiropyran homopolymer and random copolymer by copolymerizing Spiropyran and diglyme solubilizing monomer. This copolymer is water-soluble and capable of binding transition-metal ions in aqueous solution. We will evaluate transition-metal binding ability of the synthesized polymer and copolymers using model cathode solutions in next year.

#### **Soft Chemistry Coprecipitation of Battery Precursors**

In this work, we will develop novel polyolometallurgy process with the usage of green chemicals as dual functional solution for both leaching and coprecipitation. The use of the dual-functional solution significantly simplifies the overall recycling process with efficient separation and precipitation.

In FY23, we successfully demonstrated a novel polyolometallurgy method for simplified separation and precipitation. This method utilized the dual-functionality solution (CAEG) both as the leaching and precipitation agent. The detailed process conditions have been optimized for LCO cathode. We achieved a leaching efficiency of over 95% for both Co and Li within just 1 hour of reaction, maintaining nearly 100% efficiency between 1 to 2 hours. The resulting metal leachate could be easily separated from Al foil and PVDF/carbon black films. With the collected metal leachate, continued reaction initiated precipitation through

poly-esterification reactions between metal citrate and ethylene glycol. Notably, the use of CAEG enabled self-precipitation without the need for any additional chemicals. The developed precipitates have been characterized via ICP, XRD, FTIR, TGA, XPS and SEM. ICP results confirmed that more than 96% of Co could be precipitated and recovered, and the precipitates could be directly used as precursor for cathode resynthesis. We also applied this process to NMC cathodes (NMC111 and NMC622) and were able to produce NMC coprecipitates at selective NMC ratios, which confirmed that process is adaptable to both LCO and NMC cathodes (shown in Figure III.3.44). With the developed precipitates, we successfully resynthesized LCO cathode, and we are in process of optimizing the synthesis conditions for NMC cathodes.



Figure III.3.44 Images of flow sheet demonstrating the process for LCO and NMC111

The EverBatt model was employed to analyze the cost and revenue of the polyolmetallurgy process. The results indicate a high cost (approximately \$200 per kg of feedstock processed) for the overall processes at the current stage. This elevated cost is primarily attributed to the consumption of materials, such as ethylene glycol as a solvent and IPA for washing. We will explore the recycled use of ethylene glycol and IPA to lower the cost of the process for the next step.

### **Synthesis and Performance testing of Cathodes from Recycled Raw Materials**

Hydrometallurgical recycling approaches to generate the transition metal salts needed to synthesize new cathode materials is gaining popularity due to its high recovery efficiency, scalability, and low energy requirement. The hydrometallurgical process begins with acidic leaching to dissolve and extract the materials from shredded batteries. From the leachate, the transition metals are extracted with solvents and precipitated by forming the salts that are used in coprecipitation to synthesize cathode materials. Unfortunately, the complete separation of these valuable metals is challenging, and the industry lacks guidance on purity levels needed to ensure that cathode materials synthesized from recycled salts have the same morphological, density, and electrochemical performance compared to those synthesized with pristine salts. Through this project, we collect salt sources from hydrometallurgical streams and synthesize cathode materials using continuous coprecipitation to identify which impurities carry over into the cathode and affect the particle growth and electrochemical performance. The cathode materials synthesized from recycled sources will be compared to pristine cathodes synthesized in the same reactor. The recycled cathodes will be reoptimized to match morphological metrics of the pristine particle size, density, and surface area to identify impurity effects deconvoluted from morphological change. These results will advise the recycling industry on which impurities should be targeted for removal during hydrometallurgical recovery.

In FY23, a 4L continuous stirred tank reactor (CSTR) was assembled for dedicated use in this project to prevent material contamination. Baseline Ni<sub>0.6</sub>Co<sub>0.2</sub>Mn<sub>0.2</sub>(OH)<sub>2</sub> (NMC622) material was synthesized using coprecipitation and previously determined optimized conditions. Troubleshooting and fine-tuning of the reactor equipment (i.e., reactant pumps, pH controller, etc.) needed to be accomplished to ensure the baseline precursor material met previous chemical and physical characteristics reported in equivalent commercial



material. The resulting baseline material exhibited a D50 particle size of 16  $\mu\text{m}$  and a tap density of 2.06 g/cc. Li-metal half-cells were assembled with the baseline NMC622. They were electrochemically cycled using a 3.0 to 4.3 V Li/Li<sup>+</sup> voltage window with four formation cycles at C/10 immediately followed by a rate capability test. The initial discharge at C/10 was 168.7 $\pm$ 0.5 mAh/g with a coulombic efficiency of 90.63 $\pm$ 0.05% and 85% capacity retention after 50 cycles at C/3. A complete impurity profile of the cathode material was collected through ICP-OES and compared to the impurity profiles of the virgin reactants used in the synthesis. Comparison of these profiles showed carryover of various impurities such as potassium, silicon, phosphorus, molybdenum, and calcium. Additionally, the precursor synthesis introduced impurities of sodium and sulfur. This analysis will be repeated on both the baseline and the reactants to calculate the carryover yields of the impurities.

While synthesizing the baseline NMC622, we discovered fluctuations in our pump rates upon repeated reactions. These fluctuations were as high as 20%, which caused variations in the elemental content and morphology of the precursors. Before moving on to our first impurity profile, it was imperative to correct this issue to ensure differences in particle growth and performance are based on impurity content and not equipment deviation. At the Materials Engineering Research Facility (MERF) at Argonne National Lab, we have another type of reactor called the Taylor Vortex Reactor (TVR) used for coprecipitation. The advantages of the TVR over the CSTR include shorter residence times and the ability to produce material with narrower size distributions due to the higher shear mixing environment. We plan to transfer the impurity study to the TVR reactor in FY24. The improved homogeneity of elemental content, morphologies, and size will ensure that performance differences can be accurately ascribed to impurity content.

We attained our first sample of hydrometallurgical recycled Ni salts and the preceding black mass, leachate, and purified leachate from which the Ni salt was synthesized. Comparisons of the recycled Ni salt and the pristine Ni sulfate used in the baseline synthesis show greater amounts of aluminum (0.0022 wt%), cobalt (0.9829 wt%), manganese (0.0553 wt%), iron (0.0104 wt%), magnesium (0.0022 wt%), and zinc (0.0031 wt%). These results will guide our first cathode synthesis with representative impurity profiles.

### ***Design for Sustainability***

#### ***End of Life Battery Passivation for Safe Transport***

For transportation purposes, lithium-ion batteries (LIBs) are categorized as class-9 hazardous materials, which introduces costly labor and packaging requirements into large-scale LIB recycling schemes. The goal of this project is to explore two possible battery passivation strategies, ultimately in the interest of working with the Department of Transportation to lift certain requirements for LIBs and reduce transportation costs. The first passivation technique is a modest heat treatment. The second technique is discharging cells using a transportable electrical circuit.

During this past year, a small oven was assembled to safely bake individual 18650s for a specified duration. At elevated temperatures, lithium-consuming reactions are accelerated and this thicker SEI potentially reduces the risk of thermal runaway propagation while transporting cells en masse. After much trial and error, a certain temperature and time condition were chosen. Two of the four cells selected for this project were able to withstand the heat treatment without activating their current interrupter devices (CIDs). Following heat treatment, the cells were evaluated via EIS and GITT, and will soon be disassembled for a more thorough analysis of the individual electrodes. A large increase in internal resistance was observed in the cells following heat treatment, particularly in terms of mass transport (Figure III.3.68 b) located in the conclusion section). Thus far, the external short circuit tests (Figure III.3.68 c) located in the conclusion section) have proven to be relatively benign, likely due to the activation of the cells' CIDs following the short. At a 50m $\Omega$  short resistance, the voltage in either cell dropped to approximately 2.5V before temporarily leveling off, indicating that the flow of current had been stopped. At 25m $\Omega$ , the same thing happened at around 2V. Since the safety features of the cell prevent an excessive temperature rise, nail penetration may be the only remaining destructive test method.

### **Secondary Use Energy Storage Technology use Cases for Behind the Meter Applications**

Energy storage systems are currently cost prohibitive for most residential applications. However, with the development of systems that utilize secondary use batteries can reduce the costs. Batteries reach end-of-first life for several reasons, mostly calendar aging. Calendar aging is a natural reduction in capacity around 80% of original manufacture. A 20+ mile range reduction could cause a consumer to replace their battery which still has significant value and capacity. This discarded battery is ideal for direct reuse applications such as energy storage. Some major challenges include the state of charge and state of health for each battery. Since the batteries are not specifically manufactured for energy storage there are diagnostic tests that need to be performed on them to characterize their state of charge and state of health in addition to the specific chemistry characteristics.

The objective of this project is to develop and demonstrate a secondary use energy storage system for behind the meter (residential) applications from extracted battery modules. Reduce the cost associated with energy storage systems for residential applications to enable more adoption. Design a system that can use a variety of battery chemistries with diverse state of health and charge characteristics. Integrate the system into existing ORNL test beds for validation.

The approach is to select battery modules that are nominally 48V building blocks and design a flexible system around them. Assume the batteries will have a variety of power, signal, and fluid connections. Assume the batteries will have variable states of health and charge/discharge profiles. Design a system that takes these variables and challenges into account with flexibility in mind for swapping out batteries once they reach the next end of use.

The Volkswagen ID battery module was selected to build up the energy storage system. The VW battery modules are nominally 48V and have datasheets and literature to support the design of the energy storage system. ORNL received 2 modules of unknown state of health and low (30%) state of charge. Each battery module has a positive and negative connection for power, a BMS connector, and inlet/outlet fluid ports. To connect these batteries into the system we needed a flexible connection. Staubli interconnects (Figure III.3.45) are configurable connectors used for a variety of industrial applications and the ORNL team has used them in earlier projects. Using an online configurator, we could quickly prototype a connector that would adapt the battery to the energy storage system. Figure III.3.46 shows how the secondary energy storage system is tied to the grid and a home via a residential transfer switch. In more detail, Figure III.3.47 shows a schematic of the energy storage system and how the batteries will be interconnected to a common bus. Each battery is being treated like a “black box” with regulation of DC power to the bus with a common bus voltage of 400. The prototype system is designed to have multiple inputs, as to emulate a home equipped with solar and other distributed energy resources. Additionally, the system will feature grid tie hardware to integrate into existing ORNL test beds for testing energy storage systems.

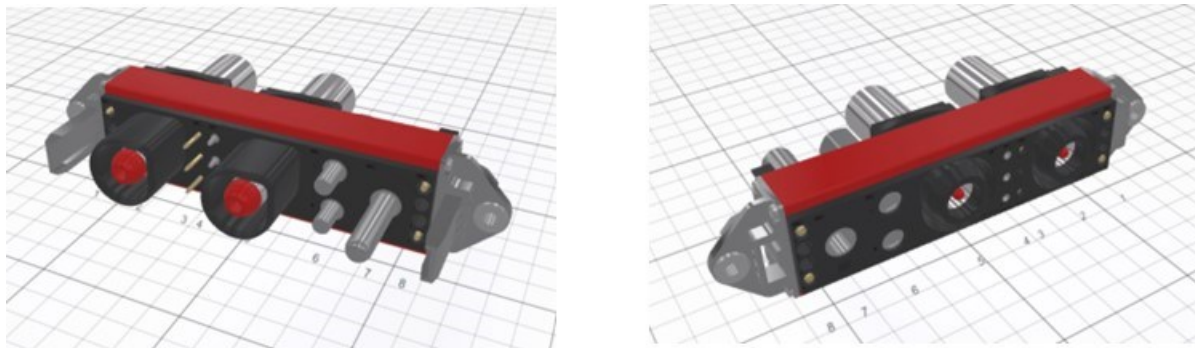


**Figure III.3.45 (Staubli Male (left) and female (right) configurable interconnect for secondary use battery application/Jonathan Harter)**

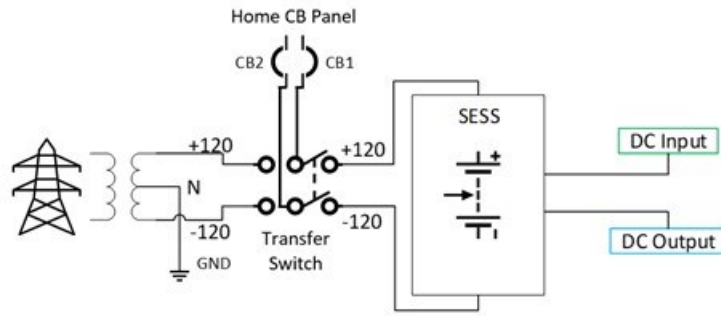


Figure III.3.46 (Secondary Use Energy Storage System Line Diagram for Residential Application/Jonathan Harter)

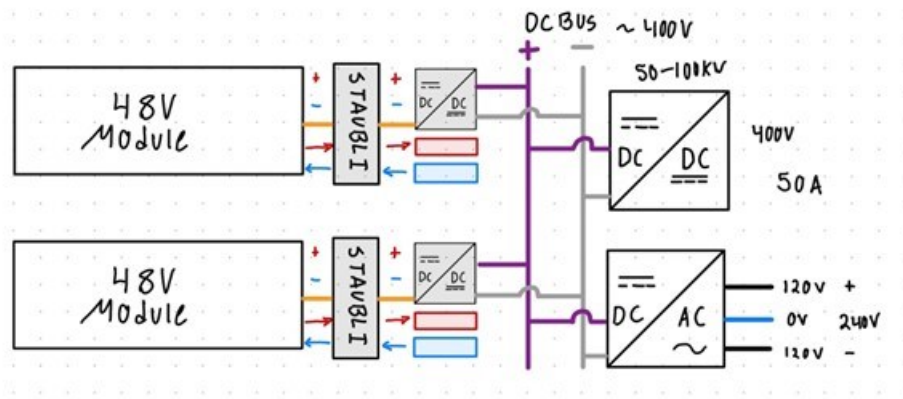


Figure III.3.47 (Secondary Use Energy Storage System Schematic Jonathan Harter)

**Sustainable Recovery of Si from PV Panels for Applications in LIBs**

As PV devices reach the end of their ~30-year lifetimes, an emerging challenge is how to handle the waste from large volumes of end-of-life (EoL) PV modules. It is projected that the cumulative mass of EoL PV modules could be up to 8 million tonnes (Mt) by 2030. The goal of this project is to recover Si from EoL solar panels for reuse in LIBs. This includes removing contaminants inherent to PV modules such as silver, tin, lead and copper and conducting electrochemical tests on the recovered silicon to enhance understanding of the effects of the PV dopant materials on the calendar life and performance. We are working with industry partners to obtain EoL Si PV material recovered from industrial scale PV recycling processes.

In FY23, we negotiated commercial EoL PV silicon material from a PV module recycler and sent 20g of material for wet ball milling to collaborators at ORNL. The ICP OES analysis of the EoL PV Si powder as well as powder from a pristine boule of silicon that was ball milled by the same process is shown in Figure III.3.48.

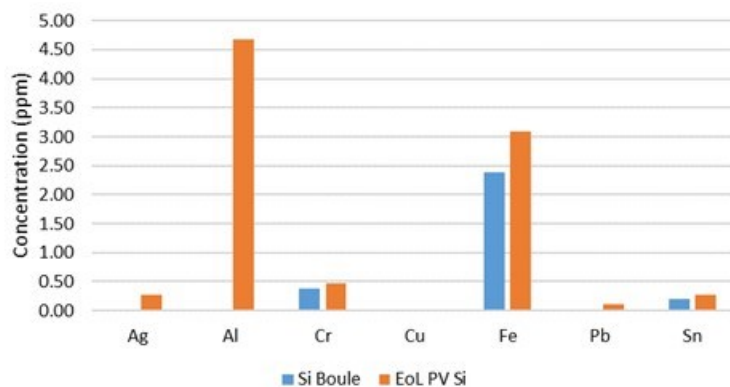


Figure III.3.48 ICP OES analysis of contaminants in ball milled silicon

Both types of silicon exhibited Fe and Cr from the ball milling process. EoL PV Silicon has significant Al and Fe with small amounts of Ag, Pb and Sn. Electrodes were cast using aqueous PAA binder, C45 carbon additive and three types of ball milled silicon: B-doped silicon boule, non-doped silicon boule and untreated EoL PV Si. Half cells were made using these ball milled silicon electrodes to compare initial electrode stability and capacity retention at C/20. The first two cycles at C/20 for each types of silicon are shown in Figure III.3.49.

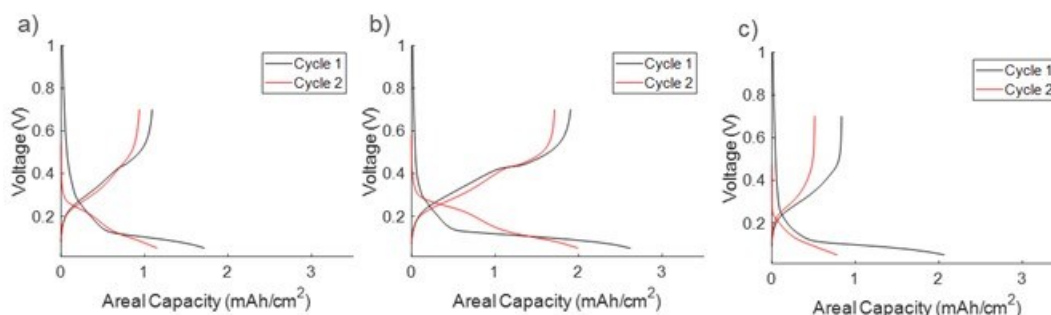


Figure III.3.49 Charge and discharge curves of C/20 cycling in half cells of ball milled silicon electrodes from a) non-doped silicon boules, b) boron-doped silicon boules and c) boron-doped EoL PV silicon

#### Battery Lifetime as a Service: New Business Model and Battery Design

The battery-as-a-service (BaaS) business concept seeks to electrify challenging applications and improve battery circularity by increasing utilization in 1<sup>st</sup> and 2<sup>nd</sup> life applications. Under the concept, the battery is owned by a single vertically integrated company throughout its lifetime. The BaaS company owning the battery is responsible for 1<sup>st</sup> life/primary application, warranty, refurbishment, 2<sup>nd</sup> life/secondary application, and recycling. By designing the battery for 1<sup>st</sup> and 2<sup>nd</sup> use at the outset, recertification costs can be avoided. By keeping the battery under ownership of one business, costs associated with ownership transfer can be avoided and the full value of the battery can be unlocked. Given the synergy with 2<sup>nd</sup> use, DOE management requested towards the end of FY23 that the team also revisit & update previous NREL analysis on the techno-economic value of battery 2<sup>nd</sup> use (Neubauer, 2015: <https://www.osti.gov/biblio/1215098>).

The objectives of this work include:

- Identify technical and business approaches to increase battery utilization over a longer battery lifetime, thus improving life-cycle value and sustainability.
- Update previous (~2015) calculations around degradation and business value of battery 2<sup>nd</sup> use.

The approach to this work:

- Perform stakeholder interviews, identify candidate BaaS applications, perform technoeconomic modeling, and draft reports. Share results with stakeholders and DOE to determine next steps.
- Document barriers and enablers of battery circularity, for example safety codes and standards (e.g. recertification and how these expenses can be reduced), long-life battery cell and pack designs, health/life estimation, digital tracking, and battery passport concepts

The team met with stakeholders throughout industry (EV applications, vehicle-to-grid (V2G), recycling), academia (state-of-health, state-of-safety) and labs (second-use, recycling) to identify possible applications for BaaS, to collect ideas and assumptions to apply in technoeconomic analysis models that account for battery lifetime, lifecycle costs, and revenues, and identify present technical and legislative barriers to BaaS. The team identified three compelling applications for BaaS:

1. Stacked use – EVs performing V2G services during the first life of the battery,
2. Cycling-intense applications with mid-life battery replacement (e.g. medium-/heavy-duty EV, electric aircraft), and
3. Second use of retired EV or aircraft batteries.

The stacked-use/V2G application is most appropriate for EV fleets whose batteries are lightly cycled (<50% depth of discharge each day) and/or spend much of their life parked (>90%). Based on data from DOE's Alternative Fuels Data Center (AFDC), the most relevant vehicles and vocations include light-duty cars/trucks/vans, low-mileage delivery trucks, and school buses. These batteries' low throughput provide opportunity to earn additional income through V2G, while still meeting the EV's lifetime requirement. Under BaaS, the BaaS provider would either lower the first cost of the vehicle or provide monthly payments to the vehicle owner/lessee to provide V2G services. The BaaS company would provide a warranty that accounts for the additional V2G cycling and re-use the battery at end of 1<sup>st</sup> life.

Candidate vehicles/vocations for mid-life battery replacement (application 2) are those with high mileage and/or high cycling-intensity, namely class 8 trucks, transit buses, shuttle buses, refuse trucks, and EV aircraft. One example application space is transit buses which presently suffer from high up-front costs, frequent fast charging, and difficult 12-year/500k-mi federal lifetime/warranty requirements. For the transit bus application, a BaaS company could lease the battery to the transit agency, schedule one planned replacement of the battery during the vehicle's lifetime, and place the used batteries into 2<sup>nd</sup> use applications.

In FY23, a technoeconomic analysis model was formulated and partly developed. The model incorporates NREL's BLAST lifetime-predictive model populated for graphite/NMC622, graphite/LFP, and LTO/NMC chemistries. Capacity fade is a function of calendar time, full-equivalent cycles, temperature, SOC, DOD, and C-rate. Preliminary analysis of battery life on drive cycles from NREL's Fleet DNA confirmed that today's transit bus batteries are unable to meet federal lifetime/warranty requirements in all situations. Rather than excessively oversizing the battery to meet life requirements, it is economically preferable to "right size" the battery just 30% greater than its route requirement and perform mid-day fast-charging of the battery late in life. Additional results will be shown in future publication.

The team cataloged barriers and synergetic enablers of BaaS. BaaS enabling technologies include (1) improved 1<sup>st</sup>- and 2<sup>nd</sup>-use safety codes and standards, (2) health/life estimation, (3) battery passport/digital tracking, and (4) life-extending battery cell and pack designs. Example life-extending/fast-charge cell technologies include advanced binders such as CNTs, single-crystal cathode materials, cathode coatings, advanced electrolytes, anode coatings, supplemental lithium, low-voltage LFP cathodes & high-voltage LTO anode (albeit with energy density penalty), dual-layer and laser-ablated electrodes. At the pack level, life-extending/fast-charge enabling technologies include internal heaters to pre-heat before fast charge, rapid cooling following fast charge, cell and module active balancing, state-of-health and -safety sensing, electrochemical charge control

protocols, and digital tracking of batteries. For life extension, each of these technologies is more cost effective than simply oversizing the pack energy content.

In reviewing safety codes and standards, the largest present barrier to BaaS and 2<sup>nd</sup> use is the lack of a 2nd use certification. The present standard, UL 1974, lays out an expensive process requiring that each individual module/pack be re-certified, for each application. In the future, with well-known battery aging processes and health documentation, our team envisions updated standards where safety certification is performed on representative aged battery samples. Further research is needed to establish the connection between state-of-health (SoH) and state-of-safety (SoS) of used batteries. (Note that other DOE ReCell projects in this report are actively working on rapid SoH estimation, but none on SoS.)

### ***Investigation of Reused EV Packs on Future Renewable Grid through ARIES***

Evaluate the performance of spent EV cells/packs in future, complex grid containing multiple forms of renewable production and energy storage. Used EV packs will be integrated with NREL's unique Advanced Research on Integrated Energy Systems (ARIES) platform. ARIES is a 20 MW microgrid designed to overcome challenges associated with the future renewable grid. ARIES' core capabilities include unique, state-of-the-art research equipment to support integrated energy research, analysis, modeling, and hardware experiments, including six research pads, advanced distribution management system test bed, cyber range, power electronic grid interface, a megawatt controllable grid interface, digital real-time simulation, and behind-the-meter storage capabilities. ARIES allows us to create, prove, and validate complex energy systems by interconnecting hardware and software that imitate renewable energy configurations and solutions for carbon-free energy and transportation systems.

In FY2023, NREL acquired two Ford fusion packs – one from New York with 69k miles and one from Texas with 109k miles. The Ford Fusion/C-Max Energi packs were selected as the best candidate for this focused research based off four metrics:

1. NREL has significant beginning of life data available from a previous program in 2013.
2. The pack and cell design allows dis-assembly and re-assembly without compromising the packs themselves.
3. Ford used NMC-111 as the cathode material for the cells within these packs.
4. Used packs are readily available through auto recyclers.

During FY23, our initial work focused on reading the CAN signals from the Ford Fusion pack. In order to cycle the pack to determine the state-of-health (SOH), we needed the cell voltage and temperature data from the CAN bus. Initial techno-economic analyses performed at NREL have shown that breaking down the pack to the cell or even module level would not be an economical solution. Rather, the pack needs to be retained in its present form and needs to have minimal modifications to determine its remaining useful life (RUL). Thus, we focused our efforts on attempting to read the controller area network (CAN) signals to understand the SOH of the cells and pack. NREL was successful in reading the CAN signals from the pack but without the DBC (CAN Database) we had limited success in translating the signals to a useful form to determine the SOH. Our efforts highlight the need for a battery passport to track the SOH of a used pack or have a means to access the cell voltage and temperature data through the onboard diagnostic system. After being unable to assess the SOH at the pack level, NREL dismantled the packs to the cell level to determine the SOH as a function of position within the pack. We also hope to understand how usage in different geographic locations (Texas vs. New York) affects the life cycle of the cells.

### ***Machine Learning RUL and SOH Classification***

Lithium-ion batteries in real world applications often have the potential for further use in less demanding roles at the 'end of first life', giving them a 'second life' and providing energy storage services, improving the environmental and economic sustainability of the lithium-ion battery market overall. However, second-life use of lithium-ion batteries requires validating the system performance and ensuring safety and reliability. While

batteries can simply be fully charged and discharged to measure their capacity, this process is very time-consuming (6-12 hours), energy intensive, and may not necessarily detect all possible safety risks. Instead, rapid characterization tests, such as DC pulses or AC impedance measurements, may be conducted in seconds or minutes, allowing cheap and scalable recertification of batteries at the end of their first life. But little research exists to inform the design of a ‘rapid characterization test’, and the accuracy of these tests for predicting battery performance and safety under different operating conditions is unknown.

This work will test commercial lithium-ion batteries using a comprehensive characterization procedure to fully diagnose battery performance and safety, using both electrochemical and ex-situ characterization methods. A variety of ‘rapid characterization’ methods will be studied to understand the role of test design on the accuracy of trained machine-learning models when predicting a large set of different performance metrics. Both lab- and field-aged batteries will be pursued to get as wide a set of aged batteries as possible.

The objectives of this work:

- Acquire aged commercial lithium-batteries for electrochemical characterization
- Define experimental procedure for comprehensive evaluation of battery health
- Develop machine-learning pipeline to extract feature and target variables from electrochemical characterization procedure and evaluate performance of models for predicting battery health and safety

The approach for this work:

- Acquire aged commercial lithium-batteries for electrochemical characterization
- Define experimental procedure for comprehensive evaluation of battery health
- Develop machine-learning pipeline to extract feature and target variables from electrochemical characterization procedure and evaluate performance of models for predicting battery health and safety

During the first year, three different sets of commercial lithium-ion batteries were acquired:

- Field aged prismatic NMC-Gr 24 Ah cells (Ford Fusion)
- Lab aged pouch NMC-Gr 64 Ah cells (aged at NREL)
- Field aged 2S-2P 64 Ah 7 V (2S-2P) LMO-Gr modules (Nissan Leaf)

All cells were physically characterized to search for potential degradation or safety issues due to mechanical expansion or gas generation. Electrochemical characterization has been performed on all the ‘NMC-Gr 64 Ah’ cells and all of the Nissan Leaf modules. The electrochemical characterization procedure was designed to collect a wide variety of performance metrics for machine-learning models to predict, and a variety of different types of pulse measurements to evaluate as potential rapid characterization techniques. The full characterization test requires ~6 days on a nominal cell. The performance metrics measured include:

- Charge and discharge capacity at  $C/10$ ,  $C/5$ ,  $C/3$ ,  $C/2$ , and  $1C$ .
- Charge depleting drive cycle performance using a US06 protocol for mobile applications.
- Charge sustaining application performance using a real-world frequency-containment reserve power profile for stationary storage applications.

Rapid characterization tests include pulses performed after rests as well as pulses overlaid on higher rate charge and discharge. Pulses after rests include ‘standard’ HPPC pulses (10s discharge, 40s rest, 10s charge) at  $C/10$ ,  $C/2$ ,  $1C$ , and  $2C$  rates as well as ‘Pseudo-Random Pulse’ (PsRP) sequences, which use randomly sampled currents and pulse durations to create a complex voltage response. Two PsRP sequences were defined, one ‘simple’ and one ‘complex’, with more current magnitudes and step durations. These simple and complex PsRP pulses were also overlaid on top of the  $C/2$  and  $1C$  charge and discharges to examine the possibility of on-line diagnostics. All pulses are repeated across the voltage window of each cell in both charge and discharge directions. The electrochemical characterization procedure is repeated for all cells at  $15\text{ }^{\circ}\text{C}$ ,  $30\text{ }^{\circ}\text{C}$ ,

and 45 °C. In total, 68 characterization tests have been performed so far. (Figure III.3.50, Figure III.3.51, Figure III.3.52)

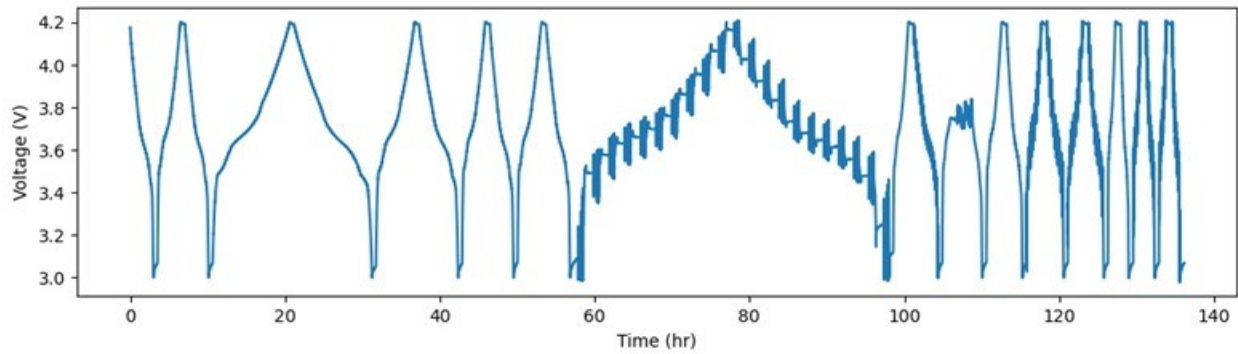


Figure III.3.50 Example voltage response from the electrochemical characterization procedure.

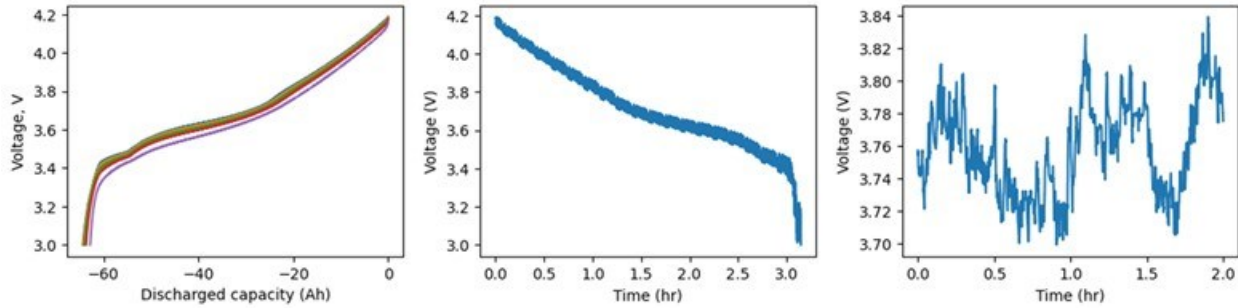
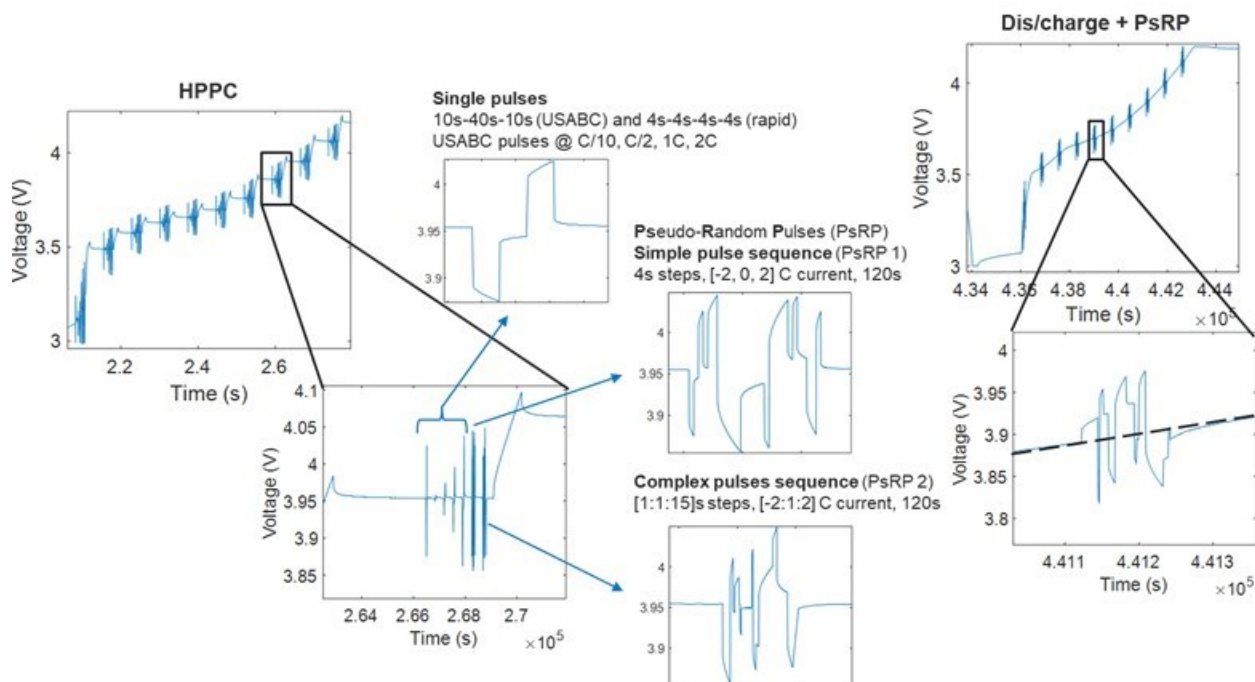


Figure III.3.51 Measurement of performance metrics. (Left) Rate capability. (Middle) Charge-depleting drive cycle. (Right) Charge-sustaining application cycle.





**Figure III.3.52 Rapid diagnostic pulses recorded across the voltage window. Examples are just from the charge direction, pulses were also performed in the discharge direction. ‘Dynamic’ PsRP measurements, overlaid on the C/2 and 1 C charges and discharge, are summarized at right, showing that the average voltage throughout the pulse is increasing, as the average current during the pulse sequence is unchanged. In total, the current data set has about 13,000 independent pulse measurements.**

Safety was quantified by fitting the post-charge voltage relaxation data with an exponential relaxation curve. Prior research has shown that when plated lithium is present, the post-charge voltage relaxation curve of lithium-ion batteries deviates from its nominal shape, which should be very near that of an ideal exponential relaxation. The error of the fit of the voltage relaxation using the exponential relaxation equation can then be used to quantify the ‘non-ideality’ of the battery, with high error suggesting potential safety issues. When fit to the electrochemical data, high error was observed for the ‘NMC-Gr 64 Ah’ cells after charging at higher rates and low temperatures, suggestive that this metric is useful for quantifying occurrence of plated lithium, while for the Nissan Leaf cells, high error was observed in some cells at high temperature but independent of rate; correlating with physical analysis showed substantial gas generation in cells with high error, which can also present safety risks due to pouch bursting or gas venting.

The usefulness of various pulses was then studied using machine-learning (ML). The ML approach uses best practices but is currently fairly straightforward to demonstrate results without any physical modeling or complex feature engineering approaches, and should be treated as a ‘baseline’ for the potential usefulness of the rapid characterization pulses:

- Input features are raw voltage and current measurements from the pulse sequences
  - Dimensionality of the input features is reduced using principal component analysis to speed model training
- XGBoost model architecture
  - Hyperparameter optimization via 50-iteration randomized grid search using 5-fold cross-validation on the training set
- 80:20 train:test data split, results averaged over 100 random splits

The resulting model performance shows that rapid diagnostic pulses can be readily used to predict most performance metrics, though there are some interesting details. For instance, the PsRP pulses predict all performance metrics with lower average error than the simpler ‘HPPC’ style pulses, demonstrating that the more complicated pulse sequences contain more information on the state of the cell than a pulse of similar length but lower complexity. Also, predicting capacity at high rates is difficult when pulses are performed after rest or at lower rates, demonstrating the challenge of predicting cell performance at extreme limits. Charge-depleting drive cycle performance can be predicted with high accuracy, while charge-sustaining drive-cycle performance is more challenging to predict. The quantified safety metric is not predicted accurately at all, however, it is suspected that improving the machine-learning pipeline should improve this prediction substantially, as the safety metric is about 70% correlated with the discharge capacity, and should be easier to predict. (Figure III.3.53, Figure III.3.54)

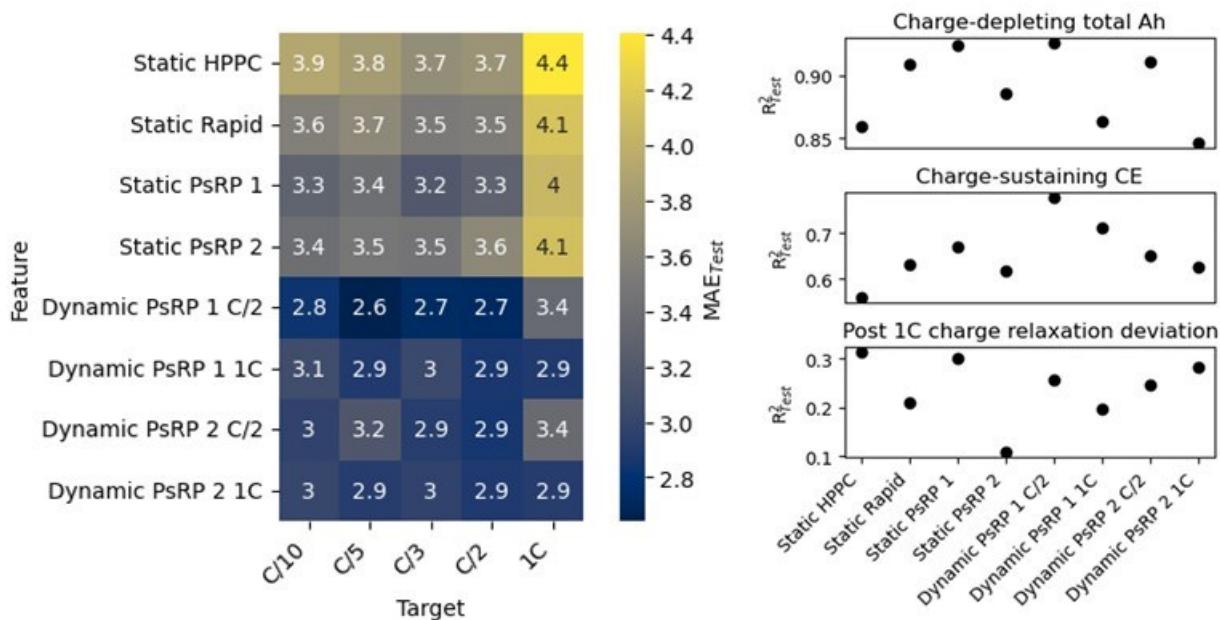


Figure III.3.53 Performance of various diagnostic pulses at predicting the measured performance metrics.

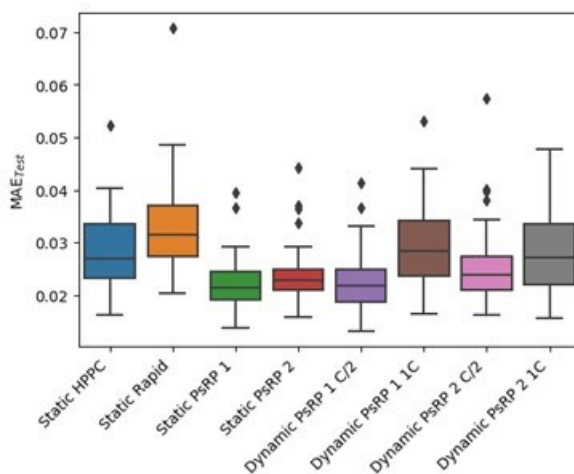


Figure III.3.54 Estimation of state-of-charge using various rapid diagnostic pulses.

Using this data set, it is also possible to answer other research questions. For instance, it can be shown that the PsRP pulses improve estimation of state-of-charge, compared to the simple ‘HPPC’ pulses, reducing the average state-of-charge estimation error from ~3% to ~2%.

### ***Advanced Fasteners that enable Rapid Disassembly of Li-Ion Battery Stacks***

EV batteries are a target for disassembly and recycling methods that do not involve shredding due to their component reusability and material composition. A challenge of economically recycling EV packs is in the way they are manufactured and the fasteners that assemble them. Packs are designed to last beyond their warranty periods which could range a decade on the road in various conditions. Therefore, packs are typically completely sealed to prevent corrosion and assembled with hundreds of screws and other challenging to separate joineries like ultrasonic welds, adhesive, and bolts. Furthering the challenge is the fastener condition such as being rusted or otherwise damaged beyond normal removal methods. This project investigates the challenges of extracting fasteners and components from electric vehicle battery stacks. ORNL is developing novel tools and processes to identify, locate, and extract fasteners and components from LIBs to enable automated disassembly, and thus provide economically viable reuse/recycle opportunities.

This project aims to achieve the development and demonstration of tooling and processes that enable automated disassembly of EV battery packs. The research provided in this annual project report aims to summarize the challenges related to disassembling lithium-ion battery stacks in an automated fashion.

ORNL is procuring and receiving end of first life battery stacks and performing condition evaluations and manual teardowns. The only way to understand and observe realistic samples is to work with them hands on and get them from the source, which is salvaged auto yards and warehouses. This project does not model or simulate the packs, rather it looks firsthand at the end-of-life products condition from being exposed to natural elements over time. First, the scope of challenges beginning at the lid were evaluated. Second, the internal components and architecture were evaluated. And lastly, the variety of packs currently available for recycling which would introduce variety to the objective were evaluated. Next, a high speed-torque tooling system was designed and developed to extract the fasteners observed from the packs. Next quarter ORNL will begin integrating the tooling into the automated system and begin testing. The ORNL team is also working on a prototype tool, IP submitted, that aims to extract a wide variety of screws without changing end effector tooling.

Key findings include a majority use of metric sized fasteners in the range of 8mm to 13mm. Additionally, the use of internal and external torx fasteners in the t10-t35 range. There are some outlier fasteners internal to the pack that are outliers, but they not widely used. ORNL has designed and procured an initial tool that will extract fasteners and are investigating the automated classification of fastener size, condition, etc using machine vision. (Figure III.3.55, Table III.3.4)



Figure III.3.55 (Estic custom ordered 80Nm high speed nutrunner with axial compensation connected on benchtop prior to robotic integration/Jonathan Harter)

Table III.3.4 Joining Type Rating Table.

Joining Method	Time	Risk	Debris	Heat	Rating
Pristine Screw	0	1	0	0	.25
Rusted Screw	3	4	3	4	3.5
Rounded Screw	5	6	5	4	5
Ultrasonic Weld	10	10	10	10	10
Adhesive	8	6	1	1	4
Captured Bolt	4	6	0	0	2.5
Stud and Nut	1	1	0	0	.5
Lock-Tite Screw	2	2	1	1	1.5

**Precise Cell/Group Diagnostics, Removal and Replacement**

EV batteries are limited in on board diagnostic capabilities and there are limited off-the-shelf products that allow advanced testing of end-of-first-life batteries. EV batteries are limited to measuring voltages of cell groups/modules and current when the contacts are closed with a charger or load. These measurements alone are not indicative of potential failures within the cells. A cell may function properly and fail abruptly. On board control limitations help prevent extreme charging/discharging events from happening but other factors

such as manufacturing defects could be responsible for issues. ORNL is exploring methods and instrument gaps that will enable advanced diagnostics of EV batteries to more accurately determine their value, safety, and life expectancy.

Design and develop new experiments with end of first life EV lithium-ion batteries to more accurately determine their state-of-health. Additionally, we are trying to isolate failing or already failed cells within a pack without removing the lid.

Cells in groups appear to have the same potential when they are connected, but when separated they show differences. Techniques such as electrochemical impedance spectroscopy are being used to measure certain characteristics of the cells stand-alone and connected in different topologies. The idea is that we can perform EIS on a known “bad” cell independently and then insert it into a group of “good” cells and learn how to identify the bad cell.

Initial findings show that 6 extracted cells from a 2017 Chevy Volt battery stack show completely different EIS results when separated from a module. Figure III.3.56 shows the EIS data of the 6 cells alone and in series (1&2, 3&4, 5&6). To maintain safe voltage levels and limited ampacity we chose to experiment with 2s3p configuration. The 2s3p configuration was unable to be tested with EIS due to the amount of inductance and added impedance of our connections. The signals were drowned out because the resistance of the connections exceeded the internal cell resistances attempting to be measured. Low inductance connections will be identified in the next quarter to continue EIS testing.

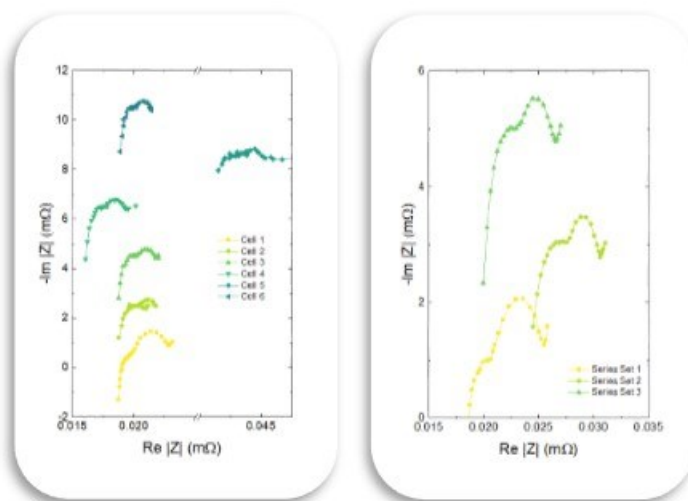


Figure III.3.56 (EIS data from 6 cells and cells 1&2, 3&4, 5&6 in series/Jonathan Harter)

### Modeling and Analysis

#### Requirements for Separation Processes through Electrochemical Modeling

The purpose of this project is to evaluate the impact of incomplete active material separation on cathode and anode performance to establish rational target metrics for active material purity. We will achieve this through advanced electrochemical modeling and analysis of mixed-electrode systems. The full separation of distinct cathode chemistries has proven challenging and may require expensive multi-stage processing. The exact benefit of improved compositional purity on cell performance has not been established. An Edisonian approach for determining optimal purity levels is impractical for a large matrix of possible compositional blends. Thus, we plan to use experimentally validated advanced electrochemical models to identify target purity levels for a broad range of mixed electrodes.

This year, we modified previously developed electrochemical models to consider some of the complexities of electrodes made with recycled materials. Figure III.3.57 illustrates how the standard Newman model has been modified to have multiple active materials within an anode or cathode. Current from each particle type is summed based on individual fractions and used within electrode domain equations. Each electrode can have multiple active materials present. For the blended electrode model to be accurate, the team performed GITT testing for different active materials in electrodes cast at NREL. After processing, the solid-state diffusivity and exchange current density as function of intercalation fraction are extracted and Figure III.3.57 illustrates results for NMC 111. Rather than interpolating parameters from the raw GITT output, the model stability and computational speed are increased by using algebraic functions. After processing the GITT data, the resulting parameters are first smoothed, before being fit with empirical expressions.

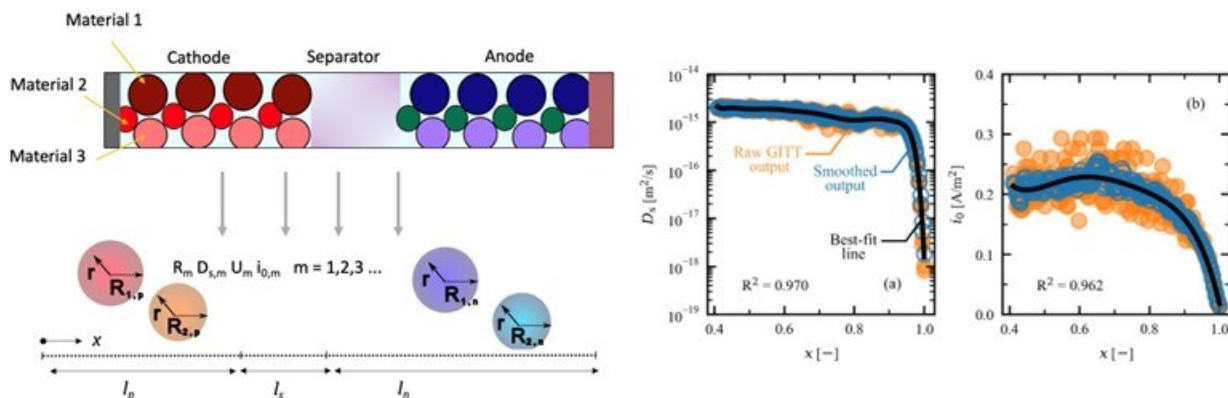


Figure III.3.57 Left.) Schematic of electrochemical model with multiple active materials per electrode Right) Electrochemical model parameters: solid-state diffusivity and exchange current density for NMC 111

### AMUSE Process Modeling

The Argonne Model for Universal Solvent Extraction (AMUSE) is used to design solvent extraction flowsheets for the recovery of metal ions and related species from acidic solutions. The standard AMUSE code was developed for spent nuclear fuel dissolved in nitric acid systems and neutral extractants. This project adds the capability for AMUSE to directly design solvent extraction flowsheets for recovery of Co, Mn, Ni and other metals from spent batteries using commercial acidic extractants. The code was modified to include Mn, Ni, and Co with the other species already included. In addition, the ability to calculate distribution coefficients for metal species from on in-process acidities was automated with correlations developed from literature data. With these changes the user can develop flowsheets for metal recovery with acidic extractants and the acid balance for the process for systems for which data on the extent of extraction as a function of acidity are available.

In commercial extraction of Ni, Mn or Co, the metals are typically dissolved in sulfuric or hydrochloric acid and acidic extractants are typically used for the solvent extraction. The standard AMUSE code was developed for nitric acid systems and neutral extractants. To address this gap, the existing AMUSE process design code has now been reconfigured to use sulfate or chloride as the balance ion in addition to nitrate, and to accommodate ion exchange extraction chemistry. In addition, the calculation of distribution coefficients as a function of the in-process acidity was developed and implemented in the code for solvent systems that used acidic extractants. The user simply inputs the parameter values required in the correlation equations.

Steady-state AMUSE normally iterates between a mass balance calculation and partitioning calculations to develop the aqueous and organic concentrations of system components at steady-state. For the new approach with acidic extractants, power law fits are first derived for literature data for equilibrium extraction. These functions calculate the distribution of metal components between the organic and aqueous phases, given by the distribution coefficients ( $D = [M]_{org}/[M]_{aq}$  at equilibrium), as a function of the aqueous-phase acid

concentration. In the scheme, the distribution coefficients (D values) are first used to identify favorable feed compositions and relative flows. Next, the hydrogen distribution between the organic and aqueous phases is determined from the extent of metal extraction. A base or buffer is introduced in-process to regulate pH based on the hydrogen ion exchange reaction.

Several simple flowsheets were run to test the approach using extraction data from different references. The notional feed consists of equimolar amounts of Ni, Mn, and Co dissolved in sulfuric acid, or another acid. A simple process flowsheet consisting of five extraction stages, two scrub stages, and five strip stages is used as an example. The number of stages and flow rates employed in an actual process will depend on a number of factors, but this range is useful to capture the basic flowsheet behavior.

The example case below uses extraction data from the literature (Guimares, Hydrometallurgy, 150 (2014) 173-177). The feed comprises 0.1M Co, Mn, and Ni in pH 6.4 sulfuric acid. The addition of NaOH solution as a feed to selected extraction and scrub stages was also simulated, though the efficacy needs to be better verified. Figure III.3.58 shows the resulting Co, Mn, and Ni stage profiles. Based on these plots Co and Mn are effectively extracted to generate a product containing >99% of the Mn and Co originally present in the feed. Similarly, >99% of the Ni reports to the raffinate. The hydrogen ion profiles show the final [H<sup>+</sup>] in each phase with the aqueous phase concentration held at the targeted value.

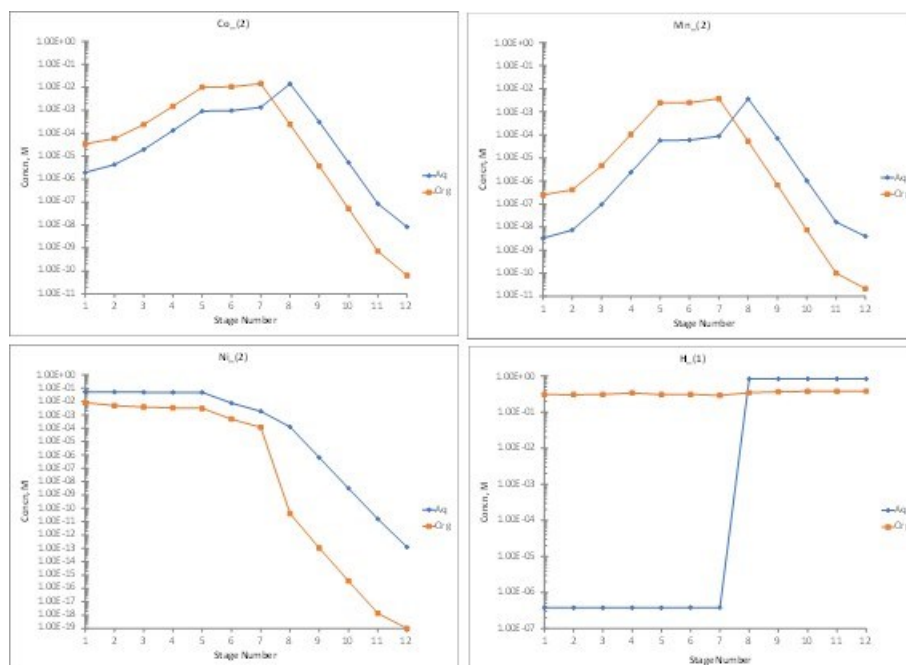


**Figure III.3.58 Stage Composition Diagrams for a run with 10% (v/v) Cyanex 272. (Distribution correlations derived from Guimares, Hydrometallurgy, 150 (2014) 173-177).**

Results from a run with the same structure but a different solvent, 10% DEHPA and 5% TBP in an aliphatic solvent (Cheng, Hydrometallurgy 56 (2000) 369-386) showed the extraction of Mn favored over both Co and Ni. In this case, the Ni and Co reside together in the raffinate. The lower pH used in this second process would make it easier to control pH in practice.

Other parameters in the AMUSE code that also impact process effectiveness include phase carryover, efficiency and solvent loading. In the examples, the solvent loading was kept within desired levels by using the

relative ratios of organic and aqueous flows, but no attempt was made to optimize conditions or capture processing efficiencies. The flowsheets described here are meant to be illustrative of process design capabilities, but the effectiveness of a given flowsheet will depend on the behavior of all of the components present in the feed. The relative extractability of these other species will impact the selection of extractant and the ultimate flowsheet design.

### **GCMAT**

To better understand how resource constraints could impact the growth in battery production and EV deployment, we have adapted Argonne's GCMat model to battery materials (GCMat-Bat), using LDRD funds. In FY23, we continued to develop and test the GCMat-Bat model, expanding its capability to model recycling and improving its data inputs. Working with NREL's LIBRA model and Argonne's EverBatt model, we initiated analysis of different scenarios with constrained resource availability.

The project will help to complement and inform existing ReCell programs and models by improving understanding of how resource constraints and disruptions to supply could impact lithium, nickel and cobalt markets, and how this in turn could impact battery recycling. GCMat-Bat can be used to help guide technology development and R&D pathways to alleviate potential impacts of resource constraints and avoid future material criticality.

Our approach to accomplishing this objective is to first complete development of the GCMat-Bat model through completion of recycling modeling capabilities, input data improvement and model testing and calibration. In parallel, we are developing capabilities to conduct integrated runs with LIBRA and GCMat. Once these developments are completed, we will conduct thorough analysis of potential outcomes under different scenarios developed with input from ReCell program managers.

We made significant progress in FY23 towards completing model development. First, we completed a preliminary version of a direct recycling module for GCMat-Bat that allows the separation of the supply of end-of-life vehicles into cathodes of different types, with tracking of the material composition of each cathode type. Second, we improved on input data in several areas. A major focus of these data updates was on current and future potential mining projects. Eighteen individual domestic lithium, cobalt and nickel development projects were added to the model, and the potential for additional mine development outside of the US was tied to USGS data on reserve and resource levels. Additional data improvements and updates were made to country-level estimates of current mining capacity, shares of production in different regions, vehicle demand projections, cathode use and material inputs, and lithium hydroxide production from brines. We also initiated analysis of trade data for estimating costs of insurance and freight, as well as for testing and calibration of material flows between regions. A third area of focus was model testing, including scenario runs to test how the model responds to different supply disruptions, such as a cut-off to cobalt supply from the Democratic Republic of Congo (DRC) and a restriction of exports from China. Selected results of the cut-off of cobalt supply from DRC are shown in Figure III.3.59. These runs demonstrated that the model was properly responding to the supply cut-offs in several ways. The cut-off in cobalt supplies led to spikes in cobalt prices, which propagated through the model to prices of other downstream products such as cathodes, battery cells and electric vehicles. Agent responses to these price signals were also observed, such as shifts toward low or no cobalt cathode types.



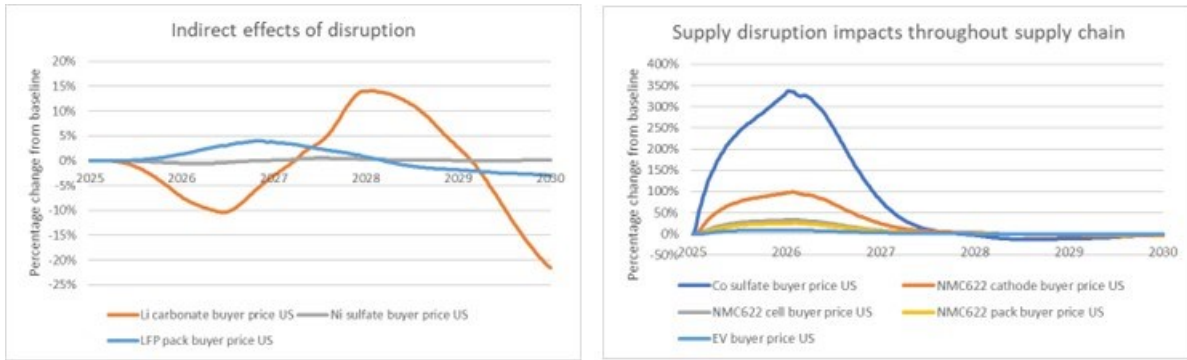


Figure III.3.59 Impacts of cut-off of cobalt supply from DRC

A fourth area of focus was working with the LIBRA modeling team to develop integrated modeling capabilities. We established a plan for initial joint modeling runs and prepared GCMat outputs showing trajectories for the maximum potential new material supply over time, shown in Figure III.3.60. LIBRA analysis combining these material supply limits with battery demand scenarios showed the most potential for global nickel supply not being able to keep up with demand, followed by cobalt with lithium in the least danger of global shortages due to high reserve values for lithium.

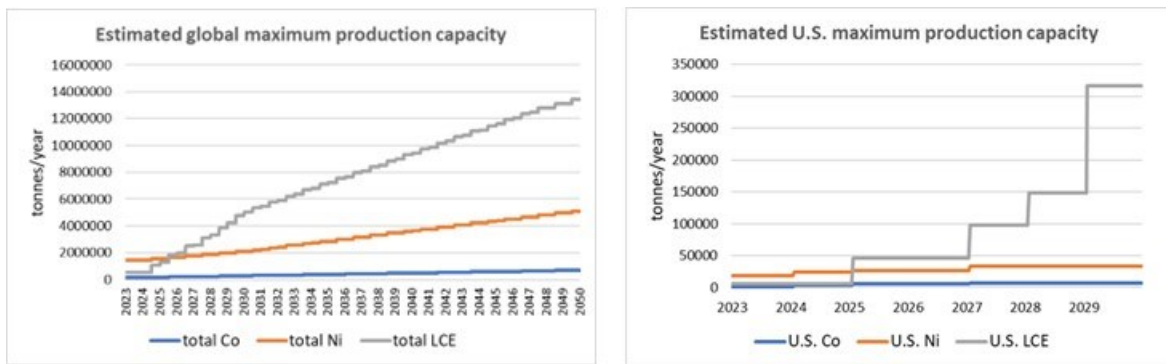


Figure III.3.60 US and global maximum production capacity

**A Combined Approach to Understanding Upcycling Diffusion Issues – NMR**

Understanding the structure and composition of end-of-life battery materials is crucial to develop and optimize relithiation and upcycling processes. The build up and impurities on electrode surfaces, lithium content on the surface and in the bulk and lithium local structure may all play a role in utilizing an effective and efficient recycling method. A complete characterization of the end product, the recycled materials, is equally crucial to understand if the targeted composition is achieved and the processes used are optimized. Solid state NMR is a powerful characterization technique to study surface and bulk composition as well as bulk local structure, and can track before and after changes, quantitatively.

The focus of solid-state NMR effort within ReCell program is to understand end-of-life and recycled battery components (anode, cathode and electrolyte) in terms their composition, surface/ interface/ bulk structure, lithium content and impurities and provide continuous feedback to direct recycling and upcycling focus areas. The goal is to build characterization guided recycling and upcycling processes where the methods used are optimized through understanding the recycled material properties/ structure and correlating these with synthesis conditions. The effort utilizes application of multinuclear solid-state NMR to understand surface composition, surface and bulk lithium content, bulk local structure and lithium and cation insertion/ diffusion into the structure after different recycling processes

In FY23, as part of our characterization focus, we utilized  $6,7\text{Li}$  NMR to study surface and bulk lithium local environments and content for EoL cathodes and after relithiation and upcycling processes. Within this effort, we reached out multiple synthesis groups within the program, working on hydrothermal, ionothermal, redox flow and solid state relithiation and upcycling; and studied a variety of samples.  $1\text{H}$  and  $19\text{F}$  solid state NMR was also utilized to understand surface impurities and possible protonation. Variety of samples were carefully studied, analyzed and before/ after data comparison was performed to understand the effect of each different step and parameter such as the effect of washing, the use of different transition metal salts, the effect annealing temperature, effectiveness of relithiation versus upcycling. The findings are used to correlate the recycled cathode's structure and composition with electrochemical performance.

As part of our model systems effort, we studied the effect of acid etching on possible H/Li exchange and proton insertion into the bulk. Model samples were prepared with  $\text{D}_2\text{SO}_4$ , washed with  $\text{D}_2\text{O}$  and then characterized by XRD, SEM and  $2\text{H}$ ,  $6\text{Li}$  solid state NMR after acid treatment and relithiation/ annealing to study the structural and compositional changes.

$6\text{Li}$  solid state NMR has been effectively used to understand the lithium loss and irreversible/ reversible structural changes in EoL cathode materials. Since the lithium-6 peak positions are sensitive to lithium coordination, nature and oxidation state of transition metals in the structure, the data provides useful information on cation diffusion and distribution after recycling processes. All the data are carefully normalized, deconvoluted and compared to track the changes within the different steps of relithiation or upcycling steps. The peak shape, width, intensity and position changes provide information on; if the end material is at the targeted cathode composition, if there is any transition metal segregation, if there is any surface lithium and if material had gone through an irreversible structural change at end of life.  $7\text{Li}$  NMR has also been utilized to quantify surface lithium within the recycled cathodes. The information is crucial to understand the efficiency of relithiation step, possible lithium loss during washing/ etching, and understand the initial capacity losses of the recycled material in comparison to the targeted composition.  $1\text{H}$  and  $19\text{F}$  NMR data collected on the samples, provide information of if there are any surface impurities left on the surface after washing, if the binder is successfully removed after solvent treatments and heating and if there is any LiF formation on the surface which can effect electrochemical performance of the recycled cathode. Examples of data comparison are given in Figure III.3.61.

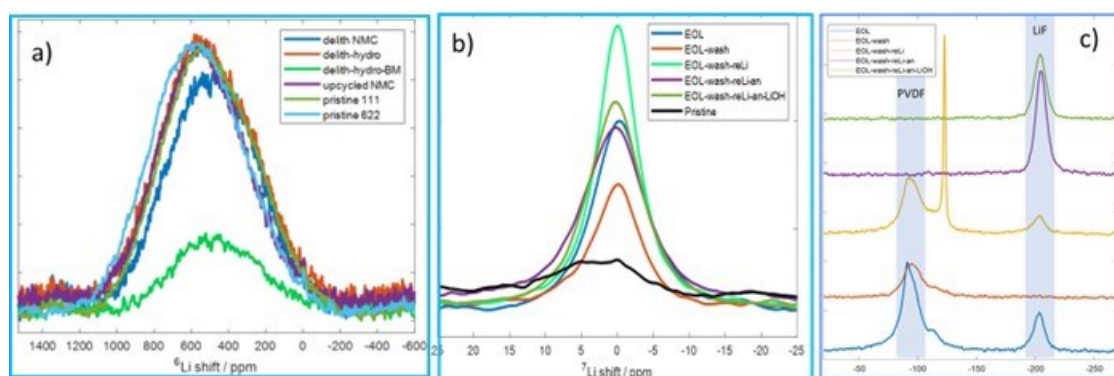


**Figure III.3.61** Solid state NMR data comparison of different recycled and relithiated samples. a)  $6\text{Li}$  NMR of upcycled NMC 111 with hydrothermal synthesis. b)  $7\text{Li}$  NMR data comparison of redox relithiated samples at different stages. c)  $19\text{F}$  NMR data of NMC 111 samples after washing and relithiation with redox chemistry.

The results on the effect of washing and surface etching on upcycled NMC 111 cathode surface and bulk is summarized in Figure III.3.62.  $2\text{H}$ ,  $6\text{Li}$  solid state NMR data show presence of both surface and structural protons after acid etching and structural lithium loss right after acid treatment, respectively. With relithiation and heat treatment lithiums are restored back and protons are removed from the structure. The etched samples

show better retention rates than non-etched samples in electrochemical performance, especially after a short but high temperature annealing.

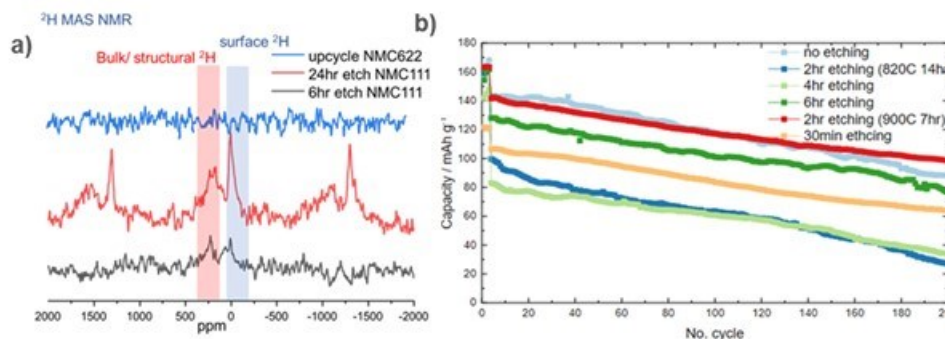


**Figure III.3.62 The effect of washing and acid etching on upcycled NMC 111. a)  $^2\text{H}$  MAS NMR on samples after acid etching b) Electrochemical performance comparison of the etched NMC111 after upcycling to NMC 622 with different heat treatments**

### ***A Combined Approach to Understanding Upcycling Diffusion Issues – APS***

Battery upcycling is a relatively new process for converting older generation cathode materials (i.e. NMC333) mixed with nickel-rich precursors to a more marketable cathode with higher Ni content, such as NMC622 or NMC811. This process requires optimization of temperature and hold times to allow for transition metal interdiffusion without significant primary particle ripening. Higher Ni content also can also lead to decomposition via cation (Li/TM) mixing or lithium loss at these high temperature conditions. Working with Jack Vaughney (CSE) and Fulya Dogan (CSE), we have studied changes in diffraction during the upcycling process for a variety of nickel-based coatings, as well as approaches for relithiation. This work has largely focused on the NMC333  $\rightarrow$  NMC622 upcycling process, but we have also ran preliminary studies on NMC811 upcycling and LFP/LMP mixtures. We also collaborated with the Coyle (NREL) and Chen (UCSD) groups on alternative approaches for relithiation and hydrothermal-based upcycling.

In FY22, we identified temperatures where a variety of Ni- and NMC-based precursors volatilize, typically forming a highly defective, (Li,Ni)O rock salt intermediate. As seen Figure III.3.63 a), this product has characteristically broad diffraction peaks associated with the domain size (i.e. primary particle) of the intermediate as well as substantial small angle x-ray scattering (SAXS) due to lattice defects. The gradual ordering of the rock salt intermediate to the final cathode can be seen by the broad 003 layered phase peak that overlaps the sharper diffraction line from the original cathode. At higher temperature, the lines coalesce and the overall diffraction intensity increases from the combined, upcycled material.

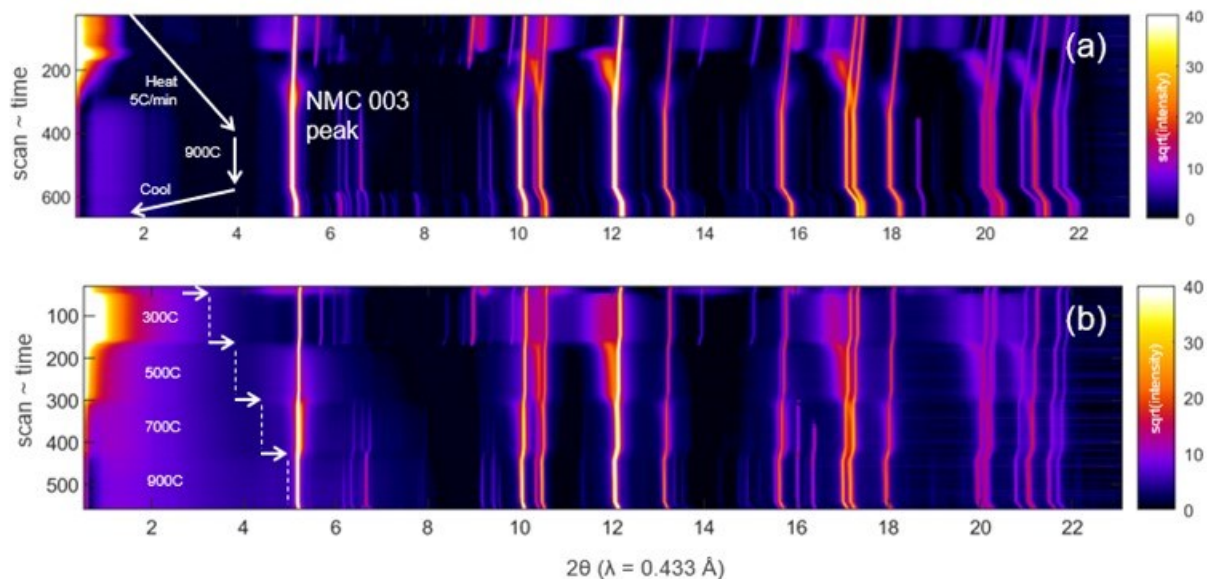


**Figure III.3.63** (a) Example of upcycling to NMC811 using a Ni sulfate-based precursor under standard heating conditions (5C/min ramp to 900C, 1 hr. hold, and cool). (b) Example of temperature step studies for understanding kinetics for upcycling processes.

Having identified the temperature for several of the reaction steps required to react the Ni- and Li-based precursors and inter-diffuse the resulting nanoscale LiNiO<sub>2</sub> phase into the cathode feedstock, we developed an alternative approach to study the kinetics of these steps. As seen in Figure III.3.62 b), we studied the time dependent changes in diffraction following thermal steps at 300, 500, 700, and 900C which correspond to (i) decomposition of the Ni coating; (ii) lithiation of the NiO intermediate; (iii) ordering and formation of LiNiO<sub>2</sub> phase and (iv) interdiffusion with the initial NMC material. This process was studied for both sulfate- and acetate-based precursors.

#### **EverBatt: Cost and Environmental Impact Modeling**

Recycling has the potential to reduce the cost and environmental footprint of lithium-ion batteries (LIBs). Argonne has developed the EverBatt model to estimate the cost and environmental impacts associated with closed-loop recycling of LIBs, and we have been using the model to help inform and direct R&D efforts at the ReCell Center.

In FY23 we developed and released a new version of EverBatt in which we updated process, cost, and environmental impacts data and the cost modeling methodology. EverBatt2023 also allows us to model preprocessing and critical material recovery steps separately or combined. In FY23 we also updated comparison of relithiation processes based on newly available information, developed models for induction delamination, polyol metallurgical relithiation, and polyol metallurgical upcycling, and evaluated ReCell's patented direct recycling process.

EverBatt modeling of ReCell's patented direct recycling process shows that the process outperforms pyrometallurgical recycling, hydrometallurgical recycling, and virgin production in terms of cost and carbon footprint. This is mostly because the structure of the cathode active material (CAM) is preserved throughout the recycling process, but also thanks to the innovative process design that can achieve satisfactory material separation with fewer processing steps compared with conventional technologies and its minimal requirements for reagents and solvents. The CAM yield of the process, however, is lower than what can be achieved for critical minerals (e.g., Ni and Co) with conventional technologies. Mechanisms for CAM loss throughout the process and design modifications that could improve the CAM yield should be explored, to further improve the cost and environmental impacts of the process.

### **Modeling the Reverse Supply Chain**

Electronic devices containing lithium-ion batteries (LIBs) are widely consumed in the United States. To improve LIB recycling performance in the U.S., a thorough understanding of the end-of-life (EOL) LIB reverse supply chain is essential. This project examines consumer behavior, geographical considerations, and regulations at state and national levels. LIB collection from households to e-waste collection locations is evaluated at the census tract level by utilizing GIS in conjunction with agent-based model (ABM) and system dynamics (SD) modeling methods. Finding supply chain bottlenecks and inefficiencies is the goal of this work, which will serve as a foundation for creating more effective incentives to increase LIB recycling.

The objective of this research is to enhance the recycling of LIBs in the United States by gaining a deeper comprehension of the existing structures and operations of EOL LIB reverse supply chains. The evaluation will encompass consumer electronics such as laptops and electric vehicles (EVs).

In the first year, the project selected laptop batteries and an e-waste regulated state to study consumer behavior and investigate any inefficiencies in e-waste recycling. We created a hybrid model that combines SD and ABM at the census tract level for the state of New York. SD model was employed to minimize computational time in tracking laptop lifespan. Cohort-based tracking of sales, rather than individual laptops, is better suited for SD. In the ABM model, the recycling behavior and decision-making progress of agents on the obverse play an important role in determining the number of laptops that are recycled. This behavior is then incorporated into the SD model, where it directly affects the quantity of laptops that undergo recycling. Data on socio-economic, demographic, and spatial aspects of the year 2021 were gathered, encompassing the locations of retailers, collection centers, and recyclers within 5,295 census tracts in New York. This comprehensive dataset was utilized for the purpose of model development and parameterization. In addition to using SD to mitigate the computational challenge, we have constructed the model at the census tract level rather than the household level. This approach allows for future scalability at the national level. With this approach, we assume that people in the same tract behave homogeneously. Agents were placed at the centroids of the census tracts and provided with representative demographic parameters. Agents' recycling decisions, in the model, depend on their socio-economic status and their proximity to recyclers or recycling centers.

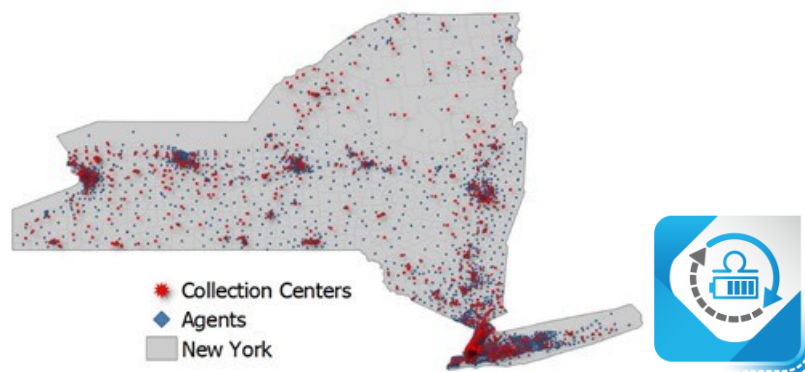


**Figure III.3.64 Map of collection centers and agents (placed at centroids of census tracts) in the state of New York.**

We modeled 5295 census tract social economic data, about 673 collection locations and approximate 506,238 in use laptops for the state of New York (Figure III.3.64) using a hybrid model (ABM and SD). This model considered various factors, including distance matrices and socio-economic indicators such as median income, education level, and age. The decision-making process of agents can be influenced by their socioeconomic characteristics. For instance, agents with higher household income may choose a more costly recycling option to save time. Additionally, the proximity of collection locations can impact agents' inclination to engage in recycling activities. It is assumed that if the recycling collection location is located over 10 miles away, agents may be less willing to make the effort to drop off their e-waste. These behaviors ultimately have an impact on

the overall recycling rate. Additionally, the model incorporated e-waste collection events, which offered strategies to improve the collection rate. The impact of these collection events on the drop-off method is depicted in Figure III.3.65, revealing a notable 23% increase in the number of census tracts participating in recycling activities.

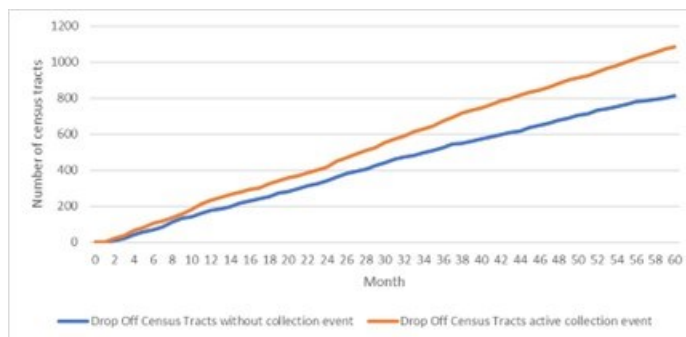


Figure III.3.65 Comparing battery collection with and without collection events.

***LIBRA: Supply Chain Analysis for Battery Recycling (falls under supply chain)***

NREL is analyzing the material and component supply chain for lithium-ion battery (LIB) manufacturing and recycling to determine the dynamic factors driving the economic viability of this nascent industry. Material availability, supply shocks, and technology adoption all impact the continued operation of this supply chain, which in turn enables the rapid electrification of the transportation sector that has been identified as a cornerstone of the global strategy to mitigate greenhouse gas emissions. NREL conducts many types of analyses for the LIB supply chain, including trade flow analyses, global resource assessments and projections of regional industry growth patterns. For this report, we will focus on NREL's systems dynamics model, Lithium-ion Battery Resources Assessment (LIBRA). The LIBRA Model identifies and explores the critical factors for the successful buildout of LIB manufacturing and recycling capacity both domestically and globally. LIBRA tracks the flows and stocks of battery materials, financing, and industrial maturity leading to more efficient plant operations through 2050 under varying policy scenarios and LIB demand conditions. The model has been used to evaluate the material circularity of the LIB industry with a particular focus on how that can lead to the achievement of established climate goals and benchmark projections. The various modules included in LIBRA are shown in Figure III.3.66.

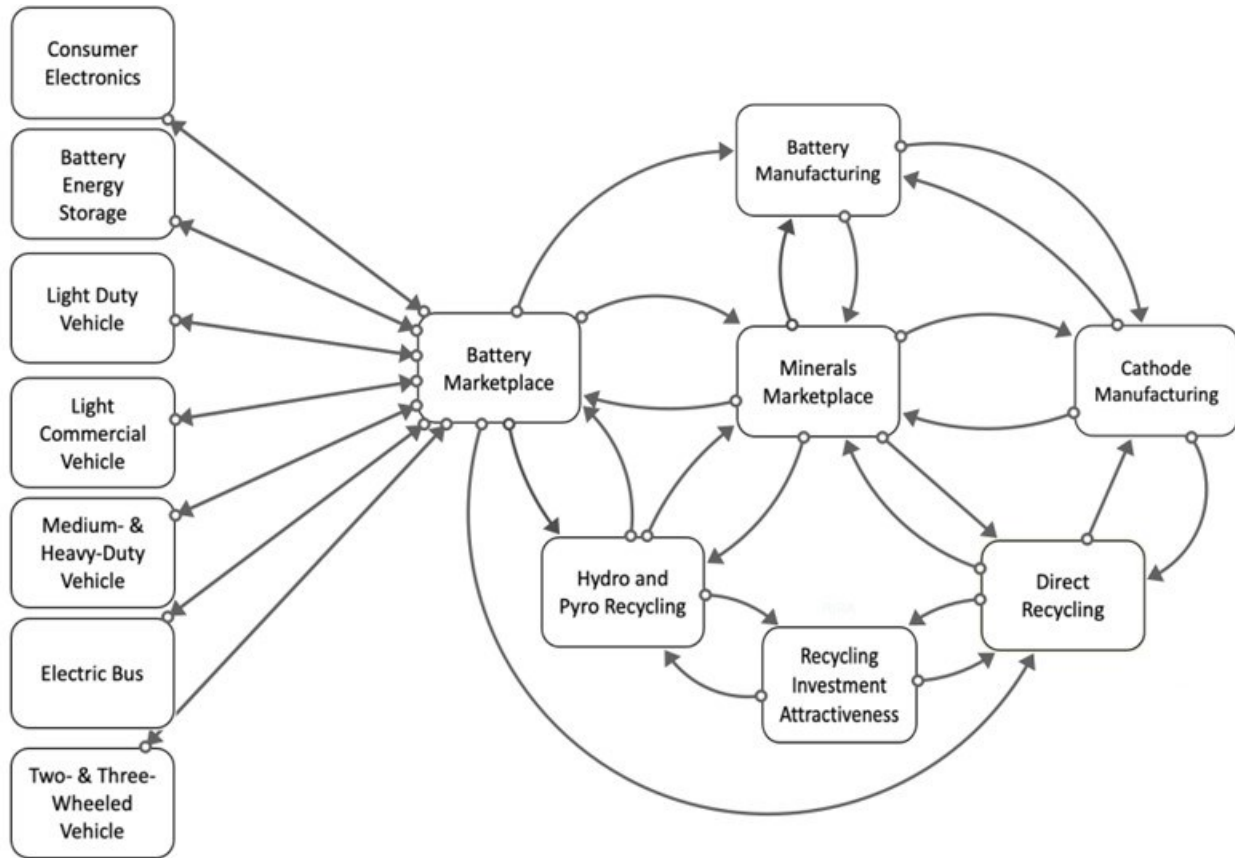


Figure III.3.66 LIBRA model top level modular structure

The objectives of this project are to evaluate the most impactful barriers and drivers of the LIB supply chain in the United States and globally. More specifically, these modeling efforts are designed to answer questions similar to those below. While the questions below are illustrative of the types of questions LIBRA can be used to answer, they are not exhaustive.

Sample key questions:

- To what extent can LIB recycling contribute to the domestic battery industry development?
- What are the top hurdles for economic development of the domestic battery manufacturing and recycling industries?
- How can we work with partner countries to enhance the domestic supply chain?
- What aspect of the supply chain exerts the most leverage on the development of the domestic industry's development?
- What impact would investment and external market shocks have on the growth of the industry?
- How might evolving chemistries impact recycling and the evolution of the recycling industry?
- How do variations in demand for LIBs impact the development of battery manufacturing and recycling capacities in the United States and globally?
- How do various factors such as policy decisions, plant financing, material constraints, or market shifts impact the potential circularity of the LIB supply chain?
  
- How does battery second life change the outlook for battery material demand, end-of-life treatment, and the recycling industry?

The LIBRA team uses system dynamics modeling, sensitivity analysis, and data aggregation and interpretation to evaluate battery supply chain outcomes under different conditions out to 2050. With projections extending out multiple decades, uncertainty in the inputs can be high and lead to significant variation in modeled outcomes. Sensitivity analysis is useful for evaluating the range and extent of these variations and determining which inputs are the most important. NREL also relies upon a number of sources for predictions of how battery demand will change over time with adoption of EVs and electrification of the grid. The range in these sources forms a useful basis for sensitivity and scenario analysis.

Work with the LIBRA model the NREL battery supply chain team this quarter had a few different areas of focus over FY23. First, the team expanded analysis around the impact of different feedstock sources on the initiation of the battery recycling industry. The first component of this feedstock, consumer electronics, have shorter lifetimes and higher cobalt concentration than EV or BES batteries. Consumer electronics therefore represent both a more valuable source of recycling feedstock and is available in greater quantities until 2035 when more significant quantities of EV batteries reach end of life (EOL) in the US. Next, this analysis considered the quantity of manufacturing scrap generated from battery production. This comprises a greater quantity of battery material for recycling than EOL EV or storage batteries until 2035. Together, consumer electronics and manufacturing scrap are critical feedstock sources for the buildout of domestic recycling capacity in the near-term, prior to the expected sharp increase in EOL EV batteries.

Figure III.3.67 shows the modeled projection of EOL batteries from different sources from LIBRA based primarily on the demand projection from BNEF 2022. EOL EV batteries become the primary feedstock beyond 2035 but manufacturing scrap and consumer electronics batteries dominate the feedstock stream until 2030 when LIBRA projects EV batteries will become a more significant source of EOL material in terms of MWh of packs reaching recycling plants.

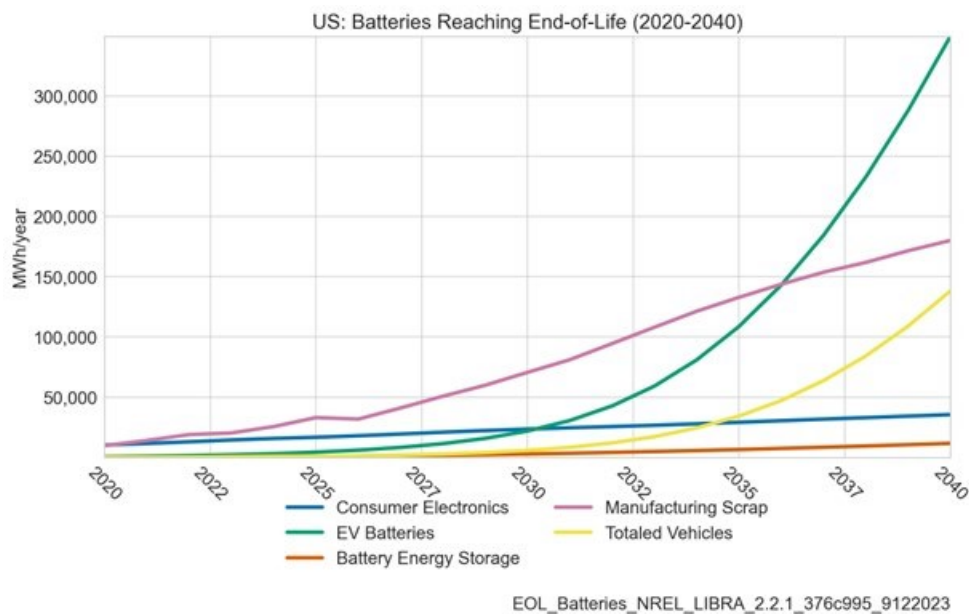


**Figure III.3.67 Projected availability of end-of-life batteries for recycling from different sources**

The team also ran analysis in other areas such as the impact of an Extended Producer Responsibility (EPR) policy that would require the recycling of 100% of end-of-life batteries. The mechanism for this policy in LIBRA is represented by payments between recyclers and the owners of the batteries at EOL (battery collectors, OEMs, or others). Payments go *to* recyclers to ensure batteries are processed that may not be profitable to the recycler such as LFP batteries. In contrast, LIBRA models payments *from* recyclers to



purchase high value chemistries such as LCO. This analysis is working to determine the range in value of these payments to maximize the percentage of batteries that are processed.

There were also significant model developments this FY including updating the data across all aspects of the model both in terms of inputs and parameters to ensure model outputs are validated against the current state of the industry for manufacturing and recycling buildout in the US. The team also added new model structure to evaluate the impact of battery second life. Second life batteries can be sourced from and used for LDV, LCV, MHDV, EBus, and BES batteries. The share of batteries allocated to second life can vary by vehicle type and battery chemistry, with the intensity of some first life duty cycles (commercial vehicles for example) likely resulting in a lower share of batteries moving into second life than for end uses with less intensive duty cycles. Likewise, different battery chemistries have longer or shorter cycle lives that might make them more appropriate for second life. Initial runs indicate that the availability of second life applications can reduce the amount of mineral that is landfilled or exported from end-of-life batteries and reduce the mineral demanded for new battery manufacturing as shown in the figures below for cobalt and nickel respectively. These reductions are linked to the extended useful life of battery materials used in second life batteries, reducing both the total quantity of material required to meet demand and reducing the amount reaching end-of-life generally in a given year. This also results in a reduction in feedstock for recycling plants, and therefore a corresponding reduction in recycling plant buildout.

## **Conclusions**

### ***Direct Recycling***

#### ***Cell Preprocessing***

A custom-designed shredding, washing, and drying system has been purchased. In addition, other unit operations for pre-processing (e.g., material processing and separations) were purchased and have arrived at Argonne. All of this equipment will be installed in the pilot facility that is currently being renovated at Argonne National Laboratory. When the pilot scale facility is up and running, we will have scalable capabilities for our pre-processing unit operations.

#### ***Electrolyte Component Removal and Recovery***

The recovery and reuse of electrolyte has been scaled up using a scalable process. In addition, the reuse of the solvent does not appear to cause significant problems on its own. There is still a lot of variability in the process that needs to be controlled as the process is scaled up further. Equipment that will be able to rinse and dry at least 20 kg/hr of shred is currently on order and is expected to be installed by the end of FY24.

#### ***Recycling Electrolytes by Precipitation and Distillation Process***

We have successfully demonstrated the recycling of low boiling-point electrolyte solvent EMC from the aged electrolyte using the developed vacuum distillation process. It is a feasible process and could be easily scaled up by chemical industry. This process is being transferred to MERF for a large quantify demonstration. In FY23, we also conducted the quantification of transition metal ion concentration in the spent electrolyte by ion chromatography (IC) method developed in FY23. Transition metal ions including Mn, Ni, Co, and Cu have been detected and their concentration was determined with high accuracy.

#### ***Thermal Binder Removal***

We have currently scaled the binder removal process to 400 g of recovered cathode material. The graphite process was scaled to a 1 kg batch. LiFePO<sub>4</sub> recycling has been funded via an AMMTO funded CRADA and will use the processes developed in this project to do the binder removal. Going forward work is ongoing to modify an alumina tube for the rotary kiln to create ridges to allow for all thermal treatments to be done effectively in the rotary kiln. Further optimization of the NMC process and processing of the graphite in the rotary kiln will be done once this tube is ready.

**Recycling through Spot Heating Treatment**

We demonstrated that high yield recovery of anode materials can be achieved by high-frequency induction heating delamination process which requires low energy consumption and fluid-free. Batch processing demonstrated recovery yield of 97% the starting anode materials with a graphite fraction of ~70% by weight in the processed materials. High purity copper foils and high-quality graphite were obtained from HFIH delamination with inert gas flowing during processing. Electrochemical cell testing revealed similar charging/discharging performance when compared to these cells constructed using pristine anode materials.

**Solvent-Based Electrode Recovery**

The SolveX process was updated to facilitate the direct recycling and remanufacturing of commercial anode scraps. By tuning the type of alkali hydroxide, LiOH concentration, reaction time, and washing conditions, the delaminated anode films were successfully reprocessed into new anode with similar electrochemical performance as the baseline anode. In addition, SolveZ process was evaluated by EverBatt modeling and published. Both SolveY and SolveZ processes have been granted patents in FY23.

**Aqueous Sequential Separation**

In summary, the aqueous sequential separation process has been successfully demonstrated to recover materials from commercial spent cells. A manuscript studying the aqueous sequential separation process was submitted and under review. The recovered graphite was reintroduced into new electrode manufacturing and exhibited good electrochemical performance. Additionally, an ethylene glycol based sequential separation process was developed to deal with the commercial electrodes.

**Solvent-Based Dual Process**

The regeneration process has been optimized to reduce processing cost by increasing the solid to solvent ratio. The process has been scaled up to produce 25 g of regenerated NMC111. When combining the delamination and relithiation in one pot, the defluorination reaction between LiOH and PVDF needs to be better understood.

**Anode/Cathode Separation and Purification**

The large-scale RE Roll and optical sorter separation processes can be further optimized on manufacturing scrap shreds and other types of battery materials. These processes are high-throughput (kg/hour) and will be included in the pilot recycling facility being installed at Argonne National Laboratory.

**Cathode/Cathode Separation**

More complex mixtures of cathode materials (e.g., three different chemistries) typically require more separation steps to achieve higher purity and optimize material recovery. Separation processes can be further optimized for cathode mixtures.

**Cathode/Cathode Separation via Froth Flotation**

During this fiscal year, we have investigated the impact of various recycling and pre-treatment processes on both bulk and surface properties of the recycled cathode active materials (CAM). Results showed that both the mechanic separation and pyrolysis treatment methods can remove and/or decompose PVDF binders from the recycled cathode composite materials. However, both surface and bulk properties of recycled cathode active materials varied with the pretreatment processes. It was found that the thermal pyrolysis at 600 °C resulted in a structural change, particularly on the surface of the recycled cathode materials, associated with a lithium loss. The presence of anode materials in the feed materials further damaged the structure of recycled cathode materials.

**Molten-Salt Assisted Flotation for Separation of Electrode Materials**

An IL based high density liquid has been developed for flotation separation of graphite and NMC from black mass. Benefit from the low melting point of IL, the molten-salt assisted flotation could be performed under room temperature. The formula of IL will be optimized to achieve higher NMC purities. Separation

performance on the other commercial black mass (V1A) will be evaluated. IL-based room-temperature separation will be scaled up from 10 g to 20 g.

### ***Solvent-Based Gravity Separation***

During this FY, the effect of process medium on the separation efficiency between anode and cathode materials by centrifugal gravity separation process was investigated. Compared with DMSO, NMP was a better solvent for PVDF binders resulting a better liberation between individual cathode particles. The result obtained from the centrifugal gravity separation experiments showed that the percentage of cathode active materials in the concentrate product reached 94.0% - 95.2% after two cleaner stages, demonstrating the effectiveness in separation of two electrode materials from the feed materials.

### ***Role of Impurities in Recycled Cathodes***

The work reveals that silicon impurity has a minimal adverse effect on hydrometallurgy recycling. Obviously, managing silicon impurity is not the primary concern in regard to recycling optimization.

### ***Purification of Black Mass***

Substantial progress has been made in FY23 to facilitate scale-up of the black mass purification process. A 1 L reactor has been installed along with supporting infrastructure and auxiliary equipment, which enables processing of 50 g batches of black mass. Design and installation of the reactor and auxiliaries was a highly intensive effort that involved coordination with several ESH&Q teams. Following installation, the reactor performance has been validated with a series of pristine NMCs, which in addition to verifying functional reactor operation has also allowed us to achieve several scientific goals. Results include verifying “no impact” of treatment conditions on NMC with varying Ni content; baselining pH response with temperature for each solution matrix; and obtaining sufficient quantities of material to evaluate a series of post-treatment rinse conditions. We have updated the EverBatt model of our process to enable sensitivity analysis of post-treatment rinse conditions, and have used the results to inform our solvent choices/treatment times/etc. We have also collaborated with the Argonne team to prepare a series of cathode-rich manufacturing scrap fines with and without thermal binder removal for initial at-scale testing of “real world” BM; we plan to prioritize upstream and downstream integration of the BMP process with other ReCell methods in FY24. Finally, we have brought a new hire onto our team and published a journal article that highlights project results from FY21-FY22.

### ***Hydrothermal Relithiation***

In FY23, we identified several vital parameters for hydrothermal relithiation scaling-up process, such as solid-liquid ratio impact, Li residue, and space occupancy impact of reactants in the hydrothermal reactor. We successfully demonstrated that the hydrothermal relithiation process could be successfully scaled up to relithiate D-NCM111 in 4M LiOH solution with an increased solid/liquid volume ratio of 1:1 at 100 oC and fully utilizing the Li source to achieve efficient and cost-effective regeneration. The optimized process is promising for developing large-scale regeneration for clean cathodes.

### ***Ionothermal Relithiation***

An ionothermal relithiation method based on RTMS flux has been successfully developed to relithiate spent NMC622. By reusing 90% of RTMS for once, the cathode regeneration cost is \$14.88/kg, much lower than those of conventional recycling technologies (\$25.22~30.11/kg). The topotactic relithiation of in RTMS can achieve relithiation and recrystallination of EoL-NMC, simultaneously remove impurities without morphology changes.

### ***Relithiation via Redox Chemistry***

We identified a key pre-relithiation step to facilitate chemical relithiation of commercial EoL NMC 622 material. The washing step can be tailored in the upstream material recovery process to prevent PVDF byproducts from preventing full relithiation. This could cut cost and improve material recovery by minimizing material loss from multiple washing steps.

### ***Chemical Relithiation***

Relithiation studies of the cycled commercial cathode powders focused on material recovered using the solvent Y process (ORNL) and final studies using the RAM method of Relithiation and lowering the costs.

Characterization results and electrochemical performance appeared consistent between the two methods showed the materials produced were consistent with the initial pristine samples. Using the RAM method allows scalability and reduces liquid wastes associated with the relithiation process. Issues with surface impurities on scale-up, noted by CAMP, were corrected by adding a DMC washing step.

### ***Hydrothermal Upcycling***

In FY23, we successfully demonstrated a two-step lithiation strategy for upcycling chemical delithiated NCMs in different SOHs into single crystal NCM 622. We propose that the process is dominated by the Ostwald ripening phenomenon, which promotes NCM crystal merging and growth at the expense of smaller crystals through dissolution and precipitation during high-temperature holding.

### ***Ionothermal Upcycling***

An ionothermal relithiation method based on RTMS flux has been successfully developed to upcycle pure NMC 111 to NMC 622 or 811. The upcycling of NMC mixtures is more challenging. The effect of SolveY-NMC 622 on the ionothermal upcycling process will be further investigated for better upcycling performance.

### ***Solid State Cathode Upcycling***

In this FY23 effort, we were sought to better understand, in association with the Fister group, the role of the nickel salt used to upcycle NMC333 to NMC622 (or NMC811). We showed that the salt anion needed to decompose completely in the needed temperature window. Previous studies had used sulfate salts with the assumed decomposition to sulfur oxides, however we were able to show that the sulfate was re-precipitating as lithium sulfate and crystalizing on colling to block the active surface. Acetate salts were found to decompose more cleanly but issues with surface reduction are being investigated as part of FY24. An annealing study on the in-situ formed material indicated that an ideal temperature time for the anneal to homogenize the upcycled product was 900 °C for 1h. Previous studies have indicated that high temperatures are an issue for final cost and the lower times at temperature is an advantage based on EverBatt.

### ***Upcycling via Co-Precipitation Process***

The diffusion limitations identified through TXM show the coprecipitation and relithiation process for cathode upcycling requires further optimization to improve the homogeneity of the Ni-rich phase to improve capacity and cycle life. The optimization will be guided by feedback provided by TXM and HR-XRD collected at the APS. Additionally, we will use these characterization techniques to evaluate how changes in porosity and composition of recycled EOL cathode may affect the Ni-diffusion during coprecipitation upcycling and relithiation compared to the pristine baseline.

### ***Anode upcycling via tailored solvent treatment***

In the first year of this task, we have developed a novel treatment approach for spent graphite that provides unique added value to what has traditionally been considered a hard-to-recycle material. We have demonstrated the ability to selectively remove certain classes of SEI species while retaining others by tuning the properties of the treatment solvent. We have identified that as-received end-of-life graphite cannot be directly recast, such that some form of solvent treatment is essential in order to directly recycle spent graphite. Robust symmetric cell protocols coupled with advanced electrochemical modeling were developed and applied to probe the electrochemistry of both baseline and upcycled material without artificially altering the SEI. Further, in collaboration with the Argonne Post-Test team, we utilized a suite of complementary advanced characterization tools and associated data analysis techniques to identify quantitative physico-chemical metrics reflecting the performance upcycled material. We produced detailed correlation plots that indicate which electrochemical and physico-chemical properties are the most relevant indicators for material performance, and how varying the treatment solvent properties affects these metrics. This FY, we thoroughly evaluated a series of single solvent systems with rationally varying chemical properties, which has revealed several distinct

solvent properties that appear to be well-correlated with performance. Our ongoing efforts are aimed at applying these findings to an expanded set of binary and perhaps ternary solvent systems. We are also probing the influence of process parameters, including treatment solvent concentration, on performance. Finally, we have brought a new hire onto our team this FY to support our ongoing progress. We are preparing a publication around our results to date, which we aim to submit in Q1 FY24.

#### ***Single Crystal Cathode Production***

In FY 23, we successfully applied the etching process to Ni-rich cathode materials for Ni-rich single-crystal cathode fabrication. The obtained single-crystal cathode has a self-coated Mn layer, which can reduce the degradation of structure and side reactions between electrodes and electrolytes. This process provides a new method to fabricate Ni-rich single crystal cathode with self-coated Mn, which reduces the cost and energy cost of extra coating or doping procedure.

#### ***Mechanical Method of Damage Mitigation***

The overall goal of this project is to optimize the annealing process to minimize cost while still repairing the EoL material enough to get comparable electrochemical performance to pristine. Multiple mechanical characterization techniques have been developed to measure cathode mechanical properties throughout the recycling process to determine whether the annealing process is sufficient to fix mechanical degradation.

#### ***Advanced Resource Recovery***

##### ***Graphite to Graphene***

The graphene process has been scaled to produce 50 g of graphene per batch. This graphene is still being tested in various applications. This includes testing it as an additive for lubricants, which we will be doing shortly. Optical sorting is an effective means of separating out copper foil from pouch and other gray metals. An understanding of the price differential is needed to see if this sorting process is economically viable or not.

##### ***Microwave assisted extraction***

In FY23 we showed that full digestion of NMC622 in low concentrations of citric acid utilizing MAE in as low a time as 1 minute can be achieved even without an additional reducing agent such as hydrogen peroxide. Batch tests have been used to identify optimal minimal and maximum temperature ranges as well as energy consumed. Future work will be focused on scalability of this technique.

##### ***Electrometallurgical Extraction and Recycling using Molten Hydroxide Salts***

In FY23, we demonstrated the viability of a two-step process using molten hydroxide salts to extract critical metals from Li-ion cathode materials. Feasibility tests successfully recovered transition metals from NMC materials and from black mass material. These results suggest that the alloy composition can be controlled by controlling the deposition voltage. Further development and refinement of the molten hydroxide systems may result in a commercializable low-temperature pyrometallurgical route for metals recovery from used Li-ion cathodes. In FY24, work will focus on determining processing conditions to achieve selective separation of the transition metals and demonstrating scalability of the process.

##### ***Ionic liquid based supported membranes for Li/Co/Mn separation***

The successful separation of Li/Co/Ni ions has been achieved using complexation driven ion exchange polymer membrane via proton pumping.

##### ***Separation and Recovery of Cathode Active Materials from End-of-life LIBs using Membrane Solvent Extraction***

MSX is a technologically promising and economically viable process for recovery and recycling of cathode active materials from EOL Lithium-Ion Batteries. The project has met the desired milestone, demonstrating the ability to generate 100g quantities of Co, Li, and Ni at >99.5 wt.% purity and >90% recovery from LIB black mass. Further exploration into the mechanism of Li/Ni recovery, possibly through precipitation in their

sulphate forms, may offer additional recovery of each of the components from the remaining low-cobalt solution.

#### ***Electrodialysis to Extract Lithium from Recycling Process Streams***

Lithium was successfully recovered from recycling waste solutions. The processes to recover lithium and convert it to lithium hydroxides can be further optimized and scaled using larger systems available at Argonne National Laboratory.

#### ***Using Sorbents to Recover Critical Materials from Leachate Solution***

Aluminum hydroxide,  $\text{Al}(\text{OH})_3$  sorbent has been successfully developed to recovery lithium from the downstream NMC black mass leachate solution. The lithiation, delithiation and relithiation process will be further optimized to determine the best process conditions. Further life cycle analysis and technoeconomic analysis will be carried out.

#### ***Continuous Extraction - Hydro Process***

The Zaiput membrane separator demonstrated high extraction efficiency in extraction of metals from a simulated black mass leachate, using relatively little solvent. Several metals (Fe, Cu, and Al) and Mn were readily extracted from the leach liquor using D2EPHA in kerosene and produced a raffinate rich in Ni, Co, and Li, which will be further separated using CYANEX 272.

The metal impurities (Fe, Al, Cu) that co-extracted with Mn were selectively removed prior to stripping of Mn using  $\text{H}_2\text{SO}_4$  solution, generating a  $\text{MnSO}_4$  solution with relatively high purity. The extractant was regenerated and reused repeatedly.

#### ***Photo-Controlled Recovery of Nickel Cobalt Manganese for Sustainable Recycling of Batteries***

We have identified an optimal photo-sensitive monomer structure for the transition metal recycling research and successfully synthesized 10 g of the monomer by a multi-step reaction. The Spiropyran monomer isomerizes when subject to UV irradiation, a prerequisite for the proposed cathode recycling approach. The concept of photo-controlled recovery benefits in reduction of cost, time, and the complexity of recycling thanks to the replacement of pH-sensitive ligands, solvents (multi-stage hydrometallurgical solvent extraction) with light source and minimal amount of polymer materials.

#### ***Soft Chemistry Coprecipitation of Battery Precursors***

In summary, we introduced a novel polyolmetallurgical approach, taking the advantages of the CAEG green solution, to simplify cathode recycling process. Benefits from the unique properties of CAEG combination, the CAEG solution serves both as leaching agent and precipitation agent, facilitating the precipitation and recovery process. The usage of CAEG solution also prevents the introduction of impurities and greatly simplifies the following separation process without comprising efficiency. This process is adaptable to both LCO and NMC cathodes and able to produce Co and NMC coprecipitates at selective NMC ratios. The produced precipitates could be directly used for cathode resynthesis.

#### ***Synthesis and Performance testing of Cathodes from Recycled Raw Materials***

We have identified that more precise control of the particle size and morphology of the cathode material is required to ensure effects in electrochemical performance are rightfully assigned to impurities present in hydrometallurgical salts. It was concluded that a shift to the TVR over the CSTR will improve the mixing environment, resulting in narrower distributions in cathode morphology. We continue to reach out to companies and national laboratories to attain information on impurity profiles and regulatory standards of materials attained from the latest hydrometallurgical processes and commercial materials from virgin sources. We are also continuing to contact industry partners for potential sources of hydrometallurgical-attained TM salts.

## Design for Sustainability

### End of Life Battery Passivation for Safe Transport

Heat treatment has demonstrably increased the cells' internal resistance, as predicted. However, the process may not be enough to render the cells safe, especially given their novel, energy-dense chemistries. Nail penetration will be conducted to properly evaluate the effectiveness of the heat treatment. In addition, older, lower energy cells are in the process of being sourced, as these may be more representative of the first-generation LIBs that will be entering the recycling stream in large quantities.

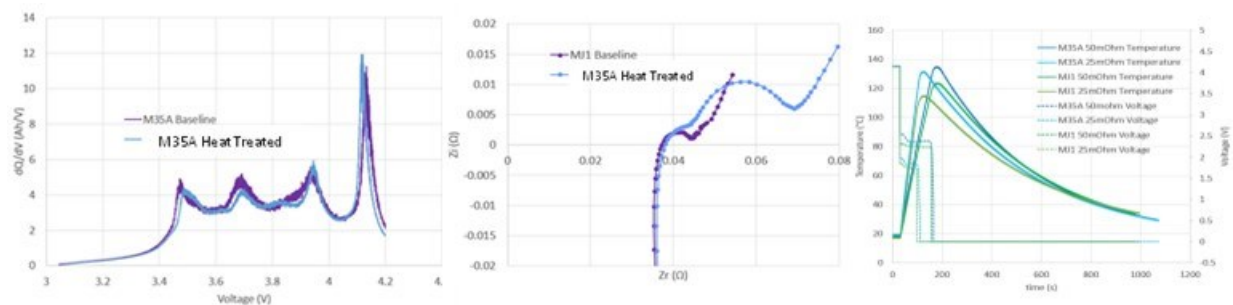


Figure III.3.68 differential capacity of a M35A (NCA/graphite) 18650 charging before and after heat treatment b) EIS of a MJ1 (NMC811/graphite + silicon) 18650 before and after heat treatment c) external short circuit results of M325A and MJ1 cells before heat treatment, at both 25 and 50mOhm short resistance

### Secondary Use Energy Storage Technology use Cases for Behind the Meter Applications

This project aims to reduce the challenges and costs associated with residential energy storage systems by enabling the integration of secondary use batteries from electric vehicles. Presented in this report are the beginnings of a hardware demonstration which will be followed by a techno-economic analysis to support the scale up and deployment of a demonstrated system with the functionality described above. Completed items include design of a scalable- residential secondary use energy storage system, design of flexible interconnects that can be configured to a variety of battery manufacturers, and a schematic of the electronics required to make the system functional with batteries of unknown state of health.

### Sustainable Recovery of Si from PV Panels for Applications in LIBs

The best silicon utilization and lowest capacity loss during initial C/20 cycling from milled boron-doped Si boule material which is promising for boron-doped PV silicon material that has been fully cleansed of contaminants. EoL material suffered high initial capacity loss and cell failure during C/20 cycling, likely due to Ag, Al, Fe contaminants.

### Battery Lifetime as a Service: New Business Model and Battery Design

The team introduced the BaaS concept, interviewed stakeholders, and began technoeconomic analysis. The technoeconomic analysis model will be completed in FY24. Key questions to answer include: To what extent does BaaS improve battery economic value and circularity? What BaaS applications are most promising? Key metrics for success from multiple stakeholder perspectives include minimizing cost/mile (or cost/ton-mile for trucking), maximizing revenue from V2G services, and maximizing battery circularity by maximizing total energy throughput across a single battery's lifetime. Additional goals include enabling difficult-to-electrify transportation applications and supporting renewable energy growth by making vehicle batteries available for V2G services. In addition to understanding viable BaaS business models, significant hurdles to increasing battery 2<sup>nd</sup> use include connecting SoH with SoS and estimating both. This is key to answer the question from several stakeholders, "When can batteries be used down to 60% and not just 80% remaining capacity?".

Next year the team will publish a whitepaper on BaaS introducing the concept and how it can be used to improve battery utilization, lifetime, and thus sustainability. After that, the team will engage stakeholders for feedback, refine the analysis and publish it. Pending resources, the team will then focus on identifying

technical solutions and modifying codes and standards to better serve BaaS and battery sustainability. The team will also revisit and update previous 2<sup>nd</sup> use technoeconomic studies.

#### ***Investigation of Reused EV Packs on Future Renewable Grid through ARIES***

In FY24, NREL will continue assessing the SOH of the Ford Fusion cells while acquiring packs with known CAN signal databases such as Nissan Leaf or Tesla Model 3 modules to allow for simpler interactions with used packs. Eventually, NREL will collect SOH data at pack, module, and cell level and how it differs from vehicle location and age (years and miles) ~10 kWh. Combining pack level data with more detailed cell level data will be used to determine at what level packs need to be deconstructed/re-assembled before used in second use applications. NREL will also perform technical economic analysis on state of reuse at levels of disassembly for comparison to direct recycling. Analysis in this area will be used to determine at what price (\$/kwh) second life packs need to be purchased at to be cost competitive with direct recycling – including transportation costs, disassembly, and state of life analysis.

#### ***Machine Learning RUL and SOH Classification***

A comprehensive data set of lithium-ion battery performance and response to a variety of rapid characterization measurements has been developed to study the potential for using rapid characterization tests to monitor lithium-ion batteries during use as well as to rapidly recertify batteries at their ‘end of first life’. Machine-learning has been used to demonstrate that battery performance can be predicted with reasonable accuracy using even simple rapid pulses, but that more complex pulse sequences inherently contain more information and are thus more useful.

#### ***Advanced Fasteners that enable Rapid Disassembly of Li-Ion Battery Stacks***

In conclusion, the project is progressing towards the objectives of enabling automation. ORNL has manually disassembled several full EV stacks and made Table III.3.4 for reference. The table will be updated periodically and updated when new joining technologies are encountered and measured. The previous year has been primarily focused on identifying problem points and designing tooling. The next year will be more focused on validating and demonstrating the tooling and developing processes and robotic routines that enable fastener extraction.

#### ***Precise Cell/Group Diagnostics, Removal and Replacement***

EIS is a valuable measurement method and may be able to assist in identifying bad or failing cells within a group, module, or even pack. Low inductance/impedance connections are necessary to perform EIS on groups of cells. High power testing may be necessary to explore higher capacity battery configurations. Cells that have been cycled and calendar aged for over 6 years show different EIS results even though they have been connected since manufacture.

#### ***Modeling and Analysis***

##### ***Requirements for Separation Processes through Electrochemical Modeling***

Substantial progress was made in developing electrochemical models to simulate electrodes made of recycled materials. A library of electrochemical parameters was developed by performing extensive GITT experiments for a variety of electrode materials. Next steps will be to compare model predicted rate performance for blended electrodes versus experimental measurements to validate blended electrode model. After validation, the model will be used to explore how electrochemical performance changes with incomplete material separation.

##### ***AMUSE Process Modeling***

The AMUSE code has been expanded to include species specific to battery materials that were not previously available within the code. The added species include Ni, Mn, Co, sulfate and chloride. The user can now define the acidic solvent used for the process and input parameters that calculate distribution coefficients for various metals as a function of acidity. The code can now also simulate the ion exchange behavior of acidic extractants based on the distribution coefficients to provide an in-process hydrogen balance. This capability informs the



addition of neutralizing bases such as NaOH or NaCO<sub>3</sub>, or the selection of buffers to control process acidity. With these added capabilities AMUSE can be better used to develop and optimize detailed flowsheets that use acidic extractants to recovery and purify valuable species present in battery materials.

### **GCMAT**

This project builds on an existing model, GCMat-Bat that has been developed at the LDRD level, which can be used to evaluate likely market responses under different supply and demand scenarios. In FY23, GCMat development focused on completing model development and establishing mechanisms for integrated runs with LIBRA, as well as preliminary scenario analysis for testing purposes. This work has set us up to conduct additional scenario analysis in future fiscal years that can be used to inform recycling technology development.

### **A Combined Approach to Understanding Upcycling Diffusion Issues – NMR**

Our solid-state NMR efforts on comparison on different recycling methods on local structure, surface and bulk lithium content and surface impurities provides crucial information and guidance on method development and improvement as well as scaling up the materials with the specific upcycling techniques. Our studies will continue on providing characterization support to the whole team, as well as comparison of the characterization data with electrochemical performance. The NMR studies will also help us to understand lithium and transition metal insertion and diffusion into the bulk and help to understand the recycling process mechanisms. The aim of our effort is to provide characterization guided recycling techniques.

### **A Combined Approach to Understanding Upcycling Diffusion Issues – APS**

In this FY23 effort, we worked to understand the chemical steps and evolving morphology of upcycling treatments using *in situ* synchrotron powder diffraction. Cathode precursors were largely developed by the Vaughey group. We also developed new characterization approaches to better quantify the time required to inter-diffuse Li and Ni species to form the final upcycled product, an important factor for optimizing the cost efficiency of the upcycling process. Additional experiments on re-lithiation processes and alternative cathode feedstocks were measured and will be analyzed in FY24.

### **EverBatt: Cost and Environmental Impact Modeling**

A better understanding of the costs for both individual processes and direct recycling will help identify possible barriers to technology scale-up and commercialization. We will continue to model the cost for ReCell unit processes once data become available, and will also provide cost estimates for promising configurations of direct recycling for both (end-of-life) EOL batteries and manufacturing scrap. Through our modeling efforts in FY23 we confirm again that consumables and capital investment are the major contributors to the cost at the recycling plant, but we also find that disposal of spent organic solvents may incur substantial cost. For processes that involve the use of organic solvents, we therefore recommend PIs consider solvents reuse or on-site combustion for energy recovery during process design or optimization.

### **Modeling the Reverse Supply Chain**

There is limited data available regarding e-waste recycling. Specifically, the general public's perception and behavior towards e-waste recycling remains largely unknown but these factors drive collection and recycling performance. To enhance our comprehension in this area, we have employed a hybrid model combining ABM and SD approaches to investigate the recycling patterns of e-waste. The utilization of a hybrid model offers the advantage of creating a comprehensive environment that encompasses both macro and micro-scale interactions, enabling us to observe and analyze the dynamics within both systems. The SD model is specifically designed to monitor the overall quantity of recycled laptops at a macro level, while individual actions significantly influence the recycling rate within the SD model. This preliminary study provides valuable insights into the collective behaviors associated with e-waste collection at the census tract level. Our next step is to adapt the model to an unregulated state. After that, we intend to apply this model to gain further understanding of EV battery collection behaviors at the household level.

**LIBRA: Supply Chain Analysis for Battery Recycling (falls under supply chain)**

NREL has developed the LIBRA system dynamics model to create a robust and data-based analysis platform to better understand the U.S. and global lithium-ion battery supply chain with a particular focus on the buildout of battery manufacturing and recycling capacity. The primary objective of LIBRA is to ask and answer questions about the future trajectory of the supply chain under varying circumstances using sensitivity and scenario analysis. Areas of analysis from this past year include variations in EV deployment, the future distribution of battery chemistries used in LIB applications, the impact of battery sorting, and the value of manufacturing scrap to the industry. These systems are dynamic and interconnected- our system dynamics framework is designed to capture the feedback between these systems, especially as it develops and evolves over time.

**Key Publications****Solvent-based Electrode Recovery**

1. Bai, Y., Li, M., Jafta, C. J., Dai, Q., Essehli, R., Polzin, B. J., & Belharouak, I. (2023). Direct recycling and remanufacturing of anode scraps. *Sustainable Materials and Technologies*, 35, e00542.
2. Bai, Y., Belharouak, I., and Essehli, R. "Direct recycling of lithium-ion battery scraps for manufacturing a new anode." US11721850B2 (granted, Aug 2023)
3. Belharouak, I., Bai, Y., and Essehli, R. "Recovery of materials from electrode scraps and spent lithium-ion batteries via a green solvent-based separation process." US11664542B2 (granted, May 2023)

**Cathode/Cathode Separation via Froth Flotation**

1. Folyan, T. O., Zhan, R., Huang, K., & Pan, L. (2023). Improved Separation between Recycled Anode and Cathode Materials from Li-Ion Batteries Using Coarse Flake Particle Flotation. *ACS Sustainable Chemistry & Engineering*, 11(7), 2917-2926.
2. Folyan, T. O., Lipson, A. L., Durham, J. L., Pinegar, H., Liu, D., & Pan, L. (2021). Direct recycling of blended cathode materials by froth flotation. *Energy Technology*, 9(10), 2100468.

**Solvent-based Gravity Separation**

1. Zhan, R., & Pan, L. (2022). A cycling-insensitive recycling method for producing lithium transition metal oxide from Li-ion batteries using centrifugal gravity separation. *Sustainable Materials and Technologies*, 32, e00399.

**Purification of Black Mass**

1. Fink, Kae Paul Gasper, Joshua Major, Ryan Brow, Maxwell C. Schulze, Andrew M. Colclasure, and Matthew A. Keyser, "Optimized purification methods for metallic contaminant removal from directly recycled Li-ion battery cathodes," *Front. Chem.* 11 (2023): 1094198, doi: 10.3389/fchem.2023.1094198
2. Coyle, Jaelyn, Kae Fink, Andrew Colclasure, and Matthew Keyser, "Recycling Electric Vehicle Batteries: Opportunities and Challenges," *AM&P Technical Articles* 181, no. 5 (2023): 19-23, <https://doi.org/10.31399/asm.amp.2023-05.p019>

**Single Crystal Cathode Production**

1. Ma, X., Vanaphuti, P., Fu, J., Hou, J., Liu, Y., Zhang, R., Bong, S., Yao, Z., Yang, Z. and Wang, Y., 2021. A universal etching method for synthesizing high-performance single crystal cathode materials. *Nano Energy*, 87, p.106194.

## References

### Roll of Impurities in Recycled Cathodes

1. Chen, M. Y.; Ma, X. T.; Chen, B.; Arsenault, R.; Karlson, P.; Simon, N.; Wang, Y., Recycling End-of-Life Electric Vehicle Lithium-Ion Batteries. *Joule* **2019**, 3 (11), 2622-2646.
2. Jin, Y.; Zhu, B.; Lu, Z.; Liu, N.; Zhu, J., Challenges and Recent Progress in the Development of Si Anodes for Lithium-ion Battery. *Adv. Energy Mater.* **2017**, 7 (23), 1700715.

### Hydrothermal Relithiation

1. Shi, Yang, Gen Chen, and Zheng Chen. "Effective regeneration of LiCoO<sub>2</sub> from spent lithium-ion batteries: a direct approach towards high-performance active particles." *Green chemistry* 20, no. 4 (2018): 851-862.
2. Shi, Yang, Gen Chen, Fang Liu, Xiujun Yue, and Zheng Chen. "Resolving the compositional and structural defects of degraded LiNi<sub>x</sub>Co<sub>y</sub>Mn<sub>z</sub>O<sub>2</sub> particles to directly regenerate high-performance lithium-ion battery cathodes." *ACS Energy Letters* 3, no. 7 (2018): 1683-1692.
3. Xu, Panpan, Zhenzhen Yang, Xiaolu Yu, John Holoubek, Hongpeng Gao, Mingqian Li, Guorui Cai et al. "Design and optimization of the direct recycling of spent Li-ion battery cathode materials." *ACS Sustainable Chemistry & Engineering* 9, no. 12 (2021): 4543-4553.
4. Yu, Xiaolu, Sicen Yu, Zhenzhen Yang, Hongpeng Gao, Panpan Xu, Guorui Cai, Satchit Rose, Christopher Brooks, Ping Liu, and Zheng Chen. "Achieving low-temperature hydrothermal relithiation by redox mediation for direct recycling of spent lithium-ion battery cathodes." *Energy Storage Materials* 51 (2022): 54-62.

### Anode Upcycling via Tailored Solvent Treatment

1. An, Seong Jin, Jianlin Li, Claus Daniel, Debasish Mohanty, Shrikant Nagpure, and David L. Wood. 2016. "The State of Understanding of the Lithium-Ion-Battery Graphite Solid Electrolyte Interphase (SEI) and Its Relationship to Formation Cycling." *Carbon* 105 (August): 52–76. <https://doi.org/10.1016/j.carbon.2016.04.008>.
2. Liu, Yangtao, Ruihan Zhang, Jun Wang, and Yan Wang. 2021. "Current and Future Lithium-Ion Battery Manufacturing." *IScience* 24 (4): 102332. <https://doi.org/10.1016/j.isci.2021.102332>.
3. Shim, Joongpyo, and Kathryn A Striebel. 2003. "Effect of Electrode Density on Cycle Performance and Irreversible Capacity Loss for Natural Graphite Anode in Lithium-Ion Batteries." *Journal of Power Sources*, Selected papers presented at the 11th International Meeting on Lithium Batteries, 119–121 (June): 934–37. [https://doi.org/10.1016/S0378-7753\(03\)00235-0](https://doi.org/10.1016/S0378-7753(03)00235-0).

### Single Crystal Cathode Production

1. Billy, E., Joulié, M., Laucournet, R., Boulineau, A., De Vito, E. and Meyer, D., 2018. Dissolution mechanisms of LiNi<sub>1/3</sub>Mn<sub>1/3</sub>Co<sub>1/3</sub>O<sub>2</sub> positive electrode material from lithium-ion batteries in acid solution. *ACS applied materials & interfaces*, 10(19), pp.16424-16435.
2. Ma, X., Vanaphuti, P., Fu, J., Hou, J., Liu, Y., Zhang, R., Bong, S., Yao, Z., Yang, Z. and Wang, Y., 2021. A universal etching method for synthesizing high-performance single crystal cathode materials. *Nano Energy*, 87, p.106194.
3. Huang, X., Zhu, W., Yao, J., Bu, L., Li, X., Tian, K., Lu, H., Quan, C., Xu, S., Xu, K. and Jiang, Z., 2020. Suppressing structural degradation of Ni-rich cathode materials towards improved cycling stability enabled by a Li<sub>2</sub>MnO<sub>3</sub> coating. *Journal of Materials Chemistry A*, 8(34), pp.17429-17441.

### Ionic Liquid Based Supported Membranes for Li/Co/Mn Separation

1. Henckens, M.; Driessen, P.; Worrell, E. Metal scarcity and sustainability, analyzing the necessity to reduce the extraction of scarce metals. *Resources, Conservation and recycling* **2014**, 93, 1-8.
2. Reuter, M.; Hudson, C.; Van Schaik, A.; Heiskanen, K.; Meskers, C.; Hagelüken, C. Metal recycling: Opportunities, limits, infrastructure. *A report of the working group on the global metal flows to the international resource panel* **2013**.

3. Femi Badigun, Bishnu P Thapaliya, Huimin, Luo, Sheng Dai, Complexation driven ion-exchange polymer inclusion membranes for separation of Co and Ni ions from Li ion via proton pumping. Separation and Purification Technology, Submitted (under review).

### Acknowledgements

The following individuals worked as individual task leaders/members for the tasks described in this project and ReCell in general: Eva Allen (ANL), Maura Appleberry (UCSD), Yaocai Bai (ORNL), Ilias Belharouak (ORNL), Tom Bethel (NREL), Ramesh Bhave (ORNL), Zheng Chen (UCSD), Andrew Colclasure (NREL), Jaclyn Coyle (NREL), Qiang Dai (ANL), Sheng Dai (ORNL), Shailesh Dangwal (ORNL), Fulya Dogan (ANL), Eric Dufek (INL), Alison Dunlop (ANL), Trevor Dzwiniel (ANL), Jakob Elias (ANL), Rachid Essehli (ORNL), Donal Finegan (NREL), Kae Fink (NREL), Tim Fister (ANL), Tinu Folayan (MTU), Hongpeng Gao (UCSD), Andrea Gardiner (TSU), Paul Gasper (NREL), Diane Graziano (ANL), Jonathan Harter (ORNL), AHM Golam Hyder (ANL), Brian Ingram (ANL), Syed Islam (ORNL), Allison Bennett Irion (ANL), Andy Jansen (ANL), Ozge Kahvecioglu (ANL), Yana Karslyan (ANL), Matt Keyser (NREL), Tiffany Kinnibrugh (ANL), Cyrus Kirwa (NREL), Jayanthi Kumar (ORNL), Kaushal Kumar (NREL), Yuan-Yuan Lee (INL), Menya Li (ORNL), Timothy Lichtenstein (ANL), Albert Lipson (ANL), Huimin Luo (ORNL), Beihai Ma (ANL), Xiaotu Ma (WPI), Jessica Durham Macholz (ANL), Margaret Mann (NREL), Trevor Martin (NREL), Colin Moore (ANL), Ruby Nguyen (INL), Lei Pan (MTU), Parans Paranthaman (ORNL), Sohyun Park (ANL), Jasmine Pattany (NREL), Candido Pereira (ANL), Saurab Prakash Pethe (ORNL), Haruka Pinegar (ANL), Bryant Polzin (ANL), Melissa Popeil (NREL), Juliane Preimesberger (NREL), Kris Pupek (ANL), Vicky Putsche (NREL), Matthew Riddle (ANL), Brian Rowden (ORNL), Andrew Schiek (NREL), Max Schulze (NREL), Mike Severson (INL), Carrie Siu (ANL), Braeton Smith (ANL), Kandler Smith (NREL), Seoung-Bum Son (ANL), Jeff Spangenberger (ANL), Venkat Srinivasan (ANL), Katherine Stasior (ANL), Xiao-Guang Sun (ORNL), Nathaniel Sunderlin (NREL), Bishnu Prasad Thapaliya (ORNL), Steve Trask (ANL), Jack Vaughney (ANL), Ankit Verma (NREL), Evelyn Wang (ANL), Tao Wang (ORNL), Yan Wang (WPI), Dustin Weigl (NREL), Nevi Cahya Winofa (NREL), Eliot Woods (ANL), Lu Yu (ORNL), Xiaolu Yu (UCSD), Yadong Zheng (WPI), Zhengcheng Zhang (ANL), Mateusz Zuba (ANL).

## IV Extreme Fast Charging (XFC)

Over the last ten years, lithium-ion batteries for plug-in electric vehicle applications have reached near high volume production levels and, as a result, costs have decreased significantly. Reduced battery costs have allowed EV manufacturers to offer a wide variety of vehicles with driving ranges comparable to traditional ICE vehicles. The Tesla Model 3 and S, Chevy Bolt, Ford Mustang Mach E, and many others, offer well over 200 miles of range per charge, and most offer over 300 miles per charge with battery upgrades.

However, the time needed to recharge these EVs remains a challenge. Gas powered cars can be refueled in minutes, whereby a 100kWh EV battery takes anywhere from 30 minutes to overnight to fully recharge which limits even broader consumer acceptance of electric vehicles.

Charging infrastructure is a challenge being addressed through large investments enabled by the Bipartisan Infrastructure Law (BIL). However, today's high energy cells use relatively thick (for high energy density) and porous graphite anodes and transition metal cathodes. These thick electrodes lead to relatively high polarization impedance (which makes charging at high rates inherently difficult), and they result in large salt concentration gradients which can lead to lithium plating on the anode surface. Lithium plating can cause rapid capacity fade and internal shorts leading to potentially catastrophic thermal runaway.

The “eXtreme fast Charge cell Evaluation of Lithium-ion batteries” (XCEL) program was formed to address this fast charge issue. Specifically, it is working to both identify the issues with and improve the fast charge acceptance of graphite/NMC based cells. Silicon containing cells often enable fast charging due to the much thinner silicon anode electrode. However, silicon exhibits poor calendar life which has inhibited its use in automotive batteries. Thus, this fast charge program is focused exclusively on graphite anode cells.

The program is led by Argonne National Laboratory, with significant support from Idaho National Laboratory, Lawrence Berkeley National Laboratory, National Renewable Energy Laboratory, SLAC National Accelerator Laboratory, and several universities.

The focus areas of the program are electrode and cell design, electrolyte development, electrochemical and thermal performance evaluation, and modeling and diagnostics. One of the main conclusions of the XCEL program has been that an “all solutions” approach may be required to enable fast charge (10-15 minutes) in high energy graphite anode cells. Early results showed the ability of a combination of improved binder, use of a more porous separator, and an enhanced electrolyte, worked collaboratively to greatly improve fast charge capability, Figure IV.1.

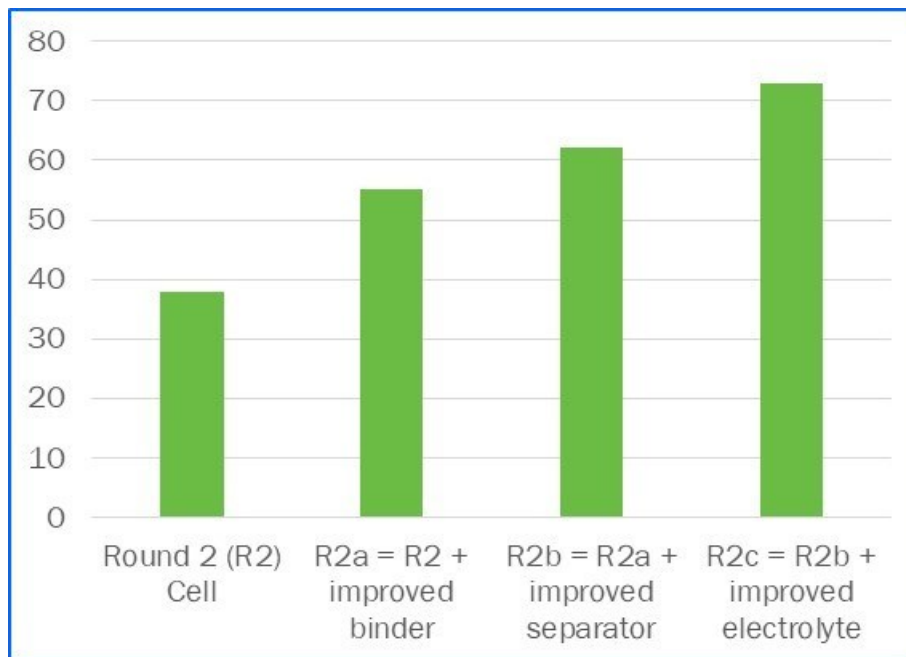


**Figure IV.1 Energy delivered during a 15-minute fast charge and improvements seen with the incorporation of an improved binder, an improved separator, and an improved electrolyte.**

The rest of this chapter contains detailed reports on the status of the following individual projects.

- Extreme Fast Charge Cell Evaluation (XCEL) Thrust-1: Electrolytes for fast charging
- XCEL Thrust-2: Electrode & Cell Design for Fast Charging
- XCEL Thrust 3: Electrochemical and Thermal Performance.

## IV.1 Extreme Fast Charge Cell Evaluation (XCEL) Thrust-1: Electrolytes for fast charging (ANL, LBNL)

### Venkat Srinivasan, Principal Investigator

Argonne National Laboratory  
9700 South Cass Avenue  
Lemont, IL 60439  
E-mail: [vsrinivasan@anl.gov](mailto:vsrinivasan@anl.gov)

### Bryan D. McCloskey, Co-Principal Investigator

Lawrence Berkeley National Laboratory and University of California, Berkeley  
201-D Gilman Hall  
Berkeley, CA 94720  
E-mail: [bmcclosk@berkeley.edu](mailto:bmcclosk@berkeley.edu)

### Jake Herb, DOE Technology Development Manager

U.S. Department of Energy  
E-mail: [Jake.Herb@ee.doe.gov](mailto:Jake.Herb@ee.doe.gov)

Start Date: October 1, 2022	End Date: September 30, 2023	
Project Funding (FY23): \$1,480,000	DOE share: \$1,480,000	Non-DOE share: \$0

### Project Introduction

Rapid charging of lithium-ion batteries is a crucial step towards electrifying our transportation system and reducing harmful greenhouse gas emissions. Electric vehicle (EV) fast charging is primarily limited by the deposition of metallic lithium on graphite anodes, or ‘Li plating’, which can cause capacity fade and catastrophic cell shorting. It has now been established that the electrolyte serves an important role in controlling battery rate capabilities and battery lifetime, particularly when operating repeatedly under extreme conditions (e.g., fast charging rates and low or high temperatures). The aim of this thrust in the Extreme Fast Charging Program (XCEL) is to understand how to design more effective electrolytes that eliminate bottlenecks to allow Li-ion batteries to be charged in 10 minutes or less to 80% capacity. As discussed below, three different classes of electrolytes are being pursued, each of which could potentially improve upon current state-of-art compositions by improving ion transport or interfacial properties that control charge transfer kinetics and longterm stability. Furthermore, this thrust interfaces with modelling and characterization teams in XCEL that allow us to understand thermal and mass transport and interfacial properties of our electrolyte systems, which then help guide further development.

### Objectives

The overarching goal was to discover new extreme fast-charge (XFC) electrolytes that enable high charge acceptance at a 6C charge rate ( $\geq 80\%$  of the 1C capacity basis), demonstrate competitive cycle-life ( $\leq 20\%$  capacity loss over anticipated lifecycle), and that exhibit good performance and survivability from 10 to 45 °C. To do so, we aim to develop electrolyte formulations with high Li ion transference number and high ionic conductivity, which will significantly increase the Li ion mass transport from cathode to anode during fast charging. In many cases, we compare the performance of our developed electrolytes against a baseline of Gen2 (1.2M LiPF<sub>6</sub> in 3:7 wt:wt ethylene carbonate:ethyl methyl carbonate) + 2-3 wt% fluoroethylene carbonate (FEC), which we reported as having excellent rate capability in prior years.

Other additional objectives included:

- Providing an experimental highly concentrated electrolyte (HCE) to the Cell Analysis, Modelling and Protocol (CAMP) facility for use in early testing of R4 materials.

- Starting development of a computational method to cover electrolyte diffusional consequences within cells during rest periods.
- Measure transport properties of electrolyte being developed within the project
- Identify lithium depletion at the back of highly loaded anodes during fast charge using spectroscopic analysis.
- Develop an experimental technique, utilizing electrospray ionization mass spectroscopy (ESI-MS) in conjunction with the van't Hoff equation, to estimate desolvation energies.
- Obtain insights into the thermodynamics of lithium desolvation and its relationship to the performance of lithium-ion batteries, particularly in fast charging condition.

### Approach

Multiple approaches were implemented to achieve our objectives, including modifying electrolyte compositions (various solvents, salts, and additives were tested). The following specific approaches were implemented across the 5 national laboratories (INL, ORNL, NREL, ANL, and LBNL) involved in the project:

- We employed battery testing methods to determine performance and aging behavior for utilizing new electrolytes with the CAMP round-3 (R3) electrode materials. Of particular interest in FY23 was the rate capability for charge acceptance of the R3 cells with electrolytes as a function of C-rate and temperature.
- We applied chemical-physics based modeling architecture (Advanced Electrolyte Model, AEM) to determine molecular and macroscale properties of HCE systems designed for R3 and the new generation R4 materials. Properties of immediate value for XFC systems are the transport suite (viscosity, conductivity, diffusivity, cation transference number) and molecular-scale properties linked to lithium desolvation energy and kinetics. New for FY23 in AEM was the addition of several metrics that speak to microstate structure in electrolytes, which are highly informative toward how local electrolyte properties may be impacted from concentration polarization (CP) during fast charge conditions.
- A steady-state polarization technique was used measure the diffusion coefficient with lithium-lithium symmetric cells containing the various electrolytes as well as NREL's "sol C" electrolyte. The long- and short-term relaxation curves were fit to equations developed by Newman and Chapman and refined by Erhl.
- An experimental approach to assess the desolvation energy of lithium solvates in the electrolyte by analyzing the changes in the concentration of ionic species under varying  $[\text{LiPF}_6]$  concentrations and temperatures through direct-injection Electrospray Ionization Mass Spectrometry (ESI-MS). By utilizing the concentration and temperature data, we derive valuable insights into the thermodynamics of lithium desolvation in the electrolyte and establish correlations with the performance of cells incorporating these electrolytes during fast charging conditions.

### Results

#### ***Fast charging improvements using highly concentrated electrolyte formulations.***

Figure IV.1.1a and b are charge acceptance plots for two of our finalist HCE electrolytes tested with Round 3 CAMP pouch cells. These test results cover the net amount from constant current and constant voltage charge conditions (CCCV), and are a roadmap for assigning a performance envelope over charge rate and temperature. We see in some cases that charge acceptance at 6C achieves approximately 58, 76 and 87 percent for temperatures of 10, 30 and 45 °C, all of which are remarkably high values. Figure IV.1.2a and b show the calculated ligand-wise lithium desolvation energies and corresponding lithium solvation numbers for electrolyte HCE-18B at 30 °C. Summation of the ligand-wise values gives the net energy (black curve in (a)), where appropriate concentration regions thereof apply to the anode during XFC. Lastly, Figure IV.1.3a and b demonstrate microstate structure effects on cation net desolvation energies for the Gen2 electrolyte versus INL HCE-13. Values are compared for a free-ion basis and complexed solvation (CS) basis, where the proportional average accounts for relative amounts of both in solution.



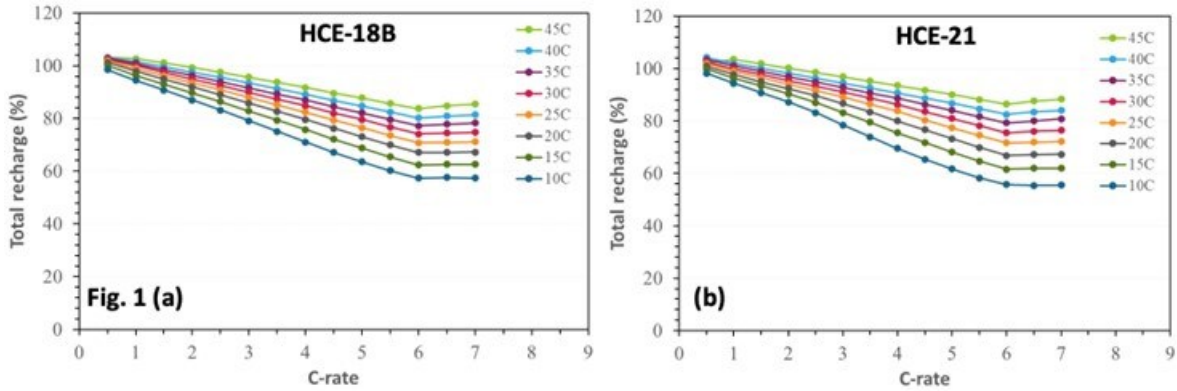


Figure IV.1.1 Charge acceptance during a CCCV (4.2V cutoff, time cutoff equivalent to given C-rate) charge of graphite | NMC811 pouch cells employing two highly concentrated electrolytes: HCE-18B (a) and HCE-21 (b).

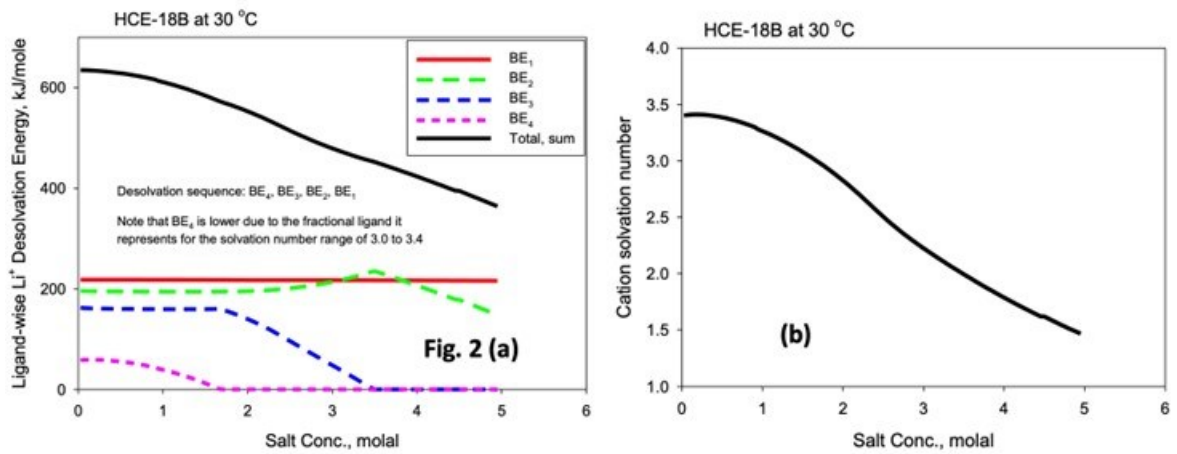


Figure IV.1.2 Ligand-wise desolvation energies, and b. cation solvation number for highly concentrated electrolyte HCE-18B at 30 °C as a function of total salt concentration as calculated using the advanced electrolyte model.

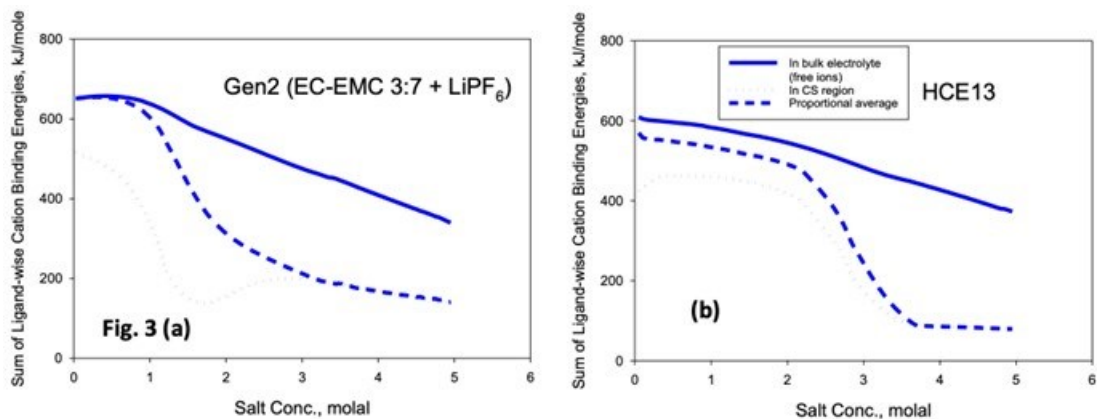


Figure IV.1.3 Ligand-wise binding energies for Gen2 electrolyte and a highly concentrated electrolyte, HCE13.

**Fast charging improvements using ORNL's HPE electrolyte.**

Figure IV.1.4a shows ORNL HPE electrolyte has improved ionic conductivity compared to Gen2 electrolyte. Figure IV.1.4b shows the voltage and current curves for 2-Ah pouch cells filled with the HPE and Gen2 electrolyte. Under the 6C charging rate, the cell voltages gradually increase during the constant current (CC)

charging and reached the cutoff voltage (4.2 V) in around 2.6 min (Gen2) and 5.6 min (HPE). The cells are further charged using the constant voltage mode with a decreasing trickle current until the overall charging time reaches 10 min. The large gap (shaded areas in Figure IV.1.4b) between the plots of current vs. time indicates that more capacity can be stored when the cell has a longer CC charging time. Figure IV.1.4c shows the cycling performance of the 2-Ah pouch cells under different C rates. HPE electrolyte shows excellent cycling performance under standard C/3 charge/discharge with 92.2% of capacity retention after 700 cycles. This demonstrates HPE electrolyte has no adverse effect on standard C/3 battery operations. Under 10-minute XFC protocol, 2-Ah pouch cell with HPE electrolyte delivers 1.54 Ah capacity, which is ~15% higher than 1.34 Ah from the cell with Gen2 electrolyte. With further cycling of the cells, HPE-based cell can still deliver 80.2% of capacity after 1500 cycles, which triples the cycle life of capacity retention criteria in DOE's target (80% after 500 cycles). It is also much higher than that of the Gen2-based cells, which has 72.1% capacity retention after 1500 cycles.

Figure IV.1.4d-i show the optical and SEM images of graphite electrodes in 2-Ah pouch cell with different electrolytes after 1500 XFC cycles. For Gen2 electrolyte, small areas of Li plating can be clearly seen across the electrode surface. The graphite electrode with Li plating and without Li plating can be easily distinguished by SEM as area ② and ①, respectively. No Li plating is spotted for electrodes with HPE electrolyte, which is mainly ascribed to its improved  $\text{Li}^+$  mass transfer properties.

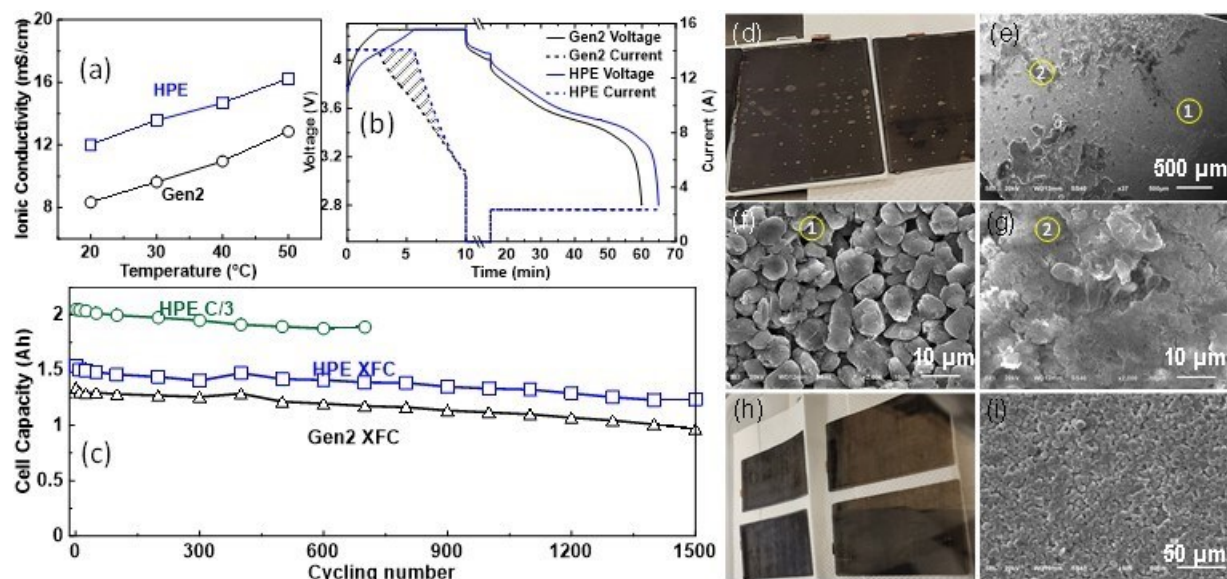


Figure IV.1.4 a. Ionic conductivities of HPE electrolyte and Gen2 electrolyte at different temperatures. b. Voltage and current versus charging time for cells charged at the 6C with a time cutoff of 10 min and discharged at the 1C rate. c. Long-term cycling performance of 2-Ah pouch cells filled with different electrolytes cycled at C/3 standard rate and XFC protocols. d. Optical and (e, f and g) SEM images of graphite electrode from Gen2 cell after 1500 XFC cycles (① is area without Li plating, and ② is area with Li plating). h. Optical and i. SEM images of graphite electrode from HPE cell.

#### Enabling low viscosity acetonitrile electrolytes using additives.

Recent studies suggest the addition of acetonitrile (AN) in lithium-ion battery electrolytes could reduce electrolyte viscosity, increase conductivity, and significantly enhance rate capabilities. To harness the benefits of AN without exacerbating known irreversible side reactions caused by AN at the electrode-electrolyte interface, an improved interface passivation strategy needs to be developed concurrently. Initial candidates were selected from different AN and additive combinations via conductivity, viscosity, cycling stability, and formation cycle capacity losses. Their fast charging performance was evaluated by overpotentials and charge acceptance at varying C-rates.

To verify acetonitrile's ability to improve ion transport and thereby fast charging, the ionic conductivity and viscosity data of ACN-containing electrolytes were measured. The conductivity at both dilute 0.1 M and concentrated 2M regimes are also measured in addition to 1.2 M. These extreme concentrations are relevant during fast charging due to the formation of a large concentration gradient and usually limits ion transport and lowers electrode utilization. Our measurements show that ACN-containing electrolytes have significantly higher conductivity and lower viscosity at all concentration ranges. With the addition of roughly 20 vol% AN, the 1.2 M electrolyte conductivity increased by 54% and the viscosity decreased by 33%.

Electrolytes made with 1.2 M LiPF<sub>6</sub>, LiFSI, LiTFSI in 3:7 (w/w) EC:EMC solvents were tested with 10, 20, and 40 vol% AN added to replace portion of EMC. 3 wt% FEC additives and varying amount of pyridine, lithium hexamethyldisilazide (LiHMDS), and lithium difluoro(oxalate)borate (LiDFOB) were included to improve interface passivation. Based on their cycling stability and capacity retention, we determined an optimal composition of 1.2 M LiPF<sub>6</sub> in 3:7 (w/w) EC:EMC with 20 vol% AN plus 3 wt% FEC and 1 wt% LiDFOB (20AN for short). A baseline electrolyte of 1.2 M LiPF<sub>6</sub> in 3:7 (w/w) EC:EMC plus 3 wt% FEC (BL for short) is selected to represent commercial electrolyte performance. The 20AN electrolyte exhibits similar capacity retention as the BL electrolyte after 100 1C CC-CV (constant current-constant voltage) cycles from 3-4.2 V. This supports our hypothesis that additives included in the 20AN electrolyte are effective at preventing significant side reactions at the interfaces.

To evaluate the possible improvements of 20AN electrolyte during fast charging, we decoupled the transport overpotential from the sum of kinetic and ohmic overpotentials (impedance overpotential) based on their difference in relaxation time. Overpotential analysis on the 20AN electrolyte demonstrates improved lithium-ion transport at high C-rates. In Figure IV.1.5a, the transport overpotential at 6C for the 20AN electrolyte is about 50 mV lower than in the BL electrolyte. This is a significant amount since the battery voltage profile is flatter at higher SOC, so slight changes in overpotential could result in large changes in charge acceptance. The impedance overpotentials remains the same for 20AN and BL electrolytes. Here, we hypothesize that the increase in ionic conductivity in AN-containing electrolytes is offset by higher resistance at electrode interfaces both due to possible AN side reactions and the addition of LiDFOB additives. A net reduction in charging overpotentials is therefore achieved with 20AN electrolyte. This reduction would allow more battery capacity to be charged with high current fast charge, thereby lowering the total charging time needed to recharge a battery.

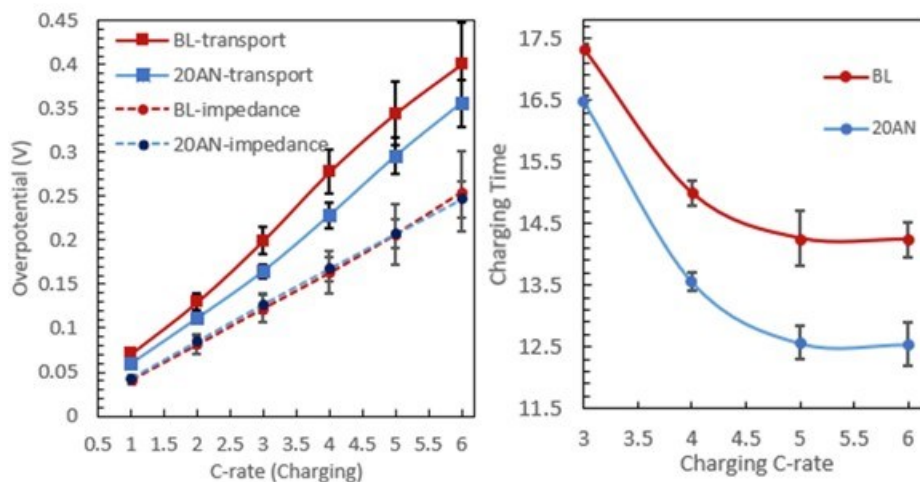


Figure IV.1.5 A comparison of Gen2 + 3wt% FEC (BL) and a cell with 20% of the EMC replaced with AN (20AN) at 30 °C. a. Overpotential measurements collected at 40% SOC after CC charging at various C-rates with relaxed upper cutoff voltage. b. Charging time of batteries with different electrolytes at varying C-rate with CC-CV protocol to 80% SOC between 3-4.2 V.

The charging time of batteries at varying C-rate with CC-CV protocol to 80% SOC between 3–4.2 V were measured. Figure IV.1.5b highlights the CC-CV charging time reduction in 20AN electrolyte. During 5C CC-CV charging, the 20AN electrolyte takes 2 mins less to reach 80 SOC% compared to the BL electrolyte. The 14% shorter charging time is correlated with a higher 6C CC charge acceptance of 45% SOC. However, ion transport continues to limit battery rate capabilities during fast charging, where increasing the constant current charging C-rate from 5C to 6C still yields no distinguishable improved charge acceptance results.

### Characterizing $\text{Li}^+$ desolvation energies experimentally.

Electrolyte samples with varied lithium salt concentrations (ranging from 0.012 M to 4.8 M) were analyzed via electrospray ionization-mass spectrometry (ESI-MS) at different gas temperatures. The MS analysis (Figure IV.1.6a) identified various complexes like LiEC, LiEMC, Li(EC)<sub>2</sub>, Li(EC)(EMC), Li(EMC)<sub>2</sub>, and Li(EC)<sub>3</sub>. Their concentrations fluctuated with gas temperature, suggesting adaptability to temperature changes. Equilibrium constants ( $\ln(K_{\text{eq}})$ ) were calculated for desolvation reactions (Figure IV.1.6b), allowing estimation of  $\Delta H$  and  $\Delta S$  through the van't Hoff equation, revealing the Gibbs free energy.

Figure IV.1.6 c demonstrates  $\Delta G$  changes with temperature for 1.2 M LiPF<sub>6</sub> in EC:EMC solutions and their response to LiPF<sub>6</sub> concentration at 30°C. The  $\Delta G$  values remain steady across various [LiPF<sub>6</sub>] concentrations, with slight changes in desolvation energies observed. Notably, the lowest  $\Delta G$  values were observed at 2.4 M. Additionally, a significant dependency of  $\Delta G$  on [LiPF<sub>6</sub>] is observed for the formation of [Li(PF<sub>6</sub>)<sub>2</sub>]<sup>-</sup>. This suggests that the quantity of free [PF<sub>6</sub>]<sup>-</sup> anion rapidly decreases as [LiPF<sub>6</sub>] increases, making the formation of [Li(PF<sub>6</sub>)<sub>2</sub>]<sup>-</sup> thermodynamically favorable.

As our study with ESI-MS clearly revealed dependency of the desolvation energy of lithium solvates in the electrolyte to the [LiPF<sub>6</sub>] concentrations, we further investigate how an electrolyte with lower desolvation energy can enhance the performance of LIBs. Testing electrolytes with varying [LiPF<sub>6</sub>] concentrations revealed that the 2.4 M solution exhibited the highest capacity retention. This outcome suggests that an electrolyte with lower desolvation energy demonstrated improved cycle retention during fast charging protocols.

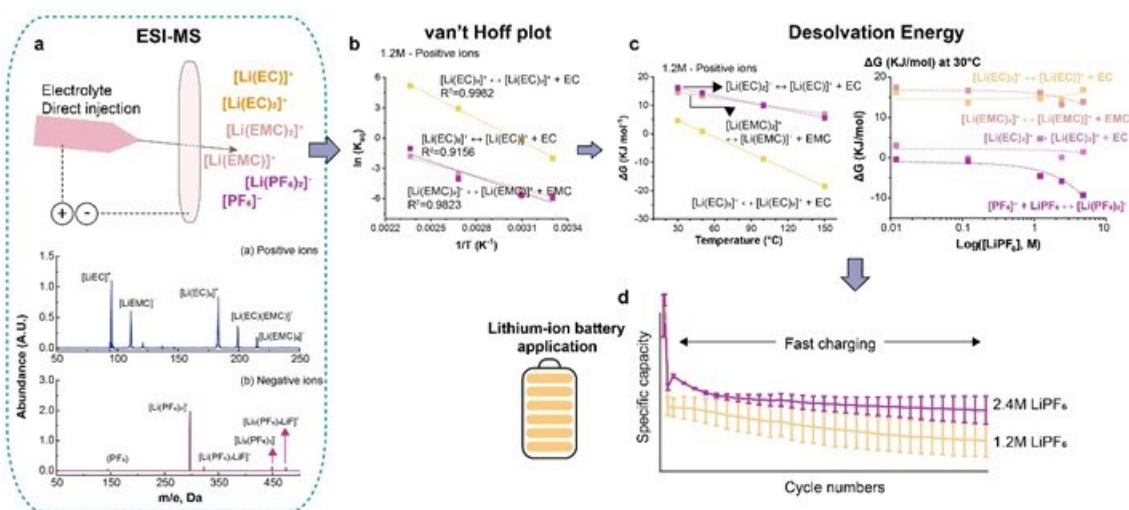


Figure IV.1.6 A novel detailed experimental workflow to estimate the desolvation energy of the electrolyte.

### Measurement of electrolyte diffusion coefficients.

The diffusion coefficient for several electrolytes was determined using the restricted diffusion experiment. Lithium-lithium symmetric cells were flooded with various electrolytes, polarized to ~100 mV, and allowed to relax. The open circuit potential was then recorded as a function of time (Figure IV.1.7). The diffusion coefficients were calculated according to well established ion-transport equations. The experimental method

was validated by first calculating the diffusion coefficient for Gen-2 electrolyte. The value for both the short-term and long-term relaxation agree with values currently accepted by the research community. In general, the diffusion coefficients do not vary widely from the Gen-2 baseline. All three of the XCEL electrolytes demonstrate higher diffusion than the Gen-2 baseline. The long-term diffusion of the electrolyte from ORNL suggests that a small corrosive current may have been present, but more investigation is needed to confirm that claim.

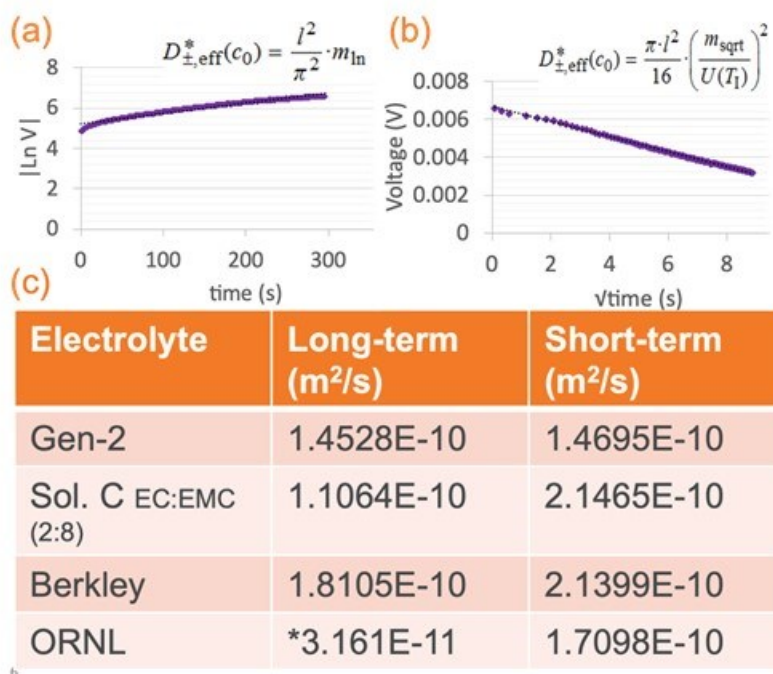


Figure IV.1.7 a) Long-term relaxation profiles for the restricted diffusion measure of Gen-2. The short-term relaxation behavior exhibits the expected linear concentration profile when plotted vs the square root of time (b). A table of the various diffusion coefficients (c).

## Conclusions

Key conclusions from the XCEL electrolyte thrust include:

- The development of multiple highly concentrated electrolyte compositions that outperform our baseline Gen2 + 2-3 wt% FEC electrolyte when fast charging at rates of 6C and above.
- The development of a novel high-performance electrolyte (HPE) which was tested in pilot-scale, 2-Ah pouch cells. The HPE-based pouch cells deliver improved discharge specific capacity and excellent long-term cyclability up to 1500 cycles under XFC conditions compared to the baseline electrolyte.
- Acetonitrile (AN) can be used as an electrolyte co-solvent to increase conductivity and lower viscosity. The addition of AN improved lithium-ion transport during fast charging, particularly a reduction in transport overpotential is observed. The 20AN electrolyte increased 6C CC charge acceptance and reduced the charging time needed to reach 80% using a 6C CC-CV protocol.
- The introduction of an innovative technique using direct-injection ESI-MS to assess electrolyte desolvation energy. We demonstrated a correlation between desolvation energy, [LiPF<sub>6</sub>] concentration, and improved cycle retention during fast-charging cycles, highlighting its importance in developing future LIBs with fast-charging capabilities.
- The diffusion coefficients for various electrolytes were calculated from electrochemical experiments. These values help reveal the connection between electrolyte design and transport properties. They also increase the accuracy of computational efforts.

### Key Publications

1. Konz, Z. M.; Wirtz, B. M.; Verma, A.; Huang, T.-Y.; Bergstrom, H. K.; Crafton, M. J.; Brown, D. E.; McShane, E. J.; Colclasure, A. M.; McCloskey, B. D. "High-throughput Li plating quantification for fast charging battery design." *Nature Energy* (2023) 8, 450-461.
2. Du, Zhijia, et al. "A Novel High-Performance Electrolyte for Extreme Fast Charging in Pilot Scale Lithium-Ion Pouch Cells." *Batteries & Supercaps* (2023) 6(10), e202300292.
3. Tanim, T. R. et al. "Rational designs to enable 10-min fast charging and long cycle life in lithium-ion batteries." *Journal of Power Sources* (2023) 582, 233519.

### Acknowledgements

Contributions to this report involved many XCEL members, including Andrew Colclasure, Kevin Gering, Zhijia Du, Seoung-Bum Kim, Brian Ingram, Ning Guo, Ryan Brow, Lydia Meyer, Sangwook Kim, and Pete Barnes.

## IV.2 XCEL Thrust-2: Electrode & Cell Design for Fast Charging (ANL, SLAC)

### Venkat Srinivasan, Principal Investigator

Argonne National Laboratory  
9700 South Cass Avenue  
Lemont, IL 60439  
E-mail: [vsrinivasan@anl.gov](mailto:vsrinivasan@anl.gov)

### Andrew Jansen, Principal Investigator

Argonne National Laboratory  
9700 South Cass Avenue  
Lemont, IL 60439  
E-mail: [jansen@anl.gov](mailto:jansen@anl.gov)

### Johanna Nelson Weker, Principal Investigator

SLAC National Accelerator Laboratory  
2575 Sand Hill Road  
Menlo Park, CA 94025  
E-mail: [jnelson@slac.stanford.edu](mailto:jnelson@slac.stanford.edu)

### Jake Herb, DOE Technology Development Manager

U.S. Department of Energy  
E-mail: [Jake.Herb@ee.doe.gov](mailto:Jake.Herb@ee.doe.gov)

Start Date: October 1, 2022	End Date: September 30, 2023	
Project Funding (FY23): \$4,500,000	DOE share: \$4,500,000	Non-DOE share: \$0

### Project Introduction

The XCEL Program in FY 2018-2021 (Phase I) centered on the influence of areal capacity loading on lithium plating during extreme fast charging (XFC). Two sets of capacity-matched electrodes were designed and fabricated with identical compositions – only the capacity loading was changed. The low loading electrode set (Round 1) utilized a 2 mAh/cm<sup>2</sup> graphite loading and the higher loading set utilized a 3 mAh/cm<sup>2</sup> graphite loading. Numerous pouch cells were fabricated and delivered to the national laboratory and university teams. These two cell builds were the early baselines for the XCEL Program. It became clear after extensive testing that lithium plating is rare on the Round 1 anodes, but is abundant on the Round 2 anodes during 6C charging. In FY 2020, a multi-thrust approach was formed to solve the problems related to XFC, the chief of which is lithium plating. One of these thrusts, the XCEL-Electrode & Electrolyte Thrust was directed to determine impact of carbon and binder domains in the positive and negative electrodes, and the impact of improved electrolyte compositions. The XCEL Program began Phase II at the start of FY 2022 with three main thrusts with the singular goal of achieving fast charge cycles (6C rate) with >4 mAh/cm<sup>2</sup> loading on the anode. This report summarizes the activities of one of the thrusts, the Electrode & Cell Design Thrust.

### Objectives

The main goal of the XCEL Electrode & Cell Design Thrust in FY 2023 was to demonstrate the impact of advanced graphite anode architectures based on dual-layer and laser-ablation using NMC811 cathodes with low carbon and binder content, and with loadings over 4 mAh/cm<sup>2</sup> loading (anode). The performance of an improved electrolyte composition was also explored in a pouch cell build. It is anticipated that an optimized cell system will be able to achieve >600 cycles at 4C charge with minimal lithium-plating.

## Approach

The Electrode & Cell Design Thrust enlists a multi-prong approach with coordinated efforts between several national labs:

- NREL's modeling tools are used to investigate strategies to reduce electrode level limitations to extreme fast charging. Novel microstructure tools are used to study the effect of changing carbon binder content on both ionic and electronic conductivity. P2D models are used to investigate the effect of dual layer electrodes on fast charge acceptance/lithium plating. The models are used to project how far electrode loadings can be increased while maintaining high fast charge acceptance/avoiding lithium plating with solutions already demonstrated by XCEL team.
- Electrodes and cells are fabricated by the CAMP Facility (Argonne) that best approximate the electrode architectures predicted by modeling effort. Cells will be made with graphite vs. NMC811 electrodes with anode loadings near 4 mAh/cm<sup>2</sup>. Latest advanced electrolytes from the Electrolyte Thrust teams will be utilized in a final cell build each year and compared to baseline.
- Post-Test Facility (Argonne) conducts post-mortem analysis of cells for presence of lithium plating and provides analysis of electrode architecture via SEM, etc. during electrode development.
- Operando x-ray characterization are conducted to detect lithium plating/stripping during cycling, and degradation of cathode material (UC-Berkeley, SLAC, Argonne).

## Results

### *Model Predictions of Ideal Electrode Architecture (NREL Focus)*

NREL used its well validated electrochemical model to summarize how improvements to cell design that improve ion transport in the electrolyte phase could enhance fast charge acceptance (see Figure IV.2.1). The standard R2/moderate loading cell only achieves around 35% fast charge acceptance during 6C CC charging. Also, the cell is predicted to plate significant amounts of lithium even at this low SOC with the anode plating potential hitting - 24 mV. The first change made to enhance transport is switching NMC 532 to 811. The higher nickel cathode has higher specific capacity and results in a thinner cathode. Also, NMC 811 has enhanced solid-state diffusion/kinetics compared to NMC 532. Replacing the standard tri-layer separator (Celgard 2325) with a more open monolayer (Celgard 2500) is predicted to significantly improve fast charge acceptance/delay lithium plating. NREL's microstructure model suggested reducing the amount of carbon and binder in the cathode from 10% to 4% would reduce tortuosity/cathode thickness while still maintaining sufficient electrical conductivity. The macrostructure model predicts reducing the carbon and binder contact improves 6C capacity by about 4%. NREL modeling also suggested replacing the standard monolayer anode with a dual layer anode with different porosities/particle size in each layer would improve fast charge capacity by another 5%. Lastly, the model predicts replacing standard Gen2 electrolyte with B26 would give a 10-minute 6C capacity of 68% (almost double the standard cell). Experimental results have shown the expected improvements and fast charge performance and this work was recently published in a journal article [1].



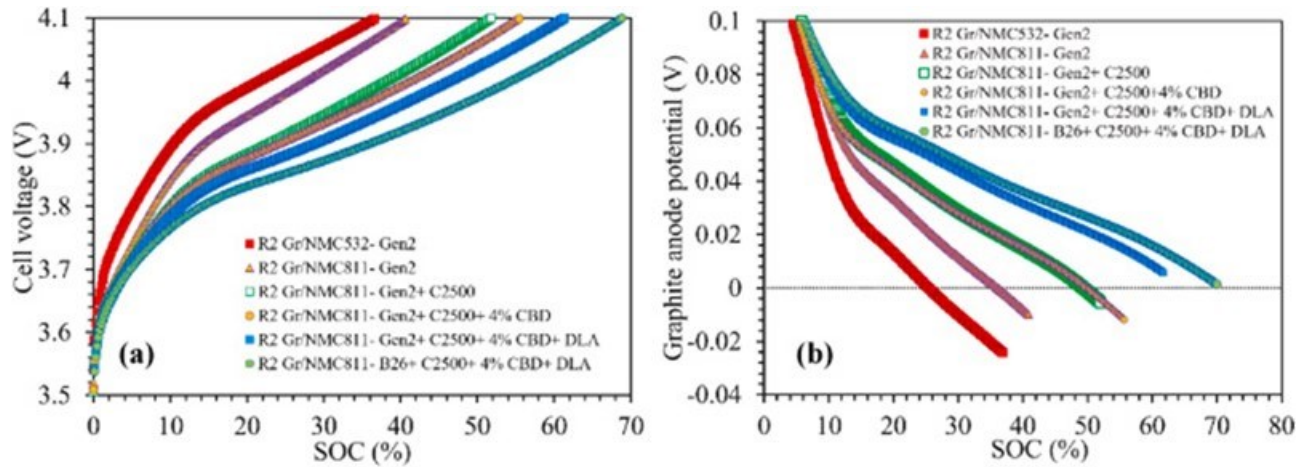


Figure IV.2.1 Electrochemical model predictions for a.) cell voltage and b.) lithium plating onset at 6C for different cell designs.

**High-Capacity Loading with High-Nickel NMC Scoping Study (Argonne Focus)**

For fast charging of lithium-ion batteries to be cost effective, they need to have capacity loadings typical of commercial EVs, in the range of 3-5 mAh/cm<sup>2</sup>. This has been the long-term goal of the XCEL Program since its start. Higher capacity-loading electrodes were made and explored in an on-going scoping study using 92% Superior Graphite SLC1506T and 96% NMC811 (also NMC90-5-5) in single-layer pouch cells. The anodes and cathodes used the traditional mono-layer structure. The cells were formed, put on rate study, an initial HPPC, and then cycled through a fast 6C cycle life protocol with two C/3 cycles after every 150 fast charge cycles (Figure IV.2.2). As can be seen from these results, traditional electrodes and electrolytes will not result in satisfactory utilization at extremely fast charges.

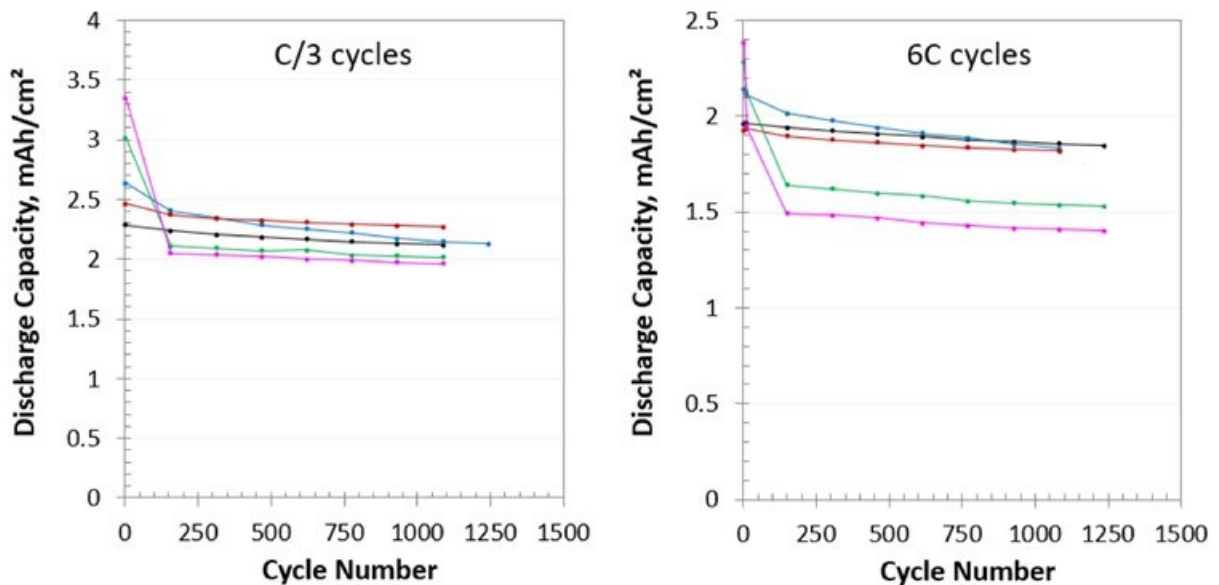


Figure IV.2.2 Scoping study of effect of capacity loading for mono-layer graphite anodes versus high-nickel NMC (NMC811 and NMC90-5-5 (red curves)) with 96% active material in cathode, Celgard 2500 separator and Gen2 + 2wt% FEC electrolyte.

***Milestones: Fabrication of Pouch Cell Deliverables Including R4 & R4+ Loadings, Laser Ablated Anode, Dual-Layer Anode, Mixed Anode, and Mono-Layer Anode; FY22 Baseline Electrolyte & Electrolyte Thrust's Best Electrolyte (Argonne-CAMP Focus)***

CAMP Facility delivered to INL 68 single-layer pouch cells using a variety of anodes that included laser ablation, mixed graphites (standard size and smaller-size graphite powders) and dual layer. All loadings were higher than that used in FY22. NMC811 was used as the common baseline cathode material in electrodes capacity matched to each anode. Celgard 2500 was used as the separator with the Gen2 +2 wt% FEC as the FY22 baseline electrolyte in all cell builds except the last one, which used the candidate electrolyte labelled HCE18. All cells were filled, formed, degassed, impedance tested at 1 kHz, capacity checked, and then shipped to INL for further electrochemical testing. See Table IV.2.1 for a summary of the cell deliverables.

**Table IV.2.1 Single-layer Pouch Cell Deliverables Fabricated at the CAMP Facility in FY23.**

R4+ Loading Cells Made & Distributed in FY23	# of cells	Build Name	Electrolyte
Mono-layer anode, 0% Ablated, (4.8 mAh/cm <sup>2</sup> )	4	CFF-B67A	Gen2 + 2wt% FEC
Mono-layer anode, 6% Ablated, (4.5 mAh/cm <sup>2</sup> )	5	CFF-B67B	Gen2 + 2wt% FEC
Mono-layer anode, 0% Ablated, (4.3 mAh/cm <sup>2</sup> )	4	CFF-B67C	Gen2 + 2wt% FEC
Mono-layer anode, 9% Ablated, (4.3 mAh/cm <sup>2</sup> )	5	CFF-B67D	Gen2 + 2wt% FEC
Mono-layer anode, 12% Ablated, (4.2 mAh/cm <sup>2</sup> )	5	CFF-B67E	Gen2 + 2wt% FEC
Mono-layer anode, 15% Ablated, (4.1 mAh/cm <sup>2</sup> )	4	CFF-B67F	Gen2 + 2wt% FEC
Mono-layer anode, 0% Ablated, (3.9 mAh/cm <sup>2</sup> )	5	CFF-B67G	Gen2 + 2wt% FEC
Mono-layer anode (5.2 mAh/cm <sup>2</sup> )	11	CFF-B68A	Gen2 + 2wt% FEC
Mixed graphites anode (5.2 mAh/cm <sup>2</sup> )	8	CFF-B68B	Gen2 + 2wt% FEC
Dual-layer anode (5.2 mAh/cm <sup>2</sup> )	8	CFF-B68C	Gen2 + 2wt% FEC
Mono-layer anode (5.2 mAh/cm <sup>2</sup> )	9	CFF-B68D	INL HCE18

***Visualizing Electrode Potentials during Fast Charge using a Reference Electrode Cell (Argonne-CAMP)***

Electrochemical tests were conducted with a reference electrode (RE) cell using electrodes fabricated at the CAMP Facility. The positive electrode had a 58 μm thick coating with 96 wt% LiNi<sub>0.8</sub>Mn<sub>0.1</sub>Co<sub>0.1</sub>O<sub>2</sub> (NMC811), 2 wt% C45 carbons and 2 wt% polyvinylidene fluoride (PVdF) on a 20 μm thick Al current collector: the electrode had ~33.7% porosity and 3.07 mAh/cm<sup>2</sup> areal capacity. The negative electrode had a 85 μm thick coating with ~92 wt% graphite, 2 wt% C45 carbons and 6 wt% PVDF binder, on a 10 μm thick Cu current collector: the electrode had ~35.4% porosity and 3.62 mAh/cm<sup>2</sup> areal capacity. The electrolyte (aka Gen 2) was a solution of 1.2 M lithium hexafluorophosphate (LiPF<sub>6</sub>) salt dissolved in a 3:7 w/w solvent mixture of ethylene carbonate (EC) and ethyl methyl carbonate (EMC) and the separator was Celgard 2500. The RE was a copper wire (25 μm dia.) with a thin layer of Li metal plated in-situ on the exposed tip; it was placed between two separators, sandwiched between 20.3 cm<sup>2</sup> disks of the oxide-positive and graphite-

negative electrodes. All tests were conducted with a Maccor cycler; test temperature was maintained at 30 °C using heating plates and a controller that monitored a thermocouple inside the cell assembly.

After initial tests, which included cycles to determine cell capacity and impedance, the cells were aged according to the standard CAMP protocol. This protocol includes a constant-current (CC) constant-voltage (CV) charge with a maximum rate of 6C for 10 minutes followed by C/2 discharge to 3 V. Expanded views of the 10-minute charge for cycles 120 and 260 are shown in Figure IV.2.3 to highlight the changes in electrode potentials. For cycle 120 (*left panel* of figure), the negative electrode potential dips below the lithium plating potential (LPC) after ~0.6 minutes during the CC charge. The CC portion at 6C lasts 1 minute at which time the cell reaches the upper cutoff voltage (UCV) of 4.1 V; the C-rate decreases thereafter and reaches 1.9C at the 10 minute mark. Note that the positive potential remains < 4.02 V vs. Li/Li<sup>+</sup> during the entire charge sequence. In contrast, for cycle 260 (*right panel* of figure), the positive potential rises rapidly and reaches 4.4 V vs. Li/Li<sup>+</sup> at ~0.67 minutes, at which time the cell reaches 4.1 V and the CC segment ends; the C-rate decreases thereafter during the CV segment and reaches 1.8C at the 10 minute mark. During the CV segment, the negative potential decreases along with the positive electrode to keep the cell voltage at 4.1 V; its value dips below the LPC after ~2.2 minutes of charge. The key message from these data is the following: positive electrode polarization determines the *onset* of lithium-plating at the negative electrode. Positive electrode polarization delays lithium plating at the negative electrode.

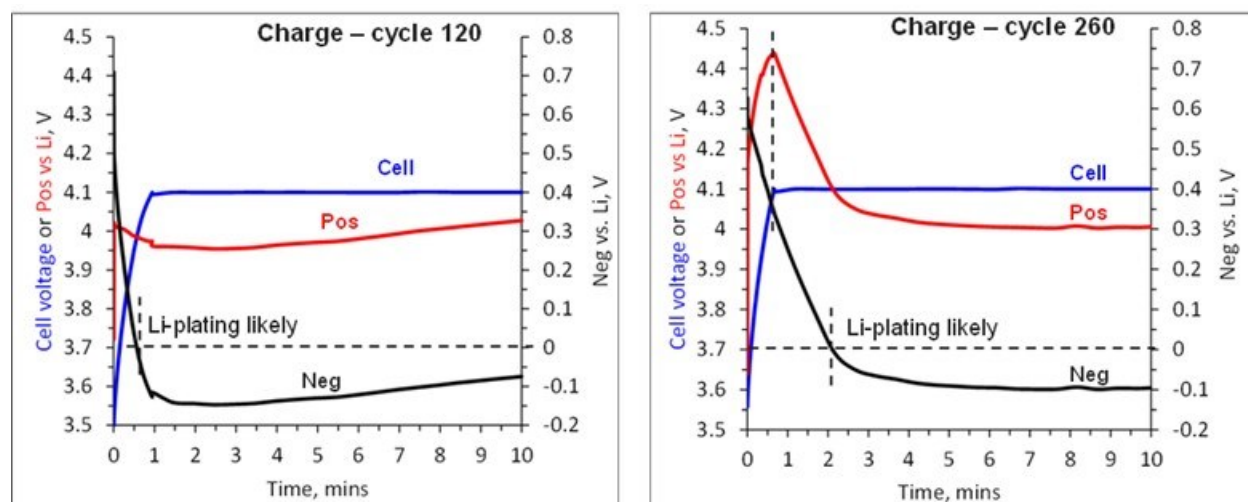


Figure IV.2.3 Data from a reference electrode cell with NMC811 positive electrode (Pos), Graphite negative electrode (Neg), Celgard 2500 separator and Gen2 electrolyte. The left and right panels show data from cycle 120 and cycle 260, respectively.

#### Mapping the Degradation of NMC Cathodes Cycled Under XFC Conditions (SLAC-Weker Focus)

The SLAC team is studying the heterogeneity of the NMC811 cathode degradation under extreme fast charging (XFC) conditions (XFC, ≤10-15 min charging) in a full single-layer graphite pouch cell with NMC811 cathodes after extensive cycling. Micro X-ray fluorescence ( $\mu$ -XRF) and micro X-ray absorption spectroscopy ( $\mu$ -XAS) on the full cells are used to investigate the effects of XFC on the cathode state of charge (SOC) without disassembling the cells.  $\mu$ -XRF provides elemental maps of the three transition metals that are present.  $\mu$ -XAS provides the electronic structure or chemistry of the transition metals. We can use the near edge features of the XAS to distinguish differences in SOC across the cathode.

*In-situ* measurements were performed on two different XFC cycled cells with B26 electrolyte after 600 cycles. The first cell was cycled with a voltage cutoff of 4.1 V with 6C charging, while the second cell had a voltage cutoff of 4.15 V with the MSR charging protocol. Electrochemical analysis suggested Li plating on second cell

but not the first. Before  $\mu$ XAS mapping at SSRL, the cells were mapped with X-ray diffraction (XRD) at APS by the Argonne team. The XRD mapping is complementary to the  $\mu$ -XAS.

Figure IV.2.4a shows elemental maps corresponding to Ni, Mn and Co taken simultaneously on the 4.15 V cutoff MSR charging cell with a 100- $\mu$ m focused X-ray beam. The  $\mu$ -XRF maps corresponding to Ni, Co, and Mn from the 4.1 V cutoff 6C charging cell are shown in Figure IV.2.4b.  $\mu$ -XRF is capable of non-destructively measuring both cathode thickness and composition simultaneously, while still observing the uniformity of the thickness and composition. Using complementary micron computed tomography ( $\mu$ -CT) imaging, it was confirmed that the variation in the measured fluorescence intensity across a cell can be correlated to topology differences of the cathode within the pouch. In other words, the non-uniform spacing between the electrodes and the pouch material dominate the changes in the XRF maps.

Guided by the XRD maps,  $\mu$ XAS were collected at regions of interest across the Ni and Mn edges. Analysis of these near edge spectra show no differences suggesting the cathode state of charge has equilibrated during storage. To confirm this, radiography images were collected across the Co and Mn edges before and after charging the cell and after discharging. The radiography has a field of view of  $\sim$ 1.7 mm and imaging resolution  $\sim$ 4  $\mu$ m. Initial analysis shows a bulk change in the near edge structure that agrees with the expected oxidation state change with charging and discharging. Analysis of the radiography data to map the heterogeneity of the SOC changes is ongoing.

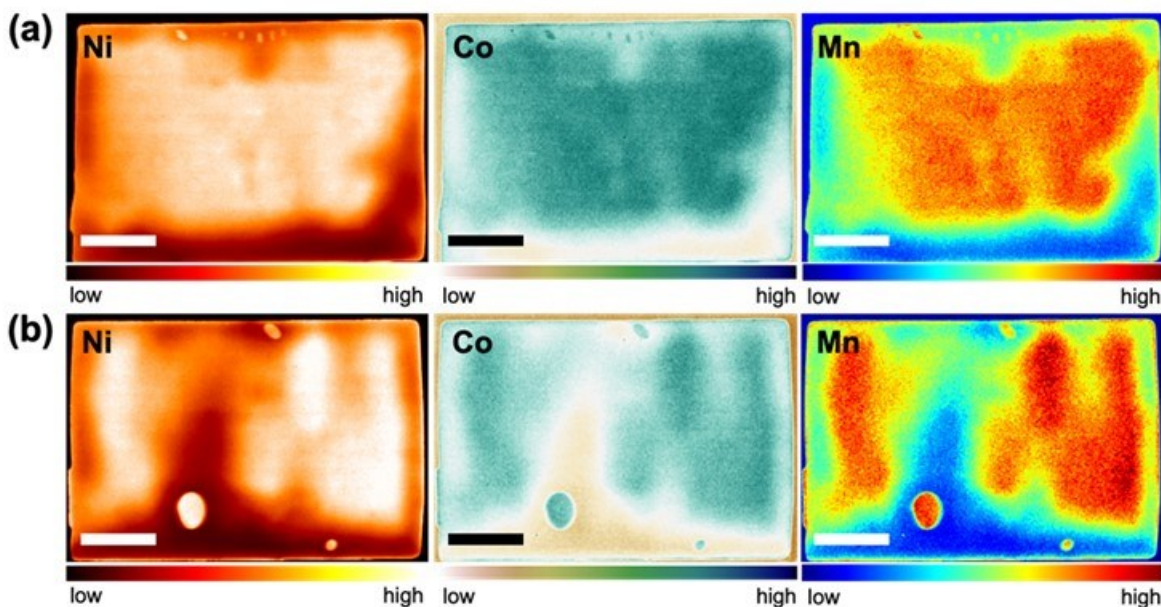


Figure IV.2.4  $\mu$ -XRF maps corresponding to Ni, Co, and Mn (a) of cell with a voltage cutoff of 4.1 V and 6C charging and (b) of cell with a voltage cutoff of 4.15 V and the MSR charging protocol after 600 XFC cycles. Regions of higher fluorescence signal correspond to more NMC material in the cathode thickness. All scale bars in the figure are 10 mm.

#### ***Cathode Particle Engineering for Fast Charge (LBNL Focus)***

The LBNL team synthesized single-crystal (SC) NMC811 with the same particle size ( $\sim$  1  $\mu$ m) and two different morphologies: octahedron-shape with predominating (012)-family surface (referred to as Oct-SC811) and polyhedron-shape with predominating (104)-family surface (referred to as Poly-SC811). Figure IV.2.5 compares electrochemical performance of the SC cathodes with the baseline polycrystalline (PC) NMC811 (referred to as PC811) cathode from the XCEL program, all cycled in half-cell coin cells between 3.0 - 4.3 V (vs. Li<sup>+</sup>/Li). Similar initial discharge capacities of  $\sim$  180-185 mAh/g were obtained at 1C rate (Figure IV.2.5a), however, both SC cathodes demonstrated improved cycling stability compared to PC811 which delivered a

performance similar to what was reported in the literature. After 100 cycles, the remaining capacities were 162, 166 and 173 mAh/g for PC811, Oct-SC811 and Poly-SC811, respectively, corresponding to a capacity fade of 10%, 8.8% and 6.3% (Figure IV.2.5d). Upon increasing the rate to 6C, all cathodes experienced an increase in polarization and a reduction in 1<sup>st</sup> cycle coulombic efficiency. Compared to PC811, much lower 1<sup>st</sup> cycle polarization was found on Poly-SC811 sample, especially during the 1<sup>st</sup> charge. The initial discharge capacity was significantly reduced but to a varying degree, with 133, 159 and 169 mAh/g obtained on PC811, Oct-SC811 and Poly-SC811, respectively. After 100 cycles, the remaining capacities were 108, 134 and 159 mAh/g for PC811, Oct-SC811 and Poly-SC811, respectively (Figure IV.2.5b), corresponding to a capacity fade of ~ 19%, 15.7% and 5.9% (Figure IV.2.5e). Figure IV.2.5c and Figure IV.2.5f compare the charge and discharge rate capabilities of the cathodes cycled between 3.0 - 4.3 V at various current densities. While all NMC811 cathodes delivered similar charge and discharge capacity of ~ 200 mAh/g at 0.1C, SC samples significantly outperformed PC-NMC811 at higher rates. Especially, Poly-SC811 delivered a reversible capacity of ~ 165 mAh/g even at 10C rate whereas the PC sample had about 38% capacity loss going from 0.1C to 10C rate. The study not only demonstrates improved stability and rate capacity of SC cathodes, it also shows the importance of SC morphology control as Poly-SC811 with the (104) surface clearly outperforms Oct-SC811 with the (012) surface under fast charge conditions.

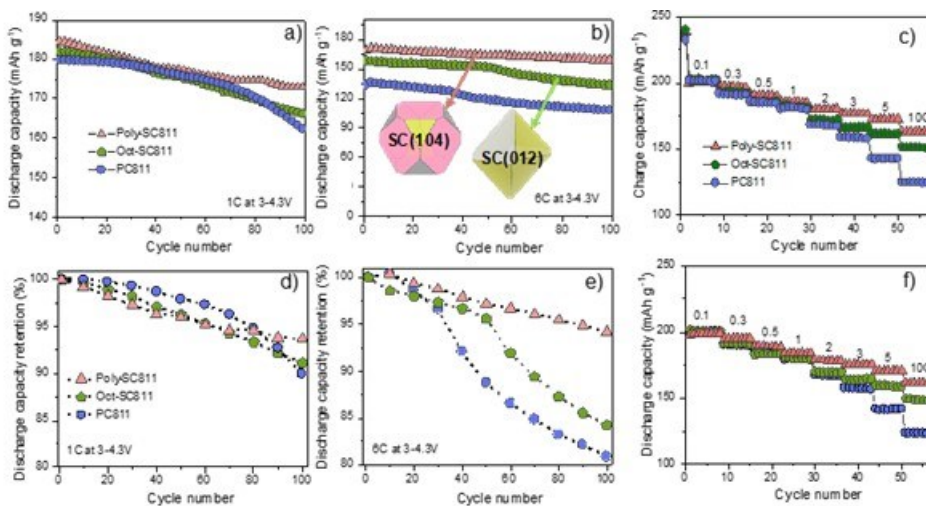


Figure IV.2.5 Comparison of discharge capacity (a, b) and capacity retention (d, e) at 1C (a, d) and 6C (b, e) cycling of NMC811 samples in the voltage window of 3-4.3V, c, f) comparison of charge and discharge rate capability, respectively.

#### Rapid-scan X-Ray Tomography in Fast Charged Batteries (LBNL Focus)

X-ray microtomography is a non-invasive technique that can yield high-resolution spatial information about materials and systems in three dimensions (3D). Experiments use a monochromatic beam as the source with energies in the 22 keV range. Cells are rotated through 180 degrees and about 1000 projection images are collected and magnified. Both ex situ and operando experiments are performed. Exposure times for each image obtained range from 100 to 225 ms. 3D reconstruction algorithms are used to synthesize the projection images to produce the morphology of the cell with a resolution of 1-5  $\mu\text{m}$ . Imaging the same cell at different time points during and after charging adds a temporal component to the analysis, allowing for the quantification of local state-of-charge and ionic current densities as well as the characterization of lithium plating nucleation and growth pathways by comparing successive tomograms. To this end, digital volume correlation has been used to quantify the spatial deformations experienced across the electrode during both charging and rest periods.

The development of lithium plating and lithiation in traditional graphite electrodes was studied using time-resolved X-ray microtomography. Previously, time constraints associated with image acquisition limited the temporal resolution of the scans such that operando experiments could only be conducted during slow charging and the rest periods immediately following fast charging. However, we are now able to scan our cells at a rate

rapid enough to capture the development of lithium plating across the electrode as well as lithiation within it throughout the fast charging process (Figure IV.2.6). During a 4C charge, lithium plating is not observed until over 60% of the charge is complete, at which point it grows exponentially until the charge completes. A secondary intercalation phase is then observed, whereby 69% of the plated lithium enters into the graphite anode. Ex-situ measurements and rest scans taken using traditional X-ray tomography support both the quantity and distribution of lithiation and lithium plating across the electrode (Figure IV.2.7a-c).

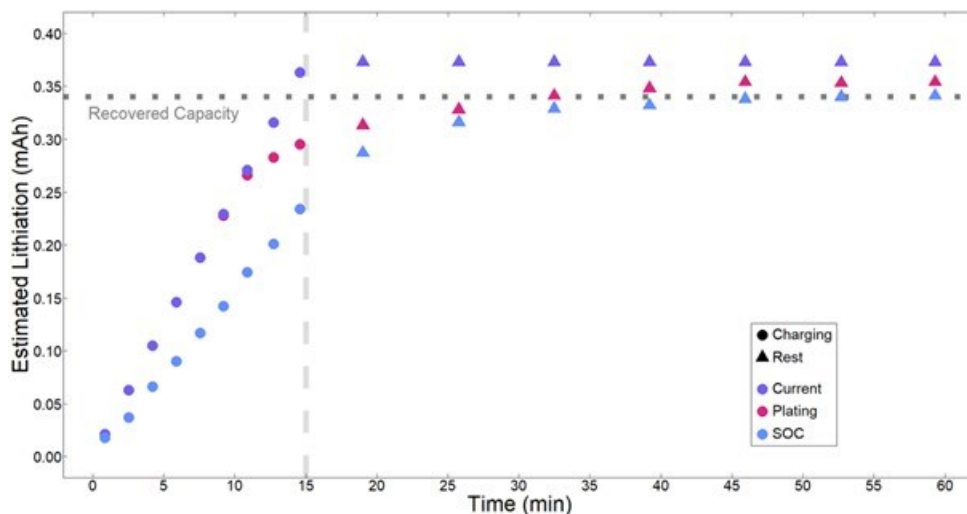


Figure IV.2.6 Quantification of Lithium Plating and Lithiation during and after a 4C Fast Charge. Plot of lithiation based on state-of-charge analysis (blue) and lithium plating (pink) during (circle) and after (triangle) a 4C fast charge. Scans taken during charge were obtained using rapid-scan tomography. The total current passed (purple) represents ideal behavior. Recovered capacity was determined after discharging the cell at C/5.

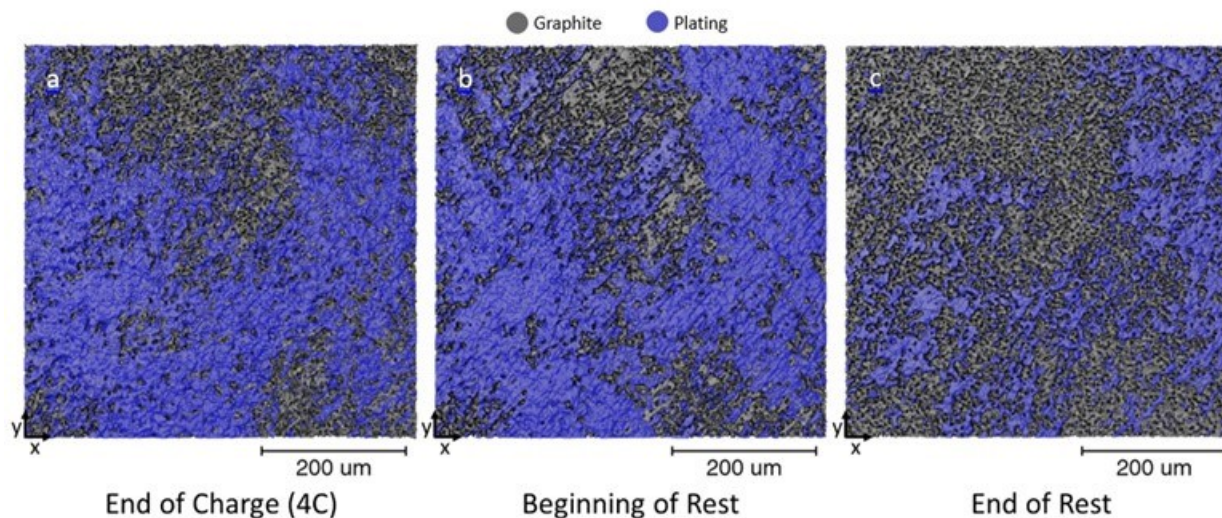
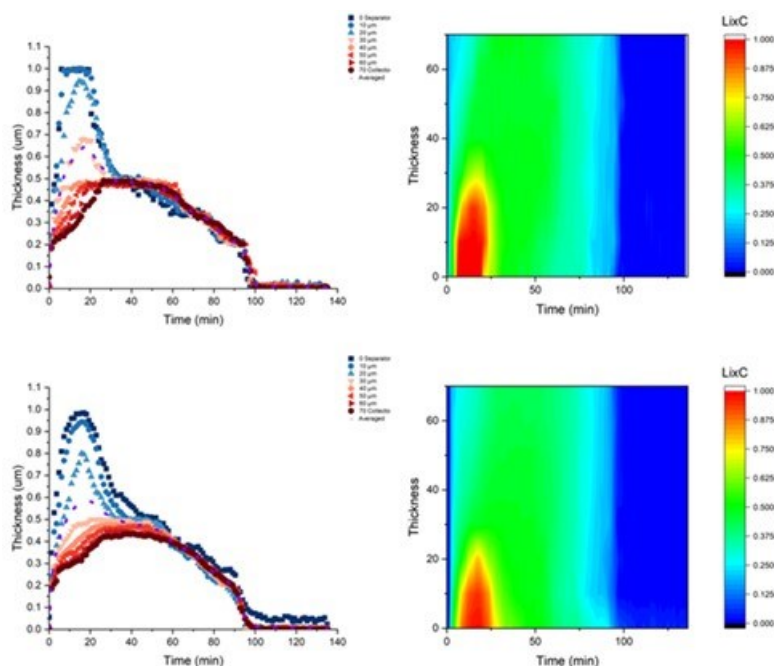


Figure IV.2.7 Distribution of lithium plating during and after a 4C charge. Top-down view of segmented lithium plating (purple) on a graphite electrode (gray) for (a) the final charge scan, (b) the first rest scan, and (c) the final rest scan.

### ***In-situ and Operando Investigation of NMC811-based Cells Subjected to Fast Charge (Argonne-APS Focus)***

One of the proposed strategies to mitigate variations in the structure and properties of electrodes, both within and across the electrode plane, involves designing configurations that incorporate microstructural diversity. One such method is the creation of engineered porosity through laser ablation. The recent enhancement at the 11-ID-C station of the Advanced Photon Source (105keV) enabled focusing capability, allowing real-time measurements of unmodified full-cell coin cells during fast charging. This enhancement enabled the development of a streamlined process for operando evaluations of the impact of cell configurations and engineering solutions on electrode utilization throughout its depth. For example, as shown in Figure IV.2.8, laser ablation effectively slows down overcharging across the top layer of the electrode, facilitating more efficient utilization of the anode throughout its depth.



**Figure IV.2.8 Comparison of LixC content in the baseline sample (top) vs. laser ablated (bottom). Li in graphite at multiple depths is shown as lines (left) or contour plots (right).**

Over the past year, this team has explored various engineered solutions intended to enhance uniform performance in thicker electrodes, with the goal of improving transport throughout the electrode's depth. The data indicates that the composition of the electrolyte can influence the extent of electrode utilization depth and either constrain or promote surface layer overcharging.

### **Conclusions**

The Electrode & Cell Design Thrust of the XCEL Phase II Program successfully coordinated its efforts to develop the ideal structured electrode to enable fast charging with minimal lithium plating. In particular:

- Model results indicate that cells with EV relevant loadings can be re-charged in 15 minutes without lithium plating if a multi-prong approach is used that improves electrode architecture, high porosity separator, and improved electrolyte.
- Cell systems with traditional mono-layer structure have poor capacity utilization above 3 mAh/cm<sup>2</sup> during extreme fast charging.
- Single-layer pouch cells were fabricated and delivered to INL to meet requested deliverables.
- Reference electrode study showed that positive electrode polarization has large effect on lithium-plating at the negative electrode.

- Micron computed tomography ( $\mu$ -CT) imaging confirmed that variation in the measured fluorescence intensity across a cell can be correlated to topology differences of the cathode.
- Single-crystal particles improved stability and rate capacity with morphological dependence.
- Time-resolved X-ray microtomography can quantify lithium plating and lithiation in graphite electrodes.
- Operando evaluations at APS showed that laser ablation effectively slows down overcharging across the top layer of the electrode.

### Key Publications

1. Tanvir R. Tanim, Sangwook Kim, Andrew M. Colclasure, Zhenzhen Yang, Kevin Gering, Peter J. Weddle, Michael Evans, Eric J. Dufek, Yulin Lin, Jianguo Wen, Francois Usseglio-Viretta, Alison R. Dunlop, Stephen E. Trask, Kandler Smith, Brian J. Ingram, Andrew N. Jansen, “Rational designs to enable 10-min fast charging and long cycle life in lithium-ion batteries” *J. Power Sources*, 582, 2023.
2. Zachary M. Konz, Brendan M. Wirtz, Ankit Verma, Tzu-Yang Huang, Helen K. Bergstrom, Matthew J. Crafton, David E. Brown, Eric J. McShane, Andrew M. Colclasure, Bryan D. McCloskey, “High-throughput Li plating quantification for fast-charging battery design” *Nature Energy*, 1-12, 2023.
3. Abigale P. Monasterial, Peter J. Weddle, Kristen Atkinson, David Wragg, Andrew Colclasure, Francois Usseglio-Viretta, Natalie Seitzman, Jun-Sang Park, Jonathan Almer, Kandler Smith, Donal Finegan, “Dynamic in-plane heterogenous and inverted response of graphite to fast charging and discharging conditions in lithium-ion pouch cells” *Small Science*, 2200067, 2023.
4. Maha Yusuf, Jacob M. LaManna, Partha P. Paul, David N. Agyeman-Budu, Chuntian Cao, Alison R. Dunlop, Andrew N. Jansen, Bryant J. Polzin, Stephen E. Trask, Tanvir R. Tanim, Eric J. Dufek, Vivek Thampy, Hans-Georg Steinrück, Michael F. Toney, Johanna Nelson Weker, “Simultaneous neutron and X-ray tomography for visualization of graphite electrode degradation in fast-charged lithium-ion batteries”, *Cell Reports Physical Science*, 3, 2023
5. O. Furat, D.P. Finegan, Z. Yang, M. Neumann, S. Kim, T.R. Tanim, P. Weddle, K. Smith, V. Schmidt, “Quantifying the impact of operating temperature on structural degeneration of Li-ion battery electrodes,” submitted.
6. O. Furat, D.P. Finegan, Z. Yang, T. Tanim, K. Smith, V. Schmidt, “Quantifying the Impact of Charge Rate and Number of Cycles on Structural Degeneration of Li-ion Battery Electrodes,” *J. Echem. Society*, 169, 100541, 2022.
7. Tanvir R. Tanim, Peter J. Weddle, Zhenzhen Yang, Andrew M. Colclasure, Harry Charalambous, Donal P. Finegan, Yanying Lu, Molleigh Preefer, Sangwook Kim, Jeffery M. Allen, Francois L.E. Usseglio-Viretta, Parameswara R. Chinnam, Ira Bloom, Eric J. Dufek, Kandler Smith, Guoying Chen, Kamila M. Wiaderek, Johanna Nelson Weker, Yang Ren, “Enabling Extreme Fast-Charging: Challenges at the Cathode and Mitigation Strategies” *Advanced Energy Materials*, 12, 2202795, 2022.
8. Sangwook Kim, Tanvir R. Tanim, Eric J. Dufek, Don Scoffield, Timothy D. Pennington, Kevin L. Gering, Andrew M. Colclasure, Weijie Mai, Andrew Meintz, Jesse Bennett. “Projecting Recent Advancements in Battery Technology to Next-Generation Electric Vehicles” *Energy Technology* 10, 2200303 (2022).
9. Nathan Dunlap, Dana B. Sulas-Kern, Peter J. Weddle, Francois Usseglio-Viretta, Patrick Walker, Paul Todd, David Boone, Andrew M. Colclasure, Kandler Smith, Bertrand J. Tremolet de Villers, Donal P. Finegan. “Laser ablation of Li-ion electrodes for fast charging: Material properties, rate capability, Li plating, and wetting” *Journal of Power Sources* 537, 231464 (2022).
10. Eric J. McShane, Helen K. Bergstrom, Peter J. Weddle, David E. Brown, Andrew M. Colclasure, Bryan D. McCloskey. “Quantifying Graphite Solid-Electrolyte Interphase Chemistry and its Impact on Fast Charging” *ACS Energy Letters*, 7, 2734-2744 (2022).

### References

1. T. Tanim et al. “Rational designs to enable 10-min fast charging and long cycle life in lithium-ion batteries” *J. Power Sources*, 582:233519 (2023)



**Acknowledgements**

Key contributors (alphabetical order per Lab) to the XCEL Electrode & Cell Design Thrust work include: Daniel Abraham, Shabbir Ahmed, Pavan Badami, Harry Charalambous, Alison Dunlop, Brian Ingram, Tianyi Li, Marco Rodrigues, Seoung-Bum Son, Steve Trask, Kamila Wiaderek, Zhenzhen Yang (Argonne); Nitash Balsara, Michael Bowen, Guoying Chen, Alec Ho, Vivekanantha Murugan, Faxing Wang (LBNL); Andrew Colclasure, Donal Finegan, Kandler Smith, Francois Usseglio-Viretta (NREL); and Yi Cui, Tony Li, Fang Liu, Johanna Weker Nelson, Molleigh Preefer, Erick Espinosa Villatoro (Stanford/SLAC)

## IV.3 XCEL Thrust 3: Electrochemical and Thermal Performance (INL)

### Eric Dufek, Principal Investigator

Idaho National Laboratory  
2525 Fremont Ave  
Idaho Falls, ID 83415  
E-mail: [eric.dufek@inl.gov](mailto:eric.dufek@inl.gov)

### Jake Herb, DOE Technology Development Manager

U.S. Department of Energy  
E-mail: [Jake.Herb@ee.doe.gov](mailto:Jake.Herb@ee.doe.gov)

Start Date: October 1, 2022	End Date: September 30, 2023	
Project Funding (FY23): \$1,480,000	DOE share: \$1,480,000	Non-DOE share: \$0

### Project Introduction

Extreme fast charging (XFC) of Li-ion batteries can create life and safety issues (Ahmed et al. 2017). With respect to performance loss one of the key complications is plating of Li metal on the negative electrode during fast charging. When this occurs, there is a pronounced loss of Li inventory and subsequent enhanced electrolyte degradation due to the reaction of electrolyte molecules with Li metal. Additional degradation modes including cathode aging can complicate analysis as new charging protocols are developed. As part of this thrust a team consisting of researchers at Idaho National Laboratory (INL), the National Renewable Energy Laboratory (NREL), Ford, the Stanford Linear Accelerator (SLAC) and Argonne National Laboratory (Argonne) looked to develop methods to both more clearly understand life and failure mode analysis for cells undergoing fast charge and to use understanding of cell design to develop new fast charge protocols. Using a combination of experimental and physics-based models, which incorporate both electrochemical and thermal performance, the team was able to develop methods and validate performance which showed a 25% increase in charge acceptance in a 10 min charge and a 3x improvement in charge acceptance for charging segments that did not include a constant voltage component.

### Objectives

Key objectives during FY23 were to continue to increase knowledge on the limitations of fast charge using graphite-based Li-ion batteries and to use that knowledge to provide improvements in performance. Overall objectives were to increase charge acceptance in cells with a fixed charge time of 10 minutes, identification of failure modes and development of means to facilitate early identification of failure modes using electrochemical signatures. The team also looked to verify the efficacy of different modes of improving charge acceptance including the use of different temperatures or cell design aspects. This thrust also evaluated the performance of solutions developed in the other XCEL thrusts including electrolyte and electrode design solutions.

### Approach

Using existing and expanding knowledge the team developed advanced charging algorithms using both experimental work and physics-based models. Both 3-electrode and pseudo-2D (P2D) model outputs provided understanding on when issues with Li metal plating or non-uniform thermal distribution could emerge in cells undergoing fast charge. Using this knowledge specific protocols were developed that limited Li plating. Using protocols researchers validated performance using single layer pouch cells. The electrochemical data from those cells was used for advanced cell analysis on overall performance and key failure modes were validated using post-test characterization including analysis of the electrolyte, optical imaging and advanced characterization using different scientific user facilities.

## Results

### Comparison of Advanced Methods to Increase Charge Acceptance.

Over the course of the XCEL program several advances have occurred which have led to increased charge acceptance. These include different electrode designs, advanced electrolytes, and different charge protocols. As shown in Figure IV.3.1 these advances directly impact the cell impedance and charge acceptance. Moving to advanced electrolytes, dual layer electrodes and NMC811 allows plating at rates above 8C without plating lithium while achieving 92% charge acceptance in 10 minutes when paired with a voltage ramping (VR) charge protocol. In total five solution sets can achieve greater than 87% in the same time duration.

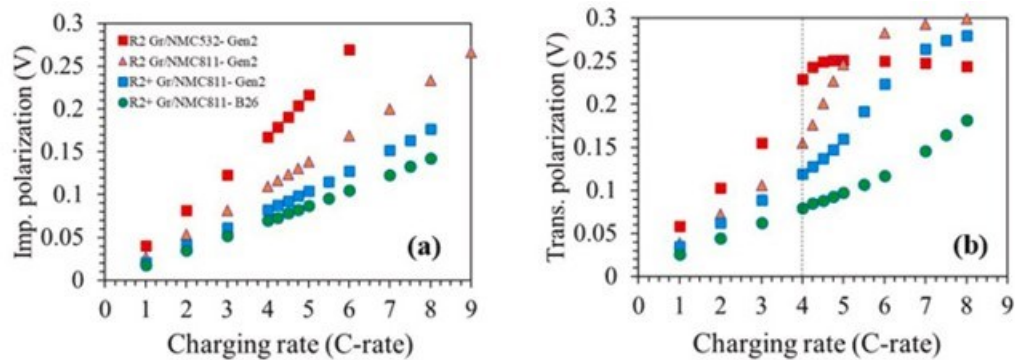


**Figure IV.3.1 Impedance and transportation polarization for cells incorporating different fast charge solutions.**

The advances including the use of B26 electrolyte, and the VR charge protocols also helped minimize aging with only ~10% capacity fade observed over 600 fast charge cycles. Even when charge using a constant current constant voltage (CCCV) regime the cells had minimal fade, though the total charge accepted was lower. To understand the fade electrochemical analysis and post-test characterization was performed which showed that for the best performing samples that Li was plated during the extended cycling. There was some cathode degradation including fracturing of the NMC811 secondary particles, but the overall impact of the degradation was lower than observed earlier in the XCEL program for NMC532.

Other posttest analysis looked at the chemical composition of the electrode surfaces and electrolyte degradation species observed. The work found slight variations in the composition of the solid electrolyte interphase (SEI) as cycling rate increased. Changes in electrolyte composition were also seen. Overall, in conditions where Li plating was more prevalent the thickness of the SEI increased, included more  $\text{Li}_x\text{POyF}_2$  species, and became more resistive. (Figure IV.3.2)

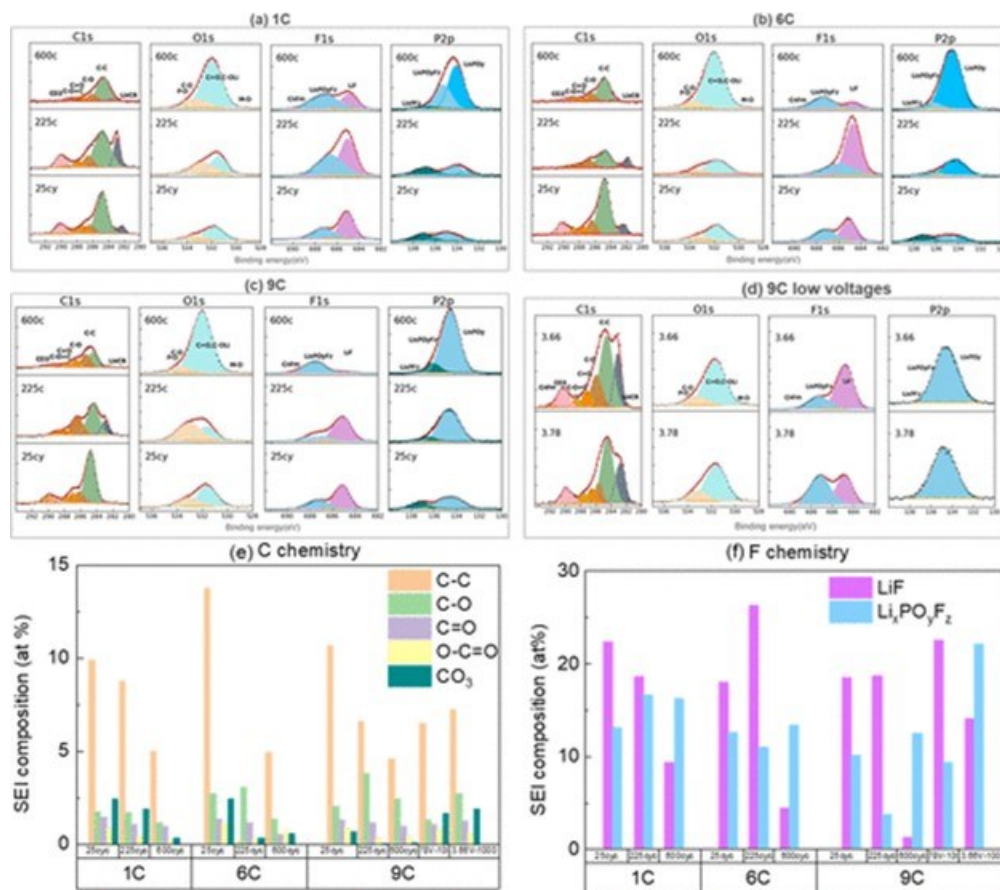


Figure IV.3.2 Comparison of SEI components for cells cycled at different fast charging rates.

### Co-optimization of Solutions.

The electrochemical/thermal solutions team is developing and demonstrating technologies that help advance battery fast-charge capability. These include:

1. Faster electrolyte transport through advanced electrolytes (described in electrolyte thrust chapters)
2. Faster electrolyte transport via low-tortuosity electrode architectures (described in electrode design thrust chapter)
3. Temperature control including elevated temperature for fast electrolyte transport and cooling to meet calendar-life requirements (previously developed in FY22 with thermal property updates below)
4. Charge protocols including voltage ramp and aging dependent Li-plating avoidance (described below)
5. Combined strategies

In FY24, the team will perform an electrochemical/thermal model-guided study propose optimal combinations of these strategies. To support this effort, in FY23 the team developed a platform for capturing the life/performance benefits of the multiple technologies, with the key submodel being a pseudo-2D electrochemical/thermal/aging model capable of making life projections for different electrode designs and duty cycles. A brief summary of the coupled electrochemical/thermal/aging model and next steps are:

- Degradation physics: The chemistry-dependent pseudo-2D model incorporates particle fracture, SEI growth and (ir)reversible Li plating. These mechanisms are also coupled with surface area increase, electrode expansion, side reaction rates, porosity changes observed in XCEL and other data
- Example simulations: Figure IV.3.3 shows example simulations from the model for XCEL Round 2 moderate loading graphite/NMC811 cells. In addition to the data shown, the model reasonably

reproduces charge capacity versus temperature and C-rate, capacity fade, loss of lithium inventory, and loss of active material.

- Computational speed: The model achieves clock time of 24 hours for 600 cycles on single processor. While suitable for parametric design studies, the team expects to further speed-up the model in the coming months.
- Next: Finish validation versus XCEL Gr/NMC811 Rounds 2 & 3 cells including variants (multiple electrolytes, dual/ablated electrodes, etc.). Study and propose cost-/fast-charge-optimal design.

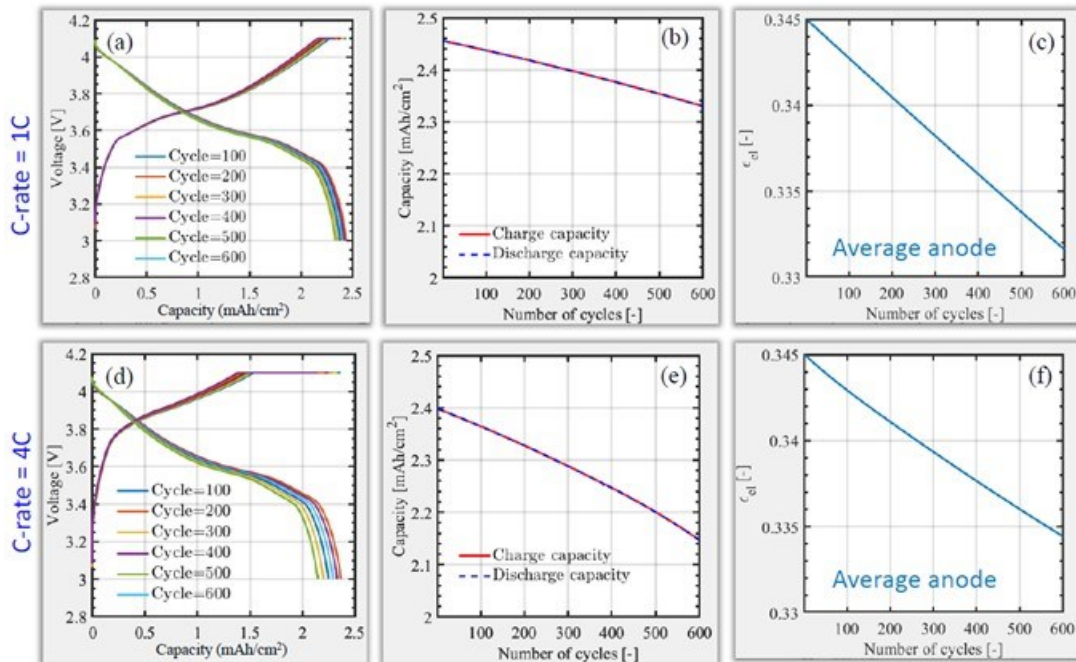


Figure IV.3.3 Electrochemical/thermal/aging model of XCEL Gr/NMC811 Round 2 cell.

#### ***Aging-Adaptive Charge Protocols.***

Researchers at NREL and LBNL jointly investigated strategies to avoid lithium plating during extreme fast charging using well-validated electrochemical models (Konz, 2023). The team combined pseudo-2D electrochemical modeling with data visualization methods to reveal important relationships between the measurable cell voltage and difficult-to-predict Li-plating onset criteria. A wide range of operating conditions were investigated including advanced charging protocols and various thermal conditions. Through several thousand electrochemical simulations, the team determined simple voltage limits as a function of state of charge can be used to avoid damage from lithium plating (see Figure IV.3.4). Simulations also revealed the capacity difference at 4V between two different charge protocols is proportional to the plating onset capacity. The team then used models to investigate how the plating onset voltage changed with aging. Aging was approximated by modifying several different model parameters to represent different aging mechanisms. The lithium plating onset becomes more variable with increased aging and the threshold for plating can be significantly reduced with cell aging/capacity fade.

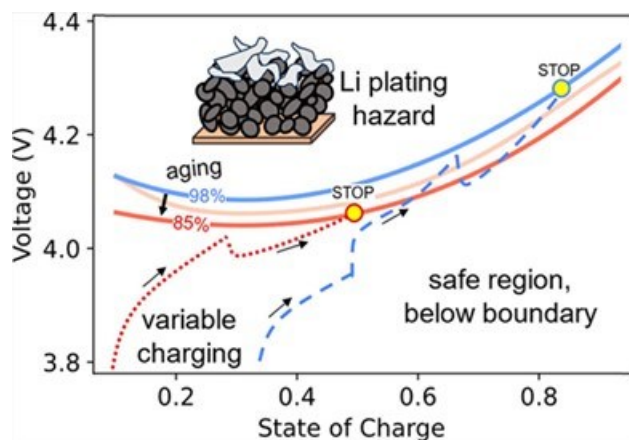


Figure IV.3.4 Empirical voltage threshold for lithium plating as function of SOC determined using electrochemical modeling.

### 3D Cell-Level Modeling.

Using a cell-cooling-coefficient (CCC) metric/approach from the literature, the team performed thermal modeling analysis to quantify impact of improved electrolyte heat transport on cell-internal temperature gradient during fast charge. Analytical and 3D thermal models simulated the cell-level heat removal benefit of raising electrolyte thermal conductivity from 0.26 W/mK (Gen2, measured) to 0.32 W/mK (ORNL, measured) or beyond, 0.52 W/mK (target). If this target is achieved, cross-plane cell-internal temperature gradients will drop by ~30%. Reduction of in-plane temperature gradients will be negligible due to the dominance of current collectors for in-plane heat transport. This mainly benefits systems that employ cell surface-cooling, rather than bottom-cooling strategies.

### Cathode Cracking 3D Modeling & Diagnostics.

The previously developed 3D chemo-mechanical model was enhanced to include electrolyte infiltration into cracks. The model then simulated various magnitudes of cracking in NMC particles and mapped the damage to effective cathode properties (surface area and solid-state diffusivity). Together with loss of cathode active material, those effective properties are being applied in pseudo 2D electrochemical/aging models to co-optimize designs for fast-charge and lifetime, as well as develop SOH-adaptive charge protocols. The 3D chemo-mechanical model is also being validated versus cracks observed in SEM images, interpreted by Univ. of Ulm using AI algorithms. Objectives of this physics-guided modeling workflow are to understand and optimize future cathode architecture and cell design with less test data. The University of Ulm published one paper and has a second paper accepted on using AI algorithms to quantitatively interpret SEM images.

### Conclusions

The electrochemical and thermal performance thrust of the XCEL program had multiple key advances during FY23. Different solutions were evaluated showing that over 90% charge acceptance could be achieved in 10 minutes, advanced coupled electrochemical, mechanical and thermal models were advanced. Characterization of both positive and negative electrodes also advanced. These found differences in SEI composition for cells undergoing high rate charging and differences in cathode particle structure as determined using tomography.

### Key Publications

1. T. Tanim, S. Kim, A. Colclasure, Z. Yang, K. Gering, P. Weddle, M. Evans, E. Dufek, Y. Lin, J. Wen, F. Usseglio-Viretta, A. Dunlop, S. Trask, K. Smith, B. Ingram, A. Jansen, "Rational Designs to enable 10-min fast charging and long cycle life in lithium-ion batteries" *J. Power Sources*, 552 (2023)
2. Z. Yang, T. Tanim, H. Liu, I. Bloom, E. Dufek, B. Key, B. Ingram, "Quantitative analysis of origin of lithium inventory loss and interface evolution over extended fast charge aging in Li-ion batteries" *ACS Appl. Materials & Interfaces*, 15, 2023.

3. O. Furat, D.P. Finegan, Z. Yang, M. Neumann, S. Kim, T.R. Tanim, P. Weddle, K. Smith, V. Schmidt, “Quantifying the impact of operating temperature on structural degeneration of Li-ion battery electrodes,” accepted
4. O. Furat, D.P. Finegan, Z. Yang, T. Tanim, K. Smith, V. Schmidt, “Quantifying the Impact of Charge Rate and Number of Cycles on Structural Degeneration of Li-ion Battery Electrodes,” *J. Echem. Society* 169 (2022) 100541.
5. Z. Konz, P.J. Weddle, P. Gasper, B.D. McCloskey, and A.M. Colclasure. “Voltage-Based Strategies for Preventing Battery Degradation under Diverse Fast-Charging Conditions” *ACS Energy Letters*, **8**:4069-4077 (2023).

### References

1. Ahmed, S., I. Bloom, A.N. Jansen, T. Tanim, E.J. Dufek, A. Pesaran, A. Burnham, et al. (2017) Enabling Fast Charging – A Battery Technology Gap Assessment. *Journal of Power Sources* 367.
2. Z. Konz, P.J. Weddle, P. Gasper, B.D. McCloskey, and A.M. Colclasure. “Voltage-Based Strategies for Preventing Battery Degradation under Diverse Fast-Charging Conditions” *ACS Energy Letters*, **8**:4069-4077 (2023).

### Acknowledgements

The activities described were a collaborative effort utilizing the capabilities of many researchers. Key contributors across the different national laboratories include Daniel P. Abraham, Ira Bloom, Bor-Rong Chen, Brian Ingram, Andrew M. Colclasure, Kevin L. Gering, Matthew Keyser, Sangwook Kim, David Robertson, Marco-Tulio F. Rodrigues, Kandler Smith, Tanvir R. Tanim, Francois L. E. Usseglio-Viretta, Peter Weddle, Molleigh B. Preefer, Johanna Nelson Weker, Alison R. Dunlop, Stephen E. Trask, Andrew N. Jansen, David N. Agyeman-Budu, Chuanbo Zhang, Yeyoung Ha, Maha Yusuf, Partha P. Paul, Chuntian Cao, and Vivek Thampy. Donal P. Finegan, Eric J. McShane, Bryan D. McCloskey, Seong-bum Son, Zhenzhen Yang and Michael Evans.

## V Testing, Analysis, High-Performance Computing, Lab-I4

The *battery testing, analysis, high-performance computing, and Lab-I4* activity develops requirements and test procedures for batteries (to evaluate battery performance, battery life and abuse tolerance). Battery technologies are evaluated according to USABC-stipulated battery test procedures. Benchmark testing of an emerging technology is performed to remain abreast of the latest industry developments. The *battery testing* activity includes performance, life and safety testing, and thermal analysis and characterization. The testing activity also supports cell analysis, modeling, and prototyping (CAMP) projects at ANL, which include benchmarking and post-test analysis of lithium-ion battery materials at three labs (ANL, ORNL, and SNL). Projects include testing (for performance, life and abuse tolerance) of cells (for contract, laboratory-developed and university-developed cells), and benchmarking systems from industry; thermal analysis, thermal testing, and modeling; cost modeling; and other battery use and life studies. *Cost assessments and requirements analysis* includes the ANL project on developing the performance and cost model BatPaC. This rigorously peer-reviewed model developed at ANL is used to design automotive lithium-ion batteries to meet the specifications for a given vehicle and estimate its cost of manufacture. An analysis using BatPaC compared the estimated costs of cells and packs for different electrode chemistries (Figure V.1).

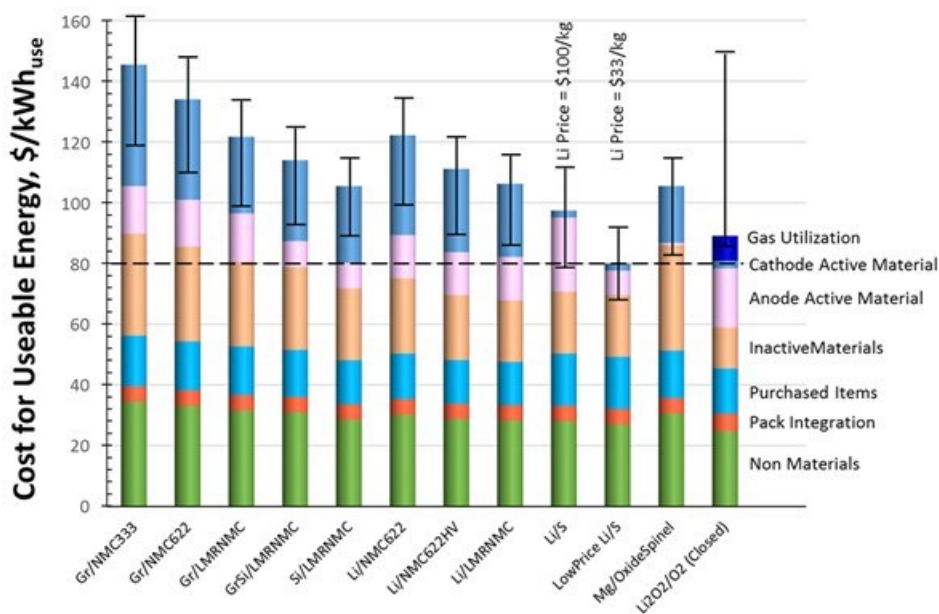


**Figure V.1** Estimated costs of cells in automotive battery packs with different combination of electrodes. The packs are rated for 100 kWh<sub>Total</sub> (85 kWh<sub>Useable</sub>), 300 kW, 315 V, 168 cells, and produced at a plant volume of 100K packs/year

The rest of this chapter contains detailed reports on the status of the following individual projects.

- BatPaC Model Development (ANL)
- Battery Performance and Life Testing (ANL)
- Battery Abuse Testing (SNL)
- Battery Thermal Analysis and Characterization Activities (NREL)
- Cell Analysis, Modeling, and Prototyping (CAMP) Facility Research Activities (ANL)
- Materials Benchmarking Activities for CAMP Facility (ANL)
- Electrochemical Performance Testing (INL)
- Machine Learning for Accelerated Life Prediction and Cell Design (INL, NREL).



## V.1 BatPaC Model Development (ANL)

### Shabbir Ahmed, Principal Investigator

Argonne National Laboratory  
9700 South Cass Avenue  
Lemont, IL 60439  
E-mail: [Shabbir.Ahmed@anl.gov](mailto:Shabbir.Ahmed@anl.gov)

### Thomas Do, DOE Technology Development Manager

U.S. Department of Energy  
E-mail: [Thomas.Do@ee.doe.gov](mailto:Thomas.Do@ee.doe.gov)

Start Date: October 1, 2022	End Date: September 30, 2023	
Project Funding (FY23): \$900,000	DOE share: \$900,000	Non-DOE share: \$0

### Project Introduction

A performance and cost model (Knehr *et al.* 2022) was developed at Argonne to design automotive Li-ion batteries that can meet the specification of a given vehicle, and then to estimate the cost of manufacturing such batteries. It is the product of long-term research and development at Argonne through sponsorship by the U.S. Department of Energy.

Over a decade, Argonne has developed methods to design Li-ion batteries for electric-drive vehicles based on modeling with Microsoft® Office Excel spreadsheets. These design models provided all the data needed to estimate the annual materials requirements for manufacturing the batteries being designed. This facilitated the next step, which was to include the manufacturing costs of the batteries.

The BatPaC model has been peer reviewed and is available on the web (<https://www.anl.gov/cse/batpac-model-software>). It captures the interplay between design and cost of Li-ion batteries for transportation applications. BatPaC helps estimate the impact of R&D advances on the mass, volume, and cost of lithium-ion cells and battery packs. Moreover, BatPaC is the basis for the quantification of battery costs in U.S. EPA and NHTSA 2017-2025 Light-Duty Vehicle Technical Assessment. This assessment is used to guide the mileage (i.e., CAFE) and CO<sub>2</sub> emission standards.

### Objectives

To develop and utilize efficient simulation and design tools for lithium-ion batteries

- to meet energy storage capacity, pulse power, and fast charge specifications
- to predict mass, dimensions, and volume
- to estimate the cost and performance metrics when manufactured in large volume, such as
  - Cell and pack costs,
  - Breakdown of cost contributors
  - Specific Energy (Wh/kg), Energy Density (Wh/L)
  - Inventory of key materials needed for manufacturing the battery and that available in the final product

### Approach

The battery pack design and cost calculated in BatPaC represent projections for a specified level of annual battery production (50 GWH plant capacity). As the goal is to predict the near future (less than 7 years) cost of manufacturing batteries, a mature manufacturing process is assumed. The model designs a manufacturing plant with the sole purpose of producing the battery being modeled. The assumed battery design and manufacturing facility are based on common practice today but also assume some problems have been solved to result in a more efficient production process and a more energy dense battery. The proposed solutions do not have to be

the same methods used in the future by industry. It is assumed that leading battery manufacturers, those having successful operations in the near future, will reach these ends by some means.

For a selected battery chemistry, BatPaC solves the governing equations to determine the size of each layer, cell, and module that make up the battery pack that can meet the desired requirements for power and energy. This allows the calculation of the mass of each material, the volume of the components, and the heat removal needed during discharge. The cost of the pack is then estimated based on a predefined manufacturing process.

Current effort is directed at

- Improving the design capability by including correlations derived from continuum modeling and updating the default material properties to reflect recent experimental and industrial performance data
- Reducing the uncertainty of model predictions by setting up independent models of the manufacturing processes
- Validating the results through discussions with manufacturers and component developers
- Updating the default price of materials used in BatPaC calculations

## Results

### Key Accomplishments

- Released BatPaC v5.1 with an accompanying document describing the updates since version 5.0
  - Included the energy required for each processing step
  - Restructured the cost calculations
  - Added new electrode chemistry couples
- Published a perspective paper that identifies the key parameters that affect the cost and performance metrics
- Developed a silicon cell model which predicts the expansion/contraction during lithiation
- Studied the cooling effect on the temperature distribution on cylindrical cells in a module

### BatPaC 5.1 Key Features and Capabilities

Several new features and capabilities have been added into this newest version (5.1) of BatPaC. For the manufacturing process, a significant improvement is the accounting of energy demand. Earlier versions used a lumped parameter that included energy and other utility costs; this version accounts for the energy demand for each manufacturing step. This information is available in the “Manufacturing Costs” tab. This additional information accounting required an overall restructuring of the manufacturing costs. Another important capability added is that one can now have different size cell and pack plants, a practice that is becoming common place in industry. Cells can be produced at higher volumes and distributed to different packs, leading to cost reductions via economies of scale.

On pack designs, the user can now select either a cost or mass-sensitive design, with a toggle that exists on the dashboard. The two options are: *cost-sensitive* – uses cheaper metal components for pack containment, at the cost of extra mass (this is the standard design); *Mass-sensitive design* – uses more expensive carbon-fiber composites and materials for pack containment to decrease the pack's weight. This allows users to get a range of metrics depending on other desired performance metrics.

This new version has also included some additional electrode definitions, with the added ability to select from several weight percent of silicon in the graphite anode – A toggle on the dashboard allows the user to add between 5 to 20% silicon to a graphite-based anode. In addition, the NMC955/G couple was added.

### Comparison of BatPaC 4.0 vs. 5.1 Results

The release of BatPaC v5.1 included modifications to the pack design and manufacturing processes to maintain alignment with industry trends. The decision was also made to switch from v4.0 to v5.1 when generating the pack cost results for the Department of Energy's Government Performance and Results Act (GPRA) analysis

in 2023. These two changes made it necessary to benchmark the v5.1 results against the results from v4.0. The Figure V.1.1 below is a waterfall plot that describes the cost changes between v4.0 and v5.1 for a pack with identical specifications (*i.e.*, 94 kWh/200 kW all-electric vehicle pack, NMC811-G active materials, and a production rate of 100,000 packs per year). Results indicate that the total pack cost had an overall increase of ~\$15/kWh from v4.0 to v5.1. Most of the cost increases (blue bars in the Figure V.1.1) are attributed to increases in the cost of the capital equipment used in the manufacturing process (“CapEx-related” = +\$7.3/kWh), a better representation of the solvent economics that led to a cost increase (“Solvent” = +\$4.5/kWh), and an increase in total profits (“Profits” = +\$4.5/kWh). The profits in BatPaC are calculated based on the total fixed capital investment used to build the plant, which is also influenced by the increase in “CapEx-related” costs. Cost decreases (orange bars in Figure V.1.1) resulted from more efficient designs of the cell, module, and pack. These changes provided a total decrease of \$6.8/kWh.

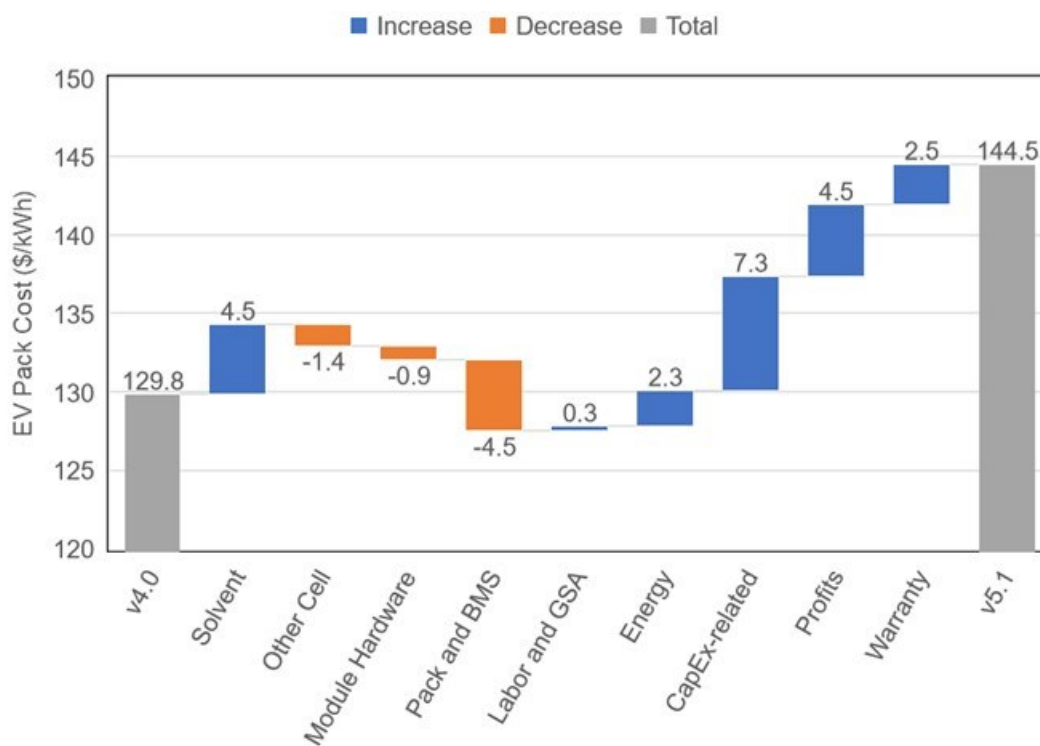


Figure V.1.1 Waterfall plot detailing the changes in costs between BatPaC v4.0 and v5.1. Results are for a 94 kWh, 200 kW, NMC811-G pack manufactured at 100,000 packs per year.

#### Key Drivers Affecting Performance and Cost Metrics (from Perspective Paper)

A study was undertaken to understand the key material properties, cell design decisions, and manufacturing costs that influence the metrics used to benchmark batteries. These metrics are related to cell energy (Wh/kg and/or Wh/L), power (W/kg and/or W/L), cost (\$/kWh), lifetime (cycles and/or years), and safety. The study was conducted using BatPaC to generate 200,000+ Monte Carlo simulations. Statistical analyses were conducted on the resulting dataset to generate correlation plots that highlighted the important parameters (see Figure V.1.2). The results were disseminated in an invited perspective paper published in *Energy Advances* [1]. Overall, a cell with optimal energy, power, and cost is best achieved with a high voltage and a low area specific impedance. If the focus is only on optimal energy and/or cost (*i.e.*, where power is less critical), cells also benefit from active materials with high specific capacities. The values of other parameters (*e.g.*, thicknesses, densities, and material costs) are shown to have less influence on achieving cell metrics. The study suggested that the best way to achieve optimal energy, power, and/or cost while maintaining long lifetimes and safe operation is through modification of these other parameters to facilitate the stable operation of materials with high voltage, high capacity, and low area specific impedance.

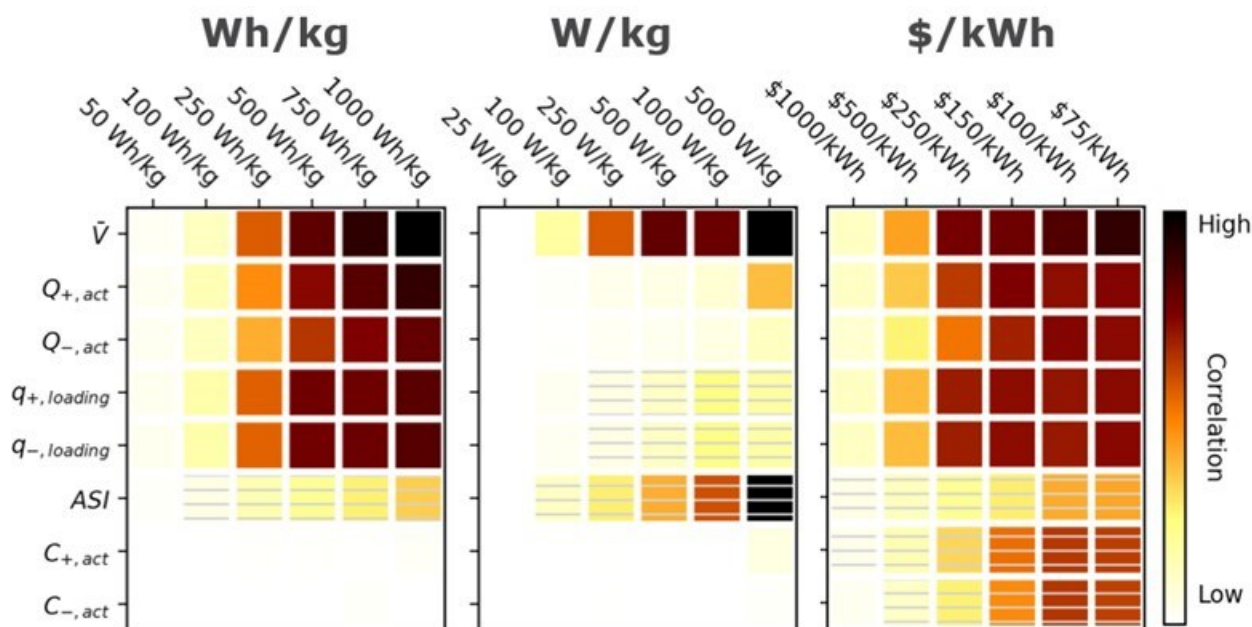


Figure V.1.2 Correlation plots showing the relative importance of parameters to achieving selected specific energy (Wh/kg), specific power (W/kg), and cost (\$/kWh) targets. Solid darker colors indicate the variable has a high degree of positive correlation, where higher values are necessary to achieve the goal. Hatched darker colors indicate strong negative correlation, where lower values are needed to meet the target. Light colors indicate the variable has minimal or no correlation, and its value has a limited impact on achieving the target.

### Energy Distribution in the Manufacturing Plant

An analysis was conducted to estimate the electricity and natural gas consumption at each processing step in a lithium-ion cell manufacturing plant. The study was performed at three production volumes (5, 25, and 50 GWh/year, see Figure V.1.3). Results at the three production volumes were used to develop correlations that were incorporated into BatPaC 5.1. The correlations estimate the energy consumption with respect to the appropriate production rates at each processing step (e.g., electrode slurry per year, coated electrode surface area per year, number of cells per year, etc.) The analysis shows that the coating-drying and the formation process are the most energy intensive steps on the manufacturing floor, with both being around 20% (depending on chemistries) of the total energy required in the pack manufacturing process. In addition to the energy need, the drying step also requires considerable floor space and processing time. The energy demand shown for the formation process in Figure V.1.3 is the net demand, after recycling part of the energy available during the cell discharge step.

The energy consumption estimates are combined with the capital equipment, labor, and plant area estimates to provide a more complete picture of the manufacturing costs in BatPaC 5.1. A manuscript is under development that reports on the use of BatPaC 5.1 to study the impact of cell material properties and cell design decisions on energy consumption within lithium-ion gigafactories.

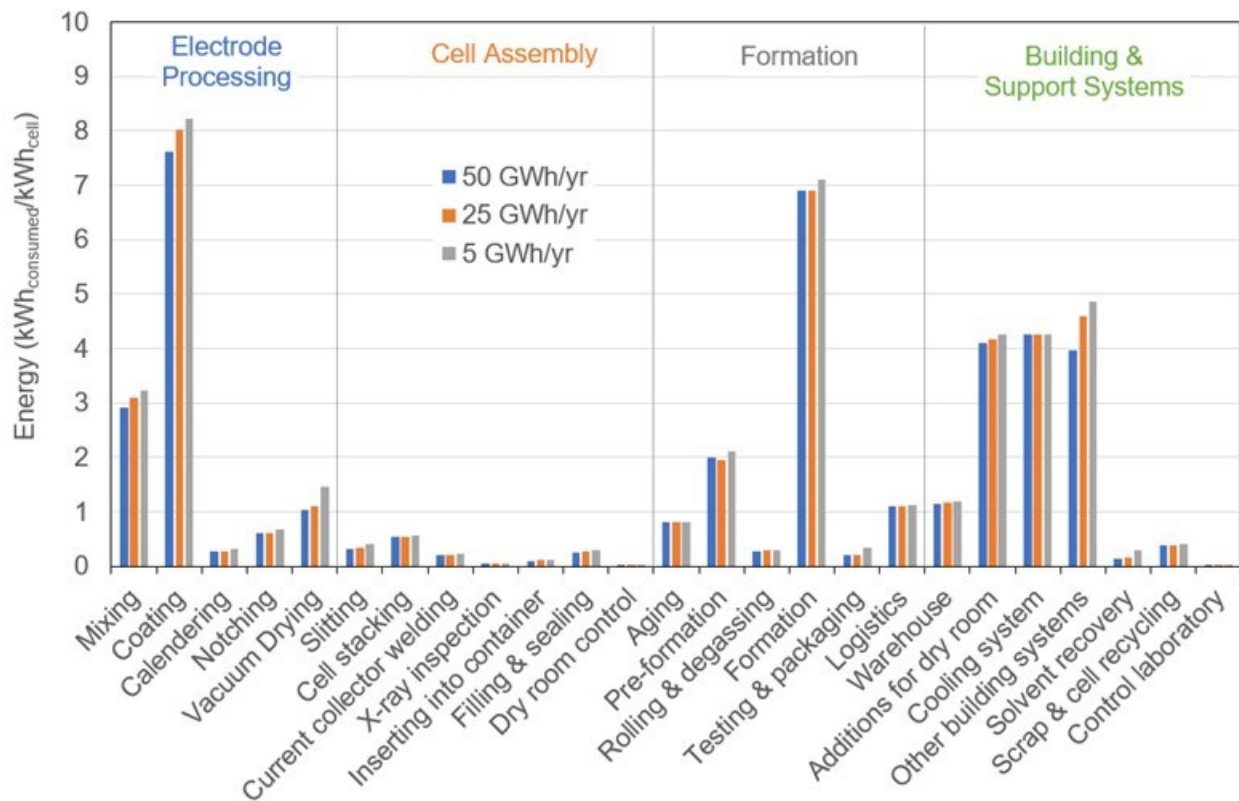


Figure V.1.3 Distribution of energy consumption in three lithium-ion gigafactories, each making NMC-G pouch cells at production volumes of 5, 25, and 50 GWh per year, respectively.

### Expansion-Contraction of a Silicon Cell

Over the last decade, Silicon has become an increasingly attractive anode active material due to its high specific capacity, low cost, and well-developed supply chain [2]. However, the lithiation of silicon is accompanied by excessive volume expansion which has remained a major bottleneck in its wide-scale commercialization [3]. Engineering solutions to mitigate the deleterious effects of this expansion require a detailed understanding of the effect of various electrode design parameters such as loading, initial porosity, thickness, external pressure on the performance and reliability of Silicon based electrodes [2-3].

Current understanding of the effect of electrode design parameters on the performance of rechargeable battery electrodes is based on porous electrode theory [4]. However, such models traditionally ignore lithiation-induced volume expansion and, as such, are insufficient to accurately capture the electrochemistry of Silicon. We have developed a detailed electrochemical model by combining traditional porous electrode theory with large deformation mechanics that enables to systematically analyze the effect of electrode design parameters on the performance of silicon based porous electrodes.

Figure V.1.4 (a) – (d) show the simulated swelling of a single Si particle during charging. During lithiation, regions close to the particle surface become lithium rich and begin to swell while the core of the particle remains lithium deficient. The particle swelling directly affects the transport of lithium inside the particle as well as in the surrounding electrolyte. Figure V.1.4 shows the comparison of simulated (blue) and experimentally measured (red) electrode thickness (e) and voltage (f) for a  $\sim C/20$  charge as highlighted by the gray shaded region in (g). Overall thickness and voltage profiles show a good match with experimental data. Differences in the charging time between experimentally measured and simulated data arise due to unaccounted capacity fade mechanisms in the model. A manuscript based on this work is in development.

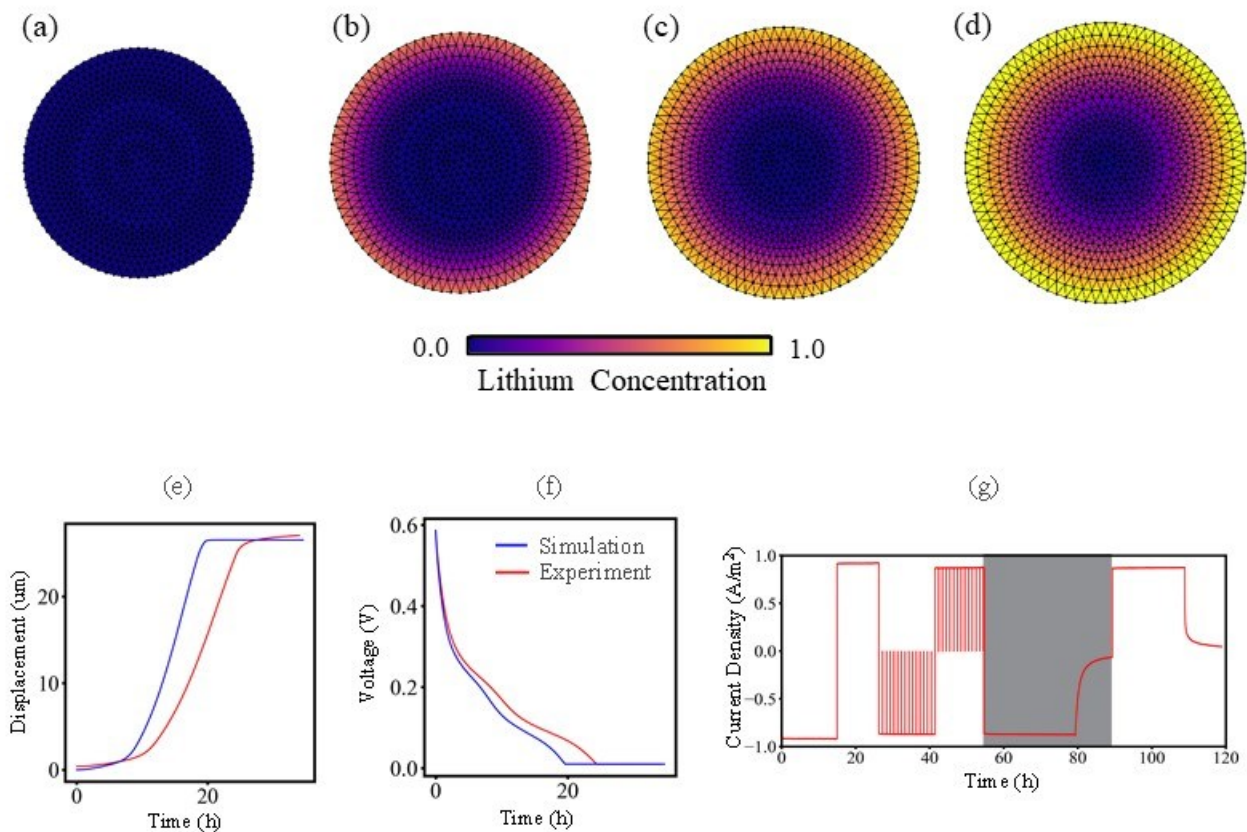


**Figure V.1.4 Simulated swelling of a single Silicon particle, (a) – (d). Comparison of simulated (blue) and experimentally measured (red) electrode thickness (e) and voltage (f) for the current profile for a  $\sim C/20$  charge as highlighted by the gray shaded region in inset (e).**

### Cooling Effects on a Module of Cylindrical Cells

Cooling plates are a popular choice for thermal management of lithium-ion battery modules to control the temperature of battery cells through pumping a coolant across the plate. Internal geometric features of cooling plates come with different topologies, see examples in

Figure V.1.5 (a) [5-7]. Irrespective of the complexity of the features, basically, the fluid passes a finite length through a finite cross section of a flow path. Based on this understanding, a simple mathematical model was built to enable the prediction of the maximum temperature of cells in a module and the pressure drop across the cooling plate. The model was validated with CFD simulations performed using COMSOL Multiphysics®, as in

Figure V.1.5 (b).

To investigate the effect of cooling plate flow-field complexity on performance, a parametric study was conducted using the developed simple model. Panels (c and d) show cells' maximum temperature and coolant pressure drop across the cooling plate, respectively, for a case when heat generated per cell,  $q_{\text{cell}}$ , was 3.6 W (corresponds to 3C discharge of a 4 Ah cell with a 25 mΩ internal resistance). The coolant inlet temperature was 15 °C and a 3 °C difference was allowed between inlet and outlet coolant temperatures. Panel (c) shows that cells' maximum temperature can be decreased by increasing the number of channels in the cooling plate (e.g., increasing the mass flow rate/channel and/or adding more complex topological features to the plates). Panel (d) shows that the pressure drop increases with increasing number of cells in the module, particularly

when number of channels increase (*i.e.*, when more control of temperature is needed). However, there is a range of  $N_{ch}$  (20-30) where an acceptable value of cells' maximum temperature is achieved, *i.e.*,  $\sim 30$  °C (see panel c), at a reasonable cost of pressure drop, *i.e.*,  $\sim 5$  kPa (see panel d). This suggests that high-complexity of flow-field features in some designs is unnecessary.

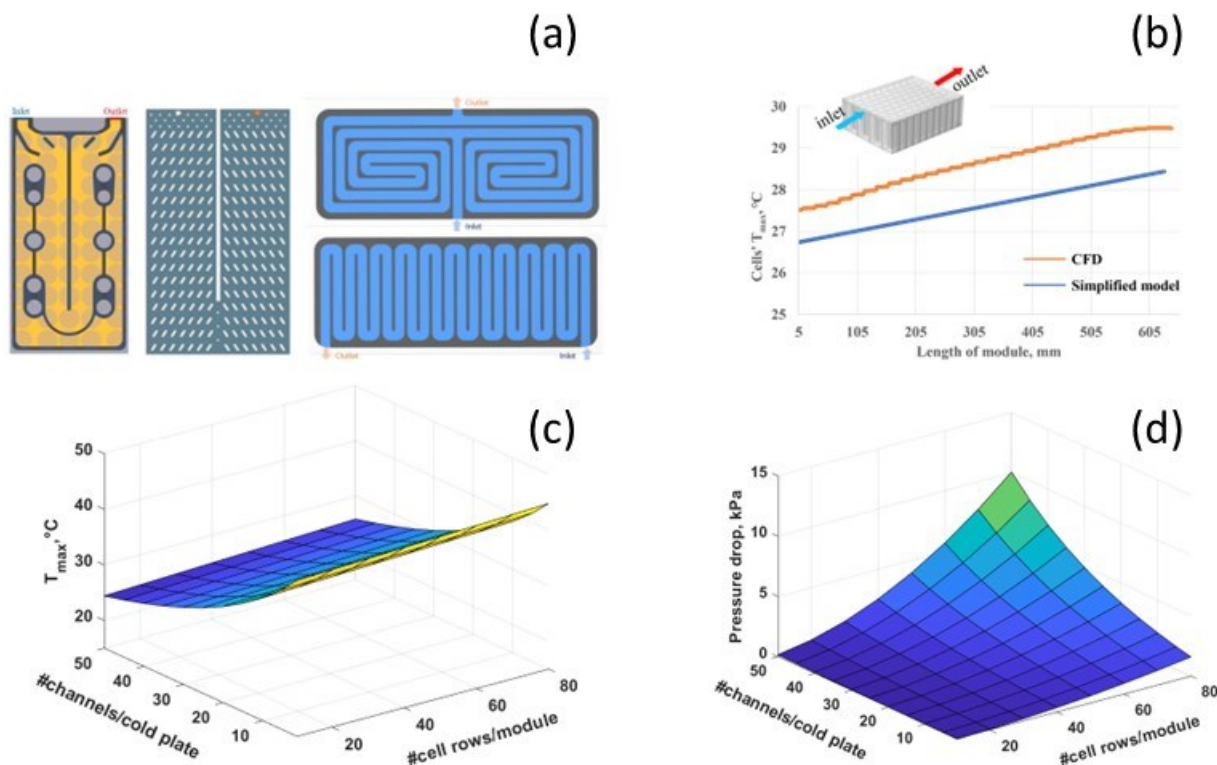


Figure V.1.5 Study of cooling plates performance for cooling cylindrical lithium-ion battery cells in a module.

(a) different designs of cooling plates, (b) validation of a developed simple mathematical model with a computational fluid dynamics (CFD) study, (c) prediction of cells' maximum temperature as a function of number of flow channels,  $N_{ch}$  in the cooling plate (left axis) and number of cell rows,  $N_{row}$  per module (right axis). In this study, 10 cells per row were assumed, giving 800 cells in the module, (d) prediction of the pressure drop across the cooling plate as a function of  $N_{ch}$  and  $N_{row}$ .

## Conclusions

A new version of BatPaC (5.1) was created, with new features at the manufacturing, pack design, and chemistry levels. While many features were built in, two key ones include the ability to select different size cell and pack production levels and have the energy requirements at each step be broken out. Using this version, a comparison of cost contributions between BatPaC versions 4 and 5.1 show that the newer version adds a total of  $\sim \$15/\text{kWh}$ , with additions of  $\$7.3/\text{kWh}$  from CapEx related factors,  $\$4.5/\text{kWh}$  from solvent use/recovery,  $\$4.5/\text{kWh}$  from profits, while cell design improvements result in  $\$6.8/\text{kWh}$  cost reductions.

Analysis of the numerous parameters that contribute to the cost, mass, and volume of the pack shows that higher cell voltage and active material specific capacities can lead to lighter, smaller, and cheaper cells; and lower prices of active materials are key to lowering the cost.

BatPaC version 5.1 has added the accounting of energy consumption at the various processing steps in the manufacturing plant. Results indicate that the coating-drying and the formation process are the two most energy intensive steps, each being  $\sim 20\%$  of the plant energy needs.

The development of a validated electrochemical-mechanical model for cells with silicon anodes will enhance the estimation of key properties such as cell impedance and stress-strain during cycling, leading to durable cell designs of silicon anode cells.

A thermal model of the cooling plate and its flow parameters (pattern, dimensions, and flow rate) will ensure that BatPaC pack designs will maintain temperature differences within an acceptable tolerance.

### Key Publications

1. K.W. Knehr, J.J. Kubal, A. Deva, M.B. Effat, S. Ahmed, "From Material Properties to Device Metrics: A Data-Driven Guide to Battery Design," *Energy Advances*, 2023, 2, 1326-1350.
2. K.W. Knehr, S. Ahmed, "A New Analytical Expression for Estimating the Adiabatic Temperature Rise in Lithium-Ion Batteries During High-Power Pulses," *Journal of The Electrochemical Society*, 170, 2023.
3. S. Ahmed, K.W. Knehr, J. Kubal, E. Islam, "Parametric Study of Lithium-Ion Batteries using BatPaC," Argonne Report ANL/CSE-23/1, 2023.
4. S. Ahmed, J. Kubal, K. Knehr, "Estimated Cost of EV Batteries 2018-2022, BatPaC Model Software, <https://www.anl.gov/cse/batpac-model-software>.

### References

1. K.W. Knehr, J.J. Kubal, A. Deva, M.B. Effat, S. Ahmed, "From Material Properties to Device Metrics: A Data-Driven Guide to Battery Design," *Energy Advances*, 2023, 2, 1326-1350.
2. Huang, Y., C. Wei, and Y. Fang, Numerical investigation on optimal design of battery cooling plate for uneven heat generation conditions in electric vehicles. *Applied Thermal Engineering*, 2022. 211.
3. Uxa, Daniel, Bujar Jerliu, Erwin Hüger, Lars Dörrer, Michael Horisberger, Jochen Stahn, and Harald Schmidt. "On the lithiation mechanism of amorphous silicon electrodes in Li-ion batteries." *The Journal of Physical Chemistry C* 123, no. 36 (2019): 22027-22039.
4. Doyle, Marc, Thomas F. Fuller, and John Newman. "Modeling of galvanostatic charge and discharge of the lithium/polymer/insertion cell." *Journal of the Electrochemical society* 140, no. 6 (1993): 1526.
5. Li, M., et al., Numerical Analysis of Cooling Plates with Different Structures for Electric Vehicle Battery Thermal Management Systems. *Journal of Energy Engineering*, 2020. 146(4).
6. Guo, R. and L. Li, Heat dissipation analysis and optimization of lithium-ion batteries with a novel parallel-spiral serpentine channel liquid cooling plate. *International Journal of Heat and Mass Transfer*, 2022. 189.
7. Zuo, Xiuxia, Jin Zhu, Peter Müller-Buschbaum, and Ya-Jun Cheng. "Silicon based lithium-ion battery anodes: A chronicle perspective review." *Nano Energy* 31 (2017): 113-143.

### Acknowledgements

K. Knehr, J. Kubal, D. Dees, A. Deva, M. Effat, Andy Jansen, Cell Analysis Modeling and Prototyping Facility (CAMP), E. Islam.



## V.2 Battery Performance and Life Testing (ANL)

### **Brian J. Ingram, Principal Investigator**

Argonne National Laboratory  
9700 South Cass Avenue  
Lemont, IL 60439  
E-mail: [ingram@anl.gov](mailto:ingram@anl.gov)

### **Haiyan Croft, DOE Technology Development Manager**

U.S. Department of Energy  
E-mail: [Haiyan.Croft@ee.doe.gov](mailto:Haiyan.Croft@ee.doe.gov)

Start Date: October 1, 2022	End Date: September 30, 2023	
Project Funding (FY23): \$850,000	DOE share: \$850,000	Non-DOE share: \$0

### **Project Introduction**

The development and commercialization of new battery technology for a diverse set of applications is important for transportation, communications, and infrastructure advancements. In particular, the Vehicle Technologies Office (VTO) supports low cost, secure, and clean energy technologies to transport people and goods throughout the United States. Electrified transportation drives research into high energy battery chemistries and high-power systems (i.e., fast charge). An independent evaluation and assessment of performance and lifetime is critical to meaningful establish meaningful technology and scientific breakthroughs. The Electrochemical Analysis and Diagnostics Laboratory (EADL) at Argonne National Laboratory provides a vast set of capabilities and knowledge to evaluate batteries using standard tests and protocols, based on those developed by the U.S. Advanced Battery Consortium (USABC). [1-4] The EADL supports VTO and USABC supported battery development projects to guide R&D priorities and an independent technology evaluation.

### **Objectives**

The EADL at Argonne has two objectives in support of the Battery Performance and Life Testing. The first is to provide DOE, USABC, and battery developers with reliable, independent, and unbiased performance and life evaluations of cells, modules, or battery packs. The second is to benchmark battery technologies that were not developed with DOE/USABC funding to ascertain their level of maturity.

### **Approach**

The EADL is committed to collecting accurate, reproducible, and reliable data sets. The EADL has over 200 test channels with a range of available sizes from (10 V, 2 A) to (60 V, 250 A). The hardware is calibrated to ensure accurate results. All battery cell and pack tests are performed within environmental chambers, which enables evaluation at thermal conditions consistent to typical battery usage conditions (i.e., -70°C to 180°C) controlled within  $\pm 1^\circ\text{C}$ . The EADL evaluates batteries using standardized and unbiased protocols, allowing a direct comparison of performance within a technology, between developers, and across technologies. The EADL controls all testing conditions with custom programmable test equipment and software and provides flexibility to partners interested in a wide range of operation conditions. For instance, tailored test profile protocols that meet specific developer requirements or energy storage applications can be designed in consultation with DOE, USABC, or developer input and approval.

### **Results**

Cells, which were fabricated during programs with developers, are sent to Argonne for evaluation. Cells tested at the EADL under the USABC benchmarking programs were aged and tested against the appropriate application target (LCFC-EV, HP-EV, etc) or specific targets developed for battery chemistries under development. Here, the purpose of evaluation is two-fold: to provide confirmation of other test information and

to provide an independent assessment of the state of the given battery technology, that is, how does it compare to the USABC [1-4] and/or project goals.

**Table V.2.1 Status of Cell Testing Deliverables in FY2023.**

Developer	Sponsor	Application	Quantity (nominal cell size)	Status at year end
WPI / Farasis / Ascend	USABC	Recycle / EV	24 (10 Ah)	On-going
WPI / Microvast	USABC	LCFC / EV	18 (0.45 Ah)	On-going
24M	USABC	LCFC / EV	18 (52 Ah)	Completed
Group 14	DOE	Silicon / EV	15 (0.4 Ah)	On-going
Enovix	DOE	Silicon / EV	15 (0.266 Ah)	On-going
Sila Power	DOE	Silicon / EV	12 (1 Ah)	On-going
Solid Power	DOE	Silicon / EV	12 (0.25 Ah)	On-going
Earth Abundant Cathode Materials	DOE	EV	various	On-going
Extreme Fast Charging	DOE	XFC / EV	18 (0.03 Ah)	On-going
Behind-the-Meter Storage	DOE	BTMS	8 (2 Ah)	On-going

The EADL supported numerous applications in development in FY2023. For instance, the technological goal of utilizing silicon in lithium-ion anodes is attractive for improved energy density. However, key challenges are being addressed by developers. Some of these challenges are first charge expansion, first charge efficiency, cycle swelling and the subsequent cycle life limits. EADL evaluates several Si-based from developers. Other USABC and DOE goals of low-cost fast charge technology and cell manufactured from recycled materials feedstock streams are evaluated. In addition to cells received from battery developers, several VTO programs are supported by the EADL: Earth Abundant Cathode Materials, Extreme Fast Charging, and Behind-the-Meter Storage were supported in FY23. A list of program deliverables associated with Argonne during fiscal year 2022 is given in Table V.2.1, along with their status.

The EADL developed and provides Battery Life Estimator software, which is based on statistical evaluation of capacity (or other measurable metric of merit), temperature, and time. Lifetime predictions inform developers of a statistically rigorous evaluation, without requiring years of data collection. In particular, LIBs based on graphite are well understood and typically follow and can be fit with the equation shown in Figure V.2.1. New chemistries and cell designs, however, have been shown to deviate from this typical lifetime degradation model. Several such investigations are highlight in Figure V.2.1, which compares representative data collected at EADL. The relative capacity change normalized to the beginning of life (BOL) vs. normalized calendar aging time, from BOL to end of testing (EOT), indicates a behavior which varies from the model. Lifetime predictions are made more challenging in these cases. The results shown in Figure V.2.1 do meet the USABC goals for the application target but emphasize the need for enhanced prediction capabilities.

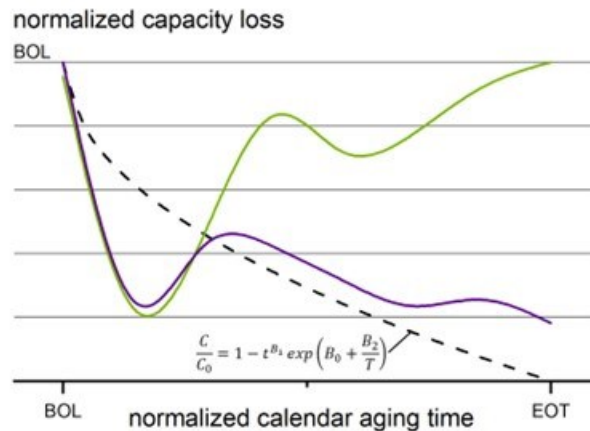


Figure V.2.1 Representative data collected at the EADL on advanced batteries. The capacity change normalized to the beginning of life (BOL) is plotted against the normalized calendar aging time, from BOL to end of testing (EOT). The dash curve represents a typical lifetime degradation model as a frame of reference.

### Conclusions

The EADL will continue to support DOE's and the USABC's cell development efforts by providing unbiased evaluation of cell performance. In FY23, further evaluation of lifetime predictions will be established in consultation with USABC, DOE, and developers to meet the needs of developing chemistries, cell designs, and applications.

### References

1. FreedomCAR Battery Test Manual for Power-Assist Hybrid Electric Vehicles, DOE/ID-11069, October 2003.
2. FreedomCAR Battery Test Manual for Plug-In Hybrid Electric Vehicles, June 2010.
3. Electric Vehicle Battery Test Procedures Manual, Revision 3.1, October 2020.
4. Battery Test Manual for 12 Volt Start/Stop Vehicles, Rev. 1, May 2015, INL/EXT-12026503.

### Acknowledgements

The following EADL staff contributed and supported this program: LeRoy Flores and Ira Bloom.

## V.3 Battery Abuse Testing (SNL)

### **Lorraine Torres-Castro, Principal Investigator**

Sandia National Laboratories  
1515 Eubank Dr. SE, M/S 0613  
Albuquerque, NM, 87185  
E-mail: [ltorre@sandia.gov](mailto:ltorre@sandia.gov)

### **Haiyan Croft, DOE Technology Development Manager**

U.S. Department of Energy  
E-mail: [Haiyan.Croft@ee.doe.gov](mailto:Haiyan.Croft@ee.doe.gov)

Start Date: October 1, 2022	End Date: September 30, 2023	
Project Funding (FY23): \$350,000	DOE share: \$350,000	Non-DOE share: \$0

### **Project Introduction**

Abuse tests are designed to determine the safe operating limits of EV and HEV energy storage devices. The tests are performed with the intention to achieve worst-case scenarios to yield quantitative data on cell/module/pack response to allow determination of failure modes and guide developers toward improved materials and designs. Standard abuse tests with defined start and end conditions are performed on all devices to provide comparison between technologies aligned with abuse hazard ratings. New tests and protocols are developed and evaluated to simulate real-world failure conditions.

In scaling from the cell to the battery level, it is important that understanding safety performance includes a detailed understanding of cell interactions. Single point failures from a single cell or group of cells can be initiated by several triggers including an internal short circuit, misuse or abuse, or a component failure at the battery or system level. Propagation of that single failure event (regardless of the initiation trigger) through an entire battery, system, or vehicle is an unacceptable outcome to ensure EV battery safety. As these batteries are scaled up in size from Wh to kWh the safety issues associated with these battery systems merit increasing concern and reevaluating testing methods to ensure all relevant data is collected. As a result, Sandia National Laboratories continues to use the United States Advanced Battery Consortium (USABC) Battery Abuse Testing Manual for Electric and Hybrid Vehicle Applications, which was updated and published by Sandia last FY.

Newer anode materials in FY23 cells include Li-metal anodes. Understanding the potential failure modes of these higher energy cells could lead to an emphasis on different testing protocol to handle the higher temperatures during thermal runaway. The physics of the failure mechanisms may be discovered as testing plans develop to capture the advanced materials interactions during off-normal operating conditions.

### **Objectives**

- Provide independent abuse testing support for DOE and USABC
- Abuse testing of all deliverables in accordance with the USABC testing procedures
- Provide battery safety testing support for DOE VTO programs

### **Accomplishments**

- Worked with TAC lead, OEMs, and other National Labs to appropriately develop testing concept based upon stated cell or battery deliverables to meet the USABC target and adequately represent the failure mechanisms related to the type of batteries being developed.
- Developed and presented test plans to each working group for each deliverable.
- Completed testing of USABC deliverables and reported results to the USABC TAC to inform EUCAR rating.
- Attended all TAC meetings throughout the year.

- Provided support to Behind the Meter Storage Program using tools developed as part of this testing program.
- Provided support for the Lithium-ion recycling prize through the voucher program.

### Approach

Abuse tolerance tests evaluate the response to expected abuse conditions. The goals of abuse and safety testing include a) testing to failure of energy storage devices and documentation of conditions that caused failure, b) systematic evaluation of failure modes and abuse conditions using destructive physical analysis (DPA), c) provide quantitative measurements of cell/module response, d) document improvements in abuse response, and e) develop new abuse test procedures that more accurately determine cell performance under most probable abuse conditions. Electrical (overcharge/overvoltage, short circuit, over discharge/voltage reversal, and partial short circuit), mechanical (controlled crush, penetration, blunt rod, drop, water immersion, laser induced short circuit, mechanical shock and vibration) and thermal abuse (thermal stability, simulated fuel fire, elevated temperature storage, rapid charge/discharge, and thermal shock cycling) cover the main categories of possible conditions evaluated. These techniques are applied to USABC deliverables, and the results reported to DOE and USABC.

### Results

Testing of deliverables was performed for USABC development programs, including testing deliverables from Farasis, Microvast, Gotion, and Zenlabs. Test results have been reported to the USABC Technical Advisory Committee. Sandia continues to make functional improvements to battery testing to enable the testing of new high energy materials and to simulate newly discovered failure mechanisms.

The development and maintenance of Battery Safety and Abuse Testing at Sandia has also allowed support for other DOE VTO programs. This has included support of the Behind the Meter Storage (BTMS) program performing testing of cells of interest for the program and support of the Lithium-Ion Battery Recycling Prize voucher program.

### Conclusions

Development and testing of higher energy, larger format cells and modules continues for USABC developers. We provide a means to field the most inherently safe chemistries and designs to help address the challenges in scaling up lithium-ion technologies of interest. This has required careful control and monitoring of tests with the potential of high energy release as well as standing up a larger facility at SNL to support module level testing. This has provided critical information to cell developers to aid in the development of increasingly abuse tolerant cell chemistries and module designs. This independent testing is also necessary to perform objective evaluations of these various designs and chemistries by the DOE and US automobile manufacturers.

SNL continues to provide safety testing support to DOE programs as needed. The capabilities developed as part of this battery safety testing program currently support work done as part of the Behind the Meter Storage program and the Lithium-ion Recycling program.

### Key Publications

1. L. Lin, J. Li, I. Fishman, L. Torres-Castro, Y. Preger, V. De Angelis, J. Lamb, XQ Zhu, S. Allu, H. Wang, **Mechanically induced thermal runaway severity analysis for Li-ion batteries**, *Journal of Energy Storage* 61 (2023)
2. L. Torres-Castro, S. Kalnaus, H. Wang, J. Lamb, **Experimental Simulations of Field-Induced Mechanical Abuse Conditions**. In: Santhanagopalan, S. (eds) *Computer Aided Engineering of Batteries. Modern Aspects of Electrochemistry, vol 62. Springer, Cham. (2023)*
3. J. Kim, C. Yang, J. Lamb, A. Kurzawski, J. Hewson, L. Torres-Castro, A. Mallarapu, and A. Santhanagopalan, **A Comprehensive Numerical and Experimental Study for the Passive Thermal Management in Battery Modules and Packs**, *Journal of The Electrochemical Society* 169 (2022)

## **Acknowledgements**

Sandia Contributors include Lucas Gray, Genaro Quintana, Alex Bates, Kyle Fenton, Jill Langendorf, and Emily Kowalchuk. National Lab and Industry Partners include the USABC TAC Team. Sandia National Laboratories is a multi-mission laboratory managed and operated by National Technology and Engineering Solutions of Sandia, LLC., a wholly owned subsidiary of Honeywell International, Inc., for the U.S. Department of Energy's National Nuclear Security Administration under contract DE-NA0003525.

## V.4 Battery Thermal Analysis and Characterization Activities (NREL)

### **Matthew Keyser, Principal Investigator**

National Renewable Energy Laboratory  
15013 Denver West Parkway  
Golden, CO 80401  
E-mail: [Matthew.Keyser@nrel.gov](mailto:Matthew.Keyser@nrel.gov)

### **Haiyan Croft, DOE Technology Development Manager**

U.S. Department of Energy  
E-mail: [Haiyan.Croft@ee.doe.gov](mailto:Haiyan.Croft@ee.doe.gov)

Start Date: October 1, 2022

End Date: September 30, 2023

Project Funding (FY23): \$500,000

DOE share: \$500,000

Non-DOE share: \$0

### **Project Introduction**

While EDVs promise to curb America’s need for imported oil, designing high-performance, cost-effective, safe, and affordable energy-storage systems for these cars can present challenges, especially in the critical area of battery thermal control. As manufacturers strive to make batteries more compact and powerful, knowing how and where heat is generated becomes even more essential to the design of effective thermal-management systems. NREL’s thermal characterization activities provide developers, manufacturers, and OEMs with the knowledge necessary to assure that batteries are designed to perform strongly, last a long time, and operate at maximum efficiency.

The Vehicle Technologies Office has a goal to reduce the cost of electric vehicle battery packs to less than \$100/kWh for graphite/NMC (short term), \$75/kWh for silicon/NMC (next-gen lithium ion), and \$50/kWh for Li metal/NMC or Sulfur (long term target) with technologies that significantly reduce or eliminate the dependency on critical materials (such as cobalt) and utilize recycled material feedstocks [1]. To meet these metrics, the battery packs will need to have higher energy densities resulting in a very compact system. Even if the energy efficiency of the next generation of batteries increases, because of the compactness of these batteries more heat is being generated per unit volume with less heat transfer area. Thus, more advanced heat rejection systems are needed to keep the battery temperatures in the “goldilocks” zone that prevents acceleration of the aging mechanisms within the battery.

The chemistries of advanced energy-storage devices—such as lithium-based batteries—are very sensitive to operating temperature. High temperatures degrade batteries faster while low temperatures decrease their power and capacity, affecting vehicle range, performance, and cost. Understanding heat generation in battery systems—from the individual cells within a module, to the inter-connects between the cells, and across the entire battery system—is imperative for designing effective thermal-management systems and battery packs.

Inadequate or inaccurate knowledge of the thermal characteristics of batteries makes it difficult to design effective thermal-control systems. This can negatively affect lifespan, safety, and cost, ultimately resulting in negative consumer perception and reduced marketability. In 2012, Nissan had to address problems with the battery for its Leaf fully electric vehicle (EV) losing capacity in the hot Arizona climate. Many attributed this issue to inadequate battery-thermal management.

Accurately measuring battery thermal performance under various electrical loads and boundary conditions makes it possible for battery-system engineers to design effective thermal-management systems. NREL, with the funding from DOE VTO, has developed unique capabilities to measure the thermal properties of cells and evaluate thermal performance of active, air, and liquid cooled battery packs. Researchers also use electro-

thermal finite element models to analyze the thermal performance of battery systems in order to aid battery developers with improved thermal designs. In addition, our lumped capacitance multi-node battery-vehicle-ambient model can predict the temporal temperature of batteries as a function drive cycle, ambient temperature, and solar radiation. These one-of-a-kind tools allow NREL to work with the battery manufacturers and OEMs to meet stringent EDV life, performance, cost, and safety goals

### Objectives

- Thermally characterize battery cells and evaluate thermal performance of battery packs provided by USABC developers.
- Provide technical assistance and modeling support to USDRIVE/USABC and developers to improve thermal design and performance of energy storage systems.
- Evaluate extreme fast charging effects on battery thermal performance.
- Quantify the impact of temperature and duty-cycle on energy storage system life and cost.
- Address high energy storage cost due to battery packaging and integration costs
- Reduce the cost, size, complexity, and energy consumption of thermal management systems
- Optimize the design of passive/active thermal management systems—explore new cooling strategies to extend the life of the battery pack.

### Approach

NREL has measured the thermal properties of the cells and batteries with many different chemistries (lead acid, NiMH, and many versions of lithium cells) through heat generation, heat capacity, and infrared thermal imaging; conducted performance thermal testing of battery and ultracapacitor modules and packs; analyzed the thermal performance of cells and modules; and developed thermal models. Researchers perform thermal testing, analysis, and modeling (1) to assist DOE/USABC battery developers in designing cells/modules/packs for improved thermal performance, and (2) to evaluate and validate the thermal performance of cell/module/pack deliverables from DOE/USABC battery developers and suppliers.

NREL's equipment can benchmark how changing the design of the cell using a different cathode, anode, current collector, electrolyte, additive, or separator affects the overall performance of the cell. The information garnered from these tests helps battery and advanced vehicle manufacturers improve their designs, while providing critical data for the development of thermal management systems that will reduce the life-cycle cost of battery systems. Using NREL's unique R&D 100 Award-winning calorimeters and infrared thermal imaging equipment, we obtain thermal characteristics of batteries and ultracapacitors developed by USABC battery developers and other industry partners. NREL supports the Energy Storage Technical Team by participating in various work groups such as the Zenlabs, Farasis, and USABC Electric Vehicle Cell Development and Beyond Lithium Ion Working Groups.

### Results

#### Calorimeter Testing

Figure V.4.1 shows the efficiency of cells tested in FY23 and prior to FY23 at NREL with a calorimeter temperature of 30°C. The lithium-ion cells were fully discharged from 100% SOC to 0% SOC under a C/2, C/1, and 2C currents. The cells in this figure have been developed under the LCFC programs within USABC. These cells are designed for mainly high energy applications (the LCFC program maintains aggressive energy level targets). It should be noted that as the specific energy of these graphite systems increases, the efficiency decreases. This is primarily due to the impact of thicker electrodes have on the thermal performance. In contrast, the efficiency of the silicon blend cells is increasing due to chemistry optimization. Silicon containing cells can maintain high energy content with lower electrode thickness due to the much greater material energy density when compared to graphite. The general trend shows that silicon containing systems still need improvements to reach the heat efficiency of graphite cells with similar electrode thickness. DOE and USABC are investigating both graphite and silicon to improve energy density, power density, cycle life and/or cost benefits. NREL's calorimeters provide the fundamental understanding of whether the inefficiencies shown below are due to chemistry or cell design.



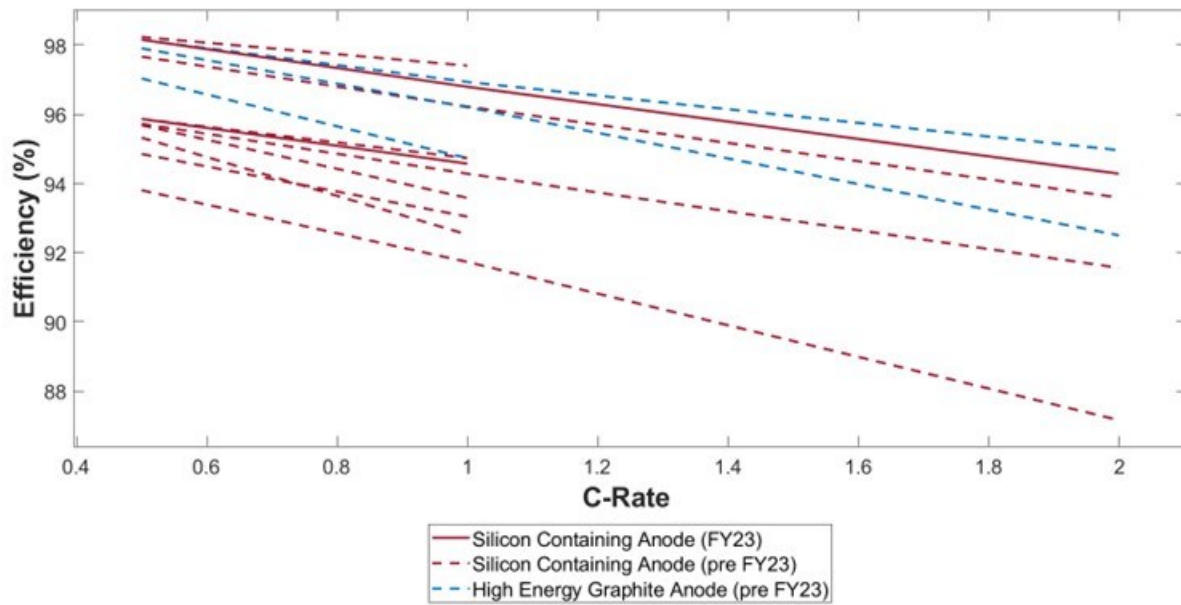


**Figure V.4.1** Efficiency summary of cells tested in NREL’s calorimeters. Caption Credits/Source: NREL-Andrew Schiek

NREL utilized our microcalorimeter technology to characterize how aging affects the heat generation of graphite/NMC cells. We thermally characterized existing NMC cathode compositions to understand how the thermal signature of a battery changes from the beginning of life to the end of life. NREL received ANL CAMP cells for the thermal characterization. A list of available cells is given in Table V.4.1. The batteries supplied by CAMP are a combination of NMC and graphite—standard material used in electric vehicles today.

**Table V.4.1** CAMP Cells to be Used for Thermal Characterization—Cathode Material was Supplied by Toda and Anode material was Supplied by Superior Graphite.

Cathode Material	Anode Material
NMC - 111	1520P
NMC - 532	1520P
NMC - 622	1520P
NMC - 811	1520P

NREL measured the heat generation of two of each of the pristine/fresh 1520P/NMC cell versions (NMC - 111, 532, 622, and 811). Figure V.4.2a shows the measured BOL heat generation of the four types of cells under a 2C constant current discharge. As expected, the heat generation is at a maximum at the end of the discharge – typical for graphite cells. Unexpectedly, the 2C heat generation was the highest for the 1520P/NMC-111 and the lowest for the 1520P/NMC-811 for a given SOC at BOL. The heat generation difference between the two cells varied by as much as 200% over the discharge curve. Since both cells are using the same anode, the heat generation difference between the test runs originates from the cathode. Figure V.4.2b shows the heat generation of the four variants of cells under a 2C constant current charge. The difference in heat generation between the four different types of cells under charge was less than that for the discharge over the entire SOC range. Finally, the heat generation trend reversed under charge as expected – in general, the 1520P/NMC-111 produced the least amount of heat for a given SOC and the 1520P/NMC-811 produced the most.

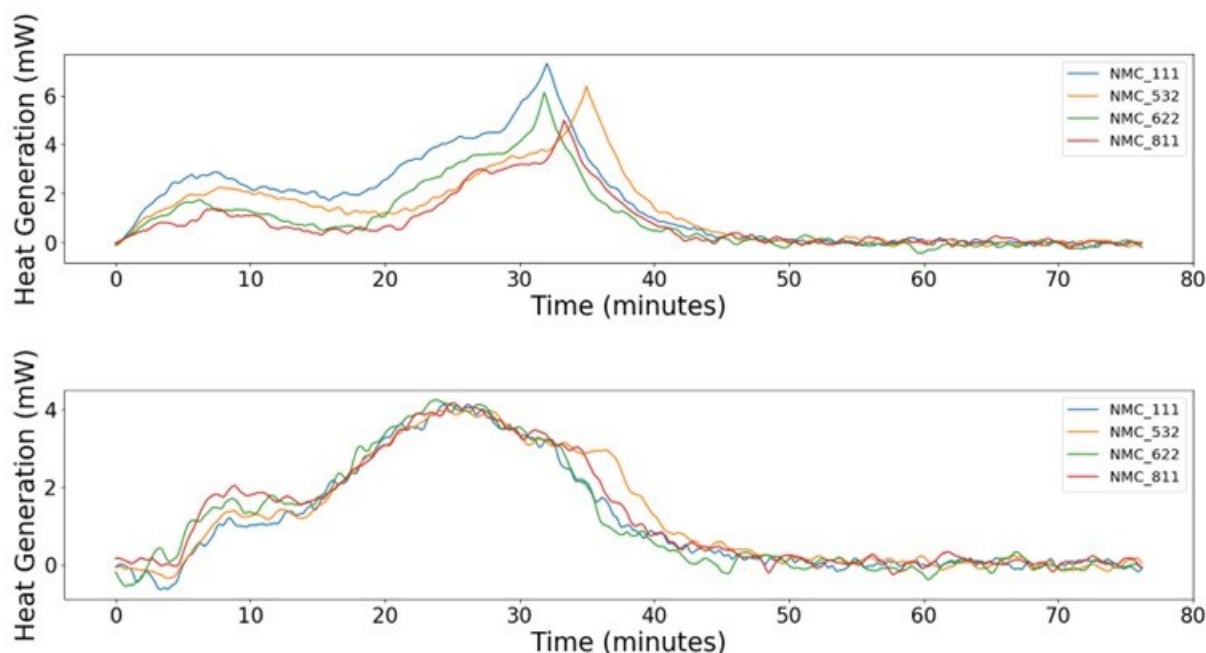


**Figure V.4.2 Superior Graphite/Toda 120P/NMC-111, 532, 622, and 811 heat generation curves for a 2C full discharge (2a-top) and 2C full charge (2b – bottom) Caption Credits/Source: NREL-Josh Major**

NREL cycled the graphite/NMC cells versions until 80% of the initial capacity remains or end-of-life (EOL). We wanted to measure the heat generation and efficiency at the EOL and use the BOL and EOL data to bracket the performance of graphite/NMC cells. The data will be used to determine the efficacy of future recycled material and processes. We aged the cells by applying a C/1 charge/discharge profile until the cells reached 80% of their initial capacity. Table V.4.2 shows the percent capacity that remains as compared to the beginning-of-life for each of the cells. Unfortunately, the graphite/NMC811 cells aged/degraded much faster than the other cells and its EOL heat generation and efficiency tests are biased due to the increased capacity loss.

**Table V.4.2 Percentage of Capacity Remaining After Aging the CAMP Cells for EOL Thermal Characterization—Cathode Material was Supplied by Toda and Anode Material was Supplied by Superior Graphite.**

Cathode Material	% of BOL Capacity	Number of cycles to reach EOL
NMC - 111	79.0	1602
NMC - 532	78.4	1411
NMC - 622	80.4	2447
NMC - 811	63.8	799

NREL also measured the heat generation and efficiency of the four types of cells at various charge and discharge currents over several SOC ranges. The data shown in Figure V.4.3 is for a constant current discharge from 4.1 V to 3.0V –discharging the cells from 100% to 0% SOC. As expected, the heat efficiency decreases as the discharge rate is increased. Furthermore, the heat efficiency of the 111, 532, and 622 cathodes are similar in magnitude and decrease the most under a 3C discharge current, the maximum discharge current used for this study. The 811-cathode cell showed the largest decrease in efficiency from BOL to EOL since it was aged to around 64% of its initial capacity. Finally, we show the full charge efficiency (only CC/no CV) from 3.0V to 4.1V in Figure V.4.4. The charge efficiencies for a given c-rate are slightly higher than those for

discharge since we eliminated the CV portion of the charge. Also, the higher resistance cells such as the graphite/NMC811 only accepted charge over the lower SOC range before limiting at the upper voltage of 4.1V; thus, the higher efficiencies as compared to discharge.

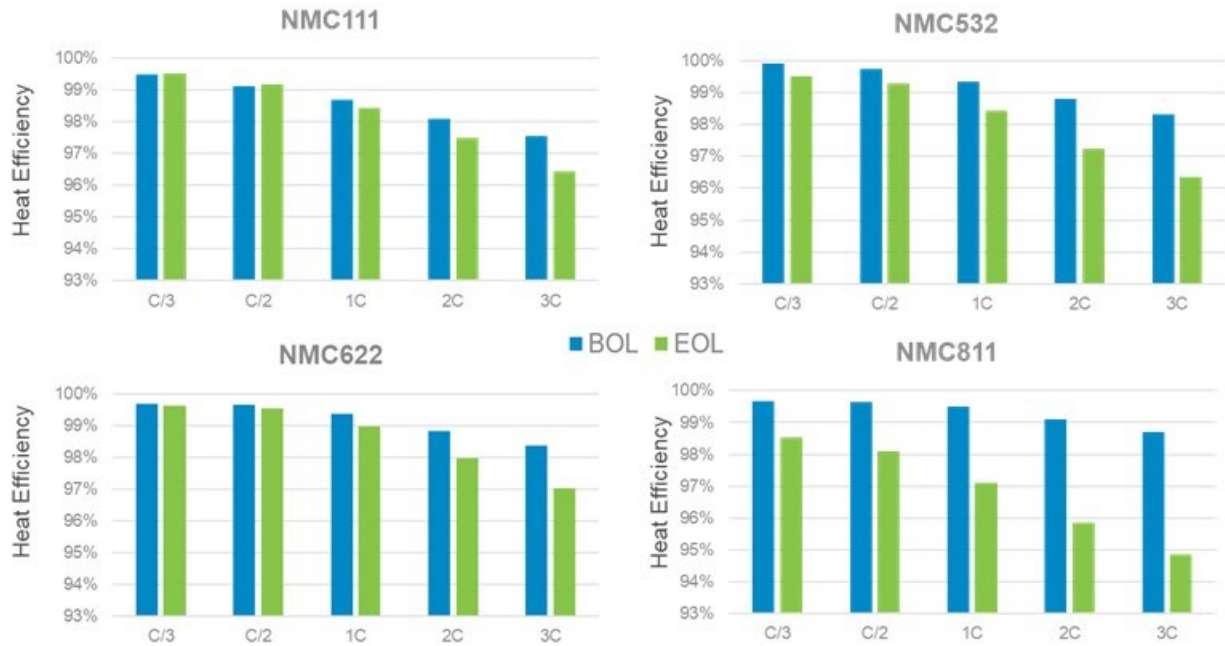


Figure V.4.3 BOL and EOL heat efficiency of 1520P/NMC cells under various discharge currents over an SOC range from 100% to 0%. Caption Credits/Source: NREL-Josh Major

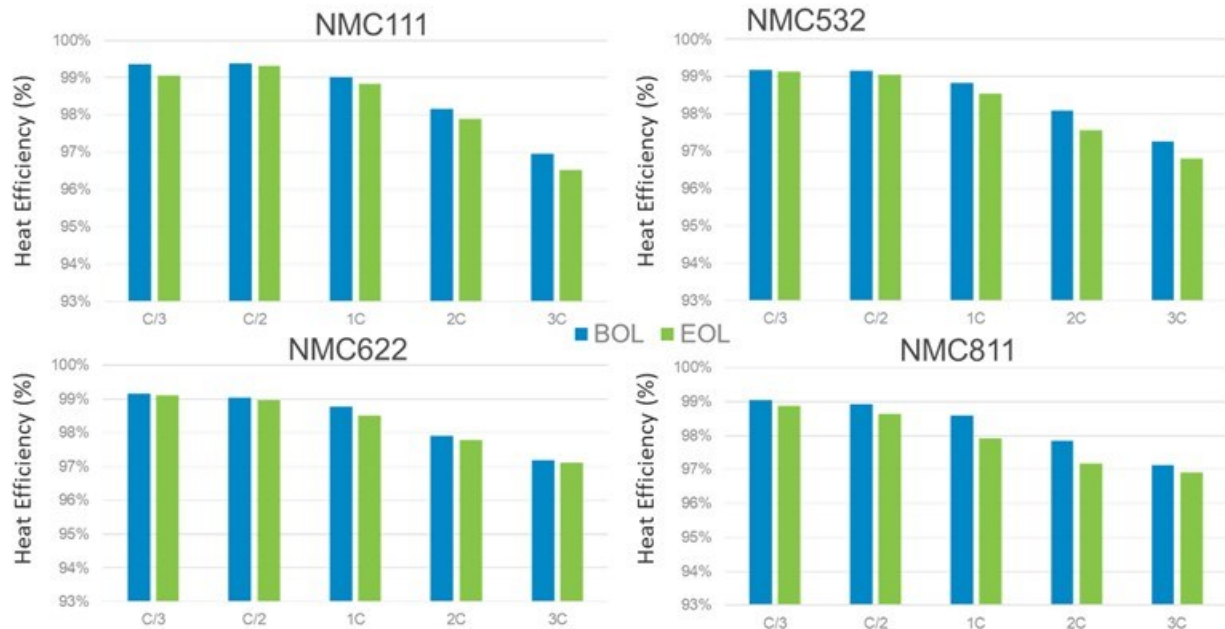


Figure V.4.4 BOL and EOL heat efficiency of 1520P/NMC cells under various charge currents over an SOC range from 100% to 0%. Caption Credits/Source: NREL-Josh Major

The microcalorimeter developed by NREL has been designed to measure the heat generation from both the cathode and anode when a single pair of electrodes is used – typical for coin cells but also for the pouch cells provided to NREL by CAMP. Figure V.4.5 compares the BOL and EOL heat generation of the NMC111 cell over a 3C full discharge from 100% to 0% SOC. Figure V.4.5 shows that the heat generation from the anode was greater than the heat from the cathode at the beginning of life. However, after the cell was aged, the heat from the cathode was much greater than that of the anode. The increased heat generation from the cathode at end of life can probably be attributed to cathode cracking, a known failure mechanism of NMC material, and will be verified with EBSD in the future. As a comparison, Figure V.4.6 compares the BOL and EOL heat generation of a NMC811 cell over a 3C full discharge from 100% to 0% SOC. Similar heat generation trends were observed in the NMC811 as compared to the NMC111.

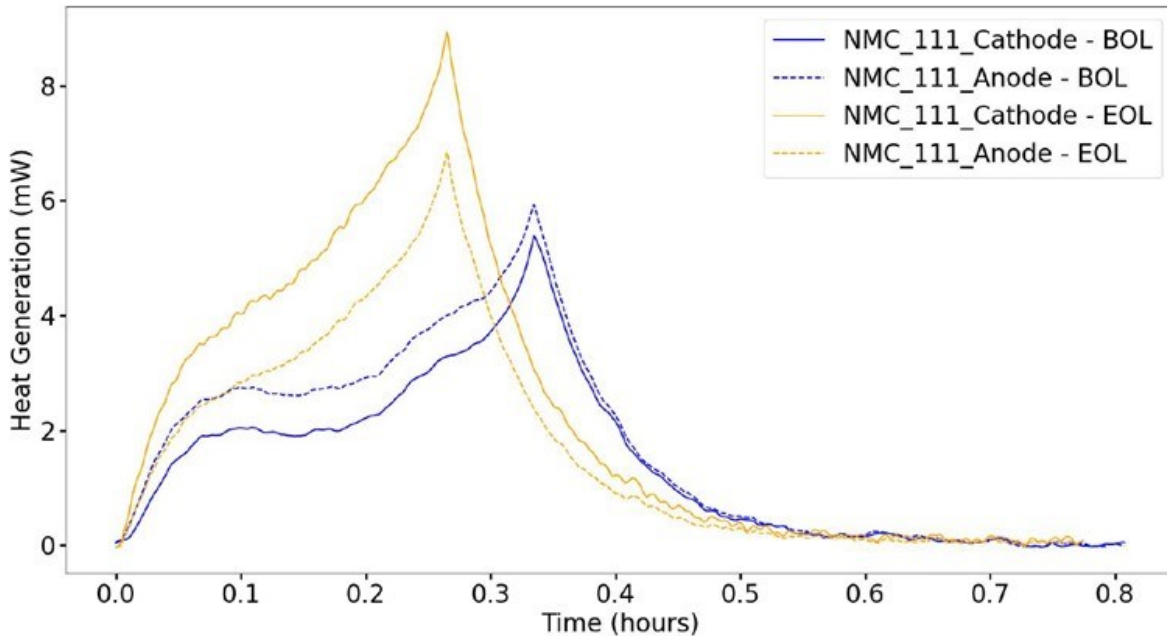


Figure V.4.5 BOL and EOL heat efficiency of a 1520P/NMC111 cell under a 3C full charge. Caption Credits/Source: NREL-Josh Major

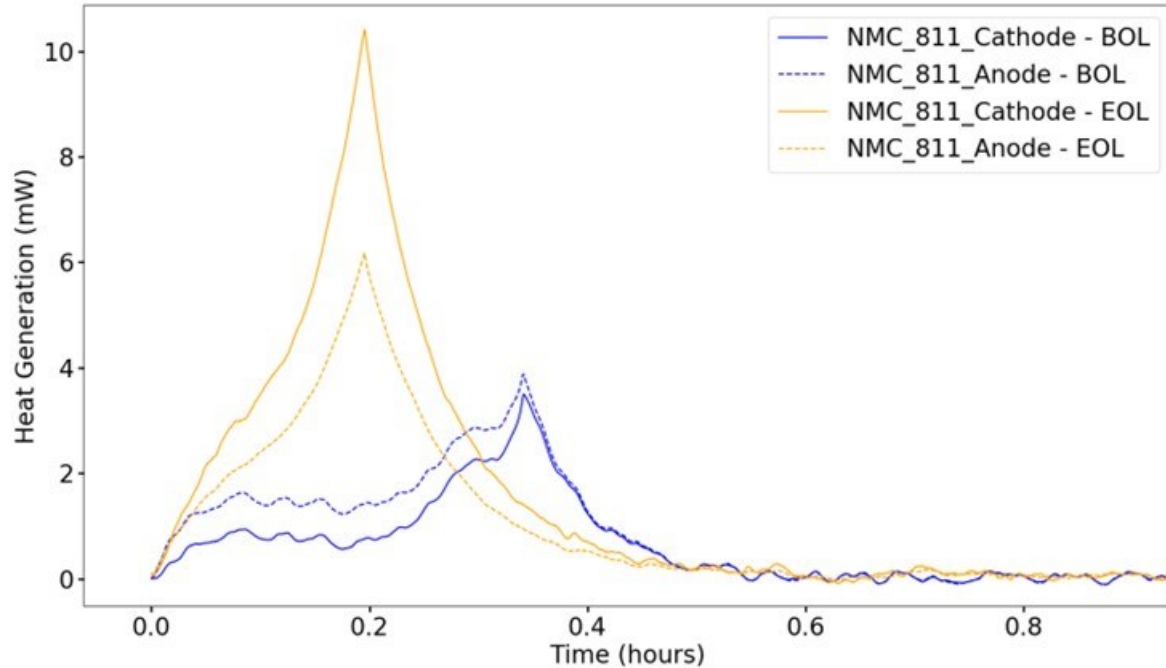
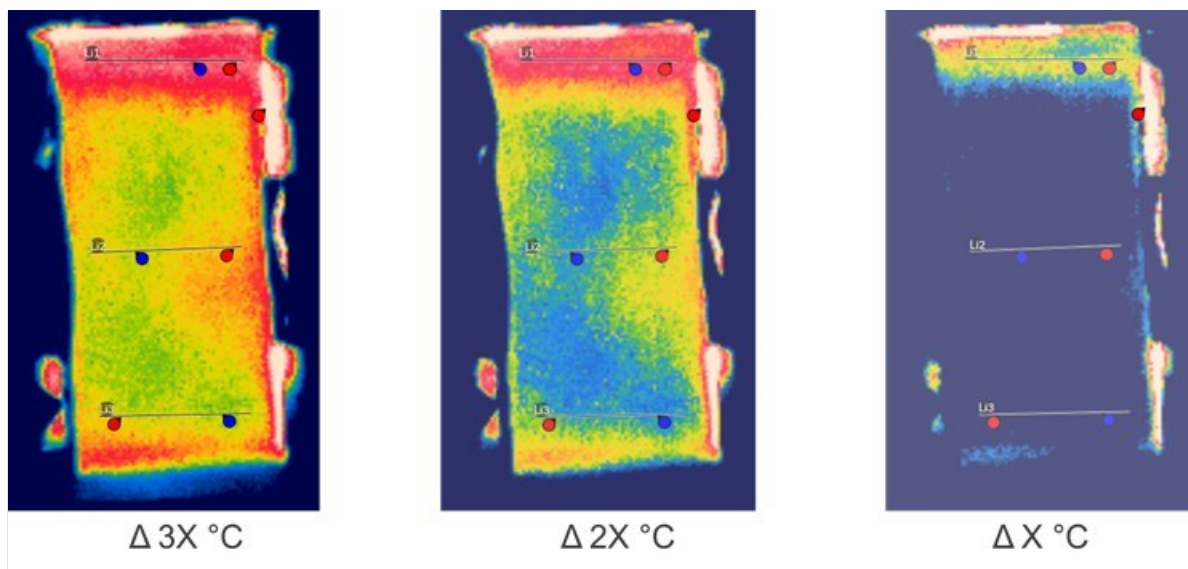


Figure V.4.6 BOL and EOL heat efficiency of a 1520P/NMC811 cell under a 3C full discharge. Caption Credits/Source: NREL-Josh Major

### ***Infrared Imaging of Cells***

NREL performs infrared (IR) thermal imaging of battery manufacturer's cells to determine areas of thermal concern. We conduct IR thermal imaging under a set of prescribed procedures and environments to minimize the error from different sources such as reflective cell surfaces, radiation from surrounding surfaces, and cooling from the power cables attached to the cell. NREL combines the IR imaging equipment with a battery cycler to place the cells under various drive cycles, such as the USABC fast charge protocol to understand the temperature differences within the cell. We then make recommendations to the battery manufacturers and USABC on how to improve the thermal design of the cell to increase its cycle life and safety.



**Figure V.4.7 Infrared image of lithium battery cell at the end of a fast charge, 3.2C. Caption Credits/Source: NREL- Aron Saxon**

Figure V.4.7 shows a lithium battery at the end of a high-rate charge, 3.2C. Each IR image has a temperature spread associated with it – by decreasing the temperature spread while maintaining the maximum set temperature, a visual reference can be used to determine where the heat is preferentially being generated within the cell. For this cell, the heat generation is biased towards the top of the cell where the terminals are located indicating the connection between the tabs and the current collectors could be an area for improvement. When the cell temperature is not uniform and consistent or symmetrical, individual cells within modules and packs age differently affecting the cycle life of the module. NREL is working with battery developers to understand how temperature non-uniformities affect the efficiency and cost of the cell over its life.

### Conclusions

NREL has thermally tested cells and modules from Zenlabs and Farasis during FY23 across multiple USABC programs. We have provided critical data to the battery manufacturers and OEMs that can be used to improve the thermal design of the cell, module, pack, and their respective thermal management systems. The data included heat generation of cells under typical EV profiles which is essential for designing the appropriately sized battery thermal management system. In FY24, NREL will continue to thermally characterize cells and modules for USABC, DOE, and USDRIVE but with a focus on fast charging applications and the heat generation for battery chemistries beyond lithium ion.

### Acknowledgements

We wish to acknowledge Haiyan Croft, Brian Cunningham, and DOE for sponsoring these efforts. We would also like to acknowledge ANL/CAMP for fabricating the cells for the NMC study as well as the support from the DOE/VTO ReCell program for funding the initial heat generation testing presented here. We would also like to acknowledge ANL's Bryant Polzin and Andy Jansen for their assistance in cell fabrication and direction guidance. Finally, we would like to acknowledge NREL's Aron Saxon as well as Andrew Schiek, Josh Major and Tom Bethel for their program support.

## V.5 Cell Analysis, Modeling, and Prototyping (CAMP) Facility Research Activities (ANL)

### **Andrew N. Jansen, Principal Investigator**

Argonne National Laboratory  
9700 South Cass Avenue  
Lemont, IL 60439  
E-mail: [Jansen@anl.gov](mailto:Jansen@anl.gov)

### **Stephen E. Trask, Co-Principal Investigator**

Argonne National Laboratory  
9700 South Cass Avenue  
Lemont, IL 60439  
E-mail: [STrask@anl.gov](mailto:STrask@anl.gov)

### **Haiyan Croft, DOE Technology Development Manager**

U.S. Department of Energy  
E-mail: [Haiyan.Croft@ee.doe.gov](mailto:Haiyan.Croft@ee.doe.gov)

Start Date: October 1, 2022	End Date: September 30, 2023	
Project Funding (FY23): \$800,000	DOE share: \$800,000	Non-DOE share: \$0

### **Project Introduction**

The “valley of death” is a phrase often used to describe the path a new discovery must traverse to become a commercial product. This is especially true for novel battery materials invented in research laboratories around the world. Often researchers are resource limited and are only able to make gram quantities of their new material. The CAMP Facility is appropriately sized to enable the design, fabrication, and characterization of high-quality prototype cells using just a few hundred grams of the latest discoveries involving high energy battery materials. Prototype cells made in the CAMP Facility generally have 400-mAh capacity, which straddles the gap between coin cells and industrially-sized cells nicely – two orders of magnitude from each end point. Thus, a realistic and consistent evaluation of candidate chemistries is enabled in a time-effective manner with practical quantities of novel materials in cell formats commonly used in industry.

The CAMP Facility is an integrated team effort designed to support the production of prototype electrodes and cells, and includes activities in materials validation (benchmarking), modeling, and diagnostics. It is not the aim of this facility to become a small battery manufacturer, but instead to be a laboratory research facility with cell production capabilities that adequately evaluate the merits and limitations of new lithium-ion chemistries in a close-to-realistic industrial format. The source of these materials (anodes, cathodes, electrolytes, additives, separators, and binders) may originate from DOE Battery Programs, as well as from other R&D organizations such as universities, national labs, and industrial vendors.

The CAMP Facility has the capability to make two prototype pouch cell formats in their 150 m<sup>2</sup> dry room: xx3450 format, with capacity around 0.5 Ah; and xx6395, with capacity around 2 Ah. Pouch cells are generally easier to assemble and are a useful indicator of gassing problems in a cell during cell aging and cycling. Central to this effort is a pilot-scale coating machine that operates with slurry sizes that range from 20 mL to 2 L. These key features of the CAMP Facility enable a professional evaluation of both novel materials (typically limited quantities) and commercial materials for benchmarking. In addition, the Materials Engineering Research Facility (MERF) is available for scaling up materials for these prototype cell builds.

## Objectives

The objective of this core-funded effort is to design, fabricate, and characterize high-quality prototype electrodes and cells that are based on the latest discoveries involving high-energy anode and cathode battery materials. Using this multi-disciplined facility, analytical diagnostic results can be correlated with the electrochemical performance of advanced lithium-ion battery technologies for electric vehicle (EV) applications.

In FY23, the CAMP Facility milestone objectives were to:

- Evaluate novel battery materials for use in electric vehicles (efforts described in Section VI.6)
- Coat thin layer of ceramic using gravure coating head on multifunctional coater
- Provide supply of advanced prototype electrodes in Electrode Library
- Develop operando X-ray techniques to study cells with solid-state electrolytes.

## Approach

The general approach used in this effort is to start small and grow large in terms of cell size and amount of resources devoted to each novel battery material. At various points in the development process, decisions are made to either advance, modify, or terminate studies to maximize utilization of available resources. Coin cells (2032 size) are used for materials validation purposes with initial studies performed at 30°C. After formation cycles, the coin cells go through rate capability testing, HPPC testing, and limited cycle life testing. Additional temperatures and test conditions are employed, if warranted.

Using the results obtained by the materials validation of promising materials (also refer to Section VI.6), single-sided electrodes are fabricated on the larger dry-room coater for diagnostic study. The new cell chemistries are studied in detail using advanced electrochemical and analytical techniques, including the employment of micro-reference electrode cells. Factors are identified that determine cell performance and performance degradation (capacity fade, impedance rise) on storage and on extensive deep-discharge cycling. The results of these tests are used to formulate data-driven recommendations to improve the electrochemical performance/life of materials and electrodes that will be incorporated in the prototype cells that are later fabricated in the dry room. This information also lays the foundation for electrochemical modeling focused on correlating the electrochemical and analytical studies, in order to identify performance limitations and aging mechanisms.

If the results from diagnostics and modeling still look promising, full cell builds are conducted using double-sided electrodes. The electrodes are then punched and assembled into full cells in the dry room using semi-automated cell assembly equipment. Formation procedures are developed for the cells to encourage electrolyte wetting and uniform solid-electrolyte-interface (SEI) formation. These cells undergo rigorous electrochemical evaluation and aging studies under the combined effort of the CAMP Facility team and Argonne's Electrochemical Analysis and Diagnostic Laboratory (EADL). After testing, select cells are destructively examined by the Post-Test Facility to elucidate failure mechanisms. This information is then used to further improve the new chemistry, as well as future electrode and cell builds.

## Results

The CAMP Facility is designed to work closely with materials researchers across the many electrochemical energy storage programs throughout the DOE-EERE-VTO. In addition to its own yearly R&D tasks, it actively coordinates its efforts to provide support to other national lab team programs such as: Silicon Consortium Project (SCP), ReCell Advanced Battery Recycling Center, eXtreme Fast Charge Cell Evaluation of Lithium-Ion Batteries (XCEL), Earth-abundant Cathode Active Material (EaCAM), Behind-the-Meter-Storage (BTMS), and Liquid Electrolyte Projects. The Materials Benchmarking Activities (in a different APR Section) is a segment of the CAMP Facility. The CAMP Facility also complements the capabilities of other DOE support facilities such as: Materials Engineering Research Facility (MERF - Argonne), Post-Test Facility (PTF - Argonne), Battery Abuse Testing Lab (BATLab - SNL), and Battery Manufacturing Facility (BMF - ORNL).



More information about these programs can be found in the relevant chapters and sections of this annual report. The remainder of this CAMP Facility section will discuss the results of the CAMP Facility deliverables and related topics for FY23.

#### ***Multifunctional Coater Specifications Confirmed during Factory Acceptance Test***

The new multifunctional roll-to-roll coater from Frontier (Delta ModTech) in Argonne's CAMP Facility dry room was installed in FY22. This coater provides many new capabilities to the CAMP Facility: interchangeable coating heads, gravure coating, single-slot die coating, progressive cavity pump, corona treatment of substrates, and an IR drying zone. Modifications were made to the dry room facility to meet the ventilation requirements of the coater and to address safety concerns that were raised by Argonne's safety committee. The corona treater in particular required a unique design for fresh air supply and air+ozone exhaust to the outside. Four blowers were installed permanently from the ceiling support structure. Training from Frontier staff was provided to several CAMP staff over the course of a week. A work planning and control safety assessment was conducted and approved in the fourth quarter of FY23. The coater is now available for use by those trained and authorized in the CAMP Facility (Figure V.5.1).



**Figure V.5.1** Images of the multifunctional coater installed in the CAMP Facility's dry room.

#### ***Electrochemical Behavior of Single-wall Carbon nanotubes in the Cathode***

Single-wall carbon nanotubes (SWCNTs) are being increasingly used in slurries used for cathode coatings. Prior research has shown that SWCNTs provide mechanical reinforcement to the electrode composite and improves electronic conduction pathways by forming conducting bridges between the oxide particles. The CAMP Facility has also started including a small amount (0.05 wt%) of SWCNTs in the CAMP cathodes. For example, data from  $\text{LiNi}_{0.5-x}\text{Mn}_{1.5+x}\text{O}_4$  (LNMO) cells, which are cycled at voltages up to 5V vs.  $\text{Li/Li}^+$ , indicate that SWCNT-containing electrodes display half the impedance of electrodes with only C45 carbons.

Are the SWCNTs electrochemically active at high voltages and what is their contribution to cell capacity fade? To answer these questions electrodes were prepared containing 16.7 wt% SWCNTs and 83.3 wt% PVdF and cycled at 30 °C in cells with a Li-metal counter electrode and EC:EMC (1:9 v/v) + 1 M  $\text{LiPF}_6$  electrolyte. Representative data from the cells are shown in Figure V.5.2 below.

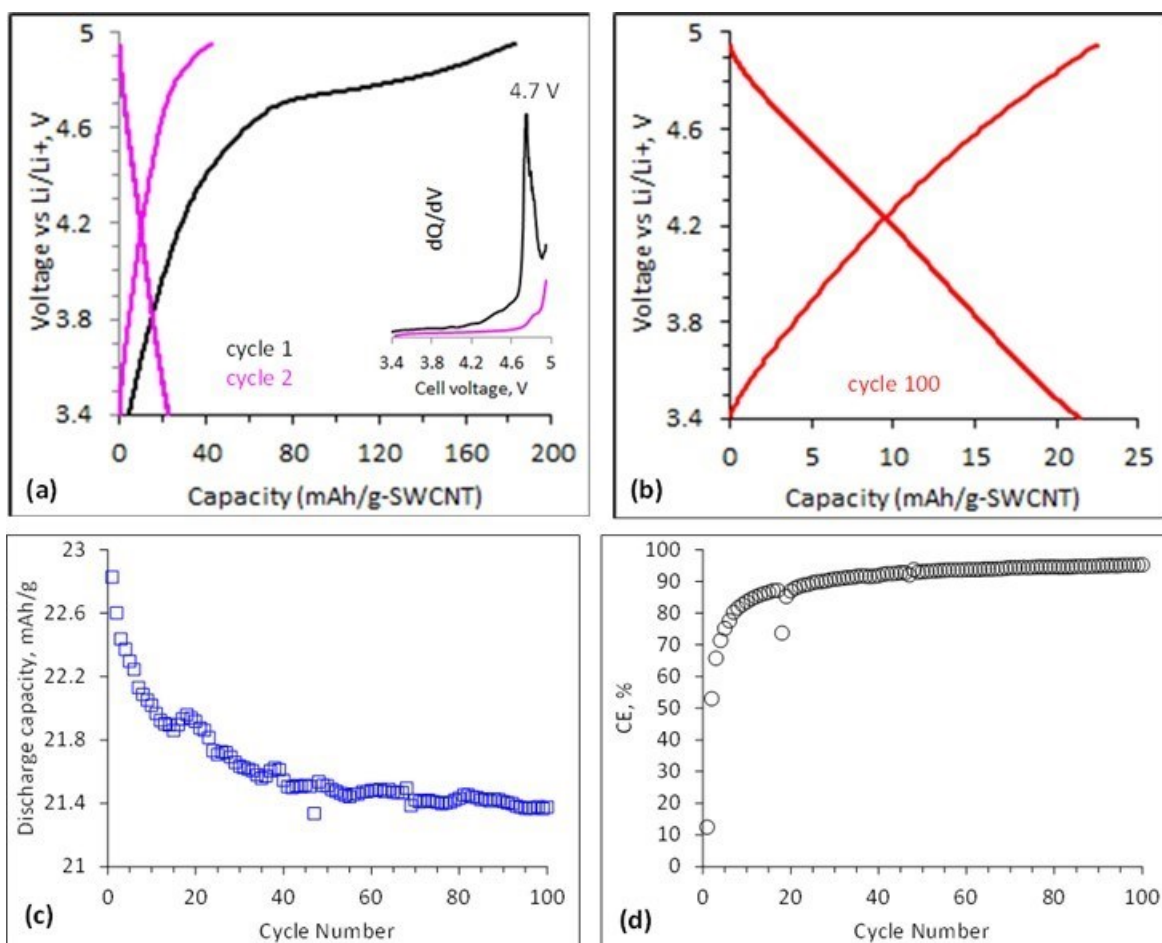


**Figure V.5.2** Electrochemical behavior of electrodes containing SWCNTs cycled vs. Li-metal in the 3.4 – 5.0 V range at 30 °C. (a) shows profiles of cycle 1 and 2 and (b) shows profile of cycle 100. (c) Discharge capacity and (d) Coulombic efficiency as a function of cycle number. The g refers to grams of SWCNTs in the electrode.

Key observations from the data include the following: (i) The cycle 1 charge capacity is  $\sim 160$  mAh/g<sub>SWCNT</sub>. The dQ/dV plot (inset Figure VI.5.2a), shows a peak around 4.7 V vs. Li/Li<sup>+</sup>, which likely arises from insertion of PF<sub>6</sub><sup>-</sup> ions into the SWCNTs. The cycle 1 discharge capacity is  $\sim 23$  mAh/g<sub>SWCNT</sub>, i.e., the cycle 1 efficiency is only  $\sim 14.3\%$ . (ii) Cell capacity decreases gradually on further cycling in the 3.4–5.0 V range (Figure VI.5.2c); the cycle 100 discharge capacity is  $\sim 21.4$  mAh/g<sub>SWCNT</sub> (Figure VI.5.2b). (iii) The coulombic efficiency (CE) increases with cycling and reaches  $\sim 95\%$  at cycle 100 (Figure VI.5.2d). The data indicate that the SWCNTs are electrochemically active but mostly at voltages  $>4.7$  V vs. Li/Li<sup>+</sup>.

With regard to influencing cell capacity fade, our cathode typically contain  $\sim 0.05$  wt% SWCNTs. In LNMO//Li cells for example, they contribute only  $\sim 0.12$  mAh/g to the 1<sup>st</sup> charge and  $< 0.017$  mAh/g to subsequent cycles. These values are negligible compared to the  $\sim 138$  mAh/g capacity of the LNMO electrode. Hence, all things considered, the effect of SWCNTs on cell capacity fade is likely to be small.

### Summary of Electrode Library Activities

Table V.5.1 highlights the distribution of electrodes from the Electrode Library, which is maintained by the CAMP Facility. The Electrode Library serves as a supply of standard electrode samples that are designed to be interchangeable with one another (capacity matched). Electrodes can be made with as little as 20 g of experimental material and can be made to match an existing counter electrode. In the first half of FY23, 936 sheets of electrode were fabricated and distributed by the CAMP Facility, which is  $>22$  square meters of

electrodes. These electrodes were supplied by the CAMP Facility in support of DOE’s numerous activities in advanced battery R&D. In addition to these electrodes, the CAMP Facility fabricated ~160 pouch cells in the first half of FY23 for DOE projects (consisting of many unique combinations of electrodes, electrolytes, and separators).

**Table V.5.1 Summary of Electrode Library Distributions**

Electrodes Delivered	FY19		FY20		FY21		FY22		FY23 First 6 months only	
	Argonne	160	15 %	245	25 %	302	17 %	704	40 %	156
Other National Labs	224	21 %	299	30 %	354	20 %	253	14 %	217	23%
Universities	296	28 %	333	33 %	426	23 %	243	14 %	262	28%
Industry	388	36 %	121	12 %	725	40 %	556	32 %	301	32%
<b>Total:</b>	<b>1068</b>		<b>998</b>		<b>1807</b>		<b>1756</b>		<b>936</b>	

### Conclusions

The multi-functional coating system from Frontier (Delta ModTech) is now fully approved for operation by trained Argonne CAMP Facility staff. This multi-functional coating system provides two new coating methods to the CAMP Facility (i.e., gravure and single-slot die). It also has an IR heating zone and corona treatment.

An *operando* X-ray technique developed in previous year(s) and will resume being used to study solid polymer electrolytes (being developed in Section VI.6) when the Advance Photon Source restarts in 2024.

Electrode Library continues to expand its list of available electrodes, with latest cathodes that are improved with single-wall carbon nanotubes (SWCNT).

The CAMP Facility supported numerous DOE battery programs, mainly through the CAMP Facility’s Electrode Library. Numerous prototype electrodes and pouch cells were fabricated and delivered to DOE-EERE programs.

A few of the planned tasks for FY23 were modified because of shutdown of APS for a major upgrade and delays in modification of dry room facility for new Frontier coater.

### Key Publications

1. I.A. Shkrob, P. Badami, J.S. Okasinski, M.-T.F. Rodrigues, S.E. Trask, D.P. Abraham, “Visualizing electrode assembly movement and lithiation heterogeneity in lithium-metal batteries using *operando* energy dispersive X-ray diffraction” *Journal of Power Sources* 553 (2023) 232273.
2. Additional publications related to the CAMP Facility are listed in other sections and in numerous other projects across the DOE and many universities.

### Acknowledgements

Key contributors to this work: Daniel Abraham, Shabbir Ahmed, Pavan Badami, Caleb Calvary, Alison Dunlop, Andy Jansen, Jae-Jin Kim, Chen Liao, Wenquan Lu, Yan Qin, Marco-Tulio Fonseca Rodrigues, Devashish Salpekar, Steve Trask, and Zhenzhen Yang.

## V.6 Materials Benchmarking Activities for CAMP Facility (ANL)

### Wenquan Lu, Principal Investigator

Argonne National Laboratory  
9700 South Cass Avenue  
Lemont, IL 60439  
E-mail: [LuW@anl.gov](mailto:LuW@anl.gov)

### Andrew N. Jansen, Co-Principal Investigator

Argonne National Laboratory  
9700 South Cass Avenue  
Lemont, IL 60439  
E-mail: [Jansen@anl.gov](mailto:Jansen@anl.gov)

### Haiyan Croft, DOE Technology Development Manager

U.S. Department of Energy  
E-mail: [Haiyan.Croft@ee.doe.gov](mailto:Haiyan.Croft@ee.doe.gov)

Start Date: October 1, 2022

End Date: September 30, 2023

Project Funding (FY23): \$400,000

DOE share: \$400,000

Non-DOE share: \$0

### Project Introduction

High energy density electrode materials are required to achieve the requirements for electric vehicle (EV) application within the weight and volume constraints established by DOE and the USABC. One would need a combination of anode and cathode materials that provide 420 mAh/g and 220 mAh/g, respectively, as predicted by Argonne's battery design model (BatPaC), if one uses a 20% margin for energy fade over the life of the battery assuming an average cell voltage of 3.6 volts. Therefore, the search for new high energy density materials for lithium-ion batteries (LIB) is the focus of this material benchmarking project. In addition to electrode materials, other cell components, such as separators, binders, current collectors, etc., are evaluated to establish their impact on electrochemical performance, thermal abuse, and cost.

This benchmarking effort is conducted as part of the Cell Analysis, Modeling, and Prototyping (CAMP) Facility (Refer to Chapter VI.5) to identify and support promising new materials and components across the "valley of death", which happens when pushing a new discovery towards a commercial product. The CAMP Facility is appropriately sized to enable the design, fabrication, and characterization of high-quality prototype cells, which can enable a realistic and consistent evaluation of candidate chemistries in a time-effective manner. However, the CAMP Facility is more than an arrangement of equipment, it is an integrated team effort designed to support the production of prototypes electrodes and cells. To utilize the facility more efficiently and economically, cell chemistries are validated internally using coin type cells to determine if they warrant further consideration. In addition, bench marking will advance the fundamental understanding of cell materials and facilitate advance the technology development.

### Objectives

- The primary objective is to identify and evaluate low-cost materials and cell chemistries that can simultaneously meet the life, performance, and abuse tolerance goals for batteries used in EV applications.
- The secondary objective is to enhance the understanding of the impact of advanced cell components and their processing on the electrochemical performance and safety of lithium-ion batteries.
- This project also provides support to the CAMP Facility for prototyping cell and electrode library development, and the MERF facility for material scale up.

## Approach

Though there are an overwhelming number of materials being marketed by vendors for lithium-ion batteries, there are no commercially available high energy materials that can meet all the requirements for all-electric-range (AER) vehicle within the weight, volume, cost, and safety constraints established for EVs by DOE and the USABC. Identification of new high-energy electrode materials is one of the challenges for this project.

Under materials benchmarking activities, we constantly reach out to, or are approached by, material developers to seek opportunities to test their advanced or newly released products. By leveraging Argonne's expertise in electrode design and cell testing, we can provide not only a subjective third opinion to material suppliers, but also deeper understanding on their materials, which can aid their material development. This deep understanding becomes even more important when the material developers are small companies or new players, who often overlook overall requirements of battery materials.

In addition to industrial partners, we also work closely with scientists from various research institutes, such as universities and research laboratories. They often come up with novel materials with advanced electrochemical performance, but small quantities, which is only enough for validation purposes. These test results help us to determine how much effort should be expanded to explore the material potential.

In general, we will validate any potential cell material, which has impact on the cell performance, mainly in terms of electrochemical performance, electrode optimization, and thermal stability. The electrochemical performance is the centerpiece of the materials benchmarking activities, which will be tested using 2032-sized coin-type cells under test protocols derived from USABC PHEV 40 requirements [Battery Test Manual For Plug-In Hybrid Electric Vehicles, Idaho National Laboratory]. The freshly made coin cells will undergo three formation cycles at a C/10 rate. The cells are then tested for the rate performance. For the rate test, the charging rate is set at C/5, while the discharge rate varies from C/5, C/3, C/2, 1C to 2C. Three cycles are performed for each discharge rate. After the rate test, the cells then undergo cycling test at C/3 rate. During the cycling test, we change the current rate to C/10 every 10th cycle to check the rate effect. Also, Hybrid Pulse Power Characterization (HPPC) is conducted every 10th cycle, which will be used to calculate the Area Specific Impedance (ASI).

This fiscal year, we have investigated various battery materials, such as cathode, anode, conductive additives, and solid-state electrolyte. In this report, we will report the progress on

- Various solid electrolytes were explored and studied PEGDA solid polymer electrolyte was prepared and electrochemically tested.
- Al<sub>2</sub>O<sub>3</sub> coated NCM523 was prepared using wet impregnation method and tested electrochemically.
- Optimum structure of SiO was investigated through annealing process.

## Results

Polymer electrolyte is recognized as a promising technology to overcome the safety issues of Li-based batteries. Compared to other solid-state electrolytes, polymer electrolyte is easier to process and provides a better interface. In this work, we developed a compound ("BU"), which can enable mechanical stable polymers with high ionic conductivity and high electrochemical stability (0 - 4.5 V) towards both lithium metal anodes and high-voltage cathode-electrodes. As shown in

Figure V.6.1, BU was added to PEGDA, LiTFSI, and plasticizer. After heat treatment, the mixture transformed into standalone polymer electrolyte.

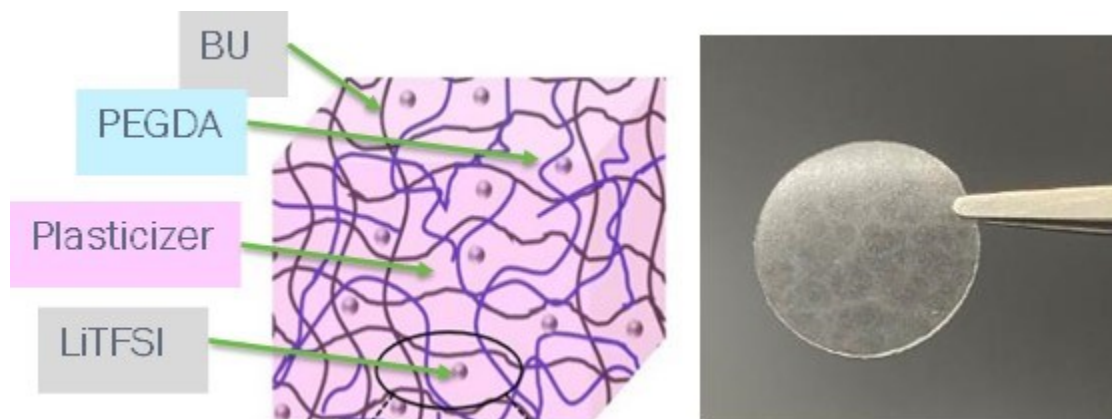


**Figure V.6.1 Schematic diagram (left) and standalone polymer film (right) of solid polymer electrolyte.**

Several BU variants were synthesized and “BU2” was selected for electrochemical testing.  $\text{LiFePO}_4$  was chosen as cathode and Li metal was used as anode. The half cells were assembled with standalone polymer electrolyte and tested under  $30^\circ\text{C}$  and  $45^\circ\text{C}$ .

Figure V.6.2 shows the rate and cycling performance of  $\text{Li}/\text{SP}/\text{LiFePO}_4$  half cells. Though the rate performance of BU2 is similar to the control solid polymer using “A2”, the cycling performance of BU2 electrolyte is much improved.

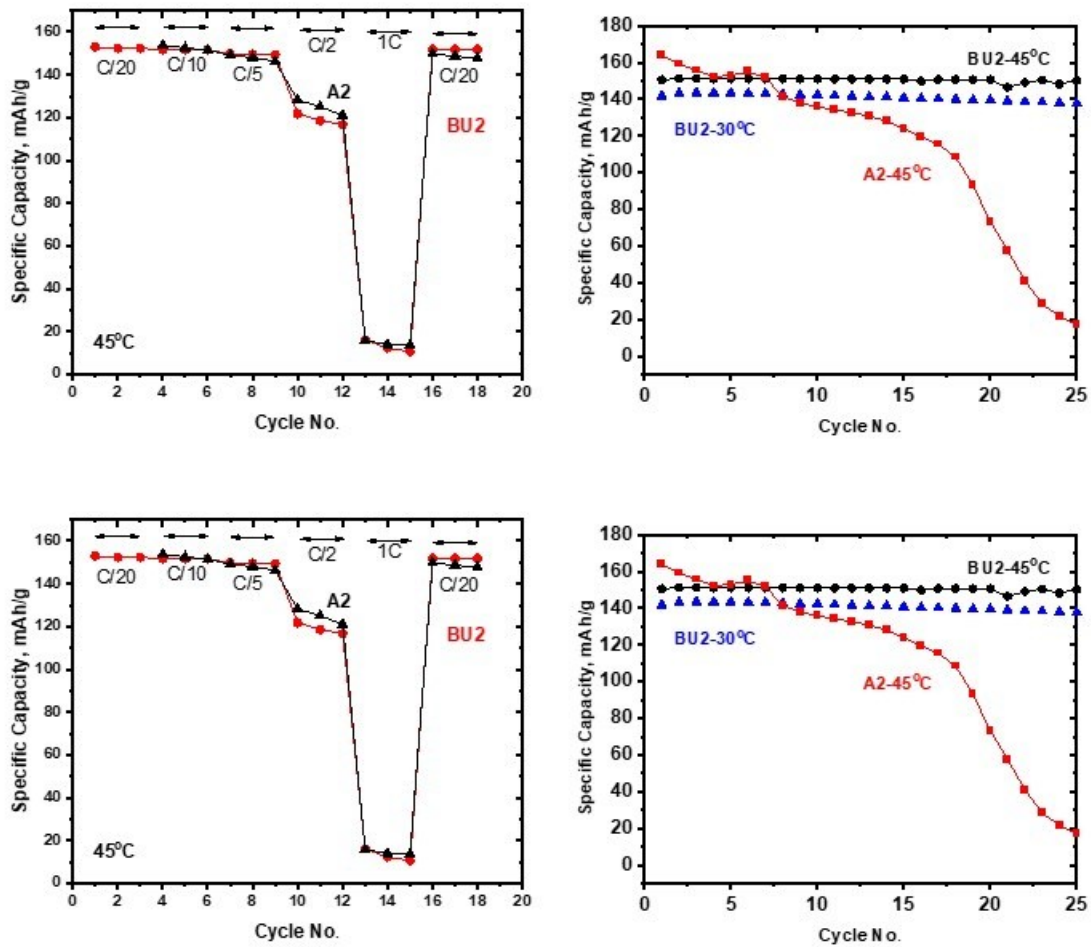
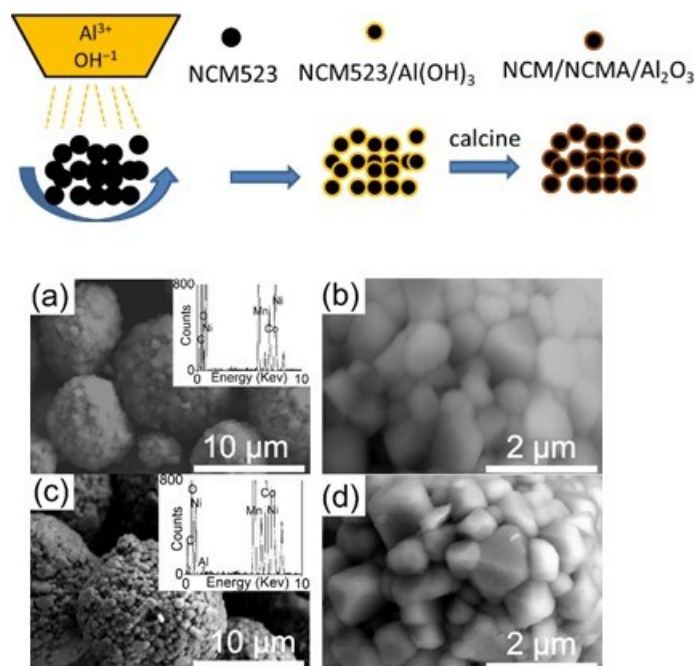


Figure V.6.2 Rate (left) and cycling (right) performance of Li/SP/LiFePO<sub>4</sub> cell.

Al<sub>2</sub>O<sub>3</sub> has been widely adopted as a coating for cathode materials due to its excellent electrochemical, chemical, and thermal stability. It can also work as an excellent protective layer for cathode materials. A cost-efficient approach with high-quality coating is highly demanded. Here, we demonstrated a facile approach, wet impregnation, to improve the surface stability of NCM523, but also reduce the surface resistance.



**Figure V.6.3** Schematic diagram of wet-impregnation coating (top) and SEM images of pristine (bottom a-b) and  $\text{Al}_2\text{O}_3$  coated (bottom c-d) NCM523 particles.

Figure V.6.3 demonstrates the schematic diagram of wet-impregnation method and SEM images of  $\text{Al}_2\text{O}_3$  coated particles. SEM images of the pristine NCM523 and the modified NCM523 suggested that the surface morphologies of the NCM523 particles before and after the surface modification process remained the same. Meanwhile, the EDS on the surface-modified NCM523 particles showed that elemental Al was on them. This indicates that the ultra-thin coating on NCM523 had been successfully created without any agglomeration.

The beneficial effect of the Al-doped layer is supported by the rate performance of NCM523 in the half-cell, which demonstrates that the increase in capacity for NCM523 after the surface modification is from 15% at C/10 to 21% at 2C. Furthermore, the cycle test of NCM523 with a cut-off voltage of 4.5 V in half-cells demonstrated that the capacity retention of NCM523 at C/3 can increase from 90% to 95% for 50 cycles. In general, the  $\text{Al}_2\text{O}_3$  surface coating on the cathode increases the surface resistance of the cathode due to the low conductivity of  $\text{Al}_2\text{O}_3$  and leads to a lower specific capacity. We attribute the higher specific capacity of the modified NCM523 to the synergetic effect of the  $\text{Al}_2\text{O}_3$  coating and the Al doping effect. The  $\text{Al}_2\text{O}_3$  coating can mitigate the side reaction between the electrolyte and NCM523, which increases the conductivity of SEI. Additionally, doped Al can stabilize the surface lattice structure of NCM523, which can also promote Li diffusion into the surface of NCM523. This leads to less electrode overpotential and thus higher capacity under the same cut-off voltage. (Figure V.6.4)



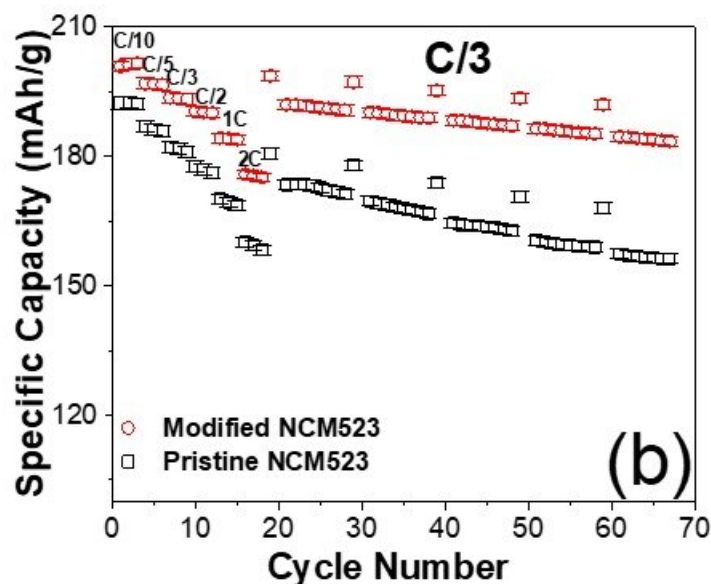


Figure V.6.4 Rate and cycling performance Li/NCM523 half cells w/ and w/o Al<sub>2</sub>O<sub>3</sub> coating.

Silicon monoxide (SiO) is a very promising anode material for next-generation high-energy lithium-ion batteries because of its high theoretical specific capacity of 1710 mAh/g and volumetric capacity of 1547 Ah/L. Compared to commercially used graphite, SiO can offer an 18% cell-stack-level improvement in volumetric energy density and an 11% improvement in gravimetric energy density (calculated on the basis of the same cell-stack model used for volumetric energy density calculation), enabling smaller and lighter batteries. It also offers more stable cycle performance compared to Si because of its smaller volume change (134% initial volume expansion and 117% reversible volume expansion), making it a more practical choice.

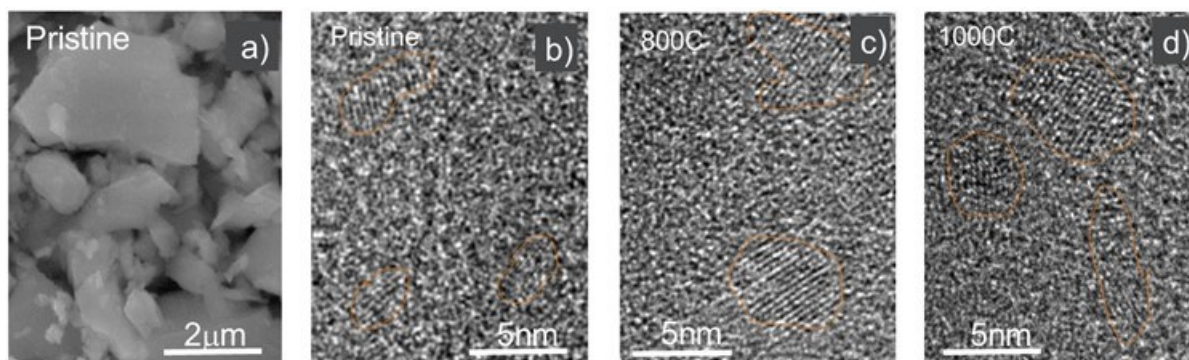
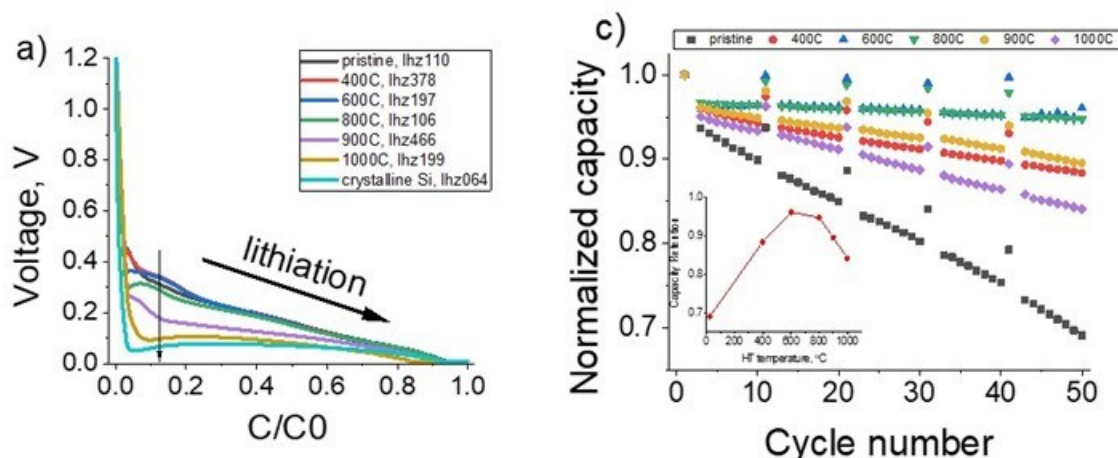


Figure V.6.5 (a) SEM image and (b–d) TEM images of pristine and heat treated SiO samples.

The SEM image in Figure V.6.5 shows that the SiO particle size varies from about several hundred nanometers to a few micrometers ( $\sim 3 \mu\text{m}$ ) with sharp edges. The HRTEM image confirms that there are nanosized crystalline domains within an amorphous matrix. The size of the Si nanodomains depends on the synthesis and processing conditions. In this study, we gradually changed the microstructure of SiO via heat treatment in an inert argon atmosphere and thoroughly studied the change in the SiO microstructure and its impact on the electrochemical performance. To obtain different microstructures, the SiO sample was annealed in an argon atmosphere at five different temperatures: 400, 600, 800, 900, and 1000 °C (SiO-400 °C, SiO-600 °C, SiO-800 °C, SiO-900 °C, and SiO-1000 °C). Compared to those of the pristine sample, the Si nanodomains of SiO-800 °C and SiO-1000 °C are much larger.



**Figure V.6.6** (left) First lithiation voltage profile and (right) Cycle tests of SiO-pristine and SiO heat-treated at different temperatures.

As shown in Figure V.6.6, the lithiation onset potential decreases, as the treatment temperature increases. The shift of redox peaks to lower potential suggests a larger kinetics barrier in the first lithiation process of SiO-900 °C and SiO-1000 °C. This figure also compares the cycle performance of pristine and annealed SiO samples. The capacity (C/C0) is normalized to the first C/10 cycle in the cycle test for better comparison. All annealed samples showed significantly improved capacity retention compared to SiO pristine. The optimal capacity retention was obtained for SiO-600 °C and SiO-800 °C. When the annealing temperature was further increased to 900 and 1000 °C, however, a decrease in capacity retention was observed. The improvement may be attributed to the interphase reduction and modification that occurred at all treatment temperatures.

### Conclusions

- PEGDA based solid polymer electrolyte was reinforced using additional cross linker. The new solid polymer electrolyte showed good electrochemical performance using Li/SPE/LiFePO<sub>4</sub> cell.
- NCM523 was coated with Al<sub>2</sub>O<sub>3</sub> using scalable and cost effective wet-impregnation method. Better performance of coated NCM523 could be attributed to synergic effect of coating and doping effects.
- The interphase of SiO was modified by an annealing approach. Good electrochemical performance of SiO was obtained with the optimum structure.

### Key Publications

1. Optimal microstructure of silicon monoxide as the anode for lithium-ion batteries, Linghong Zhang, Yuzi Liu, Fangmin Guo, Yang Ren, Wenquan Lu, ACS Appl. Mater. 2022, 14, 51965-51974 (<https://doi.org/10.1021/acsami.2c15455>).
2. Enable High-Energy LiNi<sub>0.5</sub>Co<sub>0.2</sub>Mn<sub>0.3</sub>O<sub>2</sub> by Ultra-Thin Coating through Wet Impregnation, Xin Su, Xiaoping Wang, Javier Barenó, Yan Qin, Frederic Aguesse, and Wenquan Lu, Batteries, 2022, 8, 136.
3. Materials Benchmarking Activities for CAMP Facility, Wenquan Lu, Devashish Salpekar, Yan Qin, Chen Liao, Xiaoping Wang, Kevin Mathew, Brendan Hawksley, Olivier Kasikala, Xinwei Zhou, Yuzi Liu, Caleb Calvary, Steve Trask, Alison Dunlop, and Andrew Jansen, 2023 U.S. Department of Energy Vehicle Technologies Office Annual Merit Review and Peer Evaluation, Washington DC, Jun 12<sup>th</sup> – 15<sup>th</sup>, 2023
4. Electrode Prototyping Activities in ANL's Cell Analysis, Modeling and Prototyping (CAMP) Facility. Trask, Steve, Andrew Jansen, Daniel Abraham, Shabbir Ahmed, Pavan Badami, Caleb Calvary, Kanchan Chavan, Zonghai Chen, Dennis Dees, Abhas Deva, Alison Dunlop, Mohammed Effat, James Gilbert, Brendan Hawksley, Zachary Hood, Olivier Kasikala, Hyun-Woo Kim, Jae Jin Kim, Kevin Knehr, Joseph Kubal, Chen Liao, Yuzi Liu, Wenquan Lu, Mei Luo, Kevin Mathew, Rownak Mou, John Okasinski, Yan Qin, Sathish Rajendran, Marco Rodrigues, Devashish Salpekar, Ilya Shkrob,

Deepti Tewari, Poster presented at the 2023 DOE Vehicle Technologies Office Annual Merit Review, Jun 12<sup>th</sup> – 15<sup>th</sup>, 2023.

5. Composite Polymer Electrolytes For High Performance Li Metal Batteries, Chen Liao, Bingning Wang, Yan Qin, Wenquan Lu and Andrew Jansen, 2023 Solid-State Battery Summit - (Chicago, IL, US, 08/08/23-08/09/23)

### **Acknowledgements**

First, contributions from Devashish Salpekar, Yan Qin, Chen Liao, Xiaoping Wang, Kevin Mathew, Brendan Hawksley, Olivier Kasikala, Xinwei Zhou, Yuzi Liu, Caleb Calvary, Steve Trask, Alison Dunlop are gratefully acknowledged.

## V.7 Electrochemical Performance Testing (INL)

### Lee Walker, Principal Investigator

Idaho National Laboratory  
2525 Fremont Ave  
Idaho Falls, ID 83402  
E-mail: [lee.walker@inl.gov](mailto:lee.walker@inl.gov)

### Haiyan Croft, DOE Technology Development Manager

U.S. Department of Energy  
E-mail: [Haiyan.Croft@ee.doe.gov](mailto:Haiyan.Croft@ee.doe.gov)

Start Date: October 1, 2022	End Date: September 30, 2023	
Project Funding (FY23): \$3,200,000	DOE share: \$3,200,000	Non-DOE share: \$0

### Project Introduction

The advancement of battery technologies that can meet the emerging demands for vehicle electrification requires in-depth understanding of the performance of early-stage pre-commercial batteries, state-of-the-art commercial cells and the ability to adapt evaluation methods as mobility needs change. The Battery Test Center (BTC) at Idaho National Laboratory (INL) has been supporting the evolution of electrified transportation through high-quality, independent testing of electrical energy storage systems for more than 30 years. Independent testing provides data for quantitative assessment of the fundamental technology gaps that exist in early-stage battery development. Test methods and techniques are continuously improved to offer data on relevant metrics as vehicle applications evolve and as new core gaps are identified. Advancing electrified powertrain transportation including understanding both high-energy battery chemistries and high power, extreme fast charging needs, is a top priority in advancing how people and goods are transported in the United States. As a designated core capability and lead test facility for the Vehicle Technologies Office (VTO), the BTC at INL directly supports the US Advanced Battery Consortium (USABC) and other VTO programs by providing discrete information on failure modes, mechanisms, and shortfalls in emerging technologies. Gaps in performance relative to targets are used as a metric to guide future R&D priorities.

The development and deployment of batteries in new, diverse applications requires both that the batteries function in the necessary environment as well as a deep understanding of their performance, life and expected failure mechanisms. In the past the primary means to advance knowledge on performance and life was to test batteries for extended periods of time under a range of different scenarios. Testing of batteries in this manner can take upwards of a year to make reasonable estimations of life and to clearly identify failure modes and rates. The need to shorten the design and testing cycle is critical to bringing new battery chemistries and cell designs into emerging applications such as in stationary energy storage to support electric vehicle charging stations capable of extreme fast charging.

### Objectives

The activities at the INL BTC are focused on providing high fidelity, science-based performance and life testing, analysis, modeling, and reporting. To ensure the alignment with future industry and government needs, it is a key objective to update test and analysis procedures as new concepts and design space become achievable. Refined procedures help identify promising future research paths and identify key fundamental gaps that need to be addressed.

### Approach

With 20,000 square feet of laboratory space, the INL BTC is equipped with over 800 test channels for advanced energy storage testing at the cell-level (e.g., up to 7V, 300A), module-level (e.g., up to 65V, 1200A), and pack-level (e.g., 500-1000V, 500A). Test equipment is programmed to perform distinct test profiles while

simultaneously monitoring for compliance with operating limits such as voltage, current and temperature. The output from such tests enables principles-based analysis to be performed that can aid in identification of key technology gaps.

To ensure high quality, repeatable and dependable data is used for analysis, batteries and other energy storage devices are typically subjected to specific test sequences while housed inside precision thermal chambers. To enhance performance testing across a wide range of thermal conditions, driven by automotive usage scenarios, the thermal chambers can be operated across a broad temperature range (e.g., -70 to 200°C). This temperature range enables key information to be extracted by modifying the chemical kinetic degradation rates within the evaluated items and enables accelerated aging analysis.

Successful performance testing and accurate life modeling are highly dependent on the fidelity of the acquired test data. The INL BTC has developed advanced calibration verification and uncertainty analysis methodologies to ensure that voltage, current, and temperature measurements are within the tolerance specified by the test equipment manufacturer (e.g., 0.02% of the full scale). These measured test parameters are subsequently used in various mathematical combinations to determine performance capability (e.g., resistance, energy, power, etc.). INL has also quantified the error associated with these derived parameters using the accuracy and precision of the relevant measured parameter (e.g., voltage) to ensure high-quality and repeatable results and meaningful presentation.

The INL BTC is also equipped with facilities that enable the characterization of batteries in aggressive use cases. One such use case is vibration that mimics what would be seen over the life of a battery in a typical automotive setting. Analysis of vibration on batteries at INL utilizes a high-capacity vibration table to perform non-destructive tests to understand reliability and safety of new cell topologies to mechanical vibration and shock. Emerging cell designs that vary from current state of the art cell designs are the focus of mechanical vibration and shock testing at INL.

Adjacent to the vibration table are two fire-rated isolation rooms that can be used for tests that push the known limits of battery operation. These aggressive use cases include extreme fast charging, subtle over- or under-charging, high-temperature thermal characterization for under-hood systems, among many others. The isolation rooms allow for safe testing of emerging cell technologies at or near the design limits and help characterize future use cases. The rooms also enable identification of key changes in performance fade that may emerge in aggressive use cases that can directly inform future rounds of early-stage material and cell development activities. These complimentary non-destructive evaluation capabilities comprise INL's Non-Destructive Battery Evaluation Laboratory.

## Results

The INL BTC continues to test articles of various sizes and configurations using standardized test protocols developed by INL with industry partnerships for different electric drive vehicle application. Tables 1, 2 and 3 summarize the testing activities under the USABC, Benchmarking programs and Low Cobalt FOA, respectively, for FY-23. Technologies developed through USABC contracts are aged and tested against the appropriate application target (HP-EV, LC/FC-EV, HEV, PHEV, 12V S/S, 48V HEV) and, where applicable, they are compared to previous generations of test articles from the same developer. 414 articles were tested for USABC in FY-23, including 2 modules and 412 cells. The purpose of the Benchmark program is to evaluate device technologies that are of interest to VTO within DOE but are not deliverables developed under a contract. In some cases, Benchmark devices are used to validate newly developed test procedures and analysis methodologies. Benchmark activities also are used to understand which gaps need to be fundamentally addressed to improve cell performance. 48 cells were tested for the Benchmark program in FY-23. A new testing program was started in FY-20 to evaluate deliverables from the VTO Low Cobalt FOA programs. Testing of the first round of deliverable cells was continued into FY-23, end of program deliverables were started in FY22 and are expected to conclude into FY-24. The purpose of the program is to find Li-Ion battery chemistries that have little to no cobalt content. 84 cells were tested for the Low Cobalt program in FY-23.

Analysis was performed for all articles tested, and results were presented regularly at quarterly review meetings and USABC Technical Advisory Committee (TAC) meetings to USABC representatives from different automotive manufacturers, DOE VTO representatives, developers, and national laboratory staff. INL worked with the USABC test methods committee to develop the methodology and update the manual for testing EV batteries. (See Table V.7.1, Table V.7.2, and Table V.7.3.)

**Table V.7.1 Articles Tested for USABC**

Developer	Application	System	Number of Articles Tested	Status at Year End
Farasis	Recycle	Cell	12	Completed
Farasis	Recycle	Cell	12	Completed
Farasis	Recycle	Cell	12	Completed
Gotion	HP-EV	Cell	17	Completed
Gotion	HP-EV	Cell	18	Completed
Microvast	HP-EV	Module	2	Completed
ABMC	Recycle	Cell	10	Ongoing
Amprius	LC/FC-EV	Cell	21	Ongoing
Applied Materials	HP-EV	Cell	25	Ongoing
Benchmark	LC/FC-EV	Cell	30	Ongoing
Enpower	LC/FC-EV	Cell	24	Ongoing
Farasis	HP-EV	Cell	15	Ongoing
Farasis	LV/FC-EV	Cell	15	Ongoing
Ionblox	LC/FC-EV	Cell	23	Ongoing
Ionblox	LC/FC-EV	Cell	27	Ongoing
Ionblox	LC/FC-EV	Cell	28	Ongoing
Ionblox	LC/FC-EV	Cell	5	Ongoing
Ionblox	LC/FC-EV	Cell	6	Ongoing
Microvast	LC/FC-EV	Cell	24	Ongoing
Microvast	LC/FC-EV	Cell	21	Ongoing
Microvast	HP-EV	Cell	36	Ongoing
Nanoramic	HP-EV	Cell	18	Ongoing
Saft	HEV	Cell	13	Ongoing

**Table V.7.2 Articles Tested for Benchmark**

Developer	Application	System	Number of Articles Tested	Status at Year End
Applied Materials	B500	Cell	4	Complete
U Missouri		Cell	3	Complete
Forge Nano	LC/FC-EV, FCAB	Cell	35	Ongoing
Applied Materials	LC/FC-EV	Cell	6	Ongoing

**Table V.7.3 Articles Tested for Low Cobalt**

Developer	Application	System	Number of Articles Tested	Status at Year End
Cabot	Low Co	Cell	12	Ongoing
Penn State	Low Co	Cell	12	Ongoing
UT-Austin	Low Co	Cell	12	Ongoing
UC-Irvine	Low Co	Cell	12	Ongoing
Cabot	Low Co	Cell	12	Ongoing
Penn State	Low Co	Cell	12	Ongoing
UT-Austin	Low Co	Cell	12	Ongoing

Collaborative work continued in FY-23 between the 21<sup>st</sup> Century Truck Partnership (21CTP) and INL. This work has focused on developing battery specifications for commercial trucks with electric drives. Targets were finalized for class-8 line-haul battery electric trucks, class-6 battery electric box truck, and class-4 battery electric step vans. 21CTP consists of OEM companies across the commercial vehicle market, DOE-VTO, and National Labs.

### Conclusions

The ability to perform discrete performance and life evaluation of emerging technologies in an independent, reliable manner is a direct aid to the identification of key technology gaps. Over the course of FY-23, the INL BTC was able to directly support many different endeavors within VTO with a keen focus on advancing battery technologies for emerging trends in electrified transportation. As a core capability in performance and life analysis for VTO, INL has identified key performance fade modes that exist in cells and has advanced the understanding of performance and evaluation protocols for multiple programs funded by VTO and USABC. A total of 546 devices were tested in FY-23. In FY-24 the work to develop the update of the USABC EV test manual will be concluded. In FY-24, INL plans to continue this level of support for multiple programs with broad support for the USABC and Benchmark programs. INL will also continue developing and refining standard test protocols and analysis procedures in collaboration with USABC and on providing information on core fundamental performance gaps that need to be addressed across VTO programs. Also, in FY-24, INL will continue to work with the 21<sup>st</sup> Century Truck Partnership to build battery targets for next generation electric commercial vehicles and publication of their electrification roadmap for commercial vehicles.

### Acknowledgements

The following staff at INL supported this work Matthew Shirk, Tanvir Tanim, Sergiy Sazhin, Eric Dufek, Randy Bewley, Charles Dickerson, Chinh Ho, Jordan Todd, Kevin Meudt, Michael Evans, Bianca Mak

## V.8 Machine Learning for Accelerated Life Prediction and Cell Design (INL, NREL)

### **Eric Dufek, Principal Investigator**

Idaho National Laboratory  
2525 Fremont Ave  
Idaho Falls, ID 83415  
E-mail: [eric.dufek@inl.gov](mailto:eric.dufek@inl.gov)

### **Kandler Smith, Co-Principal Investigator**

National Renewable Energy Laboratory  
15013 Denver West Pkwy  
Golden, CO 80401  
E-mail: [kandler.smith@nrel.gov](mailto:kandler.smith@nrel.gov)

### **Simon Thompson, DOE Technology Development Manager**

U.S. Department of Energy  
E-mail: [Simon.Thompson@ee.doe.gov](mailto:Simon.Thompson@ee.doe.gov)

Start Date: October 1, 2022	End Date: September 30, 2023	
Project Funding (FY23): \$1,450,000	DOE share: \$1,450,000	Non-DOE share: \$0

### **Project Introduction**

The development and deployment of batteries in new, diverse applications requires both that the batteries function in the necessary environment as well as a deep understanding of their performance, life and expected failure mechanisms. In the past the primary means to advance knowledge on performance and life was to test batteries for extended periods of time under a range of different scenarios. Testing of batteries in this manner can take upwards of a year to make reasonable estimations of life and to clearly identify failure modes and rates. The need to shorten the design and testing cycle is critical to bringing new battery chemistries and cell designs into emerging applications such as in stationary energy storage to support electric vehicle charging stations capable of extreme fast charging and the use of batteries in an assortment of different emerging areas of mobility. Connection of physics-based life models and machine learning (ML) provides the opportunity to enable more robust assessment of battery aging, failure mechanism identification and understanding as new use case scenarios are proposed. The current project is focused on means to apply ML to enhance the estimation of life while also identifying key failure pathways, building knowledge and algorithms transferrable to future designs and chemistries. During the first portion of the project existing data sets will be used for both training and validation of ML approaches to better characterize expected battery life. The work also looks to link ML with existing physics-based life models at INL and NREL.

Work in this project is focused on clearly aligning physics-based models with experimental data, synthetic data as generated from different electrochemical models and advanced data analysis methods. As a combined set of efforts, it is envisioned that the time needed for validation of both performance and key failure modes will be significantly reduced. The project also aims to develop tools that will help in the design space to more quickly align different materials and design considerations with application-specific needs. The combined set of tools are targeting a robust experimental-modeling-analysis framework which will provide more discrete information to stakeholders and battery developers to enable technology innovation with rapid turn-around.

Key contributions from this work during FY23 included the ability to expand deep learning and synthetic data generation tools to new chemistries, expansion of a protected battery datahub and a comparison of different life and failure mode prediction methods. The team also expanded synthetic data generation to include the use of high-fidelity synthetic data which can inform on the condition of a battery on a cycle-by-cycle basis.



## Objectives

Key objectives during FY23 were aligned with expanded development of the tool architecture, demonstration of the ability to not just predict and validate performance at a fixed point in aging, but also the prediction of failure mode and failure mode extent and expansion of a centralized datahub. A key priority in FY23 was the early prediction of power capability for cells undergoing different duty cycles. These outcomes and objectives were achieved through the direct linkage of physics-based life models with electrochemical models and targeted experimental characterization. The use of statistical, machine learning and deep learning methods complemented the other activities.

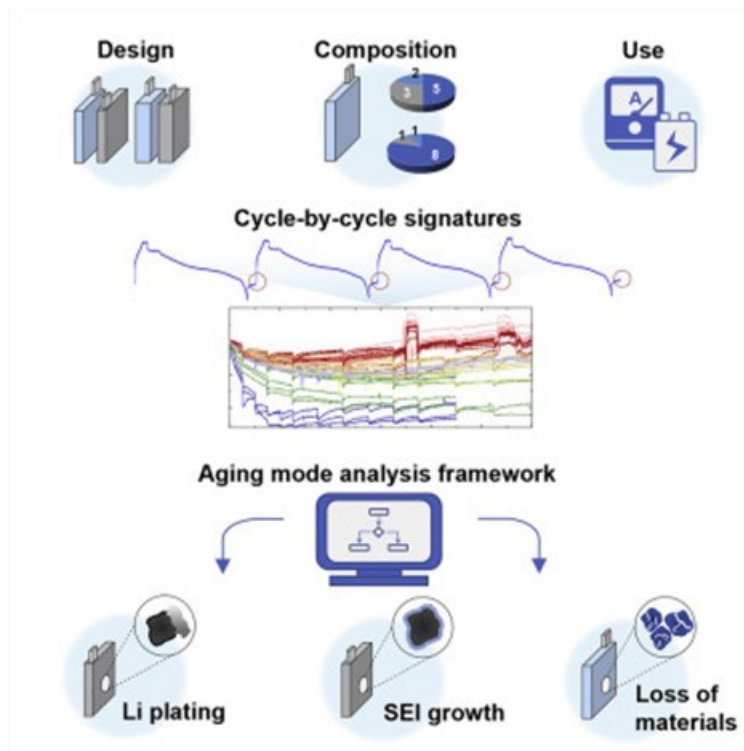
## Approach

To achieve the project objectives the team has taken an approach that blends the use of physical data acquisition, synthetic data generation using electrochemical models and battery life models. The bulk of activities focused on the use of pouch cells (either single layer or 1.1 Ah) with a graphite/NMC532 or a graphite/NMC811 chemistry that had undergone different types of fast-charging characterization. Additional analysis on Si/NMC cells was performed. Cells were characterized across different rates with post-test analysis for targeted confirmation of failure modes and extent of failure modes. Synthetic data was generated using a combination of incremental capacity (IC) models and high-fidelity electrochemical models based on a pseudo-2D (p2D) framework. Both sets of models incorporate key elements of the cell design including chemistry and electrode details and aspects of failure modes including loss of lithium inventory (LLI), loss of active materials at the positive (LAM<sub>PE</sub>) and negative (LAM<sub>NE</sub>) electrodes. The p2D model further included changes in transport and kinetic properties with aging for diagnosis of high-rate data.

Advanced analysis used a combination of techniques including a suite of machine and deep learning frameworks, physics-informed neural networks (PINNs), algebraic life models and targeted data extraction were used to analyze critical data for predictions. To maintain the link with physicality, analysis focused on using key electrochemical and environmental data points that inform both on how and why a cell is performing in a specific manner.

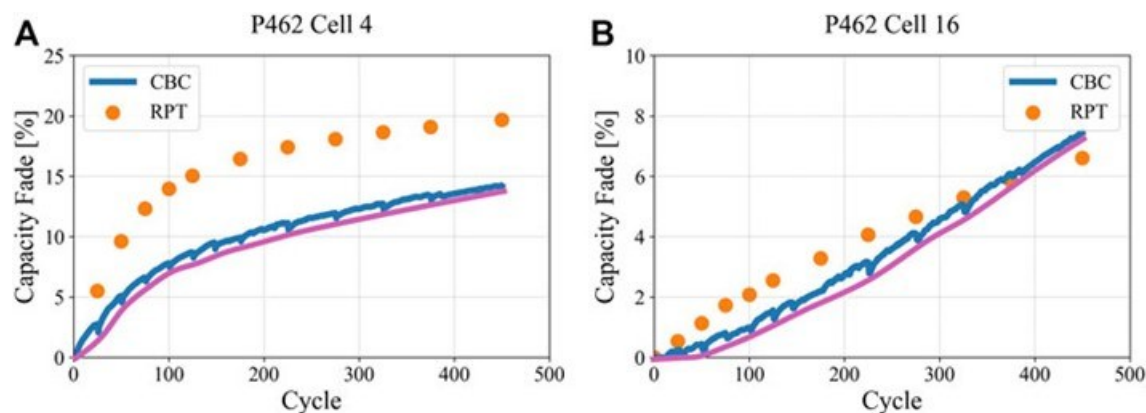
## Results

Building off of prior work the team advanced decision tree analysis for failure mode identification during FY23. This included methods to distinguish between LLI due to lithium plating, LLI due to solid electrolyte interphase (SEI) growth, and loss of active material at the positive and negative electrode. Through modification of the earlier approaches the team was able to demonstrate the ability to classify aging for each of the scenarios above as well as showing that the methods could be transferred beyond the training data in the case of different NMCs being used as the positive electrode in the cells. Using 55 cycles it was possible to classify with 86% accuracy. For LAM<sub>PE</sub> the percentage loss was quantified with an error of 4.3%. As shown in Figure V.8.1 the use of cycle-by-cycle data and especially the end-of-charge and end-of-discharge voltages were critical to the classification and assessment of cells.



**Figure V.8.1 Decision tree framework for the classification and quantification of failure modes in Li-ion batteries. The framework was demonstrated for both Graphite/NMC532 and graphite/NMC811 cells. (Chen 2023)**

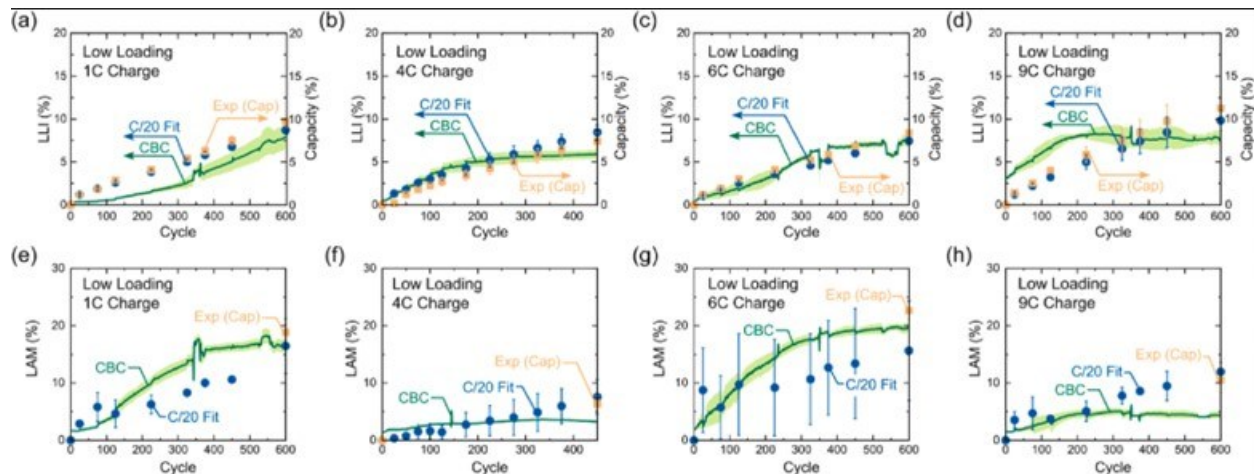
A key requirement for robust predictions and data analysis is the use of high-quality data and in understanding the impacts to the data obtained from different cycling regimes. These two areas were key focal points of a study performed looking at how polarization and capacity fade projects are manifested in cycle-by-cycle (CBC) and reference performance test cycling. Typically reference performance tests are performed at slow rates and incorporate more rest between cycles while CBC incorporates less rest and often faster cycling during both charge and discharge. When comparing the two sets of cycling the team found that often polarization can change the trend of fade and could complicate any machine learning based analysis. At a minimum it is required that values of prediction be clearly defined to mitigate confusion. As shown in Figure V.8.2 this is especially pronounced when Li metal plating occurs as part of the aging process. When plating occurred the variation between the slower rate and faster CBC capacity fade was nearly 2x different.



**Figure V.8.2 (Gering 2023)** RPT (C/20) and cycle by cycle data that show differences due to polarization effects. Pink curves represent the trendlines for CBC data just following the RPTs, effectively removing polarization hysteresis effects between RPT conditions. **(A)** Cell 4 which was charged at a 6C rate and had undergone lithium plating, while panel **(B)** shows cell 16 which was charged at a 4C rate with no signs of lithium plating.

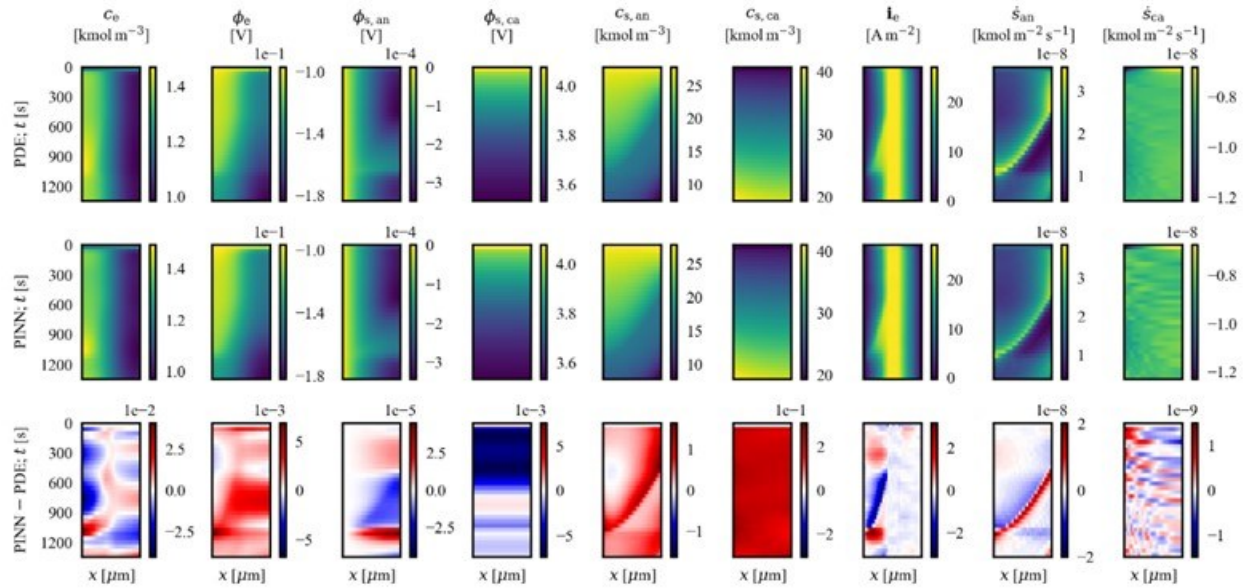
A key factor in enabling extreme fast-charging capabilities in Li-ion batteries is to ensure that fast-charge events do not significantly degrade battery performance. This project utilized several data sets from DOE's Extreme Fast Charge (XCEL) project described in separate chapters of this report. Under this project, the team developed novel electrochemical model + AI algorithms to determine a battery's aging modes during high-rate cycling. Typical state-of-the-art electrochemical diagnostic tests use relatively slow reference performance tests (RPTs) at C/20 rates. After this  $\approx 40$  h slow-cycle test, incremental capacity analysis (i.e.,  $dQ/dV$ ) maps the electrode and Li utilization to the cell's beginning-of-life performance. These thermodynamically based analysis outputs age modes such as loss-of-lithium-inventory (LLI) and loss-of-active-material (LAM) in the positive electrode ( $LAM_{PE}$ ) and the negative electrode ( $LAM_{NE}$ ). However, ideally the procedure to extract the battery's aged state would not require almost two days. Instead, this team developed a novel electrochemical model + AI workflow to determine the battery's aged state directly from high-rate cycle-by-cycle data. In this way, the battery's aged state can be determined in situ and optimal charging conditions can be adapted to ensure the battery aging does not accelerate during a fast-charge event (e.g., Li plating limits are continually avoided). To extract the battery's aged state from high-rate data, a physics-based pseudo-2D (P2D) model was developed. This model was adapted to accept aging modes as inputs (i.e., LLI,  $LAM_{PE}$ , and  $LAM_{NE}$  are inputs to the model). The age-informed P2D model was then used to simulate the high-rate response of an aged cell. A neural network was trained to the synthetic dataset and then applied to the real electrochemical data to diagnose LLI and LAM. In this way, the measured high-rate response can be correlated to aged-state responses. This work has been published in *J. Power Sources* doi: 10.2139/ssrn.4403440 (Weddle 2023) using the XCEL R1 and R2 loading data for C-rates up to 9C charging.

Figure V.8.3 shows the output of the high-rate diagnostic tool. The top row (Figure V.8.3a-d) shows estimated LLI and the bottom row shows estimated  $LAM_{PE}$ . The plots show the aged states for cells charged at 1C (Figure V.8.3a, e), 4C (Figure V.8.3b, f), 6C (Figure V.8.3c, g), and 9C (Figure V.8.3d, h). Illustrated in blue is the aged state identified using standard low-rate tests and incremental capacity analysis. Illustrated as lines is the predicted aged state from the new cycle-by-cycle (CBC) high-rate tool. Importantly, the tool can be used for every single cycle and thus the aged state is plotted for each cycle as opposed to points (which required the cell to be taken off test for a 2-day low-rate capacity measurement). Impressively, the high-rate tool can determine the aged state for cells cycled at significantly different rates. Additionally, the tool accurately predicts similar aged states as the standard C/20 testing procedure. Similar plots for the R2 loading are available in the manuscript. It is expected that by being able to determine the battery's aged state in situ, new opportunities for age-informed fast-rate protocols can be developed to extend battery life.



**Figure V.8.3 (Weddle, Kim, Chen, et al. *J. Power Sources*, 2023) [Battery aging modes determined using C/20 fits and the high-rate modeling tool. Age mode diagnostics of LLI and LAMPE are shown for the R1 XCEL cells (termed “Low Loading”) for cells cycled at 1C, 4C, 6C, and 9C.]**

The above algorithm and workflow, while offering valuable cycle-by-cycle insight from high-rate data, is slow to generate synthetic data. The generation of synthetic data requires a well-parameterized and validated P2D electrochemical model, with computations taking several days to generate the synthetic data across a wide parametric space and train a neural network to its results. Building upon the above algorithm, the team began development of a physics-informed neural network (PINN) that learns approximate solutions to the P2D model governing equations. The PINN provides a much faster alternate solution to the P2D governing equations compared to a traditional partial-differential-equation (PDE) solver. Multiple PINN models were created, including a simple single-particle model (SPM) and the full P2D model. The most accurate PINN models (Figure V.8.4) used a hierarchical learning scheme where different levels of PINNs were trained to gradually improve on simpler models, for example first the SPM with linear kinetics, next with Butler Volmer kinetics, and finally the P2D model with extra terms in the optimized loss function to ensure physical laws for conservation of charge and Li species were conserved. The resulting PINN model runs some 750x faster than the PDE model and is suitable for Bayesian inference, a type of parameter estimation which produces probability distributions for each fitted parameter. Two papers were drafted, one on the SPM PINN and the other on the P2D model PINN. The papers will be submitted in early FY24. The value of the PINN algorithm is that, once trained, the algorithm can estimate state-of-health dependent physical parameters from electrochemical data, alleviating the need for slow diagnostic tests such as C/20 and electrochemical impedance spectroscopy. The PINN is expected to speed up the development of beginning of life electrochemical performance models that help optimize electrode/cell design as well.



**Figure V.8.4** Spatiotemporal contours ( $x$ -axis is the longitudinal direction, and  $y$ -axis is the temporal direction from top to bottom) of primary and secondary variables from P2D models. Top: results from PDE integration. Middle: PINN predictions. Bottom: Absolute error between the PDE and PINN solutions. Columns from left to right are for: electrolyte Li-ion concentration, electrolyte potential, solid-phase anode potential, solid-phase cathode potential, anode particle surface concentrations, cathode particle surface concentrations, electrolyte-phase current, anode Faradaic current, and cathode Faradaic current.

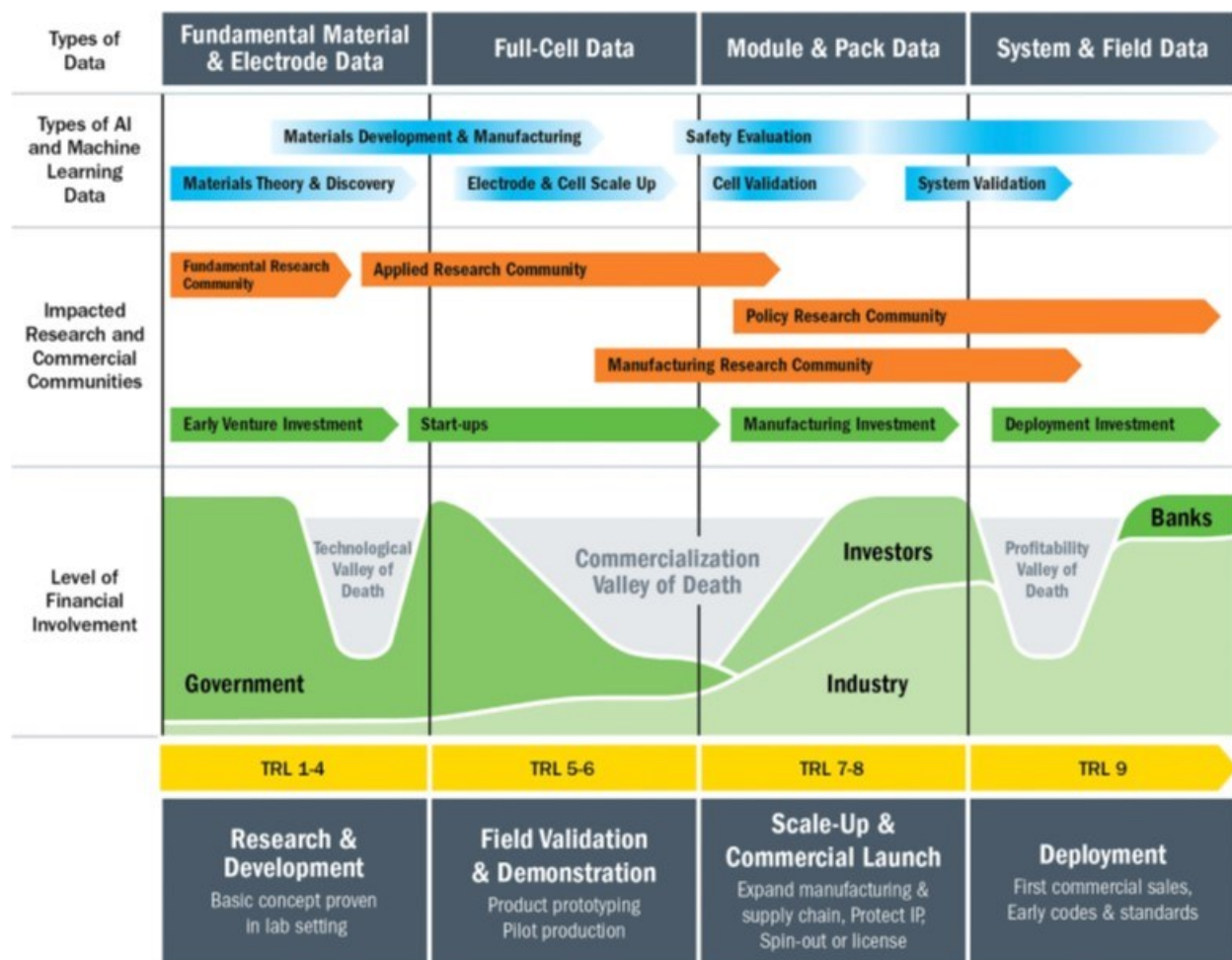


Figure V.8.5 Gaps and areas where sharing of data can aid the development process for new or modified battery technologies. (Ward, 2022)

In addition to developing new methods for analysis, life prediction and cell design it is important to advance the tools and methods used for data sharing. This is the core of the rationale for the development of different types of datahubs which can effectively aid the transition of technologies from the benchtop to commercial use. The team at INL and NREL jointly contributed with other researchers to develop the concept of the Battery Data Genome. This concept advances the possibility to use targeted data from different institutions to address the ‘Valleys of Death’ that arise in technology development, deployment, and commercialization (Figure V.8.5). By aligning the data and advancing artificial intelligence (AI) and ML techniques it is plausible to deploy energy storage more quickly aiding the transition to a more electrified globe.

In FY24, the team refined and enhanced the VTO battery data hub, [batterydata.energy.gov](https://batterydata.energy.gov). The data hub architecture uses a pre-existing DOE Energy Materials Network (EMN) platform with codebase shared across 7 other EMN data hubs. The site uses two-factor authentication, suitable for U.S. Government battery R&D. Datasets are private by default and can be released publicly when published and approved. In FY22, the team conducted stakeholder interviews, defined metadata (include prototype cell complete recipe and electrochemical test parameters), obtained DOE approvals, and went live with a prototype website. In FY23, the team completed the metadata implementation, developed standardized electrochemical data formats, and developed offline data plotting and analysis tools. The team uploaded more than 500 individual data files, including three large datasets from the XCEL program that are publicly available, complementing publications

from the XCEL team. In FY24, the team will further expand the user base to other DOE VTO programs, and develop online plotting and analysis tools. (Figure V.8.6)

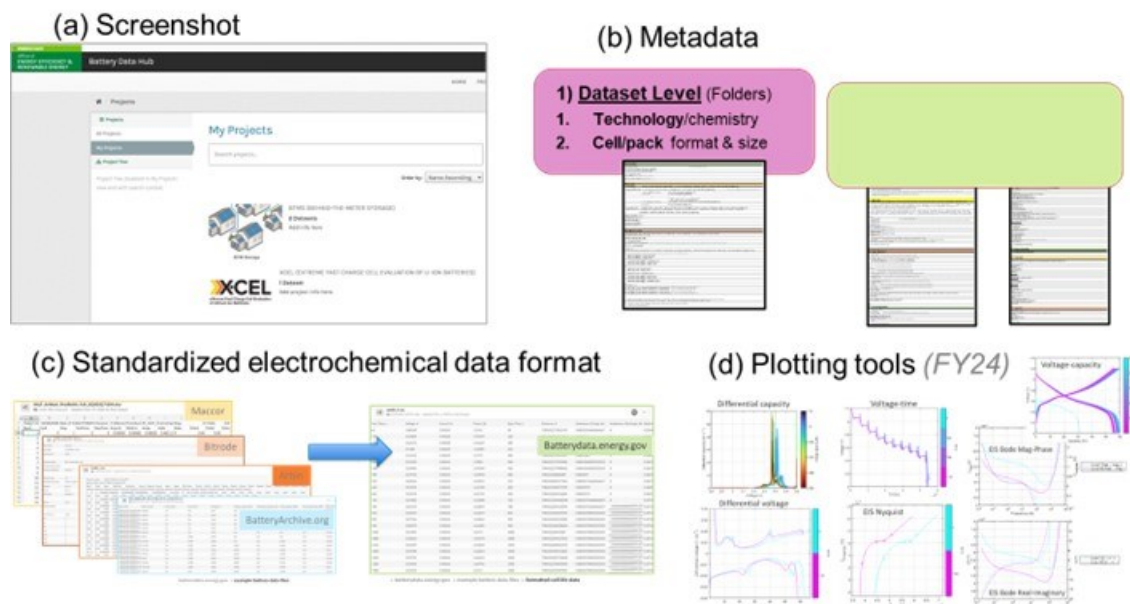


Figure V.8.6 DOE Vehicle Technologies Office Datahub, [batterydata.energy.gov](https://batterydata.energy.gov), supporting battery R&D.

### Conclusions

The physics-based machine learning (pbML) team at INL and NREL had several key advances during FY23. These included different methods that allow classification and quantification of aging modes using either adapted decision trees or the use of high-fidelity synthetic data generation coupled with deep learning. Using these methods, the ability to predict performance and failure modes to less than 5%. The team also developed PINN methods to aid in solving p2D governing equations and to identify different physical parameters needed for the equations. All of these methods were aided by understanding of appropriate data collection practices and an understanding of how CBC and reference performance tests impact cell polarization and performance.

Collecting and archiving data is also critical. Battery.data.energy.gov was further expanded in FY23 to include early plotting tools and to identify the needed tools for FY24. Common data formatting and metadata requirement were also developed that allows data collected in different location and on different testers to be standardized for easier analysis and comparison.

### Key Publications

1. P. Weddle et al, "Battery state-of-health diagnostics during fast cycling using physics-informed deep learning", *J. Power Sources*, 585, (2023)
2. A Weng, E Dufek, A Stefanopoulou, "Battery passports for promoting electric vehicle resale and repurposing" *Joule* 7 (5), 837-842 (2023)
3. K. Gering, M. Shirk, S. Kim, C. Walker, E. Dufek and Q Wang, "Battery Data Integrity and Usability: Navigating datasets and equipment limitations for efficient and accurate research into battery aging" *Frontiers in Energy Research*, 11, (2023)
4. B. Chen, Y. Police, M. Li, P. Chinnam, T. Tanim, E. Dufek, "A mathematical approach to survey electrochemical impedance spectroscopy for aging in lithium-ion batteries" *Frontiers in Energy Research*, 11 (2023)
5. B. Chen, C. Walker, S. Kim, M. Kunz, T. Tanim, E. Dufek, "Battery aging mode identification across NMC compositions and designs using machine learning" *Joule*, 12, (2022)
6. L. Ward, et al "Principles of the battery data genome", *Joule*, 10, (2022).

## References

1. K. Gering, M. Shirk, S. Kim, C. Walker, E. Dufek and Q Wang, “Battery Data Integrity and Usability: Navigating datasets and equipment limitations for efficient and accurate research into battery aging” *Frontiers in Energy Research*, 11, (2023)
2. L. Ward, et al “Principles of the battery data genome”, *Joule*, 10, (2022).
3. P. Weddle et al, “Battery state-of-health diagnostics during fast cycling using physics-informed deep learning”, *J. Power Sources*, 585, (2023)

## Acknowledgements

The activities described were a collaborative effort utilizing the capabilities of many researchers. Key contributors across the different national laboratories include Bor-Rong Chen, Andrew M. Colclasure, Paul Gasper, Kevin L. Gering, Rachel Hurst, Sangwook Kim, Tanvir R. Tanim, Cody Walker, Malik Hassanaly, Peter Weddle, Kandler Smith, Bumjun Park, and Eric Dufek. This work was also aided by collaboration with the XCEL and BTMS programs run by Venkat Srinivasan and Anthony Burrell.



## VI Small Business Innovation Research (SBIR)

### Nicolas Eidson, DOE Technology Development Manager

U.S. Department of Energy

E-mail: [Nicolas.Eidson@ee.doe.gov](mailto:Nicolas.Eidson@ee.doe.gov)

#### Project Introduction

The advanced batteries effort of the Vehicle Technologies Office supports small businesses through two focused programs: Small Business Innovation Research (SBIR) and Small Business Technology Transfer (STTR). Both programs are established by law and administered by the Small Business Administration. Grants under these programs are funded by set aside resources from all Extramural R&D budgets; 3.0% of these budgets are allocated for SBIR programs while 0.45% for STTR grants. These programs are administered for all of DOE by the SBIR Office within the Office of Science. Grants under these programs are awarded in two phases: a 6-9 month Phase I with a maximum award of \$200K and a 2 year Phase II with a maximum award of \$1.1M. Both Phase I and Phase II awards are made through a competitive solicitation and review process.

#### Objectives

Use the resources available through the Small Business Innovation Research (SBIR) and Small Business Technology Transfer (STTR) programs to conduct research and development of benefit to the advanced batteries effort within the Vehicle Technologies Office.

#### Approach

The advanced batteries team participates in this process by writing a topic which is released as part of the general DOE solicitation. Starting in FY12, the advanced batteries team decided to broaden its applicant pool by removing specific subtopics and allowing businesses to apply if their technology could help advance the state of the art by improving specific electric drive vehicle platform goals developed by the DOE with close collaboration with the United States Advanced Battery Consortium.

#### Results

##### *Phase II Awards Made in FY 2023*

Under the SBIR/STTR process, companies with Phase I awards made in FY 2022 were eligible to apply for a Phase II award in FY 2023. The following two Phase II grants were awarded:

##### ***Next Generation of High Energy Density Batteries at Low Cost (NanoHydroChem, LLC, Amherst, NY)***

NanoHydroChem, LLC is advancing the state of the art in less-expensive, longer-range lithium-based batteries for transportation based on validation and scale-up of novel silicon (Si) anode materials through the development of an innovative anode design with up to 80% Si content by mass. Si is considered as one of the promising candidates for anode materials to replace graphite in the focused effort to increase the energy density of batteries in the transportation sector. By utilizing Si waste from the solar and semiconductor industry, this technology aims to reduce industry waste and to be drop-in compatible with current battery manufacturing production lines. Phase II of the project continues the material development and electrode fabrication as well as incorporating electrolyte and formation protocol development. Additionally, the project will look at alternative methods of Si nanoparticle processing that avoids the use of silane precursor.

##### ***Domestic Novel High-Capacity Composite Anodes for the Upcycling of Spent Graphite from End-of-Life Lithium-Ion Batteries (Semplastics EHC LLC, Oviedo, FL)***

This project led by Semplastics EHC, LLC advances the state of the art in lithium-based battery recycling through novel process development. Demonstration of graphite anode upcycling with improved energy

density will ensure that less spent battery materials end up in landfills and decreases the carbon footprint of the battery supply chain. Reduction of industry reliance on foreign sources for battery-grade materials is supported through recycling/upcycling efforts. The project will accomplish graphite upcycling through transforming impure graphite material into a new polymer-derived ceramic anode materials for the next generation of lithium-based batteries. In Phase II, the project continues the optimization of the material and process and teams up with a battery recycler to incorporate realistic recycled material into the process.

### ***Phase I Awards Made in FY 2023***

Five Phase I grants were awarded in the summer of FY 2023.

#### ***Li-ion Batteries with 3-D Structured Anodes to Minimize Inactive Materials and Improve Safety (Arbor Batteries LLC, Ann Arbor, MI)***

Energy density, safety, charge time, and cost of lithium-ion batteries (LIBs) are four key areas that need to be addressed to improve batteries for widespread adoption of EVs. Through the use of laser ablation, Arbor Batteries creates 3-D structuring for thick electrodes. They aim to address all of the key research areas to produce commercially relevant anodes to provide a 15% energy density increase, 10% decrease in cell cost, and improved safety during fast charging through the controlled Li-ion intercalation without hazardous Li plating. The success of this project would allow for the improvement of current LIB chemistries already in use by the leading battery manufacturers.

#### ***Inverse Vulcanized Sulfur Cathode for Low Cost, High Energy, and Long Lasting EV Battery (Cornerstone Research Group, Inc., Miamisburg, OH)***

Sulfur based cathodes are considered one of the most promising class of cathodes to achieve both high energy density and low cost. Cornerstone Research Group's (CRG) project addresses some of the challenges of sulfur cathodes such as polysulfide dissolution by utilizing an inverse vulcanized sulfur cathode to improve cycle life and reduce costs without the need for critical materials like nickel, manganese, and cobalt. Through the use of organic crosslinkers and a sulfur polymeric backbone, CRG circumvent the low sulfur content barrier faced by many polymerized sulfur cathodes. Promising extremely high sulfur contents of 95%, >400 Wh/kg cells are proposed to hit long cycle life needed for EV applications.

#### ***Scalable Manufacturing of Multilayer Electrodes with Integrated Ceramic Separators for Improved Safety, Increased Energy Density, and Reduced Cell Assembly Cost (EnPower, Inc., Indianapolis, IN)***

The team at EnPower aim to change the way battery cells are assembled by replacing the traditional polyolefin separator with a ceramic coating that is integrated directly into the battery electrodes to provide benefits to safety, cell performance, cost, and manufacturing throughput. Phase I of this project will focus on processing and performance of both anodes and cathodes incorporating the integrated ceramic separator.

#### ***Manufacturing Earth-Abundant Layered NaMnO<sub>2</sub>-Based Sodium-Ion Cathode Materials for Low-Cost EV Batteries (Hit Nano, Inc., Princeton, NJ)***

Critical minerals (e.g. lithium, nickel, cobalt) in batteries is a growing area of concern in industry as the demand for cells grows exponentially. The Hit Nano team proposes the use of sodium-ions to replace the traditional lithium-ion chemistry. Through the use of novel waste-free, single-step aerosol processing, this project will develop a critical mineral free Na-ion battery (NIB) cathode material (NaMnO<sub>2</sub>) that will provide cost and energy density metrics that will rival lithium iron phosphate batteries that are seen as a cheaper low energy density chemistry alternative to the costly nickel and cobalt containing chemistries.

***Low Temperature Capable Catholyte for use with Garnet-Based Solid-State Electrolytes (Ion Storage Systems, Inc., Beltsville, MD)***

Ion Storage Systems has developed a garnet solid-state electrolyte for their novel Li-metal battery cell structure. Low temperature performance is critical for the EV market where low temperatures can lead to significantly reduced vehicle range and extremely long lines at charging stations. However, low temperature performance is a challenge for solid state batteries. To overcome this, the Ion Storage Systems team is developing a liquid catholyte to pair with their garnet solid-state anolyte to enable low temperature capable Li metal batteries. Their unique solution will not require external applied pressure or cell heating typical for solid-state electrolytes. They aim for >70% useable energy at -20°C at a discharge rate of C/3, sustained operation at -30°C, and cell survival at temperatures as low as -40°C.

## VII Next Generation Lithium-Ion Materials: Advanced Anodes R&D

The growing need to decarbonize the transportation sector with lower cost PEV batteries has led to the search for higher energy and lower cost materials. Silicon is an earth-abundant element that provides much higher capacity (approximately 10 times that of currently used graphite) and results in cells that are easily fast charged. However, silicon anodes undergo significant volume change (as much as 300% change per cycle), which can lead to stress buildup and particle cracking. In addition, the interface between lithiated silicon and most electrolytes appears to be unstable, leading to relatively poor calendar life.

DOE has funded both applied and fundamental research into silicon anodes for many years and the performance of those anodes have improved significantly. Just a decade ago, moderate energy density cells with majority silicon anodes achieved only 100-200 cycles. Today, some automotive sized cells (10-50 amp-hours) achieve well over 1000 cycles and over 300Wh/kg, significantly higher than most graphite-based cells. Developers and researchers are testing anodes with 100% silicon (such as Amprius and Evonix), and various blends of silicon, silicon oxide, or silicon carbide, with graphite (such as Ionblox, Farasis Energy USA, Nanograf). With the higher capacity of silicon, the anode thickness in silicon containing cells is much thinner than that in graphite cells of the same energy, leading to improved fast charge performance. While the cycle life of silicon has now improved to meet and even exceed EV targets, the calendar life remains a significant concern, driven by the lack of a stable anode/electrolyte interface.

Improving this unstable solid electrolyte interphase (SEI), is the focus of the SEISTa (Silicon Electrolyte Interface Stabilization) program. This consortium is led by researchers from the National Renewable Energy Laboratory, with participation of researchers from Argonne National Laboratory, Lawrence Berkeley National Laboratory, Oak Ridge National Laboratory, Sandia National Laboratories, and several universities.

The work in SEISTa is organized into several thrusts that are investigating: novel silicon materials; electrolyte solvents, salts, and additives; novel electrode designs; new and improved binders; advanced diagnostics and modeling; and mechanical and thermal analyses. The focus of each group and activity is to understand the root cause of the poor calendar life of Si anode containing cells and to improve it significantly.

The rest of this chapter contains detailed reports on the status of the following individual projects.

- Silicon Consortium Project (NREL, ANL, PNNL, SNL, ORNL, LBNL)
- Si-Based Li Ion Batteries with Long Cycle Life and Calendar Life (PNNL)
- Integrated Modeling and Machine Learning of Solid-Electrolyte Interface Reactions of the Si Anode (LBNL)
- Rationally Designed Lithium-Ion Batteries Towards Displacing Internal Combustion Engines (Group14 Technologies)
- Ultra-Low Volume Change Silicon-Dominant Nanocomposite Anodes for Long Calendar Life and Cycle Life (Sila Nanotechnologies)
- Solid State Li Ion Batteries Using Si Composite Anodes (Solid Power Inc.)
- Fully Fluorinated Local High Concentration Electrolytes Enabling High Energy Density Si Anodes (Stony Brook University)
- Devising mechanically compliant and chemically stable synthetic solid-electrolyte interphases on silicon using ex situ electropolymerization for long cycling Si anodes (University of Delaware)
- Rational Electrolyte Design for Li-ion Batteries with Micro-sized Si Anodes (University of Maryland, College Park)
- Free-Energy Driven Approaches to Self-Forming and Self-Terminating SEIs on Si Anodes (LBNL).

## VII.1 Silicon Consortium Project (NREL, ANL, PNNL, SNL, ORNL, LBNL)

### **Anthony K. Burrell, Principal Investigator**

National Renewable Energy Laboratory  
15013 Denver West Parkway  
Golden, CO, 80401  
E-mail: [Anthony.Burrell@nrel.gov](mailto:Anthony.Burrell@nrel.gov)

### **Brian Cunningham, DOE Technology Development Manager**

U.S. Department of Energy  
E-mail: [Brian.Cunningham@ee.doe.gov](mailto:Brian.Cunningham@ee.doe.gov)

Start Date: October 1, 2022      End Date: September 30, 2023  
Project Funding (FY23): \$7,500,000      DOE share: \$7,500,000      Non-DOE share: \$0

### **Project Introduction**

Silicon (Si) has over 10 times the theoretical capacity of graphite anodes. Problems with large volume change and short cycle life have been greatly improved using nanomaterials and other advances, such as coatings and electrolyte optimization. Poor calendar life remains a large hindrance to the commercialization of Si-containing Li-ion batteries. This year, the Silicon Consortium Project (SCP) has developed various Si materials designed for long cycle and calendar life and performed calendar aging tests on these materials. Because the focus of the SCP is understanding and mitigating calendar life issues, our FY23 Q1 milestone was, “The leading silicon electrodes that were identified in FY22 will be placed upon open circuit voltage (OCV)/reference performance test (RPT) tests to establish calendar life baseline in preparation for the Q3 milestones.” For this milestone, we identified several promising Si materials developed in the SCP, fabricated pouch cells, and tested them with an OCV/RPT test protocol.

Understanding calendar life requires both capturing data and making projections based on the data. As a time and resource consuming activity, early prediction of life is advantageous as it allows researchers to rapidly iterate and identify both new scientific solutions and critical failure modes.

### **Objectives**

#### ***Development of Calendar Life Baseline***

A prime objective of the silicon consortium project was to start testing cells with the most promising Si materials identified in FY22 to assess calendar life performance in long-term single-layer pouch cell tests. This also enabled a baseline for promising Si materials that could then serve as an initial data point to compare to future improved versions of these materials. All this data was intended to be fed into machine learning algorithms such that models could be developed that would help determine the time required to make calendar life predictions.

#### ***Calendar Life Projections***

Determining the length of time needed to assess calendar life of new materials and batteries is often time consuming and requires significant resources. The assessment also typically takes place late in the research timeline, which can lead to slowed implementation of technological solutions. The objective of the Q3 milestone was to determine the time needed to assess calendar life using existing pre-commercial cells and methods. Upon assessment, methods have been proposed to reduce the time needed and to merge with R&D level cells developed as part of the Silicon Consortium Project.

## Approach

### *Development of Calendar Life Baseline*

Electrodes tested for this project included those based on milled Si, milled B-doped Si, plasma-enhanced chemical vapor deposition (PECVD) Si coated with polyethylene oxide (Si@PEO), PECVD B-doped Si, and PECVD Si coated with pitch carbon. Electrodes comprised of these materials were fabricated into single-layer pouch cells in triplicate (68 total) using a consistent process to enable direct calendar life materials comparisons. These cells were tested with the intention that they would be analyzed as part of the calendar life projections. Cells were fabricated with both  $\text{LiFePO}_4$  (LFP) and  $\text{LiNi}_{0.8}\text{Co}_{0.1}\text{Mn}_{0.1}\text{O}_2$  (NMC811) cathodes to ensure that the impact of the cathode could also be understood from the data. These cells were then either continuously cycled or tested with the OCV/RPT calendar aging procedure. The OCV/RPT protocol that the team adopted was designed to closely mimic the standard USABC calendar testing protocol and consisted of continuous aging under OCV conditions with intermittent RPTs consisting of 3 cycles to check performance as well as pulses to evaluate impedance. Cells were generally tested with GenF3 electrolyte (1.2 M  $\text{LiPF}_6$  in 3:7 ethylene carbonate:dimethyl carbonate with 3 wt% fluoroethylene carbonate). In addition, some cells were also tested with an alternative electrolyte (electrolyte x) that is under investigation in the Electrolyte Thrust. The data was analyzed to separate the capacity loss and impedance rise related to cycling from the total capacity loss during calendar aging such that the impacts of calendar aging could be isolated. These cells were not prelithiated.

In addition to the set of 68 pouch cells described above with varied materials, another set of 30 consistently prepared cells was fabricated and tested using milled Si anodes, NMC811 cathodes, and GenF3 electrolyte. Instead of comparing various Si materials, this second set of cells included varied temperatures (30, 40, and 50°C) and states of charge (25, 50, 75, and 100%). Because the Q1 milestone was focused on determining and comparing calendar life of the most promising Si materials, the first set of data comparing materials is the focus of this report section. The second set of cells utilizing varied temperatures and states of charge will be discussed in more detail in the calendar life section.

### *Calendar Life Projections*

The ability to use different datasets, including prior testing data and synthetic aging data, allows new methods for life prediction. This work looks to identify how much data is needed for traditional analysis schemes and then improve upon that using advanced analysis tools, including machine learning (ML) and deep learning (DL) techniques. Over the course of FY23, the work has transferred learned knowledge from completed calendar tests captured as part of the Idaho National Laboratories (INL) Life and Performance Testing project to start the process of prediction of ongoing calendar life tests captured as part of the Silicon Consortium Project. To aid advance predictions, DL coupled with sigmoidal rate expression (SRE) based synthetic data and transfer learning have been used.

## Results

### *Development of Calendar Life Baseline*

Significant work in the early stages of FY23 developed the capabilities necessary to conduct these studies. Members of the Electrochemical Thrust worked extensively to devise and develop Tier 1, 2, and 3 protocols suitable for the various stages of development and testing. In addition, equipment and hardware for testing the single-layer pouch cells were developed, prototyped, and installed. As shown in Figure VII.1.1, we constructed custom pressure fixtures that allow a variable pressure to be applied to cells based on the force of the springs. We chose 4 psi as a standard pressure, consistent with fixtures at CAMP. Calendar life testing was accomplished in Associated Environmental Systems (AES) model SD-508-ATP-B atmospheric chambers at a fixed temperature of 30°C.



**Figure VII.1.1** Single layer pouch cell fixtures and a temperature-controlled chamber enables calendar aging studies for various Si materials under controlled conditions.

In general, Si materials tested all exhibited similar capacity fade within the error of the measurement except for PECVD B:Si (Figure VII.1.2). Still, two trends were beginning to emerge from these data. The capacity fade was generally faster in cells with LFP relative to NMC cathodes when paired against PEVD Si anodes, which was attributed to a higher area-specific impedance (ASI) gain in NMC811 than in LFP. Second, the cathode-dominated ASI gain was lower in PECVD Si compared with milled Si. Additional data is needed to assess and understand these trends more fully.

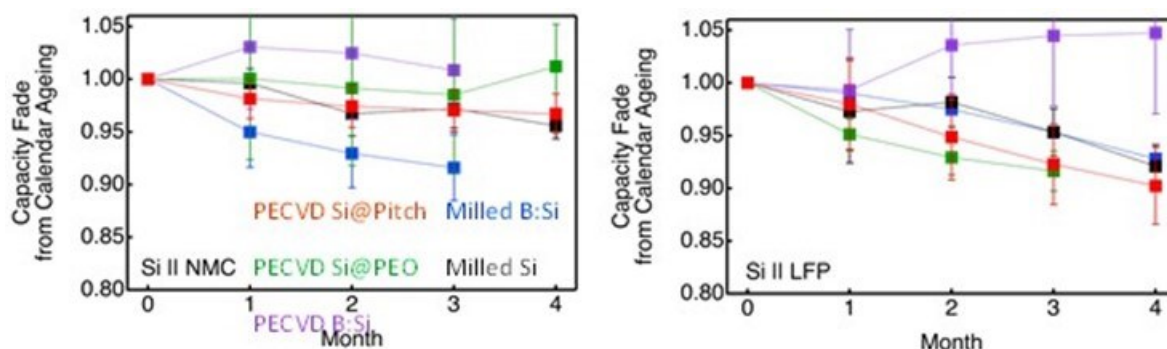


**Figure VII.1.2** Capacity fade associated with calendar aging for various Si materials paired with NMC cathodes (left) and LFP cathodes (right) with GenF3 electrolyte.

The raw data was analyzed to understand the relative contributions from cycling and calendar aging responsible for capacity fade during calendar aging tests, as shown in Figure VII.1.3. These analyses show that cycling generally impacts capacity fade more than calendar aging. Trends from these deconvoluted data also were beginning to appear. PECVD B-doped Si exhibited the best capacity retention of all the Si materials tested. Aside from PECVD B:Si cells, the contribution to capacity fade solely from calendar life (grey portions of bar plot) are similar for both  $\sim 150$  nm milled Si and  $\sim 6$  nm PECVD Si, suggesting that aging behavior is more complicated than particle surface area alone. Cells filled with a new electrolyte formulation ('electrolyte x') exhibited lower capacity fade than those containing GenF3 electrolyte, which seems to indicate that electrolyte modification is a promising strategy for slowing calendar aging effects.

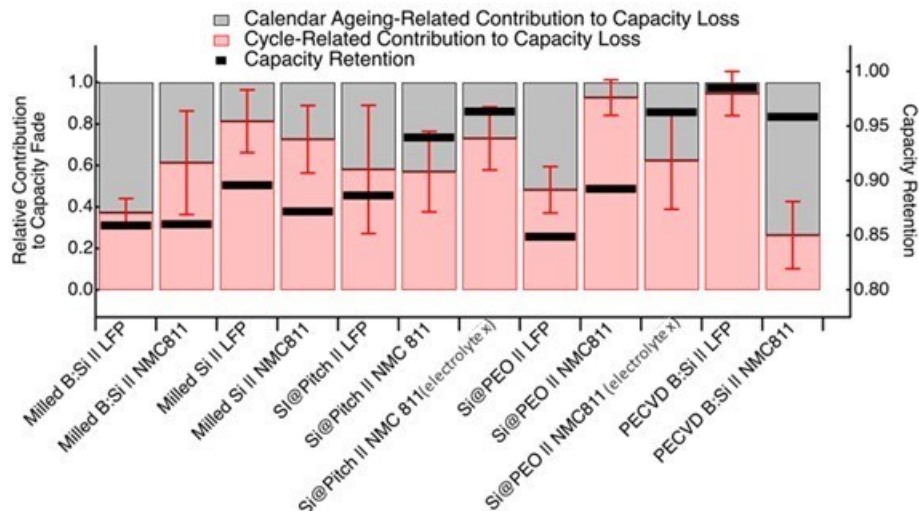


Figure VII.1.3 Deconvolution of capacity fade due to calendar aging and cycling.

### Calendar Life Projections

Prior to the development of new methods for calendar life prediction for cells and advances developed in the Silicon Consortium Project, it was necessary to first understand what the state-of-the-art for existing Si-containing cell data is and how much data is needed for current prediction methods. For data acquisition, rather than starting new experiments, data from prior Life & Performance testing efforts was first anonymized at INL and then the blinded data was analyzed by a separate group of researchers. This was done to protect the information related to the test data and to push toward more broadly transferable data analysis methods. For the analysis, cells with at least 15% Si content in the negative electrode were anonymized. To also aid in the consistency of data, only cells with some variant of  $\text{LiNi}_{1-x-y}\text{Mn}_x\text{Co}_y\text{O}_2$  as the positive electrode.

Following anonymization, different fitting techniques, including the use of sigmoidal rate expressions (SREs), were employed to determine the amount of data that was necessary to make a life prediction with high confidence. Figure VII.1.4 shows an example of one of the fitting results for a set of Si-containing cells that were calendar aged at 30°C, 40°C, and 50°C. For clarity, only some of the cells in the pack are shown. The cells all demonstrate a multi-process fade mechanism that was fitted using an SRE. Using the two-mechanism fitting, it was possible to predict life with more than 95% confidence and an  $R^2$  value in excel of 0.99 using 12–15 months of data for the different cells analyzed. This is taken as the minimum set of information that is needed to make predictions using standard testing and regression-based analysis methods.



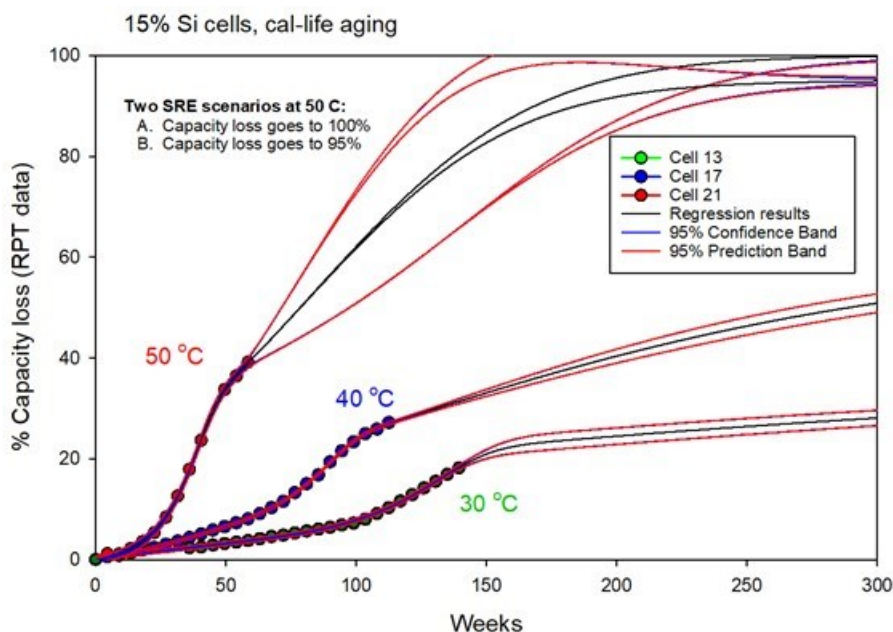


**Figure VII.1.4 SRE-based regression of Si-containing cells at three different aging temperatures. Across the different anonymized cells analysis was limited to those with at least 15% Si content in the negative electrode.**

The work extended analysis to understand the nature of the primary fade mechanisms. In the case of the cells, it was found that while loss of lithium inventory (LLI) was a key driver for the primary observable losses during early aging, loss of active material (LAM) dominated the fade later in life as the second mechanism with onset occurring between months 12 and 30 as influenced by temperature and cell set. Early efforts to reduce the time needed to make calendar life predictions have relied on the use of a DL framework. Early results using anonymized data have shown promise at reducing the time needed for a prediction to 8 months. The accuracy has been enhanced, achieving an absolute error of  $1.86 \pm 1.24$  at 30°C,  $3.73 \pm 1.55\%$  at 40°C, and  $1.78 \pm 1.40\%$  at 50°C at the end of the calendar life (ranging from 20 to 32 months). While promising, further work is needed to understand the transferability of the method to cells developed as part of the SCP.

## Conclusions

### Development of Calendar Life Baseline

Calendar aging of silicon-based anodes against both NMC811 and LFP cathodes shows that losses associated with cycling contribute more significantly to capacity fade than those from calendar aging. Power loss results primarily from impedance rise and is greater for NMC811 than LFP cathodes, suggesting that NMC811 cathodes contribute significantly to overall cell aging. While B-doped Si exhibited the most promising cycle and calendar life, other materials exhibited similar overall capacity fade within the error bars of the measurement over the 3–4 months of collected and processed data. These results could reflect the fact that all experiments conducted used non-prelithiated cells that could significantly influence the degree of Li-ion inventory loss and, therefore, the potentials experienced by anodes and cathodes in each cell format. Another key conclusion is that new electrolyte formulations are a promising strategy for reducing capacity fade and impedance rise.

### Calendar Life Projections

While completing the Q3 milestone for the SCP, we found that, using standard testing data and regression methods, 12–15 months of data is needed to make a valid calendar life prediction. The analysis of the cells identified LLI and LAM as the key drivers of fade, with LAM being responsible for failure occurring later in the aging process. Early use of DL on the same anonymized datasets suggests time can be reduced to 8 months,

but more work is still needed to reduce the prediction time, and the efforts need to be confirmed using SCP calendar datasets. Work in FY24 will focus on the transfer of methods and a further reduction in time to less than 15 months needed for robust prediction of calendar life.

## VII.2 Si-Based Li Ion Batteries with Long Cycle Life and Calendar Life (PNNL)

### **Ji-Guang Zhang, Principal Investigator**

Pacific Northwest National Laboratory  
902 Battelle Boulevard  
Richland, WA 99354  
E-mail: [jiguang.zhang@pnnl.gov](mailto:jiguang.zhang@pnnl.gov)

### **Ran Yi, Co-Principal Investigator**

Pacific Northwest National Laboratory  
902 Battelle Boulevard  
Richland, WA 99354  
E-mail: [ran.yi@pnnl.gov](mailto:ran.yi@pnnl.gov)

### **Carine Steinway, DOE Technology Development Manager**

Vehicle Technologies Office  
U.S. Department of Energy  
Phone: (202) 815-0211  
E-mail: [Carine.Steinway@ee.doe.gov](mailto:Carine.Steinway@ee.doe.gov)

### **Nicolas Eidson, DOE Technology Development Manager**

Vehicle Technologies Office  
U.S. Department of Energy  
Phone: (202) 923-0970  
E-mail: [Nicolas.Eidson@ee.doe.gov](mailto:Nicolas.Eidson@ee.doe.gov)

### **Thomas Do, DOE Technology Development Manager**

Vehicle Technologies Office  
U.S. Department of Energy  
Phone: (240) 941-4651  
E-mail: [Thomas.Do@ee.doe.gov](mailto:Thomas.Do@ee.doe.gov)

Start Date: October 1, 2022

End Date: September 30, 2023

Project Funding (FY23): \$400,000

DOE share: \$400,000

Non-DOE share: \$0

### **Project Introduction**

Silicon (Si) has been regarded as one of the most promising anode materials due to its high theoretical specific capacity (4,200 mAh/g) which is 10 times of graphite anode. Although significant progresses have been made on the cycle life of Si-based Li-ion batteries (Si-LIBs), their calendar-life is still far less than those required for electrical vehicle (EV) applications. The main barriers for the practical usage of Si anode include: 1) Severe volume change (~300%) of Si during repeated lithiation and delithiation, 2) the intrinsic low electronic conductivity, and 3) the unstable and reactive solid electrolyte interphases (SEI) layer. These intrinsic problems need to be solved to accelerate large-scale application of Si-LIBs for EV applications.

### **Objectives**

In this project, we will investigate the mechanisms behind the limited calendar life and cycle life of Si-based LIBs to accelerate the large-scale application of Si-based LIBs by 1) identifying the main factors affecting the calendar life of Si-based LIBs and 2) developing new electrolytes and electrode coatings to stabilize active materials/electrolyte interphase.

## Approach

- Investigate the mechanisms limiting the calendar life of Si-based LIBs through a systematic design of experiment to focus on one source of failure in every experiment so the main failure mechanisms can be identified. The effect of crosstalk between anode and cathode on the performance of Si-LIBs will also be investigated when different electrolytes were used.
- Using post-mortem analysis to analyze the morphology and composition of interphase layers (both solid electrolyte interphase (SEI) layer on Si anode and cathode electrolyte interphase (CEI) layer on NMC cathode. The structure and composition evolution of both cathode and anode after the calendar life test will also be investigated.
- Develop the localized high-concentration electrolytes (LHCEs) to improve the interphase properties of the Si anode and NMC cathode, especially at elevated temperatures. Demonstrate that the tailored LHCE can improve the calendar life of Si-based Li-ion batteries (LIBs) in single-layer pouch (SLP) cells.

## Results

### 1. Investigate on the Mechanisms Behind the Limited Calendar Life of Si-based LIBs

Fluoroethylene carbonate (FEC) and vinyl carbonate (VC) are frequently used as “additives” to improve the SEI/CEI properties and extend the cycle life of Si-LIBs. However, various acid species could be produced during the formation of the SEI/CEI layers. To investigate the calendar life of Si-LIBs, accelerate tests at elevated temperature (40°C, 47.5°C, and 55°C) are typically used. HF generated during the cycling/calendar test may damage SEI/CEI layers and leads to rapid impedance increase of Si-LIBs and shorten their calendar life. In FY22, we found that Si/C composite and even graphite anodes stored in FEC-containing carbonate electrolytes exhibited rapid impedance-growth at 55 °C while no impedance growth in FEC-free carbonate electrolytes was observed. In FY23, the fundamental mechanism behind the rapid increase in the impedance of Si-LIBs was systematically investigated.

First, we investigated whether the impedance growth on electrodes (both anode and cathodes) is dominated by the degradation of the bulk electrolyte stored at elevated temperature (55 °C) or by the poor electrode/electrolyte interphases (SEI/CEI layers) formed in FEC containing electrolyte at room temperature (25 °C) during formation or pre-conditioning process which are not stable during storage at elevated temperature (55 °C). To investigate the stability of typical electrolyte used for Si-LIBs, Si-baseline electrolyte (E-baseline : 1M LiPF<sub>6</sub> in EC-DEC-EMC (1:1:1 by vol) + 1 wt% VC + 5 wt% FEC) was stored at 55 °C for 8 days and then tested in Li||NMC622 half-cells as shown in Figure VII.2.1. The stored electrolyte shows no color change after storage at 55 °C for eight-days. More importantly, there is no noticeable change to the electrolyte’s ionic conductivity as shown Figure VII.2.1a. After storage test at 55 °C, the stored E-baseline electrolyte was used to test the electrochemical performance of Li||NMC622 coin-cells at room temperature (25 °C). The 1<sup>st</sup> cycle voltage profiles and the cycling performance of the cells are shown in Figure VII.2.1b and 1c, respectively. As a comparison, the performance of Li||NMC622 cells with fresh E-baseline electrolyte (without 55 °C storage) was also plotted in Figure VII.2.1b and 1c. Figure VII.2.1b shows that the voltage profiles of the cells using fresh and stored E-baseline electrolyte are almost identical, indicating the storage at 55 °C for 8 days does not lead to significant changes to the bulk properties of the electrolyte. Therefore, the rapid increase in the impedance of Si||NMC622 cells during storage at elevated temperature (55 °C for 8 days) observed in the previous works can be attributed to the evolution of cathode/electrolyte interphase properties instead of degradation of bulk electrolyte (E-baseline).

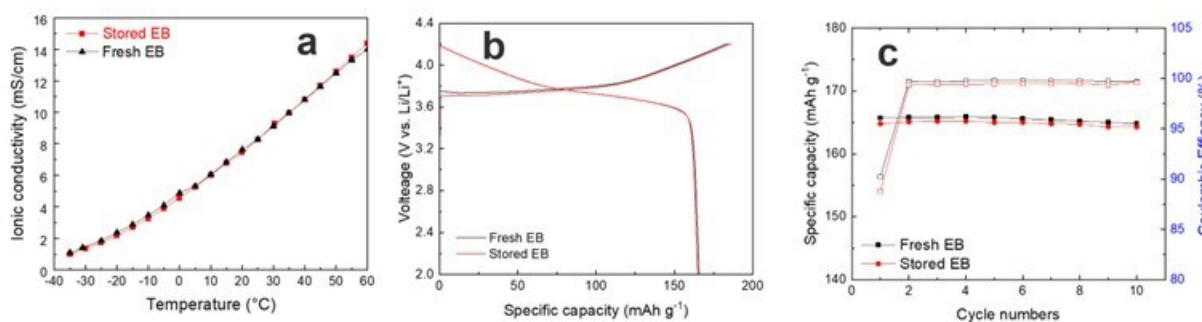


**Figure VII.2.1** (a) Ionic conductivity of E-baseline electrolyte before and after 55 °C storage for eight-days. (b) 1<sup>st</sup> cycle voltage profiles and (c) cycling performance of Li||NMC622 coin-cells in fresh and stored E-baseline electrolyte tested at room temperature.

To reveal root source affecting the calendar life of Si-based LIBs, the electrodes from the cycled Si||NMC622 coin-cells were retrieved and reassembled for storage test using the same E-baseline electrolyte which contain FEC and VC additives. The cells were preconditioned for ten cycles between 2.0 to 4.1 V at room temperature to form the SEI/CEI layers. The Si and NMC622 electrodes were then retrieved from the cycled cells at 100% state of charge (SOC) and reassembled into symmetric Si||Si and NMC622||NMC622 coin cells to eliminate the effect of the crosstalk between anode and cathode during storage at 55 °C for eight-days. To understand the effect of crosstalk between Si anode and NMC622 cathode during the full cell test, Li||Si and Li||NMC622 half-cells were also prepared using E-baseline electrolyte and tested between 2.0 to 4.2 V at room temperature for ten cycles. Si and NMC622 electrodes retrieved from pre-conditioned (ten cycles) half-cells were then reassembled into symmetric Si||Si and NMC622||NMC622 coin-cells for storage test. Because Si has a voltage of ~0.1 V vs. Li/Li<sup>+</sup> at the charged condition, NMC622 cathode retrieved from Si||NMC622 full-cell is ~ 4.2 V vs. Li/Li<sup>+</sup>, which is the same as the those of NMC622 cathode retrieved from Li||NMC622 half-cells fully charged at 4.2V. In these carefully design experiments, both NMC622 cathodes are pre-conditioned at 4.2 V vs. Li/Li<sup>+</sup> so the results of their further storage tests are more comparable. These design of experiments are illustrated in Figure VII.2.2.

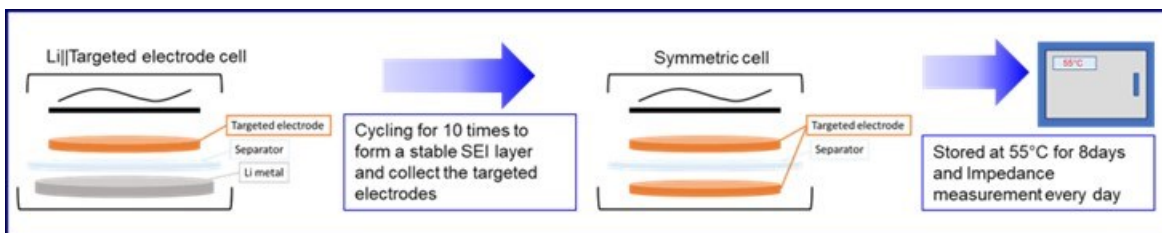


**Figure VII.2.2** Experiment design to check the crosstalk during the calendar aging.

The impedance evolution of Si||Si and NMC622||NMC622 cells using E-baseline electrolyte were recorded during 55 °C storage for eight-days as shown in Figure VII.2.3a and Figure VII.2.3b. No matter whether the Si anode was retrieved from Li||Si half-cell or from Si||NMC622 full-cell, a clear increase in impedance growth of Si||Si symmetric cells is observed in Figure VII.2.3a. The symmetric cell with Si anode retrieved from pre-conditioned Si||NMC622 full-cell shows a slightly faster impedance increase compared to those retrieved from pre-conditioned Li||Si half-cell, indicating a minimal effect of crosstalk on the Si anode during pre-conditioning of Si||NMC622 full-cells. On the other hand, nearly no impedance increase was observed in NMC622||NMC622 symmetric cells when the NMC622 cathode was retrieved from cycled Li||NMC622 half-cell as shown in Figure VII.2.3b. In contrast, a rapid impedance increase was observed in NMC622||NMC622 symmetric cells when the NMC622 cathode was retrieved from pre-conditioned Si||NMC622 full-cell as shown in Figure VII.2.3b, indicating that crosstalk between Si anode and NMC622 cathode during pre-conditioning process leads to poor quality of CEI layer which can be easily damaged during storage at 55 °C. These results clearly indicate that the rapid impedance increase in Si||NMC622 full-cells with E-baseline

electrolyte (which contains FEC) during storage at elevated temperature is mainly due to the pre-condition of NMC622 cathode when it was cycled against Si anode (Figure VII.2.3b) and the formation of a poor CEI layer, although the degradation of anode also plays a secondary role.

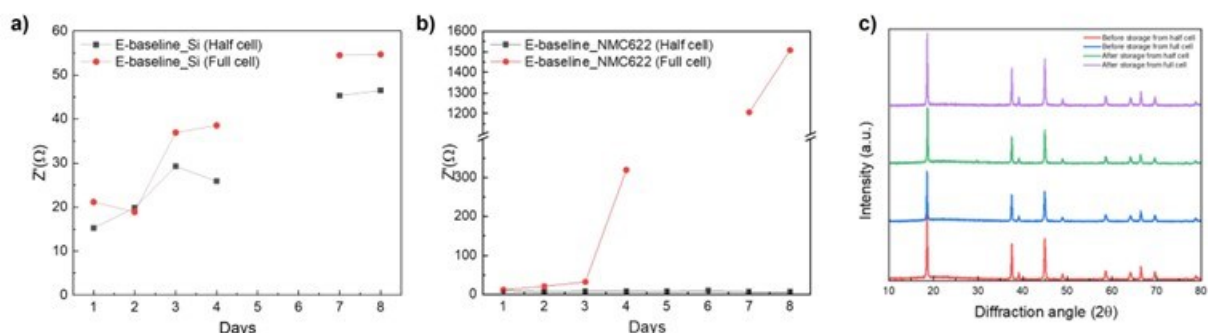


**Figure VII.2.3 Impedance growth of (a) Si||Si and (b) NMC622||NMC622 symmetric cells with FEC-containing E-baseline electrolyte during storage at 55 °C. The electrodes were retrieved from pre-conditioned half-cell or full-cells. (c) X-ray spectra of pre-conditioned NMC622 cathodes before and after storage at 55 °C.**

To further identify the source of degradation in the cathode, the structure of retrieved NMC622 cathode at different stages of storage was investigated by X-ray diffraction spectroscopy (XRD) as shown in Figure VII.2.3c. It is known that FEC and VC-containing electrolytes may generate HF during storage at elevated temperatures. HF generated in this process can migrate to the cathode side and attack the surface of the NMC622 particles leading to transition metal ions dissolution and phase transformation. Phase transformation from layered to rock-salt structure is promoted by cation mixing between  $\text{Li}^+$  and  $\text{Ni}^{2+}$  in the Li layer because  $\text{Li}^+$  (0.76 Å) and  $\text{Ni}^{2+}$  (0.69 Å) have a similar ionic radius. The rock-salt layer blocks the  $\text{Li}^+$  migration and causes inferior electrochemical performance. Table VII.2.1 summarizes the intensity ratios of I(003)/I(104) peaks of XRD spectra shown in Figure VII.2.3c taken before and after storage test. Smaller intensity ratios of I(003)/I(104) indicate a higher degree of cation mixing. Figure VII.2.3c and Table VII.2.1 indicate that the NMC622 cathode exhibits more cation mixing after storage at 55°C for eight-days than before storage. It also shows that the NMC622 cathode retrieved from the full-cell exhibits more cation mixing than those retrieved from the half-cell. These results clearly show the structure degradation of NMC622 during high-temperature storage. The crosstalk between Si anode and NMC622 during pre-conditioning of Si||NMC622 full-cells also enhanced this degradation.

**Table VII.2.1 Intensity Ratios of I(003)/I(104) from NMC622 Cathode Tested in E-baseline Electrolyte.**

	I(003)/I(104)
Before storage (After 10cycles) from half cell	1.82
Before storage (After 10cycles) from full cell	1.72
After storage (After 10cycles) from half cell	1.72
After storage (After 10cycles) from full cell	1.58

To reduce impedance increase during storage of Si||NMC622 cells at elevated temperature, a localized high concentration electrolyte (E-10: LiFSI-2.8EP-0.2EC-1TTE (in molar) with 1 wt%  $\text{LiPO}_2\text{F}_2$ ) with no FEC/VC additives has been developed to form a stable SEI/CEI layers and minimize structure damage in NMC622 particles. As a comparison to E-baseline electrolyte, the similar experiments shown in Figure VII.2.2 have been performed except replacing FEC containing E-baseline electrolyte by FEC-free electrolyte E-10. In this

case, a much slower increase in the impedance of Si||Si symmetric cells (see Figure VII.2.4a) was observed during the storage as compared with those of Figure VII.2.3a. More importantly, no significant increase in the impedance of NMC622||NMC622 symmetric cells was observed during the storage at 55°C as shown in Figure VII.2.4b. The minimal impedance-increase during storage at elevated temperatures indicates that SEI and CEI layers formed in FEC-free electrolyte E-10 during pre-conditioning process are much more stable than those formed in FEC-containing E-baseline electrolytes. In addition, much less HF is generated during storage at elevated temperature (55 °C) when FEC-free electrolyte E-10 was used. In addition, the differences in impedance evolutions of NMC622 symmetric cells with the cathodes retrieved from full-cell and half-cell is also very small. This is a clear indication that crosstalk between Si anode and NMC622 cathode was largely suppressed during the pre-conditioning process. XRD spectra of NMC622 cathodes retrieved from pre-conditioned full cells with E-10 electrode before and after storage at 55°C are shown in Figure VII.2.4c. Intensity ratios of I(003)/I(104) of NMC622 tested in E-10 electrolyte are summarized in Table VII.2.2. Although the intensity ratio of I(003)/I(104) decreased from 1.83 to 1.74 after storage (a 5% decrease), the cation mixing observed in NMC622 cathode pre-conditioned in E-10 electrolyte is not as significant as those pre-conditioned in E-baseline electrolyte where the intensity ratio of I(003)/I(104) decreased from 1.72 to 1.58 after storage (a 9% decrease). This is consistent with the results that the coin-cells with FEC-free electrolyte E-10 exhibit a much smaller impedance increase and structure degradation during storage at elevated temperatures.

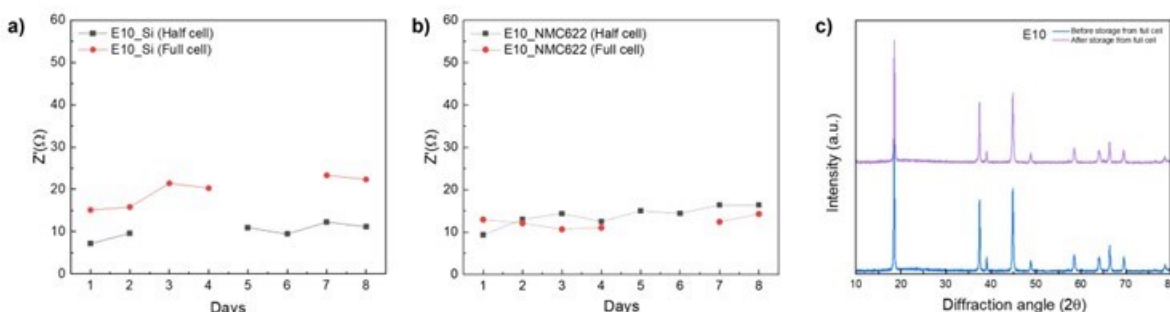


Figure VII.2.4 Impedance growth of a) Si || Si and b) NMC622 || NMC622 symmetric cells with FEC-free E-10 electrolyte during storage at 55 °C with electrodes retrieved from pre-conditioned half-cell or full cell. c) X-ray spectra of NMC622 cathodes before and after storage at 55 °C.

Table VII.2.2 Intensity Ratios of I(003)/I(104) from NMC622 Cathode Tested in E-10 Electrolyte

	I <sub>(003)</sub> /I <sub>(104)</sub>
Before storage (After 10cycles) from full cell	1.83
After storage (After 10cycles) from full cell	1.74

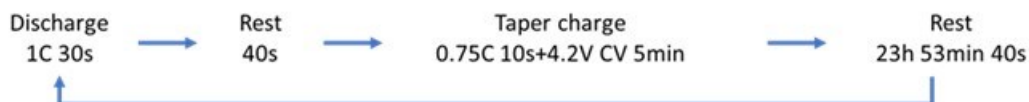
## 2. Investigate on the Calendar Life of the Si-based LIBs Using Single Layer Pouch Cells

It is well-known that the calendar life of Si-based LIBs is directly related to the increase in the cell impedance. To reduce the time required for calendar life test (from 8-10 years to less than one year), accelerated test at elevated temperature has been widely used. To further elucidate the effect of E-10 on the calendar life of the Si-LIBs in more realistic conditions, impedance evolution of Si-based LIBs at different temperatures have been tested in single layer pouch (SLP) cells. These SLP cells consist of micron-sized porous Si anode developed in PNNL, NMC622 cathode (Targray cathode powder was obtained from ANL), and FEC-free E-10 electrolyte. Si||NMC622 SLP cell preparation parameters are shown in Table VII.2.3.

**Table VII.2.3 Preparation Parameter of Single Layer Pouch Cells and their Testing Procedures.**

SLP-Cell voltage (2.0V-4.2V)	
SLP-Cell size (4.0*7.0 cm)	
Cell capacity	~63.5 mAh
Cathode	NMC 622 (Targray from ANL)
Cathode loading	2.0 mAh/cm <sup>2</sup>
PNNL anode loading	3.5 mAh/cm <sup>2</sup> (N/P ratio=1.75)
Anode binder	PI
Anode specific capacity	1000 mAh/g
Preolithiated	No
Anode formulation	Si/Gr/SP/PI=80/9/1/10
Electrolyte	LHCE E10
	LiFSI-2.8EP-0.2EC-1TTE+1 wt% LiPO <sub>2</sub> F <sub>2</sub>

The impedances of SLP cells were investigated using USABC protocol used in the determination of the calendar life of LIBs. During the formation cycle, the cells were charged at 0.1C, CVC (constant voltage charge) to C/40, and then discharged at 0.1C to 2V to determine the initial capacity of the cells. Then the cells were charged at C/3 to 4.2 V, CVC to C/40 (100% SOC) and stored at environmental chambers at 25°C, 40°C, 47.5°C, and 55°C, respectively. The cell impedance ( $R_{dc}$ ) was measured daily based on its voltage drop at a given current pulse (1C for 30s) as illustrated in Figure VII.2.5. A taper charge was used to boost the voltage of the cells to their fully charged condition after impedance measurement. The capacity of the SLP cells is also measured every 30 days after 90<sup>th</sup> day at the storage temperature to check its capacity retention by discharging the cells at 0.1C to 2 V. The combination of the impedance increase, and capacity loss during storage provides the required information on the calendar life of batteries.

**Figure VII.2.5 Calendar life test protocol**

In our previous investigation on the calendar life of Si-based LIBs using FEC-containing electrolyte (E-baseline), it was found that the impedances (represented by direct current resistance  $R_{dc}$ ) of the cells increase with increasing temperature and storage time as shown in Figure VII.2.6a (the spikes in the impedance curve are related to the capacity checkpoints).  $R_{dc}$  increases slowly with time when storage temperature is below 40 °C, but it increases dramatically at higher temperatures. The discharge resistance increases by ~22% at 30 °C and ~200% at 55 °C after 95 days. This result suggests that high temperature has a pronounced impact on cell properties. During the calendar life test, the impedance of typical LIBs using E-baseline electrolyte usually increases rapidly with increasing temperature. In direct contrast with the case when a FEC-containing



electrolyte E-baseline is used, the impedance of the SLP cells with FEC-free electrolyte (E-10) stored at elevated temperatures (40°C, 47.5°C, and 55°C) is even lower than those stored at room temperatures (25°C) in ~ 90 days as shown in Figure VII.2.6b. The calendar-life test was continued for up to 180 days to investigate the long-term impedance change of SLP cells in the FEC-free electrolyte E-10. DC impedances of the cells were continuously measured using daily pulse charge (discharge at 1C rate for 30 s, rest for 40s, then taper charge at 0.75C for 10 s and constant voltage charge at 4.2V for 5 min). In contrast to the case of FEC-containing electrolyte, Si||NMC622 single layer pouch cells with FEC-free E-10 electrolyte exhibit smaller impedance increase at 40°C and 47.5°C as compared to those observed at 25°C during long-term storage (180 days). Although the impedance of the cell stored at 55°C exhibits a similar behavior as those stored at 40°C and 47.5°C in the first ~90 days, it starts to increase more quickly after ~ 90 days.

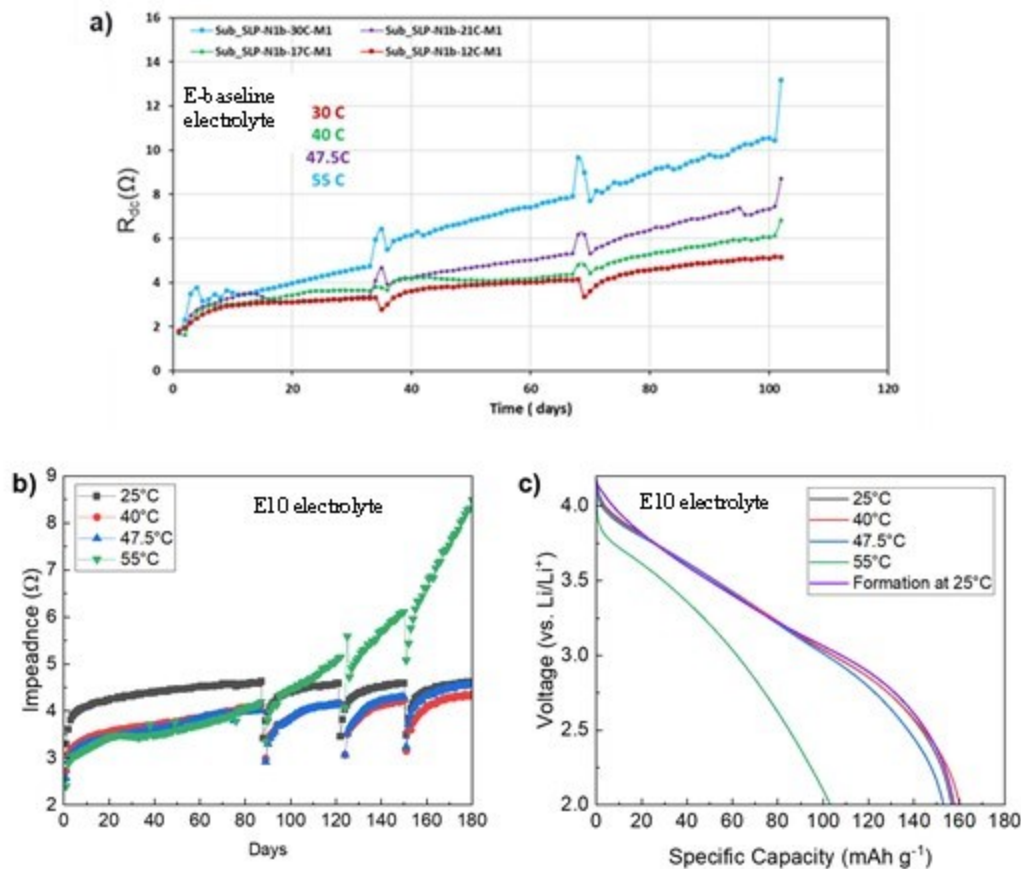


Figure VII.2.6 (a) Impedance evolution of SLP cells with FEC-containing electrolyte (E-baseline) during the calendar life test at various temperatures. (b) Impedance growth of SLP cells with FEC-free electrolyte (E-10) during the calendar life test at various temperatures, (c) Discharge capacity and voltage profiles of the SLP cells with E-10 electrolyte on the 180th day of calendar aging at various temperatures. The initial voltage profile during the formation cycle at 25°C was also plotted as a reference.

In addition to monitoring the impedance changes of the cells, an additional step has been added to the testing procedure to check the capacity of the cells every 30 days (from 90 days to 180 days) as shown in Figure VII.2.6c and Table VII.2.4. The discharge capacity and voltage profiles of SLP cells stored at the 90<sup>th</sup> day, 150<sup>th</sup> day, and 180<sup>th</sup> of the calendar aging (measured at a current density of  $C/3$ ) are shown in Figure VII.2.6c and Table VIII.2.4, respectively. After stored for 180 days, the discharge capacities of the samples are  $156.6 \text{ mAh g}^{-1}$ ,  $160.3 \text{ mAh g}^{-1}$ ,  $153.1 \text{ mAh g}^{-1}$ , and  $103.1 \text{ mAh g}^{-1}$  for the samples stored at 25°C, 40°C, 47.5°C, 55°C, respectively. Compared to the initial capacity ( $165.9 \text{ mAh g}^{-1}$ ) at 25°C, the capacity retention after 180-day storage is 94.3%, 96.6%, 92.3%, and 62.1% for the cells stored at 25°C, 40°C, 47.5°C, 55°C, respectively.

These results revealed that an FEC-free electrolyte (E-10) could largely minimize the impedance increase and extend the calendar life of Si-based LIBs, especially when the samples are stored at a temperature of 47.5°C or less. The performance of the cells at a temperature of more than 47.5°C still need to be further improved.

**Table VII.2.4 Discharge Capacities during Calendar Life Test at Various Temperatures.**

	Discharge capacity on 90days (mAhg <sup>-1</sup> )	Discharge capacity on 120days (mAhg <sup>-1</sup> )	Discharge capacity on 150days (mAhg <sup>-1</sup> )	Discharge capacity on 180days (mAhg <sup>-1</sup> )
25 °C	160.7	158.7	157.3	156.6
45 °C	165.9	164.1	162.4	160.3
47.5 °C	168.0	163.7	159.2	153.1
55 °C	157.6	143.4	128.9	103.1

### Conclusions

- The storage of the FEC-containing electrolyte itself does not affect the ionic conductivity of the bulk electrolyte. The instability of the SEI and CEI layers formed on electrode/electrolyte interphases during pre-conditioning process and storage are mainly responsible for the poor calendar life of Si-based LIBs.
- The FEC-free electrolyte E-10 can form a stable SEI and CEI layers on electrode/electrolyte interphase during pre-conditioning process and avoid crosstalk that causes the structural degradation of NMC622 cathode during the cycling and storage, therefore improving the calendar life of Si-based LIBs.
- The impedance increase in single layer pouch cells (Si||NMC622) with FEC-free electrolyte E-10 is significantly suppressed during calendar storage test. The cell impedance stored at temperatures of 47.5°C or less is even lower than those stored at room temperature and there is no significant capacity loss after 180-day storage at these temperatures.

### Key Publications

1. “Electrolytes for lithium batteries with carbon and/or silicon anodes,” Wu Xu, Ji-Guang Zhang, Hao Jia, Xianhui Zhang, Xia Cao, Sujong Chase, Ran Yi, Qiuyan Li, Won-Jin Kwak, Xiaolin Li, US11664536B2, patent granted on May 30, 2023.
2. “Si based Li Ion Batteries with Extended Cycle Life and Calendar Life,” R. Yi, J. Kim, S. Chae, Q. Li, X. Cao, W. Xu, and J. Zhang. " Presented by J. Zhang at ACS 2023 Spring Meeting, March 2023, Indianapolis, Indiana.
3. “Improving Calendar Life of Si-Based Lithium-Ion Batteries by FEC/VC-Free Electrolytes,” J. Kim, X. Cao, R. Yi, and J. Zhang. Presented by J. Kim in 243rd ECS meeting, May 2023, Boston, MA

### Acknowledgments

Key contributors include Ju-myung Kim, Xia Cao, Yaobin Xu, and Chongmin Wang.

## VII.3 Integrated Modeling and Machine Learning of Solid-Electrolyte Interface Reactions of the Si Anode (LBNL)

### **Kristin A. Persson, Principal Investigator**

Lawrence Berkeley National Laboratory  
1 Cyclotron Rd  
Berkeley, CA 94720  
E-mail: [kapersson@lbl.gov](mailto:kapersson@lbl.gov)

### **Jean-Luc Fattebert, Co-Principal Investigator**

Computational Sciences and Engineering Department  
Oak Ridge National Laboratory  
One Bethel Valley Rd  
Oak Ridge, TN 37831  
E-mail: [fattebertj@ornl.gov](mailto:fattebertj@ornl.gov)

### **Andrew Colclasure, Co-Principal Investigator**

National Renewable Energy Laboratory  
Center for Integrated Mobility Sciences  
Golden, CO 80401  
E-mail: [andrew.colclasure@nrel.gov](mailto:andrew.colclasure@nrel.gov)

### **Brian Cunningham, DOE Technology Development Manager**

U.S. Department of Energy  
E-mail: [Brian.Cunningham@ee.doe.gov](mailto:Brian.Cunningham@ee.doe.gov)

Start Date: October 1, 2022	End Date: September 30, 2023	
Project Funding (FY23): \$4,500,000	DOE share: \$4,500,000	Non-DOE share: \$0

### **Project Introduction**

Electrolyte decomposition is a critical factor in long-term lithium-ion battery (LIB) performance.[1] If decomposition products can deposit on electrode surfaces to form stable solid electrolyte interphase (SEI) layers, it is possible to cycle LIBs many hundreds or thousands of times with minimal capacity loss. On the other hand, in the absence of such a passivation film, ongoing electrolyte decomposition can lead to rapid loss of capacity and lithium inventory.

Current designs for LIBs with Si anodes exhibit poor passivation behavior, demonstrating low calendar life compared with LIBs with graphitic anodes.[2] The development of practical Si-based LIBs requires an improved control of electrolyte reactivity under reducing conditions. However, the fundamental mechanisms underlying electrolyte reactivity remain in many cases mysterious, as do the connections between these reaction mechanisms and battery performance descriptors.

This project seeks to develop and apply a range of computational models to address questions of electrolyte decomposition and SEI formation at Si anodes in LIBs. Modeling begins at the level of individual molecules and reactions, relying primarily on quantum mechanics and chemical reaction networks (CRNs). Atomistic quantum mechanical simulations inform nano- and micro-scale molecular dynamics (MD) simulations as well as continuum-scale models which can directly connect to experimental observables. Machine learning (ML) is leveraged to accelerate analysis at all levels, from the molecular to the device levels.

## Objectives

The LBNL team uses first-principles quantum chemistry, CRNs, ML, and stochastic analysis to 1) develop mechanistic understanding of electrolyte degradation and interphase formation in LIBs and 2) provide predictions of key molecular and reaction properties, such as vibrational spectra, solvation free energies, and reaction energy barriers. This work provides intrinsic benefit, helping to develop rational principles for the development of next-generation electrolytes. The reaction mechanisms identified through quantum chemical and CRN analyses also inform models that aim to study LIBs at longer length and time scales, such as those developed by the NREL team (see below). Major accomplishments of the LBNL team's atomistic approach this year include a revised understanding of electrolyte oxidation mechanisms in exemplar LIB electrolytes [3], and a ML approach to predict reaction energy barriers with high accuracy using orbital coefficients as features [4].

The ORNL team uses nanoscale simulations, primarily based on molecular dynamics (MD), to understand transport and reactive phenomena inside LIBs with silicon anodes. In FY2023, they investigated several research directions using MD, with the goals of (i) advancing the understanding of solid electrolyte interphase (SEI) growth in LIBs (ii) helping experimental teams better understand results and trends with a better picture of what is happening at the microscopic scale. Three major topics were addressed: (i) how can we overcome the timescale issue in simulating nucleation, growth, and microstructure formation in the SEI? (ii) could the calendar life issues observed experimentally be caused by diffusion and phase changes inside the silicon anodes? (iii) is the  $\text{PF}_6^-$  decomposition energy barrier as high as previously modeled?

The NREL team develops models to assist in 1) rapid electrolyte screening for calendar life, 2) and upscale fundamental (electro-)chemical reaction mechanisms, developed from atomistic-scale models to length- and time-scales relevant for studying battery degradation during cycling and calendar aging. A continuum-level model and a reduced order model are developed to meet project goals. Continuum-level models are developed to explain SEI formation and reactivity during calendar-life studies. The atomistically informed, chemically complex continuum-level model upscales competing decomposition pathways predicted from the LBNL team to length- (order nm) and time- (order hours/months) scales relevant for understanding calendar-life issues. The collaborative work resulted in a manuscript published in *Electrochem. Acta* [5]. Finally, reduced order modeling of electrochemical data from voltage-holds is performed to aid rapid calendar life screening of electrolytes for Si-based anodes.

## Approach

### LBNL

#### **First-principles electrolyte oxidation mechanisms**

Ethylene carbonate (EC) is known to react at LIB cathodes as well as anodes. These reactions at elevated potentials (depending on the electrode, between 3.8 – 4.2 V vs.  $\text{Li}/\text{Li}^+$ ) not only reduce the capacity of the cell but also can influence the anode through so-called “cross-talk” mechanisms.[6, 7] However, high-potential electrolyte oxidation is not usually considered in studies of SEI formation with either Si or graphitic anodes, and the mechanisms of electrolyte decomposition at LIB cathodes are even less well understood than those at battery anodes.

The two major mechanisms reported in the literature to describe the decomposition of EC at LIB cathodes are 1) direct electrochemical oxidation and 2) chemical oxidation by singlet oxygen ( $^1\text{O}_2$ ), which can evolve from oxide cathodes such as NMC. We examined both of these mechanisms using DFT calculations at the  $\omega\text{B97X-V}/\text{def2-TZVPPD}/\text{SMD}$  level of theory.[8-10] For electrochemical oxidation, we consider only the reaction thermodynamics, while for chemical oxidation, we identified elementary mechanisms and calculate reaction energy barriers. We also consider alternative mechanisms involving oxygen anions, which have been shown to form in the cathode bulk and at cathode surfaces.

### Orbital machine learning

Chemical reaction networks (CRNs) are a major tool that we have used to understand electrolyte decomposition and SEI formation,[11, 12] as well as to inform mesoscale [13] and continuum-scale battery models (see below for details).[5] Our current methods for CRN construction, involving filtering from the combinatorial explosion of possible stoichiometrically valid reactions,[14] is limited by our ability to accurately predict reaction kinetics. We have previously reported CRNs with tens of millions of reactions.[14,15] With networks so large, it is impossible to use DFT calculations, even at a low level of theory, to identify transition-states and calculate energy barriers for all reactions. This means that we have until now been forced to use reaction thermodynamics for most CRN analysis, performing kinetic calculations only for small numbers of important reaction mechanisms.

ML promises to accelerate predictions of molecular and reaction properties, including reaction energy barriers. But conventional ML methods are highly inefficient and require large training sets to achieve practical levels of accuracy. To improve efficiency and enable the use of ML even in small-data regimes, a model should be i) constrained by known physics, limiting the optimization space while simultaneously ensuring that all results are chemically reasonable and ii) respect symmetry (i.e., be equivariant to geometric transformations).

We have designed an equivariant graph neural network architecture for data-efficient and accurate molecular and reaction property prediction called CoeffNet (Figure VII.3.1). CoeffNet uses molecular orbital coefficients as input features. In the context of energy barrier prediction, CoeffNet first predicts the orbital coefficients at a reaction's transition-state based on the orbital coefficients of the reactants and products. Based on the predicted orbital coefficients, CoeffNet then predicts the reaction energy barrier, from which rate coefficients can be easily calculated.

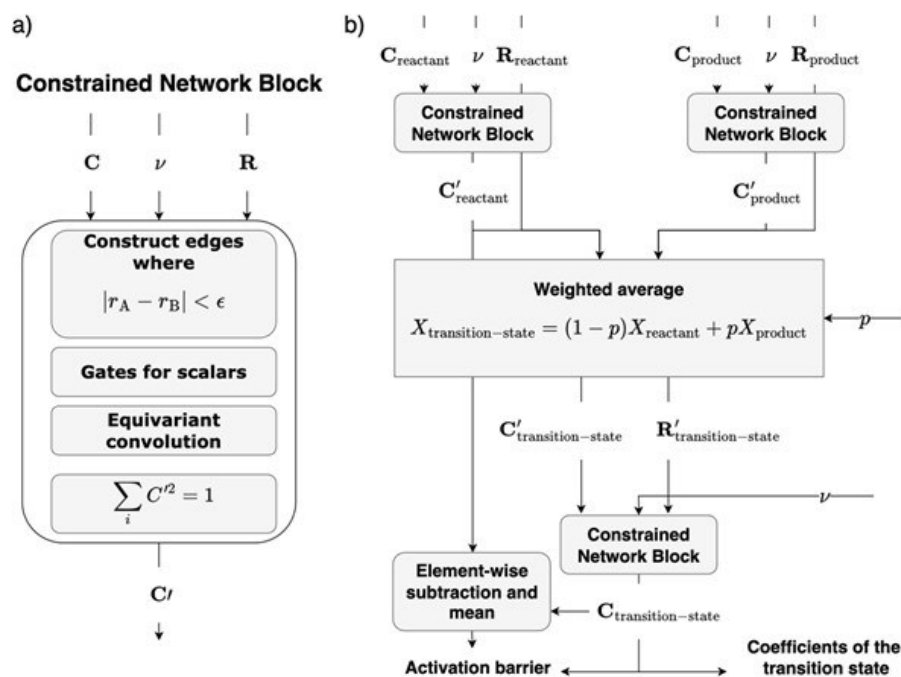
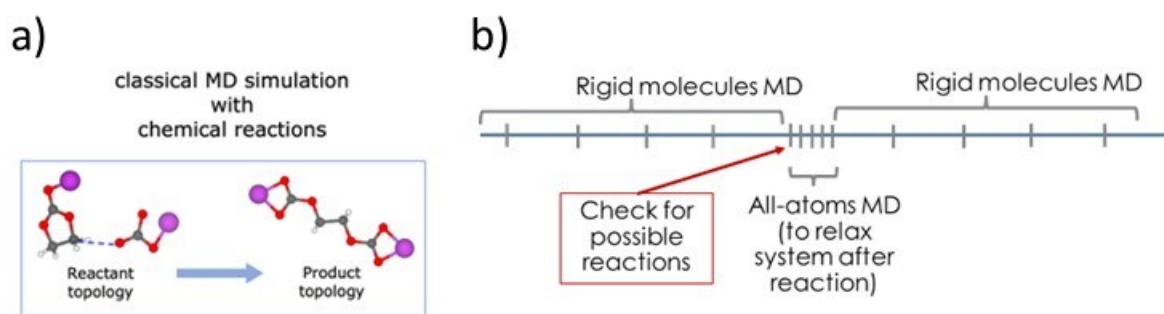


Figure VII.3.1 a) Schematic of a constrained network block with inputs of orbital coefficients  $C$ , atomic numbers  $\nu$ , and atomic positions  $R$ . b) Schematic of the architecture of CoeffNet;  $C$ ,  $\nu$ , and  $R$  for both reactants and products are passed through a constrained network block shown in a).  $C'$ , which is the output of the network, and  $R$  and linearly interpolated through  $p$  and are used as node features of the interpolated transition-state graph. Outputs of the last network are interpreted either as coefficients of the molecular orbital or are averaged after subtraction with the outputs of the constrained network block of the reactants to get the activation barrier.

## ORNL

**Time-scale issue in SEI formation**

Following what we learned from the research performed by the team during the previous three years, novel approaches are needed to understand the nucleation of growth of the different phases that co-exist in the SEI. *Ab initio* MD methods are too slow and computationally costly to enable simulations long enough to investigate SEI formation and growth. In this project, we previously investigated the early stages of SEI formation with hybrid classical MD,[16] restarting MD with new molecular components when the geometry of the atomistic system matches a template corresponding to a specific chemical reaction (This capability exists as *bond/react* in the open-source molecular dynamics code LAMMPS, <https://lammmps.sandia.gov>). Using information provided by the LBNL team to build these templates was key to enable simulations with realistic reactions. While this technique allowed us to make good progress, it is still too slow to reach a fully formed SEI. We then started investigating how using rigid molecule models could further speedup our simulations and extend the timescale of these simulations (see Figure VII.3.2). A non-negligible speed-up factor (2X-5X) was obtained through such techniques. This still falls short of reaching the target timescale to see a complete microstructure formation. In addition, classical force-field have their know shortcomings in term of accuracy. Recently developed ML interatomic potentials have the potential to improve accuracy, while requiring time-to-solution low enough to enable MD simulations at long time scales. These techniques are however still difficult to apply in the context of SEI formation, as there are many atomic species, including charged molecules that experience strong long-range interactions. To overcome these challenges, our investigations led us to the conclusion that a completely new approach is needed, which could be based on ML interatomic potentials for a coarse-grain representation of the molecules involved in the SEI formation. Our basic idea is to develop a coarse grain model that included the molecular orientations in its parameterization and to develop ML techniques to model the interaction between two rigid bodies. Realizing that there was no existing symmetric and compact representation of two-body systems with their orientation, we developed a quaternion-based representation, which we will combine with ML techniques in the near future to demonstrate the feasibility of longer and accurate molecular liquid simulations that hopefully will help us gain insights into the SEI formation and resulting microstructure.



**Figure VII.3.2 a) Illustration of change in molecular dynamics force-field when a chemical reaction happens based on precomputed templates of the reactants and products. b) Schematic representation of MD algorithm combining “coarse grain” (rigid molecules) MD with reactions now possible with LAMMPS.**

**Diffusion rates and phase changes inside the Si anodes**

LIBs with Si anodes have poor calendar lifetimes, with capacity fading rapidly within months at the shortest to 1-2 years at the longest. From an atomistic perspective, we hypothesized that slow diffusion in the solid phase could cause changes over this long time scale. A solid phase may be stable only for some specific alloy composition and may degrade as atoms migrate and change the local composition. Within a Si anode, such phenomena could lead to dead lithium being trapped in one solid phase, or even a whole Li cluster composing the anode changing into a phase from which one cannot reverse lithium flow in ambient conditions. To gain some insights into that possible scenario, we have been using a combination of classical MD simulations using LAMMPS and DFT computations using Quantum Espresso (<https://www.quantum-espresso.org>).

***LiPF<sub>6</sub> dissociation energy barrier***

As discussed above, LiPF<sub>6</sub> decomposition is notoriously challenging to study. In most reported mechanisms, including those proposed by the LBNL team (see Results below), LiPF<sub>6</sub> first dissociates to LiF and PF<sub>5</sub> in electrolytes composed of ethylene carbonate (EC) and ethyl methyl carbonate (EMC). This dissociation reaction is often assumed to occur spontaneously or rapidly. In 2013, Okamoto [17] found using DFT that the barrier for LiPF<sub>6</sub> dissociation is too high (about 1.75 eV) for the reaction to occur appreciably under ambient conditions. We decided to reconsider this reaction and the question of LiPF<sub>6</sub> decomposition, albeit still using simulations based on DFT. We used the continuum solvation model proposed by Fattebert and Gygi [18] as implemented in the MGmol code (<https://github.com/LLNL/mgmol>). The numerical approach differs significantly from the approach used by Okamoto, specifically using a much more accurate discretization of the Kohn-Sham equations on a finite difference mesh, combined with a continuum solvation model adapted to that discretization.

***NREL******Atomistic-informed SEI model***

Understanding and controlling SEI formation to stabilize cell performance is a significant challenge for next-generation LIB technologies including those using Si anodes. In recent years, computational modeling has become an essential tool in providing fundamental insights into SEI properties and dynamics. However, neither atomistic nor continuum-level approaches alone can capture the complexities of SEI chemistry across all relevant length and time scales. In our work, a continuum-level model is developed that is informed by reaction mechanisms obtained from first-principal calculations performed by the LBNL team. The atomistically informed continuum-level model is used to understand electrolyte degradation, including the decomposition of ethylene carbonate (EC), ethyl methyl carbonate (EMC), and fluoroethylene carbonate (FEC). The model is the most chemically complex continuum-level SEI model in literature to date. The SEI model is calibrated against experimental irreversible leakage currents measured in the Si Consortium Project and shows qualitative agreement with expected SEI growth trends. The model framework is expected to accelerate fundamental understanding of SEI formation, facilitate mechanism development feedback, and dynamically interact with experimental insights.

The primary goal of the continuum-level model developed in this work, is to communicate atomistic knowledge (e.g., reaction pathways, rates, species transport properties) to time- and length scales that are experimentally relevant. Additionally, the model is meant to act as a bridge to validate (electro)chemical mechanisms proposed from experimentally observed signals. More specifically, it is common for the atomistic modeling community to propose reaction mechanisms, rates, species transport properties, etc. that seek to explain initial Li-ion SEI formation. However, translating these predictions to long timescales has been challenging, preventing significant experimental validation. Additionally, it is common for the experimental community to detect atom/bond/molecule signals and propose (typically global) reactions that would logically produce these measured signals. However, the mechanisms proposed from experimental observation are not typically predictive, i.e., they struggle with answering: “What would occur if additive *X* was included in the system?”.

A major strength of the present continuum-level model is its ability to operate bidirectionally, such that atomistic insights can be upscaled to experimentally measurable signals and experimental observations can be used to refine atomistic insights. In particular, the model framework enables the use of first-principles atomistic insights to deconvolute competing reaction pathways that produce the same resultant species. Such deconvolution has traditionally challenged the experimental community. For example, vinylene carbonate (VC) is a well-documented component present in aged electrolyte whose origin is typically attributed to FEC and/or EC reduction. Multiple distinct mechanistic pathways have been proposed that could feasibly result in VC evolution, and which are supported by complementary experimental analysis. Notable proposed mechanisms include the reaction of FEC with alkoxide products and the concurrent loss of HF to form VC and LiF, or alternatively the radical disproportionation of EC to form VC. The “correct” mechanistic attribution for

VC formation remains contested in the experimental literature, as well as consumption of VC to form additional species.  $\text{CO}_2$  presents a similar challenge, with experimentally supported pathways to produce (and consume)  $\text{CO}_2$  associated with all standard electrolyte solvents, as well as multiple downstream intermediates and – in the case of Li metal anodes – even the electrode surface itself. Clearly, for such complex systems, deconvolution of all potential pathways based solely on (electro)chemical intuition is impractical. It is also unfeasible to attempt deconvolution through precise experimental detection of all complementary evolved species, when the number of relevant species is on the order of dozens to hundreds across three phases. The model, thus, offers a complementary approach to experimental measurements, whereby the favorability of competing and complex mechanistic pathways can be evaluated to both explain and help predict experimental observations.

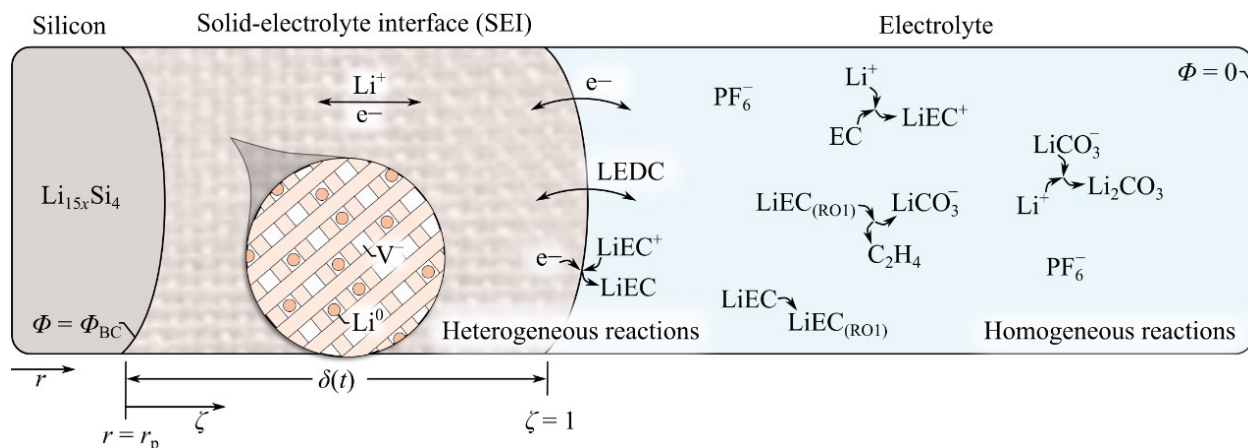


**Figure VII.3.3** Continuum-level model domain with representative physics, electrochemical/chemical reactions, independent coordinates, and select boundary conditions.

Figure VII.3.3 illustrates the continuum-level model. Three domains are illustrated: the Si particle, the SEI, and the electrolyte. To demonstrate SEI growth dynamics, Si alloying physics are not captured. The model is primarily concerned with SEI and electrolyte dynamics at a given voltage-hold. As illustrated, the SEI is assumed to form a lattice structure with mobile Li-ion and electron species interstitial. At the SEI/electrolyte interface, heterogeneous reactions including reduction and deposition/dissolution are simulated. In the electrolyte, species migration, diffusion, and production are simulated. The reaction mechanism primarily includes homogeneous reactions in the electrolyte-phase. The model internal variables are species concentrations  $[X_k]$ , electrostatic potential  $\Phi$ , and SEI thickness  $\delta$ .

#### **Rapid Electrolyte Screening for Calendar Life using Potentiostatic Holds**

Potentiostatic-hold protocols have been explored for rapid battery calendar life screening to obviate the needs for years-long testing [19] (Figure VII.3.4). This provides an avenue for rapid material screening for Si calendar life. We utilize this voltage-hold (V-hold) protocol to analyze the impact of electrolyte fluorination on calendar lifetime of Si anodes. The V-hold protocol has signatures from reversible as well as irreversible capacity that is exchanged during the hold; our work devises a deconvolution algorithm to estimate the irreversible proportion and extrapolate the estimates to predict semi-quantitative calendar lifetime of the cell [20]. This numerical approach is especially important for Si cells, as this material has been shown to exhibit slow reversible relaxation that could affect the interpretation of V-hold experiments. The combined experiment-modeling approach provides a pathway towards rapid (<2 months test duration) screening of electrode and electrolyte materials for calendar life.



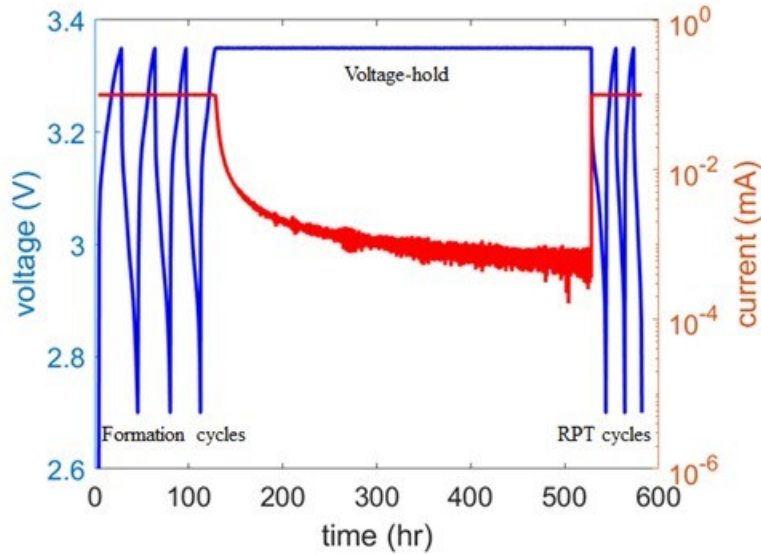


Figure VII.3.4 Example potentiostatic-hold protocol for Si-LFP cell with formation cycles, voltage hold portion and reference performance test (RPT) cycles highlighted.

Capacity during the hold is fit to a reduced order model comprising of reversible and irreversible capacity terms. Irreversible capacity losses during calendar aging show a power law nature with time, hence we use  $Q_{irrev} = at^p$  to estimate the irreversible capacity lost to SEI growth. The form of reversible capacity,  $Q_{rev}$ , is chosen to replicate the plateauing behavior of reversible lithiation of Si.

$$Q_{hold}(t) = Q_{irrev}(t) + Q_{rev}(t) = at^p + \frac{(Q_{hold}^{final} - at_{final}^p)(c + t_{final})t}{t_{final}^{c+t}} \quad (1)$$

$$Q_{hold}^{final} = Q_{rev}^{final} + Q_{irrev}^{final} \quad (2)$$

## Results

### LBNL

#### First-principles electrolyte oxidation mechanisms

Figure VII.3.5 shows the Gibbs free energy change ( $\Delta G$ ) of electrochemical EC oxidation at a range of potentials (4.0 – 5.4 V vs. Li/Li<sup>+</sup>). For each potential, we calculate  $\Delta G$  under non-standard conditions, where the concentration of oxidized EC (EC<sup>+</sup>) is less than that of EC. Because the exact steady-state concentration of EC<sup>+</sup> is not known *a priori*, we consider a range of concentration ratios  $c_{EC^+}/c_{EC}$ , as low as  $10^{-9}$ . We find that electrochemical oxidation is never thermodynamically favorable at potentials relevant to typical NMC cathodes or next-generation high-voltage cathodes such as disordered rock salts (DRX). However, oxidation could occur at potentials > 5.5 V vs. Li/Li<sup>+</sup>, in agreement with previous studies conducted using non-reactive electrodes such as platinum.[21]

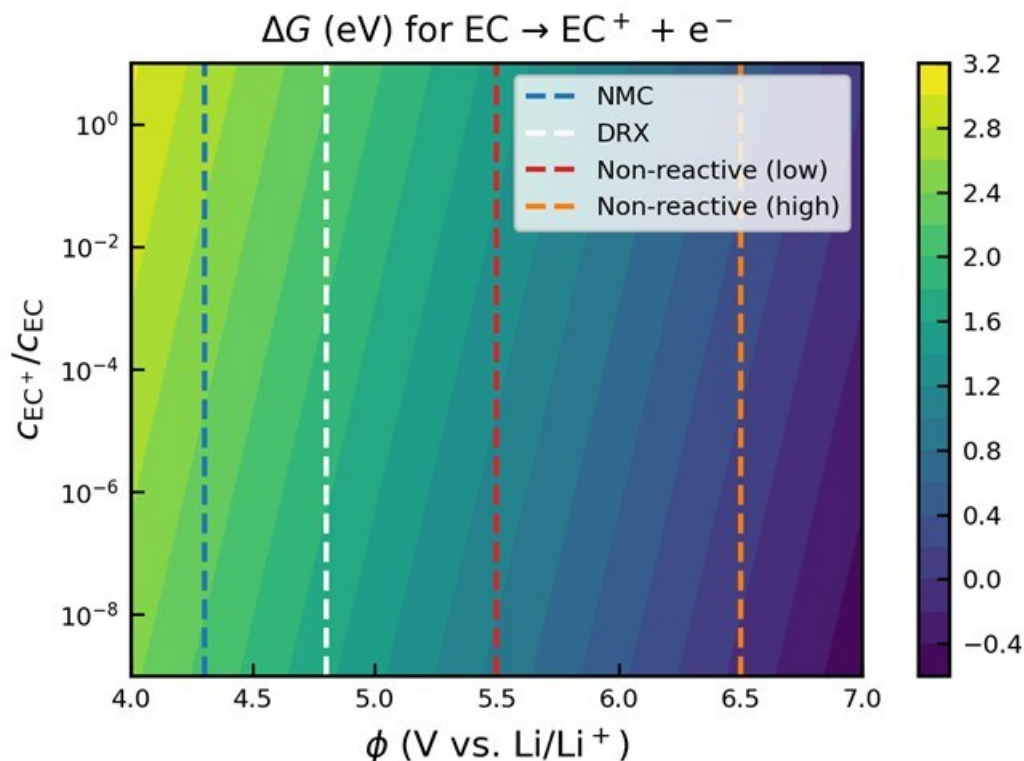


**Figure VII.3.5** Gibbs free energy change ( $\Delta G$ ) for electrochemical oxidation of EC based on DFT calculations, accounting for the effect of applied potential and the relative concentration of  $EC^+$ .

Two pathways for reactions between  $^1O_2$  and EC have been reported in the literature: an addition-elimination reaction that results in the formation of  $H_2O$  as a byproduct [22] and a double hydrogen abstraction leading to  $H_2O_2$  and vinylene carbonate (VC).[23] As Figure VII.3.6 shows, neither of these mechanisms are at all kinetically viable under ambient conditions, suffering from high energy barriers considerably greater than 1 eV.

In contrast, reactions with both superoxide ( $O_2^{-1}$ ) and peroxide ( $O_2^{-2}$ ) appear plausible (Figure VII.3.7-Figure VII.3.8). We predict that superoxide can attack EC in a nucleophilic substitution reaction, while peroxide can react in numerous ways, including nucleophilic substitution, proton abstraction, and addition. We note that these findings are preliminary, looking only at the initial steps of EC decomposition. It is not yet known what stable products could be formed through reactions between EC and oxygen anions. However, our findings suggest that such mechanisms are likely to dominate over either electrochemical or chemical oxidation routes.

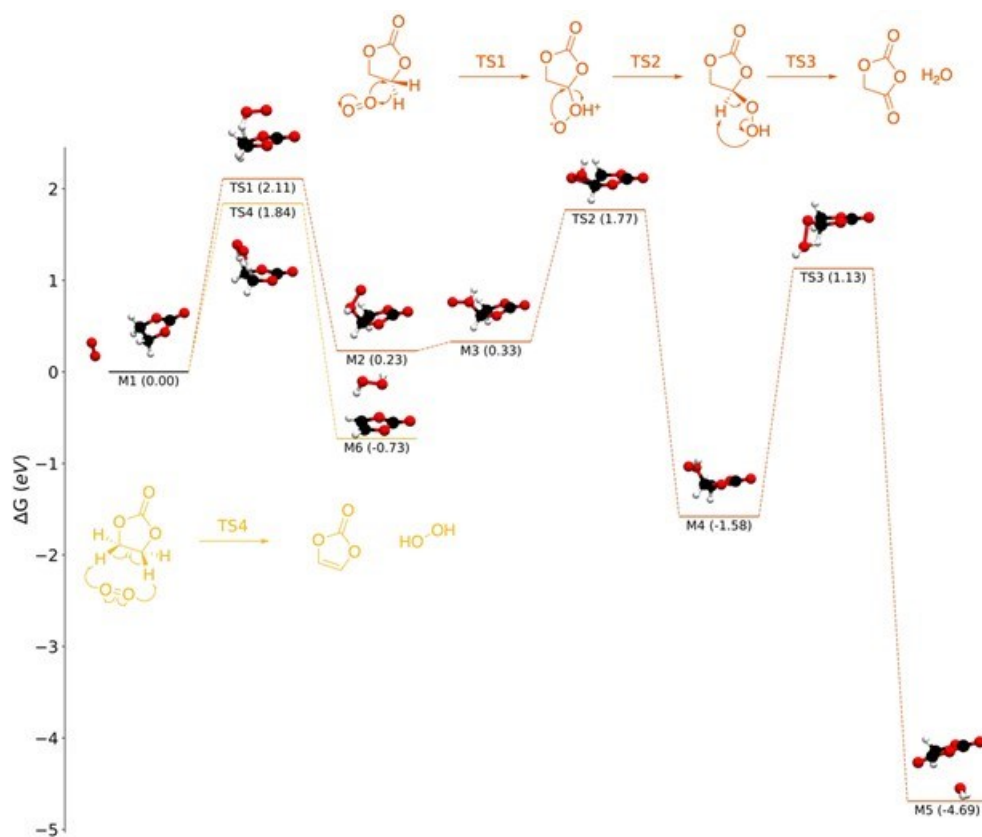


Figure VII.3.6 Energy diagrams for reactions between EC and  $^1\text{O}_2$ , based on mechanisms reported in the literature. Both pathways considered suffer from high barriers and are therefore implausible under ambient or near-ambient conditions.

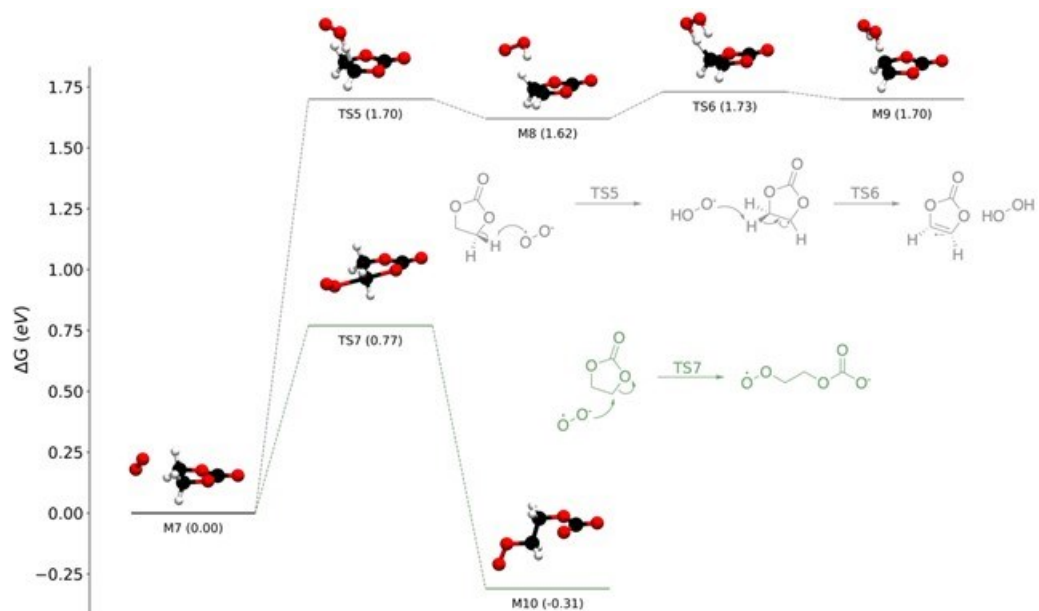


Figure VII.3.7 Energy diagrams for reactions between EC and superoxide. A hydrogen/proton abstraction mechanism (gray) is energetically unfavorable, while nucleophilic substitution (green) has a moderate barrier and is thermodynamically favored.

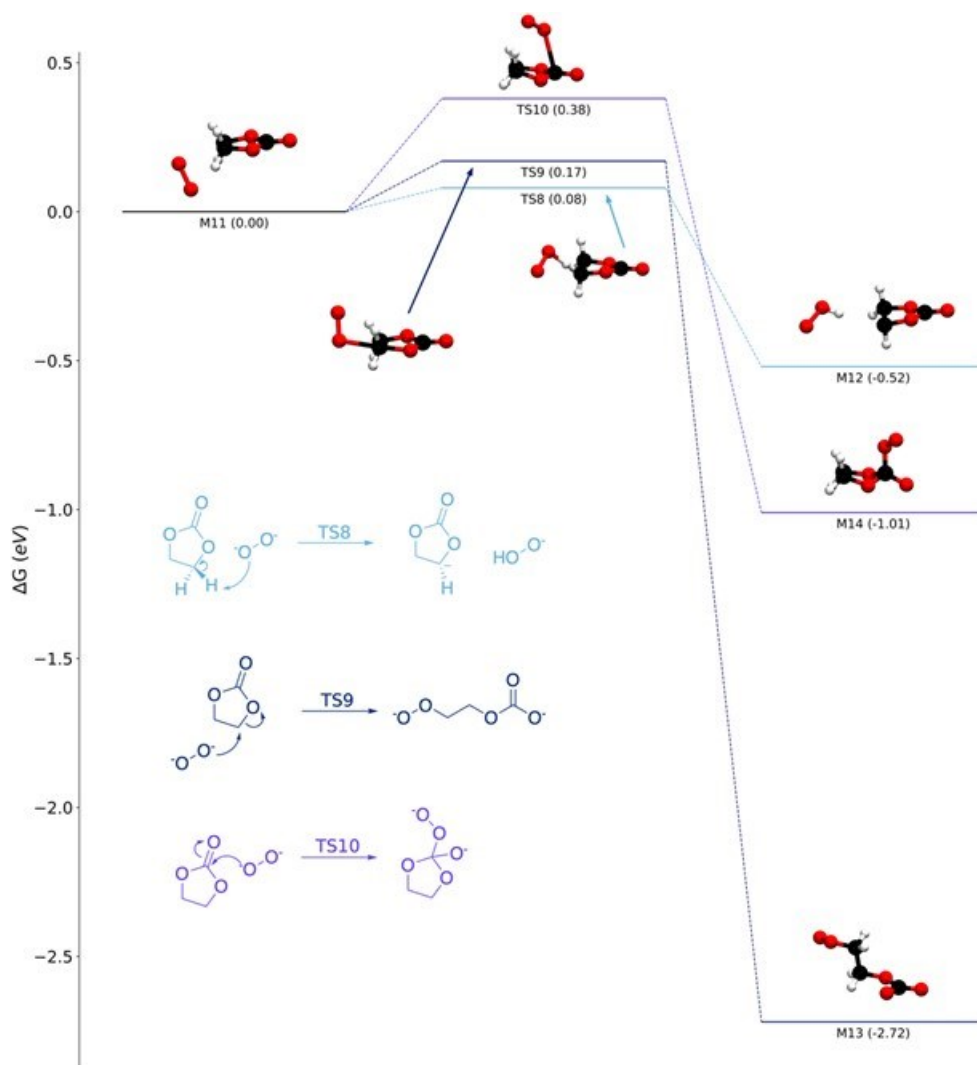


Figure VII.3.8 Energy diagrams for reactions between EC and peroxide. All three reactions shown – proton abstraction, nucleophilic substitution, and addition – can occur rapidly under ambient conditions.

### Orbital machine learning

As a proof of concept, we trained CoeffNet on a dataset of organic SN2 reactions published by von Rudorff et al.[24] We used orbital coefficients obtained from a minimal basis representation and with a relatively large def2-SVP basis set. As seen in Figure VII.3.9, both the minimal and the full basis can be used to accurately predict reaction energy barriers, with MAE 0.021 eV and 0.022 eV, respectively. This suggests that molecular orbital representations can be effective in predicting reaction properties and that input features can be generated using extremely cheap DFT calculations.

As shown in Figure VII.3.10, CoeffNet is also able to accurately predict orbital coefficients on average, though the distribution of errors is much higher for individual orbital coefficients than for energy barriers. We suspect that energy barrier prediction is somewhat less error-prone because, in our model architecture, we average the difference between the transition-state and reactant coefficient features, meaning that we may experience error cancellation.

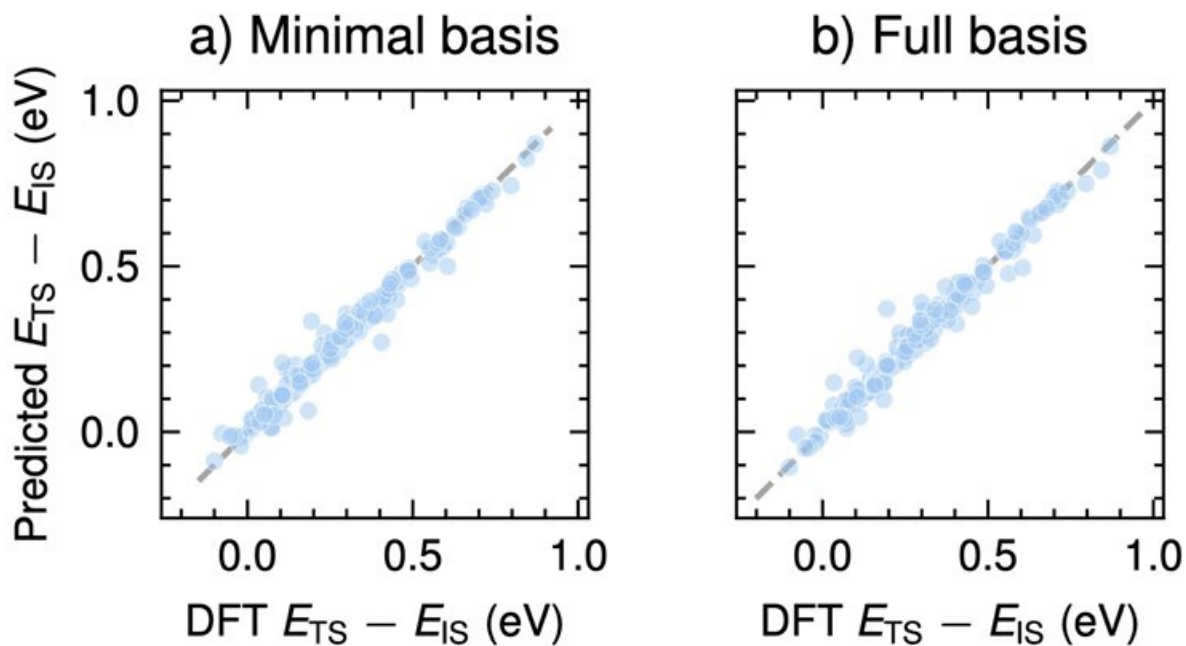


Figure VII.3.9 Comparison of predicted and DFT-computed reaction energy barriers on the test set for a) a minimal basis representation (i.e. only s and p basis functions) and b) a full basis (using the def2-SVP basis set).

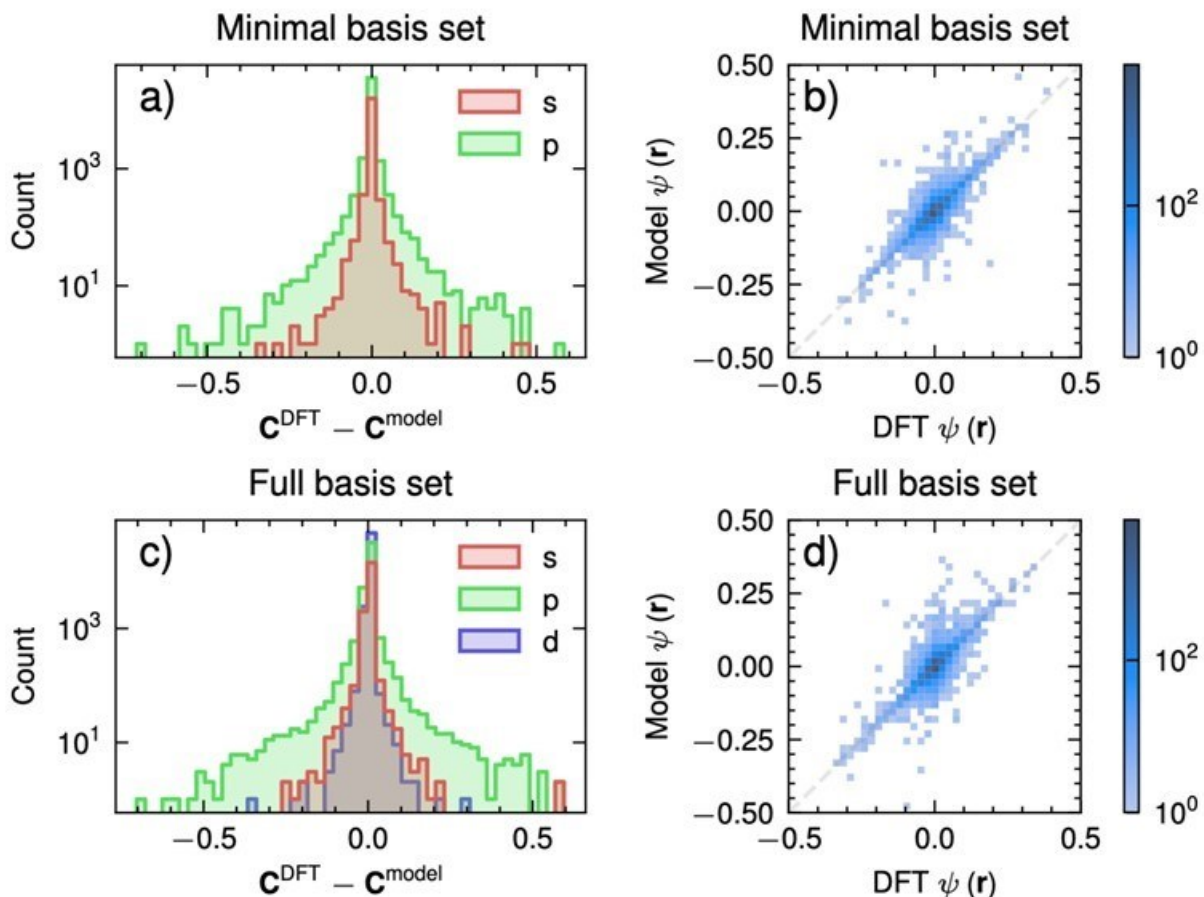


Figure VII.3.10 Residual between the C from DFT and from CoeffNet predictions for a) a minimal basis set and c) a full basis. Comparison of predicted and DFT values of the HOMO of the transition-state sampled on a  $4 \times 4 \times 4$  grid for a bounding box of  $1.25 \text{ \AA}$  away from the farthest atom of each molecule in each direction for b) minimal-basis representation and d) the full basis representation.

## ORNL

### *Timescale issue in SEI formation*

A new representation of two interacting rigid bodies was developed based on quaternions (Figure VII.3.11). This representation is symmetric with respect to the two bodies, in the sense that swapping the two bodies would lead to the same energy of interactions. It is compact in the sense that it requires only six variables to fully describe the system. A demonstration potential was implemented in the HOOMD-blue code (<https://github.com/glotzerlab/hoomd-blue>). A manuscript describing the approach in detail is in preparation. Future plans include using that new representation as a descriptor for a coarse grain Machine Learning potential and apply it to study mixtures made of the major species composing the SEI, that is  $\text{LiF}$ ,  $\text{LiO}_2$  and  $\text{Li}_2\text{CO}_3$ .

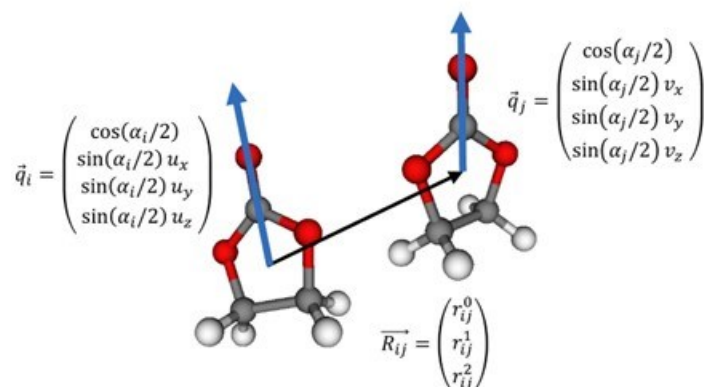


Figure VII.3.11 Quaternion-based representation of two interacting molecules. A scheme to reduce this representation to the minimal six degrees of freedom has been developed to be used to build a Machine Learning interatomic potential.

### Diffusion rates and phase changes inside the Si anodes

We investigated the stability of  $\text{Li}_{15}\text{Si}_4$  by classical molecular dynamics (EAM potentials). One interesting finding is the appearance and growth of an unknown phase when simulating a seed made of  $\text{Li}_{13}\text{Si}_4$  (76.4% Li) inside a matrix of  $\text{Li}_{15}\text{Si}_{14}$  (79% Li). This new phase comes out of the simulation with the stoichiometry  $\text{Li}_3\text{Si}$  (see Figure VII.3.12). We confirmed through DFT structural relaxation/energy minimization that this new phase is stable and has a negative formation energy. Based on the formation energy from DFT calculation, this new phase is not as stable as  $\text{Li}_{15}\text{Si}_4$ . It may indicate that this new phase is induced by Li-diffusion.

Further investigations on this topic could include using ML potentials, as well as using atomistic data obtained from those simulations in a mesoscale phase-field model of coexisting phases to understand their dynamics.

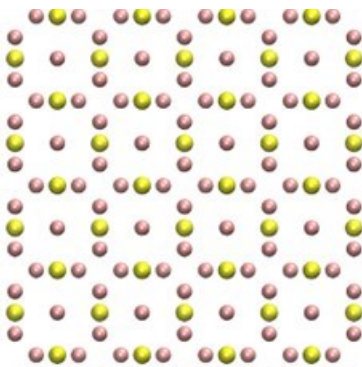


Figure VII.3.12 Representation of the new Li-Si phase emerging from Li diffusion when embedding a seed of  $\text{Li}_{13}\text{Si}_4$  inside a matrix made of  $\text{Li}_{15}\text{Si}_{14}$ . Color scheme: Si: yellow, Li: pink.

### $\text{LiPF}_6$ dissociation energy barrier

There is not much data in the literature to tune continuum solvation model. Therefore, we simply use a model parameterized for water with a different dielectric constant. In addition, we ran the model for several dielectric constants to get insights into how these affects the results. The reaction  $\text{LiPF}_6 \rightarrow \text{PF}_5 + \text{LiF}$  in EC+EMC electrolyte was modeled with three different dielectric constants (20.5, 80., 95.2). For each one, the atoms in the system  $\text{LiPF}_6$  system were fully relaxed under a constraint on the difference in distances between P and F, and Li and F, for the F reacting with Li. We use that difference as reaction coordinate. Our results are plotted in Figure VII.3.13. Our continuum solvation result for a dielectric of 20.5 is in very good agreement with the 2013 theoretical result by Okamoto result of 1.74 eV,[17] where the same dielectric constant was used. The results with a larger dielectric constant though show a slightly lower energy barrier. First-Principles MD simulations were also carried out for 7 ps for each reaction coordinate. Integrating the force on the constraint



for the last 5 ps of each of these runs shows an energy barrier even lower, about 30% below Okamoto's result. This is however still too high for a spontaneous decomposition to happen at room temperature, implying that  $\text{LiPF}_6$  decomposition likely does not occur in the bulk electrolyte but may be mediated by e.g. electrode surfaces. A publication describing these simulations and results is in preparation.

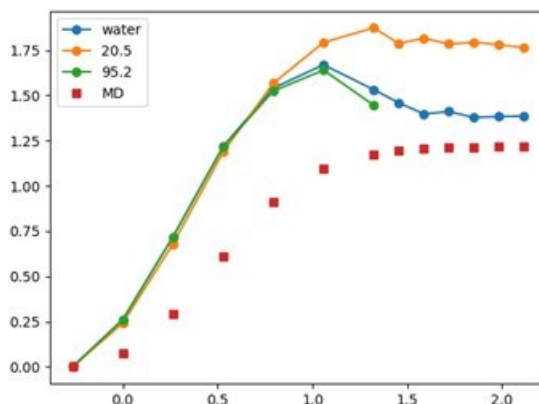
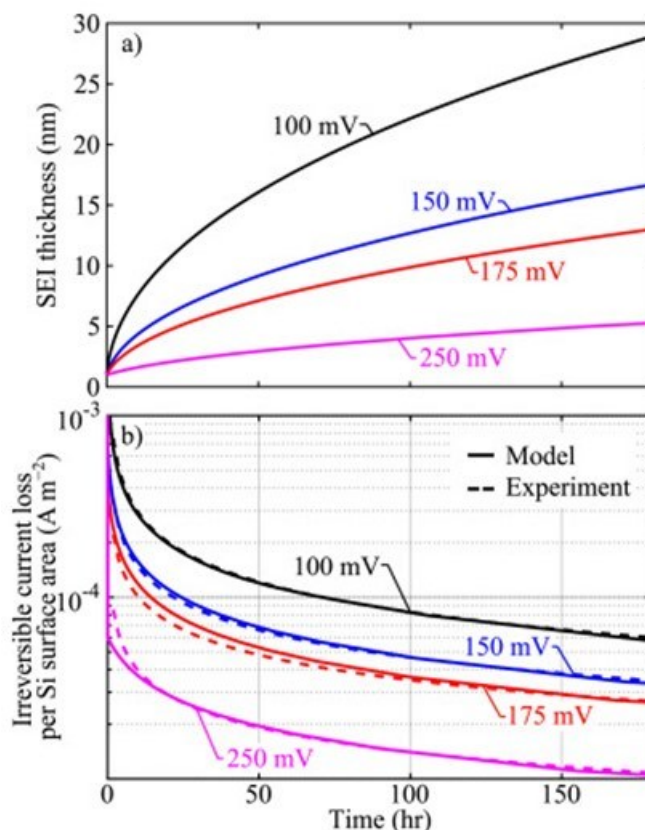


Figure VII.3.13 Energy barrier for  $\text{PF}_6+\text{Li}^+ \rightarrow \text{PF}_5+\text{LiF}$  reaction using a continuum solvation model (with three different dielectric constants) compared to First-Principles MD. The reaction coordinate is the difference in distances between P-F and Li-F. Energies are in eV and reaction coordinates in Angstrom.

## NREL

### Atomistic-informed SEI model

The continuum-level model has been developed with a specific emphasis on evaluating the passivation behavior of Si anodes. A somewhat confounding observation when considering SEI formation and passivation is the obvious difference between SEI passivation on graphite and the lack of passivation on Si and Li surfaces. Further, while both Si and Li electrodes have significantly more volume-change on cycling than graphite, Si and Li surfaces themselves seem to have different passivation characteristics. For example, Li metal has rapid cycling fade, while nano-Si can cycle for hundreds to thousands of cycles but has reduced calendar-life. The following paragraphs discuss the remaining challenges in understanding and simulating SEI formation in next generation Li-ion battery materials. Some of these challenges can be addressed by the current chemically complex continuum-level model framework, while others may require incorporating additional physics. Such modifications are possible within the inherently flexible model framework, although the complexity of physics required to capture certain behaviors is high in several cases. The additional phenomena considered below are listed in rough order of increasing intensity of the adjustment(s) that would be required for the present model framework to capture.



**Figure VII.3.14 (a) Predicted SEI thickness dynamics for at each voltage during the 180 h hold. (b) Measured irreversible leakage current and model predicted responses at several voltage-holds of Si half-cells**

Figure VII.3.14b illustrates the irreversible leakage current from the experiments and the predicted responses after calibration. Figure VII.3.14a illustrates the predicted SEI thickness increase during the 180 h voltage hold. The SEI has a growth rate that approximates trends, which is expected for (electron) diffusion-limited growth. As illustrated, the model-predicted irreversible current accurately captures the change in magnitude and relative trends at each voltage hold.

The present model and associated atomistic reaction mechanisms together represent the most chemically complex continuum-level model reported to date. However, even with the addition of orders of magnitude more chemical complexity, it is unrealistic to suggest that all possible chemical pathways will be captured. In the case of the next-generation anodes (e.g., Si and Li), important additional reactive pathways include salt decomposition; reactions of trace water; and homogeneous SEI-phase reactions (i.e., continued reactivity of species following deposition). The nature of the salt has been experimentally demonstrated to drastically influence the resulting SEI composition, particularly since salt decomposition is believed to contribute to the formation of the “pre-SEI” layer (herein assigned via initial condition to be a 1 nm layer of LiF). Further, even in the most carefully prepared systems, the presence of trace water has been detected in both the electrolyte and as hydration water within the electrodes. In the case of Si, HF formed through reactions between water and  $\text{LiPF}_6$  salt can directly etch the Si surface. Finally, the reported changes to SEI composition and morphology over repeated cycling of next-generation cells suggest that homogeneous reactions may be occurring within the SEI solid phase. Of these additional reactive pathways, incorporating salt decomposition is perhaps the most readily accessible, and this effort is already underway. Including water introduces drastically expanded mechanistic complexity and is likely to introduce numerical stability challenges, since water readily reacts with nearly all electrolyte species initially present in the system, as well as many of the reactive intermediates and products. Incorporating homogeneous SEI reactions is feasible but would require first-principles calculations

and/or experimental measurements of the thermodynamic properties and kinetic barriers to form SEI products, many of which have not yet even been conclusively identified.

In the present continuum-level model framework, although all reactions are fundamentally reversible, the species thermodynamics of primary deposition products has been chosen such that deposition is thermodynamically favorable, i.e., the SEI only grows. However, there is experimental evidence for dynamic SEI deposition/dissolution under conditions of both electrode cycling and storage. In next-generation Si and Li materials, the electrode surface is also believed to (electro-)chemically react with the SEI, such that the SEI grows into the underlying electrode active material. Specifically for Si, cryogenic scanning transmission electron microscopy (cryo-STEM) and energy dispersive X-ray spectroscopy (EDS) elemental mapping have recently shown that the expected core-shell structure for the Si-SEI is seen after the first cycle, but after sufficient cycling, the Si-SEI becomes increasingly blended. This behavior is in contrast to graphite, where it is believed that the SEI surface layer does not react with the underlying C<sub>6</sub> structure, and a core-shell structure is maintained. The SEI's inward growth on Si may cause additional capacity fade. In the continuum-level modeling framework, treating the first of these additional SEI dynamics (i.e., including dissolution as well as deposition) is relatively straightforward. However, this requires formulation of additional inputs including solubility values and kinetic barriers of various complex reduction products. Incorporating SEI blending with the underlying electrode would involve introducing an additional reactive boundary, which would be handled similarly to the SEI/electrolyte boundary. Instead of assuming only electrons and Li cross the electrode/SEI boundary, additional heterogeneous reactions could occur that eat away at the electrode structure and “blend” the SEI with the electrode. Adding this additional reactive boundary requires a robust understanding of the relevant heterogeneous solid-solid reactions, which is difficult to predict from first principles and a possible reformulation to handle two moving boundaries (at the Si/SEI and SEI/electrolyte interfaces) as opposed to one (at the SEI/electrolyte interface).

In contrast to graphite, which undergoes relatively minor volume-change dynamics, the substantial volume change occurring in both Li and Si can influence SEI passivation via SEI cracking or thinning. However, the connection between electrode strain and SEI growth dynamics is not straightforward. In the case of Li metal, there is an “infinitely large volume expansion”, and in the case of Si, lithiation results in an expansion of ≈280%. If these large volume changes influence SEI growth, the volume-change dependence would most likely influence cycling performance. This conclusion is supported by the reduced cycle life observed in Li-metal electrodes. For Si, efforts have been made to mitigate these volume-change effects by reducing the active particle size to the nanoscale. Such nano-Si materials demonstrate improved cycle life but still suffer from reduced calendar life, likely due to the highly increased surface to-volume ratios realized by the stress-reducing nanostructures. Thus, volume-change behavior alone cannot fully explain why Si exhibits reduced calendar life, since the Si expansion/contraction is relatively small during calendar-aging as compared to the expansion/contraction during cycle-aging. Including simulated finite-strain chemo-mechanics on the particle- and electrode-levels may be necessary for the continuum-level model framework to fully capture the factors influencing SEI stability. Such addition of chemo-mechanics is not the focus of the present model - which emphasizes upscaling significantly complex reaction networks from atomistic theory - but future iterations will include finite-strain chemo-mechanics.

### ***Rapid Electrolyte Screening for Calendar Life using Potentiostatic Holds***

Figure VII.3.15 (a-b) shows the normalized capacities and currents during a 400 hour hold voltage hold on Si-LFP cell with five different electrolytes: (i) Gen 2 electrolyte: 1.2M LiPF<sub>6</sub> in EC:EMC (3:7 w/w), (ii) Gen2F3: 1.2M LiPF<sub>6</sub> in EC:EMC (3:7 w/w) + 3 wt. % FEC (current baseline of the Silicon Consortium), (iii) 0.7M LiBOB in EC:EMC (3:7 w/w), (iv) 1.2M LiDFOB in EC:EMC (3:7 w/w), and (v) 1.5 M LiPF<sub>6</sub> in FEC:EMC (1:9 w/w). Gen2, Gen2F3 and LiBOB electrolyte show similar capacity gain during V-hold. LiDFOB electrolyte has the largest capacity gain during V-hold while 1.5 M LiPF<sub>6</sub> in FEC:EMC (1:9 w/w) has least capacity rise showing promise for extension of calendar life over baseline electrolyte. FEC decomposition reaction favors passivating SEI components of LiF and poly(VC) combining beneficial characteristics of electron insulation and elastomeric stretchy polymers, respectively  $\text{FEC} + (\text{Li}^+ + \text{e}^-) \leftrightarrow \text{LiF} + \text{VC} +$

$0.5\text{H}_2(\text{g})$ ,  $\text{VC} \leftrightarrow \text{poly}(\text{VC})$ ). The reduced order model fit for total capacity and current shows good match with the experimental data.

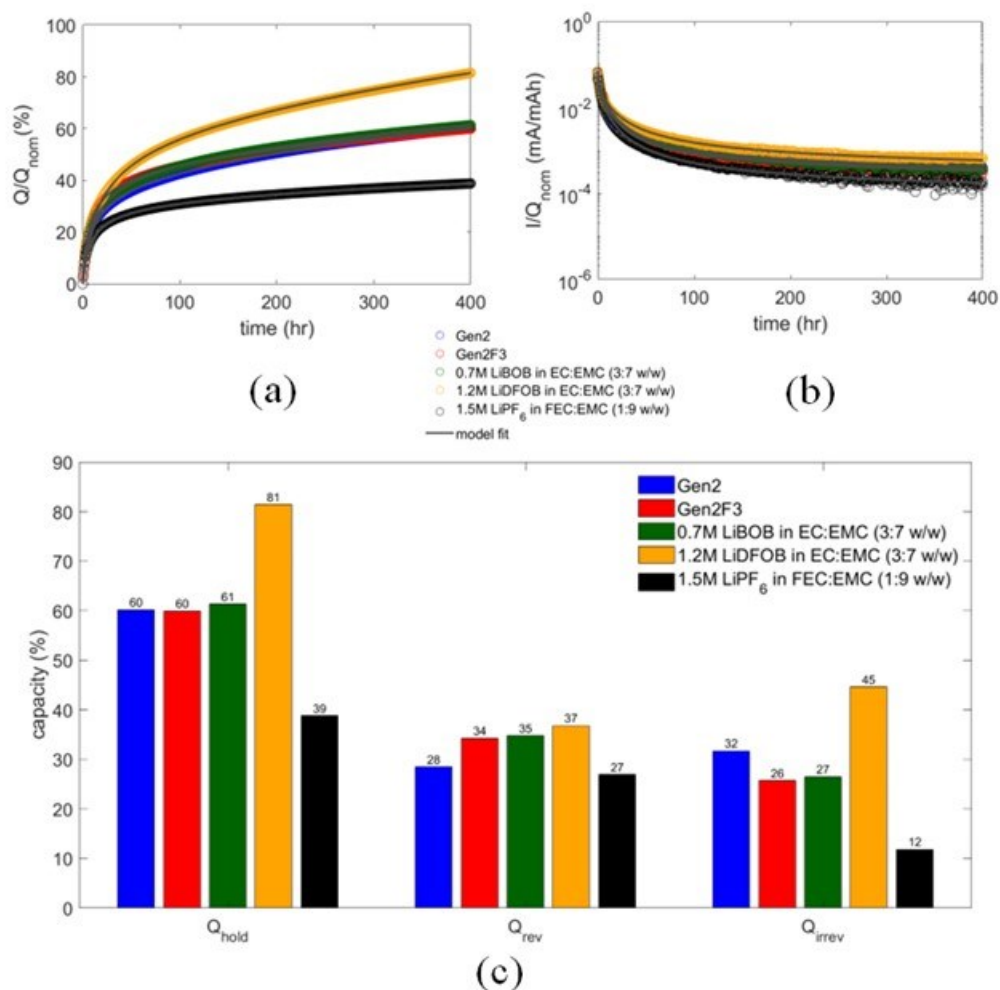


**Figure VII.3.15** (a) Normalized capacity, (b) normalized current during 400 hr voltage-hold on Si-LFP cells with five different electrolytes (data: symbols, lines: model fit). (c) Total, reversible (lithiation) and irreversible (SEI) capacities during the hold.

Total and deconvoluted reversible and irreversible capacities are shown in Figure VII.3.14(c). Irreversible capacities are lowest for the new 1.5 M LiPF<sub>6</sub> in FEC:EMC (1:9 w/w) electrolyte. Replacing the primary solvent EC in the baseline electrolyte with FEC is a promising pathway to improve calendar life. EC decomposition can form organic lithium alkyl carbonates (LEDC) and inorganic lithium carbonate, oxide (Li<sub>2</sub>CO<sub>3</sub>, Li<sub>2</sub>O) which seem to be not as favorable for parasitic currents as LiF and poly(VC) from FEC decomposition.

Finally, the model fits are extrapolated to delineate the calendar life for these electrolytes (Figure VII.3.16(a)). Here, the calendar life is normalized to the Gen2F3 baseline electrolyte. FEC:EMC electrolyte outperforms baseline Gen2F3 electrolyte by nearly 300%. LiBOB electrolyte performs like the baseline electrolyte while LiDFOB salt is bad for calendar life of Si cells. We find that FEC is important and much better than EC as the primary solvent for calendar life with Si. Reference performance test cycles after the voltage-hold are also indicative of the capacity fade in these electrolyte systems as compared to the nominal capacity. Baseline and FEC:EMC electrolyte systems have >100% capacity retention (Figure VII.3.16(b)) indicative of dominant

reversible lithiation as opposed to irreversible SEI growth during the 400 hour long hold. Over 100% capacity retention is possible through combined effects of (i) higher magnitude of reversible lithiation as compared to irreversible lithiation during the 400 hour hold for baseline and FEC:EMC system and (ii) use of oversized LFP in voltage-hold tests which can compensate for the irreversible losses for good electrolytes with low irreversible SEI capacity losses.

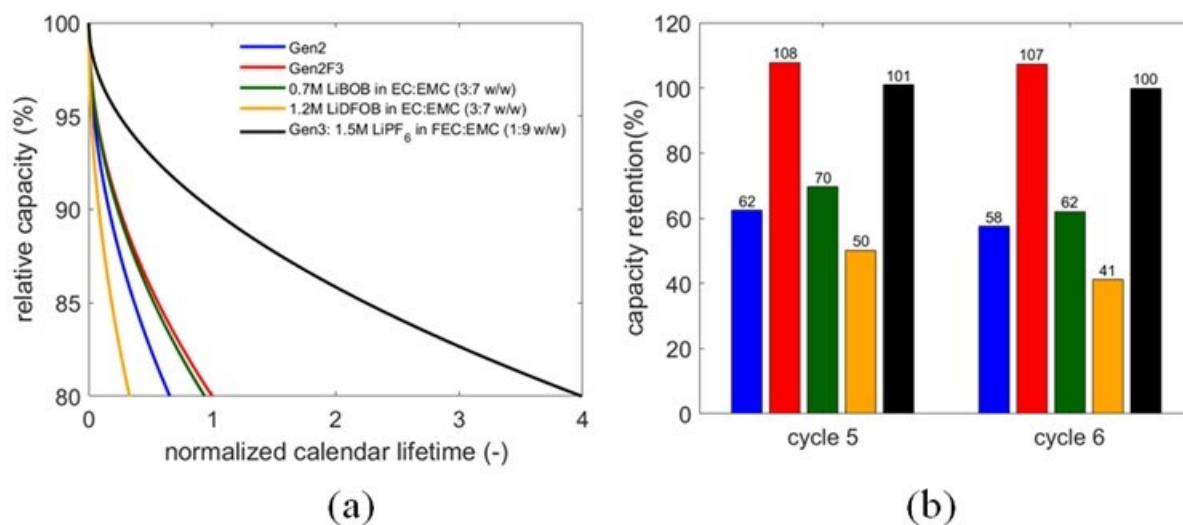


Figure VII.3.16 Comparison of (a) calendar life, and (b) reference performance test cycle capacities for the electrolytes investigated.

## Conclusions

### LBNL

- We used DFT to study EC decomposition at LIB cathodes, which has implications for SEI function due to cross-talk reactions. We found that the major reported reactions in the literature – electrochemical and chemical oxidation – are not favored under ambient conditions, while reactions between EC and oxygen anions are predicted to occur rapidly. We are continuing to explore electrolyte decomposition at LIB cathodes and intend in the future to create a reaction network that simultaneously considers reactions at cathodes and Si anodes.
- We developed an ML model to predict reaction energy barriers using orbital coefficients as input features. This model has been tested on a small dataset of SN2 reactions, and we intend in the near future to leverage the same model to predict the properties of reactions relevant to SEI formation at Si electrodes.

### ORNL

- We developed a new mathematical approach to describe interacting rigid molecules with the goal of enabling faster MD simulations of molecular liquids. We believe this approach has great potential for new ML coarse-grains potentials.
- We investigated the coexistence of various phases in Si anodes and discovered a new phase for this alloy that may play a role in the dynamics of Lithium in these anodes.
- We revisited a theoretical result on the energy barrier for the LiPF<sub>6</sub> decomposition and found qualitatively similar results, even if quantitatively our MD results indicate that the energy barrier for that decomposition to be about 30% lower than previously thought.

**NREL**

- We constructed a chemically complex, continuum-level single particle model to understand electrolyte decomposition and SEI formation on a Si nano-particle. The model considers facile decomposition for EC, EMC, and FEC to form common SEI species (e.g., LEDC, Li<sub>2</sub>CO<sub>3</sub>, LiF) and gaseous byproducts (e.g., CO, CO<sub>2</sub>, CH<sub>4</sub>, C<sub>2</sub>H<sub>2</sub>, C<sub>2</sub>H<sub>4</sub>, C<sub>2</sub>H<sub>6</sub>, C<sub>3</sub>H<sub>6</sub>, C<sub>3</sub>H<sub>8</sub>, and C<sub>4</sub>H<sub>8</sub>) based on atomistic mechanisms from LBNL.
- We used the continuum model to predict electrolyte and SEI composition during a 180 hr voltage hold. After calibration, the model correctly captures the irreversible leakage currents due to parasitic reactions at a variety of voltage holds (e.g., 100 mV, 150 mV, 175 mV, and 250 mV). The model is expected to be a key tool to communicate between atomistic predictions and experiment observations. Future work will include model/mechanism validation with gas-phase detection techniques after voltage-holds alongside required species solubility measurements.
- We developed a rapid calendar life screening method, which indicates that replacing ethylene carbonate (EC) with fluoroethylene carbonate (FEC) primary solvent alongside ethyl methyl carbonate (EMC) co-solvent enhances Si calendar life. FEC decomposition reaction can lead to lithium fluoride (LiF) and polymeric vinylene carbonate (poly(VC)) formation, combining beneficial passivating characteristics of electron insulation and elastomeric polymers, respectively.

**Key Publications****LBNL**

1. Daniel Barter, Evan Walter Clark Spotte-Smith, Nikita S. Redkar, Aniruddh Khanwale, Shyam Dwaraknath, Kristin A. Persson, Samuel M. Blau. “Predictive stochastic analysis of massive filter-based electrochemical reaction networks”. *Dig. Disc.* 2:123–137 (2023).
2. Evan Walter Clark Spotte-Smith, Thea Bee Petrocelli, Hetal D. Patel, Samuel M. Blau, Kristin A. Persson. “Elementary Decomposition Mechanisms of Lithium Hexafluorophosphate in Battery Electrolytes and Interphases”. *ACS Energy Lett.*, 8 no. 1:347–355 (2023).
3. Mingjian Wen, Evan Walter Clark Spotte-Smith, Samuel M. Blau, Matthew J. McDermott, Aditi S. Krishnapriyan, Kristin A. Persson. “Chemical reaction networks and opportunities for machine learning”. *Nat. Comput. Sci.*, 3:12–24 (2023).
4. Evan Walter Clark Spotte-Smith, Samuel M. Blau, Daniel Barter, Noel J. Leon, Nathan T. Hahn, Nikita S. Redkar, Kevin R. Zavadil, Chen Liao, Kristin A. Persson. “Chemical Reaction Networks Explain Gas Evolution Mechanisms in Mg-Ion Batteries”. *J. Am. Chem. Soc.*, 145 no. 22:12181–12192 (2023).
5. Evan Walter Clark Spotte-Smith, Orion Archer Cohen, Samuel M. Blau, Jason M. Munro, Ruoxi Yang, Rishabh D. Guha, Hetal D. Patel, Sudarshan Vijay, Patrick Huck, Ryan Kingsbury, Matthew K. Horton, Kristin A. Persson. “A database of molecular properties integrated in the Materials Project”. *Dig. Disc.* (2023).
6. Sudarshan Vijay, Maxwell C. Venetos, Evan Walter Clark Spotte-Smith, Aaron D. Kaplan, Mingjian Wen, Kristin A. Persson. “CoeffNet: Predicting activation barriers through a chemically-interpretable, equivariant and physically constrained graph neural network”. *In review* (2023).
7. Evan Walter Clark Spotte-Smith, Sudarshan Vijay, Thea Bee Petrocelli, Bernardine L.D. Rinkel, Bryan D. McCloskey, Kristin A. Persson. “A critical analysis of chemical and electrochemical oxidation mechanisms in Li-ion batteries”. *In preparation* (2023).

**ORNL**

1. Jean-Luc Fattebert. “A compact and symmetric quaternion-based representation of two interacting bodies”. *In preparation* (2023).
2. Jean-Luc Fattebert, Lorena Alzate-Vargas. “First-principles molecular dynamics and continuum solvent modeling of LiPF<sub>6</sub> decomposition”. *In preparation* (2023).

**NREL**

1. Maxwell C. Schulze, Marco-Tulio F. Rodrigues, Josefine D. McBrayer, Daniel P. Abraham, Christopher A. Apblett, Ira Bloom, Zonghai Chen, Andrew M. Colclasure, Alison R. Dunlop, Chen Fang, Katharine L. Harrison, Gao Liu, Shelley D. Minter, Nathan R. Neale, David Robertson, Adam P. Tornheim, Stephen E. Trask, Gabriel M. Veith, Ankit Verma, Zhenzhen Yang and Christopher Johnson. “Critical Evaluation of Potentiostatic Holds as Accelerated Predictors of Capacity Fade during Calendar Aging”. *J. Electrochem. Soc.*, 169 no. 5: 050531 (2022).
2. Peter J. Weddle, Evan Walter Clark Spotte-Smith, Ankit Verma, Hetal D. Patel, Kae Fink, Bertrand J. Tremolet de Villers, Maxwell C. Schulze, Samuel M. Blau, Kandler A. Smith, Kristin A. Persson, and Andrew M. Colclasure. “Continuum-level modeling of Li-ion battery SEI by upscaling atomistically informed reaction mechanisms”. *Electrochim. Acta*, 468:143121 (2023).
3. Ankit Verma, Maxwell C. Schulze, Andrew Colclasure, Marco-Tulio Fonseca Rodrigues, Stephen E. Trask, Krzysztof Pupek, Christopher S. Johnson, Daniel P. Abraham, “Assessing Electrolyte Fluorination Impact on Calendar Aging of Blended Silicon-Graphite Lithium-Ion Cells Using Potentiostatic Holds”. *J. Electrochem. Soc.*, 170 no. 7 (2023): 070516.
4. Ankit Verma, Avtar Singh, Andrew Colclasure. “On the Impact of Mechanics on Electrochemistry of Lithium-ion Battery Anodes” *JOM* (accepted) (2023).

**References**

1. Kang Xu. “Nonaqueous liquid electrolytes for lithium-based rechargeable batteries”. *Chem. Rev.*, 104 no. 10:4303-4418 (2004).
2. Josefine D. McBrayer, Marco-Tulio F. Rodrigues, Maxwell C. Schulze, Daniel P. Abraham, Christopher A. Apblett, Ira Bloom, Gerard Michael Carroll, Andrew M. Colclasure, Chen Feng, Katherine L. Harrison, Gao Liu, Shelley D. Minter, Nathan R. Neale, Gabriel M. Veith, Christopher S. Johnson, John T. Vaughey, Anthony K. Burrell, Brian Cunningham. “Calendar aging of silicon-containing batteries”. *Nat. Energy*, 6 no. 9:866-872 (2021).
3. Evan Walter Clark Spotte-Smith, Thea Bee Petrocelli, Hetal D. Patel, Samuel M. Blau, Kristin A. Persson. “Elementary Decomposition Mechanisms of Lithium Hexafluorophosphate in Battery Electrolytes and Interphases”. *ACS Energy Lett.*, 8 no. 1:347–355 (2023).
4. Sudarshan Vijay, Maxwell C. Venetos, Evan Walter Clark Spotte-Smith, Aaron D. Kaplan, Mingjian Wen, Kristin A. Persson. “CoeffNet: Predicting activation barriers through a chemically-interpretable, equivariant and physically constrained graph neural network”. *In review* (2023).
5. Peter J. Weddle, Evan Walter Clark Spotte-Smith, Ankit Verma, Hetal D. Patel, Kae Fink, Bertrand J. Tremolet de Villers, Maxwell C. Schulze, Samuel M. Blau, Kandler A. Smith, Kristin A. Persson, and Andrew M. Colclasure. “Continuum-level modeling of Li-ion battery SEI by upscaling atomistically informed reaction mechanisms”. *Electrochim. Acta*, 468:143121 (2023).
6. Bernardine L. D. Rinkel, David S. Hall, Israel Temprano, Clare P. Grey. “Electrolyte oxidation pathways in lithium-ion batteries”. *J. Am. Chem. Soc.*, 142 no. 35:15058-15074 (2020).
7. Chamithri Jayawardana, Nuwanthi Rodrigo, Bharathy Parimalam, Brett L. Lucht. “Role of Electrolyte Oxidation and Difluorophosphoric Acid Generation in Crossover and Capacity Fade in Lithium Ion Batteries”. *ACS Energy Lett.*, 6 no. 11:3788–3792 (2021).
8. Narbe Mardirossian, Martin Head-Gordon. “ $\omega$ B97X-V: A 10-parameter, range-separated hybrid, generalized gradient approximation density functional with nonlocal correlation, designed by a survival-of-the-fittest strategy”. *Phys. Chem. Chem. Phys.*, 16 no. 21:9904-9924 (2016).
9. Dmitrij Rappoport, Filipp Fursche. “Property-optimized Gaussian basis sets for molecular response calculations”. *J. Chem. Phys.*, 133(13):134105 (2010).
10. Marenich, A.V., Christopher J. Cramer, Donald G. Truhlar. “Universal solvation model based on solute electron density and on a continuum model of the solvent defined by the bulk dielectric constant and atomic surface tensions.” *J. Phys. Chem. B*, 113 no. 18:6378-6396 (2009).
11. Samuel M. Blau, Hetal D. Patel, Evan Walter Clark Spotte-Smith, Xiaowei Xie, Shyam Dwaraknath, Kristin A. Persson. “A chemically consistent graph architecture for massive reaction networks applied to solid-electrolyte interphase formation”. *Chem. Sci.*, 12 no. 13: 4931-4939 (2021).

12. Xiaowei Xie, Evan Walter Clark Spotte-Smith, Mingjian Wen, Hetal D. Patel, Samuel M. Blau, Kristin A. Persson. “Data-driven prediction of formation mechanisms of lithium ethylene monocarbonate with an automated reaction network”. *J. Am. Chem. Soc.*, 143 no. 33:13245-13258 (2021).
13. Evan Walter Clark Spotte-Smith, Ronald L. Kam, Daniel Barter, Xiaowei Xie, Tingzheng Hou, Shyam Dwaraknath, Samuel M. Blau, Kristin A. Persson. “Toward a mechanistic model of solid–electrolyte interphase formation and evolution in lithium-ion batteries”. *ACS Energy Let.*, 7 no. 4:1446-1453 (2022).
14. Daniel Barter, Evan Walter Clark Spotte-Smith, Nikita S. Redkar, Aniruddh Khanwale, Shyam Dwaraknath, Kristin A. Persson, Samuel M. Blau. “Predictive stochastic analysis of massive filter-based electrochemical reaction networks”. *Dig. Disc.*, 2:123–137 (2023).
15. Evan Walter Clark Spotte-Smith, Samuel M. Blau, Daniel Barter, Noel J. Leon, Nathan T. Hahn, Nikita S. Redkar, Kevin R. Zavadil, Chen Liao, Kristin A. Persson. “Chemical reaction networks explain gas evolution mechanisms in Mg-ion batteries”. *J. Am. Chem. Soc.*, 145 no. 22: 12181–1219 (2023).
16. Lorena Alzate-Vargas, Samuel M. Blau, Evan Walter Clark Spotte-Smith, Srikanth Allu, Kristin A. Persson, Jean-Luc Fattebert. “Insight into SEI growth in Li-ion batteries using molecular dynamics and accelerated chemical reactions”. *J. Phys. Chem. C*, 125 no. 34:18588-18596 (2021).
17. Yasuharu Okamoto. “Ab initio calculations of thermal decomposition mechanism of LiPF<sub>6</sub>-based electrolytes for lithium-ion batteries”. *J. Electrochem. Soc.*, 160 no. 2:A404.
18. Jean-Luc Fattebert, François Gygi. “Density Functional Theory for Efficient Ab Initio Molecular Dynamics Simulations in Solution”. *J. Comput. Chem.*, 23:662–666 (2002).
19. Maxwell C. Schulze, Marco-Tulio F. Rodrigues, Josefine D. McBrayer, Daniel P. Abraham, Christopher A. Ablett, Ira Bloom, Zonghai Chen, Andrew M. Colclasure, Alison R. Dunlop, Chen Fang, Katharine L. Harrison, Gao Liu, Shelley D. Minter, Nathan R. Neale, David Robertson, Adam P. Tornheim, Stephen E. Trask, Gabriel M. Veith, Ankit Verma, Zhenzhen Yang and Christopher Johnson (2022). “Critical Evaluation of Potentiostatic Holds as Accelerated Predictors of Capacity Fade during Calendar Aging”. *J. Electrochem. Soc.*, 169 no. 5 (2022): 050531.
20. Ankit Verma, Maxwell C. Schulze, Andrew Colclasure, Marco-Tulio Fonseca Rodrigues, Stephen E. Trask, Krzysztof Puppek, Christopher S. Johnson, Daniel P. Abraham, “Assessing Electrolyte Fluorination Impact on Calendar Aging of Blended Silicon-Graphite Lithium-Ion Cells Using Potentiostatic Holds”. *J. Electrochem. Soc.*, 170 no. 7 (2023): 070516.
21. Koji Abe, Yoshihiro Ushigoe, Hideya Yoshitake, Masaki Yoshio. “Functional electrolytes: Novel type additives for cathode materials, providing high cycleability performance”. *J. Power Sources*, 153 no. 2: 328-335 (2006).
22. Roland Jung, Michael Metzger, Filippo Maglia, Christoph Stinner, Hubert A. Gasteiger. “Oxygen Release and Its Effect on the Cycling Stability of Li<sub>Nix</sub>MnyCozO<sub>2</sub> (NMC) Cathode Materials for Li-Ion Batteries”. *J. Electrochem. Soc.*, 164:A1361.
23. Anna T.S. Freiberg, Matthias K. Roos, Johannes Wandt, Regina de Vivie-Riedle, Hubert A. Gasteiger. “Singlet oxygen reactivity with carbonate solvents used for Li-ion battery electrolytes”. *J. Phys. Chem. A*, 122 no. 45:8828–8839 (2018).
24. Guido Falk von Rudorff, Stefan N. Heinen, Marco Gragato, O. Anatole von Lilienfeld. “Thousands of reactants and transition states for competing e<sub>2</sub> and s<sub>2</sub> reactions”. *Mach. Learn. Sci. Tech.*, 1:045026 (2020).

## Acknowledgements

**LBNL:** Samuel M. Blau (now Research Scientist at LBNL), Mingjian Wen (now Assistant Professor at University of Houston), Hetal D. Patel, Evan Walter Clark Spotte Smith, Xiaowei Xie (now at Schrodinger, Inc.) **ORNL:** Lorena Alzate Vargas (now at Los Alamos National Laboratory), Gang Seob (G.S.) Jung, and **NREL:** Ankit Verma, Peter Weddle, Francois Usseglio-Viretta, Andrew Colclasure, Kandler Smith



## VII.4 Rationally Designed Lithium-Ion Batteries Towards Displacing Internal Combustion Engines (Group14 Technologies)

### Henry R. Costantino, Principal Investigator

Group14 Technologies, Inc.  
8502 Maltby Road  
Woodinville WA 98072  
E-mail: [rcostantino@group14.technology](mailto:rcostantino@group14.technology)

### Brian Cunningham, DOE Technology Development Manager

U.S. Department of Energy  
E-mail: [Brian.Cunningham@ee.doe.gov](mailto:Brian.Cunningham@ee.doe.gov)

Start Date: January 1, 2022                      End Date: December 31, 2023  
Project Funding: \$4,778,026                      DOE share: \$3,761,695                      Non-DOE share: \$1,016,331

### Project Introduction

Group14 Technologies is leading a world-class team composed of Cabot Corporation, Silatronix, Arkema, Pacific Northwest National Laboratories, and Farasis Energy USA to research, fabricate, test and demonstrate lithium ion batteries (LIB) implementing  $\geq 30\%$  silicon-carbon (Si-C) composite anodes achieving aggressive next generation automotive energy targets. The project's centerpiece technology is Group14's high performing Si-C composite anode material already proven to provide 35% increased energy density at 12% composite blended with graphite, >1000 cycle stability, and a projected cell cost of <\$125/kWh in conventional LIBs under a prior DOE VTO award (DE-EE0001201). This project advances this baseline by taking a holistic approach to increase silicon content for higher energy density and to improve calendar and cycle life through the optimization and incorporation of carbon additives, surface coatings and binders for the anode along with high performance co-solvent electrolyte additives. These anode improvements are being paired with high-nickel, low-cobalt, commercially available cathode to achieve the project's performance targets.

### Objectives

This three year project will culminate in a  $\geq 0.4\text{Ah}$  pouch cell which demonstrates targets of >350 Wh/kg, >750 Wh/L, >1000 cycle stability, and >10 year calendar life. This target will be achieved incrementally each year of the project with a LIB build achieving the baseline, interim and final cell targets listed below in Table VII.4.1:

**Table VII.4.1 Electrochemical Objectives for DoE Project – EE0009187.**

Objective	Metric	Baseline	Interim	Final
Useable Specific Energy at 30°C and C/3	Wh/kg	>340	>340	>340
Useable Energy Density at 30°C and C/3	Wh/L	>750	>750	>750
Calendar Life	Years to 20% fade	>3	>5	>10
Cycle Life (C/3 deep discharge to 350 Wh/kg)	Cycles to 20% fade	$\geq 300$	$\geq 600$	$\geq 1000$

### Approach

Our approach is to leverage Group14 Technologies' carbon and Si-C composite expertise in conjunction with our partnering organizations' expertise to holistically improve the performance of a LIB as measured by our

yearly electrochemical targets. Within this collaboration, each of our partners contribute a unique approach toward improving the battery:

- **Group14 Technologies:** Our core technology is to create a composite material that accounts for and overcomes the failings of traditional silicon based anode material solutions. The basis for Group14 Si-C's superior performance is its rationally designed structure. At its foundation is an amorphous carbon scaffold, with its porosity fine-tuned for promoting intra-particle growth of the desired type and size of silicon. The resulting Si-C composite includes internal void space to buffer expansion, nano-silicon to prevent particle fracture with cycling, and a carbon scaffold to enhance conductivity and particle integrity while minimizing exposed silicon surface area. Our approach for this project is to further optimize both the carbon scaffold and to modify the resulting Si-C in order to protect the surface from adverse interactions that may negatively impact cell performance.
- **Cabot Corporation:** Global leader in nanoengineered conductive carbon additives for LIBs. Their role in the project is: (1) to assist Group14 in characterization of carbon and resulting Si-C and (2) to optimize the carbon additive type and loading to maximize performance.
- **Silatronix:** Producers of organosilicon co-solvent additives that improve LIB cycle and calendar stability. Silatronix pioneered industrial relevant analytical methods for investigating silicon-electrolyte interactions, including quantitative gassing analysis and identification of degradation mechanisms. Leveraging their expertise, they will produce an optimized electrolyte formulation that will synergize with Group14 Si-C to extend battery life by controlling degradation mechanisms.
- **Arkema:** A specialty chemicals and advanced materials developer and supplier that successfully commercialized several electrode binders and separators coating resins, especially for high-energy, high-voltage LIBs. Their role in the project is to develop an optimized binder solution to maximize cohesion of Group14's Si-C composite with other anode components and to promote the long term cycling and calendar performance of the battery.
- **Farasis Energy USA:** A leading U.S. developer and supplier of LIBs for EVs. Farasis has designed and built its own Li-ion cell and battery system manufacturing plant and has been in high volume production since 2010 with fully automated production capability of 4 GWh/y. By leveraging Farasis' battery production research and experience the best design and form factor of LIB will be utilized to promote high energy density and increase cycle life.
- **Pacific Northwest National Lab (PNNL):** World-renowned experts in energy storage research. PNNL lead in mechanistic investigations regarding LIB materials and assure the guidance to the project towards success. PNNL provides critical advanced materials characterization support toward synergizing the team's optimization efforts.

## Results

In the last annual progress report, we discussed the projected interim cell cycle life and baseline calendar life data. For the current reporting period, we now have final data available for the interim build. These data are shown in Figure VII.4.1 and Figure VII.4.2 for cycle life and calendar life, respectively.

The cycling of the cells, the data collection, and data analysis were all conducted at Farasis. These data confirm the marked improvement in the interim build cell performance compared to the baseline cell performance. Specifically, the final data for the interim cells demonstrated performance exceeding 800 cycle stability, well above the interim target.

For the calendar life test, cells were stored at 30°C and 45°C with 100% state of charge (SoC) for 30 days increments. Battery performance was then measured after each 30 day interval at a C/3 rate followed by an HPPC test at C/10 rate (1C pulse) and charge-discharge at C/3 to calculate the capacity. As can be seen, there was relatively low degradation in performance observed, for example, the capacity loss after 9 months was as low as 5.5%. Performance of the interim build cells was comparable to the baseline build with respect to calendar life.

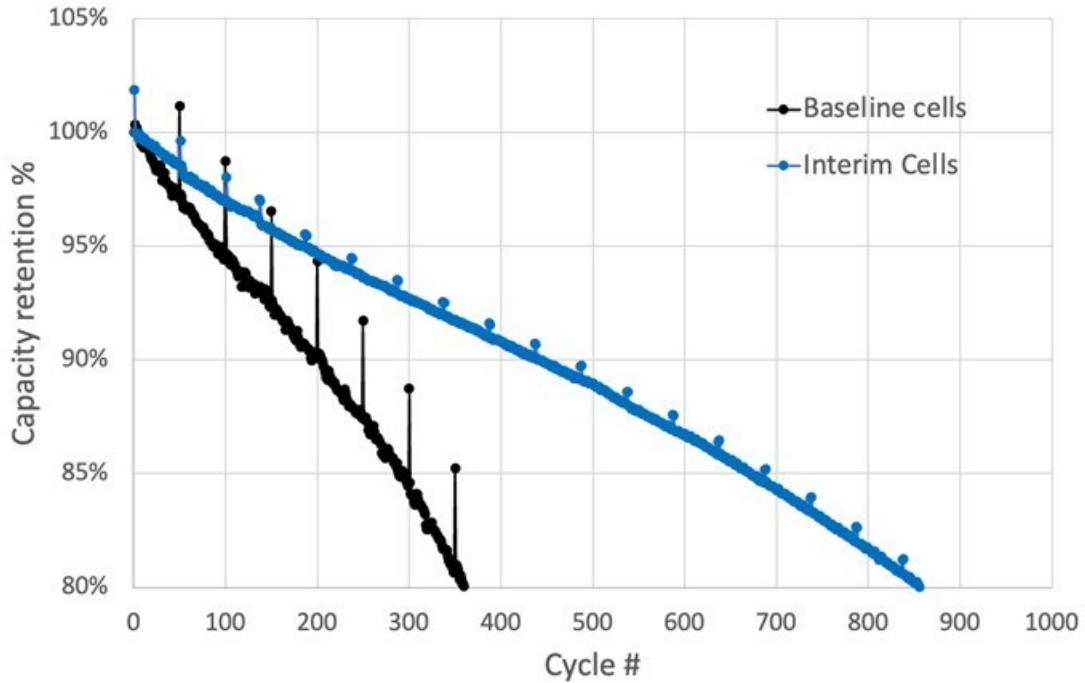


Figure VII.4.1 Interim build battery performance (Farasis cycling data) improvement over baseline.

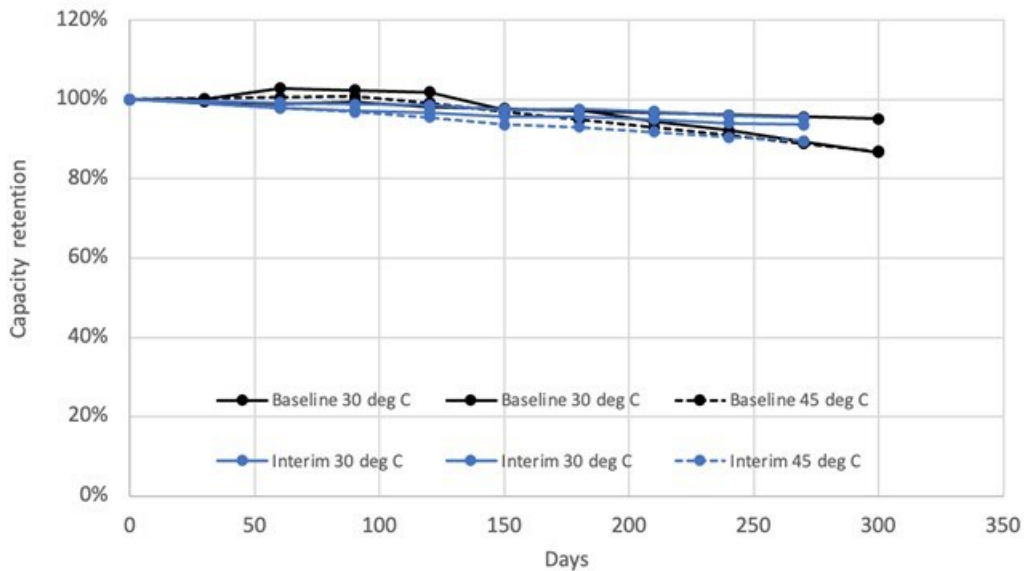


Figure VII.4.2 Calendar life update for interim & baseline batteries comprising Group14 Si-C.

The primary objective for 2023 was focused on completing the final cell build. The workstream Full cell final screening with combined down selected battery components was completed as part of the post-interim screening builds. Cell cycling data for the screening cells was supplied by Farasis and reviewed among all partners. Variants tested did not exceed the performance of the interim build cells. Based on the results of the full cell final screening, a new workstream focused on a Pre-final build was initiated and completed. This build included the planned components of the final battery build. The performance of the pre-final build cells is

projected to be lower than the interim cell build. Based on this data, additional work is planned to exceed the interim cell build performance.

### **Conclusions**

The pre-final build was completed using the planned components that will go into the final build. The performance of the pre-final build cells is projected to be lower than the interim cell build. Based on this data the project has been extended into 2024. Activities will focus on achieving and exceeding the interim build cell performance.

### **Acknowledgements**

The PI thanks Dan Casioppo for managing the project and Avery Sakshaug, Dr. Abirami Dhanabalan, Dr. Nate Phillip and Dr. Rajan Patel (Group14 Technologies) for their critical contributions to the project. The PI would also like to thank Cabot, Arkema, Farasis and Silatronix for their guidance on the project using their excellent domain expertise. Finally, the PI would like to thank Dr. Chongmin Wang of PNNL for his many contributions to the characterization of key materials throughout the project.

## VII.5 Ultra-Low Volume Change Silicon-Dominant Nanocomposite Anodes for Long Calendar Life and Cycle Life (Sila Nanotechnologies)

### Naoki Nitta, Principal Investigator

Sila Nanotechnologies  
2470 Mariner Square Loop  
Alameda, CA 94501  
E-mail: [mnitta@silanano.com](mailto:mnitta@silanano.com)

### John Tannaci, Co-Principal Investigator

Sila Nanotechnologies  
2470 Mariner Square Loop  
Alameda, CA 94501  
E-mail: [jtannaci@silanano.com](mailto:jtannaci@silanano.com)

### Carine Steinway, DOE Technology Development Manager

U.S. Department of Energy  
E-mail: [Carine.Steinway@ee.doe.gov](mailto:Carine.Steinway@ee.doe.gov)

Start Date: October 1, 2020      End Date: December 31, 2023  
Project Funding: \$4,600,000      DOE share: \$3,600,000      Non-DOE share: \$1,000,000

### Project Introduction

Today's state-of-the-art Li-ion battery cells use a small fraction of silicon in the anode to boost cell energy density. Anode silicon content is kept low because higher amounts would cause massive volume change, resulting in undesirable electrolyte reactions which have detrimental effects on both calendar and cycle life. Batteries for automotive applications have particularly stringent calendar and cycle life requirements, posing a challenging problem for high energy density cell development. However, higher energy density cells are able to deliver more energy storage per cell and therefore open a path to achieving lower cost.

Sila's silicon-dominant anode material technology is manufactured with scalable processes and inputs, and has ultra-low volume change, enabling high-capacity anodes to achieve both long calendar and cycle life. Sila Nanotechnologies has already begun commercial sales of its silicon anode material for consumer applications, starting with wearable electronics, and is scaling up production to enter larger battery markets. This project applies Sila's anode technology to research, develop, fabricate, and validate high energy density silicon-dominant Li-ion battery cells meeting automotive cycle life and calendar life requirements.

### Objectives

The objective is to research, fabricate, and test lithium battery cells that implement  $\geq 30\%$  silicon content electrodes with commercially available cathode technology and achieve cell performance identified in Table VII.5.1.

Table VII.5.1 Cell Performance Targets.

Beginning of Life Characteristics at 25 °C	Cell Level
Usable Specific Energy @ C/3	>350Wh/kg
Usable Energy Density @ C/3	>750Wh/L
Calendar Life @ C/3	>10 Years
Cycle Life (C/3 deep discharge to 350Wh/kg, <20% energy fade)	>1,000

## Approach

Sila's nano-engineered particles enable ultra-low volume change silicon-dominant anodes and are the most promising candidate for silicon-based electric vehicle Li-ion batteries. This project utilizes Sila's proprietary particles and know-how for its application in standard Li-ion battery manufacturing processes. Both the bulk and surface properties of the particle are engineered for improved performance, and the electrode construction process is optimized around the adjustments made to the particle, as are electrolyte formulations. Sila's state of the art analysis techniques are also employed, and new methods are developed to understand how material and process changes impact cell performance.

## Results

Various improvements were made to Sila's silicon Li-ion battery chemistry and production process at the particle, electrode, and electrolyte levels.

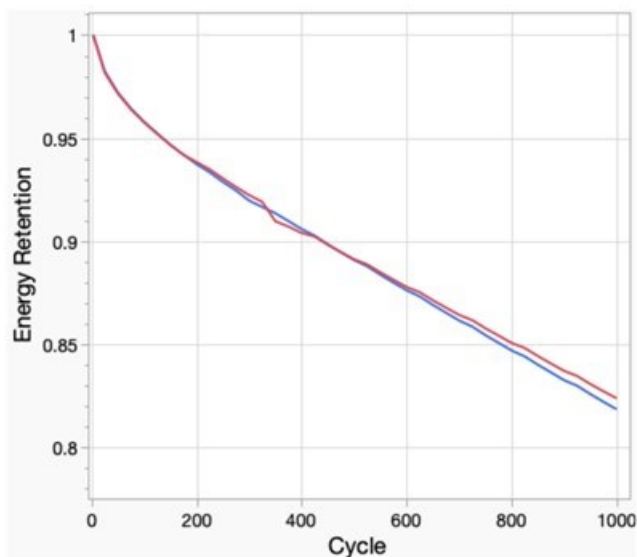


**Figure VII.5.1 Expected cycle life of Final Cells**

Figure VII.5.1 shows the cycling energy retention of the anode, electrolyte, cathode combination that will be used in final cells to be delivered at the end of the grant. When scaled to 40+ Ah cells, this design can deliver 926 Wh/L and 355 Wh/kg at the cell level, meeting the objective of the grant.

While the calendar life of this specific anode, electrolyte, cathode combination have not been tested for extended durations, the interim cells had exceptional calendar life, exhibiting 10+ years to 560 Wh/L at 30 °C. Further testing at Sila also led to the identification of a cocktail of commercial electrolyte additives that decreases calendar life losses by ~20% (for 1 month storage at 60°C and 100% SOC) (see Figure VII.5.2).

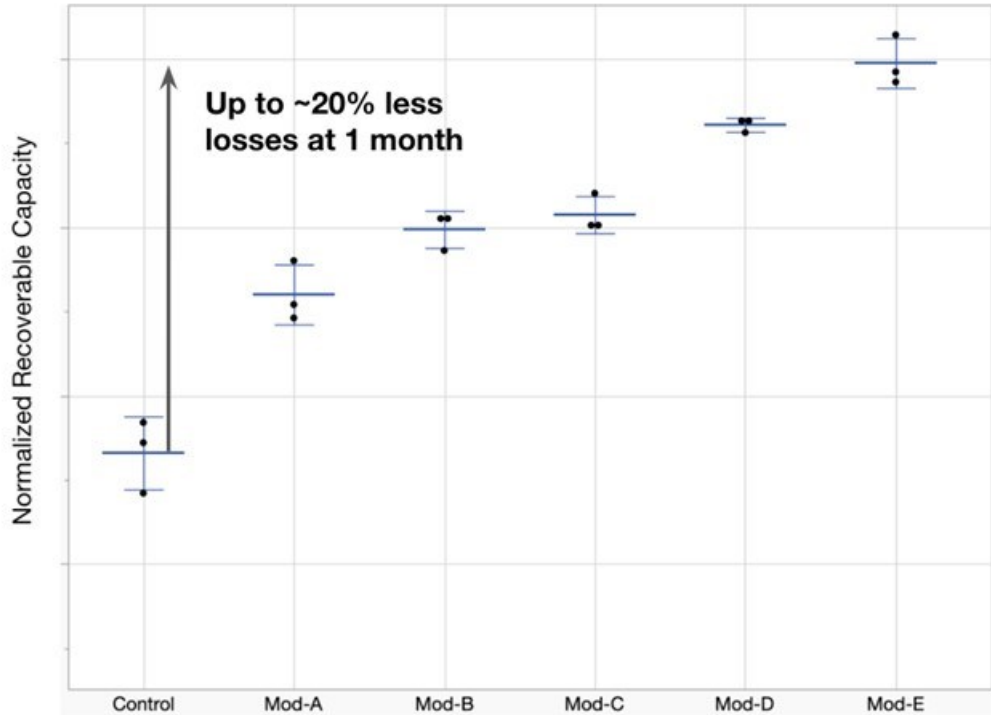


Figure VII.5.2 Improvement in normalized recoverable capacity of cells after 1 month of storage at 100% SOC and 60°C via electrolyte modification through cocktails of commercial additives.

### Conclusions

Between Sila's interim cells from the previous reporting period showing 10+ years to 560Wh/L at 30°C and 100% SOC, and the identification of the commercial electrolyte additive cocktail to extend calendar life, Sila is on track to meeting all final grant milestones.

### Acknowledgements

In earlier performance periods of the grant, Sila partnered with the Igor Luzinov from the Army Research Laboratory (ARL) to simulate reaction mechanisms to understand electrolyte decomposition mechanisms, and with Jiguang Zhang and Xia Cao from the Pacific Northwest National Laboratory (PNNL) to develop Localized High Concentration Electrolytes for higher automotive commercial readiness.

## VII.6 Solid State Li Ion Batteries Using Si Composite Anodes (Solid Power Inc.)

### **Pu Zhang, Principal Investigator**

Solid Power Inc.  
486 S Pierce Ave, Suite E  
Louisville, CO 80027  
E-mail: [pu.zhang@solidpowerbattery.com](mailto:pu.zhang@solidpowerbattery.com)

### **Thomas Do, DOE Technology Development Manager**

U.S. Department of Energy  
E-mail: [Thomas.Do@ee.doe.gov](mailto:Thomas.Do@ee.doe.gov)

Start Date: October 1, 2022	End Date: September 30, 2023	
Project Funding (FY23): \$1,672,852	DOE share: \$1,338,281	Non-DOE share: \$334,571

### **Project Introduction**

Solid Power is teaming with Argonne National Laboratory (Dr. Wenquan Lu) to develop an all-solid-state lithium-ion battery (ASSB) that will achieve high energy, long cycle life, and long calendar life. It is based on a high-capacity solid-state Si composite anode. The project will enable scalable production of large format all-solid-state batteries required by the vehicle market.

### **Objectives**

The project objective is to develop all-solid-state Li ion batteries that implement high energy silicon anodes for EV application. The all solid state battery (ASSB) cell will be able to deliver > 350 Wh/kg specific energy, > 750 Wh/L energy density, > 1000 cycle life, and > 10 years calendar life.

### **Approach**

The project will develop a solid state electrolyte (SSE) for Si anode and synthesize a Si-SSE composite anode. The solid state electrolyte system addresses the calendar life challenge of the Si anode batteries by forming highly stable SEI. A high-Ni content NMC cathode will be selected to match the Si anode. The all-solid-state cell will be assembled by scalable roll-to-roll processes developed by Solid Power.

### **Results**

#### ***Si composite anode development***

The Si composite was synthesized by integrating a Si powder and a Solid Power's sulfide solid state electrolyte (SSE). The Si-SSE composite material was mixed with a binder, a conductive carbon additive and a solvent to form an anode slurry. The slurry was then coated to Cu foil to form an electrode. A roll-to-roll process has been developed to coat the Si anode. Figure VII.6.1 shows a Si anode coated by a slot-die coater.

High energy Si composite anodes have been successfully developed with reversible capacity of >1500 mAh/g at electrode level.





**Figure VII.6.1 Continuous Si anode coating**

To verify the high energy anode capacity, Si-Li half cells were built and tested at C/5 – C/5, 0.05 – 1.0V, and 45°C. The anode was slurry-cast at a loading of 3 mAh/cm<sup>2</sup>. Performance of three generations of anodes is compared in Figure VII.6.2, the anodes developed under this project achieved capacities ranging from 1500 to 2100 mAh/g, which is 50% - 110% higher than the baseline. By evaluating the trade-off on capacity vs. cycling stability, the high energy anode with capacity of 1500 mAh/g has been selected for the pouch cell development. The comparison is shown in Table VII.6.1.

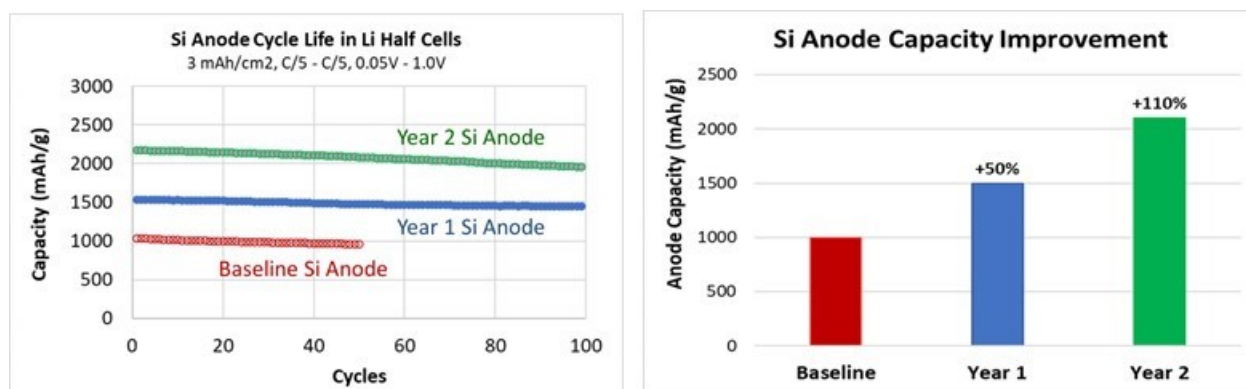


**Figure VII.6.2 Cycle life of the baseline and ultra-high energy (UHE) Si anodes in Li half cells (3 mAh/cm<sup>2</sup> loading, C/5 – C/5, 0.05 – 1.0V): (left) Si anode capacity vs. cycle; (right) capacity improvement achievement under the project.**

**Table VII.6.1 Capacity and Cycle Life of the Si Anodes**

Property	Baseline Si Anode (before the project)	High Energy Si Anode	Ultra-high Energy Si Anode
Reversible Capacity (at Electrode Level)	1000 mAh/g	1500 mAh/g	2100 mAh/g
Capacity Retention at Cycle 100	N/A	95%	90%

**Full pouch cell demonstration**

NMC622 cathode was selected to match the Si anode to form a full pouch cell. The solid state pouch cell was assembled with NMC cathode (at 3 mAh/cm<sup>2</sup> loading), SSE separator, and Si composite anode (A to C ratio of 1.10). When cycled at C/5 – C/5, 2.5 – 4.1V, and 45°C, the cell shows 90% first cycle efficiency and retains 80% capacity after 1100 cycles (Figure VII.6.3).

Calendar life of a full pouch cell was also evaluated. After storage at 4.1V and 50 °C for 256 days, the cell recovers 93% of initial energy. The cell energy over the storage period is plotted in Figure VII.6.4. The result confirms the proposed excellent calendar life of the all-solid-state Si cell.

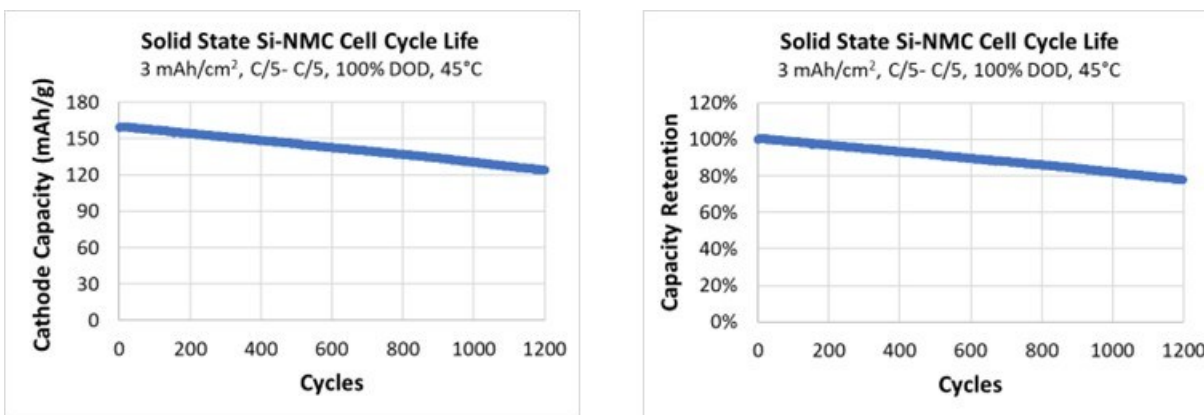


Figure VII.6.3 Cycle life of a Si-NMC full pouch cell (3 mAh/cm<sup>2</sup> loading, C/5–C/5, 2.5–4.1 V, 45°C). The cell retains 80% of initial capacity after 1100 cycles.

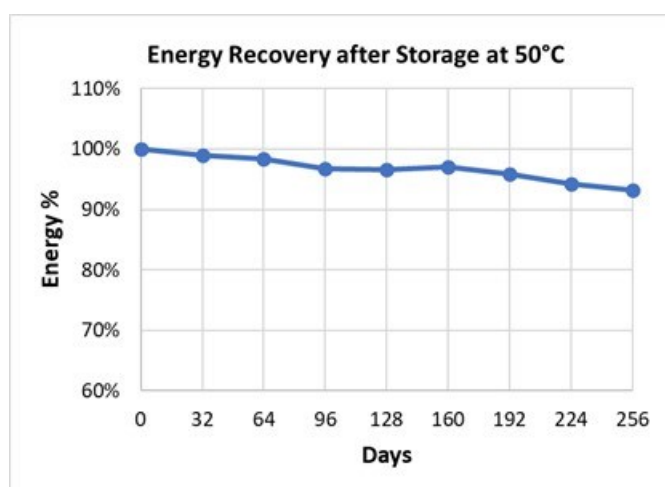


Figure VII.6.4 Calendar life of a Si-NMC full pouch cell. The cell is charged to 4.1V at C/10 and stored at 50°C. After various storage periods, the cell discharge energy is checked at C/10 and 2.5 – 4.1V. The cell recovers 93% of initial energy after 256 days.

## Conclusions

Si-SSE composite materials have been developed with a specific capacity >1500 mAh/g (at electrode level). A Si anode with the loading of 3.3 mAh/cm<sup>2</sup> was coated by using a roll-to-roll process. All-solid-state NMC-Si pouch cells have been assembled and tested. The cycle life of 1100 at 100% DOD and 45°C has been demonstrated in all-solid-state Si-NMC pouch cells. Long term stability of the all-solid-state cell is also confirmed via a high temperature storage test.

## VII.7 Fully Fluorinated Local High Concentration Electrolytes Enabling High Energy Density Si Anodes (Stony Brook University)

### Amy Marschilok, Principal Investigator

Stony Brook University  
100 Nicolls Road, 675 Chemistry  
Stony Brook, NY 11790-3400  
E-mail: [amy.marschilok@stonybrook.edu](mailto:amy.marschilok@stonybrook.edu)

### Nicolas Eidson, DOE Technology Development Manager

U.S. Department of Energy  
E-mail: [Nicolas.Eidson@ee.doe.gov](mailto:Nicolas.Eidson@ee.doe.gov)

### Thomas Do, DOE Technology Development Manager

U.S. Department of Energy  
E-mail: [Thomas.Do@ee.doe.gov](mailto:Thomas.Do@ee.doe.gov)

Start Date: October 1, 2020  
Project Funding: \$300,000

End Date: September 30, 2023  
DOE share: \$300,000

Non-DOE share: \$0

### Project Introduction

Silicon (Si) is highly desirable as an anode material for next-generation automotive battery cells due to its low operating potential and >3500 mAh/g specific capacity, ~10x graphite. However, during electrochemical cycling using conventional Li-ion electrolyte systems, the solid electrolyte interphase (SEI) which forms on Si is not stable, consuming electrolyte in each cycle and limiting cycle life.<sup>1</sup> The dynamic growth of the SEI is further aggravated by the large silicon volume change (>300%) in each (de)lithiation cycle. Thus, a critical need to enable practical Si-based anodes for high energy density is the development of novel electrolytes that result in mechanically and chemically stable SEI.

### Objectives

The objective is to research, fabricate, and test lithium battery cells that implement  $\geq 30\%$  silicon content electrodes with commercially available cathode technology and have the potential to achieve the potential to achieve 1000 cycles with >350 Wh/kg, >750 Wh/L, and <20% energy fade.

### Approach

The technological approach is to use fluorinated localized high concentration electrolytes (LHCEs), where each component of the electrolyte contains at least one fluorine in its structure, to construct a functional SEI on Si based anodes. The approach combines the SEI modification strategies of fluorinated carbonate solvents and local high concentration electrolytes. The resulting synergy of anion and fluorinated solvent decomposition will form a mechanically robust, fluorinated SEI that enables extended cycling with high capacity retention. Diluting the LiFSI/fluorinated carbonate concentrated electrolyte with inert hydrofluoroethers will reduce viscosity and increase wettability while preserving the coordination environment of the concentrated electrolyte. The strong electron withdrawing fluorine substituents on the solvents will enable high oxidative stability, permitting the Si-based anode to be paired with NMC811 cathodes.

### Results

#### 1. Microscopy Characterization of Solid Electrolyte Interphase Layer

The morphology of the solid electrolyte interphase formed on Si-graphite electrodes during cycling was using electron microscopy. Si-graphite electrodes were recovered from Si-graphite/NMC622 pouch cell batteries

after cycling 100x at a C/3 rate, using either the Generation 2 electrolyte which exhibited the highest capacity retention in a full cell configuration (Gen2 LHCE #1) or control electrolyte which incorporated fluoroethylene carbonate (1M LiPF<sub>6</sub> 3/7 EC/DMC + 10% wt. FEC). Electrochemical cycling results of the specific cells from which electrodes were harvested for analysis post 100 cycles are shown in Figure VII.7.1. After 100 cycles, the capacity retentions of the LHCE and control cells were 68% and 55%, respectively.

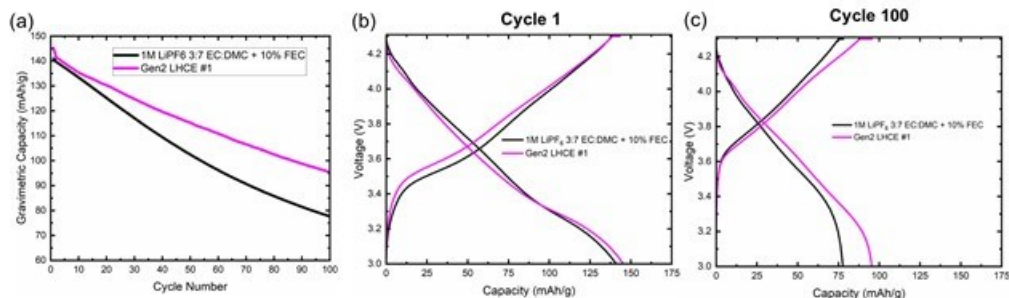


**Figure VII.7.1** Electrochemical cycling of Si-graphite/NMC622 full cells cycled using either LHCE or control electrolyte (1M LiPF<sub>6</sub> 3/7 EC/DMC +10% FEC). (a) Gravimetric capacity vs. cycle number; (b, c) Voltage profiles of (b) cycle 1 and (c) cycle 100.

The Si-graphite electrodes were recovered from the cells post cycling by rinsing with dimethyl carbonate and drying under vacuum. High resolution scanning electron microscopy images of the electrodes were collected using a JEOL 7600 instrument and are shown in Figure VII.7.2. Imaging of a pristine Si-graphite electrode shows graphite particles 6 – 10 μm in diameter intermixed with smaller Si nanoparticles with approximately 100 nm diameter. Images of the electrodes post cycling reveal that the SEI formed in the LHCE is more uniform and conformal over Si and graphite particles compared to the SEI formed in the control electrolyte.

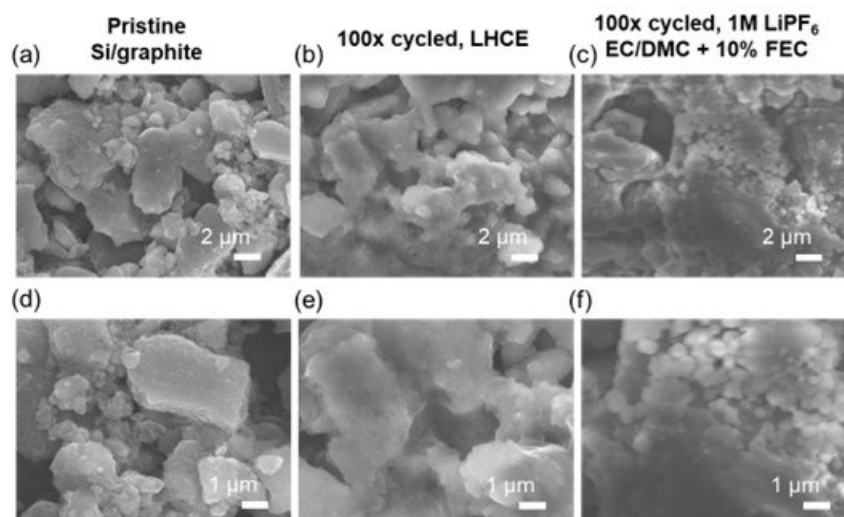


**Figure VII.7.2** Secondary electron SEM images of (a,b) pristine Si-graphite electrode, and electrode after cycling 100x in (b, e) LHCE, (c,f) 1M LiPF<sub>6</sub> EC/DMC + 10% FEC. Images are shown at magnifications of (a-c) 5000x and (d-f) 10,000x.

Energy dispersive spectroscopy measurements were also collected on the cycled electrodes (Figure VII.7.3). For electrodes cycled in either electrolyte, significant oxygen and fluorine containing species were observed within the SEI. Notably, S-containing species were observed uniformly in the SEI for the electrode cycling in the LHCE, suggesting inclusion of anion (fluorosulfonyl imide, FSI) derived species interphase layer. In contrast, for the control cycled electrode which utilized LiPF<sub>6</sub> salt, phosphorous was found to be heterogeneously distributed across the electrode surface.

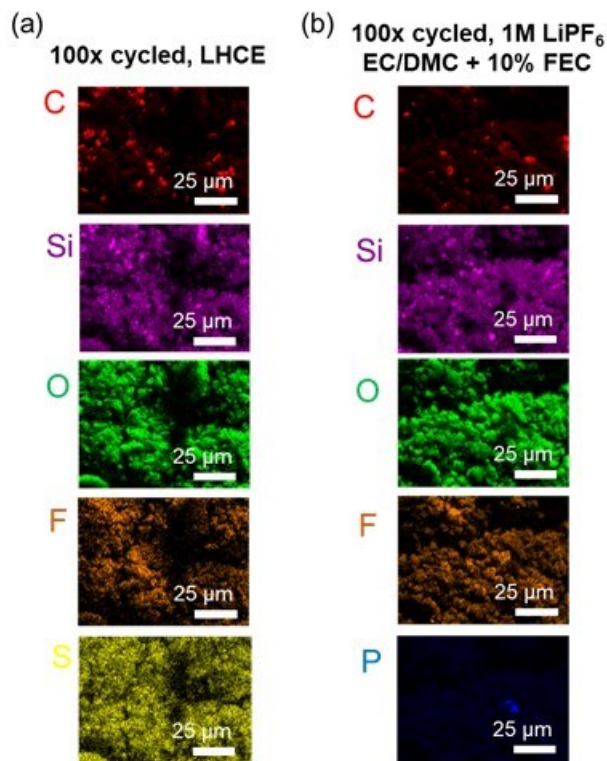


**Figure VII.7.3** Energy dispersive spectroscopy (EDS) images of Si-graphite electrodes after cycling 100x in (a) LHCE or (b) 1M LiPF<sub>6</sub> EC/DMC + 10% FEC.

Cryogenic transmission electron microscopy (cryo-TEM) was used to further characterize morphology and composition of SEI layers formed on 100x cycled Si-graphite anodes (Figure VII.7.4). Cryo-TEM stabilizes beam-sensitive and air-reactive battery materials upon beam exposure inside the microscope at liquid nitrogen temperature, enabling high-resolution structural and chemical characterization of the SEI. As shown in Figure VII.7.4, SEI layers generated in the LHCE and control electrolytes have a similar thickness of around 30-40 nm and exhibit a mosaic configuration where inorganic nanocrystals are embedded in the amorphous matrix consisting of polymeric organic component<sup>1</sup> and Li<sub>x</sub>SiO<sub>y</sub>.<sup>2</sup> The SEI layer generated in the 1M LiPF<sub>6</sub> in EC/DMC + 10%FEC (Figure VII.7.4a-b) is porous and contains nanocrystalline Li<sub>2</sub>CO<sub>3</sub>, Li<sub>2</sub>O and LiF crystals with most of the Li<sub>2</sub>CO<sub>3</sub> located in the outer layer. In contrast, the SEI layer in LHCE electrode is more uniform and smoother and contains outer layer Li<sub>2</sub>SO<sub>4</sub> species, a LiFSI decomposition product<sup>3</sup>, which encapsulate the Li<sub>2</sub>CO<sub>3</sub> component (Figure VII.7.4c-d). Li<sub>2</sub>CO<sub>3</sub> as an SEI component has been reported to be unstable against electrolyte, which decomposes to form gaseous species such as CO<sub>2</sub>, forming a dynamically evolving and porous SEI.<sup>4</sup> The Li<sub>2</sub>CO<sub>3</sub>-rich outer layer in the SEI formed in the control electrolyte can lead to continuous side reaction with electrolyte which resulted in the porous SEI (Figure VII.7.4a) and consumption of electrolyte. In contrast, the parasitic reaction may be suppressed in the LHCE by having a more stable Li<sub>2</sub>SO<sub>4</sub> SEI component<sup>4</sup> exposed to the electrolyte.

Lithium electron energy loss spectroscopy (EELS) maps and spectra collected at the SEI regions in the two electrolytes are presented in Figure VII.7.5. The EELS maps (Figure VII.7.5a, c) further confirm the similar thickness of the SEI thickness in the two electrolytes, while the spectra suggest slightly different compositions with a mixture of Li<sub>2</sub>CO<sub>3</sub>, LiF and Li<sub>2</sub>O present in the FEC control electrolyte (Figure VII.7.5b), and Li<sub>2</sub>CO<sub>3</sub>, Li<sub>2</sub>SO<sub>4</sub> and LiF in the LHCE (Figure VII.7.5d), which are assigned based on a previous EELS study of several common SEI components.<sup>5</sup>

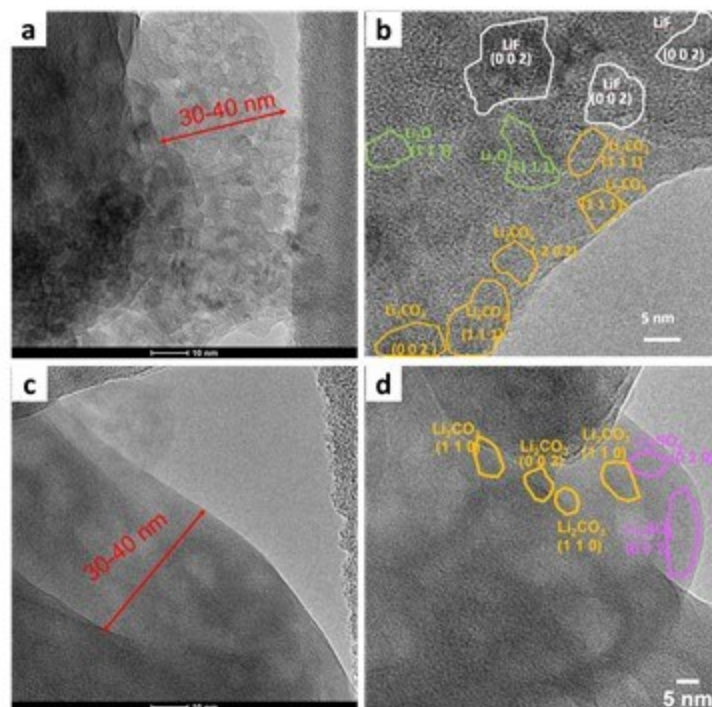


Figure VII.7.4 Cryo high-resolution (HR)TEM images of cycled Si electrodes in (a-b) 1M LiPF<sub>6</sub> in EC/DMC + 10%FEC and (c-d) LHCE.

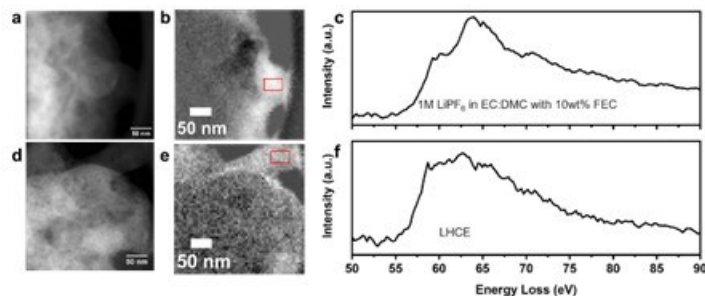


Figure VII.7.5 Cryo STEM image, Li EELS maps and spectra of SEI formed in (a-c) 1M LiPF<sub>6</sub> in EC/DMC + 10%FEC and (d-f) F-LHCE.

## 2. Hard X-ray photoelectron spectroscopy (HAXPES) characterization of interphase layers.

Synchrotron based hard X-ray photoelectron spectroscopy (HAXPES) is a non-destructive approach for probing the composition of buried interphases and uses a higher energy range enabling X-ray energy dependent inelastic mean free path (IMFP) in the  $\sim 2.5 - 10$  nm range.<sup>6</sup> Assuming an analysis depth of approximately  $3 \times \text{IMFP}$ , the technique thus enables depth probing up to 10s of nm by tuning the incident energy of the X-rays. HAXPES spectra were obtained at both 2500eV and 6000 eV to probe the interphase compositions at sampling depths of 2.5-10 nm and 25-35 nm, respectively. Measurements were collected on both the Si-graphite anodes and NMC622 cathodes recovered from the cells from Figure VII.7.1.

The fit spectra for analysis of the SEI on Si-graphite electrodes are presented in Figure VII.7.6a and Figure VII.7.6b for the control and LHCE electrolytes, respectively, and quantification of atomic composition at 2500 eV and 6000 eV is shown in Figure VII.7.6c and Figure VII.7.6d. Regardless of the electrolyte used, the C 1s spectra are comprised of five distinct peaks, assigned to the following bond types: C-C and C-H ( $\sim 284.7$  eV),

C-O (286-287 eV), O-C-O, C=O, and O-C=O (288-289 eV), CO<sub>3</sub> species (~290 eV), and C-Li (283.5 eV).<sup>7</sup> Electrodes cycled in both electrolytes exhibited lower C content with a greater probe depth, suggesting that the outer layers of the SEI have more organic content, in agreement with previous works<sup>8</sup>. O 1s spectra of both electrodes contained peaks at ~531-532 eV associated with lithium carbonates/lithium alkyl carbonates and peak at ~533 eV corresponding to the C-O species.<sup>9</sup> Peaks at 530 eV and 528 eV can be assigned to lithium alkoxides and lithium oxides, respectively.<sup>9</sup> LHCE derived SEI displayed higher O content from C-O bonds compared with the control electrolyte, which exhibited more carbonate bonds.

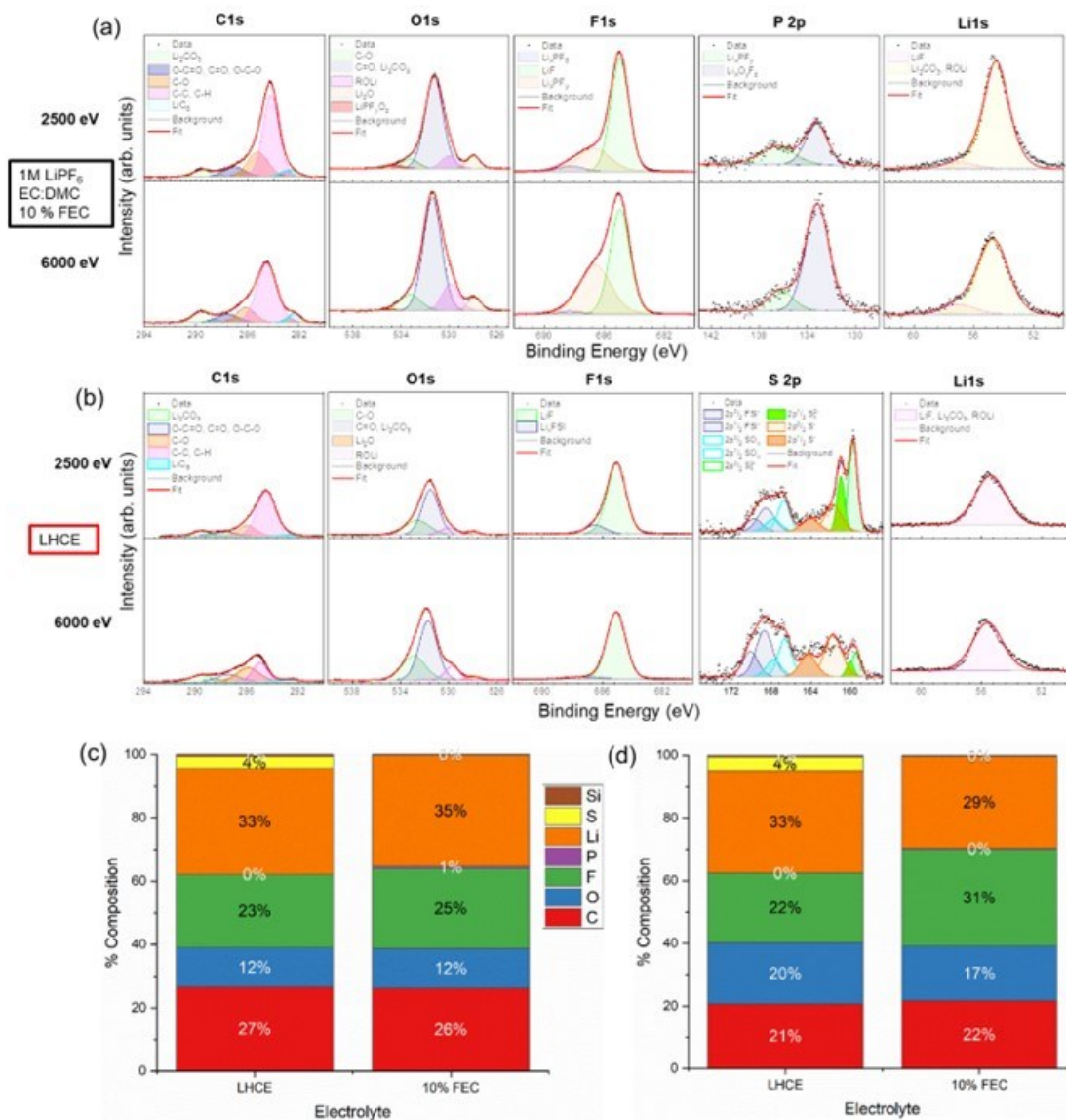


**Figure VII.7.6** HAXPES spectra of C 1s, O 1s, F 1s, P 2p, and Li 1s acquired at 2500 eV and 6000 eV measuring SEI formed on anodes cycled in (a) control electrolyte and (b) LHCE after 100 cycles. Atomic concentrations of each element in the electrodes cycled in the two electrolytes obtained at (c) 2500 eV and (d) 6000 eV.

F 1s spectra for both control and LHCE cycled electrodes show peaks corresponding to salt complexes (~ 687-688 eV)<sup>10</sup> and LiF (~685 eV)<sup>11</sup>. The relative atomic concentration of LiF, which is well known to have a beneficial impact as an SEI component for Si electrodes,<sup>12</sup> is similar in the control sample (20 at. % at 6000 eV) compared to the LHCE (19 at. % at 6000 eV). The Li 1s signal is a convolution of LiCO<sub>3</sub>, ROLi species

(~54-55 eV) as well as LiF (~56 - 57 eV). The relative atomic concentration of Li in the SEI is similar for both electrolytes, measuring 29 – 35 at %.

The most noticeable differences in the SEI derived from the LHCE vs. control electrolytes is in the anion derived species indicated by the S 2p and P 2p spectra. The control electrolyte derived SEI exhibits low concentrations of fluorophosphate ( $\text{Li}_x\text{PO}_y\text{F}_z$  and  $\text{Li}_x\text{PF}_y$ ) species. In contrast, the LHCE derived SEI also contains contributions from FSI<sup>-</sup> anions as well as FSI<sup>-</sup> decomposition species ( $\text{SO}_x$  and  $\text{Sn}^x$ ), directly indicating the significant presence of the FSI<sup>-</sup> anion and its decomposition products in the SEI layer. The concentration of these LiFSI derived species is ca. 4% at both probe depths, compared with only ca. 0.5% concentration of  $\text{LiPF}_6$  derived species in the SEI formed in the control electrolyte.

HAXPES measurements of the CEI formed on electrodes cycled in the two electrolytes were acquired at 6000 eV and are presented in Figure VII.7.7. Notably, 7x higher intensity of C 1s peaks was observed on NMC622 electrodes cycled with the control electrolyte, suggesting that the control derived CEI is more organic rich compared to the LHCE derived CEI. In agreement with the C 1s results, the O 1s spectra show less carbon to oxygen bonding in the LHCE derived CEI. Furthermore, metal to oxygen bonds associated with the NMC622 lattice at lower binding energies, approximately 528 – 529 eV, exhibited ~1/3 the intensity for LHCE cycled cathode compared to the control cycled cathode. This result suggests thicker surface films derived from the LHCE may be able to more effectively passivate the electrodes against side reactions that consume  $\text{Li}^+$  ions.

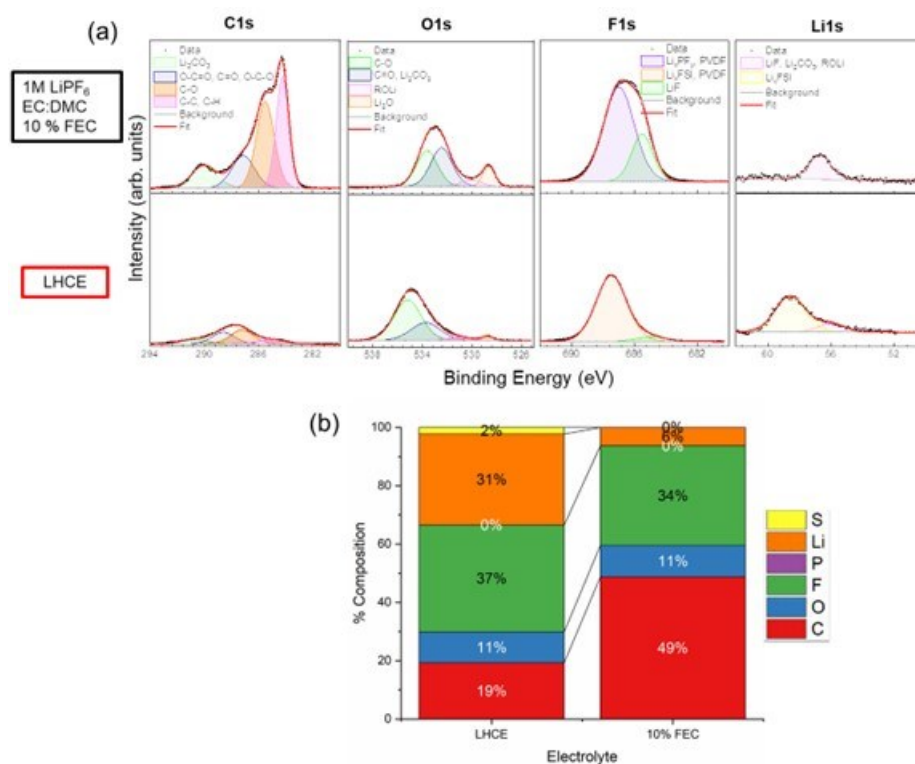


**Figure VII.7.7** HAXPES spectra of C 1s, O 1s, F 1s, and Li 1s and the corresponding atomic concentrations of each element acquired at 6000 eV measuring CEI formed on cathodes cycled in control electrolyte and LHCE after 100 cycles.

Li 1s spectra for both control and LHCE cycled electrodes show peaks corresponding to LiF,  $\text{Li}_2\text{CO}_3$  and ROLi species while the LHCE cycled electrode shows an additional peak corresponding to LiFSI derived species at higher binding energy (~59 eV). Significant differences between the control-cycled and LHCE-cycled electrolytes were also observed in P2p and S2p spectra (Figure S2). For the control electrolyte, 1M  $\text{LiPF}_6$  3:7 EC:DMC CEI contains low concentrations (< 0.1 atomic %) of fluorophosphate ( $\text{Li}_x\text{PO}_y\text{F}_z$  and



$\text{Li}_x\text{PF}_y$ ) species, while the LHCE derived SEI contains contributions from  $\text{FSI}^-$  anions as well as  $\text{FSI}^-$  decomposition species at a more significant percentage (2.4 atomic %).

The elemental composition of the CEI derived from either electrolyte was calculated based on the HAXPES results and is summarized in Figure VII.7.7b. Overall, the LHCE derived CEI is much richer in inorganic based species, including  $\text{FSI}^-$  anion derived species, compared to the mainly organic CEI formed in the control electrolyte.

### 3. Isothermal microcalorimetry characterization of parasitic heat

Isothermal microcalorimetry (IMC) was used to assess parasitic heat resulting from solid electrolyte interphase (SEI) formation on Si-graphite electrodes during cycling. *Operando* IMC is a technique that can capture real-time heat flow released from a running battery with ultra-high precision, and the evolution of parasitic reactions upon battery cycling can be determined by quantifying the dissipated heat flow associated with parasitic reactions.<sup>13</sup> Electrochemistry correlated heat flow can be attributed to a combination of polarization, entropic changes, and parasitic heat flow which can be deconvoluted to obtain insights into parasitic reactions in an operating battery. For this experiment, Si-graphite/ $\text{LiFePO}_4$  coin cells were constructed with the LHCE which exhibited the highest capacity retention previously in a full cell configuration, and conventional carbonate electrolyte with FEC additive (M  $\text{LiPF}_6$  30:70 EC:DMC + 10% wt. FEC). Cells underwent four formation cycles between 2.5 – 3.8 V at C/10 rate prior to the IMC experiment. IMC measurements were performed at a constant temperature of 30°C, with the cells cycled at a C/5 rate (based on the 140 mAh/g capacity of  $\text{LiFePO}_4$ ) with voltage limits of 2.5 – 3.8 V in the IMC for 50 cycles (Figure VII.7.8). The delivered capacity of the cell utilizing the 1M  $\text{LiPF}_6$  30:70 EC:DMC + 10% wt. FEC was initially higher than that of the cell using the LHCE (90 mAh/g vs. 88 mAh/g), but the LHCE cell demonstrated improved capacity retention over 50 cycles. The cycle 50 capacities of the 1M  $\text{LiPF}_6$  30:70 EC:DMC + 10% wt. FEC and LHCE containing cells were 67 mAh/g and 64 mAh/g, respectively.

Heat flow was collected by the IMC over the 50 cycles. Figure VII.7.9 shows the voltage profiles and corresponding heat flow for cycle 2 and cycle 50. For both electrolytes, the amount of dissipated heat was found to decrease with increasing cycle number.

Analysis of the heat flow can be advanced by considering the contributions to the total values obtained experimentally. The heat flow generated by an electrochemical cell during (de)lithiation under isothermal conditions is described by Equation 1, which shows that battery heat flow is the sum of three components: polarization heat (first term in the equation), entropic heat (second term), and heat associated with parasitic reactions (third term).

$$\dot{Q} = I(E_{load} - E_{eq}) + IT \left( \frac{dE_{eq}}{dT} \right) + \dot{Q}_p \quad (1)$$

Where  $I$  is current,  $T$  is temperature,  $E_{load}$  is the potential under current,  $E_{eq}$  is the potential at open circuit, and  $\dot{Q}_p$  is the parasitic heat flow. Polarization heat flow is always exothermic and is represented by the  $I(E_{load} - E_{eq})$  term, while entropic heat flow, is represented by the  $IT \left( \frac{dE_{eq}}{dT} \right)$  term. The remaining heat flow is attributed to parasitic reactions including SEI formation and electrolyte decomposition.

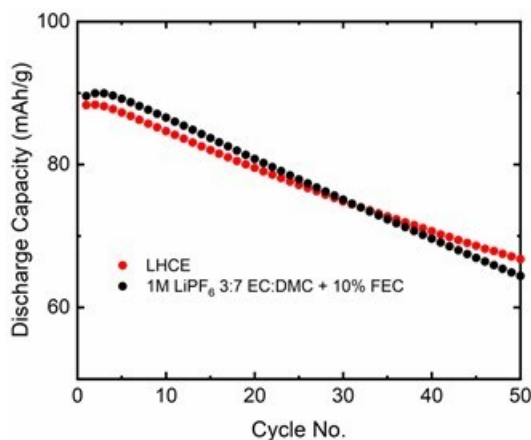


Figure VII.7.8 Discharge capacity of Si-graphite/LiFePO<sub>4</sub> coin cells galvanostatically cycled inside isothermal microcalorimeter at a C/5 rate between 2.5 – 3.8 V for 50 cycles.

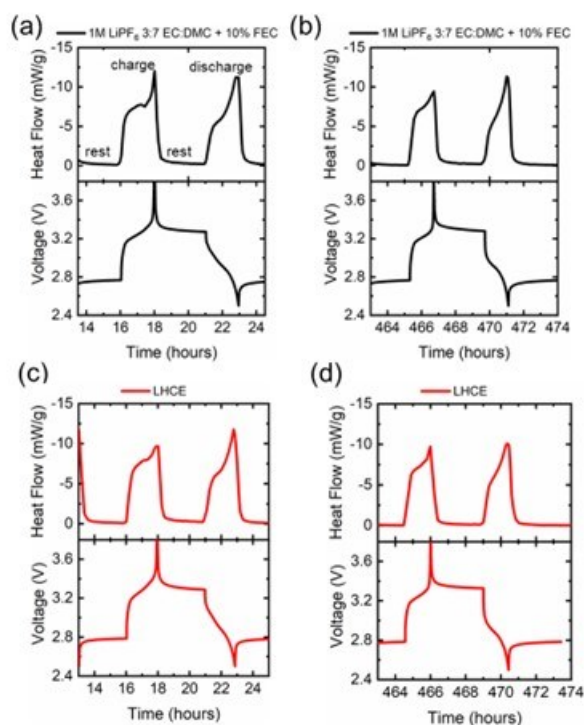


Figure VII.9 Voltage profiles and corresponding heat flow profiles during (a, c) cycle 2 and (b, d) cycle 50 for Si-graphite/LiFePO<sub>4</sub> coin cells with (a,b) 1M LiPF<sub>6</sub> 30:70 EC:DMC + 10% wt. FEC electrolyte or (c, d) LHCE electrolyte.

The polarization contribution to evolved heat was experimentally determined through pulse measurements of Si-graphite/LiFePO<sub>4</sub> cells with the two electrolytes, during charge and discharge in 10 mAh/g increments, with C/5 current used during the pulsing step. After each pulse increment the cell was rested at open circuit for 5 hours, and the polarization contribution was calculated by multiplying the current by the difference in loaded and open circuit potentials. Pulse measurements were made after cycle 2 and cycle 50 of cells cycled 50x under the same galvanostatic conditions described above.

Entropy contributions to heat flow were determined by calculating the variation of equilibrium potential with respect to temperature.<sup>13</sup> This was accomplished by measuring the open circuit potential of Si-graphite/LiFePO<sub>4</sub> cells at a given state of charge as the cell was heated from 25 °C to 35 °C. The slope of the

change in potential and the slope of the change in temperature were determined, and the quotient was multiplied by the current ( $C/5$ ) and operating temperature during cycling ( $30^{\circ}\text{C}$ ) to calculate the entropy contributions. Entropy contributions were determined in 10 mAh/g increments during (dis)charge after cycle 2 and cycle 50 of cells cycled 50x to align with the polarization measurements.

The parasitic heat during cycle 2 and cycle 50 was determined by subtracting the polarization and entropy contributions from the total heat flow measured by IMC. The summation of polarization and entropy contributions (red) compared to the measured heat flow for the charge steps of cycle 2 and cycle 50 are shown in Figure VII.7.10. Differences between the heat flow profile and the polarization + entropy contributions represent the parasitic heat flow in mW/g. Visually, less parasitic heat flow is observed in cycle 50 compared to cycle 2, with less parasitic heat also observed for the cell utilizing the LHCE electrolyte.

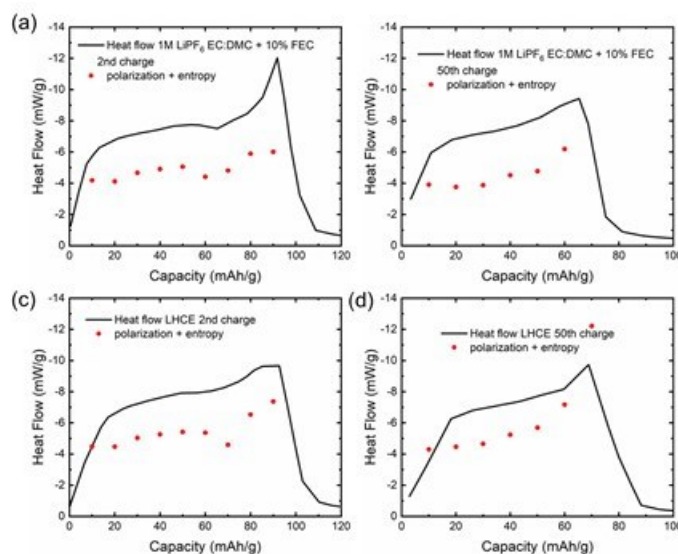


**Figure VII.7.10** Comparison of IMC measured total heat flow (black) and the sum of polarization and entropy contributions to heat flow (red) during (a, c) cycle 2 and (b, d) cycle 50 for Si-graphite/LiFePO<sub>4</sub> coin cells with (a, b) 1M LiPF<sub>6</sub> 30:70 EC:DMC + 10% wt. FEC electrolyte and (c, d) LHCE electrolyte.

The quantified parasitic heat (mWh/g) from the experiment is summarized in Figure VII.7.11. During both charge and discharge, the cell utilizing the 1M LiPF<sub>6</sub> 3:7 EC:DMC + 10% FEC electrolyte evolved more parasitic heat compared to the cell utilizing the LHCE electrolyte. Notably, the parasitic heat was significantly higher during the charging steps. This finding is consistent with solid electrolyte interphase (SEI) formation via reduction of electrolyte on the surfaces of the Si-graphite anodes as they are lithiated. The decrease in parasitic heat after 50 cycles is attributed to the reduced electrochemical reversibility of electrodes. These results provide new evidence that the LHCE is able to provide enhanced SEI stability compared to conventional electrolyte formations.

## Conclusions

The fluorinated LHCE developed under this program demonstrates improved cycling stability in Si-graphite/NMC622 pouch cells after 100 cycles at a  $C/3$  rate when compared with the counterpart cycled in a control electrolyte containing 1M LiPF<sub>6</sub> in 3:7 (v/v) EC/DMC with 10% FEC. Complementary HAXPES and electron microscopy characterizations were conducted to probe the SEI and CEI composition and morphology at different sample depths and spatial resolutions to understand the beneficial effects of LHCE. HAXPES characterizations suggested that the LHCE derived SEI contained S species associated the FSI<sup>-</sup> anion, while the CEI of the LHCE cycled electrodes had significantly greater inorganic species compared to the control-derived counterpart. The inorganic component in the SEI and CEI can collectively contribute to a more stable interphase ensuring the long-term cycling stability of the pouch cells. Isothermal microcalorimetry

investigation of the electrolytes supports the microscopy and spectroscopy studies, with quantifiably less parasitic heat evolved by cells utilizing the LHCE during cycling. Additionally, the LHCE is demonstrated to be non-flammable, making it attractive as a safer alternative to conventional electrolytes for electric vehicles.

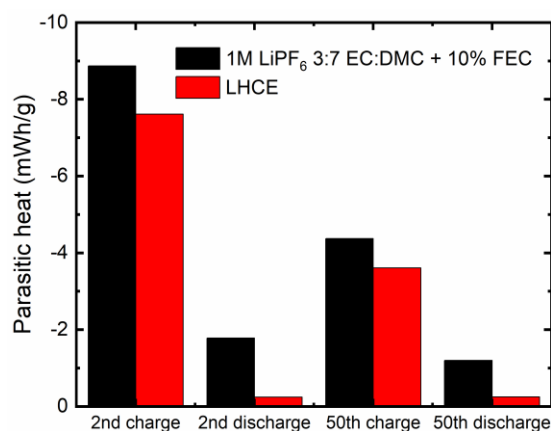


Figure VII.7.11 Summary of parasitic heat evolved during cycle 2 and cycle 50 for Si-graphite/LiFePO<sub>4</sub> coin cells with (a, b) 1M LiPF<sub>6</sub> 30:70 EC:DMC + 10% wt. FEC electrolyte or (c, d) LHCE electrolyte.

#### 4. Flammability Evaluation of Electrolytes

The flammability of the LHCE and the 1M LiPF<sub>6</sub> EC:DMC + 10% FEC electrolytes were also visually evaluated using a hand-held butane lighter. The 1M LiPF<sub>6</sub> EC:DMC + 10% FEC electrolyte is clearly flammable and burns violently after the removal of the ignitor (Figure VII.7.12a). In contrast, the LHCE is extinguished after flame removal (Figure VII.7.12b), demonstrating that the LHCE dramatically reduces electrolyte flammability compared to conventional carbonate-based electrolyte.

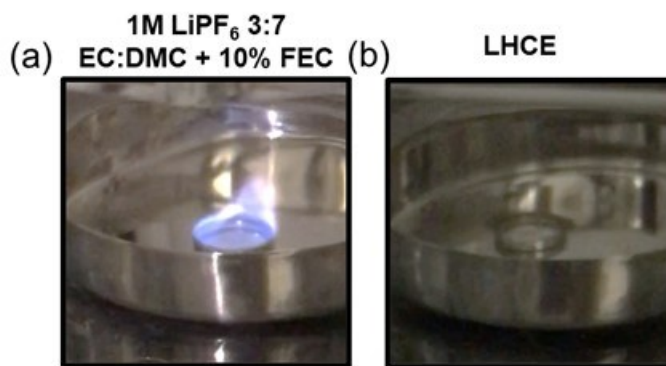


Figure VII.7.12 Flammability testing of electrolytes (a) 1M LiPF<sub>6</sub> 3/7 EC/DMC +10% FEC, (b) LHCE. Flammability measurements were collected by placing 500  $\mu$ L of electrolyte in a stainless-steel container and placing the flame from a butane lighter over the electrolyte for 2 seconds. Photos are shown after flame removal.

#### Key Publications

1. Lutz, D. M.; McCarthy, A. H.; King, S. T.; Singh, G.; Stackhouse, C. A.; Wang, L.; Quilty, C. D.; Bernardez, E. M.; Tallman, K. R.; Tong, X.; Bai, J.; Zhong, H.; Takeuchi, K. J.; Takeuchi, E. S.; Marschilok, A. C.; Bock, D. C., Progress Towards Extended Cycle Life Si-based Anodes: Investigation of Fluorinated Local High Concentration Electrolytes. *Journal of The Electrochemical Society* 2022, 169 (9), 090501.

## References

1. Zhang, X.; Weng, S.; Yang, G.; Li, Y.; Li, H.; Su, D.; Gu, L.; Wang, Z.; Wang, X.; Chen, L., Interplay between solid-electrolyte interphase and (in)active Li<sub>x</sub>Si in silicon anode. *Cell Reports Physical Science* **2021**, *2* (12), 100668.
2. Huang, W.; Wang, J.; Braun, M. R.; Zhang, Z.; Li, Y.; Boyle, D. T.; McIntyre, P. C.; Cui, Y., Dynamic Structure and Chemistry of the Silicon Solid-Electrolyte Interphase Visualized by Cryogenic Electron Microscopy. *Matter* **2019**, *1* (5), 1232-1245.
3. Piper, D. M.; Evans, T.; Leung, K.; Watkins, T.; Olson, J.; Kim, S. C.; Han, S. S.; Bhat, V.; Oh, K. H.; Buttry, D. A., et al., Stable silicon-ionic liquid interface for next-generation lithium-ion batteries. *Nature Communications* **2015**, *6* (1), 6230.
4. Han, B.; Zhang, Z.; Zou, Y.; Xu, K.; Xu, G.; Wang, H.; Meng, H.; Deng, Y.; Li, J.; Gu, M., Poor Stability of Li<sub>2</sub>CO<sub>3</sub> in the Solid Electrolyte Interphase of a Lithium-Metal Anode Revealed by Cryo-Electron Microscopy. *Advanced Materials* **2021**, *33* (22), 2100404.
5. Wang, F.; Graetz, J.; Moreno, M. S.; Ma, C.; Wu, L.; Volkov, V.; Zhu, Y., Chemical Distribution and Bonding of Lithium in Intercalated Graphite: Identification with Optimized Electron Energy Loss Spectroscopy. *ACS Nano* **2011**, *5* (2), 1190-1197.
6. Maibach, J.; Lindgren, F.; Eriksson, H.; Edström, K.; Hahlin, M., Electric Potential Gradient at the Buried Interface between Lithium-Ion Battery Electrodes and the SEI Observed Using Photoelectron Spectroscopy. *The Journal of Physical Chemistry Letters* **2016**, *7* (10), 1775-1780.
7. Briggs, D.; Beamson, G., Primary and secondary oxygen-induced C 1s binding energy shifts in x-ray photoelectron spectroscopy of polymers. *Analytical Chemistry* **1992**, *64* (15), 1729-1736.
8. Shi, S.; Lu, P.; Liu, Z.; Qi, Y.; Hector, L. G., Jr.; Li, H.; Harris, S. J., Direct Calculation of Li-Ion Transport in the Solid Electrolyte Interphase. *Journal of the American Chemical Society* **2012**, *134* (37), 15476-15487.
9. Leroy, S.; Blanchard, F.; Dedryvère, R.; Martinez, H.; Carré, B.; Lemordant, D.; Gonbeau, D., Surface film formation on a graphite electrode in Li-ion batteries: AFM and XPS study. *Surface and Interface Analysis* **2005**, *37* (10), 773-781.
10. Kang, S.-J.; Park, K.; Park, S.-H.; Lee, H., Unraveling the role of LiFSI electrolyte in the superior performance of graphite anodes for Li-ion batteries. *Electrochimica Acta* **2018**, *259*, 949-954.
11. Hennessy, J.; Nikzad, S., Atomic Layer Deposition of Lithium Fluoride Optical Coatings for the Ultraviolet. *Inorganics* **2018**, *6* (2), 46.
12. Veith, G. M.; Doucet, M.; Sacci, R. L.; Vacaliuc, B.; Baldwin, J. K.; Browning, J. F., Determination of the Solid Electrolyte Interphase Structure Grown on a Silicon Electrode Using a Fluoroethylene Carbonate Additive. *Scientific Reports* **2017**, *7* (1), 6326.
13. Housel, L. M.; Li, W.; Quilty, C. D.; Vila, M. N.; Wang, L.; Tang, C. R.; Bock, D. C.; Wu, Q.; Tong, X.; Head, A. R., et al., Insights into Reactivity of Silicon Negative Electrodes: Analysis Using Isothermal Microcalorimetry. *ACS Applied Materials & Interfaces* **2019**, *11* (41), 37567-37577.

## Acknowledgements

The co-PIs for this project include Esther S. Takeuchi (Stony Brook University and Brookhaven National Laboratory) Kenneth J. Takeuchi (Stony Brook University and Brookhaven National Laboratory), David C. Bock (Brookhaven National Laboratory) and Lei Wang (Brookhaven National Laboratory).

## VII.8 Devising mechanically compliant and chemically stable synthetic solid-electrolyte interphases on silicon using ex situ electropolymerization for long cycling Si anodes (University of Delaware)

### **Koffi Pierre Yao, Principal Investigator**

University of Delaware  
210 South College Ave.  
Newark, DE, 19716  
E-mail: [claver@udel.edu](mailto:claver@udel.edu)

### **Ajay K. Prasad, Co-Principal Investigator**

University of Delaware  
210 South College Ave.  
Newark, DE, 19716  
E-mail: [prasad@udel.edu](mailto:prasad@udel.edu)

### **Thomas Epps, Co-Principal Investigator**

University of Delaware  
210 South College Ave.  
Newark, DE, 19716  
E-mail: [thepps@udel.edu](mailto:thepps@udel.edu)

### **Daniel Abraham, Co-Principal Investigator**

Argonne National Laboratory  
9700 S Cass Ave.  
Lemont, IL, 60439  
E-mail: [abraham@anl.gov](mailto:abraham@anl.gov)

### **Carine Steinway, DOE Technology Development Manager**

U.S. Department of Energy  
E-mail: [Carine.Steinway@ee.doe.gov](mailto:Carine.Steinway@ee.doe.gov)

### **Nicolas Eidson, DOE Technology Development Manager**

U.S. Department of Energy  
E-mail: [Nicolas.Eidson@ee.doe.gov](mailto:Nicolas.Eidson@ee.doe.gov)

### **Thomas Do, DOE Technology Development Manager**

U.S. Department of Energy  
E-mail: [Thomas.Do@ee.doe.gov](mailto:Thomas.Do@ee.doe.gov)

Start Date: January 1, 2023  
Project Funding: \$1,000,000

End Date: December 31, 2023  
DOE share: \$1,000,000

Non-DOE share: \$0

### **Project Introduction**

Silicon (Si) is capable of  $\sim 3500 \text{ mAh}\cdot\text{g}^{-1}$  and operates near the lithium potential making it a potential replacement for graphite anodes ( $\sim 372 \text{ mAh}\cdot\text{g}^{-1}$ ) with a tenfold increase in capacity. Nonetheless, the reactive surface of silicon and lithium-silicide products combined with the 350% expansion of particles during cycling results in instability of the native SEI required to halt cyclical reductive degradation of battery electrolytes. Consequently, during operation, loss of lithium inventory, densification of the electrode, and loss of electrical contact curtail the cell cycling and calendar life. Cells with silicon anodes are typically unable to achieve the

DOE target of  $350 \text{ Wh}\cdot\text{kg}^{-1}$  and  $750 \text{ Wh}\cdot\text{L}^{-1}$  beyond 1000 cycles and 10 years calendar life. To solve the cycling and calendar life shortcomings of silicon as an anode, an SEI which is (i) resistant to chemical attack from the silicon surface and (ii) mechanically stable over repeated straining is needed to retain its function of protecting the electrolyte over extended cycling and/or storage.

### Objectives

The program aims to produce cells based on Si anodes paired with existing transition metal oxide cathodes capable of achieving greater than  $350 \text{ Wh}\cdot\text{kg}^{-1}$ ,  $750 \text{ Wh}\cdot\text{L}^{-1}$  at the cell level with a target calendar life of 10 years and cycle life of 1000 cycles (Table VII.8.1).

**Table VII.8.1 Summary of Program Objectives**

Beginning of Life Characteristics at 30 °C	Cell Level
Useable Specific Energy @ C/3	>350 Wh/kg
Useable Energy Density @ C/3	>750 Wh/L
Calendar Life (<20% energy fade)	>10 Years
Cycle Life (C/3 deep discharge to 350Wh/kg, <20% energy fade)	>1,000

As described in the introduction, a key to enabling long cycling silicon anodes is to devise a stable SEI to protect the electrolyte and lithium inventory against cyclical consumption in degradation processes. Our project objective is to remedy the continuous electrolyte decomposition on Si surfaces by devising a chemically stable polymer synthetic SEI capable of withstanding the expansion of Si particles with minimal damage. We aim to achieve this solution using electrodeposition methods to apply a thin elastomeric polymer film to function as a synthetic SEI.

### Approach

Externalization of the SEI application process from an operating battery environment enables the use of a wider range of precursors to search for synthetic SEIs with the requisite strain resistance to withstand the ~350% expansion/contraction of silicon during electrochemical cycling. Our project makes use of two tools available to electrochemists for surface deposition of long chain polymer on surfaces: Electropolymerization (EP) and Electrophoretic deposition (EPD). The rationale for selecting these electrochemical methods is described in the schematic shown in Figure VII.8.1. EP consists of depositing a polymer onto the electrode surface starting from a precursor solution containing monomers of the target polymer. In the specific case of silicon electrodes, a cationic growth of the target polymer is to be initiated by electroreduction of the monomer onto the electrode surface. The initiated monomer chain growth on the surface will result in a polymer coating onto the surface. EPD consists of dissolving a charged polymer to deposit in a precursor electrolyte (usually aqueous solutions). Subsequent application of an electric field between parallel working (silicon) and counter electrodes drives the charged polymer to coat onto the working electrode. In the case of silicon, cationic polymers such as Dextran and Chitosan are employed, wherein the positive charge is attracted to the surface with a negative potential at the silicon.

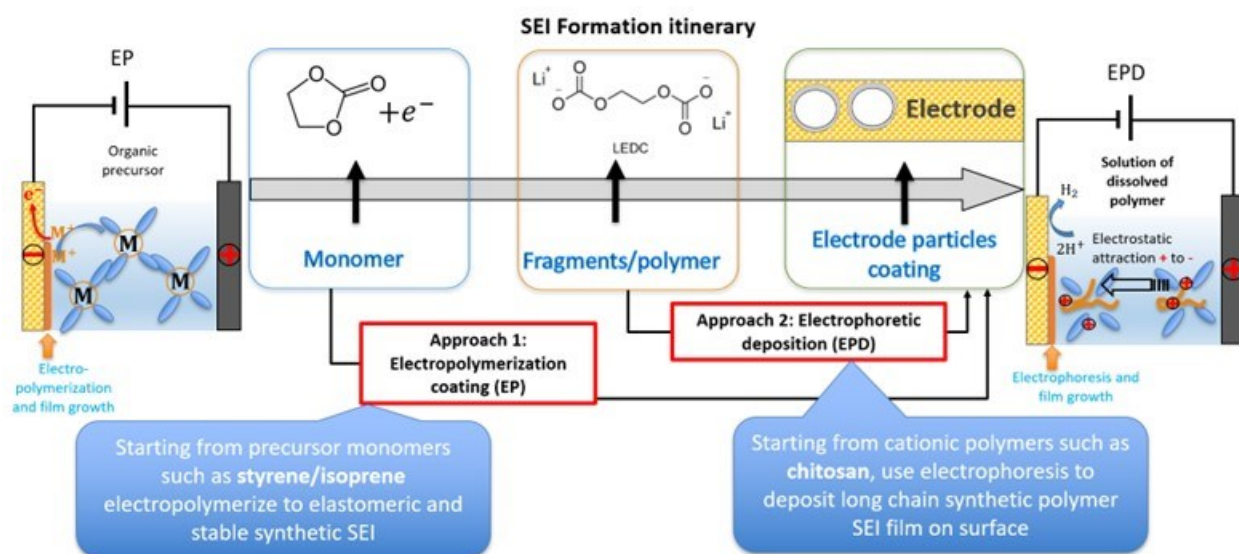


**Figure VII.8.1 Schematic description of the principles of electropolymerization and electrophoretic deposition**

As the deposition is controlled by electrochemistry, control of the deposition quantity can be achieved through control of the electric charge. The approaches therefore offer the ability to select the chemistry, chain length, conductivity, and stability of the synthetic SEI components by choice of the polymer to electrodeposit.

The workflow is as follows:

1. Utilize silicon thin film as model surfaces for polymer EPD procedure tuning.
2. Spectroscopically characterize and optimize the film growth, quality, chemistry, stability, and electrochemical properties.
3. Translate the validated electrocoating methods to coat elastomeric and ionically conductive SEIs on Si-anodes with over 30% Si loading.
4. Validate the long-term stable cycling and calendar life of cells equipped with our electrocoated Si.

## Results

To simplify characterization of the novel polymer synthetic SEIs to be generated and studied, Si thin film model surfaces were utilized. Sputtered Si thin films of ~40 nm thickness were produced by sputter deposition from an undoped silicon target in Argon atmosphere. Electropolymerization is performed in an organic supporting electrolyte containing 0.2 M LiTFSI in tetrahydrofuran (THF) with 0.1-10 wt% of the monomer for the targeted polymer added. Electropolymerization was achieved at -15 V polarization between an aluminum counter and the Si thin working electrode. For the electrophoretic deposition, an aqueous solution containing a dissolved quantity of the precursor polymer is used. In the case of Chitosan, the precursor solution contains ~0.1 M HCl and ~0.1 M NaOH to achieve an acidic pH  $\approx$  5. Approximately 0.05 wt% of Chitosan powder is then dissolved in the acidic medium. In the case of Dextran-HCl, the cationic polymer is naturally soluble in deionized (DI) water. Therefore, 1 wt% is directly dissolved in DI water and used without any other additives. The EPD depositions were achieved at -3.0 V vs. an aqueous Ag/AgCl reference electrode. FTIR was used to confirm the successful deposition of the various polymers as shown in Figure VII.2 on the Si thin film. Polyisoprene (PIP, Figure VII.8.2a), polymethylmethacrylate (PMMA, Figure VII.8.2b) were deposited by electropolymerization at -15 V; a high potential was required to successfully achieve the deposition. Evidence from EDS after EP at those potentials shows the co-deposition of Aluminum on the Si electrode surface from the Aluminum counter electrode. The Al<sup>3+</sup> cations from the “sacrificial” aluminum anode[1] may be initiating the carbocationic polymerization[2] of the monomers. Electrophoretic deposition is the most reliable and



repeatable means of electrodeposition of a long chain polymer as synthetic SEI on the silicon surface. Straightforwardly repeatable depositions of Chitosan (Figure VII.8.2c) and Dextran-HCl (Figure VII.8.2d) cationic polymers were confirmed by FTIR. The main challenge lies in controlling the thickness of the deposit to nanometer scales and is the subject of further efforts.

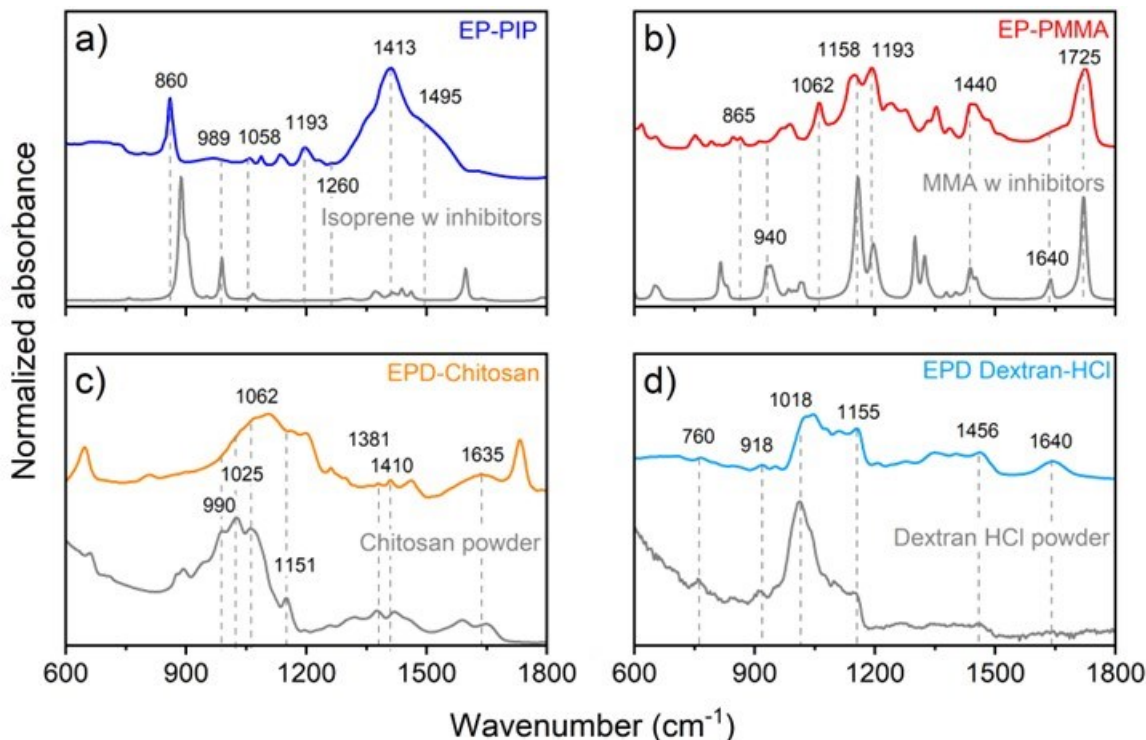


**Figure VII.8.2** Samples FTIRs of successful electrodepositions using electropolymerization and electrophoretic depositions. Electropolymerization in LiTFSI/THF precursors: (a) isoprene (IP) → polyisoprene (PIP), (b) Methyl methacrylate (MMA) → PMMA. Electrophoretic deposition of cationic polymers from aqueous precursors: (c) Chitosan, (d) Dextran-HCl.

The electrochemical cycling of Si electrodes with an applied synthetic SEI are shown in Figure VII.8.3. Figure VII.8.3a, d shows the electrochemical cycling of a LiPAA-bound silicon electrode containing 80% Si, 10% LiPAA, and 10% Carbon obtained from the Argonne National Laboratory CAMP facility. The electrochemical cycling of the electrodes after undergoing electropolymerization treatment towards a PIP coating is compared to the performance of the baseline untreated electrodes. After 100 cycles at  $C/3$  (vs. Si theoretical capacity), the baseline electrode dropped below  $1 \text{ mAh}\cdot\text{g}_{\text{Si}}^{-1}$  while the nominally EP-PIP coated electrode retains  $363 \text{ mAh}\cdot\text{g}_{\text{Si}}^{-1}$  at an average coulombic efficiency (C.E) over the 100 cycles of 98.8%. This finding is further corroborated by the coulombic inefficiency (C.I) measure (fraction of loss capacity from charge to discharge) in Figure VII.8.3d wherein the C.I of EP-PIP coated electrode remain between 0.5 and 1.7% while the baseline exceeded 10% losses after cycle 20. Figure VII.8.3b, e gauge the stabilization effect of a PMMA synthetic SEI during cycling of p84-bound electrodes sourced from Argonne National Laboratory CAMP facility. In this case, the capacity output of the EP-PMMA coated electrodes were significantly lower than the baseline (Figure VII.8.3b). Interestingly, however, the C.I of the PMMA-coated electrode is superior to that of the baseline (Figure VII.8.3e) in agreement with a calculated average C.E of 99.3% for the EP-PMMA electrode versus 97.3% for the baseline. As noted above, a significant roadblock in our synthetic SEI approach is fine control of the thickness of the SEI to nanometer scales; the lower capacity of the PMMA coated electrode may stem from clogging of the porous structure at electropolymerization coating. The cycling of Si thin films coated with Dextran-HCl is shown in Figure VII.8.3c, f and compared to a baseline uncoated film. Over 30 cycles at an

estimated rate of C/3, the capacity output of the baseline Si film exceeds that of its Dextran coated counterpart. However, once again the calculated average C.E is 95% for the coated electrode versus 93.5% for the baseline; the inter-cycle loss rate is lower for the Dextran coated electrode compared to the baseline (Figure VII.8.3f) resulting in a flatter discharge capacity per cycle in Figure VIII.9.3c. A consistent pattern is a reduction in rate of capacity loss for the electrocoated electrodes albeit the nominal cycling capacity is depressed in the case of PMMA and Dextran coatings. The loss in capacity at C/3 is attributed to a need to optimize the thickness of the coating down to tens of nanometers.

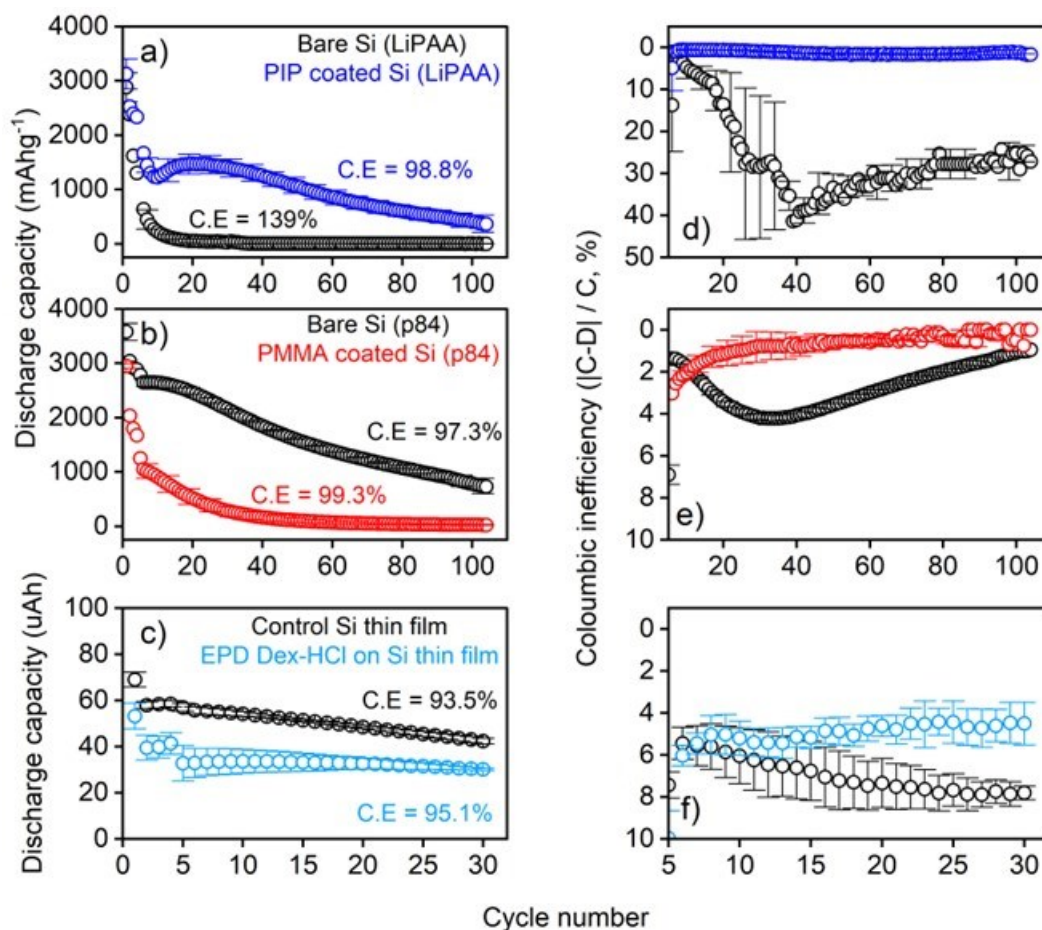


**Figure VII.8.3** Sample C/3 cycling of electrodepositions using electropolymerization and electrophoretic depositions and their corresponding coulombic efficiencies. Electropolymerization coating of porous electrodes in LiTFSI/THF precursors: (a) isoprene (IP) → polyisoprene (PIP) on LiPAA-bound electrodes, (b) Methyl methacrylate (MMA) → PMMA on p84-bound electrodes. (c) Electrophoretic deposition coating of cationic polymers Dextran-HCl on Si thin film. All cycling shown are in half-cells.

The estimation of the calendar life was performed using the so-called Tier 1 voltage hold (V-hold) protocol developed by Argonne National Lab on Si vs. LiFePO<sub>4</sub> (LFP) full cell with Gen2 (EC:EMC 3:7 w/w + 1.2M LiPF<sub>6</sub>) solution as electrolyte. The protocol includes 180 hours hold at high voltage of 3.35 V after initial 10 galvanostatic cycles at C/10. The normalized calendar life is obtained for a cell containing 3% FEC in Gen2 electrolyte for reference (Figure VII.8.4a); the method shows a threefold increase in calendar life under the FEC generated SEI as is expected. With the method validated, the normalized calendar life of LiPAA-bound electrodes with EP-PIP coating is estimated in Figure VII.8.4b. The method suggests a near tenfold increase in calendar life for the EP-PIP treated electrodes compared to the baseline, a significant gain for LiPAA bound electrodes.

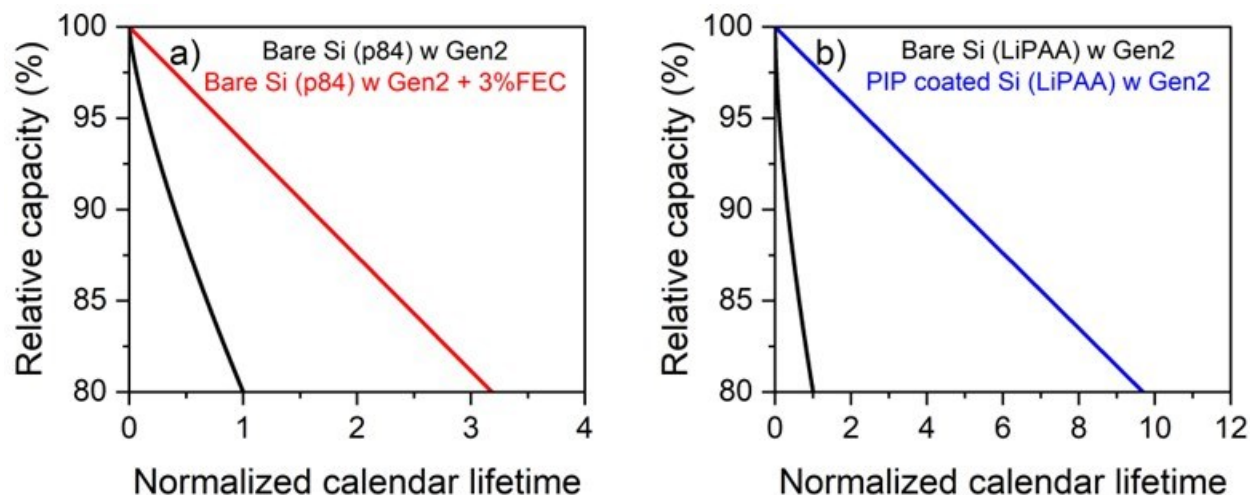


Figure VII.8.4 Sample calendar life evaluations in porous electrodes. (a) SEI generated in situ from Fluoroethylene carbonate (FEC) additive to Gen2 electrolyte and using p84-bound electrodes (b) polyisoprene (PIP) synthetic SEI in cells with LiPAA-bound electrodes and Gen2 electrolytes.

### Conclusions

Major strides have been made in achieving our goal of controlling the chemistry, morphology, and mechanical properties of the SEI on silicon electrodes to protect the battery electrolyte against cyclical reductive degradation due to the silicon surface reactivity and expansion on cycling. The following achievements signal promise for the approach to achieve the project research objectives.

1. Electropolymerization deposition of polyisoprene (PIP) and polymethylmethacrylate (PMMA) were achieved on Si at high electric fields (-15V). Electrophoretic deposition (EPD) of cationic polymers chitosan and Dextran-HCl were also achieved. More importantly, two approaches have been successfully demonstrated to construct long-chain polymer SEIs on Si electrodes.
2. A major hurdle remains in optimizing the deposition towards nanoscale thicknesses for the synthetic SEIs. Approaches such as time-controlled deposition have yielded promising reduction in charge transfer resistance for Dextran-HCl coatings on Si thin film (not shown).
3. Electrochemical cycling shows significant gains in capacity retention and calendar life for the specific case of electropolymerization applied PIP over the baseline. In the case of PMMA and Dextran-HCl a lower absolute capacity is extracted from the coated Si compared to the baseline. Nonetheless, improved coulombic efficiency is achieved. A repeated pattern of reduction in rate of capacity loss for the electrocoated electrodes is seen in cycling which indicates a potential positive impact on calendar life and overall capacity retention with the polymeric synthetic SEI.

Future effort must focus on quantifying gains in capacity retention in full cells and further quantifying the calendar life in presence of an optimized synthetic SEI. A characterization of the evolution of the synthetic SEI during calendar life storage from the perspective of gas generation and spectroscopy monitoring of the chemistry is needed.

### Key Publications

1. Rownak J. Mou, Sattajit Barua, Ajay K. Prasad, Thomas Epps III, and Koffi P.C. Yao; Electrophoretic deposition as a versatile low-cost tool to construct a synthetic polymeric solid-electrolyte interphase

on silicon anodes: A model system investigation; Submitted to ACS Applied Materials and Interfaces. Revision 2 due November 30<sup>th</sup> 2023.

2. Rownak J. Mou, Sattajit Barua, Daniel P. Abraham, and Koffi P. C. Yao; Unraveling of the morphology and chemistry dynamics in the FEC-generated silicon anode SEI across delithiated and lithiated states: Relative cycling stability enabled by an elastomeric polymer matrix. Manuscript drafted. Submission planned for the Journal of the Electrochemical Society.

## References

1. Yousef, U. S. "Electroinitiated cationic polymerization of p-chloromethyl styrene using different sacrificial anode materials in nitromethane." *European polymer journal* 34.5-6 (1998): 637-643.
2. Kostjuk, Sergei V., et al. "Carbocationic polymerization of isoprene co-initiated by B(C<sub>6</sub>F<sub>5</sub>)<sub>3</sub>: an alternative route toward natural rubber polymer analogues?" *Macromolecules* 44.6 (2011): 1372-1384.

## Acknowledgements

The P.Is acknowledge the research efforts of graduate students Rownak Jahan Mou, Sattajit Barua, and Mengying Yang. The P.Is also thank Brian Cunningham, Adrienne Riggi, Thomas Do, and Kimberly Nuhfer for productive technical discussions and project management assistance. We are thankful for the support of the ANL CAMP Facility personnels Steve Trask and Marco-Tulio Fonseca Rodrigues for the silicon electrodes.

## VII.9 Rational Electrolyte Design for Li-ion Batteries with Micro-sized Si Anodes (University of Maryland, College Park)

### **Professor Chunsheng Wang, Principal Investigator**

Department of Chemical & Biomolecular Engineering  
University of Maryland  
College Park, MD 20742  
E-mail: [cswang@umd.edu](mailto:cswang@umd.edu)

### **Oleg Borodin, Principal Investigator**

Energy Storage Branch, Sensor and Electron Devices Directorate,  
U.S. Army Combat Capabilities Development Command  
Army Research Laboratory, Adelphi, Maryland  
E-mail: [oleg.a.borodin.civ@mail.mil](mailto:oleg.a.borodin.civ@mail.mil)

### **Carine Steinway, DOE Technology Development Manager**

U.S. Department of Energy  
E-mail: [Carine.Steinway@ee.doe.gov](mailto:Carine.Steinway@ee.doe.gov)

### **Nicolas Eidson, DOE Technology Development Manager**

U.S. Department of Energy  
E-mail: [Nicolas.Eidson@ee.doe.gov](mailto:Nicolas.Eidson@ee.doe.gov)

### **Thomas Do, DOE Technology Development Manager**

U.S. Department of Energy  
E-mail: [Thomas.Do@ee.doe.gov](mailto:Thomas.Do@ee.doe.gov)

Start Date: October 1, 2019

End Date: March 31, 2023

Project Funding: \$200,000

DOE share: \$200,000

Non-DOE share: \$0

### **Project Introduction**

The success of micro-sized graphite (10  $\mu\text{m}$ ) anodes in carbonate electrolyte for Li-ion batteries is attributed to the formation of organic-inorganic solid electrolyte interphase (SEI) through simultaneous reduction of  $\text{LiPF}_6$  salt and carbonate solvents at 0.8V (vs. Li/Li+). The organic-inorganic SEI can accommodate the small volume change of graphite during lithiation/delithiation without cracking, ensuring a high Coulombic efficiency (CE) of >99.98% and cycle life of >1000. Si anodes are the most promising anode materials for next-generation Li-ion batteries (LIBs) due to favorable average potentials (0.3 V vs Li+/Li) and 10 times higher capacities than graphite anodes. However, since both Si particles and the SEI undergo larger volume changes during cycling, the SEI is more prone to be damaged and cannot effectively prevent the side reactions between Si and the electrolyte, resulting in SEI thickening and pulverization of the Si particles. Thus, the Si-based Li-ion batteries usually demonstrate rapid capacity decay and low coulombic efficiency (CE). Extensive efforts have been devoted to suppressing the Si and SEI cracking during charge/discharge cycling, and the battery community has reached a consensus that the carbon coated nano-sized Si and fluoroethylene carbonate (FEC)-contained electrolytes is the best combination to enable high-capacity Si anodes. However, the technique still suffers from high cost, low iCE and low volumetric energy density, which limits the practical applications.

### **Objectives**

Large (>10  $\mu\text{m}$ ) Si microparticles ( $\mu\text{Si}$ ) are especially attractive due to their low production cost. The objectives of this project are to research, fabricate and test lithium-ion batteries that implement  $\geq 30\%$  silicon content electrodes with commercially available cathode and have the potential to achieve cell level energy

density of  $>350$  Wh/Kg (C/3) for 1000 cycle life with  $<20\%$  energy fade. The main objective is to screen, select and investigate the solvation structures and properties of a variety of electrolytes for the  $\mu$ Si anode, and investigate the calendar life of  $\mu$ Si anode. The tasks for this budget period are: (1) electrolyte solvation investigations and SEI formation studies; (2) identify electrolyte design principles for high-energy alloy anodes through theoretical and experimental validation. (3) identify the calendar life of micro-sized silicon and understand the mechanism to improve calendar life.

## Approach

To reduce the deformation of the SEI layer, it is desirable to form an SEI layer with a low affinity to the lithiated Si particles (high interfacial energy), such that the lithiated Si can slip at the interface during volume change without damaging the SEI. Among the known components in the SEI, lithium fluoride (LiF) possesses the highest interfacial energy with  $\text{Li}_x\text{Si}/\text{Si}$ . In addition, the wide bandgap and highly insulated LiF also significantly reduce the thickness of the LiF SEI (increasing the iCE). The PIs have conducted preliminary studies and identified that 2.0 M  $\text{LiPF}_6$  in 1:1 v/v mixture of tetrahydrofuran (THF) and 2-methyl tetrahydrofuran (MTHF) electrolytes (mixTHF electrolytes) can efficiently form LiF SEI on  $\mu$ Si anode. The mixTHF electrolytes have an anodic stability of 4.2 V and enable  $\mu$ Si electrode to provide 2800 mAh  $\text{g}^{-1}$  capacity with a cycle life of  $>400$ , iCE of  $>90\%$  and cCE of  $>99.9\%$  without any pre-treatment. The mixTHF electrolytes also enable  $\mu\text{Si}||\text{LiFePO}_4$  full cells to stably charge/discharge up to 100 cycles. In the past budget period, we screened and modified all fluorinated electrolytes (1.0 M  $\text{LiPF}_6$  in FEC, FEMC, and HFE by a volume ratio of 2:6:2) by replacing FEMC with sulfone (SL), the proposed 1.0 M  $\text{LiPF}_6$ -FEC, SL, TTE (2:6:2 by volume) (abbreviated as FST) electrolytes facilitated a  $\text{Li}_2\text{O}/\text{LiF}$  composite SEI that enables high-loading  $\text{Li}||\mu\text{Si}$  half cell ( $>4.0$  mAh  $\text{cm}^{-2}$ ) for 250 cycles with high cCE of  $>99.8\%$ . The FST electrolytes also have high anodic stability of  $>5.3\text{V}$ , enabling the 4.1 mAh  $\text{cm}^{-2}$   $\mu\text{Si}||\text{NCA}$  (N/P = 1) coin cell to charge/discharge for 200 cycles with 81% capacity retention. The practical 100 mAh pouch cell also exhibited excellent cycling with a high iCE of 81.3% and cCE of  $>99.9\%$  at a current density of C/5. The 100 mAh  $\mu\text{Si}||\text{NCA}$  pouch full cell retained 83% of its capacity after 150 cycles in FST electrolytes, demonstrating its superior cycle stability in the LIBs with SiMPs as the anode. This result encourages us to further investigate the  $\text{Li}_2\text{O}/\text{LiF}$  SEI formation mechanism and its relation to the FST electrolyte solvation. Other characterization techniques like SEM, TEM, and XPS, as well as density-functional theory (DFT) and molecular dynamics (MD) simulations are also employed to fully explore the FST solvation structures and interphases (SEI/CEI) formation mechanism. Apart from the cycling performance, the voltage hold method was used to predict the calendar life of a range of electrolytes. Meantime, the associated SEI composition, and properties are investigated to understand the mechanism behind the calendar life.

## Results

### 1. Solvation and reduction investigation of FST electrolytes

As shown in Figure VII.9.1, a full exploration of the ion coordination environment of three electrolytes: 1.0 M  $\text{LiPF}_6/\text{EC-EMC}$  (EE), 1.0 M  $\text{LiPF}_6$  in FEC-FEMC-TTE (FFT), and 1.0 M  $\text{LiPF}_6$  in FEC-SL-TTE (FST), was characterized using Raman and multi-nuclear NMR ( $^7\text{Li}$ - and  $^{19}\text{F}$ -) spectroscopy. The Raman spectra around  $740 - 750$   $\text{cm}^{-1}$  probe the  $\text{PF}_6^-$  anion environment, in which the peak at a low Raman shift is assigned to an uncoordinated  $\text{PF}_6^-$ , while the peak at a high Raman shift is assigned to contact ion pairs and aggregates. FFT electrolytes show much stronger aggregation than EE electrolytes, while the interpretation of the FST spectra is complicated because the peaks around  $750$   $\text{cm}^{-1}$  could correspond to both anions coordinated to  $\text{Li}^+$  and SL/ $\text{Li}^+$  contact ion pairs. (Figure VII.9.1A) Therefore, in-situ NMR was applied to distinguish the anions coordinated to  $\text{Li}^+$  from SL/ $\text{Li}^+$  contact ion pairs. The  $^7\text{Li}$ -NMR spectra show a clear trend of the coordination with signals going upfield largely, from EE, FFT to FST, meaning increasing ion-pair or the tendency of more electron-negative ions/atoms surrounding the  $\text{Li}^+$  centers. (Figure VII.9.1B) For the  $^{19}\text{F}$ -NMR spectra, the signature  $^{19}\text{F}$  signals ( $-72$  ppm to  $-76$  ppm) first go upfield from EE to FFT electrolytes, then aggressively downfield in FST electrolytes (Figure VII.9.1C), suggesting that  $\text{PF}_6^-/\text{Li}^+$  coordination increases in all fluorinated FFT electrolyte and decreases when FEMC is replaced by SL due to stronger  $\text{Li}^+/\text{SL}$  binding

energy. Consequently, SL has the highest solvation ability and likely dominates the  $\text{Li}^+$  solvation shell, facilitating  $\text{Li}_2\text{O}$  SEI during reduction.

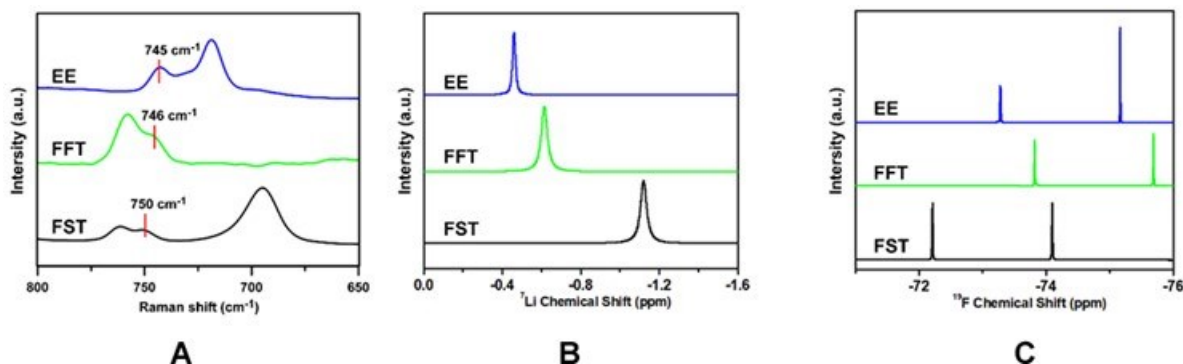


**Figure VII.9.1** Electrolytes solvation of 1.0 M  $\text{LiPF}_6/\text{EC-EMC}$  (EE), 1.0 M  $\text{LiPF}_6$  in FEC-FEMC-TTE (FFT), and 1.0 M  $\text{LiPF}_6$  in FEC-SL-TTE (FST). **A**, Raman spectra in the range of 800-650  $\text{cm}^{-1}$ . **B-C**, in-situ multi-nuclear NMR spectrum, all data were collected at r.t. NMR tuning and shimming was using external reference deuterated solvent of  $\text{D}_2\text{O}$  in a co-axis NMR tube. **B**,  $^7\text{Li}$ -NMR. **C**,  $^{19}\text{F}$ -NMR.

The solvation structure of FST electrolytes was further experimentally characterized via Pairs Distribution Functions (PDFs) with advanced synchrotron sources and simulated via molecular dynamics (MD). (Figure VII.9.2) The simulated X-ray weighted structure factor for TTE, FEC, SL solvents and FST electrolytes were well fit with experiment PDFs, validating MD simulated solvation structure. (Figure VII.9.2B). In FST electrolyte, the  $\text{Li}^+$  was primarily coordinated by 2.9 SL, 0.8 FEC and 0.7  $\text{PF}_6^-$  anions without the significant presence of TTE. These coordination numbers are consistent with the  $\text{Li}^+$  binding energy order  $\text{SL} > \text{FEC} > \text{TTE}$  in Figure VII.9.3 and radial distribution functions in Figure VII.9.4A. Importantly, non-negligible Li-F(FEC) and Li-F( $\text{PF}_6$ ) contacts are observed in Figure VII.9.4B. The  $\text{Li}^+(\text{SL})_4$ ,  $\text{Li}^+(\text{SL})_3(\text{FEC})$ ,  $\text{LiPF}_6(\text{SL})_3$  and  $\text{LiPF}_6(\text{SL})_2(\text{FEC})$  are the most probable  $\text{Li}^+$  solvates in FST electrolyte (Figure VII.9.2A). The representative solvates and aggregation of the TTE diluent in the simulation box are shown in Figure VII.9.2A, C. Further analysis of the DFT data revealed that FEC in FST electrolytes has the highest reduction potential ( $\sim 1.9$  V) among FEC, SL and TTE when its fluorine is close to  $\text{Li}^+$  (Figure VII.9.5), leading to LiF formation and initial FEC polymerization. The main  $\text{Li}^+(\text{FEC})$  reduction when  $\text{Li}^+$  is away from fluorine occurs at much lower potentials ( $\sim 1$  V v.s  $\text{Li}/\text{Li}^+$ ). Without  $\text{Li}^+$  coordination, the reduction of TTE occurs in the range of 1-1.6 V (Figure VII.9.6).  $\text{Li}^+(\text{SL})$  reduction occurs closer to 0-0.3 V with minimal deformation of the SL; however, the reduced  $\text{SL}^\bullet$  radical has a much smaller barrier of ring opening than for cycling carbonates such as PC. If this ring opening occurs simultaneously with SL reduction, the reduction potential will increase to  $\sim 1.6$  V and may serve as the precursor for  $\text{Li}_2\text{SO}_x$  species in the SEI. Alternatively,  $\sim 4\%$  of SL molecules are coordinated by 2  $\text{Li}^+$  from the MD simulations, which allows direct  $\text{Li}_2\text{O}$  formation at potentials near 2 V. The reduction of  $[\text{Li}_2\text{SL}^\bullet]^+$  ring-opened radical, however, does not release  $\text{Li}_2\text{O}$  as loss of oxygen from the terminal  $\text{SO}_2$  group is not stable. Similar reduction potentials especially for FEC and SL means LiF and  $\text{Li}_2\text{O}$  will form simultaneously, resulting in the formation of the  $\text{Li}_2\text{O}$ -LiF SEI.

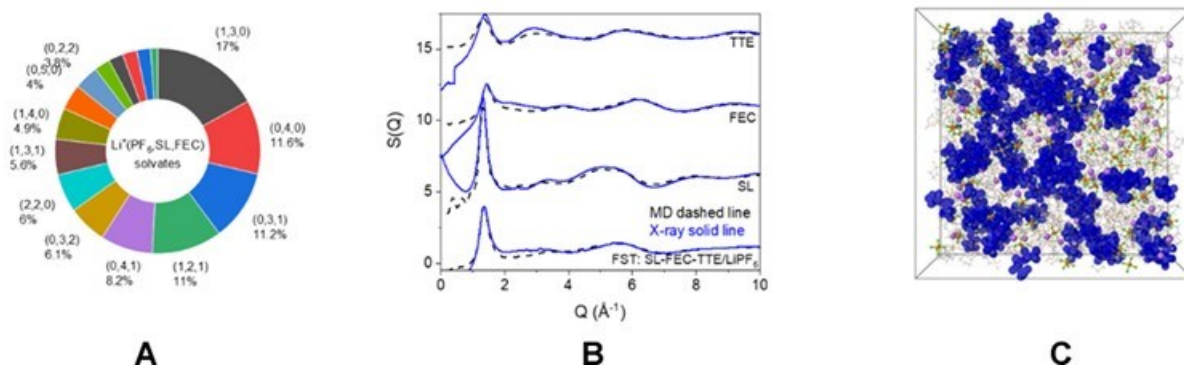


Figure VII.9.2 Solvation structure of FST electrolyte. a, distribution of the Li<sup>+</sup> solvates of FSI electrolyte from MD simulations, showing a percent for a specific solvate Li<sup>+</sup>(PF<sub>6</sub>, SL, FEC), only the solvates with more than 1% are shown for clarity. b, X-ray weighted structure factor for TTE, FEC, SL solvents and FST electrolytes from both MD simulations and experiments at room temperature with exception of SL (30 °C). c, a snapshot of MD simulation cell at 25 °C with solvent shown as a wireframe and TTE diluent highlighted using blue iso-surface.

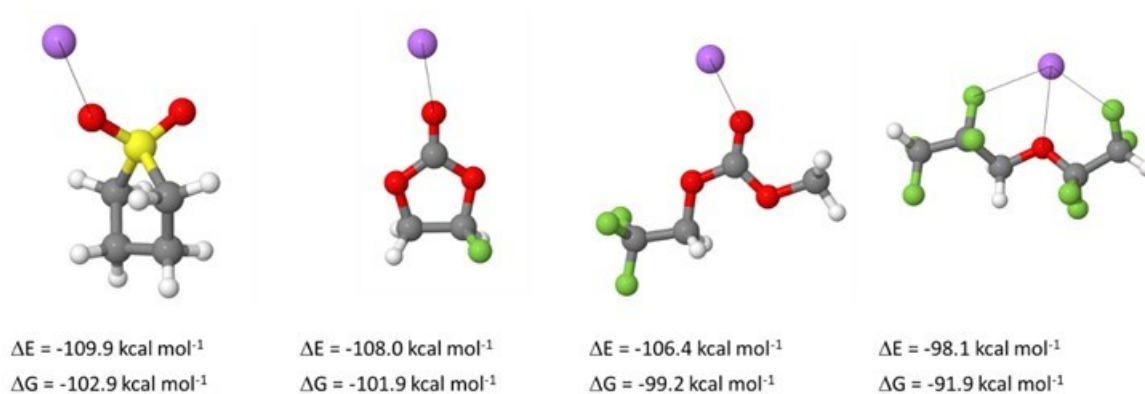


Figure VII.9.3 Binding energies of Li<sup>+</sup> to solvents from wB97XD/6-31+G(d,p) DFT calculations with all solvates immersed in implicit solvent modeled using PCM(ether) model.



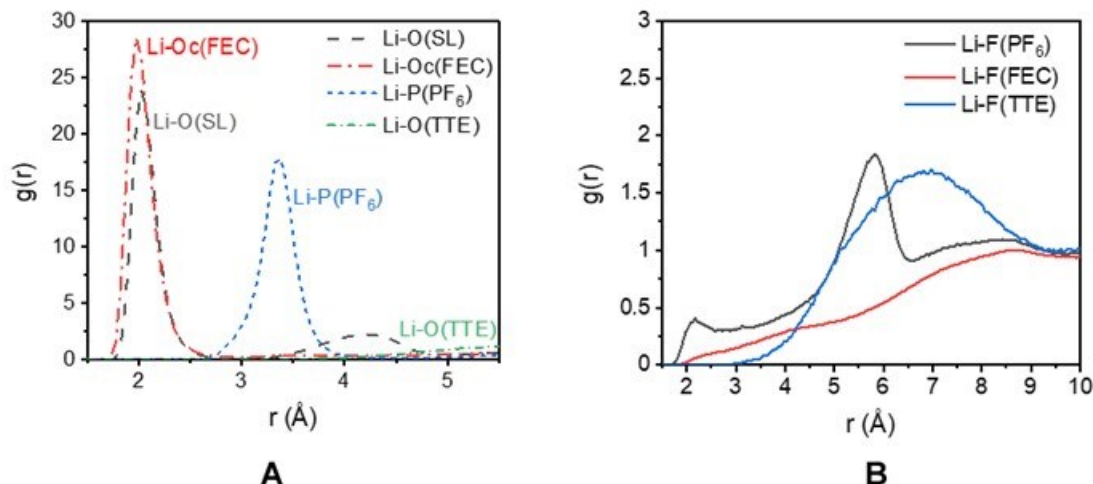


Figure VII.9.4 Radial distribution functions  $g(r)$  for FST electrolyte from MD simulations at 25 °C. Despite a slight magnitude of the higher peak for Li-Oc(FEC)  $g(r)$  compared to Li-O(SL), a significantly higher Li-O(SL) coordination number of 2.9 was observed vs. 0.8 Oc(FEC) coordination number. It is due to the higher number density of SL vs. FEC (630 SL vs. 280 FEC in the MD simulation box) and two oxygens being present in the -SO<sub>2</sub> group of SL vs. only one carbonyl Oc present in FEC.

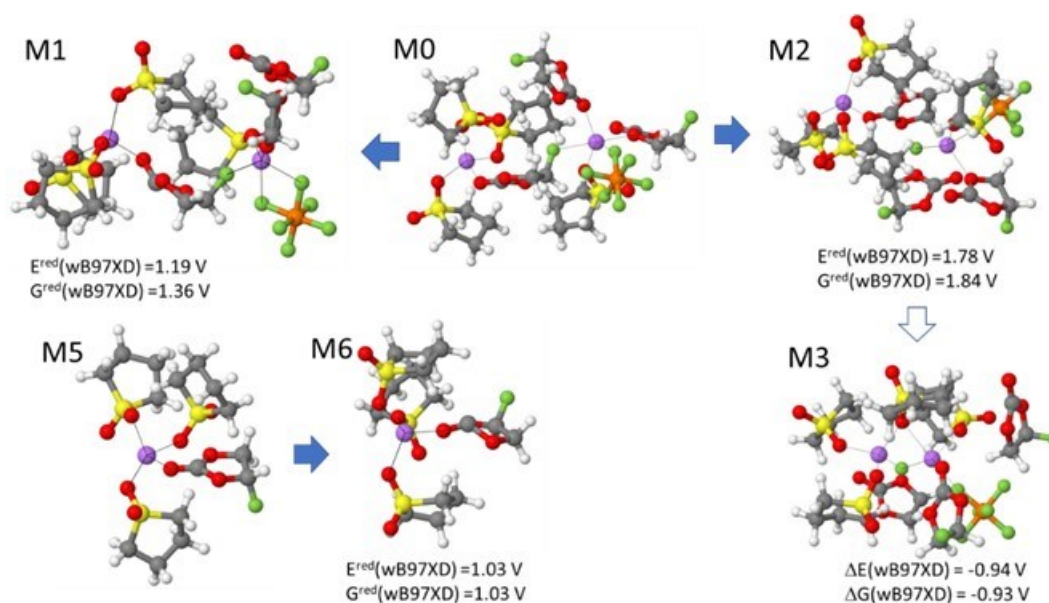


Figure VII.9.5 Reduction potentials FEC from wB97XD/6-31+G(d,p) DFT calculations with all solvates immersed in implicit solvent modeled using PCM(ether) model. The initial configurations of the representative solvates were extracted from MD simulations.

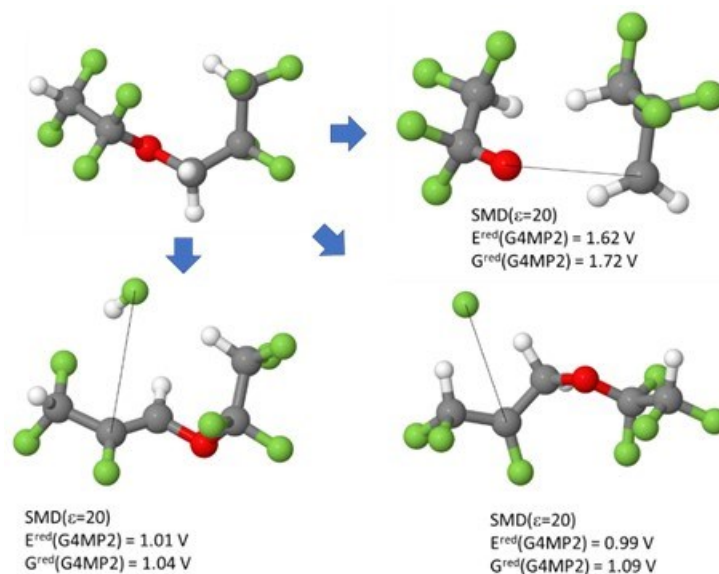


Figure VII.9.6 Reduction potentials from QC calculations using G4MP2 composite methodology TTE immersed in implicit solvent modeled using SMD( $\epsilon=20$ ) model.

## 2. Beneficial of $\text{Li}_2\text{O}$ -LiF composite SEI towards SiMPs

Weak adhesion quantified with Work of Separation (WoS) of different SEI components to  $\text{Li}_x\text{Si}$  plays a critical role in stabilizing the SiMP anode. As shown in Figure VII.9.7, the WoS for  $\text{Li}_2\text{O}$  and LiF to  $\text{Li}_x\text{Si}$  was calculated through molecular modeling and  $\text{Li}_2\text{CO}_3$  was also included as a reference, where a low WoS value corresponds to a high interface energy ( $E_{\text{int}}$ ).

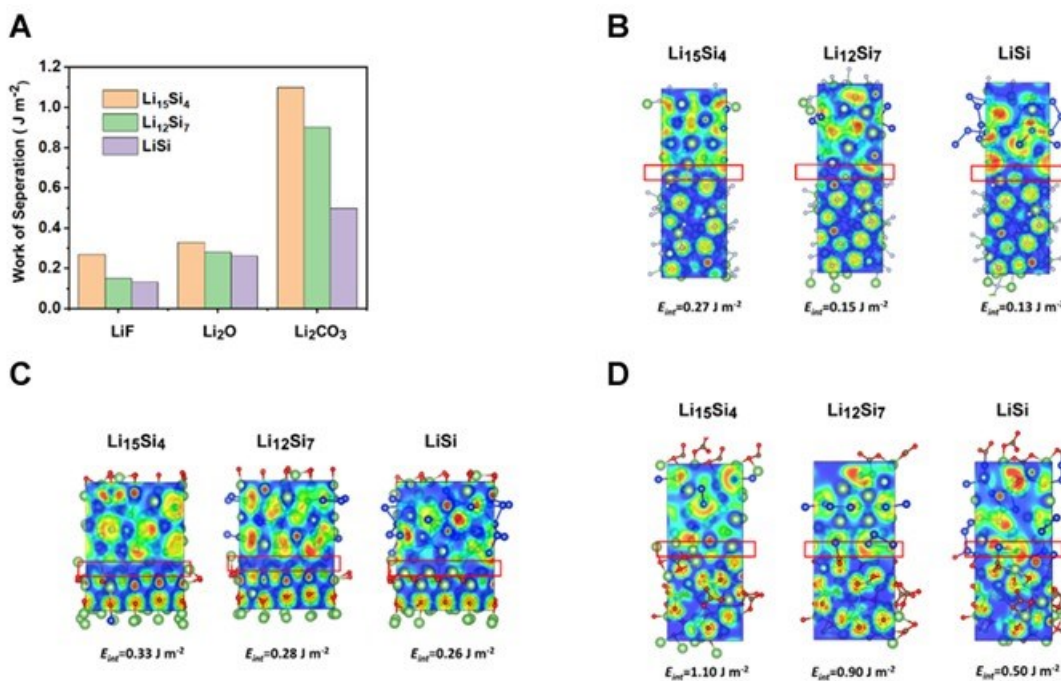


Figure VII.9.7 Effect of LiF/ $\text{Li}_2\text{O}$ / $\text{Li}_2\text{CO}_3$  SEI on the  $\text{Li}_x\text{Si}$  alloy anode. A, Work of separation for LiF/ $\text{Li}_x\text{Si}$ ,  $\text{Li}_2\text{O}$ / $\text{Li}_x\text{Si}$ , and  $\text{Li}_2\text{CO}_3$ / $\text{Li}_x\text{Si}$  interfaces. B-D, Electron localized function and  $E_{\text{int}}$  between the  $\text{Li}_x\text{Si}$  ( $\text{Li}_{15}\text{Si}_4$ ,  $\text{Li}_{12}\text{Si}_7$ , and LiSi) alloys and major SEI components (LiF,  $\text{Li}_2\text{O}$  and  $\text{Li}_2\text{CO}_3$ ). B, LiF. C,  $\text{Li}_2\text{O}$ . D,  $\text{Li}_2\text{CO}_3$ .

Figure VII.9.7A shows that both LiF and Li<sub>2</sub>O have lower WoS values ( $< 0.33 \text{ J m}^{-2}$ ) between different lithiated silicon particles (from Li<sub>15</sub>Si<sub>4</sub>, Li<sub>12</sub>Si<sub>7</sub> to LiSi) compared to a high WoS value (up to  $1.10 \text{ J m}^{-2}$ ) for Li<sub>2</sub>CO<sub>3</sub>, indicating higher interfacial energies of LiF and Li<sub>2</sub>O to the active silicon particles. Electron localization function (ELF) images between the three SEI components (LiF, Li<sub>2</sub>O, and Li<sub>2</sub>CO<sub>3</sub>) and the lithiated silicon phases are shown in Figure VII.9.7B-D. A region with an ELF value of  $< 0.2$  was observed for LiF|Li<sub>x</sub>Si and Li<sub>2</sub>O|Li<sub>x</sub>Si interfaces, referring to the absence of chemical bondings between the interfacial atoms. In contrast, the ELF value between the Li<sub>2</sub>CO<sub>3</sub>|Li<sub>x</sub>Si interface varies from 0 to 0.9, corresponding to the formation of mixed ionic and covalent bonds. The Li<sub>2</sub>O and LiF with high  $E_{int}$  to Li<sub>x</sub>Si are Si-phobic and enable the SEI to suffer less stress during the large volume change of SiMPs.

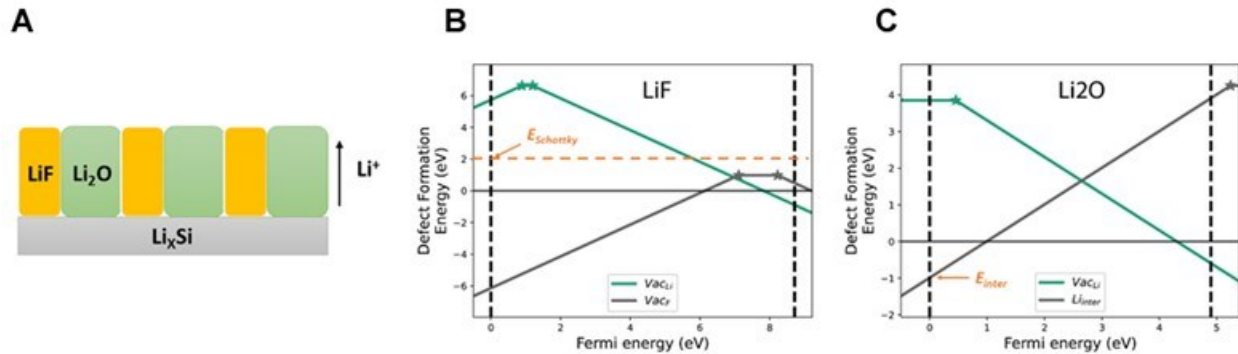


Figure VII.9.8 (A) Cartoon demonstration of the simplified model where the topological distribution of the LiF and Li<sub>2</sub>O phases was set to be parallel so that the Li<sup>+</sup> conduction path could penetrate along the SEI. (B) Formation energy v.s Fermi level (referenced to the VBM) for the most favorable native defects in LiF and Li<sub>2</sub>O under lithium-rich ( $\mu_{\text{Li}} = 0$ ) chemical potential conditions. Transitions are marked with stars. (C) The formation energy of Schottky defects was  $E^f[\text{Schottky}_{\text{LiF}}^0] = E^f[\text{vac}_{\text{Li}}] + E^f[\text{vac}_{\text{F}}]$  and its evolution with Fermi energy was plotted by a dashed orange line. Based on defect formation energy calculation, the dominant point defects of LiF and Li<sub>2</sub>O in equilibrium with the Li anode are Schottky defects and Li<sup>+</sup> interstitial defects, respectively.

In addition to SEI stabilization, the synergetic effects of LiF and Li<sub>2</sub>O also increase the Li-ion conductivity and reduce electron leakage by promoting space charge accumulation along their interfaces (Figure VII.9.8). The interstitial defect formed within the lattice Li<sup>+</sup> ion between LiF and Li<sub>2</sub>O was found to boost the interstitial Li<sup>+</sup> defect concentration in the Li<sub>2</sub>O lattice near the LiF-Li<sub>2</sub>O interface up to  $10^4$  times and reduce the electron concentration by a factor of  $10^{-4}$  compared to that of the bulk Li<sub>2</sub>O (Figure VII.9.9A).

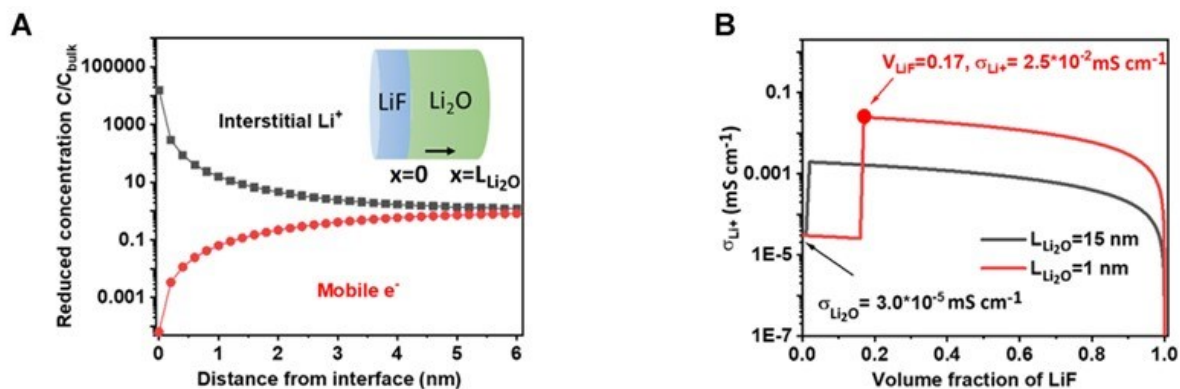
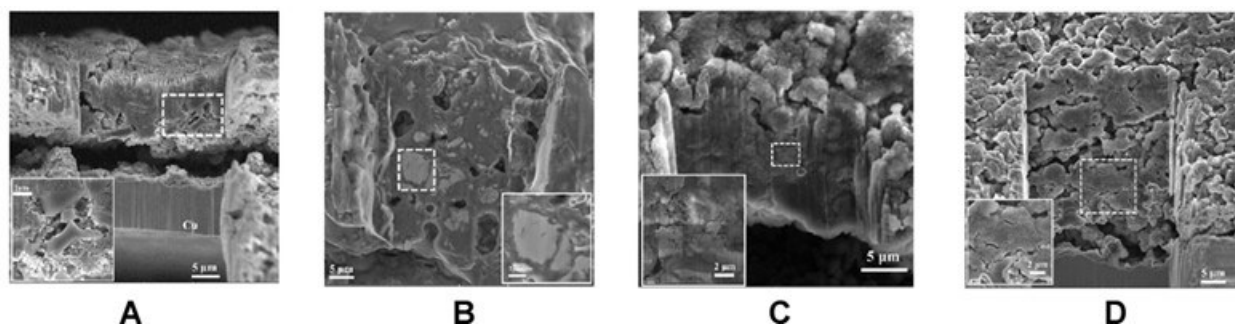


Figure VII.9.9 A, The normalized concentration profile of interstitial Li<sup>+</sup> and mobile electron Li<sub>2</sub>O within Li<sub>2</sub>O/LiF space charge region. The inserted scheme shows the configuration of the Li<sub>2</sub>O/LiF space charge model. B, The total ionic conductivity of the Li<sub>2</sub>O/LiF composite SEI as a function of the volume fraction of LiF when the grain size of Li<sub>2</sub>O is equal to 15 nm and 1 nm, respectively.

According to a simplified space charge model, when only 5% by volume of LiF was added to Li<sub>2</sub>O with a grain size of 15 nm, the ionic conductivity of the SEI increased from  $3.0 \times 10^{-5} \text{ mS cm}^{-1}$  of Li<sub>2</sub>O to  $2.0 \times 10^{-3} \text{ mS cm}^{-1}$  in the Li<sub>2</sub>O-LiF composite (Figure VII.9.9B). Further reducing the grain size of Li<sub>2</sub>O and increasing the amount of LiF can generate more Li<sub>2</sub>O-LiF interface and improve the contribution of space charge effects to total conductivity. Based on this, the total ionic conductivity of Li<sub>2</sub>O and LiF composite SEI formed in the FST electrolytes was predicted to be  $\sim 2.5 \times 10^{-2} \text{ mS cm}^{-1}$ . The interfacial calculation indicates that the high-modulus Li<sub>2</sub>O-LiF film not only ensures low bonding between SEI and Li<sub>x</sub>Si phases (Li<sub>x</sub>Si-phobic) but also promotes space charge accumulation along their interfaces. These effects suppress crackings of SiMPs during cycling and generate a high ionic-to-electronic conductivity ratio, reducing electron leakage and overall SEI thickness to enable high CE and long-cycle stability of SiMPs.

### 3. SiMPs electrode morphology and interphase characterization

SiMPs cycled in FST electrolytes show “crack-less” morphology (Figure VII.9.10B) just like the crack-free pristine Si (Figure VII.9.10A). Only minor fractures can be found in the SiMPs electrode cycled in FST electrolytes, and silicon particles larger than 5 μm could still be noticed after 50 cycles. (Figure VII.9.10 B, inset). However, large fractures have developed in SiMPs cycled in the reference electrolytes (Figure VII.9.10 C-D) with almost no micro-sized particles observed in the FIB cross-section of the electrodes.



**Figure VII.9.10** Morphology of Si particles and electrode thickness after cycling. (A-D), Focused ion beam (FIB) cross-section SEM images of the SiMP electrodes after 50 cycles of operation in different electrolytes: (A), pristine; (B), FST; (C), FFT; (D), EE.

The thickness of μSi electrodes after cycling in three electrolytes for different cycles was also monitored and evaluated. In their pristine state, the cross sections of the SiMPs electrodes showed a dense packing of the silicon particles with a thickness of 18 μm (Figure VII.9.11A), and crystalline Si particles with a size of > 5 μm can be observed. After cycling, the Si electrode cycled in FFT and EE electrolytes became loosely packed structures and the thickness continuously increased with cycling to reach 72 μm and 113 μm at 200 cycles, respectively (Figure VII.9.11B-E) due to the continuous formation of organic SEI in cracked Si. In sharp contrast, the electrode cycled in FST electrolyte showed a more confined dense layer with a thickness of 52 μm after 200 cycles, confirming the Si-phobic Li<sub>2</sub>O-LiF SEI effectively prevents the electrolyte from penetrating Si particles during lithiation/delithiation process and protects the μSi electrode from further swelling (Figure VII.9.11D-E).

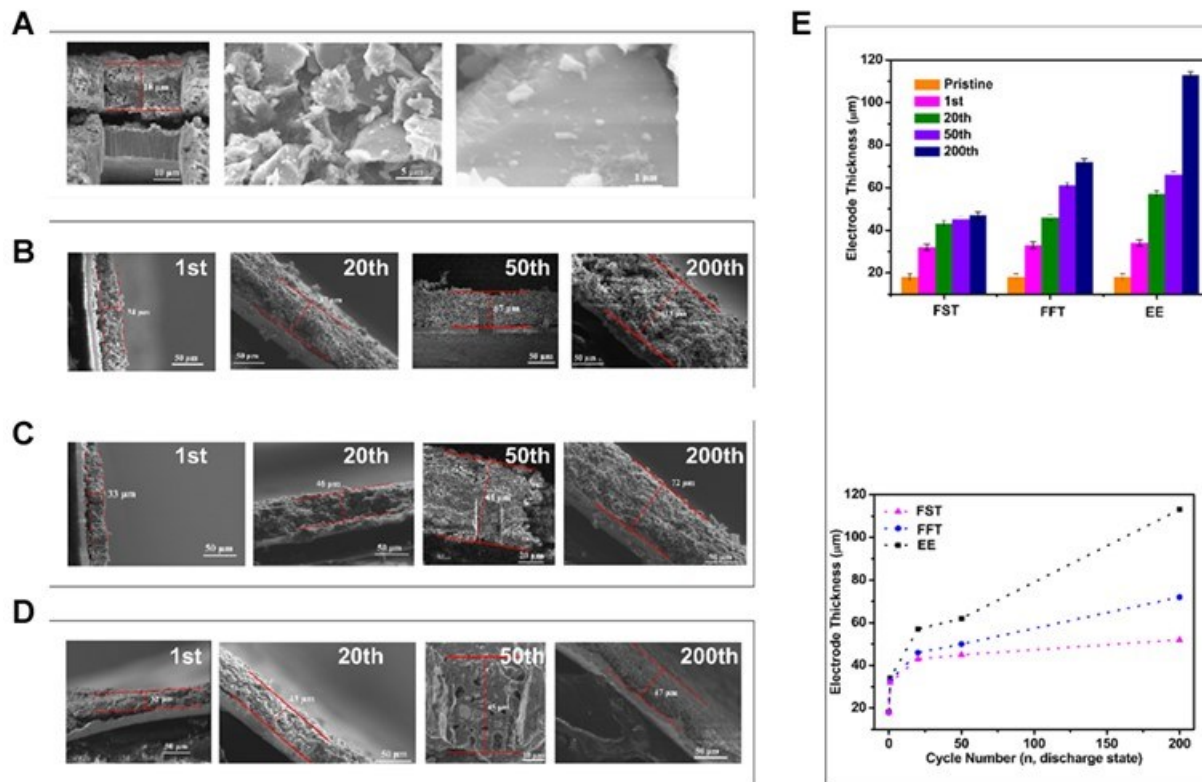


**Figure VII.9.11** (A) The SEM images of the pristine 1-5  $\mu\text{Si}$  electrodes, show the electrode thickness of pristine 4.1 mAh  $\text{cm}^{-2}$   $\mu\text{Si}$  electrode about 18  $\mu\text{m}$ . (B-D), the electrode thickness evolution under different cycled numbers (1st, 20th, 50th, and 200th) with EE (B), FFT (C), and FST (D) electrolytes. (E), the histogram of thickness evolution in the three electrolytes, and the SiMPS expansion trend. The dashed line here is only for the guidance of the eye. The  $\mu\text{Si}||\text{Li}$  cells are cycled to a specific cycle, then stopped at the discharge state to make these ex-situ measurements.

The observed SiMP electrode thickness evolution indicates the effectiveness of a fixed  $\text{Li}_2\text{O}$ -LiF SEI shell in making the expansion/contraction of the  $\text{Li}_x\text{Si}$  core more reversible with fewer cracks of the micro-sized Si particles in the designed FST electrolytes. The SEI formed on the cycled SiMPS was further explored via electron energy loss spectroscopy (EELS) spectral imaging. The FFT electrolyte was chosen as a reference. The EELS spectral images at different locations from the surface to the inside part of the SiMPS cycled in FFT and FST electrolytes were analyzed. (Figure VII.9.12) The sharp valence plasmon peak at 18.4 eV with a smooth shoulder around 34.5 eV identified the existence of  $\text{Li}_2\text{O}$  signal in SEI, while the sharp peak at 25.7 eV accompanied by a small bump of 15.3 eV is assigned as the fingerprint of LiF in the SEI layer. For SiMPS cycled in FST electrolyte (Figure VII.9.12A-B), the  $\text{Li}_2\text{O}$ -LiF was a homogeneous distribution on the Si particle surface with signatures at 15 eV, 25 eV, and 35 eV, which are in good agreement with the  $\text{Li}_2\text{O}$ -LiF SEI formation mechanism supported by the molecular modeling and XPS analysis in our previous reports. For SiMPS cycled in FFT electrolytes, a mixed organic-inorganic SEI with a broad peak centered  $\sim 23$  eV is found for almost all the near-surface spectra, which indicates that there is no substantial amount of  $\text{Li}_2\text{O}$  nor LiF on the surfaces (Figure VII.9.12D).

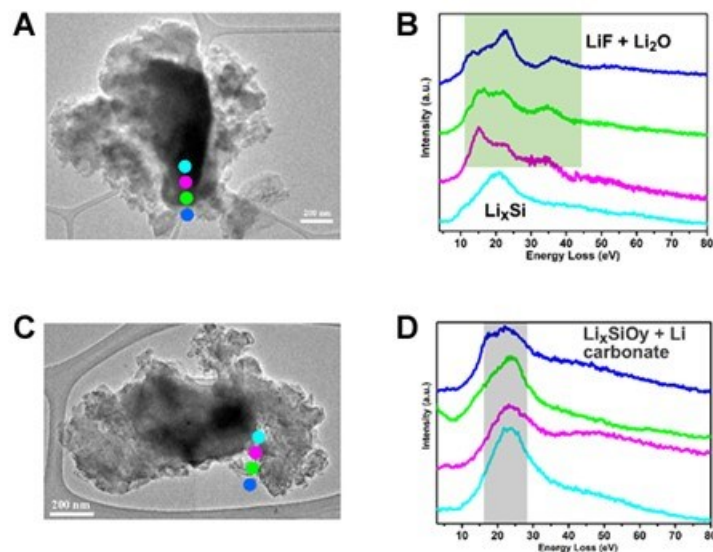
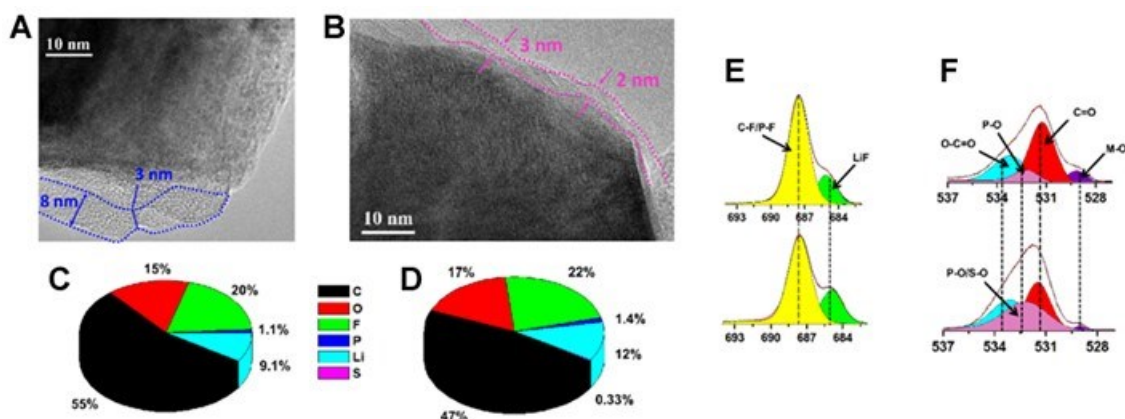


Figure VII.9.12  $\text{Li}_2\text{O}$  and  $\text{LiF}$  distribution on  $\mu\text{Si}$  anode in the FST (A-B) and FFT (C-D) electrolytes. A, C, HR-TEM images, the colored dots represent the area of corresponding EELS spectral images in b and d. B, D, typical EEL spectra near the surface of the  $\mu\text{Si}$  particles with the marked four areas in A, C (from surface to inner layer).

To understand the cathode stability of full cells cycling in the FST and FFT electrolytes, the cathode/electrolyte interphase (CEI) structure and chemistry after 50 cycles at the discharge state were characterized with scanning transmission electron microscopy (STEM) and XPS. A CEI protecting layer on the primary NCA particles was observed after 50 cycles in FFT and FST electrolytes, with a CEI thickness ranging from 2-3 nm (FST, Figure VII.9.13B) to 3-8 nm (FFT, Figure VII.9.13A). The CEI composition on cycled NCA was further examined via X-ray photoelectron spectroscopy (XPS) (Figure VII.9.13 C-F). Both CEI films formed in FFT and FST electrolytes showed high F content, as evidenced by the F/C, F/O ratio of 0.36/1.3 and 0.47/1.3, respectively, indicating LiF-dominated CEI is formed. The wide band gap (13.6 eV) and high oxidative stability (6.4 V *v.s.* Li/Li<sup>+</sup>) of LiF ensured effective suppression of the parasitic reactions between the cathode surface and electrolytes. The M-O species (~529.5 eV, O 1s, Figure VII.9.13 C-F) and high LiF in CEI formed in FST compared to FFT electrolyte ensure thin CEI thickness (Figure VII.9.13 A-B) and high anti-oxidation stability. In addition, the broad shoulder of the P-O signal (~529-535 eV) in the FST electrolytes suggests the co-existence of the S-O species, [ENREF 1](#) which might come from the decomposition of SL molecules. The sulfur-containing compounds have been proven propitious to conduct Li<sup>+</sup>, contributing to the steady cycling of the  $\mu\text{Si}/\text{NCA}$  full cell. All these findings further confirmed the ultra-stable anodic tolerance of the designed FST electrolyte. As such, the greatly improved cathode stability in the designed electrolyte guarantees the boosted steady full-cell over long-term cycling.



**Figure VII.9.13** Characterizations of Cycled NCA Electrodes in FFT and FST electrolytes. A-F, typical HR-TEM images of cycled NCA electrodes recovered from  $\mu\text{Si} \parallel \text{NCA}$  full cells after 50 cycles with FFT (A) and FST (B) electrolyte; the atomic distribution of CEI element on the surface of the NCA electrodes cycled in different electrolytes, FFT (C), FST (D); the XPS F1s (E) and O1s (F) surface spectra for NCA cathodes with FFT (upper) and FST (below) electrolytes.

#### 4. Calendar life of micro-sized Si anode

In the report of last year, we found that the micro-sized Si anode with 2.0 M  $\text{LiPF}_6$  THF/MTHF electrolytes hold great potential to have a comparable calendar life to graphite anode with 1.0 M  $\text{LiPF}_6$  EC/DEC/FEC. We also proposed that the calendar life of  $\mu\text{Si}$  anode is positively related with the CE of electrolytes because the CE can refer to the SEI stability. In order to validate our proposal, we introduce more electrolytes this year and systematically investigate the relationship between calendar life and SEI and corresponding CE. Apart from  $\text{LiPF}_6$  based electrolytes (2.0 M  $\text{LiPF}_6$  THF/MTHF and 1.0 M  $\text{LiPF}_6$  EC/DEC/FEC), we also introduce the LiFSI based high-concentration electrolytes (4.0M LiFSI DME and 1.0 M LiFSI DME/TTE). Their current response (Figure VII.9.14A) and capacity loss (Figure VII.9.14B) during voltage hold are shown below. We summarized the leakage current@180h of sample electrolytes with corresponding cycle CE in Figure VII.9.14C, the electrolytes with high CE of >98% have a leakage current at the same magnitude as standard graphite, indicating they are promising to have analogous calendar life with graphite. Moreover, for the same  $\mu\text{Si}$  electrodes, the electrolytes with higher CE are relatively consistent with the electrolytes with lower leakage current@180h. Among them, the 4.0 M LiFSI-DME electrolyte has a much lower CE of <98% and the corresponding leakage current is also much higher than other electrolytes with higher CE. Even for the three electrolytes with a high CE of >98%, there is a similar trend between CE and leakage current. Current leakage during voltage hold is generally caused by SEI growth on the Si particles, representing the SEI growth rate. When the particle size is at the same level, the SEI growth rate is directly related to the SEI passivation ability which is strongly represented by the value of CE. It is generally accepted that the electrolytes with higher CE have stronger passivating SEI. Our finding here strongly supports that a high cycle CE in a battery is a significant signal for a better calendar life of the cell. It is noted that these results do not provide absolute calendar lifetime predictions, but the comparison to standard electrodes graphite (carbonate electrolytes) with calendar lifetime well reported before should tell us their relative calendar life. Therefore, we can get a conclusion that the  $\mu\text{Si}$  electrode with high cycle CE is very promising to have a comparable calendar life with graphite.

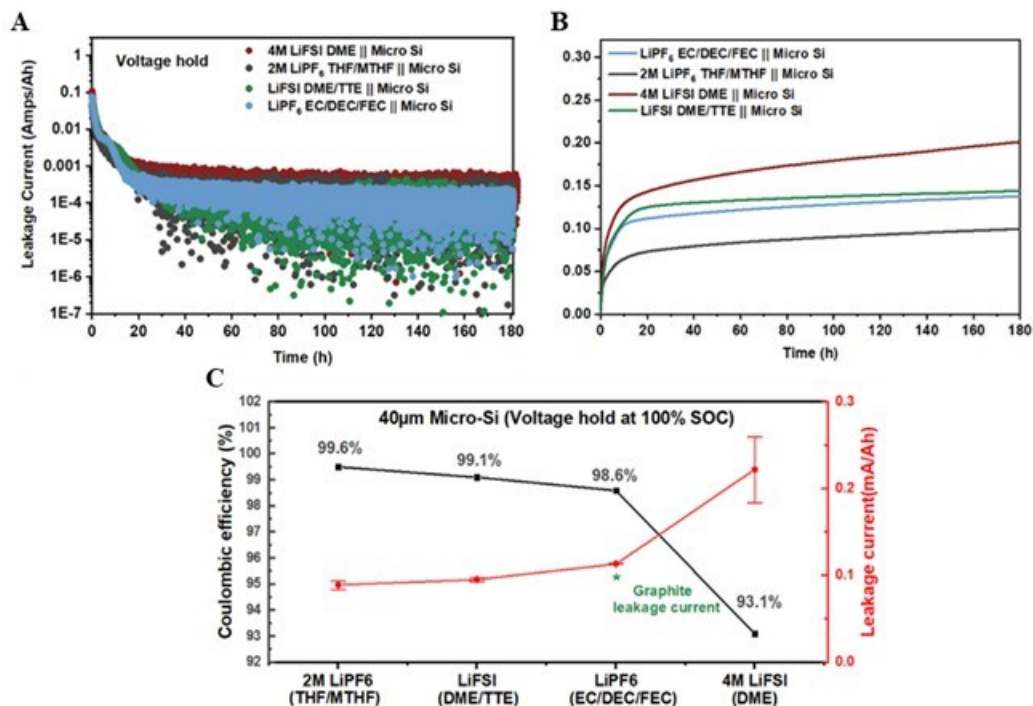


**Figure VII.9.14** (A) Leakage current of the cell using different electrolytes, including LiFSI-based electrolytes (4.0 M LiFSI DME, 1.0 M LiFSI DME/TTE), as well as LiPF<sub>6</sub>-based electrolytes (LiPF<sub>6</sub> THF/MTHF, 1.0 M LiPF<sub>6</sub> EC/DEC/FEC). (B) The capacity leakage during voltage hold is integrated by the leakage current. (C) The CE and the leakage current @180h of Li||Si and Li||graphite cells in a variety of electrolytes.

In order to figure out why the calendar life is correlated with CE (indeed SEI), we examined the SEI chemical composition via X-ray photoelectron spectroscopy (XPS) with an Ar<sup>+</sup> sputtering depth profiling for both the LiFSI-based and LiPF<sub>6</sub>-based electrolytes. Our findings are summarized below (Figure VII.9.15A):

- The SEI of 2M LiPF<sub>6</sub> THF/MTHF is LiF-rich.
- The SEI of 1M LiFSI DME/TTE is Li<sub>2</sub>O-rich.
- The SEI of 1M LiPF<sub>6</sub> EC/DEC/FEC and 4M LiFSI DME is Li<sub>2</sub>CO<sub>3</sub>-rich.

A discernible trend is evident, as the solid electrolyte interface (SEI) composition undergoes a transition from being LiF-rich to Li<sub>2</sub>CO<sub>3</sub>-rich, correlating with a reduction in calendar life. This observation agrees with recent findings published in Nature Energy (Volume 8, Pages 921–933, 2023), revealing that electrolytes incorporating FEC can mitigate side reactions, yet Si-containing cells experience a notably higher capacity loss after calendar aging compared to Si cells without FEC. This discrepancy is likely attributed to the primary decomposition product of FEC reduction, which is Li<sub>2</sub>CO<sub>3</sub>, offering a plausible explanation for the phenomenon. Initially, electrolytes display instability when coupled with silicon anodes at low voltages, leading to the formation of an SEI layer due to electrolyte reduction. However, the SEI is not an ideal barrier, as not all of its components are thermodynamically stable and electronically insulating. Variances in energy levels between the anode and electrolytes facilitate electron migration from the anode to the SEI. The SEI then conducts these electrons to the interface between the SEI and the electrolytes, contributing to further electrolyte reduction and resulting in the growth of the SEI. Consequently, SEI compositions characterized by both thermodynamic stability and low electronic conductivity are preferable for achieving an extended calendar life. While direct testing of the electrochemical stability and electronic conductivity of the SEI poses challenges, analyzing the SEI based on the properties of its main constituents yields valuable insights.



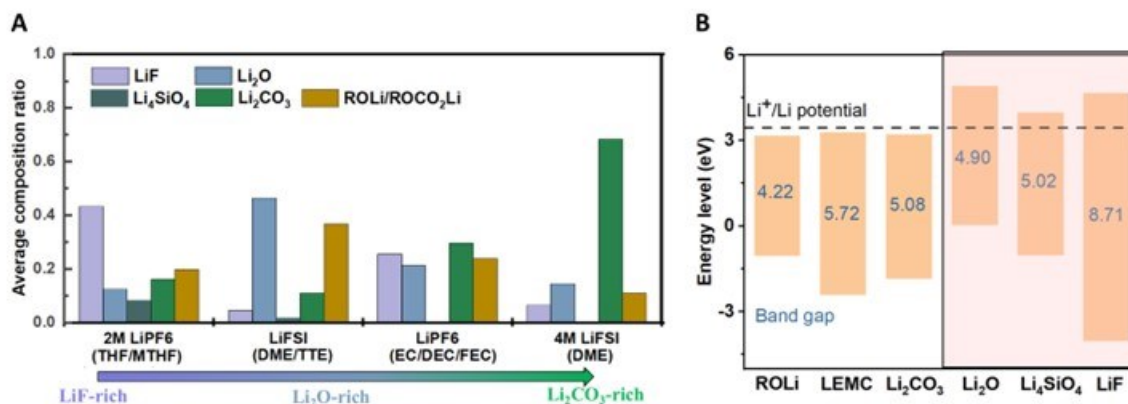


**Figure VII.9.15 (A)** The relatively molecular ratio of LiF, Li<sub>2</sub>O, Li<sub>4</sub>SiO<sub>4</sub> and Li<sub>2</sub>CO<sub>3</sub> and ROLi/ROCO<sub>2</sub>Li in SEI of 2M LiPF<sub>6</sub> THF/MTHF, 1M LiPF<sub>6</sub> EC/DEC/FEC, 1M LiFSI DME/TTE, and 4M LiFSI DME. **(B)** The calculated LUMO energy and band gap of variety SEI compositions.

To investigate the electrochemical stability and electronic conductivity of these constituents, we calculated the LUMO energy level and band gap of each component (see Figure VII.9.15B). A higher LUMO energy level indicates greater resistance to reduction. Additionally, a smaller band gap suggests better electronic conductivity, and vice versa.

Among these constituents:

- LiF demonstrates the highest LUMO energy and the widest band gap, indicating exceptional electrochemical stability and strong electron-blocking capability.
- Li<sub>2</sub>O also possesses a high LUMO energy, albeit with a narrower band gap compared to LiF, implying good stability but with a lesser ability to block electrons.
- In contrast, Li<sub>2</sub>CO<sub>3</sub> exhibits both a low LUMO energy and a narrow band gap, resembling polymer-based ROLi and ROCOLi. This implies instability and relatively poor electron-blocking capability.

The relatively elevated concentration of Li<sub>2</sub>CO<sub>3</sub> in LiPF<sub>6</sub> EC/DEC/FEC and 4M LiFSI DME elucidates their lower Coulombic efficiency (CE) and more pronounced calendar aging. Conversely, 2M LiPF<sub>6</sub> THF/MTHF forms a LiF-rich SEI with fewer organic compounds, resulting in a high CE and minimal calendar aging.

**Another pivotal factor influencing the calendar life is particle size**, specifically surface area. It is noteworthy that nano-Si electrodes exhibit a smaller average pore width compared to micro-Si electrodes. While electrolytes may not infiltrate all pore sizes uniformly, the substantial difference in surface area still yields a significantly larger available interaction surface for nano-Si with the electrolytes. Transmission Electron Microscopy (TEM) and Energy-Dispersive X-ray Spectroscopy (EDS) results on the aged nano-Si anode confirm the extensive Solid Electrolyte Interface (SEI) surface area resulting from the large electrode surface area. In contrast to the larger particles in micro-Si, the apparent "big" Si in the nano-Si electrode image is actually composed of numerous aggregated very tiny particles (Figure VII.9.16 A). Consequently, distinct C/O/F signals from the SEI are evident within the "big" Si aggregation (Figure VII.9.16 B-E), while SEI signals are predominantly concentrated on the outer layer of micro-Si anodes. Therefore, it is evident that a significantly larger amount of SEI forms in the nano-Si electrodes, leading to a substantial increase in irreversible Li<sup>+</sup> consumption. Although nano-Si may not result in a decrease in capacity retention in a Li||Si cell due to the abundance of Li<sup>+</sup>, the heightened Li<sup>+</sup> consumption poses a critical challenge in a full cell configuration where Li<sup>+</sup> availability is limited.

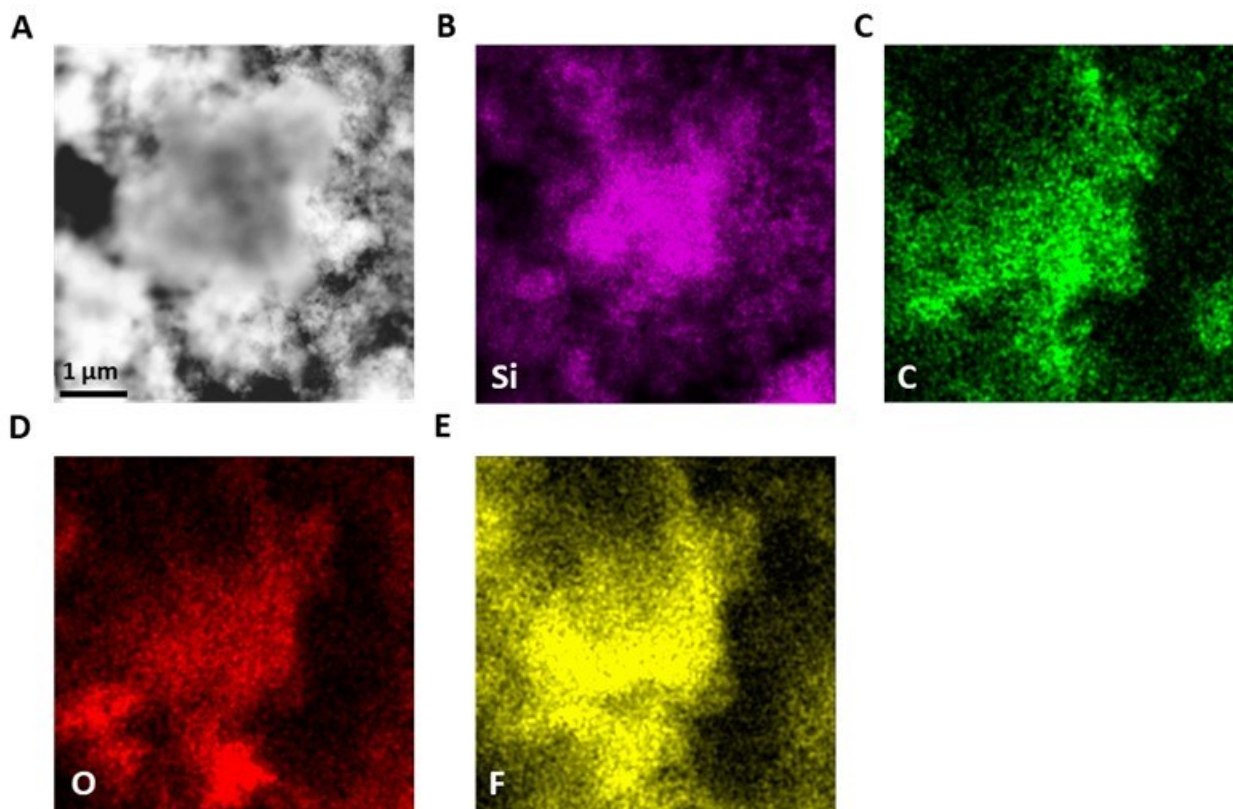


Figure VII.9.16 TEM and EDS analysis of nano silicon particles in 2M LiPF<sub>6</sub> THF/MTHF after calendar aging. (A) TEM image. (B) EDS Si map. (C) EDS C map. (D) EDS O map. (E) EDS F map.

### Conclusions

In summary, to make a stable high-energy  $\mu\text{Si}||\text{NCA}$  cell, we developed high-voltage electrolytes with high anodic stability of  $> 5.3\text{V}$ , which can form ceramic interphases on both  $\mu\text{Si}$  anode (SEI) and NCA cathode (CEI). The high-voltage FST electrolytes enable the formation of an inorganic-rich ( $\text{Li}_2\text{O}/\text{LiF}$ ) bilayer SEI layer on SiMPs, which allows the  $\mu\text{Si}||\text{NCA}$  full cell stably cycling for 200 cycles with  $>81\%$  capacity retention. The practical 100 mAh  $\mu\text{Si}||\text{NCA}$  pouch full cell retained 83% of its capacity after 150 cycles in the designed electrolyte, demonstrating the practicability of this electrolyte. We further validated the  $\text{Li}_2\text{O}/\text{LiF}$  SEI formation using DFT/MD calculations. The  $\text{Li}_2\text{O}$  is proven to be highly Si-phobic, showing high interfacial energy between the  $\text{Li}_x\text{Si}$  phases, which is comparable to the well-known LiF. The  $\text{Li}_2\text{O}/\text{LiF}$  composite SEI was also found to be beneficial for improved  $\text{Li}^+$  conductivity. A combination of SEM/TEM and XPS analysis showed that the  $\text{Li}_2\text{O}/\text{LiF}$  SEI enabled a superior cycle of  $\mu\text{Si}$  electrode with less Si particle cracking and electrode swelling. In addition, the CEI formed on the high-voltage NCA cathode after long cycling in the  $\mu\text{Si}||\text{NCA}$  full cells was validated with a portion of LiF, which is accountable for the superior high-voltage performance. These results and electrolyte design strategies identified here can be used as guidance for the electrolyte development used on micro-sized silicon anode in the next phase and further cell optimization will be performed in the next fiscal year, targeting high cycling life for high-energy  $\mu\text{Si}||\text{NMC}$  full cell.

As for the calendar life of Si-based anode, we investigated a range of electrolytes on calendar life, and we demonstrate that calendar aging is mainly derived from the  $\text{Li}^+$  consumption in SEI growth, and the rate of SEI growth is determined by the SEI surface area and the increase of SEI thickness. The SEI composition strongly affects the SEI thickness increase rate. The LiPF<sub>6</sub> THF/MTHF formed LiF-rich SEI with fewer organic compounds, which have high electrochemical stability and electron insulation ability, can significantly reduce the SEI thickness increasing. While fewer inorganic compounds and a high amount of  $\text{Li}_2\text{CO}_3$  and organic

compounds in SEI leading a much thicker SEI in the  $\text{LiPF}_6$  EC/DEC/FEC and 4M LiFSI DME. Meantime, the SEI surface area is mainly determined by the particle size of 3D silicon anodes. The nano-size particle will significantly increase the surface area of SEI, which largely increases the  $\text{Li}^+$  consumption leading to bad calendar life. Therefore, optimizing the SEI composition and developing the electrode structure to reduce the contact area between electrolytes and electrodes are future direction to minimize calendar aging.

## VII.10 Free-Energy Driven Approaches to Self-Forming and Self-Terminating SEIs on Si Anodes (LBNL)

### **Brett Helms, Principal Investigator**

Lawrence Berkeley National Lab  
1 Cyclotron Road  
Berkeley, CA, 94720  
E-mail: [bahelms@lbl.gov](mailto:bahelms@lbl.gov)

### **Carine Steinway, DOE Technology Development Manager**

U.S. Department of Energy  
E-mail: [Carine.Steinway@ee.doe.gov](mailto:Carine.Steinway@ee.doe.gov)

### **Thomas Do, DOE Technology Development Manager**

U.S. Department of Energy  
E-mail: [Thomas.Do@ee.doe.gov](mailto:Thomas.Do@ee.doe.gov)

Start Date: October 1, 2022

End Date: September 30, 2023

Project Funding (FY23): \$225,000

DOE share: \$225,000

Non-DOE share: \$0

### **Project Introduction**

Introduction of localized super-concentrated electrolytes (LSCEs) made it possible to form long-lasting passivating solid-electrolyte interface (SEI) leading stable cycle life. However, SEI from single anion electrolyte is not sufficient to protect electrodes considering calendar life. As result, continuous electrolyte decomposition and loss of Li inventory shorten battery's useful life. [1-12] High-entropy mixed anion LSCEs (HE-LSCEs) composed of multi lithium salts with different anions could take a role as more stable, electrode-protecting and self-terminating SEI former, alleviating Li loss and continuous electrolyte decomposition while situated in high voltage. The effective protection of electrodes with HE-LSCE could be a stepping stone in developing EV batteries with useable energy >350 Wh/kg, energy density >700 Wh/L, and a calendar life >10 years.

### **Concept**

To address the calendar life problem at high voltage, we proposed to design and evaluate a new class LSCE composed of multi lithium salts that forms stable surface on both anode and cathode. HE-LSCE would form stable SEI on Si anode as single anion LSCE does. LiF based inorganic SEI effectively protects anode surface during cycling and storing after charge. In the meantime, HE-LSCE form stable cathode electrolyte interface (CEI) on cathode during formation cycle in high operation voltage.

### **Objectives**

In the current reporting period, our seedling project pursued four research objectives, which are listed in turn. We aligned these research objectives to be parallel with related efforts in the Silicon Anode Research Consortium to enable direct transfer of our findings to that team.

- Objective 1: Evaluate galvanostatic cycling performance of Si-LFP cull cells using single ion LSCE, mixed ion HE-LSCE and consortium's GenF3 carbonate electrolyte. Cathode areal capacity > 1.5 mAh/cm<sup>2</sup>. Rate = C/3. Temperature = 25 °C. Using GenF 3 carbonate electrolyte as a reference, compare stable SEI formation capability on Si anode surface.
- Objective 2: Conduct post-formation and post-mortem XPS and FIB-SEM analysis of full cells cycled using LSCE, HE-LSCE electrolytes as well as the consortium's GenF 3 carbonate electrolyte. Using GenF 3 carbonate electrolyte as a reference, clarify the reason of capacity decay associated with overpotential and resistance increase, and identify components of the electrolyte that form stable SEI on the Si anode.

- Objective 3: Build a model that accounts for experimental observations for initial capacity loss and capacity fade rate on the basis of anion, solvent, diluent, and additive activity at electrified anode and cathode interfaces during interphase generation. Use model to inform final electrolyte designs, where interphases at anode and cathode are co-designed as well as the voltage cut-off and hold on charge.
- Objective 3: Evaluate full cell cycling performance for at least 300 cycles with final downselected electrolytes. Cathode areal capacity > 1.5 mAh/cm<sup>2</sup>. Rate = C/3. Temperature = 25 °C.

### Approach

To meet the above objectives, we acquired from ORNL, CAMP, and NREL or fabricated electrodes with the following specifications.

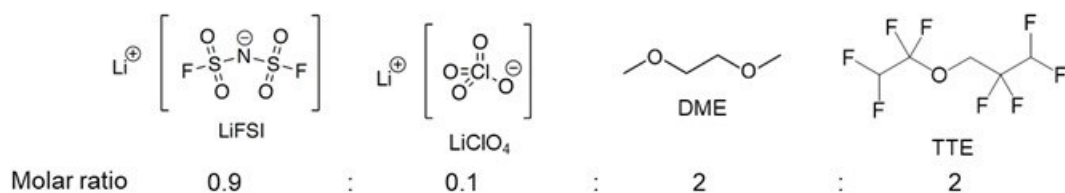
- Anodes:
  - CAMP-ORNL Si: 2.0 mAh/cm<sup>2</sup>
- Cathodes:
  - CAMP-LFP: 2.9 mAh/cm<sup>2</sup>
  - CAMP-NMC811: 2.6 mAh/cm<sup>2</sup>

These electrodes were assembled into a variety of formats, including Si|LFP and Si|NMC811 2032 coin cells, for testing our electrolytes (40 μL per coin cell) as described above. As reference electrolytes, we used Gen3 electrolyte developed by the Silicon Anode Research Consortium.

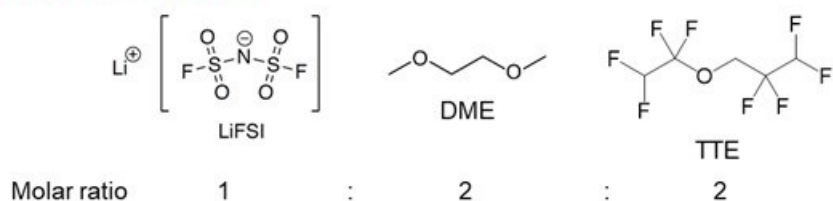
To test our hypothesis for stable SEI and CEI for anode and cathode, we prepared HE-LSCE composed of LiFSI, LiClO<sub>4</sub>, DME and TTE as lithium salt, solvent and a fluorinated diluent. As stable CEI former at high voltage, we mixed LiClO<sub>4</sub> with LiFSI. We evaluated their SEI forming capability and their compositions on Si anode and leakage current while storing the cell at high voltage to monitor and track progress toward our objectives for this reporting period. These results are discussed below in detail.

## Results

### HE-LSCE (Selected electrolyte stabilizing both Si anode and NMC811 cathode)



### LSCE (Positive control)



### Carbonate electrolyte (GenF3, Negative control)

1.2 M LiPF<sub>6</sub> in EC/EMC 3:7 w/w + 3 wt% FEC

**Figure VII.10.1 Electrolyte Downselect for Year 3. High-entropy mixed-anion locally superconcentrated electrolyte (HE-LSCE) consisting of two lithium salts of LiFSI and LiClO<sub>4</sub>, DME solvent, and TTE diluent as a downselected electrolyte for Year 3. LSCE with single LiFSI salt as a positive control electrolyte and GenF3 carbonate-based electrolyte as a negative control.**

In previous years, we found that single salt LSCE with LiFSI as a lithium salt, DME solvent, and TTE with desired ratio between them (positive control in Figure VIII.11.1) showed promising stability with Si anode. In Year 3, we designed High-entropy mixed-anion locally superconcentrated electrolyte (HE-LSCE) in Figure VII.10.1 based on our Year 1 observation that LiClO<sub>4</sub> in LSCE also provides stability with Si anode comparable to LiFSI. We evaluated the stability of Year 3 HE-LSCE in Si full cells by testing Si-LFP cells and Si-NMC811 cells and compare with LSCE (positive control) and GenF3 (negative control)

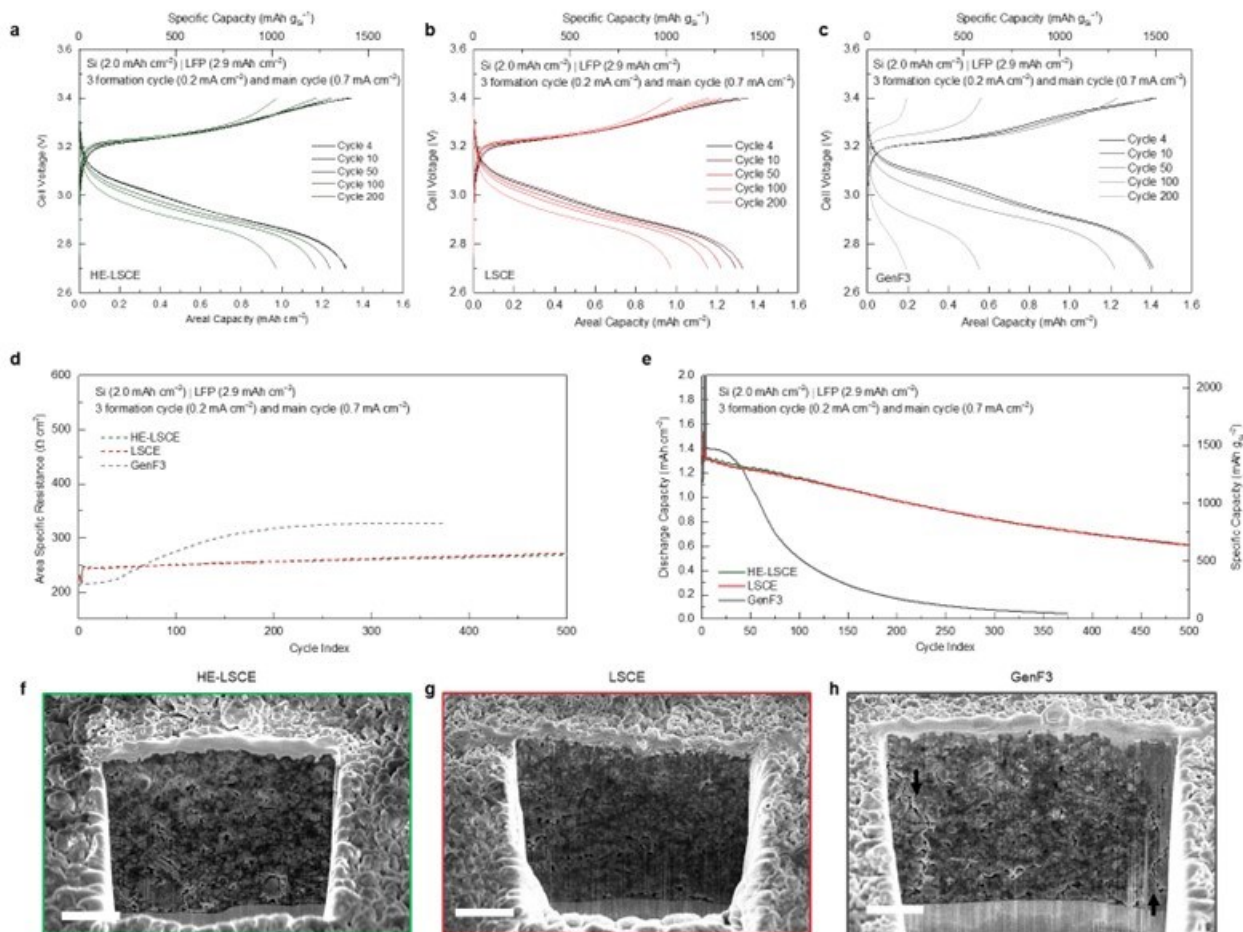


**Figure VII.10.2 Evaluation of Si-LFP Cells and Degradation of Si Anodes.** (a-c) Galvanostatic cycling profile of Si-LFP cells cycled by (a) HE-LSCE, (b) LSCE, and (c) GenF3. All cells were cycled with 3 formation cycles with C/10 followed by repeated charge and discharge with C/3. (d) Evolution of area specific resistance (ASR) during Si-LFP cycling. (e) Capacity retention of Si-LFP cells. (f-h) FIB-SEM cross-sectional images of Si anodes after 1<sup>st</sup> lithiation.

We first evaluated the compatibility of electrolytes with Si anode by testing Si-LFP cells as LFP cathode as dummy electrodes. Si-LFP cells were assembled with Si anode with the loading level of 0.95 mg cm<sup>-2</sup> and LFP cathode with areal capacity of 2.9 mAh cm<sup>-2</sup>. All cells were cycled with 3 formation cycles with C/10 followed by repeated charge and discharge with C/3 at 25°C. Galvanostatic cycling profile (Figure VII.10.2.a-c) showed that both LSCEs provide much more stable cycling performance compared to GenF3 electrolyte. Si-LFP cells with LSCEs showed much slower increase of ASR (Figure VII.10.2.d). As a result, cells with LSCEs were stably cycled up to 500 cycles without dramatic capacity decay while cells with GenF3 exhibited dramatic capacity loss only after 100 cycles. To figure out dramatic capacity decay associated with overpotential and resistance increase in case of GenF3, we collected cross-sectional FIB-SEM images from lithiated Si anode. (Figure VII.10.2.f-h) Interestingly, severe mechanical cracking is only found in Si anode composite cycled with GenF3. It suggests continuous evolution of such cracking would block efficient electrical connection through electrode composite that will eventually increase overpotential and resistance.

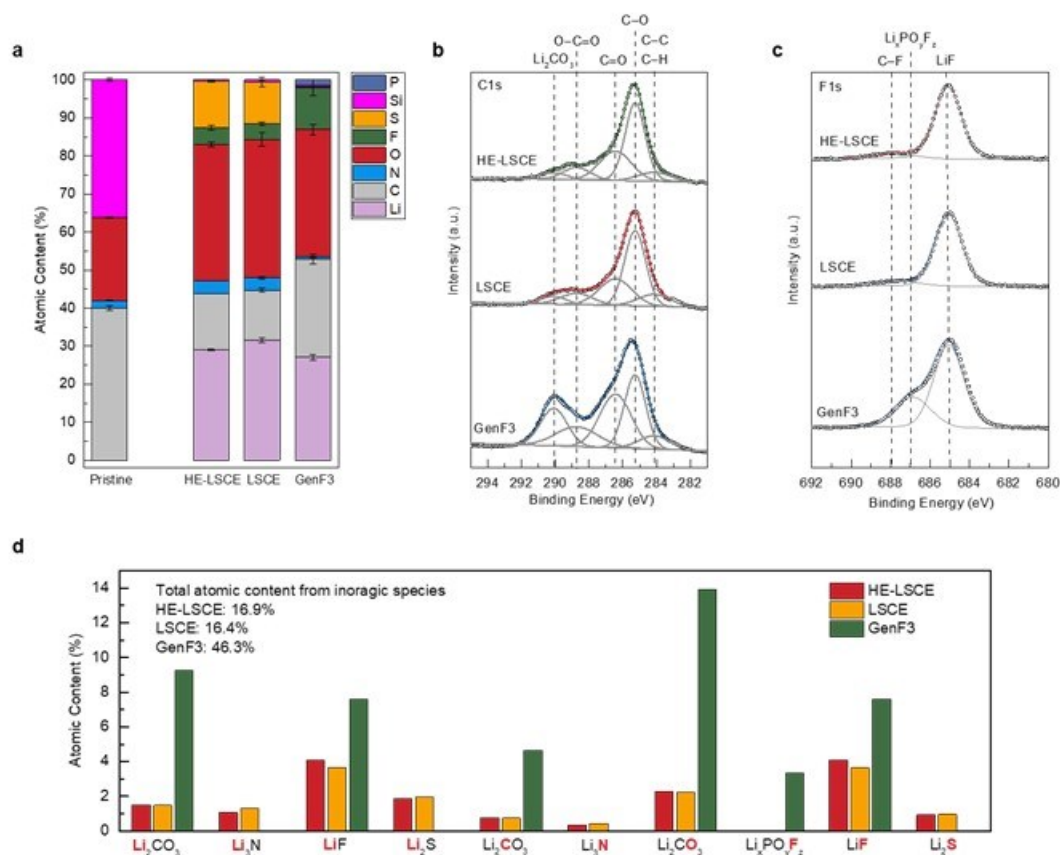


**Figure VII.10.3 Analysis of SEI on Si Anode by XPS. (a) atomic content in SEI on Si anode. (b) C1s XPS spectra from SEI on Si anode. (c) F1s XPS spectra from SEI on Si anode. (d) Atomic content assigned to inorganic SEI components determined by spectra deconvolution.**

We next tuned our attention to understanding of why Si anode composite showed different mechanical cracking behavior depending on electrolytes. We hypothesized that mechanical property of SEI governed by their composition (e.g. content of inorganic components) would control cracking. We collected XPS spectra from cycled Si anode to figure out chemistry of SEI. Contents of functionalities in SEI largely depends on electrolyte chemistry (Figure VII.10.3.a) Two LSCEs showed similar trend distinctive from GenF3. Representative XPS spectra such as C1s and F1s also shows large dependency on electrolyte chemistry (Figure VII.10.3.b-c) We deconvoluted every XPS spectra to calculate atomic content assigned to specific functionalities such as C-O, C=O, C-F, LiF, and Li<sub>2</sub>CO<sub>3</sub>. Interestingly, there is huge difference in total content of inorganic species between LSCEs and GenF3, which supports our hypothesis that inorganic-rich SEI on Si anode by GenF is vulnerable to mechanical damage during volume expansion due to lithiation.

After testing the compatibility with Si anode, we now evaluated electrolytes with NMC811 cathode. We observed leakage current evolution during cycling of Li-NMC811 cells to exclude effect from Si anode. (Figure VII.10.4.a) After 150 cycles, single-anion LSCE (red) showed dramatic evolution of leakage current 4 times higher than initial value. However, HE-LSCE showed significantly suppressed evolution of leakage current after 150 cycles even more than carbonate GenF3 electrolytes. Then, we cycled Si-NMC811 cells whose stability is concurrently affected by both Si anode and NMC811 cathode using three electrolytes. Unlike Si-LFP cells showing stable cycling with both LSCEs, Si-NMC811 cells were stably cycled only with HE-LSCE showing little overpotential increase due to its capability to suppress leakage current at NMC811 cathode surface. (Figure VII.10.4.b-c) GenF3 that fails to generate stable SEI on Si anode showed poor cycling stability of Si-NMC811 cells even with its stability with NMC811 cathode (Figure VII.10.4.d) Capacity



retention and columbic efficiency during cycling of Si-NMC811 cells suggests only HE-LSCE that build stability with both Si anode and NMC811 by suppressing mechanical cracking and leakage current evolution would achieve stable operation of Si-NMC811 full cells.

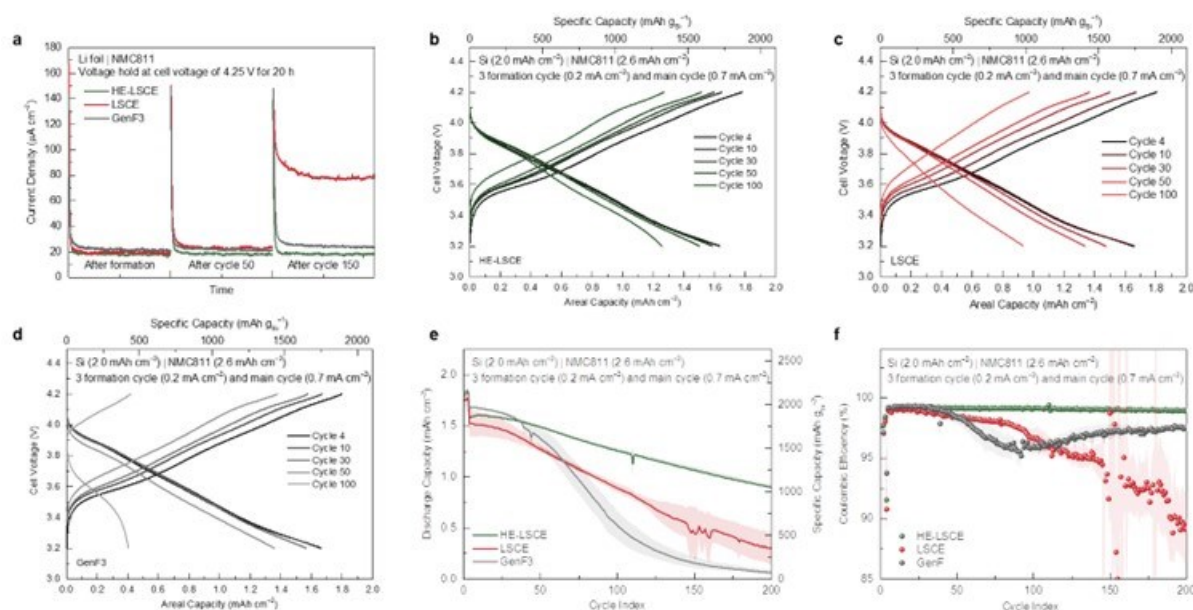


**Figure VII.10.4 Stability of Electrolytes with NMC811 cathode and Testing of Si-NMC811 cells. (a) Leakage current evolution test during cycling of Li-NMC811 cells. (b-d) galvanostatic cycling profile of Si-NMC811 cells with (b) HE-LSCE, (c) LSCE, and (d) GenF3. (e) Capacity retention of Si-NMC811 cells (f) Columbic efficiency of Si-NMC811 cells. All cells were cycled with 3 formation cycles with C/10 followed by repeated charge and discharge with C/3**

## Conclusions

For our FY24 movement, we will merge the SASP to SCP. We will move forward with pouch cell, recognizing that we have met our year 3 targets for providing superior performance over 300 cycles with cathode areal capacity  $> 1.5 \text{ mAh/cm}^2$ , rate = C/3 and temperature =  $25^\circ \text{C}$ , we have not applied to pouch cell format. We will scale the electrolyte in FY24 and provide it to performers in that program for validation in the larger pouch cell formats. We will also provide guidance for how pouch cell performance and failure is linked to the chemomechanics of the interphases and the electrodes and differentiate the outcomes on the basis of electrolyte chemistry.

## References

1. Yin, Y. *et al. ACS Appl. Mater. Interfaces* **12**, 26593 (2020)
2. Steinrück, H.-G. *et al. J. Chem. Phys.* **152**, 084702 (2020)
3. Li, Z. *et al. Adv. Energy Mater.* **10**, 1903110 (2020)
4. Huang, G. *et al. ACS Nano* **14**, 4374 (2020)
5. Coyle, J. E. *et al. J. Phys. Chem. C* **124**, 8153 (2020)
6. Schneier, D. *et al. J. Electrochem. Soc.* **166**, A4020 (2019)
7. Hu, Z. *et al. Adv. Funct. Mater.* **29**, 1906548 (2019)
8. Chen, J. *et al. Nat. Energy* **5**, 386 (2020)
9. Xie, H. *et al. ACS Appl. Energy Mater.* **3**, 1609 (2020)
10. Jin, Y. *et al. J. Am. Chem. Soc.* **140**, 9854 (2018)
11. Park, S.-J. *et al. J. Am. Chem. Soc.* **137**, 2565 (2015)
12. Lee, M. *et al. ACS Appl. Energy Mater.* **3**, 1899 (2020).

## **Acknowledgements**

Postdoctoral researchers Youngmin Ko and Dong-Min Kim performed the experiments. Liana Klivansky assisted with the XPS and Young-Woon Byeon assisted with SEM-FIB. Anthony Burrell, Nathan Neale, Marco Rodrigues, and Gabriel Veith are thanked for their helpful discussions, electrodes, and collaboration.

## VIII Next-Gen Lithium-Ion: Advanced Cathodes R&D

As a sustainable and promising store of renewable energy, lithium-ion batteries have replaced other types of batteries for many small-scale consumer devices. However, it has become clear that design and fabrication of electrode materials is necessary to meet the growing global demand for energy and the power densities needed to make electric vehicles fully commercially viable. To dramatically enhance battery performance, further advances in materials chemistry are essential, especially in novel nanomaterials chemistry. The construction of nanostructured cathode materials by reducing particle size can boost electrochemical performance.

- Earth-Abundant Cathode Active Materials (EaCAM) Consortium (ANL, ORNL, NREL, LBNL, PNNL, SLAC)
- Cation Disordered Rocksalt Materials DRX+ Consortium (LBNL, ORNL, PNNL, ANL, SLAC, UC Santa Barbara)
- Cathode-Electrolyte Interphase (CEI) Consortium (PNNL).

## VIII.1 Earth-Abundant Cathode Active Materials (EaCAM) Consortium (ANL, ORNL, NREL, LBNL, PNNL, SLAC)

### **Jason R. Croy, Principal Investigator**

Argonne National Laboratory  
9700 S. Cass Avenue  
Lemont, IL 46039  
E-mail: [croy@anl.gov](mailto:croy@anl.gov)

### **Hakim Iddir, Principal Investigator**

Argonne National Laboratory  
9700 S. Cass Avenue  
Lemont, IL 46039  
E-mail: [croy@anl.gov](mailto:croy@anl.gov)

### **Guoying Chen, Principal Investigator**

Lawrence Berkeley National Laboratory  
1 Cyclotron Road  
Berkeley, CA 94720  
E-mail: [gchen@lbl.gov](mailto:gchen@lbl.gov)

### **Chen Liao, Principal Investigator**

Argonne National Laboratory  
9700 S. Cass Avenue  
Lemont, IL 46039  
E-mail: [liaoc@anl.gov](mailto:liaoc@anl.gov)

### **Daniel P. Abraham, Principal Investigator**

Argonne National Laboratory  
9700 S. Cass Avenue  
Lemont, IL 46039  
E-mail: [abraham@anl.gov](mailto:abraham@anl.gov)

### **Tien Duong, DOE Technology Development Manager**

U.S. Department of Energy  
E-mail: [Tien.Duong@ee.doe.gov](mailto:Tien.Duong@ee.doe.gov)

### **Carine Steinway, DOE Technology Development Manager**

U.S. Department of Energy  
E-mail: [Carine.Steinway@ee.doe.gov](mailto:Carine.Steinway@ee.doe.gov)

### **Tina Chen, DOE Technology Development Manager**

U.S. Department of Energy  
E-mail: [Tina.Chen@ee.doe.gov](mailto:Tina.Chen@ee.doe.gov)

Start Date: October 1, 2022

End Date: September 30, 2023

Project Funding (FY23): \$6,650,000

DOE share: \$6,650,000

Non-DOE share: \$0

## Project Introduction

### **Design, Synthesis, and Characterization**

In response to the Department of Energy's recently released *National Blueprint for Lithium Batteries* [1], this project will explore novel materials based 100% in earth-abundant (EA) elements as competitive alternatives to state-of-the-art lithium-ion (Li-ion) cathodes, thereby directly addressing materials R&D needs pointed out in that report. Successful efforts will considerably advance the goals of diversifying supply chains as well as materials chemistries in support of sustainable lithium batteries.

It is now clear that secure, economical, and diverse supply chains are necessary to enable the growing need for sustainable electrification. In addition, the fundamental principles of sustainable development are highly correlated across social, economic, and environmental constructs [2]. In these regards, EA elements are particularly attractive and should be critically examined, as a matter of course, in such pursuits. The *Earth-abundant Cathode Active Materials (EaCAM)* consortium will pursue the design and development of Li-ion technologies based 100% in EA elements. Emphasis will be placed on a fundamental understanding of the parameters that control physiochemical properties, across all length-scales, and ultimately macroscopic electrode performance associated with *EaCAM*.

### **Atomistic Modeling**

In the pursuit of advancing sustainable energy storage solutions, this project focuses on the exploration of novel materials composed entirely of earth-abundant (EA) elements. The project aims to address critical gaps and elevate the performance of next-generation energy storage systems. The integration of theoretical Density Functional Theory (DFT) and the use of model systems play a key role in achieving our objectives. We gain insights into the atomic-scale interactions within these EA-based materials, enabling predictions of their electrochemical properties. This theoretical foundation not only accelerates the material discovery process but also guides the design of cathodes with enhanced efficiency and stability, thereby contributing to the overarching goals in advancing sustainable and high-performance energy storage technologies.

### **Surface Stabilization**

The electrolyte serves as the exclusive ion transporter between the cathode and anode, playing a pivotal role in regulating the interphase and interfaces between the electrolyte and electrodes. Its significance is pronounced in the performance of batteries employing Earth-abundant cathodes developed within the program. While there exists a plethora of knowledge regarding how electrolytes influence performance, the ability to purposefully design electrolytes tailored to specific cathodes remains elusive, necessitating time-consuming experiments.

The experiments and strategies outlined herein exemplify the systematic development of optimal electrolytes. This involves not only compositional adjustments in the bulk solvent but also the incorporation of additives tailored for a specific cathode system.

### **Analysis and Modeling**

State-of-the-art lithium-ion batteries (LIBs) being developed for transportation applications contain a transition metal (TM) oxide cathode and a graphite anode; both serve as host-matrices to house lithium ions during battery operation. The cathode typically contains  $\text{Li}_{1+x}\text{Ni}_a\text{Co}_b\text{Al}_c\text{O}_2$  (NCA) or  $\text{Li}_{1+x}\text{Ni}_a\text{Mn}_b\text{Co}_c\text{O}_2$  (NMC) oxides, where  $x \sim 0-0.05$  and  $a+b+c = 1$ . Both oxide chemistries contain Co, which is known to preserve the layered structure during lithium extraction/insertion reactions. However, the possibility of a global Co shortage and soaring costs has galvanized the LIB community to explore sustainable cathode chemistries, while maintaining cell performance (energy/power densities), safety and cycle/calendar life. In this context, the *EaCAM* program was established to discover new strategies in materials design and synthesis that allow for high-energy, sustainable cathode chemistries, based on earth-abundant elements. These oxides include the lithium and manganese rich (LMR) transition metal oxides, which have a relatively low nickel content and zero cobalt content, that can deliver high cell-energy-densities.

The goal of the analysis and modeling team is to identify constituents and mechanisms responsible for cell performance, performance loss and safety. Various diagnostic tools (electrochemical, physicochemical, etc.) are used to characterize the behavior of materials (both active and inactive) contained in the electrodes and cells; this characterization may be conducted before, during, and after electrochemical cycling. An understanding of fundamental mechanisms allows development of rational solutions to minimize performance degradation and thermal instability in the materials and electrodes, leading to safer and long-life battery cells.

## Objectives

### ***Design, Synthesis, and Characterization***

The long-term objectives of this program are the discovery and development of mechanistic insights, novel materials, new processes, and design strategies as well as dissemination of information, that enable cathode compositions based 100% in earth abundant, sustainable chemistries. The ultimate goal will be synthetic control of pre-determined particle designs, local ordering, integrated structures, dopant site-selectivity, and primary and secondary morphologies, including monolithic architectures, of high-energy earth-abundant cathode active materials (*EaCAM*). Such advancements would contribute greatly to lowering costs and increasing sustainability of next-generation technologies for transportation applications and beyond.

### ***Atomistic Modeling***

The primary objectives of the atomistic modeling research within this project are threefold. First, to determine the domain structure of LMR-NM cathodes at the atomic level, investigating the influence of Li-Mn, Mn-Ni pairs and substitutional dopants on the material total energy landscape. Second, to comprehend the implications of these domains on the structural and electronic properties of the material, focusing on the activation and behavior of  $\text{Li}_2\text{MnO}_3$  and  $\text{LiMn}_{0.5}\text{Ni}_{0.5}\text{O}_2$  domains during electrochemical processes. Third, to explore the relationship between domain structure and impedance rise, uncovering how the arrangement of Li and transition metal clusters affects the overall electrochemical performance. Furthermore, the single crystal model systems effort aims to enable a better understanding of composition-structure-property-performance correlations. Through these objectives, this study seeks to contribute nuanced insights into the design and optimization of LMR-NM materials for enhanced electrochemical applications.

### ***Surface Stabilization***

The overarching goal of this sub-team is to employ innovative synthesis and design methodologies, leveraging machine learning for both structural and quantitative predictive capabilities. The aim is to strategically design optimal electrolytes tailored for new earth-abundant cathodes. It is crucial to emphasize that the electrolyte serves as a pivotal element capable of significantly influencing key performance parameters without incurring substantial costs. By focusing on the electrolyte, the objective is to create a surface with low area-specific impedance, high electrochemical stability, and a further reduction in transition metal dissolution. The latter has been identified as a significant factor contributing to lithium inventory loss, and addressing this issue is integral to enhancing the overall performance of the system.

### ***Analysis and Modeling***

- Develop cathode constitution for testing with graphite and/or  $\text{Li}_4\text{Ti}_5\text{O}_{12}$  (LTO) anodes, ensuring optimal electrode-capacity matching to minimize cell performance degradation.
- Establish standard protocols for electrochemical testing in coin, pouch, and reference-electrode cells.
- Determine capacity fade and impedance rise behavior of full cells with LMR cathodes during cycle and calendar-life aging.
- Conduct in-depth structural and compositional characterization of LMR oxides, before and after aging, using solid state NMR techniques
- Examine thermal stability of LMR oxides using Differential Scanning Calorimetry (DSC).
- Using analytical electron microscopy, correlate microstructural evolution in the 5V spinel material with the electrochemical changes observed during electrochemical cycling in full cells

- Quantify the BoL particle morphology of LMR, LNO, and high-voltage LMNO spinel electrodes, including the distribution of particle defects, the particle size distribution, and electrode tortuosity.
- Investigate electrode-electrolyte interfacial regions formed during electrochemical cycling of full cells with LMR oxides with a spectro-electrochemical cell built for in-situ collection of ATR-FTIR spectra.

## Approach

### ***Design, Synthesis, and Characterization***

The *EaCAM* team will build on its considerable experience in areas of critical importance to advance project goals. Focused areas of collaboration will be established to gain insight on complex synthesis-structure-property relationships that govern materials properties from the atomic-scale to electrode-level performance. Atomistic, electrochemical, and techno-economic modeling will be combined with synthesis/processing, advanced structural/chemical characterization, and electrochemical analysis to establish mechanistic models of performance and degradation across length scales. Manganese, and Mn-based cathodes will serve as the initial platforms to explore the complex and broad space of *EaCAM* designs related thereto.

### ***Atomistic Modeling***

The approach involves an exploration of the domain structure's impact on the electrochemical behavior of LMR-NM materials. Utilizing spin-polarized DFT, the study systematically investigates configurations based on the number of Li-Mn and Mn-Ni pairs, emphasizing the composite nature of the material. Beyond static considerations, AIMD simulations capture dynamic responses during electrochemical activation, revealing the distinct behaviors of  $\text{Li}_2\text{MnO}_3$  and  $\text{LiMn}_{0.5}\text{Ni}_{0.5}\text{O}_2$  domains. These simulations at varying temperatures provide insights into the thermodynamic feasibility of predicted low-energy configurations, shedding light on the expected material states during synthesis and subsequent electrochemical processes. The model system efforts of this project combine single-crystals with controlled physical properties (composition, size, morphology, surface orientation, etc.) and single-particle-based diagnostic techniques to enable better understanding of composition-structure-property-performance correlations at the intrinsic materials level.

### ***Model Systems***

Combining single-crystal model systems with controlled physical properties (composition, size, morphology, surface orientation etc.) and single-particle-based diagnostic techniques to enable better understanding of composition-structure-property-performance correlations at the intrinsic material's level.

### ***Surface Stabilization***

The *EaCAM* team will build on its considerable experience in areas of electrolytes additives [1] and solvent development [2]. Combined with the strength from the System Analysis team in understanding the structural, morphological, and chemical compositional change caused by the electrolytes, we can use a feed-back loop to continuously improve the additives. The machine learning method is also implemented and will be reported in the future.

### ***Analysis and Modeling***

The approach pursued to meet the above objectives is summarized in Figure VIII.1.1. Promising oxides synthesized by the cathode team are fabricated into electrodes at Argonne's CAMP family and tested in half cells (vs. Li metal) and full cells (vs. Graphite or  $\text{Li}_4\text{Ti}_5\text{O}_{12}$  anodes) using standardized test protocols. Post-test characterization is conducted on electrodes harvested from cycled cells to determine mechanisms that degrade cell performance.

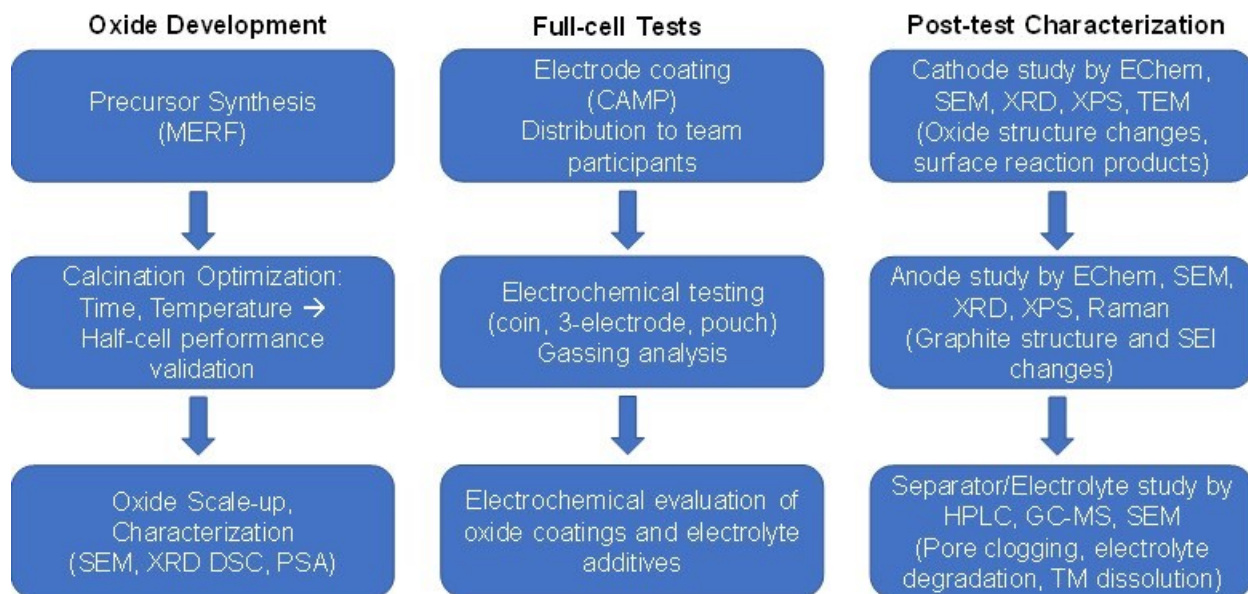


Figure VIII.1.1 Diagnostic tests are conducted at various stages of the oxide development process

## Results

### Design, Synthesis, and Characterization

The *EaCAM* consortium is exploring several categories of Mn-rich materials as baseline systems for further development. One of these systems is within the class of well-known Li- and Mn-rich NMCs (LMR, NMC = Ni, Mn, Co) where it is known that high energies can be obtained without the use of Co. The baseline composition chosen, in composite notation, is nominally  $0.3\text{Li}_2\text{MnO}_3 \cdot 0.7\text{LiMn}_{0.5}\text{Ni}_{0.5}\text{O}_2$  (LMR-NM). The advantages of such compositions, along with the major issues in need of address, have been published by the *EaCAM* cathode team in a recent article [3]. This FY, the cathode team has focused on a thorough understanding of critical performance metrics of the baseline LMR-NM. Practical electrode performance, the influence of particle synthesis, techno-economic and electrochemical modeling, as well as targeted, atomic-scale manipulations have been investigated as foundations for future advancements.

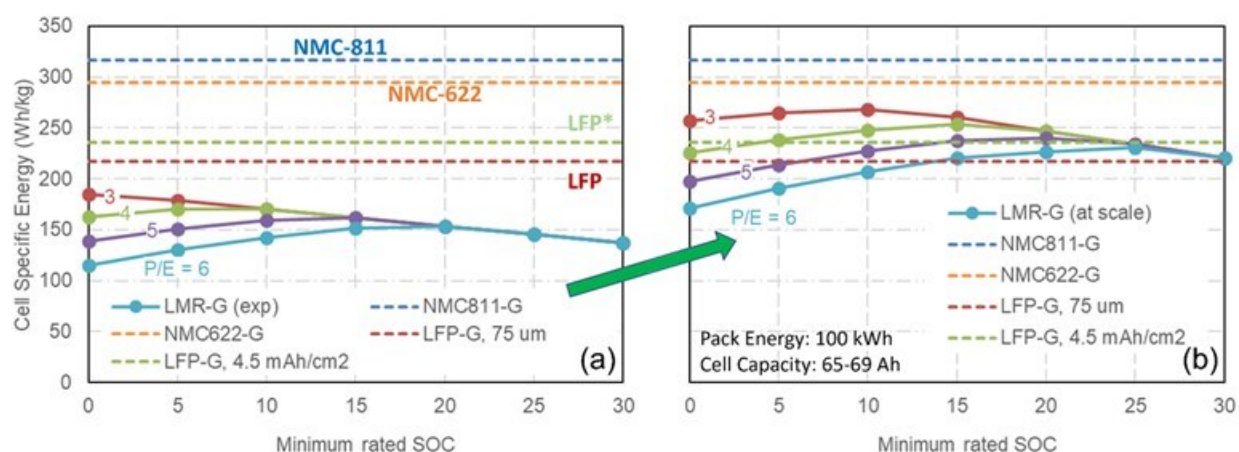


Figure VIII.1.2 (a) BatPaC techno-economic evaluation ( $\text{Wh}/\text{kg}_{\text{cell}}$ ) of the initial LMR-NM *EaCAM* baseline as a function of power-to-energy ratio (P:E) and minimum rated SOC. (b) Anticipated performance of LMR-NM through improvements in metrics identified in the analysis.



### Benchmark Studies and Evaluation of EaCAM Baseline Mn-rich Cathodes

With respect to practical electrode performance, the poor kinetics of LMR-NM electrodes was identified as a critical barrier to implementation. In order to establish baseline knowledge and prioritize research initiatives, techno-economic modeling was used to evaluate cell-level performance of the baseline LMR-NM using materials-level metrics collected on the baseline electrodes.

Figure VIII.1.2(a) shows the results of BatPaC modeling using physical and electrochemical data of a  $0.3\text{Li}_2\text{MnO}_3 \cdot 0.7\text{LiMn}_{0.5}\text{Ni}_{0.5}\text{O}_2$  material synthesized within the program (connected dots). The red and orange dashed lines mark energies bounded by  $\text{LiFePO}_4$  (LFP) and NMC-622, respectively, representing the lower and upper bounds of *EaCAM* energy targets for the baseline LMR-NM development. The data give cell-specific energies (Wh/Kg,  $\sim 67\text{Ah}$  cells) for several power:energy (P:E) ratios of the LMR-NM as a function of the lowest state-of-charge (SOC) utilized. Because of the unique low SOC impedance of LMRs, utilization of low-voltage/SOC capacity affects cell-level metrics where lower P:E ratios are generally desirable in terms of cell specific energy. As shown in Figure VIII.1.2 (a), the initial baseline material does not meet the targeted goals. Materials and electrode-level inputs to the BatPaC model identify several key parameters that hinder the baseline performance. Notably, the high porosity of the electrode, directly influencing the electrode volumetric density, is one limiting factor. Interestingly, the LMR-NM particles of this electrode were synthesized from MnNi carbonate precursors, co-precipitated in a 4L continuous stirred tank reactor (CSTR), which typically leads to additional, internal particle porosity and less than ideal particle densities (tap densities of  $\sim 2.0\text{ g/cc}$ ). Therefore, a critical element to achieving practical performance metrics is increasing the LMR-NM particle densities. However, this must be done while maintaining overall performance as highlighted below.

Figure VIII.1.3 shows electrochemical modeling of LMR particles calcined at four different temperatures. It was shown that the major change between the particle sets was the secondary particle porosities and surface areas, driven by primary particle size and agglomeration [4]. In order to accurately model discharge performance as a function of rate, two characteristic diffusion lengths were needed. One length is representative of primary particle size and the other of agglomerate size and trapped pore distribution within the secondary particle, Figure VIII.1.3 (a). Of note is the sensitivity of rate performance to primary particle size, Figure VIII.1.3 (b). Because the diffusion coefficient of LMRs is markedly lower than those of most NMCs, the effect of particle size on rate is much more pronounced and synthesis must be fully understood and controlled in this regard for optimal performance.

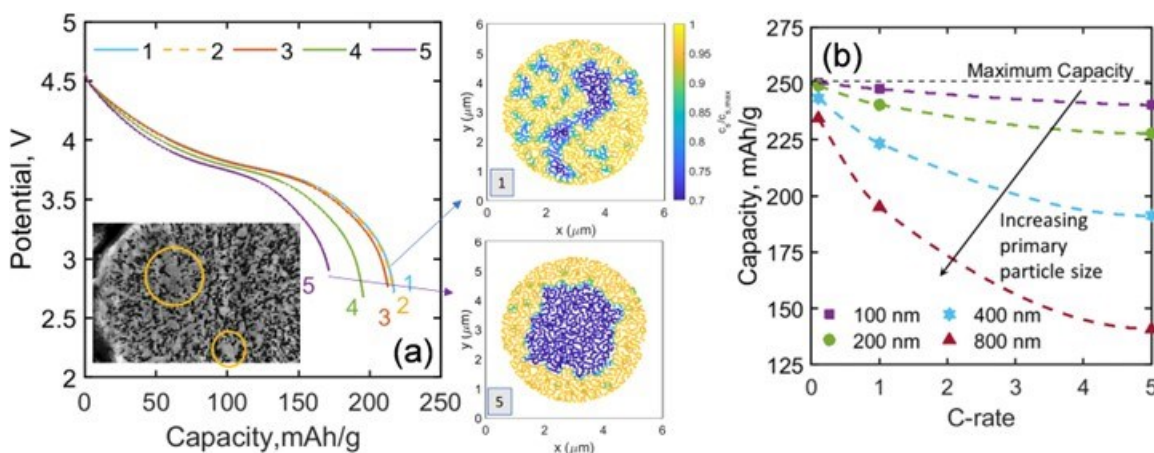
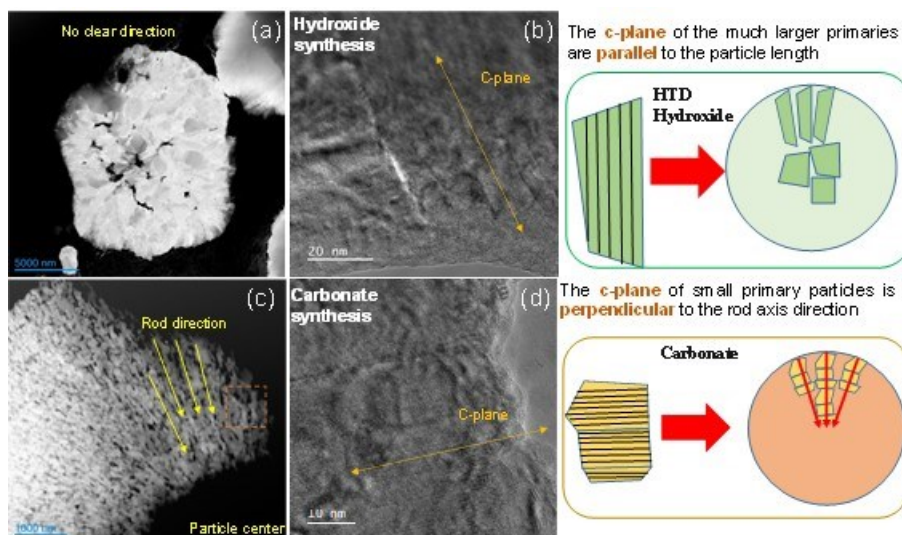


Figure VIII.1.3 (a) Electrochemical modeling of discharge capacity at 1C for LMR-NM as a function of primary size and agglomeration within secondary particles. (b) Discharge capacity of LMR-NM as a function of C-rate only considering primary particle size.

Figure VIII.1.4 (a)-(d) show particle morphologies of the baseline LMR-NM composition derived from hydroxide, (a) and (b), and carbonate, (c) and (d), precursors using CSTR co-precipitation, while specifically optimizing reaction variables for maximum particle densities. It is immediately clear that the hydroxide

process results in very large primaries compared to the carbonate-derived particles. In addition, the hydroxide particles are closely packed together with much less porosity. Perhaps most interesting is that the hydroxide particles tend to grow with the c-axis parallel to the radial axis of the secondary particle, resulting in very long channels for lithium diffusion. The carbonate process, however, results in small primaries having their c-axis perpendicular to the radial direction of the secondary particles, resulting in very short diffusion channels connected to the porous network of the secondary particle. Not surprisingly, the hydroxide-based particles/electrodes showed poor rate capability as compared to the carbonate-based particles/electrodes.



**Figure VIII.1.4** (a) High-angle annular dark-field (HAADF) image of a hydroxide-based secondary particle. (b) High-resolution TEM image of a corresponding primary particle. (c) HAADF image of a carbonate-based secondary particle. (d) HRTEM image of a corresponding primary particle.

The combined techno-economic analysis, electrochemical modeling, and experimental data reveal a challenging aspect of Mn-rich particle synthesis where particle porosity, as well as small primaries, enhance electrode performance but limit energy density. Studies are ongoing aimed at developing new synthesis routes towards greater control over secondary particle architectures for optimized density and performance. In addition, other limiting metrics identified from the initial BatPaC analysis are being systematically studied as described in the next section.

#### **Understanding Correlations Between Electrode Architecture, Formulation/Processing, and Performance**

The work on techno-economic modeling (BatPaC) of LMR-NM electrodes shows that the *EaCAM*  $0.3\text{Li}_2\text{MnO}_3 \cdot 0.7\text{LiNi}_{0.5}\text{Mn}_{0.5}\text{O}_2$  baseline material can be competitive in large cell formats, when using lower and upper bounds based on LFP and NMC-622 metrics, respectively. However, aggressive electrode formulations with respect to typical LMR formulations (active wt., carbon content, areal capacity, porosity...) are necessary. Considering the BatPaC analysis, a series of electrodes have been evaluated as a first step towards understanding the correlations between electrode formulation/processing and the resultant electrode architecture and performance.

Figure VIII.1.5(a) shows data from a series of electrodes, fabricated with increasing active material loadings (and thicknesses) of  $4\text{mg}/\text{cm}^2$  ( $57\mu\text{m}$ ),  $8\text{mg}/\text{cm}^2$  ( $93\mu\text{m}$ ),  $14\text{mg}/\text{cm}^2$  ( $130\mu\text{m}$ ), and  $19\text{mg}/\text{cm}^2$  ( $180\mu\text{m}$ ). Electrode formulations were kept constant at 84 wt.% active material, 8 wt.% Super P carbon, and 8 wt.% polyvinylidene fluoride (PVDF) binder. As expected, the thinnest electrode exhibited higher capacity at very high rates. However, loadings as high  $\sim 20\text{mg}/\text{cm}^2$  ( $\sim 180\mu\text{m}$ ) retained  $\sim 90\%$  of their slow rate ( $20\text{mA}/\text{g}$ ) capacity at  $100\text{mA}/\text{g}$ , and loadings up to  $\sim 15\text{mg}/\text{cm}^2$  ( $\sim 130\mu\text{m}$ ) are on par with the lowest loading/thinnest electrodes. We note here that the areal capacities delivered at the  $100\text{mA}/\text{g}$  rate ( $\sim C/2$ ) are  $\sim 3\text{mA}/\text{cm}^2$

(14mg/cm<sup>2</sup> loading) and ~4mA/cm<sup>2</sup> (19mg/cm<sup>2</sup> loading). These values meet BatPaC targets (~3.4mAh/cm<sup>2</sup> @ ~C/3) and the performance of these electrodes bode well for future advancements.

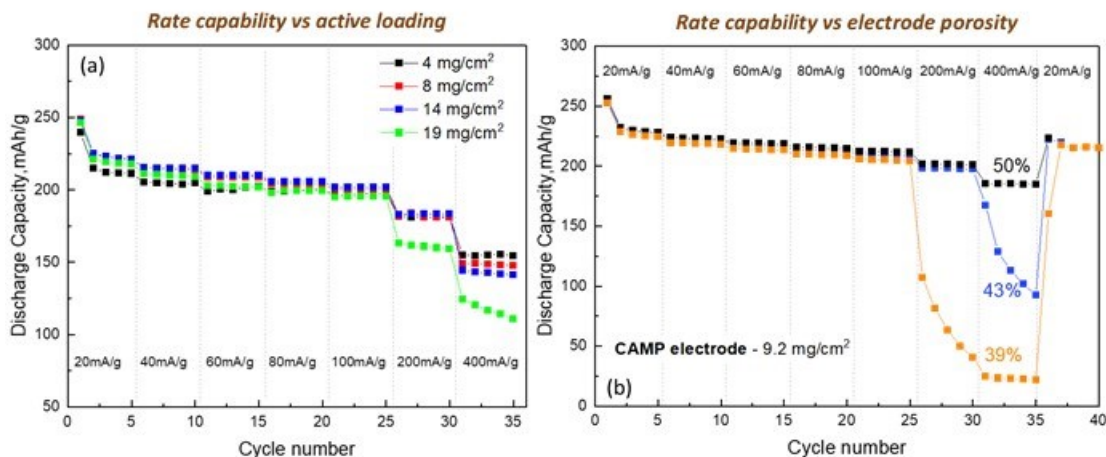


**Figure VIII.1.5 (a)** Discharge rate data from a series of electrodes with various loadings and thicknesses as described in the text. The electrodes underwent a first-cycle activation between 4.6-2.0V (vs. Li/Li<sup>+</sup>) followed by rate tests carried out between 4.5-2.5V. Charge cycle rates were constant at 20mA/g while discharge rates were increased from 20-400mA/g as listed in the figure. The electrolyte was 1.2 M LiPF<sub>6</sub> in a 3:7 wt. mixture of EC and EMC with 0.5 wt.% lithium difluoro(oxalate) borate (LiDFOB). All tests were conducted at 30°C. **(b)** Similar rate tests, as in (a), performed on electrodes with a fixed loading (9.2mg/cm<sup>2</sup>) but calendered to different porosities/thicknesses.

Despite the promising performance shown with respect to high-loadings of active material, a significant challenge remains with respect to decreasing the porosity of electrodes. Figure VIII.1.5 (b) shows rate data, similar to that of Figure VIII.1.5 (a), taken on electrodes with constant active material loadings of ~9mg/cm<sup>2</sup>, but calendered to various porosities. To help ensure consistency across samples, electrodes were fabricated at Argonne National Laboratory's Cell Analysis, Modeling and Prototyping (CAMP) facility. Porosities were estimated by comparing the measured densities (mass per unit volume) to the theoretical densities using the known electrode dimensions and densities of electrode constituents (PVDF, carbon, cathode oxide). As shown in the data, porosities below ~45-50% result in poor performance at high rates (> ~100mA/g). A challenging aspect of this analysis is the fact that the LMR-NM cathode-oxide particles, as previously discussed, can have substantial internal porosities which can negatively influence electrode tortuosity and electrochemical performance. Advanced characterization and analysis are ongoing to better understand the optimization of LMR particles and electrode architecture through formulation and processing.

#### ***In-Situ Laminography Imaging of Baseline LMR-NM Cathodes in Pouch Cells***

While tremendous effort has been devoted to studying LMR cathodes at the material level, their integration into large-format, industry-relevant pouch cells could add another layer of complexity, which is functionally very important but not well understood. To investigate this, LMR-NM cathodes-electrodes and matching graphite anode-electrodes were assembled into pouch cells for in-situ 3D laminographic imaging, Figure VIII.1.6(a), at various SOCs. When compared to the broadly applied tomography approach, this method adopts a slightly different scan geometry, in which the rotation axis is not perpendicular to the incident X-ray beam. With this configuration, the required penetration thickness through the cell is a constant and, thus, all the recorded projection images are usable for the reconstruction. A representative slice from the reconstructed volume of an LMR-NM pouch cell is shown in Figure VIII.1.6 (b), with a randomly selected region enlarged on the right-hand side for better visualization. It is interesting that a high level of heterogeneity is detected in the pristine cell prior to any electrochemical cycling. There are mainly three types of LMR-NM particles: 1) high-density particles, 2) particles with intra-particle heterogeneity, and 3) particles with pre-existing cracks. While the particle cracks can come from the calendering process, the inter-particle and intra-particle

heterogeneities are likely induced in the synthesis process as discussed above. 3D imaging at three different voltages was conducted: pristine, 4.45V, and 4.8V. Noticeable particle motions are detected at 4.45 V, indicative of a significant electrode deformation over the low voltage window during the first charge. The next step of this work is to utilize our recently developed machine learning-enabled, particle identification and tracking method [3] for statistical analysis of the particle behaviors and their relationships with cell chemistry.

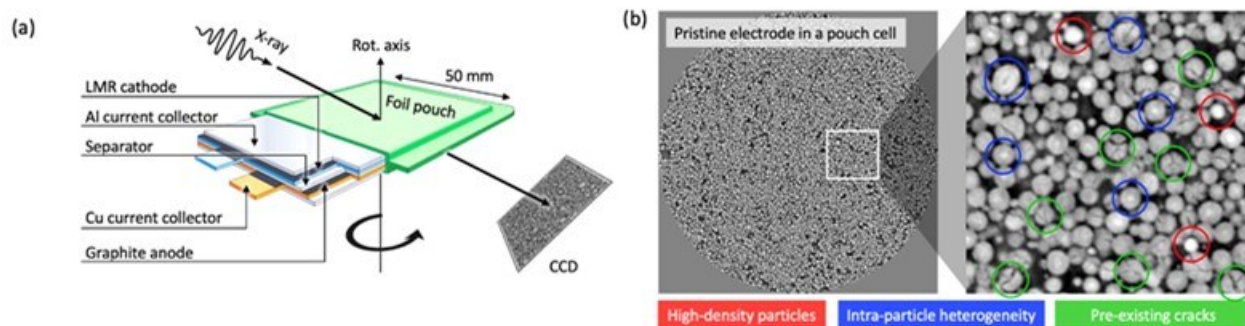


**Figure VIII.1.6** In-situ laminography imaging of an LMR-NM cathode-electrode in a pouch cell. (a) schematic of the pouch cell configuration and the laminography scan geometry. (b) a representative slice through the LMR-NM cathode-electrode in the reconstructed 3D volume of the imaged pouch cell.

#### **Effects of Cation Substitutions on Local Order, Morphology, and Low SOC Impedance of LMR Cathodes**

Voltage fade, hysteresis, and impedance at low states of charge ( $\Omega_{\text{LSOC}}$ ) represent challenging aspects of implementing LMR electrodes, as previously reviewed [4]. These processes have been shown to be correlated and directly linked to the same mechanisms [6]. Ultimately, the origin of these phenomena is the tendency for  $\text{Li}^+$  and  $\text{Mn}^{4+}$  to charge order in the pristine material where, upon an initial ‘activation’ to high SOC, a cascade of events (e.g., oxygen oxidation, M-O bond breaking, O-O bond formation, and metal migration) leads to structural changes and the onset of reversible and irreversible processes during cycling [6]. The *EaCAM* cathode team is building on those works by pursuing a strategy aimed at modifying the electrochemical response of an *activated* LMR electrode by exploiting the inherent chemical inhomogeneity and local ordering of the pristine material. In this study we begin a series of explorations based on a strategy of modifying the *activated* properties of LMR electrodes in order to improve performance metrics such as  $\Omega_{\text{LSOC}}$ . Specifically, we aim to explore the possible initial compositions, distributions of elements (e.g., among various ‘domains’), and synthesis conditions that might result in a post-activated material with improved properties (e.g., kinetics) over traditional LMRs. We focus initially on the influence of Sn as a possible modifier of  $\Omega_{\text{LSOC}}$ . Sn can form a lithium-rich  $\text{Li}_2\text{Sn}^{4+}\text{O}_3$  phase and  $\text{Sn}^{4+}$  might be expected to preferentially order with excess  $\text{Li}^+$ , as is the case for  $\text{LiMn}_6/\text{LiMn}_5\text{Ni}_1$ -type ordering found in typical LMR-NMC compositions. In addition,  $\text{Sn}^{4+}$  is not expected to migrate easily during cycling, perhaps leading to local stability. Due to the correlated nature of degradation mechanisms, as well as observable influences at all length scales (e.g., atomic-scale ordering, particle morphology, electrode properties),  $\Omega_{\text{LSOC}}$  can be used as an especially sensitive indicator of modified electrochemical behavior when probing variations of LMR materials [4-6].

Figure VIII.1.7 shows EXAFS analysis of the local environments in a series of Sn doped oxides including the LMR-NM baseline,  $3\text{Li}_2\text{Sn}_x\text{Mn}_{1-x}\text{O}_3 \cdot 0.7\text{LiNi}_{0.5}\text{Mn}_{0.5}\text{O}_2$ , as well as end-members  $\text{Li}_2\text{Mn}_{1-x}\text{Sn}_x\text{O}_3$  and  $\text{Li}[\text{Mn}_{1-x}\text{Sn}_x]_{0.5}\text{Ni}_{0.5}\text{O}_2$ , at Sn concentrations of  $x = 0.01$  and  $0.05$ . Of note here is that the local structure of the Sn-doped LMR-NM is similar at both ends of the Sn concentration ( $x = 0.01$  and  $0.05$ ). In particular, a Sn-M ( $M = \text{Mn}/\text{Ni}$ ) correlation distance of  $\sim 2.99 \text{ \AA}$  is found for each. In addition, we find no evidence of  $\text{Li}_2\text{SnO}_3$  formation in the doped LMR-NM, in agreement with high-resolution XRD data analysis (not shown). Although a  $R_{\text{Sn-M}}$  of  $\sim 2.99 \text{ \AA}$  may seem reasonable for a Sn-doped LMR-NM material, a coordination number of  $\sim 3.5$  is not. We attribute the much-lowered coordination number to excess  $\text{Li}^+$  ions clustering around  $\text{Sn}^{4+}$ .

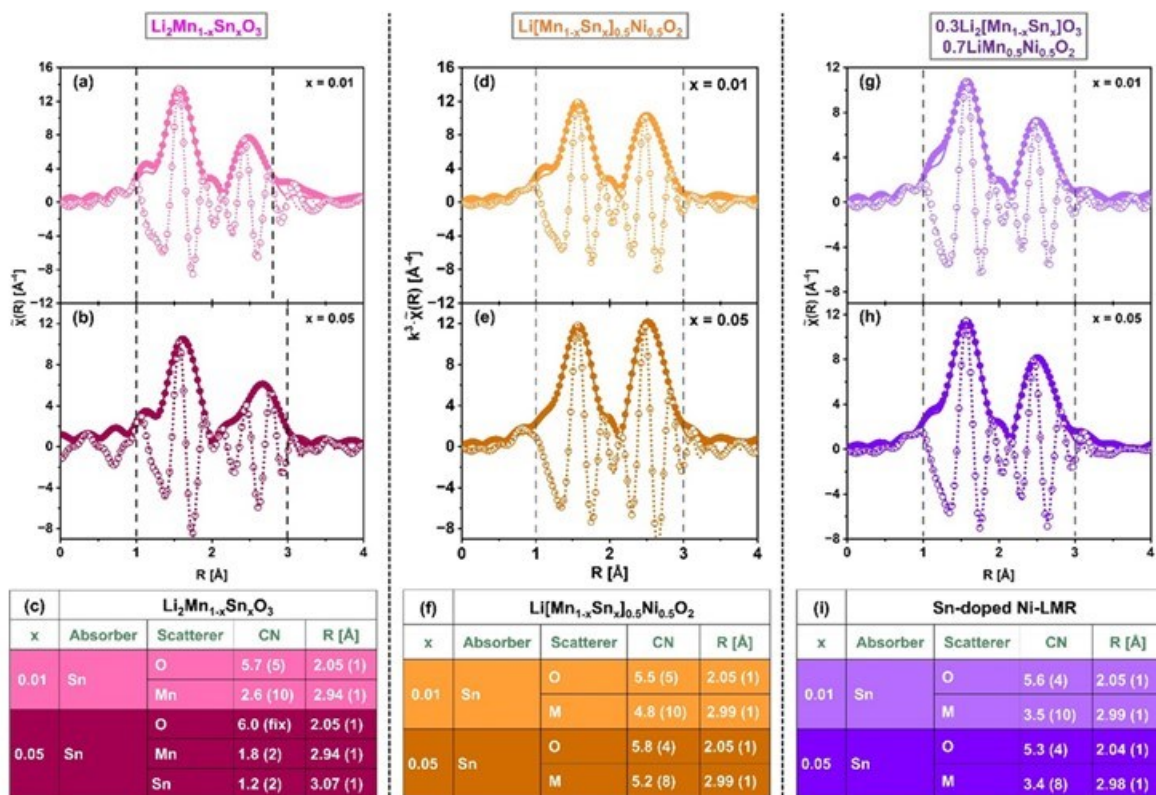
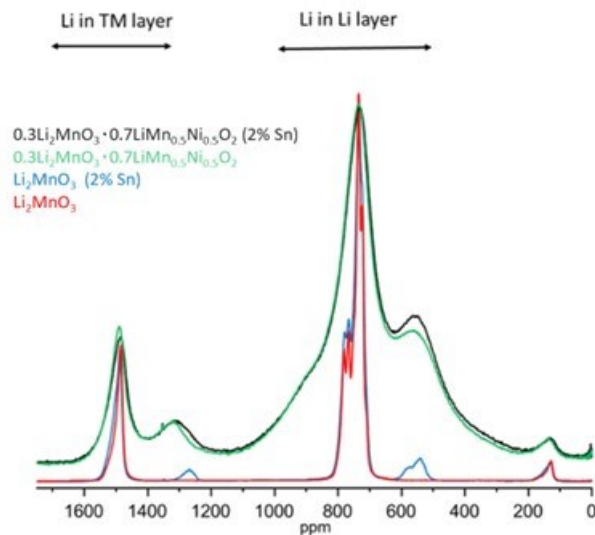


Figure VIII.1.7 EXAFS fittings for the parent compound (a-c)  $\text{Li}_2\text{Mn}_{1-x}\text{Sn}_x\text{O}_3$  and (d-f)  $\text{Li}[\text{Mn}_{1-x}\text{Sn}_x]_{0.5}\text{Ni}_{0.5}\text{O}_2$  and cathode material (g-i)  $0.3\text{Li}_2[\text{Mn}_{1-x}\text{Sn}_x]\text{O}_3 \cdot 0.7\text{LiMn}_{0.5}\text{Ni}_{0.5}\text{O}_2$  at a Sn content of  $x = 0.01$  (top panel: a, c, e) and  $x = 0.05$  (bottom panel: b, d, f). Solid and hollow circles refer to  $|\chi(R)|$  and  $\text{Re}\{\chi(R)\}$  of the dataset, respectively.

Similarly, the solid and dotted lines refer to the fitted  $|\chi(R)|$  and  $\text{Re}\{\chi(R)\}$  curve, respectively. The vertical dash line is the range of fit. A factor of  $k^3$  has been applied to these FT spectra. (c, f, i) Summarized coordination numbers and bond distances for the first and second Sn shells. Last digit error is given in the parentheses.

$^6\text{Li}$  Nuclear magnetic resonance (NMR) spectroscopy of Sn-doped materials, synthesized with  $^6\text{Li}(\text{OH})\cdot\text{H}_2\text{O}$  as a lithium source, corroborates the EXAFS analysis. As shown in Figure VIII.1.8, enhanced intensities near 1300 ppm and 550 ppm in the Sn-doped LMR-NM (black), as compared to the undoped LMR-NM (green), match well with the observed peaks of the model, Sn-substituted  $\text{Li}_2\text{MnO}_3$  (blue). Again, revealing a preference for  $\text{Sn}^{4+}$  to occupy Li-rich environments.



**Figure VIII.1.8**  ${}^6\text{Li}$  MAS NMR data comparison of  $\text{Li}_2\text{Mn}_{1-x}\text{Sn}_x\text{O}_3$  and  $0.3\text{Li}_2\text{Sn}_x\text{Mn}_{1-x}\text{O}_3 \cdot 0.7\text{LiMn}_{0.5}\text{Ni}_{0.5}\text{O}_2$ , each with  $x = 0$  and  $0.02$ .

Figure VIII.1.9(a) shows  $dQ/dV$  plots for  $0.3\text{Li}_2\text{Sn}_x\text{Mn}_{1-x}\text{O}_3 \cdot 0.7\text{LiMn}_{0.5}\text{Ni}_{0.5}\text{O}_2$  with  $x = 0, 0.01, 0.02, 0.05$ , after a first-cycle activation (4.7–2.0V vs.  $\text{Li}/\text{Li}^+$ ) and 6 cycles between 4.4–2.5V. Of significance is that all samples achieved the same capacity ( $\sim 290$  mAh/g) and extent of activation on the first-cycle charge. However, the addition of Sn shows a clear influence on the low-voltage sites that develop due to the extraction of Li from Li/Mn-rich regions on activation. Similarly, Figure VIII.1.9 (b) shows that the area specific impedance (ASI) associated with low-voltage sites ( $\Omega_{\text{L,SOC}}$ ) is strikingly different across the samples and reveals that  $\sim 1$ –2% Sn substitution apparently lowers the barrier for  $\text{Li}^+$  insertion. Detailed microscopy of the baseline and  $x = 0.01$  samples, Figure VIII.1.9 (c) and (d), highlight major morphological differences. Notably, the average grain size with just 1% Sn substitution is markedly smaller than without Sn. Analysis of high-resolution X-ray diffraction, Figure VIII.1.9 (e), corroborates this observation. Elemental mapping, Figure VIII.1.9 (f), shows that while Sn is distributed throughout the particles, a tendency for grain-boundary segregation is evident. This segregation is attributed with mitigating grain growth during the synthesis process resulting in smaller grains for Sn-containing samples.

Electrochemical and atomistic modeling by the *EaCAM* team, as discussed above and in an adjacent section of this report, clearly show the significance of particle morphology on the performance of LMR-NM electrodes and emphasize the need for strategies to control and optimize morphology across length scales (e.g., domain structure, primary, secondary, and electrode architectures). The work discussed here represents a potentially exciting strategy in that pursuit.  $\text{Sn}^{4+}$  substitution clearly has a morphological effect whereby Li diffusion lengths might be tailored. In addition, due to a tendency to order with excess Li, the domain structure (size, coherence) may well be altered. Such alterations can lead to clear changes in the properties of activated electrodes, such as low SOC ASI as reported by experimental and theoretical studies herein from the *EaCAM* team. Further analysis and modeling are ongoing and the driving force for Sn distribution and its role in altering particle properties across length-scales will be discussed in an upcoming publication, along with other cations of interest for similar studies.

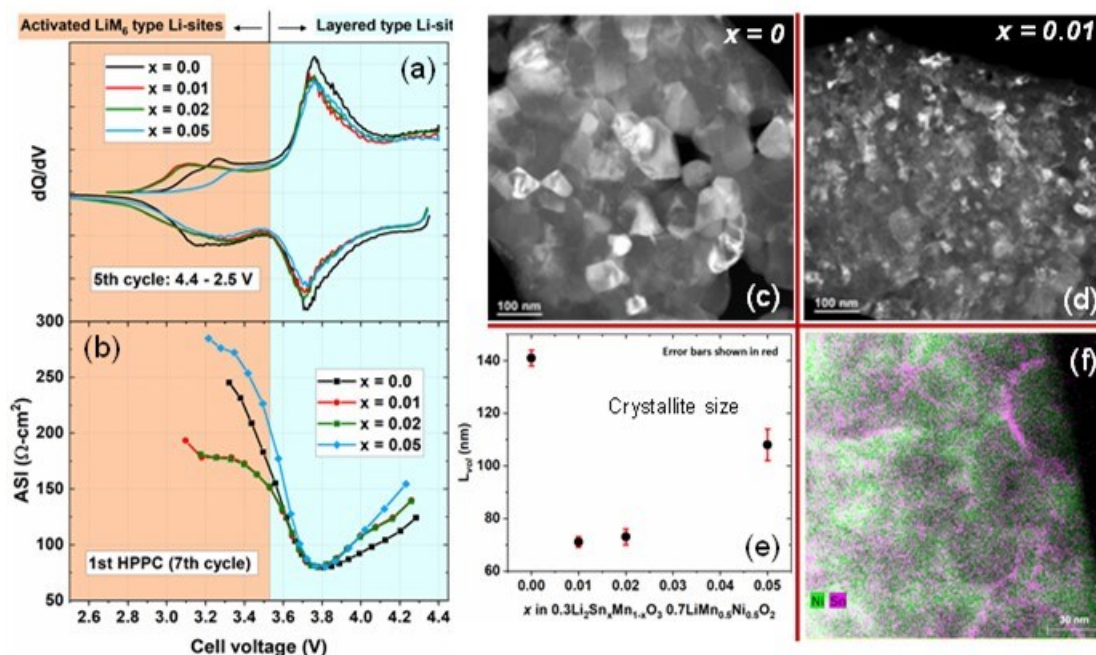


Figure VIII.1.9 (a)  $dQ/dV$  plots of  $0.3\text{Li}_2\text{Sn}_x\text{Mn}_{1-x}\text{O}_3 \cdot 0.7\text{LiNi}_{0.5}\text{Mn}_{0.5}\text{O}_2$  ( $x = 0, 0.01, 0.02, 0.05$ ). All electrodes were activated with a first-cycle charge between 4.7-2.0V at  $\sim C/20$  and subsequently cycled between 4.4-2.5V (Li metal anodes, 30C,  $\sim C/3$ ). (b) ASI comparison obtained by hybrid pulse power characterization (HPPC). (c) and (d) Transmission electron microscopy imaging revealing the difference in grain size between the baseline  $x = 0$  sample (c) and the  $x = 0.01$  sample (d). (e) Comparison of the crystallite size parameter ( $L_{\text{vol}}$ ) of the cathode materials as obtained from the analysis of high-resolution X-ray diffraction data. (f) Elemental map of Sn and Ni in the Sn = 0.01 sample.

### Structure and Performance of Novel, Lithiated Spinel (LxS) Cathode-Oxides

In addition to the study of LMR-NM cathodes, the *EaCAM* cathode team has developed a new class of cobalt-free, Mn-rich materials, designated LT-LMNO (low temperature- $\text{LiMn}_{0.5}\text{Ni}_{0.5}\text{O}_2$ ), which has a predominant, cubic-close-packed lithiated-spinel structure, interspersed with layered and rock salt domains. We refer to this new class of lithiated-spinel cathodes with coexisting layered and disordered rock salt domains as LxS materials; they are typically synthesized at a relatively low temperature, e.g., 400 °C. Our experimental observations indicate that LT-LMNO is stable at this temperature, whereas heating LT-LMNO at elevated temperatures induces a transition of this multicomponent structure towards the slightly disordered, high-temperature (HT) layered phase, HT- $\text{LiMn}_{0.5}\text{Ni}_{0.5}\text{O}_2$ , in which there is approximately 11% disorder of the lithium and transition metal ions in alternate layers when prepared at  $\sim 850$  °C. We believe that these temperature-driven phase transitions and the structural interplay between the lithiated-spinel, layered and rock salt domains exert a profound influence on the local structure and, consequently, on the electrochemical properties of these composite electrodes. Motivated by the prospect of gaining critical insights into the intricacies of these temperature-induced phase transitions, as well as local order/disorder, recent work has focused on the synthesis of a series of LMNO materials at various calcination temperatures. The primary objective is to scrutinize these phase-transitions and the impact of structural correlations on electrochemical behavior.

The X-ray diffraction patterns, and corresponding structural refinements, reveal that the LMNO LxS electrode materials display continuous topotactic transitions between the cubic and layered structural components, the extent of which is dependent on the synthesis temperature, Figure VIII.1.10 (a)-(e). A notable parabolic trend in the electrochemical properties, evident in Figure VIII.1.11 (a)-(d), is a direct consequence of the perturbation of the 3-D Li-ion diffusion channels and, on heat-treatment, an increased ordering of the lithium and transition metal ions in the layered 2-D channels. The remarkably high capacity ( $\sim 230$  mAh/g) of LT-

LMNO compositions calcined at 400°C (LMNO400), is attributed to 1) the presence of ordered 3-D Li-ion diffusion channels and 2) the structural stability of the lithiated-spinel component. In contrast, LMNO500-700 samples exhibited inferior performance, which we attribute to highly disordered layered domains that are generated at intermediate temperatures, thereby impeding Li<sup>+</sup>-ion diffusion. The gradual shift from a highly disordered to a more ordered layered structure occurs above 700 °C, thereby promoting 2-D Li<sup>+</sup>-ion diffusion and enhancing electrochemical performance, as observed for the LMNO800-LMNO900 samples. These findings highlight the opportunity to tailor novel electrode structures with lithiated-spinel and layered components. To this end, our future research will focus on improving the performance of LxS electrodes by optimizing calcination procedures and making compositional adjustments.

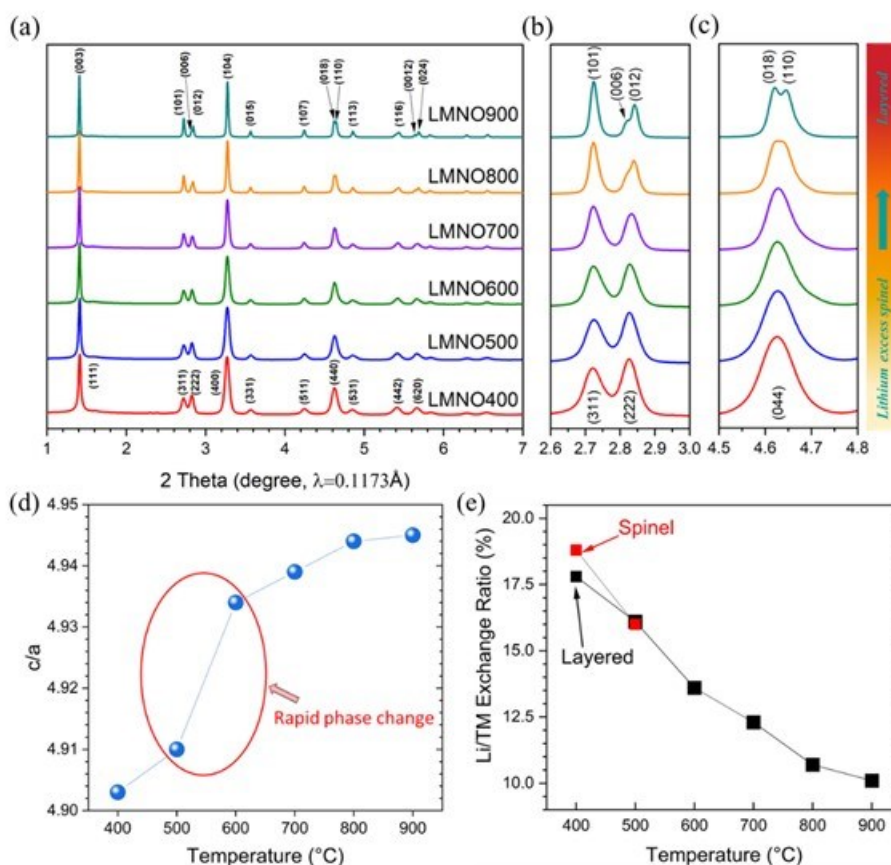


Figure VIII.1.10 (a) Synchrotron X-ray diffraction patterns of pristine 400~900 °C LMNO powders. (b) The enlarged view of the diffraction peaks of (311), (222) for LMNO400-600 and (101), (006), (012) for LMNO700-900 and (c) The enlarged view of the diffraction peaks of (444) for LMNO400-600 and (108), (110) for LMNO700-900. (e) Calculated c/a ratio for LMNO400-900. (f) The evolution of disorder level of LMNO as a function of temperature from 400 °C to 900 °C.



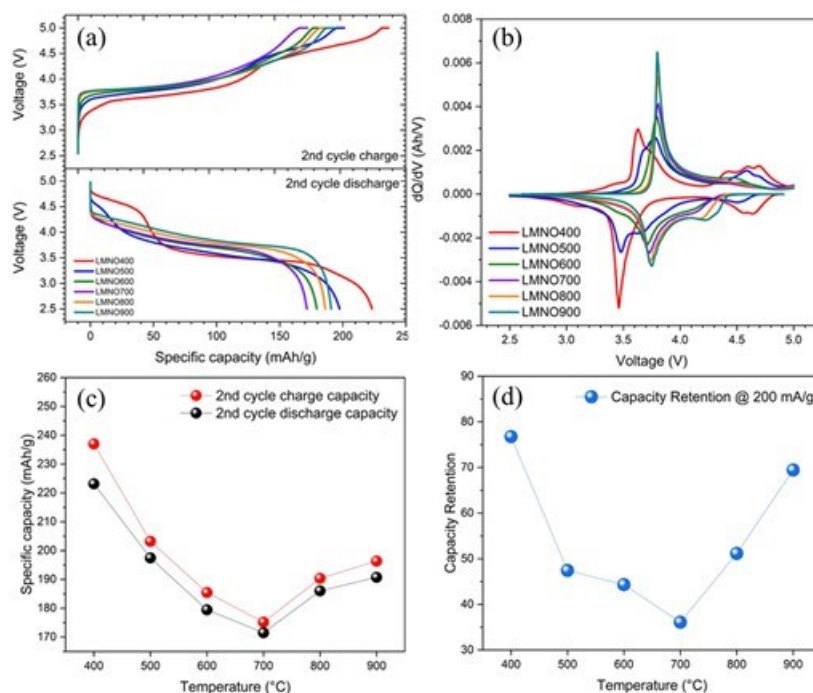


Figure VIII.1.11 (a) Comparison of electrochemical performance for LMNO400-900 samples: (a) 2nd cycle charge (top panel) and discharge (bottom panel) voltage profiles (b) 2nd cycle charge and discharge dQ/dV plot (c) Capacity evolution of 2nd cycle charge/discharge capacity. (d) Rate performance @ 200mA/g.

### Atomistic Modeling

#### Determining the Domain Structure of LMR-NM

To better understand the electrochemical properties observed for the baseline LMR-NM, as discussed above, this Focus Area seeks to uncover atomic-level insights into the mechanisms that govern phenomena such as low SOC impedance. Herein, the local domain structure of LMR-NM is investigated and initial models elucidating factors that influence low SOC impedance are presented.

As a starting point, the elemental distribution in LMR-NM materials was investigated using the spin polarized DFT methodology as implemented in the Vienna Ab Initio Simulation Package (VASP).  $\text{LiMn}_{x>4}$  clusters could be identified in Li- and Mn-rich domains ( $\text{Li}_2\text{MnO}_3$  domains) as well as an increased number of MnNi pairs in the transition metal (TM)-rich domains ( $\text{LiMn}_{0.5}\text{Ni}_{0.5}\text{O}_2$  domains). The determination of these domain sizes (i.e., the number of pairs) is important for the justification of the model system developed and used in the Ab-Initio Molecular Dynamics (AIMD) study that will be discussed below. As an initial approximation, the effect of the number of pairs on the total energy of the system was considered. Figure VIII.1.12a shows the number of Li-metal pairs and metal-metal pairs in the TM layers for each tested configuration. The lowest energy configuration is termed the composite 'ordered' ribbon model. This configuration is composed of Li-Mn pairs within the  $\text{Li}_2\text{MnO}_3$  region and Mn-Ni pairs in the  $\text{LiMn}_{0.5}\text{Ni}_{0.5}\text{O}_2$  region. Next in the energy scale are configurations with a few ions swapped between the two domains. The number of Li-Mn and Mn-Ni pairs decreases at the expense of increasing the number Mn-Mn, Ni-Ni, Li-Li and Li-Ni pairs. The trend continues while the clusters become larger and more Li-Ni pairs form. The total energy is sensitive to the number of Li-Mn pairs. Hence, they are good descriptors of each configuration. Nevertheless, the size of the simulation cell impedes a thorough exploration of other possible low energy configurations. The limited sampling manifests as a gap in Figure VIII.1.12a.

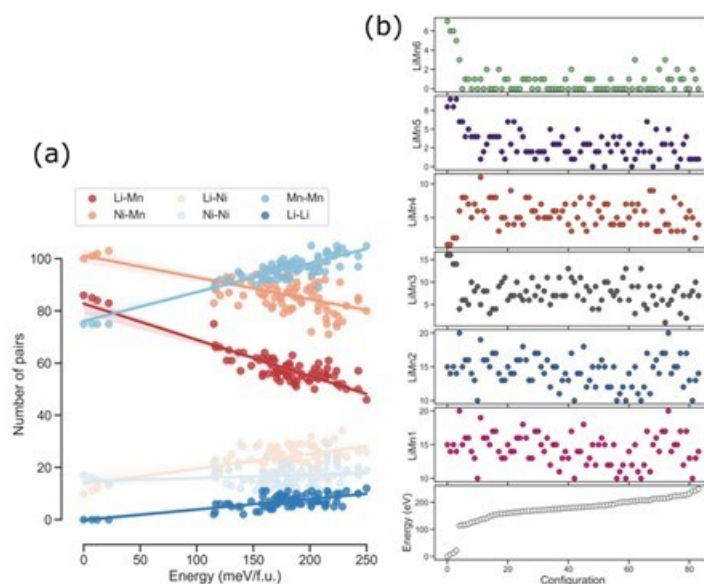


**Figure VIII.1.12** (a) Number of Li-M and M-M (M=Ni,Mn) pairs in the TM layer for each configuration. (b) LiMn<sub>x</sub> (x=6,5,4,3,2,1) clusters in the TM layer for each configuration. All configurations are sorted by total energy and referred to the lowest energy (Energy = 0).

Figure VIII.1.12b shows the distribution of LiMn<sub>x</sub> (x=6,5,4,3,2,1) clusters for each configuration. The ordered composite configuration has a larger amount of LiMn<sub>6</sub> and LiMn<sub>5</sub> clusters. The decrease in the number of LiMn<sub>6</sub> and LiMn<sub>5</sub> clusters correlates with the increase in energy. For the more disordered structures, there is no correlation with the cluster content. Thus, there are two regimes depending on the degree of disorder. Honeycomb and zigzag-like regions are evident when Li-Mn and Ni-Mn are dominant. Contrary to the high energy range, in the low energy range, the tridimensional structure of Li<sub>2</sub>MnO<sub>3</sub> regions is distinguishable. With the increase of disorder in the simulation cell, distinct Li<sub>2</sub>MnO<sub>3</sub> domains decrease. (Absence of LiMn<sub>6</sub> and LiMn<sub>5</sub> units).

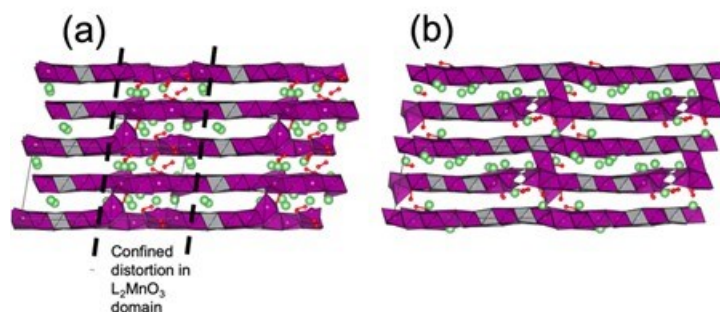
The DFT predicted low energy configuration is the ground state at 0K. Ground state configurations may be good estimations for finite temperature states. However, in multicomponent systems the configurational entropy promotes different atomic arrangements at higher temperatures. Heat treatment during synthesis influences the final configuration of elements in the material, and consequently, its electrochemical properties. At room temperature the composite ‘ribbon’ model has the highest probability of occurrence, followed by slightly disordered configurations. Highly disordered configurations are very unlikely to occur at room temperature. There is a very low probability of occurrence of configurations with energies above 100meV.

High temperatures are used during synthesis and low-energy equilibrium configurations, predicted by DFT (at 0K), might not be thermodynamically reachable, therefore, a mix of configurations should be expected. For example: at 600K the probability of occurrence increases for configurations around 200 meV higher than the ground state, at the expense of the “ordered” configurations. A mix of ordered regions and disordered regions would be present in the material at 600K. Larger Li-TM clusters remain unfavorable with very low probability of occurrence. At 900K the disordered structures have a higher probability of occurrence than the ordered ones.

### 1. Influence of Domain Structure on Low SOC Impedance

For the composite material 0.4Li<sub>2</sub>MnO<sub>3</sub>•0.6LiMn<sub>0.5</sub>Ni<sub>0.5</sub>O<sub>2</sub>, AIMD shows that, upon electrochemical activation of the ‘ordered’ ribbon model, Li<sub>2</sub>MnO<sub>3</sub> regions confined distortions of the lattice to a well-defined region, Figure VIII.1.13a. There is also formation of oxygen dimers within the Li<sub>2</sub>MnO<sub>3</sub> domains, in agreement with previous results. The LiMn<sub>0.5</sub>Ni<sub>0.5</sub>O<sub>2</sub> domains remained layered and undistorted where the calculated diffusion co-efficient of the layered domains was higher than that of the distorted Li<sub>2</sub>MnO<sub>3</sub> domains. Therefore, during

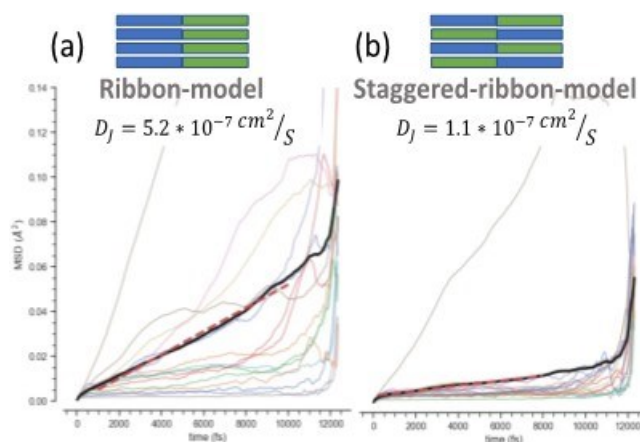
discharge the layered domains would be easier to fill first. The composite material with more disorder having ‘staggered domains’ presented distortions of the lattice spread over all the simulation cell, Figure VIII.1.13b. Wide-spread distortions resulted in a lower calculated diffusion co-efficient of the layered domains compared to the ‘ordered’ model and is expected to increase impedance rise earlier in the discharge, with respect to the ‘ordered’ model, as layered domains begin to fill. For samples with low annealing times, ill-defined  $\text{Li}_2\text{MnO}_3$  domains are thus expected to show a lower final impedance at the lowest SOC, in agreement with the experimental results.



**Figure VIII.1.13** Side view of the 60%- $\text{LiMn}_{0.5}\text{Ni}_{0.5}$ /40%- $\text{Li}_2\text{MnO}_3$  model (a) ribbon model and (b) staggered model. Transition metal sites are represented by purple and silver polyhedrons for Mn and Ni respectively. Li ions are represented by green spheres. Oxygen outside the oxygen sub-lattice structure is represented by red spheres and red sticks represent O-O bonds.

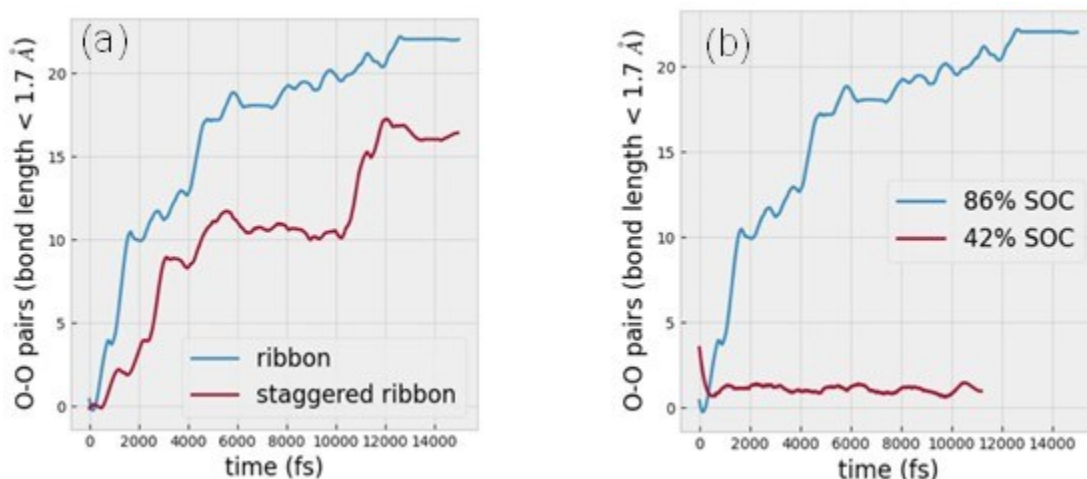
We have shown in previous reports that the composite material 60%- $\text{LiMn}_{0.5}\text{Ni}_{0.5}$ /40%- $\text{Li}_2\text{MnO}_3$  with staggered domains presented distortions of the lattice spread over all the simulation cell, albeit with limited extent compared with the distortions observed in the non-staggered model. Contrary to the non-staggered configurations, the non-localized distortions would increase the impedance earlier during discharge, but reaching a lower final impedance at low SOC, because of the limited extent of the distortions.

Figure VIII.1.14 shows the mean square displacement of Li ions moving in each model cell during activation. The colored lines represent each individual Li ion in the simulation cells. The thicker black line is the ensemble average of all the Li ions. The calculated diffusivity (during charge) in the ribbon model is almost 5 times faster than in the staggered ribbon. The increased diffusivity of Li in the ribbon model compared with that of the staggered model is due to increased Li-concentration gradient in the former: Li migrates to the Li layer first and then within the Li layer.



**Figure VIII.1.14** Mean square displacement (MSD) time evolution for (a) ribbon model (b) staggered ribbon model. Colored lines represent the evolution of the MSD for each Li ion in the simulation cell. The black line represents the ensemble average of the MSD. The red dashed line represents the linear regression used to compute the slope used to determine the jump diffusivity using the Einstein relationship. In the Inset schematics blue represent  $\text{Li}_2\text{MnO}_3$  layers and green represent  $\text{LiMn}_{0.5}\text{Ni}_{0.5}$  regions.

AIMD simulations have shown that the rate of formation of oxygen dimers is faster in the ribbon model than in the staggered model (see Figure VIII.1.15a). Furthermore, the total amount of oxygen dimers is greater for the ribbon model. For this system, the total formation of oxygen dimers is higher, and confined to a smaller area of the  $\text{Li}_2\text{MnO}_3$  region. The formation of oxygen dimers leads to undercoordinated Mn ions that are prone to migration to tetrahedral sites or octahedral sites in the Li layer [1,2]. Hence, the severity of the distortion in the 3D ordered ribbon model structure is more severe and localized. The formation of oxygen dimers only occurs at sufficiently high state of charge (see Figure VIII.1.15b).



**Figure VIII.1.15** Number of oxygen dimers formed during Ab-Initio Molecular Dynamics simulations at 900K (a) comparison of ribbon vs staggered ribbon model (b) ribbon model at two states of charge.

We have shown in previous reports from AIMD simulations that the rate of formation of oxygen dimers is faster in the ribbon model than in the staggered model. Using the oxygen dimers bond length, we were able to track the formation of peroxide, superoxide and dioxygen species. The preliminary data shows differences in the mechanism of formation of oxygen dimers. The ribbon model seems to undergo a rapid formation of superoxide to dioxygen (see Figure VIII.1.16a), whereas in the staggered ribbon model the superoxide species seems to be more stable (see Figure VIII.1.16b). This is an indication of a possible reversibility in the staggered ribbon case.

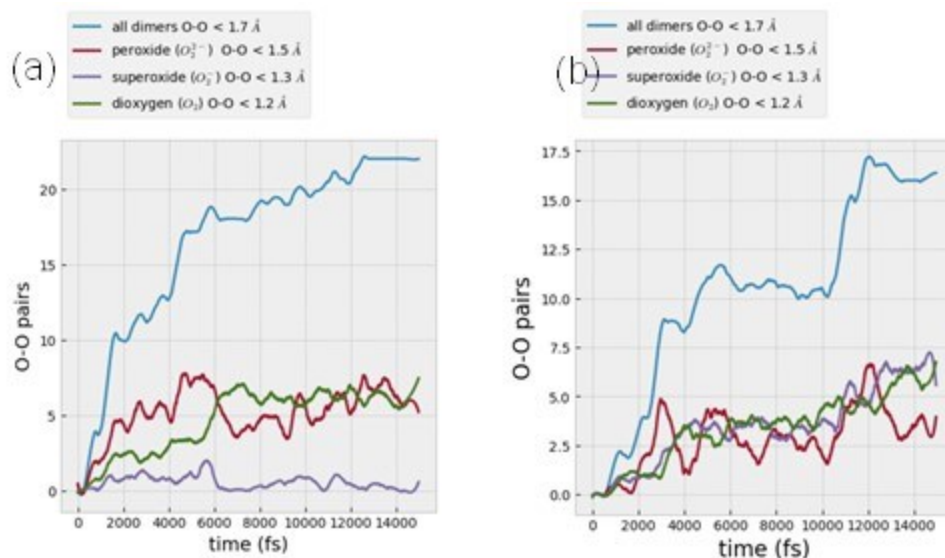


**Figure VIII.1.16** Number of oxygen dimers formed during Ab-Initio Molecular Dynamics simulations at 900K  
(a) Ribbon model at 86% SOC (b) staggered ribbon model at 86%SOC.

We have performed a theoretical analysis of NMR shifts in these materials to assist with the interpretation of the experimental peaks to assign them to a particular domain. It has been observed that  $\text{LiMn}_6$  is not considerably impacted by temperature hold (10h/staggered, 96h/non-staggered), while other shifts around 600ppm, 900ppm and  $\sim 1100$ ppm show a considerable intensity reduction with longer temperature hold (see Figure VIII.1.17). This suggests that  $\text{LiMn}_6$  units in the TM layer (Li-rich component of the LMR material) are very stable and form early in the process. The mass normalized NMR spectra also suggest some amount of Li-loss with longer holds, particularly from the Li layer (see Figure VIII.1.17).

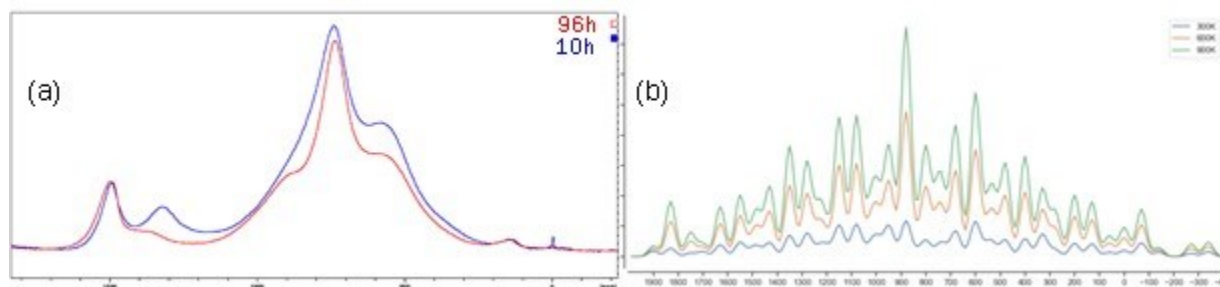


**Figure VIII.1.17** NMR spectrum of LMR-NM material (a) experimental data in blue represents the material with 10h high temperature holds and the red line the 96h high temperature hold during calcination. (b) Theoretically predicted shifts for all the possible configurations of the material at different temperatures.

The peak intensity ratios between the shift  $\sim 700$ ppm (Li in  $\text{Li}_2\text{MnO}_3$ -like environments) to the  $\sim 600$ ppm and 900ppm peaks increased with longer holds, i.e. the intensity reductions of  $\sim 600$ ppm and 900ppm shifts are more significant than the reduction at  $\sim 700$ ppm. This suggests that although there is some Li loss from the Li layer, the contributions to the shift near 700ppm remained almost at the same level. The staggering of the TM layers should reduce the intensity  $\sim 700$ ppm, i.e. longer times should increase the intensity  $\sim 700$ ppm as more 3-D like environments are created. The spectrum at 300K has higher contributions from ordered configurations MnNi domains. We continue to explore the effect of MnNi ordering, domain size, Li-Ni exchange, and in particular the relative stacking between the layers on the predicted NMR spectra, using the bond model.

## 2. Computational Li-Mn-O Phase Diagram

The Li-Mn-O composition space has proven to be an abundant source of promising earth-abundant cathode materials. In this space, a variety of phases with the stoichiometric rock salt, spinel, and defect spinel phases have been discovered with promising electrochemical properties, Figure VIII.1.18 [1]. It has also been shown that electrochemical cycling of these phases can induce phase transitions, such as layered to spinel [2]. Here, we seek to develop understanding of the finite temperature stability and metastability of important phases near the rock salt and spinel compositions to quantify the thermodynamic accessibility and driving forces for interconversion. We validate the density functional theory (DFT) techniques used to compute phase stability and compare the performance of density functionals based on the generalized gradient approximation (GGA) and meta-GGA level of theory (specifically the PBE-sol [3] and  $r^2$ SCAN [4] functionals, respectively), assess the influence of a Hubbard  $U$  term, and evaluate the energetics of specific spin orderings in describing physically accurate phase stability.

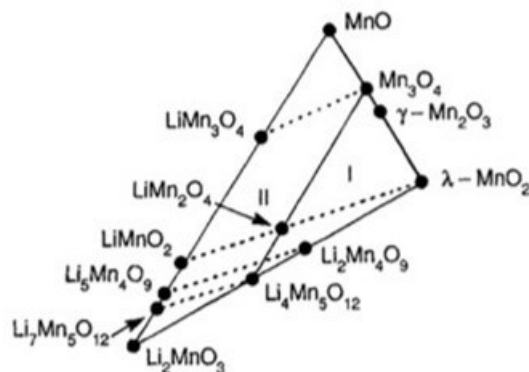
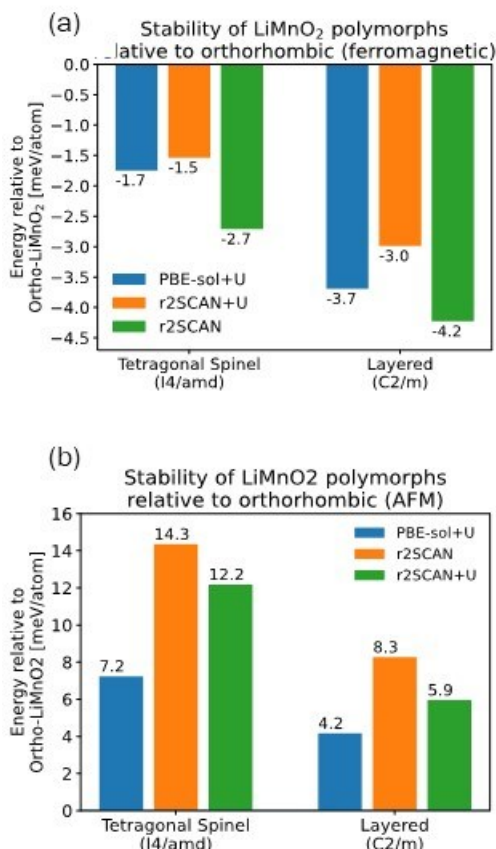


Figure VIII.1.18 Li-Mn-O phase diagram containing stoichiometric rock salt, stoichiometric spinel, and defect spinel phases. Reproduced from Thackeray et al. [8].

As a test case, we compute the phase stability of the competing orthorhombic (Pmmn), tetragonal spinel (I4/amd), and monoclinic layered (C2/m) polymorphs of  $\text{LiMnO}_2$  at 0 K using the PBE-sol+ $U$  ( $U = 3.9$  eV),  $r^2$ SCAN, and  $r^2$ SCAN+ $U$  ( $U = 1.8$  eV) functionals, with  $U$  values previously calibrated to obtain accurate Mn oxidation energies [5,6]. The  $\text{LiMnO}_2$  polymorphs are chosen because it is well-established that the phases in order of decreasing stability are orthorhombic, monoclinic layered, and tetragonal spinel at room temperature. The DFT total energies of these phases with ferromagnetic (FM) spin polarization are calculated, and the energies relative to orthorhombic  $\text{LiMnO}_2$  are shown in Figure VIII.1.19(a). When spins are FM ordered, it is predicted that the monoclinic layered phase is the ground state, being 3-4 meV/atom more stable than the orthorhombic phase, which conflicts with experimental findings. Tetragonal spinel is also predicted to be more stable than orthorhombic by 1.5-3 meV/atom.

Energies relative to the orthorhombic phase are also calculated using antiferromagnetic (AFM) spin orderings based on previously characterized magnetic ground states, and values of are shown in Figure VIII.1.19(b). Using the AFM ground states, we recover the experimental finding that the orthorhombic phase is the ground state of  $\text{LiMnO}_2$ . This phase is 4-8 meV/atom more stable than the layered phase, and 7-14 meV/atom more stable than the tetragonal spinel phase, depending on the functional used. All functionals yield qualitatively similar trends, which indicates that phase stability of  $\text{LiMnO}_2$  is significantly dictated by magnetic interaction energies and electronic structure arising from AFM spin polarization, and not differences in longer range van der Waals interactions that  $r^2$ SCAN is known to better capture.



**Figure VIII.1.19** Electronic total energies of tetragonal spinel and monoclinic layered LiMnO<sub>2</sub> phases relative to orthorhombic LiMnO<sub>2</sub>, computed with a) ferromagnetic (FM) and b) antiferromagnetic (AFM) spin polarization. The density functionals assessed are PBE-sol+U, r<sup>2</sup>SCAN, and r<sup>2</sup>SCAN+U.

Our results demonstrate that the details of magnetic ordering are vital towards obtaining physically accurate phase stability trends of LiMnO<sub>2</sub> polymorphs, which is true for all density functionals tested. This suggests that for future calculations on the rest of the Li-Mn-O space, we should similarly search for the magnetic ground state of each structure, which can be performed using established high throughput workflows [7]. To further validate the choice of density functional, we are currently assessing the voltage profile prediction of spinel LiMnO<sub>2</sub>, the results of which we will show in the next quarterly update.

#### **Model Systems: Effect of Fluorination on Li- and Mn-Rich (LMR) Layered Oxide Cathodes**

We previously synthesized a series of Li<sub>1.2</sub>Ni<sub>0.2</sub>Mn<sub>0.6</sub>O<sub>2-x</sub>F<sub>x</sub> (x=0, 0.01, 0.025 and 0.05, denoted as LNMO, LNMO-F1, LNMO-F2.5 and LNMO-F5, respectively) single crystal samples using LiF-KF as the F source. All samples adopted the same octahedron particle morphology with predominately (012) surface facets. Synchrotron X-ray diffraction (XRD) analysis confirms the absence of LiF impurities whereas a LiMn<sub>2</sub>O<sub>4</sub>-type spinel phase was found in all F-LNMO samples, with higher F content promoting the formation of more spinel secondary phase. To understand the fluorination effect on LMR, we employed X-ray photoelectron spectroscopy (XPS), synchrotron soft X-ray absorption spectroscopy (sXAS) and electron energy loss spectroscopy (EELS) to analyze the elemental and chemical distributions in this series of samples. The study aims to probe these distributions covering the entire range of surface to bulk, with the XPS probing roughly 2 nm on the top surface, sXAS in the total electron yield (TEY) mode and fluorescence yield (FY) mode probing ~ 5 nm surface and 50 nm subsurface regions, respectively, and the EELS technique combined with FIB lithography probing both surface and bulk region. Figure VIII.1.20a and b show the fitted Mn 2p and Mn 3s XPS spectra, respectively. For LNMO, surface Mn cations are at 4+. The presence of lower valence Mn<sup>3+</sup>

cation was detected on all F-LNMO crystals, with its content increasing with the increasing fluorination level. The Ni oxidation state, on the other hand, remains unchanged for all LNMO and F-LNMO samples. On the F  $1s$  XPS spectra, a broad peak centered around 684 eV was visible on LNMO-F2.5 and LNMO-F5, suggesting the presence of F on the sample. This value is much lower compared to the binding energy of LiF ( $\sim 685.4$  eV), further confirming the absence of LiF impurity in our SC samples. Mn  $L$ -edge soft XAS spectra in both TEY and FY detection modes are shown in Figure VIII.1.20c and d, respectively. Compared to that of the LNMO sample, the  $L_3$  absorption edges of the F-LNMO samples show an additional shoulder peak at  $\sim 639.5$  eV (yellow dashed lines) in both TEY and FY. This is consistent with the presence of  $Mn^{3+}$  along with  $Mn^{4+}$  in the fluorinated samples, in comparison to the reference spectra collected on various manganese oxide standards. Thus, the formation of  $Mn^{3+}$  cations from the very top surface to the subsurface region in F-LNMO is confirmed by combining XPS and sXAS analyses. We further evaluated  $Mn^{3+}$  distribution by estimating its content from principal component analysis (PCA) of the collected spectra (Figure VIII.1.20e). Again, the overall  $Mn^{3+}$  content increases with fluorination level, with the highest content detected on LNMO-F5. This is consistent with the trend in calculated bulk  $Mn^{3+}$  based on charge compensation upon replacing  $O^{2-}$  with  $F^-$  in the lattice. Furthermore, in a given F-LNMO sample, there is clearly a concentration gradient of  $Mn^{3+}$  as its content decreases from the top surface to the subsurface region of  $\sim 50$  nm.

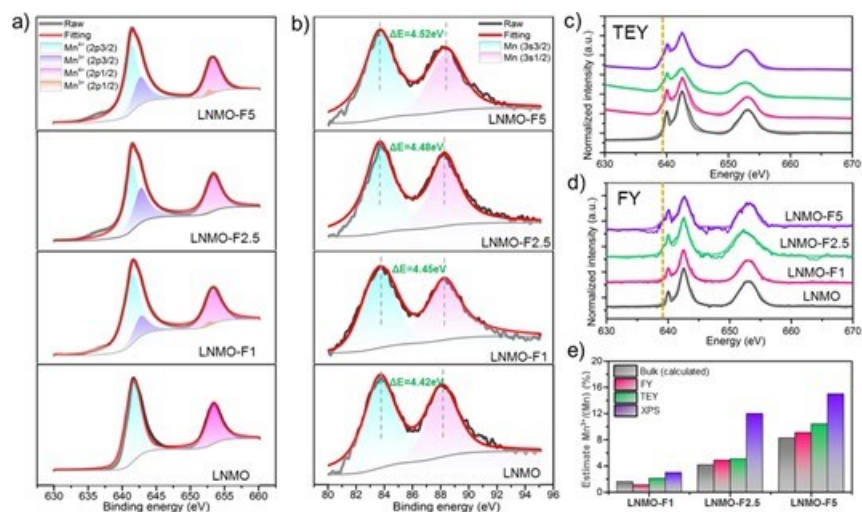


**Figure VIII.1.20** a) Mn 2p and b) Mn 3s XPS spectra of the single-crystal samples. Mn L-edge soft XAS profiles of the samples collected in c) TEY and d) FY mode. e)  $Mn^{3+}$  contents estimated from the various characterization techniques.

The surface to bulk distribution of Mn oxidation state in the LNMO-F5 crystals was further examined by the scanning transmission electron microscopy (STEM) - EELS integrated spectroscopy. Figure VIII.1.21 shows the Mn  $L_3/L_2$ -edge EELS spectra, collected in the (102) surface region of 1-31 nm and the bulk region of 120-820 nm. The peak area ratio between the  $L_3$ -edge and  $L_2$ -edge on the Mn spectra is typically used to determine the valence of Mn cations. It is clear that the Mn- $L_3/L_2$  peak area ratios near the (102) surface region (Figure VIII.1.21a) are broadly higher than that in the bulk region (Figure IX.2.10b), consistent with an overall higher  $Mn^{3+}$  cation content near the surface. The gradient distribution in  $Mn^{3+}$  content is also confirmed, with the highest content detected near the top surface and lowest content in the bulk region. The results further reveal the particle-level gradient distribution of  $Mn^{3+}$  concentration from surface to bulk of the F-LNMO crystals. Our attempt to spatially-resolve F distribution, however, was unsuccessful. In the STEM-EELS analysis, the detected F signals fall into the noise level due to its low concentration. In the STEM-EDX analysis, on the other hand, the F-K edge signal overlaps with the Mn-L edge signal in F-LNMO, resulting in difficulties in deconvoluting the signals.



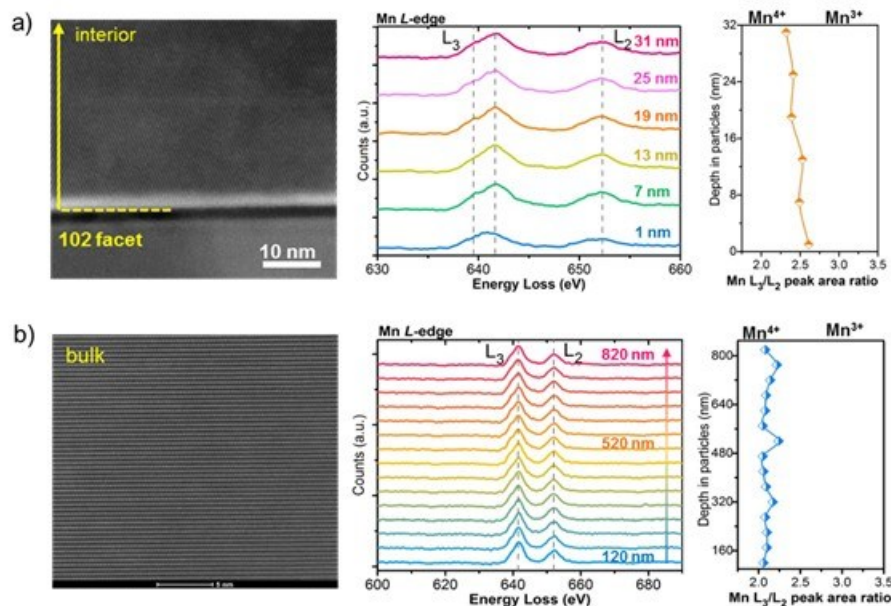
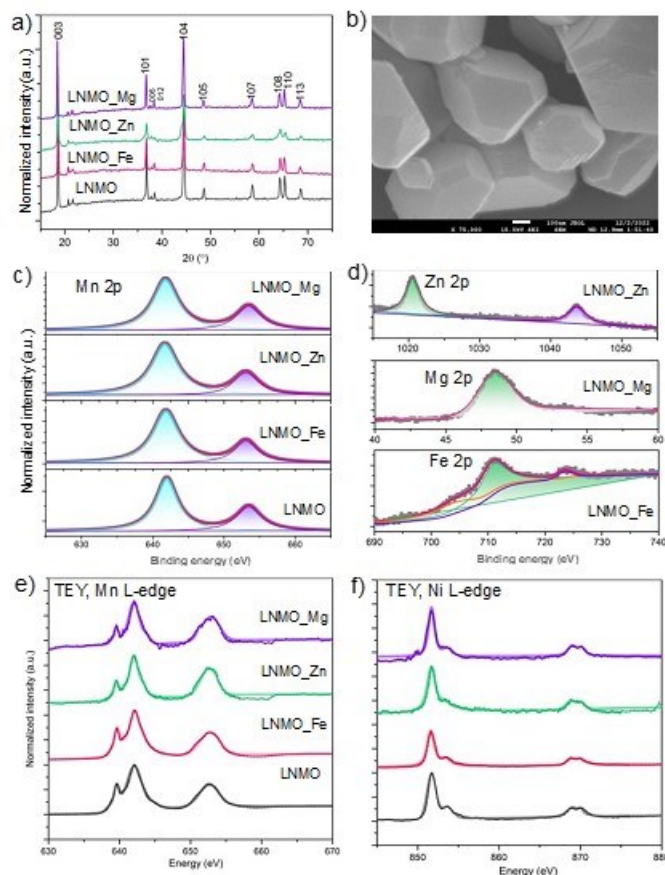


Figure VIII.1.21 STEM-HAADF and Mn L<sub>2</sub>/L<sub>3</sub>-edge STEM-EELS spectra collected on a LNMO-F5 crystal probed: a) in the (102) surface region of 1 to 31 nm at a step size of 6 nm and b) in the bulk region from 120 to 820 nm at a step size of 50 nm.

Overall, detailed characterization reveals that in LNMO single crystals, the surface is enclosed with a thin layer of spinel  $\text{LiNi}_x\text{Mn}_{2-x}\text{O}_4$  ( $x > 0.5$ ) whereas the bulk remains the layered structure. Upon fluorination, there is a concentration gradient of  $\text{Mn}^{3+}$  whose content decreases from the top surface to the subsurface region of the F-LNMO particle. This can be attributed to the formation of Ni-enriched  $\text{LiNi}_x\text{Mn}_{2-x}\text{O}_{4-y}\text{F}_y$  ( $x > 0.5$ ) where  $\text{Mn}^{3+}$  is generated upon charge compensation. Less  $\text{Mn}^{3+}$  is present in the subsurface while the bulk Mn remains at 4+, suggesting a “spinel-layered” structure where domains of the  $\text{LiNi}_{0.5}\text{Mn}_{1.5}\text{O}_4$  spinel phase are integrated into the native layered framework in the bulk.

#### Model Systems: Effect of EA Cation Doping on LMR Cathodes

Complementing the modeling effort, we aim to understand the effect of cation doping in layered LMR oxide cathode materials through well-controlled experimental studies. A variety of doped and undoped single-crystal model samples were successfully synthesized. A two-step process was used to synthesize LMR single-crystals. Transition-metal (TM) carbonate intermediates including the specific dopants were first obtained *via* a co-precipitation method, which was followed by a molten-salt synthesis procedure to convert the intermediate to the final oxide product at high temperatures. Figure VIII.1.22a shows the XRD patterns collected on the pristine LNMO as well as those doped with 2% of Fe, Mg or Zn, referred to as LNMO\_Fe, LNMO\_Mg and LNMO\_Zn, respectively. The results are consistent with those previously obtained on LMR, except for LNMO\_Zn where a small amount of spinel impurities were also detected. When CsCl is used in the molten-salt reaction, all particles adopted the same polyhedron shape with an average size of  $\sim 0.5 \mu\text{m}$ , as shown by the scanning electron microscopy (SEM) image in Figure VIII.1.22b. Structural and morphological changes due to doping were found to be negligible. Chemical analysis was also performed using XPS and synchrotron sXAS. On the XPS spectra, Mn  $2p_{3/2}$  peaks maintain the same energy as well as profile shape in all samples (Figure VIII.1.22c). The  $2p$  peaks of the dopants in LNMO\_Fe, LNMO\_Mg and LNMO\_Zn show that all dopants are at the 2+ oxidation state as expected (Figure VIII.1.22d). On the sXAS  $L$ -edge spectra, Mn and Ni were found to be at +4 and +2, respectively (Figure VIII.1.22e-f).



**Figure VIII.1.22** (a) XRD patterns of LNMO, LNMO\_Fe, LNMO\_Mg and LNMO\_Zn single-crystal samples, b) a typical SEM image showing particle morphology of the samples, (c, d) XPS spectra of Mn 2p, Zn 2p, Mg 2p and Fe 2p, (e, f) Mn and Ni L-edge soft XAS spectra collected in the TEY mode.

LNMO single crystal samples with various particle morphologies were also synthesized. Figure VIII.1.23 shows a series of 2% Fe-doped LNMO in three different morphologies of polyhedron, octahedron and rod, referred to as poly-LNMO, oct-LNMO and rod-LNMO, respectively (Figure VIII.1.23). To obtain the rod morphology, a hydrothermal method was used in the first step to prepare the intermediate which led to the final oxide particles  $\sim 1 \mu\text{m}$  long and 150 nm wide Figure VIII.1.23c). Phase purity of all samples were confirmed by XRD. In the future work, we will investigate the effect of dopant and morphology on LNMO properties and performances.

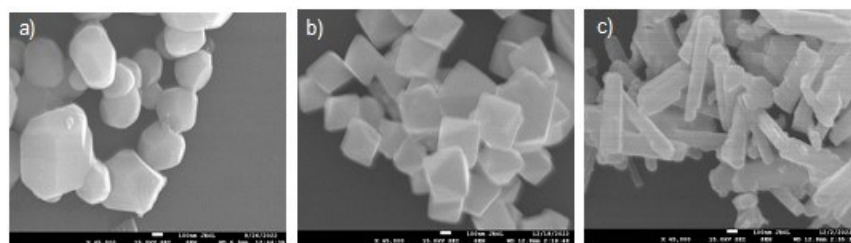


**Figure VIII.1.23** SEM images of Fe-doped LNMO in various morphologies: a) polyhedron, b) octahedron and c) rod.

The structural properties of the synthesized SC samples were further characterized. Figure VIII.1.24a shows a selected area electron diffraction (SAED) pattern, as well as transmission electron microscopy (TEM) and high-resolution TEM (HRTEM) images, collected on a rod-shaped SC-LNMO doped with 2% of Fe. The

study was carried out at the Environmental Molecular Sciences Laboratory, Pacific Northwest National Laboratory (PNNL). The SAED analysis reveals the presence of (003)-, (104)- and (102)-family of facets in the layered rhombohedral phase ( $R\bar{3}m$  space group). Further TEM imaging and the corresponding fast Fourier transform (FFT) enable the indexing of the edges of the particle labelled as 1-4 (top row, middle). The large surfaces, labelled as 1 and 4, were identified as (003)-family facets while the small edges, 2 and 3, were identified as (104) and (10 $\bar{2}$ ) facets, respectively. The results indicate that the crystal is predominately enclosed by the (003) facet on the surface. Furthermore, reconstruction layers with varying thicknesses were found on all surfaces. A thin layer of rock salt phase, 1-2 nm in thickness, was found on both (003) and (104) surfaces, while both rock salt and spinel phases were found on the (10 $\bar{2}$ ) surface. Particle-level elemental distribution was investigated by STEM - energy-dispersive X-ray spectroscopy (EDX) mapping (Figure VIII.1.24b). Mn (orange), Fe (cyan) and O (red) were uniformly distributed throughout the particle, while Ni (purple) was found to preferentially segregate on the (10 $\bar{2}$ ) facet. In the layered structure, the (102) crystal facets are terminated by both TM layers and Li layers while the (003) facets are terminated by the TM layers only. The facet-dependent Ni segregation in the (102) facets is likely a result of Ni diffusion from the bulk to the surface along the Li slab and the formation of Li-Ni anti-site defects. In future work, we will evaluate the electrochemical performance of the synthesized single-crystal samples.

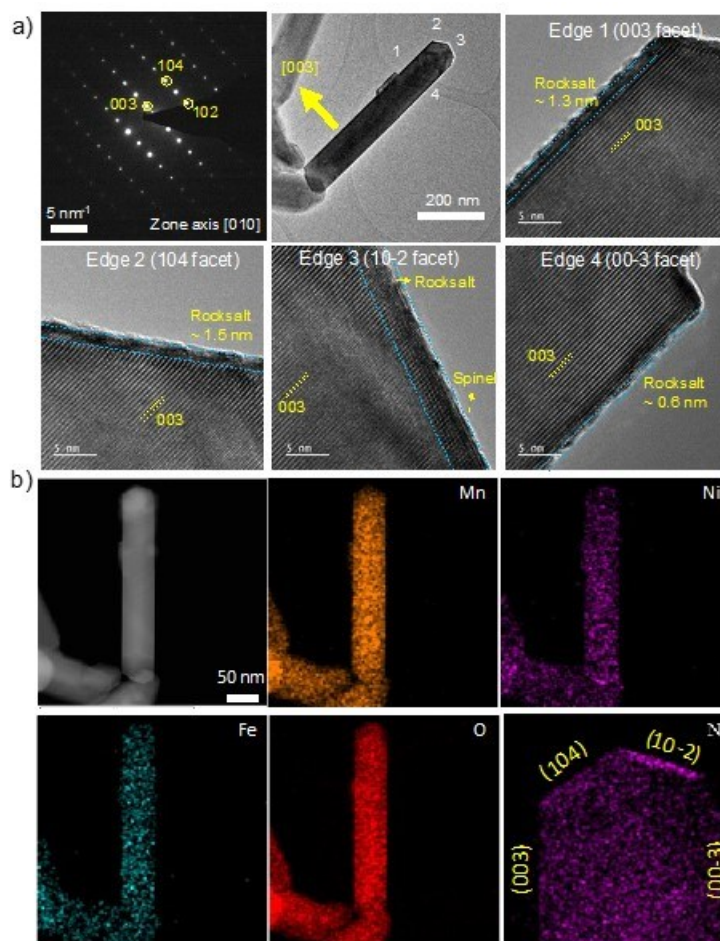


Figure VIII.1.24 (a) SAED pattern and HRTEM images collected on a rod-shaped LNMO single crystal doped with Fe. Crystal facets were determined based on SAED and FFT of the TEM images collected on the corresponding edge. (b) STEM-EDX elemental mapping of Mn (orange), Ni (purple), Fe (cyan) and O (red) at the single-particle level. Ni enrichment is seen on the (10 $\bar{2}$ ) facet.

## Surface Stabilization

### Development of Additives for High Performance LMR-NM Cathodes: Chen Liao et al. ANL

The use of additives with Mn-rich electrodes is a viable strategy for improving cell performance metrics such as energy and power. In this work, both single and dual additive formulations were systematically studied with an end-goal of establishing, with the help of machine learning, correlations between functional groups and molecular structures and surface stability of *EaCAM* systems. Further experiments showcasing the concentration effect of TMSPi and even more complicated electrolyte formulations. The selection of additives used herein is based on the *EaCAM* team's previous research and are listed in the table of Figure VIII.1.25 where each additive is initially categorized by its expected influence as a cathode or anode additive. Evaluation was done using 1.2M LiPF<sub>6</sub> in EC:EMC (3:7 wt%) (GEN2) as the base electrolyte. LMR-NM cathode-electrodes were used in coin-cells utilizing graphite anodes. Our strategy includes 3 steps: (1) test the performances of each single, dual additives; (2) optimizing the additives formulations based on an Edisonian approach and (3) using a machine learning feedback loop by dissecting the additive molecules to functional groups and moieties and correlating the performance metrics with functionalities to predict new additives structures and optimal concentrations.

Negative			Positive					
Acronym	Name	Structure	Acronym	Name	Structure	Acronym	Name	Structure
VC	vinylene carbonate		PTSI	p-toluenesulfonyl		TMSPi	tris(trimethylsilyl) phosphite	
PBE	phenylboronic acid 1,3-propanediol ester		TMSPa	tris(trimethylsilyl) phosphate		TMSB	tris(trimethylsilyl) borate	
tVCBO	phenylboronic acid 1,3-propanediol ester		MS	In situ Li Malonate or PF4		PMSL	propargyloxytrimethylsilane	
LiDFOB	lithium difluorobisoxalato borate		LDF	lithium difluorophosphate		LiBTMSPa	lithium bis(trimethylsilyl) phosphate	

Figure VIII.1.25 Chemical structures, names and acronyms for the additives tested in this study.

Figure VIII.1.26(a) shows the cycling performance of twelve single additives compared with the Gen2 baseline. Most of which are commercially available. Some are synthesized through our previous patented process (MS),[3] or an aging process of 1 day (TMSB) - 1 week (TMSPi, TMSPa).[1] We also arbitrarily assigned the single additives as either negative (working with the graphite anode) or positive (working with the LMR-NM cathode) additives. Briefly, the test protocol includes three formation cycles at a C/10 rate (1 C = 2.8 mA) from 2.5-4.3 V, followed by two activation cycles at C/20 from 2.5-4.6 V and 80 aging cycles at C/3 from 2.5-4.4 V. Right before and after every 20 aging cycles, the cell performance is checked with a slow C/25 cycle from 2.5-4.4 V to get its true capacity, a fast 1 C cycle from 2.5-4.4 V to test its cycling performance at high rate and a modified hybrid pulse power characterization (HPPC) sequence to exam its impedance. Most of the additives show improved cycling performance with this cycling protocol. Among them, the cathode additives TMSPi, MS, TMSB and LDF and the anode additives tVCBO and LiDFOB show the best cycling performance. Therefore the cathode additives are combined with anode additives to prepare the so-called dual additives, and their cycling performances are presented in Figure VIII.1.26(b). For TMSPi, 1wt% or 2wt% weight amount are applied in the dual additives, separately. It's found that all the dual additives tested have improved cycling performances compared to the Gen2 baseline and 2wt% TMSPi + 1wt% LiDFOB shows the best performance.

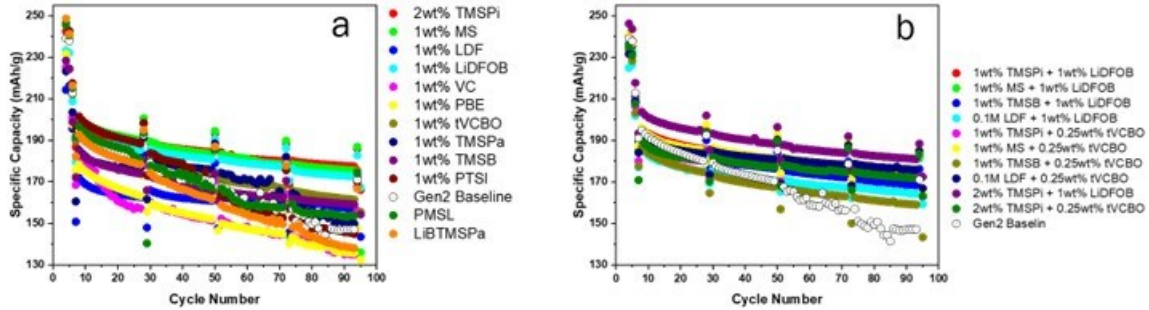


Figure VIII.1.26 Cycling performance of the LMR-NM//graphite cells containing the baseline Gen2, and Gen2 with different a) singular additives (the legends show the wt% and name of each additive) and b) dual additives.

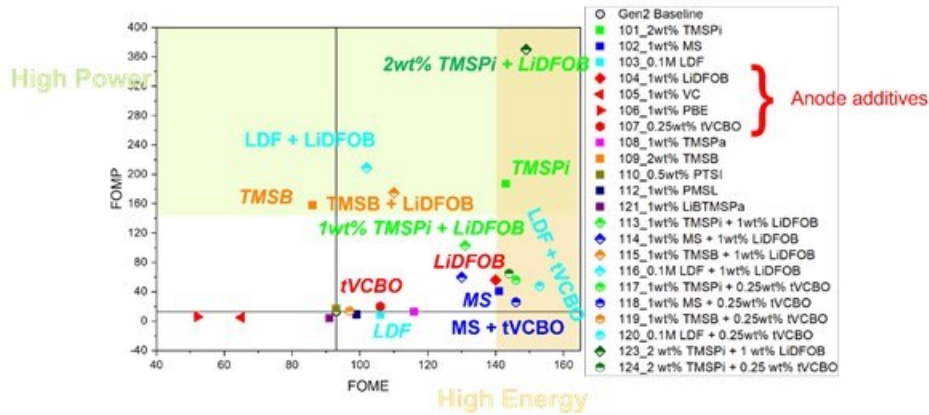
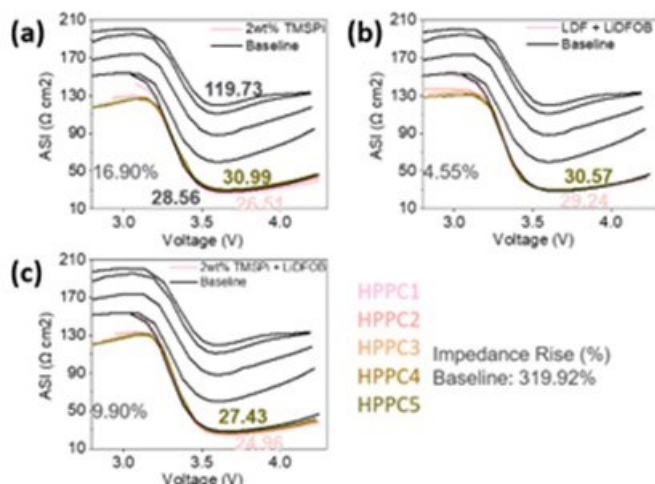


Figure VIII.1.27 FOME vs. FOMP for all single additives, dual additives, and Gen2 baseline. (The green region presents the high-power density region, and the gold region presents the high energy density region.)

To have a more straightforward exhibition of the additives performances, a figure of merit (FOM) approach is used to evaluate each single or dual additive(s) (see Figure VIII.1.27). The figure of merit energy (FOME) is evaluated based on the energy densities obtained from the 5 slow C/25 cycles and figure of merit power (FOMP) is evaluated based on the HPPC cycles from the test protocol.

To have a better understanding of the impedance rise, ASI results and analyses for the top 3 formulas with the best FOMPs are shown here: 2wt% TMSPi (as shown in Figure VIII.1.28(a)), 0.1M LDF + 1wt% LiDFOB (as shown in Figure IX.3.4(b)), and 2wt% TMSPi + 1wt% LiDFOB (as shown in Figure VIII.1.28 (c)). For the Gen2 baseline, the ASI increased from 28.56 to 119.73  $\Omega \text{ cm}^2$  with an impedance rise of 319.92%. In the presence of these three formulas the impedance rise can be significantly decreased. For example, the application of 2wt% TMSPi can not only decrease the initial impedance from 28.56 to 26.51  $\Omega \text{ cm}^2$ , but also dramatically decrease the impedance rise from 319.92% to 16.90%. Though LDF + LiDFOB slightly increases the initial impedance from 28.56 to 29.24  $\Omega \text{ cm}^2$ , its final impedance is just 30.57  $\Omega \text{ cm}^2$ , with an impedance increase of just 1.33  $\Omega \text{ cm}^2$  in value and 4.55% in percentages. And for the best performance additives of 2wt% TMSPi + 1wt% LiDFOB, its initial impedance impressively drops to 24.96  $\Omega \text{ cm}^2$  also with a low impedance rise of 9.90%. A synergistic effect in improving the cycling performance of LMR-NM//Gr is observed in the combination utilization of TMSPi and LiDFOB.



**Figure VIII.1.28** Area specific impedance (ASI) for LMR-NM//Gr cells with electrolytes containing additive(s) as shown compared to the Gen2 baseline. (The pink and brown numbers are initial and final ASI (in the unit of  $\Omega \text{ cm}^2$ ) for each additive(s) containing cell. The initial and final ASI for Gen2 baseline is 28.56 and 119.73  $\Omega \text{ cm}^2$ , respectively, as shown in black numbers. The impedance rise percentages for each sample and baseline are present in percentiles).

From the previous data, the additives amount applied in the electrolyte is proved to be very important in determining the cycling performance of LMR-NM//Gr cells. In fact, this could lead to a milestone change in the development of using Machine learning to predict both the optimal structures and the concentrations. TMSPi concentration is selected to show the synergistic improvement from concentration optimization: Gen2 electrolytes containing 0.5wt% TMSPi, 1wt% TMSPi and 3wt% TMSPi are also evaluated in the LMR-NM//Gr cells and their cycling performance compared to Gen2 baseline and 2wt% TMSPi is shown in Figure VIII.1.29. As a result, 2wt% TMSPi and 3wt% TMSPi have very similar specific capacities, slightly better than the 1wt% TMSPi while the 0.5wt% TMSPi is very close to the performance of Gen2. The ASI data for those additives compared to Gen2 baseline are shown in Figure VIII.1.30. 0.5wt% TMSPi still suffers from significant impedance rise as the Gen2 baseline. Though 1wt% TMSPi shows close specific capacities with the 2wt% TMSPi and 3wt% TMSPi, its impedance control is not as satisfying as those two. Compared with the 2wt% TMSPi, application of 3wt% TMSPi can further decrease the initial impedance from 26.51  $\Omega \text{ cm}^2$  to 25.39  $\Omega \text{ cm}^2$ , but the final impedance would increase from 30.99  $\Omega \text{ cm}^2$  to 32.50  $\Omega \text{ cm}^2$ , resulting in a higher impedance rise. So, it is concluded that 2wt% TMSPi is the optimal amount for LMR-NM//Gr cells. 0.5wt% and 1wt% TMSPi cannot give satisfying cycling performance while 3wt% TMSPi can only give a slightly lower initial impedance and the additional amount applied is thus unnecessary.

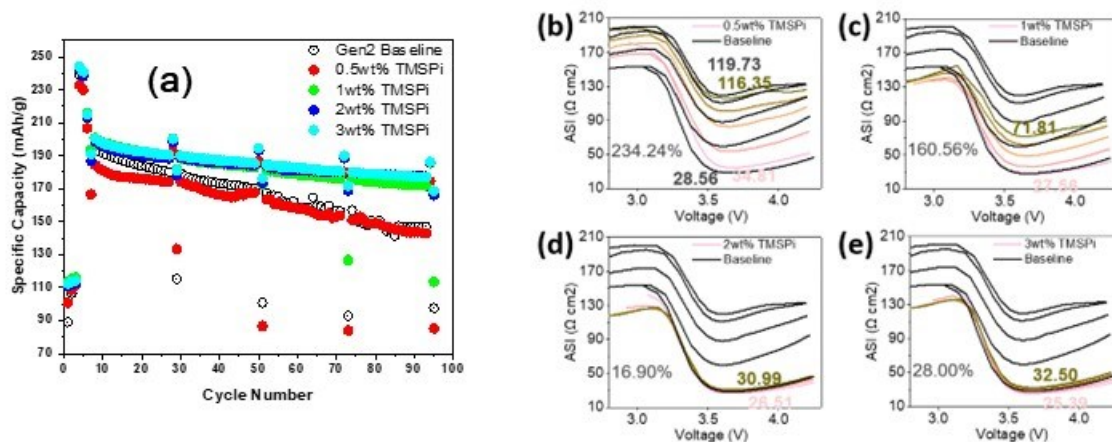


Figure VIII.1.29 a) Cycling performance of the LMR-NM//graphite cells containing Gen2 electrolyte with different amounts of TMSPI. Area specific impedance (ASI) for LMR-NM//Gr cells with electrolytes containing additives of (b) 0.5wt% TMSPI, (c) 1wt% TMSPI, (d) 2wt% TMSPI, and (e) 3wt% TMSPI compared to the Gen2 baseline. (The pink and brown numbers are initial and final ASI (in the unit of  $\Omega \text{ cm}^2$ ) for each additives containing cell. The initial and final ASI for Gen2 baseline is 28.56 and 119.73  $\Omega \text{ cm}^2$ , respectively, as shown in black numbers. The impedance rise percentages for each sample and baseline are present as denoted).

A unique case is LDF: though LDF is not outstanding when applied as a single additive in the LMR-NM//Gr cells, the dual additive of LDF + tVCBO gives the best energy density and LDF + LiDFOB gives the second-best power density. The synergistic effect of those additives thus triggers our curiosity in finding out if triple additives of 0.1M LDF + 1wt% LiDFOB + 0.25wt% tVCBO can take advantage of the good results from the dual additives. However, the triple additives do not take advantage of the synergistic effect from the dual additives. Further characterizations and performing experiments are under run to understand how the additives work on the anode or cathode and how they would give a synergistic effect in combining good merits of each single additives. In addition, with the database we have tested, machine learning will also be used to provide a model with both functional groups and optimal concentrations of the additives to improve the performance.

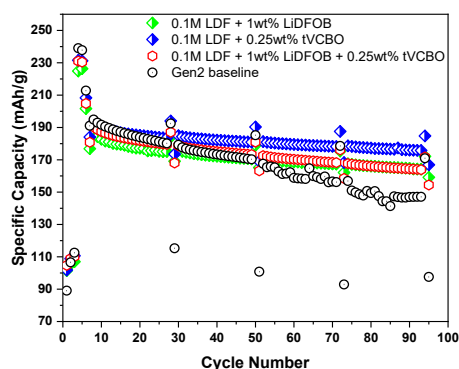
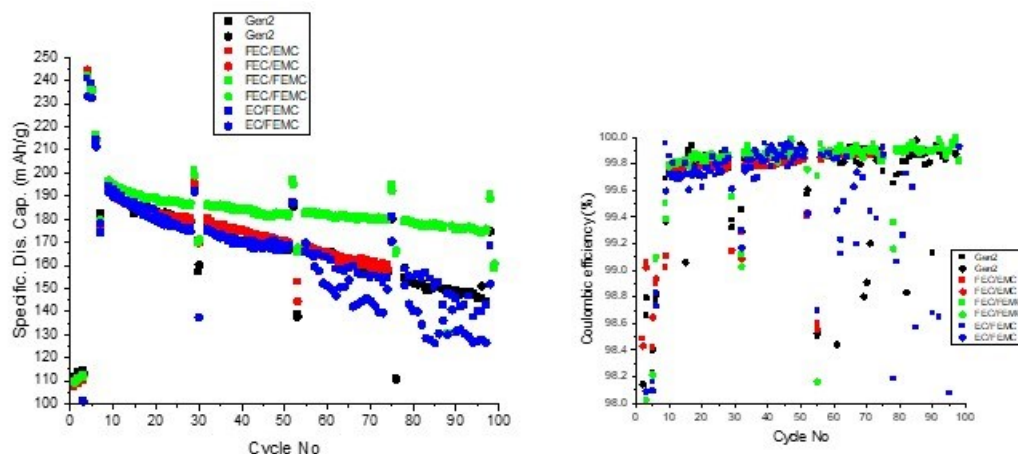


Figure VIII.1.30 Cycling performance of the LMR-NM//graphite cells containing LDF + LiDFOB + tVCBO compared to the Gen2 baseline, LDF + LiDFOB and LDF + tVCBO.

#### Development of Fluorinated Solvents for High Performance LMR-NM Cathodes: Zhengcheng Zhang et al. ANL

The electrolyte development focuses on study of the bulk electrolyte impact on LMR cathode cyclability, surface reactivity and transition metal dissolution. By replacing carbonate solvents with their fluorinated analogs, the solvation capability of electrolyte towards transition metal can be adjusted. With less solvation power from the electrolyte, migration of manganese, which is one of the main causes for capacity fading, can

be mitigated. Gen2 electrolyte and three fluorinated carbonates-based electrolytes (1.2 M LiPF<sub>6</sub> in 3/7 w/w cyclic carbonate/linear carbonate) are tested in LMR/Gr cell. The solvents used in this study are ethylene carbonate (EC), ethyl methyl carbonate (EMC), fluoroethylene carbonate (FEC), and methyl 2,2,2-trifluoroethyl carbonate (FEMC). LMR/Gr cells are assembled with Celgard 2325 separator and 40  $\mu$ L of electrolyte and the tests are conducted at 25°C.



**Figure VIII.1.31** Specific discharge capacity and coulombic efficiency of Gen2 and fluorinated carbonate electrolytes. (Testing protocol: 3 wetting cycles of constant current (CC) charge/discharge at 0.1 C from 2.5 – 4.3V, followed by 2 activation cycles of CC charge/ CCCV discharge at 0.05 C from 2.5 – 4.6 V, and 5 HPPC tests with 0.3C aging cycles.)

As shown in Figure VIII.1.31, partially replacing EC or EMC with FEC or FEMC, respectively, both FEC/EMC and EC/FEMC electrolytes showed similar capacity retention compared to Gen2 electrolyte. While completely replacing both EC and EMC, FEC/FEMC electrolyte showed an improved capacity retention of 89.4% over 100 cycles compared to 74.5% for Gen2. Moreover, while the area specific impedance (ASI) of other electrolytes increased substantially during cycling, ASI of FEC/FEMC electrolyte stayed almost unchanged (Figure VIII.1.32).

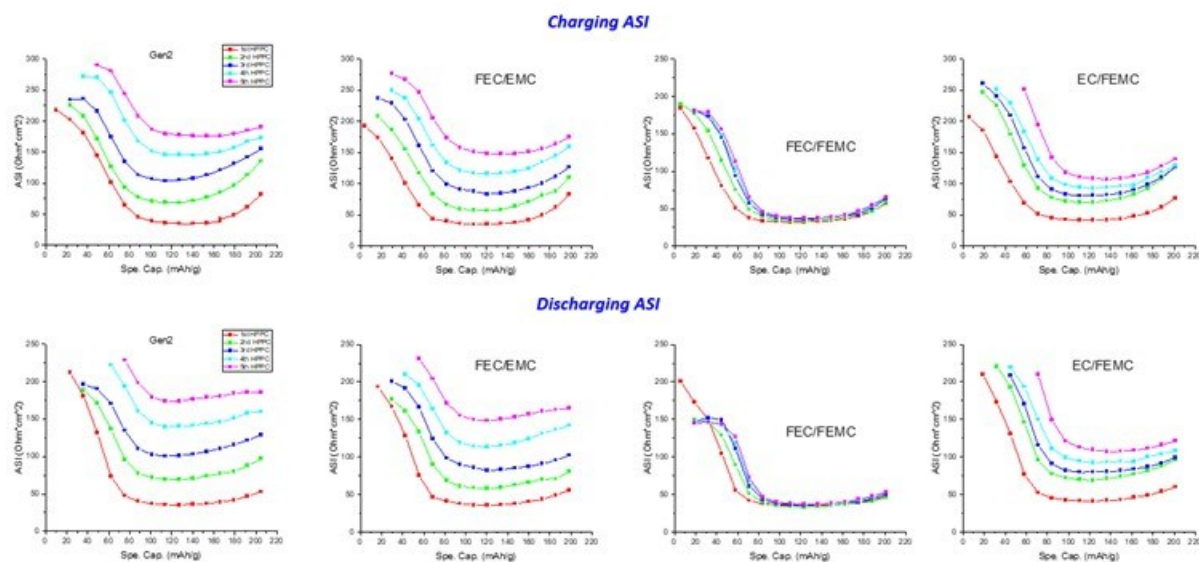


**Figure VIII.1.32** Charging and discharging ASI.



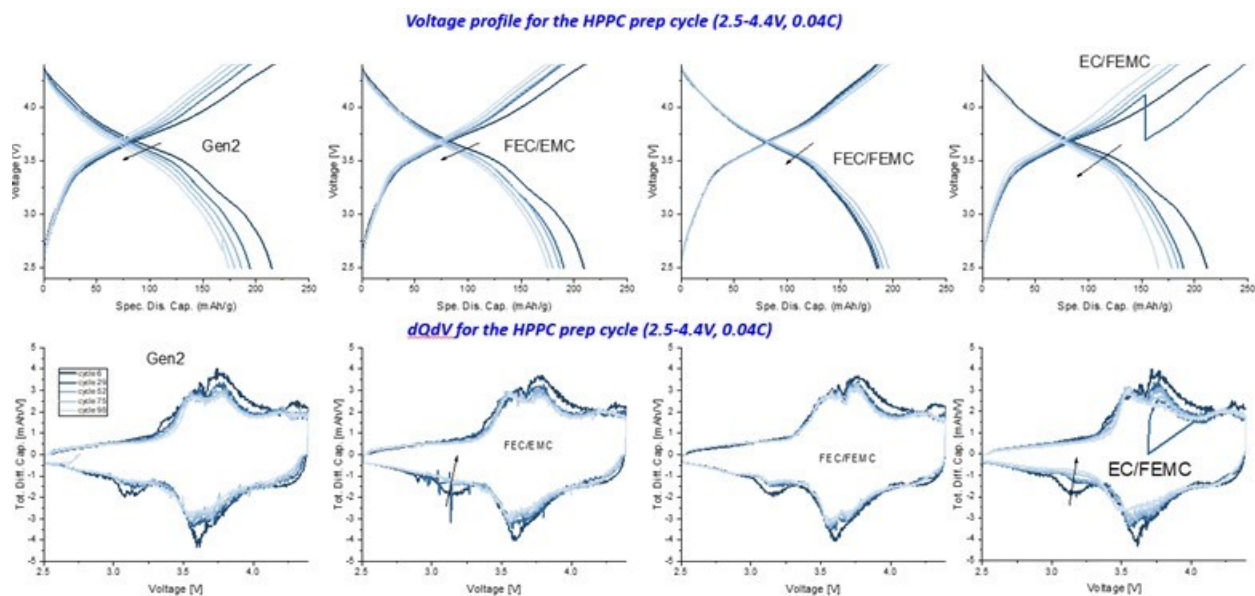


**Figure VIII.1.33 Voltage profile and dQdV of HPPC prep cycle (2.5-4.4V, 0.04 C).**

Figure VIII.1.33 shows the change of voltage profile and dQdV plots over cycling for the four electrolytes. With Gen2 electrolyte and partially fluorinated electrolytes, voltage decay was observed and the phase transition peak in the dQdV plot around 3.1 V disappeared over cycling. With FEC/FEMC electrolyte, minimum voltage fade was observed, and 3.1 V phase transition peak preserved. These results suggest that FEC/FEMC helps to preserve cathode structure over cycling.

With the four different combinations of carbonates or fluorinated carbonates tested in LMR/Gr cells, only with fluorination of both solvents (FEC/FEMC) showed the improved capacity retention. The current hypothesis is the fluorination of both solvents can effectively cut the pathway of transition metal migration, which was potentially a caused of capacity fading. To further understand the impact from the fluorinated carbonate, preformation experiment will be conducted to investigate the effect of SEI, CEI and solvation separately. Characterization of cycled electrodes and electrolytes with ICP-MS and ion chromatography (IC) are on-going to study the TM dissolution.

To further understand the superior performance of this all-fluorinated electrolyte, the transition metals (Mn and Ni) dissolved in the electrolyte and deposited on the anode were quantified through ion chromatography (IC) and inductively coupled plasma mass spectrometry (ICP-MS), respectively.

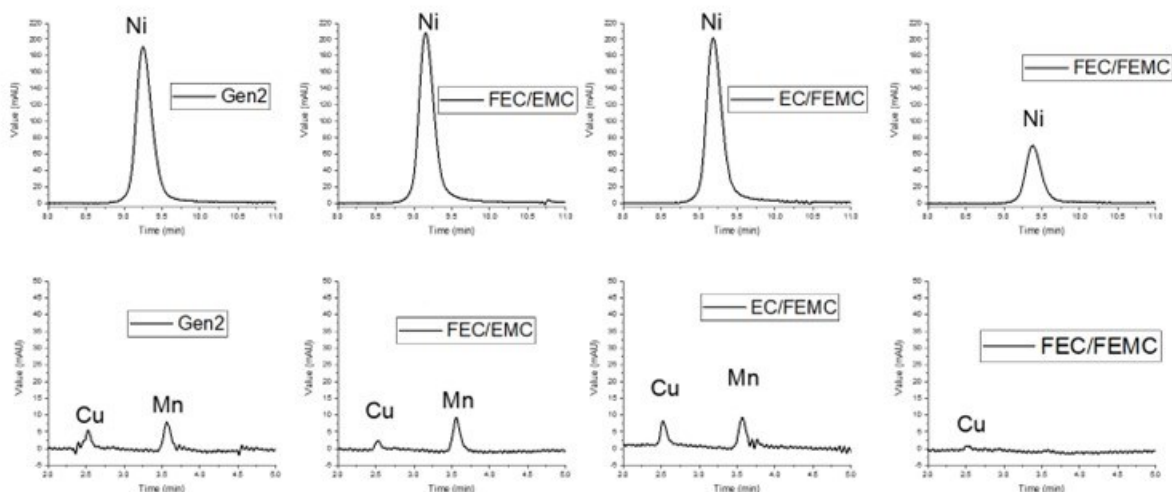


Figure VIII.1.34 IC results of electrolyte after cycling

IC analysis of harvested electrolytes (diluted 50 times) was performed through a Dionex ICS-6000 series system (Figure VIII.1.34). Mn and Ni were detected in the diluted electrolyte samples, eluting at 3.6 and 9.3 minutes, respectively. The peak at 2.5 minutes was assigned to be Cu, which corresponds to anode current collector corrosion. Calibration curves were generated to quantify Mn and Ni contents, and the results are summarized in Figure VIII.1.35. The quantification results indicate that FEC/FEMC has the lowest amount of both Mn and Ni in the electrolyte. Interestingly, a much higher amount of Ni was detected in the electrolyte, which is 2 magnitudes higher than the amount of Mn. The amount of Ni in the non-fluorinated or the partially fluorinated electrolyte varies between 9 and 10  $\mu\text{g}$ , while the amount of Mn varies between only 0.13 to 0.17  $\mu\text{g}$ .

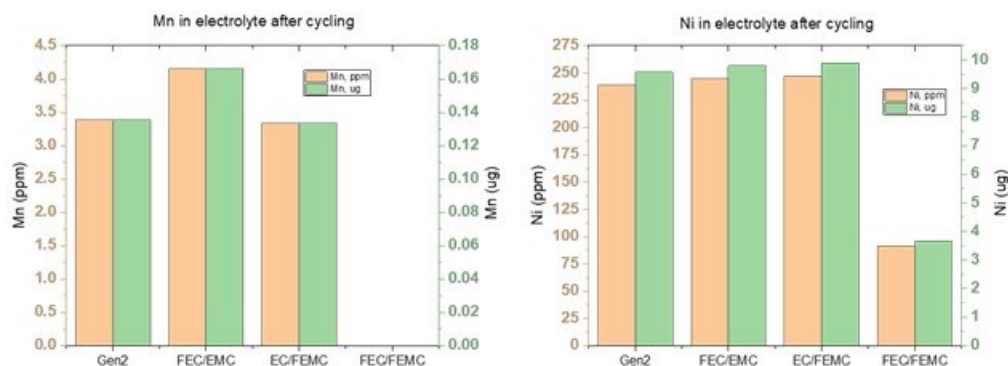
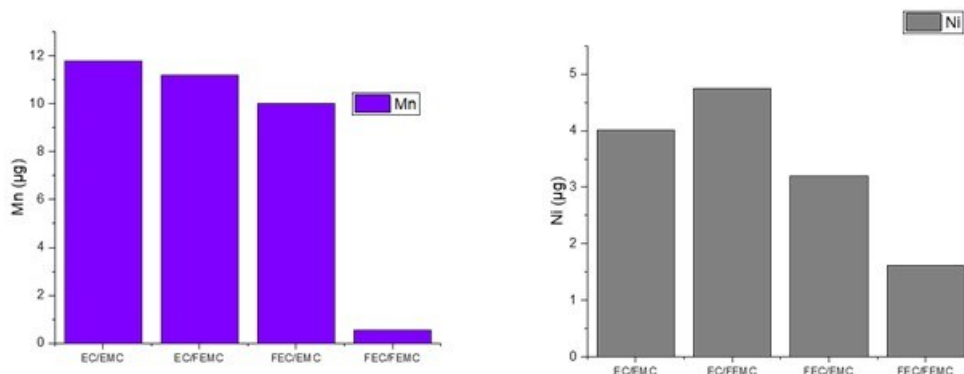


Figure VIII.1.35 IC quantification of Mn and Ni in electrolyte after cycling



**Figure VIII.1.36 ICP-MS quantification of Mn and Ni in Gr anode after cycling.**

The harvested Gr anodes were analyzed with ICP-MS for Mn and Ni. The results are displayed in Figure VIII.1.36. Mn deposited on the Gr anode with non-fluorinated or partially fluorinated electrolyte varies between 9 and 12 µg, while Ni varies between 3 and 4.5 µg. Transition metal deposition on the Gr anode is effectively mitigated by the all-fluorinated electrolyte, resulting in smaller amount of both Mn and Ni in Gr anodes cycled with FEC/FEMC. From both the ICP results and the IC results (Figure VIII.1.27 and Figure VIII.1.28), it appears that Mn is more likely to deposit on the anode, while Ni is more likely to stay dissolved in the electrolyte, suggesting different reactivity of Mn and Ni on the Gr anode.

Based on the quantification results of transition metals in both the electrolyte and the anode, the improved cycling performance of FEC/FEMC was ascribed to its effective suppression of transition metals dissolution and deposition. Additionally, Mn was found to be more likely to deposit on the Gr anode than Ni. A better comprehension of how the electrolyte impacts transition metal dissolution and deposition is still needed. Raman or IR spectroscopy of electrolytes are currently under investigation to further understand the relationship between solvation and transition metal dissolution. Surface characterization will be performed on the formed anodes and cathodes to understand the effect of electrolyte on the SEI or CEI composition.

### **Analysis and Modeling**

#### **Cycle Life Aging Study of LMR-NM//Graphite Cells: P. Badami et al., ANL**

Electrochemical tests are being conducted on cells containing LMR-NM cathodes and graphite anodes. Both the positive and negative electrodes used in the studies are fabricated at Argonne's Cell Analysis, Modeling and Prototyping (CAMP) facility. In the present study, the positive electrode had a 43 µm thick coating with 92 wt% 0.3Li<sub>2</sub>MnO<sub>3</sub>·0.7LiMn<sub>0.5</sub>Ni<sub>0.5</sub>O<sub>2</sub> (LMR-NM), 4 wt% carbons (including 0.05 wt% SWCNT) and 4 wt% polyvinylidene fluoride (PVdF) on a 20 µm thick Al current collector. The negative electrode had a 47 µm thick coating with ~92 wt% graphite, 2 wt% C45 carbon and 6 wt% PVDF binder, on a 10 µm thick Cu current collector. The cell also contained Gen 2 + 1wt% LiDFOB electrolyte and Celgard 2500 separator. The standard electrochemical tests protocol was used for the studies: this protocol includes activation cycles in the 2.5-4.4 V range and C/3 aging cycles between 2.5-4.4 V. Periodic C/25 cycles and HPPC tests are conducted to determine changes to the cell capacity and impedance.

Representative data from the tests are shown in Figure VIII.1.37. After activation, the initial cell capacities in the 2.5-4.6 V and 2.5-4.4 V range are ~255 mAh/g-oxide and ~220 mAh/g-oxide, respectively. The capacity fades during the cycle; at the end of 200 cycles the fade is ~24%. The mechanisms associated with the capacity fade are currently under investigation. Cell impedance barely changes during the cycles. After the initial cycles, the cell impedance at the lowest point (~3.66 V) is ~22.5 ohm-cm<sup>2</sup>; after 200 cycles, the value is ~24.5 ohm-cm<sup>2</sup>, which is a 2 ohm-cm<sup>2</sup> (8%) increase. At ~4.2 V, the cell impedance rises from ~43.5 to ~45.6 ohm-cm<sup>2</sup>. The cells display a higher impedance below 3.6V, rising to ~150 ohm-cm<sup>2</sup> at 3.0V; however, even in this

range, the impedance change is minimal during the cycling. The key message of this study is that the cells display capacity loss but impedance rise is very small.

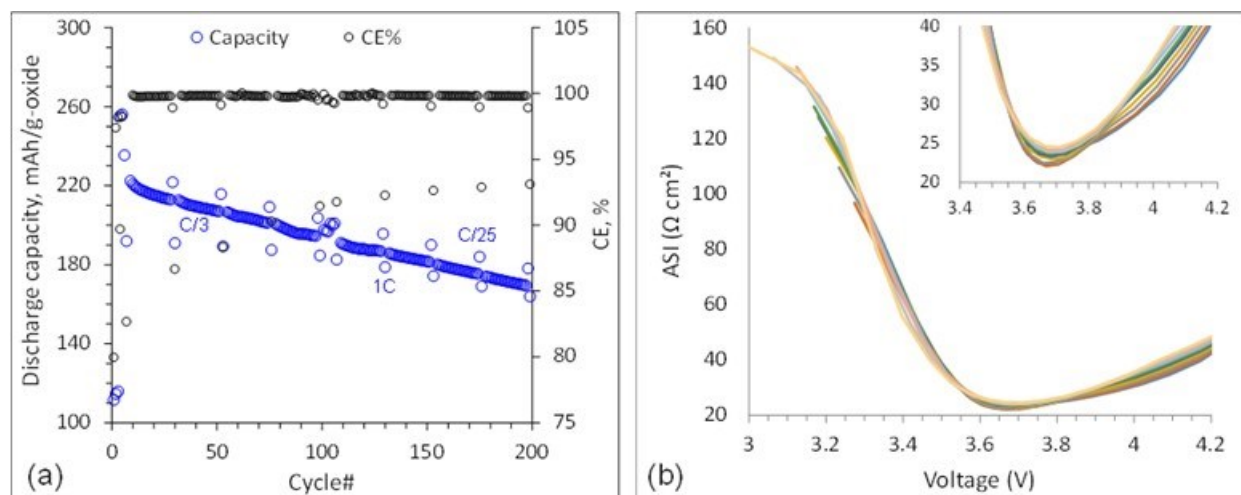


**Figure VIII.1.37** Capacity fade (a) and impedance rise (b) of cells with LMR-NM cathodes and graphite anodes. The inset in (b) is an enlarged view of the data in the 3.4-4.2 V range

#### **Agging Study of LMR-NM//LTO Cells: P. Badami et al., ANL**

Electrochemical tests were conducted on cells containing LMR-NM cathodes and  $\text{Li}_4\text{Ti}_5\text{O}_{12}$  (LTO anodes). Both the positive and negative electrodes used in the studies were fabricated at Argonne's Cell Analysis, Modeling and Prototyping (CAMP) facility. In this study, the positive electrode had a 43  $\mu\text{m}$  thick coating with 92 wt%  $0.3\text{Li}_2\text{MnO}_3 \cdot 0.7\text{LiMn}_{0.5}\text{Ni}_{0.5}\text{O}_2$  (LMR-NM), 4 wt% carbons (including 0.05 wt% SWCNT) and 4 wt% polyvinylidene fluoride (PVdF) on a 20  $\mu\text{m}$  thick Al current collector. The negative electrode had a 68  $\mu\text{m}$  thick coating with ~92 wt% LTO, 3 wt% C45 carbon and 5 wt% PVDF binder, on a 10  $\mu\text{m}$  thick Cu current collector. The cells also contained Gen 2 + 1wt% LiDFOB electrolyte and Celgard 2500 separator. The voltage ranges in the standard electrochemical test protocol were modified to make them appropriate for these studies. This protocol includes three (initial) wetting cycles (before activation) between 1.95 – 2.87 V, two activation cycles between 1.2 – 3.13 V range and subsequent C/3 aging cycles between 1.20 – 2.93 V. These ranges were determined by comparing reference electrode data between cells containing graphite and LTO anodes. Note that the LTO electrode potential is 1.55 V vs.  $\text{Li}/\text{Li}^+$ ; hence at 2.93 V and 3.13 V in LMR/LTO cell, the LMR-NM cathode is at 4.48 and 4.68 V vs.  $\text{Li}/\text{Li}^+$ , respectively.

Representative data from tests conducted at 30°C are shown in Figure VIII.1.38. After activation, the initial cell capacities (Figure VIII.1.38a) in the 1.2-3.13 V and 1.2-2.93 V ranges are ~250 mAh/g-oxide and ~237 mAh/g-oxide, respectively. The capacity fades during the cycle; at the end of 100 cycles the fade is ~4%, which is much smaller than the capacity fade (13%) for similar cells with graphite anodes. Data obtained with electrodes harvested from the cells indicate that the fade is associated with the LTO anode and not the LMR-NM cathode. The cell impedance (Figure VIII.1.38b) barely changes during the cycles. Note that the cell impedance varies from ~30  $\text{ohm}\cdot\text{cm}^2$  (at 2.24 V; cathode at 3.9 V vs.  $\text{Li}/\text{Li}^+$ ) to ~56  $\text{ohm}\cdot\text{cm}^2$  (at 2.78 V; cathode at 4.33 V vs.  $\text{Li}/\text{Li}^+$ ) and ~150  $\text{ohm}\cdot\text{cm}^2$  (at 1.8 V; cathode at 3.35 V vs.  $\text{Li}/\text{Li}^+$ ).

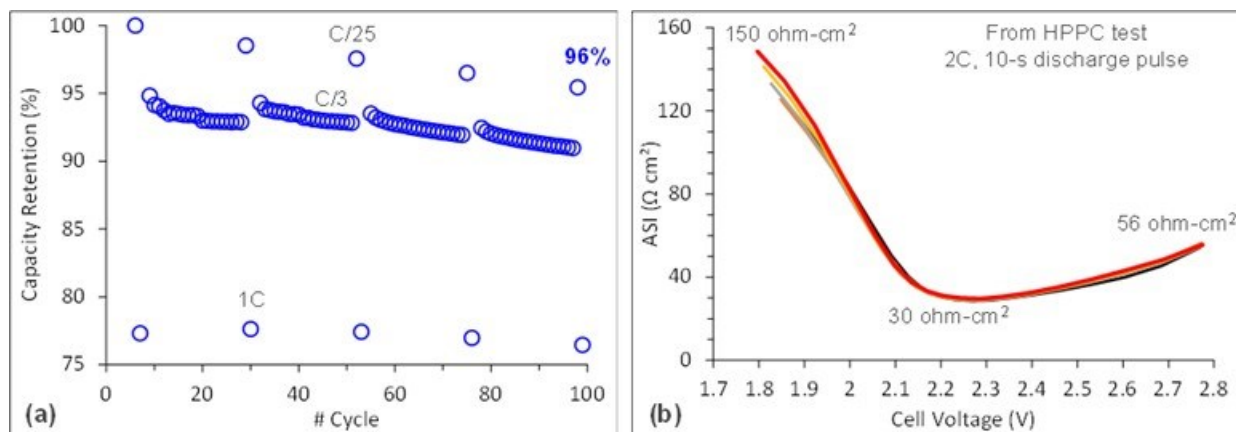


Figure VIII.1.38 Capacity fade (a) and impedance rise (b) of cells with LMR-NM cathodes and LTO anodes.

Capacity-voltage profiles from a representative LMR/LTO cell cycled in the 1.2-2.93 V range are shown in Figure VIII.1.39a. The profile changes observed during cycling reflect structural changes in the LMR oxide; observe that the changes are most significant initially (see difference between cycle 6 and cycle 30) and are smaller during the later cycles. These profiles changes are better seen in the differential capacity profiles (Figure VIII.1.39b). Relatively broad charge peaks at 1.88, 2.22, 2.78 V and discharge peaks at 2.75, 2.16 and 1.79 V are observed after the initial cycles (see cycle 6 data). The difference in peak locations for the charge and discharge profiles reflects the voltage hysteresis in the cell. On cycling, new peaks appear at 1.7 V and 1.56 V in the charge and discharge profiles, respectively, while intensities of the higher voltage peaks decrease. These profiles capacity transfer from the higher to lower voltages resulting in cell voltage fade. This voltage fade, along with the gradual capacity fade, lowers specific energy of the cell during electrochemical cycling. Overall, however, the changes are much smaller than those of the graphite-anode cells described earlier.

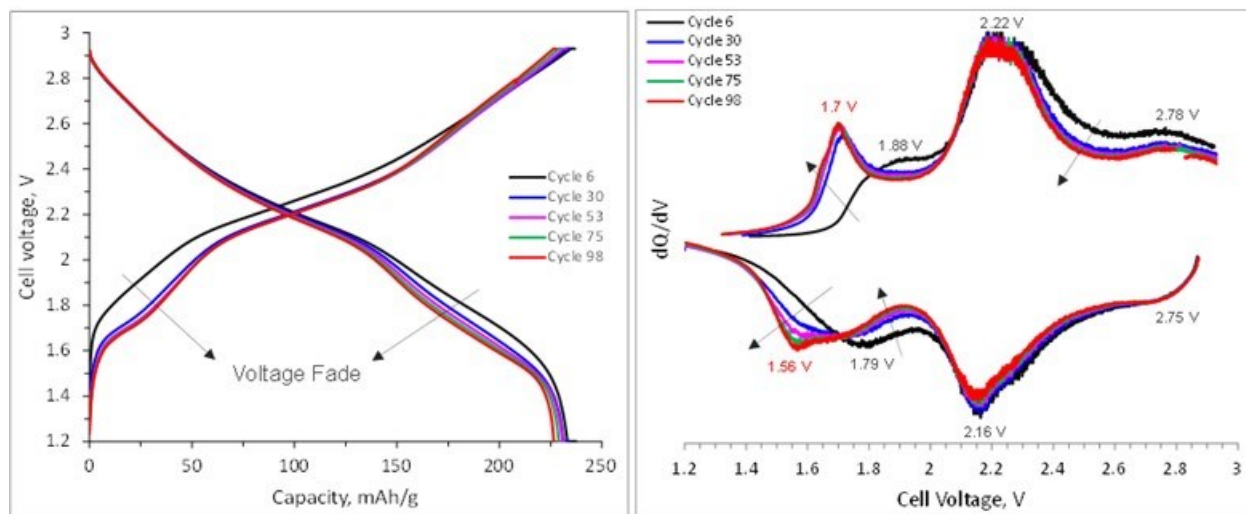


Figure VIII.1.39 Capacity-voltage (a) and differential capacity (b) profiles from cells with LMR-NM cathodes and LTO anodes cycled in the 1.2-2.93 V range. Note that these profiles are of the C/25-rate cycles.

#### Calendar Life Aging Study of LMR-NM//Graphite Cells: S. Son et al., ANL

It is crucial to comprehend the behavior of lithium-ion batteries (LIBs) during calendar aging since prolonged aging leads to a decline in both the energy and power capabilities of LIBs. While it is widely acknowledged that an undesirable parasitic reaction occurring at the surface consumes lithium ions, resulting in a loss of available lithium ions, the effects of these reactions vary depending on the employed cathode, anode and

electrolyte materials. We designed an experiment to investigate effect of calendar aging on LMR-NM//graphite cells. For calendar aging, we employed a potentiostatic hold protocol: this protocol included C/25 rate and hybrid pulse power characterization (HPPC) tests, along with the aging cycles. Note that we introduced a voltage hold after the first HPPC to assess its impact on electrochemical performance of the cell (Figure VIII.1.40a).

Capacity retention of LMR-NM/graphite cells with Gen2 + 3 wt% FEC was determined for cells, with and without a 4.4 V, 200 hr voltage hold after the 28<sup>th</sup> cycle, i.e., preceding the second HPPC (Figure VIII.1.39a). The findings (Figure VIII.1.40b) reveal that capacity retention is nearly identical, indicating that the voltage hold does not impact cell capacity retention during cycling. In Figure VIII.1.40c, area specific impedance (ASI) acquired during the HPPC test is presented. Following the first HPPC, both protocols exhibit a slight ASI increase; observe that the ASI increase is smaller for the cell with the voltage hold. The key takeaway from this study is that the implemented voltage hold has a minimal impact on cell capacity fade and impedance rise.

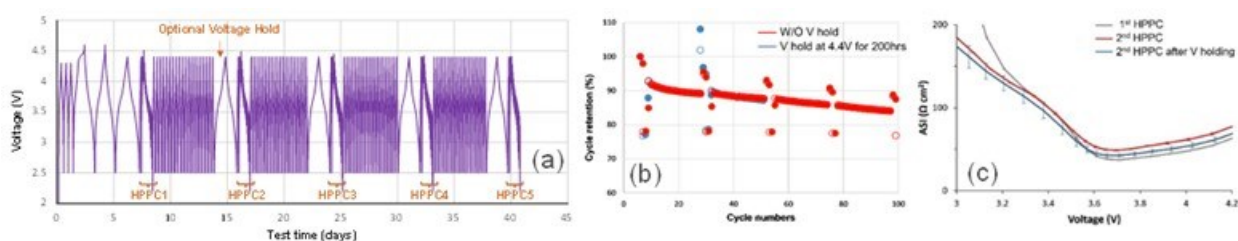


**Figure VIII.1.40** Cycling protocol (a), capacity retention (b) and ASI plots (c) of LMR-Gr cells with and without the voltage hold at 4.4V.

We also conducted experiments on LMR-NM/graphite cells at a 50 °C test temperature (Figure VIII.1.41). The cycling results indicate a decrease in capacity retention to 59.2%. An additional voltage hold at 4.4V for 200 h further reduced cycle retention to 46.7% (Figure VIII.1.41a). Figure VIII.1.41b compares the current response of cells during voltage holds at 30°C and 50°C. Observe the higher currents measured during the 50 °C voltage hold, indicating increased irreversible reactions in the cell.

To examine whether the lower capacity retention at higher temperatures was due to electrolyte depletion, we reconstructed cells using electrodes harvested from two cells, one cycled at 50°C and the other from a cell subjected to an additional 50 °C voltage hold. Fresh electrolyte was used in this reassembly process. Figure VIII.1.41c illustrates the specific capacity changes of the cells after reassembly with the new electrolyte. The results showed no increase in capacity for both cells with the fresh electrolyte. In fact, there was a slight decrease in capacity, likely due to minor material loss during the disassembly process. These findings confirm that the decrease in capacity retention at elevated temperatures was not caused by electrolyte depletion. Future studies will investigate other factors contributing to capacity decrease. This research will include surface investigations using X-ray photoelectron spectroscopy and evaluating lithium loss from the cathode by reassembling cells with a harvested cathode and lithium metal.

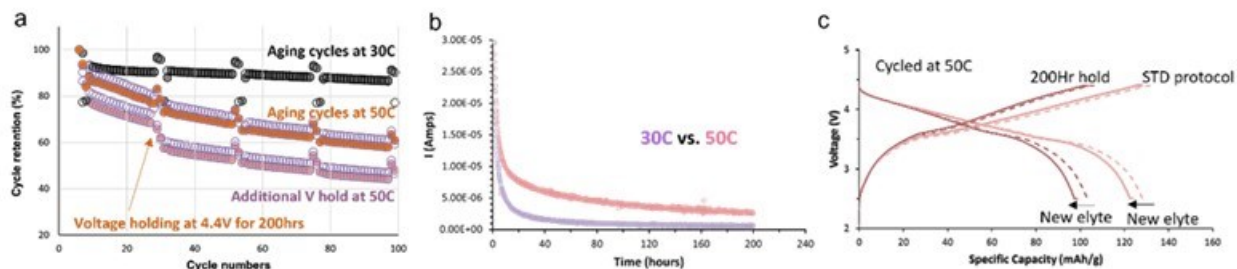


Figure VIII.1.41 (a) Capacity retention of LMR/graphite cells at 30°C and 50°C. (b) The current response measured during the voltage hold at 30°C and 50°C (c) voltage profiles of LMR/graphite cells. Dashed lines indicate the voltage profiles of the cell at the end of cycle as shown in Figure 2a. Solid lines indicate that the voltage profiles of the re-assembled cells with the fresh electrolyte.

#### ***Solid State NMR on Pristine & Harvested LMR-NM Electrodes Extracted from Cycled Cells, F. Dogan et al., ANL***

Lithium local environments of the pristine  $0.3\text{Li}_2\text{MnO}_3 \bullet 0.7\text{LiMn}_{0.5}\text{Ni}_{0.5}\text{O}_2$  (LMR-NM) oxide and the structural changes with cycling were studied by  $^6\text{Li}$  solid state NMR. The solid-state NMR effort focuses on in-depth structural and compositional characterization of the oxides, before and after aging. The changes in lithium local environments were studied with samples: (i) after formation, (ii) after activation (iii) after 200 cycles and (iv) after relithiation of the aged electrode in a half cell. The results were compared to those from a pristine electrode.

The pristine LMR-NM oxide shows combination of different lithium-6 peaks, due to the composite nature of the material (Figure VIII.1.42). The peaks within the 400-1000 ppm and 1200-1500 ppm regions can be assigned to lithiums in Li layers and lithiums in the transition metal (TM) layers, respectively. Based on prior studies, we assign the peaks at 1450 and 720 ppm to lithium environments within  $\text{Li}_2\text{MnO}_3$ -like domains, and the remaining peaks to lithium environments within Mn-Ni layered domains.

After three formation cycles, before the material is activated, the composite structure remains intact, with the same lithium-6 peak positions seen for the pristine sample. However, the peak intensity changes observed with the normalized data indicate that not all Li is reinserted into the oxide, in agreement with the 83% efficiency observed in this voltage window. After the material is activated, a profound loss of order and/or reordering in the material is observed as indicated by disappearance of  $\text{Li}_2\text{MnO}_3$ -like ordering peaks, with severe broadening of the overall spectrum and peak shift toward lower frequencies. These new lithium peak positions can be assigned to a mixture of different lithium environments, such as Li in tetrahedral sites, adjacent to vacancies and dumb bell type and spinel like Li environments.

With further cycling, more lithium loss is observed with the peak intensity decrease, however no obvious change is seen for a peak shift or formation of new lithium environments. The sharp peaks at 0 ppm observed for the cycled materials are due to presence of diamagnetic lithium environments within the electrolyte and suggest electrolyte decomposition. The irreversible structural changes and source of the lithium loss after 200 cycles was studied with relithiation of the aged cell. Comparison of the NMR data, from the relithiated sample with those from the sample after activation, suggest that almost all of the lithiums lost during aging are returned back to the new structure formed after activation. However, the structural changes after activation are irreversible.

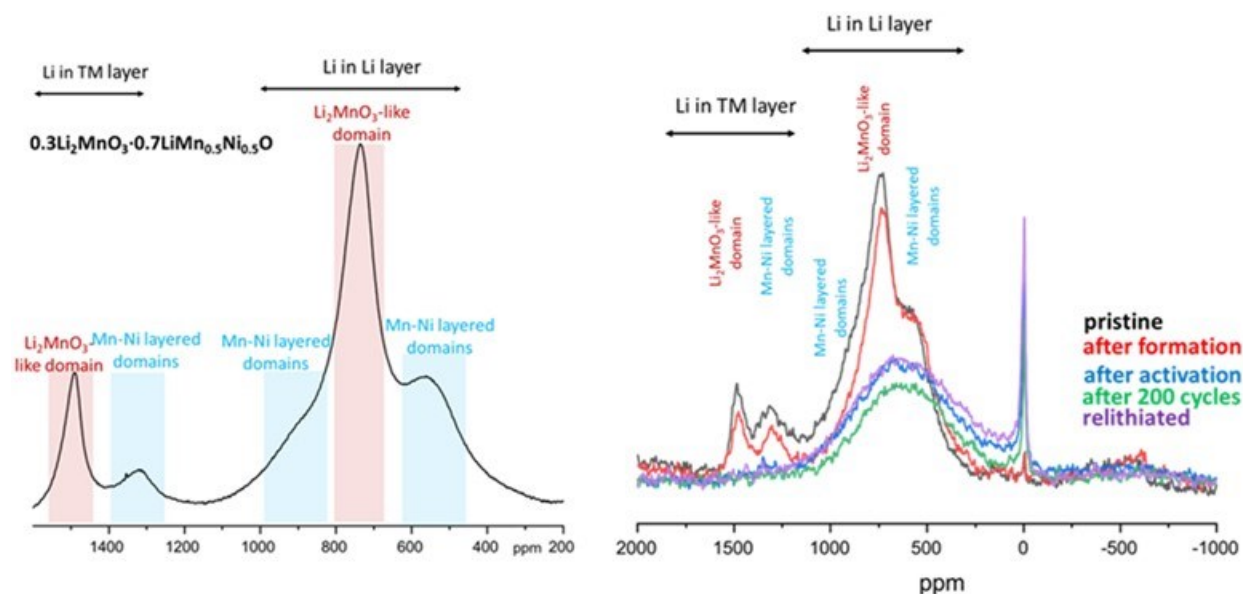


Figure VIII.1.42  $^6\text{Li}$  solid state NMR data for pristine powder (left panel) and mass normalized comparison of pristine electrode and cycled samples (right panel).

#### Thermal Stability of LMR-NM Oxides, Y. Qin et al., ANL

We used Differential Scanning Calorimetry (DSC) to examine thermal stability of the LMR-NM oxide ( $0.3\text{Li}_2\text{MnO}_3 \cdot 0.7\text{LiMn}_{0.5}\text{Ni}_{0.5}\text{O}_2$ ). Note that to obtain full capacity, the LMR-NM electrode needs to be activated by charging it to a high cut-off voltage (4.7 V vs.  $\text{Li}/\text{Li}^+$  in this study). In this work, we show how the activation process affects thermal stability of the material.

We prepared LMR-NM/Li (half) cells containing the Gen 2 + 1 wt% LiDFOB electrolyte and cycled them using the protocol shown in Figure VIII.1.43. Note that the cells first undergo 3 “wetting” cycles between 2.5–4.4 V before being cycled in the 2.5–4.7 V range at C/20 rate. Figure VIII.1.43 shows the activation plateau in the cycle 4 charge profile: the samples obtained for DSC studies from this cycle are labeled 4.4b (just before activation) and 4.7b (just after activation). We also examined samples from cycle 6: these are labeled 4.4a and 4.7a in Figure VIII.1.43. For the measurements, electrode coatings were scraped off the current collector; studies were conducted with and without the addition of fresh electrolyte.

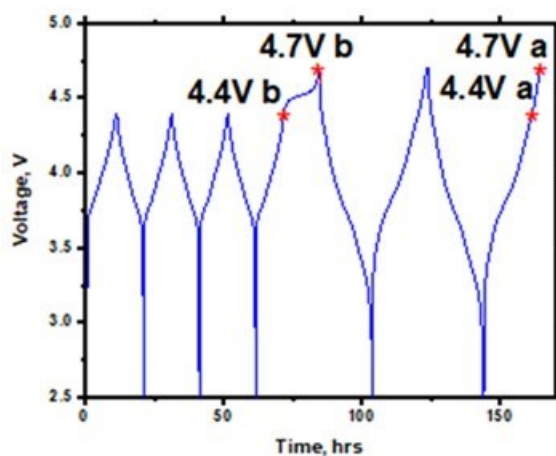


Figure VIII.1.43 Voltage vs. time profile showing locations at which LMR-NM samples were collected for DSC



As is well known, the nonaqueous electrolytes are the major contributor to thermal runaway of LiBs due to their chemical reaction with delithiated cathodes. In the presence of electrolyte, not only does thermal behavior of the delithiated cathode become complicated, but the heat generated also increases by an order of magnitude. To preclude the electrolyte effect, the DSC studies were first carried out without addition of fresh electrolyte (Figure VIII.1.44). A small heat bump before 200 °C, highlighted with a blue circle, seen for all the samples can be assigned to CEI decomposition: note that CEI (cathode electrolyte interface) refers to electrolyte decomposition products on the cathode. In addition, a major heat peak is seen between 220 °C and 300 °C regardless of the final voltage: this peak could be from a phase change in the oxide, possibly a layered to spinel structure transformation. The samples charged to 4.4V show similar peak locations (Figure VIII.1.44a) and heat flow values (Table VIII.1.1), regardless of their activation state. However, at 4.7 V (Figure VIII.1.44b), the major heat peak shifts from 250 °C (4.7V b, Cycle 4) to 270 °C (4.7V a, Cycle 6). Table VIII.1.1 shows that less heat is generated at 4.7V a than 4.7V b. That is the sample is more thermally unstable immediately after activation than in later cycles.

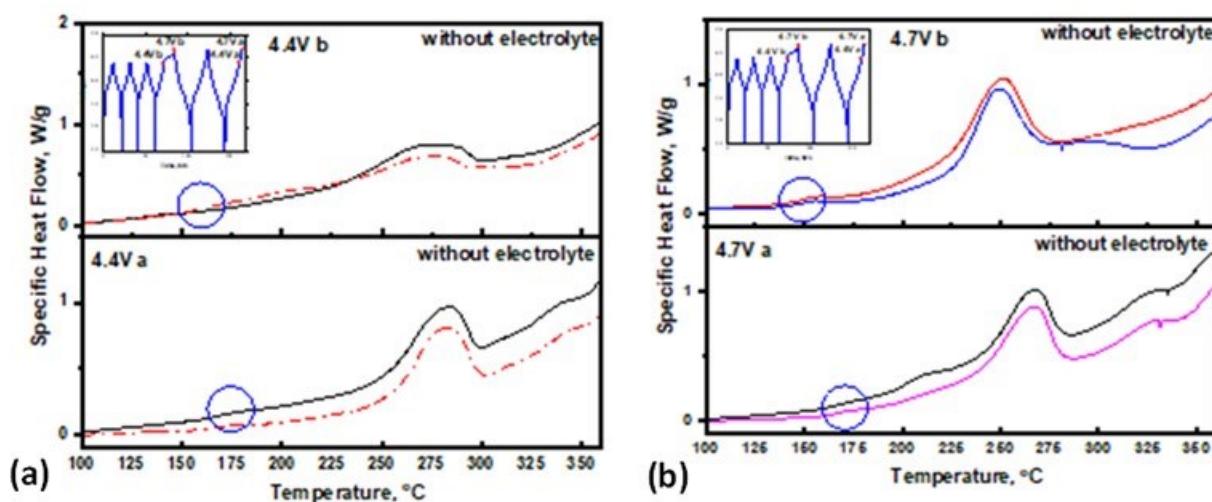


Figure VIII.1.44 DSC profiles of delithiated LMR-NM during thermal ramping from 50°C to 385°C at a scan rate of 5°C/min when charged to 4.4V (a) and 4.7V (b) before and after activation. Data from two samples are shown in each plot.

Figure VIII.1.45 shows DSC plots for the delithiated cathode with addition of fresh electrolyte. When charged to 4.4 V (Figure VIII.1.45a), the samples after activation (4.4V a) exhibit more heat peaks before 275 °C than the ones before activation (4.4V b). The after-activation samples also generate more heat (~1600 J/g) than the ones before activation (~1100 J/g); see Table VIII.1.1. This implies that the material structure after activation reacts more rigorously with the electrolyte. The difference is less dramatic for samples charged to 4.7V (Figure VIII.1.45b). The heat signatures are spread out between 150 °C and 275 °C for both 4.7V b and 4.7V a. Table VIII.1.1 shows that the 4.7a samples generate more heat and the major heat is at lower temperatures, indicating that the LMR-NM samples may become more thermally unstable with cycling; further studies are needed to confirm this observation.

Table VIII.1.1 Heat Generated during Temperature Ramping between 120°C to 350°C.

	Final Voltage b: Cycle 4 a: Cycle 6	Specific Heat J/g
Without Electrolyte	4.4V b	161.53 ± 8.02
	4.4V a	152.92 ± 14.22
	4.7V b	293.39 ± 48.99
	4.7V a	173.95 ± 17.77
With Electrolyte	4.4V b	1104.90 ± 18.44
	4.4V a	1616.81 ± 89.0
	4.7V b	1555.11 ± 72.57
	4.7V a	1794.87 ± 62.44

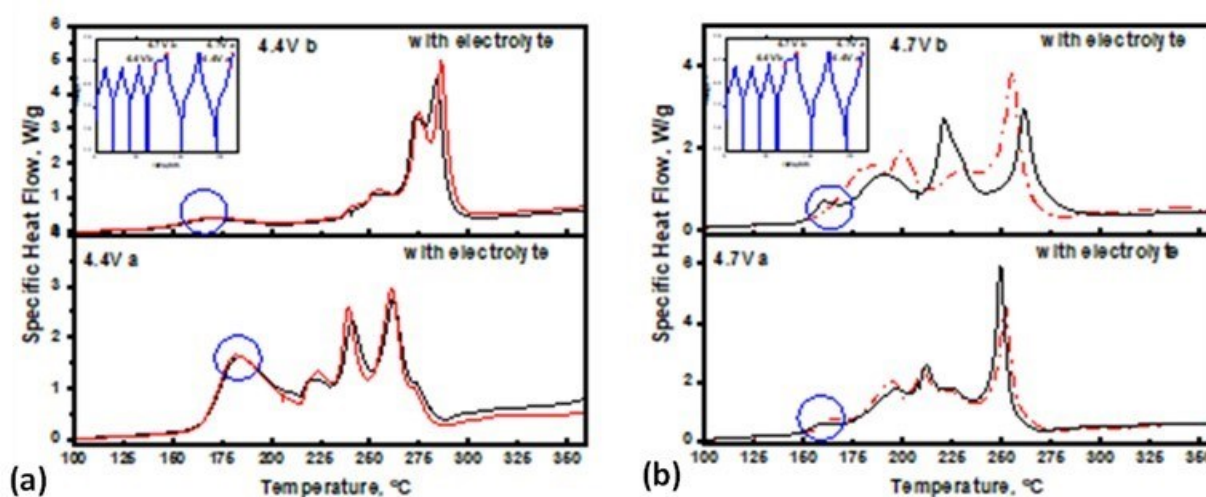


Figure VIII.1.45 DSC profiles of delithiated LMR-NM during thermal ramping from 50°C to 385°C at a scan rate of 5°C/min when charged to 4.4V (a) and 4.7V (b) before and after activation with addition of fresh electrolyte.

#### Microstructural Insights into Performance Loss of High-Voltage Spinel Cathodes for Lithium-Ion Batteries: Chongmin Wang and Peng Zuo, PNNL

Spinel-structured  $\text{LiNi}_x\text{Mn}_{2-x}\text{O}_4$  (LNMO), with low-cost earth-abundant constituents, is a promising high-voltage cathode material for lithium-ion batteries. Extensive electrochemical investigations have been conducted on these materials, in which the capacity fade has been identified to be likely associated with a range of factors. However, few studies have explored correlations between their electrochemical performance loss and associated changes in microstructure. Here, down to the atomic scale, the structural evolution of these materials is investigated upon the progressive cycling of lithium-ion cells up to 200 cycles. Three major structural degradations have been identified in the cycled LNMO cathodes, namely, transgranular cracking, secondary phase formation and void formation.

Transgranular cracking is revealed to be a key feature during cycling, and this cracking is initiated at the particle surface. Figure VIII.1.46 shows different parts of a transgranular crack, including (a) the crack open end at the primary particle surface, (b) the middle part of the crack, and (c) the crack tip. Further investigations by STEM-energy-dispersive X-ray spectroscopy (STEM-EDS) probe phases composed of electrolyte constituents F and P inside the cracked areas, indicating the penetration of electrolytes along the crack path,

thereby increasing particle exposure to the electrolyte. The transgranular cracking, along with the emergence of local lattice distortion, becomes more evident with extended cycling.

The lattice structure on the crack surface shows spatial variances, featuring a top layer of rock-salt, a sublayer of a  $\text{Mn}_3\text{O}_4$ -like arrangement, and then a mixed-cation region adjacent to the bulk lattice. As compared to the spinel structure near the crack tip in Figure VIII.1.46c, the secondary phases of rock-salt and  $\text{Mn}_3\text{O}_4$ -like can be clearly identified from the different atomic arrangements as revealed by the measured STEM- high-angle annular dark-field (STEM-HAADF) image intensities in Figure VIII.1.46a and Figure VIII.1.46b. These secondary phases are directly correlated with the LNMO performance loss upon cycling because they are less electrochemically active and can hinder  $\text{Li}^+$  ion transport. Similar secondary phases are also found at primary particle surfaces, accompanied by the formation of fluorine and phosphorous containing CEI films as revealed by STEM-EDS measurements.

Void formation through vacancy condensation of oxygens and metal cations is another key structural degradation found in the cycled samples. Such void formation can potentially degrade the structures by introducing lattice strain, cation disordering and lower Li stabilization. Eventually, all these structural effects are correlated with the LNMO performance loss, for example, lower discharge capacity and poor rate performance. All these features, transgranular cracking, secondary phase formation and void formation collectively contribute to performance degradation of the battery cells during electrochemical cycling.

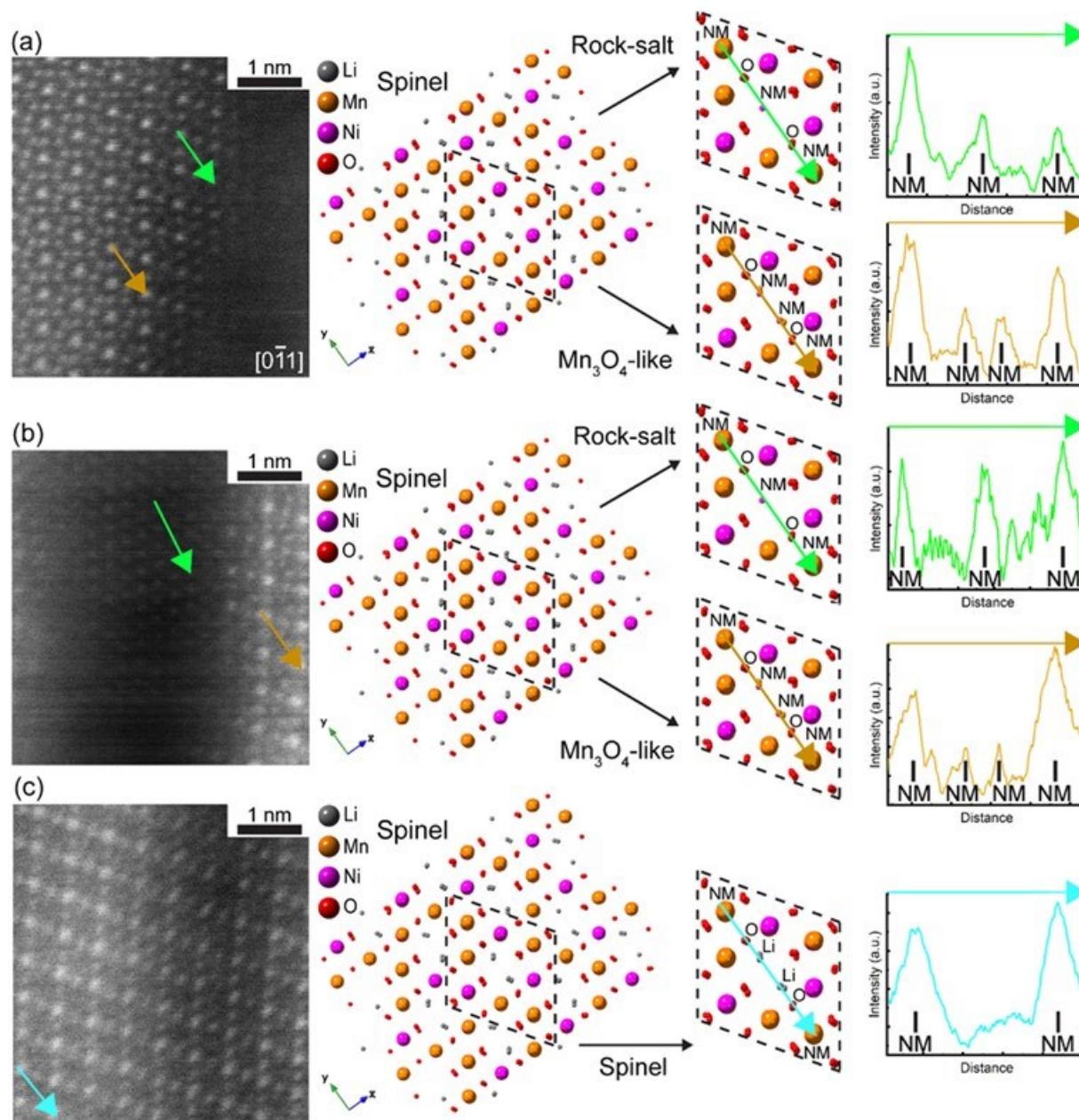
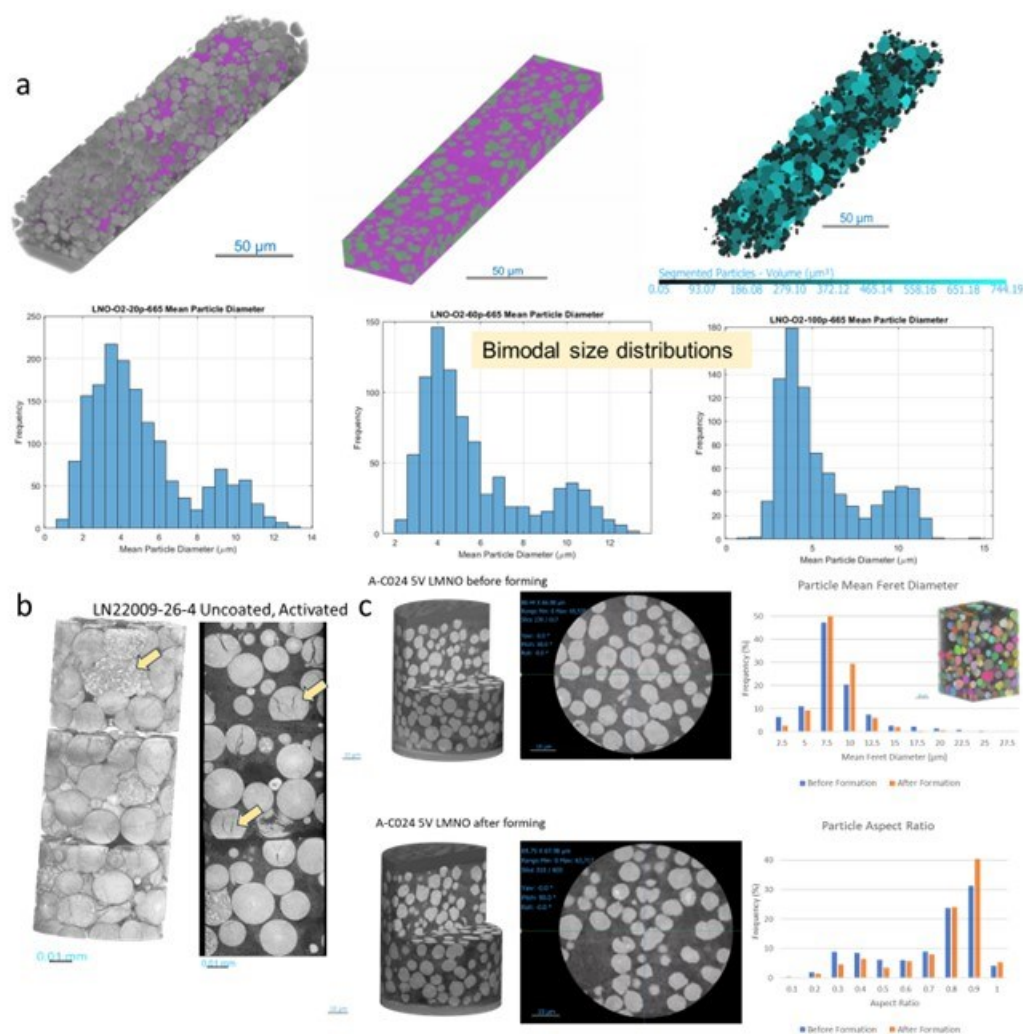


Figure VIII.1.46 Three major structural degradations, namely, transgranular cracking, secondary phase formation and void formation, are identified in the cycled LNMO cathodes. High magnification STEM-HAADF images show different parts of a transgranular crack, (a) primary particle surface where the crack ends, (b) middle part of the crack and (c) crack tip. The spinel structure in (b) and (c) is oriented in the same direction as the zone axis indicated in (a). The STEM-HAADF image intensities plotted in the right-most column, are measured along arrows in the respective images. The structural models in the middle panels are orientated in the same direction as the images to illustrate the actual atomic arrangements.

#### X-Ray Nano-CT Images of Oxide Cathodes, NREL

X-ray nano-CT was applied to LMR-NM, LiNiO<sub>2</sub> (LNO), and high-voltage LNMO spinel electrodes as shown in Figure IX.4.12 below. The LNO oxides were synthesized under different concentrations of oxygen during the sintering step (20%, 60%, and 100%) to explore role of oxygen on particle morphological properties. X-ray nano-CT provided insight into the full particle morphology but not the sub-particle grain architecture. The particle size distributions (Figure VIII.1.47a) were shown to be bimodal. The mean diameter and mean volume

of particles are provided in the Table VIII.1.2 below and show that the mean volume of particles increases with increasing concentration of oxygen. The next step for this work is to apply Electron Backscatter Diffraction (EBSD) to quantify sub-particle grain morphology that nano-CT cannot resolve.



**Figure VIII.1.47 (a) BoL morphological quantification for LNO electrodes sintered under varying concentrations of oxygen (20%, 60%, 100%) showing a consistent bi-modal size distribution. (b) CT reconstructions of multiple stacked samples of LMR-NM electrodes awaiting further image-based quantification. (c) High-voltage LMNO electrode showing slight irreversible expansion of particles following initial formation.**

LMR-NM electrodes were imaged and are shown in Figure VIII.1.47b. Around 15% of LMR electrode particles showed signs of Ni segregation. There was also clear evidence of circumferential cracking during calendaring and radial-cracking in particles following the formation and activation steps. Ongoing work is focusing on quantitatively describing the particle defects and imaging electrodes with different cycle histories.

High voltage LMNO spinel electrode material was imaged before and after formation (Figure VIII.1.47c). No evidence of particle cracking during calendaring or formation was observed. The particles displayed a highly homogeneous and narrow particle size distribution. Some particles showed highly attenuating Ni-rich cores. Quantifying the particle size distribution before and after formation showed a small irreversible increase in particle volume. Ongoing work is focusing on cycling the LMNO electrodes and quantifying the change in morphology for cathodes with different cycling histories.

**Table VIII.1.2 Table Showing the Changes in Mean Porosity, Particle Diameter, and Particle Volume for LNO Electrodes Sintered under 20%, 60%, and 100% Oxygen.**

Sample	Porosity	Mean Dia ( $\mu\text{m}$ )	Std. dev.	Mean Vol ( $\mu\text{m}^3$ )	Std. dev	Sample Size
LNO-02-20p-665	0.63	5.08	2.57	102.2	156.3	1615
LNO-02-60p-665	0.54	5.74	2.67	128.8	189.5	858
LNO-02-100p-665	0.59	5.63	2.63	134.9	187.9	870

### **Electron Microscopy Studies of Oxide Cathodes, NREL**

The goal of this work is to identify ion transport pathways in relation to nanoscale strain gradients that can cause cathode particle cracking and performance loss. 4D (2D pixel array image of a sample region to produce a 2D diffraction pattern at each pixel) scanning transmission electron microscopy (4D-STEM) was investigated for nanoscale strain mapping of LMR-NM electrodes. Overall, we are working towards comparing different grain boundaries at different lithiation states to find trends in the mechanical degradation mechanism based on grain boundary disorientation. A team member traveled to BES Molecular Foundry's National Center for Electron Microscopy to learn the 4D-STEM analysis routines and collect datasets from their microscope for an initial dataset. The completion of the Spectra 200 STEM installation at NREL in FY24Q1 will enable this data to be acquired at NREL in the future. Initial mapping of uncycled cathode particles in the electrode was conducted in the SEM with Raman spectroscopy to target particles with more strain (Figure VIII.1.48a). This was followed by EBSD mapping of the particle to identify a disorientation grain boundary (Figure VIII.1.48b). 4DSTEM results indicate that there is compressive strain at the grain boundary along with fluctuations in the strain value across the grain boundary. This work will continue to gain more information on the correlation between lithiation state and grain boundaries where cracks are forming. This nanoscale strain mapping is building NREL's multi-scale analysis capabilities to correlate to the scanning probe and nano-CT capabilities.

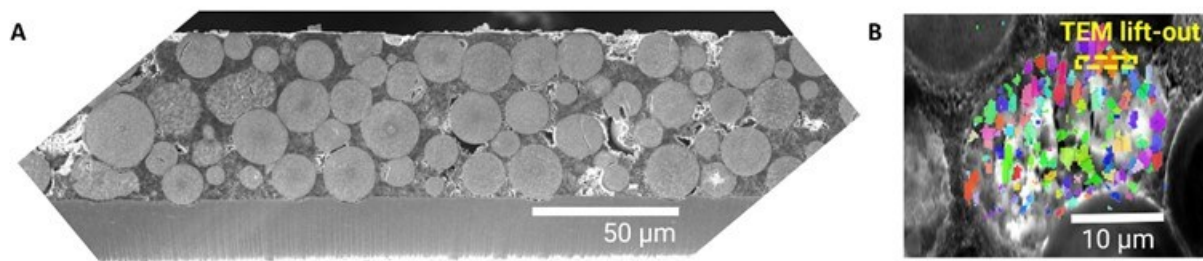


**Figure VIII.1.48 (a) Ion polished pristine LMR-NM electrode cross-section in scanning electron microscope. (b) EBSD of cross-sectioned particle shows two grains of similar orientation that can be mapped for strain along the grain boundary; a transmission electron microscopy sample was lifted out from this grain boundary.**

### **Vibrational Spectroscopy Data from LMR-NM//Graphite Cells, NREL**

NREL has developed a custom in situ ATR-FTIR spectro-electrochemical cell to incorporate a 3-electrode configuration. Using a lithium metal reference, the cell was used to test an LMR//graphite full cell, with a CC-CV electrochemical protocol. The voltage profile with individual cathode and anode potentials (vs Li ref.) and the overall cell voltage are shown in Figure VIII.1.49a. The cell was cycled for 3 cycles between 2.5 to 4.3 V at a C/5 rate, then an activation cycle from 2.5 to 4.6 V at C/10. This new 3-electrode configuration enables correlation of surface chemistry information (from FTIR) to electrochemical performance (from cell cycling) by monitoring impedance and voltage of both anode and cathode. The LMR cathode exhibits an irreversible "activation" transition when first treated between 4.3-4.6 V. In situ ATR-FTIR spectra are used to track the electrolyte solvent solvation of the  $\text{Li}^+$  ions near the surface of the cathode, which normally tracks with the

electrode behavior (differential capacity). As seen in Figure VIII.1.49b, the solution structure, represented by the ethylene carbonate (EC) coordinated to a  $\text{Li}^+$  ion (solvation shell) absorption and the pure EC (free) solvent absorption, shows significant solvent displacement during the transition when the cell voltage is  $>4.3$  V. In subsequent cycles, FTIR reveals redox-dependent solution structure of relative solvent/ $\text{Li}$ -ion solvation as expected. The disruption of the signal during the first high-voltage treatment is suspected to be due to gas evolution from the cathode or oxidation gas products from the electrolyte. This is a subject of on-going study.

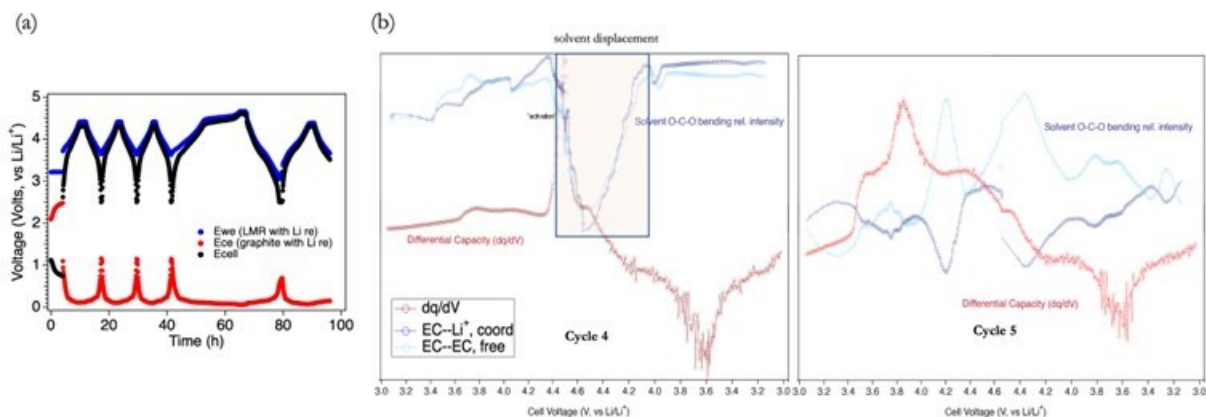


**Figure VIII.1.49 (a) Voltage profiles of anode, cathode, and total cell voltages during the first 5 cycles using the custom ATR-FTIR spectro-electrochemical cell. (b)  $dq/dV$  and FTIR absorption intensities for EC-Li (coord.) and EC (free) during cycles 4 and 5.**

$\text{Mn}^{2+}$  dissolution has been shown to occur as the LMR-NM cathode is brought to high voltage,  $>4.3$  V vs.  $\text{Li/Li}^+$ . The  $\text{Mn}^{2+}$  ions form solvated species in the  $\text{LiPF}_6$ -carbonate electrolyte, and eventually crossover through the separator and deposit on the surface of the anode and subsequently participate in adverse SEI reactions that degrade cell performance. Figure VIII.1.50 shows ex-situ ATR-FTIR spectra of a Gen 2 (1.2M  $\text{LiPF}_6$  in 3:7 EC:EMC) electrolyte compared to the same electrolyte with addition of 1%  $\text{Mn}(\text{PF}_6)_2$ . Figure VIII.1.50a and Figure VIII.1.50b show the energy region between  $1850$  and  $1600$   $\text{cm}^{-1}$ , where EC absorption occurs. It is observed that the addition of  $\text{Mn}^{2+}$  salt results in a lower-energy shift (red shift) of the EC solvent that participates in a solvation shell of cation ( $\text{Li}^+$  and  $\text{Mn}^{2+}$ ) indicating stronger solvation effects in the presence of manganese ion. Similarly, Figure VIII.1.50c and Figure VIII.1.50d show how the  $\text{PF}_6^-$  anion is affected by the addition of divalent  $\text{Mn}^{2+}$  salt, and there is also a red-shift assigned to the  $\text{PF}_6^-$  vibrational stretching modes around  $555$   $\text{cm}^{-1}$ . Interestingly, there is also a new peak that appears around  $500$   $\text{cm}^{-1}$  in the electrolyte containing  $\text{Mn}^{2+}$  salt. Moving into FY24, understanding Mn-ion dissolution will be one main focus of our vibrational spectroscopy investigations. FTIR will be used to detect the formation of Mn-ion species near the graphite anode surface using the in-situ spectro-electrochemical cell.

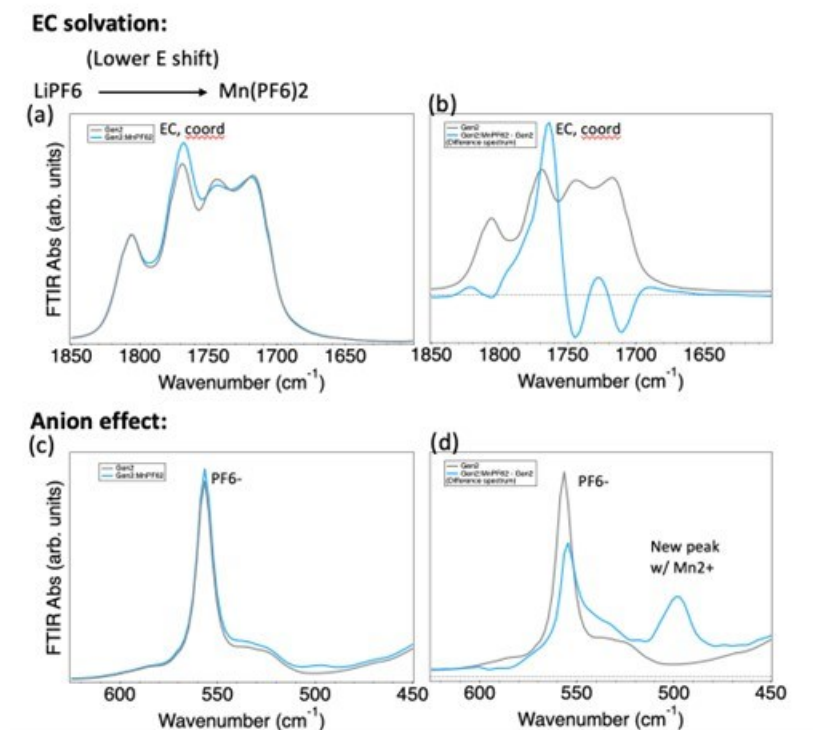


Figure VIII.1.50 (a) FTIR spectra of Gen 2 electrolyte (black) and of Gen 2 + 1 wt% Mn(PF<sub>6</sub>)<sub>2</sub> (blue)

## Conclusions

### Design, Synthesis, and Characterization

The *EaCAM* cathode team has focused efforts this FY on a fundamental understanding of the limiting factors associated with practical performance of Co-free LMR-NM electrode materials. Cost and energy targets, in the range between LFP (low end) and NMC-622 (high end) serve as a benchmark for materials evaluation. BatPac modeling has shown that the baseline LMR-NM can achieve these targets. Importantly, BatPac and electrochemical modeling, combined with experimental data, has identified and prioritized R&D efforts for FY24 and advancement in critical metrics are expected.

The cathode team has also explored the strategy of modifying the pristine LMR-NM, via targeted substitutions, with the intent of improving the performance of activated electrodes. Results from this FY clearly show that this strategy has merit. Data on Sn<sup>4+</sup> substitution, primarily into Li/Mn-rich domains, reveal the possibility of tailoring particle morphologies and low SOC ASI. Studies along these lines will be continued in FY24.

In addition to LMR-NM studies, the cathode team is continuously working to develop novel, earth-abundant cathode materials. The recent discovery of a new class of Mn-rich, lithiated-spinel cathodes by this team represents a new strategy for the design of next-generation cathodes. Detailed studies show that these predominantly lithiated-spinel materials can cycle high capacities (~250 mAh/g) while maintaining a stable structure. Furthermore, the compositional space available, coupled with synthesis and processing parameters, represents a significant opportunity to further improve the performance of this class of cathodes. This work will be undertaken in FY24.

### Atomistic Modeling

The local domain structures of a baseline LMR-NM were constructed via Density Functional Theory (DFT). The influence of various domain structures on the low SOC impedance of LMR-NM was elucidated. The formation of O-O dimers at high SOC is faster in 3D ordered ribbon model compared to the staggered model of (Li<sub>1.17</sub>Ni<sub>0.25</sub>Mn<sub>0.58</sub>O<sub>2</sub>). The total number of oxygen dimers formed because of activation is greater for the



ribbon model than the staggered ribbon model. Oxygen dimers are confined to the  $\text{Li}_2\text{MnO}_3$  region of the ribbon model (resulting in more localized distortions). The mechanism of formation of O-O dimers at high SOC's depends on the 3D structure of the 60%- $\text{LiMn}_{0.5}\text{Ni}_{0.5}$ /40%- $\text{Li}_2\text{MnO}_3$  ( $\text{Li}_{1.17}\text{Ni}_{0.25}\text{Mn}_{0.58}\text{O}_2$ ) material. Theoretically predicted NMR shifts improve the understanding of features in the experimental spectrum, showing contributions from interfaces and disordered domains.

Using well-defined single crystals as model systems, we carried out detailed characterization to understand the effect of fluorination and EA-cation doping on LMR properties. An in situ fluorination method was developed which can produce F-LNMO single-crystal samples with no apparent impurities. Our studies reveal particle-level  $\text{Mn}^{3+}$  concentration gradient from the surface to the bulk of F-LNMO crystals, in association with the formation of a Ni-rich  $\text{LiNi}_x\text{Mn}_{2-x}\text{O}_{4-y}\text{F}_y$  ( $x > 0.5$ ) spinel phase on the surface and a “spinel-layered” coherent structure in the bulk where domains of a  $\text{LiNi}_{0.5}\text{Mn}_{1.5}\text{O}_4$  high-voltage spinel phase are integrated into the native layered framework. Single-crystal model samples with a variety of EA-cation dopants and morphologies were also synthesized. Structural and morphological changes due to doping were found to be negligible. Particle-level elemental distribution analysis reveals facet-dependent Ni segregation in the (102) facets, likely a result of Ni diffusion from the bulk to the surface along the Li slab and the formation of Li-Ni anti-site defects. Our study provides fundamental understanding of the fluorination and cation doping effects on LMR and key insights for future development of high-energy Mn-based cathodes.

### **Surface Stabilization**

- TMSB is good in improving power density.
- MS and LiDFOB are good in improving energy density.
- TMSPi is the best single additive considering both the power and energy densities.
- For LDF, it is not prominent when used as a single additive, but when it is applied in dual additives, 0.1M LDF + 0.25wt% tVCBO gives the best energy density and 0.1M LDF + 1wt% LiDFOB gives the second highest power density. And for dual additives, the applied amount can also play an important role in the cycling performance of LMR-NM
- In consideration of both energy and power densities, 2wt% TMSPi + 1wt% LiDFOB is the best electrolyte formulation
- Improved cycling performance of LMR-NM was achieved with fluorinated solvents FEC/FEMC
- FEC/FEMC successfully suppressed transition metals dissolution and deposition.
- Mn was found to be more likely to deposit on the Gr anode than Ni.

### **Analysis and Modeling**

- Full cells containing the LMR-NM positive electrode and either graphite- or LTO -based negative electrode show capacity fade on accelerated aging, which is greater for the graphite cell. Impedance rise for both cell chemistries is very small. The LMR-NM electrode shows voltage fade for both types of cells; this fade is significant only during the early cycles and very small during later cycles.
- Calendar-aging studies on LMR-NM//Gr cells showed higher currents during voltage hold at 55 °C than at 30 °C indicating greater parasitic side-reactions at the higher temperature.
- Solid state NMR data from LMR-NM oxides show loss of  $\text{Li}_2\text{MnO}_3$ -like ordering after activation. The ordering is not recovered even after complete relithiation of the oxide, indicating a permanent structural change after activation.
- DSC studies on LMR-NM oxides show that thermal stability of the oxides decrease after activation. The specific heat generated increases by an order of magnitude in presence of additional electrolyte, indicating significant reactions between the delithiated oxide and electrolyte.
- Analytical electron microscopy studies on cycled 5V spinel material show transgranular cracking, secondary phase formation and void formation, all of which contribute to performance degradation of the battery cells during electrochemical cycling.
- Synthesis conditions greatly influence particle morphological properties such as by increasing the mean particle volume for LNO particles for higher concentrations of oxygen during sintering, and Ni-segregation in particles and particle cracking in LMR electrodes during synthesis and calendaring.

- In-situ ATR-FTIR studies show that the presence of  $Mn^{2+}$  in the electrolyte results in a red shift of the EC solvent that participates in a cation ( $Li^+$  and  $Mn^{2+}$ ) solvation shell, indicating stronger solvation effects. The  $PF_6^-$  anion vibrational stretching modes also show a red-shift, indicating that its solvation is affected by  $Mn^{2+}$  presence.

## Key Publications

### Design, Synthesis, and Characterization

1. Gutierrez, D. Tewari, J. Chen, V. Srinivasan, Mahalingam Balasubramanian, J. R. Croy, *Earth-Abundant, Mn-Rich Cathodes for Vehicle Applications and Beyond: Overview of Critical Barriers*, *J. Electrochem. Soc.* **170** 030509 (2023).
2. Kyojin Ku, J. Han, L. Li, J. Gim, J. Park, B. Shi, Y. Liang, A. Stark, C. Wang, J.R. Croy, M.M. Thackeray, J. Libera, and E. Lee, *LT-LiNi<sub>1/3</sub>Mn<sub>1/3</sub>Co<sub>1/3</sub>O<sub>2</sub>: A partially-disordered, composite rock salt cathode prepared by flame spray pyrolysis for Li-ion batteries*, *J. Electrochem. Soc.* **170**, 050511 (2023).
3. Tornheim, D. C. O'Hanlon, A. Vu, J. Gim, D. P. Abraham, and J. R. Croy, *Evaluation of Cathode Materials with Lithium-Metal Anodes: Baseline Performance and Protocol Standardization of Coin Cells*, *J. Electrochem. Soc.* **170** 010507 (2023).

### Atomistic Modeling

1. F. Wang, P. Zuo, Z. Xue, Y. Liu, C. Wang and G. Chen, "Fluorination Effect on Lithium- and Manganese-Rich Layered Oxide Cathodes," under review (2023).

### Surface Stabilization

1. Patent: Additives for lithium batteries and methods, Chen Liao, Ilya A Shkrob, Daniel Abraham, Zhengcheng Zhang, US11695156B2, Patent issued July 4, 2023.
2. Patent: Additives for high voltage lithium-ion batteries, Cameron Peebles, Ilya A. Shkrob, Chen Liao, Daniel Abraham, Hakim Iddir, Juan Garcia, US11757131B2 Patent granted 2023-09-12
3. Understanding and Mitigating the Dissolution and Delamination Issues Encountered with High-Voltage  $LiNi_{0.5}Mn_{1.5}O_4$ , Bingning Wang, Pavan Badami, Stephen E. Trask, Daniel Abraham, Yang Qin, Zhenzhen Yang, Xianyang Wu, Andrew Jansen, Chen Liao, *Batteries* 2023, 9(9), 435.
4. Unveiling the parasitic-reaction-driven surface reconstruction in Ni-rich cathode and the electrochemical role of  $Li_2CO_3$ , Jiyu Cai, Zhenzhen Yang, Xinwei Zhou, Bingning Wang, Ana Suzana, Jianming Bai, Chen Liao, Yuzi Liu, Yanbin Chen, Shunlin Song, Xuequan Zhang, Li Wang, Xiangming He, Xiangbo Meng, Niloofar Karami, Baasit Ali Shaik Sulaiman, Natasha A Chernova, Shailesh Upreti, Brad Prevel, Feng Wang, Zonghai Chen, *Journal of Energy Chemistry*, 85, 2023, 126-136.

### Analysis and Modeling

- Peng Zuo, Pavan Badami, Stephen E. Trask, Daniel P. Abraham, and Chongmin Wang, "Microstructural Insights into Performance Loss of High-Voltage Spinel Cathodes for Lithium-ion Batteries", *Small*, 2023, 2306807.
- C. Wang, Invited Presentation, Cryo-TEM for rechargeable battery: does cooling solve the beam sensitive problem we face? 2023 MRS Spring Meeting, San Francisco, April 10-14, 2023.
- C. Wang, Invited Presentation, *In-Situ and Ex-Situ S/TEM Probing of Interfacial Process in Rechargeable Batteries*, Workshop on Electrochemical Interfaces: Advancing the integration between multiscale modeling and multimodal characterization, Lawrence Livermore National Laboratory, Livermore, September 28-29, 2023.

## References

### Design, Synthesis, and Characterization

1. National Blueprint For Lithium Batteries, (2021), Federal Consortium of Advanced Batteries <https://energy.gov/eere/vehicles/articles/national-blueprint-lithium-bat-teries>

2. Our Common Future, Report of the World Commission on Environment and Development, United Nations (1987), <https://sustainabledevelopment.un.org/con-tent/documents/5987our-common-future.pdf>
3. J. Li, N. Sharma, Z. Jiang, Y. Yang, F. Monaco, Z. Xu, D. Hou, D. Ratner, P. Pianetta, P. Cloetens, F. Lin, K. Zhao, and Y. Liu, *Science*, **376** 517 (2022).
4. A. Gutierrez, D. Tewari, J. Chen, V. Srinivasan, Mahalingam Balasubramanian, J. R. Croy, *Earth-Abundant, Mn-Rich Cathodes for Vehicle Applications and Beyond: Overview of Critical Barriers*, *J. Electrochem. Soc.* **170** 030509 (2023).
5. A. Gutierrez, J. T. Kirner, M. T. Saray, M. Avdeev, L. Geng, R. S. Yassar, W. Lu, and J. Croy, *J. Electrochem. Soc.*, **169**, 020574 (2022).
6. J. Chen, A. Gutierrez, M. T. Saray, R. S. Yassar, M. Balasubramanian, Y. Wang, and J. R. Croy, *J. Electrochem. Soc.*, **168**, 080506 (2021).
7. J. R. Croy, M. Balasubramanian, K. G. Gallagher, and A. K. Burrell, *Acc. Chem. Res.*, **48**, 2813 (2015).
8. BatPaC – Kevin W. Knehr, Joseph J. Kubal, Paul A. Nelson, and Shabbir Ahmed, “Battery Performance and Cost Modeling for Electric-Drive Vehicles: A Manual for BatPaC v5.0”, ANL/CSE-22/1, July 2022, doi: 10.2172/1877590 <https://www.anl.gov/cse/batpac-model-software>.

### Atomistic Modeling

1. M.M. Thackeray, A. de Kock, M.H. Rosouw, D. Liles, R. Bittihn, and D. Hodge, *J. Electrochem. Soc.* **139**, 363 (1992).
2. A. R. Armstrong, N. Dupre, A.J. Paterson, C. P. Grey, and P.G. Bruce, *Chem. Mater.* **16**, 3106 (2004).
3. J.P. Perdew, A. Ruzsinszky, G.I. Csonka, O.A. Vydrov, G.E. Scuseria, L.A. Constantin, X. Zhou, and K. Burke, *Phys. Rev. Lett.* **100** 136406 (2008).
4. J.W. Furness, A.D. Kaplan, J. Ning, J.P. Perdew, and J. Sun, *J. Phys. Chem. Lett.* **11**, 8208 (2020).
5. L. Wang, T. Maxisch, and G. Ceder, *Phys. Rev. B* **73**, 195107 (2006).
6. S. Swathilakshmi, R. Devi, and G.S. Gautam, Arxiv, doi:10.48550/arkiv.2301.00535, (2023).
7. M.K. Horton, J.H. Montoya, M. Liu, and K.A. Persson, *Npj Comput. Mater.* **5**, 64 (2019).

### Surface Stabilization

1. I. A. Shkrob, B. Han, R. Sahore, A. P. Tornheim, L. Zhang, D. P. Abraham, C. Liao, *Facile in Situ Syntheses of Cathode Protective Electrolyte Additives for High Energy Density Li-Ion Cells*, *Chemistry of Materials*, 2019, 31(7), 2459-2468; C. Peebles, J. Garcia, A. P. Tornheim, R. Sahore, J. Bareño, C. Liao, *Chemical “Pickling” of Phosphite Additives Mitigates Impedance Rise in Li Ion Batteries et al. J. Phys. Chem. C* 2018, 122(18), 9811-9824
2. Zhengcheng Zhang, Libo Hu, Huiming Wu, Wei Weng, Meiten Koh, Paul C. Redfern, Larry A. Curtiss, Khalil Amine, Fluorinated electrolytes for 5 V lithium-ion battery chemistry, *Energy Environ. Sci.*, 2013,6, 1806-1810
3. J. Yang, I. Shkrob, Q. Liu, N. L. Dietz Rago, Y. Liu, K. Liu, C. Liao, Structural underpinnings of cathode protection by in situ generated lithium oxyfluorophosphates, *Journal of Power Sources* 2019 (438), 227039; Chen Liao, Ilya A Shkrob, Daniel Abraham, Zhengcheng Zhang, Additives for lithium batteries and methods, Patent number, US11695156B2

### Acknowledgements

Support from the Vehicle Technologies Office of the U.S. Department of Energy, particularly from the *Earth-abundant Cathode Active Materials (EaCAM)* consortium under Tien Duong, Carine Steinway, Tina Chen, and Brian Cunningham, is gratefully acknowledged.

### Design, Synthesis, and Characterization

Contributions in this chapter are the works of Jiajun Chen, Chun Yuen Kwok, Subhadip Mallick, Boyu Shi, Yulin Lin, Maksim Sultanov, Jianguo Wen, Anh Vu, Arturo Gutierrez, Marco Rodrigues, Kevin Knehr, Joseph Kubal, Steve Trask (CAMP), Fulya Dogan, Deepti Tewari, Venkat Srinivasan, Eungje Lee, Michael M.

Thackeray, Jihyeon Gim, Guibin Zan, Yijin Liu, Will Chueh, Jason R. Croy, and Mahalingam Balasubramanian.

***Atomistic Modeling***

Contributions in this chapter are the works of Juan Garcia, Fulya Dogan, Faxing Wang, Liang Fang, Peng Zuo, Chongmin Wang, Guoying Chen and Hakim Iddir.

***Surface Stabilization***

Contributions from the CAMP (Cell Analysis, Modeling and Prototyping) Facility at Argonne National Laboratory are acknowledged.

***Analysis and Modeling***

The CAMP (Cell Analysis, Modeling and Prototyping) Facility at Argonne National Laboratory as well as team members at the various National Laboratories are acknowledged.

## VIII.2 Cation Disordered Rocksalt Materials DRX+ Consortium (LBNL, ORNL, PNNL, ANL, SLAC, UC Santa Barbara)

### Gerbrand Ceder, Principal Investigator

Lawrence Berkeley National Laboratory  
1 Cyclotron Road  
Berkeley, CA 94720  
E-mail: [gceder@berkeley.edu](mailto:gceder@berkeley.edu)

### Tien Duong, DOE Technology Development Manager

U.S. Department of Energy  
E-mail: [Tien.Duong@ee.doe.gov](mailto:Tien.Duong@ee.doe.gov)

Start Date: October 1, 2022                      End Date: September 30, 2023  
Total Project Cost (FY23): \$3,400,000    DOE share: \$3,400,000                      Non-DOE share: \$0

### Project Introduction

The projected growth of Li-ion battery (LIB) production towards multiple TWh/year will require several million tons of Co/Ni combined, which constitutes a very sizeable fraction of the annual production of these metals. Disordered rocksalt (DRX) compounds have created the opportunity to develop high-energy cathodes from earth-abundant metals. Therefore, they can be an ideal class of materials to address the resource limitations and cost considerations posed by the use of nickel and cobalt in traditional NMC cathodes. Our previous deep-dive DRX program has considerably advanced our understanding of the intrinsic challenges related to DRX materials and has developed DRX materials with significantly improved performance. In this research program, we aim to address the remaining challenges, optimize DRX-based Gen1 cathodes that maintain 750 Wh/kg at 100 mA/g for 300 cycles, and initiate the development of Gen3 partially disordered cathodes with specific energies between 800 and 1100Wh/kg, all based on Mn as a cost-effective, abundant, and safe redox-active element. The focus of the program spans from materials development to electrode fabrication optimization, including (i) electrolyte optimization by investigating additives solvent and salt modifications, (ii) inorganic and carbonaceous coatings to DRX compounds, (iii) optimization of composition and morphology of DRX cathodes, (iv) investigation of partially disordered Mn-based materials, and (v) optimization of electrode fabrication process with DRX materials. The consortium has assembled strong expertise from national labs (ORNL, PNNL, ANL, BNL, and SLAC) and universities (USB and UCSB) to tackle these challenges.

### Objectives

This project aims to develop high-energy, high-rate Ni and Co-free DRX cathode materials based on Mn as a cost-effective, earth-abundant, and safe redox-active element. Specifically, Gen1-DRX achieving 650Wh/kg at 100mA/g for at least 100 cycles will be optimized and scaled up. Gen2-DRX achieving at least 700Wh/kg at 100mA/g for 300 cycles will be developed through the application of functional coatings on Gen1, incorporation of electrolyte improvements, and further compositional and morphological refinements. Gen3-DRX with very high specific energies between 850 and 1100Wh/kg will be explored by introducing partial disorder in the structure.

### Approach

Technical approaches in this research program span from materials development to electrode fabrication optimization, including:

- (i) Develop high-voltage electrolytes specifically optimized for the DRX materials being pursued in the consortium. Investigate additives as well as solvent and salt modifications to enable more stable cycling of Gen1 and Gen2 cathodes at high voltage.
- (ii) Apply inorganic and carbonaceous coatings to DRX surface for protection and creation of electronic pathways in cathode composites with low carbon content. Develop, evaluate, and optimize an effective, scalable process of creating carbonaceous conformal coatings on DRX powder materials.
- (iii) Evaluate synthesis approaches and conditions, optimize composition and morphology of Gen1-DRX. Scale up the synthesis to produce larger quantity of materials needed in the consortium.
- (iv) Explore partially disordered Mn-based materials as high energy, high rate cathodes made with scalable synthesis methods. Investigate in detail the structure and synthesis pathways of these metastable materials, leading to materials with  $> 1000\text{Wh/kg}$ .
- (v) Optimize and improve DRX electrode fabrication by lowering the carbon content as well as optimizing particle size and morphology of electrode components. Establish optimal voltage limits and cycling protocols for DRX cathodes.

### Summary

In its first year of operation, the DRX+ consortium has been able to report multiple successes towards the adoption of earth-abundant Mn-based Disordered Rocksalt Cathodes. Synthesis scale-up through traditional solid-state processes has been achieved so that all of the consortium can work on materials from the same source, thereby ensuring compatibility of results. During the same period, alternative synthesis approaches with better control of morphology have been explored and further developed. The consortium has been transitioning to higher Mn-content materials which results in higher energy content and better cycle life. These materials undergo a slow transition to a  $\delta$  structure with improved rate capability and higher capacity. Analysis of parasitic processes in half cells is pointing at carbonate solvent breakdown and nefarious processes on the carbon additive as playing an important role in capacity loss with cycling. As a result of this finding, we have established proof of concept that using graphitic carbon on the composite cathode can show very significant improvement in cycle life, and lead to lowering of the total cathode carbon content, thereby increasing cell level energy density. Our findings also indicate formation of Li-carbonate due to solvent breakdown, and subsequent reaction of that carbonate with the  $\text{PF}_6$  salt. Improvements with LHCE electrolytes are particularly noteworthy. Specific energies up to  $800\text{Wh/kg}$  (cathode) have been achieved but need to be stabilized for more cycles. Initial safety evaluation indicates that high Mn content DRX may have extremely low heat release, hinting at potential benefits at the pack level integration.

### Results

#### Task 1: Synthesis and Scale-up

##### 1) Scale-up of solid-state synthesis.

Most DRX materials are synthesized *via* a classic solid-state synthesis method around  $700\text{-}1100^\circ\text{C}$  followed by high-energy ball milling prior to electrode fabrication. This can result in poorly controlled, inhomogeneous, non-ideal particle morphologies and distributions as well as batch-to-batch irreproducibility. To ensure a common baseline cathode material for multiple consortium tasks as well as reduce batch-to-batch reproducibility, the MERF team carried out scale-up of  $\text{Li}_{1.2}\text{Mn}_{0.6}\text{Ti}_{0.2}\text{O}_{1.8}\text{F}_{0.2}$  (LMTF2622) using conventional solid-state synthesis method.  $\text{Mn}_2\text{O}_3$ ,  $\text{TiO}_2$ ,  $\text{Li}_2\text{CO}_3$ , and  $\text{LiF}$  precursors adding up to  $\sim 200\text{g}$  were ball-milled together with Y-stabilized  $\text{ZrO}_2$  in 500 mL jars at 67 RPM using Retsch Planetary Ball Mill PM 400. Figure VIII.2.1a shows the X-ray diffraction (XRD) of ball-milled precursor material with no evidence of mechanochemical activation prior to calcination. Initially calcinations were done at 50-60g scale at  $1000^\circ\text{C}$  for 4 hours under Argon atmosphere. Figure VIII.2.1b shows XRD of the final calcined product, which visibly shows the DRX phase (Fm-3m) but also some small LiF (Fm-3m) impurity. The calcined DRX material was subsequently ball-milled at 400 RPM in an organic solvent for 4 hours without any carbon. Ball-milling resulted in a nano-sized DRX with bimodal particle size distribution (Figure VIII.2.1c). When reducing the primary particle size, the XRD pattern exhibits peak broadening as evident in Figure VIII.2.1b. This material was shared with the consortium to support other tasks.  $^{19}\text{F}$  nuclear magnetic resonance spectroscopy ( $^{19}\text{F}$ -

NMR) of the nano-sized DRX material was done at University of California, Santa Barbara (UCSB). Initial results showed very little fluorine content imbedded in the DRX structure (Figure VIII.2.2b), while the small fluorine signal represented trace amounts of LiF.

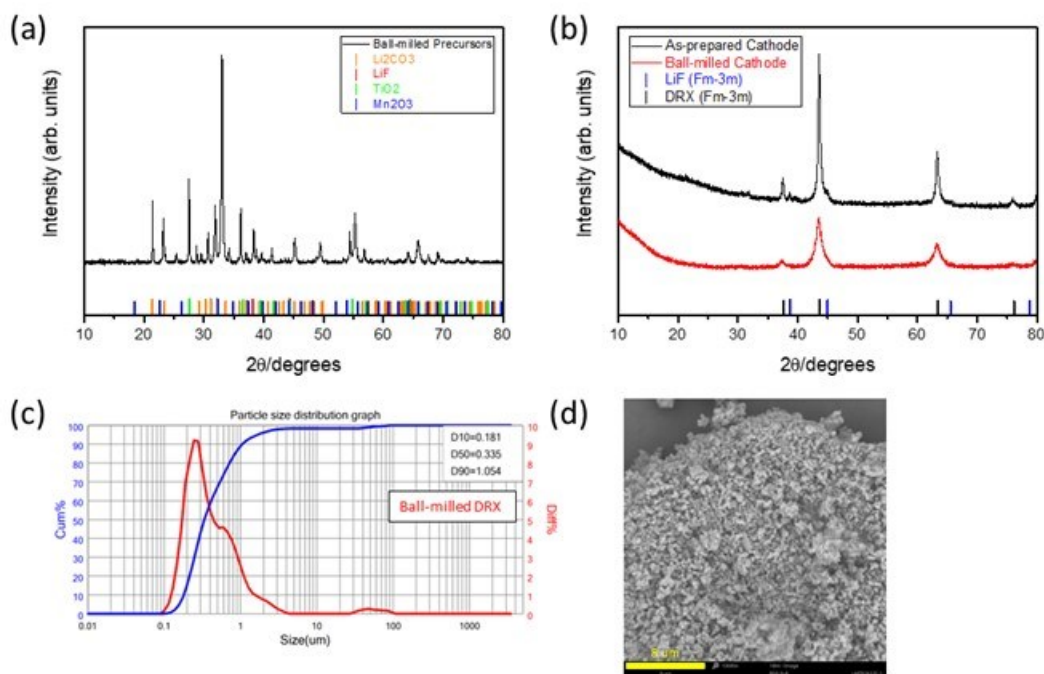


**Figure VIII.2.1** (a) XRD of ball-milled precursors, (b) as-prepared and ball-milled DRX cathode material, (c) particle size distribution and (d) SEM of ball-milled DRX cathode material.

Fluorine is notoriously challenging to incorporate into the DRX materials in solid-state synthesis. In general, higher temperature should increase fluorine solubility, but LiF becomes volatile at high temperatures. This tends to lead to an under-fluorinated DRX material. Additionally, the majority of small scale DRX synthesis was done using precursors pressed into pellets. This may have a beneficial effect of encouraging more fluorine solubility during the calcination reaction because pelletization ensures intimate contact of precursors. This may also reduce LiF volatility, however, large scale pelletization remains unpractical. To investigate why the scaled-up material shows significantly less fluorine than the small-scale synthesis, we undertook two approaches. 1) Calcining precursors at lower temperature (900°C) for select periods of time (0.5h, 4.0h, 12.0h). Calcinations at lower temperatures should reduce LiF volatility. 2) Calcining precursors as loose powder and pellets. One main question is whether pelletization is necessary to reach high fluorine content. Each loose powder sample and pellet (40 mm diameter) consisted of 10 grams of ball-milled precursor. Figure VIII.2.2a shows SEM images of DRX materials calcined as either loose powder or pellet for 0.5h, 4.0h, and 12.0h at 900°C under Argon atmosphere. When increasing the duration of calcination for the loose powder sample, a clear trend is observed where longer time leads to larger particles. For the case of the pellet samples, the 0.5h pellet sample resembles that of the 0.5h loose powder sample. However, longer duration results in more aggregated and less distinguishable particles in pellet samples. To help obtain qualitative information on the fluorine content, NMR was performed on these samples. Figure VIII.2.2b shows the normalized fluorine signal. In all case, samples calcined at 900°C showed significantly more fluorine incorporated into the bulk DRX structure than the previous material synthesized at 1000°C. This shows that temperature having a significant effect on the final fluorine content. For 0.5h calcined powder and pellet samples, the fluorine signal displays similar bulk fluorine and LiF intensity. Longer calcination time (12.0h) does not change the relative intensity of the bulk fluorine signal. However, the LiF intensity is significantly weaker for the case of the powder sample. This means that the fluorine solubility limit is reached quickly in 0.5h where longer

calcination times only serve to remove residual LiF impurities. Additionally, pelletization can reduce LiF volatility but does not influence the fluorine solubility limit.

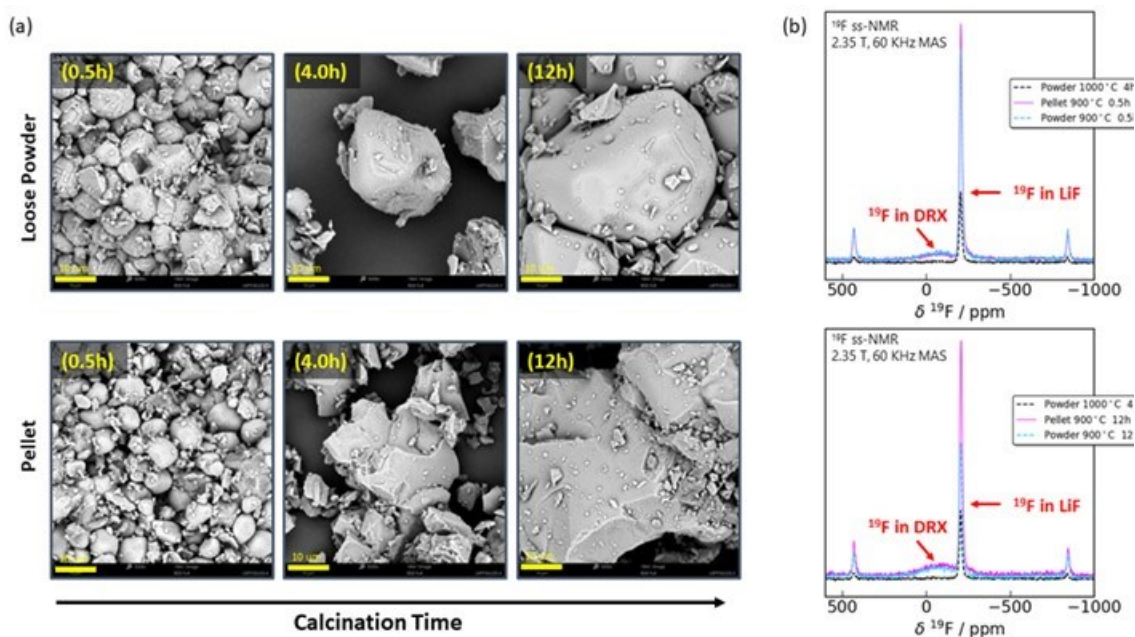
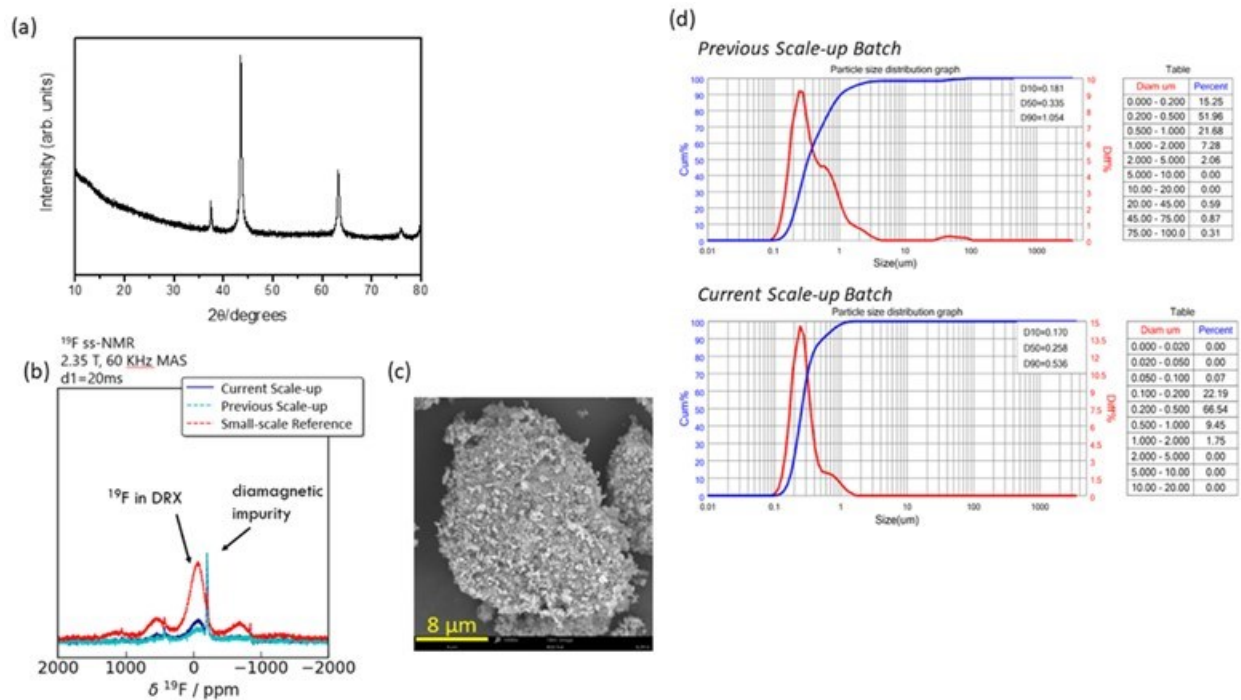


Figure VIII.2.2 (a) SEM images of as-prepared DRX cathode material calcined at 0.5h, 4.0h, and 12.0h as both loose powder and pellet. (b, c)  $^{19}\text{F}$ -NMR of as-prepared DRX calcined as pellets and loose powder.

To produce the baseline cathode material LMTF2622, the MERF team carried out cathode scale-up by using a modified solid state synthesis method.  $\text{Mn}_2\text{O}_3$ ,  $\text{TiO}_2$ ,  $\text{Li}_2\text{CO}_3$ , and LiF precursors adding up to  $\sim 200\text{g}$  were ball-milled together with Y-stabilized  $\text{ZrO}_2$  in 500 mL jars at 100 RPM using Retsch Planetary Ball Mill PM 400. The rotation speed was increased from previous batch syntheses to further decrease precursor size and encourage more fluorine incorporation. Several calcinations were done with  $\sim 40\text{g}$  of precursor at a time as loose powders to not deviate from optimal calcination conditions obtained in the previous quarter. Calcinations were done at 900 °C for 12 h under Argon atmosphere. The calcined DRX material batches were combined and subsequently ball-milled at 400 RPM in an organic solvent for 4 h without any carbon, resulting in nano-size primary particles (Figure VIII.2.3c). Figure VIII.2.3a shows XRD of the final product, which clearly shows the DRX phase (Fm-3m).  $^{19}\text{F}$ -NMR was done on this material to qualitatively measure the F-content (Figure VIII.2.3b). Compared to the previous scale-up batch, the current batch shows significant improvement in terms of F incorporation into the DRX structure. However, compared to  $\text{Li}_{1.2}\text{Mn}_{0.6}\text{Ti}_{0.2}\text{O}_{1.8}\text{F}_{0.2}$  synthesized in small scale; the F-content of the current batch is still much lower. Thus, fluorine incorporation remains a challenge and requires further investigation. Particle size analysis on the scale-up materials were also performed. Interestingly, this current batch of DRX material showed a narrower size distribution compared to that of the previous batch (Figure VIII.2.3d). Differences in calcination temperatures may produce DRX materials with different mechanical properties. This may influence the rate of nano-sizing during the ball-milling process. In any case, a narrow distribution is beneficial for more uniform material properties at the particle level.





**Figure VIII.2.3 (a) XRD patterns and (c) SEM image of DRX material synthesized through solid-state method. (b)  $^{19}\text{F}$ -NMR and (d) PSA of previous and current DRX scale-up batches.**

The phase progression during solid state synthesis of DRX materials was further investigated at SLAC. Using in-situ X-ray powder diffraction, we are able to observe changes to the crystalline phases as the material progresses from precursors, through intermediate phases, and finally forms the DRX endpoint. By tracking this phase progression our data sheds light on the formation mechanism of the DRX material. Experiments were conducted at SSRL BL2-1 using an Anton Paar furnace integrated onto the beamline for solid state synthesis. Precursors were prepared according to protocols developed by the Clement group and heated under flowing argon with powder diffraction data collected continuously during the annealing process. We conducted in-situ measurements during synthesis of several DRX compositions,  $\text{Li}_{1.2}\text{Mn}_{0.4}\text{Ti}_{0.4}\text{O}_2$  (LMT-244),  $\text{Li}_{1.2}\text{Mn}_{0.5}\text{Ti}_{0.3}\text{O}_{1.8}\text{F}_{0.2}$  (LMTF-2532),  $\text{Li}_{1.2}\text{Mn}_{0.6}\text{Ti}_{0.2}\text{O}_{1.8}\text{F}_{0.2}$  (LMTF-2622), and  $\text{Li}_{1.1}\text{Mn}_{0.8}\text{Ti}_{0.1}\text{O}_{1.9}\text{F}_{0.1}$  (LMTF-1811). Several crystalline intermediates were observed for all compositions during heating as seen in Figure VIII.2.4.

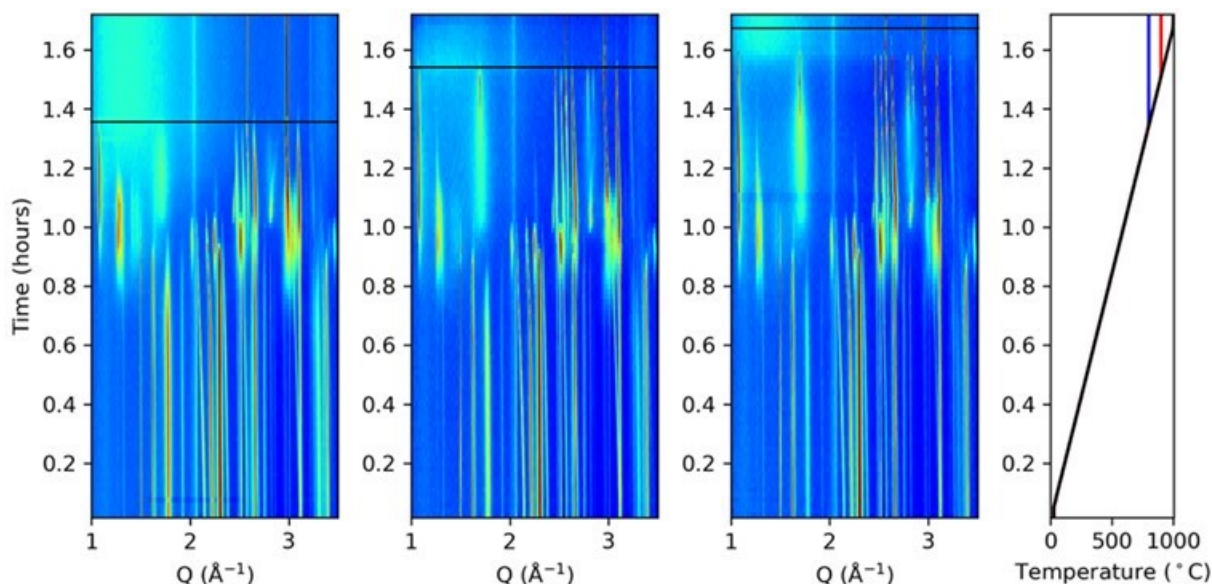


**Figure VIII.2.4** Waterfall plots showing the in-situ powder diffraction data for the solid state synthesis of LMTF-2532 (left), LMTF-2622 (middle), and LMTF-1811 (right) DRX materials. The different compositions were annealed to different temperatures, so the temperature profile at the right shows the temperature plateaus in colors matching the plot labels and the point at which the hold temperature was reached is indicated by the black line on the waterfall plots. The formation of several short lived intermediates can be seen. The overall phase progression appears to be similar between different compositions.

These intermediates appear to be the same for all compositions although the details of the various transformation temperatures and the crystal structures for these intermediates is still to be determined.

We also evaluated the potential of X-ray Absorption Spectroscopy (XAS) to probe and capture the local electronic structure effects of fluorination on DRX cathodes. We performed preliminary experiments at beamline 7.3.1 of the Advanced Light Source (ALS) on three systems:  $\text{Li}_{1.2}\text{Mn}_{0.5}\text{Ti}_{0.3}\text{O}_{1.9}\text{F}_{0.1}$  (LMTF2531), LMTF2622 and LMTF1811, as well as on their respective precursors. All precursors F K-edge spectra exhibit the characteristic fluorine K-edge feature around 698 eV, which closely resembles that of LiF, as shown in Figure VIII.2.5 (red solid line). Differences are observed, however, in the intensity and spectral shape of the feature around 710 eV between the different precursors (and potential Fe contamination). These differences are further investigated with ongoing experiments. Upon synthesis, the LMTF2531 and LMTF2622 samples also exhibit the characteristic fluorine feature at  $\approx 698$  eV, indicating effective fluorination on these compounds. For LMTF1811, however, this feature is not observed. The latter was synthesized at higher temperatures than LMTF2531 and LMTF2622. Similar dependence on the fluorination with synthesis temperature were observed in Li-Mn-Nb-O-F DRX materials.

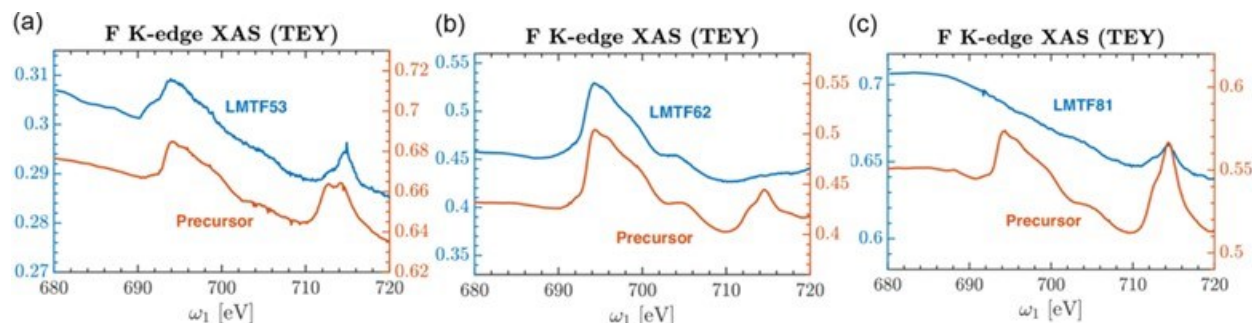


**Figure VIII.2.5** Normalized Total electron Yield (TEY) soft X-ray Absorption spectra (sXAS) of LMTF2531 (a), LMTF2622 (b) and LMTF1811 (c) along with the spectra of their respective precursors, as indicated. Left (right) y-axis corresponds to the normalized intensity of the synthesized sample (precursor).

Further XAS experiments on the F K-edge and a more detailed analysis are necessary to investigate these subtle changes in the fine structure of the F K-edge spectra with F content. Particularly, these changes could potentially reveal modifications in the fluorine local atomic environment upon synthesis and F content. Additional experiments on the Mn and Ti L-edges are also planned for the near future which could potentially provide complementary information regarding the fluorine incorporation on the DRX materials. Simultaneously, we have initiated DFT based simulations via the OCEAN code for interrogating the experimental X-ray spectral features. As we move forward a close collaboration with consortium co-PIs focused on theoretical geometrical structures of the disorder will enable us to evaluate the sensitivity and limitations of these experimental methods. Ultimately, and based on the evaluation of these benchmarking activities, we will be able to transfer this experimental study into the hard x-ray regime via X-ray Raman Spectroscopy at SSRL so that we can follow the Fluorine electronic structure evolution during the *in-situ* synthesis of materials.

## 2) Alternative scalable synthesis: solution-based coprecipitation method.

To evaluate different DRX scale-up methods, we utilize a novel aqueous coprecipitation method as a viable pathway toward commercialization. DRX synthesis through co-precipitation relies on producing a Mn-Ti precursor material, which has inherently high atomic mixing. Preliminary synthesis was done using a 1L Taylor Vortex Reactor (TVR) by mixing water soluble Mn and Ti reagents with NaOH and ammonia to form a  $\text{Mn}_{0.5}\text{Ti}_{0.5}$ -hydroxide precursor. Figure VIII.2.6a shows the XRD pattern of the resulting hydroxide precursor, which takes on an amorphous quality apart from a small amount of Mn oxide impurity. Mn hydroxide is not air stable and readily oxidizes in air. To form the targeted  $\text{Li}_{1.2}\text{Mn}_{0.4}\text{Ti}_{0.4}\text{O}_2$  DRX cathode, the DRX hydroxide precursor was mixed with LiOH anhydrous before being calcined at 600°C under Argon atmosphere. This material was recovered, reground, and calcined again using same conditions. XRD pattern of the final material shows it has mostly DRX structure but with small MnO impurity. Precursor pre-treatment and calcination optimization to minimize impurities are ongoing. Figure VIII.2.6b shows SEM image of the DRX precursor, which are irregularly shaped secondary particles made up of small nano-sized primaries. After calcination, the primary particles remain nano-sized but noticeably larger than that of the precursor. Future coprecipitation efforts will focus on the optimization of the DRX precursor synthesis to get more uniform secondary particles, use of different chelating/precipitating agents, and moving towards high-Mn content systems to be more in-line with other efforts in the consortium.

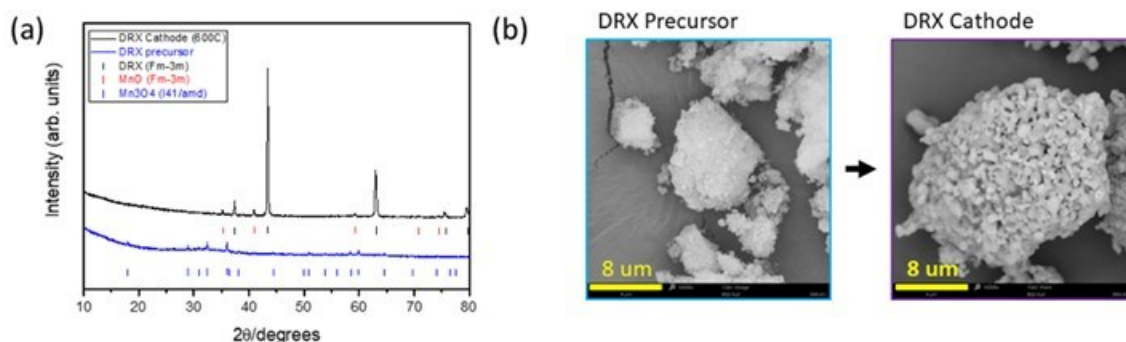


Figure VIII.2.6 (a) XRD and (b) SEM images of coprecipitated DRX precursor and calcined DRX cathode material.

Building onto this work, we attempt to synthesize the LMTF2622 baseline cathode material using the developed aqueous co-precipitation method. Preliminary synthesis was done using a 1L Taylor Vortex Reactor (TVR) by mixing water soluble Mn and Ti reagents with NaOH and ammonia to form a  $Mn_{0.70}Ti_{0.30}$ -hydroxide precursor, based on ICP. This precursor is Mn-deficient from the ideal  $Mn_{0.75}Ti_{0.25}$ -hydroxide precursor. Further optimization studies will be carried out to obtain the ideal transition metal stoichiometry. Figure VIII.2.7a shows the XRD pattern of the resulting hydroxide precursor, which displays broad and weak peaks related to  $Mn_3O_4$  (I41/amd). Previously synthesized  $Mn_{0.50}Ti_{0.50}$ -hydroxide precursor showed to have an amorphous structure with less  $Mn_3O_4$  impurities. Manganese-rich hydroxides are air sensitive and readily oxidized. The higher Mn-content as well as the inherently nano-sized nature of DRX precursor primary particles (Figure VIII.2.7b) leads to the rapid formation of  $Mn_3O_4$ . It is not clear if Mn atoms oxidize and segregate from Ti completely to form  $Mn_3O_4$  or Ti exists partially within the  $Mn_3O_4$  structure.

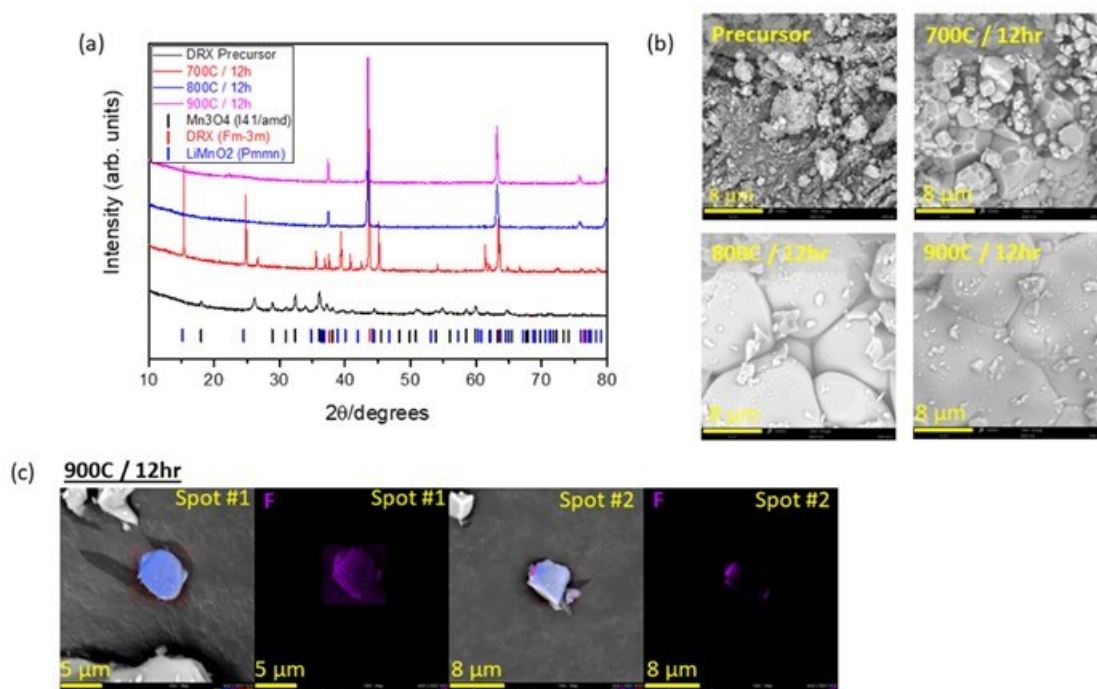


Figure VIII.2.7 (a) XRD patterns and (b) SEM images of DRX precursor and samples calcined at 700 °C, 800 °C, and 900 °C. (c) SEM/EDS analysis of DRX materials calcined at 900°C.

The DRX hydroxide precursor was mixed with LiOH anhydrous and LiF before being calcined at 700 °C, 800 °C, and 900 °C for 12 h under Argon atmosphere. The XRD patterns of the calcined materials are also shown

in Figure VIII.2.7a. Calcination at 700 °C produced a mixed phase of LiMnO<sub>2</sub> (Pmmn) and DRX (Fm-3m) structure whereas the 800 °C and 900 °C calcinations produced a single phase DRX structure. Compared to previous calcinations on Mn<sub>0.50</sub>Ti<sub>0.50</sub>-hydroxide precursor, this higher Mn precursor requires higher calcination temperature to form the pure DRX phase. Increased particle growth is also observed when increasing calcination temperature (Figure VIII.2.7b). Similar to the solid-state synthesis route, LiF was used as the source of fluorine. To investigate whether F is retained in the bulk, SEM/EDS was done on the 900 °C calcined sample. Figure VIII.2.7c shows Spot#1 with the appearance of a well distributed F in the particle, which initially suggests successful fluorination in this material. However, Spot#2 shows the presence of localized fluorine hotspots. This suggests that the fluorine is unevenly distributed and may exist as an impurity phase on the surface that may be too small to detect in XRD. Follow up studies using in-situ XRD during calcinations and F-NMR will be pursued to better understand the synthesis mechanism.

### 3) Alternative scalable synthesis: wet milling method.

The small-scale synthesis in the laboratory often uses a high energy planetary ball-milling method, which is less scalable. To this end, wet ball-milling where ethanol is used as a solvent was also investigated. Standard precursors of LiF, Li<sub>2</sub>CO<sub>3</sub> (10 wt.% excess), Mn<sub>2</sub>O<sub>3</sub> and TiO<sub>2</sub> were used. The precursor mixture was dried and pelletized before the mixture was heated in a large furnace (inset of Figure VIII.2.8a). The precursor mixture was heated at 600 °C for 2 hours and the temperature was increased up to 1000 °C (dwelling for 2 hours) under continuous Ar gas flow. To confirm the reproducibility of the scale-up synthesis, we attempted three synthesis experiments and compare their crystal structures by XRD as shown in Figure VIII.2.8a. These three experimental results show different levels of impurities of LiF and spinel-like phase. We identified that the inconsistency of Ar gas flow and gas leakage significantly affect the phase purity of the DRX compound. In our lab setup, all Ar gas lines are inter-connected and used for multiple furnaces simultaneously. Therefore, the use of each furnace affects the Ar gas flow of other furnaces. In contrast to the small scale, such a deviation of Ar gas flow could affect the large-scale synthesis. Therefore, we have installed a separate Ar gas line and O<sub>2</sub>/moisture traps for scale-up synthesis experiments (Figure VIII.2.8b), which will provide improved control of Ar gas flow. In the future work, we will optimize the scale-up synthesis conditions of DRX compounds.

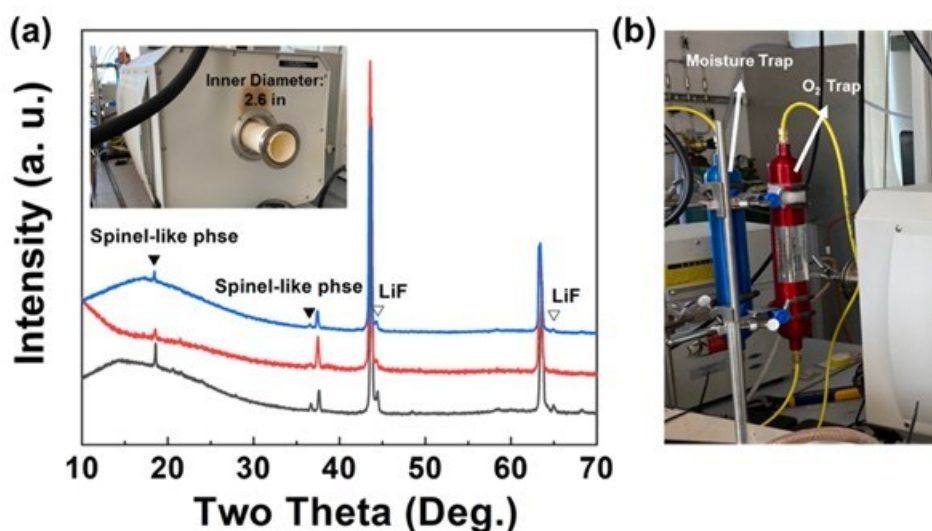


Figure VIII.2.8 (a) XRD patterns of scaled up DRX compounds using a large size tube furnace (Inset: photo of the large tube furnace, inner diameter: 2.6 inch) and (b) connection of moisture and O<sub>2</sub> traps to the large tube furnace.

### 4) Development of combustion synthesis method.

The team at Oak Ridge National Laboratory (ORNL) developed a combustion synthesis route to produce Mn/Ti-based DRX powders. Briefly, this method involves heating an aqueous solution containing oxidizing

reagents (e.g., metal nitrates) and a fuel (e.g., glycine) to its autoignition temperature. After the combustion reaction, powders were further heat treated (up to 1,000 °C under argon) to increase the crystallinity and grain size. While the results shown here are for gram-scale batches, the process is scalable and capable of producing large quantities (kg+) of crystalline powders.

This route was used to prepare several DRX oxides and oxyfluorides where the Mn/Ti molar ratio was either 5/3 or 7/1. Figure VIII.2.9a shows powder XRD data for a material with the nominal composition  $\text{Li}_{1.2}\text{Mn}_{0.5}\text{Ti}_{0.3}\text{O}_{1.95}$  (assuming  $\text{Mn}^{3+}/\text{Ti}^{4+}$  valence states and 2.5% anionic vacancies) which was heated to 1,000 °C for 4 h. In addition to the desired DRX phase, Rietveld refinement indicates the presence of monoclinic secondary phase(s) (e.g.,  $\text{Li}_2\text{TiO}_3$  and/or  $\text{Li}_2\text{MnO}_3$ ). It should be noted that  $\text{Li}_2\text{TiO}_3$  and  $\text{Li}_2\text{MnO}_3$  are isostructural, and due to the similar X-ray scattering power of  $\text{Mn}^{4+}$  and  $\text{Ti}^{4+}$ , these two phases are difficult to distinguish with the present dataset. While the oxide synthesis yielded a mixture of phases, an oxyfluoride powder with the nominal composition  $\text{Li}_{1.25}\text{Mn}_{0.5}\text{Ti}_{0.3}\text{O}_{1.95}\text{F}_{0.05}$  was nearly phase-pure DRX after heat treatment at 1,000 °C (see Figure VIII.2.9b). A similar trend was observed for Mn-rich powders including  $\text{Li}_{1.2}\text{Mn}_{0.7}\text{Ti}_{0.1}\text{O}_{1.85}$  vs.  $\text{Li}_{1.35}\text{Mn}_{0.7}\text{Ti}_{0.1}\text{O}_{1.85}\text{F}_{0.15}$  (see Figure VIII.2.10). These intriguing results suggest that F incorporation stabilizes the DRX phase due to formation of different intermediates during heating.

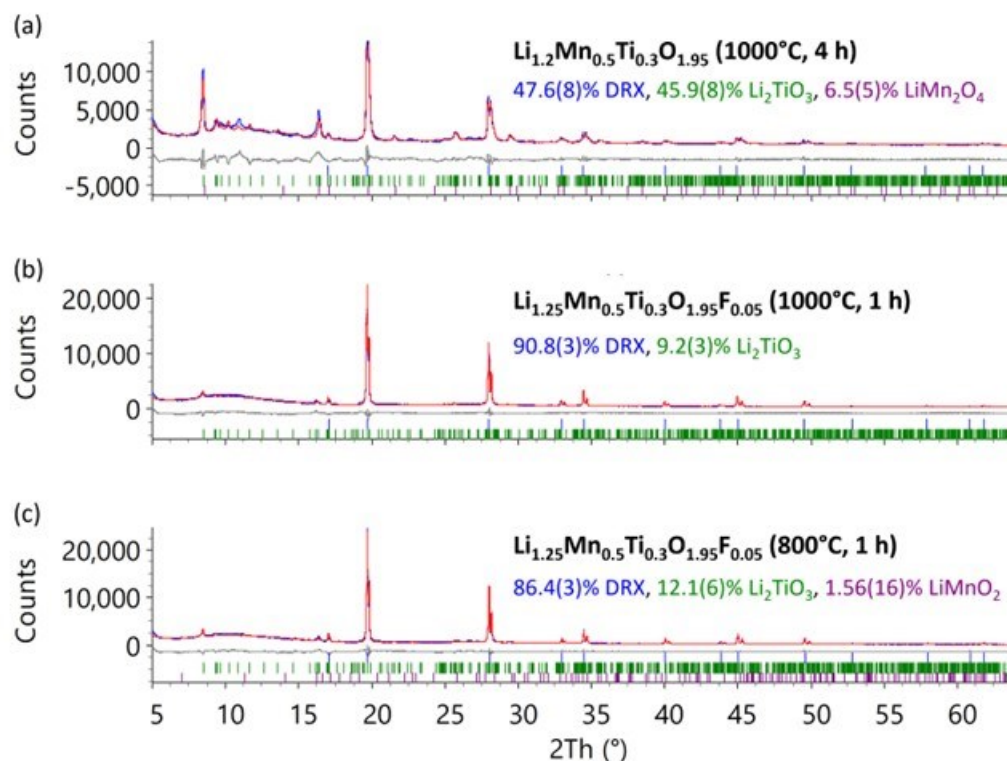


**Figure VIII.2.9** Powder XRD data and corresponding Rietveld plots obtained for DRX powders (Mn/Ti = 5/3) prepared through a combustion synthesis route. Results are shown for (a) metal oxide and (b-c) metal oxyfluoride compositions. All samples were heat-treated under flowing Ar using the conditions indicated. Data were collected on a lab diffractometer using a Mo radiation source with a 2 : 1 mixture of  $\text{K}\alpha_1$  :  $\text{K}\alpha_2$  ( $\lambda_1 = 0.70930$  Å;  $\lambda_2 = 0.71359$  Å)

The effect of synthesis temperature on DRX phase formation was also explored. Since the combustion route involves atomistic mixing of precursors in solution, the DRX phase can be formed at much lower temperatures (e.g., 800 °C, see Figure VIII.2.10c) compared to traditional solid-state reactions (typically 900–1,000 °C). The lower temperature of the combustion route is advantageous for two key reasons: (i) decreasing energy requirements to synthesize high purity materials and (ii) potentially providing more intimate control over the final powder's stoichiometry by reducing Li/F loss, which is problematic at temperatures  $\geq 900$  °C. To further

explore this topic, preliminary *in-situ* XRD data were collected to assess the onset temperature for DRX phase formation in the  $\text{Li}_{1.25}\text{Mn}_{0.5}\text{Ti}_{0.3}\text{O}_{1.95}\text{F}_{0.05}$  powder (see Figure VIII.2.11). These data indicate that DRX phase formation begins as early as 700 °C, and the phase-purity increases to 73.1(12) wt% after 10 min heating at 800 °C. It should be noted that the refinement values reported here serve only as a semi-quantitative metric, and more detailed compositional analysis (e.g., ICP and F-ISE) is currently underway. Nonetheless, these results indicate that the combustion route enables DRX phase formation at lower temperatures and shorter times compared to conventional solid-state routes.

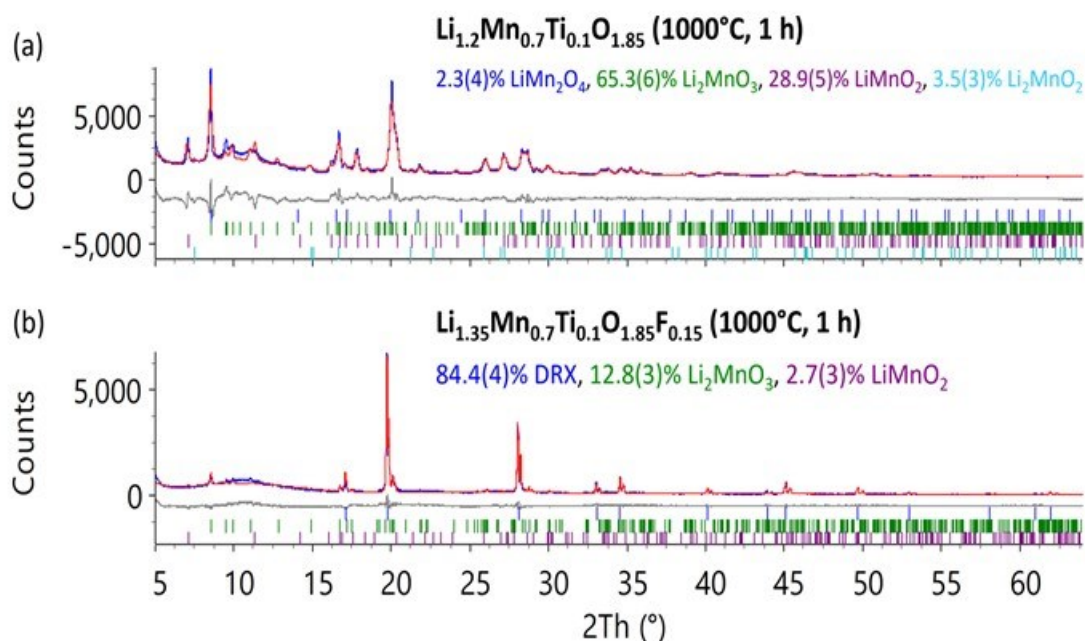


**Figure VIII.2.10** XRD data and corresponding Rietveld plots obtained for Mn-rich DRX powders (Mn/Ti = 7/1) prepared through a combustion synthesis route. Results are shown for (a) metal oxide and (b-c) metal oxyfluoride compositions heated for 1 h at 1,000 °C under flowing Ar. Data were collected on a lab diffractometer using a Mo radiation source with a 2 : 1 mixture of  $\text{K}\alpha_1$  :  $\text{K}\alpha_2$  ( $\lambda_1 = 0.70930 \text{ \AA}$ ;  $\lambda_2 = 0.71359 \text{ \AA}$ )

Electrochemical cycling data for the Mn-rich oxyfluoride DRX powder were evaluated in Li metal half cells containing a liquid electrolyte (1.2M LiFP<sub>6</sub> in EC/EMC, 3/7 w/w). Composite cathodes were prepared in a two-step process where: (i) high energy milling was used to coat the active material with graphite (7/2 w/w) followed by (ii) slurry mixing and electrode casting. The dried cathode contained 70 wt% DRX, 20 wt% graphite, and 10 wt% PVDF binder. As described in previous quarterly reports, graphite is a preferable conductive additive due to formation of a robust electronically conductive network and a more stable cathode/electrolyte interface, especially at high states of charge. Figure VIII.2.12 shows the cathode had a high initial charge capacity ~270 mAh/g and reversible capacity ~220 mAh/g. These results are consistent with those obtained for materials prepared through solid-state routes and indicate charge compensation occurs through Mn and O redox centers. While the initial cycles exhibited a sloping voltage profile, extended cycling yielded a plateau ~3V vs. Li/Li<sup>+</sup> due to formation of the spinel-like phase which is well-known for Mn-rich DRX phases. The material also showed good cycling stability with negligible fade over 30 cycles (test is ongoing).

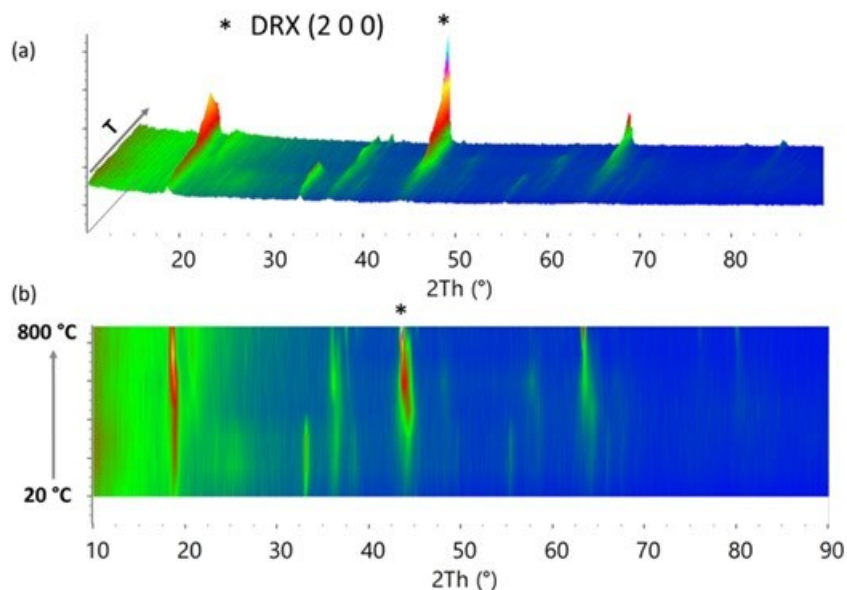


Figure VIII.2.11 Surface plots of the in-situ XRD patterns obtained for the  $\text{Li}_{1.25}\text{Mn}_{0.5}\text{Ti}_{0.3}\text{O}_{1.95}\text{F}_{0.05}$  powder. Data were acquired on a lab diffractometer using a Cu radiation source with  $2 : 1 \text{ K}\alpha_1 : \text{K}\alpha_2$  ( $\lambda_1 = 1.54056 \text{ \AA}$ ;  $\lambda_2 = 1.54439 \text{ \AA}$ ). Scans were collected at room temperature and 100 – 800 °C with a total scan time of 10 minutes at each temperature.

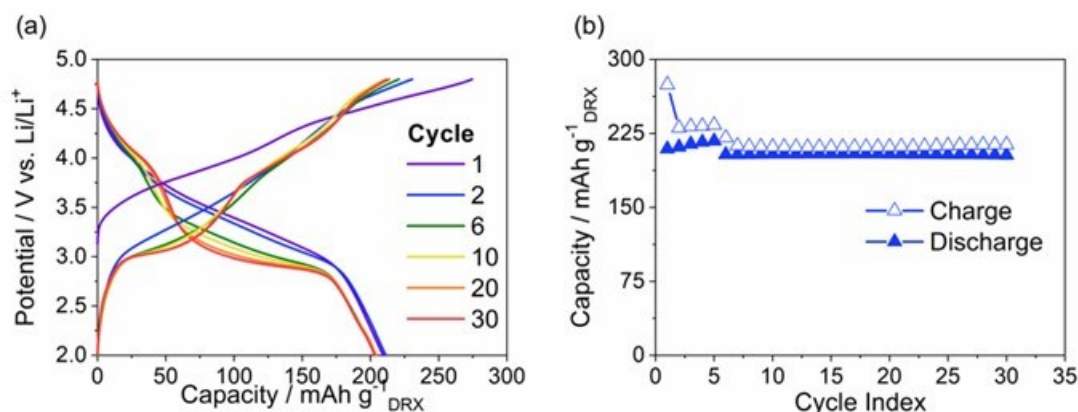


Figure VIII.2.12 Galvanostatic cycling performance of DRX cathodes prepared through a combustion synthesis route. The nominal cathode powder composition is  $\text{Li}_{1.35}\text{Mn}_{0.7}\text{Ti}_{0.1}\text{O}_{1.85}\text{F}_{0.15}$ . (a) Voltage profiles for various cycles and (b) charge/discharge capacity over 30 cycles. All cells were cycled between 2.0 V and 4.8 V at a specific current of 10 mA  $\text{g}^{-1}$  for the first 5 cycles and 20 mA  $\text{g}^{-1}$  for subsequent cycles.

Overall, the scalable combustion synthesis route is capable of producing high purity, high performance Mn/Ti-based DRX oxides and oxyfluorides. These results indicate that F incorporation stabilizes DRX phase formation during annealing. Furthermore, due to atomistic mixing of precursor elements in solution, the combustion route enables DRX phase formation at lower temperatures (700–800 °C) and shorter reaction times ( $\leq 1$  h) compared to traditional solid-state reactions. Cycling measurements in Li metal half cells demonstrate the Mn-rich DRX cathodes have attractive electrochemical properties with reversible capacities  $\sim 220$  mAh/g and stable performance over 30 cycles. Furthermore, these results show that advancements from the carbon coating subgroup (e.g., graphite coatings to improve cycling stability) readily translate to DRX materials prepared through alternate synthesis routes. Ongoing efforts are focused on collaborative measurements across the consortium. For example, cycling performance of cathodes prepared through the combustion route will be tested using new high voltage electrolyte formulations (collaboration with PNNL). Similarly, advanced



characterization methods available at other institutions (e.g., SLAC, PNNL, UC-B, and UC-SB) will provide valuable insights on the reaction mechanism and material structure.

### 5) Thermal properties.

It is well known that charged lithium transition-metal oxide (LTMO) cathodes such as layered  $\text{LiNi}_{0.8}\text{Co}_{0.15}\text{Al}_{0.05}\text{O}_2$  (NCA) and  $\text{LiNi}_x\text{Mn}_y\text{Co}_{1-x-y}\text{O}_2$  (NMC) are highly reactive towards liquid electrolytes, leading to significant heat generation that subject lithium-ion batteries (LIBs) to thermal runaway and other safety issues. For example, in the presence of a 1.0 M  $\text{LiPF}_6$  in ethylene carbonate (EC)/ diethyl carbonate (DEC) electrolyte,  $\text{LiNiO}_2$  cathode charged to 4.2 V can release  $\sim 1600$  J/g heat with an onset temperature of 184 °C. In this regard, the remarkable thermal stability of  $\text{LiFePO}_4$  and its charged counterpart ( $\text{FePO}_4$ ) was instrumental to its commercial success, despite its relatively low energy density compared to the traditional layered LTMO cathodes. The charged  $\text{LiFePO}_4$  electrode has a high onset temperature of 250 °C and peak exotherm at 280 and 315 °C on the DSC profile, with a total heat generation of about 145 J/g.

To evaluate the prospect of DRX cathodes, we investigated the thermal properties of a Gen 1 DRX cathode ( $\text{Li}_{1.1}\text{Mn}_{0.8}\text{Ti}_{0.1}\text{O}_{1.9}\text{F}_{0.1}$ , M80) and compared its behavior to a commercial  $\text{LiNi}_{0.8}\text{Co}_{0.1}\text{Mn}_{0.1}\text{O}_2$  (NMC811) cathode. Prior to electrode fabrication, M80 active material was ball milled with a carbon black additive to reduce the particle size and improve electronic conduction. The resulting particles are significantly smaller compared to the commercial NMC811 cathode particles, which are submicron and tens of microns, respectively (Figure VIII.2.13a and b). Figure VIII.2.13c shows the 1<sup>st</sup> charge  $dQ/dV$  profile of the M80 cathode as well as gas evolution measured by operando differential electrochemical mass spectrometry (DEMS). At a current density of 10 mA/g, broad peaks centered at  $\sim 3.75$  and  $\sim 4.5$  V were observed on  $dQ/dV$ . Oxygen gas was not detected even at a high charging voltage of 4.8 V. Evolution of  $\text{CO}_2$  begins around 3.5 V and peaks at  $\sim 4.15$  V, likely arising from decomposition of residue carbonate on the DRX surface as well as electrolyte degradation. Further analysis on the redox processes was carried out using *ex situ* synchrotron hard X-ray absorption spectroscopy (XAS). On the XANES spectra (Figure VIII.2.13d), the average Mn oxidation state changed from 3+ to 4+ upon changing to 4.8 V.

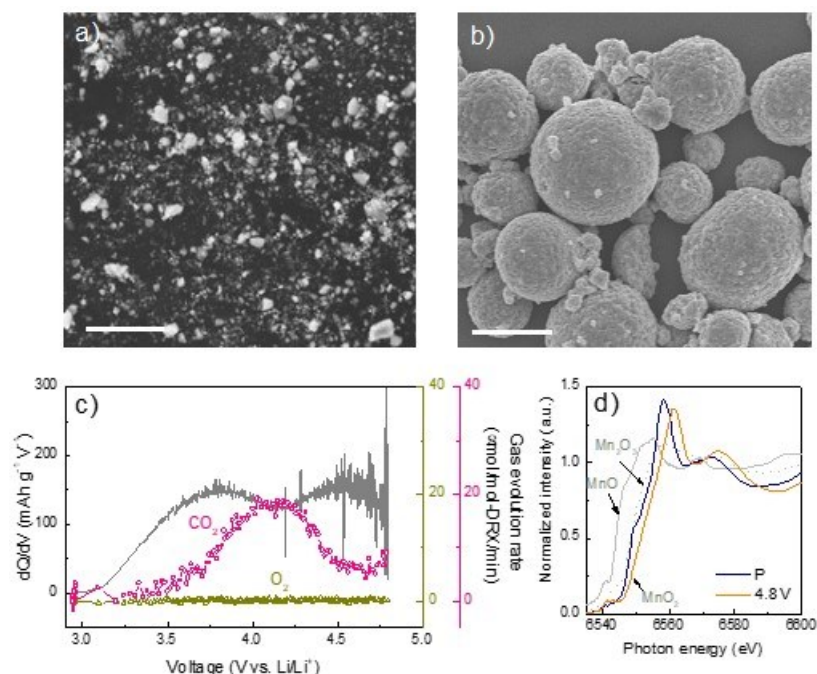


**Figure VIII.2.13** SEM images of M80 (a) and NMC811 (b) particles. Scale bars are 10  $\mu\text{m}$ , (c) operando DEMS results collected during the 1<sup>st</sup> charge of M80 cathode to 4.8 V. The  $dQ/dV$  curve (grey) as well as gas evolution profiles of  $\text{O}_2$  (olive) and  $\text{CO}_2$  (pink) are plotted as a function of voltage. (d) Mn L-edge XANES profiles collected on the pristine and recovered M80 electrode at 4.8 V.

The thermal properties of cathode materials are typically evaluated by differential scanning calorimetry (DSC), accelerating rate calorimetry (ARC), or microcalorimetry. Here *ex situ* DSC measurements were carried out to compare the thermal stability of M80 and NMC811 cathodes at various state of charge. Figure VIII.2.14a shows the 1<sup>st</sup> charge voltage profiles in the presence of a 1.0 M  $\text{LiPF}_6$  in EC and DEC (50:50 v/v) electrolyte. At a cutoff voltage of 4.4, 4.6, and 4.8 V, charge capacities of  $\sim 187$ , 208, and 254 mA/h/g were obtained on M80, respectively. Assuming no capacity contribution from side reactions, the extracted Li contents are approximately 0.56, 0.63 and 0.77, respectively (based on the theoretical capacities of 332 from total Li extraction). For the NMC811 cathode charged to 4.4 V, the specific capacity is 231 mA/g, corresponding to an estimated 0.82 Li extraction (based on a theoretical capacity of 280 mA/g). For DSC measurements, the recovered cathodes were loaded into hermetically sealed stainless steel capsules in the glovebox without rinsing, and tested from 30 to 400  $^\circ\text{C}$  at a 10  $^\circ\text{C}/\text{min}$  heating rate. The capsules with a gold-coated Cu gasket can withstand an internal pressure up to 150 atm, which suppresses the volatilization of solvent and ensures no weight loss during the experiment. Figure VIII.2.14b shows the DSC profiles of the M80 cathode charged to various cutoff voltages. For the pristine M80 electrode, an exothermic peak center at 210  $^\circ\text{C}$  leads to a total heat generation of about 130 J/g. This value remains nearly unchanged upon charging the cathode to 4.4 and 4.6 V, although the peak heat generation temperature decreases to  $\sim 190$  and 170  $^\circ\text{C}$ , respectively. Further increasing the charging voltage to 5.0 V leads to a significant reduction of heat to 49 J/g, with the peak centered at  $\sim 150$   $^\circ\text{C}$ . For comparison, the NMC811 cathode charged to 4.4 V is shown in Figure VIII.2.14c. A broad double peak centered at 218  $^\circ\text{C}$  and 238  $^\circ\text{C}$  were observed on the DSC profile. The total heat evolved is 844 J/g, which is consistent with the high reactivity of high-Ni cathodes such as NCA.

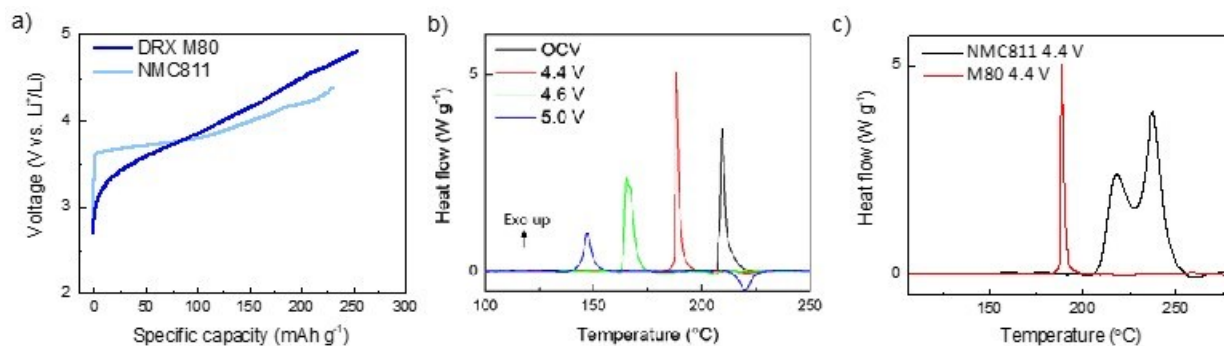


**Figure VIII.2.14** a) The 1<sup>st</sup> charge voltage profiles of M80 and NMC811 cathodes at a current density of 10 mA/g, (b) DSC profiles collected on M80 cathodes recovered at OCV, 4.4, 4.6, 5.0 V, respectively, and (c) DSC profiles collected on M80 and NMC811 cathodes recovered at 4.4 V.

When a liquid electrolyte is present, the solvents can be oxidized by the highly oxidative transition-metals (TMs) as well as the oxygen released from the cathode material at high voltages. The amount of heat generated is directly related to the combustion heat of the solvents. For NMCs, the presence of reactive Ni<sup>4+</sup> and oxygen released upon structural damages at high voltages can lead to extensive reactivities and a large amount of heat release. Whereas in the Mn-Ti based DRX oxyfluorides, the overall low heat generation indicates excellent thermal stability, consistent with low oxygen release and less reactive TMs at high voltages. The lower onset temperatures of the exothermic peaks in the M80 electrodes are likely associated with electrolyte decomposition products on DRX surface, as the samples were collected without rinsing or additional treatment prior to the DSC measurements.

## Task 2: Electrolytes

### 1) Localized high concentration electrolytes.

The PNNL team tested four different electrolytes, ED01 (baseline), ED02, ED03 and ED04 in Li||DRX half cells in the voltage range of 2.0 – 4.8 V, where the DRX electrode has the composition of Li<sub>1.2</sub>Mn<sub>0.6</sub>Ti<sub>0.2</sub>O<sub>1.8</sub>F<sub>0.2</sub>. ED01, ED02 and ED03 are conventional LiPF<sub>6</sub>/carbonate electrolytes, while ED04 is a non-conventional localized high concentration electrolyte (LHCE). The electrolyte formulations are shown in Table VIII.2.1.

**Table VIII.2.1 Electrolyte Formulations for ED01-ED04.**

Electrolyte code	Electrolyte formulation
ED01	1 M LiPF <sub>6</sub> in EC-DMC (1:2 by wt.)
ED02	1 M LiPF <sub>6</sub> in EC-EMC (3:7 by wt.)
ED03	1 M LiPF <sub>6</sub> in EC-EMC (3:7 by wt.) + 2 wt.% VC
ED04	LiFSI-2DMC-0.2EC-3TTE

For the Li||DRX coin cells, each was assembled with a DRX cathode, a polyethylene (PE) separator, a 250 μm thick Li metal anode, and 75 μL ED electrolyte. The cells first underwent four formation cycles at a current density of 10 mA/g, then cycled at 20 mA/g at 30 °C. As shown in Figure VIII.2.15a for the first cycle charge and discharge voltage profiles, the three conventional electrolytes ED01 to ED03 show very similar discharge capacity of 214.2 mAh/g at 10 mA/g, with the first cycle Coulombic efficiency (CE) of 60.7% for ED01,

64.9% for ED02 and 64.8% for ED03. However, the LHCE ED04 shows slightly higher discharge capacity of 221.4 mAh/g with the first cycle CE of 66.9%. At the current density of 20 mA/g, Li||DRX cells with ED04 deliver the highest capacity and the most stable cycling compared to that of the conventional electrolytes (ED01 to ED03) (Figure VIII.2.15b). Among the three conventional electrolytes, ED02 results in a higher capacity than ED01, probably because of the better wettability of EC-EMC in ED02 to the PE separator than that of EC-DMC in ED01. ED03 shows faster capacity decay than ED02, indicating the additive VC in ED03 is not stable at high voltages. These results suggest that ED04, an LHCE with unique solvation structure, could be a promising electrolyte formulation for a high-voltage DRX cathode.

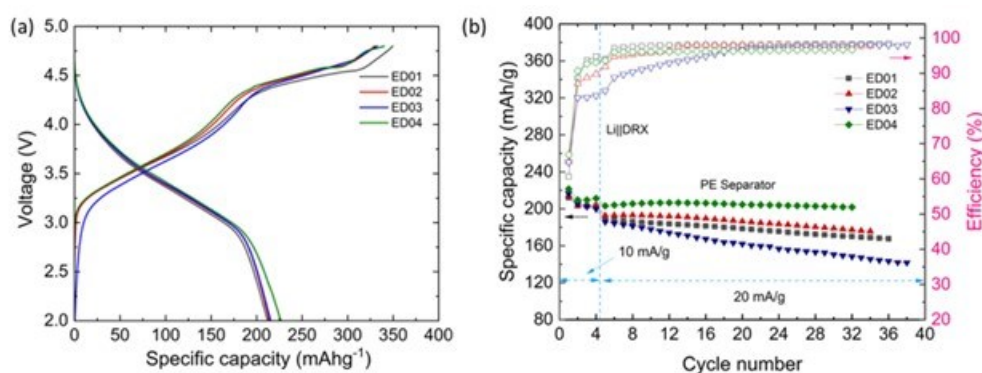


**Figure VIII.2.15** (a) Voltage profiles for the 1st formation cycle at 10 mA/g. (b) Cycling performance of Li||DRX cells at 20 mA/g charging and discharging, after four formation cycles at 10 mA/g. The voltage range is 2.0 – 4.8 V (vs Li/Li+).

The performance of a localized high-concentration electrolyte (LHCE) ED04 of LiFSI-2DMC-0.2EC-3TTE (by mol.) was further evaluated in DRX half-cells, in comparison with the baseline electrolyte ED01 of 1 M LiPF<sub>6</sub> in EC-DMC (1:2 by wt.). The DRX electrode laminates were fabricated by the LBNL team with carbon-coated LMTF2622 powder. Each of the DRX half-cell coin cell was assembled with a piece of DRX cathode, a piece of PE separator, a 250 μm thick Li metal anode, and 75 μL of electrolyte. For the electrochemical cycling stability test, the cells first underwent 4 formation cycles at a current density of 10 mA/g, then were cycled at 20 mA/g. For the rate capability test, the cells were first subjected to 3 formation cycles at a current density of 10 mA/g, then cycled at a constant charge current density of 20 mA/g and various discharge current densities. The charge and discharge voltage range was 4.8-2.0 V, and the testing temperature was 30 °C.

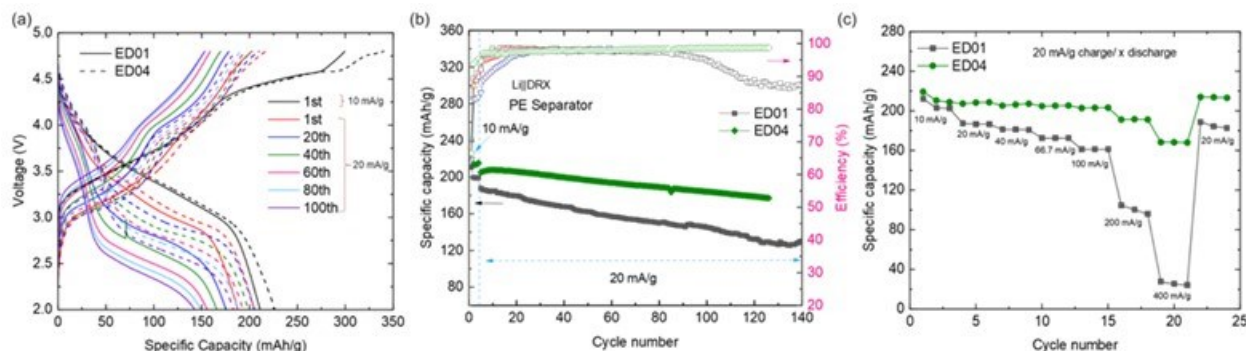


**Figure VIII.2.16** Performance of DRX half-cells with ED01 and ED04 electrolytes: (a) voltage profiles at selected cycle numbers, (b) cycling performance at 20 mA/g charging and discharging after four formation cycles at 10 mA/g, and (c) discharge rate capability with 20 mA/g charging current after three formation cycles at 10 mA/g.

The voltage profiles in Figure VIII.2.16a show that the voltage polarization is more pronounced for cells with ED01 than with ED04 electrolyte. In addition, at a current density of 20 mA/g on charge and discharge, DRX

half-cells with ED04 deliver much higher capacity and more stable cycling compared with ED01 (Figure VIII.2.16b), having a capacity retention of  $\sim 87.2\%$ , as compared with  $\sim 70.5\%$  for ED01, after 120 cycles. Furthermore, discharge rate capability results reveal much higher capacities for DRX half-cells with ED04 compared with ED01 (Figure VIII.2.16c). For instance, at a discharge current density of 400 mA/g, a discharge capacity of 170 mAh/g was obtained for DRX half-cells with ED04 compared with 25 mAh/g for ED01. ED04 electrolyte also led to high stability of the Coulombic efficiency (CE) compared to the significant drop in CE observed for ED01 at high discharge current densities. This outstanding performance of the DRX half-cells with ED04 may be attributed to the high stability of the ED04 electrolyte and the formation of a stable and robust cathode electrolyte interphase (CEI) on the DRX cathode and thus, suggesting that ED04 is a promising electrolyte formulation for high voltage DRX cathodes.

The UCSB team used  $^7\text{Li}$  solid state nuclear magnetic resonance (ssNMR) spectroscopy to characterize the pristine DRX cathode and cycled cathode samples collected at the 100<sup>th</sup> discharged state when cycled with ED01 and ED04 electrolytes. As shown in Figure VIII.2.17a, the ED01 DRX sample underwent significant change in the bulk structure, which seem to result in greater cation ordering (the narrower resonance indicates a narrower distribution of chemical environments for  $^7\text{Li}$ ). On the other hand, the ED04 DRX sample showed a rather similar  $^7\text{Li}$  resonance as the pristine sample, suggesting little change in bulk structure. However, there is clearly some loss of  $^7\text{Li}$  signal intensity for both DRX samples, but it is hard to tell its origin. More characterization (including *ex situ* X-ray diffraction) is planned.

The ALS (LBNL) team characterized the surface of the cycled DRX electrodes ( $< 5$  nm for C-K edge) by total electron yield (TEY) mode of the C K-edge soft X-ray absorption spectroscopy (sXAS). As shown in Figure VIII.2.17b, the sXAS-TEY spectra from the ED01 DRX sample showed a significant difference between the first and second cycle but became similar to the pristine sample after 100 cycles, suggesting parasitic reactions after the first and second cycles and passivation after 100 cycles. According to previous report, compounds with carbonates, ketone, and alkyl functional groups could be candidates for the surface products. On the other hand, all sXAS-TEY spectra from the ED04 DRX sample highly resemble the pristine electrode. The results suggest that the parasitic reactions that happened with ED01 are limited in the ED04 environment. More characterization for ED04 cycled samples will be performed in the future.

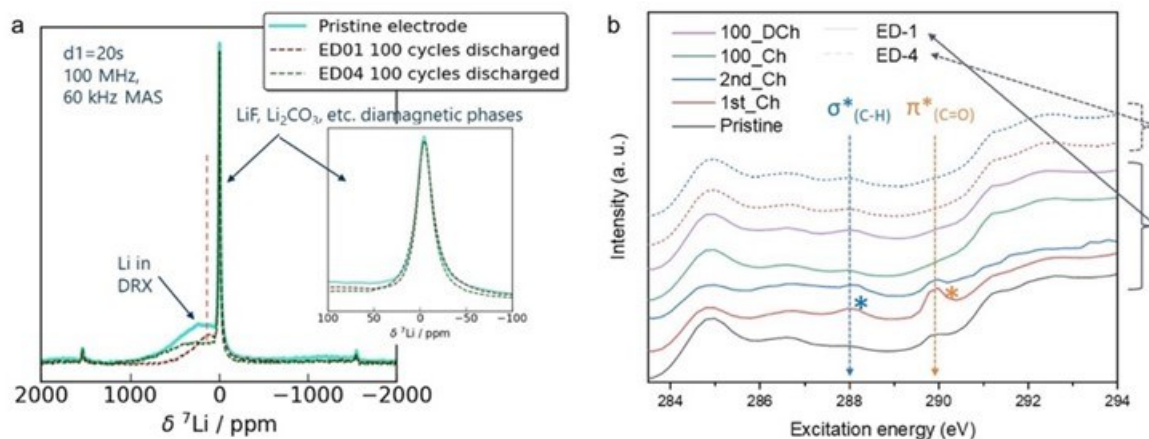
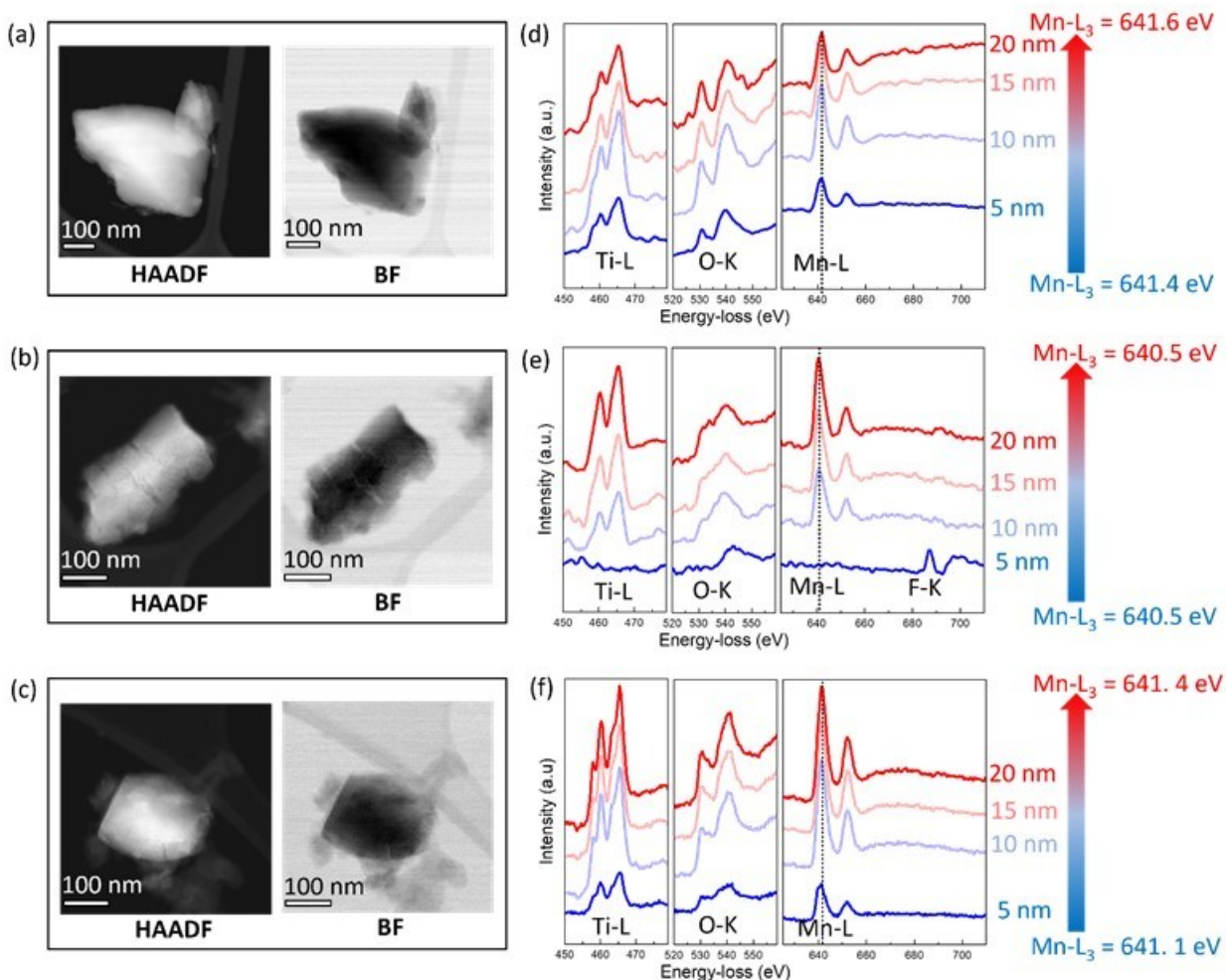


Figure VIII.2.17 (a)  $^7\text{Li}$  spin echo solid-state NMR spectra collected at 100 MHz and under 60 kHz MAS and (b) C K-edge sXAS-TEY spectra of pristine electrodes and DRX electrodes cycled in ED01 and ED04 electrolytes.

Microstructural and chemical composition analyses were also performed using scanning transmission electron microscopy (S(TEM)) and electron energy loss spectroscopy (EELS) on these cycled DRX electrodes and the results are presented in Figure VIII.2.18. The comparison of the STEM images in Figure VIII.2.18a-c reveals that the DRX electrode cycled in baseline electrolyte (ED01) becomes cracked and porous (Figure VIII.2.18b), while the DRX cathode cycled in LHCE (ED04) shows less cracks and porosity (Figure VIII.2.18c).



**Figure VIII.2.18** (a-c) STEM images and (d-f) EELS results of (a,d) pristine DRX, (b,e) DRX cycled in ED01 (after 100 cycles) and (c,f) DRX cycled in ED04 (after 100 cycles).

In addition, as shown in Figure VIII.2.18d-f for the electronic structures of the pristine and two cycled electrodes in both ED01 and ED04, a slight oxygen (O) loss and a reduction of manganese (Mn) are observed near the surface of the pristine DRX electrode. The high energy shift for fluorine (F)-K suggests the F in complex form (Figure VIII.2.18d), which likely comes from the PVDF binder used in the electrode. A thick F, O, carbon (C) (not shown in the Figure) containing structure is obvious on the surface of the DRX electrode cycled in ED01. Moreover, a significant reduction in Mn compared to the pristine (~1.1 eV peak shift) and a much broader O-K peak are observed in the DRX electrode cycled in ED01. The Mn reduction and the chemical change of DRX penetrate to the bulk region in DRX cycled in ED01. In the case of DRX cycled in ED04, the F, O, C (not shown in the Figure) containing complex structure is very thin, a gradient of Mn reduction is observed, and the bulk closely mimics the pristine state. Furthermore, Mn on the surface of DRX cycled in ED04 is less reduced than that on DRX cycled in ED01. The results demonstrate that the cathode electrolyte interphase (CEI) layer formed in the LHCE (ED04), as contrasted with that in the baseline electrolyte (ED01), can effectively protect DRX electrode. The result based on microstructural features captured by the STEM is consistent with the results of ssNMR and sXAS. Meanwhile, the PNNL team extended the cycling stability test of ED01 and ED04 in Li||DRX half cells in the voltage range of 2.0 – 4.8 V. As shown in Figure VIII.2.19a, Li||DRX cells with ED04 deliver much higher capacity and more stable

cycling than with ED01, having a capacity retention of ~75.5%, as compared with ~21.2% for ED01, after 200 cycles.

New LHCEs with the formulation of LiFSI-xDMC-yTTE (where  $1.6 \leq x \leq 5$ ,  $1 \leq y \leq 3$ ) were tested in Li||DRX half cells in the voltage range of 2.0 – 4.8 V with the purpose of finding out the optimal electrolyte formulation for DRX cathodes. These LHCEs were coded as ED05 to ED19. The DRX electrodes were prepared by the LBNL team (Dr. Yanbao Fu and Dr. Vincent Battaglia) using the 2nd batch of Argonne DRX powders ( $\text{Li}_{1.2}\text{Mn}_{0.6}\text{Ti}_{0.2}\text{O}_{1.8}\text{F}_{0.2}$ ). The preliminary cycling results for the new electrolytes show that higher content of DMC ( $x > 2$ ) is not good for the cycling performance, and hence we focused on LHCEs with lower DMC content, ED05 – ED07 and ED17 – ED19. The cycling stability of Li||DRX cells with these electrolytes and ED01 and ED04 are presented in Figure VIII.2.19b,c. As shown in Figure VIII.2.19b, for the first cycle charge and discharge voltage profiles, ED01 shows a discharge capacity of 184.5 mAh/g at 10 mA/g, with the first Coulombic efficiency (FCE) of 58.7%. However, the LHCEs (ED04 – ED07, ED17 – ED19) show slightly higher discharge capacities compared with ED01, with ED17 delivering the highest discharge capacity of 202.6 mAh/g and the FCE of 61.6%. At the current density of 20 mA/g for charging and discharging, Li||DRX cells with these LHCEs deliver higher capacities than those with the conventional electrolyte (ED01). The Coulombic efficiencies (CEs) at this current density (20 mA/g) are within the range of 95% – 98%. In addition, Li||DRX cells with ED17 show the highest capacity and the most stable cycling compared with those of other electrolytes. More duplicated cells are currently under testing to confirm the exceptional cycling performance observed for ED17. Overall, the obtained results suggest that LHCEs with less DMC content are promising for high-voltage DRX cathodes.

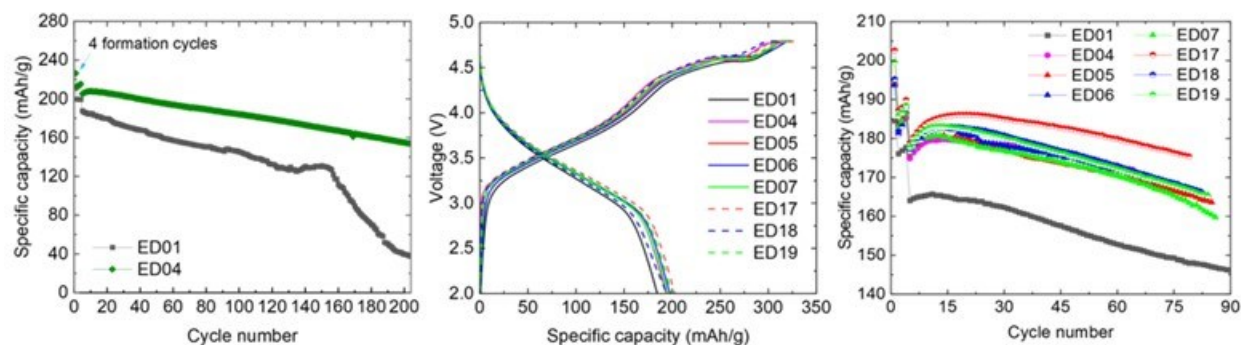


**Figure VIII.2.19** (a) Long-term cycling performance of Li || DRX cells with ED01 and ED04 at 20 mA/g charging and discharging, after four formation cycles at 10 mA/g (1st batch Argonne DRX). (b) Voltage profiles for the 1st formation cycle at 10 mA/g and (c) cycling performance at 20 mA/g charging and discharging of Li || DRX cells with new LHCEs in comparison with ED01 and ED04, after four formation cycles at 10 mA/g (2nd batch of Argonne DRX).

## 2) Gas evolution analysis.

Differential electrochemical mass spectrometry (DEMS) was used to examine interfacial degradation processes that occur during the first four cycles of  $\text{Li}_{1.2}\text{Mn}_{0.4}\text{Ti}_{0.4}\text{O}_2$  (LMTO). LMTO was cycled at a constant rate of  $0.1 \text{ Li hr}^{-1}$  ( $32.9 \text{ mA g}^{-1}$ ) in a voltage window of 4.8 – 1.5 V vs. Li/Li<sup>+</sup> with 1M LiPF<sub>6</sub> in 3:7 (v:v) ethylene carbonate (EC):ethyl methyl carbonate (EMC) as the electrolyte. As shown in Figure VIII.2.20a, significant CO<sub>2</sub> evolution was observed for all four cycles, arising primarily from decomposition of the carbonate solvents in the electrolyte. The manner in which the CO<sub>2</sub> evolution persists throughout the first four cycles indicates that the electrolyte degradation processes remain unpassivated during cycling within this voltage window.

To evaluate the effects of the observed interfacial degradation on long-term cycling, cycling experiments were conducted in full cells containing LMTO cathodes and pre-formed, pre-lithiated graphite anodes. The full cells were cycled with the same current, voltage window, and electrolyte as the DEMS cells described previously. Periodically, electrochemical impedance spectroscopy (EIS) was used to measure the impedance of the full cell in the fully charged state. As shown in the Nyquist plot in Figure VIII.2.20b, the cell impedance grows

consistently throughout cycling, suggesting that the sustained interfacial degradation drives impedance rise through deposition of insulating degradation products. These results underscore the need to identify new electrolyte compositions that provide better stability, particularly at high voltages. We also plan to vary the voltage window to understand how both low and high voltage cutoffs impact gas evolution and impedance evolution in a cell.

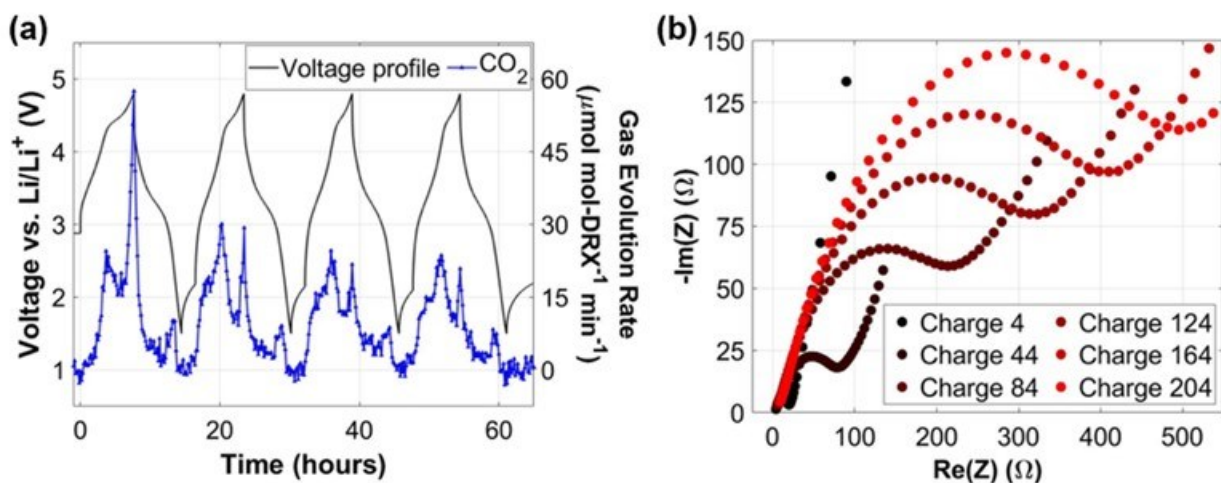


Figure VIII.2.20 (a) DEMS results depicting CO<sub>2</sub> evolution during cycling of LMTO in half cell, and (b) Nyquist plot depicting growth in impedance over long-term cycling of LMTO in a full cell. Impedance measurements were taken after each charge listed. For both experiments, the cells were charged at a constant rate of 0.1 Li hr<sup>-1</sup> (32.9 mA g<sup>-1</sup>) in a voltage window of 4.8 – 1.5 V vs. Li/Li<sup>+</sup> and the electrolyte was 1M LiPF<sub>6</sub> in 3:7 EC:EMC. The EIS scan employed an amplitude of 5 mV and a frequency range of 20 MHz to 100 kHz.

As a way to correlate outgassing of EC-based electrolytes with carbon black surface area, we performed isotopic labelling measurements to trace the origin of CO<sub>2</sub> evolution during cycling. We tested three cells: one in which the Li<sub>1.2</sub>Mn<sub>0.6</sub>Ti<sub>0.2</sub>O<sub>1.8</sub> (LMTO) active material was synthesized using a Li<sub>2</sub><sup>13</sup>CO<sub>3</sub> precursor (to tag any residual carbonate left after the synthesis procedure), one in which the carbon black was predominantly <sup>13</sup>C enriched, and one in which both the DRX and carbon black were <sup>13</sup>C labelled. When preparing these three cells, we used slightly different carbon-to-DRX ratios in the electrodes, and noted that the <sup>13</sup>C carbon black and typical carbon black (Super P) had fairly different weight-averaged surface areas (63 vs 145 m<sup>2</sup>/g for Super P and <sup>13</sup>C, respectively), such that the carbon surface area contained in each cathode tested was substantially different. When plotting the cumulative CO<sub>2</sub> evolution over the first ten cycles from each of these cells (Figure VIII.2.21), we note that when normalized to the LMTO content in the cathode, the electrolyte-originating CO<sub>2</sub> (EC+CBK-CO<sub>2</sub> in Figure VIII.2.9a, <sup>12</sup>CO<sub>2</sub> in Figure VIII.2.9b, c) varies between 550 and 1350 μmol/g<sub>LMTO</sub>. However, when normalized to the surface area of the carbon black contained in each electrode, the electrolyte-originating CO<sub>2</sub> in each cell is very similar, ranging between 19 and 21 μmol/m<sup>2</sup>. This result suggests that the carbon black plays a more predominant role in electrolyte degradation than the DRX material. Future strategies to reduce its surface area could result in dramatically improved long-term performance.



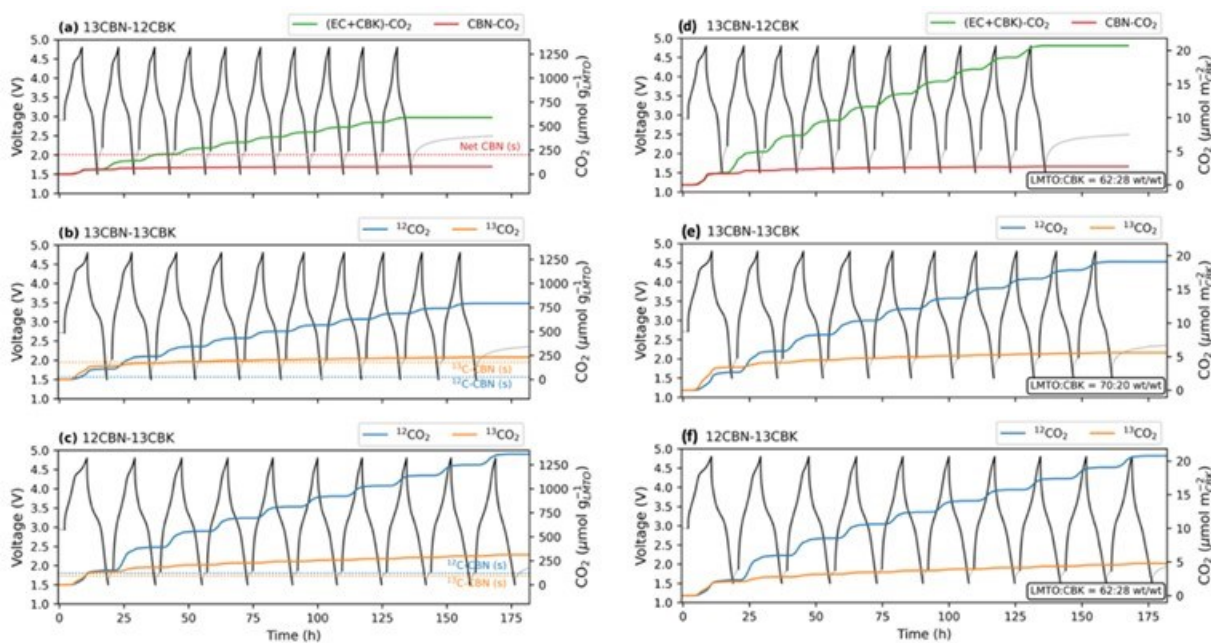


Figure VIII.2.21 (a) Cumulative CO<sub>2</sub> evolution from a DRX material prepared using <sup>13</sup>C labelled Li<sub>2</sub>CO<sub>3</sub> (<sup>13</sup>CBN) and Super P carbon (<sup>12</sup>CBK). (b) Cumulative CO<sub>2</sub> evolution from a <sup>13</sup>CBN DRX and <sup>13</sup>C labelled carbon black (<sup>13</sup>CBK) cathode. (c) Cumulative CO<sub>2</sub> evolution from a <sup>12</sup>CBN DRX and a <sup>13</sup>CBK cathode. (a-c) are all normalized to the weight loading of the DRX material (LMTD). Horizontal dotted lines mark the initial amounts of solid native carbonate in LMTD. (d-f) are the same cumulative CO<sub>2</sub> evolution profiles as (a-c), but instead normalized to the carbon black surface area. In each case, the electrolyte-originating CO<sub>2</sub> is nearly identical when normalized to the carbon black surface area rather than the LMTD loading, implying that the carbon black governs electrolyte stability.

We also examined three battery additives, lithium bis(oxalato)borate (LiBOB), tris(trimethylsilyl) phosphate (TMSPa), and fluoroethylene carbonate (FEC), and studied the H<sub>2</sub>, Me<sub>3</sub>SiF, and CO<sub>2</sub> outgassing that occurs from each cell over the first 8 cycles, noting that any Me<sub>3</sub>SiF evolution is specific to TMSPa cells. In

Figure VIII.2.22, H<sub>2</sub> and Me<sub>3</sub>SiF evolution are multiplied by a factor of 10 for easier viewing. We added 3wt% of these additives to 1.5M LiPF<sub>6</sub> in an EC lean electrolyte (15 vol% EC, 85 vol% DMC) and tested them in Li||DRX cells with LMTF2622C-1 DRX (Li<sub>1.2</sub>Mn<sub>0.6</sub>Ti<sub>0.2</sub>O<sub>1.8</sub>F<sub>0.2</sub>) supplied from Argonne National Laboratory. The DRX was mixed with C65 and PVDF in a 70:20:10 ratio and had very similar loading (+/- 0.1mg) across all samples. The LiBOB additive showed the worst performance with continuous capacity fade, a result that is surprising given LiBOB's typical use to promote cathode stabilization. TMSPa is an additive that scavenges F<sup>-</sup> ions and reacts to form Me<sub>3</sub>SiF, a gas that can be detected. The first peak shows the most Me<sub>3</sub>SiF evolution, but repeated cycles show minor continuous evolution at high voltages. FEC shows small, low-voltage (~4.2V) CO<sub>2</sub> evolution during charge, likely the reduction of FEC. This reduced product likely forms H<sub>2</sub> at high voltages during later cycles, with H<sub>2</sub> evolution slowly increasing over cycling. All cells observed similar small O<sub>2</sub> evolution around 4.6V on their first cycle (not shown), indicating that O<sub>2</sub> evolution was not impacted by additive inclusion. It should be noted that this DRX batch (LMTF2622C-1) has different CO<sub>2</sub> outgassing behavior than other DRX tested, with the onset voltage being higher than other DRX material, and total CO<sub>2</sub> outgassing being higher. Understanding the origin of this different behavior is still being investigated. In the end, among all additives characterized, TMSPa appears to be the most promising in stabilizing the cathode surface while maintaining good cycle life and capacity retention; we will continue to characterize TMSPa-containing cells to understand this performance improvement in the future work.

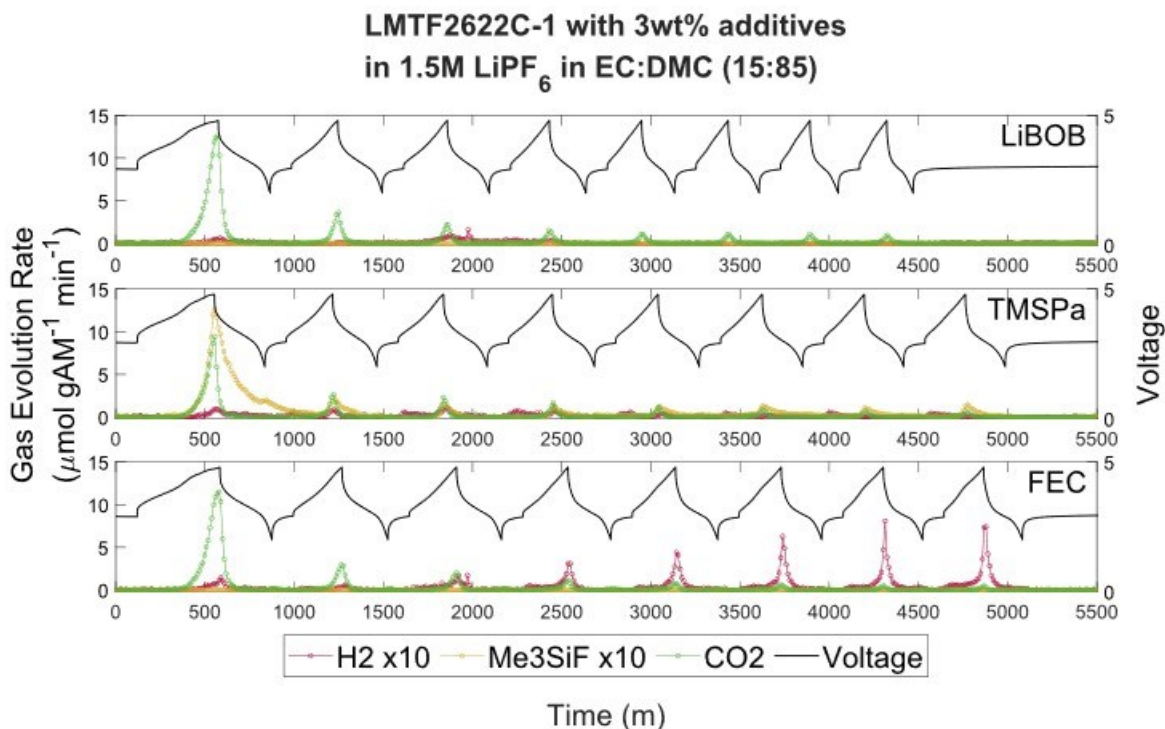


Figure VIII.2.22 Outgassing from a Li || DRX (LMTF2622) cell employing EC-lean electrolytes with three different additives.

### 3) Simulations to elucidate degradation mechanisms involving reactive oxygen.

We are currently investigating chemical oxidation reactions taking place at the cathode of Li-ion batteries. By studying the feasibility of these reactions, we illustrate which decomposition products are formed at the cathode-electrolyte interphase of DRX electrodes and the mechanisms responsible for their formation in Figure VIII.2.23. The decomposition pathways for reactions of ethylene carbonate (EC) with singlet oxygen was investigated. The decomposition of EC-based electrolytes causes gas (carbon dioxide, carbon monoxide and hydrogen) evolution. Since this gas evolution is observed at potentials much lower than the oxidation potential of EC, it has been suggested that the mechanisms leading to decomposition are primarily chemical in nature (i.e., not related to the electrochemical oxidation of EC) and related to the reaction of *singlet* oxygen with EC. We computed the activation barriers for the first decomposition step of EC with singlet oxygen. We find that the activation barriers for all proposed mechanisms in the literature are highly endergonic, suggesting that the reaction is unlikely to occur on the timescale in which it is observed in experiments.

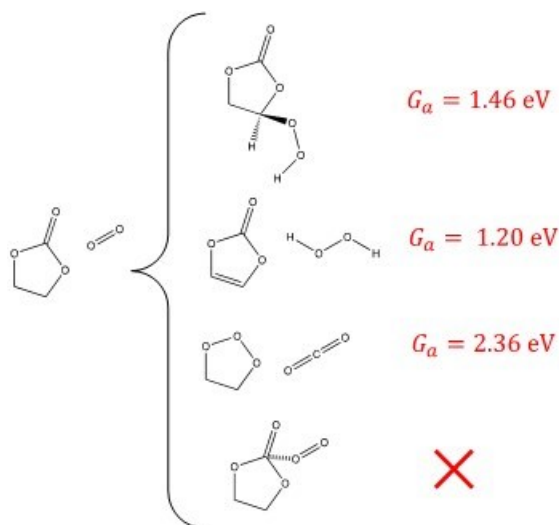


Figure VIII.2.23 Activation barriers (in red) for the decomposition of EC with singlet oxygen

Using density functional theory (DFT), we have pursued mechanistic explanations for the decomposition of common carbonate-based electrolytes at Li-ion battery positive electrodes. In recent years, it has been widely reported that oxygen in the singlet excited state ( $^1\text{O}_2$ ) is responsible to decomposing ethylene carbonate (EC) solvent molecules via a chemical oxidation reaction. While this is consistent with the observation of  $\text{O}_2$  evolving from high-voltage positive electrodes (including some DRX materials) at potentials  $> 4.2\text{V}$ , we do not believe that explanations based on  $^1\text{O}_2$  are plausible. Figure VIII.2.24a shows elementary mechanisms for the two most commonly cited reactions between EC and  $^1\text{O}_2$ : a single-step concerted reaction forming hydrogen peroxide ( $\text{H}_2\text{O}_2$ ) and vinylene carbonate (VC) and an addition-elimination reaction yielding water and 1,3-dioxolane-2,4-dione. DFT calculations at the  $\omega\text{B97X-V}/\text{def2-TZVPPD}/\text{SMD}$  level of theory predict that these reactions both have high free energy barriers ( $\Delta G^\ddagger \gg 1 \text{ eV}$ ), suggesting that they will be extremely slow under normal battery operating conditions. However, our calculations suggest that the superoxide radical ( $\text{O}_2^{-1}$ ) can more easily react with EC (Figure VIII.2.24b), particularly through a nucleophilic substitution. Further computational studies examining reactions between EC and oxygen anions – including superoxide as well as peroxide ( $\text{O}_2^{-2}$ ) – are ongoing. We are also collaborating with the McCloskey group, who are performing experiments aiming to detect decomposition products for reactions between EC-based electrolytes and superoxide/peroxide species.

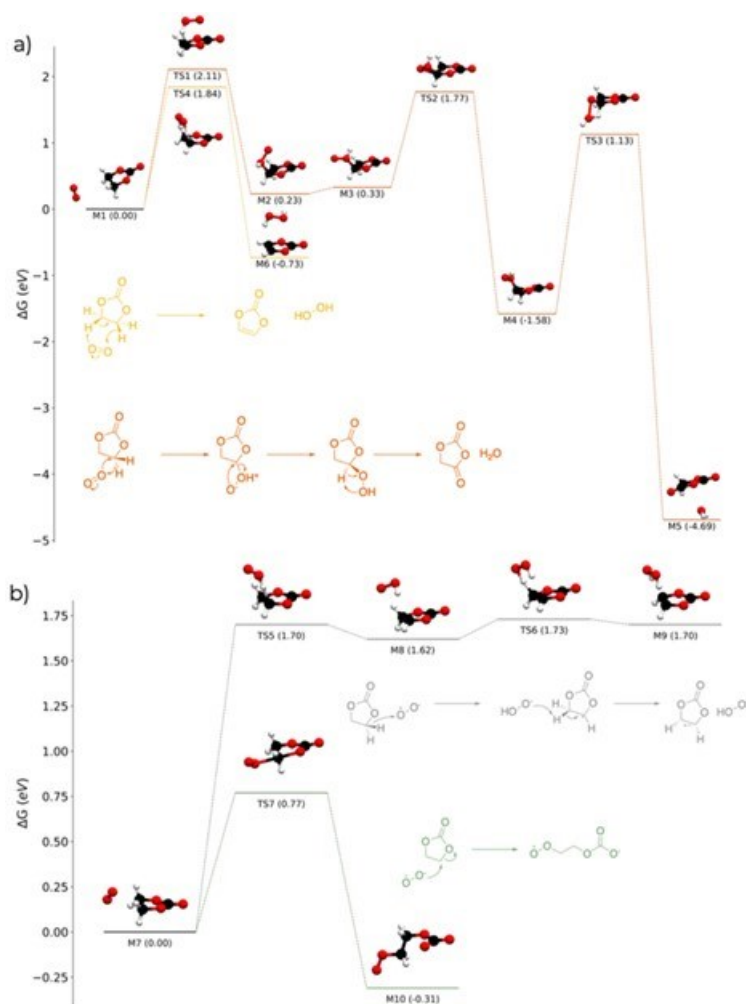


Figure VIII.2.24 energy diagrams for reactions between ethylene carbonate (EC) and a) singlet oxygen ( $^1O_2$ ); or b) superoxide ( $O_2^-$ ).

### Task 3: Coatings

A major goal of the carbon coating task is to develop materials/processes to reduce the carbon content in DRX cathodes and thus increase the electrode/cell level energy density. Carbon coating of cathode particles can effectively increase electrical conductivity and cycle performance by changing the ion transport mechanism and preventing them from direct contact with electrolytes. In addition, cathodes coated with graphite has been reported to exhibit superior electrochemical properties than other forms of carbon such as carbon black or acetylene black. In general, high temperature treatment is required to make a graphitic carbon coating. However, in contrast to the conventional layered oxide cathodes, the DRX cathodes can decompose under the highly reducing environment at high temperature. Therefore, a low temperature synthesis route for graphitic carbon coating needs to be developed. The most viable approach for applying a carbon coating is by ball milling a mixture of DRX with a carbon material. However, it has never been clear how the ball milling process affects the DRX.

#### 1) Effect of carbon coating.

In FY23, PNNL investigated the morphology of carbon coated DRX cathode particles. For this study, solid-state synthesized  $Li_{1.2}Mn_{0.5}Ti_{0.3}O_{1.9}F_{0.1}$  DRX cathode particles were coated with C-65, graphite and ketjenblack using mechanical mixing (ball milling). The morphology of carbon coated DRX cathode surface was probed by transmission electron microscopy (TEM). Figure VIII.2.25 shows TEM images of DRX surface

coated with C-65, Graphite and ketjenblack. In case of DRX surface coated with C-65 and ketjenblack, nonuniform carbon layers were apparent near the surface as evidenced by Figure VIII.2.25a and Figure VIII.2.25c. However, in case of graphite coated DRX, virtually uniform layer with thickness about  $\sim 15$  nm was observed. The more uniform coating layer of graphite compared to C-65 and ketjenblack could be attributed to the lubricating effect of graphite which is mechanical in nature.

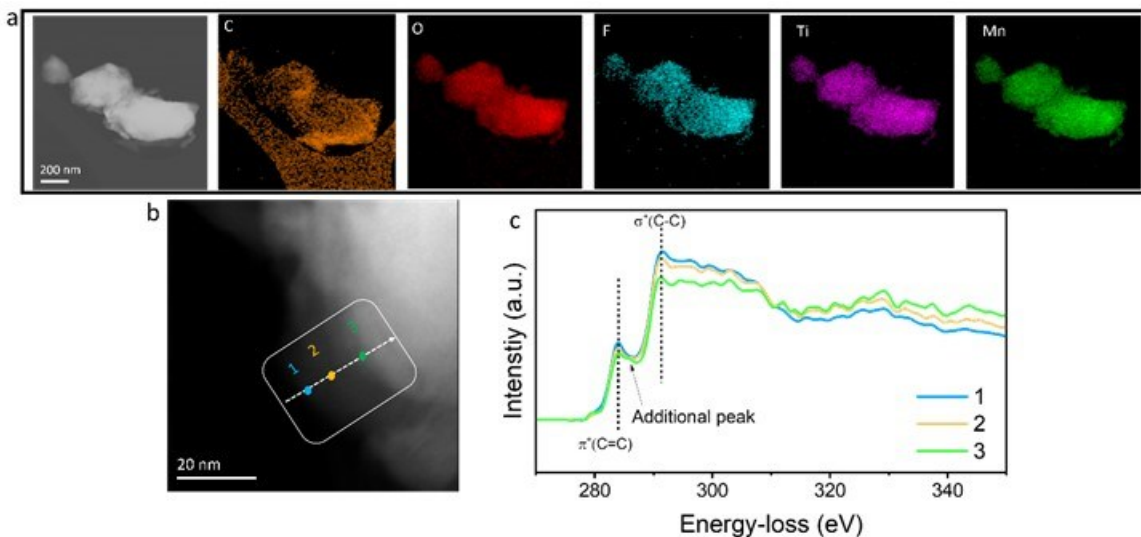


**Figure VIII.2.25 Morphology and chemical state of graphite coated DRX cathodes (a) HAADF-STEM image and energy dispersive spectroscopy (EDS) map of graphite coated cathodes. (b) HAADF image showing the position where EELS signals were taken (c) EELS taken from marked regions in (b).**

To further understand the elemental composition and chemical state of coated graphite which showed a uniform distribution within the particle, we used high-angle annular dark field (HAADF) imaging, X-ray energy dispersive spectroscopy (EDS) and electron energy-loss spectroscopy (EELS) in scanning transmission electron microscope (STEM). Figure VIII.2.25a is the HAADF-STEM image and EDS mapping of constituent elements of DRX cathode. Apparent feature from the EDS mapping is the presence of additional chunks of residual graphite near the particles. However, other elements such as O, F, Ti and Mn were uniformly distributed in the graphite coated DRX cathode. In order to further understand the chemical nature of coated graphite, we employed electron energy-loss spectroscopy. Figure VIII.2.25c shows the EELS signals observed for the regions indicated in Figure VIII.2.25b. In all probed regions, we observed the sharp  $\pi^*$  ( $\sim 284.6$  eV) and  $\sigma^*$  ( $\sim 292.4$  eV) peaks at C-K edge, indicating the preservation of graphitic nature of coated graphite. However, near the interface (region 3) between coated graphite and cathode, we observed an additional peak at  $\sim 287.2$  eV, suggesting the carbon complex formation possibly due to interaction with Li, O, or transition metals from the cathode. A detail analysis on additional peak observed near the interface with reference to change in Li-K, O-K and transition metal (TM)-L edges will be the future study. Irrespective of that, this study reveals the possibility of uniform carbon coating of cathode particles required to enhance conductivity and stability of cathode materials.

Experiments on mapping the spatial distribution of different carbon additive including graphite and C-65 on DRX particles were also conducted. To fabricate the DRX particles compatible for electrode fabrication, solid state synthesized  $\text{Li}_{1.1}\text{Mn}_{0.8}\text{Ti}_{0.1}\text{O}_{1.9}\text{F}_{0.1}$  cathode particles were subjected to ball milling at a speed of 300 rpm. Two different milling conditions were employed: one with acetylene black as a carbon source (20%) and another without any carbon source. Scanning electron microscopy (SEM) images of the resultant DRX particles with and without carbon are presented in Figure VIII.2.26a and b respectively. It was observed that the DRX particles milled without carbon source led to smaller particle sizes and greater agglomeration as apparent from SEM images. To further investigate this phenomenon, scanning transmission electron

microscopy (STEM) and energy dispersive X-ray spectroscopy (EDS) techniques was employed, as depicted in Figure VIII.2.26c and d. STEM-EDS mapping clearly reveals coating of carbon on the DRX particle surface with simultaneous existence of bulk residual carbon as shown in Figure VIII.2.26c. Additionally, Figure VIII.2.26d supports the SEM results, demonstrating the particle agglomeration for the case of ball milling without carbon.

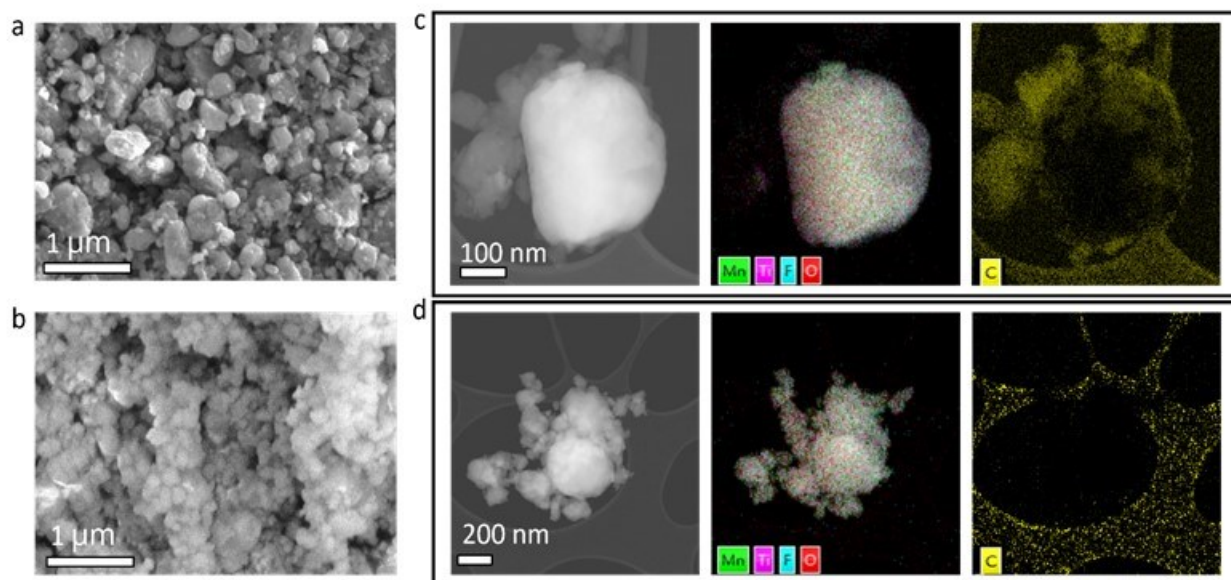
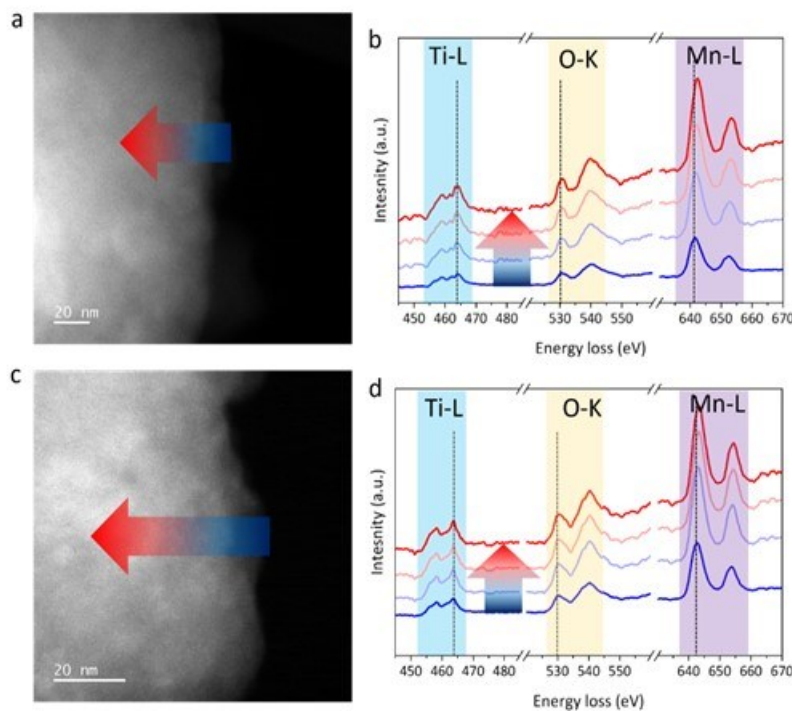
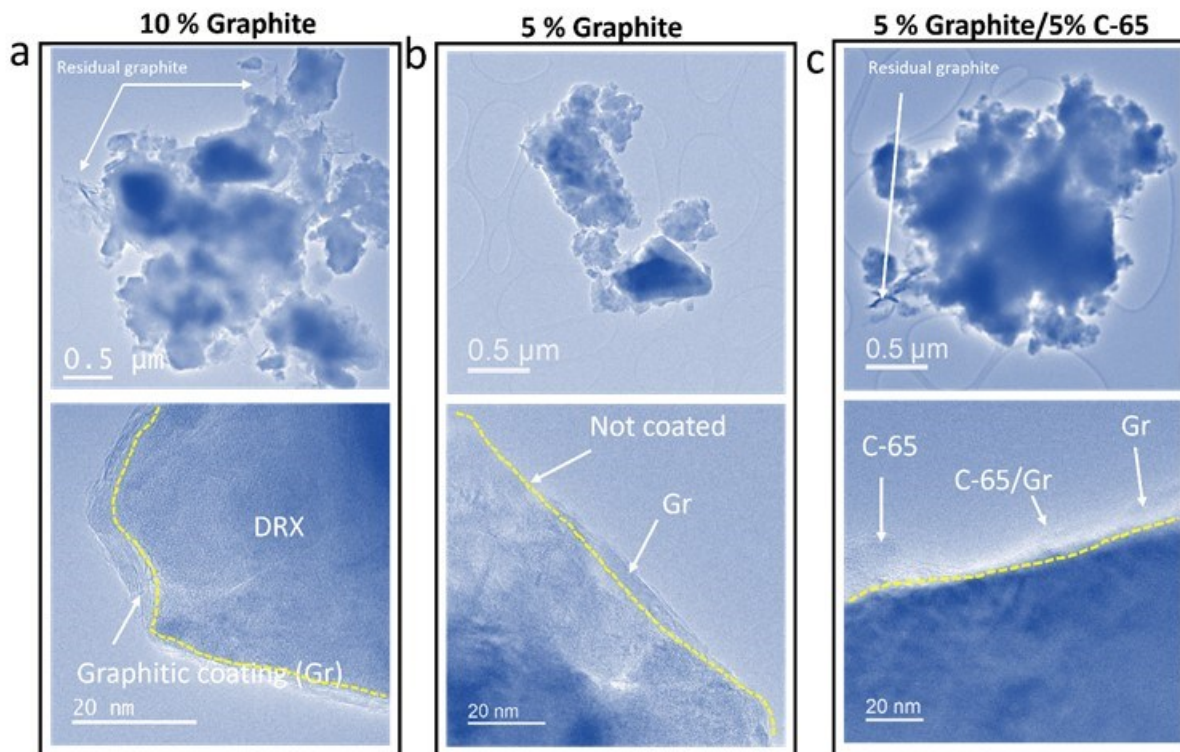


Figure VIII.2.26 Effect of ball milling with and without carbon on DRX morphology. (a) SEM image of the particle milled with carbon, (b) SEM image of the particle milled without carbon, (c) HAADF image and corresponding EDS elemental map showing the carbon distribution on the DRX particle milled with carbon, (d) HAADF image and EDS elemental map showing the particle agglomeration on the particle milled without carbon (the carbon map in d indicates the carbon film on TEM grid).



**Figure VIII.2.27** A comparison of chemical nature of cations for DRX particles milled with and without carbon. (a) HAADF image indicating the position and direction of EELS acquisition, (b) EELS acquired at Ti-L, O-K and Mn-L edges for the particle milled with carbon. (c) HAADF image indicating the position and direction of EELS acquisition for the particle milled without carbon, (d) EELS acquired at Ti-L, O-K and Mn-L edges for the particle milled without carbon.

The morphology of carbon coated DRX cathode particles using large scale synthesized  $\text{Li}_{1.2}\text{Mn}_{0.6}\text{Ti}_{0.2}\text{O}_{1.8}\text{F}_{0.2}$  particles (made at ANL facilities) was also investigated. These particles were coated with different carbon materials, including 10% graphite (Gr), 5%Gr and 5%(Gr)+5%(C-65) using ball milling. Figure VIII.2.28 presents the TEM images of carbon coated DRX surfaces. In case of DRX surface coated with 10%Gr, a relatively uniform layer with thickness 5-10 nm was observed as presented in Figure VIII.2.28a. This indicates that the graphite coating provides a consistent coverage on the DRX surface. For the DRX surface coated with 5%Gr, uncoated surfaces can be seen. For the 5%Gr+5%C-65, the presence of both Gr and C-65 was noted. Notably, C-65 coating appeared thicker compared to the graphite coating, as depicted in Figure VIII.2.28c. Evidently, carbon source characteristics and overall carbon concentration play a role for the coating quality. These findings provide insight into optimizing the carbon coating parameters for DRX cathode particles, aiding in the development of improved DRX electrode materials.



**Figure VIII.2.28** Spatial distribution of different carbon species on DRX particle surface; (a) Gr (10%) coated DRX, showing a coating layer thickness of 5-10 nm with residual graphite, (b) Gr (5%) coated DRX, showing a coating layer thickness of 5-10 nm at some regions, while some regions are uncoated. (c) 5%(Gr)+5%(C-65) coated DRX; Gr coating ranges from 5-20 nm and C-65 coating ~25 nm; some residual chunks of graphite are evident.

## 2) Developing carbon coating method.

LBNL explored the solution-based carbon coating route that utilizes an electrostatic interaction between DRX particles and few-layer reduced graphene oxide (rGO) sheets by controlling the surface charge. Using this process, two different rGO-DRX composites were synthesized and characterized. The scaleup sample of  $\text{Li}_{1.2}\text{Mn}_{0.6}\text{Ti}_{0.2}\text{O}_{1.8}\text{F}_{0.2}$  which were synthesized by ANL was used for the rGO coating. Initially, the surface charges of the particles and graphene are determined from the zeta potential measurement and it was observed that the  $\text{Li}_{1.2}\text{Mn}_{0.6}\text{Ti}_{0.2}\text{O}_{1.8}\text{F}_{0.2}$  is positively charged at pH-2 while graphene has a negative charge at pH 2-12. One approach is to adjust the pH of solution to maintain the surface charges of  $\text{Li}_{1.2}\text{Mn}_{0.6}\text{Ti}_{0.2}\text{O}_{1.8}\text{F}_{0.2}$  and rGO oppositely for an electrostatic attraction. In this method, graphite oxide (20 mm) was dissolved in deionized (DI) water ( $1 \text{ mg mL}^{-1}$ , 200 mL) and exfoliated to produce graphene oxide by sonication for 100 min. To reduce graphene oxide, urea (0.15 M) was slowly added to the graphene oxide solution and stirred for 10 h at  $80^\circ\text{C}$  in an oil bath. Then,  $\text{Li}_{1.2}\text{Mn}_{0.6}\text{Ti}_{0.2}\text{O}_{1.8}\text{F}_{0.2}$  powder was added to the above solution and stirred for 1 h at room temperature. Finally, pH of the solution was adjusted to 2, where the  $\text{Li}_{1.2}\text{Mn}_{0.6}\text{Ti}_{0.2}\text{O}_{1.8}\text{F}_{0.2}$  and rGO have opposite surface charges. At this low pH, the negatively charged rGO nanosheets electrostatically attract positively charged DRX particles, resulting in the uniform wrapping that was confirmed by SEM images in Figure VIII.2.29a. X-ray diffraction (XRD) peaks (Figure VIII.2.29b) of rGO-DRX exhibited a small right shift compared to DRX, which might indicate the extraction of Li-ions from the DRX structure, which is under investigation.



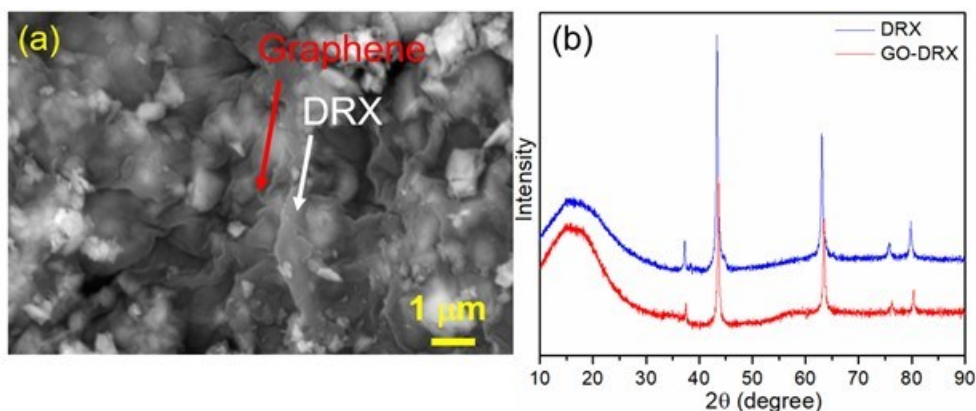


Figure VIII.2.29 (a) SEM image of DRX particles wrapped by reduced graphene oxide and (b) XRD of DRX particles wrapped by reduced graphene oxide compared with DRX.

The other approach is a two-step process that involves (1) coating of  $\text{Li}_{1.2}\text{Mn}_{0.6}\text{Ti}_{0.2}\text{O}_{1.8}\text{F}_{0.2}$  particles by a polyethylenimine (PEI) with positive surface charges and (2) wrapping the polymer coated DRX particles in rGO sheets. In a typical process, 1 g of PEI and 0.8 g polyvinylpyrrolidone (PVP) were dissolved in 20 mL of ethanol and methanol (1:1) mixture solution and then 1 g of LMTOF02 were dispersed in the solution at 50 mg/mL concentration. The dispersion was subjected to sonication for 60 min and stirred at 600 rpm for 24 h at room temperature. PEI coated DRX is attained by washing the resultant products using the methanol and acetone followed by drying at 70 °C. The rGO wrapped PEI coated DRX is obtained by exfoliating graphite oxide to graphene oxide and then reducing it by urea followed by the addition of PEI coated DRX. Hence, positively charged PEI coated DRX is wrapped by negatively charged rGO through electrostatic interactions in a neutral pH, which is evidenced by SEM (Figure VIII.2.30a and b). In this case, it was observed that some of LMTOF02 particles are uncovered by rGO, indicating that more optimization is further required for a uniform coating. XRD pattern (Figure VIII.2.30c) of PEI-DRX is identical to DRX peaks while a slight shift is observed from rGO-PEI-DRX which could be due to the reaction of  $\text{Li}_{1.2}\text{Mn}_{0.6}\text{Ti}_{0.2}\text{O}_{1.8}\text{F}_{0.2}$  with water, which is under investigation. It is also noteworthy that the shift of XRD peak detected from rGO-PEI-DRX is not significant as observed at pH 2 in Figure VIII.2.29b.

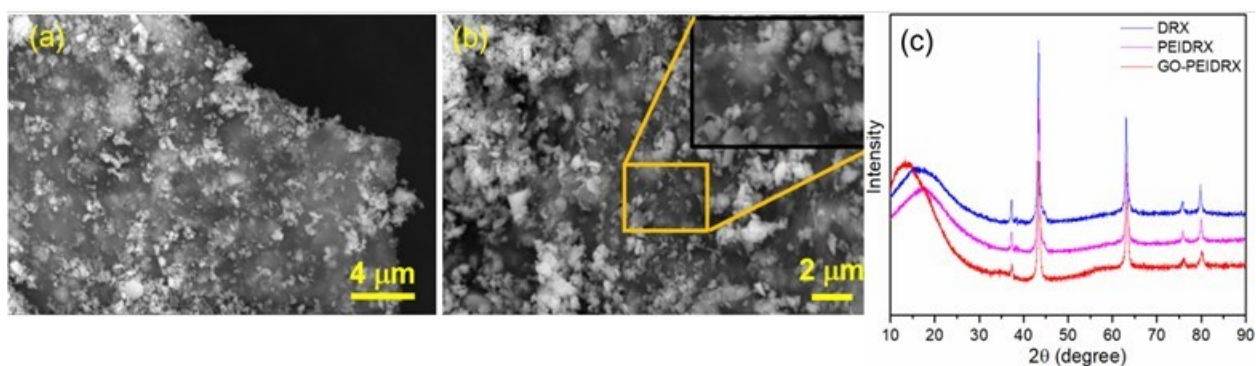


Figure VIII.2.30 (a)(b) SEM images of PEI coated DRX particles wrapped by reduced graphene oxide and (c) XRD of PEI-DRX particles wrapped by reduced graphene oxide compared with DRX and PEI coated DRX.

In addition, detailed analysis and screening of the solvents to be used for the graphene-wrapped polyethylenimine (PEI) coated DRX synthesis was studied. For this study, the dispersion of graphene is initially verified in various aqueous and organic solvents. We observed that the graphene is well dispersed in dimethylformamide (DMF), ethylene glycol (EG), tetrahydrofuran (THF) and N-methyl-2-pyrrolidone (NMP) similar with that in water. Hence, the stability of the scaleup sample of  $\text{Li}_{1.2}\text{Mn}_{0.6}\text{Ti}_{0.2}\text{O}_{1.8}\text{F}_{0.2}$  which was synthesized by Argonne National Laboratory was investigated in these solvents using inductively coupled

plasma mass spectrometry (ICP-MS) analysis. In this process, 1 mg  $\text{Li}_{1.2}\text{Mn}_{0.6}\text{Ti}_{0.2}\text{O}_{1.8}\text{F}_{0.2}$  was dispersed in 1 mL of the solvent and left the suspension for different time intervals. For the analysis, we collected 20  $\mu\text{L}$  of the solution after all the DRX particles were completely settled and the collected solution was added to the 10 mL of nitric acid for the ICP-MS measurements. It was detected that  $<8$  at% of Li and  $<1$  at% of Mn, and Ti were removed from the DRX in water after 1 h and  $\sim 16$  at% of Li and  $\sim 1$  at% of Mn and Ti were dissolved in water after 24 h (Figure VIII.2.31). In contrast, in the case of other solvents, the dissolution of the DRX particles was 4 times less than in water after 24 h. Here, we want to highlight that there is no dissolution of Li, and Mn in the case of THF solvent and it was observed that the dissolution of Ti is only  $<0.1$  at% after 24 h. Therefore, in the following quarters, we will use THF to synthesize the graphene wrapped PEI coated DRX and test their electrochemical performance.

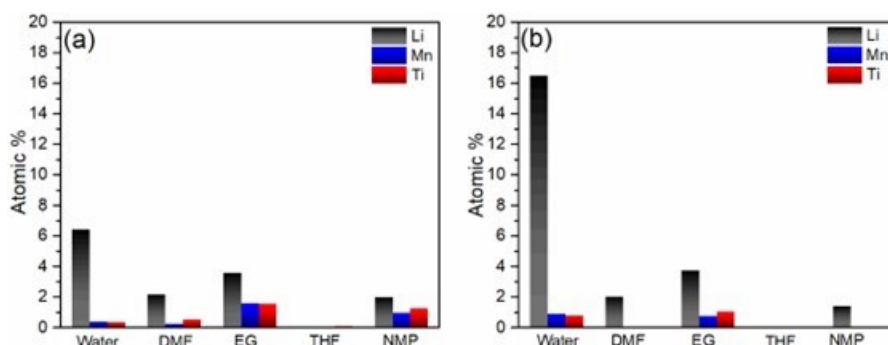


Figure VIII.2.31 ICP-MS signal of  $\text{Li}_{1.2}\text{Mn}_{0.6}\text{Ti}_{0.2}\text{O}_{1.8}\text{F}_{0.2}$  particles dispersed in various solvents at (a) 1 h and (b) 24 h.

### 3) Effect of carbon additive in composite cathode.

At LBNL, DRX was coated with Denka black and carbon nanotubes *via* high energy ball milling. The electrodes with 15 wt% DB+CNT showed the best performance. the ratio of Denka black and CNT was further investigated. The content of the DRX active material and PVDF were fixed at 75 wt% and 10 wt%, respectively, then electrodes were fabricated with three different ratios of DB to CNT: 10/5, 5/10 and 0/15. The electrochemical performance of the electrodes is shown in Figure VIII.2.32. The capacity and energy of the cells were improved with increasing the ratio of CNT to DB. An increase in the ratio of CNT to DB reduced the charge transfer resistance. However, high levels of CNT in the electrode resulted in more side reactions and a decrease in the coulombic efficiency.

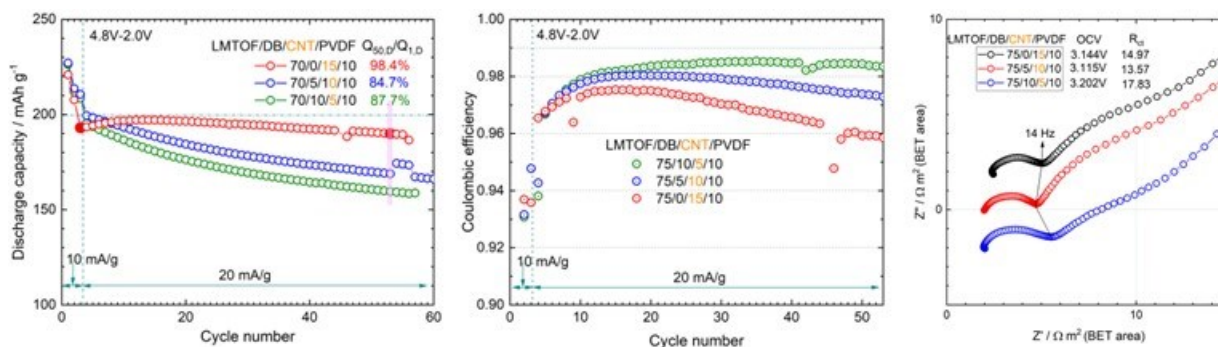
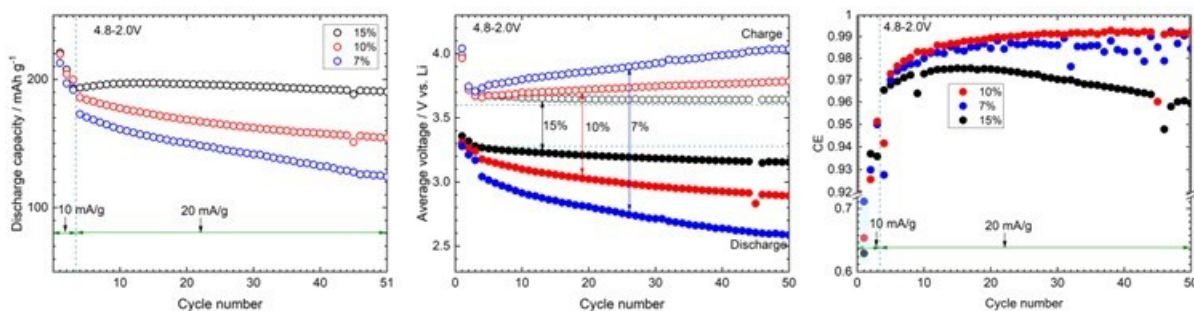


Figure VIII.2.32 The electrochemical performance of the electrodes with different ratios of DB to CNT: discharge capacity, coulombic efficiency and electrochemical impedance spectroscopy from left to right.



**Figure VIII.2.33** The electrochemical performance of the electrodes with different amounts of CNT.

In addition, the reduction of the CNT content from 15 to 7% in the absence of Denka black was studied. The electrochemical performance of the electrodes *versus* CNT content is shown in Figure VIII.2.33. The electrode with 15% CNT delivered high capacity and shows stable cycling performance, although the reduction of CNT improved the coulombic efficiency.

Ten percent CNT is better than 7%, as the capacity fade is less, the difference in the average voltage on charge and discharge is less. The coulombic efficiency is improved, but this may be a result of less capacity decay with the 10% CNT. The 15% CNT-cell first shows an increase in capacity and a higher capacity than the other two cells, then levels off and begins to fall after 15 cycles. This is a much-improved capacity cyclability. However, the coulombic efficiency is significantly worse, which is likely to have a detrimental impact on cycle performance at later cycles. It is possible that this worse coulombic efficiency allowed for longer charging times which resulted in higher capacities on each charge. An optimum has to be found to get the high coulombic efficiency of 10% CNT and the slow capacity fade and low resistance rise of the 15% CNT. These changes are only reducing the carbon from 20% to 15%. The goal is to reduce the overall carbon content to 5%. It is possible to achieve it by adjusting the binder content and moving toward a more uniform particle size distribution.

We further investigated the impact of use carbon nanotubes at different weight fractions relative to the active material. The binder content was essentially held constant around 10%. The work presented here is on the first batch of DRX supplied by ANL. In Figure VIII.2.34, *Left*, the capacity *versus* cycle number for batch 1 for three loadings of carbon (8, 10, and 15% by weight) is presented. Clearly, the electrode with the highest level of carbon, 15 wt%, demonstrates the best cycling performance. One sees that the capacity at a charge-discharge current of 20 mA/g starts at around 189 mAh/g, rises to 194 mAh/g by the 15<sup>th</sup> cycle, then experiences a fairly linear decline to 172 mAh/g by the 100<sup>th</sup> cycle. Figure VIII.2.13, *Center*, provides the voltage profiles for the first 15 cycles and additional profiles for cycles 50, 75, and 100. Overall, one sees that the voltage curve is evolving from the very first cycle. The interpretation is that during the entire time of cycling the material's structure is changing from rock salt to partial spinel, otherwise referred to as  $\delta$ -phase. It appears that early on the change in structure is leading to slightly more capacity between 2 and 4.8 V. After this initial capacity rise from structure change we begin to see impedance rise in the Nyquist plots of Figure VIII.2.34, *Right*, and the associated capacity loss in Figure VIII.2.34, *Left*. Close inspection of the impedance rise points to three time regimes. The first is the mid-frequency region that ranges from 1 to 1000 Hz. This impedance is typically associated with charge transfer resistance. The second time regime of impedance rise is between 0.005 and 0.2 Hz. We believe that this rise of impedance could be due to the development of a barrier layer on the CNTs and active material. The third source of impedance rise is below 0.003 Hz and could be attributed either to slower solid-state lithium diffusion or longer diffusion pathways. (Disclaimer: since the impedance is taken at 60% DOD based on the initial capacity, the impedance is being taken at an ever-lower depth of discharge as the capacity declines after the first 15 cycles. Charge transfer and diffusion can be SOC dependent in crystalline materials so the increase in resistance could be due to the changes in Li-ion fraction in the material with cycling.)

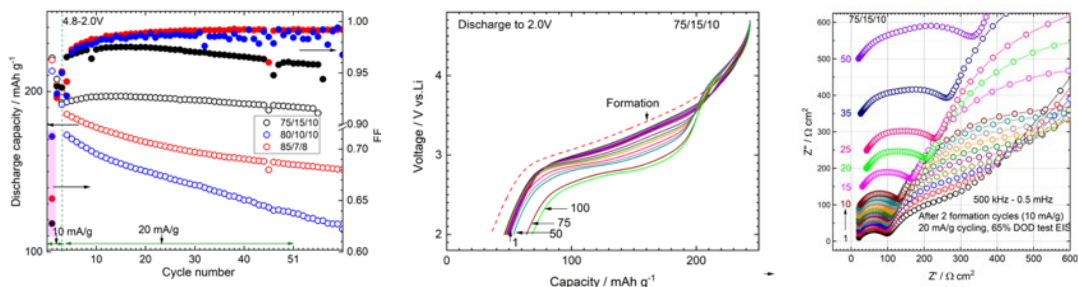


Figure VIII.2.34 (Left) the active-area specific-capacity and coulombic efficiency versus cycle number, (Center) the discharge voltage curves versus specific capacity at a discharge rate of 20 mAh/g, and (Right) Nyquist plot of electrochemical impedance spectroscopy data taken over the first 50 cycles.

#### Task 4: Bulk Studies and Design

##### 1) Cluster expansion studies on disorder effect in partially disordered spinel systems.

DRX GEN3 will be sought among partially disordered materials with specific focus on spinels. Cation disorder on the octahedral sites of a spinel been demonstrated to remove the two-phase reaction around 3 V leading to more stable cycling. In FY23 we saw the successful simulation of the electrochemical profile as function of disorder. By using cluster expansion in conjunction with Monte Carlo (MC) simulations, voltage curves for (de)lithiation within spinel frameworks with varying levels of Mn 16c/16d disorder ( $d$ , where  $d$  indicates the 16c sites occupancy) were calculated. Figure VIII.2.35 shows the calculated voltage profile from semi-grand-canonical (sgc) MC. At  $d=0$ , the characteristic plateaus at  $\sim 4.3$  V and  $\sim 3$  V in the ordered spinel phase are similar to experimental results. With higher  $d$ , the  $\sim 4$  V and  $\sim 3$  V plateaus shorten and disappears at  $d=0.25$ . We find that disorder on 16c/16d lowers the energy of the solid-solution phase through Li occupancy of non-Mn-occupied 16d sites, which stabilizes face-sharing environments.

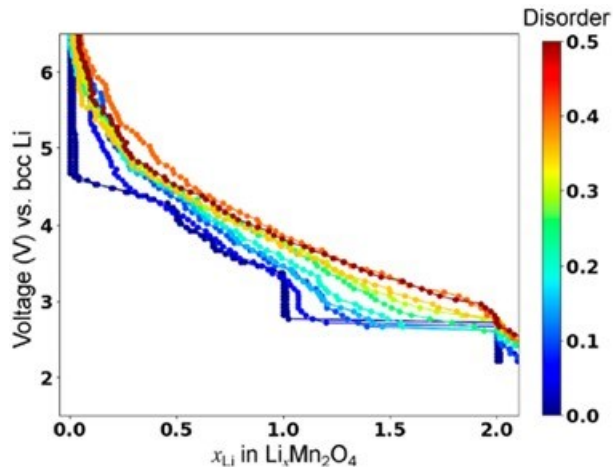


Figure VIII.2.35 sgc MC-simulated voltage curves of spinel  $\text{Li}_x\text{Mn}_2\text{O}_4$  with varying disorder from  $d = 0.0$  (ordered spinel, dark blue) to  $d = 0.5$  (fully disordered spinel, dark red).

Data on the specific local configurations that occur as a partially disordered spinel is lithiated are shown in Figure VIII.2.36. At low level of disorder ( $d = 0.1$ ) lithiation initially proceeds the same as in the ordered system ( $d = 0$ ), where Li is inserted into isolated tet (8a) sites (left inset in Figure VIII.2.36c) until fully occupied, and a phase transition (transparent blue regime) occurs with occupancy shifting from tet to oct occupancy. From  $x_{\text{Li}} \approx 0.4$  to  $x_{\text{Li}} \approx 1.2$ , Li begins to occupy oct sites (left inset in Figure VIII.2.36d), (red in Figure VIII.2.36b) and Mn-face-sharing tet sites (right inset in Figure VIII.2.36d), as evidenced by the increase in tet Li with Mn-face-sharing environments (purple in Figure VIII.2.36d) and oct Li concentration. The larger population of tetrahedral environments that singly face-share with Mn leads to more face-sharing

Li–Mn configurations, which increases the Li site energy. Further lithiation until  $x_{\text{Li}} \approx 1.4$  involves Li occupying Li-face-sharing tet sites (blue in Figure VIII.2.36d). For  $d=0.1$ , the two-phase region is significantly reduced and appears between  $x_{\text{Li}} \approx 1.4$  and  $x_{\text{Li}} 2.0$ .

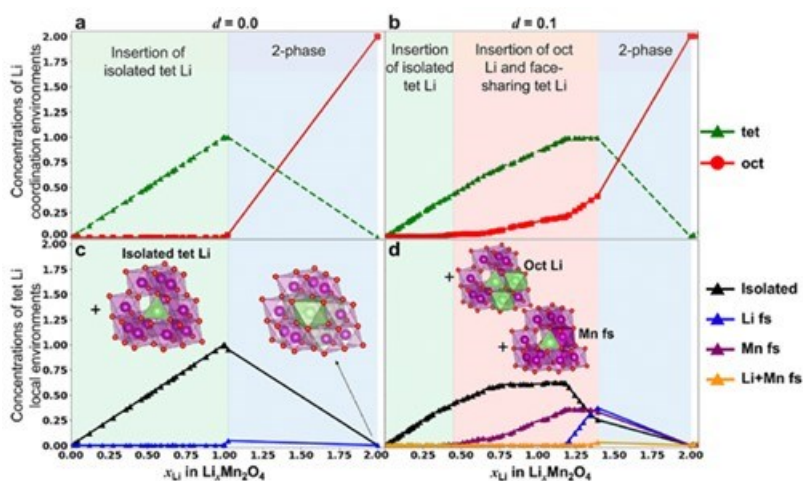
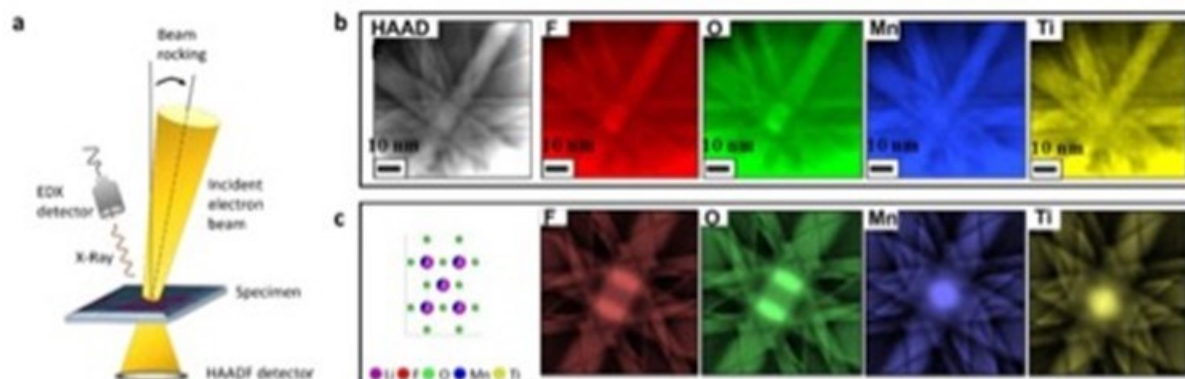


Figure VIII.2.36 Averaged concentrations of  $\text{Li}_x\text{Mn}_2\text{O}_4$  tet (green triangles) and oct (red circles) coordination at  $d = 0.0$  (a) and  $d = 0.1$  (b); and averaged concentrations of tet Li categorized by the species in their face-sharing nearest neighbor oct sites, including isolated with no face-sharing (black triangles), face-sharing with Li (blue), face-sharing with Mn (purple), and face-sharing with both Li and Mn (orange) at  $d=0$  (c) and  $d=0.1$  (d). Insets show local Li environments, including isolated tet Li inserted during the green regime and the fully lithiated spinel's oct Li in panel c, and oct Li and face-sharing tet Li inserted during the red regime in panel d.

## 2) Direct experimental identification of fluorine in DRX lattice.

Fluorination DRX has been demonstrated to enhance the lattice stability upon charge and discharge cycling. We have developed a novel capability to demonstrate that O and F are homogeneously mixed in DRX. Although NMR and synchrotron based XAS have been used for probing the coordination chemistry of F in DRX, these two techniques are bulk materials based techniques, and inherently lack the spatial resolution. In collaboration with Thermofisher Scientific, University of Melbourne, and Forschungszentrum at Julich, we have used an electron beam rocking technique to directly reveal the lattice position of F in DRX. In this technique, a focused electron beam is rocked at certain angle with respect to the lattice plane in a material, which leads to a phenomenon of Atom Location by Channeling-Enhanced Microanalysis (ALCHEMI). During the rocking of the electron beam, the electron channeling pattern (ECP) was recorded with the high angle annular dark field (HAADF) detector. From this the ionic channeling pattern (ICP) can be separated and recorded with characteristic x-ray energy dispersive spectroscopy (XEDS). Consequently, comparison of the ICP with different atomic species allows us to identify the atomic location of different atomic species at the lattice.

$\text{Li}_{1.2}\text{Mn}_{0.7}\text{Ti}_{0.1}\text{O}_{1.7}\text{F}_{0.3}$  DRX cathode particles synthesized using sol-gel route were used as a representative sample to demonstrate this technique for locating the position of F in DRX. For the DRX lattice, the cation and anion column are separated along the  $[110]$  zone axis. Therefore, as shown in Figure VIII.2.37, we captured the ECP and ICP along  $[110]$  zone axis. At the same time, we also calculated the ICP with each atomic species. It is apparent that ICP pattern of F and O are similar, while the ICP Mn and Ti are similar. Because the experimental ICP is consistent with the simulated one, the electron rocking beam results provide direct evidence that F and O atoms occupy the same atomic site in the DRX lattice.



**Figure VIII.2.37** A comparison of experimentally captured and simulated ionic channeling pattern (CP) associated with different atomic species along (110) direction for  $\text{Li}_{1.2}\text{Mn}_{0.7}\text{Ti}_{0.1}\text{O}_{1.7}\text{F}_{0.3}$  DRX. (a) Schematic to illustrate the electron rocking beam technique and recording of electron channeling pattern (ECP) with high angle annular dark field (HAADF) detector, while the ICP associated with each atomic species is recorded with characteristic x-ray energy dispersive spectroscopy (XEDS) technique. (b) ECP image recorded by HAADF and ICP images for F, O, Mn and Ti detected by XEDS. (c) Atomic model viewing along the [110] zone axis and correspondingly the simulated ICP images.

### 3) Investigating factors influencing the delta phase transformation in high-Mn DRX.

In high-Mn DRX, phase transformation from DRX to a new phase (named  $\delta$ ) can occur during electrochemical cycling. The  $\delta$  phase has a general composition of Li-Mn-Ti-O, and forms from Mn-rich DRX synthesized via a solid-state method. This phase displays partial spinel-like order after cycling due to high Mn mobility and exhibits high energy density and rate capability.

From the voltage profile of the  $\delta$  phase during the first 20 cycles between 1.5-4.8 V at 20 mA/g (Figure VIII.2.38), we can observe the material undergoes a gradual phase transformation during electrochemical cycling. In cycle 1 (Red), the material exhibits a slopy voltage profile, which resembles typical DRX materials. In cycle 20 (Blue), the material shows a flattened  $\sim 4$  V and  $\sim 3$  V regions, indicating a transformation from DRX to a partial spinel-like phase. Further ex-situ XRD collected at 3.5 V during the 20th discharge (Figure VIII.2.39) confirms the formation of spinel-like environments with both 16d and 16c sites partially occupied by transition metals. The broad spinel peaks and sharp rocksalt peaks also suggest that the long-range anion lattice remains intact after transformation to the  $\delta$  phase, whereas the spinel-like cation ordering has short coherence length.

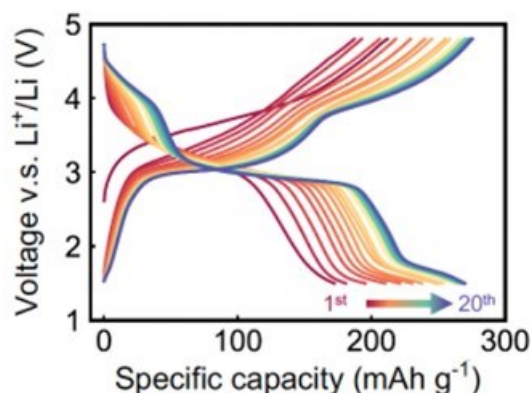


**Figure VIII.2.38** Electrochemical voltage profile of the  $\delta$  phase cycled between 1.5 and 4.8 V for the first 20 cycles.

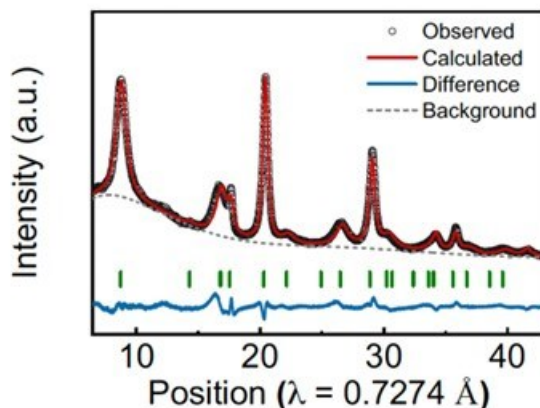


Figure VIII.2.39 Rietveld refinement of synchrotron XRD discharged to 3.5 V at the 20<sup>th</sup> cycle.

The electrochemical performance of the  $\delta$  phase materials was evaluated using galvanostatic cycling between different voltage ranges at 20 mAh/g (Figure VIII.2.40). Between 2 and 4.8 V, the discharge capacity increases from 138 mAh/g in the first cycle to 211 mAh/g in cycle 20, and the average discharge voltage increases from 3.128 V to 3.191 V during the first 40 cycles. Extending the voltage range to 1.5-5 V can further increase the capacity to over 250 mAh/g while maintaining the high voltage retention, with a decrease from its maximum of 2.889 V to 2.806 V after 100 cycles. The high discharge capacity and great retention performance of the  $\delta$  phase, combined with the low cost of Mn and Ti-based oxide precursors, make it an excellent candidate to create abundant and inexpensive Li-ion energy storage materials.

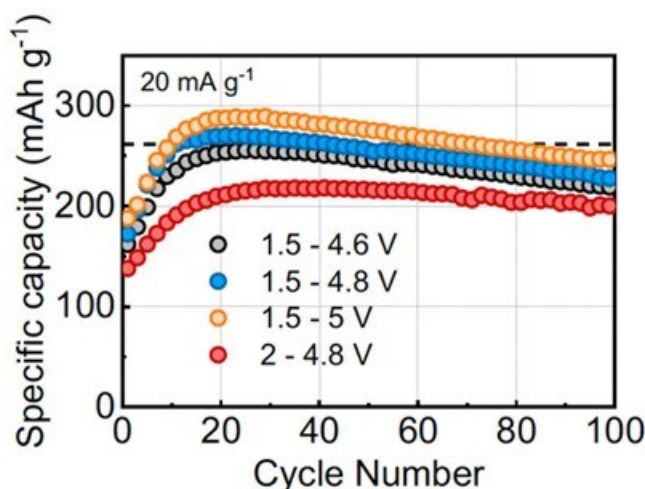
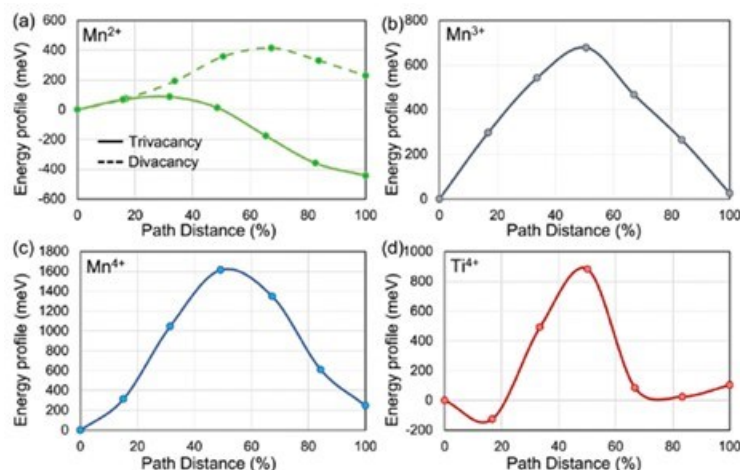


Figure VIII.2.40 Capacity retention over 100 cycles when cycled in different voltage windows at 20 mA/g.

We further studied the driving force and kinetics for the phase transformation of the high Mn-content ( $\text{Mn} > 0.6$  f.u.) DRX oxides with a general formula of Li-Mn-Ti-O. Through density functional theory (DFT) calculations and the nudged-elastic band (NEB) method, we established the design guidelines for Li-rich and Mn-rich compositions that combine high energy density, high rate-capability, and good cyclability.

Figure VIII.2.41 shows the escape energy for  $\text{Mn}^{2+}$ ,  $\text{Mn}^{3+}$ ,  $\text{Mn}^{4+}$ , and  $\text{Ti}^{4+}$  in a DRX configuration calculated using NEB DFT. The migration assumes the presence of a trivacancy for the transition metals (TM) with higher charge state ( $\text{Mn}^{3+}$ ,  $\text{Mn}^{4+}$ ,  $\text{Ti}^{4+}$ ) and a divacancy for  $\text{Mn}^{2+}$ .  $\text{Mn}^{4+}$  and  $\text{Ti}^{4+}$  show very high escape energies of  $\sim 1000$  meV or higher, indicating that they are highly likely to remain immobile during cycling.

However, reducing  $\text{Mn}^{4+}$  to  $\text{Mn}^{3+}$  or  $\text{Mn}^{2+}$ , decreases the barrier to  $\sim 700$  meV and  $\sim 400$  meV, respectively. Therefore, the Mn ions are mainly responsible for the TM reordering to form the  $\delta$  phase.



**Figure VIII.2.41 Migration barrier of different TM species. The energy profile of (a)  $\text{Mn}^{2+}$ , (b)  $\text{Mn}^{3+}$ , (c)  $\text{Mn}^{4+}$  and (d)  $\text{Ti}^{4+}$  when migrating from one octahedral site to another.**

Though high Mn-content contributes to the DRX-to- $\delta$  phase transformation, it is the thermodynamic energy difference between the original DRX phase and the  $\delta$  phase that provides the driving force for the transformation. We estimated this driving force from the energetic difference between structures with  $\gamma$ - $\text{LiFeO}_2$ -type ordering ( $E_\gamma$ ) and spinel-type ordering ( $E_S$ ). Figure VIII.2.36a shows this calculated energy difference ( $E_S - E_\gamma$ ) along the  $\text{LiMnO}_2$ - $\text{Li}_2\text{TiO}_3$  compositional line.  $E_S - E_\gamma$  becomes more negative as the  $\text{Mn}^{3+}$  increases, indicating a stronger driving force for the DRX-to- $\delta$  transformation. This finding is consistent with our experimental observation that a high  $\text{Mn}^{3+}$  content generally promotes phase transformation. As the Mn valence is kept constant at 3+ in Figure VIII.2.42a, an increase in Mn content is coupled with a decrease in the amount of Li excess. To deconvolute these effects, we compared two groups of composition at fixed Li content in Figure VIII.2.42b with the  $\text{Li}_{1.208}\text{Mn}_{0.791-x}\text{Ti}_x\text{O}_2$  family of materials. The compositions have fixed  $\text{Mn}^{3+}$  content at 0.372/f.u., and  $\text{Mn}^{4+}$  is gradually replaced with  $\text{Ti}^{4+}$ . In the  $\text{Li}_{1.208}\text{Mn}_{0.791-x}\text{Ti}_x\text{O}_{1.75}\text{F}_{0.25}$ , we replace  $\text{Mn}^{4+}$  with  $\text{Ti}^{4+}$  when  $x \leq 0.169$ . When the  $\text{Ti}^{4+} \geq 0.169$ /f.u., we also replaced  $\text{Mn}^{3+}$  with  $\text{Mn}^{2+}$  and  $\text{Ti}^{4+}$  to compensate for the charge to understand the effect of the Mn valence. The  $E_S - E_\gamma$  when delithiated to a typical spinel composition (cation/anion = 3/4) for both groups of compositions, were computed. The results in Figure VIII.2.42 confirm that a larger  $\text{Ti}^{4+}$  content leads to a lower driving force (less negative  $E_S - E_\gamma$ ), and the Mn content directly affects the thermodynamic driving force for transforming to the  $\delta$  phase.

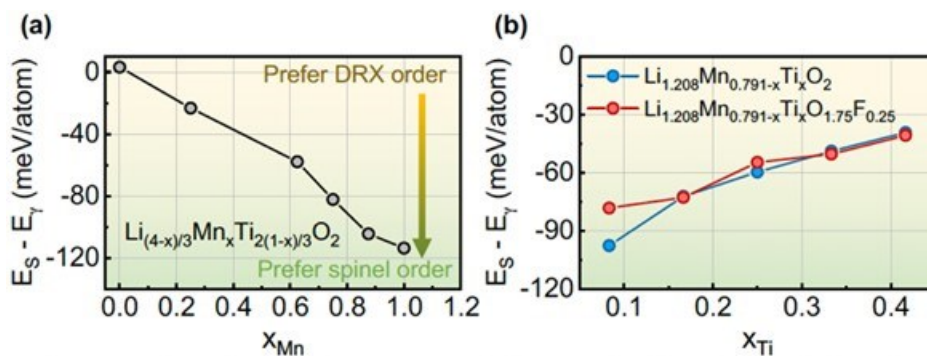


**Figure VIII.2.42 Thermodynamic driving force evaluations of DRX-to- $\delta$  phase transformation. (a) Calculated thermodynamic driving force ( $E_S - E_\gamma$ ) at  $\text{LiMnO}_2$ - $\text{Li}_2\text{TiO}_3$  composition tie line. (b) Calculated thermodynamic driving force ( $E_S - E_\gamma$ ) of composition with  $\text{Li}_{1.208}$ /f.u. and two different  $F=0$ /f.u. and  $F=0.25$ /f.u.**



We hypothesize that relaxation of the unstable delithiated DRX structure is one of the major driving forces for delta phase formation during electrochemical cycling. The results presented below focus on the  $\text{Li}_{1.1}\text{Ti}_{0.7}\text{Mn}_{0.2}\text{O}_2$  DRX composition.

To isolate the impact of the lithium content on the DRX to delta phase transformation, and to maximize sample crystallinity for ease of characterization, we prepared a series of chemically-delithiated  $\text{Li}_{1.1-x}\text{Ti}_{0.7}\text{Mn}_{0.2}\text{O}_2$  samples. ICP indicates that up to 80% of the Li can be removed from the DRX structure using  $\text{NO}_2\text{BF}_4$ . We tracked the evolution of a pristine and chemically delithiated  $\text{Li}_{0.57}\text{Ti}_{0.7}\text{Mn}_{0.2}\text{O}_2$  sample upon heating, whereby chemical delithiation and heat treatment is used as a proxy for structural relaxation processes taking place during battery cycling. In-situ heating diffraction experiments (Figure VIII.2.43a) (under Ar) reveal the gradual evolution of new diffraction peaks in the case of the chemically delithiated sample. These newly evolved peaks are consistent with those reported for the delta phase and for spinel structures. In contrast, no major changes in the diffraction pattern of the pristine  $\text{Li}_{1.1}\text{Ti}_{0.7}\text{Mn}_{0.2}\text{O}_2$  DRX sample are observed upon heating (Figure VIII.2.43b). Our in-situ heating experiments demonstrate that delithiated Mn-rich DRXs are not thermodynamically stable, and this instability drives relaxation of the DRX structure to a much more stable phase (delta phase or spinel).

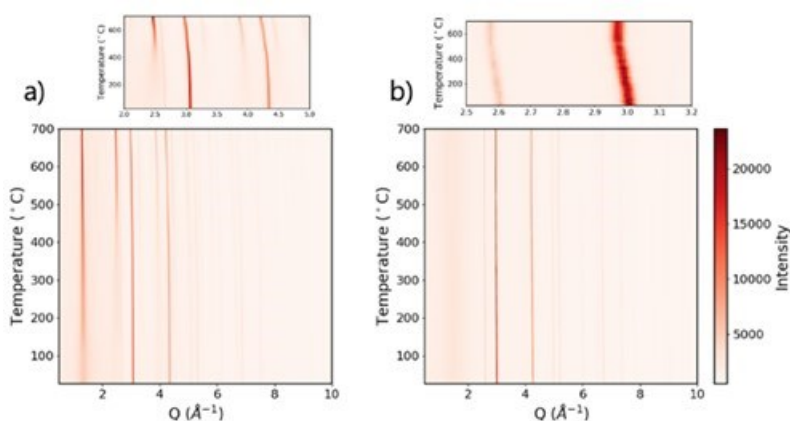


**Figure VIII.2.43** In-situ heating diffraction experiments conducted on a) chemically-delithiated  $\text{Li}_{0.57}\text{Ti}_{0.7}\text{Mn}_{0.2}\text{O}_2$  and b) pristine  $\text{Li}_{1.1}\text{Ti}_{0.7}\text{Mn}_{0.2}\text{O}_2$  under Ar.

Further, high-resolution TEM and electron diffraction results (Figure VIII.2.44a) indicate that the newly-formed structure consists of nanosized spinel-like domains within the disordered rocksalt matrix. The observed spinel-like domains highly resemble those reported for the delta phase formed during electrochemical cycling. Moreover, the voltage profile of the thermally-relaxed and chemically delithiated  $\text{Li}_{0.57}\text{Ti}_{0.7}\text{Mn}_{0.2}\text{O}_2$  cathode clearly exhibits two plateaus at  $\sim 4.0$  and  $\sim 3.0$  V vs.  $\text{Li}/\text{Li}^+$  (Figure VIII.2.44b), characteristic of Mn-based spinel cathodes or DRX cathodes after in situ cycling transformation to the delta phase. Those results suggest that thermal relaxation of chemically-delithiated Mn-rich DRXs leads to similar local structure rearrangements as those observed during electrochemical cycling and lend credence to our experimental approach. Thermally-relaxed, chemically-delithiated  $\text{Li}_{1-x}\text{Mn}_{0.7}\text{Ti}_{0.2}\text{O}_2$  samples are much more crystalline than electrochemically-cycled cathode samples, allowing us to perform Rietveld refinement of both synchrotron and neutron diffraction patterns. For this, a disordered rocksalt-spinel two-phase structural model was built. The refinement of the data collected on the heat treated  $\text{Li}_{0.57}\text{Ti}_{0.7}\text{Mn}_{0.2}\text{O}_2$  sample (Figure VIII.2.44c) indicates that, in the relaxed structure, octahedral Mn/Ti/Li sites in the initial DRX structure split into 2 sites. Mn/Ti species migrate to one of the sites, leaving the other site vacant and breaking the FCC symmetry of the original DRX unit cell. Li species migrate from the original octahedral sites to tetrahedral sites. Selective migration of Li and Mn/Ti species leads to the formation of spinel-like domains in the DRX structure, as illustrated in Figure VIII.2.44d. We did not find any evidence for a change in Mn/Ti content or their ratio in the DRX average structure before and after thermal relaxation, suggesting no Mn/Ti redistribution happening between DRX and

spinel domains. However, the contraction of the DRX lattice parameters upon heating suggests that Li preferentially occupies DRX domains after thermal relaxation.

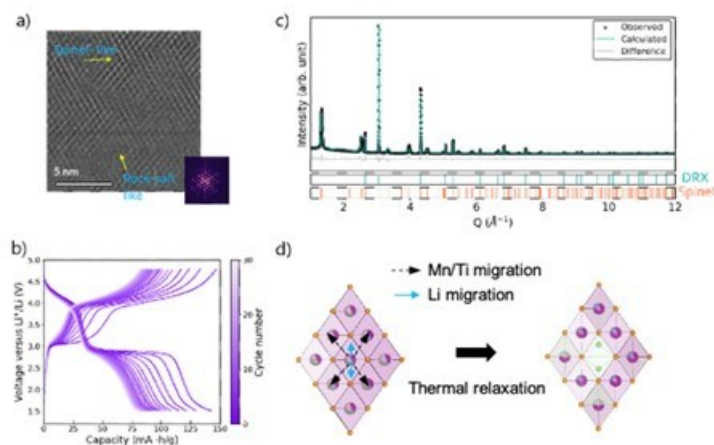


**Figure VIII.2.44** Analysis of thermally-relaxed, chemically-delithiated  $\text{Li}_{0.57}\text{Mn}_{0.7}\text{Ti}_{0.2}\text{O}_2$ . a) TEM image and selected area electron diffraction, b) Voltage profile (1.5–4.8 V, 20 mA/g), and c) Synchrotron XRD pattern and Rietveld refinement fit. d) Illustration of the local structure transformation from Mn-rich delithiated DRX to spinel-like phase.

We also formulated a computational framework to model the intercalation voltage profiles of DRX materials, counting the complex disordered structures and multiple redox behaviors. We introduce an approach that combines sparse regression to construct cluster-expansion Hamiltonian and semigrand-canonical Monte Carlo simulations to sample the energies of charge-balanced ionic configurations. These techniques are applied to DRX oxyfluoride  $\text{Li}_{1.3-x}\text{Mn}_{0.4}\text{Nb}_{0.3}\text{O}_{1.6}\text{F}_{0.4}$  to predict its voltage profile with lithium intercalation. Figure VIII.2.45a presents the simulated profile (green dots), which agrees well with experimental data (green solid line). Figure VIII.2.45b shows the content of redox-active species during the intercalation, which provides a clear demonstration of the manganese and oxygen contributions to the redox potential as a function of Li content. The methods developed here for DRX cathodes will be useful for modeling other complex ionic materials with multiple redox-active species and a disordered structure.

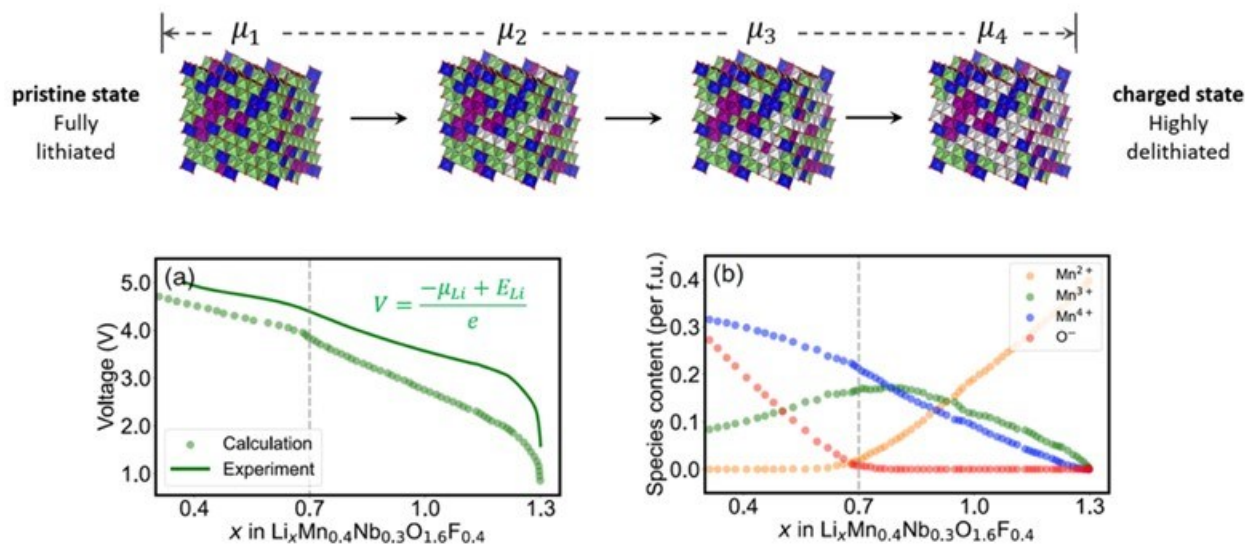


Figure VIII.2.45 Illustration of the intercalation calculation of DRX structures. (a) Calculated (circle) and experimental (solid line) voltage profiles of  $\text{Li}_{1.3-x}\text{Mn}_{0.4}\text{Nb}_{0.3}\text{O}_{1.6}\text{F}_{0.4}$ . (b) Calculated content of  $\text{Mn}^{2+}$ ,  $\text{Mn}^{3+}$ ,  $\text{Mn}^{4+}$ , and  $\text{O}^-$  per formula unit (f.u.) as a function of Li content (x).

## Conclusions

In FY23, the DRX+ consortium focused on four main tasks to address outstanding challenges, including synthesis optimization, electrolyte formulation, coating development and bulk design. In Synthesis and Scale-up, parameters in solid-state synthesis were refined for large-scale production. Solid-state synthesis of DRX at 50-60g scale was demonstrated. Alternative scalable synthesis methods, including solution-based and combustion synthesis routes were developed. In the Electrolyte task, new localized high-concentration electrolytes with the formulation of  $\text{LiFSI-xDMC-yTTE}$  were developed and evaluated in DRX cells. The use of these LHCEs enables higher capacity, lower polarization and better cycling of DRX cathode. Compared to the equivalent cells with a conventional  $\text{LiPF}_6$ -based electrolyte, post-mortem analysis reveals improved bulk structural stability and the formation of a more stable cathode-electrolyte interphase with LHCEs. High-voltage stability was also evaluated on EC-lean electrolytes with three additives. TMSPa was identified as the most promising in stabilizing DRX surface while maintaining good cycle life and capacity retention. In the Coating task, various carbon coating techniques were investigated. The efficacy of carbon coatings strongly depends on the carbon structure and processing route. Carbon additives play a critical role in composite cathode performance, particularly the weight fraction of carbon nanotube used in DRX cathodes was optimized. In Bulk studies, the effect of disorder on partially disordered spinel systems was investigated via cluster expansion studies which confirmed that the 3V two-phase region can be removed by 16c/16d cation disorder. A new technique based on electron rocking beam was developed, providing direct evidence on F position in DRX lattice. In addition, DFT calculations revealed the thermodynamic energy difference is the driving force for DRX phase to the  $\delta$  phase transformation. Mn content has a direct effect on the thermodynamic driving force. Experimentally, relaxation of delithiated Mn-rich DRX structure was shown as a driving force for  $\delta$  phase formation during electrochemical cycling.

## Key Publications

1. J. Ahn, R. Giovine, V. C. Wu, K. P. Koriala, C. Wang, R. J. Clement and G. Chen, "Ultrahigh-Capacity Rocksalt Cathodes Enabled by Cycling-Activated Structural Changes," *Advanced Energy Materials*, 2300221 (2023). DOI: 10.1002/aenm.202300221.
2. S. Patil, K. P. Koirala, M. J. Crafton, G. Yang, W.-Y. Tsai, B. D. McCloskey, C. Wang, J. Nanda, E. C. Self "Enhanced Electrochemical Performance of Disordered Rocksalt Cathodes Enabled by a Graphite Conductive Additive" *ACS Appl. Mater. Interfaces*, **2023** (Under Review)

3. S. Patil, D. Darbar, E. C. Self, T. Malkowski, V. C. Wu, R. Giovine, N. J. Szymanski, R. D. McAuliffe, B. Jiang, J. K. Keum, K. P. Koirala, B. Ouyang, K. Page, C. Wang, G. Ceder, R. J. Clément, J. Nanda “Alternate Synthesis Method for High-Performance Manganese Rich Cation Disordered Rocksalt Cathodes” *Adv. Energy Mater.* **2023**, 13, 2203207.
4. T Chen, J. Yang, L. Barroso-Luque, G Ceder, “Removing the Two-Phase Transition in Spinel LiMn2O4 through Cation Disorder” *ACS Energy Lett.* **2023**, 8, 314-319, DOI: 10.1021/acseenergylett.2c02141 (2023)
5. Huang, J., Ouyang, B., Zhang, Y. *et al.* Inhibiting collective cation migration in Li-rich cathode materials as a strategy to mitigate voltage hysteresis. *Nat. Mater.* **22**, 353–361 (2023).
6. Nathan J. Szymanski, Zhengyan Lun, Jue Liu, Ethan C. Self, Christopher J. Bartel, Jagjit Nanda, Bin Ouyang, and Gerbrand Ceder” Modeling Short-Range Order in Disordered Rocksalt Cathodes by Pair Distribution Function Analysis”, *Chem. Mater.* **2023**, DOI: 10.1021/acs.chemmater.2c03827 (2023)
7. Huang, T.-Y.; Crafton, M. J.; Kaufman, L. A.; Konz, Z. M.; Bergstrom, H. K.; Kedzie, E. A.; Hao, H.-M.; Ceder, G.; McCloskey, B. D. “Quantitative decoupling of oxygen-redox and manganese-redox voltage hysteresis in a cathode-disordered rock salt cathode.” *Advanced Energy Materials* (2023) **13**, 2300241.
8. Crafton, M. J.; Huang, T.-Y.; Yue, Y.; Giovine, R.; Wu, V.; Dun, C.; Urban, J. J.; Clement, R. J.; Tong, W.; McCloskey, B. D. “Tuning bulk redox and altering interfacial reactivity in highly fluorinated cation-disordered rocksalt cathodes.” *ACS Applied Materials & Interfaces* (2023) **15**(15), 18747-18762.
9. S. Patil, K. P. Koirala, M. J. Crafton, G. Yang, W.-Y. Tsai, B. D. McCloskey, C. Wang, J. Nanda, E. C. Self “Enhanced Electrochemical Performance of Disordered Rocksalt Cathodes Enabled by a Graphite Conductive Additive” *ACS Appl. Mater. Interfaces*, **2023**, *15*, 39253.
10. Z. Cai, B. Ouyang, H.-M. Hau, T. Chen, R. Giovine, K. P. Koirala, L. Li, H. Ji, Y. Ha, Y. Sun, J. Huang, Y. Chen, V. Wu, W. Yang, C. Wang, R. J. Clément, Z. Lun, and G. Ceder, *In Situ Formed Partially Disordered Phases as Earth-Abundant Mn-Rich Cathode Materials*, *Nat. Energy* (2023).
11. P. Zhong, F. Xie, L. Barroso-Luque, L. Huang, and G. Ceder, Modeling Intercalation Chemistry with Multiredox Reactions by Sparse Lattice Models in Disordered Rocksalt Cathodes, *PRX Energy* **2**, 043005 (2023).
12. S. Anand, B. Ouyang, T. Chen, and G. Ceder, *Impact of the Energy Landscape on the Ionic Transport of Disordered Rocksalt Cathodes*, *Phys. Rev. Mater.* **7**, 095801 (2023).
13. Z. Jadidi, J. H. Yang, T. Chen, L. Barroso-Luque, and G. Ceder, *Ab Initio Study of Short-Range Ordering in Vanadium-Based Disordered Rocksalt Structures*, *J. Mater. Chem. A* **11**, 17728 (2023).
14. N. J. Szymanski, Z. Lun, J. Liu, E. C. Self, C. J. Bartel, J. Nanda, B. Ouyang, and G. Ceder, *Modeling Short-Range Order in Disordered Rocksalt Cathodes by Pair Distribution Function Analysis*, *Chem. Mater.* **35**, 4922 (2023).

### Acknowledgements

Vincent Battaglia, Jordan Burns, Gerbrand Ceder, Guoying Chen, Raphaele Clement, Matthew Crafton, Yanbao Fu, Yang Ha, Kenny Higa, Tzu-Yang Huang, Jianan Xu, Vincent Wu, Shripad Patil, Haegyum Kim, Ethan Self, Ozge Kahvecioglu, Adam Tornheim, Wu Xu, Samson Jenekhe, Johanna Weker, William Chueh, Robert Kostecki, Bryan McCloskey, Jagjit Nanda, Joseph Papp, Kristin Persson, Rohit Satish, Ethan Self, Chongmin Wang, Wanli Yang, Tyler Bennet, P. M. Ajayan, Ganguli Babu, Eric Yoshida, Katherine Page, Juhyeon Ahn, Yijin Liu, Dimosthenis Sokaras, Kevin Stone, Sudarshan Vijay, Evan Spotte-Smith, Guang Yang, Mateusz Zuba, Krishna Prasad Koirala, Venkata Sai Avvaru, Rebecca McAuliffe, Beth Armstrong, Matthew Chambers, Carrie Siu, Nathan Szymanski, Tianyu Li, Tucker Holstun, Zijian Cai, Rohith Srinivaas Mohanakrishnan, Nessa Majaya, Gihyeok Lee

## VIII.3 Cathode-Electrolyte Interphase (CEI) Consortium (PNNL)

### **Jie Xiao, Principal Investigator**

Pacific Northwest National Laboratory  
902 Battelle Blvd  
Richland, WA, 99354  
E-mail: [jie.xiao@pnnl.gov](mailto:jie.xiao@pnnl.gov)

### **Tien Duong, DOE Technology Development Manager**

U.S. Department of Energy  
E-mails: [Tien.Duong@ee.doe.gov](mailto:Tien.Duong@ee.doe.gov)

### **Carine Steinway, DOE Technology Development Manager**

U.S. Department of Energy  
E-mails: [Carine.Steinway@ee.doe.gov](mailto:Carine.Steinway@ee.doe.gov)

### **Nicolas Eidson, DOE Technology Development Manager**

U.S. Department of Energy  
E-mails: [Nicolas.Eidson@ee.doe.gov](mailto:Nicolas.Eidson@ee.doe.gov)

Start Date: October 1, 2022

End Date: December 31, 2025

Project Funding: \$4,700,000

DOE share: \$4,700,000

Non-DOE share: \$0

### **Project Introduction**

Cathodes, and particularly high-energy and low-cost cathodes, are leading the materials innovation value chain towards vehicle electrification. Enhancing stability of CEI at high voltages is not only critical to stabilize cathode and therefore battery cycle life but helps to extract more energy from the same materials without increasing the cost. Almost all electrode couples in electrochemical cells operate beyond the thermodynamic stability limits of the electrolytes [1]. In many cases, these cells only operate because electrode-electrolyte reactions result in the formation of new phases (or interphases) at the electrode-electrolyte interfaces. On the cathode side, CEI is generated through the decomposition of electrolytes at high voltages and passivates cathode surfaces especially [2]. CEI directly determines the reversibility of ion transport and dictates the kinetics of the cathode and thus overall cell reactions. In addition to electrolyte recipes, cathode surface chemistry [3], morphologies [4], and electrochemical potential [5] all profoundly impact CEI components and properties. Many complicated and interrelated chemical and physical processes occur on/near the cathode surfaces [6]. A full understanding of CEI formation and evolution at varied length and time scales, especially at high voltages, is still lacking but urgently needed to better tune CEI properties at the atomic scale to further stabilize the electrochemical energy storage system.

The goal of the CEI Consortium is to identify and address fundamental challenges in stabilizing CEI at high voltage to accelerate the development of next-generation cathode materials such as nickel-rich  $\text{LiNi}_{1-x-y}\text{Mn}_x\text{Co}_y\text{O}_2$  (NMC), polycrystal and/or single crystals and beyond. The Consortium will revisit fundamentals of CEI in the model system tested at relevant experimental conditions and cross-validate new discoveries to ensure that knowledge gathered from this project is valuable for industry to accelerate R&D, demonstration, and large-scale deployment of advanced cathode materials for future lithium-based batteries.

Led by PNNL, the CEI Consortium consists of ten national labs and ten universities that have been categorized into three focused groups (Figure VIII.3.1): (1) Model Cathode Materials, (2) Electrolyte and (3) Characterization & Modeling, to address the scientific challenges of CEI stability from different aspects. The new insights developed from the CEI consortium will not only be utilized to enhance CEI properties, but it will

also provide guidelines for designing compatible electrolytes and stabilizing cathode materials at high voltages.

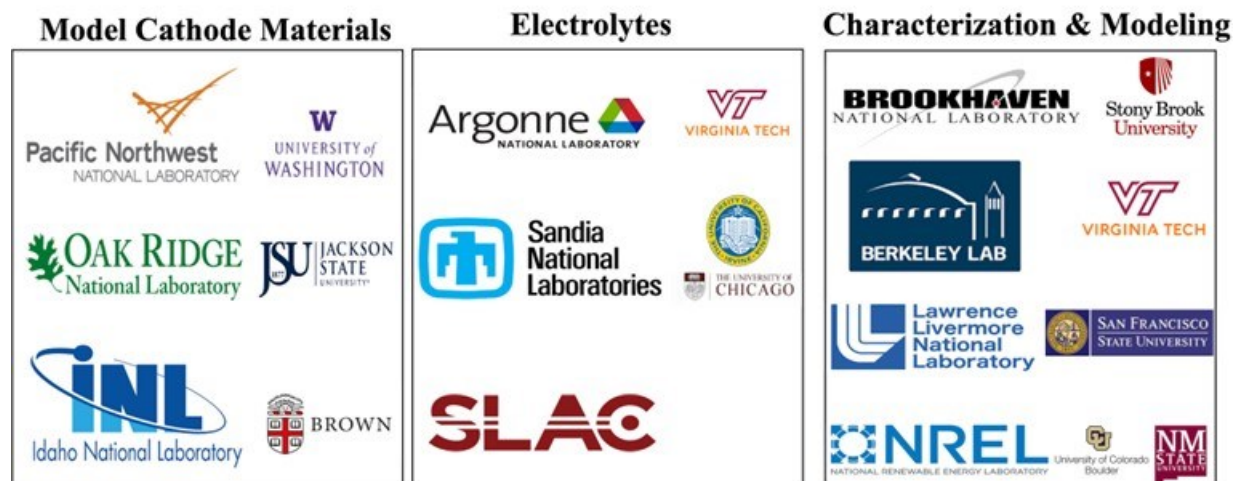


Figure VIII.3.1 The CEI Consortium has three focused groups working on Model Cathode Materials (left), Electrolytes (middle) and Characterization & Modeling (right).

### Objectives

The objective of the CEI Consortium is to integrate different scientific tools and expertise in these organizations to develop a platform to quickly identify, understand, and tackle key challenges of CEI relevant to realistic Li-ion batteries. The CEI Consortium examines the interfacial reactions between cathode and electrolytes at high voltages, which critically dictate the observed performances of Li-ion batteries. The capabilities developed and integrated within the CEI Consortium also directly support the Earth-Abundant Cathode Active Materials (EaCAM) Consortium and the Cation Disordered Rocksalt (DRX<sup>+</sup>) Cathode Consortium, which both focus on cathode materials development.

### Approach

- Integrate various characterization and modeling tools to probe CEI stability at high voltages and at different time scales to develop new theories or hypothesis.
- Develop full coin cell protocols to cross validate hypothesis developed from the CEI consortium at industry-relevant conditions.
- Establish baseline performances by using baseline materials and full coin cell protocols for teams to benchmark their new results.

### Results

#### Consortium level:

In year 1, the CEI Consortium has established a full coin cell protocol using stable graphite as the anode to effectively assess CEI properties. The full coin cell protocol, being shared with the Consortium, includes detailed information from step-by-step coin cell assembly to the parameters needed to construct cathode and anode (Table VIII.3.1). For example, the mass loading of NMC811 is ~15 mg/cm<sup>2</sup> corresponding to an areal capacity of ca.3 mAh/cm<sup>2</sup>. The cathode and anode are also calendared to have controlled porosities, relevant to practical Li-ion battery conditions.

Based on the full coin cell protocol, the consortium has also established baseline performances of commercial polycrystal NMC811, which are used to benchmark future CEI modification and/or new cathode/electrolyte materials for fair comparison across different groups in the consortium. Figure VIII.3.2 shows the cycling stability of commercial polycrystal NMC811 coupled with graphite anode. When the full coin cell is cycled between 2.6 and 4.2 V vs. Graphite (Figure VIII.3.2a) in the baseline electrolyte (1M LiPF<sub>6</sub> in EC/EMC+2%

VC), the capacity retention is about 80% after 416 cycles. At increased cutoff voltage of 4.3 V vs. Graphite (Figure VIII.3.2b), cell degradation is accelerated. At 130<sup>th</sup> cycle, capacity retention has reached 80% within this expanded electrochemical window. Baseline performances for single crystal NMC811 are also being developed under the consortium.

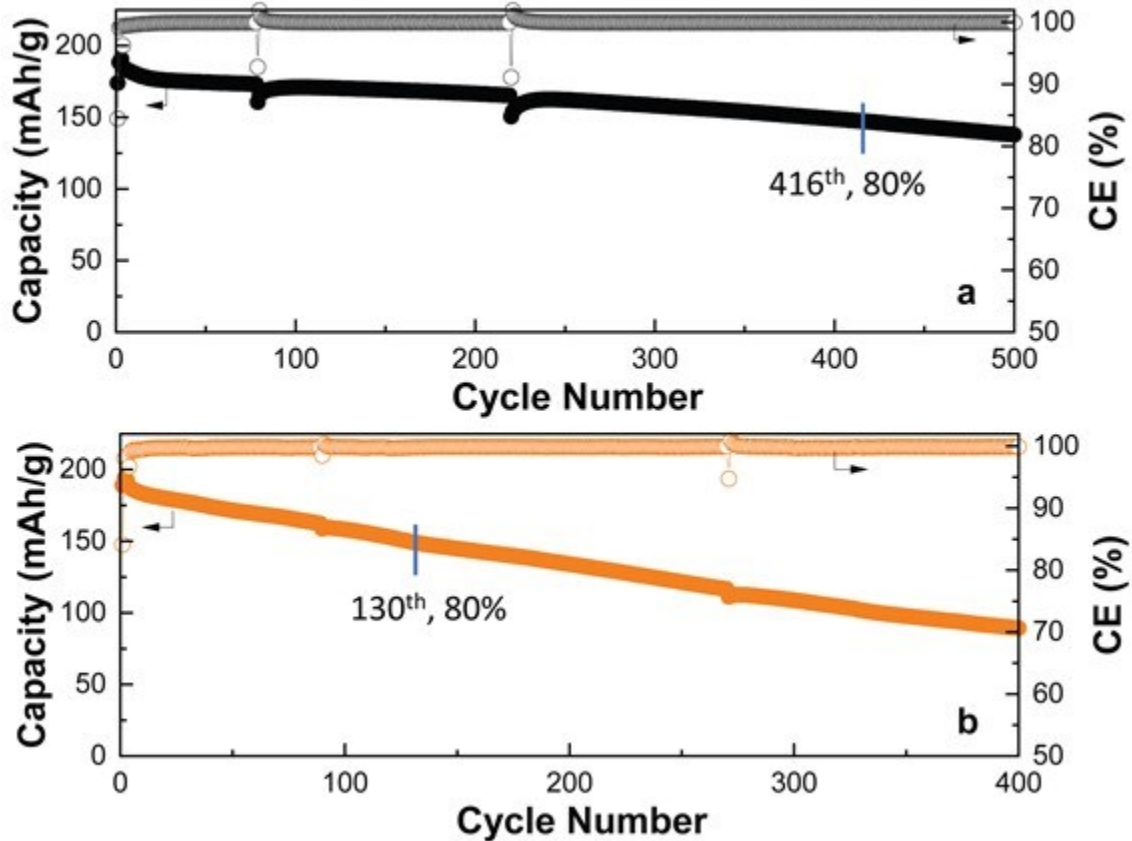


Figure VIII.3.2 Baseline performances of commercial polycrystal NMC811 and graphite (Gr) cycled between (a) 2.6 and 4.2 V, and (b) 2.6 and 4.3 V. All the rest testing conditions are similar to those listed in the table below.

Table VIII.3.1 Key Parameters from the Full Coin Cell Protocol

<b>Cathode: NMC811 (polycrystals or single crystals)</b>	
Active material %	96%
Carbon %	2%
PVDF %	2%
Mass loading (NMC only)	~15 mg/cm <sup>2</sup>
Specific Capacity	~200 mAh/g (C/10)
Areal Capacity	~ 3 mAh/cm <sup>2</sup>
Voltage Window	2.6 V-4.3 V <b>vs. Gr</b> (2.7 V-4.4 V <b>vs. Li</b> )
Porosity	~ 35%
<b>Anode: Graphite (without prelithiation)</b>	
Areal Capacity	~3.6 mAh/cm <sup>2</sup>
N/P	~1.2
<b>Baseline Electrolyte (Gen1)</b>	1M LiPF <sub>6</sub> in EC/EMC(3:7)+2% VC
Formation Cycle	C/10 for charge & discharge for 3 cycles
Charge	CC-CV: C/3 to 4.3 V (vs. Gr) then constant voltage until $I \leq C/20$
Discharge	C/3

**Focused Group 1:****Pacific Northwest National Laboratory (PNNL) and University of Washington: Completed storage study of NMC811 in different environments**

PNNL team has completed the storage tests of commercial NMC811 in different environments including argon, N<sub>2</sub>, dry air with 0.1% relative humidity (RH) and at 20°C, ambient environment (33% RH, 20°C), pure CO<sub>2</sub>, mixture of CO<sub>2</sub> and H<sub>2</sub>O (~70% RH, 20°C) and mixture of argon and H<sub>2</sub>O (~70% RH, 20°C). It was found that as long as moisture (H<sub>2</sub>O) exists, the surface morphology change always happens even only one day of storage. Focus has then been narrowed on the storage of NMC811 in ambient, dry air and N<sub>2</sub> in order to identify a cost-efficient solution for long-term storage of Ni-rich NMC. Figure VIII.3.3 compares the surface evolution of NMC811 after storing in ambient air (Figure VIII.3.3a1-a3), dry air (Figure VIII.3.3b1-b3) and N<sub>2</sub> (Figure VIII.3.3c1-c3) for various days. In ambient air with 33% RH, after only one day, there is readily surface particles showing up with noticeable population on NMC811 (Figure VIII.3.3a1), while in dry air (Figure VIII.3.3b1) or N<sub>2</sub> (Figure VIII.3.3c1) the surface of NMC811 polycrystals are still “clean”. After five days of storage, an increased number of impurities on NMC811 particles is seen (Figure VIII.3.3a2). After 10 days of storage in ambient environment, it seems the surface impurities grow and merge into bigger particles (Figure VIII.3.3a3). Polycrystal NMC811 stored in dry air (Figure VIII.3.3 3b2-b3) or N<sub>2</sub> (Figure VIII.3.3 c2-c3) still display no obvious change after being stored for 5 or 10 days.



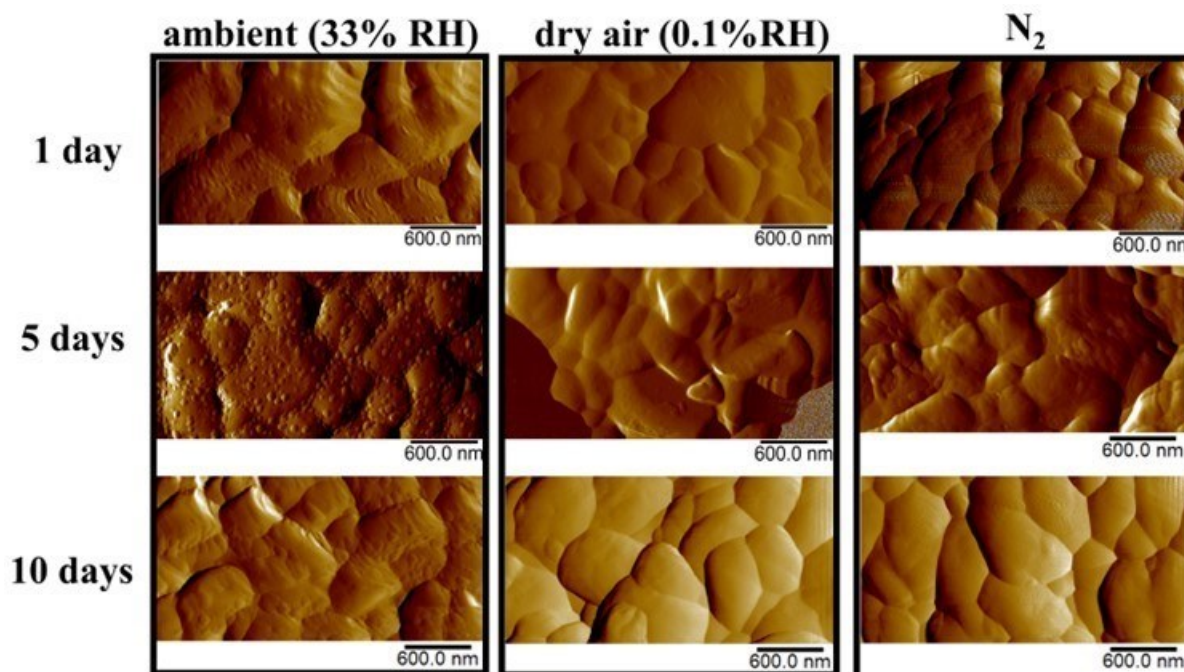


**Figure VIII.3.3** Atomic Force Microscope (AFM) images of NMC811 stored in different environments after various days. (a1-a3) are NMC811 stored in ambient environment for 1, 5 and 10 days, respectively. (b1-b3) are those stored in dry air (with 0.1% RH) for 1, 5 and 10 days, respectively. (c1-c3) are NMC811 stored in  $N_2$  for 1, 5 and 10 days, respectively.

The observation of the morphological change on NMC811 surfaces in different gases is consistent with the electrochemical performances of those stored NMC811 (Figure VIII.3.4). In  $N_2$ , after even one month storage, the capacity variation is minimal, if any, from NMC811 which still delivers  $>200$  mAh/g discharge capacity after 30 days of storage (Figure VIII.3.4a). In dry air with 0.1% humidity, the capacity of NMC811 shows slightly more variations than those stored in  $N_2$  but is still close to each other regardless of the time of storage (Figure VIII.3.4b). It is in the ambient environment (Figure VIII.3.4c) that NMC811 capacity continues to decrease during storage and becomes less than 200 mAh/g after only 5 days. The development of surface impurities on NMC811 stored in ambient environment mainly involves the growth of LiOH and  $Li_2CO_3$  which impacts the cathode performances. Interestingly, the lost capacity and damaged surface seem to be fully recoverable after appropriate treatment. Figure VIII.3.5a is the Scanning Electron Microscope (SEM) image for NMC811 stored in ambient environment for 30 days. Consistent with AFM images, impurities such as LiOH and  $Li_2CO_3$  [7] significantly develop and cover the surfaces of NMC811 particles. However, after appropriate treatment, the impurities are all gone and the surfaces of NMC811 become clean again (Figure VIII.3.5b). There are some fine grains found on “refreshed” NMC811 which are still under investigation. However, the discharge capacity of stored NMC811 is fully recovered to 203 mAh/g (Figure VIII.3.5c) after the treatment, indicating a potential solution to rejuvenate the damaged NMC811 that may have been temporarily exposed to air during long-time storage or transport process.

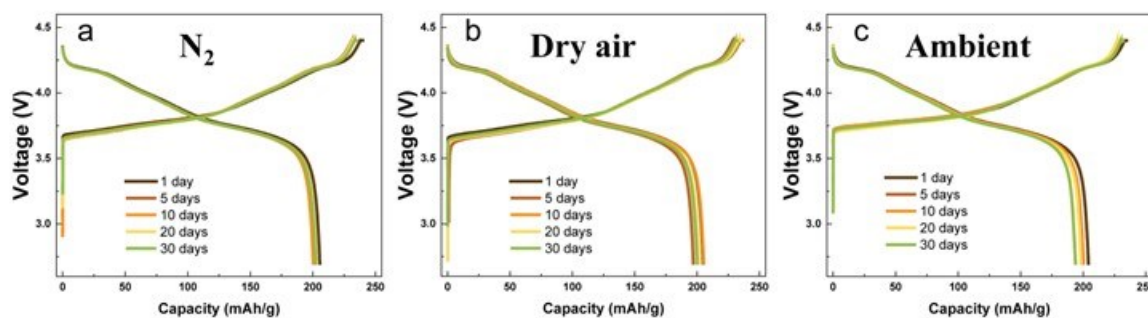


Figure VIII.3.4 The first charge-discharge curves of NMC811 stored in (a)  $N_2$ , (b) dry air and (c) ambient environment for different days. For each sample after storage,  $60^\circ C$  overnight drying in vacuum is conducted before slurry coating process.

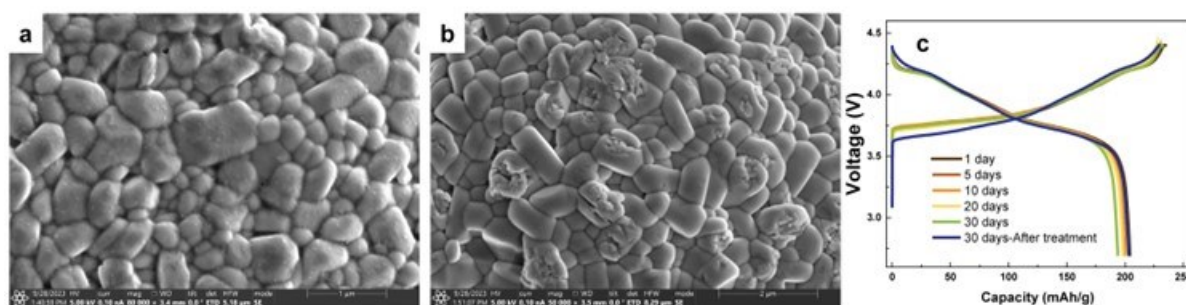


Figure VIII.3.5 (a) SEM image of NMC811 stored in ambient environment for 30 days, (b) SEM image of the stored NMC811 after certain treatment, (c) The first charge-discharge curves of NMC811 stored in ambient environment for different days. Stored NMC811 are tested in half coin cells between 2.7-4.4 V. Relatively low mass loading of ca.  $5 \text{ mg/cm}^2$  of NMC811 is used since the goal is to only to check the usable capacity after storage.

**Idaho National Laboratory (INL) and Brown University: Optimized thickness of ceria coating layer on NMC811 for electrochemical performance improvement of Ni-rich cathode materials.**

The INL team has successfully optimized thickness of ceria layer coating on the surfaces of NMC811 powders by atomic layer deposition (ALD). According to XPS results, in as-synthesized ceria ( $CeO_{2-x}$ ) coating, oxygen vacancies still exist due to the presence of  $Ce^{3+}$ . The growth per cycle (GPC) by ALD for  $CeO_{2-x}$  coating is evaluated to be around  $0.06 \text{ nm/cycle}$ . Using ALD,  $CeO_{2-x}$  layers with different thicknesses (2 nm and 4 nm) have been grown on NMC811 powders.

The electrochemical performances of bare NMC811 and 2 nm  $CeO_2$  coated NMC811 with active material mass loading of  $9.69 \text{ mg/cm}^2$  and  $10.56 \text{ mg/cm}^2$  are evaluated in coin cells for comparison (Figure VIII.3.6a). The upper cut-off voltage is 4.4 V vs.  $Li/Li^+$ . The constant charge rate and discharge rate are C/10 and C/3, respectively. Localized high-concentration electrolyte (LHCE) was used to ensure the Li metal anode is stable during the initial assessment of NMC811. It was found that NMC811 coated with 2 nm-thick  $CeO_{2-x}$  shows higher specific capacity and Coulombic Efficiency (CE) than bare NMC811. Because of sufficient Li inventory at the Li metal anode side, CE value can reflect the reversibility of cathode structures and its interface. Higher CE in the Li metal half-cell with coated NMC811 suggests improved electrochemical stability of CEI at high voltage (e.g., 4.4 V).

Then, graphite/NMC811 full coin cells are also tested in carbonate-based electrolyte with a cutoff voltage of 4.3V, using the baseline electrolyte recommended by CEI Consortium. The constant charge /discharge rates are both C/3 for full coin cells. As shown in Figure VIII.3.6b, NMC811 coated with 2 nm-thick  $CeO_2$  layers

greatly outperforms the others in terms of specific capacity and cyclability in full coin cells. The bare NMC811 electrode exhibits the worst cycling performances. The thicker  $\text{CeO}_2$  coating would lead to higher charge transfer resistances at the interface leading to poorer rate performances. The bare NMC811 powders in INL are commercial available from Targrey. The more significant fading of the bare NMC811 than baseline performances PNNL shared is mainly due to different N/P ratio, which is 1.8 in INL (vs. 1.2 in PNNL's protocol in Table VIII.3.2). In addition to this, the electrodes prepared by INL is in atmosphere environments rather in dry room. Since NMC is very sensitive to moisture, we will prepare electrodes in dry room in the future for comparison studies.

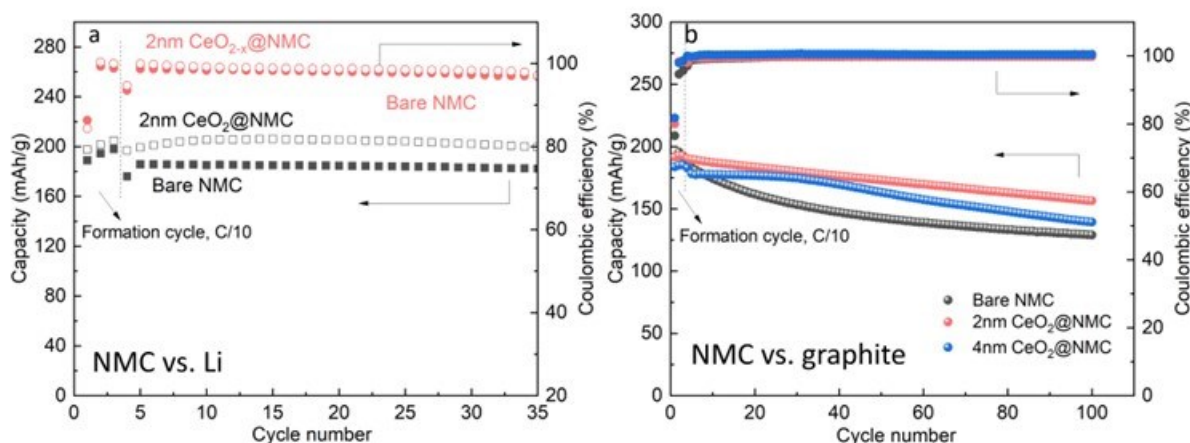


**Figure VIII.3.6** Cycling performances of (a) Li/NMC811 (bare vs. coated) and (b) graphite/NMC811 (bare vs. coated) coin cells. Testing conditions for half cells in (a): 2.8 V-4.4 V vs. Li/Li<sup>+</sup>; C/10 for charge and C/3 for discharge. Mass loading for bare NMC811: 9.69 mg/cm<sup>2</sup>; mass loading of NMC811 coated by 2 nm  $\text{CeO}_2$ : 10.56 mg/cm<sup>2</sup>. Testing conditions for full cells in (b): 2.7 V-4.3 V vs. graphite, C/3 for both charge and discharge. The active material mass loading of bare NMC811, NMC811 coated by 2 nm  $\text{CeO}_2$ , and NMC811 coated with 4 nm  $\text{CeO}_2$  are 9.40 mg/cm<sup>2</sup>, 10.97 mg/cm<sup>2</sup>, and 9.21 mg/cm<sup>2</sup>, respectively. N/P ratio in the full coin cell: 1.8. The initial testing conditions for materials understanding are not exactly the same as the Consortium's coin cell protocol and will be repeated later when more knowledge is gathered.

In addition, rate performance of graphite/NMC811 (bare vs. coated) full coin cells are tested and compared. The mass loading of the bare NMC811, 2 nm  $\text{CeO}_2$  coated NMC811, and 4 nm  $\text{CeO}_2$  coated NMC811 are 9.84 mg/cm<sup>2</sup>, 10.55 mg/cm<sup>2</sup>, and 9.31 mg/cm<sup>2</sup>, respectively. The charge /discharge rates change following the charge rate of C/10 (formation cycle), C/5, C/3, C/2, C/1, C/2, C/3, as shown in Figure VIII.3.7. 2 nm-thick  $\text{CeO}_2$ -x layers coating NMC811 shows the best performance with high specific capacity and cyclability. The NMC811 coated with 4 nm-thick ceria layers shows the worst rate performance.

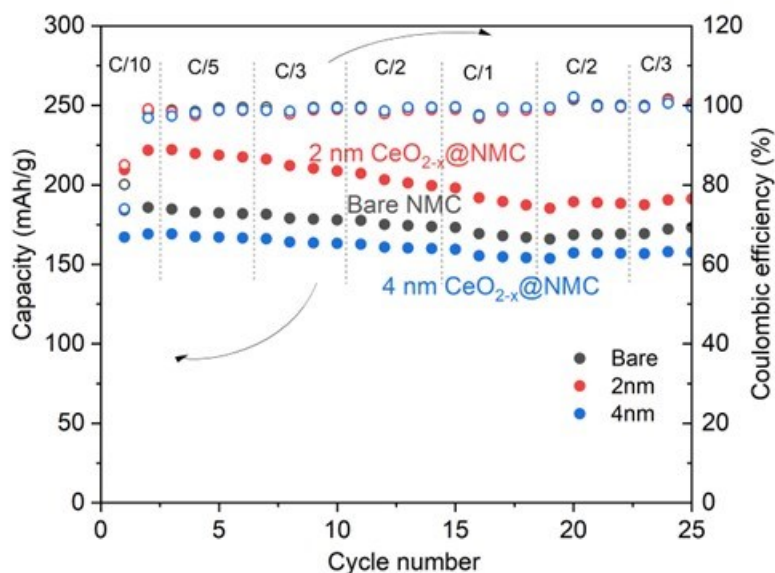


**Figure VIII.3.7 Rate performances of graphite/NMC811 (bare vs. coated) coin cells. Testing conditions for half cells in 2.7 V-4.3 V vs. graphite, C/5, C/5, C/3, C/2, C/1, C/2, C/3 for both charge and discharge.**

In order to study the role of oxygen vacancies on the surface of NMC811 and in coating, the INL team partnering with Brown University tried to demonstrate the roles from the view of oxygen vacancy formation energy. To perform the simulations of oxygen vacancy formation energy in NMC811, the model structure for NMC811 was determined first by density functional theory (DFT) calculations. To computationally represent the high-Nickel NMC cathode, it is intuitive to start with  $\text{LiNiO}_2$ , and then apply the most stable  $\text{LiNiO}_2$  structure as a parent structure for high-Ni NMC by substituting certain Ni sites with Mn or Co. A space group with rhombohedral symmetry ( $R\bar{3}m$ ) under an  $\alpha\text{-NaFeO}_2$ -type framework, in which oxygen layers pack in an ABCABC sequence, is frequently reported as a representative structure of  $\text{LiNiO}_2$ . However, the  $\text{LiNiO}_2$ - $R\bar{3}m$  structure with Ni being octahedrally coordinated to six oxygen atoms through equivalent Ni-O bonds conflicts with the renowned Jahn-Teller (JT) activity of low-spin trivalent Ni. By means of X-ray absorption techniques and pair distribution functions, the presence of local JT distortions with four short and two long Ni-O bonds in  $\text{LiNiO}_2$  has been experimentally observed. Additionally, the calculated band structures confirm the  $\text{LiNiO}_2$ - $R\bar{3}m$  structure is metallic regardless of computational methods, contrary to the experimentally reported semiconducting behavior, suggesting the  $R\bar{3}m$  structure may not be the best starting point to study  $\text{LiNiO}_2$ . Some previous works suggested three possible crystal structures for  $\text{LiNiO}_2$ :  $P2/c$ ,  $P2_1/c$  and  $C2/m$ . The  $C2/m$  and  $P2_1/c$  structures are JT distorted. The  $P2/c$  structure does not have distorted transition metal-oxygen octahedrons, but it does allow a disproportionation of the oxidation state of Ni ( $\text{Ni}^{2+}$  and  $\text{Ni}^{4+}$ ). Furthermore, Ab initio molecular dynamics (AIMD) simulations and electron spin resonance studies have proposed that the dynamic and non-cooperativity JT effect in  $\text{LiNiO}_2$  led to an overall averaged macroscopic  $R\bar{3}m$  symmetry. Due to this conflicting information in the literature, to identify the base structure of pure  $\text{LiNiO}_2$ , DFT calculations were performed based on four different space groups, namely  $R\bar{3}m$ ,  $P2/c$ ,  $P2_1/c$ , and  $C2/m$ .

In this work, First-principles calculations were performed within the framework of DFT by the projector augmented wave (PAW) method using the Vienna ab initio simulation package (VASP). The generalized gradient approximation (GGA) by Perdew, Burke, and Ernzerhof (PBE) was used for the exchange-correlation functional. The GGA + U approach was adopted to describe the strongly correlated d-electrons of the transition metals. The selection of Hubbard U parameters of 6.5 eV for Ni. The plane-wave cutoff is set to be 500 eV. The gamma-centered Monkhorst-Pack scheme of k-point generation is applied, with k-point spacing

less than  $0.03 \text{ \AA}^{-1}$  in the Brillouin zone. Structural optimization was performed for all the cases until the maximum residual force on all atoms becomes less than  $0.02 \text{ eV} \cdot \text{\AA}^{-1}$  while the cell was allowed to relax.

**Table VIII.3.2 The Unit Cell Parameters and Normalized Stabilization Energies (Relative to the  $R\bar{3}m$  Cell).**

LiNiO <sub>2</sub>									
		w/o vdW				w/ vdW			
	Exp.	$R\bar{3}m$	$P2/c$	$P2_1/c$	$C2/m$	$R\bar{3}m$	$P2/c$	$P2_1/c$	$C2/m$
$a$ (Å)	2.88	2.87	4.92	5.83	5.13	2.88	4.94	5.83	5.13
$b$ (Å)	2.88	2.87	5.78	2.92	2.78	2.88	5.80	2.92	2.79
$c$ (Å)	14.18	14.33	5.01	4.89	5.12	14.33	5.00	4.91	5.12
Energy relative to $R\bar{3}m$ /f.u. (meV)			-77.1	-70.5	-64.2		-68.7	-60.7	-56.3
NiO <sub>2</sub>									
		w/o vdW				w/ vdW			
	Exp.	$R\bar{3}m$	$P2/c$	$P2_1/c$	$C2/m$	$R\bar{3}m$	$P2/c$	$P2_1/c$	$C2/m$
$a$ (Å)	2.81	2.76	4.79	5.83	4.78	2.77	4.81	5.53	4.80
$b$ (Å)	2.81	2.76	5.53	2.77	2.77	2.77	5.55	2.78	2.78
$c$ (Å)	13.36	14.73	5.14	4.79	5.12	13.65	4.79	4.81	4.72
Energy relative to $R\bar{3}m$ /f.u. (meV)			-0.8	0.3	-1.9		-1.5	-0.6	-1.1

In Table VIII.3.2, the DFT calculated energies of the  $P2/c$ ,  $P2_1/c$  and  $C2/m$  LiNiO<sub>2</sub> without considering Van der Waals (vdW)-corrections are lower than the  $R\bar{3}m$  structure by 77.1, 70.5 and 64.2 meV, respectively, similar to that reported by Chen et.al. [8]. Although the energy difference among the four structures is only less than 0.1 eV, their band structures show drastic differences. The total density of states suggests that LiNiO<sub>2</sub> with an  $R\bar{3}m$  symmetry should be metallic, while LiNiO<sub>2</sub> with  $P2/c$ ,  $P2_1/c$  and  $C2/m$  symmetries all agree to the experimentally reported semiconducting behavior. Furthermore, the calculated energies of NiO<sub>2</sub> also indicate that  $R\bar{3}m$  is not the ground state structure (Table VIII.3.2). Hence, in this work,  $P2/c$  symmetry is applied for the following computations.

Experiments frequently observed that during charging, the cathode undergoes a structural transition from H1 to M, H2, and H3, successively, where H1, H2, and H3 are rhombohedral while M is monoclinic. Notably, during the H2 to H3 transition, a drastic construction occurs along the c-axis, accompanied by the shorter Li-O distance because of the collapse of the layer. Figure VIII.3.8 shows the estimated lattice relaxations during delithiation. When the vdW-correction was considered, at  $x = 0.25$ , a remarkable contraction of volume and c-axis was observed as well as the Li-O distance began to decrease, which agrees with the experiment [9]. However, when the vdW interaction was ignored, the evolution of the volume, c-lattice parameter, and Li-O distance cannot be well described. Compared to the experimental results, when the vdW interaction was ignored, the NiO<sub>2</sub>-  $R\bar{3}m$  c-lattice parameter was significantly overestimated (Table VIII.3.2). As a result, vdW-

correction is needed at the low Li content stages. Therefore, the oxygen vacancy formation energy will be simulated based on  $P2/c$  symmetry and the consideration of vdW-correction, which will be reported later.

Oxygen vacancies exist in as-synthesized  $\text{CeO}_{2-x}$  layers due to the presence of  $\text{Ce}^{3+}$ . In order to further reveal the roles of oxygen vacancy in  $\text{CeO}_{2-x}$  layers, the coated NMC811 powders will be annealed at elevated temperatures in dry air to remove oxygen vacancy through the oxidation process from Ce(III) to Ce(IV). The corresponding electrochemical performances are being evaluated by the team.

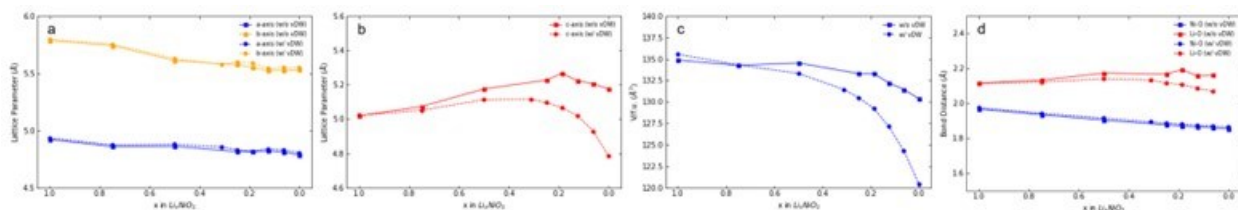


**Figure VIII.3.8** Evolution of (a) a- and b-lattice parameters, (b) c-lattice parameter, (c) unit-cell volume, and (d) Li-O and Ni-O bond distances for the different  $\text{Li}_x\text{NiO}_2$  phases with a comparison between calculations with and without vdW-correction.

#### **Oak Ridge National Laboratory (ORNL) and Jackson State University: Completed eutectic synthesis of single-crystal NMC622 and NMC9055 particles**

ORNL team has validated the baseline electrochemical performance on commercial single-crystal (SC) NMC622 from Targray following the full-cell protocols introduced by PNNL. With a mass loading of  $16.6 \text{ mg/cm}^2$  and an N/P ratio of 1.17, we have obtained full coin cell capacity of  $168 \text{ mAh/g}$  at  $0.1 \text{ C}$  between  $2.7 \text{ V}$ - $4.3 \text{ V}$  and a capacity retention of  $77\%$  after 100 cycles at  $0.33 \text{ C}$  ( $1 \text{ C} = 180 \text{ mAh/g}$ ). This NMC622 baseline performances help the team benchmark future results of lab synthesized NMC622 SCs.

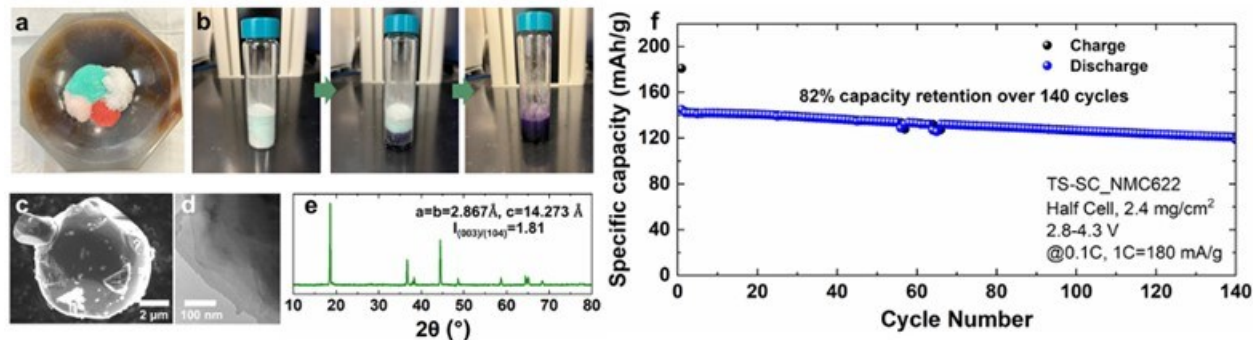


**Figure VIII.3.9** (a) Metal acetate precursor powders; (b) Spontaneous solid to molten transition of the mixed powder at above  $80 \text{ }^\circ\text{C}$ ; (c) SEM and (d) TEM image and (e) XRD of the NMC622 single crystals synthesized by eutectic method with a temperature-swing annealing. (f) Half-cell cycling data using SC-NMC622 synthesized by eutectic method.

ORNL team has developed eutectic synthesis of layered transitional metal oxide cathodes previously [10,11], and has successfully adopted this synthesis method to obtain SC-NMC622 using metal acetate precursors (Figure VIII.3.9a). The mixture of precursor powders went through a spontaneous solid to molten transition at  $80 \text{ }^\circ\text{C}$ , thus a uniform mixing down to the atomic level is realized (Figure VIII.3.9b). A temperature-swing annealing between  $900 \text{ }^\circ\text{C}$ - $1000 \text{ }^\circ\text{C}$  in oxygen is adopted, and after grinding and sieving, SC-NMC622 particles have been obtained. The SC-NMC622 morphology and microstructure are investigated by scanning electron microscopy (SEM) and transmission electron microscopy (TEM) (Figure VIII.3.9 c-d). X-ray diffraction (XRD) data (Figure VIII.3.9 e) has confirmed the crystallinity of the SC particles. The half-cell performance (Figure VIII.3.9 f) indicates an initial reversible capacity of  $145 \text{ mAh/g}$  with a capacity retention of  $82\%$  over 140 cycles. ORNL team also has synthesized NMC9055 SC particles using eutectic method.

Jackson State University is parallelly developing SC particles with sub-micron sizes and octahedral-shape using solution-combustion method. To enhance the CEI stability associated with high Ni-content NMC particles, ORNL aims to develop NMC622-coated NMC9055 SC particles with a diluted eutectic mixture and evaporation coating process (Figure VIII.3.10a). The coated NMC9055 exhibited an initial charge and discharge capacities of 207 and 164 mAh g<sup>-1</sup> at 0.1 C between 2.8 V-4.3 V. Interestingly, ORNL found that when the coated NMC9055 cycled between 2.8 V-4.7 V, not only cell specific capacities increased, but also the capacity retention improved from 80% to 92% over 20 cycles in comparison with the cell cycled between 2.8 V-4.3 V (Figure VIII.3.10b).

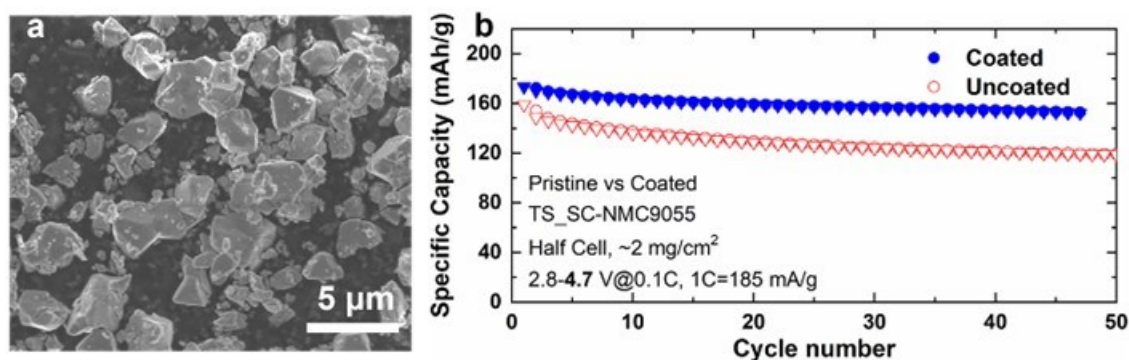


Figure VIII.3.10 (a) SEM image of NMC622-coated NMC9055 SC particles synthesized by eutectic method; (b) Half-cell performance of the pristine NMC9055 and NMC622-coated NMC9055 SC particles synthesized by eutectic method.

Parallelly, under the broad scope of understanding the role of cross-talk on CEI evolution, ORNL undertook a deep-dive study in elucidating the mechanism of transition-metal dissolution that is commonly observed to occur at a severe rate upon high-voltage cycling. In order to study whether or not transition metal cations from NMC will dissolve during potentiostatic hold at upper cut-off voltage (UCV), the team has utilized two different targeted cell aging protocols on graphite//NMC622 full cells. In one protocol, cells undergoes either a long (>450 h) potentiostatic hold at 4.4 V (full-cell voltage) upon first charge with no discharge prior to cell disassembly. In the other test, similar long potentiostatic hold (cumulative) at UCV was applied but with discharge steps also included (Figure VIII.3.11a-b). Electrochemical Impedance Spectroscopy (EIS) of full cells as a function of aging protocol presents interesting trends where the cell showed a minimal impedance growth during the long potentiostatic hold at UCV, but it experienced a continuous impedance growth at the cathode/electrolyte interface (2<sup>nd</sup> semicircle) when the discharge steps were included (Figure VIII.3.11c-d). SEM with energy dispersive X-ray spectroscopy (EDX) mapping was performed on graphite anodes extracted in the charged state (rinsed 3 times with dimethyl carbonate (DMC)). Mn signal is clearly detected in the anode from full cell that had discharge steps included. In contrast, no Mn signal was observed in the anode from full cell that underwent only a charge followed by a long potentiostatic hold (Figure VIII.3.11e-f). Future work will focus on repeating the study at a higher cut-off voltage (4.6 V full cell) where the H2 → H3 phase transformation is known to occur for NMC622 cathode.

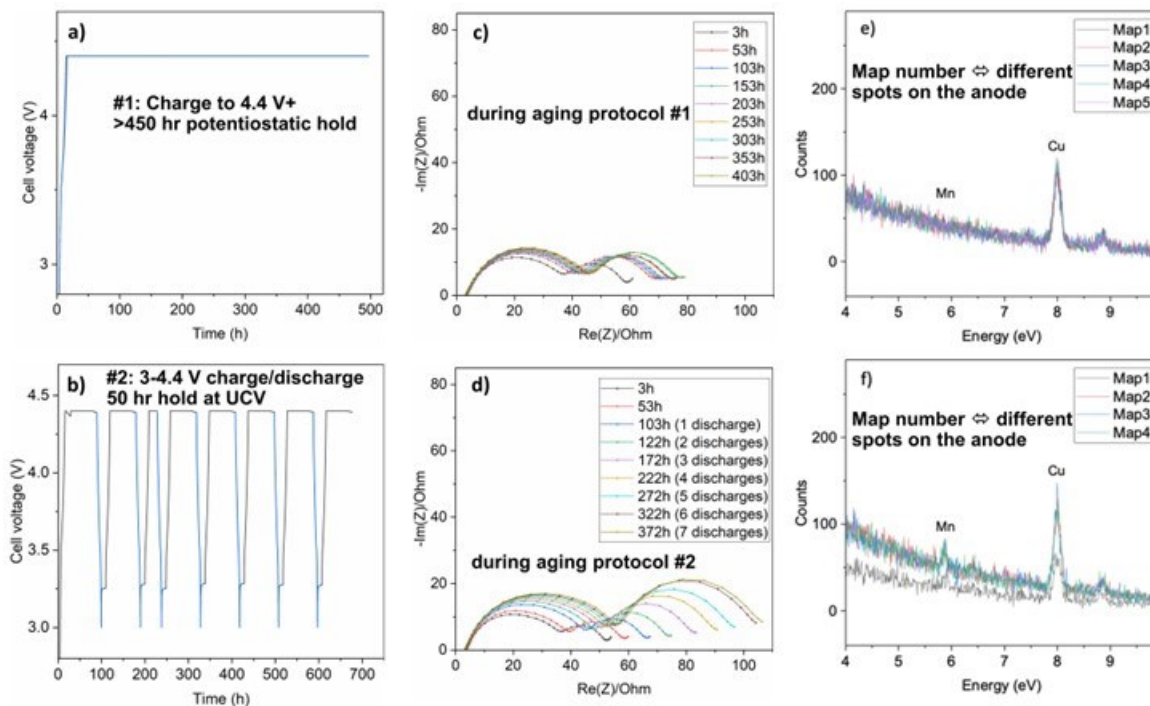


Figure VIII.3.11 (a, b) Voltage profiles showing the two types of cathode aging protocols in graphite//NMC622 full cells. Protocol #1: charge cells to 4.4 V followed by a >450 h potentiostatic hold at 4.4 V. Protocol #2: cycle the full cell between 3 V-4.4 V. At the end of each charge, constant voltage is held at 4.4 V for 50 h. (c, d) Impedance spectra of full cells cycled using protocols #1, and #2, respectively, measured at UCV at various increments. (e, f) SEM/EDX spectra of the charged graphite anodes (rinsed) extracted from cells that underwent the protocol #1, and #2, respectively. Different map numbers represent different spots on the anode.

### Focused Group 2:

#### Argonne National Laboratory (ANL) and Virginia Tech: Fundamental understanding of electrolyte decomposition at high voltage cathode-electrolyte interfaces (CEI)

During FY23, ANL articulated and implemented a framework of analysis of the fundamentals of electrolyte decomposition that combines electrolytes with controlled levels of purity, simplified model systems and the use of cathode particles with well-defined surface motifs. Implementation has already yielded valuable insight. In particular, it established the elementary reaction of oxidation of ethylene carbonate (EC) at high potential as being a “reverse” proton-coupled electron transfer (PCET). Analysis of products from this initial step coupling electroanalysis with liquid nuclear magnetic resonance (NMR) revealed that the protons generated are superacidic (Figure VIII.3.12). A second step of reverse PCET is accessible to form vinylene carbonate (VC), thus rationalizing the observations of this product commonly available in the literature. By leveraging solvents of high purity, isotope enrichment and rigorous sample manipulation, NMR results clearly indicated that the evolution from EC to VC involves a complex and dynamic collection of intermediates, including highly unstable radical species (Figure VIII.3.12).

The generation of catalytic superacidic protons was incontrovertibly linked to other products commonly found in batteries during CEI formation, including  $\text{CO}_2$ , dioxolane and polymers. This work mapped a long cascade of reactions that lead to the complex CEI reported in the literature, but that are not all directly the result of the initial oxidation at high potential. The detrimental role of superacidic protons in battery cycling was established by controlled additions in both fluorine-free and Gen 1 electrolytes, using a protocol of  $\text{H}_2$  oxidation that decouples them from the oxidation of the electrolyte. In all cases, the presence of protons led to abnormal voltage profiles in the initial cycles. Preliminary evidence also points to a lower capacity and faster fading in



the presence of protons. The work has highlighted the critical role of proton formation from electrolyte dissolution in the dynamic evolution of the CEI and points at the need to curb these species in future strategies aimed at avoiding degradation.

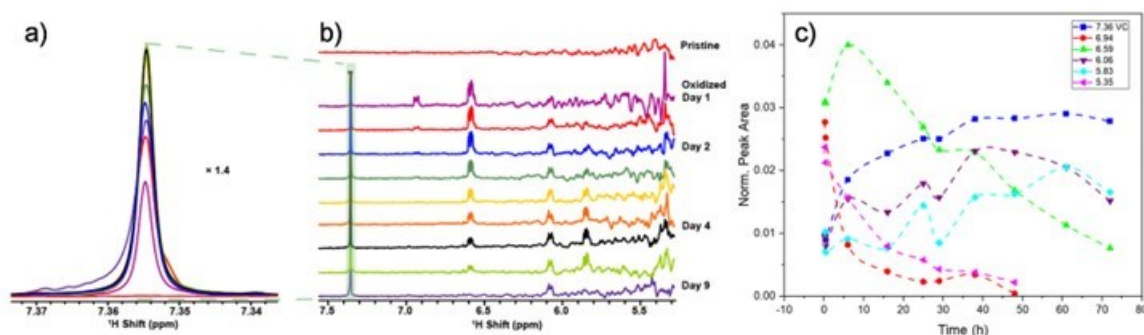


**Figure VIII.3.12** Evolution of the  $^{13}\text{C}$  NMR of solutions of  $\text{LiClO}_4/\text{EC}$  solutions after electrolysis at high potential. The measurements tracked (a) the appearance and growth of VC simultaneous to (b) the evolution of a complex set of intermediates from EC oxidation, which (c) could be quantified as a function of time.

**Sandia National Laboratories (SNL), University of Chicago, and University of California at Irvine: Redefining the Electrolyte Space to Enable High Voltage Cathode Materials via CEI Elucidation**

Open cell configurations for NMC811 are equilibrated at a series of potentials and X-ray photoelectron spectroscopy (XPS) was performed to characterize the surface chemistry *in operando*. We found that the amount of  $\text{Li}_2\text{CO}_3$  initially increases with increasing voltage, presumably via vapor phase transport of organic electrolyte species to the cathode surface, where it is oxidized. Above 4.3 V this carbonate decomposes, leaving surface lithium oxide species remaining.

To tune CEI properties, Li-borate salts are evaluated for their ability to stabilize the CEI on NMC811 under high-loading ( $\sim 15 \text{ mg/cm}^2$ ) but in half cells first. When cycled under high voltage conditions (4.6 V upper cutoff vs.  $\text{Li}/\text{Li}^+$ ),  $\text{CB}_{11}\text{H}_{12}^-$ ,  $\text{B}(\text{OCH}(\text{CF}_3)_2)_4^-$ , and  $\text{B}(\text{C}_2\text{O}_4)_2^-$  (BOB) significantly improve the capacity retention at 50 cycles compared to additive-free baseline, Gen2 (Figure VIII.3.13). The most oxidatively stable anion,  $\text{BF}_4^-$ , does not. XPS shows that the highest performing additive,  $\text{B}(\text{C}_2\text{O}_4)_2^-$  (86% retention), is most adept at minimizing carbonate solvent and  $\text{PF}_6^-$  anion decomposition based on minimization of C-O and P-F character within the CEI.

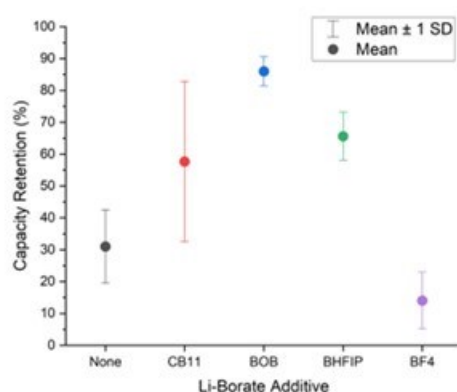


**Figure VIII.3.13** Impact of Li-borate salt additives on high-loading NMC811 capacity retention measured after 50 cycles at C/3 rate using a 4.6 V upper voltage cutoff. Error bars represent the standard deviation of three cells in each case. (SNL Unpublished data)

University of Chicago utilizes high loading NMC811 and formulated liquified gas electrolyte (LGE), i.e., 0.9M Lithium bis(trifluoromethanesulfonyl)imide (LiTFSI) in N-propyl-N-methyl-Pyrrolidinium

bis(trifluoromethanesulfonyl)imide) :FM (Fluoromethane) (C3mpyrTFSI), to compare with the team's previous baseline electrolyte (Gen2+VC) plus LiBOB additive, as depicted in Figure VIII.3.14. LGE w/o LiBOB additive showed the best performance with capacity retention of 99.5% over 50 cycles and with average C.E of 99.7%. LiBOB being a sacrificial agent and an HF scavenger [12], seems not helpful to further improve the performance of LGE-based electrolyte, due to the absence of HF generating (like LiPF<sub>6</sub>) or H<sub>2</sub>O generating (like esters) agents. Computationally, we used DFT/HSE06 to compute the reaction barriers (DE\*) associated with O<sub>2</sub><sup>2-</sup> formation on Li<sub>x</sub>NiO<sub>2</sub> (LNO) facets. The (104) facet, with 2-coordinated O anions yields a 0.6 eV barrier towards formation of a peroxide-like O<sub>2</sub><sup>2-</sup> species with both O atoms coordinated to the same surface Ni. Subsequent reaction to yield a more oxidized, quasi-spin-triplet O<sub>2</sub> species, exhibits DE\*=0.85 eV. However, hydrogen abstraction from EC by LNO (104) exhibits a much lower barrier of 0.3 eV.

The team plans to use the consortium's full coin cell protocol to validate the new findings and apply the knowledge learned from in open cell XPS, roles of electrolyte additives and favorable LNO facets to release O<sub>2</sub> from modeling to investigate CEI stability and develop new strategies for enlarging the voltage window for cycling.

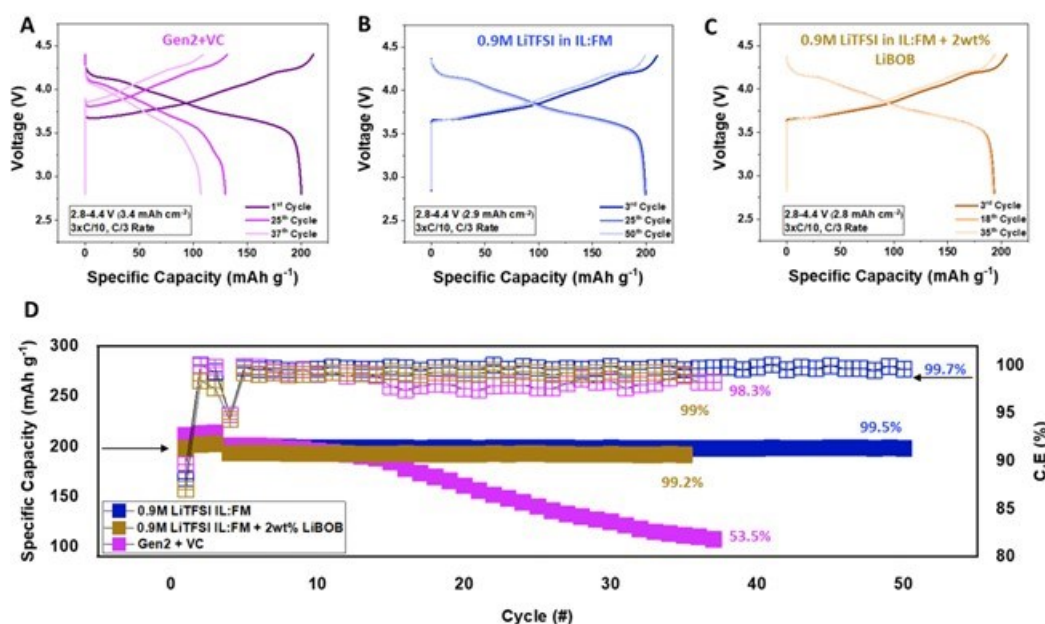


Figure VIII.3.14 High voltage cycling of high loading NMC 811 cathode in half cells using Li metal as the counter electrode. C/3 charge-discharge curves using the electrolytes (A) Gen2 + VC, 0.9M LiTFSI-C3mpyrTFSI-FM (B) w/o LiBOB additive (C) with LiBOB additive. (D) Li/NMC811 performance curves of electrolyte (A), (B), and (C). All tests are in half cells between 2.8 V and 4.4 V. The active mass loading of the cathodes with electrolyte (A)-(C) are 16.95 mg/cm<sup>2</sup>, 14.6 mg/cm<sup>2</sup>, 14 mg/cm<sup>2</sup>, respectively. (Univ. Chicago unpublished data)

#### SLAC National Accelerator Laboratory and Stanford University: Resolving and tuning high-voltage cathode electrolyte interfaces

SLAC is trying to develop a foundational understanding of the CEI for high-voltage cathode systems and guide the rational manipulation of interfacial chemistry and structure. We are pursuing this goal from three different approaches: i) interphase characterization using cryo-EM, ii) electrolyte design, and iii) electrolyte surface modification. The team has already developed cryo-EM capability for cathode characterization; The ongoing efforts are mainly focused on 3D tomography protocol development. The electrolyte design is focused on new solvent design toward high voltage battery operations.

For the surface modification, the corrosion mechanism of the Al current collector has been studied to understand its impact on performance as a first step. The team is leveraging with their previously developed capability of Atomic Level Deposition (ALD) coating to improve high-voltage operation of NMC cathodes. Specifically, the team has optimized the Li-containing ALD film recipe:  $\text{LiAl}_x\text{O}_y$ . For any Li-containing thin films, the relative content of Li can highly impact the film quality,  $\text{Li}^+$  ion transport, growth rate, and film stability. So, we systematically studied short and long Li-precursor pulse processes and optimized the number of ALD cycles required to obtain improved performance in the battery. We have completed the preliminary testing in Li || NMC cells up to 4.3 V vs.  $\text{Li}/\text{Li}^+$  in baseline LP40 electrolyte using a 50 mA/g (C/3) rate for a fast throughput screening.

Figure VIII.3.15a shows the most optimized cycling performance obtained with short Li-precursor pulses, and Figure VIII.3.15b displays the results obtained with long Li-precursor pulses. The long exposure process results in 61.9% capacity retention after 60 cycles; the short exposure process results in 42.8% capacity retention after 60 cycles, both higher than bare cathode (10.9% after 60 cycles). These results show that our optimized  $\text{LiAl}_x\text{O}_y$  coating is promising and can cause significant improvement during high-voltage battery operations. Note that for long Li-precursor exposure processes, a smaller number of ALD cycles is required for significant performance improvement.

We plan to test our best-performing coating (long Li-exposure, 3-12 cycles ALD) in full coin cells by using consortium-declared baseline conditions. CEI properties modified by ALD coating, if any, will be further characterized by cryo-EM and understand the impacts of surface treatment on high-voltage CEI.

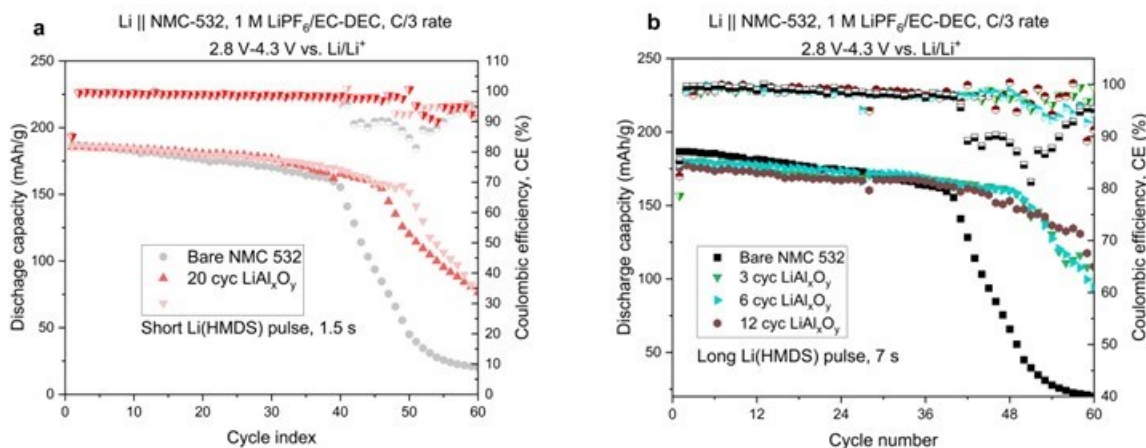


Figure VIII.3.15 Cycling stability of Li||NMC 532-coin cells using Li as the anode cycled between 2.8 and 4.3 V vs.  $\text{Li}/\text{Li}^+$  at C/3 charge and discharge rate. a) short ALD Li-precursor exposure and b) long ALD Li-precursor exposure. Mass loading of NMC532:  $12.1\text{mg}/\text{cm}^2$  ( $\sim 1.88\text{mAh}/\text{cm}^2$ ).

### Focused Group 3:

#### Brookhaven National Laboratory (BNL) and Stony Brook University (SBU): Elucidating cathode electrolyte interphase via isothermal microcalorimetry and spectroscopy investigations

The BNL-SBU team aims to discover new fundamental insights into the CEI through a synergistic approach integrating operando characterization of CEI parasitic heat with advanced spectroscopic approaches in order to gain new fundamental insights regarding CEI formation and evolution at short and long time scales.

During FY23, BNL achieved quantification of parasitic heat associated with CEI formation during formation cycling. Li/NMC811 cells were assembled and cycled in two voltage ranges for three cycles at a C/10 rate. Isothermal microcalorimetry was used to measure the total heat dissipated during electrochemical cycling, where contributions from polarization, entropic change, and parasitic heat were quantified. Results indicate that parasitic heat is most significant during cycle 1 during the charge process (Figure VIII.3.16). The data

show that polarization contributions are significant at end of discharge/ beginning of charge (low Li content). The results further indicate that changes in entropy are important and necessary to explain the overall heat flow of the system. Interestingly, in cycle 3 parasitic heat is still 3x greater during charge compared to discharge.

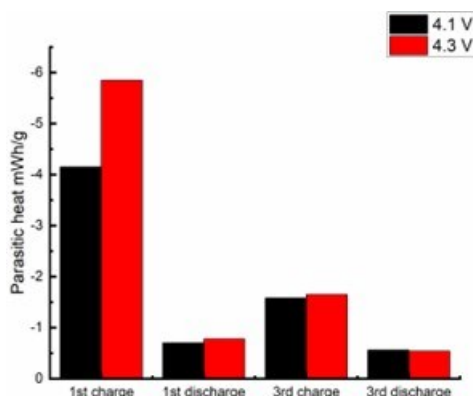


**Figure VIII.3.16 Comparison of parasitic heat resulting during cycling of Li/NMC811 cells cycled in two voltage ranges (3.0 V–4.1 V and 3.0 V–4.3 V).**

In addition, BNL completed the analysis of entropic heat flow associated with CEI formation of Li/NMC811 cells assembled and cycled in two voltage ranges (between 3 V–4.1 V and 3 V–4.3 V) for three cycles at a C/10 rate. When the entropic heat flow is negative this indicates that heat is being released due to a thermodynamically favorable process and as such indicates that the entropy of the system is increasing, while when the entropic heat flow is positive the entropy of the system is decreasing. During the first charge, the entropic heat flow is initially negative but becomes positive after 0.1 equivalents of lithium are removed ( $\text{Li}_{0.9}\text{NMC811}$ ) suggesting that the entropy of the system is initially increasing but then quickly starts decreasing during delithiation (Figure VIII.3.17a-b). The heat flow becomes progressively more positive until it peaks at  $\text{Li}_{0.7}\text{NMC811}$ . The heat flow remains positive until the cell is charged to 4.1 V ( $\text{Li}_{0.33}\text{NMC811}$ ); however, when the NMC is delithiated to  $\text{Li}_{<0.25}\text{NMC811}$ , the entropic heat flow changes sign to negative and remains negative through charge to 4.3 V ( $\text{Li}_{0.17}\text{NMC811}$ ). During discharge 1 (Figure VIII.3.17a-b), the changes in entropy are generally mirrored, indicating a reversible process, where the entropic heat flow is positive until the material is lithiated to  $\text{Li}_{0.4}\text{NMC811}$  and then negative for the remainder of the discharge, once again peaking at around  $\text{Li}_{0.7}\text{NMC811}$ . The changes in cycle 3 (Figure VIII.3.17c-d) are very comparable which confirms the entropic reversibility of the system.

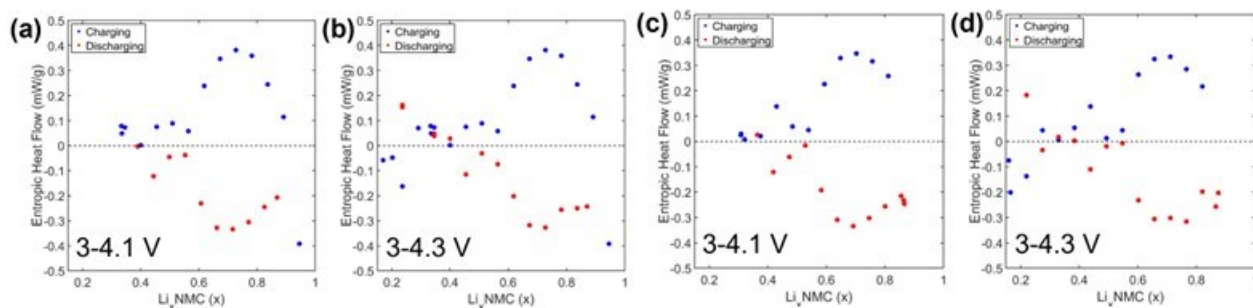


**Figure VIII.3.17 Entropic heat flow determination of Li/NMC811 coin cells. Entropic heat flow vs.  $x$  ( $\text{Li}_x\text{Ni}_{0.8}\text{Mn}_{0.1}\text{Co}_{0.1}\text{O}_2$ ) for (a) the 1st cycle from 3.0 V to 4.1 V, (b) the 1st cycle from 3.0 V to 4.3 V, (c) the 3rd cycle from 3.0 V to 4.1 V, and (d) the 3rd cycle from 3.0 V to 4.3 V.**

SBU focused on using Hard X-ray Photoelectron Spectroscopy (HAXPES) to study the composition of interfaces, including buried interfaces. HAXPES data were collected on post cycling NMC811 cathodes

recovered from Li/NMC811 cells after cycle 1-3 formation as well as after 100x cycles at C/2 rate, with measurements collected in both the discharged and charged states.

In the post formation electrodes, after three formation cycles between 3.0 V-4.1 V or 3.0 V-4.3 V at C/10 rate, HAXPES measurements were collected at both 2500 and 6000 eV. In the C1s region, the HAXPES data (Figure VIII.3.18 top) of all samples exhibit similar C1s bonds: C-C and C-H (~284.2 eV), CH<sub>2</sub> (~285 eV) C-O (~286 eV), O-C-O, C=O, and O-C=O (287-288 eV), CO<sub>3</sub> species (~289 eV), and CF<sub>2</sub> (~290.5 eV) independent of charge voltage or (dis)charge state. At 6000 eV, concentration of CF<sub>2</sub> (PVDF binder) component increases (from ~4 at. % to ~7 at. %) attributed to greater probe depth. In the O1s region, the HAXPES data (Figure VIII.3.18 bottom) shows peaks at 528-529 eV (NMC lattice oxygen, M-O bonds), ~530 eV (lithium alkoxides), 531-532 eV (lithium carbonates, lithium alkyl carbonates), and 533 eV (C-O species). M-O bonds have higher intensity at 6000 eV due to deeper probe depth. No significant differences in chemistry of CEI between 3.0 V-4.1 V and 3.0 V-4.3 V ranges post formation.

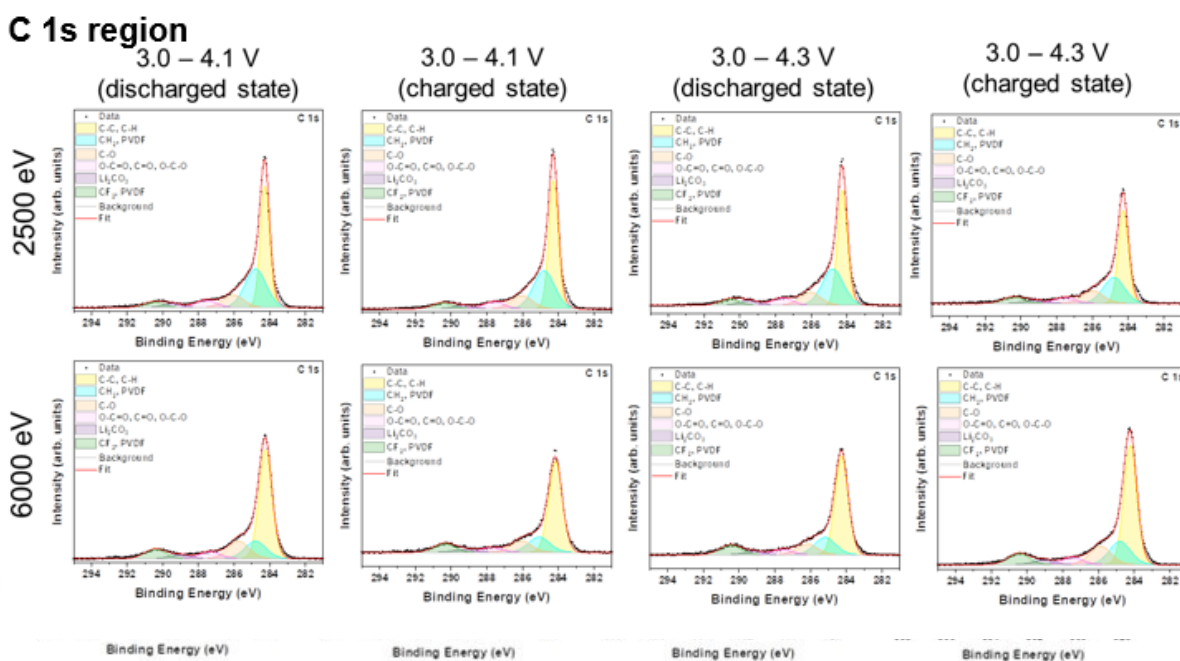


**Figure VIII.3.18 HAXPES Characterization of Interfaces Post Formation from NMC811 cathodes recovered from Li/NMC811 cells after three formation cycles between 3.0 V-4.1 V or 3.0 V-4.3 V at C/10 rate, with measurements collected in both the discharged and charged states (3.0 V-4.1 V and 3.0 V-4.3 V).**

After 100x cycles at C/2 rate, M-O and PVDF bonds are more apparent at higher beam energy, consistent with the formation cycling data, reflective of deeper probe depth (Figure VIII.3.19 a). A greater relative intensity of C-O species post-100x cycles compared to post formation was observed, suggesting formation of a thicker CEI over extended cycling (Figure VIII.3.19b). The appearance of the C-O species after 100 cycles at the two voltage windows was similar. At F 1s, the cathodes cycled between 3.0 V-4.1 V showed a comparably greater evolution of LiF component with >2x higher atomic concentration in the discharged state relative to the cathodes cycled between 3.0 V-4.3 V (Figure VIII.3.19c).

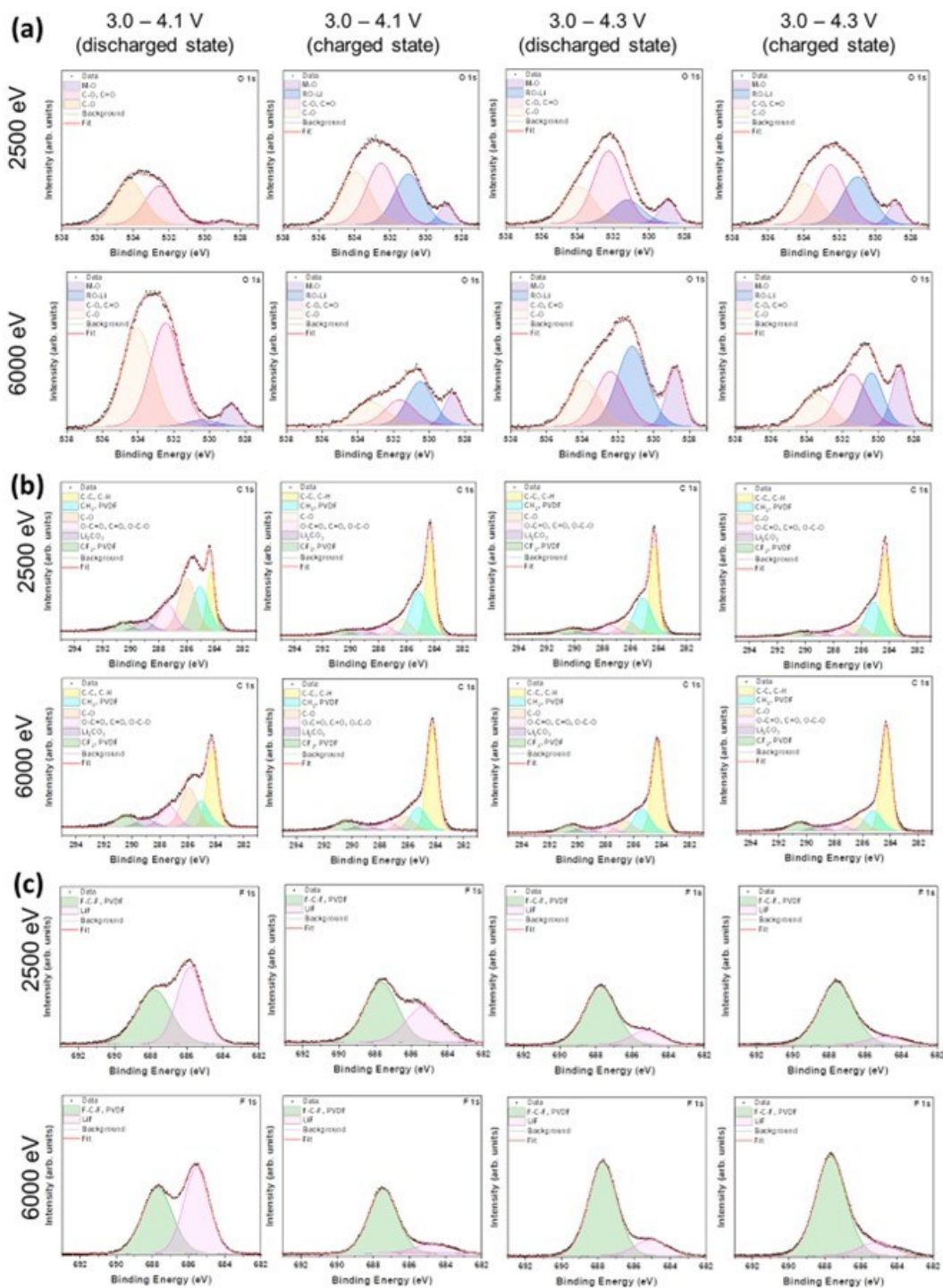
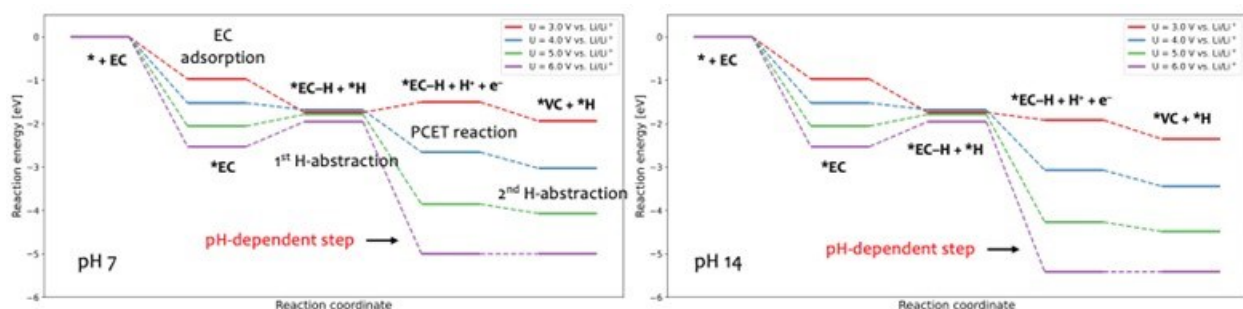


Figure VIII.3.19 HAXPES measurements collected on post NMC811 cathodes recovered from Li/NMC811 cells after 100x cycles at C/2 rate (a) O 1s data, (b) C 1s data, (c) F 1s data.

In summary, analysis of HAXPES measurements of NMC811 cathodes cycled in two voltage ranges (3.0 V-4.1 V and 3.0 V-4.3 V) for 3 cycles at C/10 rate and ending in the charged or discharged state show similar CEI chemistry. M-O and PVDF bonds are more apparent at higher beam energy, reflective of deeper probe depth. LiF species have lower concentration in CEI at (1) deeper probe depths, (2) in the charged state, and (3) at higher charge voltage.

**Lawrence Livermore National Laboratory (LLNL) and San Francisco State University: Elucidation of interfacial degradation mechanism from multiscale modeling**

In collaboration with ANL/ University of Illinois Chicago (UIC), the LLNL team performed the grand canonical density functional theory (DFT) simulations to compute potential energy profiles (shown in Figure VIII.3.20) of ethylene carbonate (EC) degradation towards vinylene carbonate (VC) on a model Pt (111) surface as a function of applied electrode potential. Our results show that EC is predicted to bind favorably to Pt (111) surfaces at electrode potentials between 3 V-6 V vs.  $\text{Li}/\text{Li}^+$ . Once bound to the surface, EC readily undergoes H-abstraction to produce an intermediate EC-H species, either a hydrogen adatom or a dissolved proton following a proton coupled electron transfer (PCET) reaction. Once the intermediate EC-H species is formed, the conversion to VC is thermodynamically favorable at all potentials between 3 V-6 V vs.  $\text{Li}/\text{Li}^+$ . Overall, the predicted onset potential of EC decomposition agrees well with the experiment measurements conducted by the ANL/UIC team.



**Figure VIII.3.20 Voltage-dependent potential energy profiles showing degradation of ethylene carbonate towards vinylene carbonate on Pt (111) surface.**

In addition to the model Pt (111) surface, we are examining the thermodynamic propensity of EC decomposition on the  $\text{LiNiO}_2$  surfaces, as proxies of NMC surfaces with high Ni content. To determine the most stable surface structures, we calculated the surface energies of (104), (110), (100), and (101) facets and identified the (104) and (110) surfaces are the most stable surfaces with a surface energy of 0.69 and 1.86  $\text{J}/\text{m}^2$ , respectively. To further investigate EC adsorption on these surfaces, we performed a grid search to identify the most favorable adsorption site and orientation of the EC molecule. It is found that EC prefers to be adsorbed on the (110) surface as expected due to its more reactive nature (higher surface energy). Subsequently, we explored different decomposition pathways of EC on  $\text{LiNiO}_2$  (104) and (110) surfaces, following either the ring-opening or  $\text{H}^+$ -abstraction mechanism. Our results reveal that both reactions are thermodynamically unfavorable due to the large reaction energies observed. Our next step is to compare these results with simulations performed on  $\text{Li}_x\text{NiO}_2$  surfaces (different charged states) and evaluate the impact of surface defects, such as Li and O vacancies or dopants, such as Mn and Co.

In collaboration with PNNL, we developed a micromechanics model to address the origin of steplike cracks formed in cycled NMC76 single crystals as observed in the post-mortem TEM measurement (Figure VIII.3.21c). We parameterized the model using the anisotropic elastic modulus of hexagonal  $\text{LiNiO}_2$  and the anisotropic volume expansion values of  $\text{LiNiO}_2$  during lithiation calculated from DFT. Based on the quasi-static model, we mapped the mechanical stress distribution near the (001) crack tips at fully discharged state and varied the distance between two neighboring (001) cracks. It is found that there is a strong compressive stress at the (001) crack tips suppressing its further propagation within the (001) plane (Figure VIII.3.21a). When there exist two (001) cracks close in distance, a significant buildup of shear stress between the crack tips is observed (Figure VIII.3.21b), which can drive new crack opening along the (101) plane. These simulation results unravel the underlying mechanism of steplike crack formation in cycled NMC materials and support the experimental observations. We plan to further refine our model by incorporating phase-field fracture mechanics to understand the dynamical behavior of crack formation and propagation.

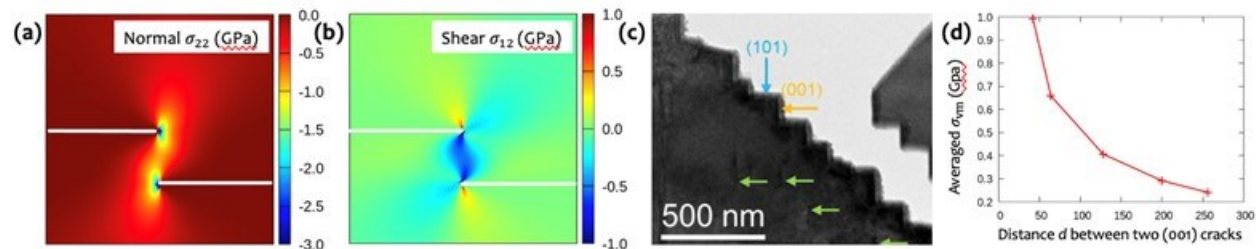


**Figure VIII.3.21** (a) and (b) Predicted stress distribution at pre-existing crack tips; (c) Post-mortem TEM image highlighting the formation of steplike cracks in cycled NMC76 single crystals (PNNL unpublished results); (d) Predicted local stress as a function of distance between two pre-existing cracks.

To determine the structure of CEI, we performed sensitivity tests to assess whether common experimental probes, such as X-ray absorption spectroscopy (XAS) can distinguish the crystalline and highly disordered phases of major CEI components. Figure VIII.3.22 demonstrates that crystalline  $\text{Li}_2\text{O}$  exhibits strong distinct XAS features whereas the amorphous-like phase washes out all major features in both Li K-edge and O K-edge spectrum. In contrast, XAS remains sensitive for capturing the structural features of  $\text{Li}_2\text{CO}_3$ , especially for O K-edge. When the structure of  $\text{Li}_2\text{CO}_3$  become highly disordered, a new feature at  $\sim 536$  eV emerge, which is attributed to a unique local bonding environment of O in this highly disordered phase. We are currently performing first-principles based XAS simulations of more complex structures, including  $\text{Li}_2\text{CO}_3/\text{Li}_2\text{O}$ ,  $\text{Li}_2\text{O}/\text{LiF}$ ,  $\text{Li}_2\text{CO}_3/\text{LiF}$  interfaces or mixtures and other relevant compositions containing P and S as identified in the scanning transmission electron microscopy/electron energy loss spectroscopy (STEM/EELS) measurement from PNNL.

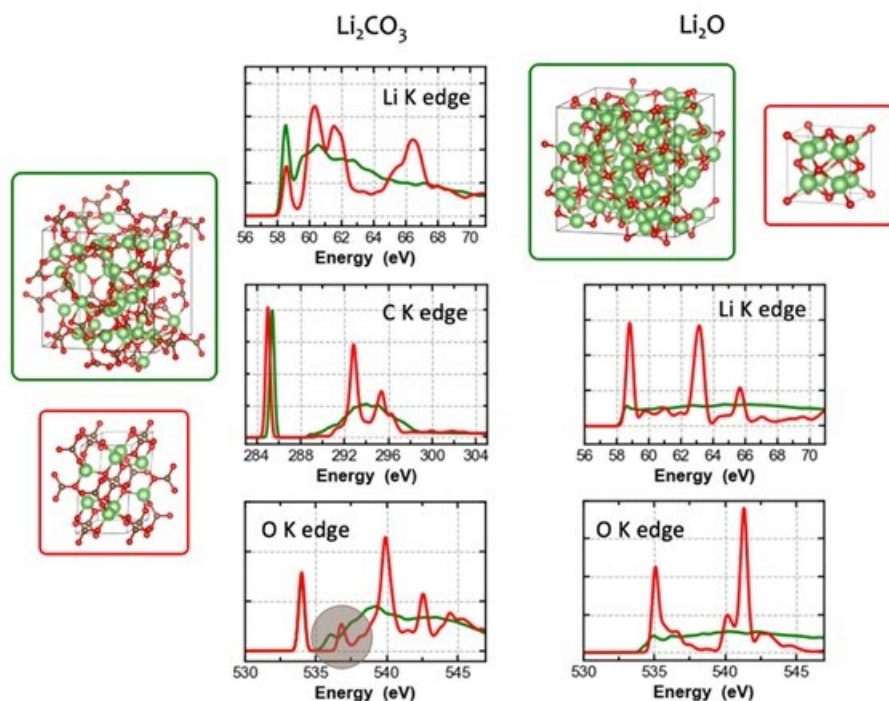


**Figure VIII.3.22** Calculated XAS spectrum of crystalline (red inset) and highly disordered phases (green inset) of  $\text{Li}_2\text{CO}_3$  (left) and  $\text{Li}_2\text{O}$  (right). In the structure representation, Li, O and C are shown as green, red and brown spheres, respectively.



**Lawrence Berkeley National Laboratory (LBNL) and Virginia Tech: Understanding and quantifying metal dissolution in candidate cathode materials as they undergo cycling**

LBNL has finished a study of “ $\text{Li}_4\text{Mn}_2\text{O}_5$ ” (LMO) a nanocomposite disordered rock salt material and published a paper (see Key Publications section) supported by CEI Consortium. Cells cycled for this study are disassembled and copious deposits of a dark material are found on the separator, suggesting a high degree of Mn dissolution even at room temperature. We now plan to study the effects of voltage limit and temperature on Mn dissolution using various analytic tools such as ICP (to measure Mn content on the separators), hard X-ray absorption spectroscopy (XAS) to determine the oxidation state of the Mn, and other spectroscopic and analytic techniques. We will then compare results to those found for  $\text{Li}_{1.167}\text{Mn}_{0.7}\text{Ti}_{0.133}\text{O}_{1.8}\text{F}_{0.2}$  (LMTOF), a better-performing DRX material, a spinel-modified LMO material, and high nickel content NMCs. LBNL also plans to prepare thin films of candidate DRX materials by pulsed laser deposition and study their properties. This allows observation of CEI formation in the absence of confounding factors like carbon and binders, which are commonly present in conventional composite electrodes and complicate interpretation of results.

Virginia Tech has developed an *in situ* X-ray fluorescence microscopy (XFM) experiment to monitor transition metal dissolution and re-deposition dynamics, using an NMC cathode ( $\text{LiNi}_{0.9}\text{Mn}_{0.05}\text{Co}_{0.05}\text{O}_2$ ). As an example, Figure VIII.3.23 shows the median nickel fluorescence intensity as a function of time and voltage during charging in a cell with 1M LiTFSI in 3:7 volume% EC:TEGDME. The increase in fluorescence intensity after the initial measurement is attributed to transition metals that dissolved into the electrolyte during cell rest and later were redeposited onto the electrode surface during charging.

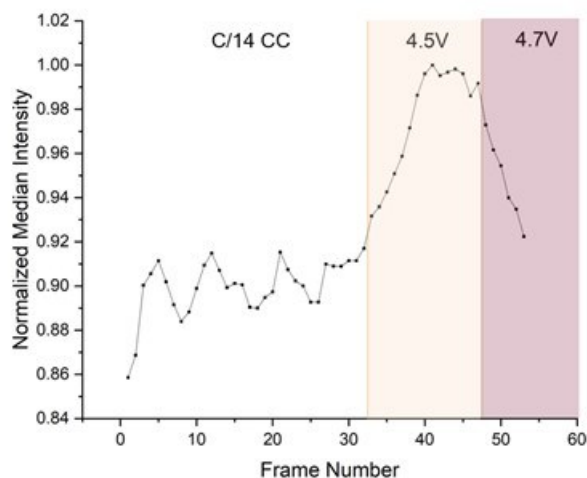


**Figure VIII.3.23 Median nickel fluorescence intensity as a function of time and voltage during charging of a half-cell containing  $\text{LiNi}_{0.9}\text{Mn}_{0.05}\text{Co}_{0.05}\text{O}_2$  and 1M LiTFSI in 3:7 volume % EC:TEGDME.**

An analysis of the operando XFM data collected at ANL on  $\text{LiNi}_{0.9}\text{Mn}_{0.05}\text{Co}_{0.05}\text{O}_2$  after a 4.5 V hold was carried out. There are large amounts of transition metal redeposition from the Ni, Co, and Mn under these conditions. For each pixel, the initial intensity was matched at the beginning of the redeposition period to its change in fluorescence intensity over the redeposition period. The data was then plotted as a function of initial intensity. This allowed visualization of where the Ni, Mn, and Co were redepositing on the cathode (Figure VIII.3.24). Notably, Mn and Co showed a preference to redeposit on the low fluorescence intensity regions of the cathode. Conversely, nickel shows redeposition on the higher intensity regions of the cathode. This suggests that Ni may have a different driving force for redeposition than Mn and Co.

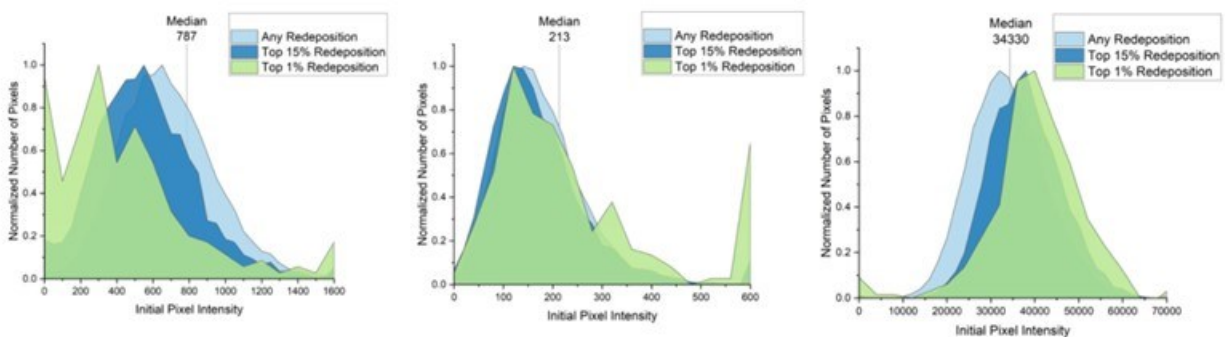


**Figure VIII.3.24** Redeposition behavior of cobalt (left), manganese (center), and nickel (right) as a function of initial pixel intensity. The median intensity of the initial redeposition frame is shown as a vertical line. Peaks falling to the left of the line represent redeposition at low intensity regions. Peaks falling to the right of the line represent redeposition at high intensity regions. “Any redeposition” refers to the behavior of all pixels experiencing TM redeposition. “Top 15%” and “Top 1% Redeposition” refer to initial intensities of the pixels with the most aggressive (top 15% and 1%) increases in fluorescence intensity.

Virginia Tech plans to continue data analysis and to determine what factors drive when and how the transition metals redeposit and how this affects the CEI. The techniques developed for this study will then be transferred to cells containing DRX materials.

***National Renewable Energy Laboratory (NREL), University of Colorado, and New Mexico State University: Investigating high-voltage Li cathode-electrolyte interfacial processes***

This team focuses on a multi-technique approach toward to the characterization of processes occurring at CEI that lead to film formation as well as the generation of products that have deleterious effects elsewhere in the cell. The complexity of the challenge is illustrated in Figure VIII.3.25 which shows a schematic representation of the multiple overlapping involved processes occurring at the CEI. Cathode/electrolyte interfacial properties develop through degradation of both the cathode material as well as electrolyte components, likely in coupled processes.

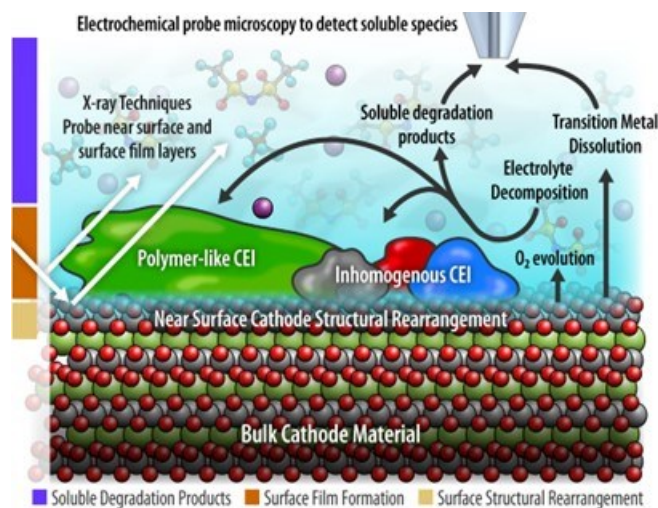


**Figure VIII.3.25** Schematic showing relevant interfacial processes to be studied and planned evaluation methods. Interfacial/ surface and near-surface analysis techniques will be paired with modeling to deconvolute CEI formation mechanisms.

Our effort focuses on the combination of X-Ray surface spectroscopy, electrochemical probe microscopy and molecular dynamic simulations to better understand CEI processes and associated cell degradation processes.

The long-term goal is to characterize CEI processes occurring at a NMC811 model cathode material. In this year, we have focused on initial method development and demonstrating efficacy of our methods using simplified “non-intercalating” electrodes (platinum, Pt and glassy carbon, GC) as well as initial evaluation of  $\text{LiMn}_2\text{O}_4$  (LMO). Subsequent work is pivoting to the NMC 811 material which will be reported on in future efforts.

Initial work using x-ray spectroscopic methods to probe surface film formation and cathode structural rearrangement has focused on  $\text{LiMn}_2\text{O}_4$  (LMO) model materials. The team has successfully synthesized LMO thin films on N-type Si with conductive layers on both sides by using polymer-assisted deposition method (PAD). The LMO model surface serves as the cathode in our test cell, while Li metal is used as the counter and reference. We observed a slow but continuous decay in capacity in cyclic voltammetry for our LMO model surface. We believe this is associated with the well-known issue of Mn dissolution. Via surface sensitive near edge X-ray absorption fine structure (NEXAFS) total electron yield (TEY) and linear combination fitting (LCF), we observed that the suspected Mn dissolution is associated with an irreversible surface reconstruction in the CEI of LMO. The soluble species, which we believe is mainly  $\text{Mn}_3\text{O}_4$ , is predominantly formed during the discharge process.

Figure VIII.3.26a shows CV data for LMO in our LP58 model electrolyte after its 2<sup>nd</sup>, 45<sup>th</sup>, 60<sup>th</sup> and 80<sup>th</sup> cycles. It is noted that a continuous decay occurs during cycling, and the decrease in the overall charge capacity shown in the CV data (area under the oxidation and reduction peaks). This decay is further studied via NEXAFS, which is shown in Figure VIII.3.26b. The NEXAFS data indicates the accumulation of  $\text{Mn}^{2+}$  and  $\text{Mn}^{3+}$  species occurring on the model cathode surface. This data is mostly similar to the pattern of the  $\text{Mn}_3\text{O}_4$  reference indicating the likely presence of that material. The shifting of the spectrum is more dramatic between 45<sup>th</sup> and 60<sup>th</sup> cycles, which is in line with the decay observed in CV data. To further investigate the potential dependence of the Mn species in the CEI, we also acquired the oxidation state of the LMO surface at both charged and discharged state in various cycles, as shown in Figure VIII.3.26c. When LMO is charged to 4.3 V, the oxidation state of the surface is between 3.6 V-3.7 V over 60 cycles. This indicates that the previously formed  $\text{Mn}_3\text{O}_4$  species appear to be removed from the surface during charging. The ever-increasing gap of oxidation state between charged and discharged state potentially indicates that the  $\text{Mn}_3\text{O}_4$  altered layer is accumulating during the discharging process, and its formation is very likely accelerating with continued cycling.

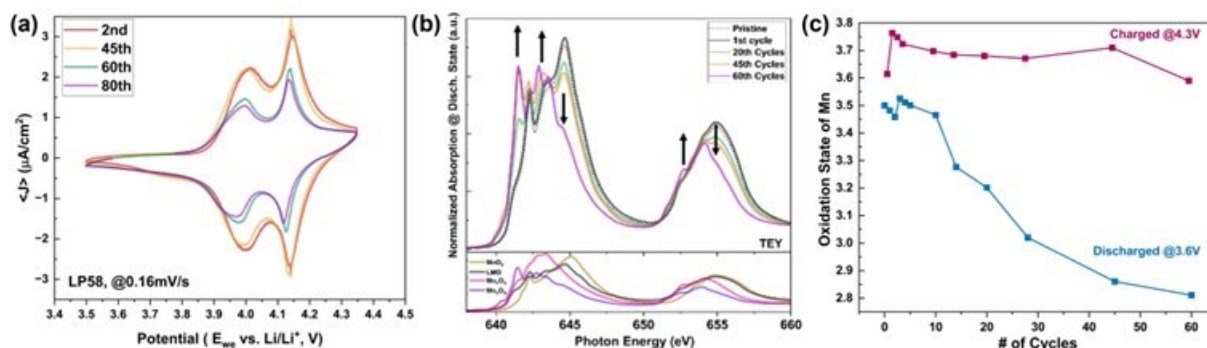


**Figure VIII.3.26 (a) Cyclic Voltammetry of PAD-LMO in LP58 model electrolytes (1.2M  $\text{LiPF}_6$  in EC:EMC=3:7), (b) Mn L-edge NEXAFS of Cycled PAD-LMO in TEY mode and (c) Comparison of the Oxidation States of PAD-LMO in Charged/Discharged State.**

Figure VIII.3.27 shows a simple schematic of a typical scanning electrochemical microscopy (SECM) apparatus. SECM is a scanning probe microscopy that can be used to perform electrochemical analysis of species evolving from or being consumed at an electrode surface. Analysis occurs by using a small electrode as a sensing “tip” in an active four-electrode electrochemical cell containing an electrolyte solution. The applied potential at both the substrate and the tip electrode is controlled versus the same reference and counter

electrodes by a bi-potentiostat. The tip electrode commonly consists of a conductive wire (micron-nanometer in diameter) embedded in glass and ground/polished to a point. The instrument can be used both as an imaging technique, as implied by its name, as well as a measurement technique. This report is focused on the use of SECM measurement methods to detect electrochemically active materials leaving the CEI.

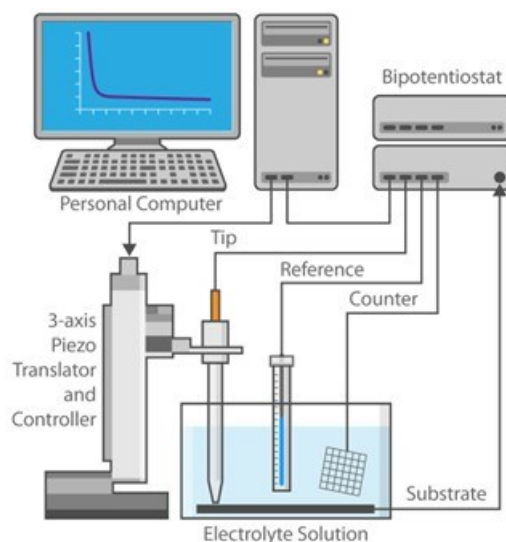


**Figure VIII.3.27 Schematic showing a typical scanning electrochemical microscope.**

Generation/Collection SECM (G/C SECM) is an *in-situ* measurement method in which the tip electrode is used to conduct experimental measurements of species evolving from a substrate surface similar to the rotating ring-disk electrode method. In this work, the tip electrode can be used to perform analysis at varying distances from the underlying substrate to characterize species evolving from the CEI formation process as well as their stability as they diffuse away from the CEI. The use of a small tip electrode for characterization enables measurements to be made very near the active cathode-electrolyte interface and allows the examination of short-lived transient species that may only be observed prior to further solution phase reactions. The G/C SECM technique is ideal for probing both direct electron transfer between the cathode and the electrolyte (electrochemical oxidation) as well as the properties of highly reactive species released during the CEI formation process that subsequently react with the electrolyte in a chemical oxidation.

To isolate direct electrolyte oxidation from potential chemical oxidation processes we have paired studies at an initial model cathode material (LMO) with those using “non-intercalating” electrodes such as Pt or GC. This work attempts to gain understanding of the direct oxidation of our LP58 electrolyte and begins to compare this to oxidation processes observed in the presence of a model cathode material. A combination of CV and G/C SECM was used to study the oxidation behavior of the LP58 electrolyte on non-intercalating electrodes as well as LMO. Data from these efforts are summarized in Figure VIII.3.28. Figure VIII.3.28a-b show CV data collected using Pt (a) and GC (b) electrodes. The different colors shown represent varying voltage sweep ranges. Both the Pt and GC data show multiple oxidation processes occurring at high voltage due to oxidation of the LP58 electrolyte material. Oxidation of the LP58 electrolyte at the Pt electrode appears to lead to the formation of a reducible product observed at voltages below 3.1 V while data collected at the GC electrode does not show a similar product. The reduction product detected using the Pt electrode may be consistent with proton reduction from de-protonation of the carbonate solvents (ethylene and ethylmethyl carbonates) as has been reported by the Cabana team. Pt electrodes typically are more reactive toward proton reduction than glassy carbon. Based on this, the lack of the reduction product detected with glassy carbon may well point toward the proton as the origin of the observed reduction on Pt.

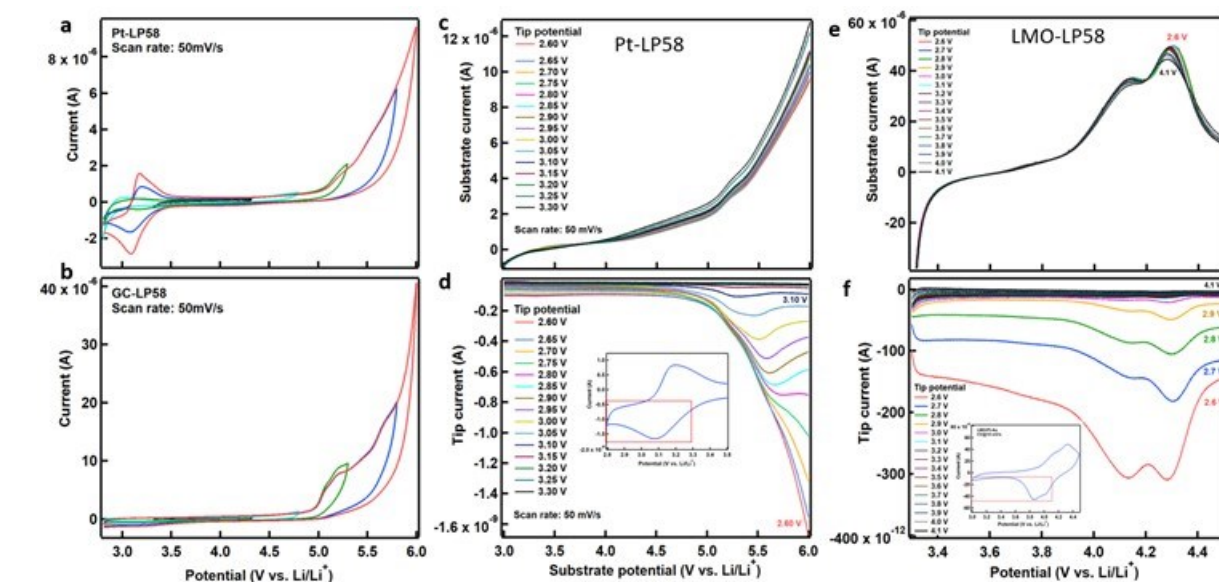


Figure VIII.3.28 (a) cyclic voltammetry (CV) for oxidation of LP58 at a 2 mm Pt disk. (b) CV for LP58 at a 3 mm GC electrode. (c) linear sweep voltammetry (LSV) collected at a 2 mm Pt disk electrode for oxidation of LP58 (d) Generation/collection SECM (GC-SECM) tip current collected for a 10 mm Pt tip electrode near the 2 mm Pt disk substrate. Tip voltage was varied from 3.3 V to 2.6 V (e) LSV for a LMO model cathode material in LP58 (f) GC-SECM tip current collected for a 10 mm Pt disk tip electrode near a LMO substrate undergoing voltage sweep.

Figure VIII.3.28c-d show G/C SECM data collected for the direct electrochemical oxidation of the LP58 electrolyte at a Pt electrode. A 2 mm Pt disk electrode was used as the substrate in our SECM cell and a 10 mm Pt SECM tip was placed near the substrate surface to detect any species generated at the substrate. In this experiment the Pt substrate electrode voltage was swept from 3 V to 6 V while the tip electrode voltage was held at constant values ranging from 3.3 V to 2.6 V. Figure VIII.3.28c shows the current measured at the Pt substrate electrode during the voltage sweep and is similar to that seen in the CV data for oxidation of LP58 in Figure VIII.3.28a as would be expected. Figure VIII.3.28d shows the measured tip current collected during the associated voltage sweep at the Pt substrate electrode. The x-axis in Figure VIII.3.28c-d are both for the voltage at the substrate electrode during the voltage sweep. The multiple traces shown in Figure VIII.3.28d are tip current values collected at various fixed tip potentials as the substrate voltage is swept positive. The range of tip potentials from 3.3 V to 2.6 V was selected based on potential detection of the expected reduction product shown at low voltage on Pt in Figure IX.3.28a. The inset in Figure VIII.3.28d highlights in a red square the range of tip detection voltages and shows the overlap with the expected reduction process mentioned. Figure VIII.3.28d, initially, when the tip voltage was held at greater than  $\sim 3.1$  V no significant increase in tip current is detected when the oxidation of LP58 is driven at high voltage on the Pt substrate. However, as the tip bias is moved to lower voltages, a noticeable reduction current is detected during the oxidation process when the substrate is at high voltage. The reduction current at the tip continues to increase as the tip voltage is shifted further and further negative. The fact that a tip reduction product is only detected at voltages consistent the reduction product detected by CV in Figure IX.3.28a indicates that this is likely the same product, potentially coming from deprotonation of the carbonates in the electrolyte. This result is not entirely surprising given the earlier CV results, but does serve to demonstrate how the G/C SECM method can be used to detect species generated at the substrate as well as what voltage they may be reduced at. In the case of identical materials for the tip and substrate electrodes, the response detected by G/C SECM and CV would be expected to be similar.

However, the situation is not as clear cut when the substrate material differs from the tip material.

Figure VIII.3.28e-f show data from a similar experiment to that in Figure VIII.3.28c-d but with LMO as the substrate electrode and a 10 mm Pt SECM tip electrode. Figure VIII.3.28e shows the current measured at the LMO substrate when swept from 3.3 V to 4.5 V in the LP58 electrolyte. Excursions to voltages greater than 4.5 V led to catastrophic destruction of the LMO substrate and were, hence, avoided. To identify any reducible products formed during the oxidation of the LMO substrate, the voltage of the tip electrode was held varying potentials between 4.1 V and 2.6 V as shown in the red box in the insert in Figure VIII.3.28f. Figure VIII.3.28f shows tip current traces collected at these varied voltages as the oxidation of LMO is driven at the substrate. As the tip voltage is shifted to lower potentials in Figure VIII.3.28f, the reduction current detected at the tip increases. Notably, the detected reduction current appears to show a “peaked” response that correlates with the oxidation processes observed for the LMO. The origin on the reduction process detected at the tip is not clear, but does appear to be most prominently observed at the same low voltages shown for Figure VIII.3.28 (c) and (d). This may indicate that the same oxidation product is being formed at lower voltage (and concurrently with Mn oxidation) in the presence of the model cathode material. This system is under substantial further study to better understand the origin of this process and its relationship with the LMO oxidation.

Initial work from the theory team has focused on simulations of model electrolytes above a non-intercalating electrode with the Reaxff molecular dynamics force field, as well as bulk electrolyte simulations. Our team has also initiated a new collaboration with Sabrina Wan and Stephen Weitzner, to enable simulations with more realistic NMC cathodes. Sabrina and Stephen will provide us DFT-generated data on electrolyte/NMC interactions, which will be used to parameterize the first Reaxff force fields ever developed for simulating NMC cathodes.

## Conclusions

The CEI Consortium had a delayed start in year one but the three focused groups have made great progress towards deepening the fundamental understanding of CEI at high voltages from different angles.

**PNNL/University of Washington** tackles the CEI challenges from the original storage environments of commercial NMC811, while **ORNL/Jackson State University** apply eutectic synthesis approach to modify the surface properties of single crystals and studies the roles of “cross-talk” on CEI properties. **INL/Brown University** explores the feasibility of creating an artificial CEI layer to mitigate oxygen release from cathode by using both experimental and simulation approaches. **ANL/Virginia Tech** utilizes classical rotating disk electrode to understand electrolyte decomposition pathway at high voltages and its implication for CEI stability. The electroanalysis results from ANL are shared with **LLNL/San Francisco State University** to examine the thermodynamic propensity of EC decomposition on model surfaces. **LLNL** is also in collaboration with PNNL to develop a micromechanics model to address the origin of steplike cracks formed in cycled NMC76 single crystals. **SLAC** studies the corrosion mechanism of aluminum current collector and plans to further stabilize high voltage CEI by leveraging their ALD capability. The team of **SNL/University of Chicago/University of California Irvine** investigates the fundamental roles of borate additive in conventional electrolyte and LGE to develop strategies to stabilize CEI at high voltages. The **BNL/Stony Brook University** team has achieved quantification of parasitic heat associated with CEI formation during formation cycling, which investigates CEI properties from different aspects. In addition to probe the dissolution and redeposition of transition metals from Ni-rich NMC (led by **Virginia Tech**) by using *in situ* XFM, **LBNL** is studying “Li<sub>4</sub>Mn<sub>2</sub>O<sub>5</sub>” (LMO) a nanocomposite disordered rock salt material in support of the DRX<sup>+</sup> Consortium. The team of **NREL/University of Colorado/New Mexico State University** focuses on a multi-technique approach towards the characterization of processes occurring at CEI that lead to film formation as well as the generation of products that have deleterious effects elsewhere in the cell.

At consortium level, a full coin cell protocol has been established and shared within the consortium to ensure fair comparisons when reporting experimental results. Commercial NMC811 and lab-made single crystals (synthesized at PNNL) have been shared within the CEI Consortium to accelerate research innovation. Baseline performance of commercial NMC811 is also established by using the full coin cell protocol to benchmark the work developed under the consortium. While thin-film cathodes or half coin cells are still

flexibly used for different purposes such as characterization and modeling, it is expected that functional materials or new electrolytes targeted to enhance CEI stability will be cross validated by using the consortium's protocol making the fundamental research meaningful for and adaptable by industry.

### Key Publications

1. Yin, Wei. et al., "Li-Mn-O Li-Rich Cation Disordered Rock-salt Cathode Materials Do Not Undergo Reversible Oxygen Redox during Cycling." *Journal of Materials Chemistry A* 11 (2023): 23048-23061. <https://doi.org/10.1039/D3TA04873J>.
2. He, Rong, Larissa Zhou, Robert Tenent, and Meng Zhou, "Basics of the Scanning Electrochemical Microscope and Its Application in the Characterization of Lithium-ion Batteries: A Brief Review." *Materials Chemistry Frontiers* 7 (2023): 662-678. <https://doi.org/10.1039/D2QM01079H>.
3. Xiao, Jie. et al., "From Laboratory Innovations to Materials Manufacturing for Lithium-based Batteries." *Nature Energy* 8 (2023): 329-339. <https://doi.org/10.1038/s41560-023-01221-y>.

### References

1. Xu, Kang. "Electrolytes and Interphases in Li-Ion Batteries and Beyond." *Chemical Reviews* 114 (2014): 11503-11618. <https://doi.org/10.1021/cr500003w>.
2. Nelson, Kathlyne. et al., "Studies of the Effect of High Voltage on the Impedance and Cycling Performance of Li[Ni<sub>0.4</sub>Mn<sub>0.4</sub>Co<sub>0.2</sub>]O<sub>2</sub>/Graphite Lithium-Ion Pouch Cells." *Journal of The Electrochemical Society* 162 (2015): A1046-A1054. <https://doi.org/10.1149/2.0831506jes>.
3. Yan, Pengfei. et al., "Tailoring Grain Boundary Structures and Chemistry of Ni-Rich Layered Cathodes for Enhanced Cycle Stability of Lithium-Ion Batteries." *Nature Energy* 3 (2018): 600-605. <https://doi.org/10.1038/s41560-018-0191-3>.
4. Hu, Jiangtao. et al., "Locking Oxygen in Lattice: A Quantifiable Comparison of Gas Generation in Polycrystalline and Single Crystal Ni-Rich Cathodes." *Energy Storage Materials* 47 (2022): 195-202. <https://doi.org/10.1016/j.ensm.2022.02.025>.
5. Bi, Yujing. et al., "Reversible Planar Gliding and Microcracking in a Single-Crystalline Ni-Rich Cathode." *Science* 370 (2020): 1313-1317. <https://doi.org/10.1126/science.abc3167>.
6. Jiang, Ming, Dmitri Danilov, Rüdiger-A Eichel, and Peter Notten. "A Review of Degradation Mechanisms and Recent Achievements for Ni-Rich Cathode Based Li-Ion Batteries." *Advanced Energy Materials* 11 (2021): 2103005. <https://doi.org/10.1002/aenm.202103005>.
7. Liu, Hansan, Yong Yang, and Jiujun Zhang, "Investigation and Improvement on the Storage Property of LiNi<sub>0.8</sub>Co<sub>0.2</sub>O<sub>2</sub> as a Cathode Material for Lithium-Ion Batteries." *Journal of Power Sources* 162 (2006): 644-650. <https://doi.org/10.1016/j.jpowsour.2006.07.028>.
8. Cheng, Huangru, Colin Freeman, and John Harding, "Charge Disproportionation and Jahn-Teller Distortion in LiNiO<sub>2</sub> and NaNiO<sub>2</sub>: A Density Functional Theory Study." *Physical Review B* 84 (2011): 085108. <https://doi.org/10.1103/PhysRevB.84.085108>.
9. Biasi, Lea. et al., "Phase Transformation Behavior and Stability of LiNiO<sub>2</sub> Cathode Material for Li-Ion Batteries Obtained from In Situ Gas Analysis and Operando X-Ray Diffraction." *ChemSusChem* 12 (2019): 2240-2250. <https://doi.org/10.1002/cssc.201900032>.
10. Li, Mengya. et al., "Correlation of Oxygen Anion Redox Activity to In-Plane Honeycomb Cation Ordering in Na<sub>x</sub>Ni<sub>y</sub>Mn<sub>1-y</sub>O<sub>2</sub> Cathodes." *Advanced Energy and Sustainability Research* 3 (2022): 2200027. <https://doi.org/10.1002/aesr.202200027>.
11. Li, Mengya. et al., "Eutectic Synthesis of P2-Type Na<sub>x</sub>Fe<sub>1/2</sub>Mn<sub>1/2</sub>O<sub>2</sub> Cathode with Improved Cell Design for Sodium-Ion Batteries." *ACS Applied Materials & Interfaces* 12 (2020): 23951-23958. <https://doi.org/10.1021/acsami.0c04513>.
12. Li, Yixuan. et al., "Elucidating the Effect of Borate Additive in High-Voltage Electrolyte for Li-Rich Layered Oxide Materials." *Advanced Energy Materials* 12 (2022): 2103033. <https://doi.org/10.1002/aenm.202103033>.

**Acknowledgements**

PNNL: Yujing Bi, Yaobin Xu, Witness Martin and Chongmin Wang; University of Washington: Corie Cobb, Michelle Katz, Jun Liu; INL: Wenjuan Bian, Eric Dufek and Bin Li (former PI at INL); Brown University: Yue Qi, I-Ta Hsieh; ORNL: Mengya Li, Ritu Sahore; Jackson State University: Saiful Islam, Subrata Roy; ANL: Jordi Cabana, Key Baris, Haoyu Liu, Zhengcheng Zhang, Justin Connell, Stefan Ilic, Qian Liu, Jingtian Yang; Virginia Tech: Feng Lin, Chenguang Shi, Weibo Huang, Katelyn Meyer; SLAC: Yi Cui, Sanzeeda Baig Shuchi; SNL: Kevin Leung, Nathan Hahn, Kevin Zavadil; University of Chicago: Shirley Meng, Sven Burke; UC Irvine: Shen Dillon; BNL: Amy Marschilok, Lei Wang, Shan Yan; Stony Brook University: Kenneth Takeuchi, Esther Takeuchi, Armando Rodriguez Campos; LBNL: Marca Doeff, Wei Tong, Monica Theibault, Robert Kostecki; LLNL: Liwen (Sabrina) Wan, Stephen Weitzner, Wonseok Jeong, Bo Wang; San Francisco State University: Nicole Adelstein; NREL: Robert Tenet; Colorado University-Boulder: Michael Toney, Kayla Sprenger, Wenhan Qu, Rafael Ferreira de Menezes; and New Mexico State: Hongmei Luo, Meng Zhou, Rong He.



## IX Next Generation Lithium-Ion Materials: Diagnostics

The increasing demand for lithium-ion batteries requires advancements in diagnostics to observe capacity loss to maintain reliability as the capacity declines, identify anomalies to prevent catastrophic failures, and predict the end of battery life when the battery fades to a set capacity threshold. Well-developed battery test technologies must recognize all battery conditions and provide reliable results, even if the charge is low.

The rest of this chapter contains detailed reports on the status of the following individual projects.

- Interfacial Processes (LBNL)
- Advanced in situ Diagnostic Techniques for Battery Materials (BNL)
- Microscopy Investigation on the Fading Mechanism of Electrode Materials (PNNL)
- In-Operando Thermal Diagnostics of Electrochemical Cells (LBNL)
- Pre-Lithiation of Silicon Anode for High Energy Li-Ion Batteries (Stanford U).

## IX.1 Interfacial Processes (LBNL)

### **Robert Kostecki, Principal Investigator**

Lawrence Berkeley National Laboratory  
1 Cyclotron Rd.  
Berkeley, CA 94720  
E-mail: [r\\_kostecki@lbl.gov](mailto:r_kostecki@lbl.gov)

### **Tien Duong, DOE Technology Development Manager**

U.S. Department of Energy  
E-mail: [Tien.Duong@ee.doe.gov](mailto:Tien.Duong@ee.doe.gov)

Start Date: October 1, 2022	End Date: September 30, 2023	
Project Funding (FY23): \$440,000	DOE share: \$440,000	Non-DOE share: \$0

### **Project Introduction**

Li-based batteries are inherently complex and dynamic systems. Although often viewed as simple devices, their successful operation relies heavily on a series of complex mechanisms, involving thermodynamic instability in many parts of the charge/discharge cycle and the formation of metastable phases. This paradigm of Li-battery system operation usually drives the battery toward irreversible physical and chemical conditions that lead to battery degradation and failure.

The requirements for long-term stability of Li batteries are extremely stringent and necessitate control of the chemistry at a wide variety of temporal and structural length scales. Progress towards identifying the most efficient mechanisms for electrical energy storage and the ideal material depends on a fundamental understanding of how battery materials function and what structural/electronic properties limit their performance. This in turn necessitates the development and use of new characterization tools to monitor these processes.

The design of the next generation of Li batteries requires a fundamental understanding of the physical and chemical processes that govern these complex systems. Although some significant advances have been made to prepare and utilize new materials efforts towards the understanding of their operation mechanisms and degradation modes have been insufficient and/or unsuccessful.

Instability and/or high resistance at the interface of battery electrodes limit electrochemical performance of high-energy density batteries. A better understanding of the underlying principles that govern these phenomena is inextricably linked with successful implementation of high energy density materials in Li-based cells for PHEVs and EVs. Pristine and cycled composite and thin film model electrodes are investigated using a variety of state-of-the-art techniques to identify, characterize and monitor changes in materials structure and composition that take place during battery operation and/or storage. This project constitutes an integral part of the concerted effort within the BMR Program and it supports development of new electrode materials for high-energy Li-metal based rechargeable cells.

### **Objectives**

This collaborative project involves the development and application of advanced experimental methodologies to study and understand the mechanism of operation and degradation of high-capacity materials for rechargeable cells for PHEV and EV applications. The project objective is to establish specific design rules toward the next generation of low-impedance Li-metal rechargeable batteries that are capable of performing 1000 deep discharge cycles at Coulombic efficiency > 99.9% and suppressing lithium dendrite formation at high current densities (> 2 mA/cm<sup>2</sup>). This project aims at the following: (1) establishing general rules between

Li<sup>+</sup> transport properties in novel liquid/solid electrolytes, and (2) determining the mechanism of the solid electrolyte interphase (SEI) layer (re)formation.

The other goal is development and application of far- and near-field optical probes and synchrotron-based advanced X-ray techniques that are capable of unveiling the function and operation of hidden or buried interfaces and interphases to obtain insight into the mechanism of Li<sup>+</sup> transport and interfacial reactions in lithium/liquid model systems and determine material, electrode and battery cell electrochemical performance and failure modes.

Through an integrated synthesis, characterization, and electrochemistry effort, this project aims to develop a better understanding of lithium / liquid electrolyte (LE) interface so that rational decisions can be made as to their further development into commercially viable Li-metal cells and propose effective remedies to address inadequate Li-metal rechargeable batteries calendar/cycle performance for PHV and EV applications.

### Approach

- The pristine and cycled composite electrode and model thin-film electrodes were probed using various surface- and bulk-sensitive techniques, including FTIR, ATR-FTIR, near-field IR and Raman spectroscopy/microscopy, and SPM to identify and characterize changes in materials structure and composition.
- Novel in situ / ex situ far- and near-field optical multi-functional probes in combination with standard electrochemical and analytical techniques are developed to unveil the structure and reactivity at interfaces and interphases that determine materials electrochemical performance and failure modes.

### Results

A sample preparation protocol was established for studying the SEI on Li metal in contact with GEN2 electrolyte (EC/EMC 1.2 M LiPF<sub>6</sub>) with nano-FTIR spectroscopy. A piece of Li metal was cut out of cleaned Li rod in a solvent-free glovebox via razorblade wrapped in Celgard and rolled between two plastic plates wrapped in Celgard to obtain a shiny metallic Li surfaces free of contaminants.

ATR-FTIR spectra of Li after interacting with GEN 2 electrolyte consists of a mix of IR bands from the electrolyte and LEDC. The presence of EC and EMC bands indicates electrolyte/solvent trapping inside SEI layer. Systematic attempts to remove excess of residual electrolyte without simultaneous removal of the SEI were carried out. Contrary to washing with 30 μL of EMC, using a Kimwipe to collect the electrolyte from the surface preserves the peaks of the SEI components are present and effectively removes EC/EMC. (Figure IX.1.1)

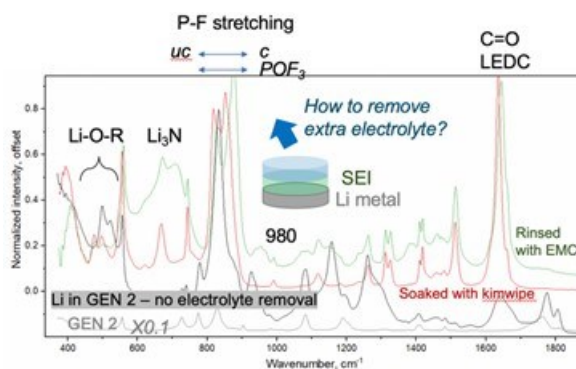
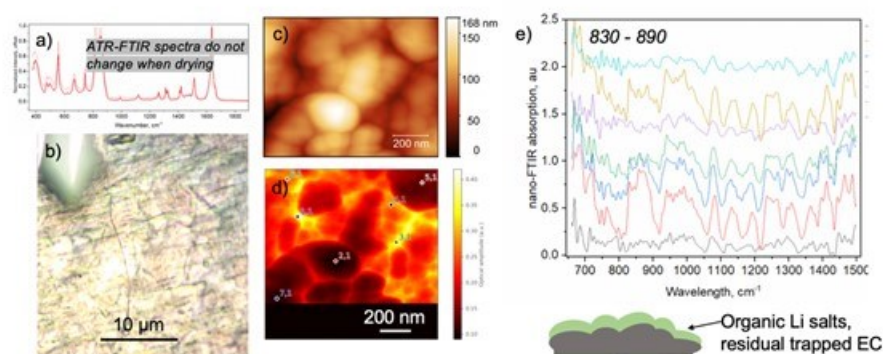


Figure IX.1.1 ATR-FTIR spectra of Li metal after exposure to GEN2 electrolyte. The residual electrolyte was removed by drying (black), kimwipe (red), rinsing with 30 μL EMC (green). ATR spectrum of GEN2 electrolyte dried on Cu (grey) is included for reference.

On the micro scale, an iridescent film was found on top of the Li metal surface. When attempting to perform non-contact AFM measurements, the tip was immediately contaminated, indicating that loosely bound particles of electrolyte or its decomposition products were picked up from the surface. Moreover, a signal from residual  $\text{LiPF}_6$  salt at  $834\text{ cm}^{-1}$  dominated local FTIR spectra.

After prolonged drying under low vacuum ( $10^{-3}$  Torr, 48 hours), ATR-FTIR spectra of the Li surface, after reacting with GEN 2, looks identical. However, on the micro scale, the Li surface does not have the same iridescent film previously observed. AFM topography measurements revealed a surface structure of a collection of quasi-spherical particles with sizes ranging from  $\sim 50$  to  $\sim 300$  nm (Figure IX.1.2). While white light imaging showed nanoscale IR reflectivity heterogeneities which correlated with the topography features. The nano-FTIR spectra revealed broad features in the  $830\text{-}890\text{ cm}^{-1}$  region, indicating the presence of P-F or  $\text{POF}_3$  vibrations. These sample preparation protocols which are essential to preserving the SEI structure and chemistry were employed in *ex situ* investigations of post cycling Li electrodes.



**Figure IX.1.2** Characterization of a Li surface after reaction with GEN2 electrolyte: effect of vacuum drying a) ATR-FTIR spectra of Li sample after 30 min and 48 hrs of drying under vacuum b) optical image of the Li surface after drying electrolyte with Kimwipe and drying for 48hr under vacuum c) AFM topography image of the Li surface after exposure to GEN2 d) white light (WL) image corresponding to c) and e) nano-FTIR spectra from 7 different locations on the sample.

Evolution of Li metal surface was studied *ex situ* 24 hours after exposure to GEN2 electrolyte. ATR-FTIR measurements (Figure IX.1.3) reveals a surface film forms immediately after contact with the electrolyte, which contain a mixture of organic alkyl carbonates and  $\text{Li}_2\text{CO}_3$ . Prolonged exposure to the electrolyte leads to emergence of a new peak at  $463\text{ cm}^{-1}$ . The amount of  $\text{Li}_2\text{CO}_3$  in the film also increases significantly. The peak at  $667\text{ cm}^{-1}$  that is a characteristic for Li-O vibrations in organic lithium carbonates grows in intensity. Region between  $800\text{-}900\text{ cm}^{-1}$  contain overlapping vibrations of P-F,  $\text{OCO}_2$  (organic/inorganic carbonates) as well as PEO ( $843\text{ cm}^{-1}$ ). The P-F vibration at  $840\text{ cm}^{-1}$  originates from  $\text{PF}_6^-$  shifts to lower wavenumbers indicating formation and accumulation of -POF compounds. FTIR peaks between  $1309\text{-}1325\text{ cm}^{-1}$  correspond to  $-\text{OCO}_2-$  stretching. The increase of the  $1309\text{ cm}^{-1}$  peak after 24 hr indicates increased ratio of LiEDC dimerization. Moreover, the increase of signal at  $1453\text{-}1477\text{ cm}^{-1}$  also indicates of presence of lithium methyl carbonate (LiMC). Similar experiments were performed using nano-FTIR spectroscopy. Unlike ATR FTIR which senses the film a few hundreds of nm deep, nano-FTIR is more surface sensitive and probes with lateral resolution of  $\sim 20$  nm just a few tens of nanometers deep. In this case we observed that the P-F vibrations disappeared after prolonged exposure to the electrolyte. Instead, vibrations from epoxy ring at ca.  $1150\text{ cm}^{-1}$  from EC decomposition appeared in the spectrum.

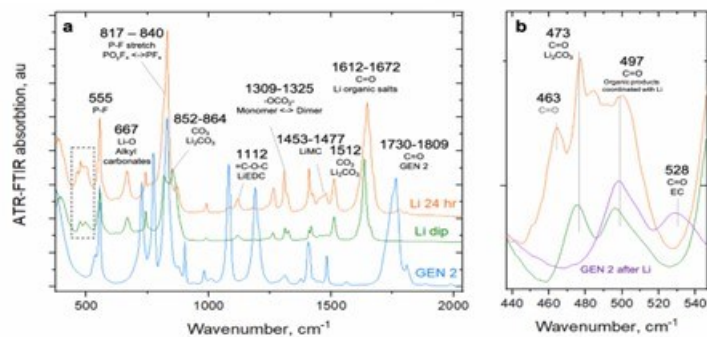


**Figure IX.1.3** a) ATR-FTIR spectra of Li metal surface after reaction with GEN2 electrolyte immediately after exposure (green), after 24hr exposure (orange); b) close up plot of C=O deformation vibrations generated from species on Li surface and in electrolyte after reaction with Li metal (purple)

Regarding *in situ* nano-FTIR experiments, fabrication protocols of *in situ* electrochemical/optical cells were developed and pursued. The custom-built cell should enable simultaneous electrochemical measurements and *in situ* nano-FITR characterization via of buried graphene/Li-liquid electrolyte interfaces. Custom 200 nm thick silicon nitride windows with a matrix of one-micron holes that was amenable for graphene transfer were obtained. These have been designed and manufactured after an extensive consultation with a vendor. The multi-step transfer process of a single sheet graphene on Cu base includes, plasma etching one side of the Cu base, supporting the graphene with an Al mask, etching Cu in sodium persulfate solution to free and isolate graphene, and vacuum pumping/heating for removal of residual liquid etchant and/or water followed by positioning graphene layer on top of the silicon nitride window, capping the holes with atomically-thin sheets of graphene. The process can be reproduced for deposition of bi-, tri-, etc. graphene films. Figure IX.1.4 displays AFM images of a representative window, with array of holes, blanketed with two graphene layers. While the graphene layers droop slightly into the holes (darker centers on the AFM topography data), the constant AFM tapping amplitude data indicates that the graphene surface covers the hole.

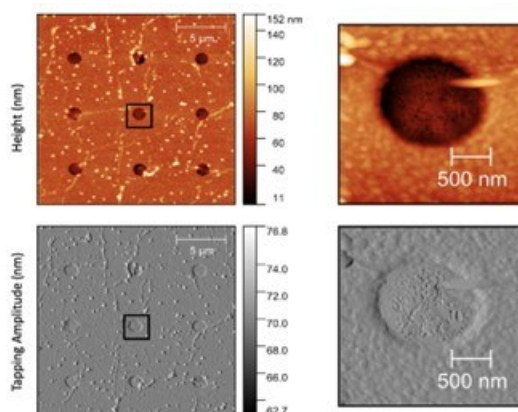


**Figure IX.1.4** Atomic force microscopy: topography (top) and tapping amplitude (bottom) of a silicon nitride window capped with two layers of graphene. The right column are zoom-ins on the black boxes in the left column of the figure.

Figure IX.1.5 shows *in situ* nano-FTIR spectrum of graphene/GEN 2 electrolyte interface. The peaks at 844 and 547  $\text{cm}^{-1}$  correspond to P-F vibrations from  $\text{PF}_6^-$  anions. Ethylene carbonate (EC) vibrations from the Gr/GEN2 interface are matching those of GEN2 electrolyte. However, C(O)-O vibration, located at 1118  $\text{cm}^{-1}$ , is absent from the spectrum. This could be related to specific orientation of EC molecules at graphene interface, which suppresses C(O)-O vibrations. Prominent peak at 1303  $\text{cm}^{-1}$  corresponds to C(O)-O vibration in ethyl methyl carbonate (EMC). The intensity of this peak is an indication of higher concentration of EMC molecules at the interface compared to EC. Interestingly, graphene/GEN2 interface shows a band at 1620  $\text{cm}^{-1}$ ,

which is assigned to C=O vibrations of LEDC, a product of SEI and electrolyte decomposition. C=O vibrations of graphene, EC and EMC overlap and form a broad peak 1700-1800  $\text{cm}^{-1}$ . Notably, suspended graphene signature at 1577  $\text{cm}^{-1}$  is also present in graphene-GEN2 spectrum. The nano-FTIR spectra over the Gr/GEN2 interface revealed new EMC vibrations is observed (914 and 1368  $\text{cm}^{-1}$ ), while the intensity of C(O)-O EMC vibration, located at 1303  $\text{cm}^{-1}$  stayed unchanged. This discrepancy hints on difference in orientation and coordination of EMC molecule at the interface.

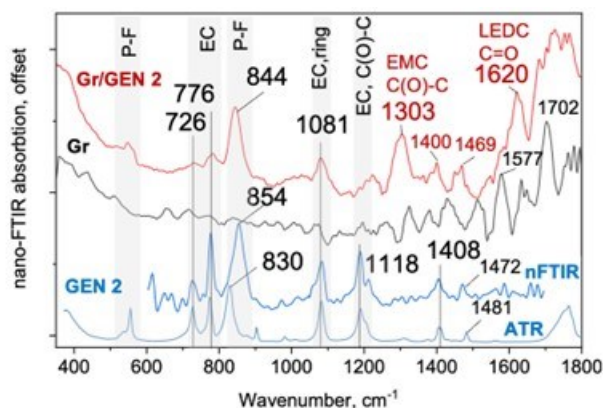


Figure IX.1.5 ATR and nano-FTIR of dried GEN2 electrolyte (blue), suspended graphene (black) and graphene/GEN2 interface (red)

To facilitate interpretation of nano-FTIR results, the key detection and processing steps involved in producing scattering-type near-field nano-FTIR were outlined. This was done to optimize our ability to understand the complex valued spectra to be collected at electrochemically active interfaces supporting interphases in upcoming quarters. The self-contained mathematical and experimental work derives and explains: (i) how normalized complex-valued nano-FTIR spectra are generated, (ii) why the real and imaginary components of spectra qualitatively relate to dispersion and absorption respectively, (iii) a new and generally valid equation for spectra which can be used as a springboard for additional modeling of the scattering processes, and (iv) an algebraic expression that can be used to extract the sample's local extinction coefficient from nano-FTIR. The algebraic expression was validated with nano-FTIR and attenuated total reflectance Fourier transform infrared (ATR-FTIR) spectra on samples of polystyrene and Kapton (Figure IX.1.6).

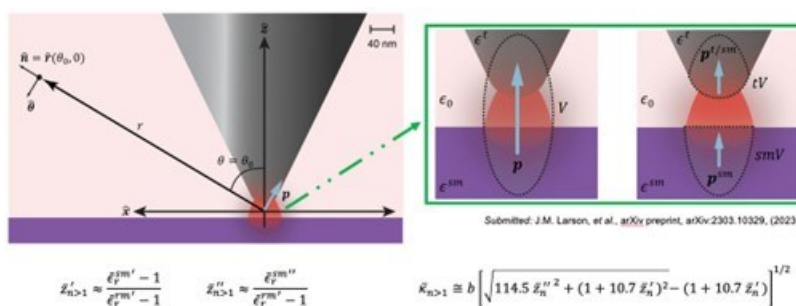


Figure IX.1.6 Illustration of the tip-sample region in which the near-field-induced dipole moment,  $p$ , is visualized as both a net dipole and a sum of two dipoles (top). Equations relating the real and imaginary parts of the complex valued nano-FTIR spectrum to the local dielectric properties of the sample material (bottom left) and an algebraic expression for the local extinction coefficient as a function of the real and imaginary parts of the nano-FTIR spectrum (bottom right).

## Conclusions

- Investigated SEI layer formed between Li metal and GEN2 electrolyte at nanometer resolution using *in situ* near-field IR spectroscopy

- Developed an effective strategy for analysis of pristine SEI with optical probes
- Showed nanometer-scale inhomogeneities in Li metal SEI formed upon immediate contact with electrolyte
- Designed a custom device design for in-situ analysis of buried interfaces via nano-FTIR spectroscopy
- Modeled the detection & signal processing steps for nano-FTIR spectra to aid in nanoscale characterization of heterogenous battery interphases [2]
  - Demonstrated how  $\bar{z}'_n$  ( $\bar{z}''_n$ ) relate to dispersion (absorption)
  - Derived expression for extinction coefficient for superior chemical fingerprinting:
- $\bar{\kappa}_{n>1} \cong b \left[ \sqrt{114.5 \bar{z}''_n{}^2 + (1 + 10.7 \bar{z}'_n)^2} - (1 + 10.7 \bar{z}'_n) \right]^{1/2}$

### Key Publications

1. Lukas Karapin-Springorum, Asia Sarycheva, Andrew Dopilka, Hyungyeon Cha, Muhammad Ihsan-Ul-Haq, Jonathan M. Larson, and Robert Kostecki; *An infrared, Raman, and X-ray database of battery interphase components*, submitted to arXiv
2. Asia Sarycheva, Robert Kostecki “Nanoscale Chemical Characterization of Early Stages of SEI In Li Metal Anodes”, International Battery Association meeting (IBA 2023), Austin, TX, USA (manuscript in preparation)
3. Robert Kostecki, “Infrared Near-Field Nano-Spectroscopy of Electrochemical Interfaces in Li Batteries”, Pittcon 2023, Philadelphia, PA, March 20-24, 2022, (invited lecture) (manuscript in preparation)

### Acknowledgements

This work has been performed in close collaboration with: V. Battaglia: ABMR program leads; ABMR Cathode and Anode Task Groups; ANL, LBNL, SUNY, UP, HQ, NREL and UU (R-C. Lee, J. Franklin, G. Chen, V. Battaglia, M. Doeff, K. Persson, V. Zorba, W. Yang, C. Ban, N. Balsara, B. McCloskey); Advanced Light Source (H. Bechtel, E. Rotenberg, E. Crumlin); University of Liverpool (UK) (L. Hardwick); Central Laser Facility, Research Complex at Harwell (UK); and University of California, Berkeley.

## IX.2 Advanced *in situ* Diagnostic Techniques for Battery Materials (BNL)

### **Xiao-Qing Yang, Principal Investigator**

Chemistry Division, Brookhaven National laboratory  
Bldg. 555, Brookhaven National Lab.  
Upton, NY 11973  
E-mail: [xyang@bnl.gov](mailto:xyang@bnl.gov)

### **Enyuan Hu, Co-Principal Investigator**

Chemistry Division, Brookhaven National laboratory  
Bldg. 555, Brookhaven National Lab.  
Upton, NY 11973  
E-mail: [enhu@bnl.gov](mailto:enhu@bnl.gov)

### **Tien Duong, DOE Technology Development Manager**

U.S. Department of Energy  
E-mail: [Tien.Duong@ee.doe.gov](mailto:Tien.Duong@ee.doe.gov)

Start Date: October 1, 2022	End Date: September 30, 2023	
Project Funding (FY23): \$425,000	DOE share: \$425,000	Non-DOE share: \$0

### **Project Introduction**

In order to meet the challenges of powering the EVs, advanced Li-ion batteries with high energy and high power density, low cost, good abuse tolerance, and long calendar and cycle life need be developed. In addition, it is very important to develop beyond Li-ion battery systems, such as Li-metal, Li-S, Na-ion, and solid-state batteries. To overcome the current barriers, in-depth understanding of the structural changes of the cathode and anode materials in the bulk and at the surface, the interactions between the electrode material and the electrolyte during cycling and the formation and functionality of the electrode/electrolyte interphase (solid electrolyte interphase or SEI on anode and cathode electrolyte interphase or CEI on cathode), the effects of the additives and the surface coatings are critically important. The goal of this project is to develop and apply various advanced diagnostics techniques to investigate these issues, to obtain fundamental understanding of the mechanisms governing the relationship between the structure and the performance, and to provide guidance and approaches to solve these problems. The characterizations are focusing on materials such as lithium metal anode, sulfur cathode, sodium-ion battery cathodes, solid-state electrolytes, Ni-rich  $\text{Li}(\text{Ni}_x\text{Mn}_y\text{Co}_{1-x-y})\text{O}_2$  (NMC) cathode etc.

In this project, we aim to develop and apply multi-scale and multi-modal approaches using combinations of various synchrotron-based x-ray techniques, as well as selected neutron- and electron-based methods, with good time and spatial resolution to study battery materials *ex situ* and *in situ* or *in operando* at relevant scales of length. A multi-modal approach is critical for comprehensive understanding of complex physical and chemical changes governing battery performance. Primary methods are: x-ray total scattering including x-ray diffraction (XRD) and x-ray pair distribution function (x-PDF), neutron total scattering including neutron diffraction (ND) and neutron pair distribution function (n-PDF); x-ray spectroscopies including hard/tender/soft x-ray absorption spectroscopies (XAS), resonant inelastic x-ray scattering (RIXS), x-ray photon emission spectroscopy (XPS), especially synchrotron-based XPS with depth profiling capability; and imaging techniques including x-ray fluorescence (XRF) microscopy, transmission x-ray microscopy (TXM), and transmission electron microscopy (TEM). The results of this project will enhance the ability to interrogate the “buried” interphase and push the boundaries of diagnostic techniques and to apply these techniques on relevant problems of interest. In summary, this project supports the goals of VTO BMR program by



developing new diagnostic technologies and applying them to beyond Li-ion battery systems to provide guidance for new material development.

### Objectives

Diagnostic studies are aimed at understanding the complicated physical, chemical and mechanical phenomena in batteries and providing guidance on material design for beyond Li-ion battery systems. The first objective is to study the sulfur cathode for Li-S batteries. The materials include both elemental sulfur and polymeric sulfur. We will use various scattering, spectroscopic and microscopic tools, especially sulfur XAS, sulfur XRF and xPDF developed at BNL to obtain understanding on a series of issues in Li-S batteries. For example, the polysulfide formation, dissolution, and reaction with lithium metal; the sulfur redox mechanism involving possible disproportionation reactions; the structure and the redox mechanism of polymeric sulfur; the stability of polymeric sulfur against various types of electrolytes.

We will also use the diverse tools to study the lithium metal anode. The emphasis will be on characterizing the lithium metal interphase in various systems. We aim to obtain an understanding of lithium metal interphase in terms of chemical composition and spatial distribution. We will characterize both the crystalline and amorphous components in the interphase using XRD, xPDF, soft XAS, TEM and other techniques. The goal also includes characterizing the lithium stripping and plating process during charge-discharge and understanding the interactions among lithium metal anode, electrolyte, and the cathode.

The third objective is to characterize the sodium-ion battery cathodes, aiming to understand the complicated phase transitions in these cathode materials. By collaborating with other national Labs, academic institutions and industry partners in the US, we aim to understand the structure-performance relationship for various sodium-ion battery cathodes such as P type, O type oxides and different kinds of polyanion cathodes. Oxygen activity in these materials can potentially increase the capacity and the energy density of sodium-ion batteries. We will use tools such as RIXS, ND and nPDF to understand the oxygen redox mechanism in the mentioned cathode materials.

The fourth objective is to characterize the solid-state electrolytes for solid-state batteries. We aim to understand the atomic structure and the micro-structure of ceramic, polymeric and composite electrolytes using xPDF, TXM and TEM. We will also leverage the tools such as soft XAS and synchrotron XPS to understand the interface and the interphase between different components in the solid electrolytes. In addition, we will also develop tools to understand the stabilities of these solid electrolytes against lithium metal anode and NMC cathode.

### Approach

- Develop and apply advanced diagnostic techniques to study and improve the performance of high energy density LIBs and Li/S batteries.
- Using nano-probe beamline at NSLSII to study the elemental distribution of new solid electrolyte materials for Li-ion and Na-ion batteries.
- Using hard X-ray fluorescence (XRF) imaging on the concentration gradient Ni-rich NCM cathode particles in a noninvasive manner with 3D reconstructed images through tomography scans to study the 3D Ni, Co, and Mn elemental distribution from surface to the bulk.
- Using transmission X-ray Microscopy (TXM) studies on the concentration gradient Ni-rich NCM cathode particles with 3D reconstructed images through tomography scans.
- Using the S K-edge XRF imaging and XAS studies with examination of the reaction products on the sulfur cathode and Li-metal anode in high energy density Li/S cell.

### Results

In FY2023, BNL has been focused on the development of new diagnostic techniques to study and improve the performance of beyond Li-ion batteries. We used PDF to characterize the SEI on Li/Cu in Cu||Li, NMC||Li and NMC||Cu cells. The electrolyte used is 1M lithium bis(fluorosulfonyl) imide (LiFSI) in 1,2-dimethoxyethane

(DME). PDF probes both the crystalline and amorphous phases and the peaks correspond to atomic pairs which can be either chemical bonds or two indirectly-connected atoms. As shown in Figure IX.2.1, The left panel shows measured PDF of SEI from Cu||Li cells, with the calculated PDF patterns of possible SEI components also shown for data analysis. It clearly indicates that the SEIs on Cu foil and that on lithium foil have basically the same crystalline and amorphous components. The only difference is the residue copper that was accidentally introduced into SEI during sample collection. The first peak in the blue region corresponds to carbon-based bonds which are relatively short. These include C=O bond in  $\text{Li}_2\text{CO}_3$  and C-O and C-O bond in DME oligomers. The second peak in the blue region corresponds to sulfur-based bonds which are longer than the carbon-based bonds. These include S-F, S-N and S-O in the chemical species resulting from FSI anion decomposition. For example, it could be  $\text{Li}_2(\text{FSI}_{(-F)})_2$  (-F means one fluorine atom is lost from FSI). The first peak in the red region corresponds to the Li-O bond that can only be originated from inorganic SEI components such as  $\text{Li}_2\text{O}$ , LiF,  $\text{Li}_2\text{CO}_3$  and LiOH. Because of its uniqueness, this peak is a good indication of the relative content of inorganic species in the SEI. The second peak in the red region corresponds to the indirect O-O pair in the  $\text{CO}_3^{2-}$  motif which is from  $\text{Li}_2\text{CO}_3$ . It can be concluded that 1M LiFSI in DME electrolyte is not fully stable on Li or Cu electrode. It can decompose, leading to SEI having a similar amount of organic and inorganic species. LiFSI is very likely decomposed during the process. While SEI components are the same for Li and Cu in Cu||Li cells, they are quite different in Li||NMC and Cu||NMC cells, which is indicated by the middle and the right panels. In Li||NMC cells, the SEI on Li foil has a large amount of organic species resulting from anion decomposition, which is indicated by the dominant peak in the blue region. The amount of inorganic species, which is indicated by the peak in the red region, is relatively small. In Cu||NMC cells, the organic species in SEI come from decompositions of both solvents and anions. In contrast to the SEI on Li foil in Li||NMC cells, the SEI on Cu foil in Cu||NMC is dominated by inorganic species, which is indicated by the strong peak in the red region. This study demonstrates PDF is capable of probing both crystalline and amorphous phases in SEI, revealing the relative content of organics from solvent decomposition, organics from anion decomposition and overall inorganics.

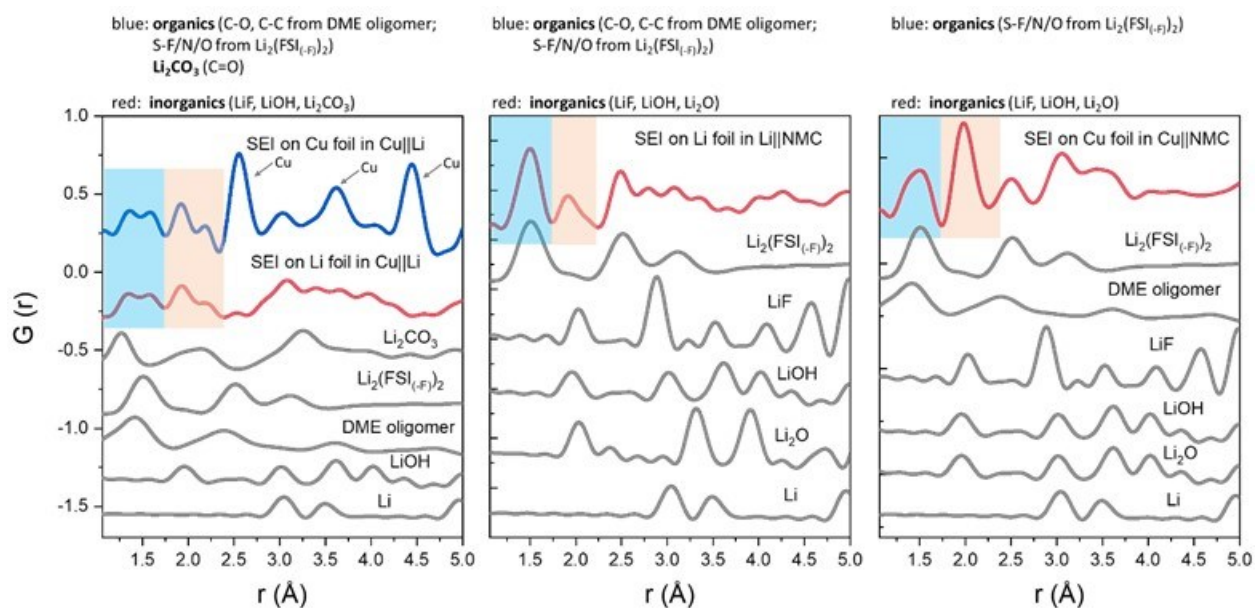
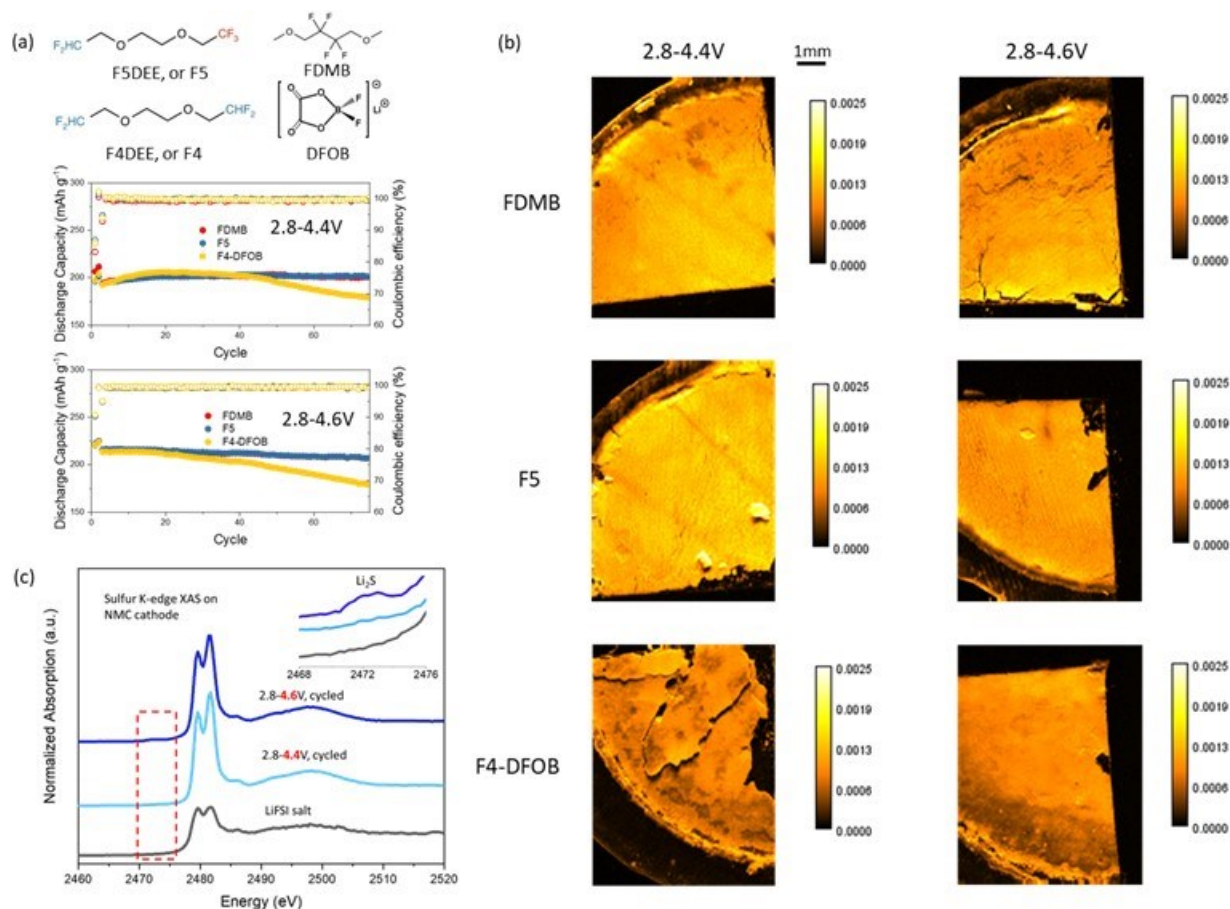


Figure IX.2.1 Left panel, measured PDF data of SEIs on Cu foil and on Li foil in Cu || Li cells. Middle panel, PDF data of SEI on Li foil in Li || NMC cells. Right panel, PDF data of SEI on Cu foil in Cu || NMC cells. Calculated PDF patterns of possible SEI components are also shown for data analysis.

In FY2023, the BNL team also collaborated with **Stanford University** to study the interphases. The interphases in the lithium metal cell (Li||NMC811) using various fluorinated ether electrolytes were characterized by synchrotron-based imaging and spectroscopy techniques to gain insight into the morphology

and chemical composition of them. Three kinds of electrolytes were tested: 1.2 M lithium bis(fluorosulfonyl) imide (LiFSI) in fluorinated dimethoxybutane (FDMB); 1.2 M LiFSI in diethoxyethane with five fluorine substitutions (F5DEE, or F5); 1.2 M LiFSI in diethoxyethane with four fluorine substitutions (F4DEE, or F4) and using lithium difluoro(oxalato)borate (DFOB) as additive. Detailed molecular structures are shown in the upper panel of Figure IX.2.2a. The lower panel of Figure IX.2.2a shows the cyclabilities of Li||NMC811 coin cells using these electrolytes. Two cycling voltage windows (2.8V-4.4V and 2.8V-4.6V) were applied and the test results are consistent with the data provided by our collaborators at Stanford University. For 2.8V-4.4V cycling protocol, cells using F5 and FDMB electrolytes have better cyclability than cells using F4+DFOB electrolyte. Increasing the charging voltage to 4.6V leads to an increased discharge capacity of around 20 mAh/g. Cells using F5 and FDMB still show stable cycling even at high voltage while cells using F4+DFOB electrolyte experience fast capacity decay.

X-ray fluorescence mapping was carried out on the cycled (50 cycles) lithium metal anode to understand the distribution of sulfur species at the electrode level (Figure IX.2.2b). As FSI<sup>-</sup> anion is the only electrolyte component that contains sulfur element, sulfur distribution shown in Figure 1b provides information of both the amount of anion decomposition and heterogeneity of these anion-derived species. When cycled in the voltage range 2.8V-4.4V, F4+DFOB electrolyte has the least anion decomposition. Considering that anion-derived decomposition products are the desired interphase components, little anion decomposition suggests the lithium metal solid-electrolyte-interphase (SEI) is not well formed. In addition, the SEI from F4+DFOB electrolyte has large heterogeneity in sulfur distribution and the cracks are clearly visible. These results suggest that F4+DFOB electrolyte cannot effectively form an anion-derived SEI and explain the reason why cells using this electrolyte show the fastest capacity fade. In contrast, both FDMB and F5 electrolytes can produce good amounts of anion-derived species for the interphase. The sulfur distribution is also in general much more uniform for these two electrolytes. The combined properties contribute to the good SEI from FDMB and F5 electrolytes and stable cycling of the cells using these electrolytes. Increasing the charging voltage to 4.6V leads to in general more heterogeneities in the distribution of sulfur-containing species for all the three studied electrolytes. This suggests a more complicated SEI formation mechanism at high voltages and more experiments are being planned to obtain a good understanding.



**Figure IX.2.2 (a) Cyclabilities of the NMC811 | Li coin cells using three kinds of electrolytes: 1.2 M LiFSI in F5; 1.2 M LiFSI in F4 with DFOB additive; 1.2 M LiFSI in FDMB. The molecular structures of involved solvents and additives are shown in the top panel. (b) Sulfur x-ray fluorescence mapping on lithium metal anode. Due to the relatively high concentration of sulfur species, quantification of absolute sulfur amount cannot be obtained. Instead, only relative sulfur amount can be known as shown in the color scale bar. (c) Sulfur K-edge XAS of NMC cathode for CEI study using 1.2 M LiFSI in F5 electrolyte.**

Sulfur K-edge x-ray absorption spectroscopy (XAS) was employed to study the cycled NMC811 electrode to understand the chemical composition of cathode-electrolyte-interphase (CEI) as shown in Figure IX.2.2c. As F5 shows the greatest promise among the three tested electrolytes (slightly better than FDMB at high voltage), it was chosen to be the focus of CEI study. As Figure IX.2.2c shows, the sulfur-containing species in CEI is mainly the FSI<sup>-</sup> anion decomposition products. This is clearly indicated by the similarity between the XAS spectra of CEI and that of LiFSI salt. The relative ratio between the two major peaks is different in CEI spectra from that in LiFSI salt spectrum. This is likely attributed to the local structural change from FSI<sup>-</sup> anion to its decomposition products. When high voltage charging (4.6V) is applied, a new shoulder peak, which is located at around 2472 eV and has weak intensity, appears in the CEI XAS spectrum. This peak arises from the presence of Li<sub>2</sub>S and its appearance suggests that the anion derived CEI is further decomposed at high voltage. These studies on the SEI and CEI of lithium metal batteries (Li||NMC811) gain insight into the interphase formation mechanism and its dependence on the charging voltage. Such knowledge will help to guide the material design for high energy lithium metal batteries.

In FY2023, the BNL team also further developed the *in situ* TXM experiment. We identified the beam damage issue in the experiment and found the mitigation method. In situ coin cells with NMC622 cathode and Li metal anode were assembled and cycled in the beamline 18-ID at NSLS-II for *in situ* transmission X-ray microscopy (TXM) characterizations, which can reveal the evolutions of both morphology and chemical distribution of

NMC cathode materials during battery cycling. A schematic diagram of an *in situ* coin cell used in this study is shown in Figure IX.2.3a. The cells have two windows on both ends covered by Kapton tapes.

The cells were probed by the X-ray beam at 8.4 keV (just above Ni K-edge) to evaluate the effect of X-ray on battery materials. Tomographic images of NMC622 cathode particles were collected during the exposure to X-ray beam (Figure IX.2.3b). Upon exposure to X-ray for several seconds, bubble formation can be observed as indicated by the red arrow in Figure IX.2.3b. The bubble formation is likely caused by the decomposition of electrolyte induced by X-ray beam. The bubble expands over prolonged exposure to X-ray beam. Bubble formation can be detrimental to in situ experimentation because bubbles can electrochemically deactivate cathode particles within the field of view by cutting off the lithium-ion supply from the electrolyte to the NMC622 particles.

We further evaluated the beam damage effect on in-situ battery cycling. The coin cell was charged at a rate of C/10 and 2D X-ray absorption near-edge spectroscopy (XANES) mapping at Ni K-edge was simultaneously carried out (Figure IX.2.3c). The collected 2D XANES were fitted using Ni white-line energy to get a distribution of the Ni oxidation states within the particles (top panel of Figure IX.2.3c). The bottom panel of Figure IX.2.3c shows the population density of the pixels with various energies, which describes the distribution of Ni oxidation states within the cathode material. The results indicate that upon charging, the maximum of the pixel distribution does not change, suggesting the particles are inert during the charging process.

Significant beam damage was observed upon prolonged charging of the battery with continuous exposure to the X-ray beam. Displacement of particles within the field of view was observed during the period of data acquisition (Figure IX.2.3d). Such displacement might be caused by the propagating bubbles formed during X-ray radiation. Particle displacement also has significant implications for data analysis as TXM data processing requires the images collected from different energies (and hence at different times) to be perfectly aligned with each other. Once the particle moves, the perfect alignment cannot be done which will result in artifacts for the 2D XANES fitting (Figure IX.2.3e). Such artifacts can make the particle appear to be highly oxidized. In summary, we found that beam damage effects need to be considered for in situ TXM experiments for NMC materials. Such effects might be able to partially explain the discrepancies on NMC TXM results reported in the literature. Careful inspection of the data needs to be done before drawing any conclusions about the evolution of morphologies and chemical distribution of NMC particles. In the next quarter, we will design ways to address this issue and provide general guidelines for reliable *in situ* TXM experiments.

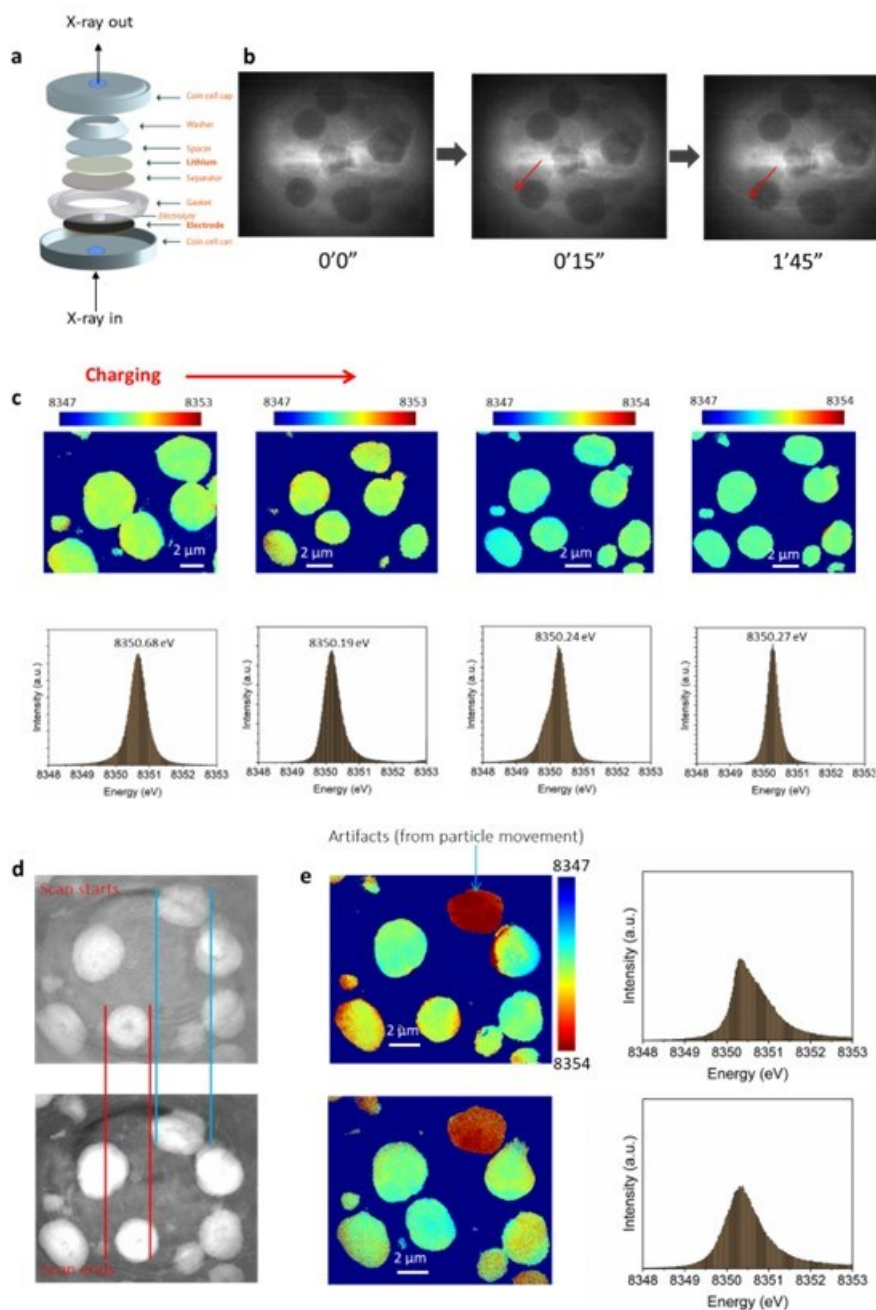


**Figure IX.2.3** (a) Schematic diagram of an in-situ coin cell used in this study. (b) Bubble formation in the in situ NMC|Li coin cells upon exposure to X-ray beam at 8.4 keV energy. (c) 2D-XANES maps at Ni K-edge collected from the in-situ coin cells upon charging (top) and the corresponding energy histogram (bottom) of the 2D XANES maps. (d) Particle movement caused by extensive beam damage during in-situ experiments. (e) Artifacts generated from data analysis due to particle movement on the 2D-XANES map (left) and the corresponding energy histograms generated from the 2D XANES maps (right).

To address these issues, we redesigned the in situ cell and used the pouch cell configuration as shown in Figure IX.2.4a. To guarantee the pressure, we sandwiched the pouch cell with stainless steel plate on both sides. A very narrow slit is opened in the stainless steel plate to serve as X-ray window. The *in situ* TXM setup is shown in Figure IX.2.4b and the experiment was carried out at beamline 18-ID, NSLS-II of BNL.

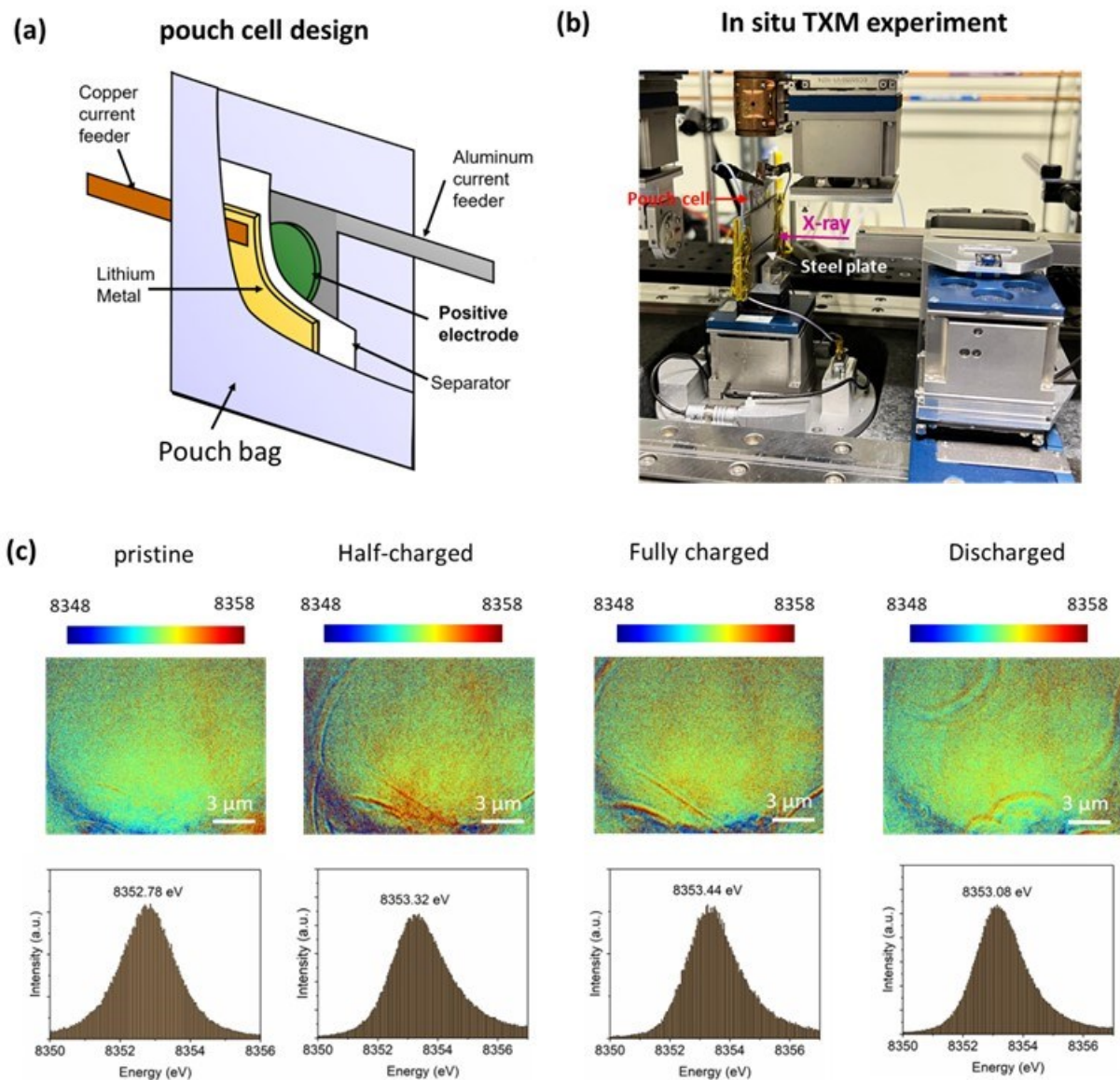


Figure IX.2.4 (a) illustration of the single-layer pouch cell configuration. (b) the *in situ* TXM experiment setup. (c) 2D Ni K-edge XANES mapping of Li/Mn-rich NMC during charge-discharge. The top panel, distribution of white line energies in the file of view. The bottom panel, the histogram of the white line energies.

*In situ* 2D Ni XANES (X-ray absorption near edge spectroscopy) mapping was carried out and the data was analyzed to study the evolution of Ni oxidation state. The effectiveness of mitigating beam damage can be seen from the ability of monitoring reversible Ni oxidation change during charge-discharge as discussed below. Figure IX.2.4c shows the 2D Ni XANES mapping of the Li/Mn-rich NMC cathodes during charge-discharge at a rate of  $C/2$  in an *in situ* TXM pouch cell. The collected raw data was processed and fitted to identify the white line energy at each pixel (top panel in Figure IX.2.4c). Since white line energy is a good indicator of the oxidation state for nickel (the higher white line energy corresponds to higher oxidation state of nickel and vice versa), such identification also reveals the oxidation state of nickel at each pixel. A histogram of the energy distribution in the field of view is shown in the bottom panels of Figure IX.2.4c. The x axis is the white line energy and the y axis is normalized probability, or the occurrence, of specific energies. The maximum occurrence indicates the dominating species and the corresponding white line energy is shown for each stage during charge-discharge. Upon charge, this white line energy increases, indicating the oxidation of Ni. Upon

discharge, the white line energy decreases and suggests Ni reduction. Such reversible change in the oxidation state of nickel suggests the issue of beam damage has been effectively addressed. Our conclusion is that pouch cell with appropriately applied pressure is the recommended cell configuration for *in situ* TXM experiment. Such configuration suppresses the bubble formation, particle movement and deactivation problems that are commonly seen when the coin cell configuration is used.

### Conclusions

This project, “Advanced *in situ* Diagnostic Techniques for Battery Materials (BNL)”, has been successfully completed in FY2023. All milestones have been completed. The publication records are very good. Extensive collaboration with other national Labs, US universities and international research institutions were maintained and strengthened.

### Key Publications

#### Publications

1. Sha Tan, Muhammad Mominur Rahman, Zhaohui Wu, Haodong Liu, Shen Wang, Sanjit Ghose, Hui Zhong, Iradwikanari Waluyo, Adrian Hunt, Ping Liu, Xiao-Qing Yang, and Enyuan Hu\*, Structural and Interphasial Stabilities of Sulfurized Polyacrylonitrile (SPAN) Cathode. *ACS Energy Letters* 2023, 8, 2496–2504. Publication Date: May 8, 2023.
2. Muhammad Mominur Rahman, Kangxuan Xia, Xiao-Qing Yang, Kingo Ariyoshi, and Enyuan Hu\*, Asymmetric Lithium Extraction and Insertion in High Voltage Spinel at Fast Rate. *Nano Letters* 2023, 23, 7135–7142. Publication Date: July 18, 2023.

#### Presentations

1. E. Hu, *Anode interphase, cathode interphase and their interactions in lithium metal batteries*. International Battery Association (IBA) meeting, Austin, TX. March 9, 2023. Invited keynote talk.
2. E. Hu, *Roles of oxygen, hydrogen and fluorine in lithium batteries*. University of Houston Electrical and Computer Engineering Department Seminar (online). March 27, 2023. Invited talk.
3. E. Hu, *Characterization of lithium metal interphase and amorphous battery materials*, Thermo Fisher Scientific Clean Energy Forum, La Jolla, CA, September 26, 2023. Invited talk.



## IX.3 Microscopy Investigation on the Fading Mechanism of Electrode Materials (PNNL)

### Chongmin Wang, Principal Investigator

Pacific Northwest National Laboratory  
902 Battelle Boulevard, Mail Stop K8-93  
Richland, WA 99352  
E-mail: [Chongmin.wang@pnnl.gov](mailto:Chongmin.wang@pnnl.gov)

### Tien Duong, DOE Technology Development Manager

U.S. Department of Energy  
E-mail: [Tien.Duong@ee.doe.gov](mailto:Tien.Duong@ee.doe.gov)

Start Date: October 1, 2022

End Date: September 30, 2023

Project Funding (FY23): \$400,000

DOE share: \$400,000

Non-DOE share: \$0

### Project Introduction

Functioning of an electrochemical cell, typically such as a rechargeable battery, depends on the synergy of three major components in the cell: anode, electrolyte and cathode. The electrolyte, in either solid state or liquid state, is sandwiched between the cathode and the anode to facilitate ion transport. Electron transfer across the interface leads to the formation of an interfacial layer, which is termed as solid electrolyte interphase (SEI) layer. It is the characteristics of the SEI layer, including chemical, structural, morphological and mechanical properties, that determine a series of key properties of rechargeable batteries. For better battery performances, the SEI is expected to possess three ideal characteristics: electrically insulative, ionically conductive, and constant thickness. These three characteristics are interactively correlated, typically, the thickness of SEI layer is controlled by the electrical properties of SEI layer. Despite the critical importance of the electrical properties of SEIs, quantitative measurement of this parameter remains unsolved due to the lack of a proper and reliable method. The four-point Hebb-Wagner polarization and electrochemical impedance spectroscopy (EIS) methods for mixed ionic-electronic conductors cannot be readily applied to quantify the electrical conductivity of SEIs, because SEIs are not only highly air-sensitive but also very thin that is beyond the high spatial resolution of the method. In spite of the lack of concrete experimental evidence, it is widely assumed that an SEI layer behaves as an insulator, as such assumption helps to interpret, at some degrees, the electrochemical performances of rechargeable batteries. In essence, for all types of cell chemistries that are enabled by SEI, the electrical and ionic properties of SEIs remain as the most challenging mystery, leading to a range of behaviors of rechargeable battery being uninterpreted. This project focuses on probing interfacial process in rechargeable batteries. We aim to gain critical insights regarding the structural and chemical evolution of interfaces and their effect on electrode stability, which will form the foundation for addressing the key challenges of rechargeable batteries. The outcome of the proposed study will feed back to the battery materials fabrication group to aid in designing better materials with enhanced battery performance.

### Objectives

The main objective is to explore interfacial phenomena in rechargeable Li-ion batteries of both solid-state electrolyte (SSE) and liquid electrolyte (LE) configuration to identify the critical parameters that control the stability of interface and electrodes as well as solid electrolyte (SE). The outcome will be establishing correlations between structural-chemical evolution of active components of batteries and their properties. These correlations will provide insight and guidance to battery materials development groups for work on high-performance battery materials.

### Approach

The project will use integrated advanced microscopic and spectroscopic techniques, including *in situ* and *ex situ* scanning transmission electron microscopy (STEM), environmental STEM, cryogenic electron

microscopy, and *in situ* liquid secondary ion mass spectrometry, in collaboration with theoretical modeling, to directly probe the structural and chemical information of active materials in rechargeable batteries. Cryogenic STEM with analytical tools, such as energy dispersive X-ray spectroscopy (EDS) and electron energy loss spectroscopy (EELS), will be used to gain chemical and electronic structural information at the interface between lithium metal and electrolyte of both solid-state and liquid configuration, which will allow direct correlation between the morphology and chemistry. STEM – high-angle annular dark-field atomic-level imaging and EDS/EELS will be used to probe the interface and bulk lattice stability of cathode and SE in solid-state batteries (SSBs). The work will be in close collaboration with the battery development group within the BMR and U. S. – Germany Collaboration on Energy Storage.

## Results

### **Developed *in-situ* bias transmission electron microscopy to directly measure the electrical properties of solid electrolyte interphase layer on Li and Cu**

We developed a novel *in situ* bias transmission electron microscopy (TEM) method, which enable us to measure the electrical properties of beam sensitive SEIs formed on the Cu and Li substrates inside TEM. As shown in Figure IX.3.1a, we integrated *in situ* bias TEM with scanning tunneling microscopy (STM) technique. There is a dual-probe design in the holder (Figure IX.3.1b): one probe uses a W probe as the electrode, another Cu wire with SEI is moveable inside the TEM column. It is driven by a piezo-motor capable of 3D positioning with a step-size of 1 nm. Inside an Ar-filled glove box, the Cu wire with SEI/Li particles formed on (Figure IX.3.1c and d) was taken out from the coin cell and affixed on the TEM holder. The TEM holder was transferred and inserted into the TEM column with limited exposure to air. As ion-blocking Cu and W electrodes are used, the measured I-V data directly reflect the electron transport behavior of SEI. As SEI is very sensitive to electron beam, we performed the I-V measurements at very low magnification of electron dose rate of  $1 \text{ e}^- \text{ \AA}^{-2} \text{ s}^{-1}$  to avoid electron beam induced damage to SEIs.

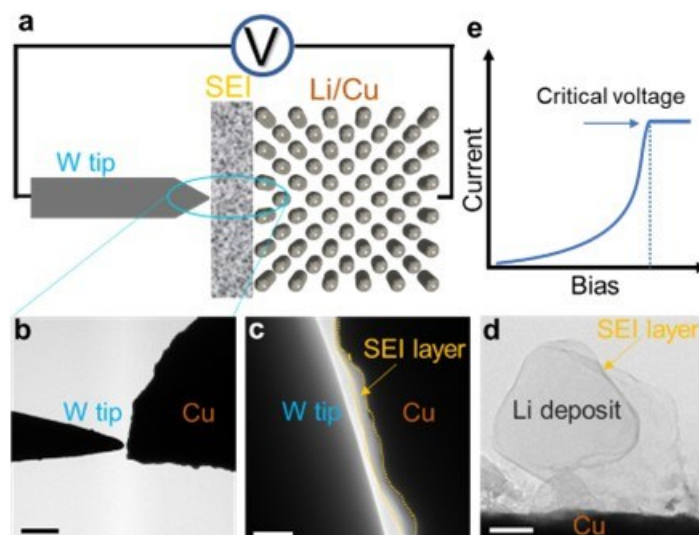


**Figure IX.3.1** *In situ* bias TEM measurement of electrical properties of solid electrolyte interphase. **a**, Schematic of experiment setup. **b-d**, TEM images showing W wire with sharp tip and Cu wire with SEI layer on the surface. **e**, Typical I-V curves showing the critical voltage. Scale bars, 50  $\mu\text{m}$  in **c** and 100 nm in **b** and **d**.

### **The electrical properties of solid electrolyte interphase layer on Li and Cu in terms of I-V curve**

With our developed *in situ* bias TEM method, we measured the electrical properties of beam sensitive SEIs formed on the Cu and Li substrates. To systematically study different SEIs, Li bis(fluorosulfonyl)imide (LiFSI) and 1,2-dimethoxyethane (DME) were chosen to make four electrolytes with designed microscopic solvation structures: (1) a low concentration electrolyte (LCE) comprised of 1 M LiFSI in DME with a molar ratio of 1:9; (2) a high concentration electrolyte (HCE) of LiFSI and DME with a molar ratio of 1:1.2; (3) a

localized high concentration electrolyte (LHCE) formed by adding bis(2,2,2-trifluoroethyl) ether (BTFE) diluent into the HCE to yield LiFSI-DME-BTFE=1:1.2:3 by mol. (LHCE-BTFE); and (4) an LHCE with bis(2,2,2-trifluoroethyl) ether carbonate (BT FEC): LiFSI-DME-BT FEC=1.0:1.2:3.0 by mol. (PLHCE, as free DME molecules are not closely coordinated with  $\text{Li}^+$  and making it a pseudo-LHCE).

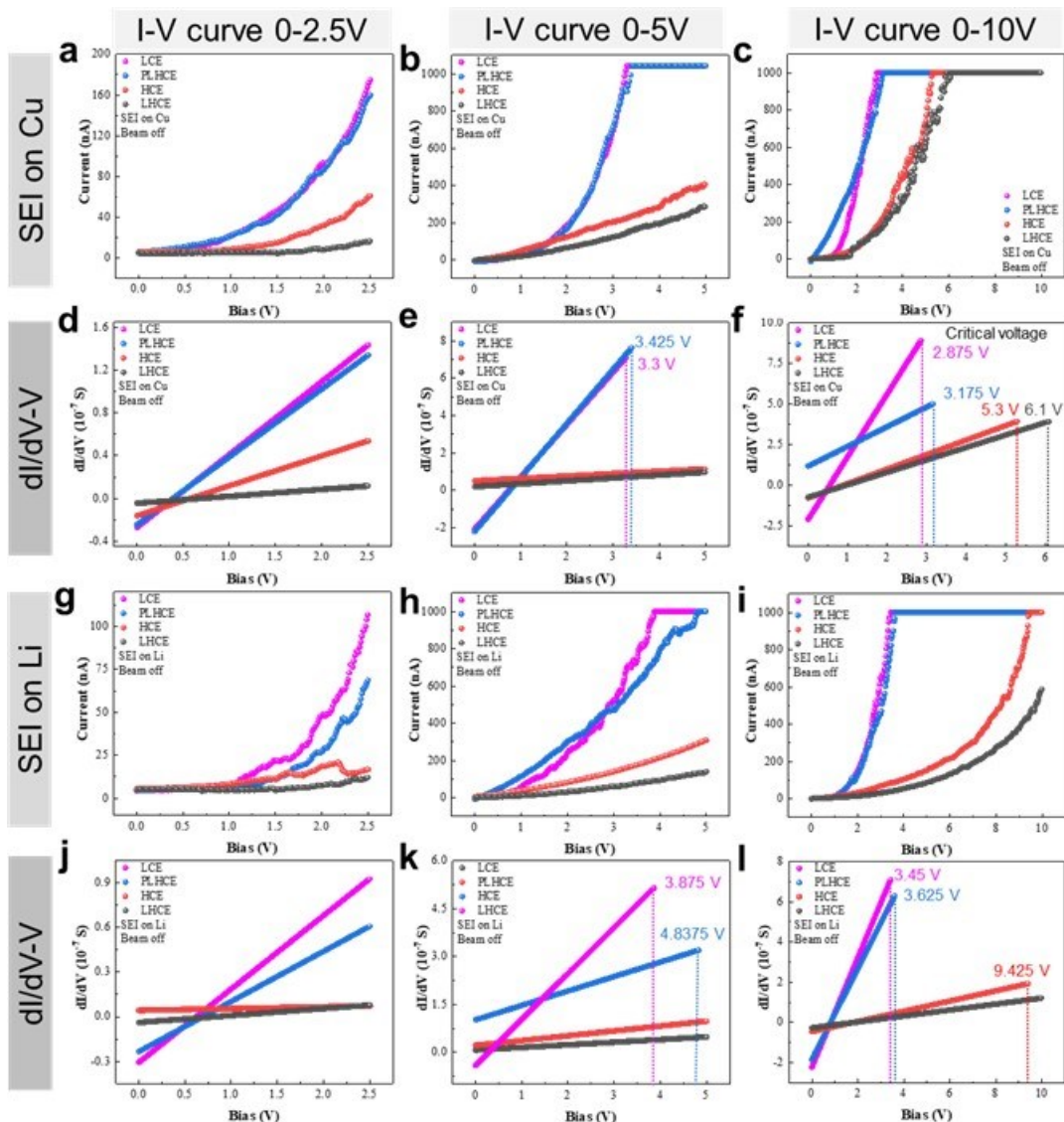


**Figure IX.3.2** I-V curves and  $dI/dV$ -V curves taken from SEI layers formed on Cu and Li. a-c, I-V curves measured from SEI on Cu formed in the different electrolytes under electron beam off condition with bias range from (a) 0-2.5 V, (b) 0-5 V and (c) 0-10 V. d-f, Corresponding differential conductance derived from the above I-V curves (a-c). g-i, I-V curves measured from SEI on Li formed in the different electrolytes under electron beam off condition with bias range from (g) 0-2.5 V, (h) 0-5 V and (i) 0-10 V. j-l, Corresponding differential conductance derived from the above I-V curves (g-i). Insets of (e-f) and (k-l): critical voltage.

The I-V curves of SEI layers formed on Cu and Li with the four different electrolytes are shown in Figure IX.3.2a-c and g-i. It is apparent that the I-V curves of SEIs on both Cu and Li are similar to that of semiconductor but distinctively different from that of electrical insulator, revealing that the electrical properties of SEIs resemble that of a semiconductor. Two characteristic parameters can be extracted from the I-V curves to quantitatively interpret the I-V curves. One is the differential conductance,  $dI/dV$ , which is plotted as a function of applied voltage, V (Figure IX.3.2d-f and j-l). Another one is the critical field strength

for the breakdown of SEI layer. The differential conductance of all samples unanimously shows a linear relationship with the applied voltage. However, the slopes of the linear relationship, which can be termed as the rate of differential conductance, are significantly different for different samples. The differential conductance ( $dI/dV$ ) of all SEIs on both Cu and Li shows linear positive correlations to the applied voltage, while the values of slopes follow a decreasing order from LCE ( $3.86 \times 10^{-7}$  S/V and  $2.72 \times 10^{-7}$  S/V) to PLHCE ( $1.22 \times 10^{-7}$  S/V and  $2.26 \times 10^{-7}$  S/V), HCE ( $8.93 \times 10^{-8}$  S/V and  $2.53 \times 10^{-8}$  S/V) and LHCE ( $7.67 \times 10^{-8}$  S/V and  $1.48 \times 10^{-8}$  S/V), where the values in the parentheses correspond to the slopes of  $dI/dV$ -V on Cu and Li, respectively. Since the differential conductance represents the electron density of state at the local position of the SEI layer, the positive linear relationship between  $dI/dV$  and voltage indicates that the electrical conductance increases with increasing voltage, implying that the formation of SEI during battery cycling shows dependence on the voltage difference between the electrode/SEI interface and the SEI/electrolyte interface. The larger the rate of the differential conductance against voltage is, the stronger the SEI responds to the voltage increase. As illustrated in Figure IX.3.2f and 2l, regardless of the type of the substrate (Cu or Li), the SEIs formed by LHCE and HCE electrolytes show much lower rate of differential conductance than those by PLHCE and LCE electrolytes.

### ***Correlation of electrical properties of SEI with Li morphology***

Consistent with above electrochemical property differences among these four electrolytes is the significant difference of morphological features of both SEI and the deposited Li. The deposited Li in these four electrolytes all exhibits crystalline structure and granular morphology (Figure IX.3.3a and inset of Figure IX.3.3b). However, the particle size distributions and topographic features vary significantly. Figure IX.3.3a shows the morphologies of the deposited Li particles using high angle annular dark field imaging (HAADF) in scanning transmission electron microscopy (STEM) by which the image intensity is proportional to the square of atomic number of the sample. The elemental compositions of SEI, such as O, C, F, S and N, each has large atomic number as compared with Li, leading to a large contrast between SEI and Li, therefore lending the convenience of delineating the spatial distribution of SEI. Based on the SEI configuration maps (Figure IX.3.3b) derived from the STEM-HAADF images (Figure IX.3.3a), it can be seen that SEI with a high rate of differential conductance is corresponded with a high SEI:Li metal ratio.

Three-dimensional (3D) visualization of Li deposits yields details of Li topography. It is evident that for the SEI with a high rate of differential conductance and a low critical field strength, as representatively shown for the case of LCE (Figure IX.3.3c), the deposited Li particles exhibit a wide size distribution, large fraction of isolated small particles (possible “dead” Li), and a high topographical tortuosity, leading to high specific surface area of the SEI. In contrast, for the SEI with a low rate of differential conductance and a high critical field strength, as represented by the case of LHCE (Figure IX.3.3c), the deposited Li particles are large, uniformly distributed, and topographically smooth, leading to a low specific surface area of the SEI and less “dead” Li.

It is apparent that the non-negligible electrical conductance governs the SEI formation and Li deposition and consequently affecting battery performance. A higher electrical conductance of SEI could facilitate electron transport inside SEI, especially at the initial stage of SEI formation, leading to reduction of  $Li^+$  in SEI and consequently formation of metallic Li inside the SEI. This reduced Li is isolated by SEI, leading to the formation of “dead” Li and moss Li.

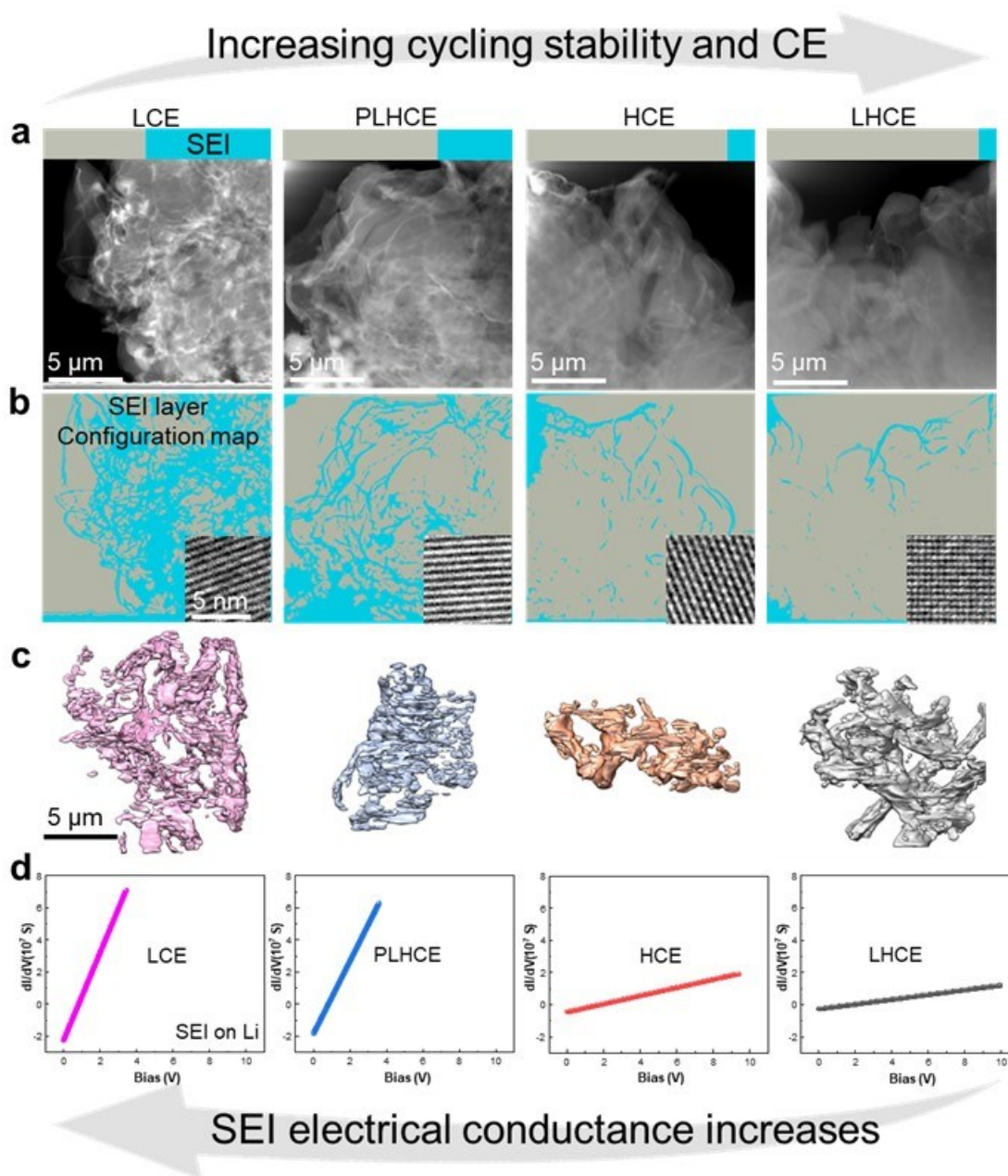


Figure IX.3.3 Dependence of microstructure of Li deposits on rate of differential conductance. a, Low magnification cryo-scanning transmission electron microscopy-high angle annular dark field (STEM-HAADF) images of Li deposits formed in low concentration electrolyte (LCE), pseudo-localized high concentration electrolyte (PLHCE), high concentration electrolyte (HCE), and localized high concentration electrolyte (LHCE) electrolytes; gray and blue bar indicates the area fraction of Li and solid electrolyte interphase (SEI). b, SEI layer configuration maps derived from the STEM-HAADF images, the inset at each image is the high-resolution TEM images of Li deposits; c, 3D reconstruction of Li deposits. d,  $dI/dV$ -V curves of SEI on Li formed in those four electrolytes, where the slope of  $dI/dV$  as a function of V is termed as rate of differential conductance.

#### *Correlation of electrochemical properties with SEI electrical conductivities*

One of the key questions is how the voltage-dependent differential conductance of SEI correlates with the electrochemical properties. To answer this question, we explore the direct correlation between SEI electrical

property and battery performance. The electrochemical performances in terms of Coulombic efficiency (CE) and cycle life of the four electrolytes were evaluated in Li||Cu cells and Li||LiNi<sub>0.8</sub>Mn<sub>0.1</sub>Co<sub>0.1</sub>O<sub>2</sub> (NMC811) batteries. The Li||Cu cells were assembled for the Li CE determination using the CE testing protocol. 5 mAh cm<sup>-2</sup> Li was first deposited on Cu electrode and fully stripped till 1 V to determine the initial Li CE. Another 5 mAh cm<sup>-2</sup> Li was deposited on the Cu electrode followed by 10 times repeated stripping and depositing of 1 mAh cm<sup>-2</sup> Li on Cu electrode and fully stripped the Li till 1 V at the end to get the average Li CE. The Li||NMC811 cells were assembled and an Al-clad cathode case was used to avoid stainless steel corrosion at high voltages. Another Al foil with a diameter of 1.9 cm was placed between the cathode disk and the Al-clad case for further protection. The cells were charged/discharged in a voltage window of 2.8 to 4.4 V on Land battery testers (Wuhan Land) at 25 °C and at C/3 rate (a constant-voltage charge at 4.4 V was applied after the cell was charged to 4.4 V until the current reached C/20 or the time reached 1 h) after two formation cycles at C/10.

As shown in Figure IX.3.4, the first cycle CEs of Li||Cu cells show the following orders: LHCE (99.2%) > HCE (98.6%) > PLHCE (98.3%) > LCE (90.3%). In terms of cycling stability, Li||NMC811 cell with LCE dropped to 80% initial capacity after 10 cycles, cell with PLHCE dropped to 80% initial capacity retention after 41 cycles, while cells with HCE and LHCE maintained 80% initial capacity after 57 and 110 cycles, respectively. Combined with our previous results, apparently, an increased differential conductance of SEI correlates to a decreased Li CE and battery cycling stability, indicating the governing role of SEI electrical property on the battery performance.

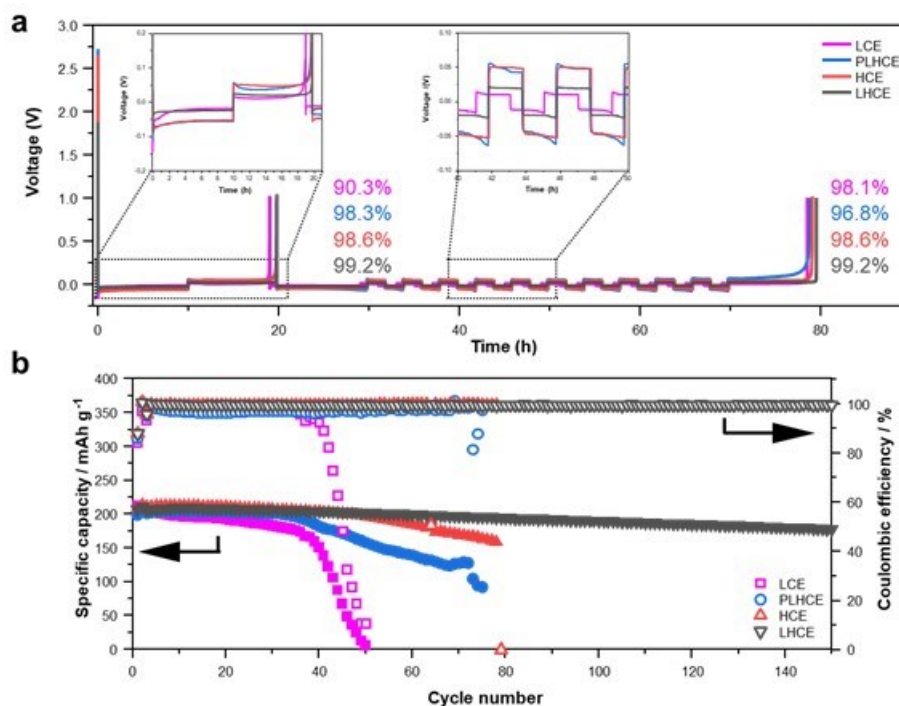


Figure IX.3.4 Electrochemical cell performances. a, Coulombic efficiency (CE) of Li||Cu cells. b, Long-term cycling stability of Li||NMC811 cells in low concentration electrolyte (LCE), pseudo-localized high concentration electrolyte (PLHCE), high concentration electrolyte (HCE), and localized high concentration electrolyte (LHCE) electrolytes. Inset numbers: initial CE and average CEs from 10 cycles

### Conclusions

- Established an in-situ transmission electron microscopy method for measuring the electrical properties of SEI layer on Li and Cu.

- Measured the electrical properties of SEI layer on Li and Cu, revealing that SEI layer shows semiconductive properties, rather than as an insulator, featuring a voltage-dependent differential conductance.
- A higher rate of differential conductance induces a thicker SEI with an intricate topographic feature, leading to an inferior Coulombic efficiency and cycling stability in Li||Cu and Li||LiNi<sub>0.8</sub>Mn<sub>0.1</sub>Co<sub>0.1</sub>O<sub>2</sub> (NMC811) cells.
- Reveals that SEI components with high content of inorganic species show high electron resistance, while those in rich of organic species exhibit higher electron leakage, providing insight as how to design SEI layer with low electrical conductivity.
- A very recent modelling work on SEI growth showed that it is more reasonable to use a voltage-dependent electron conductivity to interpret the SEI growth rate than to assume a constant electron conductivity in the SEI. Our measured electrical properties of SEI layer in terms of  $I$ - $V$  curve aligns well with the modeling prediction.
- Our work provides insight into the targeted design of SEI with desired characteristics toward better battery performance.

### Key Publications

1. Yaobin Xu, Hao Jia, Peiyuan Gao, Diego E. Galvez-Aranda, Saul Perez Beltran, Xia Cao, Phung M. L. Le, Jianfang Liu, Mark H. Engelhard, Shuang Li, Gang Ren, Jorge M. Seminario, Perla B. Balbuena, Ji-Guang Zhang, Wu Xu, Chongmin Wang. Direct in situ measurements of electrical properties of solid–electrolyte interphase on lithium metal anodes, **Nature Energy**, (2023) online publication, doi: 10.1038/s41560-023-01361-1.
2. Werres M, Y. B. Xu, H. Jia, C. M. Wang, W. Xu, A. Latz, B. Horstmann. Origin of heterogeneous stripping of lithium in liquid electrolytes. **ACS Nano** **17**, 10218-10228 (2023).
3. Liu, G. D, Y. He, Z. X. Liu, H. Wan, Y. B. Xu, H. Q. Deng, H. Yang, J.-G. Zhang, P. V. Sushko, F. Gao, C. M. Wang, Y. G. Du. In situ visualization of the pinning effect of planar defects on Li ion insertion. **Nano Lett.** **23**, 6839-6844(2023).
4. Kautz, D. J, X. Cao, P. Y. Gao, B. E. Matthews, Y. B. Xu, K. S. Han, F. Omenya, M. H. Engelhard, H. Jia, C. M. Wang, J.-G. Zhang, W. Xu. Designing electrolytes with controlled solvation structure for fast-charging lithium-ion batteries. **Adv. Energy Mater.** **13**, 2301199 (2023).
5. Liu, Q, W. Jiang, J. Y. Xu, Y. B. Xu, Z. Z. Yang, D.-J. Yoo, K. Z. Pupek, C. M. Wang, C. Liu, K. Xu, Z. C. Zhang. A fluorinated cation introduces new interphasial chemistries to enable high-voltage lithium metal batteries. **Nat. Commun.** **14**, 3678(2023).
6. Hao Jia, Ju-Myung Kim, Peiyuan Gao, Yaobin Xu, Mark H. Engelhard, Bethany E. Matthews, Chongmin Wang, and Wu Xu, “A Systematic Study on the Effects of Solvating Solvents and Additives in Localized High-Concentration Electrolytes over Electrochemical Performance of Lithium-Ion Batteries”, **Angew. Chem. Int. Ed.** **E202218005** (2023).
7. Hao Jia, Zhijie Yang, Yaobin Xu, Peiyuan Gao, Lirong Zhong, David J. Kautz, Dengguo Wu, Ben Fliegler, Mark H. Engelhard, Bethany E. Matthews, Benjamin Broekhuis, Xia Cao, Jiang Fan, Chongmin Wang, Feng Lin, and Wu Xu, “Is Nonflammability of Electrolyte Overrated in the Overall Safety Performance of Lithium Ion Batteries? A Sobering Revelation from a Completely Nonflammable Electrolyte”, **Adv. Energy Mater.** **13**, 2203144 (2023).
8. Xia Cao, Yaobin Xu, Lianfeng Zou, Jie Bao, Yunxiang Chen, Bethany E. Matthews, Jiangtao Hu, Xinzi He, Mark H. Engelhard, Chaojiang Niu, Bruce W. Arey, Chunsheng Wang, Jie Xiao, Jun Liu, Chongmin Wang, Wu Xu and Ji-Guang Zhang, “Stability of solid electrolyte interphases and calendar life of lithium metal batteries”, **Energy Environ. Sci.**, **16**, 1548-1559 (2023).
9. Yan Jin, Phung M. L. Le, Peiyuan Gao, Yaobin Xu, Biwei Xiao, Mark H. Engelhard, Xia Cao, Thanh D. Vo, Jiangtao Hu, Lirong Zhong, Bethany E. Matthews, Ran Yi, Chongmin Wang, Xiaolin Li, Jun Liu and Ji-Guang Zhang, “Low-solvation electrolytes for high-voltage sodium-ion batteries”, **Nature Energy**, **7**, 718–725 (2022).

10. Zhang, X. H., P. Y. Gao, Z. H. Wu, M. H. Engelhard, X. Cao, H. Jia, Y. B. Xu, H. D. Liu, C. M. Wang, J. Liu, J.-G. Zhang, P. Liu, and W. Xu. "Pinned Electrode/Electrolyte Interphase and Its Formation Origin for Sulfurized Polyacrylonitrile Cathode in Stable Lithium Batteries." **ACS Appl. Mater. Interfaces** **14**, 52046–52057 (2022).
11. J.-M. Kim, Y. B. Xu, M. H. Engelhard, J. T. Hu, H.-S. Lim, H. Jia, Z. J. Yang, B. E. Matthews, S. Tripathi, X. H. Zhang, L. R. Zhong, F. Lin, C. M. Wang, W. Xu. Facile Dual-Protection Layer Enhancing Performances of Cobalt-Free/Nickel-Rich Cathodes in Lithium-Ion Batteries. **ACS Appl. Mater. Interface**, **14**, 17405-17414 (2022).
12. E. Sebti, H. A. Evans, H. N. Chen, P. M. Richardson, K. M. White, R. Giovine, K. P. Koirala, Y. B. Xu, E. Gonzalez-Correa, C. M. Wang, C. M. Brown, A. K. Cheetham, P. Canepa, R. J. Clément. Stacking Faults Assist Lithium-Ion Conduction in a Halide-Based Superionic Conductor. **J. Am. Chem. Soc.**, **144**, 5795–5811 (2022).

### Acknowledgements

Support from the U. S. Department of Energy (DOE), Vehicle Technologies Office, specifically from Tien Duong and David Howell is gratefully acknowledged.



## IX.4 In-Operando Thermal Diagnostics of Electrochemical Cells (LBNL)

### Ravi Prasher, Principal Investigator

Lawrence Berkeley National Lab  
1 Cyclotron Rd  
Berkeley, CA 94720  
E-mail: [RSPrasher@lbl.gov](mailto:RSPrasher@lbl.gov)

### Tien Duong, DOE Technology Development Manager

U.S. Department of Energy  
E-mail: [Tien.Duong@ee.doe.gov](mailto:Tien.Duong@ee.doe.gov)

Start Date: October 1, 2022

End Date: September 30, 2023

Project Funding (FY23): \$300,000

DOE share: \$300,000

Non-DOE share: \$0

### Project Introduction

Characterizing electrochemical processes in Li-metal cells such as lithium deposition and dendrite growth at interfaces is of great significance for understanding and enhancing their electrochemical performance and reliability. In situ and operando 3-omega micro thermal sensors can provide significant information regarding the impact of buried interfaces as a function of time, material, voltage, current, and temperature, etc. Therefore, it is important to develop operando 3-omega micro thermal sensors and develop models relating those signals to electrochemical performance for beyond lithium-ion cells. The physics-based model relating thermal and electrochemical properties based on these measurements can facilitate future design of Li metal batteries.

### Objectives

Transport at various interfaces in beyond lithium-ion cells will play a major role in electrochemical performance and reliability. It has not yet been possible to thermally profile a Li-metal cell during operation to provide a spatially resolved map of thermal transport properties throughout the cell. The objective of this research is to create a metrology capable of spatially resolved in operando thermal property profiling, and then relate thermal property to the quality of electrodes and interfaces and use the developed thermal metrology to understand electrochemical processes in Li-metal batteries such as dendrite growth, interface kinetics, and ionic transport.

### Approach

To accomplish project goals, the team will utilize an in-house adapted 3-omega technique to probe thermal properties of a Li-metal cell while it is in operation, without affecting the operation of the cell. The 3 omega sensors will be deposited and fabricated on Li-metal cells based on previous learning on 3-omega sensor fabrication. The characteristic depth of the thermally probed region is defined by the wave's "thermal penetration depth,  $\delta = \sqrt{D/2\omega}$ , where D is the sample's thermal diffusivity, and  $2\omega$  is the heating frequency of the thermal wave (Lubner et al. 2020). By depositing the project's  $3\omega$  sensors on the battery's outer surface and adjusting  $\omega$ , the team controls  $\delta$  to span the full range from the top to the bottom layer, thereby noninvasively probing the thermal transport in subsurface layers and interfaces within the bulk of the battery. Thermal transport can be related to quality of the interface. By doing concurrent thermal transport and electrochemical performance measurements, the team plans to relate thermal transport to electrochemical performance. As frequency based thermal measurement techniques provide excellent spatial resolution within the cell, the team also plans to study heat generation at the electrolyte–Li-metal interface and relate the thermal signals to the interface kinetics and ionic transport. The frequency dependence of heat generated due to transport resistance is different from that due to kinetic resistance. The team plans to utilize this difference to separate the contributions of kinetic and transport resistance at the interface, which will enable understanding of interface kinetics and transport at the Li-metal–Solid-state electrolyte (SSE) interface.

## Results

The thermal energy group is building operando  $3\omega$  micro thermal sensors and developing models relating thermal signals to electrochemical performance for beyond lithium-ion cells. The anode-side  $3\omega$  sensor will be used to probe thermal properties of Li metal anodes and related interfaces. The group is also developing a general frequency based thermal metrology to probe the interface kinetics and transport. We described our approach of studying thermal signatures of the heat generated at multiple harmonics of the excitation current to extract the electrochemical properties of buried interfaces and named the method Multi-harmonic ElectroThermal Spectroscopy (METS). We also presented a prototype design for a METS sensor and laid out an experimental plan for the verification of METS by comparing the electrochemical properties obtained from METS to those obtained from Electrochemical Impedance Spectroscopy (EIS).

In the first and second quarter of this year, to verify METS, we designed a model system (an electrochemical cell) with a lithium foil electrode and electrodeposited lithium electrode. We performed METS measurement using a sensor near the electrodeposited electrode and tried to resolve the contribution of electrode kinetics versus the transport overpotential at the interface due to the presence of surface passivation layer (solid-electrolyte interphase, SEI). To show the effect of SEI growth on the interface overpotential, we performed METS and electrochemical impedance spectroscopy (EIS) simultaneously on a cell freshly after preparation (pre-SEI growth) and after cycling the cell and letting the SEI grow under  $40\text{ }^{\circ}\text{C}$  for 12 hours (post-SEI growth). Both EIS and METS showed increase in the interface resistance attributable to the SEI growth. However, since the information from EIS is limited we could not differentiate or quantify the amount of the increase in SEI resistance to any particular electrode. Unlike with EIS, as METS provides spatial information as well, we were also able to resolve the contribution of each electrode on the apparent interface resistance. Figure IX.4.1 (a) shows the schematic of the fabricated model cell and Figure IX.4.1 (b) shows the EIS spectra before and after SEI growth. As seen in Figure IX.4.1 (a), although the two electrodes are chemically identical (lithium), one is electrodeposited whereas the other is foil lithium. We expect the electrodeposited lithium to be more pristine while the foil lithium should contain surface contaminants and therefore should have a higher interface resistance. In the EIS plots (Figure IX.4.1 (b)), we do see two semi-circles possibly pertaining to the two electrodes. But, there is no certain way of quantifying the apparent interface resistance to any particular electrode.

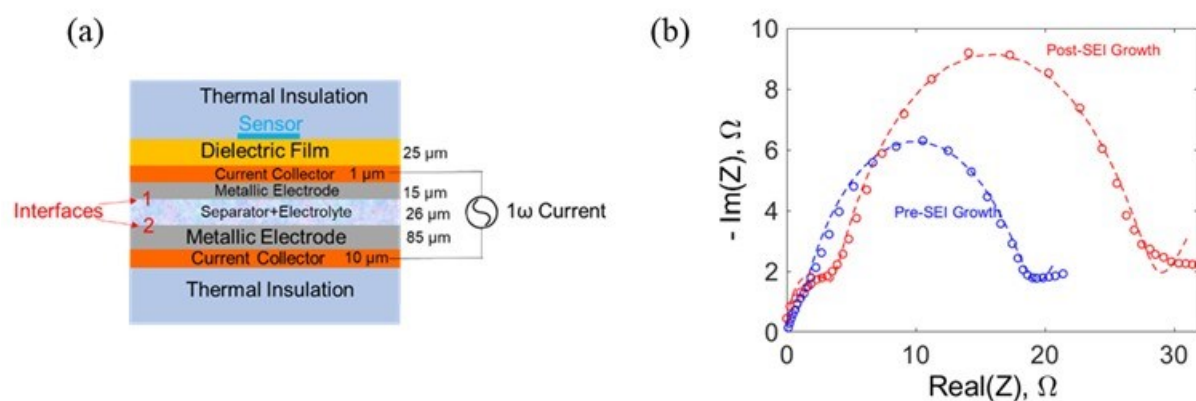


**Figure IX.4.1** (a) Schematic of the model cell with electrodeposited and foil lithium electrodes. The METS sensor is deposited on the dielectric film with a thin film copper current collector on which  $15\text{ }\mu\text{m}$  lithium is electrodeposited. (b) EIS spectra of the cell measured after cell assembly (pre-SEI, blue) and after cycling to allow SEI growth (post-SEI, red). Two semi-circles are visible on both spectra but attributing each semi-circle to particular electrodes is ambiguous because of the lack of spatial information with EIS.

Unlike in the case of EIS, from the frequency dependence of the thermal penetration depth, and from the non-linearity in the generation of thermal signature, METS can resolve both the kinetic overpotential vs transport overpotential at the interface and the contribution of each electrode towards the transport and kinetic

overpotential. Figure IX.4.2 shows the experimentally obtained METS spectrum for different current magnitudes for the model cell pre-SEI growth (top) and post-SEI growth (bottom).

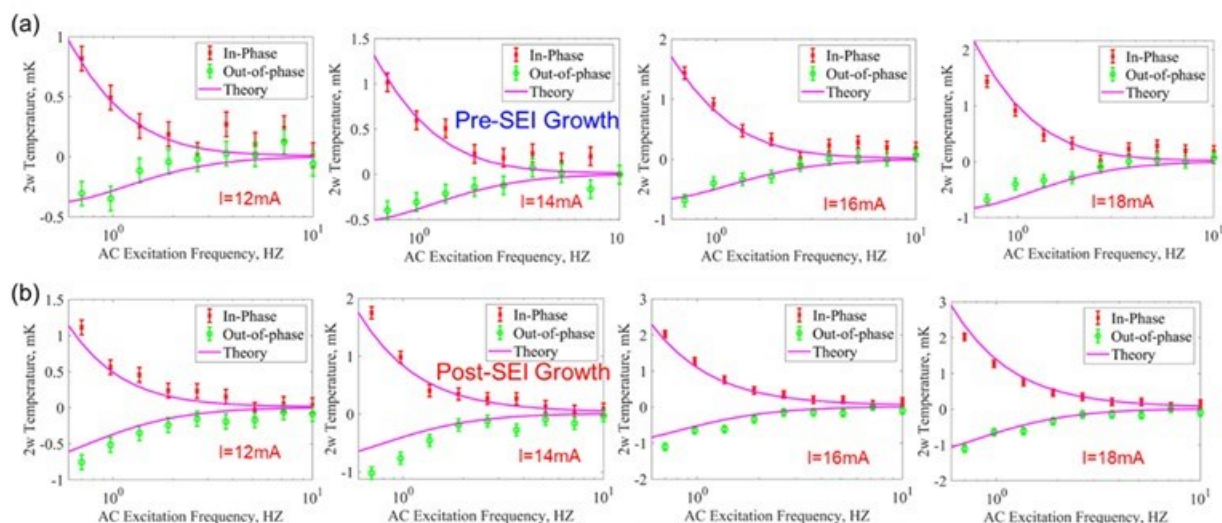


**Figure IX.4.2 METS Spectrum and the best-fit lines (purple) at different current magnitudes for pre-SEI growth (a, top) and post-SEI growth (b, bottom) cases. From the frequency dependence of the thermal penetration depth, the spatial resolution i.e. resolution of the contribution of each electrode is achieved. From the non-linear dependence of electrode kinetics on the current, the resolution of transport (SEI resistance) and the kinetic overpotential is achieved.**

From the best-fit to METS spectrum at different current magnitudes, we were able to deduce the contribution of kinetics and transport overpotentials at each electrode (summarized in Table IX.4.1 and Table IX.4.2). The total resistance due to kinetics and SEI at both the electrodes should sum up to the apparent low frequency impedance in the EIS spectra. As seen in the comparison (Table IX.4.1), the total impedance measured from EIS and METS agree well and therefore validate the METS method.

**Table IX.4.1 Summary of Impedances Related to Kinetic and Transport Overpotentials at the Interface Measured using METS and EIS for the Cell Pre-SEI Growth.**

	Electrode 1, Transport	Electrode 1, Kinetics	Electrode 2, Transport	Electrode 2, Kinetics	Total
<b>METS</b>	1.9 $\Omega$	0.1 $\Omega$	17.2 $\Omega$	0.8 $\Omega$	20 $\Omega$
<b>EIS</b>	Unknown	Unknown	Unknown	Unknown	18.8 $\Omega$

**Table IX.4.2 Summary of Impedances Related to Kinetic and Transport Overpotentials at the Interface Measured using METS and EIS for the Cell Post-SEI Growth.**

	Electrode 1, Transport	Electrode 1, Kinetics	Electrode 2, Transport	Electrode 2, Kinetics	Total
<b>METS</b>	5.9 $\Omega$	0.2 $\Omega$	23.7 $\Omega$	0.8 $\Omega$	30.6 $\Omega$
<b>EIS</b>	Unknown	Unknown	Unknown	Unknown	28.2 $\Omega$

In the third quarter, we were continuing to work on making the solid-state cells to perform the METS experiment. Meanwhile we focused on the self-heating study of lithium metal solid state cells. We choose lithium aluminum germanium phosphate (LAGP) instead of lithium lanthanum zirconium oxide (LLZO) as the electrolyte in the self-heating study. Currently the cycling of solid-state cells was investigated under the excitation of high frequency alternate current (AC) using a function generator. The symmetric cells which have

lithium metal at each side were assembled at first. To do the thermal insulation, the cell stacks were sandwiched by aerogel material and the power is supplied through copper wires instead of aluminum tabs. A small thermocouple was inserted between the aerogel and the Kapton film to monitor the temperature rise. The LAGP-Lithium cell was placed the Kapton film with additional Kapton tape used for fastening. The solid-state cell was cycled under around 300 kPa pressure to enable good contact and electrochemical performance. Here, three different settings were tested, they are: base case, more insulated case and two-layered case. Their temperature rise curves are shown in Figure IX.4.3 (h). Their heating performances are shown in Figure IX.4.3 (e), (f), (g) respectively. As shown in the results, from the measured impedance and the thermal transport properties, we have simulated the temperature rise as a function of the frequency and verified the simulations with the experimental temperature measurement. From the results, we have developed an understanding of the heat generation rate, heat loss and temperature rise.

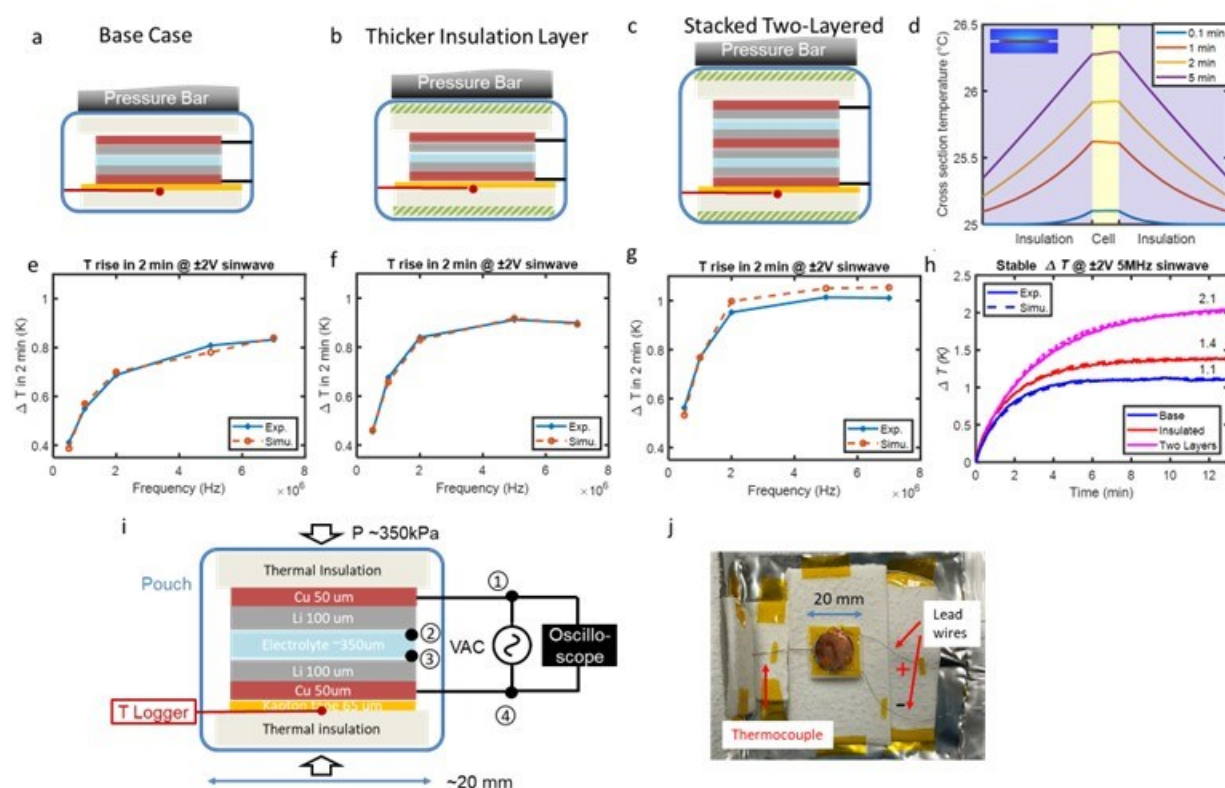
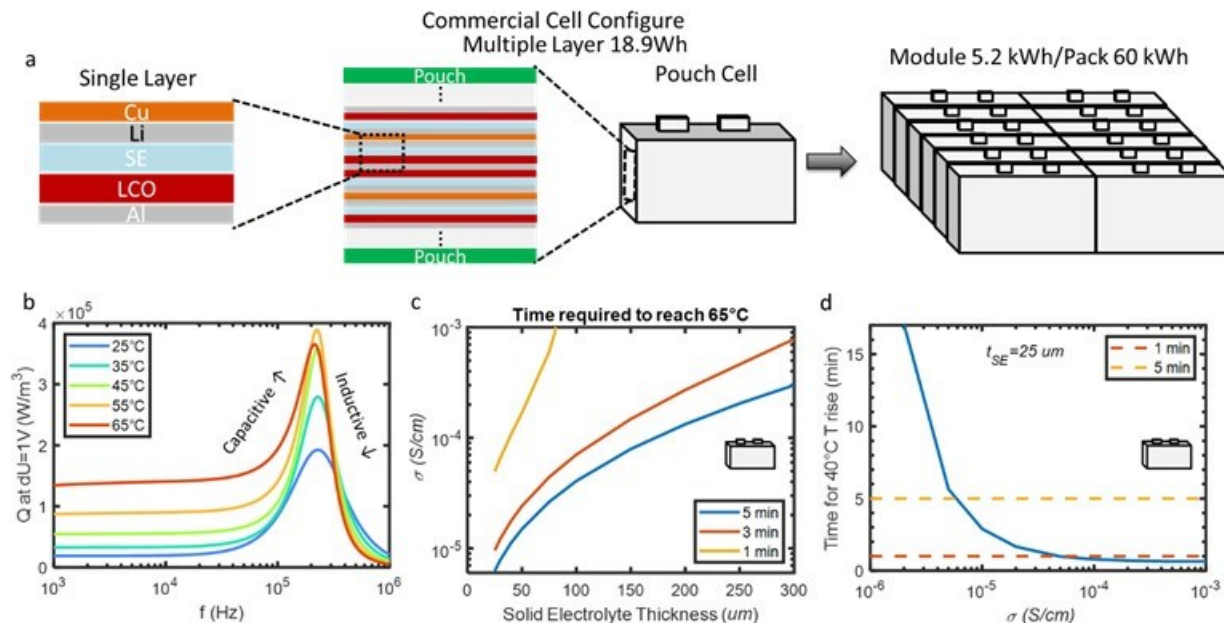


**Figure IX.4.3** Schematics of the LAGP symmetric cell (a) Base Case, (b) Thicker Thermal Insulation Layer, (c) Double Layer and (e), (f), (g) their corresponding temperature rise in 2 mins at different current frequencies. (d) Schematic illustration shows the simulated temperature distribution of the SSBs at cross section using COMSOL. (h) Temperature evolution for the above different configurations showing both experiments and simulation results. (i) Experiments setup for the alternating current heating of LAGP symmetric cell and the images of the cell.

In the fourth quarter, we continued the work and did the simulations for the cell level to pack level electrochemical-thermal simulation. We have developed an understanding of the heat generation rate, heat loss and temperature rise. This information helps us quantifying that how the electrochemical interface resistance decayed after the temperature increase caused by high frequency alternating current heating. Following figures are showing the heating performance on cell and pack level. We assumed the cell with single layer composed of lithium metal anode and lithium cobalt oxide cathode. The characteristic of heating power on frequency are shown in the Figure IX.4.4 (b). For each cell, there exists an optimal current frequency to give largest heating rate. Then with varying the solid electrolyte thickness and the ionic electrolyte conductivity, the time required to reach 40 °C temperature rise is shown. In the final subplot, we fix the solid-state electrolyte at 25 μm which

is reasonable to achieve comparable energy density. Then we are showing how the heating time will be reduced with respect to the ionic conductivity growing. In conclusion, if we can achieve heating quickly, the interface resistance of solid-state batteries will be largely reduced and the obtainable capacity can be increased to the theoretical capacity of lithium metal batteries. Moreover, higher temperature is beneficial to do fast charging for these high energy density cells and operating at cold environment.



## Conclusions

This year we published the results of in-situ monitoring of lithium-solid state electrolyte interface morphology from thermal interface resistance measurement enabled by thermal wave sensing based on the  $3\omega$  method. In our METS experiments on lithium-ion cell with liquid electrolyte and separator, morphological parameters such as the transport resistance and transport resistance were extracted from the thermal measurements by considering the effect of morphology and contact mechanics on solid-solid thermal interface resistance. By utilizing the frequency dependence of the thermal penetration depth, the method provided spatial resolution to attribute the observed interface resistance to specific interfaces, an ability not available with techniques such as Electrochemical Impedance Spectroscopy (EIS). METS works on the principle that different electrochemical processes have thermal signatures in different harmonics of the AC current passed through an electrochemical cell. It also utilizes the concept of thermal penetration depth to achieve spatial resolution. Finally, by considering the frequency-dependent heat generation rate and the thermal resistance of the cell, we studied self-heating of lithium-solid state electrolyte cell and were able to predict the magnitude of the temperature rise using combined electrochemical-thermal simulations on cell and pack level.

## Key Publications

### Journal articles:

1. Chalise, Divya, Richard Tee, Yuqiang Zeng, Sumanjeet Kaur, Himanshu Pokharna, and Ravi S. Prasher. 2023. "High Throughput, Spatially Resolved Thermal Properties Measurement Using Attachable and Reusable  $3\omega$  Sensors." *Review of Scientific Instruments* 94 (9): 094901. <https://doi.org/10.1063/5.0151160>.

2. Chalise, Divya, Robert Jonson, Joseph Schaadt, Pallab Barai, Yuqiang Zeng, Sumanjeet Kaur, Sean D. Lubner, Venkat Srinivasan, Michael C. Tucker, and Ravi S. Prasher. 2023. "Using Thermal Interface Resistance for Noninvasive Operando Mapping of Buried Interfacial Lithium Morphology in Solid-State Batteries." *ACS Applied Materials & Interfaces* 15 (13): 17344–52. <https://doi.org/10.1021/acsami.2c23038>.

**Presentations:**

1. Multi-Harmonic Electrothermal Spectroscopy (METS), a New Technique for Spatially Resolved Electrochemical Measurements, D Chalise, J Schaadt, A Dhar, V Srinivasan, S Lubner, S Kaur, R Prasher, 242nd ECS Meeting, Atlanta, GA
2. Measurement of entropy change of a half-cell electrochemical reaction using Multi-harmonic ElectroThermal Spectroscopy (METS); APS March Meeting (virtual), Las Vegas, NV, 2023
3. "Thermal Probes for understanding thermodynamics, transport and kinetics in electrochemical systems", Divya Chalise, Graduate Seminar Series, UT Arlington, Arlington, TX, September 2023

**References**

1. Lubner, Sean D., Sumanjeet Kaur, Yanbao Fu, Vince Battaglia and Ravi Prasher. 2020. "Identification and Characterization of the Dominant Thermal Resistance in Lithium-Ion Batteries Using Operando 3-Omega Sensors." *Journal of Applied Physics* 127 (10). <https://doi.org/10.1063/1.5134459>.

**Acknowledgements**

We thank Divya Chalise, Buyi Zhang, Dr. Yuqiang Zeng, Dr. Sean Lubner, Dr. Suman Kaur, Dr. Yanbao Fu, Dr. Vince Battaglia for their help in carrying out the research in this project.

## IX.5 Pre-Lithiation of Silicon Anode for High Energy Li-Ion Batteries (Stanford U)

### Yi Cui, Principal Investigator

Stanford University

Department of Materials Science and Engineering, Stanford University  
Stanford, CA 94305

E-mail: [yicui@stanford.edu](mailto:yicui@stanford.edu)

### Tien Duong, DOE Program Manager

U.S. Department of Energy

E-mail: [Tien.Duong@ee.doe.gov](mailto:Tien.Duong@ee.doe.gov)

Start Date: Oct.1, 2022

End Date: Sep.30, 2023

Project Funding (FY23): \$500,000

DOE share: \$500,000

Non-DOE share: \$0

### Project Introduction

Lithium Ion Batteries (LIBs) offer superior performance among all rechargeable battery technologies, and are the main power sources for portable electronic devices and electric vehicles. Silicon is a high-performance anode material for next generation lithium ion batteries, with an order of magnitude higher capacity than traditional graphite anode. In our lab, challenges of Si anode materials associated with large volume change (>300%) during lithium insertion and extraction are largely addressed by well-designed nanostructures[1]. However, the common issue associated with these anode materials is the increased solid electrolyte interphase (SEI) formation on high-surface-area nanostructures during the first cycle. The process consumes an appreciable amount of lithium, resulting in irreversible loss of capacity and low 1st CE (50-80%)[2], while a value of at least 90% is needed for real applications. Such capacity loss is usually compensated by additional loading of cathode materials in commercial lithium ion batteries. However, the lithium metal oxide cathodes have much lower specific capacity than the anodes. The excessive loading of cathode material causes appreciable reduction of battery energy density. It is therefore highly desirable to suppress such loss and consequently increase the 1st CE through prelithiation. In addition, pre-storing lithium inside anodes enable the opportunity to pair with Li-free cathodes such as sulfur and oxygen cathodes. This project's success will make high-energy-density Li ion batteries for EVs.

### Objectives

Prelithiation of high-capacity electrode materials is an important means to enable those materials in high-energy batteries. This study pursues three main directions: (1) developing facile and practical methods to increase 1st cycle CE of anodes, (2) synthesizing fully lithiated anode to pair with high-capacity Li free cathode materials, and (3) prelithiation from the cathode side. The challenge associated with the anode prelithiation is the high chemical reactivity of prelithiation materials, which are hard to survive multiple processing steps (exposure to air and solvent, slurry mixing, coating and baking) during battery electrode fabrication. A protective coating is therefore needed. Different passivation coatings have been used to increase the dry-air and solvent stability of prelithiation reagents. At the end of battery assembly, the coatings are activated to ensure quick lithium ions diffusion for prelithiation. The passivation coatings can improve the dry-air stability of prelithiation materials to a certain extent, but much study is still needed to improve solvent stability to better compatible with practical battery fabrication. We plan to explore a new solvent-free dry method for anode prelithiation through *in situ* prelithiation. Prelithiation reagents are added to the battery in the assembly step, to avoid the concern of solvent compatibility. We also plan to design prelithiation reagents for this solvent-free method, and accurately control the prelithiation amount of anode materials to pair with different-capacities cathode materials.

## Approach

Three main approaches have been developed for prelithiation: 1) Synthesizing lithium alloying  $\text{Li}_x\text{M}$  particles as novel prelithiation reagents to provide a low-cost and general strategy for prelithiation. The synthesized Li-rich compounds should be able to mix with various anode or cathode materials during slurry process and serve as prelithiation reagents. 2) Developing new prelithiation process based-on pressure-induced prelithiation. By direct contact with Li and Si under pressure, heat-free and solvent-free prelithiation can be achieved without the concern of solvent compatibility. Also, prelithiation amount is controllable through contact time and pressure. 3) Developing new *in situ* prelithiation process based on shorting-mechanism. A layer of thin lithium is inserted above Si anode in cell fabrication to achieve *in situ* prelithiation during battery resting period. Prelithiation reagents need to carefully designed for this approach to control prelithiation amount and avoid excessive Li. 4) Developing lithium-containing copper current collector with dual function of current collector and prelithiation. This strategy transfers the current collectors from dead weight in batteries to dry prelithiation reagents. Besides prelithiation step, a series of morphological and chemical composition characterizations including SEM, TEM, XPS, Raman spectroscopy, XRD, etc. and electrochemical testing are conducted for performance characterization.

## Results

This year, we propose a new concept of storing lithium in the anode current collectors. We develop lithium-containing current collectors as new dry prelithiation reagents. This dual-function current collector can utilize the dead weight in batteries for excessive lithium storage and achieve one-step, dry prelithiation. Lithium-containing current collectors are fabricated by annealing Li and Cu foils where Li atoms gradually diffuse into the Cu lattices. In this way, we store sacrificial lithium to the Cu current collectors which can be extracted in anode delithiation. Prelithiation with lithium-containing current collectors compensates the initial battery capacity loss and increases initial Coulombic efficiency. This lithium-containing current collector demonstrates a dry one-step prelithiation strategy as a promising prelithiation approach towards practical applications.

The lithium-containing current collectors are prepared by annealing Li and Cu foil (Figure IX.5.1a). First, thin Li foil of desired capacity is placed on top of Cu foil, a conventional current collector for anodes. Then aligning foils, we placed these set of foils into an oven for annealing and observed changes. During annealing, Li foil on top starts to liquefy due to temperature above its melting temperature, and lithium atoms start to diffuse into Cu current collector (Figure IX.5.1a, center). This process allows lithium atoms to transport into Cu lattices and change their crystal structure. After annealing, prelithiated current collector was collected from oven and cooled down for further experiments (Figure IX.5.1a, right). As depicted in Figure IX.5.1b, colors of layered foils exhibit goldish color on both sides and this change implies possible formation of a new phase. XRD analysis results in Figure IX.5.1c show direct evidence of changes in Cu crystal lattices. Compared to XRD peaks of Cu foil, those of prelithiated current collectors are shifted towards lower angle of diffraction. Since  $2\theta$  is inversely proportional to interplanar spacing under the same incident beam, this data indicates that lattice parameters have increased after annealing, possibly due to insertion of Li into lattices. Therefore, we could suggest that Li atoms can be stored inside Cu current collector for prelithiation. The most important part of this work is that we were able to utilize current collectors, which are electrochemically inactive and considered as 'dead weight', to store lithium by one-step thermal reactions.



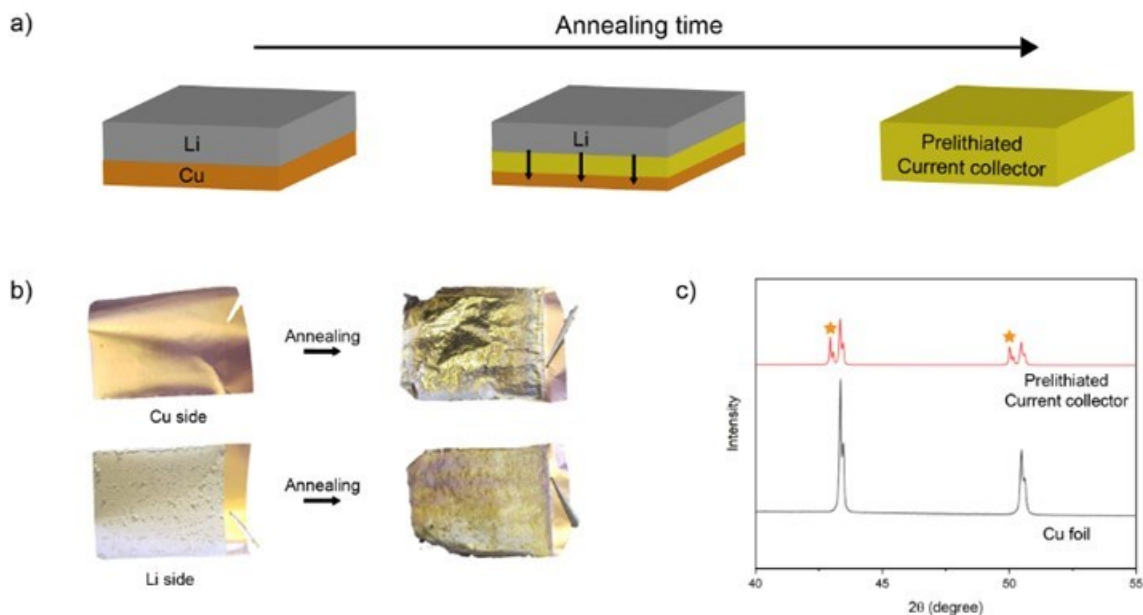


Figure IX.5.1 a, Schematic of preparing lithium-containing Cu current collector by annealing. b, Digital photos of the Li on Cu foil before (left) and after (right) prelithiation by annealing. c, XRD analysis results of bare Cu foil and prelithiated current collector. New peaks observed from Li-containing current collector are marked with yellow symbols.

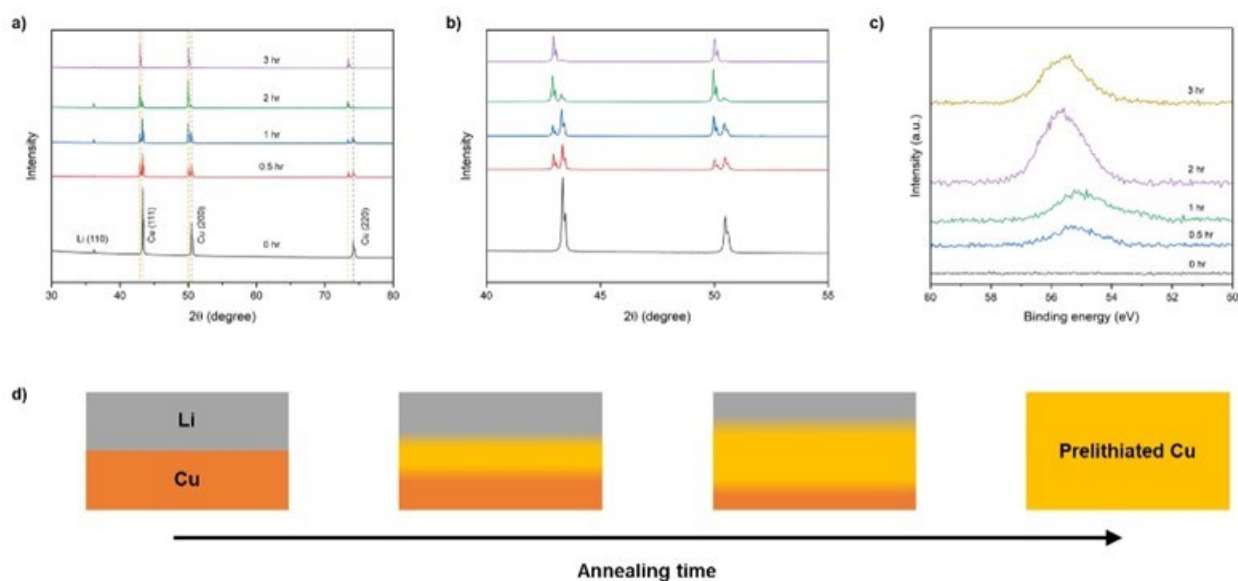
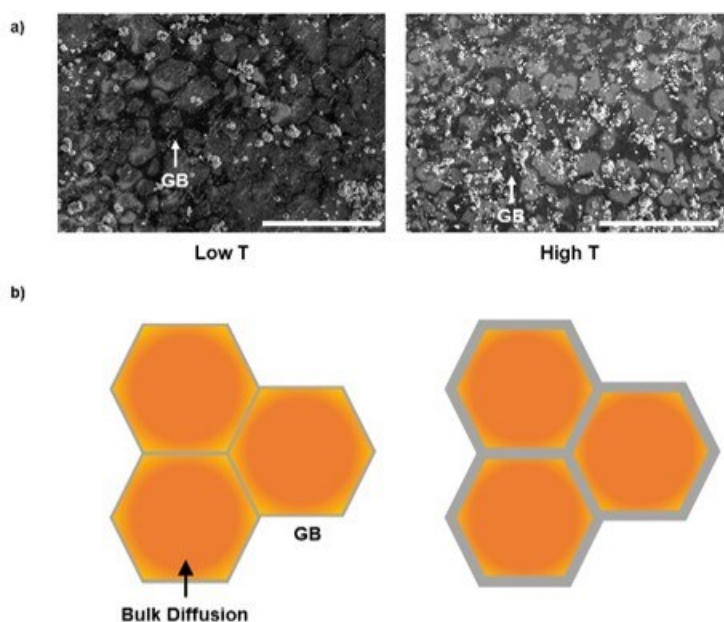


Figure IX.5.2 a) XRD analysis of lithium containing Cu current collectors with different time of annealing (0, 0.5, 1, 2, and 3 hours) and b) enlarged plot of XRD results for  $2\theta = 40 - 55^\circ$  Li 1s XPS on Cu side of samples before and after annealing. d) Corresponding schematic diagram showing the progress of prelithiation from Li on Cu foil.

The effect of annealing time to the prelithiation of Cu current collector is further investigated. From the previous results, changes in crystal structure of Cu after annealing was observed by X-ray diffraction (XRD) results and it was an indirect evidence of prelithiation. However, the optimal time for the annealing was still not clear for the fabrication of current collectors with stored Li. Therefore, samples with various annealing

time were prepared and conducted XRD to have a better understanding of their crystal structures (Figure IX.5.2a). Before annealing, XRD plot exhibited peaks of pristine Li and Cu, as expected. As the foil was heated longer inside the oven, intensities of peaks corresponding to Cu (111), (200), and (220) decreased. Meanwhile, representative peaks of prelithiated Cu phase start to evolve. From Figure IX.5.2b, it is clear that these peaks have slightly smaller refractive angles compared to all Cu peaks and this implies that lattice parameters of Cu are increasing while maintaining its structure. This may be due to insertion of Li atoms into Cu lattices. The increasing ratio of new peaks over those of pristine Cu after longer annealing represents the degree of prelithiation in Cu foils. Similar trend was observed from X-ray photoelectron spectroscopy (XPS) (Figure IX.5.2c). Li 1s XPS plot of 0 hr samples on the copper side did not show any peaks due to lack of lithium. However, a peak at around 55 eV was visible after 0.5 hr annealing and small portion of lithium may have diffused to the copper side during this process. Surprisingly, 2 hr annealed sample showed a peak located at a higher binding energy. This may be due to the formation of prelithiated phases on the surface after sufficient time of annealing. The peak location was consistent in 3 hr-annealed sample as well, possibly representing complete transformation into Cu current collector with prelithiation. Therefore, it is reasonable to state that the time of annealing has a huge impact on the degree of prelithiation on Cu foil and it was confirmed with XRD and XPS. This is also depicted in Figure IX.5.2d. As a conclusion, it may be possible to control the capacity stored by manipulating annealing time.



**Figure IX.5.3 a) SEM analysis of lithium containing Cu current collectors after annealing at various temperatures (scale bar = 50  $\mu\text{m}$ ) and b) schematic diagram of the possible diffusion mechanism of Li into Cu, respectively (orange : Cu, silver : Li).**

To get a better understanding of the mechanism, we studied the effect of the annealing temperature. The formation of a new phase by annealing is already observed from our earlier reports and this phenomenon could be an indirect evidence of Li intercalation in Cu. Even with this information, it is still necessary to optimize appropriate conditions for stability and performance. To study the effect of annealing temperature, we varied the temperature of annealing for Li on Cu samples and studied how morphologies could be different (Figure IX.5.3a). As depicted from scanning electron microscopy (SEM) images, samples annealing at higher temperature showed larger grains and more pores. It is speculated that increasing the annealing temperature seem to accelerate both grain boundaries (GB) and bulk diffusion of Li into copper foil. By comparing portion of grain boundaries (marked with white arrows) at various temperatures, more lithium is located on the grain boundaries at higher temperature due to the faster diffusion. However, since bulk diffusion is slower than the grain boundary diffusion, it is postulated that more lithium is accumulated on GB at higher temperature while

some of them diffuse into grains (Figure IX.5.3b). This higher concentration gradient around the boundaries of grains might be helpful for the uniform synthesis of Li-containing current collectors. In conclusion, we suggest that faster diffusion of Li through GBs of copper foil occurs at higher temperature and this could be beneficial for the fabrication process.

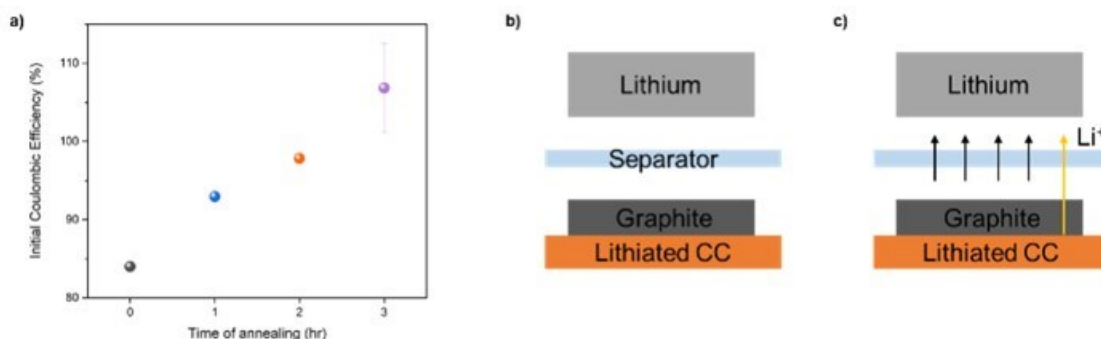


**Figure IX.5.4** a) Initial coulombic efficiency of graphite anodes with lithiated current collectors. Time of annealing describes the degree of lithiation. b) A schematic of coin cell setup with lithiated current collectors and c) extraction of Li during cycling.

With this current collector, our goal was to investigate the impact of additional Li capacity on the ICE of graphite anodes. Based on structural changes to Cu lattices resulting from annealing, we could observe successful infusion of lithium into Cu unit cells. Consequently, we could also presume this new current collector works as a reservoir for additional amount of lithium inside batteries. In order to test its applicability in coin cells, we integrated graphite anodes onto the lithiated current collectors and tested their performance in half cells (Figure IX.5.4). When we first cycled bare graphite anodes against Li without lithiated current collectors, their ICEs were around 83% (depicted as '0 hr' in Figure IX.5.4a). Then graphite anodes were placed on top of our current collectors and supplementary lithium was extracted during the first charging steps (Figure IX.5.4b). With 1hr annealed samples, ICEs of graphite anodes were about 93% which was 10% increase from bare graphite anodes. As a result, it was clear that lithiated current collectors can successfully supply extra amount of lithium for anodes during the first cycle (Figure IX.5.4c). Based on our analysis that samples with longer annealing time can store more lithium, we further investigated on the changes of ICEs with various current collectors. As we increased the annealing time from 1 hr to 2, and 3 hrs, we observed gradual increase in ICEs from 93% to 97% and 106%, respectively. This result not only supports the previous data but also exhibits possibilities of fine-tuning lithium capacities in current collectors and reaching close to 100 % ICEs in diverse types of anodes. In conclusion, we postulate that this novel method of using current collectors as a lithium source might be beneficial for achieving high ICEs in the next generation of lithium batteries.

## Conclusions

In the past year, we have developed dual-function lithium-containing current collectors as new dry prelithiation reagents for facile and controllable prelithiation. Using copper collectors as excessive Li source can utilize the dead weight of current collectors for Li storage and prelithiate anode in one-step, dry prelithiation process. The lithium-containing current collectors are fabricated by annealing Li and Cu foils where Li atoms diffuse into Cu lattices at elevated temperature. The optical images show the clear color change of Cu foil after annealing. XRD and XPS results verify the formation of new Li-Cu phase. The study of annealing time shows that increased Li storage into Cu foils with longer annealing time, providing varied prelithiation capacity. We also studied the impact of annealing temperature that faster diffusion of Li through grain boundaries of copper foil are observed at higher temperature. Utilizing Li-containing copper foils for battery prelithiation, we increase

the initial CE of graphite anodes from 83% to close to 100% initial CE. In sum, this work provides new insights for studying and designing prelithiation strategies.

### Key Publications

1. Zhao, Jie, Zhenda Lu, Nian Liu, Hyun-Wook Lee, Matthew T. McDowell, and Yi Cui. "Dry-air-stable lithium silicide–lithium oxide core–shell nanoparticles as high-capacity prelithiation reagents." *Nature communications* 5, no. 1 (2014): 1-8.
2. Zhao, Jie, Zhenda Lu, Haotian Wang, Wei Liu, Hyun-Wook Lee, Kai Yan, Denys Zhuo, Dingchang Lin, Nian Liu, and Yi Cui. "Artificial solid electrolyte interphase-protected  $\text{Li}_x\text{Si}$  nanoparticles: an efficient and stable prelithiation reagent for lithium-ion batteries." *Journal of the American Chemical Society* 137, no. 26 (2015): 8372-8375.
3. Zhao, Jie, Hyun-Wook Lee, Jie Sun, Kai Yan, Yayuan Liu, Wei Liu, Zhenda Lu, Dingchang Lin, Guangmin Zhou, and Yi Cui. "Metallurgically lithiated  $\text{SiO}_x$  anode with high capacity and ambient air compatibility." *Proceedings of the National Academy of Sciences* 113, no. 27 (2016): 7408-7413.
4. Sun, Yongming, Hyun-Wook Lee, Zhi Wei Seh, Nian Liu, Jie Sun, Yuzhang Li, and Yi Cui. "High-capacity battery cathode prelithiation to offset initial lithium loss." *Nature Energy* 1, no. 1 (2016): 1-7.
5. Sun, Yongming, Hyun-Wook Lee, Guangyuan Zheng, Zhi Wei Seh, Jie Sun, Yanbin Li, and Yi Cui. "In situ chemical synthesis of lithium fluoride/metal nanocomposite for high capacity prelithiation of cathodes." *Nano letters* 16, no. 2 (2016): 1497-1501.
6. Sun, Yongming, Hyun-Wook Lee, Zhi Wei Seh, Guangyuan Zheng, Jie Sun, Yanbin Li, and Yi Cui. "Lithium Sulfide/Metal Nanocomposite as a High-Capacity Cathode Prelithiation Material." *Advanced Energy Materials* 6, no. 12 (2016): 1600154.
7. Sun, Yongming, Yanbin Li, Jie Sun, Yuzhang Li, Allen Pei, and Yi Cui. "Stabilized  $\text{Li}_3\text{N}$  for efficient battery cathode prelithiation." *Energy Storage Materials* 6 (2017): 119-124.
8. Zhao, Jie, Jie Sun, Allen Pei, Guangmin Zhou, Kai Yan, Yayuan Liu, Dingchang Lin, and Yi Cui. "A general prelithiation approach for group IV elements and corresponding oxides." *Energy Storage Materials* 10 (2018): 275-281.
9. Chen, Hao, Yufei Yang, David T. Boyle, You Kyeong Jeong, Rong Xu, Luiz Scalco de Vasconcelos, Zhuojun Huang et al. "Free-standing ultrathin lithium metal–graphene oxide host foils with controllable thickness for lithium batteries." *Nature Energy* (2021): 1-9.
10. Yang, Yufei, Jiangyan Wang, Sang Cheol Kim, Wenbo Zhang, Yucan Peng, Pu Zhang, Rafael A. Vilá, Yinxing Ma, You Kyeong Jeong, and Yi Cui. "In Situ Prelithiation by Direct Integration of Lithium Mesh into Battery Cells." *Nano Letters* 23, no. 11 (2023): 5042-5047.

### References

1. Liu, Yayuan, Guangmin Zhou, Kai Liu, and Yi Cui. "Design of complex nanomaterials for energy storage: past success and future opportunity." *Accounts of chemical research* 50, no. 12 (2017): 2895-2905.
2. Zhao, Jie, Zhenda Lu, Nian Liu, Hyun-Wook Lee, Matthew T. McDowell, and Yi Cui. "Dry-air-stable lithium silicide–lithium oxide core–shell nanoparticles as high-capacity prelithiation reagents." *Nature communications* 5, no. 1 (2014): 1-8.

## X Next-Gen Lithium-Ion: Modeling Advanced Materials

Development of accurate, real-time models for rechargeable batteries is essential to ensure efficient battery management and safe operation. Using battery models, battery design parameters can be leveraged in developing strategies for optimal battery operation and improved efficiency. Optimal operation of battery results in prolonged battery life with maximum capacity by reducing losses while maintaining safety. This optimal operation is achieved by operating a battery with optimal charge discharge cycles (provided by an optimizer), through a controller. A model (representative of a battery) is involved as an integral component in the optimizer, controller, as well as state of charge (SOC) estimator. There are different states associated with batteries such as, SOC, voltage, current, capacity etc. – which all must be monitored and maintained at desired levels for optimal battery operation, and real time battery models can help realize such desirable performance. For a model to be useful, it should include all the significant phenomena that occur inside a rechargeable battery.

The rest of this chapter contains detailed reports on the status of the following individual projects.

- Electrode Materials Design and Failure Prediction (ANL)
- Characterization and Modeling of Li-Metal Batteries: Model-system Synthesis and Advanced Characterization (LBNL)
- Design of High-Energy, High-Voltage Lithium Batteries through First-Principles Modeling (LBNL)
- Modeling of Solid-State Conductors (LBNL).

## X.1 Electrode Materials Design and Failure Prediction (ANL)

### Venkat Srinivasan, Principal Investigator

Argonne National Laboratory  
9700 South Cass Avenue  
Lemont, IL 60439  
E-mail: [vsrinivasan@anl.gov](mailto:vsrinivasan@anl.gov)

### Tien Duong, DOE Technology Development Manager

U.S. Department of Energy  
E-mail: [Tien.Duong@ee.doe.gov](mailto:Tien.Duong@ee.doe.gov)

Start Date: October 1, 2022	End Date: September 30, 2023	
Project Funding (FY23): \$550,000	DOE share: \$550,000	Non-DOE share: \$0

### Project Introduction

Solid-electrolytes (SEs) are expected to enable high-energy-density and liquid-free, safe, next-generation Li-ion batteries, while combined with thin Li-metal anodes. During charge, lithium dendrites are observed through the SEs, which are supposed to occur because of the non-uniform current distribution at the Li/electrolyte interface. Due to their lack of conformability, hard-ceramic-based SEs [such as, lithium lanthanum zirconium oxide ( $\text{Li}_7\text{La}_3\text{Zr}_2\text{O}_{12}$  or LLZO) and lithium aluminum titanium phosphate (LATP)] are expected to experience loss of electrochemically active surface area during lithium plating and stripping, which can eventually lead to current focusing and subsequent dendrite growth. Softer sulfide based solid electrolytes, such as, thiophosphate type lithium phosphorous sulfide ( $\text{Li}_3\text{PS}_4$  or LPS) or argyrodite type lithium phosphorous sulfide chloride ( $\text{Li}_6\text{PS}_5\text{Cl}$  or LPSCl), are expected to demonstrate better interface with lithium metal anodes. However, severe side reaction induced thick solid-electrolyte-interphase (SEI) formation has been observed in sulfide based solid electrolytes, and growth of lithium dendrites are still observed under higher current densities. It is also known that stripping induced void formation in lithium metal anodes is a challenge, which needs to be addressed along with the dendrite growth related problems.

The positive electrode containing active material and solid electrolytes are also not easy to stabilize during fabrication and operation. Interdiffusion of ions at the time of co-sintering process tend to form resistive interphase, which can substantially limit cell performance. Even if interdiffusion during cathode fabrication can be prevented, possibly through the application of high pressure at around room temperature conditions, interfacial delamination induced degradation observed during operation are ubiquitous in the solid state battery literature. Propensity of interdiffusion of ions during the charged state becomes higher because of the inherent instability of the delithiated cathode active particles. The delamination related issues were investigated in previous years. This year, a mathematical model will be developed that is capable of predicting the propensity of interdiffusion during sintering, as well as at the time of charge-discharge operation.

### Objectives

The main project objective is to develop computational models for understanding the various degradation mechanisms for next-generation solid state lithium-ion batteries (LIBs). This year's goal is to use the continuum-based mathematical model to estimate the lithium plating and stripping processes with non-ideal interfaces, such as, an interphase layer with an alloying material, with pre-existing voids at the interface, composite electrode (such as, lithium/carbon-nanotube or Li/CNT), etc. Electrolytes comprised of soft polymers, hard ceramics, and a combination of the two in the form of polymer-ceramic composites, are possible.

On the cathode side, interdiffusion of ions between the cathode active material and the solid electrolyte is a possibility, which leads to the formation of resistive cathode electrolyte interphase (CEI) layers with very high

resistance. Elucidation of factors that influence the extent of interdiffusion is another objective of this project. Accordingly, a computational methodology is devised to capture the formation and thickness of the resistive CEI layers for different types of oxide based cathode and oxide/sulfide based solid electrolytes.

### Approach

In the present project, mesoscale models are developed based on mass conservation, charge balance, and force balance relations at the continuum level to describe the physical processes occurring in the electrochemical systems during charge and discharge, which is then compared with the experimental observations for appropriate validation. The models are then used to provide insights and guidance for strategizing new design concepts and materials for the stabilization of Li-metal anodes.

### Results

#### *Develop computational model for lithium deposition and stripping with alloying anodes.*

In order to stabilize lithium deposition at the anode side during the charging process, various metals have been attempted as the anode capable of alloying with lithium and possibly eliminate the growth of dendrites. However, depending on the open circuit potential of the alloying anode, and the extent of lithiation experienced by the alloying metal, it is possible to obtain either alloying of lithium, or plating of lithium, on top of the anode. In the present context, a computational model is developed capable of predicting the propensity of alloying or plating reactions. The alloying reaction shows some positive value of the open circuit potential, whereas the lithium plating reaction occurs under zero volts. Lithiation of the alloying anode is assumed to occur through a solid solution mechanism. The concentration dependent variation in open circuit potential of the alloying anode material is assumed to follow the Nernst equation, where the impact of the activity coefficients is neglected. The computationally predicted voltage vs. time curve during the lithium deposition on top of the alloying anode is shown in Figure X.1.1, where both alloying and plating is successfully captured. Changes in the computational domain during the alloying and plating process is shown in the left by the images marked A – F.

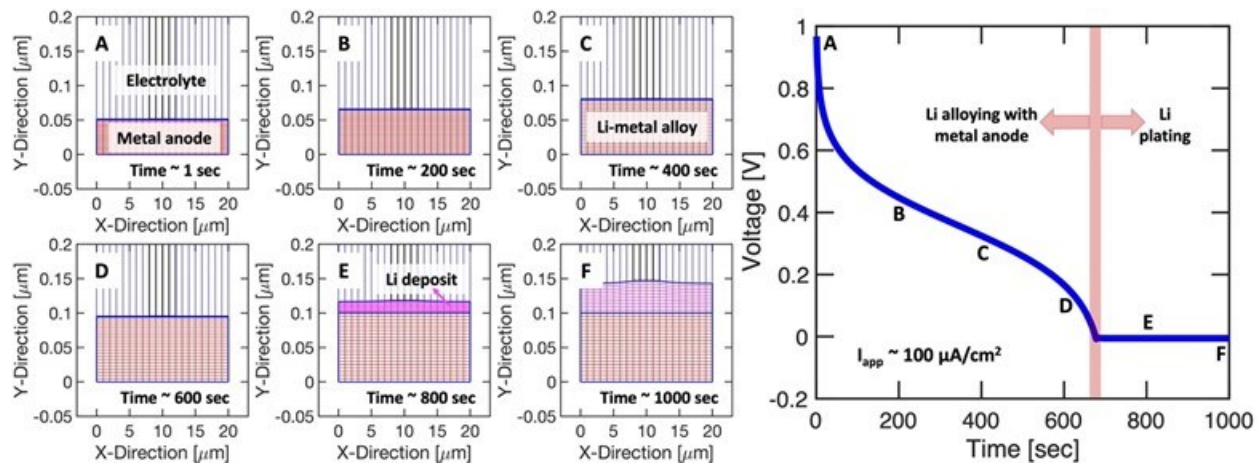


**Figure X.1.1** Computationally predicted voltage vs. time curves for lithium alloying and plating phenomena. Time evolution of the domain containing lithium metal alloy (red) and deposited lithium (magenta) is shown in the left. The electrolyte on top is also denoted in blue. The applied current density is  $100 \mu\text{A}/\text{cm}^2$ .

A separate one dimensional model is developed for capturing the stripping process that occurs after the deposition of lithium. Figure X.1.2 shows the voltage vs. capacity curves obtained during plating and stripping of lithium for different thickness of the alloying anode material.

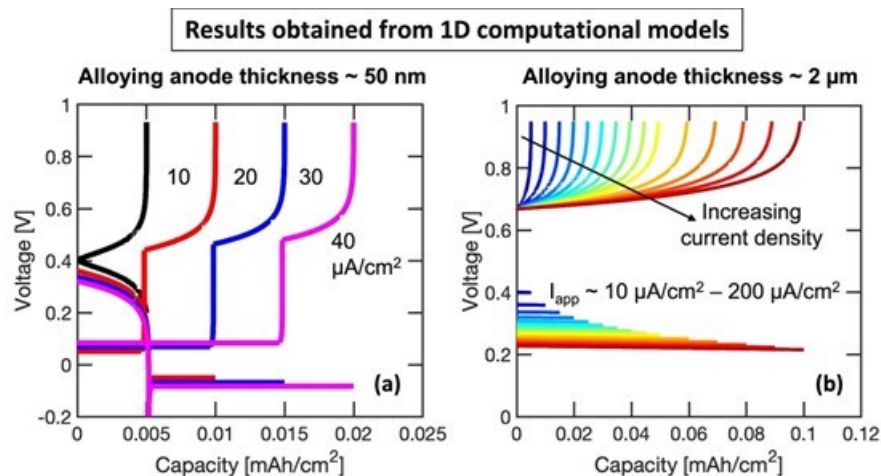


**Figure X.1.2** Computation predicted voltage vs. capacity curves obtained during plating and stripping of lithium with alloying metal anodes. (a) Thinner alloying anode layer is used with thickness around 50 nm, which experiences both alloying and plating reactions. During stripping, the plated lithium strips first and the dealloying process starts later. (b) With 2 μm thick metal foil, all the deposited lithium ends up alloying with the metal. No plating of lithium is observed. During stripping only dealloying is observed.

#### **Modeling the interdiffusion of ions at the cathode/solid-electrolyte interface.**

A major challenge experienced by the cathode particles located adjacent to solid electrolytes is the interdiffusion of ions and formation of passivation layers. It is important to understand the mechanism to devise strategies capable of limiting, or completely eliminating, the intermixing of ions. Ionic interdiffusion have already been observed in solid oxide fuel cells during operation at higher temperatures, and there exist established theories for capturing those phenomena (see Hu et al., *App. Phys. Lett.* (2014) 213907). In the present context, existing theories for predicting the interdiffusion of ions between the electrode and electrolyte of solid oxide fuel cells are extended to investigate the ionic intermixing phenomena observed in lithium ion batteries with layered oxide cathodes and solid electrolytes.

Interdiffusion of ions between lithium cobalt oxide cathodes (LiCoO<sub>2</sub>, LCO) and Li<sub>2</sub>S-P<sub>2</sub>S<sub>5</sub> based sulfide type solid electrolytes (LPS) have already been investigated experimentally (see Sakuda et al., *Chem. Mater.* (2010) 949 – 956), where distribution of atoms at the electrode/electrolyte interface were estimated using scanning transmission electron microscopy (STEM) techniques combined with energy dispersive X-ray diffraction (EDX) measurements (also shown in Figure X.1.3(a)). From a computational standpoint, ionic transport is estimated using a dilute solution theory, while maintaining charge neutrality and zero flux of ions across the interface. Evolution of a separate phase parameter is solved to capture the thickness and movement of the interphase layer. Figure X.1.3 (b) demonstrates the initial distribution of Co, S and P ions near the cathode/electrolyte interface. After simulating interdiffusion for 2.75 hours, the ionic distribution is demonstrated in Figure X.1.3 (c), which correlates well with the experiments.



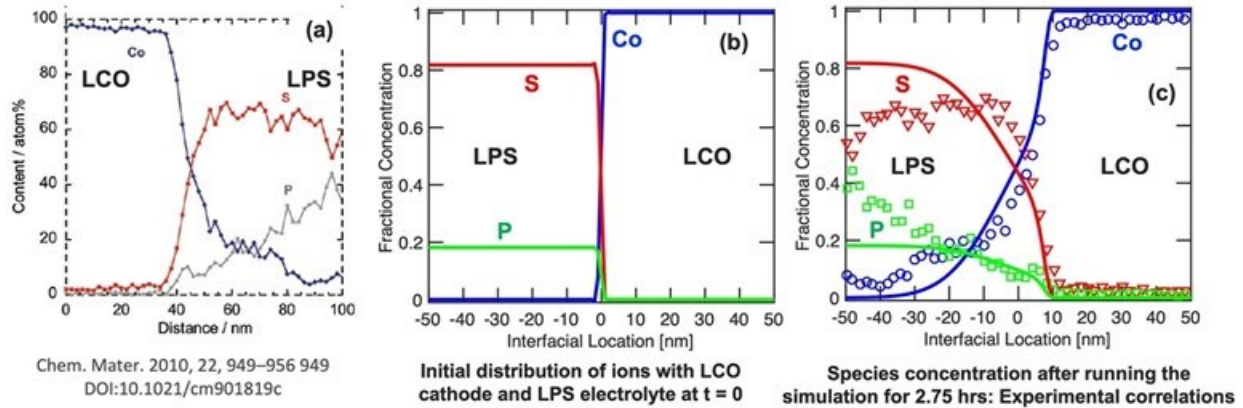


Figure X.1.3 (a) Experimentally observed interdiffusion of ions at the LCO cathode and LPS solid-electrolyte interface (adopted from Sakuda et al., Chem. Mater. 2010 949 – 956). (b) Initial distribution of Co (blue), P (green), and S (red) atoms near the interface used in the computational model. (c) Distribution of Co, P, and S at the interface after simulating the interdiffusion of ions for 2.7 hours. Similar distributions of atoms as observed in experiments are also predicted by the computational models.

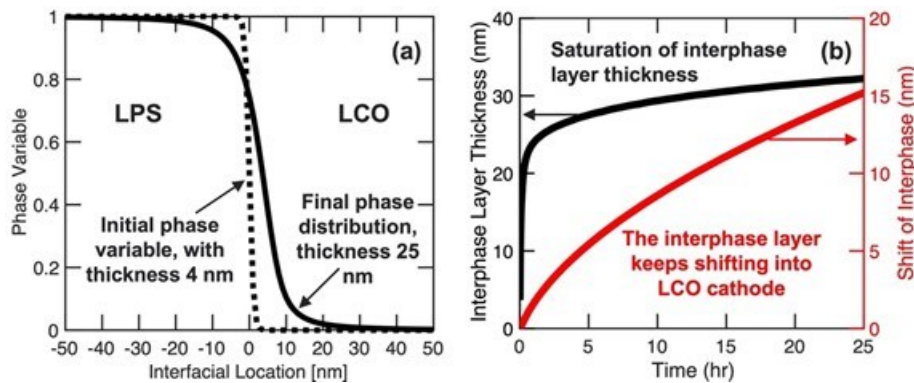


Figure X.1.4 Model predicted evolution of the interphase region with time is reported here. (a) The initial interphase layer is denoted by the dotted line. The interphase after interdiffusion for 2.7 hours is shown by the solid line. (b) Computational model predicted increase in interphase layer thickness with time is denoted by the black line along the left axis. Shift of the LCO/LPS interface into the cathode with time is shown by the red line.

Computationally predicted phase variable at  $t = 0$  and after 2.75 hours is shown in Figure X.1.4(a). Model predicted increase in interphase layer thickness and corresponding shift of the interface into the LCO cathode is shown in Figure X.1.4 (b). Development of a computational model for interdiffusion was completed successfully.

Investigate lithium deposition at a Li|electrolyte interface with pre-existing voids.

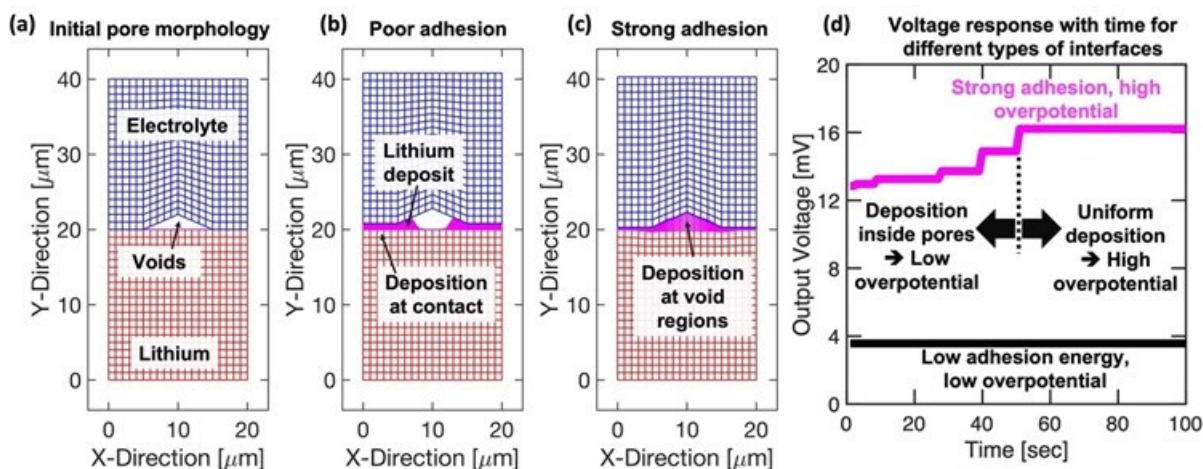


Figure X.1.5 Impact of adhesion strength on the Li deposition near void domains. (a) Initial mesh of a porous Li|SE interface. (b) Li deposit at the contact points for weak adhesion between the electrode and electrolyte. (c) For well adhered Li|SE interface, majority of the initial deposition happens at the pore domain. (d) Output voltage response for strong and weak adhesion between the anode and electrolyte, where strong adhesion leads to higher overpotential.

Due to the inherent roughness of the lithium|solid-electrolyte (Li|SE) interface, it is important to understand how the deposition of Li is expected to occur under the presence of stiff homogeneous electrolytes. It has been hypothesized in the recent literature that Li can either nucleate at the porous domains (Kazyak et al., Matter (2022) 3912) or plate at the contact points (Fuchs et al., Adv. Energy Mater. (2023) 2203174). In the present quarter, Li deposition at the Li|SE interface is simulated. If the adhesion strength of Li|SE interface is small, deposition of Li at the contact points is possible, which is depicted in Figure X.1.5(b). For stronger interface, initial deposition within the pores become more favorable, because the overpotential associated with fracturing the Li|SE interface far exceeds the kinetic overpotential of plating Li adjacent to voids with decreased electroactive area (Figure X.1.5 (c)). Variation in voltage response with time during the lithium deposition process is shown in Figure X.1.5 (d), where the overpotential for strongly adhered surfaces are observed to be large.

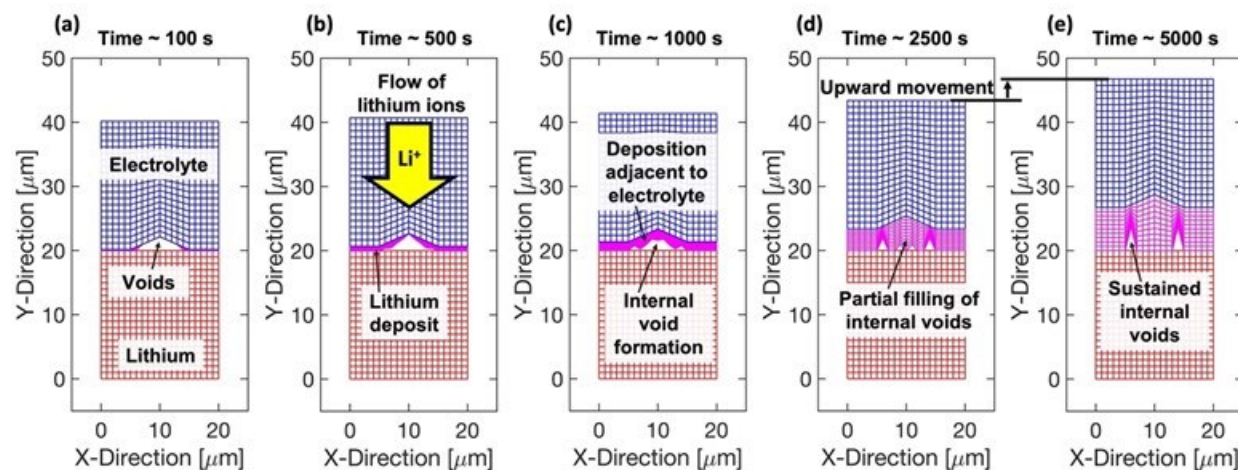


Figure X.1.6 Under the assumption that Li can deposit inside the pores adjacent to solid electrolytes, without direct contact with the metal electrode, it is possible to demonstrate the formation and evolution of internal voids within the lithium electrode from the interfacial pores. (a - e) Evolution of lithium deposits at the

interface after plating for 100s, 500s, 1000s, 2500s, and 5000s, respectively, at a current density of 1 mA/cm<sup>2</sup>.

Formation of internal voids inside Li metal due to Li deposition at the interfacial pores was reported by Kasemchainan et al., (Nat. Mater. (2019) 1105). Similar formation of internal voids can be simulated if very high electronic conductivity of the deposit is assumed, and Li is allowed to plate adjacent to the SE without touching the metal electrode, which is demonstrated in Figure X.1.6(a – e) in a step-by-step fashion. Computational simulation of the Li deposition at Li|SE interface was successfully completed here.

### **Study the effect of external materials (such as carbon nanotube) on the overall lithium stripping phenomena.**

Interfacial instabilities due to the formation of voids are observed during the stripping of lithium at lithium-metal-electrode/solid-electrolyte interfaces. Limiting current associated with the stripping process can be several factors smaller than the critical current density observed during the lithium plating process. Usually, the capacity of Li that can be stripped prior to interfacial detachment is limited to 1 – 1.5 mAh/cm<sup>2</sup> during operation without the application of external pressures, which is about a factor of three (or factor of four) smaller than the 5 mAh/cm<sup>2</sup> required in realistic cells with lithium metal anodes. In order to improve the pressure less stripping capacity of lithium metal anodes, foreign materials, such as, carbon-nanotubes (CNTs) have been mixed with metallic lithium to form composite electrodes (see Fuchs et al., Adv. Energy Mater. 2022, 12, 2201125). Substantial increase in the stripping capacity of lithium metal anodes, by a factor of 5x to 25x, were reported due to the incorporation of CNT based fillers. In the present quarter, a computational framework is developed that is capable of capturing the electrochemical stripping of lithium from the Li/CNT composite electrode. The computational mesh used for the analysis is shown in Figure X.1.7(a), and the corresponding voltage vs time response is depicted in Figure X.1.7(b). The open circuit potential for stripping of lithium from the CNT is assumed to be around 12 mV, which ensures initially only the lithium metal gets depleted. Delithiation of CNT only occurs after the Li metal surface is completely depleted, and the overpotential starts to rise. Transport of Li from the metal electrode to the CNT is also taken into consideration, which is controlled by the reaction rate constant,  $k_{\text{reac}}$ , shown in the flux expression in Figure XIII.1.7(b).

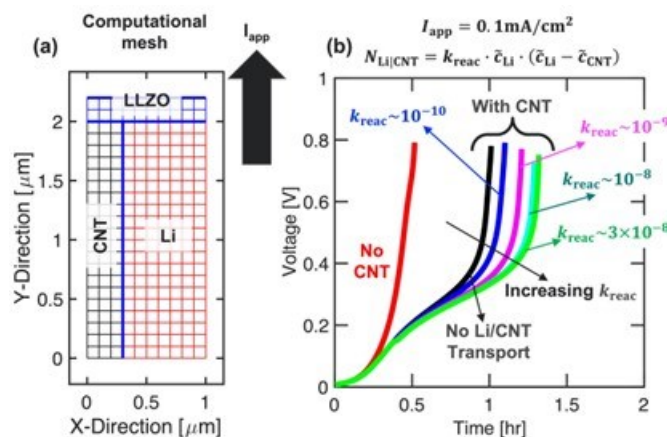


**Figure X.1.7 (a) Computational mesh used for simulating the stripping of lithium from the Li/CNT composite electrode. The LLZO solid electrolyte is located on top and shown in blue, the CNT is shown in black, and the Li metal is denoted in red. (b) Increase in voltage with time during the stripping process. Without any CNT, the voltage response is shown in red. The black curve shows the voltage response with CNT, but Li transport from metal to CNT is not considered. Blue to green lines indicate voltage response under different magnitudes of the reaction rate constant ( $k_{\text{reac}}$ ).**

Concentration of Li within the composite electrode is shown in Figure X.1.8(a), Figure X.1.8 (b) and Figure X.1.8 (c) after 10, 40 and 70 minutes, respectively. Initially, majority of the current acts on Li metal electrode (Figure X.1.8 (a)), which eventually shifts towards the CNT (Figure X.1.8 (b)), and finally the overpotential

shoots up when both the components are fully depleted (Figure X.1.8 (c)). Deciphering the stripping mechanism of Li from Li/CNT composite electrode is completed here.

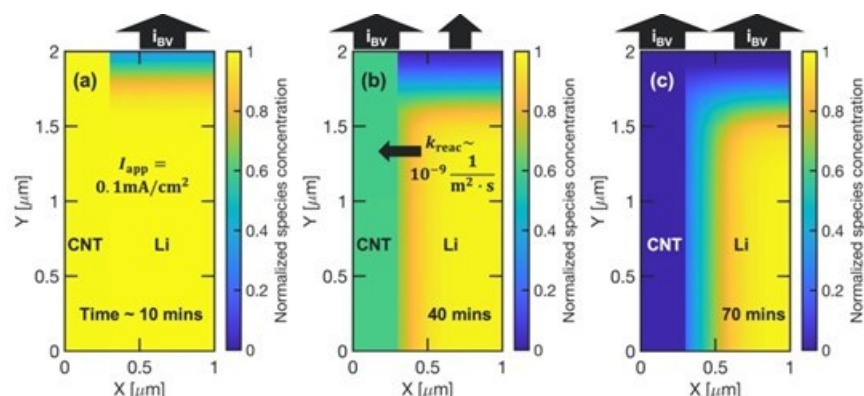


**Figure X.1.8** Lithium concentration profile within the Li/CNT composite at different times. (a) At around 10 mins majority of the stripping happens from the Li metal anode, without any depletion from the CNTs. (b) After 40 mins, the Li metal surface is almost completely depleted, and the CNT experiences delithiation. Li moves from metal to the CNT. (c) Li concentration profile after 70 mins when both the metal and CNT are depleted.

## Conclusions

Detailed mathematical frameworks are developed for deciphering the various physicochemical phenomena occurring at the anode/solid-electrolyte as well as the cathode/solid-electrolyte interfaces. Physical significance behind the experimentally investigated strategies used for stabilizing the interface between lithium metal anode and solid electrolytes are elucidated through computational means. Alloying anodes are a possibility to stabilize the lithium plating, but lithium deposition on top of the interphase layer can significantly worsen the situation that can eventually lead to formation of dendrites. Lithium deposition with the presence of interfacial voids can lead to suppression of pores if the interface between the anode and solid electrolyte is strongly adhered to each other. Also, mixing some form of carbon with lithium metal can help to enhance the stripping capacity due to faster transport of lithium through the carbon based inclusions. Interdiffusion of ions at the cathode/solid-electrolyte interface is also a challenge, which needs to be addressed through the incorporation of interphase layers that can minimize the interdiffusion of ions.

## Key Publications

1. P. Barai, T. Fuchs, E. Trevisanello, H. K. Kim, F. H. Richter, J. Janek, and V. Srinivasan. Reaction Current Heterogeneity at the Interface between a Lithium Electrode and Polymer/Ceramic Composite Electrolytes. *ACS Applied Energy Materials* (2023) 6 4 2160 – 2177.
2. J. A. Maslyn, P. Barai, K. D. McEntush, K. J. Harry, L. Frenck, W. S. Loo, A. S. Ho, D. Y. Parkinson, V. Srinivasan, N. P. Balsara. Plating and Stripping of Lithium Metal Stabilized by a Block Copolymer Electrolyte: Local Current Density Measurement and Modeling. *Journal of the Electrochemical Society* (2023) 170 7 070510

## Acknowledgements

This research is supported by the Vehicle Technologies Office (VTO), Department of Energy (DOE), USA, through the Battery Materials Research (BMR) program. Argonne National Laboratory is operated for DOE Office of Science by UChicago Argonne, LLC under the contract number DE-AC02-06CH11357. The project contributors also thank the US-German collaboration with the group of Prof. Jürgen Janek from the Justus Leibig University, Giessen, Germany.

## X.2 Characterization and Modeling of Li-Metal Batteries: Model-system Synthesis and Advanced Characterization (LBNL)

### Guoying Chen, Principal Investigator

Lawrence Berkeley National Laboratory  
1 Cyclotron Road  
Berkeley, CA 94720  
E-mail: [GChen@lbl.gov](mailto:GChen@lbl.gov)

### Tien Duong, DOE Technology Development Manager

U.S. Department of Energy  
E-mail: [Tien.Duong@ee.doe.gov](mailto:Tien.Duong@ee.doe.gov)

Start Date: October 1, 2022

End Date: September 30, 2023

Project Funding (FY23): \$400,000

DOE share: \$400,000

Non-DOE share: \$0

### Project Introduction

In order to develop mitigating approaches and rationally design advanced functional materials, a deep understanding of the relationships among structure, properties and function is essential. For Li-metal batteries employing a solid-state electrolyte (SE), significant challenges, both at the material level and system level, prevent them from practical applications. It is well recognized that fundamental knowledge on the role of SE microstructure in solid-state ion conduction and Li dendrite formation/propagation, performance-limiting processes and phase transition mechanisms in SEs, and the dynamic evolution of the SE/electrode interfaces are key to the development of high-energy Li-metal batteries with improved commercial viability. This project addresses these challenges in a systematic way, by synthesizing well-controlled SE model systems and SE/electrode model interfaces, obtaining new insights into the model materials and interfaces utilizing state-of-the-art analytical techniques, and subsequently establishing the correlations between specific property and function. The goal is to use these findings to properly design and synthesize advanced SE materials and SE/electrode interfaces with improved performance.

### Objectives

This project will use a rational, non-empirical approach to design and develop SE materials and interfaces for the next-generation Li-metal batteries. Combining a suite of advanced diagnostic techniques with well-controlled model-system samples, the project will perform systematic studies to achieve the following goals: 1) obtain understanding on the role of SE grain and grain boundaries on Li ion conduction and dendrite formation, 2) obtain fundamental knowledge on rate- and stability-limiting properties and processes in SEs when used in Li-metal batteries, 3) investigate the reactivities between SE and electrodes and gain insights on the dynamic evolution of the interfaces, and 4) design and synthesize improved SE materials and interfaces for safer and more stable high-energy Li-metal batteries.

### Approach

The project will combine model-system synthesis and advanced diagnostic studies to investigate ion conduction and interfacial chemistry of SE in Li-metal batteries. Single crystalline, polycrystalline and amorphous model samples with various grain and grain boundary properties will be synthesized. Model interfaces between the SE and electrodes with controlled properties will also be developed. Both bulk-level and single-grain level characterization will be performed. Global properties and performance of the samples will be established from the bulk sample analysis, while the single-grain-based studies will utilize time- and spatially-resolved analytical techniques to probe the intrinsic redox transformation processes and failure mechanisms under Li-metal battery operating conditions.

## Results

While the  $\text{Li}_3\text{MCl}_6$ -family ( $\text{M} = \text{Sc}, \text{In}, \text{Y}, \text{Er}$  and  $\text{Yb}$  etc.) halide solid electrolytes have shown good stability towards 4 V-class cathode materials, their thermodynamic instability towards Li-metal anode remains a significant challenge. Theory studies indicated that upon direct contact with Li metal,  $\text{Li}_3\text{YCl}_6$  (LYC) decomposes to  $\text{LiCl}$ ,  $\text{YCl}_3$  and metallic Y, leading to dendrite growth, internal shorting and safety issues. To experimentally evaluate the reactivities at the anode-electrolyte interface, we carried out comparative studies of LYC SE interfacing a Li-metal anode vs. a Li-In alloy (3:7 molar ratio) anode.  $\text{Li} | \text{LYC} | \text{Li}$  and  $\text{Li-In} | \text{LYC} | \text{Li-In}$  symmetric cells were assembled and galvanostatically charged and discharged at a current density of  $0.2 \text{ mA/cm}^2$ . As shown in Figure X.2.1a, the Li cell experienced a gradual increase in potential during the first 12 cycles, reaching  $\sim 150 \text{ mV}$  after 25 hr. Following that, the potential gradually decreased and reached  $\sim 2 \text{ mV}$  after 60 hr, which remained constant afterwards. The electrochemical results suggest rapid reactions at the LYC/Li interface prior to cell internal shorting. Further evidence is shown by the scanning electron microscopy (SEM) image collected on the anode-electrolyte interphase (AEI) region of the recovered LYC SE pellet where a large amount of black deposits is clearly present (Figure X.2.1b). While the X-ray diffraction (XRD) pattern of the same sample (Figure X.2.1c) is dominated by peaks from the LYC phase,  $\text{LiCl}$  was found to be the main decomposition product in the AEI. Due to the poor detection limit of XRD, it is unclear whether metallic Y was also present.

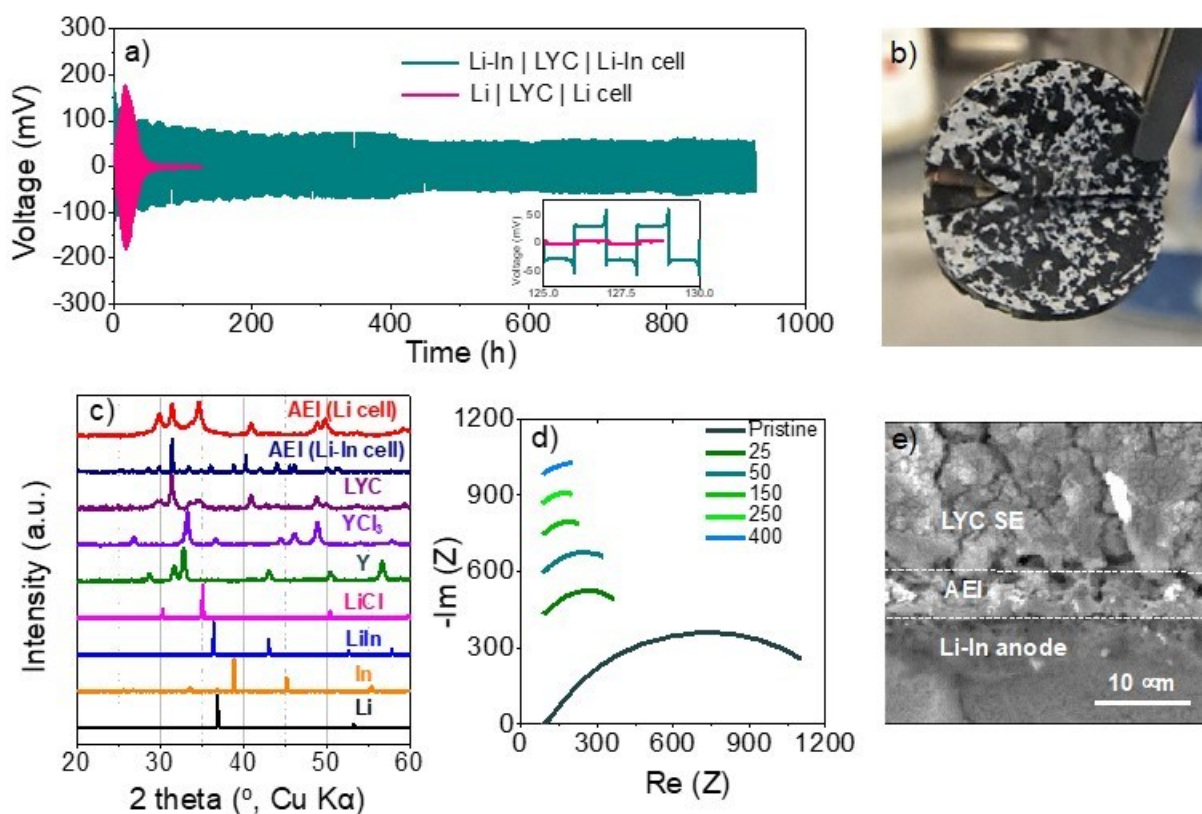
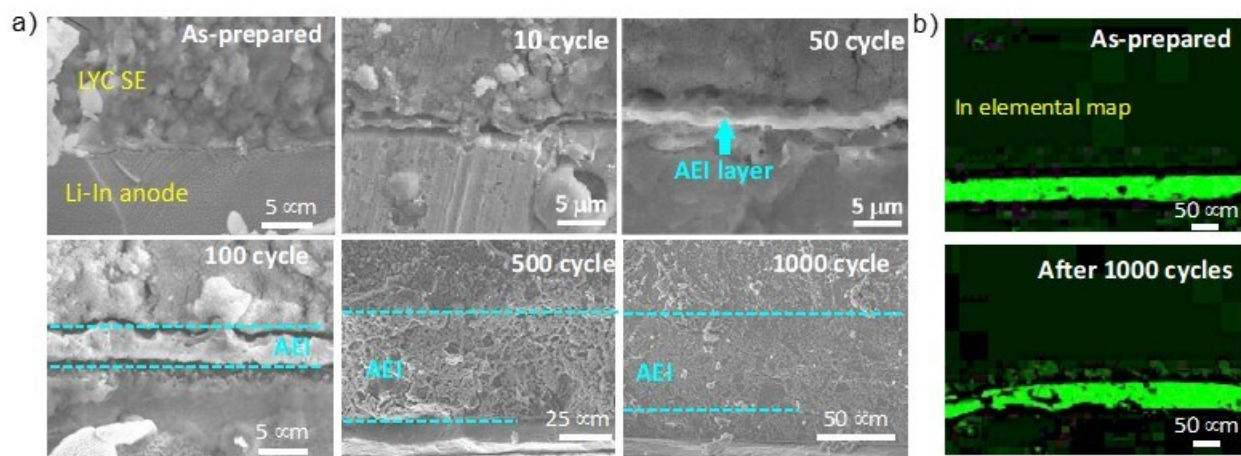


Figure X.2.1 (a) Voltage profiles of  $\text{Li} | \text{LYC} | \text{Li}$  and  $\text{Li-In} | \text{LYC} | \text{Li-In}$  symmetrical cells when cycled at a constant current density of  $0.2 \text{ mA/cm}^2$ . (b) SEM image collected from the recovered AEI region of the cycled  $\text{Li} | \text{LYC} | \text{Li}$  cell. (c) XRD patterns collected on various samples as indicated. (d) EIS data collected at the OCV of the  $\text{Li-In} | \text{LYC} | \text{Li-In}$  cell after various cycles, in the frequency range between 1 MHz – 100 mHz. (e) Cross-sectional SEM image collected from the recovered AEI region of the cycled  $\text{Li-In} | \text{LYC} | \text{Li-In}$  cell.

In comparison, the voltage response of the Li-In symmetric cell is also shown in Figure X.2.1a. At  $0.2 \text{ mA/cm}^2$ , the cell quickly reached a constant voltage of  $\sim 35 \text{ mV}$  during both charge and discharge. The

potential increased slightly at the end of each step, reaching  $\sim 50$  mV. However, the process is highly reversible and stable cycling was maintained throughout the test, suggesting the presence of a passivating AEI between LYC and the Li-In alloy anode. We further performed electrochemical impedance spectroscopy (EIS) measurements to monitor the evolution of the AEI during cycling. The data was collected at the open circuit voltage (OCV) after various cycles, using a constant voltage of 10 mV. As shown in the Nyquist plot (Figure X.2.1d), a depressed semi-circle was obtained from the pristine Li-In | LYC | Li-In cell. The size of the semi-circle decreased quickly upon initial cycling which stabilized and remained constant during the rest of cell testing, confirming the formation of a stable AEI following the initial reactions between LYC and Li-In in early cycles. In contrast, the impedance responses from the Li symmetric cell was largely unstable, especially after 50 hr, EIS measurement was not possible due to the internal shorting in the cell. Figure X.2.1e shows the cross-sectional SEM image collected on the recovered interface region of LYC and the Li-In anode. After  $\sim 460$  cycles, the presence of an AEI layer with an average thickness of  $\sim 8$ - $10$   $\mu\text{m}$  is clearly shown. A comparison of the XRD patterns collected at the AEI regions of LYC/Li and LYC/Li-In (Figure 1c) shows significant differences in reaction products.

To further analyze the chemical and structural nature of the AEI formed between LYC and Li-In alloy anode, we performed detailed investigation on the anode-electrolyte interface evolution upon cycling of the halide-based all solid-state battery (ASSB) full cells. Cathode composites were prepared by combining  $\text{LiNi}_{0.8}\text{Mn}_{0.1}\text{Co}_{0.1}\text{O}_2$  (NMC811),  $\text{Li}_3\text{YCl}_6$  (LYC) and carbon black, which were then assembled into ASSBs with an LYC solid electrolyte (SE) and a Li-In anode and cycled between 3.0 and 4.3 V (V vs.  $\text{Li}^+/\text{Li}$ ). Figure X.2.2a shows the SEM cross-sectional images collected at the LYC/Li-In anode interface before and after cycling to various cycle numbers. The pristine interface shows a clean boundary between LYC and Li-In anode. After 50 cycles, a distinct AEI layer with a thickness of  $\sim 3$ - $5$   $\mu\text{m}$  is clearly seen between the separator and the anode. Further cycling leads to AEI growth, with the thickness increased to  $\sim 8$ - $10$   $\mu\text{m}$  after 100 cycles and  $\sim 60$   $\mu\text{m}$  after 500 cycles. No changes in the AEI layer thickness were observed afterwards. Figure X.2.2b compares the In elemental distribution at the interface, obtained using micro X-ray fluorescence ( $\mu\text{XRF}$ ) mapping. While In was confined to the anode only in the as-prepared LYC/Li-In anode interface, its presence in the AEI layer was detected after 1000 cycles. The results suggest In diffusion and incorporation into the AEI chemistry upon cycling.



**Figure X.2.2 (a) SEM images collected at the LYC/Li-In anode interface before and after cycling to various cycle numbers and b) XRF mapping of In distribution at the LYC/Li-In anode interface before and after 1000 cycles.**

The oxidation states of Y and In were examined by synchrotron hard X-ray absorption (XAS) spectroscopy. Figure X.2.3a and b show the X-ray absorption near-edge structure (XANES) profiles of Y and In, respectively, collected on various reference compounds as well as the cycled Li-In anode recovered after 1000 cycles at 0.5 C. In comparison to the Y *K*-edge XANES spectra collected on Y metal and LYC, the energy

edge of Y in the AEI layer resembles that in LYC (Figure X.2.3a), suggesting an oxidation state of 3+. Compared to the spectra collected on the In metal, the In *K*-edge XANES profile from the cycled anode show an energy edge shift of  $\sim 1$  eV towards higher energy, similar to that of the InCl reference. The results indicate the presence of oxidized In in the cycled anode. As hard XAS examines bulk properties of the sample which include contributions from both AEI component as well as the Li-In alloy anode in this case, we further probed the chemical nature of the AEI layer using spatially-resolved micro X-ray absorption spectroscopy ( $\mu$ XAS). The technique was employed to collect Cl *K*-edge XAS data at a spot size of  $\sim 2 \times 2 \mu\text{m}^2$ , at the various locations in the cross-section of the cycled ASSB cell. Figure X.2.3c shows the  $\mu$ XRF elemental maps of Cl, In, and Y (red, green and blue, respectively) at the cross-section where a distinct boundary between LYC SE and the Li-In anode is shown. The specific locations for  $\mu$ XAS analysis are indicated in the expanded view in Figure X.2.3c (right), which include the regions containing the AEI layer (p1 - p3), LYC SE (p4) and the cathode (p5 and p6). Unlike the weak and broad Cl pre-edge peak at 2823.3 eV observed on LYC (p4, guideline a in Figure X.2.3d and e), the spectra of p1, p2 and p3, especially that of p2, show a prominent pre-edge peak at 2824.5 eV (guideline b in Figure X.2.3d and e), indicating changes in Cl chemical environment in the AEI layer. Further comparison with the spectra collected on various Cl containing reference compounds suggests the presence of Cl in InCl<sub>3</sub>- and/or InCl-type of surroundings (Figure X.2.3e).

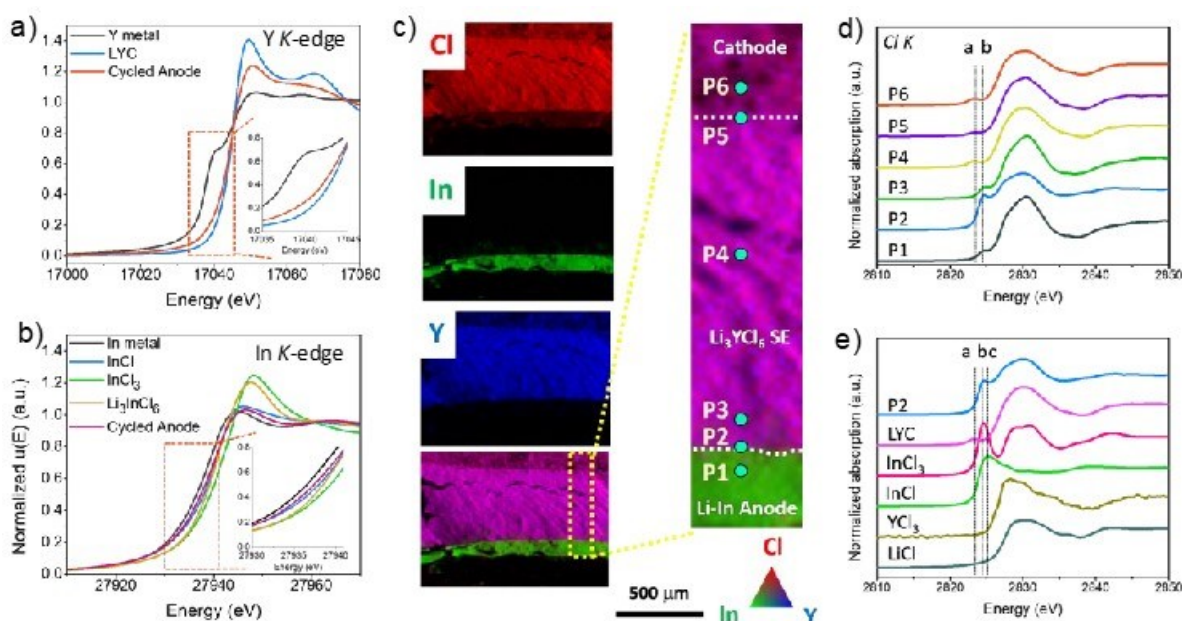


**Figure X.2.3** *K*-edge XANES spectra of Y (a) and In (b) collected on various reference compounds and recovered Li-In anode after 1000 cycles. (c) XRF elemental maps of Cl, In and Y collected from the cross-section of the NMC811-LYC|LYC|Li-In ASSB cell after 1000 cycles. The expanded view of the cross section is shown on the right. (d) Cl *K*-edge  $\mu$ XAS spectra collected from the p1-p6 locations as indicated in the expanded view in c), and (e) comparison of Cl *K*-edge  $\mu$ XAS spectra of p2 and reference compounds.

Based on these understanding, we then developed alternative approaches to stabilize the anode interface of halide SEs. Compared to chloride compounds, the iodide-based counterparts are often more stable at low voltages. We therefore introduced I substitution into the LYC-family SEs and synthesized a series of Li<sub>3</sub>YCl<sub>6-x</sub>I<sub>x</sub> (LYCI) compounds using the high-energy ball milling method. Figure 4a shows the XRD patterns collected on the samples with  $x = 0, 0.5, 1.0$  and  $1.5$ , denoted as LYC, LYCI-0.5, LYCI-1.0 and LYCI-1.5, respectively. Compared to the baseline LYC, the main peaks at  $\sim 32, 41$  and  $49$  degrees ( $2\theta$ ) gradually shift towards lower value with the increasing  $x$ . This is consistent with the expansion in the lattice parameters upon iodide incorporation into the anion lattice. Iodide substitution also leads to an overall broadening and intensity reduction of the XRD peaks, suggesting a reduction in crystallinity in LYCI. The effect becomes more



pronounced at a higher iodide substitution level. For LYCI-1.5, the XRD pattern indicates that the material is composed of nearly amorphous phase(s).

The ionic conductivity of the LYCI samples were evaluated by EIS measurements and the results are displayed in Figure X.2.4b. The measured room temperature ionic conductivity of the samples are 0.21, 1.64, 2.02, and 0.45  $\text{mS}\cdot\text{cm}^{-1}$  for LYC, LYCI-0.5, LYCI-1.0 and LYCI-1.5, respectively. The study revealed a significant improvement in conductivity upon I substitution, reaching the highest value and an order of magnitude increase from the baseline value in LYC to that in LYCI-1.0. Further increasing the I content to  $x = 1.5$  leads to a decrease in conductivity, likely a result of phase changes in the sample as indicated by the XRD analysis in Figure X.2.4a.

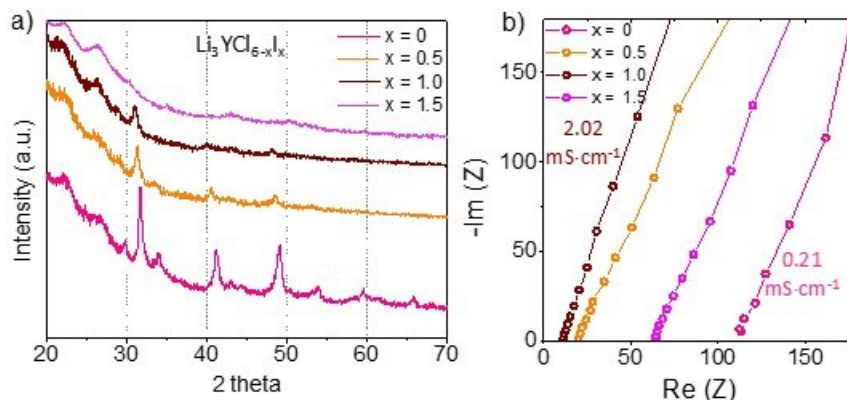


**Figure X.2.4 (a) XRD patterns and (b) Nyquist plots of the  $\text{Li}_3\text{YCl}_{6-x}\text{I}_x$  ( $x = 0, 0.5, 1.0$  and  $1.5$ ) solid electrolytes synthesized using the high-energy ball-milling method.**

ASSB full cells consisting of a composite cathode of single-crystal  $\text{LiNi}_{0.8}\text{Mn}_{0.1}\text{Co}_{0.1}\text{O}_2$  (SC-NMC811), LYCI and carbon (weight ratio = 57:40.5:2.5), an LYCI SE separator and a Li-In alloy anode were assembled and cycled between 3.0 and 4.3 V (vs.  $\text{Li}^+/\text{Li}$ ) at a rate of 0.2 C ( $1\text{C} = 200 \text{ mAh/g}$ ). The first two cycle voltage profiles of the cells with an LYC SE or an LYCI-1.0 SE are compared in Figure X.2.5. While the former cell delivered a discharge capacity of  $\sim 141 \text{ mA/g}$  and a coulombic efficiency of 77 % in the first cycle (Figure X.2.5a), the values for the LYCI-1.0 cell are  $\sim 64 \text{ mA/g}$  and 36 %, respectively (Figure X.2.5b). Similar 1<sup>st</sup> charge capacities were obtained from both cells, although the internal resistance in the LYCI-1.0 cell is significantly higher. The slopy voltage profile below 3.7 V in the latter (Figure X.2.5c) also suggests considerable side reactions occurring in the voltage window, likely between NMC811 and the LYCI-1.0 SE. It is conceivable that I substitution of Cl decreases the overall high-voltage stability of LYCI SE at the cathode side. Improvement in cell performance is likely by optimizing the substitution level of I as well as the ASSB cell configuration.

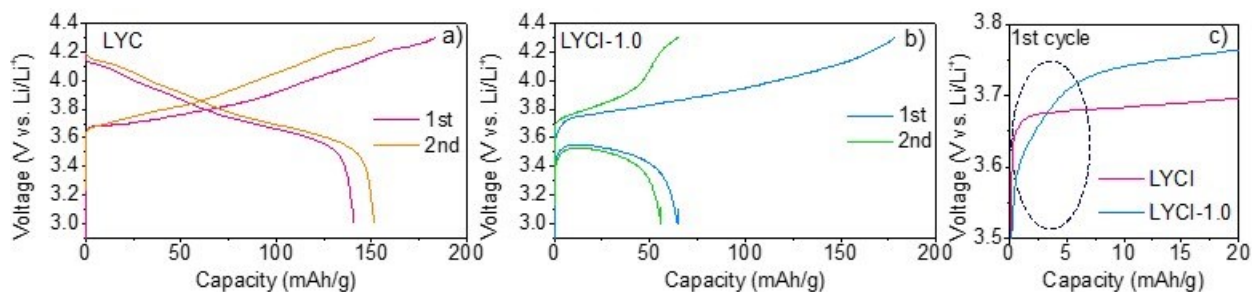


**Figure X.2.5 Charge/discharge voltage profiles of the ASSB cells during the 1<sup>st</sup> and 2<sup>nd</sup> cycles: a) LYC as the SE and b) LYCI-1.0 as the SE. c) Comparison of the 1<sup>st</sup> charge voltage profile of the cells.**

In our second approach, we evaluated the use of Li-M alloys in stabilizing the interface between the halide SE and the anode. In the literature, halide-based ASSB cells are often cycled with an Li-In alloy anode along with a sulfide buffer layer such as  $\text{Li}_6\text{PS}_5\text{Cl}$ . Our studies demonstrated that stable cycling of NMC811 | LYC | Li-In ASSB cells can be achieved without the presence of a sulfide buffer layer. Compared to the Li-metal anode, the higher redox potentials of the alloys reduce the energy density of the ASSB. However, they may also reduce the reactivities at the anode-SE interface and lead to alternative interfacial reaction pathways for a more stable interphase layer. Extracting and inserting Li with a “host” can also minimize dendrite and void formations at the anode-SE interface. As In is a very expensive metal impractical for commercial application, we evaluated the use of Li-Ga alloys as alternative anodes. Ga-rich Li-Ga alloys can be expected to have soft mechanical properties due to the low melting point of Ga ( $\sim 30^\circ\text{C}$ ). Our initial study focuses on the solid solution region between  $\text{Li}_3\text{Ga}_{14}$  and  $\text{Li}_5\text{Ga}_9$  (Figure X.2.6a) which has a flat voltage of  $\sim 0.6\text{ V vs. Li}^+/\text{Li}$ .  $\text{Li}_3\text{Ga}_7$  alloy was prepared by heating the stoichiometric mixture of Li and Ga metals at  $550^\circ\text{C}$  for 8 hours under Ar atmosphere and then evaluated in a  $\text{Li}_3\text{Ga}_7$  | LYC |  $\text{Li}_3\text{Ga}_7$  symmetric cell. As shown in Figure X.2.6b, at a current density of  $0.2\text{ mA/cm}^2$ , the cell voltage gradually increased upon the initial cycling and varied in the range of 180-650 mV during the first 500 cycles. After that, stable voltage was maintained at  $\sim 250\text{ mV}$ , suggesting the formation of stable interphase between LYC and the Li-Ga anode. We further evaluated the ASSB performance in a full cell configuration (Figure X.2.6c) consisting of a composite cathode of single-crystal  $\text{LiNi}_{0.8}\text{Mn}_{0.1}\text{Co}_{0.1}\text{O}_2$  (SC-NMC811), LYC and carbon (weight ratio = 57:40.5:2.5), an LYC SE separator, and a composite anode of  $\text{Li}_3\text{Ga}_7$  alloy, LYC and carbon (weight ratio = 75:24:1). The cell delivered excellent performance at low rate, reaching a discharge capacity of  $\sim 210\text{ mAh/g}$  at 0.2C which is similar to what was reported on the equivalent liquid cell with an NMC811 cathode (Figure X.2.6d). There is a fast decay in capacity with increasing rate, which was reduced to  $50\text{ mAh/g}$  at 1C. However, the initial capacity obtained at 0.2 C was fully recoverable after lowering the cycling rate. These results are consistent with the previous reports that attributed the poor rate capability to the resistive nature of ASSB cells without the presence of any liquid. We further evaluated the cycling stability of the full cell and the results obtained at 0.5 C are shown in Figure X.2.6e and f. During the first 40 cycles, the discharge capacity decreased from  $\sim 150\text{ mAh/g}$  to  $130\text{ mAh/g}$ , corresponding to a capacity retention of  $\sim 87\%$ .

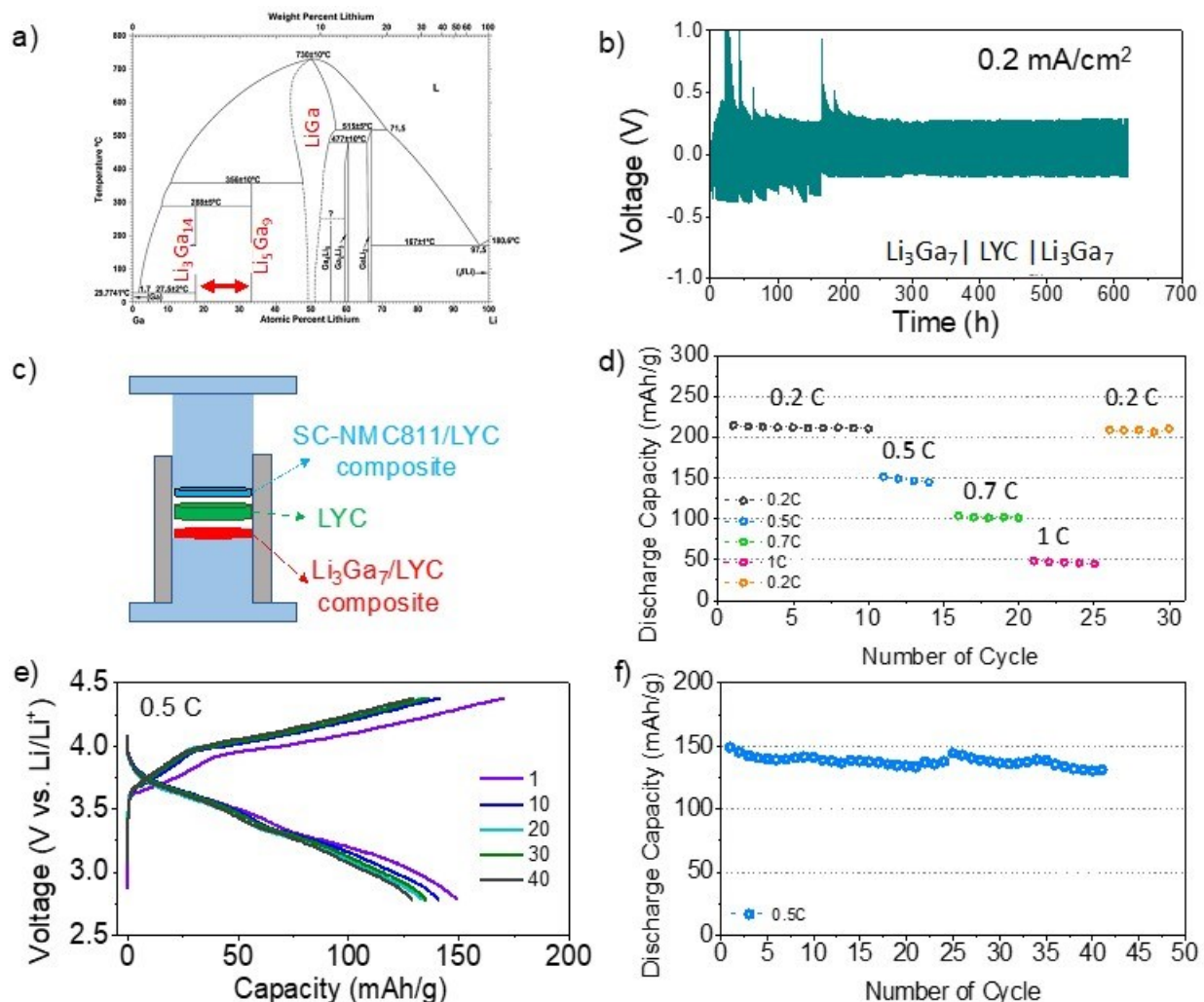
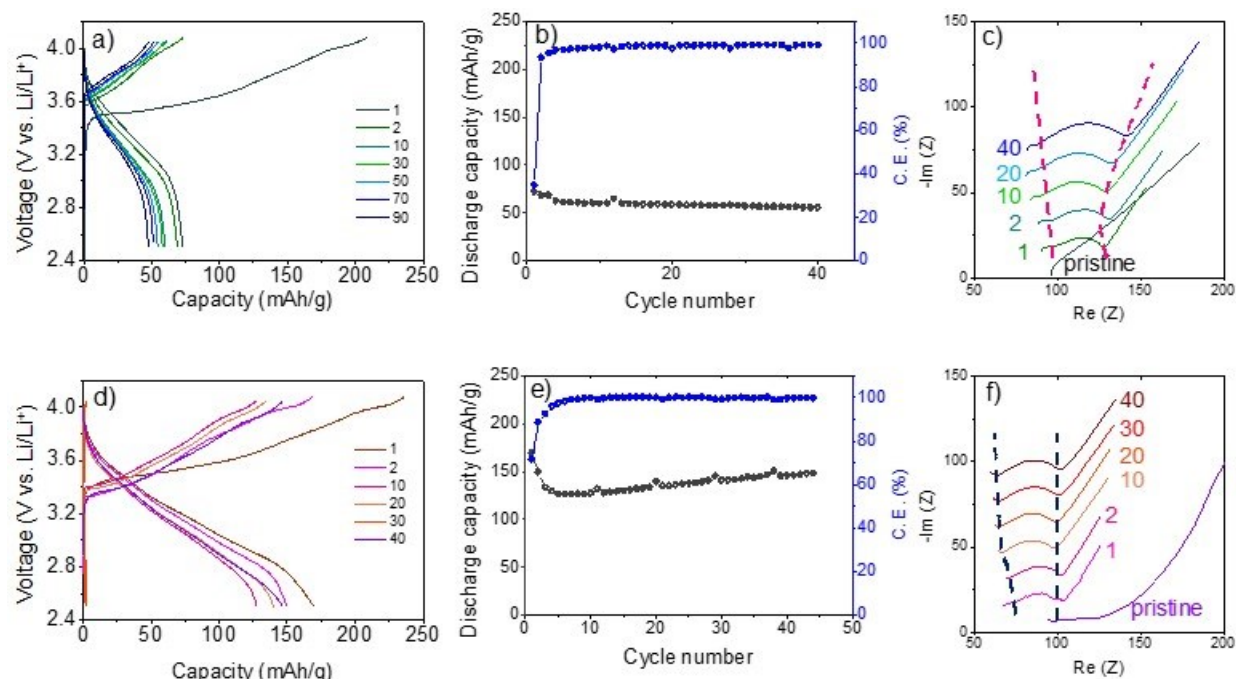


Figure X.2.6 (a) The phase diagram of Li-Ga, (b) galvanostatic cycling data obtained on a  $\text{Li}_3\text{Ga}_7 \mid \text{LYC} \mid \text{Li}_3\text{Ga}_7$  symmetric cell, (c) schematic of the ASSB cell with a NMC811 composite cathode, a LYC SE separator and a  $\text{Li}_3\text{Ga}_7$  composite anode, and (d, e, f) rate capability, voltage profiles and capacity retention at  $0.5 \text{ C}$  of the ASSB cell shown in (c).

ASSB cells consisting of a composite cathode of single-crystal  $\text{LiNi}_{0.8}\text{Mn}_{0.1}\text{Co}_{0.1}\text{O}_2$  (SC-NMC811), LYC and carbon, an LYC SE separator, and a composite anode containing Si, LYC and carbon were also constructed and evaluated. Figure 7 compares the electrochemical performance obtained on cells with a Si anode material (Figure X.2.7a-c) or a pre-synthesized Li-Si alloy anode material (Figure X.2.7d-f). The cells were cycled between 2.5 and 4.1 V (vs.  $\text{Li}^+/\text{Li}$ ) at a rate of  $0.2 \text{ C}$ . For the Si cell, while the 1<sup>st</sup> charge capacity reached over 220 mAh/g, only  $\sim 65 \text{ mAh/g}$  discharge capacity was obtained (Figure X.2.7a). The value further decreased to  $\sim 50 \text{ mAh/g}$  after 40 cycles, corresponding to a capacity retention of  $\sim 76\%$  (Figure X.2.7b). On the Nyquist plot obtained from the EIS measurements carried out at the discharged state (Figure X.2.7c), the typical semi-circle along with the Warburg element appear in the examined frequency region (1 MHz - 1 mHz) after the 1<sup>st</sup> cycle. As the semi-circles at the low-frequency region ( $< 10 \text{ Hz}$ ) is often associated with the interfacial resistance between the SE layer and the anode, the gradual increase in its size during the first 40 cycles suggests continuous side reactions at the anode. In contrast, the Li-Si alloy cell shows much improved cycling performance. While a similar 1<sup>st</sup> charge capacity of  $\sim 230 \text{ mAh/g}$  was obtained, the discharge capacity reached  $\sim 162 \text{ mAh/g}$  after the 1<sup>st</sup> cycle. The capacity retention was also improved, reaching  $\sim 93\%$  after 45 cycles with  $\sim 150 \text{ mAh/g}$  of discharge capacity remaining. The results from the EIS measurements (Figure X.2.7f) further indicate improved interfacial stability between the SE and the anode. On the Nyquist plot obtained on the

initial 40 cycles, the size of the semi-circle remained nearly unchanged after the 1<sup>st</sup> cycle, suggesting the establishment of a stable anode-electrolyte interphase upon cycling. The chemical and structural nature of the interphase will be investigated to better understand its formation mechanism and its role in ASSB performance.



**Figure X.2.7** (a, d) Voltage profiles of the SC-NMC811 ASSB cells cycled at 0.2 C. (b, e) Discharge capacity retention and coulomb efficiency of the ASSB cycled at 0.2 C. (c, f) Nyquist plots collected at the discharged state after various cycles as indicated. (a, b, c) are obtained from the cell with a Si anode material whereas (d, e, f) are obtained from the cell with a pre-synthesized Li-Si alloy anode.

## Conclusions

Halide solid electrolytes have shown excellent high-voltage stabilities at the cathode side, however, their reactivities at the Li-metal anode present significant challenges in ASSB development. In FY23, we show that in contrast to the decomposition reactions observed at the LYC and Li metal anode interface, a stable AEI layer develops at the interface of LYC and Li-In alloy anode. The thickness of the AEI layer grows upon initial cycling but eventually stabilizes, indicating passivation by equilibrium. Detailed elemental and chemical analyses reveal In migration into the AEI layer and subsequent formation of a Li-Y-In-Cl phase or phases. Alternative approaches to stabilize the interface of halide SEs at the anode were then developed and evaluated. Iodine substitution in LYC results in up to an order-of-magnitude increase in the ionic conductivity of LYCI samples, however, the ASSB full cell cycling stability is largely limited by the diminished high-voltage stability of LYCI SE at the cathode side. We further evaluated Li-M alloy compounds as anodes and demonstrated their great promise in ASSB cell development. Both Li-Ga and Li-Si alloy anode based cells delivered excellent cycling performance, including large discharge capacity similar to what was obtained on the equivalent liquid cells, and stable cycling with excellent capacity retention. Our study highlights the importance of both materials and engineering design in stabilizing the interface between halide SE and Li-metal based anode in ASSB cells.

## Key Publications

1. S. Y. Kim, H. Cha, R. Kostecki and G. Chen, "Composite Cathode Design for High-Energy All-Solid-State Lithium Batteries with Long Cycle Life," *ACS Energy Lett.* 8, 521 (2023). DOI: 10.1021/acsenerylett.2c02414

2. M. Jung, S. Y. Kim, S.-B. Lee, M.-J. Kim, I.-J. Yang, W. Cho, J. Yu, G. Chen, K. Kim and K.-H. Park, “Anion Engineering for Halide Solid Electrolytes,” under review (2023).
3. L. Li, B. Ouyang, Z. Lun, H. Huo, D. Chen, Y. Yue, C. Ophus, W. Tong, G. Chen, G. Ceder and C. Wang, “Atomic-Scale Probing of Short-Range Order and Its Impact on Electrochemical Properties in Cation-Disordered Oxide Cathodes,” Nature Communications, accepted (2023).
4. S. Yang, S. Y. Kim and G. Chen, “Halide Superionic Conductors for All-Solid-State Batteries: Effects of Synthesis and Composition on Lithium-Ion Conductivity,” under review (2023).

### **Acknowledgements**

This work was conducted by Se Young Kim and Shuhao Yang at LBNL. We acknowledge the support from the Vehicle Technologies Office of U. S. Department of Energy.

## X.3 Design of High-Energy, High-Voltage Lithium Batteries through First-Principles Modeling (LBNL)

### Kristin A. Persson, Principal Investigator

Lawrence Berkeley National Laboratory  
1 Cyclotron Rd  
Berkeley, CA 94720  
E-mail: [kapersson@lbl.gov](mailto:kapersson@lbl.gov)

### Tien Duong, DOE Technology Development Manager

U.S. Department of Energy  
E-mail: [Tien.Duong@ee.doe.gov](mailto:Tien.Duong@ee.doe.gov)

Start Date: October 1, 2022	End Date: September 30, 2023	
Project Funding (FY23): \$500,000	DOE share: \$500,000	Non-DOE share: \$0

### Project Introduction

This project supports Vehicle Technologies Office programmatic goals by developing next-generation, high-energy cathode materials and enabling stable cathode operation at high voltages through target particle morphology design, functional coatings, and rational design of electrolytes. The end-of-project goals include the following: (1) understanding of the factors that govern charge transport in nonaqueous, superconcentrated liquid electrolytes (LEs), (2) critical surface and coating design and optimization strategies that will improve cycling of Li-ion battery cathodes by reducing cathode degradation from oxygen loss, and (3) simulation and machine learning (ML) of the early formation of the solid-electrolyte interphase (SEI) on Li-metal electrodes.

### Objectives

The end-of-project goals include the following:

- Understanding of the factors that govern charge transport in nonaqueous, superconcentrated LEs.
- Critical surface and coating design and optimization strategies that will improve cycling of Li-ion battery cathodes by reducing cathode degradation from oxygen loss.
- Simulation and ML of the early formation of the SEI on Li-metal electrodes.

### Approach

- First-principles calculations, both static and dynamic approaches, are used to model SSE material thermodynamics and kinetics. LEs are modeled through coupled classical MD and first principles methods to accurately capture solvation structure as well as reactivity of the liquid system.
- Examine different transport models to study the electron and ion mobility through the amorphous coating layer.
- The reaction network is built on large-scale first-principles data, using graph theory and machine learning (ML) models.

### Results

#### *Design of Cathode Coatings in Li batteries*

We report our recent progress in high-throughput computational screening of amorphous cathode coatings for lithium-ion battery applications. Besides providing facile  $\text{Li}^+$  diffusion pathways, an optimal cathode coating should block  $\text{O}^{2-}$  diffusion such that the oxygen-loss-induced cathode surface reconstruction can be mitigated. Therefore, to evaluate  $\text{Li}^+$  and  $\text{O}^{2-}$  transport in the screened amorphous coatings, we calculate ionic diffusivity, flux, and transport time through the coating materials using *ab initio* molecular dynamics (AIMD) simulations and Onsager transport models.

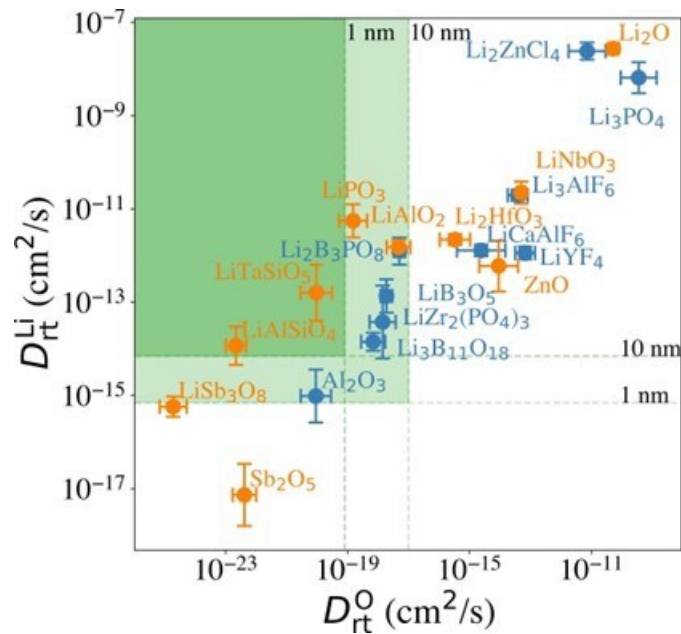


**Figure X.3.1** The distribution of  $D_{rt}^{Li}$  and  $D_{rt}^O$  of 20 selected compounds.

Figure X.3.1 illustrates the distribution of  $D_{rt}^{Li}$  and  $D_{rt}^O$  of 20 selected compounds. Our calculations show that in general,  $Li^+$  and  $O^{2-}$  diffusion is correlated, i.e., a compound with a higher  $D_{rt}^{Li}$  also has a higher  $D_{rt}^O$ . In addition, we find that for compounds consisting of the same species, a compound with a higher  $Li^+$  concentration also has a higher  $Li^+$  and  $O^{2-}$  diffusion. For example, comparing  $Li_3B_{11}O_{18}$  and  $LiB_3O_5$ , we find that  $LiB_3O_5$ , which has a higher  $Li^+$  concentration, exhibits a higher  $D_{rt}^{Li}$  and  $D_{rt}^O$ . Similar behavior is found in  $LiPO_3$  and  $Li_3PO_4$ , relating to their  $D_{rt}^{Li}$  and  $D_{rt}^O$ .

From the calculated  $D_{rt}^{Li}$  and  $D_{rt}^O$ , we evaluate the coating suitability of the selected compounds in terms of their ability to facilitate  $Li^+$  transport while blocking  $O^{2-}$  transport. We estimate the overpotential,  $\Delta V$ , at the cathode surface. We set the criterion for overpotential imposed by the coating as  $\Delta V \leq 0.1$  V, above which the  $Li^+$  transport across the coating will be significantly compromised. Figure X.3.2a shows that for 1 nm surface coatings, all the selected compounds, except  $Sb_2O_5$  (23 V) and  $LiSb_3O_8$  (0.18 V), result in overpotentials below 0.1 V, which indicates a sufficient  $Li^+$  transport in these compounds. The overpotential of the  $Al_2O_3$  coating is found to be 0.07 V. When the coating thickness is increased to 10 nm, the overpotentials of  $Sb_2O_5$ ,  $LiSb_3O_8$  and  $Al_2O_3$  coatings increase to 230 V, 1.8 V and 0.7 V, respectively, while the overpotentials of other compounds are still below 0.1 V. Next, we estimate the minimum  $Li^+$  diffusivity  $D_{rt}^{Li}$  to meet the overpotential criterion of  $\Delta V \leq 0.1$  V, which are represented by the horizontal dashed lines in Figure X.3.1.

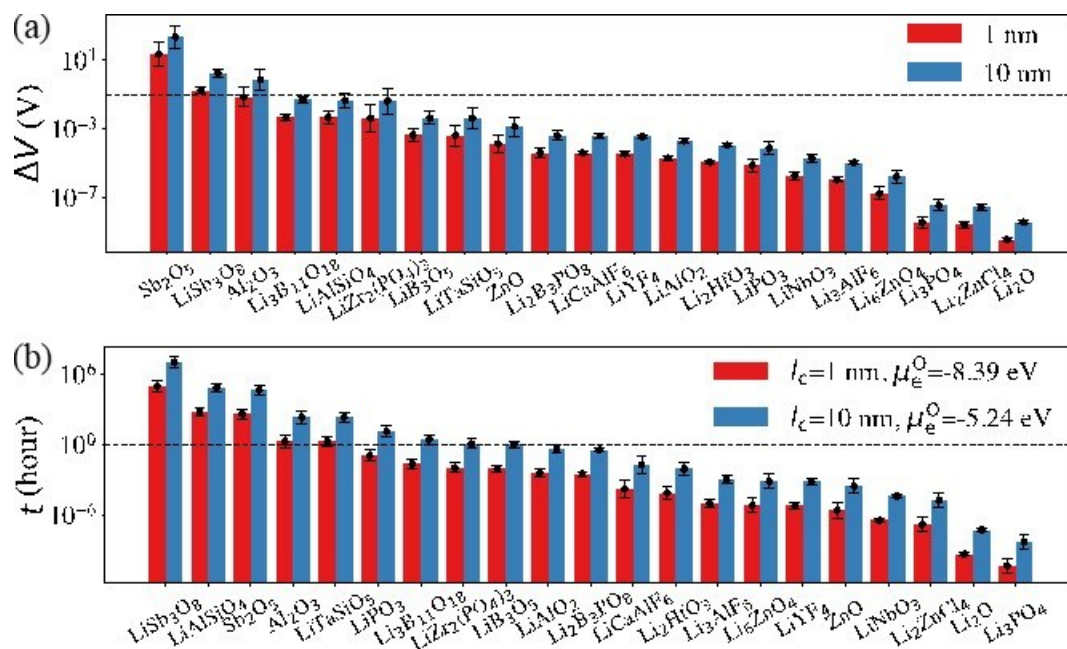


Figure X.3.2 (a) Calculated overpotentials ( $\Delta V$ ) for a current density of  $0.044 \text{ mA cm}^{-2}$  across room temperature cathode coatings of  $l_c = 1$  and  $10 \text{ nm}$ . The dashed line represents  $\Delta V = 0.1 \text{ V}$ . (b) Calculated  $\text{O}^{2-}$  diffusion time  $t$  in the selected compounds assuming an  $r = 1 \text{ }\mu\text{m}$  primary particle and an  $l_s = 2 \text{ nm}$  surface rocksalt phase. The dashed line represents  $t = 1 \text{ h}$ . The green regions represent favorable  $\Delta V$  and  $t$ .

To evaluate the effectiveness of these coatings in blocking  $\text{O}^{2-}$  transport, we estimate the  $\text{O}^{2-}$  flux  $J^0$  and the time  $t$  required for  $\text{O}^{2-}$  to diffuse through the coating. Figure X.3.2b shows the calculated  $\text{O}^{2-}$  diffusion time  $t$  in the selected compounds. We select the compounds with an estimated  $\text{O}^{2-}$  diffusion time longer than 1 h such that not all  $\text{O}^{2-}$  ions that are evolved from surface  $\text{NiO}_2$  layer have diffused through the coating under 1C rate. We find that  $\text{LiSb}_3\text{O}_8$ ,  $\text{LiAlSiO}_4$ ,  $\text{Sb}_2\text{O}_5$ ,  $\text{Al}_2\text{O}_3$ ,  $\text{LiTaSiO}_5$ ,  $\text{LiPO}_3$ ,  $\text{Li}_3\text{B}_{11}\text{O}_{18}$ ,  $\text{LiZr}_2(\text{PO}_4)_3$  and  $\text{LiB}_3\text{O}_5$  exhibit an estimated  $\text{O}^{2-}$  diffusion time longer than 1 h. Next, we estimate the upper limit of  $\text{O}^{2-}$  diffusivity to have  $t \geq 1\text{h}$ , which are represented by the vertical dashed lines in Figure X.3.1. Therefore, the green region in Figure X.3.1 represents the favorable  $\text{Li}^+$  and  $\text{O}^{2-}$  diffusivity window, and a compound falling on the top left area is more desirable in terms of facilitating  $\text{Li}^+$  transport while blocking  $\text{O}^{2-}$  transport.

Next, we carried out an extensive high-throughput computational study to develop materials design principles governing amorphous cathode coating selections for Li-ion battery applications (see Figure X.3.3). Our high-throughput screening includes descriptors to evaluate the thermodynamic stability, electrochemical stability, chemical reactivity with electrolytes and cathodes, and ionic diffusion in the cathode coatings. An optimal amorphous cathode coating should not only exhibit sufficient thermodynamic stability, electrochemical stability, and chemical stability, but also a low  $\text{O}^{2-}$  diffusivity and a high  $\text{Li}^+$  diffusivity to achieve oxygen-retaining and surface-protective functions while avoiding significant losses in rate capability. Combing the screening results and ionic diffusion analysis, we summarize the promising cathode coatings and general materials design principles:

(1)  $\text{Li}^+$  and  $\text{O}^{2-}$  diffusion are highly correlated, therefore, a higher  $\text{Li}^+$  transport promotes higher  $\text{O}^{2-}$  transport. In Li containing compounds, the  $\text{Li}^+$  diffusion rate is generally fast enough to avoid a large overpotential. As a higher  $\text{Li}^+$  diffusion may compromise a coating's ability to block  $\text{O}^{2-}$  diffusion, when selecting cathode coatings with same chemistry, a compound with a lower Li concentration is preferred. It exhibits an improved oxygen retention as well as a higher oxidation limit. For example, the  $\text{Li}^+$  concentrations in  $\text{LiPO}_3$  and  $\text{Li}_3\text{PO}_4$  are 20% and 37.5%, respectively. Both  $\text{LiPO}_3$  and  $\text{Li}_3\text{PO}_4$  exhibit a facile  $\text{Li}^+$  diffusion, but  $\text{LiPO}_3$  exhibits an improved oxygen retention as compared to  $\text{Li}_3\text{PO}_4$ . In addition, the oxidation limit of  $\text{LiPO}_3$  (4.9 V) is higher than that of  $\text{Li}_3\text{PO}_4$  (4.0 V).



(2) Mitigating  $O^{2-}$  diffusion is a formidable challenge when selecting an ideal cathode coating as most thin conformal coatings will transport oxygen under prolonged cycling and high voltage. Our results show that in addition to the four experimentally confirmed cathode coatings:  $Li_3B_{11}O_{18}$ ,  $LiZr_2(PO_4)_3$ ,  $LiPO_3$  and  $LiAlSiO_4$ , we also identify three new promising cathode coatings:  $LiB_3O_5$ ,  $LiSb_3O_8$  and  $LiTaSiO_5$ .

(3) Based on our ionic diffusion analysis, we find that  $BO_x^{y-}$ ,  $SiO_x^{y-}$ ,  $PO_x^{y-}$  and  $SbO_x^{y-}$  anion groups tend to exhibit an improved oxygen retention. Therefore, we expect that compounds such as  $LiBa(B_3O_5)_3$ ,  $LiAl(Si_2O_5)_2$ ,  $LiTi_2(PO_4)_3$ ,  $LiScP_2O_7$ ,  $LiK(PO_3)_2$ , and  $LiCs(PO_3)_2$  could also be potentially effective cathode coatings. On the other hand,  $F^-$  and  $Cl^-$  anion groups tend to exhibit faster  $Li^+$  and  $O^{2-}$  diffusion as compared to the oxides. Thus, they are not ideal for high-voltage cathode coatings where the driving force for oxygen loss is high. However, their inherent fast  $Li^+$  diffusivity may render them promising candidates as the solid-state electrolytes or lithium metal coatings.

(4) A non-Li-containing compound generally exhibits slower  $Li^+$  diffusion but better oxygen retention ability as compared to its lithiated counterpart. We mainly consider Li-containing compounds in this study, however, we expect that effective cathode coatings can also be found in non-lithiated compounds, such as  $Al_2O_3$ . Based on our identified anion groups above, we expect that compounds, such as  $ScBO_3$ ,  $HfSiO_4$ ,  $ZrP_2O_7$  and  $AlPO_4$ , could be potentially effective cathode coatings.

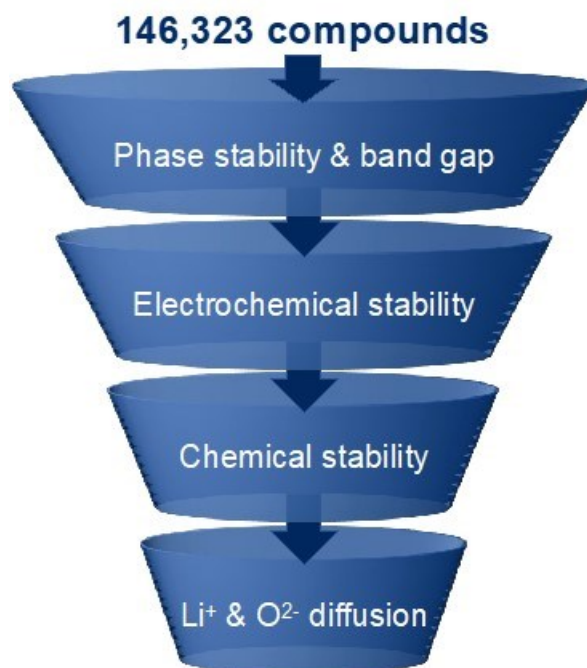


**Figure X.3.3 High-throughput computational screening procedure to select cathode coatings for Li-ion battery.**

#### **Interface formation in Li-based batteries**

We are developing methods to predict interface formation in liquid- as well as solid-based electrolyte Li energy storage systems. First principles methods such as density functional theory (DFT) give us an accurate depiction of the thermodynamics of a given chemical space, and it corroborates well with phase identification in experimental studies of solid-state batteries; but the dynamics of forming new phases is a convoluted process where the morphology of the resulting interface is determined by both thermodynamics and kinetics. Recent advances in machine learned interatomic potentials (MLP) has led to an increase of using DFT-informed data to train atomic force fields for MD simulations. MLPs has shown promising results in extrapolating ab initio molecular dynamics (AIMD) simulations into MD length scales for accurate ionic diffusivity, structure, and property predictions. We are developing and employing MLPs to study the

thermodynamics and kinetics that determine the formation of the solid electrolyte interphase (SEI) on Li-metal anodes. Our objective is to use ML-informed MD to gain fundamental understanding of the atomic-level mechanisms that drive surface reactivity and influence the performance of materials and electrolytes in Li metal batteries.

(1) For this project we have developed an active, high-throughput training data generation scheme that leverages the existing computational infrastructure built by Materials Project. The high-throughput training data generation scheme is designed to curate large batches of accurate DFT-level calculations of a given system that samples the potential energy landscape of the chemical system proposed. This includes perturbing atomic configurations into non-equilibrium configurations that contain important structure-property information for MLPs. By generating extensive DFT data of explicit interface structures, our scheme is focused on capturing the kinetics governing the formation of Solid-State Electrolyte (SSE) - Li anode interphases.

(2) Recently developed universal interatomic potentials (UIPs) are benchmarked to be efficient at quick-sampling MD at low temperatures for highly crystalline structures but contain slight inaccuracies for high temperature structures. We benchmarked UIPs (without fine tuning) with AIMD, where we performed NVT calculations at low to moderate temperatures with a batch of binary and ternary structures selected from the Materials project. Our results show that highly crystalline binary structures were accurately simulated according to radial distribution function and coordination numbers. The short-range ordering of ternary structures is highly accurate for UIPs but smears out details for long range interactions. Structures with non-crystalline characteristics were inaccurate with UIPs. More benchmarking is required to establish the efficacy extent of these UIP simulations.

(3) We utilized the data generation scheme outlined in reference (1) to create a customized MLP model for a solid-state electrolyte (SSE) system, specifically interfaced with a Li metal anode. Our MLP model demonstrated its predictive capability even in the absence of explicit training data from DFT predicted stable structures. The model can identify interphase products that are thermodynamically stable under ambient conditions. We conducted simulations using classical MD via our trained MLP. These simulations revealed observations of various phases' formation and we assessed their chemical reactivity. The results of our analysis align closely with experimental expectations, validating the reliability and accuracy of our approach.

In liquid-based electrolyte systems, we have developed a reaction network-based model which leverages a growing database of bond-breaking/bond-formation energetics and transition state data from high-throughput DFT calculations. Prior work shows that species like  $\text{LiPF}_6$  and EC (Ethylene Carbonate) react at relatively low potentials. Specifically,  $\text{LiPF}_6$  reacts to form  $\text{LiF}$  which precipitates and contributes to the solid-electrolyte interface (SEI). A range of other products including  $\text{POF}_3$ ,  $\text{PF}_2\text{OOH}$  have been identified experimentally. As an initial investigation, we attempted to understand the thermodynamically and kinetically feasible reactions leading to the formation of  $\text{LiF}$  and  $\text{CO}_2$  using a transition state search. The reaction involving  $\text{Li}_2\text{CO}_3$  and  $\text{PF}_5$  leading to the formation of  $\text{LiF}$ ,  $\text{POF}_3$  and  $\text{CO}_2$  was found to be both thermodynamically and kinetically feasible. However, this reaction is purely chemical in nature and requires  $\text{Li}_2\text{CO}_3$  a priori, which is formed by the electrochemical reduction of EC, and therefore indirectly, the rate of formation of  $\text{LiF}$ ,  $\text{POF}_3$  will have a potential dependence. To understand the potential dependence of the rate of formation, efforts towards creating reaction networks with starting species as EC,  $\text{LiPF}_6$ ,  $\text{Li}^+$  ion were made. The reaction networks thus developed were unable to predict the formation pathways for  $\text{CO}_2$ , as the reaction networks are built under the assumption of single bond breaking or bond formation. However, the transition state search study previously conducted, showed that both  $\text{LiF}$  and  $\text{CO}_2$  gets formed due to multiple concerted bond breakages. Due to these shortcomings, the reaction network including  $\text{LiPF}_6$  is delayed.

To overcome the issue of multiple bond breakages and avoid the combinatorial explosion of reaction networks, several strategies are being investigated in the current reaction network generation process. As one example, we have explored using chemically informed machine learning of activation barriers to early on identify

kinetically unfeasible reaction pathways. To predict the activation barriers in a chemically interpretable way, we have developed an equivariant graph neural network that predicts activation barriers using coefficients of a frontier molecular orbital (such as the highest occupied molecular orbital) of reactant and product complexes as graph node features (see Figure X.3.4 for example performance).

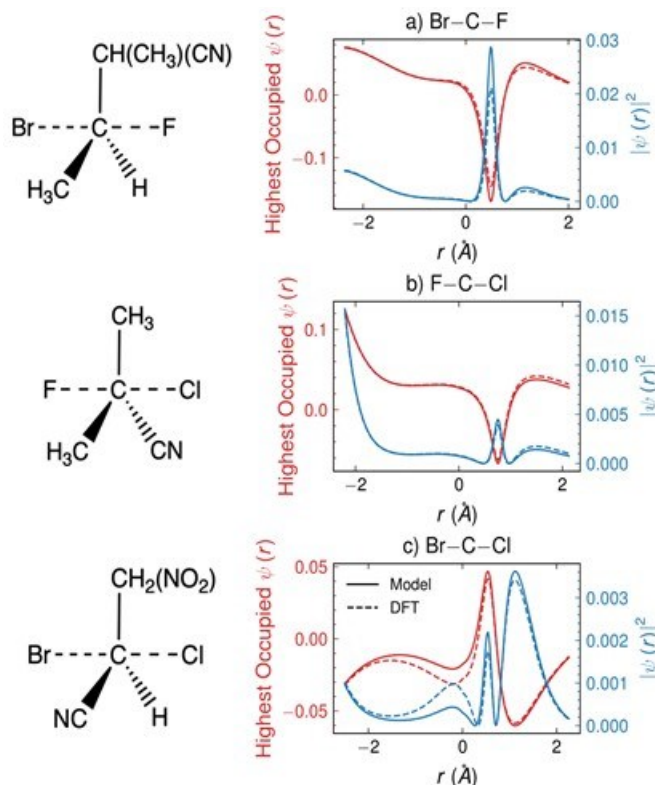


Figure X.3.4 Comparison of model predicted and DFT (red) HOMO of the transition state and (b) orbital density along the reaction axis of three representative SN2 reactions.

As a proof of concept, the methodology predicted activation barriers with a mean absolute error of less than 0.025 eV on a dataset of S<sub>N</sub>2 reactions. Training the architecture on a much broader range of reaction classes will allow us use this as a filter reaction while expanding the reaction network.

### Conclusions

- Onsager transport model elucidates correlation in Li<sup>+</sup> and O<sup>-</sup> diffusivity in cathode coating materials.
- High-throughput computational screening procedure to select cathode coating for Li-ion batteries.
- Machine learned interatomic potential infrastructure development for thermodynamic and kinetic analysis of solid-state electrolyte – Li anode systems.
- Shortcomings of reaction network findings for LiPF<sub>6</sub> resulted in a strategy shift to develop machine-learned reaction barriers.

### Key Publications

1. E. Sivonxay and Kristin A. Persson, *Density functional theory assessment of the lithiation thermodynamics and phase evolution in Si-based amorphous binary alloys*, Energy Storage Materials, 52, 42-50, (2022)
2. J. Cheng, Kara D. Fong, Kristin A. Persson, *Materials Design Principles of Amorphous Cathode Coatings for Lithium-ion Battery Applications*, J. Mater. Chem. A, 10, 22245, (2022).

**Acknowledgements**

This work was supported in part by the Advanced Battery Materials Research (BMR) program directed by Tien Duong and in part by the U.S. Department of Energy's Vehicle Technologies Office under the Silicon Consortium Project, directed by Brian Cunningham, and managed by Anthony Burrell. This research utilized resources at the National Energy Research Scientific Computing Center (NERSC), a U.S. Department of Energy Office of Science User Facility located at Lawrence Berkeley National Laboratory and the Lawrencium computational cluster resource provided by the IT Division at the Lawrence Berkeley National Laboratory, operated under Contract No. DE-AC02-05CH11231. Additionally, a portion of this research was performed using computational resources sponsored by the Department of Energy's Office of Energy Efficiency and Renewable Energy and located at the National Renewable Energy Laboratory (NREL). We gratefully acknowledge Shyam Dwaraknath and Jianli Cheng for valuable discussion.

This work was intellectually led by the Battery Materials Research (BMR) program under the Assistant Secretary for Energy Efficiency and Renewable Energy, Office of Vehicle Technologies of the U.S. Department of Energy, Contract DE-AC02-05CH11231. This research used resources of the National Energy Research Scientific Computing Center; a DOE Office of Science User Facility supported by the Office of Science of the U.S. Department of Energy under Contract No. DE-AC02-05CH11231. This research also used the Lawrencium computational cluster resource provided by the IT Division at the Lawrence Berkeley National Laboratory (Supported by the Director, Office of Science, Office of Basic Energy Sciences, of the U.S. Department of Energy under Contract No. DE-AC02-05CH11231)

## X.4 Modeling of Solid-State Conductors (LBNL)

### Gerbrand Ceder, Principal Investigator

Lawrence Berkeley National Laboratory  
1 Cyclotron Rd, MS: 33-146  
Berkeley, CA, 94720  
E-mail: [gceder@berkeley.edu](mailto:gceder@berkeley.edu)

### Tien.Duong, DOE Technology Development Manager

U.S. Department of Energy  
E-mail: [Tien.Duong@ee.doe.gov](mailto:Tien.Duong@ee.doe.gov)

Start Date: October 1, 2022	End Date: September 30, 2023	
Project Funding (FY23): \$400,000	DOE share: \$400,000	Non-DOE share: \$0

### Project Introduction

Solid-state batteries promise to increase the safety and energy density of current Li batteries [1]. To enable their development and deployment, superionic conductor (SIC) electrolytes with high Li conductivity and electrochemical stability must be discovered and optimized. Oxide SIC materials have been commonly explored, as they tend to have greater electrochemical stability than sulfide SICs [2]. However, there is still a lack of known oxide SICs with Li conductivity that can match that of sulfides. Thus, we explore a new class of oxide SICs that are derived from Li-excess rocksalt oxide structures, which have been commonly investigated as cathode materials. We establish design principles for these phases, which can open new avenues towards the discovery of novel oxide SICs.

We also continue to enhance the performance and develop the understanding of sulfide SICs. Specifically, we seek to enhance the Li conductivity of argyrodite phases through tuning the anion sublattice. Furthermore, we apply first-principles calculations to quantify and understand the thermodynamic stability of several promising superionic conductors in the  $\text{Li}_2\text{S-P}_2\text{S}_5$  pseudo-binary space, which includes the  $\alpha\text{-Li}_3\text{PS}_4$ ,  $\beta\text{-Li}_3\text{PS}_4$ , HT- $\text{Li}_7\text{PS}_6$ , and  $\text{Li}_7\text{P}_3\text{S}_{11}$  phases.

### Objectives

Solid-state batteries are promising to achieve high energy density. The project objective is to determine the design principles needed to create solid-state electrolytes (SSEs) with high Li-ion conductivity, while also achieving stability against common Li-ion cathodes and Li-metal anodes.

### Approach

High-throughput (HT) computation is used to screen suitable solid electrolytes (SEs) with high electrochemical stability and high ionic conductivity, by incorporating nudged elastic band and an *ab initio* molecular dynamics method. Meanwhile, density functional theory (DFT) is used to calculate bulk elastic constants of materials, surface energies, and interface decohesion energies of grain boundaries. Thermodynamic interface stability is assessed from *ab initio* computed grand potential phase diagrams in which the lithium voltage can be controlled. Kinetic limits for SE decomposition are assessed by topotactic lithium insertion and removal from the SE. Materials are synthesized and experimentally tested for conductivity and stability.

### Results

#### Designing overlithiated rocksalt-based Li superionic conductors

Li-metal-oxides with a face-centered cubic (*fcc*) anion sublattice constitute a large family of compounds, but their potential of serving as superionic conductors is rarely explored. Recently, the formation of distorted face-sharing Li polyhedra at intermediate states upon Li insertion has emerged as a key mechanism to account for

the fast kinetics observed in several Li-ion anodes (e.g.,  $\text{Li}_4\text{Ti}_5\text{O}_{12}$  [3],  $\text{Li}_3\text{V}_2\text{O}_5$  [4]). We propose that constructing a face-sharing Li configuration, in which Li ions simultaneously occupy an octahedral site and its face-sharing tetrahedral site (Figure X.4.1a), could be a general strategy to enhance the Li-ion conductivity in *fcc*-type oxides. Such a face-sharing configuration leads to strong Li-Li interactions, which will lift the Li site energy and potentially activate ion migration with low barriers. However, the face-sharing Li environment is typically absent in stoichiometric *fcc* oxides such as rocksalt. To create a face-sharing Li configuration, we attempted to introduce over-stoichiometric Li in the rocksalt structure, which may naturally drive Li to occupy the tetrahedral sites that are face-sharing with the octahedral Li.

To find potential metal compositions that enable excess Li in a rocksalt, we used density-functional theory (DFT) calculations to evaluate the phase stability of various redox-inactive metal couples in the presence of over-stoichiometric Li. The calculated compositions share the general formula of  $\text{Li}_{1+x+2y}\text{M}_1\text{M}_2\text{M}_{1-x-z}\text{O}_2$ , where  $y$  is the overlithiation level ( $y = 1/6$  or  $1/12$ ) and  $x$  is the Li-excess level ( $x = 0, 1/6, 1/3$ ). We tested 16 redox-inactive metal cations that are commonly used in solid-state electrolytes. The resulting metal compatibility heatmap is shown in Figure X.4.1b, where each pixel represents the average  $E_{\text{hull}}$  of all the computed compounds for the selected metal pairs. A lower  $E_{\text{hull}}$  value suggests that the metal couples can better accommodate the face-sharing configuration induced by over-stoichiometric Li. From this heatmap, it can be inferred that larger metal cations (e.g.,  $\text{In}^{3+}$ ) generally lead to better stability of overstoichiometric compositions. This trend can be rationalized because larger cations can better tolerate structural distortions caused by face-sharing configuration.  $\text{La}^{3+}$  is an exception as it is too large to accommodate the six-fold cation coordination in a rocksalt. Based on these modeling results, we plan to further investigate the In-based overlithiated rocksalt system and examine the Li-ion conductivity both computationally and experimentally.

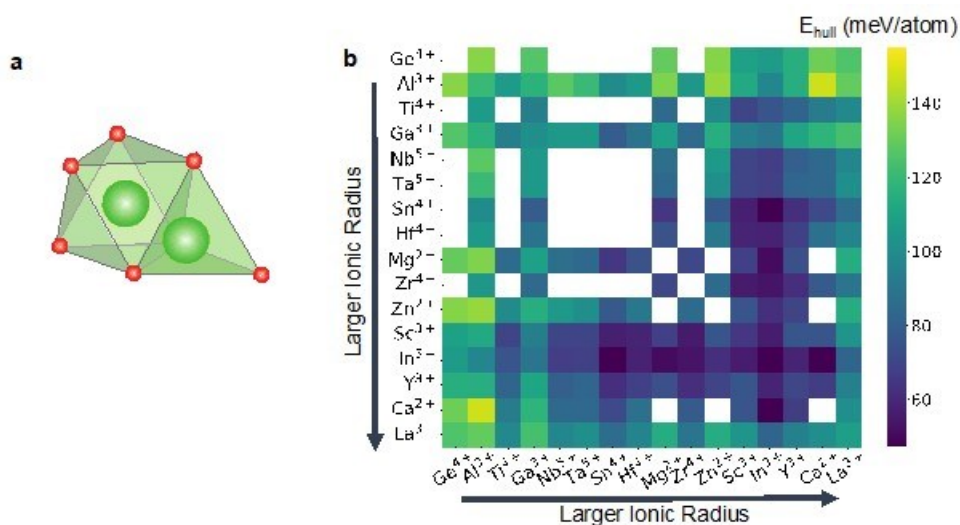


Figure X.4.1 (a) A schematic of tetrahedral-octahedral face-sharing Li configuration. (b) A metal compatibility heatmap extracted from high-throughput DFT calculations.

#### Design and synthesize novel sulfide superionic conductor

The cubic polymorph of lithium (Li) argyrodite ( $\text{Li}_7\text{PS}_6$ , F-43m) is a promising superionic conductor with room temperature Li conductivity  $> 0.1$  mS/cm [5]. Doping argyrodite with halogen atoms ( $X=\text{Cl}, \text{Br}, \text{I}$ ) to form  $\text{Li}_6\text{PS}_5\text{X}$  increases room temperature Li conductivity to  $\sim 1$  mS/cm [6]. Thus, engineering the anion sublattice can have significant impact on Li mobility, motivating further material designs in this area. Recent studies on anti-perovskite superionic conductors have shown that cluster-ion substitution can increase ionic conductivity by orders of magnitude, which was attributed to cluster-ions providing greater degrees of freedom, such as bond stretching and bending, allowing alkali ions to preserve coordination as they migrate

[7]. In this study, we apply cluster-ion substitution to computationally screen and experimentally realize a novel Li superionic conductor.

We have explored the feasibility of enhancing Li conductivity through pseudohalogen substitution through applying an *ab initio* computational screening. We substituted a range of pseudohalogen units ( $\text{BH}_4$ ,  $\text{BF}_4$ ,  $\text{AlH}_4$ ,  $\text{AlF}_4$ , and  $\text{NH}_2$ ) and halogen atoms (Cl, Br, I) into the argyrodite structure (Figure X.4.2A) and evaluated their thermodynamic stability from density functional theory (DFT) calculations [8]. All halide-substituted structures are found to be more stable than the pseudohalogen-substituted structures. Among the pseudohalogen-substituted structures, the most stable compounds are found with  $\text{BH}_4$  substitution, with energy above hull ( $E_{\text{hull}}$ ) of roughly 50 meV/atom at 0 K (Figure X.4.2B). Thus, we used the  $\text{BH}_4$ -substituted phase as a target for experimental synthesis.

We used a mechanochemical synthesis process, as  $\text{LiBH}_4$  precursors decompose at high temperature. Through applying high-energy ball milling on  $\text{LiBH}_4$  and  $\beta\text{-Li}_3\text{PS}_4$  precursors, we successfully synthesized a target structure, with composition  $\text{Li}_{5.91}\text{PS}_{4.91}(\text{BH}_4)_{1.09}$  [8]. Synchrotron X-ray diffraction (XRD) refinement confirmed that the structure crystallizes in the cubic F-43m space group. The fractional occupancies of B were refined to determine the amount of  $\text{BH}_4$  incorporation into the crystal. Transmission electron microscopy and Raman response of the structure were also applied to verify the formation of argyrodite and incorporation of  $\text{BH}_4$ .

Using electrochemical impedance spectroscopy (EIS) the ionic conductivity of  $\text{Li}_{5.91}\text{PS}_{4.91}(\text{BH}_4)_{1.09}$  and the conventional halide-substituted structures  $\text{Li}_6\text{PS}_5\text{Cl}$  and  $\text{Li}_6\text{PS}_5\text{Br}$  can be compared. Arrhenius plots are shown in Figure X.4.3 and demonstrate that  $\text{BH}_4$  substitution indeed increases the room temperature Li conductivity (4.8 mS/cm) compared to Cl and Br-doped argyrodites (0.95 and 0.87 mS/cm, respectively) [8].

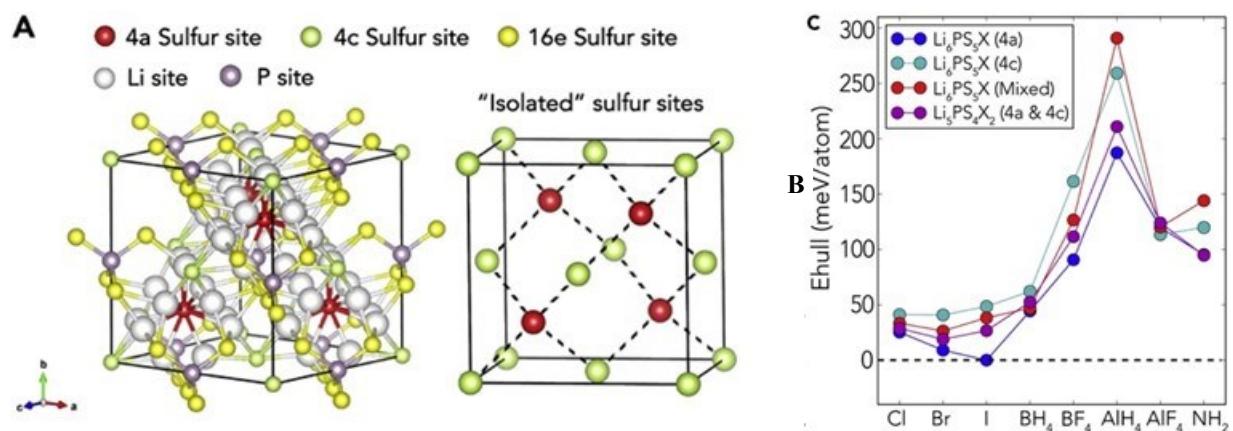


Figure X.4.2 (A) General structure of argyrodite with different sulfur (S) sites (4a – red, 4c – green, 16e – yellow). (B) Energy above the hull with different substitutions.

$\text{BH}_4$  substitution also leads to a lower activation energy of 0.27 eV. Since the Li concentration of  $\text{BH}_4$ -substituted argyrodite is only slightly smaller than that in the Cl and Br-substituted structures, the difference in Li conductivity cannot be attributed to this factor. Future studies using *ab initio* modeling will seek to clarify the mechanisms underlying this improvement in Li conductivity.

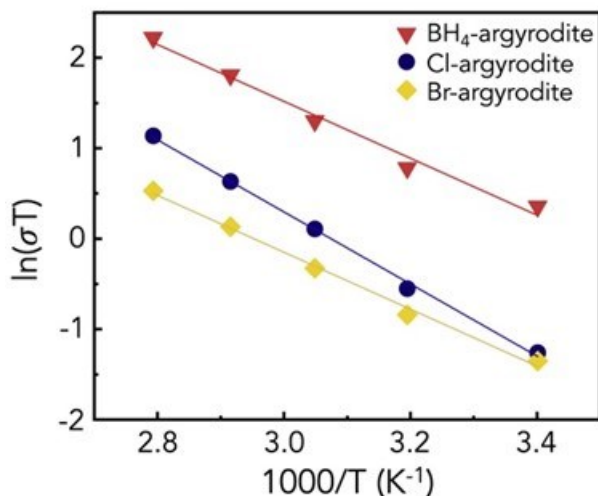


Figure X.4.3 Arrhenius plots of  $\text{Li}_{5.91}\text{PS}_{4.91}(\text{BH}_4)_{1.09}$ ,  $\text{Li}_6\text{PS}_5\text{Cl}$ , and  $\text{Li}_6\text{PS}_5\text{Br}$  from electrochemical impedance spectroscopy (EIS) measurements.

#### Clarifying the Crystal Structure and Modeling Disorder in $\beta\text{-Li}_3\text{PS}_4$

The  $\beta$  polymorph of  $\text{Li}_3\text{PS}_4$  is a promising sulfide Li superionic conductor with high Li-ion conductivity  $\sim 0.1$  mS/cm at room temperature [9, 10]. It has been experimentally shown that this phase is metastable at ambient temperature, with the  $\gamma$  polymorph being the ground state for  $T < 525$  K. The metastability of  $\beta\text{-Li}_3\text{PS}_4$  motivates our *ab initio* study with the objective to understand its thermodynamic accessibility at finite temperature and rationalize experimental trends in this system. To understand temperature related stability difference between the various polymorphs of  $\text{Li}_3\text{PS}_4$  one needs to capture the phenomena that control the entropy of each phase. Crystallographic refinements have shown that  $\beta\text{-Li}_3\text{PS}_4$  contains configurational Li-vacancy disorder, which we can model from first principles using the established cluster expansion (CE) and Monte Carlo (MC) approach [11]. To properly model the configurational disorder, we require accurate structural models to define the set of distinct sites that Li can occupy, which we refer to as the Li sublattice. However, previous reports of the Li sublattice of  $\beta\text{-Li}_3\text{PS}_4$  from X-ray diffraction (XRD) and neutron diffraction (ND) refinements have been conflicting [10, 12]. XRD reports a structure containing 3 distinct Li sites ( $\text{Li}1'$  (8d),  $\text{Li}2'$  (4b), and  $\text{Li}3'$  (4c)) with Pnma symmetry, while neutron diffraction (ND) identifies splitting of  $\text{Li}1'$  (8d) to distinct  $\text{Li}1\text{A}$  (8d) and  $\text{Li}1\text{B}$  (8d) sites, and splitting of  $\text{Li}2'$  (4b) to  $\text{Li}2$  (8d) [12]. We show the ND-refined unit cell of  $\beta\text{-Li}_3\text{PS}_4$  in Figure X11.4.4(i), and the splitting of  $\text{Li}1$  (8d) and  $\text{Li}2$  (4b) in Figure X.4.4(ii) and Figure X.4.4(iii), respectively.



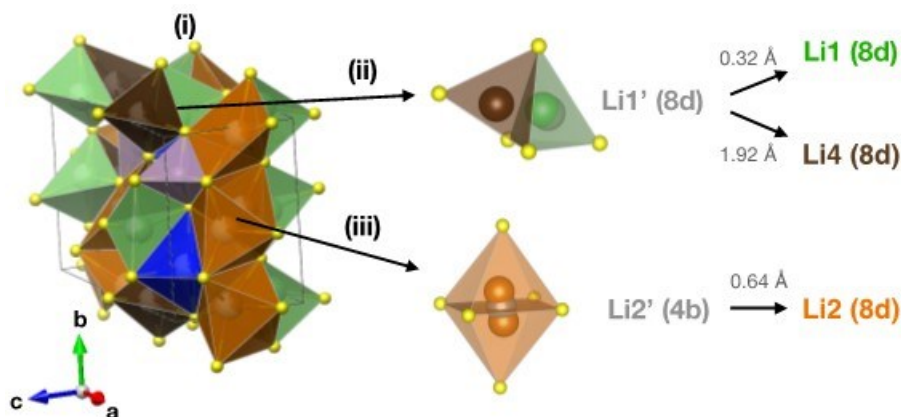


Figure X.4.4 Structure of  $\beta$ - $\text{Li}_3\text{PS}_4$ . (i) The unit cell from ND refinement, (ii) splitting of  $\text{Li1}'$  (8d) site, and (iii) splitting of  $\text{Li2}'$  (4b).

We evaluate the accuracy of the XRD and ND refinements by using the positions from these refinements as starting configurations for density functional theory (DFT) optimizations and evaluate how much the atomic coordinates relax from their XRD and ND refined sites. This is measured by calculating the normalized root mean squared (NRMS) displacement of relaxed atomic locations from the ND and XRD refined  $\beta$ - $\text{Li}_3\text{PS}_4$  lattice sites. The distribution of NRMS displacements from the ND and XRD refined structures are shown in Figure X.4.5. We can observe that there is significantly smaller NRMS distance from the ND structure, as the 3<sup>rd</sup> quartile of the ND distribution and 2<sup>nd</sup> quartile of the XRD distribution do not overlap. This indicates that the Neutron determined positions are likely more correct.

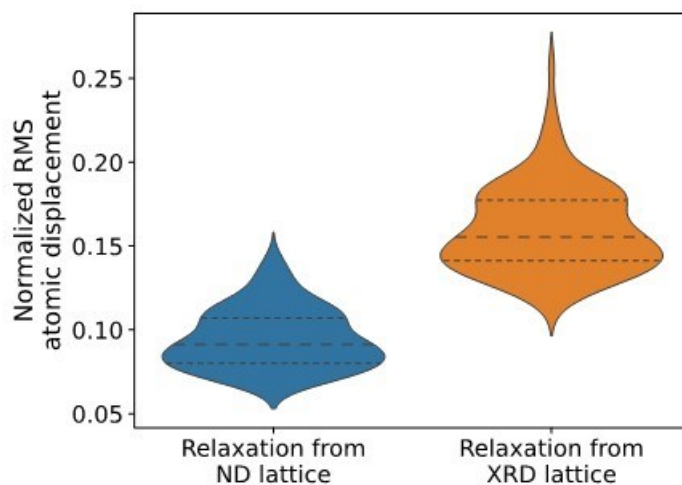


Figure X.4.5 Distributions of NRMS atomic displacements for each DFT-relaxed structure from refined XRD and ND sites.

The thermodynamic disorder created in the XRD and ND refined structures at elevated temperature are also compared. We fit separate ab-initio cluster expansions on each lattice and perform MC simulations to predict the Li site disorder as a function of temperature. In Figure X.4.6, the fractional occupancies on each Li site across temperature are shown. The XRD structure only begins to disorder at approximately 900 K, and by 1000 K changes in the Li fractional occupancies are still relatively small, yielding poor agreement with the experimental XRD refinement (Figure X.4.6a). In contrast, the ND structure begins to disorder at a lower temperature of about 600 K, and by 1000 K has significant changes in its Li fractional occupancies, highlighted by  $\text{Li1}$  (8d) and  $\text{Li3}$  (4c) having occupancies of 0.8 and 0.3, respectively. These values show reasonable agreement with the ND refinement at 620 K (0.7 and 0.3) (triangles in Figure X.4.6b). Our

simulations on both the XRD and ND structures underestimate the experimentally reported configurational disorder. However, the ND structure is predicted to have greater disorder and thus better agreement with experiment, suggesting that the ND refinement is more accurate.

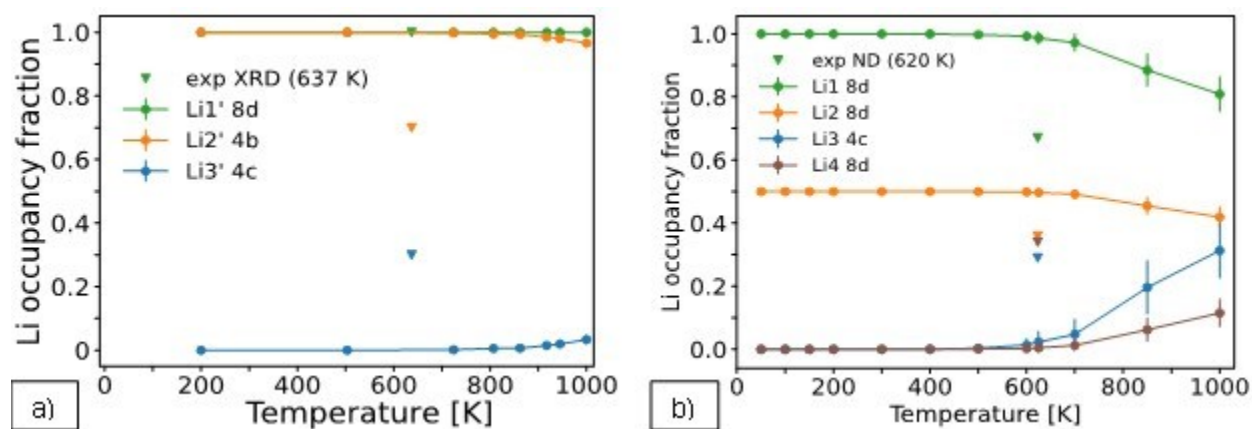


Figure X.4.6 Li fractional occupancies as a function of temperature for the a) XRD structure and b) ND structure of  $\beta$ -Li<sub>3</sub>PS<sub>4</sub>.

Our analysis demonstrates that the increased details of the ND refinement of  $\beta$ -Li<sub>3</sub>PS<sub>4</sub> are more physically accurate and lead to significant differences in predicted thermodynamic behavior. After identifying the more accurate structural model of this phase, we will perform similar analysis to verify the structure of  $\alpha$ -Li<sub>3</sub>PS<sub>4</sub> and other superionic conductors in the Li<sub>2</sub>S-P<sub>2</sub>S<sub>5</sub> pseudo-binary space. Upon obtaining accurate structural models of each polymorph, we can assess the phase stability of this composition space by calculating and comparing their free energy.

#### Phase Diagram of the Li<sub>2</sub>S-P<sub>2</sub>S<sub>5</sub> System from First Principles

The Li<sub>2</sub>S-P<sub>2</sub>S<sub>5</sub> pseudo-binary system has been a rich source of promising Li superionic conductors, encompassing the  $\alpha$ -Li<sub>3</sub>PS<sub>4</sub>,  $\beta$ -Li<sub>3</sub>PS<sub>4</sub>, HT-Li<sub>7</sub>PS<sub>6</sub>, and Li<sub>7</sub>P<sub>3</sub>S<sub>11</sub> phases [5, 13, 14]. According to previous experimental and computational studies, these superionic conductors are all metastable at ambient temperature [13]. Their metastability motivates our *ab initio* study with the objective to quantify their thermodynamic accessibility at finite temperature, rationalize experimental trends, and potentially propose new synthesis procedures. To model the free energy of each phase, we consider contributions from the electronic structure, configurational disorder, and vibrational modes. Configurational Li-vacancy disorder, which we assume to be significant in the superionic conductors, is treated with the cluster expansion (CE) and Monte Carlo (MC) sampling approach. To construct the CE models, we require detailed descriptions of the Li sublattices in each structure, which we obtain from performing analysis similar to the methods applied to clarify the  $\beta$ -Li<sub>3</sub>PS<sub>4</sub> structure, as described in the previous section. The vibrational free energies are computed with harmonic phonon calculations on the ground-state of each phase.

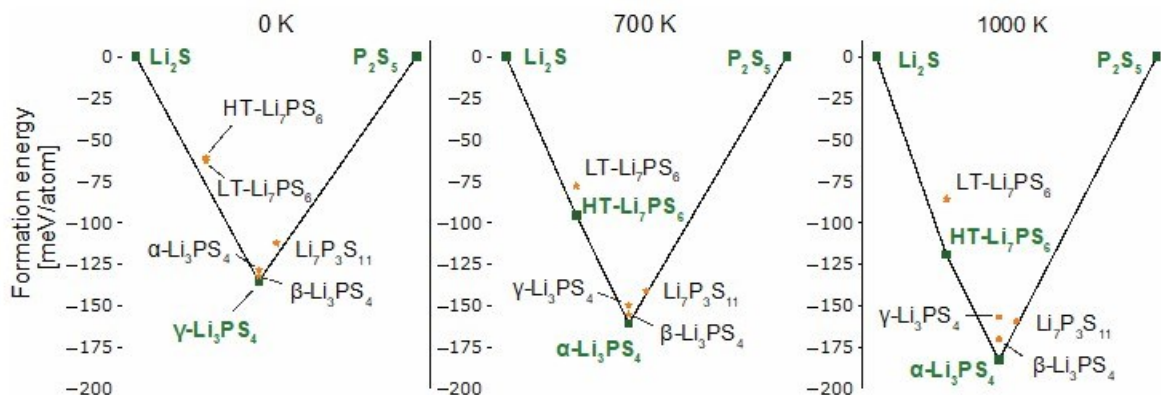


Figure X.4.7 Phase diagram of the  $\text{Li}_2\text{S}-\text{P}_2\text{S}_5$  system at 0, 700, and 1000 K. Solid lines denote the convex hull. Stable phases are marked with green squares and unstable phases with gold stars.

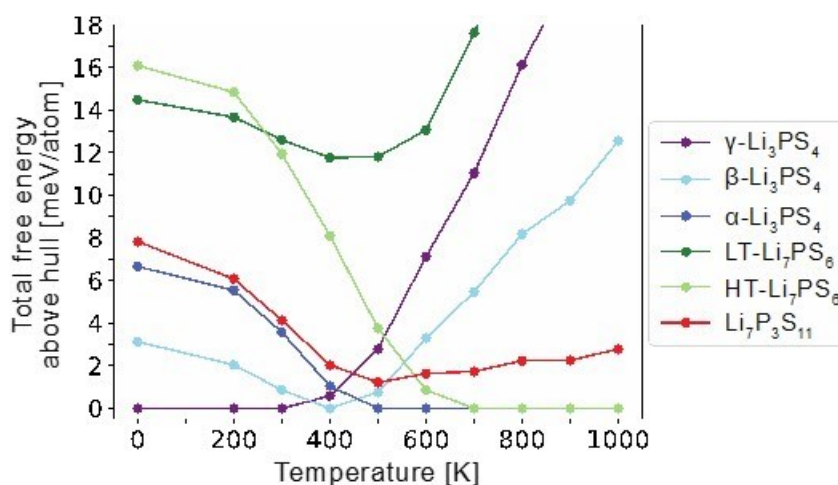


Figure X.4.8 Free energy above the hull ( $E_{\text{hull}}$ ) for all phases from 0 to 1000 K.

Using these free energy contributions for each phase, we construct the pseudo-binary  $\text{Li}_2\text{S}-\text{P}_2\text{S}_5$  phase diagram, which is shown in Figure X.4.7. The energies above the hull ( $E_{\text{hull}}$ ) as a function of temperature are shown in Figure X.4.8. The convex hull is a typical construction to obtain stable phases and represents the collection of thermodynamic ground states into which all other phases have a driving force to convert. At 0 K, the only stable phases on the convex hull are  $\gamma\text{-Li}_3\text{PS}_4$  and the endpoints,  $\text{Li}_2\text{S}$  and  $\text{P}_2\text{S}_5$  (Figure X.4.7). At 700 K,  $\text{HT-Li}_7\text{PS}_6$  is stabilized and appears on the hull. Since reported synthesis procedures for LT- and  $\text{HT-Li}_7\text{PS}_6$  typically do not require mechanical milling or quenching [13], it may be surprising that they are unstable at 300 K—13 and 12 meV/atom above the hull respectively (Figure X.4.8). It is likely that the thermodynamically favored phase separation of  $\text{HT-Li}_7\text{PS}_6$  to  $\text{Li}_2\text{S}$  and  $\text{Li}_3\text{PS}_4$  is kinetically hindered at room temperature. Instead,  $\text{HT-Li}_7\text{PS}_6$  is found to transform to  $\text{LT-Li}_7\text{PS}_6$  upon cooling, a potentially more facile process as it merely involves shifting the  $\text{PS}_4$  locations. Thus, an appropriate solid-state synthesis procedure would be to perform sufficiently high temperature ( $T > 600$  K) synthesis to stabilize  $\text{HT-Li}_7\text{PS}_6$ , before a relatively rapid cooling process to bypass the phase separation to  $\text{Li}_2\text{S}$  and  $\text{Li}_3\text{PS}_4$ .

For the  $\text{Li}_3\text{PS}_4$  composition, our calculations in Figure X.4.8 predict phase transformations from  $\gamma \rightarrow \beta \rightarrow \alpha$  with increasing temperature, which is consistent with experiments. Since  $\beta\text{-Li}_3\text{PS}_4$  is less than 1 meV/atom above the hull at 300 K (Figure X.4.8), it is plausible that nanoporous synthesis and mechanical milling techniques can lead to its stabilization at room temperature [9]. The  $\alpha\text{-Li}_3\text{PS}_4$  polymorph is only slightly less

stable than  $\beta$  at 300 K ( $E_{\text{hull}} = 4$  meV/atom), which explains why  $\alpha$  can also be stabilized at ambient temperature through a rapid heating and quenching procedure [16]. Rapid heating of the  $\text{Li}_3\text{PS}_4$  glass to temperatures in the stability range of  $\beta$  enables nucleation of metastable  $\alpha$  particles that are only slightly less stable than  $\beta$ , which is possible by the Ostwald step rule. Rapid quenching can then obstruct the commonly observed direct transition from  $\alpha$  to  $\gamma$  [12], which is possible as their energy difference is only 4 meV/atom at 300 K.

$\text{Li}_7\text{P}_3\text{S}_{11}$  (red curve in Figure X.4.8) is metastable across all temperatures as its energy is never low enough to be on the convex hull, which agrees with prior experimental studies [17]. At 300 K, it is 4 meV/atom above the convex hull. As temperature increases to 500 K, its  $E_{\text{hull}}$  decreases to a minimum of 1.4 meV/atom. Further increases in temperature lead to greater  $E_{\text{hull}}$ . Thus, an ideal synthesis temperature should be around 500 K, corresponding to the minimum  $E_{\text{hull}}$ . This temperature is remarkably close to its experimentally observed glass transition temperature and helps rationalize why heat treatments near this temperature have been successful for recrystallization [17]. The increasing instability with respect to temperature helps explain the experimentally observed tendency to phase separate to  $\text{Li}_3\text{PS}_4$  and  $\text{Li}_4\text{P}_2\text{S}_6$  at temperatures greater than 800 K. The source of this instability is the competition with  $\alpha\text{-Li}_3\text{PS}_4$ , its neighboring stable point, which lowers its free energy more with increasing temperature, therefore increasing the convex hull depth (Figure X.4.8).

In summary, we have computed the phase diagram of the  $\text{Li}_2\text{S}\text{-P}_2\text{S}_5$  pseudo-binary system, which recovers key trends observed from experiment. We have quantified the thermodynamic accessibility of the promising  $\alpha\text{-Li}_3\text{PS}_4$ ,  $\beta\text{-Li}_3\text{PS}_4$ , HT- $\text{Li}_7\text{PS}_6$ , and  $\text{Li}_7\text{P}_3\text{S}_{11}$  superionic conductors as a function of temperature. At ambient temperature, we predict them to be metastable, but thermodynamically accessible due to their relatively small energies above the hull. New synthesis procedures are also proposed that can assist experimental efforts to stabilize these phases.

## Conclusions

We have proposed a new design principle for oxide superionic conductors, in which Li-excess and face-sharing Li configurations are introduced into rock-salt crystal structures with an fcc oxygen sublattice, with the goal to enhance Li conductivity in these structures. From high throughput DFT calculations, we have identified that larger redox-inactive metals, such as  $\text{In}^{3+}$ , can stabilize the face-sharing cation configurations, as these ions can better tolerate the structural distortions arising from face-sharing configurations. These insights will guide further computational and experimental investigation to design and optimize the In-based over-lithiated rocksalt superionic conductors.

In the realm of sulfide superionic conductors, we have also improved the performance of known phases and derived new understanding of their phase stability. We discovered that pseudohalogen substitution into the cubic argyrodite phase to form the  $\text{Li}_{5.91}\text{PS}_{4.91}(\text{BH}_4)_{1.09}$  composition can lead to substantial improvement in Li conductivity at room temperature (4.8 mS/cm) compared to the conventional halide-substituted argyrodites  $\text{Li}_6\text{PS}_5\text{Cl}$  and  $\text{Li}_6\text{PS}_5\text{Br}$  (0.95 and 0.87 mS/cm, respectively). We attribute this improvement to the cluster-ions providing greater degrees of freedom, such as bond-stretching and bending, allowing alkali ions to preserve coordination as they migrate.

We have also clarified the crystal structures and constructed a phase diagram of the  $\text{Li}_2\text{S}\text{-P}_2\text{S}_5$  system. This phase diagram recovers many experimentally observed phase stability trends in the  $\alpha\text{-Li}_3\text{PS}_4$ ,  $\beta\text{-Li}_3\text{PS}_4$ , HT- $\text{Li}_7\text{PS}_6$ , and  $\text{Li}_7\text{P}_3\text{S}_{11}$  superionic conductors. We have verified that the precise details of the Li sublattices obtained from ND refinements are essential towards accurately modeling the configurational disorder. All superionic conductors in this space are predicted to be metastable, but thermodynamically accessible due to their small energy above the convex hull at ambient temperature. New synthesis procedures for these superionic conductors are proposed, which can guide future experimental efforts to optimize these phases and their derivatives.

### Key Publications

1. Sun, Y., Ouyang, B., Wang, Y., Zhang, Y., Sun, S., Cai, Z., & Ceder, G. (2022). Enhanced ionic conductivity and lack of paddle-wheel effect in pseudohalogen-substituted Li argyrodites. *Matter*, 5(12), 4379-4395.
2. Lee, B. J., Jun, K. J., Ouyang, B., and Ceder, G. Weak Correlation between the Polyanion Environment and Ionic Conductivity in Amorphous Li-P-S Superionic Conductors *Chem. Mater.*, 35, 3, 891–899 (2023)
3. Huang, J.; Ouyang, B.; Zhang, Y.; Yin, L.; Kwon, D.-H.; Cai, Z.; Lun, Z.; Zeng, G.; Balasubramanian, M.; Ceder, G. Inhibiting Collective Cation Migration in Li-Rich Cathode Materials as a Strategy to Mitigate Voltage Hysteresis. *Nat Mater*, 1–9 (2023)
4. Kam, R., Jun, K. J., Barroso-Luque, L., Yang, J. H., Xie, F. Y., Ceder, G. Crystal Structures and Phase Stability of the Li<sub>2</sub>S-P<sub>2</sub>S<sub>5</sub> System from First Principles. *Chemistry of Materials* (accepted October 11, 2023)
5. Jun, K. J., Lee, B., Kam, R., Ceder, G. The Non-existence of a Paddlewheel Effect in Superionic Conductors. (submitted)

### References

1. Janek, Jürgen, and Wolfgang G. Zeier. "A Solid Future for Battery Development." *Nature Energy* 1, no. 9 (2016): 16141.
2. Jun, KyuJung, Yingzhi Sun, Yihan Xiao, Yan Zeng, Ryounghee Kim, Haegyeom Kim, Lincoln J. Miara, Dongmin Im, Yan Wang, and Gerbrand Ceder. "Lithium Superionic Conductors with Corner-Sharing Frameworks." *Nature Materials*, 2022, 1–8.
3. Zhang, Wei, Dong-Hwa Seo, Tina Chen, Lijun Wu, Mehmet Topsakal, Yimei Zhu, Deyu Lu, Gerbrand Ceder, and Feng Wang. "Kinetic Pathways of Ionic Transport in Fast-Charging Lithium Titanate." *Science* 367, no. 6481 (2020): 1030–34.
4. Liu, Haodong, Zhuoying Zhu, Qizhang Yan, Sicen Yu, Xin He, Yan Chen, Rui Zhang, et al. "A Disordered Rock Salt Anode for Fast-Charging Lithium-Ion Batteries." *Nature* 585, no. 7823 (2020): 63–67.
5. Ziolkowska, Dominika A., William Arnold, Thad Druffel, Mahendra Sunkara, and Hui Wang. "Rapid and Economic Synthesis of a Li7PS6 Solid Electrolyte from a Liquid Approach." *ACS Applied Materials & Interfaces* 11, no. 6 (2019): 6015–21.
6. Deiseroth, Hans-Jörg, Shiao-Tong Kong, Hellmut Eckert, Julia Vannahme, Christof Reiner, Torsten Zaiß, and Marc Schlosser. "Li6PS5X: A Class of Crystalline Li-Rich Solids With an Unusually High Li+ Mobility." *Angewandte Chemie International Edition* 47, no. 4 (2008): 755–58.
7. Fang, Hong, and Puru Jena. "Li-Rich Antiperovskite Superionic Conductors Based on Cluster Ions." *Proceedings of the National Academy of Sciences* 114, no. 42 (2017): 11046–51.
8. Sun, Yingzhi, Bin Ouyang, Yan Wang, Yaqian Zhang, Shuo Sun, Zijian Cai, Valentina Lacivita, Yinsheng Guo, and Gerbrand Ceder. "Enhanced Ionic Conductivity and Lack of Paddle-Wheel Effect in Pseudohalogen-Substituted Li Argyrodites." *Matter* 5, no. 12 (2022): 4379–95.
9. Liu, Zengcai, Wujun Fu, E. Andrew Payzant, Xiang Yu, Zili Wu, Nancy J. Dudney, Jim Kiggans, Kunlun Hong, Adam J. Rondinone, and Chengdu Liang. "Anomalous High Ionic Conductivity of Nanoporous  $\beta$ -Li3PS4." *Journal of the American Chemical Society* 135, no. 3 (2013): 975–78.
10. Homma, Kenji, Masao Yonemura, Takeshi Kobayashi, Miki Nagao, Masaaki Hirayama, and Ryoji Kanno. "Crystal Structure and Phase Transitions of the Lithium Ionic Conductor Li3PS4." *Solid State Ionics* 182, no. 1 (2011): 53–58.
11. Barroso-Luque, Luis, Peichen Zhong, Julia H. Yang, Fengyu Xie, Tina Chen, Bin Ouyang, and Gerbrand Ceder. "Cluster Expansions of Multicomponent Ionic Materials: Formalism and Methodology." *Physical Review B* 106, no. 14 (2022): 144202.
12. Kaup, Kavish, Laidong Zhou, Ashfia Huq, and Linda F. Nazar. "Impact of the Li Substructure on the Diffusion Pathways in Alpha and Beta Li3PS4: An in Situ High Temperature Neutron Diffraction Study." *Journal of Materials Chemistry A* 8, no. 25 (2020): 12446–56.

13. Kudu, Ömer Ulaş, Theodosios Famprakis, Benoit Fleutot, Marc-David Braidia, Thierry Le Mercier, M. Saiful Islam, and Christian Masquelier. “A Review of Structural Properties and Synthesis Methods of Solid Electrolyte Materials in the Li<sub>2</sub>S – P<sub>2</sub>S<sub>5</sub> Binary System.” *Journal of Power Sources* 407 (2018): 31–43.
14. Seino, Yoshikatsu, Tsuyoshi Ota, Kazunori Takada, Akitoshi Hayashi, and Masahiro Tatsumisago. “A Sulphide Lithium Super Ion Conductor Is Superior to Liquid Ion Conductors for Use in Rechargeable Batteries.” *Energy & Environmental Science* 7, no. 2 (2014): 627–31.
15. Kong, Shiao-Tong, Hans-Jörg Deiseroth, Christof Reiner, Özgül Gün, Elmar Neumann, Clemens Ritter, and Dirk Zahn. “Lithium Argyrodites with Phosphorus and Arsenic: Order and Disorder of Lithium Atoms, Crystal Chemistry, and Phase Transitions.” *Chemistry - A European Journal* 16, no. 7 (2010): 2198–2206.
16. Kimura, Takuya, Takeaki Inaoka, Ryo Izawa, Takumi Nakano, Chie Hotehama, Atsushi Sakuda, Masahiro Tatsumisago, and Akitoshi Hayashi. “Stabilizing High-Temperature  $\alpha$ -Li<sub>3</sub>PS<sub>4</sub> by Rapidly Heating the Glass.” *Journal of the American Chemical Society*, 2023.
17. Mizuno, F., A. Hayashi, K. Tadanaga, and M. Tatsumisago. “New, Highly Ion-Conductive Crystals Precipitated from Li<sub>2</sub>S–P<sub>2</sub>S<sub>5</sub> Glasses.” *Advanced Materials* 17, no. 7 (2005): 918–21.

## XI Next-Gen Li-ion: Low Temperature Electrolytes

Current Li-ion cells have demonstrated significant performance improvements in increasingly extreme conditions, including higher voltages, wider temperature range, and intense abuse conditions, and more recently, extreme fast charging. Yet, performance under these more extreme uses is often limited by the stability and properties of the liquid electrolytes within the cells. Traditional liquid electrolytes are composed of lithiumhexafluorophosphate ( $\text{LiPF}_6$ ) salt dissolved in mixed carbonate solvents, which include ethylene carbonate (EC), propylene carbonate (PC), ethyl methyl carbonate (EMC), dimethyl carbonate (DMC) and/or diethyl carbonate (DEC), and an array of additives included to improve performance against the utilized electrodes. These volatile and flammable organic solvents can easily undergo drastic degradation processes, often act as a limiting factor in the performance under extreme conditions including operating at high voltage, in a wide temperature range, under extreme fast charging, and/or under extreme abuse. As such, there is a need to develop novel liquid electrolytes which can operate under those extreme conditions and can retain their enhanced performance and stability.

The rest of this chapter contains detailed reports on the status of the following individual projects.

- Ethylene Carbonate-Lean Electrolytes for Low Temperature, Safe Li-ion batteries (LBNL)
- Fluorinated Solvent-Based Electrolytes for Low Temperature Li-ion Battery (ANL)
- Synthesis, Screening and Characterization of Novel Low-temperature Electrolyte for Lithium-ion Batteries (BNL)
- Extending the Operating Range and Safety of Li-Ion Batteries with New Fluorinated Electrolytes (Koura)
- Fluorinated Ester Local High Concentration Electrolytes for Operation of Li-Ion Batteries under Extreme Conditions (Stony Brook Univ)
- Novel Organosulfur-Based Electrolytes for Safe Operation of High Voltage Li-Ion Batteries Over a Wide Operating Temperature (GM).

## XI.1 Ethylene Carbonate-Lean Electrolytes for Low Temperature, Safe Li-ion batteries (LBNL)

### **Bryan D. McCloskey, Principal Investigator**

Lawrence Berkeley National Laboratory and University of California, Berkeley  
201-D Gilman Hall  
Berkeley, CA 94720  
E-mail: [bmcclosk@berkeley.edu](mailto:bmcclosk@berkeley.edu)

### **Haiyan Croft, DOE Technology Development Manager**

U.S. Department of Energy  
E-mail: [Haiyan.Croft@ee.doe.gov](mailto:Haiyan.Croft@ee.doe.gov)

Start Date: October 1, 2022

End Date: September 30, 2023

Project Funding (FY23): \$150,000

DOE share: \$150,000

Non-DOE share: \$0

### **Project Introduction**

Li-ion batteries suffer from performance limitations at low temperatures (sub- 0 °C) due to a large rise in overall cell impedance. In prior years, we identified charge transfer resistance—an interfacial process—as the dominant limitation for low temperature battery performance, and that while charge transfer resistance is dominated by processes at the anode, the cathode charge transfer resistance also contributes substantially. We also previously identified an additive ‘A’ which greatly improved the performance of the cell at lower temperatures by significantly decreasing the impedance. In FY23, we aimed to understand how electrolyte composition impacts charge transfer resistance at both electrodes, with the ultimate goal of identifying an electrolyte that enables 70% of 30 °C energy during a C/3 discharge at -20 °C. Our work has primarily focused on exploring new solvents to replace EC, that impact the interfacial compositions. We also focus on trying to understand how additive ‘A’ improves battery performance at low temperatures by looking at the solid electrolyte interface (SEI) composition.

### **Objectives**

The research this year centered on investigating a new class of electrolyte solvents to improve low temperature performance of Li-ion cells. Our objectives were to investigate several analogs of this solvent chemistry to understand its impact on the low temperature cell resistance to confirm that the new compositions did not have a negative impact on cycle life or coulombic efficiency. We further aimed to understand how cell resistance was influenced by these new compositions, and to perform a quantitative analysis of the solid electrolyte interface (SEI) and find the relation between the SEI composition and the resistance of the cell. We also looked at the effect of additive ‘A’ on the SEI composition and ultimately the cell performance.

### **Approach**

We selected different wt% of the solvent in our electrolyte and compared the respective cell performance. For the additive, we performed mass spectrometry and impedance analysis for 0.75wt% additive in the electrolyte. We tested graphite/NMC622 cells, with electrodes provided by Argonne’s CAMP facility and electrolytes with novel additives prepared at LBNL. We used battery testers and impedance-capable potentiostats to conduct the work. In-situ and ex-situ mass spectrometry techniques are used for quantitative analysis of the SEI. Galvanostatic Electrochemical Impedance Spectroscopy (GEIS) is used to find the resistance of the cell during charge/discharge of the cell, and EIS spectra are deconvoluted using the distribution of relaxation times to quantify charge transfer and SEI resistances. Differential electrochemical mass spectrometry (DEMS) is used to quantify outgassing during formation cycling of cells comprised of various electrolytes.



## Results

### Capacity characterization of electrolytes containing a new class of low-temperature solvent.

This year we moved away from  $\gamma$ -butyrolactone and started considering a new solvent, acetonitrile, as a means of affecting the charge transfer resistance, whose rise limits the access of capacity at low temperature. From previous studies, we saw that despite its excellent properties like high dielectric constant and low viscosity,  $\gamma$ -butyrolactone is unable to improve the cell performance because it reduces at a potential very close to FEC reduction potential in the cell. This leads to  $\gamma$ -butyrolactone reduced products in the SEI, which is unstable and has a higher impedance (thus lower capacities) at low temperatures. We chose acetonitrile as a co-solvent since it has very low viscosity and high dielectric strength when compared to conventional linear carbonates.

We tried different amounts of acetonitrile (ACN) in our electrolyte, with it replacing EC and EMC in our baseline electrolyte, 1.0M LiPF<sub>6</sub>, 3:7 EC:EMC (Gen 2 or baseline). A small amount of FEC (3wt%) was added to all of the ACN-containing electrolyte, without which the cells lose all of their capacity as early as the first two cycles. Figure XI.1.1 gives the capacity removed at -20°C from cells of different ACN concentrations that were brought to the top of charge at 30 °C. Table XI.1.1 shows the different solvent compositions tested.

**Table XI.1.1 Solvent Compositions(ACN:EC:EMC wt ratio) That were Tested for Low Temperature Performance**

	ACN	EC	EMC	FEC
<b>Baseline</b>	0	3	7	0wt%
<b>ACN1</b>	1	2	7	3wt%
<b>ACN2</b>	2	1	7	3wt%
<b>ACN3</b>	3	0	7	3wt%
<b>ACN4</b>	1	3	6	3wt%
<b>ACN5</b>	1	0	0	1

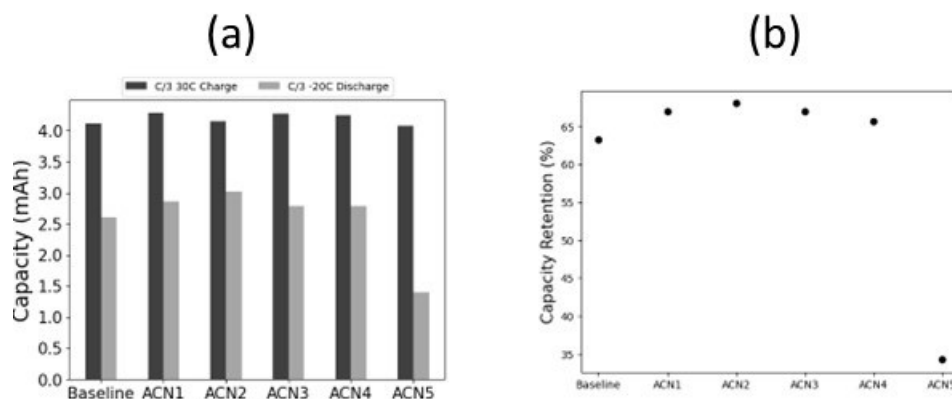


**Figure XI.1.1 (a) C/3 Charge and Discharge Capacities (2.8-4.2 V operating window) at 30 °C and -20 °C respectively, for different electrolyte compositions. (b) Capacity Retention (on the basis of Discharge Capacities) at -20 °C for different electrolyte compositions, given as a percentage of 30 °C capacity.**

We can see from the plot above that higher capacities can be removed from ACN-containing electrolytes compared to Gen 2 at 30 °C. We are also able to recover higher energies from ACN-containing electrolytes compared to Gen 2 electrolyte because the ACN-containing electrolytes have lower overall resistance than the

Gen 2 electrolyte (see Figure XI.1.2), resulting in lower overpotentials and therefore higher discharge voltages. We see from above that ACN2 performs best in terms of capacity retention, and we retain about 70.1% capacity at -20°C as compared to 63.1% retained for Baseline electrolyte at -20°C compared to 30°C. 70% of the energy recovered at 30°C is the stated USABC target and the overall objective of our project.

Replacing EMC with ACN (ACN4) also leads to an improvement in the capacity retention compared to the Baseline electrolyte, but not to the same extent as ACN3, in which ACN replaces EC. ACN5, which has only ACN and FEC (1:1 ratio by wt) has the worst performance of all, presumably a result of a poor SEI due to the lack of EC in the electrolyte composition. We see further capacity degradation with cell cycling for ACN5, and this seems to again highlight the need for EC to form a stable, low impedance SEI.

### **Electrochemical impedance analysis of cell employing ACN.**

Previously acquired data indicated that low temperature energy improvement is associated with significant improvement in interfacial charge transfer resistance. To verify this, we measured the electrochemical impedance spectroscopy of cells with different electrolytes at 20°C and -20°C. This data is presented in Figure XI.1.2.

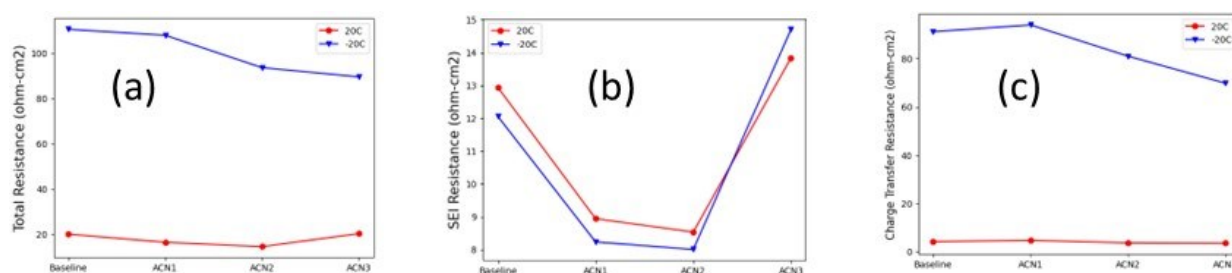


**Figure XI.1.2 (a) Total resistance of cells with ACN-containing electrolyte and baseline electrolyte at 20°C and -20°C, deconvoluted into (b) SEI Resistance and (c) Charge Transfer Resistance**

We measured the resistance using Galvanostatic Electrochemical Impedance Spectroscopy (GEIS) and the total resistance was deconvoluted into the bulk, SEI and charge-transfer resistance using distribution of relaxation times. The resistances reported above are at 50% state-of-charge (SoC). It can be seen that the total resistance is lower for ACN-based electrolytes compared to the baseline electrolyte. ACN containing electrolytes perform better at both 20°C and -20°C. The decrease in impedance is due to the significant improvement in the charge transfer resistance. As we replace EC with ACN, the charge transfer resistance decreases. It is interesting to note that for ACN3, we have the highest SEI resistance but the lowest charge transfer resistance. This points to the fact that in the absence of EC, the SEI formed on our anode is different in composition than SEI formed in the presence of EC.

Figure XI.1.3 shows the dQ/dV plots for cells with ACN electrolytes. In Figure XI.1.3 a, we can see one peak, which corresponds to FEC reduction. dQ/dV for the baseline electrolyte has 2 peaks – the first one (starting 2.5V) corresponds to LiF formation from PF<sub>6</sub><sup>-</sup> degradation and the second (starting at 2.8V) corresponds to EC reduction, as was confirmed by DEMS, wherein H<sub>2</sub> evolution start at ~2.5V and ethylene evolution starts at ~2.8V. The latter peak is absent in the presence of ACN. These observations seem to point to the fact that in ACN based electrolytes, ACN doesn't play a role in SEI formation, and it is majorly FEC that forms the SEI. Similarly, EC also seems to play a muted role in SEI formation in the FEC-containing electrolytes. To reinforce this, we performed in-situ mass spectrometry on cells with ACN-containing electrolytes.

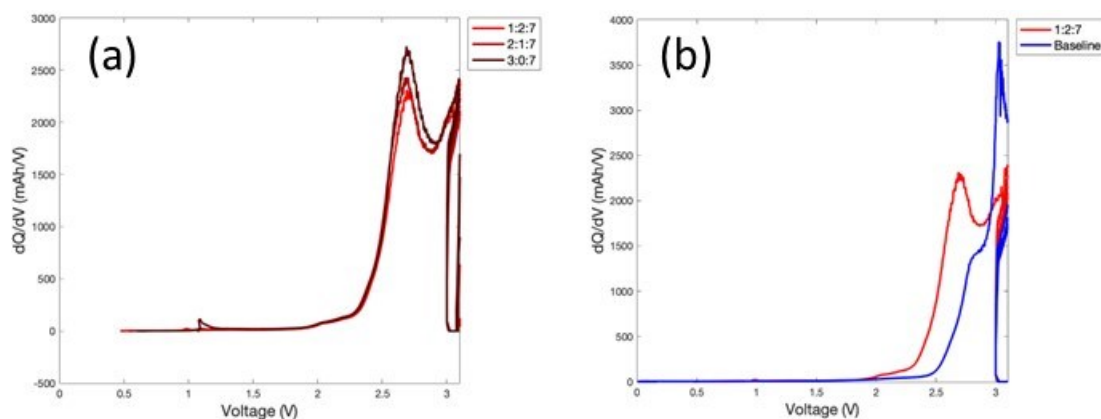


Figure XI.1.3 (a) dQ/dV for ACN-based electrolytes, peaks for all of which correspond to FEC reduction. (b) dQ/dV for Baseline vs ACN-based electrolyte. The ratios in the legend correspond to ACN1 (1:2:7), ACN2 (2:1:7), and ACN3 (3:0:7).

#### Quantification of outgassing during cell formation.

On performing Differential Electrochemical Mass Spectrometry (DEMS) on two-electrode full cells with the ACN containing electrolytes, we see that the ethylene evolution decreases, and CO<sub>2</sub> evolution increases (due to FEC reduction) (see

Figure XI.1.4). No other gas evolution is observed, which likely means that ACN is not leading to formation of any new gaseous products. These results are in line with what is observed in the dQ/dV plots above.

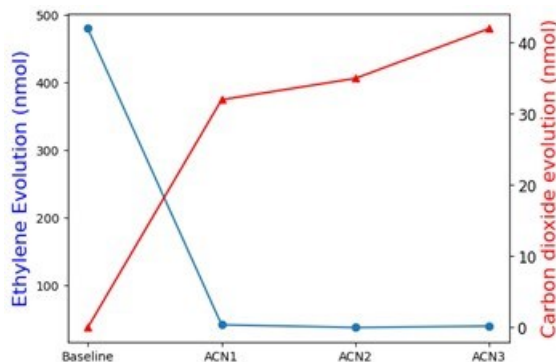


Figure XI.1.4 Ethylene (C<sub>2</sub>H<sub>4</sub>) and Carbon dioxide (CO<sub>2</sub>) evolution during the first formation cycle for ACN-based and Baseline electrolyte.

Experiments were also performed by adding 0.75wt% of additive 'A' to acetonitrile containing electrolyte but we observed that additive 'A' does not help low temperature performance in this case (in terms of both capacity and impedance).

Next steps for this work include combining results from GEIS and DEMS studies with titration mass spectrometry experiments on formed electrodes in order to quantify components of the SEI and observe how the SEI component quantities change in the presence of ACN. We also aim to perform GEIS experiments on 3-electrode cells to understand the effect of ACN on Gr and NMC electrodes, to learn which electrode is affected more by ACN. This can help us understand how ACN helps improve the cell performance at low temperatures at a structural level and increase our understanding of interfaces.

## Conclusions

The key conclusions from our research this year are:

1. On replacing EC with acetonitrile in our baseline electrolyte, we are able to achieve higher discharge energies at -20 °C, with some -20 °C energy densities being above 70% of the 30 °C energy densities, thereby achieving the target capacity of this project.
2. We confirm that the improved low temperature performance of our ACN-based electrolyte is a result of a sizable decrease in charge transfer resistance in the cell compared to the Baseline electrolyte. Only a modest rise in SEI resistance is observed when employing ACN.
3. The chemistry of the formation cycling is clearly impacted in the presence of ACN, as a decrease in C<sub>2</sub>H<sub>4</sub> evolution is observed with increasing ACN amounts.

## Key Publications

1. Fang, C.; Tran, T.-N.; Ahmed, F.; Hubble, D.; Fu, Y.; McCloskey, B. D.; Battaglia, V. S.; Liu, G. “Silicic acid electrolyte additive reduces charge transfer impedance at sub-ambient temperature for lithium-ion rechargeable batteries.” *Electrochemistry Communications* (2023) 150, 107489.

## Acknowledgements

We thank Stephen Trask, Andrew Jansen, Alison Dunlop, and their CAMP Facility colleagues for providing the graphite and NMC622 electrodes used in our studies.

## XI.2 Fluorinated Solvent-Based Electrolytes for Low Temperature Li-ion Battery (ANL)

### Zhengcheng (John) Zhang, Principal Investigator

Argonne National Laboratory  
9700 South Cass Avenue  
Lemont, IL 60439  
E-mail: [zzhang@anl.gov](mailto:zzhang@anl.gov)

### Tien Duong, DOE Technology Development Manager

U.S. Department of Energy  
E-mail: [Tien.Duong@ee.doe.gov](mailto:Tien.Duong@ee.doe.gov)

Start Date: October 1, 2022

End Date: September 30, 2023

Project Funding (FY23): \$300,000

DOE share: \$300,000

Non-DOE share: \$0

### Project Introduction

Electric vehicles require Li-ion batteries (LIB) that not only have high energy/power densities at low cost, but also can achieve superior performances at low temperature (LT) environment ( $< 0^{\circ}\text{C}$ ). However, current battery technology has not yet met the satisfactory LT performance requirement, in large part due to the limitation in the electrolyte and the electrolyte-derived electrode/electrolyte interfaces. Particularly at LT, the electrolyte ionic conductivity is significantly reduced, and the interface impedances are significantly increased, severely limiting the energy/power of LIB and potentially causing undesired lithium plating.[1] This project aims to improve the electrolyte performances at LT using fluorinated solvents.

### Objectives

The objective is to develop electrolytes that enable LIB to deliver  $>70\%$  of usable energy at  $-20^{\circ}\text{C}$  compared to the normal battery operating temperature ( $30^{\circ}\text{C}$ ) at C/3 rate, and to achieve excellent cycling performances and calendar life at high temperatures ( $40\sim 60^{\circ}\text{C}$ ).

### Approach

Our first approach is to use fluorinated carbonates as co-solvents for the state-of-the-art (SOA) electrolyte. Due to the weaker polar-polar interaction in fluorine-containing groups, fluorinated carbonates are anticipated to show lower melting points than their non-fluorinated counterparts, which can be beneficial for LT application. Moreover, our previous studies demonstrated that fluorinated carbonates can significantly improve high temperature cycling performances of LIB.[2-4] Thus, incorporating fluorinated carbonates into the SOA electrolyte can potentially improve the performances of LIB at both low and high temperature.

Our second approach is to use fluorinated carboxylate esters as single solvents with solid-electrolyte interphases (SEI)-forming additives. Carboxylate esters generally have very low melting points, good dielectric constants, and low viscosities; thus, it is anticipated that carboxylate esters and its fluorinated derivatives can likely maintain excellent ionic conductivities at LT. Previous studies have reported the use of carboxylate esters or fluorinated carboxylate esters as co-solvents in the SOA electrolyte for LIB;[5, 6] however, their use as single solvents is less explored. The major challenge of using carboxylate esters is that carboxylate esters cannot form stable graphite SEI and thus SEI-forming additives are required.

### Results

#### *Physical property and modeling results for fluorinated ester-based electrolytes*

The state-of-the-art electrolyte for low temperature performances is based on a carboxylate ester solvent with fluoroethylene carbonate (FEC) co-solvent and additive. Although EA has a low melting point and high ionic conductivity, it exhibits a stronger binding to  $\text{Li}^+$  ions than EMC due to the absence of an electron-

withdrawing ester group, resulting in a higher desolvation energy. To decrease the desolvation energy, one of the limiting factors of  $\text{Li}^+$  ion kinetics at low temperatures, we functionalized the terminal methyl group ( $-\text{CH}_3$ ) to trifluoro methyl group ( $-\text{CF}_3$ ), a strong electron-withdrawing group. In addition, the fluorination enhances high voltage stability with reduced the highest occupied molecular orbital (HOMO) levels, preventing the possible oxidation of hydrogen at high voltage. The design of the electrolyte and the physical properties of all fluorinated esters are shown in Figure XI.2.1(a) and its Table.

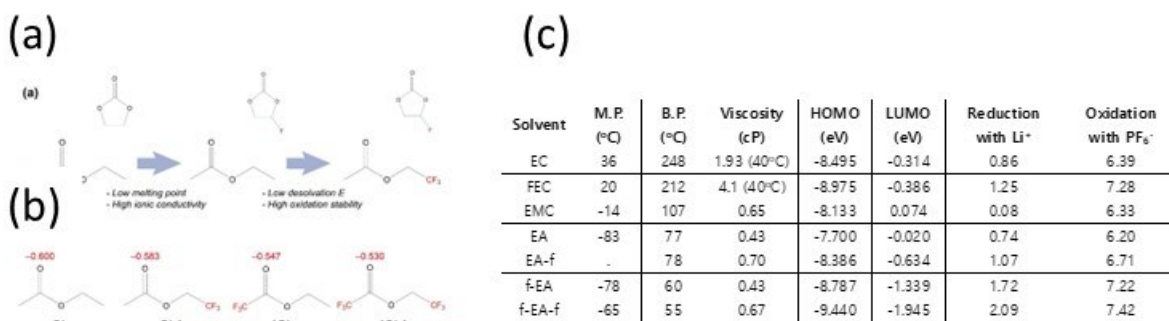


**Figure XI.2.1** (a) Scheme of solvent design transition from carbonates to fluorinated esters. (b) Atomic charge analysis of carbonyl groups in EA, EA-f, f-EA, and f-EA-f. (c) Physical properties of electrolyte solvents used in this study.

Understanding the solvation structures of the fluorinated electrolytes is important because the solvents coordinated with Li are likely to be reduced to form the SEI layer and therefore impact the low temperature performance. The degree of ion-pairing also affects solubility and ionic conductivity. 10% FEC was formulated with F-ester solvents since pure EA or EA-f solvents cannot stabilize the SEI layer. To analyze the  $\text{Li}^+$  solvation structures of F-ester/FEC electrolytes, we conducted MD simulation to calculate the solvation species and their distribution.

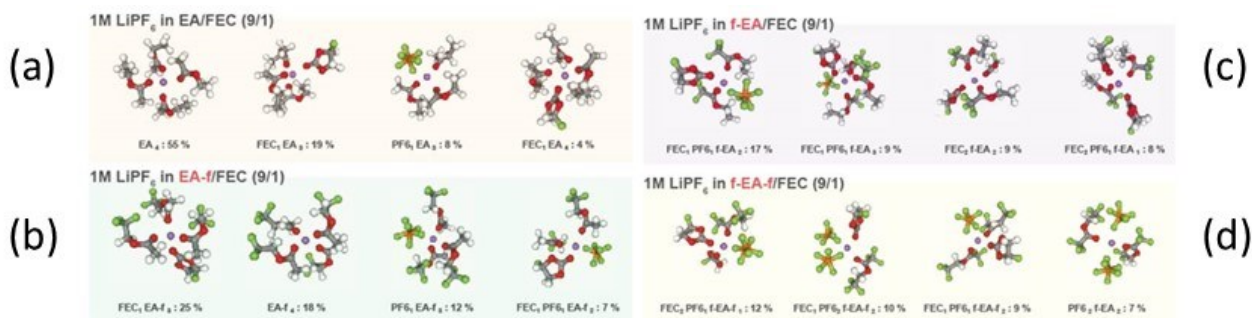


**Figure XI.2.2** Representative solvation structures from MD simulations. (a) 1 M  $\text{LiPF}_6$  in EA/FEC (9/1); (b) 1 M  $\text{LiPF}_6$  in EA-f/FEC (9/1); (c) 1 M  $\text{LiPF}_6$  in f-EA/FEC (9/1); and (d) 1 M  $\text{LiPF}_6$  in f-EA-f/FEC (9/1).

As shown in Figure XI.2.2(a), fluorine-free EA solvent has strong solvation energy and high coordination number and dominates the  $\text{Li}^+$  solvation sheath (55%), which requires higher energy for  $\text{Li}^+$  to desolvate and intercalate in graphite anode. This process becomes even more sluggish at low temperatures. However, when fluorinated EA solvents are used as main solvents, their solvation structure and solvation species distribution is completely changes. Figure XI.2.2(b), (c) and (d) show the  $\text{Li}^+$  solvation structures of the main species for EA-f, f-EA and f-EA-f, respectively. As the fluorination degree increases, the diversity of  $\text{Li}^+$  solvation shells increase due to the weak solvating power. FEC and  $\text{PF}_6^-$  anion become nearly equal shell participants for f-EA and high fluorinated f-EA-f electrolyte.

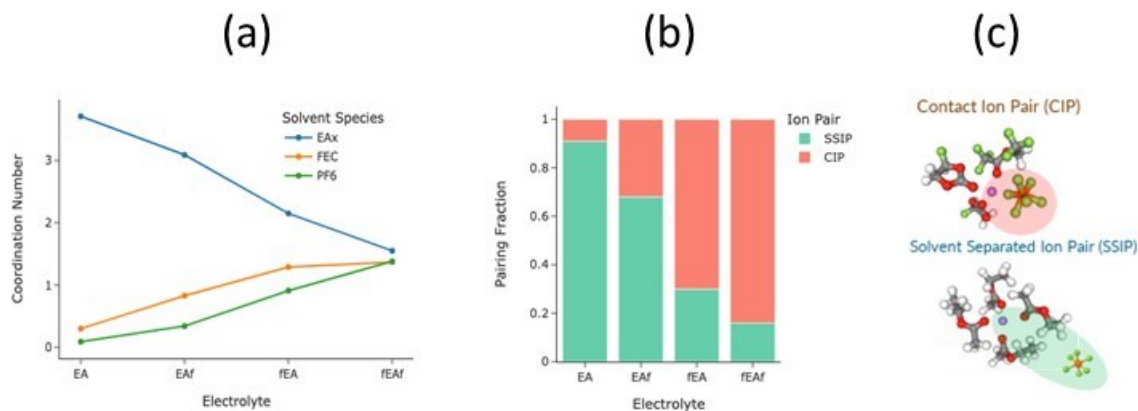


Figure XI.2.3 (a) Coordination number of fluorinated ester EA-f, f-EA and f-EA-f and FEC from MD simulations; (b) quantification of contact ion pairs (CIP) and solvent separated ion pairs (SSIP) for 1 M LiPF<sub>6</sub> in EA/FEC (9/1), 1 M LiPF<sub>6</sub> in EA-f/FEC (9/1), 1 M LiPF<sub>6</sub> in f-EA/FEC (9/1) and 1 M LiPF<sub>6</sub> in f-EA-f/FEC (9/1) electrolyte; (c) indicative structure of CIP and SSIP.

Increasing fluorination of EA decreases solvating strength with Li<sup>+</sup> with the order of f-EA-f < f-EA < EA-f < EA. With increasing fluorination degree, Li<sup>+</sup>-EA-x solvation shell becomes more balanced. It is observed that weaker binding of f-EA and f-EA-f created more space for FEC and PF<sub>6</sub><sup>-</sup> to participate in the Li<sup>+</sup> solvation, leading to the formation of high concentration of contact ion pairs (CIP). MD simulation explain the modified solvation structures and energies in the EA-derivative electrolytes. The MD simulation data are showed in Figure XI.2.3. This MD results are consistent with the solubility experiment at low temperature shown in Figure XI.2.4(a) and (b). At RT, fluorinated esters can dissolve 1 M LiPF<sub>6</sub> salt and showed comparable ionic conductivity with Gen 2 electrolyte; however, when temperature drops to -20°C and -40°C, LiPF<sub>6</sub> salt starts to precipitate out from the f-EA and f-EA-f solution. Only EA-f electrolyte exhibits the optimal low temperature property for cell performance testing.

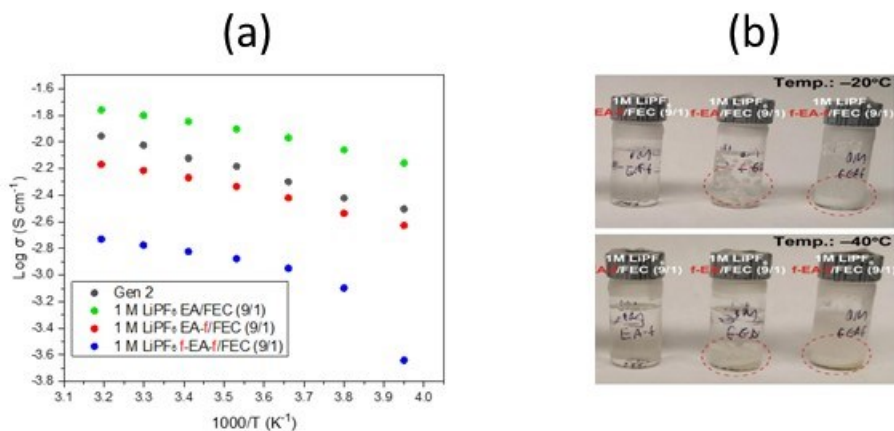


Figure XI.2.4 (a) Arrhenius plots of electrolytes with different fluorinated solvents and Gen 2 and (b) lithium salt solubility test for 1M LiPF<sub>6</sub> in EA-f/FEC (9/1) (left), 1M LiPF<sub>6</sub> in f-EA/FEC (9/1) (center), and 1M LiPF<sub>6</sub> f-EA-f/FEC (9/1) (right) electrolytes at -20°C and -40°C.

## Electrochemical performances

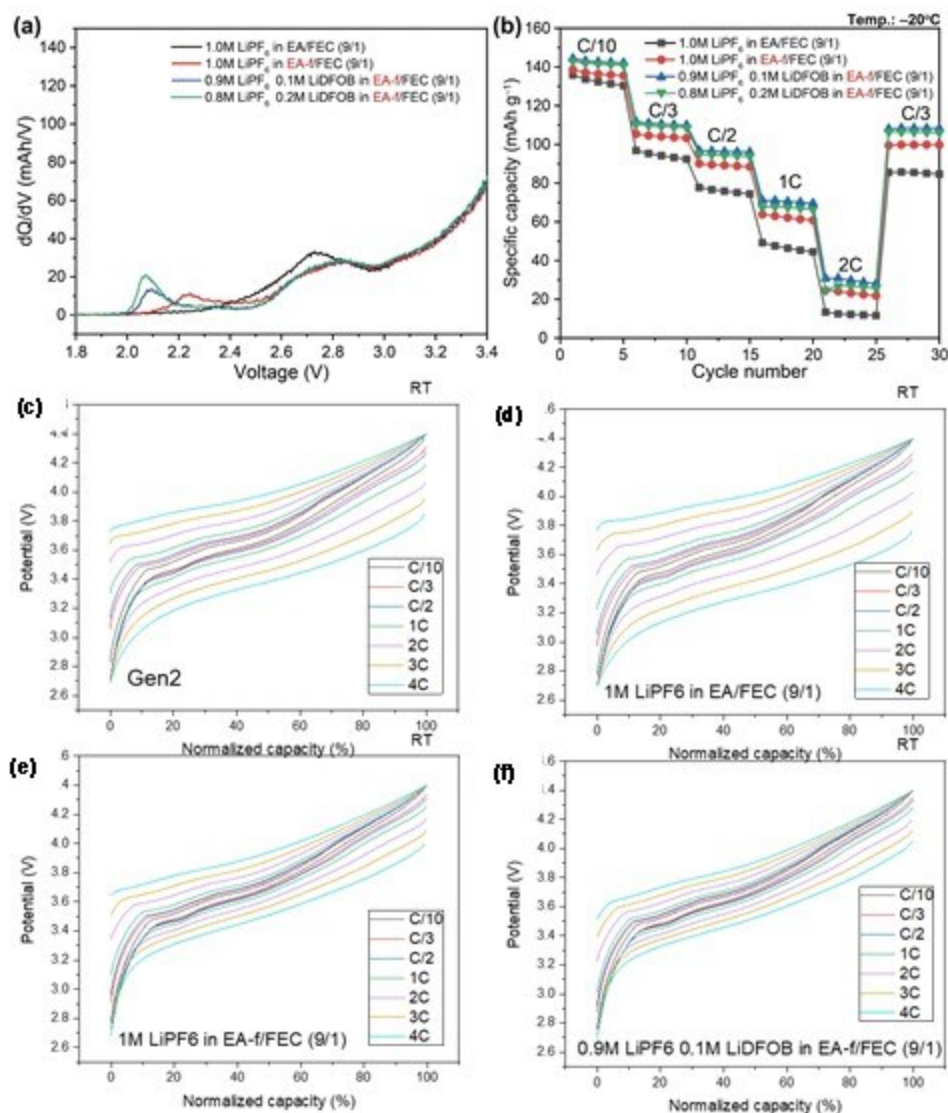


Figure XI.2.5 (a)  $dQ/dV$  profiles of graphite|NMC622 cells with different electrolytes during the 1<sup>st</sup> charging; (b) C-rate capability with different electrolytes at  $-20^{\circ}\text{C}$ . Normalized voltage profiles at various C-rates with (c) Gen 2, (d) 1 M LiPF<sub>6</sub> in EA/FEC (9/1), (e) 1 M LiPF<sub>6</sub> in EA-f/FEC (9/1), and (f) 0.9 M LiPF<sub>6</sub> + 0.1 M LiDFOB in EA-f/FEC (9/1) electrolyte.

In our previous report, we unveiled that the SEI formation plays a crucial role in rate capability and stability at low temperatures. With that in mind, 0.1 M LiDFOB was used as an SEI formation co-additive to EA-f based electrolyte to further strengthen the SEI layer. The effect of LiDFOB additive was verified in  $dQ/dV$  analysis (Figure XI.2.5(a)) and its concentration was optimized from the rate capability test results (Figure XI.2.5(b-f)). The optimized electrolyte was 0.9 M LiPF<sub>6</sub> + 0.1 M LiDFOB in EA-f/FEC (9/1). The SEI layer formation can be seen in  $dQ/dV$  profiles of NMC622/graphite cells at the first charging step. There was an EC reduction peak at 3.0 V in Gen 2. While there was a free FEC reduction peak at 2.7 V in EA electrolyte, Li<sup>+</sup>-coordinated FEC was reduced earlier at 2.3 V in EA-f electrolyte. This is well matched with the coordination number change of FEC in electrolytes from MD simulations. In the EA-f electrolyte with LiDFOB additive, DFOB<sup>-</sup> was reduced earlier than Li<sup>+</sup>-coordinated FEC, forming an ion-conductive SEI layer. In contrast, for f-EA electrolyte-based



electrolyte, f-EA solvent was reduced earlier than FEC and showed high peaks at 2.6 and 2.7 V due to the high reduction potential which could not stabilize the surface of graphite anode.

### Conclusions

We have systematically investigated the effect of the position and degree of fluorination in EA solvent on electrochemical performances. We reveal that a high degree of fluorination or fluorination close to ester group imposes more electron-withdrawing effect, resulting in low atomic charges, low binding energies to Li<sup>+</sup> ions, low ionic conductivities, and poor solubilities at low temperatures. Since interfacial resistance is governed by the kinetics of Li<sup>+</sup> ion desolvation, charge transfer across the SEI and ion conductivity, EA-f electrolyte shows the best electrochemical performance at sub-zero temperature. EA-f effectively balances the property trade-offs associated with fluorination, outperforming both f-EA and f-EA-f based electrolytes. This study provides a deep insight on design principles of novel fluorinated electrolytes for LIBs operating at low temperatures.

### Key Publications

1. Dong-Joo Yoo, Qian Liu, Orion Cohen, Minkyu Kim, Kristin A. Persson, and Zhengcheng Zhang. Rational Design of Fluorinated Electrolytes for Low Temperature Lithium-Ion Batteries. *Adv. Energy Mater.*, 2023, 2204182.
2. Xin Su, Ying Xu, Jianzhong Yang, and Zhengcheng, Zhang. Liquid electrolyte for low-temperature lithium batteries: main limitations, current advances, and future perspectives. *Energy Storage Materials* 2023, 56, 642-663.
3. Dong-Joo Yoo, Qian Liu, Orion Cohen, Minkyu Kim, Kristin A. Persson, and Zhengcheng Zhang. Understanding the Role of SEI Layer in Low-Temperature Performance of Lithium-Ion Batteries. *ACS Applied Material & Interfaces* 2022, 14, 9, 11910–11918.

### References

1. Choi, J. W.; Aurbach, D., Promise and reality of post-lithium-ion batteries with high energy densities. *Nature Reviews Materials* 2016, 1 (4), 16013.
2. Etacheri, V.; Marom, R.; Elazari, R.; Salitra, G.; Aurbach, D., Challenges in the development of advanced Li-ion batteries: a review. *Energy & Environmental Science* 2011, 4 (9), 3243-3262.
3. Dunn, B.; Kamath, H.; Tarascon, J.-M., Electrical Energy Storage for the Grid: A Battery of Choices. *Science* 2011, 334 (6058), 928-935.
4. Bandhauer, T. M.; Garimella, S.; Fuller, T. F., A Critical Review of Thermal Issues in Lithium-Ion Batteries. *Journal of The Electrochemical Society* 2011, 158 (3), R1-R25.
5. Gupta, A.; Manthiram, A., Designing advanced lithium - based batteries for low - temperature Conditions. *Advanced energy materials* 2020, 10 (38), 2001972.
6. Jow, T. R.; Delp, S. A.; Allen, J. L.; Jones, J.-P.; Smart, M. C., Factors Limiting Li+Charge Transfer Kinetics in Li-Ion Batteries. *Journal of The Electrochemical Society* 2018, 165 (2), A361-A367.

### Acknowledgements

This work was funded by the U.S. Department of Energy (DOE), Office of Energy Efficiency and Renewable Energy, Vehicle Technologies Office. Support from Haiyan Croft and Tien Duong of Office of Vehicle Technology Office is gratefully acknowledged. The submitted manuscript has been created by UChicago Argonne, LLC, Operator of Argonne National Laboratory, which is supported by DOE Office of Science under Contract No. DE-AC02-06CH11357.

## XI.3 Synthesis, Screening and Characterization of Novel Low-temperature Electrolyte for Lithium-ion Batteries (BNL)

### **Xiao-Qing Yang, Principal Investigator**

Chemistry division, Brookhaven National laboratory  
Bldg. 555, Brookhaven National Lab.  
Upton, NY 11973  
E-mail: [xyang@bnl.gov](mailto:xyang@bnl.gov)

### **Enyuan Hu,, Co-Principal Investigator**

Chemistry division, Brookhaven National laboratory  
Bldg. 555, Brookhaven National Lab.  
Upton, NY 11973  
E-mail: [enhu@bnl.gov](mailto:enhu@bnl.gov)

### **Tien Duong, DOE Technology Development Manager**

U.S. Department of Energy  
E-mail: [Tien.Duong@ee.doe.gov](mailto:Tien.Duong@ee.doe.gov)

Start Date: October 1, 2022	End Date: September 30, 2023	
Project Funding (FY23) : \$1,000,000	DOE share: \$1,000,000	Non-DOE share: \$0

### **Project Introduction**

This project did not receive new funding for FY2023. It used the carryover fund from FY2024 to wrap up some uncompleted research work left from the FY2022 efforts, and analyzed the results of studies, organized them into manuscripts and submitted them for scientific publications.

While the energy density and cost of batteries powering electric vehicles are becoming competitive with internal combustion engines, there are still several critical issues that need to be addressed. The low temperature performance of the batteries and the fast charge capability are two of them. Current lithium-ion batteries (LIB) experience a significant capacity drop down to about one fifth of its room temperature capacity at -30 °C. Current LIB electrolyte is often based on ethylene carbonate (EC) as a major solvent component due to the high dielectric constant and formation of an excellent solid-electrolyte-interphase (SEI) on the graphite anode. Unfortunately, EC has a rather high melting point (37 °C), leading to significantly increased viscosity and severely decreased Li<sup>+</sup> conductivity at low temperatures. LIB also has high impedance at low temperature due to the sluggish Li<sup>+</sup> transport through SEI. These issues result in the much-decreased capacity and poor cyclability at low temperature. Therefore, to improve the low temperature performance of LIB, it is critical to develop new electrolyte system that has low viscosity, high Li<sup>+</sup> conductivity, and is able to form stable and low-impedance interphase on both anode and cathode. This consortium, with team members of Brookhaven National Laboratory (**BNL**), DEVCOM Army Research Laboratory (**ARL**), University of Maryland (**UMD**), and University of Rhode Island (**URI**), addresses the low temperature electrolyte challenge through integrated molecular modeling, electrolyte components design, synthesis, testing, and advanced characterization.

### **Objectives**

The project objective is to develop next generation electrolyte formulations that enable the Li-ion batteries to deliver >70% of room temperature energy at -20 °C, while still meeting the United States Advanced Battery Consortium (USABC) Operating Environment Conditions (-30 to +52 °C), fast charge capability, calendar life testing at 30, 40, 50, and 60 °C.

## Approach

Up to date, most low temperature electrolyte development efforts have been focused on adjusting a combination of different commercially available solvents only, and a decent low-temperature performance can only be achieved by sacrificing other properties such as high-temperature and high voltage performance. Keeping the goals of automobile application in mind, to achieve the desired low temperature performance while maintaining other performance, we need to design new electrolyte systems using an integrated approach starting from theoretical calculations of the new electrolytes, understanding the electrolyte-electrode interphases, to the synthesis of new solvents, salts, and additives, as well as advanced characterizations of the electrolyte systems in actual battery environments. Molecular modeling has been used to predict the transport property, electronic structure and the initial solid electrolyte interphase (SEI) formation mechanisms to propose possible candidates that have high  $\text{Li}^+$  conductivity, good stability, as well as low-impedance SEI. These candidates have been or will be synthesized and purified for experimental validation. The new electrolyte system is subject to a series of electrochemical testing and diagnostic studies for performance evaluation and mechanistic studies. This knowledge provides feedback to the theoretical model for better understanding and more accurate predictions.

Solvent candidates to be explored include but are not limited to ethers, esters, nitriles and their fluorine-substituted derivatives. Salt candidates include lithium tetrafluoroborate ( $\text{LiBF}_4$ ), lithium hexafluorophosphate ( $\text{LiPF}_6$ ), lithium bis(fluorosulfonyl) imide ( $\text{LiFSI}$ ), lithium bis(trifluoromethanesulfonyl) imide ( $\text{LiTFSI}$ ), lithium bis(oxalato) borate ( $\text{LiBOB}$ ), and lithium difluoroxyalato borate ( $\text{LiDFOB}$ ) etc. Additive candidates include vinylene carbonate (VC), fluoro ethylene carbonate (FEC), phosphites, phosphates, sulfones, sultones, and sulfates.

New electrolyte systems are subject to a series of characterizations and theoretical calculations such as Infrared and Raman spectroscopies as well as x-ray and neutron pair distribution function (xPDF and nPDF) analysis. The results have been analyzed together with molecular dynamic (MD) calculations to understand the structure of the electrolyte. The SEI and cathode-electrolyte-interphase (CEI) components are subject to characterizations such as high energy x-ray photoelectron spectroscopy (HAXPES), resonant inelastic x-ray scattering (RIXS), x-ray absorption spectroscopy (XAS), x-ray photoemission electron microscopy (XPEEM), as well as cryo transmission electron microscopy (Cryo TEM) to obtain the structure, depth-profiling, and chemical distribution in the battery interphases.

## Results

The **BNL** team coordinated the research works carried out by the **ARL**, **UMD** and **URI** teams, participated in the preparations of several research papers for scientific publications with these teams in FY2023. **BNL** team also took the lead in preparation of a review paper on “Low Temperature Electrolytes for Lithium-ion and Lithium Metal Batteries”. This paper has been accepted by the *Electrochemical Energy Reviews* for publication in 2023. The Graphic Abstract of this paper is shown in Figure XI.3.1.

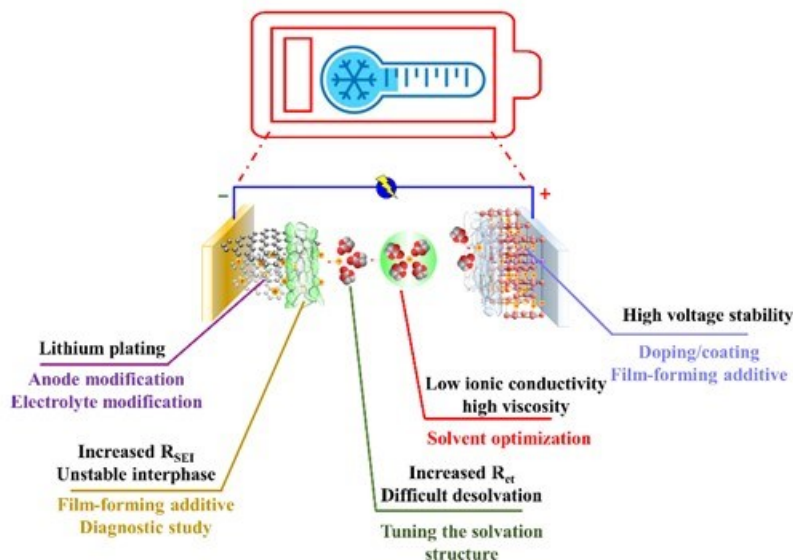
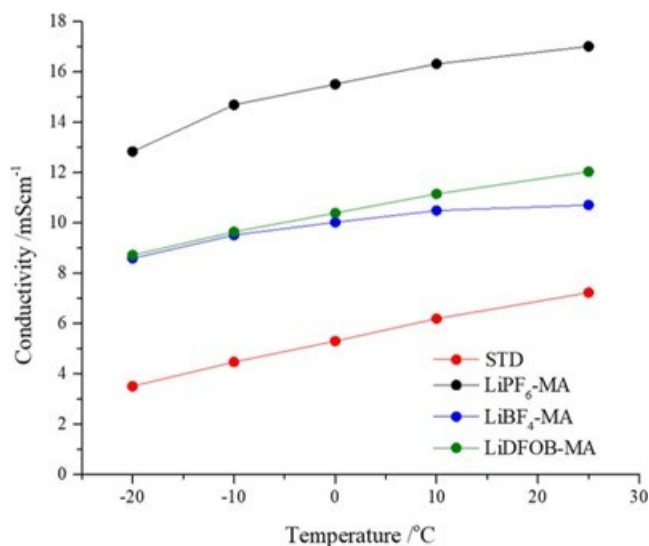


Figure XI.3.1 The graphic Abstract of a review paper to be published on *Electrochemical Energy Reviews*

The University of Rhode Island (URI) team continued their efforts on the development and studies on the novel methyl acetate (MA)-based electrolyte systems and their potential applications in low-temperature electrolytes. The effects of three lithium salts,  $\text{LiBF}_4$ ,  $\text{LiPF}_6$ , and lithium bis(oxalato)borate (LiBOB), were first investigated, and then, three different electrolyte additives, lithium bis(oxalato)borate (LiBOB), lithium difluorophosphate ( $\text{LiF}_2\text{PO}_2$ ), and lithium bis-(trimethylsilyl) phosphate (LiTMSP), were investigated with the ester-based electrolyte formulation, aiming to specifically address the poor SEI properties and improve the low-temperature and room-temperature battery performance. The surface films generated in the presence of the novel electrolyte formulations were studied via ex situ surface analysis using (LiBOB) additive to understand the effect of additives on the cycling performance at each temperature.

To understand the influences of the three different salts in the MA-based electrolyte formulations on battery performance, ionic conductivities of the electrolyte systems were measured at different temperatures and are given in Figure XI.3.2. The ionic conductivity of the  $\text{LiPF}_6$ -MA electrolyte ( $17.01 \text{ mS cm}^{-1}$ ) is higher than that of the other two MA-based electrolyte formulations which have ionic conductivities of  $10.70 \text{ mS cm}^{-1}$  ( $\text{LiBF}_4$ -MA) and  $12.04 \text{ mS cm}^{-1}$  ( $\text{LiDFOB}$ -MA) at  $25^\circ\text{C}$ . This can be attributed to the low dissociation energy of  $\text{LiPF}_6$  due to the larger size of the  $\text{PF}_6^-$  anion which is known to form solvent solvated ion pairs. Considering the two formulations with  $\text{LiPF}_6$  as the salt, the ester formulation has a much higher ionic conductivity compared to the carbonate at  $25^\circ\text{C}$  ( $17.01$  vs  $7.23 \text{ mS cm}^{-1}$ ). This implies that solvents influence the ion transport properties through different intramolecular inter- actions and through properties related to melting points, viscosity, etc. Previous reports suggest that  $\text{LiPF}_6$  in carbonate-based electrolytes has a much higher ionic conductivity than  $\text{LiBF}_4$  and that  $\text{LiDFOB}$  has an ionic conductivity in between that of  $\text{LiPF}_6$  and  $\text{LiBF}_4$ .  $\text{BF}_4^-$  is known to strongly coordinate with  $\text{Li}^+$ , resulting in more contact ion pairs. However, in the novel ester-based electrolyte system, when the temperature decreases, the ionic conductivity change of the  $\text{LiPF}_6$ -MA electrolyte is greatest and the change in that of the  $\text{LiBF}_4$ -MA electrolyte is the smallest, though the relative dimension of the ionic conductivity does not change. Overall, a clear trend in higher ionic conductivity for all three Li salts in ester-based electrolytes was observed compared to the standard electrolyte (STD) used in this study of  $1 \text{ M LiPF}_6$  in EC: ethylmethyl carbonate (3:7, v/v) over the temperature range of  $20^\circ\text{C}$  to  $-20^\circ\text{C}$ . The improved low-temperature performance observed with the ester-based electrolytes compared to the STD carbonate electrolyte is related to the increased ionic conductivity of the electrolyte formulations containing esters.



**Figure XI.3.2** Ionic conductivities of the three salts in the MA–FEC solvent system and the STD electrolyte measured at different electrolytes.

The charge–discharge cycling performance of NCM622 || graphite cells with the alternative lithium salts along with the STD electrolyte at low temperature ( $-20\text{ }^{\circ}\text{C}$ ) and room temperature ( $25\text{ }^{\circ}\text{C}$ ) is given in Figure XI.3.3 a, b, respectively. For low-temperature cycling, all three MA/FEC-based solvent systems reveal higher reversible capacities than the carbonate-based STD electrolyte system. At low temperature, among the three MA-based formulations, the one containing  $\text{LiBF}_4$  gives the best cycling performance with an average capacity of  $99.9\text{ mAh g}^{-1}$  over 50 cycles. Both  $\text{LiDFOB}$  and  $\text{LiPF}_6$  in MA have better cycling performance at  $-20\text{ }^{\circ}\text{C}$  compared to the STD electrolyte. However, at room temperature, the STD electrolyte outperforms all three salts in the MA-based electrolyte as depicted in Figure XI.3.3b. When comparing the three Li salts in MA/FEC-based formulations, only the formulation containing  $\text{LiPF}_6$  has comparable reversible capacities ( $133\text{ mAh g}^{-1}$ ) to the STD ( $141\text{ mAh g}^{-1}$ ). Despite the lower initial capacity, both  $\text{LiBF}_4$  and  $\text{LiDFOB}$  electrolytes, as previously reported, have good capacity retention after 100 cycles, retaining 84 and 94% of their initial capacities, respectively.

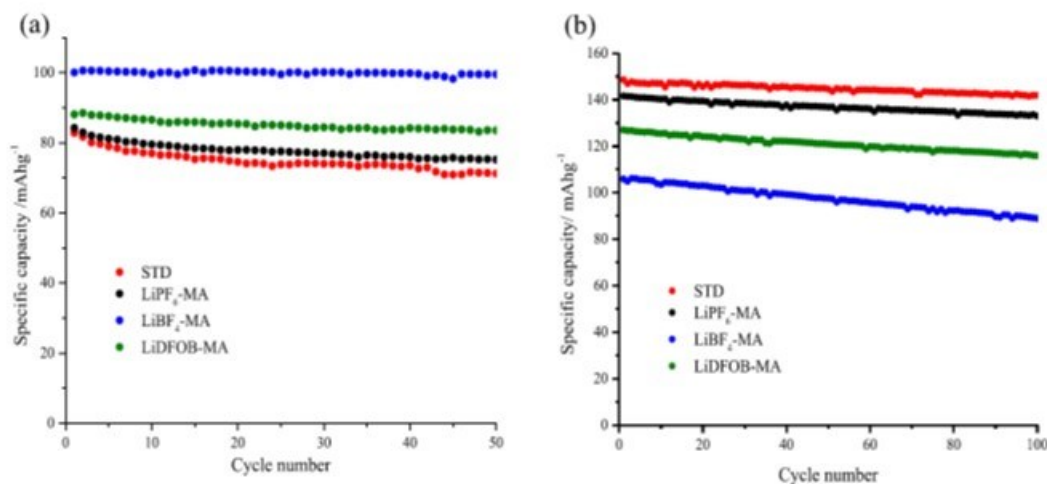


**Figure XI.3.3** Charge–discharge cycling performance of NCM 622 || graphite cells with 3 salts in the MA–FEC solvent system and the STD electrolyte at (a)  $-20\text{ }^{\circ}\text{C}$  and (b)  $25\text{ }^{\circ}\text{C}$ .

Since the  $\text{LiBF}_4$ -MA electrolyte formulation provided the best capacities at  $-20\text{ }^\circ\text{C}$ , a further investigation has been conducted to improve room-temperature performance in  $\text{LiBF}_4$ -MA electrolyte-containing cells without compromising low-temperature performance. The  $\text{LiBF}_4$ -MA electrolyte formulation was modified by introducing electrolyte additives to generate a more stable SEI on the anode surface. Long-term cycling performance results of the  $\text{LiBF}_4$ -MA electrolyte containing various additives at low temperature ( $-20\text{ }^\circ\text{C}$ ) and room temperature ( $25\text{ }^\circ\text{C}$ ) are shown in Figure XI.3.4. Cells with ester-based electrolyte have superior performance compared to the STD electrolyte formulations for cells cycled at low temperature ( $-20\text{ }^\circ\text{C}$ ). Cells containing the STD electrolyte have an average capacity of  $\sim 72\text{ mAh g}^{-1}$  after 100 cycles, whereas  $\text{LiBF}_4$ -MA, the base electrolyte (blue), has an average capacity of  $\sim 99\text{ mAh g}^{-1}$ . Incorporation of 1% LiBOB (gray) and 1%  $\text{LiF}_2\text{PO}_2$  (orange) resulted in a slight decrease in the overall capacity of the cells at low temperature, while addition of 1% LiTMSP (green) improves the low-temperature capacity with the highest average capacity of  $\sim 105\text{ mAh g}^{-1}$  over 100 cycles.

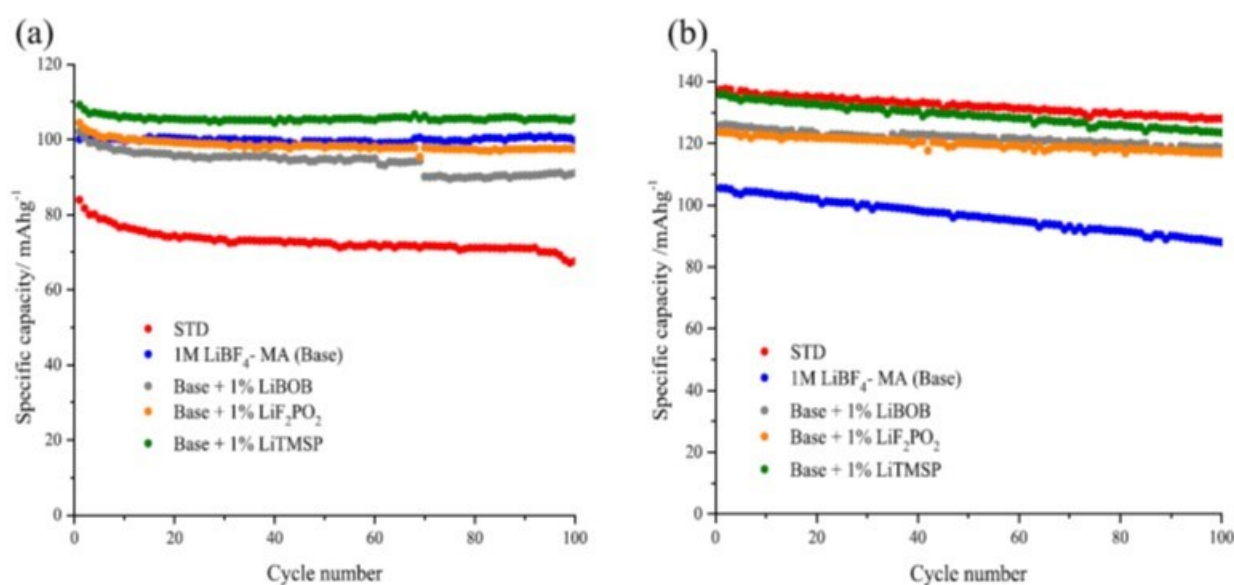


**Figure XI.3.4** Charge–discharge cycling performance of NCM 622 || graphite cells with STD;  $\text{LiBF}_4$ -MA (base); and electrolytes with 1% LiBOB, 1%  $\text{LiF}_2\text{PO}_2$ , and 1% LiTMSP additives at (a)  $-20\text{ }^\circ\text{C}$  and (b)  $25\text{ }^\circ\text{C}$ .  $\text{LiF}_2\text{PO}_2$ , and 1% LiTMSP electrolyte formulations at (a)  $-20$  and (b)  $25\text{ }^\circ\text{C}$ .

To understand how the incorporation of the different additives leads to improved low- and room-temperature cycling performance, XPS was conducted on the graphite anodes of the cells after formation cycling and 50 cycle cycling at room temperature and at  $-20\text{ }^\circ\text{C}$ . As shown in Figure XI.3.5, the surface films generated with the STD electrolyte after formation cycling appear to differ from the surface film derived from ester containing electrolytes. The anode surface films generated from the ester-containing electrolytes contain peaks characteristic of boron-containing species (B–F at 192 eV). Moreover, additional differences are observed for the ester-based electrolyte formulations which contain different additives. Compared to the electrolytes containing additives, increased intensities for F 1s (LiF at 685 eV), and B 1s (B–O at 192 eV, B–F at 193 eV) spectra observed for the base ester electrolyte ( $\text{LiBF}_4$ -MA) suggesting that more decomposition of the  $\text{LiBF}_4$  salt has occurred to form a thicker SEI in the absence of additives. A thinner SEI was observed with the different electrolytes containing additives as suggested by reduced peak intensities for (LiF at 685 eV,  $\text{Li}_x\text{PF}_y\text{O}_z$  at 687 eV). In addition, significant differences in surface film composition were observed for electrolytes containing 1% LiTMSP or 1% LiBOB. A phosphate-rich SEI (134 eV) is observed with added 1% LiTMSP, while an SEI rich in oxalato-borates (B–O and B–F at 192/193 eV) is observed for electrolytes containing 1% LiBOB. Similar to the electrolyte containing LiTMSP, the surface film generated from the 1%

LiF<sub>2</sub>PO<sub>2</sub> electrolyte consists of an inorganic-rich SEI which primarily consists of LiF and Li<sub>x</sub>PF<sub>y</sub>O<sub>z</sub> and boron-containing decomposition products from BF<sub>4</sub><sup>-</sup>.

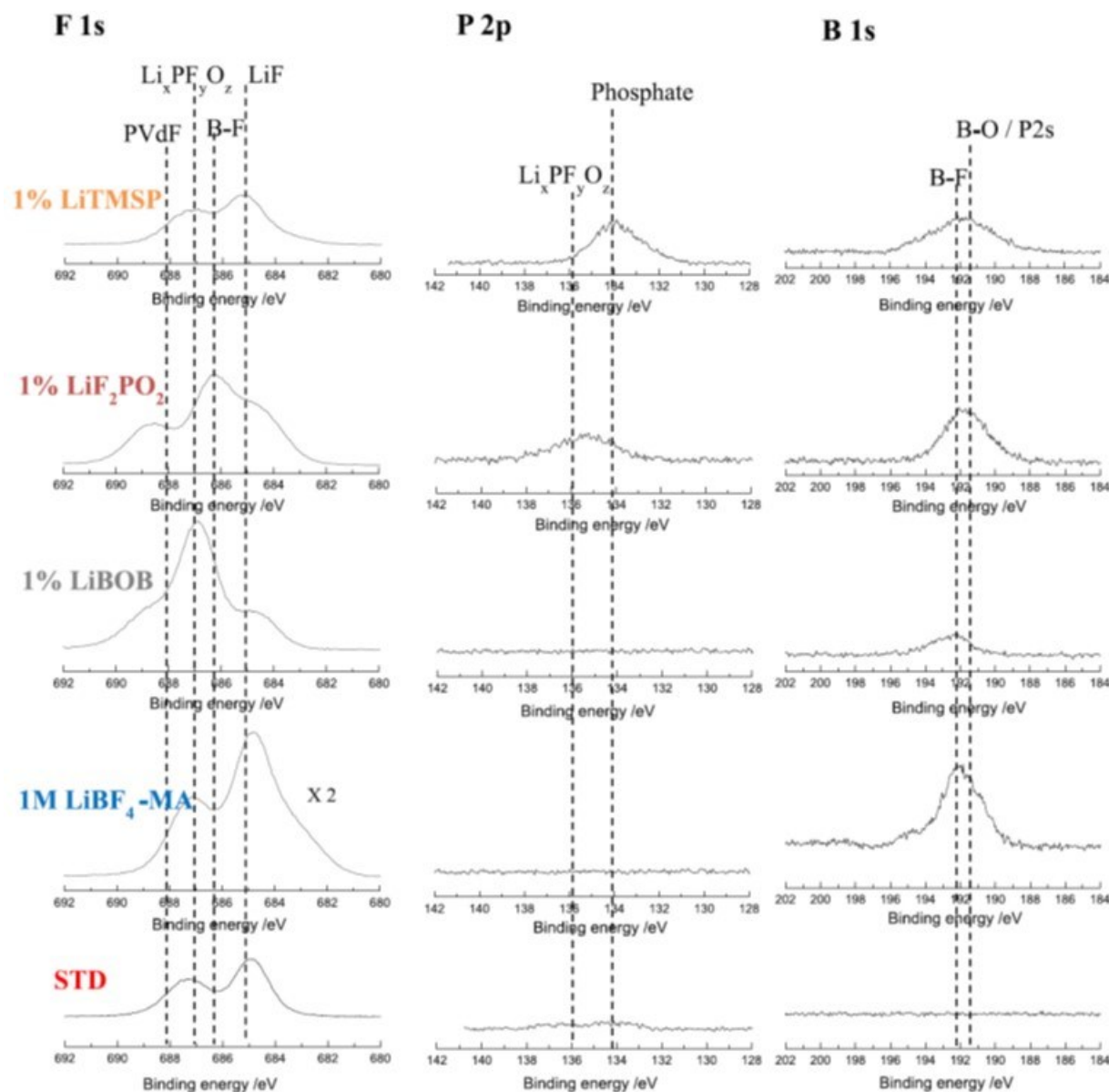


Figure XI.3.5 F 1s (left), P 2p (center), and B 1s (right) XPS spectra of the graphite anodes after 5 formation cycles at 25 °C with different electrolyte formulations.

As shown in Figure XI.3.6, upon cycling at 25 °C for 50 cycles, the chemical composition of surface films on the graphite electrodes with the base ester (LiBF<sub>4</sub>-MA), 1% LiBOB, and 1% LiF<sub>2</sub>PO<sub>2</sub> electrolytes changed significantly and generated thicker surface films. For the base electrolyte (LiBF<sub>4</sub>-MA) and the 1% LiBOB electrolyte, increased intensities for peaks characteristic of LiF (685 eV) and boron species (133 eV) suggest more decomposition products on the graphite electrode. The SEI generated from the base electrolyte is primarily composed of the reduction products of LiBF<sub>4</sub> and FEC, while the SEI generated from the 1% LiBOB-containing electrolyte is dominated by LiBOB reduction products. Similarly, when electrolytes containing 1% LiF<sub>2</sub>PO<sub>2</sub> are utilized, the SEI is dominated by the decomposition products of LiF<sub>2</sub>PO<sub>2</sub> as

supported by increased intensities for LiF (685 eV) and  $\text{Li}_x\text{PF}_y\text{O}_z$  (687 eV in F 1s and 136 eV in P 2p). Alternatively, a lower LiF to  $\text{Li}_x\text{PF}_y\text{O}_z$  ratio in the F 1s spectrum for the STD electrolyte suggests that the carbonate solvent decomposition is more dominant compared to salt decomposition as the SEI changes during room-temperature cycling. However, minimal changes to the surface composition upon extended cycling are observed for cells cycled with 1% LiTMPS suggesting less evolution of the SEI over a wide operating temperature.

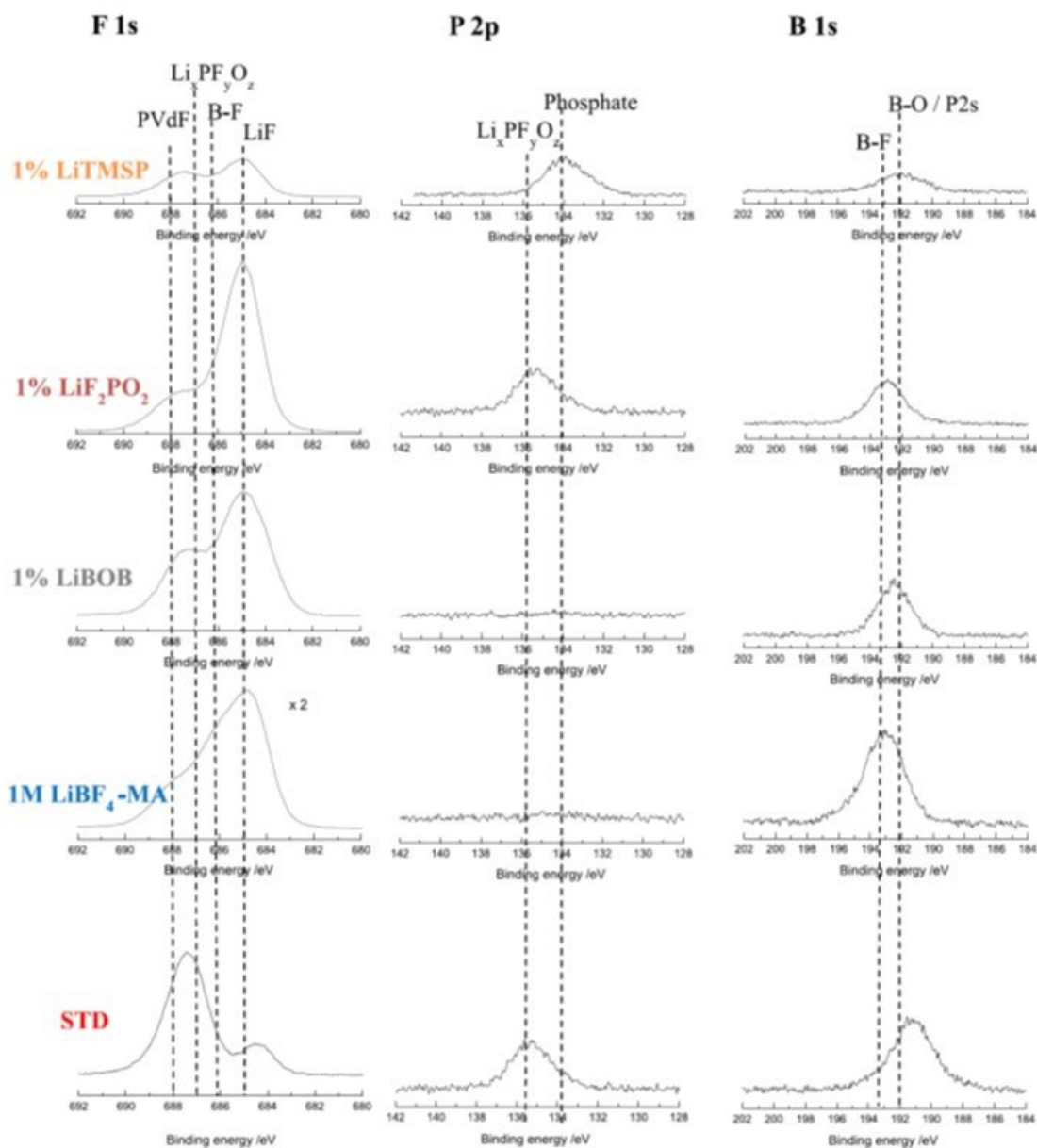


Figure XI.3.6 F 1s (left), P 2p (center), and B 1s (right) XPS spectra of the graphite anodes after 50 cycles at 25 °C with different electrolyte formulations..

The University of Maryland at College Park (UMD) team investigated the compatibility of a baseline electrolyte towards lithium plating which might happen at fast charge and/or low temperature conditions. To study it, a  $\sim 2.0 \text{ mAh cm}^{-2}$  graphite was used with 20% extra lithium of the desired electrode capacity plated on the electrode. As shown in Figure XI.3.7a, the reversibility of the lithium metal || Graphite/Lithium hybrid electrode cell with the baseline electrolyte became worse with the increase of cycling number (after 25 cycles).



Besides, it is seen that the overpotential of the cell increases continuously from 10 to 50 cycles, indicating the gradual increase of the internal resistance which could be attributed to the continuous growth of SEI. While for the cell with the designed electrolyte that is modified based on the baseline electrolyte, as shown in Figure XI.3.7b, the reversibility of the cell maintained well within 50 cycles & the increase in the overpotential is limited, inferring the possibility to regulate the lithium plating on the graphite anode at extreme conditions with advanced electrolyte design strategies.

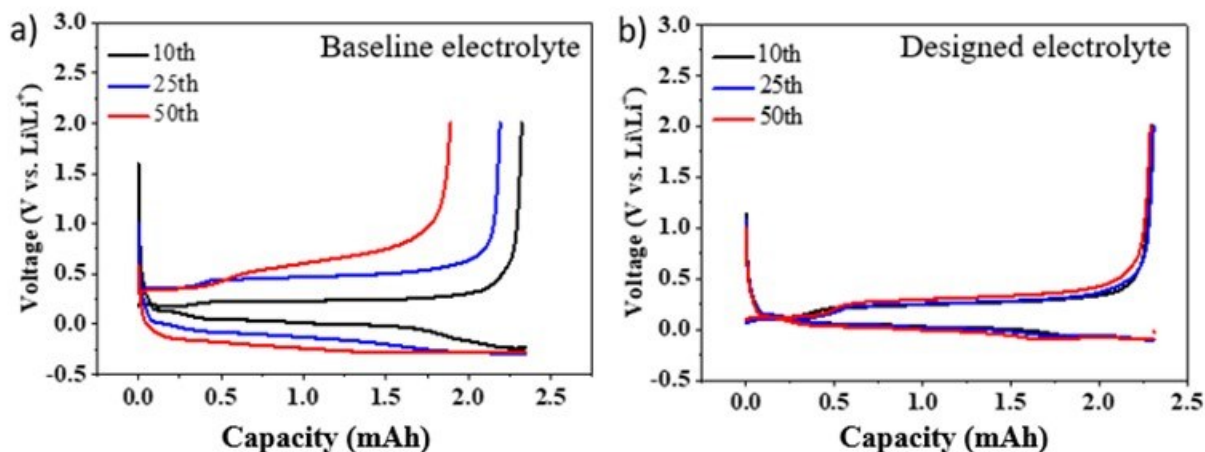


Figure XI.3.7 Cycling performance of Li || Gr half cell with 20% extra lithium plating on the graphite anode at -20 °C with (a) baseline electrolyte (8), (b) designed electrolyte (861) at 0.1 C charge/0.2 C discharge condition

To further evaluate the compatibility of the electrolytes with both the graphite anode and possible lithium plating on it, NMC811 || Gr cells with N/P of 1: 1 were assembled with these two electrolytes. In Figure XI.3.8a, the cycling stability of the cells with different electrolytes were shown. It can be seen that the modification of the baseline electrolyte led to no harm on the cycling stability of the NMC811 || Gr with the exhibition of a better capacity retention of 77% after 350 cycles. In the meanwhile, the cells with the baseline electrolyte shows a worse capacity retention of ~70% within the cycling number. The discrepancy in cycling stability of these two electrolytes with the NMC811 || Gr cells becomes larger at -20 °C. In Figure XI.3.8b, the NMC811||Gr with the designed electrolyte shows no obvious attenuation in the capacity within 100 cycles while that with the baseline electrolyte decays very fast, with ~60% capacity retention after 70 cycles. This inferior cycling performance of the cell with baseline electrolyte could be explained by the worse tolerance of the electrolyte toward the lithium plating, which is evident by Figure XI.3.7a, too.

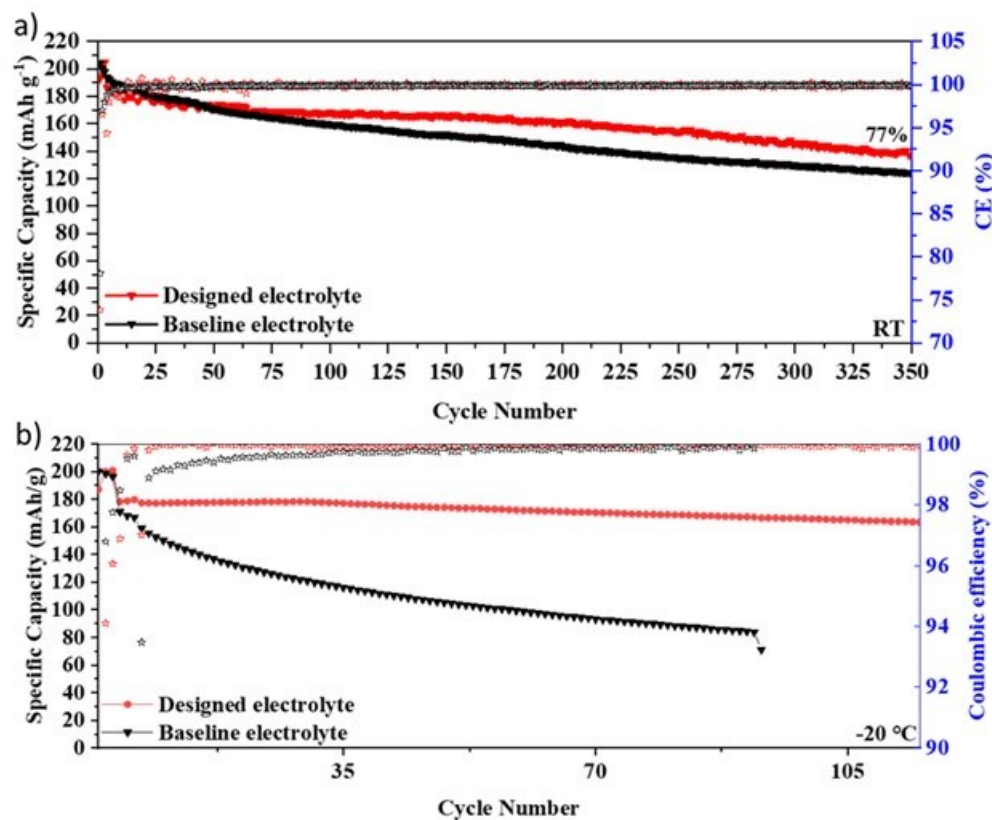


Figure XI.3.8 Cycling performance of NMC811|Gr cell at (a) room temperature (b) -20 °C with baseline electrolyte and designed electrolyte (861) at 0.2 C discharge/0.2 C charge condition.

The solid/electrolyte interphase (SEI) on the graphite anode that were cycled with both electrolytes was studied to decipher the improved reaction kinetics (low overpotential) and enhanced cycling stability, as shown in Figure XI.3.9. The pristine graphite has no amorphous film at the edge of the graphite lattice, indicating a clear graphite surface. For the graphite that was cycled with baseline electrolyte, it has a thick SEI film (~5 nm) covering on the graphite surface, which could account for the larger overpotential of the cells. On the contrary, the SEI layer on the graphite that was cycled with design electrolyte is much thinner with a thickness of ~1-2 nm, suggesting a shortened lithium-ion transport pathway which is beneficial for the reduction of the SEI resistance. The solid/electrolyte interphase (SEI) on the graphite anode that were cycled with both electrolytes was studied to decipher the improved reaction kinetics (low overpotential) and enhanced cycling stability, as shown in Figure XI.3.9. The pristine graphite has no amorphous film at the edge of the graphite lattice, indicating a clear graphite surface. For the graphite that was cycled with baseline electrolyte, it has a thick SEI film (~5 nm) covering on the graphite surface, which could account for the larger overpotential of the cells. On the contrary, the SEI layer on the graphite that was cycled with design electrolyte is much thinner with a thickness of ~1-2 nm, suggesting a shortened lithium-ion transport pathway which is beneficial for the reduction of the SEI resistance. The manuscript for this work is under preparation.

In addition, UMD team also prepared a review paper on “Low-temperature electrolytes development strategies: from lithium-ion transport kinetics of the whole cell to individual transport process perspectives”. This manuscript is ready to submit. The Graphic Abstract of this paper is shown in Figure XI.3.9.

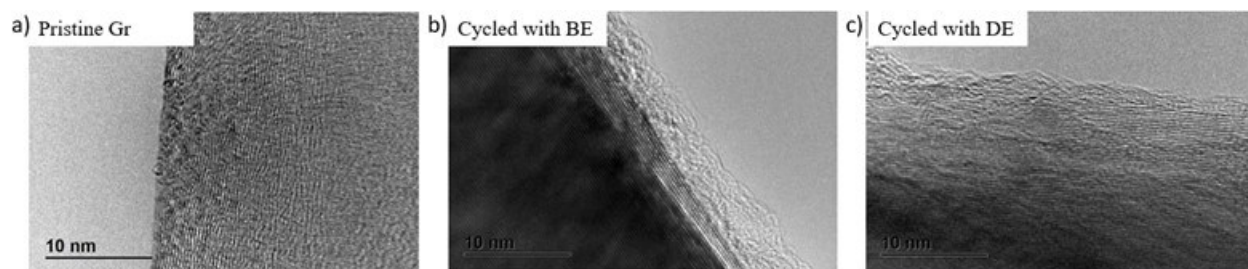


Figure XI.3.9 The TEM images of the (a) pristine graphite; (b) graphite cycled with baseline electrolyte (BE) and (c) graphite cycled with designed electrolyte (DE)

In addition, UMD team also prepared a review paper on “Low-temperature electrolytes development strategies: from lithium-ion transport kinetics of the whole cell to individual transport process perspectives”. This manuscript is ready to submit. The Graphic Abstract of this paper is shown in Figure XI.3.10.

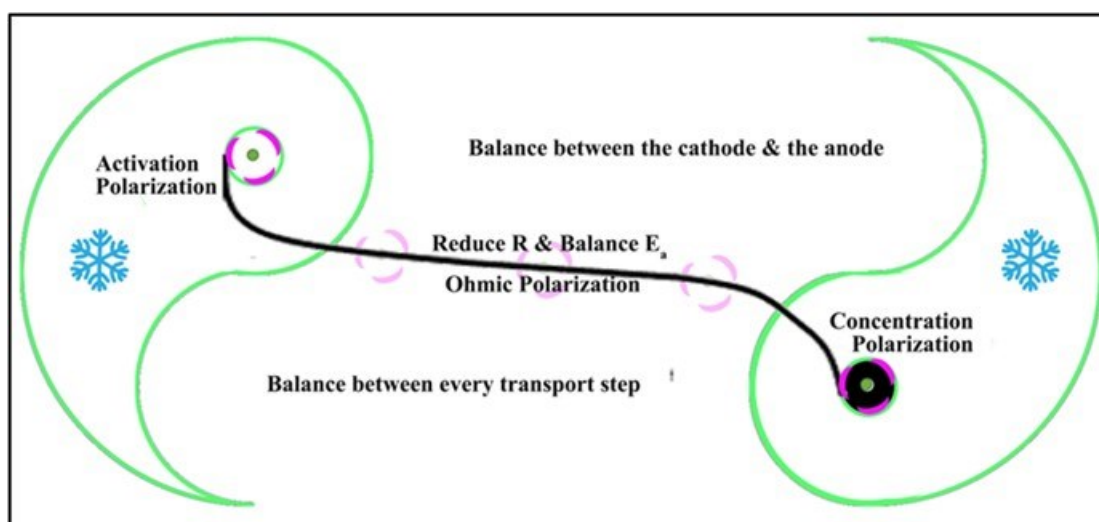


Figure XI.3.10 The graphic Abstract of a review paper that is ready to be submitted to a scientific journal for publication.

## Conclusions

This project, “Synthesis, screening and characterization of novel low temperature electrolyte for lithium-ion batteries (BNL)”, has been successfully completed in FY2023. All milestones have been completed with results being prepared for publications/patents. Extensive collaboration with other national Labs, US universities and international research institutions were well established.

## Key Publications

### Publications

1. Nuwanthi D. Rodrigo, Chamithri Jayawardana, Leah Rynearson, Enyuan Hu, Xiao-Qing Yang, and Brett L.Lucht, “Use of Ethylene Carbonate Free Ester Solvent Systems with Alternative Lithium Salts for Improved Low-Temperature Performance in NCM622/Graphite Li-ion Batteries”, *J. Electrochem. Soc.*, DOI: 10.1149/1945-7111/ac9d0a, Publication date (web): November 03, 2022.
2. Jijian Xu, Jiaxun Zhang, Travis P. Pollard, Qingdong Li, Sha Tan, Singyuk Hou, Hongli Wan, Fu Chen, Huixin He, Enyuan Hu, Kang Xu, Xiao-Qing Yang, Oleg Borodin\* and Chunsheng Wang\*, “Electrolyte Design for Li-ion Batteries under Extreme Operating Conditions”, *Nature*, DOI: 10.1038/s41586-022-05627-8, Publication date (web): February 08, 2023.

3. Chamithri Jayawardana, Nuwanthi D. Rodrigo, Munaiah Yeddala, Bo Nan, Leah Rynearson, Chunsheng Wang, and Brett L. Lucht\*, “Lithium Tetrafluoroborate-Based Ester Electrolyte Formulations to Improve the Operating Temperature Range in NCM 622 || Graphite Li-Ion Batteries”, *ACS Applied Energy Materials*, DOI: 10.1021/acsaem.3c00261. Publication date: May 1<sup>st</sup>, 2023
4. Sha Tan, Zulipiya Shadike\*, Xinyin Cai, Ruoqian Lin, Atsu Kludze, Oleg Borodin, Brett L. Lucht, Chunsheng Wang, Enyuan Hu\*, Kang Xu\*, Xiao-Qing Yang\*, “Review on low temperature electrolytes for lithium-ion and lithium metal batteries”, Accepted by *Electrochemical Energy Reviews*.
5. Bo Nan, Singyuk Hou, An Phan, Hongli Wan, Weiran Zhang, Chunsheng Wang. “Low-temperature electrolytes development strategies: from lithium-ion transport kinetics of the whole cell to individual transport process perspectives”. Ready to be submitted to a scientific journal for publication.

## XI.4 Extending the Operating Range and Safety of Li-Ion Batteries with New Fluorinated Electrolytes (Koura)

### **Suresh Sriramulu, Principal Investigator**

Mexichem Fluor Inc. (Koura)  
950 Winter Street  
South Entrance 1st Floor  
Waltham, MA 02451  
United States  
E-mail: [suresh.sriramulu@kouraglobal.com](mailto:suresh.sriramulu@kouraglobal.com)

### **Andrew Jansen, co-Principal Investigator**

Argonne National Laboratory  
9700 South Cass Avenue  
Lemont, IL 60439  
E-mail: [jansen@anl.gov](mailto:jansen@anl.gov)

### **Wenquan Lu, co-Principal Investigator**

Argonne National Laboratory  
9700 South Cass Avenue  
Lemont, IL 60439  
E-mail: [wenquan.lu@anl.gov](mailto:wenquan.lu@anl.gov)

### **Sarah Guillot, co-Principal Investigator**

Silatronix (wholly owned by Mexichem Fluor Inc.)  
3587 Anderson St, Suite 108  
Madison, WI 53703  
E-mail: [sarah.guillot@kouraglobal.com](mailto:sarah.guillot@kouraglobal.com)

### **Monica Usrey, co-Principal Investigator**

Silatronix (wholly owned by Mexichem Fluor Inc.)  
3587 Anderson St, Suite 108  
Madison, WI 53703  
E-mail: [monica.usrey@orbia.com](mailto:monica.usrey@orbia.com)

### **Haiyan Croft, DOE Technology Development Manager**

U.S. Department of Energy  
E-mail: [Haiyan.Croft@ee.doe.gov](mailto:Haiyan.Croft@ee.doe.gov)

Start Date: October 1, 2022	End Date: September 30, 2023	
Project Funding (FY23): \$1,579,905	DOE share: \$1,261,554	Non-DOE share: \$318,351

### **Project Introduction**

Li-ion batteries have seen significant improvements in energy density, cycling stability and power metrics over the last decade; however, traditional electrolytes continue to limit performance under extreme conditions such as wide temperature, fast charge, and high voltage operation [1, 2]. While electrolyte solvents have been identified that can enable superior low-temperature performance (such as short-chain esters), these solvents often reduce high-temperature storage performance and cycle life [3]. Electrolyte selection can have a big impact on the fast charge capability of the Li-ion cell. Essentially, poorly designed electrolytes can promote Li-plating under some conditions that can result in rapid performance loss. Electrolytes also remain a challenge in advancing battery safety, due to their flammability and for fast-charge cells, influencing lithium plating, which may then lead to safety incidents. To improve the performance, reliability, and safety of Li-ion

batteries, new advanced electrolytes must be integrated into the cell design to extend the operating window of Li-ion batteries. These electrolytes must enable stable operation of batteries under conditions of low and high temperatures as well as during fast-charge cycling. These requirements demand innovation of novel electrolyte components with superior stability and transport properties.

Fluorinated electrolyte components are known to provide multiple benefits to Li-ion battery. Koura is leveraging its expertise in fluorine chemistry to develop and produce a wide range of fluorinated molecules that have the potential to further enhance Li-ion performance. In this project, we are aiming to develop electrolyte formulations that include fluorinated compounds to enhance Li-ion battery performance.

### Objectives

The objective of the project is for Koura, in collaboration with Silatronix and Argonne National Laboratory, to develop and validate advanced fluorinated liquid electrolytes to meet critical battery requirements of stable performance over a wide range of temperatures as well as during fast charge cycling. To reach these targets, Koura is developing fluorinated solvents, integrating them into fully functional electrolytes to demonstrate improved performance in NMC811/Gr cells under extreme conditions. Target performance for these electrolytes include electrochemical stability of fluorinated solvents up to 4.5V with a temperature window from -40°C to 40°C, demonstrate  $\geq 80\%$  capacity retention ( $\geq 1000$  cycles at  $\sim C/3$  at  $\sim 0^\circ\text{C}$ ) and  $\geq 70\%$  capacity retention ( $\geq 1000$  cycles at  $\sim 4C$  charge at  $\sim 30^\circ\text{C}$ ) with reduced gas generation for improved safety.

At the end of this project, the project team will deliver 12 2 Ah cells with the top-performing electrolyte(s) as well as a baseline carbonate electrolyte to the appropriate DOE test facility.

The proposed fluorinated electrolyte technology has the potential to address both safety and performance challenges to enable next generation Li-ion batteries for transportation applications. If successful, the proposed project will have a significant impact on enabling operation under extreme conditions including operating over a wide temperature range, under intense abuse conditions, and utilizing extreme fast charging. This will enable wider adoption of electric vehicles in the US and globally.

### Approach

To accomplish these objectives, Koura, Silatronix, and Argonne National Laboratory are working together to develop and optimize Li-ion battery electrolytes with fluorinated electrolytes. Koura has been a global leader in the development, manufacture, and supply of fluoroproducts. Koura's research and development capabilities, along with an integrated North American supply chain for fluorine, allow the design and synthesis of proprietary fluorinated materials with unique properties. As a result, Koura's portfolio of fluorinated structures includes a wide variety of functionalities, characteristics, and physical properties that are being tested and screened as potential electrolyte battery components.

Silatronix, wholly owned by Mexichem Fluor Inc. since 2021, has been focused on developing unique advanced electrolyte solvents for over a decade and has built up extensive electrolyte characterization and testing expertise and capabilities over the years. These capabilities include the development of a rigorous process to relate electrolyte-level properties to observed performance in Li-ion cells through comprehensive post-test analysis. Silatronix has facilities for chemical synthesis and purification, blending of electrolyte, physical properties characterization, multi-layer pouch cell filling and electrochemical testing, coin cell assembly, and direct access to the instrumentation required for post-test analysis of electrodes, electrolytes, and gas. Silatronix's capabilities are employed on this project for completing characterization of Koura's fluorinated products, formulating the solvents into battery electrolytes and performing initial battery cell testing.

The Cell Analysis, Modeling, and Prototyping (CAMP) Facility at Argonne National Laboratory has been developing and testing Li-ion battery materials for more than 20 years. Their expertise includes battery cell design and battery materials characterization and testing. The CAMP facility has the capability for

manufacturing and testing multiple cell formats, including coin cells, single layer pouch cells, and multi-layer pouch cells with a wide variety of capacities, including the 2 Ah deliverable pouch cells for this project.

The objectives of this project will be met by leveraging the strengths of each collaborator participating in this program. Koura is developing novel fluorinated electrolyte solvents. Silatronix is characterizing these materials and testing in coin cell and small pouch cell batteries. Argonne is designing and validating cell designs towards the final deliverable builds.

Fluorinated materials for electrolytes have been tested and evaluated in complex electrolyte formulations. Testing has targeted optimization of the electrolyte formulation for superior performance as well as development of a fundamental understanding of how these materials operate mechanistically. Cell testing includes low temperature rate measurement, fast charge cycling, low temperature cycling, standard rate room temperature cycling, and wide operating temperature testing. Fundamental evaluations include post-test studies of the composition of extracted cell components (gas, electrolyte, and electrode), solubility and solvation studies of pristine electrolytes, and thermal stability analysis of electrolytes in contact with charged active materials. The insights from these tests and characterizations are informing the continued development of additional unique fluorinated structures by Koura. Guidance from Argonne on cell design and testing procedures influence the nature of screening tests by Silatronix. The most promising electrolyte design(s) will be sent to Argonne for testing in the 2 Ah deliverable build to benchmark performance against established targets.

## Results

### Overview

In the first budget period, more than 25 fluorinated materials were synthesized and characterized by Koura and Silatronix. Of these, 10 molecules were selected for detailed characterization using measurements of thermophysical properties and electrochemical stability. Initial screening of these materials led to a down-selection from the original ten molecules to four molecules (KDC-713, KDC-502, KDC-403, and KDC-301). In FY 23, Budget Period 2 (BP2), Koura and Silatronix continued to test and optimize fluorinated solvents and demonstrate their feasibility as battery electrolytes through pouch cell performance testing. Key activities included:

- Koura synthesized and delivered fluorinated solvents to Silatronix and aided in material assessment, down-selection, structure optimization. Koura began synthesis process development to scale-up promising molecules.
- Silatronix characterized the fluorinated solvents from Koura, formulated these solvents into electrolytes, and carried out electrochemical performance testing in pouch cells. In BP2, more than 300 pouch cells (with NMC811 cathode and graphite anode) were assembled and tested to help down-select promising candidates, evaluate electrolyte formulations, and carry out electrolyte optimization studies.
- Argonne continued to develop their cell design, progressing from coin cells to single-layer pouch cells using NMC811 cathode and graphite anode. They are on track to validate the deliverable 2Ah cells in BP3 for the program deliverables.

The work carried out in BP2 identified two promising fluorinated solvents for improving Li-ion battery performance. One of these, KDC-403 – a fluorinated dioxolane – showed measurable improvement in widening the operating temperature range and fast-charge capability of graphite/NMC811 Li-ion pouch cells. The primary benefit of KDC-403 appears to be in reducing the anode SEI thickness, resulting in

- improved rate capability and cycle life at low temperatures;
- improved cycle life, reduced impedance growth and gas generation at high temperatures; and
- enhanced fast-charge cycle life.

The other fluorinated solvent was KDC-301 – a fluorinated carbonate –also showed improvement in high temperature cycling and fast-charge capability against the baseline carbonate electrolyte; however, the benefit was greater with KDC-403.

Optimization of electrolytes containing KDC-403 was initiated in BP2, including investigating the effect of concentration and combination of KDC-403 with non-carbonate cosolvents.

### Initial Pouch Testing of Refined Molecular Structures

One of the goals of this program is to develop electrolytes that have superior performance under extreme temperature operation – that is, at both low and high temperatures. In the initial wide operating temperature test, four fluorinated materials were tested at 20 v% compared to the control (EC/DEC/EMC + 1M LiPF<sub>6</sub> + 1v% VC). These were the most promising solvent candidates tested from the ten Round 1 molecules screened in FY22: KDC-713 (ether nitrile), KDC-502 (ester), KDC-403 (dioxolane), and KDC-301 (carbonate). These electrolytes were tested in 230 mAh multilayer pouch cells with single-crystal NMC811 cathodes and artificial graphite anodes. The cells were cycled between 4.3V and 2.75V, and with a C/2 charge rate and constant voltage charging at 4.3V until the current dropped below C/20. The discharge rate was C/2, except during the rate test, where the discharge rate was varied from C/2 to 2C. After undergoing formation, the cells were cycled at 30 °C for 10 cycles followed by a rate test at 0 °C with 3 cycles at each subsequent discharge rate of C/2, 1C, and 2C. The following 10 cycles were at 0 °C, after which they were brought to 30 °C for a capacity check over 10 cycles. Finally, the cells were cycled for 300 cycles at 45 °C.

The cycling data is shown in Figure XI.4.1. During the low temperature rate test, 20% 713 performed poorly, while at the C/2 and 1C discharge rates all other electrolytes had similar capacities. At the higher 2C discharge rate, there was more noticeable differences in discharge capacity based on the electrolyte, with the control and 20% 403 electrolytes performing best followed by 20% 502 (Figure XI.4.1a). During the subsequent high temperature (45 °C) cycling (Figure XI.4.1b), 20% 713 again showed poor cycling stability. The other fluorinated materials outperformed the control, showing improved high temperature cycling stability, with 20% 403 retaining the highest capacity of all the electrolytes.

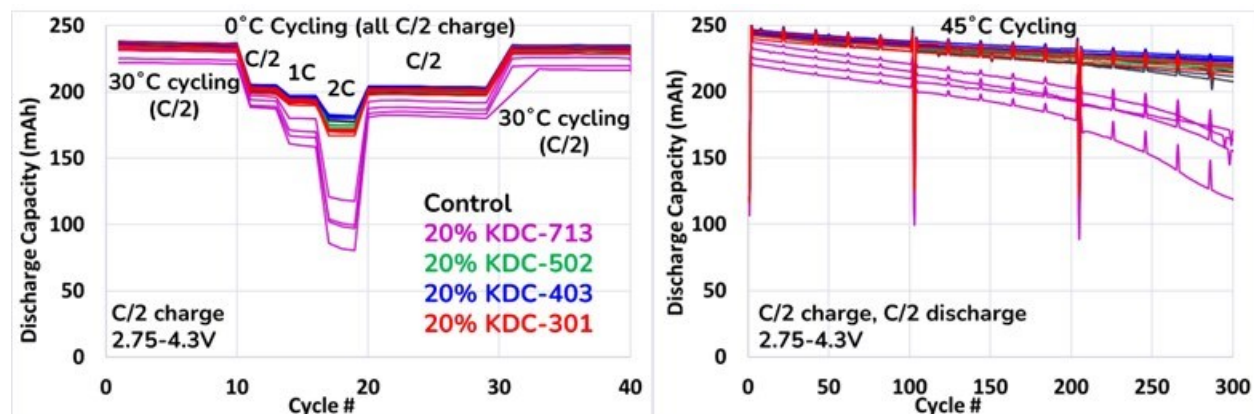
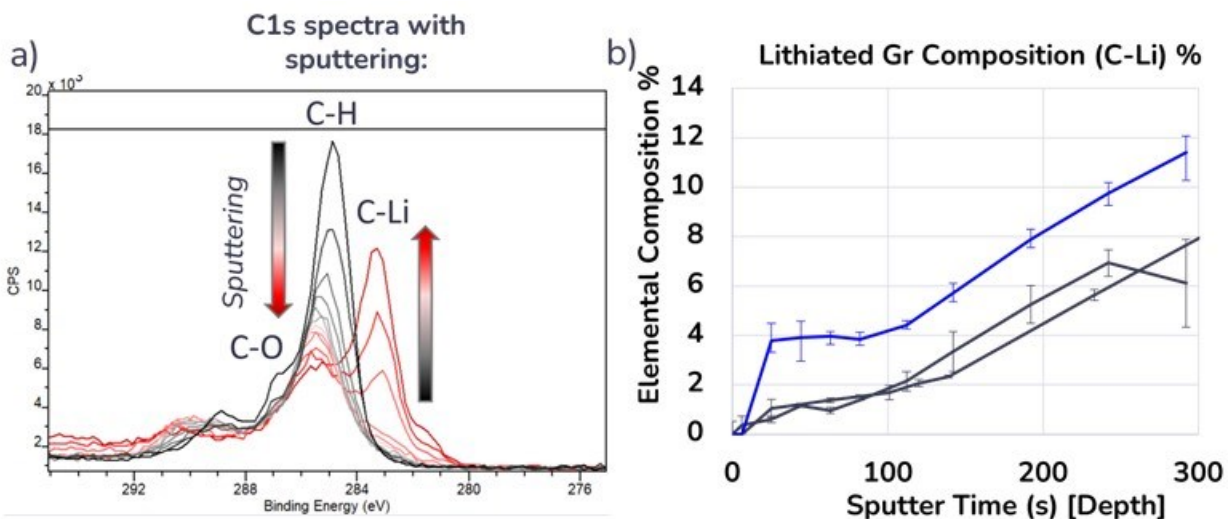


Figure XI.4.1 Wide operating temperature characterization of electrolytes in 230 mAh pouch cells with artificial graphite anode and NMC811 single crystal cathode. a) initial cycling at 30 °C, followed by rate characterization at 0 °C, and continued 30 °C cycling followed by b) 45 °C high temperature cycling. Electrolyte compositions tested: control (black traces, EC/DEC/EMC 1/1/1 v/v + 1v% VC + 1M LiPF<sub>6</sub>), 20v% KDC-713 (pink traces), 20v% KDC-502 (green traces), 20v% KDC-403 (blue traces), and 20v% KDC-301 (red traces) electrolytes. The fluorinated electrolytes were added at 20 v% to the control electrolyte. The salt was 1M LiPF<sub>6</sub> and VC was at 1% in all electrolytes. Operating voltage range: 4.3V – 2.75V.



After 300 cycles of the 45 °C cycling phase of the wide operating temperature test, graphite anodes were extracted from the cells and analyzed by XPS. Depth profiling was performed via argon ion sputtering in order to estimate the thickness of the anode decomposition layer or SEI (Figure XI.4.2). The lithiated graphite peak (C-Li) shown in Figure XI.4.2a appears as the SEI layer is sputtered away, and a larger C-Li composition at an earlier sputtering timepoint indicates a thinner SEI layer. Figure XI.4.2 shows that 20% 403 has a significantly greater C-Li composition after just 25 seconds of sputtering, suggesting a thinner SEI with 20% 403.



**Figure XI.4.2 XPS with sputtering for depth profile of graphite anodes after wide operating temperature test**  
 a) overlaid representative carbon C1s spectra from each level of sputtering and b) percent total anode composition of C-Li (lithiated graphite) peak throughout sputtering for 20% 403 and control anodes

The same electrolyte formulations (20% of each of the down selected fluorinated materials KDC-713, KDC-403, KDC-502, and KDC-301) were tested in a separate experiment under fast charge cycling conditions. After formation, the pouches were cycled at 30°C and 4C charge rate and C/2 discharge for 500 cycles (Figure XI.4.3). Similar to the wide operating temperature results in Figure XI.4.3, 20% KDC-713 did not cycle stably, while the other three fluorinated electrolytes (KDC-502, KDC-403, and KDC-301) had higher capacities at the end of cycling compared to the control. Overall, in both the wide operating temperature 45 °C cycling and 30 °C fast charge cycling, 20% KDC-403 performed the best and significantly improved cycling stability over the control. Throughout the fast charge cycling, 20% KDC-403 and 20% KDC-301 had much lower impedance compared to the control, while 20% KDC-503 had higher impedance vs control despite having greater cycling stability (Figure XI.4.3b).

After the fast charge cycling test, pouch cells with the control and 20% KDC-403 electrolytes were opened in an argon-atmosphere glovebox and the graphite anodes were photographed (see Figure XI.4.4). Both anodes showed evidence of plated lithium, as expected after extended fast charge cycling. However, the anode with 20% KDC-403 had significantly less plated lithium than the control. Greater amounts of plated lithium indicate greater loss of lithium inventory in the cell, which often leads to capacity loss. Additionally, lithium plating can lead to increased electrolyte consumption through decomposition reactions and increased cell failure due to formation of lithium dendrites and cell shorting [4].

Based on these initial pouch testing results (wide operating temperature and fast charge), KDC-403 was selected as the most promising candidate by far, providing superior fast charge and high temperature cycling stability. Follow-up deep dive and optimization experiments focused on KDC-403. KDC-713 was eliminated from further testing due to poor cycling stability, while KDC-502 and KDC-301 showed moderate promise and were investigated further in limited experiments.

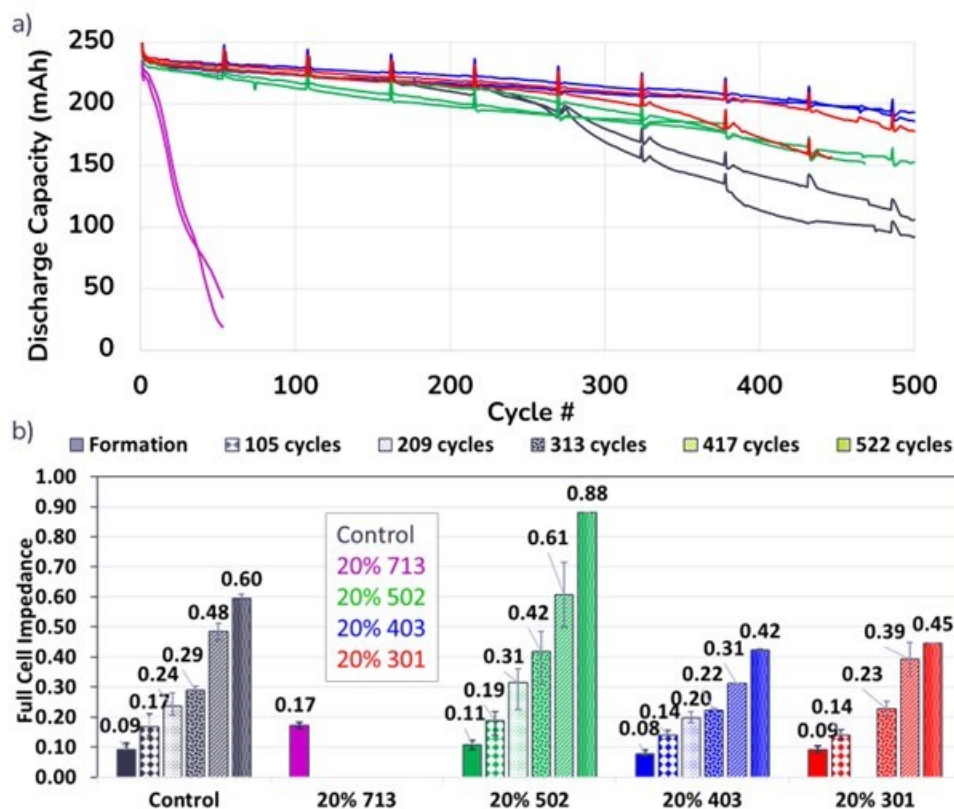


Figure XI.4.3 Fast charge cycling test in 230 mAh single crystal NMC811/artificial graphite pouch cells, with a cathode capacity loading of  $\sim 2.2$  mAh/cm<sup>2</sup> a) discharge capacity measured during 4C charge (CCCV) and 1C discharge and b) impedance for cells with control (black traces, EC/DEC/EMC 1/1/1 v/v + 1v% VC + 1M LiPF<sub>6</sub>), 20v% KDC-713 (pink traces), 20v% KDC-502 (green traces), 20v% KDC-403 (blue traces), and 20v% KDC-301 (red traces) electrolytes

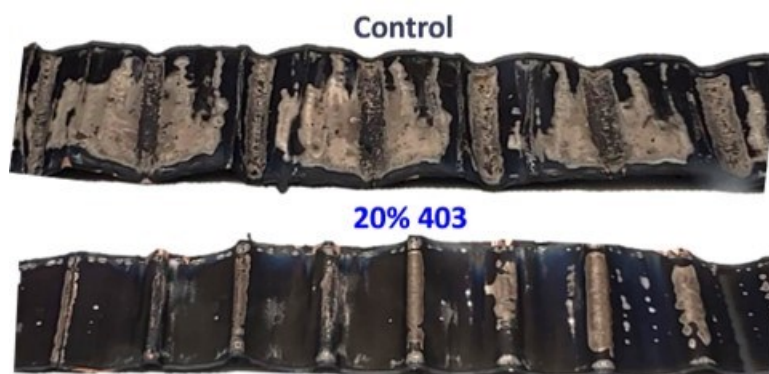


Figure XI.4.4 Graphite anodes (7.78 mg/cm<sup>2</sup>) after fast charge cycling test in 230 mAh single crystal NMC811/artificial graphite pouch cells with either control (EC/DEC/EMC 1/1/1 v/v + 1v% VC + 1M LiPF<sub>6</sub>) or 20% KDC-403 electrolytes.

#### Electrolyte Optimization Pouch Testing

Figure XI.4.5 shows the results of the low temperature rate test validating 20% 403 as an electrolyte to improve low temperature performance by comparison to three commercially available short-chain esters (methyl acetate, methyl propionate, and methyl butyrate) which have good low-temperature performance.

Electrolytes with 20% of each ester were compared to 20% 403 and the control electrolyte (EC/DEC/EMC 1/1/1 + 1M LiPF<sub>6</sub> + 1% VC) in 230 mAh NMC811/Gr pouch cells (discharge capacity and impedance) and their bulk electrolyte transport properties were measured (conductivity and viscosity). All esters had higher impedance than the control, while the cells with 20% 403 had the lowest impedance at all temperatures, indicating improved interfacial transport at all temperatures tested (0-20 °C). By contrast, all esters had higher electrolyte conductivity and lower viscosity than the control and 20% 403, indicating improved bulk transport with the esters over 20% 403.

This data provided insights into the performance differences of the electrolytes during the LT rate test (Figure XI.4.5d-f). At all temperatures with C/2 discharge, 20% 403 improves capacity over the control and ester electrolytes, indicating that the improved interfacial transport dominates the performance at these temperatures and rate. At 0 °C to -10 °C and 1C discharge, 20% 403 also had the best performance, suggesting again that improved interfacial properties benefit under those conditions. By contrast, at higher C-rates combined with lower temperatures (1C and -20 °C; -10 °C to -20 °C and 2C discharge), the esters have the best performance, suggesting that improved bulk transport properties dominate performance under those conditions.

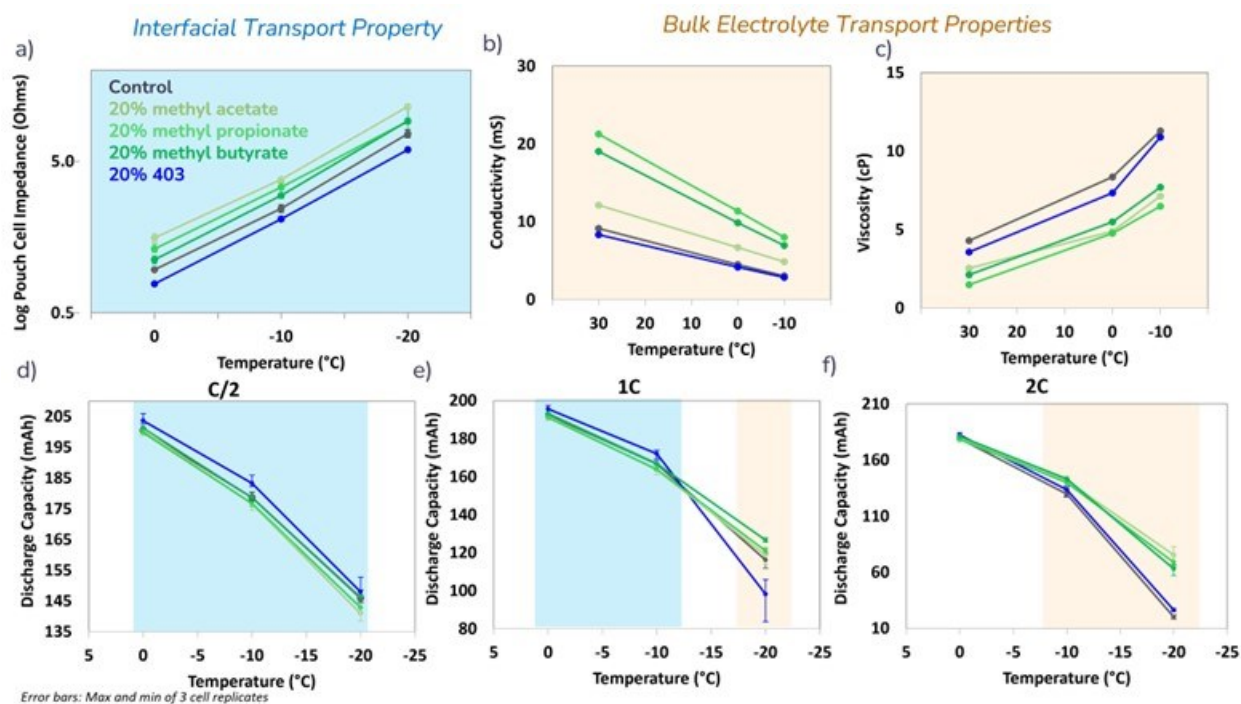


**Figure XI.4.5** Connection between interfacial vs bulk transport property measurements and discharge capacity of 230 mAh NMC811/Gr multilayer pouch cells with control, 20% methyl acetate, 20% methyl propionate, 20% methyl butyrate, or 20% 403 electrolytes with a) pouch cell impedance from 0 °C to -20 °C, b) electrolyte conductivity from 30 °C to -10 °C, c) electrolyte viscosity from 30 °C to -10 °C, and pouch cell discharge capacities during rate tests at 0 °C to -20 °C with d) C/2 discharge rate, e) 1C discharge rate, and f) 2C discharge rate where regions shaded in blue are where benefits from improved interfacial transport appear to dominate discharge capacity and regions shaded in gold are where benefits from improved bulk electrolyte transport appear to dominate discharge capacity.

Low temperature performance is understood to be limited by both interfacial diffusion resistance and reduced bulk conductivity. However, these effects become the controlling effect under different conditions. Here, we attempt to quantify these effects using the data shown in Figure XI.4.5. For these cells 1C rate would correspond to about 2.2 mA/cm<sup>2</sup> and C/2 about 1.1 mA/cm<sup>2</sup>. Referring to Figure XI.4.5, we can infer the following:

- At current density  $< 1.1 \text{ mA/cm}^2$  (or less than C/2 rate) and temperatures above  $-20 \text{ }^\circ\text{C}$ , the interfacial resistance dictates the discharge capacity (as evidenced by the slightly higher performance of the cells)
- At current density  $> 4.4 \text{ mA/cm}^2$  (or 2C or higher discharge rate), and temperature below  $-10 \text{ }^\circ\text{C}$ , the bulk conductivity of the electrolyte dictates performance (as evidenced by the higher performance of the cells with the ester electrolytes).
- For an intermediate current density of  $2.2 \text{ mA/cm}^2$  (or 1C rate), for temperatures below  $-10 \text{ }^\circ\text{C}$  bulk conductivity dictates performance whereas for temperatures above  $-10 \text{ }^\circ\text{C}$ , interfacial resistance dictates performance.

Additional well-designed experimentation would be needed to further quantify the current densities at which bulk or interfacial effects dominate.

Following the low temperature rate test, optimization of the KDC-403 electrolyte composition for C/2 cycling at  $0 \text{ }^\circ\text{C}$  was performed. This investigation explored the optimal concentration of KDC-403 (2% to 20%) as well as the effect of combining KDC-403 with methyl propionate, with the goal of obtaining an electrolyte with both the excellent conductivity/viscosity of 20% MP and the improved impedance of 20% 403 (Figure XI.4.5). The pouch cells (230 mAh NMC811/Gr) with these electrolytes underwent formation followed by 350 cycles at  $0 \text{ }^\circ\text{C}$ . Figure XI.4.6a shows that the highest concentration tested of 403 (20%) had the highest percent capacity retention during  $0 \text{ }^\circ\text{C}$  cycling, significantly improved over the control electrolyte (EC/DEC/EMC 1/1/1 v/v + 1v% VC + 1M LiPF<sub>6</sub>). 5% and 10% KDC-403 also improved capacity retention relative to the control, to a minor degree. Figure XI.4.6b shows 20% KDC-403, 20% MP, and the combination of 20% MP + 20% 403. 20% MP slightly improved capacity retention compared to the control (similar to 5% and 10% KDC-403), while 20% 403 + 20% MP showed the most stable cycling of all the electrolytes tested. These data indicate that the superior low temperature cycling performance of KDC-403 can be further advanced through optimization of the other electrolyte components.

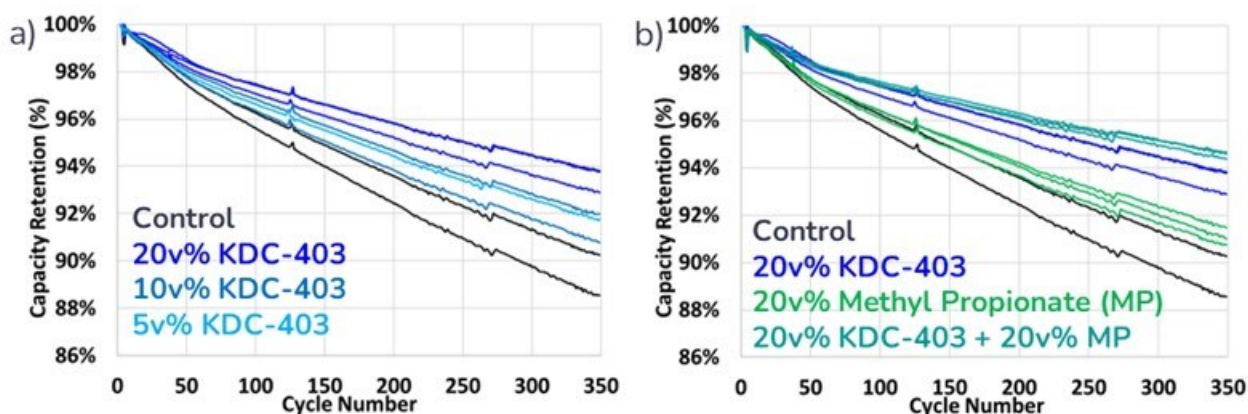


Figure XI.4.6  $0 \text{ }^\circ\text{C}$  cycling test in 230 mAh single crystal NMC811/artificial graphite pouch cells with a) control (black), 20v% KDC-403 (bright blue), 20v% KDC-403 (steel blue), and 20v% KDC-403 (sky blue) electrolytes ; b) control (black), 20v% KDC-403 (bright blue), 20v% methyl propionate (green), and 20v% KDC-403+20v% methyl propionate (teal) electrolytes; . The control electrolyte is EC/DEC/EMC 1/1/1 v/v + 1v% VC + 1M LiPF<sub>6</sub>.

#### Cell Format Development – Argonne National Laboratory

Argonne investigated the effects of electrode loading and porosity during BP2. The Cell Analysis, Modeling, and Prototyping (CAMP) Facility at Argonne made anode and cathode electrodes (Table XI.4.1), and three different loadings were tested in coin half cells. For the cathodes, the loadings were  $8.21 \text{ mg/cm}^2$  (A-C019A),  $9.08 \text{ mg/cm}^2$  (A-C020A), and  $15.81 \text{ mg/cm}^2$  (LN3174-179-4). The Silatronix baseline electrolyte (1 M LiPF<sub>6</sub> in 1/1/1 EC: EMC: DEC with 1% VC, v/v/v) was used for these half cells. The results showed that the higher loading electrodes had higher capacities on average at all C-rates tested (Figure XI.4.7). For the anodes, the

loadings tested were 8.85 mg/cm<sup>2</sup> (CFF-B28), 10.84 mg/cm<sup>2</sup> (LN3024-141-5), and 12.4 mg/cm<sup>2</sup> (LN3107-105-8). The higher loading anodes had a better capacity retention at higher c-rates (Figure XI.4.8).

**Table XI.4.1 Summary Of Electrodes Tested By Argonne**

Material	Loading (mg/cm <sup>2</sup> )	Coating Thickness (μm)	Label
NMC811	8.21	32	A-C019A
	9.08	33	A-C020A
	15.81	54	LN3174-179-4 MC
	15.81	59	LN3174-179-4
	15.81	64	LN3174-179-4 LC
	18.63	71	LN3237-100-3
Artificial Graphite	6.38	52	A-A016
	8.85	60	CFF-828
	10.84	68	LN3024-141-5 MC
	10.84	74	LN3024-141-5
	10.84	81	LN3024-141-5 LC
	12.40	90	LN3107-108-8

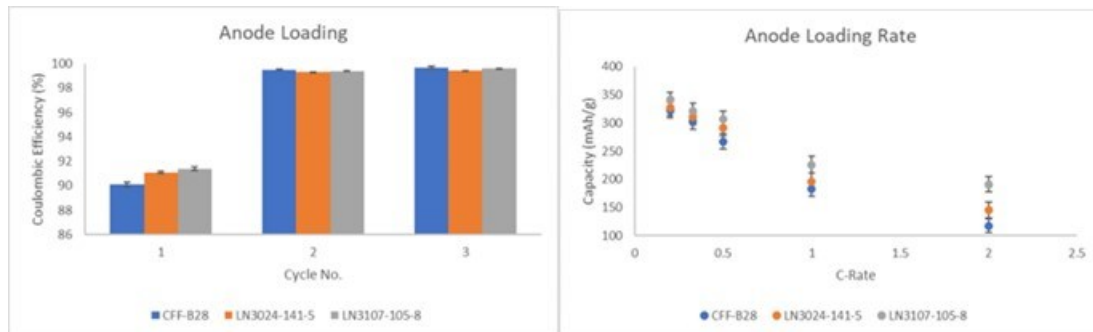


**Figure XI.4.7 Coulombic efficiency and rate performance of Li/NMC811 with various loadings in half cells with Silatronix baseline electrolyte**

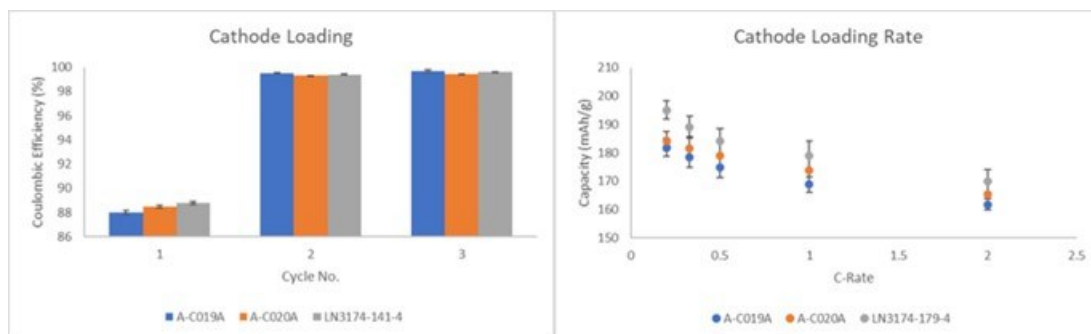


**Figure XI.4.8 Coulombic efficiency and rate performance of Li/Graphite with various loadings in half cells with Silatronix baseline electrolyte**

Using uncalendared anode and cathode electrodes that were sourced from CAMP, the impact of  $\pm 5\%$  change in porosity was examined. For the cathodes, LN3174-179-4 MC had the lowest porosity (29.3% and 54  $\mu\text{m}$  thickness), LN3174-179-4 had moderate porosity (34.7% and 59  $\mu\text{m}$  thickness), and LN3174-179-4 LC had the highest porosity (40.1% and 64  $\mu\text{m}$  thickness). When the rate studies were performed for this study, all cathodes had similar capacities. The cathodes with 34.7-40.1% porosity performed better on average than the cathode with 29.3% porosity, and the first cycle coulombic efficiency was higher with higher cathode porosity (Figure XI.4.9).

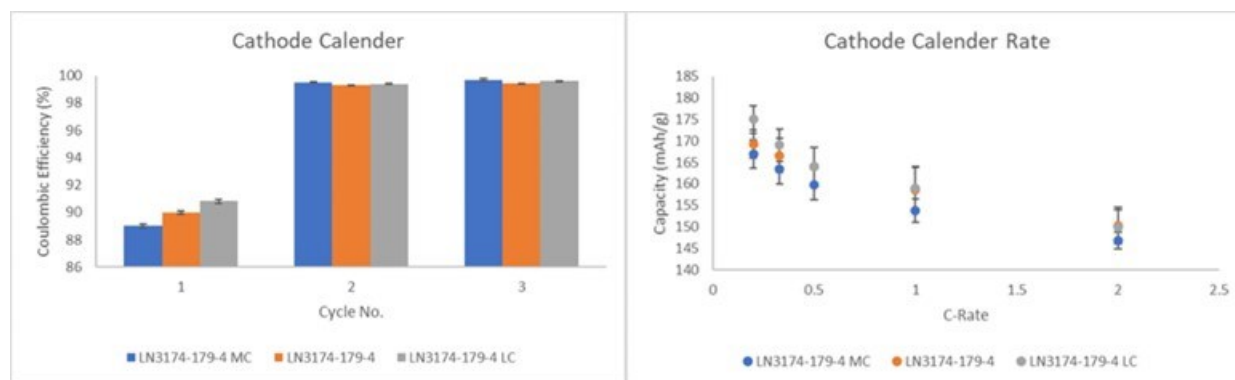


**Figure XI.4.9 Coulombic efficiency and rate performance of Li/NMC811 with various loadings in half cells with Silatronix baseline electrolyte**

The normal porosity of the anode, LN3024-141-5, was 35.4% at a 74  $\mu\text{m}$  thickness (L3024-141-5). A higher porosity anode L3024-141-5 LC (39.6% and 81  $\mu\text{m}$  thickness) and a lower porosity anode L3024-141-5 MC (30.4% and 68  $\mu\text{m}$  thickness) were also studied. As with the cathode, the rate capabilities of all anodes were similar regardless of porosity but the first cycle coulombic efficiency increased with porosity (Figure XI.4.10).

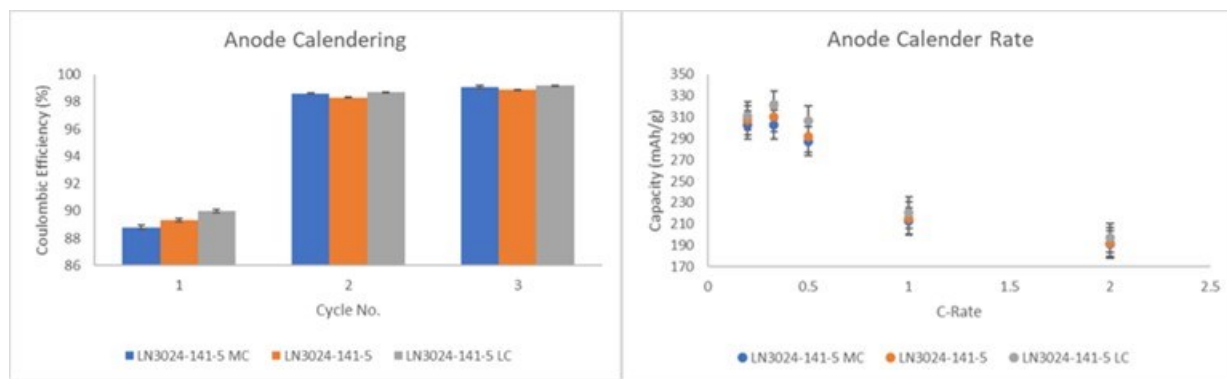


**Figure XI.4.10 Coulombic efficiency and rate performance of Li/Graphite with various loadings in half cells with Silatronix baseline electrolyte**

Full coin cells were made from higher loading artificial graphite MAGE 3 (LN3024-141-5) and NMC811 (LN3174-179-4) and tested with the baseline and Gen 2 (1.2 M LiPF<sub>6</sub> in EC/EMC (3/7 wt.%) electrolytes. This combination had an N/P ratio of 1.23 according to half-cell testing results. Gen 2 and baseline electrolyte were used for these full cells. All the full cells were cycled between 3.0 V and 4.2 V.

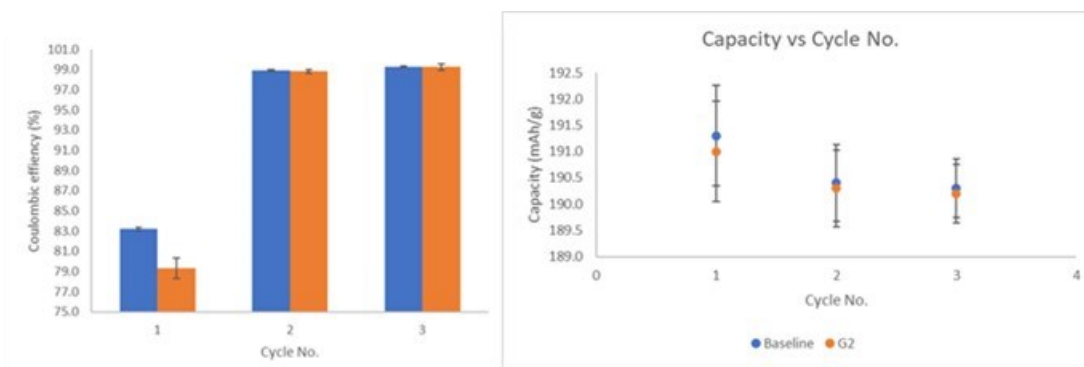


**Figure XI.4.11 Coulombic efficiency and rate cycle performance of Graphite (LN3024-141-5) /NMC811 (LN3174-179-4) full cell with Silatronix baseline and Gen 2 (G2) electrolytes.**

The first cycle coulombic efficiency for the Silatronix baseline electrolyte was higher than for Gen 2 (Figure XI.4.11). Subsequent, rate testing demonstrated that the Silatronix baseline electrolyte had higher capacity and less capacity fade than the Gen 2 electrolyte at all c-rates (Figure XI.4.12).

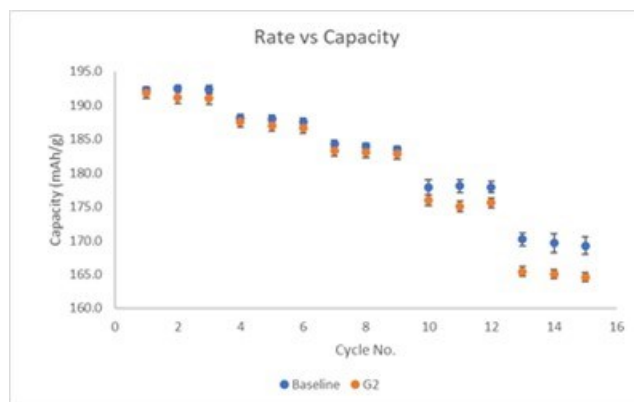


**Figure XI.4.12 Rate performance of MAGE3/NMC811 coin cells with Gen 2 and Silatronix baseline electrolytes**

Rate studies for these electrodes showed the least capacity fade at higher c-rates with the Silatronix baseline electrolyte. Hybrid Pulse Power Characterization (HPPC) experiments were conducted for these full cells as well. HPPC allowed for the examination of impedance (area specific impedance, ASI) at different states of charge. When the ASI at a 50% SOC was plotted from the HPPC, both electrolytes showed a rise in impedance after 50 cycles (Figure XI.4.13). The plot shows that these two electrolytes are similar, when it comes to impedance.

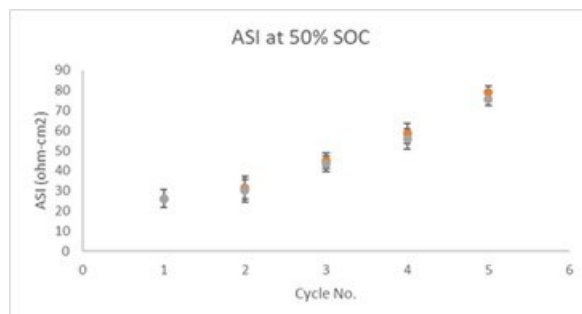


**Figure XI.4.13 ASI plots at 50% SOC of Graphite (LN3024-141-5) / NMC811 (LN3174-179-4) full cell with baseline (grey) and Gen 2 (orange).**

Overall, both baseline and Gen 2 electrolytes cycled well in full coin cells, validating the use of these electrolytes as benchmarks in larger cell format testing.

The results in coin cells were used to inform the build format of single layer pouch cells at Argonne. 32 single layer size 3450 (34mm x 50mm) dummy pouch cells were fabricated. These dummy cells consist of plastic place holders to be swapped later with single layer anode and cathode. This approach will ensure the quality and consistency of single layer pouch cell performance. The same approach will be applied to multilayer pouch cells. Single layer pouch cells will be tested with baseline, Gen 2, and fluorinated electrolytes to validate the cell format and understand the effects of electrolyte formulation.

## Conclusions

Early in FY23, the results of initial pouch cell testing at Silatronix revealed KDC-403, a fluorinated molecule, as the most promising candidate for improved stability and performance under extreme operating conditions. The continuing work throughout FY23 focused on 1) validating 403 against current commercially available electrolyte cosolvents commonly used low temperature and fast charge cycling; 2) optimizing the electrolyte formulation with KDC-403 for best performance; and 3) developing a mechanistic understanding of how KDC-403 operates in cells and provides the observed performance improvements.

The validation of 403 vs commercial cosolvent materials (short-chain esters) has been completed, with KDC-403 demonstrating superior fast charge and high temperature cycling stability, as well as improved low temperature cycling down to -20 °C and improved high-rate discharge at low temperatures down to -10 °C up with up to 1C discharge rate. Significant progress has been made in the effort to optimize the electrolyte composition with KDC-403, showing beneficial results with higher concentrations of 403 up to 20% and excellent low temperature stability with the combination of 20% 403 + 20% methyl propionate.

Initial post-test analysis results in FY23 have provided important insight into the origin of improved performance with 20% 403. These data together point to a thinner SEI layer on the graphite anode with 403 as the source of the observed reduced impedance growth, faster charging, and low-temperature cycle life. Argonne National Laboratory continued their cell design development towards the deliverable, assessing the effects of electrode loading and porosity and validating both Gen 2 and the Silatronix baseline electrolytes in test cells.



Further testing with electrolyte components will be performed in FY24 to optimally enhance cell performance under extreme operating conditions. In the remainder of the program, investigations will be carried out to further understand the role played by fluorinated solvents in improving cell performance. The program efforts will focus on continued optimization of fluorinated electrolytes, and demonstration in multi-Ah cells to be built at Argonne National Laboratory.

### Key Publications

1. Guillot, Sarah L.; Usrey, Monica L.; Du, Peng; Kerber, Brian; Zhou, Liu; Garg, Shipra; Sriramulu, Suresh. 2023. "Fluorinated Battery Electrolytes for Low Temperature Cycling." In *243<sup>rd</sup> Electrochemical Society Meeting, Boston, MA, USA, May 30, 2023*.
2. Sriramulu, Suresh. 2023. "Fluorinated Battery Electrolytes for Wide Temperature Range Performance." In *49<sup>th</sup> Power Sources Conference, Fort Washington, MD, USA, June 27-30, 2023*.
3. Kerber, Brian; Guillot, Sarah L.; Usrey, Du, Peng; Zhou, Liu; Garg, Shipra; Usrey, Monica L. 2023. "Improving Extreme Temperature and Charge Rate Performance in Li-Ion Batteries through Addition of Fluorinated Electrolyte Cosolvents." In *244<sup>th</sup> Electrochemical Society Meeting, Boston, MA, USA, May 30, 2023*.

### References

1. Li, Qiuyan; Jiao, Shuhong; Luo, Langli; Ding, Michael S.; Zheng, Jianming; Cartmell, Samuel S.; Wang, Chong-Min; Xu, Kang; Zhang, Ji-Guang; Xu, Wu, "Wide-Temperature Electrolytes for Lithium-Ion Batteries," *ACS Applied Materials & Interfaces* 9, (2017): 18826-18835, <https://doi.org/10.1021/acsami.7b04099>.
2. Li, Shiyong; Zhao, Wei; Zhou, Zhifang; Cui, Xiaoling; Liu, Haining; Zhang, Dongqiang, "Studies on Electrochemical Performances of Novel Electrolytes for Wide-Temperature-Range Lithium-Ion Batteries," *ACS Applied Materials & Interfaces* 6, (2014): 4920-4926, <https://doi.org/10.1021/am405973x>
3. Li, Qian; Liu, Gang; Cheng, Haoran; Sun, Quijiang; Zhang, Junil, "Low-Temperature Electrolyte Design for Lithium-Ion Batteries: Prospect and Challenges," *Chemistry A European Journal* 27, (2021): 15842-15865, <https://doi.org/10.1002/chem.202101407>
4. Waldmann, T.; Hogg, B-I.; Wohlfahrt-Mehrens, M. "Li plating as unwanted side reaction in commercial Li-ion cells – A review," *Journal of Power Sources* 384, (2018): 107-124, <https://doi.org/10.1016/j.jpowsour.2018.02.063>

### Acknowledgements

The efforts and accomplishments described in this summary relied on the work and insights of many people at Koura, Silatronix, and Argonne National Laboratory, including Andy Sharratt, Maxine Doran, Joshua Walton, Joe Lowson, Caleb Calvary, Diana Sadowski, Amy Zhou, Peng Du, Tobias Johnson, Drew Lehmann, Shipra Garg, John Hecht, David Arnett, Janiel Meier, and Brian Kerber.

## XI.5 Fluorinated Ester Local High Concentration Electrolytes for Operation of Li-Ion Batteries under Extreme Conditions (Stony Brook Univ)

### Esther Takeuchi, Principal Investigator

Stony Brook University  
100 Nicolls Road, 675 Chemistry  
Stony Brook, NY 11790-3400  
E-mail: [esther.takeuchi@stonybrook.edu](mailto:esther.takeuchi@stonybrook.edu)

### Haiyan Croft, DOE Technology Development Manager

U.S. Department of Energy  
E-mail: [Haiyan.Croft@ee.doe.gov](mailto:Haiyan.Croft@ee.doe.gov)

Start Date: October 1, 2022	End Date: September 30, 2023
Project Funding (FY23): \$866,461	DOE share: \$686,168      Non-DOE share: \$180,293

### Project Introduction

Lithium-ion batteries (LIB) are the battery technology of choice for hybrid/electric vehicles as they can provide high capacity and power capability due to the low reduction potential and the small ionic radii of lithium ions. LIBs are increasingly required to operate under a broad range of operational conditions pushing the limits of the current state of the art. Extreme conditions of high operating voltage, wide temperature range, fast charge, and abuse present stability and safety problems, primarily due to the limitations of Li-ion carbonate based electrolytes. Thus, there is a critical need to develop novel electrolytes with expanded functionality to meet this diverse set of environments and operating parameters.

### Objectives

The objective is to research, fabricate, and test liquid electrolytes for next-generation Li-ion cells (liquid electrolytes against graphite anodes and moderate/high voltage cathodes) with improved performance under an array of extreme conditions including high voltage, wide operating temperature, under extreme fast charging, and/or under extreme abuse.

### Approach

The technological approach is to use a modified electrolyte that will enable the operation under fast charge, wide temperature range, and high voltage conditions, with the added benefit of low flammability. The electrolyte will provide high oxidative stability, and integration of non-flammable diluents offers the opportunity to reduce or eliminate the flammability.

### Results

During this budget period, accomplishments were made in four areas: (1) Formulation of Generation 2 electrolytes and characterization of transport and stability properties, (2) Evaluation of morphology and chemical composition of interphases, (3) Evaluation of electrochemical behavior of Gen2 electrolytes under baseline and extreme conditions, and (4) Development of a computational model to predict electrolyte properties.

#### **1. Formulation of Generation 2 Electrolytes and Characterization of LHCE Transport and Stability Properties.**

Generation 2 (Gen2) were formulated with variation of ratios, and the transport and stability properties were characterized. Generation 2 formulations were prepared using solvent II, diluents VI and VII, and additives. The components were down selected based on the electrochemical cycling data collected previously on Generation I electrolytes. A total of 8 Gen2 formulations were tested.

Transport properties (conductivity and viscosity) of the Gen2 LHCEs are shown in Figure XI.5.1. LHCEs utilizing diluent VI (LHCEs E – H) are more conductive than those utilizing diluent VII (LHCEs A - D). A maximum conductivity of  $7.2 \pm 0.5$  mS/cm is achieved with LHCE E. Measured viscosities show that LHCEs A - D are more viscous than LHCEs E - H. The relationship of viscosity and conductivity with temperature is shown in Arrhenius plots (Figure XI.5.1**b, d**). All samples follow a nearly linear relationship ( $R^2 \geq 0.98$ ), where conductivity increases and viscosity decreases with increasing temperature.

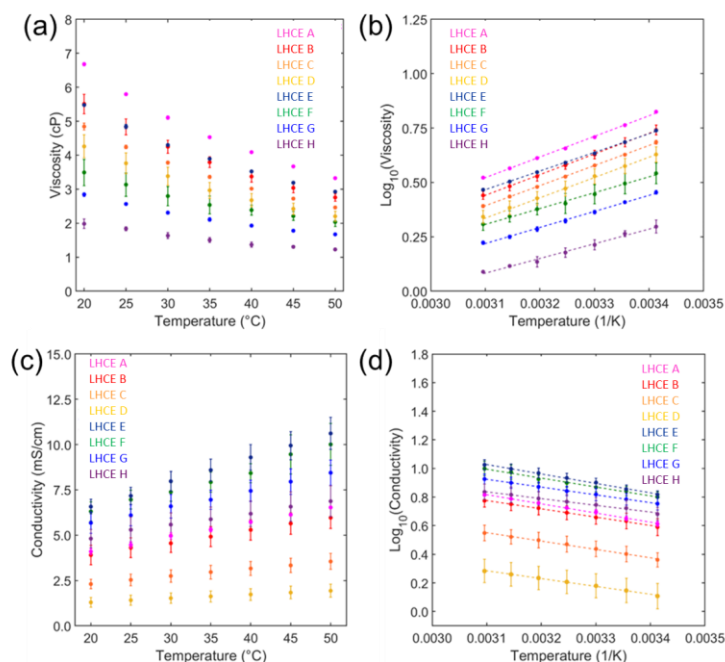


**Figure XI.5.1 (a, b) Conductivity and (c, d) viscosity measurements of Gen2 LHCEs over a temperature range of 20-50 °C. (b, d) show Arrhenius plots.**

Voltage stability of the Gen2 electrolytes was assessed using cyclic voltammetry in a 3-electrode cell configuration with Pt working electrode and Li reference and counter electrodes. Cyclic voltammograms were collected at a scan rate of 20 mV/s, with the voltage incrementally increased or decreased for upper or lower voltage limit testing, respectively, until the current density reached  $1 \times 10^{-4}$  A/cm<sup>2</sup> or a lower voltage cutoff of 0.05 V. Results are shown in Figure XI.5.2. All LHCEs had upper voltage limits between 4.6 – 4.8 V. All LHCEs were found to be stable down to the lower voltage cutoff of 0.05 V.

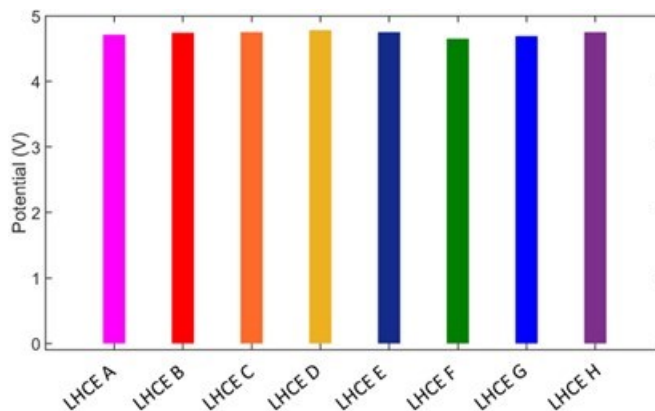


**Figure XI.5.2 Voltage stability of Gen2 LHCEs where the limiting current density was defined as  $1 \times 10^{-4}$  A/cm<sup>2</sup>. A lower voltage cutoff of 0.05 V vs. Li/Li<sup>+</sup> was used.**

The flammability of the Gen2 LHCEs was also tested and is shown in Figure XI.5.3. The flammability of the 8 Gen2 electrolytes (Figure XI.5.3a b-i) was compared against that of conventional Li-ion battery electrolyte as a control, 1M LiPF<sub>6</sub> in 3:7 (v:v) ethylene carbonate: dimethyl carbonate (EC:DMC) (Figure XI.5.3a). The control electrolyte immediately ignites when exposed to a flame and continues to burn after flame removal until only a highly viscous residue remains. On the other hand, both LHCEs could not be ignited when a flame was applied. This notable result shows that the LHCEs are significantly less flammable than current state-of-the-art carbonate based electrolytes.

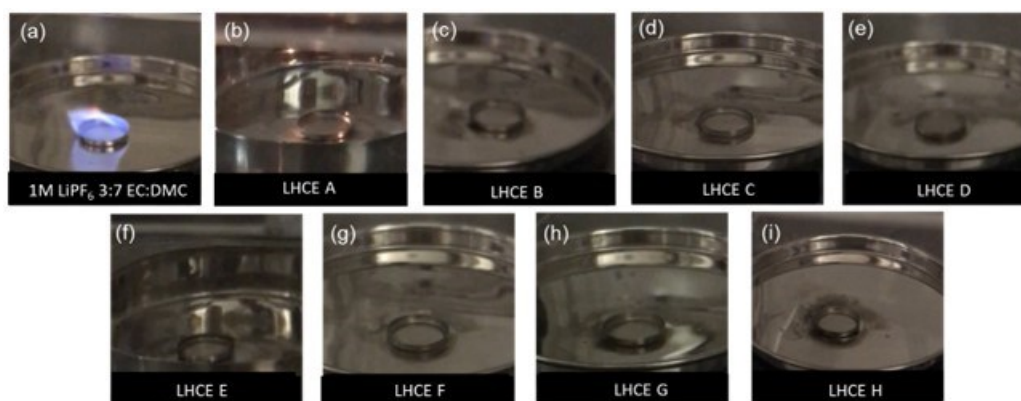


**Figure XI.5.3 Flammability testing of the electrolytes: (a) 1M LiPF<sub>6</sub> in 3:7 EC:DMC, (b-i) Gen2 LHCEs.**

## 2. Evaluation of Morphology and Chemical Composition of LHCE Derived Interphases

The morphology and chemical composition of the LHCE derived interphases was characterized. To characterize the chemical composition, X-ray photoelectron spectroscopy (XPS) measurements were collected on graphite anodes and NMC811 cathodes after recovered from cells cycled 200x under baseline cycling conditions (4.3 V, 30°C, 1C (dis)charge rate). Figure XI.5.4 compares the XPS results for electrodes recovered from cells cycled with either 1M LiPF<sub>6</sub> 3:7 EC:DMC or LHCE F. Notable differences in the cathode electrolyte interphase (CEI), (Figure XI.5.4a-d) were observed after cycling in the two electrolytes with the EC:DMC electrolyte exhibiting almost double the carbon content (69 atomic (at) % for the LiPF<sub>6</sub> EC:DMC vs. 32 at. % for LHCE F, with the LHCE F electrolyte showing a substantial reduction in carbonate type species at ~290 eV.<sup>1-3</sup> Comparison of the F1s spectra indicate significantly higher levels of LiF (~684 eV) species for the (LHCE F electrolyte (3 at. % for LiPF<sub>6</sub> EC:DMC vs. 13% for LHCE F. Meanwhile, the Li 1s spectra indicate a higher Li content for the LHCE F derived CEI (11 at. % for LiPF<sub>6</sub> EC:DMC vs. 25% for LHCE F. Analysis of the S2p, N1s regions revealed that the LHCE F CEI also contains contributions from anions as well as anion decomposition species (SO<sub>x</sub> and S<sub>n</sub><sup>x-</sup>)<sup>4-6</sup> while the LiPF<sub>6</sub> EC:DMC contains fluorophosphate (Li<sub>x</sub>PO<sub>y</sub>F<sub>z</sub> and Li<sub>x</sub>PF<sub>y</sub>) species. Overall, the analysis reveals that the LHCE derived CEI is rich in inorganic species including LiF and anion derived species, which have been shown to be associated with improved capacity retention for metal oxide cathodes.<sup>7, 8</sup>

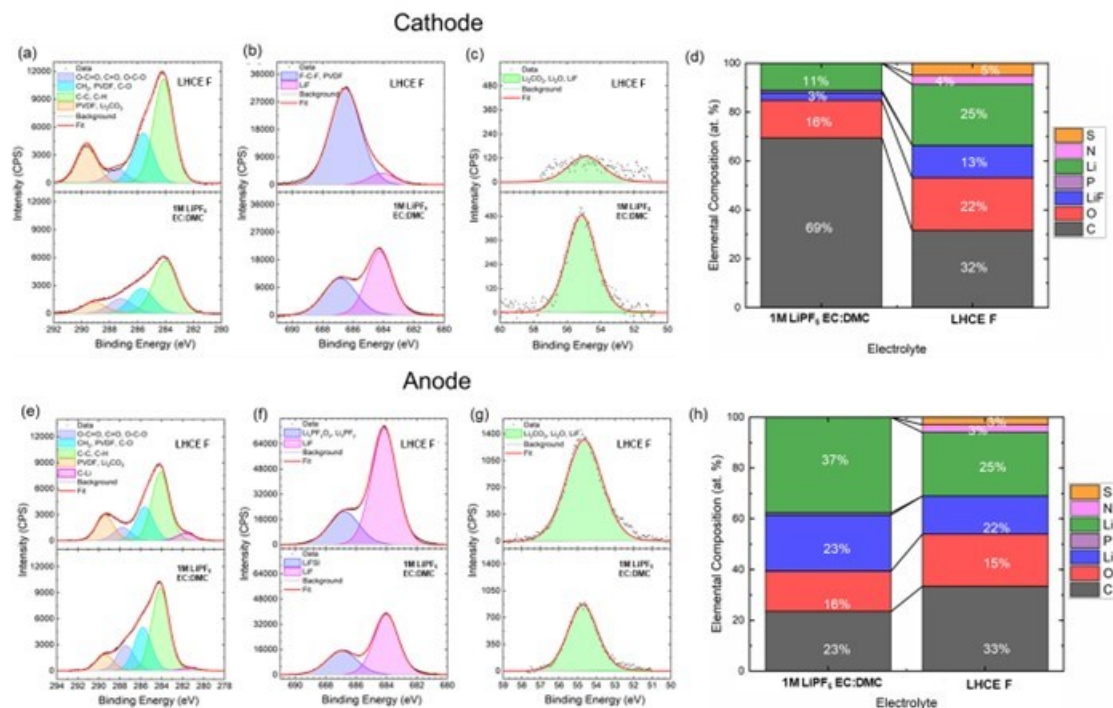


**Figure XI.5.4** XPS (a, e) C 1s (b, f) F 1s and (c, g) Li 1s spectra of recovered (a-c) NMC811 cathodes and (e-g) graphite anodes after 200x cycles under 1C/1C CCCV cycling condition with either LiPF<sub>6</sub> EC:DMC or LHCE F. (d, h) Elemental composition of interphases formed on (d) cathodes and (h) anodes.

Morphology of the interphases formed on the electrodes was characterized using scanning electron microscopy on electrodes recovered after cycling 200x under the baseline condition cycling condition (4.3 V, 30°C, 1C (dis)charge rate) with the LiPF<sub>6</sub> EC:DMC and LHCE F electrolytes. SEM images of the recovered cathodes are presented in Figure XI.5.5. CEI formation can be observed for both electrolytes. In the case of the cathode cycled in LiPF<sub>6</sub> EC:DMC electrolyte, a dark, amorphous film can be seen on top of the particles (Figure XI.5.5a-c). An energy-r filter was used which allows for acquisition of both backscattered and secondary electrons; the dark color suggests that the film is composed of lower z atoms (i.e. organic matter). On the other hand, the cathode particles cycled in LHCE F are covered with a new film of particles (Figure XI.5.5d-f). These particles are significantly smaller than the NMC811 primary crystallites, 210 +/- 50 nm vs. 520 +/- 80 nm, suggesting that they are a different inorganic species. SEM-energy dispersive X-ray spectroscopy (EDS) was used to determine the relative atomic percentages of species formed on the two cathodes and revealed that the LiPF<sub>6</sub> EC:DMC electrolyte led to significantly more C and O in the CEI, while the LHCE F electrolyte led to significantly higher fluorine content, in good agreement with the XPS results. Taken together, the SEM and EDX suggest that the CEI film on the LiPF<sub>6</sub> EC:DMC cycled cathode is an organic rich film while the CEI on the LHCE F cathode is crystalline fluoride and contains distinct particles; this is consistent with the XPS findings of an organic rich CEI on the LiPF<sub>6</sub> EC:DMC cycled cathode and a LiF rich CEI on the LHCE F cycled cathode.

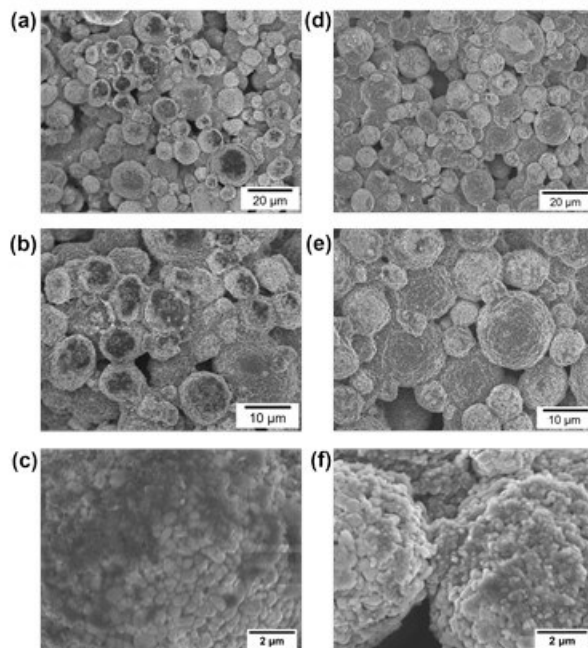


**Figure XI.5.5 SEM images of NMC811 cathodes post cycling 200x under the 1C/1C CCCV condition in either (a-c) LiPF<sub>6</sub> EC:DMC electrolyte or (d-f) LHCE F electrolyte, at (a, d) 1000X, (b, e) 2000X, and (c, f) 5000X magnification.**

### **3. Evaluation of Electrochemical Behavior of Gen2 Electrolytes Under Baseline and Extreme Conditions**

The cycling performance of the Gen2 LHCE formulations in a full cell configuration was tested under baseline and extreme conditions. Single layer graphite/NMC811 pouch cells were utilized. Graphite anodes were prepared with composition of 90% SLC 1506T natural graphite, 3% carbon black, and 7% KF-9300 Kureha PVDF binder. Electrode loading was 5 mg/cm<sup>2</sup>. The graphite electrodes were paired with LiNi<sub>0.8</sub>Mn<sub>0.1</sub>Co<sub>0.1</sub>O<sub>2</sub> (NMC811) cathodes (90% NMC811, 5% carbon black, 5% PVDF, 9 mg/cm<sup>2</sup> loading) with N : P ratio of 1.15 : 1. The areal capacity of the NMC811 cathodes was 1.8 mAh/cm<sup>2</sup>. The pouch cells were fabricated using the pilot pouch cell fabrication line at Brookhaven National Laboratory. A control carbonate-based electrolyte (1M LiPF<sub>6</sub> in 30:70 ethylene carbonate : dimethyl carbonate (EC:DMC)) was tested in addition to the LHCEs. Formation cycling of the cells was performed at a C/10 rate (based on 200 mAh/g NMC811) for four cycles. Voltage limits were 3.0 – 4.3 V. Duplicate cells were tested per condition.

Baseline cycling of the cells post-formation was performed under a constant current constant voltage (CCCV) protocol with 1C charge rate until an upper voltage limit of 4.3 V was reached, with the voltage held at 4.3 V until the current dropped below the equivalent C/10 rate. The discharge rate was 1C with a lower voltage limit of 3.0 V. The cycling protocol was performed at temperatures of 30° C for 200 cycles, with two C/10 cycles collected every 100 cycles. Results are shown in Figure XI.5.6. After 200 cycles, the average 1C capacities were 165 ± 9 mAh/g and 168 ± 1 mAh/g for LHCE A and LHCE E, respectively, compared to 144 ± 3 mAh/g for 1M LiPF<sub>6</sub> in 3:7 EC:DMC. Corresponding capacity retention values were 92 ± 2, 93 ± 3 %, and 78 ± 2 % for LHCE A, LHCE E, and 1M LiPF<sub>6</sub> in 3:7 EC:DMC, respectively.

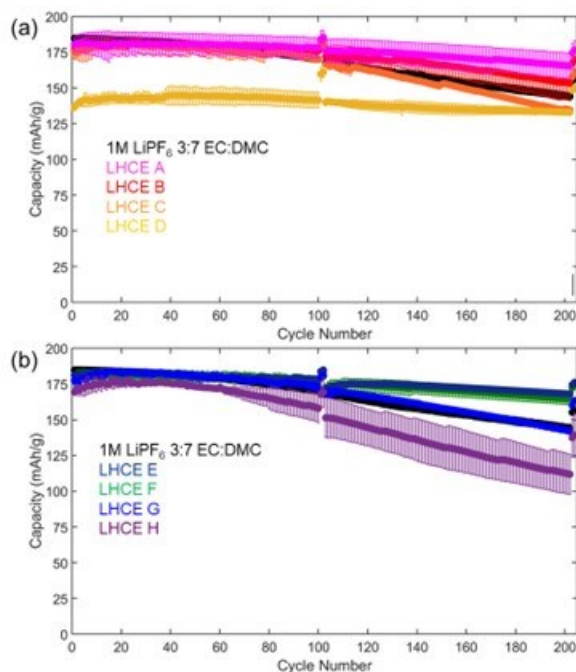


**Figure XI.5.6 Baseline cycling of NMC811/graphite pouch cells with Gen2 electrolyte and a control electrolyte 1M LiPF<sub>6</sub> 3:7 EC:DMC. (a) LHCEs A - D (b) LHCEs E - H.**

High voltage cycling of the cells post-formation was performed under a constant current constant voltage (CCCV) protocol with 1C charge rate until an upper voltage limit of 4.5 V was reached, with the voltage held at 4.5 V until the current dropped below the equivalent C/10 rate. The discharge rate was 1C with a lower voltage limit of 3.0 V. The cycling protocol was performed at 30° C for 200 cycles. Results are shown in Figure XI.5.7. After 200 cycles, multiple formulations demonstrated improvement in capacity retention compared to the control electrolyte. The LHCE E formulation had capacity of  $135 \pm 5$  mAh/g after 200 cycles, with capacity retention of  $73 \pm 1$  %. In comparison, the control electrolyte exhibited 200x cycle capacity of only  $114 \pm 2$  mAh/g and capacity retention of 57.4 mAh/g.

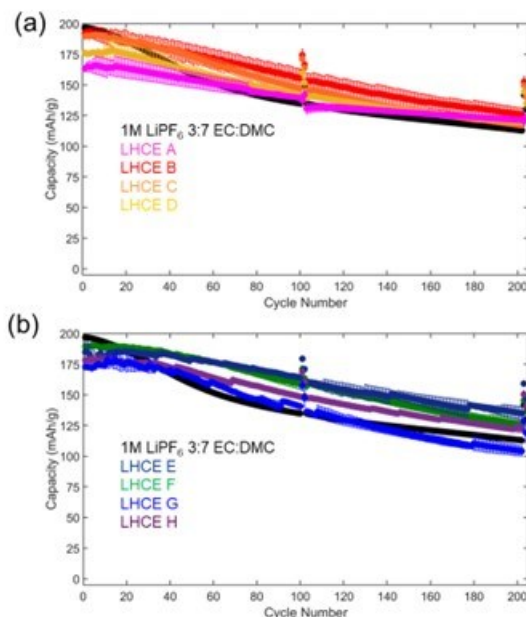


**Figure XI.5.7** High voltage cycling of NMC811/graphite pouch cells with Gen2 electrolyte and a control electrolyte 1M LiPF<sub>6</sub> 3:7 EC:DMC. (a) LHCEs A - D (b) LHCEs E - H.

High temperature (40° C) cycling of the cells post-formation was performed under a constant current constant voltage (CCCV) protocol with 1C charge rate until an upper voltage limit of 4.3 V was reached, with the voltage held at 4.3 V until the current dropped below the equivalent C/10 rate. The discharge rate was 1C with a lower voltage limit of 3.0 V. Results are shown in Figure XI.5.8. After 200 cycles, LHCEs A, B, C, E, F, G had delivered capacities which were within error of the control electrolyte (154 ± 7 mAh/g). LHCEs D and H exhibited higher levels of capacity fade with 200x capacity retention < 75%.

Low temperature testing was performed under a constant current constant voltage (CCCV) protocol with 1C charge rate until an upper voltage limit of 4.3 V was reached, with the voltage held at 4.3 V until the current dropped below the equivalent C/10 rate. The cells were held at -20° C in an environmental chamber for the test. The results of the low temperature test are shown in Figure XI.5.9. At -20° C, cells utilizing the control carbonate based electrolytes are only able to deliver ca. 30 - 40 mAh/g of capacity initially, falling to < 20 mAh/g by cycle 20. In contrast, cells utilizing LHCEs E - H delivered average capacities between 94 - 105 mAh/g in the first cycle, with >90% capacity retention over 100 cycles. The results demonstrate a significant improvement over the control electrolyte. LHCEs A - D were found to exhibit low initial capacities during initial cycling and, due to the comparably higher viscosity and lower conductivity of those formulations, were not tested over extended cycling.



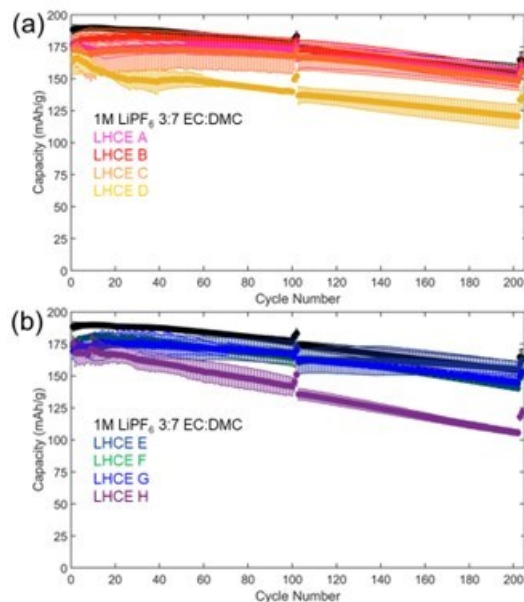


Figure XI.5.8 High temperature cycling of NMC811/graphite pouch cells with Gen2 electrolyte and a control electrolyte 1M LiPF<sub>6</sub> 3:7 EC:DMC. (a) LHCEs A - D (b) LHCEs E - H.

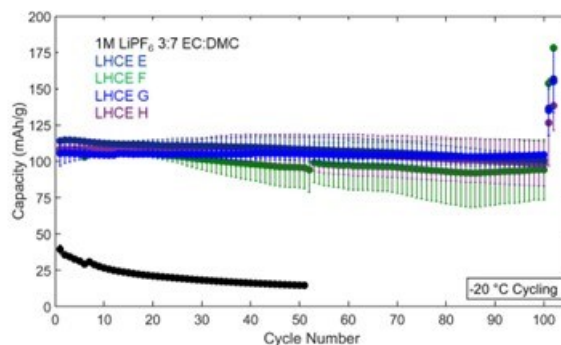


Figure XI.5.9 Low temperature cycling of NMC811/graphite pouch cells: discharge capacity vs. cycle number over 100 cycles at -20 ° C.

Fast charge cycling of the cells post-formation was performed under a constant current constant voltage (CCCV) protocol with 4C charge rate until an upper voltage limit of 4.3 V was reached, with the voltage held at 4.3 V until the total charge time was fifteen minutes. The discharge rate was 1C with a lower voltage limit of 3.0 V. Cells utilizing control electrolyte delivered capacity of  $132 \pm 8$  mAh/g after 200 cycles, corresponding to a capacity retention of  $72 \pm 4$  %. Significant improvement in capacity retention compared to the control cells was observed for Gen2 electrolytes having higher solvent to diluent ratios (Figure XI.5.10). For Gen2 electrolytes LHCE A and LHCE E, which exhibit the highest conductivity of all the formulations, average capacities of the cells at 200 cycles were  $167 \pm 2$  mAh/g and  $167 \pm 3$  mAh/g, corresponding to capacity retention values of  $95 \pm 5$  mAh/g and  $95 \pm 3$  mAh/g, respectively.

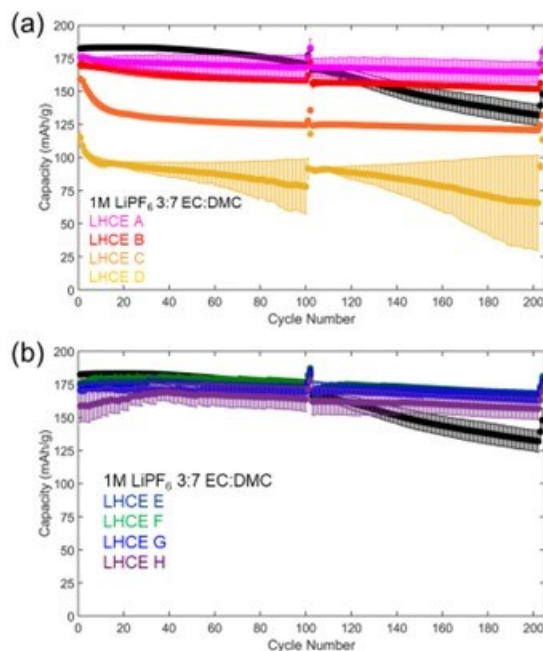


Figure XI.5.10 Fast charge cycling of NMC811/graphite with Gen2 electrolyte and a control electrolyte 1M LiPF<sub>6</sub> 3:7 EC:DMC. (a) LHCEs A - D (b) LHCEs E - H.

#### 4. Development of a Computational Model to Predict Electrolyte Properties

Computational work used Molecular Dynamics (MD) to simulate the properties of the electrolyte systems. Specifically, the work focused on identifying the selection rules for diluents incorporated into LHCEs and analysis of ionic conductivities as a function of diluent type and diluent molar ratio. The purpose of diluting an HCE to form an LHCE is to reduce the overall salt concentration but retain the highly concentrated salt-solvent clusters of the HCE. The diluent molecules should offer minimal solubility to the salt; i.e., the diluent should have poor solvating capacity for Li<sup>+</sup> ions to retain the local coordination environment of the inner solvation shell of HCE. The diluent should not enter the high concentration salt-solvent cluster since this will reduce the salt concentration in the cluster. However, the diluent should still be miscible with the solvating solvent in the HCE. Lastly, the diluent should have low viscosity, to reduce the overall viscosity of the electrolyte while improving ion conductivity.

LHCEs consisting of different diluents were simulated to understand their properties in retaining or improving the structures of the high concentration salt-solvent clusters and improving ionic conductivity. The LHCEs were based on based on lithium salt, solvent II and diluents V and VI. were studied in a comparative fashion to understand their effectiveness as a diluent. Based on the two aforementioned diluents, several LHCE structures were created (Figure XI.5.11e,f and Figure XI.5.12e,f) as well as the HCE structure (Figure XI.5.11b and Figure XI.5.12b) for comparison. The HCE structure was simulated by completely mixing Li<sup>+</sup>, salt anion and fluorinated solvent II at 1:1:3.2 molar ratio, which formed a uniform solution and gave a concentration of 2.4 M. The simulation cell consisted of a total of 80 Li<sup>+</sup>, 80 anions and 256 solvent II molecules.

For the LHCE structures, small cluster units consisting of 5 salt and 16 solvent II molecules were placed in a network of diluents so that in the initial configuration the salt is not in contact with diluent molecules. Based on a previous test the 5salt-16II unit clusters resulted in the most energetically favorable configuration. 16 of these unit clusters were placed in the simulation cell such that there was a total number of 80 salt, 256 II and either 128 or 25 diluent molecules depending on which molar ratio was considered. Throughout the simulation time, the LHCE structures consisted of many salt-solvent clusters of different sizes.

Figure XI.5.11 and Figure XI.5.12 show ternary phase diagrams for salt-solvent-diluent ternary phases. Figure XI.5.11 corresponds to the ternary phase diagram consisting of diluent V whereas Figure XI.5.12 corresponds to diluent VI. Each corner of the ternary phase diagram corresponds to a single phase, either the salt, the solvent II or the diluents V/VI. Each edge of the diagram corresponds to a binary phase, for example, the left edge corresponds to a binary phase of salt and solvent II. The HCE system (salt-3.2 II) lies on this edge as shown in Figure XI.5.11b and Figure XI.5.12b and it is close to the solubility limit of the salt in the solvent. The bottom edge corresponds to the binary phase of solvents and diluents. Figure XI.5.11c and Figure XI.5.12c show the binary solutions of II-V and II-VI, respectively. The right edge corresponds to the binary phases of salt and diluents. In the simulations of salt and diluent V binary systems there was found to be some level of salt solubility in the diluent. The salt-V binary system shown in Figure XI.5.11d corresponds to a point near the solubility limit shown in the right edge of the ternary phase diagram in Figure XI.5.11. The diluent VI on the other hand does not show any salt solubility, thus the solubility limit of salt in VI merges at the corner of the ternary phase diagram which corresponds to the pure diluent VI phase (Figure XI.5.12). Any region inside the diagram corresponds to ternary systems. The gray region above the line connecting the salt-solvent solubility limit and the salt-diluent solubility limit corresponds to the salt-precipitation region. The light green region under this line corresponds to the stable solution region where salt-solvent clusters in diluent network could exist. Any point on the dashed line corresponds to constant salt:II molar ratio of 1:3.2. The LHCE systems (salt-3.2 II-1.6/3.2 V/VI) shown in the figures are from points from the dashed line.

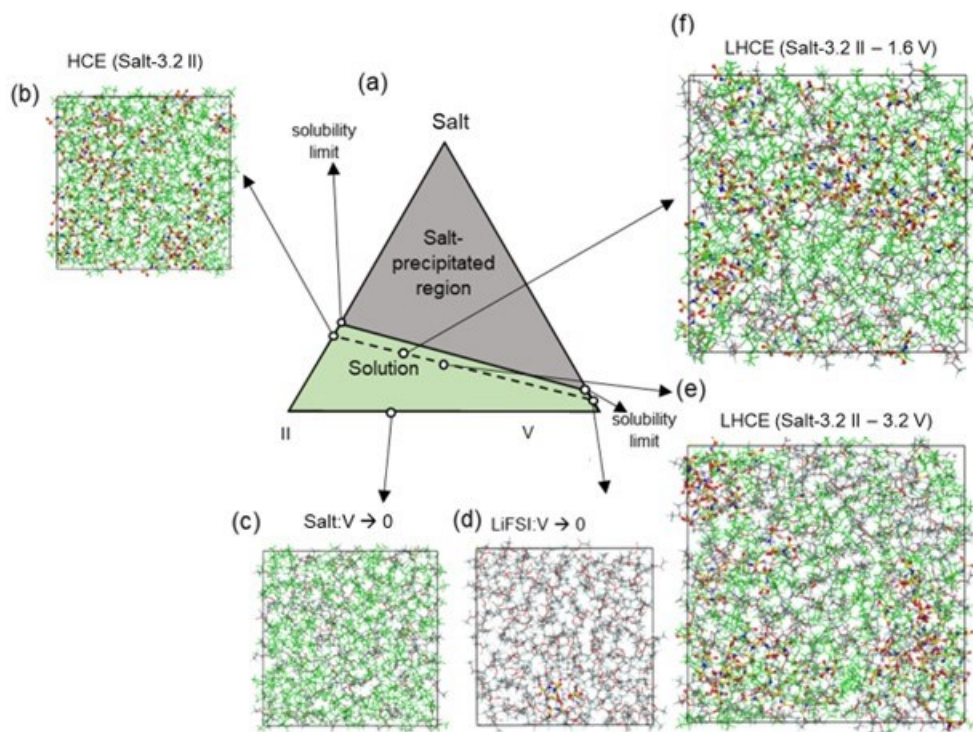


Figure XI.5.11 Ternary phase diagram of salt, solvent II, and diluent V.

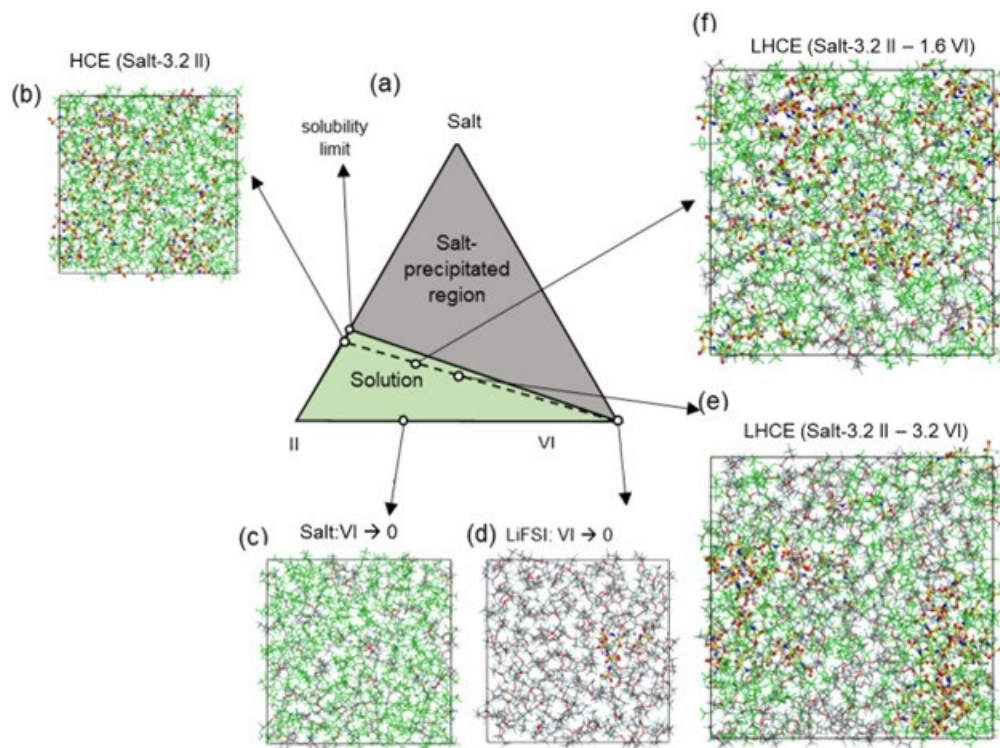


Figure XI.5.12 Ternary phase diagram of salt, solvent II, and diluent VI.

The time averaged number of electrolyte constituents (and their fraction of the total number of constituents shown in parenthesis) surrounding a single  $\text{Li}^+$  ion in the solvation shells in HCE and LHCEs were calculated. For the HCE system, on average the  $\text{Li}^+$  is coordinated to 2.65 salt anions and 2.12 solvent (II) molecules. This translates to 56% of anion contribution in the salt-solvent clusters. When adding diluent to the HCE to form LHCE, the salt anion coordination should either retain or ideally increase since at the optimized temperature. The  $\text{Li}^+$  solvation structure of LHCE can have a higher concentration of salt anion than that of its HCE counterpart due to some solvent molecules moving away from the salt-solvent clusters and entering and mixing with the diluent network. When diluent V molecules are added to the HCE system to form LHCE consisting of salt-3.2II-1.6V (Figure XI.5.11f), the percentage of anions in the solvation shell does not change significantly; however, the diluent V enters the salt-solvent clusters and replaces some of the solvent. This results in a decrease in solvent coordination to 1.67 and an undesirable diluent coordination of 0.49, which corresponds to a 10% contribution in the  $\text{Li}^+$  ion solvation shell from the diluent. The more diluent V in the LHCE, the more the diluent enters and replaces the solvent from the salt-solvent clusters, as simulated for the LHCE consisting of salt-3.2II-3.2V (Figure XI.5.11e), which has an increased diluent-coordination of 0.69. The diluent VI on the other hand maintains almost zero coordination with the diluent and thus does not participate in the solvation shell, but dissolves and removes solvents from the salt-solvent cluster, effectively increasing the salt anion contribution to coordination from 56% to 65%. The more the VI diluent, the higher the anion concentration in the cluster becomes. Thus, the results indicate that diluent VI is a more effective diluent than V, forming higher local concentrated salt clusters.

Ionic conductivity of the LHCEs was predicted using two different methods – namely the Nernst-Einstein equation which is more applicable to dilute electrolytes and the Green-Kubo method which takes into account ion correlations and is more applicable for high concentration electrolytes. The goal was to find a method that can reproduce experimentally obtained ionic conductivity. The Nernst-Einstein equation is widely applied to dilute cases and strong electrolytes. In low concentration electrolytes, the ion pairs are separated by solvents and thus, the diffusion of individual ions contributes entirely to the total ionic conductivity. In high concentration electrolytes or localized high concentration electrolytes, the ions move as contact ion pairs or

aggregates. Thus, concerted migration of ions must be accounted for in computing ionic conductivity for HCEs and LHCEs. We calculated ionic conductivity using the following Green-Kubo relation that accounts for correlation between ions,

$$\sigma = \frac{1}{6k_BTV} \lim_{t \rightarrow \infty} \frac{d}{dt} \left\langle \sum_i \sum_j q_i q_j [r_i(t) - r_i(0)] \cdot [r_j(t) - r_j(0)] \right\rangle \quad (\text{Eq 1})$$

where  $V$  is the volume,  $q_i$  is the charge of species  $i$  and  $r_i(t)$  is the position vector of ion  $i$  at time  $t$ . Ionic conductivity is computed by obtaining the slope of the linear regime of the bracketed term of Eq 1. Figure XI.5.13 shows the calculated ionic conductivity plotted alongside the experimentally obtained ionic conductivity. For these calculations, the diluent molar ratio was varied from  $x = 0$  to 6.4 in the LHCE systems (Salt-3.2 Solvent II-  $x$ Diluent). The calculated ionic conductivities show similar qualitative trends with the two distinct slopes as seen in the experimental results and are of similar order of magnitude.

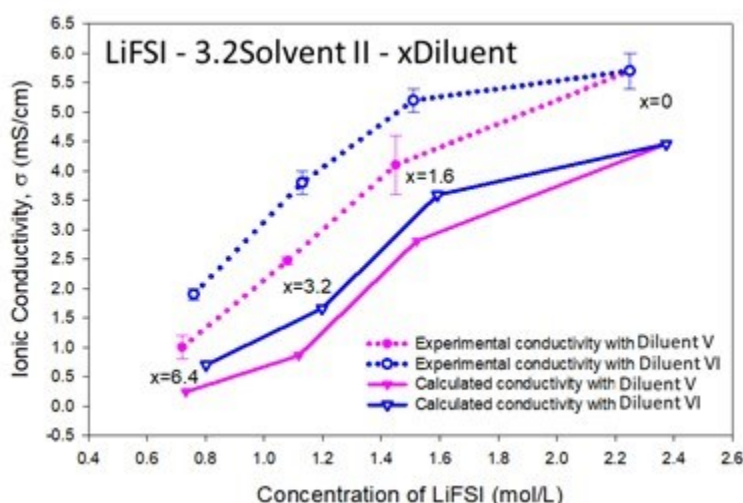


Figure XI.5.13 Calculated and experimentally determined conductivity at 25 °C as a function of salt concentration for electrolyte formulations with Salt : Solvent II : diluent molar ratios of 1 : 3.2 :  $x$  ( $x = 0, 1.6, 3.2, 6.4$ ).

## Conclusions

2<sup>nd</sup> Generation LHCEs have been developed and characterized with variation of diluent type and solvent : diluent ratio. LHCEs with higher solvent : diluent ratio have high conductivity and improved capacity retention compared to formulations with lower solvent: diluent ratio. The Gen2 LHCEs improve capacity retention compared to conventional carbonate based electrolyte after 200 cycles in a full cell under multiple extreme conditions of high voltage, fast charge, and low temperature, while maintaining performance under high temperature. The electrolytes also demonstrate significantly reduced flammability. Study of LHCE derived interphases by XPS and SEM indicate that they incorporate high levels of LiF and anion derived species. Furthermore, a computational model has been developed that can accurately predict the ionic conductivity of the LHCEs.

## Key Publications

- Hossain, Md Jamil; Wu, Qisheng; Marin Bernardez, Edelmy; Quilty, Calvin; Marschilok, Amy; Takeuchi, Esther; Bock, David; Takeuchi, Kenneth; Qi, Yue. "The Relationship between Ionic Conductivity and Solvation Structures of Localized High-Concentration Fluorinated Electrolytes for Lithium-Ion Batteries" *J. Phys. Chem. Lett.* **2023**, 14, 7718-7731

## Acknowledgements

The co-PIs for this project include Kenneth J. Takeuchi (Stony Brook University and Brookhaven National Laboratory), Amy C. Marschilok (Stony Brook University and Brookhaven National Laboratory), David C. Bock (Brookhaven National Laboratory), Lei Wang (Brookhaven National Laboratory), Yue Qi (Brown University).

## References

1. Briggs, D. Beamson, G., Primary and secondary oxygen-induced C1s binding energy shifts in x-ray photoelectron spectroscopy of polymers. *Analytical Chemistry* **1992**, *64* (15), 1729-1736.
2. Leroy, S.; Blanchard, F.; Dedryvere, R.; Martinez, H.; Carre, B.; Lemordant, D. Gonbeau, D., Surface film formation on a graphite electrode in Li-ion batteries: AFM and XPS study. *Surface and Interface Analysis* **2005**, *37*, 773-781.
3. Moulder, J. F., Stickle, W. F., Sobol, P. E. and Bomben, K. D., *Handbook of X-ray Photoelectron Spectroscopy*. ULVAC-PHI: 1995.
4. Chae, S.; Kwak, W.-J.; Han, K. S.; Li, S.; Engelhard, M. H.; Hu, J.; Wang, C.; Li, X. Zhang, J.-G., Rational Design of Electrolytes for Long-Term Cycling of Si Anodes over a Wide Temperature Range. *ACS Energy Letters* **2021**, *6* (2), 387-394.
5. Xue, W.; Shi, Z.; Huang, M.; Feng, S.; Wang, C.; Wang, F.; Lopez, J.; Qiao, B.; Xu, G.; Zhang, W., et al., FSI-inspired solvent and “full fluorosulfonyl” electrolyte for 4 V class lithium-metal batteries. *Energy & Environmental Science* **2020**, *13* (1), 212-220.
6. He, J.; Bhargav, A.; Shin, W. Manthiram, A., Stable Dendrite-Free Sodium–Sulfur Batteries Enabled by a Localized High-Concentration Electrolyte. *Journal of the American Chemical Society* **2021**.
7. Bai, P.; Ji, X.; Zhang, J.; Zhang, W.; Hou, S.; Su, H.; Li, M.; Deng, T.; Cao, L.; Liu, S., et al., Formation of LiF-rich Cathode-Electrolyte Interphase by Electrolyte Reduction. *Angewandte Chemie International Edition* **2022**, *61* (26), e202202731.
8. Ren, X.; Zou, L.; Cao, X.; Engelhard, M. H.; Liu, W.; Burton, S. D.; Lee, H.; Niu, C.; Matthews, B. E.; Zhu, Z., et al., Enabling High-Voltage Lithium-Metal Batteries under Practical Conditions. *Joule* **2019**, *3* (7), 1662-1676.

## XI.6 Novel Organosulfur-Based Electrolytes for Safe Operation of High Voltage Li-Ion Batteries Over a Wide Operating Temperature (GM)

### Meinan He, Principal Investigator

General Motors Research and Development Center  
30470 Harley Earl Blvd  
Warren, MI 48092  
E-mail: [Meinan.he@gm.com](mailto:Meinan.he@gm.com)

### Haiyan Croft, DOE Technology Development Manager

U.S. Department of Energy  
E-mail: [Haiyan.Croft@ee.doe.gov](mailto:Haiyan.Croft@ee.doe.gov)

Start Date: October 1, 2022	End Date: September 30, 2023
Project Funding (FY23): \$1,033,313	DOE share: \$807,855      Non-DOE share: \$225,458

### Project Introduction

This project proposes a new electrolyte system based on organosulfur solvents for high voltage lithium-ion batteries (LIBs). Due to their high anodic stability and intrinsic safety, several organosulfur solvents such as sulfones and sulfonamides were successfully applied to LIBs.<sup>1-3</sup> However, in exploring new electrolyte systems, researchers typically focus on a single property and synthesize molecules that are outstanding in that property while neglecting other features that are essential for the stable cycling of LIBs.<sup>3,4</sup>

In this work, we will (1) Design and synthesize new organosulfur solvents functionalized by strong electron withdrawing groups such as fluoroalkyl and cyano groups. With regio-specific molecular engineering, supported by theoretical calculation, we will lower the HOMO energy level of the molecules to increase the anodic stability for high voltage charging. (2) Optimize the formulation of the organosulfur-based electrolyte with co-solvents and salts specific to the new electrolyte system. (3) Use advanced spectroscopic techniques to thoroughly understand the mechanisms of interaction between the electrolyte and the electrode materials. (4) Test pouch cell under engineering protocols with normal and extreme conditions.

### Objectives

The objective of this proposal is to develop a new electrolyte system based on organosulfur solvents for high voltage lithium-ion batteries (LIBs). Through the region-specific molecular engineering, organosulfur molecules having the most stable organosulfur backbone with the best functional group attached at the optimum position will be invented to enable very stable high voltage cycling of graphite||high-Ni cathode full cells. In the meantime, by formulating the organosulfur based solvents with different co-solvents and lithium salts, the wide temperature operation capability of the cell can be further enhanced. Combining the advantages of their intrinsic high anodic stability and non-flammability nature, several organosulfur solvents such as sulfones and sulfates will be applied to LIBs.

### Approach

To achieve our goal, we will (1) design and synthesize new organosulfur solvents functionalized with strong electron withdrawing groups such as fluoroalkyl and cyano groups. With regio-specific molecular engineering, supported by theoretical calculation, we will lower the HOMO (highest occupied molecule orbital) energy level of the molecules to increase the anodic stability for high voltage charging. (2) We will optimize the formulation of the organosulfur-based electrolyte with co-solvents and salts specific to the newly synthesized solvent molecules. (3) We will use advanced spectroscopic techniques to thoroughly understand the mechanisms of interaction between the electrolyte and the electrode materials. Finally, we will (4) test pouch cell under engineering protocols with normal and extreme conditions. The pouch cell with the newly

developed electrolyte system will be tested to allow 2 Ah Gr||NMC811 cells to operate at extreme conditions with  $\geq 4.5$  V cutoff with high stability (1000 cycles with 80 % capacity retention), high safety (non-flammability during puncture test) and wide temperature range (-40 °C to +40 °C).

## Results

### Baseline electrode materials selection

At the beginning of this project, both anode and cathode additives are systematic studied. Three types of  $\text{LiNi}_x\text{Co}_y\text{Mn}_z\text{Al}_{(1-x-y-z)}\text{O}_2$  (NCMA) cathode active materials with >80% Ni content and four types of  $\text{LiNi}_{0.8}\text{Co}_{0.1}\text{Mn}_{0.1}\text{O}_2$  (NCM811) were purchased in powder format and their high voltage stability was determined via cycling tests. NCMA materials generally possess higher stability than NCM materials, as seen from Figure XI.6.1 below. After 500 cycles with an upper cutoff voltage of 4.2V, NCMA 3 has a capacity retention of 87%. While showing slightly less capacity retention, NCM 1 shows the best performance among the NCM candidates, with a capacity retention of 85% after 500 cycles. When ultimately down selecting for the 1<sup>st</sup> batch roll to roll electrode and pouch cell fabrication, performance as well as availability of materials was considered. As available NCMA material stock is extremely limited and difficult to procure in necessary amounts, NCM 1 was chosen, due to its relatively strong cycling performance and ensured availability for purchase and procurement.

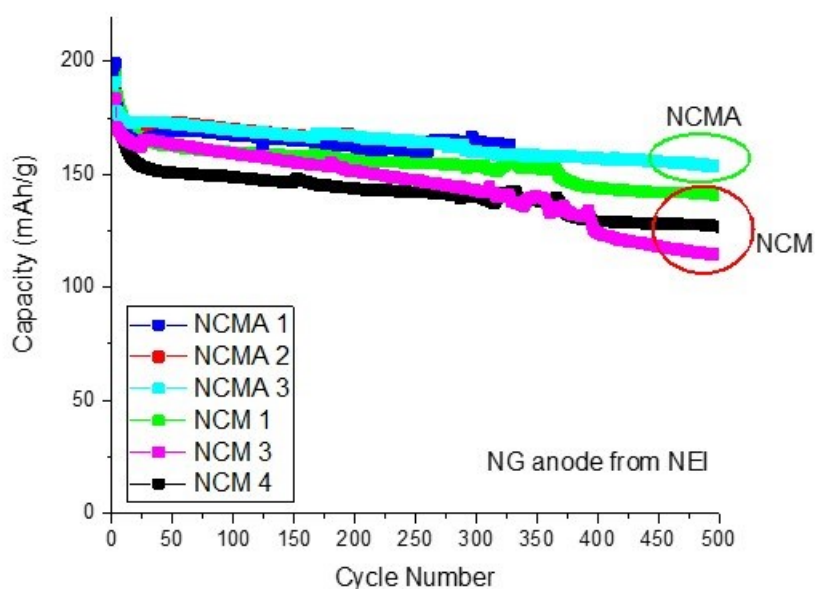


**Figure XI.6.1** The capacity retention of full cells using the as-fabricated cathodes and NEI graphite anode under 4.2V upper cutoff voltage.

Graphite is the foremost commercial anode for lithium-ion batteries (LIBs) due to its good cyclability and affordability, and therefore has become the first choice for EV LIBs. In this study, both natural graphite (NG) and artificial graphite (AG) were tested to select an anode for roll-to-roll electrode coating. Anodes were constructed by creating a NG or AG-based slurry, coating a copper current collector, and pressing to form the final electrode. More experimental details regarding electrode fabrication were previously reported and can be found in our Q3 report. Stability of the as-fabricated electrodes were determined by cycling tests of cells with our previously selected cathode, NCM 1, and an AG or NG anode, with various cutoff voltages of 3.0V to 4.5V. Results are shown in Figure XI.6.2. Cells with AG show better initial capacity retention than cells with NG over the first 50 cycles. However, upon further cycling, cells with AG anodes experience an abrupt loss in



capacity approaching end of cycle life. As seen in Figure XI.6.3, we additionally observe an associated dramatic and sudden loss of coulombic efficiency (CE) and increase in surface resistance upon extensive cycling for cells with AG anodes. Cells with NG anodes, on the other hand, showed steadier capacity losses over the extended cycling tests, without the sudden abrupt capacity and CE loss that was observed for the cell with NG-based anodes. Overall, we conclude that NG-based anodes offer superior long-term cyclability and maintain high coulombic efficiency throughout cycling tests. We therefore selected NG as the preferred anode graphite to use in our studies moving forward in the project.

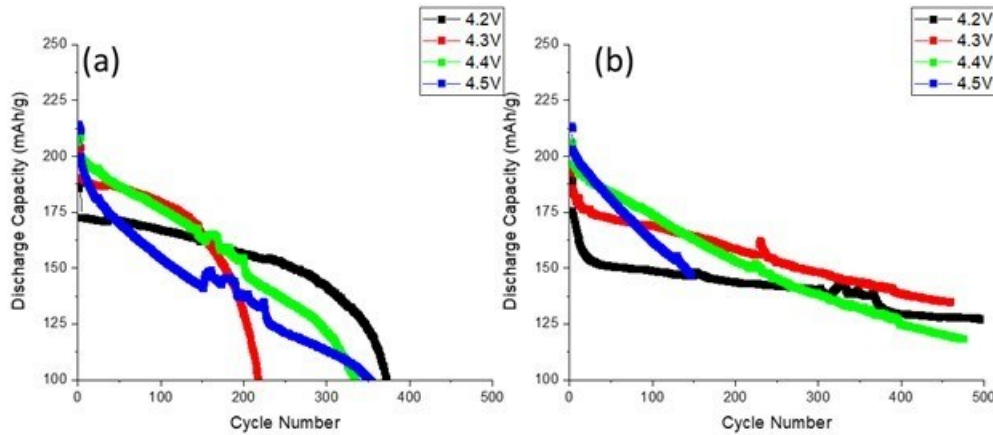


Figure XI.6.2 Capacity retention using AG or NG as anode and NCM1 as cathode under different upper cutoff voltages. a) artificial graphite; b) natural graphite

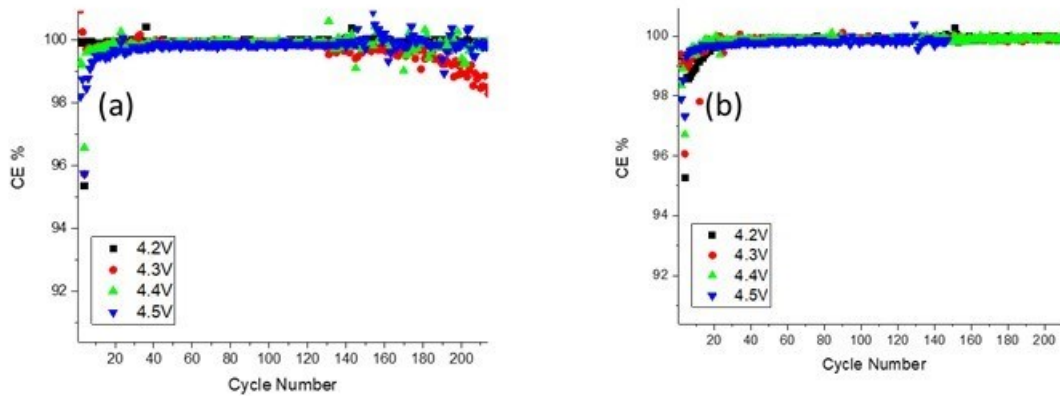


Figure XI.6.3 Coulombic efficiency using AG or NG as anode and NCM1 as cathode under different upper cutoff voltages. a) artificial graphite; b) natural graphite

As outlined previously, both NCM1 and NG were selected for 1<sup>st</sup> batch electrode roll and pouch cell fabrication. As noted in our Q2 report, cathode slurry formulation was optimized and addressed. The electrode loadings for different cell designs are displayed in Table XI.6.1. Cells with 4.3V and 4.4V operation voltage share same electrode design, as a result, the N/P of 4.3V design is slightly higher than 4.4V design.

Table XI.6.1 Electrode Roll Loading Information for Pouch Cell Design.

Cell design	Anode AM loading	Cathode AM loading	Anode capacity loading	1st charge capacity/Voltage	1st discharge capacity/voltage	N/P
4.5V	10.8mg/cm <sup>2</sup>	13.75mg/cm <sup>2</sup>	3.9mAh/cm <sup>2</sup>	250mAh/g@4.5V	218mAh/g@3V	1.1
4.4V	10.8mg/cm <sup>2</sup>	15.05mg/cm <sup>2</sup>	3.9mAh/cm <sup>2</sup>	238mAh/g@4.4V	211mAh/g@3V	1.1
4.3V	10.8mg/cm <sup>2</sup>	15.05mg/cm <sup>2</sup>	3.9mAh/cm <sup>2</sup>	231mAh/g@4.3V	205mAh/g@3V	1.12
4.2V	10.8mg/cm <sup>2</sup>	16.5mg/cm <sup>2</sup>	3.9mAh/cm <sup>2</sup>	221mAh/g@4.2V	198mAh/g@3V	1.08

The cathode electrode has a single side coating thickness of 45  $\mu\text{m}$ , porosity was controlled to 25%, and the electrode density was controlled to 3.2g/cm<sup>3</sup>. The anode has a single side coating thickness of 75  $\mu\text{m}$  and the anode porosity was controlled to 33%. Images of the as-fabricated cathode and anodes are shown below in Figure XI.6.4 and Figure XI.6.5. The as-fabricated double-sided coated electrode was tested in a coin cell by removing one side of the coating before pouch cell assembling. When measuring the full cell voltage profiles, all cells showed 88-90% CE during their first cycle, indicating a reasonable N/P ratio design. Capacity reversible percentage between C/10 and C/3 is  $\sim$ 95% for all upper cutoff voltage cells, indicating a good rate capability for our as-fabricated electrodes.

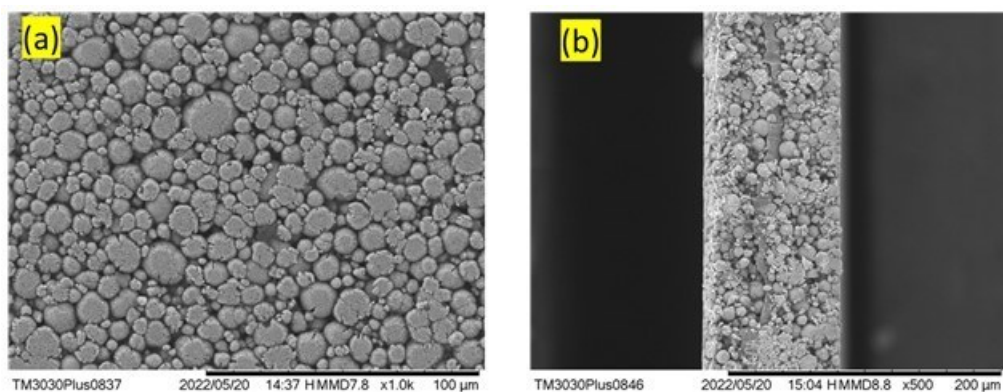


Figure XI.6.4 SEM images of the as-fabricated cathode for 4.2V design (a). Top view and (b). cross section view

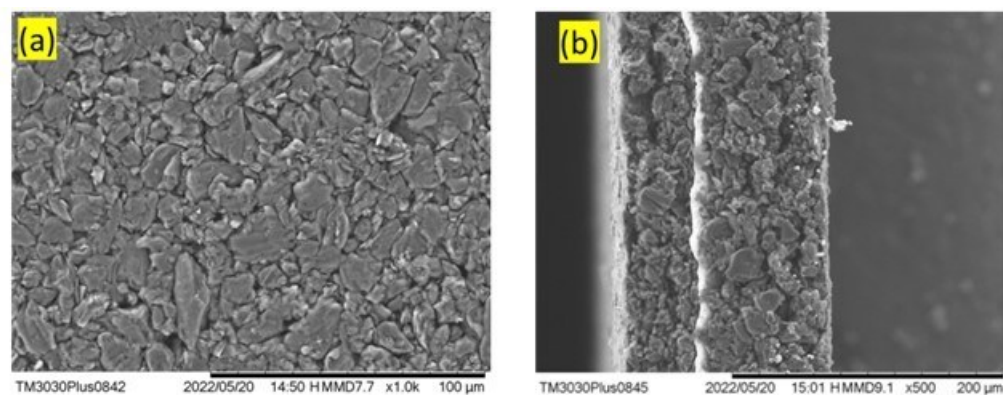


Figure XI.6.5 SEM images of the as-fabricated graphite anode for all upper cutoff voltage design (a). Top view and (b). cross section view

**Baseline cell data collection at the coin cell level**

Applying the optimized electrode design determined earlier in this section, we have now conducted baseline cell data collection at the coin cell level.

Experiments were completed to understand the relationship between upper cutoff voltage, temperature, and discharge capacity over extended cycling. A control sample cell was cycled at 25°C at a discharge rate of C/3 for 300 cycles following three C/10 formation cycles, as shown by the pink markers in Figure XI.6.6. Meanwhile, a sister set of coin cells (blue and red markers) was cycled at a specified upper voltage cutoff condition at varying temperatures and alternating discharge rates of C/3 and C/10. At each temperature condition, three cycles with a C/10 discharge rate were performed, after which 25 cycles were performed at a C/3 discharge rate, with an exception for the column designated “-30C C/10-C/10”, which shows results where the sister cells were simply discharged at a C/10 rate for all cycles shown. Results are shown in Figure XI.6.7 and tabulated in Table XI.6.2. The sister cells demonstrated good sample similarity and reproducibility at each voltage and temperature condition. We find that temperature has a drastic impact on the discharge capacity of the cells. To a lesser extent, discharge capacity is also impacted by the discharge rate, with the greatest impact seen for the lower temperature conditions, particularly for the -35°C condition, where the discharge capacity is effectively zero with a C/3 rate, but reaches ~20-80 mAh/g with a reduced discharge rate of C/10. Overall, we can conclude a few key trends from the data: 1. As upper cutoff voltage is increased, discharge capacity increases. 2. As temperature increases, discharge capacity increases. 3. As discharge rate is reduced, discharge capacity increases.

Coulombic efficiency (CE) was also calculated for each cycle reported. Complimentary CE data are displayed in Figure XI.6.7. The control cell cycled at C/10 and 25°C boasts a consistent ~99.9% CE throughout the extensive cycling following formation, however the sister experimental cells cycled at varying temperatures and rates show significant deviation from a 99.9% CE. Reduction of the sister cells' CE is most notable and consistently observed at high cycle numbers after the cells have seen a variety of temperatures. This suggests exposing the cells to a variety of temperatures over extended cycling may negatively impact the cell performance and cause undesirable parasitic reactions. This degradation of cell performance can also be seen in Figure XI.6.6, where capacity is seen to drop more rapidly after the varied temperature test compared to that of the control cell. This is most notable for the high voltage condition of 4.5V and high temperature operation of 45°C. Further experimentation and analysis is needed to understand why and how the CE is negatively impacted by the varied temperature test controlled to a constant temperature test.

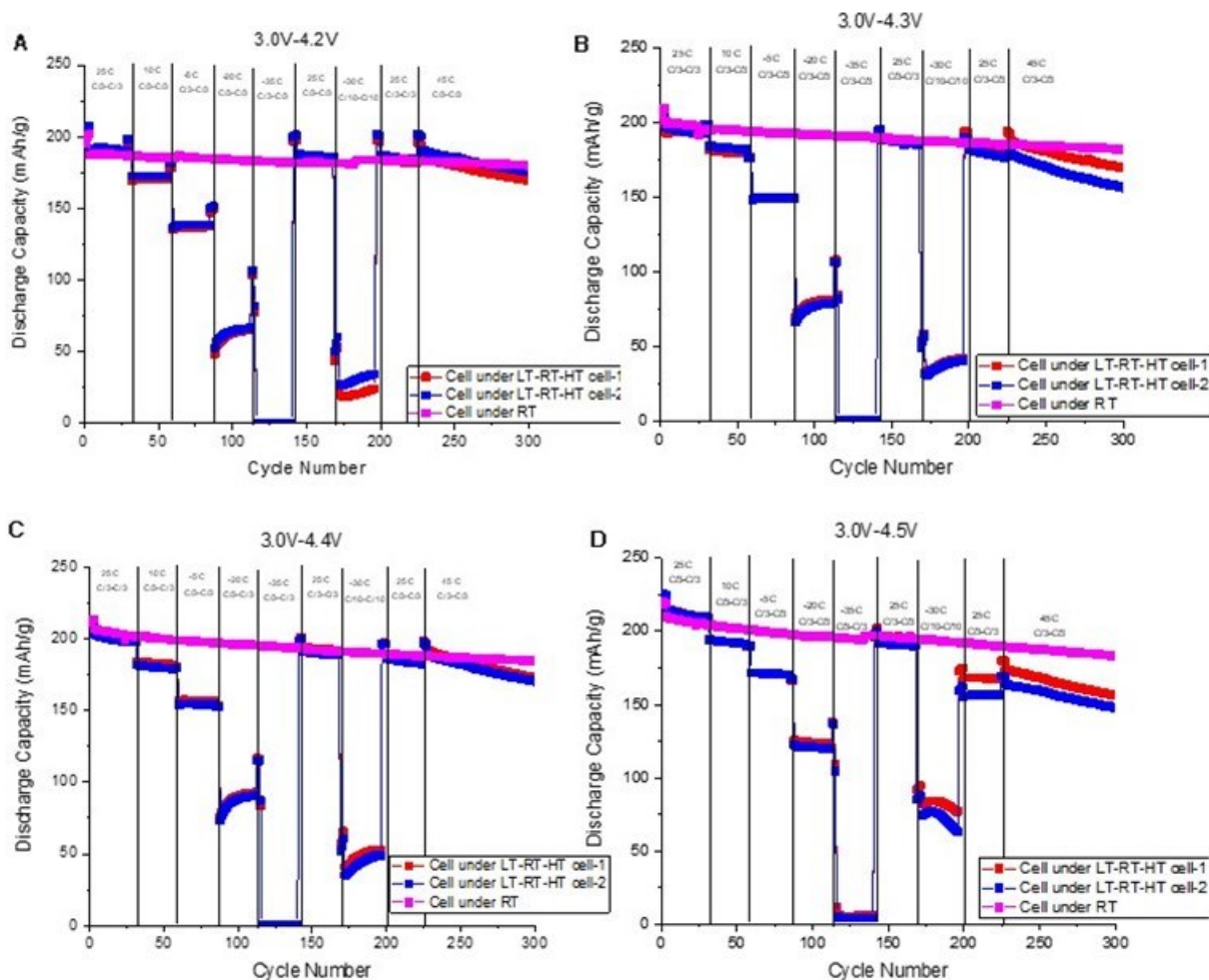


Figure XI.6.6 Discharge capacity versus cycle number throughout the variable temperature and cycling rate test for upper cutoff voltage conditions of (A) 4.2V, (B) 4.3V, (C) 4.4V, and (D) 4.5V. The control cell (pink markers) is discharged at C/3 and 25 °C throughout the entire test while the sister test cells (blue and red markers) were discharged at C/10 for three cycles, then at a C/3 rate for 25 cycles under varying temperature conditions, as specified for each column of designated cycle numbers.

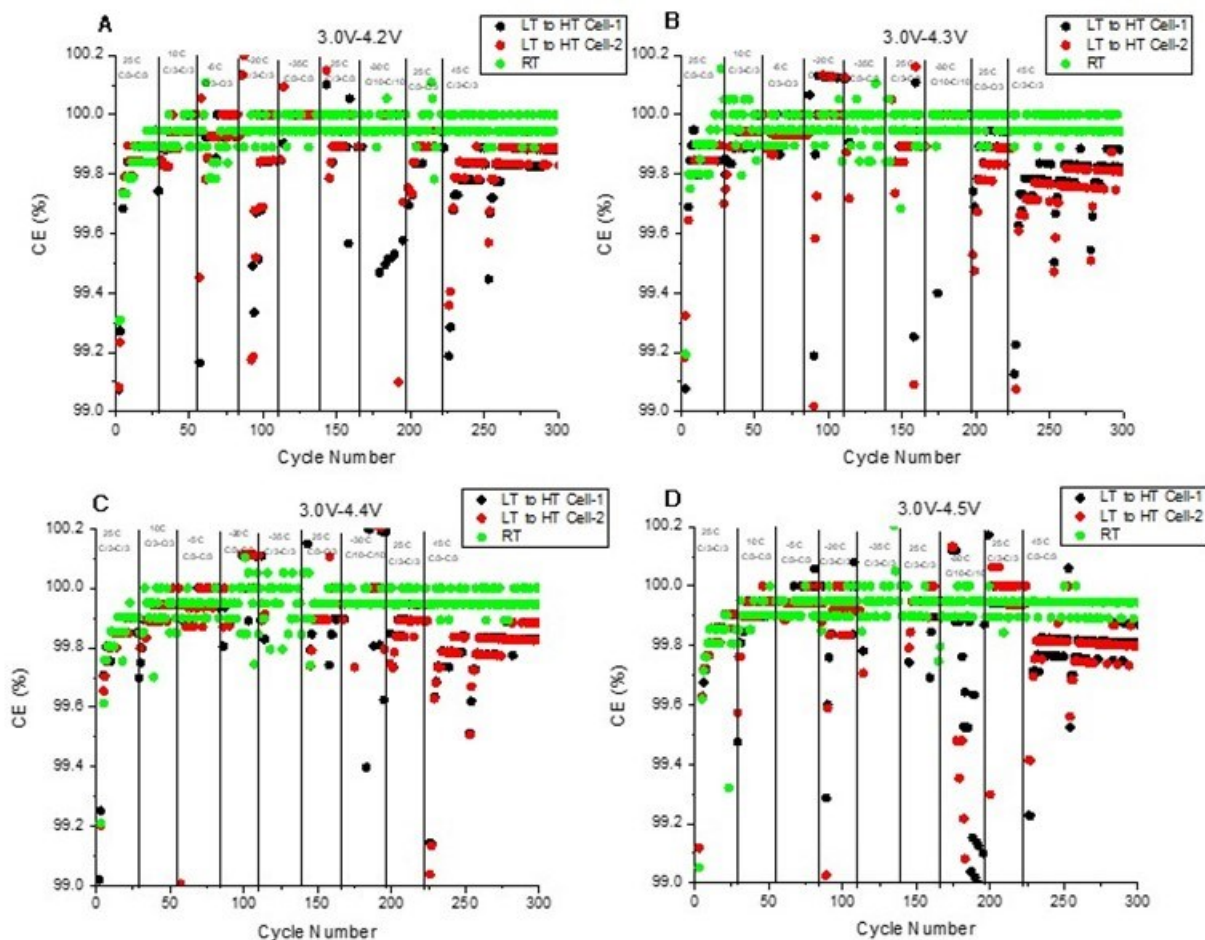


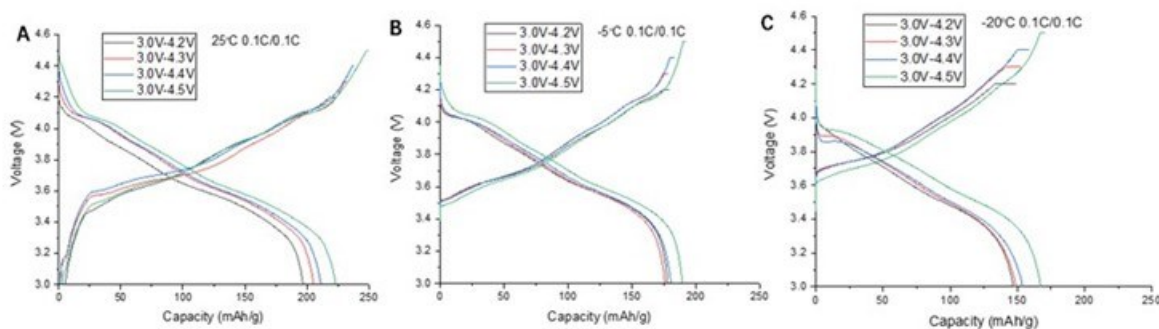
Figure XI.6.7 Coulombic efficiency data versus cycle number throughout the variable temperature and cycling rate test for upper cutoff voltage conditions of (A) 4.2V, (B) 4.3V, (C) 4.4V, and (D) 4.5V. The control cell (green markers) is discharged at C/10 and 25 °C throughout the entire test while the sister test cells (red and black markers) were discharged at varying rates under varying temperature conditions, as specified for each column of designated cycle numbers.

Table XI.6.2 Discharge Capacity Values at Specified Discharge Rates, Temperatures, and Upper Cutoff Voltage Conditions.

	25 °C Discharge capacity (mAh/g)		10 °C Discharge capacity (mAh/g)		-5 °C Discharge capacity (mAh/g)		-20 °C Discharge capacity (mAh/g)		-35 °C Discharge capacity (mAh/g)		Capacity reversibility (- 35 °C/25 °C)
	C/10	C/3	C/10	C/3	C/10	C/3	C/10	C/3	C/10	C/3	
4.2V	195		187		198		170		178		n/a
4.3V	210		200		200		180		177		148
4.4V	212		205		198		182		185		157
4.5V	218		208		208		192		189		171

To further characterize the impact of temperature and upper cutoff voltage on capacity and cell performance, we report the voltage profile, as shown in Figure XI.6.8, after formation during charge and discharge at 25°C, -5°C, and -20°C with varied upper cutoff voltage conditions under a C/10 discharge rate. Consistent with previous results, we see that the higher the temperature, the greater the achieved capacity during cycling.

Additionally, the greater the upper cutoff voltage, the greater the achieved capacity. Interestingly, at the lower temperature conditions of  $-5^{\circ}\text{C}$  and especially  $-20^{\circ}\text{C}$ , the 4.5V condition is observed to significantly outperform all other voltage conditions (which appear to reduce to very similar curves) for achieved capacity. While further characterization and experimentation is required to understand why, we hypothesize that the high cutoff voltage during low temperature may assist to release the overpotential in battery.



**Figure XI.6.8** Initial voltage versus capacity curves after formation for specified upper voltage cutoff conditions at (A)  $25^{\circ}\text{C}$ , (B)  $-5^{\circ}\text{C}$ , and (C)  $-20^{\circ}\text{C}$  with a charge/discharge rate of  $10/\text{C}$ .

We conducted extended cycling tests of coin cells with baseline electrolyte for various upper cutoff voltage conditions of 4.2, 4.3, 4.4, and 4.5V at  $25^{\circ}\text{C}$ . For each upper voltage cutoff condition, three sister coin cells were assembled and cycled for  $\sim 600$ -700 cycles. While this cycling magnitude is lower than the 1000 cycles specified for the subtask due to time constraints, we are currently undergoing further cycling and data collection to reach the 1000 cycle goal. Cells were cycled at  $25^{\circ}\text{C}$  at a discharge rate of  $C/3$  up to 1000 cycles following three  $C/10$  formation cycles. Discharge capacity and capacity retention results for each upper cutoff voltage condition are shown below in Figure XI.6.9. As seen in Figure XI.6.9 A-D, cells show excellent repeatability, with capacity curves laying atop each other for a given upper cutoff voltage condition. Discharge capacity for each voltage condition is observed to steadily decline over the course of the test, in an approximately linear nature following the first formation cycles. As seen in Figure XI.6.9E, lower cutoff voltages show better capacity retention over extensive cycling, with an impressive average capacity retention of 90% for the 4.2V upper cutoff voltage condition at 600 cycles, while cells with a 4.5V condition retained on average of 78% capacity.

The extended cycling experiments are conducted with  $C/3$  and  $C/10$  rates, with results are tabulated below in Table XI.6.3. When comparing average capacity for  $C/3$  and  $C/10$  rates, the slower rate of  $C/10$  consistently outperforms the  $C/3$  rate for each upper cutoff voltage condition, although the differences are minor, with capacities at each rate within 6% of each other. And while the highest upper cutoff voltage condition of 4.5V has the greatest average capacity over 600 cycles, it displays the worst capacity retention by the 600<sup>th</sup> cycle. To conclude, consistent trends are observed over extended cycling: 1. Reduced cycling rates improve capacity, and 2. Higher cutoff voltages display higher initial capacity but have reduced long-term capacity retention.

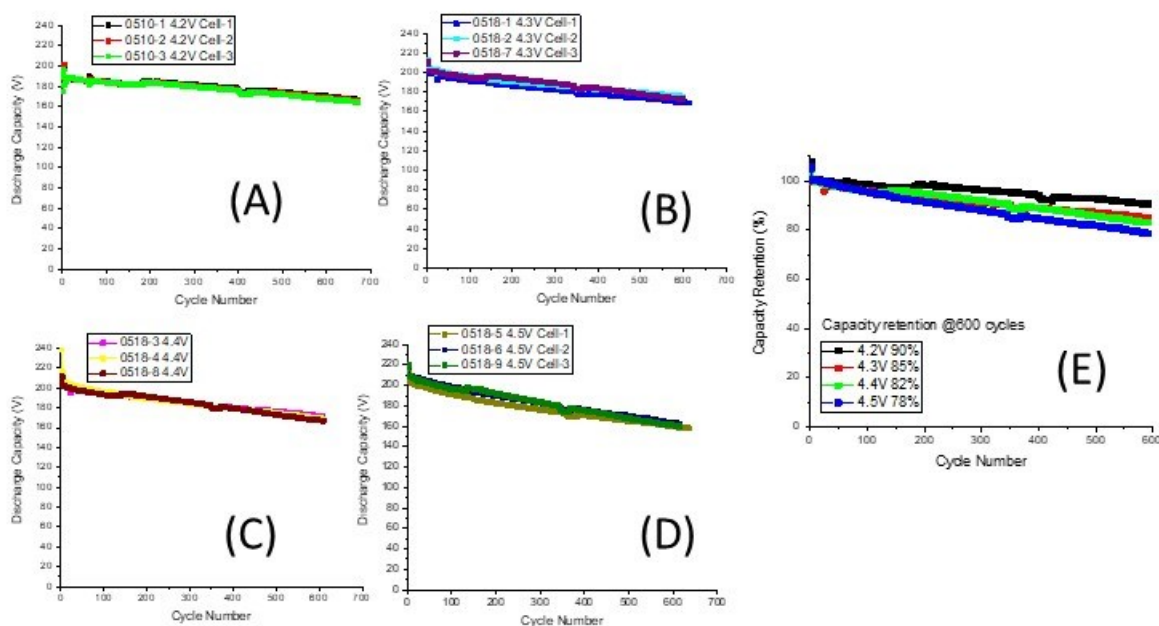


**Figure XI.6.9** Discharge capacity versus cycle number of three sister coin cells with a charge/discharge rate of C/10 for formation and C/3 for cycling and an upper cutoff voltage of (A) 4.2V, (B) 4.3V, (C) 4.4V, and (D) 4.5V. (E) Averaged discharge capacity versus cycle number for each set of three cells at each upper cutoff voltage. Average capacity retention at 600 cycles is also specified in the legend for each upper cutoff voltage.

**Table XI.6.3** Discharge Capacity, Reversibility, and Retention Values of Cells at Specified Discharge Rates and Upper Cutoff Voltage Conditions.

Upper Cutoff Voltage	C/10 Discharge Capacity (mAh/g)	C/3 Discharge Capacity (mAh/g)	Capacity Reversibility Between C/10 And C/3	C/3 Discharge Capacity At 600 <sup>th</sup> Cycles (mAh/g)	Capacity Retention At 600 <sup>th</sup> Cycles
4.2V	195	187	95.89%	168	90.8%
4.3V	210	200	95.23%	170	85%
4.4V	212	205	96.69%	167	81.46%
4.5V	218	208	95.41%	161	77.4%

#### ***Dry pouch cell design, failure analysis and thermal stability validation***

We conducted X-ray diffraction (XRD) to characterize the cathode after our various upper cutoff voltage conditions to probe any material changes to the cathode that may be causing the varied performance, we observe at different upper cutoff voltage conditions. As seen in Figure XI.6.10, cells underwent formation before a 2 hr hold at a specified applied voltage, after which XRD patterns were immediately obtained. When examining the (003) Bragg peak of the pattern, we observe a clear trend with voltage. As voltage is changed from 4.2 to 4.5, the (003) Bragg peak moves to a higher 2theta position. Additional differences are found when comparing the patterns at varied voltages: the peak shift of phase (003), the disappearing of peak (006), as well as the split of peak (108) and (110). These XRD results indicate that the cathode has different lattice parameters depending on the upper cut off voltage. Overall, we find that the cathode undergoes material

changes that we hypothesize impact its capacity under various upper cutoff voltage conditions. We plan to continue to conduct material characterization at varied voltage conditions to further understand this relationship. Additionally, we propose the use of Hybrid Pulse Power Characterization (HPPC) to study the resistance effect under different upper cutoff voltage.

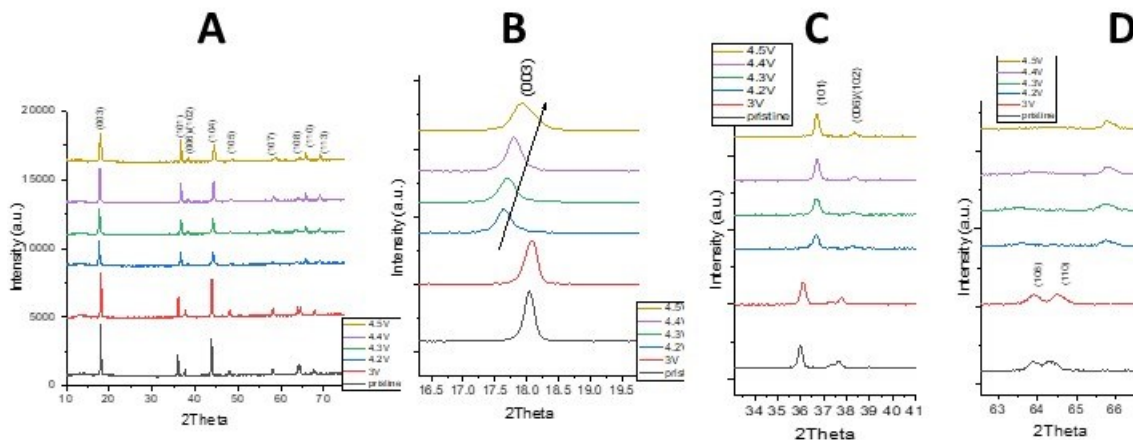


**Figure XI.6.10** (A) X-ray diffraction patterns of the cathode measured immediately after formation and a 2 hr hold at the specified applied voltage. (B) Magnified view of the (003) Bragg peak. (C) Magnified view of the (101), (006), and (102) Bragg peaks. (D) Magnified view of the (108) and (110) Bragg peaks.

We have completed this subtask and have finalized a roll-to-roll type electrode fabrication process, dry pouch cell assembly, and a testing fixture design. As displayed in Figure XI.6.11, our design for the pouch cell is consistent with a standard pouch cell design, with a compartment for the roll-to-roll type electrode, and compartments for electrolyte fill and degassing. We can test our first batch as-fabricated pouch cells in our testing fixture, which features pressure sensing capabilities, easy potentiostat connection, and a secondary storage/safety box to measure the cell in during testing. Our design enables us to track key electrochemical data throughout performance testing and cycling, as well as pressure buildup throughout testing, which can be correlated to gas formation and CE data.

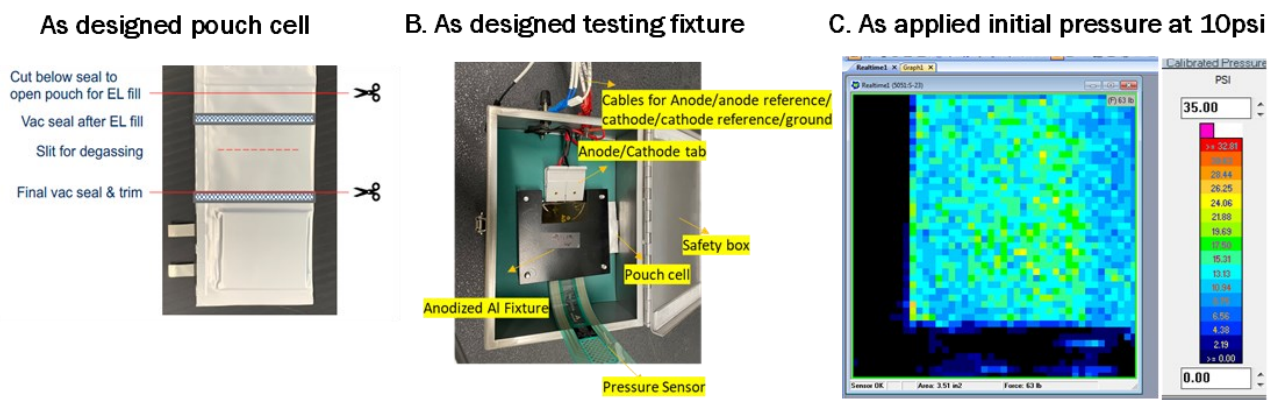


**Figure XI.6.11** A. Our designed pouch cell, with labeled compartments. B. Our designed testing fixture. C. Example initial pressure data of a pouch cell.



To probe the impact of upper cutoff voltage conditions on capacity and capacity retention of our pouch cells with the baseline electrolyte, we conducted extensive cycling of our pouch cells at 25°C with a discharge rate of C/3 over 275 cycles. As seen in Figure XI.6.12A, while cells with voltage conditions of 4.4V and below perform comparably over 275 cycles with capacities maintained between ~2250-2500 throughout testing, the cells with a 4.5V condition steadily and dramatically decline in capacity throughout the testing. Similarly, the CE of Cell 1 reported throughout testing with the 4.5V condition is reduced when compared to the CE of cells with voltage conditions of 4.4V and below, as shown in Figure XI.6.12B. When assessing capacity retention, we observe a clear trend that higher voltage conditions lead to reduced capacity retention over cycling, with cells at 4.4V and 4.5V retaining 90% and 77% of their capacities, respectively. Meanwhile, cells with voltage conditions of 4.2V and 4.3V have impressive capacity retentions of 98% and 96%, respectively, as seen in Figure XI.6.12C.

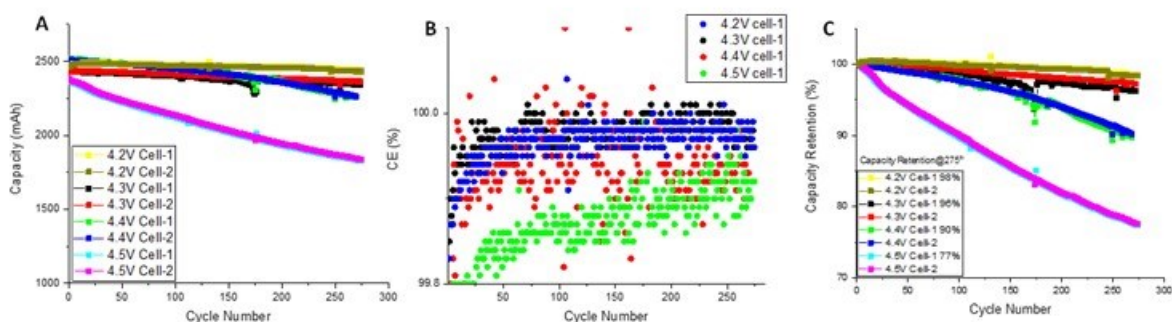


**Figure XI.6.12 (A) Capacity, (B) coulombic efficiency, and (C) capacity retention of pouch cells tested at 25 °C and a discharge rate of C/3 with specified upper cutoff voltage conditions over 275 cycles. Each voltage condition was tested with two sister cells, cell 1 and 2, as shown in (A) and (C). Capacity retention after 275 cycles is calculated for cell 1 at each voltage condition and is specified in the legend of (C).**

We additionally conducted preliminary pressure mapping of pouch cells after cycle testing. As seen in Figure XI.6.13, the pressure in each pouch cell increases overall after cycling. For cells with 4.2 and 4.3V upper voltage cutoff conditions, pressure increase is slight, but no difference can be discerned between these two cells. For 4.4V and 4.5V conditions, there is a discernable increase in overall pressure accumulated, with the 4.5V sample clearly experiencing the most severe pressure buildup. The pressure buildup is understood to be caused by gas formation throughout cycling, as a product of undesirable parasitic electrochemical reactions with the electrolyte at the anode and cathode throughout testing. The comparatively reduced CE of the 4.5V cell, reported in Figure XI.6.13B, points to an increased magnitude of parasitic reactions occurring throughout the cycling, consistent with the increased pressure and gas evolution observed in Figure XII.6.3.4. We aim to further investigate the relationships between upper voltage cutoff condition, CE, and pressure buildup in pouch cells in our future work.

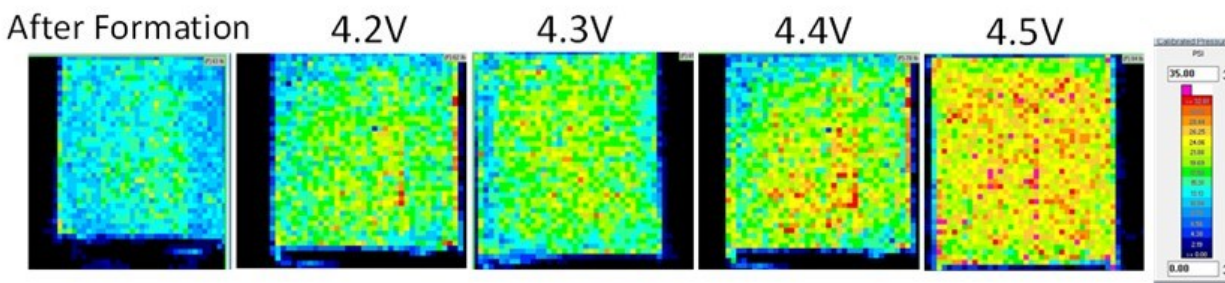


Figure XI.6.13 Pressure maps of pouch cells before (as prepared, after formation under 3.0V) and after 275 cycles at each specified upper voltage cutoff condition at 25 °C. Corresponding pressure map legend is shown to the right.

#### *Theoretical calculation build up for electrolyte solvent*

First-principles calculations based on Density Functional Theory (DFT) have been employed to understand the anodic stability of various solvent molecules and salt ions that compose selected carbonate and organosulfur electrolytes. The DFT based free energies as well as solvation energies of neutral and charged species are calculated and used to predict oxidation potentials and various electronic structure properties such as HOMO/LUMO levels, Mulliken charge and electrostatic potential analyses. Our theoretical model aims to explain the role of different functionalized groups in oxidation behavior of electrolyte molecules suitable for high voltage battery applications. The methodology developed herein can be further used to explore underlying mechanisms that control electrolyte high-voltage behavior with signature chemical and structural trends and to narrow down the molecular space by rank ordering electrolytes under investigation according to their anodic stability.

All DFT calculations are being conducted with the NWChem code<sup>1</sup>. A systematic benchmarking methodology has been developed by considering several previous studies<sup>2-5</sup>. Following the study of He et al.<sup>2</sup>, an initial set of calculations were performed on a group of electrolyte solvent molecules consisting of four cyclic carbonates (EC, FEC, TFPC, and TFP-PC-E) and four linear carbonates (DMC, F-EMC, HF-DEC, and TF-DEC). The DFT structure optimization and the total energies were carried out for the neutral and charged molecules with the B3LYP functional with both the 6-31G\* and 6-31+G\* basis sets. The solvation energies were then calculated on the optimized structures with the Solvation Model Based on the Density (SMD) method<sup>6</sup> implemented in NWChem code. Following the method reported by He et al.<sup>2</sup>, we approximated the solvation effect with a dielectric constant of 55.725 which represents a solvent with 25% EC, 25% EMC and 50% PC. The zero-point energy and thermal corrections were also computed to account for vibrational effects on molecular structure and energies along with the gas phase free energy and solvation energy calculations.

Considering the oxidation process to be a one-electron transfer from a solvent molecule to the electrode<sup>4,5</sup>, the free energy cycle of the oxidation reaction can be illustrated as shown in Figure XI.6.14.

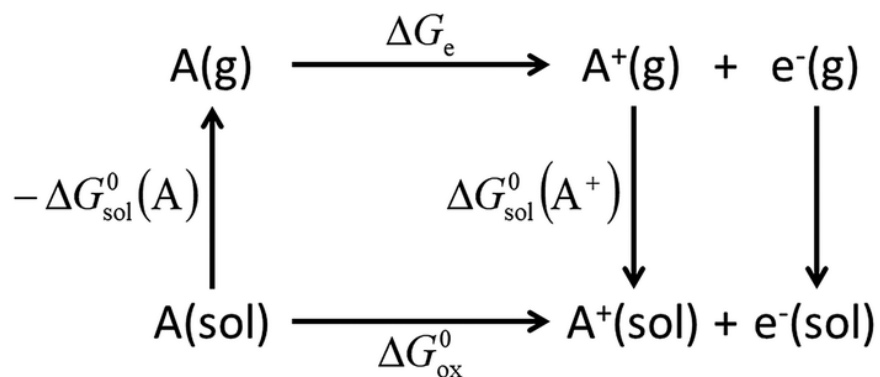


**Figure XI.6.14** Free energy cycle of the oxidation reaction ( $A \rightarrow A^+ + e^-$ ). Here  $A(g)$  and  $A(sol)$  denote molecule A in gas phase and solvated phase, respectively.  $A^+$  denotes the oxidized cation of A.

Using the thermodynamic cycle of oxidation reaction as shown in Figure XI.6.14, the oxidation potential is calculated using the absolute free energy differences between the neutral and ionic species and expressed relative to the Li<sup>+</sup>/Li reference electrode. Following IUPAC recommendations<sup>5</sup>, the conversion from the absolute potential scale to the standard Li<sup>+</sup>/Li scale in aqueous solution is given by Eq 1:

$$E_{ox}^0 \left( vS. \frac{Li}{Li^+} \right) = \frac{\Delta G_{ox}^0}{F} - 1.37 = \frac{1}{F} \left( \Delta G_e(A) + \Delta G_{sol}^0(A^+) - \Delta G_{sol}^0(A) \right) - 1.37 \quad (1)$$

where  $\Delta G_e(A)$  and  $\Delta G_{sol}^0(A)$  are the free energy of ionization of the gas phase and the solvation energy of molecule A, respectively,  $\Delta G_{sol}^0(A^+)$  is the solvation energy of oxidized species  $A^+$  and  $F$  is the Faraday constant (=1 eV/V). The value of 1.37 V is obtained considering the standard Li<sup>+</sup>/Li potential of -3.05 V versus the Standard Hydrogen Electrode (HSE) potential of 4.42 V for aqueous solutions<sup>5</sup>.

The calculated oxidation potentials for the eight solvent molecules are shown in Figure XI.6.15. The computed oxidation potentials using both 6-31G\* and 6-31+G\* basis sets show a very similar trend as reported earlier by He et al. We find that the theoretical oxidative stabilities of the cyclic carbonates follow: TFPC > FEC > EC >> TFP-PC-E while the linear carbonates follow: HF-DEC > F-EMC > TF-DEC > DMC, which agree well with earlier results. As expected, the 6-31+G\* basis set improves the overall results relative to those from the 6-31G\* basis set by treating polarization and diffuse functions on the heavier atoms. The only exception we find is TF-DEC which shows a reduction of oxidation potential using the 6-31+G\* basis: this needs further study. While the trend is very similar between our calculations and previous literature, our results show a slight decrease in oxidation potential for all the molecules which could be related to the differences between methods implemented in our model versus the theoretical model of He et al. Especially, the solvation effects are treated differently in these two approaches, where our model computes the solvation free energies using the SMD<sup>6</sup> method implemented in NWChem, and He et al. used the Polarizable Continuum Model (PCM)<sup>7</sup> method implemented in Gaussian 09 code.

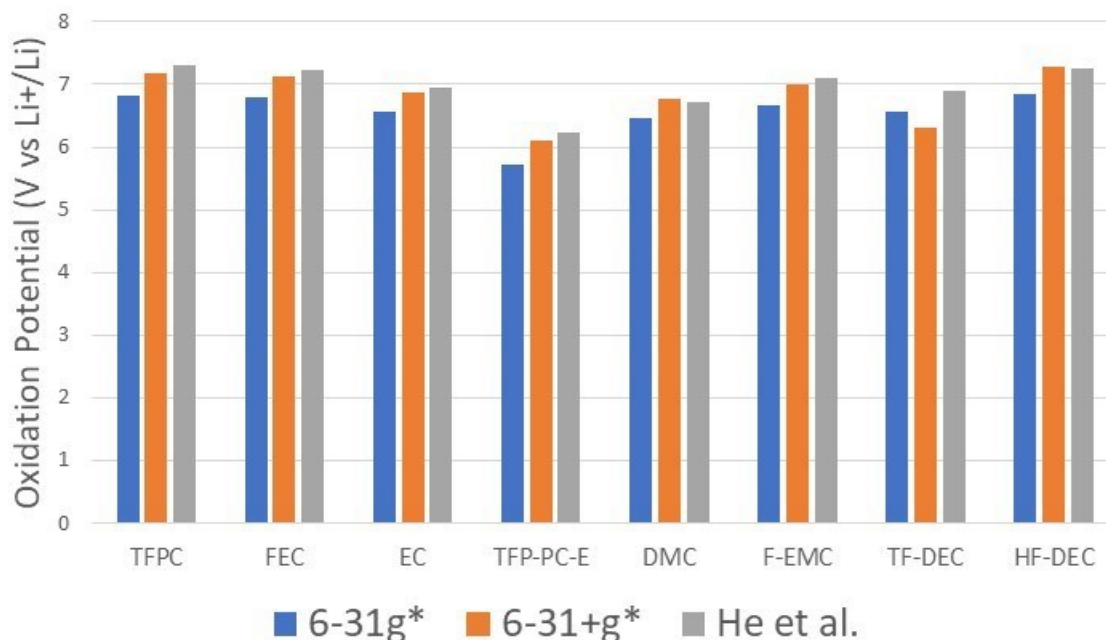


**Figure XI.6.15 Oxidation potentials of eight carbonate based solvent molecules calculated from DFT simulations. Benchmarking calculations done with B3LYP functional and 6-31g\* and 6-31+g\* basis sets successfully reproduced the oxidation potentials previously reported by He et al.2**

In addition to the calculation of oxidation potentials, we also developed a methodology to visualize the molecular orbitals such as the HOMO and LUMO orbitals as shown for neutral DMC molecules in Figure XI.6.16. This provides electronic structure information such as the hybridization of atoms and the nature of the bonding environment as well as the contribution of atomic states at the Fermi level that participates in electron transfer during oxidation. Such description of molecular orbitals along with Mulliken charge analysis (currently under development) can provide a quantitative picture of the role of different functional groups and atomic contributions in the oxidation potentials.

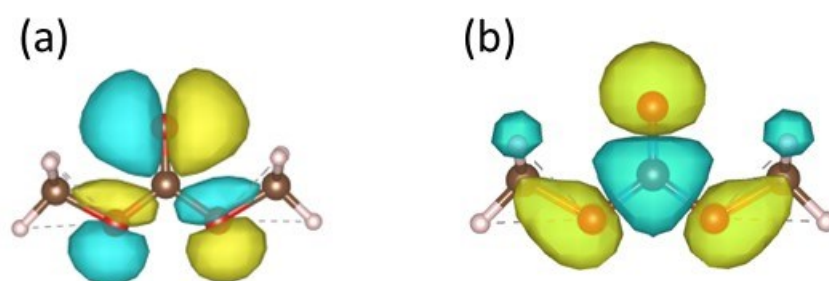


**Figure XI.6.16 Molecular (a) HOMO and (b) LUMO orbitals of neutral DMC molecule. The yellow and blue regions show the positive and negative isosurfaces. The iso value is 0.02 au.**

Current experimental measurement with linear scan voltammetry (LSV) reports that the EMS and TMS demonstrate the highest anodic stability among various organosulfur solvents with onset potentials at approximately 4.75 V vs. Li<sup>+</sup>/Li at low anodic current. The experimental results on seven organosulfur molecules (TMS, EMS, DMMA, DMS, MSF, MMS and PS) proposed for the DOE project indicate that while all the electrolytes experienced charging specific capacity higher than the theoretical capacity of the cathode,

the first discharge from all the cells show capacities significantly lower than the theoretical capacity. To improve the overall performance, Fluoroethylene Carbonate (FEC) co-solvent was added in the electrolytes which demonstrates that the TMS/FEC and EMS/FEC have the highest discharge capacity after the first charging, which is much higher than those without FEC co-solvent.

#### **Coin cell level data collection with as synthesized organosulfur based electrolyte under wide operation temperature and high voltage**

To evaluate the performance of regular sulfone electrolyte in high voltage Li-ion batteries, we implement the cycling test with A12 graphite (AA002, CAMP facility) as the anode,  $\text{LiNi}_{0.8}\text{Co}_{0.1}\text{Mn}_{0.1}\text{O}_2$  (NMC811, AC019, CAMP) as the cathode and glass fiber as the separator. The reason for using glass fiber as separator is its good wettability towards sulfone electrolytes, which may not be wetted by traditionally PP-PE separator. Conventional Gen2 electrolyte (1.2M  $\text{LiPF}_6$  in EC/EMC 3/7) was used as the baseline electrolyte for this study. Figure XI.6.17a and 1b depict respectively the long-term (500 cycles) cycling results and Coulombic efficiency (CE) of AA002||AC019 full cells using Gen2 electrolyte with cutoff voltages at 4.2 V and 4.5 V. Despite the initial lower specific capacity (180 mAh/g), the cell with low cutoff voltage (4.2 V) displayed much higher cycling stability while the cell with high cutoff voltage (4.5 V) showed significantly larger initial capacity (210 mAh/g), but faded quickly. The average CE of the cell with low cutoff voltage was significantly higher than that of high cutoff voltage. Obviously, Gen2 electrolyte is not suitable for high voltage cycling.

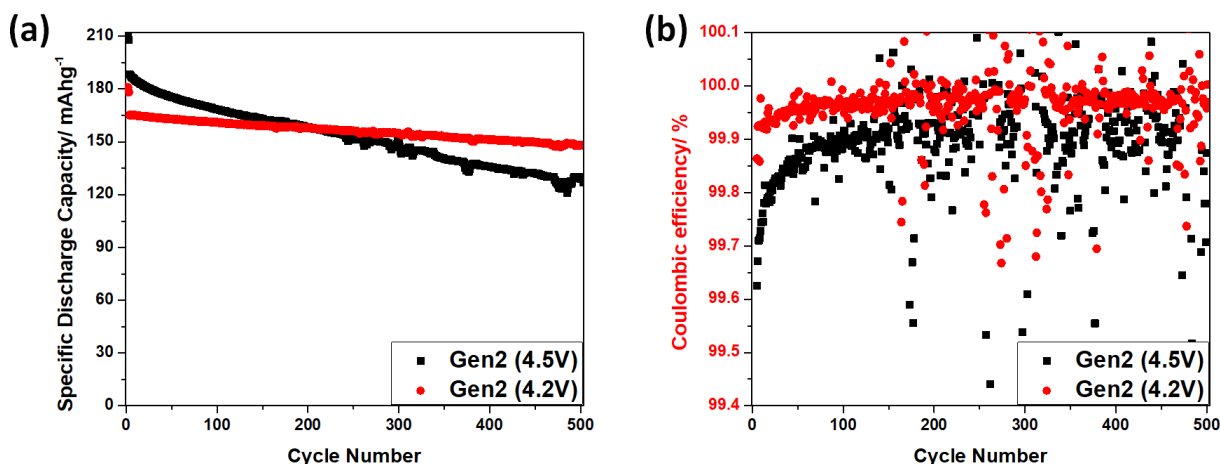


**Figure XI.6.17 Long-term capacity retention (a) and Coulombic efficiency (b) of AA002||AC019 full cells using conventional electrolyte cycling at different cutoff voltages.**

We first used 1.2M lithium bis(fluorosulfonyl)imide ( $\text{LiFSI}$ ) dissolved in ethyl methyl sulfone (EMS) or tetramethylene sulfone (TMS) to probe the cycling performance of regular sulfone electrolytes on AA002||AC019 full cells. Figure XI.6.18a and b represent respectively the long-term capacity retention and Coulombic efficiency (CE) of AA002||AC019 full cells using sulfone electrolytes with cutoff voltages at 4.2 V and 4.5 V. The details of cycling were summarized in Table XI.6.4. It is noteworthy that the capacity retention of the cells employing sulfone electrolytes was significantly better than the cell using Gen2 electrolyte, probably due to the higher anodic stability of sulfone electrolytes. However, the initial specific capacity of the full cell using sulfone electrolytes were all very low (around 15% lower) compared to the cell employing Gen2. Contrary to the Gen2 cells, the sulfone cells with 4.5V cutoff voltage displayed better long-term 500-cycle capacity retentions than the cells with 4.2V cutoff voltage and the difference was more significant in the cells using TMS electrolyte. This is probably due to the inability of sulfone electrolytes in forming robust SEI surface on the graphite anode, evidenced by the low initial specific capacity of the full cells. Apparently, the cycling performance of EMS cells is better than that of TMS cells. Yet, the initial specific capacity for EMS cell with 4.5V cutoff voltage was only 190 mAh/g, which is much lower than that of Gen2 cell (210 mAh/g). Again, the low initial capacity majorly originates from the poor solid-electrolyte interphase (SEI) formation by

the sulfone electrolytes. Taken together, we conclude that the sulfone electrolyte, especially EMS electrolyte, possesses higher anodic ability but much worse SEI forming capability than Gen2 electrolyte for the full cells.

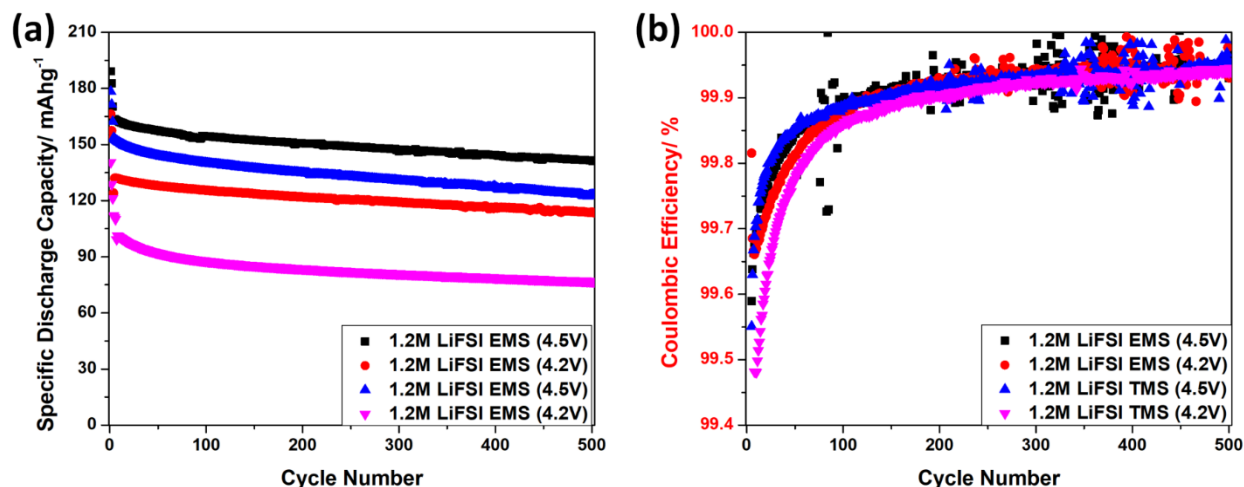


Figure XI.6.18 Long-term capacity retention (a) and Coulombic efficiency (b) of AA002 || AC019 full cells using sulfone electrolytes cycling at different cutoff voltages.

Table XI.6.4 Data Associated with Two Figures for AA002 || AC019 Full Cells Various Electrolytes: 1st-Cycle Coulombic Efficiency (1st CE), 1st-cycle Discharge Capacity (1st DC), Capacity Retention after 500 Cycles (CR-500), Average 500-Cycle Discharge Capacity (AC-500) and Average CE of 500 Cycles (ACE).

Electrolyte	1st CE	1st DC (mAh/g)	AC-500 (mAh/g)	CR-500	ACE
Gen2 (4.5 V)	85.71%	210.2	152.3	67.8%	99.90%
Gen2 (4.2 V)	84.85%	181.0	156.0	89.6%	99.97%
1.2M LiFSI EMS (4.5 V)	71.86%	189.1	149.3	86.4%	99.91%
1.2M LiFSI EMS (4.2 V)	70.88%	166.2	120.9	85.9%	99.91%
1.2M LiFSI TMS (4.5 V)	69.38%	178.4	133.4	80.4%	99.91%
1.2M LiFSI TMS (4.2 V)	60.16%	140.5	83.6	69.3%	99.86%

#### Stable long-term cycling enabled by functional additives:

To facilitate better cycling of sulfone electrolytes for high voltage operation, we implemented study for effective additives. As mentioned above, the insufficient capability of sulfone electrolytes in forming robust SEI on graphite surface led to low initial and average capacity of the full cells. Therefore, the ability to assist the formation of stable SEI before the sacrificial decomposition of sulfone molecules should be the utmost important criterion in selecting effective additive for the sulfone electrolyte. In this additive study, 1.2M LiFSI EMS was used as the baseline because it displayed significantly better cell performance than TMS electrolyte. Common additives vinylene carbonate (VC), lithium difluoro (oxalate) borate (LiDFOB) and fluoroethylene carbonate (FEC) were introduced into the EMS electrolyte, attempting to improve the cycling performance of the full cells. Figure 3a displayed the 500-cycle capacity retention of AA002||AC019 full cells using 1.2M LiFSI EMS electrolytes with 2 wt. % VC, LiDFOB, ANL  $\delta$  and FEC cycled at 4.5V cutoff voltage and the details of the cycling tests were summarized in Table XI.6.5. It is clear that VC and FEC provide significant beneficial effect towards the high voltage cycling of the full cell. Moreover, the beneficial effect of VC as an additive was slightly better than that of FEC. With the addition of VC, the initial capacity of EMS electrolyte increased from 190 mAh/g to 205 mAh/g and the average 500-cycle capacity (AC-500) increased from 149 mAh/g to 164 mAh/g. It is noteworthy that the 500-cycle capacity retention (CR-500) actually decreased from

86% to 78% with the addition of VC, because the initial capacity of the plain LiFSI-EMS cell was significantly lower (around 10%) than that of VC cell. Figure XI.6.19b shows the capacity retention of the cells using sulfone electrolytes with VC and ANL  $\chi$  additives, as well as a mixture of VC and ANL  $\delta$  cycled at high voltage. It is noteworthy that ANL  $\chi$  is a synthetic additive developed at Argonne and is currently under patent application. The cell using ANL  $\chi$  additive undoubtedly showed the best performance around all the cells using EMS based electrolytes. The AC-500 and CR-500 for the ANL  $\chi$  cell are 169 mAh/g and 84% respectively, which are significantly higher than those cells using other additives. To further improve the cycling performance of the high voltage full cell, we investigated the synergistic effect of VC with commercially available additive ANL  $\delta$  and our newly developed ANL  $\chi$ , which share similar chemical structure. Unfortunately, there was no synergistic effect observed for the dual additives VC-ANL  $\delta$  cell as shown in Figure XI.6.19b. The cycling performance of this dual additives cell was very similar to the VC cell with no significant improvement. Figure XI.6.20a and b represent respectively the long-term capacity retention and Coulombic efficiency (CE) of AA002||AC019 full cells using EMS electrolytes with different additives. Undeniably, the cycling performance of the full cell employing EMS electrolyte with both VC and ANL  $\chi$  additives exhibits not only the best CR-500 with high initial capacity (210 mAh/g), but also the highest AC-500 (180 mAh/g), which is 6% higher than the cell using only ANL  $\delta$  and 10% higher than the cell using only VC. Moreover, highly stable CEs were obtained for the cell using both ANL and VC (Figure XI.6.20b), further supporting its exceptional cycling stability. All in all, the newly developed additive ANL  $\chi$  is highly beneficial for the cycling performance of high voltage cell using sulfone electrolytes. With the addition of VC, the synergistic effect is impressive. The mechanistic study of the effectiveness of additives is still on-going and we are going to present our SEM, XPS and ICP results in the near future.

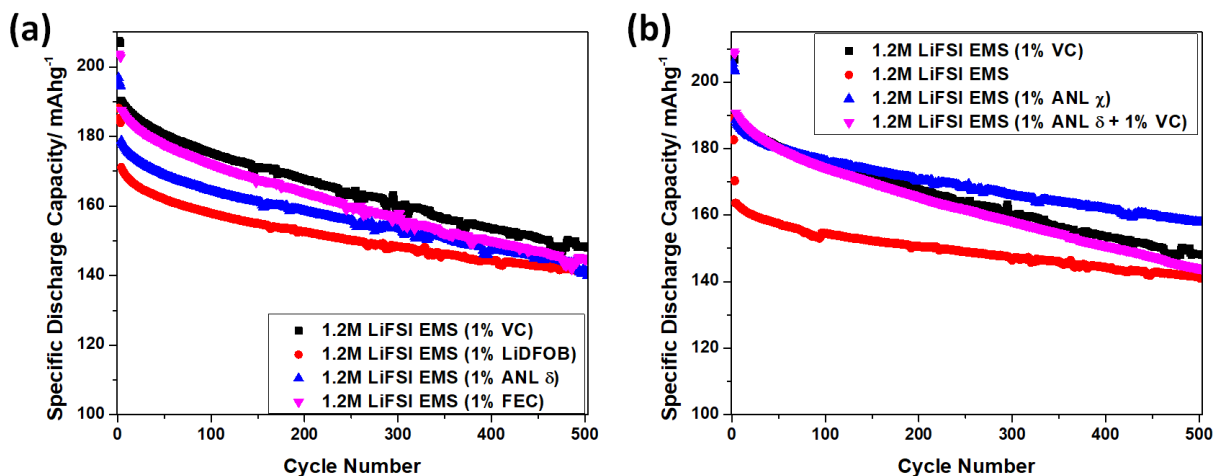


Figure XI.6.19 Long-term capacity retention of AA002||AC019 full cells using EMS electrolytes with additives (a) VC, LiDFOB, ANL  $\delta$ , FEC; and (b) VC, ANL  $\chi$ , ANL  $\delta$  cycled at 4.5V.

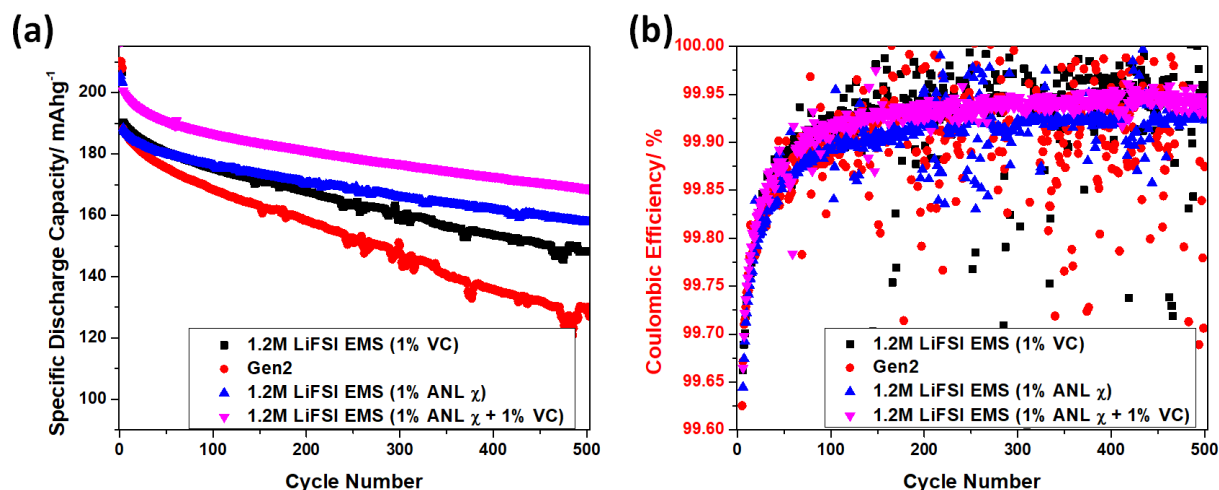


Figure XI.6.20 Capacity retention (a) and Coulombic efficiency (b) of AA002 | AC019 full cells using Gen2 and sulfone electrolytes with additives cycling at different cutoff voltages cycled at 4.5V.

Table XI.6.5 Data Associated with Two Earlier Figures for AA002 | AC019 Full Cells Various Electrolytes: 1st-cycle Coulombic efficiency (1st CE), 1st-cycle Discharge Capacity (1st DC), Capacity Retention after 500 Cycles (CR-500), Average 500-Cycle Discharge Capacity (AC-500) and Average CE of 500 Cycles (ACE).

1.2M LiFSI EMS	1st CE	1st DC (mAh/g)	AC-500 (mAh/g)	CR-500	ACE
No Additive	71.86%	189.1	149.3	86.4%	99.91%
+ 2% VC	80.05%	207.5	164.4	78.1%	99.93%
+ 2% LiDFOB	72.33%	188.1	151.1	82.3%	99.91%
+ 2% FEC	78.51%	203.8	160.8	77.3%	99.88%
+ 2% ANL $\delta$	78.39%	196.8	156.2	78.6%	99.90%
+ 2% ANL $\chi$	75.50%	205.6	169.0	84.0%	99.90%
+ 2% ANL $\delta$ + 2% VC	82.01%	209.1	162.5	75.7%	99.91%
+ 2% ANL $\chi$ + 2% VC	80.82%	216.6	179.7	84.4%	99.92%

**Design rule for functional additives in achieving synergistic effect:**

The chemical structures of the solvents and lithium salts used in this study were depicted in Figure XI.6.21 except for ANL  $\delta$  and ANL  $\chi$ .



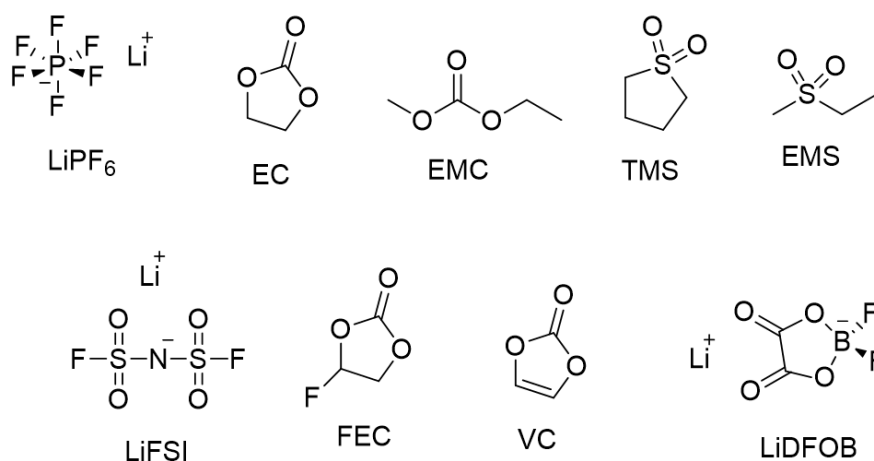


**Figure XI.6.21 Chemical structures of LiPF<sub>6</sub>, LiFSI, EMS, TMS, EC, EMC, LiDFOB, VC and FEC.**

To investigate the origin of this drastic synergistic effect of combining new synthetic additive ANL  $\chi$  with VC, we first carried out a variety of electrochemical analyses. Figure XI.6.22 displays the differential capacity profiles of Li||Graphite half cells using LiFSI-EMS based electrolytes with various additives. The reduction potential of VC is at 0.7 V vs. Li/Li<sup>+</sup>, which is slightly lower than that of EC. As a result, VC is not a highly effective anode additive, especially for organosulfur electrolyte, which can generate detrimental by-products on anode without the protection of robust solid-electrolyte interphase (SEI). On the contrary, all the other additives including FEC, ANL  $\delta$  and ANL  $\chi$  reduced at voltage > 1.0 V vs. Li/Li<sup>+</sup>, and the newly synthesized ANL  $\chi$  additive possessed the highest reduction potential, which is able to minimize the sulfone decomposition on graphite in the SEI formation process. By incorporating the functional groups for forming robust SEI and enhancing reduction potential, ANL  $\chi$  is proved to be a highly effective anode additive. As depicted in Figure XI.6.22b, the early SEI formation of ANL  $\chi$  actually mitigate the VC reductive decomposition in the Li||Graphite cell using both VC and ANL  $\chi$  additives. However, it is also important to consider the side reactions on the cathode electrolyte interface for high voltage cycling and thus, additive that can sacrificially decompose before the sulfone solvent to form a protective layer on the cathode surface is desirable. Unfortunately, ANL  $\chi$  also possesses relatively high anodic stability, evidenced by the linear sweep voltammetry results displayed in Figure XI.6.23. The on-set oxidation potentials for LiFSI-EMS electrolytes with and without ANL  $\chi$  are exactly the same, implying the oxidation potential of ANL  $\chi$  is higher than that of LiFSI-EMS. In contrast, the onset oxidation potential of VC added electrolyte is around 4.5 V vs. Li/Li<sup>+</sup>, which is significantly lower than the plain LiFSI-EMS electrolyte. As a result, the preferential oxidative decomposition of VC renders its capability to form protective layer on cathode surface while ANL  $\chi$  does not possess this ability. Therefore, it is plausible to attribute the significant synergistic effect observed by using both VC and ANL  $\chi$  additives to the ability of forming cathode protective layer by VC and the uniqueness in forming highly effective SEI by ANL  $\chi$ .

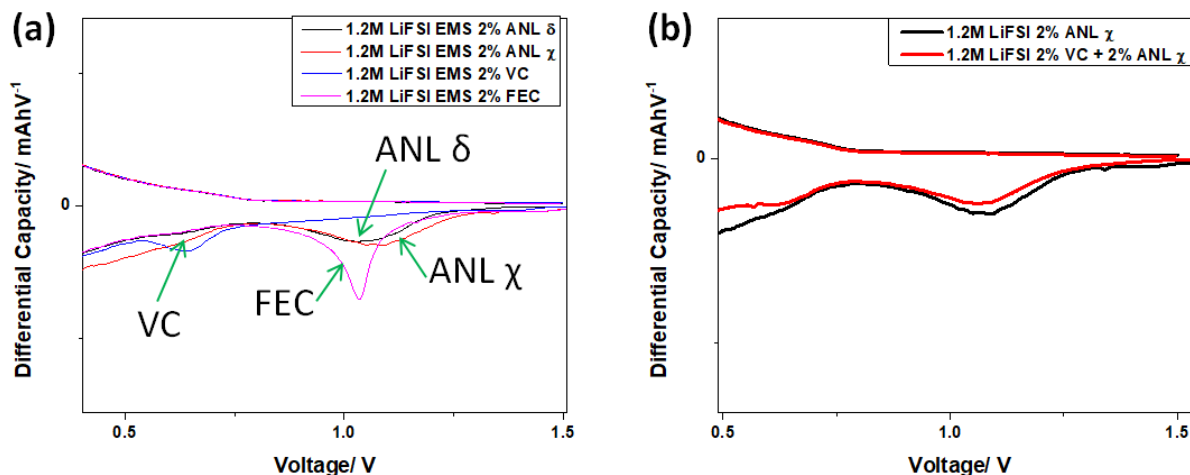


Figure XI.6.22 The differential capacity profiles of Li | Graphite half cells using 1.2M LiFSI EMS electrolytes with (a) 2 wt.% VC, FEC, ANL  $\delta$  and ANL  $\chi$ ; and (b) ANL  $\chi$  and both ANL  $\chi$  and VC.

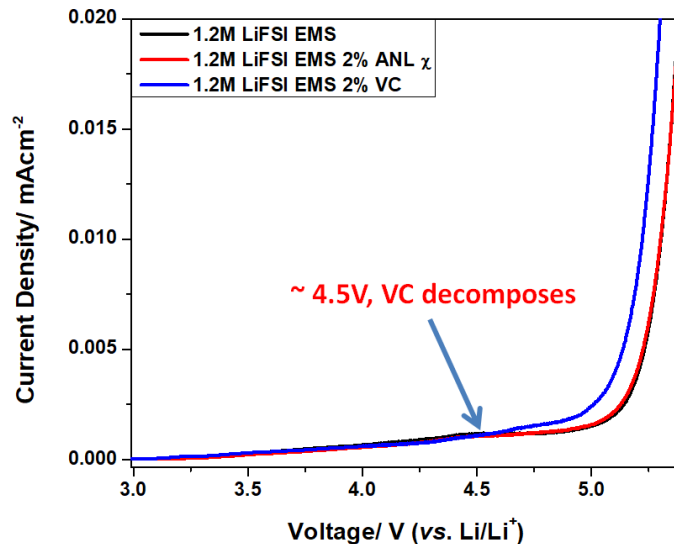


Figure XI.6.23 Linear sweep voltammograms (LSVs) of various EMS based electrolytes without additive or with 2 wt.% VC or TFDTD, scan rate 0.2 mV/s, aluminum as the working electrode and lithium metal as both the reference and counter electrodes.

The synergistic effect of using both VC and ANL  $\chi$  is also revealed by lowered over-potential of the dual additives cell. Figure XI.6.24a and b depict respectively the 5<sup>th</sup> cycle and 500<sup>th</sup> cycle voltage profiles of the full cells employing 1.2M LiFSI EMS electrolyte with VC, ANL  $\chi$  and VC + ANL  $\chi$  additives. Clearly, the over-potentials of all the cells are relatively similar during the 5<sup>th</sup> cycle, with ANL  $\chi$  cell showing slightly higher over-potential. However, the over-potential of the VC cell increased drastically after 500 cycles, displaying extremely huge over-potential compared to the over-potentials of the other two cells. This result is possibly originated from the insufficient capability of VC in protecting the graphite anode and thus, the impedance of the cell increased largely over the course of long-term cycling.

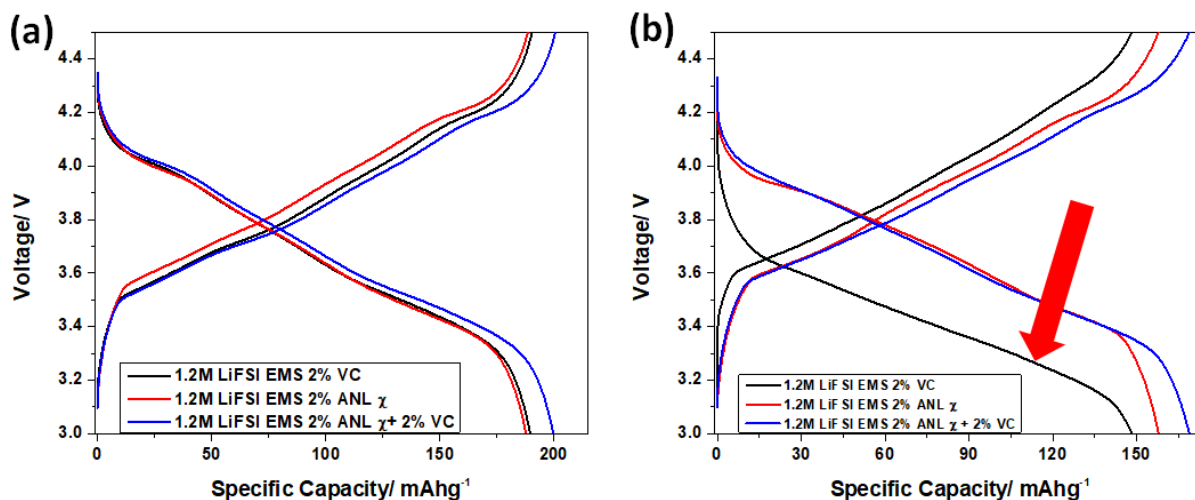


Figure XI.6.24 (a) 5th cycle and (b) 500th cycle voltage profiles of AA002 | AC019 full cells using 1.2M LiFSI EMS electrolyte with VC, ANL  $\chi$  and VC + ANL  $\chi$  additives.

### Conclusions

- **The 1<sup>st</sup> Go/No-Go decision have been passed.**
- **The Tasks and milestone below have been completed and demonstrated successfully.**
- Task 1.1: Baseline electrode materials selection.
  - Coin cell parts supplier and cell testing were aligned between 4 teams.
  - Cathode slurry formulation optimization was addressed.
  - Cathode materials were validated (NCM811 and NCMA).
  - Anode materials were validated (Natural graphite and Artificial graphite).
- Task 1.2 Baseline cell data collection at the coin cell level and milestone.
  - Cathode and Anode candidate for 1st batch roll to roll electrode fabrication was nailed down.
  - The as-fabricated electrode was tested under different upper cutoff voltage.
- Task 1.3 Dry pouch cell design, failure analysis and thermal stability.
  - 2.5Ah pouch cell with different upper cutoff voltage design was fabricated and tested.
  - Low temperature performance of the baseline electrolyte was tested in both coin cell and pouch cell format.
  - Thermal behavior was quantified under both coin cell and pouch cell level.
- Task 1.4 Molecular design/ prototype synthesis/theoretical calculation of new organosulfur based solvents
  - A new model to calculate the HOMO-LUMO of as formulated electrolyte was established.
  - Molecular level calculation of organosulfur based material has been established.
- Task 1.5 Coin cell level data collection with as synthesized organosulfur based electrolyte under wide operation temperature and high voltage.
  - Coin cell level data collection with organosulfur based electrolyte up to 1000 cycles.
  - Electrolyte with new as-designed additive shows good high voltage stability against our baseline cell design in coin cell level.
  - New organosulfur solvent was synthesized and characterized.
  - New as-designed additive was synthesized and characterized.
  - Coin cell with new as-designed electrolyte have been tested.
- Milestone 1.1.1 Defined electrode material supplier and electrode design for electrolyte validation.
- Milestone 1.2.1 Demonstrate electrochemical data in coin cell level with baseline electrolyte under different operation voltages and temperatures.
- Milestone 1.3.1 Demonstrate electrochemical data in pouch cell level with baseline electrolyte under different operation voltages and temperatures.

- Milestone 1.4.1 Demonstrate electrochemical stability, thermostability, and physical properties of the synthesized prototype organosulfur electrolyte.
- Milestone 1.5 Coin cell level data collection with as synthesized organosulfur based electrolyte under wide operation temperature and high voltage.
- Milestone 1.5.2 Demonstrate the capability to synthesize the organosulfur solvent with enhanced performance in lab scale.

### Key Publications

1. One review paper named “Organosulfur Electrolytes for Lithium Batteries: Promising Candidates for Stable and Safer High Voltage Operation” is under revision between all PIs.
2. An GM internal report named “Structure and Stability of Electrolytes for High Voltage Batteries” is under preparing. Will publish it externally after internal process.
3. An GM internal report named “Differential Electrochemical Mass Spectrometry for Online Gas Evolution Analysis of High Voltage Graphite/NMC Pouch Cells: Instrumentation Development, Experiments, and Preliminary Analysis” is under preparing. Will publish it externally after internal process.
4. Two patents under filing (USPTO filing number TBD).

### References

1. Abouimrane, A.; *et al.*, *Electrochem. Commun.*, **2009**, *11*, 1073.
2. Xue, W.; *et al.*, *Ener. Environ. Sci.* **2020**, *13*, 212.
3. Su, C.-C.; *et al.* *Ener. Environ. Sci.* **2017**, *10*, 900.
4. He, M.; *et al.*, *J. Electrochem. Soc.* **2015**, *162*, A1725.

### Acknowledgements [Use EERE\_Head\_03\_Shaded]

The PI (Dr. Meinan He) and co-PIs (Dr. Chi-Cheung Su, Dr. Hasnain Hafiz, Prof. Jeffrey Lopez and Juchen Guo) would like to thank financial support from the Assistant Secretary for Energy Efficiency and Renewable Energy, Office of Vehicle Technologies of the U.S. Department of Energy (DOE) under contract no. DE-EE0009644. They also would like to thank Haiyan Croft, Barbara Nitz and Mallory Clites at DOE for program management, and all the students and postdocs involved in this project.

## XII Beyond Li-ion R&D: Metallic Lithium

Rechargeable lithium metal batteries use metallic lithium as the negative electrode. The high specific capacity of lithium (3,860 mAh/g), very low redox potential ( $-3.040$  V versus standard hydrogen electrode) and low density ( $0.59$  g/cm<sup>3</sup>) make it the ideal anode material for high energy density battery technologies. Rechargeable lithium metal batteries could have a long run time due to the high charge density of lithium.

The rest of this chapter contains detailed reports on the status of the following individual projects.

- Lithium Dendrite Prevention for Lithium Batteries (PNNL)
- Integrated Multiscale Model for Design of Robust 3-D Solid-state Lithium Batteries (LLNL)
- Advanced Polymer Materials for Li-ion (SLAC)
- Anode-Free Lithium Batteries (PNNL).

## XII.1 Lithium Dendrite Prevention for Lithium Batteries (PNNL)

### Wu Xu, Principal Investigator

Pacific Northwest National Laboratory  
902 Battelle Boulevard  
Richland, WA 99354  
E-mail: [wu.xu@pnnl.gov](mailto:wu.xu@pnnl.gov)

### Tien Duong, DOE Technology Development Manager

U.S. Department of Energy  
E-mail: [Tien.Duong@ee.doe.gov](mailto:Tien.Duong@ee.doe.gov)

Start Date: October 1, 2022

End Date: September 30, 2023

Project Funding (FY23): \$400,000

DOE share: \$400,000

Non-DOE share: \$0

### Project Introduction

Lithium (Li) metal is an ideal anode material for the next-generation, high-energy-density, rechargeable batteries. However, the application of Li metal as an anode has been hindered by the short cycle life and safety concerns. The short cycle life of Li metal batteries is mainly associated with the high reactivity of Li metal with electrolytes and the Li loss due to the formation of solid electrolyte interphase (SEI) and electrochemically inactive or “dead” Li during cycling. The safety concern of Li metal batteries mainly arises from the Li dendrite growth and the flammability of the liquid electrolytes. Although much progress has been achieved in suppressing Li dendrites and increasing Li Coulombic efficiency (CE) in liquid electrolytes (LEs) in recent years, the intrinsic problems of Li-metal anode still exist. In FY23, we will continue to develop three-dimensional (3D) porous current collectors for Li metal anode to suppress Li dendrite growth, increase the utilization of Li metal, reduce the Li loss during cycling, and consequently enhance the safety and cycle life of Li-metal batteries. In addition, we will develop artificial dual-layers (DL) to protect Li metal anode. Finally, we will further investigate mechanisms affecting Li deposition and stripping behaviors to lay the groundwork for future improvement of electrolytes (salts, solvents, and additives) for Li metal batteries. The success of this project will increase the safety and cycle life of Li batteries and accelerate market acceptance of electric vehicles.

### Objectives

The objective of this project is to enable practical application of Li metal as an effective anode in Li-metal batteries with good electrochemical performance and safety. The investigation in FY23 focused on the following aspects: (1) continuing development of the 3D-structured, lightweight, flexible current collectors for Li-metal anode and Li-metal batteries, and (2) developing a stable DL as an artificial protection layer on Li metal anode to improve the cycling stability of Li-metal batteries, and (3) obtaining mechanistic insight on Li-metal deposition/stripping behavior.

### Approach

The approach has encompassed the following areas: (1) optimize current collectors with a 3D structure based on polymeric scaffold for Li-metal anode to suppress Li dendrite growth, increase Li utilization, and extend the cycle life of Li-metal batteries, (2) develop artificial protection layers not only to improve the electrochemical performance of  $\text{Li}|\text{LiNi}_x\text{Mn}_y\text{Co}_{1-x-y}\text{O}_2$  (NMC) batteries, but also to alleviate the side reactions between the electrolyte and Li metal anode, and (3) conduct mechanistic studies on Li deposition behavior to lay groundwork for future improvement of Li-metal batteries.

## Results

### 1. Development of 3D current collectors

Even though a 3D current collector has great potential to suppress Li dendrite growth due to its increased surface area and pore volume that can improve Li utilization and therefore increase the cycle life of Li-metal batteries, the mainstream 3D current collectors are carbonaceous materials, which suffer from poor wettability with metallic Li and poor flexibility. In FY22, we had developed a 3D current collector based on polymer fibers with electroless plating to transform the insulating polymer fibers into an electronically conductive matrix. Electrospun polyimide (PI) was selected as the precursor because of its high thermal stability. The copper (Cu)-coated PI (Cu@PI) current collector was fabricated via electroless plating of Cu nanoparticles on PI porous membrane in an appropriate electroless plating solution containing Cu ions. In FY23, we further optimized these 3D pristine Cu@PI current collectors to improve their electronic conductivity and enhance the uniformity of Li deposition. We found that heat treatment of Cu@PI at optimized temperature leads to smoother surface morphology of Cu coating than that of pristine coating as shown in the scanning electron microscopy (SEM) images (see Figure XII.1.1a). The heat treatment also increased electronic conductivity ( $2.69 \times 10^3 \text{ S cm}^{-1}$ ) of the 3D substrate compared to that of the pristine Cu@PI ( $1.97 \times 10^3 \text{ S cm}^{-1}$ , Figure XIII.1.1b). The cross-sectional SEM images were obtained from Cu@PI substrates (with or without heat treatment) after initial deposition of Li (at a current density of  $0.4 \text{ mA cm}^{-2}$  for a capacity of  $4 \text{ mAh cm}^{-2}$ ) in Li||Cu@PI cells with  $75 \mu\text{L}$  electrolyte (Li bis(fluorosulfonyl)imide (LiFSI) in 1,2-dimethoxyethane (DME) and 1,1,2,2-tetrafluoroethyl-2,2,3,3-tetrafluoropropyl ether (TTE) (at 1:1.2:3 by mol.)). Figure XII.1.1c-d shows the SEM images (left figures) and energy-dispersive X-ray spectroscopy (EDS) mapping (middle figures) taken on the backside of the 3D substrates after initial Li deposition. The SEM image on the heat-treated Cu@PI shows full coverage of Li deposition up to the back side of Cu@PI, but most Li was deposited in the front side of pristine Cu@PI. EDS mappings show that Cu is still exposed on the backside of untreated Cu@PI after Li deposition, but no Cu is exposed on the backside of heat-treated Cu@PI after Li deposition, indicating a more uniform Li coverage through the whole heat-treated 3D Cu@PI current collector. The difference in uniformity of Li deposition between pristine Cu@PI and heat-treated Cu@PI on the Li deposition through the thickness direction can also be observed from the cross-sectional images as shown on the right side of Figure XII.1.1c and Figure XII.1.1d. For heat-treated Cu@PI substrate, Li has been deposited through the full thickness of the substrate, while most Li was deposited on the top surface of pristine Cu@PI. It demonstrates that the heat treatment of Cu@PI increased electronic conductivity of the substrate and enabled full utilization of the 3D substrate.

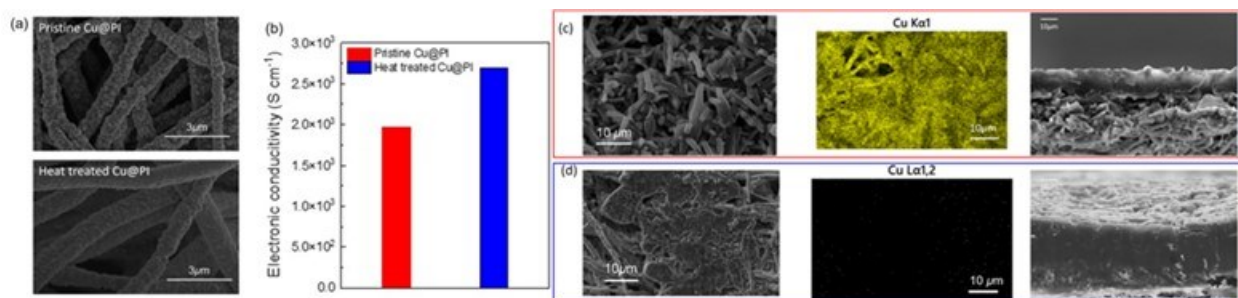


**Figure XII.1.1** a) SEM images and (b) electronic conductivities of pristine and heat-treated Cu@PI. (c, d) SEM and EDS mapping images for the backside and cross-sectional SEM images of Li deposited for  $4 \text{ mAh cm}^{-2}$  on (c) pristine Cu@PI and (d) heat-treated Cu@PI at a current density of  $0.4 \text{ mA cm}^{-2}$ .

To investigate the effect of the Cu@PI on the electrochemical performance of Li metal batteries (LMBs), Li||NMC622 coin cells were assembled with electrochemically deposited Li (EDLi) ( $5 \text{ mAh cm}^{-2}$ ) on Cu@PI 3D substrates as anode, NMC622 ( $4.5 \text{ mAh cm}^{-2}$ ) as cathode, and a localized high concentration electrolyte (LiFSI-1.2DME-3TTE). The cells were charged at C/10 and discharged at C/3 discharging ( $1\text{C} = 4.5 \text{ mA cm}^{-2}$ ) after two cycles of formation at C/10 in the voltage range of 2.8 to 4.4 V (vs. Li/Li<sup>+</sup>). As shown in Figure XII.1.2, the cell with heat-treated Cu@PI shows a higher initial capacity ( $192.1 \text{ mAh g}^{-1}$ ) than those with bare

Cu substrate ( $189.0 \text{ mAh g}^{-1}$ ) or pristine Cu@PI substrate ( $188.0 \text{ mAh g}^{-1}$ ). The heat-treated Cu@PI also leads to improved capacity retention of 95.2% after 100 cycles compared to those of bare Cu (92.8%) and pristine Cu@PI (84.0%). In addition, EDLi||NMC622 with the heat-treated Cu@PI demonstrates 80% capacity retention after 180 cycles, while the cells with bare Cu exhibit only 51.5% of capacity retention under the same condition. The cells with pristine Cu@PI also show poor cycling performance, possibly because the Cu particles cannot well cover the PI fibers and allow the continuous side reactions between PI and Li during cycling. This result demonstrates that LMBs with an optimized 3D anode current collector can lead to better cycling performance than those with bare Cu substrate.

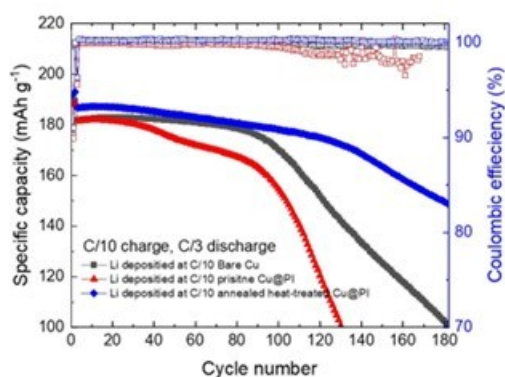


**Figure XII.1.2** Cycling performance of EDLi||NMC622 coin cells with EDLi on Bare Cu, Pristine Cu@PI, and Heat-treated Cu@PI.

Another significant advantage of the 3D Cu@PI current collector is its light weight which could further improve the specific energy density of the batteries. As shown in Figure XII.1.3a, the mass of Cu@PI is 14.5% of the bare Cu. When the total mass of the cathode, separator, and EDLi was used to calculate the specific energy density of the EDLi||NMC622 cells, EDLi||NMC622 with the heat-treated Cu@PI shows 20% higher specific energy ( $212.0 \text{ Wh kg}^{-1}$ ) than that with the bare Cu substrate ( $178.9 \text{ Wh kg}^{-1}$ ) at the first cycle (Figure XII.1.3b). This result indicates that a LMB using a lighter 3D current collector made of Cu-coated PI nanomat can improve both the cyclability and energy density of the batteries as compared to similar batteries using bare Cu as the anode current collector.

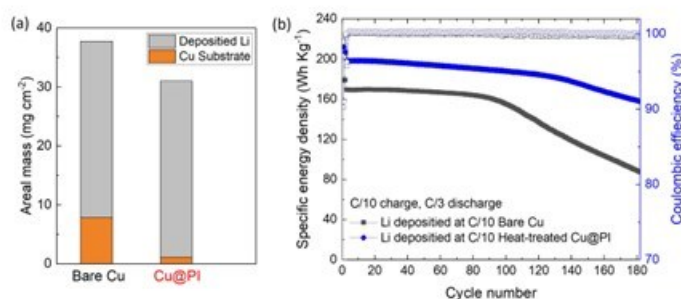


**Figure XII.1.3 a)** Comparison of areal mass of EDLi ( $5 \text{ mAh cm}^{-2}$ ) on bare Cu and Cu@PI. **B)** Cycling performance of EDLi||NMC622 cells based on specific energy density ( $\text{Wh kg}^{-1}$ ) for bare Cu and Cu@PI.

To further reveal the positive effect of the Cu@PI over bare Cu foil on the performance of Li metal anode and LMBs, the surface morphologies and compositions of the EDLi after 180 cycles were examined by SEM and X-ray photoelectron spectroscopy (XPS). As shown in Figure XII.1.4a,b, Li deposited on bare Cu has a porous surface with smaller Li particles while Li deposited on Cu@PI shows a much denser Li deposition. This result indicates that Li dendrite growth would be suppressed by the uniform Li deposition on Cu@PI current collector during cycling. In addition, the XPS Ni 3p spectra present a much higher intensity of



deposited Ni on the surface of bare Cu when compared to the Cu@PI (Figure XII.1.4c and Figure XII.1.4d). The dissolution of the heavy transition metal ions (e.g. Ni, Co, or Mn) from the NMC cathode into the electrolyte could migrate through the liquid electrolyte and deposit on the Li metal anode surface. Likewise, the reduction species of the electrolyte on Li metal surface could also migrate through the electrolyte to reach the cathode side and cause side reactions. Such behavior is called “crosstalk” which is known as one of the reasons for battery failure. This is an evidence that the cells with 3D Cu@PI anode current collector could lead to better Li morphology (as shown in in Figure XII.1.3 a-b) which can reduce the crosstalk between anode and cathode and improve the cycling stability of cells. Based on these results, it is confirmed that the well-developed Cu@PI 3D current collector can prevent Li dendrite growth and side reactions in LMBs as well.

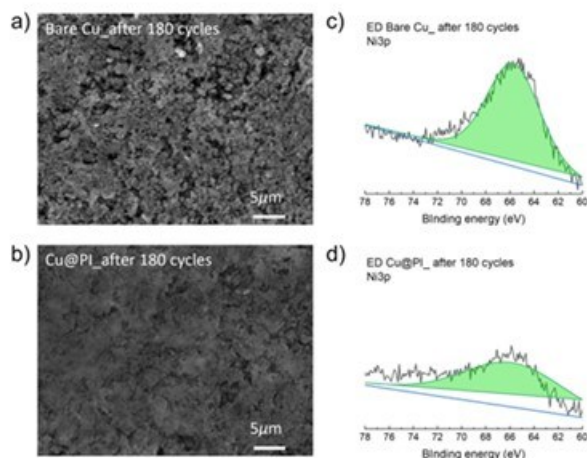


Figure XII.1.4 a,b) SEM images and c,d) XPS Ni 3p spectra of the EDLi surfaces after 180 cycles in EDLi || NMC622 cells with a,c) Bare Cu and b,d) Cu@PI.

## 2. Artificial protection layers for Li metal anode

### 2.1. Dual protection layer

To prevent side reactions between the Li metal anode and the electrolytes, an artificial dual protection layer has been developed. Polyethylene oxide (PEO) has been widely studied as a material in the protection layers due to its high stability against Li metal, high donor number for Li ion and high chain flexibility, which are important for having long stability and promoting ion transport. However, dimensional instability of PEO in liquid electrolytes due to dissolution or swelling is considered a big obstacle. To bring the advantage from PEO, a dual layer (DL) configuration is designed. The DL consists of a PEO-based composite bottom layer (CBL) with additional ionic conductive material to enhance the Li ion transport through this layer and a top layer (TL) composed of a cross-linked polymer that is expected to enhance the mechanical strength of the PEO-based CBL after electrolyte penetration.

The effect of the DL on the morphologies of deposited Li was studied. Li deposition on Cu substrate was conducted in Li||TL@CBL@Cu and Li||Bare Cu cells with the electrolyte of LiFSI-1.2DME-3TTE (by mol) at a current density of  $C/2$  and a capacity of  $4 \text{ mAh cm}^{-2}$ . As shown in Figure XII.1.5a,b, a more uniform Li morphology with larger particles was observed on the surface of the TL@CBL@Cu. Furthermore, the cross-sectional image of Li deposited on TL@CBL@Cu shows a dense morphology with  $35 \mu\text{m}$  thickness (Figure XII.1.5c) as compared with that on bare Cu that leads to porous and thicker Li deposition (Figure XII.1.5d), indicating that this dual protection layer could effectively improve the Li deposition morphology and alleviate dendritic Li growth on the Cu as well.

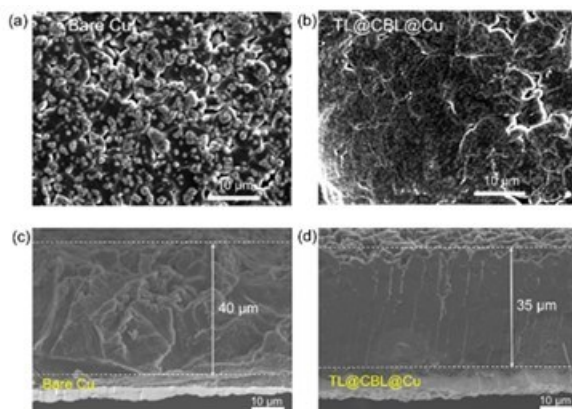


**Figure XII.1.5** SEM images (top and cross-sectional views) of deposited Li (at C/2 for 4 mAh cm<sup>-2</sup>) on (a,c) bare Cu and (b,d) TL@CBL@Cu.

To study the effect of the DL on LMB performance, the Li||NMC811 coin cells using the bare Li and the TL/CBL-coated Li (TL@CBL@Li) were assembled with PE separator and 75 μL electrolyte of LiFSI-1.2DME-3TTE (by mol.). After the formation cycles at C/10 rate, the cells were cycled at a current rate of C/2. The TL@CBL@Li||NMC811 cells delivered a capacity and capacity retention of 132 mAh g<sup>-1</sup> and 73.4%, respectively, after 200 cycles, much higher than the those of bare Li||NMC811 cells (65 mAh g<sup>-1</sup> and 60.1%, respectively) (Figure XIII.1.6a). Besides, the TL@CBL@Li||NMC811 cells also have a lower polarization compared with bare Li||NMC811 cells (Figure XII.1.6b). Figure XII.1.6c shows that the TL@CBL@Li||NMC811 cells also exhibit improved discharge capacities even at higher charge current densities (C/2, 1C, 3/2 C). These results demonstrate that TL@CBL@Li could be a promising candidate to enhance the electrochemical performance of LMBs in terms of cycling stability and charge rate capability, possibility due to the reduced side reactions between electrolyte and Li metal by the double protection layer. To deeply understand the double protection layer strategy, more characterizations are currently conducted and will be reported in FY24.

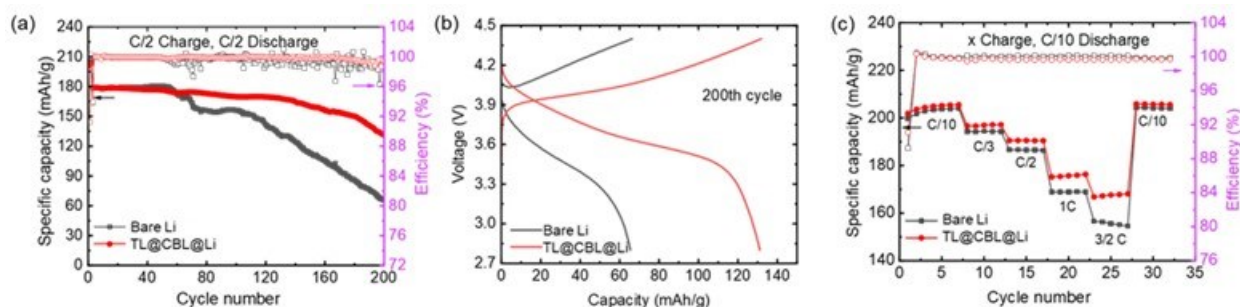


**Figure XII.1.6** a) Cycling performance of Li||NMC811 cells at C/2 for charging and discharging, b) Charge/discharge voltage profiles at 200<sup>th</sup> cycle. c) Charging rate capability at various charge rates (x) with a constant discharge current rate of C/10. The cells were first conducted in two formation cycles at C/10, where 1C = 4.8 mA cm<sup>-2</sup>. The voltage range was from 2.8 to 4.4 V (vs. Li/Li<sup>+</sup>).

## 2.2. Li ion conductive protection layer via molecular layer deposition

In FY23, a single layer of Li glycerol (GL) coated Li metal (GL@Li) was prepared by using molecular layer deposition (MLD) on a 50 μm of Li metal surface, with the aim of using the GL layer as an artificial SEI layer to prevent side reactions between Li metal anode and the electrolyte. Furthermore, a top layer coated Li metal (TL@GL@Li) was prepared by coating a crosslinked polymer layer on the GL@Li. These coatings are expected to improve the cycling stability of Li metal anode at high charge current densities. To investigate the effect of GL and TL@GL coating layers on the cycling performance of LMBs, the cycling performance and charge rate capability of Li||NMC622 coin cells using the bare and coated Li metal anodes were assembled,

with 75  $\mu\text{L}$  electrolyte of LiFSI-1.2DME-3TTE (by mol). At a current density of C/10 for charging and C/3 for discharging, TL@GL@Li delivers a better capacity retention of 94.8% after 160 cycles compared to GL@Li (91.2%) and bare Li (86.5%) (Figure XII.1.7a). While at a current density of C/2, GL@Li showed more stable cycling performance with capacity retention of 98.7% after 120 cycles than TL@GL@Li (94.5%) and bare Li (56.1%) (Figure XII.1.7b). More testing on TL@GL@Li is needed. In the charge rate capability testing, both GL@Li and TL@GL@Li show improved charge rate capability compared with bare Li as shown in Figure XII.1.7c. These results demonstrate that GL@Li and TL@GL@Li could be promising candidates for high electrochemical performance of Li metal batteries. The performance of GL@Li and TL@GL@Li will be further optimized in the next fiscal year.

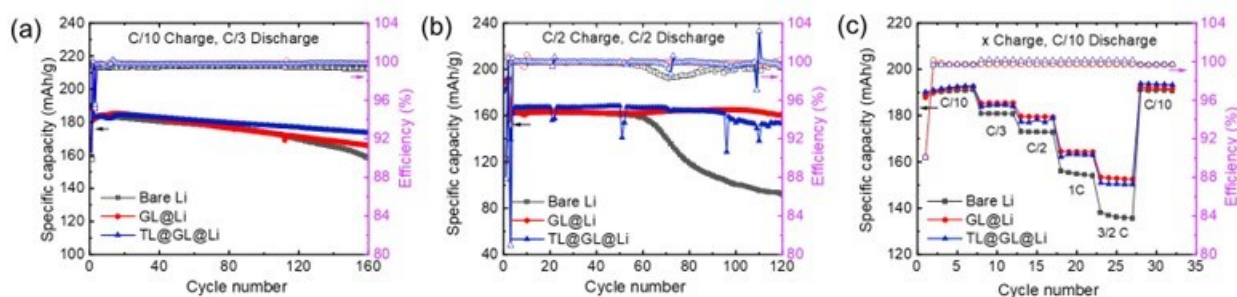


**Figure XII.1.7** Cycling performance of Li||NMC622 cells at (a) C/10 for charging and C/3 for discharging, (b) C/2 for charging and discharging, (c) various charge current densities (x) with a constant discharge current density (C/10). The cells were first conducted two formation cycles at C/10, where  $1\text{C} = 4.0 \text{ mA cm}^{-2}$ . The voltage range is from 2.8 to 4.4 V (vs. Li/Li<sup>+</sup>).

### 3. Direct measurement of electrical properties of SEI on Li metal anode

SEI has been investigated significantly since it was proposed in 1979 by Peled, but it is still not well understood because it is generated from the electrochemical reduction and chemical reaction of electrolyte components. The variation of electrolyte components and compositions would greatly change the SEI components, compositions and morphologies, then affect the battery performance. An ideal SEI is considered electronic insulation but ionic conduction. However, the electrical properties of the SEI have long been unable to measure due to its ultrathin and fragile nature and the lack of appropriate characterization tools.

In this fiscal year, we collaborated with the electron microscopic team at PNNL and the simulation team at Texas A&M University and for the first time directly measured the electrical properties of SEIs on Cu and Li surfaces by using in-situ bias transmission electron microscopy (TEM). By employing the setup exhibited in Figure XII.1.8a-e and the *ab initio* dynamic simulations to study the SEIs formed in four electrolytes based on LiFSI in DME with various solvation structures, namely low concentration electrolyte (LCE), high concentration electrolyte (HCE), localized high concentration electrolyte (LHCE) and pseudo localized high concentration electrolyte (PLHCE), we revealed that the SEIs formed in the four typical electrolytes showed varied voltage-dependent differential conductance, i.e. the electrical behaviors. This is contrary to the conventional understanding. In reality, the SEI does not act as perfect electrical insulators, and instead, it shows non-negligible electrical conductance, which governs the SEI formation and Li deposition and consequently affects battery performance. A higher rate of differential conductance induces a thicker SEI with an intricate topographic feature, leading to an inferior Coulombic efficiency and cycling stability in Li batteries. Meanwhile, the electrical properties of the SEI are determined by the microstructure and chemistry of SEI components formed by the reduction and reaction of electrolyte solvent and Li salt. The SEI with high content of inorganic species shows good electrical insulation, then thin and uniform thickness (Figure XII.1.8f). This work provides a direct method to quantify the electrical properties of the SEI and their effects on the electrochemical performances of rechargeable Li-based batteries.

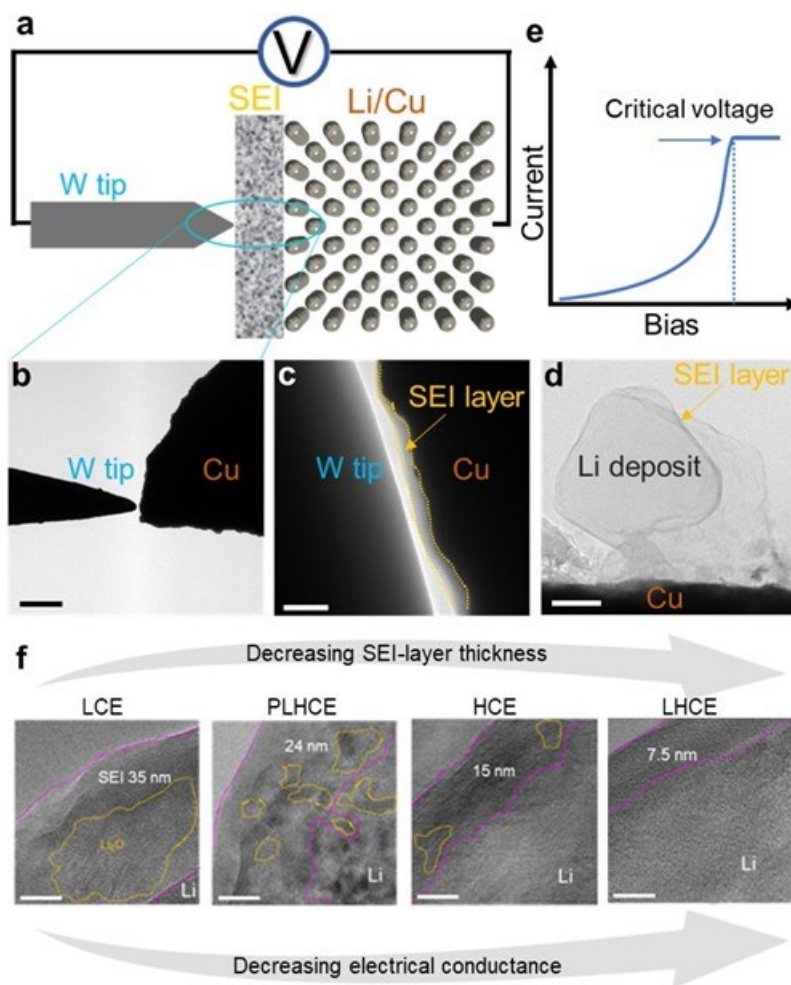


Figure XII.1.8 (a-e) In situ bias TEM measurement of electrical properties of SEI. (a) Schematic of experiment setup. (b-d) TEM images showing W wire with sharp tip and Cu wire with SEI layer on the surface. (e) Typical I-V curves showing the critical voltage. Scale bars, 50  $\mu\text{m}$  in (c) and 100 nm in (b) and (d). (f) Correlation between SEI structure and its electrical property. Atomic structure of SEI layers on the Li deposits formed in LCE, PLHCE, HCE, and LHCE.

## Conclusions

- The heat treatment on a 3D current collector based on Cu-coated PI fibers (Cu@PI) improved its electronic conductivity and led to uniform Li deposition through the full thickness of the 3D substrate. The Cu@PI-based EDLi||NMC622 LMB showed not only a longer cycle life but also an improved specific energy compared to the bare Cu-based EDLi||NMC622. These results indicate that a well-developed lightweight 3D current collector could enhance the cell performance of high energy density LMBs.
- A dual protection layer that consists of a PEO-based composite bottom layer (CBL) and the cross-linked polymer-based top layer (TL) was successfully developed. The Li||NMC811 cells with Li anode protected by TL/CBL-coating delivered better cell performance at a higher current density than those with bare Li anode because the dual layer protection minimized the side reactions between Li metal anode and electrolytes.
- For the first time, the electrical properties of the SEIs formed on Cu and Li substrates in four electrolytes with different solvation structures were directly characterized by using an *in-situ* bias TEM method. All SEIs exhibited a voltage-dependent differential conductance. A higher rate of differential conductance induced a thicker SEI with an intricate topographic feature, leading to an inferior Coulombic efficiency

and cycling stability in Li batteries. This work provides insight into the targeted design of the SEI with desired characteristics towards better battery performance.

### Key Publications

1. Y. Xu<sup>†</sup>, H. Jia<sup>†</sup>, P. Gao, D. E. Galvez-Aranda, S. P. Beltran, X. Cao, P. M. L. Le, J. Liu, M. H. Engelhard, S. Li, G. Ren, J. M. Seminario\*, P. B. Balbuena\*, J.-G. Zhang, W. Xu\*, C. Wang\*, “Direct in-situ measurement of electrical properties of solid electrolyte interphase on lithium metal anode”, *Nature Energy*, 2023, DOI:10.1038/s41560-023-01361-1.
2. M. Werres, Y. Xu, H. Jia, C. Wang, W. Xu, A. Latz, and B. Horstmann\*, “Origin of heterogeneous stripping of lithium in liquid electrolytes”, *ACS Nano*, 2023, **17**(11), 10218-10228. DOI:10.1021/acsnano.3c00329.
3. G. Feng, Y. Shi, H. Jia, S. Risal, X. Yang, Z. Fan, W. Xu\*, X. Shan\*, “Imaging Lithium Nucleation Dynamics and Localized Overpotential Using Operando Reflection Interference Microscope”, *Advanced Sciences*, 2023, **9**(21), eadg6813. DOI:10.1126/sciadv.adg6813.
4. G. Feng<sup>†</sup>, H. Jia<sup>†</sup>, Y. Shi<sup>†</sup>, X. Yang, Y. Liang, M. H. Engelhard, Y. Zhang, C. Yang, K. Xu\*, Y. Yao\*, W. Xu\*, X. Shan\*, “Imaging Solid-Electrolyte-Interphase Dynamics Using Operando Reflection Interference Microscopy”, *Nature Nanotechnology*, 2023, **18**(7), 780–789. DOI:10.1038/s41565-023-01316-3.

### Acknowledgments

Key contributors to this project include Ji-Guang (Jason) Zhang, Ju-Myung Kim, and Ridwan Ahmed. Collaborators include (1) Chongmin Wang and Yaobin Xu of PNNL on characterization by TEM/SEM; (2) Mark Engelhard of PNNL on characterization by XPS; (3) Yuepeng Zhang and Ashley Simmons of Argonne National Laboratory on electrospinning polyimide porous membranes; (4) Xiangbo Meng of University of Arkansas on MLD-protected Li; (5) Jorge Seminario and Perla Balbuena of Texas A&M University on performing *ab initio* dynamic simulations; and (6) Martin Werres, Arnulf Latz, and Birger Horstmann of Helmholtz Institute Ulm on Li dendrite simulations.

## XII.2 Integrated Multiscale Model for Design of Robust 3-D Solid-state Lithium Batteries (LLNL)

### Brandon C. Wood, Principal Investigator

Lawrence Livermore National Laboratory  
7000 East Avenue  
Livermore, CA 94550  
E-mail: [wood37@llnl.gov](mailto:wood37@llnl.gov)

### Simon Thompson, DOE Technology Development Manager

U.S. Department of Energy  
E-mail: [Simon.Thompson@ee.doe.gov](mailto:Simon.Thompson@ee.doe.gov)

Start Date: October 1, 2022	End Date: September 30, 2023	
Project Funding(FY23): \$375,000	DOE share: \$375,000	Non-DOE share: \$0

### Project Introduction

Interfaces in solid-state batteries present critical impediments for both performance and cyclability. Particularly challenging is the cathode-electrolyte interface, which is often characterized by formation of unwanted chemical products and interphases, as well as the appearance of voids, gaps, or cracks that can accumulate during cycling. Chemical evolution and mechanical behavior at cathode-electrolyte interfaces are intrinsically linked and intimately connected to cycling behavior of solid-state batteries, as stresses accumulate within the solid electrolyte and in the cathode-electrolyte composite matrix. These interfacial stresses and reaction intermediates in turn affect desired transport properties, accelerate further chemical evolution, and promote mechanical failure. To advance and accelerate the development of solid-state batteries with high cyclability and lifetime, it is critical to understand how these degradation and failure modes are connected to specific interfacial features. Such understanding can aid in the development of more accurate and predictive lifetime models, as well as motivate changes in composition or processing. This project develops and applies advanced multiscale modeling approaches to assesses how chemical and microstructural evolution during cycling impact solid mechanics and transport at the cathode-electrolyte interface in solid-state batteries, with a view towards predicting conditions and materials features that ultimately lead to failure via fracture or catastrophic performance loss.

### Objectives

The goal of the project is the development and application of multiscale, multiphysics models that connect composition, microstructure, and architecture to chemomechanical integrity at interfaces in 3-D solid-state batteries. The focus is on cathode-electrolyte interfaces and internal electrolyte interfaces in ceramic ( $\text{Li}_{1-x}\text{La}_x\text{ZrO}_2$  [LLZO]) solid electrolytes, as well as other electrolyte formulations including halides ( $\text{Li}_3\text{InCl}_6$ ) and/or inorganic/organic composites. The models integrate multiple computational methods from the atomistic to continuum scales, informed and validated through collaborations with complementary experimental efforts.

The project addresses three objectives:

1. Develop multiphysics, multiscale chemomechanics models of cathode-electrolyte interfaces in solid-state batteries;
2. Assess interface- and microstructure-induced mechanical failure thresholds and high impedance;
3. Simulate chemomechanical evolution under battery operating conditions.

### Approach

The team's approach integrates diverse computational methods—including density functional theory (DFT) calculations, molecular dynamics, machine learning, micromechanical modeling, and phase-field models—to predict the chemomechanical properties of cathode-electrolyte interfaces and internal grain boundaries at

different charge/discharge states. DFT and *ab initio* molecular dynamics are used to simulate interfacial chemistry and mechanical response with high accuracy, as well as to train interatomic potentials using machine learning methods for accessing much longer simulation times. These data parameterize micromechanics models and microstructure-aware continuum simulations, which establish microstructure-property relationships for ion transport and fracture. Phase-field simulations of cathode evolution during cycling provide a connection to battery operation. The integrated simulation techniques are also used to predict chemomechanical hotspots that are likely failure initiation zones under different operation conditions.

## Results

### ***Atomistic simulations of mechanical fracture and interfacial evolution in ceramic solid electrolytes***

Because the computational cost of DFT-based approaches limits application to relatively simple systems and short times, the team developed a force field capable of simulating both LLZO and LLZO|LiCoO<sub>2</sub> (LCO) interfaces based on machine learning (MLFF), trained on extensive DFT and *ab initio* molecular dynamics (AIMD) simulation data.<sup>1</sup> Previously, the team had demonstrated an LLZO MLFF capable of simulating atomically disordered interfaces; this year, the effort was expanded to also account for the presence of LCO interfaces. This MLFF can enable molecular dynamics simulations (MLMD) that are hundreds or thousands of times faster than fully first-principles approaches, while reproducing structural, vibrational, and dynamical properties of model systems close to first-principles calculations.

The team used the validated MLFF to perform large-scale molecular dynamics (MD) simulations of crack tip propagation behavior in cubic LLZO. Figure XII.2.1a depicts the schematic illustration of LLZO simulation preparation and crack generation. In Figure XII.2.1b, the sample is preloaded hydrostatically to its yield point; here, the crack consistently propagates along the {100} plane, resulting in a flat fracture surface. Comparable crack behavior can be found in Figure XII.2.1c, for which the crack is initialized at the free surface of the sample and uniaxially preloaded along the [010] direction. A notable difference arises when the crack is introduced along the {1 $\bar{1}$ 0} plane and the sample is preloaded hydrostatically (or along the [1 $\bar{1}$ 0] direction for the free surface scenario); in this case, the crack deviates and propagates along the {100} plane (Figure XII.2.1d). This observation indicates fracture anisotropy in single-crystal cubic LLZO and lower cleavage energy of the {100} plane. Figure XII.2.1e highlights local Li redistribution along the cracking plane, indicating higher Li concentration on the crack surfaces. Interestingly, during crack propagation, a cubic-to-tetragonal phase transformation is observed in the vicinity of the crack (Figure XII.2.1b). The team plans to utilize these data to inform mechanical failure thresholds for mesoscale models, which can then be coupled to the computed local stress distributions and cycling profiles.

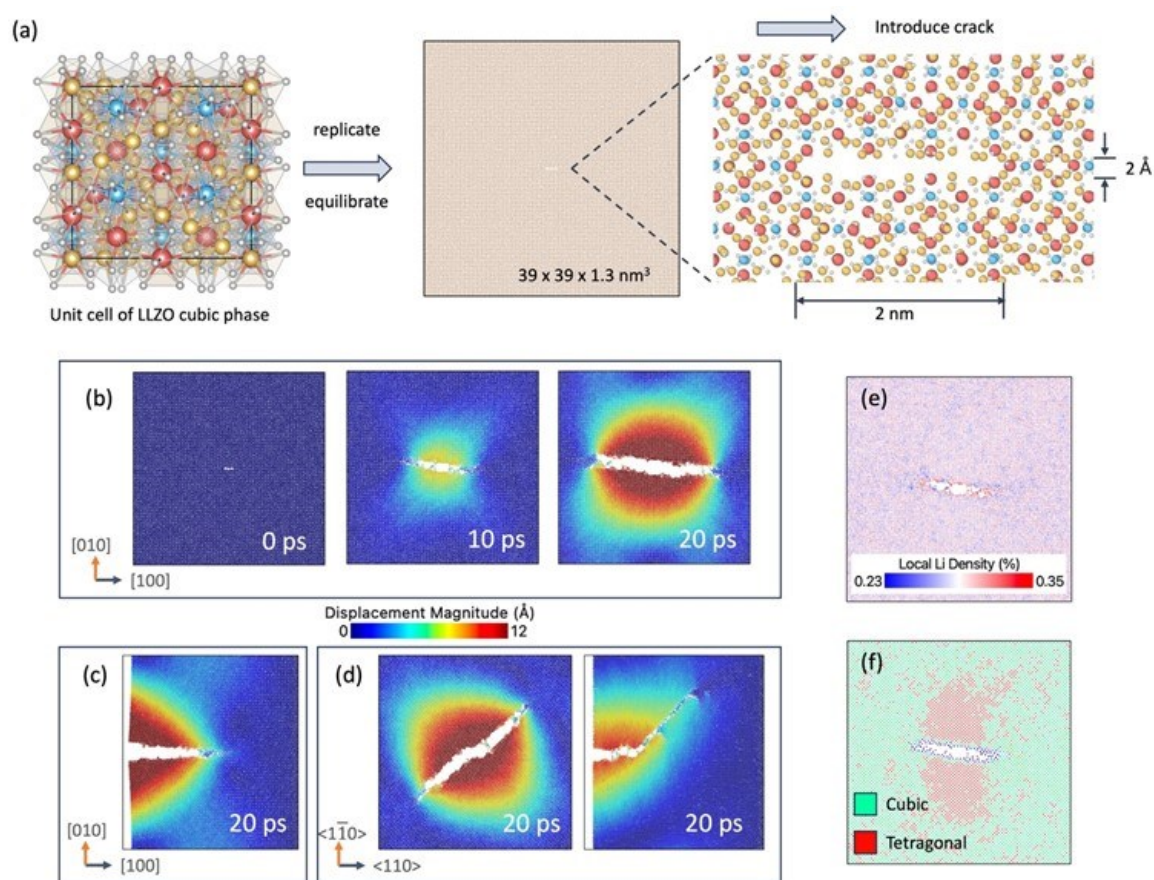


**Figure XII.2.1 Crack tip propagation behavior in cubic LLZO. (a) Schematic illustration of LLZO sample preparation and crack generation. (b) Crack propagation within bulk LLZO along the {100} plane. (c) Crack propagation from the surface of the {100} plane. (d) Crack introduced along the {110} plane and its propagation within the bulk (left) and from the surface (right). (e) Local Li redistribution during crack propagation. (f) Phase evolution of LLZO in the vicinity of the crack.**

The team also used the new MLFFs to perform large-scale MD simulations of LLZO|LCO interfaces to study their evolution at the atomic scale. Figure XII.2.2 presents their LLZO(001)|LCO(104) interface models, which featured two interfacial regions: one Li-deficient and the other Li-rich, corresponding to different states of discharge. These two interfaces show different propensities of chemical evolution after 10 ns of simulation time. In particular, local Li-deficiency results in more severe interfacial disordering, which in turn leads to significant cation mixing and interdiffusion of Co ions from LCO into LLZO. In contrast, the Li-rich interface shows far less cation mixing, with local ordering of Zr and O ions maintained in the near-interface region. This may imply that additional Li sources may alleviate interfacial degradation during co-sintering. At the same time, segregation was observed between La and Zr at the Li-sufficient interface during the initial stages of interfacial evolution. Note that the team found a similar evolution tendency in the LLZO|LCO interfaces with other LCO planes. Therefore, the results reveal a correlation between interface chemistry and the propensity of interfacial evolution towards degradation.



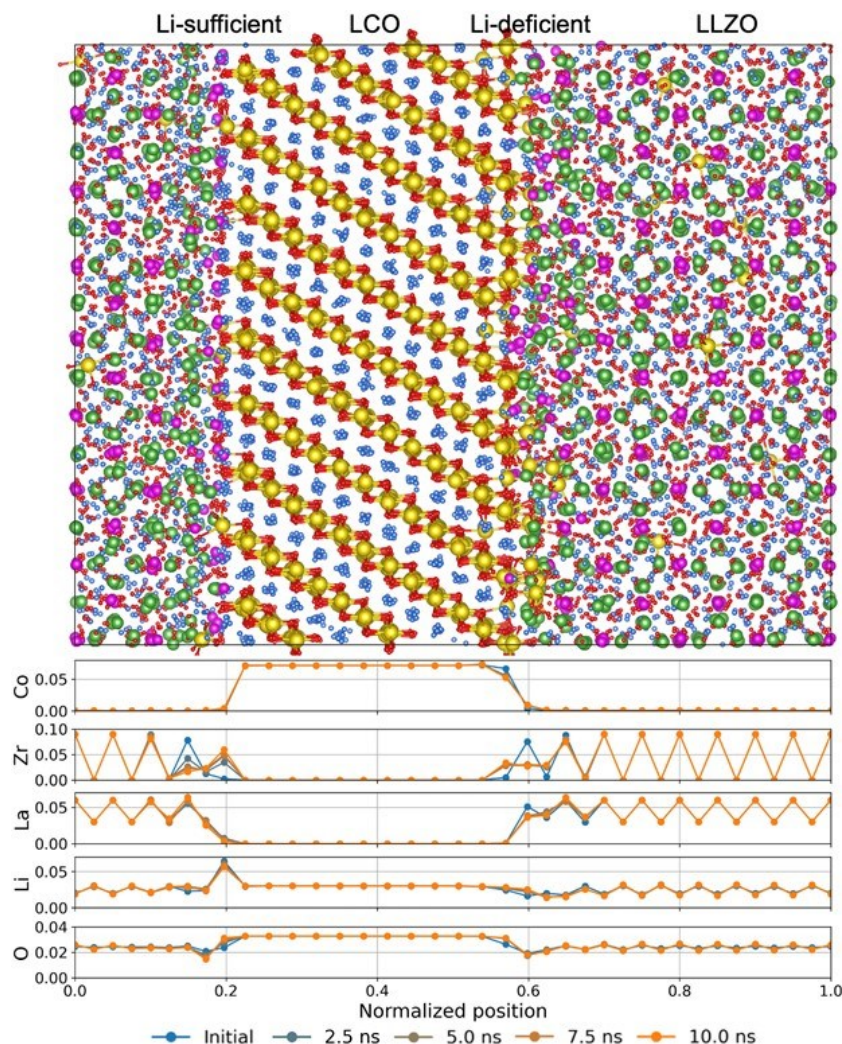


**Figure XII.2.2 LLZO(001)|LCO(104) interface after 10 ns of large-scale molecular dynamic simulation at 1500 K using the developed machine-learning force field. The atomic model shows two interfacial regions with different initial chemical compositions (Li-rich on the left side; Li-deficient on the right side). Li is blue, La is green, Zr is magenta, O is red, and Co is yellow. The concentration profiles of each species are also presented as a function of position normal to the interface.**

Recognizing that Co diffusion from LCO may indeed occur into LLZO at the Li-deficient interface, the team further investigated the subsequent behavior of Co ions within LLZO. These MD simulations showed that Co ions diffuse via Li sites in cubic LLZO, as shown in Figure XII.2.3a. In addition, the residence time of Co ions in Li sites were found to be about 100 times longer than that of Li ions, translating to only 1-2 orders of magnitude slower diffusivity of Co ions compared to Li ions (Figure XII.2.3a). This implies reasonably rapid Co diffusion in LLZO at high temperatures, which should translate to long-range diffusion into LLZO during co-sintering. At the same time, Co ions were also predicted to segregate to grain boundaries (GBs) in LLZO, where the atomic disorder appears to trap the ions (Figure XII.2.3b). In these regions, Co ions are likely to form clusters in disordered/amorphous LLZO structures (Figure XII.2.3c), which could serve as eventual nucleation sites for Co-rich secondary phases at GBs. As such, the simulations revealed the mechanism of Co diffusion across the LLZO|LCO interfaces as well as the formation of Co-rich secondary phases at the GBs in LLZO, both of which were observed experimentally by the team's partners within the U.S.-Germany collaboration on solid-state cathode-electrolyte interfaces.<sup>2</sup> Overall, the results highlight the elaborate

relationship between physicochemical properties and complex interface geometries, suggesting guidelines for interface design that can minimize interfacial degradation and improve cycling performance.

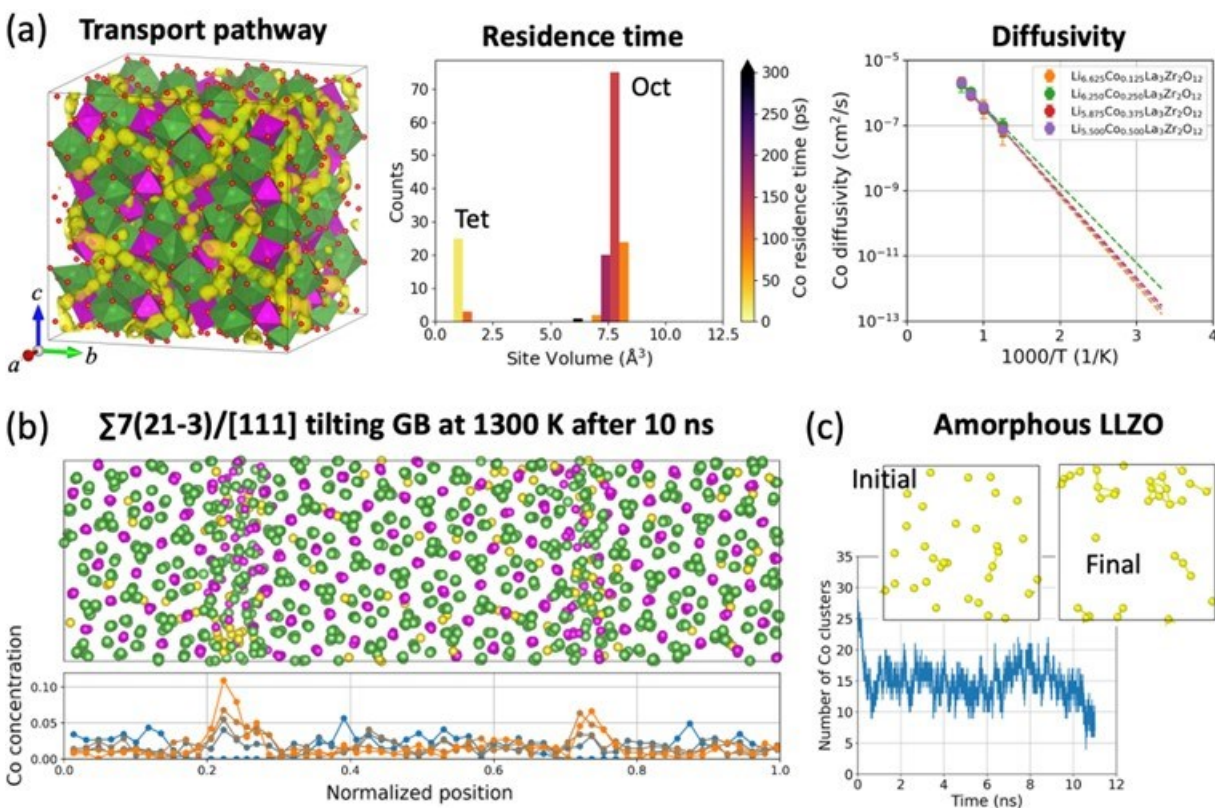
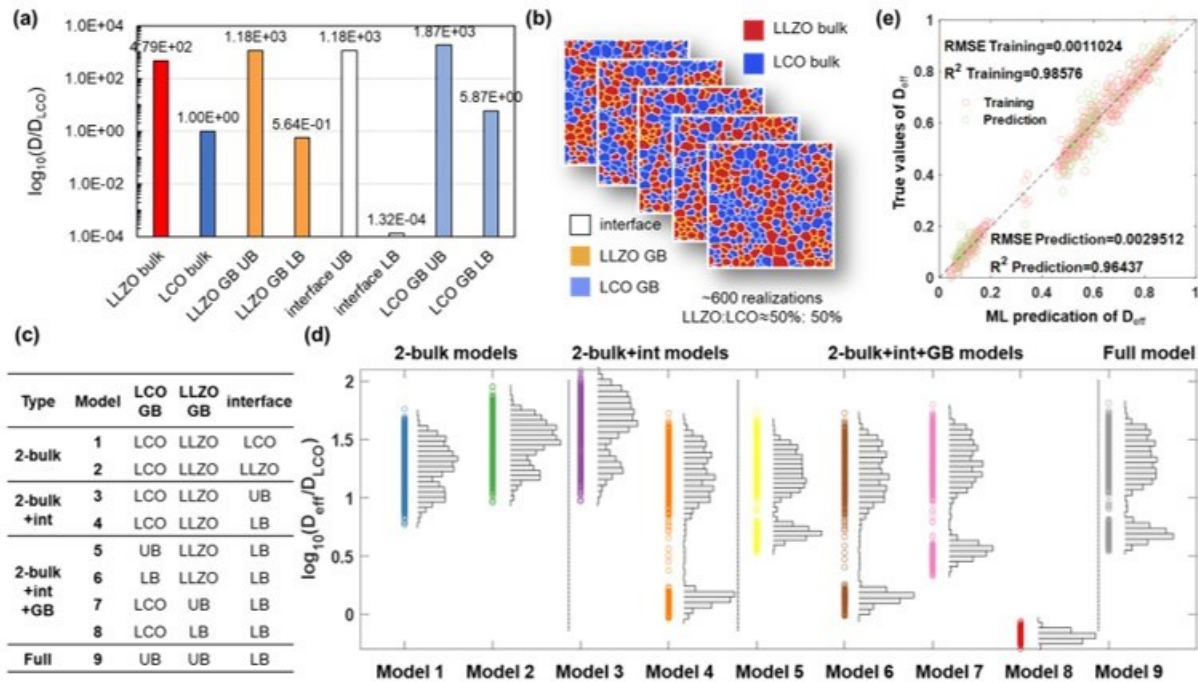


Figure XII.2.3 (a) (Left) positional probability density of Co-ions in cubic LLZO showing diffusion pathways with yellow isosurface (red spheres represent O ions, and green and magenta polyhedra are  $\text{LaO}_8$  and  $\text{ZrO}_6$ , respectively), (middle) histogram for volume of sites where Co ions resided in LLZO with a colormap showing average residence time at each histogram bin (two distinct volume ranges correspond to tetrahedral and octahedral Li sites in LLZO, respectively), and (right) Arrhenius plots for Co diffusivities with various Co contents. (b) Atomic structure of LLZO  $\Sigma 7$  GB with (213) GB plane and [111] axis after 10 ns, showing Co segregation at GB areas. Co concentration as a function of time is also shown below the atomic structure. (c) The number of Co clusters in an amorphous LLZO as a function of time with the structures before and after the MD simulation.

### Mesoscale modeling of microstructure effects on chemomechanical properties

This year, the team's mesoscale modeling effort was focused on two objectives: first, expanding their library of representative digital microstructures of co-sintered solid electrolyte-cathode particle mixtures; and second, determining the effect of microstructure on the effective ionic diffusivity and lithiation/delithiation-induced mechanical stress evolution in the cathode active materials during the discharge/charge processes. The team worked closely with Jianchao Ye as part of his VTO companion project to isolate the observed LLZO + LCO microstructures, which were found to exhibit a bi-continuous and polycrystalline nature. A new approach was debuted to capture this behavior, combining a physics-based spinodal microstructure simulator, an image analysis toolkit, and a stochastic microstructure generation method. First, the team generated a bi-continuous spinodal microstructure using a phase-field model, following which the profile of each phase was extracted using a skeleton transform image analysis. The regions along the skeletons were then used as centers for stochastically generated particles, effectively confining the positions of these new particles to the connected pathways. This approach was able to realistically capture the primary ionic conduction pathways in the LLZTO-LCO mixture.

In total, the team generated 600 realizations of the LCO-LLZO composite microstructure (Figure XII.2.4b) for statistically reliable analysis and comprehensive exploration of the high-dimensional space of probable microstructural configurations. They then computed the effective ionic diffusivity ( $D_{\text{eff}}$ ) through each sample in this digital microstructure library, based on the diffusivities within individual grain, grain boundary, and interfacial regions obtained from MLFF-based atomistic simulations (Figure XII.2.4a). Because these local diffusivities themselves were found to be highly dependent on atomic structural details, the team incorporated this variability by considering a range of model scenarios, each corresponding to different assumed bounds in the statistical distribution (Figure XII.2.4c). Physically, the use of multiple models can be roughly mapped to different conditions of densification, processing, and compositional variation, and also can reveal the importance of individual features in operating devices. Interestingly, the results indicate that the computed  $D_{\text{eff}}$  values through the complex microstructures tend to exhibit bimodal distributions (Figure XII.2.4d). This suggests that there are two distinct classes of microstructures in the database of 600—one type being more conductive than the other. Further analyses verified that those two types are determined by whether channels of oriented LLZO grains can successfully percolate through the system. To probe critical microstructural factors that determine the effective diffusivity, the team applied a random-forest model to analyze the computed  $D_{\text{eff}}$  values (based on Model 9). The trained ML model performed very well (Figure XII.2.4e) and could capture two distinct types of microstructural and parameter configurations, confirming that the most critical factors are the area and connectivity of the largest LLZO particle.



**Figure XII.2.4** Assessing the variability and statistical behavior of the computed effective transport properties arising from microstructural configuration and local property variation. (a) Input local diffusivity ( $D$ ) at 300K as calculated using MLFF for the bulk and grain boundaries (GBs) of LCO, LLZO, and their interfaces. UB and LB stand for upper-bound and lower-bound, respectively. (b) Generation of 600 2D microstructures with varied configurations for the LCO-LLZO composite. The volume fractions are approximately 50%:50%, and the presence of GBs and interfaces are considered. (c) A list of models with different assumptions for the local diffusivities at the GBs and interfaces. (d) The calculated effective diffusivities ( $D_{\text{eff}}$ ) of all 600 microstructures by assuming different models listed in (c). Each dataset of  $D_{\text{eff}}$  is plotted with the corresponding histograms aside. (e) Performance of a random forest ML model (22 descriptors) in predicting the  $D_{\text{eff}}$ .

The team also developed a mesoscale model to simulate the chemomechanical response during lithiation/delithiation via the interplay between diffusion-induced stress and stress-gradient driven transport. In

Figure XII.2.5a, the team considered the lithiation of a model polycrystalline agglomerate embedded within the LLZO solid electrolyte matrix. Figure XII.2.5b shows the time evolution of the depth of discharge (DOD) for cases without and with the stress effect on Li transport. The corresponding spatial profiles of the Li concentration and stress at DOD = 45% are shown in Figure XII.2.5 c,e and d,f, respectively. The simulations clearly show that the evolving stress makes the overall lithiation of the cathode particle more sluggish, which also results in a more uniform Li distribution in the cathode agglomerate (compare Figure XII.2.5 c and d). The local von Mises stress magnitudes in the intercalated grains and at the heterointerface are also reduced (compare Figure XII.2.5 e and f). The observed behavior (the retardation of lithiation and the more uniform Li distribution) can be rationalized as follows. The high local stresses in the intercalated grains create high elastic strain energy density, which increases the resistance against further lithiation from the exterior heterointerface, while simultaneously promoting energetically favorable diffusion of segregated Li into the unintercalated grains within the interior of the agglomerate. As a result, the Li distribution becomes more homogeneous in the stress-diffusion coupled case than in the uncoupled counterpart. Simultaneously, the number of highly concentrated residual mechanical stress hotspots is also reduced by stress-driven diffusion, indicating its importance for maintaining robustness against fracture during cycling.

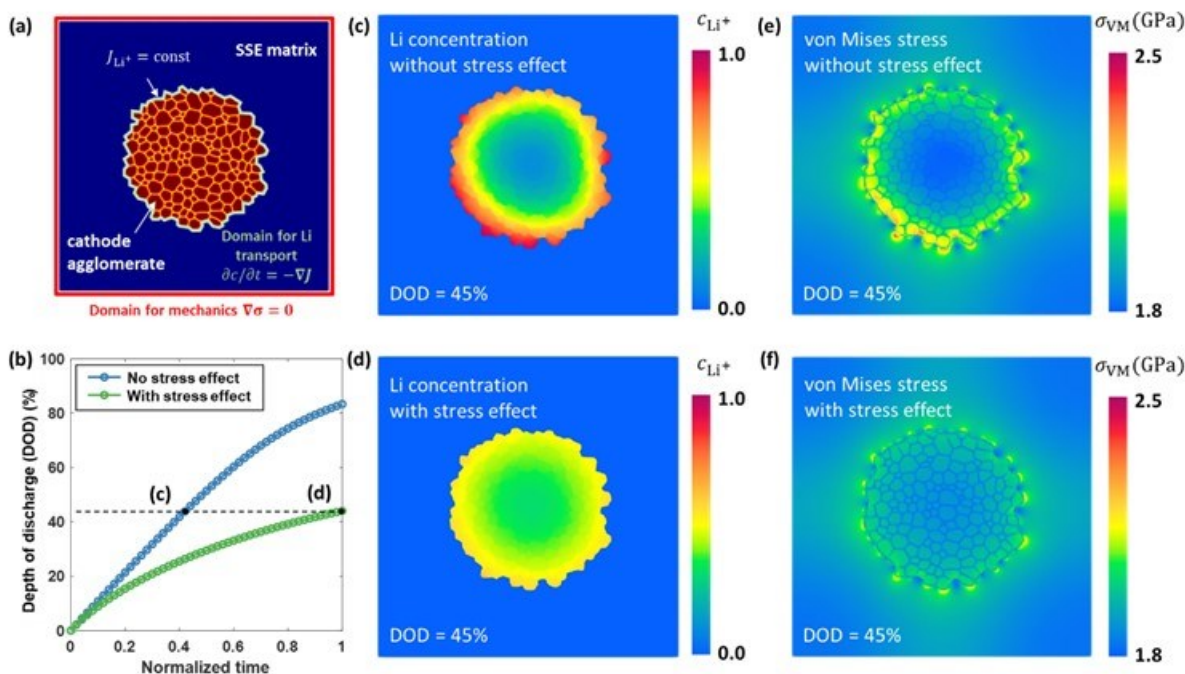


Figure XII.2.5 Mesoscale modeling of Li transport and mechanical stress distribution in LLZO-cathode composite during lithiation. (a) Model setup. The inset schematically shows the volume expansion of a unit cell of the cathode active material after Li insertion. (b) Depth of discharge (DOD) as a function of normalized simulation time. (c,d) Distributions of normalized Li concentration ( $c_{Li^+}$ ) at DOD=45% (c) without and (d) without considering the stress effect on Li transport. (e,f) The corresponding distributions of von Mises stress ( $\sigma_{VM}$ ) at DOD=45% (e) without and (f) with considering the stress effect on Li transport.

## Conclusions

The team's progress this year centered on two primary activities. First, validated MLFFs were used to investigate the mechanical fracture in LLZO and the chemical evolution as well as Co interdiffusion at LLZO|LCO interfaces by large-scale atomic simulations with quantum-level accuracy. The mechanical simulations suggest that fracture anisotropy in single-crystal cubic LLZO and the crack-induced cubic-to-tetragonal phase transformation may affect the ionic transport, with possible implications for processing the ceramic materials. The direct observation of interfacial evolution at atomic scale reveals the correlation between interface chemistry and the propensity of interfacial evolution as well as the mechanisms of Co

interdiffusion and the formation of Co-rich secondary phases at grain boundaries. The team next plans to apply its MLFF capability to doped LLZO and halide solid electrolytes to evaluate dopant segregation, secondary phase formation, and ion transport kinetics, leveraging partnerships through the U.S.-Germany solid-state cathode-electrolyte collaboration. Second, at the microstructural scale, mesoscale modeling was applied to cathode/electrolyte composites to generate representative digital microstructures and investigate their effect on the effective ionic diffusivity and lithiation/delithiation-induced mechanical stress evolution in the cathode active materials during the discharge/charge processes. These mesoscale capabilities were shown to enable the prediction of effective ionic diffusivity and mechanical stress, as well as to correctly describe the interplay between the diffusion-induced stress and the stress-gradient driven transport in a self-consistent manner. The team will continue to refine their models by considering diffusion and elastic anisotropy, and by employing a full suite of atomistically derived parameters to more accurately quantify the interplay among microstructure, chemomechanics, and diffusion during (de)lithiation cycles.

### Key Publications

1. Ren, Y., Danner, T., Moy, A., Finsterbusch, M., Hamann, T., Dippell, J., Fuchs, T., Müller, M., Hoft, R., Weber, A., Curtiss, L.A., Zapol, P., Klenk, M., Ngo, A.T., Barai, P., Wood, B.C., Shi, R., Wan, L.F., Heo, T.W., Engels, M., Nanda, J., Richter, F.H., Latz, A., Srinivasan, V., Janek, J., Sakamoto, J., Wachsman, E.D., and Fattakhova-Rohlfing, D. "Oxide-based solid-state batteries: A perspective on composite cathode architecture," *Adv. Energy Mater.* **13**, 2201939 (2023).
2. Scheld, W.S., Kim, K., Schwab, C., Moy, A.C., Jiang, S-K., Mann, M., Dellen, C., Sohn, Y.J., Lobe, S., Ihrig, M., Danner, M.G., Chang, C-Y., Uhlenbruck, S., Wachsman, E., Hwang, B.J., Sakamoto, J., Wan, L.F., Wood, B.C., Finsterbusch, M., and Fattakhova-Rohlfing, D., "The riddle of dark LLZO: Cobalt diffusion in garnet separators of solid-state lithium batteries," *Adv. Funct. Mater.* **33**, 2302939 (2023).
3. Dive, A., Kim, K., Kang, S., Wan, L.F., and Wood, B.C. "First-principles evaluation of dopant impact on structural deformability and processability of  $\text{Li}_7\text{La}_3\text{Zr}_2\text{O}_{12}$ ." *Phys. Chem. Chem. Phys.*, Advanced Article (2023). DOI: 10.1039/D2CP04382C
4. S. Yu, K. Kim, B.C. Wood, H.-G. Jung, and K.Y. Chung, "Structural design strategies for superionic sodium halide solid electrolytes," *J. Mater. Chem. A* **10**, 24301 (2022).

### References

1. Kim, K., A. Dive, A. Grieder, N. Adelstein, S. Kang, L.F. Wan, and B.C. Wood, "Flexible machine-learning interatomic potential for simulating structural disordering behavior of  $\text{Li}_7\text{La}_3\text{Zr}_2\text{O}_{12}$  solid electrolytes," *J. Chem. Phys.* **156** (2022): 221101.
2. Scheld, W.S., Kim, K., Schwab, C., Moy, A.C., Jiang, S-K., Mann, M., Dellen, C., Sohn, Y.J., Lobe, S., Ihrig, M., Danner, M.G., Chang, C-Y., Uhlenbruck, S., Wachsman, E., Hwang, B.J., Sakamoto, J., Wan, L.F., Wood, B.C., Finsterbusch, M., and Fattakhova-Rohlfing, D., "The riddle of dark LLZO: Cobalt diffusion in garnet separators of solid-state lithium batteries," *Advanced Functional Materials*, **33** (2023): 2302939.

### Acknowledgements

This work was performed under the auspices of the U.S. Department of Energy by Lawrence Livermore National Laboratory under contract DE-AC52-07NA27344. The team gratefully acknowledges collaborations with Professor Nicole Adelstein (San Francisco State University) for modeling transport through disordered regions, Dr. Jianchao Ye (LLNL) for experimental results on LLZO/polymer composites, and the U.S.-Germany partnership on solid-state battery research for the multiscale modeling with the integration between atomic/mesoscale modeling capabilities at LLNL and continuum-level modeling capabilities at ANL (Dr. Pallab Barai) and Deutsches Zentrum für Luft- und Raumfahrt (Dr. Timo Danner in Germany) as well as the theory-experiment collaboration regarding interfacial characteristics with University of Maryland (Prof. Eric Wachsman), University of Michigan (Prof. Jeff Sakamoto), and Forschungszentrum Jülich (Prof. Dina Fattakhova-Rohlfing in Germany).

## XII.3 Advanced Polymer Materials for Li-ion (SLAC)

### Zhenan Bao, Principal Investigator

Stanford University  
 Department of Chemical Engineering, Stanford University  
 Stanford, CA 94305  
 E-mail: [zbao@stanford.edu](mailto:zbao@stanford.edu)

### Yi Cui, Co-Principal Investigator

Stanford University  
 Department of Chemical Engineering, Stanford University  
 Stanford, CA 94305  
 E-mail: [yicui@stanford.edu](mailto:yicui@stanford.edu)

### Tien Duong, DOE Technology Development Manager

U.S. Department of Energy  
 E-mail: [Tien.Duong@ee.doe.gov](mailto:Tien.Duong@ee.doe.gov)

Start Date: October 1, 2022

End Date: September 30, 2023

Project Funding (FY23): \$500,000

DOE share: \$500,000

Non-DOE share: \$0

### Project Introduction

Batteries with lithium A key challenge to enable Li metal batteries as next-generation energy storage devices is to stabilize the interface between the Li metal and the electrolyte. When Li metal is in direct contact with the electrolyte, it typically reacts with both the lithium salt and the solvent to form a SEI. Many recent electrolyte designs populate the concept of an anion-rich inner solvation sheath. The resulting salt derived SEIs are robust and promote stable long-term operation of the battery.

A parallel route to achieve a stable SEI is interface engineering. A coating layer on Li electrode surface could stabilize this interface and promote the long-term operation of LMBs. Polymers are promising coating materials due to their tunable chemical and physical properties. The polymer coating layer is expected to have both physical and chemical interactions with the underlying Li metal.

### Objectives

This project aims to develop new polymer coatings for Li metal anode. The polymers should have appropriate mechanical properties that can accommodate the volume change during charging and discharging. At the same time, the polymers should modulate the interfacial reactions between electrolyte and Li metal to promote the formation of stable solid electrolyte interface.

### Approach

We hypothesize that, if a polymer coating allows the selective transport of lithium salts instead of solvent molecules, salts would have a higher probability of being in physical contact with the Li metal. This can promote salt-derived SEI formation. Our strategy intercepts the self-amplifying process of heterogeneous Li deposition by tuning the chemical composition of the SEI. Our polymer design incorporates both salt-philic and solvent-phobic (SP<sup>2</sup>) moieties as polymer side chains to facilitate the selective transport. The molecular design requirements for this coating are selective transport of salt over solvent, viscoelasticity to maintain electrode coverage, and chemical stability.

### Results

**Stanford team** developed a polymer coating capable of tuning the solid electrolyte interphase (SEI) composition. Recent research findings indicated that a salt-derived SEI is beneficial for the performance of Li

metal anode. Therefore, the team designed polymer coatings capable of selectively transporting salt over solvent molecules to the interface, which leads to preferentially salt-derived SEI. This series of polymers were named SP<sup>2</sup> (salt-philic solvent-phobic). The team has arrived at a desirable composition, SP<sup>2</sup><sub>perF</sub>, where the “perF” indicates the addition of a perfluorinated side chain (Figure XII.3.1).

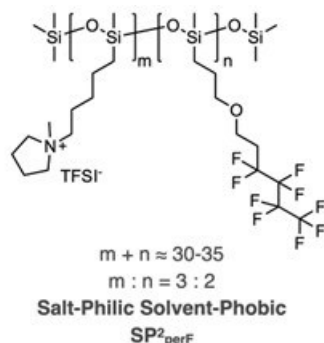


**Figure XII.3.1 Chemical structure of SP<sup>2</sup><sub>perF</sub>**

The SEI chemistry under the influence of polymer coating was characterized by X-ray photoelectron spectroscopy (XPS). The SEI was formed on bare or SP<sup>2</sup><sub>perF</sub> coated Cu by cycling Li||Cu cells at 0.5 mA cm<sup>-2</sup>, 1 mAh cm<sup>-2</sup> for 10 cycles. In 1 M lithium bis(trifluoromethanesulfonyl)imide (LiTFSI) in 1,3-dioxolane / 1,2-dimethoxyethane (DOL/DME) with 1 wt% LiNO<sub>3</sub> electrolyte, the SP<sup>2</sup><sub>perF</sub> coating increased the salt-derived oxygen content in the SEI from 14% to around 30% (Figure XII.3.2 a-c). In addition, the S/C and F/C elemental ratios can indicate the relative contribution from solvent and salt to SEI. In both 1 M LiTFSI DOL/DME electrolyte and 1 M lithium hexafluorophosphate (LiPF<sub>6</sub>) in ethylene carbonate / diethyl carbonate (EC/DEC) electrolyte, the SP<sup>2</sup><sub>perF</sub> coated samples showed three times higher S/C or F/C ratio than the uncoated samples (Figure XII.3.2d, e). Overall, the XPS results indicated the impact of SP<sup>2</sup><sub>perF</sub> coating on promoting salt-derived SEI and suppressing solvent-derived SEI.

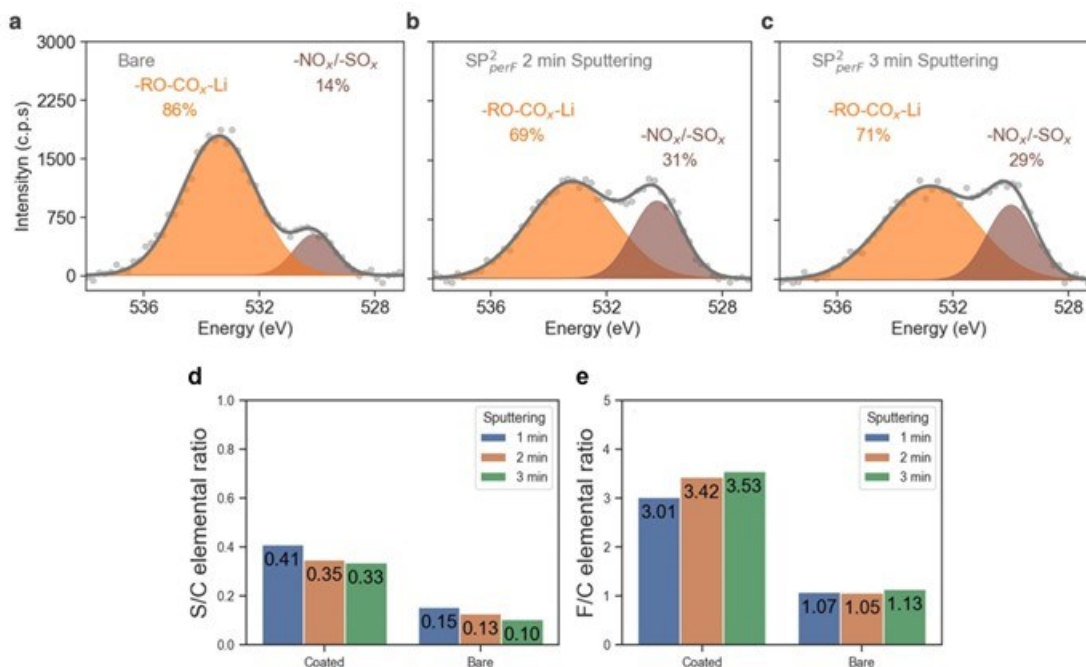


**Figure XII.3.2 (a-c)** The O1s spectra of SEI from 1 M LiTFSI DOL/DME with 1wt% LiNO<sub>3</sub> electrolyte. (a) bare Cu, sputtered for 2 min; (b) SP<sup>2</sup><sub>perF</sub> coated Cu after 2 min of sputtering; (c) SP<sup>2</sup><sub>perF</sub> coated Cu after 3 min of sputtering. (d) The S/C elemental ratio of SEI from 1 M LiTFSI DOL/DME electrolyte at different sputtering time. (e) The F/C elemental ratio of SEI from 1 M LiPF<sub>6</sub> EC/DEC electrolyte at different sputtering time. The Li||Cu cells were cycled at 0.5 mA cm<sup>-2</sup>, 1 mAh cm<sup>-2</sup> for 10 cycles. The samples were rinsed with 200  $\mu$ L DME. The sputtering power was 2 kV  $\mu$ A.

To understand the stability of coating on the electrode surface during cycling, the team constructed an optical Li||Cu cell containing 1 M LiPF<sub>6</sub> EC/DEC with 10% fluoroethylene carbonate (FEC) (Figure XII.3.3a). On the bare Cu electrode, non-uniform and dendritic Li preferentially deposited at the edge of the Cu facing Li (Figure XII.3.3c). This may be because this location has the highest curvature and the most concentrated electric field. In comparison, on the SP<sup>2</sup><sub>perF</sub> coated Cu foil, homogeneous Li deposition was observed across the electrode surface (Figure XII.3.3b). This was attributed to the coating reducing the electric field concentration at the Cu edge due to its dielectric nature. The results above also demonstrated that the coating maintained macroscopic coverage of the surface during Li deposition.



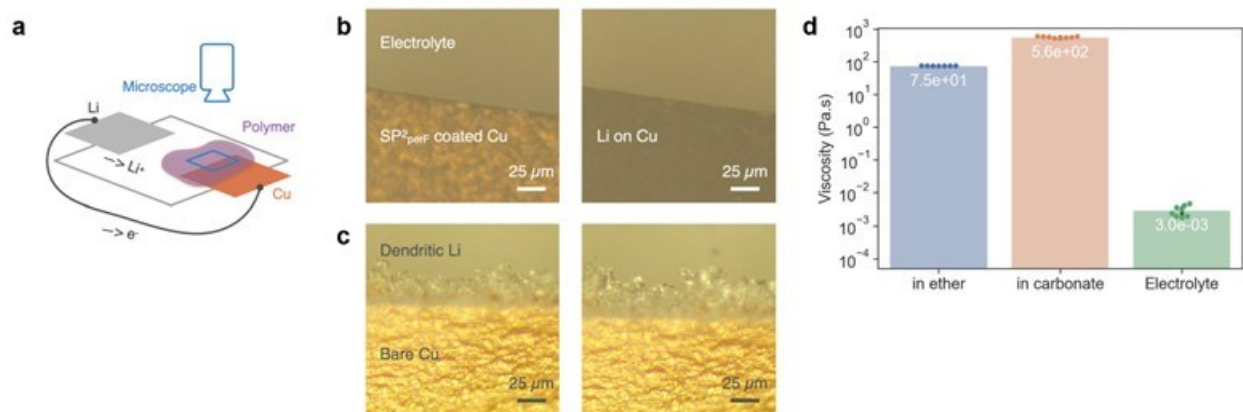


**Figure XII.3.3** (a) Experimental setup for optical cell. Images were taken from the top-down view on the Cu electrode as Li was deposited on it. (b-c) Optical microscope images of Li deposited on Cu at  $0.2 \text{ mA cm}^{-2}$  current density: (b)  $\text{SP}^2_{\text{perF}}$  coated Cu; (c) bare Cu. Scale bar:  $25 \mu\text{m}$ . (d) Steady-state viscosity of  $\text{SP}^2_{\text{perF}}$  soaked in ether ( $1 \text{ M LiTFSI DOL/DME}$  with  $1\text{wt}\%$   $\text{LiNO}_3$ ) and carbonate ( $1 \text{ M LiPF}_6 \text{ EC/DEC}$  with  $10\%$  FEC) electrolytes at room temperature, as well as  $1 \text{ M LiTFSI}$  in DME (labeled as Electrolyte).

To further explain the stable coverage of  $\text{SP}^2_{\text{perF}}$  on electrode during Li plating, the steady-state viscosity of the polymer was measured after soaking it in different electrolytes (Figure XII.3.3d). The viscosity of the soaked polymer complex was 4-5 orders higher than that of the ether solvent, which contributed to the stable coverage of polymer on electrode.

The electrochemical performance of  $\text{SP}^2_{\text{perF}}$  coating was evaluated in various electrolytes: ether ( $1 \text{ M LiTFSI DOL/DME}$  with  $1\text{wt}\%$   $\text{LiNO}_3$ ), carbonate ( $1 \text{ M LiPF}_6 \text{ EC/DEC}$  with  $10\%$  FEC), and FDMB ( $1 \text{ M LiFSI FDMB}$ ). The CE of  $\text{Li}||\text{Cu}$  half cells were improved by  $\text{SP}^2_{\text{perF}}$  in all three electrolytes (Figure XII.3.4a). The Li metal anode stabilization was also observed by the impedance evolution of  $\text{Li}||\text{Li}$  cells (Figure XII.3.4b). For the first 100 hours of resting in open circuit,  $\text{SP}^2_{\text{perF}}$  reduced the impedance increase from  $104\%$  to  $33\%$  in carbonate electrolyte, and from  $153\%$  to  $42\%$  in FDMB electrolyte (Figure XII.3.4c). This demonstrated the capability of  $\text{SP}^2_{\text{perF}}$  to suppress electrolyte degradation.

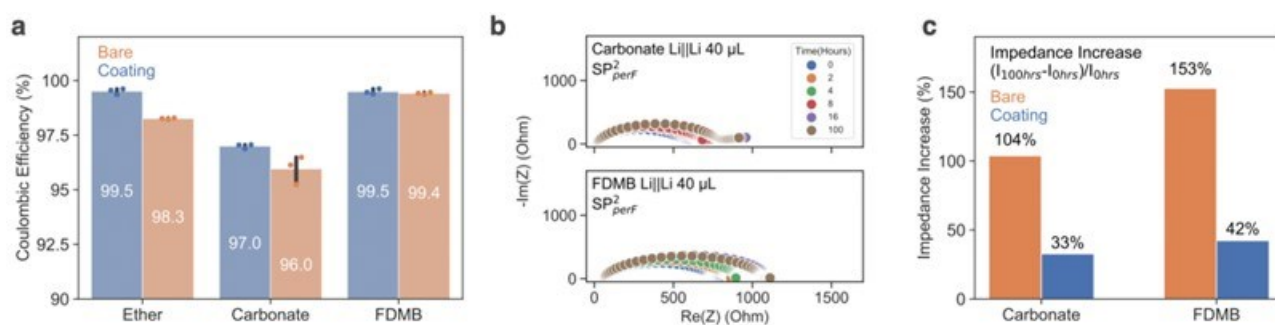


**Figure XII.3.4** Electrochemical characterizations of  $\text{SP}^2_{\text{perF}}$  with different electrolytes. (a) CE measured on coated Cu in  $\text{Li}||\text{Cu}$  cells with  $40 \mu\text{L}$  of ether ( $1 \text{ M LiTFSI DOL/DME}$   $1\text{wt}\%$   $\text{LiNO}_3$ ), carbonate ( $1 \text{ M LiPF}_6 \text{ EC/DEC}$   $10\%$  FEC), or FDMB ( $1 \text{ M LiFSI FDMB}$ ) electrolyte. (b) Electrochemical impedance spectroscopy (EIS) measurement overtime with coated  $\text{Li}||\text{Li}$  symmetric cell in electrolytes. (c) Calculated impedance increase (%) over 100 hours of resting procedure in an open circuit.

The effects of  $\text{SP}^2_{\text{perF}}$  on full-cell performance were evaluated in carbonate electrolyte ( $1 \text{ M LiPF}_6 \text{ EC/DEC}$  with  $10\%$  FEC).  $\text{Li}||\text{NMC811}$  full cells were constructed with high-loading cathodes ( $5 \text{ mAh cm}^{-2}$ ) and limited excess Li ( $50 \mu\text{m}$  thick). Reasonable rate capability was observed (Figure XII.3.5a).  $\text{Li}||\text{NMC811}$  long-term cycling was performed under lean electrolyte ( $3 \text{ g Ah}^{-1}$ ) condition. The  $\text{SP}^2_{\text{perF}}$  coating improved cycle life by 2-4 folds (Figure XII.3.5b-d).

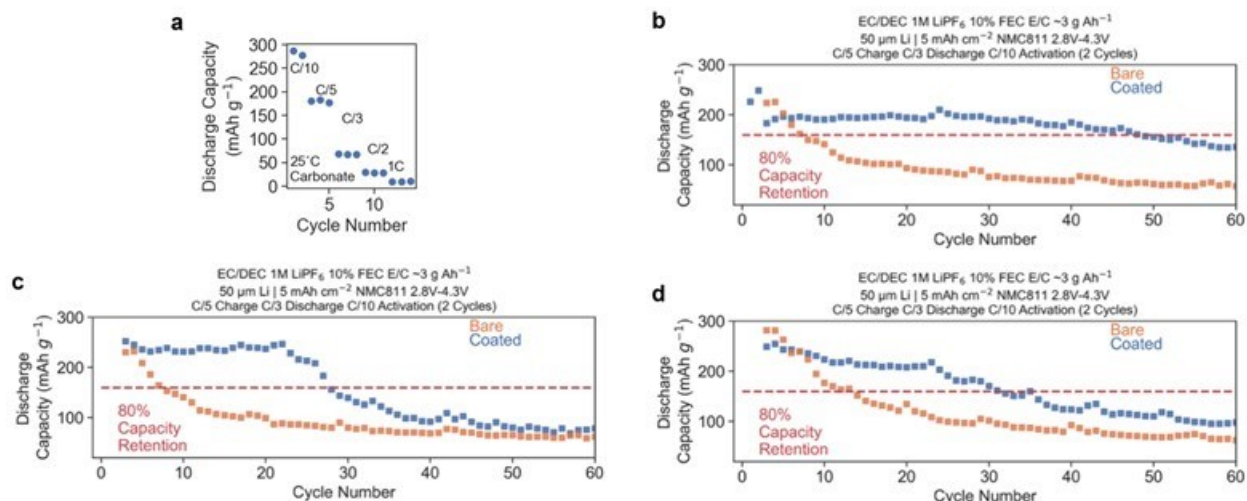


Figure XII.3.5 (a) Rate-capability of Li||NMC811 cells at high cathode loading of 5 mAh cm<sup>-2</sup>. (b-d) Cycling performance of Li||NMC811 coin cells in lean electrolyte condition (3 g Ah<sup>-1</sup>) with and without SP<sup>2</sup><sub>perF</sub> coating. Three repetitions are shown.

The Li||NMC811 full cell performance was further evaluated in FDMB electrolyte. With 2.5 mAh cm<sup>-2</sup> areal capacity, reasonable capacity can be achieved below C/2 (Figure XII.3.6a). Long-term cycling at C/5 charging and C/3 discharging achieved around 400 cycles (till 80% capacity retention) with SP<sup>2</sup><sub>perF</sub>, more than doubling the cycle life of bare electrodes (Figure XII.3.6b). At the 100<sup>th</sup> cycle, the coated sample showed a higher overpotential (Figure XII.3.6c) likely due to the increased mass transport hindrance as a result of the salt-over-solvent selectivity of the coating. Li||NMC811 cells with higher areal capacity (5 mAh cm<sup>-2</sup>) were tested, and a 2-fold increase in cycle life was observed (Figure XII.3.6d).

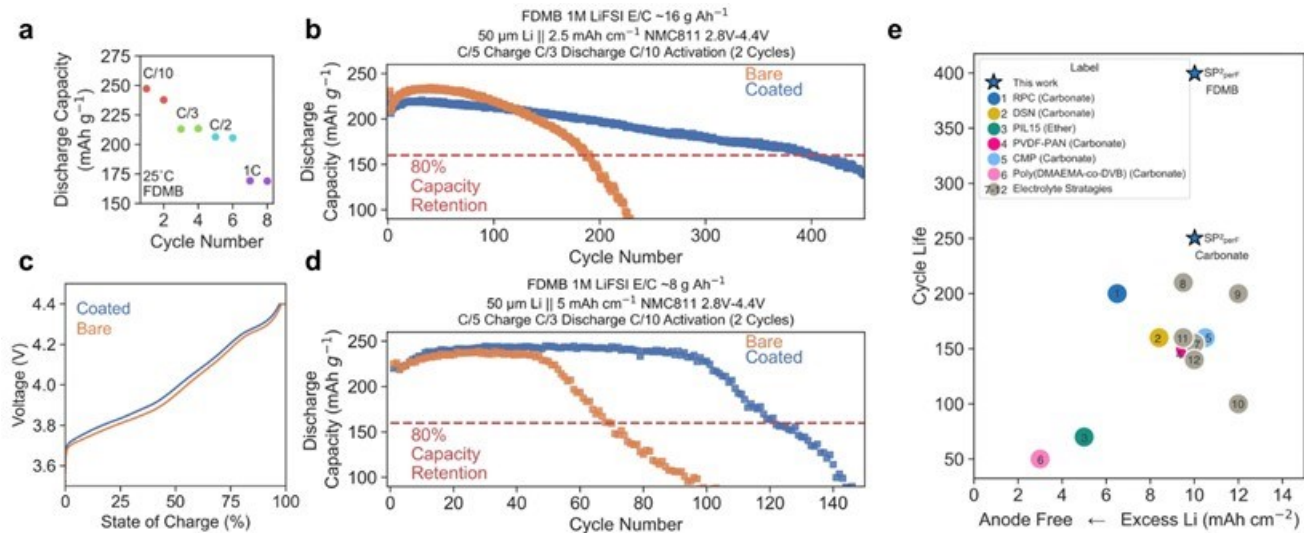


Figure XII.3.6 Cycling of SP<sup>2</sup><sub>perF</sub>-coated Li in Li||NMC811 cells with 1 M LiFSI FDMB electrolyte. (a) Rate capabilities. (b) Long-term cycling with 2.5 mAh cm<sup>-2</sup> positive electrodes. (c) Charging voltage curve at 100<sup>th</sup> cycle at C/5 charging rate. (d) Long-term cycling with 5 mAh cm<sup>-2</sup> electrodes. (e) Cycle life (80% capacity retention) plotted against excess lithium amount. The SP<sup>2</sup><sub>perF</sub> coating is compared with other coatings or electrolyte strategies. The x axis locations of Point 4, 5, 7, 11, and 12 are 10 mAh cm<sup>-2</sup>, and they are offset slightly for visualization.

Overall, the SP<sup>2</sup><sub>perF</sub> polymer design is applicable to various electrolyte chemistries. It showed marked improvement in cell cycle life vs. excess Li amount compared to other state-of-the-art strategies (Figure

XII.3.6e). The salt-philic and solvent-phobic interfacial design promoted the formation of beneficial salt-derived SEI and improved the cycling performance. Through physical interactions, the chemical reactions were tuned at the electrode-electrolyte interface. It is envisioned that the SP<sup>2</sup> design concept can be extended to other polymer chemistries and potentially paired with emerging electrolytes.

## Conclusions

Here we report a salt-philic, solvent-phobic (SP<sup>2</sup>) polymer coating for Li metal electrode that selectively transports salt over solvent and thus promotes salt-derived SEI formation. Unlike previously reported artificial SEIs, this SP<sup>2</sup> coating approach resulted in enhanced cycling performance in several types of solvent, such as ether, carbonate and fluorinated ether. Specifically, the SP<sup>2</sup> coating further enhanced the cycle life of a recently reported high-performance fluorinated ether electrolyte to give a ~400 cycle life (50  $\mu\text{m}$  Li, 2.5 mAh cm<sup>-2</sup> NMC811 and 80% capacity retention). Our coating design concept can be further fine tuned as promising electrolytes become available.

## Key Publications

### Publications

1. David T Boyle, Yuzhang Li, Allen Pei, Rafael A Vilá, Zewen Zhang, Philaphon Sayavong, Mun Sek Kim, William Huang, Hongxia Wang, Yunzhi Liu, Rong Xu, Robert Sinclair, Jian Qin, Zhenan Bao and Yi Cui, "Resolving current-dependent regimes of electroplating mechanisms for fast charging lithium metal anodes," *Nano Letter*, DOI: 10.1021/acs.nanolett.2c02792. Publication date: October 10, 2022.
2. David T Boyle, Sang Cheol Kim, Solomon T Oyakhire, Rafael A Vilá, Zhuojun Huang, Philaphon Sayavong, Jian Qin, Zhenan Bao and Yi Cui, "Correlating kinetics to cyclability reveals thermodynamic origin of lithium anode morphology in liquid electrolytes," *Journal of the American Chemical Society*, DOI: 10.1021/jacs.2c08182. Publication date: November 1, 2022.
3. Zhuojun Huang, Jian-Cheng Lai, Xian Kong, Ivan Rajkovic, Xin Xiao, Hasan Celik, Hongping Yan, Huaxin Gong, Paul E. Rudnicki, Yangju Lin, Yusheng Ye, Yanbin Li, Yuelang Chen, Xin Gao, Yuanwen Jiang, Snehashis Choudhury, Jian Qin, Jeffrey B.-H. Tok, Yi Cui and Zhenan Bao, "A solvent-anchored non-flammable electrolyte," *Matter*, DOI: 10.1016/j.matt.2022.11.003. Publication date: November 30, 2022.
4. Mun Sek Kim, Zewen Zhang, Jingyang Wang, Solomon T. Oyakhire, Sang Cheol Kim, Zhiao Yu, Yuelang Chen, David T. Boyle, Yusheng Ye, Zhuojun Huang, Wenbo Zhang, Rong Xu, Philaphon Sayavong, Stacey F. Bent, Jian Qin, Zhenan Bao and Yi Cui, "Revealing the multifunctions of Li<sub>3</sub>N in the suspension electrolyte for lithium metal batteries," *ACS Nano*, DOI: 10.1021/acsnano.2c12470. Publication date: January 26, 2023.
5. Sang Cheol Kim, Solomon T Oyakhire, Constantine Athanitis, Jingyang Wang, Zewen Zhang, Wenbo Zhang, David T Boyle, Mun Sek Kim, Zhiao Yu, Xin Gao, Tomi Sogade, Esther Wu, Jian Qin, Zhenan Bao, Stacey F Bent and Yi Cui, "Data-driven electrolyte design for lithium metal anodes," *Proceedings of the National Academy of Sciences*, DOI: 10.1073/pnas.2214357120. Publication date: February 27, 2023.
6. Isik Su Buyuker, Ben Pei, Hui Zhou, Xia Cao, Zhiao Yu, Sufu Liu, Weiran Zhang, Wu Xu, Ji-Guang Zhang, Zhenan Bao, Yi Cui, Chunsheng Wang and M Stanley Whittingham, "Voltage and temperature limits of advanced electrolytes for lithium-metal batteries," *ACS Energy Letters*, DOI: 10.1021/acsenerylett.3c00235. Publication date: March 13, 2023.
7. Zhuojun Huang, Jian-Cheng Lai, Sheng-Lun Liao, Zhiao Yu, Yuelang Chen, Weilai Yu, Huaxin Gong, Xin Gao, Yufei Yang, Jian Qin, Yi Cui and Zhenan Bao, "A salt-philic, solvent-phobic interfacial coating design for lithium metal electrodes," *Nature Energy*, DOI: 10.1038/s41560-023-01252-5. Publication date: April 24, 2023.
8. Chibueze V Amanchukwu, Anna B Gunnarsdóttir, Snehashis Choudhury, Tamsin L Newlove, Pieter CMM Magusin, Zhenan Bao and Clare P Grey, "Understanding lithium-ion dynamics in single-ion

- and salt-in-polymer perfluoropolyethers and polyethyleneglycol electrolytes using solid-state NMR,” *Macromolecules*, DOI: 10.1021/acs.macromol.2c02160. Publication date: April 28, 2023.
9. Philaphon Sayavong, Wenbo Zhang, Solomon T Oyakhire, David T Boyle, Yuelang Chen, Sang Cheol Kim, Rafael A Vilá, Sarah E Holmes, Mun Sek Kim, Stacey F Bent, Zhenan Bao and Yi Cui, “Dissolution of the solid electrolyte interphase and its effects on lithium metal anode cyclability,” *Journal of the American Chemical Society*, DOI: 10.1021/jacs.3c03195. Publication date: May 23, 2023.
  10. Elizabeth Zhang, Yuelang Chen, Zhiao Yu, Yi Cui and Zhenan Bao, “Monofluorinated ether electrolyte with acetal backbone for high-performance lithium metal batteries,” arXiv, DOI: 10.48550/arXiv.2305.19580. Publication date: May 31, 2023.
  11. Sang Cheol Kim, Jingyang Wang, Rong Xu, Pu Zhang, Yuelang Chen, Zhuojun Huang, Yufei Yang, Zhiao Yu, Solomon Oyakhire, Wenbo Zhang, Louisa Greenburg, Mun Sek Kim, David Boyle, Philaphon Sayavong, Yusheng Ye, Jian Qin, Zhenan Bao and Yi Cui, “High entropy electrolytes for practical lithium metal batteries,” *Nature Energy*, DOI: 10.1038/s41560-023-01280-1. Publication date: July 6, 2023.
  12. Yangju Lin, Zhiao Yu, Weilai Yu, Sheng-Lun Liao, Zhuojun Huang, Yuelang Chen, Elizabeth Zhang, Jian Qin, Yi Cui and Zhenan Bao, “Impact of fluorination degree of ether-based electrolyte solvent on Li-metal battery performance,” *ChemRxiv*, DOI: 10.26434/chemrxiv-2023-ppgxx. Publication date: July 19, 2023.
  13. Xin Gao, Zhiao Yu, Jingyang Wang, Xueli Zheng, Yusheng Ye, Huaxin Gong, Xin Xiao, Yufei Yang, Yuelang Chen, Sharon E Bone, Louisa C Greenburg, Pu Zhang, Hance Su, Jordan Affeld, Zhenan Bao and Yi Cui, “Electrolytes with moderate lithium polysulfide solubility for high-performance long-calendar-life lithium-sulfur batteries,” *Proceedings of the National Academy of Sciences*, DOI: 10.1073/pnas.2301260120. Publication date: July 24, 2023.
  14. Snehashis Choudhury, Zhuojun Huang, Chibueze V Amanchukwu, Paul E Rudnicki, Yuelang Chen, David Thomas Boyle, Jian Qin, Yi Cui and Zhenan Bao, “Ion conducting polymer interfaces for lithium metal anodes: impact on the electrodeposition kinetics,” *Advanced Energy Materials*, DOI: 10.1002/aenm.202301899. Publication date: July 28, 2023.

### Presentations

1. Zhuojun Huang, Yi Cui, Zhenan Bao, “Designing polymer coatings for Li metal anodes,” International Symposium of Stimuli Responsive Materials, Napa Valley, CA, October 24, 2022.
2. Zhuojun Huang, Yi Cui, Zhenan Bao, “Polymer materials design for Li metal anode,” Electrochemistry Gordon, Santa Barbara, CA, September 10, 2022.
3. Zhuojun Huang, Yi Cui, Zhenan Bao, “Polymer materials design for Li batteries”, International Battery Materials Association, Austin, TX, March 8, 2023.
4. Weilai, Yi Cui, Zhenan Bao, “Understanding the solid-electrolyte interphase (SEI) of Li-metal anode by XPS,” CAMCOR workshop on Advanced Battery Characterization, Eugene, OR, March 8, 2023.
5. Zhuojun Huang, Yi Cui, Zhenan Bao, “Polymer materials design for Li batteries,” International Battery Materials Association, Austin, TX, March 8, 2023.
6. Zhuojun Huang, Yi Cui, Zhenan Bao, “A solvent-anchored non-flammable electrolyte (SAFE),” Materials Research Society, San Francisco, CA, April 12, 2023.
7. Zhuojun Huang, Yi Cui, Zhenan Bao, “A salt-philic solvent-phobic (SP2) interfacial coating design for lithium metal electrodes,” Materials Research Society, San Francisco, CA, April 12, 2023.
8. Zhenan Bao, “Understanding molecular design for stable lithium metal electrolyte interface,” Materials Research Society, San Francisco, CA, April 12, 2023.
9. Yuelang Chen, Yi Cui, Zhenan Bao, “Fast-charging limitations of advanced electrolytes for lithium metal batteries,” Stanford Energy Student Lectures, Stanford, CA, August 21, 2023.



## XII.4 Anode-Free Lithium Batteries (PNNL)

### Ji-Guang Zhang, Principal Investigator

Pacific Northwest National Laboratory  
902 Battelle Boulevard  
Richland, WA 99354  
E-mail: [jiguang.zhang@pnnl.gov](mailto:jiguang.zhang@pnnl.gov)

### Xia Cao, Co-Principal Investigator

Pacific Northwest National Laboratory  
902 Battelle Boulevard  
Richland, WA 99354  
E-mail: [xia.cao@pnnl.gov](mailto:xia.cao@pnnl.gov)

### Tien Duong, DOE Technology Development Manager

U.S. Department of Energy  
E-mail: [Tien.Duong@ee.doe.gov](mailto:Tien.Duong@ee.doe.gov)

Start Date: October 1, 2022

End Date: September 30, 2023

Project Funding (FY23): \$300,000

DOE share: \$300,000

Non-DOE share: \$0

### Project Introduction

Although lithium (Li) ion batteries (LIBs) based on graphite anode and high voltage cathodes has been widely adopted in electrical vehicles (EVs), the state-of-the-art LIBs still cannot satisfy the energy demand for the next generation of EVs. By replacing graphite anode with Li metal anode (LMA), specific energy density of Li metal batteries (LMBs) can increase more than 50% because LMA has a much higher specific capacity ( $3820 \text{ mAh g}^{-1}$ ) than that of graphite ( $372 \text{ mAh g}^{-1}$ ).<sup>1</sup> To further increase the energy density of Li batteries, the concept of “anode-free” Li batteries (AFLBs) has been explored. An as-assembled or fully discharged AFLB consists of a Li-containing cathode and an anode current collector (such as copper (Cu)).<sup>2</sup> All Li source is stored in cathode. This cell design not only increases energy density of the battery, but also improves the safety of the battery because there is no Li metal present in the battery in its as-assembled or discharged state. Neudecker et al. first demonstrated the feasibility of this concept in solid state thin film batteries based on LiPON electrolyte.<sup>3</sup> Adams and Zhang et al. demonstrated the feasibility of AFLB in coin-cells with non-aqueous liquid electrolytes.<sup>2</sup> However, many significant barriers (such as fast capacity fade, first cycle loss etc) still need to be overcome before the practical application of AFLBs. In addition, new approaches developed in AFLBs can also be applied to LMBs to accelerate their market penetration. Therefore, there is an urgent need to have a better understanding on the factors that affect the performance of AFLBs and develop new approaches to improve their cycle life and safety.

### Objectives

The main objective of this project is to explore the feasibility of anode-free lithium batteries (AFLBs) for high-energy-density energy storage systems. In this project, we will investigate the main factors affecting the performance of AFLBs and identify the solutions to enable long-term cycling and safety of these batteries. The Li dendrite suppressing principles and strategies for both liquid and solid-state AFLBs, including materials design (electrolytes, cathodes, current collectors), cell fabrication, and operation controls will be investigated to enable a high CE of AFLB to be above 99.7% and maximize the cycling stability of the AFLBs. Because of the many similarities among AFLBs, Li-metal batteries, and Li-ion batteries, experiences and approaches developed for AFLBs may also be applied to Li-metal and Li-ion batteries, thus accelerating the market penetration of other Li-based rechargeable batteries.

## Approaches

1. Investigate the effect of pressure value and its uniformity on the morphology/uniformity of deposited Li film and solid electrolyte interphase (SEI) during cycling of AFLBs.
2. Develop localized high concentration electrolytes (LHCEs) to improve the thermal stability of AFLB pouch cells.
3. Develop advanced artificial protective layers on Cu substrate.

## Results

### *Effect of the pressure distribution on Li deposition/SEI formation in AFLB coin-cells*

For the anode-free batteries, the uniform/dense lithium (Li) deposition is critical for long-term cycling stability of their operations. Thus, the effect of internal pressure on lithium (Li) deposition was investigated using 2032-coin cells. It is found that the morphology of the deposited Li layer is very sensitive to the internal pressures (controlled by the number and thickness of stainless spacers (SSS) where 1t represent 1 mm thick spacer) applied on the copper (Cu) (Figure XII.4.1a). The uniformity/density of Li deposition and associated SEI quality vary significant under different internal pressures controlled by the total thickness of spacers as shown in Figure XII.4.1b. The thickness of Li layers deposited on the Cu electrode decreases with increasing pressure (which is proportional to the thickness of the spacers) as shown in Figure XII.4.1c. The cell at optimized pressure (with 2 mm thick spacer (SSS–2t)) shows the best cycling stability with a capacity retention of 72% after 100 cycles, while cells with lower internal pressures (with 1mm (SSS–1t) or 1.5 mm (SSS–1.5t) thick spacers) exhibit faster capacity decays. It is also found that the cell with too high a pressure (with 3 mm thick spacer (SSS–3t)) without a buffer from spring leads to unstable cycling and early cell failure after ~ 40 cycles (Figure XII.4.1g) because too high an internal pressure may lead to mechanical/physical failure of the cell components (including separator) in the coin-cells. After Li is fully stripped from anode in the first cycle, EDX mapping (see Figure XII.4.1d-f) is used to examine the coverage of SEI layers on the Cu substrate under different cell pressures. Figure XII.4.1e shows that no Cu can be detected on the anode cycled under high pressures (SSS–2t and SSS – 3t). This means the Li deposited at these conditions can fully cover Cu substrate and the residual SEI layer after Li stripping can still fully cover Cu substrate. On the other hand, significant amount of Cu can be detected on the anode of the cells under smaller pressure (SSS–1t and SSS–1.5t) after Li is fully stripped. This indicates a non-uniform coverage of Li deposition at relatively low pressures. The SEI layer formed under optimized pressure of SSS–2t exhibits the highest sulfur element content of 36% (which is derived from the salt decomposition shown in Figure XII.4.1h) and leads to the best cycling stability of AFLBs as shown in Figure XII.4.1g.

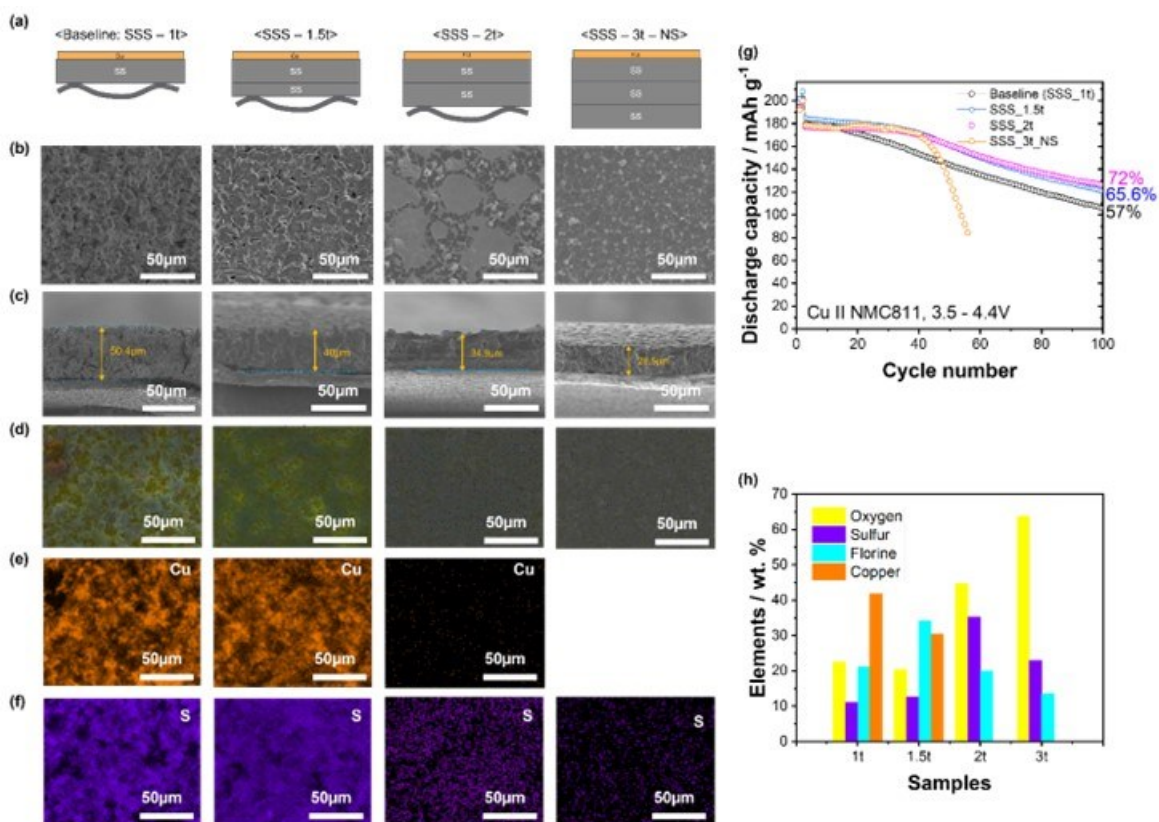


**Figure XII.4.1** (a) Schematic illustration for the internal pressure effect on density and uniformity of the lithium layer deposited on copper (Cu) electrode in 2032 coin-cells. Corresponding SEM images (b) for the top (c) and cross-sectional views of the Cu electrodes after the 1<sup>st</sup> Li deposition to 4.5V and EDS mappings for SEIs (d) all elements and (e) Cu element and (f) S element after 1<sup>st</sup> cycle Li deposition and stripping. (g) Cycling performance of NMC811||Cu cells with different internal pressures cycled between 3.5V – 4.4V. (h) Quantified elements distribution in SEIs formed at different internal pressures.

The stabilities of as-formed initial SEI layers under different internal pressures in the Cu||NMC811 anode-free coin cells (AFCs) were investigated by scanning electron spectroscopy (SEM) and X-ray photoelectron spectroscopy (XPS) with Ar sputtering after 1<sup>st</sup> charge (Li was deposited on the Cu substrate and covered by SEI layer) and discharge processes (Li stripped from deposited Li film and a residual SEI layer left on Cu substrate). The uniformity and stability of the solid electrolyte interphase (SEI) layers remained on Cu current collector after the 1<sup>st</sup> Li stripping are significantly dependent on the internal pressures of cells as illustrated in Figure XII.4.2a. Figure XII.4.2b shows the mapping of oxygen-containing species in the samples (area: 400 $\mu$ m \* 400 $\mu$ m) from AFCs with a spacer thickness of 1 mm (1t, shown in the left side of Figure XII.4.2b) and 2 mm (2t, shown in the right side of Figure XII.4.2b) after 5 minutes of sputtering. In the sample retrieved from AFC-2t cell, both Li<sub>2</sub>O and Li<sub>2</sub>CO<sub>3</sub> are uniformly distributed with lower concentrations (indicating a thinner SEI film) compared to the sample from AFC-1t cell. The Li 1s spectra of AFC-1t and AFC-2t samples are shown in Figure XII.4.2c and d, respectively. The top and bottom panels in Figure XII.4.2c and d are the XPS-spectra taken before and after 5 min sputtering, respectively. Compared to the AFC-1t electrode, the AFC-2t electrode shows significantly higher amount of Li after sputtering, (Figure XII.4.2c and d). These XPS results indicate that a thinner and more uniform SEI layer is formed under a higher internal pressure. The mechanical stability of the SEI layers was also examined by longer time sputtering up to 20 min before and after the Li stripping from the Cu current collectors. The XPS depth profiles shown in Figure XII.4.2e and f are obtained on the sample AFC-1t and AFC-2t, respectively, where the solid symbol and open symbol represent the data collected after first charge (Li deposited on Cu substrate) and after first discharge (Li stripped from Cu substrate).



Figure XII.4.2f shows that the atomic percentages of different components in SEI layers formed in the AFC-2t cell are similar before (solid symbol) and after Li stripping (open symbol), while those formed in the AFC-1t cell shows a significant change before and after Li stripping as shown in Figure XII.4.2e. These results indicate that the porous SEI layer (see Figure XII.4.2a) formed under lower pressure is much less stable than the film-like dense SEI layer (see Figure XII.4.2b) formed under higher pressure. The higher internal pressure contributes to the formation of a uniform and stable initial 2D SEI layer which in turn minimizes the surface area and reduces surface reactions. This is consistent with the better cycling stability of AFLBs with higher internal pressure as shown in Figure XII.4.1g.

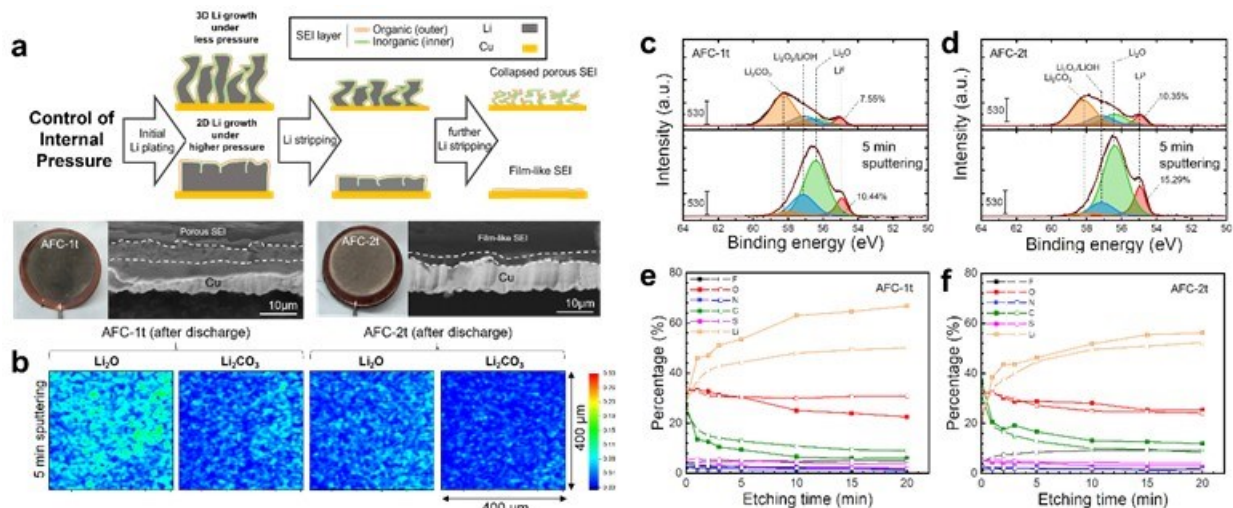
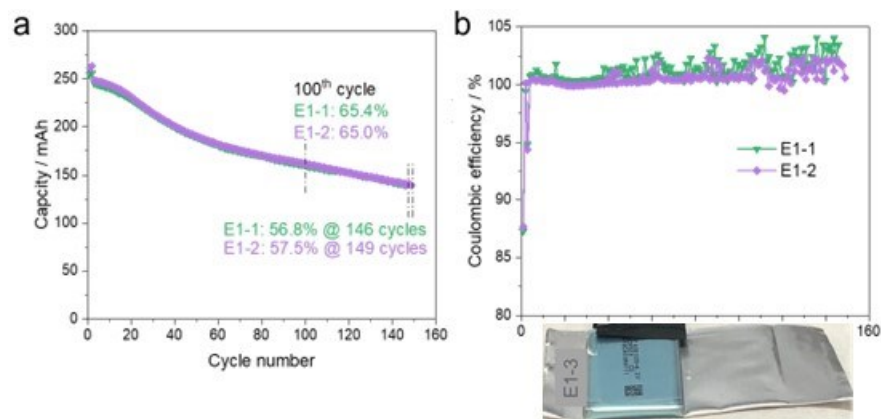


Figure XII.4.2 (a) Schematic illustration of the SEI formation depending on the different morphologies of the initial metallic Li deposited on the Cu current collectors under the different internal pressures, digital photographs, and SEM images of Li/SEI layers on Cu substrates formed after 1st cycle. (b) XPS mappings of peak components (Li<sub>2</sub>O and Li<sub>2</sub>CO<sub>3</sub>), fitted XPS Li 1s spectra of the SEI layers formed on the Li depositions on the Cu substrate collected from Cu || NMC811 cells (c: AFC-1t and d: AFC-2t) and depth profiles of the elements (e: AFC-1t and f: AFC-2t, solid: after charge and empty: after discharge) in the SEI layers formed after the 1st formation cycle (at C/10, 3.5-4.5V).

#### Improve thermal stability of AFLB pouch cells with localized high concentration electrolyte (LHCE)

The thermal stability of AFLBs was investigated in multilayer pouch cells with a newly developed localized high concentration electrolyte (LHCE) (named E1 in this report). The dry cells (Cu||NMC532, 250 mAh) were acquired from Li-Fun Technology Co. LTD, and filled with LHCE electrolyte (E1) in a dry room and sealed in PNNL. As shown in Figure XII.4.3a, the capacity retention of the AFLB pouch cells after 100 cycles were 65.4% and 65.0% respectively for two parallel cells, and were reduced to 56.8% after 146 cycles for cell 1 and 57.5% after 149 cycles for cell 2. Figure XII.4.3b shows the Coulombic efficiency (CE) of the two cells, with an initial CE of 87.5%. There was no apparent gas release in both cells after about 150 cycles as shown in the insert of Figure XII.4.3.



**Figure XII.4.3** Cycling performance, (a) capacity and (b) Coulombic efficiency of the 250 mAh Cu|NMC532 pouch cells with E1 electrolyte cycled between 3.5V – 4.4V at C/10 charge and C/3 discharge after 2 formation cycles at C/10. The insert in (b) shows the image of the cell after cycling.

After cycling, the thermal stability of the AFLB cells with E1 electrolyte was evaluated by nail penetration test in fully charged condition by EIC Laboratory (Norwood, MA). As shown in Figure XII.4.4a and Figure XII.4.4e, the cycled cells were first charged to 4.4 V before the nail penetration test. During the nail penetration test, an infrared camera was used to monitor the temperature change of the cells. As shown in Figure XII.4.4b and Figure XII.4.4f, the temperatures of the cell E1-1 and E1-2 before nail penetration were 19.1 and 19.5 °C, respectively. The maximum temperature of the cell E1-1 and E1-2 were 89.1 and 84.2 °C, respectively after nail penetration. The temperature started to decrease in ~ 3 min and reached room temperature in about 30 minutes. No apparent changes were observed between the cells after nail penetration (see Figure XII.4.4d and Figure XII.4.4h) and before nail penetration (see Figure XII.4.4b). Thermal stability of AFLB cells with E1 electrolyte in other operating conditions will be further evaluated.

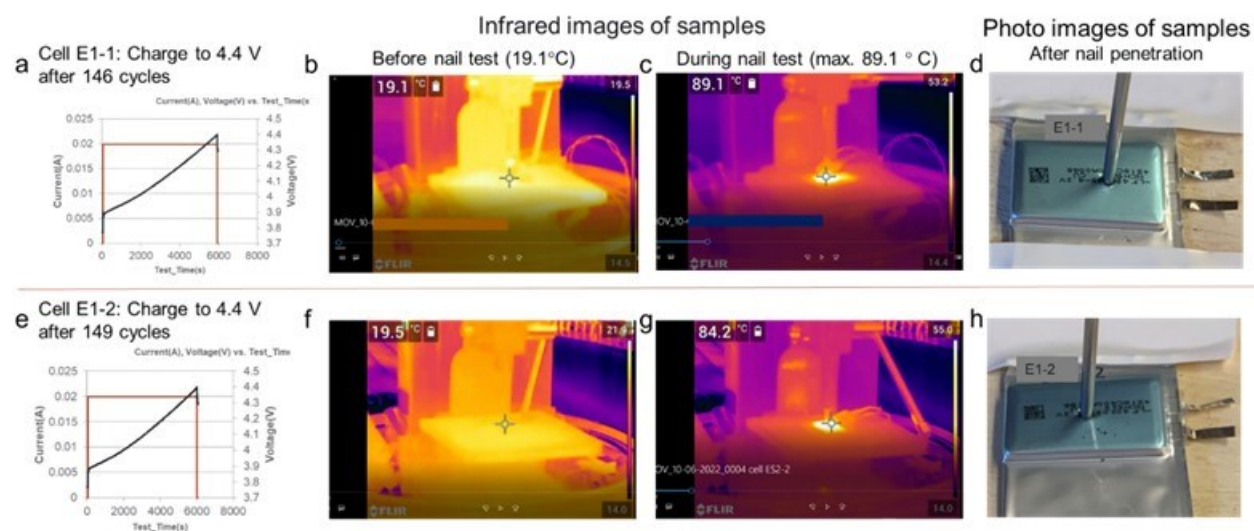


**Figure XII.4.4** Nail penetration of the 250 mAh Cu|NMC532 cells at full charged state after 146 cycles for E1-1 and 149 cycles for E1-2, (a, e) charge voltage profile before nail penetration, snapshots of the infrared images for the cells (b, f) before nail penetration and (c, g) after nail penetration when the maximum temperatures were reached. (d, h) photos of the cells after nail penetration.

### Develop new protection layer on Cu current collector to improve cycling stability of AFLBs

To further improve the performance of AFLBs, we have developed floatable protection layers (FPLs) on the Cu current collector using a facile method. Several groups have reported different protection layers before. However, most of these protection layers are only effective in the early stage of Li deposition. These protection layers are often quickly broken after a few cycles and most Li will be deposited on the top of the protection layer in the subsequent cycles. The FPLs developed in this work has good mechanical stability to tolerate repeated cycling. More importantly, the binding between these FPLs and Cu substrate can be easily tuned to optimized value which is stronger enough to enable an intimate contact with Li to enable good protection, but also weak enough to allow Li to be deposited underneath the FPL under the desired pressure. Figure XII.4.5a illustrate the deposition of Li with FPL coatings under different pressures. Figure XII.4.5b1 and b2 shows the photo image of a FPL layer (black) coated Cu substrate used in coin-cell before and after initial Li deposition, respectively. The white part in the center and black dots along the edge of the deposited Li film indicate the region where Li deposited on the top and bottom of protection layer, respectively. Figure XII.4.5b3 shows the pressure distribution inside of coin-cell measured by pressure sensitive films. The non-uniform pressure distribution observed in Figure XII.4.5b3 can be attributed to the spring used in coin-cells (see Figure XII.4.1a). Comparing Figure XII.4.5b2 and 3, it is found that Li was deposited underneath of FPL layer at higher pressure. In contrast, Li was deposited on the top of FPL layer at lower pressure region. To enable more Li to be deposited underneath of FPL, a pouch cell configuration with more uniform pressure control is required and will be further investigated. The scanning electron microscope (SEM) images in Figure XII.4.5c (1 and 2) shows the top views of Li deposited on FPL-Cu substrate and retrieved from an FPL-Cu||NMC811 cell after initial Li deposition under low pressures (1) and high pressure (2). Figure XII.4.5c2 clearly shows that FPL can be easily detached from Cu surface after Li deposition at high pressure. Figure XII.4.5c3 and c4 show that Li was deposited on the top of the FCL at low pressure region (3) while deposited underneath of FPL at higher pressure (4). The FPL-Cu||NMC811 cell exhibits significantly improved cycling stability (80% of capacity retention in 100 cycles) with more stable Coulombic efficiency (CE) compared with those of the baseline cells (with un-coated Cu anode current collector), as demonstrated in Figure XII.4.5d and Figure XII.4.5e.

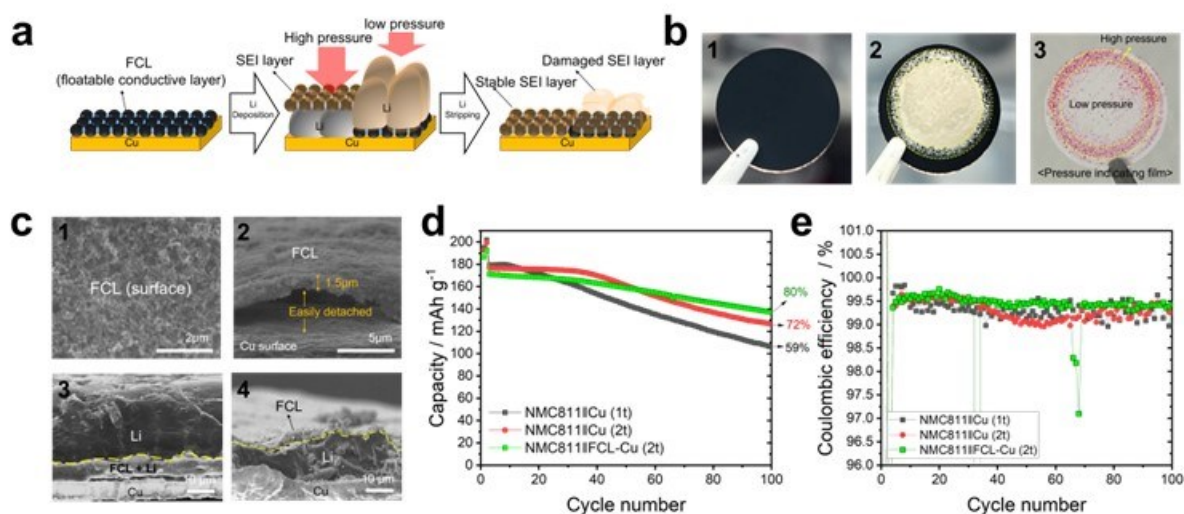


Figure XII.4.5 (a) Schematic illustration of the floatable protective layer (FPL) coated on Cu current collector for the uniform Li deposition and stable SEI layer under high internal pressures, digital photographs of (b1) FPL coated Cu, (b2) after 1<sup>st</sup> Li deposition and (b3) the pressure domain on the pressure indicating film, and SEM images of (c1) the surface of FPL layer, (c2) cross-sectional images of detachable FPL from Cu current collector, after Li deposition under (c3) high and (c4) low internal pressures, respectively. (d) Cycling stabilities of Cu || NMC811 cells with pristine Cu under different pressures (1t and 2t), and FCL coated Cu (2t) and their (e) Coulombic efficiency at C/10 in the cut-off voltage range of 3.5-4.4V after two formation cycles in 3.5-4.5V.

## Conclusions

- Pressure effect on Li deposition and AFLB performance is investigated using a LHCE electrolyte in Cu||NMC811 cells. The pressure of the cells was tuned by using different thickness of spacers. The best capacity retention (72% at 100<sup>th</sup> cycle) were obtained when 2mm thick spacers was used in the coin cells. A uniform and complete SEI layer was obtained under the optimized pressure, which can minimize continuous loss of active Li loss and electrolyte depletion.
- Thermal stability of the multilayer pouch Cu||NMC532 cells (250 mAh) was improved by a newly developed LHCE electrolyte (E1). After ~ 140 cycles fully charged cells can still pass the nail penetration test. The maximum temperatures of the two parallel cells were 89.4 and 84.2°C during nail penetration as monitored by infrared camera.
- A stable and uniform SEI layer was obtained under the optimized internal pressure. Non-porous film-like SEI layer exhibits a stable mechanical stability even after Li stripping, while a porous SEI layer formed under low pressure was broken down.
- A floatable protective layer (FPL) with a weak adhesion to Cu surface was developed which allows the Li to deposited underneath FPL layer at high internal pressure. Large Li particles formed under FPL layer can minimize surface area of Li and improve the long-term cycling stability of AFLBs. The properties of FPL will be further improved in the next year.

## Key Publications

### Publications/Presentations

1. “Improving Cycling Performance of Anode-Free Lithium Batteries by Pressure and Voltage Control,” Hyung-Seok Lim, Dan Thien Nguyen, Joshua A Lochlala, Xia Cao, Ji-Guang Zhang. ACS Energy Letters, under revision.
2. “Improving Cycling Performance of Anode-Free Lithium Batteries by Pressure Control,” Lim H., D. Nguyen, W. Xu, X. Cao, and J. Zhang. 05/30/2023. Presented by H. Lim at 243rd ECS Meeting, May 2023, Boston, MA

## References

1. J. Liu, Z. Bao, Y. Cui, E. J. Dufek, J. B. Goodenough, P. Khalifah, Q. Li, B. Y. Liaw, P. Liu, A. Manthiram, Y. S. Meng, V. R. Subramanian, M. F. Toney, V. V. Viswanathan, M. S. Whittingham, J. Xiao, W. Xu, J. Yang, X.-Q. Yang and J.-G. Zhang, Nature Energy, 2019, 4, 180-186.
2. J. Qian, B. D. Adams, J. Zheng, W. Xu, W. A. Henderson, J. Wang, M. E. Bowden, S. Xu, J. Hu and J.-G. Zhang, Advanced Functional Materials, 2016, 26, 7094-7102.
3. B. J. Neudecker, N. J. Dudney and J. B. Bates, Journal of The Electrochemical Society, 2000, 147, 517.
4. C. Niu, D. Liu, J. A. Lochala, C. S. Anderson, X. Cao, M. E. Gross, W. Xu, J.-G. Zhang, M. S. Whittingham, J. Xiao and J. Liu, Nature Energy, 2021, 6, 723-732.

## Acknowledgements

Key contributor: Hyung-Seok Lim.

## XIII Beyond Li-ion R&D: Solid-State Batteries

Lithium-ion batteries have made tremendous progress in the last two decades and are now instrumental in creating worldwide demand for electric vehicle (EVs), but the liquid organic electrolyte in lithium-ion battery cells is highly reactive and flammable. There is growing interest in the use of solid lithium-ion conducting materials in place of the liquid electrolyte. Solid electrolyte materials are non-flammable, and they not only allow more robust cell operation but also the integration of metal-based anodes needed to achieve VTO's aggressive cost, energy density, and cycle life targets. Solid electrolyte materials face challenges, however, including low conductivity, poor voltage stability, and inadequate mechanical properties. VTO research in this area attempts to overcome these challenges by research of new solid electrolytes that can address materials challenges and enable next-generation chemistries, complementary diagnostics, and modeling techniques to ensure materials development progress.

The rest of this chapter contains detailed reports on the status of the following individual projects.

- Lithium Dendrite-Free Solid Electrolytes for High Energy Lithium Batteries (University of Maryland, College Park)
- Development of Thin, Robust, Lithium-Impenetrable, High-Conductivity, Electrochemically Stable, Scalable, and Low-Cost Glassy Solid Electrolytes for Solid-State Lithium Batteries (Iowa State University)
- Molecular Ionic Composites: A New Class of Polymer Electrolytes to Enable All Solid-State and High Voltage Lithium Batteries (Virginia Polytechnic Institute and State University)
- Hot Pressing of Reinforced All-solid-state Batteries with Sulfide Glass Electrolyte (General Motors LLC)
- Developing Materials for High-Energy-Density Solid State Lithium-Sulfur Batteries (Penn State University, University Park)
- Fundamental Understanding of Interfacial Phenomena in Solid-State Batteries (General Motors)
- Multidimensional Diagnostics of the Interface Evolutions in Solid-State Lithium Batteries (University of Houston)
- First-Principles Modeling of Cluster-Based Solid Electrolytes (Virginia Commonwealth University)
- Predictive Engineering of Interfaces and Cathodes for High-Performance All Solid-State Lithium-Sulfur Batteries (University of Louisville)
- Enabling Continuous Production of Defect-free, Ultrathin Sulfide Glass Electrolytes for Next Generation Solid-state Lithium Metal Batteries (ANL)
- Stable Solid-State Electrolyte and Interface for High-Energy All-Solid-State Lithium-Sulfur Battery (PNNL)
- Scale-Up of Novel Li-Conducting Halide Solid State Battery Electrolyte (LBNL)
- Low-Pressure All Solid State Cells (NREL)
- 3D Printing of All-Solid-State Lithium Batteries (LLNL)
- Substituted Argyrodite Solid Electrolytes and High-Capacity Conversion Cathodes for All-Solid-State Batteries (Oak Ridge National Laboratory)
- Multifunctional Gradient Coatings for Scalable, High-Energy-Density Sulfide-Based Solid-State Batteries (ANL)
- Thick Selenium-Sulfur Cathode Supported Ultra-thin Sulfide Electrolytes for High-energy All-solid-state Lithium Metal Batteries (ANL)
- Synthesis of Composite Electrolytes with Integrated Interface Design (ANL)
- Polymer Electrolytes for Stable Low Impedance Solid State Battery Interfaces (ORNL)
- Inorganic-Polymer-Composite Electrolyte with Architecture Design for Lithium Metal Solid State Batteries (BNL)
- Ion-Conductive High Li<sup>+</sup> Transference Number Polymer Composites for Solid-State Batteries (LBNL)

- Precision Control of the Li Surface for Solid-state Batteries (Oak Ridge National Laboratory)
- Lithium Halide-Based Superionic Solid Electrolytes and High-Voltage Cathode Interfaces (ANL)
- Polyester-Based Block Copolymer Electrolytes for Lithium-Metal Batteries (University of California, Berkeley)
- Development of All Solid-State Battery using Anti-Perovskite Electrolytes (ANL)
- High-Conductivity and Electrochemically Stable Lithium Thioborate Solid-State Electrolytes for Practical All-Solid-State Batteries (SLAC/Stanford University)
- Solid state batteries with long cycle life and high energy density through materials design and integration (LBNL).

## XIII.1 Lithium Dendrite-Free Solid Electrolytes for High Energy Lithium Batteries (University of Maryland, College Park)

### Chunsheng Wang, Principal Investigator

University of Maryland, College Park  
 Room 3236 Jeong H. Kim Engineering Building  
 College Park, MD 20742  
 E-mail: [cswang@umd.edu](mailto:cswang@umd.edu)

### Tien Duong, DOE Technology Development Manager

U.S. Department of Energy  
 E-mail: [Tien.Duong@ee.doe.gov](mailto:Tien.Duong@ee.doe.gov)

Start Date: October 1, 2019

End Date: December 30, 2022

Project Funding: \$1,250,000

DOE share: \$1,000,000

Non-DOE share: \$250,000

### Project Introduction

The development of all solid-state Li metal batteries (ASSLBs) using nonflammable inorganic or organic solid-state electrolytes (SSEs) was reckoned as the promising direction due to their enhanced safety and high energy density. However, lithium dendrite growth during charge/discharge cycles still limits the use of all solid-state batteries.

In our project, a criterion for lithium dendrite suppression that is developed through systematical investigation on thermodynamics and kinetics of lithium dendrite growth was proposed to guide the SSE design and Li/SSE interface modification.  $\text{Li}_7\text{N}_2\text{I-LiOH}$  and  $\text{Li}_3\text{YCl}_6$  solid electrolyte with high ionic conductivity and low electronic conductivity was used to validate the criterion for lithium dendrite suppression and achieve the project objective. Different surface modifications were also explored to enhance the dendrite suppression capability of SSEs.

### Objectives

The objective of this project is to research, develop, and test Li-metal-based batteries that implement solid Li-ion conductors (LICs) equipped with  $\text{Li}_7\text{N}_2\text{I-LiOH}$  SSE capable of achieving cell performance of 350 Wh/Kg energy density for 1000 cycle life with a cost of  $\leq$  \$100/kWh. To achieve these, the team will 1) establish the relationship among interface energy, lithium plating/stripping overpotential, interface resistance, SSE stability with lithium, and critical current density (CCD). 2) The dendrite suppression criterion will be developed based on the relationship. 3) The dendrite suppression capability for the  $\text{Li}_7\text{N}_2\text{I-LiOH}$  pellet will be evaluated by testing the CCD. 4) The  $\text{Li}_7\text{N}_2\text{I-LiOH}$  electrolytes and  $\text{Li}_7\text{N}_2\text{I-LiOH/Li}_3\text{YCl}_6$  bi-layer electrolytes will be used to validate the developed dendrite suppression criterion and support Nickel Manganese Cobalt oxides (NCM) cathodes. 5) New engineering methods would be developed to suppress the Li dendrite to realize ASSLB.

### Approach

Li metal surface will be engineered with the interface to suppress dendrite growth and maintain cycling stability. Thin-film solid electrolyte will be fabricated from solid electrolyte with modified particle size and polymer binder. A high energy density solid-state battery will be assembled by combining Li modification, thin-film solid electrolyte and thick and stable positive electrode.

### Results

#### ***Modeling the Li plating and stripping behaviours in the interlayer with different lithiophobicity.***

Lithiophobicity of the interlayer significantly changes the Li growth from Li anode and nucleation inside the interlayer. Interlayers with different lithiophobicity exert different capillary forces on protruded Li. To analyze the influence of lithiophobicity on Li penetration, Li penetration into a cylindrical shape pore was modeled as

Figure XIII.1.1a-b by phase field methods. Li easily fills the conical shape surface flaw if the interlayer is lithiophilic (Figure XIII.1.1a). In contrast, Li penetration into conical shape surface flaw is self-limited in lithiophobic interlayer (Figure XIII.1.1b). Lithiophobicity of the interlayer significantly also changes the Li nucleation inside the interlayer. Li nucleation rate in mixed conductive interlayer was determined based on classical nucleation theory. As can be seen from Figure XIII.1.1c, the nucleation rate is a function of overpotential. When the overpotential reaches a certain value, the nucleation rate suddenly rises. The overpotential where observable nucleation occurs is defined as the critical nucleation overpotential  $\eta_c$ . The lithiophobicity of the interlayers, which was indicated by the contact angle of Li on the substrate, influences the critical nucleation overpotential  $\eta_c$ . Increasing the lithiophobicity of the interlayer can suppress the Li nucleation. For interlayer with a contact angle of  $60^\circ$ , the Li nucleation occurs with overpotential  $> 0.5$  V and Li nucleation only occurs in the region close to Li anode (inserted). Further increasing the contact angle to  $120^\circ$  increase the overpotential to  $\sim 0.9$  V in a small channel. Therefore, the lithiophobicity of the interlayer is a vital parameter to control Li nucleation and achieve stable plating.

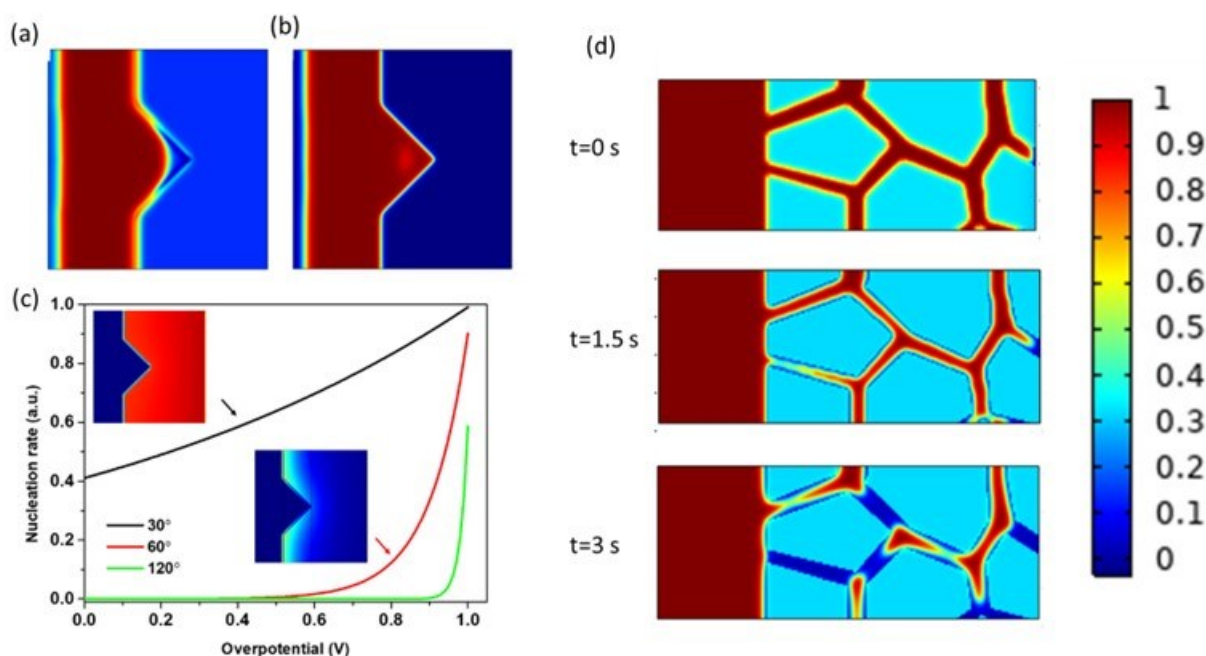


**Figure XIII.1.1** Phase field simulations of Li penetration into interlayer with different lithiophobicity. Li growth on a simplified conical shape surface flaw of the (a) lithiophobic interlayer and (b) lithiophilic interlayer. (c) Nucleation rate as a function of overpotential at electrolyte with different contact angle against Li. The inserted figure shows the simulated Li nucleation rate distribution in the corresponding interlayer. (d) Li stripping from porous interlayer at 0, 1.5 and 3 s.

Li stripping from the porous interlayer was also studied with phase field methods. Figure XIII.1.1d shows the Li stripping from the porous interlayer. To simulate Li stripping, the electrolyte channels are first filled with Li. The stripping was initiated by setting the potential as 0.1 mV. As we can see, the stripping behavior is quite non-uniform. From 0 – 1.5 s, Li stripping is concentrated on the bottom left region and right region. The fast stripping at the bottom left region is due to a smaller channel, which can provide more intimate contact. The right region also stripped fast, which can be explained by the short diffusion length to the counter electrode. When Li stripping continued from 1.5 – 3 s, some part of Li is isolated from current collect due to non-uniform stripping. Due to loss of contact with current collector, those Li cannot be stripped anymore. This is so called “dead lithium”, which will cause low efficiency in ASSB. Therefore, dead lithium is a critical issue for porous interlayer. Designing a mixed ionic and electronic conductive interlayer can solve this problem.



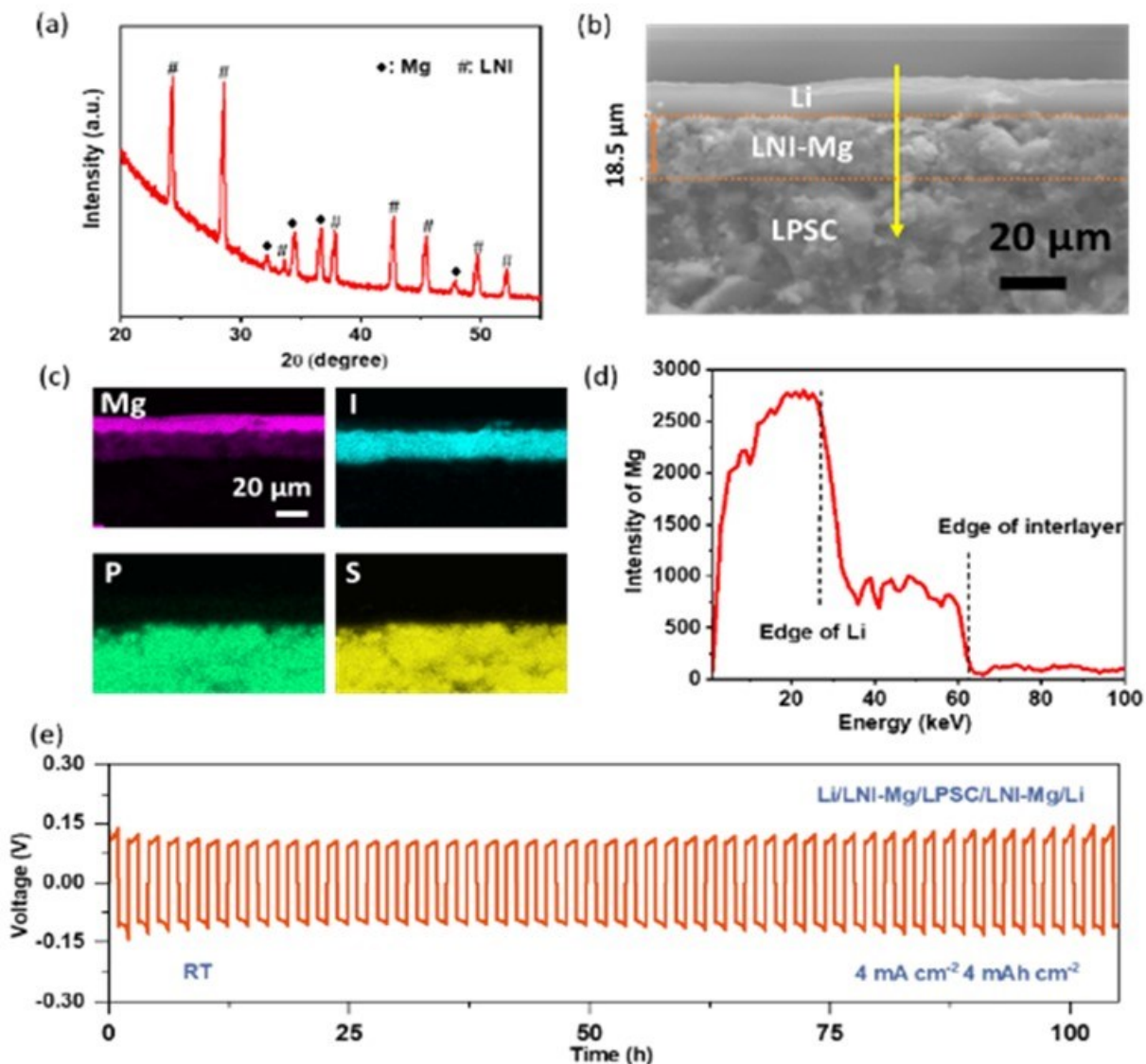


Figure XIII.1.2 (a) XRD of LNI-25%Mg powder. (b) SEM, (c) EDS mapping and (d) Mg element line scan of activated Li/LNI/Mg interface in Li/LNI-Mg/LPSC/Li cells. The thickness of the LNI-Mg interlayer is 18.5  $\mu\text{m}$ . The Mg element line scan in (d) is captured along the yellow line of Figure (b). (e) Galvanostatic cycling of Li/LPSC/Li cells sandwiched with LNI-25% Mg composite at constant current densities/capacity of  $4\text{mA cm}^{-2} / 4\text{mAh cm}^{-2}$  at 25  $^{\circ}\text{C}$ .

#### **Designing a thin $\text{Li}_7\text{N}_2\text{l-Mg}$ interlayer with gradient electronic conductivity.**

Reducing the thickness of the interlayer is important to increase the energy density of batteries for their practical applications. We fabricate a new type of interlayer that has gradient electronic conductivity between Li and solid electrolyte. This strategy can reduce the interlayer thickness, and increase the cell energy density and Li dendrite suppression capability.

LNI-Mg was prepared by ball-milling the LNI electrolyte and 25 wt% of Mg metal gently. The ball milling process does not change the main phase structure of LNI and Mg. As we can see from Figure XIII.1.2 a, in XRD pattern of milled LNI-Mg, all the peaks can be assigned to LNI and Mg and no extra peak was observed. To assemble Li/LNI-Mg/LPSC/LNI-Mg/Li batteries, 3 mg of LNI-Mg was spread on each side of LPSC electrolyte, pressed at 180 MPa and then attached Li on each side. The batteries were heated at 60  $^{\circ}\text{C}$  for 12 h.

The LNI-Mg interlayer after activation was characterized. The SEM image (Figure XIII.1.2b) shows that the thickness of the LNI-Mg interlayer is 18.5  $\mu\text{m}$ , which is much thinner than the 90  $\mu\text{m}$  LNI-5%CNT interlayer. EDS mapping (Figure XIII.1.2c) shows that in the LNI-25%Mg interlayer Mg element diffuses to the Li anode side after activation at 60  $^{\circ}\text{C}$  for 12 hours, while I, P and S elements stay at their original position. To observe the Mg distribution in the interlayer more clearly, the line scan of the Mg element (Figure XIII.1.2d) was conducted along the yellow line of Figure XIII.1.2b. A high Mg intensity of 2500 was detected in the Li anode, suggesting the diffusion of Mg from interlayer to anode. In the interlayer, the Mg signal gradually decreases from the Li anode side to the solid electrolyte side. At the interface of the interlayer/SSE boundary, Mg intensity becomes nearly 0. Therefore, most Mg diffuses towards the Li anode side. The remaining Mg in the interlayer spontaneously forms an Mg concentration gradient (Figure XIII.1.2d), which generates a gradient of electronic conductivity. Briefly, by activating the Li/LPSC/Li cell with LNI-25%Mg interlayer, a gradient electronic conductive LNI-Mg interlayer was formed in situ. The Li dendrite suppression capability of the 18.5  $\mu\text{m}$  gradient electronic conductive LNI-Mg interlayer was evaluated. As we can see from Figure XIII.1.2, The Li/LPSC/Li symmetric cell with activated 18.5  $\mu\text{m}$  LNI-Mg interlayer cycle at 4  $\text{mA cm}^{-2}$  with a capacity of 4  $\text{mAh cm}^{-2}$  for more than 100 hours at room temperature without short circuit (Figure XIII.1.2e). This performance is much better than CCD of 1.4  $\text{mA cm}^{-2}$  / 1.4  $\text{mAh cm}^{-2}$  for 14.8  $\mu\text{m}$  LNI-5%CNT interlayer.

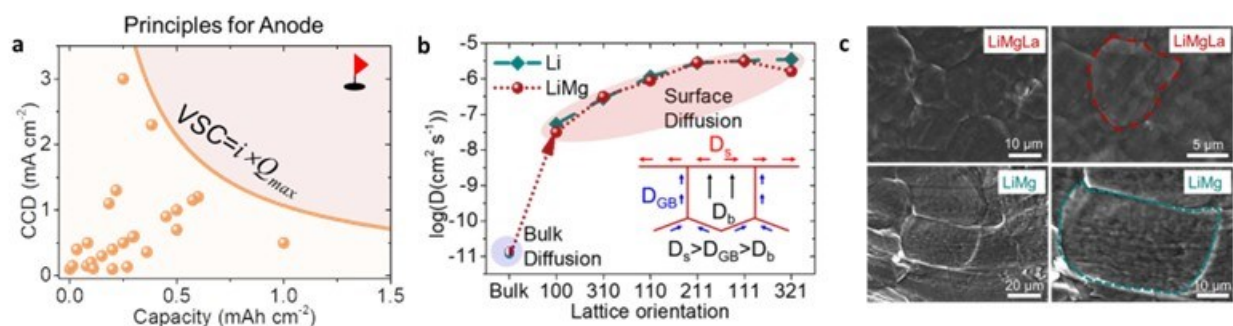


**Figure XIII.1.3** (a) The predicted upper limit of CCD (orange line) and reported CCDs (orange scatters) as a function of capacity. The red target on the top right represents a target of high rate and high energy density ASSLMB. (b) Molecular dynamics-calculated diffusion coefficients of bulk and differently oriented surfaces for Li metal and LiMg alloy at room temperature. The inset scheme illustrates different diffusion mechanisms. (c) SEM showing the grain distributions and sizes of the LiMgLa and LiMg alloys.

**Void suppression capability (VSC) is defined to analyze the void evolution mechanism.**

For a Li|SSE interface without the formation of voids, the ideal situation of stable stripping-plating process is that the mass-transfer controlled overpotential ( $\eta$ ) increases slowly and remains smaller than the critical overpotential (COP) of the SSE. However, with voids formation, the voids at Li|SSE interface reduce the effective contact area at the interface and partially block lithium paths into the SSE, making the mass-transfer controlled overpotential ( $\eta$ ) increase rapidly with the lithium stripping time. For the subsequent lithium plating process, the initial overpotential may be larger than the COP of an SSE (less stable against lithium) due to the formed voids, driving lithium dendrite formation and propagation. It should be noted that even for an ideal dendrite-free electrolyte with a high COP, the high interface overpotential due to the formed void will finally block the charge/discharge process. Here, we define Void suppression capability (VSC) as the product of the applied current ( $i$ ) and full depletion capacity ( $Q_{max}$ ), which is related to the production of Li diffusivity ( $D_{eff}$ ) and initial concentration. Since the effective diffusion coefficient and initial lithium concentration for the anode are the intrinsic properties of the anode, the VSC should be a constant for certain lithium metal or alloy anodes. The relative void suppression capability (RVSC) is obtained by defining the VSC of Li metal as 1.

To simultaneously reach the goal of fast charging and high energy density (star in Figure XIII.1.3a), the VSC should be raised by improving  $c_0$  at the interface and  $D_{eff}$  of the anode. The lithium diffusion coefficients of the bulk and surfaces with different orientations for Li and LiMg are calculated via molecular dynamics (Figure

XIII.1.3b). LiMg and Li show close diffusion coefficients for both bulk and surface cases because of the low ratio of Mg and the same lattice type. The bulk LiMg shows a similar diffusion coefficient of  $1.4 \times 10^{-11} \text{ cm}^2 \cdot \text{s}^{-1}$  to that of bulk Li ( $1.1 \times 10^{-11} \text{ cm}^2 \cdot \text{s}^{-1}$ ). The calculated diffusion coefficients of LiMg are consistent with the measured  $D_{\text{eff}}$  ( $3.42 \times 10^{-11} \text{ cm}^2 \cdot \text{s}^{-1}$ ) obtained by experimental data. However, the surface diffusion coefficients of Li and LiMg are over 3 magnitudes higher than those in the bulk. LiMgLa anodes have a higher specific surface and grain boundary area than Li and LiMg, enabling faster Li diffusion because of the higher defect concentration at surfaces and grain boundaries. Here, we use Mg-La as excellent inoculant for lithium crystallization, which results in a reduced grain size, from approximately  $40 \mu\text{m}$  for Li-Mg alloy to around 5-10 for Li-Mg-La alloy (Figure XIII.1.3c).

#### ***Li-Mg-La alloy anode was developed to suppress void formation in SSBs.***

For a Li|SSE interface without the formation of voids, the ideal situation of stable stripping-plating process is that the Li-Mg-La alloy has good wettability with LLZTO as shown in Figure XIII.1.4a. In the SEM image (Figure XIII.1.4b), LiMgLa has intimate contact with LLZTO due to good wettability. To assess the quality of the interface between these alloy anodes and the LLZTO solid-state electrolyte, we conducted electrochemical impedance spectroscopy (EIS) measurements. As shown in Figure XIII.1.4c, the bulk resistance of LLZTO was determined to be approximately  $155 \Omega \cdot \text{cm}^2$  and the interface resistances of LiMg, LiLa, and LiMgLa alloy anodes to LLZTO were fall within the range of  $20\text{-}35 \Omega \cdot \text{cm}^2$ . We further investigated the lithium stripping behavior of symmetric cells equipped with different electrodes (LiMg, LiLa, and LiMgLa) at a constant current density of  $1.0 \text{ mA} \cdot \text{cm}^{-2}$ , as illustrated in Figure XIII.1.4d. The voltage profiles displayed stable plateaus at small capacity and showed a sharp increase at the end of the lithium stripping process. The voltage rise is attributed to the detachment of anodes from LLZTO solid electrolyte due to the formation of voids at LLZTO/anode interface. The symmetric cells with LiMgLa electrodes have ten times higher stripping capacity ( $4.0 \text{ mAh} \cdot \text{cm}^{-2}$ ) before voltage rise comparing with that with Li electrodes ( $0.4 \text{ mAh} \cdot \text{cm}^{-2}$ ) at the same stripping current ( $1.0 \text{ mA} \cdot \text{cm}^{-2}$ ). This suggests a substantial improvement in the VSC with LiMgLa electrodes. We further optimized the ratio of magnesium and lanthanum in LiMgLa to maximize the VSC. We first fix the ratio of Mg to La but change the doping amount of Mg-La. For the  $\text{Li}_{95}(\text{Mg-La})_5$  anodes (Figure XIII.1.4e), the composite with a Mg/La ratio of 97/3 leads to a high stripped capacity above  $1.5 \text{ mAh} \cdot \text{cm}^{-2}$  at a current density of  $1 \text{ mA} \cdot \text{cm}^{-2}$ . Then we adjust the ratios of magnesium to lanthanum, while keeping the total amount of Mg-La constant. When the Mg/La weight ratio is fixed, the VSC of  $\text{Li}_{97.5}(\text{Mg-La})_{2.5}$  anodes consistently outperform that of  $\text{Li}_{95}(\text{Mg-La})_5$  anodes. Specifically, the  $\text{Li}_{97.5}(\text{Mg-La})_{2.5}$  anodes can deliver a stripped capacity of  $> 3 \text{ mAh} \cdot \text{cm}^{-2}$  at a current density of  $1 \text{ mA} \cdot \text{cm}^{-2}$ . In Figure 2f, we can see the voltage profiles of LiMgLa anodes at various current densities, with a cutoff voltage of 5.0 V. The LiMgLa anodes demonstrate a significantly higher depletion capacity compared to LiMg anodes at the same current density. LiMgLa anodes consistently outperform LiMg anodes in terms of full depletion time at various current densities. For the LiMgLa anodes (Figure XIII.1.4f), it can deliver a capacity over 1.5, 3.5 and  $6 \text{ mAh} \cdot \text{cm}^{-2}$  at the current densities of 2, 1 and  $0.1 \text{ mA} \cdot \text{cm}^{-2}$ , respectively. We further evaluated the cycling performance of the LiMgLa anode at  $0.8 \text{ mA} \cdot \text{cm}^{-2}$  and from 0.25 to  $1.0 \text{ mA} \cdot \text{cm}^{-2}$  (Figure XIII.1.4g-h). A stable cycling of  $0.8 \text{ mAh} \cdot \text{cm}^{-2}$  and  $0.4 \text{ mAh} \cdot \text{cm}^{-2}$  can be realized over 200 hours, which corresponds to a VSC of 0.32. Furthermore, when the current increased to  $1 \text{ mA} \cdot \text{cm}^{-2}$ , the LiMgLa symmetric cell exhibited stable cycling over 100 hours, corresponding to a VSC of 0.5, which is much closer to the simulation result of 0.83. This confirms a significant improvement of VSC for the LiMgLa anodes.

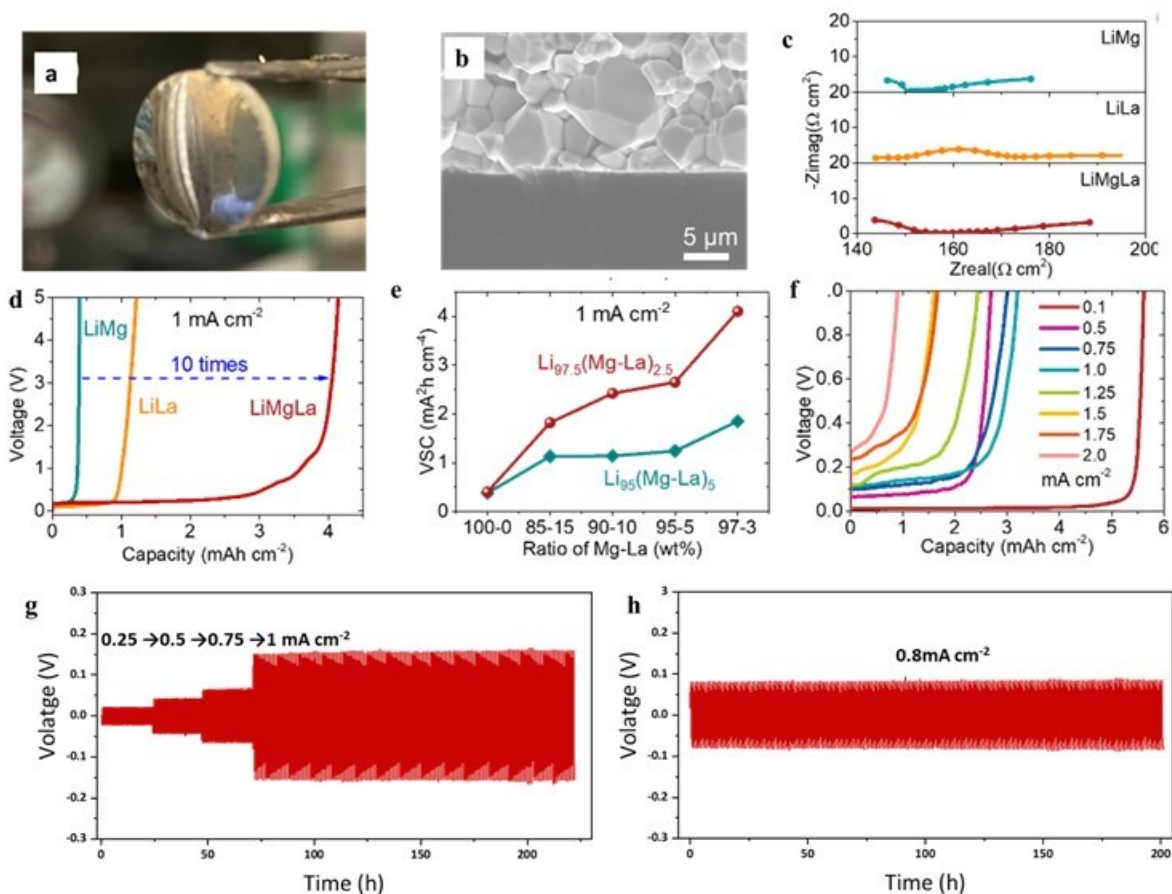


Figure XIII.1.4 (a) Digital pictures of the wettability of molten Li-Mg-La against LLZTO pellets. (b) Scanning electronic microscope (SEM) images for the cross-section of the LiMgLa|LLZTO interface before cycling at different scales, showing decent contact. (c) Electrochemical impedance spectra of anode/LLZTO/anode symmetric cells with LiMgLa, LiLa, and LiMg anodes from 1 MHz to 0.1 without an external pressure at room temperature. (d) Delivered maximum capacity of LiMgLa, LiLa, and LiMg anodes during stripping at a current density of 1.0 mA·cm<sup>-2</sup> with a voltage cut-off of 5.0 V. (e) VSC of LiMgLa anodes with different compositions during stripping at a current density of 1.0 mA·cm<sup>-2</sup>. (g, h) Galvanostatic cycling of the LiMgLa|LLZTO|LiMgLa symmetric cell at various current densities at room temperature.

#### High-performance cathode was designed for thin-film solid-state batteries.

To achieve the energy density target of 350 Wh/kg and cycle life of 1000 cycles, LiNi<sub>0.8</sub>Co<sub>0.1</sub>Mn<sub>0.1</sub>O<sub>2</sub> (NCM811) is employed as the cathode active material because of its high specific capacity. The particle size of NCM811 significantly affects the performance of the solid-state batteries. Two sizes of NCM811 (5 μm and 10 μm, denoted as SNCM811 and LNCM811) were explored. NCM811 was synthesized using a hydroxide coprecipitation method. LNCM811 is the product after coprecipitation for 15 hours while SNCM811 is obtained from coprecipitation for a shorter time. For both kinds of cells, the SSB was cycled at 0.1 C for the first 3 cycles and then cycled at 0.33 C, as depicted in Figure XIII.1.5a-b. The first cycle charge/discharge capacity of two sizes NCM811 are 216.6/168.8 mAh g<sup>-1</sup> and 232.6/187.8 mAh g<sup>-1</sup> at 0.1 C, respectively. The increased ICE and initial specific capacities can be attributed to the better interfacial contact between SE and SNCM811 particles than that between SE and LNCM811. When cycled at 0.33 C from the fourth cycle, the capacity of SSB with SNCM811 dropped from 156.8 to 142.7 mAh g<sup>-1</sup> after 40 cycles, while that with LNCM811 dropped from 135.1 to 109.9 mAh g<sup>-1</sup>. The capacity retentions for SNCM811 and LNCM811 are 91.0 % and 81.3 %, respectively. All these results demonstrate that the utilization of small particle size NCM811 is a good choice to achieve a high energy density and long cycle life for SSB.

To achieve the final goal of 350 Wh/kg, the battery structure needs further to be modified. The thickness of the electrolyte membrane which occupied the most weight ratio of the whole battery needs to be reduced. Here, we successfully fabricated a thin film electrolyte composed of LPSCl electrolyte and NBR binder. The thickness of the thin film can be less than 100  $\mu\text{m}$  by controlling the weight amount of the powder. To evaluate the electrochemical performance, the SE film was tested in the Li symmetric cell. The cell tested at 0.2  $\text{mA cm}^{-2}$  (Figure XIII.1.5c) exhibited stable cycle performance over 100 hours, indicating the stability of SE film with Li. The inset cross-sectional image shows the intimate contact between SE film and Li. Then the SE film was further evaluated in the full cell with a structure of Li|SE|NMC/SE (Figure XIII.1.5d). The cells cycled at 0.1, 0.15 and 0.2 C show a capacity of about 153, 135 and 107  $\text{mAh g}^{-1}$  (Figure XIII.1.5e), respectively. The cell cycled at 0.1 afterward decreased from 153 to 142  $\text{mAh g}^{-1}$  after 50 cycles. These results demonstrated the feasibility of using NBR and LPSCl to fabricate thin film electrolytes for high energy density. The electrochemical performance of the SE film can be further improved by reducing the thickness, incorporating high conductive SE particles and using Li salt to enhance the Li mobility in the polymer binders.

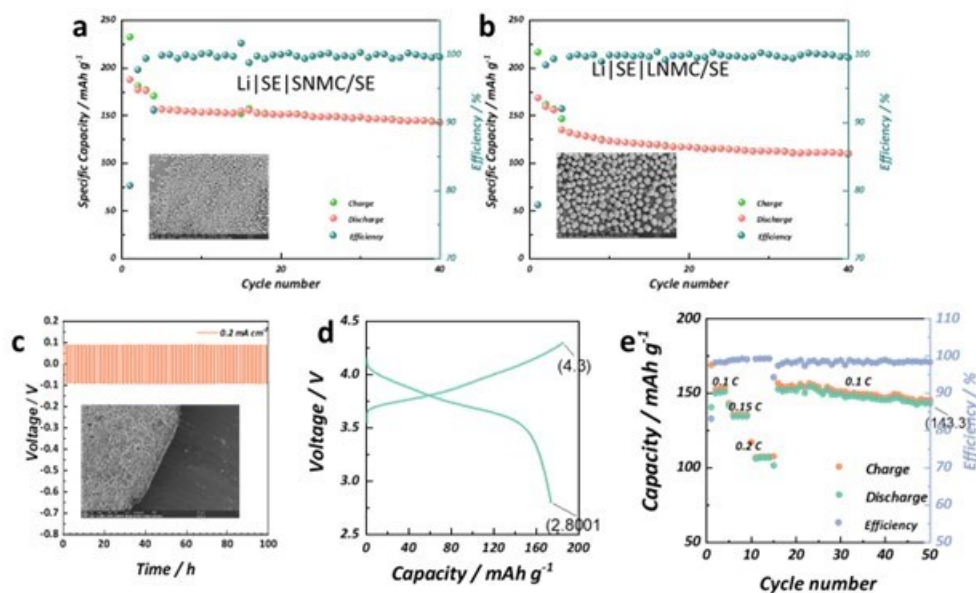


Figure XIII.1.5 Cycle performance of the all-solid-state Li metal cells with (a) Small ( $\sim 5 \mu\text{m}$ ) and (b) large ( $10\sim 15 \mu\text{m}$ ) NMC811 particles. Inset are SEM images with corresponding NMC811 particles. (c) Cycling curves of the Li symmetric cell using thin film electrolyte. Inset is the cross-sectional image of the interface between Li and SE. (d) Charge and discharge curve of the SSB with thin film electrolyte at 0.1 C and (e) corresponding cycling performance.

## Conclusions

1. The impact of lithiophobicity to Li plating and striping in the porous interlayer was simulated. It was found that increasing the lithiophobicity of the interlayer is essential to promote Li striping/plating cycling stability. Li tends to grow into or nucleate inside the interlayer if the interlayer is lithiophilic interlayer. However, Li plating and striping are self-limited in the porous lithiophobic interlayer.
2. The concept of interlayer with gradient electronic conductivity was proposed to reduce interlayer thickness and improve Li dendrite suppression capability. LNI-25%Mg interlayer was prepared and formed interlayer with gradient electronic conductivity. A stable cycling of Li/LPSC/Li cell with LNI-25%Mg interlayer at a current density of 4  $\text{mA/cm}^2$  at a fixed capacity of 4.0  $\text{mAh/cm}^2$  was achieved.
3. The concept of void suppression capability was proposed to evaluate the performance of Li anode. The design principle of refining grain size to boost the Li diffusivity, which is experimentally realized by the use of Mg-La inoculant into Li to form small size ( $\sim 5\mu\text{m}$ ) grain. The designed Li-Mg-La anode

outperforms both Li and Li-Mg alloy anode, which delivered a high stripped capacity over 4 mAh/cm<sup>2</sup> at 0.1 mA/cm<sup>2</sup>. The Li symmetric cell with Li-Mg-La anode showed stable cycling at 0.8 mA/cm<sup>2</sup>.

4. Different NMC size was explored to improve the coulombic efficiency and cycle life. Solid-state battery with 5 μm size NCM811 cathode can deliver 91.0 % capacity retention after 40 cycles at 0.33 C. Further utilization of NBR polymer enabled the fabrication of thin film electrolyte (<100 μm). The solid-state battery with such film electrolyte can cycle stably at 0.1 C over 50 cycles.

### Key Publications

1. Hongli Wan, Zeyi Wang, Weiran Zhang, Xinzi He, Chunsheng Wang, Interface design for all-solid-state lithium batteries. *Nature*, **2023**.
2. Hongli Wan, Zeyi Wang, Sufu Liu, Tao Deng, Xinzi He, Weiran Zhang, Chunsheng Wang, Critical Interphase Overpotential as a Lithium Dendrite Suppression Criterion for All-Solid-State Lithium Battery Design. *Nat. Energy*, **2023**, 8, 473-481.
3. Zeyi Wang, J. Xia et al. Lithium Anode Interlayer Design for All-Solid-State Lithium-Metal Batteries. *Nat. Energy*. (Accepted: Nov. 2023)
4. Xiao Ji, Xinzi He, Chi Chen, Singyuk Hou, Jijian Xu, Bao Zhang, Yunjun Ruan, Jiaxun Zhang, Tao Deng, Ji Chen, Chunsheng Wang, Void Suppressive Lithium Anodes for All-Solid-State Batteries, *Nature Materials*. (Under Revision)
5. X. He, X. Ji, B. Zhang, N. Rodrigo, S. Hou, K. Gaskell, T. Deng, H. Wan, S. Liu, J. Xu, B. Nan, B. Lucht, C. Wang, Tuning interface lithiophobicity for lithium metal solid-state batteries, *ACS Energy Lett.*, **2022**, 7 131-139.
6. T. Deng, X. Ji, L. Zou, O. Chiekezi, X. Fan, L. Cao, T. R. Adebisi, H. Chang, H. Wang, B. Li, X. Li, C. Wang, D. Reed, J.-G. Zhang, V. Sprenkle, C. Wang, X. Lu, Interfacial engineering enabled practical low-temperature sodium metal battery, *Nat. Nanotechnol.*, **2022**, 17, 269-277.
7. H. Wan, B. Zhang, S. Liu, J. Zhang, X. Yao, C. Wang, Understanding LiI-LiBr Catalyst Activity for Solid State Li<sub>2</sub>S/S Reactions in an All-Solid-State Lithium Battery, *Nano Lett.* **2021**, 21, 8488-8494.
8. H. Wan, S. Liu, T. Deng, J. Xu, J. Zhang, X. He, X. Ji, X. Yao, C. Wang, Bifunctional Interphase-Enabled Li<sub>10</sub>GeP<sub>2</sub>S<sub>12</sub> Electrolytes for Lithium-Sulfur Battery, *ACS Energy Lett.*, **2021**, 6, 862-868.
9. X. Ji, S. Hou, P-F. Wang, X. He, N. Piao, X. Fan, C. Wang, Solid-State Electrolyte Design for Lithium Dendrite Suppression, *Adv. Mater.* **2020**, 2002741.

### Acknowledgements

We acknowledge the financial support from the Department of Energy (DOE) under Award number DEEE0008856.

## XIII.2 Development of Thin, Robust, Lithium-Impenetrable, High-Conductivity, Electrochemically Stable, Scalable, and Low-Cost Glassy Solid Electrolytes for Solid-State Lithium Batteries (Iowa State University)

### Steve W. Martin, Principal Investigator

Iowa State University  
528 Bissell Rd  
Ames, IA, 50011-1096  
E-mail: [swmartin@iastate.edu](mailto:swmartin@iastate.edu)

### Tien Duong, DOE Technology Development Manager

U.S. Department of Energy  
E-mail: [Tien.Duong@ee.doe.gov](mailto:Tien.Duong@ee.doe.gov)

Start Date: October 1, 2019	End Date: September 30, 2023	
Project Funding: \$431,154	DOE share: \$344,710	Non-DOE share: \$86,444

### Project Introduction

The development of thin, < 50 microns, mixed oxy-sulfide-nitride (MOSN) mixed glass former (MGF) glassy solid electrolyte (GSE) films that yield superior performance in a safer, lower-cost, and Li-dendrite impenetrable form will be used to develop new solid-state lithium batteries (SSLBs). It is expected that high rate and long cycle life SSLBs can be achieved using thin-film MOSN GSEs. The new GSEs in SSLBs are anticipated to increase the energy density (anode basis) from ~ 300 mAh/g to ~ 4,000 mAh/g, enabling replacement of internal combustion engines in both light and heavy-duty vehicles. Each 20% reduction in the ~ 1.6 billion liters of gasoline used per day in the United States would reduce CO<sub>2</sub> emissions by ~ 4 billion kg CO<sub>2</sub> per day. The team will also increase scientific and engineering knowledge of thin-film GSEs in SSLBs.

### Objectives

The objective of this project is to develop new high Li<sup>+</sup>-conducting MOSN GSE thin-films, < 50µm, that are impermeable to lithium dendrites, scalable through low-cost glass manufacturing, chemically and electrochemically stable, and will enable low-cost, high-energy-density SSLBs. It is expected that the SSLBs constructed from these new MGF MOSN GSEs will meet and exceed all program objectives: useable specific energy @ C/3 ≥ 350 Wh/kg, calendar life 15 years, cycle life (C/3 deep discharge with < 20% energy fade) 1,000, and cost ≤ \$100/kWh.

### Approach

The MOSN MGF GSEs studied in previous work has been further characterized to determine not only the electrochemical properties, but also the viscosity and crystallization behavior in order to best ascertain the best candidate glass composition for thin film drawing. New compositions were explored to increase the resistance to crystallization and improve electrochemical behavior. Small batches were quality tested and cast into a large preform and drawing conditions have started to be optimized to generate thin films for use at the cell level.

### Results

#### *Compositional optimization and characterization of MOSN MGF GSEs:*

Several glass compositions have been studied in the past year of the project. The previously determined best glass composition for thin film drawing based on electrochemical measurements and thermal properties is the ISU-6 composition in the Li<sub>2</sub>S – SiS<sub>2</sub> – LiPO<sub>3</sub> phase space. This glass composition has demonstrated a high conductivity near 10<sup>-3</sup> S/cm, good stability against lithium metal at both oxidizing and reducing potentials, and stable cycling at low current densities. Additionally, this glass presents a high working range (difference

between the crystallization temperature ( $T_c$ ) and glass transition temperature ( $T_g$ ) greater than  $100^\circ\text{C}$ ) and modest resistance to crystallization. Last fiscal year, a new method was used to determine the crystallization resistance of this glass and its sulfide and MOSN analogues, where  $\text{LiPO}_3$  is replaced with  $\text{LiPS}_3$  or  $\text{LiPON}$  respectively. Of these glasses, the MOS ISU-6 showed the best resistance to crystallization.

Several other glass chemistries have been studied, particularly to best understand the impact of the lithium dopants such as  $\text{LiPO}_3$ ,  $\text{LiPON}$ , and  $\text{Li}_x\text{SiO}_y$  on thermal and electrical properties. One of the most promising systems is the  $\text{Li}_2\text{S} - \text{SiS}_2 - \text{Li}_{3.48}\text{SiO}_{3.74}$  system. The glasses synthesized are shown on the pseudo-ternary phase diagram in Figure XIII.2.1. Some of the glasses in this system show working ranges of more than  $150^\circ\text{C}$ , conductivities of nearly  $0.9\text{ mS/cm}$ , and viscosity and crystallization behaviors that are more promising than even the ISU-6 composition. These glasses are still being studied to determine which composition presents the best properties for scaling up into a preform for thin film drawing.

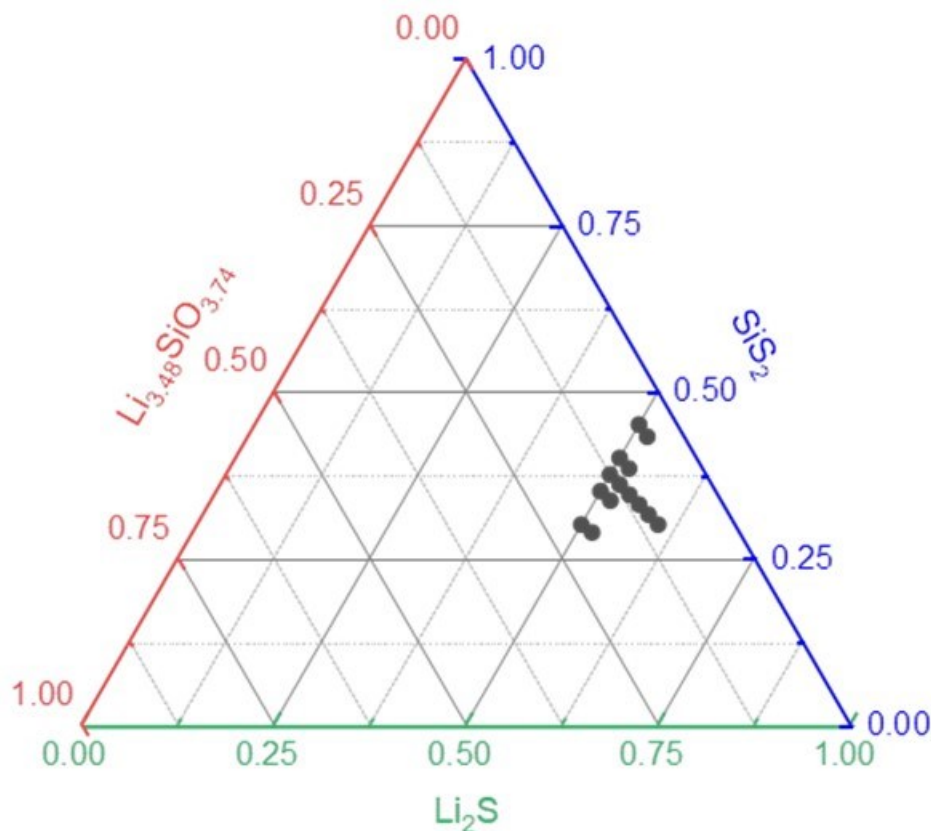


Figure XIII.2.1 Pseudo-ternary phase diagram detailing some of the new glass compositions synthesized in the  $\text{Li}_2\text{S} - \text{SiS}_2 - \text{Li}_{3.48}\text{SiO}_{3.74}$  system.

#### **Optimization of processing conditions for the production of thin-film MOS MGF GSE ribbons:**

A new preform was synthesized through small-scale batches with rigorous quality control. Thirty-three 10 g glass samples were synthesized, and each sample was tested using differential scanning calorimetry (DSC) to determine the  $T_g$ ,  $T_c$ , working range, and crystallization resistance at  $355^\circ\text{C}$ . Raman spectra were taken of each glass sample as well, and down selected from there. Due to poor crystallization resistance and presence of a defect structure in the Raman spectra, 13 samples were rejected, and the other 20 samples were melted into a  $\sim 200\text{ g}$  preform. Several attempts have been made to draw this preform into a film, with the most recent being successful to obtain film of  $\sim 300\ \mu\text{m}$  in thickness, as seen in Figure XIII.2.2. The remaining amount of preform was remelted and will continue to be drawn into film. The preform has been melted and cast into a preform seven times, with no substantial change in properties, highlighting the recyclability and reusability of



these GSEs made through thin film drawing. Future work will continue to optimization of the thin film drawing process to generate films of less than 50  $\mu\text{m}$  in thickness.

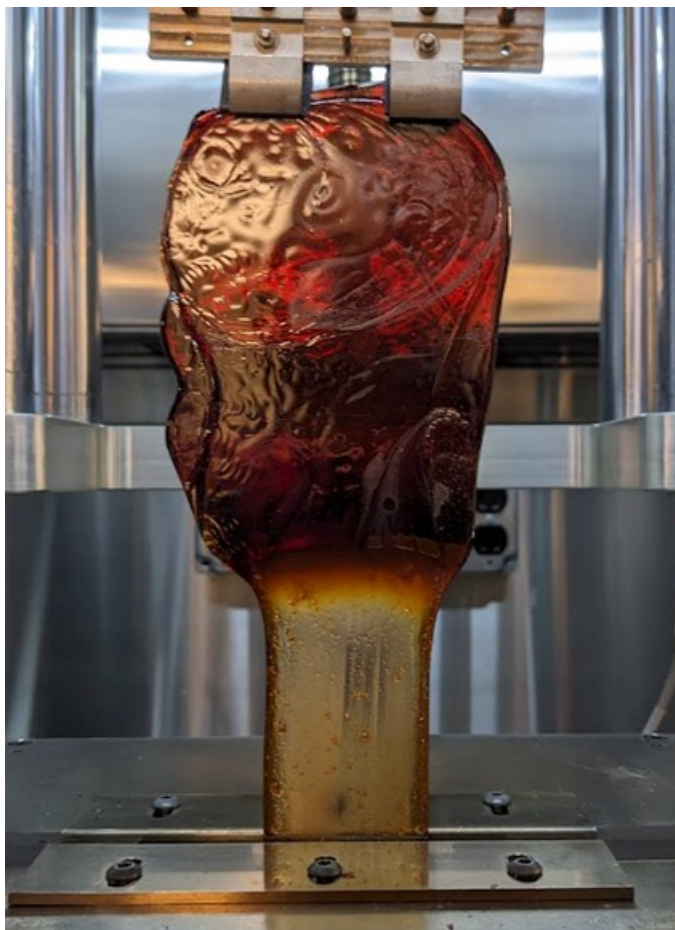


Figure XIII.2.2 Preform #3 with a small section of drawn thin film of around 300  $\mu\text{m}$  after drawing.

***Fabricate and test ASSLBs utilizing GSEs in small-area planar format:***

Composite cathodes were synthesized during this period through planetary milling of the active material, vapor-grown carbon fiber (VGCF), and ISU-6 GSE. The cathode composites were made using either  $\text{Li}_2\text{S}$  or sulfur as the active material with the ratios set to be 3:6:1, sulfur:ISU-6:VGCF. From literature, this seems to be a common starting point to obtain cathode composites for Li-S batteries that have adequate ionic and electronic conductivity for high sulfur utilization. To determine which would be the best starting point to pair with ISU-6 electrolytes, pellets were pressed and alternating current conductivity measurements were conducted with samples taken at different milling times, shown in Figure XIII.2.3. The conductivity of the sulfur active material was higher at nearly every milling time, as such, this was decided to be the first composition to optimize the cell testing procedure. The first few cells of this cathode synthesized through various methods is ongoing. Future work will entail a design-of-experiments approach to optimizing the cathode composition to eventually pair the cathode with a drawn thin film GSE.

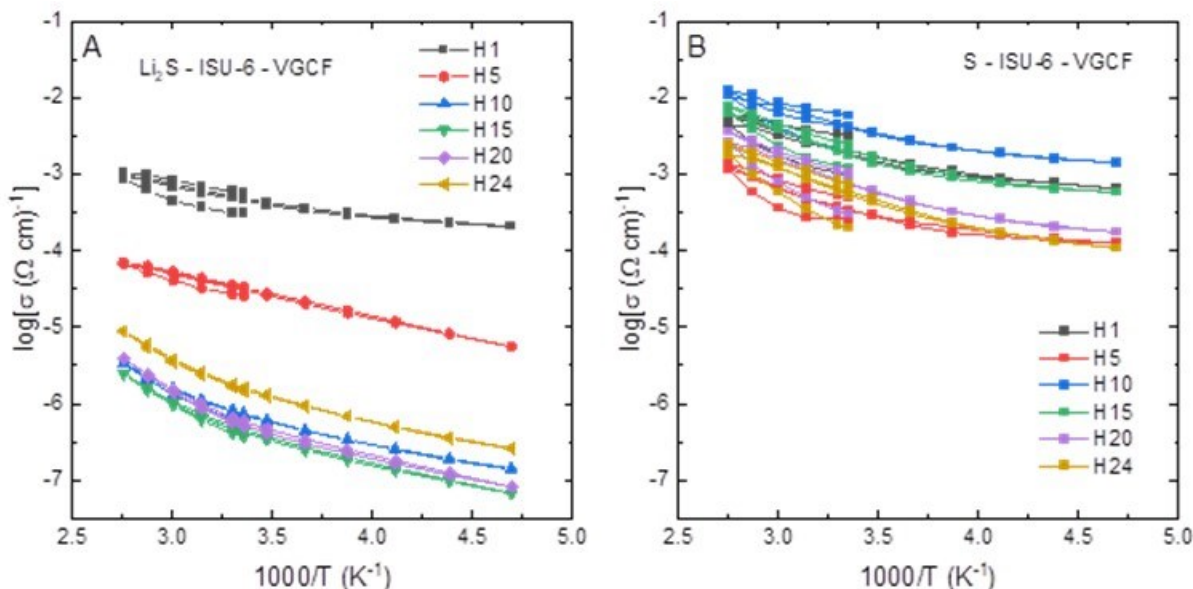


Figure XIII.2.3 A.C. Conductivity results from cathode composites with mass ratios of S:ISU-6:VGCF of 3:6:1 when charged. (A) From  $\text{Li}_2\text{S}$  starting material. (B) From sulfur starting material.

### Conclusions

In FY 2023, we have started to improve our glass quality control, and through that have been able to synthesize a new preform of ISU-6 glass, while continuing our compositional exploration to potentially find an even better glass composition. More thin film has been drawn from the new preform, but further optimization of the drawing process is in progress. Furthermore, a preliminary investigation has begun on Li-S composite cathodes using the ISU-6 glass composition. In the next fiscal year, this work will continue, and the cathode composite will be paired with the thin film glass once the processing and compositions for each are optimized.

### Key Publications

1. "Short Range Order Structures of Lithium Oxy-ThioSilicate Glasses," Guantai Hu, Victor M. Torres III, Steve W. Martin, *Journal of Non-Crystalline Solids: X*, Vol. 19, pp. 100198, 2023  
<https://doi.org/10.1016/j.nocx.2023.100198>
2. "Structure-mechanical properties correlation in bulk LiPON glass produced by nitridation of metaphosphate melts," Victor M. Torres III, Sergiy Kalnaus, Steve W. Martin, Caitlin Duggan, Andrew S. Westover, *Journal of the American Ceramic Society*, Vol.106, No. 11, pps.6565-6576, 2023, <http://doi.org/10.1111/jace.19327>.

### Acknowledgements

The PI would like to acknowledge the newly started collaboration with Drs. Gabriel Veith, Andrew Westover, and Sergiy Kalnaus at Oak Ridge National Laboratory for their work to begin the study of the mechanical moduli, fracture strength, and surface properties of the GSEs being studied in this project. This collaboration has already resulted in one publication that we report above.

### XIII.3 Molecular Ionic Composites: A New Class of Polymer Electrolytes to Enable All Solid-State and High Voltage Lithium Batteries (Virginia Polytechnic Institute and State University)

#### Louis A. Madsen, Principal Investigator

Department of Chemistry  
Virginia Tech  
319 Davidson Hall  
1040 Drillfield Dr.  
Blacksburg, VA 24061  
E-mail: [lmadsen@vt.edu](mailto:lmadsen@vt.edu)

#### Feng Lin, Co-Principal Investigator

Department of Chemistry  
Virginia Tech  
323 Davidson Hall  
1040 Drillfield Dr.  
Blacksburg, VA 24061  
E-mail: [fenglin@vt.edu](mailto:fenglin@vt.edu)

#### Tien Duong, DOE Technology Development Manager

U.S. Department of Energy  
E-mail: [Tien.Duong@ee.doe.gov](mailto:Tien.Duong@ee.doe.gov)

Start Date: January 1, 2022  
Project Funding: \$130,600

End Date: June 30, 2023  
DOE share: \$121,548

Non-DOE share: \$9,052

#### Project Introduction

Based on a newly discovered class of solid polymer electrolyte materials, which we term molecular ionic composites (MICs), we are developing Li solid electrolytes targeted for use in transportation applications. MICs form a mechanically stiff (~ 1 GPa modulus), electrochemically stable, and highly thermally stable matrix that can resist dendrite formation with metal anodes, allow high voltage operation, provide robust safety against fire, and enable fast charging/discharging over a wide temperature range. The component molecules in MICs are inexpensive and MICs can be processed to yield a large area format at room temperature and generally in ambient atmosphere and with relatively safe solvents. Our team is advancing this class of polymer electrolytes to promote uniform lithium plating, inherent safety, and long term stability against both lithium metal anodes and high voltage layered oxide cathodes.

#### Objectives

Utilizing molecular ionic composite (MIC) solid polymer electrolytes, the overall objective is to develop solid-state lithium conductors targeted for use in transportation applications. MICs form a mechanically stiff, electrochemically stable, and thermally stable matrix.

Specific objectives include the following: (1) Development of robust MIC electrolyte thin films (down to ~ 20  $\mu\text{m}$ ) to serve as simultaneous nonflammable separators and dendrite-blocking  $\text{Li}^+$  conductors that enable the use of Li metal anodes, (2) electrochemical quantification of key performance metrics including electrolyte stability, interfacial reactions, and suitability/compatibility with a range of electrode materials, and (3) comprehensive investigation of ion transport mechanisms and electrode-electrolyte interfacial reactivity under practical operating conditions using NMR and synchrotron X-ray analyses.

## Approach

MICs rely on a unique polymer “PBDT” that is similar to Kevlar® in its strength, stiffness, and thermal stability, but with densely spaced and ordered ionic groups that serve to form an electrostatic network that permeates mobile ions in the MIC. The team can tailor the ion concentrations and types to yield MIC electrolyte films that are electrochemically compatible with Li-metal anode as well as a range of high-voltage layered cathodes. The team is searching the composition space of lithium salts, electrochemically compatible ionic liquids, and polymer (PBDT) molecular weight to determine the best composition windows for MIC electrolytes. The team is also investigating the best methods for casting or spraying thin films in terms of temperature, solvent/evaporation conditions, and control over the initial liquid crystalline gel formation point. Concurrently, the team is testing MIC films in various electrochemical cells, quantifying transport and structural/morphology parameters with NMR and X-ray techniques, and measuring key mechanical (dynamic mechanical thermal analysis, stress-strain) and thermal (DSC, TGA) properties.

## Results

In this period, the team reported on the fundamental investigation of interfacial processes in the Li|MIC|NMC cells. The work was done at NSLS-II at Brookhaven National Laboratory. We have successfully collected data for the cross-section of the solid electrolyte after various stages of battery cycling. Figure XIII.3.1 shows the schematic representation of the beamline experiments. We are now able to chemically resolve the species at the electrode-electrolyte interface. In particular, the team has made more progress since the earlier report on this technique in our previous annual report. With these new insights, the team has developed a solid understanding of the anodic and cathodic side reactions in this new solid battery cell. We plan to use such understanding to implement compositional changes to improve battery performance.

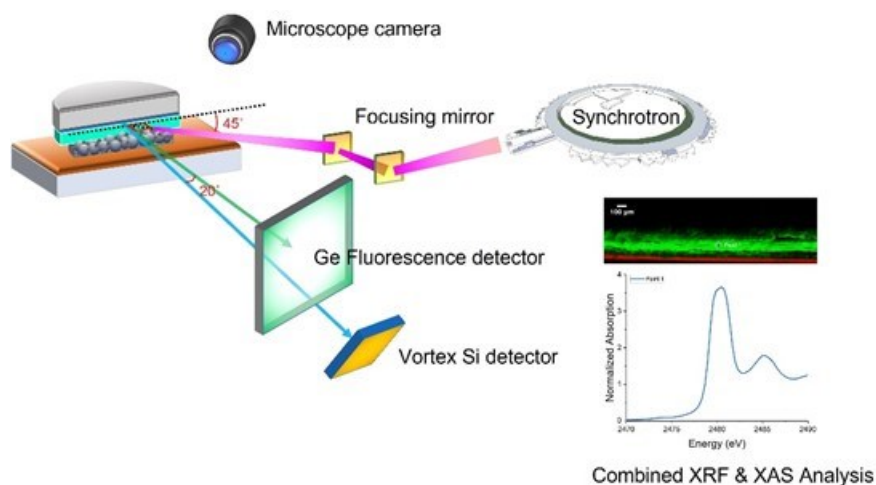


**Figure XIII.3.1** Schematic representation of the combined XRF and XAS experiments, which allow us to identify the local concentration and chemical structure of the interested element at the cross-section.

The team has also made further progress on a new formulation of this solid-state rigid polymer electrolyte. We use both Li/Li and Li/LiFePO<sub>4</sub> cells to evaluate the limiting current density of the prepared rigid polymer electrolyte. For the Li/LiFePO<sub>4</sub> cells, the cathode, containing 3 wt% PBDT, 10 wt% carbon additive and 87 wt% LiFePO<sub>4</sub> is used directly here. Figure XIII.3.2a shows the voltage profile of a Li/Li cell cycled at 22 °C at different current densities. When the applied current density is below 0.3 mA cm<sup>-2</sup>, the cell cycles stably. After 2.5 cycles (10 hours) at 0.3 mA cm<sup>-2</sup>, the voltage increases drastically and eventually reaches the safety limit (5 V), indicating that the limiting current density is about 0.3 mA cm<sup>-2</sup> at 22 °C for the rigid polymer electrolyte membrane. Li/LiFePO<sub>4</sub> cells demonstrate similar results (Figure XIII.3.2b and Figure XIII.3.2c). Increasing the cycling current density from 0.05 to 0.3 mA cm<sup>-2</sup> leads to the specific capacity decreasing from 150 to 120 mAh g<sup>-1</sup>. Further increasing the current density causes significant polarization and drastic capacity decay. The limiting current density of an electrolyte is closely related to its thickness. Under the same salt polarization

profile, the obtainable current density is inversely proportional to the thickness of the electrolyte. Since the rigid polymer electrolyte used in this study is very thick ( $130 \pm 20 \mu\text{m}$ ), reducing its thickness to  $25 \mu\text{m}$  should lead to an increase of the limiting current density by a factor of about 5.

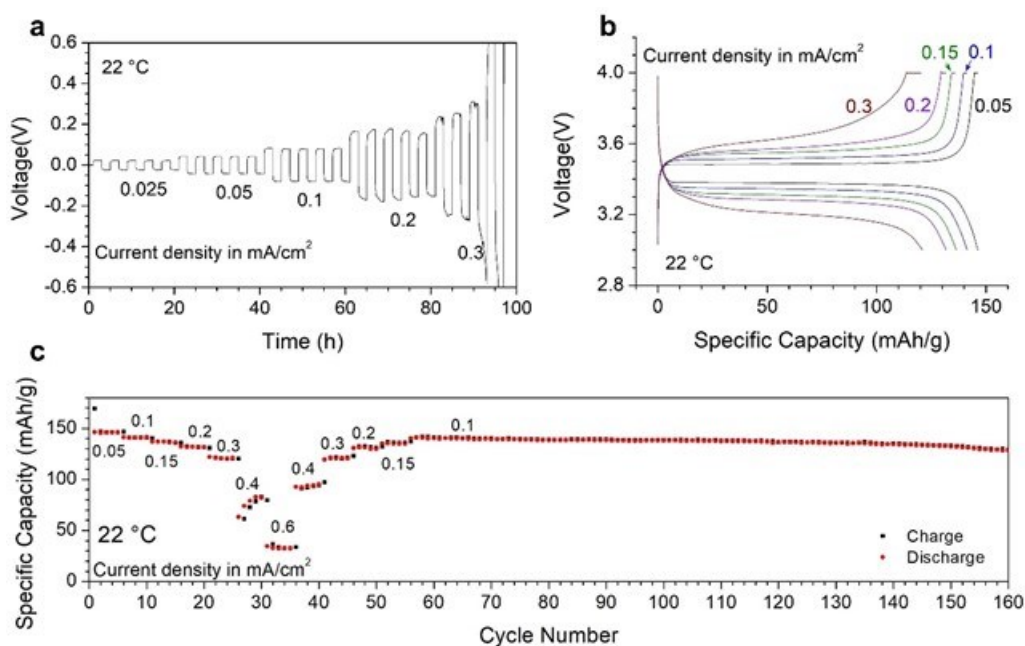


**Figure XIII.3.2** Rate capability of Li/Li and Li/LiFePO<sub>4</sub> cells using the new formulation for the solid-state rigid polymer electrolyte at 22 °C. (a) Voltage profile of a Li/Li cell cycled at various current densities. Both charging and discharging time are 2 hours for each cycle and the current density increases from 0.025 to 0.3 mA cm<sup>-2</sup> with 5 cycles for each step. (b) Typical voltage profiles of the Li/LiFePO<sub>4</sub> cell cycled at different current densities. (c) Specific charge and discharge capacities of LiFePO<sub>4</sub> when cycled at various current densities. The thickness of the rigid polymer electrolyte used in this study is  $130 \pm 20 \mu\text{m}$ , and the LiFePO<sub>4</sub> mass loading in the cathode is  $3.6 \pm 0.4 \text{ mg cm}^{-2}$ . Li/Li and Li/LiFePO<sub>4</sub> cycling tests reveal a limiting current density of about 0.3 mA cm<sup>-2</sup> and stable long-term cycling at 0.1 mA cm<sup>-2</sup> of the rigid polymer electrolyte at 22 °C.

Our team published an article in *ACS Energy Letters* on a new transport mechanism for Li<sup>+</sup> in hydroxyl-containing electrolytes (glycerol with Li salt). While these may not be feasible for current battery designs, coated or specialized electrodes may enable their use in the future. Lithium batteries rely crucially on fast charge and mass transport of Li<sup>+</sup> in the electrolyte. For liquid and polymer electrolytes with added lithium salts, Li<sup>+</sup> couples to the counter-anion to form ionic clusters that produce inefficient Li<sup>+</sup> transport, leading to Li dendrite formation. Quantification of Li<sup>+</sup> transport in glycerol-salt electrolytes via NMR experiments and MD simulations reveals a surprising ion-hopping mechanism. The Li<sup>+</sup> transference number, measured by ion-specific electrophoretic NMR, can reach 0.7, and Li<sup>+</sup> diffusion does not correlate with nearby ion motions even at high salt concentration. Glycerol's high density of hydroxyl groups increases ion dissociation and slows anion diffusion, while the close proximity of hydroxyls and anions lowers local energy barriers, facilitating Li<sup>+</sup> hopping. This system represents a bridge between liquid and inorganic solid electrolytes, thus motivating new molecular designs for liquid and polymer electrolytes to enable the uncorrelated Li<sup>+</sup> hopping transport needed for fast-charging and all-solid-state batteries.

In order to comprehensively understand transport of solvent and ions, the team directly measured Li<sup>+</sup>, counterion, and solvent self-diffusion ( $D$ ), ionic conductivity ( $\sigma$ ), and Li<sup>+</sup> and counterion electrophoretic mobility ( $\mu$ ). The team then analyzed these quantities (notably with the Onsager coefficient formalism) to draw critical conclusions about associations among ions and solvent molecules. We further combined these results with MD simulations to gain further insights into Li<sup>+</sup> hopping and decoupling from counteranions. Figure

XIII.3.3 shows representative  $\text{Li}^+$  hop simulations from this study. This study incorporated work from our key collaborator groups Prof. Diego Troya (VT) and Ralph Colby (PSU).

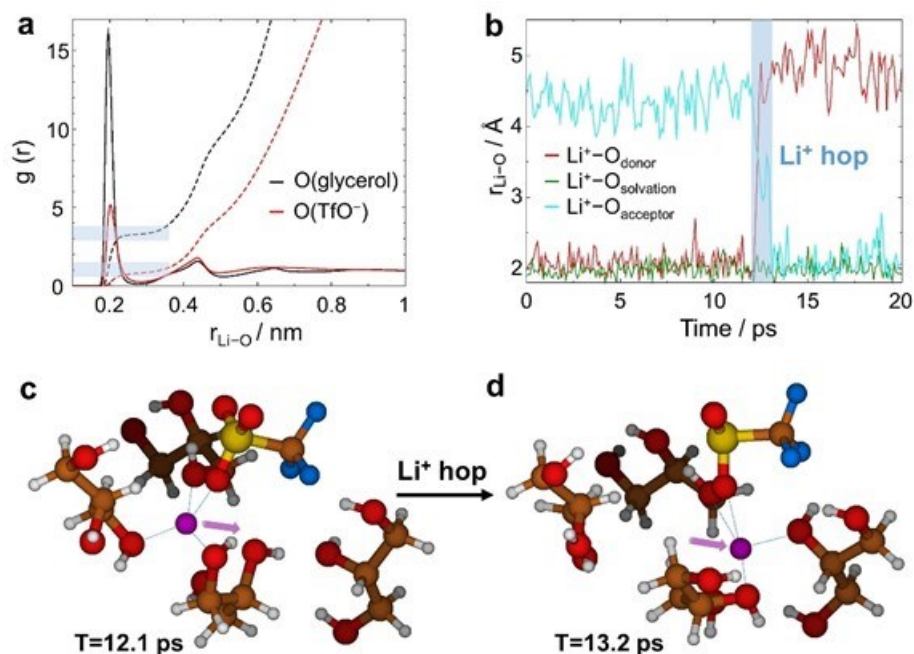
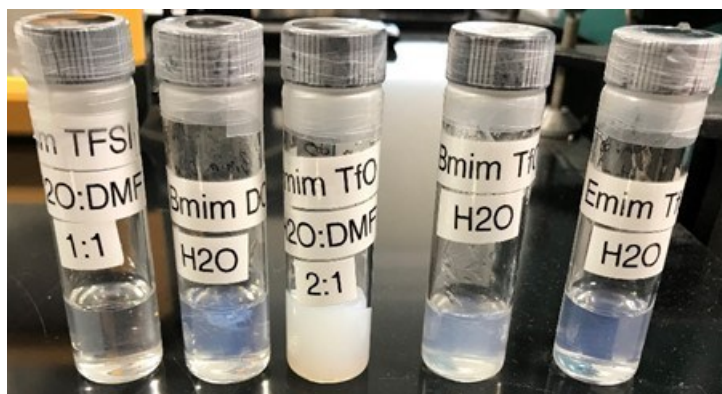


Figure XIII.3.3 Lithium-ion hopping in MD simulations of salt-in-glycerol electrolytes. (a) Radial distribution functions (rdfs) of the O atoms of glycerol and  $\text{TfO}^-$  to  $\text{Li}^+$  at 50 °C in glycerol/ $\text{LiTfO} = 2$ . Dashed lines represent the cumulative coordination number and shaded bars highlight rdf plateaus at  $\approx 1$ , and 3 O-Li coordination numbers. (b) Internuclear distances between a  $\text{Li}^+$  and representative O atoms in the inner solvation shell, highlighting the ligand exchange of  $\text{Li}^+$  in a 2 to 4 Å and ~ 1 ps duration hop between donor (red trace) and acceptor (cyan) molecules. A spectator  $\text{Li}^+$ -O distance is shown for reference (green trace). (c and d) Snapshots of the inner solvation shell of the  $\text{Li}^+$  before and after a hopping event.

The other area of activity in this period was exploration of solvent effects during MIC electrolyte casting, including hydrogel/solvogel behaviors to study the liquid crystalline gel precursors to dry MIC film formation. In order for us to form dry MIC films, they must reach a liquid crystalline gel state, which then shrinks when the remaining casting solvent is removed. We now believe that some disruption of the gel network may take place upon solvent removal, depending on casting solvent and temperature. We work to identify the fundamentals of this process. A first step is to find what choice of solvent and/or component IL can yield the lowest solvent content (volume fraction) at the gel point. Figure XIII.3.4 shows variations of ionic liquid type and solvent mixtures to modulate the solid gel properties. The team has filed a full US patent on these hydrogels/solvogels on their own merits.



**Figure XIII.3.4 Hydro/solvogels formed from PBDT charged double helix polymer, ionic liquid (IL) and water and/or DMF. Gel properties vary widely based on solvent content (water + DMF) and IL type. Much stiffer gels result from ~ 1:1 DMF-H<sub>2</sub>O casting solvent. More milky gels appear to be more strongly liquid crystalline (rods aligned) and more mechanically robust. *Left to right:* BmimTFSI in 1:1 water-DMF, BmimDCA in water, BmimTfO in 2:1 water-DMF, BmimTfO in water, and EmimTfO in water. These gels carry critical implications for final mechanical properties of fully dried MIC battery electrolyte films.**

The team has continued to push interfacial engineering and characterization, as well as investigate other material compositions. Major results for this period involve a new system (related to our MIC electrolytes) that is a composite of PEG oligomers (400 g/mol) with PBDT polymer. While these materials may not achieve sufficient properties for most battery applications, they hold exciting features that may be applicable with suitable modifications. The team has just published these results. The key advantages of these systems are that they are single-ion conductors (for Li<sup>+</sup> and/or Na<sup>+</sup>), and they possess nearly the highest conductivities of all polymer-based single-ion conductors, as well as the highest moduli of previous systems. Figure XIII.3.5, Figure XIII.3.6, and Figure XIII.3.7 and their captions summarize this new solid electrolyte.

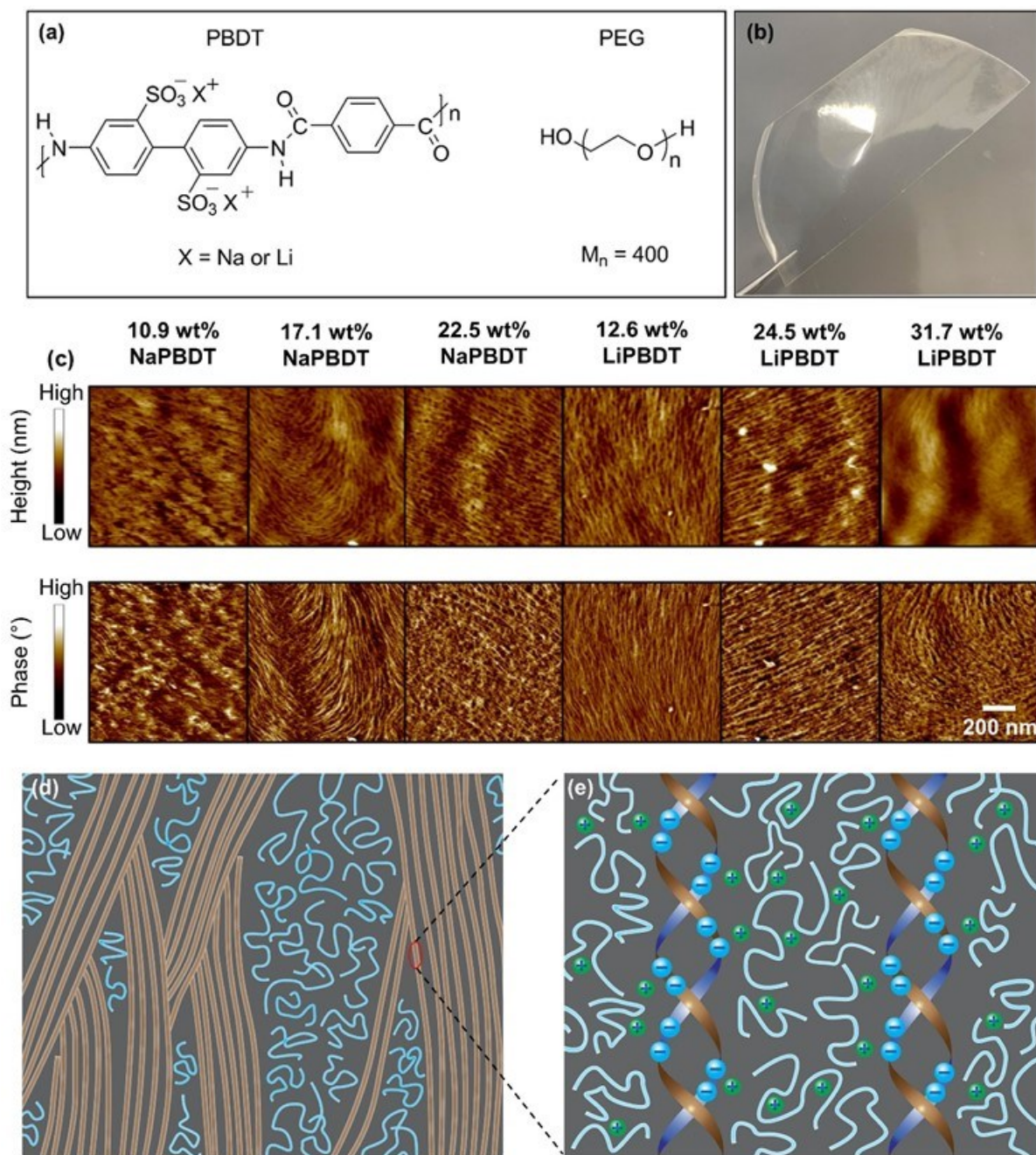


**Figure XIII.3.5 Morphology of PBDT-PEG membranes.** (a) Molecular structures of PBDT with Na<sup>+</sup> or Li<sup>+</sup> counterions and PEG400. (b) Image of a single-ion-conducting solid polymer electrolyte film containing 24.5 wt% LiPBDT with a thickness of  $80 \pm 10 \mu\text{m}$ . (c) Atomic force microscopy (AFM) tapping mode images of the PBDT-PEG membranes over a  $1 \mu\text{m}^2$  area. Increasing the PBDT concentration in the membranes leads to the formation of a single-bundle phase. (d) Conceptual  $\sim 100 \text{ nm}$  scale model of the biphasic internal network of PBDT-PEG membranes (Li<sup>+</sup> or Na<sup>+</sup> form) where PBDT-rich bundles (orange lines) interact with PEG (blue lines). (e) Conceptual nanometer-scale model of the ionic interactions within a PBDT bundle. At a rod-rod distance of  $\sim 2 \text{ nm}$ , the counterions interact with both the sulfonate anion from the PBDT double helix and low molecular weight PEG. This proposed model gives a framework to discuss mechanical and conductivity results.



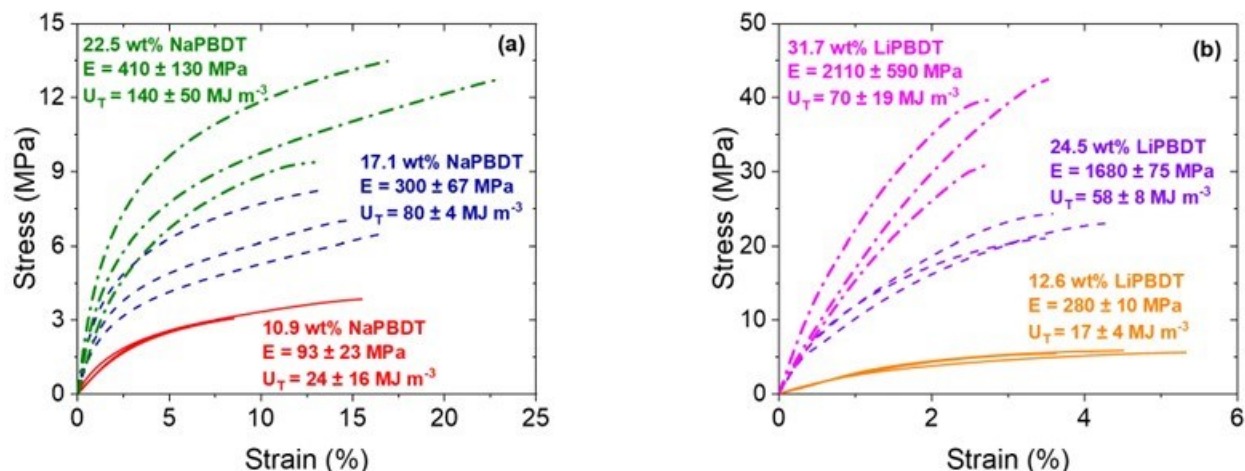


Figure XIII.3.6 Mechanical robustness of the PBDT-PEG membranes. Uniaxial stress-strain curves for the PBDT-PEG membranes with (a)  $\text{Na}^+$  counterions and (b)  $\text{Li}^+$  counterions at a force ramp rate of  $1 \text{ N min}^{-1}$  at  $30^\circ\text{C}$ . All membranes were repeated by cutting three test samples from each PBDT-PEG membrane. The slope of the stress-strain curves at  $< 0.5\%$  strain yields the Young's modulus ( $E$ ), with values of  $E$  and the toughness ( $U_T$ ) with standard deviations. In general, the Li-based membranes have higher modulus and lower strain at break than the Na-based membranes and are comparable to or better than our IL-based MIC materials. The Na-based membranes show 3-10X higher conductivity than comparable Li-based membranes.

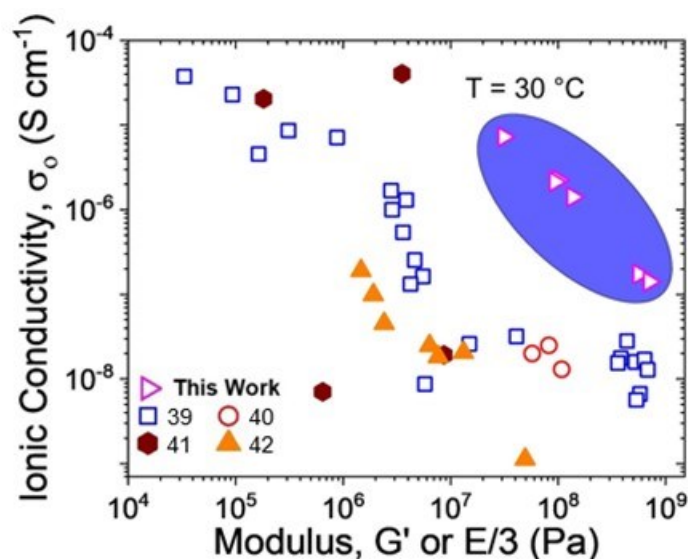


Figure XIII.3.7 Relationship between ionic conductivity ( $\sigma_0$ ) and modulus (either  $G'$  or  $E/3$ ) for PBDT-PEG membranes and various polymeric single-ion conducting electrolytes at  $30^\circ\text{C}$ . Filled symbols represent materials with recorded shear moduli ( $G'$ ) and open symbols materials with recorded tensile moduli ( $E$ ). The PBDT-PEG membranes (pink open triangles) consistently show higher moduli and/or  $\sigma_0$  when compared to other single-ion polymeric electrolytes. Experimental errors are smaller than symbol sizes. The published article reported below lists the external references involved in this plot.

## Conclusions

The team has successfully completed the project with the discoveries of multiple new compositions for solid state polymer electrolytes, the development of new analytical techniques to investigate buried interfaces, and understanding new transport mechanisms. Lithium batteries rely crucially on fast charge and mass transport of  $\text{Li}^+$  in the electrolyte. For liquid and polymer electrolytes with added lithium salts,  $\text{Li}^+$  couples to the counter-

anion to form ionic clusters that produce inefficient  $\text{Li}^+$  transport and lead to Li dendrite formation. Quantification of  $\text{Li}^+$  transport in glycerol–salt electrolytes via NMR experiments and MD simulations reveals a surprising  $\text{Li}^+$ -hopping mechanism. The  $\text{Li}^+$  transference number, measured by ion-specific electrophoretic NMR, can reach 0.7, and  $\text{Li}^+$  diffusion does not correlate with nearby ion motions, even at high salt concentration. Glycerol’s high density of hydroxyl groups increases ion dissociation and slows anion diffusion, while the close proximity of hydroxyls and anions lowers local energy barriers, facilitating  $\text{Li}^+$  hopping. This system represents a bridge between liquid and inorganic solid electrolytes, thus motivating new molecular designs for liquid and polymer electrolytes to enable the uncorrelated  $\text{Li}^+$ -hopping transport needed for fast-charging and all-solid-state batteries. We also report solid electrolytes that combine a rigid-rod polyanion, poly(2,2'-disulfonyl-4,4'-benzidine terephthalamide) (PBDT), with  $\text{Na}^+$  or  $\text{Li}^+$  counterions, and poly(ethylene glycol) (PEG,  $M_n = 400 \text{ g mol}^{-1}$ ). PBDT-PEG membranes show Young’s modulus from 90 to 2110 MPa that increases with the PBDT content and is  $>4\times$  higher for Li-based vs Na-based electrolytes. We attribute this dramatically higher modulus in LiPBDT–PEG to poorer ion dissociation between  $\text{Li}^+$  and PBDT sulfonate groups and stronger interactions between LiPBDT and PEG. These membranes show an increase in ionic conductivity with increasing PEG concentration ( $0.1\text{--}7 \mu\text{S cm}^{-1}$  at  $30 \text{ }^\circ\text{C}$ ), reaching  $0.13 \text{ mS cm}^{-1}$  at  $120 \text{ }^\circ\text{C}$ . These materials use highly rigid and charged PBDT double helices to “solidify” low-molecular-weight PEG into mechanically strong and highly single-ion-conductive solid polymer electrolytes with high thermal stability. Their combination of high cation conductivity and high modulus exceeds those of competing single-ion conductors at  $30 \text{ }^\circ\text{C}$ .

### Key Publications

1. "Uncorrelated lithium-ion hopping in a dynamic solvent-anion network" Deyang Yu, Diego Troya, Andrew G. Korovich, Joshua E. Bostwick, Colby, Ralph; Louis A. Madsen. *ACS Energy Letters* (2023), 8, 1944–1951. doi: 10.1021/acseenergylett.3c00454.
2. “High Modulus Single-Ion-Conducting Electrolytes Based on a Rigid-Rod Polyanion” Joshua E. Bostwick,† Deyang Yu,† Curt J. Zanelotti, Theo J. Dingemans, Louis A. Madsen, and Ralph H. Colby. *ACS Applied Energy Materials* 2023, 6, 6910–6916. doi: 10.1021/acsaem.3c00243.

### Patents

1. Full US/international patent application filed: “Rechargeable Solid State Lithium Batteries Working Over A Wide Temperature Range” PCT/US22/39656.
2. US/international patent application filed: “Hydrogel Compositions Comprising Polymer-Salt Composites And Methods Of Making The Same” Application number 63316302.

### Acknowledgements

The team acknowledges collaborations with T. J. Dingemans’ group at University of North Carolina (UNC) Chapel Hill in which they are forming composites based on PBDT polymer with carbon materials such as graphene oxide and are beginning to develop new charged rigid-rod polymers that build on PBDT. The team also acknowledges collaborations with Prof. R. H. Colby at PSU on shear rheology and broadband dielectric spectroscopy to understand mechanical properties and conduction mechanisms. The team also acknowledges collaborations with Dr. D. Nordlund and Dr. Y. Liu at SLAC National Accelerator Laboratory (SLAC), and S.-M. Bak of Brookhaven National Lab, for conducting synchrotron X ray studies on MIC films and composite electrodes. The team also appreciates the collaboration with Prof. Y. Yao at University of Houston for establishing the solid-state battery testing platform and Prof. P. Dong, George Mason University (GMU) for advanced mechanical testing, and Prof. D. Troya for molecular dynamics simulations of ion transport processes.

## XIII.4 Hot Pressing of Reinforced All-solid-state Batteries with Sulfide Glass Electrolyte (General Motors LLC)

### Thomas A. Yersak, Principal Investigator

General Motors LLC  
 GM Global Research and Development  
 30470 Harley Earl Blvd.  
 Warren, MI 48092  
 E-mail: [thomas.yersak@gm.com](mailto:thomas.yersak@gm.com)

### Tien Duong, DOE Technology Development Manager

U.S. Department of Energy  
 E-mail: [Tien.Duong@ee.doe.gov](mailto:Tien.Duong@ee.doe.gov)

Start Date: October 1, 2019

End Date: September 30, 2023

Project Funding: \$1,250,000

DOE share: \$1,000,000

Non-DOE share: \$250,000

### Project Introduction

The performance of solid-state batteries (SSBs) with sulfide solid-state electrolytes (SSEs) is limited because they are 10 - 30% porous. Porosity limits energy density of the composite cathode and provides a conduit for Li-metal deposits through the separator if operating specifications (*e.g.* current density, operating temperature, and pressure) are not strictly controlled. This project intends to demonstrate that hot press cell processing and appropriately formulated sulfide glass SSEs can eliminate porosity to enable SSBs with energy density of  $\geq 350$  Wh/kg.

### Objectives

The objective of this project is to research, develop, and test SSBs capable of achieving program performance metrics by implementing appropriately formulated sulfide glass SSEs and hot press cell processing in a dry room environment. In the composite cathode, hot pressing eliminates porosity to increase energy density by enabling thick composite cathodes with high active material loading. In the separator, hot pressing eliminates porosity that may otherwise provide a conduit for Li metal deposits to short the cell.

### Approach

Some glassy sulfides SSEs soften when heated above their glass transition temperature. This project takes advantage of that effect to study how to consolidate SSBs by hot pressing. The sulfide SSE used in the composite cathode, otherwise known as the catholyte, dictates the processing specifications for ASSB hot pressing. Thermal stability can be achieved by NCM passivation and proper catholyte formulation. Work conducted during this project's first budget period systematically evaluated different NCM coatings, catholyte formulations, and hot press cell processing conditions (*i.e.* temperature, time, and pressure). Having established the feasibility of hot-pressed composite cathodes, work transitioned to this project's second budget period, which focused solely on the separator. Separator glass electrolyte compositions were systematically studied for processability and compatibility with secondary electrolyte phases. The functional characteristics of processed glass electrolyte separators such as ionic conductivity and critical current density were determined. In the final budget period of this project, full ASSB stacks were realized.

## Results

### Outline

This project's final report will be divided into three sections. In the first section, a Li/S semi-solid cell design will be described that shows program performance metrics can be met [1]. The technical achievements enabling this cell design will then be described; namely, fabrication of a reinforced LiPSiS glass SSE separator by hot pressing [1] and chemical compatibility between LiPSiS glass SSE and DME:DOL based liquid electrolyte [2]. In the second section, we will outline several opportunities for how the aforementioned cell design can be improved. In the third and final section, we then go on to describe progress towards an improved cell design including evaluation of sulfide SSE moisture stability in a dry room environment [3], development of a highly processable oxysulfide glass SSE composition, development of hot-pressed all-solid-state cathode composites [4], and development of a semi-solid electrolyte system comprising oxysulfide SSE and solvate ionic liquid (SIL) electrolyte.

### Cell Design

The performance of Li/S battery cells can be improved by integrating solid-state electrolytes (SSEs) into the cell design. In Li/S cells with highly solvating electrolytes, a major problem is the migration of dissolved polysulfide species to the anode [5], which results in a parasitic polysulfide shuttle that reduces cell coulombic efficiency. A  $\text{LiNO}_3$  co-salt may be used to inhibit the polysulfide redox shuttle, however, its continual consumption generates gas and increases cell impedance over time [6, 7]. Impermeable SSE separators have been used to physically block the migration of polysulfide and eliminate the need for  $\text{LiNO}_3$  co-salt. Previous reports utilize thick oxide ceramic SSE pellets composed of  $\text{Li}_{1.3}\text{Al}_{0.3}\text{Ti}_{1.7}(\text{PO}_4)_3$  (LATP) [8-10],  $\text{Li}_{1+x}\text{Y}_x\text{Zr}_{2-x}(\text{PO}_4)_3$  (LYZP) [11],  $\text{Li}_{1.5}\text{Al}_{0.5}\text{Ge}_{1.5}(\text{PO}_4)_3$  (LAGP) [12], and  $\text{Li}_7\text{La}_3\text{Zr}_2\text{O}_{12}$  (LLZO) [13]. Unfortunately, these aforementioned oxide SSE separators greatly reduce cell energy density because they are thick ( $\sim 1\text{mm}$ ) and dense ( $> 3\text{g cm}^{-3}$ ). The SSE separator developed for this project's semi-solid Li/S cell design is pictured in Figure XIII.4.1. It is a reinforced film of  $(\text{Li}_2\text{S})_{60}(\text{SiS}_2)_{28}(\text{P}_2\text{S}_5)_{12}$  (LiPSiS) glass SSE that is insoluble in DME:DOL based liquid electrolytes, largely impermeable to polysulfides, flexible, thin ( $\sim 100\ \mu\text{m}$  thick), light ( $< 2\text{g cm}^{-3}$ ), and large enough for evaluation in a pouch cell format. To the author's knowledge, this project's semi-solid Li/S cell design is the first to utilize a sulfide SSE separator and the first to be demonstrated in a pouch cell format.

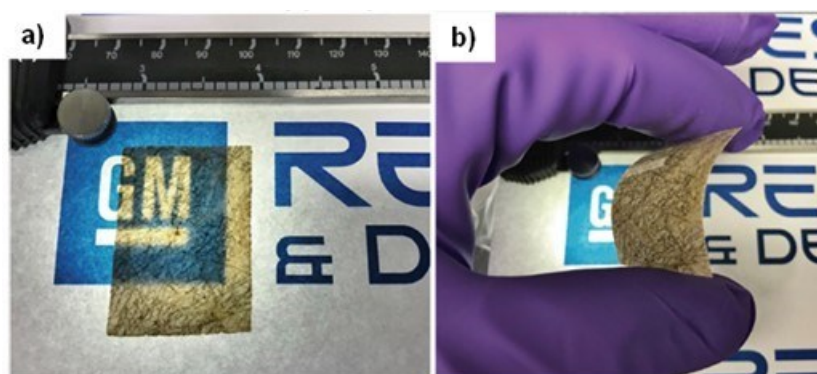


**Figure XIII.4.1** Pictures of reinforced LiPSiS glass SSE separators, which are translucent, bendable, and 135 – 180  $\mu\text{m}$  thick. The dark brown crosshatch pattern is attributed to the underlying non-woven fiberglass reinforcement. Figures reproduced from [1].

Our cell designs utilizing a LiPSiS SSE separator are depicted in Figure XIII.4.2. Cells were evaluated in both coin cell and single layer pouch cell formats. The conventional sulfur cathode had a nominal capacity of approximately  $2.5\ \text{mAh cm}^{-2}$ , the anode was  $60\ \mu\text{m}$  thick Li on stainless steel foil, and the liquid electrolyte was either 1:1 (v/v) DME:DOL + 1M LiTFSI or 1:1 (v/v) DME:DOL + 0.4M LiTFSI + 0.6M  $\text{LiNO}_3$ . More details are reported elsewhere [1].

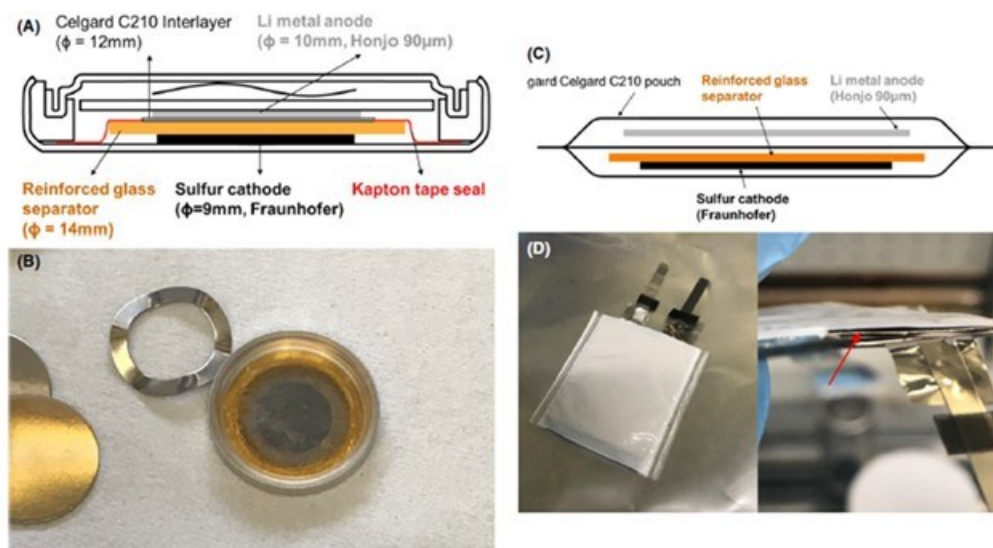


**Figure XIII.4.2 Schematics and pictures of the semi-solid Li/S cell designs developed for this project. a) Schematic of a semi-solid coin cell design. b) Top-down picture of a semi-solid coin cell with sulfur cathode sealed using an annular Kapton tape disc and a reinforced LiPSiS glass film separator. c) Schematic of a single layer semi-solid pouch cell design. The pouch cell casing is not included in the schematic. d) Top-down picture of a single layer semi-solid pouch cell core and a side-view picture of the same with the reinforced LiPSiS glass film separator indicated by a red arrow. Figures reproduced from [1].**

Cycling data for this project's semi-solid Li/S cells are provided in Figure XIII.4.3 and reported elsewhere [1]. In a first experiment utilizing the coin cell format (Figure XIII.4.2a,b), a control cell and a semi-solid cell were cycled with DME:DOL electrolyte containing no LiNO<sub>3</sub>. The control cell (blue) never completed its first charge cycle due to the parasitic polysulfide shuttle. On the other hand, the semi-solid cell with LiPSiS SSE separator (red) quickly completed its first charge cycle and went on to cycle 300 cycles at a C/10 rate thereafter. An H-cell experiment with 0.1M Li<sub>2</sub>S<sub>4</sub> solution confirmed that the LiPSiS separator acted as an impermeable barrier to polysulfides. Having shown that LiPSiS SSE separators block the polysulfide shuttle, a second experiment was conducted utilizing the single layer pouch cell format (Figure XIII.4.2c,d). A LiPSiS SSE separator was shown to increase both cycle life and efficiency. We note that the semi-solid cell design presented here is a proof-of-concept and not fully optimized. Better design of the E/S and N/P ratios and the use of a thinner SSE separator are expected to improve cell cycle life and energy density to meet program targets.

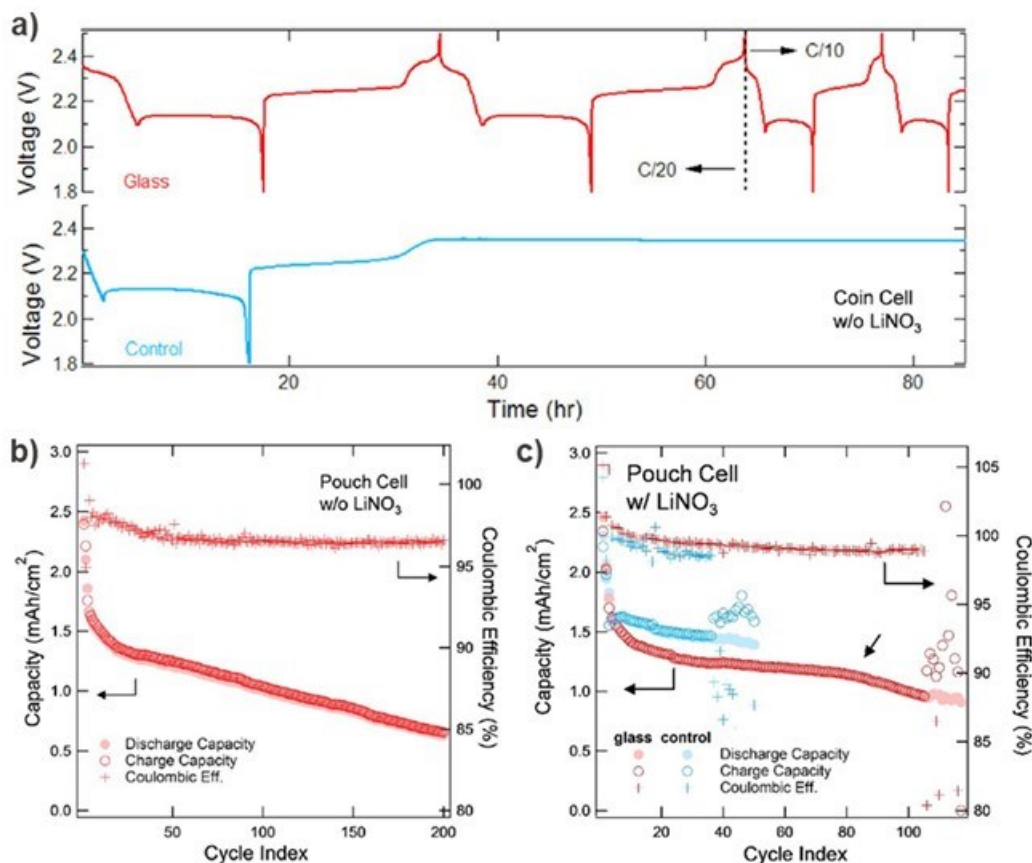
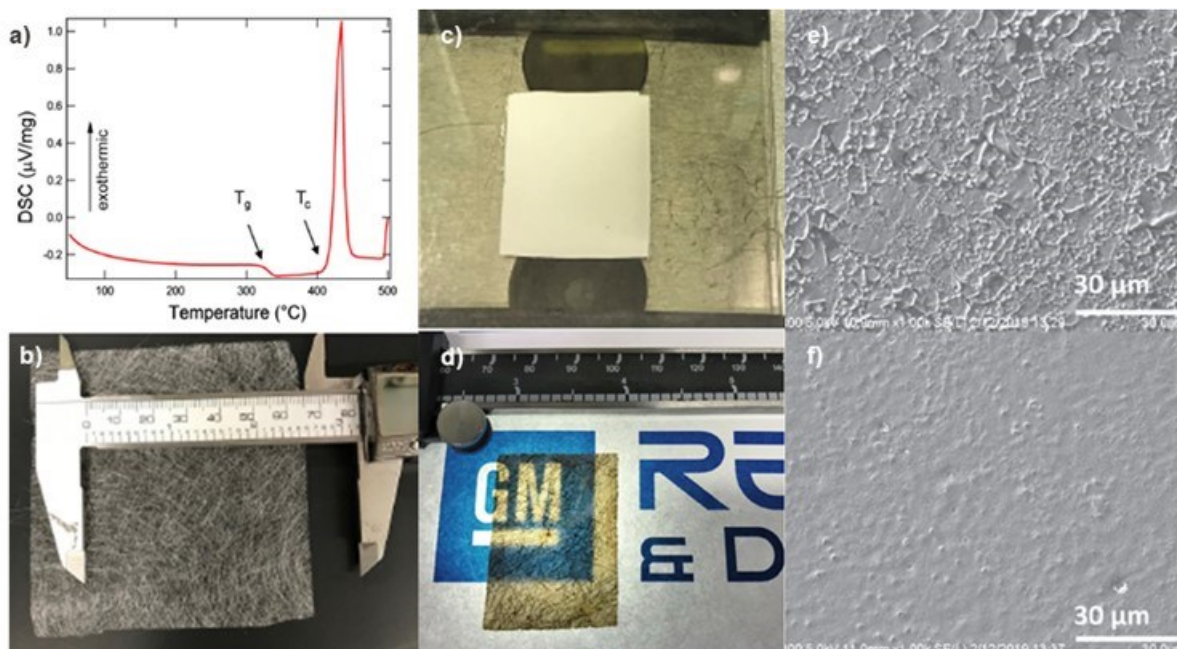


Figure XIII.4.3 Cycling data for semi-solid Li/S coin and pouch cells with 1:1 (v/v) DME:DOL + 1M LiTFSI liquid electrolyte. a) Initial cycling behavior of coin cells without LiNO<sub>3</sub> co-salt. The semi-solid cell cycles normally while the control cell does not complete its first charge due to the parasitic polysulfide shuttle. b) Cycling data for a semi-solid pouch cell without LiNO<sub>3</sub> co-salt. c) Cycling data for control and semi-solid pouch cells with LiNO<sub>3</sub> co-salt. The LiPSiS SSE separator improves both cell cycle life and coulombic efficiency. Figures reproduced from [1].

The aforementioned semi-solid Li/S cell design was enabled by two technical achievements:

- 1) Fabrication of LiPSiS glass SSE separators and
- 2) Chemical compatibility of LiPSiS glass SSE with DME:DOL based liquid electrolyte.

In previous work, it was recognized that the moldability of glassy sulfide SSEs improved when consolidated at elevated temperature [14, 15]. Consolidation of glassy sulfide SSEs at elevated temperature will be referred to as hot pressing (HP). Similarly, consolidation of glassy SSEs at room temperature will be referred to as cold pressing (CP). The differential scanning calorimetry (DSC) scan for LiPSiS glass SSE is provided in Figure XIII.4.4a and it shows two features; namely, a glass transition,  $T_g$ , at 322 °C and a crystallization onset,  $T_c$ , at 408 °C. When heated above the  $T_g$ , glasses enter a supercooled liquid state and viscosity drops dramatically [16]. This project utilized this effect to hot press tape cast films of LiPSiS glass SSE for 30 minutes at 330 °C and 12 MPa. The process is detailed in Figure XIII.4.4 and elsewhere [1]. We note that a process temperature of only 330 °C is hundreds of degrees lower than that required to sinter oxide ceramic SSEs. A fiberglass non-woven paper was used to reinforce the brittle LiPSiS glass SSE. SEM images of the LiPSiS glass SSE film before and after hot pressing show that porosity was largely eliminated. In fact, the separator was over 93% dense and had an ionic conductivity of 0.7 mS cm<sup>-1</sup> at room temperature.



**Figure XIII.4.4** a) DSC scan for LiPSiS glass SSE with glass transition,  $T_g$ , and crystallization onset,  $T_c$ , indicated with arrows. b) A picture of the fiberglass non-woven (NW) paper used to reinforced the SSE separator. c) Picture of the green SSE/NW/SSE stack prior to hot pressing. d) Picture of the finished reinforced SSE separator after hot pressing. e) A SEM micrograph of a green SSE separator surface shows considerable porosity. f) A SEM micrograph of a hot-pressed SSE separator surface shows that the pores are largely eliminated. Figures reproduced from [1].

It is a generally held view that sulfide SSEs are not chemically compatible with ether-based solvents. In fact, there have been at least two reports of sulfide SSEs deposited from solutions composed of ether-based solvents [17, 18]. These SSE formulations,  $(\text{Li}_2\text{S})_{75}(\text{P}_2\text{S}_5)_{25}$  and  $\text{Li}_{10}\text{GeP}_2\text{S}_{12}$ , were also found to be soluble in triglyme [19]. Therefore, it was non-obvious that LiPSiS glass SSE would be chemically compatible with a

DME:DOL based liquid electrolyte (LE). To provide evidence of chemical compatibility, a series of  $(\text{Li}_2\text{S})_{60}(\text{SiS}_2)_x(\text{P}_2\text{S}_5)_{40-x}$  ( $x = 0, 4, 20, 28, 40$ ) glass SSE compositions were soaked in 1:1 (v/v) DME:DOL and the results are provided in

Figure XIII.4.5 and reported elsewhere [2]. SiS<sub>2</sub>-rich glass compositions  $x = 28$  and 40 were insoluble in DME:DOL. This result was achieved because the Si-S bond (619 kJ mol<sup>-1</sup>) is comparatively stronger than the P-S bond (346 kJ mol<sup>-1</sup>). To demonstrate the utility of a semi-solid electrolyte system an experiment was conducted to determine the critical current densities (CCDs) of an all-solid-state Li/SSE/Li test cell and a semi-solid Li/LE/SSE/LE/Li test cell. As shown in Figure XIII.4.6, the all-solid-state test cell required a stack pressure of 3 MPa to achieve a CCD of 1.8 mA cm<sup>-2</sup>. The semi-solid test cell not only achieved a higher CCD of 3.0 mA cm<sup>-2</sup>, but it did so at a stack pressure of only 0.1 MPa. This result is significant because it demonstrates how semi-solid cells have advantageous performance and operating specifications compared to all-solid-state cells.

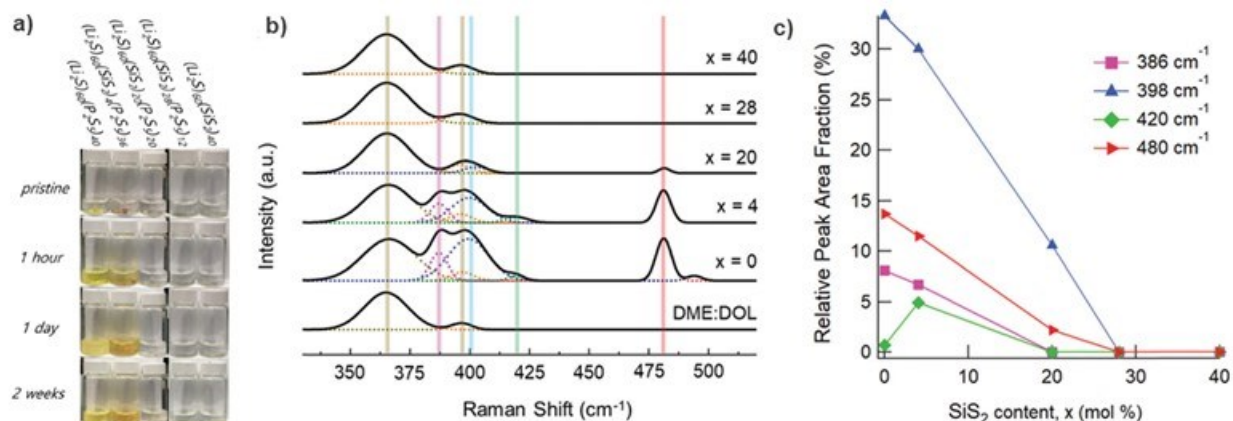


Figure XIII.4.5 a) Solubility times series for  $(\text{Li}_2\text{S})_{60}(\text{SiS}_2)_x(\text{P}_2\text{S}_5)_{40-x}$  ( $x = 0, 4, 20, 28, 40$ ) glasses soaked in DME:DOL. After 2 weeks the  $x = 0, 4$  and  $20$  sample solutions showed signs of discoloration, which is attributed to dissolution of the glass. The  $x = 28$  and  $40$  sample solutions remain clear over the course of the experiment. b) Raman spectra of pristine DOL:DME solvent and solutions obtained by soaking  $(\text{Li}_2\text{S})_{60}(\text{SiS}_2)_x(\text{P}_2\text{S}_5)_{40-x}$  ( $x = 0, 4, 20, 28, 40$ ) glasses in DME:DOL. The location of structural unit vibrational modes are indicated with colored bars from left to right; namely,  $\text{P}_2\text{S}_7^{4-}$  (pink),  $\text{P}_2\text{S}_6^{4-}$  (blue),  $\text{PS}_4^{3-}$  (green), and  $\text{S}_8$  (orange). Two vibrational modes of DME:DOL are also indicated (brown). c) Summary of dissolved species as a function of glass composition. Figures reproduced from [2].

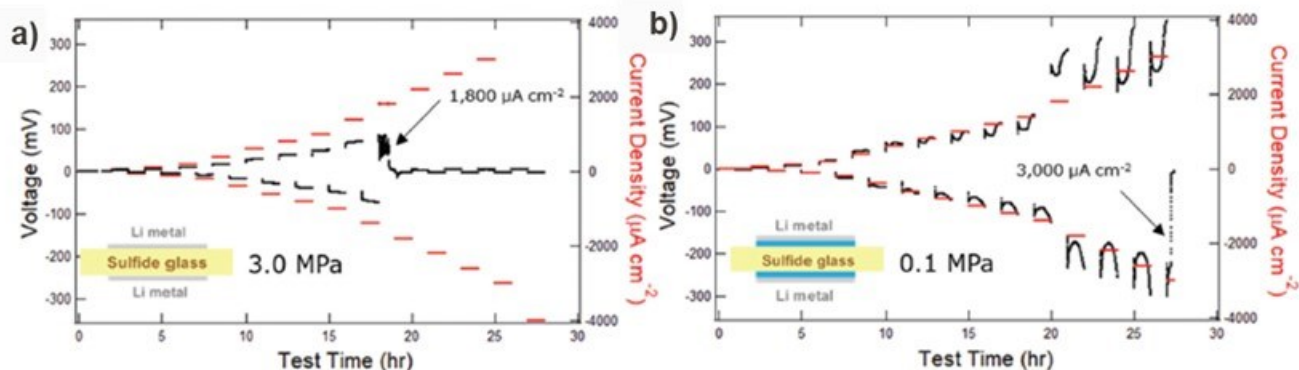


Figure XIII.4.6 CCDs of symmetric Li/SSE/Li test cells with or without a liquid electrolyte interlayer and a different stack pressures at  $25^\circ\text{C}$ . The SSE separators are  $(\text{Li}_2\text{S})_{60}(\text{SiS}_2)_{28}(\text{P}_2\text{S}_5)_{12}$  glass wafers of approximately  $600\ \mu\text{m}$  thickness. a) An all-solid-state test cell with direct Li/SSE contact and  $3\ \text{MPa}$  stack pressure experiences shorting failure at a CCD of  $1.8\ \text{mA cm}^{-2}$ . b) A semi-solid test cell with liquid electrolyte Li/SSE interlayer and a  $0.1\ \text{MPa}$  stack pressure experiences shorting failure at a CCD of  $3.0\ \text{mA cm}^{-2}$ . Note: the test was paused for two days at 20 hours due to a planned facility power outage. Figures reproduced from [2].

### Cell Design Opportunities

There are several opportunities to improve upon the cell design outlined in the first section and they will now be described to motivate the work described in the third section.

The primary benefit of an all-solid-state battery (ASSB) is improved abuse and thermal tolerance [20]. Unfortunately, a liquid or gel electrolyte used in a semi-solid battery design may reduce this tolerance somewhat. The first opportunity involves replacing the flammable and volatile DME:DOL based liquid electrolyte with a non-flammable alternative.

The second opportunity involves improving the moisture stability of sulfide SSEs. The semi-solid Li/S battery described in the first section was fabricated entirely inside an argon filled glovebox ( $<1\ \text{ppm H}_2\text{O}$ ), however,



cell manufacturing typically takes place in dry rooms with a  $-40\text{ }^{\circ}\text{C}$  dewpoint (127 ppm). To gauge the manufacturing readiness level of our cell technology, the stability of sulfide SSEs in a dry room environment must be evaluated and improved if necessary.

The third opportunity involves improving SSE separator design and there are several ways to do so. Glass thermal stability describes the tendency of a glass to devitrify (i.e. crystallize) once it is heated to a supercooled liquid state above its  $T_g$ . A glass that is thermal stability remains vitreous. The viscosity of a partially devitrified glass increases rapidly once the crystallites start to physically interact. Both LiPS and LiPSiS glasses have poor thermal stability and devitrify after hot pressing as shown in Figure XIII.4.7 [1, 14]. As a result, a pressure of 12 MPa was required to consolidate the LiPSiS glass SSE separator to 93% density and 200 MPa to fully consolidate LiPS. Design of a thermally stable glass SSE composition would facilitate processing at lower pressures, which would allow the use of existing Li-ion battery calendaring equipment. The standalone LiPSiS glass SSE separator presented above also limits cell energy density because it is too thick. To meet energy density targets it is required that the separator thickness be reduced to less than  $40\text{ }\mu\text{m}$  [21]. To do so it is best to support the separator by the cathode. It follows that the cathode will also need to undergo the same hot pressing process required to consolidate the supported separator.

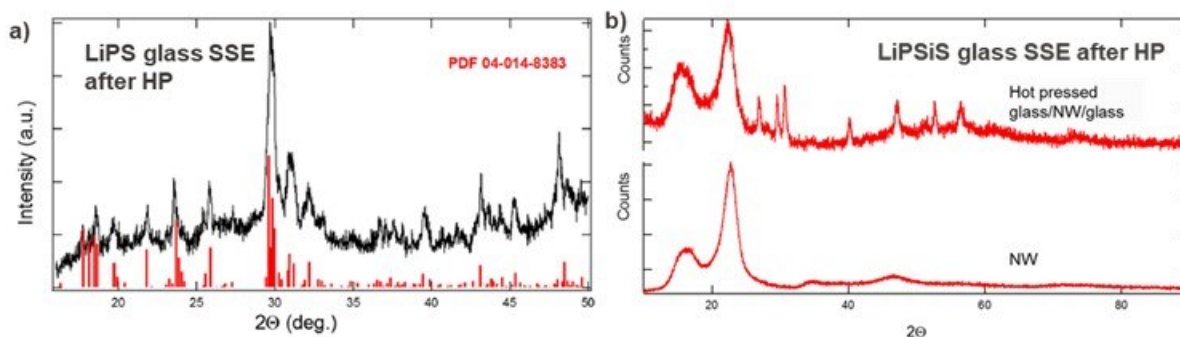


Figure XIII.4.7 Both LiPS and LiPSiS glass SSEs exhibit poor thermal stability and devitrify when hot-pressed. Devitrification during hot pressing increases the viscosity of the glass in the supercooled liquid state. As a result, much higher pressures are required to consolidate the glasses. a) pXRD spectrum of LiPS glass SSE after hot pressing. b) pXRD spectrum of LiPSiS glass after hot pressing. Figures reproduced from [1, 14].

### Cell Design Opportunities

#### Moisture Stability Evaluated

The moisture stability of sulfide SSEs was systematically investigated as a function of SSE composition and dry room moisture setpoint [3]. A glovebox was retrofitted with a custom moisture control system as shown in Figure XIII.4.8a,b to control water level to different moisture setpoints ranging from  $-76\text{ }^{\circ}\text{C}$  ( $<1\text{ ppm H}_2\text{O}$ ) to  $40\text{ }^{\circ}\text{C}$  ( $127\text{ ppm H}_2\text{O}$ ) dewpoint. The setup consisted of an Arduino microcontroller, a moisture probe, and a cartridge-based desiccant system (VAC). A variety of different SSE compositions were studied; namely,  $(\text{Li}_2\text{S})_{75}(\text{P}_2\text{S}_5)_{25}$ ,  $(\text{Li}_2\text{S})_{70}(\text{P}_2\text{S}_5)_{30}$ ,  $(\text{Li}_2\text{O})_7(\text{Li}_2\text{S})_{68}(\text{P}_2\text{S}_5)_{25}$ ,  $(\text{Li}_2\text{O})_7(\text{Li}_2\text{S})_{63}(\text{P}_2\text{S}_5)_{30}$ , and  $(\text{Li}_2\text{S})_{75}(\text{P}_2\text{S}_5)_{25} + 20\text{ mol\% LiI}$  (LPSI). It was found that moisture stability improved with 75 mol%  $\text{Li}_2\text{S}$  modifier content and the introduction of a  $\text{Li}_2\text{O}$  co-modifier (Figure XIII.4.8c,d). After a 30 min exposure in a  $-40\text{ }^{\circ}\text{C}$  dewpoint dry room environment the LPSI SSE powder generated  $0.1\text{ cc g}^{-1}\text{ H}_2\text{S}$  and its ionic conductivity decreased by over 50%. However, when the LPSI SSE powder was exposed as a slurry in an anhydrous dodecane carrier the same SSE generated  $0\text{ cc g}^{-1}\text{ H}_2\text{S}$  and its ionic conductivity only dropped by 14% (Figure XIII.4.8e). Our results show that sulfide SSEs have acceptable moisture stability when appropriately processed in a dry room environment with anhydrous solvents and binders.

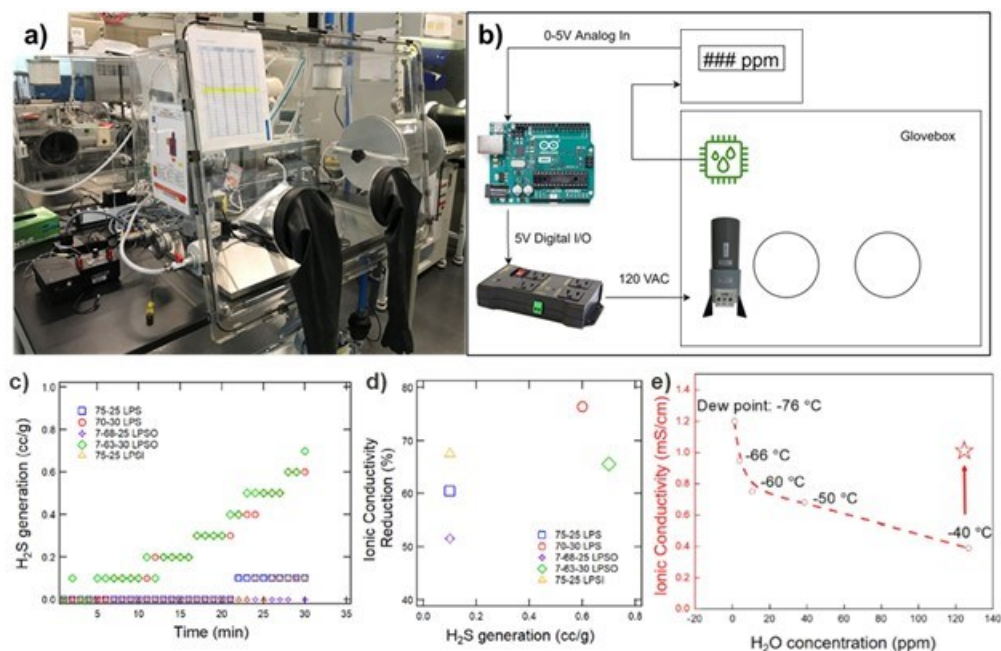


Figure XIII.4.8 a) A picture of the experimental setup used to expose sulfide SSE powders to a dry room environment. The setup includes a 300L volume tabletop glovebox, a cartridge-based desiccant system, a microcontroller system to control the moisture setpoint, a personal H<sub>2</sub>S detector, and a fan to continuously mix the glovebox air. b) Diagram of the experimental setup's control system to maintain moisture setpoints. c) H<sub>2</sub>S generation of different SSEs in a -40 °C dewpoint dry room as a function of time. d) Reduction in ionic conductivity versus maximum H<sub>2</sub>S reading for different sulfide SSEs. e) Ionic conductivity of LPSI sulfide SSE after exposure as a dry powder to different dry room environments for 30 min. The star marks the ionic conductivity of LPSI sulfide SSE after exposure to a -40 °C dewpoint dry room for 30 min while immersed in anhydrous dodecane. Figures were reproduced from [3].

### Oxysulfide SSE Processability

To improve the processability of glass SSE separators, it was desired to develop a more thermally stable SSE composition. As a reminder, thermal stability defines a glass' resistance to devitrification (i.e. crystallization). As shown in Figure XIII.4.9a,  $(\text{Li}_2\text{S})_{70}(\text{P}_2\text{S}_5)_{30}$  sulfide glass SSE (LPS, 70:30) devitrifies extensively to the  $\text{Li}_7\text{P}_3\text{S}_{11}$  ceramic phase after hot pressing. As mentioned earlier, this results in the need for a high processing pressure (200 MPa) to fully consolidate the material because devitrified glasses are highly viscous. Oxygen can be added to  $(\text{Li}_2\text{S})_{70}(\text{P}_2\text{S}_5)_{30}$  glasses by including a  $\text{P}_2\text{O}_5$  co-former. When 5 mol%  $\text{P}_2\text{O}_5$  is added, it was found that  $(\text{Li}_2\text{S})_{70}(\text{P}_2\text{S}_5)_{25}(\text{P}_2\text{O}_5)_5$  oxysulfide glass SSE (LPSO, 70:25:5) remained largely vitreous after hot pressing (Figure XIII.4.9b). In fact, when hot-pressed at 230°C, LPSO, 70:25:5 had a devitrification rate that was 10 times slower than that of LPS, 70:30 (Figure XIII.4.9c). Oxygen atoms in LPSO, 70:25:5 are accommodated into a  $\text{Li}_7\text{P}_3\text{S}_9.75\text{O}_{1.25}$  ceramic phase that is isostructural with the  $\text{Li}_7\text{P}_3\text{S}_{11}$  ceramic phase [22]. The devitrification rate of LPSO, 70:25:5 is slower because the smaller radius of the  $\text{O}^{2-}$  anion (140 pm) compared to the  $\text{S}^{2-}$  anion (184 pm) sterically hinders atomic rearrangement during the crystallization process (Inset Figure XIII.4.9c).

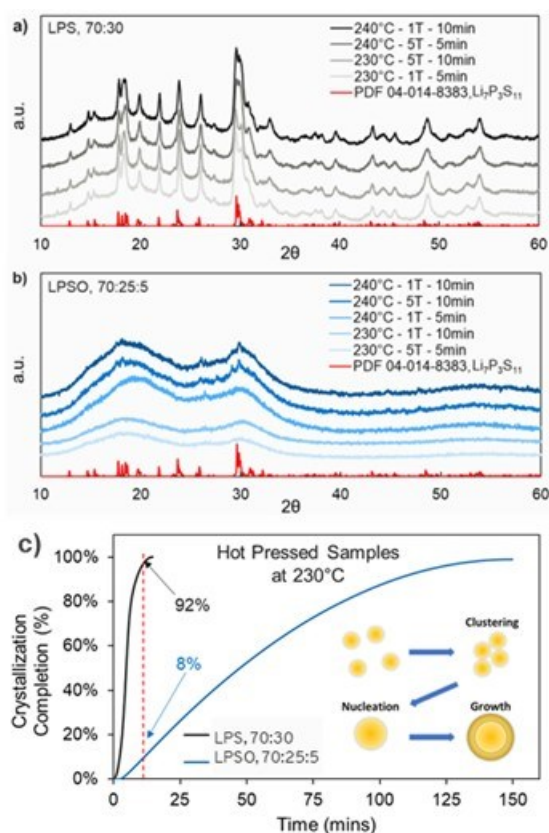


Figure XIII.4.9 a) pXRD of LPS, 70:30 samples after hot-pressing using various protocols. b) pXRD of LPSO, 70:25:5 samples after hot-pressing using various protocols c) DSC crystallization completion of LPS, 70:30 vs. LPSO, 70:25:5 at 230 °C. Bottom right inset graphic illustrates the crystallization process of crystallite nucleation and growth. The poor thermal stability of the LiPS glass leads to extensive devitrification, whereas the thermally stable LiPSO glass remains largely vitreous.

Having established that the LPSO, 70:25:5 oxysulfide glass SSE is thermally stable, a series of hot pressing trials were conducted using a variety of different processing conditions (Figure XIII.4.10a). In each case, the oxysulfide SSE was more deformable than the sulfide SSE. Informed by the optimal process condition, a 40  $\text{cm}^2$  separator film of LPSO, 70:25:5 oxysulfide glass SSE was prepared by hot pressing at a temperature of 230 °C and a pressure of only 2.75 MPa. The film was 110  $\mu\text{m}$  thick, 91.4% dense, and had an ionic

conductivity of 0.75 mS/cm after annealing. We conclude that the LPSO, 70:25:5 oxysulfide glass SSE is highly processable and sought to apply it next as a catholyte in all-solid-state cathodes.



Figure XIII.4.10 a) Picture of LPS, 70:30 and LPSO, 70:25:5 reinforced pellets after hot pressing using various protocols. In general, the LPSO, 70:25:5 samples are much more deformable than the LPS, 70:30 samples. b) Picture of a hot-pressed standalone, reinforced LPSO, 70:25:5 SSE separator film. The film is flexible and translucent. c) Close up picture of the same film after being cut into a disc. The crosshatch pattern is attributed to the underlying non-woven fiber reinforcement.

#### Hot-Pressed Cathode Composites

All-solid-state cathodes are advantageous for two reasons. First, the utilization of a SSE catholyte improves SSB abuse and thermal tolerance because it displaces liquid electrolyte, which may be volatile and flammable. Second, an all-solid-state cathode is better suited at supporting a SSE separator. As mentioned in the second section, cathode-support provides a means to reduce the thickness of SSE separators to an extent that cell energy targets are met. It follows that the cathode support must also undergo the same hot pressing process as the supported separator. Therefore, the goal of this work was to show that hot pressing can also improve the performance of all-solid-state electrodes by increasing the solid-solid interface between active material (AM) and SSE. In the first phase of work, we investigated the hot pressing of NCM cathode composites. In the second phase of work, we investigated the hot pressing of low voltage AM cathode composites.

The effectiveness of hot pressing NCM cathode composites was explored by systematically evaluating combinations of NCM622 and NCM85105 AMs with glassy  $\text{Li}_3\text{PS}_4$ , glassy  $\text{Li}_7\text{P}_3\text{S}_{11}$ , and  $\beta\text{-Li}_3\text{PS}_4$  SSEs [4]. As shown in Figure XIII.4.11, the performance of a NCM622 +  $\beta\text{-Li}_3\text{PS}_4$  composite cathode was improved by hot-pressing at 200 °C and 370 MPa for 10 minutes. While the hot-pressed (HP) cathode initially delivered a lower specific capacity (Figure XIII.4.11a), its capacity retention at a C/10 rate was much improved compared to a cold-pressed (CP) control cell (Figure XIII.4.11b). It was found that NCM reacted with certain SSE compositions, producing insulating interfacial decomposition products that increased cell impedance and reduced specific capacity (Figure XIII.4.12a). Unfortunately, the SSE that was the most stable versus NCM (i.e.  $\beta\text{-Li}_3\text{PS}_4$ ), was also the least moldable SSE. As shown in Table XIII.4.1, the cathode composite with  $\beta\text{-Li}_3\text{PS}_4$  was still 26.7% porous after hot-pressing. It is advantageous to reduce cathode composite porosity as much as possible because it increases cell energy density. In addition, secondary NCM particles were susceptible to cracking at the pressures required to consolidate  $\beta\text{-Li}_3\text{PS}_4$  (Figure XIII.4.12b,c). In conclusion, it was desired to replace high voltage NCM AM with a stable and mechanically robust low voltage AM so that the most moldable SSE catholyte could be utilized.

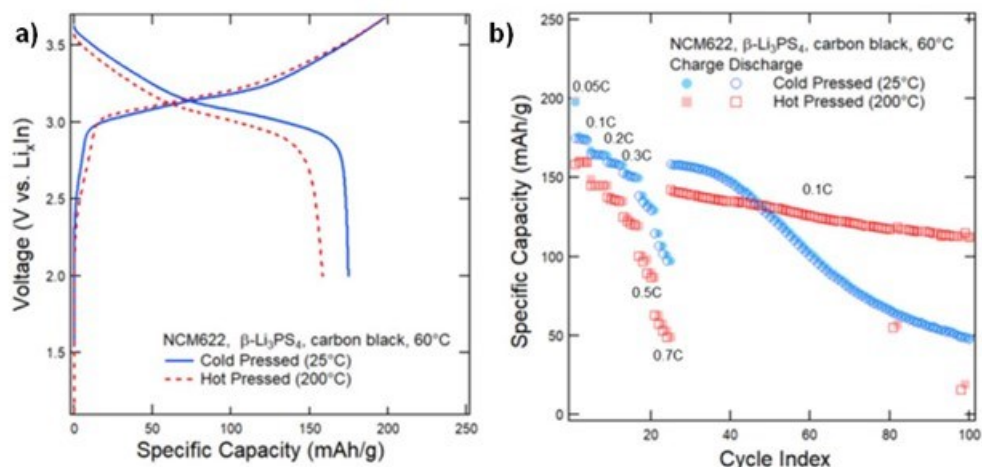


Figure XIII.4.11 a) First cycle voltage profiles for cold-pressed (blue) and hot-pressed (red) cathode composites with NCM622 active material,  $\beta\text{-Li}_3\text{PS}_4$  SSE, and carbon black conductive additive. b) Cyclic capacities for the same. Though the hot-pressed cell initially delivers lower capacity, it goes on to retain its capacity better than the cold-pressed cell. Figures reproduced from [4].

Table XIII.4.1 Densities and Porosities of Cold-pressed and Hot-pressed NCM Cathode Composites.

Material System	CP density (g/cc)	HP density (g/cc)	CP porosity (%)	HP porosity (%)
Glassy $\text{Li}_3\text{PS}_4$ + NCM85105	2.95	3.19	13.5	6.5
Glassy $\text{Li}_3\text{PS}_4$ + NCM622	2.863	3.149	17.1	8.86
$\beta\text{-Li}_3\text{PS}_4$ + NCM85105	2.36	2.47	29.7	26.7
Glassy $\text{Li}_7\text{P}_3\text{S}_{11}$ + NCM622	2.863	3.499	17.8	0

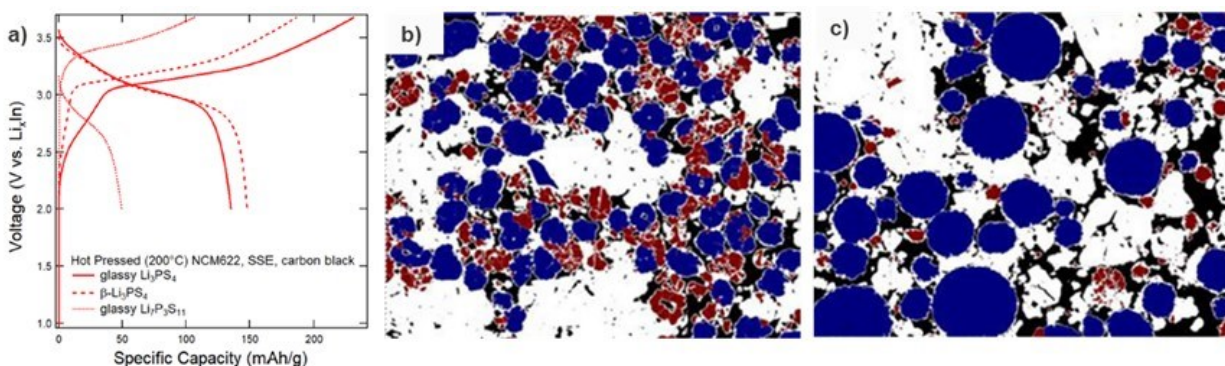


Figure XIII.4.12 a) First cycle voltage profiles for NCM622 composites with either glassy  $\text{Li}_3\text{PS}_4$  (solid),  $\beta\text{-Li}_3\text{PS}_4$  (dash), or glassy  $\text{Li}_7\text{P}_3\text{S}_{11}$  (dot) SSEs and 2 wt.% carbon black additive. b) Processed SEM image of a hot-pressed NCM85105/ $\beta\text{Li}_3\text{PS}_4$  cathode composite. c) Processed SEM image of a hot-pressed NCM622/ $\beta\text{-Li}_3\text{PS}_4$  cathode composite. The color scheme for the processed images is as follows: white = SSE particle, black = pore, blue = intact NCM particle, and red = damaged NCM particle. Figures reproduced from [4].

In the second phase of the all-solid-state cathode work, NCM was replaced with a low voltage AM. Furthermore, highly processable LPSO oxysulfide glass SSE was used as the catholyte. Hot pressing at 240 °C and 47 MPa for 10 minutes reduced the porosity of low voltage AM + LPSO cathode composites from ~30% to ~20% (Figure XIII.4.13). DSC scans of NCM and low voltage AM cathode composites are provided in Figure XIII.4.13d. The NCM cathode composites reveal large exothermic signals that are attributed to an interfacial reaction between the NCM and the sulfide SSE. On the other hand, the low voltage AM cathode composites exhibit no exothermic signals related to interfacial decomposition. Small exothermic signals at

approximately 250 °C are attributed to devitrification of the LPSO glass SSE. The electrochemical performance of CP and HP cells with low voltage AM + LPSO cathode composites are provided in Table XIII.4.2. When cycled at 25 °C, a CP cell delivered negligible capacity whereas a HP cell delivered a 1<sup>st</sup> cycle discharge capacity in excess of 600 mAh g<sup>-1</sup>. Furthermore, the cell impedance was reduced from 4010 Ω to 127 Ω by hot pressing. When cycled at 60°C, the HP cell also shows improved performance up to 50 cycles (Figure XIII.4.14). Improved HP cell performance is attributed to better AM/SSE interfacial contact and the absence of insulating interfacial decomposition products. This result was achieved by selecting mechanically robust and stable low voltage AM and highly processable LPSO glass SSE catholyte. In conclusion, we demonstrated a viable cathode support for hot-pressed SSE separators.

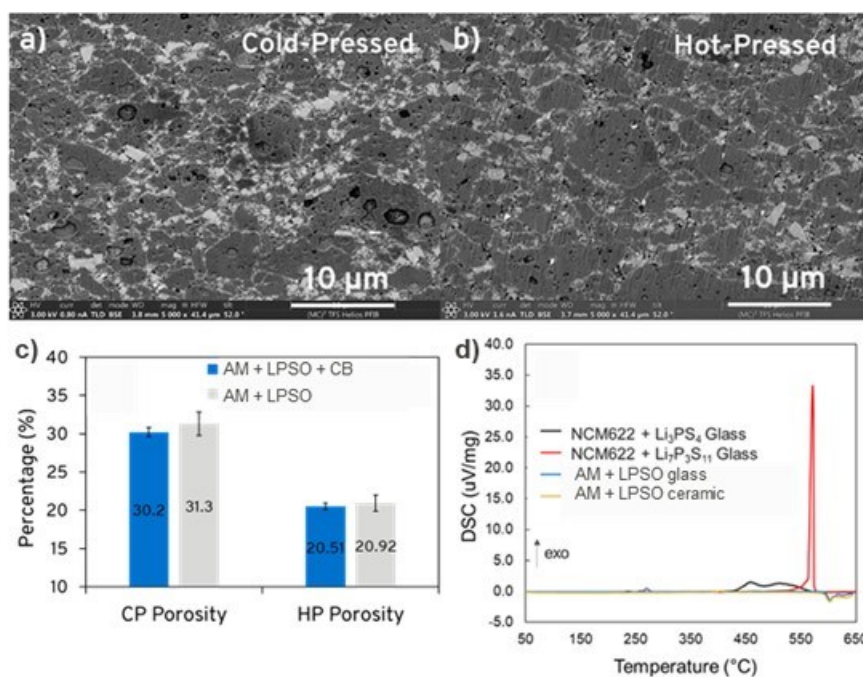
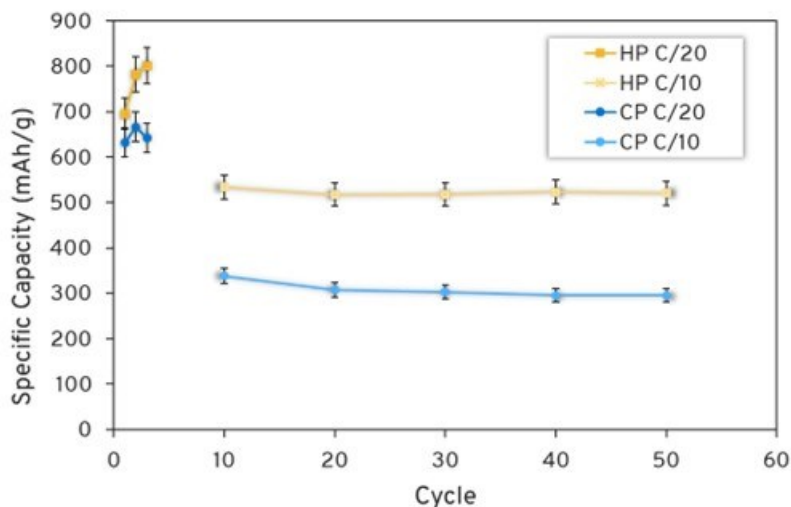


Figure XIII.4.13 SEM images of cathode composite composed of a low voltage active material (AM) and LPSO glass SSE a) before and b) after hot pressing. c) Porosity of cathode composites before and after hot pressing. d) DSC scans of NCM622 and low voltage AM cathode composites. The NCM622 cathode composites exhibit large exothermic reactions indicative a reaction between the NCM622 and the LPS SSE. On the other hand, the low voltage AM cathode composite exhibit no exothermic reactions in the same temperature range. Small exothermic signals around 250 °C are attributed to the devitrification of the glassy SSEs.

Table XIII.4.2 Summary of Electrochemical Characterization of Cells with Cathode Composites Composed of Low Voltage Active Material (AM) and Highly Processable LPSO Glassy SSE.

Press	Temperature (°C)	Spec. Cap. @ C/20 (mAh/g)	EIS (Ω)
CP	25	0	4010
CP	60	588.9	150
HP	25	657.8	127
HP	60	801.3	47



**Figure XIII.4.14** Cyclic capacity of cells with cathode composites composed of low voltage active material (AM) and highly processable LPSO glassy SSE cycled at 60 °C. Hot pressing (HP) improves the utilization of AM by nearly 70% compared to cold pressing (CP).

### **Semi-Solid Electrolyte**

The final avenue explored to improve upon our semi-solid Li/S cell design involved replacing the DME:DOL based liquid electrolyte with a solvate ionic liquid (SIL) electrolyte. As shown in Figure XIII.4.15, SIL electrolyte is less flammable than DME:DOL based liquid electrolyte, which will improve future cell abuse and thermal tolerance. As before, chemical compatibility between the SSE and the LE is of the utmost importance. Fortunately, it was previously reported that  $\text{Li}_{10}\text{GeP}_2\text{S}_{12}$  is stable in SIL [19], however, SIL are often highly viscous and cause poor reaction kinetics. Consequently, it may be desirable to utilize dilute SIL for improved wettability and enhanced reaction kinetics. In Figure XIII.4.16 we show that oxysulfide SSE are more stable in dilute SIL than sulfide SSE. A variety of (oxy)sulfide glass SSE samples were soaked in SIL for 7 days. It was found that sample mass loss decreased with increasing oxygen content (Figure XIII.4.16b). SILs were also characterized with UV-Vis spectroscopy after 7 days and reduced absorbance was associated increased oxygen content. We conclude that a combination of oxysulfide SSE and SIL provides a promising semi-solid electrolyte system for future semi-solid battery designs.

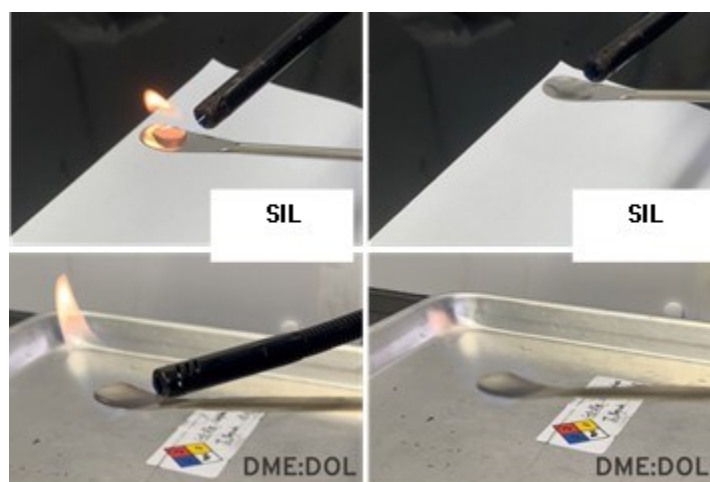


**Figure XIII.4.15** Pictures of a solvate ionic liquid (SIL) electrolyte and a DME:DOL + 1M LiTFSI electrolyte under an exposed flame. The DME:DOL electrolyte readily ignites whereas the SIL does not.

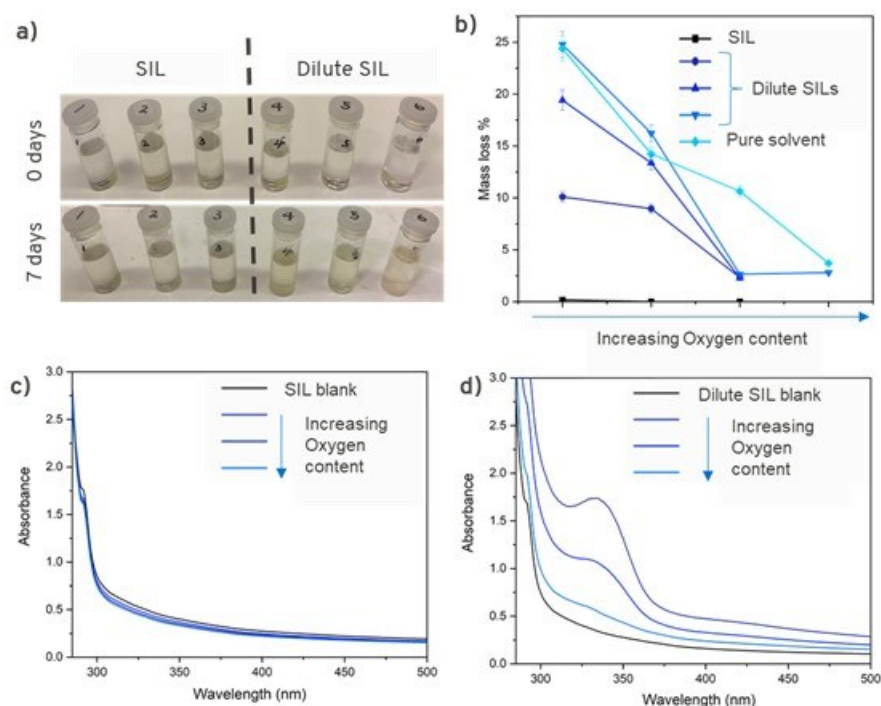


**Figure XIII.4.16** a) Picture of (oxy)sulfide glass SSE samples soaked in SIL and dilute SIL. b) Mass loss of (oxy)sulfide glass SSE samples after soaking in a variety of SIL for 7 days. Reduced mass loss is associated with increased SSE oxygen content. c) UV-Vis spectra of (oxy)sulfide SSE samples after soaking in SIL for 7 days. d) UV-Vis spectra for (oxy)sulfide SSE samples after soaking in dilute SIL for 7 days. Reduced absorbance is associated with increased SSE oxygen content.

## Conclusions

High profile research on solid-state electrolytes typically focuses on alluring attributes like high ionic conductivity and the discovery of new ceramic phases. In this project, we focused on the often neglected attributes of processability (i.e. crystallization kinetics), chemical stability, and moisture stability. As a result, we were rewarded with the demonstration of a semi-solid Li/S cell design capable of meeting program targets.

## Key Publications

1. Yersak, Thomas, James R. Salvador, Robert D. Schmidt, and Mei Cai. "Hybrid Li-S pouch cell with a reinforced sulfide glass solid-state electrolyte film separator." *International Journal of Applied Glass Science* 12.1 (2021): 124-134.
2. Albertus, Paul, et al. "Challenges for and pathways toward Li-metal-based all-solid-state batteries." *ACS Energy Letters* 6.4 (2021): 1399-1404.
3. Yersak, Thomas A., Fang Hao, Chansoon Kang, James R. Salvador, Qinglin Zhang, Hernando Jesus Gonzalez Malabet, and Mei Cai. "Consolidation of composite cathodes with NCM and sulfide solid-state electrolytes by hot pressing for all-solid-state Li metal batteries." *Journal of Solid State Electrochemistry* 26.3 (2022): 709-718.
4. Yersak, Thomas A., Chansoon Kang, James R. Salvador, Nicholas PW Pieczonka, and Mei Cai. "Sulfide glass solid-state electrolyte separators for Li metal batteries: using an interlayer to increase rate performance and reduce stack pressure." *Materials Advances* 3.8 (2022): 3562-3570.
5. Yersak, Thomas A., Yubin Zhang, Fang Hao, and Mei Cai. "Moisture Stability of Sulfide Solid-State Electrolytes." *Frontiers in Energy Research* 10:882508 (2022).



## References

1. Yersak, T., et al., Hybrid Li-S pouch cell with a reinforced sulfide glass solid-state electrolyte film separator. *International Journal of Applied Glass Science*, 2021. 12(1): p. 124-134.
2. Yersak, T.A., et al., Sulfide glass solid-state electrolyte separators for Li metal batteries: using an interlayer to increase rate performance and reduce stack pressure. *Materials Advances*, 2022. 3(8): p. 3562-3570.
3. Yersak, T.A., et al., Moisture Stability of Sulfide Solid-State Electrolytes. *Frontiers in Energy Research*, 2022. 10: p. 882508.
2. Yersak, T.A., et al., Consolidation of composite cathodes with NCM and sulfide solid-state electrolytes by hot pressing for all-solid-state Li metal batteries. *Journal of Solid State Electrochemistry*, 2022. 26(3): p. 709-718.
3. Ye, H. and Y. Li, Towards practical lean-electrolyte Li-S batteries: Highly solvating electrolytes or sparingly solvating electrolytes? *Nano Research Energy*, 2022. 1(1): p. e9120012.
4. Jozwiuk, A., et al., The critical role of lithium nitrate in the gas evolution of lithium-sulfur batteries. *Energy & Environmental Science*, 2016. 9(8): p. 2603-2608.
5. Zhang, S.S., Role of LiNO<sub>3</sub> in rechargeable lithium/sulfur battery. *Electrochimica Acta*, 2012. 70: p. 344-348.
6. Wang, L., Y. Wang, and Y. Xia, A high performance lithium-ion sulfur battery based on a Li<sub>2</sub>S cathode using a dual-phase electrolyte. *Energy & Environmental Science*, 2015. 8(5): p. 1551-1558.
7. Yu, X., et al., Hybrid lithium-sulfur batteries with a solid electrolyte membrane and lithium polysulfide catholyte. *ACS applied materials & interfaces*, 2015. 7(30): p. 16625-16631.
8. Zhou, W., et al., Plating a dendrite-free lithium anode with a polymer/ceramic/polymer sandwich electrolyte. *Journal of the American Chemical Society*, 2016. 138(30): p. 9385-9388.
9. Yu, X., et al., Polysulfide-shuttle control in lithium-sulfur batteries with a chemically/electrochemically compatible NASICON-type solid electrolyte. *Advanced Energy Materials*, 2016. 6(24): p. 1601392.
10. Wang, Q., et al., A gel-ceramic multi-layer electrolyte for long-life lithium sulfur batteries. *Chemical communications*, 2016. 52(8): p. 1637-1640.
11. Li, Y., et al., Hybrid polymer/garnet electrolyte with a small interfacial resistance for lithium-ion batteries. *Angewandte Chemie International Edition*, 2017. 56(3): p. 753-756.
12. Yersak, T., et al., Hot pressed, fiber-reinforced (Li<sub>2</sub>S)<sub>70</sub>(P<sub>2</sub>S<sub>5</sub>)<sub>30</sub> solid-state electrolyte separators for Li metal batteries. *ACS Applied Energy Materials*, 2019. 2(5): p. 3523-3531.
13. Garcia-Mendez, R., et al., Correlating macro and atomic structure with elastic properties and ionic transport of glassy Li<sub>2</sub>S-P<sub>2</sub>S<sub>5</sub> (LPS) solid electrolyte for solid-state Li metal batteries. *Advanced Energy Materials*, 2020. 10(19): p. 2000335.
14. Shelby, J.E., *Introduction to glass science and technology*. 2020: Royal society of chemistry.
15. Lim, H.D., et al., Solid electrolyte layers by solution deposition. *Advanced Materials Interfaces*, 2018. 5(8): p. 1701328.
16. Xiao, Q., et al., *Electrolyte and Electrode Structure*. 2016, GM Global Technology Operations LLC.
17. Oh, D.Y., et al., Excellent compatibility of solvate ionic liquids with sulfide solid electrolytes: toward favorable ionic contacts in bulk-type all-solid-state lithium-ion batteries. *Advanced Energy Materials*, 2015. 5(22): p. 1500865.
18. Inoue, T. and K. Mukai, Are all-solid-state lithium-ion batteries really safe?—verification by differential scanning calorimetry with an all-inclusive microcell. *ACS Applied Materials & Interfaces*, 2017. 9(2): p. 1507-1515.
19. Berg, E.J. and S. Trabesinger, Viability of polysulfide-retaining barriers in Li-S battery. *Journal of The Electrochemical Society*, 2017. 165(1): p. A5001.
20. Minami, K., et al., Structure and properties of the 70Li<sub>2</sub>S·(30-x)P<sub>2</sub>S<sub>5</sub>·xP<sub>2</sub>O<sub>5</sub> oxysulfide glasses and glass-ceramics. *Journal of non-crystalline solids*, 2008. 354(2-9): p. 370-373.

## Acknowledgements

The PI (Thomas A. Yersak) would like to recognize our NETL managers, Adrienne L Riggi and Coriana H. Fitz, and our GM Government Contracts Manager, Aida Rodrigues. Special thanks is also given to Drs. James

R. Salvador, Yubin Zhang, Hernando Jesus Gonzalez Malabet, Robert Schmidt, Nicholas P. W. Pieczonka, Fang Hao, and Chansoon Kang for their important contributions to the project.

## XIII.5 Developing Materials for High-Energy-Density Solid State Lithium-Sulfur Batteries (Penn State University, University Park)

### Donghai Wang, Principal Investigator

Penn State University  
134 Energy & Environmental Laboratory  
University Park, PA 16802  
E-mail: [dwang@psu.edu](mailto:dwang@psu.edu)

### Tien Duong, DOE Technology Development Manager

U.S. Department of Energy  
E-mail: [Tien.Duong@ee.doe.gov](mailto:Tien.Duong@ee.doe.gov)

Start Date: October 1, 2019  
Project Funding: \$425,259

End Date: September 30, 2023  
DOE share: \$339,358

Non-DOE share: \$85,901

### Project Introduction

Lithium-sulfur (Li-S) all-solid-state battery (ASSB) is a promising candidate to replace existing Li-ion batteries for application in electric and plug-in hybrid electric vehicles (EVs and PHEVs) due to its high energy density and superior safety. Moreover, recent advances in improving ionic conductivities ( $\approx 10^{-2} \text{ S cm}^{-1}$ ) of sulfide-based solid-state electrolytes (SSEs) put us one step closer to the practical application of Li-S ASSBs<sup>1</sup>. In Li-S ASSBs, the polysulfide shuttling and self-discharges in liquid-type Li-S batteries could be fundamentally resolved<sup>2</sup>. Furthermore, as added benefits, sulfide-based SSEs possess improved safety due to the absence of flammable organic electrolytes<sup>3,4</sup>. However, despite those encouraging characteristics of ASSBs, there are technological challenges such as low sulfur utilization and increased interfacial resistance due to poor contact, large volume expansion of sulfur upon cycling and unoptimized microstructure of sulfur-carbon-SSEs composites in the solid cathode, poor charge/discharge rate due to the low conductivity of SSEs, and SSEs' chemical instability against moisture and lithium/lithium alloy anodes. The challenges are fundamentally attributed to the properties of the solid materials and their interfaces in electrodes.

In brief, we shall address the following three problems of Li-S ASSBs in this project. First, we aim to construct electron and ionic transport pathways in the cathode to improve sulfur utilization upon cycling and boost overall energy density. Second, we target generating a favorable interface between carbon-sulfur composite and solid-state electrolytes with novel solid additives or approaches. Third, we plan to develop new sulfide-based solid electrolytes with high ionic conductivity and improved stability against moisture and lithium alloys for all.

### Objectives

The project objectives are to develop materials involving advanced S-C composite materials, solid additives, and sulfide-based SSEs and acquire knowledge of Li-S ASSBs. Li-S ASSBs with high areal sulfur loading ( $\geq 5 \text{ mg cm}^{-2}$ ) and high sulfur content ( $\geq 50 \text{ wt\%}$  in cathode), pairing with lithium or lithium alloy anode, shall deliver a high initial specific capacity of over  $1200 \text{ mAh g}^{-1}$  at high charge/discharge rate ( $> 0.3 \text{ C}$ ) for 500 cycles with over 80% capacity retention. The out-year goals are as follows: (1) develop and optimize sulfur cathode materials and synthesize new solid electrolytes (ionic conductivity  $> 5 \text{ mS cm}^{-1}$  at room temperature) (2) conduct characterization and performance tests on both material and electrode levels. The final demonstration will be all-solid-state sulfur cathodes with  $> 1200 \text{ mAh g}^{-1}$  discharge capacity at  $0.3 \text{ C}$  discharge rate and 50 wt% sulfur content for 500 cycles at room temperature.

## Approach

The project goal will be accomplished by developing new materials, together with the in-depth characterization of sulfur cathodes. Specifically, approaches to realize the project objectives include the following:

- (1) development of new carbon material with unique structure, high surface area, and large pore volume;
- (2) development of new S-C and S-C-M<sub>x</sub>S<sub>y</sub> materials (M = Li, Co, Ti, Mo, etc.) to facilitate electron/ion transport;
- (3) development of novel additives to tune interfacial behavior among components in the cathode;
- (4) development and optimization of new SSE through cation and anion doping with superior properties such as high ionic conductivity, good moisture, and stability; and
- (5) diagnostics, characterization, and cell tests on the developed new material or advanced sulfur cathode.

## Results

### 1. Electrochemical characterization of sulfur cathodes

In the previous year, we found that the new solid electrolyte (SSE) we prepared could effectively improve the performance of high-sulfur-content cathodes (60wt% of sulfur). To explicate sulfur cathodes' electrochemical behaviors during charge/discharge, we performed the galvanostatic intermittent titration technique (GITT) using Li-S ASSBs with sulfur cathodes using conventional 75Li<sub>2</sub>S-25P<sub>2</sub>S<sub>5</sub> (LPS) solid electrolyte (S-C-LPS) and the new solid electrolyte we prepared (S-C-SSE). As shown in Figure XIII.5.1, S-C-SSE cathode delivered significantly higher specific capacity and lower overpotential than S-C-LPS cathode, suggesting more active sulfur, lower reaction resistance and improved Li<sup>+</sup> transport kinetics in the S-C-SSE cathode than in the S-C-LPS cathode. Together, the analysis demonstrates that sufficient Li<sup>+</sup> transport pathways and fast Li<sup>+</sup> transport kinetics are achieved in the S-C-SSE cathode.

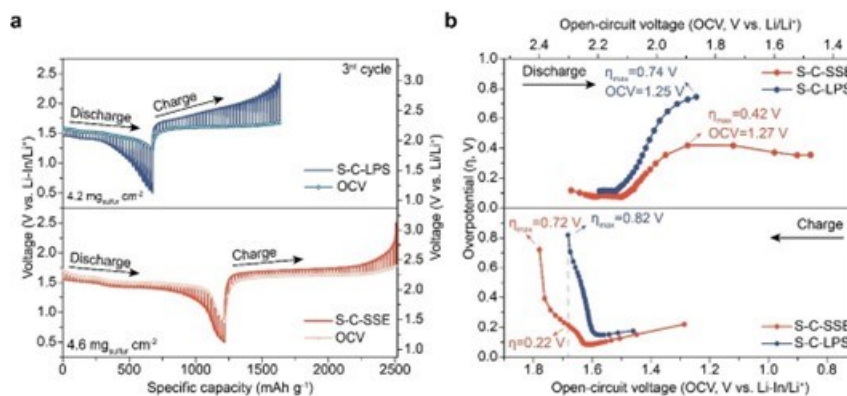


Figure XIII.5.1 (a) GITT and open circuit voltage (OCV) curves of S-C-SSE and S-C-LPS cathodes at the third cycle. Current pulses of 0.03 C for 30 mins were employed, followed by 4-hour resting. (b) Overpotential profiles of S-C-SSE and S-C-LPS cathodes from the GITT measurement.

### 2. Development of new additive for sulfur cathodes

Based on our previous findings, we identified a new additive for sulfur cathodes to improve the ionic conductivity of sulfur cathodes. As shown in Figure XIII.5.2, within a limited electrochemical voltage window of 1.0-2.5 V vs. Li-In/Li<sup>+</sup> (or 1.62-3.12 V vs. Li/Li<sup>+</sup>), the sulfur cathode with an areal sulfur loading of 2.175 mg cm<sup>-2</sup> and a high sulfur content of 50 wt% exhibited a high discharge specific capacity over 1200 mAh g<sup>-1</sup> at 0.1 C. After continuing screening different additives for use in sulfur cathodes, the cell with additive 2 delivered the best rate performance. At 0.1 C, the discharge capacity of the cell with additive 2 could reach as high as 1548 mAh g<sup>-1</sup>, close to the theoretical capacity of sulfur. When the current rate increased to 0.4 C, the discharge capacity of the cell remained at 1196 mAh g<sup>-1</sup>. The improved performance might be induced by the improved ionic transport in the sulfur cathode and at sulfur/SE interfaces.

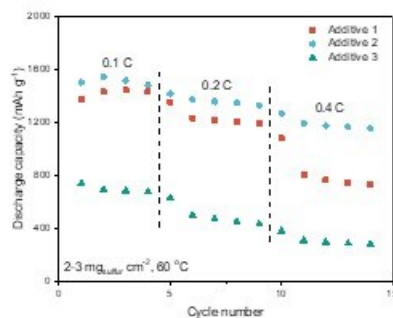


Figure XIII.5.2 Rate performance of all-solid-state Li-In | S batteries with different additives in sulfur cathodes. The areal sulfur loading of sulfur cathodes is controlled between 2-3  $\text{mg}_{\text{sulfur}} \text{cm}^{-2}$ . The cells were tested at 60 °C.

### 3.XPS analysis of sulfur cathodes

In addition, we also performed XPS quantitative analysis and collected the high-resolution S 2p spectra of the lithiated electrodes to understand the lithiation states of the sulfur cathodes. To do so, we first carried out the XPS survey scan of 25 different spots on the surface of the lithiated S-C-LPS cathode and the lithiated ‘new cathode’, and the survey spectrum of the S-C-LPS cathode is shown in Figure XIII.5.3a. The XPS quantitative results (Figure XIII.5.3b) revealed the nonuniform lithiation states on the cathode surface and the relatively higher lithiation states of the lithiated new electrode, attributed to the higher discharge capacity of the cell with new electrode than the cell with control S-C-LPS cathode. XPS S 2p spectra (Figure XIII.5.3c) further revealed that some sulfur remains inactive in the lithiated S-C-LPS cathodes.

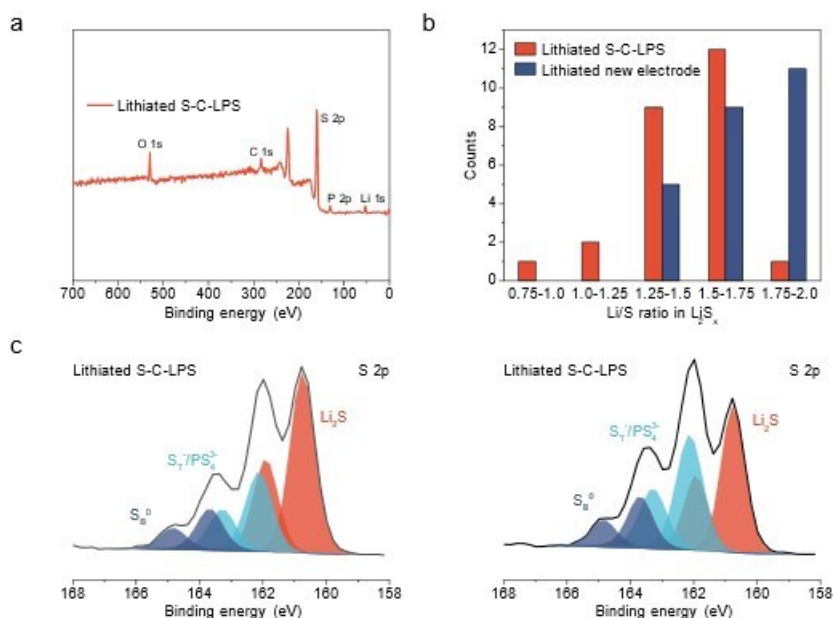
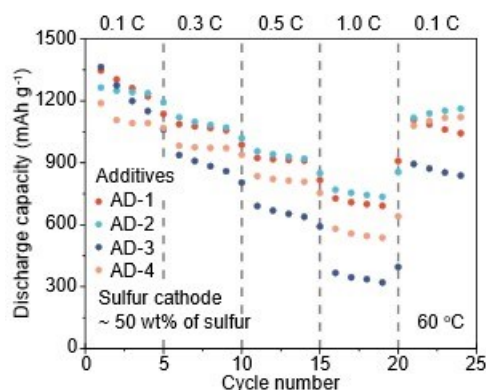


Figure XIII.5.3 (a) XPS survey spectra of lithiated S-C-LPS. (b) Distribution of lithium to sulfur atomic ratios in the active material at different sites on S-C-LPS and developed new electrode surfaces. (c) High-resolution S 2p spectra of two sites on S-C-LPS cathode surfaces.

### 4.Screening of various cathode additives for Li-S all-solid-state batteries

We further continue the screening of various cathode additives aiming to promote the interfacial ion transport. Four different cathode additives were selected and evaluated in sulfur cathodes with 50wt% of sulfur and areal sulfur loading of 2-3  $\text{mg cm}^{-2}$ . As shown in Figure XIII.5.4, while all additives can help promote initial

discharge capacity to above  $1000 \text{ mAh g}^{-1}$  at  $0.1 \text{ C}$ , AD-2 additive enabled sulfur cathodes with the best rate performance and reversibility. Such improvement might be caused by the improved robust interfacial contact as well as faster interfacial ion transport between sulfur and solid-state electrolyte (SSE) due to the use of additives. It demonstrates improved results from Figure XIII.5.4.



**Figure XIII.5.4** Rate performance of sulfur cathodes using different cathode additives at  $60 \text{ }^\circ\text{C}$  with an areal sulfur loading of  $2\text{-}3 \text{ mg cm}^{-2}$ .

### 5. Investigation on the origin of low sulfur utilization

As the two-electron conversion reaction between  $\text{S}_8$  and  $\text{Li}_2\text{S}$  involves the formation of  $\text{Li}_2\text{S}_2$  as an intermediate state, it is not clear whether the low sulfur utilization is induced by unreacted sulfur or insufficient conversion of  $\text{S}_8$  to  $\text{Li}_2\text{S}$ . Therefore, we carried out Raman spectral imaging characterization of lithiated sulfur cathodes to understand the low sulfur utilization in conventional sulfur cathodes with a sulfur content of  $50 \text{ wt}\%$  and  $75\text{Li}_2\text{S}\cdot 25\text{P}_2\text{S}_5$  (LPS) SSE. As shown in Figure XIII.5.5, elemental sulfur with several micrometers in size can be clearly observed on the surface of the lithiated sulfur cathode. Because of the low electronic and ionic conductivity of sulfur, the sulfur, which is isolated from electronic conductive carbon framework (carbon) or ionic conductive carbon framework, cannot be reduced and thus induce the low sulfur utilization of the cell.

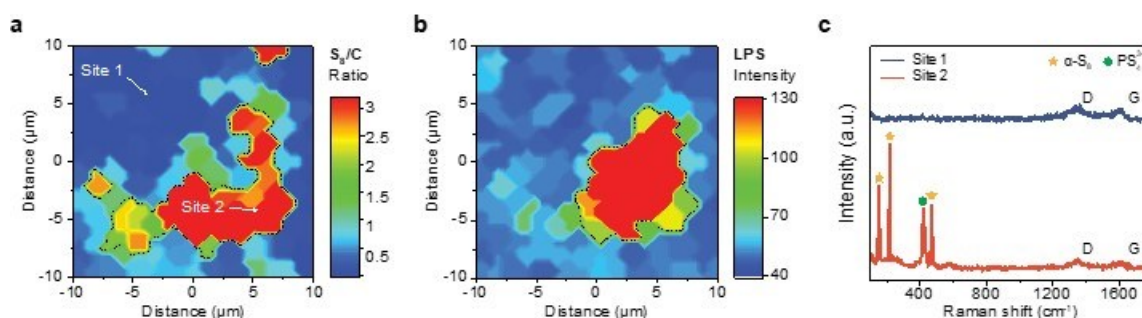


**Figure XIII.5.5** Raman spectral mapping images ( $10\times 10 \text{ }\mu\text{m}$ ) of the sulfur electrode surface after first discharge at  $0.1 \text{ C}$  and  $60 \text{ }^\circ\text{C}$  showing the distribution of sulfur/carbon ratio (based on intensity) (a) and LPS SSE (b). (c) Raman spectra of the sulfur cathode surface at two different sites.

### 6. Optimization of sulfur cathodes with high areal sulfur loading

Finally, we continued working on optimizing sulfur cathodes in terms of compositions and preparation process. The new SSE we developed previously with high ionic conductivity of  $\sim 4 \text{ mS cm}^{-1}$  was used for sulfur cathode preparation. As a result, the sulfur cathode with optimized compositions, high sulfur content of  $\geq 50 \text{ wt}\%$ , high areal sulfur loading of  $5.16 \text{ mg}_\text{s} \text{ cm}^{-2}$  and preparation procedure delivered initial discharge capacity of  $905.3 \text{ mAh g}^{-1}$  at  $0.1 \text{ C}$  ( $1 \text{ C}=1675 \text{ mAh g}^{-1}$ ). Upon increasing the discharge current rate to  $0.3 \text{ C}$ , the discharge capacity first decreased to  $\sim 782.8 \text{ mAh g}^{-1}$  then gradually increased to over  $1000 \text{ mAh g}^{-1}$  in 16 cycles (Figure XIII.5.6a). The highest discharge capacity reached  $\sim 1085 \text{ mAh g}^{-1}$ . After 100 cycles, the

discharge capacity remained  $993.4 \text{ mAh g}^{-1}$ . The performance meets the requirements for the milestone of the third quarter. As shown in the galvanostatic charge-discharge profiles (Figure XIII.5.6b), the voltage polarization is  $\sim 800 \text{ mV}$  which is quite high. It indicates that ionic and electron transport in sulfur cathodes need further improvement toward better electrochemical performance of Li-S all-solid-state batteries with high areal sulfur loading at room temperature.

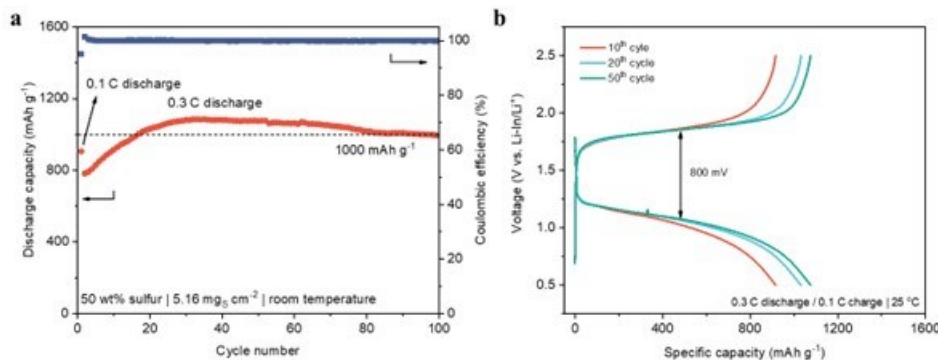


Figure XIII.5.6 (a) Cycling performance and (b) corresponding galvanostatic charge-discharge profiles of sulfur cathodes using the new SSE we developed at room temperature.

### 7. Lithium alloy anodes for Li-S all-solid-state batteries and their electrochemical performance

Besides, to prolong the lifetime of Li-S all-solid-state batteries and increase their energy density, we synthesized different types of lithium alloy anodes to replace Li-In anode. Utilizing the high-energy ball-milling method, we could fabricate lithium alloys with different lithiated states, which possess various electrochemical potentials versus lithium metal. We found that the electrochemical potentials are important in preventing lithium dendrite formation and propagation. Also, to improve the interfacial issues such as side reactions between solid-state electrolytes and lithium metal, using alloy anodes could not only suppress the undesired products but also improve the interfacial contact between the two. We developed three types of lithium alloys and performed a series of electrochemical tests. For the long-cycling performance (Figure XIII.5.7), the Lithium alloy-2 with a moderate lithiated state outperforms the Lithium alloy-1 and Lithium alloy-3. It can cycle stably and enable all-solid-state Li-S batteries with high discharge capacities over 200 cycles and sustain a high capacity retention of around 90%. However, Lithium alloy-1 suffers from short-circuiting after 20 cycles, while Lithium alloy-2 and Lithium alloy-3 could deliver high discharge capacities and prevent dendrite formation. It implies that suitable lithiated state of the applied alloy anode could avoid short-circuiting, and still maintain high energy density.

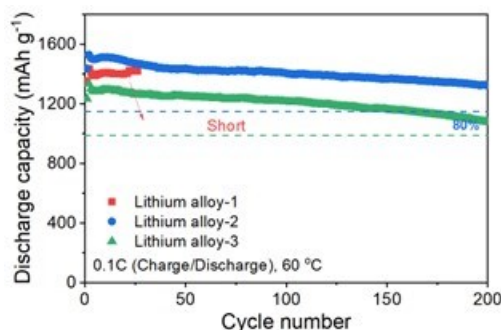


Figure XIII.5.7 Cycling performance of the Li-S ASSBs with alloy anodes. The cells were tested at 0.1C under 60 °C, and the specific capacity is based on the weight of sulfur.

### 8. Cycling performance of Li-S batteries using Li alloy anodes at high loadings or under high currents

To achieve a high loading cell with over  $5 \text{ mg cm}^{-2}$  and high discharge capacity of over  $1000 \text{ mAh g}^{-1}$  at  $0.3 \text{ C}$  rate, all-solid-state Li alloy anodes were also studied because of the high theoretical capacity of Li alloy anodes and their potential of suppressing dendrites. The alloy anodes we prepared have higher energy density than conventional Li-In alloy anode and improved cycling stability. The alloy anodes we prepared have higher energy density than conventional Li-In alloy anode and improved cycling stability. The optimized lithium alloy with better lithium diffusion and lower impedance enables a superior electrochemical performance. As shown in Figure XIII.5.8a, a cell composed of lithium alloy anode and high loading sulfur cathode ( $5.45 \text{ mg cm}^{-2}$ ) achieved an initial capacity of  $1176.9 \text{ mAh g}^{-1}$  at  $0.1 \text{ C}$  rate and  $60^\circ \text{C}$ . It can maintain above  $5 \text{ mAh cm}^{-2}$  until 72<sup>th</sup> cycle. Moreover, the optimized lithium alloy anode paired with normal capacity loading around  $2.5 \text{ mg cm}^{-2}$  was also fabricated and tested under step-increased currents from  $0.1\text{C}$ ,  $0.2\text{C}$ , and  $0.5\text{C}$  after every 3 cycles and then  $1\text{C}$  hereafter (Figure XIII.5.8b). The long-term cycling test under  $1\text{C}$  shows stable discharge capacity retention over 1000 cycles. The results imply that the cell performance is promising and possible to replace conventional Li-In alloy anode.

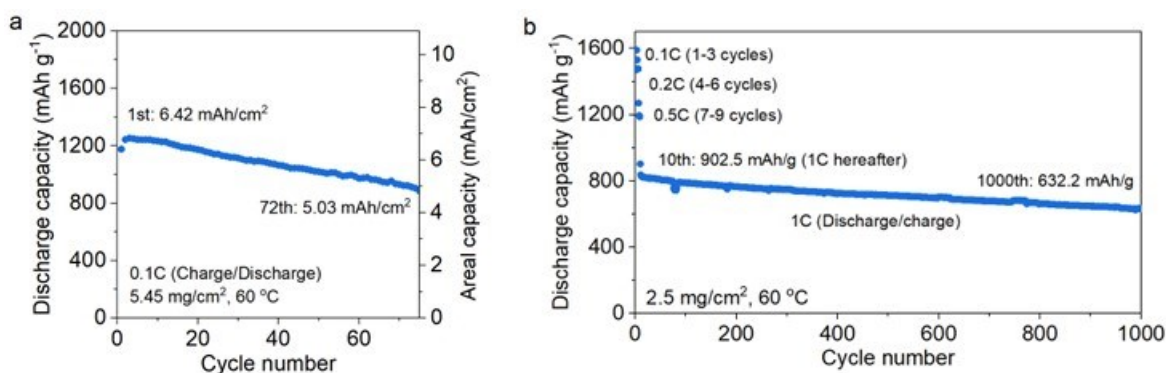


Figure XIII.5.8 (a) Cycling performance of the high loading cell with  $5.45 \text{ mg cm}^{-2}$  sulfur cathode using the lithium alloy anode under  $0.1\text{C}$ , (b) cycling performance of the cell with  $2.5 \text{ mg cm}^{-2}$  sulfur loading tested under  $1\text{C}$  rate for over 1000 cycles.

### Conclusions

In conclusion, we have accomplished our goals for the budget period 1-3 and obtained the following main achievements: (1) We successfully synthesized an effective additive for sulfur cathodes and obtained superior electrochemical performance. (2) The effects of ion/electron transport within sulfur cathodes were investigated through GITT, Raman technique, and XPS analysis. (3) We developed advanced sulfur cathodes for all-solid-state batteries with high sulfur content of  $\geq 50 \text{ wt}\%$ , high areal sulfur loading of  $5.16 \text{ mgs cm}^{-2}$  which could deliver initial discharge capacity of  $905.3 \text{ mAh g}^{-1}$  at  $0.1 \text{ C}$  and maintain high discharge capacity at  $0.3 \text{ C}$  for over 100 cycles. (4) Alloy anodes were utilized to facilitate Li-S all-solid-state batteries, which performed stable cycling over 200 cycles, and showed good performance at high loadings or under high current conditions.

### Key Publications

1. Wang, D., Jhang, L.J., Kou, R. *et al.* Realizing high-capacity all-solid-state lithium-sulfur batteries using a low-density inorganic solid-state electrolyte. *Nature Communication* **14**, 1895 (2023).

### References

1. Kamaya, Noriaki, Kenji Homma, Yuichiro Yamakawa, Masaaki Hirayama, Ryoji Kanno, Masao Yonemura, Takashi Kamiyama, Yuki Kato, Shigenori Hama, Koji Kawamoto, and Akio Mitsui. 2011. "A lithium superionic conductor." *Nature Material* **10**: 682-686.
2. Hayashi, Akitoshi, Takamasa Ohtomo, Fuminori Mizuno, Kiyoharu Tadanaga, and Masahiro Tatsumisago. 2003. "All-solid-state Li/S batteries with highly conductive glass-ceramic electrolytes." *Electrochemistry Communications* **5**, no. 8 (August): 701-705.



3. Inoue, Takao, and Kazuhiko Mukai. 2017. "Are All-Solid-State Lithium-Ion Batteries Really Safe? – Verification by Differential Scanning Calorimetry with an All-Inclusive Microcell." *ACS Applied Materials & Interfaces* 9, no. 2 (January): 1507-1515.
4. Tatsumisago, Masahiro, Motohiro Nagao, and Akitoshi Hayashi. 2013. "Recent development of sulfide solid electrolytes and interfacial modification for all-solid-state rechargeable lithium batteries." *Journal of Asian Ceramic Societies* 1, no. 1 (March): 17-25.

### **Acknowledgements**

The work was supported by the Department of Energy, under Award Number DE- EE0008862. We appreciate the support from Colleen Butcher at National Energy Technology Laboratory, and Simon Thompson and Patricia Smith from DOE.

## XIII.6 Fundamental Understanding of Interfacial Phenomena in Solid-State Batteries (General Motors)

### Xingcheng Xiao, Principal Investigator

General Motors Research and Development Center  
30470 Harley Earl Blvd.  
Warren, MI 48092-2031  
E-mail: [xingcheng.xiao@gm.com](mailto:xingcheng.xiao@gm.com)

### Tien Duong, DOE Technology Development Manager

U.S. Department of Energy  
E-mail: [Tien.Duong@ee.doe.gov](mailto:Tien.Duong@ee.doe.gov)

Start Date: October 1, 2019  
Project Funding: \$200,000

End Date: May 31, 2023  
DOE share: \$150,000

Non-DOE share: \$50,000

### Project Introduction

Solid-state batteries (SSBs) are considered the next generation battery technology for resolving the intrinsic limitations of current lithium-ion batteries, such as poor abuse tolerance, insufficient energy density, and short cycle life. However, the main hurdle for SSB in electric vehicle (EV) applications is the complexity caused by material interfaces, such as Li metal/solid electrolyte (SE) and SE/cathode interfaces, leading to increased impedance and shortened cycle life. Although interfaces in SSBs are one of the key factors, a clear understanding of their properties and functions is still unavailable, partly due to the difficulty in characterizing buried solid-solid interfaces and interphases formed during battery cycling. Solid-state batteries (SSBs) are considered the next generation battery technology for resolving the intrinsic limitations of current lithium-ion batteries, such as poor abuse tolerance, insufficient energy density, and short cycle life. However, the main hurdle for SSB in electric vehicle (EV) applications is the complexity caused by material interfaces, such as Li metal/solid electrolyte (SE) and SE/cathode interfaces, leading to increased impedance and shortened cycle life. Although interfaces in SSBs are one of the key factors, a clear understanding of their properties and functions is still unavailable, partly due to the difficulty in characterizing buried solid-solid interfaces and interphases formed during battery cycling.

### Objectives

The project objective is to develop a comprehensive set of in situ diagnostic techniques combined with atomic/continuum modeling schemes to investigate and understand the coupled mechanical/chemical degradation associated with dynamic interfacial phenomena in SSBs. Specifically, in situ observations and characterizations of lithium plating-stripping processes, lithium dendrite formation, interphase formation, and the induced interfacial stresses, as well as the mechanical and electrochemical properties of interfaces and interphases, are paramount. The study will provide useful guidelines for optimizing cell structure design and engineering interfaces and interphases to enable SSBs. In addition, it will establish a critical guideline to design safe and durable SSBs with energy density > 500 wh/kg for EV applications.

### Approach

The multiscale in situ diagnostic tools, including AFM, nanoindentation, dilatometer, stress sensors, and pressure cells, will be used to investigate mechanical behavior and microstructure evolution at interface/interphase during lithium plating and stripping. The information (along with Li-ion transport properties and microstructure evolution obtained using the advanced spectroscopic ellipsometry, and in situ TEM) will be correlated with electrochemical performance toward high cycle efficiency and dendrite-free SSBs. The goal of this understanding is to develop strategies for surface and interface engineering, apply them to commercially available SEs (including powder, pellets, and foils), and assemble SSBs for further validation and optimization, eventually extending cycle life for EV application.

## Results

### Development of the kinetic Monte Carlo (KMC) stripping code for the Li/solid electrolyte (Li/SE) interface

The KMC code has been employed to simulate the vacancy evolution near different Li/SE interfaces using the DFT calculated Li hopping barriers. To gain more accurate insight for the surface morphology after stripping, the implementation of stripping in the KMC simulation is further developed to impose the constant current density at the interface in this quarter. The developed code is tested among Li/LiF, Li/Li<sub>2</sub>O and Li/LLZO interfaces, which can provide input for the simulation of the contact loss at the interface at larger length scale and time scale on the continuum level.

### Implementation of the stripping code:

In the KMC simulation, the Li diffusion within the anode, SE and the stripping of Li atoms from the anode to the SE are assisted by the Li vacancy hopping. As the number of lattice sites in the simulation cell is fixed and the shortest hopping is considered, the lattice diffusion model can help explain the hopping events in the KMC simulation. In the Li anode, assuming the Li surface is the first plane ( $j=1$ ), the Li flux across a plane  $j$  considering the 2-direction hopping events is calculated using

$$\frac{dLi_j}{dt} = \frac{1}{2N_0} (k_f^{i+1} N_{i+1} V_i + k_b^{i-1} N_{i-1} V_i - k_f^i N_i V_{i-1} - k_b^i N_i V_{i+1}), \quad (1)$$

where  $N_0$  is the total number of lattice sites on the plane  $j$ ,  $k_f^i$  and  $k_b^i$  are the forward and backward hopping rates for forward (towards the interface) and backward (away from the interface) hopping event, and  $N_i$  and  $V_i$  are the number of Li atoms and vacancies on the plane  $i$ , where  $N_0 = N_i + V_i$ .

The hopping events in KMC simulation are also related to the numbers of both Li atoms and vacancies. In the anode, a hopping event is a Li atom moves from its current position to the nearest vacancy along the (111) direction ( $\sim 3\text{\AA}$ ). The DFT calculated hopping barriers ( $E_a$ ) were converted to the hopping rate ( $k_i$ ,  $i$  stand for the intergers between 1 and 10.) for each possible hopping event within the anode according to the transition state theory

$$k_i = v_0 \exp\left(\frac{-E_a}{k_B T}\right), \quad (2)$$

where  $v_0$  is the jumping frequency,  $k_B$  and  $T$  are the Boltzmann constant and the temperature, respectively. For hopping events in the interface region (except for the first two layers), the hopping barriers were fitted to exponential functions and then converted to hopping rates.

At the interface, the diffusion model can be applied to the first plane according to

$$\frac{dLi_1}{dt} = \frac{1}{2} (k_f^2 N_2 \frac{V_1}{N_0} - k_b^1 N_1 \frac{V_2}{N_0} - k_s N_1 \frac{V_s}{N_s}), \quad (3)$$

where  $k_s$  is the rate for each stripping event,  $V_s$  is the number of vacancy sites on the anode surface and  $N_s$  is the number of lattice sites on the anode surface.  $N_s$  is around  $1.56N_0$  in the current SE reservoir. In the KMC simulation, since the Li ions in the SE are removed before the simulation,  $V_s$  is equal to the Li sites in the SE reservoir. A stripping/hopping event here is a Li atom on the anode surface jumps to a nearest vacancy site on the SE surface. The cutoff distance for this kind of hopping is  $3.5\text{\AA}$ .

To apply the constant current density at the interface,  $\frac{dLi_1}{dt}$  (or the flux in the SE,  $\dot{N}$ ,  $ms^{-1}$ ) can be calculated from the current density ( $i_s$ , mA/cm<sup>2</sup>) using

$$\dot{N} = \frac{i_s A}{1000q}, \quad (4)$$

where  $A$  is the area of the interface cross section and  $q$  is the electric charge for one electron.

For testing purposes, the Li hopping was firstly neglected to focus on the stripping process at the interface, which can be verified by the number of stripped Li atoms and the stripping time. Assuming all the stripping events are equivalent, it leads to the condition

$$\dot{N} = \frac{k_s N_1 V_s}{2N_s}. \quad (5)$$

For Li hopping within the SE reservoir, only the diffusion to vacancy sites within the cutoff distance (3.5 Å) on adjacent planes are considered, which also has the hopping rate  $k_s$  ( $k_s = k_9$ ). The backward hopping ( $k_{10} = 0$ ) was set to be 0.

The KMC code was developed based on the Bortz-Kalos-Lebowitz (BKL) algorithm. Each KMC step consists of 5 operations. (1) All the possible hopping events (cutoff distance 3.5 Å) are determined in the evolving structure. (2) The corresponding hopping rates are assigned to the hopping events. (3) The  $q$ th event is picked to occur according to the criteria  $\sum_{m=1}^q k_m \geq \rho_1 k_{tot} \geq \sum_{m=1}^{q-1} k_m$ , where  $\rho_1$  is a random number between 0 and 1. (4) The positions of the Li atom and the vacancy in the  $j$ th event are switched to update the evolving structure. (5) The simulation time is evolved by  $\Delta t = -\frac{\ln \rho_2}{k_{tot}}$ , where  $\rho_2$  is another random number between 0 and 1. The KMC simulation is finished after  $10^4$  steps for current densities larger than  $10^3$  A/cm<sup>2</sup>.

#### Effect of DTL coating layer on hot pressed $\text{Li}_{6.24}\text{Al}_{0.24}\text{La}_3\text{Zr}_2\text{O}_{11.98}$

To investigate the DTL coating as the interlayer in solid state batteries, bare and coated Li electrodes were studied in symmetrical cells with  $\text{Li}_{6.24}\text{Al}_{0.24}\text{La}_3\text{Zr}_2\text{O}_{11.98}$  (LLZO) solid state electrolyte pellets. Li symmetrical cells were assembled in using split test cell (MTI) for electrochemical characterization. Electrochemical impedance spectroscopy (EIS) was performed 7MHz-1Hz with 10mV perturbation. Critical current density (Jc) test was performed starting at 10uA/cm<sup>2</sup> with 10μA/cm<sup>2</sup> increment. For each current density, there were 5 mins stripping or plating process for 5 cycles.

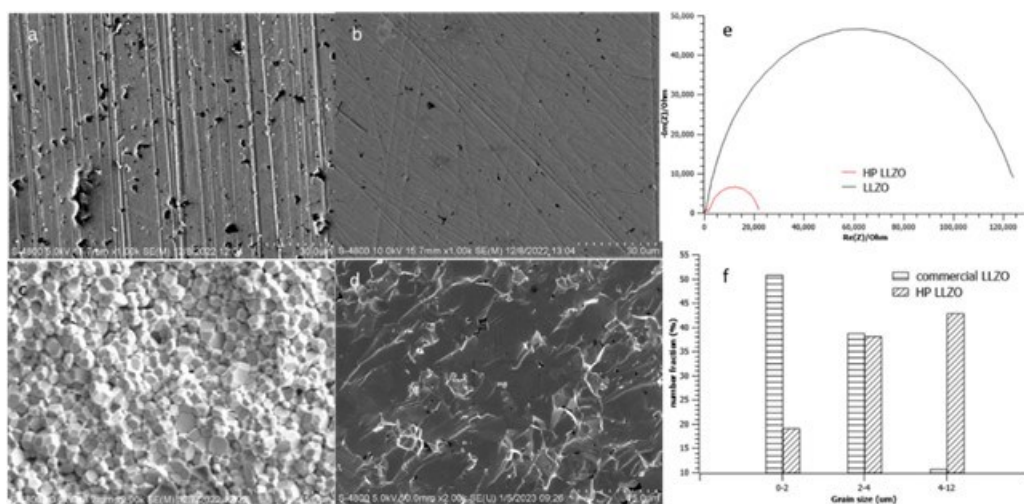


Figure XIII.6.1 SEM surface image of a) Commercial LLZO, b) Hot pressed LLZO. Fracture image of c) Commercial LLZO, d) Hot pressed LLZO. e) Nyquist plots obtained from EIS. f) Grain size distribution.

As shown in the surface SEM image of LLZO (Figure XIII.6.1 a and b), more dark spots were noted as pore for the c-LLZO. No matter how intensive polish process was performed, these intrinsic pores will cause contact loss and lead to large contact resistance and low critical current density. Even though DTL coating layer could fill the void of pellets and improve contact resistance as reported in our previous report. The cell total impedance is still too large to perform critical current density test or long-time cycling. So, we decided to use HP-LLZO instead of c-LLZO for our future experiments. Clear difference could be told from impedance measurement as shown in Figure XIII.6.1e. With same surface polishing method, total impedance of cell with c-LLZO showed six times higher than the cell with HP-LLZO.

Another important aspect of the microstructural difference was the fracture mode as shown in Figure XIII.6.1 c and d. The commercial LLZO showed intergranular fracture. While majority of HP-LLZO showed intragranular fracture. Which indicated strong grain boundaries for the HP-LLZO pellets. Relative densities were calculated based on the ratio between measured density and theoretical density. Relative density for c-LLZO is 90.6%, while the HP-LLZO could achieve 95%. The increase in grain size (Figure XIII.6.1 f) and decrease in porosity at grain boundaries would lead to an increase in percentage of intragranular fracture.

#### **Multiscale simulations of the contact loss at the Li/solid electrolyte (Li/SE) interface**

For solid state batteries, maintaining a flat Li surface and good interfacial contact during stripping are important to mitigate the uneven Li deposition in the following plating process and further impede the Li dendrite growth during cycling. In this quarter, a mechanical FEM model (mesoscale) was developed to get the contact area fraction at the interface. The obtained surface contact area fraction was then used to construct initial configurations to get more realistic contact fractions from KMC simulations (nanoscale).

Although the iteration of the KMC-FEM has not been performed yet, positions of the equilibrium contact area fraction (filled markers, LiF: triangle, Li<sub>2</sub>O: circle, LLZO: square) at different length scales can be estimated based on current data.

Figure XIII.6.2 shows the positions of contact area fractions for the three interfaces with varying  $P_{hold}/Y_0$  ratios, Data points obtained for  $\frac{P_{hold}}{Y_0} = 4$  are marked in red, while for  $\frac{P_{hold}}{Y_0} = 2$  and 1, the data points are in green and blue, respectively. The dashed arrows start from the FEM calculated contact area fractions ( $t = 1s$ ) and point to the fractions from KMC simulations (unfilled markers).

For the lithiophobic Li/LiF interface, at high current densities (Figure XIII.6.2a), based on KMC simulations, the contact is rapidly decreased to 0 in all three cases regardless of the initial surface contact, suggesting all the Li atoms on the surface are depleted. Given the time to remove the whole Li surface at high current densities (within  $\mu s$ ), the contact recover due to the local pressure is insufficient to increase the contact. Therefore, the equilibrium contact area fraction for the Li/LiF interface is 0. No unfilled markers are plotted as they overlap with the filled ones.

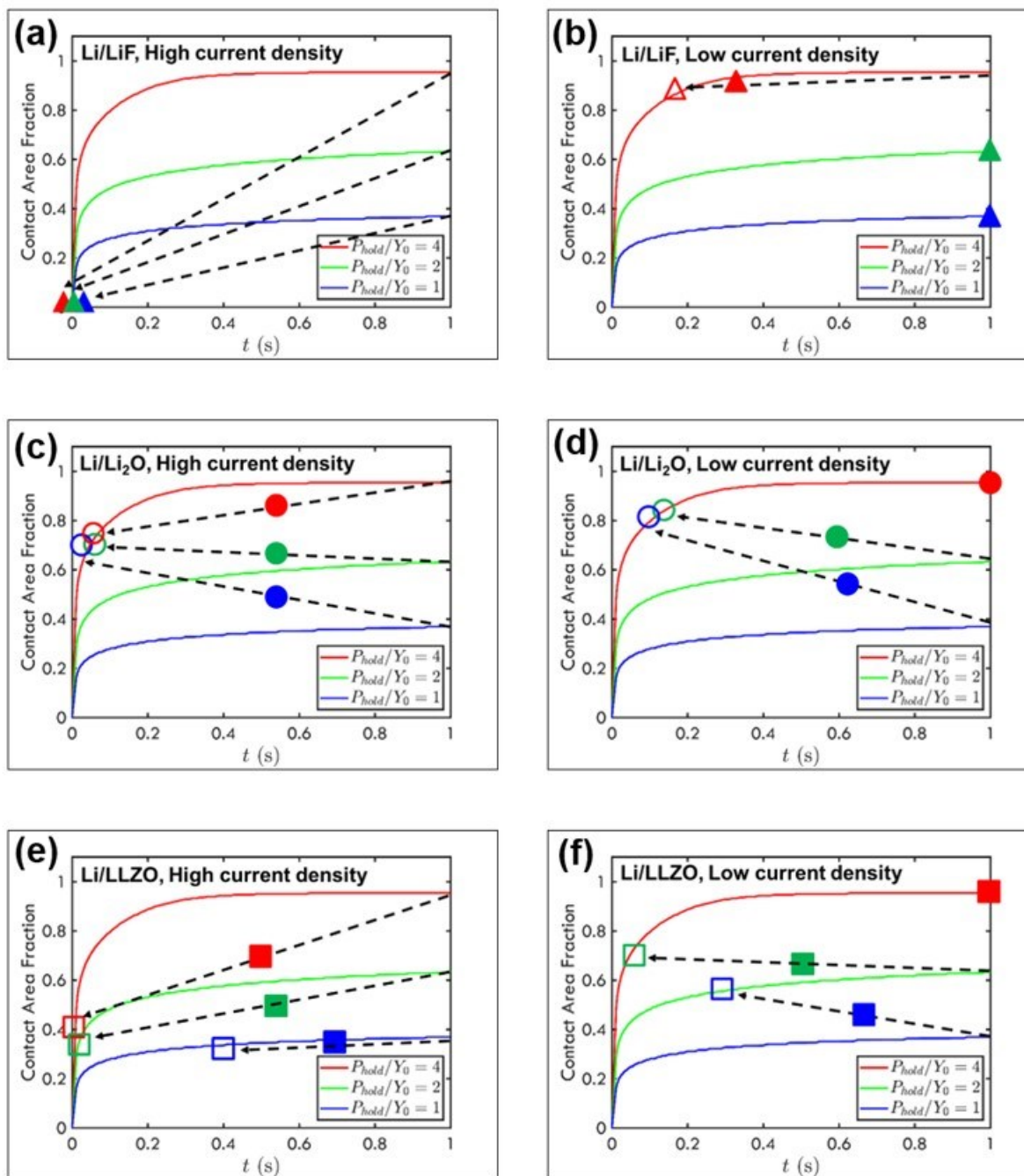


Figure XIII.6.2 The schematics of estimated equilibrium contact area fractions (filled markers) for the LiF, Li<sub>2</sub>O and LLZO at high (a,c,e,  $10^3$  A/cm<sup>2</sup>) and low (b,d,f, 1 mA/cm<sup>2</sup>) current densities with different  $P_{hold}/Y_0$  ratios. The dashed arrows start from the contact area fraction in FEM towards the contact area fraction in KMC (unfilled markers). Triangles: LiF, Circles: Li<sub>2</sub>O, Squares: LLZO.

At low current densities (Figure XIII.6.2b), with  $\frac{P_{hold}}{Y_0} = 4$  (red), the contact area fraction is decreased from 0.95 to 0.90 after stripping. When the contact loss due to stripping and contact recover due to creep reach an equilibrium, the final position (filled red triangle) will be between 0.90 and 0.95. For other cases, contact area is not altered after KMC simulations. Therefore, the equilibrium condition is satisfied at both length scales

(filled green triangle at 0.62, filled blue triangle at 0.38). This means the Li hopping flux will not fill vacancies on the surface, as expected for a lithiophobic interface.

In contrast, even at high current densities, the lithiophilic Li/Li<sub>2</sub>O interface ((Figure XIII.6.2c) reaches around 0.8 of contact, regardless of initial contact area fractions, which is attributed to fast Li hopping from the second layer to the surface. Then the estimated equilibrium contact area fraction is between the initial and final states ((Figure XIII.6.2c, filled circles). At low current densities ((Figure XIII.6.2d), the contact area fractions after stripping increase by 0.04 compared to cases at high current densities for  $\frac{P_{hold}}{Y_0} = 2$  and 1. On the other hand, due to the good Li wettability, the contact is maintained when starting with a 0.95 initial contact ( $\frac{P_{hold}}{Y_0} = 4$ ). Overall, the lithiophilic Li/Li<sub>2</sub>O interface shows much higher contact retention than the lithiophobic Li/LiF interface at different current densities. Based on the estimated equilibrium contact area fractions (filled markers), at both high and low current densities, the surface contact is ranked as Li<sub>2</sub>O > LLZO > LiF when the initial contact area fractions are the same. The high current density will significantly decrease the surface contact for less lithiophilic interfaces (Li/LLZO, Li/LiF). Hence, the KMC-FEM simulation scheme captures the impacts of different interface interactions and current densities on the surface contact.

Using the FEM calculated surface contact area fractions to construct initial surface configurations, KMC simulations demonstrated the evolution of surface contact for different Li/SE interfaces. The regions for the equilibrium contact are estimated across different length scales at high and low current densities. The model is still being developed to further resolve the different time scales in KMC and FEM and eventually build the KMC-FEM loop to obtain the converged contact area fraction.

For solid state batteries, maintaining a flat Li surface and good interfacial contact during stripping are important to mitigate the uneven Li deposition in the following plating process and further impede the Li dendrite growth during cycling. During cycling, the Li/SE interface contact is altered at different length scales. Macroscopically (mesoscale), the stripping process removes Li atoms from the surface, forming voids and decreasing the contact area. In addition, the Li creep due to the applied stack pressure ( $P_{hold}$ ) also changes the contact by pushing Li atoms towards the interface. The contact across different length scales should be considered to study the interface contact evolution. In our work, the kinetic Monte Carlo-Finite Element Modeling (KMC-FEM) multiscale simulation scheme is employed.

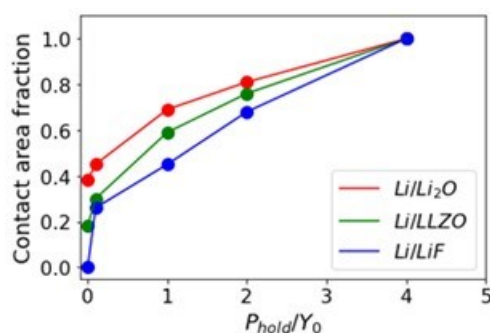


**Figure XIII.6.3** The schematics of estimated equilibrium contact area fractions for the LiF, Li<sub>2</sub>O and LLZO at 10 mA/cm<sup>2</sup> with different  $P_{hold}/Y_0$  ratios.

With the FEM and KMC calculated contact fractions, the equilibrium states of contact at meso and nanoscales is predicted. It shows that the creep effects can always lead to better contact, but the interface interactions will not be completely overcome until  $P_{hold}/Y_0 = 4$  (Figure XIII.6.3). Lower stack pressures and higher current densities are being studied using the KMC-FEM iterations to get the equilibrium contact across meso and nano

length scales to provide suggestions for optimal battery operating conditions with good contact at the Li/SE interface.

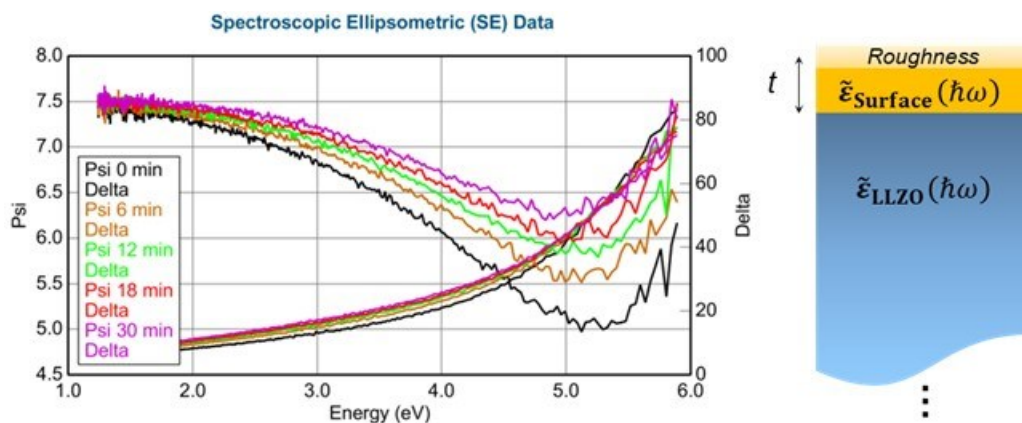


**Figure XIII.6.4** Optical ellipsometry spectra of the new LLZO pellet after exposure to air. This spectral change is explained by the formation of the surface layer as shown on the right.

We present here the results of a spectral model analysis based on in situ spectroscopic ellipsometry data. To ensure reliable optical spectra, we meticulously polished the pellet's surface within an Ar-filled glovebox and then transferred it to a vacuum chamber to prevent any exposure to air. The in situ optical ellipsometry spectra ( $\Psi$  and  $\Delta$ ) in Figure XIII.6.4 exhibit a systematic change as the LLZO pellet is exposed to air. This spectral variation can be attributed to the formation of a surface passivation layer. By employing a spectral model fit, we derived the dielectric functions ( $\tilde{\epsilon}(\omega) = \epsilon_1(\omega) + i\epsilon_2(\omega)$ ) of both LLZO and the surface passivation layer. It is important to note that the  $\epsilon_1$  values of the surface layer are smaller than those of LLZO, indicating that the surface layer is composed of an electronically more insulating material with larger optical bandgap energies ( $> 4.6$  eV). To determine the composition of the surface layer, additional sample characterizations such as x-ray photoemission spectroscopy are required.

## Conclusions

- Multiscale models have been developed to gain insights into the intricate interplay among interfaces, diffusion, stripping current density, stack pressure, and the evolution of contact area during Li-stripping. These models have convincingly demonstrated that the utilization of a lithiophilic interlayer can effectively mitigate stack pressure and elevate the critical current density required to thwart lithium dendrite growth.
- Pressure studies have unveiled that a soft and compliant artificial SEI (solid electrolyte interphase) layer, characterized by a modulus significantly lower than that of LLZO, can further enhance the initial interfacial impedance. These discoveries underscore the advantages of a softer, viscoelastic interface between lithium and LLZO in terms of improving interfacial impedance.
- Interlayer design strategies have been meticulously formulated and subsequently validated through the coating of lithium anodes. Additionally, various approaches have been explored to engineer grain boundaries with the objective of reducing sintering temperatures and augmenting ionic conductivity.

## Key Publications

1. J. Cho, K. Kim, S. Chakravarthy, X. Xiao, J. L. M. Rupp, B. W. Sheldon, An Investigation of Chemo-Mechanical Phenomena and Li Metal Penetration in All-Solid-State Lithium Metal Batteries Using In Situ Optical Curvature Measurements, *Adv Energy Mater* 12, 2200369 (2022)
2. T. Cai, A. S Westover, S. Kalnaus, J. Cho, C.E. Athanasiou, N. Dudney, and B. W. Sheldon, In-situ Thermo-Mechanical Characterization and Strain Engineering of Lipon Thin Films, to be submitted (June 2023).



3. A Meyer, X Xiao, M Chen, A Seo, YT Cheng, A Power-Law Decrease in Interfacial Resistance Between  $\text{Li}_7\text{La}_3\text{Zr}_2\text{O}_{12}$  and Lithium Metal After Removing Stack Pressure, *Journal of The Electrochemical Society* 168 (10), 100522
4. A Seo, A Meyer, S Shrestha, M Wang, X Xiao, YT Cheng, Observation of the surface layer of lithium metal using in situ spectroscopy, *Applied Physics Letters* 120 (21), 211602
5. M. Feng, C. Yang, and Y. Qi, The Critical Stack Pressure to Alter Void Generation at Li/Solid-Electrolyte Interfaces during Stripping, *Journal of The Electrochemical Society*, 2022, 169, 090526

### Patents

1. Xingcheng Xiao, Robert Schmidt, Yifan Zhao, A simplified process to improve the ionic conductivity of solid electrolyte, Application-P104736-PRI-NP-US01 GM6372
2. Xingcheng Xiao, Yang-Tse Cheng, Thomas Yersak, Self-healing solid-state battery configuration and the method of manufacturing thereof. GM Ref. No. P104629-PRI-NP-US01
3. Xingcheng Xiao, A process to reduce the interfacial impedance in all solid-state batteries, Application-P103667-PRI-NP-US01 GM6265

### Acknowledgements

The Principal Investigator (PI) wishes to express gratitude for the invaluable contributions made by the Co-Principal Investigators, Professors Brian W. Sheldon, Yue Qi, Yang-Tse Cheng, Ambrose Seo, and their dedicated students and postdoctoral researchers, including Dr. Yifan Zhao, Min Feng, Sydney Morris, and Jacob Hempel.

The entire team also extends its heartfelt appreciation for the financial support received from the Assistant Secretary for Energy Efficiency and Renewable Energy, specifically from the Office of Vehicle Technologies and the Advanced Battery Materials Research (BMR) programs of the U.S. Department of Energy (DOE), under contract number DE-EE0008863. Special thanks go to Tien Duong, Tricia Smith, and Coriana H. Fitz at DOE for their outstanding program management.

## XIII.7 Multidimensional Diagnostics of the Interface Evolutions in Solid-State Lithium Batteries (University of Houston)

### Yan Yao, Principal Investigator

University of Houston  
4800 Calhoun Rd  
Houston, TX 77004  
E-mail: [yyao4@uh.edu](mailto:yyao4@uh.edu)

### Tien Duong, DOE Technology Development Manager

U.S. Department of Energy  
E-mail: [Tien.Duong@ee.doe.gov](mailto:Tien.Duong@ee.doe.gov)

Start Date: October 1, 2019

End Date: March 31, 2023

Project Funding: \$1,2500,000

DOE share: \$1,000,000

Non-DOE share: \$250,000

### Project Introduction

The failure of a solid-state Li battery may be briefly attributed to two main causes: interfacial resistance increase and Li dendrites growth. The former may be further attributed to electrolyte decomposition and interfacial void formation (i.e. loss of physical contact). Electrolyte decomposition happens in two ways: oxidative decomposition at the cathode active material–electrolyte interface and reductive decomposition at the Li (including dendrites)–electrolyte interface. Void formation occurs at the same two interfaces. The complex origins of battery failure call for multidimensional diagnostics utilizing not one but a combination of tools that can quantify the formed void and dendrites, identify the chemical and mechanical natures of the Li dendrites and electrolyte decomposition products, and in situ monitor the evolution of the processes. The tools also need to cover a sufficiently large scale (up to ~100  $\mu\text{m}$ ), have spatial resolutions of a few nanometers, and be sensitive enough to detect subtle changes in chemical and mechanical properties. These considerations lead us to a toolset of FIB-SEM tomography, ToF-SIMS, and nanoindentation (inside SEM chamber, i.e. in-SEM nanoindentation) and atomic force microscopy (AFM; inside SIMS chamber, e.g. in-SIMS AFM)-based stiffness mapping for structural, chemical, and mechanical characterizations, respectively. We will acquire detailed information of interfaces and dendrites evolutions including but not limited to (1) real-time visualization of Li dendrites growth within the whole thickness of electrolyte layer, (2) chemical composition, mechanical property, and evolution of electrolyte decomposition products, including intermediate and metastable ones, at both cathode and anode interfaces, (3) potential correlation of the induction and propagation of Li dendrites with electrolyte decomposition, and, (4) quantitative correlation between electrolyte decomposition, void formation, and cell performance. These in-depth understandings will allow us to effectively predict and optimize the physical and chemical changes of components within solid-state Li batteries during charge and discharge.

### Objectives

The project objective is to develop a platform in combination of FIB-SEM tomography, ToF-SIMS, and in-SEM nanoindentation-based stiffness mapping for structural, chemical, and mechanical characterizations in solid-state Li batteries. Assessment of the influence of cell design and testing conditions (external pressure, current density, temperature) on the evolutions of interfaces will be performed.

### Approach

Space- and time-resolved structural, chemical, and mechanical characterizations of the cathode-electrolyte and anode-electrolyte interfaces will be performed on all-solid-state Li batteries using FIB-SEM, ToF-SIMS, in-SEM nanoindentation. Tasks include (1) development of solid-state cell thin stacks and test-cell configurations that are suitable for in-situ characterizations, (2) quantitative characterization and in-situ tracking of interfacial voids formation within composite cathode and electrolyte layer; (3) identification and in-situ tracking of the

chemical composition, spatial distribution, and mechanical properties of electrolyte decomposition products at the Li- and cathode-electrolyte interfaces; (4) visualization, chemo-mechanical properties detection, and in-situ tracking of Li dendrites grown within solid electrolyte layer.

## Results

The project objective is to develop a platform in combination of structural, chemical, and mechanical characterizations in solid-state Li batteries. Our previous operando SEM and in situ ToF-SIMS analyses successfully showcased the morphological and chemical evolution of solid-state battery interface during lithiation and delithiation. This year, we further extended our characterization capability to acquire mechanical information at the electrolyte–electrode interface during cell operation, as well as to link chemical and mechanical properties together.

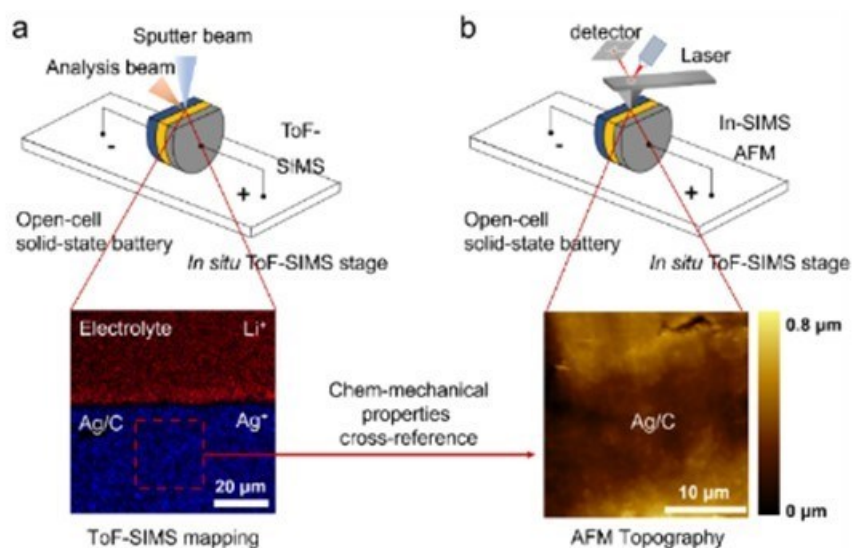


**Figure XIII.7.1** Illustration of the in situ ToF-SIMS and in-SIMS AFM measurements. a, schematic illustration of ToF-SIMS analysis on Ag-C/Li<sub>6</sub>PS<sub>5</sub>Cl interface. b, schematic illustration of AFM measurement on selected Ag-C region.

The effects of chemo-mechanical coupling on solid-state batteries were investigated by combining ToF-SIMS with an Atomic Force Microscope (AFM). As shown in Figure XIII.7.1, a polished open-cell solid-state battery (Ag-C/Li<sub>6</sub>PS<sub>5</sub>Cl/Li) was mounted on our custom-made ToF-SIMS stage for chemical and mechanical analysis. Here, Ag-C was chosen as a model system to study its role on stabilizing metal–electrolyte interface.[1] The ultra-low detection limit (ppm-ppb) of lithium-related species in the ToF-SIMS allowed for the acquisition of chemical evolution at the electrolyte-anode interface in the as-prepared sample. Figure XIII.7.1a shows a surface secondary ion mapping of the pristine Ag-C/ Li<sub>6</sub>PS<sub>5</sub>Cl interface, where the Ag<sup>+</sup> (blue) mapping displays the distribution of the Ag-C layer and the Li<sup>+</sup> (red) mapping indicates the presence of Li-related species (Li<sub>6</sub>PS<sub>5</sub>Cl) in the sample. In-situ topography and stiffness mapping on a selected region were also performed using an AFM instrument. Figure XIII.7.1b shows the AFM topography of the selected Ag-C region, providing insight into the morphological evolution of the Ag-C layer during electrochemical operation.

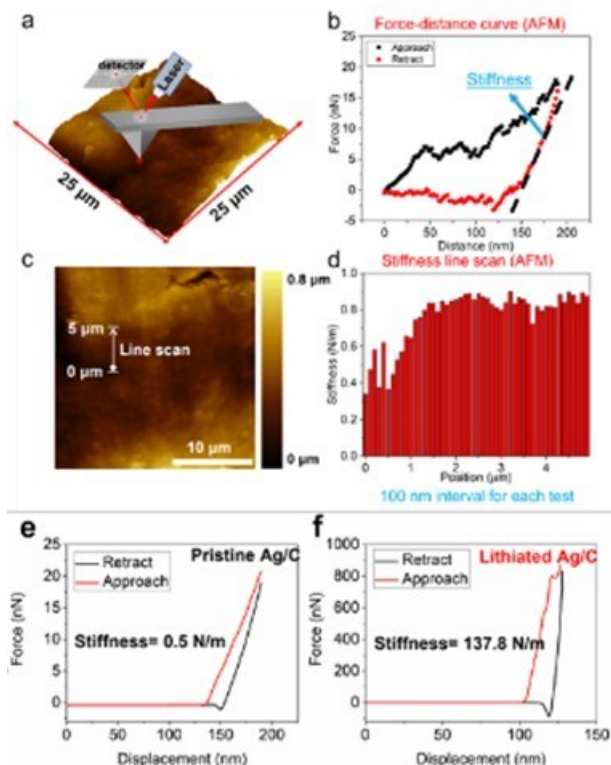


**Figure XIII.7.2** Stiffness measurements of selected Ag-C region. **a**, schematic illustration of single point stiffness measurement. **b**, force-distance curve on Ag-C layer. **c**, line scan of stiffness measurements on Ag-C layer. **d**, stiffness plot along the scan line displays in **c**, with 100 nm interval for each test. **e-f**, force-distance curve on pristine and lithiated Ag-C layers.

The stiffness of the Ag-C layer is measured using force-distance curves obtained with an AFM. The AFM tip is moved in a vertical direction rather than scanning along the surface, as shown in Figure XIII.7.2a. The force between AFM probe and sample is collected as the tip approaches and retracts from the surface. Figure XIII.7.2b shows a single-point force-distance curve on the Ag-C sample, where the stiffness can be obtained from the retraction curve. The AFM tip can probe an extremely small interaction area (tip radius  $\sim 5\text{--}50$  nm) with a high force sensitivity, allowing for mapping of microstructure evolution in the Ag-C layer with high spatial resolution. Here, a 5- $\mu\text{m}$  line scan of stiffness measurements was performed on the Ag-C layer, with a 100 nm interval between each force-distance test, as shown in Figure XIII.7.2c. We observe a stiffness difference along the scanning line, plotted in Figure XIII.7.2d, which may originate from inhomogeneous composition and microstructure. As previously reported in in-situ ToF-SIMS tests, we observed a gradient distribution of lithium-related species in the Ag-C layer during lithiation, indicating a gradual and possibly multi-step lithiation process. Figure XIII.7.2e shows a typical force-distance curve of Ag-C layer before lithiation, showing a stiffness of  $0.5\text{ N m}^{-1}$ . In contrast, after the lithiation of Ag-C, the stiffness increased dramatically to around  $137.8\text{ N m}^{-1}$ . This increase in stiffness is attributed to the decrease in porosity of the Ag-C layer or the lithiation process occurring in the Ag-C layer.

Figure XIII.7.3a shows the optical image of the Ag-C and  $\text{Li}_6\text{PS}_5\text{Cl}$  interface, where the  $\text{Li}_6\text{PS}_5\text{Cl}$  domain is visible and the lithiated Ag-C layer exhibits metallic reflection. AFM topography characterization was performed on the same area shown in Figure XIII.7.3b, and the scratches seen in the optical image were also observed in the AFM topography, confirming good alignment between the AFM and optical image. Stiffness mapping was conducted at the interface across the Ag-C and  $\text{Li}_6\text{PS}_5\text{Cl}$  domain, as indicated in the red box region, with a 1000 nm interval for each force-distance test. The stiffness mapping of the selected region is shown in Figure XIII.7.3c, revealing a stiffness gradient covering both Ag-C and  $\text{Li}_6\text{PS}_5\text{Cl}$  electrolyte

domains. The high stiffness values were observed close to the interfacial area, which may be attributed to the highest lithium concentration at the interface during the lithiation of the Ag-C layer.

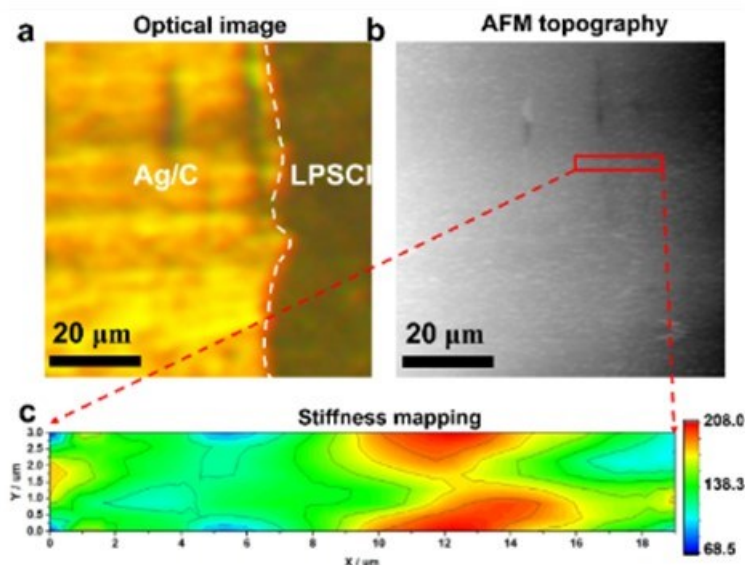


**Figure XIII.7.3** Stiffness measurements of selected Ag-C/Li<sub>6</sub>PS<sub>5</sub>Cl interface. a, Optical image of selected region for AFM characterization. b, AFM topography of the identical area as shown in optical image. c, stiffness mapping of boxed region in red, with 1000 nm interval for each test.

We previously characterized the Ag-C layer lithiation through operando SEM and ToF-SIMS, which successfully visualized morphological and chemical evolution during the electrochemical process. This AFM measurement is the last piece of the platform capability that enables us to establish an electro-chemo-mechanical framework to rationalize the working mechanisms of Ag-C layer. The results explain phenomena observed in previous tasks, such as cracks in the Ag-C layer at the lithiation front, which can be attributed to the drastic drop in stiffness from the lithiated to the unlithiated region.

The implementation of the multiscale characterization technique has yielded valuable insights into cell failure mechanisms and has led to the development of a solid-state lithium cell that exhibits exceptional durability. We have successfully demonstrated all-solid-state full cells with a thin lithium metal anode, capable of cycling at a current density of 2.8 mA cm<sup>-2</sup> at 30 °C. Remarkably, the cell maintained an average coulombic efficiency of 99.98% and retained 83% of its initial capacity after 2500 cycles. This achievement showcases how the knowledge obtained from multiscale characterization can be effectively applied to the design of materials, resulting in improved battery performance.

## Conclusions

We have developed an in-situ AFM setup to serve as a platform for investigating the evolution of mechanical properties of interfaces in all-solid-state lithium batteries with a high spatial resolution. The stiffness of interlayer at anode–electrolyte interface is mapped and compared before and after lithiation. We report a drastic increase in stiffness after the porous interlayer becomes lithiated. Mechanical property mapping serves as a complement to our previous research on space- and time-resolved, chemical and morphological characterizations. Probing chemo-mechanical properties and their evolution during cycling allows us to understand cell kinetics and rationally design solid-state batteries to achieve improved performance.

## Key Publications

1. L. Zhao, W. Li, C. Wu, Q. Ai, L. Guo, Z. Chen, J. Zheng, M. Anderson, H. Guo, J. Lou, Y. Liang, Z. Fan, J. Zhu, Y. Yao\*, Taming metal-solid electrolyte interface instability via metal strain hardening. *Adv. Energy Mater.*, **2023**, 202300679. OSTI: 1987597

2. C. Wu\*, B. Emley\*, L. Zhao, Y. Liang, Q. Ai, Z. Chen, F.C.R. Hernández, F. Wang, S. Risal, H. Guo, J. Lou, Y. Yao\*, Z. Fan\*, Understanding the chemomechanical function of silver-carbon interlayer in sheet-type all-solid-state lithium-metal batteries, *Nano Lett.*, **2023**, 23, 4415. OSTI: 1985464
3. G. Feng, H. Jia, Y. Shi, X. Yang, Y. Zhang, C. Yang, K. Xu\*, Y. Yao\*, W. Xu\*, X. Shan\*, Imaging solid-electrolyte-interphase dynamics using in-operando reflection interference microscopy. *Nature Nanotechnol.*, 2023, doi.org/10.1038/s41565-023-01316-3 OSTI: 1985460
4. S. Risal, C. Wu, F. Wang, S. Risal, F.C.R. Hernandez, Y. Yao\*, and Z. Fan\*, Silver-carbon interlayers in anode-free solidstate lithium metal batteries: current development, interfacial issues and instability challenges, *Carbon*, **2023**, 213, 118225. OSTI: 1985465
2. Q. Ai, Z. Chen, B. Zhang, F. Wang, T. Zhai, Y. Liu, Y. Zhu, T. Terlier, Q. Fang, Y. Liang, L. Zhao, C. Wu, H. Guo\*, Z. Fan, M. Tang, Y. Yao\*, J. Lou\*, High-spatial-resolution quantitative chemo-mechanical mapping of organic composite cathodes for sulfide-based solid-state batteries. *ACS Energy Letter*, **2023**, 8, 1107. OSTI: 1985466

### References

1. Y.G. Lee, S. Fujiki, C. Jung, N. Suzuki, N. Yashiro, R. Omoda, D.S. Ko, T. Shiratsuchi, T. Sugimoto, S. Ryu, J.H. Ku, T. Watanabe, Y. Park, Y. Aihara, D. Im, I.T. Han, High-energy long-cycling all-solid-state lithium metal batteries enabled by silver-carbon composite anodes. *Nature Energy*, **2020**, 5, 299.

### Acknowledgements

This is a collaborative project between University of Houston (Profs. Yan Yao and Zheng Fan) and Rice University (Prof. Jun Lou). We appreciate the support from Tien Duong, DOE Technology Development Manager, and Ms. Colleen Butcher at NETL for project management.

## XIII.8 First-Principles Modeling of Cluster-Based Solid Electrolytes (Virginia Commonwealth University)

### **Puru Jena, Principal Investigator**

Virginia Commonwealth University  
Department of Physics  
701 W Grace St  
Richmond, VA 23284  
E-mail: [pjena@vcu.edu](mailto:pjena@vcu.edu)

### **Hong Fang, Co-Principal Investigator**

Rutgers University (Camden campus)  
303 Cooper St  
Camden, NJ 08102  
E-mail: [hfangtom@gmail.com](mailto:hfangtom@gmail.com)

### **Tien Duong, DOE Technology Development Manager**

U.S. Department of Energy  
E-mail: [Tien.Duong@ee.doe.gov](mailto:Tien.Duong@ee.doe.gov)

Start Date: October 1, 2022  
Project Funding: \$991,335

End Date: September 30, 2023  
DOE share: \$793,040

Non-DOE share: \$198,295

### **Project Introduction**

Given the trend of global warming and the urgent need to transition from fossil fuels to green energy, lithium-ion batteries will continue to be an integral part of our lives. Design, development, and understanding of novel solid-state electrolyte materials play the key role for achieving next-generation all-solid-state batteries with high energy and great safety. The current modeling schemes to develop advanced solid electrolytes are focusing on materials in which the building blocks are individual atoms. Our theoretical approach is a paradigm shift in solid-state electrolyte design. Instead of atoms, we focus on clusters as the building blocks and model these solid electrolytes and their interfaces with electrodes, especially Li-metal anode, for their successful implementation in solid-state batteries. The advantage of using the cluster-ions to replace elemental ions is that the size, composition, and shape of the former can be tailored to achieve higher ionic conductivity at room temperature, electrochemical stability and charge transfer across solid-solid interfaces than conventional materials. Specifically, the project includes: (1) Developing cluster-based solid electrolytes, where the halogen components are replaced by cluster-ions that mimic the chemistry of halogens but are characterized by additional degrees of freedom, including the size, shape, and composition. (2) Providing a fundamental understanding of the ionic conduction mechanism in the newly-developed cluster-based solid electrolytes; (3) Modeling the interfacial properties (i.e., structural, chemical and transport) between the cluster-based solid electrolytes and electrodes at the atomic level. For the cluster-based solid electrolytes incompatible with the Li-metal anode or cathode materials, potential candidates for interfacial coatings will be identified and studied. (4) Providing a theoretical framework towards optimizing critical parameters of the solid-state electrolytes that will guide experimentalists to attain desired cathode-electrode interface for cluster-based solid-state electrolytes.

### **Objectives**

The objective of the project is to use cluster-ions, which are stable atomic clusters that mimic the chemistry of individual atoms, as the building blocks of new solid electrolytes (SEs) for Li-ion batteries and the corresponding battery system. The advantages of using cluster-ions to replace elemental ions is that the size, shape, and composition of the former can be tailored to achieve higher superionic conductivity, electrochemical stability, and charge transfer across the solid-solid interfaces than the conventional materials.

More specifically, the goal is to develop superior SEs based on cluster-ions and to model these SEs and their interfaces with electrodes, especially with the Li-metal anode, for successful integration into high performance SSBs for EVs. The team will model and screen cluster-based SEs that, compared to conventional SEs, have low activation energies, practical room-temperature ionic conductivities, wide electrochemical stability windows, and desired mechanical properties that, for example, can inhibit the Li-metal anode dendrite growth. They will provide a fundamental understanding of the ionic conduction mechanism in the newly developed, cluster-based SEs and identify means to further improve property metrics via chemical and defect engineering. The team will model the interfacial properties, such as the structural, chemical, electrochemical, and ion/charge transfer properties, between the cluster-based SEs and electrodes at the atomic level, as well as find the interfacial coating materials with desired properties. Based on accumulated data from modeling, they will establish links between the basic parameters of the cluster-ions and the bulk/interface properties, which can directly guide experiments. Meanwhile, the team will work closely with experimentalists in the BMR Program to complement the project's theoretical efforts and to guide them in focused development of the predicted cluster-based SEs and the interfaces.

## Approach

### **1. Developing new cluster-based solid electrolyte materials using selected cluster-ions from the established database of clusters.**

The possible crystal structures of the newly developed materials are determined using structure prediction techniques, such as the particle swarm optimization and the evolutionary algorithm [1-2]. The most stable phases that contain the cluster-ion from the search are considered as the initial structures, subject to further investigation. Each cluster-based solid electrolyte material with the determined crystal structure is fully optimized (for both the ion positions and lattice parameters) to its energy minimum using DFT calculations [3-4]. The lattice dynamic stability of the structure is then tested by phonon calculations based on the optimized structure; absence of imaginary frequency would define a stable structure. The formation energy of the lattice-dynamically stable cluster-based solid electrolyte material is then calculated. Its thermodynamics stability is investigated by calculating the pair correlation function and the position correlation function using the structural data from MD simulations at different temperatures. For each cluster-based solid electrolyte that is thermally stable, possible defects involving  $\text{Li}^+$  in the material is studied by calculating their formation and binding energies. Next, for each cluster-ion based solid electrolyte, a supercell system with the relevant defect is subjected to MD simulations with constant volume at different temperatures. MSD of the Li-ions is calculated using our own programs. The diffusion coefficients and the ionic conductivity at different temperatures are calculated from the MSD using the Nernst-Einstein relation. The room temperature ionic conductivity and the activation energy of the material is obtained by fitting to the Arrhenius relationship. The relevant electronic properties, including the bandgap, the band edges and the electronic conductivity are calculated using DFT. The hybrid functional (e.g. HSE [5]) and meta-GGA (e.g. mBJ [6]) is applied. All the obtained results from the above process are collected into a database.

### **2. Modeling the ionic conduction mechanism in the cluster-based solid electrolyte materials.**

To study the ionic conduction mechanism, we first investigate the channel size inside the solid electrolyte for  $\text{Li}^+$  migration, created by different cluster-ions. Next, the migration routes of  $\text{Li}^+$  in the presence of the chosen defect are studied. Given the non-spherical nature of the cluster-ion, there are a number of inequivalent migration routes. The energy barrier for each of these is calculated using the NEB method. The effect of the changing orientation of the cluster-ions on the ionic conductivity of the material is studied by building a Boltzmann model for different orientational configurations and selective dynamic simulations. The pattern of  $\text{Li}^+$  motions inside the cluster-based solid electrolytes is investigated using statistical analysis, such as computing the distinct van Hove time correlation function in the modeled system. From the above studies, the dependence of the solid electrolyte performance on the size, shape (symmetry), internal charge distribution, electron affinity, as well as the dynamics of the cluster-ion is established.



### **3. Modeling and optimizing the chemical mixing and doping in the cluster-based solid electrolyte materials.**

Different phases with mixed halides and clusters are created via chemical mixing. Their structures with different ratio are fully optimized using DFT energy calculations. Each optimized system is then investigated using DFT calculations and MD simulations to reveal its formation energy, ionic conduction properties, electrochemical properties, and mechanical properties against the original phase. The ratio that can enable the highest ionic conductivity while maintaining merits in other aspects is recorded in the database.

### **4. Modeling and optimizing the defect formation and concentration.**

Models are built for the cation-doped cluster-based solid electrolyte systems with supercells that contain different concentrations of the Li-vacancy defects. The structures of these systems are first energetically optimized using DFT calculations. Then, the structures are studied using MD simulations at fixed temperature. The ionic conduction properties of the resulting structures are investigated. The defect concentration that can entail the highest ionic conductivity in the cluster-based solid electrolyte can be revealed.

### **5. Modeling the electrolyte-electrode interfaces.**

Given that many of the cluster-based solid electrolytes material are metastable, the possible equilibrium phases at the interfaces when the solid electrolyte is in contact with the electrode are first identified by building lithium grand potential diagrams at different battery voltages (modeled by the lithium chemical potential) using the crystal data from the material database, e.g. the Materials Project [7]. Next, DFT calculations and MD simulations are conducted to study the stability, electronic and ionic conduction properties of the obtained equilibrium phase at the interface. The interface between the cluster-based solid electrolyte and the equilibrium phase, or between the equilibrium phase and the electrode are modeled using stacked slabs of the active materials. The local bonding reconstruction and charge transfer, as well as possible amorphization of the interface are then studied using MD simulations. If the interface cannot form a Li-conducting layer, or destroys the structure of the solid electrolyte through reaction, potential coating materials that are chemically/electrochemically stable, Li-conducting and having little lattice mismatch with the active materials, are identified. The structural, electrochemical and transport properties of the coating materials are studied using DFT calculations and MD simulations.

### **6. Modeling and optimizing the interface between the cluster-based solid electrolyte and the identified coating materials.**

Possible alloying phases between the cluster-based solid electrolyte and the coating material are investigated using the cluster expansion method [8-9]. The alloys that appear on or near the built convex hull are selected as the stable phases and their relevant properties, e.g., the ionic conductivity, are studied using DFT calculations and MD simulations. The alloying phase that can entail the highest ionic conductivity can serve as a good candidate for coating. The results regarding the identified coating materials and their possible alloying phases are included in our database.

### **7. Establishing links between the key parameters of the cluster-ion and the bulk and interfacial properties of the cluster-based solid electrolyte materials.**

With the data accumulated in our database, links between the key parameters (such as the size, shape, composition, charge distribution, and electron affinity) of the cluster-ion and the cluster-based solid electrolyte as well as its interfaces can now be drawn by using machine learning techniques. The established links aim to guide experiments in terms of which cluster-ions to choose that can entail high-performance cluster-based solid electrolytes and interfaces with the electrodes, especially with the Li-metal anode. The PI and team at VCU work in close collaboration and coordination (unfunded) with VTO-BMR (Vehicle Technology Office's Battery Materials Research) Program PIs working at multiple DOE National Laboratories on solid electrolyte modeling and interfaces and specifically with experimental groups working on synthesis and interfacial characterization of Li-based solid electrolytes.

## Results

We have completed two studies targeted in FY2023, as planned in SOPO. One is on understanding the ionic conductivity of a mixed phase with both cluster and halogen ions. A new program is developed to characterize the dynamically-changed channel space and Li-anion interactions in systems containing different ratios of cluster-ions and halogens. The dynamical channel space method is found to be a simple yet effective way to qualitatively evaluate the ionic conductivity and the activation energy of the cluster-based solid-state electrolytes (SSEs). We also studied the kinetic effect of the cluster-ions on the SSE-Li interface, and showed that the cluster-ions can inhibit the detrimental reaction at the interface by in-situ formations of interphases that are electronically insulating and ion-conductive.

Our previous studies show that the ionic conductivity and activation energy of a cluster-based SSE with halogen dopants do not change monotonically with the dopant concentration. For example, for a  $\text{Li}_6\text{PS}_5(\text{BH}_4)_{1-x}\text{Cl}_x$ , the system exhibits the lowest activation energy and the highest ionic conductivity at  $x = 0.875$ . This is orders of magnitude higher than that at  $x = 0.125$  or  $0.675$ . This suggests that the ionic conductivity is independent from the concentration of the halogen and cluster ion. The ionic conductivity is closely related to the available channel space for Li-ion migration in the structure. For the channel space, conventional studies have focused on characterizing the "static" spaces in an SSE using topology analysis. However, given the presence of non-spherical cluster ions and their motional dynamics in our studied SSEs, it is necessary to characterize the dynamically-changing channel space or the voids inside an SSE. We have developed a method to evaluate the dynamical channel space inside a given SSE by going through the "snapshots" from the molecular dynamics simulations. For each snapshot structure, the cell is first filled by dots with each dot carrying a tiny volume unit. Then, the dots that can accommodate at least one Li ion is identified using a specific algorithm. The total void space in a structure that can hold at least one Li ion is then determined. The channel spaces around each Li ion and between the neighboring Li ions are further evaluated, as shown schematically

The ionic conductivity is also closely related to the Li-anion and Li-cation interactions in the system. A Li ion will deviate from its equilibrium position (at the ground state) against the anion during diffusions. The deviation will strain the Li-anion interaction and cost energy which is related to the activation energy of an SSE. For a system with "soft" Li-anion interactions (small force constant of a Li-anion spring, per Figure XIII.8.1A), large deviations can be accessible during the thermally-excited Li ion diffusion, corresponding to relatively low activation energy. For systems with "stiff" Li-anion interactions (large force constant of a Li-anion spring), relatively small deviations can be accessible, corresponding to relatively high activation energy. Reduction in the neighboring Li-Li distance from its equilibrium value (at the ground state) would suggest increased Li ion correlation during the diffusion.

Figure XIII.8.1B shows the calculated channel spaces and deviations against the Cl-doping concentration at room temperature. It is found that Li ions always approach the  $\text{Cl}^-$  during the diffusion and reduce the Li-Cl distance from the equilibrium value at the ground state. As mentioned above, this will strain the Li-Cl interaction and cost energy. On the other hand, the Li-H ( $@\text{BH}_4^-$ ) distance is largely maintained. This is because, although the Li ions will approach  $\text{BH}_4^-$  during the diffusion, the anion cluster can accommodate the passing Li ion using its large rotational and translational degrees of freedom, maintaining the equilibrium Li-H distance to lower the energy cost. This agrees well with our previous discoveries. We have found before that the dynamics of anion cluster can be categorized into two types. The first one is called "responsive" dynamics, where the cluster can rotate and translate to accommodate a passing Li ion to lower the pathway energy. The other one is called "active" dynamics, where the clusters randomly rotate due to direct thermal excitations. These latter dynamics may inhibit the ion diffusion. Therefore, to make the high ionic conductivity in a cluster-based SSE is to introduce a "right amount of" cluster compositions and cluster dynamics. Excessive cluster dynamics can also lead to high activation energy and low ionic conductivity.

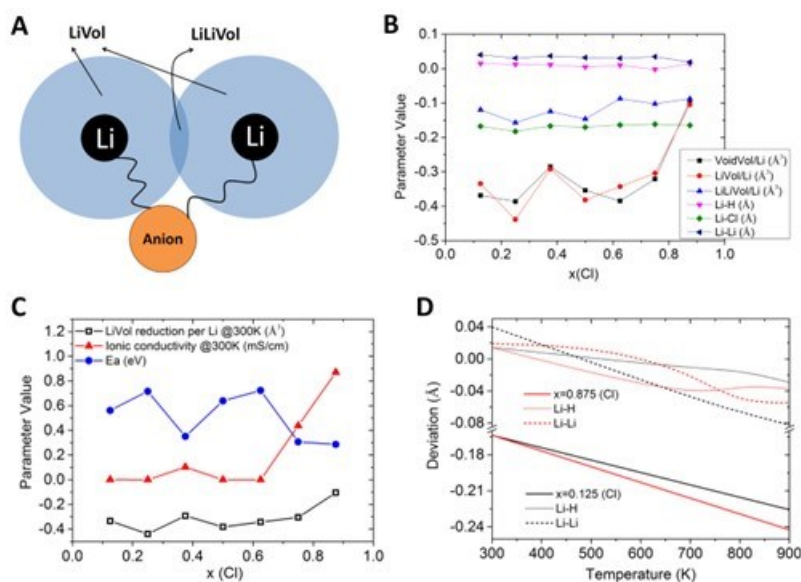


**Figure XIII.8.1** (A) Schematics show the channel spaces around each Li ion (LiVol) and between the neighboring Li ions (LiLiVol). It also shows the simple spring model capturing the Li-anion interaction in the system. (B) The calculated total void space (VoidVol), channel space surrounding each Li-ion (LiVol), channel space between neighboring Li ions (LiLiVol), deviation of Li ion from its equilibrium against  $\text{BH}_4^-$  (Li-H), deviation of Li ion from its equilibrium against  $\text{Cl}^-$  (Li-Cl), and deviation of the neighboring Li-Li distance from equilibrium. (C) Strong correlation between the channel space LiVol and the ionic conductivity/activation energy of the SSE. (D) Deviations of Li ion from its equilibrium against  $\text{Cl}^-$  (solid lines),  $\text{BH}_4^-$  (dotted lines), and neighboring Li (dashed lines) with elevated temperature at two Cl concentrations  $x = 0.875$  and  $x = 0.125$ .  
[Use EERE\_Figure\_Caption]

Figure XIII.8.1C shows that the defined channel space surrounding each Li (LiVol) correlates well with the ionic conductivity and activation energy of an SSE, and can serve as an effective descriptor for these quantities. Such dynamical channel space can be evaluated in a short time period and can be applied to qualitatively prescreen the compositions that can lead to high ionic conductivities. On the other hand, directly calculating the ionic conductivity at room temperature is very hard to converge, requiring a very long simulation time. Any shortage of the simulation time may result in the computed ionic conductivities with orders of magnitude difference. Figure XIII.8.1D shows that the Li-Cl (solid lines) and Li-H (dotted lines) deviations for  $x = 0.875$  are significantly greater than those of  $x = 0.125$ . This explains why the former exhibits the high ionic conductivity and low activation energy per Figure 1, i.e., the system with  $x = 0.875$  exhibits "soft" Li-anion interactions and small energy cost for the ion diffusion. The figure also shows that the Li-cluster (Li-H) distance deviates slightly from the equilibrium value (put at zero in the figure) with elevated temperature, due to the large deviation caused by the Li ion diffusion that cannot be completely accommodated by the cluster dynamics at high temperatures. The reduction in the Li-Li distance also increases with elevated temperature, suggesting a stronger Li-Li correlation during the diffusion.

Our previous studies have shown that the CBSE can entail a much more stable interface against Li metal anode than its halogen counterpart (e.g.,  $\text{Li}_6\text{PS}_5\text{Cl}$ ). We identified the decomposed phases at the interface composed by the clusters based on explicit interface simulations. These cluster-based interphases exhibit large bandgaps and very low electron mobility, leading to sluggish reduction reactions. To further confirm these and directly show the passivating behavior of the cluster-containing interphases, we completed the following in the last quarter. First, we greatly extended the simulation time to over 200 ps for the interface modeling. For example, Figure XIII.8.2 shows the results of the  $\text{Li}_6\text{PS}_5(\text{BH}_4)$ -Li interface model (Figure XIII.8.2A). Figure XIII.8.2B shows that, after 200 ps, more than 75% of P-S bonds remained in  $\text{Li}_6\text{PS}_5(\text{BH}_4)$  compared to only 65% in  $\text{Li}_6\text{PS}_5\text{Cl}$ . After about 100 ps, the reduction of P and the breaking up of P-S bonds stop in  $\text{Li}_6\text{PS}_5(\text{BH}_4)$ . The

radial distribution function analysis in Figure XIII.8.2C suggests the formation of  $\text{Li}(\text{BH}_4)$  at the interface, which is responsible for the inhibited reduction reaction

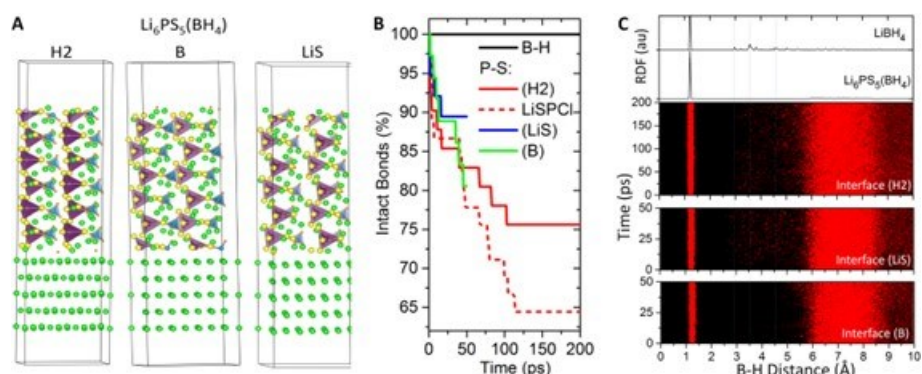


**Figure XIII.8.2 (A)** Explicit interface models of  $\text{Li}_6\text{PS}_5(\text{BH}_4)$ -Li with three different terminating species in close contact with Li metal surface. **(B)** Bond analyses for the interface models based on molecular dynamics simulations up to 200 ps. The  $\text{BH}_4^-$  clusters are stable throughout the simulation, while some  $\text{PS}_4^{3-}$  units are breaking up due to the reduction of P by the Li metal. **(C)** Radial distribution function analyses at the interface showing the formation of  $\text{LiBH}_4$  with the characteristic peaks around 3-4.5 Å. [Use EERE\_Figure\_Caption]

Second, we conducted new analyses to directly show the charge transfer leading to the reduction of P in  $\text{PS}_4^{3-}$  units in the solid electrolytes. The charge transfer from Li metal to P is the key reason for the instability of the argyrodite solid electrolytes against Li metal anode. We make a program that can compute the averaged charge state of P in a CBSE layer by layer parallel to the interface using the Bader charges of each 'snapshot' structure at certain simulation time. Based on this, the charge transfer from the Li metal to the CBSE across the interface can be obtained against the simulation time. For example, as shown in Figure XIII.8.3, the charge transfer to P from Li metal is much more limited in the CBSEs compared that in  $\text{Li}_6\text{PS}_5\text{Cl}$ . As indicated by the contour lines in the figure, electrons permeate and distributed across the interphase of  $\text{Li}_6\text{PS}_5\text{Cl}$ , while the electrons are only concentrated at the bottom of the interphases in the CBSEs. Here,  $\text{Li}_6\text{PS}_5(\text{BH}_4)$  with the interphase  $\text{LiBH}_4$  exhibits the best passivating ability among the three, where the electron transfer is clearly inhibited in both time and space.

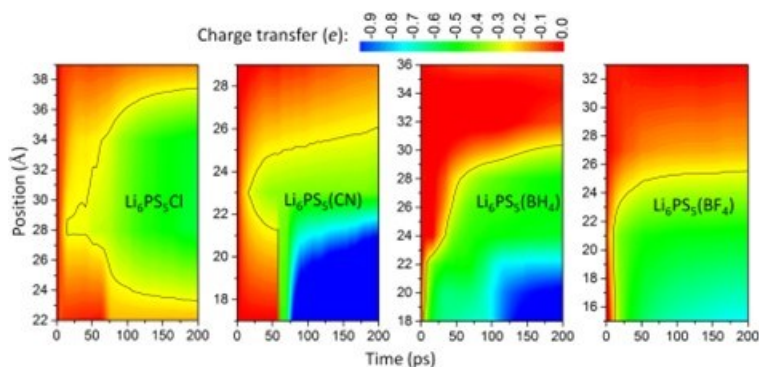


**Figure XIII.8.3** Direct showing of charge (electron) transfer from Li metal to P in the solid electrolytes. The bottom position (e.g., at 22 Å in the case of  $\text{Li}_6\text{PS}_5\text{Cl}$ ) corresponds to the top of the Li metal surface of each case. The color bar corresponds to the amount of charge transfer from Li metal to P. [Use EERE\_Figure\_Caption]

Besides the charge transfer from Li metal to the solid electrolyte, there will be also mass transfer across the interface if the reduction reaction continues. Li atom will transfer into the solid electrolyte and the reduced P

will move away from its original crystalline site. These will be reflected in the change of atomic distribution across the interface. The atomic distribution can be measured by the position deviation of the atoms along the z-axis perpendicular to the interface defined as,

$$\sigma = \sqrt{\frac{1}{N} \sum_{i=1}^N (z_i - \bar{z})^2}, \quad \bar{z} = \frac{1}{N} \sum_{i=1}^N z_i. \quad (1)$$

Figure XIII.8.4 shows the change of  $\sigma$  against the simulation time for P and Li. Besides  $\text{Li}_6\text{PS}_5\text{Cl}$ ,  $\text{Li}_6\text{PS}_5(\text{CN})$ , and  $\text{Li}_6\text{PS}_5(\text{BH}_4)$ , the results for  $\text{Li}_6\text{PS}_5(\text{BF}_4)$  are also included in the figure. It shows that the distribution of P is maintained in the interfaces with the CBSEs, while greatly increases in  $\text{Li}_6\text{PS}_5\text{Cl}$ . This corresponds to the sharp decrease of Li distribution in  $\text{Li}_6\text{PS}_5\text{Cl}$  due to some of the Li metal moving into the electrolyte due to the reduction reaction. For the  $\text{Li}_6\text{PS}_5(\text{CN})$ , and  $\text{Li}_6\text{PS}_5(\text{BH}_4)$  interfaces, the change of Li distribution is much more limited, while the Li distribution for  $\text{Li}_6\text{PS}_5(\text{BF}_4)$  is nearly unchanged throughout the time. This suggests that, while the cluster-containing interphases can effectively inhibit the reduction reaction at the interface, the cluster  $\text{BF}_4^-$  can passivate the interface most rapidly by forming the interphase  $\text{LiBF}_4$ .

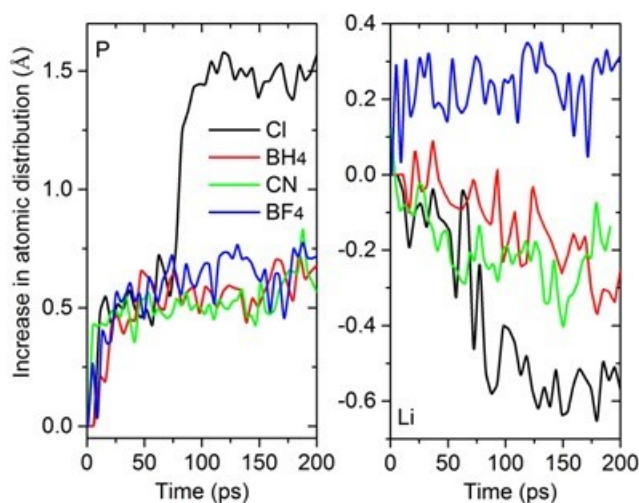


Figure XIII.8.4 Change of atomic distribution across the interface measured by the calculated change of atomic deviation ( $\sigma$ ). [Use EERE\_Figure\_Caption]

## Conclusions

We have systematically designed and modeled a new family of solid-state electrolyte materials based on substitution of cluster ions. Both the bulk physicochemical properties of the new solid electrolytes and their interface properties against electrodes, especially Li metal anode, have been unraveled. A theoretical framework to study the structure and dynamics of the cluster ions inside lattice has been established. The results of this project show that the cluster ions serving as the building block of solid electrolytes is a viable way to produce good performance in both ion transports and interface stabilities. Indeed, a number of very recent experiments have confirmed our designed solid electrolytes based on cluster ions and their working mechanisms [e.g., 10-14]. We are currently working with our experimental collaborators to further the range of synthesized materials based on different cluster ions and explore new synthetic and processing methods for even better properties.

## Key Publications

1. H. Fang and P. Jena, Kinetic effects of anion cluster on the interfacial stability between solid-state electrolyte and metal anode, *Phys. Rev. X Energy*, 2023, Revision under Review.
2. R. L. Sacci, T. H. Bennett, H. Fang, P. Jena, J. Nanda et al., Halide sublattice dynamics drive Li-ion transport in antiperovskites, *J. Mater. Chem. A* 10, 15731, 2022.

3. H. Fang, P. Jena, Argyrodite-type advanced lithium conductors and transport mechanisms beyond paddle-wheel effect, *Nature Communications* 13, 2078, 2022.
4. Xuyong Feng, Hong Fang, Nan Wu, Pengcheng Liu, Puru Jena, Jagjit Nanda, and David Mitlin, Review of modification strategies in emerging inorganic solid-state electrolytes for lithium, sodium, and potassium batteries, *Joule* 6, 543-587, 2022.

## References

1. Y. Wang, J. Lv, L. Zhu, Y. Ma, CALYPSO: A Method for Crystal Structure Prediction, *Comput. Phys. Commun.* 2012, 183, 2063.
2. A. R. Oganov, C. W. Glass, *Crystal Structure Prediction Using Evolutionary Algorithms: Principles and Applications*, *J. Chem. Phys.* 2006, 124, 244704.
3. S. J. Clark, M. D. Segall, C. J. Pickard, P. J. Hasnip, M. J. Probert, K. Refson, M. C. Payne, *First Principles Methods Using CASTEP*, *Zeitschrift fuer Kristallographie.* 2005, 220, 567.
4. G. Kresse, J. Furthmuller, Efficiency of Ab Initio Total Energy Calculations for Metals and Semiconductors Using a Plane-Wave Basis Set, *Int. J. Comput. Mater. Sci. Eng.* 1996, 6, 15.
5. A. V. Krukau, O. A. Vydrov, A. F. Izmaylov, G. E. Scuseria, Influence of the Exchange Screening Parameter on the Performance of Screened Hybrid Functionals, *J. Chem. Phys.* 2006, 125, 224106.
6. J. Sun, A. Ruzsinszky, J. P. Perdew, Strongly Constrained and Appropriately Normed Semilocal Density Functional, *Phys. Rev. Lett.* 2015, 115, 036402.
7. A. Jain, S. P. Ong, G. Hautier, W. Chen, W.D. Richards, S. Dacek, S. Cholia, D. Gunter, D. Skinner, G. Ceder, K.A. Persson, The Materials Project: A Materials Genome Approach to Accelerating Materials Innovation, *APL Materials.* 2013, 1, 011002.
8. A. V. D. Walle, G. Ceder, Automating First-Principles Phase Diagram Calculations, *J. Phase Equilib.* 2002, 23, 348.
9. A. V. D. Walle, M. Asta, G. Ceder, The Alloy Theoretic Automated Toolkit: A User Guide, *Calphad.* 2002, 26, 539.
10. Y. Sun, Y. Wang, X. Liang, Y. Xia, L. Peng, H. Jia, H. Li, L. Bai, J. Feng, H. Jiang, J. Xie, Rotational Cluster Anion Enabling Superionic Conductivity in Sodium-Rich Antiperovskite Na<sub>3</sub>OBH<sub>4</sub>, 2019, *J. Am. Chem. Soc.* 141, 5640–5644.
11. A. E. Maughan, Y. Ha, R. T. Pekarek, C. M. Schulze, Lowering the activation barriers for lithium-ion conductivity through orientational disorder in the cyanide argyrodite Li<sub>6</sub>PS<sub>5</sub>CN, 2021, *Chem. Mater.* 33, 5127–5136.
12. Y. Sun, B. Ouyang, Y. Wang, Y. Zhang, S. Sun, Z. Cai, V. Lacivita, Y. Guo, G. Ceder, Enhanced ionic conductivity and lack of paddle-wheel effect in pseudohalogen- substituted Li argyrodites, 2022, *Matter* 5, 1-17.
13. A. Sakuda et al. Mechanochemically prepared Li<sub>2</sub>S–P<sub>2</sub>S<sub>5</sub>–LiBH<sub>4</sub> solid electrolytes with an argyrodite structure, 2018, *ACS Omega* 3, 5453–5458.
14. Yong-Jin Jang, Hyungeun Seo, Young-Su Lee, Sora Kang, Woosuk Cho, Young Whan Cho, and Jae-Hun Kim, Lithium Superionic Conduction in BH<sub>4</sub>-Substituted Thiophosphate Solid Electrolytes, 2023, *Adv. Sci.* 2023,10, 2204942.

## XIII.9 Predictive Engineering of Interfaces and Cathodes for High-Performance All Solid-State Lithium-Sulfur Batteries (University of Louisville)

### Badri Narayanan, Principal Investigator

University of Louisville  
332 Eastern Parkway  
Louisville, KY 40292  
E-mail: [badri.narayanan@louisville.edu](mailto:badri.narayanan@louisville.edu)

### Tien Duong, DOE Technology Development Manager

U.S. Department of Energy  
E-mail: [Tien.Duong@ee.doe.gov](mailto:Tien.Duong@ee.doe.gov)

Start Date: October 1, 2019	End Date: December 31, 2022	
Project Funding: \$1,250,000	DOE share: \$1,000,000	Non-DOE share: \$250,000

### Project Introduction

All solid lithium-sulfur battery (ASLSB) is a promising next-generation energy storage technology due to its high theoretical capacity (~1675 Ah/kg; ~5-6 times higher than state-of-the-art Li-ion batteries), high promised energy density (400 Wh/kg), safety, no polysulfide-shuttling, and natural abundance of sulfur. Sulfide ( $\text{Li}_2\text{S-P}_2\text{S}_5$ ) solid electrolytes (SSEs) possess high Li-ion conductivity ( $\sim 10^{-3}$  S/cm), good elastic stiffness (~30 GPa), good stability against Li metal, and low flammability. Such a collection of unique properties makes them lucrative for use in long-lived, safe, high-capacity Li-S batteries for all-electric transportation. Despite this promise, ASLSBs (even using SSEs) remain far from commercialization due to unresolved issues at the electrode-electrolyte interfaces, including (a) poor contact, and high resistance to  $\text{Li}^+$  ion transport across the cathode/SSE interface, (b) poor ionic/electronic conduction within the cathode, and (c) dendrite growth at the Li/SSE interface. Most of these daunting challenges arise primarily from a lack of fundamental understanding of electrochemical/chemical and transport processes that occur at electrode/electrolyte interfaces, especially at atomic to mesoscopic scales.

Here, we propose to bridge this knowledge gap and address the interfacial issues by developing highly accurate materials models at atomic-to-mesoscopic length/time scales using data-centric and machine learning methods. Successful development of these models will significantly advance the current state-of-the-art in fundamental understanding of reaction chemistry, kinetics, charge transfer, and dendrite growth at electrified solid-solid interfaces. Multi-scale simulations based on the newly developed models, alongside our wet-chemistry synthesis and advanced characterization will unravel novel strategies to mitigate interfacial resistance, enable precise control over the composition/morphology of solid electrolyte interphase (SEI) and design cathodes with high sulfur loading. Broadly, fundamental knowledge gained by this work will enable development of high-performance ASLSBs that meet DOE targets of specific energy (350 Wh/kg @C/3), sulfur loading (> 6 mg/cm<sup>2</sup>), and high cycle life (1000).

### Objectives

The primary goal of this project is to leverage data-driven methods and ML strategies to develop accurate multi-physics models for all-solid-state Li-S battery (ASLSB) materials that can capture electrochemical and transport phenomena over atomic-to-mesoscopic length/timescales; these models will be rigorously validated by synthesis and advanced characterization experiments. The team will leverage the predictive power of these models, alongside synthesis/characterization experiments and battery fabrication to address longstanding issues at the electrode/electrolyte interfaces in ASLSBs. The project's proposed technology involves the following: (1) halide-doped solid sulfide electrolytes that can concurrently provide high  $\text{Li}^+$  ion conductivity and suppress dendrite growth; (2) novel mesoporous cathode composed of interconnected carbon nano-cages co-infiltrated

with sulfur and sulfide electrolyte, which hold potential to allow high sulfur loading and optimal ion/electron pathways; and (3) functionalization of sulfide electrolyte with ionic liquids to improve physical contact and minimize impedance at the cathode/electrolyte interface.

## Approach

The project brings together innovative solutions in multi-scale materials modeling, electrolyte synthesis, fabrication of cathode architecture, and electrolyte functionalization to overcome the issues at electrode-electrolyte interfaces in ASLSBs. The central idea is to employ a data-driven and ML-based approach to develop accurate multi-physics battery models at atomic-to-mesoscopic scales. This approach overcomes critical problems with existing model development methods by foregoing need for pre-defined functional forms, introducing deep-learning technique to describe reactivity, and employing optimization methods that do not require human intuition. Multi-scale simulations based on the newly developed models will provide insights into electrochemical phenomena at electrode/electrolyte interfaces.

## Results

### Synthesis and Structure of F/I hybrid doped argyrodite electrolytes:

State-of-the-art solid-state techniques to synthesize SSEs offer excellent control over composition.<sup>1</sup> However, these methods are energy-intensive and time consuming, typically requiring long periods of ball-milling and heat treatments of  $\geq 550$  °C; which, severely limits their scalability. To address this issue, we developed a scalable, efficient, and economic solvent-based method to produce SSEs.<sup>2-4</sup> Briefly, in this technique, a stoichiometric mixture of  $\text{Li}_2\text{S}$ ,  $\text{Li}_3\text{PS}_4$  and  $\text{LiX}$  ( $\text{X} = \text{F}, \text{Cl}, \text{Br}, \text{I}$ ) in anhydrous ethanol solvent; followed by evaporation and heat-treatment to achieve the desired halide doped SSE with prescribed composition. Note, we have also extended this technique to introduce multiple halogens into  $\text{Li}_7\text{PS}_6$  structure.

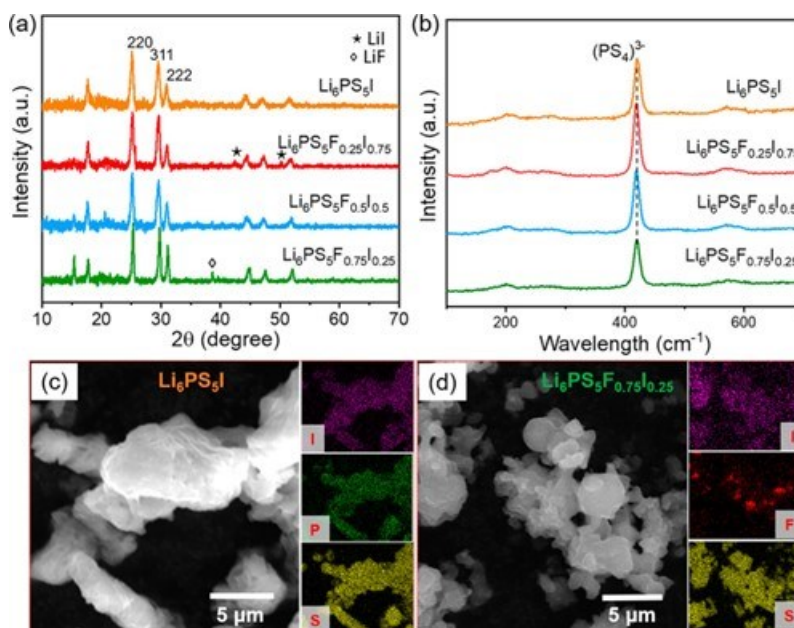


**Figure XIII.9.1 Scalable synthesis of F/I hybrid doped argyrodite electrolytes. (a) XRD patterns and (b) Raman spectra of solvent-synthesized  $\text{Li}_6\text{PS}_5\text{I}$  and  $\text{Li}_6\text{PS}_5\text{F}_x\text{I}_{1-x}$  ( $x = 0.25, 0.5, 0.75$ ) argyrodites. SEM images and EDS mapping of (c)  $\text{Li}_6\text{PS}_5\text{I}$  and (d)  $\text{Li}_6\text{PS}_5\text{F}_{0.75}\text{I}_{0.25}$ . It is noted that the  $x$  value only refers to the amount of F from the precursor and does not reflect the accurate F-doping content in argyrodites.**

Importantly, our newly developed solvent-based technique provides SSEs with excellent phase purity and composition control, as highlighted by one of our representative works on fluorinated argyrodites (Figure XIII.9.1). X-ray characterization of samples of  $\text{Li}_6\text{PS}_5\text{F}_x\text{I}_{1-x}$  ( $x=0.25, 0.5, 0.75$ ) produced by our solvent-based method (followed by a heat treatment at 200°C) show strong characteristic diffraction peaks at  $2\theta = 25.2^\circ$ ,



29.6°, and 31.0°, corresponding to the (220), (311), and (222) crystal planes<sup>3</sup> in the cubic argyrodite structure (space group  $F\bar{4}3m$ ), respectively (Figure XIII.9.1(a)). The pristine  $\text{Li}_6\text{PS}_5\text{I}$  possesses slightly higher lattice parameter (10.12 Å) than  $\text{Li}_6\text{PS}_5\text{Cl}$  (9.85 Å) and  $\text{Li}_6\text{PS}_5\text{Br}$  (9.98 Å) owing to the large size of  $\text{I}^-$  ions. Consistent with this observation, we also noted that upon hybrid doping with  $\text{I}^-$  and  $\text{F}^-$  ions, the lattice parameter decrease slightly (e.g., 9.94 Å for  $\text{Li}_6\text{PS}_5\text{F}_{0.75}\text{I}_{0.25}$ ) owing to the smaller ionic radius of  $\text{F}^-$  as compared to  $\text{I}^-$  ions ( $\text{F}^-$ : 1.33 Å,  $\text{I}^-$ : 2.16 Å). Although the X-ray diffraction (XRD) pattern indicate a dominant argyrodite phase, we also observe a minor secondary phase is also observed in hybrid-doped samples (Figure XIII.9.1(a)). For example, the  $\text{Li}_6\text{PS}_5\text{F}_{0.75}\text{I}_{0.25}$  sample shows minor peaks at  $2\theta = 42.4^\circ$  and  $50.2^\circ$  (indexed to  $\text{LiI}^5$ ), while  $\text{Li}_6\text{PS}_5\text{F}_{0.25}\text{I}_{0.75}$  sample shows weak peak at  $2\theta = 39.1^\circ$  that can be attributed to small amount of secondary phase of  $\text{LiF}$  (possibly due to the low temperature annealing in our synthesis).<sup>2</sup> Furthermore, the XRD refinements indicate that in  $\text{Li}_6\text{PS}_5\text{I}$  the  $\text{I}^-$  anion completely occupies the  $4a$  site, while the S atoms occupy the  $4d$  site in the argyrodite crystal. Conversely, the  $\text{I}^-$  anion in  $\text{Li}_6\text{PS}_5\text{F}_{0.75}\text{I}_{0.25}$  shows a  $4a$  occupancy of only 0.4534, indicating a greater frequency of halogen disorder in this composition.

Notably, all the  $\text{Li}_6\text{PS}_5\text{F}_x\text{I}_{1-x}$  ( $x=0.25,0.5,0.75$ ) samples show strong bands around  $420\text{ cm}^{-1}$  with smaller bands at  $575\text{ cm}^{-1}$  and  $200\text{ cm}^{-1}$  (Figure XIII.9.1(b)). The frequency range around  $420\text{ cm}^{-1}$  corresponds to the stretching vibration of the P–S bond in  $\text{PS}_4^{3-}$  (ortho-thiophosphate), as reported by previous studies on argyrodite electrolytes ( $\text{Li}_7\text{PS}_6$ ,  $\text{Li}_6\text{PS}_5\text{Br}$  and  $\text{Li}_6\text{PS}_5\text{Cl}$ ).<sup>6,7</sup> Furthermore, scanning electron microscopy (SEM) images indicate a granular morphology with particle size around 1–10  $\mu\text{m}$ , as exemplified for  $\text{Li}_6\text{PS}_5\text{I}$  and  $\text{Li}_6\text{PS}_5\text{F}_{0.75}\text{I}_{0.25}$  in Figure XIII.9.1(c,d) respectively. While  $\text{Li}_6\text{PS}_5\text{I}$  shows homogeneous elemental distribution of I, P, and S, the aggregation of F is observed for the  $\text{Li}_6\text{PS}_5\text{F}_{0.75}\text{I}_{0.25}$  sample in some local areas (see Energy Dispersive Spectroscopy (EDS) mapping in Figure XIII.9.1(c,d)), which may come from the secondary phase.

#### **Introduction of anion-site disorder via F/I hybrid doping, and its impact on ionic conductivity:**

Impedance spectroscopy measurements show that  $\text{Li}_6\text{PS}_5\text{F}_{0.25}\text{I}_{0.75}$  exhibits the highest RT ionic conductivity of  $3.5 \times 10^{-4}\text{ S cm}^{-1}$ , which is 40% higher than that of  $\text{Li}_6\text{PS}_5\text{I}$  ( $2.5 \times 10^{-4}\text{ S cm}^{-1}$ ) (Figure XIII.9.2(a-c)). On the other side,  $\text{Li}_6\text{PS}_5\text{F}_{0.75}\text{I}_{0.25}$  sample shows the lowest ionic conductivity of  $1.5 \times 10^{-4}\text{ S cm}^{-1}$ , which is possibly due to the minor secondary  $\text{LiF}$  phase (~9 wt% as observed in our XRD results). To gain further insights into the effect of hybrid-doping on the atomic-structure of argyrodite electrolytes, we performed density functional theory (DFT) calculations to elucidate the energetics of anion-disorder of  $\text{Li}_6\text{PS}_5\text{I}$  and  $\text{Li}_6\text{PS}_5\text{F}_{0.25}\text{I}_{0.75}$ . We found that  $\text{Li}_6\text{PS}_5\text{I}$  exhibits a perfect argyrodite structure with face-centered cubic symmetry (space group:  $F4\bar{3}m$ ) consisting of  $\text{PS}_4^{3-}$  building blocks (Figure XIII.9.2 (d)). In ordered configuration, the I atoms occupy only the corners/face centers (i.e.,  $4a$  Wyckoff sites). The S atoms belonging to the  $\text{PS}_4^{3-}$  occupy the Wyckoff  $16e$  sites; while other S occupy the  $4d$  sites. The Li atoms partially occupy the  $48h/24g$  positions, which form a cage-like structure around the S-atoms placed at the  $4d$  sites (Figure XIII.9.2 (e)) consistent with previous DFT works.<sup>8,9</sup> Notably, our DFT-predicted lattice parameter (10.3 Å) of  $\text{Li}_6\text{PS}_5\text{I}$  is close (within 2%) to those obtained from the XRD measurements (10.12 Å). For pure  $\text{Li}_6\text{PS}_5\text{I}$ , our DFT calculations show that anion-disordered structures (with varying distribution of  $\text{S}^{2-}$  and  $\text{I}^-$  ions among  $4a$  and  $4d$  sites) are significantly less stable than the ordered counterpart. For instance, creating an anti-site by swapping a pair of S and I between  $4a$  and  $4d$  sites in the ordered structure is endothermic ~0.3 eV/u.f (Figure XIII.9.2 (d)). Such energetic penalty against anion-disorder in  $\text{Li}_6\text{PS}_5\text{I}$  can be attributed to the substantial larger size of  $\text{I}^-$  (2.06 Å) as compared to  $\text{S}^{2-}$  (1.85 Å). On the other hand, in dual-doped  $\text{Li}_6\text{PS}_5\text{F}_{0.25}\text{I}_{0.75}$ , our DFT calculations on several structures with varying distributions of  $\text{S}^{2-}$ ,  $\text{F}^-$ , and  $\text{I}^-$  ions among  $4a$  and  $4d$  sites elucidate that anion-disordering is thermodynamically favorable (swapping a pair of S and F between  $4a$  and  $4d$  sites in the ordered argyrodite is mildly exothermic about -0.27 eV/u.f.) owing to the small ionic radius of  $\text{F}^-$  (1.33 Å) and strong Li-F interactions (representative example shown in Figure XIII.9.2 (e)). This energetic preference for halogen disorder in  $\text{Li}_6\text{PS}_5\text{F}_{0.25}\text{I}_{0.75}$  would enhance the frequency of inter-cage hops, owing to difference in electronegativity between S and F ions as suggested by previous DFT studies.<sup>8</sup> Indeed, our ab initio molecular dynamics (AIMD) simulations also indicate that anion disorder enables ~10 times faster Li-ion conduction in  $\text{Li}_6\text{PS}_5\text{F}_{0.25}\text{I}_{0.75}$  as compared to  $\text{Li}_6\text{PS}_5\text{I}$ , which qualitatively matches with our impedance spectroscopy measurements (Figure XIII.9.2(a-c)).

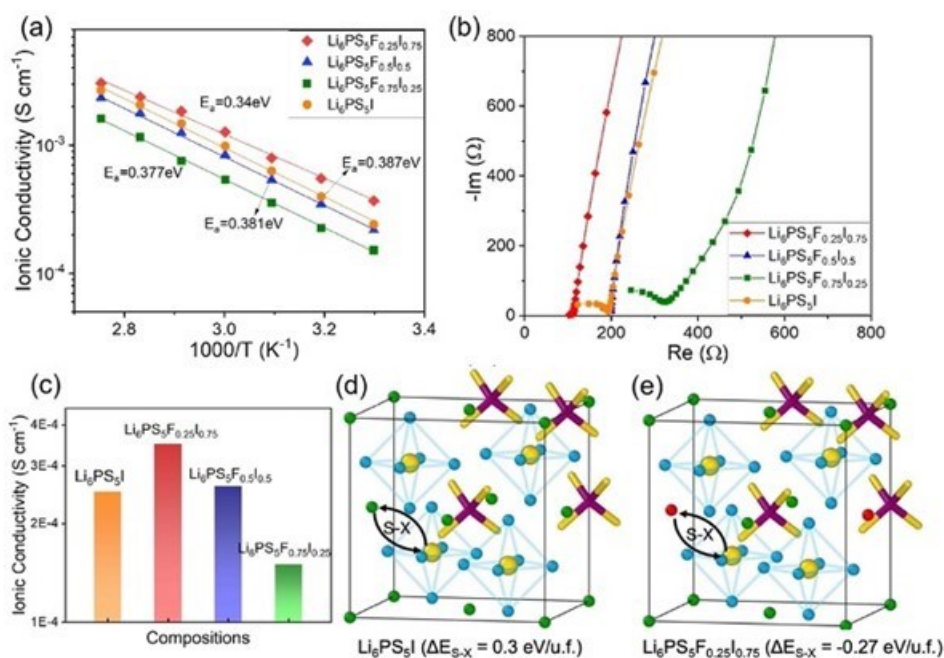


**Figure XIII.9.2** Anion-disorder in dual-doped argyrodite SEs and its impact on Li-ion conduction. (a) Arrhenius plots (30-90 °C) of Li<sub>6</sub>PS<sub>5</sub>I and hybrid-doped Li<sub>6</sub>PS<sub>5</sub>F<sub>x</sub>I<sub>1-x</sub> ( $x = 0.25, 0.5, 0.75$ ) argyrodites; (b) Nyquist plots and (c) composition dependent ionic conductivity of Li<sub>6</sub>PS<sub>5</sub>I and hybrid-doped Li<sub>6</sub>PS<sub>5</sub>F<sub>x</sub>I<sub>1-x</sub> argyrodites at RT; Atomic-scale structures of (d) Li<sub>6</sub>PS<sub>5</sub>I, and (e) Li<sub>6</sub>PS<sub>5</sub>F<sub>0.25</sub>I<sub>0.75</sub> optimized by density functional theory (DFT) calculations. In each panel, the energy change associated with swapping a S atom at 4d site (cage-center) with a halogen (I in panel (a), and F in panel (b)) are indicated. The Li, P, S, F and I atoms are depicted as blue, purple, yellow, red, and green spheres, respectively.

#### **Electrochemical stability of F/I hybrid doped argyrodites in Li symmetric cells and Li metal batteries:**

Electrochemical cycling tests of Li symmetric cells indicate that F/I co-doped argyrodites show a nearly flat polarization voltage profile (Li<sub>6</sub>PS<sub>5</sub>F<sub>0.75</sub>I<sub>0.25</sub> better than Li<sub>6</sub>PS<sub>5</sub>F<sub>0.25</sub>I<sub>0.75</sub>) over 100 cycles, while Li<sub>6</sub>PS<sub>5</sub>I shows an increasing polarizing voltage from 0.18 V to 0.37 V (Figure XIII.9.3(a)). This is indicative of a more stable Li/electrolyte interface with the hybrid doped argyrodites. Furthermore, the impedance of Li symmetric cell with Li<sub>6</sub>PS<sub>5</sub>F<sub>0.75</sub>I<sub>0.25</sub> solid electrolyte (SE) slightly changes from 2950 to 2780 Ω after 100 cycles, which further indicates the formation of a stable solid electrolyte interphase (SEI) layer between Li<sub>6</sub>PS<sub>5</sub>F<sub>0.75</sub>I<sub>0.25</sub> SE and Li metal. The long-term cycling stability of Li<sub>6</sub>PS<sub>5</sub>F<sub>0.75</sub>I<sub>0.25</sub> SE in Li symmetric cell is presented in Figure XIII.9.3(c), which runs continuously for 1100 h without any obvious voltage jumps or short circuiting. X-ray photoelectron spectroscopy (XPS) indicates that a SEI layer containing both LiF and LiI at the interface between Li<sub>6</sub>PS<sub>5</sub>F<sub>0.75</sub>I<sub>0.25</sub> SE and Li metal during the electrochemical cycling (Figure XIII.9.3(d-f)).<sup>2,10</sup> Both LiF and LiI have been previously reported to enhance interfacial stability, with LiF specifically known to prevent proliferation of Li-dendrites.<sup>11,12</sup>

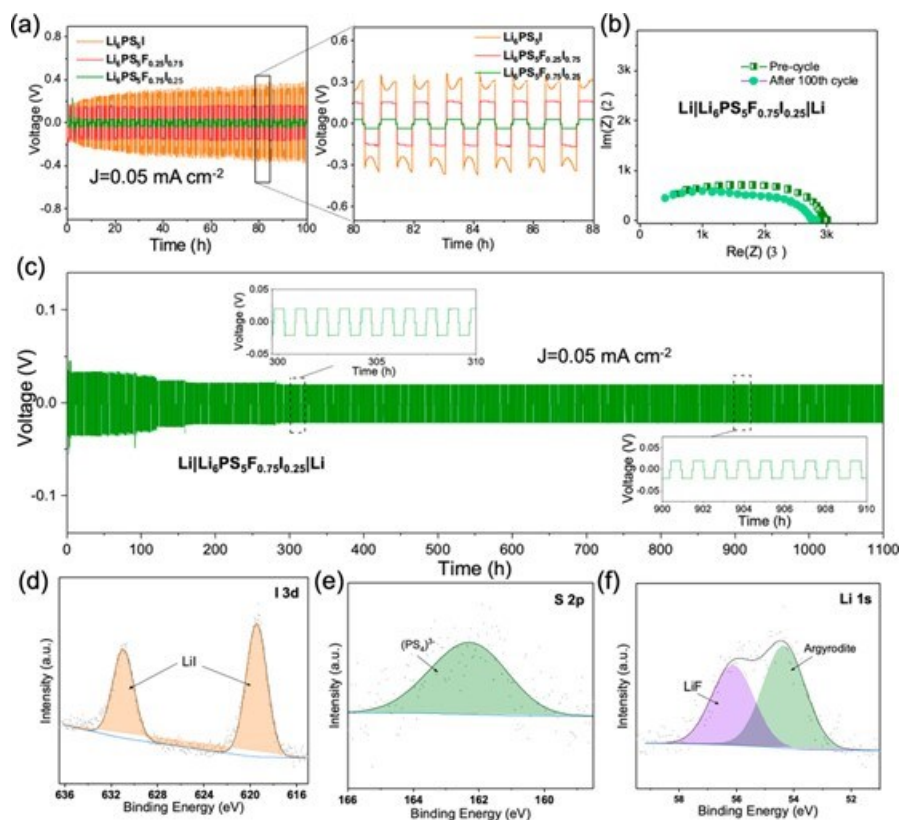


**Figure XIII.9.3** Electrochemical stability of F/I hybrid-doped argyrodites against lithium metal. (a) Cycling performance of Li symmetric cells with  $\text{Li}_6\text{PS}_5\text{I}$ , and hybrid-doped  $\text{Li}_6\text{PS}_5\text{F}_x\text{I}_{1-x}$  ( $x = 0.25, 0.75$ ) argyrodites as SEs under current density of  $0.05 \text{ mA cm}^{-2}$ . (b) Nyquist plots of  $\text{Li}_6\text{PS}_5\text{F}_{0.75}\text{I}_{0.25}$ -based symmetric cell before and after cycling for 100 cycles. (c) Voltage profiles of  $\text{Li}_6\text{PS}_5\text{F}_{0.75}\text{I}_{0.25}$ -based symmetric cell cycling up to 1100 h (current density of  $0.05 \text{ mA cm}^{-2}$ ) and XPS spectra of cycled symmetric cell with  $\text{Li}_6\text{PS}_5\text{F}_{0.75}\text{I}_{0.25}$  SE: (d) I 3d, (e) S 2p, and (f) Li 1s. In the XPS, the doublet peaks for I 3d at 619.4 and 630.5 eV (panel (d)) originate from Li-I bonding, while the peak at 56.2 eV for Li 1s (panel (f)) can be attributed to Li-F bonding. This clearly indicates presence of LiI and LiF.

Inspired by the long time stable cycling of Li-symmetric cells with  $\text{Li}_6\text{PS}_5\text{F}_{0.75}\text{I}_{0.25}$  SE, we assembled a solid state Li-metal battery with lithium titanate (LTO) positive electrode and  $\text{Li}_6\text{PS}_5\text{F}_{0.75}\text{I}_{0.25}$  SE. We found that this full cell delivers an initial specific capacity of about  $140 \text{ mAh g}^{-1}$ , which slightly decreases to  $128 \text{ mAh g}^{-1}$  at the 50th cycle (91.5% capacity retention), within an electrochemical window of 1.0–2.8 V under a C-rate of 0.1 C (Figure XIII.9.4(a)). Even after 200 cycles, the cell retains a respectable a specific capacity values of  $105 \text{ mAh g}^{-1}$  (Figure XIII.9.4(a)). Additionally, the cycling can be achieved with a high Coulombic efficiency  $\sim 99.95\%$  presents the charge–discharge voltage profiles within an electrochemical window of 1.0–2.8 V under a C-rate of 0.1 C. The cell delivers an initial specific capacity of about  $140 \text{ mAh g}^{-1}$ , which slightly decreases to  $128 \text{ mAh g}^{-1}$  at the 50th cycle (91.5% capacity retain). After the 100th and 200th cycles, the cell maintains decent specific capacity values of 115 and  $105 \text{ mAh g}^{-1}$ , respectively. In Figure XIII.9.4(b), a stable cycling performance with high Coulombic efficiency close to 99.95% is observed for the  $\text{Li}_6\text{PS}_5\text{F}_{0.75}\text{I}_{0.25}$ -based solid-state Li metal batteries. When cycled under higher C-rate, such a cell retains a high specific capacity of  $121 \text{ mAh g}^{-1}$  at 0.2 C. While the cell displays a large drop to low capacity at 0.6 C, the specific capacity of the cell returns to values above  $120 \text{ mAh g}^{-1}$  when the battery cycling is returned to 0.1 C. The battery cycling performance proves the great electrochemical stability of  $\text{Li}_6\text{PS}_5\text{F}_{0.75}\text{I}_{0.25}$  argyrodite in solid-state Li metal batteries.

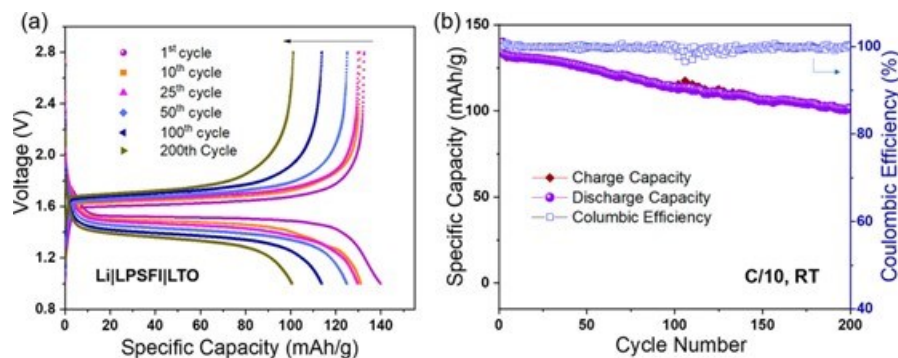


**Figure XIII.9.4** Performance of F/I hybrid-doped argyrodites in solid-state lithium battery. (a) Charge-discharge voltage profiles and (b) cycling performance of Li metal batteries with  $\text{Li}_6\text{PS}_5\text{F}_{0.75}\text{I}_{0.25}$  as the SE and LTO as the active cathode cycled at 0.1 C rate (current density of  $0.02 \text{ mA cm}^{-2}$ ) at room temperature.

***Fabrication of ASLSB with Optimized Cathode at high S-loading, solid sulfide electrolyte, and Li anode:***

At high S-loading, the low capacity of solid-state lithium-sulfur battery can be attributed to poor sulfur utilization and lower ionic (Li) conductivity of the S-cathode. In previous years of this project, we successfully addressed this issue incorporated SE ( $\text{Li}_6\text{PS}_5\text{F}_{0.5}\text{Cl}_2$ ) into the cathode (Super-P carbon-sulfur) at high S-loading ( $4 \text{ mg/cm}^2$ ) by pressing it together. This was possible after we learned how to handle the entire battery assembly including the cathode formulation inside the glove box. In all cases, cathode containing SSE powder (balled milled together) was pressed together with the SSE powder in a stainless-steel pellet die inside the glove box, and a prescribed amount of ionic liquid (IL made up of LiTFSI in N-butyl-N-methyl pyrrolidinium (PYR-14):1,3 dioxalane (DOL) (1:3) at 3M) to ensure sufficient wetting. We also found that a low volume  $\sim 5 \mu\text{L}$  of IL provides sufficient wetting, while still maintaining a near-all-solid-state like discharge profile. Notably, although the quasi-solid-state behavior in the batteries containing high amount of functionalizing IL affords a higher initial discharge capacity  $\sim 1000 \text{ mAh/g}$ , the capacity fades quickly and yields  $\sim 200 \text{ mAh/g}$  after 100 cycles, possibly due to burn out of the IL. In contrast, using lower amounts of IL ( $\sim 5 \mu\text{L}$ ) reduces the initial discharge capacity reduces to  $\sim 650 \text{ mAh/g}$ , but offers excellent capacity retention.

We optimized the amount of SE in the cathode, while keeping the amount of IL fixed at  $5 \mu\text{L}$  to further enhance the  $\text{Li}^+$  ion conductivity of the cathode, and consequently, its capacity (Figure XIII.9.5). We find that the battery with 25% SSE in the cathode showed the best performance with an initial discharge capacity of  $\sim 700 \text{ mAh/g}$ , and retention of  $\sim 430 \text{ mAh/g}$  after 100 cycles (@C/20) at  $60^\circ\text{C}$  (Figure XIII.9.5(a)). Indeed, the discharge profiles show a solid-state-like behavior, which shows that the  $5 \mu\text{L}$  of IL is still low enough to suppress formation of higher-order polysulfides (Figure XIII.9.5(b)). Interesting, the capacity fade is appreciable only over the initial 5 cycles (where it drops from  $\sim 700 \text{ mAh/g}$  to  $\sim 480 \text{ mAh/g}$ ); thereafter, the capacity remains nearly stable, with a slow drop down to  $\sim 430 \text{ mAh/g}$  at 100 cycles. This indicates that the interphase at the cathode-electrolyte interface does not form fully in the first few cycles; we are currently running a few battery tests with slow-rate for the initial discharge; before beginning the cycling tests.

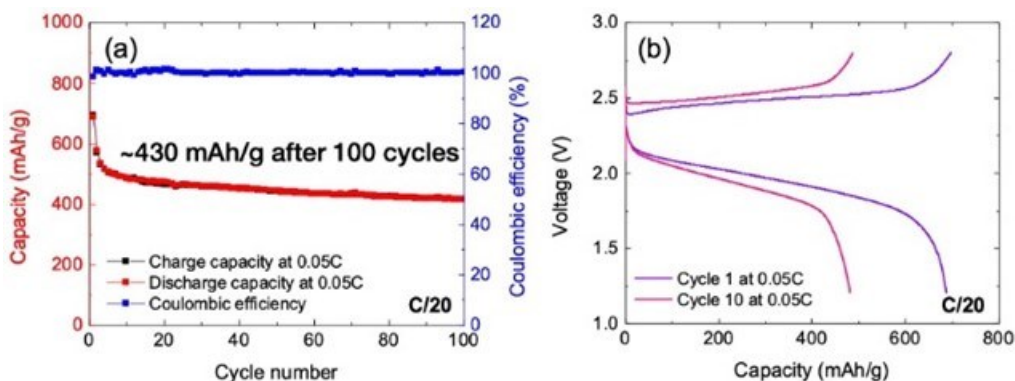


**Figure XIII.9.5** Electrochemical cycling performance of batteries consisting of Li anode, SP-S cathode with 4.0 mg/cm<sup>2</sup> loading pressed with 25% SE, Li<sub>6</sub>PS<sub>5</sub>F<sub>0.5</sub>Cl<sub>2</sub> SE with 5 μL of ionic liquid (LiTFSI in PYR:DOL(1:3) at 3M) at the cathode-SSE interface. (a) Capacity variation, and Coulombic efficiency as a function of cycles at 60 °C at C/20, (b) Discharge profiles at selected cycles.

### Conclusions

We developed a simple, economic, scalable, and energy-efficient method to synthesize argyrodite electrolytes with precise control over composition and microstructure. Using this method, we synthesized F/I hybrid doped argyrodite solid electrolytes (Li<sub>6</sub>PS<sub>5</sub>F<sub>x</sub>I<sub>1-x</sub>; x = 0, 0.25, 0.75); the as-synthesized primarily consisted of argyrodite phase (as evidenced by XRD and Raman spectra) with minor amounts of secondary LiI or LiF phases in the hybrid F/I doped cases. Our wet-chemistry technique enables synthesis of nanostructured Li<sub>6</sub>PS<sub>5</sub>I (with I rich regions in the grain boundaries) that provides fast Li-ion conduction (~0.25 mS/cm), which is ~3–4 orders of magnitude higher than that for Li<sub>6</sub>PS<sub>5</sub>I prepared by state-of-the-art solid state methods. Interestingly, our DFT calculations show that anion site disorder becomes more energetically stable in F/I hybrid doped cases; which, in turn, enables much faster Li-ion diffusion as indicated by our AIMD simulations. Indeed, impedance spectroscopy measurements reveal that Li<sub>6</sub>PS<sub>5</sub>F<sub>0.75</sub>I<sub>0.25</sub> has an ionic conductivity of 0.35 mS/cm (~40% higher than that for nanostructured Li<sub>6</sub>PS<sub>5</sub>I). With a higher F content, Li<sub>6</sub>PS<sub>5</sub>F<sub>0.75</sub>I<sub>0.25</sub> exhibited the best electrochemical stability and long-term cycling ability up to 1100 h in Li symmetric cells under 0.05 mA cm<sup>-2</sup>. Moreover, the assembled solid-state Li metal battery (LTO as cathode) delivered the first discharge capacity of 140 mAh g<sup>-1</sup> and retained a decent specific capacity of 105 mAh g<sup>-1</sup> after 200 cycles under 0.1 C. This work has resulted in the synthesis of novel compositions in the argyrodite SE family, demonstrating great potential in the future development of solid-state Li metal batteries. Finally, we developed novel mesoporous cathodes containing super-P carbon and multi-walled carbon nanotubes that host both sulfur and SSE to enable stable battery cycling at high S-loading. Using 25% SSE in cathode with high S-loading (4 mg/cm<sup>2</sup>) and 5 μL ionic liquid (2M LiTFSI in 1:1 (volume) PYR:DOL), we demonstrated stable cycling of Li-S batteries with all-solid-state like behavior (i.e., suppressing formation of higher-order polysulfides). This battery showed an initial discharge capacity of ~700 mAh/g, and retention of ~430 mAh/g after 100 cycles (@C/20) at 60°C.

### Key Publications

1. W. Arnold, V. Shreyas, S. Akter, Y. Li, S. Halacoglu, M. Koralalage, X. Guo, D. Vithange, W. Wei, G. Sumanasekera, J. Jasinski, B. Narayanan, and H. Wang. Highly Conductive Iodine and Fluorine Dual-Doped Argyrodite Solid Electrolyte for Lithium Metal Batteries. *Journal of Physical Chemistry C* 127, 11801 – 11809 (2023). DOI: <https://doi.org/10.1021/acs.jpcc.3c00962>
2. W. Arnold, Y. Li, B. Narayanan and H. Wang, “A simple and economic synthesis method for fluorine-doped lithium-argyrodite solid electrolyte”, Invention Disclosure filed with Office of Technology Transfer, University of Louisville (2022).
3. W. Arnold. Wet chemical synthesis and properties of argyrodite sulfide solid electrolytes for solid state lithium batteries. Ph.D. Dissertation, University of Louisville (2022). *Electronic Theses and Dissertations*. Paper 4014. DOI: <https://doi.org/10.18297/etd/4014>

4. M. Korallalage. Super p-sulfur cathodes for quasi-solid-state lithium-sulfur-batteries. Ph.D. Dissertation, University of Louisville (2023). *Electronic Theses and Dissertations*. Paper 4054. DOI: <https://doi.org/10.18297/etd/4054>
5. M. Jaishi, V. Shreyas, and B. Narayanan, Reactive force field for Li-P-S system with application to sulfide Li-ion conductors. *Manuscript under preparation*
6. M. Korallalage, Varun Shreyas, W. Arnold, S. Akter, A. Thapa, J. Jasinski, H. Wang, G. Sumanasekera, B. Narayanan. Mesoporous composite cathodes for solid-state lithium sulfur batteries at high sulfur loading. *Manuscript under preparation*

## References

1. Zhao, F.; Sun, Q.; Yu, C.; Zhang, S.; Adair, K.; Wang, S.; Liu, Y.; Zhao, Y.; Liang, J.; Wang, C.; Li, X.; Li, X.; Xia, W.; Li, R.; Huang, H.; Zhang, L.; Zhao, S.; Lu, S.; Sun, X. Ultrastable Anode Interface Achieved by Fluorinating Electrolytes for All-Solid-State Li Metal Batteries. *ACS Energy Letters* 2020, 5 (4), 1035-1043. DOI: 10.1021/acsenergylett.0c00207.
2. Arnold, W.; Shreyas, V.; Li, Y.; Korallalage, M. K.; Jasinski, J. B.; Thapa, A.; Sumanasekera, G.; Ngo, A. T.; Narayanan, B.; Wang, H. Synthesis of Fluorine-Doped Lithium Argyrodite Solid Electrolytes for Solid-State Lithium Metal Batteries. *ACS Applied Materials & Interfaces* 2022. DOI: 10.1021/acsaami.1c24468.
3. Arnold, W.; Buchberger, D. A.; Li, Y.; Sunkara, M.; Druffel, T.; Wang, H. Halide doping effect on solvent-synthesized lithium argyrodites Li<sub>6</sub>PS<sub>5</sub>X (X= Cl, Br, I) superionic conductors. *Journal of Power Sources* 2020, 464, 228158. DOI: <https://doi.org/10.1016/j.jpowsour.2020.228158>.
4. Li, Y.; Arnold, W.; Jasinski, J. B.; Thapa, A.; Sumanasekera, G.; Sunkara, M.; Narayanan, B.; Druffel, T.; Wang, H. Interface stability of LiCl-rich argyrodite Li<sub>6</sub>PS<sub>5</sub>Cl with propylene carbonate boosts high-performance lithium batteries. *Electrochimica Acta* 2020, 363, 137128. DOI: <https://doi.org/10.1016/j.electacta.2020.137128>.
5. Zhang, Z.; Zhang, J.; Jia, H.; Peng, L.; An, T.; Xie, J. Enhancing ionic conductivity of solid electrolyte by lithium substitution in halogenated Li-Argyrodite. *Journal of Power Sources* 2020, 450, 227601. DOI: <https://doi.org/10.1016/j.jpowsour.2019.227601>.
6. Zhang, J.; Zheng, C.; Li, L.; Xia, Y.; Huang, H.; Gan, Y.; Liang, C.; He, X.; Tao, X.; Zhang, W. Unraveling the Intra and Intercycle Interfacial Evolution of Li<sub>6</sub>PS<sub>5</sub>Cl-Based All-Solid-State Lithium Batteries. *Advanced Energy Materials* 2020, 10 (4), 1903311, <https://doi.org/10.1002/aenm.201903311>. DOI: <https://doi.org/10.1002/aenm.201903311>.
7. Zhang, Z.; Zhang, L.; Yan, X.; Wang, H.; Liu, Y.; Yu, C.; Cao, X.; van Eijck, L.; Wen, B. All-in-one improvement toward Li<sub>6</sub>PS<sub>5</sub>Br-Based solid electrolytes triggered by compositional tune. *Journal of Power Sources* 2019, 410-411, 162-170. DOI: <https://doi.org/10.1016/j.jpowsour.2018.11.016>.
8. de Klerk, N. J. J.; Rosłoń, I.; Wagemaker, M. Diffusion Mechanism of Li Argyrodite Solid Electrolytes for Li-Ion Batteries and Prediction of Optimized Halogen Doping: The Effect of Li Vacancies, Halogens, and Halogen Disorder. *Chemistry of Materials* 2016, 28 (21), 7955-7963. DOI: 10.1021/acs.chemmater.6b03630.
9. Baktash, A.; Reid, J. C.; Roman, T.; Searles, D. J. Diffusion of lithium ions in Lithium-argyrodite solid-state electrolytes. *npj Computational Materials* 2020, 6 (1), 162. DOI: 10.1038/s41524-020-00432-1.
10. Zhang, J.; Zheng, C.; Lou, J.; Xia, Y.; Liang, C.; Huang, H.; Gan, Y.; Tao, X.; Zhang, W. Poly(ethylene oxide) reinforced Li<sub>6</sub>PS<sub>5</sub>Cl composite solid electrolyte for all-solid-state lithium battery: Enhanced electrochemical performance, mechanical property and interfacial stability. *Journal of Power Sources* 2019, 412, 78-85. DOI: <https://doi.org/10.1016/j.jpowsour.2018.11.036>.
11. Yang, Q.; Li, C. Li metal batteries and solid state batteries benefiting from halogen-based strategies. *Energy Storage Materials* 2018, 14, 100-117. DOI: <https://doi.org/10.1016/j.ensm.2018.02.017>.
12. Chen, Y.; Li, W.; Sun, C.; Jin, J.; Wang, Q.; Chen, X.; Zha, W.; Wen, Z. Sustained Release-Driven Formation of Ultrastable SEI between Li<sub>6</sub>PS<sub>5</sub>Cl and Lithium Anode for Sulfide-Based Solid-State

Batteries. *Advanced Energy Materials* 2021, 11 (4), 2002545. DOI:  
<https://doi.org/10.1002/aenm.202002545>.

### **Acknowledgements**

This project involves three co-investigators: Dr. Hui Wang, Dr. Gamini Sumanasekera, and Dr. Jacek Jasinski at the University of Louisville. A part of this work was performed in collaboration with Prof. Anh Ngo (University of Illinois-Chicago, Argonne National Laboratory), Prof. Subramanian Sankaranarayanan (University of Illinois-Chicago, Argonne National Laboratory), and Prof. Arunkumar Subramanian (University of Illinois-Chicago). This research used resources of the National Energy Research Scientific Computing Center; a DOE Office of Science User Facility supported by the Office of Science of the U.S. Department of Energy under Contract No. DE-AC02-05CH11231. Use of the Center for Nanoscale Materials was supported by the U. S. Department of Energy, Office of Science, Office of Basic Energy Sciences, under Contract No. DE-AC02-06CH11357.

## XIII.10 Enabling Continuous Production of Defect-free, Ultrathin Sulfide Glass Electrolytes for Next Generation Solid-state Lithium Metal Batteries (ANL)

### **Tim Fister, Principal Investigator**

Argonne National Laboratory  
9700 South Cass Avenue  
Lemont, IL 60439  
E-mail: [fister@anl.gov](mailto:fister@anl.gov)

### **Simon Thompson, DOE Technology Development Manager**

U.S. Department of Energy  
E-mail: [Simon.Thompson@ee.doe.gov](mailto:Simon.Thompson@ee.doe.gov)

Start Date: October 1, 2020

End Date: September 30, 2023

Project Funding (FY23): \$167,000

DOE share: \$167,000

Non-DOE share: \$0

### **Project Introduction**

Sulfide glass materials are one of the most appealing candidates for solid state batteries due to their superior performance using relatively inexpensive raw materials. Glass materials prepared from a melt, unlike ball milled sulfides or polycrystalline electrolytes, also lack the void space and grain boundaries that are often weak points for lithium dendrites or decomposition species. In practice these glasses are not entirely defect free and can have isolated defects such as bubbles or crystalline inclusions formed during manufacture and processing. Recent advances from PolyPlus have demonstrated the ability to draw glasses to thicknesses approaching 10-20 microns. These thicknesses produce a flexible glass that is compatible with roll-to-roll manufacturing, but impurities become an even more negative design parameter in this regime.

### **Objectives**

The goal of this project is to identify the source of defects in sulfide glasses and understand their impact on the mechanical and electrochemical stability of the solid electrolyte. Understanding the distribution, size, and composition of these defects, and identifying ways to mitigate them, is a critical requirement for achieving ultrathin glass sheets necessary for a roll-to-roll manufacturer to build them into cylindrical format cells.

### **Approach**

This project focuses on sulfide glasses developed and produced at PolyPlus and uses advanced synchrotron and optical methods at Argonne National Laboratory to identify and analyze defects in glass samples ranging from 20-1000  $\mu\text{m}$  in thickness. Analytical methods developed in this project will focus on buried defects within the glass and reactions that form at the surface and electrode interface, both from processing and electrochemical treatments, as illustrated in Figure XIII.10.1.



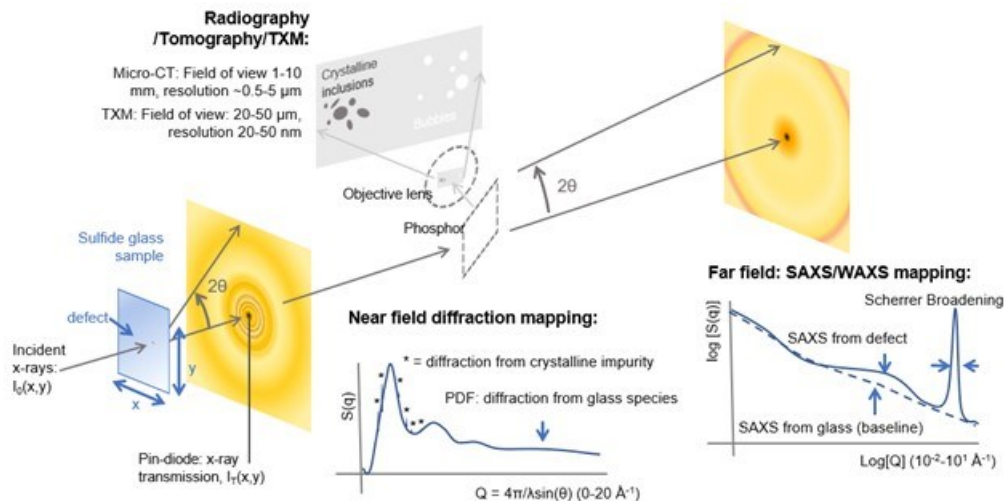


Figure XIII.10.1 Schematic of multimodal synchrotron analysis of sulfide glass samples.

During the first two quarters of this project, Argonne and PolyPlus evaluated the processing steps, to identify the steps where impurities were incorporated into the glass (Figure XIII.10.2). The phase analysis approaches developed by Argonne, were used to screen for crystalline impurities or phase heterogeneity in the sulfide glass using the x-ray diffraction measurements that mapped over the entire volume of sulfide glass samples provided by PolyPlus. These feasibility measurements showed that these techniques are uniquely sensitive to the atomic structure of the glasses and that the x-rays were easily capable of measuring 100 μm thick glass samples and will be able to resolve structure in the final ultrathin samples.

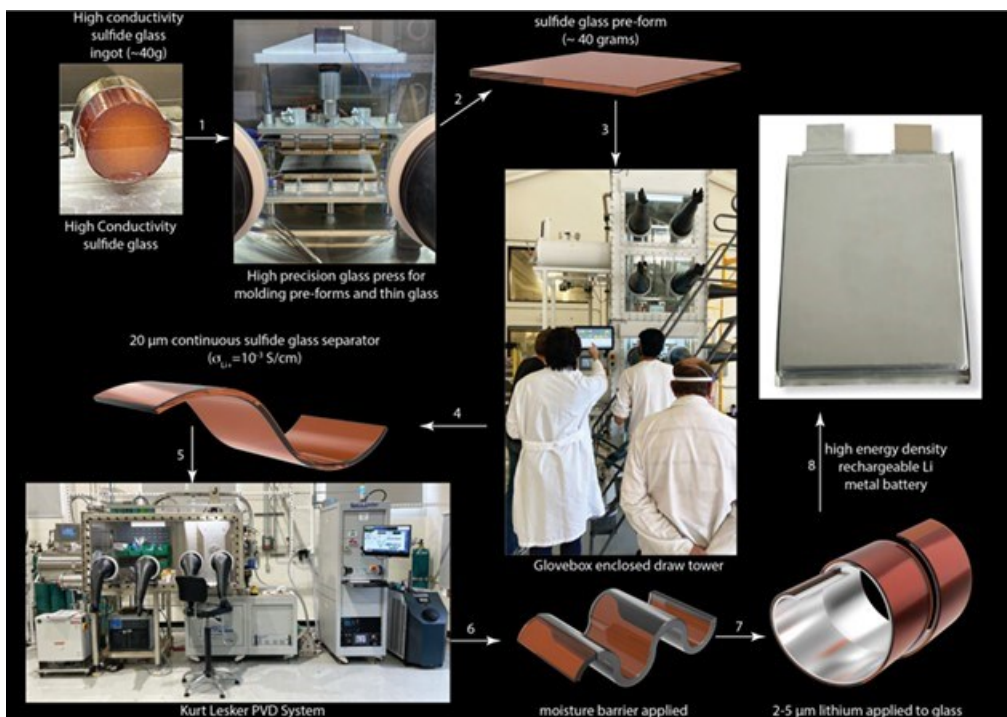


Figure XIII.10.2 Schematic of the processing steps for developing ultrathin glass.

In the last two quarters, processing of lithium phosphorus sulfide (LPS) and  $\text{Li}_3\text{BS}_3$  (LBS) were evaluated for the ease of manufacturing impurity free glass. The different glass compositions were tested to improve homogeneity and reduce impurities in processing. Polyplus and Argonne used the optimized processing procedures developed to minimize crystalline impurities, post-treatment processes previously accessed, and developed analysis approaches to compare the two glass compositions.

## Results

Synchrotron x-ray experiments at the Advanced Photon Source (APS) focused on determining the differences in glass manufacture and processing using a phase analysis approach to identify possible sources for impurity inclusions and ways to mitigate removal. The phase analysis approach maps the impurities with x-ray scattering from the sulfides in XRD regimes as shown in Figure XIII.10.3. The phase analysis approach developed uses principal component analysis or a K-means clustering algorithm to screen for crystalline impurities or phase heterogeneity in the sulfide glass itself.

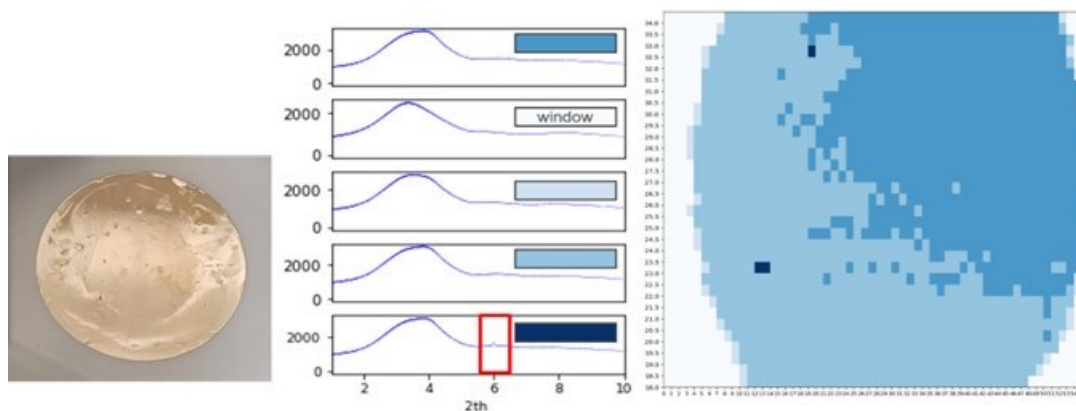


Figure XIII.10.3 K-means clustering phase analysis of a Li-B-S glass with both phase heterogeneity due glass thickness and noncrystalline impurities.

Polyplus and Argonne evaluated the processing steps to determine at which step crystalline impurities are incorporated into the glass. Impurities were found to be introduced during the preforming, when a slice of core is pressed to the intermediate thickness (Figure XIII.10.4). The cores had no significant concentration of impurities. Improvement in decreasing the concentration of crystalline impurities is attributed to identifying and improving the processing steps that were the source of the impurities and incorporating post-processing procedures (Figure XIII.10.5).

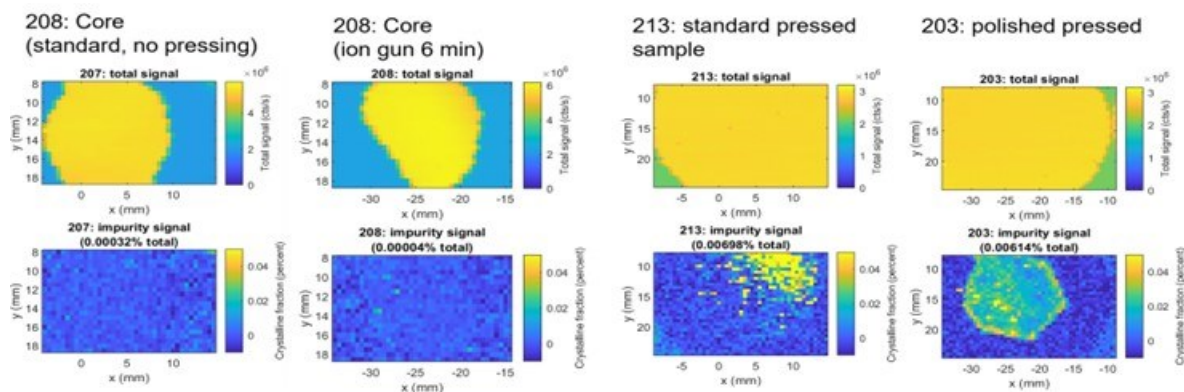
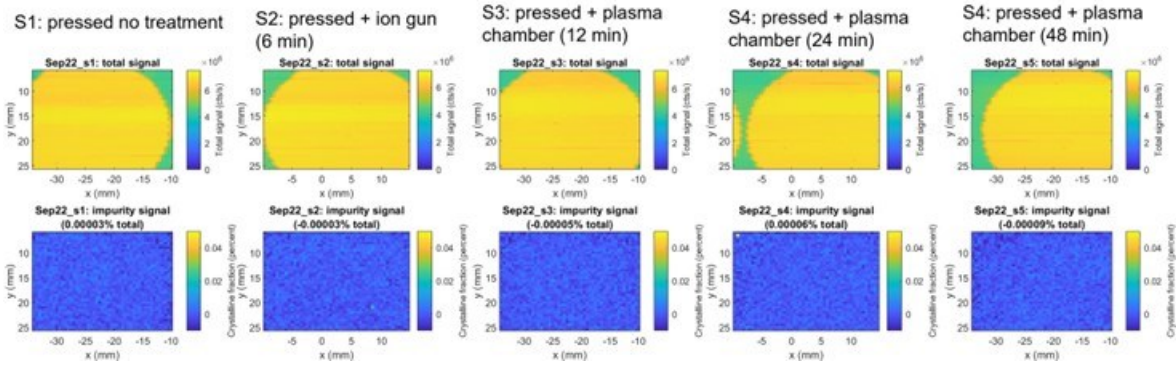


Figure XIII.10.4 Comparison of impurity concentration of the core and after the core is pressed to the desired thickness (preforming). Impurity concentration increase with preforming.



**Figure XIII.10.5 Optimization of processing conditions significantly reduced the concentration of crystalline inclusions. Post-processing treatments can further decrease the impurity concentration.**

Using the optimized processing steps, post-treatment procedures, and analysis approaches, LBS and LPS were evaluated for the ease of manufacturing impurity free glass (Figure XIII.10.6). LPS is a more mature glass with a higher glass transition temperature than LBS. The optimized processing procedure were found to produce less impurities for the LPS glass than the LBS glass owing to the higher glass transition temperature. Post-treatment of the LPS glass was still required to ensure impurity free glass.

Evaluation of the glass transition temperature was carried out using in situ X-ray diffraction experiments at the Advanced Photon Source (APS) with the sample heated at  $5^{\circ}\text{C}/\text{min}$  to  $300^{\circ}\text{C}$  (Figure XIII.10.7). The diffraction experiment can directly monitor the onset of crystalline phases. The crystalline impurities were found to be the same impurities as the processed LBS glass disks. This indicates heating during the processing steps may be the factor for influencing crystalline impurities.

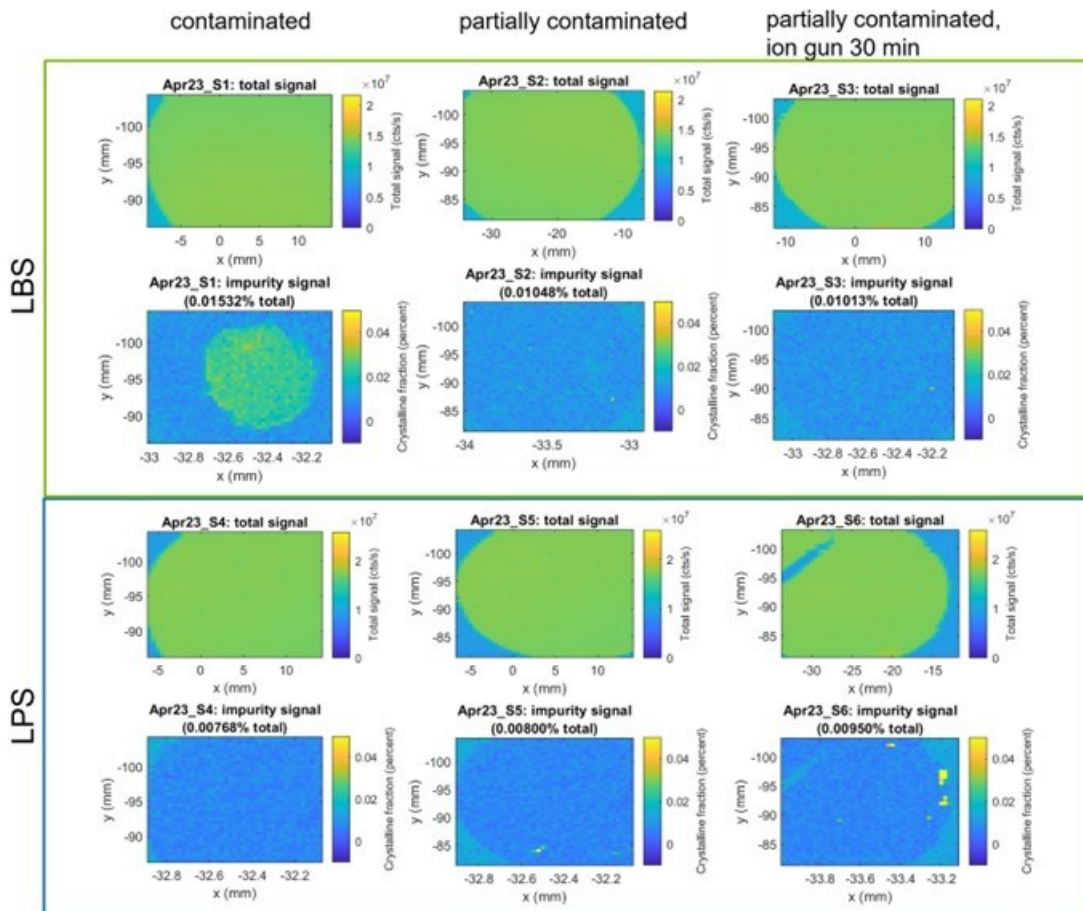


Figure XIII.10.6 Comparison impurity concentration of contaminated LPS and LBS glass disks.

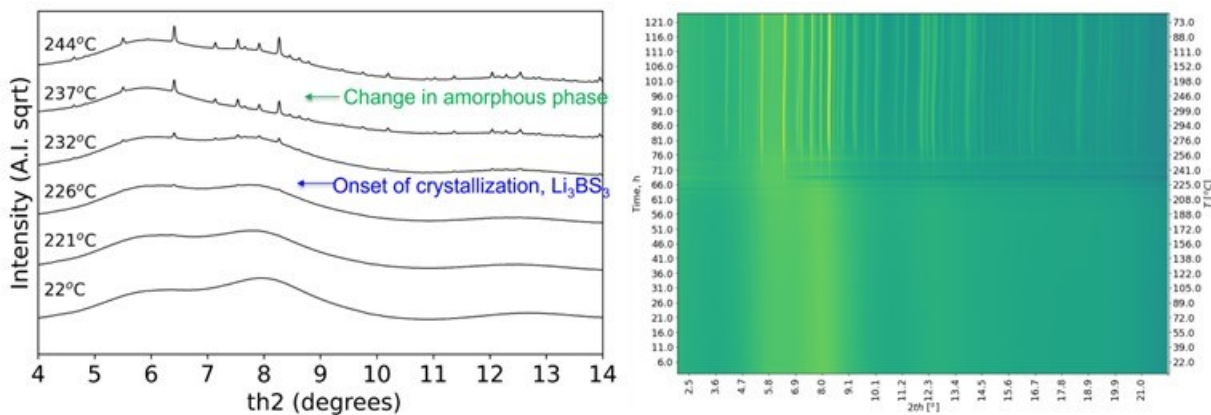


Figure XIII.10.7 A PXRD waterfall plot for the in situ diffraction experiment for LBS (right). Selected PXRD indicating the crystalline impurities (left).

**Conclusions**

1. Determined pre- and post-processing treatments that improve homogeneity by reducing crystalline impurities: ion gun, plasma chamber, etc
2. Identified and optimized processing steps where crystalline inclusions occurred.

3. Evaluated the ease of manufacturing impurity free LBS and LPS glass using the optimized processing steps and post-processing treatments.

#### References

1. Tatsumisago, M. et al. *J. Am. Ceram. Soc.*, 71 (9) 766-769 (1988)

## XIII.11 Stable Solid-State Electrolyte and Interface for High-Energy All-Solid-State Lithium-Sulfur Battery (PNNL)

### Dongping Lu, Principal Investigator

Pacific Northwest National Laboratory  
902 Battelle Blvd.  
Richland, WA 99354  
E-mail: [dongping.lu@pnnl.gov](mailto:dongping.lu@pnnl.gov)

### Simon Thompson, DOE Technology Development Manager

U.S. Department of Energy  
E-mail: [Simon.Thompson@ee.doe.gov](mailto:Simon.Thompson@ee.doe.gov)

Start Date: October 1, 2022

End Date: September 30, 2023

Project Funding (FY23): \$700,000

DOE share: \$700,000

Non-DOE share: \$0

### Project Introduction

All solid-state-lithium batteries (ASSLBs) hold potential to achieve superior energy and power densities, thereby extending the range of electric vehicles and simultaneously reducing charging time. While oxides are intrinsically more stable than sulfides, sulfide solid state electrolytes (S-SSEs) arguably present a more viable option for bulk-type ASSLBs. This is due to the low material density, low elastic modulus, and high ionic conductivity, which facilitate intimate contact with active materials and practical processibility through industrial slurry or dry processing. A series of sulfide-based compounds with extremely high ionic conductivities ( $> 10^{-2}$  S/cm) have been developed. By using surface coated cathodes and S-SSEs, stable cycling of LiCoO<sub>2</sub> cells and high energy LiNi<sub>x</sub>Mn<sub>y</sub>Co<sub>(1-x-y)</sub> cells have been demonstrated, proving viability of S-SSEs for high performance ASSLBs.

Given the advantages of low cost and resource availability, all solid-state lithium-sulfur (Li-S) is emerging as a promising next-generation energy storage technology. More promisingly, the S-SSEs are chemically and electrochemically compatible with sulfur, making them feasible for direct sulfur cathode application without any protective cathode coating. Despite high expectations for S-SSEs, there are significant materials and interfacial challenges that need to be addressed before practical technology deployment. These challenges include materials moisture sensitivity, Li/SSE interfacial stability, and scalable processing of SSE film and SSE contained cathodes. Moreover, to improve energy in ASSLBs, the SSE membrane thickness should be minimized while the cathode mass loading should be practically high. This is especially important in all solid-state Li-S battery due to the relative low working voltage of S (1.9 V vs. Li). To reach a cell level energy  $> 500$  Wh/kg in a 2 Ah pouch cell, the S cathode areal capacity should be  $> 8$  mAh/cm<sup>2</sup>, which must in turn be charge balanced by the same amount of Li stripping/plating at the anode side. However, such deep Li cycling causes significant challenges to the metallic Li anode including large volume change, reaction nonuniformity, pressure variation, and Li dendrite formation. Although S-SSEs allow Li metal cycling at certain current densities and areal capacities, stable Li cycling at the capacities matching high-areal-capacity S cathodes is still beyond reach. This is why most long cycling of Li-S cells had to use Li-In or other alloy-based anodes, which unfortunately sacrifices cell energy due to the heavy material (In: 7.3 g/cm<sup>3</sup>) and its high working voltage (0.6 V vs. Li). Thus, in addition to the challenges of ionic conductivity, chemical stability, and interfacial properties, achieving highly reversible Li plating/stripping at high areal capacities is another key step toward stable operation of ASSLBs. Comprehensive strategies built on innovations of material development, interfacial design, chemo-mechanical management, and viable processing are essential to overcome the existing barriers faced by the practical ASSLBs.

## Objectives

This project focuses on addressing material and interfacial challenges of sulfide-based solid-state electrolyte (SSE) for deep cycling of Li metal anode in all-solid-state Li batteries (ASSLBs). The ultimate goals are:

1. Development of Li metal compatible S-SSEs with low Li/SSE interfacial resistance and  $\text{Li}^+$  conductivity.
2. Facilitation of stable and enduring Li plating/stripping at a critical current density exceeding  $1 \text{ mA/cm}^2$ .
3. Development of ultra-thin multifunctional interlayer to promote deep and stable Li cycling.
4. Dry processing of a SSE/interlayer bilayer assembly ( $<100 \text{ }\mu\text{m}$ ) with an overall ionic conductivity  $>1 \text{ mS/cm}$ .
5. Performance validation of solid electrolytes and processing technology in realistic Li-S pouch cells, aiming for an energy target of  $500 \text{ Wh/Kg}$ .

## Approach

1. Develop functional Li metal interphase or interlayer to enable stable Li stripping/plating.
2. Understand Li nucleation and growth and effect of the functional interfacial layer.
3. Identify compatible binder and method for processing of the Li interlayer.
4. Optimize external pressure to further improve deep and stable Li cycling.

## Results

### **1. Developed optimal materials for the fabrication of Li metal interphase to enable Li stripping/plating at $> 2 \text{ mAh/cm}^2$ for over 200 cycles in Li-S full cells.**

Lithium iodide (LiI) is considered a unique component for stable Li interface due to its chemical stability against Li and decent ionic conductivity. To understand the effects of LiI on the Li plating/stripping, Li/solid-state electrolyte (SSE)/Cu cells using SSEs with various content of LiI ( $\text{Li}_7\text{P}_2\text{S}_8\text{Br}_{1-x}\text{I}_x$ ,  $x = 0, 0.5, 1$ ) were assembled and tested with an areal capacity of  $2 \text{ mAh cm}^{-2}$  (corresponding to approximately  $10 \text{ }\mu\text{m}$  of Li). At a current density of  $0.2 \text{ mA cm}^{-2}$ , the Li plating in the Li/ $\text{Li}_7\text{P}_2\text{S}_8\text{Br}$ /Cu cell begins at an big overpotential of  $-18.5 \text{ mV}$ , indicating a large Li nucleation barrier at the beginning, and then the voltage increases to  $-7.7 \text{ mV}$  and keeps constant (not shown here). The second cycle plating starts with a lower overpotential of  $-11.8 \text{ mV}$ , probably due to the Li residual serving as nucleation sites. In contrast, the Li/ $\text{Li}_7\text{P}_2\text{S}_8\text{Br}_{0.5}\text{I}_{0.5}$ /Cu cell, where LiI exists in the SSE, does not show such high overpotential for both first and second plating, indicating a much smaller energy barrier for Li nucleation, which may be due to the favorable SSE/Li interface with presence of the LiI. This is confirmed by increasing LiI content in the Li/ $\text{Li}_7\text{P}_2\text{S}_8\text{I}$ /Cu cell, where even smaller overpotential (i.e.,  $-4 \text{ mV}$ ) and easier Li plating were observed. These results suggest that the higher the LiI content is, the lower will be the overpotential for Li nucleation and plating. To track the LiI evolution during Li plating/stripping, cells after the first plating were cross-sectioned and subjected to SEM and EDS characterizations (Figure XIII.11.1 a-c). Oxygen (O) signal was detected on the surface of the deposited Li, which is due to the short exposure of samples to the ambient environment when loading samples and could be used as an indicator of metallic Li. Fig. XVI.16.1a presents the cross-sectional SEM of the plated Li on the surface of  $\text{Li}_7\text{P}_2\text{S}_8\text{Br}$ . The plated Li metal is slightly loose, suggesting void formation and corresponding to the high polarization of Li plating. Much denser Li plating is observed for  $\text{Li}_7\text{P}_2\text{S}_8\text{Br}_{0.5}\text{I}_{0.5}$ /Li and  $\text{Li}_7\text{P}_2\text{S}_8\text{I}$ /Li, which agrees well with the lower Li plating polarization. Interestingly, the migration and accumulation of I from the SSE to the Li surface is clearly observed at both interfaces of  $\text{Li}_7\text{P}_2\text{S}_8\text{Br}_{0.5}\text{I}_{0.5}$ /Li and  $\text{Li}_7\text{P}_2\text{S}_8\text{I}$ /Li. Surprisingly, Br does not migrate in the Li/ $\text{Li}_7\text{P}_2\text{S}_8\text{Br}$ /Cu cell, but its migration toward Li is detected in the  $\text{Li}_7\text{P}_2\text{S}_8\text{Br}_{0.5}\text{I}_{0.5}$ /Li cell. These results suggest that  $\text{I}^-$  not only has higher diffusivity than  $\text{Br}^-$  but also spurs the diffusion of  $\text{Br}^-$ . Accompanying I migration to Li metal, more LiI-rich SEI is expected to be formed on the interfaces of  $\text{Li}_7\text{P}_2\text{S}_8\text{Br}_{0.5}\text{I}_{0.5}$ /Li and  $\text{Li}_7\text{P}_2\text{S}_8\text{I}$ /Li during Li plating. Further understanding of how the I element migrates during Li plating is still being gained through experimental and theoretical study. During the subsequent Li stripping, the I is released and reaccumulated at the SSE/Cu interface (data was not shown here), which will promote subsequent Li plating/stripping. Both electrochemical and morphological characterizations

demonstrate that LiI can be enriched and released reversibly, functioning as an artificial interlayer to facilitate dense Li plating/stripping.

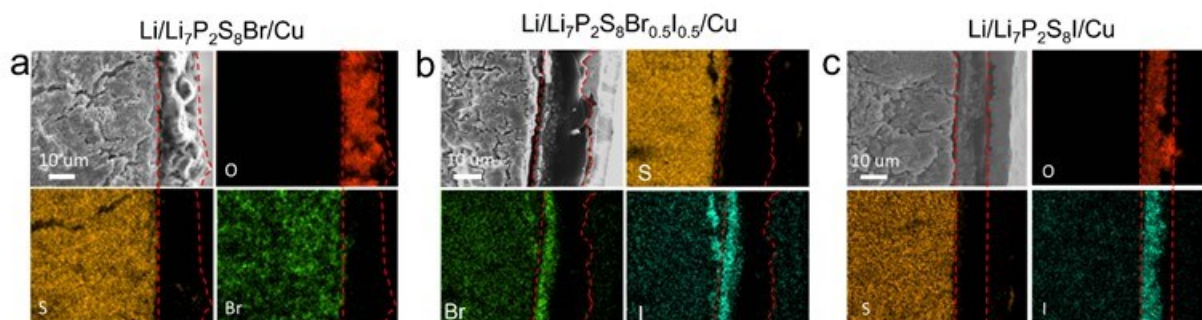


**Figure XIII.11.1** Li/Li<sub>7</sub>P<sub>2</sub>S<sub>8</sub>Br<sub>1-x</sub>I<sub>x</sub>/Cu ( $x=0, 0.5, \text{ and } 1$ ) cross-sectional SEM images and corresponding elemental mappings after Li plating: (a) Li/Li<sub>7</sub>P<sub>2</sub>S<sub>8</sub>Br/Cu, (b) Li/Li<sub>7</sub>P<sub>2</sub>S<sub>8</sub>Br<sub>0.5</sub>I<sub>0.5</sub>/Cu, and (c) Li/Li<sub>7</sub>P<sub>2</sub>S<sub>8</sub>I/Cu.

To validate the applicability of the LiI based interface for long-term cycling of the metallic Li anode the SSE Li<sub>7</sub>P<sub>2</sub>S<sub>8</sub>Br<sub>0.5</sub>I<sub>0.5</sub> was used to fabricate all solid-state S/Li<sub>7</sub>P<sub>2</sub>S<sub>8</sub>Br<sub>0.5</sub>I<sub>0.5</sub>/Li-full cells. Sulfur (S) was used as the cathode and the metallic Li was used as the anode directly without any surface treatment or use of additional interlayers. Figure XIII.11.2 a and b present the voltage profiles and cycling performance of the S/Li<sub>7</sub>P<sub>2</sub>S<sub>8</sub>Br<sub>0.5</sub>I<sub>0.5</sub>/Li under 0.1 C ( $1\text{ C} = 1600\text{ mA g}^{-1}$ ) at 20 °C. An areal capacity of  $\sim 2\text{ mAh cm}^{-2}$  and a high reversible capacity of  $1440\text{ mAh g}^{-1}$  were achieved after a gradual activation process. The Li-S solid cell demonstrates a stable cycling for 250 cycles without any capacity decay and short circuiting, which is among the best cycling performance for all-solid-state sulfur batteries with metallic Li as the anode. This further validates the extraordinary robustness of the Li/SSE interface benefiting from the artificial LiI-rich interlayer.

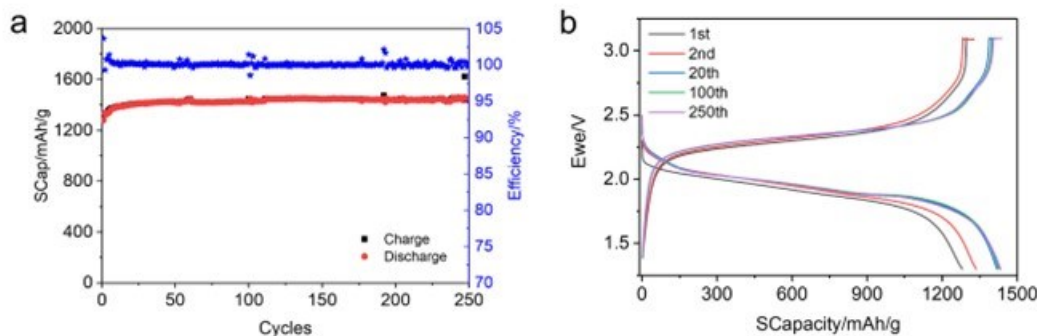


**Figure XIII.11.2** (a) Cycling performance and (b) voltage profiles of the cell S/Li<sub>7</sub>P<sub>2</sub>S<sub>8</sub>Br<sub>0.5</sub>I<sub>0.5</sub>/Li under 0.1 C ( $1\text{ C} = 1600\text{ mA g}^{-1}$ ) at  $2\text{ mAh cm}^{-2}$  and 20 °C.

For scalable processing of SSE membrane and solid-state cathode, our collaboration team at University of Wisconsin-Milwaukee developed a modified dry process method for film type solid cell fabrication. Please note the Argyrodite Li<sub>6</sub>PS<sub>5</sub>Cl (LPSCl) SSE was used as an example solid electrolyte for the processing demonstration. The SSE film was fabricated by using dry SSE powders and 0.75 wt.% PTFE at an elevated temperature. As shown in Figure XIII.11.3a, the thickness of the finished SSE film can be controlled between 100~140 μm. The S cathodes consisting of S, carbon, and LPSCl with a weight ratio of 2:1:3 were also fabricated through the dry process using 1.0 wt.% of PTFE. The thickness of the S cathode film can be controlled between 70~150 μm. The all-film solid-state pouch cells were assembled by stacking the processed S cathode, SSE membrane and LiIn anode, and pressed at 20 MPa for 4 min (Figure XIII.11.3). The pouch cell was tested at 60°C by clamping the cell with a home-made fixture. Figure XIII.11.3d shows the charge/discharge curves of the first three cycles of the all-solid-state S pouch cell. In initial discharge, the cell delivers a specific capacity of  $904\text{ mAh g}^{-1}$ , which increases to 1270 and 1129  $\text{mAh g}^{-1}$  in the subsequent



second and third cycles, respectively. Research to further improve the processability, cathode mass loading and S utilization rate needs further efforts and is in progress.

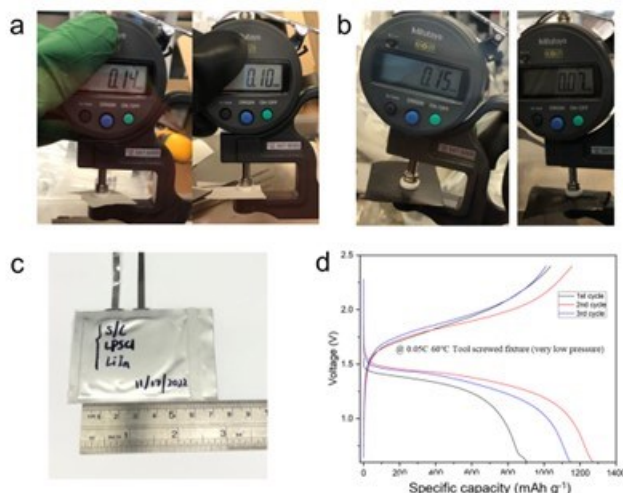


**Figure XIII.11.3** Photo image and thickness measurement of the processed (a) dry SSE film and (b) dry sulfur cathode. (c) Photo image of all-solid-state pouch cell and (d) typical charge/discharge curves at 60 °C.

## 2. Identified unique mechanical behaviors of LiI as a functional Li interfacial layer through experimental and modeling study.

To understand how the LiI-interface forms and affects Li plating/stripping, we employed both experimental and theoretical modeling methods to examine mechanical properties of LiI and its effect on Li transport. The plastic flow of LiI in the SSE during compaction was identified experimentally and studied by modeling using the material point method (MPM). A 3D contact model of SSE was constructed to mimic the microstructure of the SSE and to study the pellet densification of the SSE as well as Li-ion transportation paths (not shown here). For simplification, we extracted and compared diagonal slices of the 3D models with and without different pressures to illustrate LiI migration, SSE pellet densification, and changes in current distribution in SSE (Figure XIII.11.4 a-d). Each large grain of  $\text{Li}_{6.7}\text{P}_2\text{S}_8\text{Br}_{0.5}\text{I}_{0.2}$  is surrounded by multiple small grains of lithium halides, such as LiI, LiBr, LiCl, and LiF for comparison of various of lithium halides. We simulated the current streamline (white line with arrow) through the SSE pellet under different pressures to compare the ionic conductivity/connectivity; longer and denser lines indicate better connectivity and higher ionic conductivity. Without pressure, both  $\text{Li}_{6.7}\text{P}_2\text{S}_8\text{Br}_{0.5}\text{I}_{0.2}$  and LiI grains are loosely packed and retain their initial shape (not shown here). In this case, the resulting pellet has a very high porosity (49.37%) and a very low overall conductivity. This agrees with the interrupted current streamlines (Figure XIII.11.4a) and the large potential difference between the bottom and top plates (maximum potential 7.69 V). As the pressure increases, the pellet thickness decreases, the void spaces shrink, and both the  $\text{Li}_{6.7}\text{P}_2\text{S}_8\text{Br}_{0.5}\text{I}_{0.2}$  and LiI grains start to deform gradually (Figure XIII.11.4 b-d). Connected current pathways between the top and bottom plates start to form as neighboring grains in the domain connect. The smoother color transition indicates better connection with surrounding grains. For example, at a final pressure of 575.6 MPa (Figure XIII.11.4d), most void spaces are filled, the resulting overall porosity drops to 7%, the maximum potential difference falls from 7.69 V at zero pressure to  $3.28 \times 10^{-3}$  V at 575.6 MPa, and the corresponding conductivity rises to  $2.2 \text{ mS cm}^{-1}$ . It was also observed that compared to sulfides, the LiI grains have a higher deformation under high pressure and the grains prefer to flow to fill the voids. The sulfide grains have a smoother color transition, which implies better connectivity with neighboring grains from top and bottom. This is consistent with the denser and continuous current streamlines.

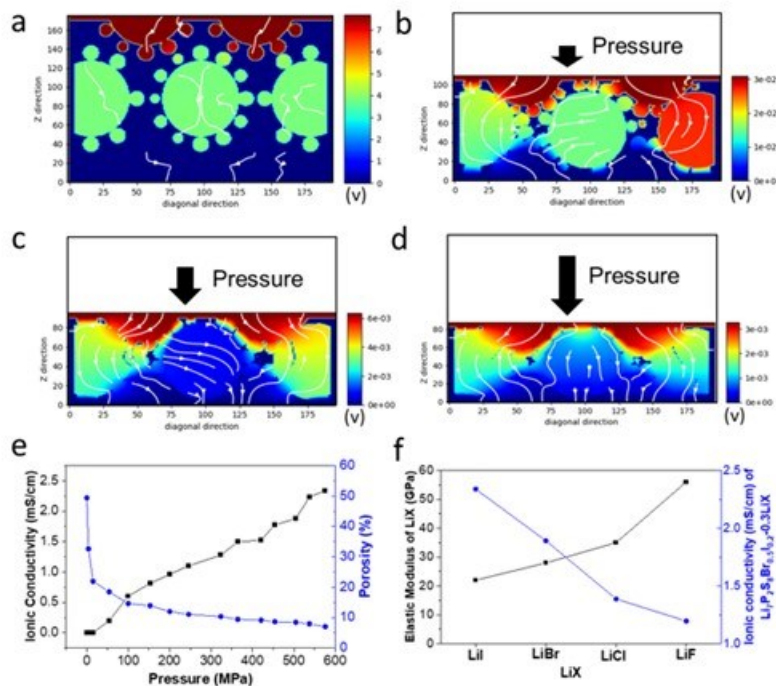


**Figure XIII.11.4** Electrical field and current path in  $\text{Li}_{6.7}\text{P}_2\text{S}_8\text{Br}_{0.5}\text{I}_{0.2}-0.3\text{LiI}$  pellet under constant current and different pressure: (a) no pressure, (b) 54 MPa, (c) 245 MPa, and (d) 575 MPa. (e) Effective ionic conductivity and porosity of  $\text{Li}_{6.7}\text{P}_2\text{S}_8\text{Br}_{0.5}\text{I}_{0.2}-0.3\text{LiI}$  pellet as a function of pressure. (f) Elastic modulus and effective ionic conductivity of  $\text{Li}_{6.7}\text{P}_2\text{S}_8\text{Br}_{0.5}\text{I}_{0.2}-0.3\text{LiX}$  ( $X = \text{I, Br, Cl, F}$ ).

For comparison, we also simulated other halides LiX ( $X = \text{Br, Cl, and F}$ ) with the same setup and pressure conditions. Figure XIII.11.4f shows the elastic modulus of each halide and the effective conductivities of the pellet pressed at 575.6 MPa. The LiX halides have increasing elastic modulus from LiI to LiF, and their yield strength has the same trend. Under pressure, the deformation of LiX shows an inverse correlation with its yield strength. Nanosized LiI has the lowest yield strength and highest ionic conductivity among all the Li halides. It reduces interfacial resistance of the SSE and enhances the pellet overall ionic conductivity, as Figure XIII.11.4f shows. This study suggests LiI has unique mechanical and transport properties, making it a good candidate as an interfacial layer ingredient for Li metal anode.

### 3. Developed functional Li interfacial layer and optimized external pressure for stable Li plating/stripping

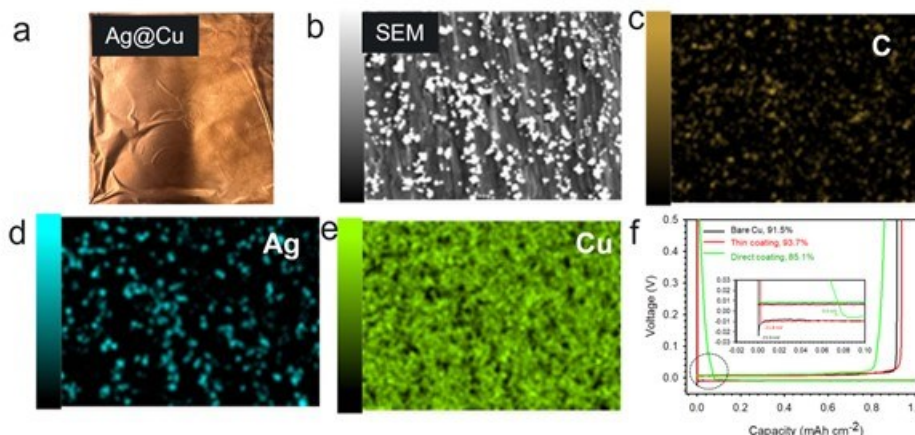


**Figure XIII.11.5** a) Photo image of the Ag coated Cu current collector, b) SEM image of the Ag coated Cu, c-e) EDS of Ag coated Cu, and f) Initial plating/stripping profiles of Li/SSE/Cu cells using Cu with/without Ag coating.

Li plating and stripping processes involve complex chemical, electrochemical, and mechanical interactions. In particular, changes in Li morphology accompanies with all these processes. Nonuniform Li stripping can lead to the formation of voids, while uneven Li plating can result in the generation of Li dendrites. Such nonuniformity is exacerbated with an increase in applied current densities or Li stripping/plating depth (areal capacity). To address these issues, we attempted two approaches to homogenize Li plating/stripping along the Li/SSE interface: 1) constructing a functional interlayer on the current collector to uniform the Li plating and stripping, and 2) optimizing external pressure by investigating the impacts of pressure for pellet fabrication, Li attaching, and cell operation on cell cycling.

We synthesized carbon-coated nanosized silver particles (Ag@C) using a chemical method. These particles were then coated onto a current collector (Cu) either by in situ deposition during synthesis (direct coating) or through a slurry coating method (thin coating). Unlike the Ag/C composites prepared by mixing Ag nanoparticles with carbon, this chemical synthesis approach allows for control over the morphology of Ag particles, thereby tuning the kinetics of the Li-Ag alloy/de-alloy processes. Additionally, the in-situ carbon coating confines the Ag nanoparticles and prevents them from migrating and agglomerating during the Ag-Li alloy/de-alloy processes. As shown in Figure XIII.11.5a, the Cu foil after Ag coating appears very similar in color to pristine Cu, indicating a very thin and uniform coating layer. Scanning electron microscopy (SEM) characterization reveals that the Ag@C particles are not only uniform but also nanosized. X-Ray diffraction (XRD) analysis confirmed the formation of an Ag phase (not shown here), and energy-dispersive X-ray spectroscopy (EDS) results approve the uniform distribution of Ag nanoparticles across the Cu substrate. It has been reported that using Ag/C as an interlayer between SSE and the current collector can improve conductivity and lower Li nucleation energy, resulting in uniform Li plating. Accordingly, we used the Ag@C-coated Cu collector to assemble Li/SSE/Cu cells to study its effect on Li plating/stripping. We compared three types of Cu current collectors: bare Cu, Ag-coated Cu by direct coating, and Ag-coated Cu by thin coating (Figure XIII.11.5f). Preliminary comparisons and conclusions can be drawn from the Li plating and stripping profiles. Compared to bare Cu, the presence of Ag@C can reduce the Li nucleation energy at room temperature, as evidenced by the reduced Li plating overpotential from -24 mV to -12 mV. This is likely due to improved conductivity and the presence of nano Ag. The initial Coulombic efficiency improved from 91.5% for bare Cu to 93.7% for Ag-coated Cu, confirming a positive effect of Ag coating. A detailed study of the function of Ag coating on long-term Li cycling at various areal capacities and current densities is still in progress.

External pressure has been reported to significantly influence Li cycling, primarily due to its impact on Li/SSE interfacial contact and Li creeping behaviors. We have investigated the effects of pressure by decoupling

fabrication pressure, Li attaching pressure, and cell operation stack pressure. In addition to pellet densification, we found that pellet fabrication pressure plays a critical role in Li metal cycling, specifically in plating/stripping. At given cycling conditions, a higher fabrication pressure supports a longer cycle life. As shown in Figure XIII.11.6a and b, if the pellet is fabricated at a relatively low pressure like 300 MPa or lower, the Li/SSE/Li cell will easily short circuit. However, when the fabrication pressure is increased to 700 MPa or higher, the cell can be cycled stably for over 500 hours at  $0.5 \text{ mAcm}^{-2}$  without any internal short circuiting. This can be explained by the correlations of Li growth and pellet porosity. High pellet porosity, fabricated at lower pressure, may induce Li creep and filament growth into the pellet, which propagates through the pellets and leads to an internal short. Increasing fabrication pressure lowers porosity and increases pore tortuosity, both of which slow down the rate of Li propagation. For pellets fabricated under a same pressure, the cell operation pressure plays a significant role in cell cycling. Figure XIII.11.6c and d compares the cycling of Li/SSE/Li cells at different operation pressures. All the pellets used for cell test were fabricated at 700 MPa. If the cell operation pressure is 3MPa or lower, the cell exhibits a relatively high Li plating/stripping overpotential, which is attributed to high interfacial contact resistance. Increasing the operation pressures to 5 MPa or 10 MPa significantly reduces the Li plating/stripping voltage, indicating that an appropriate cell operation pressure is required to enhance the contact between Li and SSE. A more significant effect of cell operation pressure is observed on Li cycling. Contrary to previous understanding that higher stacking pressure leads to faster Li dendrite formation and earlier cell failure, we found that low pressures such as those below 3 MPa easily induced cell failure by internal short circuit. This is because, due to insufficient stack pressure, the Li morphology grown along the Li/SSE interface is porous and nonuniform, leading to inhomogeneous Li deposits during plating or void formation after stripping. Upon repeated cycling, such inhomogeneous morphology could lead to increased local current densities, causing dendrite formation and short circuit. This study suggests that for a specific SSE, in order to improve cell cycle life with a Li metal anode, optimal pressure ranges should be identified for pellet fabrication, Li attaching, and cell operation.

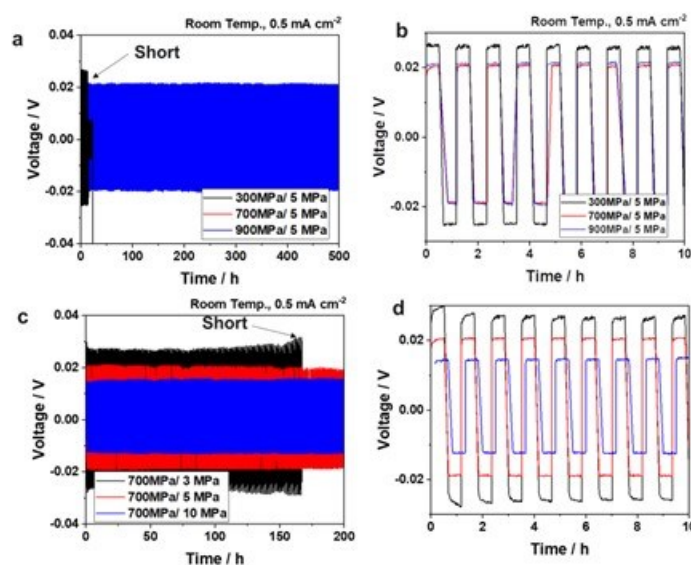


Figure XIII.11.6 Impact of pressure on Li stripping/plating: a, b) Cycling of Li/SSE/Li cells with SSE pellets fabricated at different pressures (cell testing is performed at a constant stack pressure of 5 MPa and room temperature,  $0.5 \text{ mAcm}^{-2}$  for each step of plating or stripping). c, d) Cycling of Li/SSE/Li cells at different stack pressures (SSE pellets were fabricated at constant pressure of 700 MPa).

#### 4. Studied functional mechanism of C-M interlayer for Li plating/stripping

The Li/solid state electrolyte (SSE) interfacial properties impact early-stage Li nucleation, which dictates subsequent Li growth and cycling stability. For this aspect, uniform Li/SSE interface both in chemistry and morphology can help even and reduce local current density, promoting uniform bulk Li growth. For sulfide

based solid state electrolytes (S-SSE), the Li/S-SSE interface is composed of  $\text{Li}_3\text{P}$ ,  $\text{Li}_2\text{S}$ , and Li-halides after contact and chemical interactions. Once formed, such an interface is thermodynamically stable against Li metal at a static status, but is challenged by dynamics upon repeated Li cycling, particularly at practically high current density and areal capacity conditions. A high current density may induce a much faster Li plating and stripping than Li creeping along the interfaces. This would boost the potentials of inhomogeneous Li growth and even dendrite formation, which is exaggerated if heterogeneous Li/SSE interfaces pre-exist. This may lead to a high local current density and internal-short-circuit. Moreover, at a high areal capacity, Li stripping/plating stimulates a large volume change (1 mAh  $\text{cm}^{-2}$  corresponds to  $\sim 5 \mu\text{m}$  thickness change) and may cause SEI fracture, local-contact loss, and local-pressure variation, which further deteriorates the Li/SSE interface and Li cycling stability. To overcome these issues, a comprehensive strategy is needed to both enable a dynamically stable Li/SSE interface and tailor bulk Li plating/stripping (e.g., high areal capacity). To address the issue, we developed a thin Li/SSE interlayer (carbon-metal, C-M) with functions tailoring Li nucleation and growth, promoting reversible cycling of thick Li. To achieve such a design, the interlayer should 1) have a low Li nucleation energy and can react or alloy with Li readily prior bulk Li metal plating; 2) be thin and light without introducing significant parasitic volume and weight to the cell, and 3) be mechanically robust to withstand the volume change upon Li alloying and dealloying. Figure XIII.11.7a shows an example C-M interlayer ( $< 5 \mu\text{m}$ ), which help dense Li plating with an areal capacity up to 10 mAh/ $\text{cm}^2$ . Mechanism study indicates that Li plating follows a multi-step alloy-nucleation-growth process. The Li-M alloying is the first-step reaction and starts at a voltage  $\sim 100 \text{ mV}$  vs. Li and proceeds with gradual voltage decrease. Accompanying the alloying process, the porous C-M interlayer gets filled up and densified due to the volume expansion and turns into a smooth surface eventually when the lithiation capacity reaches to 4 mAh  $\text{cm}^{-2}$  (Figure XIII.11.7c). Then Li starts to nucleate on the flat C-M-Li surface (Figure XIII.11.7d) and grows up gradually into large particles and then dense Li layer (Figure XIII.11.7e). A clear evolution process of M-Li alloying, Li nucleation, Li particle growth, and merging into a Li film as a function of plating capacity was captured by SEM and XRD (not shown here) characterization. This C-M interlayer is expected to not only homogenize Li nucleation but also regulate bulk Li growth in between the C-M layer and Cu current collector, helping reduce Li dendrite formation. Such a thin C-M interlayer can be tuned in chemistry and architecture and fabricated by either wet coating or in situ deposition on Cu substrate.

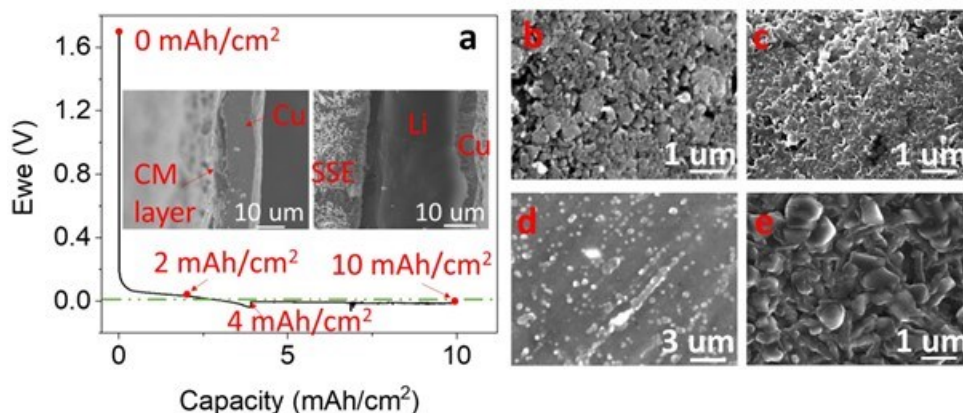


Figure XIII.11.7 Morphological changes of Li plating with presence of C-M interlayer. (a) Voltage profiles during  $0.5 \text{ mA cm}^{-2}$  discharging (Li plating) of Li/SSE/C-M/Cu cell (Inset: cross-section SEM images C-M before and after Li plating). (b-e) Top-view SEM images of the C-M interlayer when (b) pristine, (c)  $2 \text{ mAh cm}^{-2}$ , (d)  $4 \text{ mAh cm}^{-2}$ , and (e)  $10 \text{ mAh cm}^{-2}$ .

## Conclusions

1. LiI-rich interface on Li facilitates Li plating/stripping at a low overpotential and with a dense morphology.

2. The Li/Li symmetric cells with  $\text{Li}_7\text{P}_2\text{S}_8\text{Br}_{0.5}\text{I}_{0.5}$  were realized for 1000 hours cycling under conditions of  $0.5 \text{ mA cm}^{-2}$  at  $20 \text{ }^\circ\text{C}$ ,  $1 \text{ mA cm}^{-2}$  at  $60 \text{ }^\circ\text{C}$ , and  $2 \text{ mA cm}^{-2}$  at  $100 \text{ }^\circ\text{C}$  (0.5h for each step Li stripping or plating).
3. All-solid-state Li-S cells with metallic Li as anode demonstrate stable cycling for >250 cycles; high area-capacity cathode of  $6 \text{ mAh cm}^{-2}$  was developed.
4. Functional Li interfacial layer (C-M) was developed to improve Li cycling and its mechanism was studied.
5. Dry processing of cell components was demonstrated, and all-film solid cell integration was started for full cell fabrication and evaluation.

#### Key Publications

1. Z. Yu, J. Xiao, D. Lu. "Lithium-metal compatible solid electrolyte for all-solid-state battery", Patent Application No. 17/945,447
2. M. Kindle, Z. Yu, D. Marty, Y. Xu, C. Zeng, J. Bao, C. Wang, Z. Xu, and D. Lu, Optimizing Sulfur Utilization in High Loading Cathode for All-Solid-State Lithium-Sulfur Battery, The 243 ECS Meeting and 18th International Symposium on Solid Oxide Fuel Cells (SOFC-XVIII), 2023, May 28-June 2, Boston
3. D. Lu, Stable Solid-State Electrolyte and Interface for High-Energy-Density Lithium-Sulfur Battery, The 2023 Vehicle Technologies Office (VTO) Annual Merit Review, 2023, June 12-15
4. D. Lu, Dry Processing Technology for Advanced Battery Manufacturing, Roundtable: Battery Manufacturing Science in Accelerating Technology Translation from Lab to Market, 2023, September 26-27, Seattle
5. T. Ding, D. Zheng, H. Qu, W. Ji, X. Zhang, D. Lu, G. Wang, and D. Qu, In-situ electrochemical optical techniques in the investigation of lithium interfacial phenomena with a liquid and a solid-state electrolyte, *Journal of Power Sources*, 589 (2024) 233746.

#### Acknowledgements

Michael Kindle, Zhaoxin Yu, Dahee Jin, Un Hyuck Kim, Jing Wu, Daniel Marty, Yaobin Xu, Chao Zeng, Chongmin Wang, Jie Bao and Zhijie Xu (PNNL); Deyang Qu (University of Wisconsin-Milwaukee);

## XIII.12 Scale-Up of Novel Li-Conducting Halide Solid State Battery Electrolyte (LBNL)

### Mike Tucker, Principal Investigator

Lawrence Berkeley National Laboratory  
1 Cyclotron Rd  
Berkeley, CA 94720  
E-mail: [MCTucker@LBL.gov](mailto:MCTucker@LBL.gov)

### Simon Thompson, DOE Technology Development Manager

U.S. Department of Energy  
E-mail: [Simon.Thompson@ee.doe.gov](mailto:Simon.Thompson@ee.doe.gov)

Start Date: October 1, 2022

End Date: September 30, 2023

Project Funding (FY23): \$400,000

DOE share: \$400,000

Non-DOE share: \$0

### Project Introduction

LBNL and project partner Saint Gobain (SG) will demonstrate scalable processing of halide-based solid state batteries. SG's innovative halide-based SSE utilized in this project is inherently scalable: it can be compressed into a dense electrolyte sheet at room temperature under moderate pressure, can be processed in dry air, and does not present any safety issues during processing or end use. The halide material will form the dense electrolyte layer, and be dispersed in the thick cathode to form a highly conductive path for Li ions. The halide will also be in contact with various environments and other materials (solvents, binders, processing equipment, etc.) throughout the battery manufacturing process, and must be stable in contact with cathode and anode materials during operation. R&D efforts commonly use thick pellets of SSE materials to interrogate the relevant interactions, however such studies do not usually reflect the challenges and processing constraints of commercially-relevant thin electrolyte layers. To establish the scalability of this promising material, full cells must be fabricated using a thin electrolyte layer and scalable processing techniques, and any issues encountered during scale-up and processing must be thoroughly characterized and addressed before pilot manufacturing can commence. In this project, SG produces halide powders with  $\text{Li}_3\text{YBr}_6$  (LYB) and proprietary compositions, and LBNL focuses on fabricating thin electrolyte and thick cathode layers incorporating these powders.

### Objectives

The key objectives are: identification of processing and cell materials that are compatible with the halide material; demonstration of full cells with thin electrolyte and thick cathode prepared by scalable techniques; and, scale-up to pouch-size cells. The final objective is a 10 mAh,  $\sim 3 \times 4 \text{ cm}^2$  pouch cell providing 300 Wh/kg.

### Approach

Initially, the compatibility of the halide powder with processing materials (solvents, binders, processing equipment surfaces) and cell materials (current collectors, cathode active materials, carbon, anode-side solid secondary electrolytes (SSE-A)) will be evaluated. Tape casting will be used to prepare thin ( $< 40 \mu\text{m}$ ) electrolyte and SSE-A layers, and thick ( $> 100 \mu\text{m}$ ) cathode layers, which will be laminated for adhesion and densification. Once compatible materials and processing techniques are identified, the processing parameters and cell architecture will be optimized for performance and cycling stability at the coin cell level. Finally, pouch cells will be fabricated to demonstrate scalability. Throughout the project, advanced characterization techniques will be used as needed to evaluate materials interactions and cell architecture.

### Results

In the previous FY, toluene was selected as the solvent for halide material tape casting through a compatibility study. Binder for the tape casting was screened in this FY. Binders used in the battery industry, such as

polyvinylidene fluoride (PVDF), and many common tape casting binders, such as polyvinyl acetate (PVA) or polyvinyl butyral (PVB), do not dissolve in toluene. More than 10 candidate binders were ball milled separately with LYB powder in toluene. All the selected binders, QPAC100, QPAC130, ethyl cellulose, PEO, PMMA, polyethylenimine, MSB1-13, polystyrene, polybutadiene and poly(acrylonitrile-co-butadiene) show good compatibility with LYB. The ionic conductivity of the LYB tapes is 1 to 4 orders of magnitude lower than the fresh powder, depending on the binder type and content. The tapes with PEO, polyethylenimine, MSB1-13, polystyrene or poly(acrylonitrile-co-butadiene) as the binder show good ionic conductivity (Table XIII.12.1). Considering mechanical properties, such as strength, elongation, flexibility and robustness after lamination, MSB1-13 was selected as the binder for further tape casting optimization.

**Table XIII.12.1 Ionic Conductivity of LYB Tapes with Binders, Cast from Toluene Slurries.**

Binder	Ionic conductivity (S cm <sup>-1</sup> )	Tape quality
2% QPAC100+1.7% polycarbonate	3.4x10 <sup>-5</sup>	Cracked
3% QPAC130	9.7x10 <sup>-5</sup>	Brittle
2.5% ethyl cellulose (300 cP)	9.1x10 <sup>-5</sup>	Cracked
3% PEO	1.5x10 <sup>-4</sup>	Brittle
3% PMMA	1.0x10 <sup>-5</sup>	Brittle
2.5% polyethylenimine	2.2x10 <sup>-4</sup>	Cracked
2% MSB1-13	2.0x10 <sup>-4</sup>	Flexible
2.5% polystyrene	3.2x10 <sup>-4</sup>	Brittle
3% polystyrene	1.4x10 <sup>-4</sup>	Brittle
3% polybutadiene	6.2x10 <sup>-6</sup>	Flexible
3% poly(acrylonitrile-co-butadiene)	1.1x10 <sup>-4</sup>	Flexible

The impact of MSB1-13 content on tape quality and ionic conductivity is shown in Figure XIII.12.1. With increasing binder content there is a trade-off: mechanical properties improve significantly, but ionic conductivity decreases approximately logarithmically. At 1 and 1.5 wt% MSB1-13 loading, the tapes are very challenging to peel off from the Al substrate. When the binder content is increased to 2 wt%, the tape is still not free-standing in large area but it can be peeled off from the Al substrate when it is punched into a small area (<1.6 cm<sup>2</sup>). Large area tapes could be successfully stripped from the substrate by first laminating with a cathode tape. When the binder content is further increased to 5 wt% or 10 wt%, large-area free-standing tapes are achieved, but with an unacceptable sacrifice of ionic conductivity.



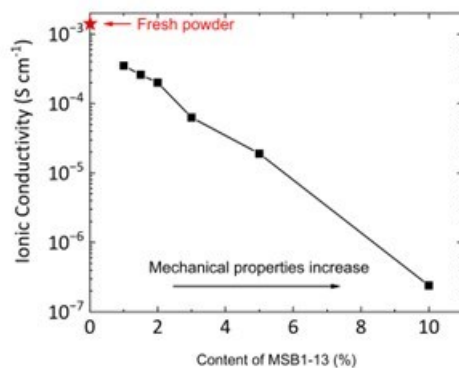


**Figure XIII.12.1 Impact of binder loading for MSB1-13. Ionic conductivity vs. MSB1-13 content.**

Several NMC cathode active material (CAM) candidates were compared and single crystal NMC811 with a particle size of 3 to 5  $\mu\text{m}$  from MSE Supplies LLC was selected. The ratio of the cathode components was also optimized. Results show that 70% NMC811 with 29% raw Gen2.2 catholyte and 1% C65 is optimal. Saint-Gobain also provided Gen2.2 powder with particle size decreased from  $\sim 20 \mu\text{m}$  to  $\sim 3 \mu\text{m}$ . Replacing the raw Gen2.2 catholyte with fine Gen2.2 catholyte, the capacity increased. With 24 wt% catholyte, the capacity increased from 120 mAh/g for raw Gen2.2 catholyte to 169 mAh/g for fine Gen2.2 catholyte. Even with 19 wt% fine Gen2.2 catholyte, the capacity is 145 mAh/g at 0.05 C. Less catholyte is needed when the catholyte particle size is smaller, thereby improving energy density. To further decrease particle size, we synthesized  $\text{Li}_3\text{InCl}_6$  (LIC) with particle size less than 500 nm, even smaller than the fine Gen2.2 particle size. Cells were prepared with very fine halide as catholyte (LIC) and fine halide as separator (Gen2.2). With fine Gen2.2 catholyte replaced by LIC and a cathode interlayer loaded between cathode and pellet electrolyte, the cell shows discharge capacity of 186, 169, 153 and 122 mAh/g at 0.02, 0.05, 0.1 and 0.2 C, respectively. The cathode was composed of 80% NMC811, 19% LIC and 1% C65. After cycling at different C rates, the cell was further cycled at a constant C rate of 0.1 C for almost 40 cycles. The retention is 55% and the coulombic efficiency is  $\sim 97\%$  (Figure XIII.12.2 (Left)). LIC catholyte provides better ionic conduction in the cathode due to the smaller particle size.

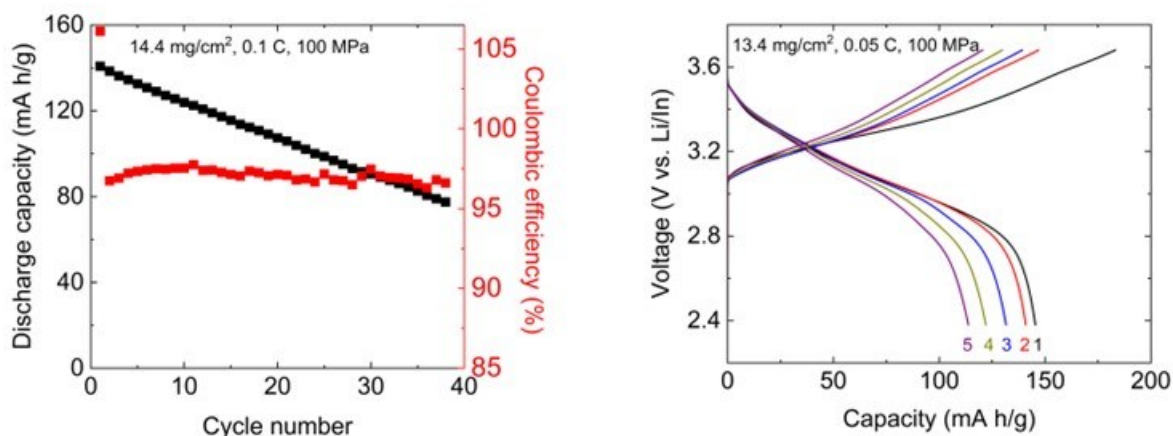


**Figure XIII.12.2 (Left) The retention of a pellet cell with LIC catholyte and cathode interlayer in  $\sim 40$  cycles at 0.1 C. Cell structure: Li-In( $150\mu\text{m}$ )/Gen2.2( $300\mu\text{m}$ )/LIC( $300\mu\text{m}$ )/NMC-LIC-C( $100\mu\text{m}$ ). (Right) Charge/discharge curves of a tape cast cell with cell structure: Li-In( $150\mu\text{m}$ )/Gen2.2-MSB( $40\mu\text{m}$ )/LIC-MSB( $40\mu\text{m}$ )/NMC-LIC-C-MSB( $100\mu\text{m}$ ).**

To scale up, a cathode was tape cast with 80% NMC811, 18% LIC catholyte, 1% C65 and 1% MSB1-13 binder (100  $\mu\text{m}$  thick). LIC cathode interlayer (40  $\mu\text{m}$  thick) and Gen2.2 electrolyte (40  $\mu\text{m}$  thick) were tape cast with 3% MSB binder. A cell with each layer punched to 0.5  $\text{cm}^2$  and Li-In alloy anode was assembled and tested in a Sphere Energy setup at 100 MPa. The 1<sup>st</sup> cycle discharge capacity is 145 mAh/g at 0.05 C (Figure XIII.12.2 (Right)), ~14% lower than the comparable pellet cell. This illustrates that tape casting binder enables scalable thin layers, but moderately impacts performance.

A cell with an area of 5.7  $\text{cm}^2$  was assembled from tapes and cycled in a glove box with a compressing jig (stack pressure <2 MPa). The structure and composition of the cell are the same as the above button cells, with cathode loading of 4.1  $\text{mg}/\text{cm}^2$ . The interfacial resistance is larger and the discharge capacity lower than the 0.5  $\text{cm}^2$  button cell, due to the much lower stack pressure. The retention of the large cell is good, although it fluctuates due to room temperature variation (Figure XIII.12.3). The large cell performance shows the feasibility of cell scaling-up. Pouch cells with an area of 12  $\text{cm}^2$  will be assembled in the next FY and will be cycled in a constant temperature oven.

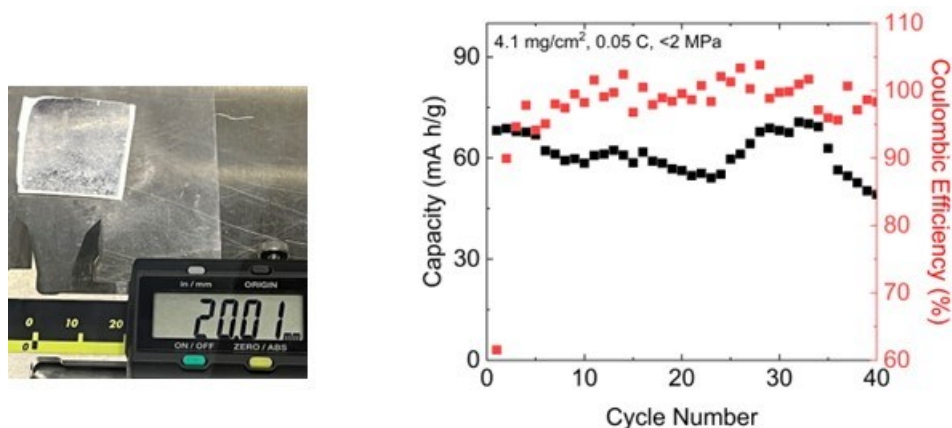


**Figure XIII.12.3** Li-In(150 $\mu\text{m}$ )/Gen2.2-MSB(40 $\mu\text{m}$ )/LIC-MSB(40 $\mu\text{m}$ )/NMC-LIC-C-MSB(30 $\mu\text{m}$ ) cell structure. Retention of a tape-cast large area (5.7  $\text{cm}^2$ ) cell with a stack pressure of <2 MPa.

Li metal anode is our ultimate goal for halide electrolyte-based solid state batteries. In this FY, anode interlayer materials were screened and found to be relatively stable in the Li metal symmetric cells. All-solid-state batteries with NMC811 cathode, LIC cathode interlayer, Gen2.2 electrolyte, anode interlayer, and Li metal anode will be presented in the next FY.

## Conclusions

Binder MSB1-13 was down-selected from more than 10 candidates for halide tape casting. A loading of 2 to 3wt% MSB1-13 binder was used for tape casting halide electrolyte according to a trade-off between ionic conductivity and mechanical properties. A CAM was selected and the cathode components ratio was optimized. LIC halide was synthesized by a freeze-dry method and it improves the discharge capacity due to its small particle size. NMC811 cathode, LIC catholyte layer and Gen2.2 electrolyte were successfully tape cast with a small amount of MSB1-13 binder and a thickness of ~100  $\mu\text{m}$ , 40  $\mu\text{m}$  and 40  $\mu\text{m}$  respectively. The assembled button cells with these tapes show good performance. A larger cell with an area of 5.7  $\text{cm}^2$  was assembled with the same structure and composition, showing half of discharge capacity of the button cells, due to low stack pressure.

## Key Publications

1. F. Shen, M. McGahan, J.D. Pietras, G.Y. Lau, M.M. Doeff, V.S. Battaglia, M.C. Tucker, *Journal of The Electrochemical Society*, 170(2023) 100505.

## **Acknowledgements**

We thank Mike McGahan, Michelle Sugimoto, and John Pietras at Saint Gobain for helpful discussion and providing powder samples. Kris Shen produced all of the results presented in this report. Marca Doeff and Vince Battaglia are key personnel on this project.

## XIII.13 Low-Pressure All Solid State Cells (NREL)

**Anthony K. Burrell, Principal Investigator**

National Renewable Energy Laboratory  
15013 Denver West Parkway  
Golden, CO, 80401  
E-mail: [Anthony.Burrell@nrel.gov](mailto:Anthony.Burrell@nrel.gov)

**Simon Thompson, DOE Technology Development Manager**

U.S. Department of Energy  
E-mail: [Simon.Thompson@ee.doe.gov](mailto:Simon.Thompson@ee.doe.gov)

Start Date: October 1, 2022      End Date: September 30, 2023  
Project Funding (FY23): \$1,240,000      DOE share: \$1,240,000      Non-DOE share: \$0

### Project Introduction

To achieve the goal of low-pressure solid-state cells, the team is utilizing three classes of solid ion conductors, sulfide materials, melt-processable lithium carboranes, and multinary metal halides. These materials can be chemically modified to optimize ionic conductivity and voltage stability in single conductor modes or in combinations to effect interface modification for full-cell development. Specifically, the use of flexible ionic conductors at the cathode interface will enable the mechanical effects of cathode expansion and contraction to be mitigated. In combination with the materials discovery work, the project has an extensive characterization team to help determine the impacts of interface, chemical, electrochemical, and mechanical factors on system performance. Full-cell assembly and development, targeting approaches that are readily scalable and compatible with roll-to-roll process, will drive the materials innovation and development.

### Objective

The goal of this project is to develop all-solid-state batteries (ASSBs) using four classes of solid-state electrolytes (SSEs), and/or electrode modifiers, that can be used to achieve the final 500 Wh/kg cell target. These materials will be down selected using full-cell testing and advanced characterization to achieve cell targets at cell pressures less than 100 psi.

### Approach

Many factors limit ASSB performance, and this project seeks to address the interface stability of both the lithium interface and the high-voltage cathode. The combination of multiple ionic conductors coupled is specifically targeted to allow solution processing, and low-pressure cell outcome will enable lower cost deployment of solid-state cells in automotive applications.

### Results

**Full Cell Development**

In this quarter, the NREL cell build team focused on demonstrating high cathode active material utilization in a full cell configuration. The all-solid-state full-cell configuration used Si as the active material for the anode and a novel high nickel/cobalt-free cathode active material. These two active materials can support very high cell level energy densities with further cell optimization. Figure XIII.13.1 shows the electrochemical performance for this Si/high nickel cathode cell operating at room temperature. The initial C/20 discharge achieves 92% utilization of the high nickel cathode capacity. Moving forward, the cell build team will work to stabilize capacity utilization during continued cycling using novel materials with enhanced chemical and mechanical stability.

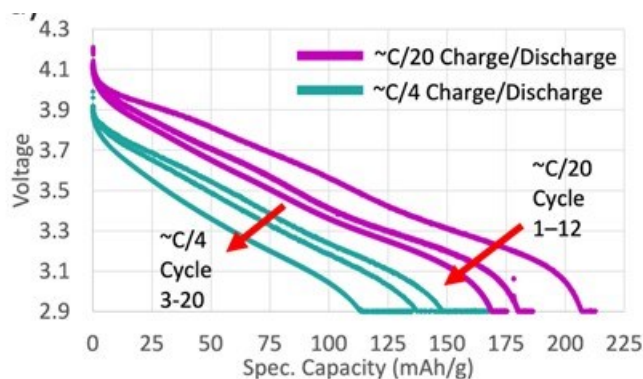
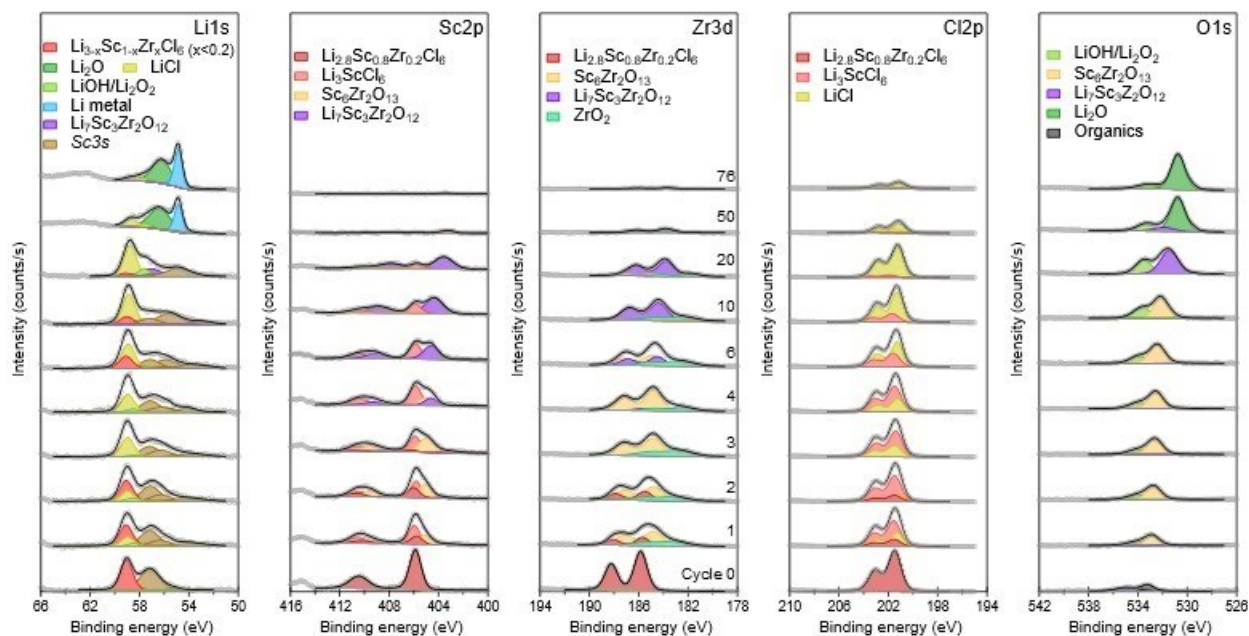


Figure XIII.13.1 Voltage profiles for all-solid-state Si/hi nickel cathode cell cycled at RT

#### ***Virtual-electrode X-ray photoelectron spectroscopy.***

The consortium has focused on understanding SEI formation in the Li-halide solid-state electrolyte (SSE)  $\text{Li}_{2.8}\text{Sc}_{0.8}\text{Zr}_{0.2}\text{Cl}_6$  (LSZC). In the previous report, we presented data from virtual-electrode X-ray photoelectron spectroscopy (VE-XPS) experiments for three different materials: two cation-substituted argyrodite-based SSEs,  $\text{Li}_{6.5}\text{Sb}_{0.5}\text{Ge}_{0.5}\text{S}_5\text{I}$  and  $\text{Li}_6\text{PS}_5\text{Cl}_{0.9}(\text{BH}_4)_{0.1}$ , and the Li-metal-halide LSZC. While we had a clearer understanding of the argyrodite materials, we had not yet identified all relevant peaks and phases in the SEI of LSZC. Recent work has focused on extending and refining the XPS data analysis to provide a more complete and accurate picture of SEI formation in this system.

To provide a quick summary of the VE-XPS experiments, SSE samples are mechanically bonded to a piece of grounded Li foil. The SSE sample surfaces are biased with a flux of either electrons (reduction), or ultraviolet radiation ( $h\nu = 21.2$  eV) that produces an outgoing flux of photoelectrons (oxidation). The reduction experiment brings  $\text{Li}^+$  to the surface due to the negative surface charge associated with the electron flux. When the  $\text{Li}^+$  ions reach the surfaces, they are neutralized and, presumably, converted to short-lived  $\text{Li}^0$  atoms that rapidly react with reducible species, thus forming the solid-electrolyte interphase (SEI). The oxidation experiment, on the other hand, drives  $\text{Li}^+$  ions away from the surface, providing a means for studying the decomposition of SSE material under oxidative stress. Thus, the VE-XPS approach provides a means for studying (electro)chemical changes at the SSE| $\text{Li}^0$  and SSE|cathode interfaces without the need for direct contact with a macroscopic electrode (hence, a virtual electrode).



**Figure XIII.13.2 VE-XPS reduction results on  $\text{Li}_{2.8}\text{Sc}_{0.8}\text{Zr}_{0.2}\text{Cl}_6$  showing formation of a passivating SEI followed by plating of metallic lithium.**

Figure XIII.13.2 shows updated results from the VE-XPS reduction experiment on the LSZC sample. Decomposition proceeds initially via the formation of  $\text{Li}_3\text{ScCl}_6$ , a Sc-Zr oxide phase (tentatively identified as  $\text{Sc}_6\text{Zr}_2\text{O}_{13}$ ),  $\text{ZrO}_2$ , and  $\text{LiCl}$ . The oxygen detected in the SSE decomposition phases might originate either in the form of contaminant species within the SSE bulk or from trace residual gases (primarily  $\text{H}_2\text{O}$ ) that are present in the XPS vacuum chamber during measurements. Further work will be needed to distinguish between these possibilities. Peaks associated with the initial SSE phase are substantially reduced beginning with cycle 1, but persist for several cycles until they are eventually fully attenuated by the growing SEI. Following these initial decomposition processes, the Sc-Zr oxide appears to become increasingly lithiated over the course of the experiment, eventually forming a Li-Sc-Zr oxide phase or phases, as evidenced by the purple peaks in Figure 3. Lastly, in VE-XPS experiments, the SEI eventually passivates such that pure Li metal begins to plate on the surface, which happens around cycle 30. This passivation occurs simultaneously with the growth of  $\text{Li}_2\text{O}$ . This is expected based on the presence of trace amounts of  $\text{H}_2\text{O}$  and other oxygen-containing species in the XPS vacuum chamber (base pressure  $\sim 5 \times 10^{-10}$  torr).

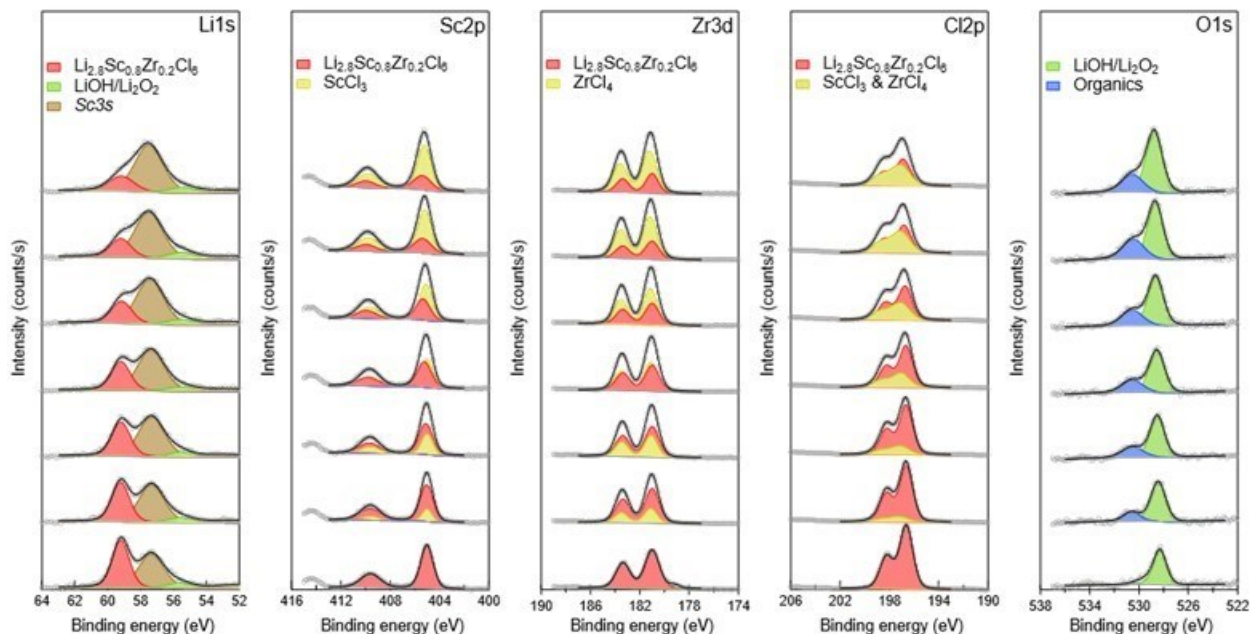


**Figure XIII.13.3** VE-XPS oxidation results on  $\text{Li}_{2.8}\text{Sc}_{0.8}\text{Zr}_{0.2}\text{Cl}_6$ . Throughout the experiment, the lithium signal decreases as it migrates away from the surface. The resulting decomposition products,  $\text{ScCl}_3$  and  $\text{ZrCl}_4$ , form as expected. Over the course of the experiment, the net Cl 2p signal decreases, suggesting the formation of fugitive  $\text{Cl}_2$  gas, also as expected.

To improve our understanding of the phases that form during SSE reduction, we also performed the VE-XPS oxidation experiment on the same sample (Figure XIII.13.3). In this experiment,  $\text{Li}^+$  is driven away from the surface, and consequently, the SSE is expected to decompose into Li-free chloride phases. One of the key challenges of elucidating the lithium-containing phases in the reduction experiment is that the Li 1s and Sc 3s core levels overlap. The oxidation experiment shows that the Sc 3s peak is a significant signal in the Li 1s core scan, and the latter spectra in this series enable us to accurately model Sc 3s peaks in the previously described VE-XPS reduction experiment. Furthermore, we can clearly identify the metal chloride peaks in the oxidation experiment, and observe them at nearly the same binding energies as in the bulk LSZC phase. This supports our identification of Sc- and Zr-containing oxides in the VE-XPS, as opposed to chlorides, as the observed oxide peaks are shifted by up to several eV to lower binding energies.

Our results here indicate that the formation of a passivating SEI on  $\text{Li}_{2.8}\text{Sc}_{0.8}\text{Zr}_{0.2}\text{Cl}_6$  is driven by the formation of Sc- and Zr-containing oxides. Further experiments are required to determine the extent to which SEI formation differs without the presence of any oxygen.

## Conclusions

The development of solid-state electrochemical cells relies on new materials and significant understanding of materials properties and interface stability. While simply forming a solid-state cell represents both a scientific and technological challenge, it is important to consider the requirements of a functional cell. To compete with existing lithium-ion cells, ASSB must achieve increased energy density at comparable costs. One major issue is the formation of functional cells at pressures that can be managed using reasonable technology. To enable this goal, this project is preparing full cells as a primary method of understanding the science challenges.

## XIII.14 3D Printing of All-Solid-State Lithium Batteries (LLNL)

### Jianchao Ye, Principal Investigator

Lawrence Livermore National Laboratory  
7000 East Avenue  
Livermore, CA, 94550  
E-mail: [ye3@llnl.gov](mailto:ye3@llnl.gov)

### Simon Thompson, DOE Technology Development Manager

U.S. Department of Energy  
E-mail: [Simon.Thompson@ee.doe.gov](mailto:Simon.Thompson@ee.doe.gov)

Start Date: October 1, 2022

End Date: September 30, 2023

Project Funding (FY23): \$375,000

DOE share: \$375,000

Non-DOE share: \$0

### Project Introduction

All-solid-state lithium metal batteries (ASSLBs) have attracted attention due to their potential for mitigating safety issues and addressing energy density limitations of conventional lithium-ion batteries (LIBs). While solid-state electrolytes (SSEs) with room-temperature ionic conductivities greater than that of their liquid electrolyte counterparts have been discovered, integration of the different solid components of ASSLBs is not trivial. Taking garnet  $\text{Li}_7\text{La}_3\text{Zr}_2\text{O}_{12}$  (LLZO) electrolyte as an example, problems for this SSE include brittleness, high temperature processing for densification, poor contact with electrodes, and lack of scalable manufacturing methods. These obstacles must be overcome before LLZO becomes commercially viable for ASSLB applications.

Realistic shape factors. Commercially available or lab-developed SSE discs must be thick (e.g., hundreds of micrometers to millimeters) to be mechanically robust enough to overcome their brittle nature, which unfortunately increases the cell impedance and accounts for the majority of overall cell weight and volume, leading to dramatically decreased power and energy densities. To increase energy density, membrane thickness has to be less than 100  $\mu\text{m}$  and ideally  $< 20 \mu\text{m}$ . However, poor mechanical properties such as brittleness for pure oxide SSEs and low stiffness for polymer SSEs increase processing difficulty and promote defect-induced Li penetration. Ultrathin, flat and dense SSE membranes show high flexibility and thus can be stacked together with other electrode components for large scale battery assembly, though that the community suffers from a lack of cost-effective precision manufacturing methods for this purpose. Alternatively, composite polymer electrolytes with requisite active filler content and proper organization may increase mechanical flexibility while reducing manufacturing cost. However, these materials still suffer from conductivity, mechanical stiffness, and electrochemical stability issues which all must be addressed.

Electrode integration. Wetting of SSEs with metallic Li has been partially addressed by introducing lithiophilic interfaces, while the uniformity and cost of the artificial layer still need to be optimized. In addition, achieving good contact of SSEs with the cathode is still an issue. On one hand, co-sintering has been investigated to enhance the cathode contact via solid-state densification while kinetically limiting the chemical reactions. Our work on composite pellet co-sintering and slurry-based co-sintering has shown reasonable thermal stability between Ta-doped LLZO (LLZTO) and NMC 622 at 900 °C. However, issues like mechanical robustness due to relatively high porosity still need to be solved. In addition, carbon additives need to be introduced to provide electronically conductive pathways for these relatively thick electrodes. On the other hand, cathode slurries with polymer binders have often been spread on the sintered LLZO films for cell assembly. The use of polymer binder may sacrifice the operational temperature and lower electrochemical stability. A small amount of liquid electrolyte/solvent is usually applied to enhance the contact, which negates some of the safety benefits of all-solid-state batteries. A highly conductive solid catholyte with stable and good contact with cathode will be necessary to facilitate  $\text{Li}^+$  transport.



Scaling up approach. Unlike liquid electrolyte-based LIBs for which roll-to-roll (R2R) methods have been developed for large scale manufacturing, scaling up of SSBs is likely different. Although soft and glassy sulfide-based SSBs are promising candidates for R2R manufacturing, their interfacial stability with electrodes must be resolved. For garnet LLZO-based SSBs, composite polymer electrolytes may be most ready for meaningful demonstrations of scaling up, though their Li<sup>+</sup> conductivity still needs improvement. Pure ceramic-based SSBs will likely require one-step formation to avoid repeated deformation induced cracking.

Cycling stability. Even with successful manufacturing of an ASSLB, poor cycling stability can still limit performance. Several failure mechanisms must be overcome include (but are not limited to): 1) void formation at the Li anode side during Li stripping; 2) Li dendrite nucleation and penetration; and 3) cracking/delamination on the cathode side. Effective characterization methods that help shed light on the failure mechanisms will be critical for designing better materials and manufacturing approaches that stabilize the long-term cycling performance.

### Objectives

Specific Objective 1: Down select 3D printing and post processing approaches for SSE/cathode integration  
Specific Objective 2: Understand battery failure mechanisms via ex situ and in situ characterization

### Approach

The technical approaches include advanced manufacturing based on 3D printing and related techniques, ex situ/in situ characterizations, and battery testing. In addition to experimental efforts, the team will work closely with the computational partner (PI: Brandon Wood) to better understand battery failure mechanisms and design new battery architectures and chemistries for performance improvement. 3D printing approaches will be optimized and down selected to fabricate 3D interfaces for battery performance evaluation. Three approaches including sintering-free, hybrid, and co-sintering will be studied. Ex situ and in situ characterizations will be developed to understand battery failure mechanisms. Routine electrochemical and basic characterizations will be used for troubleshooting. In situ Raman and KPFM techniques will be conducted to analyze the electro-chemo-mechanical evolution of printed ASSLBs.

### Results

#### *UV-curable PEGDA/PEGMEA/PEO-LLZTO composite polymer electrolytes*

The team used UV curable PEGDA/PEGMEA/PEO-LLZTO as a model system to study the relationship of ionic conductivity and Young's modulus with LLZTO particle content, and explore different strategies to integrate the resulted CPE with LFP cathode and Li anode for cell performance test.

The CPE membranes were prepared by tape casting of homogeneous slurries composed of PEGDA, PEGMEA, PEO, LiTFSI, LLZTO, and other additives. After UV curing and 80°C vacuum drying overnight, freestanding films were formed (Figure XIII.14.1a). Modulus of the CPE with LLZTO content up to 10wt% was measured by AFM nanoindentation in Ar glovebox. Figure XIV.19.1b shows the modulus decreases from 6 MPa without LLZTO to 1 MPa at 7 wt%. Correspondingly, Li symmetric cells show the ionic conductivity of CPE increases from  $2 \times 10^{-5}$  S/cm to  $2 \times 10^{-4}$  S/cm (Figure XIII.14.1b). Strong trade-off between modulus and ionic conductivity can be explained by the reduced crosslinking degree and amorphization. The CPE with 7wt% LLZTO (CPE7) can be cycled in Li symmetric cells (Figure XIII.14.1c) at room temperature, although the overpotential at 0.1 mA/cm<sup>2</sup> increases gradually from 0.14V up to 1V after 76 cycles.

FEC has been found to improve the SEI quality in liquid electrolyte based LIBs and was recently found to be beneficial for polymer electrolytes [1]. Here, the team added 1wt% of FEC in the CPE and studied its effects in the mechanical, electrochemical properties and cell performance. AFM nanoindentation reveals the improvement of Young's modulus, from 1 MPa to 5 MPa, making the casted film easy to peel off from the glass slide substrate. This improved mechanical property is beneficial to mitigating dendrite penetration issue and reduce the chance of short circuit during cell assembly and testing. With the increase of mechanical properties, trade-off is observed with ionic conductivity reduced to  $2\sim 5 \times 10^{-5}$  S/cm at room temperature.

However, heating it up to 60 °C gives a 10 times higher conductivity ( $4 \times 10^{-4}$  S/cm). Li symmetric cells show Li plating/stripping overpotentials gradually increase from 24 mV to 50 mV at 0.1 mA/cm<sup>2</sup> after 33 cycles. Lower the temperature to 45 °C leads to an increase of overpotential to 140 mV and gradually to 270 mV after 35 cycles.

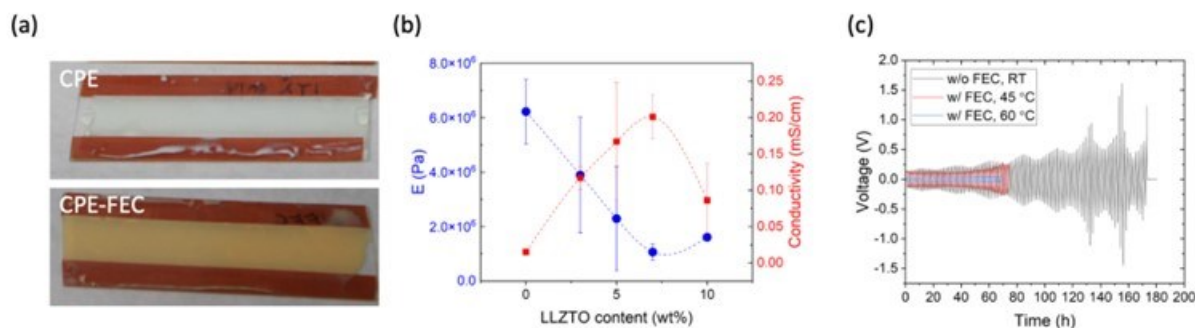


**Figure XIII.14.1** Composite polymer electrolytes. (a) Tape casted CPE films with (bottom) and without (top) FEC additive. (b) Young's modulus (E) and ionic conductivity as functions of LLZTO weight percentage in PEGDA/PEGMEA/PEO-LiTFSI polymer electrolytes. (c) The Li plating/stripping cycling stability test with 0.1 mA/cm<sup>2</sup> current density and 1h plating/stripping period.

The team assembled solid state cells using the developed CPEs, with LFP as cathode and Li as anode. Tape casted LFP films were employed before diving into 3D printed counterparts. The CPE were either infilled into as casted or calendered LFP films, or directly attached to calendered LFP films for coin cell assembly (Figure XIII.14.2). The comparison reveals the importance of forming and maintaining intimate contact for facile Li<sup>+</sup> and electron transport.

For example, as shown in Figure XIV.19.2a, infilling CPE into uncalendered LFP film could break down the connections between LFP particles, leading to the loss of materials and therefore lower capacity. This can be a serious issue when the solvents in the CPE precursors attack the PVDF binder. To improve physical contact in the cathode, the as tape casted cathode was calendered using a hot roller press. CPE was infilled into calendered cathodes to compare with the as-casted cathode (Figure XIV.19.2c). Free-standing CPE film was stacked onto calendered cathode to make another cell without catholyte infilling for performance comparison (Figure XIII.14.2b). Generally calendered cells show higher capacity than as casted cell, suggesting some active materials in the as casted cathode are not in good contact with the current collector or adjacent carbon black particles after CPE infilling. Upon cycling, volume change may further weaken the particle-particle contact and therefore leads to continuous material loss. Using freestanding CPE in the calendered cell with LFP mass loading of 5 mg/cm<sup>2</sup>, the team demonstrated a cell with high initial capacity of 145 mAh/g at RT, but the value dropped quickly to 110 mAh/g in the third cycle. It is likely that insufficient ion transport pathway in this case led to fast capacity decay. By infilling the CPE into calendered cathode to provide ion transport medium, the capacity reaches 150 mAh/g, and maintains that value in the following two cycles. Compared with as casted electrodes, the IR drop decreases from 168 mV to 48 mV after calendering. EIS also shows the reduction of interfacial resistance by adopting infilled calendered cathode, suggesting the gain of electrochemical surface area. Calendering strengthens the bonding between active materials and therefore can maintain good electrical contact during processes including CPE infilling, vacuum drying, and UV cure. However, due to the weak mechanical properties of the CPE7 electrolyte, Li dendrite penetration leads to micro-shorts that cause the voltage noise in the charging period (Figure XIII.14.2c).

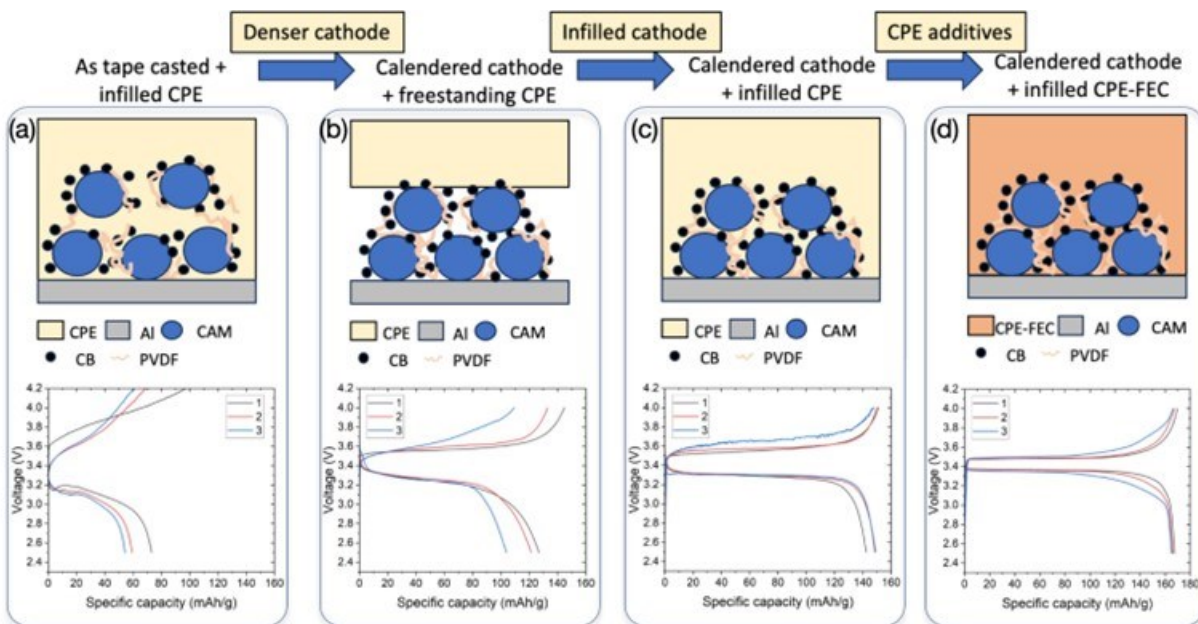


**Figure XIII.14.2 Four LFP-Li cells with different integration methods showing the improvement of charge/discharge capacity at C/10 rate.**

By adding 1 wt% FEC in process of CPE7F, The LFP-CPE7F-Li Cell (as casted LFP) shows stable cycling with capacity of 115 mAh/g at C/20, and ~ 90 mAh/g at C/10 at 45 °C. Stable charging/discharging with no overpotential increase or microshorts was observed in the current 13 cycles at slow rates. Further increasing the temperature to 60 °C led to a capacity of 135 mAh/g at C/20. EIS shows that both the bulk and interfacial impedance decreased 10 times with increasing temperature to 45 °C, which is in contrast to the CPE without FEC that showed interfacial resistance decrease of only 22 % with increase temperature to 60 °C. This strongly indicates that FEC stabilizes the SEI layer with metallic Li anode. Using a calendered LFP for the CEP7F cell (Figure XIV.19.2.d) leads to further enhancement of the cell performance with close to 170 mAh/g specific capacity at C/10 rate at 60 °C and smooth voltage profiles.

#### **Co-sintering of LLZTO/LiCoO<sub>2</sub>.**

Co-sintering the cathode and electrolyte together has the potential to improve interfacial contact. However, the team observed that the  $\text{Li}_{6.4}\text{La}_3\text{Zr}_{1.4}\text{T}_{0.6}\text{O}_{12}$  (LLZTO) solid electrolyte changed color from white to green when it was co-sintered with an  $\text{LiCoO}_2$  (LCO) cathode using conventional furnace sintering (Figure XIV.19.3a). The team conducted experiments to determine the cause of this color change and its effect on the structure, mechanical properties, and conductivity of the LLZTO.

Element analysis was conducted using inductively coupled plasma-optical emission spectroscopy (ICP-OES) and instrumental gas analysis (IGA for oxygen), on the LLZTO pellet after co-sintering with a layer of  $\text{LiCoO}_2$ . The table in Figure XIII.14.3b confirm the presence of a very small amount of cobalt (0.11 wt%) in the LLZTO pellet after co-sintering, resulting in a composition of  $\text{Li}_{6.3}\text{La}_3\text{Ta}_{0.6}\text{Zr}_{1.4}\text{Co}_{0.02}\text{O}_{11.3}$ . These results suggest that in addition to cobalt entering the LLZTO structure, some lithium and oxygen may have been lost during co-sintering. These Co-doped LLZTO pellets were also analyzed by XRD to identify any structural changes that may have taken place as a result of the Co diffusion into the LLZTO lattice. The XRD results are shown in Figure XIII.14.3c. Overall, the small level of Co-doping does not seem to have much of an effect on the overall structure of the LLZTO.

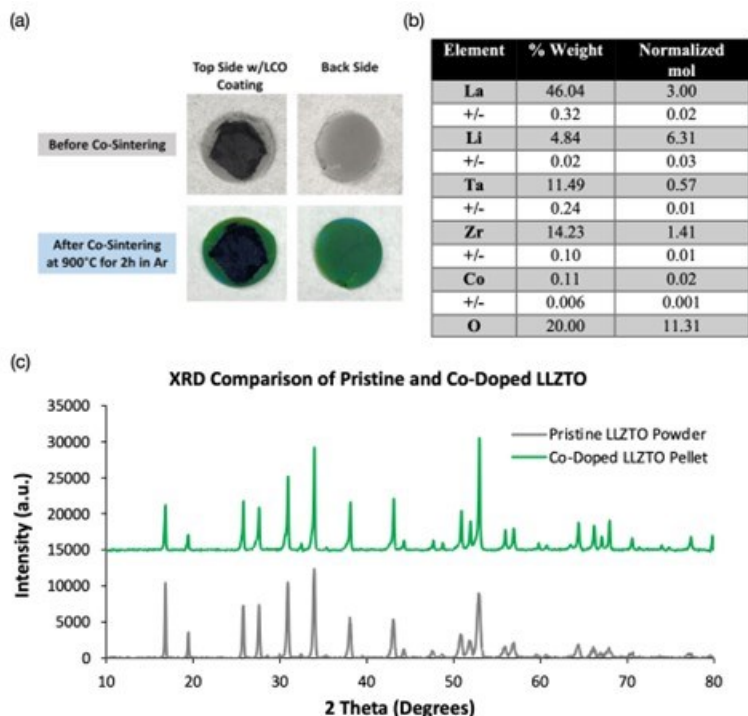


Figure XIII.14.3 (a) Pictures of sintered LLZTO pellets coated with a layer of LCO before and after co-sintering at 900 °C for 2h in Ar. (b) ICP-OES (all elements except for oxygen) and IGA analysis (oxygen) of LLZTO pellets after co-sintering with LCO. The LCO layer was removed before analysis. (c) XRD comparison of pristine LLZTO powder and Co-doped LLZTO pellets (prepared by removing the LCO layer after co-sintering with LCO at 900 °C for 2h in Ar).

Nanoindentation tests were performed on the Co-doped LLZTO pellets to determine the effect of Co diffusion on the mechanical properties. Nanoindentation tests reveal a decrease of Young's modulus and hardness with Co diffusion. Pristine LLZTO pellets show a Young's modulus of  $156.5 \pm 5.1$  GPa and hardness of  $8.81 \pm 0.75$  GPa. With Co diffusion, the Young's modulus decreases to  $139.9 \pm 4.3$  GPa and the hardness to  $7.31 \pm 0.41$  GPa. Nanoindentation load-displacement curves (Figure XIII.14.4a) also show viscoplastic creep behavior changes with Co diffusion. The increased creep displacement for a given load holding time (10s) suggests microstructural variation that introduces an additional deformation mechanism after Co diffusion. It is hypothesized that Co accumulation in the LLZTO grain and grain boundaries may lead to a higher degree of amorphization, weaken the grain boundaries and cause grain sliding/rotation under load, but detailed atomic scale characterization may be necessary to reveal the underlying physics.

Electrochemical impedance spectroscopy (EIS) was used to determine the effect of Co-doping on the ionic and electronic conductivities of LLZTO. Gold paste was applied to the surfaces of the LLZTO pellets to serve as ion-blocking electrodes. EIS plots (Figure XIII.14.4b) were fit by a simple (Q1+Q2/R2) equivalent circuit model to obtain the solid state electrolyte resistance R2. The measured ionic conductivity of pristine LLZTO at RT was 0.35 mS/cm. After co-sintering with LCO, the conductivity decreased to 0.21 mS/cm. This result implies that co-sintering induced Co diffusion may adversely impact the LLZTO separator. The electronic conductivity was measured by applying a DC voltage bias (0.3V) for 3 hours (Figure XIII.14.4c). It was found that with Co doping, the electronic conductivity also decreased from 2.5 nS/cm to 1.9 nS/cm. The decrease of electronic conductivity is beneficial for LLZTO separator but may reduce electron transport in the LLZTO/LCO composite cathode.

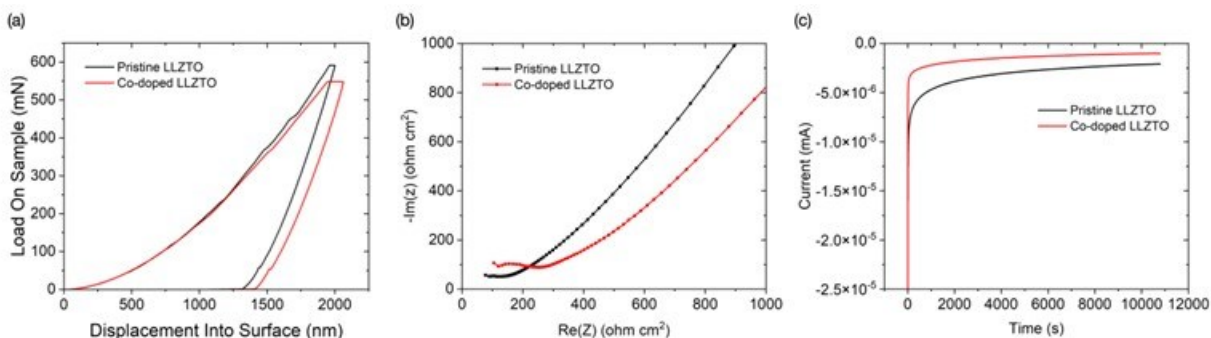


Figure XIII.14.4 (a) EIS plots and (b) DC polarization curves of pristine and Co-doped LLZTO pellets with Au as ion blocking electrodes.

### Conclusions

In FY23,  $> 10^{-4}$  S/cm ionic conductivity at room temperature was achieved in UV-curable PEGDA/PEGMEA/PEO-LLZTO composite polymer electrolytes. The ionic conductivity reaches a peak value  $2 \times 10^{-4}$  S/cm with 7wt% LLZTO additive. In the meantime, the modulus is down to a valley value of 1 MPa. The Li symmetric cells show a gradual increase of over potential, suggesting the accumulation of SEI or mossy lithium. The low modulus of the CPE also adds challenge to assemble cells with 3D printed electrodes due to the local high pressure induced short circuit. The addition of 1wt% FEC significantly increases modulus (5x) and interfacial stability. With further strengthening of electrode films by calendaring, the cell performance was dramatically improved. In a parallel study, the team found that co-sintering LLZTO/LCO using conventional furnace sintering leads to a decrease in the ionic conductivity, electronic conductivity, modulus, and hardness of LLZTO. The findings provide important information in the failure mechanisms of solid-state batteries with co-sintered cathode.

### Key Publications

#### Talks

1. UC Davis chemical engineering seminar, Davis, California (January 12, 2023): “Additive Manufacturing for Energy Applications”. Invited.
2. 2nd Edition of TechBlick's Next Generation & Beyond Li-Ion Battery Materials Conference, virtual (February 15, 2023): “Laser Sintering of Solid-State Electrolytes”. Invited.
3. 40<sup>th</sup> International Battery Seminar & Exhibit, Orlando, Florida (March 20-23, 2023): “Additive Manufacturing for Battery Applications”. Invited.
4. ACS Spring 2023, Indianapolis, Indiana (March 26-30, 2023): “Laser Sintering of Solid-State Electrolytes”. Invited.
5. Workshop on Electrochemical Interfaces: Advancing the integration between multiscale modeling and multimodal characterization. Livermore, CA. (September 28-29, 2023): “Additive Manufacturing Tools to Facilitate Battery Research and Manufacturing”.
6. FY23 Solid State Engineering Lab Review Meeting. Berkeley, California (August 30-31, 2023): “Three-Dimensional Printing of All-Solid-State Lithium Batteries”.

### References

1. Lin, R., et al., *Characterization of the structure and chemistry of the solid–electrolyte interface by cryo-EM leads to high-performance solid-state Li-metal batteries*. Nature Nanotechnology, 2022. 17(7): p. 768-776.

### Acknowledgements

LLNL Team members who have contributed to the project in FY23 include Asya Orhan, Erika Ramos, Marissa Wood, Yuliang Zhang, and Sijia Huang. We also acknowledge Bo Wang, Tae Wook Heo, and

Brandon Wood from LLNL simulation group, as well as Sangil Kim from University of Illinois at Chicago, Huolin Xin from University of California at Irvine for discussions and collaborations.

## XIII.15 Substituted Argyrodite Solid Electrolytes and High-Capacity Conversion Cathodes for All-Solid-State Batteries (ORNL)

### Jagjit Nanda, Principal Investigator

SLAC National Accelerator Laboratory  
2575 Sand Hill Rd, Mailstop 0027,  
Menlo Park, California 94025  
E-mail: [jnanda@stanford.edu](mailto:jnanda@stanford.edu)

### Guang Yang, Principal Investigator

Oak Ridge National Laboratory  
G162, 4500S, 1 Bethel Valley Rd,  
Oak Ridge, Tennessee 37830  
E-mail: [yangg@ornl.gov](mailto:yangg@ornl.gov)

### Simon Thompson, DOE Technology Development Manager

U.S. Department of Energy  
E-mail: [Simon.Thompson@ee.doe.gov](mailto:Simon.Thompson@ee.doe.gov)

Start Date: January 1, 2022

End Date: September 30, 2023

Project Funding (FY23): \$650,000

DOE share: \$650,000

Non-DOE share: \$0

### Project Introduction

Advances in solid electrolytes (SEs) with superionic conductivity and stabilized electrode-electrolyte interfaces are key enablers for all-solid-state batteries (SSBs) to meet the energy density and cost targets for next-generation batteries for electric vehicles. Argyrodite SEs are crucial due to their high ionic conductivity and stability, making them ideal for use in safer, next-generation SSBs. This project aims at synthesis and fabrication of Li-ion conducting argyrodite SEs with nominal composition  $\text{Li}_6\text{PS}_5\text{X}$ , where X = chlorine and/or bromine. The team will combine alternating current (AC) impedance with complementary *in situ* spectroscopy and microscopy to identify buried interfacial side-reaction products and quantify the voltage losses associated with these side reactions. Specifically, we plan to investigate the interfacial reaction between various  $\text{Li}_6\text{PS}_5\text{X}$  SE and Li-ion cathodes belonging to different structural families [transition-metal-based sulfides and fluorides (for example,  $\text{FeS}_2$  and  $\text{FeF}_2$ ) and high-voltage layered oxides (for example,  $\text{LiNi}_{0.8}\text{Mn}_{0.1}\text{Co}_{0.1}\text{O}_2$ )]. New dopants such as niobium and partial substitution of sulfur with oxygen will be explored to improve stability of argyrodite SEs against lithium metal and high-voltage cathodes.

### Objectives

Develop thin, free standing argyrodite SEs by (1) identifying compatible solvents and binders for processing; (2) optimizing binder type and loading to produce free-standing films with thickness  $< 50 \mu\text{m}$  and ionic conductivity  $\sim 1 \text{ mS/cm}$  at room temperature; (3) evaluate the ionic conductivity using electrochemical impedance spectroscopy; (4) utilize interfacial coatings to stabilize the cathode as needed; use various AC / direct current electroanalytical methods to identify degradation mechanisms during cycling. Targets: produce a free-standing thin-film sulfide SSE with thickness  $< 50 \mu\text{m}$  and critical current density  $> 500 \mu\text{A/cm}^2$ ; and integrate thin-film SSE with a cathode and thin lithium anode to cycle at reduced pressure.

### Approach

A key focus of this program is to develop scalable, wet chemistry processing routes for producing free-standing, sulfide-based SEs for high-energy lithium metal SSBs. In FY23, we developed scalable solution-based processing routes to produce freestanding sulfide/binder solid-state separators. These separators have thicknesses less than  $70 \mu\text{m}$  and an area-specific resistance (ASR) of less than  $50 \Omega \text{ cm}^2$ . This achievement

was enabled by developing a general method based on the Hansen Solubility Parameter space, which helps to interrogate the interactions between solvents, polymer binders, and SE particles systematically. We also explored the interfacial stability between the argyrodite SE and the Li metal anode, as well as the high-voltage  $\text{LiNi}_{0.8}\text{Mn}_{0.1}\text{Co}_{0.1}\text{O}_2$  (NMC811) cathode, using Raman imaging and X-ray absorption spectroscopy and imaging. Additionally, we initiated efforts to explore the cycling performance of the thin-film SEs with  $\text{Li}_x\text{In}$  alloy and NMC811 cathode.

## Results

We started with systematically exploring and optimizing scalable, solution processing procedure for making quality  $\text{Li}_6\text{PS}_5\text{Cl}$  (LPSCl) solid-state electrolyte thin films. We established a paradigm of solvent and binder selection for solution processing LPSCl solid-state electrolyte (SSE) particles based on Hansen solubility parameters (details are shown in our recent publication<sup>1</sup>). Treatment of the  $\text{Li}_6\text{PS}_5\text{Cl}$  in selected solvents results in particle morphological change, but crystallographic structure remains intact. Although solution processing reduced the  $\text{Li}_6\text{PS}_5\text{Cl}$  ionic conductivity, it promotes the interfacial stability by alleviating its reduction decomposition against Li metal. Solvent treatment of neat LPSCl is found to decrease room temperature ionic conductivity regardless of solvent choice. Herein, we show that two key criteria for solution processing sulfide SSEs include: (i) good dispersion of the polymer binder and sulfide  $\text{Li}_6\text{PS}_5\text{Cl}$  SSE in a solvent and (ii) chemical compatibility of the  $\text{Li}_6\text{PS}_5\text{Cl}$  SSE with the solvents, including cyclohexane (CHex), toluene (TOL) ethyl acetate (EA) and ethyl propionate (EP). Poly(isobutylene), or PIB (850 kg/mol) was used as the binder.

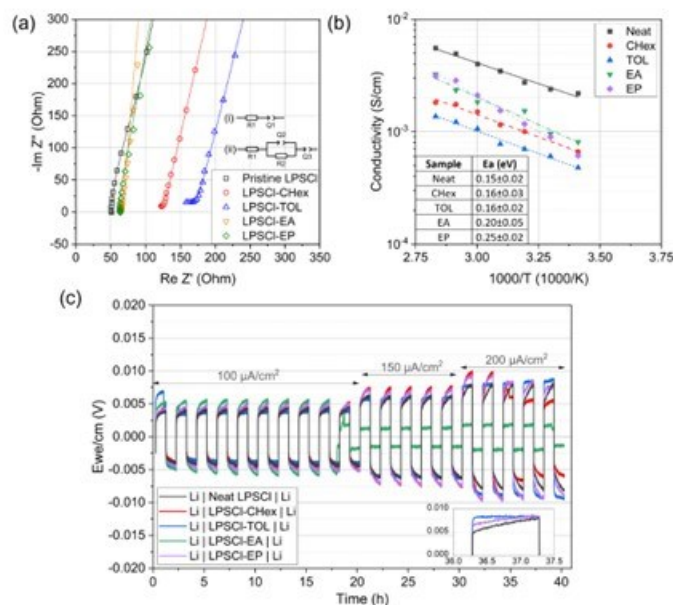


**Figure XIII.15.1** Solvent-treated LPSCl powders were electrochemically characterized by (a) room temperature ionic conductivity, (b) temperature-dependent ionic conductivity, and (c) stability against lithium metal at 100  $\mu\text{A}/\text{cm}^2$ , 150  $\mu\text{A}/\text{cm}^2$ , and 200  $\mu\text{A}/\text{cm}^2$ .

Symmetric cells composed of carbon coated aluminum foil (C@Al) were used to determine room temperature ionic conductivity and activation energy of LPSCl processed by different solvents. We found that treating LPSCl with different solvents altered its ionic conductivity (Figure XIII.15.1a). LPSCl SEs treated with solvents EA and EP, had similar ionic conductivities, while two other SEs treated with TOL and CHex had higher ionic resistance. The EA and EP samples conducted ions almost as well as untreated LPSCl. However, the CHex and TOL samples conducted ions less effectively, possibly because their solvent molecules were more likely to get stuck in the free volume of the LPSCl SE.<sup>2</sup> Arrhenius plots of the four solvent-treated samples and neat control are shown in Figure XIII.15.1b. Solvent treatment decreased ionic conductivity at all



temperatures. LPSCI-EP had a significantly larger activation energy than the neat LPSCI, LPSCI-CHex, and LPSCI-TOL samples. The LPSCI stability against Li metal anode were further explored. Shown in Figure XIII.15.1c, voltage profile of Li|SSE|Li symmetric cells indicates that LPSCI-EA sample failed first ( $100 \mu\text{A}/\text{cm}^2$ , hour 18), followed by LPSCI-CHex ( $200 \mu\text{A}/\text{cm}^2$ , hour 25). The LPSCI-TOL sample experienced early instability, and then stabilized and worked more stable than untreated LPSCI.

We further explored how these solvent treatments affected the LPSCI|Li interfacial chemistry by Raman mapping (Figure XIII.15.2). Our analysis showed that when LPSCI is in contact with lithium, it undergoes chemical changes, forming various decomposition products at the interface. These changes were more pronounced in the untreated LPSCI, indicating the existence of a thick layer of reaction products (or solid/electrolyte interphase, SEI), including LiCl, lithium sulfide ( $\text{Li}_2\text{S}$ ) and lithium phosphide ( $\text{Li}_3\text{P}$ ) as indicated by Raman peaks different that bulk LPSCI shown in Figure XIII.15.2c.<sup>3</sup> It's also worth noting that these reduction byproducts protrude into the bulk LPSCI that is  $>20 \mu\text{m}$  away from the Li/neat LPSCI interface. This indicates the SEI layer is thicker than that stemmed from liquid electrolyte. In this context, there is the non-passivation behavior of the LPSCI against Li due to SE chemical reduction. Our finding suggests that neat LPSCI is more prone to decomposed against chemical reactions with lithium anode and form a thick SEI layer. On the other hand, toluene processing alleviates the interfacial decomposition of the LPSCI, corroborating the stable potential profile at a higher striping/plating current shown in the inset in Figure XIII.15.1c.

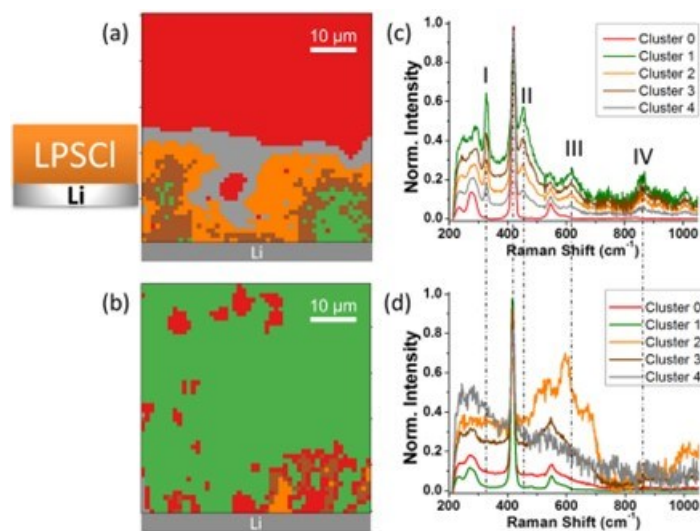


**Figure XIII.15.2** Raman mapping based on the K-means clustering analysis respectively for (a) Li/neat LPSCI interface and (b) Li/ LPSCI-TOL interface. (c-d) The corresponding centroid spectra of the clusters shown in (a). Each color stands for a chemistry or structure, with red in (a) and green in (b) representing bulk LPSCI.

After developing knowledge on solvent and binder selections, we then focus on developing scalable method to fabricate sheet-type, free-standing argyrodite SE films. Tape-casting substrates play an essential role in determining the dimensional integrity of the standalone separator upon film release. We explore the effects of poly(isobutylene) (PIB), a non-polar binder, content at 1, 2, and 5 wt% on the properties of PIB-LPSCI composite separators. Toluene was chosen as the processing solvent. Shown in Figure XIII.15.3, the slurry was first mixed by a low-energy roller mill to obtain a homogeneous paste-like dispersion, followed by tape casting on a Mylar film using a doctor blade. The calendaring process was applied to densify the film. Figure XIII.15.3 shows the as-fabricated film has a thickness of  $\sim 66 \mu\text{m}$ .

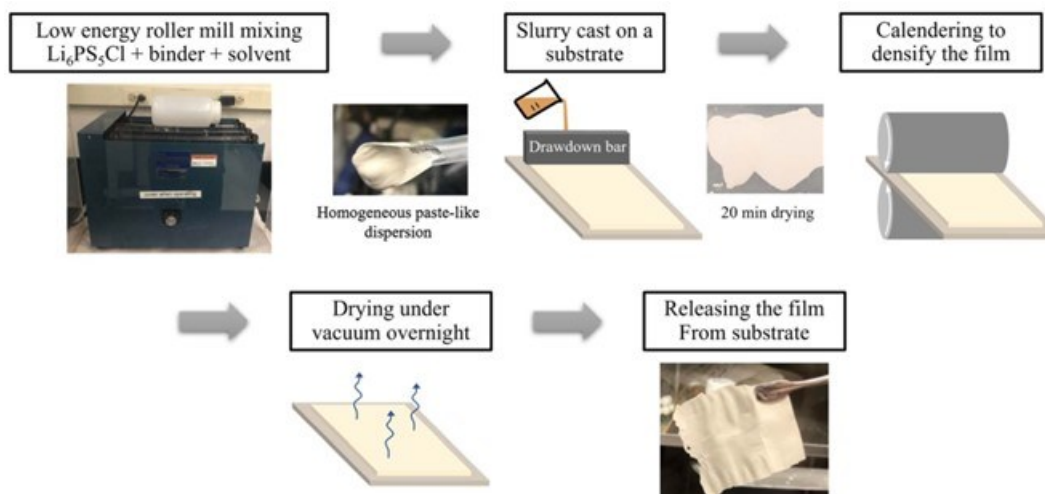


Figure XIII.15.3 Process schematic depicting PIB-LPSCI composite film fabrication.

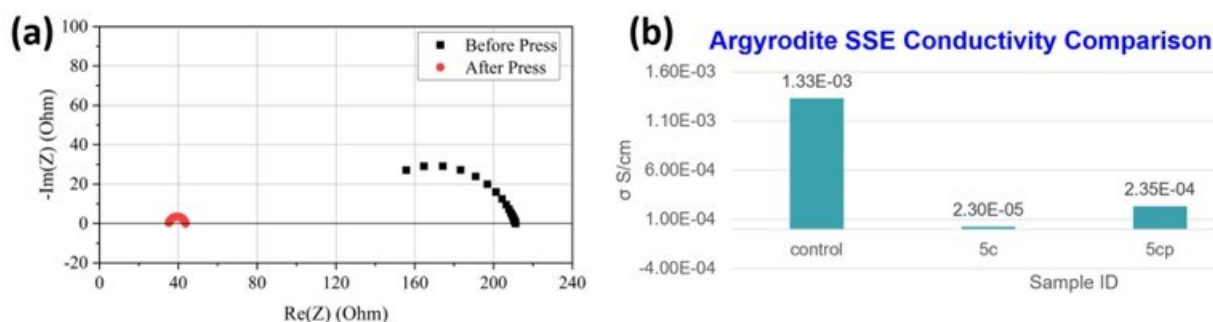
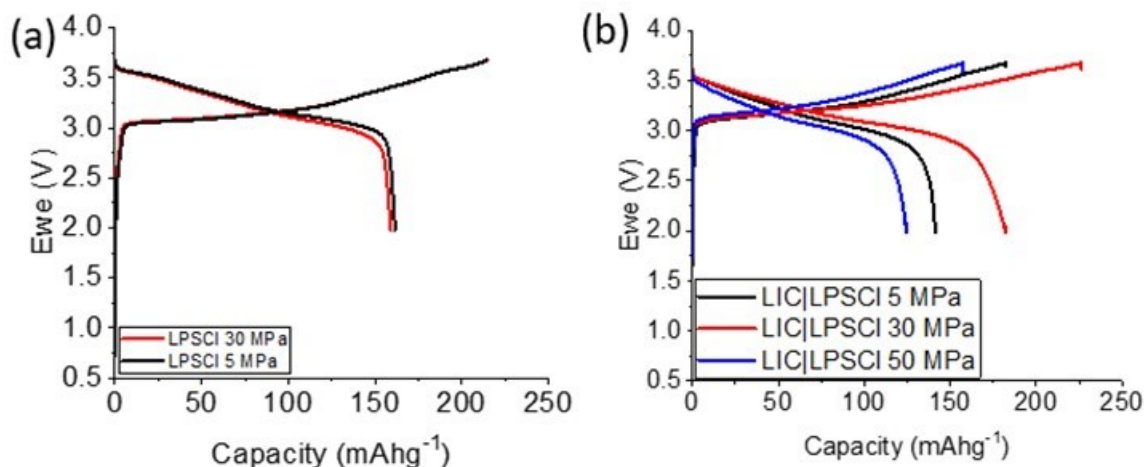


Figure XIII.15.4 (a) Nyquist plots showing decreased interfacial resistance after cold pressing of a C@Al | 5 wt% PIB-LPSCI | C@Al cell. (b) Comparison of the ionic conductivity of various LPSCI separators. The control sample is a cold-pressed pellet with a thickness of 490  $\mu\text{m}$ . Sample 5c stands for calendered LPSCI thin film separator with 5wt% PIB binder (average thickness = 64  $\mu\text{m}$ ). Sample 5cp stands for 5wt% PIB LPSCI thin film separator after cold pressing (average thickness = 48  $\mu\text{m}$ )

Film quality appeared to increase with increasing binder content. Upon calendering, thickness was reduced by around 40%, leading to SE film densification. Additional film thickness reduction can be achieved by cold pressing. Both measurements assist in alleviating the interfacial resistance while promoting ionic conductivity (Figure XIII.15.4) As such, the areal-specific resistance of the cold-pressed standalone LPSCI film could be reduced to 25  $\Omega \text{ cm}^2$ , reduced by 80% benchmarked to the as-released film without cold pressing. Therefore, the post-mortem process, such as cold pressing is essential for the ion transport properties of the free-standing sulfide separators.



**Figure XIII.15.5 (a) Initial galvanostatic cycling profiles of the In|LPSCI|NMC cells at 5 and 30 MPa stack pressures. (b) Initial galvanostatic cycling profiles of the In|LPSCI|LIC|NMC cells at 5, 15, and 30 MPa stack pressures.**

It is well known that LPSCI SE is prone to experience oxidation decomposition when in touch with high voltage NMC cathode. Such an issue could be addressed by using halide SEs, such as lithium indium chloride ( $\text{Li}_3\text{InCl}_6$ , LIC) to NMC side. Two SSB configurations were studied: In|LPSCI|NMC (with LPSCI catholyte) and In|LPSCI|LIC|NMC (with LIC catholyte), both tested in a custom-made PEEK cell (1/2-inch inner diameter). The NMC cathode was composed of NMC811, solid-state electrolyte (SSE) (LIC or LPSCI), and vapor-grown carbon fiber (VGCF) (mass ratio 70:27:3, 10.5mg active material loading). The mass of the SSE was set at 200 mg for LPSCI and 100 mg LPSCI + 100 mg LIC for the bilayer cell. Each cell was uniaxially pressed at 500 MPa for 5 minutes. All SSBs were cycled at a C/10 equivalent rate.

For the single-layer indium (In)|LPSCI|NMC SSB, the initial charge capacity reaches up to 215 mAh/gNMC for both 5 and 30 MPa stack pressures, with a similar initial capacity loss of 26% (Figure XIII.15.5a). In contrast, the In|LPSCI|LIC|NMC SSB displays distinguishable pressure-dependent cycling performance, achieving the highest initial charge capacity of 226 mAh at 30 MPa. Compared to the In|LPSCI|NMC SSB, the bilayer cell exhibits a 5.1% improvement in initial discharge capacity at 30 MPa, likely due to the less oxidation reactions of LIC on NMC and improved NMC utilization. It is known that LPSCI has a limited electrochemical window and is prone to irreversible oxidation at the NMC cathode surface when the voltage increases to  $>4\text{V}$  vs.  $\text{Li}/\text{Li}^+$ .<sup>4</sup> In our study, it is demonstrated that without the LIC buffer layer, oxide decomposition occurs at 3.1V vs.  $\text{Li}/\text{Li}^+$  during the initial charge cycles for both 5 and 30 MPa stack pressures. This oxidation decomposition is not observed for the bilayer cells, indicating that LIC stabilizes the NMC cathode more effectively. The long-term cycling profile of the In|LPSCI|NMC SSB reveals that improving stack pressure does not benefit cycling performance (not shown here). However, for the In|LPSCI|LIC|NMC SSB, there exists an optimal stack pressure of 30 MPa, although the capacity retention is close to that of 50 MPa. The low-capacity retention of 28% for the first 50 cycles necessitates further cell optimization. Our finding underscores the importance of stack pressure in SSB performance, particularly in In|LPSCI|NMC configurations.

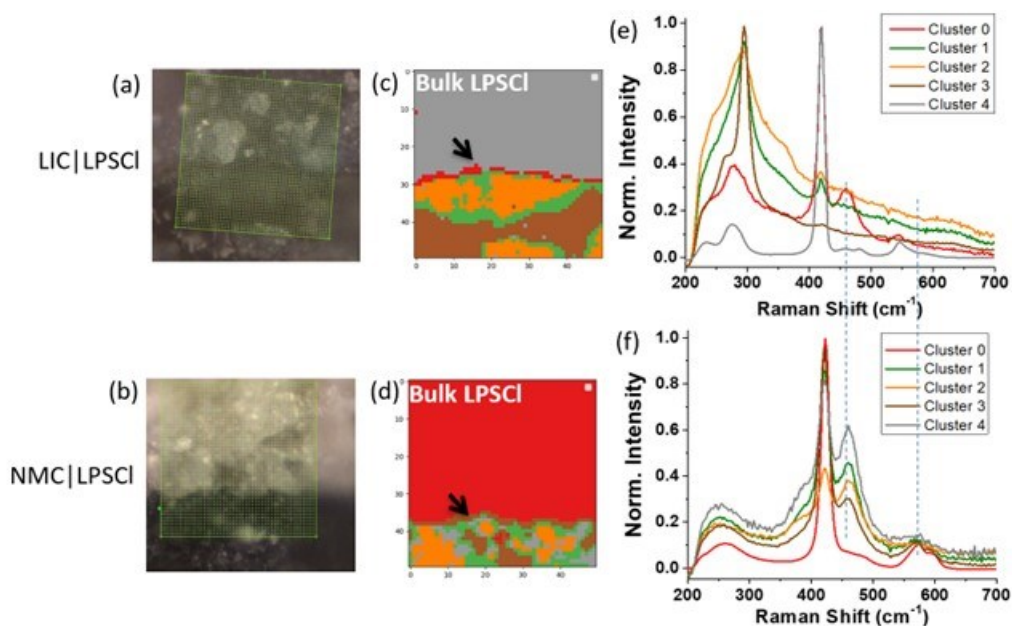


**Figure XIII.15.6** The cross-sectional optical microscopic images of the (a) LIC|LPSCI interface and (b) NMC|LPSCI interface. The green box represents the mapping region. Raman imaging (following K-means clustering analysis) of the (c) LIC|LPSCI interface and (d) NMC|LPSCI interface is also displayed. The black arrow indicates the interface for each Raman mapping. Each color-coded zone represents a region with similar structure and chemistry, and the corresponding centroid spectra, following the same color-coding, are shown in (e) and (f), respectively. Dash lines mark peaks different from those in bulk LPSCI, stemming from the LPSCI oxidation decomposition.

In our study, we employed Raman imaging combined with an unsupervised learning algorithm to investigate the interfacial chemistry between nickel manganese cobalt oxide (NMC) and solid electrolytes (SEs) in two cell configurations. Using K-means clustering analysis on Raman mapping data ( $40 \times 40 \mu\text{m}^2$  area,  $1 \mu\text{m}/\text{pixel}$  resolution), we identified structural heterogeneities and chemical variations at these interfaces (Figure XIII.15.6). This approach revealed distinct interfacial layers in both LIC|LPSCI and NMC|LPSCI samples, marked by unique vibrational modes absent in pristine LPSCI, suggesting side reactions at the NMC|LPSCI interface post-cycling. The interfacial chemistry between LIC and LPSCI differs significantly from that between NMC and LPSCI, with LIC showing a better stabilizing effect on the NMC surface.

To investigate capacity loss in NMC cathodes with argyrodite solid electrolytes (SEs), we utilized Synchrotron X-ray absorption spectroscopy (XAS) and Transmission X-ray Microscopy (TXM). This analysis focused on the chemical phase, oxidation state, and morphology changes in NMC811 cathodes and LPSCI solid electrolytes. Conducted at the Stanford Synchrotron Radiation Light Source (SSRL), Ni K-edge XAS helped identify the chemical states of Ni in NMC811 cathodes post charge and discharge cycles. Our XAS experimental setup involved X-rays reflecting off a silicon crystal and passing through various detectors, with the fluorescence detector positioned perpendicularly (Figure XIII.15.7). We examined pristine NMC811 cathodes, alongside those cycled with argyrodite SEs and Li-In alloy anodes. These included once-charged and fully cycled (charged-discharged) samples, prepared in an argon-filled glovebox and enclosed in polycarbonate films on the sample holder. XAS results (Figure XIII.15.7c) showed higher oxidation states in charged NMC-811 cathodes, indicating Ni oxidation during the charge cycle. The rising edge of the spectra for charged samples shifted to higher energy, reflecting  $\text{Ni}^{2+}/\text{Ni}^{3+}$  and  $\text{Ni}^{3+}/\text{Ni}^{4+}$  redox reactions. In contrast, the charged-discharged samples' spectra returned to energies close to the pristine sample, suggesting a reversal during lithiation.

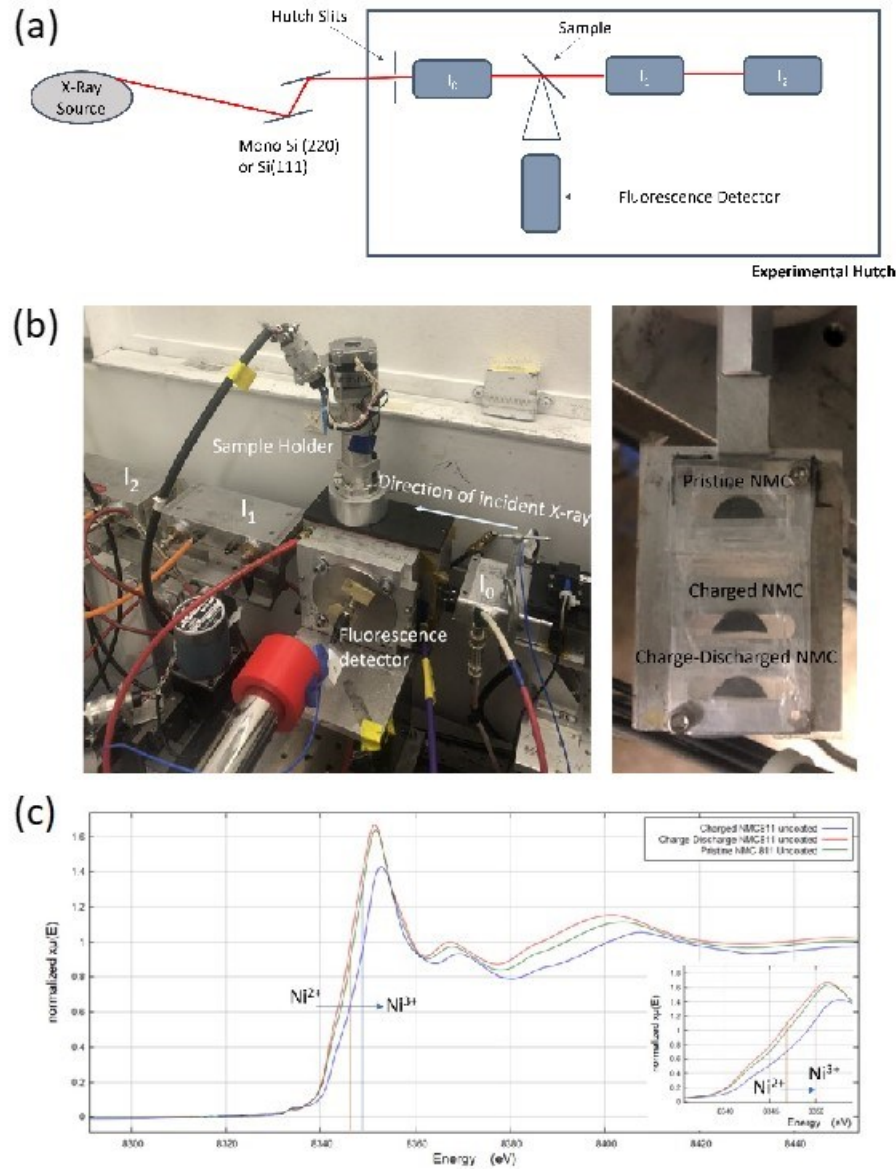
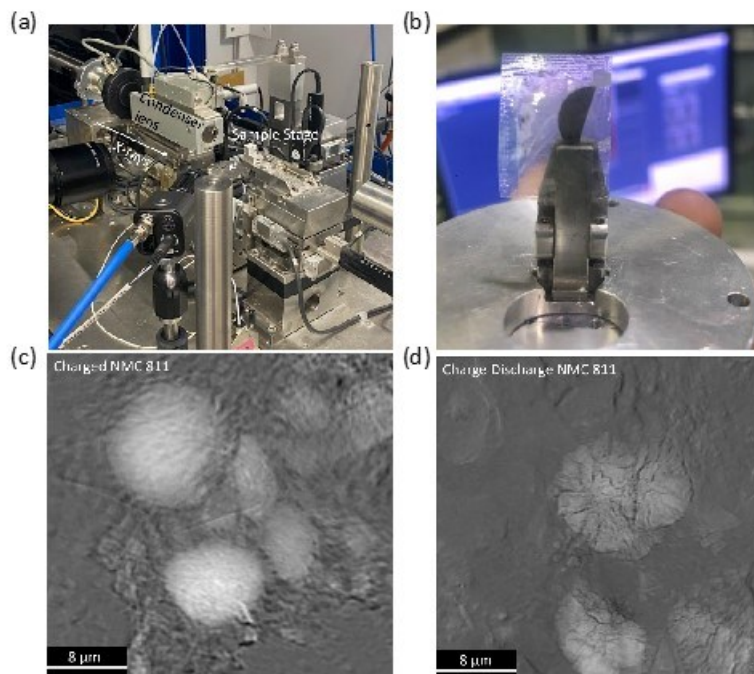


Figure XIII.15.7 X-ray absorption studies to reveal the capacity loss mechanism in NMC811 cathodes using argyrodite solid electrolytes. (a) Schematic of the basic components of a XAS measurement setup. (b) Experimental setup of the XAS instrument and the part of the sample holder containing NMC811 cathode samples (pristine, charged and charged-discharged). (c) Ni K-edge spectrum of Pristine (green), Charged (blue), and Charged-discharged (red) Ni-rich NMC811 cathodes that were in contact with an argyrodite sulfide solid state electrolyte.



**Figure XIII.15.8** Transmission X-ray Microscope (TXM) to visualize the morphological change of NMC-811 cathodes change at different cycling conditions. (a) Experimental setup of the TXM instrument. (b) The sample holder containing Charged NMC-811 sample that have been cycled using argyrodite solid electrolytes. TXM images of NMC-811 (c) charged sample, (d) charged-discharged sample.

TXM at the SSRL's beamline 6-2 was used to examine the morphological changes in NMC811 cathodes under different cycling conditions. The TXM setup involved X-rays passing through components like wigglers, mirrors, and a monochromator, focusing on the sample sealed in polycarbonate films to prevent atmospheric interaction. We achieved high-resolution imaging (30 nm) by scanning the energy across the Ni absorption K edge, with varying energy steps for different regions to normalize the X-ray absorption spectra. Using TXM Wizard software, we processed the images for analysis. Each sample was imaged separately at fixed energy steps around the Ni K-edge. TXM images (Figure XIII.15.8c and d) of NMC811 in fully charged and charged-discharged states revealed significant differences. Captured above the Ni K-edge energy, these images showed the NMC811 particles encased in argyrodite solid electrolytes, with clear microstructural changes like cracking and degradation post-discharge. This suggests that cracking and overcharging of Ni in NMC811 cathodes are key factors in the capacity decay observed in the first cycle when using argyrodite solid electrolytes.

### Conclusions

In summary, our research has advanced the development of thin and free-standing  $\text{Li}_6\text{PS}_5\text{Cl}$  (LPSCl) sulfide solid electrolytes. Key to this advancement is the optimal selection of polymer binder and solvent, guided by Hansen Solubility Parameters (HSPs), which ensures effective LPSCl dispersion and maintains its structural integrity. The scalable tape casting method for creating thin sulfide SE separators with low binder content has led to reduced resistance and maintained ionic conductivity, though these properties are sensitive to fabrication conditions like binder loading and processing pressure. Furthermore, we've observed that solid-state batteries incorporating halide SE,  $\text{Li}_3\text{InCl}_6$  buffer layer exhibit variable performance based on stack pressure, especially in configurations involving nickel manganese cobalt oxide (NMC). Using advanced impedance spectroscopy (EIS), Raman imaging and synchrotron X-ray absorption spectroscopy (XAS) we show electrode|LPSCl interfaces play a significant role in determining the sulfide SSB performance.

Our ongoing research is now focused on (a) fine-tuning binder types for LPSCl films and exploring bilayer SSEs combining LPSCl and LIC, aiming to enhance the overall performance and efficiency of SSBs; (b)

Integration thin Li anode in the thin film LPSCI full cell to evaluate and optimize the cell performance and (c) developing solvent mediated routes to synthesize new argyrodite sulfide SSE with halide and aliovalent substitutions using both mechano-chemical and solid-state methods.

### Key Publications

1. Self, Ethan C., Wan-Yu Tsai, Andrew S. Westover, Katie L. Browning, Guang Yang, and Jagjit Nanda. "Benchmarking Solid-State Batteries Containing Sulfide Separators: Effects of Electrode Composition and Stack Pressure." *Journal of The Electrochemical Society* 169, no. 10 (2022): 100510.
2. Mills, Anna, Guang Yang, Wan-Yu Tsai, X. Chelsea Chen, Robert L. Sacci, Beth L. Armstrong, Daniel T. Hallinan, and Jagjit Nanda. "Adverse Effects of Trace Non-polar Binder on Ion Transport in Free-standing Sulfide Solid Electrolyte Separators." *Journal of the Electrochemical Society* 170, no. 8 (2023): 080513.
3. Mills, Anna, Wan-Yu Tsai, Teerth Brahmabhatt, Ethan C. Self, Beth L. Armstrong, Daniel T. Hallinan, Jagjit Nanda, and Guang Yang. "Navigating the complexities of solvent and binder selection for solution processing of sulfide solid-state electrolytes." *MRS Communications* (2023): 1-8.
4. Hao, Hongchang, Yijie Liu, Samuel M. Greene, Guang Yang, Kaustubh G. Naik, Bairav S. Vishnugopi, Yixian Wang et al. "Tuned Reactivity at the Lithium Metal–Argyrodite Solid State Electrolyte Interphase." *Advanced Energy Materials* (2023): 2301338.

### Patent

1. Yang, Nanda, Hallinan, Mills, and Chen, "Fabrication of thin film sulfide solid-state electrolyte through slurry processing route" US Provisional Patent Application Serial No. 63/455,305

### Presentations

1. (invited) Yang, Guang, Ethan Self, Teerth Brahmabhatt, Anna Mills, Wan-Yu Tsai, Daniel Hallinan, Xi Chen, Frank Delnick, and Jagjit Nanda. "Development of Argyrodite-Based Sulfide Electrolytes for Next-Generation Solid-State Li Batteries." In Electrochemical Society Meeting Abstracts 242, no. 4, pp. 537-537. The Electrochemical Society, Inc., 2022.
2. (invited) Jagjit Nanda, Guang Yang. Current Progress and Challenges in Development of Sulfide and Halide Based Solid Electrolytes for All Solid-State Batteries EN08.02.01 2023 MRS Spring Meeting
3. (invited) Yang, Guang, and Jagjit Nanda. "Investigating multiscale interfaces and interphases using advanced spectroscopy for electrochemical energy storage (Conference Presentation). In Enhanced Spectroscopies and Nanoimaging 2022, p. PC122030E. SPIE, 2022.
4. (invited) Mills, A., Yang, G., Tsai, W.Y., Chen, X., Sacci, R., Armstrong, B., Hallinan, D.T., Nanda, J., 2023, February. Thin Film Sulfide Solid Electrolyte Composites. 2023, Second Annual Polymer Research Symposium. ACS POLY/PMSE at FAMU-FSU.

### References

1. Mills, A., Tsai, W., Brahmabhatt T., Self, E., Armstrong B., Hallinan D.T., Nanda, J., and Yang, G., Navigating the Complexities of Solvent and Binder Selection for Solution Processing of Sulfide Solid-state Electrolytes (Early Career Materials Researcher Special Issue) *MRS Communications* **2023**.
2. Xu, R. C.; Xia, X. H.; Yao, Z. J.; Wang, X. L.; Gu, C. D.; Tu, J. P., Preparation of Li<sub>7</sub>P<sub>3</sub>S<sub>11</sub> glass-ceramic electrolyte by dissolution-evaporation method for all-solid-state lithium ion batteries. *Electrochimica Acta* **2016**, *219*, 235-240.
3. Banerjee, A.; Tang, H.; Wang, X.; Cheng, J.-H.; Nguyen, H.; Zhang, M.; Tan, D. H. S.; Wynn, T. A.; Wu, E. A.; Doux, J.-M.; Wu, T.; Ma, L.; Sterbinsky, G. E.; D'Souza, M. S.; Ong, S. P.; Meng, Y. S., Revealing Nanoscale Solid–Solid Interfacial Phenomena for Long-Life and High-Energy All-Solid-State Batteries. *ACS Applied Materials & Interfaces* **2019**, *11* (46), 43138-43145.
4. Tan, D. H.; Wu, E. A.; Nguyen, H.; Chen, Z.; Marple, M. A.; Doux, J.-M.; Wang, X.; Yang, H.; Banerjee, A.; Meng, Y. S., Elucidating reversible electrochemical redox of Li<sub>6</sub>PS<sub>5</sub>Cl solid electrolyte. *ACS Energy Letters* **2019**, *4* (10), 2418-2427.

## **Acknowledgements**

This research is sponsored by the United States Department of Energy through the Office of Energy Efficiency and Renewable Energy (EERE) and Vehicle Technologies Office (VTO, Program Managers: Simon Thompson and Tien Duong). ORNL team members include Drs. Ethan Self, Wan-Yu Tsai, Mrs. Anna Mills, and Mr. Teerth Brahmhatt. SLAC team members include Dr. Xueli Zheng. University collaborators include Prof. Daniel Hallinan from Florida State University and Prof. David Mitlin from UT Austin. The team also thanks Dr. Andrew Westover (ORNL) for providing the vapor deposited Li metal anodes.



## XIII.16 Multifunctional Gradient Coatings for Scalable, High-Energy-Density Sulfide-Based Solid-State Batteries (ANL)

### Justin Connell, Principal Investigator

Argonne National Laboratory  
9700 South Cass Avenue  
Lemont, IL 60439  
E-mail: [jconnell@anl.gov](mailto:jconnell@anl.gov)

### Simon Thompson, DOE Technology Development Manager

U.S. Department of Energy  
E-mail: [Simon.Thompson@ee.doe.gov](mailto:Simon.Thompson@ee.doe.gov)

Start Date: November 1, 2021

End Date: December 31, 2026

Project Funding (FY23): \$530,000

DOE share: \$530,000

Non-DOE share: \$0

### Project Introduction

All-solid-state batteries (ASSBs) have great potential to significantly improve the safety of lithium batteries by replacing flammable liquid electrolytes with solid-state electrolytes (SSEs), but interfacial stability remains a key barrier to commercialization. Among various classes of solid electrolytes that have been investigated, sulfide-based SSEs deliver the highest Li-ion conductivities ( $\geq 10$  mS/cm) compared to polymer and oxide SSEs across a wide range of temperatures with favorable mechanical properties and low temperature processability. The majority of recent developments in ASSBs have focused primarily on improving cycle life by protecting the lithium metal and suppressing lithium dendrites on the anode side. Significantly less has been done to improve the integration of cathode materials into ASSBs; however, for ASSBs to compete in the electric vehicle (EV) market, they must incorporate stable, high-energy cathodes and utilize low-cost processes. In particular, industry needs a strategy to stabilize ASSBs integrating both Li metal anodes and high energy density cathodes, and manufacturability is paramount.

Sulfide SSEs face three primary limitations to their large-scale deployment. The first is their incompatibility with environmental conditions, even those in dry room environments, due to the high reactivity of sulfide materials with both H<sub>2</sub>O and O<sub>2</sub>, which leads to material degradation and toxic H<sub>2</sub>S evolution. The extent of this reactivity can be mitigated depending on the specific chemistry of the material, but in all cases some degree of air-sensitivity is present, motivating new strategies to make sulfide SSEs more amenable to processing at scale. The second limitation is the intrinsic instability of the anode and cathode interface with sulfide SSEs. Particularly concerning is evidence that direct contact between oxide cathodes and sulfide SSEs leads to chemical intermixing and electrochemical reactivity to form deleterious interfaces that block lithium ion transport. Due to this incompatibility, coatings are required to stabilize the anode and cathode interfaces, with direct coating of the oxide and Li metal surfaces serving as the primary approach for stabilization to date. Despite some success of such coating strategies, the need for separate coating steps for each interface adds significant cost and complexity when considering scalability of this technology. The third, less explored but equally critical issue that must be mitigated is the formation of space-charge layers at oxide-sulfide interfaces, which can lead to high interfacial impedance at the SSE-cathode interface. Such space charge layers are formed due to the mismatch in chemical potential between oxide and sulfide materials, and result in the formation of a Li depletion region within the sulfide during charging of the cathode.

### Objectives

This task seeks to develop scalable approaches to synthesize gradient-coated sulfide solid-state-electrolyte (SSE) particles to improve their air/moisture tolerance and provide chemical compatibility with Li-metal anodes and high-voltage oxide cathodes. The compositional gradient is targeted to provide the additional

advantage of lower interfacial impedance due to mitigation of detrimental, spontaneously formed space-charge layers and/or elemental interdiffusion at the sulfide SSE-oxide cathode interface.

### Approach

The team will leverage a surface science-based, integrated experimental-theoretical approach to synthesize gradient-coated SSE powders, characterize the structure, composition, and intrinsic stability of coated SSEs in contact with reactive electrodes, and directly correlate this understanding with their electrochemical performance. Gradient coatings will be developed using atomic layer deposition (ALD) and/or physical mixing methodologies viable at the kg/ton scale, ensuring technical and commercial relevance of the final, optimized coating process. Well characterized, model surfaces will be used to understand the electronic structure and chemical stability of the gradient coatings as a function of gradient composition and thickness to understand the effect of space-charge layers and chemical reactions on interface resistance. They will accelerate development and optimization of the gradient coatings for improved performance in full cells by establishing a tight feedback loop between materials synthesis and experimental/computational characterization of interfacial (electro)chemistry.

### Results

Sulfide-based solid-state electrolytes (SSEs) with an argyrodite-type cubic structure and  $\text{Li}_{7-y}\text{PS}_{6-y}\text{X}_y$  (LPSX; X = Cl, Br, I) composition have high ionic conductivities ( $>1$  mS/cm), wide band gaps, and favorable mechanical and processing properties, making them particularly promising candidate materials for all-solid-state batteries. As a result, we have focused our efforts on this family of materials as a platform for developing our gradient coating chemistries. All materials studied have the nominal formula  $\text{Li}_6\text{PS}_5\text{Cl}$  (LPSCl), and we have evaluated LPSCl materials synthesized in-house at ANL, as well as material obtained from the commercial suppliers NEI and Ampcera. Experimental and computational results from FY22 demonstrated the stability of LPSCl materials to ALD processing and contact with Li metal, as well as an initial assessment of their electrochemical properties. In FY23, we have further developed our understanding of these coatings, demonstrating their significant benefits to environmental stability, electrochemical properties and cycling performance in symmetric and full cells. We have also developed a computational methodology for evaluating the stability of candidate coatings in order to narrow down the chemistries selected for experimental exploration and accelerate materials optimization.

***Stability of ALD-Coated LPSCl to Environmental Exposure.*** We began our investigation with argyrodite powders coated with ALD  $\text{Al}_2\text{O}_3$ , as our team has extensively investigated this chemistry during the first year of this program. We leveraged the power of thermogravimetric analysis (TGA) to better understand the impact of the ALD  $\text{Al}_2\text{O}_3$  coatings on LPSCl when these electrolytes were subjected to oxidizing conditions. Specifically, we probed the mass change of the powders under a flow of dry and humidified  $\text{O}_2$ , as argyrodites are notoriously unstable under humid and oxidizing conditions.[1,2] The mass gain was collected on a thermogravimetric analyzer (TGA, TA Instruments) under a flow of  $\text{O}_2$  as well as under a flow of  $\text{O}_2$  bubbled through deionized  $\text{H}_2\text{O}$ . Mass gains for argyrodites under oxidizing and humid conditions can be correlated with the decomposition of the electrolyte into  $\text{H}_2\text{S}$ , Li sulfates, etc., in combination with  $\text{H}_2\text{O}$  adsorption. The argyrodite powders coated with ALD  $\text{Al}_2\text{O}_3$  showed significantly lower weight gain under dry and humidified  $\text{O}_2$  exposure compared to the uncoated LPSCl (Figure XIII.16.1). Specifically, argyrodite powders coated with 10 cycles of ALD  $\text{Al}_2\text{O}_3$  exhibited negligible ( $\leq 1\%$ ) weight changes following 240 min of dry  $\text{O}_2$  exposure, and only a  $\sim 17\%$  weight gain following 240 min of wet  $\text{O}_2$  exposure ( $\sim 100\%$  relative humidity). This compares to  $\sim 19$  and  $\sim 100\%$  weight gains for the uncoated argyrodite exposed to dry and humidified  $\text{O}_2$ , respectively. It is remarkable that even one ALD  $\text{Al}_2\text{O}_3$  cycle can significantly suppress weight gain under these conditions, particularly during humidified  $\text{O}_2$  exposure.

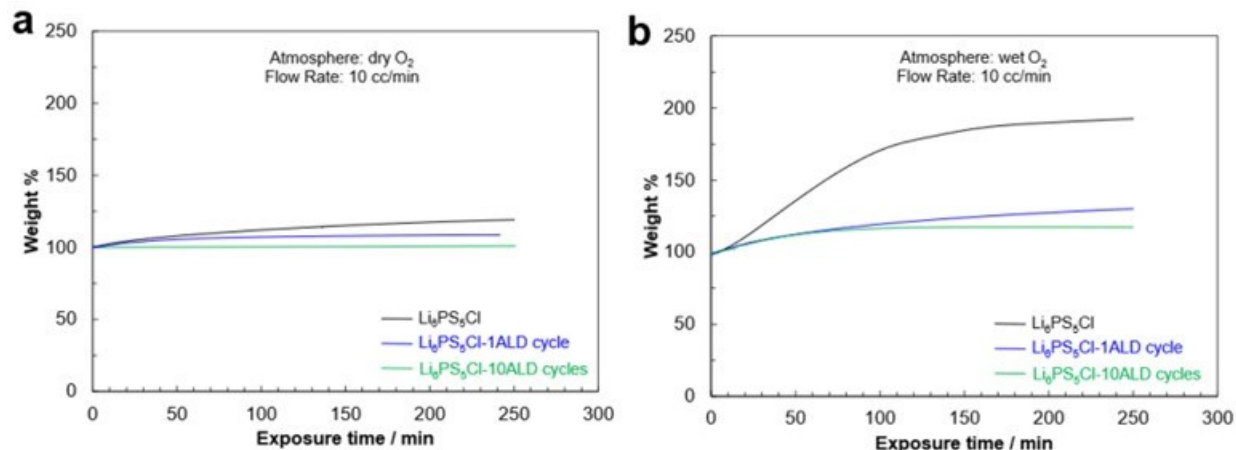


Figure XIII.16.1 Weight gain of uncoated  $\text{Li}_6\text{PS}_5\text{Cl}$  powders and  $\text{Li}_6\text{PS}_5\text{Cl}$  powders after 1 and 10 ALD  $\text{Al}_2\text{O}_3$  cycles during exposure to (a) pure  $\text{O}_2$  and (b) humidified  $\text{O}_2$ .

To gain a more holistic understanding of the impact of the ALD coatings on argyrodites under humid and oxidizing conditions, we compared our results for ALD  $\text{Al}_2\text{O}_3$  coatings to our recently-developed process to grow ZnO and ZnS coatings on LPSCl. These new chemistries were grown onto LPSCl by first depositing a thin  $\text{Al}_2\text{O}_3$  seed layer (with one ALD  $\text{Al}_2\text{O}_3$  cycle) followed by 10 ALD ZnO or ZnS cycles. The ALD  $\text{Al}_2\text{O}_3$  seed layers were used because we discovered that the ALD ZnO and ZnS do not readily nucleate on the argyrodite surface. The argyrodite powders coated with both ALD ZnO and ZnS showed significantly improved stability under humidified  $\text{O}_2$  exposure compared to the uncoated LPSCl (Figure XIII.16.2), achieving >50% reduction in weight gain relative to uncoated material after ~80 minutes. This metric is particularly important for the development of solid-state electrolyte coatings that are compatible with realistic processing environments, as the solid-state electrolyte may be in contact with ambient conditions for approximately 60-80 minutes, for example in a dry room.[3] While the ZnS and ZnO coatings appear to affect the reaction kinetics between LPSCl and humidified  $\text{O}_2$ , the ALD  $\text{Al}_2\text{O}_3$  coatings appear to be most effective for protecting the argyrodite powders against decomposition reactions. This conclusion is corroborated by calculated reaction energies for ZnO and  $\text{Al}_2\text{O}_3$  with LPSCl and water.  $\text{Al}_2\text{O}_3$  is less reactive (reaction energy of -0.05 eV/atom) towards LPSCl than ZnO, which reacts to form  $\text{Li}_2\text{S}$ ,  $\text{Li}_3\text{PO}_4$ , ZnS and LiCl with energy of -0.38 eV/atom. However, the reaction of ZnO with water to form hydroxides is not very favorable, with an energy of approximately 0 eV/atom.

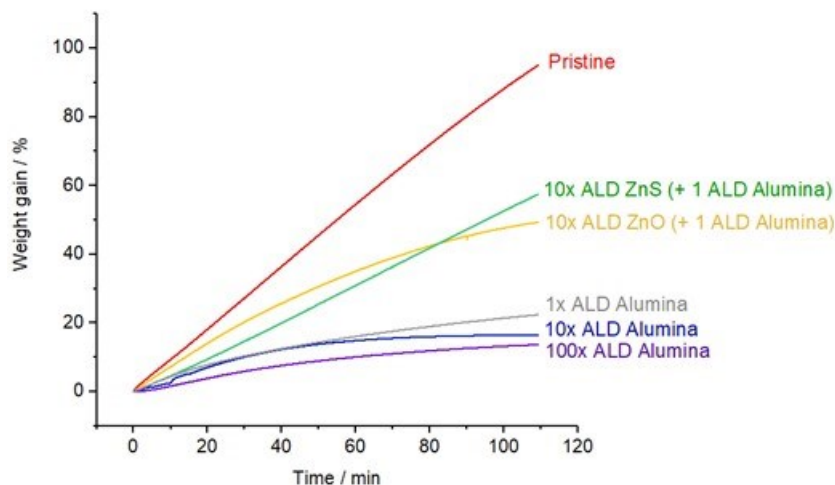


Figure XIII.16.2 Weight gain of uncoated  $\text{Li}_6\text{PS}_5\text{Cl}$  powders and  $\text{Li}_6\text{PS}_5\text{Cl}$  powders after 1, 10, and 100 ALD  $\text{Al}_2\text{O}_3$  cycles, 10 ALD ZnS cycles, and 10 ALD ZnS cycles during exposure to humidified  $\text{O}_2$ .

These results demonstrate that precise control of the thickness of ALD coatings on  $\text{Li}_6\text{PS}_5\text{Cl}$  powders provides a number of significant benefits to the chemical stability of these materials. Specifically, ALD coatings improve the stability of argyrodites under both humid and oxidizing conditions, a benefit that is demonstrated for three distinct coating chemistries, suggesting there is likely a broad spectrum of coatings that can realize similar benefits to sulfide SSE stability against environmental conditions. Density functional theory (DFT) calculations further suggest favorable ionic and electronic transport properties through interfacial layers formed on coated materials that may facilitate Li-ion migration across the interface and improve interfacial contact, motivating detailed studies of the electrochemical properties of coated LPSCl.

**Electrochemical Properties of ALD-Coated LPSCl.** We assessed the impact of ALD coating on the electrochemical properties of LPSCl by measuring the ionic conductivity and Arrhenius activation energies of dense (>95%) pellets pressed from ALD-coated powders (coated by 1, 10 and 100 cycles of ALD  $\text{Al}_2\text{O}_3$ ) and compared these results with those obtained from the uncoated material (Figure XIII.16.3a-b). Surprisingly, we observe up to a factor of 2 increase in ionic conductivity for coated materials relative to uncoated materials ( $0.9 \pm 0.05 \times 10^{-3}$  vs.  $1.7 \pm 0.05 \times 10^{-3}$  S/cm at 25 °C for uncoated and 10 cycles ALD-coated materials, respectively). These changes in ionic conductivity are accompanied by slight decreases in the Arrhenius activation energies ( $0.31 \pm 0.03$  vs.  $0.28 \pm 0.02$  eV for uncoated vs. 10 cycles ALD-coated materials, respectively). We observe that increases in ionic conductivity are maximum for 10 ALD cycles, and further increases in coating thickness to 100 cycles result in a factor of 3 decrease in ionic conductivity relative to uncoated material, indicating there is an optimal coating thickness for enhancing the electrochemical properties of coated LPSCl powders. We hypothesize that the improved electrochemical properties, including both the room-temperature ionic conductivity and Arrhenius activation energy, are a combination of matrix and grain boundary effects due to a redistribution of the vacancies and interstitial sites (e.g., space-charge effects) across the interface between the ALD coating and the argyrodite.

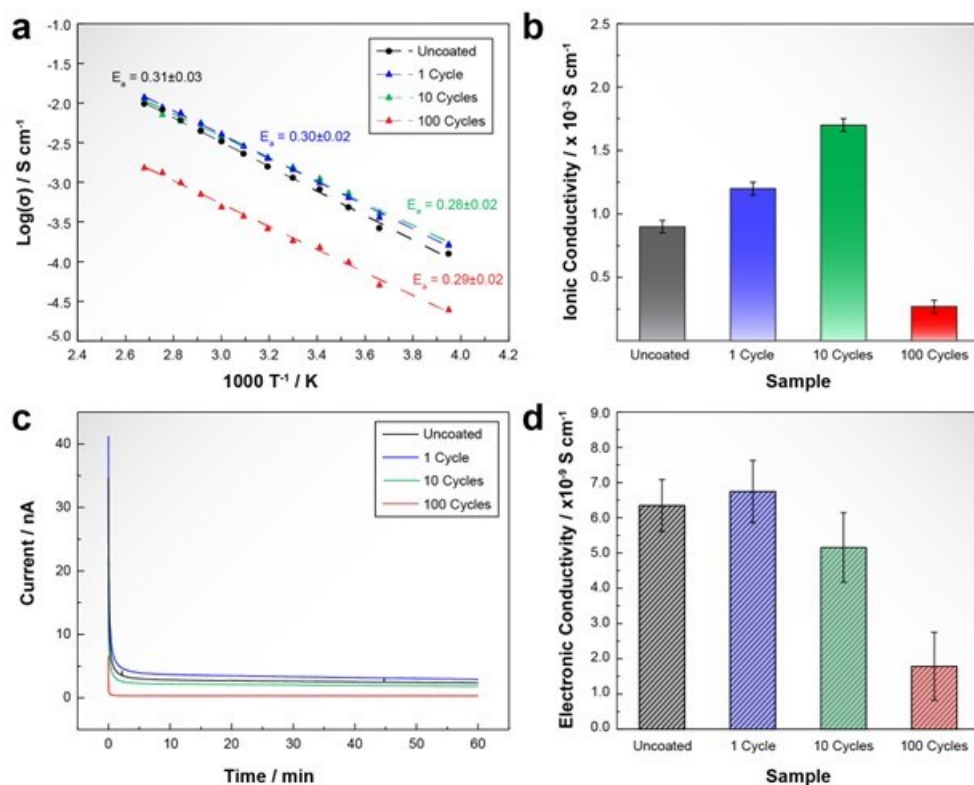


Figure XIII.16.3 (a) Arrhenius plots, (b) ionic conductivity at 25°C, (c) current-time curves (DC polarization at 200 mV, 25°C) and (d) electronic conductivity at 25°C for  $\text{Li}_6\text{PS}_5\text{Cl}$  pellets pressed from powders coated by 1, 10, and 100 ALD alumina cycles in comparison to pellets pressed from uncoated powders.

The measured improvements in ionic conductivity are coupled with a systematic decrease in electronic conductivity with increasing ALD coating thickness (Figure XIII.16.3c-d). The electronic conductivity of the powders was evaluated for each material in a symmetric cell configuration with a bias of 200 mV. These measurements reveal up to a factor of 3 *decrease* in electronic conductivity for LPSCl coated with 100 cycles ALD Al<sub>2</sub>O<sub>3</sub> relative to uncoated material ( $1.7 \pm 0.05 \times 10^{-9}$  vs.  $6.3 \pm 0.05 \times 10^{-9}$  S/cm at 25 °C, respectively). This indicates that tuning the thickness and chemistry of the ALD coating on the argyrodite electrolytes allows for one to not only control the Li<sup>+</sup> transport properties, but also to control undesired electron leakage through the solid electrolyte membrane.

Having established the significant benefit of ALD coatings to the bulk ionic and electronic properties of SSE pellets, we then assessed the performance of coated and uncoated materials in Li||Li symmetric cells to determine whether the favorable bulk properties translate to improved cycling performance. Critical current density (CCD) tests at 25 °C using uncoated LPSCl and LPSCl coated with 10 cycles of ALD Al<sub>2</sub>O<sub>3</sub> indicate that the uncoated argyrodite can cycle up to 0.6 mA/cm<sup>2</sup> while the coated argyrodite can cycle up to 0.8 mA/cm<sup>2</sup>. Extended cycling of uncoated materials at 0.5 mA cm<sup>-2</sup> and 1 mAh cm<sup>-2</sup> and 25°C (Figure XIII.16.4a) yields uniform stripping and plating up to ~115 cycles, together with an increase in the DC polarization of nearly 2×. At cycle 116, an overpotential is observed, indicative of non-uniform Li metal plating/stripping. Cycling of LPSCl materials coated with 10 cycles of ALD Al<sub>2</sub>O<sub>3</sub> yield significantly more stable behavior, with uniform plating and stripping to at least 150 cycles and a 2× lower DC polarization relative to uncoated material (

Figure XIII.16.4b). This significant improvement in the cycling performance is consistent with the bulk ionic/electronic property measurements discussed above. It is further consistent with X-ray photoelectron spectroscopy (XPS) measurements of interfacial stability performed in FY22, which detailed significant improvements to the chemical stability of coated LPSCl to contact with Li metal. We note that ALD Al<sub>2</sub>O<sub>3</sub> has been previously shown to improve Li metal wetting via conversion to the more ionically conducting LiAlO<sub>2</sub> under electrochemical cycling in conventional lithium-ion batteries, a result that is also consistent with our previously reported XPS results. We further note that prior demonstrations of ALD Al<sub>2</sub>O<sub>3</sub> coatings in solid-state systems were limited to improvements in charge transfer resistance at the SSE-Li *interface*. Pellets pressed from our coated materials exhibit improvements in their *bulk* properties, in addition to interfacial properties with Li metal, resulting in significant improvements to cycling performance. These results clearly demonstrate the multifaceted benefits to our ALD coating strategy, with significant implications for the extent to which bulk *and* interfacial properties of sulfide SSEs can be tuned by modifying the surface chemistry of precursor powders.

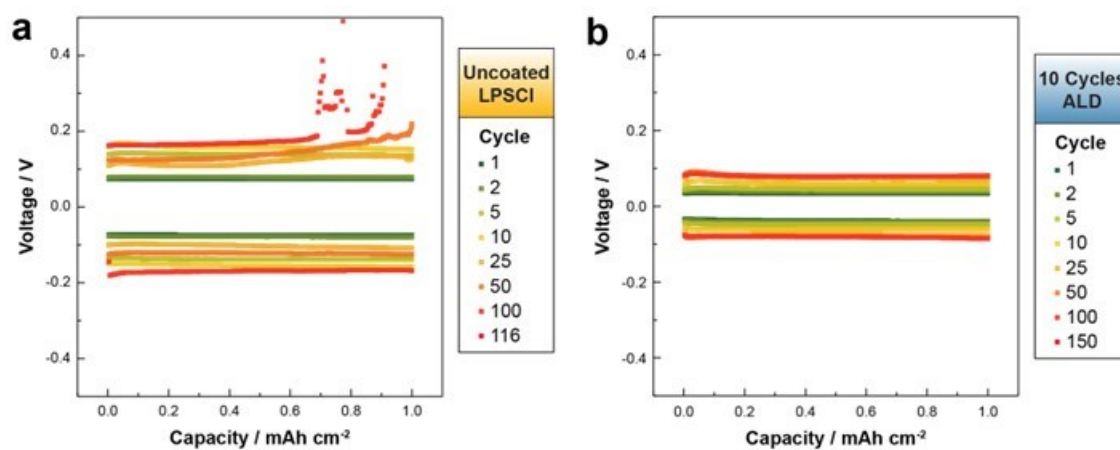


Figure XIII.16.4 Li || Li Symmetric cell cycling performance at an applied current density of 0.5 mA/cm<sup>2</sup> at 25 °C and 6 MPa stack pressure of (a) uncoated Li<sub>6</sub>PS<sub>5</sub>Cl and (b) Li<sub>6</sub>PS<sub>5</sub>Cl after 10 cycles of ALD Al<sub>2</sub>O<sub>3</sub>. Total Li thickness is 20 μm.

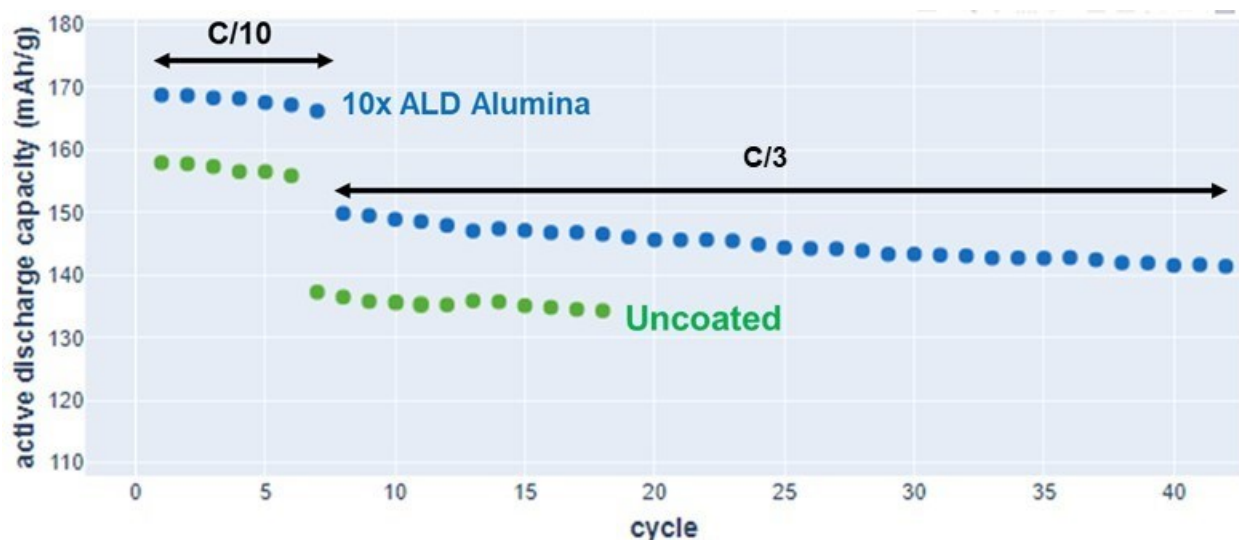


Figure XIII.16.5 Full cell cycling data comparing performance of LPSCI coated with 10 cycles ALD Al<sub>2</sub>O<sub>3</sub> (blue) with cells assembled from uncoated material (green).

**Full Cell Cycling Performance.** LPSCI materials were synthesized at ANL, and a fraction of material from the same synthesis batch was subsequently coated with 10 cycles of ALD Al<sub>2</sub>O<sub>3</sub>, as this coating thickness exhibits the optimal enhancement in materials properties (i.e., ionic/electronic conductivity and environmental stability, detailed above). Coated and uncoated materials were then sent to Solid Power, where they were assembled and cycled in a full cell as a catholyte and separator material. Specifically, the powders were processed into a pelletized separator with a lithium metal anode and a sprinkled cathode composite. The cathode composite contained LiNi<sub>0.6</sub>Mn<sub>0.2</sub>Co<sub>0.2</sub>O<sub>2</sub> (NMC 622) cathode active material, coated or uncoated SSE from ANL, and carbon. The cell was then cycled from 2.5-4.2V at 45°C. A symmetrical charge/discharge rate of C/10 was used for the first 6 cycles and then increased to C/3 (

Figure XIII.16.5). The results indicate significant improvements in performance for cells assembled from coated materials as compared to uncoated materials, with improved capacity, regardless of rate, as well as improved first cycle efficiency (FCE, Table XIII.16.1). Specifically, cells assembled from coated materials exhibit up to a ~10% improvement in discharge capacity relative to uncoated materials (150 vs. 138 mAh g<sup>-1</sup> at C/3). Equally, if not more significant is the increased FCE of 91.4 vs. 85.9% for coated vs. uncoated materials, respectively. This is consistent with the improved stability of ALD-coated LPSCI against Li metal and, in combination with the improved discharge capacity, suggests that these materials have improved stability against NMC 622 as well. This improved stability is corroborated by the observation of overall very similar total cell impedance as a function of cycle number for cells assembled using coated vs. uncoated material (Figure XIII.16.6). Overall, these data highlight a significant benefit to full cell performance from the ALD-coated materials. These results are particularly significant given that we have yet to optimize the coating chemistry to better match the chemistry of the cathode active material, suggesting that there is significant room to further improve the performance of full cells incorporating ALD-coated SSE materials as catholytes.

Table XIII.16.1 Summary of Relevant Performance Metrics for Full Cells Assembled Using Coated and Uncoated LPSCI.

Catholyte Coating	C/10, First Discharge Capacity (mAh g <sup>-1</sup> )	First Cycle Efficiency (%)	C/3 Discharge Capacity (mAh g <sup>-1</sup> )
Uncoated	158	85.9	137
10x ALD Al <sub>2</sub> O <sub>3</sub>	169	91.4	150

We will build on these results to further explore the interplay between SSE coating chemistry and full cell performance, both from the perspective of improving accessible capacity and capacity retention, as well as improving processability for scale-up. Longer-term cycling measurements will be performed in order to monitor changes in cell impedance during extended cycling that may reveal additional benefits to cell lifetime and/or capacity retention. Furthermore, optimization of the particle size distribution of ANL-synthesized LPSCI should yield additional improvements in overall cell performance, regardless of coating chemistry. Finally, co-optimization of the coating chemistry to improve the processability of coated SSEs in scalable manufacturing methods (e.g., slurry casting) will further enable the integration of these coated materials with roll-to-roll processing capabilities at Solid Power.

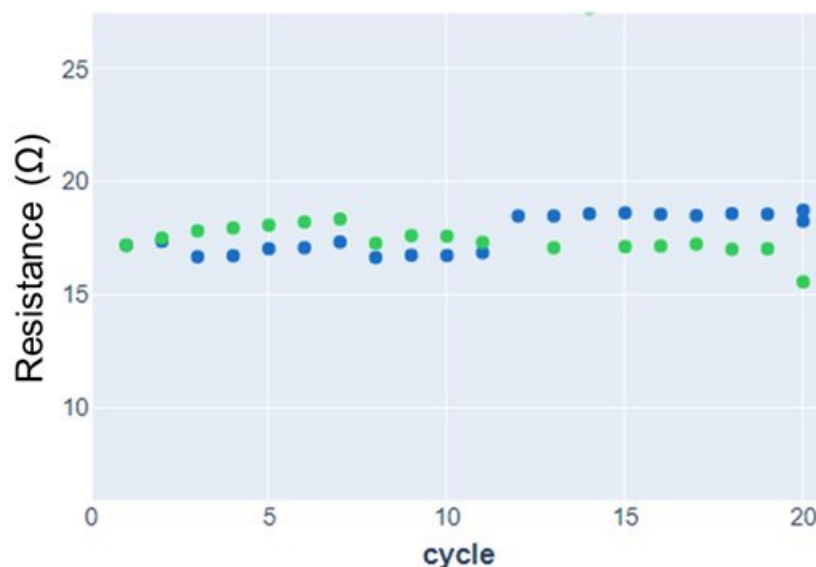
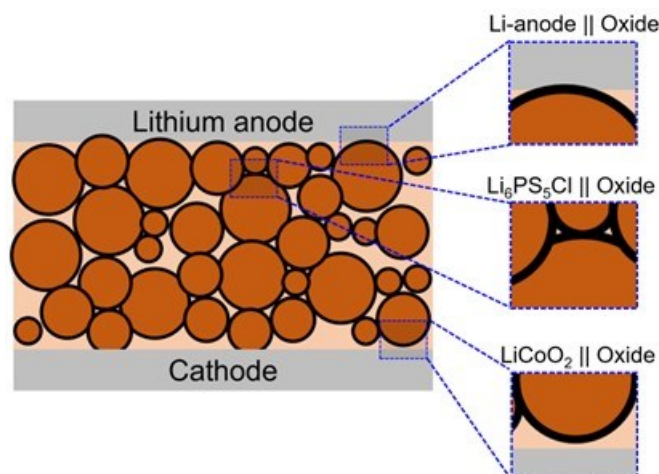


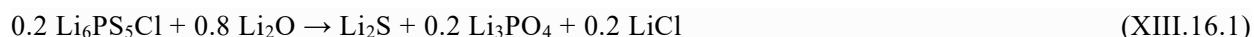
Figure XIII.16.6 Total cell impedance as a function of cycle number for full cells assembled from uncoated (green) and 10x ALD Al<sub>2</sub>O<sub>3</sub>-coated LPSCI, corresponding to the cycling data in Figure XIV.21.5.

**Computational Evaluation of Candidate Coating Chemistries.** Given the myriad benefits of ALD alumina coatings to the (electro)chemical performance of LPSCI detailed above, it is likely that additional ALD coating chemistries can provide similar or enhanced benefits. In order to effectively and efficiently determine which coatings may provide benefits, however, it is necessary to leverage computational methodologies to screen the reactivity of candidate coating materials towards active electrodes, as well as to LPSCI itself. This will enable detailed assessments of which candidate chemistries will likely form beneficial (or problematic) interfacial species that can enhance (or degrade) battery performance, narrowing the pool of materials to be synthesized for detailed experimental exploration. To this end, we used DFT calculations to model reactivity at three distinct interfaces (Figure XIII.16.7): 1) electrolyte || coating, 2) anode || coating and 3) cathode || coating. Among the materials chosen for this study, we use Li<sub>6</sub>PS<sub>3</sub>Cl argyrodite as the electrolyte, various types of experimentally synthesizable oxides, in particular those suitable for ALD, as electrolyte coatings, while metallic Li and LiCoO<sub>2</sub> serve as the anode and cathode materials, respectively.



**Figure XIII.16.7** Interfaces modeled in this work. The left image shows the all-solid-state battery containing  $\text{Li}_6\text{PS}_5\text{Cl}$  electrolyte powders coating with ALD-grown oxides. The three smaller schematics on the right are the magnified representation of the Li-anode || Coating and  $\text{Li}_6\text{PS}_5\text{Cl}$  || Coating and  $\text{LiCoO}_2$ -cathode || Coating interfaces.

The thermodynamic stability of electrolyte-coating interfaces against decomposition reactions was modeled by calculating the reaction enthalpy (denoted as  $\Delta E$ , computed using DFT energies at 0 K) for all possible reactions. One such reaction between  $\text{Li}_6\text{PS}_5\text{Cl}$  and  $\text{Li}_2\text{O}$  is shown in Equation XIV.21.1, with  $\Delta E = -0.278$  eV/atom.



Thermodynamic reaction data for Eq. XIII.16.1 were obtained from the Materials Project database. Analogously, for each oxide chemistry, we calculate several possible types of reactions with the LPSCl electrolyte. Depending on the stoichiometry or the relative concentrations of the electrolyte and oxide, each electrolyte-oxide pair can have multiple reactions. Table XIII.16.2 lists the electrolyte-oxide reactions with the lowest value of reaction enthalpy  $\Delta E$ . The three most stable oxides according to this criterion are  $\text{Al}_2\text{O}_3$ ,  $\text{ZrO}_2$ , and  $\text{TiO}_2$ . These correspond to elements with valence electronic configuration  $s^2p^1$  or early transition-metals ( $d^2$ ). Generally, it is expected that elements with a single s-orbital valence electron or high d-orbital occupancies result in very reactive electrolyte-oxide interfaces.

**Table XIII.16.2** The Three Most Stable LPSCl || Oxide Interfaces, with the Lowest Driving Forces for Interface Reactions.

Coating	$\text{Li}_6\text{PS}_5\text{Cl}$    Coating reaction	$\Delta E$ (eV/atom)
$\text{Al}_2\text{O}_3$	$0.2 \text{Li}_6\text{PS}_5\text{Cl} + 0.8 \text{Al}_2\text{O}_3 \rightarrow 0.2 \text{Li}_3\text{PS}_4 + 0.2 \text{LiCl} + 0.1 \text{LiAlSi}_2 + 0.3 \text{LiAl}_5\text{O}_8$	-0.044
$\text{ZrO}_2$	$0.3333 \text{Li}_6\text{PS}_5\text{Cl} + 0.6667 \text{ZrO}_2 \rightarrow 0.3333 \text{Li}_2\text{S} + 0.6667 \text{ZrS}_2 + 0.3333 \text{Li}_3\text{PO}_4 + 0.3333 \text{LiCl}$	-0.097
$\text{TiO}_2$	$0.3333 \text{Li}_6\text{PS}_5\text{Cl} + 0.6667 \text{TiO}_2 \rightarrow 0.1111 \text{Li}_4\text{TiS}_4 + 0.2222 \text{Li}(\text{TiS}_2)_2 + 0.1111 \text{TiS}_3 + 0.3333 \text{LiCl} + 0.3333 \text{Li}_3\text{PO}_4$	-0.126

The stability of the anode-coating interface was modeled similar to the procedure described above, with a specific focus on the three coating chemistries listed in Table XIII.16.2. For each oxide type ( $\text{Al}_2\text{O}_3$ ,  $\text{ZrO}_2$ , and  $\text{TiO}_2$ ), enthalpy changes at 0 K were computed for all possible reactions between the oxide and Li metal, which is the anode in our study. Table XIII.16.3 lists these reactions and their  $\Delta E$  values. In case of multiple



reactions for an oxide chemistry, the table shows the reaction with the largest  $\Delta E$  value. It is evident that due to the higher reactivity of metallic Li, the reaction enthalpies at the Li-anode || coating interface are 5-10 times larger than the reaction enthalpies at the  $\text{Li}_6\text{PS}_5\text{Cl}$  || coating interface. Also, the stability order is not the same at both interfaces. The potential benefit of coating LPSCl with oxides is evident by comparing against the interface between the bare electrolyte and anode. For  $\text{Li}_6\text{PS}_5\text{Cl}$  || Li,  $\Delta E = -0.539$  eV/atom with  $\text{Li}_3\text{P}$ ,  $\text{LiCl}$  and  $\text{Li}_2\text{S}$  formed as the reaction products. This enthalpy is 2-3 times larger than the values reported in Table XIII.16.3.

**Table XIII.16.3 Reaction Thermodynamics at Li || Oxide Interfaces, with a Specific Focus on Oxide Chemistries in an Adjacent Table.**

Coating	Li-anode    Coating reaction	$\Delta E$ (eV/atom)
$\text{ZrO}_2$	$0.6122 \text{ Li} + 0.3878 \text{ ZrO}_2 \rightarrow 0.06122 \text{ Zr}_3\text{O} + 0.102 \text{ Li}_6\text{Zr}_2\text{O}_7$	-0.185
$\text{Al}_2\text{O}_3$	$0.6667 \text{ Li} + 0.3333 \text{ Al}_2\text{O}_3 \rightarrow 0.1667 \text{ LiAl} + 0.5 \text{ LiAlO}_2$	-0.220
$\text{TiO}_2$	$0.6316 \text{ Li} + 0.3684 \text{ TiO}_2 \rightarrow 0.1053 \text{ Ti}_2\text{O} + 0.1579 \text{ Li}_4\text{TiO}_4$	-0.357

Finally, Table XIII.16.4 shows the reaction enthalpies for the  $\text{LiCoO}_2$  || coating interface. There are no known reactions between the  $\text{LiCoO}_2$  (LCO) and zirconia. LCO reacts with titania and alumina to form complex Ti-Co and Al-Co oxides. We note that additional calculations are required for other oxide coating chemistries for a complete evaluation of the stability of the LCO || coating interface. Alumina, zirconia, and titania were selected since they are found to be compatible with LPSCl.

**Table XIII.16.4 Reaction Thermodynamics at  $\text{LiCoO}_2$  || Oxide Interfaces, with a Specific Focus on Oxide Chemistries in a Previous Table.**

Coating	$\text{LiCoO}_2$ -cathode    Coating reaction	$\Delta E$ (eV/atom)
$\text{ZrO}_2$	No reaction	---
$\text{TiO}_2$	$0.5 \text{ LiCoO}_2 + 0.5 \text{ TiO}_2 \rightarrow 0.167 \text{ Li}(\text{CoO}_2)_2 + 0.167 \text{ Li}_2\text{Ti}_3\text{CoO}_8$	-0.012
$\text{Al}_2\text{O}_3$	$0.333 \text{ LiCoO}_2 + 0.667 \text{ Al}_2\text{O}_3 \rightarrow 0.111 \text{ Li}(\text{CoO}_2)_2 + 0.111 \text{ Al}_2\text{CoO}_4 + 0.222 \text{ LiAl}_5\text{O}_8$	-0.03

The results are corroborated by our previous results that coating LPSCl electrolyte powders with ALD alumina improve chemical stability of coated LPSCl upon  $\text{O}_2$ /humidified  $\text{O}_2$  exposure as well as its stability against Li metal in symmetric Li || Li cells. Tables XIV.21.2 and XIV.21.3 show that  $\text{Al}_2\text{O}_3$  coating has small thermodynamic driving forces for reactions with LPSCl and Li. Overall, our screening provides guidance to our ALD coating strategy, suggesting additional candidate compositions for in-depth computational studies and experimental modification of sulfide SSE powders. We plan to build on these results by investigating the extent to which different coating chemistries can realize benefits to bulk LPSCl properties, as well as to the stability of coatings against cathode materials and the performance of full cells containing coated SSE materials. Computational studies of the reactivity of LPSCl with ALD precursors are also of interest to better understand how best to optimize the ALD processing and resulting coating quality for a given chemistry.

## Conclusions

Utilizing a surface science-based, integrated experimental-theoretical approach, we have demonstrated the significant benefits of our ALD powder coating strategy to the environmental stability and electrochemical performance of argyrodite-type sulfide-based SSEs. Specifically, multiple ALD coating chemistries have been shown to significantly stabilize LPSCl powders to environmental exposure, with  $\geq 50\%$  lower observed weight gains upon exposure to humidified  $\text{O}_2$  for coated vs. uncoated materials. We have further demonstrated that coatings with optimized thickness can realize up to a 2x increase in the ionic conductivity and up to a 3x decrease in the electronic conductivity. These improvements in electrochemical properties result in dramatic improvements to the cycling performance of Li||Li symmetric cells that utilize ALD-coated powders as the

separator, as well as to the accessible capacity of Li||NMC622 full cells that utilize ALD-coated powders as both separator and catholyte. DFT calculations have enabled the screening of additional candidate ALD coating chemistries across a number of metrics for stability, suggesting promising directions for experimental exploration to further improve the performance of ALD-coated SSEs in symmetric and full cell configurations. Leveraging our combined experimental-theoretical approach, we anticipate the continued development of new coating chemistries, and, based on our promising results in symmetric and full cells, we plan to begin optimizing and scaling up one to two selected materials to prepare our approach for integration into realistic, roll-to-roll compatible manufacturing processes for pouch cell assembly.

### Key Publications

1. Multifunctional Coatings on Sulfide-Based Solid Electrolyte Powders with Enhanced Processability, Stability, and Performance for Solid-State Batteries. Hood, Z. D.; Mane, A. U.; Sundar, A.; Tepavcevic, S.; Zapol, P.; Eze, U. D.; Adhikari, S. P.; Lee, E.; Sterbinsky, G. E.; Elam, J. W.; Connell, J. G. *Advanced Materials* 35, 2023, 2300673. <https://doi.org/10.1002/adma.202300673>
2. **OXISULFIDE PROTECTIVE LAYERS ON SOLID STATE ELECTROLYTE.** Zapol, P.; Sundar, A.; Connell, J. G.; Elam, J. W.; Mane, A.; Hood, Z. D. Invention Disclosure ANL-IN-23-028.

### References

1. Y. Nikodimos, C.-J. Huang, B. W. Taklu, W.-N. Su, B. J. Hwang, *Energy Environ. Sci.* **2022**, 15, 991.
2. Banik, Y. Liu, S. Ohno, Y. Rudel, A. Jiménez-Solano, A. Gloskovskii, N. M. Vargas-Barbosa, Y. Mo, W. G. Zeier, *ACS Appl. Energy Mater.* 2022, 5, 2045.
3. Internal presentation from the VTO Solid-State Review Meeting in Berkeley, CA on August 17 -18, 2022.

### Acknowledgements

The PI is grateful to his collaborators Collin Becker (Solid Power), Josh Buettner-Garrett (Solid Power), Jeffery Elam (ANL), Zachary Hood (ANL), Taewoo Kim (ANL), Eungje Lee (ANL), Anil Mane (ANL), Jason Roberts (Solid Power), Aditya Sundar (ANL), Sanja Tepavcevic (ANL), Peter Zapol (ANL) and Pu Zhang (Solid Power), for materials synthesis, data collection and analysis, and their many other valuable contributions to the project.

## XIII.17 Thick Selenium-Sulfur Cathode Supported Ultra-thin Sulfide Electrolytes for High-energy All-solid-state Lithium Metal Batteries (ANL)

### Guiliang Xu, Principal Investigator

Argonne National Laboratory  
9700 South Cass Avenue  
Lemont, IL 60439  
E-mail: [xug@anl.gov](mailto:xug@anl.gov)

### Simon Thompson, DOE Technology Development Manager

U.S. Department of Energy  
E-mail: [Simon.Thompson@ee.doe.gov](mailto:Simon.Thompson@ee.doe.gov)

Start Date: October 1, 2022

End Date: September 30, 2023

Project Funding (FY23): \$500,000

DOE share: \$500,000

Non-DOE share: \$0

### Project Introduction

Lithium-sulfur (Li-S) battery constitute a serious contender for energy storage application because of its high theoretical energy density ( $\sim 2600$  Wh/kg) and the nature abundance of sulfur.[1] All solid-state lithium/sulfur batteries (ASSLSBs) using solid-state electrolytes (SSEs) can effectively eliminate the polysulfide shuttle and stabilize Li metal anode to improve the cycling stability and safety.[2] However, the lack of SSEs that can improve their power characteristics and energy densities significantly hinders their implementation. Two essential criteria for SSEs to achieve 500 Wh/kg are (1) comparable RT ionic conductivity ( $>10^{-2}$  S/cm) with liquid electrolytes that can boost the utilization of cathode active materials; and (2) thin and lightweight that can reduce the percentage of inactive components in the whole cells. Nevertheless, the fabrication of ultra-thin and mechanically stable sulfides SSEs remain technically challenging.[3] In particular, most sulfides SSEs are not stable under ambient condition, limiting the conventional processing approaches.[4] Moreover, stabilization of the SSE/cathode interface and the SSE/Li anode interface to maintain intimate solid-solid contact and negligible interfacial resistance during charge/discharge remain formidable challenge.[5]

The team led by Dr. Guiliang Xu at Argonne National Laboratory is focusing on the development of ultra-thin sulfides SSEs with high RT ionic conductivity and high air/mechanical/electrochemical stability as well as intimate solid-solid contact when coupling with high-capacity Li metal anode and Se-S cathode.

### Objectives

The objective of this project is to develop ultra-thin ( $< 30$   $\mu\text{m}$ ) sulfide SSEs with high room temperature ionic conductivity ( $> 10^{-2}$  S/cm) and high chemical/mechanical/electrochemical stability, and further integrate them with lithium metal and high-loading selenium-doped sulfur (Se-S) cathodes through rational interface engineering to develop all-solid-state Li-S batteries (ASSLSBs) with high cell energy density of  $> 500$  Wh/kg and stable cycle life of  $> 300$  cycles at a current density of  $> 1$  mA/cm<sup>2</sup>.

### Approach

The thickness and chemical/interfacial stability of sulfide SSEs are the critical challenges for energy density, cycle life, and mass production of all-solid-state Li-S pouch cells. The team will combine innovative material design, electrode architecture fabrication, and advanced diagnostics tools to address these challenges. Specifically, the approaches include: (1) improving air stability and ionic conductivity of sulfides through synthetic control and cation/anion doping, (2) fabrication of flexible thick SeS cathode supported thin sulfide electrolytes to ensure intimate contact and increase the energy density, (3) stabilizing Li-metal/sulfide electrolytes interface via interlayer and additives design to increase the critical current density (CCD) of lithium stripping/plating, (4) advanced Li-S pouch cell design, and (5) multiscale advanced diagnostic such as

in situ X-ray diffraction (XRD), X ray absorption spectroscopy (XAS), X-ray tomography, and focused ion beam-scanning electron microscopy (FIB-SEM) to understand and overcome the degradation pathways.

#### TEAM MEMBER:

- Processing of sulfides: Dr. Jieun Lee (CSE, ANL)
- Synthesis of sulfides: Dr. Chen Zhao (CSE, ANL), Dr. Xingkang Huang (UChicago)
- Synchrotron X-ray diffraction: Dr. Dongzhou Zhang, Dr. Wenqian Xu (APS of ANL)
- Synchrotron X-ray absorption spectroscopy: Dr. Cheng-Jun Sun (APS of ANL)
- Electron microscopy: Dr. Yuzi Liu (CNM of ANL)
- X-ray tomography: Dr. Dula (Dilworth) Parkinson (ALS of LBNL)

## Results

### *Developing Br/O co-doped $\text{Li}_{1-x}\text{PS}_{5-x-y}\text{O}_y\text{Br}_{1+x}$ solid electrolyte with high room temperature ionic conductivity*

Last year, we used in situ synchrotron X-ray diffraction (XRD) to probe the solid state synthesis of  $\text{Li}_{1-x}\text{PS}_{5-x-y}\text{O}_y\text{Br}_{1+x}$  solid electrolyte and evaluated the effect of temperature, dopants, holding time and cooling process on the crystal and local structures of final products. Following these guidance, we have synthesized Br/O co-doped  $\text{Li}_{6-x}\text{PS}_{5-x-y}\text{O}_y\text{Br}_{1+x}$  through synthetic control and evaluated their crystal structures, morphologies, ionic conductivity, and critical current density of Li/Li stripping/plating.

Figure XIII.17.1a shows the XRD pattern of  $\text{Li}_{5.5}\text{PS}_{4.5}\text{Br}_{1.5}$  synthesized at 500 °C for 12h with natural cooling, which is mostly in accordance with the standard XRD pattern of  $\text{Li}_6\text{PS}_5\text{Br}$ . Nevertheless, XRD peaks belong to LiBr impurity can be also seen. When introducing oxygen dopants into  $\text{Li}_{5.5}\text{PS}_{4.5}\text{Br}_{1.5}$ , the LiBr impurity was decreased and no impurity peaks belong to  $\text{Li}_2\text{O}$  can be found in the  $\text{Li}_{5.5}\text{PS}_{4.4}\text{O}_{0.1}\text{Br}_{1.5}$  at 500 °C, indicating that oxygen has been successfully doped into the lattice (Figure XIII.17.1b). However, when calcinated at a higher temperature of 600 °C, the amount of LiBr impurity was significantly increased (Figure XIII.17.1c). The results highlight the importance of temperature control.

We further characterized their morphologies by SEM. As shown in Figure XIII.17.1d, the as-prepared  $\text{Li}_{5.5}\text{PS}_{4.5}\text{Br}_{1.5}$  shows secondary aggregates that are further comprising of primary particles with hundreds of nanometers. After introducing oxygen, the size of primary particles was increased (Figure XIII.17.1e and 1f), which can impact their ionic conductivity.

Electrochemical impedance spectroscopy was used to measure the room temperature ionic conductivity of these three electrolytes. The pressure to fabricate the pellets (10 mm diameter) was 400 MPa and the corresponding thickness is ~ 800  $\mu\text{m}$ . During testing, the stack pressure was controlled at 20 MPa. As shown in Figure XIII.17.2a, the ionic conductivity of  $\text{Li}_{5.5}\text{PS}_{4.5}\text{Br}_{1.5}$ ,  $\text{Li}_{5.5}\text{PS}_{4.4}\text{O}_{0.1}\text{Br}_{1.5}@500\text{ }^\circ\text{C}$  and  $\text{Li}_{5.5}\text{PS}_{4.4}\text{O}_{0.1}\text{Br}_{1.5}@600\text{ }^\circ\text{C}$  were 0.45, 0.40 and 0.32 mS/cm. The difference could come from both LiBr impurity and particle size. We have used the same process to measure the ionic conductivity of commercial  $\text{Li}_6\text{PS}_5\text{Cl}$  material from vendor. As shown in Figure XIII.17.2b, the ionic conductivity of commercial  $\text{Li}_6\text{PS}_5\text{Cl}$  was measured to be 0.4 mS/cm, which is similar to our materials.

Li stripping/plating behaviour of  $\text{Li}_{5.5}\text{PS}_{4.5}\text{Br}_{1.5}$  and commercial  $\text{Li}_6\text{PS}_5\text{Cl}$  was further conducted. The cells were tested at continuously increased current densities for 1 hour per stripping or plating process with a stack pressure of 20 MPa. As shown in Figure XIII.17.2c and 2d, commercial  $\text{Li}_6\text{PS}_5\text{Cl}$  shows slightly higher critical current density of 1.4 mA/cm<sup>2</sup> than that of  $\text{Li}_{5.5}\text{PS}_{4.5}\text{Br}_{1.5}$  (1.0 mA/cm<sup>2</sup>).

The optimization on the solid-state synthesis of  $\text{Li}_{6-x}\text{PS}_{5-x-y}\text{O}_y\text{Br}_{1+x}$  takes quite a long time. And we will further investigate the effect of quenching process, ball milling time/speed and ratio of Br/O dopants. We will continue to optimize these process to increase the ionic conductivity/critical current densities.

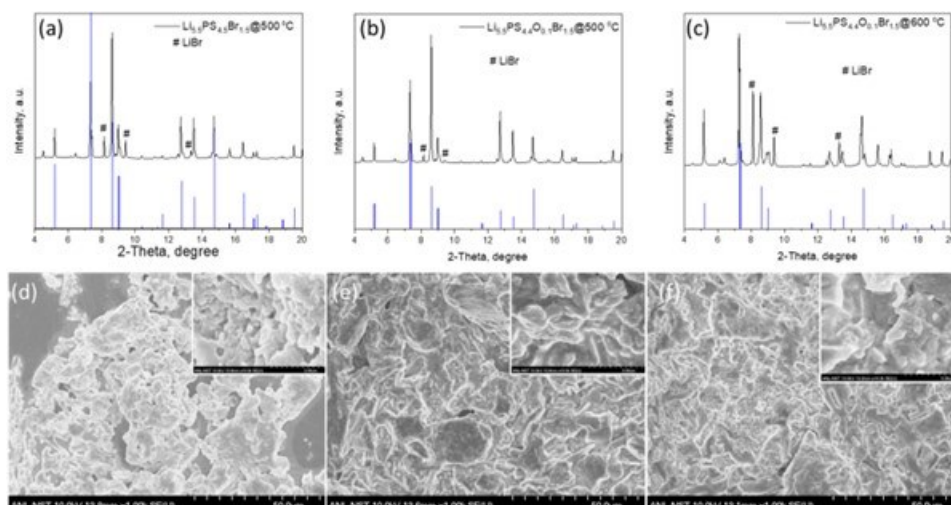


Figure XIII.17.1 Synchrotron XRD patterns of (a)  $\text{Li}_{5.5}\text{PS}_{4.5}\text{Br}_{1.5}$  synthesized at 500 °C for 12h,  $\text{Li}_{5.5}\text{PS}_{4.4}\text{O}_{0.1}\text{Br}_{1.5}$  synthesized at (b) 500 °C for 12h and (c) 600 °C for 12h. SEM images of (c)  $\text{Li}_{5.5}\text{PS}_{4.5}\text{Br}_{1.5}$  synthesized at 500 °C for 12h,  $\text{Li}_{5.5}\text{PS}_{4.4}\text{O}_{0.1}\text{Br}_{1.5}$  synthesized at (d) 500 °C for 12h and (e) 600 °C for 12h. Insets in (d-f) shows the corresponding high magnification SEM images.

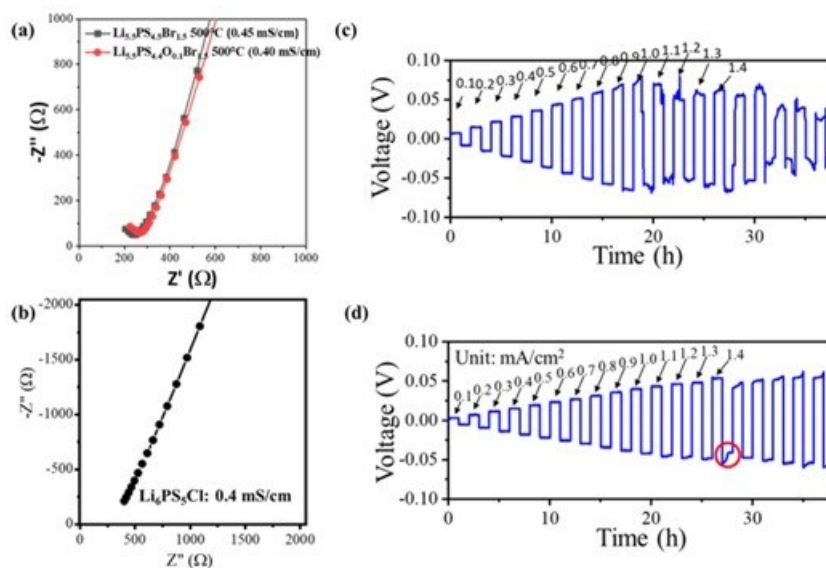


Figure XIII.17.2 (a) Room temperature ionic conductivity measurement of  $\text{Li}_{5.5}\text{PS}_{4.5}\text{Br}_{1.5}$  synthesized at 500 °C for 12h,  $\text{Li}_{5.5}\text{PS}_{4.4}\text{O}_{0.1}\text{Br}_{1.5}$  synthesized at 500 °C for 12h and 600 °C for 12h. (b) Room temperature ionic conductivity measurement of commercial  $\text{Li}_6\text{PS}_5\text{Cl}$  from vendor. Lithium stripping/plating behavior of symmetrical cells using solid electrolytes of  $\text{Li}_{5.5}\text{PS}_{4.5}\text{Br}_{1.5}$  synthesized at 500 °C for 12h (c) and commercial  $\text{Li}_6\text{PS}_5\text{Cl}$  (d). The current densities were increased gradually from 0.1  $\text{mA}/\text{cm}^2$  to 1.4  $\text{mA}/\text{cm}^2$ .

#### Probing the moisture stability of sulfide solid electrolyte by in situ synchrotron X-ray diffraction

Another challenge of argyrodites sulfide electrolytes is their inherent instability against moisture, which will not only undergo severe morphology changes (color, physical form), but also release toxic  $\text{H}_2\text{S}$  together with severe crystal structure change. As a result, the ionic conductivity of argyrodite electrolytes tend to decrease significantly after exposure to moisture. And the synthesis and processing of argyrodite electrolytes are now mostly conducted inside glovebox and dry room, which increases the manufacture cost of this electrolytes.

Through Br and O co-doping, we are aiming to achieve a balanced ionic conductivity and moisture stability. We have used in situ synchrotron XRD to track the phase transition of the developed solid electrolytes at

different levels of humidity to evaluate their moisture stability. However, the physical form change (solid to gel) of the sulfide electrolytes after exposure to moisture will cause the collapse of the sulfide electrolytes powder or pellet, making it move out of the beam center and hence losing the XRD signal. To address this issue, we have designed a new set up shown in Figure XIII.17.3, in which we have loaded the sulfide electrolyte pellet into the bottom of a sealed pouch bag. An observation window sealed with Kapton tape was created to allow better identification of the sample position. An inlet tubing was put close to the pellet while the outlet was on the top of the pouch bag to make sure the inlet gas has good contact with the pellet. The gas was a mixture of dry helium and wet helium, which can achieve different humidity by controlling the flow rates. Currently, we can control the humidity from 10% to 90%. Meanwhile, synchrotron XRD can be collected when the samples are exposed to different humidity.

Figure XIII.17.4 shows the XRD patterns of the synthesized  $\text{Li}_{5.5}\text{PS}_{4.5}\text{Br}_{1.5}$  and  $\text{Li}_{5.5}\text{PS}_{4.4}\text{O}_{0.1}\text{Br}_{1.5}$  electrolyte under 20% humidity. The time interval of XRD patterns was 1 minute. As verified by the increase of XRD peaks highlighted by the blue boxes, the  $\text{Li}_{5.5}\text{PS}_{4.5}\text{Br}_{1.5}$  without oxygen doping exhibited rapid phase transition after exposure to moisture for only 5 minutes. By sharp contrast, the  $\text{Li}_{5.5}\text{PS}_{4.4}\text{O}_{0.1}\text{Br}_{1.5}$  did not show visible phase transition till 40 minutes. Such results demonstrate that oxygen doping can significantly improve the moisture stability of the Argyrodite electrolytes.

In brief, we have established an approach to evaluate the moisture stability of Argyrodite electrolytes and show that Br and O doping could achieve a balanced ionic conductivity and moisture stability.

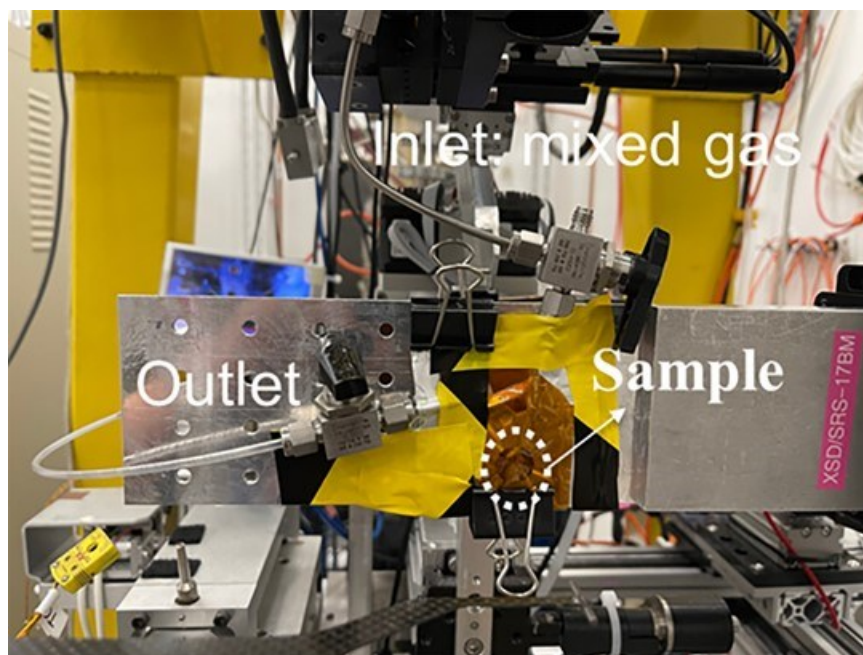


Figure XIII.17.3 Image for the in situ synchrotron XRD set up for the measurement of moisture stability of solid state electrolytes.

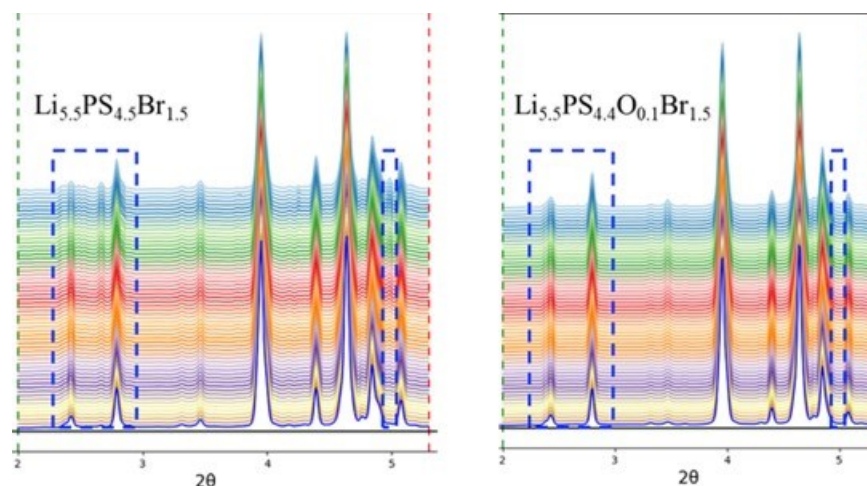
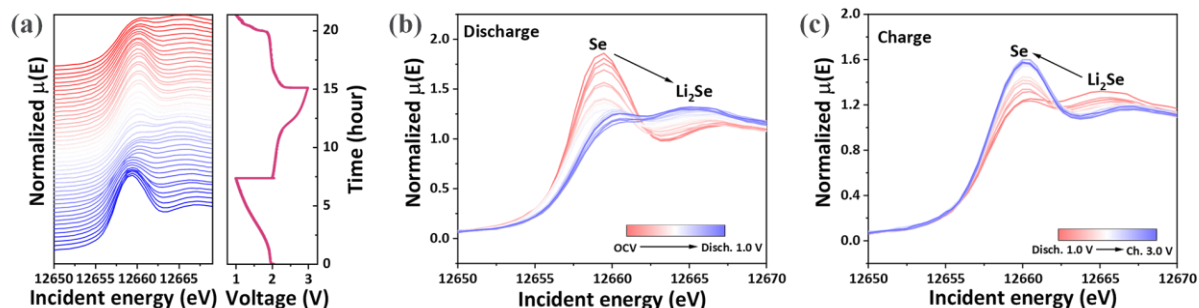


Figure XIII.17.4 Synchrotron XRD patterns of the synthesized  $\text{Li}_{5.5}\text{PS}_{4.4}\text{O}_{0.1}\text{Br}_{1.5}$  and  $\text{Li}_{5.5}\text{PS}_{4.5}\text{Br}_{1.5}$  electrolyte under 20% humidity. The time interval of XRD patterns was 1 minute.

#### ***Probing the redox mechanism of all-solid-state lithium-sulfur batteries by in situ X-ray absorption spectroscopy***

To understand the redox mechanism during charge/discharge, we have conducted in situ synchrotron X-ray absorption near edge spectroscopy (XANES) to investigate the (de) lithiation mechanism of all-solid-state Li-Se batteries. XANES is sensitive to the electronic changes and/or oxidation state of all the atoms of the targeted type in the samples involves liquid and solid, as well as crystalline and/or amorphous phases, which is ideal tool to probe if there is formation of soluble polysulfides or polyselenides intermediates during cycling. Se cathode was used to differentiate the sulfur signal from sulfide solid electrolytes. The in situ all-solid-state Li-Se cell was fabricated using ANL's composite Se cathode,  $\text{Li}_6\text{PS}_5\text{Cl}$  sulfide solid electrolyte and Li anode; synchrotron Se K-edge XANES was conducted during the charge/discharge process.

Figure XIII.17.5a shows the in situ XANES data for the discharge and charge process of composite Se cathode at 0.1 C ( $1\text{C} = 675\text{ mA g}^{-1}$ ) in the first and half cycle. The voltage profile is also displayed and correlated with the evolution of the XANES data. For example, the inflection point observed in the contour plot of the XANES data coincides well with the critical point in the fully discharge state. The apparent symmetry of the data set emphasizes that the discharging and charging proceed through a reversible sequence of reactions in the first cycle. The typical Se K-edge XANES spectra during discharge and charge process are shown in Figure XIII.17.5b and 5c, respectively. The Se K-edge absorption energy before cycling matched well with that of Selenium powder (12658 eV), which is assigned to the transition of Se 1s core electrons to the unoccupied 4p state. Upon discharge, the absorption peaks belonging to selenium have a relatively large decrease, while the signal for  $\text{Li}_2\text{Se}$  gradually increased. Nevertheless, we do not observe a significant Se K-edge shift at the end of discharge process, which is consistent with our previous results in the carbonate-based and fluorinated ether-based electrolytes that are free of shuttle effect. The results indicate that there is no formation of soluble polyselenides during charge/discharge of all-solid-state Li-Se batteries. Therefore, a solid-solid (de) lithiation mechanism is confirmed, which can be further validated by the single voltage plateau in the voltage profiles. Upon charge, we can see the intensity of Se gradually recovered, corresponding to a reversible (de) lithiation process. This understanding is important for the future design of composite cathode materials for all-solid-state Li-S and Li-Se batteries.



**Figure XIII.17.5** (a) In situ Se K-edge X-ray absorption near edge spectroscopy (XANES) of composite Se cathode during charge/discharge of all-solid-state Li-Se cells using Li metal anode and  $\text{Li}_6\text{PS}_5\text{Cl}$  sulfide solid electrolytes at C/10 ( $1\text{C}=675\text{ mA g}^{-1}$ ). Selected Se XANES of composite Se cathode during (b) discharge and (c) charge process.

#### **Developing thin sulfide solid electrolytes through electrospinning**

In FY23, we also started to explore the fabrication of thin sulfide solid state electrolytes. Our idea is to use electrospinning to fabricate polymer scaffold on top of sulfur electrode, and then infuse sulfides solution to form a thin solid electrolyte layer. Our first step is to identify a polymer with high elasticity to improve the mechanical integrity of the thin solid electrolyte.

Spandex has attracted our attention because of its extraordinary elasticity, which comes from its bimodal segments (both soft and hard). The soft segments allow the entire polymer matrix to be stretchable, while the hard segments mechanically sustain the overall network. It has been used as binder for various electrode materials such as Si anode and  $\text{LiNi}_x\text{Co}_y\text{Mn}_{1-x-y}\text{O}_2$  cathode in lithium-ion batteries. When used as scaffold in solid-state batteries, it not only improves the mechanical strength of the thin solid electrolyte membrane, but also helps to improve the cohesion between solid electrolytes particles and active material particles through hydrogen bonding.

Our group has set up in-house electrospinning capability for thin solid electrolyte development. We started with the optimization of electrospinning process (feeding rate, concentration of solutions, solvent/co-solvents) to obtain fine nanofiber network. Spandex is dissolved into different organic solvents to prepare solutions for electrospinning. The working voltage was set to 18 kV for all electrospinning experiments.

N-Methyl-2-pyrrolidone (NMP) solution was selected as the solvent to dissolve spandex given it has been widely used as binder for batteries. The concentration was controlled at 5 wt.%. The feeding rate has an influence on the evaporation rate of the electrospinning jet and thus significantly affects the morphology of the formed nanofibers. As shown in Figure XIII.17.6, at a lower feeding rate of 0.21 ml/h, a small amount of solution was ejected from the capillary tips, leading to formation of small droplet size. By increasing the feeding rate to 0.42 ml/h, the ratio of nanofiber was significantly increased. As a result, the feeding rate was set to 0.42 ml/h for the subsequent experiments.

Due to the higher dielectric constant, lower vapor pressure, and higher electric conductivity of dimethylformamide (DMF), we have investigated the effect of solvents on the morphology of electrospun samples. The results show sharp contrast when we switched the solvent from NMP to DMF. As shown in Figure XIII.17.7, in addition to the nanofibers, large beads formed in the case of NMP solvent, while well-dispersed nanofibers were obtained in the case of DMF solvent. DMF was not easy to volatilize during the electrospinning process, which made it easier to form a branching fiber. The evaporation rate of the solvent had effects on the formation of electrospun fibers from the polymer jet. A jet with a strong dielectric ability can produce a large electrostatic drafting force in the stable electrospinning, and ultrafine fiber can be formed after solvent volatilization.



However, the solubility of spandex in DMF is low, which takes up to one week for complete dissolution. To resolve this issue, we have added cosolvent such as tetrahydrofuran (THF) to increase the solubility. Meanwhile the ratio of cosolvent could also change the surface tension of spandex solution. As shown in Figure XIII.17.8, with high content (40 vol%) of THF solvent, winding and thick fibers with large pore were formed, while straight and thin nanofiber with small pores were produced in the case of low-content (10 vol%) THF.

Through optimization of electrospinning parameters, we are now able to produce fine spandex nanofiber with highly porous interconnected fibrous structures, which is suitable for the uptake of a sufficient amount of liquefied argyrodite sulfide solid electrolytes. We will fabricate the cathode-supported sulfide solid electrolytes and control the thickness in FY24. We will further evaluate their performance in all-solid-state Li-sulfur batteries.

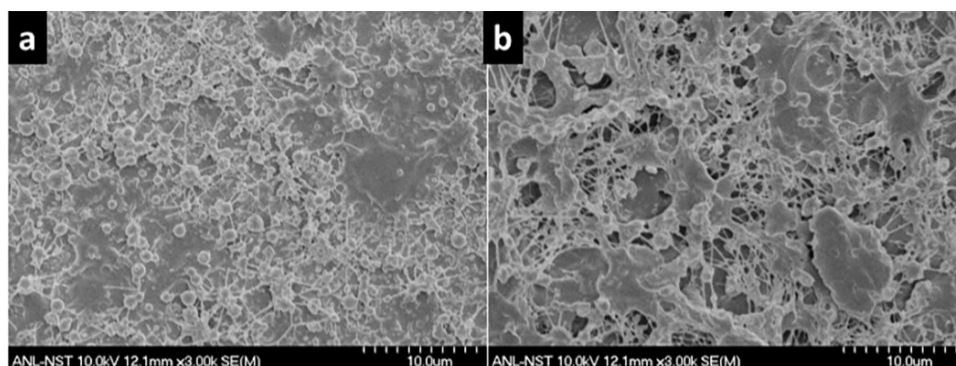


Figure XIII.17.6 SEM images of Spandex prepared by electrospinning at a feeding rate of (a) 0.21 ml/h and (b) 0.42 ml/h.

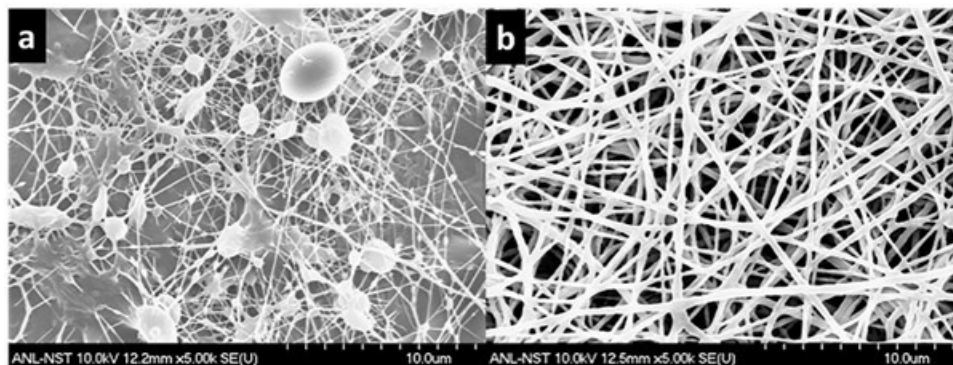


Figure XIII.17.7 SEM images of Spandex by electrospinning with a feeding rate of 0.42 ml/h using different solvents: (a) NMP; (b) DMF. The concentration of solution is 10 wt.%.

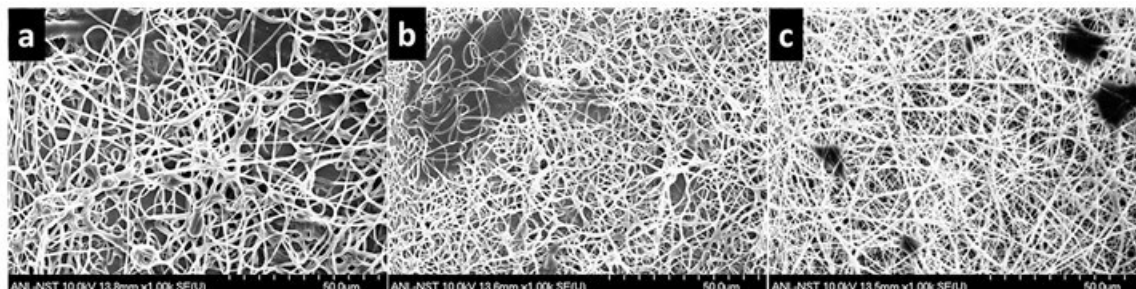


Figure XIII.17.8 SEM images of Spandex nanofibers by electrospinning with a feeding rate of 0.42 ml/h using THF cosolvent: (a) DMF/THF=3:2, v/v; (b) DMF/THF=8:2, v/v; (c) DMF/THF=9:1, v/v. The concentration of solution is 10 wt.%.

### Conclusions

In summary, we have developed Br/O co-doped  $\text{Li}_6\text{PS}_5\text{Br}$  sulfide solid electrolyte with improved ionic conductivity through careful synthetic control. In situ synchrotron X-ray diffraction characterization showed no phase transition under humidity of 20% in the case of  $\text{Li}_{5.5}\text{PS}_{4.4}\text{O}_{0.1}\text{Br}_{1.5}$ , indicating enhanced moisture stability. In situ synchrotron X-ray absorption near edge spectroscopy revealed a solid-solid (de) lithiation mechanism during charge/discharge of all-solid-state lithium-selenium batteries using sulfide solid electrolytes. And we have successfully fabricated elastic Spandex nanofiber as scaffold of thin sulfide solid electrolytes through optimization of electrospinning conditions.

### Key Publications

#### Patents

1. Guiliang Xu, Jieun Lee and Khali Amine. A METHOD FOR MAKING COMPOSITE CATHODE USING BULK ACTIVE MATERIALS. IN-23-094.

#### Presentations

1. Xu, G. L. Thick Selenium-Sulfur Cathode Supported Ultra-thin Sulfide Electrolytes for High-Energy All-Solid-State Batteries. The 2023 Vehicle Technologies Office (VTO) Annual Merit Review, 2023, June 12-15.
2. Guiliang Xu, Jieun Lee and Khalil Amine. Solid State Review meeting, Berkeley, Aug 30-31, 2023.

### References

1. Zhao, C.; Xu, G. L.; Yu, Z.; Zhang, L.; Hwang, I.; Mo, Y.-X.; Ren, Y.; Cheng, L.; Sun, C. -J.; Ren, Y.; Zuo, X.; Li, J.-T.; Sun, S.-G.; Amine, K. and Zhao, T. A high-energy and long-cycling lithium-sulfur pouch cell via a macroporous catalytic cathode with double-end binding sites. *Nature Nanotechnol.*, 2021, 16, 166-173.
2. Ding, B.; Wang, J.; Fan, Z.; Chen, S.; Lin, Q.; Lu, X.; Dou, H.; Nanjundan, A. K.; Yushin, G.; Zhang, X.; Yamauchi, Y. Solid-state lithium-sulfur batteries: Advances, challenges and perspectives. *Mater. Today* 2020, 40, 114-131.
3. Yang, X.; Adair, K. R.; Gao, X.; Sun, X. Recent advances and perspectives on thin electrolytes for high-energy-density solid-state lithium batteries. *Energy Environ. Sci.* 2021, 14, 643.
4. Li, Y.; Daikuhar, S.; Hori, S.; Sun, X.; Suzuki, K.; Hirayama, M.; Kanno, R. Oxygen Substitution for Li-Si-P-S-Cl Solid Electrolytes toward Purified  $\text{Li}_{10}\text{GeP}_2\text{S}_{12}$ -Type Phase with Enhanced Electrochemical Stabilities for All-Solid-State Batteries. *Chem. Mater.* 2020, 32, 8860-8867.
5. Wang, C.; Liang, J.; Zhao, Y.; Zheng, M.; Li, X. and Sun, X. All-solid-state lithium batteries enabled by sulfide electrolytes: from fundamental research to practical engineering design. *Energy Environ. Sci.* 2021, 14, 2577.

**Acknowledgements**

Support from Simon T. Thompson of the U.S. DOE's Office of Vehicle Technologies Program is gratefully acknowledged. Use of the Advanced Photon Source, an Office of Science User Facility operated for the DOE Office of Science by Argonne National Laboratory, was supported by DOE under contract no. DE-AC02-06CH11357.

## XIII.18 Synthesis of Composite Electrolytes with Integrated Interface Design (ANL)

### Sanja Tepavcevic, Principal Investigator

Argonne National Laboratory  
9700 South Cass Avenue  
Lemont, IL 60439  
E-mail: [sanja@anl.gov](mailto:sanja@anl.gov)

### Simon Thompson, DOE Technology Development Manager

U.S. Department of Energy  
E-mail: [Simon.Thompson@ee.doe.gov](mailto:Simon.Thompson@ee.doe.gov)

Start Date: October 1, 2022

End Date: October 1, 2027

Project Funding (FY23): \$550,000

DOE share: \$550,000

Non-DOE share: \$0

### Project Introduction

Making safe, strong, and stable solid-state electrolytes (SSEs) is essential for high density Li metal batteries. Using combined experimental- and computational-based methodologies, we previously gained interdisciplinary, atomic-level insights into solid electrolyte interfaces with metallic Li by studying LLZO and PEO thin films as model systems. This proposal will transfer and build upon the knowledge gained on thin films to create more refined composite ceramic-polymer electrolytes (CPEs) that can be synthesized in a real-world manufacturing process. We will focus on an integrated design of critical interfaces to improve CPE ionic conductivity and guide homogeneous ion distribution across both anode and cathode interfaces. The study will be focused on the LLZO-PEO system, where nanofiber LLZO will be used to improve ion transport and electrochemical stability. Investigations into CPEs based on polyethylene oxide (PEO) showed that integrating ceramic fillers with polymers increased Li<sup>+</sup> transport by decreasing the crystallinity of the conducting polymer and creating space charge regions that can enhance Li<sup>+</sup> diffusion. The combination of Li<sup>+</sup>-conducting ceramics and polymers offers a new pathway to create better electrolytes with both high ionic conductivity and good mechanical properties.

### Objectives

This project aims to develop well-controlled, scalable LLZO nanofiber and CPE synthesis processes that will address the manufacturing challenges of current SSEs and demonstrate the fabrication of large-area, thin CPE membranes with outstanding electro-chemomechanical properties. The outcome of this proposal will be a transformative manufacturing solution that can create large-area, mechanically and (electro)chemically stable SSEs (0 V to 4.5 V versus Li/Li<sup>+</sup>) with Li<sup>+</sup> conductivity of  $\geq 10^{-3}$  S/cm at room temperature enabling  $\geq 1$ C charging rates.

### Approach

To commercialize all-solid-state lithium-ion battery technology, further advances will require the application of knowledge, concepts, and tools from a variety of fields including materials science, physics, engineering, theory, and interfacial electrochemistry. The team's research philosophy is to establish a synthesis-material characterization-computation cycle that advances synthesis, chemistry, microstructure, interfaces, and transport in CPEs by a coordinated, interdisciplinary approach. The team's diverse expertise will allow them to understand, create, and rapidly scale up composite electrolytes to meet ambitious conductivity, energy, and power density targets.

## Results

### Interphase Control.

In our previous work, we investigated the chemistry of the solid electrolyte interphase (SEI) in composite polymer electrolytes with and without  $\text{Li}_7\text{La}_3\text{Zr}_2\text{O}_{12}$  (LLZO) nanofibers. We demonstrated that the LLZO plays no role in the SEI, and only the PEO polymer and lithium bis(trifluoromethane-sulfonyl) imide (LiTFSI) salt decompose when exposed to lithium to generate the interphase. To optimize the SEI and increase charging rates and Coulombic efficiencies,[1] we used computation of SEI mechanics and experimental design to improve the anode interface.

Mesoscale modeling was employed to compare two SEI characteristics: modulus and uniformity. A poor SEI will be heterogeneous in coverage, thin, and made of weak/soft chemical components; a quality SEI will be thick and uniform and contain a large portion of hard components (Figure XIII.18.1a). As current is applied and lithium metal plates, dendritic filaments can grow through defects in the SEI at certain rates, which can be quantified as dendrite growth velocity. As seen in Figure XIII.18.1b, quality SEIs slow the effective dendrite growth velocity under all conditions relative to weak SEIs. Also of note is that the growth velocity is constant and high until the shear modulus of the bulk electrolyte,  $G_{\text{Elec}}$ , approaches and exceeds that of lithium metal,  $G_{\text{Li}}$ . As noted, the moduli of all PEO-based composite electrolytes with and without LLZO nanofibers are well below the moduli of lithium metals.

The conductivity of the SEI layer can also impact the propensity for dendrite growth by altering the reaction current density at the defect zone. Figure XIII.18.1c is a phase map demonstrating the dendrite growth velocity as a function of conductivity and mechanical stiffness of the SEI layer. It is evident that increasing the overall conductivity of the SEI layer helps minimize the extent of current focusing at the imperfections where dendrites are expected to initiate. This implies that either a sufficiently strong or a highly conductive SEI should be able to fully prevent dendrite growth in CPEs. Various commonly observed SEI components are pointed out in the phase map shown in Figure 1c. Inorganic SEI components ( $\text{Li}_2\text{O}$ ,  $\text{LiF}$ ) deposited in a uniform fashion are expected to stabilize the lithium deposition process due to higher elastic stiffness. On the other side, uniform layers of organic SEI components ( $\text{Li}_2\text{EDC}$ ,  $\text{Li}$ -alkoxides) may also reduce dendrite growth velocity due to a higher SEI ionic conductivity. Unfortunately, the actual SEI layer consists of both organic and inorganic components, which leads to inherent heterogeneities in both transport and mechanical properties of the SEI layer. These inhomogeneities act as hot spots for current focusing as well as fracture of the SEI layer, which can lead to dendrite growth and subsequent shorting of the cell.

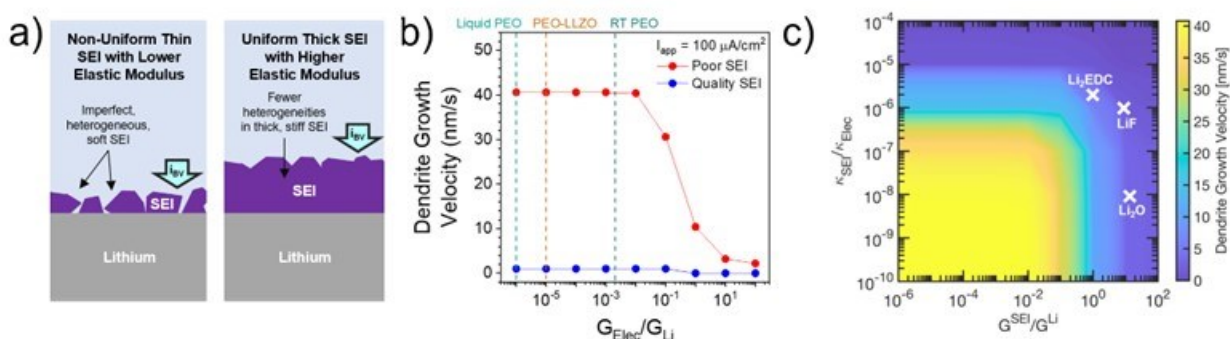


**Figure XIII.18.1** a) Schematic of the mesoscale model used for modeling lithium plating through soft and heterogeneous SEI vs. strong and uniform SEI. b) Computed dendrite velocity as a function of relative bulk electrolyte modulus for the weak and strong SEIs. c) A phase map demonstrating the competition between conductivity and elastic modulus of the SEI layer in determining the stability of lithium deposition process.

To further ensure inorganic SEI characteristics, we developed salt-rich thin film coatings on copper foil electrodes. Putting these in contact with freestanding bulk electrolyte membranes with lower salt contents and controlling the temperature and potential of SEI formation should allow control over inorganic vs. organic SEI

components (Figure XIII.18.2a) while limiting the cost of using large salt quantities. Our hypothesis is that SEI formed electrochemically (in the absence of lithium metal) at higher potentials would yield more inorganic species and improve cell characteristics. Using a Li salt-PEO coated interlayer with 2:1 Li:EO ratio, potentials of 0.05 V and 1.0 V were applied at room temperature (Figure XIII.18.2b). Surprisingly, cells with SEI formed at lower potentials performed better with lower SEI resistance, higher CCD, and better CE before shorting. Notably, cell shorting seems to still be determined by the bulk electrolyte, PEO-LiTFSI, indicating the need for more SEI studies.

To optimize other characteristics of this interlayer, we adjusted the thickness of the coating from 150 to 600 nm, which are all achievable in uniform layers with our slot-die technique. Interestingly, thicker layers of LiTFSI-PEO with 2:1 Li:EO showed enhanced performance, with lower SEI resistance and higher critical current density (Figure XIII.18.2c). This may be due to more salt being present in the diffusion layer during SEI formation, leading to more salt-derived SEI. Finally, we incorporated LLZO nanofibers as an additional interfacial layer between the salt-rich coatings and bulk PEO-LiTFSI electrolyte followed by SEI formation at 0.05 V. This produced the lowest interface resistance in our cells to date, with an 86% decrease in impedance compared to the typical freestanding samples (Figure XIII.18.2b).

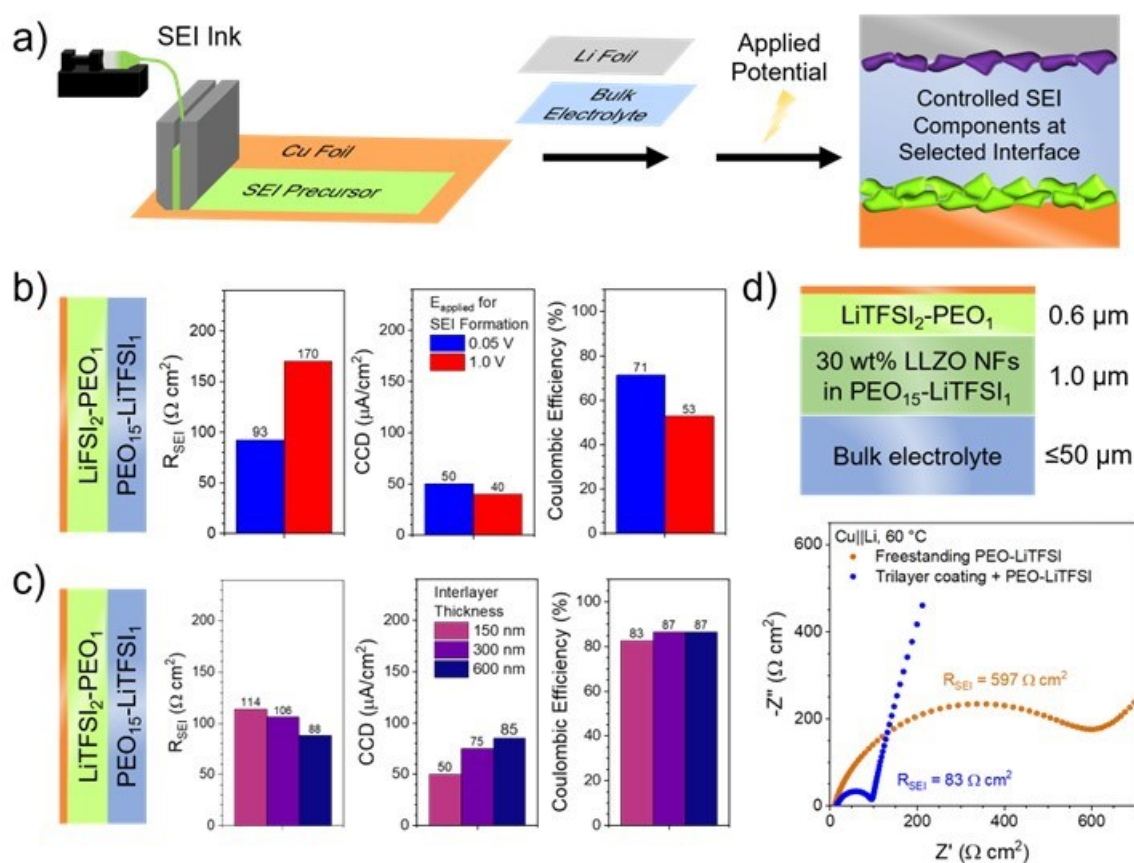


Figure XIII.18.2 a) Schematic of slot-die coating salt-rich SEI precursor layers and generating SEI under controlled conditions on copper electrodes. b) Applying potentials of 0.05 V and 1.0 V for 2 hours at 25 °C with lithium bis(fluorosulfonyl)imide (LiFSI)-rich interlayers shows that lower potentials generate better cell characteristics. c) Varying the thickness of LiTFSI-rich interlayers shows that thicker 600 nm layers have better performance. d) Incorporating LLZO nanofibers in a coated trilayer structure can decrease the effective interface resistance by >85% compared to typical cells assembled with freestanding membranes.

### Ultra-thin Anode Coatings.

In another attempt to create an inorganic anode interphase that prevents further lithium reactivity and improves Coulombic efficiency, we used atomic layer deposition (ALD) to deposit ultra-thin (5-20 nm) layers of  $\text{Al}_2\text{O}_3$  and ZnO on Cu current collectors.[2] X-ray photoelectron spectroscopy, time-of-flight secondary ion mass spectrometry, and scanning electron microscopy revealed that  $\text{Al}_2\text{O}_3$  only partially reacts with lithium to form a lithiated  $\text{Li}_y\text{AlO}_x$  phase, while ZnO reacts completely to form a LiZn alloy and  $\text{Li}_2\text{O}$  (Figure XIII.18.3a). The insulating nature of  $\text{Al}_2\text{O}_3$  limits the lithium inventory loss in the cell during formation steps, while ZnO remains conductive and leads to more Li loss than bare Cu with PEO-LiTFSI solid polymer electrolytes (Figure XIII.18.3b). Despite this initial performance improvement,  $\text{Al}_2\text{O}_3$  coatings short faster than bare Cu, while ZnO coatings increase the critical current density (Figure XIII.18.3c).

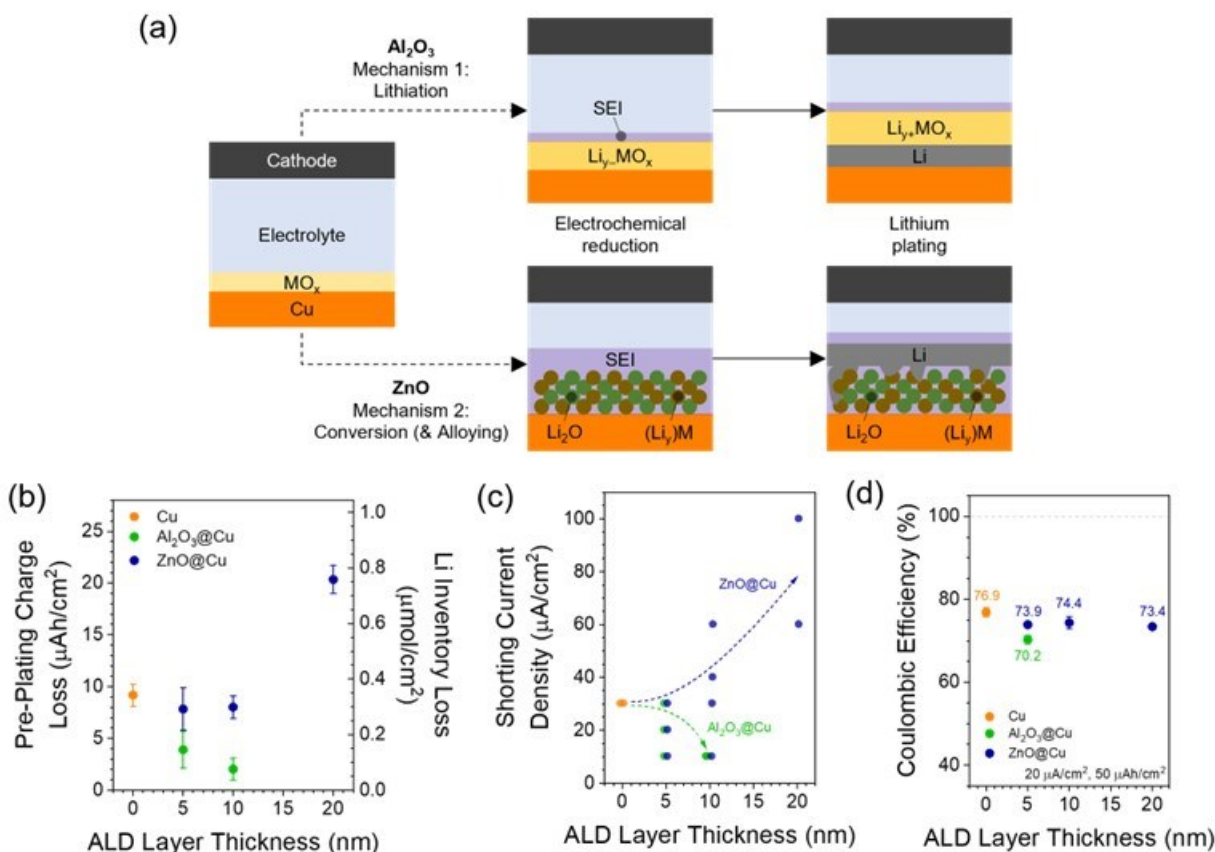


Figure XIII.18.3 a) Schematics of metal oxide ALD coatings on copper electrodes during the initial formation and lithium plating steps. b) Charge loss in a Cu || Li half-cell with PEO-LiTFSI solid polymer electrolyte cell before the onset of lithium plating. c) Current density at which different cells shorted. d) Coulombic efficiency of lithium plating and stripping.

However, neither coating improved Coulombic efficiency relative to the unmodified Cu electrodes (Figure XIII.18.3d) due to the lithium plating mechanisms dictated by defects in the coatings. Given the industrial application of ALD and the wide range of materials available, there is a rich space to explore these mechanisms further and improve Coulombic efficiency in anode-free lithium metal batteries with any type of electrolyte.

### LLZO Nanofiber Synthesis and Modification.

Apart from the SEI formation dependent on the polymer phase in composite electrolyte, we investigated the LLZO nanofiber structure, composition, and processability in ambient environment to increase bulk lithium

ion conductivity. To optimize the LLZO nanofibers, the Li content of the nanofibers was investigated and calibrated by adding extra Li source in the precursor. The composition of LLZO nanofiber with 0% excess Li is expected to be  $\text{Al}_{0.25}\text{Li}_{6.25}\text{La}_3\text{Zr}_2\text{O}_{12}$  based on the precursor composition. However, the actual Li content was  $\text{Li}_{3.8}$ , as measured by inductive coupled plasma (ICP) analysis (Figure XIII.18.4a), which can be attributed to Li loss during the thermal annealing process (750 °C for 2 h). To compensate for Li loss during annealing, excess Li was incorporated in the precursor proportionally to  $\text{Li}_{6.3}$  with 25% excess Li, which is close to the target composition ( $\text{Li}_{6.25}$ ). The prepared LLZO nanofibers showed a well-maintained nanofiber structure, and all elements were evenly distributed throughout the fiber as confirmed by scanning transmission electron microscopy (STEM) and element mapping from energy dispersive X-ray spectroscopy (EDS) (Figure XIII.18.4b). In addition, the LLZO nanofiber showed better crystallinity with increasing the amount of excess Li, accompanied by the decrease of impurity phase ( $\text{La}_2\text{Zr}_2\text{O}_7$ ) (Figure XIII.18.4c). Only in LLZO with 25% excess Li did the  $\text{La}_2\text{Zr}_2\text{O}_7$  peak disappear, indicating a high-crystallinity cubic LLZO phase. Notably, LLZO nanofibers rapidly formed  $\text{Li}_2\text{CO}_3$  when exposed to ambient air as shown by both X-ray diffraction and Raman spectroscopy, along with proton exchange with lithium ions in the cubic LLZO lattice.

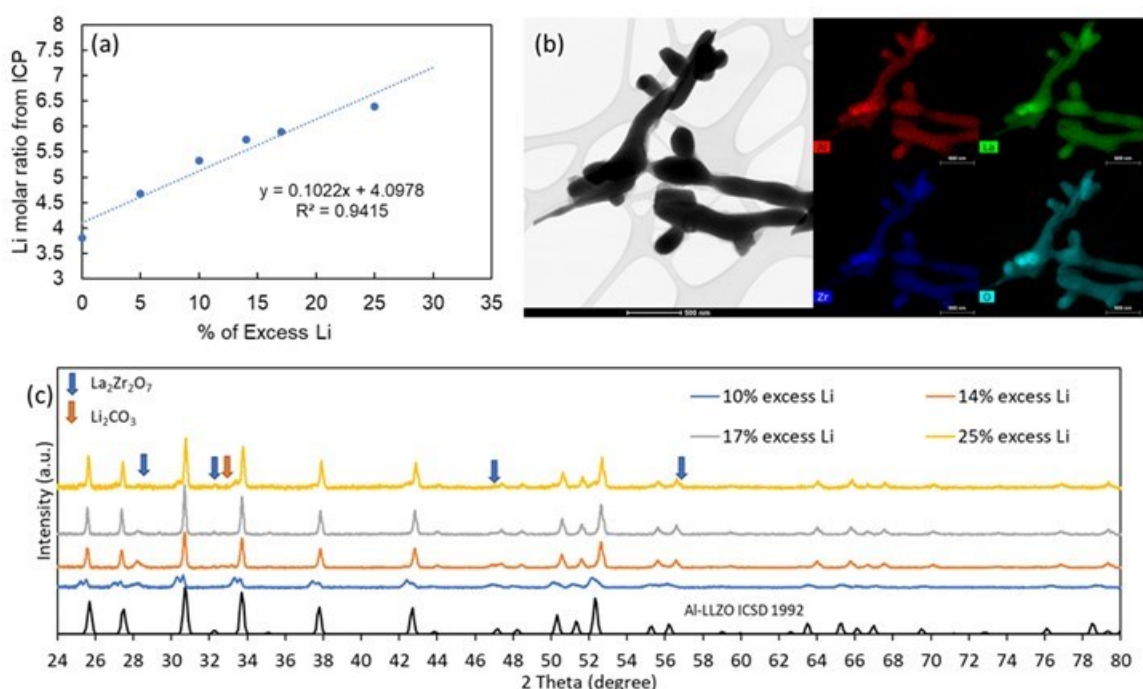


**Figure XIII.18.4** (a) Calibration curve of Li content in Al-LLZO nanofiber synthesis. (b) STEM-EDS images of Al-LLZO with 25% excess Li. (c) X-ray diffraction patterns of Al-LLZO with varied contents of excess Li.

Since ionic conductivity in CPEs mainly relies on the LLZO nanofiller conductors, it is necessary to verify the conductivity of our nanofibers. Previously, this determination was challenging because of the low density of the cold pressed nanofiber pellets. This technical difficulty has been solved by sintering the LLZO nanofiber pellet at elevated temperatures above 1000 °C in collaboration with LBNL. Recently, an ionic conductivity of  $3 \times 10^{-4}$  S/cm was measured for the Al-doped LLZO nanofiber pellet that was densified into 80% density (Figure XIII.18.5a-b). The Arrhenius activation energy for  $\text{Li}^+$  transport was consistent across two different nanofiber syntheses and pellet densification tests, with an  $E_a \sim 0.39$  eV (Figure XIII.18.5c). This bulk conductivity and activation energy are close to those of bulk Al-doped LLZO pellets with micron-sized grains (typically  $2\text{-}5 \times 10^{-4}$  S/cm and 0.34-0.38 eV, respectively) processed at higher temperatures, demonstrating the advantage of our low temperature cubic LLZO nanofiber synthesis. There was an order of magnitude loss in conductivity of the nanofiber pellets over time due to air exposure of the high-surface area LLZO nanofibers,



leading to proton exchange and carbonate formation. This highlights the importance of protecting the surface of LLZO nanofillers.

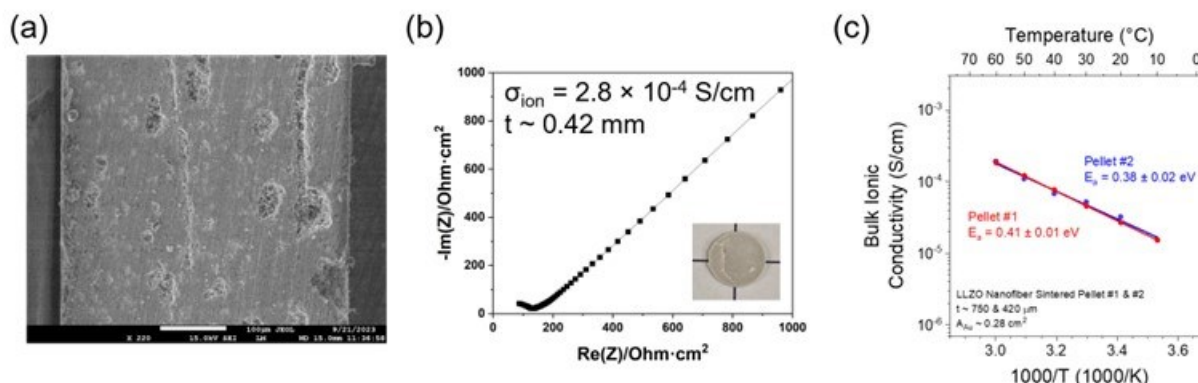


**Figure XIII.18.5 (a) Scanning electron micrograph of the cross-section of the 83% dense pellet made with Al-doped LLZO nanofibers. (b) Impedance spectrum of the pellet (photo inset) with sputtered Au blocking electrodes. (c) Arrhenius plots of two different densified Al-doped LLZO nanofiber pellets.**

To protect the LLZO surface, increase its interaction with the polymer matrix, and provide surface chemistries for further composite modification, we covalently bound functionalized silanes to the surface of LLZO nanofibers and nanoparticles. The use of the (acidic) water-based silane solutions would exacerbate the proton exchange seen above and lower LLZO conductivity. Therefore, we developed a LLZO surface modification method using aprotic organic solvent instead.

A simple reflux method with toluene solvent was developed for this new surface modification method (Figure XIII.18.6a). LLZO nanofibers were added to a mixture of silane precursor and toluene, then heated at 80 °C for 16-24 h. The blue shift of the Raman spectrum Zr-O peak is significant for bare LLZO fibers over several hours due to proton exchange, but this remains stable when protected by silane (Figure XIII.18.6b-c). This shows that this silane treatment effectively coats the LLZO surface to protect it from air, but the treatment itself does not significantly disrupt the LLZO structure. We found this method to work for multiple silanes with different functional groups. Figure XIII.18.6d shows FT-IR spectra of LLZO nanoparticles and (3-Aminopropyl)triethoxysilane (APTES)-modified LLZO nanoparticles. After the APTES modification, N-H vibrations at 3550 and 1575  $\text{cm}^{-1}$  were observed, and the intensity of the O-H vibration from the LLZO surface and surface contaminant LiOH was decreased. This result indicates that the -OH group on the surface of LLZO is replaced by the APTES, which protects the surface from then on.

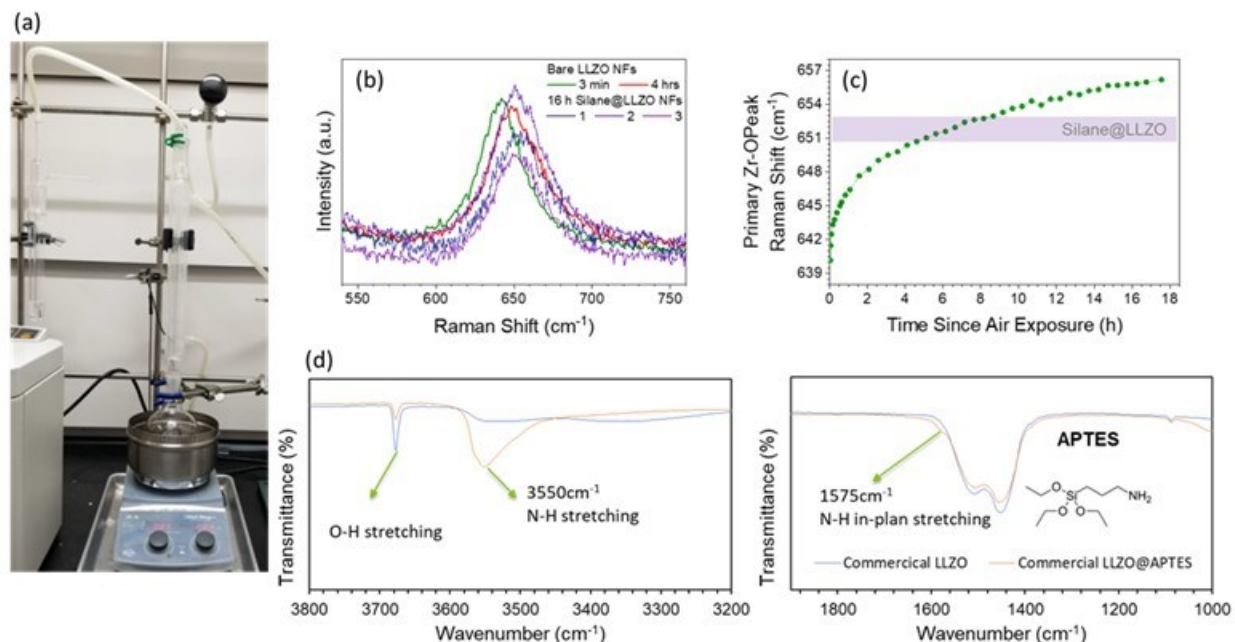


**Figure XIII.18.6** (a) Photograph of reflux surface modification set-up. (b) Raman spectra of bare LLZO and silane-modified LLZO over time. (c) Comparison of the Zr-O peak shift with bare LLZO and silane-modified LLZO nanoparticles after exposure to air. (d) FT-IR spectrum of LLZO nanoparticles and APTES-modified LLZO nanoparticles showing surface functional groups.

These surface-modified LLZO particles were tested in composite polymer electrolytes to determine their effect on total ionic conductivity and lithium ion transference number. Figure XIII.18.7 compares these values for pure PEO-LiTFSI electrolyte, as well as composites with un-modified LLZO (Neat LLZO), LLZO with APTES coating prepared by the reflux method (APTES@LLZO), and LLZO coated with an ionically insulating Al<sub>2</sub>O<sub>3</sub> layer (Al<sub>2</sub>O<sub>3</sub>@LLZO) that was fabricated via atomic layer deposition. Al<sub>2</sub>O<sub>3</sub>@LLZO composites are a control experiment to show what a “non-functional” interface that does not transport Li<sup>+</sup> would look like, while still incorporating the same particle morphologies into the composite membranes. At 10 wt % LLZO loading (Figure XIII.18.7a), the conductivities of all LLZO composites are increased above the baseline electrolyte, as expected, but have only minor changes in activation energy, implying little change in ion transport mechanism. At 50 wt % LLZO loading (Figure XIII.18.7b), Neat LLZO is very similar to PEO-LiTFSI, while more drastic changes are seen as the LLZO surface changes. APTES@LLZO shows much different activation energies, indicating changes in the ion transport at certain temperatures. Al<sub>2</sub>O<sub>3</sub>@LLZO is more similar to Neat LLZO in terms of activation energy, although with an order-and-a-half magnitude lower conductivity overall.

Lithium ion transference numbers ( $t_{Li^+}$ ) calculated by the Bruce-Vincent method (Figure XIII.18.7c) shed light on these differences. Adding LLZO with any surface at 10 wt % slightly increases  $t_{Li^+}$ , possibly due to a non-surface-specific plasticizing effect. At 50 wt % LLZO,  $t_{Li^+}$  is the highest of any sample with APTES@LLZO ( $t_{Li^+} = 0.211$ ), which we attribute to better interaction of the particles with the polymer and lithium salt matrix. By completely shutting down the LLZO-PEO-LiTFSI interaction with an ionically insulating Al<sub>2</sub>O<sub>3</sub> layer, transference plummets to  $t_{Li^+} = 0.054$ , even lower than the baseline electrolyte despite having a higher global lithium concentration. This points to the importance of the LLZO-PEO-LiTFSI interface for increasing Li<sup>+</sup> transport in these CPEs.

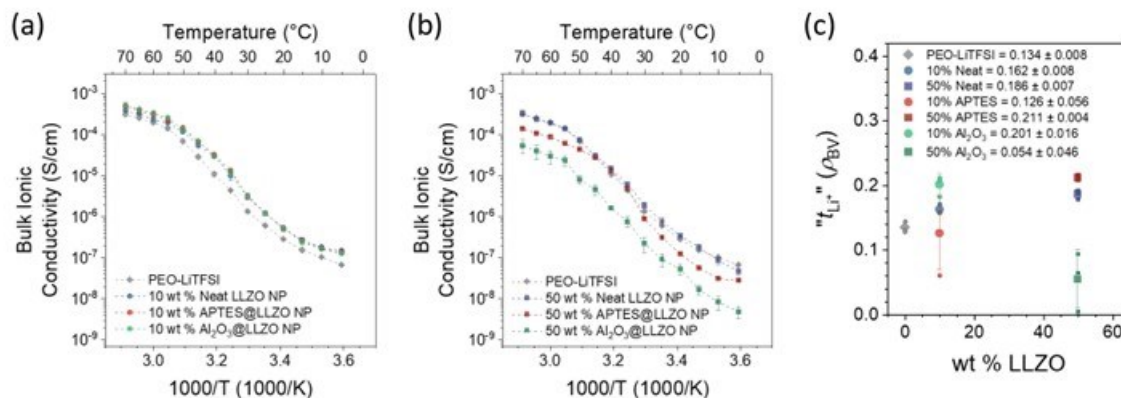


**Figure XIII.18.7** Ionic conductivity of (a) 10 wt % and (b) 50 wt% LLZO nanoparticle composite electrolytes with different surface modifications compared to the baseline PEO-LiTFSI polymer electrolyte. (c) Estimated transference number of the electrolytes vs. LLZO loading. Small dots represent single measurements; large dots and error bars represent the average and standard deviation of three cells.

#### **Bridging PEO-LLZO for $Li^+$ Transport.**

We next sought to incorporate our surface modification of LLZO nanofillers into a crosslinked PEO-LiTFSI composite membrane. To expedite the synthesis and testing process, we used commercial Al-doped LLZO nanoparticles (NPs), which have similar conductivity to our nanofibers. Treating the LLZO NPs with APTES, a silane with a primary amine end-group, allows us to initiate PEO crosslinking from the particle surface. Ethylene oxide oligomers of trimethylolpropane ethoxylate triacrylate 912 (T) and Jeffamine ED-2003 (J) were mixed with LiTFSI, PEO (Mw ~ 600 kDa), and APTES-treated LLZO NPs, and then casted by slot-die coating, followed with a curing step at 80 °C for up to 24 hours. The aza-Michael addition reaction between acrylates and amines led to a highly crosslinked structure (xTJ, Figure XIII.18.8a) that is mechanically stronger than the standard PEO-LiTFSI. The ionic conductivity of these crosslinked composites was tested and compared to non-crosslinked electrolytes using PEO alone (Figure XIII.18.8b-c). An order of magnitude improvement in the room temperature conductivity ( $\sim 2 \times 10^{-5}$  S/cm) was observed for the crosslinked electrolytes regardless of LLZO content ( $\sim 2 \times 10^{-6}$  S/cm). The apparent activation energy is also lower after crosslinking. We attribute these improvements to the lack of PEO chain crystallization in xTJ, which can only be achieved in normal PEO by adding plasticizing additives or increasing operating temperatures. However, adding pristine or functionalized LLZO to the crosslinked electrolyte does not appreciably increase conductivity, especially at 25 °C (Figure XIII.18.8b). This disproves our hypothesis that covalent linking of the polymer matrix to the ceramic LLZO fillers would activate their interface and increase  $Li^+$  conductivity by facilitating  $Li^+$  transport between the polymer and ceramic phases.

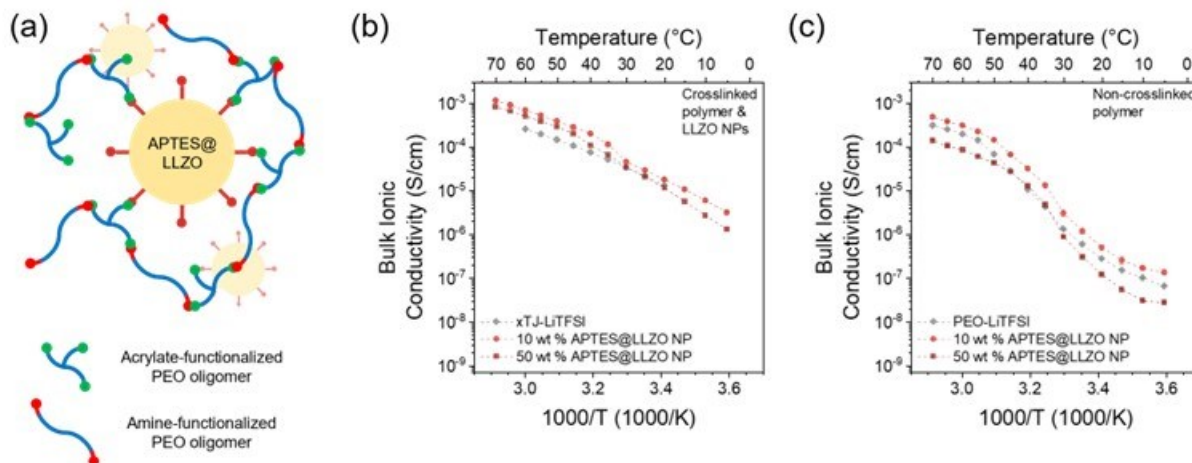


**Figure XIII.18.8** (a) Schematic of crosslinked xTJ composite membrane chemistry, where PEO oligomers with acrylate end-groups (T) covalently bond to the amines on APTES@LLZO and the end-groups of other PEO oligomers (J). (b) Arrhenius plots of this crosslinked membrane with no LLZO (xTJ-LiTFSI) and with 10 and 50 wt % APTES@LLZO nanoparticles. (c) Arrhenius plots of linear PEO (600 kDa) and LiTFSI with 0, 10, and 50 wt % APTES@LLZO nanoparticles to compare the effects of crosslinking.

Computational modelling has shed some light on this observation. We modeled our composite electrolytes with two Li<sup>+</sup>-conductive phases (PEO and LLZO) and two interphases, one conductive and one resistive (Figure XIII.18.9a). This two-interphase layer model was able to capture the change in experimental ionic conductivity with variable LLZO content (Figure XIII.18.9b). The conductive interphase is attributed to the LLZO nanofiller's disruption of PEO crystallization, essentially acting as a plasticizer. The resistive interphase is attributed to the adsorption of PEO on LLZO and the limited segmental motion of the polymer chains when near the LLZO surface. At small LLZO contents (<20 wt %), the plasticizing effect improves conductivity by removing crystallinity in the PEO matrix. At higher LLZO contents, the volume fraction of resistive interphases increases significantly, which hinders ion transport through the bulk of the composite and lowers conductivity, sometimes even below that of normal PEO-LiTFSI. Our current estimation is that the resistive interphase limits conductivity by an order of magnitude more than the conductive interphase aids conductivity (Figure XIII.18.9b) leading to a net loss with high LLZO fractions. The interfacial resistance between PEO and LLZO is most probably extremely high, which prevents the movement of lithium ions from the polymer to the ceramic particles. There can be various sources for the high resistance observed at the PEO-LLZO interface:

- Presence of resistive foreign materials at the PEO-LLZO interface, such as lithium carbonate (Li<sub>2</sub>CO<sub>3</sub>), lithium oxide (Li<sub>2</sub>O), and lithium hydroxide (LiOH);
- High activation energy barrier between PEO and LLZO, which is a kinetic barrier;
- High thermodynamic energy barrier, which can be attributed to the difference in lithium concentration within the PEO and LLZO as well as difference in their reference chemical potentials.

Either one, or a combination of multiple factors, leads to very high interfacial resistance between PEO and LLZO (or possibly other ceramic particles), which most probably prevents transport of lithium ions from the polymer phase to the LLZO.

We aim to address these interfacial issues in a few ways, in addition to our continued silane surface functionalization. Changing the lithium salt anion (e.g., ClO<sub>4</sub><sup>-</sup> instead of TFSI<sup>-</sup>) may influence the interfacial ion exchange as well as allow higher lithium molar loadings to match the chemical potential between filler and polymer phase. We will also investigate the influence of polymer molecular weight and chemistry on this interfacial resistance by (partially) replacing the 600 kDa PEO with lower M<sub>w</sub> PEO and other polymers like poly(vinylidene difluoride) (PVDF). Finally, we will change the chemistry of the nanofiller itself by testing

lithium lanthanum titanate (LLTO) in replacement of LLZO, which is chemically similar to LLZO but has lower lithium concentrations and fewer issues with surface degradation products like  $\text{Li}_2\text{CO}_3$ .

These revelations led to our new design of composite structures where  $\text{Li}^+$  percolation is achieved among conductive LLZO nanofibers alone, without the hindrance of PEO. This requires direct contact among LLZO crystals, which is free of surface contaminants ( $\text{Li}_2\text{CO}_3$ ,  $\text{LiOH}$ , and PEO) and grain-to-grain resistance. We are currently developing LLZO scaffolds made of highly interconnected, sintered nanofibers. Figure XVIII.18.9c shows the transformation of typically prepared LLZO nanofibers (annealed at  $750^\circ\text{C}$ ) into well connected flakes through modified thermal treatment conditions, which utilized small heating rates and higher annealing temperatures (e.g., up to  $950^\circ\text{C}$ ). The average fiber diameter more than doubles, and the inter-fiber contact is greatly increased as fibers are sintered together instead of just physically contacting. Importantly, we can achieve this transformation at temperatures that are still below those used for regular powder sintering of LLZO (usually  $\sim 1100^\circ\text{C}$ ). Our next step is to infiltrate polymers into the ceramic scaffolds to generate freestanding membranes with good electrode contact for cell testing.

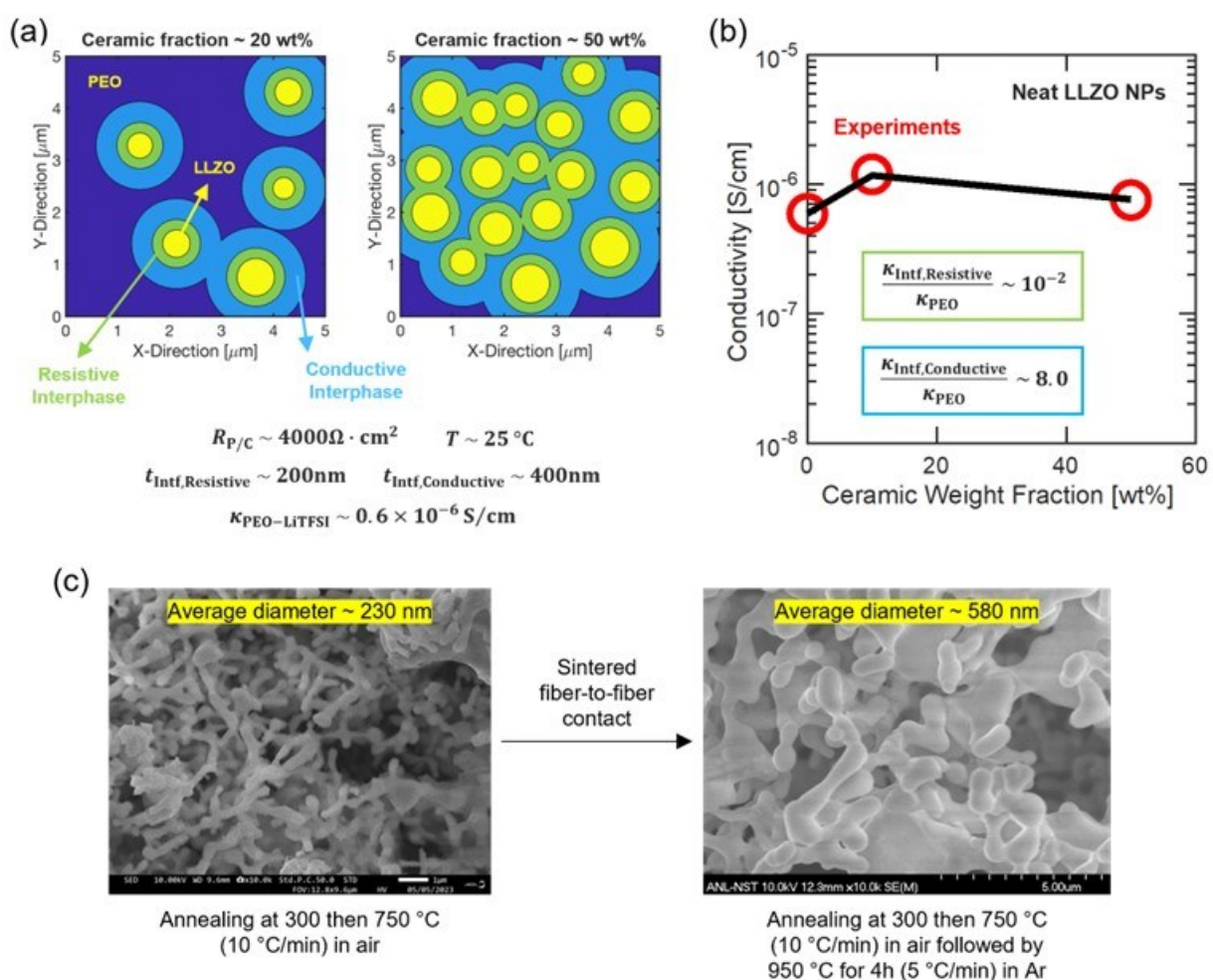


Figure XIII.18.9 (a) Schematics of the computational model used to model conductivity in composites, using multiple interphases that enhance or disrupt  $\text{Li}^+$  transport. (b) Fit of experimental data with unmodified LLZO NPs in PEO-LiTFSI to the model, showing that improvement in PEO conductivity from small LLZO contents is outweighed by more resistive interphases at higher LLZO contents. (c) Further heat treatment of LLZO nanofibers (left) can ensure fiber-to-fiber contact and build a percolation network with sintered scaffolds (right).

## Conclusions

Our work this year focused on improving two critical interfaces in solid-state batteries with composite polymer electrolytes: the anode-electrolyte interface and the polymer-ceramic interface. Coating copper current collectors with salt-rich coatings to dictate the chemistry of the SEI and with nanometer-thick metal oxide thin films show two ways that the solid electrolyte interphase resistance, reactivity, and other performance characteristics can be tuned in these composite polymer electrolyte systems. Optimization of our LLZO nanofiber synthesis yielded conductivities and activation energies near that of bulk Al-doped LLZO. A new silane treatment of the LLZO surface protects the LLZO from further reaction with air, increases the lithium ion transference number, and provides functionality for covalent bonding to the polymer matrix. Despite these improvements, there is still a large inherent resistance to transporting  $\text{Li}^+$  between the ceramic and polymer phases, as probed by the computational modelling. Future work will focus on building LLZO interconnected network through scaffolds and determining the chemical origin of ceramic-polymer resistance to achieve usable room temperature conductivity and high transference number of the composites.

## Key Publications

1. Counihan, Powers, Barai, Hu, Zagorac, Zhou, Lee, Connell, Chavan, Gilmore, Hanley, Srinivasan, Zhang, and Sanja Tepavcevic. 2023. "Understanding the Influence of  $\text{Li}_7\text{La}_3\text{Zr}_2\text{O}_{12}$  Nanofibers on Critical Current Density and Coulombic Efficiency in Composite Polymer Electrolytes." *ACS Applied Materials & Interfaces* 15, no. 21, 26047-26059.
2. Counihan, Kim, Pathak, Zagorac, Yang, Burns, Cabana, Klie, Hanley, Connell, Mane, Elam, and Sanja Tepavcevic. 2023. "Insights into the reactivity and lithium plating mechanisms of ultra-thin metal oxide coatings for anode-free solid-state lithium metal batteries." *Frontiers in Batteries and Electrochemistry* 2, 1292622.
3. Woodahl, Jamnuch, Amado, Uzundal, Berger, Manset, Zhu, Li, Fong, Connell, Hirata, Kubota, Owada, Tono, Yabashi, te Velthuis, Tepavcevic, Matsuda, Drisdell, Schwartz, Freeland, Pascal, Zong, and Michael Zuerch. 2023. "Probing lithium mobility at a solid electrolyte surface." *Nature Materials* 22, 848-852.

## References

1. Counihan, Powers, Barai, Hu, Zagorac, Zhou, Lee, Connell, Chavan, Gilmore, Hanley, Srinivasan, Zhang, and Sanja Tepavcevic. 2023. "Understanding the Influence of  $\text{Li}_7\text{La}_3\text{Zr}_2\text{O}_{12}$  Nanofibers on Critical Current Density and Coulombic Efficiency in Composite Polymer Electrolytes." *ACS Applied Materials & Interfaces* 15, no. 21, 26047-26059.
2. Counihan, Kim, Pathak, Zagorac, Yang, Burns, Cabana, Klie, Hanley, Connell, Mane, Elam, and Sanja Tepavcevic. 2023. "Insights into the reactivity and lithium plating mechanisms of ultra-thin metal oxide coatings for anode-free solid-state lithium metal batteries." *Frontiers in Batteries and Electrochemistry* 2, 1292622.

## Acknowledgements

The PI is grateful to our team members Yuepeng Zhang, Michael Counihan, Jungkuk Lee, Pallab Barai, Meghan Burns, Taewoo Kim, Rajesh Pathak, Teodora Zagorac, Yingjie Yang, Devon Powers, Luke Hanley, Robert Klie, Jordi Cabana, Justin Connell, Jeff Elam, Anil Mane, Kanchan Chavan, Larry Curtiss, and Venkat Srinivasan for data collection and analysis and their valuable contributions to the project. We also thank Xinwei Zhou, Yuzi Liu, Ashley Simmons, Shiyu Hu, and Byeongdu Lee for help with materials synthesis and characterization.

## XIII.19 Polymer Electrolytes for Stable Low Impedance Solid State Battery Interfaces (ORNL)

### Xi (Chelsea) Chen, Principal Investigator

Oak Ridge National Laboratory  
PO Box 2008, MS6124  
Oak Ridge, TN, 37830  
E-mail: [chenx@ornl.gov](mailto:chenx@ornl.gov)

### Simon Thompson, DOE Technology Development Manager

U.S. Department of Energy  
E-mail: [Simon.Thompson@ee.doe.gov](mailto:Simon.Thompson@ee.doe.gov)

Start Date: October 1, 2022	End Date: September 30, 2026	
Project Funding (FY23): \$650,000	DOE share: \$650,000	Non-DOE share: \$0

### Project Introduction

This work aims at developing stable and low impedance polymer/electrode interfaces for the integration of a thin solid composite electrolyte into a battery, to achieve chemical stability at the electrodes, high energy density (500 Wh/kg), high rate (1 mA/cm<sup>2</sup>) and long cycle life (80% capacity retention for 300 cycles), demonstrated in pouch cells.

Our main design principle is to use an oxide ceramic as the main ion transporting phase in the electrolyte and a polymer electrolyte to form optimized interfaces with the electrodes as well as to provide flexibility to the electrolyte membrane. Oxide ceramics have the advantages of high ionic conductivity, high Li ion transference number and high mechanical modulus. Polymer electrolytes are soft and flexible and capable of maintaining good contact at interfaces. However, the adoption of composite electrolyte in a solid-state battery has two main technical barriers:

1. Internal interface: a large interfacial resistance between the polymer and the ceramic electrolyte must be overcome. Even with an interconnected ceramic pathway to deliver good conductivity, the polymer-ceramic interface issue cannot be bypassed. Because we still rely on polymer to make contact and bridge the ceramic with the electrodes.
2. External interface: stable and low impedance interfaces between the polymer and the electrodes (including the anode and the cathode) must be achieved, as this is crucial for high rate and long cyclability of a solid-state battery.

### Objectives

The overall objective of this project is developing stable and low impedance polymer/electrode interfaces for the integration of a thin solid composite electrolyte into a battery, to achieve chemical stability at the electrodes, high energy density (500 Wh/kg), high rate (1 mA/cm<sup>2</sup>) and long cycle life (80% capacity retention for 300 cycles), demonstrated in pouch cells.

The main objective can be dissected into 4 tasks: Task 1 is the synthesis and characterization of fluoropolyether polymers, or other model polymer electrolytes. Task 2 focuses on understanding and optimizing polymer-cathode interface. Task 3 focuses on understanding and optimizing polymer-anode interface. Task 4 is the integration of a thin composite electrolyte into a solid-state battery.

### Approach

The team's main design principle is to use an oxide ceramic as the main ion transporting phase in the electrolyte and a fluorinated polyether-based polymer electrolyte to form optimized interfaces as well as to

provide flexibility to the electrolyte membrane. In FY22, we synthesized a series of fluorinated polyether (PFPE) polymer electrolytes and characterized their physical, thermal, structural and electrochemical properties. We discovered that the conductivity of these PFPE electrolytes was too low and the PFPE/Li interfacial resistance was too high to reach DOE's performance targets. Given FY22's findings, in FY23 we modified task 1 to synthesize a model single-ion-conducting (SIC) polymer electrolyte. Single-ion-conducting polymer electrolytes with their immobilized anions further improved the transference number of our interconnected composite electrolyte and have resulted in significantly improved rate capabilities. In FY23, we continue investigating external and internal interfaces in the interconnected composites. We quantify the interface resistance between the new SIC polymer and the ceramic scaffold. We also use combined electrochemical characterizations and postmortem scanning electron microscopy (SEM) to understand lithium stripping/plating morphology, dendrite growth and cell failure mechanisms in dry solid polymer electrolyte full cells.

## Results

In FY23, efforts were focused on Task 1 and 4, the synthesis of SIC polymer electrolytes and the development of 3D composite electrolyte with the new SIC polymer, and Task 3, understanding polymer-anode interface. Results on the progress of these three tasks are summarized below.

### **1. The synthesis of SIC polymers and formation of Gen 2 interconnected composite electrolyte**

We synthesized a series of SIC polymer electrolytes and evaluated their ionic conductivity. These electrolyte membranes are referred to as 60VEC-SIC, 70VEC-SIC, 80VEC-SIC and 60EC-SIC, respectively. First, the monomers were mixed in an argon filled glovebox. Then the polymerization reaction was carried out between two glass plates separated by cover glass slips with a thickness of 0.17 mm, on a hotplate inside the glovebox. After a desired reaction time, the membrane was peeled off from the glass plates and stored in the glovebox. Measurements were done without further treatments.

Figure XIII.19.1a shows the ionic conductivity of the SIC polymer membranes. 60EC-SIC had much lower ionic conductivity than 60VEC-SIC ( $3.4 \times 10^{-8}$  vs  $6.0 \times 10^{-7}$  S/cm at 20 °C). Comparing 60, 70 and 80VEC-SIC, 80VEC-SIC had the highest ionic conductivity. However, the high conductivity is the result of low degree of polymerization and large amounts of unreacted monomers. The resulting membrane was not a complete solid. We chose 70VEC-SIC to go forward with the 3D composite development because its ionic conductivity was higher than 60VEC-SIC ( $1.7 \times 10^{-6}$  S/cm vs.  $6.0 \times 10^{-7}$  S/cm at 20 °C) and was a solid membrane. For the rest of this report, SIC polymer refers to 70VEC-SIC.

The 70VEC-SIC precursor mixture was infiltrated into an interconnected doped lithium aluminum titanium phosphate ceramic (LATP, Ohara Corp.) scaffold to prepare the interconnected ceramic/polymer composite electrolyte. Roughly 50% excess of the calculated amount of precursor was infiltrated to leave a thin surface polymer layer on both sides. The surface polymer layers are intended to promote conformal contact at the electrolyte|electrode interfaces as well as protecting LATP from reacting with lithium (Li) anode. This 3D composite is referred to as the **Gen2 3D composite**. This is to differentiate from Gen1 3D composite we developed in FY22 which consists of a different polymer electrolyte (crosslinked poly(ethylene oxide) - lithium bis(trifluoromethane)sulfonimide, xPEO-LiTFSI), and the same LATP ceramic scaffold. We also prepared a trilayered composite electrolyte with a fully dense LATP plate (Ohara Corp.), where the SIC polymer (70VEC-SIC) is thinly coated on both the surfaces. The thickness of surface polymer layers in both 3D composite and the dense plate trilayer composites is ~30-35 um. The schematics of the two composites are shown as the insets of Figure XIII.19.1b.



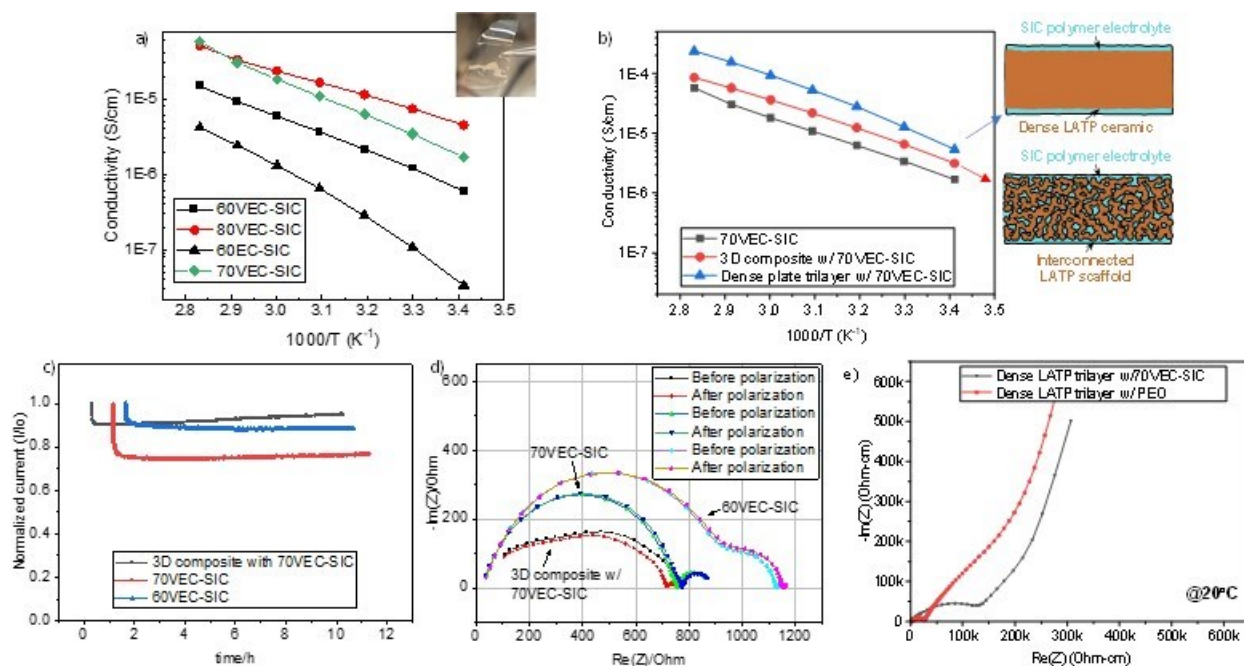


**Figure XIII.19.1** Ion transport characteristics of SIC polymer and the resulting 3D composite. (a) Ionic conductivity of 60VEC-SIC, 70 VEC-SIC, 80VEC-SIC, and 60EC-SIC as a function of inverse temperature. Inset, a digital photograph of 60VEC-SIC membrane. (b) Ionic conductivity of 70 VEC-SIC, 3D composite with 70VEC-SIC, and Dense LAMP plate trilayer with 70VEC-SIC, as a function of inverse temperature. (c) and (d)  $\text{Li}^+$  transference number ( $t_+$ ) measurement results of 60VEC-SIC, 70VEC-SIC, and 3D composite with 70VEC-SIC at 70 °C. (c) Chronoamperometry with an applied potential of 10 mV. Current is normalized to initial current. (d) The impedance spectra before and after the applied potential. (e) Impedance spectra at 20 °C of Dense LAMP trilayer w/ 70VEC-SIC, and Dense LAMP trilayer w/ linear PEO-LiTFSI.

Figure XIII.19.1b plots the Arrhenius plots of ionic conductivity of Gen2 3D composite and is compared with the pure SIC polymer and the trilayer with dense plate. Ionic conductivities of Gen 2 3D composite and the trilayer with dense plate are  $\sim 2$  and  $\sim 6$  times higher, compared to the neat polymer, owing to the contributions of LAMP ceramic scaffold and the dense plate, which has one and two orders higher ionic conductivities compared to the neat SIC polymer. The suppressed enhancement of ionic conductivity is due to both the low ionic conductivity of the 70VEC-SIC surface polymer (even if only  $\sim 30$   $\mu\text{m}$  thick), and the polymer/ceramic interfacial impedance present at the membrane surfaces. The polymer/ceramic interfacial impedance is measured to be much smaller with 70VEC-SIC compared to linear PEO-LiTFSI that was reported in the last year (see the second semicircle in Figure XIII.19.1e). The impedance is normalized to area and thickness of the membranes ( $R \times \text{Area}/\text{thickness}$ ).

We also measured the  $\text{Li}^+$  transference number ( $t_+$ ) of the 3D composite, and neat 60 and 70VEC-SIC in a Li symmetric cell at 70 °C using the Bruce-Vincent method (Figure XIII.19.1c and d). The current profiles obtained during the chronoamperometry step are normalized to the initial current. The steady-state current of the 70VEC-SIC showed a greater decay compared to 60VEC-SIC for unknown reason. However, the Gen2 3D composite showed little decay from the initial value, suggesting very low concentration gradient formation within the electrolyte and participation of the ceramic phase.

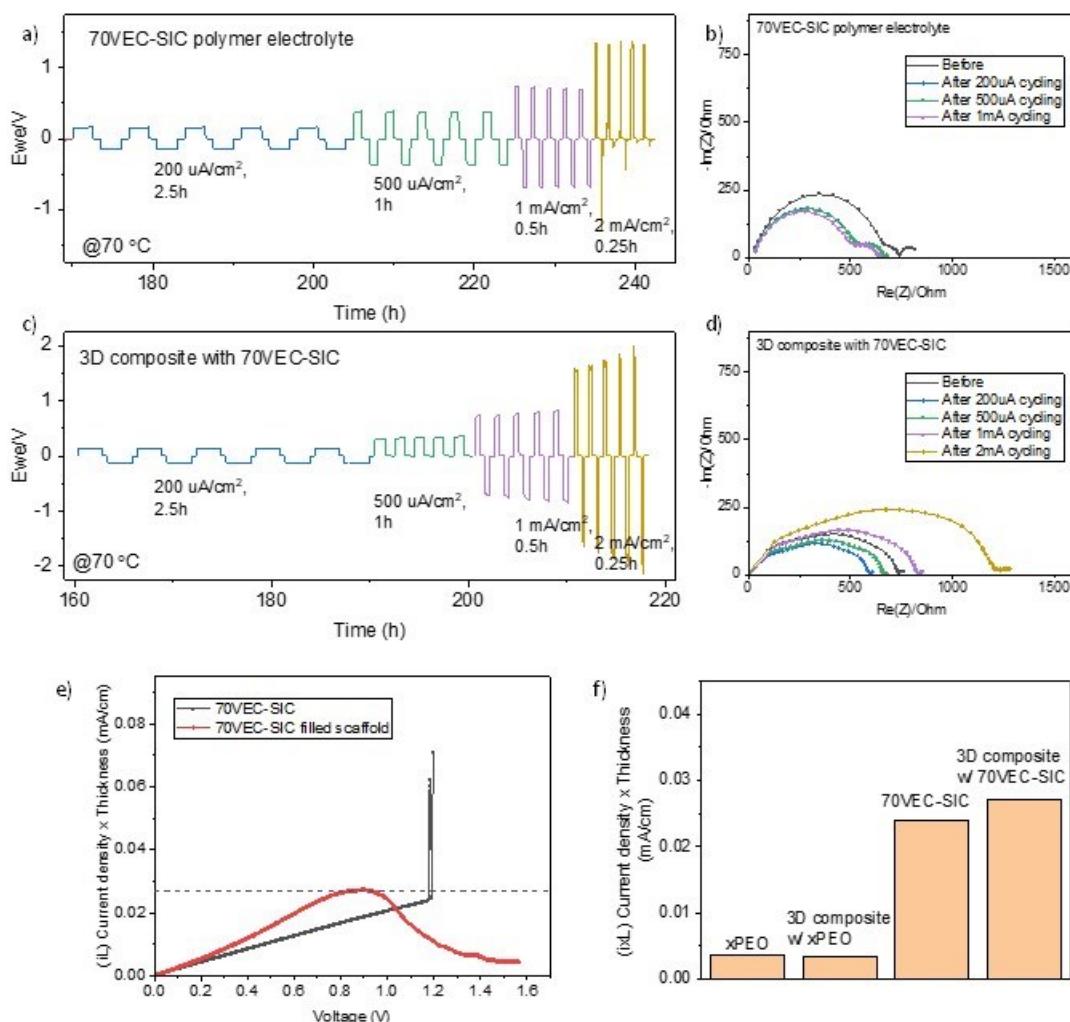


**Figure XIII.19.2** Rate performance in SIC polymer and Gen2 3D composite. (a, c) Li//Li stripping/plating test of 70VEC-SIC and 3D composite electrolyte at increasing currents while keeping the capacity cycled per cycle constant at 0.5 mAh/cm<sup>2</sup>. (b, d) Evolution of the impedance spectra before and after cycling (shown in a, c) at various currents. (e) Linear sweep voltammetry (LSV) of 70VEC-SIC, 70VEC-SIC filled LAMP scaffold, at 0.05 mV/s and 70 °C. (f) Bar chart comparing the normalized limiting current (i x L) of xPEO-LiTFSI, 3D composite with xPEO-LiTFSI, 70VEC-SIC, and 3D composite with 70VEC-SIC, measured via LSV at 0.05 mV/s and 70 °C.

We investigated the rate performance of the neat 70VEC-SIC polymer as well as the Gen2 3D composite in a Li//Li symmetric cell at 70 °C (Figure XIII.19.2). The 70VEC-SIC electrolyte survived up to 1 mA/cm<sup>2</sup> before shorting at 2 mA/cm<sup>2</sup> (Figure XIII.19.2a). These currents are much greater than what the prior non-single-ion polymer electrolyte formulations could be cycled at. The cell showed stable impedance until shorting (Figure XIII.19.2b). The Gen2 3D composite did not show any shorting even at 2 mA/cm<sup>2</sup> based on the voltage profiles (Figure XIII.19.2c). Note that the absence of negative half cycles at 500  $\mu\text{A}/\text{cm}^2$  was a mistake in programming. However, the impedance continued to significantly increase, especially after cycling at 2 mA/cm<sup>2</sup> (Figure XIII.19.2d). This is an indication of the reaction of Li metal dendrites with LAMP ceramic scaffold which is unstable with Li and forms electronically conductive reaction products which can further perpetuate the reaction.

Limiting current density of the Gen2 3D composite as compared with the pure SIC polymer electrolyte (70VEC-SIC) was measured via linear sweep voltammetry (LSV) at a scan rate of 0.05 mV/s. In this test, the voltage is increased at a constant rate while the current is recorded. The value of current at which it plateaus is

extracted as the limiting current of the electrolyte. Since it is dependent on the electrolyte thickness, a normalized value plotted in Figure XIII.19.2e. The current profiles are dramatically different between the two electrolytes. A sudden spike in the pure polymer curve is due to a complete Li dendrite penetration causing a short, and therefore it never reaches a plateau. This current is then noted as its limiting current. Whereas, the Gen2 3D composite reaches a plateau before it starts to go downwards suggesting a different failure mechanism, where the cell resistance increases (compared to decrease with a short). Figure XIII.19.2f compares the limiting currents observed for Gen 2 3D composite prepared with 70VEC-SIC with the Gen 1 3D composite prepared in the last fiscal year with a dual-ion polymer electrolyte (xPEO-LiTFSI), along with the corresponding neat polymers. We note two observations from this comparison: 1) the limiting current density of the composite seems to be dictated by the neat polymer; 2) Gen 2 composite achieved an 8-fold increase in the limiting current density compared with Gen 1 composite, owing to the high rate capability of the SIC polymer.

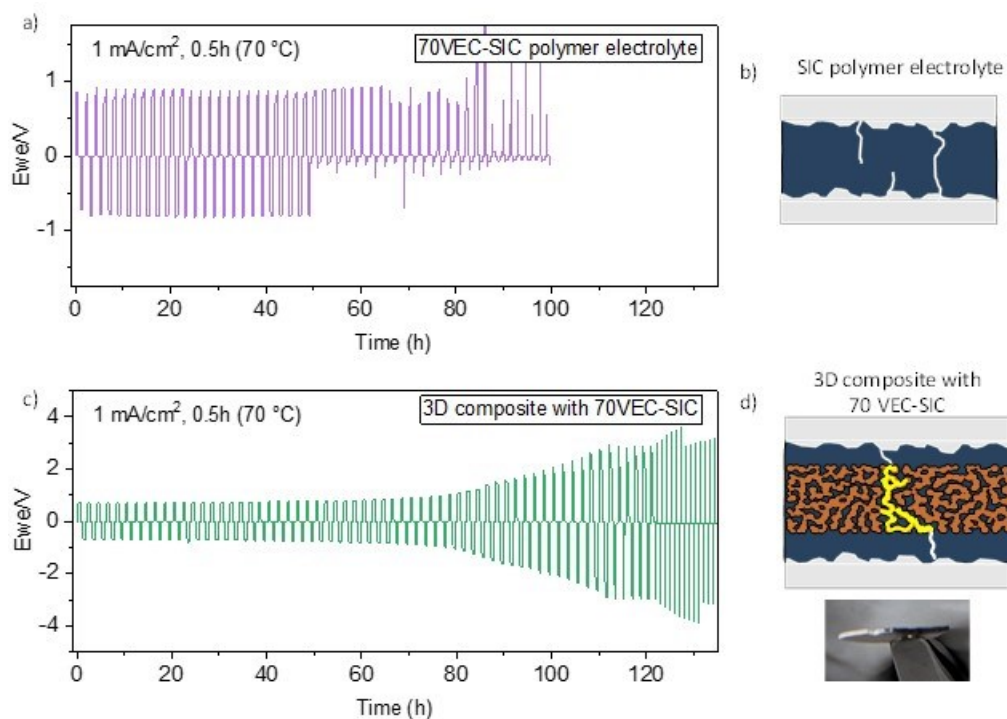


**Figure XIII.19.3** Failure mechanisms in SIC polymer and Gen2 3D composite. (a, c) Li//Li symmetric cell cycling of cells made with 70VEC-SIC and the 3D composite with 70VEC-SIC, respectively. Cycling is done at 1 mA/cm<sup>2</sup> and 70 °C with each half cycle being 0.5 h long. (b, d), Proposed failure mechanisms in a and c, respectively.

Long term cycling at a current density of 1 mA/cm<sup>2</sup> was performed to further evaluate the failure mechanisms of the SIC polymer and Gen2 3D composite (Figure XIII.19.3). When cycled a current density of 1 mA/cm<sup>2</sup>, which is slightly lower than the limiting current of both the electrolytes, the pure polymer cell shorts in about 50 h of cycling, whereas the composite cell cycled stably for almost 70 h (consistent with its slightly higher limiting current), after which the cell overpotential increased continuously (Figure XIII.19.3a, c). This also seems consistent with the failure mechanism described above, where likely the membrane impedance increased instead of a complete short. A photograph of the composite membrane extracted from a Li//Li symmetric cell after rate-test cycling is shown in Figure XIII.19.3d where the cross-section had turned black and membrane was fractured. The schematics in Figure XIII.19.3b and d illustrates proposed failure mechanisms of the SIC polymer and the Gen2 composite: for the SIC polymer, dendrite growth leading to cell shorting is the failure mechanisms; whereas for the composite, partial dendrite propagation through the surface

polymer layer followed by their consumption via chemical reaction with the Li-unstable LATP ceramic as well as fracturing of the composite membrane is the failure mechanism.

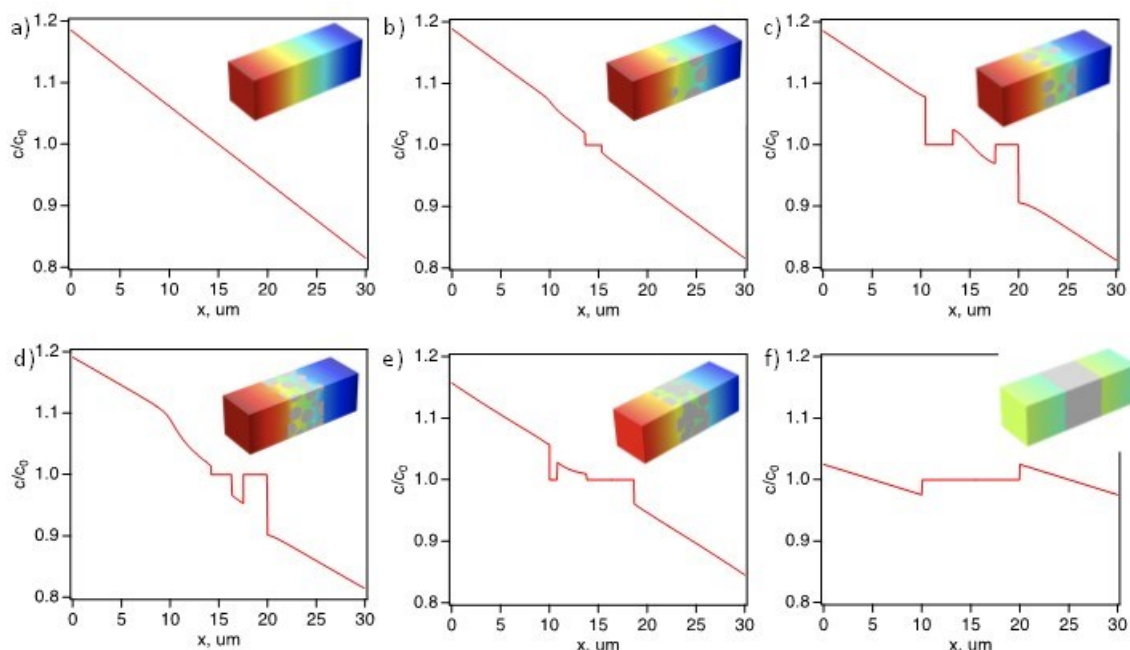


**Figure XIII.19.4** Normalized lithium concentration in PE at steady state current under 10 mV applied potential: a) fully PE domain; b) 15 vol% LATP particles; c) 30 vol% LATP particles; d) 50 vol% particles; e) 50 vol% particles connected via partial sintering; f) fully dense LATP block. The line plots represent normalized concentration along the line passing through the center of the domain.

In addition to experiments, we used numerical simulations to study effect of particle loading and particle connectivity on ion distribution and transient behavior of composite polymer electrolytes. In Figure XIII.19.4, normalized concentration gradients were computed in a dual-ion-conducting polymer electrolyte with the addition of ceramic particles of a series of loadings and connectivity. The concentration gradients in the polymer electrolyte phase form due to the additional diffusional ion flux. It can be seen that the highest concentration gradients develop in all of the scenarios from 0% to 50% by volume of LATP loading. With interconnected particles (Figure XIII.19.4e), the concentration gradient only decreased slightly. The most uniform distribution of Li cations is achieved in the scenario where the PE domains are separated by a fully dense LATP insert which fully blocks the migration of anions thus resulting in overall reduction of concentration gradients, Figure XIII.19.4f.

**Table XIII.19.1** Comparison between Gen2 and Gen1 3D Composite Electrolytes.

	Gen 2 3D composite	Gen 1 3D composite	Gen 2 polymer	Gen 1 polymer
<b>Polymer</b>	70 VEC-SIC	xPEO-LiTFSI (filling) Linear PEO-LiTFSI (surface layer)	70 VEC-SIC	xPEO-LiTFSI, Linear PEO-LiTFSI
<b>Ceramic</b>	LATP	LATP	-	-
<b>t+ (Bruce-Vincent)</b>	0.76	0.29	0.75	0.05
<b>Interface resistance between polymer and ceramic (<math>\Omega\cdot\text{cm}^2</math>) at 25 °C</b>	1512	1294 (xPEO-LiTFSI/LATP) 4110 (Linear PEO-LiTFSI/LATP)	-	-

	Gen 2 3D composite	Gen 1 3D composite	Gen 2 polymer	Gen 1 polymer
Conductivity at 70 °C (S/cm)	$5.7 \times 10^{-5}$	$1.0 \times 10^{-4}$	$3.1 \times 10^{-5}$	$2.6 \times 10^{-4}$ (xPEO-LiTFSI) $4.7 \times 10^{-4}$ (Linear PEO-LiTFSI)
Limiting current density normalized by thickness (mA/cm)	0.027	0.0034	0.024	0.0036 (xPEO-LiTFSI)

In Table XIII.19.1, we summarize and compare the characteristics of Gen2 and Gen1 3D composites. Gen2 3D composite features the following improvements compared to Gen1 3D composite: 1) its  $\text{Li}^+$  transference number is 0.76, much higher than Gen 1 composite, due to the use of an SIC polymer electrolyte; 2) the interface resistance between SIC polymer and LATP ceramic is lower than that between linear PEO-LiTFSI and LATP; 3) Gen2 composite has higher ionic conductivity compared to the neat SIC polymer, whereas Gen1 composite's conductivity was lower than the neat polymer electrolytes (PEO-LiTFSI) and 4) 8-fold improved limiting current density compared to Gen 1 composite.

## 2. Lithium morphology evolution and cell failure mechanism in dry polymer electrolytes

In order to understand lithium stripping/plating morphology, and cell failure mechanisms in dry solid polymer electrolyte, we fabricated full cells made with dry polymer electrolyte, xPEO-LiTFSI. The cell configurations are shown in Figure XIII.19.5a. Two types of Li anodes were used, a Li chip with 600  $\mu\text{m}$  thickness from MTI corp., and a Li foil that is 40  $\mu\text{m}$  thick on a copper substrate from MSE Supplies. We refer to these two configurations as the Li chip cells and Li foil cells, respectively. The cells were first conditioned at 70 °C for 48 hrs, followed by cycling at 70 °C between 2.8 and 4.2 V at a current density of 50  $\mu\text{A}/\text{cm}^2$ . Representative voltage profiles are shown in Figure XIII.19.5b. The time to complete each cycle decreases as cycling goes on, indicating capacity decay of the cells. Figure XIII.19.5c shows average charge and discharge capacity of Li chip and Li foil cells, each averaged over 6 cells. The first cycle discharge capacity of Li chip cells is higher (106 mAh/g) than that with Li foil (88 mAh/g). However, the Li chip cells' capacity on average faded much faster than the Li foil cells. To better visualize capacity decay, we normalized the capacities to the discharge capacity of the first cycle (Figure XIII.19.5d). We considered a cell to be dead once 90% of the initial capacity was lost. On average, Li foil cells (56 cycles) were able to cycle for almost 20 cycles longer than Li chip cells (37 cycles). This difference is statistically significant, as shown by Figure XIII.19.5d.

The interface impedance evolution of a representative cell with each of the lithium anodes was monitored as by taking impedance measurements after each charge and discharge half cycles. The interface resistance at the anode interface was obtained by fitting the high frequency semicircle of the impedance spectra and is shown in Figure XIII.19.5e. After first charge, the anode interface impedance for Li chip and Li foil cells was similar, 48 and 43  $\Omega \cdot \text{cm}^2$ , respectively. Slowly, the interface impedance grew. At the end of 15 cycles, the interface impedance grew to be 94 and 83  $\Omega \cdot \text{cm}^2$ , respectively. The anode interface impedance grew faster in Li chip cells.

The cathode interface impedance, including interface resistance and charge transfer resistance, was obtained by fitting the low frequency semicircle, as shown in Figure XIII.19.5f. Similar to the initial anode interface, the cathode interface impedance after first charge was similar, with 206  $\Omega \cdot \text{cm}^2$  for the Li chip cell and 250  $\Omega \cdot \text{cm}^2$  for the Li foil cell. However, the cathode interface impedance in the Li chip cell grew by over an order of magnitude in 15 cycles, to 2921  $\Omega \cdot \text{cm}^2$ , while that of the Li foil cell grew by sixfold to 1593  $\Omega \cdot \text{cm}^2$ . The substantial increase in the cathode interface impedance correlates well with the capacity fade of the cells. This analysis shows that even with the same cathode-electrolyte interface, the lithium anode has profound impact on the cathode charge transfer process.

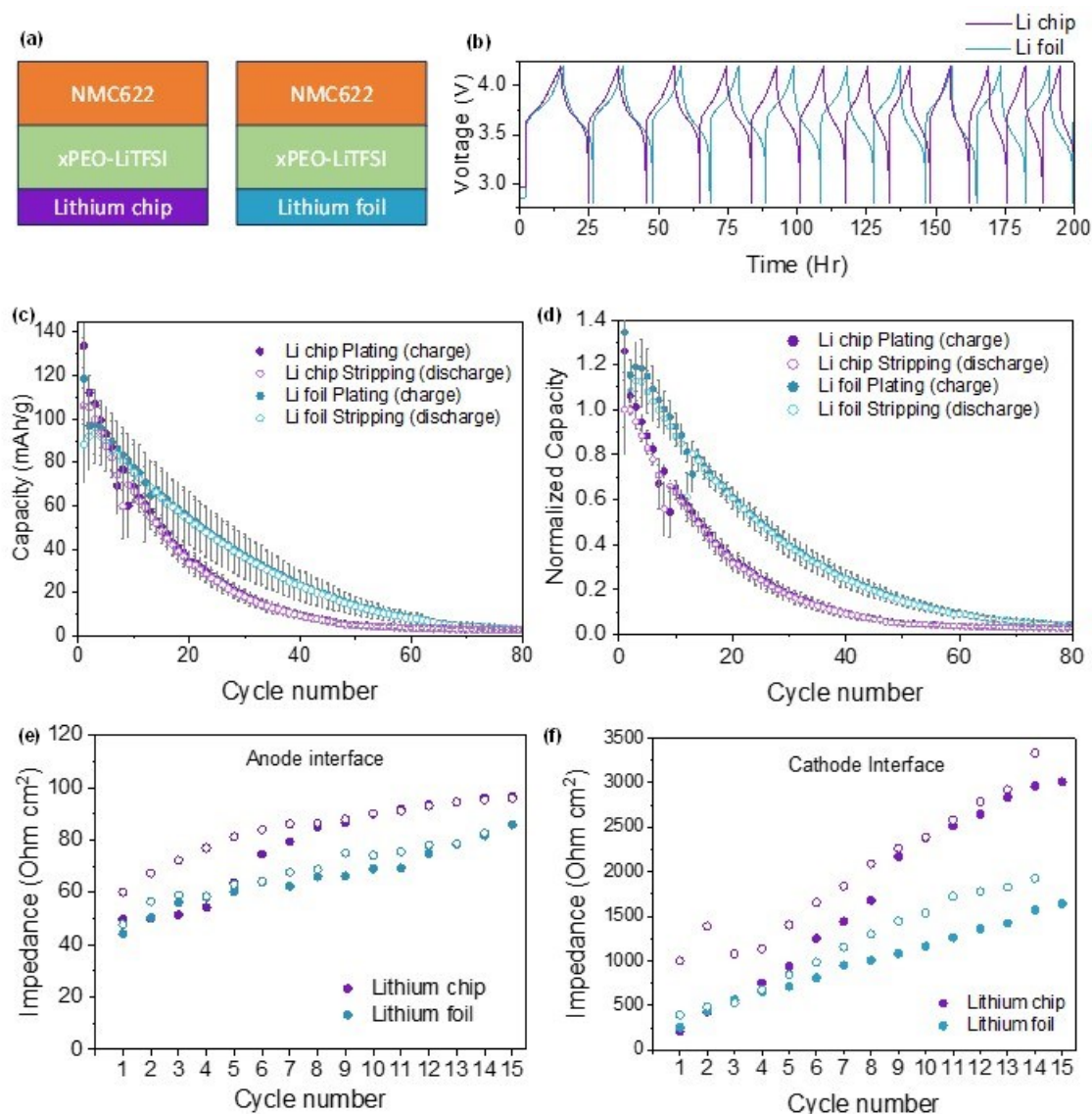


**Figure XIII.19.5** Full cell cycling results using xPEO-LiTFSI and two lithium anode sources at current density of  $50 \mu\text{A}/\text{cm}^2$  at  $70^\circ\text{C}$ . (a) Cell configurations; (b) Voltage profiles; (c) Average charge and discharge capacity as a function of cycle number; averaged over 6 cells for each type of lithium; (d) Normalized average charge and discharge capacity, normalized to the discharge capacity of the first cycle. (e) Anode interface impedance evolution as a function of cycle number; open symbols, after plating (charge to 4.2V); solid symbols, after stripping (discharge to 2.8 V) (f) Cathode interface impedance evolution as a function of cycle number. Symbols follow the same rule as Panel e.

Figure XIII.19.6 compares the Li anode morphologies before cycling and at different stages of cycling for each Li source. Pristine uncycled Li chip has smooth areas and rough areas but overall more rough than Li foil (Figure XIII.19.6a). This has been confirmed with atomic force microscopy measurements (AFM, results not shown). Li foil's surface morphology, on the other hand, is very uniform with striations across its surface. After conditioning in assembled cell at  $70^\circ\text{C}$  for 48 hrs, solid electrolyte interphase (SEI) formed on both Li chip and Li foil's surface (Figure XIII.19.6b). The morphology of the conditioned Li chip surface appears to be very different from the pristine surface. Grains with approximate size of  $5 \mu\text{m}$  have formed. Conditioned Li foil, in contrast, is similar to pristine Li foil.

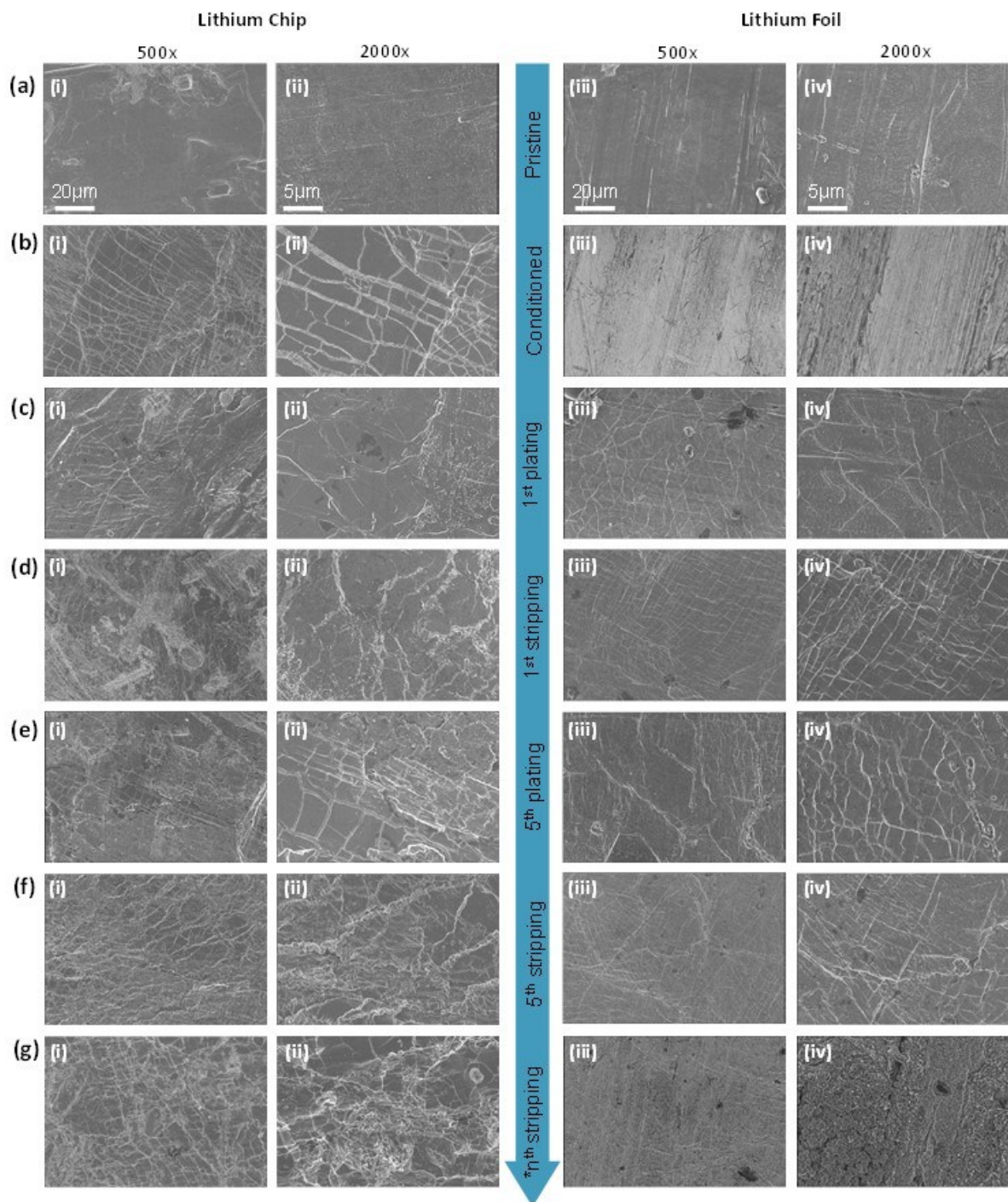


**Figure XIII.19.6 SEM images of Li anode morphology at different cycling stages. Row (a) – Row (g): Pristine (a), conditioned (b), after first plating (charge to 4.2 V) (c), after first stripping (discharge to 2.8 V) (d), after 5<sup>th</sup> plating (e), after 5<sup>th</sup> stripping (f), and after cell capacity faded to < 10% (g). Column (i, ii), morphology of Li chip at two different magnifications; Column (iii, iv), morphology of Li foil at two different magnifications. The scale bar at the top of the columns applies to all the images in the same column.**

As cycling proceeds, we did not observe significant roughening on either Li chip or Li foil anodes. In our previous study investigating the Li electrodeposition morphology of the gel composite electrolyte paired with Li chip<sup>1</sup>, we observed severe pitting as early as the second stripping cycle. This indicates much better chemical

stability between the dry xPEO-LiTFSI with Li. Taking a closer look at the plating morphology, there is a noticeable difference between the 5<sup>th</sup> plating and the 1<sup>st</sup> plating morphology for Li chip. While 1<sup>st</sup> plating is homogenous with a new layer of lithium covering all the surface uniformly (Figure XIII.19.6c, **i and ii**), 5<sup>th</sup> plating appears to be less uniform (Figure XIII.19.6e, **i and ii**). There are areas that look very similar to the grains first seen in the conditioned Li. This can also be seen in the SEM image after cell death (Figure XIII.19.6g, **i and ii**). This leads us to believe that there are parts of the Li chip that did not participate in cycling. It is possible that Li chip gradually lost contact with xPEO-LiTFSI. This is further supported by the lack of Li chip lodged in the polymer (results not shown) as we peeled them apart. For Li foil, plating morphology remains uniform throughout cycling. The Li morphology study results seems to indicate that Li foil has better adhesion with xPEO-LiTFSI than Li chip.

The above results on the cell performance and impedance analysis, together with the Li morphology study, demonstrated that the primary failure mode from these cells is capacity fade (instead of dendrite growth), as none of the 12 cells shorted. The Li foil cells lasted longer (56 cycles) than Li chip cells (37 cycles). This difference is statistically significant. Impedance analysis suggested that the anode interface resistance slowly grew for both cells, but not nearly as much as the cathode interface impedance growth. We believe that the capacity decay originates primarily from unoptimized cathode-electrolyte interface. However, the two forms of Li sources lead to different decay rates. Li morphology study seems to indicate that Li foil has better adhesion with the polymer electrolyte than Li chip. XPS analysis shows that Li foil has a thinner SEI layer richer in fluorine (results not shown). We also note that although dry xPEO-LiTFSI and the gel composite electrolyte<sup>1</sup> have very similar mechanical modulus and ionic conductivity at their respective cycling conditions, the failure modes are drastically different. In dry xPEO-LiTFSI, polymer-cathode interface drives cell failure while in the gel composite electrolyte, dendrite growth is the primary cell failure mode.

## Conclusions

In Tasks 1 and 4, we synthesized a single-ion-conducting polymer electrolyte. By adjusting the monomer ratios, the degree of polymerization was optimized to have the highest ionic conductivity ( $1.7 \times 10^{-6}$  S/cm at 20 °C) while still maintaining a solid membrane. A representative SIC polymer, 70VEC-SIC, was used to infiltrate the 3D LATP ceramic scaffold to form interconnected composite (Gen2 composite). Compared with Gen1 composite consisting of xPEO-LiTFSI and LATP scaffold, Gen2 composite with 70VEC-SIC and LATP scaffold boasts 8-fold increase in limiting current density. Gen2 composite can cycle stably for 70 cycles at 1 mA/cm<sup>2</sup>. This current density is the DOE target for solid-state batteries. The significant improvement in limiting current density is the combined results of greatly improved Li<sup>+</sup> transference number and decreased interfacial resistance between 70VEC-SIC and LATP ceramic, compared to Gen 1 composites.

In Task 3, we studied lithium stripping/plating morphology and cell failure mechanisms in dry solid polymer electrolyte full cells made with xPEO-LiTFSI electrolyte, NMC622 cathode and two forms of lithium – Li chip and Li foil. The long-term cycling assessment demonstrated that the primary failure mode from these cells is capacity fade. The Li foil cells' lifetime is 50% longer than Li chip cells (56 cycles vs 37 cycles). This difference is statistically significant. We believe that the capacity decay originates primarily from unoptimized cathode-electrolyte interface. However, the two forms of Li sources lead to different decay rates. Li morphology study seems to indicate that Li foil has maintained better contact with the polymer electrolyte than Li chip. XPS analysis shows that Li foil has a thinner SEI layer richer in fluorine. This study indicates that while unoptimized cathode-electrolyte interface causes capacity decay, Li anode also plays a role in cell's capacity fade and failure mechanism.

## Key Publications

1. Sahore, R.\*; Armstrong, B. L.; Tang, X.; Liu, C.; Owensby, K.; Kalnaus, S.; Chen, X. C., Role of Scaffold Architecture and Excess Surface Polymer Layers in a 3D-Interconnected Ceramic/Polymer Composite Electrolyte. *Adv. Energy Mater.* 2023, 2203663.
2. Bocharova, V.\*; Chen, X. C.; Jeong, S. P.; Zhou, Z.; Sacci, R. L.; Keum, J. K.; Gainaru, C.; Rahman, M. A.; Sahori, R.; Sun, X.-G.; et al. Single Ion Conducting Hairy Nanoparticle Additive to



Improve Cycling Stability of Solid Polymer Electrolytes. *ACS Applied Energy Materials* **2023**, *6*, 8042-8052. DOI: 10.1021/acsaem.3c01106

3. Owensby, K. D.; Sahore, R.; Tsai, W.-Y.; Chen, X. C.\* Understanding and controlling lithium morphology in solid polymer and gel polymer systems: mechanisms, strategies, and gaps. *Materials Advances* **2023**, 10.1039/D3MA00274H.
4. R. Sahore, B. Armstrong, X. C. Chen, S. Kalnaus, “Self-standing Interconnected Polymer/Ceramic Composite Solid Electrolyte”, US Provisional Patent Application Serial No. 63/532,107, filed 08/11/2023.

## References

1. (1) Tsai, W.-Y.; Chen, X. C.; Kalnaus, S.; Sahore, R.; Du, Z.; Westover, A. S. Li Morphology Evolution during Initial Cycles in a Gel Composite Polymer Electrolyte. *ACS Applied Energy Materials* 2022. DOI: 10.1021/acsaem.2c01856.

## XIII.20 Inorganic-Polymer-Composite Electrolyte with Architecture Design for Lithium Metal Solid State Batteries (BNL)

### Enyuan Hu Principal Investigator

Chemistry division, Brookhaven National laboratory  
Bldg. 555, Brookhaven National Lab.  
Upton, NY 11973  
E-mail: [enhu@bnl.gov](mailto:enhu@bnl.gov)

### Simon Thompson, DOE Technology Development Manager

U.S. Department of Energy  
E-mail: [Simon.Thompson@ee.doe.gov](mailto:Simon.Thompson@ee.doe.gov)

Start Date: October 1, 2022

End Date: September 30, 2023

Project Funding (FY23): \$500,000

DOE share: \$500,000

Non-DOE share: \$0

### Project Introduction

This project aims to leverage the strong expertise and close collaboration of the team (**Brookhaven National Laboratory, Harvard University and University of California, Irvine**) to address issues facing solid electrolyte lithium metal batteries and achieve goals set by DOE. We propose to use inorganic-polymer-composite electrolyte coupled with architecture design to address the issue. Composite electrolyte can inherit the merits of both the inorganic electrolyte part (high ionic conductivity, compatibility with cathode, good mechanical strength and so on) and the polymer part (good interfacial contact, tunable stability with lithium metal, facile thickness control, flexibility, easy roll-to-roll processing and so on). It is worth noting that the proposed organic-inorganic hybrid strategy is built upon the demonstrated success of a ‘combination’ strategy for liquid electrolyte optimizations in which combines ethylene carbonate (excellent interphase formation capability but poor conductivity) and some linear carbonate (great conductivity but cannot form good interphase).

The importance and success of the architecture design for solid electrolyte, especially in addressing the lithium dendrite penetration issue, has been recently demonstrated by the team. We will generalize this strategy to composite electrolytes that include broad types of ceramic and polymer electrolytes. We will optimize the composite electrolyte structure—sandwiched, interpenetrated, or dispersed to strike a balance between ionic conductivity, mechanical stability, and electrochemical (interface) stability.

The advantage of high energy density of solid-state batteries can only be realized by a lithium metal anode. Therefore, stability against lithium metal is a key property required for solid electrolyte and lithium metal protection is needed if the electrolyte does not have sufficient thermodynamic stability against lithium. The lithium metal stability issue can be addressed by engineering the interphase, a strategy that has been proven to be successful in liquid-electrolyte-based lithium metal batteries. It was shown that through tuning the solvation structure and the additive, the property of solid-electrolyte-interphase (SEI) can be engineered to favor lithium-ion transport across the interphase and stabilize the lithium metal anode. We propose to use similar strategies for the composite solid electrolyte and engineer the lithium metal SEI through the optimization of the polymer electrolyte composition, especially the choice of additives.

We also aim to apply the advanced characterization tools including synchrotron and cryoEM, to help us understand both the interphases and the bulk properties. The interphases include lithium metal SEI, cathode-electrolyte-interphase (CEI), and also very importantly, the interphase between polymer and ceramic in the solid electrolyte which is critical to the overall electrolyte performance but was very little characterized and understood.

## Objectives

This project targets the following goal: the composite electrolytes will be thin ( $< 100 \mu\text{m}$ ) and have high Li-ion conductivity ( $\geq 10^{-3} \text{ S/cm}$  at room temperature), low interfacial impedance, and desirable mechanical properties. When used in the solid electrolyte (SE) Li-metal battery, a current density  $> 1 \text{ mA/cm}^2$  and an areal capacity of  $2\text{-}3 \text{ mAh/cm}^2$  can be achieved with more than 300 cycles. The constructed  $\text{LiNi}_x\text{Mn}_y\text{Co}_{1-x-y}\text{O}_2$  (NMC)/ $\text{LiCoO}_2$  || composite electrolyte || Li-metal cell can be operated at up to  $4.5 \text{ V}$  versus  $\text{Li}^+/\text{Li}$ . The SE will also be compatible with high loading cathodes in achieving high energy density at the coin or pouch-cell level.

## Approach

The project approaches are as follows: (1) design and synthesize polymer with anion-tether strategy for high transference number, (2) through theories and experiments, design hierarchical inorganic electrolyte for suppressing lithium dendrite penetration, (3) optimize the composite electrolyte composition and structure, (4) use additives for Li-metal anode and NMC cathode protection, and (5) use synchrotron and cryogenic electron microscopy characterization to understand the bulk electrolyte and interphases.

## Results

In FY2023, the BNL team fabricated polyvinylidene difluoride (PVDF) based polymer electrolyte and characterized it systematically in various cell configurations to understand its stability against the electrodes. Figure XIII.20.1a shows the structure of PVDF and the fabrication process of the PVDF-lithium bis(trifluoromethanesulfonyl)imide (LiTFSI) polymer electrolyte using the solvent casting method. Several common solvents were tried and it turned out that the highly polar solvent, N-Methylpyrrolidone (NMP), has good solubility of PVDF polymer and was therefore used as the solvent. 600 mg of PVDF powder and LiTFSI salt (weight ratio 1:1) were added to 10ml NMP solution, which was then stirred for 24 hours to obtain a uniform slurry. The slurry was added to glass Petri dishes and vacuum dried at  $60 \text{ }^\circ\text{C}$  for 24 hours to remove the solvent and form the solid electrolyte film. The obtained PVDF polymer electrolyte is around  $100 \mu\text{m}$  in thickness.

The PVDF polymer electrolyte has an ionic conductivity of around  $10^{-4} \text{ S/cm}$  at room temperature. It was assembled into solid state battery (coin cell) together with various cathodes and lithium metal anodes. NMC811(NMC)||Li,  $\text{LiFePO}_4$ (LFP)||Li,  $\text{LiMn}_2\text{O}_4$ (LMO)||Li and  $\text{LiCoO}_2$ (LCO)||Li cells were tested and selected charge-discharge profiles from the initial 15 cycles are shown in Figure XIII.20.1b. Both NMC||Li and LCO||Li cells experience rapid capacity fade even within 15 cycles while LFP||Li and LMO||Li cells show good stability.

To understand the capacity fade mechanism, synchrotron-based soft x-ray absorption spectroscopy (XAS) was carried out for ex situ polymer electrolytes. Nitrogen, carbon and oxygen XAS spectra are shown in Figure XIII.20.1c and Figure XIII.20.1d. From the nitrogen and carbon XAS data, it is clear that signals from the LiTFSI salt are still strong for the cycled polymer electrolytes harvested from LFP||Li and LMO||Li cells. In contrast, the LiTFSI salt signals are mostly gone for cycled polymer electrolytes harvested from NMC||Li and LCO||Li cells. As the experiment was done in fluorescence mode which has a probing depth of around  $100 \text{ nm}$  for the polymer materials, the absence of LiTFSI salt peaks in the XAS data suggests that a considerable amount of salt (upon contact with the cathode and at least  $100 \text{ nm}$  in depth) was consumed during cycling. While this is the case for NMC||Li and LCO||Li cells, LiTFSI seems to be well maintained in LFP||Li and LMO||Li cells.

Figure XIII.20.2d shows the oxygen XAS for the PVDF polymer electrolyte (without adding LiTFSI salt). The presence of the peak at around  $533 \text{ eV}$  suggests that pristine electrolyte contains oxygen element. This is unexpected as PVDF itself does not contain any oxygen. The only possible oxygen source is the solvent NMP which has oxygen in the carbonyl group. Therefore, this result indicates that NMP solvent cannot be fully removed during the electrolyte fabrication process. The carbonyl group in NMP may cause instability issue against lithium metal and this was verified by the experiment shown in the right panel of Figure XIII.20.2d. A

piece of lithium metal anode was placed in a vial containing NMP solvents. After 12 hours, the solution that was initially transparent became yellowish, suggesting the reactivity of NMP with lithium metal. In summary, PVDF/LiTFSI polymer electrolyte was fabricated using the solvent casting method. The electrolyte shows relatively good ionic conductivity and enables cycling of various solid state battery cells at room temperature. While LFP||Li and LMO||Li cells show stable cycling, NMC||Li and LCO||Li cells do not. The degradation may be attributed to both the salt consumption by NMC and LCO and the incompatibility between lithium metal and NMP which is the solvent residual that cannot be fully removed during the fabrication process. Learning from these lessons, the team is now actively exploring solvent-free method for making polymer electrolytes.

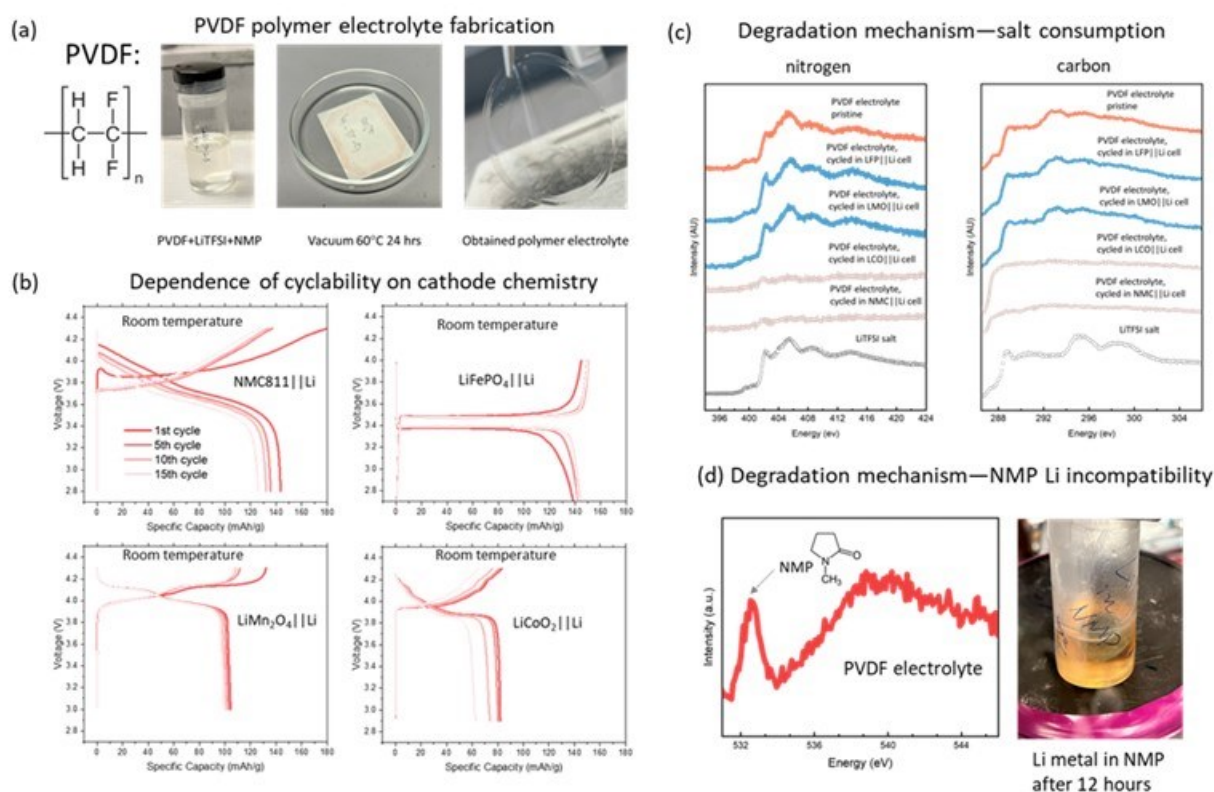


**Figure XIII.20.1** (a) Fabrication of PVDF/LiTFSI polymer electrolyte using NMP based solvent casting method. (b) Cyclabilities of NMC811 || Li, LiFePO<sub>4</sub> || Li, LiMn<sub>2</sub>O<sub>4</sub> || Li and LiCoO<sub>2</sub> || Li cells using the fabricated PVDF polymer electrolyte. (c) Degradation mechanism probed by the soft x-ray absorption spectroscopy (XAS) both at nitrogen and carbon K-edges. The fluorescence mode, which has a probing depth of around 100nm, is used. (d) left, degradation mechanism probed by soft XAS at oxygen K-edge; right, the reactivity between NMP and lithium metal anode indicated by the solution which turned from transparent to yellowish after putting lithium disk in NMP solvent after 12 hours. The vial was placed in the Ar-filled glove box.

In FY2023, the BNL team also designed and fabricated an *in situ* solid-state cell to study the interphase between solid state electrolyte (SSE) and the cathode. The cell design was done in collaboration with Prof. Fudong Han from Rensselaer Polytechnic Institute. As shown in Figure XIII.20.2a, catholyte, SSE and anode are sandwiched between two stainless steel plates. Catholyte is a composite of NCA (LiNi<sub>0.8</sub>Co<sub>0.15</sub>Al<sub>0.05</sub>O<sub>2</sub>) cathode and ceramic SSE. The anode is LiIn alloy which has good stability with most of the SSE to be studied. Au coating is applied on the top of catholyte to serve as both current collector and an X-ray window. To strike a balance between electric conductivity and X-ray signal, the thickness of the Au coating was optimized to be around 100 nm. The whole system is sealed with rubber rings and pressured through the screws through the holes. The incoming X-ray shines upon the catholyte and resulting fluorescence spectroscopy reveals information about the interphase between the cathode and the SSE in the catholyte.

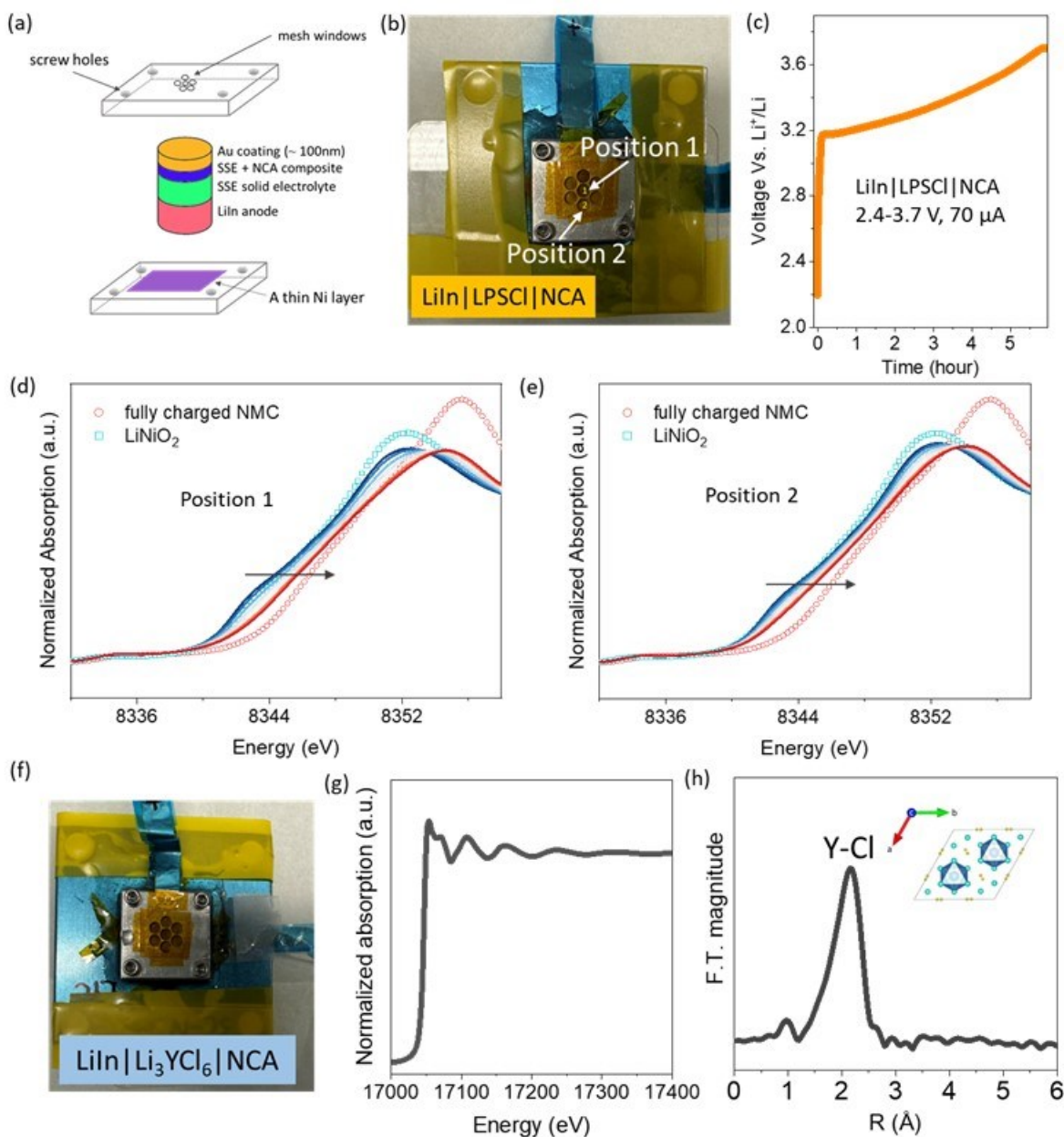


Figure XIII.20.2 (a) Schematic of the *in situ* solid-state cell design. (b) The *in situ* solid-state cell using argyrodite as the SSE. (c) The first cycle charging curve of the *in situ* solid-state cell mentioned in (b). (d) The *in situ* Ni K-edge XANES data collected from position 1 in the *in situ* cell. (e) The *in situ* Ni K-edge XANES data collected from position 2 in the *in situ* cell. (f) The *in situ* solid-state cell using  $\text{Li}_3\text{YCl}_6$  as the SSE. (g) Y K-edge XANES data of the pristine catholyte measured in the cell. (h) Y K-edge ft-EXAFS data of the pristine catholyte measured in the cell.

At NSLS-II (National Synchrotron Light Source II) of BNL, two *in operando* XAS (X-ray absorption spectroscopy) experiments were carried out for two *in situ* solid-state cells. In the first cell, argyrodite  $\text{Li}_6\text{PS}_5\text{Cl}$  SSE is used (Figure XIII.20.2b). Probably due to its high ionic conductivity, the *in situ* cell was able to be charged even at room temperature. The charging curve is shown in Figure XIII.20.2c. As the voltage of LiIn is around 0.6 V Vs.  $\text{Li}^+/\text{Li}$ , the voltage of the *in situ* cell is around 0.6 V lower than that of the conventional cell using Li metal as the anode. Therefore, charging the *in situ* cell to 3.7 V is equal to charging

conventional cell to 4.3 V from the perspective of the depth of delithiation. At this voltage, most of the lithium is extracted. During discharge (not shown in the Figure), much less capacity was delivered. This is probably because charging induces a higher pressure than discharging as the former process involves lithium plating while the latter involves stripping. The higher pressure means better physical contact among cell components and better overall kinetics. Even though a full charge-discharge cycle was not successful, *in situ* data for the charging part was obtained. The results are shown in Figure XIII.20.2d and Figure XIII.20.2e, corresponding to the data from point 1 and point 2 in the *in situ* cell. Different locations were selected to test the homogeneity of the reaction. The *in situ* data from both points suggest Ni is oxidized to the fully charged state, indicating that at the current density ( $70 \mu\text{A}/\text{cm}^2$ ) used for the experiment, the reaction is in general homogeneous.

The second *in situ* solid-state cell we tested is the cell in which  $\text{Li}_3\text{YCl}_6$  is used as the SSE (Figure XIII.20.2f). Because the energy of yttrium K-edge is within the accessible range of the beamline, XAS of Y K-edge was measured for the *in situ* cell at the pristine state and the results are shown in Figure XIII.20.2g and Figure XIII.20.2h, corresponding to the XANES (X-ray absorption near edge spectroscopy) and the ft-EXAFS (Fourier transformed extended X-ray absorption fine structure) of XAS. The XANES data is consistent with those in the literature report. In the ft-EXAFS, the first peak corresponds to the Y-Cl bond in the  $\text{YCl}_6$  octahedra in  $\text{Li}_3\text{YCl}_6$ . There are no additional peaks in the ft-EXAFS because the  $\text{YCl}_6$  octahedra are far apart from each other as shown in the inset graph of Figure 1h. Attempts to charge the *in situ* cell failed probably because the ionic conductivity of the used  $\text{Li}_3\text{YCl}_6$  is not high enough to guarantee charge-discharge at room temperature. A possible remedy may be adding heating element to the *in situ* cell, which is the ongoing effort to improve the *in situ* solid-state cell. To sum, we have tested the feasibility of the *in situ* solid-state cell to study the interphase between SSE and cathode as in the catholyte. High quality XAS data can be obtained for both 3d transition metal and those elements whose energies are accessible such as Zr, Y and Br. These are important elements for oxide, sulfide and halide SSE. We have realized that kinetics may be an issue for the *in situ* solid-state cells and heating elements may need to be added to guarantee charge-discharge for all cells with various SSE. We will keep improving the *in situ* cell to achieve a fully successful XAS experiment in the future.

In FY2023, the UCI team developed an ultra-thin, single-ion conducting solid polymer electrolyte (SIC-SPE) prepared by a modified UV polymerization approach (Figure XIII.20.3a). Typically, a 20- $\mu\text{m}$ -thick Celgard® PP separator was employed as the mechanical reinforcement to ensure compatibility with conventional battery fabrication technology. The SPE chemistry was also carefully tuned for better wettability towards the PP reinforcement as well as avoiding macroscopic phase separation. The achieved thickness of 20- $\mu\text{m}$  is comparable to state-of-the-art liquid electrolytes and is significantly reduced compared with other reported SSEs<sup>1</sup>. More excitingly, we further demonstrate in Figure XIII.20.3b that the 20- $\mu\text{m}$  SIC-SPE still possesses excellent dendrite blocking capability as evidenced by a high critical current density (CCD) of  $2.4 \text{ mA}/\text{cm}^2$ . For comparison, the CCD for inorganic solid electrolytes<sup>2</sup> is typically  $\sim 1 \text{ mA}/\text{cm}^2$ . In addition, a low charge transfer resistance of  $100 \text{ ohm}\cdot\text{cm}^2$  (Figure XIII.20.3c) also suggests excellent interfacial stability with the  $\text{Li}^0$  anode. Limiting current density (LCD) is the largest sustainable current density that can be drawn across the electrolyte. Above this value, the concentration of lithium salt near the cathode reaches zero and causes cell failure<sup>3</sup>. We first investigated the LCD of the mixed ion conducting SPE (MIC-SPE, both the  $\text{Li}^+$  and anion are mobile) by applying step-up current densities to a  $\text{Li}^0$ - $\text{Li}^0$  cell and then recording the time-dependence of cell potential (Figure XIII.20.3d). At small current densities ( $< 1.2 \text{ mA}/\text{cm}^2$ ), the voltage gradually ramps up with charging time and then reached a steady value. While at a higher current density of  $1.6 \text{ mA}/\text{cm}^2$ , the potential first exponentially increases with time due to salt accumulation near the anode and depletion near the cathode. After reaching a maximum value, a voltage drop was observed, suggesting soft-shortening inside the battery. The above trend became more obvious with increasing current densities, thus the LCD of MIC-SPE was determined to be  $1.2 \text{ mA}/\text{cm}^2$ . For the SIC-SPE (Figure XIII.20.3e), a higher LCD of  $2 \text{ mA}/\text{cm}^2$  was observed due to the homogenous distribution of covalently tethered anion within the membrane matrix (i.e. no concentration gradient). In Figure XIII.20.3f, Figure XIII.20.3g and Figure XIII.20.3h, we further tested the durability of the 20  $\mu\text{m}$  SIC-SPE. At  $0.2 \text{ mA}/\text{cm}^2$ , the  $\text{Li}^0$ - $\text{Li}^0$  cell shows a low overpotential of  $< 100 \text{ mV}$  and the cycling life is  $> 550$  hours. The preliminary full cell result using a  $\text{Li}$ - $\text{LiFePO}_4$

configuration shows a high initial capacity of 161 mAh/g, which is quite close to the theoretical value of 170 mAh/g. The capacity retention after 65 cycles is 96.3 %, and the stable charge-discharge curves in Figure XIII.20.3h suggest no short-circuiting occurred.

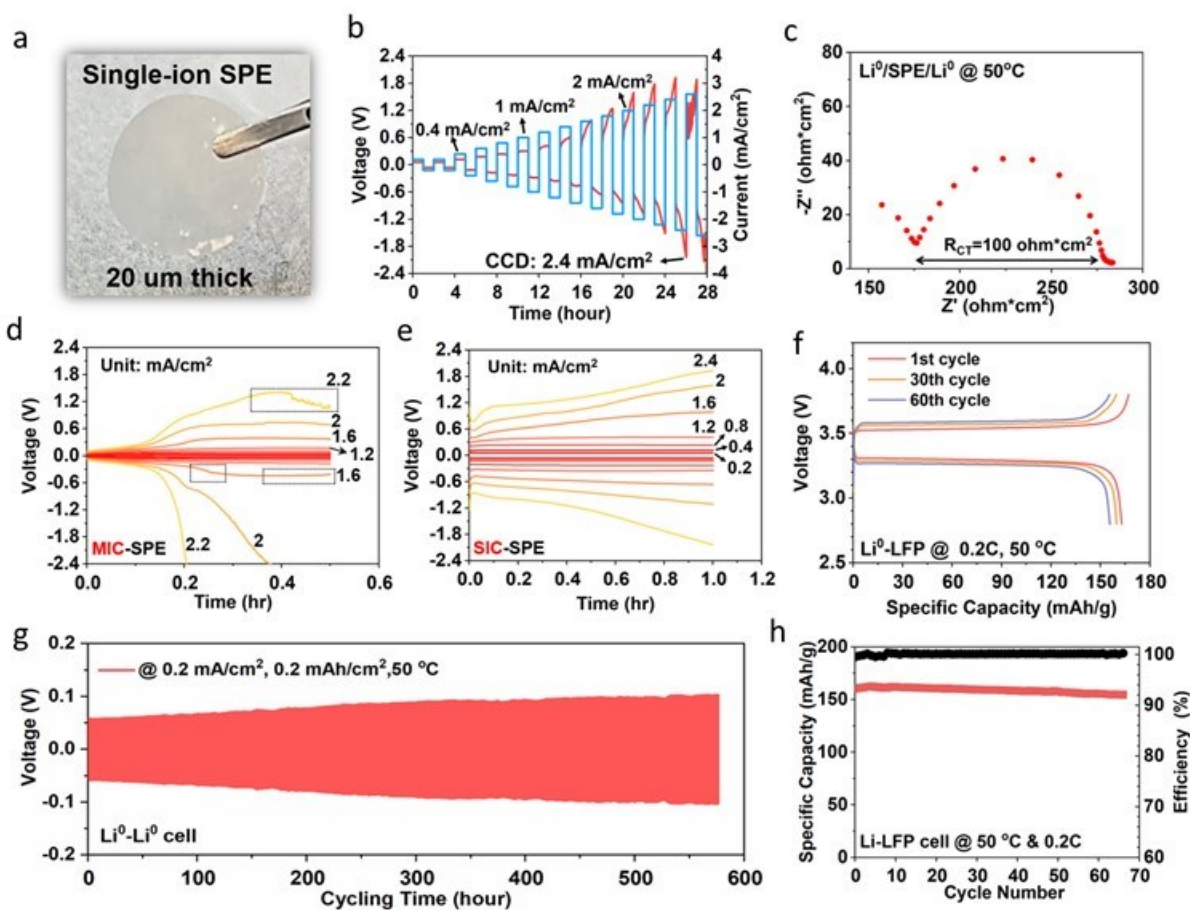


Figure XIII.20.3 (a) Photograph of 20- $\mu\text{m}$ -thick SIC-SPE; (b) Critical current density of SIC-SPE measured at 50  $^{\circ}\text{C}$ ; (c) EIS plot of a  $\text{Li}^0/\text{SIC-SPE}/\text{Li}^0$  cell showing the charge transfer resistance; (d,e) Limiting current density of MIC-SPE (d) and SIC-SPE (e) measured at 50  $^{\circ}\text{C}$ ; (f) Selected charge-discharge curves of Li-LiFePO<sub>4</sub> cell. The cathode loading is 2.2 mg/cm<sup>2</sup>; (g) Long-term cycling performance of SIC-SPE tested under Li<sup>0</sup>-Li<sup>0</sup> symmetric cell configuration; (h) Cycling stability of Li-LiFePO<sub>4</sub> cell at 50  $^{\circ}\text{C}$  and 0.2C.

In FY2023, the **Harvard** team tested solid-state batteries with hierarchical ceramic electrolytes using various solid electrolyte combinations. When lithium metal is applied as the anode, the performance of solid-state battery usually is worse than most of other anodes. Lithium dendrite forms at the anode during cycling and lithium penetrates through the solid electrolyte. As the cathode loading is increased, more lithium metal is deposited and higher areal current density is incurred, which further promotes the lithium dendrite growth from the anode. Preventing lithium dendrite penetration is the focus in this quarter's work. Mechanical suppression of lithium dendrite using very dense ceramic electrolyte layer has been proven challenging. We instead applied the hierarchical ceramic electrolytes as the separator, using their chemical and electrochemical properties to ensure the stability of lithium metal anode.

It is found that the performance varies depending on the solid electrolyte used. When the cathode loading is high ( $>8$  mg/cm<sup>2</sup>), some battery structure short circuit quickly, while some others keep good stability with no short circuit. Figure XIII.20.4a shows the short circuit of battery using the solid-state electrolyte A at loading at 10 mg/cm<sup>2</sup>, with pure lithium metal as an anode. After the solid electrolyte is changed to Electrolyte A + B

+ A (Figure XIII.20.4b), the short circuit is prevented, meaning lithium dendrite penetration is prohibited using such an electrolyte structure (A and B are different sulfide electrolytes). For long cycling of solid-state electrolyte, more combinations are tested at cathode loading of  $>8 \text{ mg/cm}^2$  for different electrolytes. Figure XIII.20.5 shows the rate capability and the cycling performance of batteries using Electrolyte ABA, ACA, and ADA. All three show no short circuit at different rates. ABA structure with Electrolyte B as a middle layer shows the highest specific capacity at the same rates compared to other structures. The battery using hierarchical ceramic electrolytes show stable cycling at a high rate of 2C (A, B, C, D are different sulfide electrolytes). For proprietary reasons, the specific formulas of A, B, C and D are not disclosed).

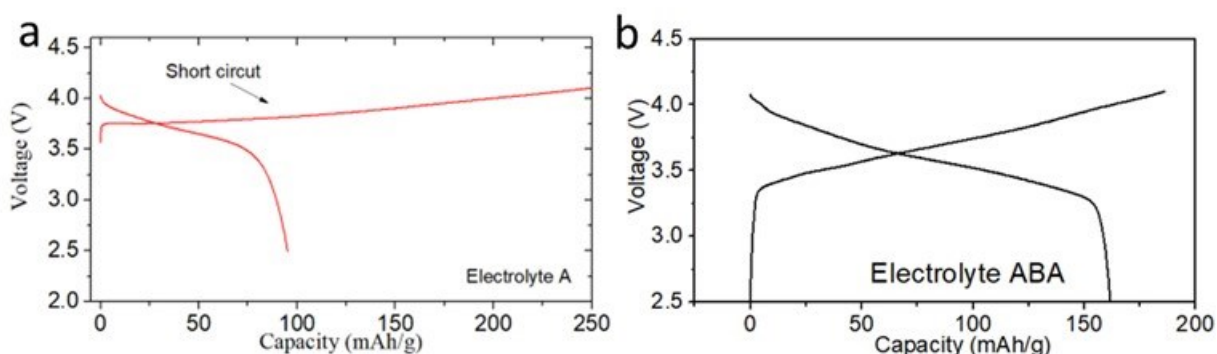


Figure XIII.20.4 Charge and discharge curves for Electrolyte A with NMC-Electrolyte-Lithium structure. Electrolyte in (a) is Electrolyte A and in (b) is hierarchical ceramic electrolytes denoted as ABA. Both batteries are with  $>8 \text{ mg/cm}^2$  loading and cycled at 0.5C.

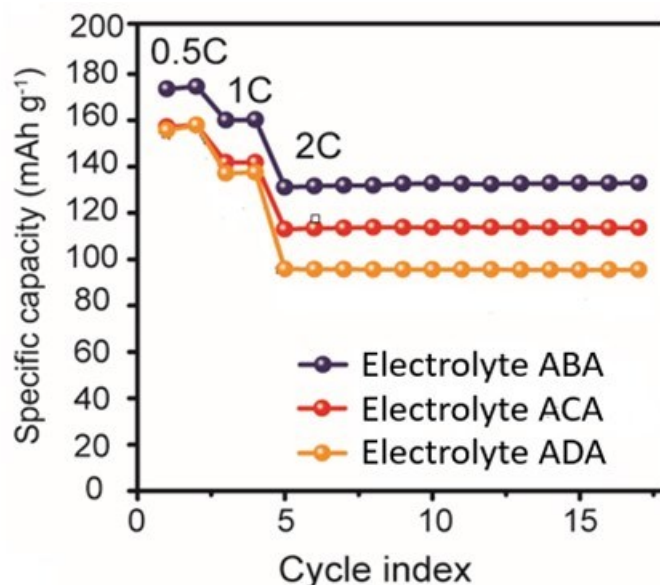


Figure XIII.20.5 Specific capacity of three batteries at different C-rates at  $>8 \text{ mg/cm}^2$  cathode loading.

## Conclusions

In conclusion, we fabricated PVDF polymer-based solid electrolyte through slurry casting method and used synchrotron characterization to understand its stability against lithium metal and NMC cathode. We also designed and tested the in situ XAS solid-state cell for understanding the electrode-electrolyte interphases. We optimized the composition of single ion conducting solid polymer electrolyte (SPE) to achieve interfacial resistance  $<200 \text{ ohm cm}^2$ , limiting current density  $>1 \text{ mA/cm}^2$ , and membrane thickness  $<20 \text{ }\mu\text{m}$  under



stacking pressure < 0.1 MPa. We have also increased the cathode loading in NMC||hierarchical ceramic electrolyte||Li cells to 8 mg/cm<sup>2</sup> and test the performance of cells using various electrolytes.

### **Key Publications**

#### **Patents**

1. Xin Li et al. Fast Cycling Of Lithium Metal Solid State Battery At High Loading, US 63/428,634

#### **Publications**

1. Yubin He, Chunyang Wang, Peichao Zou, Ruoqian Lin, Enyuan Hu, Huolin L. Xin\*. Anion-tethered Single Lithium-ion Conducting Polyelectrolytes through UV-induced Free Radical Polymerization for Improved Morphological Stability of Lithium Metal Anodes. *Angewandte Chemie*. 2023, 135, e202308309. Publication date: August 07, 2023.

#### **Presentations**

1. Xin Li, Dynamic stability design of solid electrolytes for solid-state batteries, MRS Spring Meeting, April 13, 2023, San Francisco, invited talk.

## XIII.21 Ion-Conductive High Li<sup>+</sup> Transference Number Polymer Composites for Solid-State Batteries (LBNL)

### Bryan D. McCloskey, Principal Investigator

Lawrence Berkeley National Laboratory and University of California, Berkeley  
201-D Gilman Hall  
Berkeley, CA 94720  
E-mail: [bmcclosk@berkeley.edu](mailto:bmcclosk@berkeley.edu)

### Simon Thompson, DOE Technology Development Manager

U.S. Department of Energy  
E-mail: [Simon.Thompson@ee.doe.gov](mailto:Simon.Thompson@ee.doe.gov)

Start Date: October 1, 2022

End Date: September 30, 2023

Project Funding (FY23): \$280,000

DOE share: \$280,000

Non-DOE share: \$0

### Project Introduction

This project seeks to develop polymer-inorganic composites that have an optimal combination of conductivity, processability, and low interfacial resistance at both a Li metal anode and a porous Li[Ni, Co, Mn]O<sub>2</sub> (NMC) cathode. In an effort to enable Li metal anodes, mechanically rigid solid-state Li<sup>+</sup> conductors, such as Li<sub>7</sub>La<sub>3</sub>Zr<sub>2</sub>O<sub>12</sub> (LLZO), Li<sub>1+x</sub>Al<sub>x</sub>Ti<sub>2-x</sub>(PO<sub>4</sub>)<sub>3</sub> (LATP), and Li<sub>2</sub>S-P<sub>2</sub>S<sub>5</sub> glasses (LPS), have been employed due to their high Li<sup>+</sup> ion conductivity and, when engineered to eliminate interfacial defects, appropriate stiffness to suppress Li metal dendrite formation. However, for these materials to result in batteries that compete against current commercial cells in terms of energy density and cost per kWh, they would need to be manufactured at no more than 50 microns thickness and cost no more than \$5 per square meter. The materials would also need to be engineered to be defect free (to disallow Li dendrite growth) and have anode and cathode interfacial resistances that remained low over 100s of cycles. These metrics are daunting for pure thin-film inorganic ion conductors, particularly when a porous, thick cathode also needs to be used to achieve competitive cell energy densities.

To overcome these challenges, this project aims to develop polymer-inorganic composites, where high Li<sup>+</sup> transference number polymer electrolytes serve as a binder for inorganic ion conducting particles. By optimizing the composition of this composite electrolyte, we aim to marry the processability and interfacial mechanical compliance of polymers with the impressive transport properties of inorganic composites, thereby enabling roll-to-roll manufacturing to allow thin (<50 micron) layers of high conductivity solid-state conductors to be cost-effectively incorporated into batteries.

### Objectives

Our objectives in FY23 have focused on understanding the formation and removal of impurities from solid state particles, particularly the H<sup>+</sup> exchange with Li<sup>+</sup> from LLZO particles immersed in aqueous solutions, as well as the ion transport across the solid state particle-liquid electrolyte interfaces using electrochemical impedance spectroscopy and the initial formation and conductivity characterization of single-ion conducting polymer-inorganic particle composites.

### Approach

The project approach relies on the following key steps: (1) using monomers with (trifluoromethanesulfone) imide anions appended to them, synthesize and characterize polyanionic PEs with high Li<sup>+</sup> transference number and conductivity; (2) through systematic material structure-property characterization, understand how to reduce interfacial ion transport impedance between inorganic ion conductors (specifically, thin-film inorganic conductors such as Li-La-Zr-Ta-O, LATP, and LPS) and high Li<sup>+</sup> transference number PEs; and (3) characterize electrode-polymer and electrode-inorganic conductor interfacial resistances at a Li-metal anode.

We purchased LLZO and LTP powders from reputable vendors. Single-ion conducting polymers, specifically poly((trifluoromethane)sulfonimide lithium methacrylate) (PLiMTFSI), were synthesized using radical addition fragmentation polymerization and purified through dialysis. LLZO and LTP powders were characterized for carbonate impurities through titration mass spectrometry, a technique developed in our laboratory that quantifies gas evolution after immersing the powders into acid.

## Results

Impedance analysis suggests  $\text{Li}^+$  moves through the interface of certain LTP powders immersed highly concentrated liquid electrolytes. Studying the  $\text{Li}^+$  exchange process between inorganic filler particles and the polymer phase is critical in the design of composite electrolytes. The improvement of conductivity by adding inorganic fillers to a polymer electrolyte is generally attributed to the highly conductive  $\text{Li}^+$  pathways through the filler particles and/or the reduced glass transition temperature of the polymer phase. To remove the effect of glass transition temperature and focus on the  $\text{Li}^+$  exchange process, we studied the effect of LTP powder inclusion on a highly concentrated liquid electrolyte prepared by dissolving LiTFSI in EC in a 1:2 molar ratio.

Figure XIII.21.1 shows the Nyquist plots of the pure liquid electrolyte and mixtures of LTP and the liquid electrolyte. LTP was provided by two different suppliers. LTP from MSE has a particle size of 600 nm, while LTP from Toshiba has a particle size of 5~15  $\mu\text{m}$ . The ionic conductivity of the pure liquid electrolyte is 0.22 mS/cm, agreeing well with literature values. After adding 30 wt% LTP with small particle sizes, the conductivity dropped to 0.16 mS/cm, suggesting the  $\text{Li}^+$  exchange process is slow. However, when using the large particle size LTP, the conductivity is slightly increased with two semicircles shown in the Nyquist plot, which is distinctly different from the other two plots. Some recent publications have shown that the particle size is a critical factor in determining the effective conductivity of composite electrolytes, which is a question we endeavor to answer in FY 2024.

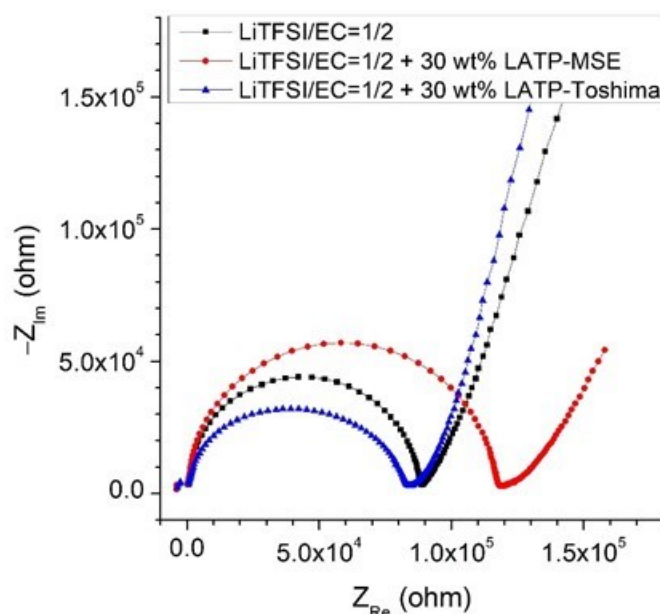
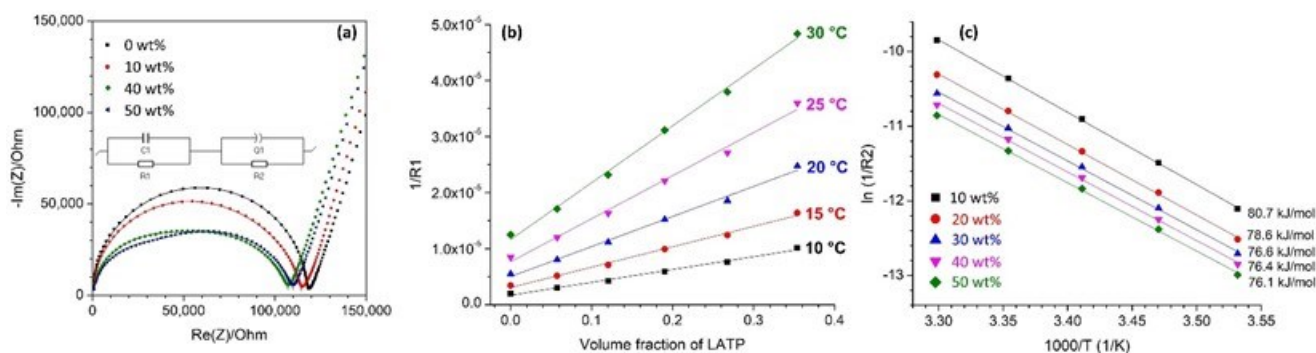


Figure XIII.21.1 Nyquist plots of a concentrated liquid electrolyte, LiTFSI dissolved in EC in a 1:2 molar ratio, and two mixtures of this liquid electrolyte with LTP. LTP-MSE has a particle size of 600 nm, and the LTP-Toshiba has a particle size of 5~15  $\mu\text{m}$ . The impedance spectra were measured using a cell with two copper wire electrodes separated by 22 mm with a calibrated cell constant of 19.5  $\text{cm}^{-1}$ .

We further studied the ‘large particle’ Toshiba LTP system at different temperature and LTP content.

Figure XIII.21.2a shows that the single semicircle of pure liquid electrolyte in the Nyquist plot is replaced by two semicircles after adding LTP. The Nyquist plots after adding LTP are fitted using a R1/C1+R2/Q1 equivalent circuit, where R1/C1 fits the semicircle at higher frequency and R2/Q1 fits the semicircle at lower frequency. R1 decreases when increasing the LTP content, and the inverse of R1 ( $1/R1$ ) shows almost a linear relationship with the volume fraction of LTP (Figure XIII.21.2b) within the studied region. In contrast, R2 increases with LTP content. We think R1 likely corresponds to ion translational motions at higher frequency both in the liquid phase and inside the LTP particles, while R2 corresponds to the slow  $\text{Li}^+$  exchange process at the liquid/ceramic interface. When increasing LTP content, more  $\text{Li}^+$  in the liquid phase are involved in the exchange process due to increased ceramic/liquid contact area, and thus this process dominates the overall resistance of the sample at high LTP content. In order to gain more insight into this  $\text{Li}^+$  exchange process, we demonstrate the Arrhenius plots of  $1/R2$  in Figure XIII.21.2c. Within the studied 10 – 30 °C temperature range, an activation energy of 76 ~ 81 kJ/mol was obtained. This activation energy is consistent with reported  $\text{Li}^+$  de-solvation energies in carbonate-based electrolytes, further supporting that R2 is related to the  $\text{Li}^+$  exchange process on the ceramic/liquid surface.



**Figure XIII.21.2 Impedance study of the effect of LTP to a concentrated liquid electrolyte EC/LiTFSI=2/1. (a) Nyquist plots of the concentrated electrolyte at different LTP content at 25 °C. The inset shows the equivalent circuit used to fit the data when LTP is added to the liquid electrolyte. The pure liquid electrolyte is fitted using a simple R/C circuit. (b) The evolution of  $1/R1$  as a function of LTP volume fraction and temperature. (c) Arrhenius plot of  $1/R2$  shows that  $R2$  is related to a physical process with an activation energy of 76 ~ 81 kJ/mol.**

We further studied whether the two-semicircle phenomenon, which we believe is indicative of ion transfer across particle-liquid interfaces, also occurs in other systems. We first replaced the LiTFSI in the liquid electrolyte with LiFSI, which leads to a higher conductivity of the liquid electrolyte. Figure XIII.21.3a shows the Nyquist plots of concentrated liquid electrolyte EC/LiFSI=2/1 with 0 and 30 wt% LTP at 0 °C. Without LTP, the electrolyte shows only one semicircle. After adding 30 wt% LTP, the Nyquist plot demonstrates two semicircles and the plot can be fitted with the same equivalent circuit as shown in Figure XIII.21.2a. We then further replaced LTP with LPSCI ( $\text{Li}_6\text{PS}_5\text{Cl}$ ). Again, similar two-semicircle phenomenon was obtained as shown in Figure XIII.21.3b. Overall, our study suggests that in concentrated electrolyte-ceramic mixtures, the ion transport behavior includes two sections: ion transport at higher frequency that can be ascribed to a combination of transport in the liquid phase and inside the ceramic particles, and ion transport at lower frequency which is likely a result of the  $\text{Li}^+$  exchange at the liquid/ceramic interface. We will continue to probe the impact of both particle and liquid electrolyte composition on the ability of  $\text{Li}^+$  to transfer across an interface between them in FY 2024.

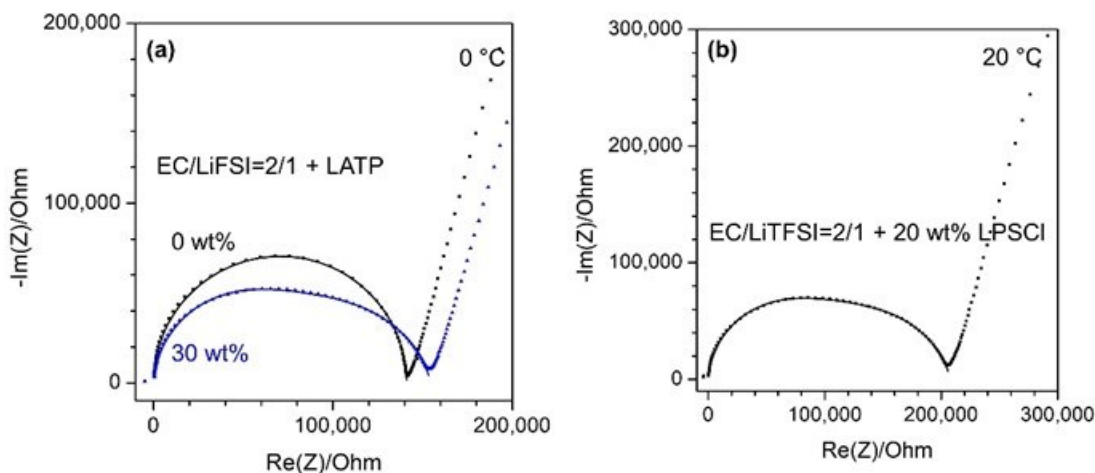


Figure XIII.21.3 (a) Nyquist plots of EC/LiFSI=2/1 with 0 and 30 wt% LATP at 0 °C. (b) Nyquist plot of EC/LiFSI=2/1 with 20 wt% LPSCI at 20 °C.

#### Controlling carbonate content in LLZO powders.

In FY23, we began examining how to control the removal of lithium carbonate from LLZO particles to facilitate ion transport and decrease interfacial resistance between ceramic and polymer phase. To quantify carbonate content, we monitored CO<sub>2</sub> evolution from LLZO powder immersed in a strong acid solution using a technique developed in our laboratory which we call titration mass spectrometry (TiMS). We have characterized numerous oxide materials using TiMS, including Ni-rich NMCs, Li/Mn-rich NMCs, Li-excess disordered rocksalts, and LLZO, and we always find some carbonate on every oxide surface, with typical carbonate amounts ranging from a few tenths of a weight percent to 10 wt.%. The LLZO powder from MSE is no different, as it was found to contain 5.6 wt% carbonate as-received. Upon a 24 hr exposure to air, 16.2 wt% carbonate was found in the material due to the known reaction of the LLZO with ambient CO<sub>2</sub>. Removing carbonate from the particle surfaces is likely necessary to result in any Li<sup>+</sup> transfer between the LLZO particles and any adjacent electrolyte phase.

While sintering is a possible method for removing carbonate from LLZO, we have primarily been examining a more scalable and energy-efficient process – washing. We began using Inductively Coupled Plasma (ICP) to measure the lithium content in the supernatant after washing, in combination with TiMS to measure carbonate content, and the data suggests extreme protonation of the LLZO structure when using both weak and strong acids. Even diluting the acid into alternate solvents like methanol results in this same level of rapid protonation. By measuring secondary ions such as zirconium and lanthanum, we confirmed that the ceramic was not being dissolved by the acid. This suggests that any acid-based attempt at cleaning LLZO, while successfully removing the majority of the carbonate surface impurities, will protonate the ceramic structure, leading to undesirable effects on dendrite formation and bulk conductivity. Table XIII.21.1 below shows the preparation conditions, LLZO concentration from ICP, and extent of protonation. In an attempt to avoid protonation of the LLZO material, we also utilized alkaline washes, although still saw substantial Li<sup>+</sup> exchange (Table 2). The ICP data shows that even for basic solutions there is excess lithium after washing, suggesting that protons are not the only ions capable of exchanging with the lithium in LLZO. Increasing the cation size (from Na<sup>+</sup> to K<sup>+</sup>) was found not to impact the lithium exchange significantly; however, increasing the cation oxidation state (from Na<sup>+</sup> to Ca<sup>2+</sup>) led to lower lithium exchange, although it was still present. We intend to continue exploring how different salt and solvent combinations may lead to an effective removal of Li<sub>2</sub>CO<sub>3</sub> without compromising the underlying ceramic structure in FY 2024. Table XIII.21.2 below shows preparation conditions, Li<sup>+</sup> concentration from ICP, and the extent of Li<sup>+</sup> exchange. We suspect that while Ca(OH)<sub>2</sub> washes show carbonate still present, this carbonate is CaCO<sub>3</sub> rather than Li<sub>2</sub>CO<sub>3</sub> given calcium carbonate's limited solubility in organic solvents.

Table XIII.21.1 Acidic Washing Impact on LLZO (All Acid Concentrations are 0.1 M).

Washing Agent (solvent)	Preparation Notes	Li concentration in ICP (mM)	Post-wash $\text{Li}_2\text{CO}_3$ (wt. %)	% of Li exchanged from LLZO
HCl (Methanol)	10-minute wash	110.8	0.41	58.20
HCl (Methanol)	40-minute wash	102.1	0.34	51.56
HCl (Water)	10 min	93.5	0.94	47.59
HCl (Water)	2.5 min	87.6	0.89	43.04
HCl (Water)	10 min; high concentration	466.8	0.38	45.25
HCl (Water)	40 min	106.1	0.61	55.51
Acetic Acid (Water)	10 min	99.5	0.6	50.66
Acetic Acid (Water)	40 min	99.1	0.58	50.29
Acetic Acid (Methanol)	10 min	101.2	0.31	50.74
Acetic Acid (Methanol)	40 min	121.4	0.35	65.75
Acetic Acid (Water)	10 min; equimolar $\text{H}^+/\text{Li}_2\text{CO}_3$	157.7	0.26	53.46
Acetic Acid (Water)	40 min; equimolar $\text{H}^+/\text{Li}_2\text{CO}_3$	162.7	0.26	55.92
Acetic Acid (Methanol)	10 min; equimolar $\text{H}^+/\text{Li}_2\text{CO}_3$	116.2	5.35	53.34
Acetic Acid (Methanol)	40 min; equimolar $\text{H}^+/\text{Li}_2\text{CO}_3$	121.9	4.44	52.52
HCl (Water)	10 min; equimolar $\text{H}^+/\text{Li}_2\text{CO}_3$	177.7	0.32	63.50
HCl (Water)	40 min; equimolar $\text{H}^+/\text{Li}_2\text{CO}_3$	168.4	0.28	58.75

Table XIII.21.2 Basic Washing Solution Impact on LLZO.

Washing Agent (conc.)	Preparation Notes	Li concentration in ICP (mM)	Post-wash Li <sub>2</sub> CO <sub>3</sub> (wt. %)	% of Li exchanged from LLZO
NaOH (0.1 M)	10 minute wash	160	0.6	56
NaOH (0.1 M)	40 minute wash	170	-	58
NaOH (0.05 M)	10 minute wash	165	0.6	57
NaOH (0.05 M)	40 minute wash	164	-	55
KOH (0.05 M)	10 minute wash	211	-	78
KOH (0.05 M)	40 minute wash	202	-	74
KOH (0.1 M)	10 minute wash	212	-	78
KOH (0.1 M)	40 minute wash	218	-	81
CaOH <sub>2</sub> (0.05 M)	In IPA; 1.5 hr. wash	3.6	5.5	-
CaOH <sub>2</sub> (0.05 M)	In IPA; 3 hr. wash	3.1	5.1	-
CaOH <sub>2</sub> (0.05 M)	In IPA + 10vol% glycerol; 1.5 hr. wash	80.	5.4	33
CaOH <sub>2</sub> (0.05 M)	In IPA + 10vol% glycerol; 3 hr. wash	63	4.6	21

**Initial studies on full-cell testing.**

We also developed a new platform to study organic-inorganic composite electrolytes. We explored the possibility of preparing a tetraglyme-plasticized composite polymer electrolyte with Li<sub>1.3</sub>Al<sub>0.3</sub>Ti<sub>1.7</sub>(PO<sub>4</sub>)<sub>3</sub> (LATP) as the inorganic filler and PVDF as the polymer matrix. Free-standing composite polymer electrolyte membranes are prepared via a one-step solvent casting method and the preliminary tests indicate that the prepared solid electrolyte supports a critical current density > 0.3 mA/cm<sup>2</sup> when cycled in a Li/LiFePO<sub>4</sub> cell at ambient temperature (22 °C). Figure XIII.21.4 shows the voltage profiles of the cell when cycled at 0.1, 0.2, and 0.3 mA/cm<sup>2</sup>. The LiFePO<sub>4</sub> cathode coating layer has a thickness of 67 μm and an areal capacity of 1.81 mAh/cm<sup>2</sup>. No additional liquid component is used when assembling the cell. We believe the critical current density could be potentially further improved by optimizing the electrolyte composition and cell assembling process, such as casting the electrolyte membrane on the cathode directly and thus preparing cathode-supported solid electrolyte with low interfacial resistance.

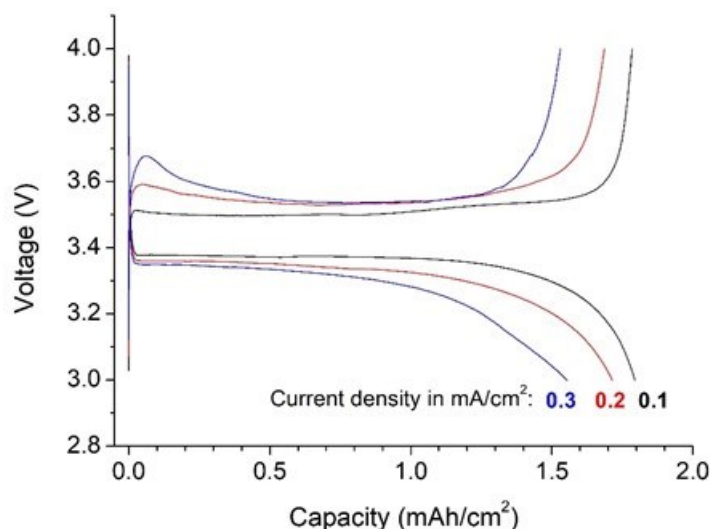


Figure XIII.21.4 Voltage profiles of a Li/LiFePO<sub>4</sub> cell with a PVDF/LATP-based composite polymer electrolyte cycled at ambient temperature at 0.1, 0.2, and 0.3 mA/cm<sup>2</sup>.

### Conclusions

Key conclusions from our work this year were:

1. Impedance analysis suggests that Li<sup>+</sup> can transfer between certain ceramic particles and an organic, liquid electrolyte. The impact of the composition of each phase on ion transfer across these interphases is still to be determined.
2. In instances where ion transport does occur across particle-liquid interfaces, 2 semicircles are observed a Nyquist plot, where one appears to be related to a weighted average of the conductivities of each phase, and the second is related to the ion transfer resistance across the particle-liquid interface. Both scale as expected with respect to particle loading and temperature. When no ion transport across the particle-liquid interfaces, only a single semicircle is present, with it agreeing with the conductivity of the liquid phase.
3. Carbonate content in LLZO materials was 5.6 wt% in as-received powders from vendors. It is unclear whether this carbonate originates from poor handling or was left over from the material synthesis.
4. In agreement with prior studies, rapid protonation and Li exchange was found to occur when LLZO was immersed in aqueous systems, both acidic and alkaline. Organic washes are being explored instead to allow carbonate to be removed from surfaces while eliminating protonation.

### Key Publications and Presentations

1. Bergstrom, H. K.; Fong, K. D.; Halat, D. M.; Karouta, C. A.; Celik, H. C.; Reimer, J. A.; McCloskey, B. D. "Ion correlation and negative lithium transference in polyelectrolyte solutions." *Chemical Science* (2023) 14, 6546-6557.
2. McCloskey, B. D. "Ion Transport in Li<sup>+</sup> Polyelectrolytes and Concentrated Binary Salt Electrolytes." Invited presentation, American Institute of Chemical Engineers Annual Conference, Nov. 2023.
3. Tronstad, Z., McCloskey, B. D. "Ion Conductive High Li<sup>+</sup> Transference Number Polymer Composites for Solid-State Batteries." Poster presentation, American Institute of Chemical Engineers Annual Conference, Nov. 2022.
4. McCloskey, B. D. Department of Chemical Engineering seminar, University of Wisconsin. Sept. 2023. "Ion transport in charged polymer electrolytes: the pursuit of high transference number."
5. McCloskey, B. D. Department of Energy Engineering seminar, Hanyang University. Aug. 2023. "Ion transport in charged polymer electrolytes: the pursuit of high transference number."
6. McCloskey, B. D. Sila Nanotechnologies academic seminar series. July 2023. "Ion transport in charged polymer electrolytes: the pursuit of high transference number."



7. McCloskey, B. D. NASA/DOE workshop on batteries for flight, NASA Glenn Research Center. Apr. 2023. “Li-air batteries: a status report.”
8. McCloskey, B. D. Department of Chemical Engineering seminar, University of Florida. Mar. 2023. “Ion transport in charged polymer electrolytes: the pursuit of high transference number.”
9. McCloskey, B. D. Physical Chemistry seminar, Department of Chemistry, University of California, Santa Barbara. Feb. 2023. “Ion transport in charged polymer electrolytes: the pursuit of high transference number.”
10. McCloskey, B. D. The Vaughan Lecture, Department of Chemical Engineering, Caltech. Oct. 2022. “Ion transport in charged polymer electrolytes: the pursuit of high transference number.”
11. McCloskey, B. D. Department of Chemical Engineering seminar, Columbia University. Oct. 2022. “Ion transport in charged polymer electrolytes: the pursuit of high transference number.”

### **Acknowledgements**

This section was coauthored by Zachary Tronstad and Deyang Yu (LBNL).

## XIII.22 Precision Control of the Li Surface for Solid-state Batteries (ORNL)

### Andrew S. Westover, Principal Investigator

Oak Ridge National Laboratory  
PO Box 2008, MS6124  
Oak Ridge, TN 37830  
E-mail: [westoveras@ornl.gov](mailto:westoveras@ornl.gov)

### Simon Thompson, DOE Technology Development Manager

U.S. Department of Energy  
E-mail: [Simon.Thompson@ee.doe.gov](mailto:Simon.Thompson@ee.doe.gov)

Start Date: October 1, 2022	End Date: September 30, 2023	
Project Funding (FY23): \$650,000	DOE share: \$650,000	Non-DOE share: \$0

### Project Introduction

The knowledge of lithium surface engineering and the implications for cell design of Li-metal-batteries will improve commercialization efforts for solid-state Li-metal batteries. There is very little standard knowledge about variations in the impurity level in different lithium sources, the surface chemistry of different lithium surfaces, and their impact on performance. Furthermore, the strategies developed to engineer the surface of the lithium metal for integration into Li-metal batteries will provide significant performance increases, ideally enabling successful commercialization.

### Objectives

This project has three primary objectives. 1) Understand the chemistry and mechanics of native Li and its surfaces and correlate with electrochemical performance 2) engineer the Li surfaces to minimize interfacial resistance and optimize stress relief along the interface and 3) demonstrate that the engineered surface coating can enable batteries with a specific energy of 500 Wh/kg for at least 300 cycles.

### Approach

This project is broken into two parts. First, the team is focused on thoroughly understanding the purity, mechanics, and surface chemistry of multiple lithium sources and how these parameters impact performance. Second, they will focus on intentionally engineering the lithium purity and surface chemistry to control the mechanical properties, electrochemical stability, and electrochemical performance. They will explore three approaches to engineering the surfaces: gas-phase passivation, deposition of thin metal coatings, and deposition of thin inorganic coatings. To test electrochemical performance, they will use standard ceramic and polymer electrolytes to demonstrate the impact of purity and surface chemistry. The program will also employ a range of standard and specialized characterization techniques, including a significant focus on understanding the mechanics of lithium metal using nanoindentation and adhesion measurements using surface probe microscopy.

### Results

The first goal of FY23 was to connect the performance of different Li sources with solid electrolytes in terms of surface composition, microstructure, and mechanics. In FY22 Q4 we established that the thickness of the surface layer directly correlated to the interfacial resistance of standard PEO-LiTFSI electrolytes. Surprisingly, the cleanest Li surface performed the worst in terms of cycling performance before shorting. This data suggests that the microstructure also plays a key role in the performance. In Q1 our focus was on testing the performance of different Li sources with an argyrodite solid electrolyte  $\text{Li}_6\text{PS}_5\text{Cl}$  purchased from NEI corporation. To this end, we developed Li/Argyrodite/Li cells. The cells were made by taking 1/2" Li discs and placing them in the PEEK die first. This was followed by 200 mg Argyrodite powder poured on top. With an

SS plunger, the powder was pressed to 50 bars of pressure for ~15 secs. Then the plunger was taken out, and the second Li disc (7/16") was placed on top. The whole stack was then pressed with an SS plunger on top at 200 bars (~80 MPa) for 5 mins. This cell is then tested at 5-6 MPa and RT. The cells were cycled at a current density of  $100 \mu\text{A}/\text{cm}^2$  for 10 hours per cycle for a total capacity of  $1 \text{ mAh}/\text{cm}^2$ . In total, we compared three different Li sources. To maintain the quality of the comparison all three sources consisted of Li deposited on battery-grade Cu foil ~10  $\mu\text{m}$  thick. For the evaporated Li we compared Li of 10 and 30  $\mu\text{m}$  thick. For the commercial source, we used a source that was rolled onto Cu foil and was approximately 40  $\mu\text{m}$  thick. In Figure XIII.22.1 we can clearly see that both evaporated Li metal sources fail first. Notably, the failure mechanism is not dendritic shorting but rather a sharp rise in the overpotential. This overpotential results from a loss of Li contact with the solid electrolyte. This can occur due to voiding at the Li surface, or due to continuous reactions between the solid electrolyte and Li metal, or due to a combination of both. As there is a difference in the Li, the first possibility is that voiding is exacerbated because there is less pressure in the cells with the evaporated Li. To rule this out as a possible explanation we performed a similar set of tests but with a higher pressure of 17 MPa vs. 5 MPa of the standard tests. There was very little difference in performance for the 10  $\mu\text{m}$  evaporated Li tested at higher pressure from the initial tests at 5 MPa suggesting that pressure is not the reason for the difference in performance. With the difference in pressure due to the thicker Li ruled out, there are two possible reasons for the difference in performance. First, the surface layer on the commercial Li, which is characterized by a silicone signature, helps to mitigate the reactions between the Li metal and the solid electrolyte.

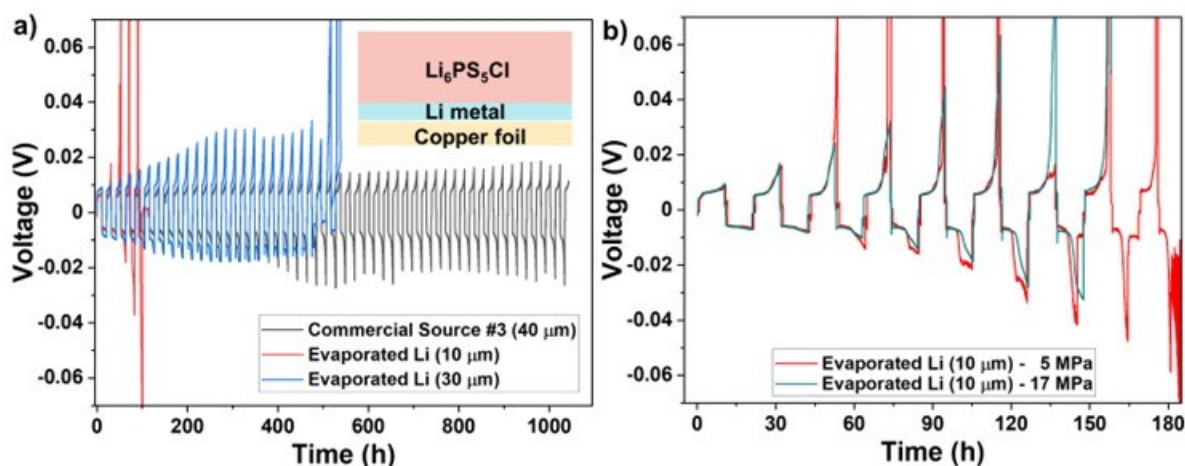


**Figure XIII.22.1 (a)** Cu/Li/Li<sub>6</sub>PS<sub>5</sub>Cl/Li/Cu cells tested with 3 different types of Li. First from a commercial source dubbed #3 in prior quarterly reports on Cu and evaporated Li of 2 different thicknesses (10 and 30  $\mu\text{m}$ ). **(b)** Two cells tested at 5 MPa and 17 MPa, both with the 10  $\mu\text{m}$  thick Li metal.

As demonstrated by the loss of contact observed in Figure XIII.22.1, maintaining the solid/solid contact between the electrode and electrolyte during electrochemical cycling is essential for all-solid-state batteries. The common strategy for combatting the contact issue is applying stack pressure, which is a sort of scientific shortcut that masks the real challenges of maintaining adhesion between the different electrodes and the electrolyte. A more effective and commercially viable strategy is improving the adhesion between different battery components. We hypothesized that increasing the adhesion between electrode and electrolyte will improve the electrode integrity, mitigate contact loss, and hence increase the Coulombic efficiency and cycle life. There are very few studies on the adhesion of battery materials. This is primarily due to limited techniques to measure adhesion at the nanometer and micrometer scales that are relevant to the battery operation. In this project, we proposed to use atomic force microscopy (AFM) with customized probes to investigate adhesion between electrodes and electrolytes *at the nano and micro scale*. In this FY, we successfully developed a protocol to measure adhesion between Li metal and oxide electrolytes. First, we screened and selected AFM probes that have the right stiffness to perform force-distance (F-D) measurements using AFM and will not

react with Li metal. We then coated the AFM probes with a thin layer of Li metal (~500 nm). The adhesion forces between Li metal and solid electrolytes are extracted via F-D measurements. During the F-D measurements, the AFM probes were first brought into contact with the solid electrolyte samples and then withdrawn from the sample surface. During the probe withdrawal, if there is a strong adhesion force between the Li and the sample, the AFM probe will stick to the surface and bend toward the sample (Fig. 1a, probe position in light gray). When the force from the bent cantilever is larger than the adhesion force between the Li metal and the sample, the probe will snap out of contact (Figure XIII.22.2a, probe position in dark gray), creating a sharp jump in the F-D curve, which provides the adhesion force of the system (Figure XIII.22.2b). The adhesion force increases with the probe-sample contact area. As Li metal is a relatively soft material, it is crucial to control the F-D parameters to minimize changes in the Li morphology on the probe during F-D measurements (Figure XIII.22.2d-f). Our preliminary results (Figure XIII.22.2c) showed that Li metal has a stronger adhesion force to LiPON (~90 nN) than to borosilicate glass (~10 nN). In order to, compare the adhesion force between different class of materials quantitatively, the adhesion force needs to be normalized by the probe-substrate contact area. Therefore, careful calibration of the customized probes and characterization of the Li probe morphology after F-D measurements is essential and will be our next focus. We suspect that the nitrogen in LiPON improves the adhesion of Li to the electrolytes. In the next few quarters, we will compare different oxide-based solid electrolytes with and without N to prove this hypothesis.

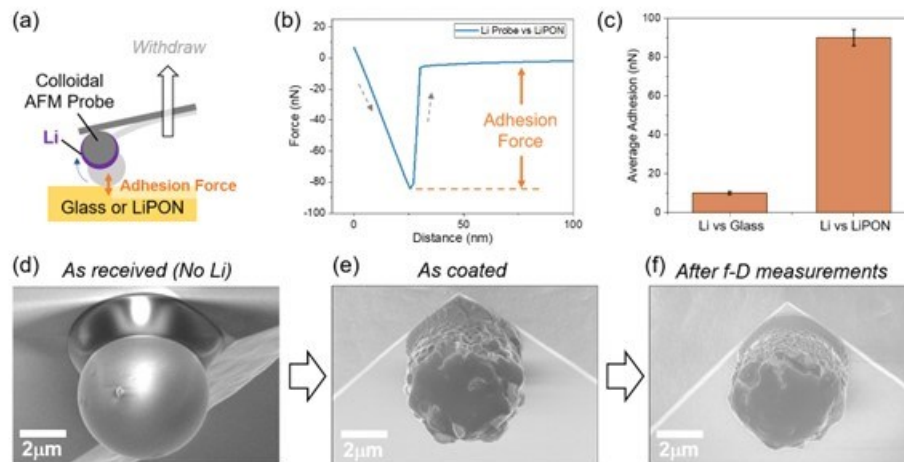


**Figure XIII.22.2** (a) Schematics of adhesion measurements using AFM; (b) An average withdraw curve of a Li-coated probe from LiPON surface; (c) Adhesion forces of Li to glass and Li to LiPON; SEM images of (d) an as-received AFM probe, (e) an as-coated probe, and (f) a post F-D measurement probe.

The third key achievement for this FY relates to the ability to engineer the surface of Li metal. In the previous FY, we discovered that different Li metal sources can have dramatically different surfaces. Furthermore, many electrolytes are unstable with Li metal and do not form kinetically passivating layers. To have successful Li metal batteries it is critical that 1) the surfaces of Li metal be carefully controlled and 2) that a kinetically stable interphase be formed, artificially if needed. One of the key goals of this program is to explore multiple different pathways to form consistent and kinetically stabilized interphases. To do this we are using our standard evaporated Li metal as a baseline that forms a very thin passivating layer. Using this untreated Li metal, we then performed three different types of passivation 1) a gas phase passivation utilizing an etch in an Ar/O<sub>2</sub> plasma, 2) a Cu metal coating via standard radio frequency magnetron sputtering, and 3) an inorganic amorphous Li<sub>3</sub>PO<sub>4</sub> (LiPO) coating. Pictures of the untreated Li metal and three coated Li metals are shown in Figure XIII.22.3a-d. The untreated Li has the classic Li metallic sheen, the Ar/O<sub>2</sub> etched Li had a slightly golden tint to the surface, the Cu coated had a deep blue/purple coloration, and the LiPO coated Li had a yellow-green coloring. In each case, a different passivation layer has been formed on the surface. Figure XIII.22.3e-h shows scanning electron microscopy images (SEM) of the four Li metals. The untreated Li metal

had a clean surface. The Ar/O<sub>2</sub> plasma-treated Li also had a relatively uniform surface but with different spots with lighter coloring under the electron beam. These spots may correspond to impurities from the etching process and showed an excess of O in EDX data. The copper-coated Li had a unique texture with micron-scale features. This may be indicative of an incomplete copper coating, so further tuning may be needed. Finally, the LPO-coated Li showed texturing very similar to the grain structure of the bulk Li metal. Notably, the EDX of the LPO-coated samples showed a distinct P signal that was absent in the other three Li metal films.

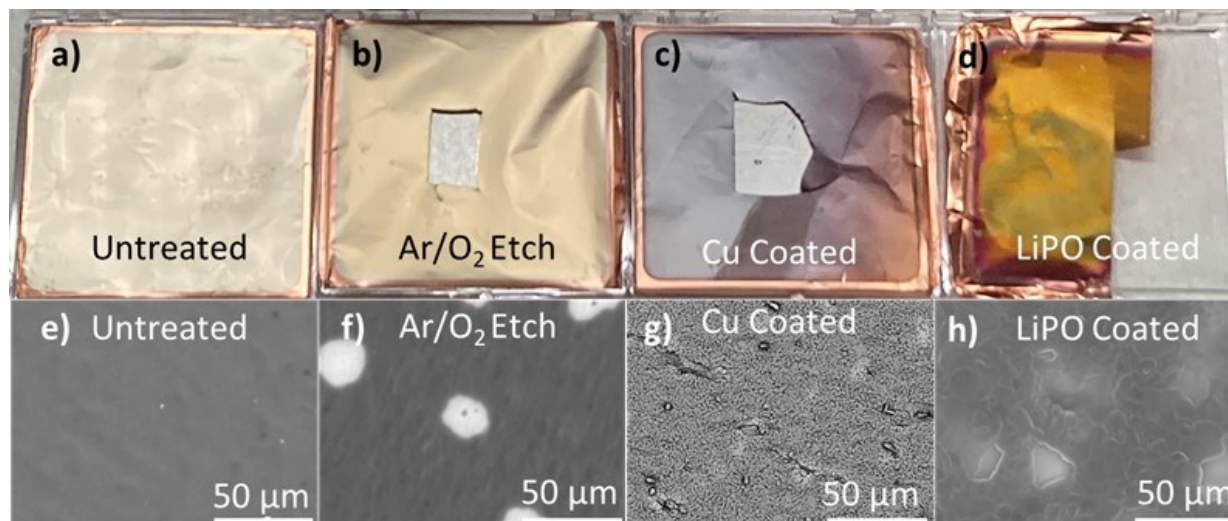


**Figure XIII.22.3 a-d) pictures of four Li metal films with a) untreated, b) Ar/O<sub>2</sub> etched, c) Cu coated, and d) LiPO coated. e-h) SEM images of the same four Li metal films with e) untreated, f) Ar/O<sub>2</sub> etched, g) Cu coated, and h) LiPO coated.**

While the surface clearly had different coatings, we also performed infrared spectroscopy of the different coated Li metal films. In Figure XIII.22.4, we can see the IR data for the four films. In line with previous results, the IR of the untreated Li metal shows a minimal surface species that includes Li<sub>2</sub>CO<sub>3</sub> as characterized by the peak at ~880 cm<sup>-1</sup>. The Ar/O<sub>2</sub> treated Li unsurprisingly shows a much more distinct surface, that includes both a Li<sub>2</sub>CO<sub>3</sub> signature seen in the uncoated film and a very distinct Li-O signature from 400-700 cm<sup>-1</sup>. Surprisingly, the Cu-coated sample has a very similar IR signature to that of the Ar/O<sub>2</sub> treated sample. As both processes were subjected to the same Ar source for sputtering/etching this may be indicative of a reaction with residual impurities in the Ar gas. As Cu metal is not IR active, we would not expect to see an IR signal from the Cu. The easiest explanation for this data is there is a Li-O and Li<sub>2</sub>CO<sub>3</sub> layer underneath the Cu coating. The LiPO coated signal showed the signature that indicates a similar Li-O and Li<sub>2</sub>CO<sub>3</sub> coating underneath the LiPO, but also shows a distinct signature of the LiPO coating with a broad phosphate peak from 1000-1200 cm<sup>-1</sup> and an additional signature in the Li-O regime from 400-700 cm<sup>-1</sup> that is also found in isolated LiPO films.

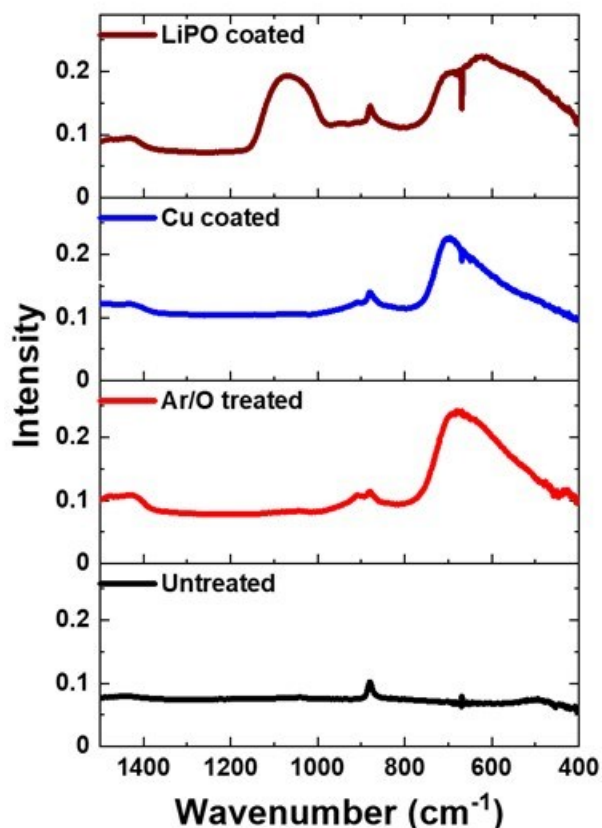


Figure XIII.22.4 IR data for the four Li films shown in Figure 1 from 400-1500  $\text{cm}^{-1}$  as measured by attenuated total internal reflection (ATR).

Currently, we are pursuing testing these different coated Li metals with a crosslinked PEO-LiTFSI electrolyte and a standard argyrodite sulfide solid electrolyte. While the argyrodite results are ongoing, Figure XIII.22.5 shows the results for the PEO-LiTFSI polymer electrolytes cycled in symmetric cells with pristine Li metal, the etched Li metal, and LiPON-coated Li metal. The cells were made using standard coin cells with the polymer layers cut to 5/8 of an inch and the Li metal foils cut to 1/2 an inch. In all cases, 3 spacers were used due to the thin 20  $\mu\text{m}$  Li metal used on both sides of the cells. The cells were allowed to condition for 2 or more days until the electrochemical impedance spectroscopy (EIS) profile stabilized at 70°C. After conditioning, the cells were set to cycle at 70°C at a current density of 50  $\mu\text{A}/\text{cm}^2$  for 10 hours per cycle with a 1-hour rest period between each half cycle.

Figure XIV.27.5 shows the initial EIS data after preconditioning for each of the Pristine,  $\text{O}_2$  etched, and LiPON-coated samples and the cycling behavior of representative cells for each. From the EIS data, we can clearly see that the lowest resistance was observed for the pristine sample at 330  $\Omega$ . The  $\text{O}_2$  etched and LiPON coated both had significantly higher initial resistances of 800 and 1200  $\Omega$  respectively. These two samples also both had a distinct second semicircle indicating a second interfacial layer. This aligns with the IR data from last quarter which showed that the etched sample had a significant  $\text{Li}_2\text{O}$  layer, and the LiPON coated also had a phosphate signature. The initial plating overpotential for the three cells was 63 mV, 131 mV, and 110 mV respectively. For the pristine cell, there is initially stable Li plating and stripping for about 800 hours with only a gradual increase in the overpotential from 63 mV to 150 mV. But from 800 hours, the overpotential dramatically increases and reaches overpotentials as high as 430 mV by 1200 hours of cycling. The  $\text{O}_2$  sample had relatively stable cycling performance with a slight decrease in overpotential from 131 mV to 98 mV over 400 hours followed by a slow return to 130 mV by about 600 hours of cycling. After 600 hours the overpotential quickly increases beyond 500 mV at about 800 hours of cycling. The LiPON-coated Li had the

best performance with stable Li plating and stripping for 2000 hours and counting. After 2000 hours of cycling the LiPON-coated Li overpotential has only risen from the initial 110 mV to 150 mV with no indications of a sharp increase in overpotential. Testing of this cell is still ongoing. While this data needs to be repeated several times to ensure the accuracy of the results, this suggests that the LiPON-coated Li can significantly increase the stability of Li metal cycling for this crosslinked PEO-LiTFSI electrolyte under these test conditions.

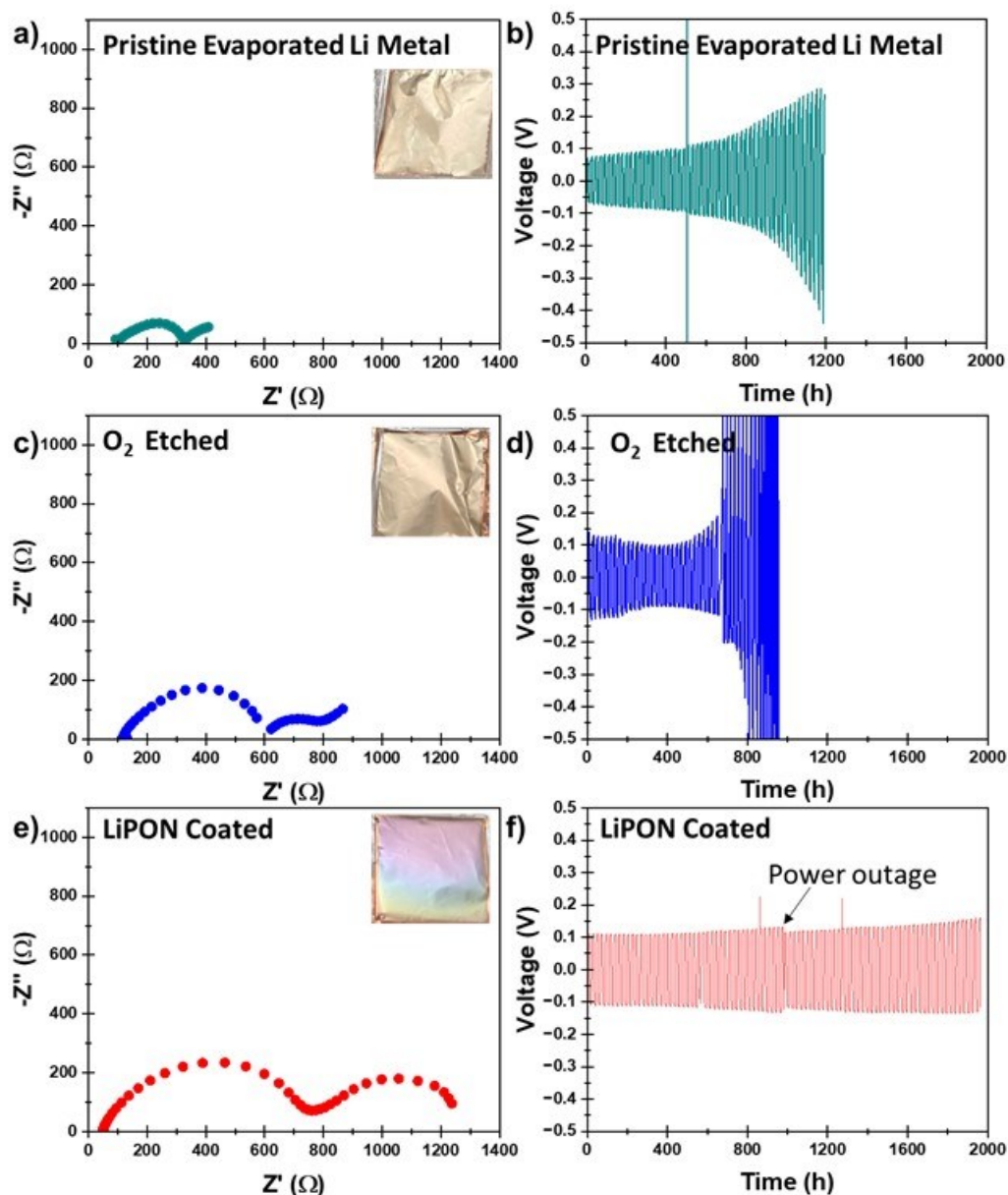


Figure XIII.22.5 Nyquist plots and Li//Li cycling data with a dry crosslinked PEO-LiTFSI polymer electrolyte with pristine Li metal (a-b), O<sub>2</sub> etched Li (c-d), and LiPON coated Li (e-f).

### Conclusions

1. For argyrodite sulfide solid electrolytes, the reactivity with Li metal causes rapid consumption of the thin Li metal anodes. Implementation of these electrolytes will require an engineered surface coating between the Li metal and the argyrodite.

2. The adhesion of the Li metal to various solid electrolytes can be measured using surface probe microscopy using Li-coated tips. This technique will provide significant insight into how to improve the adhesion of Li to solid electrolytes to improve cycle life and the critical current density.
3. Surface coatings on Li metal can either have a very positive effect or can have a detrimental effect, and this is likely electrolyte dependent. For cross-linked PEO-LiTFSI films Li metal with thin LiPON solid electrolyte coatings significantly improves the cycling stability of Li with this electrolyte.

#### **Key Publications**

1. E. C. Self, W.-Y. Tsai, A. S. Westover, K. L. Browning, G. Yang, J. Nanda “Benchmarking Solid-State Batteries Containing Sulfide Separators: Effects of Electrode Composition and Stack Pressure” *J. Electrochem. Soc.* 2022, 169, 100510.
2. Kalnaus, S; Dudney, N. J.; Westover, A. S.; Herbert. E.; Hackney, S.; “Solid-State Batteries: The critical role of mechanics”, *Science* 2023 381 (6664), eabg5998.
3. Torres, V. M.; Kalnaus, S.; Martin, S. W.; Duggan, C.; Westover, A. S., “Structure-mechanical properties correlation in bulk LiPON glass produced by nitridation of metaphosphate melts”, *Journal of the American Ceramic Society* 2023, 106 (11), 6565-6576

#### **Acknowledgments**

Key work in this project was performed by ORNL researchers Wan-Yu Tsai, Kyra Owensby, Katie Browning, Ritu Sahore, Sergiy Kalnaus, and Erik Herbert.



## XIII.23 Lithium Halide-Based Superionic Solid Electrolytes and High-Voltage Cathode Interfaces (ANL)

### Robert L. Sacci, Principal Investigator

Oak Ridge National Laboratory  
P.O. Box 2008, MS6124  
Oak Ridge, TN 37830  
E-mail: [saccirl@ornl.gov](mailto:saccirl@ornl.gov)

### Jagjit Nanda, Co-Principal Investigator

SLAC National Accelerator  
2575 Sand Hill Rd  
Menlo Park, CA 94025  
E-mail: [jnanda@slac.stanford.edu](mailto:jnanda@slac.stanford.edu)

### Simon Thompson, DOE Technology Development Manager

U.S. Department of Energy  
E-mail: [Simon.Thompson@ee.doe.gov](mailto:Simon.Thompson@ee.doe.gov)

Start Date: October 1, 2022      End Date: September 30, 2026  
Project Funding (FY23): \$1,250,000      DOE share: \$1,250,000      Non-DOE share: \$0

### Project Introduction

The realization of practical SSBs requires addressing several critical gaps in materials, synthesis, and processing, simultaneously. Advances in scalable processing of superionic solid electrolytes (SEs), stabilizing electrode-electrolyte interfaces and promoting long cycle life are all needed to meet the energy density and cost targets for next-generation batteries for electric vehicles. For SSBs to attain both high energy density and long cycle life, one of the most critical issues to solve is the electrolyte-cathode interface, where significant losses occur due to oxidative instabilities, poor wettability, and interfacial contact loss during cathode volumetric expansion. This problem is exacerbated in the case of high voltage cathodes, where the electrolyte instability leads to the formation of reactive interphase that could block lithium transport and increase area-specific resistance (ASR) between the cathode-SE.

### Objectives

The project aims to develop low-temperature solution-based synthesis strategy for high ionic conducting halide-based solid electrolyte (SE) and to enable approaches to develop a scalable process for integrating halide-based SE within porous high-voltage Li-ion cathode matrix. The proposed tasks and metrics aim at addressing the long-term Vehicle Technologies Office goal for developing SSBs at ambient temperature with energy density in the range of 500 Wh/Kg and 1000 Wh/L for electric drive vehicles. We will demonstrate single-layer, pouch-cell SSB containing a thin halide SE separator coupled with high-voltage cathodes with 70% capacity retention over 300 cycles at 2 mA/cm<sup>2</sup> in an anode-free SSB configuration that can attain 1000 Wh/L in prototype cells. If successful, then we will decrease the cost of SSB manufacturing while enabling high energy density cathode architectures.

### Approach

The project employs a multifaceted approach: (1) conduct solution-based synthesis of the metal halide superionic conductor as the platform to enable robust cathode-electrolyte interface processing for SSBs, (2) infiltrate pore structures using solution-based processing that deposits high-conductivity SEs within cathode pores, and (3) facilitate lithium transport and improve stability using cation doping (divalent to introduce lithium vacancies, and lanthanum to prevent indium redox). Our approach for the Years 1 and 2 aim at developing low-cost,

solution-based synthesis routes to produce a halide class of superionic conductor belonging to  $\text{Li}_3\text{MX}_6$  (where  $\text{M} = \text{Sc}, \text{Y}, \text{La}, \text{Er}, \text{In}$ , and  $\text{X} = \text{Cl}, \text{Br}, \text{I}$ ) along with enabling electrochemical and structural characterization.

## Results

To-Date Milestone overview is as follows:

1. Demonstration of synthesis of doped  $\text{Li}_3\text{InCl}_6$  for improved stability and conductivity. (Completed)
2. Compare conductivity between different casting methodologies. (Completed)
3. Obtain free-standing SE and SE/cathode composite films  $< 100\text{-}\mu\text{m}$ -thick. (Completed)
4. Demonstrate 50 cycles of SE/NMC-type cathode composites and Li-P-S (LPS)-coated anodes. (Completed)

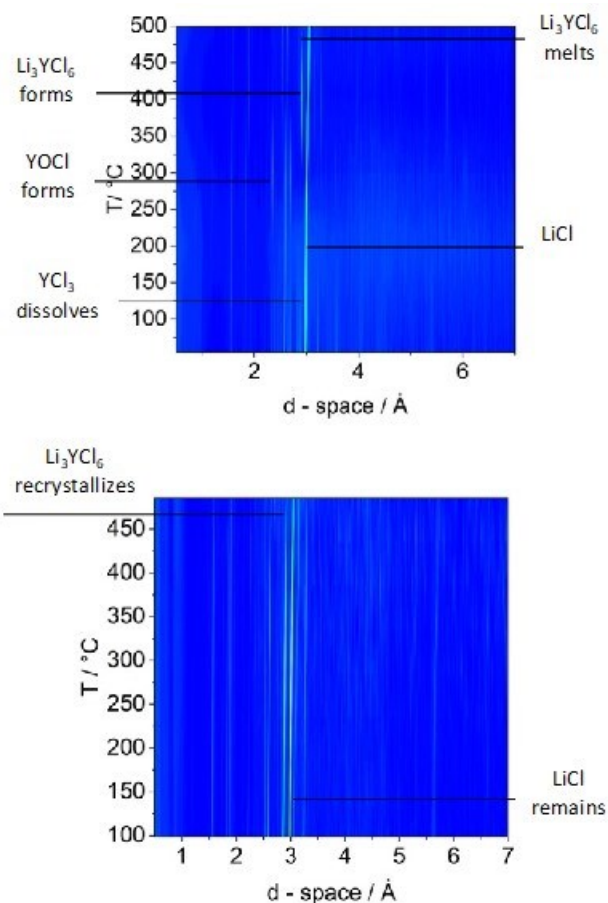


**Figure XIII.23.1** *In situ* Neutron diffraction contour plots of the direct water synthesis pathway: (top) heating from RT to 500 °C and (bottom) cooling from 500 °C to RT.

We expanded the synthesis of lithium halide-based electrolytes to include  $\text{Li}_3\text{YCl}_6$ . The purpose of changing the multivalent metal site is to increase the operating voltage window. By replacing  $\text{In}^{3+}$  with  $\text{Y}^{3+}$ , the voltage window is expected to increase by upwards to 0.5 V toward the anode. We attempted to replace  $\text{InCl}_3$  with  $\text{YCl}_3$ , dissolving it in water along with  $\text{LiCl}$  and synthesizing it through dehydration similar to  $\text{Li}_3\text{InCl}_6$ . This pathway failed to result in pure  $\text{Li}_3\text{YCl}_6$ . Instead, the product was a mixture of  $\text{YOCl}$  and  $\text{LiCl}$ , with little  $\text{Li}_3\text{YCl}_6$ . We followed this reaction using neutron diffraction, which is shown in Figure XIII.23.1. Here, the precursors were dissolved in water and dried under vacuum at 80 °C.  $\text{YCl}_3$  vanishes when the dried pellet is heated to 200 °C, and  $\text{Li}_3\text{YCl}_6$  begins to form around 300 °C. The impurity phase  $\text{YOCl}$  is also observed around 300 °C, which is in line with reports in the literature, which show that  $\text{YOCl}$  can be synthesized from

$\text{YCl}_3 \cdot 6\text{H}_2\text{O}$  by heating the precursor to  $350\text{ }^\circ\text{C}$  for 4 hours in the air.<sup>1</sup> Surprisingly, the sample melts at  $500\text{ }^\circ\text{C}$ , leaving behind unreacted  $\text{LiCl}$ . Upon cooling, the  $\text{Li}_3\text{YCl}_6$  reforms around  $475\text{ }^\circ\text{C}$  resulting in a large  $\text{LiCl}$  impurity. This result is likely due to the significant consumption of the  $\text{YCl}_3$  precursor in the formation of  $\text{YOCl}$  impurities during heating.

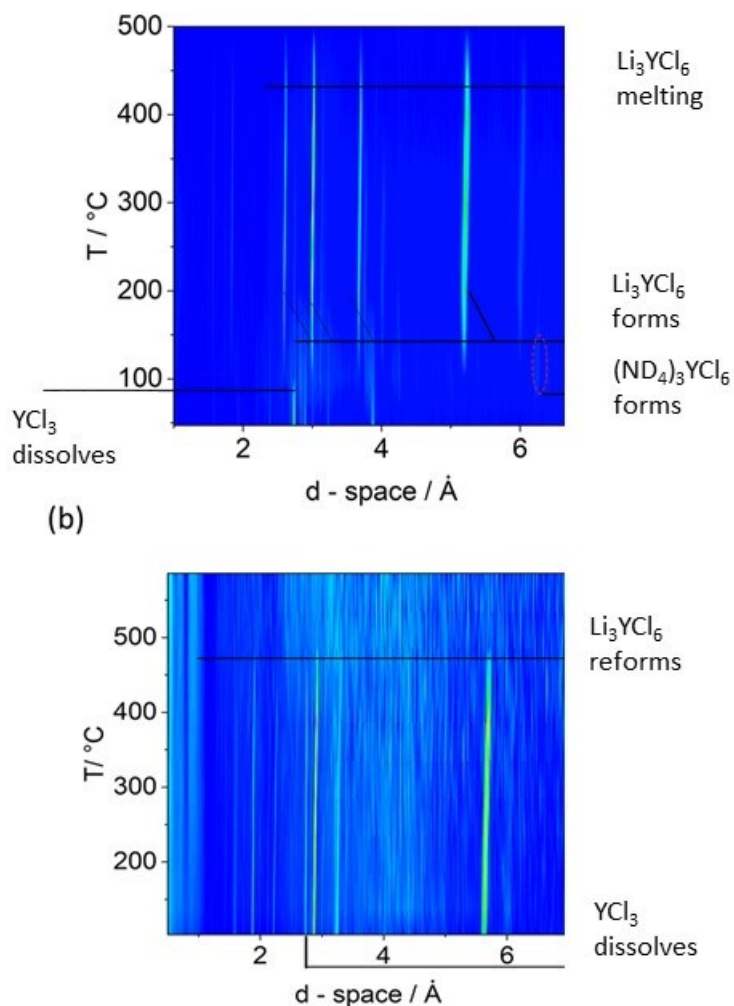


**Figure XIII.23.2** *In situ* Neutron diffraction contour plots of the ammonium-assisted synthesis pathway: (top) heating from RT to  $500\text{ }^\circ\text{C}$  and (bottom) cooling from  $500\text{ }^\circ\text{C}$  to RT. (top) depicts the presence of  $\text{YCl}_3$  precursors along with the early formation of  $(\text{ND}_4\text{Cl})_3[\text{YCl}_6]$  intermediate at  $\sim 100\text{ }^\circ\text{C}$ .

Given the strong coordination between  $\text{H}_2\text{O}$  and  $\text{Y}^{3+}$ , we attempted to shift the equilibrium towards the  $[\text{YCl}_6]^{3-}$  complex by adding excess  $\text{NH}_4\text{Cl}$ .  $\text{NH}_4\text{Cl}$  increases the concentration of chloride ions and undergoes clean sublimation at  $\sim 375\text{ }^\circ\text{C}$ . Figure XIII.23.2 shows the *in situ* neutron scattering data that seems to confirm our hypothesis. Here, the mixture of  $\text{YCl}_3$ ,  $\text{LiCl}$ , and  $\text{NH}_4\text{Cl}$  quickly forms the desired  $\text{Li}_3\text{YCl}_6$  product  $\sim 200\text{ }^\circ\text{C}$ . The comparison of the two synthetic routes clearly shows that  $\text{NH}_4\text{Cl}$  is required to protect the  $\text{YCl}_3$  precursor from hydrolysis during heating.

We also synthesized the  $\text{Li}_3\text{YCl}_6$  from a purely mechanochemical method. Here we ground anhydrous  $\text{YCl}_3$  and  $\text{LiCl}$  together for 16 h in a planetary mill. From here, we divided the batch between amorphized (unannealed) and crystalline (annealed). The annealed sample was pelletized and heated at  $500\text{ }^\circ\text{C}$  (ramp rate  $5\text{ }^\circ\text{C}/\text{min}$ ) for 5 h under argon flow in a glovebox.

We compared the conductivity of the three pure products (ammonium assisted (AA), mechanochemical (MC), and mechanochemical annealed (MCA)) in Figure XIII.23.3. The AA product showed the greatest room temperature conductivity of the three samples at 0.65 mS/cm, with MC and MCA being 0.37 and 0.13 mS/cm, respectively. The  $\text{Li}^+$  transport activation energy as derived from (Eq.1):

$$\sigma_{ionic} = \sigma_0 \exp\left(-\frac{E_a}{k_B T}\right) \quad (\text{Eq. 1})$$

where  $\sigma_0$ ,  $k_B$ , and  $T$  are the temperature-independent Arrhenius scalar, the Boltzmann constant, and the absolute temperature, respectively. The activation energy for the total conductivity for the mechanochemical products was 0.35 eV, while that of the AA product was 0.39 eV. The MCA product's conductivity is lower than that of the MC sample and is likely driven by annealing-induced ordering within the sample. This is in line with previous reports regarding the effect of annealing time on the mechanochemically derived  $\text{Li}_3\text{YCl}_6$  where it was observed that the conductivity decreased as the milled sample was annealed for longer periods of time ranging from 1 minute to 1 hour.<sup>2</sup> This was attributed to the large amount of cation site disorder induced during milling and the subsequent reordering caused by annealing.

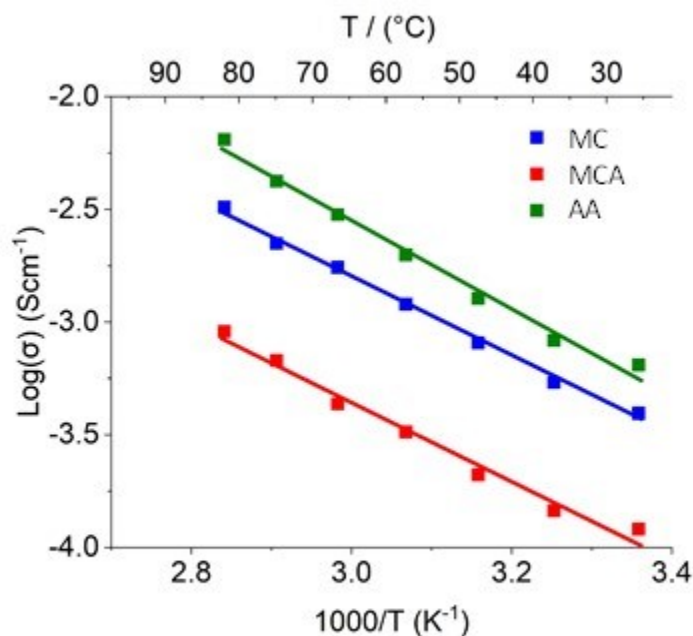


**Figure XIII.23.3 Arrhenius plot comparison for the  $\text{Li}_3\text{YCl}_6$  M, PMA, and AC samples**

Recent work has shown that electrochemical performance can be affected by the choice of a synthesis route for sulfide and halide solid electrolytes.<sup>3</sup> To understand this relationship for  $\text{Li}_3\text{YCl}_6$ ,  $\text{LiNi}_{0.8}\text{Mn}_{0.1}\text{Co}_{0.1}\text{O}_2$  (NMC811)/ $\text{Li}_3\text{YCl}_6$ /Li-In cells were constructed for the MC, MCA, and AA samples. A lithium-indium anode was used in place of lithium metal because  $\text{Li}_3\text{YCl}_6$  has been shown to be unstable against lithium metal.<sup>24</sup> The alloy was formed by lithiating indium foil on the first charge cycle of each cell. Figure XIII.23.4 presents the initial charge-discharge capacities for each cell at  $66 \mu\text{A}/\text{cm}^2$ , in which the  $\text{Li}_3\text{YCl}_6$ -MCA cell has a much higher initial charge capacity, 188 mAh/g, compared to just 148 mAh/g for the  $\text{Li}_3\text{YCl}_6$ -MC but the initial loss between the 1<sup>st</sup> charge and discharge is also substantially higher for the  $\text{Li}_3\text{YCl}_6$ -MCA cell, ~29% compared to just 0.7% capacity fade for the  $\text{Li}_3\text{YCl}_6$ -M cell. These cells were cycled at ~6 MPa; Yan Yao at the University of Houston is cycling these cells in parallel at greater stack pressures to understand the effect of contact loss during cycling.

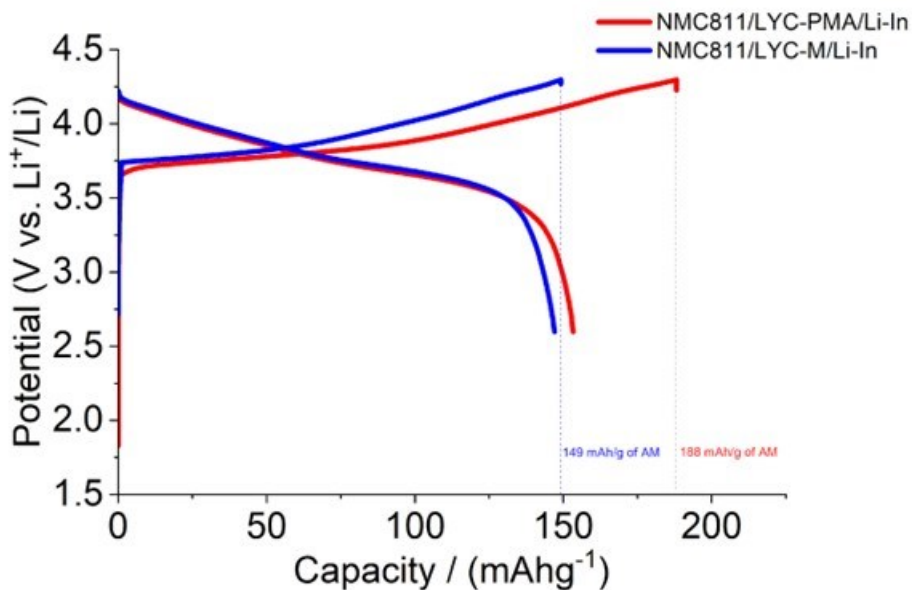


Figure XIII.23.4 Initial charge-discharge comparison for NMC811/Li<sub>3</sub>YCl<sub>6</sub>/Li-In cells.

Scalable fabrication of thin Li<sub>3</sub>InCl<sub>6</sub> (LIC) membrane: The goal was to fabricate electrolyte membrane with its thickness below 100 μm to enable high cell-level energy density. Here, we demonstrate a 15 cm × 8 cm thin LIC membrane with a thickness of 20±2 μm in Figure 5a-b. LIC membrane was prepared by tape-casting slurry comprised of LIC, hydrogenated nitrile butadiene rubber (HNBR) binder in isobutyl isobutyrate (IBIB) solvent onto a non-woven fabric, followed by vacuum-drying. The dimensions of the tape casted LIC membrane are shown in Figure XIII.23.5. Remarkably, the film maintains uniformity over a large area of 15×8 cm<sup>2</sup>. After densification, the LIC membrane shows a smooth surface and a controlled thickness of 20±2 μm. The as-prepared electrolyte membrane is scalable and satisfies the thickness requirement for high-energy-density batteries.

We evaluated the impact of solvent effect during tape-casting on membrane chemistry. Fourier transform infrared spectroscopy (FT-IR) shows the absence of C=O and C-O-C bonds, indicating complete removal of IBIB solvent after the drying (Figure XIII.23.1c). Distinct peaks at 1633 cm<sup>-1</sup> can be attributed to C=C stretching, and peaks at 1004 and 949 cm<sup>-1</sup> are associated with the alkenyl C-H bending, both originating from the HNBR binder. To assess any phase changes of LIC during the processing, X-ray diffraction (XRD) of LIC membrane shows an identical pattern with LIC powder, suggesting the addition of binder and solvent-processing do not affect the halide electrolyte structure.

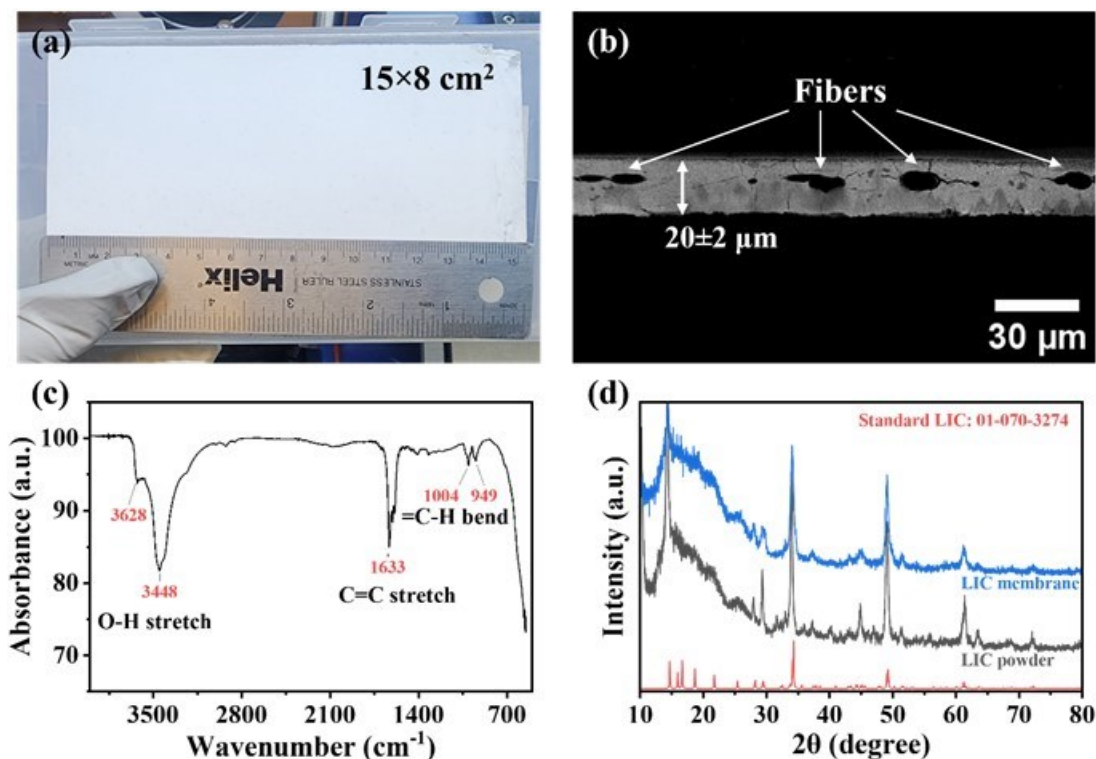
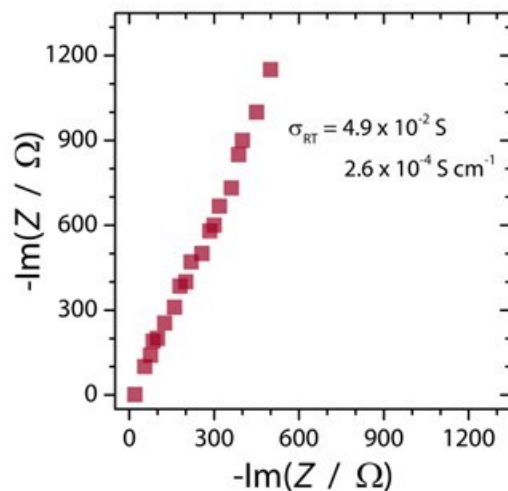


Figure XIII.23.5 Tape-casted LIC membrane and characterization. a) Optical image and dimensions. b) Cross-section of LIC membrane reinforced by non-woven fabric. c) FT-IR spectrum of LIC membrane showing complete removal of solvent. O-H bond comes from air exposure during FTIR characterization. d) XRD pattern of LIC powder and LIC membrane showing the identical phase.

We also attempted to cast a bilayer, argyrodite and LIC, membrane. Guang Yang at ORNL aided and we used his protocol to tape cast an 8 x 8 cm<sup>2</sup> thin bilayer membrane with a thickness of 77±3 μm. This formulation utilizes 5 wt% poly(isobutylene) dissolved in toluene. Impedance spectroscopy was conducted at room temperature to check the overall conductivity after pressing to 50 MPa and relaxing back to ambient pressure. As can be seen from the Nyquist plot in Figure XIII.23.6, the conductivity of the bilayer was 4.9 x 10<sup>-2</sup> S, which corresponded to a specific conductivity of 2.6 x 10<sup>-4</sup> S cm<sup>-1</sup>.



**Figure XIII.23.6** Nyquist plot of LPSC/LIC bilayer membrane at room temperature between two carbon coated aluminum current collectors. Data collected by Anna Mills and Guang Yang from FSU and ORNL, respectively.

Lastly, we have compared separator methodologies for both  $\text{Li}_3\text{InCl}_6$  and  $\text{Li}_3\text{YCl}_6$ . The purpose of this study conducted at University of Houston was to ascertain the inherent differences between  $\text{Li}_3\text{InCl}_6$  and  $\text{Li}_3\text{YCl}_6$  as far as the need and utility of a sublayer between the electrolyte and Li-In alloy anode. The solid cell NMC85 |LYC|Li-In with an 88.9% capacity retention after 50 cycles have been demonstrated.

In  $\text{Li}_3\text{InCl}_6$ -based cells (Figure XIII.23.7a), electrolyte  $\text{Li}_3\text{InCl}_6$  reacts with Li-metal or Li-In alloy anode and leads to unstable halide solid-electrolyte/anode interface. A bi-layer structure with Li-metal-stable argyrodite electrolyte was adopted to avoid reductive decomposition of  $\text{Li}_3\text{InCl}_6$ . The cathode composite was prepared by mechanically mixing 70%  $\text{LiNi}_{0.85}\text{Mn}_{0.05}\text{Co}_{0.1}\text{O}_2$  (NMC85) with 27%  $\text{Li}_3\text{InCl}_6$  and 3% graphitic carbon fibers. The cell showed a high initial cycling capacity of  $205 \text{ mAh g}^{-1}$ , but it gradually decayed to 84.6% after 10 cycles (Figure XIII.23.7a, d). The  $\text{Li}_3\text{YCl}_6$  counterpart with the same cell architecture and cathode composition showed an inferior stability, with capacity decay to 69% over 7 cycles. We speculate that cumulative cathode volume change at high active material fraction might mechanically deteriorate cathode–electrolyte interface. Moreover,  $\text{Li}_3\text{YCl}_6$  has a lower ionic conductivity  $1.4 \text{ mS/cm}$  at  $60^\circ\text{C}$  compared to  $\text{Li}_3\text{InCl}_6$   $2.05 \text{ mS/cm}$  which requires higher electrolyte fraction in the composite cathode to achieve sufficient ion conduction. Decreasing the cathode active material fraction to 50% drastically improves the cycling stability (Figure XIII.23.7b), with a capacity retention of 86.3% after 10 cycles (Figure XIII.23.1e). It is also noteworthy that the cell impedance continuously increased in the bi-layer cells with both electrolytes  $\text{Li}_3\text{InCl}_6$  (Figure XIII.23.7g) and  $\text{Li}_3\text{YCl}_6$  (Figure XIII.23.7h). For the  $\text{Li}_3\text{InCl}_6$  bilayer cell the high frequency resistance, which correlates to electrolyte conductivity, stays the same and the low frequency resistance that corresponds to interfacial impedance increases. For the  $\text{Li}_3\text{YCl}_6$  bilayer cell both resistances increase. Because both NMC–halide interface and argyrodite–metal interfaces are reported to be stable, it is likely that the impedance increase originates from the reactions between halide electrolyte and argyrodite electrolyte at  $60^\circ\text{C}$ .

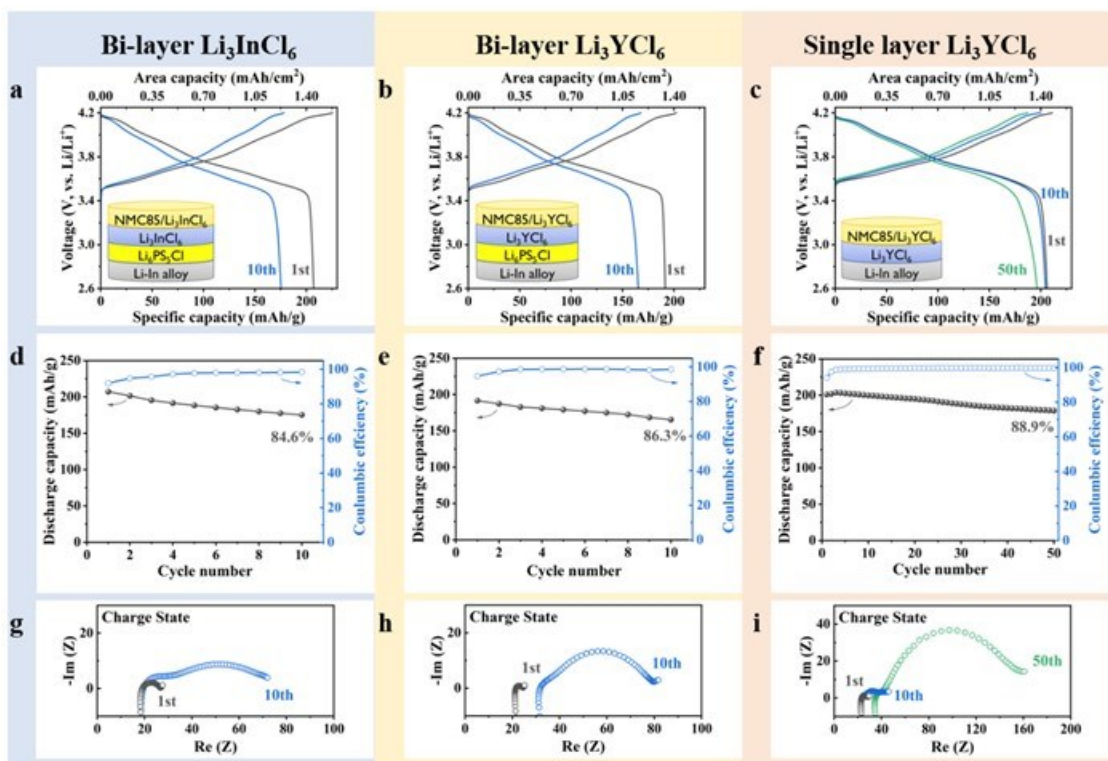


**Figure XIII.23.7** Electrochemical profile of solid-state batteries with halide electrolyte. a-c) Cell architecture and corresponding charge and discharge voltage profiles. d-f) Capacity retention. g-i) Impedance profiles measured at charge state. All cells were tested at 60 °C, under 50 MPa stacking pressure and at 10 mg/cm<sup>2</sup> cathode loading.

Unlike  $\text{Li}_3\text{InCl}_6$  that shows reductive instability,  $\text{Li}_3\text{YCl}_6$  is relatively stable against the Li/In alloy anode with mild and reversible decomposition reaction. To avoid possible reactions between two electrolytes, we removed the separating argyrodite layer and simplified the cell design back to single layer cell with direct  $\text{Li}_3\text{YCl}_6$ -Li/In contact. The new cell design resulted in a dramatic improvement in both cathode active material utilization (Figure XIII.23.7c) and capacity retention (Figure XIII.23.7f), with an initial charge capacity of 205 mAh g<sup>-1</sup> and 88.9% capacity retention after 50 cycles. The relatively stable cycling performance is the result of (1) decreased active material fraction to mitigate volume change and resultant mechanical failure; (2) improved separator stability by using single-component electrolyte to avoid side reactions; (3) improved anode-electrolyte stability by the choice of relatively stable electrolyte material against reductive decomposition. Lastly, Figure 7c shows that our year out goal has been accomplished.

## Conclusions

1. We confirmed that aqueous synthesis of  $\text{Li}_3\text{YCl}_6$  does not result in pure product unless ammonium chloride is added to direct the reaction pathway to an  $(\text{NH}_4)_3\text{YCl}_6$  intermediate.
2. There is difference between mechanochemical synthesized  $\text{Li}_3\text{YCl}_6$  and the aqueous phase.
3. We have used 5 wt% poly(isobutylene) dissolved in toluene to form <100 um thick LIC membranes and have pressed <200 um of composite cathode electrodes.
4. The use of LYC enables cycling to 4.2 V and beyond when integrating with LPSC anolyte. This improvement seems to be driven by better chemical stability between the LYC and LPSC. LIC reacts with LPSC resulting in delamination as the cathode cycles.

For year 3, we will focus on understanding the mechanical and interfacial instabilities of LYC and LIC with the high voltage cathodes.



## Key Publications

### Invited Presentations

1. Sacci et al., How Halide sub-lattice affects Li ion transport in antiperovskites and solution phase synthesis of Li Halide electrolytes, 242<sup>nd</sup> ECS Meeting, Atlanta GA

### Publications

1. Liqun Guo, Jie Zheng, Lihong Zhao\*, Yan Yao\*, **Interfacial instabilities in halide-based solid-state batteries**, *MRS Bulletin*, **2023**, 48, 1-10.

## References

1. Todd, P. K.; McDermott, M. J.; Rom, C. L.; Corrao, A. A.; Denney, J. J.; Dwaraknath, S. S.; Khalifah, P. G.; Persson, K. A.; Neilson, J. R. Selectivity in Yttrium Manganese Oxide Synthesis via Local Chemical Potentials in Hyperdimensional Phase Space. *J. Am. Chem. Soc.* **2021**, *143* (37), 15185–15194. <https://doi.org/10.1021/jacs.1c06229>.
2. Schlem, R.; Muy, S.; Prinz, N.; Banik, A.; Shao-Horn, Y.; Zobel, M.; Zeier, W. G. Mechanochemical Synthesis: A Tool to Tune Cation Site Disorder and Ionic Transport Properties of  $\text{Li}_3\text{MCl}_6$  (M = Y, Er) Superionic Conductors. *Adv. Energy Mater.* **2020**, *10* (6), 1903719. <https://doi.org/10.1002/aenm.201903719>.
3. Koç, T.; Marchini, F.; Rouse, G.; Dugas, R.; Tarascon, J.-M. In Search of the Best Solid Electrolyte-Layered Oxide Pairing for Assembling Practical All-Solid-State Batteries. **2021**, 11.

## Acknowledgements

These researchers provided important insights and assistance with the programs: Teerth Brahmabhatt, Bredesen Center, University of Tennessee, Knoxville, Prof. Yan Yao, Liqun Guo, and Jie Zheng, University of Houston.

## XIII.24 Polyester-Based Block Copolymer Electrolytes for Lithium-Metal Batteries (University of California, Berkeley)

### Dr. Nitash P. Balsara, Principal Investigator

Department of Chemical and Biomolecular Engineering  
University of California, Berkeley  
Berkeley, CA 94720  
E-mail: [nbalsara@berkeley.edu](mailto:nbalsara@berkeley.edu)

### Tien Duong, DOE Technology Development Manager

U.S. Department of Energy  
E-mail: [Tien.Duong@ee.doe.gov](mailto:Tien.Duong@ee.doe.gov)

Start Date: October 1, 2022

End Date: September 30, 2023

Project Funding (FY23): \$400,000

DOE share: \$400,000

Non-DOE share: \$0

### Project Introduction

Polymer electrolytes offer increased stability in lithium batteries in comparison to more widely used liquid electrolytes. Block copolymer-based electrolytes containing both soft, ion-conducting domains and rigid, nonconducting domains offer the opportunity to tune both mechanical and electrical properties separately. Most block copolymer electrolytes studied thus far comprise poly(ethylene oxide) (PEO) as the conducting domain. The team hopes to develop polyester-based (PES) electrolytes that exhibit much higher transport properties and limiting currents than PEO-based electrolytes. An all-solid full cell with this new block copolymer electrolyte, a Li-metal anode, and an NMC cathode will have much higher energy density than current Li-ion technology.

### Objectives

The project objective is to design and synthesize polyester-based block copolymer electrolytes that can enable full-cell cycling at 1 mA/cm<sup>2</sup> or greater for 300 cycles. The cell comprises Li-metal anode, 4.5 V Ni-Mn-C (NMC) cathode, and thin separators (20-50 μm) casted from the block copolymer.

### Approach

The team will begin by synthesizing several series of polyester homopolymers and fully characterizing their blends with lithium salts as polymer electrolytes in Li-Li symmetric cells. Next, they will make block copolymer electrolytes based on the most promising candidate and measure the electrochemical and mechanical properties thoroughly. Finally, they will assemble full cells with the optimum block copolymer electrolytes together with lithium metal and a 4.5 V NMC cathode.

### Results

#### Measuring Limiting Current

We measured the limiting current ( $i_L$ ) of three PES/LiTFSI electrolytes using lithium-lithium symmetric cells. In Figure XIII.24.1a and Figure XIII.24.1b we show the voltage ( $V$ ) as a function of time ( $t$ ) for various applied current densities for electrolytes with an  $r$  value of 0.02 and 0.04 respectively. For this study it is useful to determine the largest current density that results in a stable voltage response and the smallest current density that results in an unstable voltage response. These two values are averaged together to find the limiting current. As seen in Figure XIII.24.1a, an applied current density of 0.25 mA/cm<sup>2</sup> results in a stable voltage response where over time the voltage goes to a constant value. An applied current density of 0.3 mA/cm<sup>2</sup> results in an unsteady voltage response. In Figure XIII.24.1b we see the same phenomenon for current densities of 0.9 mA/cm<sup>2</sup> and 1.1 mA/cm<sup>2</sup>.

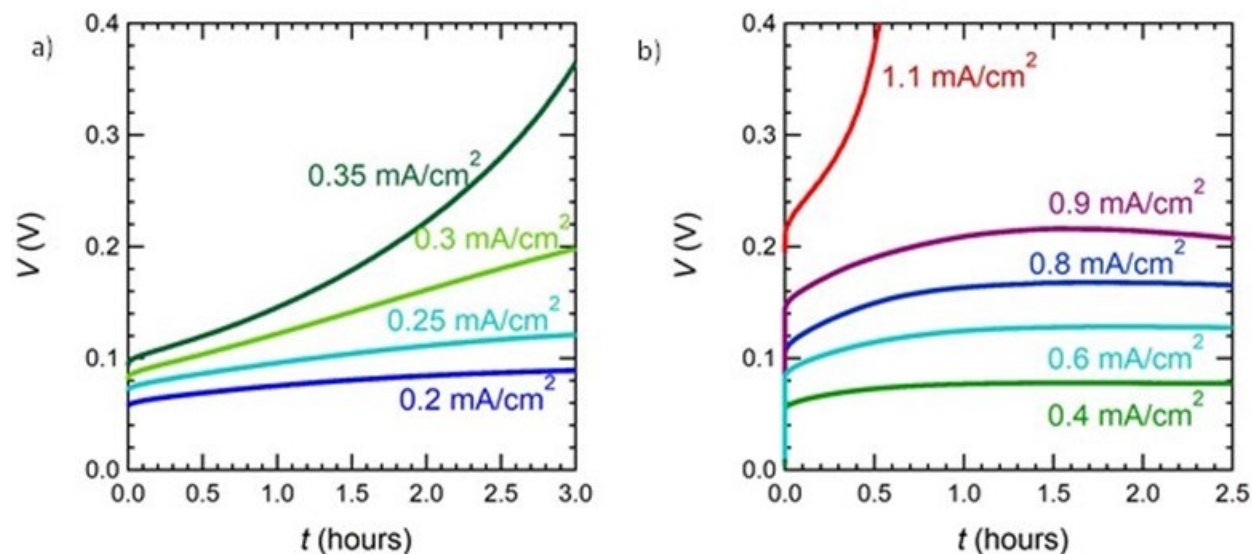


Figure XIII.24.1 Voltage (V) behavior as a function of time (t) for various applied current densities at 90 °C for PES/LiTFSI electrolytes with salt concentrations of a)  $r = 0.02$ , and b)  $r = 0.04$ .

In our studies we also measured the limiting current of PES/LiTFSI electrolytes of salt concentration  $r = 0.06$ . The limiting current of these three electrolytes allows for a comparison of the performance limitations of PPM/LiTFSI electrolytes and PEO/LiTFSI electrolytes.

Figure XIII.24.2 shows the normalized limiting current, where the limiting current density is multiplied by the thickness of our electrolytes, to compare the limiting current of PES/LiTFSI electrolytes to previously determined limiting currents of PEO/LiTFSI electrolytes.<sup>1</sup> At the lowest salt concentration of  $r = 0.02$ , the limiting current of the two systems are very similar. However, at higher salt concentrations the limiting current of the PES/LiTFSI electrolytes is more than double that of PEO/LiTFSI. This shows that PES/LiTFSI electrolytes can be subjected to higher currents compared to PEO/LiTFSI electrolytes, making this material more attractive for real world applications compared to PEO.

According to concentrated solution theory the limiting current should be a linear function of salt concentration. In Figure XIII.24.2, linear fits of the limiting current data are shown, with the intercept held at zero since no current will be passed through a neat polymer. For PES/LiTFSI electrolytes,  $i_L L = 1.16r$ , and for PEO/LiTFSI electrolytes,  $i_L L = 0.42r$ . Again, this is indicative that PES/LiTFSI electrolytes can operate under higher applied currents than PEO/LiTFSI electrolytes for most salt concentrations above the lower limit of  $r = 0.02$ .

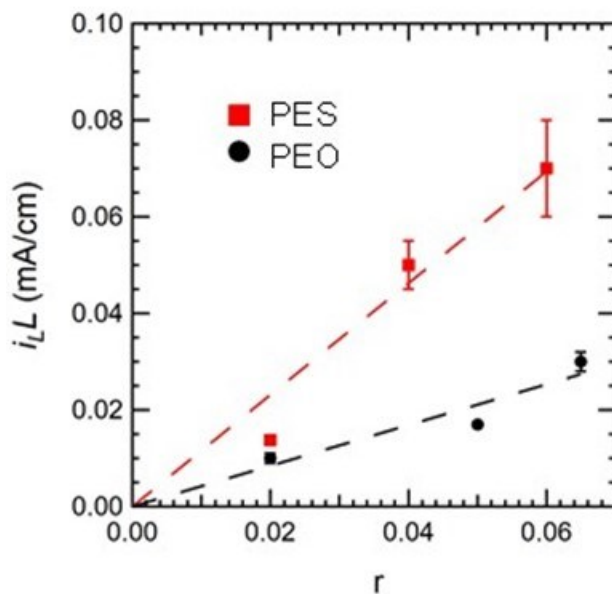


Figure XIII.24.2 Normalized limiting current,  $i_L$  of PES/LiTFSI and PEO/LiTFSI electrolytes as a function of salt concentration,  $r$ . The dashed lines are linear fits of the data with the intercept constrained at zero. The red data represents PES/LiTFSI electrolytes, and the black data represents PEO/LiTFSI electrolytes. All data was collected at 90 °C.

#### Molecular Weight Effects on Ion Transport Properties

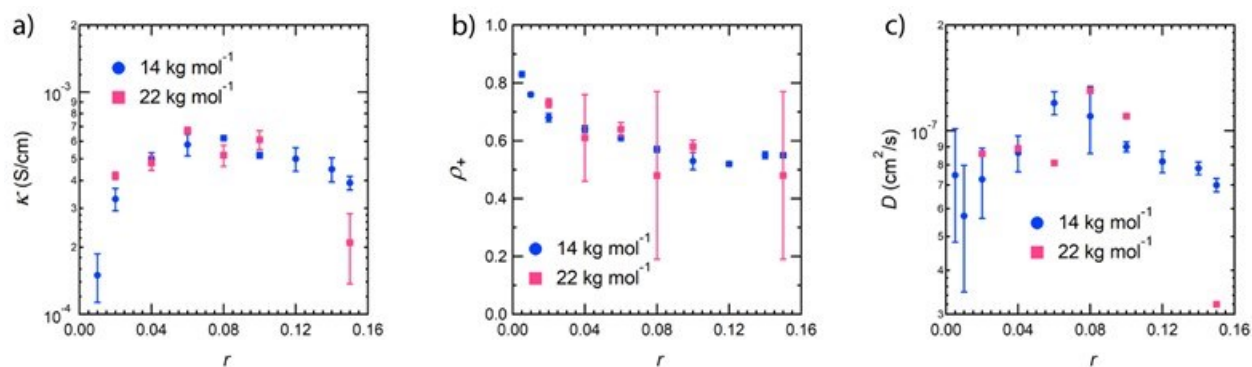


Figure XIII.24.3 a) Ionic conductivity ( $\kappa$ ), b) current fraction, ( $\rho_+$ ), and c) restricted diffusion coefficient ( $D$ ) as a function of salt concentration ( $0.005 \leq r \leq 0.15$  (where  $r = [\text{Li}^+]/[\text{O}]$ )) for two molecular weights of PES at 90 °C. Three data points at each salt concentration represents reproducibility of the data. The low molecular weight (14 kg mol<sup>-1</sup>) is shown in blue circles, while the high molecular weight is shown in pink squares (22 kg mol<sup>-1</sup>).

We studied how lithium-ion transport varies with molecular weight in PES electrolytes. Figure XIII.24.3 shows the electrochemical properties as a function of salt concentration of two PES electrolytes with different molecular weights: 14 and 22 kg mol<sup>-1</sup>. The values of ionic conductivity shown in Figure XIII.24.3a exhibit minor changes when the molecular weight is increased by 12 kg mol<sup>-1</sup>. Similar to ionic conductivity, the current fractions for each molecular weight are within experimental error of each other. (Figure XIII.24.3b) Lastly, Figure XIII.24.3c shows only slight differences in the restricted diffusion coefficient between each molecular weight across most salt concentrations. The largest deviations are seen at high salt concentrations.

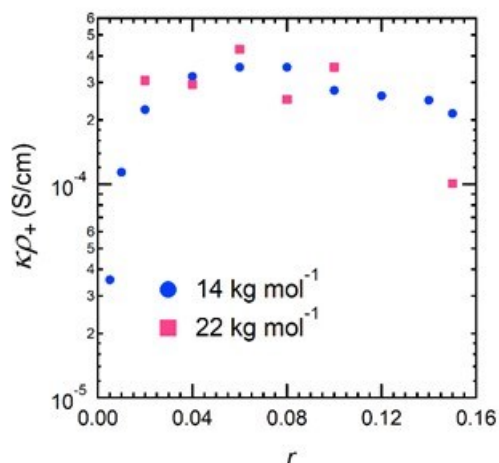


Figure XIII.24.4 Efficacy ( $\kappa\rho_+$ ) as a function of salt concentration for two molecular weights of PES at 90 °C. The low molecular weight (14 kg mol<sup>-1</sup>) is shown in blue circles, while the high molecular weight is shown in pink squares (22 kg mol<sup>-1</sup>).

Figure XIII.24.4 plots the efficacy of the PES electrolytes as a function of salt concentration for two molecular weights. The efficacy captures the tradeoff between ionic conductivity and current fraction in limit of low current densities. Overall, changing the molecular weight of PES has no impact on the overall efficacy and performance of the polyester electrolytes.

### PES Block Copolymer Synthesis

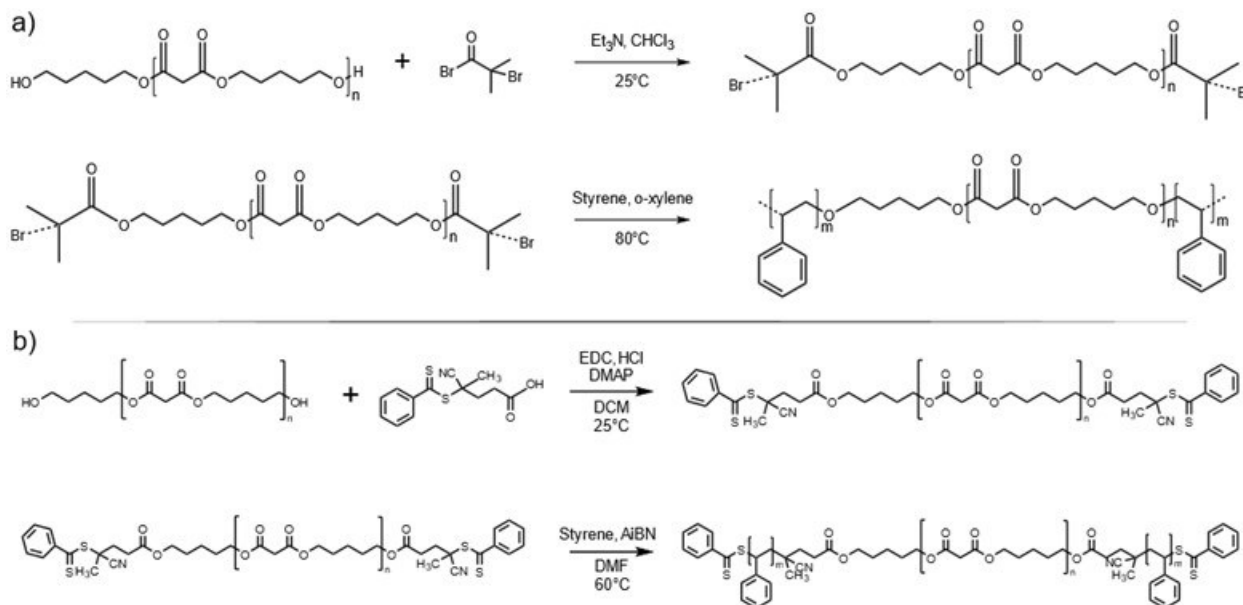
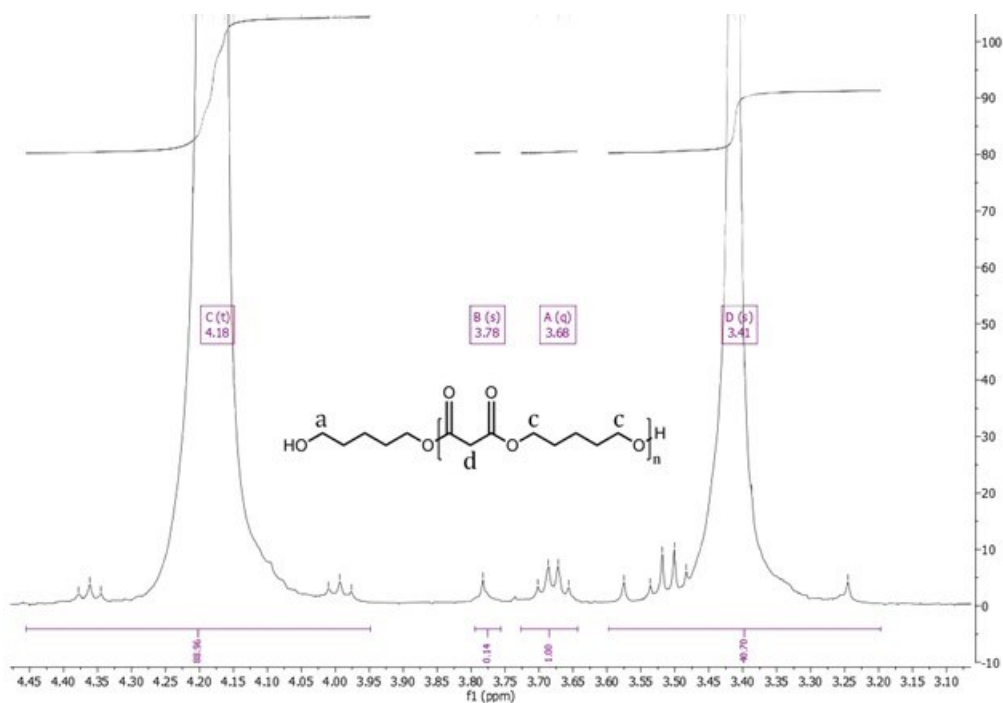


Figure XIII.24.5 (a) Atom transfer radical polymerization reaction scheme and (b) reversible addition fragmentation chain transfer polymerization scheme for synthesizing PS-PES-PS block copolymers.

We explored the synthesis of a polystyrene-*b*-polyester-*b*-polystyrene (PS-PES-PS) using two polymerization techniques: atom transfer radical polymerization (ATRP) and reversible addition fragmentation chain transfer (RAFT) polymerization. Figure XIII.24.5a and Figure XIII.24.5b show the reaction schemes for the ATRP and

RAFT synthesis, respectively. Currently, we have only been able to produce a viable PS-PES-PS product using the ATRP mechanism at the given conditions.



**Figure XIII.24.6**  $^1\text{H}$  NMR of a polyester homopolymer synthesized using a condensation reaction. The molecular weight of the homopolymer was approximately  $13 \text{ kg mol}^{-1}$ . The peak shifts are correlated with the corresponding hydrogens on the molecular structure except for peak B which is correlated to the methyl terminated end-group.

Figure XIII.24.6 shows the starting  $^1\text{H}$  NMR data of the polyester homopolymer with majority OH- end functional groups. The 3.68 ppm shift relates to the terminal end-group hydrogens, the 3.41 ppm shift corresponds to the  $\alpha$ -hydrogens, and the 4.18 ppm shift is correlated to the ester hydrogens. The shift at 3.78 ppm indicates the presence of small amounts of methyl terminated polymer chains. As a result, the resulting molecular weight of the homopolymer is approximately  $13 \text{ kg mol}^{-1}$ .

Figure XIII.24.7 shows the final  $^1\text{H}$  NMR data of the PS-PES-PS block copolymer using the ATRP reaction scheme. The peak at 4.15 ppm corresponds to the ester  $\text{CH}_2$ - hydrogens, while the peaks in the 6.52-7.36 range correspond to the styrene  $\text{CH}$ - hydrogens. Based on the peak integrations, the molecular weight of the attached styrene block is approximately  $15 \text{ kg mol}^{-1}$ . This corresponds to approximately 67 styrene repeat units. Using this as a steppingstone, we hope to complete a more controlled synthesis of a PS-PES-PS block copolymer to produce higher molecular weight products.

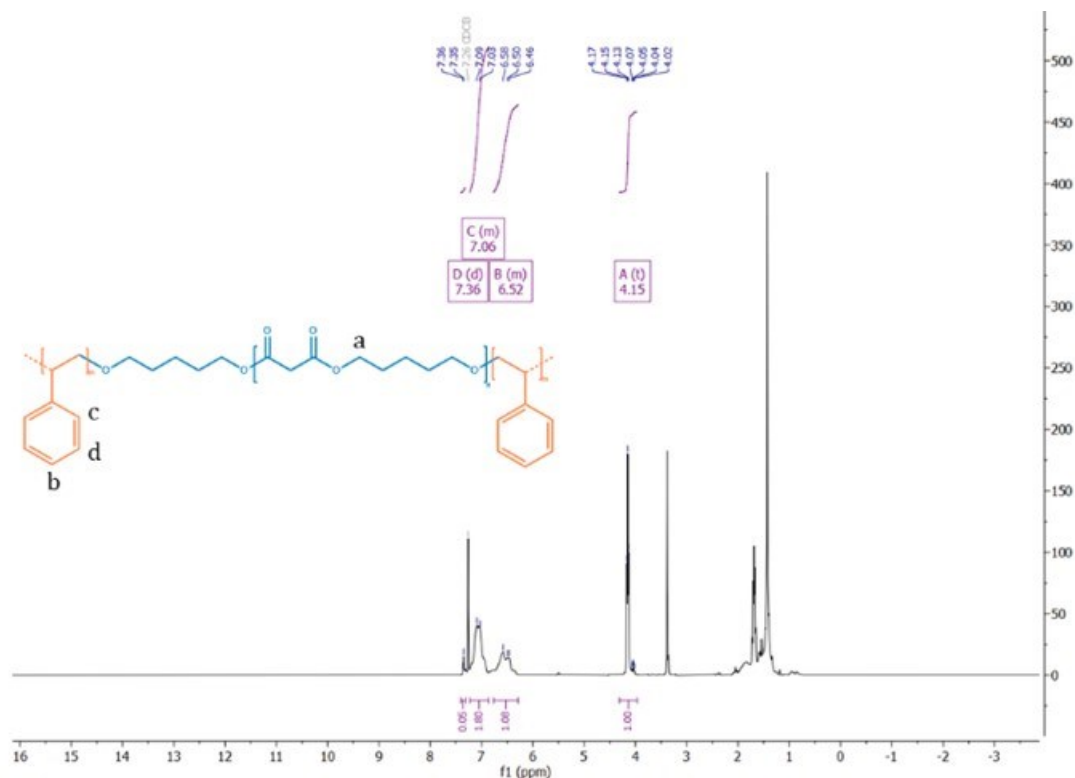


Figure XIII.24.7  $^1\text{H}$  NMR of a PS-PES-PS block copolymer synthesized with ATRP. The molecular weight of the polyester block and the styrene block was approximately  $13 \text{ kg mol}^{-1}$  and  $15 \text{ kg mol}^{-1}$ , respectively. The peak shifts are correlated with the corresponding hydrogens on the molecular structure.

#### Physical Properties of Cross-linked PES Electrolytes

The main goal of this project was to make an all-solid battery with polymer electrolytes and a lithium metal anode. When we wrote the proposal, we had identified PES as a promising polymer electrolyte, and proposed to solidify this polymer by attaching the chain to a polystyrene (PS) block. We made significant efforts over the past 6 months to synthesize the block copolymer but we were only able to synthesize low molecular samples with poor mechanical properties. We abandoned that approach and decided to pursue crosslinking PES to create the polymeric solid.

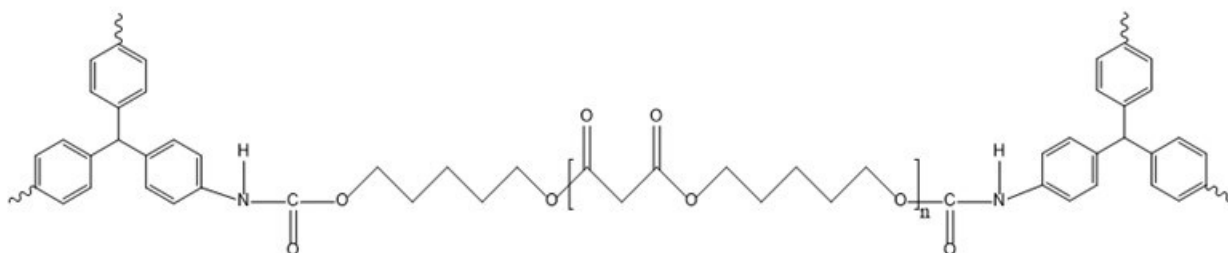
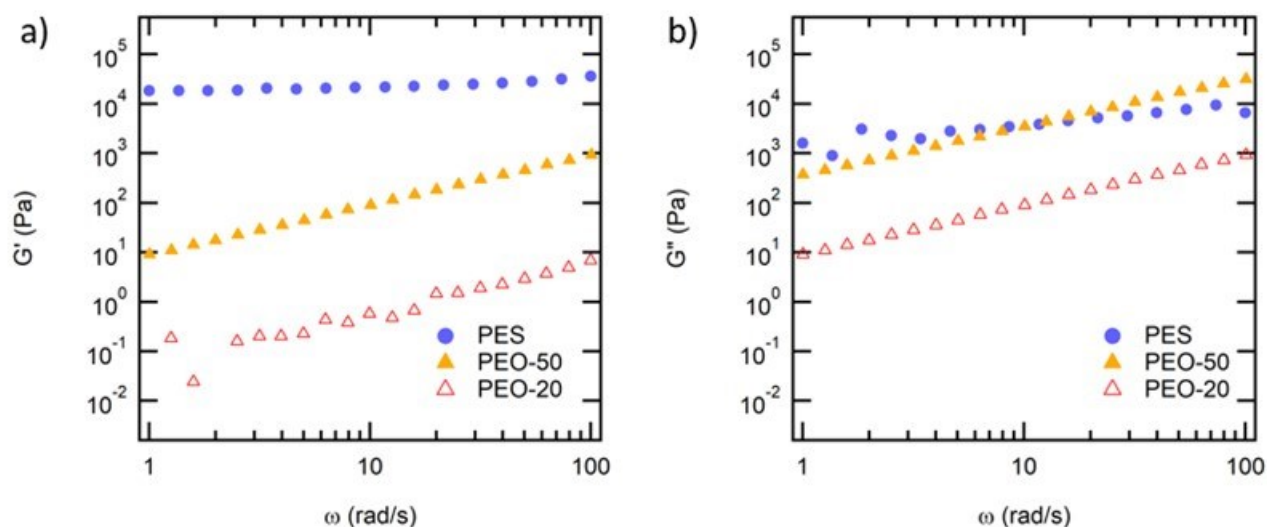


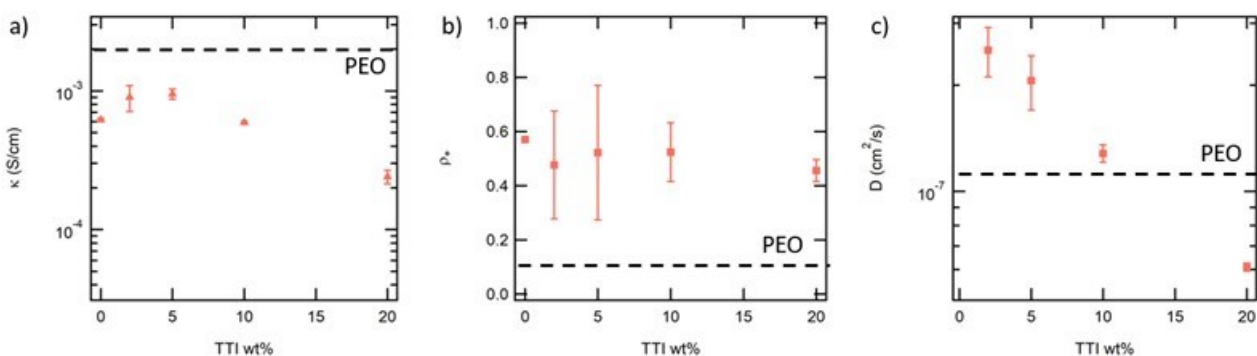
Figure XIII.24.8 Final reaction product obtained after reaction of PES with TTI in 1-methyl 2-pyrrolidine at  $120^\circ\text{C}$ .

Figure XIII.24.8 shows the final reaction product of the crosslinked PES polymer. Using triphenylmethane trisocyanate (TTI) as our crosslinking agent, we were able to preliminary synthesize several freestanding films of PES electrolyte with varying amounts crosslinking ratios.



**Figure XIII.24.9** a) Storage modulus ( $G'$ ) and b) loss modulus ( $G''$ ) as a function of frequency for PES (26 kg mol<sup>-1</sup>)/10 wt% TTI, PEO (20 kg mol<sup>-1</sup>), and PEO (50 kg mol<sup>-1</sup>) at 90°C. The measurements were taken in the absence of salt. PES/TTI is shown in blue circles, PEO-20 is shown in open red triangles, and PEO-50 is shown in yellow triangles.

Figure XIII.24.9a and Figure XIII.24.9b show the storage modulus ( $G'$ ) and loss modulus ( $G''$ ) of poly(ethylene oxide) (PEO) with different molecular weights and PES/10 wt% TTI at 90°C.  $G'$  for the PES polymer is orders of magnitude larger than the PEO polymers with similar molecular weights. The  $G'$  values are greater than the  $G''$  for PES across the frequency range, which indicates more solid-like behavior. The inverse relationship is observed for both PEO polymers indicating more liquid like behavior. This shows that crosslinking is a promising route for achieving higher mechanical stability without the use of a block copolymer.



**Figure XIII.24.10** a) Ionic conductivity ( $\kappa$ ), b) current fraction, ( $\rho_+$ ), and c) restricted diffusion coefficient ( $D$ ) of PES electrolyte as a function of TTI weight percent at 90°C. The salt concentration ( $r = [\text{Li}^+]/[\text{O}]$ ) was fixed to 0.08. Two data points at each weight percent represent reproducibility of the data.

Next, we characterized the electrochemical properties of PES electrolytes with salt. The salt concentration,  $r = [\text{Li}^+]/[\text{O}]$ , was fixed relative to the amount of PES polymer. Figure XIII.24.10a, Figure XIII.24.10b, and Figure XIII.24.10c show the ionic conductivity, current fraction, and restricted diffusion coefficient as a function of TTI wt% measured using Li-Li symmetric cells. At small TTI wt%, the ionic conductivity does not change drastically, but upon significant addition of TTI, there is a drop in conductivity. While there is a slight decrease in current fraction upon crosslinking, the change is within error of the homopolymer PES electrolyte.



The restricted diffusion coefficient shows a steady reduction in magnitude with increasing TTI content as expected with chemical crosslinked systems. In the future, we plan on implementing a purification process of the crosslinked PES electrolytes through solvent washing to remove unreacted monomer and TTI and help improve their stability towards lithium metal. We expect this will aid in reducing error in our electrochemical measurements.

### Conclusions

In the present research, the efficiency of new polyester-based electrolyte against lithium metal has been investigated. The major conclusions are summarized below:

- PES/LiTFSI electrolytes were shown to have considerably higher limiting currents than state-of-the-art PEO/LiTFSI electrolytes.
- Ion-transport properties of PES electrolytes did not show any molecular weight dependence.
- Two block copolymer synthesis methods were explored, but only resulted in irreproducible low molecular products. We therefore shifted our approach to designing crosslinked PES electrolytes.
- Crosslinked PES polymer demonstrated large improvements in mechanical stability compared to PEO polymer. Increasing the weight percent of crosslinking agent results in deterioration of ion transport properties.

### Key Publications

1. Maslyn, Jacqueline A., Pallab Barai, Kyle D. McEntush, Katherine J. Harry, Louise Frenck, Whitney S. Loo, Alec S. Ho, Dilworth Y. Parkinson, Venkat Srinivasan, and Nitash P. Balsara. 2023. "Plating and Stripping of Lithium Metal Stabilized by a Block Copolymer Electrolyte: Local Current Density Measurement and Modeling." *Journal of The Electrochemical Society* 170 (7): 070510. <https://doi.org/10.1149/1945-7111/ace12f>.

### References

Gribble, Daniel A., Louise Frenck, Deep B. Shah, Jacqueline A. Maslyn, Whitney S. Loo, Katrina Irene S. Mongcopa, Danielle M. Pesko, and Nitash P. Balsara. 2019. "Comparing Experimental Measurements of Limiting Current in Polymer Electrolytes with Theoretical Predictions." *Journal of The Electrochemical Society* 166 (14): A3228. <https://doi.org/10.1149/2.0391914jes>.

## XIII.25 Development of All Solid-State Battery using Anti-Perovskite Electrolytes (ANL)

### Zonghai Chen, Principal Investigator

Argonne National Laboratory  
9700 South Cass Avenue  
Lemont, IL, 60439  
E-mail: [Zonghai.chen@anl.gov](mailto:Zonghai.chen@anl.gov)

### Tao Li, Co-Principal Investigator

Argonne National Laboratory  
9700 South Cass Avenue  
Lemont, IL, 60439  
E-mail: [taoli@anl.gov](mailto:taoli@anl.gov)

### Simon Thompson, DOE Technology Development Manager

U.S. Department of Energy  
E-mail: [Simon.Thompson@ee.doe.gov](mailto:Simon.Thompson@ee.doe.gov)

Start Date: October 1, 2022	End Date: September 30, 2023	
Project Funding (FY23): \$585,000	DOE share: \$585,000	Non-DOE share: \$0

### Project Introduction

In the past decades, a continuous effort has been paid to developing high-energy density lithium-ion chemistries without sacrificing their safety performance for automobile applications. Conventional non-aqueous electrolytes have been the bottleneck for further increase in both the energy density and safety while solid-state electrolytes are promising to take the seat and continue the journey. Giving top priority to the processability of the electrolyte material for scalable manufacturing, the project team will develop a high-performance anti-perovskite solid-state electrolyte with stabilized electrode/electrolyte interfaces for scalable fabrication of liquid-free solid-state batteries. In line with this project's objectives, the project consists of four over-arching goals.

- Development of high-performance anti-perovskite electrolytes.
- Accessing the air stability and proton mobility.
- Stabilizing the solid/solid interface through interfacial engineering.
- Prototyping liquid free cells using anti-perovskite electrolyte.

### Objectives

The objective of this project is to develop an optimized anti-perovskite electrolyte with a stabilized interface for scalable fabrication of liquid-free solid-state batteries.

### Approach

The project approach is multifold: (1) chemistry design: multiple doping at anion sites will be pursued to improve structural stability, ionic conductivity and environmental compatibility; (2) interfacial design: surface coating will be deployed to improve the chemical and mechanical stability of solid/solid interface; and (3) process development: a scalable fabrication process based on melt-infiltration or dry lamination will be developed for the fabrication of all solid state lithium batteries.

## Results

### Composite electrolyte for better conductivity

In the previous year, we were able to synthesize phase pure anti-perovskite electrolytes using simple solid-state reaction at a relatively low processing temperature ( $\sim 300$  °C). It is also well recognized that one of bottlenecks of anti-perovskite electrolytes is their relatively low lithium-ion conductivity. We all observed that the lithium-ion conductivity could be improved by partially replace Cl with Br. However, the lithium-ion conductivity is quite low ( $\sim 10^{-5}$  S/cm). Searching for alternative electrolyte formulas and alternative approaches to fabricate electrolyte pellets is needed to further improve the lithium-ion conductivity of anti-perovskite electrolytes. Figure XIII.25.1 shows the measured lithium-ion conductivity of the latest electrolyte formula, a composite electrolyte between  $\text{Li}_2\text{HOCl}_{0.75}\text{Br}_{0.25}$  (AP) and garnet  $\text{Li}_{6.4}\text{La}_3\text{Zr}_{1.4}\text{Ta}_{0.6}\text{O}_{12}$  (LLZTO). The electrolyte pellets were fabricated using a warn press ( $\sim 250$  MPa at  $\sim 250$  °C). The latest formula (AP-5 and AP-6) demonstrated a lithium-ion conductivity of  $\sim 0.1$  mS/cm at 25 °C, and  $\sim 1$  mS/cm at 75 °C.

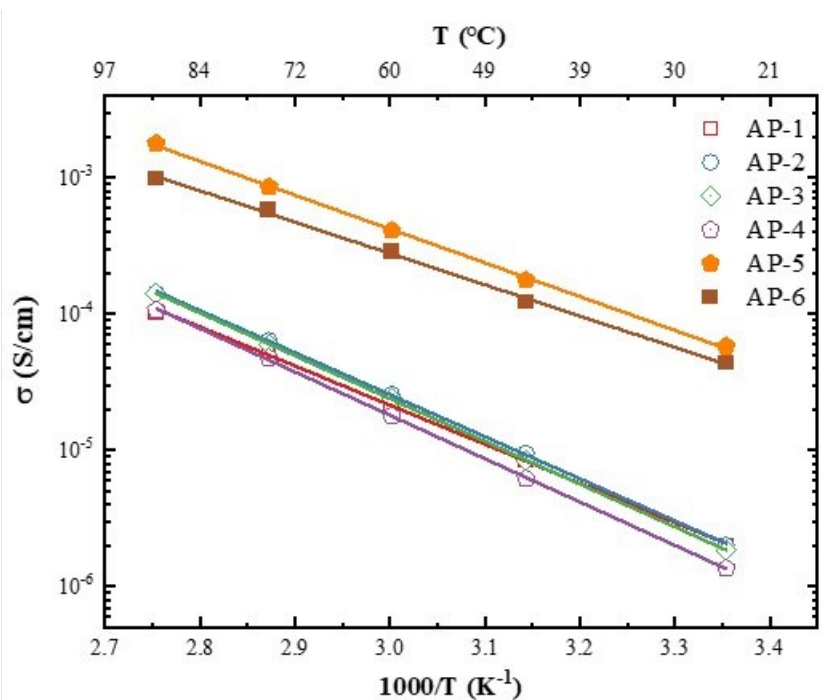
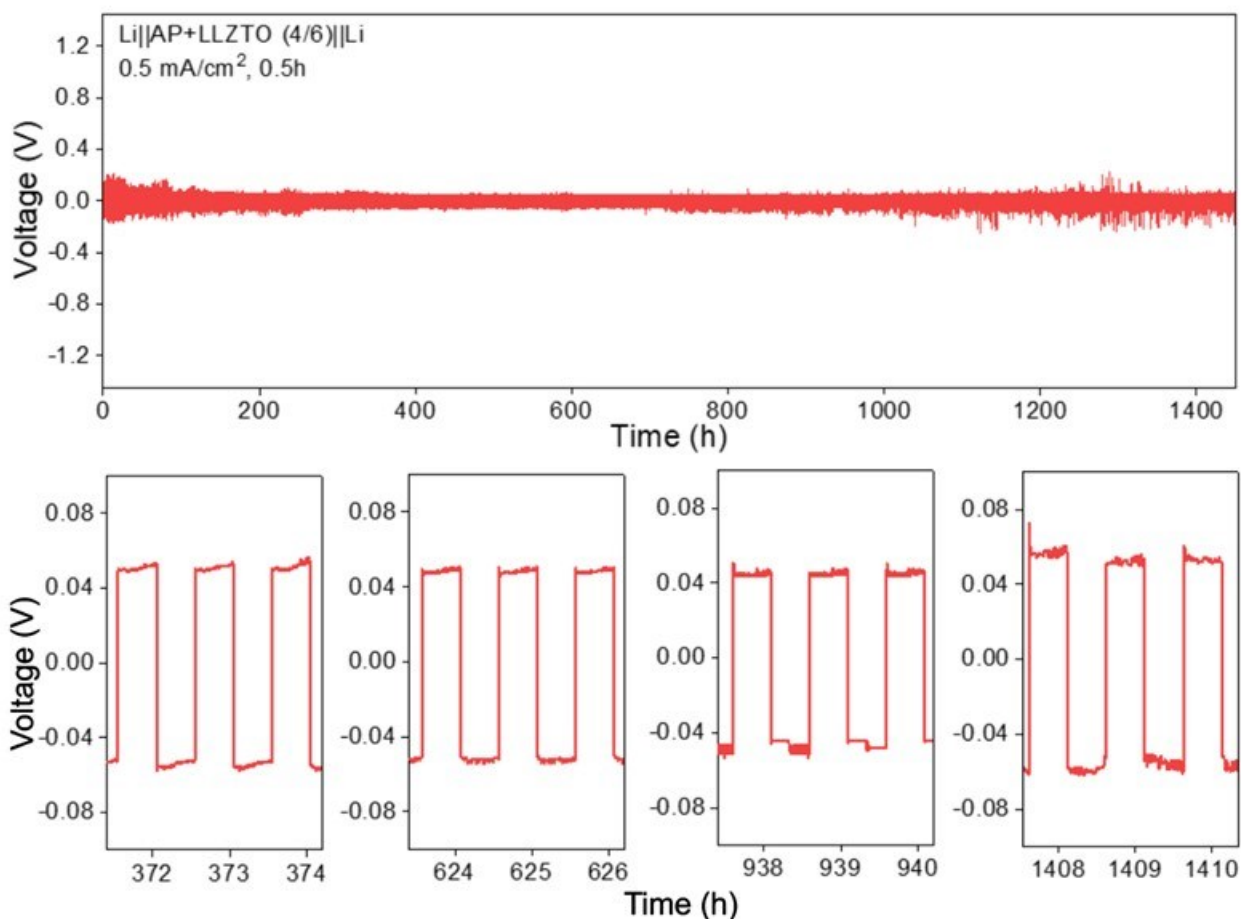


Figure XIII.25.1 Temperature dependent lithium-ion conductivity measured for different electrolyte formulations. AP-5 has the best lithium-ion conductivity.

### Electrochemical stability of symmetrical cells

Taking advantage of the low melting point of anti-perovskite electrolytes, we were able to fabricate dense composite electrolyte pellet at a temperature as low as 300 °C. Figure XIII.25.2 shows a typical voltage profile of a symmetrical cell using  $\text{Li}_2\text{HOCl}_{0.75}\text{Br}_{0.25}$  (AP)/  $\text{Li}_{6.4}\text{La}_3\text{Zr}_{1.4}\text{Ta}_{0.6}\text{O}_{12}$  (LLZTO) composite electrolyte during repeating lithium stripping/plating experiment up to 1500 hours at 0.5 mA/cm<sup>2</sup>. It is shown that the symmetrical cell properly functions up to 1500 hours without any sign of internal short. It can also be seen that the voltage polarization is initially high, and it gradually decreases with the experiment up to 600 hours, after which the voltage polarization increases with the experimental time. The initially high voltage polarization can be attributed to the poor contact between the lithium foil and the composite electrolyte after the cell assembling. The lithium/electrolyte contact was improved with the repeating lithium stripping/plating, resulting in improved lithium/electrolyte contact and a reduced voltage polarization. The slow increases in the voltage polarization at a later phase (>600 hours) suggests a slow side reaction between the composite electrolyte and the lithium foil, causing a steady increase on the interfacial impedance.



**Figure XIII.25.2** Voltage profile of symmetrical cells using  $\text{Li}_2\text{HOCl}_{0.75}\text{Br}_{0.25}$  (AP)/  $\text{Li}_{6.4}\text{La}_3\text{Zr}_{1.4}\text{Ta}_{0.6}\text{O}_{12}$  (LLZTO) composite electrolyte.

The results on symmetrical cells showed a good compatibility between the metallic lithium and the composite electrolyte, it is also important to validate the chemical/electrochemical stability of the electrolyte at high potentials. For this study, metallic foils (Al, Ni, and Ti) were used as the working electrode and paired with lithium anode to form dummy cells. High precision leakage current (HpLC) measurement was conducted to quantify the rate of side reactions occurring on the electrical conducting surface (see Figure XIII.25.3). When Al foil was used as the working electrode, a strong cathodic reaction was observed within the potential range of 3.8–4.2 V vs.  $\text{Li}^+/\text{Li}$ , and the steady leakage current dropped when the potential is higher than 4.2 V. This behavior is very similar to corrosion of Al foil in liquid electrolytes (*J. Phys. Chem. Lett.* **2017**, 8, 5, 1072–1077). When Al foil was replaced with Ni foil and Ti foil, the side reaction was completely suppressed as shown in Figure XIII.25.3 This suggests that Al foil needs to be protected, or be replaced with other current collectors like Ni, to achieve a higher electrochemical stability of the solid-state electrolyte.

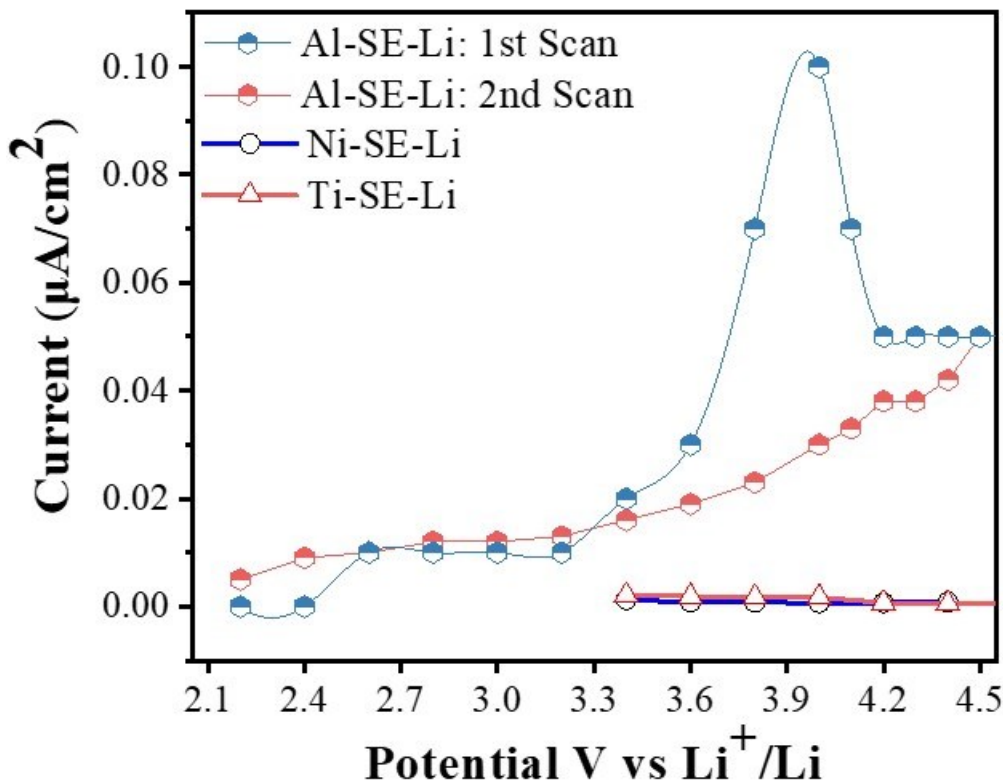


Figure XIII.25.3 Steady leakage current measured as a function of working potential to show the potential reaction between the Al foil with the electrolyte.

#### **Chemical stability of cathode/electrolyte interface**

The chemical compatibility between the solid-state electrolyte and the delithiated cathode is crucial to ensure long term stability of solid-state batteries. In his exercise,  $\text{LiNi}_{0.6}\text{Mn}_{0.2}\text{Co}_{0.2}\text{O}_2$  (NMC622) was used as the model cathode material, and  $\text{Li}_2\text{HOCl}_{0.75}\text{Br}_{0.25}$  was used as the catholyte. After the cell was convent-voltage charged to 4.2 V, the cell was disassembled, and the cathode was harvested and gently ground into powder for transmission X-ray microscopy study. Figure XIII.25.4 shows the 3D image of an NMC622 particle collected at the Ni absorption edge. The color of each pixel represents the white line energy of the Ni absorption spectra; a higher absorption energy indicates a higher valence state of Ni element. Figure XIII.25.4 clearly shows that the valence state of Ni at the interface is consistently lower than those in the core of the particle. This gradient on the valence state implies a slow reaction between the electrolyte and the delithiated NMC particle, causing the partially reduction of Ni element at the cathode electrolyte interface.

To evaluate the significance of this side reaction, accelerating rate calorimeter (ARC) was utilized to study the reaction kinetics between the delithiated cathode and the electrolyte. For this exercise, the cathode material ( $\text{LiNi}_{0.8}\text{Mn}_{0.1}\text{Co}_{0.1}\text{O}_2$ , NMC811) was charged to 4.2 V using a liquid electrolyte. Then the cell was disassembled, and the cathode electrode was harvested for the ARC study. Figure XIII.25.5 shows the ARC profiles of the delithiated NMC811 with the presence of either carbonate-based liquid electrolyte or the composite solid electrolyte. The ARC data clearly show that samples with the presence of solid-state electrolyte had a much lower self-heating rate, or a slower reaction kinetics, than samples with the presence of liquid electrolytes. This result implies an improved safety performance at the cathode side by replacing the liquid electrolyte with solid state electrolytes.

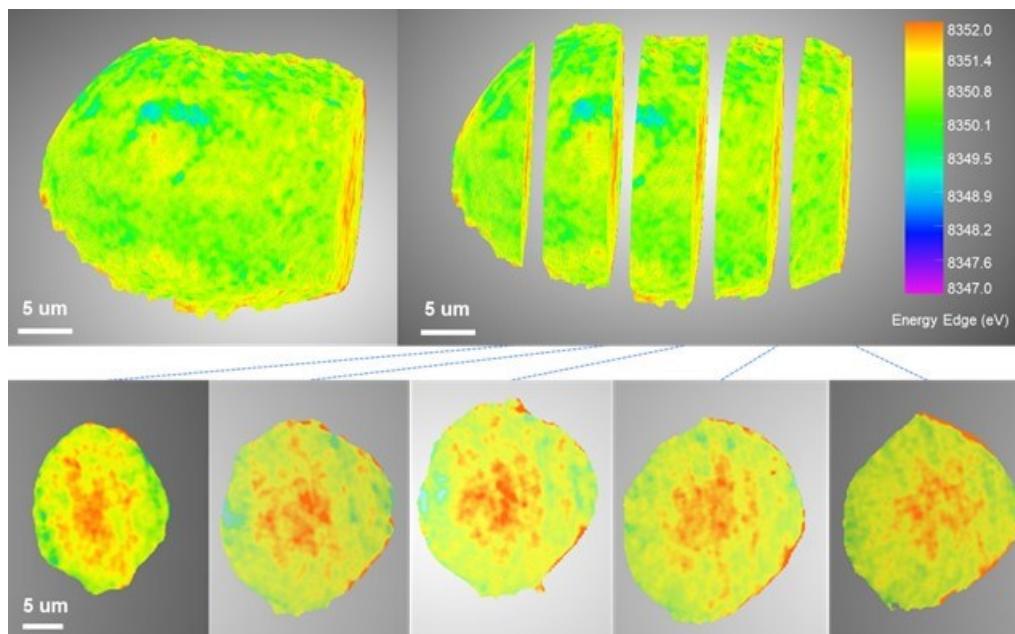


Figure XIII.25.4 Transmission X-ray microscopy (TXM) image of a  $\text{LiNi}_{0.6}\text{Mn}_{0.2}\text{Co}_{0.2}\text{O}_2$  (NMC622) after being charged to 4.2 V. The color in the 3D map is the white line energy of Ni absorption edge. A red color means a higher oxidation state on Ni.

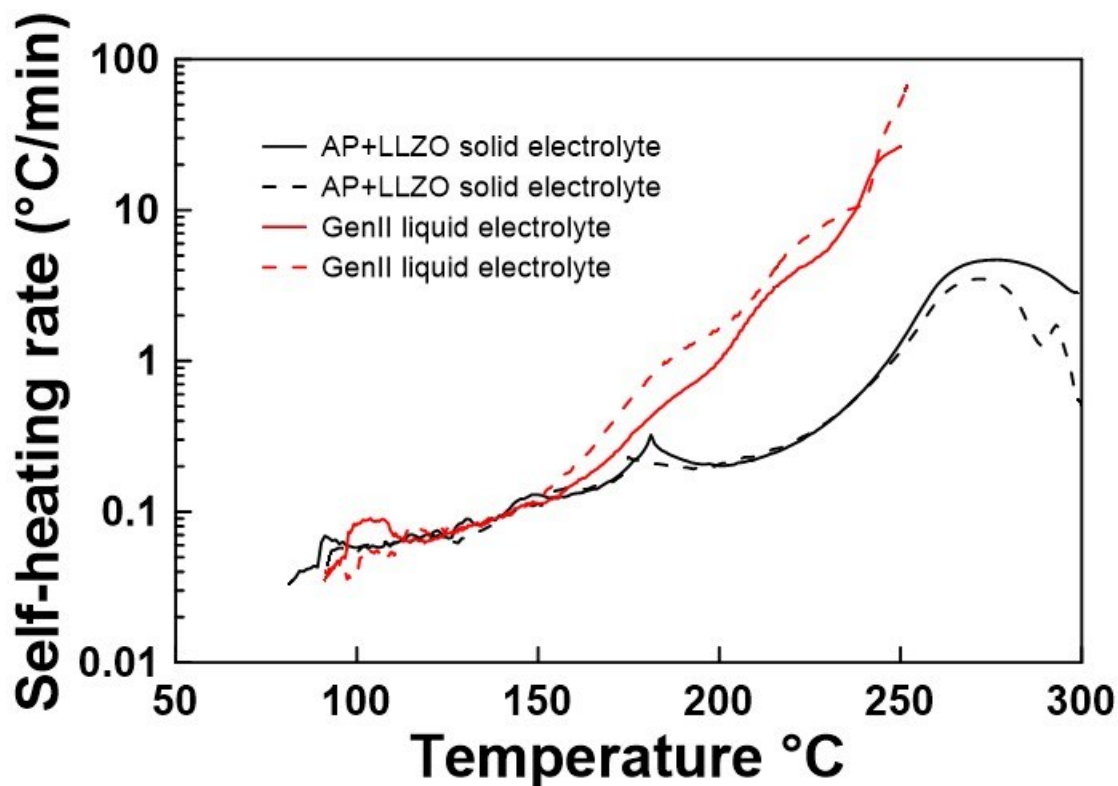


Figure XIII.25.5 Comparison of accelerating rate calorimeter (ARC) profiles for delithiated  $\text{LiNi}_{0.8}\text{Mn}_{0.1}\text{Co}_{0.1}\text{O}_2$  (4.2V) mixed with conventional carbonate-based liquid electrolyte, and  $\text{Li}_2\text{HOClO}_{0.75}\text{Br}_{0.25}$  (AP)/ $\text{Li}_{6.4}\text{La}_3\text{Zr}_{1.4}\text{Ta}_{0.6}\text{O}_{12}$  (LLZTO) composite electrolyte.

### Frication of thin electrolyte film

The scalable process to fabricate thin electrolyte film, below 100 microns, is crucial to enhance the energy density of all solid-state batteries. By collaborating with ORNL team, a wet casting process was used to fabricate thin and free-standing electrolyte film as shown in Figure XIII.25.6a. The scanning electron microscopy (SEM) image (Figure XIII.25.6b) of the free-standing film shows that the film is quite porous, and the morphology of the electrolyte powder is maintained. The energy dispersive spectroscopy images of the electrolyte film (Figure XIII.25.6c-Figure XIII.25.6g) show a homogeneous distribution of electrolyte elements, showing no clear segregation of elements or phase separation after the wet casting process.

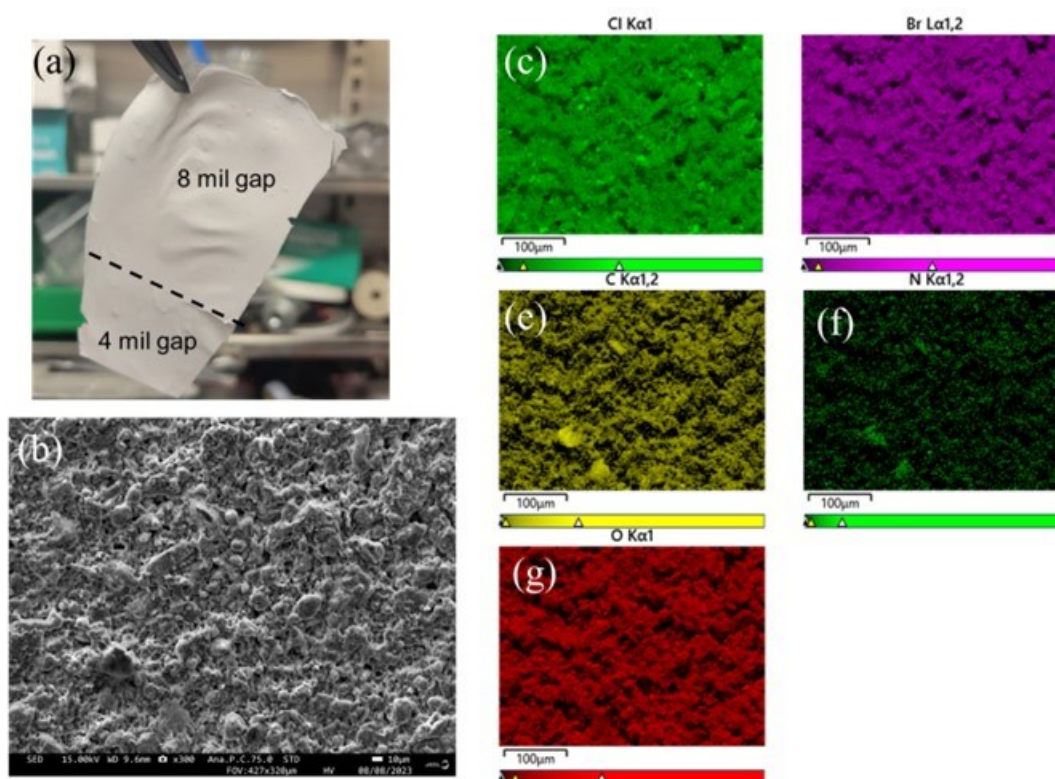


Figure XIII.25.6 (a) Digital image, (b) scanning electron microscopy image of a wet cast free standing electrolyte film composing of  $\text{Li}_2\text{HOCl}_{0.75}\text{Br}_{0.25}$ ; (c)-(g) energy dispersive spectroscopy (EDS) image of the electrolyte film showing the homogeneous distribution of elements.

To reduce the porosity of the electrolyte film, both cold oppress, both warm press and thermal annealing were performed to reduce the grain boundary resistance. Figure XIII.25.7 shows a typical image of electrolyte film after thermal annealing at 250°C. A clear leafy structure was formed after the thermal annealing. This type of leafy structure can also be found in samples experiencing both cold press and hot press, but with a smaller domain size. Therefore, the transport properties of the electrolyte film were also investigated under different stacking pressures. It was found that the lithium-ion conductivity of the wet-cast and cold pressed electrolyte film is comparable with the pellets prepared using a warm press approach. The electric resistance of the electrolyte film was also conducted by stacking the electrolyte film between two stainless steel blocking electrodes, and the leakage current was collected by applying 1V bias on the blocking electrodes. Figure XIII.25.8a shows that the leakage current surprisingly decreases with the stacking pressure. Figure XIII.25.8a **b** shows that the leakage current increases with the measuring temperature. At a temperature as high as 90°C, the steady leakage current is about  $0.3\mu\text{A}/\text{cm}^2$ , which is very low compared to the normal operation rate of a lithium cell ( $\sim 1\text{mA}/\text{cm}^2$ ). It can at least conclude that the stacking pressure has no adverse effect on the transport properties of the anti-perovskite electrolyte.



Figure XIII.25.7 SEM image of an electrolyte film after thermal annealing at 250°C.

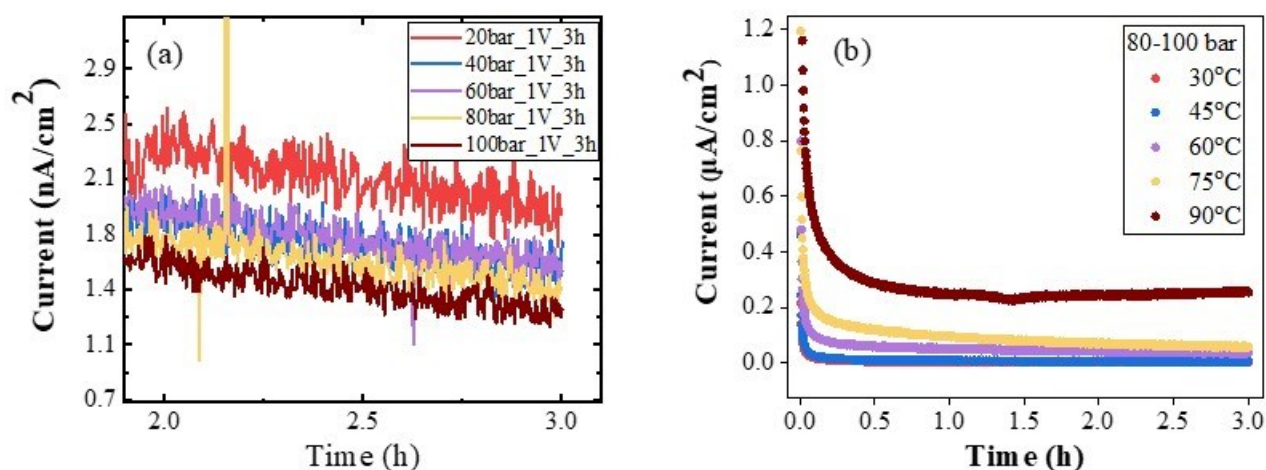


Figure XIII.25.8 Measurement of electric resistance as a function of the stacking pressure (a) and temperature (b).

### Conclusions

The current anti-perovskite electrolyte,  $\text{Li}_2\text{HOCl}_{0.75}\text{Br}_{0.25}$  has an intrinsically low lithium-ion conductivity, which can be partially overcome by compositing with garnet ceramic electrolyte. It has been demonstrated that the composite electrolyte has a good compatibility against metallic lithium. Symmetrical cells using the composite electrolyte can be repeatedly stripping/plating for >1400 cycles without causing internal short. The electrolyte stability at the cathode sides includes the side reactions with both Al current collector and the delithiated cathode material. A Ti or Ni current collector can be an alternative candidate to Al foil. Comparing to the liquid electrolyte, the composite electrolyte has low reactivity towards delithiated cathodes. Finally, a thin electrolyte film can be fabricated through a wet casting process.



**Key publications**

1. Jiantao Li, Jiyu Cai, Zonghai Chen, Composite Inorganic Electrolytes for Solid-State Batteries, US Pat. Appl., filed, **2023**.
2. Jiyu Cai, Xinwei Zhou, Yuzi Li, and Zonghai Chen, Probing Electronic Conductivity in Solid State Electrolyte, the 20<sup>th</sup> International Microscopy Congress, Busan, Sep. 9<sup>th</sup> -16<sup>th</sup>, **2023**.

**Acknowledgements**

This report is coauthored by Dr. Jiantao Li, Dr. Yingying Xie, Dr. Jiyu Cai, and Ms. Xinyi Liu. Dr. Yuzi Liu and Dr. Xinwei Zhou are also acknowledged for their help in electron microscopy characterization. We thank Dr. Tianyi Li and Dr. Wenqian Xu of Advanced Photon Source (APS) at ANL for assistance in structural characterization using high energy X-ray diffraction. Dr. Lin Ma (UNCC) is acknowledged for safety study using accelerating rate calorimeter (ARC). We also sincerely acknowledge the collaboration with Dr. Xianghui Xiao of Brookhaven National Laboratory for Transmission X-ray Microscopy characterization and Dr. Xiangbo Meng of Arkansas University for material protection using atomic layer deposition.

## XIII.26 High-Conductivity and Electrochemically Stable Lithium Thioborate Solid-State Electrolytes for Practical All-Solid-State Batteries (SLAC/Stanford University)

### Yi Cui, Principal Investigator

Stanford University  
450 Serra Mall  
Stanford, CA, 94305  
E-mail: [yicui@stanford.edu](mailto:yicui@stanford.edu)

### Simon Thompson, DOE Technology Development Manager

U.S. Department of Energy  
E-mail: [Simon.Thompson@ee.doe.gov](mailto:Simon.Thompson@ee.doe.gov)

Start Date: October 1, 2022	End Date: September 30, 2023	
Project Funding (FY23): \$200,000	DOE share: \$200,000	Non-DOE share: \$0

### Project Introduction

This project aims to develop novel lithium thioborates (Li-B-S, LBS) as a new class of solid-state electrolytes (SSEs) to realize high-performance all-solid-state batteries (ASSBs), with a particular focus on addressing the technical challenges in electrolyte synthesis, cell integration, failure diagnostics, and scale-up. The approach will be technologically transformative to the current solutions for ASSB development.

### Objectives

We plan to develop doped and undoped lithium thioborates for high-energy-density, all-solid-state lithium metal batteries. For the final deliverables, ASSBs with the ability to reach an energy density of 500 Wh/kg and maintain 80% capacity for at least 300 cycles will be demonstrated.

### Approach

The long-term project has a multistep approach toward integration of LBS with high-voltage cathodes, with steps 4 and 5 as the focus for this year:

1. Fabricate undoped LBS powders using an all-solid-state synthesis method to achieve high ionic conductivity, low electronic conductivity, and a wide operational voltage window.
2. Integrate LBS SSEs into symmetric Li/LBS/Li cells and into full batteries using high-voltage cathodes including lithium Ni-Mn-Co (NMC) oxide.
3. Study atomic, particle, and cell-scale Li-metal-SSE interface development and dendrite growth mechanisms in SSEs using advanced characterization tools. Use knowledge to better develop SSEs and modify interfaces for stable cycling in full cells.
4. Fabricate doped LBS powders and develop particle/surface modifications to increase ionic conductivity as well as stability in full batteries and in air for glovebox-free synthesis.
5. Investigate catholytes for high-voltage batteries using NMC cathodes.

### Results

We developed a synthesis to produce  $\text{Li}_{10}\text{B}_{10}\text{S}_{20}$  with lithium halide species in the grain boundaries. The synthesis involves ball milling of the precursor materials,  $\text{Li}_2\text{S}$ , S, B, and  $\text{LiX}$  ( $X=\text{Cl}$ , Br, I); loading the precursors into a boron nitride crucible; sealing the crucible in a quartz tube under vacuum; sintering; and unloading the material to retrieve the powders. Electrochemical impedance spectroscopy (EIS) revealed that  $\text{LiCl}$  and  $\text{LiBr}$  reduced the ionic conductivity of the SSE relative to the undoped LBS, while  $\text{LiI}$  increased the ionic conductivity by over two times (Figure XIII.26.1a). With this promising result using iodine, we synthesized LBS with  $\text{LiI}$  in four stoichiometries:  $\text{Li}_{10}\text{B}_{10}\text{S}_{20}\text{-LiI}$  (LBS-LiI),  $\text{Li}_{10}\text{B}_{10}\text{S}_{20}\text{-2LiI}$  (LBS-2LiI),

$\text{Li}_{10}\text{B}_{10}\text{S}_{20}\text{-4LiI}$  (LBS-4LiI), and  $\text{Li}_{10}\text{B}_{10}\text{S}_{20}\text{-6LiI}$  (LBS-6LiI). LBS-2LiI had the highest ionic conductivity, followed by LBS-4LiI, LBS-LiI, and LBS-6LiI, suggesting that too much LiI will begin to slow ion transport pathways (Figure XIII.26.1b-c). As such, LBS-2LiI had the highest ionic conductivity of all SSEs, over  $1.0 \text{ mS cm}^{-1}$  (Figure XIII.26.1c).

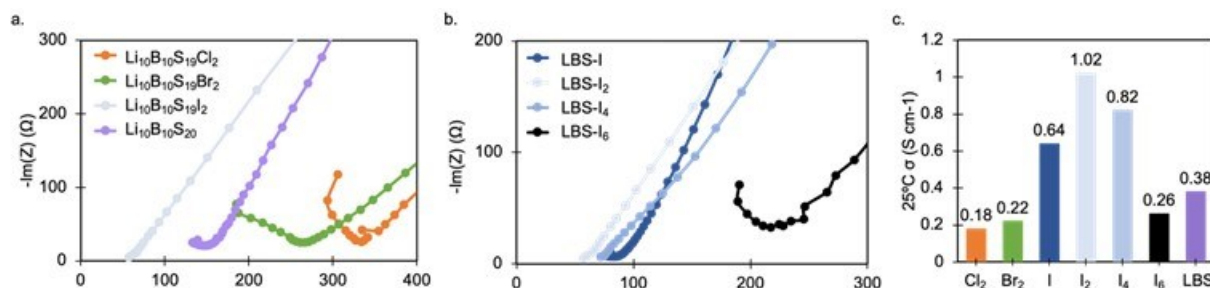


**Figure XIII.26.1** Lithium thioborate-lithium halide electrochemical evaluation. (a) EIS of SS- $\text{Li}_{10}\text{B}_{10}\text{S}_{19}\text{X}_2$ -SS ( $\text{X}=\text{Cl}$ , Br, and I) and SS- $\text{Li}_{10}\text{B}_{10}\text{S}_{20}$ -SS cells at 360 MPa, room temperature. (b) EIS of SS- $\text{Li}_{10}\text{B}_{10}\text{S}_{20}\text{-yI}_y$ -SS cells,  $y=1, 2, 4$ , and 6 at 360 MPa, room temperature. (c) Ionic conductivity of each lithium thioborate at 360 MPa, room temperature.

We performed scanning electron microscopy (SEM) with energy dispersive X-ray spectroscopy (EDS) to resolve the location of iodine/LiI in the powder. We observed clusters of iodine signal in the pellet (Figure XIII.26.2a, top row) and as well as surrounding an LBS polycrystal (Figure XIII.26.2a, bottom row) with no signal in the bulk of the polycrystal. We identify this as lithium iodide, and to confirm whether there was iodine in the LBS polycrystal, we performed TEM with EELS (Figure XIII.26.2b), which showed no iodine signal within a crystal.

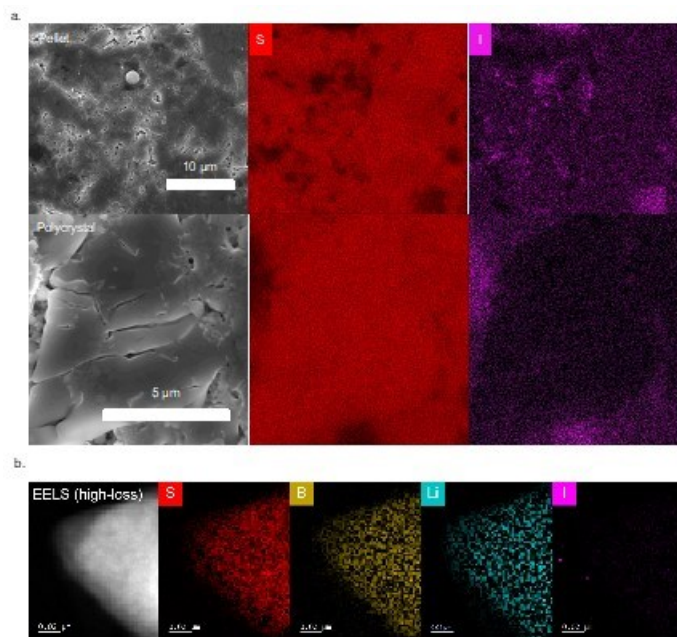


**Figure XIII.26.2** (a) SEM image of pressed LBS-LiI pellet (top row) and polycrystal in pellet (bottom row) with EDS mapping of sulfur and iodine. (b) TEM image with EELS (high-loss) and corresponding EDS mapping of sulfur, boron, lithium, and iodine.

From our candidate LBS-LiI electrolytes, we sought to find which exhibited the most stable cycling. We cycled the Li-SSE-Li cells at room temperature with a high current density of  $0.25 \text{ mA cm}^{-2}$  to exaggerate the effects of SEI and void/dendrite formation. Within 25 hours, LBS-2LiI, -4LiI, and -6LiI had significant

overpotential growth, while LBS-LiI had uniform plating with a low overpotential ( $\sim 35$  mV) (Figure XIII.26.3a). Although LiI clearly has superior interfacial contact with Li metal, too much LiI appears to block ion pathways from the Li to the more ionically conductive regions of the SSE. As such, we proceeded to characterize and use LBS-LiI as an SSE in Li metal batteries. At  $0.1$  mA cm $^{-2}$ , LBS-LiI cycled stably for  $>100$  hours with a gradual increase in overpotential due to contact loss and SEI growth (Figure XIII.26.3b).

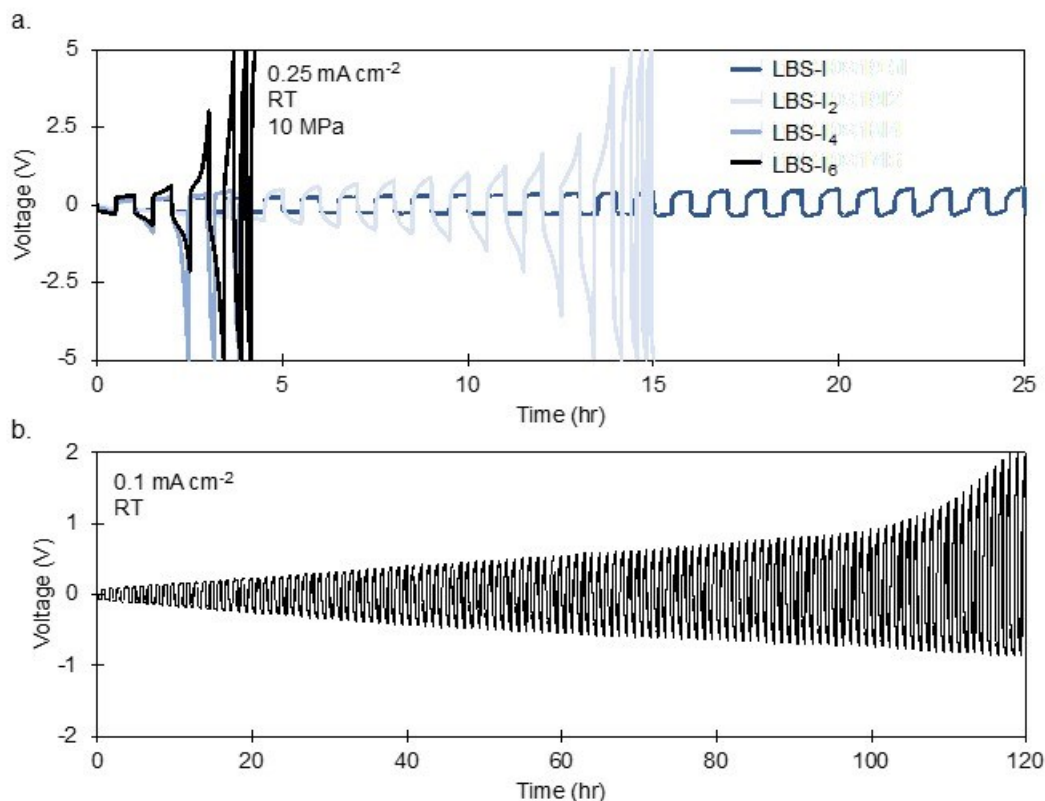


**Figure XIII.26.3** LiI-lithium thioborate electrochemical evaluation. (a) Symmetric cell cycling at  $0.25$  mA cm $^{-2}$  of Li-Li $_{10}$ B $_{10}$ S $_{20}$ -YLiI-Li (Y=1, 2, 4, 6) at 10 MPa, room temperature. (b) Symmetric cell cycling of LBS-LiI at  $0.1$  mA cm $^{-2}$ , 10 MPa, room temperature.

We tested the critical current density (CCD) in steps of  $0.2$  mA cm $^{-2}$ , and Li plated up to current densities of  $2.0$  mA cm $^{-2}$  (Figure XIII.26.4a). There was some asymmetry in the voltage profile during plating due to differences in the initial condition of the Li electrodes such as amount of Li. The source of cell failure was not shorting or even microshorting, but instead was high overpotential polarization owing to loss of contact and SEI growth. The CCD of LBS-LiI is clearly higher than that of LBS,  $1.2$  mA cm $^{-2}$ , and the overpotential of the cell during CCD testing was far lower of LBS-LiI than of LBS. The Li-LBS-LiI-Li cell resistance increased from  $605$   $\Omega$  cm $^{-2}$  before to  $2749$   $\Omega$  cm $^{-2}$  after cycling, and a Warburg impedance tail appeared, suggestive of the growth of ion-blocking species at the interface of the SSE with Li metal, such as Li $_2$ S (Figure XIII.26.4b).

To understand the morphology and chemistry of the anode in LBS-LiI cells after cycling, we performed SEM and XPS, respectively. SEM exposed a  $30$ - $40$ - $\mu$ m thick, host-like, and porous but uniform anode after cycling (Figure XIII.26.4c). XPS analysis revealed that the anode contained mostly Li metal with LiI and Li $_2$ S and some LBS and S (Figure XIII.26.4d). While Li $_2$ S is electronically and ionically insulating, LiI has been shown to induce uniform plating of Li metal, explaining the long-term stable cycling. Other works also report the accumulation of LiI at the interface of SSEs with LiI with Li metal during cycling and report a benefit to cycling performance. The LBS-LiI pellet remains dense and largely crack-free after cycling, corroborating that high interfacial impedance, rather than shorting, is the source of cell failure. The finding of Li $_2$ S, a Li+

blocking species, at the anode corroborates the appearance of the Warburg impedance tail seen in the EIS after cycling.

Because Li metal was still present at the anode but the overpotential grew, cell failure can be attributed to loss of interfacial contact and inadequate ion pathways between Li metal and LBS-LiI, likely due to  $\text{Li}_2\text{S}$  (no ion conduction) and LiI (slow ion conduction) accumulating at the interface of Li and LBS-LiI. From the constant current cycling and CCD testing, it can be concluded that both calendar aging and degradation induced by high currents cause loss of contact and SEI growth.

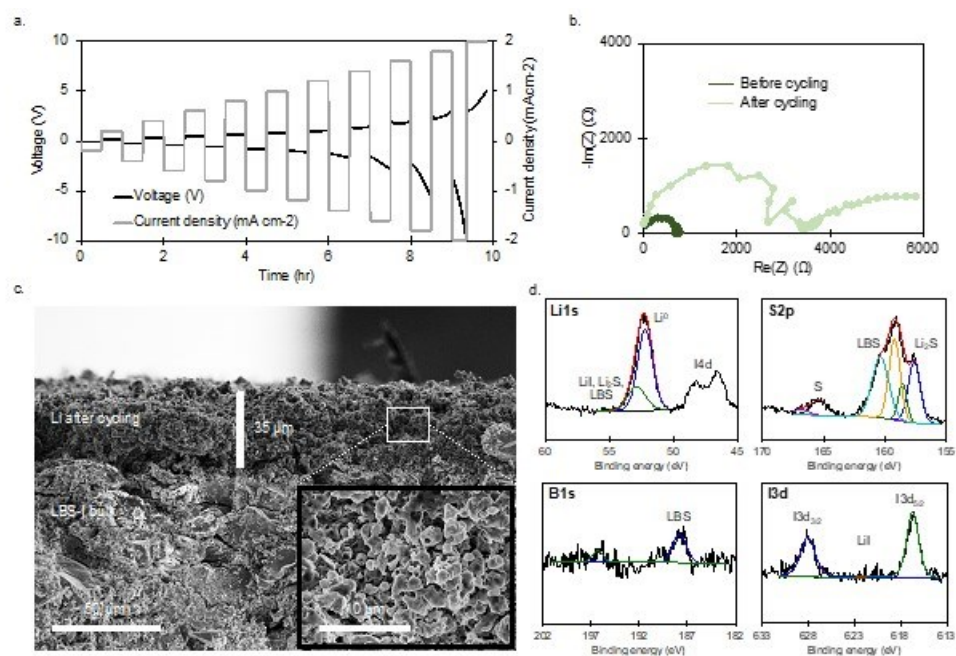


**Figure XIII.26.4** Electrochemical performance and anode analysis of Li-LBS-LiI-Li symmetric cells. (a) Critical current density testing of cell in steps of 0.2 mA cm<sup>-2</sup> at room temperature, 10 MPa. (b) EIS of symmetric cell before and after cycling. (c) SEM image of the Li interface with the LBS-LiI pellet after cycling. Inset: a high-resolution image of the porous Li interface, showing small particles. (d) XPS of the same Li interface after cycling.

We assembled full cells with NMC 622 cathodes to assess the practicality of LBS-LiI in lithium metal batteries. To identify the best cathode composition for LBS-LiI, an SSE that has never been used in a full cell, we explored three catholytes: PEO/LiTFSI, ball-milled LBS-LiI, and  $\text{Li}_2\text{ZrCl}_6$ . To minimize the number of variables and focus on identifying the appropriate catholyte, all cells contained 0.25 mAh capacity and were cycled at C/10 rates, room temperature, and ~70 MPa pressure (Figure XIII.26.5).

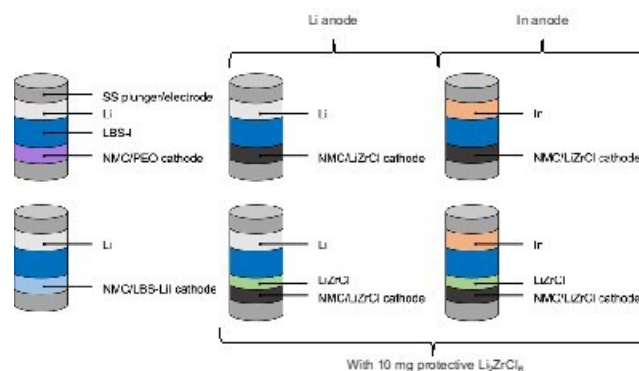


Figure XIII.26.5 Schematic representation of the six cell types tested in this study.

For the PEO-based cathode, we used the composition of 90% NMC, 7.5% PEO/LiTFSI, and 2.5% C65 conductive carbon. The capacity retained after 15 cycles was only ~33% of the theoretical capacity, and the capacity decayed over time, likely resulting from loss of contact between the catholyte and NMC, degradation of the PEO/LiTFSI, and degradation at the anode. Aiming to provide compatibility with the SSE, we then tested LBS-LiI in the cathode. We used particles ball-milled for 30 minutes as the catholyte for a balance of high ionic conductivity and small particle size. We did not include carbon in the cathode since tests showed that carbon, although it enabled full capacity utilization upon the first charge, severely degraded the cell's capacity (Figure XIII.26.6, top). Cells with a ratio of 70:30 NMC:LBS-LiI in the cathode had reasonable initial discharge capacity and capacity retention (Figure XIII.26.6., bottom), and this ratio has been confirmed in the literature to provide the optimal ratio of balanced ionic and electronic conductivity in the cathode. Even with this optimized ratio, the capacity utilized initially and retained over 15 cycles was low, suggesting that the low oxidation voltage of LBS-LiI (~2.4 V), low ionic conductivity of the small particles, and poor NMC-LBS-LiI contact is insufficient for good cycling.

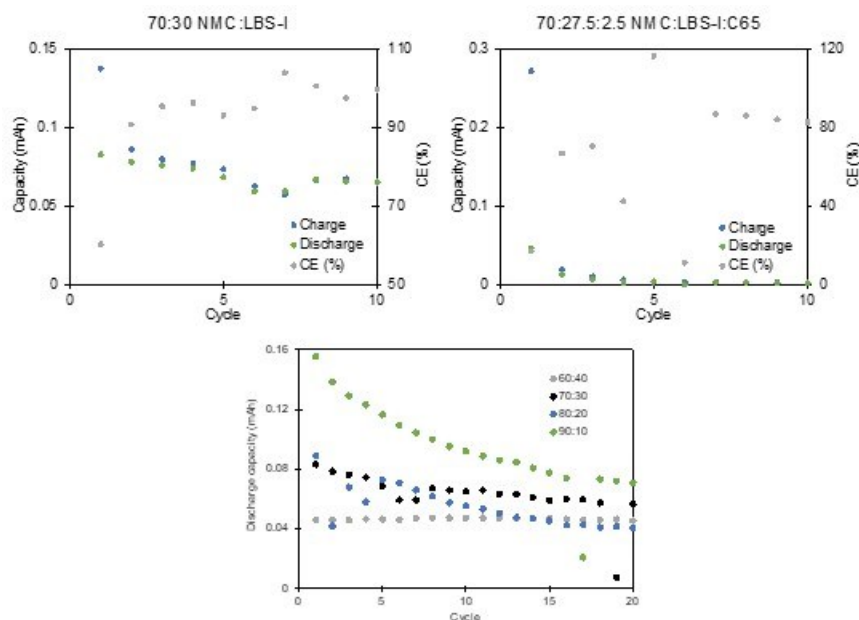
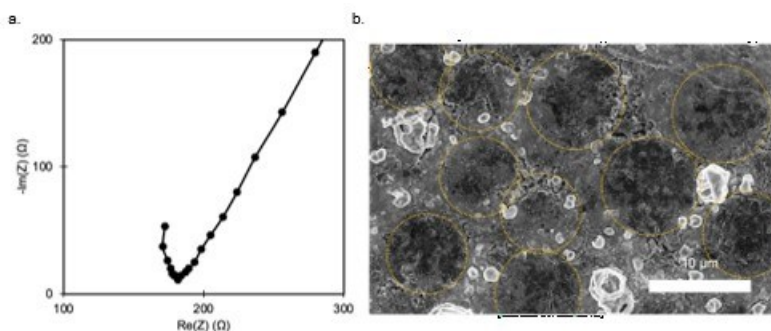


Figure XIII.26.6 Top: Charge and discharge capacity and CE (%) of full cells with 0.25 mAh NMC cathode as designated (with and without C65 carbon). All cells had 450-micron LBS-LiI SSE, Li anode, and were cycled at C/20 rate, room temperature, and 70 MPa pressure. Bottom: Optimization of four ratios of NMC:LBS-LiI in cathode: 60:40, 70:30, 80:20, and 90:10. Cells were cycled at 0.05C, 70 MPa pressure, room temperature.

For these reasons, we searched for other potential catholytes that would have a higher oxidation potential, small particle size, and compatibility with NMC and LBS-LiI. Recent reports of halide-based SSEs show excellent oxidative stability and high ionic conductivity, although most halides are not stable at the anode. As such, we synthesized the SSE  $\text{Li}_2\text{ZrCl}_6$  (LiZrCl) via ball-milling for 24 hours. With no post-mill treatment, the ionic conductivity of LiZrCl with extremely small particle size is  $3.2 \times 10^{-4} \text{ S cm}^{-1}$  (Figure XIII.26.7a-b). To ensure good compatibility with the cathode, we performed linear sweep voltammetry (LSV) of the electrolytes. The oxidation voltage of LiZrCl began  $\sim 3.4 \text{ V}$  and peaked  $\sim 5.4 \text{ V}$ , a significant improvement from  $\sim 2.4$  and  $\sim 3.4 \text{ V}$ , respectively, for LBS-LiI (Figure XIII.26.8af), making LiZrCl suitable as a catholyte.



**Figure XIII.26.7 a. Room-temperature EIS of LiZrCl. b. SEM of NMC with LiZrCl in a 70:30 ratio. NMC particles are highlighted in yellow.**

Using a pressed LBS-LiI pellet as the SSE and a cathode with a 70:30 ratio of NMC: LiZrCl, we assembled four cell types: with Li anode, with Li anode and 10 mg LiZrCl between the cathode and SSE, with In anode, and with In anode and 10 mg LiZrCl between the cathode and SSE (Figure XIII.26.5b.). Lithium alloys with indium upon charging, and indium can reduce the reactions of the SSE with the anode. Additionally, using a thin protect layer of a halide SSE between the cathode and SSE has been shown to reduce SSE decay near the cathode, which is critical for preventing LBS-LiI degradation and low ionic conductivity.

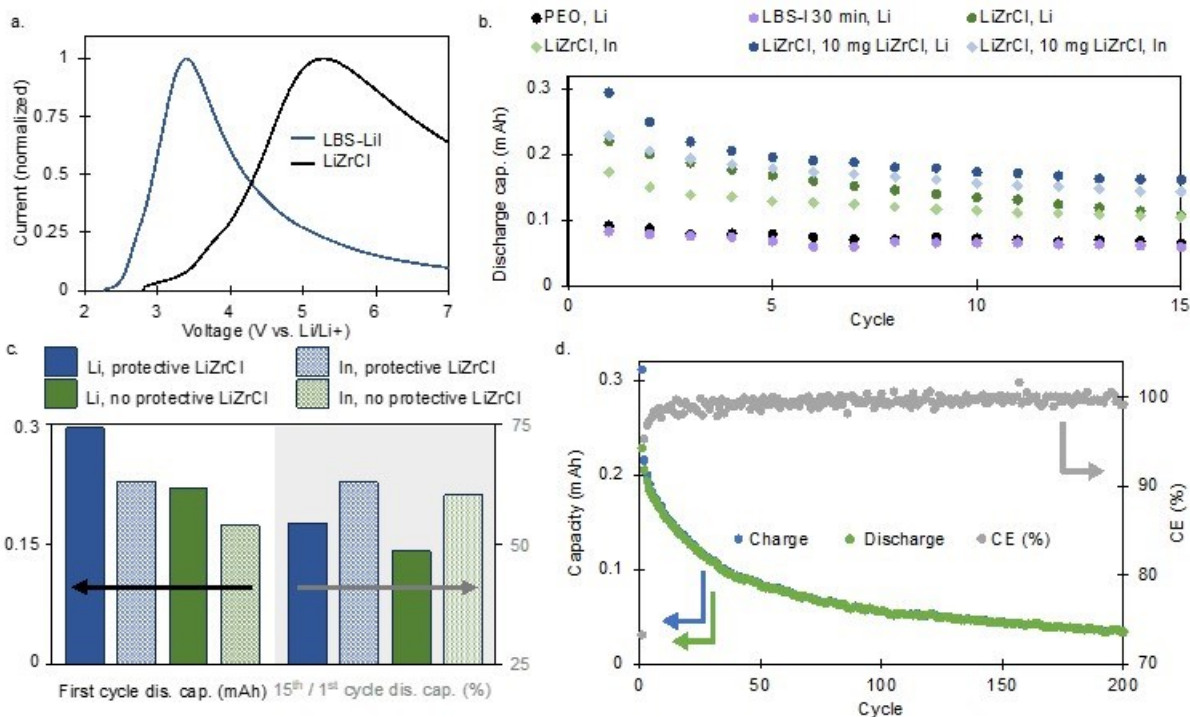


**Figure XIII.26.8** Full cell cycling of cells with NMC cathodes and LBS-LiI SSE. (a) Current-voltage plot of LBS-LiI and LiZrCl in Li-SSE-SSE/C65 composite pressed pellet. Sweep rate: 1 mV/s. (b) Discharge capacity vs. cycle of 6 cell types with 70:30 NMC:SSE ratio in cathode. (c) First cycle discharge capacity (mAh) and 15<sup>th</sup> / 1<sup>st</sup> cycle discharge capacity (%) for all cells with LiZrCl catholyte. (d) 200 cycles of full cell with NMC:LiZrCl 70:30 ratio cathode, LBS-LiI pellet SSE, and In anode.

In all cells, most of the capacity loss occurred in the first cycle, where the coulombic efficiency (CE %) was around ~60-75% (Figure XIII.26.8 b-c). The cells with the LiZrCl protective layer had first-cycle CE greater than those without: Li without protective LiZrCl 67% and with protective LiZrCl 73%; In without protective LiZrCl 64% and with protective LiZrCl 73%. Cells with Li at the anode had higher initial discharge capacity than those with In: Li without protective LiZrCl 0.2203 mAh and with protective LiZrCl 0.2954 mAh; In without protective LiZrCl 0.1736 mAh and with protective LiZrCl 0.2283 mAh. However, capacity fade was greater in cells with Li anodes, owing to void formation and the continuous reaction of Li with LBS-LiI to form Li<sub>2</sub>S (Figure XIII.26.8 b-c). Capacity fade still occurred in cells with In anodes, likely owing to the oxidation of the Li<sub>2</sub>ZrCl<sub>6</sub> at high potentials, LBS-LiI degradation, and loss of contact between the electrodes and LBS-LiI (Figure XIII.26.4 c-d, 8 b-c). In anode with protective LiZrCl had the highest 15<sup>th</sup>/1<sup>st</sup> cycle discharge capacity retention percentage at 62.9%, followed with In without protective LiZrCl at 60.3%, Li with protective LiZrCl at 54.6%, and Li without protective LiZrCl at 48.5% (Fig. 8c)

The best-performing cell in the long term had the protective layer of LiZrCl between the cathode and LBS-LiI, preventing oxidation of the LBS-LiI and thus maintaining high ionic conductivity at the cathode, and In at the anode, providing a lower cell potential of 3.9 V and reducing the interaction of the LBS-LiI with the anode (Figure XIII.26.8d). The cell cycled over 200 cycles with high CE (average of 98.8% after 3<sup>rd</sup> cycle). While this study shows promising results for using LBS-LiI as the SSE in full cells with NMC cathodes, a more thorough investigation must be done to enable high-loading cathodes and faster charging rates.

## Conclusions

We performed a full investigation into Li<sub>10</sub>B<sub>10</sub>S<sub>20</sub> with LiI (LBS-LiI) and its use as an SSE in Li metal batteries. We found that LiI increased the ionic conductivity of the SSE to over 1.0 mS cm<sup>-1</sup> by inducing the formation of crystalline Li<sub>10</sub>B<sub>10</sub>S<sub>20</sub> with LiI residing in the grain boundaries. Even a small amount of LiI



resulted in improved interfacial contact with Li anodes, high critical current density ( $2.0 \text{ mA cm}^{-2}$ ), and stable symmetric cell cycling. Analysis of the cell after cycling revealed a porous, host-like anode consisting of Li,  $\text{Li}_2\text{S}$ , and LiI. Finally, we used LBS-LiI as the SSE in cells with NMC cathodes using three different catholytes and found that  $\text{Li}_2\text{ZrCl}_6$  is the most stable catholyte. This work provides an understanding of the cyclability of LBS in all-solid-state batteries and lays the groundwork for future work in both increasing the ionic conductivity of LBS and incorporating LBS into working batteries with high-energy-density cathodes. Although we observed no major differences in the LBS grain structure between electrolytes with or without LiI using lab-based characterization, a deeper investigation into the lithium substructure and other properties that are challenging to characterize should be carried out to fully elucidate differences in the SSEs are the subsequent influences on ionic conductivity. EIS studies at ultra-low temperatures as well as lithium diffusion studies via solid-state NMR will be necessary to resolve the grain and grain boundary impedances and to confirm the ion conduction mechanism. Finally, a more thorough investigation must be done to enable high-loading cathodes and faster charging rates.

### Key Publications

1. Ma, Y.; Wan, J.; Xu, X.; Sendek, A. D.; Holmes, S. E.; Ransom, B.; Jiang, Z.; Zhang, P.; Xiao, X.; Zhang, W.; Xu, R.; Liu, F.; Ye, Y.; Kaeli, E.; Reed, E. J.; Chueh, W. C.; Cui, Y. Experimental Discovery of a Fast and Stable Lithium Thioborate Solid Electrolyte,  $\text{Li}_{6+2x}[\text{B}_{10}\text{S}_{18}]_x$  ( $x \approx 1$ ). *ACS Energy Lett.* **2023**, 2762–2771. <https://doi.org/10.1021/acsenergylett.3c00560>.

## XIII.27 Solid state batteries with long cycle life and high energy density through materials design and integration (LBNL)

### Haegyum Kim, Principal Investigator

Lawrence Berkeley National Laboratory  
1 Cyclotron Rd.  
Berkeley, CA, 94720  
E-mail: [haegyumkim@lbl.gov](mailto:haegyumkim@lbl.gov)

### Simon Thompson, DOE Technology Development Manager

U.S. Department of Energy  
E-mail: [Simon.Thompson@ee.doe.gov](mailto:Simon.Thompson@ee.doe.gov)

Start Date: October 1, 2022      End Date: September 30, 2023  
Project Funding (FY23): \$1,875,000      DOE share: \$1,875,000      Non-DOE share: \$0

### Project Introduction

Solid-state Li metal batteries hold tremendous promise as a safer and higher energy-density technology than current Li-ion systems. By replacing the liquid electrolyte with a solid electrolyte (SE), the temperature at which a cell experiences thermal runaway can be increased, thereby preventing fire. In addition, the use of a Li metal anode can lead to a significant increase in energy density. However, several challenges need to be addressed before any solid-state lithium metal battery can be competitive and surpass the specific energy, energy density, and cycle life of lithium-ion batteries.

### Objectives

This project aims to create solid-state Li-metal batteries (SSLMBs) with high specific energy, high energy density, and long cycle life using scalable processing techniques. The team will achieve this by addressing fundamental challenges associated with (1) interfacial reactivity, (2) Li-metal plating, and (3) cathode loading. Addressing these challenges supports the broader Vehicle Technologies Office goal of solid-state batteries with increased cycle life and energy density. Ultimately, this project will develop an understanding of how to prevent interfacial reactions, make uniform Li-metal plating, and increase cathode loading significantly. The knowledge obtained from this project will be used to design SSLMBs with high specific energy of 500 Wh/kg, 80% capacity retention for at least 300 cycles, and critical current density (CCD) > 1 mA/cm<sup>2</sup>.

### Approach

This project addresses several fundamental challenges and makes the SSLMB competitive, surpassing the specific energy, energy density, and cycle life of Li-ion batteries:

- Create *homogeneous lithium deposition* on the anode without penetration of lithium metal through the separator to achieve **high cycle life** and **high safety**. The team will achieve this with the use of an active buffer layer (hereafter, ABL or BL) that combines active and inactive components to homogenize lithium plating and to keep the lithium plating potential away from the solid electrolyte (SE) separator.
- Limit *chemical reactivity* and *mechanical decohesion* between the SE, carbon, and cathode material in the composite cathode so that **high cycle life** can be achieved. The team will limit chemical reactivity by protecting the carbon from the SE, by using novel cathode coatings designed to be stable to high voltage and that do not react with the SE, by using novel solid halide catholyte conductors, and by using inorganic/organic solid composite electrolytes in the cathode.
- Achieve *high volumetric loading* of the active cathode material in the composite cathode to achieve **high energy density** and **high specific energy**. The team will achieve high volumetric cathode loading by creating thin highly porous conductor scaffolds that are infiltrated with cathode, by tailored particle size distributions of deformable lightweight conductors, and by the use of organic/inorganic hybrids.

- Create *inexpensive materials* and *processes* to fabricate SSBs so that they can be **cost-competitive** with Li-ion batteries. The team will create solution-processable organic/inorganic hybrids to be used as a separator and to blend in the composite cathode; they will use inexpensive, scalable ceramics processing techniques to create high-loading composite cathodes.

## Results

### **Task 1: Buffer layers to stabilize the lithium/SE interface and create uniform lithium plating.**

#### **Computational investigation to understand the role Ag nanoparticles in ABL:**

This task aims to understand the roles of ABLs and develop new ABLs that can create uniform lithium metal plating. In FY23, we investigated lithiation processes in silver (Ag) by using a cluster expansion analysis, which will help us to understand and rationalize the phase transformation mechanisms during lithiation in the Ag-C composite ABL. In this study, we computed a total of 227 configurations (73 for body-centered cubic (BCC), 79 for face-centered cubic (FCC), and 75 for  $\gamma$ -brass) using density functional theory (DFT) and fit the electronic energy to the cluster expansion models built on the three structural prototypes. With the fitted energy models, we performed Monte Carlo simulations to integrate the configurational entropy and calculate the free energy of each structural prototype. Figure XIII.27.1a and b show the free energy of the FCC, BCC, and  $\gamma$  structures for varied Li contents at  $T=300$  K. In our computations, considering only the electronic energy and the configurational entropy, we found that at  $x \geq 0.6$ , the free energy of all types of phases is remarkably similar, with a difference of less than 6 meV/atom. In this region, our results show that the BCC phase is slightly more stable than  $\gamma$ . The similarity in free energy between BCC and  $\gamma$  phases can be attributed to their close structural relationship, as  $\gamma$ -brass structures can be considered a specific type of BCC structure with slight structural rearrangements (Figure XIII.27.1c). Figure XIII.27.1d displays the calculated electrochemical potential and over-potential of Ag-Li at varied Li contents. As the Ag particles are lithiated beyond  $x = 1$  at  $\text{Li}_x\text{Ag}$ , the alloy transforms from the FCC to the BCC phase, traversing through  $\gamma$  phases that have energies extremely close to BCC. We found that the Ag-Li will maintain a positive potential for a large Li content, which might make a homogeneous solid solution of Li and Ag until the very end of the lithiation process.

We have further embarked on an in-depth exploration of the intricate microscopic processes within solid-state batteries featuring an Ag (silver)-C (carbon) composite BL. Employing first-principle thermodynamic calculations, we have been able to precisely gauge the free energy profiles of Ag-Li alloy systems. Our investigation also encompasses continuum modeling, focusing on the mechanisms governing Li transport within the BL. Additionally, we have conducted detailed simulations to examine the electrochemical and mechanical factors dictating the direction of Li plating during lithiation.

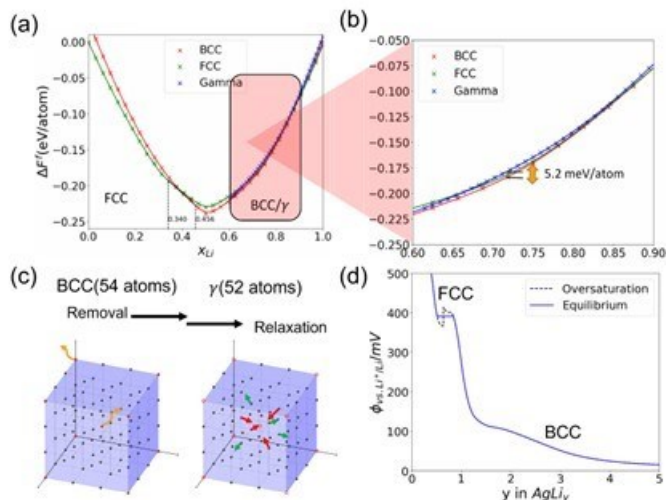


**Figure XIII.27.1** (a) Free energy of the BCC (red), FCC (green) and  $\gamma$  (blue) phases as a function of Li content ( $x_{Li}$ ) at  $T=300K$ . (b) Free energy functions in (a), enlarged in the range  $x_{Li} = 0.6\sim 0.9$ . (c) The relationship between BCC and  $\gamma$  structures. The structure of  $\gamma$  is obtained from removing one corner atom and one center atom in the  $3*3*3$  super-cell of BCC structure and relax neighboring atoms around the vacancies. (d) The equilibrium and over electrochemical potential of Li in the Ag-Li system as functions of  $y$  in formula  $AgLi_y$ .

The analysis of Li transport within the Ag-C BL is illustrated in Figure XIII.27.2. Figure XIII.27.2a offers a schematic view of our BL model, showcasing a Ag particle embedded within an amorphous carbon matrix. Figure XIII.27.2b tracks the progression of the Ag particle's potential throughout the lithiation process. To delve deeper into Li transport, we performed continuous simulations under two conditions: (1) assuming equivalent interfacial charge-transfer area specific resistance (ASR) at both BL/SE and BL/current collector (CC) interfaces, with a focus on the influence of Ag-Li alloying, and (2) considering non-equivalent charge-transfer ASR, emulating real-world conditions where the ASR at the BL/CC interface is lower than at the BL/SE interface. In the scenario of equal ASRs at both interfaces (Figure XIII.27.2c), we observe a balanced deposition of Li on both. However, in a more realistic scenario (Figure XIII.27.2d), Li predominantly deposits at the BL/CC interface, aligning with the expected behavior in an actual BL environment. This analysis provides invaluable insights into the complex dynamics of Li transport within the Ag-C BL, shedding light on critical factors influencing the preferential plating of Li at the BL/CC interface.

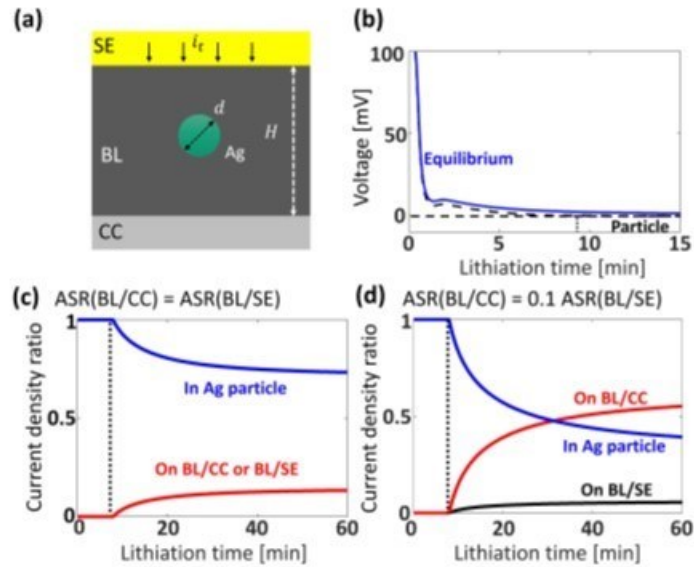


Figure XIII.27.2 (a) schematic of the continuum simulation model. (b) Simulated electrochemical potential of Ag particle (black dashes) and equilibrium bulk potential (solid blue) as functions of lithiation time. (c)-(d) Ratio of Li current flowing into Ag particle, depositing on BL/CC and BL/SE interfaces as functions of lithiation time, assuming (c) equal ASR on both interfaces and (d) lower ASR on BL/CC interface.

To further enhance our understanding of the preferential plating of lithium at the BL/CC interface, we conducted additional simulations, detailed in Figure XIII.27.3, to ascertain the extrusion behavior of Li within the BL and gain insight into the favored extrusion direction. Figure XIII.27.3a presents the relative volume percentage that Ag-Li occupies within the BL over time, at a charge rate of  $0.68 \text{ mA/cm}^2$ . It is evident that Ag particles are expected to expand and fill the pores within the BL after approximately 15 minutes. With the BL completely densified, any excess lithium plated must be deposited either at the BL/SE or BL/CC interface as represented in Figure XIII.27.3b. Figure XIII.27.3c quantifies the evolution of internal hydrostatic pressure within the BL as a function of lithiation time. Under this assumption, the internal pressure can reach a maximum of approximately 8 MPa. It becomes evident that once this internal stress becomes substantial enough to counterbalance the adhesion strength of the BL/CC interface, estimated at approximately 2 MPa, in addition to the externally applied 1 MPa stack pressure, the BL/CC interface will separate, causing Li-Ag to extrude towards the CC. Figure XIII.27.3d combines both electrochemical factors (ASR) and mechanical factors (volume expansion, surface adhesion, plastic flow) to portray the evolution of the Li deposition thickness at the BL/CC and BL/SE interfaces. The lithiation of Ag particles and densification of the BL occur within the initial 20 minutes of the lithiation process, accompanied by the formation and volume expansion of Ag-Li alloy. Subsequently, the Ag-Li alloy extrudes towards the CC for the remainder of the lithiation time due to the lower adhesion strength of the BL/CC interface compared to the BL/SE interface. In summary, the preference for Li metal to deposit on the BL/CC interface can be attributed to both the lower interfacial charge transfer resistance and the lower adhesion strength at the BL.

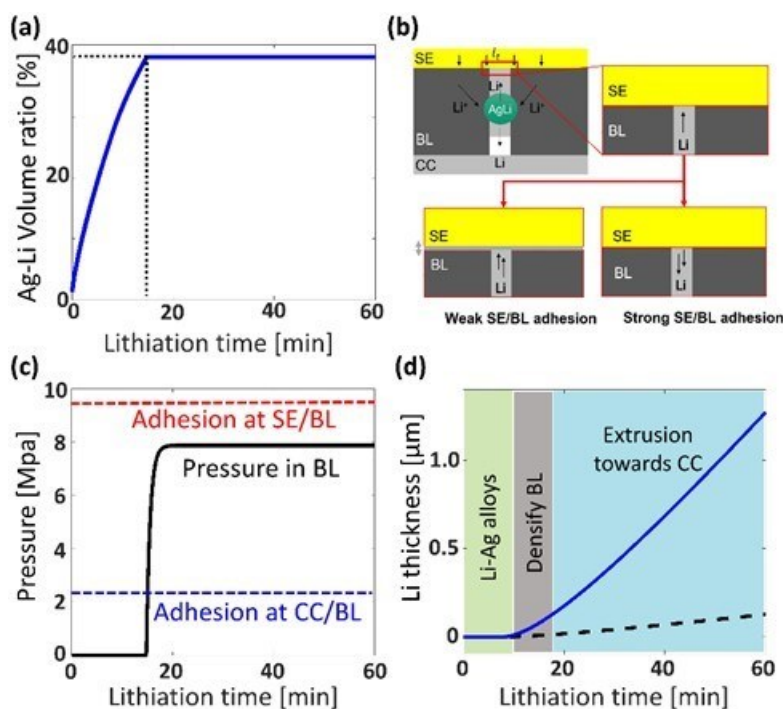
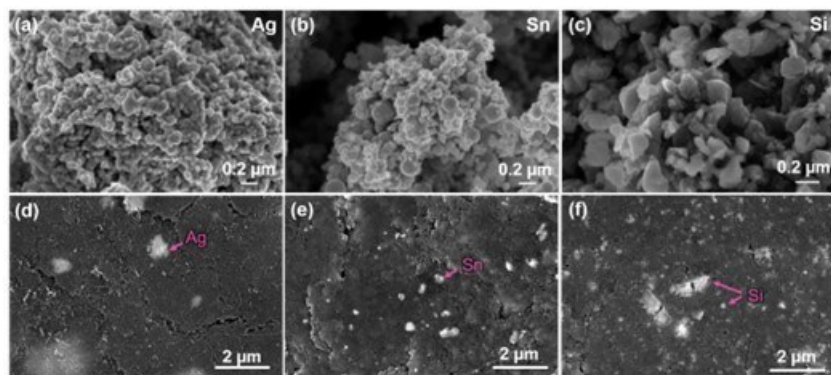


Figure XIII.27.3 (a) Volume percentage of Ag-Li alloy in the BL as a function of lithiation time. (b) Mechanism for interface separation between the BL/CC and BL/SE. (c) Calculated internal stress as a function of lithiation time in an anode-free setup. (d) Calculated evolution of deposited Li thickness as a function of lithiation time on BL/CC and BL/SE interfaces combining electrochemical and mechanical effects.

**Experimental search for alternative ABL components that can replace expensive Ag:**

LBNL team has been testing several metallic components to investigate what materials can replace expensive Ag in the ABL but also understand what properties enable uniform Li metal plating and prevent dendritic Li metal formation. We used composite ABLs including metal nanoparticles like silver (Ag), tin (Sn), and silicon (Si) that can alloy with Li before nucleating Li metal. Initially, the particle size of the metal nanoparticles is determined using the scanning electron microscope (SEM) and the particle sizes of Ag (100 nm), Sn (100-200 nm) and Si (~150 nm) (Figure XIII.27.4a-c) are confirmed. For metal-carbon composite ABL fabrication, metal nanoparticles and ketjenblack carbon were mixed at a weight ratio of 25:75 respectively, and planetary ball milled at 300 rpm for 3 h under argon atmosphere. ABL films were prepared by hand mixing 90% of the metal-carbon composite and 10% of polytetrafluoroethylene (PTFE) binder and then rolled into a 20  $\mu\text{m}$  thin film inside an argon-filled glovebox. Particle agglomeration over the ABL surface is evidenced from SEM (Figure XIII.27.4d-f) that might be caused due to the milling and/or hand-mixing of ABL with PTFE.



**Figure XIII.27.4 SEM images of (a) Ag, (b) Sn, and (c) Si nanoparticles as received from vendors. SEM images of (d) Ag-C, (e) Sn-C and (f) Si-C composites after rolling to ABL thin film.**

To investigate the electrochemical performance, half cells were constructed using our customized cells that consist of a 6.35 mm of polyetheretherketone (PEEK) die and two steel rods that are placed between two steel plates and a stack pressure was applied between them. In this assembly, 50 mg of an argyrodite type lithium phosphorous sulfur chloride ( $\text{Li}_6\text{PS}_5\text{Cl}$ ) SSE was loaded into the PEEK die and pressed between the two rods at 300 MPa for 10 min to form a 1mm thick pellet. ABL (M-C) and Li metal of 6.35 mm dia. were pressed on either side of SSE at 300 MPa and 20 MPa respectively and a stainless steel (hereafter, SUS) foil is used as the current collector. Once fully assembled, the entire cell stack was then compressed at 20 MPa for 15 min and stack pressure of 5 MPa was applied during the cell operation at 50°C. Loading density and thickness of 0.6 mg and 20  $\mu\text{m}$  respectively are maintained constant for each ABL and cells were limited by voltage (-1,1) during the discharge/charge cycles. In our experiments, cells were precycled at 0.5  $\text{mA cm}^{-2}$  for 3 complete discharge/charge cycles and cycled at 1  $\text{mA cm}^{-2}$  until a short circuit was observed by maintaining a constant areal capacity of 1  $\text{mAh cm}^{-2}$ . In this study, plots representing negative voltage value refer to the Li plating behavior at the ABL side and positive voltage is the Li stripping process. It was observed that the cell with no ABL (Figure XIII.27.5a) was short-circuited within 10 cycles at a current rate of 1  $\text{mA cm}^{-2}$  after initial precycling at 0.5  $\text{mA cm}^{-2}$ . Under the same conditions, Ag-C ABL (Figure XIII.27.5b, c) exhibited stable 343 cycles before short-circuiting. Sn-C ABL (Figure XIII.27.5d, e) also showed stable Li plating/stripping cycles over 290 cycles without short-circuit. In contrast, Si-C ABL (Figure XIII.27.5f) short-circuited completely after 4 cycles at similar experimental conditions. Although further investigation is required to address the failure mechanisms, it is found that the ABL consisting of Sn-C exhibited good performance compared to Si-C and is analogous to Ag-C.

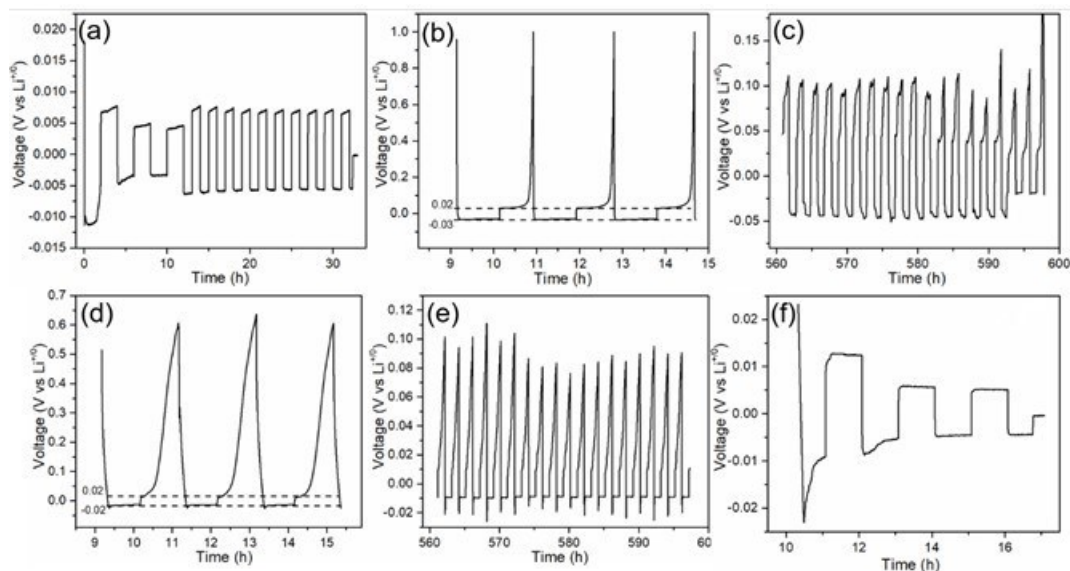


Figure XIII.27.5 Voltage curves during galvanostatic discharge/charge cycles in half cells with (a) No ABL, (b) first 3, and (c) last 15 discharge-charge cycles of Ag-C ABL, (d) first 3, and (e) last 15 cycles of Sn-C ABL and (f) Si-C ABL, at current density of  $1 \text{ mA cm}^{-2}$  after precycling at  $0.5 \text{ mA cm}^{-2}$ .

**Task 2: Composite cathode: high voltage stability, chemical and mechanical degradation issue.**

**A hybrid cathode-carbon composite development:**

Currently, there are two main fundamental challenges, limiting the cyclability of composite cathodes: (1) chemical and electrochemical degradation at the cathode/SE and SE/carbon interfaces and (2) mechanical contact loss at the cathode/SE interface due to repeated expansion and contraction of the cathode particles. In FY23, we aimed to evaluate the strategy of tailoring coatings to the chemistry of the cathode. The novel 3-dimensional (3D) composite developed in this task consists of 3D carbon frame as a core, which is coated with the cathode particles. This structure limits (or at least reduces) direct contact between carbon and SE and therefore minimizes the degradation of cathode composite. In addition, the soft and pliable carbon framework can accommodate the volume change of cathode active material (CAM) thus can prevent the mechanical contact loss at the cathode/SE interface. In FY23, we developed a composite of NMC811 ( $\text{LiNi}_{0.8}\text{Mn}_{0.1}\text{Co}_{0.1}\text{O}_2$ ) hybridized with a reduced graphene oxide (rGO) framework. SEM images of this hybrid composite of NMC811 with rGO, and its mechanically mixed equivalent, are displayed in Figure XIII.27.6a and 6b, respectively. The superior coverage of NMC811 on rGO in the hybrid composite compared to the mechanical mix is clearly evidenced in these SEM images. The hybridized sample shows successful compositing of all NMC811 particles with rGO where all the NMC811 particles are attached on rGO surface. In contrast, we found that, in the mechanically mixed sample, some NMC811 particles are not attached on rGO.

We assessed the impact of hybridization by constructing cells with various NMC+carbon cathode composites, each with equivalent carbon content. In these experiments,  $\text{Li}_6\text{PS}_5\text{Cl}$  (LPSCl) is used as a SSE and Li-In alloy is used as an anode. Figure XIII.27.6c illustrates the charge-discharge voltage profiles of the cathode composite samples at  $4 \text{ mA g}^{-1}$  ( $0.02 \text{ C}$ ,  $1 \text{ C} = 200 \text{ mA g}^{-1}$ ) within a voltage cut-off range of 4.3 to 2.5 V (vs.  $\text{Li/Li}^+$ ) at  $50^\circ\text{C}$ . Initial charge capacities were found to be 214, 180, 218, and 271  $\text{mAh g}^{-1}$  for NMC+carbon nano fiber (CNF), NMC+rGO+CNF, NMC+rGO, and  $\text{LiNbO}_3$  (LNO) coated NMC+rGO respectively. We found that the capacity obtained in low-voltage regions below 3.6V decreases as the CNF is replaced by rGO in the composite. This behavior demonstrates that the material decomposition at the interface between SE and carbon is reduced when the NMC-rGO hybrid composite is used. The reversible discharge capacities for the samples, in descending order of CNF content, were: 94, 110, and 146  $\text{mAh g}^{-1}$ . In addition, we achieved an enhanced charge/discharge capacity by introducing an LNO coating to NMC with the rGO composite sample



(refer to the red curve in Figure XIII.27.6c). The LNO-coated NMC-rGO hybrid cathode exhibits  $209 \text{ mAh g}^{-1}$ , which is equivalent to the conventional liquid cells ( $210\text{-}220 \text{ mAh g}^{-1}$ ). The improved discharge capacity is attributable to the fact that the hybrid cathode composite limits the unwanted side reactions between the SE/carbon and SE/NMC interfaces. As we progress, our focus will be on optimizing the carbon content to further improve the cyclability of the cell.

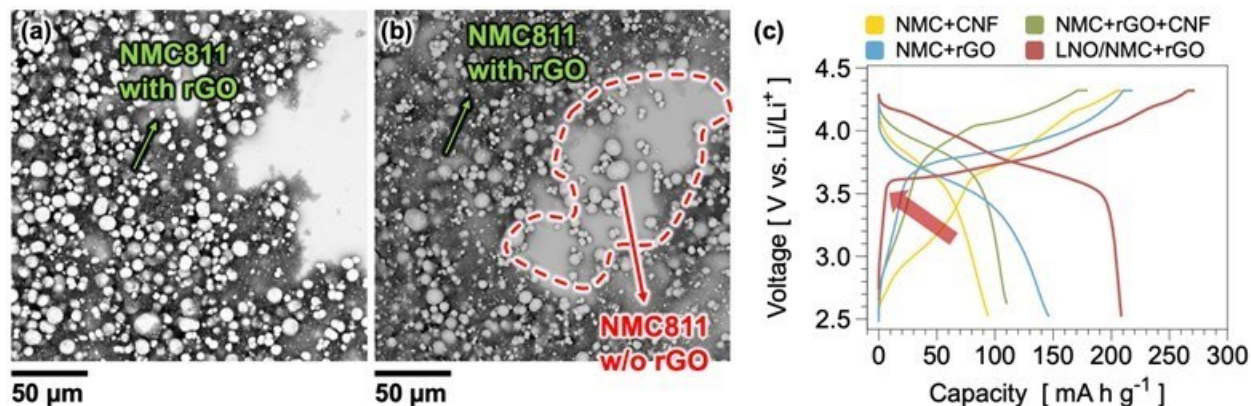


Figure XIII.27.6 (a-b) SEM images of NMC811/rGO composites by (a) hybridization method and (b) mechanical ball-mill mixing. (c) Charge-discharge profiles of various cathode composite (carbon contents:  $\sim 2 \text{ wt}\%$ ).

#### Halide-based SE development for high-voltage stability:

New  $\text{Li}_3\text{MX}_6$  halides containing rare earth (RE) elements are being developed as high-voltage stable SEs. So far a number of  $\text{Li}_3\text{MCl}_6$  ( $\text{M} = \text{Sc}, \text{In}, \text{Y}, \text{Er}, \text{Yb}$ ) chlorides have been reported to have a high ionic conductivity (up to  $10^{-3}\text{-}10^{-4} \text{ S}\cdot\text{cm}^{-1}$ ) and a wide electrochemical stability window (up to  $4.3 \text{ V vs. Li/Li}^+$ ). In the  $\text{Li}_3\text{REX}_6$ -family of compounds, it is fairly common for the halides to go through polymorphic transformations, especially under thermal treatments. For example, by means of the solid-state reactions using relatively low annealing temperatures, metastable phases of  $\text{Li}_3\text{RECl}_6$  (such as  $\beta\text{-Li}_3\text{YCl}_6$  and trigonal  $\text{Li}_3\text{YbCl}_6$ ) can be obtained, which were found to have higher ionic conductivities compared to their corresponding thermodynamically stable phases ( $\alpha\text{-Li}_3\text{YCl}_6$  and orthorhombic  $\text{Li}_3\text{YbCl}_6$ ). In this subtask, we aim to engineer new compositions and phases of  $\text{Li}_3\text{REX}_6$  that may have better ionic transport properties, wider electrochemical stability windows and/or better mechanical properties.

In FY23, we investigated the effect of chemical composition on non-stoichiometric LYX (n-LYC) samples prepared by the mechanochemical (MC) method. Figure XIII.27.7a shows the X-ray diffraction (XRD) patterns collected on a series of n-LYC and LYC synthesized by high-energy ball milling. Unlike these made by the solid-state (SS) synthesis, all samples prepared by the MC method adopted the trigonal phase, regardless of the  $x$  value in  $\text{Li}_{3-3x}\text{Y}_{1+x}\text{Cl}_6$ . The room-temperature ionic conductivity ( $\sigma_{25}$ ), determined from the electrochemical impedance spectroscopy (EIS) measurements, is  $\sim 0.4 \text{ mS cm}^{-1}$  for  $0 \leq x \leq 0.15$  (Figure XIII.27.7b). We observed the highest  $\sigma_{25}$  value ( $0.46 \text{ mS cm}^{-1}$ ) on  $\text{Li}_{2.55}\text{Y}_{1.15}\text{Cl}_6$  ( $x = 0.15$ ) that has an activation energy of  $0.37 \text{ eV}$ . Further increasing Y content to  $x > 0.15$  leads to a significant reduction in ionic conductivity. The anodic stability was also evaluated using the linear sweep voltammetry (LSV) measurements. Figure XIV.32.7c shows the results obtained on the SE+C | SE | Li-In cells at a scan rate of  $0.02 \text{ mV s}^{-1}$ . In all cases, anodic currents arising from the reactivities of the SE were observed at approximately  $4.2 \text{ V}$ . The oxidation current of n-LYC becomes smaller with higher  $x$  value, implying enhanced oxidation stability in n-LYC with increasing Li deficiency. We further explored the effect of F-substitution in halide SE properties. A series of  $\text{Li}_{3-3x}\text{Y}_{1+x}\text{Cl}_{6-y}\text{F}_y$  (n-LYCF,  $x = 0.15, 0 \leq y \leq 1.5$ ) were mechanochemically synthesized from mixtures of  $\text{LiCl}$ ,  $\text{YCl}_3$  and  $\text{YF}_3$  with various ratios. We found that the fluorinated sample appears more disordered, with broader and less defined peaks. F anions are expected to occupy the chlorine sites in the lattice. We found that fluorination leads to a reduction in ionic conductivity,

which decreases continuously with the increasing F content. On the other hand, the oxidation stability is significantly improved with F incorporation.

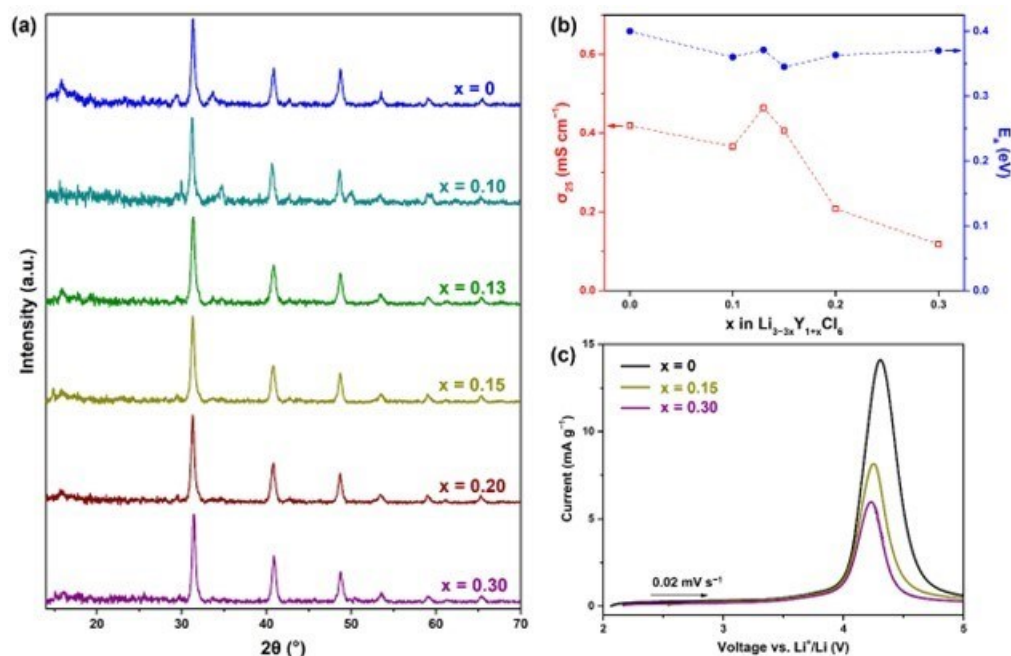


**Figure XIII.27.7** (a) XRD patterns of LYC and n-LYC prepared by mechanochemical synthesis, (b) Room-temperature ionic conductivity and activation energy of LYC and n-LYC, and (c) LSV profiles collected on the SE+ $C|SE|Li-In$  cells (SE = LYC or n-LYC). The sweep rate is  $0.02\text{ mV s}^{-1}$ .

Here, we evaluated their electrochemical performance in all-solid-state battery (ASSB) cells equipped with an uncoated 4 V class cathode material with a non-stoichiometric  $Li_{2.61}Y_{1.13}Cl_6$  SE. Figure XIII.27.8 shows the results obtained on a cell with a NMC811 composite cathode, a non-stoichiometric  $Li_{2.61}Y_{1.13}Cl_6$  SE separator synthesized using the solid-state method (SS-nLYC), and a Li-In alloy anode. The cathode composite was composed of NMC811, SS-nLYC and a carbon additive (Super C65) in a weight ratio of 58:38:5 (Figure XIII.27.8a). The mass loading of the active material was  $8\text{ mg cm}^{-2}$ , significantly higher than that in typical liquid electrolyte cells with an NMC811 composite cathode ( $\sim 6\text{ mg cm}^{-2}$ ). Figure XIII.27.8b shows the first and second charge–discharge profiles of the ASSB cell cycled between 3.0 and 4.3 V vs.  $Li^+/Li$  at room temperature. At 0.1 C rate ( $1\text{ C} = 200\text{ mA g}^{-1}$ ), the cell delivered an initial discharge capacity of  $171\text{ mAh g}^{-1}$  and a coulombic efficiency of  $\sim 82\%$ . The relatively low coulombic efficiency is attributed to the *in situ* formation of Li-In alloy on the anode as well as the initial “break-in” process or the establishment of solid-state  $Li^+$  diffusion pathways in the cathode composite. After that, the coulombic efficiency increased to  $\sim 95\%$  in the second cycle and the cell delivered a discharge capacity of  $181\text{ mAh g}^{-1}$ , corresponding to an areal capacity of  $1.45\text{ mAh cm}^{-2}$  at 0.1 C. We note that although discharge capacities up to  $\sim 200\text{ mAh g}^{-1}$  (at 0.1 C) were reported on the equivalent NMC811 liquid electrolyte cells, the areal capacity is often much lower ( $\sim 1.2\text{ mAh cm}^{-2}$ ). In the following cycles, the coulombic efficiency further increases to  $\sim 99\%$ . The ASSB cell also showed good rate capability, delivering discharge capacities of 176, 142, and  $105\text{ mAh g}^{-1}$  at 0.2, 0.5, and 1 C, respectively (Figure XIV.32.8c). In the future work, we will optimize cathode composite formulation as well as cell configuration to further improve the ASSB cell performance.

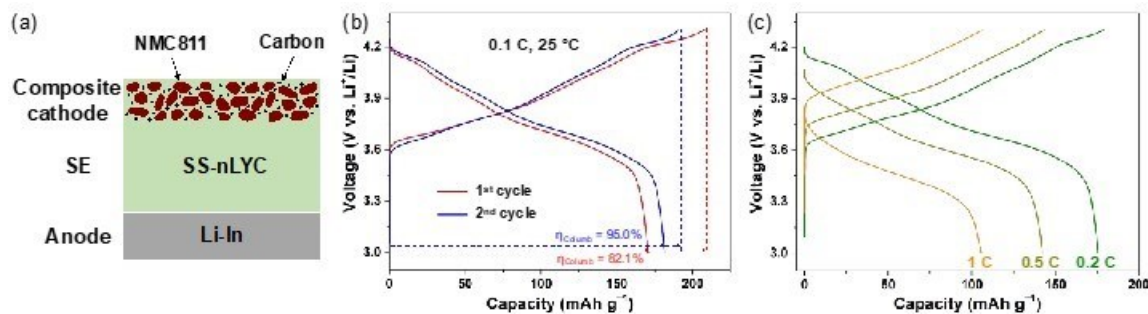
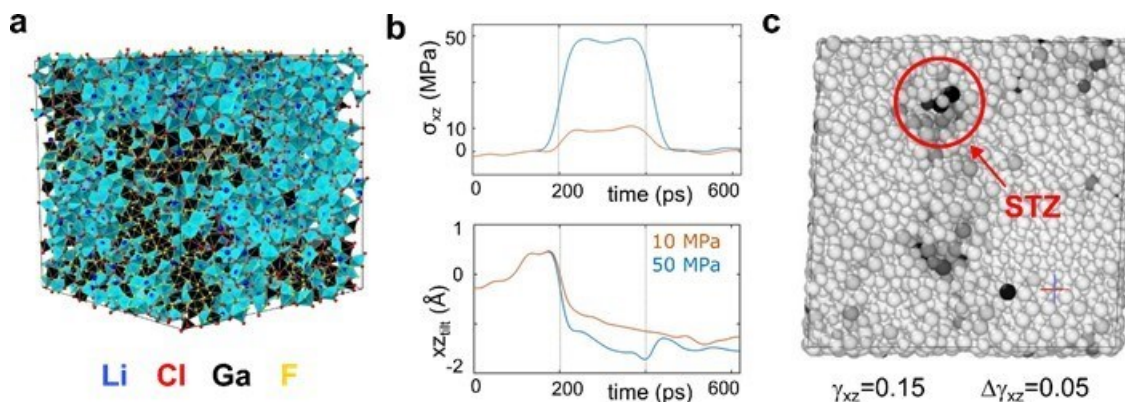


Figure XIII.27.8 (a) A schematic of the Li-In|SS-nLYC|NMC811 ASSB cell configuration, (b, c) charge-discharge profiles of the ASSB cell during the first two cycles at 0.1 C and the subsequent cycles at 0.2, 0.5 C and 1 C, respectively. Cycling was performed at room temperature in the voltage window of 3.0–4.3 V vs. Li<sup>+</sup>/Li.

#### Formation of pliable lithium superionic conductor from rigid-salts mixture:

A family of pliable electrolytes with a general formula of  $x\text{LiCl-GaF}_3$  ( $2 \leq x \leq 4$ ) were recently reported with soft mechanical properties and high room temperature ionic conductivity of  $3.6 \text{ mS cm}^{-1}$ .<sup>[1]</sup> These clay-like ionic conductors enable intimate contact to be maintained between a cathode and a SE during the cycling of solid-state batteries without external stack pressure. This subtask aims to develop new rigid-salts mixtures with pliable mechanical properties and high lithium ionic conductivity. In FY23, we first verified the mechanochemical synthesis of  $x\text{LiCl-GaF}_3$ , which was reported by Samsung researchers.<sup>[1]</sup> After 24 hours of high-energy ball-milling, the mixture of  $3\text{LiCl-GaF}_3$  turned to a clay-like state with high mechanical formability. We found it can be rolled into a film and further bent into shapes without cracking. The room-temperature ionic conductivity was measured at  $2.9 \text{ mS cm}^{-1}$  using EIS, which is consistent with the reported value in the literature.

After confirming the synthesis and high ionic conductivity of the material, we next wanted to understand why this material shows a soft mechanical response. Since the material is amorphous, modeling its properties with conventional DFT-based ab initio molecular dynamics (AIMD) is not tractable. We thus employed a multiscale theoretical approach to study the properties. We first trained an interatomic potential energy (PE) model of the Li-Cl-Ga-F chemical system using deep learning. The training was performed on >1 million AIMD trajectories. The PE model was subsequently used to construct a representative amorphous structure with >10k atoms. Figure XIII.27.9a shows the constructed amorphous structure. The structure was equilibrated in a classical MD simulation at a high temperature of  $T=850 \text{ K}$  for  $t=20 \text{ ps}$  to allow anion exchange and enhanced mixing. Thermodynamically, it is expected that when LiCl and GaF<sub>3</sub> react, the thermodynamic driving force is maximum for the reaction:  $2\text{LiCl} + 3\text{GaF}_3 \rightarrow 2\text{LiF} + 3\text{GaCl}_3$ . We found as expected that anion exchange occurs and GaCl<sub>3</sub>-like units are formed.



**Figure XIII.27.9** (a) An amorphous Li-Cl-Ga-F structure constructed for theoretical modelling. (b) The evolution of the applied external shear stress ( $\sigma_{xz}$ ) and xz-tilt distance of the amorphous structure as a function of time in the classical MD simulation. The xz-tilt distance is a representative of shear strain. A maximum of 10 and 50 MPa of external periodic stress was applied to the amorphous structure to study its mechanical response. (c) A snapshot of the amorphous structure at an external shear strain  $\gamma_{xz} = 0.15$ . The grey-scale color (white-low and black-high) represents value of non-affine displacement, at an interval of  $\Delta\gamma_{xz} = 0.05$ . The shear transformation zone (STZ) formed is circled in red.

We next explored the mechanical properties of the amorphous structure by performing classical MD simulations with the trained PE model. To understand if our structure is mechanically soft as in experiments, the shear response of the amorphous structure was explored under a low periodic external stress of 10 and 50 MPa. Figure XIII.27.9b shows the time evolution of the periodic external shear stress and the resulting change in xz-tilt distance, which is representative of shear strain. The xz-tilt distance does not revert to its original value even when the external stress is removed. This permanent deformation corresponds to plastic deformation behavior. It is interesting to see plastic behavior at low stresses of 10 MPa, which is in an agreement with the experimental observations. Then, we studied the microscopic features which are responsible for such soft-plastic behavior. It is widely known that plastic behavior in amorphous materials occurs through the formation of shear transformation zones (STZ). STZs are usually a collection of a few molecular units which get activated during the onset of plastic deformation. Non-affine displacement, which is a measure of deviation from elastic deformation is routinely used to track plastic behavior. Figure XIII.27.9c shows a snapshot of the amorphous structure at a shear strain of 0.15, where the color represents the value of non-affine displacement. The dark regions are the formed STZs. On closely looking at the atomic structure, we found that these STZs are  $\text{GaCl}_3$ -like molecular units.  $\text{GaCl}_3$  is a molecular solid, and in comparison, with  $\text{LiCl}$  and  $\text{GaF}_3$ , is very soft.  $\text{GaCl}_3$  bulk solid is just an aggregate of  $\text{Ga}_2\text{Cl}_6$  molecules connected by a weak van der Waals bond. Our results show that the formation of these weakly bonded molecular solids is linked to the clay-like soft mechanical response. These molecular solids formed during anion exchange ( $2\text{LiCl} + 3\text{GaF}_3 \rightarrow 2\text{LiF} + 3\text{GaCl}_3$ ) get activated at low stresses to form STZs and are responsible for the soft plastic behavior. Even in natural clay, the soft water molecules lead to the soft plastic response and the mechanism for the soft mechanical behavior in both these systems are very similar. Since the formation of molecular solids is responsible for clay-like mechanical response, finding other salt combinations where there is a maximum thermodynamic driving force for molecular solid formation might also show similar behavior. Apart from thermodynamics, the kinetics of the anion exchange is also important, e.g., a complete anion exchange will lead to phase separation of molecular solid units and will not lead to clay-like material.

### **Task 3. High-loading composite cathodes.**

#### **Thin SE layer development:**

This task aims to achieve high energy density and specific energy by developing a thick cathode composite with a good rate capability and a thin SE membrane through scalable processing techniques. In FY23, we developed thin lithium lanthanum zirconium oxide (hereafter, LLZO) SE membranes and tested their mechanical properties. We prepared LLZO and MgO-added LLZO (LLZO-MgO) thin SE membranes at varied

sintering times (2-10 hours) at 1050 °C. We ensure that all the specimens have a relative density of ~95 % and a thickness of 125  $\mu\text{m}$ . We used 3-point bending tests to study the fracture strengths of LLZO and LLZO-MgO SE membranes and the results are shown in Figure XIII.27.10a. The LLZO showed a fracture strength of 152.8 MPa when the LLZO SE membrane is sintered for 2 hours and the fracture strength decreases to 103.26 MPa when the sintering time increases up to 10 hours. We found that the LLZO-MgO showed a higher fracture strength and narrower error bar than LLZO at all sintering times while it shows the same trend of fracture strength decrease at longer sintering time. The fracture strength of LLZO-MgO is 247.8 MPa when the sintering time is 2 hours and it reduces to 172.9 MPa when the sintering time is longer (10 hours). In general, it is known that smaller grain size can make higher fracture strength. Therefore, we investigated the grain size of LLZO and LLZO-MgO SE membranes using SEM. We found that the grain size of LLZO sample sintered for 2 hours is smaller than the one sintered for 10 hours as shown in Figure XIII.27.10b. A similar trend is also confirmed in LLZO-MgO samples. In addition, we found that the addition of MgO in the fabrication of LLZO SE membrane reduces the grain size of LLZO.

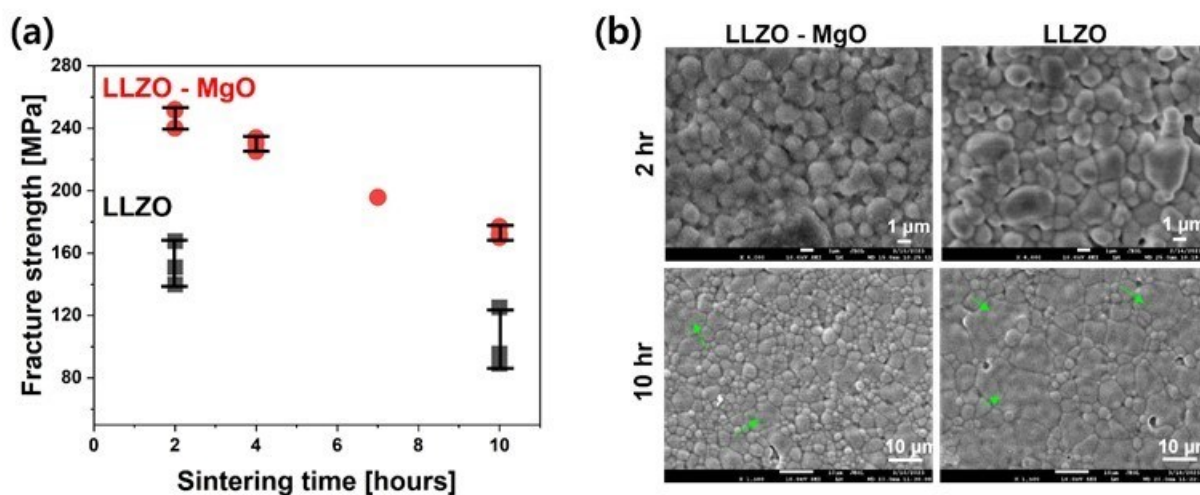


Figure XIII.27.10 (a) Fracture strengths of LLZO (Black) and LLZO-MgO (Red). (b) SEM image of the LLZO electrolyte. Green arrows point to abnormally grown grains.

#### Scale-up to large area and mechanical testing:

We prepared large-area MgO-modified LLZO composite electrolytes and tested their mechanical properties (Figure XIII.27.11). The LLZO's area was scaled up from 1.1 to 8.4  $\text{cm}^2$  (Figure XIII.27.11 a-c) with a fixed thickness of 80  $\mu\text{m}$ . Our conventional tape-casting process was used for this scaling-up, but some modifications were necessary including extending the binder burning time and using a large-area sintering furnace. Mechanical properties of large and small-area LLZOs were compared using 3-point bending (Figure XIII.27.11 d). The small area LLZO ( $\sim 1 \text{ cm}^2$ ) showed a fracture strength of 223.3 MPa, and the large area LLZO ( $\sim 4.8 \text{ cm}^2$ ) exhibited a relatively lower strength of 206.2 MPa. The strength of the largest area LLZO ( $\sim 8.4 \text{ cm}^2$ ) could not be tested because it was too fragile to handle as shown in Figure XIII.27.11c. We could observe that the larger area LLZO is more fragile than the smaller area LLZO, and further scaling up would be too difficult. Through our work, we successfully improved the mechanical properties of LLZO, increasing the fracture strength by almost 75%. However, it was still not enough to make robust thin and large-area LLZO sheets in a free-standing configuration. Therefore, we will continue working with porous LLZO scaffolds as a support for thin LLZO electrolyte.

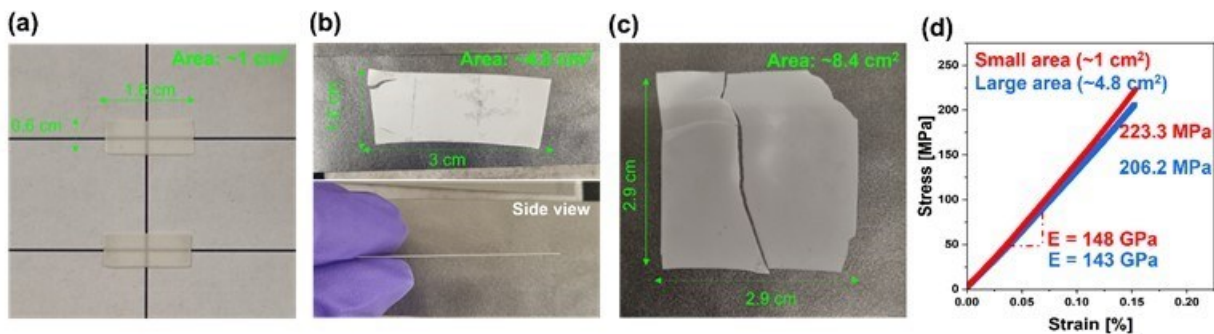


Figure XIII.27.11 Prepared thin (80  $\mu\text{m}$ ) LLZO electrolytes with area of (a) 1  $\text{cm}^2$ , (b) 4.8  $\text{cm}^2$  and (c) 8.4  $\text{cm}^2$ . (d) Stress/strain curve for the small and large area LLZOs.

#### Secondary SE development and integration:

The team investigated three different Succinonitrile (SN)-Lithium salt mixtures for use as catholytes in LLZO-based ASSBs: (i) LiTFSI+SN, (ii) LiBOB+SN, and (iii) LiTFSI+LiBOBN+SN. The SN and Li salts were mixed at 80 °C in the glove box, and the mixtures were cooled down to room temperature. We confirmed that the mixtures are in a plastic crystal phase. Then, we evaluated the required properties of the catholyte, including ionic conductivity, oxidative stability, and compatibility with LLZO. The ionic conductivities of the mixtures were evaluated in symmetric cells (SUS/SN+Li salts mixture/SUS) using EIS. Figure XIII.27.12a shows the Nyquist plots of the three mixtures. The LiBOB+SN exhibits a distinguishably higher impedance than LiTFSI+SN and its conductivity was  $5.58 \times 10^{-5}$  S/cm which is  $\sim 100$  times lower than that of LiTFSI+SN ( $3.46 \times 10^{-3}$  S/cm). The oxidation stability was tested in a coin cell (SUS/SN+Li salts mixture/Li metal) using the LSV method in Figure XIII.27.12b. The scanned voltage range was 3.0 ~ 5.5 V vs. Li/Li<sup>+</sup> with a scanning speed of 1 mV/sec. For the LSV plot of the LiTFSI+SN (Figure XIII.27.12b), little current was detected ( $< 10$   $\mu\text{A}$ ) before  $\sim 4.7$  V, which implies that it is stable to oxidation up to  $\sim 4.7$  V. The plot also showed a noticeable current flowing at  $> 4.7$  V, suggesting that the LiTFSI+SN can be oxidized at such a high voltage ( $> 4.7$  V). In contrast, the LiBOB+SN exhibited negligible current flowing until the end of the measurement (5.5 V). We also found that the mixed salt system (LiTFSI+LiBOB+SN) exhibits both good ionic conductivity and high oxidation stability compared to single salt systems.

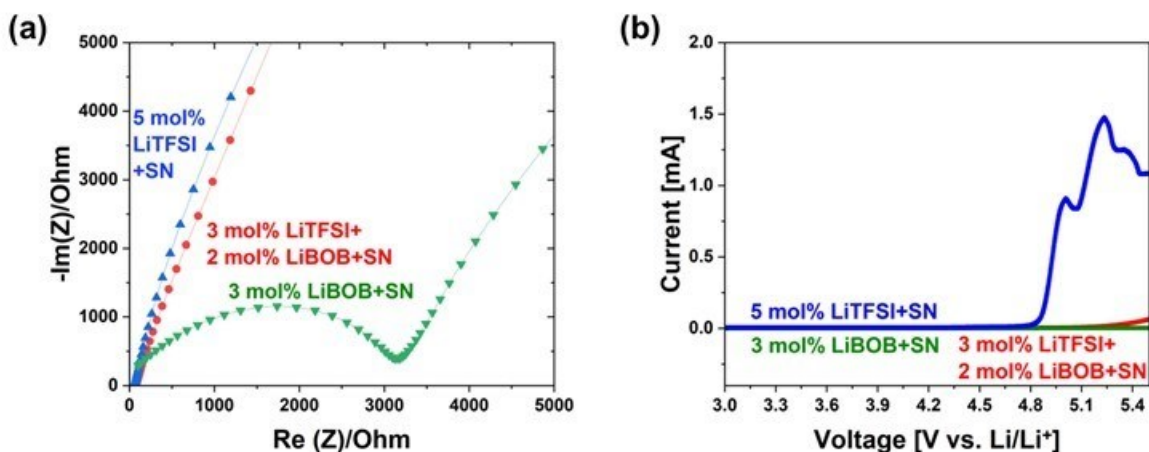


Figure XIII.27.12 Ionic conductivity and oxidation stability test. (a) Nyquist plots of SN+Li salts mixtures. (b) Linear Sweep Voltammetry (LSV) of the SN+Li salts mixtures in the range of 3.0 ~ 5.5 V vs. Li/Li<sup>+</sup>.

We further tested solid catholytes of succinonitrile (SN)-Lithium salt mixture in ASSB. Figure XIII.27.13a shows the tested cell configuration: a thin LLZO (80  $\mu\text{m}$ ) electrolyte was used, and the catholyte melt infiltrated into a conventional  $\text{LiNi}_{1/3}\text{Mn}_{1/3}\text{Co}_{1/3}\text{O}_2$  (NMC111) cathode (NMC111: carbon black: PVDF = 8:1:1

wt%) at 80 °C. The cells were cycled with no exogenous pressure at a 0.1 C current rate at 25 °C (1 C = 150 mA/g). Among the three cells, SN+LiBOB cell could not be cycled possibly due to the low ionic conductivity ( $5.58 \times 10^{-5}$  S/cm) of the SN+LiBOB mixture. Figure XIII.27.13b and c show the charge-discharge profiles of the cells with SN+LiTFSI and SN+LiTFSI+LiBOB catholytes, respectively. The SN+LiTFSI cell exhibits a capacity of ~100 mAh/g for more than 30 cycles (Figure XIII.27.13b). The capacity is relatively smaller than a typical NMC111 cathode (~150 mAh/g), and it also exhibits a high polarization in its charge/discharge voltage profiles. In contrast, the SN+LiTFSI+LiBOB cell (Figure XIII.27.13c) shows a higher capacity of ~125 mAh/g for more than 9 cycles. The charge/discharge profiles also show smaller polarization and better cycle retention than that of SN+LiTFSI cell. While the SN+LiTFSI+LiBOB cell exhibits better performance than SN+LiTFSI cell in initial few cycles, its long-term cycle life still needs to be evaluated.

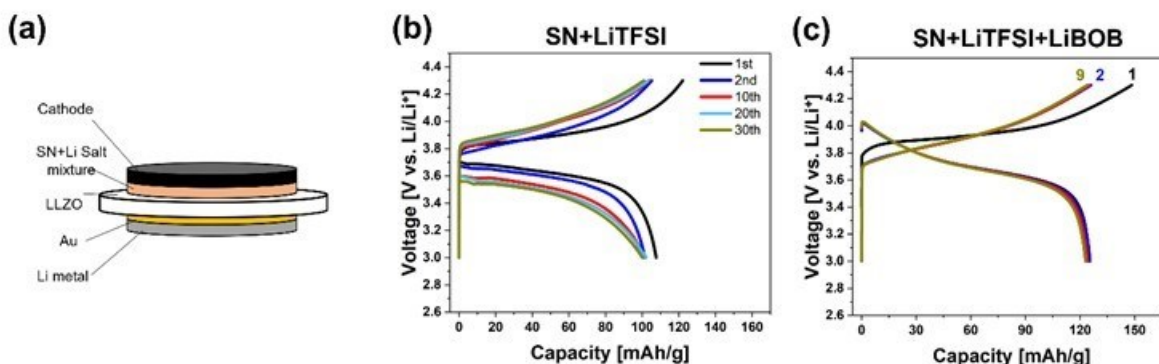


Figure XIII.27.13 (a) Cell configuration for the solid state cells with SN-based catholytes. Charge and discharge curve of the (b) SN+LiTFSI and (c) SN+LiTFSI+LiBOB.

#### Task 4. Glass composite solid electrolyte by low-temperature solution-phase synthesis.

This task aims to develop a sulfide separator that is both thin and resisting a Li dendrite penetration from the lithium metal anode. Solution processable separators would be more easily integrated with solid-state batteries through low-cost processing. In addition, solution-processable solid electrolytes could be directly integrated with cathode materials to form a composite cathode through the conventional slurry coating process. Our objective is therefore to develop the processes to synthesize hybrid solid electrolytes from inorganic conductors and polymers through solution-based processes, which combine high ionic conductivity ( $>10^{-3}$  S  $\text{cm}^{-1}$ ) and high fracture toughness ( $>10$  MPa  $\text{m}^{1/2}$ ). The combination of non-ionic conducting polymer and  $\text{Li}_6\text{PS}_5\text{Cl}$  (LPSCl) ceramic SE enhances the mechanical properties, but it tends to reduce the ion conductivity of the composites. Therefore, the development of processes to integrate polymers and LPSCl, and create uniform mixing of the two is necessary. In FY23, we investigated the post ball-milling process to control the crystallinity and morphology of LPSCl and understand their effect on the formation of composite structure with polymer. We found that the as-received commercial LPSCl has irregular morphology (Figure XIII.27.14a). The integration of such irregular shaped- and sized- LPSCl with polymers tends to create large impedance due to the uncontrolled distribution of the polymer along the irregular shaped LPSCl ceramic particles. A post material ball-milling processing improves crystallinity of the LPSCl powder and creates more uniformized size distribution of rectangular shaped LPSCl particles as shown in Figure XIII.27.14b. The ball-milled LPSCl exhibits higher ionic conductivity than the as-received LPSCl (Figure XIII.27.14c). We made polymer-LPSCl composites by mixing 1:1 weight ratio of triethylene glycol dimethacrylate (TEGDMA) and LPSCl, followed by a polymer crosslinking reaction to form the composites. While the ionic conductivities are lower for the polymer composites than the LPSCl samples, the composite of ball-milling processed LPSCl with TEGDMA shows higher ionic conductivity than that of the as-received LPSCl polymer composite (Figure XIII.27.14d and e).

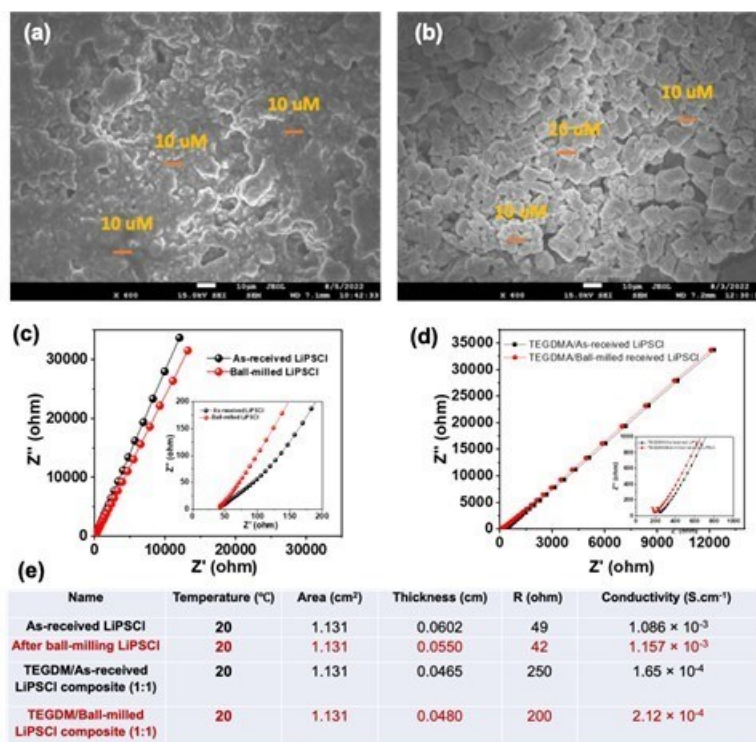


Figure XIII.27.14 (a) SEM image of commercial as-received LPSCI particles. (b) SEM image of lab ball-milled processed LPSCI particles. (c) EIS measurement of the two LPSCI materials with blocking electrodes. (d) EIS measurement of the two TEGDMA/LPSCI composites with blocking electrodes. (e) Details of the measurement conditions and calculated results.

We fabricated and performed a full-cell battery testing. The battery performance of the prepared electrolytes was examined using an all-solid-state cell that had a coated NMC811/SE/Li-In configuration at a temperature of 25 °C. The choice of coated NMC811 as the cathode material was based on its high energy density, cycling performance, and theoretical capacity. Figure XIII.27.15a illustrates the charge-discharge (CD) plots of the cells at 0.1 C, up to a potential of 4.2 V and Figure XIII.27.15b and c show the changes in discharge specific capacity (C<sub>sp</sub>) and coulombic efficiency as the number of CD cycles increases at 0.1C. At a rate of 0.1C, the C<sub>sp</sub> values of the solid-state cells with ALPSCI, BLPSCI, ALPSCI-P, and BLPSCI-P electrolytes were approximately 115, 125, 134, and 138 mAh/g, respectively (Figure XIII.27.15a). (Note: as-received LPSCI, ball-milled LPSCI, as-received LPSCI-TEGDMA polymer, ball-milled LPSCI-TEGDMA polymer are denoted as ALPSCI, BLPSCI, ALPSCI-P, and BLPSCI-P, respectively.) These values are comparable to or higher than those reported for other SEs. Furthermore, after 50 CD cycles, the cells with these electrolytes exhibited C<sub>sp</sub> values of around 65, 73, 87, and 90 mAh/g for ALPSCI, BLPSCI, ALPSCI-P, and BLPSCI-P electrolytes, respectively, at 0.1 C. The capacity was decreased by approximately 44%, 42%, 37%, and 38% of the initial C<sub>sp</sub> (Figure XIII.27.15b). The coulombic efficiencies of the half-cell using ALPSCI, BLPSCI, ALPSCI-P, and BLPSCI-P electrolytes were approximately 94.05%, 95.82 %, 99.85%, and 99.97%, respectively, during the first CD cycle (Figure XIII.27.15c). These efficiencies significantly improved to approximately 98.08%, 99.80%, 99.98%, and 99.99%, respectively, after 50 CD cycles, owing to the enhanced interfacial contact between the electrode and electrolyte. More importantly, both at the initial and following 50 cycles, the cells utilizing composite electrolytes, specifically ALPSCI-P and BLPSCI-P, demonstrated higher coulombic efficiencies compared to cells employing individual ALPSCI and BLPSCI electrolytes. These observations strongly suggest that the composite electrolytes exhibit substantial electrochemical stability and enduring cycling performance within the potential range of up to 4.2 V. Additionally, the rate capability of the cells was investigated at various current densities from 0.1 C to 0.5 C. The cell with BLPSCI-P electrolyte delivered a capacity of over 59 mAh/g at a high current density of 0.5C, and no short circuit was observed. In



conclusion, the BLPSCI-P electrolyte demonstrated excellent cycling and electrochemical stability, showing promise for the development of high-voltage solid-state batteries.

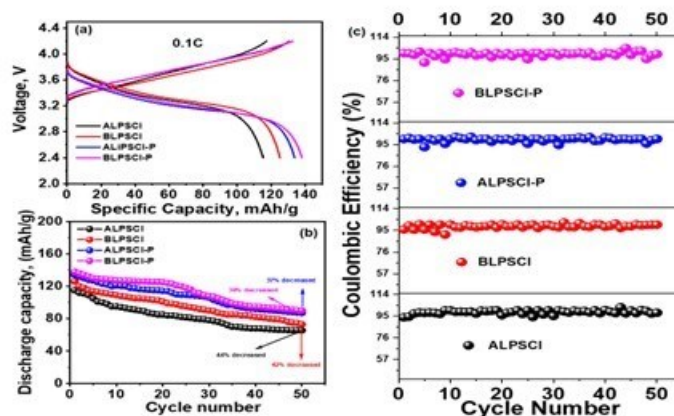


Figure XIII.27.15 (a) Charge and discharge (CD) plots of the as-prepared electrolyte solutions based on the coated NMC811//SE//Li-In cell at 0.1C rate. (b) Specific discharge capacity plots of the cells as a function of the CD cycles at 0.1C (c) Coulombic efficiency of the cells with as-prepared SEs as a function of the CD cycles.

## Conclusions

This project has four main tasks: (1) ABL development, (2) chemically and mechanically stable cathode composite development, (3) high-loading cathode composite design, and (4) glass composite solid electrolyte development. For task 1, the team has investigated the lithiation and lithium metal plating mechanisms in Ag/C composite ABL and identified an alternative ABL system of Sn/C composite. For task 2, the team has evaluated their approaches to create CAM-carbon composite electrodes that can provide high electronic conductivity but minimize detrimental carbon-SE interfaces. In addition, the team developed non-stoichiometric  $\text{Li}_{3-x}\text{Y}_{1+x}\text{Cl}_6$  ( $0 \leq x \leq 0.13$ ) SE that can exhibit high ionic conductivity and excellent oxidation stability, which were demonstrated in a solid-state battery cell. The team also revealed that partial (incomplete) anion exchange forms molecular-solid that enables clay-like mechanical properties. Task 3 focuses on the optimization of thin and large area LLZO separators and development of the secondary SE for the cathode composite. While we developed thin ( $<100 \mu\text{m}$ ) LLZO separators, we found that the thin LLZO separators are too fragile when they are processed for a large-area separator. Therefore, the team decided to use supporting materials on one or both sides of LLZO separators. The team also developed SN-based plastic crystal SEs that have high ionic conductivity and oxidation stability. In the efforts of Task 4, the team developed glass-ceramic hybrid SEs consisting of TEGDME and LPSCI. The hybrid SE exhibits improved cycling stability in a solid-state battery cell.

## Key Publications

1. "Lithium Batteries with Small-Molecule Quinone Cathode Enabled by Lithium Garnet Separators" R. Jonson, V. Battaglia, M. Tucker, ACS Appl. Energy Mater., DOI: 10.1021/acsaem.2c02932 (2023)
2. "Lithium Phosphorus Sulfide Chloride-Polymer Composite via the Solution-Precipitation Process for Improving Stability toward Dendrite Formation of Li-Ion Solid Electrolyte" R. Khomein, Y. -W. Byeon, D. Liu, J. Yu, A. M. Minor, H. Kim, G. Liu, ACS Appl. Mater. Interfaces, DOI: <https://doi.org/10.1021/acsaem.2c21302> (2023)
3. "The impact of residual solvent on the performance of catholyte for solid-state batteries", F. Shen, R. Jonson, M. Tucker, 242<sup>nd</sup> ECS Meeting, October 2022, Atlanta, GA

4. “The Mechanism by which a Ag-Carbon Buffer Layers Improves Li Plating in Solid-State Batteries”, G. Ceder and H. Tu. 2023 MRS Spring Meeting & Exhibit, April, 2023, San Francisco, CA
5. “Manufacturing Considerations for Solid-State Batteries based on LLZO”, M. M. Doeff, M. Tucker, T. Deng, W. Go, 2023 MRS Spring Meeting & Exhibit, April 2023, San Francisco, CA
6. “Succinonitrile-Lithium Salt Composite as a Solid Catholyte for LLZO-Based All-Solid-State Batteries”, W. Go, M. Tucker, M. M. Doeff, 2023 MRS Spring Meeting, April 2023, San Francisco, CA
7. “Succinonitrile-Lithium Salt Composite as a Solid Catholyte for LLZO-Based Solid-State Batteries”, W. Go, M. Tucker, M. M. Doeff, 243<sup>rd</sup> ECS Meeting, May 2023, Boston, MA
8. “Organic Cathode for Lithium Batteries, Enabled by Solid-State LLZO Separator”, M.C. Tucker, R. Jonson, V.S. Battaglia, 243<sup>rd</sup> ECS Meeting, May 2023, Boston, MA
9. “Design Considerations for Batteries based on LLZO” Marca M. Doeff, Michael Tucker, Wooseok Go, and Tao Deng, The Fourth World Conference on Solid Electrolytes for Advanced Applications: Garnets and Competitors, Sept. 4-7, 2023 Trømso, Norway (invited).

### References

1. Sung-Kyun Jung, Hyeokjo Gwon, Gabin Yoon, Lincoln J. Miara, Valentina Lacivita, and Ju-Sik Kim. “Pliable Lithium Superionic Conductor for All-Solid-State Batteries” ACS Energy Lett. 6, 2006-2015 (2021)

### Acknowledgements

This project collaborates with the following co-PIs: G. Ceder, V. Battaglia, G. Chen, M. M. Doeff, G. Liu, M. Scott, M. Tucker, and J. Urban, all at LBNL. We appreciate graduate students and postdoctoral researchers who contribute to this project: Y. -W. Byeon, F. Ahmed, S. Yang, V. S. Avvaru, W. Go, K. Higa, Y. Fu, D. Collins-Wildman, F. Shen, S. Yang, T. Ogunfunmi, S. Gupta, X. Yang.

## XIV Beyond Li-Ion R&D: Lithium Sulfur Batteries

Lithium-sulfur (Li-S) battery technology has the potential to offer affordable, lighter-weight batteries that also have a safety advantage over present systems. In these batteries, the metal-rich cathode of Li-ion cells is replaced with a comparatively cheap and abundant elemental sulfur, a material that offers the theoretical potential for a five-fold improvement in capacity for the same weight. By using sulfur, lightweight cells can be produced using more cost-effective materials, while also reducing the environmental and social concerns surrounding the production of nickel and cobalt. Whereas such battery types as Li-ion and Na-ion employ an intercalation mechanism for Li-ions to shuttle between electrodes, Li-S batteries operate by a ‘conversion mechanism’ in which elemental sulfur and lithium react to form a series of lithium-containing sulfur compounds (polysulfides) to deliver the energy stored in the cell. There are several key challenges associated with this technology including the poor electronic conductivity of sulfur, the dissolution of discharge products (shuttle effect) and the poor reversibility of lithium.

The rest of this chapter contains detailed reports on the status of the following individual projects.

- A Novel Chemistry: Lithium-Selenium and Selenium-Sulfur Couple (ANL)
- Development of High Energy Lithium-Sulfur Batteries (PNNL)
- Mechanistic Investigation for the Rechargeable Li-Sulfur Batteries (BNL, U of Wisconsin Milwaukee)
- New electrolyte binder for Lithium sulfur battery (LBNL)
- Strategies to Enable Lean Electrolytes for High Loading and Stable Lithium-Sulfur Batteries (UCSD)
- New Engineering Concepts for High Energy Density Li-S Batteries (UPitt)
- Development of Li-S Battery Cells with High Energy Density and Long Cycling Life (PSU)
- Nanostructured Design of Sulfur Cathodes for High Energy Lithium-Sulfur Batteries (Stanford University)
- Fluorinated Glyme Solvents to Extend Lithium-Sulfur Battery Life Fluorinated Glyme Solvents to Extend Lithium-Sulfur Battery Life (Navitas Advanced Solutions Group)
- Liquid Electrolytes for Lithium-Sulfur Batteries with Enhanced Cycle Life and Energy Density Performance (Giner)
- Development of Functional Electrolytes for Li-S Battery Cells (PSU).

## XIV.1 A Novel Chemistry: Lithium-Selenium and Selenium-Sulfur Couple (ANL)

### **Khalil Amine, Principal Investigator**

Argonne National Laboratory  
9700 South Cass Avenue  
Lemont, IL 60439  
E-mail: [amine@anl.gov](mailto:amine@anl.gov)

### **Tien Duong, DOE Technology Development Manager**

U.S. Department of Energy  
E-mail: [Tien.Duong@ee.doe.gov](mailto:Tien.Duong@ee.doe.gov)

Start Date: October 1, 2022

End Date: September 30, 2023

Project Funding (FY23): \$500,000

DOE share: \$500,000

Non-DOE share: \$0

### **Project Introduction**

Lithium/sulfur (Li/S) batteries have attracted extensive attention for energy storage applications due to the high theoretical energy density ( $2600 \text{ Wh kg}^{-1}$ ) and earth abundance of sulfur.[1] Recently, selenium and selenium-sulfur systems have also received considerable attention as cathode materials for rechargeable batteries because of the high electronic conductivity (20 orders of magnitude higher than sulfur) and high volumetric capacity ( $3254 \text{ mAh cm}^{-3}$ ) of selenium.[2] Selenium-sulfur (Se-S) mixtures are miscible in a wide concentration range, and many Se-S composites can be prepared, including  $\text{Se}_5\text{S}$ ,  $\text{Se}_5\text{S}_2$ ,  $\text{Se}_5\text{S}_4$ ,  $\text{SeS}$ ,  $\text{Se}_3\text{S}_5$ ,  $\text{SeS}_2$ ,  $\text{SeS}_7$ , and even materials with a small amount of Se such as  $\text{SeS}_{20}$ . [2] These Se-S composites offer higher theoretical specific capacities than Se alone and improved conductivity compared to pure S. However, similar to Li/S batteries, two major obstacles resulting from lithium polysulfides/polyselenides (LiPSs/LiPSes) shuttle and lithium dendrite formation remain huge challenges for long-life Li/Se-S batteries.[3] The former is due to the dissolution and migration of polysulfides/polyselenides intermediates in the conventional ether-based electrolytes, which could induce severe parasitic reactions with Li metal and hence formation of porous or mossy Li metal. The latter originates from the parasitic reactions of lithium metal with the electrolytes, leading to the formation of fragile solid electrolyte interphase (SEI) on Li metal, further uncontrolled lithium dendrite growth and eventually dead lithium. These parasitic reactions are the direct cause for the rapid capacity fade and poor coulombic efficiency of Li/S and Li/Se-S batteries.

Via advanced diagnostic tools including synchrotron X-ray probes and computational modeling, the team led by Dr. Khalil Amine and Dr. Guiliang Xu at Argonne National Laboratory (ANL) is focusing on the development of rational cathode structure designs and exploration of novel electrolytes to effectively eliminate these parasitic reactions and simultaneously suppress the shuttle effect and lithium dendrite formation during long-term cycling.

### **Objectives**

The objective of this project is to develop novel Li/Se-S batteries with high energy density ( $500 \text{ Wh kg}^{-1}$ ) and long life (>500 cycles) along with low cost and high safety.

### **Approach**

To prevent the dissolution of polysulfides and increase the active material utilization, S or  $\text{Li}_2\text{S}$  is generally impregnated in a conducting carbon matrix. However, this approach makes it difficult to increase the loading density of practical electrodes. It is proposed here to solve the above barriers by the following approaches: (1) partial replacement of S with Se, (2) confinement of the Se-S in a porous conductive matrix with high pore volume, and (3) exploration of advanced electrolytes that can suppress shuttle effect and lithium dendrite growth.

## Results

### *Pushing Lithium–Sulfur Batteries towards Practical Working Conditions through a Cathode–Electrolyte Synergy*

In order to enable the operation of Li/S batteries towards more practical conditions such as wide-temperature, high areal S loading and low electrolyte/sulfur (E/S) ratio, the synergistic cooperation of rational host design and advanced electrolytes is critical to simultaneously suppress the shuttle effect and stabilize Li stripping/plating process.

In FY23, we have designed an order macroporous sulfur host (OMSH) with a pore diameter of 180 nm, which further consists of Co-N-C single atom catalyst and ZnS polar sites. Such design could immobilize and catalytically convert polysulfide intermediates during cycling, even with a high  $S_{22.2}Se$  loading of 80 wt%. The cathode is therefore denoted as OMSH-Se/S. On the other hand, we have invented an HFE-based electrolyte (1.0 m LiTFSI in the mixture of dioxolane and 1,1,2,2-tetrafluoroethyl-2,2,3,3-tetrafluoropropyl ether (1/1 volume ratio) with 0.1 m  $LiNO_3$  additive) to suppress lithium dendrite and polysulfides dissolution.

First, we tested the OMSH-Se/S cathode with high areal loading under both low (0 °C) and high (55 °C) temperature conditions to evaluate the wide-temperature operating performance. At low temperature, the ion diffusion coefficient and the redox kinetics will decrease and deteriorate the electrochemical performance, particularly for thick electrodes. Meanwhile, the accumulation of polysulfides (LiPSs) and polyselenides (LiPSes) intermediates during cycling caused by the slower redox kinetics will also lead to the loss of active material and thus affects the cycling stability of Li-S cells. As a result, most of the previously reported low-temperature Li-S cells were still based on thin S cathode.

In contrast, due to the introduction of the ordered macroporous host material and Se doping, the electrochemical redox kinetics of the OMSH-Se/S cathode was effectively boosted. As shown in Figure XIV.1.1a, when cycling the thick OMSH-Se/S cathode ( $5.2 \text{ mg cm}^{-2}$ ) in HFE-based electrolyte under 0 °C, the cathode can still deliver and maintain a reversible high areal capacity of  $> 4.2 \text{ mAh cm}^{-2}$  after 100 cycles at a current density of  $100 \text{ mA g}^{-1}$ . We then evaluated the electrochemical performance of thick OMSH-Se/S cathode ( $5.0 \text{ mg cm}^{-2}$ ) in HFE-based electrolyte at an elevated temperature of 55 °C. As shown in Figure XIV.1.1b, the higher temperature can further enhance the electrochemical redox kinetics of the OMSH-Se/S cathode, resulting in a high specific capacity of  $1215.97 \text{ mAh g}^{-1}$ , and it can maintain a specific capacity of  $750.94 \text{ mAh g}^{-1}$  after 50 cycles even with high areal Se/S loading.

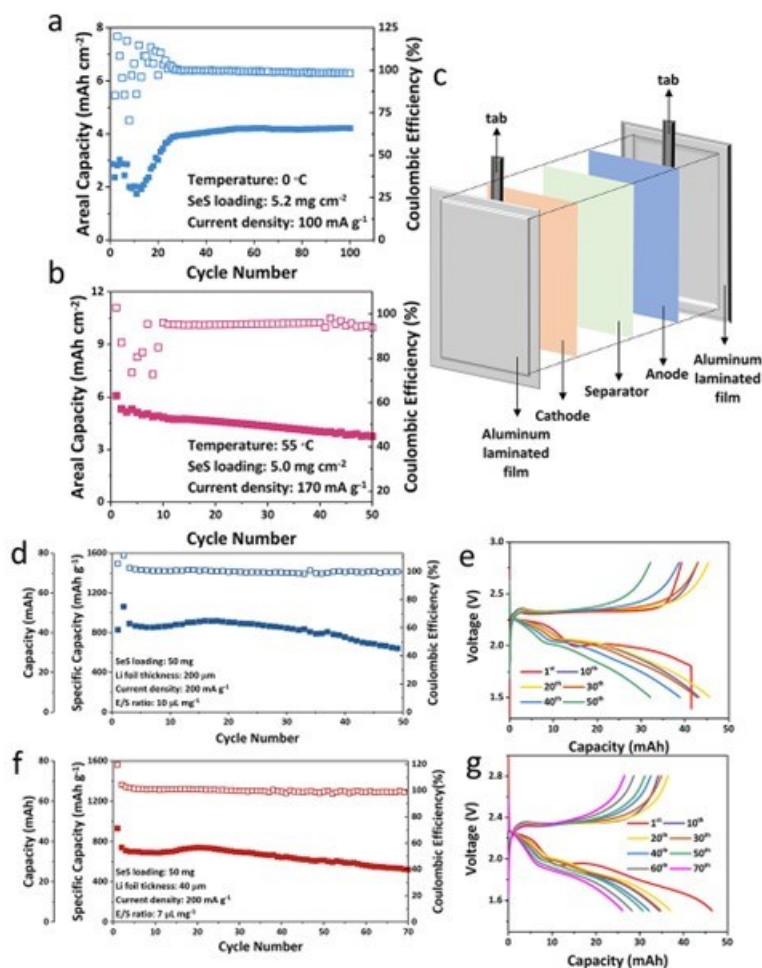


**Figure XIV.1.1** Practical application validation for the combination of OMSH-Se/S cathode with HFE-based electrolyte. Cycling performance of OMSH-Se/S cathode in HFE-based electrolyte under a) 0 °C condition, b) 55 °C condition. c) Schematic graph of Li-Se/S pouch cell configuration. d) Cycling performance of Li-Se/S pouch cell with thick Li metal anode (200 μm). e) Charge/discharge voltage profiles of various cycles of Li-Se/S pouch cell with 200 μm Li metal anode. f) Cycling performance of Li-Se/S pouch cell with thin Li metal anode (40 μm). g) Charge/discharge profiles of various cycles of Li-Se/S pouch cell with 40 μm Li metal anode.

Furthermore, we then investigated the electrochemical performance of OMSH-Se/S cathode in HFE-based electrolyte using a practical pouch cell configuration. The pouch cell configuration is shown in Figure XIV.1.1.c. We firstly evaluated the performance of the Li-Se/S pouch cell based on OMSH-Se/S cathode and HFE-based electrolyte with 200 μm-thick Li metal foil as the anode, and the E/S ratio was controlled to be 10 μL mg<sup>-1</sup>. As shown in Figure XIV.1.1.d & 1e, the as-assembled Li-Se/S pouch cell can deliver an initial specific capacity of 830.76 mAh g<sup>-1</sup> at a current density of 200 mA g<sup>-1</sup>. Meanwhile, it can well maintain a specific capacity of 650.23 mAh g<sup>-1</sup> after 50 cycles, corresponding to a capacity retention rate of 78.27%.

To deliver a high realistic cell specific energy, the amount of Li metal anode and the electrolytes should also be carefully controlled. However, since the parasitic reaction in a practical pouch cell is much more severe than that of a small-scale coin cell, it remains challenging to achieve a stable cycling performance in a Li-S pouch cell. And most of the reported Li-S pouch cells utilized the Li metal anode with the thickness of > 100 μm. As a result, we applied thin Li metal foil (40 μm) as the anode and controlled the E/S ratio to 7 μL mg<sup>-1</sup> for the Li-Se/S pouch cell to validate the effectiveness of our sulfur host in limiting the parasitic reaction and thus enhance the stability of the Li-Se/S pouch cell. As shown in Figure XIV.1.1.f & 1g, the as-assembled Li-

Se/S pouch cell can deliver an initial specific capacity of  $931.12 \text{ mAh g}^{-1}$  at  $200 \text{ mA g}^{-1}$ . Moreover, the cell can well maintain a high coulombic efficiency of  $> 99.3 \%$  for 70 cycles.

Furthermore, to reveal the underlying mechanism, we have conducted advanced characterization including in situ high-energy X-ray diffraction (XRD), X-ray near-edge absorption spectroscopy (XANES), time-of-flight secondary ion mass spectrometry (ToF-SIMS) and electron microscopy (SEM and TEM) during or after charge/discharge of batteries.

In situ HEXRD of the OMSH-Se/S cathode during charge/discharge in HFE-based electrolyte was carried out to track the phase transformation. As shown in Figure XIV.1.2a, the peaks located at  $4.48^\circ$ ,  $6.39^\circ$ ,  $6.71^\circ$ ,  $7.48^\circ$ ,  $7.75^\circ$ ,  $8.03^\circ$ ,  $8.33^\circ$ , and  $8.39^\circ$  can be assigned to crystalline Se-doped S phase, whose intensities began to decrease as the depth of discharge increase, indicating the continuous reduction of Se/S cathode during the discharge process. At the discharge cut-off voltage of  $\sim 1.5 \text{ V}$ , some of the Se-doped S peaks have almost diminished ( $4.48^\circ$ ,  $7.2^\circ$ ,  $8.33^\circ$ ,  $8.39^\circ$ , and  $9.9^\circ$ ), while some peaks ( $7.5^\circ$ ,  $7.8^\circ$ , and  $9.1^\circ$ ) remained, which however are overlapped with the peaks of standard  $\text{Li}_2\text{Se}$  and  $\text{Li}_2\text{S}$ . Such overlap makes it difficult to clearly clarify the peak assignment. Nevertheless, it can be seen that the intensity of the peak at  $7.8^\circ$  was increased from 3.33 h to 4.8 h (1.5 V), which should be due to the formation of  $\text{Li}_2\text{S}$ . Moreover, given the high discharge specific capacity ( $1206 \text{ mAh g}^{-1}$ ) of the cell during in situ XRD measurement, it was believed that most of the Se-doped S was reduced to form  $\text{Li}_2\text{S}$  and  $\text{Li}_2\text{Se}$  during discharge. Meanwhile, the intensity of the peak located at  $10.43^\circ$  began to increase at  $\sim 1.0 \text{ h}$ , indicating the gradual formation of a kind of crystalline intermediate. Afterward, this peak intensity began to decrease near the end of the discharge process and almost disappeared at the cut-off voltage. During the charging process, the  $10.43^\circ$  peak intensity began to increase at  $\sim 7.0 \text{ h}$  and then quickly faded, suggesting this crystalline intermediate also exist during the charging process. This peak could be highly likely assigned to be  $\text{Li}_2\text{S}_2$ . Further charging process has led to the recovery of sulfur signal, indicating the continuous conversion of  $\text{Li}_2\text{S}$  ( $\text{Li}_2\text{Se}$ ) to form Se-doped S during charge.

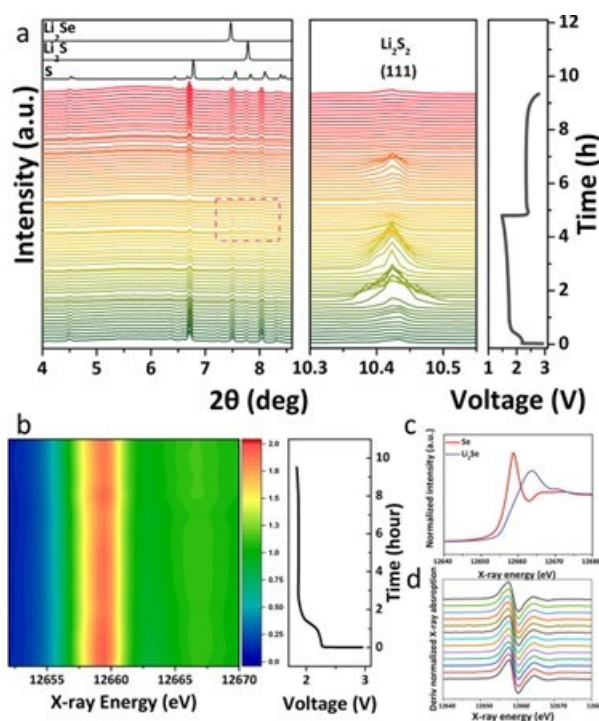


Figure XIV.1.2 In situ phase transformation analysis of cathode material. a) Charge and discharge curve of OMSH-Se/S cathode at 0.15 C in HFE-based electrolyte and the corresponding in situ HEXRD patterns. b) Discharge curve of OMSH-Se/S cathode at 0.1 C in HFE-based electrolyte and the corresponding in situ XANES spectra. c) The standard Se and  $\text{Li}_2\text{Se}$  XANES spectra. d) First derivatives of in situ XANES spectra.

In situ Se K-edge XANES characterization was further conducted to probe the environment around the Se atom during the discharge process to 1.8 V. As shown in Figure XIV.1.2b & Figure XIV.1.2c, the adsorption intensity of Se ( $\sim 12658.7$  eV) gradually decreased as the depth of discharge increased, indicating the continuous reduction of Se/S. Meanwhile, the adsorption intensity of  $\text{Li}_2\text{Se}$  ( $\sim 12663.6$  eV) gradually increased during the discharge process, suggesting the formation of  $\text{Li}_2\text{Se}$  product during the discharge process. Moreover, as shown in Figure XIV.1.2b & Figure XIV.1.2d, there is no energy shift for the Se atom between 12658.7 eV and 12663.6 eV, which is consistent with the previously reported behavior of Se/S cathode in carbonate-based electrolyte while different from that in DME-based electrolyte. Therefore, it can be concluded that the OMSH-Se/S cathode in HFE-based electrolyte undergoes a quasi-solid-solid (de)lithiation process to bypass the formation of LiPSs intermediates and thus eliminate the capacity decay caused by shuttling.

We further conducted ToF-SIMS and TEM characterization to gain an in-depth understanding of the interphase and morphology properties of cycled Se/S cathode and Li metal anode in different electrolytes. All the characterized cathodes and anodes were collected after galvanostatic cycling at a charge/discharge rate 0.1 C for 100 cycles in the corresponding HFE- and conventional ether (DME)-based electrolytes. In the DME-based electrolyte, due to the formation of highly soluble lithium polyselenides (LiPSes), the repeated dissolution/re-deposition process during long-term cycling will cause the migration of Se from the inner part of the cathode to the outer surface and thus lead to the non-uniform distribution of Se on the cycled cathode (Figure XIV.1.3a). In the case with HFE-based electrolyte (Figure XIV.1.3b), no Se agglomerates can be found on the surface of the cycled cathode. Similar to Se, the signal of S for the cycled cathode in DME-based electrolyte also exhibits more inhomogeneity than that of the cycled cathode in HFE-based electrolyte (Figure XIV.1.3a & Figure XIV.1.3b), further confirming the effectiveness of HFE-based electrolyte in preventing shuttling effect. The depth profile ( $\text{Se}^-$ ) of cycled OMSH-Se/S cathode in the DME-based electrolytes (Figure XIV.1.3c) exhibited a strong  $\text{Se}^-$  signal on the outmost surface and became weaker as depth increased, confirming the formation of Se migration layer on the surface of the cycled cathode. In the case with HFE-based electrolyte, the  $\text{Se}^-$  signal showed a reverse trend. Meanwhile, the TEM image and corresponding EDS results of cycled OMSH-Se/S cathode in HFE-based electrolyte (Figure XIV.1.4) confirmed that the ordered macroporous structure can be well maintained after long-term cycling. Similar results can be found in the cycled Li metal anode. In comparison with pristine Li metal, after cycling the Li-Se/S cell in the DME-based electrolyte, an uneven surface with lots of agglomerates can be found on the surface of cycled Li metal anode (Figure XIV.1.3d). While in the case of HFE-based electrolyte (Figure XIV.1.3f), a uniform surface with no agglomerates can be observed.



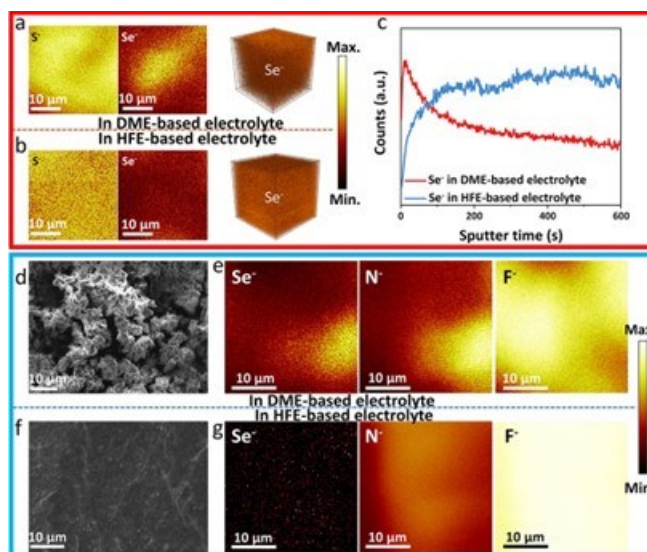


Figure XIV.1.3 Interphase and morphology characterizations of cycled electrodes. ToF-SIMS chemical mappings (S- and Se-) and 3D element reconstructions (Se-) of cycled OMSH-Se/S cathode in a) DME- and b) HFE-based electrolytes. c) Depth profile (Se-) of cycled OMSH-Se/S cathode in both DME- and HFE-based electrolytes. d) SEM image of cycled Li metal anode in Li-Se/S cell with DME-based electrolyte. e) ToF-SIMS chemical mappings (Se-, N-, and F-) of cycled Li metal anode in Li-Se/S cell with DME-based electrolyte. f) SEM image of cycled Li metal anode in Li-Se/S cell with HFE-based electrolyte. g) ToF-SIMS chemical mappings (Se-, N-, and F-) of cycled Li metal anode in Li-Se/S cell with HFE-based electrolyte.

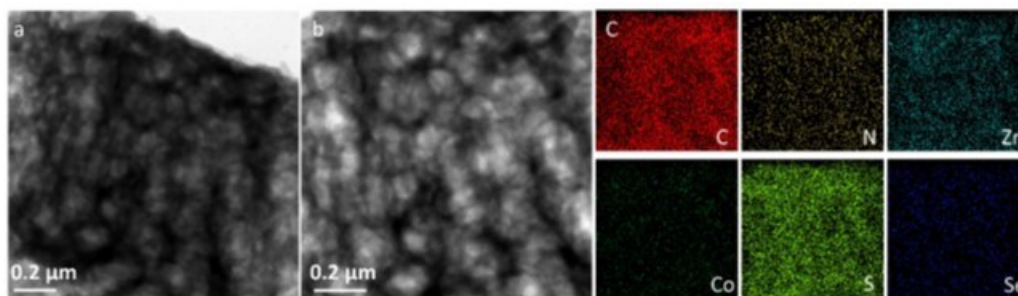


Figure XIV.1.4 TEM image of cycled OMSH-Se/S cathode in HFE-based electrolyte. b, c) TEM image and corresponding EDS elements mappings (C, N, Zn, Co, S, Se) of cycled OMSH-Se/S cathode in HFE-based electrolyte.

ToF-SIMS characterizations of cycled Li metal anode in both electrolytes were further carried out. As shown in Figure XIV.1.3e, in the case of DME-based electrolyte, Se<sup>-</sup> signal can be detected on the surface of cycled Li metal anode. By contrast, no visible Se<sup>-</sup> can be detected on the surface of cycled Li metal anode using HFE-based electrolyte (Figure XIV.1.3g). Moreover, since Li-N and Li-F compounds have been considered the main components of SEI on the surface of Li metal anode, we chose N<sup>-</sup> and F<sup>-</sup> signals as the indicators to analyze the as-formed SEI in two different electrolytes. As shown in Figure XIV.1.3e, both the N<sup>-</sup> and F<sup>-</sup> signals were non-uniformly distributed in conventional DME-based electrolyte, indicating that the as-formed SEI was rather fragile to maintain its shape during cycling. In HFE-based electrolyte, the N<sup>-</sup> and F<sup>-</sup> signals were uniformly distributed (Figure XIV.1.3g), suggesting the formation of robust SEI on the surface of the Li metal anode. Moreover, the ToF-SIMS depth profiles of cycled Li metal anode in both DME- and HFE-based electrolytes further revealed that a layer of F-rich SEI was formed on the surface of Li metal anode in HFE-

based electrolyte. However, in the case with DME-based electrolyte, the gradually increased intensity of F-signal suggests the continuous formation/decomposition process of SEI.

In brief, the synergy of cathode structure tailoring and electrolytes modulation could simultaneously mitigate the shuttle effect and Li dendrite problem in Li-S batteries through tailoring the cathode and anode interface.

### Suppressing Polysulfides Crossover in High-Energy Lithium Sulfur Batteries via a Versatile Interlayer Design

In FY23, we have also designed a versatile and thin ( $\sim 25\ \mu\text{m}$ ) interlayer consisting of multifunctional active sites, with a goal to simultaneously regulate the Li deposition process and suppress the polysulfides crossover (Figure XIV.1.5a). The interlayer contains N-rich core part and wide-spread CoZn dual active sites within a unique yolk-shell framework (denoted as CoZn-YSIL). Therefore, it can effectively regulate the Li deposition even high areal capacity and high current densities. More importantly, the strong binding ability of CoZn dual active sites and the N-rich framework can significantly suppress the detrimental chemical crossover during the long-term cycling.

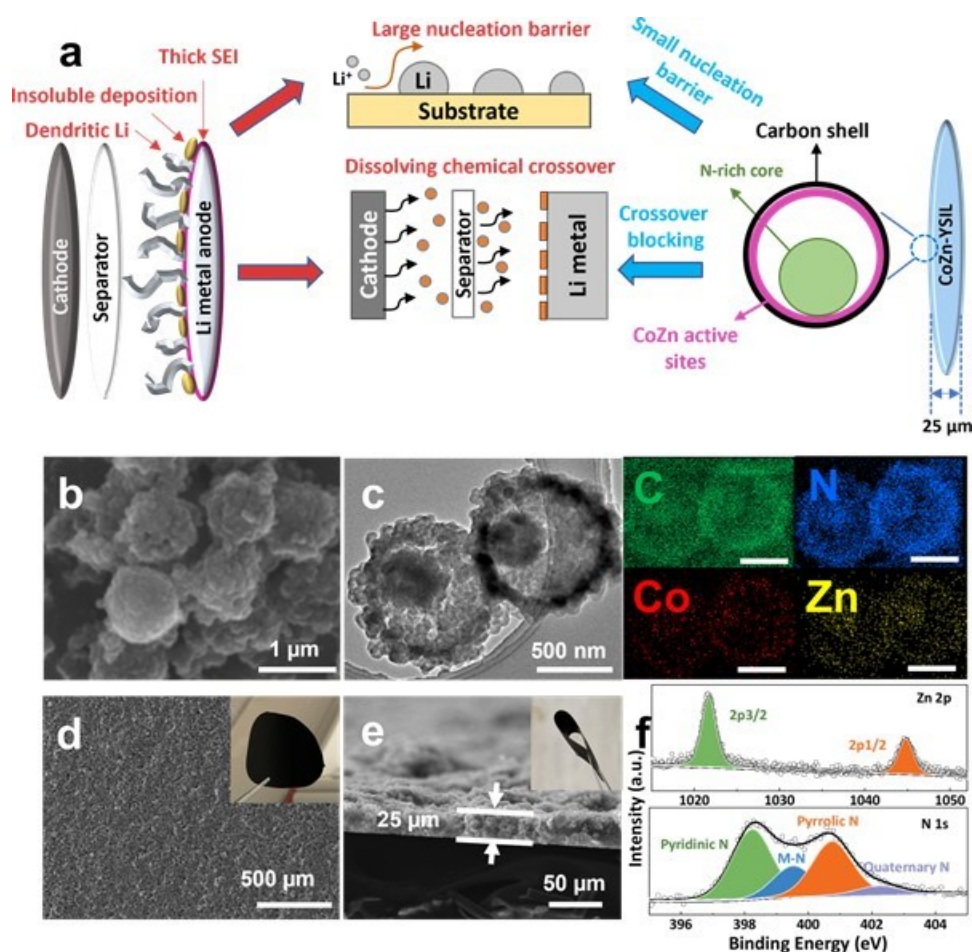


Figure XIV.1.5 (a) Schematic of working principles of CoZn-YSIL in regulating the Li deposition behavior and preventing the Li side reaction with cathode dissolving species. (b) SEM image of CoZn-YSs. (c) TEM image and corresponding EDS element mappings of CoZn-YSs (interesting elements are C, N, Co, and Zn). (d) Top-view SEM image of CoZn-YSIL (inset: digital photograph of CoZn-YSIL). (e) Cross section-view SEM image of CoZn-YSIL (inset: digital photograph of folded CoZn-YSIL). (f) High-resolution Zn 2p and N 1s XPS spectra of CoZn-YSIL.

As characterized by scanning electron microscopy (SEM), the CoZn yolk-shell spheres (CoZn-YSs) exhibit spherical morphology, and the size of the as-prepared CoZn-YSs is measured to be  $\sim 1.0 \mu\text{m}$  (Figure XIV.1.5b). The transmission electron microscopy (TEM) and the corresponding energy dispersive spectroscopy (EDS) in Figure XIV.1.5c further show that a typical yolk-shell structure with a  $\sim 400 \text{ nm}$  diameter core part and a  $\sim 100 \text{ nm}$  thick shell structure can be clearly identified. Moreover, an N-containing framework was successfully constructed, which can improve the  $\text{Li}^+$  affinity of the yolk-shell sphere. Meanwhile, the widespread ZnCo active sites inside the yolk-shell spheres can effectively lower the Li nucleation overpotential and enhance the Li deposition inside the yolk-shell spheres.

After the rolling-pressing process, the free-standing thin film CoZn-YSIL was successfully fabricated. As shown in the top-view SEM image of CoZn-YSIL (Figure XIV.1.5d), the as-fabricated CoZn-YSIL exhibited continuous and uniform surface features. In addition, as shown in the cross-section SEM image and the digital photograph of the CoZn-YSIL (Figure XIV.1.5e), the CoZn-YSIL demonstrated good mechanical strength. The thickness of the interlayer is only  $25 \mu\text{m}$ , which is comparable with the commercial Celgard separator. To further confirm the existence of elementary Zn and N-containing lithiophilic sites inside the CoZn-YSIL, X-ray photoelectron spectroscopy (XPS) characterization was conducted. As shown in Figure XIV.1.5f, the Zn 2p<sub>3/2</sub> (1021.7 eV) and 2p<sub>1/2</sub> (1044.8 eV) can be identified, confirming the existence of elementary Zn. Moreover, the N 1s spectrum was deconvoluted into four peaks at 398.2 eV, 399.5 eV, 400.7 eV, and 402.2 eV, which can be assigned to pyridinic-N, metal-N, pyrrolic-N, and quaternary-N, respectively.

The effectiveness of CoZn-YSIL interlayer has been evaluated in Li-S cells. The interlayer was placed on both anode and cathode side. As shown in Figure XIV.1.6, due to the severe side reaction between Li metal anode and dissolved polysulfides, the areal capacity of bare Li-S cell without the interlayer quickly faded to  $0.67 \text{ mAh cm}^{-2}$  after only 50 cycles, and it can only maintain an areal capacity of  $0.17 \text{ mAh cm}^{-2}$  after 100 cycles. By contrast, the Li-S cell with the CoZn-YSIL can deliver a high initial specific capacity of  $1327 \text{ mAh g}^{-1}$  and areal capacity of  $6.90 \text{ mAh cm}^{-2}$  at  $0.1 \text{ C}$ , and can maintain a high areal capacity of  $5.32 \text{ mAh cm}^{-2}$  after 100 cycles, confirming that the CoZn-YSIL can effectively confine and catalyze the dissolved LiPSs to prevent the side reactions with lithium metal anode.

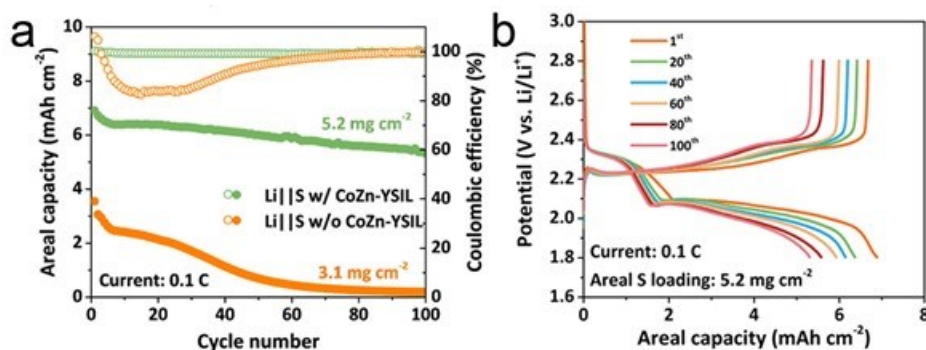


Figure XIV.1.6 Cycling performance of high-loading Li/S cells with and without CoZn-YSIL at the cathode side under the current of  $0.1 \text{ C}$ . (f) Charge and discharge voltage profiles of various cycles of high-loading Li/S cell with CoZn-YSIL under the current of  $0.1 \text{ C}$ .

## Conclusions

We have explored the use of ordered macroporous carbon with double-end binding sites as a sulfur cathode host and an interlayer for Li-S batteries. Combining with fluorinated ether based electrolytes, we show that the shuttle effect and lithium dendrite growth problem could be effectively suppressed, leading to significantly improved cycling stability under high areal S loading, thin Li metal, reduced electrolyte/sulfur ratio and wide temperature, in both coin cells and single-layer pouch cells. Moreover, we have performed a suite of advanced characterization including synchrotron X-ray technique, advanced electron microscopy and surface probes to

reveal the structural evolution during battery cycling. Our results highlight the importance of rational host design and electrolyte formulation to push Li-S batteries towards practical applications.

## Key Publications

### Publications

1. Zhou, S.; Shi, J.; Liu, S.; Li, G.; Pei, F.; Chen, Y.; Deng, J.; Zheng, Q.; Li, J.; Zhao, C.; Hwang, I.; Sun, C.; Liu, Y.; Deng, Y.; Hung, L.; Qiao, Y.; Xu, G. L.\*; Chen, J. F.; Amine, K.\*; Sun, S. G.; Liao, H.\*. Visualizing Interfacial Collective Reaction Behaviour of Li-S Batteries. *Nature*, 2023, 621, 75-81.
2. Zhao, C.; Amine, K.\*; Xu, G. L.\* Non-traditional Approaches to Enable High-Energy and Long-Life Lithium-Sulfur Batteries. *Acc. Chem. Res.* 2023, 56, 2700-2712.
3. Xie, C.; Zhao, C.; Jeong, H.; Li, T.; Li, L.; Xu, W.; Yang, Z.; Lin, C.; Liu, Q.; Cheng, L.; Huang, X.; Xu, G. L.\*; Amine, K.\*; Chen, G.\* Suppressing Universal Cathode Crossover in High-Energy Lithium Metal Batteries via a Versatile Interlayer Design. *Angew. Chem. Int. Ed.* 2023, e202217476.

### Presentation

1. Gui-Liang Xu and Khalil Amine. Advance high-energy and long-life lithium-sulfur batteries: from fundamental to application. Invited talk at Lawrence Livermore National Laboratory. Sep 1<sup>st</sup>, 2023.
2. Xu, G. L. and Amine, K. Novel Chemistry: Lithium Selenium and Selenium Sulfur Couples. The 2023 Vehicle Technologies Office (VTO) Annual Merit Review, June 12-15, 2023
3. Gui-Liang Xu. "Advanced Cathode, Electrolyte and Interlayer Strategies to enable High Energy Li S Batteries." Invited presentation at the 2023 SAE Battery and Electrification Summit, April 4, 2023 - April 5, 2023
4. Gui-Liang Xu and Khalil Amine. "Advanced lithium-ion batteries and beyond for automotive application." Invited Institutional Talk at University of Illinois - Chicago, Mar 2, 2023
5. Gui-Liang Xu. "Advanced Cathode, Electrolyte and Interlayer Strategies to enable High Energy Li S Batteries." Invited presentation at the 2023 American Chemical Society Spring Meeting, Indianapolis, Mar 26-30, 2023.

### Patents

1. Method of electrolyte-less batteries. Chen Zhao, Gui-Liang Xu and Khalil Amine. Patent invention (ANL-22-150).
2. Gui-Liang Xu, Jianzhao Liu, Zonghai Chen and Khalil Amine. Poly(alkylene oxide) siloxane-based electrolytes for rechargeable batteries. US11,769,905 B2. Date of Patent Sep 26, 2023.

## References

1. Z.W. Seh, Y. M. Sun, Q. F. Zhang, and Y. Cui. "Designing High-Energy Lithium-Sulfur Batteries." *Chemical Society Reviews* 45, no. 20 (2016): 5605-34. DOI:10.1039/c5cs00410a.
2. A. Abouimrane, D. Dambournet, K. W. Chapman, P. J. Chupas, W. Weng, and K. Amine. "A New Class of Lithium and Sodium Rechargeable Batteries Based on Selenium and Selenium-Sulfur as a Positive Electrode." *Journal of the American Chemical Society* 134, no. 10 (2012): 4505-08. DOI: 10.1021/ja211766q.
3. Y. Cui, A. Abouimrane, J. Lu, T. Bolin, Y. Ren, W. Weng, C. Sun, et al. "(De)Lithiation Mechanism of Li/SeS<sub>x</sub> (X = 0-7) Batteries Determined by in Situ Synchrotron X-Ray Diffraction and X-Ray Absorption Spectroscopy." *Journal of the American Chemical Society* 135, no. 21: 8047-56. DOI: 10.1021/ja402597g.

## Acknowledgements

Support from Tien Duong of the U.S. DOE's Office of Vehicle Technologies Program is gratefully acknowledged. Use of the Advanced Photon Source, an Office of Science User Facility operated for the DOE Office of Science by Argonne National Laboratory, was supported by DOE under contract no. DE-AC02-06CH11357. We would like to thank our team members and collaborators at Argonne National Laboratory

who made significant contribution to this project, including Guiliang Xu, Chen Zhao, Chengjun Sun, Inhui Hwang, Wenqian Xu, Tianyi Li, Luxi Li, Lei Cheng and Heonjae Jeong.

## XIV.2 Development of High Energy Lithium-Sulfur Batteries (PNNL)

### **Dongping Lu, Principal Investigator**

Pacific Northwest National Laboratory  
902 Battelle Blvd.  
Richland, WA 99354  
E-mail: [dongping.lu@pnnl.gov](mailto:dongping.lu@pnnl.gov)

### **Lili Shi, Co-Principal Investigator**

Pacific Northwest National Laboratory  
902 Battelle Blvd.  
Richland, WA 99354  
E-mail: [lili.shi@pnnl.gov](mailto:lili.shi@pnnl.gov)

### **Tien Duong, DOE Technology Development Manager**

U.S. Department of Energy  
E-mail: [Tien.Duong@ee.doe.gov](mailto:Tien.Duong@ee.doe.gov)

Start Date: October 1, 2015

End Date: September 30, 2024

Project Funding (FY23): \$300,000

DOE share: \$300,000

Non-DOE share: \$0

### **Project Introduction**

Lithium-sulfur (Li-S) battery has a high theoretical energy and low cost, making it one of the most promising battery technologies to meet the DOE battery cost target of < \$80/kWh for vehicle electrification. Despite advances in Li-S battery, deployment of the technology is still hindered by the low practical energy and limited cycle life. Achieving a high energy Li-S cell is feasible only through the simultaneous integration of a high-loading S cathode, thin Li anode, and most importantly a very lean amount of electrolyte. However, a simple combination of these parameters in a high-energy cell often leads to both a low reversible capacity and a very limited cycling life. Clear understanding of fundamental mechanisms of the cell failure at realistic conditions still need more efforts. Our study of high-energy Li-S pouch cells indicates that 1) electrolyte amount has a nearly linear correlation with the cumulative cell capacity (i.e., overall capacities delivered during the lifespan); and 2) electrolyte diffusion/ redistribution is hindered by the high tortuosity sulfur electrodes, which leads to the reaction heterogeneity and accelerated cell-failure. To improve cell cycle life and maintain high energy density of the cell at the same time, new designs of materials and electrode architectures addressing the above issues are essentially needed. Rational designs should be targeted to increase effective electrolyte supply, facilitate electrolyte infiltration and distribution, reduce electrolyte consumption, maintaining a durable Li-ion conduction network under realistic cell operation conditions. First, reducing electrode porosity is critical to conserving more electrolyte for cell cycling. For a given areal capacity, sulfur cathodes are much thicker and more porous (>60%) compared to the dense Li-ion battery cathodes due to the use of low density and porous S/C materials. This severely diminishes cell energy while also requiring more electrolyte for pore filling. However, reducing electrode porosity through direct pressing proves challenging if using the materials originally designed for highly porous cathodes. This is because the electrodes featuring low porosity and high tortuosity have slow electrolyte diffusivity, reducing the sulfur reaction kinetics and utilization rate. Therefore, a clear understanding of the effect that electrode porosity/tortuosity has on the electrolyte transport, sulfur reaction kinetics and cell life is critical for the rational design of materials and electrode architectures. Approaches that reduce the tortuosity in a low-porosity cathode are required to ensure the quick electrode wetting. Second, Li-ion conduction pathways should be maintained by either developing stable electrolytes/additives or through building durable quasi-solid Li<sup>+</sup> conduction networks. So far, the ether-based liquid solutions combined with LiNO<sub>3</sub> additive remain the most viable option for Li-S electrolytes. However, consumption and depletion continue through chemical and electrochemical reactions. The “non-solvating” electrolytes, localized concentrated electrolytes, and solid electrolytes received widespread attention for

prolonging the cycle life of the Li metal batteries. These electrolytes may also be helpful in Li-S cells but need an optimal electrode architecture that can take advantages of novel electrolytes.

The objective of this project is to develop high-energy Li-S batteries with a long lifespan. In FY23, we focused on the development of cathode materials, electrode architecture, and processing to realize operation of low-porosity electrodes at very lean electrolyte conditions.

### Objectives

- Realize S utilization rate  $>1100$  mAh/g in low-porosity (porosity  $\leq 40\%$ ) and high-loading ( $> 4$  mg cm<sup>-2</sup>) S electrodes through optimization of materials and electrode architectures.
- Scale-up preparation of the optimized materials and high-loading and dense sulfur electrodes to support Li-S pouch cell demonstration and evaluation.

### Approach

1. Study effects of cathode architecture/topography on sulfur reactivity and reaction uniformity under conditions of high-mass-loading cathode and lean electrolyte conditions.
2. Investigate the effects of cathode architecture on Li plating/stripping and cell cycling stability at practical conditions.
3. Understand electrolyte transport and sulfur reactions in high-loading and low-porosity electrodes.
4. Develop secondary-phase electrolyte reservoir into the dense electrode to extend cell cycle life.

### Results

#### **1. Fabricated model electrodes with controlled architecture/topography to study their effects on sulfur reactivity and reaction uniformity at high-mass-loading electrode and lean electrolyte conditions ( $>4$ mg/cm<sup>2</sup>, E/S $<4$ mL g<sup>-1</sup>)**

It is well-known that lithium (Li) plating during the charging of lithium-sulfur (Li-S) batteries is affected by the local current density, Li-ion concentration gradient, and electrolyte mass transfer, etc. Thus, any change in these factors would affect the morphology of the Li plating and cell cycle life. This is particularly important in Li-S cell, because S cathode are not only highly rough and porous, but also involve dynamic redistribution of S species during discharging/charging. To study the impact of the cathode structure on Li growth and cycling, the patterned sulfur cathodes (PSC), which have patterned surface structures, were prepared to represent the amplified rough surface and were studied at practical high S loading and lean electrolyte conditions. The PSC with a S loading of 6 mg cm<sup>-2</sup> was prepared by applying a double-layer coating using aluminum (Al) mesh as a template for the second layer coating (Figure XIV.2.1a). Copying the Al mesh template, the PSC showed diamond-shaped peak regions (PR) and linear valley regions (VR) (Figure XIV.2.1b and c). The optical profilometry measurement indicates that the PR resides  $\sim 60$   $\mu\text{m}$  higher than the VR, and the average roughness of the whole electrode is  $\sim 25$   $\mu\text{m}$  (Figure XIV.2.1 d and g). For comparison, the baseline S cathode (BSC) without any patterns was also prepared, which has an overall flatter surface (Figure XIV.2.1e) and an average surface roughness of 20  $\mu\text{m}$  (Figure XIV.2.1f). The BSC and PSC were assembled into coin cells and tested under lean electrolyte conditions (E/S=4 mL g<sup>-1</sup>) (Figure XIV.2.1h). It was found that compared to PSC, the BSC showed higher specific capacity and a longer cycle life under the lean electrolyte conditions. The charge failure occurred after 563 hours' cycling. However, in the PSC cell, the cell failure occurred much earlier during the fourth cycle ( $\sim 70$  hours), featuring an internal short circuit (ISC) (highlighted in grey in Figure XIV.2.1h). The cell was recovered after a prolonged and fluctuated charge cycle, indicating the occurrence of a micro or soft ISC. Despite the recovery, the cell failed after 303 hours of cycling. Increasing the electrolyte amount (E/S ratio) helped extend the cycle life for both electrodes (results were not shown here), but the trend in charge failure, i.e., PSC had much shorter cycle life than BSC, remained the same. This suggests the prevailing role of S electrode topography in cell cycling, where a rougher surface leads to quicker formation of Li dendrites, and thus earlier cell failure.

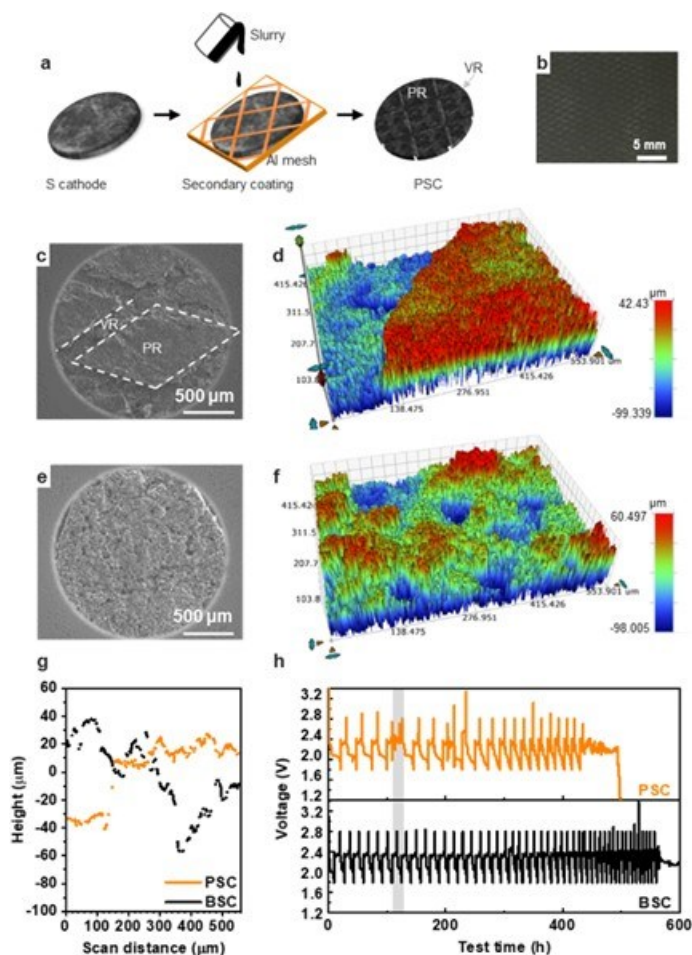


**Figure XIV.2.1** (a) Schematic illustration of PSC preparation. (b) Digital photograph of the PSC, Scanning Electron Microscope (SEM), and surface profilometric images of PSC (c and d) and BSC (e and f). The color from blue to red represents the height from low to high. (g) X line-scan profiles of PSC and BSC. (h) Discharge and charge profiles of the PSC and BSC upon cycling at an E/S of  $4 \text{ mL g}^{-1}$ . The grey bar highlights the early occurrence of ISC in PSC.

Based on the understanding, any approaches that could homogenize cathode reactions and lower the variation of local currents would help to delay or even eliminate an ISC event, thereby extending cell cycle life. Control of electrode topography is one of the most straightforward ways to accomplish this. To verify its effectiveness, a mild calendared electrode with a smoother surface was prepared. Only 10% compression was used to prepare the compressed S cathode (CSC) and the measured average roughness was decreased by 20% compared to that of BSC (Figure XIV.2.2a). Without calendaring, the BSC failed by ISC at 557 and 570 hours (Figure XIV.2.2b, d) at a S loading of  $6 \text{ mg cm}^{-2}$  and  $4 \text{ mg cm}^{-2}$ , respectively. Promisingly, the CSC shows a significantly improved cycle life from 557 h to 790 h at the same E/S of  $4 \text{ mL g}^{-1}$  (Figure XIV.2.2b). By lowering the areal loading from 6 to  $4 \text{ mg cm}^{-2}$ , the cycle life improvement was even more profound, improving by 124% to 1251 h (Figure XIV.2.2c and d). This further proves the importance of electrode topography on cell cycle life, where high electrode uniformity and low roughness are desired for long cycling Li batteries. These understandings and improvement have been incorporated to the Li-S pouch cell assembly and test.



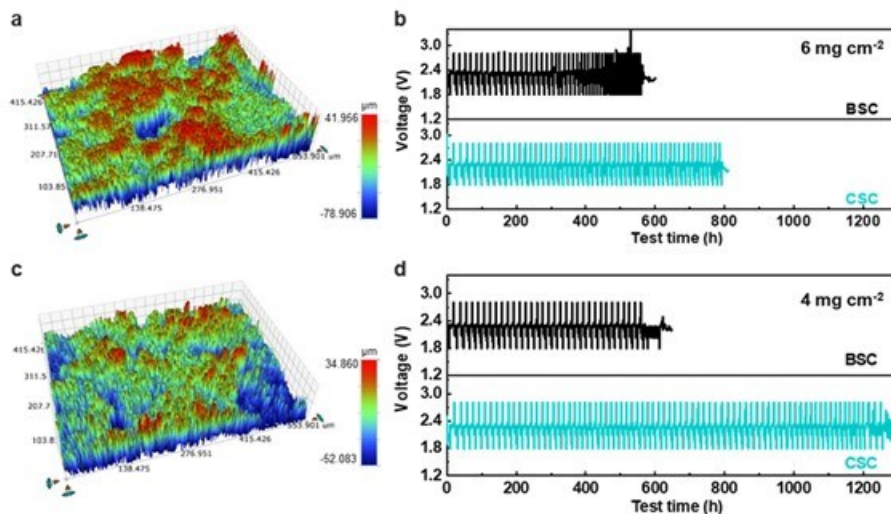


Figure XIV.2.2 Optical profilometric images of CSC at S loading of  $6 \text{ mg cm}^{-2}$  (a) and  $4 \text{ mg cm}^{-2}$  (c). Discharge and charge profiles of the BSC and CSC at S loading of  $6 \text{ mg cm}^{-2}$  (b) and  $4 \text{ mg cm}^{-2}$  (d) in  $E/S = 4 \text{ mL g}^{-1}$ .

## 2. Investigated the effects of cathode architecture on Li plating/stripping and cell cycling stability at practical conditions and mechanism behind.

To understand the effects of cathode topography on Li electrodeposition, the Li anodes before and after cycling with the surfaced patterned sulfur cathode (PSC) were analyzed at three scenarios: (1) the pristine Li anode before assembly, (2) after assembly into a coin cell with the PSC before cycling, and (3) after cycling with the PSC. The pristine Li anode showed a flat and smooth surface (Figure XIV.2.3 a and d). After cell assembly with the PSC, the cathode morphology imprinted onto the Li anode, showing diamond-shaped dents, and raised lines. This means that the diamond-shaped region of the cathode have better contact with Li metal due to the higher local pressure (Figure XIV.2.3b and e). After cycling, the Li from the diamond dents transformed into diamond peak region (PR) (Figure XIV.2.3 c, f, g), suggesting extensive reactions and volume expansion. SEM characterizations indicated the PR regions were very porous and composed of entangled powders and wires (Figure XIV.2.3h), while the linear valley regions (VR) remained flat and dense as the pristine Li (Figure XIV.2.3i). The chemical compositions of the PR and VR were further analyzed by XPS (not shown). More C, O, and S species were identified in PR than in the VR. These results suggest that because of the better contact, the Li with better contact with the cathode participated more in the Li striping/plating and thus in more side reactions with the electrolyte, thereby generating significant volume expansion.

To understand Li anode evolution and the local current density ( $i_{\text{local}}$ ) distribution when working with a rough cathode, a two-dimensional Li-S cell including mass and charge transport were simulated (Figure XIV.2.4). A part of PSC containing both VR and PR was extracted and used as the cathode topography (Figure XIV.2.4). First, a simplified model was used to study the effect of cathode topography where the cathode and anode were assumed as reaction surfaces. The distance between the cathode and anode affects the electrical field and the electromigration. As Figure XIV.2.4b shows, the  $i_{\text{local}}$  of the cathode is directly correlated to the cathode topography. During the first discharge ( $t=5 \text{ h}$ ), the  $i_{\text{(PR,cathode)}}$  was averagely higher than  $i_{\text{(VR,cathode)}}$ , especially in the junction region that a more than three times  $i_{\text{(junction,cathode)}}$  of  $i_{\text{(VR,cathode)}}$  was observed. For the anode surface, although the cathode topography heterogeneity was buffered by the porous separator, the  $i_{\text{(PR,anode)}}$  was still higher than  $i_{\text{(VR,anode)}}$  (Figure XIV.2.4d). During the subsequent charging process ( $t=15 \text{ h}$ ), although the  $i_{\text{(local,cathode)}}$  was not changed much, the anode current density differences ( $i_{\text{(PR,anode)}} - i_{\text{(VR,anode)}}$ ) became larger, suggesting the current density heterogeneity on the anode is exacerbated upon the cycling. This heterogeneity of current density causes the uneven Li plating (Figure XIV.2.4c). More Li plated on the PR than VR, causing the boundary of PR of Li moves much closer to the cathode than VR after one cycle ( $t=20 \text{ h}$ , Figure XIV.2.4c). These results were consistent with the SEM characterization (Figure XIV.2.4f). A similar current distribution and morphological evolution trend was confirmed on cathode and anode by using a more

detailed model where both a porous cathode and polysulfide dissolution were considered (not shown here). Based on the study of cathode topography and its effects on the Li anode, a sulfur cathode and Li anode crosstalk mechanism was proposed. Given the high porosity and roughness of the S cathode, there are always high and low regions distributed locally along the electrode surface (Figure XIV.2.4e). When the soft Li foil is used as the anode, the rough cathode easily creates indentations on the Li anode surface under pressure during cell assembly (Figure XIV.2.4f), causing uneven contact between the two electrodes. These highly indented regions have better contact and thus smaller local resistance. While for the valley regions, loose contact, even small gaps, may exist locally, resulting a higher local resistance. When current is applied, electrochemical reactions will preferentially occur along the lower resistance regions, resulting uneven Li stripping/plating, as observed by SEM (Figure XIV.2.3). This leads to local Li volume expansion and pulverization, and thus causes electrolyte redistribution, which further exacerbates variation of local resistance and current density (Figure XIV.2.4g). Under certain circumstances, Li dendrites may be formed at locations having extremely high local current densities (Figure XIV.2.4h).

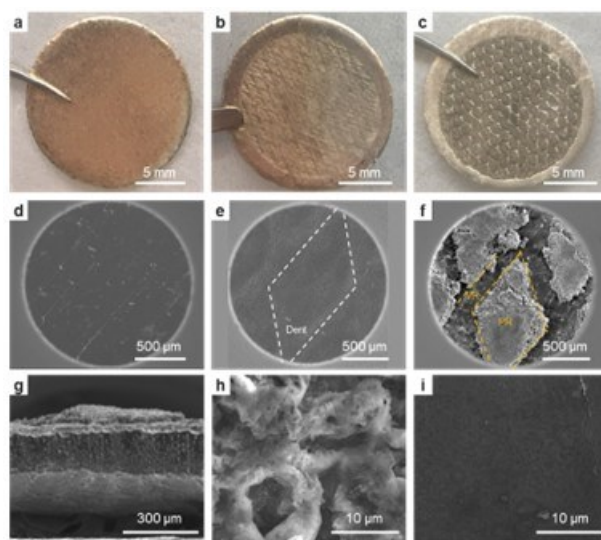


**Figure XIV.2.3** Digital photographs (a-c) and SEM images (d-i) of the pristine Li anode (a and d), the Li anode after assembly but before cycling (b and e), and the Li anode after cycling with PSC (c, f-i). (g) Cross-section of (f). Higher-resolution images of PR (h) and VR (i) of (f).

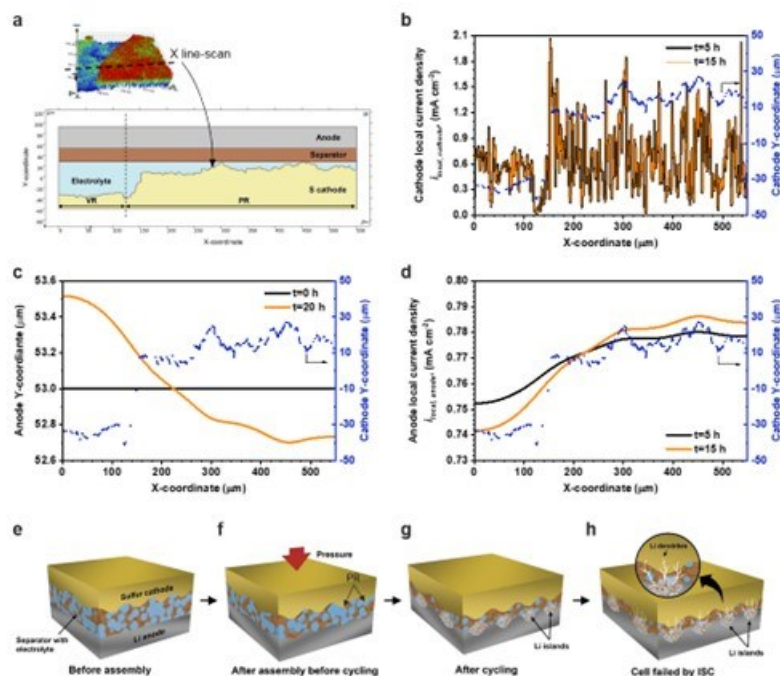


**Figure XIV.2.4** Simulation (a-d) and schematic illustration (e-f) of the  $i_{local}$  distribution and Li anode evolution in the Li-S cell with a rough cathode. (a) Geometry of the model. (b)  $i_{local,cathode}$  distribution. (c)  $i_{local,anode}$  distribution in the first discharge ( $t=5$  h) and charge ( $t=15$  h).  $t=0-10$  h is the first charge.  $t=10-20$  h is the first discharge. (d) The moving boundary of Li anode at the beginning ( $t=0$  h) and the end of first cycle ( $t=20$  h). (e) The rough cathode, separator, and Li metal anode before they are assembled in a cell. (f) The rough cathode imprints its pattern on the soft Li metal anode. (g) During cycling, Li islands form in the PR protruding from Li metal anode. (h) Sharp Li metal dendrites penetrate through the separator causing an ISC.

### 3. Understood electrolyte transport and S reactions in high-loading and low-porosity electrodes through 3D electrode modeling.

Direct use of a low-porosity cathode for Li-S battery results in poor electrode wetting, nonuniform electrode reactions, and thus early cell failure. To understand and mitigate the barriers associated with the use of low-porosity electrodes, in this quarter, we performed multiscale modeling to predict electrode wetting, electrolyte diffusion, and their impacts on sulfur reactions in Li-S cells by explicitly considering the electrode wettability impacts and electrode morphologies.

For practical high-mass-loading sulfur electrodes, the nonuniform distribution of electrolytes is one of the most challenging issues, particularly for low-porosity electrodes. The absence of electrolytes in local regions (i.e., electrode wetting issue) can potentially reduce sulfur reaction kinetics and utilization rate. The previously reported numerical models focus on the ideal condition of high porosity ( $>70\%$ ) or do not consider electrolyte wetting. Under those conditions, the electrode is “ideally” assumed to be fully wetted with constant sulfur loading and mass transport properties along all directions. However, this condition is not true in the realistic conditions of high sulfur loading and low-porosity electrodes (e.g.,  $\sim 45\%$  porosity), electrolyte wetting becomes a limiting factor. To bridge the gap between practical needs and models, we proposed a new multiscale modeling approach (Figure XIV.2.5) for a Li-S battery with low-porosity electrodes and correlated it to the experimental results at the same conditions. In the proposed framework, three-dimensional (3-D) pore-scale model has been integrated with the 1-D device-scale electrochemical model to investigate the effects of cathode structure on the battery performance. The 3-D pore-scale model simulates the electrolyte infiltration process with multiphase Computational Fluid Dynamics (CFD) to inform the 1-D electrochemical model of the electrode wetting and electrolyte-distribution conditions. With that information, the effective species-diffusion coefficient, electrode specific area, and other related parameters become a function of the electrolyte wetting

conditions along the cell thickness direction. Informed by the 3-D electrode model, the 1 D device-scale model then calculates the electrochemical reactions of sulfur species inside the partially wetted electrode at different locations. The multiscale model explicitly considers the electrode wettability impact and electrode morphology change to predict the Li-S battery performance. With this integration, the developed multiscale Li-S model can help us understand the advantages and trade-offs of low-porosity electrodes and help optimize the sulfur electrode design.

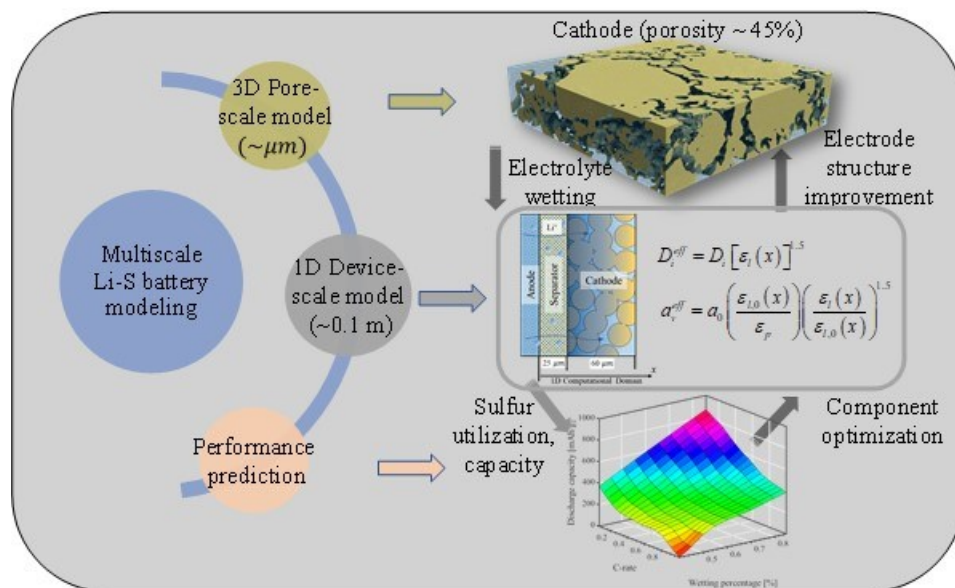


Figure XIV.2.5 Strategy for multiscale model development for a Li-S battery.

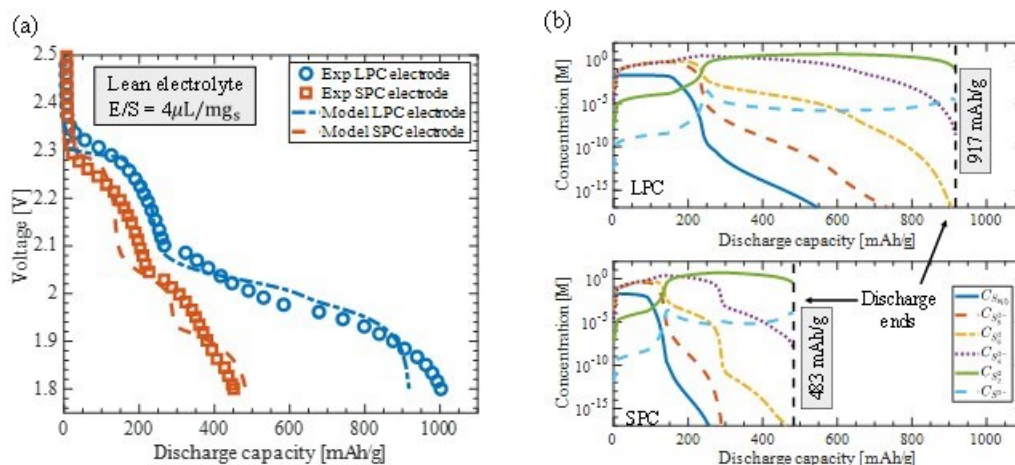


Figure XIV.2.6 (a) Comparison of the Li-S discharge curves between experimental data and the multiscale model for the 20  $\mu\text{m}$  and 90  $\mu\text{m}$  electrodes at 0.1C. (b) The polysulfides concentration profiles during the discharge for both LPC (up) and SPC (down).

Through the multiscale modeling approach, the Li-S discharging behavior in low porosity electrode was predicted and compared with experimentally measured discharge curves (Figure XIV.2.6). Two types of sulfur/carbon particles were used for electrodes: large particle cathode (LPC, 90  $\mu\text{m}$ ) and small particle cathode (SPC, 20  $\mu\text{m}$ ). As shown by experimental curves, cells with LPC and SPC at a 45% porosity achieve a specific capacity of 1001 mAh/g and 451 mAh/g, respectively, at a discharge rate of 0.1C. The model-predicted discharge curves match the experimental curve with a discharge capacity difference under 9%. The

two typical discharge plateaus are observed in both experimental and simulation curves in the LPC. With a low-porosity electrode, the lower plateau in the discharge curve has an inclined slope, and the voltage drops from 2.1 V at a capacity of 250 mAh/g to 1.93 V at a capacity of 900 mAh/g before a sharply decreasing tail appears at the end of discharge. The multiscale model can capture these decrease trends by considering the electrode morphology and electrolyte distribution factors. Figure XIV.2.6b shows the polysulfides concentration profiles during the whole discharge process. In the LPC, the  $S_{8(l)}$ ,  $S_8^{2-}$  and  $S_6^{2-}$  concentrations show a drastic decrease at around 200 mAh/g, which corresponds to the higher plateau transition to the lower plateau in the discharge curve. At this stage, all the accessible sulfur is dissolved and converted to polysulfides. After 250 mAh/g, the  $S_4^{2-}$  becomes one of the important species that dictate the lower plateau voltage trends. The  $S_2^{2-}$  remains a relatively constant concentration during the lower plateau regions in the discharge process. At the end of discharge, the data from the multiscale model predicted that the voltage decreases to 1.8 V earlier than the experimental data. The multiscale model calculates the species diffusion properties following Bruggeman's correlation, which assumes the electrode particles are nearly spherical. With the deposition of  $Li_2S$  inside the low-porosity electrode, the electrode structure can change noticeably, making it possible to deviate from Bruggeman's correlation. The  $Li_2S$  precipitation microstructures can vary at different operation conditions, which results in a change of the discharge curve tails. For the SPC with 20  $\mu m$  secondary particles, the battery specific capacity is more significantly decreased. The two plateaus become much narrower than seen from the LPC. Specifically, the high plateau region from the multiscale model matches well with the experimental discharge profile. For the lower plateau region, blockage of the pores becomes more severe when the  $Li_2S$  solid deposition starts to occur inside the narrow pore channels, thus leading to early termination of the discharging process. Those voltage curve trends are also reflected in the SPC polysulfides concentration profiles as shown in Figure XIV.2.6 b. Because of the entangled evolutions of electrolyte distribution, electrode passivation, and pore blockage, it has been very challenging to effectively predict the second discharge plateau in a Li-S battery. Through this multiscale model, the prediction of the second discharge plateau was successfully achieved with decent accuracy, further indicating the necessity of incorporating the input of the 3-D electrode for an electrochemical simulation, which is used to guide experimental optimization of electrodes.

#### ***4. Developed secondary-phase electrolyte reservoir for the dense electrode to extend cell cycle in high loading electrodes at lean electrolyte conditions***

Fabricating high-volumetric-energy sulfur (S) cathodes through direct calendaring often leads to low S utilization rate and reaction kinetics, due to the reduced electrode porosity and tortuosity that hinder electrolyte infiltration and uptake. To overcome this challenge, previous methods have created low tortuosity vertically aligned channels by freezing drying, magnetic templates or laser patterning, but at the cost of increasing electrode porosity. We propose a novel strategy of introducing a liquid electrolyte reservoir additive into the electrode structure during fabrication, which can enhance electrolyte infiltration and storage to facilitate sulfur conversion reactions and cycling. The additive reservoir is a polymeric material that has high affinity with the ether-based liquid electrolyte. Before cell operation, the additive reservoir helps electrolyte infiltration into the electrode after electrolyte injection. During electrode wetting, the additive interacts with the liquid electrolyte, dissolves or swells, and forms a semi-solid interfacial layer that covers the active S/C particles along with other polymeric binder. With this approach, the sulfur cathode with a very low porosity of 30% can still deliver a large discharge capacity of  $\sim 1100$  mAh/g under very lean electrolyte conditions, doubling the volumetric capacity of the sulfur cathode from 612 to 1262 mAh  $cm^{-3}$ . Micro computed tomography (Micro-CT) was used to analyze the structure of electrodes both with and without the additive (Figure XIV.2.7). The baseline electrode was fabricated by mixing the S/C active materials with a polymeric binder Polyacrylic Acid (PAA) (10 wt.%). The additive-contained electrode, on the other hand, was prepared by substituting 40% of PAA with the additive reservoir. In the baseline electrode, the presence and distribution of PAA binder can be identified by micro-CT due to its lower contrast compared to S/C. It is evident that PAA aggregates are present not only on the surface of S/C particles but also within the voids/channels throughout the electrode. When 40% of PAA was replaced by the polymeric additive, a similar electrode structure and component distribution were observed. This is because the added polymeric additive has a similar chemistry to PAA, thus it has a similar X-

ray contrast. However, after rinsing the electrodes in liquid electrolyte (1M LiTFSI/DOL/DME), distinct morphologies were observed under Micro-CT. To better compare the electrode components and their distribution, we color-coded the components based on their contrast (red-S/C, yello-PAA, green-voids). It was observed that PAA binder maintains its morphology within the electrode without additive even after contact with liquid electrolyte, due to its stability against the solvent or electrolyte. In contrast, rinsing in liquid electrolyte causes significant changes to the electrode with embedded additive. The original aggregates become fewer and smaller. This is because the used additive is partially soluble or can swell when exposed to liquid electrolyte due to its high affinity. As a result, this would generate a gel-hybrid interface on S/C particle surface. After the electrode was dried and the additive was redistributed across the electrode framework but with a more loose or amorphous morphology, which could not be clearly detected by micro-CT. The high electrolyte affinity to electrolyte and morphology evolution would enhance electrode wetting and help to trap electrolyte within the electrode architecture.

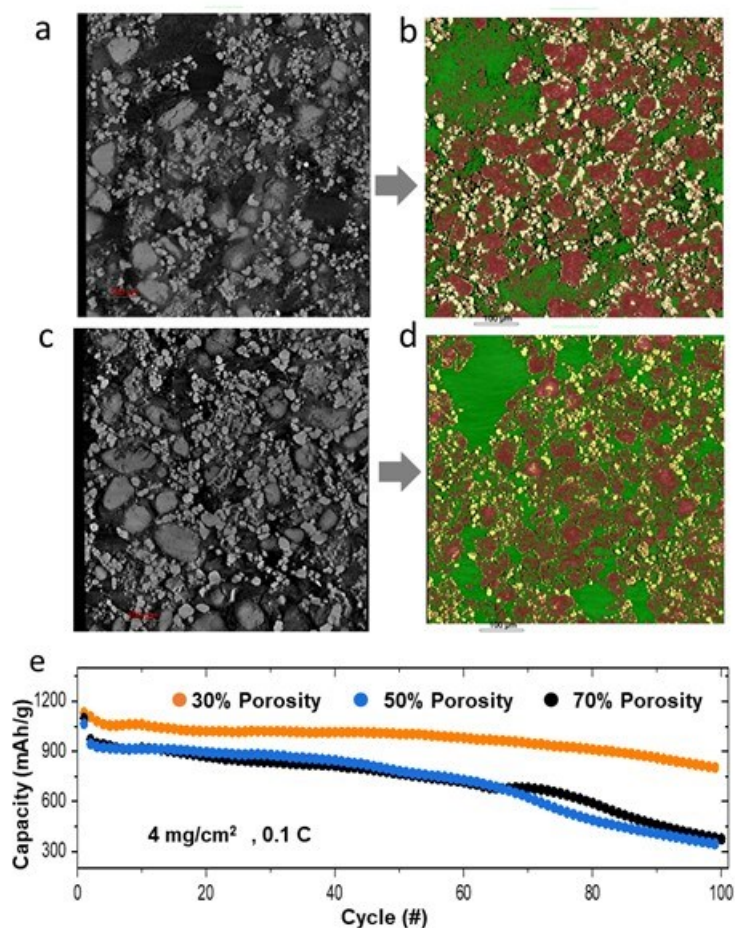


**Figure XIV.2.7** Micro-CT characterization: sulfur electrodes without additive (a) before and (b) after rinsed in electrolyte; sulfur electrodes with additive (c) before and (d) after rinsed in electrolyte. (e) Cycling performance of 30% porosity sulfur electrode with additive and comparison with baseline electrodes without additive at 50% and 70% porosities,  $E/S=10 \text{ mLg}^{-1} \text{ S}$ .

By forming a gel-hybrid interface on S/C with additive, we can achieve a balance between enhanced electrolyte wetting and suppressed polysulfide shuttling in low porosity electrodes. Low-porosity sulfur electrodes have several advantages. First, they require less pore-filling electrolyte at a given E/S ratio, leaving more electrolyte for cell cycling. Second, they block polysulfide diffusion and shuttling. Third, they have a

smooth surface that improves the reaction uniformity of Li anode and delays Li dendrite formation. To verify this, we prepared 30% porosity additive-contained electrodes and compared them with baseline electrodes at 50% and 70% porosities. Of note, the baseline electrode at 30% porosity can be cycled. As shown in Fig. XV.2.7e, the 70% and 50% porosity electrodes both have a rapid capacity drop in the second cycle and the capacity drops to <500 mAh/g after 100 cycles. For the additive-contained electrode with even very low porosity of 30%, a high specific capacity of 1130 mAh/g can be obtained. Moreover, it shows a more stable cycling. After 100 cycles, the reversible capacity is still around 900 mAh/g. This study provides an effective approach to tackle the electrode wetting issue in low-porosity electrodes.

### Conclusions

1. Nitrogen doped secondary carbon particles (NKB) were developed and scaled up for high loading S electrodes; Integration degree of the NKB affects pore structure and connectivity; High specific capacity > 1000 mAh/g was obtained with S loading up to 7 mg/cm<sup>2</sup> and porosity down to 50%.
2. Impacts of electrode architecture/topography on S cathode, Li anode and cell cycling were studied at practical conditions; Rough topography affects electrolyte distribution and cathode reaction heterogeneity; Li anode copies cathode and preferably reacts at the low resistant regions, inducing inhomogeneous Li reaction and early dendrite formation.
3. Multiscale modeling integrating electrode wettability impacts and electrode morphologies was performed to predict electrode wetting, electrolyte diffusion, and their impacts on sulfur reactions at practical cell operation conditions.

### Key Publications

1. Shi L., Anderson C., Liu D., Xiao J., and Lu D., Effects of Sulfur Cathode Topography on Cycling of Practical Li-S Batteries, 242nd ECS Meeting, October 9-13, 2022, Atlanta, GA
2. Feng S., Liu J., Zhang X., Shi L., Anderson C., Lin Y., Song M., Liu J. Xiao J., Lu D. Rationalizing nitrogen-doped secondary carbon particles for practical lithium-sulfur batteries, *Nano Energy*, 2022, 103, 107794.
3. Fu Y., Singh R., Feng S., Liu J., Xiao J., Bao J., Xu Z., Lu D. Understanding of Low-Porosity Sulfur Electrode for High-Energy Lithium-Sulfur Batteries, *Advanced Energy Materials*, 2023, 13, 2203386.
4. Lu D. and Liu J., Development of High Energy Li-S Battery, Department of Energy's (DOE) Vehicle Technologies Office (VTO) Annual Merit Review (AMR), virtually, June 12-15, 2023.
5. Feng S, Fu Y., Shi L. Anderson C. and Lu D., Low-Tortuous and Dense Electrode for High-Energy Lithium-Sulfur Batteries, 243rd ECS Meeting with SOFC-XVIII, Boston, May 28- June 2, 2023.
6. Fu Y, Bao J, Feng S, Singh R, Zeng C, Chen Y, Lu D, and Xu Z, Characterization of Emerging Porous Electrode Designs with High-Fidelity Pore-Scale Models, 243rd ECS Meeting with SOFC-XVIII, Boston, May 28- June 2, 2023.

### Acknowledgements

Shuo Feng, Yucheng Fu, Jie Bao, Zhijie Xu, Jie Xiao, Jun Liu, and Ji-Guang Zhang (PNNL); Venkat Subramanian (The University of Texas, Austin)

## XIV.3 Mechanistic Investigation for the Rechargeable Li-Sulfur Batteries (BNL, U of Wisconsin Milwaukee)

### Enyuan Hu, Principal Investigator

Chemistry division, Brookhaven National Laboratory  
Bldg. 555, Brookhaven National Lab.  
Upton, NY 11973  
E-mail: [enhu@bnl.gov](mailto:enhu@bnl.gov)

### Deyang Qu, Co-Principal Investigator

University of Wisconsin Milwaukee  
3200 N Cramer Street  
Milwaukee, WI, 53211  
E-mail: [qud@uwm.edu](mailto:qud@uwm.edu)

### Tien Duong, DOE Technology Development Manager

U.S. Department of Energy  
E-mail: [Tien.Duong@ee.doe.gov](mailto:Tien.Duong@ee.doe.gov)

Start Date: October 1, 2022

End Date: September 30, 2023

Project Funding (FY23): \$500,000

DOE share: \$500,000

Non-DOE share: \$0

### Project Introduction

Rechargeable lithium-sulfur (Li-S) battery technology have been considered as a potential candidate of beyond Li-ion chemistry to replace the state-of-art Li-ion battery in EV applications, owing to the high theoretical energy density ( $1672\text{mAhg}^{-1}$ ), safety, low cost, and sustainable material resource. The energy density of a Li-S battery could potentially reach 2-3 times higher than that of a state-of-art Li-ion battery. However, to realize the full potential of Li-S chemistry, the “shuttle-effect” problem caused by the dissolved polysulfide ions needs to be solved. On the Li-S cell level, this phenomenon causes high self-discharge rate, low Coulombic efficiency, low active materials utilization, and short cycle life. The dendrite growth and “dead” Li formation on a Li anode are other major technical difficulties.

In the past few years, we have developed the MS-HPLC essays for the quantitative and qualitative identification of dissolved polysulfide ions in various electrolytes. Coupling with in-situ electrochemical method, evolution of the dissolved polysulfides during the battery operation was determined. The mechanisms for the sulfur redox reaction including the equilibrium between dissolved polysulfide ions and elemental sulfur were revealed. As a result, the continuous decay of the capacity during cycling, “shuttle-effect” and high self-discharge rate during the storage are better understood. We also started the investigation of all solid-state Li-S battery (ASSLSB) research considering the electrochemical window of sulfide solid-state electrolyte (SSE) matches that of Li-S chemistry well. We have demonstrated ASSLSB full cells (using either elemental sulfur or small organosulfur compounds) with a long cycle life and high energy density. We concluded that 1) The shuttle-effect can be mitigated by forming short-chain polysulfide (SCP) ions, which are much less reactive than longer chain polysulfide (LCP) ions; 2) Owing to the elastic nature of the materials, small organosulfur compounds are suitable for a large format ASSLSB pouch cell without compromising much energy density in comparison with elemental sulfur cathode and/or polymeric sulfur cathode.

We accomplished the goal of FY 2023. We have demonstrated:

1.  $600\text{mAh g}^{-1}$  capacity in an ASSLSB at  $17\text{ mg cm}^{-2}$  active material loading over 50 cycles.
2. The feasibility of the cell design was demonstrated through a reversible cell breathing.



3. A catalytic carbon host capable of facilitating the disproportionation of dissolved polysulfides into solid  $\text{Li}_2\text{S}_2$  and elemental sulfur was discovered. The distinctive carbon porosity facilitates the uniform deposition of  $\text{Li}_2\text{S}_2$  within the matrix, thereby promoting the catalytic conversion of  $\text{Li}_2\text{S}_2$  to  $\text{Li}_2\text{S}$  in a solid-solid reaction. When integrated into a Li-S pouch cell with a  $1.3 \text{ mg cm}^{-2}$  loading, a Li-S pouch cell with this catalytic carbon host can maintain a  $900 \text{ mAh g}^{-2}$  capacity over 100 cycles. Even at higher loading of  $5 \text{ mg cm}^{-2}$ , it still delivered a  $600 \text{ mAh g}^{-1}$  over 50 cycles.

## Objectives

The primary objectives were as follows:

- To synthesize, optimize and down select small organosulfur electrode for ASSLSBs.
- To investigate the interface and physical compatibility e.g. elasticity between the small organosulfur electrode and solid-state electrolyte.
- To develop surface protective Li anode so it can be compatible with PTFE binder.
- To continue investigating the interaction of polysulfides in the cathode solid phase.

## Approach

In this collaborative project, our primary focus was to complete the investigation of the use of small organosulfur compounds in ASSLSBs. Our efforts extended to scrutinizing and enhancing the interphase between the sulfur, including organo-sulfur cathode, and the electrolyte. Furthermore, we continued our research into developing host and catalytic materials designed to curtail the migration of long-chain polysulfides. The synergy of our collaborative research efforts leveraged the capabilities of BNL's synchrotron-based techniques and UWM's electrochemical analytical tools, allowing us to delve deeper into the intricacies of the sulfur redox reactions occurring in the solid phase.

## Results

### 1) Small OrganoSulfur Compound Cathode.

In FY 2022, we reported the investigation of small organosulfur compounds as cathode materials for an ASSLSB. We down selected thiuram polysulfide as the organic cathode material for ASSLSB application, particularly dipentamethylenethiuram hexasulfide (PMTH) was selected as a representative cathode material. The chemical structure and proposed redox reaction mechanism are shown in Figure XIV.3.1 E. Figure XIV.3.1 D compares the gravimetric energy density of PMTH with the previously reported organic cathodes for Li-organic and organosulfide all solid-state batteries (ASSBs). The PMTH material-level energy density was  $1140 \text{ Wh kg}^{-1}$ , surpassing the records of all literatures. The theoretical capacity of organosulfide could be further improved by devising the end caps and increasing the number of linear S atoms. The electrode-level energy density was  $376.2 \text{ Wh kg}^{-1}$ , which was the highest among sulfide-based ASSBs but the second highest when compared with solid-polymer electrolytes (SPE)-based ASSBs. This is due to the lightweight property of SPEs compared with sulfide electrolytes. To further enhance the electrode-level energy density of PMTH, future work can reduce the SSE fraction within the composite cathode through adopting more ionically conductive sulfide SSEs. The comparison of the discharge and recharge profiles of moderate PMTH loading electrode ( $2 \text{ mg cm}^{-2}$ ) and high PMTH loading electrode are shown in Figure XIV.3.1 A and Figure XIV.3.1 B. The cell was cycled at  $60^\circ\text{C}$  and  $0.03 \text{ C}$  rate. A good capacity can be achieved in both moderate and high loading. In addition, a good rate performance is demonstrated in Figure XIV.3.1 C.

One of the major advantages of using organosulfur compounds in an ASSLSB is the elasticity of the organic material, which is critical to maintaining a good interface between the cathode and SSE during the volume change. Galvanostatic intermittent titration technique (GITT) and electrical impedance spectra (EIS) were employed to study the evolution of cathode interface during cycling. A series of current pulses were applied to the cell, followed by a 4 h relaxation for each step. As shown in Figure XIV.3.2 a, the voltage polarization ( $\Delta V$ ) of each current pulse was estimated from the relaxation curve. The voltage polarization shown in Figure XIV.3.2 b decreases slightly at the beginning followed by a drastic increase at the end of a charging and a discharging process, especially for the latter. The voltage polarization is the sum of  $iR$  drop and a relaxation

process. The former is caused by the ohmic resistance and the charge transfer resistance at the cathode|SSE interface while the latter is a process that  $\text{Li}^+$  concentration tends to reach an equilibrium.

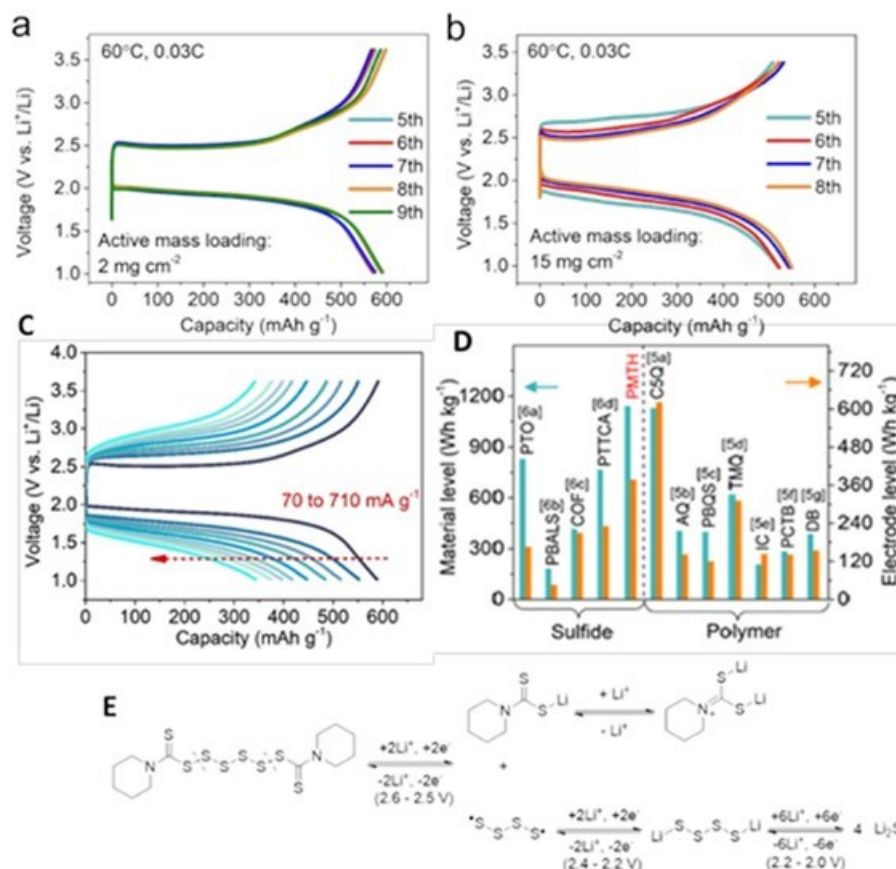


**Figure XIV.3.1** The performance of PMTH|Li<sub>6</sub>PS<sub>5</sub>Cl|Li cell under A) moderate active mass loading condition; B) high active mass loading condition; C) Charge/discharge profiles of PMTH|Li<sub>6</sub>PS<sub>5</sub>Cl|LiIn cell at different current densities at 25 °C; D) Energy density comparison of the state-of-the-art organic cathodes reported in Li-organic ASSBs; E) Proposed reaction mechanism for PMTH cathode during battery operation.

EIS spectra were collected every 3 hours sequentially during a complete discharge/recharge cycle at 0.07C. As shown in Figure XIV.3.2 c, the overall impedance decreases gradually at first followed by an increase when approaching the cut-off potentials. The cell impedance reached the highest level at the lower cut-off potential, which was consistent with the GITT result. The increased polarization during charging can be assigned to a partial oxidation of Li<sub>6</sub>PS<sub>5</sub>Cl, forming S, LiCl, Li<sub>3</sub>PS<sub>4</sub>, and P<sub>2</sub>S<sub>5</sub> as decomposition products. Such oxidative degradation is inevitable in a Li-organosulfide cell, due to their largely overlapped potential ranges. The increased polarization upon discharging, however, is attributed to a partial reduction of Li<sub>6</sub>PS<sub>5</sub>Cl, forming Li<sub>3</sub>P, Li<sub>2</sub>S, and LiCl as decomposition products. As marked by the purple arrow in Figure XIV.3.2 c, the impedance spectra at the lower cut-off potential between two consecutive cycles remains almost unchanged, implying a reversible evolution of the cell impedance collectively. Since the cathode side contributed to the majority of overall cell impedance, the evolution of cathode interfacial layer was reversible, consistent with the conclusion made in previous study.

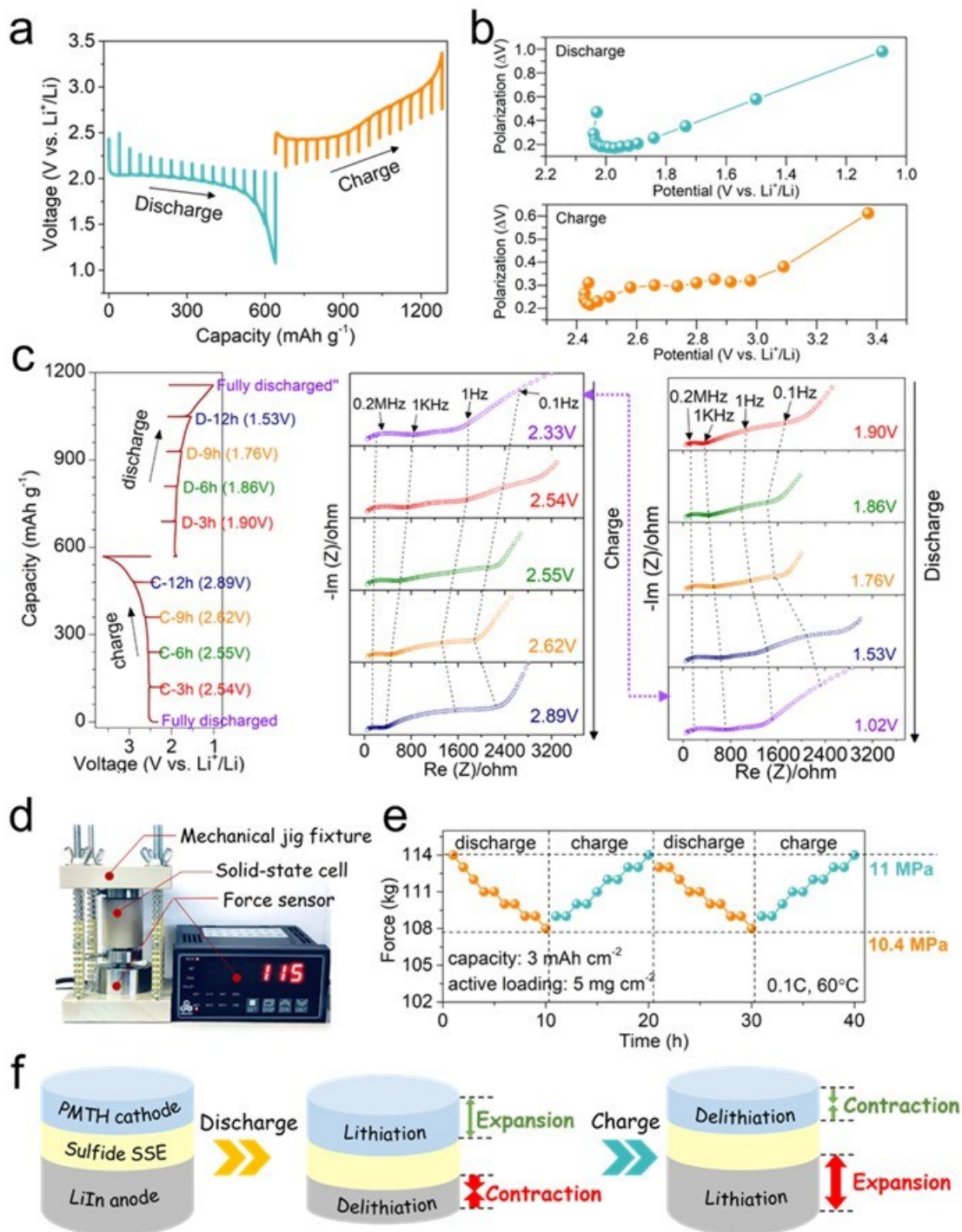


Figure XIV.3.2 a) GITT profile and b) polarization plots of PMTH|Li<sub>6</sub>PS<sub>5</sub>Cl|LiIn cell upon one discharge/recharge cycle at 0.07C. c) EIS evolution at different SOC states upon one charge/discharge cycle. d) A schematic cell setup for in-situ stack pressure measurement. e) The variation of cell stack pressure upon two consecutive cycles. f) Schematic illustration of volumetric change within the cell upon one discharge/recharge cycle.

The stress evolution upon cycling was further investigated through *in-situ* monitoring the stress change during two consecutive cycles. As shown in Figure XIV.3.2 d, a mechanical jig fixture was used to exert an initial stack pressure (~10 MPa) on the cell. A force sensor, with a measurement resolution of 1 kg, was then

integrated into the jig to monitor the change of cell stack pressure upon cycling. Figure XIV.3.2 e reveals an oscillating stress change up to 0.6 MPa during the two consecutive cycles, implying a relationship between the redox reaction and the mechanical stress evolution of the entire cell. Particularly, the stress reduced to 10.4 MPa at the fully discharged state and recovered to 11 MPa at the fully charged state. Figure XIV.3.2 f illustrates that active materials within both the electrodes undergo volumetric change upon cycling. Upon charging, LiIn anode experienced a more significant volumetric expansion compared with the contraction of PMTH cathode, leading to a net increase of the overall volume and a rise of internal pressure by 0.6 MPa. Overall, the magnitude of cell stress change was predominated by the anode side rather than the cathode side. Besides, the variation of stack pressure was quite reversible from cycle to cycle, indicating a stable chemo-mechanical environment upon cycling.

## 2) A catalytic carbon host facilitates the disproportionation of dissolved polysulfides, thus mitigating polysulfide shuttling.

In the latter part of FY 2022, we conducted research involving a newly developed nitrogen-doped carbon material with a unique pore structure. This carbon was utilized as a sulfur host in both coin cells and pouch cells, where it displayed impressive performance. We utilized *in-situ* HPLC-Electrochemical techniques to investigate the reaction mechanisms. Our findings suggest that nitrogen-doped carbon has the potential to convert dissolved polysulfides in the electrolyte into elemental sulfur and potentially  $\text{Li}_2\text{S}_x$  ( $X \leq 2$ ). In FY 2023, we have proven the hypothesis and confirmed that the unique catalytic carbon host can mitigate the shuttle effect by a fast and complete catalytic disproportionation of long-chain polysulfide ions dissolved in the electrolyte.

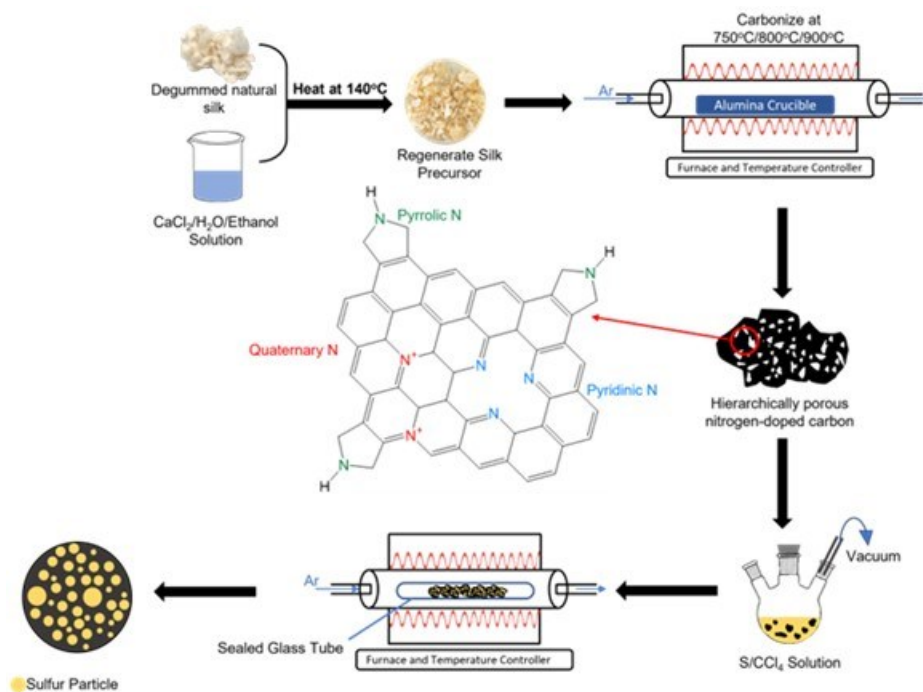


Figure XIV.3.3 Schematic illustration of the preparation of NC/S

As shown in Figure XIV.3.3, we synthesized a novel bi-functional carbon (BFC) as the carbon host for sulfur cathodes by using a degummed silk as a precursor through a facile carbonization process. Natural silks produced by silkworms are protein polymers enriched by a nitrogen element and are very easy to obtain because of their abundant resources on the earth. Therefore, silks are expected to be an ideal raw material to produce the nitrogen-doped carbon (NC) host through a facile carbonization process without any additional doping process. The obtained NC not only possesses a high surface area with optimized mesopore structures, but also exhibited activity to facilitate the disproportionation of polysulfide to short-chain polysulfide and

elemental sulfur. The content of nitrogen doped in the carbon usually changes with the pyrolysis temperature. We prepared NCs at various carbonization temperatures to examine its influence on the composition and the structure of the carbon as well as the sulfur cathode properties. In addition, a high-performance liquid chromatography (HPLC) analysis was applied to investigate the interaction between NC and PS.

Figure XIV.3.4 shows the morphologies of the NCs prepared at different carbonization temperatures by a field scanning electron microscopy (FESEM). Figures XV 3.4 (a)-(d) show the SEM images of NC750, NC800, NC900, and NC950 at the same magnification. NCs that formed at 750 and 800 °C display an aggregated morphology with a clear porous structure, particularly NC800 in which a honeycomb or a beehive structure is clearly observed in Figure XIV.3.4 (b) demonstrated a better development of porosity. However, as the carbonization temperature increased to 900 and 950 °C, the compact structure disintegrated, and a more dispersed structure emerged along with a reduction in pore structures on the NC surface. The  $N_2$  adsorption/desorption isothermal analysis was then performed to explore the porosity of the obtained NCs. The isotherm curves are depicted in Figure XIV.3.4 (e) for NC800. According to the IUPAC categorization, the as-prepared materials exhibited collective isotherm curves of types II and IV. The adsorption/ desorption hysteresis loop (H3) indicated a mesopores and macropores hybrid structure. The H3 hysteresis loop attributed to capillary condensation was typically observed in materials with mesopores. It suggested a broad pore size distribution of the shed-like aggregates, which was consistent with that observed from the SEM images. The BJH pore size distribution curves shown in Figure XIV.3.4 (f) further demonstrate the hierarchical porosity of the NCs with a vast pore size distribution in the range of 2-60 nm. Even though all materials displayed comparable pore size distribution characteristics, NC800 had a larger distribution of the pores with an opening larger than 5 nm. Among the NCs carbonized at different temperatures, NC800 has the largest BET specific surface area of  $835 \text{ m}^2 \text{ g}^{-1}$  and a total pore volume of  $1.74 \text{ cm}^3 \text{ g}^{-1}$ . The results are tabulated in Table XIV.3.1. With a greater pore capacity and a balanced pore size, NC800 has the potential to encapsulate more polysulfides within the mesopores, better accommodate the volume change of sulfur cathode, and thus inhibit the migration of the high-order lithium polysulfides during discharge.

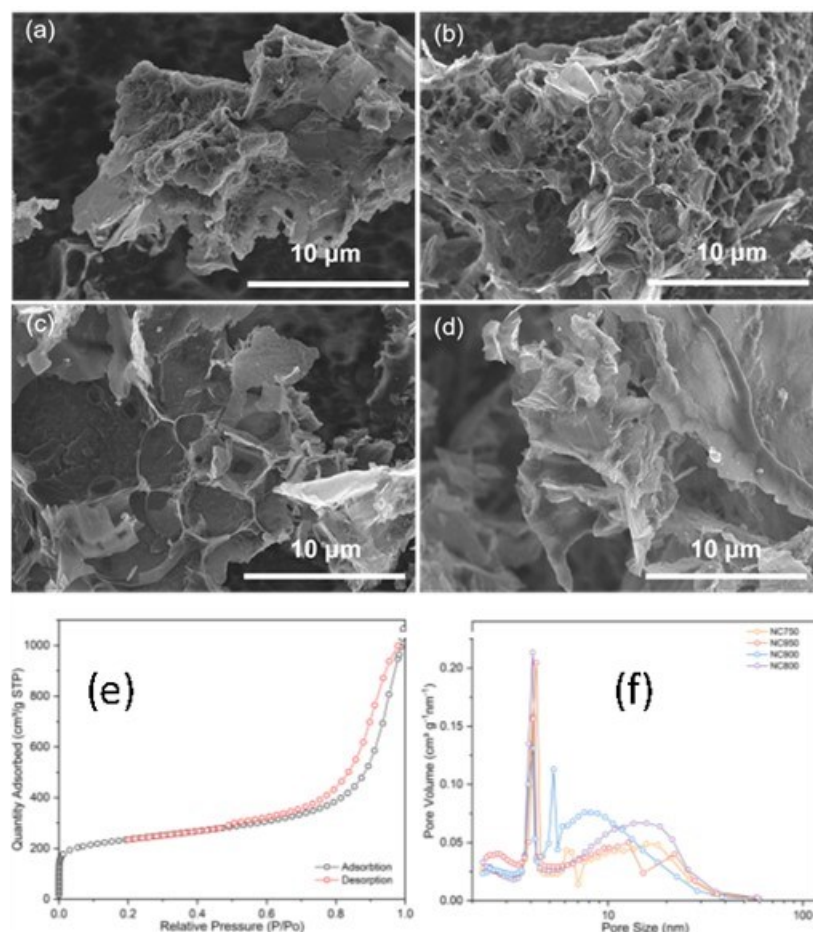


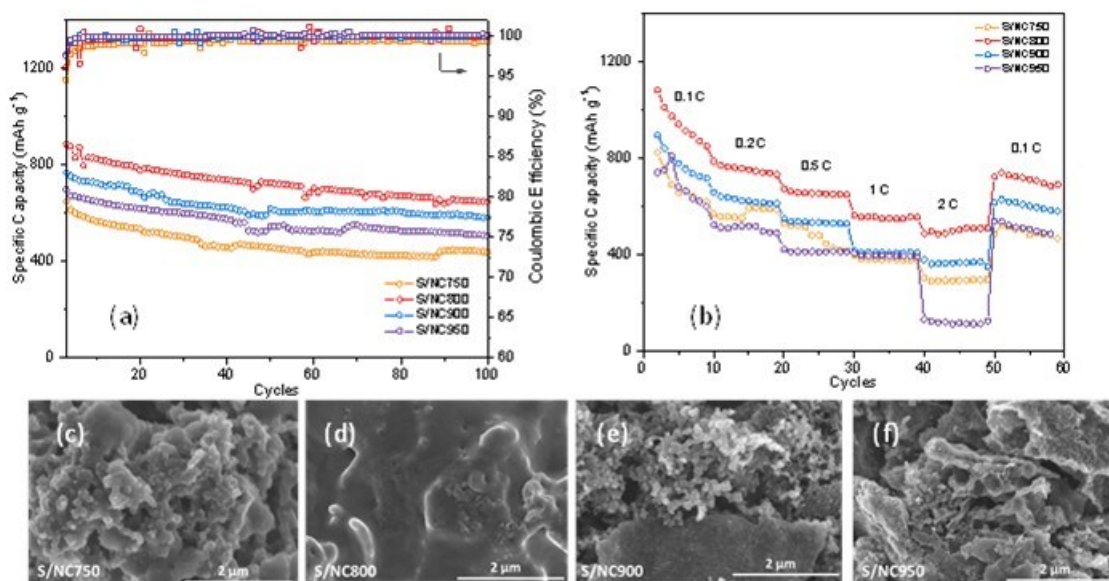
Figure XIV.3.4 FESEM images of (a) NC750, (b) NC800, (c) NC900, and (d) NC950. Nitrogen adsorption/desorption isotherm of NC800; (e) Corresponding pore size distribution curves of NC750, NC800, NC900, and NC950.

Table XIV.3.1 Nitrogen Content and Porosity of Different Samples.

Samples	Specific Surface Area (m <sup>2</sup> g <sup>-1</sup> )	Pore Volume (cm <sup>3</sup> g <sup>-1</sup> )	Average Pore Size (nm)	Nitrogen content (XPS, at %)
NC700	636.6	1.34	12.5	4.9
NC800	835.9	1.74	13.5	7.4
NC900	644.7	1.58	10.2	4.3
NC950	575.4	1.52	12.2	2.6

The electrochemical performance of an Li-S cell with the NC carbons made with various carbonization temperatures were further investigated. Figure XIV.3.5 (a) compares the cycling behaviors of the sulfur cathodes with various NC hosts. The cells were first activated at a low rate of 0.1 C for 2 cycles, and then cycled at the rate of 0.5 C between the voltage range of 1.7 and 2.9 V for 100 cycles. For the first cycle at 0.5 C, the S/NC800 delivered a discharge capacity of 919 mAh g<sup>-1</sup>, which was higher than 647, 766, and 697 mAh g<sup>-1</sup> delivered by the S/NC750, S/NC900, and S/NC 950, respectively. After 100 cycles, the reversible capacities of the S/NC800, S/NC750, S/NC900, and S/NC950 remained at 647, 439, 581, and 503 mAh g<sup>-1</sup>, respectively. All the cells exhibited a satisfactory capacity retention around 70%, demonstrating the synergistic effect of porous structures and doped nitrogen atoms in the NCs on mitigating the shuttle effect and enhancing

the cycling performance of the cells. Cells with different cathodes were then cycled at various current densities from 0.1 to 2 C to evaluate the rate capability of the S/NC composites. As shown in Figure XIV.3.5 (b), the S/NC800 displays the best rate performance among all the samples. The S/NC800 delivered an initial discharge capacity of 1410 mAh g<sup>-1</sup> at 0.1 C. When the current rates were increased to 0.2, 0.5, and 1C, the corresponding reversible discharge capacities reduced to 786, 672, and 563 mAh g<sup>-1</sup>, respectively. Even at a high rate of 2C, the S/NC800 still remained the highest specific capacity of 497 mAh g<sup>-1</sup> among all the samples. As the current density was reduced back to 0.1C, the specific capacity of the S/NC800 recovered to 740 mAh g<sup>-1</sup>, indicating a good stability of the cathode. We believed that the N800 can better catalyze the sulfur redox reaction and induce a homogeneous distribution of sulfide compounds deposition on the host carbon material. The hypothesis was supported by the comparison of the SEM images of the cycled cathode at a discharged state as shown in Figure XIV.3.5 (c)-(f). While the grape-shape lithium sulfide deposited on the carbon hosts of N750, N900 and N950, a smooth deposition of sulfides was formed on N800, which was like a “honey filled honeycomb” (referring to Figure XIV.3.4 (b), in which a beehive meso-porous structure was shown for N800). The more uniform distribution of Li<sub>2</sub>S/Li<sub>2</sub>S<sub>2</sub> on S/N800 compared to other NCs, indicated that it underwent a homogeneous conversion process from S<sub>8</sub> to Li<sub>2</sub>S/Li<sub>2</sub>S<sub>2</sub> on the surface. These morphological changes may be ascribed to the polarity of the special nitrogen-containing groups formed on the surface of NCs, and the catalytic characteristics of NC in the disproportionation reaction of PS in the electrolyte during cycling. It was speculated that NC800 possesses a higher density of nitrogen-contained functional groups with higher polarity, evenly distributed on its surface. This results in more nucleation sites for Li<sub>2</sub>S/Li<sub>2</sub>S<sub>2</sub>, which are favorable to the electrochemical performance of the battery.



**Figure XIV.3.5 (a) Cycling performance and Coulombic Efficiency at 0.5 C, and (b) Rate capability cathodes at different C-rate of S/NC750, S/NC800, S/NC900, and S/NC950 composite; FESEM images of the discharged electrodes with (c) NC750, (d) NC800, (e) NC900, and (f) NC950. All the carbons were tested in coin cells.**

Figure XIV.3.6 (a) displays the cycling performance of a pouch cell with the E/S ratio of 10  $\mu\text{L mg}^{-1}$  electrolyte. After being activated at 0.05C for two cycles, the cell delivered an initial specific capacity of 905 mAh g<sup>-1</sup> at the rate of 0.2 C and displayed an incremental capacity increase during the first 50 cycles. The capacity increase can be ascribed to the slow penetration of the electrolyte during the discharge and charge processes. The capacity of the pouch cell was stabilized after 50 cycles and remained at 1031 mAh g<sup>-1</sup> after 100 cycles. Figure XIV.3.6 (b) shows the discharge and recharge curves of the cell.

HPLC analysis was then carried out to determine polysulfide species in the electrolyte during cycling. A pouch cell with S/Ketjenblack cathode was also assembled for a comparison. Both pouch cells were disassembled after cycling for three cycles. The electrolyte was then taken out from the separators and derivatized with the methyl triflate to form stable dimethyl polysulfides. The results of the experiment, as shown in the HPLC chromatographs in Figure XIV.3.6 (c), indicate that the S/NC800 sample had a high content of  $S_8$  in the electrolyte and almost no polysulfide ions. On the other hand, the S/Ketjenblack sample had a distribution of high concentration of polysulfide ions but no  $S_8$ . These results suggested that NC800 exhibited a high catalytic activity to the disproportionation of polysulfide ions to the elemental sulfur. The solubility of  $S_8$  in electrolyte is much lower than that of the polysulfide species, hence it can be better absorbed in the porous cathode matrix instead of shuttling to the anode. The *in-situ* analytical results unveiled that nearly all of the dissolved polysulfide ions in the electrolyte underwent catalytic disproportionation, forming  $Li_2S_x$  ( $x \leq 2$ ) and elemental sulfur. Given that dissolved polysulfides are the primary contributors to the adverse shuttle effect, the introduction of NC800 carbon effectively mitigated this detrimental phenomenon.

The utilization of a high sulfur loading cathode in Li-S battery is critical for the improvement of energy density in the practical application of the battery. Therefore, the S/NC800 cathode with a high sulfur loading of  $5 \text{ mg cm}^{-2}$  was made in a pouch cell. The cycle result is shown in Figure XIV.3.6 (d). The battery delivered an initial specific capacity of  $742 \text{ mAh g}^{-1}$  and a well remained specific capacity of  $580 \text{ mAh g}^{-1}$  after cycling at  $0.2 \text{ C}$  for 50 cycles, which demonstrates a stable and consistent cycling performance of S/NC800 cathode. In addition, the nearly unchanged upper plateau of the charge/discharge curves shown in Figure XIV.3.6 (e) also demonstrates the ability of NC800 to mitigate the shuttle effect that occurred during the cycling process.

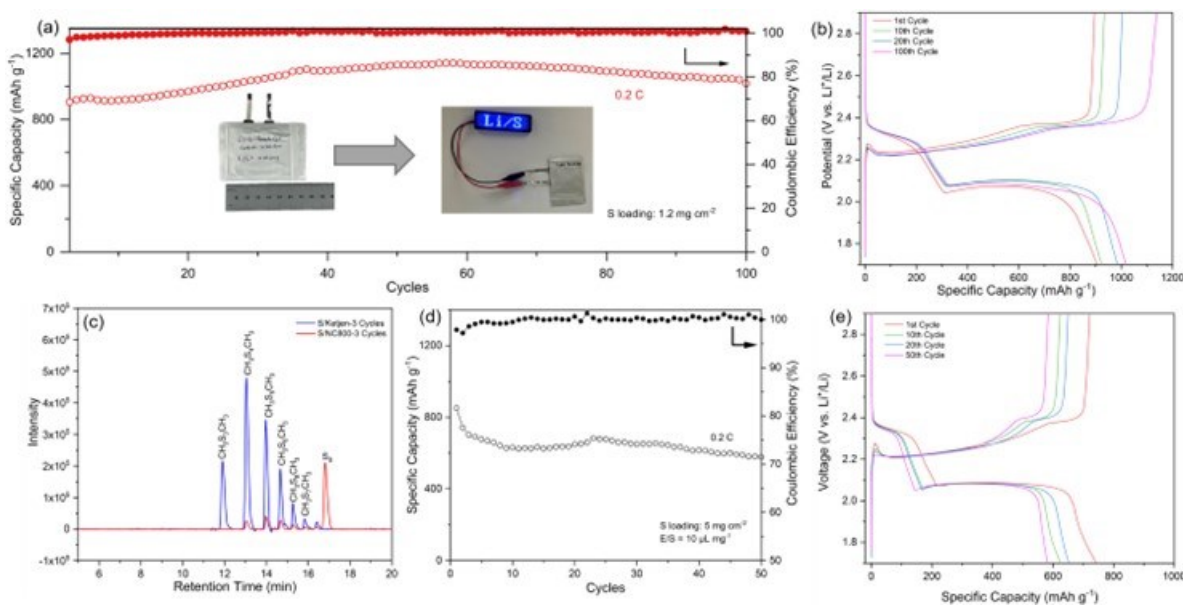


**Figure XIV.3.6** (a) Cycling performance of S/NC800 pouch cell with sulfur loading of  $1.2 \text{ mg cm}^{-2}$  and E/S ratio of  $10 \text{ } \mu\text{L mg}^{-1}$ ; (b) corresponding discharge/charge profile; (c) HPLC chromatograms of S/NC800 and S/Ketjenblack pouch cells after 3 cycles; (d) Cycling performance of S/NC800 pouch cell with sulfur loading of  $5 \text{ mg cm}^{-2}$  and E/S ratio of  $10 \text{ } \mu\text{L mg}^{-1}$ ; (e) Corresponding discharge/charge profile.

## Conclusions

In conclusion, the exploration of thiuram polysulfide has shown promise as a cost-effective and high-capacity cathode material for the realization of commercially viable all-solid-state organic batteries utilizing sulfide electrolytes. The viability of the thiuram hexasulfide (PMTH) cathode has been successfully demonstrated in a PMTH|Li<sub>6</sub>PS<sub>5</sub>Cl|LiIn cell, achieving an impressive capacity of approximately  $600 \text{ mAh g}^{-1}$  maintaining long cycle life, even in the presence of oscillating-stress changes up to  $0.6 \text{ MPa}$  during cycling. Moreover, the reversible evolution of the cathode interface over cycles has been confirmed. Specific energy calculations reveal values of  $1140 \text{ Wh kg}^{-1}$  at the material level and  $376 \text{ Wh kg}^{-1}$  at the electrode level, with an areal



capacity of 10.4 mAh cm<sup>-2</sup> achieved under high active mass loading conditions. This research represents a significant step towards the development of commercially accessible organic all-solid-state batteries by optimizing material, electrode, and cell-level designs.

A bifunctional carbon material boasting unique attributes was synthesized which mitigated the polysulfide shuttle effect in a Li-S battery. This carbon material, derived from a raw silk precursor, exhibits a porous honeycomb structure that serves as a reservoir for sulfur, while also catalyzing the transformation of long-chain polysulfide ions into elemental sulfur. Furthermore, it ensures the uniform deposition of lithium sulfide on its surface. Experimental results confirm that very few dissolved polysulfides are present in the electrolyte during cycling, with only dissolved elemental sulfur being detected. These synergistic advantages culminate in outstanding performance, as demonstrated by the sulfur/carbon composite using the carbon material synthesized at 800 °C, delivering a remarkable reversible capacity of over 1000 mAh g<sup>-1</sup> after 100 cycles in a pouch cell, with a sulfur content of 60 wt%. This research offers a promising approach for the development of high-performance Li-S batteries with enhanced cycle life and minimal shuttle effect.

### Key Publications

1. Dantong Qiu, Xiaoxiao Zhang, Dong Zheng, Weixiao Ji, Tianyao Ding, Huainan Qu, Miao Liu, Deyang Qu. “High performance Li-S batteries with minimum shuttle-effect – disproportionation of dissolved polysulfide to elemental sulfur catalyzed by a bi-functional carbon host”, ACS Appl. Mater. & Interface <https://doi.org/10.1021/acsami.3c06459>.
2. Tianyao Ding, Huainan Qu, Xiaoxiao Zhang, Dong Zheng, Weixiao Ji, Deyang Qu. “Dynamic Surface Protective Layer on a Metallic Lithium Anode with Electronic and Ionic Dual Conductivity”, J. Power Source 580(2023)233344.

### Acknowledgements

The University of Wisconsin Milwaukee principal investigator is grateful to Professor T.H. Lambert and Dr. H Huang of Cornell for the synthesis of the organo-sulfur materials.

## XIV.4 New electrolyte binder for Lithium sulfur battery (LBNL)

### **Gao Liu, Principal Investigator**

Lawrence Berkeley National Laboratory  
Berkeley, California, 94720  
E-mail: [gliu@lbl.gov](mailto:gliu@lbl.gov)

### **Tien Duong, DOE Technology Development Manager**

U.S. Department of Energy  
E-mail: [Tien.Duong@ee.doe.gov](mailto:Tien.Duong@ee.doe.gov)

Start Date: October 1, 2022

End Date: September 30, 2023

Project Funding (FY23): \$750,000

DOE share: \$750,000

Non-DOE share: \$0

### **Project Introduction**

A strong demand for low-cost and high-energy-density rechargeable batteries has spurred lithium-sulfur (Li-S) rechargeable battery research. First, sulfur is an abundant and low-cost material. Second, the Gibbs energy of the lithium (Li) and sulfur reaction is approximately 2,600 Wh/kg, assuming the complete reaction of Li with sulfur to form  $\text{Li}_2\text{S}$ , more than five times the theoretical energy of transition metal oxide cathode materials and graphite coupling. With these advantages, Li-S batteries could be both high energy density and low cost, satisfying demand in energy storage for transportation application. The major obstacle is the loss of sulfur cathode material as a result of polysulfide dissolution into common electrolytes, which causes a shuttle effect and significant capacity fade. The polysulfide shuttle effect leads to poor sulfur utilization and fast-capacity fade, which have hindered widespread use of rechargeable Li-S batteries. This proposed work of new electrolyte development in understanding the thermodynamics and kinetics of polysulfide dissolution and precipitation will yield new approaches for electrolytes of Li-S rechargeable batteries.

### **Objectives**

This project aims to develop new electrolytes and additives and electrode binders for Li-S battery. The properties of the ideal electrolyte for sulfur electrode would be high ion conductivity, stable towards polysulfide, and promoting the polysulfide affiliation with the electrode substrate to prevent polysulfide dissolution. The first objective is to understand the electrode substrate interaction with the polysulfides in different electrolytes. This will lead to better understandings of the polysulfide nucleation and precipitation mechanisms in common electrolytes. The second objective is chemically modifying the structures of the solvent and salt electrolyte molecules, as well as formulations to increase electrolyte stability and ionic conductivity and to prevent polysulfide dissolution, promote polysulfides precipitation, and enhance lithium metal electrode stability.

### **Approach**

This project aims to develop new electrolytes and additives, and electrode binders for Li-S battery. The properties of the ideal electrolyte for sulfur electrode and lithium metal anode would be high ion conductivity, stable towards polysulfide, promoting the polysulfide affiliation with the electrode substrate to prevent polysulfide dissolution, and enhance lithium metal electrode stability. The project is designed to first understand the electrode substrate and binder interaction with the polysulfides in different electrolytes. This leads to better understandings of the polysulfide nucleation and precipitation mechanisms in common electrolytes. The second stage of the project will focus on chemically modifying the structures of the solvent and salt electrolyte molecules, and electrode binders to increase electrolyte stability and ionic conductivity and to prevent polysulfide dissolution and promote polysulfides precipitation, and enhance lithium metal electrode stability.

## Results

Lithium-sulfur batteries (LSBs) have received extensive attention as next-generation energy storage technologies due to their outstanding energy density (ca. 2600 Whk/g), low cost (ca. 36-130 dollars k/Wh), abundance, eco-friendliness, and high specific capacity (ca. 1675 mAh/g).<sup>1-3</sup> Despite these advantages, LSBs confront many critical challenges in practical applications, such as the large volume change of the sulfur (S) cathode, poor Coulombic efficiency, dissolved polysulfides (that arise during the discharge process) in the electrolyte, dendrite formation on the Li-anode, and low conductivity of the S cathode.<sup>4-6</sup> To overcome these limitations, several strategies have been developed, mainly focusing on the synthesis of new additives to improve the electrochemical performance of LSBs and modifying the S cathode to reduce the volume changes after cycling and improve the conductivity.<sup>7-11</sup> Moreover, considerable attention has been given to investigating and creating new binding agents to enhance the performance of LSBs, as well as to the synthesis of catalytic materials and hierarchical porous carbon for use in LSBs.<sup>12-15</sup> However, LSBs still face a long journey to achieve practical utility and commercialization. Therefore, there is ample scope for further research in developing high energy-density LSBs through the engineering of electrolyte additives, co-solvents, and modifications of the S cathode.

Until now, researchers have extensively studied non-aqueous liquid electrolytes to improve the cycling performances of LSBs.<sup>16-18</sup> The addition of functional molecules and co-solvents, such as ionic liquids and fluorinated ethers, can effectively minimize side reactions between polysulfides and Li-metal and suppress dendrite formation by producing a good solid-electrolyte interface (SEI) layer on the Li-metal surface.<sup>19-22</sup> Polysulfide additives, as functional molecules, are used in non-aqueous LSBs to minimize the dissolution of polysulfides by creating a concentration gradient of polysulfide species at the cathode/electrolytes interface.<sup>23-24</sup> Additionally, lithium nitrate, a well-known electrolyte additive, develops a good passivation layer on the Li-metal anode surface and restricts the shuttle effect.<sup>25-26</sup> However, side reactions among these additives, electrolytes, and electrodes are still uncertain.<sup>27</sup> Highly concentrated electrolytes, solvate ionic liquids, and solvents in salt concepts are being significantly executed to overcome these challenges.<sup>28-31</sup> Recently, highly concentrated imide-based electrolyte solutions have been reported to reduce side reactions in battery systems. Specifically, solutions containing 3M LiTFSI, 7M LiTFSI, and 3M LiFSI in 1,3 dioxane (DOL)/dimethoxyethane (DME) solvent have shown significant promise in this regard.<sup>32-33</sup> However, despite their excellent electrochemical stability, ability to form a favorable SEI layer, and relatively high  $\sigma$ , highly concentrated and viscous electrolytes would not be a good choice for commercial applications. Therefore, many researchers have used diluted electrolyte solutions with poorly-coordinating solvents, such as hexyl methyl ether in DOL, fluoroalkyl ether in DME, and hydrofluoroethers, etc., to reduce the polysulfide dissolution during CD cycling.<sup>34-35</sup> Among all the solvents, hydrofluoroethers show excellent performance due to their moderate polarity and low solvation ability to Li-metal.<sup>36</sup> The use of hydrofluoroethers-type solvents significantly reduces the corrosion of the Li-anode during CD cycling and improves cell safety, electrochemical stability, and Coulombic efficiency of the LSBs.<sup>36</sup> 1,1,2,2-tetrafluoroethyl-2,2,3,3-tetrafluoropropyl ether (TTE), a hydrofluoroether solvent, is commonly used in LSBs, even though it can barely dissolve Li-salts.<sup>8,37</sup> Therefore, a co-solvent is always used with TTE to achieve better LSB performances.<sup>38</sup> In our previous work, we reported a new technique to suppress polysulfide dissolution using micelle-based additives with TTE and observed a unique solvation mechanism in which Li-ion easily coordinated with additives and formed micelle structures.<sup>8</sup> The prepared electrolyte solution (0.5M LiTFSI in F<sub>3</sub>EO<sub>1</sub>/TTE) showed excellent compatibility with Li-metal anode, formed a uniform SEI layer on the Li-metal anode surface after CD cycling, and significantly suppressed the polysulfide dissolution.<sup>8</sup> However, the effect of the anions (TFSI and FSI anion) and F<sub>4</sub>EO<sub>2</sub> additive on the overall LSB battery performance was not significantly studied in our previous work. There is currently a lack of adequate research on the design and synthesis of highly fluorinated electrolyte additives, as well as the impact of additives ratios on electrolyte compositions.

Herein we have synthesized a highly fluorinated ether-based bifunctional (lithiophilic head and fluorinate lithiophobic tail) electrolyte additive, 1,1,1,2,2,3,3,4,4-nonafluoro-6-(2-methoxyethoxy)hexane (F<sub>4</sub>EO<sub>2</sub>), for LSB application. Furthermore, we assessed the influence of the completely new electrolyte solutions on LSB

performance by varying the composition of TTE, F<sub>4</sub>EO<sub>2</sub>, LiTFSI, LiFSI, and DOL, respectively. We also discovered the micelle-structured F<sub>4</sub>EO<sub>2</sub> additive reinforced Li-ion transport behavior and prevented polysulfide dissolution by constructing a stable SEI layer on the Li-anode surface (shown in Scheme 1 in Figure XIV.4.1). Additionally, the LSBs exhibited a superior cycling performance when harnessing the electrolyte solutions containing LiTFSI salt in comparison to LiFSI salt. The TFSI anion, produced from the LiTFSI salt, exhibits greater electrochemical stability compared to the FSI anion generated from the LiFSI salt. This enhances the electrochemical stability of the Li salt towards various reactive intermediates generated during the CD cycling of LSB. The surface morphology of the cycled electrodes was analyzed using scanning electron microscope (SEM), and X-ray photoelectron spectroscopy (XPS), respective

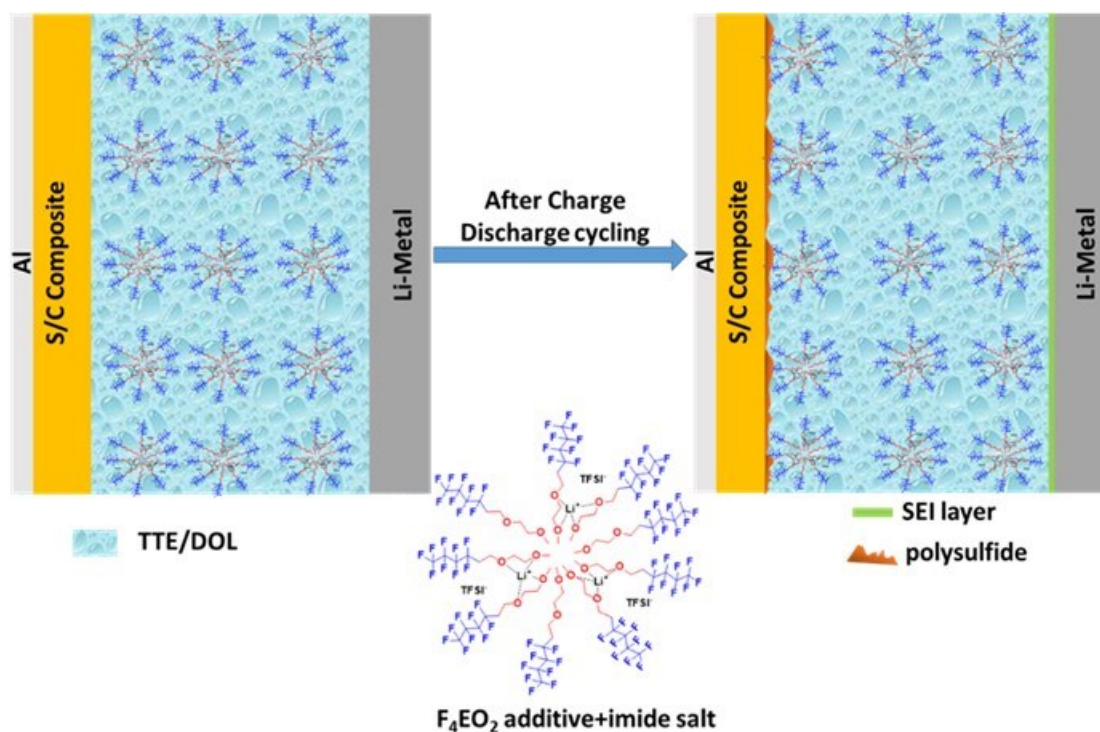


Figure XIV.4.1 **Scheme 1.** Schematic diagram of the role of micelle-structured additive and imide salt.

## DISCUSSION OF EXPERIMENTS

### Materials.

The following chemicals were purchased from Sigma Aldrich and used as received without any additional purification: Dichloromethane (DCM), 2-methoxyethanol, 4-toluenesulfonyl chloride, triethylamine (TEA), hydrochloric acid (HCl), sodium bicarbonate (NaHCO<sub>3</sub>), potassium hydroxide (KOH), 1-methyl-2-pyrrolidinone (NMP), LiTFSI, diethyl ether, brine, magnesium sulfate (MgSO<sub>4</sub>), poly(vinylidene fluoride) (PVDF, M<sub>w</sub> = ~534000), sulfur, LiFSI, DOL, DME, denka black, and ketjen carbon black. TTE and 1H,1H,2H,2H-perfluorohexan-1-ol were purchased from TCI America and Oakwood Products, Inc., respectively. The Li-Metal disk and polypropylene separator were received from Albemarle and Celgard, respectively, and stored inside the glove box.

### Instrumentations and measurements.

The prepared compound's chemical structure was confirmed using <sup>1</sup>H-NMR spectroscopy (Bruker DRX, 500 MHz), where deuterated chloroform (CDCl<sub>3</sub>) and tetramethylsilane (TMS) were used as the solvent and internal reference, respectively. The surface morphologies, elemental compositions, and topographies of the electrodes were analyzed using SEM (JEOL JSM-750F). Additionally, XPS was used for further analysis, where an air-free sample holder with Ag-tape on Si-substrate was kept inside the Ar-filled glove box and the

electrodes were secured with the Ag-tape. The XPS analyses were performed using a Thermo-Fisher K-Alpha Plus XPS/UPS analyzer (operating pressure of  $2.0 \times 10^{-7}$  Pa) with a monochromatic Al K $\alpha$  X-rays (1.486 eV) source at The Molecular Foundry. The cyclic voltammetry (CV) test was conducted using a VMP3 (BioLogic) potentiostat to investigate the electrochemical stability of the electrolyte solutions at a scan rate of  $0.1 \text{ mV}\cdot\text{s}^{-1}$  with the coin cell configuration of Li metal//electrolyte//S/C composite (Celgard was used as a separator) at 30 °C. Electrochemical impedance spectroscopy (EIS) was performed on an impedance analyzer (Biologic, Claix, France) with an AC amplitude of 5 mV over a frequency range of 0.1-10<sup>5</sup> Hz at different temperature conditions (-20 to 80 °C).

#### Synthesis of 1,1,1,2,2,3,3,4,4-nonafluoro-6-(2-methoxyethoxy)hexane (F<sub>4</sub>EO<sub>2</sub>).

The synthesis of the F<sub>4</sub>EO<sub>2</sub> electrolyte additive was carried out according to the previously reported method,<sup>8</sup> and the synthesis scheme is presented in Scheme 2 (Figure XIV.4.2). In brief, 13.70 g (0.180 mol) of 2-methoxy ethanol in 540 mL DCM and 36.03 g of (0.189 mol) 4-toluenesulfonyl chloride were mixed into a 1000 mL two-neck round bottom flask, and equipped with an air condenser, argon flow, and a magnetic stirrer. Then, 50 mL (0.360 mol) of dried TEA (distilled from CaH<sub>2</sub>) was slowly added via a dropping funnel and the mixture was stirred for 12 h at 25 °C. The resulting crude product was washed with distilled H<sub>2</sub>O, diluted HCl, and saturated NaHCO<sub>3</sub>, respectively. After evaporation of the DCM, the yellowish liquid product (2-methoxyethyl 4-methylbenzenesulfonate) was obtained with a yield of 96% (42 g) and used for the next step without any additional purification.

42.00 g (0.182 mol) of 2-methoxyethyl 4-methylbenzenesulfonate and 18.2 g (0.091 mol) of 1H,1H,2H,2H-perfluorohexan-1-ol were mixed in 55 mL NMP and 55 mL aqueous KOH (45 wt%). The reaction mixture was stirred for 5 h at 50 °C and then the temperature was increased to 70 °C and stirred for 2 h. After completion of the reaction, the product was extracted with ether, washed with water and brine, and dried over MgSO<sub>4</sub>. Finally, a colorless liquid F<sub>4</sub>EO<sub>2</sub> product with high purity (22.02 g, 75% yield) was obtained by distillation under high vacuum pressure. The prepared electrolyte additive was further dried with molecular sieves and stored inside the glove box.

For F<sub>4</sub>EO<sub>2</sub>: <sup>1</sup>H NMR (500 MHz, CDCl<sub>3</sub>):  $\delta = 2.40\text{-}2.50$  (m, 2H); 3.39 (s, 3H); 3.54-3.70 (m, 4H), 3.80 (t, 2H)

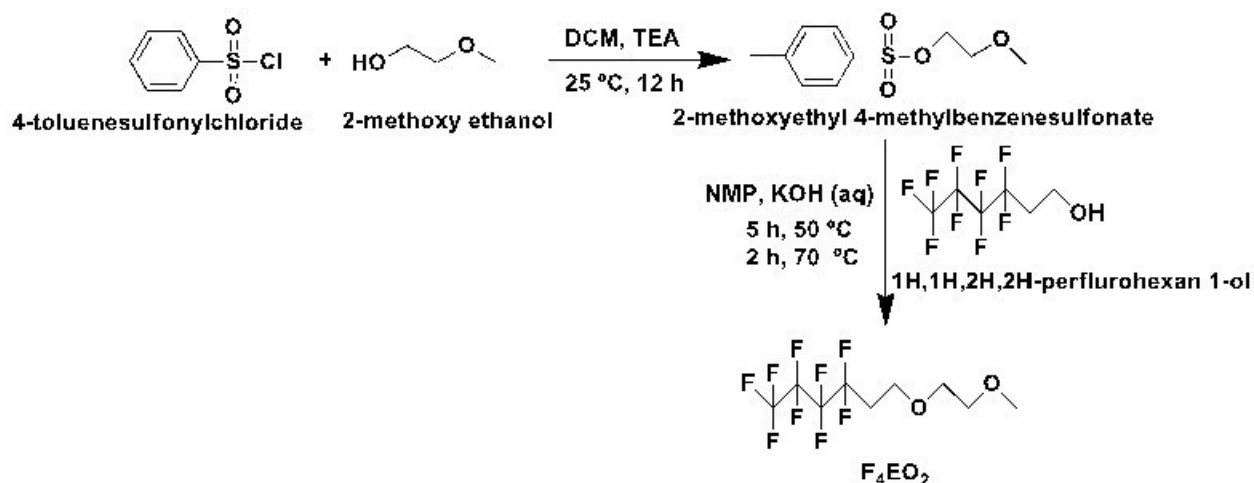


Figure XIV.4.2 Scheme 2. The synthesis route of 1,1,1,2,2,3,3,4,4-nonafluoro-6-(2-methoxyethoxy)hexane (F<sub>4</sub>EO<sub>2</sub>).

#### Preparation of electrolyte solutions, S/C composite electrodes, and coin cells.

To prepare electrolyte solutions, we used TTE, DOL, LiFSI, LiTFSI, and F<sub>4</sub>EO<sub>2</sub> respectively, and the solutions are denoted as TDLiTFSI, T5FDLiTFSI, T10FDLiTFSI, T20FDLiTFSI, T5FDLiTFSI-FSI, and T5FDLiFSI,

respectively. The details of the composition of the electrolyte solutions are shown in Table XIV.4.1. In addition, the S/C composite electrode was prepared according to our previous work.<sup>8</sup> At first, ketjen carbon black and sulfur were mixed with a ratio of 3:7 (wt%) using a mechanical ball mixing (CryoMill) for 20 min. Thereafter, the prepared mixture was sealed in a container (Teflon) and annealed at ca. (150-155) °C for 20 h in a furnace to form S/C composite.

**Table XIV.4.1 Compositions of the Prepared Electrolyte Solutions.**

Acronym of the Electrolyte Solution	Ratio TTE:F <sub>4</sub> EO <sub>2</sub>		DOL (vol%) in the electrolyte	Concentration LiTFSI (M)	Concentration LiFSI (M)
	TTE	F <sub>4</sub> EO <sub>2</sub>			
TDLiTFSI	5	-	10%	0.5	-
T5FDLiTFSI	5	1	10%	0.5	-
T10FDLiTFSI	10	1	10%	0.5	-
T20FDLiTFSI	20	1	10%	0.5	-
T5FDLiFSI	5	1	10%	-	0.5
T5FDLiTFSI-FSI	5	1	10%	0.5	0.25

To prepare electrode slurry, S/C composite, denka black, and PVDF binder was taken with the weight ratio of 6:3:1. Then 10 wt% of NMP solvent was added and pestle and mortar were used to mix the slurry. The electrode slurry was doctor-bladed on a current collector (aluminum foil, 20 μm) and dried overnight at 40 °C. The prepared S/C composite cathode disk was additionally dried under vacuum for 20 h and transferred into an Ar-filled glovebox. The S/C cathode disk (diameter 12.7 mm, 0.75 mg/cm<sup>2</sup> S loading), Li-metal anode disk (diameter 14 mm), an appropriate amount of as-prepared electrolyte solution, and Celgard separator (diameter 18 mm) were used to assemble CR2032 coin cells. The CD capacity of the coin cells was tested by using a Maccor series 4000 cell tester at the voltage range of 1.7 and 2.8 V (at 0.1 C rate) at 30 °C.

## DISCUSSION OF RESULTS

### **Electrochemical Performance and Ionic Conductivity of the Prepared Electrolyte Solutions.**

The CV results of the LSBs using both the prepared and standard electrolyte solutions are shown in Figure XIV.4.3. The voltage range was (1.8-2.8) V, and the scan rate was 0.1 mA/s. The LSBs with the prepared electrolyte solutions showed one broad reduction current peak in the cathodic scan (Figure XIV.4.3), which is associated with the solid-solid phase transition (S/C to Li<sub>2</sub>S).<sup>39</sup> On the other hand, the LSB with the standard electrolyte solution showed two reduction peaks at ca. 2.3 and 2.0 V, which correspond to the solid-liquid (elemental S to dissolved Li<sub>2</sub>S<sub>8</sub>) and liquid-solid (dissolved Li<sub>2</sub>S<sub>6</sub> to Li<sub>2</sub>S<sub>2</sub> or Li<sub>2</sub>S) phase transition.<sup>40-42</sup> Therefore, the prepared electrolyte solutions can suppress polysulfide dissolution.

The slight over potential in the initial cathodic and anodic sweep of the LSBs with the T5FDLiTFSI-FSI and T5FDLiFSI electrolyte solutions is attributed to the polarization caused by the phase transition in the conversion-dissolution-diffusion process of S and polysulfides.<sup>40</sup> More importantly, the EIS of the LSBs with T5FDLiTFSI-FSI and T5FDLiFSI electrolyte solutions changed significantly after CV cycling, which can be attributed to the less stable FSI anion present in the electrolyte solutions. However, the LSBs with the T5FDLiTFSI electrolyte solution showed excellent cycling performance, with well-overlapping anodic and cathodic peaks in the CV curves, and no changes were observed in EIS after CV cycling, indicating low polarization and high reversibility in subsequent cycles.<sup>40-42</sup> Additionally, as the amount of F<sub>4</sub>EO<sub>2</sub> additive in the electrolyte solution increases, the LSB showed less polarization and good reversibility in the CV cycles,

demonstrating the positive effect of the  $F_4EO_2$  additive and LITFSI salt on both the S electrode and Li-metal electrode, resulting in better cell performance.

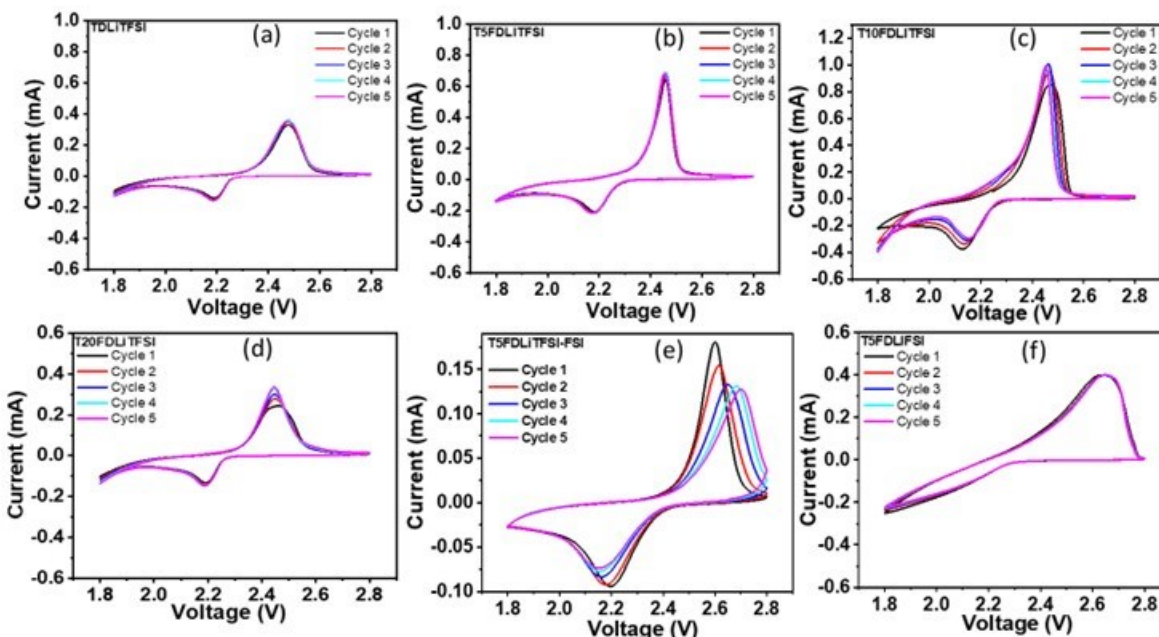


Figure XIV.4.3 CV curves of the (a) TDLiTFSI, (b) T5FDLiTFSI, (c) T10FDLiTFSI, (d) T20FDLiTFSI, (e) T5FDLiTFSI-FSI, and (f) T5FDLiFSI electrolyte solutions with the Li//electrolyte//S/C cell configuration at 0.1mV/s.

The  $\sigma$  of the prepared electrolytes were ca.  $1.39 \times 10^{-4}$ ,  $2.14 \times 10^{-4}$ ,  $1.59 \times 10^{-4}$ ,  $1.50 \times 10^{-4}$ ,  $2.21 \times 10^{-4}$  and  $2.41 \times 10^{-4}$  S/cm for TDLiTFSI, T5FDLiTFSI, T10FDLiTFSI, T20FDLiTFSI, T5FDLiTFSI-FSI, and T5FDLiFSI electrolyte solutions, respectively, at 30°C. These results are comparable to or greater than other reported organic electrolytes.<sup>8,38</sup> As the temperature increased, all of the electrolytes exhibited higher  $\sigma$  values. At 80 °C, TDLiTFSI, T5FDLiTFSI, T10FDLiTFSI, T20FDLiTFSI, T5FDLiTFSI-FSI, and T5FDLiFSI electrolyte solutions exhibited enhanced  $\sigma$  values of ca.  $1.83 \times 10^{-4}$ ,  $3.03 \times 10^{-4}$ ,  $2.53 \times 10^{-4}$ ,  $2.43 \times 10^{-4}$ ,  $3.13 \times 10^{-4}$  and  $3.33 \times 10^{-4}$  S/cm, respectively, which is due to the change of the viscosity of the electrolyte solutions with the increase of temperature.<sup>43-45</sup> Furthermore, the addition of the  $F_4EO_2$  additive to the electrolyte solution improved the  $\sigma$  of the solution by forming larger complexes that reduce the overall ion diffusion path and enhance  $Li^+$  conductivity.<sup>8</sup>

#### Cell Performance based on the Composition of the Electrolytes.

The cell performance of the prepared electrolyte solutions was evaluated using a coin cell configuration of Li//electrolyte//S/C composite cathode at 30 °C. The S was chosen as an active cathode material due to its high theoretical specific capacity (1675 mAh/g), low cost, abundance, and safety.<sup>1</sup> The CD capacity was measured over a voltage range of 1.7 to 2.8 V at 0.1 C (current density, 1.42 mA/cm<sup>2</sup>). Figure XIV.4.4a and b depict the galvanostatic CD plots of the LSBs at the first cycle and after 20 cycles, respectively, while Figure 2c displays the variation of specific discharge capacity ( $C_{sp}$ ) concerning the number of CD cycles at 0.1 C. The actual charging capacity of the LSB cells with TDLiTFSI, T5FDLiTFSI, T10FDLiTFSI, T20FDLiTFSI, T5FDLiTFSI-FSI, and T5FDLiFSI electrolyte solutions were ca. 0.81, 1.23, 1.05, 0.93, 0.95, and 0.94 mAh, respectively, at the first CD cycle (Figure XIV.4.4a), and ca. 0.65, 1.17, 1.08, 1.07, 0.66, and 0.55, mAh, respectively, after 20 cycles (Figure XIV.4.4b). In addition, the  $C_{sp}$  of the LSB cell with these electrolyte solutions were ca. 866, 1331, 1124, 1013, 1025, and 982 mAh/g, respectively, at the first CD cycle (Figure XIV.4.4c), which are comparable to or higher than other reported LSB battery system. Furthermore, the  $C_{sp}$  value of LSBs with TDLiTFSI, T5FDLiTFSI, T10FDLiTFSI, T20FDLiTFSI, T5FDLiTFSI-FSI, and

T5FDLiFSI electrolytes were ca. 691, 1222, 1129, 1128, 692, and 576 mAh/g, respectively, after 20 CD cycle (Figure XIV.4.4c). The LSB with TDLiTFSI electrolyte solution (without F<sub>4</sub>EO<sub>2</sub> additive) showed lower capacity than that of LSB with other electrolyte solutions due to the polysulfide dissolution and shuttling.<sup>8</sup> And the polysulfide dissolution and shuttling were consistently suppressed as the amount of F<sub>4</sub>EO<sub>2</sub> additive increased in the electrolyte solution, indicating that the F<sub>4</sub>EO<sub>2</sub> additive positively affects the movement of Li-ion and on the anode passivation in the LSB system. The performance of the LSB with the prepared electrolyte solutions is consistent with their electrochemical stability (CV cycling) and  $\sigma$  results. More importantly, the LSBs with T5FDLiTFSI, T10FDLiTFSI, and T20FDLiTFSI electrolyte solutions showed excellent capacity retention (Figure XIV.4.4c), and rate capability and reversibility (Figure XIV.4.4), even though only 0.5 M LiTFSI salt concentration was used (lower than the standard salt concentration for LSB), which may correspond to the formation of a good SEI layer by F<sub>4</sub>EO<sub>2</sub> additive on the surface of the Li anode and protect the degradation of TF<sub>5</sub>SI anion. The Coulombic efficiencies of the LSBs with TDLiTFSI, T5FDLiTFSI, T10FDLiTFSI, and T20FDLiTFSI electrolyte solutions were ca. 99.32, 99.98, 99.93, and 99.92%, respectively, after 20 cycles (Figure XIV.4.4d). Correspondingly, the Coulombic efficiencies were significantly decreased after 20 cycles of the LSBs with T5FDLiTFSI-FSI, and T5FDLiTFSI electrolyte solutions, were ca. 88.18, and 88.79%, respectively. However, the LSB cell with T5FDLiTFSI electrolyte solution exhibited superior performances in both the initial C<sub>sp</sub> and Coulombic efficiency compared to the LSB cells with T5FDLiTFSI-FSI, and T5FDLiTFSI electrolyte solutions. This improvement can be attributed to the presence of different anions in the electrolyte solutions, leading to distinct surface chemistry on the Li-metal anode after charge-discharge (CD) cycling. The TF<sub>5</sub>SI anion demonstrates higher chemical stability compared to the FSI anion, thus contributing to enhanced electrochemical stability of the Li salt against various reactive intermediates formed during the CD cycle of LSBs.<sup>32</sup> The LSB with T5FDLiTFSI electrolyte solution showed good cycling stability (ca. C<sub>sp</sub> 948 mAh/g) and Coulombic efficiency (ca. 99.99%) after 100 cycles (Figure XIV.4.4) and the obtained results are comparable to or better than other reported LSBs.<sup>46-48</sup> Figure XIV.4.4 displays the results of the solubility test for S, Li<sub>2</sub>S, Li<sub>2</sub>S<sub>x</sub> (x=2,4,6,8) in T5FDLiTFSI electrolyte. The measurements indicate that polysulfide has very limited solubility in the electrolyte, with solubility up to Li<sub>2</sub>S<sub>6</sub>. Even at Li<sub>2</sub>S<sub>8</sub>, the solubility of polysulfide in the T5FDLiTFSI electrolyte remains significantly lower than that in DOL-based electrolyte, where the solubility of S species can reach above 6M in a typical ether solvent electrolyte.<sup>49</sup> These findings suggest that polysulfide dissolution is effectively suppressed by the T5FDLiTFSI electrolyte, which is consistent with the electrochemical performance of the T5FDLiTFSI electrolyte.



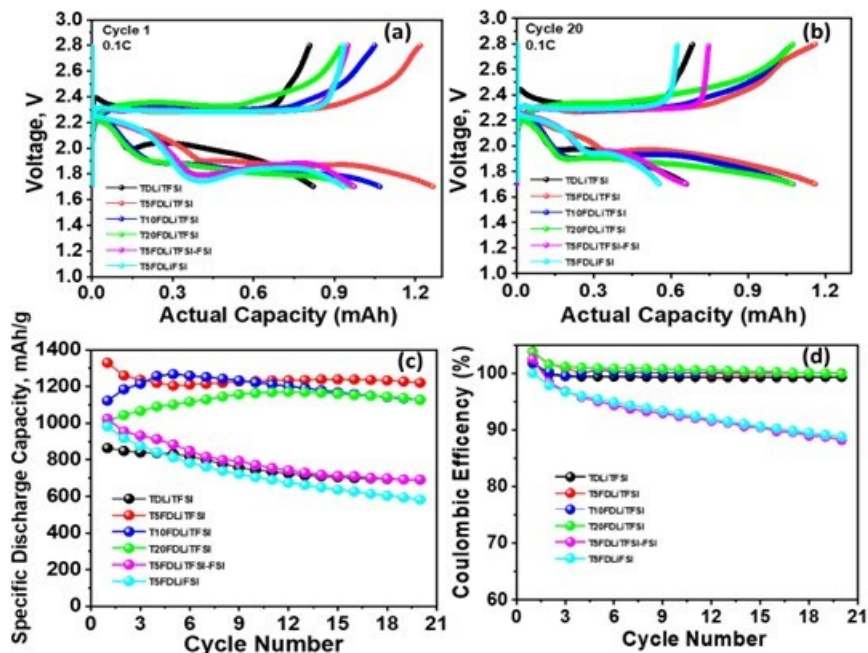
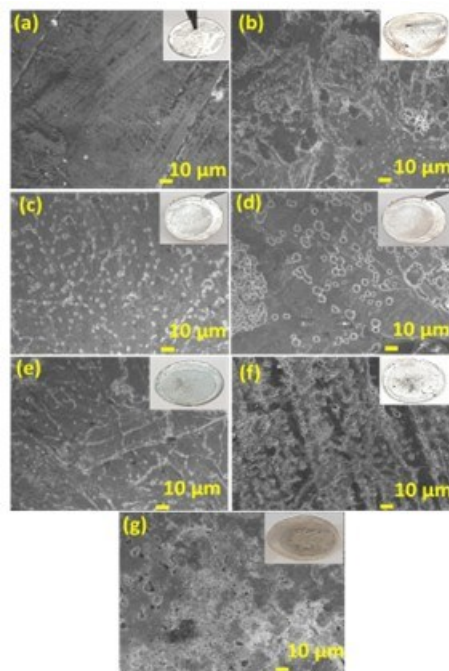


Figure XIV.4.4 CD plots of the as-prepared electrolyte solutions based S/C//electrolyte//Li half-cell at 0.1 C rate, (a) at first cycle and (b) after 20 cycles. (c) Specific discharge capacity plots of the cells as a function of CD cycles at 0.1 C. (d) Coulombic efficiency of the LSBs with as-prepared electrolyte solutions as a function of CD cycles.

#### Morphological Analysis of the Electrodes.

The surface of the electrodes was analyzed using SEM and XPS to better understand the impact of the  $F_4EO_2$  additive and anionic structure of the imide salts in LSBs. Prior to SEM and XPS analyses, all of the cycled Li-metal anodes were washed with DOL and dried for 24 h. Figure XIV.4.5 (a-g) displays the SEM images of Li-metal anodes before and after 20 CD cycle. The surface of the bare Li-metal anode was neat and smooth (Figure XIV.4.5a). In contrast, the Li-metal anode with T5FDLiTFSi-FSI, and T5FDLiFSi electrolyte solutions exhibited rough and irregular surfaces after CD cycling because of the regrowth of SEI layers and dissolution (Figure XIV.4.5f and g),<sup>32</sup> whereas the Li-metal anode with T5FDLiTFSi electrolyte solution exhibited a much smoother, less crack, and relatively compact surface (Figure XIV.4.5c). These results suggesting that Li-metal anodes easily degrade in the LiFSi containing electrolyte solution, which is an important signature of less stable SEI layers formed on the L-metal anode with LiFSi electrolyte salts in LSB. This is also very consistent with the other reported LSBs system.<sup>32</sup> However, the results from CD cycling and morphology tests indicate that LiTFSi and  $F_4EO_2$  additive have an excellent capability to form a good SEI layer on the Li-metal anode by tailoring the structures and morphology of SEI layers, which is better than that of LiFSi electrolyte salt in the LSBs.



**Figure XIV.4.5** FE-SEM images of the (a) bare Li-anode and cycled Li-anode with (b) TDLiFSI (c) T5FDLiFSI, (d) T10FDLiFSI, (e) T20FDLiFSI, (f) T5FDLiFSI-FSI, and (g) T5FDLiFSI electrolyte solutions. (Photographic images of the Li-anodes are shown as inset in the SEM images).

Moreover, the surface of the cycled S/C composite cathodes was also characterized by SEM to evaluate the effect of cathode/electrolyte interphases on the CD cycling performance of LSBs. Figure XIV.4.6 (a-g) display the SEM images and EDS of the S/C composite cathodes (bare and after 20 CD cycles at 0.1 C). No significant changes were observed on the surfaces of S/C composite cathodes before and after cycling the LSBs with all of the electrolyte salts. This suggests that the electrode/electrolyte interphases on the S/C cathode do not significantly affect the cycling performance of LSBs with all of the electrolyte solutions. However, some changes were observed on the cathode surface after CD cycling, possibly due to the S/C cathode's volume change during the CD cycling.<sup>7</sup> Therefore, it is clear that the cycling stability of the SEI layers formed on the Li-metal anode plays a significant role in improving the cycling performance of the LSBs.

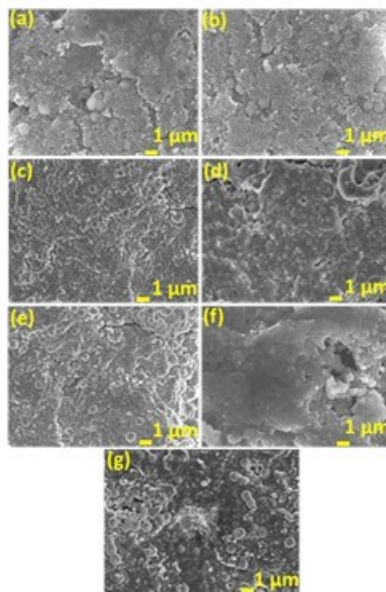


**Figure XIV.4.6 FE-SEM images of the (a) bare S/C composite cathode and cycled S/C cathodes with (b) TDLiTFSI (c) T5FDLiTFSI, (d) T10FDLiTFSI, (e) T20FDLiTFSI, (f) T5FDLiTFSI-FSI, and (g) T5FDLiFSI electrolyte solutions.**

Figure XIV.4.7 and Figure XIV.4.8 show the full XPS survey and high narrow scan spectra of deposited elements on the Li-anode surface. The chemical composition on the cycled S/C electrodes was nearly the same for all electrolytes, while significant differences were found on the cycled Li-metal anode surface (Figure XIV.4.7). Figure 6a depicts the F 1s spectra of the cycled Li-metal anode with TDLiTFSI, T5FDLiTFSI, T10FDLiTFSI, T20FDLiTFSI, T5FDLiTFSILiFSI, and T5FDLiFSI electrolytes. The main intense peak was observed at ca. 685.51 eV for cycled Li-metal anode with T5FDLiFSI electrolyte (Figure XIV.4.8a), which corresponds to LiF, produced from the degradation of FSI anion.<sup>32</sup> The intensity of the LiF peak consistently decreased with the increased amount of LiTFSI salt and F<sub>4</sub>EO<sub>2</sub> additive in the electrolyte solutions (Figure XIV.4.8a), suggesting that compared to TFSI anion, FSI anion can easily be degraded and form LiF. In addition, one extra peak appeared at ca. 689.20 and 690.01 eV for cycled Li anode with T5FDLiTFSI-FSI and T5FDLiFSI electrolyte solutions, which may be responsible for the presence of the S-F group.<sup>50</sup> The obtained results indicated that an electrolyte additive, F<sub>4</sub>EO<sub>2</sub>, prevents the degradation of electrolyte salt anion during CD cycling.

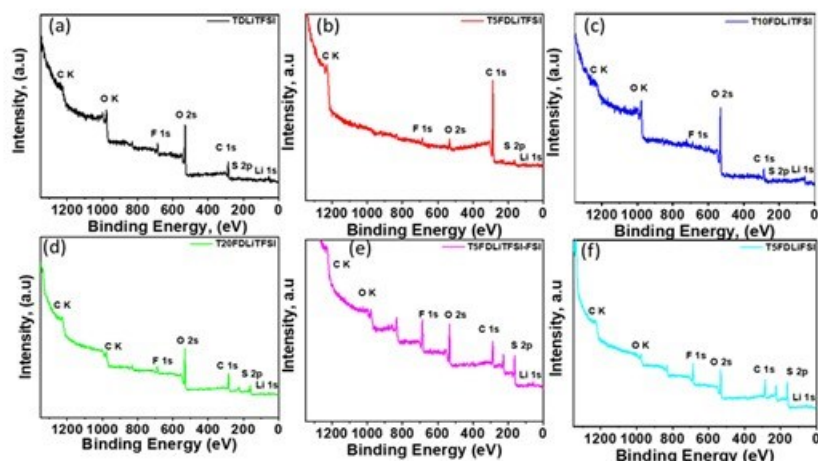


Figure XIV.4.7 XPS survey spectra of cyclized Li-anode with (a) TDLiTFSI (b) T5FDLiTFSI, (c) T10FDLiTFSI, (d) T20FDLiTFSI, (e) T5FDLiTFSI-FSI, and (f) T5FDLiFSI electrolyte solutions.

The S 2p spectra of the cyclized Li-metal anode in TDLiTFSI, T5FDLiTFSI, T10FDLiTFSI, T20FDLiTFSI, T5FDLiTFSILiFSI, and T5FDLiFSI electrolytes are shown in Figure XIV.4.8b. The cyclized Li-anode in TDLiTFSI, T5FDLiTFSI, T10FDLiTFSI, and T20FDLiTFSI electrolytes showed intense peaks in ca. 163 eV, which can be associated with polysulfide ( $\text{Li}_2\text{S}_x$ ) on the surface of the anode.<sup>51-52</sup> Therefore, sulfur-containing chemical species on the cyclized anode in TDLiTFSI, T5FDLiTFSI, T10FDLiTFSI, and T20FDLiTFSI electrolyte is associated with polysulfide formation (reversible in LSB).<sup>51</sup> On the other hand, Li-metal anode in T5FDLiTFSI-FSI, and T5FDLiFSI electrolytes exhibited very strong sulfide peaks (ca. 161.14 eV, irreversible in LSB) in the XPS spectra.<sup>51</sup> These obtained XPS results can be used to explain the cyclized performances of the LSB with as-prepared electrolyte solutions. The LSB in T5FDLiTFSI, T10FDLiTFSI, and T20FDLiTFSI electrolytes, the dominant discharge products are reversible lithium polysulfides. Therefore, these LSBs showed a good cycling performance compared to LSB with T5FDLiTFSILiFSI, and T5FDLiFSI electrolytes. In the LSBs with LiFSI salt, many side reactions occurred and formed many irreversible chemical products on the Li-metal anode surface, which directly affect the cycling performance of the LSBs.

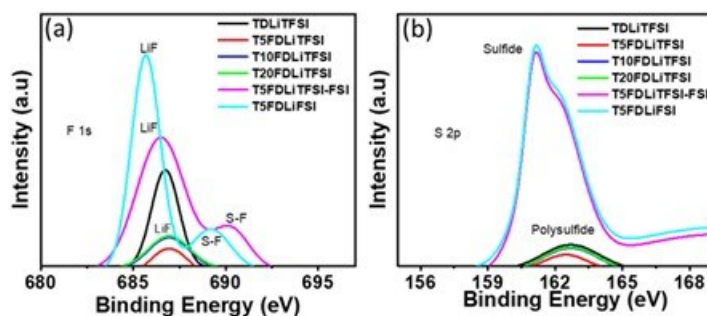


Figure XIV.4.8 High-resolution XPS spectra of (a) F 1s and (b) S 2p for cyclized Li-anode with as-prepared electrolyte solutions.

## Conclusions

We have synthesized a highly fluorinated ether-based bifunctional micelle electrolyte additive,  $\text{F}_4\text{EO}_2$ , and applied a unique strategy to suppress polysulfide dissolution in LSB. We have also prepared different electrolyte solutions by using  $\text{F}_4\text{EO}_2$ , TTE, LiTFSI, LiTFSI, and DOL, respectively, for LSB application. The LiTFSI imide electrolyte with  $\text{F}_4\text{EO}_2$  additive showed excellent compatibility with Li-metal anode, good electrochemical stability, cycling stability, and high  $C_{\text{sp}}$  of ca.  $1331 \text{ mAhg}^{-1}$  with the battery configuration of

S/C composite//electrolytes//Li-metal at 0.1C than that of LiFSI electrolyte. The chemically unstable FSI anion reacted with the Li-metal anode, depositing a large amount of LiF and sulfides on the surface, and reducing the overall cell performance. Concurrently, the micelle-structured F<sub>4</sub>EO<sub>2</sub> additive improves the battery performance significantly. The obtained results demonstrated that the LSB in T5FDLiTFSI electrolyte showed excellent cycling performance by suppressing polysulfide dissolution along with excellent capacity retention and Coulombic efficiency (99.98%) after 20 CD cycles. Therefore, it is evident that our technique, along with the F<sub>4</sub>EO<sub>2</sub> additive, holds great potential for the advancement of high-performance LSBs in the future. In our future endeavors, we plan to enhance battery performance by optimizing the concentration of salt in the electrolyte solutions and conducting battery tests.

### Key Publications

1. Faiz Ahmed, Chen Fang, Defu Li, Yangzhi Zhao, and Gao Liu, Lithium–Sulfur Batteries with Micelle-Structured Electrolytes and Imide-Based Salts *ACS Appl. Energy Mater.* **2023**, 6, 13, 7212–7220.

### References

1. Zhou, G.; Chen, H.; Cui, Y. Lithium–Sulfur Batteries. *Nat. Energy* **2022**, 7 (4), 312–319. <https://doi.org/10.1038/s41560-022-01001-0>.
2. Wang, N.; Zhang, X.; Ju, Z.; Yu, X.; Wang, Y.; Du, Y.; Bai, Z.; Dou, S.; Yu, G. Thickness-Independent Scalable High-Performance Li-S Batteries with High Areal Sulfur Loading via Electron-Enriched Carbon Framework. *Nat. Communications* **2021**, 12 (1), 1–10. <https://doi.org/10.1038/s41467-021-24873-4>.
3. Lee, B. J.; Zhao, C.; Yu, J. H.; Kang, T. H.; Park, H. Y.; Kang, J.; Jung, Y.; Liu, X.; Li, T.; Xu, W.; Zuo, X. B.; Xu, G. L.; Amine, K.; Yu, J. S. Development of High-Energy Non-Aqueous Lithium-Sulfur Batteries via Redox-Active Interlayer Strategy. *Nat. Communications* **2022**, 13 (1), 1–11. <https://doi.org/10.1038/s41467-022-31943-8>.
4. Zhao, M.; Li, B. Q.; Zhang, X. Q.; Huang, J. Q.; Zhang, Q. A Perspective toward Practical Lithium-Sulfur Batteries. *ACS Cent. Sci.* **2020**, 6 (7), 1095–1104. <https://doi.org/10.1021/acscentsci.0c00449>.
5. Pang, Q.; Liang, X.; Kwok, C. Y.; Nazar, L. F. Advances in Lithium-Sulfur Batteries based on Multifunctional Cathodes and Electrolytes. *Nat. Energy* **2016**, 1 (9), 1–11. <https://doi.org/10.1038/nenergy.2016.132>.
6. Lei, J.; Liu, T.; Chen, J.; Zheng, M.; Zhang, Q.; Mao, B.; Dong, Q. Exploring and Understanding the Roles of Li<sub>2</sub>Sn and the Strategies to beyond Present Li-S Batteries. *Chem* **2020**, 6 (10), 2533–2557. <https://doi.org/10.1016/j.chempr.2020.06.032>.
7. Ma, Q.; Tong, B.; Fang, Z.; Qi, X.; Feng, W.; Nie, J.; Hu, Y.-S.; Li, H.; Huang, X.; Chen, L.; Zhou, Z. Impact of Anionic Structure of Lithium Salt on the Cycling Stability of Lithium-Metal Anode in Li-S Batteries. *J. Electrochem. Soc.* **2016**, 163 (8), A1776–A1783. <https://doi.org/10.1149/2.1301608jes>.
8. Zhao, Y.; Fang, C.; Zhang, G.; Hubble, D.; Nallapaneni, A.; Zhu, C.; Zhao, Z.; Liu, Z.; Lau, J.; Fu, Y.; Liu, G. A Micelle Electrolyte Enabled by Fluorinated Ether Additives for Polysulfide Suppression and Li Metal Stabilization in Li-S Battery. *Front. Chem.* **2020**, 8 (6), 1–9. <https://doi.org/10.3389/fchem.2020.00484>.
9. Xue, W.; Shi, Z.; Suo, L.; Wang, C.; Wang, Z.; Wang, H.; So, K. P.; Maurano, A.; Yu, D.; Chen, Y.; Qie, L.; Zhu, Z.; Xu, G.; Kong, J.; Li, J. Intercalation-Conversion Hybrid Cathodes Enabling Li–S Full-Cell Architectures with Jointly Superior Gravimetric and Volumetric Energy Densities. *Nat. Energy* **2019**, 4 (5), 374–382. <https://doi.org/10.1038/s41560-019-0351-0>.
10. Sun, J.; Zhang, K.; Fu, Y.; Guo, W. Benzoselenol as an Organic Electrolyte Additive in Li-S Battery. *Nano Res.* **2022**. <https://doi.org/10.1007/s12274-022-4361-z>.
11. Van Ree, T. Electrolyte Additives for Improved Lithium-Ion Battery Performance and Overcharge Protection. *Curr. Opin. Electrochem.* **2020**, 21, 22–30. <https://doi.org/10.1016/j.coelec.2020.01.001>.
12. Chen, H.; Ling, M.; Hencz, L.; Ling, H. Y.; Li, G.; Lin, Z.; Liu, G.; Zhang, S. Exploring Chemical, Mechanical, and Electrical Functionalities of Binders for Advanced Energy-Storage Devices. *Chem. Rev.* **2018**, 118 (18), 8936–8982. <https://doi.org/10.1021/acs.chemrev.8b00241>.

13. Hencz, L.; Chen, H.; Wu, Z.; Qian, S.; Chen, S.; Gu, X.; Liu, X.; Yan, C.; Zhang, S. Highly Branched Amylopectin Binder for Sulfur Cathodes with Enhanced Performance and Longevity. *Exploration* **2022**, *2* (1), 20210131. <https://doi.org/10.1002/exp.20210131>.
14. Hencz, L.; Wu, Z.; Zheng, M.; Bat-Erdene, M.; Qian, S.; Su, Z.; Gu, X.; Liu, X.; Zhang, S.; Chen, H. Sustainable “Sweet and Salty” Synthesis of Hierarchical Porous Carbon for Lithium–Sulfur Batteries. *ACS Appl. Energy Mater.* **2022**, *5* (4), 4991–5001. <https://doi.org/10.1021/acsaem.2c00367>.
15. Chen, H.; Wu, Z.; Zheng, M.; Liu, T.; Yan, C.; Lu, J.; Zhang, S. Catalytic Materials for Lithium–Sulfur Batteries: Mechanisms, Design Strategies, and Future Perspective. *Mater. Today* **2022**, *52* (02), 364–388. <https://doi.org/10.1016/j.mattod.2021.10.026>.
16. Gu, S.; Sun, C.; Xu, D.; Lu, Y.; Jin, J.; Wen, Z. Recent Progress in Liquid Electrolyte-Based Li–S Batteries: Shuttle Problem and Solutions. *Electrochem. Energy Rev.* **2018**, *1* (4), 599–624. <https://doi.org/10.1007/s41918-018-0021-0>.
17. Li, X.; Banis, M.; Lushington, A.; Yang, X.; Sun, Q.; Zhao, Y.; Liu, C.; Li, Q.; Wang, B.; Xiao, W.; Wang, C.; Li, M.; Liang, J.; Li, R.; Hu, Y.; Goncharova, L.; Zhang, H.; Sham, T. K.; Sun, X. A High-Energy Sulfur Cathode in Carbonate Electrolyte by Eliminating Polysulfides via Solid-Phase Lithium–Sulfur Transformation. *Nat. Commun.* **2018**, *9* (1), 1–10. <https://doi.org/10.1038/s41467-018-06877-9>.
18. Sun, K.; Wu, Q.; Tong, X.; Gan, H. Electrolyte with Low Polysulfide Solubility for Li–S Batteries. *ACS Appl. Energy Mater.* **2018**, *1* (6), 2608–2618. <https://doi.org/10.1021/acsaem.8b00317>.
19. Fang, C.; Zhang, G.; Lau, J.; Liu, G. Recent Advances in Polysulfide Mediation of Lithium–Sulfur Batteries via Facile Cathode and Electrolyte Modification. *APL Mater.* **2019**, *7* (8). <https://doi.org/10.1063/1.5110525>.
20. Zhang, S. S. Liquid Electrolyte Lithium/Sulfur Battery: Fundamental Chemistry, Problems, and Solutions. *J. Power Sources* **2013**, *231*, 153–162. <https://doi.org/10.1016/j.jpowsour.2012.12.102>.
21. Scheers, J.; Fantini, S.; Johansson, P. A Review of Electrolytes for Lithium–Sulphur Batteries. *J. Power Sources* **2014**, *255*, 204–218. <https://doi.org/10.1016/j.jpowsour.2014.01.023>.
22. Zhang, S.; Ueno, K.; Dokko, K.; Watanabe, M. Recent Advances in Electrolytes for Lithium–Sulfur Batteries. *Adv. Energy Mater.* **2015**, *5* (16). <https://doi.org/10.1002/aenm.201500117>.
23. Xu, R.; Belharouak, I.; Li, J. C. M.; Zhang, X.; Bloom, I.; Bareño, J. Role of Polysulfides in Self-Healing Lithium–Sulfur Batteries. *Adv. Energy Mater.* **2013**, *3* (7), 833–838. <https://doi.org/10.1002/aenm.201200990>.
24. Lee, D. J.; Agostini, M.; Park, J. W.; Sun, Y. K.; Hassoun, J.; Scrosati, B. Progress in Lithium–Sulfur Batteries: The Effective Role of a Polysulfide-Added Electrolyte as Buffer to Prevent Cathode Dissolution. *ChemSusChem* **2013**, *6* (12), 2245–2248. <https://doi.org/10.1002/cssc.201300313>.
25. Mikhaylik, Y. V. U. S. Pat. 7,352,680. **2008**, *2* (12), U. S. Pat. 7,352,680.
26. Aurbach, D.; Pollak, E.; Elazari, R.; Salitra, G.; Kelley, C. S.; Affinito, J. On the Surface Chemical Aspects of Very High Energy Density, Rechargeable Li–Sulfur Batteries. *J. Electrochem. Soc.* **2009**, *156* (8), A694. <https://doi.org/10.1149/1.3148721>.
27. Wu, H. L.; Shin, M.; Liu, Y. M.; See, K. A.; Gewirth, A. A. Thiol-Based Electrolyte Additives for High-Performance Lithium–Sulfur Batteries. *Nano Energy* **2017**, *32* (December 2016), 50–58. <https://doi.org/10.1016/j.nanoen.2016.12.015>.
28. Suo, L.; Hu, Y. S.; Li, H.; Armand, M.; Chen, L. A New Class of Solvent-in-Salt Electrolyte for High-Energy Rechargeable Metallic Lithium Batteries. *Nat. Commun.* **2013**, *4*, 1–9. <https://doi.org/10.1038/ncomms2513>.
29. Park, J.; Ueno, K.; Tachikawa, N.; Dokko, K.; Watanabe, M. Ionic Liquid Electrolytes for Lithium–Sulfur Batteries. *J. Phys. Chem. C* **2013**, *117*, 20531–20541. <https://doi.org/10.1021/jp408037e>.
30. Park, J. W.; Yamauchi, K.; Takashima, E.; Tachikawa, N.; Ueno, K.; Dokko, K.; Watanabe, M. Solvent Effect of Room Temperature Ionic Liquids on Electrochemical Reactions in Lithium–Sulfur Batteries. *J. Phys. Chem. C* **2013**, *117* (9), 4431–4440. <https://doi.org/10.1021/jp400153m>.
31. Ren, X.; Chen, S.; Lee, H.; Mei, D.; Engelhard, M. H.; Burton, S. D.; Zhao, W.; Zheng, J.; Li, Q.; Ding, M. S.; Schroeder, M.; Alvarado, J.; Xu, K.; Meng, Y. S.; Liu, J.; Zhang, J. G.; Xu, W. Localized High-Concentration Sulfone Electrolytes for High-Efficiency Lithium–Metal Batteries. *Chem* **2018**, *4* (8), 1877–1892. <https://doi.org/10.1016/j.chempr.2018.05.002>.

32. Cao, R.; Chen, J.; Han, K. S.; Xu, W.; Mei, D.; Bhattacharya, P.; Engelhard, M. H.; Mueller, K. T.; Liu, J.; Zhang, J. G. Effect of the Anion Activity on the Stability of Li Metal Anodes in Lithium-Sulfur Batteries. *Adv. Funct. Mater.* **2016**, *26* (18), 3059–3066. <https://doi.org/10.1002/adfm.201505074>.
33. Singh, A.; Rafie, A.; Kalra, V. Revisiting the Use of Electrolyte Additives in Li-S Batteries: The Role of Porosity of Sulfur Host Materials. *Sustain. Energy Fuels* **2019**, *3* (10), 2788–2797. <https://doi.org/10.1039/c9se00277d>.
34. Weller, C.; Pampel, J.; Dörfler, S.; Althues, H.; Kaskel, S. Polysulfide Shuttle Suppression by Electrolytes with Low-Density for High-Energy Lithium–Sulfur Batteries. *Energy Technol.* **2019**, *7* (12). <https://doi.org/10.1002/ente.201900625>.
35. Zheng, J.; Ji, G.; Fan, X.; Chen, J.; Li, Q.; Wang, H.; Yang, Y.; DeMella, K. C.; Raghavan, S. R.; Wang, C. High-Fluorinated Electrolytes for Li–S Batteries. *Adv. Energy Mater.* **2019**, *9* (16). <https://doi.org/10.1002/aenm.201803774>.
36. Fang, C.; Zhang, G.; Lau, J.; Liu, G. Recent Advances in Polysulfide Mediation of Lithium-Sulfur Batteries via Facile Cathode and Electrolyte Modification. *APL Mater.* **2019**, *7* (8). <https://doi.org/10.1063/1.5110525>.
37. Lee, C. W.; Pang, Q.; Ha, S.; Cheng, L.; Han, S. D.; Zavadil, K. R.; Gallagher, K. G.; Nazar, L. F.; Balasubramanian, M. Directing the Lithium-Sulfur Reaction Pathway via Sparingly Solvating Electrolytes for High Energy Density Batteries. *ACS Cent. Sci.* **2017**, *3* (6), 605–613. <https://doi.org/10.1021/acscentsci.7b00123>.
38. Ren, X.; Chen, S.; Lee, H.; Mei, D.; Engelhard, M. H.; Burton, S. D.; Zhao, W.; Zheng, J.; Li, Q.; Ding, M. S.; Schroeder, M.; Alvarado, J.; Xu, K.; Meng, Y. S.; Liu, J.; Zhang, J. G.; Xu, W. Localized High-Concentration Sulfone Electrolytes for High-Efficiency Lithium-Metal Batteries. *Chem* **2018**, *4* (8), 1877–1892. <https://doi.org/10.1016/j.chempr.2018.05.002>.
39. Zhang, S. S. Sulfurized Carbon: A Class of Cathode Materials for High Performance Lithium/Sulfur Batteries. *Front. Energy Res.* **2013**, *1* (DEC), 1–9. <https://doi.org/10.3389/fenrg.2013.00010>.
40. Qin, F.; Zhang, K.; Fang, J.; Lai, Y.; Li, Q.; Zhang, Z.; Li, J. High Performance Lithium Sulfur Batteries with a Cassava-Derived Carbon Sheet as a Polysulfides Inhibitor. *New J. Chem.* **2014**, *38* (9), 4549–4554. <https://doi.org/10.1039/c4nj00701h>.
41. Lin, Y.; Wang, X.; Liu, J.; Miller, J. D. Natural Halloysite Nano-Clay Electrolyte for Advanced All-Solid-State Lithium-Sulfur Batteries. *Nano Energy* **2017**, *31* (11), 478–485. <https://doi.org/10.1016/j.nanoen.2016.11.045>.
42. Zhang, K.; Qin, F.; Fang, J.; Li, Q.; Jia, M.; Lai, Y.; Zhang, Z.; Li, J. Nickel Foam as Interlayer to Improve the Performance of Lithium-Sulfur Battery. *J. Solid State Electrochem.* **2014**, *18* (4), 1025–1029. <https://doi.org/10.1007/s10008-013-2351-5>.
43. Ahmed, F.; Rahman, M. M.; Sutradhar, S. C.; Lopa, N. S.; Ryu, T.; Yoon, S.; Choi, I.; Lee, Y.; Kim, W. Synthesis and Electrochemical Performance of an Imidazolium Based Li Salt as Electrolyte with Li Fluorinated Sulfonylimides as Additives for Li-Ion Batteries. *Electrochim. Acta* **2019**, *302*. <https://doi.org/10.1016/j.electacta.2019.02.040>.
44. Ahmed, F.; Choi, I.; Ryu, T.; Yoon, S.; Rahman, M. M.; Zhang, W.; Jang, H.; Kim, W. Highly Conductive Divalent Fluorosulfonyl Imide Based Electrolytes Improving Li-Ion Battery Performance: Additive Potentiating Electrolytes Action. *J. Power Sources* **2020**, *455* (2), 227980. <https://doi.org/10.1016/j.jpowsour.2020.227980>.
45. Ahmed, F.; Rahman, M. M.; Chandra Sutradhar, S.; Siraj Lopa, N.; Ryu, T.; Yoon, S.; Choi, I.; Kim, J.; Jin, Y.; Kim, W. Synthesis of an Imidazolium Functionalized Imide Based Electrolyte Salt and Its Electrochemical Performance Enhancement with Additives in Li-Ion Batteries. *J. Ind. Eng. Chem.* **2019**, *78*, 178–185. <https://doi.org/10.1016/j.jiec.2019.06.016>.
46. Kumar, R.; Liu, J.; Hwang, J. Y.; Sun, Y. K. Recent Research Trends in Li-S Batteries. *J. Mater. Chem. A* **2018**, *6* (25), 11582–11605. <https://doi.org/10.1039/c8ta01483c>.
47. Lopez, C. V.; Maladeniya, C. P.; Smith, R. C. Lithium-Sulfur Batteries: Advances and Trends. *Electrochem* **2020**, *1* (3), 226–259. <https://doi.org/10.3390/electrochem1030016>.

48. Pan, H.; Cheng, Z.; He, P.; Zhou, H. A Review of Solid-State Lithium-Sulfur Battery: Ion Transport and Polysulfide Chemistry. *Energy and Fuels* **2020**, *34* (10), 11942–11961. <https://doi.org/10.1021/acs.energyfuels.0c02647>.
49. Dibden, J. W.; Smith, J. W.; Zhou, N.; Garcia-Araez, N.; Owen, J. R. Predicting the Composition and Formation of Solid Products in Lithium-Sulfur Batteries by Using an Experimental Phase Diagram. *Chem. Commun.* **2016**, *52* (87), 12885–12888. <https://doi.org/10.1039/c6cc05881g>.
50. Zhang, X. Q.; Chen, X.; Hou, L. P.; Li, B. Q.; Cheng, X. B.; Huang, J. Q.; Zhang, Q. Regulating Anions in the Solvation Sheath of Lithium Ions for Stable Lithium Metal Batteries. *ACS Energy Lett.* **2019**, *4* (2), 411–416. <https://doi.org/10.1021/acsenergylett.8b02376>.
51. Fantauzzi, M.; Elsener, B.; Atzei, D.; Rigoldi, A.; Rossi, A. Exploiting XPS for the Identification of Sulfides and Polysulfides. *RSC Adv.* **2015**, *5* (93), 75953–75963. <https://doi.org/10.1039/c5ra14915k>.
52. Wu, Y.; Momma, T.; Ahn, S.; Yokoshima, T.; Nara, H.; Osaka, T. On-Site Chemical Pre-Lithiation of S Cathode at Room Temperature on a 3D Nano-Structured Current Collector. *J. Power Sources* **2017**, *366*, 65–71. <https://doi.org/10.1016/j.jpowsour.2017.08.113>.

### Acknowledgements

Dr. Faiz Ahmet, Dr. Thanh-Nhan Tran, Dr. Chen Fang performed experimental work, and analyzed data.



## XIV.5 Strategies to Enable Lean Electrolytes for High Loading and Stable Lithium-Sulfur Batteries (UCSD)

### Ying Shirley Meng, Principal Investigator

University of California, San Diego  
9500 Gilman Dr.  
La Jolla, CA 92093  
E-mail: [shmeng@ucsd.edu](mailto:shmeng@ucsd.edu)

### Hui Du, Co-Principal Investigator

Ampcera, Inc.  
Tucson Tech Park  
1700 E 18th St Ste 102  
Tucson, AZ 85719-6552  
E-mail: [hdu@ampcera.com](mailto:hdu@ampcera.com)

### Mei Cai, Co-Principal Investigator

General Motors.  
30470 Harley Earl Blvd.  
Warren, MI 48092  
E-mail: [mei.cai@gm.com](mailto:mei.cai@gm.com)

### Haiyan Croft, DOE Technology Development Manager

U.S. Department of Energy  
E-mail: [Haiyan.Croft@ee.doe.gov](mailto:Haiyan.Croft@ee.doe.gov)

Start Date: October 1, 2021	End Date: December 31, 2024	
Project Funding (FY23): \$1,058,769	DOE share: \$831,351	Non-DOE share: \$227,418

### Project Introduction

Lithium-sulfur (Li-S) batteries offer the potential for higher energy densities due to the high theoretical capacities of the sulfur cathode (1675 mAh g<sup>-1</sup>). Moreover, by using abundant elemental sulfur, they also benefit from lower material costs than conventional lithium-ion batteries (LIBs) which are still largely based on costly transition metal oxides materials such as nickel and cobalt.<sup>1</sup> Sulfur-based cathodes also offer improved safety factors due to their conversion-based reaction mechanisms which reduce the risks of thermal runaway typical of host-type materials.<sup>2</sup> Moreover, the environmentally benign nature of elemental sulfur also reduces the potential environmental impact of cells when they reach their end of life. However, the commercialization of Li-S still faces several technical barriers that impede its commercialization:

- 1) Inability to enable lean electrolyte conditions necessary for high energy densities.
- 2) Polysulfide dissolution resulting in sulfur inventory loss & continuous electrolyte consumption.

To achieve targets of 400 Wh/kg under realistic sulfur cathode loadings ( $\geq 64$  wt%), lean electrolyte conditions of  $< 3$  g/Ah are needed, an ambitious goal currently unachievable with the state of the art. The highly porous nature of low-density carbon-sulfur (C-S) composite cathodes makes it difficult to prepare compact electrodes with high sulfur loading, often resulting in cracking during the fabrication process. Continuous electrolyte consumption originating from high cathode porosity also results in the need for a large excess of liquid electrolytes to achieve reasonable sulfur utilization and cycle life. There is an urgent need to develop compact electrodes with high sulfur loading and low porosity, with a focus on balancing high tap density and sufficient intrinsic porosity to allow wettability as well as efficient polysulfide adsorption. Recent attempts to reduce electrolyte excess include efforts to improve electrolyte diffusion within porous electrodes, as well as the use

of 3D nanoporous sulfur host structures to improve wettability and reduce tortuosity.<sup>3</sup> However, these studies have yet to demonstrate efficacy under lean electrolyte conditions and high sulfur areal loadings ( $>10 \text{ mAh cm}^{-2}$ ). Comparatively, our promising strategies to enable lean electrolytes for high-loading and stable Lithium-Sulfur batteries are via adopting redox active dense stacking polymers as Li-S cathodes. Our bulky hexaazatrinaphthylene (HATN) polymer reduces the stacking porosity to achieve a high bulk density of  $1.6 \text{ g cm}^{-3}$  by the melting polymerization process, while its intrinsic porosity based on *s*-triazine bonding is maintained.<sup>4</sup> The bulky HATN polymer serves as a Sulfur host material, which shows high S loading with a low porosity in Li-S batteries using a limited amount of electrolyte; regulates the lithium polysulfide deposition; accommodates the cathode volume change from S to  $\text{Li}_2\text{S}$ .

This project is led by UCSD with the collaboration of Ampcera Inc. and General Motors (GM). Our UCSD team has established the baseline setup for the HATN lab-scale synthesis; built the cryogenic characterization toolbox for Li-S batteries; developed the quantitative methodologies to analyze the degradation of Li-S batteries. Ampcera Inc. is a company possessing the technology of solid-state chemical synthesis, which dedicates the effort to scaling up the synthesis of HATN polymer (kg-scale) in this project. GM contributes to the large-size Li foil supply and large-capacity cell assembly owing to their robust facilities and resources for pouch cell production. Upon effort of the entire team, we can insight into the root limitations of high-energy-density Li-S batteries and develop strategies to sort them out.

### Objectives

The objective of the project is to develop high energy density ( $>400 \text{ Wh/kg}$ ) and low cost ( $<68 \text{ \$/kWh}$ ) Li-S pouch cells. More specifically, the main goal of this project is to develop a high-performance and low-cost polymer-based S electrode (HATN-S) and novel electrolyte formulation to enable long-term stable cycling. The best combination of novel cathode synthesis process, new electrolyte formula and full cell design will provide us a high energy Li-S pouch cell. The critical success factors in achieving that goal include:

- Develop novel electrode architectures and electrolyte chemistries including HATN polymer-Sulfur composite electrode, and state-of-the-art liquid electrolyte systems to enable Li-S pouch cell that use high areal loading ( $>10 \text{ mAh cm}^{-2}$ ) and low porosity (30%) cathode with high full cell energy density ( $>400 \text{ Wh/kg}$ ).
- Utilize advanced characterization, and diagnosis tools for resolving the root causes of capacity fade and identify electrode architectures that improve the cycle life of Li-S pouch cells.
- Close collaboration between university-industry to deliver practical pouch type cells with low cost ( $<68 \text{ \$/kWh}$ ).

### Approach

To achieve that, novel electrode architectures using the HATN polymer-sulfur composite electrode will be explored to achieve the low cathode porosity and the high S active loading of the composite electrode. Additionally, advanced electrolyte systems and the optimization of Li metal anode will be applied further to increase the energy density of the Li-S pouch cell. If successful, the proposed HATN polymer-sulfur composite electrode will achieve less than 30% porosity, significantly decreasing electrolyte usage with high areal capacities of  $>10 \text{ mAh cm}^{-2}$ , enabling lean electrolyte conditions  $<3 \text{ g/Ah}$  in the full Li-S pouch cell.

### Results

In budget plan 2 (BP2), the characterization toolbox, including cryogenic focused ion beam-scanning electron microscopy (cryo-FIB-SEM), titration-gas chromatography (TGC), and High-performance liquid chromatography-ultraviolet spectroscopy (HPLC-UV), was constructed to quantify the Li and S inventory loss in Li-S batteries (Q1). It revealed that Li losses are more severe under lean electrolyte conditions (baseline electrolyte:  $1 \text{ M LiTFSI DOL/DME}$ , vol/1:1, 2 wt.%  $\text{LiNO}_3$ ) due to the consumption of limited  $\text{LiNO}_3$  reservoir in lean electrolyte conditions and polysulfide corrosion (Q2). HPLC-UV methodology was introduced to quantify the consumption additives of  $\text{LiNO}_3$  and the novel additive (NPL) compound in the baseline and the new electrolytes, and the standard curves of  $\text{LiNO}_3$  and the NPL concentration were established (Q3). The electrolyte consumption in nanostructured C-S cathode-based Li-S batteries is

tremendously larger than in bulky S cathode-based ones (Q3) due to larger cathode porosity (larger surface area). These results suggest the importance of using bulk S cathode materials to decrease the electrolyte consumption to achieve lean electrolyte usage for high-energy-density Li-S batteries. In Q3, it was demonstrated that the HATN/CNT-S cathode features a low porosity of 38% and tortuosity of 2.07, which could enable lean electrolyte usage in Li-S batteries with electrolyte-to-sulfur, E/S ratio of  $6 \mu\text{l}/\text{mg}_{\text{sulfur}}$  paired with thin lithium ( $100 \mu\text{m}$ ).

Further efforts were dedicated to the scalable synthesis of the HATN/CNT-S electrode materials by optimizing the synthetic conditions and decreasing the cost of raw materials. As decomposition-based  $\text{LiNO}_3$  is required in the charge and discharge of Li-S batteries, a stable alternative is necessary to avoid continuous depletion of its critical function. Thus, a new electrolyte (NewEle) system is proposed to avoid reliance on  $\text{LiNO}_3$ , using an alternative additive that is stable at the Li metal anode. In applying this new electrolyte system to the HATN/CNT-S cathode, stable cell cycling behavior has been achieved using lean electrolyte conditions with a capacity retention of  $\sim 70.2\%$  based on a high initial capacity of  $\sim 6 \text{ mAh cm}^{-2}$  after  $\sim 100$  cycles, compared to the baseline  $\text{LiNO}_3$  containing electrolyte that shows severe degradation after 50 cycles. The HATN/CNT-S cathode has been used in single-layered pouch cell prototyping in Q4, 2023 for electrochemical performance validation.

***Developing new electrolyte to address the bottleneck of polysulfide corrosion.***

It is crucial to identify the effect of polysulfide in practical Li-S batteries using lean electrolyte and lean lithium. A simple calculation was done to mimic the potential concentration of polysulfide under lean-electrolyte conditions (Q1, 2023) by converting the utilized S of the cathode ( $1000 \text{ mAh g}^{-1}/1675 \text{ mAh g}^{-1} = \sim 60\%$ ) into polysulfide ( $6 \text{ S} \sim \text{Li}_2\text{S}_6$ ) based on the electrolyte volume according to the E/S ratio ( $6 \mu\text{l mg}_{\text{sulfur}}^{-1}$ ). The polysulfide concentration is calculated to be  $>0.52 \text{ mol/L}$  ( $>0.52 \text{ M}$ ). The fresh Li vanished after 1 week in a  $0.5 \text{ M Li}_2\text{S}_6$  solution showing that Li is vulnerable in such a high concentration of polysulfide ((Figure XIV.5.1a). Thus, a new electrolyte has been developed to address the issue of polysulfide corrosion. The effectiveness was justified by immersing a Li foil ( $100 \mu\text{m}$ ) into the new electrolyte with  $0.5 \text{ M Li}_2\text{S}_6$  for 1 month. It shows a high Li inventory retention of  $86.43\%$  quantified by titration gas chromatography (TGC) (Figure XIV.5.1b), which means that Li features high chemical compatibility with concentrated polysulfide owing to the new electrolyte. The electrochemical stability of the new electrolyte was further compared to the baseline electrolyte by using the high-capacity HATN/CNT-S cathode and thin Li anode ( $100 \mu\text{m}$ ) with a low E/S ratio  $6 \mu\text{l mg}_{\text{sulfur}}^{-1}$  (Figure XIV.5.1c and 1d). The voltage profiles in the new electrolyte have two well-defined plateaus typically located at  $2.3 \text{ V}$  and  $2.1 \text{ V}$  ((Figure XIV.5.1d), which shows that sulfur redox also dominates the cells like the baseline counterpart. The cathode delivers a slightly higher specific capacity in the new electrolyte (attributed to the error bar), indicating that the Li inventory loss can be larger as higher Li utilization generates more inactive Li.

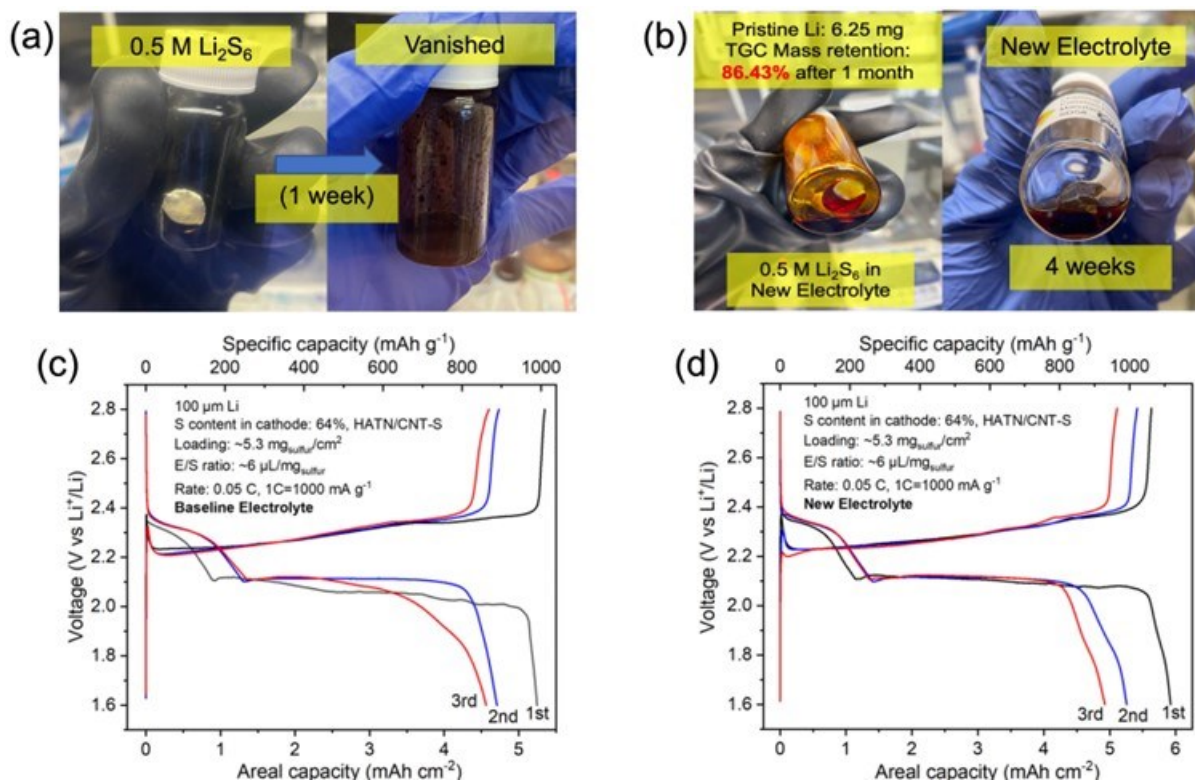


Figure XIV.5.1 (a) The photos showing the Li foil immersed into 0.5 M Li<sub>2</sub>S<sub>6</sub> before and after 1 week; (b) Photos of 100 μm Li foils inside the new electrolyte with 0.5 M Li<sub>2</sub>S<sub>6</sub> for 1 month (86.43% Li inventory retention) and the bare new electrolyte for 4 weeks (being shining); The voltage profiles of the HATN/CNT-S cathode with 5.30 mg<sub>sulfur</sub> cm<sup>-2</sup> with a low E/S ratio of 6 μL mg<sub>sulfur</sub><sup>-1</sup> in the baseline electrolyte of 1 M LiTFSI in DOL/DME (1:1, vol), 2 wt.% LiNO<sub>3</sub> (c) and the new electrolyte (d) at 0.05 C, 1 C = 1000 mA g<sup>-1</sup>.

#### Unveiling the effectiveness of polysulfide corrosion inhibition by the new electrolyte.

We also established a series of characterization tools to elucidate the root cause of short cycling life of the Li-S system. In Q2 & Q3, 2023, polysulfide corrosion has been pinpointed as the major challenge of achieving stable cyclability of Li-S batteries with a high energy density. The new electrolyte was developed and evaluated by using a high-capacity HATN/CNT-S cathode (>5 mAh cm<sup>-2</sup>, Q2, 2023) and the 100-μm lithium anode with a low E/S ratio of <6 μL mg<sub>sulfur</sub><sup>-1</sup>. The Li inventories in both electrolytes were quantified in Q2, 2023, which shows 8.31% from 6.25 mg (pristine) in the new electrolyte, much smaller than 18.26% from 7.41 mg (pristine) in the baseline electrolyte (Figure XIV.5.2b). The transparent TGC solution (Figure XIV.5.2b) of the cycled Li (Figure XIV.5.2.a) in the new electrolyte also illustrates the inhibition of polysulfide corrosion. Moreover, the morphology of the cycled Li anodes was investigated by Cryo-FIB-SEM (Q3, 2023). The large-area top-view images show bulky Li deposition in both electrolytes Figure XIV.5.2.c and Figure XIV.5.2.e). Still, the cycled Li in the new electrolyte is denser (Figure XIV.5.2.e), indicating less anode-electrolyte reaction. And the weak sulfur signal in the corresponding EDX spectrum (Figure XV.5.2f) proves that Li reaction with polysulfide is minor in the new electrolyte system compared to the baseline (Figure XIV.5.2d), indicating the successful inhibition of polysulfide corrosion.

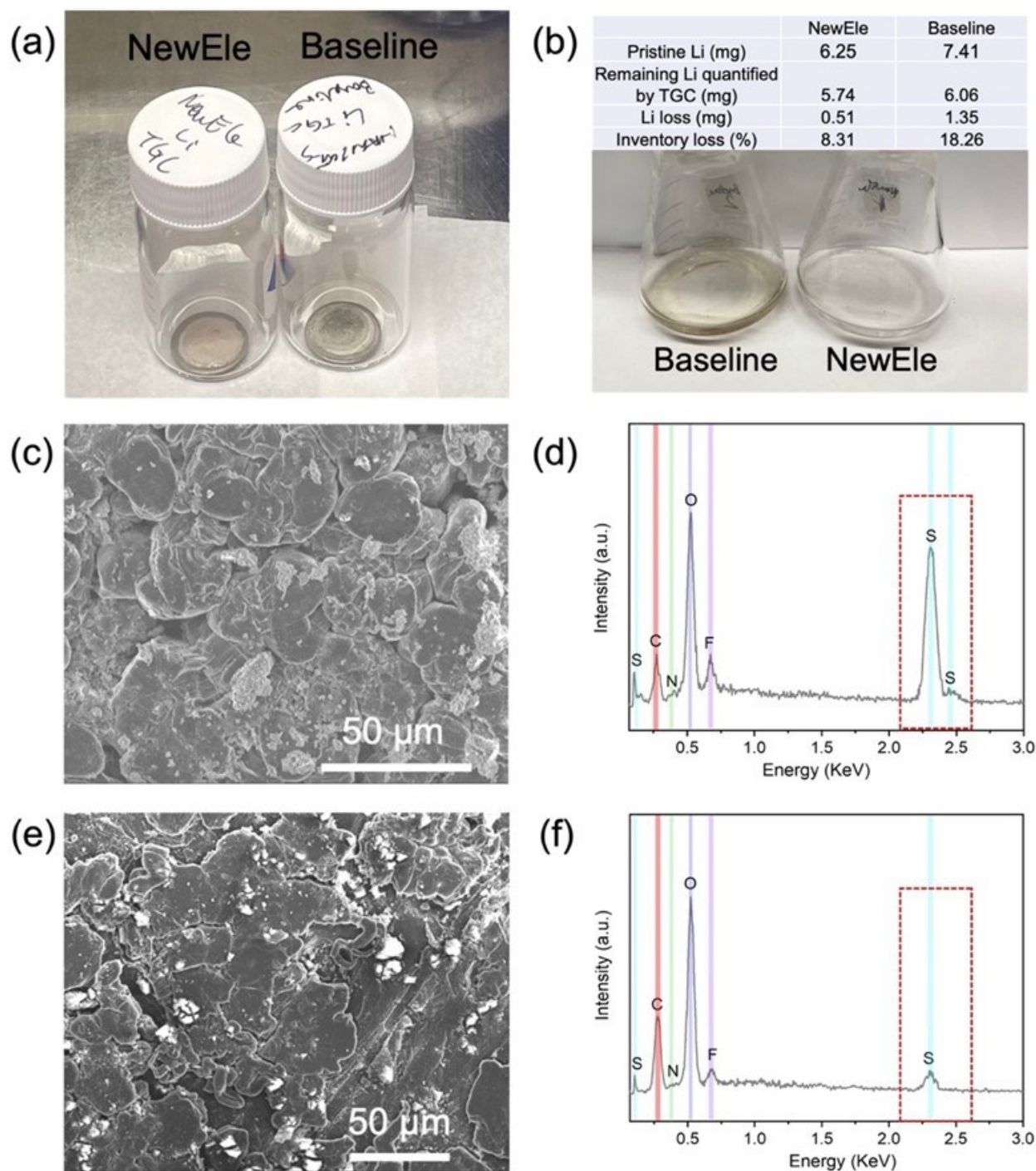
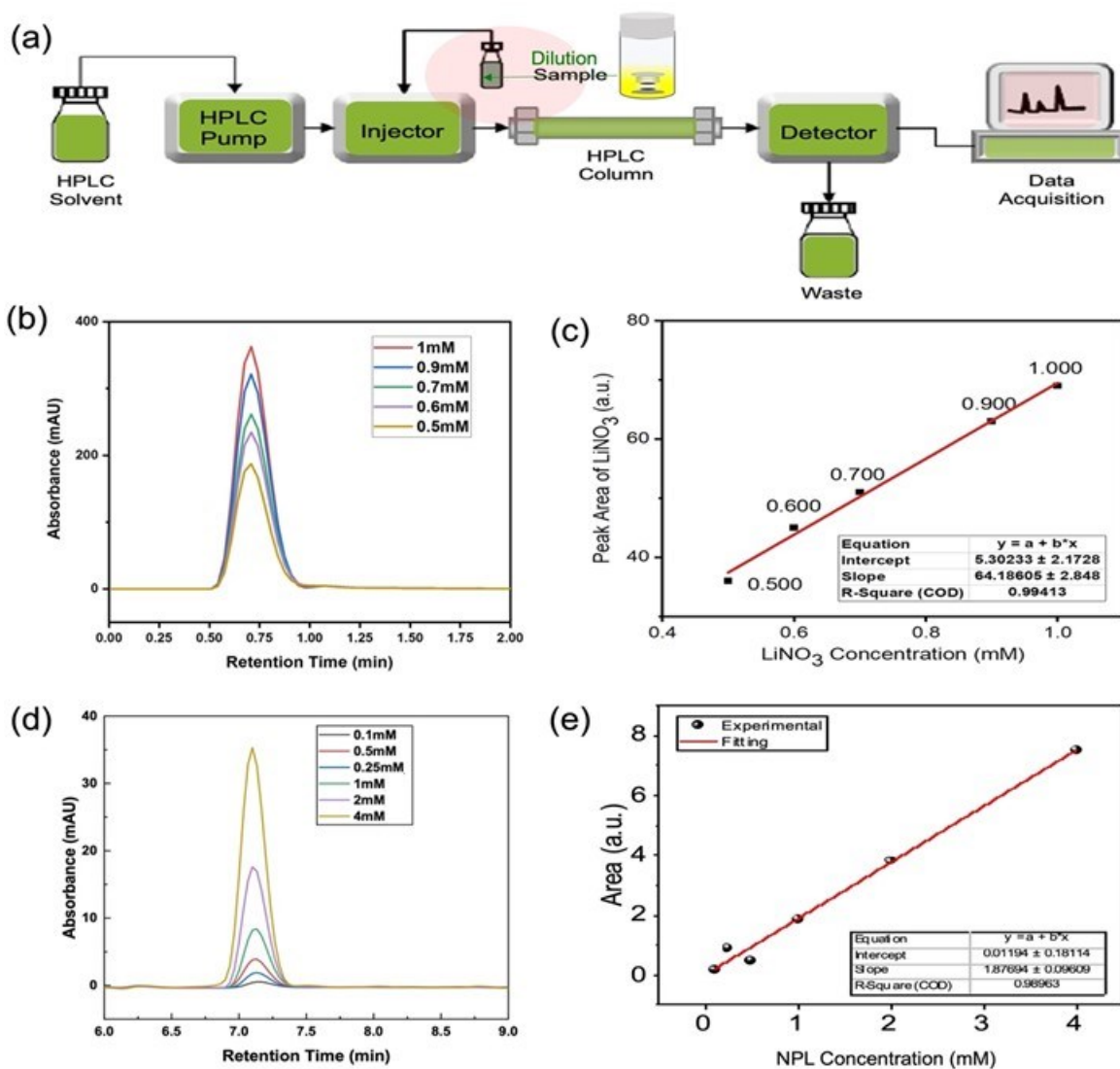


Figure XIV.5.2 (a) The photo of the cycled Li anodes in the baseline and new electrolytes (Q2, 2023); (b) The photo of the TGC solutions in the two electrolytes with the table of the correlated TGC results; The large-area cryo-SEM images of the cycled Li anodes (top-view) and the corresponding accumulated Energy-dispersive X-ray (EDX) spectra in (c & d) the baseline and (e & f) new electrolytes.

#### Quantifying the depletion of effective additives in baseline and new electrolytes

In Q2, 2023, the HPLC-UV methodology was introduced to quantify the consumption of  $\text{LiNO}_3$  in the baseline electrolyte of 1 M LiTFSI in DOL/DME (1:1, vol), 2 wt.%  $\text{LiNO}_3$  and the NPL additive in our newly developed electrolyte. In Figure XV.5.3a, the cycled cells were disassembled and dissolved by DOL/DME

solvent, which generates a homogeneous liquid sample (electrolyte). The samples were injected into the HPLC column chromatography for separation and then characterized by the UV detector. Based on the polarity of different species in the sample,  $\text{LiNO}_3$  and NPL were readily separated and eluted out.



**Figure XIV.5.3** (a) The schematic of the HPLC-UV methodology used to investigate the  $\text{LiNO}_3$  amount; (b) The HPLC-UV spectra of  $\text{LiNO}_3$  solutions ranging from 0.5 mM to 1 mM and (c) The corresponding standard curve of  $\text{LiNO}_3$ ; (d) The HPLC-UV spectra of the NPL solutions ranging from 0.1 mM to 4 mM and (e) The corresponding standard curve of the NPL additive in the new electrolyte.

It is known that cathode porosity and tortuosity impact electrolyte usage and wettability. To investigate the influence on electrolyte consumption, various S cathodes will be evaluated for comparison. Thus, a standard curve of  $\text{LiNO}_3$  concentration vs UV adsorption was established (Figure XIV.5.3b and Figure XIV.5.3c), and it can be used to retrieve the accurate concentration of the  $\text{LiNO}_3$  at different stages in various S cathodes. The remarkable  $\text{LiNO}_3$  depletion is correlated to decomposition during the charging process to facilitate polysulfide to be oxidized into S, which was verified in FY2022. The NPL compound was designed and synthesized to replace  $\text{LiNO}_3$  as features minor depletion during cycling validated in FY2022. The standard curve of the NPL additive in the new electrolyte was also established (Figure XIV.5.3d and Figure XIV.5.3e), which can be used

to monitor the NPL amount evolution alongside the cycling of Li-S cells in Q3, FY2023. Furthermore, since the S redox chemistry is an interfacial reaction on the conductive carbon host materials, the C-S cathode consumes far more additives during the charge and discharge. Hence, to achieve lean electrolyte utilization for high energy density, the S cathode should be of less porosity and tortuosity instead of the conventional cathode design principle of the nanostructured C-S cathode.

**Investigating the 3-D porosity and tortuosity of the dense-stacking HATN/CNT-S cathode.**

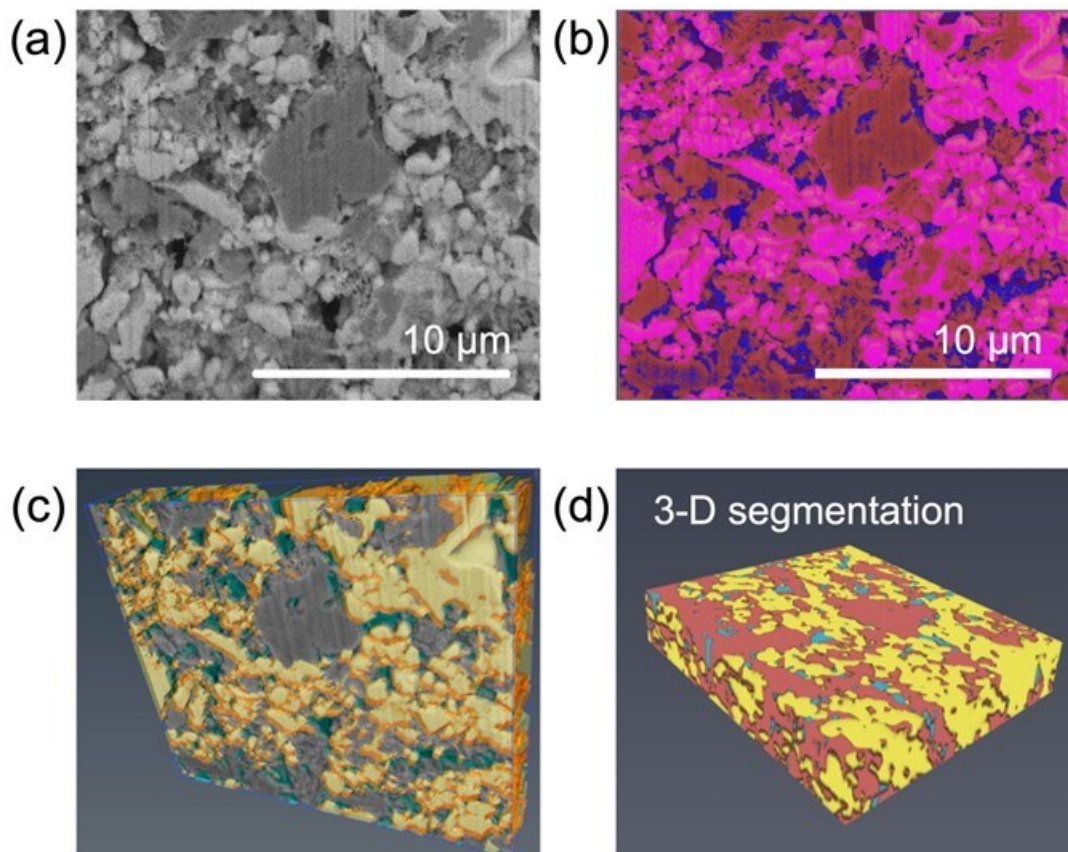


**Figure XIV.5.4** (a) The Cryo-FIB image of the cross-section view of the HATN/CNT-S cathode with a high S loading of  $\sim 9.56 \text{ mg cm}^{-2}$ . (b) The demonstration of segmentation of cathode components, including micron-sized sulfur (magenta), Voids (dark blue), and HATN/CNT + super P + binder (red) of the first slice of 40 milling slices by Cryo-FIB (slice interval of 100 nm). (c) The 3-D reconstruction of 40 Cryo-FIB slices in total using Avizo3D software, giving the distributions sulfur (yellow) and the void volume (cyan, 7.5%). (d) The 3-D segmentation of the HATN/CNT-S cathode for 3-D tortuosity ( $\tau$ ) calculation using a MatLab application of TauFactor.

This project focuses on the bulky dense-stacking HATN polymer as S host materials. In BP1, carbon nanotubes (CNTs) were incorporated into the HATN polymerization to construct a good 3D ion and electron conduction network, while maintaining the same S content and the bulky structure of the HATN host. 3-D porosity (pore volume/total volume,  $\epsilon$ ) and tortuosity (pore distribution,  $\tau$ ) are the two key factors that affect the electrolyte excess within S cathodes and their electrolyte wettability since high cathode porosity consumes more electrolyte and high electrode tortuosity deters the electrolyte wetting process (Q3). The conventional S cathodes feature high porosity originating from the nanostructured materials, including sulfur by melt infusion, carbon, and host materials. Their pores are hardly distinguished and can be squeezed by calendaring, causing high tortuosity. Thus, for conventional S cathodes, only the porosity can be measured by the portion of pore volume, i.e., (practical cathode volume-theoretical cathode volume)/practical cathode volume, as discussed in previous quarters.

However, the HATN/CNT-S cathode can be readily segmented by non-porous bulk S, voids, and the composite of HATN/CNT-super P-binder (Figure XIV.5.4b) based on the Cryo-FIB images (Figure XIV.5.4a). By 3-D reconstruction of all the Cryo-FIB slices, the spatial distribution and volumes of voids and sulfur can be identified (Figure XIV.5.4c). Considering a measured porosity ( $\epsilon$ ) of 38% and a calculated void volume of 7.5% (Figure XIV.5.4c) for the HATN/CNT-S cathode, the porosity generated by the composite of HATN/CNT-super P-binder is 30.5%. Since the electrolyte cannot permeate the micron-sized sulfur, a low 3-D tortuosity ( $\tau$ ) of 2.07 is obtained by allowing electrolyte to diffuse into voids and the pores of HATN/CNT-super P-binder using a MatLab application of TauFactor (Figure XIV.5.4d). The above characterization and calculation are based on the thick HATN/CNT-S (190  $\mu\text{m}$ ) cathode with a high S loading of  $\sim 9.56 \text{ mg cm}^{-2}$ . Upon such a low porosity and tortuosity, the as-prepared HATN/CNT-S cathode is likely to deliver rational electrochemical performance under lean lithium and electrolyte conditions, which will be discussed next.

#### ***The scaling up of the HATN/CNT synthesis.***

Ampcera has secured a multi-kg supply chain for the Triquinoyl hydrate and 3,4-diaminobenzonitrile precursors, which have been made available to UCSD and GM upon request. Background infrared (IR) spectroscopy data of the precursor material is presented in a previous report. The cost of raw materials has been decreased dramatically to \$3000/kg of Triquinoyl Hydrate and \$4500/kg of 3,4-Diaminobenzonitrile from  $> \$20\text{k/kg}$  of the ones from TCI and Sigma (Q3, 2023). Note that this is a price per kg at the current volumes we purchase. The price per kg would decrease significantly in the future when the precursors are produced at larger volumes and purchased by the barrel, or pallet. Therefore, based on future assumptions such as a precursor cost decrease of 90% ( $\$300/\text{kg}$  and  $\$450/\text{kg}$ ), the estimated cost of the HATN is  $\sim \$500/\text{kg}$  based on the synthetic reaction. Further, considering that HATN only contains 13% in our cathode recipe while other materials like CNT (13%), super P (5%), sulfur (64%), and binder (5%) are relatively inexpensive, compared to metal oxide chemistry cathode, it is promising to achieve the final goal of 68  $\$/\text{kWh}$ . Ampcera will keep working on the scaled synthesis of the HATN polymer and the HATN/CNT composite in the coming quarters. An overview of the HATN monomer synthesis (Figure XIV.5.5a), the HANT/CNT composite polymerization (Figure XIV.5.5b), and Ampcera's overall project work plan is summarized in Figure XIV.5.5c. The synthesis of the HATN monomer uses the recently purchased (kg scale) Triquinoyl hydrate and 3,4-Diaminobenzonitrile precursors. The bright yellow product (digital image on the right) along with the NMR spectrum confirms a high-purity product can be achieved (Figure XIV.5.5d). These NMR spectra have been compared with spectra from the lab scale synthesis of HATN monomer provided by UCSD in previous reports. The percent yield was also increased to 90% using a modified washing procedure. It should be noted that these results were obtained using the lab-scale synthesis developed in Budget Period One (BP1, Figure XIV.5.5b).



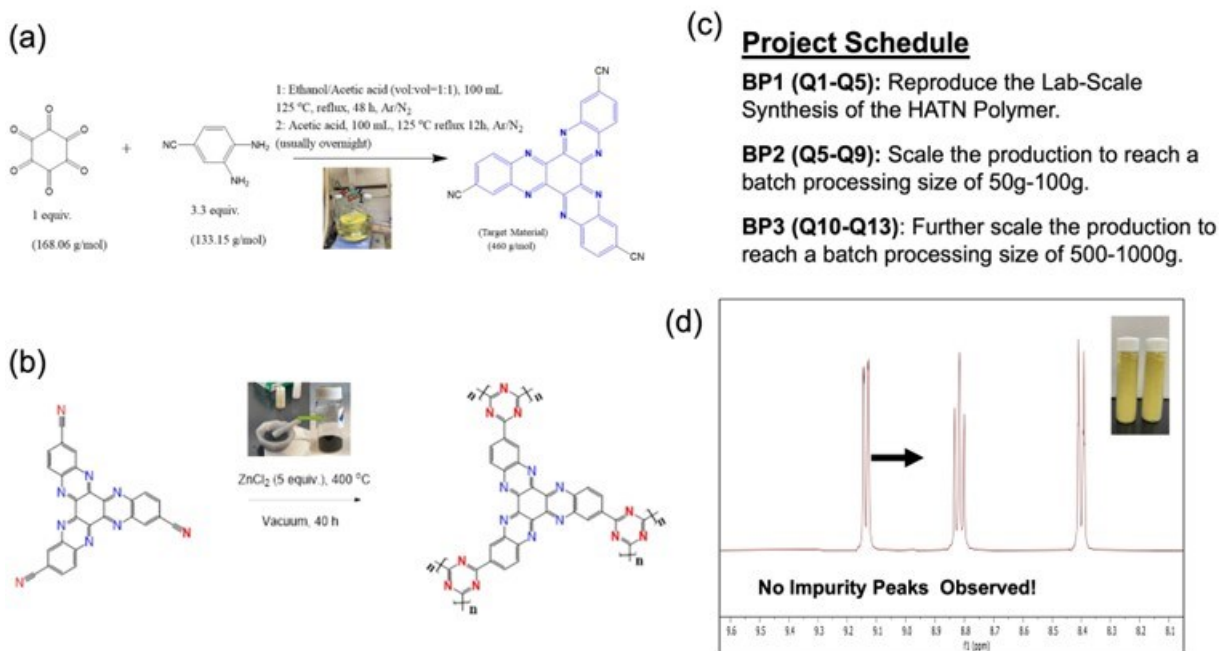


**Figure XIV.5.5 (a and b)** A summarized overview of Ampcera's overall work plan. The synthesis of the HATN monomer and polymer. (c) The project schedule of industrial production of the materials. (d) The H-NMR spectrum of the scaled HATN monomer.

Ampcera recently scaled the monomer synthesis to reach the BP2 goal of 50g as shown in the digital images in Figure XIV.5.6. The digital image in Figure XIV.5.6a is the synthesis at the initial stages before turning dark green. The digital image in Figure XIV.5.6b is the finished monomer before washing and filtration. The digital image in Figure XIV.5.6c is the final HATN monomer product (50g) in a sealed jar. The product is compared to a ruler for reference. The 50 g batch of HATN monomer still needs to be evaluated using NMR and FTIR at the University of Arizona. A small portion of the material will also be sent to UCSD for additional analysis. It should be noted that Ampcera is currently undergoing facility expansion and upgrades that are essential for its core business (solid-state electrolytes). As part of these upgrades, its wet acid lab is also getting updated with better fume hood equipment and safety features needed to carry out this project in BP3 (scaled synthesis of 500 g or more). The apparatus for the HATN/CNT polymerization is presented in Figure XIV.5.6d. It should be noted that Ampcera adopted the same setup recommended by Dr. Xiaowei Wang at UCSD. Figure XIV.5.6d shows the quartz tube inside the muffle furnace for vacuum polymerization at 400 °C. Figure XIV.5.6e is a zoomed-in image of the HATN/CNT composite after a 40-hour polymerization. The monomer to ZnCl<sub>2</sub> (anhydrous powder) mass ratio was fixed 1:3 by UCSD (Q3, 2023). It should be noted that polymerization is still at the lab scale at Ampcera. The process will be scaled once Ampcera receives confirmation that the product is qualified for electrode fabrication. So far Ampcera has sent six HATN/CNT samples to UCSD for evaluation (Trial-1, Trial-2, and Batches A-D). The HATN/CNT composite from Trial-1 was washed using a truncated washing procedure that is more scaleup-friendly to remove the ZnCl<sub>2</sub> catalyst and unreacted HATN monomer. However, severe corrosion was observed in the initial battery testing indicating that a high degree of ZnCl<sub>2</sub> was still present in the composite (Q3, 2023). The other 4 batches (A-D) are under evaluation to ultimately validate the synthesis and post-treatment of the HATN/CNT materials.

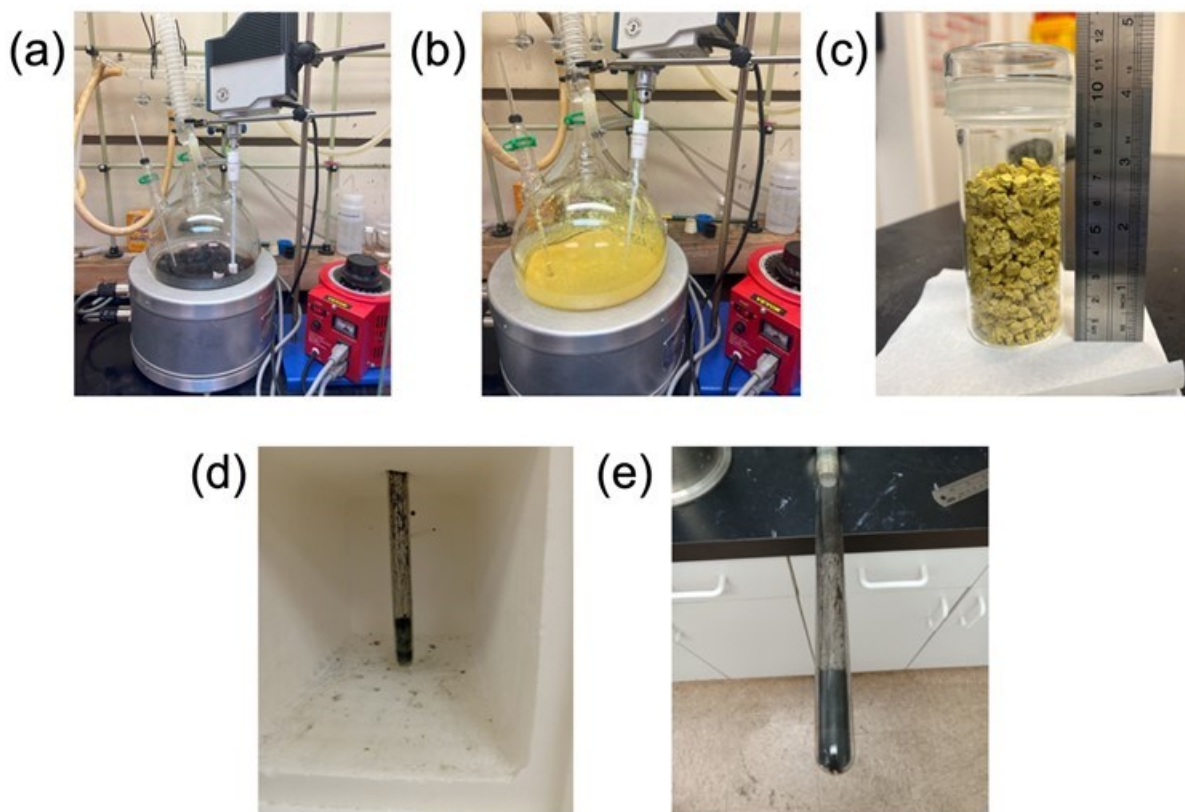


**Figure XIV.5.6** Digital images of the HATN monomer synthesis at 50-g scale (a = initial & b = final). The digital image in (c) is the HATN monomer product with a ruler for reference. (d) The image of the polymerization setup. (e) a zoomed-in view of the HATN/CNT polymer composite product.

In Q4, 2023, UCSD validated the HATN/CNT samples from Ampcera by the fabrication of HATN/CNT-S cathodes. The post-treatment of unwashed HATN/CNT (Batch A) was done at UCSD. Notably, two times of water washing must be conducted after the treatment of trifluoro acetic acid (TFA) treatment to confirm a neutral filtrate using PH paper. This suggests that TFA residues were contained within the HATN/CNT matrix while it removes the HATN monomer. Another possibility is the agglomerated HATN/CNT composite was not ground well for efficient water washing. Thus, the well-washed HATN/CNT composite allows good HATN/CNT-S cathode fabrication through slurry preparation using the same slurry recipe of (30% solid ratio), slurry casting, and vacuum drying (Figure XIV.5.7b), which presents a similar sulfur loading of  $6.2 \text{ mg cm}^{-2}$  without Al foil corrosion and electrode cracking. Comparatively, the HATN/CNT-S cathode based on the washed Ampcera HATN/CNT composite (Batch C) features minor cracking and corrosion issues (Figure XIV.5.7a). Still, it is much better than the previous trials of materials with severe corrosion issues (Q3, 2023). This demonstrates the industrial synthesis of the HATN/CNT materials is only affected by the post-treatment, Ampcera and UCSD will work closely on addressing this final obstacle to fulfil the goal of low-cost Li-S cells.

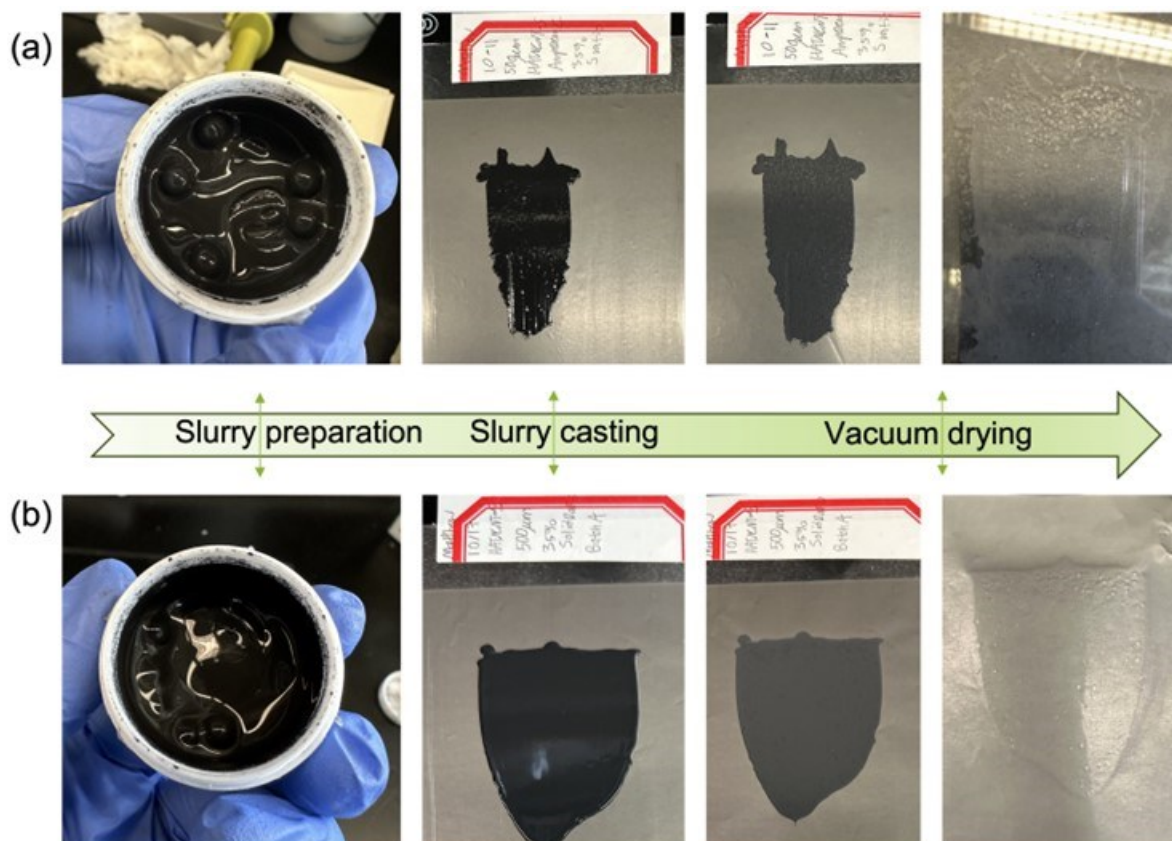


Figure XIV.5.7 Digital images of the HATNCNT-S cathode based on the HATN/CNT composite from Ampcera. (a) Batch C and (b) Batch A that followed the same polymerization process.

To further understand the impact of using the new electrolyte on cycling behavior, in this quarter, the C-S cathode with a sulfur loading of  $3.4 \text{ mg cm}^{-2}$  provided by GM was used to construct Li-S cells by pairing it with  $100 \text{ }\mu\text{m}$  Li anode using an E/S ratio of  $8 \text{ }\mu\text{l mg}_{\text{sulfur}}^{-1}$ . Besides, the post-analysis was carried out by quantifying the Li inventory loss after stable cycling in both the baseline and the new electrolytes (Figure XIV.5.8). The GM C-S cathode features limited cycling behavior with dramatic Coulombic efficiency decay after 30 cycles in the baseline electrolyte suggesting the existence of polysulfide shuttle that consumes Li (Figure XIV.5.8a). Figure XIV.5.8 exhibits the charge-discharge curves of some selected cycles of the Li-S cells in Figure XIV.5.8a. The difference between discharge capacity and charge capacity is increasing along with the cell cycling (Figure XIV.5.8b), leading the decrease of Coulombic efficiency from  $\sim 100\%$  to  $\sim 50\%$  (Figure XIV.5.8a). By sharp contrast, the cycle life in the new electrolyte has been extended twice of the baseline by referring to a point of moderately high Coulombic efficiency of  $90\%$  (Figure XIV.5.8c), while their Li inventory losses after cycling are approaching. The correlated voltage profiles also show good capacity retention in the Li-S cells using this new electrolyte (Figure XIV.5.8d). Therefore, the effect of the new electrolyte is reaffirmed by evaluating the merely S-redox-based cathode (C-S) in both electrolytes, which presents much improved electrochemical performance.

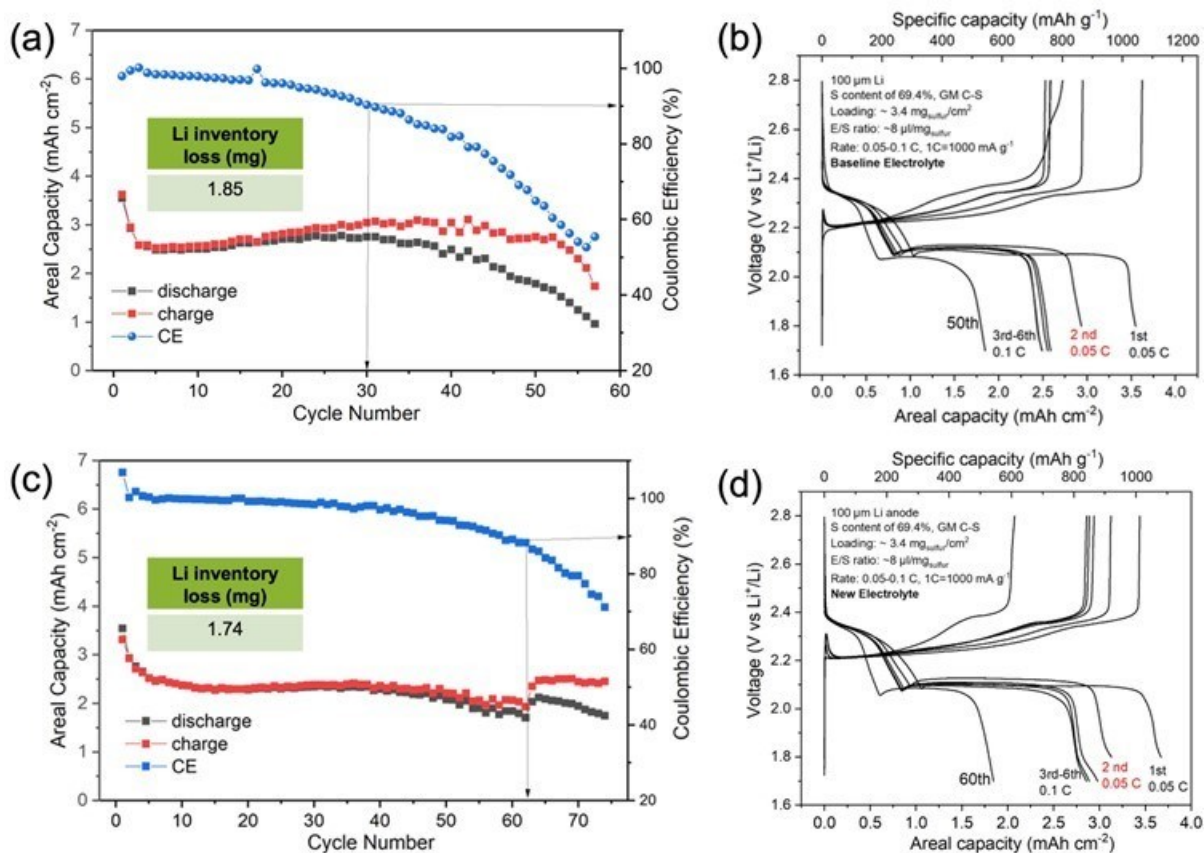
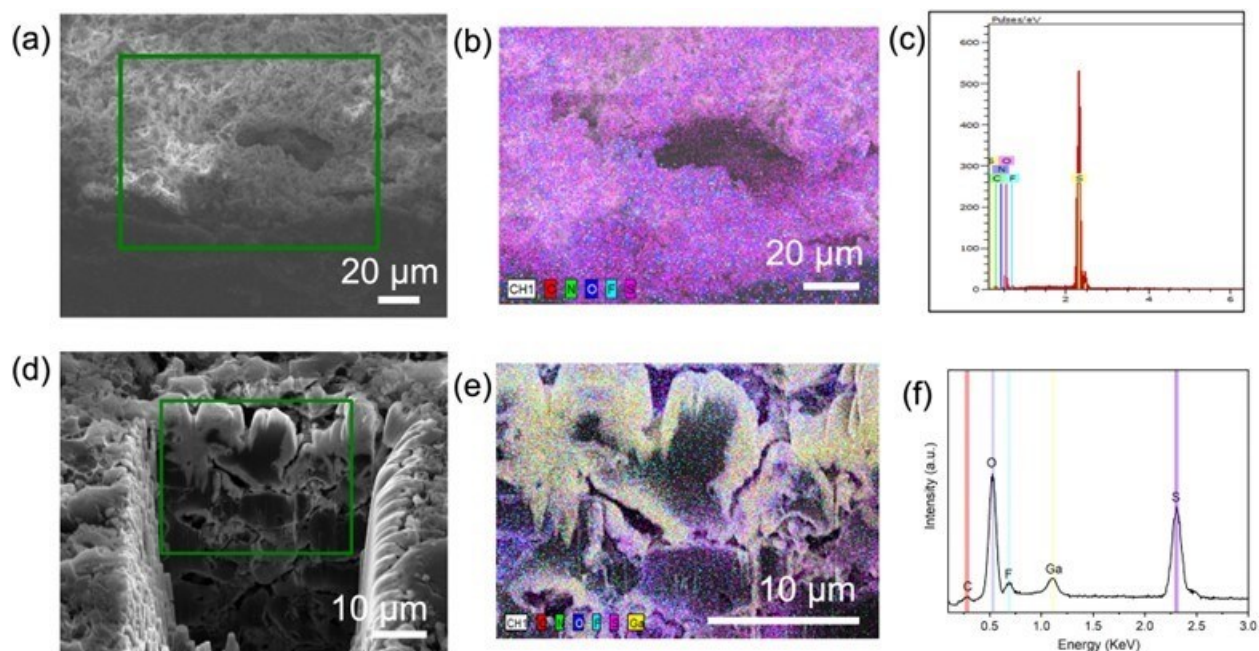


Figure XIV.5.8 (a) The cycling behavior of the GM C-S cathode with a sulfur loading of 3.4 mg cm<sup>-2</sup> and an E/S ratio of 8  $\mu\text{l mg}_{\text{sulfur}}^{-1}$  in the baseline electrolyte using 100  $\mu\text{m}$  Li anode. (b) The related voltage profiles. (c) The cycling behavior of the GM C-S cathode in the new electrolyte under the same conditions as the baseline. (d) The corresponding voltage profiles. The TGC results are inserted.



**Figure XIV.5.9** (a) The large-area cryo-SEM images of the cycled Li anode (cross-section view). (b) the Energy-dispersive X-ray (EDX) element mapping of the selected area. (c) the corresponding accumulated EDX spectra of the Li anode cycled in the baseline electrolyte. (d) The cryo-FIB cross-section image of the cycled Li anode. (e) the Energy-dispersive X-ray (EDX) element mapping of the selected area. (f) the corresponding accumulated EDX spectra of the Li anode cycled in the baseline electrolyte.

#### **Comparing the new electrolyte with the baseline electrolyte using the GM C-S and the HATN/CNT-S cathodes**

In Q2 and Q3 (FY23), GM C-S cathodes were used to validate the electrochemical performances in the baseline electrolyte and the new electrolyte, which shows the extended cycle life of Li-S cells in the new electrolyte with low Li inventory loss quantified by TGC (Q3). In Q4, 2023, the post-mortem analysis of Li anodes cycled in the two electrolytes was conducted by using cryo-FIB-SEM shown in Figure XIV.5.9. For the Li anode cycled in baseline electrolyte, it sustains severe degradation and pulverization (Figure XIV.5.9a), which is caused by the polysulfide corrosion in Li-S cells evidenced by uniform S distribution and major S peak in the accumulated EDX mapping (Figure XIV.5.9b) and its corresponding spectra in Figure XIV.5.9c. By sharp contrast, bulky Li deposition maintains after a long cycling process in the new electrolyte (Figure XIV.5.9d), and the EDX mapping of the cryo-FIB cross-section shows large bulks of unreacted Li (Figure XIV.5.9e). The EDX spectrum (Figure XIV.5.9f) shows that the S intensity is at the same level with O representing the SEI species on Li surface, further confirming the polysulfide corrosion has been inhibited by using the new electrolyte.

Furthermore, the effect of the new electrolyte is validated by evaluating the HATN/CNT-S cathode in both electrolytes, which presents much improved electrochemical performance. The baseline performance of the HATN/CNT-S cathode was reported, which shows evident capacity decay after 76 cycles despite the potential high energy density originating from using a low E/S ratio of  $6 \mu\text{l mg}_{\text{sulfur}}^{-1}$  and a very low N/P ratio of  $\sim 2.6$  in coin-cells (Figure XIV.5.10a and Figure XIV.5.10b). To achieve the desirable cycling stability of high-energy-density Li-S batteries, the high-loading HATN/CNT-S cathode ( $>6 \text{ mAh cm}^{-2}$ ) has been obtained from the new electrolyte under lean electrolyte and lithium conditions (UCSD, Q3, 2023). Figure XIV.5.10c presents the well-defined voltage profiles of Li-S batteries showing a high specific capacity of  $>1000 \text{ mAh g}^{-1}$  under a low N/P ratio of  $\sim 2.6$ . The cells are currently cycling with capacity retention of  $\sim 70.2\%$  after 98 cycles based on an initial capacity of  $\sim 6 \text{ mAh cm}^{-2}$  at  $0.1 \text{ C}$  (Figure XIV.5.10d). The coin-cell study helps the team's insight into the root causes of cell fading using quantitative methodologies like TGC and TGA. The related quantitative

results of the S inventory will be obtained in the future to rationalize the effect of the new electrolyte on the cathode side. The above results show the feasibility of using the new electrolyte to achieve Li-S batteries with long cyclability. Future endeavors will focus on prototyping single-layered or few-layered Li-S pouch cells.

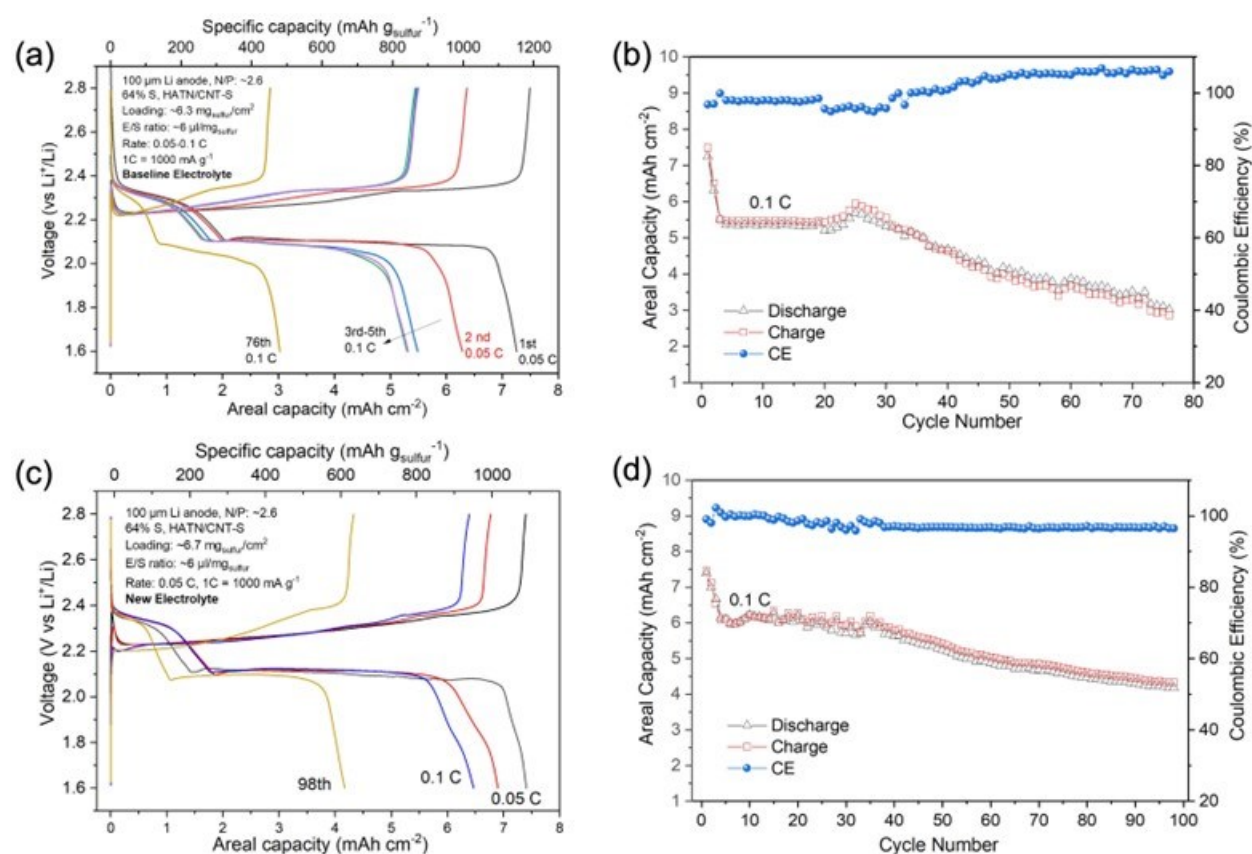


**Figure XIV.5.10** (a) The voltage profiles and cycling behavior of the HATN/CNT-S cathode with  $\sim 6.5 \text{ mg}_{\text{sulfur}} \text{ cm}^{-2}$  with a low E/S ratio of  $6 \mu\text{l mg}_{\text{sulfur}}^{-1}$  in the baseline electrolyte (a and b) and the new electrolyte (c and d) at 0.05 C, 1 C =  $1000 \text{ mA g}^{-1}$ .

In Q2, 2023, the high-capacity HATN/CNT-S cathode (no S melt infusion) was reported ( $>10 \text{ mAh cm}^{-2}$ ,  $\sim 8.48 \text{ mg}_{\text{sulfur}} \text{ cm}^{-2}$ ) with a stringently low N/P ratio of 1.85 using baseline electrolyte in coin-cell tests. This demonstrates the feasibility of the high areal capacity of our HATN/CNT-S cathode for BP3. It was evaluated using E/S of  $\sim 6 \mu\text{l mg}_{\text{sulfur}}^{-1}$  at  $0.25 \text{ mA cm}^{-2}$  and  $0.5 \text{ mA cm}^{-2}$ . The areal current density of  $0.25 \text{ mA cm}^{-2}$  is equivalent to 0.17 C of  $\text{LiFePO}_4$  with the same active loading. It is shown that the HATN/CNT-S cathode presents high S-specific capacities (high S utilization) of  $>1000 \text{ mAh g}_{\text{sulfur}}^{-1}$  under the lean electrolyte condition (Q3, 2023). It delivers a high initial areal capacity of  $10.8 \text{ mAh cm}^{-2}$  at  $0.25 \text{ mA cm}^{-2}$ , which keeps at  $9 \text{ mAh cm}^{-2}$  at  $0.5 \text{ mA cm}^{-2}$ . However, the corresponding baseline Li-S cells suffer from obvious polarization and relatively low Coulombic efficiency, which suggests severe electrode degradation of electrodes. Therefore, in Q3, 2023, the as-prepared HATN/CNT-S cathode with a high S loading of  $\sim 9.56 \text{ mg cm}^{-2}$  was directly tested in the new electrolyte to inhibit the polysulfide corrosion. It shows improved rate performance of the HATN/CNT-S cathode at current densities ranging from  $0.25 \text{ mA cm}^{-2}$  to  $1 \text{ mA cm}^{-2}$ , presenting high areal capacities from  $\sim 10 \text{ mAh cm}^{-2}$  to  $6.5 \text{ mAh cm}^{-2}$ , respectively. This demonstrates its feasibility in high-energy-density Li-S pouch cells.

Concerning the rate capability of the Li-S cells, DOE suggested lowering S loading to a moderate one of  $\sim 6 \text{ mAh cm}^{-2}$ . The rate performance of the HATN/CNT-S cathode ( $\sim 6.4 \text{ mg}_{\text{sulfur}} \text{ cm}^{-2}$ ) was evaluated in the new electrolyte for benchmarking (Q4, 2023) before fabricating the high-energy-density Li-S pouch cells in BP3.

Figure XIV.5.11a shows the voltage profiles of the HATN/CNT-S cathode with a low E/S ratio of  $6 \mu\text{L mg}_{\text{sulfur}}^{-1}$  from 0.05 C to 0.2 C, wherein 1C is  $1000 \text{ mA g}^{-1}$ . The HATN/CNT-S Li-S full cell delivers a high specific capacity of  $>1000 \text{ mAh g}^{-1}$  at a formation current density of 0.05 C and maintains a high specific capacity of  $720 \text{ mAh g}^{-1}$  at 0.2 C, showing well-defined charge-discharge plateaus. The HATN/CNT-S cathode presents good cycling stability under lean electrolyte and lithium conditions with a high capacity retention rate of 70% after 150 cycles based on an initial capacity of  $4.5 \text{ mAh cm}^{-2}$  at 0.2 C (Figure XIV.5.11b). The cell capacity quickly decays to 50% after 200 cycles indicating severe electrode degradation, which will be investigated in the upcoming quarters to insight into the root causes. The stringent cell testing conditions promises the feasibility of achieving high energy density of Li-S batteries. In Q4, single-layered pouch cells were fabricated based on the HATN/CNT-S with a moderately high S loading of  $>6 \text{ mg cm}^{-2}$ , which will be discussed next.

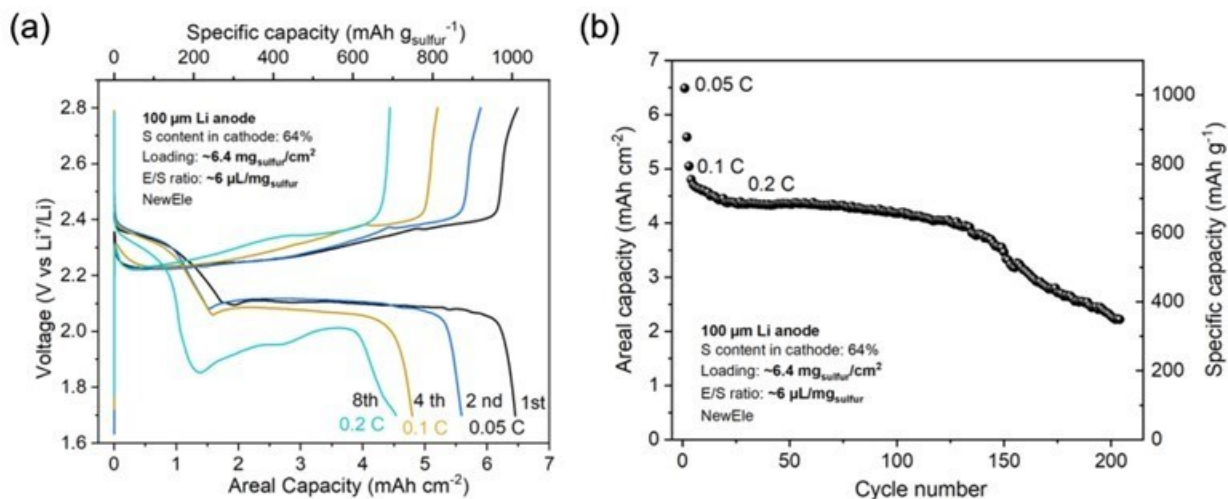


Figure XIV.5.11 (a) Voltage profiles of the HATN/CNT-S cathode with  $\sim 6.4 \text{ mg}_{\text{sulfur}} \text{ cm}^{-2}$  with a low E/S ratio of  $6 \mu\text{L mg}_{\text{sulfur}}^{-1}$  or a calculated E/C ratio of  $4.64 \text{ g Ah}^{-1}$  from 0.05 C to 0.2 C, 1 C is  $1000 \text{ mA g}^{-1}$ . The cells were assembled by pairing against  $100 \mu\text{m}$  Li anodes in the new electrolyte. (b) the cycling behavior of the HATN/CNT-S cathode in the new electrolyte.

### Single-layered pouch-cell assembly

After fixing the materials synthesis, UCSD justified slurry preparation and casting parameters like solid ratio, stirring speed, casting thickness, etc. It is crucial to identify these factors before making electrodes at GM at the final stage. Due to the restriction of safe transportation, dry pouch cells are being prepared based on the UCSD C-S (Figure XIV.5.12a), GM C-S, and HATN/CNT-S cathodes (Figure XIV.5.12b) with S loadings of  $\sim 4.2 \text{ mg cm}^{-2}$ ,  $\sim 3.5 \text{ mg cm}^{-2}$ , and  $\sim 6.5 \text{ mg cm}^{-2}$ , which was sent to UCSD in Q4 for testing. In Q4, 2023, GM formed a total of 8 single-layer dry pouch cells for later filling at UCSD with electrolyte. As shown in Figure XIV.5.12c, each cell was produced using  $100 \mu\text{m}$  lithium foil as anode, and UCSD C-S and HATN/CNT-S cathodes (Figure XIV.5.12e) or baseline GM cathode (Figure XIV.5.12d).

Electrolyte filling was performed at UCSD, and additional pouch material from the batch of pouch cells from GM has been included. Note that single-layer pouch cells (Figure XIV.5.12d and Figure XIV.5.12e) have a higher proportion of inactive surfaces surrounding the core relative to active material area, and typically require more electrolyte than multilayer cells as a result. After filling, a starting pressure of approximately 140-160 kPa is targeted for cycling. Dry cells were filled at UCSD with electrolytes, then the pouch cells were resting for 24 hours by normal sealing. The pouch cells were cut open again to do the vacuum sealing before cell testing. The UCSD team accomplished these steps by using a Fuji sealer as shown in Figure XIV.5.12f.

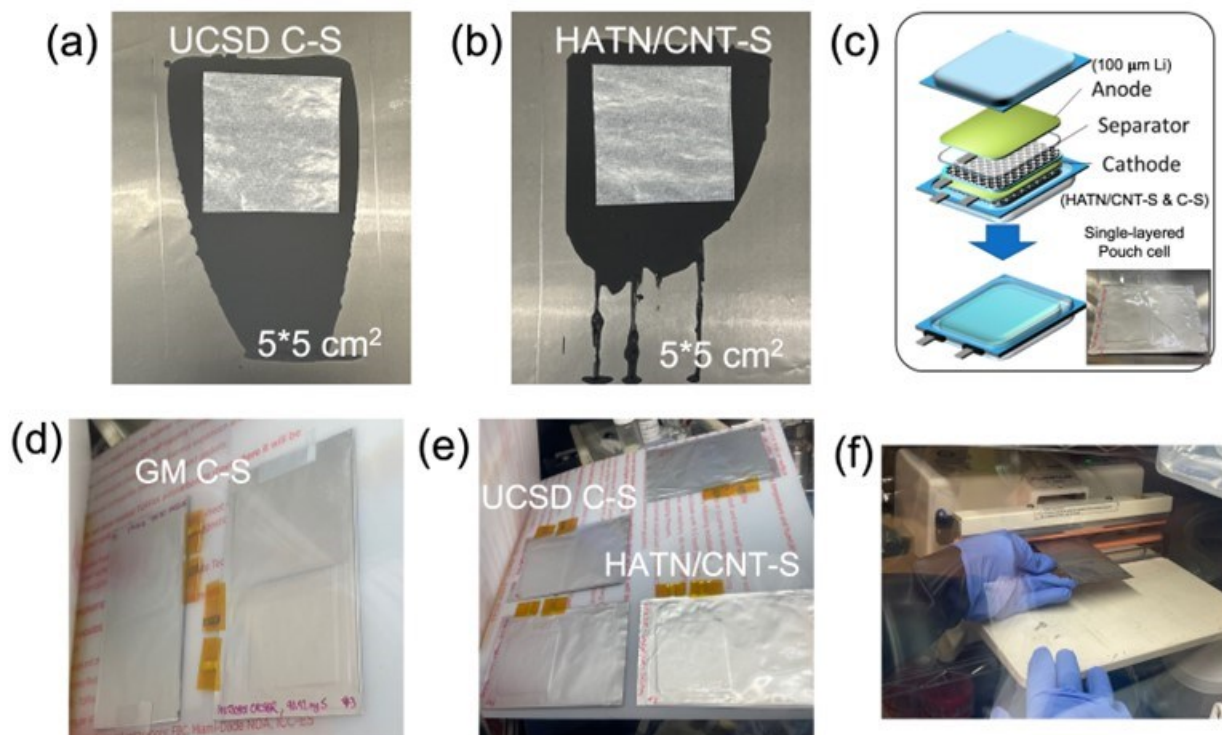


Figure XIV.5.12 (a) Photos of the synthesized UCSD C-S and HATN/CNT-S (b) cathode sheets (5x5 cm<sup>2</sup>). (c) The schematic of pouch-cell assembly details at GM. Photos of single-layer dry pouch cells produced at GM. (d) GM C-S, (e) UCSD C-S and HATN/CNT-S. (f) The vacuum sealing station was set up at UCSD.

### Conclusions

In BP2, a characterization toolbox and quantification methodologies have been utilized to investigate the Li and S inventory loss, electrolyte depletion, and electrode structural evolution. The polysulfide corrosion issue as well as the additive depletion of LiNO<sub>3</sub> in the baseline electrolyte have been identified to be culprits to the limited cycle life of Li-S batteries. Thus, a new electrolyte system containing the NPL additive has been developed to resolve the problems. Besides, to mitigate the electrolyte decomposition caused by high porosity and tortuosity of conventional C-S cathodes, our HATN/CNT-S cathode features a low porosity of 38% and tortuosity of 2.07 owing to the robust 3D ion and electron conduction network built by incorporating CNT into the polymerization of HATN. The team achieved the milestone of scalable synthesis of the electrode materials by optimizing the synthetic conditions and decreasing the cost of raw materials. Besides, to replace the decomposition based LiNO<sub>3</sub> additive, the NewEle system has been introduced. The cells based on the HATN/CNT-S cathodes are currently cycling with capacity retention of ~70.2% after 98 cycles based on an initial capacity of ~6 mAh cm<sup>-2</sup> at 0.1 C under stringent lean electrolyte (E/S ratio of ~6 µl mg<sub>sulfur</sub><sup>-1</sup>) and thin Li (100 µm). This is attributed to the low porosity of the HATN/CNT-S cathode in contrast to the highly porous C-S cathode, and the low tortuosity of the HATN/CNT-S cathode for good electrolyte wettability into its bulky structure. The NewEle has been used for the HATN/CNT-S cathode, essential to achieving stable high-energy-density Li-S batteries. The team has fabricated for the single layered pouch cells for electrochemical performance validation.

### Key Publications

The project has a non-disclosure invention submitted regarding the new electrolyte additive and formula.

1. Xiaowei Wang, Saurabh Parab, Ganesh Raghavendran, Bhargav Bhamwala, Alex Liu, Matthew Miyagishima and Ying Shirley Meng, "New Electrolyte additive design for extending cycle life of high energy Li-S batteries", manuscript preparation.



**References**

1. Mauler, L.; Duffner, F.; Zeier, W. G.; Leker, J., Battery cost forecasting: a review of methods and results with an outlook to 2050. *Energy Environ. Sci.* 2021, *14* (9), 4712-4739.
2. Manthiram, A.; Fu, Y.; Chung, S. H.; Zu, C.; Su, Y. S., Rechargeable lithium-sulfur batteries. *Chem. Rev.* 2014, *114* (23), 11751-11787.
3. Shi, L.; Bak, S.-M.; Shadike, Z.; Wang, C.; Niu, C.; Northrup, P.; Lee, H.; Baranovskiy, A. Y.; Anderson, C. S.; Qin, J.; Feng, S.; Ren, X.; Liu, D.; Yang, X.-Q.; Gao, F.; Lu, D.; Xiao, J.; Liu, J., Reaction heterogeneity in practical high-energy lithium–sulfur pouch cells. *Energy Environ. Sci.* 2020, *13* (10), 3620-3632.
4. Wang, X.; Yang, Y.; Lai, C.; Li, R.; Xu, H.; Tan, D. H. S.; Zhang, K.; Yu, W.; Fjeldberg, O.; Lin, M.; Tang, W.; Meng, Y. S.; Loh, K. P., Dense-Stacking Porous Conjugated Polymer as Reactive-Type Host for High-Performance Lithium Sulfur Batteries. *Angew. Chem. Int. Ed.* 2021, *60* (20), 11359-11369.

**Acknowledgements**

We thank Michele Foster (DOE), Haiyan Croft (DOE) and Tien Duong (DOE) for supporting our work.

## XIV.6 New Engineering Concepts for High Energy Density Li-S Batteries (UPitt)

### Prashant N. Kumta, Principal Investigator

University of Pittsburgh  
815C Benedum Hall,  
3700 O'Hara St.  
Pittsburgh, PA 15261  
E-mail: [pkumta@pitt.edu](mailto:pkumta@pitt.edu)

### George E. Blomgren, Co-Principal Investigator

Blomgren Consulting Services, Ltd.  
Oberlin, OH 44074  
E-mail: [geblomgren@prodigy.net](mailto:geblomgren@prodigy.net)

### Oleg I. Velikokhatnyi, Co-Principal Investigator

University of Pittsburgh  
815C Benedum Hall,  
3700 O'Hara st,  
Pittsburgh, PA 15261  
E-mail: [olv3@pitt.edu](mailto:olv3@pitt.edu)

### Tien Duong, DOE Technical Development Manager

U.S. Department of Energy  
E-mail: [Tien.Duong@ee.doe.gov](mailto:Tien.Duong@ee.doe.gov)

Start Date: October 1, 2022

End Date: September 30, 2023

Project Funding: \$521,913

DOE share: \$416,991

Non-DOE share: \$104,922

### Project Introduction

Li-S batteries (LSBs) with energy densities  $\geq 500$  Wh/kg @C/5 and  $>1000$  cycles, cycle life operating over wide temperatures has been identified to be critical for meeting the global energy demands. Progress is however, very much limited due to several major hurdles related to the following: (a) poor  $\text{Li}^+$  reaction kinetics (conductivity/diffusivity) enabling full reversible S conversion to  $\text{Li}_2\text{S}$ , (b) inferior electron ( $e^-$ ) conductivity, specific capacity and cycle life due to electrolyte soluble species of polysulfides (PSs) formed with the reaction of Li ions with sulfur migrating to anode, (c) unstable solid electrolyte interphase (SEI) formation and finally, (d) dendrites that are formed on the Li metal anode severely limiting the cycle life due to polarization at the solid/liquid interfaces causing safety, inferior capacity, energy density, rate, and cycle life issues. Creation of a fully functional economical  $\leq \$80/\text{kWh}$ , high energy density LSBs is vital for enabling its widespread commercial deployment and use in current and next generation electric vehicles (EVs).

### Objectives

The major objectives/goals of this project are to develop a lithium sulfur pouch cell with a cell capacity  $>300\text{mAh}$  and exhibiting an initial energy density  $\geq 300\text{Wh/kg}$ ,  $\geq 450\text{Wh/L}$  and a final energy density  $\geq 500\text{Wh/kg}$ ,  $\geq 750\text{Wh/L}$  with cycling over 1000 cycles @C/3 rate, cycle life of 1000 at C/3 and  $\leq 20\%$  fade in energy @ C/10-C/3, and  $\leq \$80/\text{kWh}$ . To achieve these proposed objectives, the following major goals will be attained in year 2 of the three-year funded project. (a) Identification of effective functional electrocatalysts (FECs) and Li-ion conductors (LICs) lowering the activation barrier; (b) In situ synthesis of FECs and LICs dispersed complex carbon-based framework materials (CFM) and sulfur (S) nanocomposite with S content  $\geq 90\text{wt. \%}$ ; (c) Achieve initial areal capacity of  $\sim 6\text{mAh/cm}^2$  and a final  $\sim 15\text{mAh/cm}^2$  areal capacity of S electrode with an initial S loading of  $\geq 6\text{mg/cm}^2$  and a final loading  $\geq 10\text{mg/cm}^2$ ; (d) Synthesis of Li-

structurally isomorphous (SIA) alloy and multicomponent alloys (MCAs) exhibiting  $\geq 1000$  cycle with initial areal capacity of  $\sim 6 \text{ mA h/cm}^2$  and a final areal capacity of  $\sim 15 \text{ mAh/cm}^2$  @C/3 rate; (e) Identification of optimal electrolyte compositions giving  $\text{Li}^+$  conductivities  $\sim 10^{-2} \text{ S/cm}$  and polysulfide (PS) dissolution  $< 1 \text{ ppm}$  in the modified electrolytes.

### Approach

Work involves executing a theory driven study directed at identification of electrocatalyst (ECs) for efficient conversion of species of polysulfides (PSs) to  $\text{Li}_2\text{S}$  during the forward discharge process and backward charge process to elemental sulfur and Li. Also, first principles computational approaches will be applied to identify solid-state LICs with conductivity  $> 10^{-4} \text{ S/cm}$ . Employing the expertise in the PI's laboratory, suitable low temperature ( $< 240^\circ \text{ C}$ ) scalable synthesis techniques will be used to generate theoretically identified FECs and LICs. Low PS solubility and stable solid electrolyte interphase (SEI) forming electrolytes will then be prepared from commercially available solvents, additives, and salts. Effectiveness of the FECs and LICs to improve the PSs to  $\text{Li}_2\text{S}$  transformation kinetics and ability to achieve the targeted specific capacity by trapping PSs including desired structural transformation during charging/discharging will be assessed, and accordingly suitable modification of FECs and LICs will be performed to generate the ideal microstructures enabling confining high sulfur loadings yielding high specific capacity and the desired cycling stability. Suitable modification if required of Li alloy as anodes will also be performed by alloying with other metals to improve the Li ion diffusivity kinetics and the Gibb's Thomson Parameter, a measure of the interfacial energy. The scalable approaches developed will be further refined to optimize the sulfur utilization in the cathode, engineer the surface and bulk structure of the novel Li-SIA and Li-MCA anodes to yield the desired areal capacity with optimal coulombic efficiency, and finally optimize the electrolyte structure to minimize and eliminate PS dissolution with desired  $\text{Li}^+$  conductivities. Finally, the developed systems will be scaled up, fabricated, and tested in pouch cell configurations to exhibit the required target performance specifications.

### Results

Throughout the last year of this funded project, a combination of experimental and computational methods was employed to work on different aspects of the Li-S batteries (LSBs), to meet the milestones of the project. Experimental investigations were conducted to evaluate the electrochemical performance of the various Complex Framework Materials (CFMs) developed and utilized as sulfur host materials to improve the cathodic performance of the carbon-sulfur (C/S) composites. Various electrolyte additives were identified and used in the baseline electrolyte to improve the interface between the electrode and electrolyte to facilitate stable and robust SEI layers resulting in improved overall electrochemical performance of the LSBs. Additionally, the potential of Multicomponent Alloy (MCA) identified by computational studies and reported in the previous annual report as dendrite-free anode materials was shown that can reversibly cycle  $\text{Li}^+$  and exhibit a stable areal capacity of more than  $15 \text{ m Ah cm}^{-2}$ . The promise of MCA to be used as anode material by standard slurry coating was shown and their ability to be used as current collectors was also demonstrated. In addition to the above experimental studies, research efforts were also directed at conducting computational calculations dedicated to identifying strategies aimed at reducing the solubility of polysulfides (PS) species in the solvents used in the electrolytes for the Li-S batteries. The progress made in the project emphasizing the above aspects is presented in this annual report in the following sections.

#### *Influence of additives on different sulfur loading of CFM-S cathodes and electrochemistry of MCA*

Initially, preliminary work was conducted to modify the chemistry of standard electrolyte (1.0 M LiTFSI, 2 wt.%  $\text{LiNO}_3$  in DOL: DME) by adding appropriate additives to improve the electrochemical performance of LSBs. Several additives were explored to identify the best-performing ones and their amount that influence the solid electrolyte interface (SEI) layers on both the electrodes, namely, the Li-anode and the baseline sulfur cathode to positively enhance the electrochemical performance of the Li-S cell. 1 wt.% of an organic chemical additive (CA) was considered. The hypothesis is that this additive not only fine-tunes and interacts with the Li-polysulfides preventing their dissolution but also serves to modify the electrode interface forming a multifunctional SEI over the electrodes. The addition of CA is anticipated to form a multifunctional, robust, and stable SEI layer on the electrodes which is capable of conforming to the Li-anode surface while also

regulating a uniform Li deposition inhibiting dendrite formation and causing extremely low polarization during cycling. Therefore, the preliminary studies conducted by the team examine the effect of the addition of 1 wt.% of CA in the standard electrolyte on the electrochemical performance of the baseline CFM-S cathode with low and high areal sulfur loading developed by the team and the Li metal anode, respectively.

#### **Effect of additives on electrochemistry of CFM-S cathodes with different sulfur loading and Li anode**

The electrochemical cycling performance of the Li-S cell with baseline CFM-S and the modified standard electrolyte containing 1 wt.% CA additive was evaluated with different sulfur loadings and the result is presented in Figure XIV.6.1. The cathodes were prepared by the standard slurry casting method by mixing the active material, conductive carbon, and PVDF in a 72:18:10 ratio using NMP as solvent. Lean electrolyte with an electrolyte to sulfur ratio (E/S) of  $8\mu\text{l mg}^{-1}$  was used to fabricate all the cells. The cell with a moderate sulfur loading of  $3.5\text{ mg cm}^{-2}$  is termed LCA1 and the cell with more than two-fold higher sulfur loading of  $7.8\text{ mg cm}^{-2}$  is labeled HCA1. The cells were cycled at 0.05 C-rate for the initial 10 cycles for stabilization followed by cycling at 0.1 C-rate for the entire test. All the cells showed an initial drop in the discharge capacity, likely due to the formation of an SEI layer over the electrodes which stabilizes after a few cycles. The LCA1 and HCA1 cells stabilize and display a discharge capacity of  $520\text{ m Ah g}^{-1}$  and  $569\text{ m Ah g}^{-1}$  after 95 cycles with coulombic efficiencies of more than 98.8% and 97.8%, respectively.

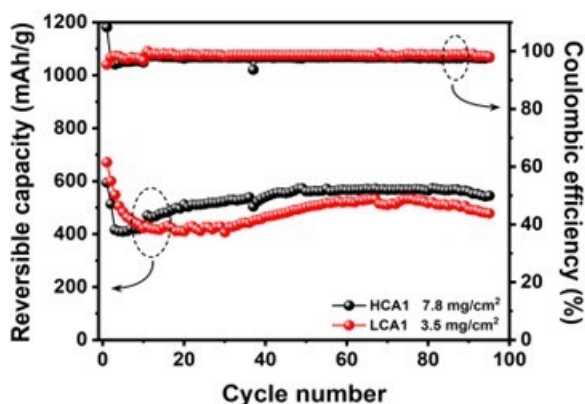


**Figure XIV.6.1** Cycling performance of baseline electrode with modified electrolyte (1 wt.% of CA) as an additive at low and high sulfur loadings.

To examine the effect of the additive on the stabilization of the Li-anode, coin cells with Li-metal as anode and bare Cu as the cathode were fabricated and tested with modified electrolyte (1 wt.% CA) at 1 mA current for 1 hour. The cells were flooded with  $60\ \mu\text{L}$  of modified electrolyte. The cells were cycled for more than 100 cycles and the results are presented in Figure XIV.6.2. The Li plating and stripping behavior stabilized after 3 cycles and the cells delivered a stable areal capacity of  $0.793\text{ m Ah cm}^{-2}$  throughout the 103 cycles with an average coulombic efficiency of 99.97%. Initially, the cells showed instabilities in Li cycling and a high overpotential (0.2V) is observed due to an unstable SEI layer. However, the Li cycling stabilizes after  $\sim 22$  cycles and the overpotential is significantly reduced (0.073V) likely due to SEI layer stabilization and desirable Li-ion conduction in the modified electrolyte. Initial results presented suggest that CA significantly influences cell chemistry by possibly forming a stable SEI layer on both electrodes and interacting with Li-polysulfides. Additionally, electrochemical testing of other plausible electrolyte additives that influence the SEI layer, Li-ion conduction, and restrict polysulfide dissolution is presented in the following sections.

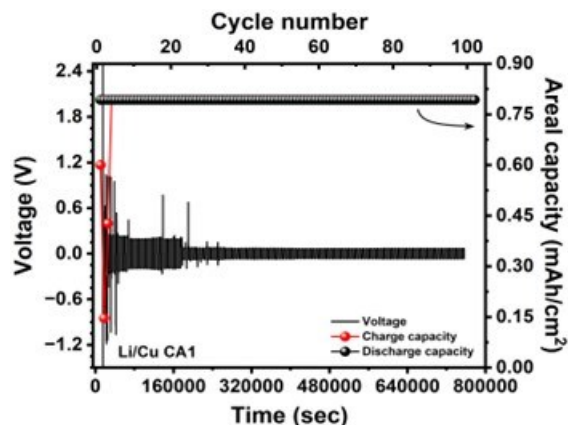
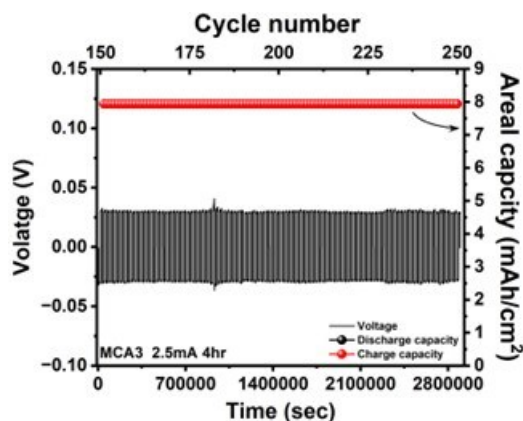


Figure XIV.6.2 Li cycling performance with modified electrolyte (1 wt.% CA additive) at 1 mA current for 1 h for 103 cycles.

#### Electrochemical performance of MCA:

Initially, MCA systems were studied electrochemically and reported in the annual report of the previous year. The MCA systems were further evaluated for their electrochemistry response and reported herein with extended cycling showing their robustness and cyclic stability. The MCA serves as dendrite-free anode material and the current collector was synthesized by a high-energy mechanical milling and alloying (HEMM/HEMA) process. The structurally isomorphous system, MCA3 having a similar lattice registry (*bcc phase*) to metallic Li, prevents Li dendrite growth by forming a solid solution with the reacting Li-ions electrochemically presented to it from the metallic Li serving as the counter electrode. The ensuing electrochemical alloying reaction occurring thereby, allows for a significant amount of Li to be solubilized into the parent MCA3 alloy causing a minimal change in volume due to the solid solution formation. The crystallographic arrangements of atoms in the MCA3 alloy being identical to that of Li metal enables it to preserve the overall crystallographic symmetry and allows the formation of a solid solution with optimal interfacial energy. The MCA3 alloy also improves the lithium diffusion preventing surface segregation while continuing to maintain dendrite-free cycling, hence, serving as effective anodes as well as current collectors for anode free cells in Li-S batteries. The MCA3 alloy was prepared by high-energy mechanical alloying (HEMA) and the anode electrode for electrochemical testing was prepared by standard slurry casting method (95 wt.% MCA3 and 5 wt.% PVDF) in NMP solvent followed by electrochemical testing in a coin cell as shown in Figure XIV.6.3. The electrode with an area of 1.26 cm<sup>2</sup> was used to assemble cells and flooded with 60 μL of standard electrolyte. The MCA3 cells with an average electrode loading of 6.2 mg cm<sup>-2</sup> were initially cycled for rate capability at different current rates *viz.* 1mA for 1h alloying and dealloying (A/D), 1mA 2h A/D, 1mA 4h A/D, 1.5mA 4h A/D for 31 cycles each and 2mA 4h A/D for 100 cycles followed by exploring cycling stability at 2.5mA 4h A/D for another 100 cycles. The cycling stability of MCA3 after 150 cycles of rate capability is depicted in Figure XIV.6.3 revealing excellent Li plating/stripping behavior affording a stable areal capacity of ~8 m Ah cm<sup>-2</sup> for continuous 100 cycles. The propensity of the MCA3 alloy electrode to demonstrate reversible Li cycling (plating/stripping) is evinced in Figure XIV.6.3 as the overpotential of the cell remains constant even after cycling for more than 250 cycles. Further electrochemical testing of cells with MCA electrodes is presented in upcoming sections. Additionally, efforts are directed at fabricating free-standing dense pellets of the MCAs to serve as dendrite-resistant anode current collectors for reversibly cycling Li ions. Results of these studies conducted on the MCAs electrodes and the electrochemical testing of the dense pellet of MCAs serving as current collectors are presented in the subsequent sections of this report.



**Figure XIV.6.3** Electrochemical cycling performance of MCA3 electrode along with areal capacities cycled at 2.5 mA current for 4 h for alloying and de-alloying, respectively from 150 to 250 cycles after rate capability test.

*Evaluation of electrolyte additive on PTA-coated CFM-S cathodes and exploring the MCA electrochemistry*

The following section includes results of studying the effect of chemical additives added to the standard electrolyte on the polysulfide trapping agent (PTA) coated sulfur (CFM-S) cathode performance compared to the standard electrolyte. This section also includes the study conducted exploring the ability of the MCAs identified and reported in the previous section to exhibit higher areal capacity with stable Li cycling without the formation of dendrites.

**Additive on PTA-coated CFM-S cathodes electrochemistry:**

Thus, as outlined above, the chemistry of the standard electrolyte (1.0 M LiTFSI, 2 wt.% LiNO<sub>3</sub> in DOL:DME, (1:1 v/v) was modified by adding appropriate chemical additives (CA) to improve the electrochemical performance of LSBs. Lean electrolyte conditions of electrolyte (E)/sulfur (S) ratio were maintained at 8  $\mu\text{l mg}^{-1}\text{s}$  throughout the testing. Various additives were also explored that would modify the SEI layers on both the Li-anode and the baseline sulfur cathode to improve the electrochemical response of the Li-S cell. Accordingly, 1 wt.% of CA added to the electrolyte displayed the most optimal influence on the electrochemical performance of the PTA-coated sulfur cathode when tested in the coin cell configuration. The PTA is also anticipated to meticulously refine and chemically interact with the Li polysulfides and inhibit their dissolution in the electrolyte. Furthermore, the CA additive expectedly facilitates the creation of multifunctional, robust, and stable SEI over the electrodes. Studies were therefore conducted to show the influence of the addition of 1 wt.% of CA on the electrochemical performance of PTA-coated sulfur cathode. This was done by testing a cathode comprising CFM infiltrated with sulfur (CFM-S) coated with PTA using a standard electrolyte as well as the standard electrolyte modified by the addition of 1 wt. % CA as the chemical additive.

As mentioned above accordingly, 10% PTA was coated on the CFM-S cathode serving to trap the polysulfides and prevent their dissolution, improving the utilization of sulfur. These PTA moieties on the CFM-S cathode contain functional groups binding to the polysulfides thereby modifying the cathode electrode interface. The electrochemical performance of the PTA-coated CFM-S electrode using standard electrolyte with and without the chemical additive of 1 wt. % CA is shown in Figure XIV.6.4 and Figure XIV.6.5, respectively. The PTA-coated CFM-S electrodes were cycled at C/20 with an average electrode loading of 4.7 mg cm<sup>2</sup> electrode area. The PTA-coated CFM-S tested with standard electrolyte shows an initial discharge capacity of ~1009 m Ah g<sup>-1</sup> at C/20 reaching a capacity of ~750 m Ah g<sup>-1</sup> at the 10<sup>th</sup> cycle, stabilizing at ~725 m Ah g<sup>-1</sup> after the 25<sup>th</sup> cycle. The electrode finally stabilizes at ~510 m Ah g<sup>-1</sup> after 70 cycles until 82 cycles with a coulombic efficiency of ~ 98.6 %. To further elucidate the influence of CA, the PTA-coated CFM-S cathode was cycled with the standard electrolyte modified with 1 wt.% CA and compare its electrochemical response with that of the standard electrolyte displayed in Figure XIV.6.4. The electrochemical cycling of the PTA-coated CFM-S

cathode using the modified standard electrolyte is shown in Figure XIV.6.5. These electrodes were initially cycled at C/20 with an average sulfur electrode loading of  $4.5 \text{ mg cm}^{-2}$  and showed a higher initial discharge capacity of  $\sim 1049 \text{ mAh g}^{-1}$  which however decreases to  $\sim 600 \text{ mAh g}^{-1}$  at the 10<sup>th</sup> cycle. The electrodes maintained a stable discharge capacity of  $\sim 625 \text{ mAh g}^{-1}$  at C/10 rate up to 82 cycles with coulombic efficiencies of  $\sim 98.6 \%$ . Therefore, considering the current findings, the addition of 1 wt.% CA to the standard electrolyte enables the cells to exhibit a higher capacity of  $\sim 625 \text{ mAh g}^{-1}$  compared to  $\sim 510 \text{ mAh g}^{-1}$  for a similar S loading in the  $\sim 4.5\text{-}4.7 \text{ mg cm}^{-2}$  range in accordance with the proposed hypothesis above.

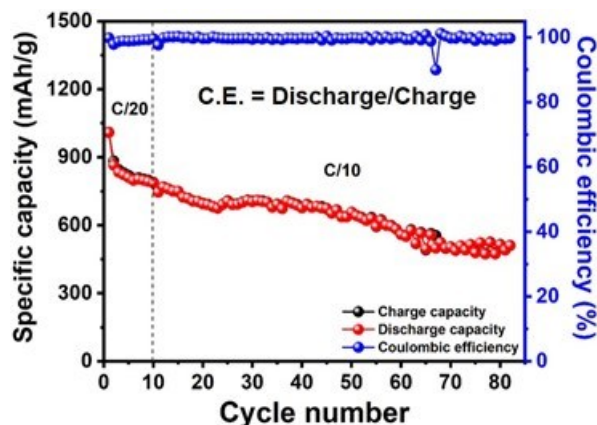


Figure XIV.6.4 Cyclic performance and Coulombic efficiency of 10% PTA coated CFM-S electrode cycled between 1.8-2.8V at C/20 and 1.7-2.8V at C/10 using standard electrolyte.

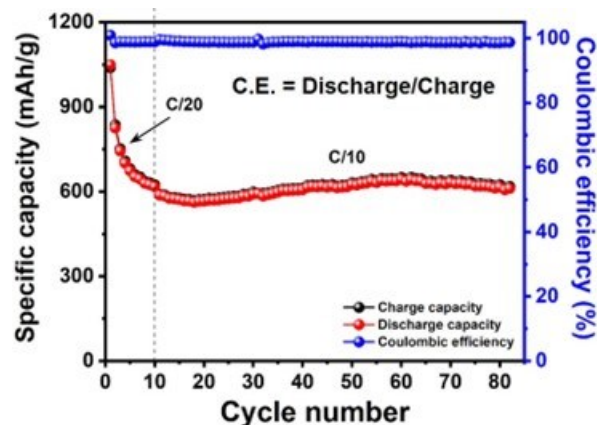
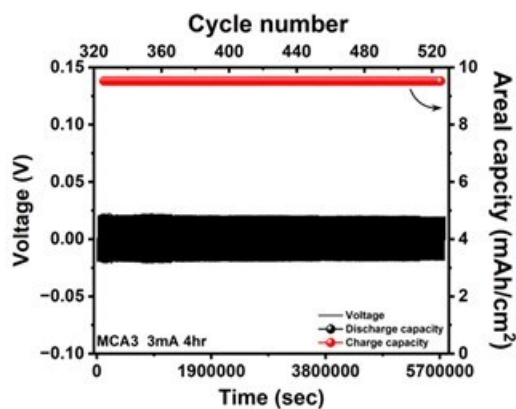


Figure XIV.6.5 Cyclic performance of 10% PTA coated CFM-S electrode cycled between 1.8-2.8V at C/20 and 1.7-2.8V at C/10 with modified electrolyte with 1wt. % of the chemical additive (CA).

#### **Pushing the boundaries of MCA alloy electrochemistry:**

The MCAs are structurally isomorphous systems as explained above, and MCA3, a specific MCA system as described earlier has a similar lattice registry (*bcc phase*) to metallic Li with an optimal interfacial energy that prevents Li dendrite growth by electrochemically forming a solid solution with the reacting Li-ions rather than plating. The crystallographic arrangements of atoms in the MCA3 alloy, being identical to that of Li metal confer the ability to preserve the overall crystallographic symmetry preventing huge volumetric changes and allowing the formation of a solid solution with Li preserving the *bcc* crystal structure. The MCA3 alloy also improves the lithium diffusion preventing surface segregation while continuing to maintain dendrite-free cycling, hence, serving as effective anodes as well as current collectors in LSBs. The HEMA-derived MCA3 alloy tested as an anode electrode was prepared by standard slurry casting method (95 wt.% MCA3 and 5 wt.% PVDF) in N-methyl pyrrolidone (NMP) solvent followed by electrochemical testing in a coin cell as shown in Figure XIV.6.6. The cells were flooded with 60  $\mu\text{L}$  of standard electrolyte. The MCA3 cells were prepared

with an average electrode loading of  $6.2 \text{ mg cm}^{-2}$  and were initially cycled for rate capability at different current rates as indicated in the previous section. To evaluate the MCA3 alloy electrochemical capability to cycle  $\text{Li}^+$ , it was tested and further studied at 3mA current for 4 hours of A/D for another 200 cycles ending at 525 cycles which is depicted in Figure XIV.6.6. The figure reveals excellent Li plating/stripping behavior affording a stable areal capacity of  $\sim 9.5 \text{ m Ah cm}^{-2}$  for continuous 200 cycles. The efficacy of the MCA3 alloy electrode to demonstrate reversible Li cycling (plating/stripping) is thus evident in Figure XIV.6.6 since the overpotential of the cell remains invariant even after cycling for more than 525 cycles. These results show the potential of the MCA3 alloy serving as dendrite-free current collectors offering its use in a pre-lithiated alloyed form as well as anode-free configuration of lithium-containing systems serving as cathodes.



**Figure XIV.6.6** Cyclic performance of MCA3 electrode along with areal capacities cycled at 3 mA current for 4 h for alloying and de-alloying, respectively from 325 to 500 cycles after cycling at various currents for different time periods described in the text.

#### *Improved cathode cyclic stability with electrolyte additive and pushing the MCA electrochemistry limits*

In this section, experimental investigations are presented focusing on the influence of electrolyte additives (EA) incorporated into the standard electrolyte on the electrochemical cycling performance of the fabricated sulfur cathodes. It also includes further investigation of MCA focusing primarily on determining their ability to demonstrate higher areal capacity during cycling Li ions while maintaining stability and preventing dendrite formation. Additionally, computational studies are also focused on identifying approaches to decrease the solubility of polysulfides (PS) in LSBs.

#### ***Influence of electrolyte additives (EA) on CFM-S cyclic stability:***

The research aimed to enhance the electrochemistry of LSBs through alterations in the chemistry of the conventional electrolyte (1.0 M LiTFSI, 2 wt.%  $\text{LiNO}_3$  in DOL:DME, 1:1 v/v). This was achieved by incorporating suitable EA to improve the overall performance of the sulfur cathodes and Li metal anodes. Among several additives examined, the most effective additives were identified for improving the electrochemical response of the Li-S cell by modifying the SEI layers on both, the Li-anode, and the baseline PTA-coated CFM-S sulfur cathode. The electrolyte made with the electrolyte additives incorporated into the standard electrolyte is, henceforth, termed a modified electrolyte. Among the electrolyte additives, 1 wt.% of EA1 and EA2 displayed the most optimal influence on the electrochemical performance of the sulfur cathode when tested in the coin cell configuration. The functional groups of the PTA interact and entrap the Li polysulfides (LPS) preventing their shuttling. Also, the EAs in the electrolyte chemically interact with the LPS, likely inhibiting their dissolution in the electrolyte. Additionally, the EAs are expected to modify the electrode interfaces creating a robust, and stable multifunctional SEI layer over the electrodes. Studies were therefore conducted to examine the influence of adding EA on the electrochemical performance of the PTA-coated CFM-S sulfur cathode by testing it in a standard electrolyte as well as a modified electrolyte containing 1 wt.% additives (EA1 & EA2).



The sulfur cathode developed comprises CFM infiltrated with sulfur (CFM-S) and coated with PTA. A 10% PTA was coated on the CFM-S cathode serving to trap the polysulfides and prevent their dissolution, improving the utilization of sulfur. These PTA moieties as explained earlier contain functional groups binding to the polysulfides species thereby modifying the cathode interface. The electrochemical performance of the PTA-coated CFM-S electrode using standard electrolyte and modified electrolyte with 1 wt.% of the additives (EA1 & EA2) is shown in Figure XIV.6.7. The PTA-coated CFM-S electrodes with an average areal sulfur loading of  $\sim 5.1 \text{ mg cm}^2$  were initially cycled at C/20 as formation cycles. Lean electrolyte conditions of electrolyte to sulfur (E/S) ratio of  $8 \mu\text{l mg}^{-1}$  was maintained consistently throughout the studies. In the standard electrolyte, the PTA-coated CFM-S cathode exhibits an initial discharge capacity of  $\sim 1009 \text{ m Ah g}^{-1}$  at C/20, reaching  $\sim 750 \text{ m Ah g}^{-1}$  at the 10<sup>th</sup> cycle and stabilizing at  $\sim 725 \text{ m Ah g}^{-1}$  after the 25<sup>th</sup> cycle. The capacity stabilizes at  $\sim 510 \text{ m Ah g}^{-1}$  after 70 cycles until 82 cycles, with a coulombic efficiency of  $\sim 98.6\%$ . To better understand the impact of the EA, the PTA-coated CFM-S cathodes were cycled using modified electrolytes containing 1 wt.% of the two different EAs, namely EA1 and EA2. The electrochemical cycling response was then compared with that of the standard electrolyte also shown in Figure XIV.6.7. The PTA-coated CFM-S electrodes cycled with modified electrolytes show higher initial discharge capacities. The electrodes with EA2 show an initial discharge capacity of  $\sim 1014 \text{ m Ah g}^{-1}$  at C/20 which stabilizes to  $\sim 785 \text{ m Ah g}^{-1}$  at the 10<sup>th</sup> cycle. These electrodes were then cycled at C/10 rates and showed good electrochemical stability exhibiting a reversible capacity of  $730 \text{ m Ah g}^{-1}$  after 61 cycles with coulombic efficiencies of  $\sim 97.8\%$ . The electrochemical performance of PTA-coated CFM-S with modified electrolyte (EA2) showed significantly improved cycling stability compared to the standard electrolyte which indicates that the addition of EA2 is influencing the electrode kinetics by forming a stable SEI layer over the electrodes. Thus, the results show that the modified electrolyte (1 wt.% EA2) exhibits a higher stable capacity of  $\sim 730 \text{ m Ah g}^{-1}$  compared to the standard electrolyte  $\sim 510 \text{ m Ah g}^{-1}$  as well as the modified electrolyte containing 1 wt. % EA1  $\sim 600 \text{ m Ah g}^{-1}$  after 70 cycles.

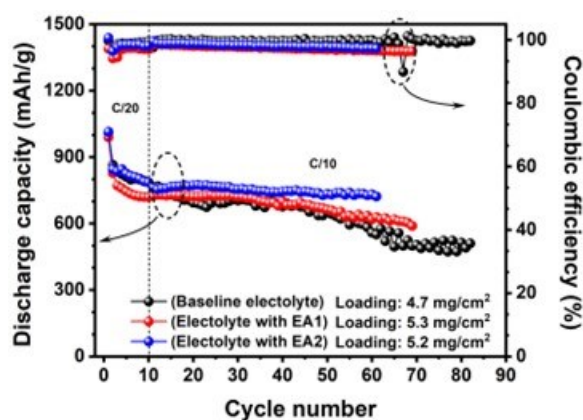
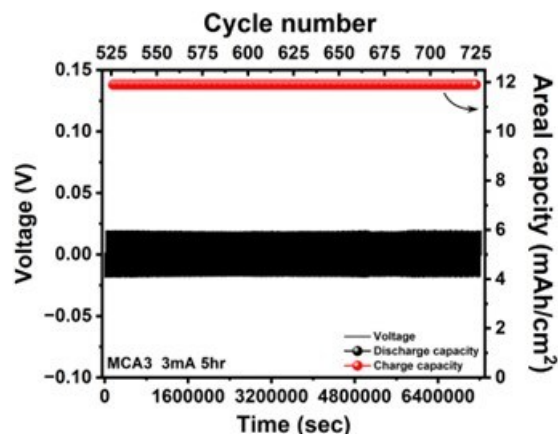


Figure XIV.6.7 Electrochemical cycling performance of 10% PTA coated CFM-S electrode cycled between 1.8-2.8V at C/20 and 1.7-2.8V at C/10 using standard electrolyte and with 1 wt.% additives EA1, EA2.

#### Testing the limits of MCA electrochemistry:

Additionally, the MCA3 alloy was further investigated to ascertain the capability of the MCA3 alloy to demonstrate higher areal capacity and maintain stable Li cyclability. The MCA3 alloy as explained earlier is structurally isomorphous in crystal structure to Li and also evinces optimal interfacial energy that prevents Li dendrite growth and forms a solid solution with the reacting Li-ions, The MCA3 alloy, accordingly, allows Li<sup>+</sup> to solubilize and causes minimal volume change due to solid solution formation. After the rate capability and cycling stability at various current rates (cycled for 3882 hours), the electrochemical performance of MCA3 alloy was further examined at 3mA current for 5 hours of A/D to determine their ability to demonstrate higher areal capacity for another 200 cycles as depicted in Figure XIV.6.8. The figure reveals excellent reversible Li cycling behavior rendering a stable areal capacity of  $\sim 11.9 \text{ m Ah cm}^{-2}$  for continuous 200 cycles. Figure XIV.6.8 also, clearly demonstrates the unique expected virtue of the MCA3 alloy electrode in showcasing

reversible Li cycling (plating/stripping). The overpotential of the cell remains unchanged even after more than 725 cycles, indicating the excellent cycling stability of the MCA3 alloy electrode.



**Figure XIV.6.8** Electrochemical cycling performance of MCA3 electrodes cycled at 3 mA for 5 h with a stable areal capacity of 11.9 m Ah cm<sup>-2</sup> for cycles after cycling at various currents for different periods described in the text.

#### *Cycling stability of CFM-S cathodes, potential of MCA3 as current collector and computation studies on LPS solubilities*

This section includes the investigations conducted to evaluate the electrochemical performance of the carbon fiber mat-sulfur (CFM-S) cathodes, and the potential of structurally isomorphous alloys, MCAs to demonstrate their ability to be used as current collectors for reversible Li cycling while maintaining stability and preventing dendrite formation showcasing their potential for anode-free cell configurations. Additionally, computational studies were conducted focused on identifying strategies to decrease the solubility of lithium polysulfides, LPS in LSBs.

#### **Electrochemistry of CFM-S cathode:**

The first part of this section is focused on evaluating the electrochemical performance of our CFM-S cathodes at higher C-rates (C/10, C/5) in the standard electrolyte (1.0 M LiTFSI, 2 wt.% LiNO<sub>3</sub> in DOL:DME, 1:1 v/v). The CFMs consist of submicron size (<2 μm) carbon fibers intertwined, forming a thick 3D conducting carbon mat utilized as a binder-less, free-standing sulfur confinement system. The CFM-S cathodes avoid the use of binder and solvent bypassing the standard procedure of slurry coating method. Moreover, the CFMs are electronically conductive and exhibit inherent N-doping in the carbon skeleton of the mats due to the nitrogen moieties present in the carbon precursor that can additionally trap the LPSs and reduce their shuttling thereby, enhancing the overall electrochemical performance of the Li-S cells. The CFM-S cathode mats were prepared by simple carbonization of electro-spun polymeric precursor and by infusing sulfur into the mats by incipient wetting with sulfur dissolved in carbon disulfide, S-CS<sub>2</sub> solution. Firstly, a polymeric mat was prepared by electrospinning a 10% PAN solution in DMF solvent. Electrospinning (e-spinning) is used to create the fine fiber mats of a submicron diameter range from a polymer solution and the characteristics of the mats can be tailored by modulating the respective e-spinning parameters. The e-spun PAN mat was stabilized in an air atmosphere for inducing the cyclization of the polymeric chains followed by carbonization at 750 °C in an inert atmosphere. The resultant carbon fiber mats (CFMs) thus obtained were cut into electrode size (1.26 cm<sup>2</sup>) and were soaked in 10% S-CS<sub>2</sub> solution for sulfur infusion to obtain the sulfur infiltrated CFM-S cathodes. Further following this, these CFM-S cathodes were evaluated for their electrochemical performance in the coin cell configuration.

The CFM-S cathodes with a range of areal sulfur loading of 3.6 – 4.5 mg cm<sup>-2</sup> were assembled in coin cell configuration and examined for their electrochemistry with an even leaner electrolyte conditions of electrolyte (E) to sulfur of E/S ratio of 5 μL/mgs. Figure XIV.6.9 shows the cycling performance of the corresponding Li-

S cell using CFM-S as cathode with  $3.6 \text{ mg cm}^{-2}$  sulfur loading cycled at various current rates for 200 cycles. The cells were initially cycled at C/20 for initiating the formation cycles and the cells showed an initial specific capacity of  $880 \text{ m Ah g}^{-1}$ . After 10 cycles of cycling, the current rate was altered, and the cells were cycled at C/10 rate for the next 90 cycles. The specific capacity as shown in Figure XIV.6.9 steadily increases after initial variation, possibly due to the electrolyte wetting issues attaining stabilization of the electrodes as the cells showed stable cycling. After the stabilization of CFM-S cathodes, the cells showed a specific capacity of  $1051 \text{ m Ah g}^{-1}$  and exhibited moderately stable cyclic performance. After 100 cycles, the cells displayed moderately stable reversible capacity of  $939 \text{ m Ah g}^{-1}$  with a coulombic efficiency of 99.8% exhibiting an extremely low capacity fading of 0.1% per cycle. The cells show excellent redox reversibility with negligible polysulfide shuttling which can be attributed to the 3D carbon fiber structure and N-moieties as explained earlier that serve to anchor the polysulfides formed with the Li ions reacting with the sulfur and enhance their conversion to redox species. The electrochemical performance of the cells was further evaluated at higher current rates (C/5) for another 100 cycles. At the C/5 rate, the cells showed an initial capacity of  $864 \text{ m Ah g}^{-1}$  and displayed moderately stable cycling without indicating any sharp decline in capacity until 200 cycles. The cells were therefore cycled for 200 cycles at various current rates and still displayed a reversible specific capacity of  $560 \text{ m Ah g}^{-1}$  demonstrating excellent cyclability of the CFM-S cathodes.

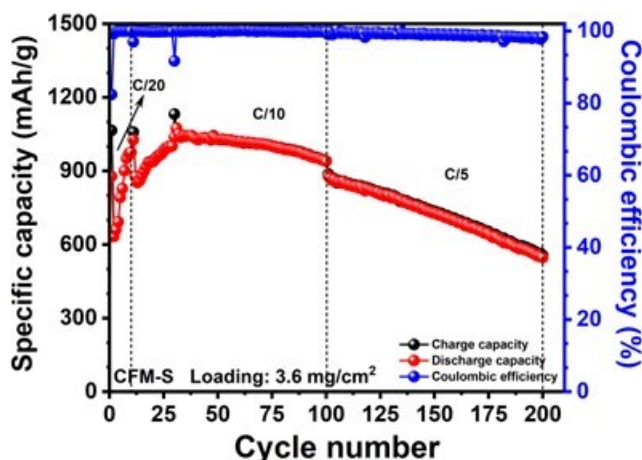


Figure XIV.6.9 Electrochemical cycling performance of CFM-S electrode cycled between 1.8-2.8V at C/20 and 1.7-2.8V at C/10 and C/5 using standard electrolyte.

#### Potential of PMCA3 alloy as current collectors:

As stated earlier, the structurally isomorphous multicomponent alloy, MCA, systems were continued to be examined to explore and demonstrate their ability to be used as current collectors for reversible Li cycling while maintaining stability and preventing dendrite formation. The MCA systems as detailed earlier, form a solid solution with the reacting Li-ions, ensuring dendrite-free anode behavior due to their optimal interfacial energy. The promise of MCA3 alloy to be used as the anode-free current collector for Li-S batteries is thus presented herein. The MCA3 alloy as mentioned above was prepared by a simple and scalable high-energy mechanical alloying and milling process. The electrochemical performance of the MCA3 alloy thus far shown earlier was explored using the slurry process (see Figure XIV.6.3, Figure XIV.6.6 and Figure XIV.6.8) wherein the electrochemical response was affected by the presence of electrochemically inactive binder. The true intrinsic electrochemical performance of the MCA3 alloy was thus examined here as an anode-free current collector using dense pellets in a coin cell configuration. The dense pellets were prepared by hot-pressing the synthesized 100% MCA3 alloy employing a pressure of 6750 psi and temperature of  $100 \text{ }^\circ\text{C}$  for 5 hours followed by subsequently subjecting the dense pellets to electrochemical testing as shown in Figure XIV.6.10. The dense pellet of MCA3 alloy (PMCA3) with a surface area of  $1.32 \text{ cm}^2$  and areal loading of  $137.8 \text{ mg cm}^{-2}$  was cycled in the coin cell using extremely lean electrolyte conditions of  $0.3 \text{ } \mu\text{L/mg}$  of MCA3 utilizing Li metal foil as the counter electrode during testing. A digital image of the PMCA3 is presented in the inset of Figure XIV.6.10. The PMCA3 cells were cycled at a current density of  $1 \text{ mA cm}^{-2}$  with an areal capacity of 5

m Ah cm<sup>-2</sup>. Figure XIV.6.10 shows the electrochemical performance of PMCA3 cells displaying the voltage profiles and cycling performance. The cells show a stable cycling of Li-ions with reversible charge and discharge energy efficiency. The variations in the energy efficiency during initial cycles may be possibly due to SEI formation over the PMCA3 surface or diffusion resistance for Li-ions to form a solid solution as the Li ions are entering into the host MCA *bcc* alloy structure. However, a stable SEI layer forms over PMCA3 after a few cycles, and thereafter, the cells exhibit a coulombic efficiency of 100% for 193 cycles. The overpotential of the cells is higher in the initial cycles due to the stable SEI formation as well as the possible diffusion barrier which reduces significantly after this initial stabilization. The overpotential remains constant for more than 130 cycles and shows a negligible increase after 193 cycles. The PMCA3 cells show excellent cycling stability as Li forms a solid solution with the host MCA3 alloy structure due to optimal interfacial energy and results in negligible volume change during cycling. These results highlight the potential of the MCA3 alloy to serve as dendrite-free current collectors, making the alloy system suitable for use in both pre-lithiated alloyed forms for non-lithium containing cathode systems such as the Li-S batteries, and as part of an anode-free configuration in lithium-containing systems functioning as cathodes. Moreover, the MCA systems demonstrate gravimetric densities over 50% lower than those of the currently employed copper current collectors, rendering them appealing as lightweight current collectors. These results therefore highlight the potential of the MCA3 alloy to serve as dendrite-free current collectors, making the alloy suitable for use in both pre-lithiated alloyed forms for Li metal batteries (LMBs) and even in anode-free configuration for lithium-containing systems functioning as cathodes such as LiCoO<sub>2</sub>, LiNiO<sub>2</sub>, and high Ni containing LiNi<sub>x</sub>Co<sub>y</sub>Mn<sub>1-x-y</sub>O<sub>2</sub>, (NMC), etc.

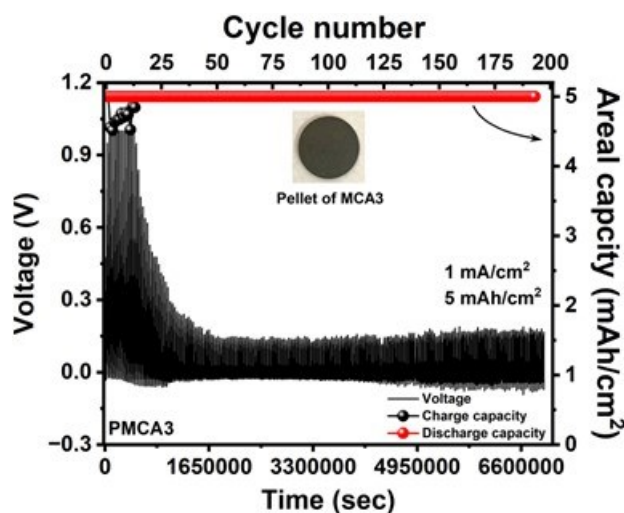


Figure XIV.6.10 Electrochemical cycling performance of PMCA3 as current collector cycled at 1 mA cm<sup>-2</sup> current density with 5 mAh cm<sup>-2</sup> areal capacity showcasing the potential of MCA alloys for current collectors in Li-based batteries. Digital image of MCA3 pellet in the inset.

#### **Effect of electrolyte additives on PSs solubility: Initial computational study**

One of the approaches to minimize the solubility of polysulfides (PS) species in the LSBs would be the identification of different electrolyte additives with the capability to suppress or at least, to hinder the rapid dissolution of PSs in the electrolyte during electrochemical cycling. For these purposes a computational study along the lines of Zhang et al. [ACS Energy Lett. 2021, 6, 537] has been initiated. The computational work takes into consideration a model system containing 1,2-dimethoxyethane (DME)/1,3-dioxolane (DOL) solvent mixture that is used in all the experimental studies in Li-S batteries along with Li<sub>2</sub>S<sub>6</sub> which is the typical PS species encountered in the Li-S batteries. In this electrolyte system the dissociation of Li<sub>2</sub>S<sub>6</sub> could occur following these two steps: 1) formation of individual species of Li<sup>+</sup> and LiS<sub>6</sub><sup>-</sup> and 2) further continuing the dissociation of LiS<sub>6</sub><sup>-</sup> into Li<sup>+</sup> and S<sub>6</sub><sup>2-</sup> species.

Thus, the solvation Gibbs free energy of species X (Li<sup>+</sup>, Li<sub>2</sub>S<sub>6</sub>, LiS<sub>6</sub><sup>-</sup>, and S<sub>6</sub><sup>2-</sup>) in DOL and DME are determined as follows:

$$\Delta G_{d1}^* = \Delta G_{d1}^\circ + \Delta G^*(\text{Li}^+) + \Delta G^*(\text{LiS}_6^-) - \Delta G^*(\text{Li}_2\text{S}_6) + 1.89 \quad \text{Reaction 1} \quad (\text{Li}_2\text{S}_6 \rightarrow \text{Li}^+ + \text{LiS}_6^-)$$

$$\Delta G_{d2}^* = \Delta G_{d2}^\circ + \Delta G^*(\text{Li}^+) + \Delta G^*(\text{S}_6^{2-}) - \Delta G^*(\text{LiS}_6^-) + 1.89 \quad \text{Reaction 2} \quad (\text{LiS}_6^- \rightarrow \text{Li}^+ + \text{S}_6^{2-})$$

$\Delta G^\circ$  - Gibbs free energies in the gas phase

$\Delta G^*(X)$  is the solvation Gibbs free energies of species X in DOL and DME.

$1.89 \text{ kcal/mol} = RT \ln(RT/P)$  – conversion of free energy from the gas phase to the solution phase.

The Gibbs free energy of solvation determines the solubility of the PSs in the solvent.

In the present study calculations of the solvation-free energy delta  $\Delta G^*(X)$  have been conducted using the cluster-continuum solvation method implemented in the *Gaussian 09* software.

**Table XIV.6.1 Calculated Free Energies of Solvation in DME Solvent (Values Given in kcal/mol)**

X	Li <sub>2</sub> S <sub>6</sub>	Li <sup>+</sup>	LiS <sub>6</sub> <sup>-</sup>	S <sub>6</sub> <sup>2-</sup>
$\Delta G^\circ[X(\text{DME})_n]$	-35.83	-86.71	-5.68	-8.21
$\Delta G^*[X(\text{DME})_n]$	-16.54	-39.35	-51.78	-135.57
$n\Delta G_{\text{vap}}(\text{DME})$	2.74	2.74	1.37	2.74
$\Delta G^*(X)$	-49.63	-123.32	-56.09	-141.04

**Table XIV.6.2 Calculated Free Energies of Solvation in DOL Solvent (Values Given in kcal/mol)**

X	Li <sub>2</sub> S <sub>6</sub>	Li <sup>+</sup>	LiS <sub>6</sub> <sup>-</sup>	S <sub>6</sub> <sup>2-</sup>
$\Delta G^\circ[X(\text{DOL})_n]$	-22.74	-48.45	-11.84	-5.97
$\Delta G^*[X(\text{DOL})_n]$	-10.34	-23.85	-32.71	-86.38
$n\Delta G_{\text{vap}}(\text{DOL})$	2.42	2.42	1.21	2.42
$\Delta G^*(X)$	-30.66	-69.88	-43.34	-89.93

$\Delta G^*(X) = \Delta G^\circ[X(\text{DME/DOL})_n] + \Delta G^*[X(\text{DME/DOL})_n] + n\Delta G_{\text{vap}}(\text{DME/DOL})$ , where  $\Delta G_{\text{vap}}(\text{DME/DOL})$  - vaporization energies of DME and DOL as is available in the literature.

From the general point of view following the accepted thermodynamic convention, a larger negative value indicates the higher stability for any particular species that is considered in the study, and therefore, correspondingly is indicative of higher solubility of the specific species in the solvent.

Table XIV.6.1 collects the solvation energies for all the different species in the DME solvent. It can be evinced from Table XIV.6.1 that DME solvent is indeed very favorable for PSs dissolution which is also observed experimentally. Furthermore, Li<sup>+</sup> and S<sub>6</sub><sup>2-</sup> are also very stable species, and thus, the most prevalent components and correspondingly, the species of PSs present and stable in dimethoxy ethane, DME solvent compared to other possible species, namely molecular Li<sub>2</sub>S<sub>6</sub> and LiS<sub>6</sub><sup>-</sup> ions. Hence, it can be construed that the PSs species can be easily dissolved in DME solvent that is commonly used in all the experimental studies of Li-S batteries in the literature.

In addition to the above, an identical study was also conducted with dioxolane, DOL solvent and correspondingly, the calculated Gibbs free energies of solvation are collectively shown in Table XIV.6.2. It can be perceived from the values tabulated in Table XIV.6.2 that compared to the calculated Gibbs free energy values,  $\Delta G^*(X)$  obtained for the DME solvent shown in Table XIV.6.1, the corresponding Gibbs free energies of solvation calculated for all the identical possible PSs components in the DOL solvent are much lower indicating less stability for all the individual species and therefore, reflecting an inferior dissolution of all the PSs in DOL solvent, although Li<sup>+</sup> and S<sub>6</sub><sup>2-</sup> are still the predominant species prevalent in comparison to the molecular species of Li<sub>2</sub>S<sub>6</sub> and LiS<sub>6</sub><sup>-</sup>, respectively.

The results of these calculations and the computational study conducted thus far, confirm that DME is the main solvent in the DME/DOL electrolyte mixture that is favorable for PS dissolution compared to DOL, and thus, identification of an optimal ratio of DME/DOL would be beneficial from the PS dissolution point of view. Additionally, it can be putatively noted that conducting the computational study comprising a comparison of PSs solubility in presence of various electrolyte additives will help identify solutions with lower PS solubility.

**Table XIV.6.3 Calculated Free Energies of Solvation in DME Solvent (Values Given in kcal/mol)**

X	Li <sub>2</sub> S <sub>6</sub>	Li <sup>+</sup>	LiS <sub>6</sub> <sup>-</sup>	S <sub>6</sub> <sup>2-</sup>
$\Delta G^*(X)$	-49.63	-123.32	-56.09	-141.04
X	Li <sub>2</sub> S <sub>4</sub>	Li <sup>+</sup>	LiS <sub>4</sub> <sup>-</sup>	S <sub>4</sub> <sup>2-</sup>
$\Delta G^\circ [X(\text{DME})_n]$	-29.38	-86.71	-3.26	6.54
$\Delta G^*[X(\text{DME})_n]$	-13.85	-39.35	-45.48	-122.15
$n\Delta G_{\text{vap}}(\text{DME})$	2.74	2.74	1.37	2.74
$\Delta G^*(X)$	-40.46	-123.32	-47.37	-125.95
X	Li <sub>2</sub> S <sub>8</sub>	Li <sup>+</sup>	LiS <sub>8</sub> <sup>-</sup>	S <sub>8</sub> <sup>2-</sup>
$\Delta G^\circ [X(\text{DME})_n]$	-41.83	-86.71	-8.51	-11.74
$\Delta G^*[X(\text{DME})_n]$	-18.22	-39.35	-54.89	-155.63
$n\Delta G_{\text{vap}}(\text{DME})$	2.74	2.74	1.37	2.74
$\Delta G^*(X)$	-57.31	-123.32	-62.03	-164.63

**Table XIV.6.4 Calculated Free Energies of Solvation in DOL Solvent (Values Given in kcal/mol)**

X	Li <sub>2</sub> S <sub>6</sub>	Li <sup>+</sup>	LiS <sub>6</sub> <sup>-</sup>	S <sub>6</sub> <sup>2-</sup>
$\Delta G^*(X)$	-30.66	-69.88	-43.34	-89.93
X	Li <sub>2</sub> S <sub>4</sub>	Li <sup>+</sup>	LiS <sub>4</sub> <sup>-</sup>	S <sub>4</sub> <sup>2-</sup>
$\Delta G^\circ [X(\text{DOL})_n]$	-18.69	-48.45	-10.06	-5.13
$\Delta G^*[X(\text{DOL})_n]$	-8.56	-23.85	-28.42	-78.18
$n\Delta G_{\text{vap}}(\text{DOL})$	2.42	2.42	1.21	2.42
$\Delta G^*(X)$	-24.83	-69.88	-37.27	-80.89
X	Li <sub>2</sub> S <sub>8</sub>	Li <sup>+</sup>	LiS <sub>8</sub> <sup>-</sup>	S <sub>8</sub> <sup>2-</sup>
$\Delta G^\circ [X(\text{DOL})_n]$	-27.65	-48.45	-14.24	-6.89
$\Delta G^*[X(\text{DOL})_n]$	-15.48	-23.85	-38.12	-101.37
$n\Delta G_{\text{vap}}(\text{DOL})$	2.42	2.42	1.21	2.42
$\Delta G^*(X)$	-40.41	-69.88	-51.14	-105.84

In addition, following the literature work [Qi He et. al., JECS, 2020, 080508] the PI and his team wanted to clarify whether Li<sub>2</sub>S<sub>4</sub> or Li<sub>2</sub>S<sub>8</sub> PSs are more stable in the electrolyte compared to the abovementioned Li<sub>2</sub>S<sub>6</sub>. Herein, the PI and his team calculated free energies of solvation of different possible species resulting from the

dissolution of  $\text{Li}_2\text{S}_4$  or  $\text{Li}_2\text{S}_8$  PSs in DME/DOL solvent. The calculated solvation energies are collected in Table XIV.6.3 and

X	$\text{Li}_2\text{S}_6$	$\text{Li}^+$	$\text{LiS}_6^-$	$\text{S}_6^{2-}$
$\Delta G^*(X)$	-49.63	-123.32	-56.09	-141.04
X	$\text{Li}_2\text{S}_4$	$\text{Li}^+$	$\text{LiS}_4^-$	$\text{S}_4^{2-}$
$\Delta G^\circ [X(\text{DME})_n]$	-29.38	-86.71	-3.26	6.54
$\Delta G^*[X(\text{DME})_n]$	-13.85	-39.35	-45.48	-122.15
$n\Delta G_{\text{vap}}(\text{DME})$	2.74	2.74	1.37	2.74
$\Delta G^*(X)$	-40.46	-123.32	-47.37	-125.95
X	$\text{Li}_2\text{S}_8$	$\text{Li}^+$	$\text{LiS}_8^-$	$\text{S}_8^{2-}$
$\Delta G^\circ [X(\text{DME})_n]$	-41.83	-86.71	-8.51	-11.74
$\Delta G^*[X(\text{DME})_n]$	-18.22	-39.35	-54.89	-155.63
$n\Delta G_{\text{vap}}(\text{DME})$	2.74	2.74	1.37	2.74
$\Delta G^*(X)$	-57.31	-123.32	-62.03	-164.63

Table XIV.6.4 for DME and DOL solvents, respectively. One can see that similar to  $\text{Li}_2\text{S}_6$ , considered previously,  $\text{Li}_2\text{S}_4$  and  $\text{Li}_2\text{S}_8$  PSs are also dissociated to the most stable and prevalent components of  $\text{Li}^+$  and  $\text{S}_4^{2-}$  or  $\text{S}_8^{2-}$  in both DME and DOL solvents. It is also important to notice that in the DME solvent,  $\text{S}_8^{2-}$  is more stable than  $\text{S}_6^{2-}$ , while  $\text{S}_4^{2-}$  is less stable in the solution than both  $\text{S}_6^{2-}$  and  $\text{S}_8^{2-}$ .

Considering the energetics of  $\text{S}_4^{2-}$ ,  $\text{S}_6^{2-}$  and  $\text{S}_8^{2-}$  species and possible disproportionation reaction of  $2\text{S}_6^{2-} \rightarrow \text{S}_4^{2-} + \text{S}_8^{2-}$  one can see that  $\Delta G^*$  for this reaction in both, DME and DOL solvents are -4.25 kcal/mol and -3.43 kcal/mol, correspondingly. Similar consideration could be applied to the disproportionation reaction  $2\text{Li}_2\text{S}_6 \rightarrow \text{Li}_2\text{S}_4 + \text{Li}_2\text{S}_8$ . Taking the corresponding solvation energy values from Tables 3 and 4 one can obtain  $\Delta G^*$  for this reaction in DME and DOL as +0.75 kcal/mol and -1.96 kcal/mol, respectively. Due to the small energy values in both the DME and DOL solvents, an experimental detection of the simultaneous presence of the  $\text{S}_4^{2-}$ ,  $\text{S}_6^{2-}$  and  $\text{S}_8^{2-}$  species as well as molecular  $\text{Li}_2\text{S}_4$ ,  $\text{Li}_2\text{S}_6$ , and  $\text{Li}_2\text{S}_8$  in the electrolyte may prove to be difficult, which is reported and, also, well corroborated in the literature as well [see Qi He et. al., JECs, 2020, 080508].

The next step of the present computation study will be the consideration of various electrolyte additives and study their effect on the solubility of polysulfides during the electrochemical cycling. This work is ongoing and will be presented in the next quarterly and annual reports.

Functional electrocatalysts (FECs) have also been successfully synthesized that were identified from the previous computational studies conducted by the group and active experimental work is currently ongoing to embed these computationally identified FECs in the carbon framework materials. The FECs lower the activation energy of the rate-limiting step during the discharging process and promote faster electro-kinetics to facilitate maximum utilization of sulfur in the CFM-S cathodes as well as other carbon framework materials identified by the PI and his team to confine the sulfur in high sulfur loaded forms. Efforts are also underway to explore other electrode fabrication approaches utilizing minimal or no solvents at all. These studies are currently ongoing. Furthermore, it is anticipated and envisaged that the CFM-S sulfur cathodes as well as other carbon framework materials embedded with the experimentally synthesized FECs that have been computationally identified would further enhance their overall electrochemical performance showing the desired specific capacity at higher sulfur loadings with longer stable cycle life enabling attaining the initial areal specific capacity of 6 m Ah  $\text{cm}^{-2}$  and then eventually attain the final desired areal specific capacity of 15

m Ah cm<sup>-2</sup>. These studies are currently ongoing and will be presented in the subsequent quarterly and annual reports.

## Conclusions

Research work was conducted both experimentally and computationally on enhancing the individual performance of the three different components (anode, cathode, and electrolyte) of the LSBs. These include experimental synthesis and optimization of the new confinement cathodes for embedding sulfur and preventing polysulfide migration. Another aspect of the project related to experimental studies for identifying the optimal electrolyte additive along with their amount (1wt.% of EA1 and EA2) for stabilizing and forming a multifunctional, robust, SEI layer influencing the electrode kinetics of LSBs was completed. The theory identified FECs were successfully synthesized that lowers the activation barriers activation barriers of the rate limiting step in LSBs. A third aspect of the work was directed on pushing the boundaries of MCA3 exhibiting 15 m Ah cm<sup>-2</sup> areal capacity forming a dendrite-free solid solution with lithium during electrochemical cycling without inducing phase separation for more than 5882 hours and 725 cycles. The potential of MCA3 alloy was highlighted to also serve as dendrite-free current collectors to be used in both pre-lithiated alloyed forms and as part of an anode-free configuration. Additionally, computational studies revealed that different intermediate anionic species of LPSs are stable in DOL and DME solvents although their experimental detection in electrolyte is difficult. Research work related to all aspects of the three components has been successfully conducted and mostly completed in this second year of the project. This project with the required deliverables could therefore be considered completed in FY2024. The electrochemical performance of sulfur cathode and MCA3 anode with lean to extremely lean E/S ratios aided by optimal EA were thoroughly quantified in 20mm coin cell configuration and are being considered for full Li-S cell testing. Major aims planned for optimizing electrolyte additives, sulfur confinement systems and achieving desired 15 m Ah cm<sup>-2</sup> areal capacity for MCA systems in year 2 have been achieved. Five invited presentations as well as two patent applications were awarded in FY2023 with one patent applications also filed in FY2023. Extensive teamwork among the team members contributed significantly to achieving the highly productive outcomes.

## Key Publications

### Publications

Manuscripts are in preparation with the key findings of the cathode, anode and electrolyte additives and are planned for submission in the coming months.

### Presentations

1. Prashant N. Kumta, Oleg Velikokhatnyi, and Ramalinga Kuruba, "From Lithiated Transition Metal Oxides to Silicon and Lithium-Sulfur Systems: An Evolution of Electrochemically Active Materials", presented at the 242<sup>nd</sup> Electrochemical Society Symposium on Research and Development of Primary and Secondary Batteries in honor of George E. Blomgren, October 9-12, 2022 (Invited).
2. Prashant N. Kumta, "Evolution of Electrochemically Active Materials – Meeting the High-energy Density Challenge", paper presented at the 4<sup>th</sup> International Conference on Materials Science & Engineering Meeting held at the Double Tree by Hilton, Houston Intercontinental Airport, Houston, Texas, April 24-26, 2023 (invited).
3. Prashant N. Kumta, "Evolution of Electrochemically Active Materials for High-Energy Density Li-S Batteries", paper presented at the Division of Energy and Fuels: Next Generation Conversion/alloying Chemistries for High-Capacity Batteries Symposium for the American Chemical Society Meeting held in Indianapolis, Indiana, March 26-30, 2023 (invited).
4. Prashant N. Kumta, "Emergent Electrochemically Active Dendrite Free Materials for High-Energy Density Li-S Batteries", Paper presented at the 47<sup>th</sup> International Conference & Exposition on Advanced Ceramics & Composites Symposium 6: Advanced Materials and Technologies for Rechargeable Energy Storage, January 22-27, 2023, Hilton Daytona Beach Resort and Ocean Center, Daytona Beach, Florida, USA. (Invited).



5. Prashant Nagesh Kumta, Oleg Velikokhatnyi, Mayur Gaikwad, Ramalinga Kuruba, George E Blomgren, [Electrochemically Active Materials: Meeting the High-Energy Density Challenge](#), 244th ECS Meeting (October 8-12, 2023), 2023 (Invited).

### Patents

1. Kumta, P.N., Gattu, B., Datta, M.K., Velikokhatnyi, O., Shanthi, P.M. and Hanumantha, P.J., University of Pittsburgh, 2023. High capacity, air-stable, structurally isomorphous lithium *alloy multilayer porous foams*. U.S. Patent 11,575,127.
2. Kumta, P.N., Talakonda, P.R., Datta, M.K., Velikokhatnyi, O., Shanthi, P.M. and Kuruba, R., University of Pittsburgh, 2023. *Identification and methods of fabrication of novel scalable, economic complex framework material (cfm) based cathodes for lithium-sulfur batteries*. U.S. Patent Application 17/781,061.
3. Kumta, P.N. Gaikwad, M., Kuruba, R., and Velikokhatnyi, O., University of Pittsburgh, 2023. *Dendrite-free anodes and current collectors for Li metal batteries and Li-ion batteries*. U.S. Provisional Patent Application filed August 22, 2023.

### Acknowledgements

The principal investigator and co-investigators graciously acknowledge the funding and support provided by DOE, vehicle technology office (VTO). The team also offer their heartfelt appreciation to Tien Duong, Yi Ding, and Haiyan Croft, the program managers for their continuous inputs and eternal encouragement. The team is also in particular, thankful to the deep scientific and technological insights and extremely useful suggestions of Tien Duong and Haiyan Croft during all the quarterly review meetings and the follow-on discussions held throughout the second year of this project. Finally, the principal investigator and co-investigators cordially acknowledge the dedication and team effort of the fellow team members, Dr. Ramalinga Kuruba and Dr. Mayur Gaikwad for their extensive, diligent, and decisive contribution to complete all aspects of the present project.

## XIV.7 Development of Li-S Battery Cells with High Energy Density and Long Cycling Life (PSU)

### Donghai Wang, Principal Investigator

Pennsylvania State University  
134 Energy & Environmental Laboratory  
University Park, PA 16802  
E-mail: [dwang@psu.edu](mailto:dwang@psu.edu)

### Haiyan Croft, DOE Technology Development Manager

U.S. Department of Energy  
E-mail: [Haiyan.Croft@ee.doe.gov](mailto:Haiyan.Croft@ee.doe.gov)

Start Date: October 1, 2022	End Date: September 30, 2023	
Project Funding (FY23): \$488,000	DOE share: \$390,213	Non-DOE share: \$97,554

### Project Introduction

The Li-S battery, based on reversible lithiation/delithiation of sulfur ( $16 \text{ Li} + \text{S}_8 \rightarrow \text{Li}_2\text{S}_n + 8 \text{ Li}_2\text{S}$ ), is believed to be a next-generation high-energy power source for electric vehicle applications due to its high theoretical energy density (specific energy density of 2450 Wh/kg and volumetric energy density of 2899 Wh/L for the cathode, 3 times that of the traditional Li-ion battery cathode) and the low cost of sulfur [1]. Despite the numerous advantages, practical application of Li-S battery technology is encountering several challenges for both sulfur cathode and lithium anode [2]. First, the electric and ionic insulating nature of sulfur makes it difficult to obtain high capacity at useful charge/discharge rates. It requires conductive additives during the fabrication of electrodes to access large portions of the sulfur which reduces the practical energy density [3]. Second, the lithium polysulfide ( $\text{Li}_2\text{S}_x$ ,  $x = 4 \sim 8$ ) can dissolve in the liquid electrolyte and be reduced on the anode surface causing multiple issues during cell cycling, such as shuttling effect, self-discharge, and continuous capacity fading [4]. Finally, electrolyte depletion due to growth of Li dendrites and electrolyte reaction with the Li anode shall lead to poor cycle life [5].

In brief, the most challenging issue is still polysulfide dissolution and its shuttling phenomena. We shall develop a new soluble-polysulfide-free sulfur cathode with high sulfur content (> 50 wt%). With this polysulfide-free cathode, accompanied with the development of functional binders, optimization of electrolyte compositions and electrode fabrication, and protected Li metal anode, advanced Li-S batteries with high energy density and long cycle life are achievable.

### Objectives

The objective of this project is to develop a new soluble-polysulfide-free sulfur cathode (*i.e.*, sulfur polymerized composite (SPC)-derived sulfur composite materials) with a high sulfur content (> 50 wt%) and high discharge specific capacity (> 700 mAh/g, based on the weight of the whole cathode), and demonstrate the performance of the sulfur electrode at high electrode capacity (> 7 mAh/cm<sup>2</sup>, low N/P ratio (< 2) and low electrolyte/sulfur (E/S) ratio (< 2.5  $\mu\text{L}/\text{mg}$ ). A prototype 0.5 Ah Li-S battery cells with the predicted energy density of 400 Wh/kg and 80% capacity retention for over 300 cycles using conventional electrolyte and lithium metal anodes with a protective layer developed from PI's group will be demonstrated.

### Approach

The overall approach will focus on synthesizing and optimizing a novel polysulfide-free sulfur composite active material and functional binders. Specifically, approaches to realize the project objectives include the following: (1) development of novel polysulfide-free sulfur composite active materials, (2) development of new functional polymer binders to facilitate Li<sup>+</sup> transport and trap residual lithium polysulfide; and (3) diagnostics, characterization, theoretical simulation, and cell tests on the developed materials in Li-S batteries.

## Results

In this budget period, we mainly focused on the following aspects: (1) optimization of the synthetic procedures for sulfur polymerized composite (SPC) with increased specific capacities as high-performing cathode materials (SPC-1) for Li-S batteries; (2) optimization of the electrolytes and binders for the high areal loading, SPC-based cathodes for Li-S batteries upon practical conditions; (3) development of sulfur polymerized composite generation-2 (SPC-2) with high sulfur content for Li-S batteries. Meanwhile, we were working on the in-depth characterization and computational simulation on our materials and systems. In the following part, we shall elucidate our accomplishments that have been achieved so far.

### 1. Optimization of the sulfur polymerized composite generation-1 (SPC-1) as sulfur cathode materials

The S content of SPC materials in this budget period was further increased because the higher S content can yield increased specific capacity. In the meanwhile, towards the cell operation at realistic conditions including lean electrolyte and limited Li metal, we aimed to decrease the specific surface area of the obtained SPC materials since the reduced specific surface area can contribute to the less exposure to the electrolyte and thus the decreased electrolyte consumption. By adjusting the heating temperature and heating in SPC-1 synthesis, along with the aftertreatment, we tried to fabricate SPC-1 materials with higher S content and minimized specific surface area. As shown in Figure XIV.7.1, compared with conventional SPAN powder ( $> 16 \text{ m}^2 \text{ g}^{-1}$ ), the optimized SPC powder demonstrated much reduced specific surface area ( $8.0 \text{ m}^2 \text{ g}^{-1}$ ) probably due to the higher S fraction in the SPC powder. Based on the optimized SPC-1 material, the corresponding Li-S cell demonstrated a high initial specific capacity over  $1000 \text{ mAh g}^{-1}$  from the first discharge at a current density of  $50 \text{ mA g}^{-1}$  as shown in Figure XIV.7.2a. In the subsequent cycling at a current density of  $200 \text{ mA g}^{-1}$ , the specific capacity of the SPC-based cell could be stabilized at  $\sim 750 \text{ mAh g}^{-1}$  for more than 120 cycles with an average CE over 99.7% as shown in Figure XIV.7.2b. Such discharge specific capacity fulfills the target for this reporting period and further optimization would be continued in next research period.

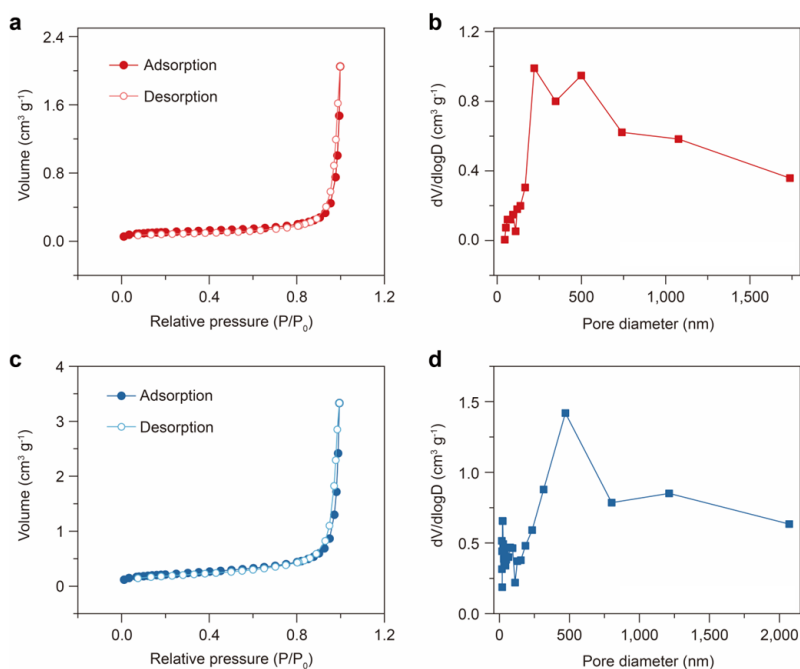
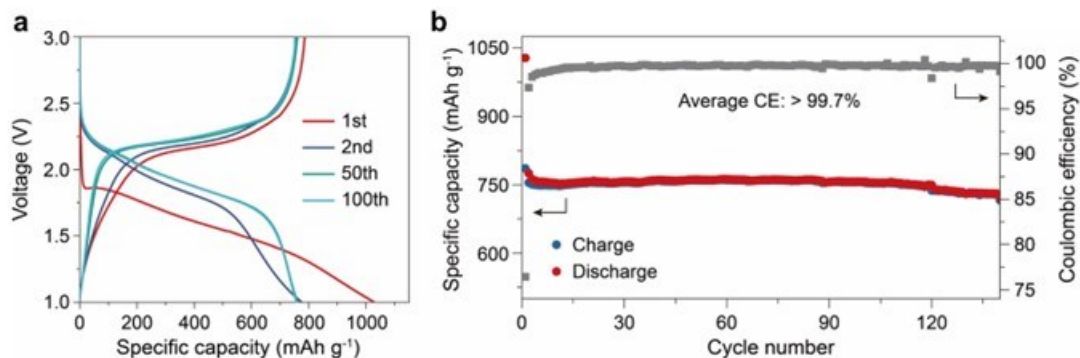
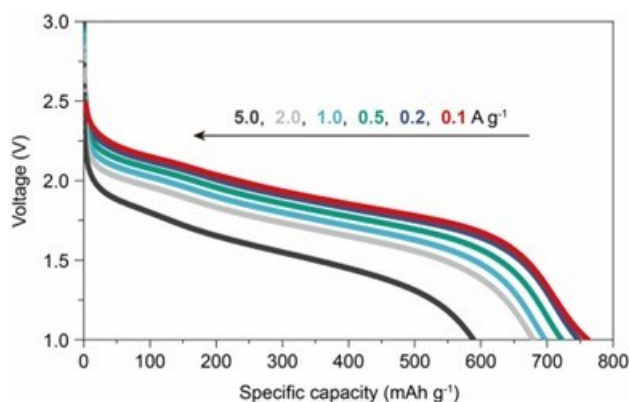


Figure XIV.7.1 (a) and (b), N<sub>2</sub> adsorption/desorption isotherms (a) and (b) pore size distribution of optimized SPC. (c) and (d), N<sub>2</sub> adsorption/desorption isotherms (c) and (d) pore size distribution of conventional SPAN.



**Figure XIV.7.2** (a) The galvanostatic charge and discharge curves of cells based on optimized SPC-1 cathodes at  $200 \text{ mA g}^{-1}$ . (b) Evolution of charge-discharge capacity and Coulombic efficiency (CE) versus cycle number at  $200 \text{ mA g}^{-1}$ .

To further increase the overall energy density of Li-S batteries at cell level, the binders and conductive agents of cathode fabrication were optimized for desirable rate capability. Optimized polymer binders and carbon additives were used to construct the SPC-1 based electrodes with areal cathode loading of  $\sim 2 \text{ mg cm}^{-2}$ . The resultant SPC-based electrodes were paired with excessive Li metal and tested at low E/S ratio of  $8 \mu\text{l mg}^{-1}$  in carbonate electrolyte. As shown in Figure XIV.7.3, upon the current densities of 0.1, 0.2, 0.5, 1.0, 2.0, and  $5.0 \text{ A g}^{-1}$ , the Li-S cells based on SPC materials with new binders and conductive agents delivered specific capacity of 753, 749, 761, 698, 668, and  $587 \text{ mAh g}^{-1}$ , respectively.



**Figure XIV.7.3** Discharge profiles of the Li-S cells based on optimized SPC-1 cathodes in carbonate electrolytes at increasing current densities from 0.1 to  $5.0 \text{ A g}^{-1}$  based on SPC-1 composite.

## 2. Optimization of electrolytes and functional polymer binders for high areal capacity SPC-1 cathodes

Following with the optimization of SPC-1 cathode materials, we also explored the dependence of the electrolyte formula on the recurring Li deposition because the uniform Li deposition is important to the stable cycling of Li-S batteries. The electrolyte formula has been previously optimized according to the electrochemical performances of SPC-1-based cathodes and in this period, we mainly focused on the behaviors of Li anodes in different electrolytes. As shown in Figure XIV.7.4a-b, the lithium in carbonate-based electrolyte developed a mossy appearance, with a relatively porous structure. While in the ether-based electrolyte, spherical and relatively uniform Li deposition was observed Figure XIV.7.4c-d. This better morphology is beneficial to the higher coulombic efficiency due to the more efficient stripping for charging processes. Therefore, although the carbonate-based electrolyte benefits the formation of a relatively stable CEI layer for the SPC cathode, the electrolyte formula still needs improvement to achieve stable cycling of Li anode and so as the desirable cycling performance of the resultant Li-S batteries.

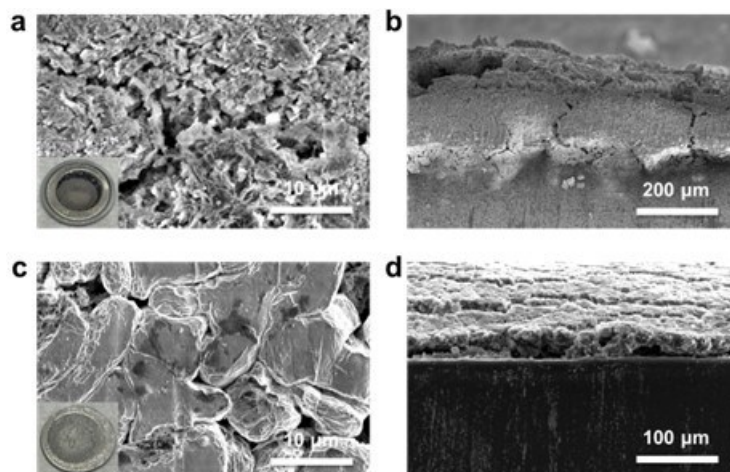


Figure XIV.7.4 (a) and (b), SEM images of Li anodes disassembled from the cycled SPC-1 cathode-based Li-S batteries in the carbonate-based electrolyte. (c) and (d), SEM images of Li anodes disassembled from the cycled SPC cathode-based Li-S batteries in the ether-based electrolyte.

Based on above results, we further optimized the formula of the electrolyte for improved compatibility and more stable operation of Li metal anodes. The new electrolyte formula was then used to construct and evaluate the SPC-based Li-S batteries upon practical conditions including high areal capacity ( $\sim 4 \text{ mAh cm}^{-2}$  in cathode) and relatively lean electrolyte (E/S ratio of 5). As shown in Figure XVII.8.5, compared with previously used electrolyte (Figure XIV.7.5a), our newly optimized electrolyte (Figure XIV.7.5b) gave the corresponding SPC-based cells improved cycling stability over 200 cycles with a high initial specific capacity over  $1000 \text{ mAh g}^{-1}$ . Such discharge specific capacity fulfills the target for this reporting period and further optimization would be continued in next steps.

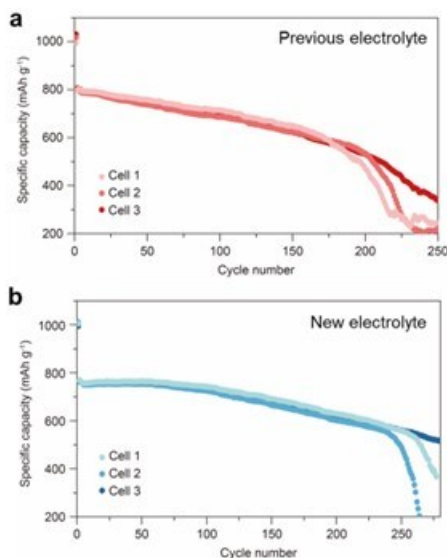


Figure XIV.7.5 (a) and (b), Cycling performances of the SPC-1-based Li-S batteries at  $200 \text{ mA g}^{-1}$  in previous electrolyte (a) and in new electrolyte (b).

To further increase the overall energy density of Li-S batteries at cell level, the binders of cathode fabrication were optimized for higher areal capacity. The resultant high areal capacity SPC-1-based cathodes were paired with excessive Li metal and tested at low E/S ratio of  $5 \mu\text{L mg}^{-1}$  in typical carbonate electrolyte (electrolyte 1). As shown in Figure XIV.7.6, the application of binder 2 afforded enhanced cycling stability compared with that of cathodes based on binder 1. The optimized binder 3 could simultaneously serve as binder and

conductive agents for cathode preparation thus a higher mass ratio of SPC-based cathode material could be achieved, which delivered an enhanced initial areal capacity. Such initial discharge capacity meets the target for this reporting period. However, the high initial discharge capacity based on binder 3 demonstrated limited cycling stability, which needed further optimization.

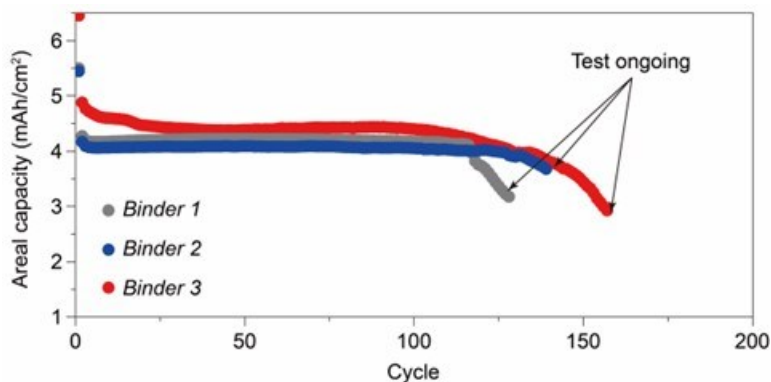


Figure XIV.7.6 Cycling performances of optimized SPC cathodes fabricated with different binders tested at low E/S ratio of  $5 \mu\text{L mg}^{-1}$  and excessive Li metal. Compared with previously used binders (binder 1), upon the construction of high areal capacity SPC cathodes, the optimized binder 2 delivered improved cycling stability and the optimized binder 3 could afford higher areal capacity in Li-S batteries.

### 3. Development and optimization of the sulfur polymerized composite generation-2 (SPC-) as sulfur cathode materials

We also developed new polymer precursors and used them to fabricate a new family of sulfurized polymer cathode materials named SPC-2. We fabricated the SPC-2-based cathodes, paired them with Li metal anodes in Li-S batteries, and evaluated the corresponding electrochemical performances upon practical conditions including high areal capacity ( $\sim 4 \text{ mAh cm}^{-2}$  in cathode) and relatively lean electrolyte (E/S ratio of 5). As shown in Figure XIV.7.7, our newly fabricated sulfur cathode SPC-2 gave the corresponding SPC-2-based cells a high initial specific capacity over  $900 \text{ mAh g}^{-1}$  in carbonate-based electrolyte. Such discharge specific capacity fulfills the target for this reporting period and further optimization would be continued in next steps.

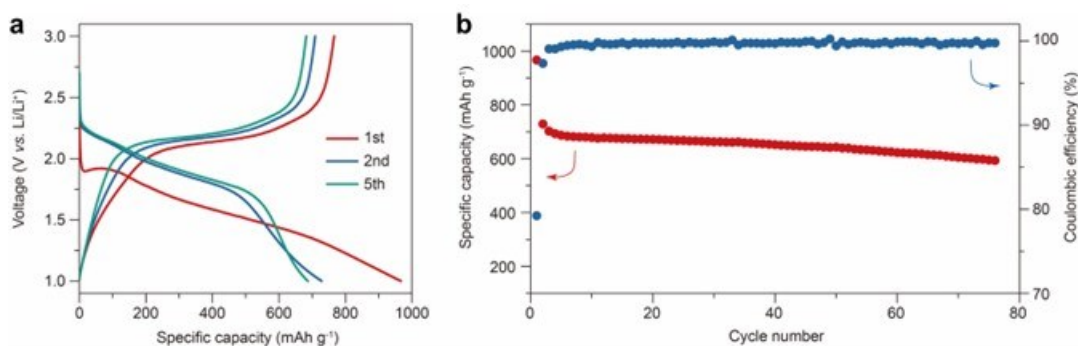


Figure XIV.7.7 (a) Galvanostatic charge and discharge curves of SPC-2-based cells at  $200 \text{ mA g}^{-1}$  cathode material in carbonate-based electrolyte. (b) Corresponding evolution of discharge capacity and Coulombic efficiency (CE) versus cycle number in (a).

## Conclusions

In conclusion, we have accomplished our goals and Go/no Go target for the budget period 2. In specific, we have developed a series of SPC materials and accordingly synthesized polysulfide-free sulfur cathodes with significantly enhanced specific capacity for Li-S batteries using both carbonate and ether-based electrolytes. We have also worked on the evaluation of the electrochemical performances, in-depth characterization, and computational simulation of our newly developed materials and systems.

**References**

1. P. G. Bruce, S. A. Freunberger, L. J. Hardwick, J. M. Tarascon, *Nature Materials* 2012, 11, 19.
2. A. Manthiram, Y. Fu, S. H. Chung, C. Zu, Y. S. Su, *Chemical Reviews* 2014, 114, 11751; Z. W. Seh, Y. Sun, Q. Zhang, Y. Cui, *Chemical Society Reviews* 2016, 45, 5605.
3. X. Ji, K. T. Lee, L. F. Nazar, *Nature Materials* 2009, 8, 500.
4. M. R. Busche, P. Adelhelm, H. Sommer, H. Schneider, K. Leitner, J. Janek, *Journal of Power Sources* 2014, 259, 289.
5. L. Qie, C. Zu, A. Manthiram, *Advanced Energy Materials* 2016, 6, 1502459.

**Acknowledgements**

The work was supported by the Department of Energy, under Award Number DE-EE0009650. We appreciate the support from Coriana Fitz at National Energy Technology Laboratory and Patricia Smith from DOE.

## XIV.8 Nanostructured Design of Sulfur Cathodes for High Energy Lithium-Sulfur Batteries (Stanford University)

### Yi Cui, Principal Investigator

Stanford University

Department of Materials Science and Engineering, Stanford University  
Stanford, CA 94305

E-mail: [yicui@stanford.edu](mailto:yicui@stanford.edu)

### Tien Duong, DOE Technology Development Manager

U.S. Department of Energy

E-mail: [Tien.Duong@ee.doe.gov](mailto:Tien.Duong@ee.doe.gov)

Start Date: October 1, 2017

End Date: September 30, 2023

Project Funding (FY23): \$500,000

DOE share: \$500,000

Non-DOE share: \$0

### Project Introduction

Lithium-sulfur (Li-S) batteries are a promising next generation energy storage technology due to their high theoretical energy density of 2500 Wh kg<sup>-1</sup>. However, Li-S batteries suffer from low electronic and ionic conductivity of sulfur and lithium sulfide, intermediate lithium polysulfide shuttling, and safety issues due in part to highly flammable liquid electrolytes. One approach to improve Li-S battery safety and target high energy density is to use non-flammable solid-state electrolytes. However, slow reaction kinetics of the sulfur conversion remain a major issue. In this project, we develop a single-atom catalyst that can be rapidly synthesized with our hydrogen substituted graphdiyne aerogel ultra-fast sparking synthesis (GAUSS). We use this GAUSS platform to prepare a single-atom cobalt/hydrogen substituted graphdiyne (HGDY) catalyst. Electrochemical testing and density functional theory calculations show that single-atom catalysts synthesized with the GAUSS platform promote Li-S conversion kinetics in all-solid-state Li-S batteries.

### Objectives

The charge capacity limitations of conventional transition metal oxide cathodes are overcome by designing optimized nano-architected sulfur cathodes. This study aims to enable sulfur cathodes with high capacity and long cycle life by developing sulfur cathodes from the perspective of nanostructured materials design, which will be used to combine with Li-metal anodes to generate high-energy Li-S batteries. In this project, we develop a hydrogen substituted graphdiyne (HGDY) aerogel assisted ultra-fast sparking synthesis to produce cobalt single atoms that catalyze the sulfur conversion reaction in Li-S batteries. High-angle annular dark-field scanning transmission electron microscopy (HAADF-STEM) and X-ray absorption fine structure are used to confirm the successful synthesis of the cobalt single-atoms. Electrochemical testing and density functional theory calculations are used to study the reaction kinetics and energetics of the HGDY/single-atom catalyst. Sulfur cathodes with the HGDY/cobalt catalyst are tested in all-solid-state Li-S batteries and deliver superior reaction kinetics and improved capacity and cycle life.

### Approach

The approach involves three main efforts: (I) Advanced nanostructured sulfur cathodes design and synthesis, including (1) engineer empty space into sulfur cathode to solve the problem of electrode volume expansion, (2) develop novel sulfur nanostructures for confinement of S/Li polysulfides to address issues of active materials loss and low conductivity, (3) develop/discover optimal nanostructured materials that can capture the polysulfide dissolved in the electrolyte, (4) develop space-efficiently-packed nanostructured sulfur cathode to increase volumetric energy density and rate capability, and (5) identify interaction mechanism between sulfur species and different types of materials, and find optimal materials to improve capacity and cycling of sulfur cathode. (II) Structure and property characterization, including *ex situ* transmission electron microscopy and



X-ray absorption fine structure. (III) Electrochemical testing including coin cells as well as a set of electrochemical techniques.

## Results

For the GAUSS process (Figure XIV.8.1a), hydrogen substituted graphdiyne (HGDY) aerogel is designed to provide micro-explosions. HGDY aerogels have high surface area, high volume to mass ratio, micropores, and unique acetylenic carbon chemistry, which provides high density sites of micro-explosions to realize ultra-high temperature. When the HGDY aerogel touches the hotplate (set to 450 °C) a sparking reaction occurs. During this reaction, red flames spread from origin quickly through the entire aerogel, transforming the HGDY from light brown to a black color. This reaction produces a large amount of heat and pressure. Synthesis of Co/HGDY with our GAUSS platform is achieved by soaking the HGDY aerogel in ethanol with dissolved metal salts and then drying to achieve a metal infused HGDY aerogel. The metal infused HGDY aerogel is then placed in contact with a hotplate (set to 450 °C), quickly initiating the spark reaction which provides the fast heating and cooling rates necessary to achieve the metastable states. The facile, scalable nature, and low costs of reagents of the GAUSS platform endow the method with promise for large-scale commercialization.

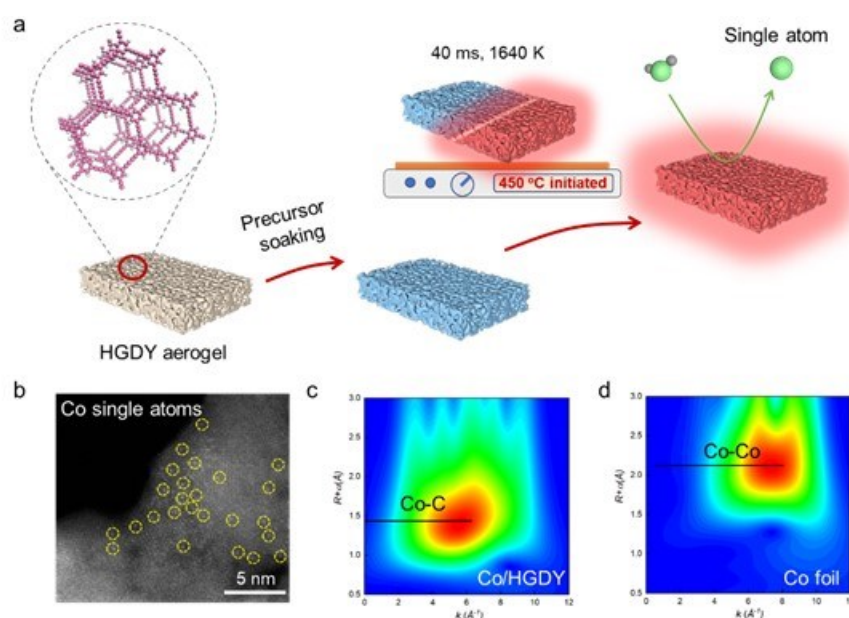


**Figure XIV.8.1** Single atoms by GAUSS for ASSLSBs. (a) Schematic of GAUSS for cobalt (Co) single atoms. Precursors are firstly dissolved in ethanol and soaked on HGDY aerogel. Solvated HGDY aerogel is dried and placed on the hotplate set at a temperature of 450 °C. Immediately, sparking reaction happens and spreads quickly through the entire aerogel, achieving an ultra-high temperature up to 1640 K within 40 milliseconds. (b-d) Characterizations of single atoms by GAUSS. b, STEM image of Co single atoms on HGDY. Wavelet transforms for d, Co/HGDY. and e, Co foil reference.

To characterize single atoms produced by our GAUSS platform, we use aberration corrected high-angle annular dark-field scanning transmission electron microscopy (HAADF-STEM) to resolve single atoms owing to large atomic number difference between metal atoms and carbon atoms in the HGDY support. The HAADF-STEM image showed localized bright spots on the HGDY support, indicating single atom Co sites are well dispersed on the HGDY support (Figure XIV.8.1b). Co K-edge extended X-ray absorption fine structure (EXAFS) further supports the HAADF-STEM measurement. Wavelet analysis clearly shows no Co-Co formation in the Co/HGDY material, indicating the successful synthesis of single atom sites on GDY (Figure XIV.8.1c and Figure XIV.8.1d). The Co loading is determined as 0.23 wt% by inductively coupled plasma (ICP) analysis.

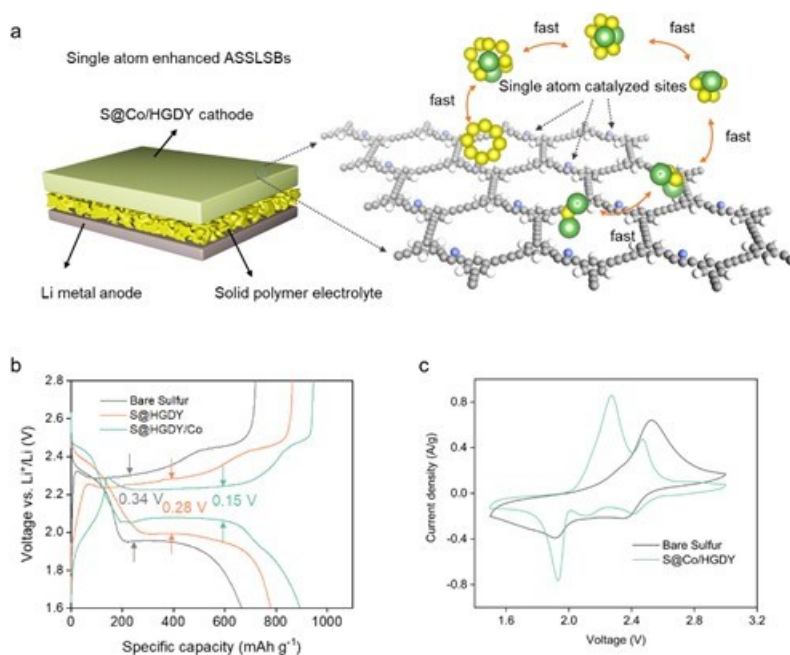


**Figure XIV.8.2** Ultrafast single atom synthesis for all-solid-state lithium-sulfur batteries (ASSLSBs). (a) Schematic of Co single atoms enabled ultra-fast Li-S conversion in ASSLSBs. (b) Charge/discharge curves of ASSLSBs using bare sulfur cathodes, S@HGDY cathodes, and S@Co/HGDY cathodes at 60 °C at 0.05 C. (c) Cyclic voltammetry profiles of ASSLSBs using bare sulfur cathodes, and S@Co/HGDY cathodes at 60 °C.

The unique structure of Co/HGDY aerogel prepared by GAUSS provides abundant active sites for enhancing the sluggish Li-S redox reaction kinetics in ASSLSBs. A schematic of the Co/HGDY enhanced ASSLSBs is shown in Figure XIV.8.2a. Here we synthesize active materials for sulfur cathodes by infiltrating sulfur into the Co/HGDY network (S@Co/HGDY) with a 9:1 mass ratio of sulfur to Co/HGDY. As a control active material, we infiltrate sulfur into carbon black with a 9:1 sulfur to carbon mass ratio. Sulfur cathodes are made by mixing active material, carbon black, and polyethylene oxide/lithium bis(trifluoromethanesulfonyl)imide (PEO@LiTFSI) binder with a mass ratio of 0.6:0.15:0.25. Polyimide (PI) infiltrated with PEO@LiTFSI is used as the solid polymer electrolyte. Incorporating Co single atoms into the HGDY support enabled a maximum discharge capacity of  $\sim 900 \text{ mA}\cdot\text{h}\cdot\text{g}^{-1}$  for ASSLSBs. A minimized overpotential of 0.14 V is obtained owing to the catalytic enhancement of Li-S conversion kinetics by Co single atoms. (Figure XIV.8.2b). Larger polarizations are observed for the bare sulfur cathode (0.34 V) and S@HGDY cathode (0.28 V). Cyclic voltammetry measurements are performed to investigate the Li-S conversion for ASSLSBs using bare sulfur cathodes, and S@Co/HGDY cathodes at 60 °C. The S@Co/HGDY cathode shows a noticeable positive shift in the cathodic peak and a negative shift in the anodic peak (Figure XIV.8.2c), indicating the improved reaction kinetics of the S@Co/HGDY cathode owing to the function of the Co single atoms on HGDY.

The catalytic enhancement of the Li-S conversion reaction is supported by density functional theory (DFT) calculations. Sulfur cathodes with Co on HGDY show a lower free energy for all steps in the conversion reaction compared with bare sulfur cathodes (Figure XIV.8.3). The optimized position for Co on HGDY, and optimized structures of the lithium polysulfide intermediates on the Co/HGDY substrate are shown in the insets of (Figure XIV.8.3). The conversion from  $\text{Li}_2\text{S}_4$  to  $\text{Li}_2\text{S}_2$  and from  $\text{Li}_2\text{S}_2$  to  $\text{Li}_2\text{S}$  have larger positive Gibbs free energy than the rest of the reaction steps, indicating that the formation of  $\text{Li}_2\text{S}_2$  and  $\text{Li}_2\text{S}$  are rate-limiting steps in the discharge process. When considering Co single atoms catalyst in this conversion reaction, the energy barrier of  $\text{Li}_2\text{S}_4$  to  $\text{Li}_2\text{S}_2$  and  $\text{Li}_2\text{S}_2$  to  $\text{Li}_2\text{S}$  is significantly reduced.

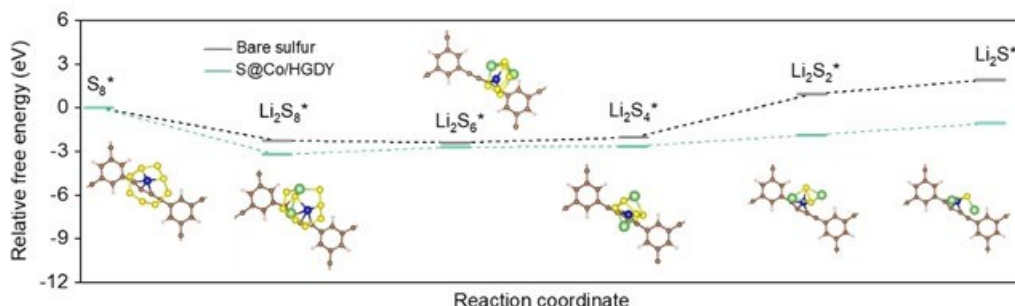


Figure XIV.8.3 Density functional theory calculations of sulfur reduction reaction. Energy profiles for the reduction of bare sulfur and sulfur@Co/HGDY. The optimized structures of the intermediates are shown in the inset.

Experimental evidence of this catalytic effect is shown in the Li-S battery with S@Co/HGDY cathodes; a smaller ratio of the first plateau to second plateau (compared to the control cathode) in the voltage profile, indicates that addition of Co/HGDY enables more  $\text{Li}_2\text{S}_4$  conversion to  $\text{Li}_2\text{S}$ .

Rate and cycling performance of sulfur cathodes with and without the Co/HGDY catalyst for ASSLSBs at 60 °C are shown in Figure XIV.8.4. After an initial activation cycle at 0.05 C, the S@Co/HGDY cathodes deliver greater capacity at 0.1 C, 0.2 C, and 0.5 C, compared to the S@HGDY cathodes. Notably, the S@Co/HGDY cathodes experience less capacity drop than S@HGDY cathodes when the rate is increased. Even without Co single-atoms, the S@HGDY cathodes deliver greater capacity compared to the bare sulfur control cathodes at all rates studied.

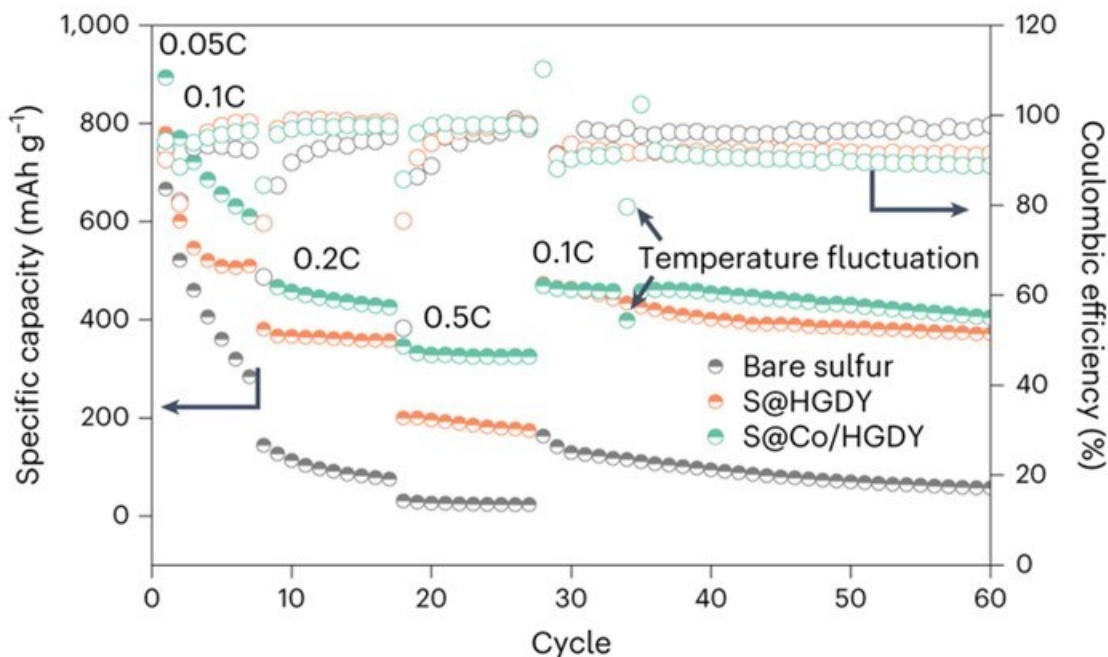


Figure XIV.8.4 Rate and cycling performance of ASSLSBs using bare sulfur cathodes, S@HGDY cathodes and S@Co/HGDY cathodes at 60 °C.

The catalytic effect of Co single atoms enhances the cycling and rate performance of the sulfur cathodes, in addition to decreasing the amount of soluble sulfur species in the solid polymer electrolytes by porous HGDY. The capacity and cycling stability of single-atom-enhanced ASSLSBs is comparable to state-of-the-art solid polymer-based ASSLSBs.

### Conclusions

We have developed the GAUSS synthesis platform which we used to fabricate Co/HGDY single-atom catalyst for sulfur cathodes. We use HAADF-STEM and EXAFS to confirm the successful preparation of single-atom Co. Electrochemical tests and density functional theory are used to understand the catalyst's effect on the reaction kinetics, cell performance, and the reaction mechanism in the presence of the catalyst in all-solid-state Li-S batteries. The Co/HGDY catalyst yields a lower reaction overpotential and superior rate and cycling performance compared to the control cells. The GAUSS synthesis method can also be used to create other metastable nanomaterials for future ASSLSBs or other cell chemistries.

### Key Publications

1. Zheng, X.; Gao, X.; Vilá, R. A.; Jiang, Y.; Wang, J.; Xu, R.; Zhang, R.; Xiao, X.; Zhang, P.; Greenburg, L. C.; Yang, Y.; Xin, H. L.; Zheng, X.; Cui, Y. Hydrogen-Substituted Graphdiyne-Assisted Ultrafast Sparking Synthesis of Metastable Nanomaterials. *Nat. Nanotechnol.* 2022. <https://doi.org/10.1038/s41565-022-01272-4>.

## XIV.9 Fluorinated Glyme Solvents to Extend Lithium-Sulfur Battery Life Fluorinated Glyme Solvents to Extend Lithium-Sulfur Battery Life (Navitas Advanced Solutions Group)

### **Taylor Xu, Principal Investigator**

Navitas Advanced Solutions Group  
4880 Venture Drive  
Ann Arbor, MI, 48108  
E-mail: [txu@navitassys.com](mailto:txu@navitassys.com)

### **John Zhang, Principal Investigator**

Argonne National Laboratory  
9700 S. Case Avenue  
Lemont, IL, 60439  
E-mail: [zzhang@anl.gov](mailto:zzhang@anl.gov)

### **Haiyan Croft, DOE Technology Development Manager**

U.S. Department of Energy  
E-mail: [Haiyan.Croft@ee.doe.gov](mailto:Haiyan.Croft@ee.doe.gov)

Start Date: Jan. 01, 2023	End Date: September 30, 2023	
Project Funding (FY23): \$1,361,192	DOE share: \$1,088,992	Non-DOE share: \$272,200

### **Project Introduction**

Navitas proposes to improve Li-S battery (LSB) life and performance by developing innovative electrolyte solutions based on partially fluorinated glymes (PFG). ('Glyme' refers to the general class of glycol ethers.) The novelty of our concept is the use of PFG as a multifunctional solvent to attain high ionic conductivity and non-flammability, while also retaining the merits of similar partially fluorinated ether (PFE) [1] in suppressing polysulfide (PS) dissolution and promoting SEI formation on electrode surfaces.

Navitas Advanced Solutions Group (Navitas) will team with Dr. Zhengcheng (John) Zhang at Argonne National Laboratory (ANL) to jointly develop a novel electrolyte solution to further extend the cycle life of Li-S batteries. ANL will design, synthesize, characterize, and scale up PFG solvents. Navitas will formulate electrolyte solutions with PFG solvent candidates, perform physical properties and cell performance testing, and then validate the electrolyte performance in prototype 2 Ah LSB pouch cells.

Lithium sulfur batteries are emerging as promising 'beyond lithium ion' energy storage systems. Sulfur-based cathodes are safe, economical, and possess a theoretical energy density of 2567 Wh/kg, 3X higher than NMC 811. However, existing LSB technology faces significant technical challenges due to the formation of lithium polysulfides as intermediate discharge products. Polysulfides are highly soluble in the organic solvents comprising established liquid electrolyte systems. This solubility leads to loss of cathode active material, reduced Coulombic Efficiency (CE), and increased self-discharge. Soluble polysulfides cross the separator and react with and degrade the lithium metal anode, which in turn dramatically reduces cycle life and/or requires large excess amounts of electrolyte and lithium.

To date, LSB cells have employed ether/glyme mixtures as electrolyte, most commonly 1,3-dioxolane (DOL) and 1,2-dimethoxyethane (DME) dissolved with LiTFSI salt. Various additives, e.g., LiNO<sub>3</sub>, are often included to create protective solid electrolyte interface (SEI) layers on the anode to improve Coulombic Efficiency. Unfortunately, these additives are slowly consumed and depleted and only temporarily remedy loss of active materials and parasitic side reactions. Therefore, the cell capacity drops dramatically with cycle number even though with a high Coulombic efficiency.

Perfluorinated ethers added as co-solvents have significantly improved the LSB CE and cycle life. The effectiveness of PFEs is attributed to reducing the solubility of polysulfide intermediates and to the formation of protective SEI on the lithium metal anode. However, limited evidence has been presented to support the latter effect, and the key traits of beneficial co-solvents or additives has remained elusive.

The ANL group has been at the forefront of addressing this gap and providing an understanding of the structure-function relationships between PFE co-solvents/additives and increased Coulombic Efficiency and the cell performance [1-3]. Based on the study, ANL has identified new group of PFG compounds as promising electrolyte candidates which are the focus of this proposal (Figure XIV.9.1).

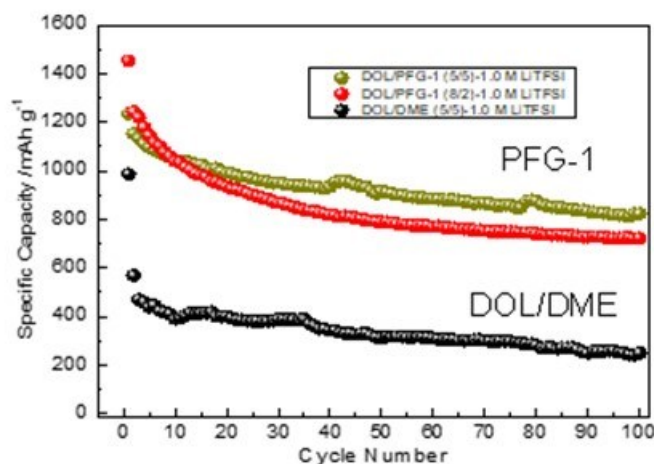


**Figure XIV.9.1** Navitas and ANL propose to develop electrolytes for Li-S batteries based on new fluorinated co-solvents (PFG). Incorporating PFG will surpass state of art DOL/DME electrolytes by reducing polysulfide solubility and protecting electrodes to improve the capacity and cycle life for EV applications.

In this program, ANL will scale up synthesis of the chosen PFG co-solvents. ANL will design and synthesize PFG solvent molecules, perform prescreening tests in coin cells, and deliver solvent samples to Navitas. Navitas will formulate electrolyte solutions including these PFG solvent candidates, perform physical properties and cell performance testing, and then validate the electrolyte performance in prototype 2 Ah LSB cells. Navitas may also incorporate innovative cathode materials and separators in development under other concurrent non-DOE programs. The Navitas' cathode and separator include proprietary porous conductive ceramic compounds whose high affinity for sulfur and polysulfides in the cathode will complement the electrolyte to further suppress the polysulfides dissolution.

### Objectives

Navitas teams with ANL to jointly develop a novel electrolyte solution to further extend the cycle life of Li-S batteries. The novel electrolyte contains partially fluorinated glyme (PFG) solvent capable of achieving  $\geq 1,000$  mAh/g in reversible sulfur specific capacity. The ionic conductivity could reach  $\geq 10$  mS/cm by adjusting the percentage of PFGs in electrolyte. Coulombic Efficiency (CE) of Li-S cells could reach  $\geq 99.5\%$  with addition of both PFGs and other additive. The final deliverable 2 Ah prototype Lithium Sulfur Battery (LSB) pouch cell can achieve  $> 600$  cycles with energy density of  $\geq 400$  Wh/kg.

### Approach

Use PFG as a multifunctional solvent. The proposed PFGs from ANL have structures as described in Figure XIV.9.2. Based on the Li-S cell performance, the different PFG candidates will be down-selected and synthesized.

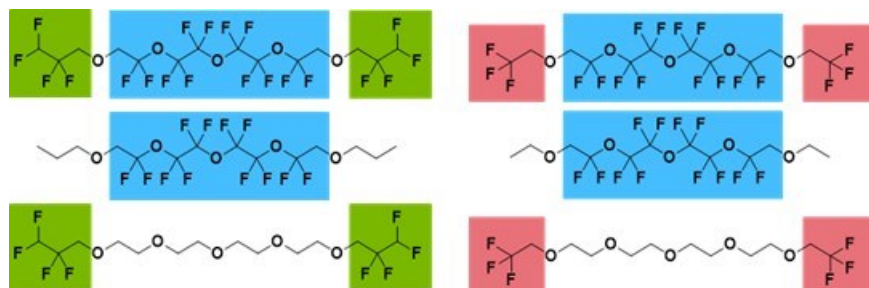


**Figure XIV.9.2** Structure of novel partially fluorinated glymes (PFG) to be synthesized by ANL for evaluation in Li-S batteries. The color shading highlights where the fluorination occurs.

The synthesized and down-selected PFGs should have the properties of high ionic conductivity and non/low flammability. On the other hand, they can suppress polysulfide (PS) dissolution, and promote SEI formation on electrode surfaces.

## Results

### Synthesize PFGs:

Navitas/ANL have synthesized two new partially fluorinated glyme (PFG) solvents with varying fluorination degrees, PFG-1 and PFG-2 (Didn't show structure here), respectively. These two solvents have the same glyme backbone with two oxygen, but with different fluorination structures.

Navitas/ANL also synthesized and evaluated other fluorinated ethers and glymes, such as PFG-3, PFG-4, and PFG-5, shown in Figure XIV.9.3, which have different structures and fluorination degrees.

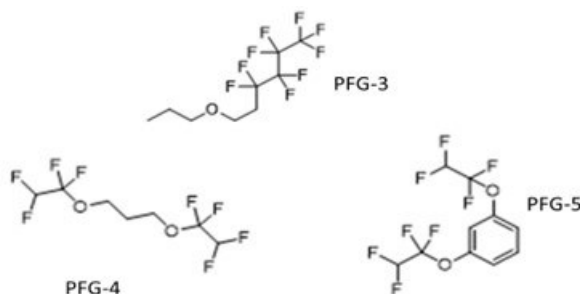


**Figure XIV.9.3** Structures of the other partially fluorinated ether and glymes (PFGs) with varying fluorination degrees.

In this report, we will only focus on test results from PFG-1 and PFG-2.

### Characterize and modify PFGs

To improve safety of electrolyte in Li-S batteries, ANL/Navitas have conducted characterization tests on the synthesized PFGs such as flash point, ionic conductivity, and polysulfide solubility of PFG solutions with LiTFSI.

Figure XIV.9.4 shows the setup of the 30000-0 Setaflash Series 3 Closed Cup Flash Point Tester, which was used to investigate the flash point of studied PFGs and corresponding electrolytes. The test results are summarized in Table XIV.9.1. For comparison, the flash points of the most widely used electrolytes in LIB are also listed in Table XIV.9.1.



**Figure XIV.9.4 30000-0 Setaflash Series 3 Closed Cup Flash Point Tester**

It can be found that the flash points of electrolytes used in LIBs depend on lithium salts, types of solvents, and the ratio (in wt. % or volume %) between the solvents. However, the flash points of those traditional LIB electrolytes are lower than 40°C, which may be a big concern for battery safety.

**Table XIV.9.1 Flash Points of the Most Widely Used LIB Electrolytes [4] and PFG Electrolyte for Li-S Batteries.**

Electrolyte	Flash Point (°C)
1 M LiPF <sub>6</sub> /EC:DMC:EA (1:1:1 wt)	10 ± 1
1 M LiPF <sub>6</sub> /EC:DMC (1:1 wt)	25.5 ± 1
1 M LiPF <sub>6</sub> /PC:DMC (1:1 wt)	26 ± 2
1 M LiTFSI/EC:DMC (1:1 wt)	26 ± 1
10.5 wt% LiBOB/EC:DMC (1:1 wt)	26 ± 1
1 M LiPF <sub>6</sub> /EC:EMC (3:7 wt)	28 ± 1
1 M LiPF <sub>6</sub> /EC:EMC (1:1 wt)	31 ± 1
1 M LiPF <sub>6</sub> /EC:DEC (1:1 wt)	38 ± 1
Baseline: 1 M LiTFSI/DOL:DME (1:1 v)	below room temperature
Pure PFG-1 solvent	66
1 M LiTFSI/DME:PFG-1 (1:2 v)	45

The flash point of the baseline electrolyte for Li-S batteries (1 M LiTFSI/DOL:DME, 1:1 v) is below room temperature, and lower than that of most LIB electrolytes. Introducing a certain amount of PFG-1 solvent to Li-S electrolyte dramatically increases the flash point. As depicted in Table XIV.9.1, 1 M LiTFSI/DME:PFG-1 (1:2 v) electrolyte has a flash point of 45°C due to a higher flash point of pure PFG-1 solvent (66°C) than that of DOL (2 °C, open cup) and DME (1 °C).

Electrolytes containing PFGs with higher flash points ensure a safer Li-S battery. However, PFG solvents with no flash point (or high flash point) as co-solvent may not be suitable for Li-S battery application due to the decrease in lower ionic conductivity, as PFGs do not solvate Li-ions very well.



Test PFGs in coin/SLP/DLP cells:

Figure XIV.9.5 shows the coin cell cycling results with 0.02 M thiourea additive in 1 M LiTFSI DME/DOL (1/1) + 3% LiNO<sub>3</sub> and in 1 M LiTFSI DME/PFG-1 (3/1) + 3% LiNO<sub>3</sub> electrolytes depicted in the last quarterly report of BP1.

The sulfur specific capacity with 0.02 M thiourea additive in 1 M LiTFSI DME/PFG-1 (3/1) + 3% LiNO<sub>3</sub> reaches ~1300 mAh/g at the first cycle at C/10 rate (Figure XIV.9.5). Also, thiourea additive helped capacity retention/cell performance for the cathodes with low S loading (1 mg S/cm<sup>2</sup>) and showed encouraging results initially, but the remarkable synergetic effect with PFG-1 appeared to be decreasing with cycling and the effect could no longer be observed after ~60-70 cycles.

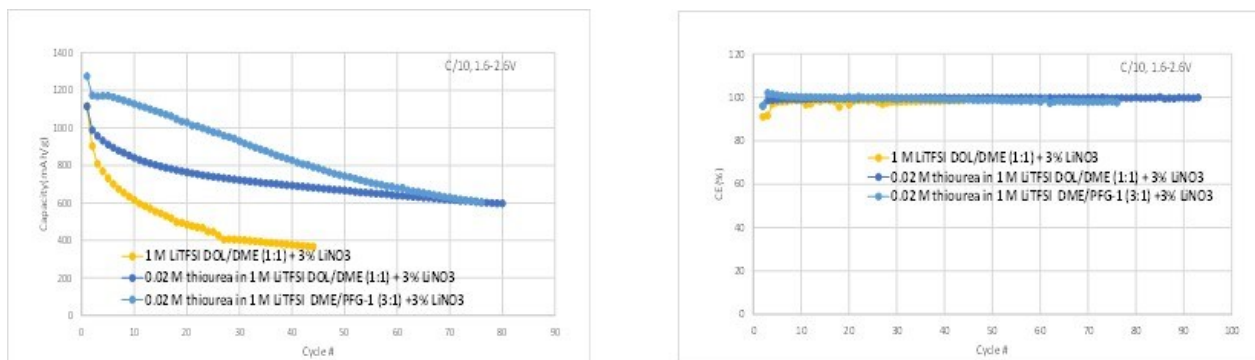


**Figure XIV.9.5 Specific capacity (Left) and Coulombic efficiency (Right) variations with cycling for coin cells with thiourea additive. CR2032, 1.0 mg S/cm<sup>2</sup> loading, 1.6-2.6V, C/10, room T. The synergetic effect of thiourea and PFG-1 appeared to be decreasing with cycling.**

As high loading cathodes ( $\geq 3$  mg S/cm<sup>2</sup>) will be the primary cathodes for BP 2 for high energy Li-S cells vs.  $\sim 1$  mg/cm<sup>2</sup> S loading cathodes used for the exploring tests in BP 1. The electrochemical performance of the high loading cathode coin cells ( $\sim 3.6$  mg S/cm<sup>2</sup>) with PFG-2 as co-solvent is shown in Figure XIV.9.6.

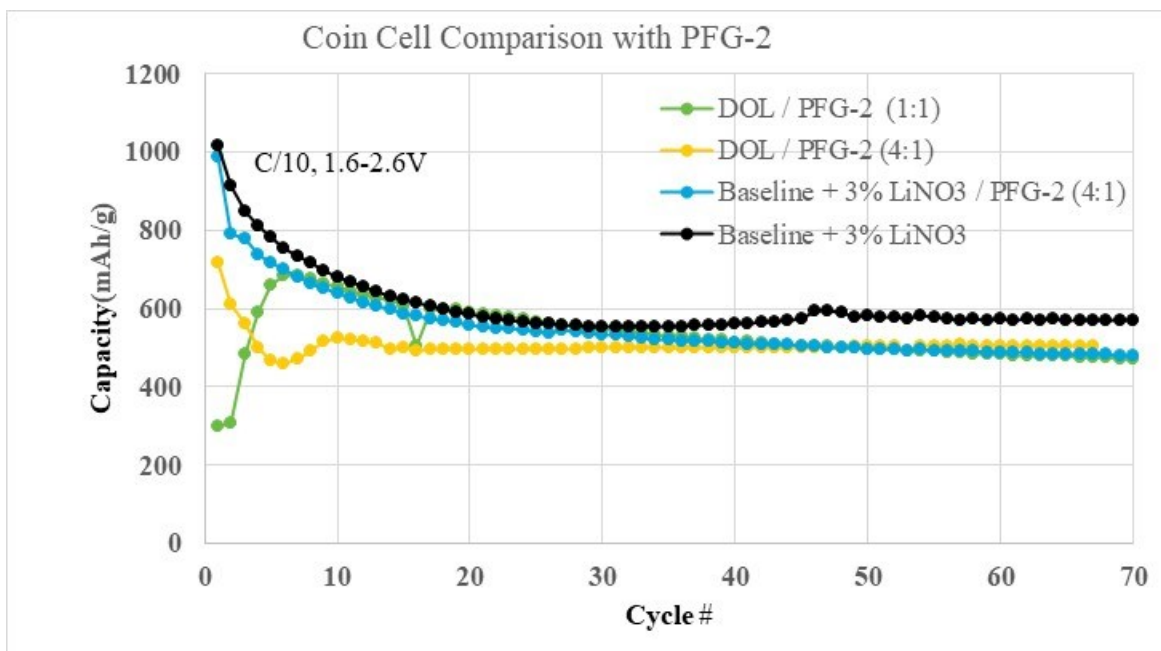


**Figure XIV.9.6** The electrochemical performance of coin cells with electrolyte PFG-2 as co-solvent and  $\text{LiNO}_3$  as additive. (PVDF binder, 80AM/14CB/6PVDF, uncalendared. CR2032, C/10, room T. E/S ratio = 6.5-7; loading  $\approx 3.5 \text{ mg S/ cm}^2$ ).

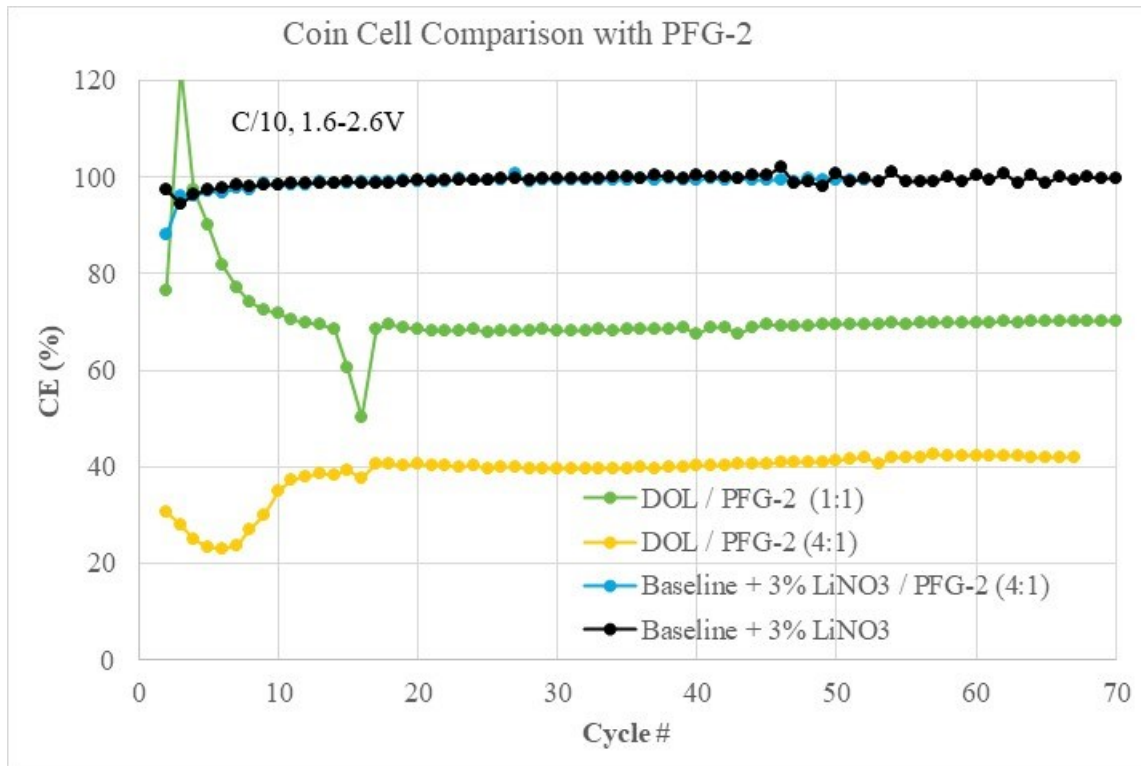
Compared to low sulfur loading cathode coin cells, the high sulfur loading coin cells showed some different behavior. First, the high loading S cathode cells in baseline electrolyte (with 3%  $\text{LiNO}_3$ ) also showed quite stable cycling performance with high Coulombic efficiency ( $\text{CE} \geq 99.5\%$ ) as depicted in

Figure XIV.9.7. After 30 cycles, the high S loading cathode cells still showed specific capacity above 500 mAh/g, which is better than that of the low S loading cathode cells ( $\sim 400 \text{ mAh/g}$ ). Second, the sulfur specific capacity is  $\sim 1000 \text{ mAh/g}$ , which is lower than that of low S loading cathode cells ( $>1100 \text{ mAh/g}$ ).

When replacing DME solvent with PFG-2 solvent and controlling DOL/PFG-2 ratio at 1:1 and 4:1; the electrochemical performance of the cells with PFG-2 co-solvent in electrolyte are slightly worse than that with baseline + 3%  $\text{LiNO}_3$  electrolyte in the beginning 30 cycles, possibly due to the difference in electrode wetting when PFGs are present in electrolyte. But after 30 cycles, the performances are comparable.

However, there is a huge difference in Coulombic efficiency for electrolyte with both  $\text{LiNO}_3$  and DOL/PFG-2 at different ratios. When there is no  $\text{LiNO}_3$  as an additive in the electrolyte, the Coulombic efficiency is dramatically lower (

Figure XIV.9.7): it is only  $\sim 40.4\%$  for electrolyte with DOL/PFG-2 at 4:1 ratio. When the percentage of PFG-2 is increased to DOL/PFG-2 ratio of 1:1, the Coulombic efficiency is  $\sim 68.1\%$ , indicating much less parasitic (side or unwanted) reactions unrelated to charge and discharge behavior of the Li-S battery.



**Figure XIV.9.7** The Coulombic efficiency (CE) of coin cells with electrolyte PFG-2 as co-solvent and LiNO<sub>3</sub> as additive. PVDF binder, 80AM/14CB/6PVDF, uncalendared. CR2032, C/10, room T. E/S ratio = 6.5-7; loading  $\approx 3.5 \text{ mg S/ cm}^2$ .

It must be noted here, increasing the percentage of PFG-2 co-solvent in electrolyte doesn't guarantee better Coulombic efficiency. To achieve Coulombic efficiency higher than 99.5% for Li-S cells, our data shows that LiNO<sub>3</sub> additive must be in the electrolyte.

The low Coulombic efficiency of Li-S cells without LiNO<sub>3</sub> in electrolyte was also verified by ANL as shown in Figure XIV.9.8.

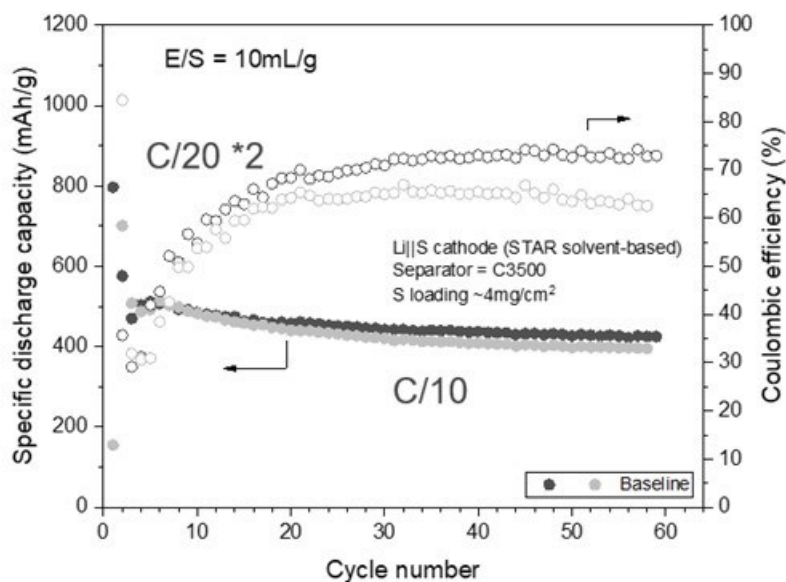


Figure XIV.9.8 The Coulombic efficiency of coin cells from ANL.

*Postmortem analysis of tested cells with PFGs:*

Navitas/ANL will continue to examine the harvested the sulfur electrode and Li anode from the Li-S cells after different numbers of charge-discharge cycles using various techniques such as XPS, SEM/EDS to determine the formation of electrode protection layers in PFG based electrolytes and the compositions of the protective layers and characterize the active species in the electrolyte after cycling using ex situ analysis methods such as UV-vis spectroscopy or FT-IR.

From the Li plating/stripping test, the CE is ~ 94.2% for the baseline electrolyte. However, the CE is much higher when electrolyte contains PFG-1, with a value of 97.4% (Figure XIV.9.9a).

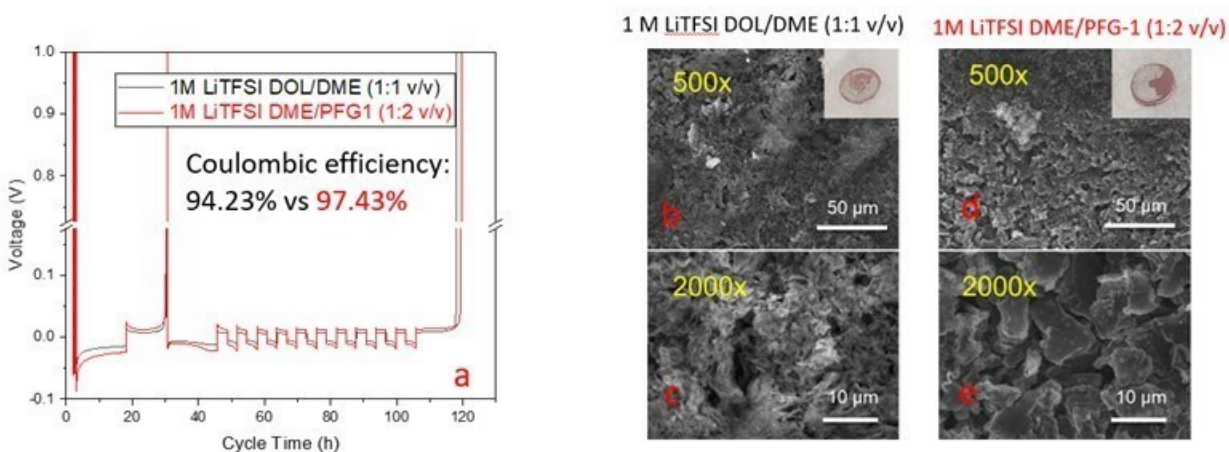


Figure XIV.9.9 (a) Li|Cu cell ( $0.2 \text{ mA/cm}^2$ ,  $3.0 \text{ mAh/cm}^2$ ), SEM images of Li anode surface after charge-discharge of Li/Cu half-cell in electrolyte (b,c) Without PFG-1, and (d,e) with PFG-1.

The deposited Li with 1 M LiTFSI DOL/DME (1:1 v/v) electrolyte shows a mossy morphology, which typically indicates dendrite growth (Figure XIV.9.9b, c).

Li morphology with 1 M LiTFSI DME/PFG-1 electrolyte is denser and more regulated in shape, which indicates better passivation of lithium anode surface (Figure XIV.9.9d, e). Different percentage of PFG-1 in electrolyte will be investigated.

*Optimize, down select PFG and scale up synthesis:*

Navitas/ANL will continue to optimize PFGs, down select PFGs for the final electrolyte formulation, and scale up synthesis of the selected PFGs.

*Optimize electrolyte formulation:*

Navitas/ANL will optimize electrolyte formulation with the selected PFGs to achieve high ionic conductivity, more reduction of polysulfide dissolution and electrolyte/sulfur ratio.

*Assemble DLP cells*

Navitas has designed and assembled DLP cells (Target: 200 mAh) with baseline electrolyte 1.0 M LiTFSI in DOL/DME with and without 3% LiNO<sub>3</sub>. Figure XIV.9.10 shows an assembled DLP cell. The anode consists of Li foil (50 μm thick) rolled onto both sides of a thin layer of copper (12 μm). The cathodes were originally pilot coated single sided on aluminum foil, then punched out using a die (55x105mm cell format). The cathodes were stacked together and then the tab (made of Al) is welded to them. A Ni tab is then welded to the anode. The anode is placed inside a separator bag. The electrodes were then stacked together cathode-anode (in separator bag)-cathode. The anode is slightly larger than the cathodes. The entire stack is then placed inside a larger separator bag (or strip). The real capacity of DLP vs cycle number was shown in Figure XIV.9.11.

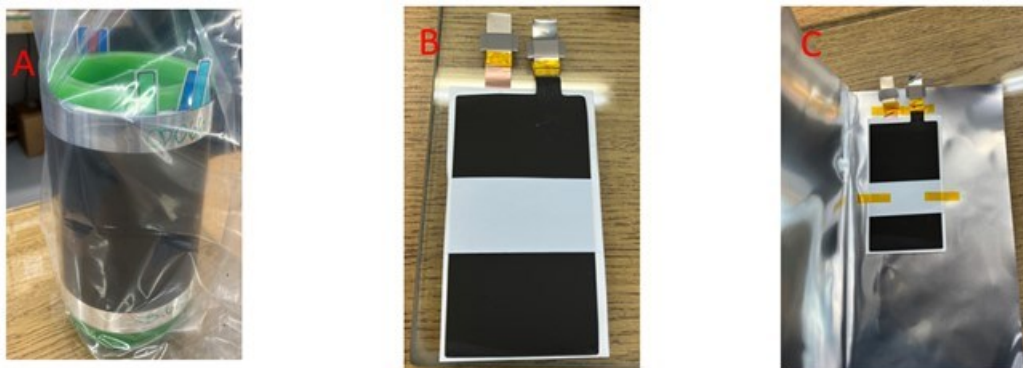


**Figure XIV.9.10 Double-Layer Pouch (DLP, 55x105mm “BB2590” cell format) cell assembly process. (A) assembled cathode-anode-cathode, (B) cell is taped inside pouch before sealing and filling, (C) The pilot coated single sided cathode before assembly.**

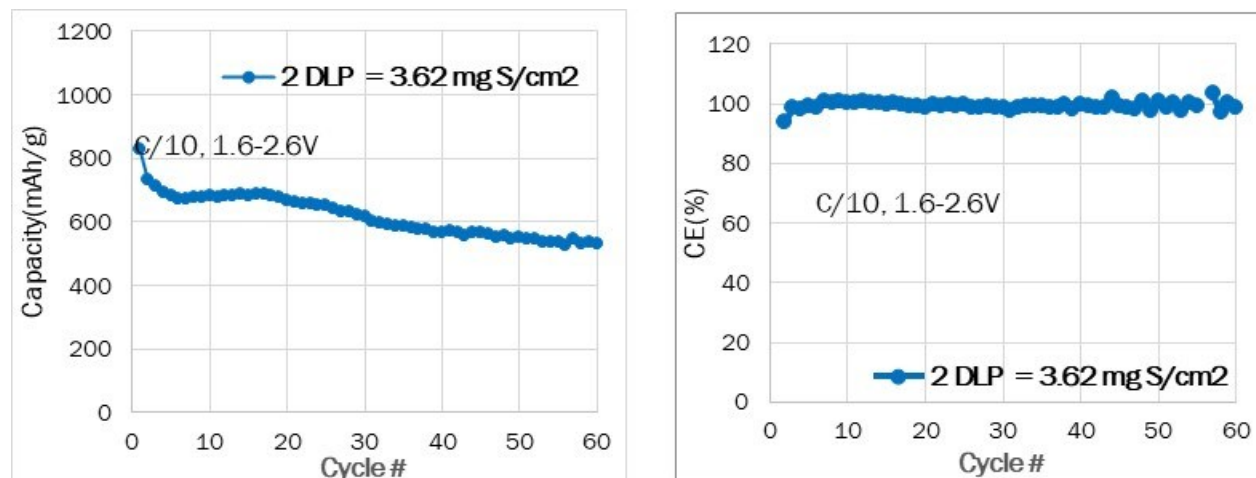
Leaving one side of pouch open for electrolyte filling, the other three sides of the pouch are joined together with heat sealing. Based on the E/S ratio, the pre-calculated amount of liquid electrolyte was added into the cell. Then, the cell is sealed using a vacuum sealing machine, and the DLP assembly is complete.

*Test DLP cells*

Navitas has assembled and tested DLP cells to determine the performance of baseline electrolyte cell as shown in Figure XIV.9.10.

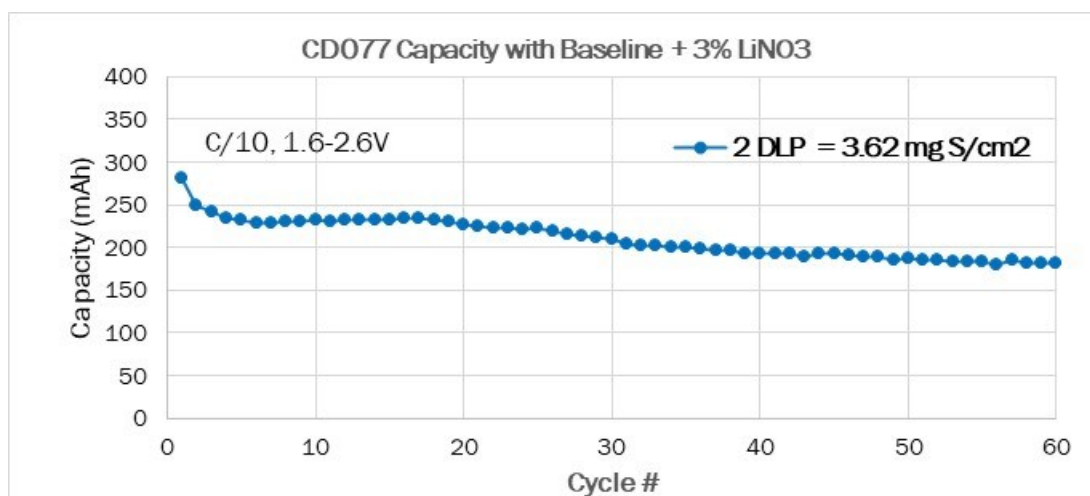
Figure XIV.9.11 shows the sulfur specific capacity variations with cycle number for high sulfur loading (~3.62 mg S/cm<sup>2</sup>) cathode DLPs. The sulfur specific capacity for DLP is ~ 800 mAh/g, which is slightly lower than that of coin cells (~1000 mAh/g). However, the overall performance of DLP is comparable with that of coin cells by comparing the specific capacity at cycle #50, indicating the cell format with high sulfur loading (3.6 mg S/cm<sup>2</sup>) electrodes is scalable without affecting the electrochemical performance.

Coulombic efficiency is also higher than 99.5% in the studied cycle life of the cell (Figure XIV.9.11 Right). Navitas will continue monitoring these cells.



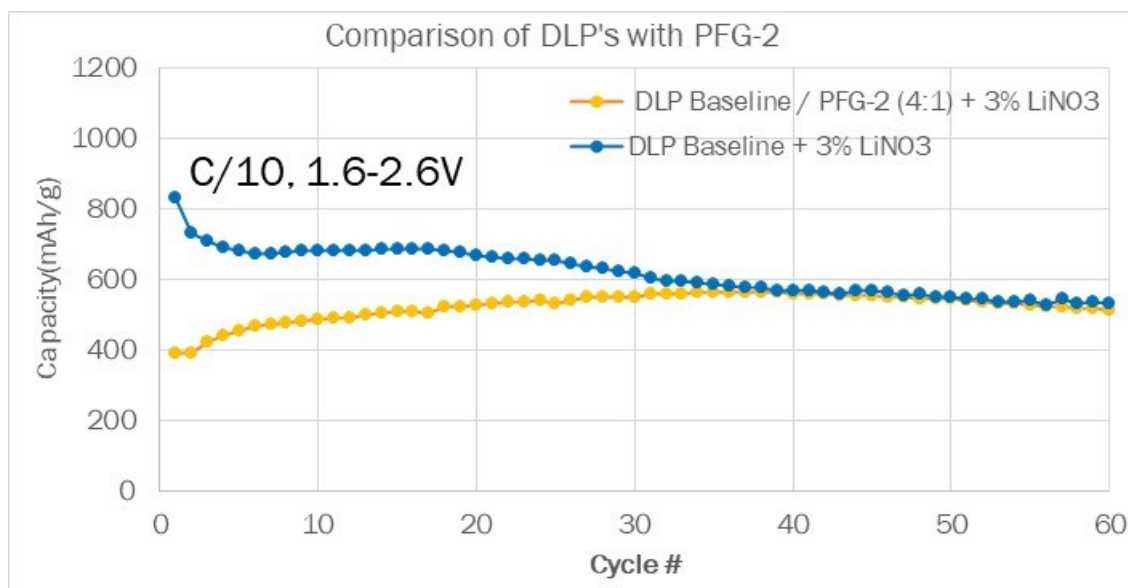
**Figure XIV.9.11** The sulfur specific capacity (Left) and Coulombic efficiency (Right) of DLP cells with baseline electrolyte with 3% LiNO<sub>3</sub> as additive. HSV 1800 PVDF binder, 80AM/14CB/6PVDF, uncalendared. C/10, room T. E/S ratio = 5; Sulfur loading  $\approx$  3.6 mg S/cm<sup>2</sup>.

Figure XIV.9.12 shows the cell capacity variations with cycle number for high sulfur loading ( $\sim$ 3.62 mg S/cm<sup>2</sup>) cathode DLPs with baseline electrolyte. The capacity reached 200 mAh at C/10 rate for the first cycle (Milestone achieved), it decayed as a function of cycle number. However, the capacity is still 530 mAh/g S after 60 cycles.



**Figure XIV.9.12** Capacity of DLP cells with baseline electrolyte with 3% LiNO<sub>3</sub> as additive. HSV 1800 PVDF binder, 80AM/14CB/6PVDF, uncalendared. C/10, room T. E/S ratio = 5; Sulfur loading  $\approx$  3.6 mg S/cm<sup>2</sup>.

Besides the electrochemical performance of coin cells with PFG-2 co-solvent electrolyte, DLP cells with PFG-2 co-solvent electrolyte was also investigated. Comparing to DLP cell performance with baseline electrolyte, it was found that initial specific capacity of sulfur is much lower when PFG-2 was introduced as a co-solvent in baseline electrolyte (Figure XIV.9.13), probably due to the electrode electrolyte wetting issues and reduction in electrolyte conductivity. However, after 39 cycles, the DLP cell performances are comparable, the sulfur specific capacity is 566 mAh/g. Navitas will continue monitoring and comparing the cycle life of these DLP cells.



**Figure XIV.9.13** The electrochemical performance of DLP cells with baseline electrolyte + 3% LiNO<sub>3</sub> and PFG-2 electrolyte {Baseline + 3% LiNO<sub>3</sub>/PFG-2 (4:1 ratio)}. PVDF (HSV 1800) binder, 80AM/14CB/6PVDF, uncalendared; DLP's are C-A-C in BB2590 format, C/10, room T; E/S ratio = 5; Sulfur loading  $\approx$  3.6 mg S/cm<sup>2</sup>.

Navitas/ANL will continue optimizing and down select the PFG electrolyte. In addition to PFG electrolyte optimization, Navitas also tested additives such as thiourea, bis(4-nitrophenyl) carbonate (BCN), 1,4-benzenedithiol (BDT), and Li<sub>2</sub>S<sub>8</sub> as depicted in BPI. Though preliminary experiments focused on baseline + 3% LiNO<sub>3</sub> electrolytes without PFGs as co-solvent, these additives may be repeated when optimized PFG electrolyte is finalized.

Navitas will fabricate more baseline cathodes, bifunctional separator, procure the Li anodes and assemble coin cells/SLP cells/DLP cells with various PFG based electrolytes and baseline electrolyte.

### Conclusions

Navitas and ANL have synthesized and down-selected partially fluorinated glyme (PFG) solvents with varying fluorination degrees PFG-1 and PFG-2.

The sulfur specific capacity achieved 1100 mAh/g with sulfur loading of  $\sim$  1.0 mg S/cm<sup>2</sup>. Coulombic efficiency of coin cell and DLPs with PFG-2 as a cosolvent in electrolyte reaches  $>$  99.5% when 3% LiNO<sub>3</sub> was added as an additive.

ANL tested the flash point of PFGs and electrolyte containing PFGs. The pure PFGs and PFGs-containing electrolyte have higher flash points comparing with traditional Li-ion battery electrolytes.

Navitas has assembled  $\geq$ 200 mAh pouch cells with baseline electrolyte and LiNO<sub>3</sub> additive. The electrolyte containing PFG-2 is under investigation.

High S-loading cathode tests targeting the high energy Li-S 2Ah cell were also initiated.

### References

1. Zhengcheng Zhang et al., Lithium-sulfur battery with partially fluorinated ether electrolytes: Interplay between capacity, coulombic efficiency and Li anode protection. *J. Power Sources*. 2019, 438(31), 226939

2. Zhengcheng Zhang et al. Fluorinated Electrolytes for 5-V Lithium-ion Battery Chemistry. *Energy Environ. Sci.*, 2013, 6, 1806-1810.
3. Zhengcheng Zhang et al. Tackling the Issues of Li-S Battery Chemistry by a Functional Additive - Hexafluorobenzene (HFB). *ACS Appl. Energy Mater.* 2020, 3, 3198-3204.
4. Steffen Hess *et al.* Flammability of Li-Ion Battery Electrolytes: Flash Point and Self-Extinguishing Time Measurements *J. Electrochem. Soc.* 2015, 162, A3084.

### **Acknowledgements**

Navitas would like to thank Coriana Fitz, Haiyan Croft for DOE for organizing the quarterly review meeting and providing constructive suggestion on this project. Laura, Amy, Grace, and Brandon from Navitas research team, Jingtian, Qian, Kevin from ANL contributed to the entire research work. The Navitas team would like to thank the financial support from USABC Projects (DE-EE0009645).



## XIV.10 Liquid Electrolytes for Lithium-Sulfur Batteries with Enhanced Cycle Life and Energy Density Performance (Giner)

### **Gauid P. Pandey, Principal Investigator**

Giner, Inc.  
89 Rumford Avenue  
Newton, MA 02466  
E-mail: [gpandey@ginerinc.com](mailto:gpandey@ginerinc.com)

### **Sanjeev Mukerjee, Co-Principal Investigator**

Northeastern University  
360 Huntington Ave  
Boston, MA 02115  
E-mail: [s.mukerjee@northeastern.edu](mailto:s.mukerjee@northeastern.edu)

### **Yury Gogotsi, Co-Principal Investigator**

Drexel University  
3141 Chestnut Street  
Philadelphia, PA 19104  
E-mail: [gogotsi@drexel.edu](mailto:gogotsi@drexel.edu)

### **Haiyan Croft, DOE Technology Development Manager**

U.S. Department of Energy  
E-mail: [Haiyan.Croft@ee.doe.gov](mailto:Haiyan.Croft@ee.doe.gov)

Start Date: October 1, 2021

End Date: September 30, 2023

Project Funding: \$959,814

DOE share: \$767,683

Non-DOE share: \$192,131

### **Project Introduction**

Lithium-sulfur (Li-S) batteries are one of the most promising next-generation energy storage technologies because of its high theoretical gravimetric energy density of 2600 Wh/kg, which is more than five times higher than the theoretical energy of transition metal oxide cathode materials and graphite coupling.<sup>1,2</sup> Li-S batteries are estimated to deliver a practical gravimetric energy density of 400 to 600 Wh/kg which is two- to three-fold higher than state of the art lithium-ion batteries (LIBs), thus demonstrating a high potential for satisfying demand in energy storage for transportation applications. However, despite their promise, several fundamental challenges have limited the commercial translation of Li-S batteries. The primary challenges limiting stable cycling of Li-S batteries are migration of dissolved lithium polysulfide species (LiPSs) to the anode, as well as electrolyte decomposition and dendrite formation at the lithium (Li) metal anode.<sup>3</sup> Continuous electrolyte consumption originating from high cathode porosity also results in the need for a large excess of liquid electrolytes to achieve reasonable sulfur utilization and cycle life. To achieve commercial readiness of Li-S battery technology, electrolytes that prevent lithium polysulfides (LiPSs) dissolution and decomposition of the Li metal anode are required to achieve the necessary cycle life, efficiency, and operational temperature range for transportation applications. In this proposed work, we are working to develop new electrolyte via several approaches involving identifying Li salts, salt concentrations, cosolvent blends, and additives that work with Giner-developed artificial solid-electrolyte-interface (ASEI)-protected Li anode to reduce LiPSs dissolution and enable long cycle life Li-S batteries.

This project is led by Giner Inc. with the collaboration of Northeastern University (NU) and Drexel University (Drexel). Our NU team focused on providing a fundamental understanding on the effect of electrolyte additives and formation of Li polysulfide intermediates using advanced characterization tools such as in-situ Raman Spectroscopy and X-ray absorption spectroscopy (XAS). Drexel contributes to evaluating the LiPSs

adsorption capability of conductive MXenes and to identify the most promising MXenes for various components (e.g., cathode interlayer) with the aim to enhance the cycle life of Li-S batteries. Upon the effort of the entire team, we can gain more information into the root limitations of high-energy-density Li-S batteries and develop suitable electrolytes and other cell components.

### Objectives

The objective of the project is to develop and validate 3.0-Ah or greater Li-S pouch cells capable of  $\geq 500$  cycles to  $\geq 80\%$  capacity retention at 100% depth-of-discharge and high energy density ( $\geq 400$  Wh/kg) and low cost ( $\leq \$80$ /kWh). More specifically, the main goal of this project is to develop electrolytes for Li-S batteries that inhibit LiPS dissolution when used in combination with Giner's ASEI-protected Li metal anodes. This program is focused on directly addressing shortcomings of traditional Li-S electrolytes by developing novel electrolytes which utilize strongly bound Li salts, fluorinated cosolvents, and additives. By reducing polysulfide dissolution and subsequent Li anode poisoning, Giner will demonstrate a high energy Li-S pouch cell with enhanced cycle life.

### Approach

This project is focused on developing new electrolytes utilizing strongly-bound Li salts, fluorinated cosolvents, and additives. The properties of the ideal electrolyte for Li-S battery chemistry would be high ion conductivity, stable towards polysulfides, and promoting the conversion of long-chain LiPSs to insoluble polysulfides. The project is designed to first develop electrolytes and understand the role of cosolvents and additives on the performance of Li-S cells as well as to develop understanding on the role of fluorinated cosolvent on the Li<sup>+</sup> solvation structure. This leads to a better understanding of the polysulfide shuttling and precipitation mechanisms in common electrolytes. The second stage of the project will focus on combining the newly developed electrolytes with Giner's ASEI-protected Li anode to demonstrate 3 Ah Li-S pouch cells with long cycling stability and high energy density of 400 Wh/kg or greater.

### Results

In budget period 1 (BP1), Giner was working to screen identified fluorinated co-solvents and Li salts. Several electrolyte compositions were prepared, characterized, and evaluated on performance in Li-S cells. Based on this screening, we down selected electrolyte compositions, fluorinated co-solvents, and strongly bound Li salts to further characterize and study in the next stage of this project. Selected electrolyte compositions were characterized in Li-S cells by in-situ Raman Spectroscopy and X-ray absorption spectroscopy (XAS).

#### *Identification of fluorinated co-solvents and strongly bound Li-salts*

We have identified several high-performance fluorinated solvents to screen for Li-S battery applications. In this screening process, the following two Li salt-based electrolyte compositions were used as baseline electrolytes:

- LiTFSI baseline: 1M LiTFSI in DME/DOL (1:1; v/v) + 0.2M LiNO<sub>3</sub>
- LiFSI baseline: 1M LiFSI in DME/DOL (1:1; v/v) + 0.2M LiNO<sub>3</sub>

Strongly bound salts with a high association energy, such as lithium trifluoroacetate (LiTFA) ( $\Delta G_{\text{ion}}$  association of -93 KJ/mol), have been shown to reduce the LiPS reduction in Li-S cells because of their ability to disrupt the formation of polysulfide clusters.<sup>4</sup> We identified a few strongly bound salts in this screening process to use as additive salt in the new electrolyte compositions. The screened fluorinated solvents and Li salts are presented in Table XIV.10.1.

Table XIV.10.1 List of Fluorinated Solvents and Li Salts Used in the Electrolyte Formulations.

Fluorinated solvents	Abbreviation
1,1,2,2- Tetrafluoroethyl 2,2,3,3- tetrafluoropropyl ether	TTE
Ethyl 1,1,2,2-tetrafluoroethyl ether	ETFE
Propyl 1,1,2,2-tetrafluoroethyl ether	PTFE
2,2,2- Trifluoroethyl 1,1,2,2- tetrafluoroethyl ether	TTFTE
1,1,1,3,3,3-hexafluoro-2-methoxypropane	HFMP
1,1,1,3,3,3-hexafluoro-2-(fluoromethoxy)propane	HFFMP
bis(2,2,2-trifluoroethoxy)methane	TFEM
2,2,2-trifluoroethyl acetate	TFEA
1,1,1,3,3,3-hexafluoropropan-2-yl acetate	HFPA
Li salts	Abbreviation
Lithium bis(trifluoromethanesulfonyl) imide	LiTFSI
Lithium bis(fluorosulfonyl)imide	LiFSI
Lithium trifluoromethanesulfonate or lithium triflate	LiTf
Lithium trifluoroacetate	LiTFA

Using the above fluorinated co-solvents and Li salts, new electrolyte compositions were prepared consisting of a blend of DME/DOL (1:1 v/v), 0.2 M LiNO<sub>3</sub>, fluorinated co-solvent, and Li salts. Data for baseline electrolytes is presented as electrolyte compositions with 0% fluorinated co-solvent. Ionic conductivity of the fluorinated co-solvent electrolyte formulations was measured at room temperature. The ionic conductivity of two electrolytes series (with TTE and TFEM fluorinated co-solvent) is shown in Figure XIV.10.1. Both series of electrolytes show similar ionic conductivity trends, a decrease in ionic conductivity with increasing volume% of fluorinated co-solvent. However, the LiFSI-based electrolytes show higher ionic conductivity values compared to electrolytes prepared with LiTFSI salt.

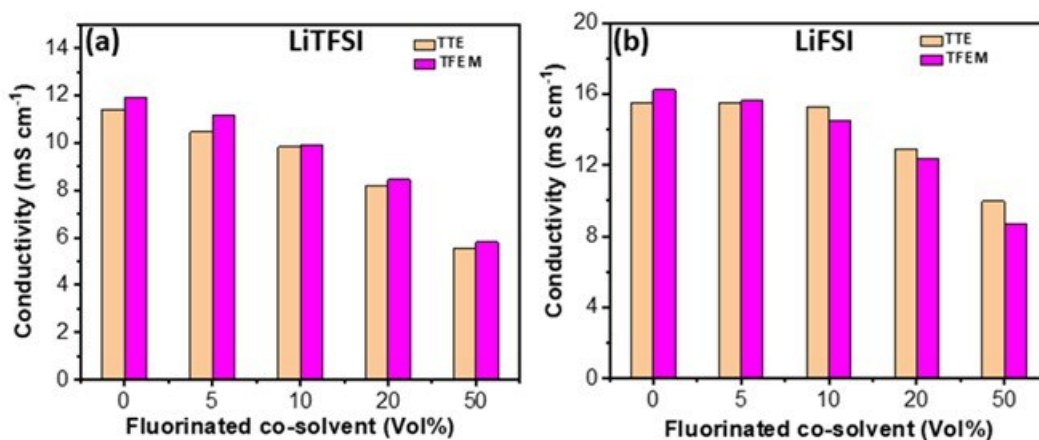


Figure XIV.10.1 Ionic conductivity of the two series of electrolytes with varying content of fluorinated co-solvents: (a) ionic conductivity of LiTFSI-based electrolytes and (b) ionic conductivity of LiFSI-based electrolytes.

### Li-S cell performances

The electrochemical performance of new electrolyte compositions was evaluated using the coin cell configuration of Li//electrolyte//sulfur cathode at room temperature. The sulfur mass loading on cathode was 3.8–4.0 mg/cm<sup>2</sup> and E/S ratio was 8 μl mgs<sup>-1</sup>. The charge-discharge capacity of the cells was measured over a voltage range of 1.6 to 2.8 V at 0.2 C after initial cell stabilization cycles (3 cycles each at 0.05 C and 0.1 C). A typical result of electrochemical performance with the HFMP fluorinated cosolvent-based electrolyte series is presented in Figure XV.10.2. Li-S cells with LiFSI/HFMP electrolyte compositions show stable discharge capacity at 0.2 C rate. Compared to the baseline electrolyte, the HFMP-containing electrolyte cells show slightly lower discharge capacity and coulombic efficiency (Figure XIV.10.2a and b), with values decreasing as the content of fluorinated co-solvent is increased from 5 to 20 vol%. Cells assembled with LiTFSI/HFMP electrolyte compositions show stable discharge capacity, but coulombic efficiency decreases with increasing volume% of HFMP (Figure XIV.10.2c and d).

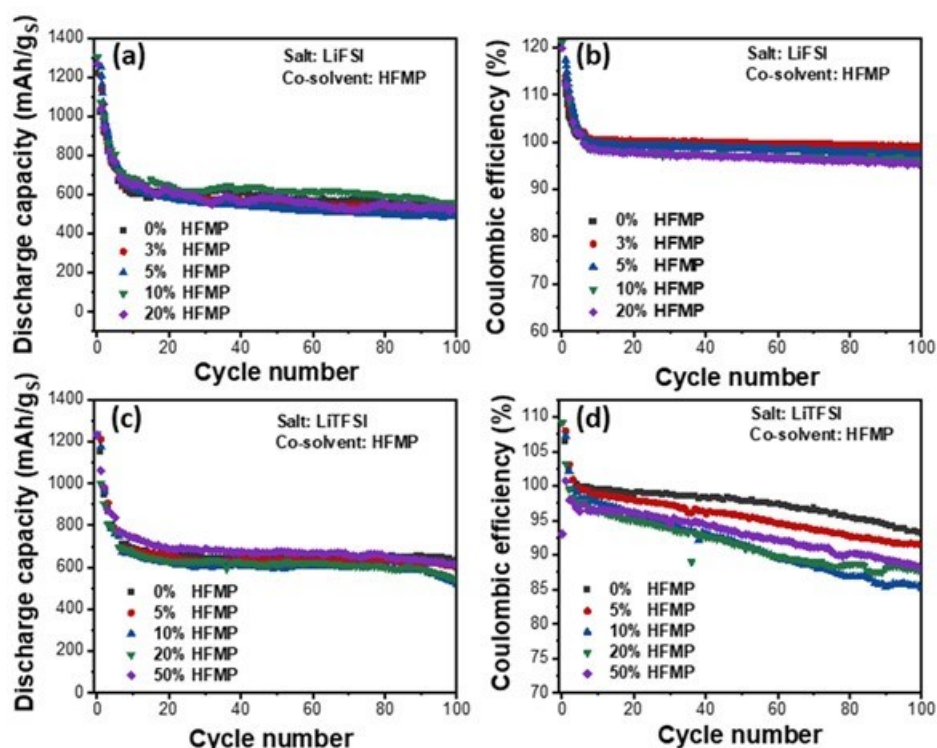


Figure XIV.10.2 Electrochemical performance of Li-S cells with electrolyte composition containing HFMP fluorinated co-solvents with both series of electrolytes: a) discharge capacity, b) coulombic efficiency (LiFSI-series), c) discharge capacity, d) coulombic efficiency (LiTFSI-series).

Li-S cells with LiFSI salt and 3% HFMP fluorinated ether co-solvent were tested for long cycle life, and performance was compared to the baseline electrolyte (0% HFMP). Cells with baseline electrolyte show slightly higher discharge capacity but failed much earlier compared to cells with 3% HFMP. Figure XIV.10.3 clearly depicts the advantage of fluorinated co-solvents in terms of enhancing cycle life and coulombic efficiency. The cell with 3% HFMP/LiFSI achieved more than 250 cycles with a specific capacity of ~600 mAh/g at 0.2 C rate.

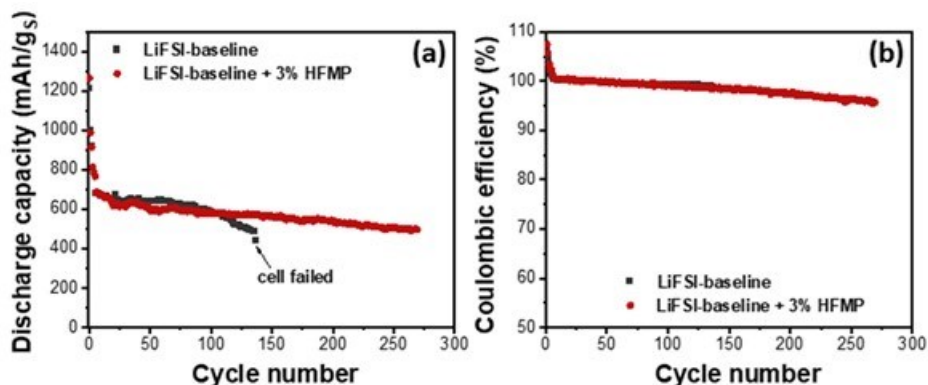


Figure XIV.10.3 Cycling performance of Li-S cells with LiFSI-baseline and with 3% HFMP fluorinated co-solvent electrolytes: a) discharge capacity, b) coulombic efficiency.

Based on work performed during BP1, results suggest that electrochemical performance of different fluorinated co-solvent additives is strongly impacted by their ability to solvate Li<sup>+</sup> ions. Overall, electrochemical performance is poor for compositions with more than 20 vol% fluorinated co-solvent despite having a conductivity of  $> 5 \text{ mS cm}^{-1}$ . Based on the screening, HFMP, TFEM, ETFE, PTFE and TTE-containing electrolyte compositions were selected for further evaluation and electrolyte characterizations.

All the electrolyte compositions were characterized by conductivity measurements, and for oxidation/reduction stability by linear sweep voltammetry (LSV) and lithium plating/stripping study. Identified fluorinated cosolvent-containing electrolytes demonstrate ionic conductivity  $> 5 \text{ mS/cm}$ . The fluorinated cosolvent-based electrolytes are electrochemically stable up to 3.65 V (versus Li/Li<sup>+</sup>) (Figure XIV.10.4a). The lithium plating/stripping studies demonstrate stable SEI formation with enhanced cycle life compared to the baseline electrolyte as shown in the Figure XV.10.4b.

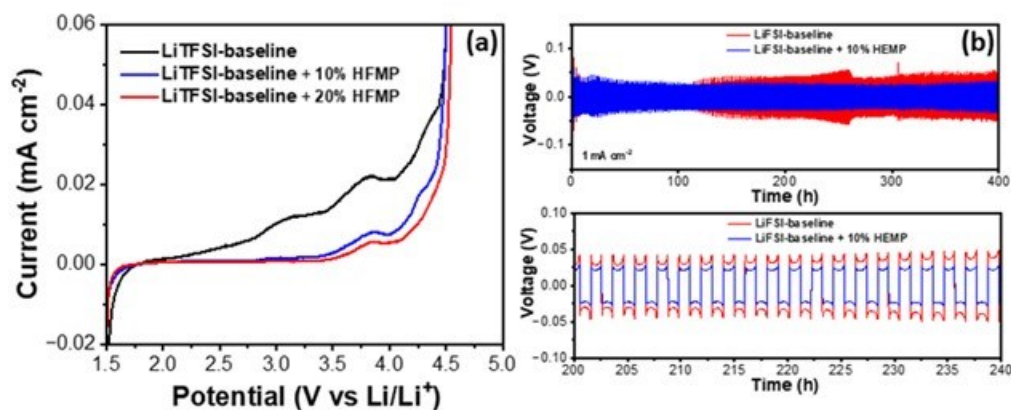


Figure XIV.10.4 (a) Linear Sweep Voltammetry curves and (b) Li plating/stripping performance of symmetrical cells containing baseline and fluorinated co-solvent based electrolyte.

#### *Operando Raman spectroscopy and X-ray absorption spectroscopy (Northeastern University)*

In this project, Northeastern University focused on providing a fundamental understanding on the effect of electrolyte additives and formation of LiPS intermediates during charging/discharging of Li-S cells. The Li-S cells, fabricated with Giner developed electrolytes, were characterized by in-situ Raman Spectroscopy and X-ray absorption spectroscopy (XAS) experiments.

Three different electrolytes were selected to characterize via *operando* Raman spectroscopy to investigate the critical issue of the formation of soluble intermediate LiPSs and polysulfide shuttling issue during Li-S cell operation.

- Baseline electrolyte: 1 M LiTFSI in DME/DOL (1:1, v/v) + 0.2 M LiNO<sub>3</sub>
- LiTFSI-baseline + 10 vol% HFMP
- LiTFSI-baseline + 10 vol% TFEM

Raman spectroscopy was conducted at a 0.05 C charge-discharge rate in *operando* mode. The *in-situ* cells (ECC-Opto-10, EL-cell) were assembled in the glovebox and rested for 24 hours prior to the measurements. All data was collected at the initial cycle, using 532 nm wavelength laser at 1% intensity (Horiba, XploRA plus Raman microscope). Raman spectra from the initial discharge process for the three representative electrolyte systems are presented in Figure XIV.10.5. To normalize the Raman spectroscopy data, the wavenumber was fixed between 100 to 600 cm<sup>-1</sup>, and the spectra were selected from 5 representative locations in the voltage profile as labeled by the rectangle boxes in Figure XIV.10.5a. A pristine Raman measurement was conducted at the location of a sulfur cluster and a typical sulfur characteristic peaks were observed at 150, 220, 245, 437 and 472 cm<sup>-1</sup>, consistent with the reported literature.<sup>5</sup> Clear Raman peak changes were observed in electrolyte containing HFMP fluorinated co-solvent compared to the baseline electrolyte. After around 16500s, a series of prominent peaks around 453 cm<sup>-1</sup> appeared (Figure XV.10.5c) whereas such changes were not observed in the baseline electrolyte cells. These changes are believed to be the result of an increasing concentration of short-chain polysulfides (S<sub>x</sub><sup>2-</sup>, 3<x<5) due to changes in the reaction kinetics of the Li-S redox reaction with the HFMP-containing electrolyte.

On the other hand, there was a distinct difference observed in the TFEM-containing electrolyte after the elemental sulfur had been converted (after 7500s). Lower intensity peaks around 400 cm<sup>-1</sup> were observed as opposed to higher intensity peaks in the baseline electrolyte cells (Figure XIV.10.5d, peaks at 400 cm<sup>-1</sup>). This is believed to be the result of long-chain polysulfides (S<sub>x</sub><sup>2-</sup>, 6<x<8) being converted to short-chain polysulfides (S<sub>x</sub><sup>2-</sup>, 3<x<5) at a higher conversion rate than in baseline electrolytes.

The Raman peak changes during the whole *operando* discharge process are presented in Figure XIV.10.6 for a HFMP-containing electrolyte system. The intensity values presented in the heatmap have been normalized between 0 and 1 for each spectrum within the *operando* Raman spectra. Consequently, these normalized intensity values are unsuitable for comparing the relative concentration on the cathode; instead, they serve the purpose of monitoring trends in Raman peak changes. The heatmap originates with three characteristic peaks, depicted in Figure XIV.10.6a, associated with elemental sulfur. These peaks rapidly diminish during the initial discharge (lithiation), giving way to a distinct peak at 400 cm<sup>-1</sup>, indicative of long-chain polysulfides. Upon entering the second plateau, the intensity of the long-chain polysulfide peak decreases, and a new peak emerges at 453 cm<sup>-1</sup>, signifying the formation of short-chain intermediate polysulfides. In the final segment of the heatmap (Li<sup>+</sup> greater than 0.6), a more diffuse feature is observed with broader peaks. This phenomenon is attributed to an increase in background noise as the intensity of all characteristic peaks decreases.

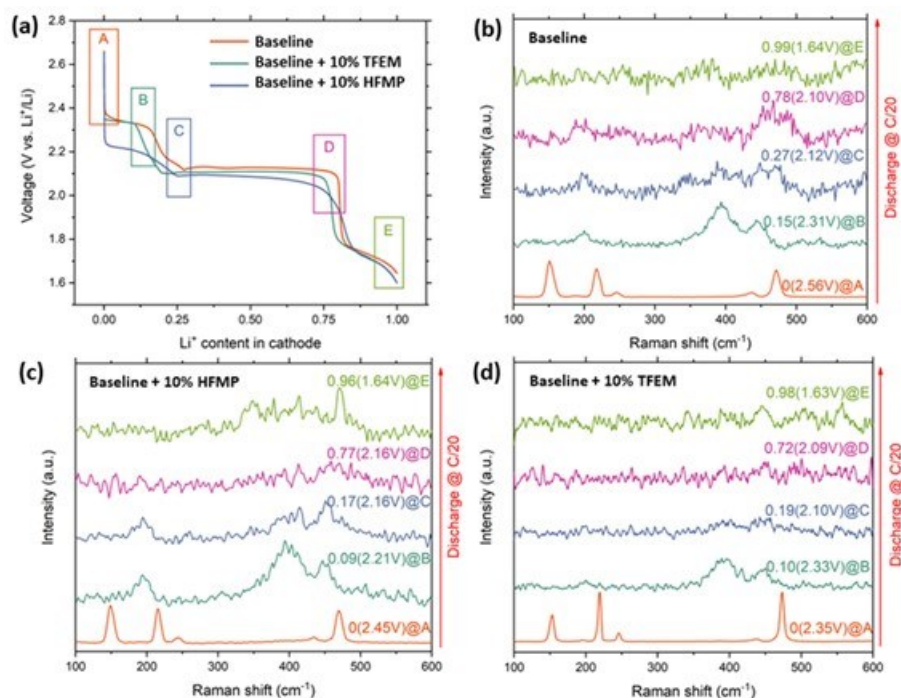


Figure XIV.10.5 In Panel (a), voltage profiles are depicted with five representative positions on the voltage curves for the baseline electrolyte, HFMP, and TFEM-containing systems during the initial discharge cycle at a 0.05 C rate. Panels (b-d) present Raman spectra corresponding to each electrolyte at the five characteristic locations indicated in Panel (a).

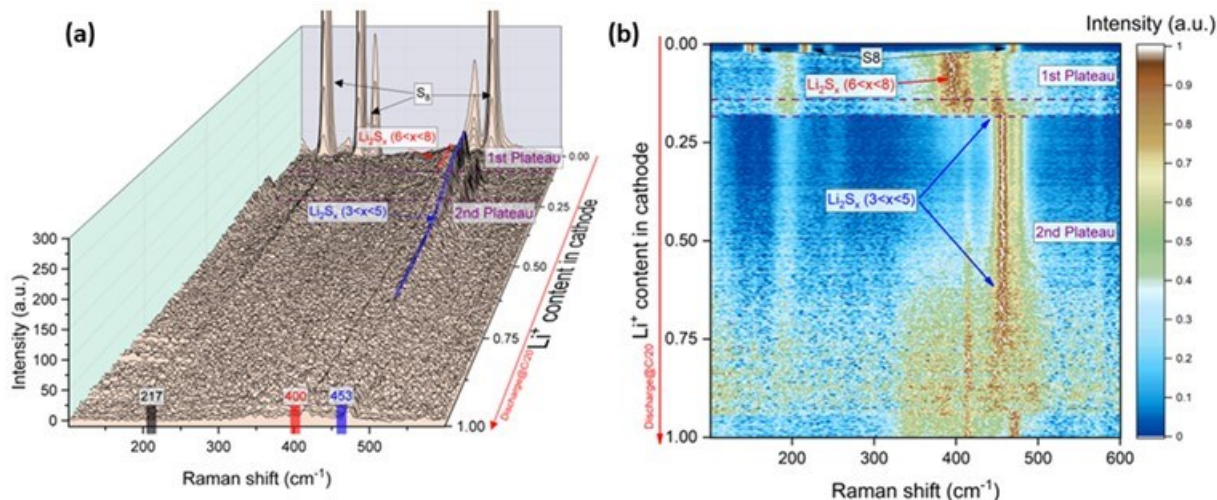


Figure XIV.10.6 (a), the *operando* Raman spectra of the HFMP-containing electrolyte are illustrated during the initial discharge at a 0.05 C rate. The X-axis and spectra were labeled with three characteristic Raman peaks, with elementary sulfur highlighted in black, long-chain polysulfides in red and intermediate polysulfides in blue. Panel (b) presents the corresponding normalized heatmap of intensity from (a), enhancing the visibility of changes in Raman peaks.

NEU team has also carried out characterization on ex-situ samples using X-ray fluorescence (XRF) mapping and X-ray absorption spectroscopy (XAS) to understand polysulfide shuttling phenomena. *Ex-situ* samples for these studies were prepared by Giner and samples were collected from coin cells fabricated with three different electrolytes and at varying cycle numbers. The electrolytes selected for these studies are as follows:

- Baseline electrolyte: 1 M LiTFSI in DME/DOL (1:1, v/v) + 0.2 M LiNO<sub>3</sub>
- LiTFSI-baseline + 10 vol% HFMP
- LiTFSI-baseline + 10 vol% TFEM

To avoid the possible interference of LiTFSI salt with the XRF mapping and XAS data, samples were rinsed in DME solvent. XRF mapping and XAS studies were conducted to analyze the sulfur distribution, concentration, and composition information on the surface. The beam size was carefully adjusted to 5 microns to achieve optimal spatial resolution.

The XRF mapping of anodes and cathodes from cells with three different electrolytes are presented in Figure XIV.10.7. It is noteworthy that a conspicuous contrast in the concentration of sulfur has been identified at the anode in fluorinated cosolvent electrolytes in comparison to the baseline electrolyte. This occurrence can be ascribed to the less severe shuttling of polysulfides in the fluorinated cosolvent-based electrolytes. Moreover, a lower sulfur intensity was observed on the cathode relative to the baseline electrolyte, which indicated a different cathode-electrolyte interface (CEI) formation with fluorinated cosolvent-based electrolytes compared to the baseline. Specifically, a different CEI layer formed on the cathode surface, consisting of non-sulfur species, which concealed the sulfur signal in the XRF mapping results. This results show that fluorinated cosolvents play a crucial role on mitigating polysulfides shuttling effect.

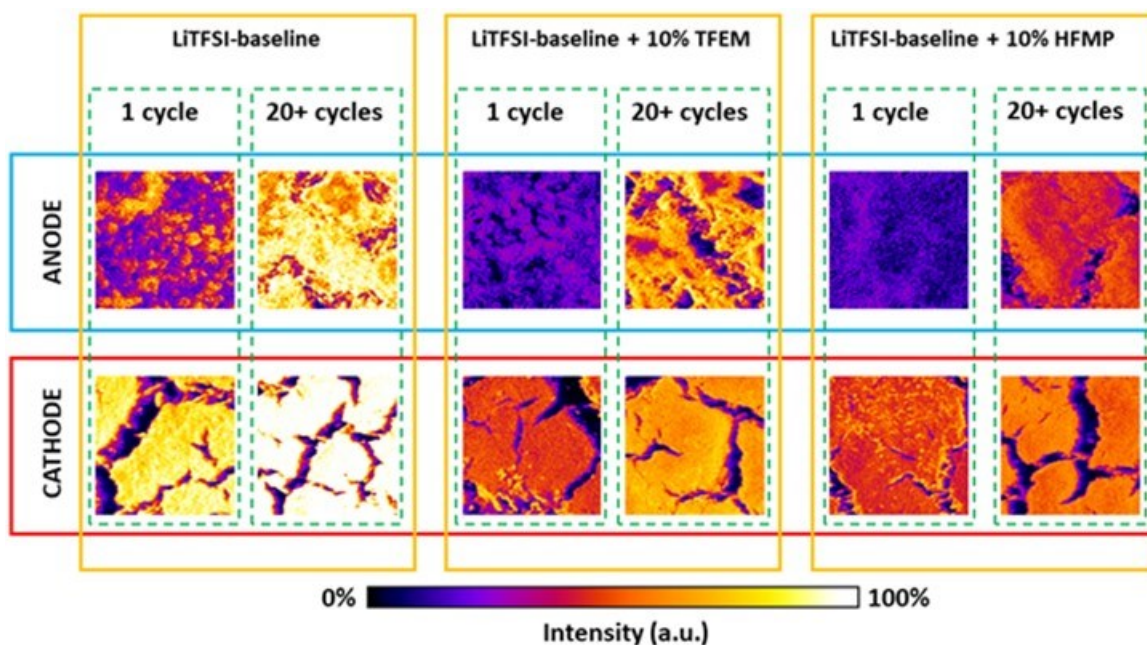


**Figure XIV.10.7** Normalized XRF mapping image of anodes and cathodes. For each electrolyte, two distinct sets of cells are featured, one having undergone 1 cycle, and the other 20 or more cycles.

In order to gain a better understanding of the complex composition of various polysulfide species, XAS analysis was conducted on several reference samples. The X-ray absorption near edge spectroscopy (XANES) result of these reference samples is presented in Figure XIV.10.8. Clear peaks were observed at 2471.5 eV and 2473.3 eV for Li<sub>2</sub>S<sub>4</sub>, Li<sub>2</sub>S<sub>6</sub>, and Li<sub>2</sub>S<sub>8</sub> samples, while an edge shift with a different peak at 2474.2 eV was detected for Li<sub>2</sub>S. The inset in Figure XV.10.8 shows the intricate change of the peak at 2471.5 eV, indicating the terminal sulfur atoms in the polysulfides. It was observed that the intensity of this specific peak increased with shorter polysulfide chains. It is worth noting that Li<sub>2</sub>S<sub>4</sub> to Li<sub>2</sub>S<sub>8</sub> samples were in solution form, while Li<sub>2</sub>S was in solid powder form. The edge shift in Li<sub>2</sub>S sample is attributed to the linearity of short-chain polysulfides and a different valence state of sulfur. This preliminary analysis will help us to better understand



the sulfur species detected in the XANES spectra from the selected locations on each anode and cathode from the XRF mapping.

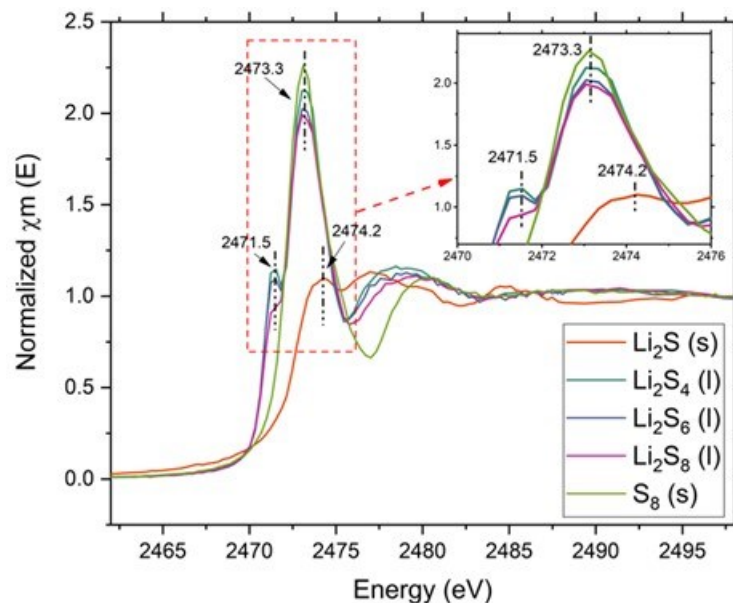


**Figure XIV.10.8 Normalized X-ray Absorption Near Edge Spectra (XANES) of the standard reference including elemental sulfur,  $\text{Li}_2\text{S}$  and various polysulfides.**

Two distinct locations were identified on electrodes, one with a higher sulfur concentration and other with a lower concentration to collect the XANES spectra. The XANES spectra of two electrolyte systems (baseline, ‘baseline + HFMP’ electrolytes) are presented in Figure XIV.10.9. A prominent peak at 2471.5 eV was detected in the baseline samples, indicating that the polysulfide shuttling effect occurs even at the early stages and persists regardless of the cycle number. As the cycle number increased, the intensity of the peak at 2471.5 eV also increased, indicating that the polysulfide shuttling effect worsened at higher cycle number. The peak at 2481.2 eV is attributed to the SEI growth on the anode side, as its intensity reaches a maximum at initial cycles and decreases at 20+ cycles. This phenomenon was caused by the ongoing polysulfides deposition resulting from the shuttling effect, leading to a lower intensity at 2481.2 eV and a higher intensity at 2471.5 eV. On the cathode side, a minor peak at 2471.5 eV was detected at 1 cycle which disappeared at higher cycle numbers due to the sluggish kinetics of solid-solid polysulfides conversion in the baseline electrolyte. As a result, unreacted solid short-chain polysulfides were observed on the cathode surface. A different evolution of the minor peak at 2471.5 eV was also observed for the ‘baseline + HFMP’ electrolyte. The peak intensity at 1 cycle was lower than that at 20+ cycles, indicating that the polysulfide shuttling effect was suppressed by the additives in the electrolyte, as also confirmed by the XRF mapping results. However, the peak intensity at 2481.2 eV varied significantly in the high and low intensity areas from the XRF mapping. This may be related to the different SEI thickness at different locations. In the cathode spectra for the baseline + HFMP’ electrolytes, it is evident that the peak at 2471.5 eV was not observable in the first cycle but appeared in the subsequent 20+ cycles. This suggests that the kinetics of the battery system with fluorinated cosolvents improved during the early cycle compared to the baseline electrolyte.

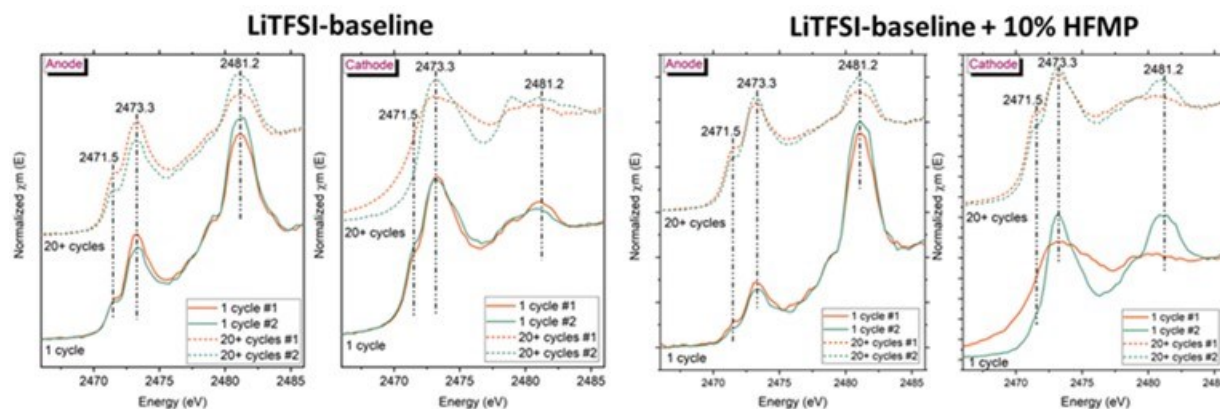


**Figure XIV.10.9** Normalized X-ray Absorption Near Edge Spectra (XANES) for the anodes and cathodes. The XANES were acquired from locations marked as number 1 (brighter, higher intensity) and number 2 (darker, lower intensity) on the electrodes, selected based on XRF mapping.

#### Screening conductive MXenes for lithium polysulfide adsorption (Drexel University)

In budget period 1 (BP1), Drexel team evaluated the lithium polysulfide adsorption capability of conductive MXenes and identified most promising MXenes to use in the various components (e.g., cathode) of Li-S cells to improve the electrochemical performance and cycling stability.

Drexel team tested seven MXene compositions,  $\text{Ti}_2\text{CT}_x$ ,  $\text{Ti}_3\text{C}_2\text{T}_x$ ,  $\text{Ti}_3\text{CNT}_x$ ,  $\text{Mo}_2\text{TiC}_2\text{T}_x$ ,  $\text{V}_2\text{CT}_x$ ,  $\text{Nb}_2\text{CT}_x$ , and  $\text{Nb}_4\text{C}_3\text{T}_x$ , to quantify polysulfide adsorption capabilities based on research interest. MXenes were soaked in the replicated environment of LiPS solution as illustrated in Figure XV.10.10a. Varying degrees of color change were observed in the LiPS solution, attributed to different degrees of LiPS adsorption and their interactions with candidate materials (Figure XV.10.10b). UV-Vis spectroscopic measurements on the MXene-soaked LiPS solution, as depicted in Figure XV.10.10c, revealed that  $\text{Ti}_2\text{CT}_x$  demonstrates polysulfide adsorption performance comparable to highly performing cathode host materials like  $\text{MnO}_2$  and  $\text{V}_2\text{O}_5$ .<sup>6</sup> The adsorption capabilities quantified using this technique indicated differences among various MXene compositions. Figure XV.10.10d shows that carbon black,  $\text{MnO}_2$ ,  $\text{V}_2\text{O}_5$ ,  $\text{Ti}_2\text{CT}_x$ ,  $\text{Ti}_3\text{C}_2\text{T}_x$ ,  $\text{Ti}_3\text{CNT}_x$ ,  $\text{Mo}_2\text{TiC}_2\text{T}_x$ ,  $\text{V}_2\text{CT}_x$ ,  $\text{Nb}_2\text{CT}_x$ , and  $\text{Nb}_4\text{C}_3\text{T}_x$  exhibit the adsorption capabilities of 8, 211, 291, 179, 92, 58, 22, 30, 27, and 46 mg/g of the candidate material, respectively, under the selected equivalent conditions. This revealed an order of magnitude of difference in polysulfide adsorption capabilities (normalized by their weights) across the candidate materials. Notably, the titanium-based MXene compositions have stronger polysulfide adsorption capability than the vanadium and niobium-based MXene compositions. Drexel team further examined the correlation between the polysulfide uptake and both the concentration of LiPSs in the DME/DOL solvent and soaking time for three effective adsorbents,  $\text{Ti}_2\text{CT}_x$ ,  $\text{Ti}_3\text{CNT}_x$ , and  $\text{Ti}_3\text{C}_2\text{T}_x$  at room temperature (Figure XV.10.10e and f). It was observed that the polysulfide uptake of MXenes increases with both increase in concentration of LiPS and soaking time. Additionally, Drexel team conducted modeling of these adsorption isotherms to understand the thermodynamics and kinetics of the adsorption process.

The team employed multiple spectroscopic techniques (XPS, FTIR and ICP-OES) to quantify and investigate complex polysulfide adsorption species to make a rational selection of materials to effectively capture polysulfides. This study demonstrated that, irrespective of MXene chemistry variations, the polysulfide adsorption mechanism followed the thiosulfate/polythionate complex formation pathway attributed to O-terminations common on all MXene surfaces prepared with acid etching. However, the extent of redox reactions and ion selectivity of adsorbed polysulfide species depended on the MXene composition. Drexel team discovered that MXene compositions exhibit different adsorption preferences for  $\text{Li}^+$  and  $\text{S}_x^{2-}$  ions, dependent on their outer transition metal layer.  $\text{Mo}_2\text{TiC}_2\text{T}_x$ , with a molybdenum outer transition metal layer, exhibited selectivity for  $\text{S}_x^{2-}$  ions, potentially retaining intermediate polysulfides formed during cycling.

Conversely, titanium outer transition metal layer MXene compositions ( $\text{Ti}_2\text{CT}_x$ ,  $\text{Ti}_3\text{CNT}_x$ , and  $\text{Ti}_3\text{C}_2\text{T}_x$ ) showed selectivity for  $\text{Li}^+$  ions of the polysulfides, facilitating selective  $\text{Li}^+$  ion transport.

There is a high potential for MXenes with Mo-based outer transition metal layer as cathode hosts, while Ti-based outer transition metal layer as separator coatings in Li-S batteries to inhibit the shuttle effect and improve the cycling performance of the Li-S cells. Selected MXene compositions will be used in various cell components in the next steps of this project.

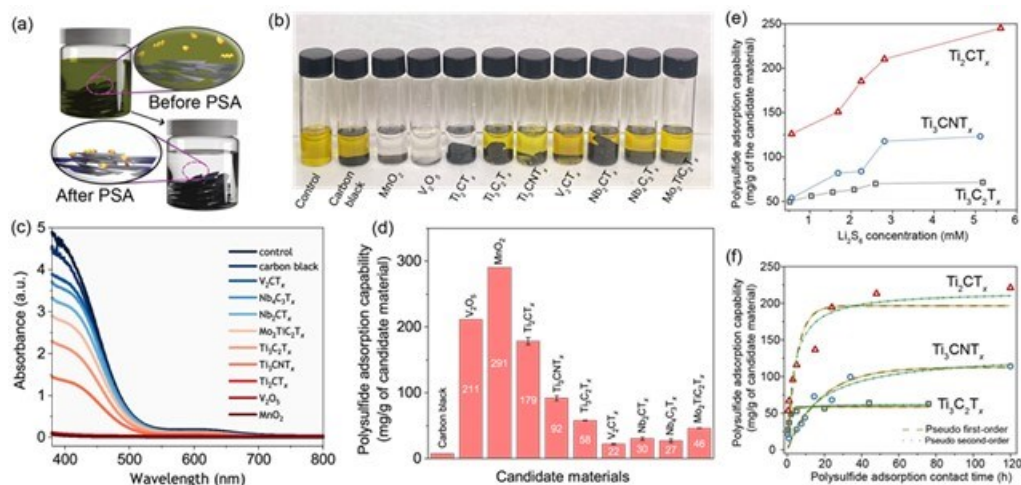


Figure XIV.10.10 (a) Schematic of the polysulfide adsorption test carried out in DME/DOL (1:1; v/v) solvent, with the inset showing the adsorption of polysulfides on the MXene flake surface. (b) Visual assessment of  $\text{Li}_2\text{S}_6$  solution color change after soaking candidate materials in  $\text{Li}_2\text{S}_6$  solution for 72 h. (c) UV-Vis absorption spectra of residual  $\text{Li}_2\text{S}_6$  solution and (d) calculated LIPS adsorption capability of candidate materials after 72 h in  $\text{Li}_2\text{S}_6$  solution. Lithium polysulfide adsorption characteristics of Ti-outer layered MXenes, (e) Adsorption isotherms of  $\text{Li}_2\text{S}_6$  in DME/DOL and (f) adsorption on  $\text{Ti}_2\text{CT}_x$ ,  $\text{Ti}_3\text{CNT}_x$  and  $\text{Ti}_3\text{C}_2\text{T}_x$  modeled using pseudo-first-order (yellow) and pseudo-second-order kinetic models (green). Experimental data points are connected by a dotted line.

## Conclusions

In BP1, we have prepared and characterized several new electrolyte compositions utilizing fluorinated cosolvents, strongly-bound Li salts, and additives. Based on the screening, electrolyte compositions containing fluorinated cosolvents such as HFMP, TFEM, ETFE, PTFE and TTE were selected for further evaluation and electrolyte characterizations. We showed that the addition of fluorinated cosolvents suppresses polysulfide dissolution and enhances Li anode stability in Li-S batteries. The LiTFSI-based electrolytes with TFEM additive showed excellent compatibility with Li anode and cycling stability, whereas LiFSI-based electrolytes showed better cycling stability with HFMP co-solvent. In this project period, several characterization tools have been established to characterize electrolytes and to investigate the effect of fluorinated cosolvents and additives on the performance of Li-S battery. Finally, the team has identified most promising MXene compositions to use in the various cell components to enhance the cycle life of Li-S batteries.

## Key Publications

1. Provisional patent regarding the new electrolyte formulation and additive (in preparation)
2. Screening Conductive MXenes for Lithium Polysulfide Adsorption, G. Valurouthu, M. Shekhirev, M. Anayee, R. Wang, K. Matthews, T. Hryhorchuk, R.W. Lord, D. Zhang, A. Inman, C.W. Ahn, Vibha Kalra, I.K. Oh and Y. Gogotsi (in preparation)

**References**

1. Lei Zhou, L.; Danilov, D. L.; Qiao, F.; Wang, J.; Li, H.; Eichel, R.-A.; Notten, P. H. L., Sulfur reduction reaction in lithium–sulfur batteries: mechanisms, catalysts, and characterization. *Adv. Energy Mater.* 2022, 12, 2202094.
2. Mauler, L.; Duffner, F.; Zeier, W. G.; Leker, J., Battery cost forecasting: a review of methods and results with an outlook to 2050. *Energy Environ. Sci.* 2021, 14 (9), 4712-4739
3. Lin, D.; Liu, Y.; Cui, Y., Reviving the lithium metal anode for high-energy batteries. *Nature Nanotech.* 2017, 12, 194-206.
4. Gupta, A.; Bhargav, A.; Jones, J.-P.; Bugga, R. V.; Manthiram, A., Influence of lithium polysulfide clustering on the kinetics of electrochemical conversion in lithium–sulfur batteries. *Chemistry of Materials* 2020, 32(5), 2070-2077
5. Lang, S.; Yu, S.-H.; Feng, X.; Krumov, M. R.; Abruña, H. D., Understanding the lithium–sulfur battery redox reactions via operando confocal Raman microscopy. *Nature comm.* 2022, 13, 4811
6. Wu, D. S.; Shi, F.; Zhou, G.; Zu, C.; Liu, C.; Liu, K.; Liu, Y.; Wang, J.; Peng, Y.; Cui, Y., Quantitative investigation of polysulfide adsorption capability of candidate materials for Li-S batteries. *Energy Storage Mater.* 2018, 13, 241-246.

**Acknowledgements**

Initial contribution of Dr. Castro Laicer on this project is thankfully acknowledged. Dr. Pavithra Shanthi (Giner, Inc.), Srinidi Badhrinathan (Giner, Inc.), Dr. Huidong Dai (Northeastern University) and Geetha Valurouthu (Drexel University) performed experimental work and analyzed data.

## XIV.11 Development of Functional Electrolytes for Li-S Battery Cells (PSU)

### Donghai Wang, Principal Investigator

The Pennsylvania State University  
134 EEL Building  
University Park, State College, PA 16802  
E-mail: [dwang@psu.edu](mailto:dwang@psu.edu)

### Haiyan Croft, DOE Technology Development Manager:

U.S. Department of Energy  
E-mail: [Haiyan.Croft@ee.doe.gov](mailto:Haiyan.Croft@ee.doe.gov)

Start Date: October 1, 2021	End Date: December 31, 2024	
Project Funding (FY23): \$781,111	DOE share: \$624,890	Non-DOE share: \$156,221

### Objectives

The objective of the project is to develop new functional electrolytes, which involve advanced co-solvent and reactive electrolyte additives and acquire knowledge for lithium-sulfur (Li-S) batteries in order to meet DOE's targets for high-energy-density battery ( $\geq 350$  Wh/kg) with long cycle life ( $< 20\%$  energy decay) and low cost ( $\leq \$100$  kWh). Li-S batteries using the advanced functional electrolytes shall achieve the sulfur-specific capacity of 1200 mAh/g at a high electrode capacity ( $> 7$  mAh/cm<sup>2</sup>) for over 300 cycles at low electrolyte/sulfur (E/S) ratio of 2 mL/g and demonstrate prototypes of 0.5 Ah Li-S battery cells with predicted energy densities of 400 Wh/kg and 80% capacity retention for 300 cycles.

### Approach

The overall approach will focus on synthesizing, modeling, optimizing, and evaluating functional electrolytes for Li-S batteries. This will be accompanied by property measurement and characterization (conductivity, electrochemical stability window, etc.) of the functional electrolyte, theoretical simulation to understand the functionality of the electrolyte, and interfacial characterization on both SEI and CEI using the electrolyte in Li-S batteries, along with cell electrochemical testing.

The task is focused on screening and optimizing the solvent, diluent, redox mediators, and additives to 1) decrease the solubility of lithium polysulfides and minimize the shuttling phenomenon, 2) facilitate the conversion kinetic of polysulfides and increase the S cathode-specific capacity, and 3) inhibit the shuttling effect and fabricating a CEI protection layer on the sulfur cathode to suppress polysulfide dissolution. This year, the team has investigated advanced electrolyte additives and co-solvents, e.g., commercial non-available ether and redox mediators, to mitigate the shuttle effect of polysulfide species during cycling.

### Results

The first approach is to optimize a new electrolyte to improve the cycling stability of Li-S cells. As shown in Figure XIV.11.1a, the high-mass loading sulfur cathode (4.0 mg S/cm<sup>2</sup>) can deliver a high discharge capacity of  $\sim 1100$  mAh/g at 0.05C. Following two cycles of the formation step at 0.05C for both charging and discharging, the Li-S coin cell remained capable of delivering a discharge capacity of up to 730 mAh/g at 0.1C for discharge. This is a remarkable achievement and a testament to the efficiency of the new electrolyte A. The newly developed electrolyte not only delivers high discharge capacity but also ensures a stable cycling performance, as illustrated in Figure XIV.11.1b. The Li-S coin cell demonstrated excellent electrochemical performance with electrolyte A, with a capacity retention rate of 84% after 24 cycles. It is worth noting that the Coulombic efficiency ramped up to over 95% within just five cycles and remained stable, showing no signs of

rapid deterioration. In conclusion, the newly developed electrolyte is promising for Li-S cells, offering stable cycling performance with high discharge capacity.

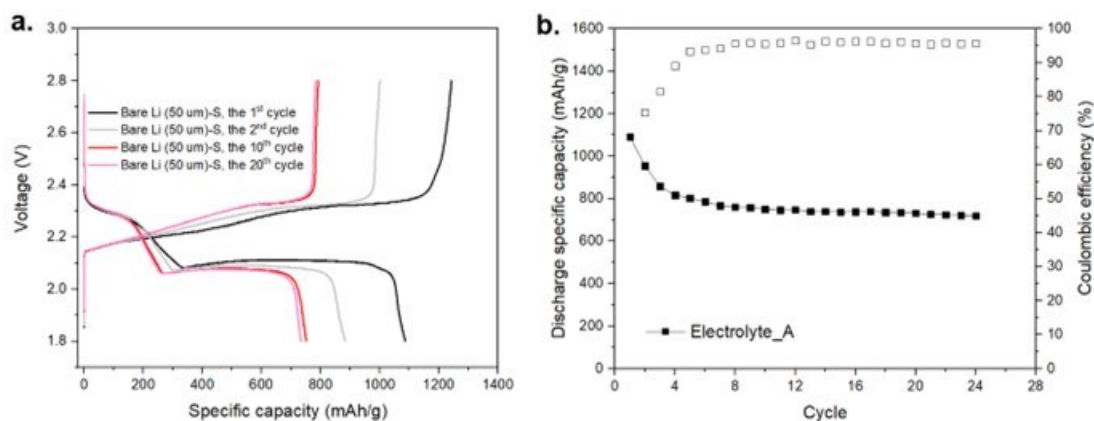


Figure XIV.11.1 (a) Voltage profiles for the Li-S coin cells at different cycles in electrolyte A; (b) Cycling performance of Li-S coin cell in electrolyte A.

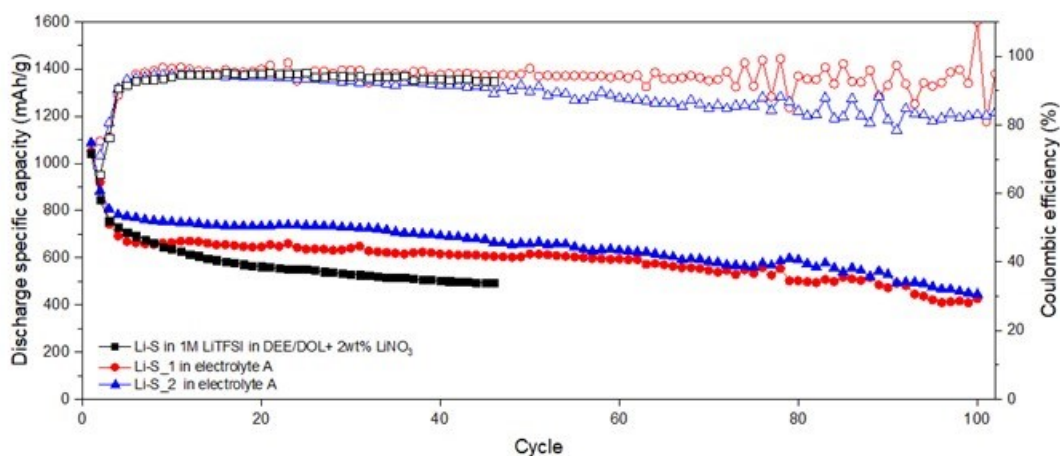
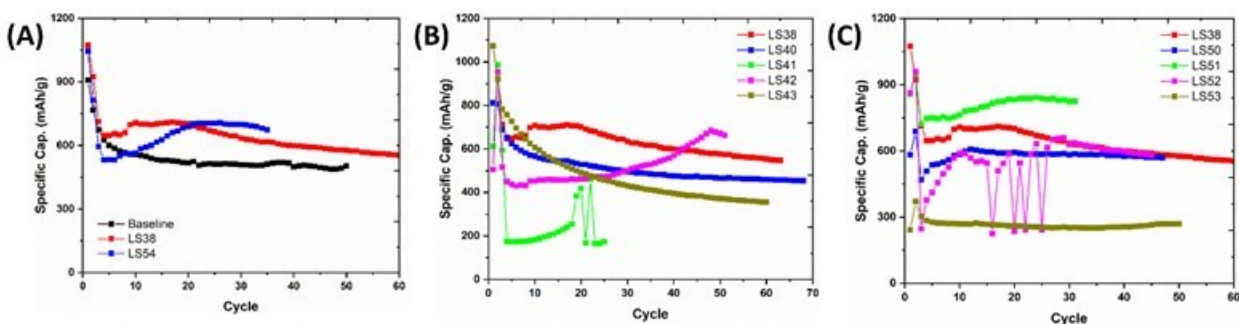


Figure XIV.11.2 Cycling performance of Li-S coin cells in baseline electrolyte 1M LiTFSI in DEE/DOL + 2 wt.% LiNO<sub>3</sub> and the newly developed electrolyte A. charge/discharge at 0.05C for the first 2 cycles for formation, then the coin cells was cycled at 0.1C for charge/discharge. 1C= 1000mAh/g; S mass loading: 4.0 mg S/cm<sup>2</sup>.

Next, the newly developed electrolyte A was further evaluated using parallel Li-S coin cells to validate its efficiency. As illustrated in Figure XIV.11.2, the new electrolyte A enables the two parallel Li-S coin cells to exhibit evidently improved cycling stability compared to the baseline ether-based electrolyte 1M LiTFSI in DEE/DOL + 2 wt% LiNO<sub>3</sub>. The electrolyte A demonstrates an 80% capacity retention after 63 cycles for coin cell Li-S<sub>1</sub> and 56 cycles for coin cell Li-S<sub>2</sub>, respectively. Moreover, the 2 parallel cells can stably cycle after 100 cycles without sudden decay. In contrast, the baseline electrolyte resulted in a fast decay and an 80% capacity retention after 14 cycles. In conclusion, the newly developed electrolyte A demonstrates its capability to enhance the performance of Li-S cells, enabling stable electrochemical performance along with high discharge capacity.



**Figure XIV.11.3 (a) Comparison of cycling profiles between the baseline (1M LiTFSI in DME/DOL 1:1 v/v + 2 wt.% LiNO<sub>3</sub>) and the new electrolytes LS38, LS54; Cycling profiles of LS38 combined with different additives at (b) 1 wt.% A1-A4 (LS40-LS43) and (c) 5 wt.% A1-A4 (LS50-LS53), respectively.**

The second approach is to create an extremely new formulation to increase Li<sup>+</sup> dissolution, sulfur utilization, and polysulfide suppression. Our proposed formulation is 1M LiTFSI in DME (solvating solvent)/co-solvent S1 (inhibit long-chain polysulfide dissolution)/diluent S2 (localize concentration of LiTFSI) + additive LiNO<sub>3</sub> (stabilize solid electrode-electrolyte interface) + additive A (promote polysulfide conversion kinetics) + additive B (enhance short-chain Li<sub>2</sub>S dissolution). Firstly, the electrolytes LS38 (1M LiTFSI in DME/S1/S2 + 2 wt.% M LiNO<sub>3</sub>) and LS54 (1M LiTFSI in DME/S1/S2 + 4 wt.% LiNO<sub>3</sub>) show much-improved cycle ability with better capacity retention and higher specific capacity (Figure XIV.11.3a). Therefore, LS38 is chosen to screen out the second additive for further optimization. Figure XIV.11.3b indicates that with 1 wt.% of additives A1-A4, all the electrolytes behaved worse than LS38 without additive A. However, when the concentration of additives A1-A4 increase to 5 wt.%, the electrolytes show much improved specific capacity and cycling stability (Figure XIV.11.3c). With 5 wt.% of A2 (LS51) exhibits the best behavior compared to the other electrolytes with other additives in terms of specific capacity and capacity retention.

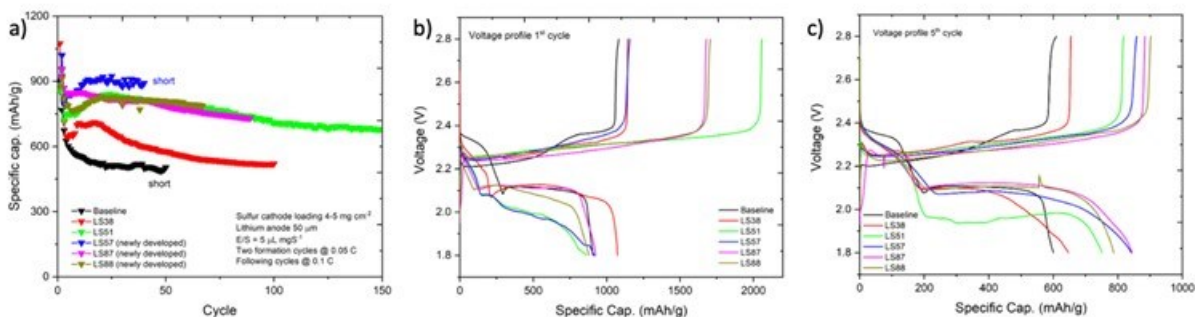


**Figure XIV.11.4 Comparison of cycling profiles between the baseline (1M LiTFSI in DME/DOL 1:1 v/v + 2 wt.% LiNO<sub>3</sub>) and the new electrolytes LS38 to LS88 (a); Voltage profiles between baseline and the new electrolytes after 1<sup>st</sup> cycle (b); and after 5<sup>th</sup> cycle (c).**

So far, we figured out the best additive A (A2) for the electrolyte formulation 1M LiTFSI in DME/S1/S2 + 2 wt.% LiNO<sub>3</sub> + 0.5 wt.% A2 (denoted as electrolyte LS51). We continued to screen out the additive B with the function to enhance short-chain Li<sub>2</sub>S dissolution in order to maximize the utilization of sulfur. We added 0.2 wt. % additive B1 to B3 into LS51 to create LS57, LS87, LS88, respectively.

Firstly, the electrolytes LS57, LS87, LS88 show much-improved cycling ability with better capacity retention and higher specific capacity (Figure XIV.11.4a) that indicated that the additive B is effective in enhancing the utilization of sulfur. Among the three additives B, LS57 shows the highest specific capacity, however got short-circuit after 40 cycles. The LS87 and LS88 show better cycling retention with a special observation of increasing capacity in LS88, thus the additive B2 and B3 are promising to fulfil our proposed electrolyte formulation.

The Figure XIV.11.4b shows that LS87 and LS88 indicated very low capacity lost and high charge capacity after 1<sup>st</sup> cycle compared to the baseline and other electrolytes. After 5<sup>th</sup> cycle, LS87 and LS88 show quite similar behavior with no severe voltage drop at around 2.1 V due to low viscosity of electrolyte with less polysulfide dissolution (Figure XIV.11.4c). So far, the LS87 and LS88 behaved quite same phenomenon, thus we keep cycling them to figure out which one is the best for our complete proposed electrolyte formulation.

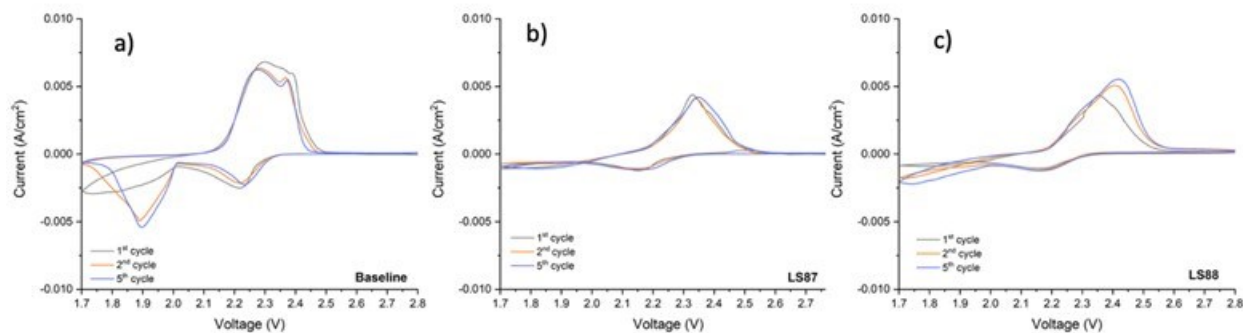


**Figure XIV.11.5 Comparison of cyclic voltammetry profiles between a) the baseline (1M LiTFSI in DME/DOL 1:1 v/v + 2 wt.% LiNO<sub>3</sub>) and the new electrolytes b) LS87, c) LS88.**

We figured out that LS87 and LS88 indicated very low capacity lost and high charge capacity after 1<sup>st</sup> cycle compared to the baseline and other electrolytes. After 5<sup>th</sup> cycle, LS87 and LS88 show quite similar behavior with no severe voltage drop at around 2.1 V due to low viscosity of electrolyte with less polysulfide dissolution. In this quarter, we studied the mechanism of the additives in the LS87 and LS88. As shown in Figure XIV.11.5, in LS87 and LS88, the redox voltages and peaks changed that indicated less polysulfide formation and high amount of sulfur reserved compared to the baseline.

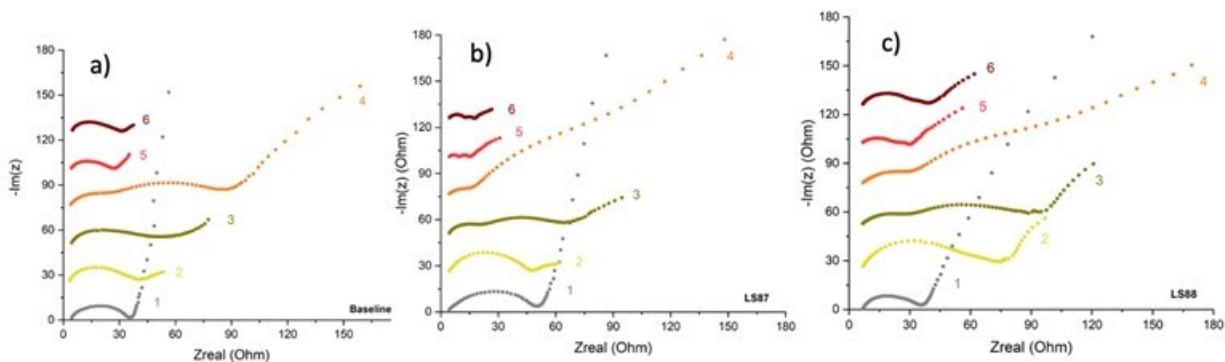


**Figure XIV.11.6 Comparison of impedance profiles between a) the baseline (1M LiTFSI in DME/DOL 1:1 v/v + 2 wt.% LiNO<sub>3</sub>) and the new electrolytes b) LS87, c) LS88.**

In the Figure XIV.11.6, we did the impedance spectra for the baseline and the two new electrolytes. The kinetics changed from step 3 to step 6 in the LS87 and LS88 with less polysulfide formation, faster rate of Li<sub>2</sub>S transfer and higher yield of sulfur, much less cell impedance than the baseline. The Li<sub>2</sub>S dissolved very fast after formed made the electrolyte less viscous and the interfaces between the electrode and electrolyte clearer without Li<sub>2</sub>S accumulation.



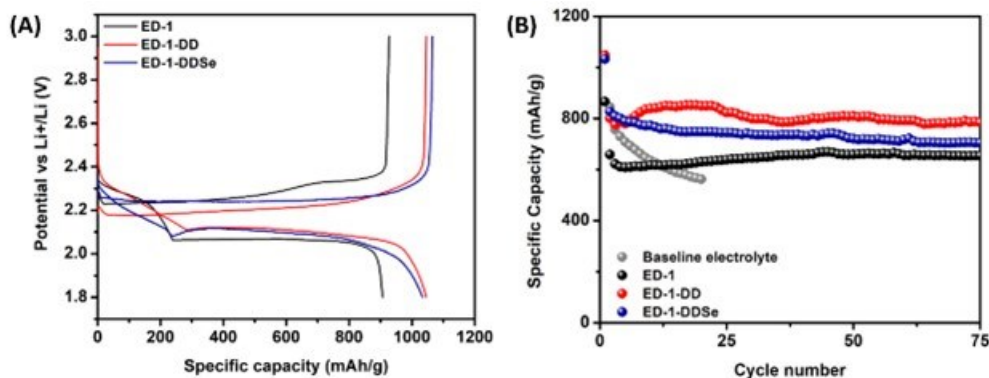


Figure XIV.11.7 (a) Galvanostatic charge/discharge potential profile of the KB/S cathode in a functional electrolyte with/without redox mediator (first cycle at 0.05 C). (b) Cycling performance of the KB/S cathode in different electrolytes (cycle at 0.1 C).

The third approach is to synthesize new commercial non-available ether to prevent polysulfide shuttling and add redox mediators to boost sulfur capacity. The unique electrolyte changes the solvation properties between Li cation and solvent molecules to suppress the lithium polysulfide dissolution and simultaneously form a stable SEI on the Li metal anode. Therefore, the cyclability and Coulombic efficiency of the KB/S cathode is improved. In the last quarter, we screened several ethers and selected ED-1 as the co-solvent for future modification. However, due to the suppression of polysulfide dissolution, the ED-1 electrolyte exhibited a low discharge capacity (907 mAh/g) and first-cycle Coulombic efficiency (98%). Therefore, we screened several redox mediators (DD, DDSe, etc.) in the selected ED-1 electrolyte as additives to facilitate the S conversion kinetically. As shown in Figure XIV.11.7a, with a high-loading sulfur cathode (4 mg/cm<sup>2</sup>) and thin Li metal anode (50 μm), the ED-1-DD and ED-1-DDSe electrolyte exhibits a higher discharge capacity (1046 mAh/g and 1033 mAh/g) and Coulombic efficiency (99.7% and 96.8%). The redox mediator, DD and DDSe, changed polysulfide formation to organic sulfur, significantly preventing the shuttling effect and prolonged the cycling performance. The ED-1-DD and ED-1-DDSe cell could both deliver a specific capacity of over 800 mAh/g at a current rate of 0.1 A/g and maintain over 99% and 85% of capacity for 75 cycles, respectively (Figure XIV.11.7b). Therefore, we need to further investigate other mediators and optimize the ratio between the redox mediator and ether electrolyte to achieve high capacity with promising capacity retention.

## Conclusions

In this year, we reported three approaches to conduct modifications to enhance the electrochemical performance of the functional additives and redox mediators as well as synthesis new solvents/co-solvents. We applied physical characterization to investigate the protection mechanism for the second approach. Moreover, we figured out which formulation is the best for Li-S system and perform the characterization to know the kinetics and the chemistry inside the batteries and the real functions of those additives. The three approaches will be explored further to meet the second-year milestone of achieving a high-load (3 mAh/cm<sup>2</sup>) sulfur-specific capacity of 800 mAh/g and superior cycle life (< 20% capacity decay in 200 cycles) at room temperature.

## Acknowledgements

The work was supported by the Department of Energy, under Award Number DE- EE0009647. We appreciate the support from Coriana Fitz at National Energy Technology Laboratory and Mallory Clites and Patricia Smith from DOE.

## XV Beyond Li-ion R&D: Lithium-Air Batteries

A lithium-air cell benefits from using oxygen molecules at the positive electrode. Oxygen reacts with positively charged lithium ions to form lithium peroxide. Electrons are drawn out of the electrode until no more lithium peroxide can be formed. For the rechargeable Li-air battery, the practical energy density could be ~800 Wh/kg. An advantage of such batteries is their open structure; that is, they can absorb the active cathode material (oxygen) from the surrounding environment instead of having to carry it within. However, their open structure also leads to several challenges. Although significant progresses have been made in recent years on the fundamental properties of lithium-air batteries, many barriers still need to be addressed before their practical application in EVs.

The rest of this chapter contains detailed reports on the status of the following individual projects.

- Lithium-Air Batteries (ANL)
- Lithium Oxygen Battery Design and Predictions (ANL)
- Development of a High-Rate Lithium-Air Battery Using a Gaseous CO<sub>2</sub> Reactant (UIC)

## XV.1 Lithium-Air Batteries (ANL)

### **Khalil Amine, Principal Investigator**

Argonne National Laboratory  
9700 South Cass Avenue  
Lemont, IL 60439  
E-mail: [amine@anl.gov](mailto:amine@anl.gov)

### **Larry Curtiss, Co-Principal Investigator**

Argonne National Laboratory  
9700 South Cass Avenue  
Lemont, IL 60439  
E-mail: [curtiss@anl.gov](mailto:curtiss@anl.gov)

### **Tien Duong, DOE Technology Development Manager**

U.S. Department of Energy  
E-mail: [Tien.Duong@ee.doe.gov](mailto:Tien.Duong@ee.doe.gov)

Start Date: October 1, 2022

End Date: September 30, 2023

Project Funding (FY23): \$450,000

DOE share: \$450,000

Non-DOE share: \$0

### **Project Introduction**

Lithium-oxygen batteries are of much interest because they offer, in principle, ten times the energy density of conventional lithium-ion systems. The inherent energy potential of lithium metal approaches that of gasoline, but there are challenges that remain to be able to unlock this potential. While today's lithium-ion batteries may provide acceptable power for hybrid electric vehicles and all-electric vehicles, they do not yet provide sufficient energy for the long distance driving desired by consumers. A breakthrough in Li-oxygen battery technology would significantly increase the possibility of extending the electric range of these vehicles with the added advantages of reducing battery cost and weight.

The successful implementation of non-aqueous Li-air cells has been hampered because of severe materials problems that have limited electrochemical performance. These include (1) the non-aqueous electrolytes can be unstable under both the charge and discharge conditions, thereby seriously limiting cycle life; (2) during discharge, the solid and insoluble  $\text{Li}_2\text{O}_2$  and/or other lithium oxide products are deposited on the surface or within the pores of the carbon cathode, thereby passivating the surface as well as clogging the pores and restricting oxygen flow; (3) degradation of the lithium anode due to oxygen crossover destroys the integrity and functioning of the cell; and (4) commonly used transition metal cathode catalysts, do not access the full capacity of the oxygen electrode or enable sufficiently high rates.

The team led by Dr. Khalil Amine at Argonne National Laboratory is working on problems that limit the electrochemical performance of the Li-oxygen battery, including the stability of the organic electrolytes, development of new cathode catalysts, and new electrolytes. This effort will lead to the development of a reversible lithium oxygen battery that provides much higher energy density than state-of-the-art lithium-ion batteries for electric vehicles

### **Objectives**

This project will develop new cathode materials and electrolytes for Li-air batteries for long cycle life, high capacity, and high efficiency. The goal is to obtain critical insight that will provide information on the charge and discharge processes in Li-air batteries to enable new advances to be made in their performance. This will be done using state-of-the-art characterization techniques combined with state-of-the-art computational methodologies to understand and design new materials and electrolytes for Li-air batteries.

## Approach

The project is using a joint theoretical/experimental approach for design and discovery of new cathode and electrolyte materials that act synergistically to reduce charge overpotentials and increase cycle life. Synthesis methods, in combination with design principles developed from computations, are used to make new cathode architectures. Computational studies are used to help understand decomposition mechanisms of electrolytes and how to design electrolytes with improved stability. The new cathodes and electrolytes are tested in Li-O<sub>2</sub> cells. Characterization, along with theory, is used to understand the performance of materials used in the cell and to make improved materials.

## Results

### New cell design to investigate electrolyte production of soluble catalysts

Lithium oxygen (Li-O<sub>2</sub>) batteries have attracted extensive research interest due to their high energy density. Single atom catalysts hosted in carbon frameworks has been reported to show promising results for the cathode. However, their functioning mechanism has always been unclear. We previously looked into the possibility that soluble homogenous catalyst can be produced from the solid cathode. These species can then help dramatically reduce the overpotential. This year we developed a cell design that can be used to detect the production of such species without significantly altering the transport properties of the cell.

As seen in Figure XV.1.1A, the cell design includes two working electrodes connected to two potentiostats. The premise of this design is to allow for the detection of electrochemically active species in the electrolyte that are generated from the cathode. This cell has been made by our in-house glass blower, with a 3- electrode connection. During operation, the carbon + catalyst cathode is subjected to a galvanostatic charging current against the Li metal reference and counter. At set intervals of times, the charging current will be halted and cyclic voltammetry will be performed between the secondary working electrode (carbon paper) and the Li metal reference and counter electrode. Figure XV.1.1B shows the charging profile observed in Potentiostat 2. Figure XV.1.1C shows the corresponding CV response indicating some redox active species are present in the electrolyte upon charging the cathode. Furthermore, the reduction current indicates that it has redox mediating properties that can be beneficial to the oxygen evolution reaction.

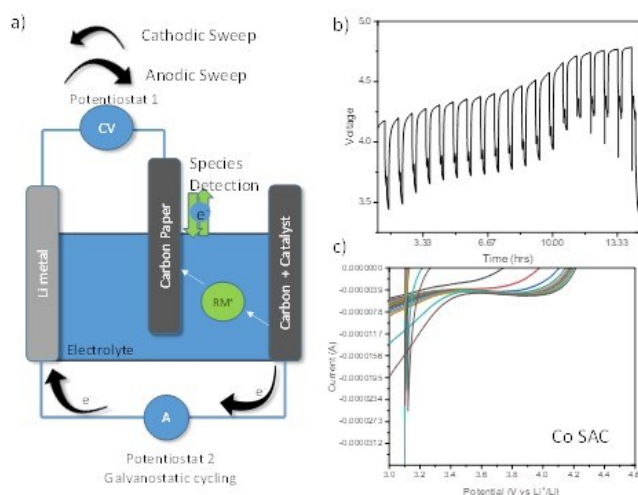


**Figure XV.1.1 (A)** Two working electrode cell design that was implemented in a Swagelok cell. The addition of an additional working electrode (i.e. carbon paper) in the electrolyte and separated from the cathode, allows for the detection of electrochemical active species generated from the cathode. Note: RM is short for redox mediator. **B)** Voltage profile during the intermittent galvanostatic charging executed between the cathode electrode and the lithium metal anode (reference and counter electrode). **C)** Cyclic voltammograms observed at different SOCs sampled between the carbon paper electrode coated with Co Single atom catalyst (SAC) and the lithium metal anode.

To summarize, a new cell design was developed that allows for the convenient electrochemical sampling of the electrolyte under relatively normal charging cell conditions. We successfully applied this new design to probe the electrochemistry of the electrolyte for redox active species and have found such species when Co single atom catalysts (SAC) were used on the cathode. This work points to changing how the Li-O<sub>2</sub> research community can understand solid-phase catalyst and also developing their relationship to liquid-phase catalysts.

*A non-precious metal catalyst for a lithium superoxide based Li-O<sub>2</sub> battery*

Lithium oxygen (Li-O<sub>2</sub>) batteries have attracted extensive research interest due to their high energy density. Iridium (Ir)-based materials including IrLi and Ir<sub>3</sub>Li have been recently studied in our group as efficient electrocatalysts in Li-O<sub>2</sub> batteries. It was demonstrated that the surface lattices of IrLi and Ir<sub>3</sub>Li catalysts were well-matched with lithium superoxide (LiO<sub>2</sub>) surfaces and supported epitaxial growth of LiO<sub>2</sub>, which can result in reduced charge potentials and give longer cycle life. However, Ir is one of the most expensive precious metals, which would increase the total cost of the Li-O<sub>2</sub> battery system. Compared to lithium peroxide (Li<sub>2</sub>O<sub>2</sub>), LiO<sub>2</sub> has better charge transport (lower charge transport resistance) due to its good electronic conductivity, which leads to the lower charge potentials and potentially longer cycle life of Li-O<sub>2</sub> batteries. Therefore, it is highly desirable to develop non-precious electrocatalysts that can support the epitaxial growth of LiO<sub>2</sub>.

Recently, we found that LiAl could have potential to be a proper non-precious electrocatalyst material through a density functional theory (DFT) simulation as some of its surfaces have a good lattice match with LiO<sub>2</sub> similar to that found for Ir<sub>3</sub>Li and IrLi. Li-O<sub>2</sub> cells were run using a reduced graphene oxide (rGO) cathode with and without LiAl nanoparticles added to it. The results are presented in Figure XV.1.2. For a Li-O<sub>2</sub> battery with LiAl/rGO as the catalyst and the use of an electrolyte composed of tetraglyme, lithium triflate, and the ionic liquid (IL) 1-Ethyl-3-methylimidazolium tetrafluoroborate (EMIM-BF<sub>4</sub>) the cell achieved 635 cycles (1270 h with a cut-off voltage of 4.0 V) as shown in Figure XV.1.2A. Without the utilization of the IL, LiAl/rGO still displayed good cyclability (460 cycles with a higher cut-off voltage of 4.6 V), although the overpotential was much larger than that with IL for the whole battery cycling as shown in Figure XV.1.2C. Specifically, the charge potential has been significantly reduced when using the IL, which illustrates that the IL probably protects the surface of LiAl that can be oxidized when purging with O<sub>2</sub> gas. Further experiments are in process to understand the effect of the IL on the performance of the LiAl based cathode. Meanwhile, rGO without the LiAl catalyst, but with IL, showed poor cyclability demonstrating the favorable catalytic capability of LiAl in the Li-O<sub>2</sub> cell as shown in Figure XV.1.1c. Furthermore, LiAl exhibited good cycle life (325 cycles, cut-off voltage: 4.1 V) at higher capacity (1000 mAh/g) as shown in Figure XV.1.2B.

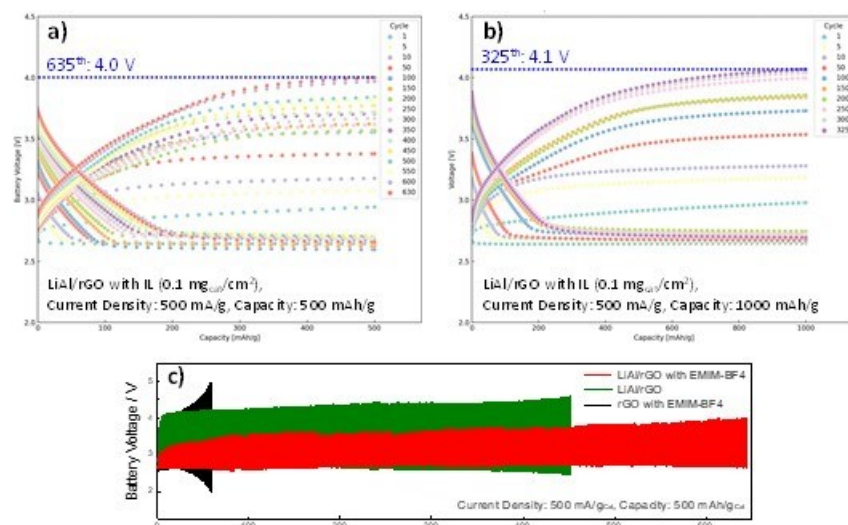


**Figure XV.1.2** Li-O<sub>2</sub> battery cycling performance: (A,B) voltage-capacity profiles of LiAl/rGO with Ionic Liquid at 500 and 1000 mAh/g<sub>Cat</sub> of capacity, (C) Galvano-static discharge/charge profiles of LiAl/rGO with Ionic Liquid (EMIM-BF<sub>4</sub>) (Red), LiAl/rGO (Green), and rGO with Ionic Liquid (EMIM-BF<sub>4</sub>) (Black).

X-ray diffraction analysis for the Li-O<sub>2</sub> cell with and without the IL has been carried out to characterize the discharge product. As shown in Figure XV.1.3, XRD patterns of discharged LiAl/rGO cathodes (with and without IL) have the major two peaks of LiO<sub>2</sub> indicating that the LiAl based cathode results in LiO<sub>2</sub> formation. The relative peak intensity is much higher with the use of IL, suggesting that IL promotes LiO<sub>2</sub> formation. Additionally, small peaks for Li<sub>2</sub>O<sub>2</sub> ((101) and (102) lattices) were obtained in both cases. We also investigated the possible presence of the discharge product on a separator that was coupled with the discharged cathode with IL. From Figure XV.1.3, it is seen that small peaks for LiO<sub>2</sub> are observed on the separator, which supports the LiO<sub>2</sub>-generating ability of LiAl cathode as a solution phase mechanism.

In future work, DFT calculations will be carried out to understand the mechanism for formation of the LiO<sub>2</sub> on the LiAl cathode and additional physicochemical characterizations such as Raman, acid-based titration, X-ray photon spectroscopy, scanning and transmission microscopies, and new analysis will be carried out to obtain more evidence of LiO<sub>2</sub> formation on the non-precious LiAl electrocatalyst.

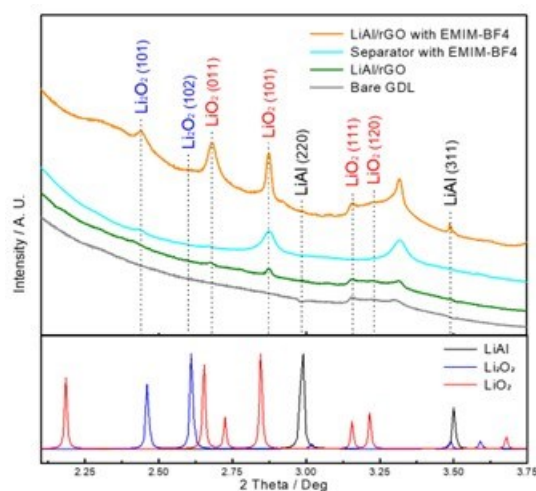


**Figure XV.1.3** Synchrotron-based High-Energy X-ray diffraction pattern (HE-XRD) of several samples

### *New redox mediators for discharge in Li-O<sub>2</sub> batteries*

Lithium oxygen (Li-O<sub>2</sub>) batteries have attracted extensive research interest due to their high energy density. Redox mediators are necessary to increase the discharge capacity by facilitating the reduction and precipitation of Li<sub>2</sub>O<sub>2</sub> in a way that reduces the possibility of passivation. While much effort has been spent on oxygen evolution reaction redox mediators, redox mediators for the reduction of O<sub>2</sub> to Li<sub>2</sub>O<sub>2</sub> have not been a well studied field with a large majority of the oxygen reduction reaction redox mediators (ORR-RM) used being a derivative of benzoquinone. Here we identified and synthesized a new class of unexplored ORR-RM in the form of triaryl methyl cation-based redox mediators.

Figure XV.1.4A shows a series of triaryl methyl cation-based redox mediators with redox potentials tuned by changing the R1, R2, R3 of the carbocation for different aryl-based functional groups labeled from (i-vii). From DFT calculations, we were able to predict the redox potential of the triaryl methyl cations before synthesis and testing and selected nine candidate molecules for use in CV measurements where the kinetics parameters of the O<sub>2</sub>/Li<sub>2</sub>O<sub>2</sub> redox were derived. Among the nine candidates, five had redox potentials that made them suitable for serving as a ORR-RM, i.e. the redox potential of the ORR-RM was around ~2.8 V vs Li<sup>+</sup>/Li.

Discharge experiments using these ORR RM at their solubility limits are shown in Figure XV.1.4B. Clearly, the baseline sample without any ORR-RM exhibited poor performance and with little Li<sub>2</sub>O<sub>2</sub> deposition capacity, which aligns well with common understanding since the surface area of the carbon paper cathode is not that large. Each of the five ORR-RM synthesized (1b, 1c, 1d, 1e, and 4) exhibited significant increases in discharge capacity with 1b at 200 mM able to deliver up to ~2.3 mAh cm<sup>-2</sup>.

Beyond the increase in performance, we also found an interesting trend of the discharge capacity with respect to the reaction rate constant derived from CV. As shown in Figure XV.1.4C, the larger reaction rate constant, as derived from CV fitting, does not seem to result in a larger discharge capacity. In fact, it seems that the lower the reaction rate, the larger the discharge capacity. This counterintuitive observation can be explained by the relationship of the reaction rate constant and the reduction potential of the ORR-RM. The ORR-RM's rate of O<sub>2</sub> reduction to Li<sub>2</sub>O<sub>2</sub> increases with a decrease in reduction potential. The lower the potential of the ORR-RM, the larger the driving force for O<sub>2</sub> reduction by the ORR-RM. However, a side feature of this is that when the reduction potential of the ORR-RM drops too low, the self reduction of O<sub>2</sub> to Li<sub>2</sub>O<sub>2</sub> is also favored due to the extra driving force from the lower potential. This results in a competition between the a ORR-RM facilitated reduction of O<sub>2</sub> and a unfavorable ORR-RM-free reduction of O<sub>2</sub>. This relationship suggests that higher potential ORR-RM should perform more favorably in Li-O<sub>2</sub> rather than lower potentials ORR-RM.

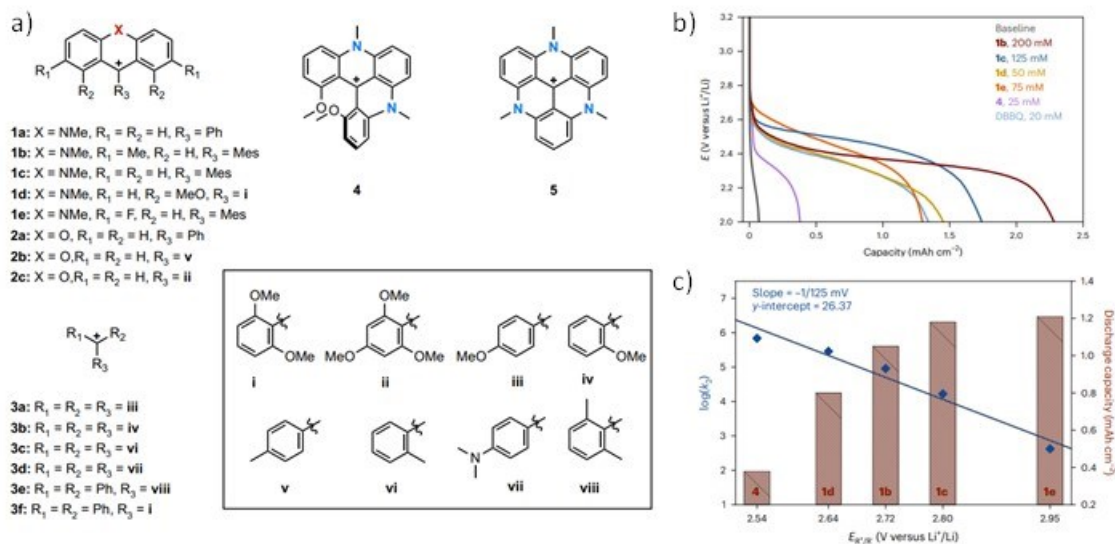


**Figure XV.1.4 (A)** A series of triaryl methyl cation redox mediators were synthesized and investigated as ORR redox mediator (RM) for Li-O<sub>2</sub> battery. Various function groups were substituted to examine their effect on the discharge capacity and redox potential. **(B)** Discharge capacity using a commercial carbon paper with various redox mediators at their solubility limit. **(C)** Relationship between RM potential and reaction rate (derived from CV).

#### Solid state Li-Air battery

A novel rechargeable solid-state electrolyte Li-air battery (RSS-LAB) that enables a lithium oxide (four electrons reaction) discharge product has been shown for the first time. The battery has excellent performance in all respects, introduces a fundamentally new concept for Li-O<sub>2</sub> batteries, and provides a real breakthrough to obtain very high energy densities far beyond what is possible from Li-ion (LIB) technology. The RSS-LAB has the following features.

First, this battery runs for 1000 cycles with a very small polarization gap (0.4 V at end of cycling) as shown in Figure XV.1.5 In addition, this is accomplished in a cell run at room temperature, at a good charge/discharge rate of 1000 mA/g (1C), a good capacity of 1000 mAh/g and in atmospheric air so no O<sub>2</sub> tanks would be required.

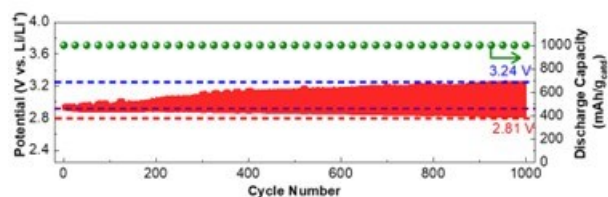


**Figure XV.1.5** Cycling results for the solid-state Li-air battery.

Second, this is the first successful Li-O<sub>2</sub> battery (pure O<sub>2</sub> or in air) that has been based on a solid-state electrolyte (SSE) as opposed to a liquid or molten salt electrolyte. This new SSE is a composite ceramic-polymer electrolyte with excellent ionic conductivity (0.52 mS/cm), electrochemical stability (5.27 V), and Li<sup>+</sup> transference number (0.73) that enables a successful and more importantly a safe operating Li-air battery.

Finally, this battery runs on a new concept for a Li-O<sub>2</sub> (pure O<sub>2</sub> or air) different from both a Li-ion battery and a liquid electrolyte-based Li-O<sub>2</sub> battery. Conventional Li-ion batteries use mixed ion-electron conductors for the intercalation processes in the cathode (oxides) and anode (graphite). In the SS-LAB, the discharge and charge bond-making and breaking processes are enabled by a mixed ion-electron conductor discharge product



located on the cathode. The four-electron reaction is enabled by this mixed ion-electron conducting discharge product and its interface with air.

### Conclusions

During the past year we have developed a Li-O<sub>2</sub> cell that can be used to detect the production of species in the electrolyte without significantly altering the transport properties of the cell. This cell was used to probe the electrochemistry of the electrolyte for redox active species and have found such species when Co single atom catalysts (SAC) were used on the cathode. This work points to changing how the Li-O<sub>2</sub> research community can understand solid-phase catalyst and also developing their relationship to liquid-phase catalysts.

Previously, we demonstrated that the surface lattices of IrLi and Ir<sub>3</sub>Li catalysts were well-matched with lithium superoxide (LiO<sub>2</sub>) surfaces and supported epitaxial growth of LiO<sub>2</sub>, which can result in reduced charge potentials and give longer cycle life. However, Ir is one of the most expensive precious metals. During the past year we have studied a non-precious metal, LiAl, for a catalyst for a Li-O<sub>2</sub> battery, and found that it results in LiO<sub>2</sub> growth also. This battery has a long cycle life of more than 600 cycles and a low charge potential.

Redox mediators are necessary to increase the discharge capacity by facilitating the reduction and precipitation of Li<sub>2</sub>O<sub>2</sub>. While much effort has been spent on oxygen evolution reaction redox mediators, redox mediators for the reduction of O<sub>2</sub> to Li<sub>2</sub>O<sub>2</sub> have not been a well studied field. During the past year we have identified and synthesized a new class of unexplored ORR-RM in the form of triaryl methyl cation-based redox mediators. Some of these new ORR-RM result in greatly increased capacity.

A novel rechargeable solid-state electrolyte Li-air battery that enables a lithium oxide (four electrons reaction) discharge product has been shown for the first time. The solid-state electrolyte is a composite based on ceramic nanoparticles embedded in a polymer. The battery can cycle in air and at room temperature for 1000 cycles with a low polarization gap. It works on a fundamentally new concept for Li-O<sub>2</sub> batteries and can attain very high energy densities far beyond what is possible from Li-ion (LIB) technology.

### Key Publications

1. Askins, E.J., Zoric, M.R., Li, M. et al. Triarylmethyl cation redox mediators enhance Li-O<sub>2</sub> battery discharge capacities. *Nat. Chem.* (2023). <https://doi.org/10.1038/s41557-023-01268-0>
2. Alireza Kondori et al., A room temperature rechargeable Li<sub>2</sub>O-based lithium-air battery enabled by a solid electrolyte. *Science* 379,499-505(2023). DOI:10.1126/science.abq1347
3. Solvents and catalyst preparations for lithium-oxygen batteries, HH Wang, R Jagatramka, S Plunkett, LA Curtiss, K. Amine - US Patent 11,658,291, 2023
4. "Template assisted lithium superoxide growth for lithium-oxygen batteries," Hsien-Hau Wang, Chengji Zhang, Jing Gao, Kah Chun Lau, Samuel T Plunkett, Moon Park, Rachid Amine, Larry A Curtiss, Faraday Discussions (2023) doi.org/10.1039/D3FD00116D

### Acknowledgements

Other participants who have contributed to this project include Mathew Li (ANL), Ksenija Glusac (UIC/ANL), Rachid Amine (ANL), Hau-Hsien Wang (ANL), Mohammad Asadi (IIT), Moon Park (ANL), Xiaozhou Huang (ANL).

## XV.2 Lithium Oxygen Battery Design and Predictions (ANL)

### Larry Curtiss, Principal Investigator

Argonne National Laboratory  
9700 South Cass Avenue  
Lemont, IL 60439  
E-mail: [curtiss@anl.gov](mailto:curtiss@anl.gov)

### Amin Salehi, Co-Principal Investigator

University of Illinois at Chicago  
Department of Mechanical and Industrial Engineering  
Chicago, IL 60607  
Email: [salehikh@uic.edu](mailto:salehikh@uic.edu)

### Ahn T. Ngo, Co-Principal Investigator

University of Illinois at Chicago  
Department of Mechanical and Industrial Engineering  
Chicago, IL 60607  
Email: [ahnngo@uic.edu](mailto:ahnngo@uic.edu)

### Tien Duong, DOE Technology Development Manager

U.S. Department of Energy  
E-mail: [Tien.Duong@ee.doe.gov](mailto:Tien.Duong@ee.doe.gov)

Start Date: October 1, 2022

End Date: September 30, 2023

Project Funding (FY23): \$450,000

DOE share: \$450,000

Non-DOE share: \$0

### Project Introduction

Lithium (Li)-oxygen (O<sub>2</sub>) batteries are considered as a potential alternative to Li-ion batteries for transportation applications due to their high theoretical specific energy. The high energy density of Li-O<sub>2</sub> batteries is made possible because of the formation of the Li<sub>2</sub>O<sub>2</sub> product, which can store significantly higher amounts of energy compared to other energy storage systems because of the Li-O bonds. However, the challenge is that the decomposition of Li<sub>2</sub>O<sub>2</sub> during the charge process requires charge transfer, which is difficult because of the large band gap of solid Li<sub>2</sub>O<sub>2</sub> likely covering catalytic sites. This leads to a sluggish charge process requiring higher potentials for Li<sub>2</sub>O<sub>2</sub> decomposition, which in turn reduces the energy efficiency of the battery and puts the electrolyte at risk of degradation. Additionally, the charge potential can depend on the morphology and size of Li<sub>2</sub>O<sub>2</sub> product. The major issues with the existing Li-O<sub>2</sub> systems include degradation of the anode electrode, reactions with air components, clogging of the cathode, and electrolyte instability. These issues are being addressed in this project.

### Objectives

The objective of this work is to develop new materials for Li-O<sub>2</sub> batteries that give longer cycle life, higher charge/discharge rates, and improved efficiencies in an air environment. New electrolyte blends and additives are being investigated that can reduce clogging and at the same time can promote the cathode functionality needed to reduce charge overpotentials and increase discharge/charge rates. The cathode materials are based on high to medium entropy two-dimensional transition metal dichalcogenides (TMDCs) that we have found to be among the best oxygen reduction and evolution catalysts. New high entropy alloys are being investigated. The objective is to design and predict new electrolytes that work with these catalysts to give longer cycle life, high charge rates, good efficiencies, and high capacities needed to make scale up possible for these types of batteries.

## Approach

The project is using a joint theoretical/experimental approach for design and discovery of new cathode and electrolyte materials that act synergistically to reduce charge overpotentials and increase cycle life. Synthesis methods, in combination with design principles developed from computations, are used to make new cathode architectures. Computational studies are used to help understand decomposition mechanisms of electrolytes and how to design electrolytes with improved stability. The new cathodes and electrolytes are tested in Li-O<sub>2</sub> cells. Characterization, along with theory, is used to understand the performance of materials used in the cell and to make improved materials.

## Results

### *Synthesis of a new di-iridium sulfur-based catalyst for a Li-O<sub>2</sub> battery*

We have been synthesizing a new class of catalysts based on bi- and tri-metallic systems with dichalcogenides for use as catalyst in Li-O<sub>2</sub> batteries including porous dichalcogenides with bridging transition metal active sites. Such alloys should have high entropy and be more likely to withstand higher rates desired in a Li-O<sub>2</sub> battery. In the work done this year we synthesized powders of SnIrS<sub>3.6</sub> crystals by the chemical vapor transport (CVT) method for use in a Li-O<sub>2</sub> cell to act as a catalyst for oxygen reduction and evolution. The powders of tin disulfide, iridium, and sulfur were mixed based on stoichiometric ratio and sealed into quartz ampoules. The synthesis process was started by heating the ampoule to 1050 °C, keeping it at this temperature for ten days, and cooling it down to room temperature naturally. A liquid-phase exfoliation method was used to exfoliate SnIrS<sub>3.6</sub> into nanoflakes.

Various characterizations were carried out on the as-synthesized SnIrS<sub>3.6</sub> to study its physical and electrochemical properties. Scanning electron micrographs (SEM) of the SnIrS<sub>3.6</sub> revealed a 1-D nanoribbon texture shown in **Figure XV.2.1A**, with a relative cross-sectional diameter ranging from 500 nm to 1 micron. The elemental mapping with energy-dispersive spectroscopy (EDS) indicates a homogeneous distribution of S, Sn, and Ir in this material, as shown in **Figure XV.2.1B**. To determine the crystal structure, the three-dimensional electron diffraction dataset and atomic resolution scanning transmission electron microscopic image were acquired. The unit cell indicates that the structure has never been discovered before for the whole chalcogenide compound family.

The arrangement of the atoms fits well with the atomic model shown in **Figure XV.2.1C**. A powder X-ray diffraction (PXRD) pattern was collected and compared with the simulated PXRD pattern from the structure model, as shown in **Figure XV.2.1D**. The structure was composed of six- and five-coordinated metal atoms, forming octahedral and triangular bipyramids, respectively. Along the b-axis of the structure, a micropore with a size of 4.4 Å is presented (shown in **Figure XV.2.1E**). The formation of the porosity structure is very intriguing since the synthesis method is chemical vapor transport and does not involve the usage of any surfactants or structure-directing agents, which are the common chemical compounds to form micropores in the structure. The overall crystal structure was also viewed from other directions, as shown in **Figure XV.2.1F**. From the structure, we can also obtain the accurate stoichiometry for this material, which is SnIrS<sub>3.6</sub>.

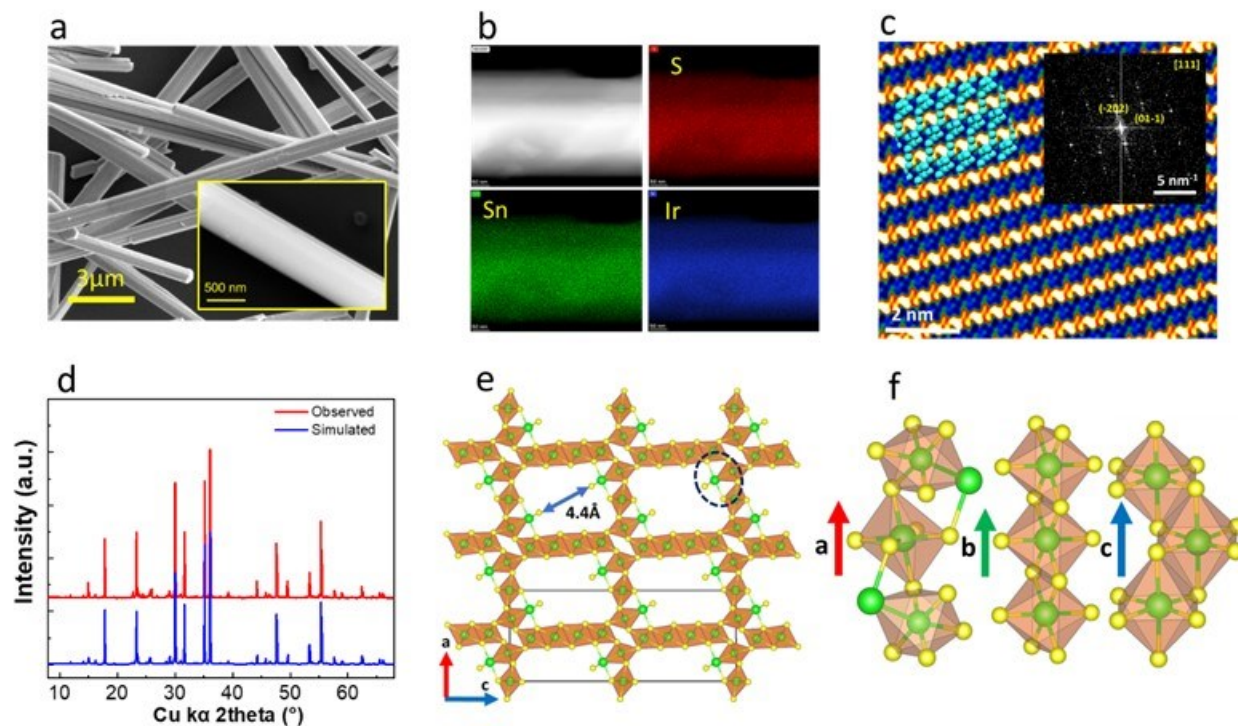


**Figure XV.2.1** (A) SEM images taken from as-synthesized SnIrS<sub>3</sub> nanorods. (B) Atomic resolution scanning transmission electron microscopic high-angle annular dark field (STEM HAADF) image and STEM-EDS spectrum image that shows the distribution of S, Sn, and Ir elements. (C) Atomic resolution STEM image was taken along the [111] direction. (D) A comparison plot between simulated and observed PXRD patterns. (E) The 3D atomic structure determined from three-dimensional electron diffraction (3DED) datasets viewed along the b axis. The six coordinated metal atoms are highlighted as square bipyramids in the structure. (F) A magnified image shows a five-coordinated metal atom in the structure, showing the triangular bipyramid shape view along the a, b, and c axis.

#### Li-O<sub>2</sub> battery performance studies

For the battery experiments, we used a Li metal foil anode, a porous glass-fiber separator, and SnIrS<sub>3.6</sub> as the cathode in 30  $\mu\text{L}$  of electrolyte blend comprised of 0.125M SnI<sub>2</sub> and 1M LiTFSI dissolved in DMSO and EMIM-BF<sub>4</sub> ionic liquid at a volumetric ratio of 9:1. The results in Figure XV.2.2 show the galvanostatic cycling of the battery at the current density of 0.5mA.cm<sup>-2</sup> with the capacity of 0.5mAh.cm<sup>-2</sup>. The charge potential of  $\sim 3.5\text{V}$  at the first cycle remained below 4.0V after 60 cycles. Figure XV.2.2 also shows a galvanostatic cycling result of the battery at a higher current density of 1 mA.cm<sup>-2</sup> where the discharge potential remained above 2.5V over 50 cycles and the charge potential is still 3.7V at the first cycle and gradually increased to 4.0V after the 50th cycle with the capacity of 0.5mAh.cm<sup>-2</sup>. At the same current density of 1mA.cm<sup>-2</sup>, we have performed the batteries with a higher capacity of 1mAh.cm<sup>-2</sup>. As shown in Figure 1, the battery was still able to run for up to 30 cycles with a discharge potential higher than 2.5V. The charge potential was 3.8V for the first cycle and increased to 3.9V after iteration cycles before reaching the cut-off potential of 4 V. Additional battery experiments were also performed with various current densities with and without SnI<sub>2</sub>. The charge profiles for the results without SnI<sub>2</sub> tend to go up in potential near the end of the charge. This indicates both that there is some Li<sub>2</sub>O<sub>2</sub> present in the discharge product for higher rates and the effectiveness of the SnI<sub>2</sub> as a redox mediator.

To identify the discharge products, we carried out various characterization techniques. Raman spectra for SnIrS<sub>3.6</sub> cathode after the 5th discharge cycle showed two peaks at 1125 cm<sup>-1</sup> and 1500 cm<sup>-1</sup> corresponding to LiO<sub>2</sub>. No other peaks were observed suggesting no other side products (e.g., LiOH, Li<sub>2</sub>CO<sub>3</sub>). Since LiO<sub>2</sub> is recognized as a metastable discharge product, we performed Raman spectroscopy over the cathode under resting

conditions for 1 and 5 days after discharge to test the stability of produced  $\text{LiO}_2$  structures. The results still show the presence of two peaks at  $1125\text{ cm}^{-1}$  and  $1500\text{ cm}^{-1}$  for  $\text{LiO}_2$ . This confirms the presence of  $\text{LiO}_2$  as a discharge product in  $\text{SnIrS}_3/\text{SnI}_2$ -based system in our Li- $\text{O}_2$  battery system.

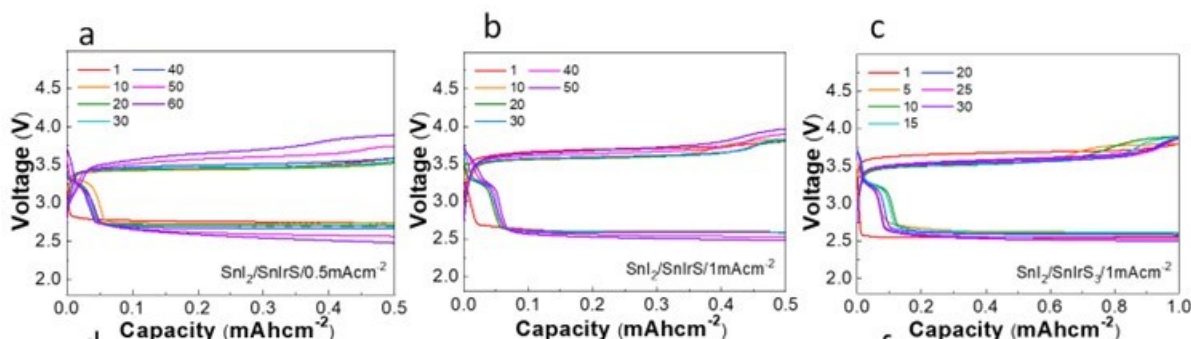


**Figure XV.2.2 Galvanostatic cycling results of Li-air cell with  $\text{SnIrS}_3$  cathodes and redox mediator of  $\text{SnI}_2$  at the current density of (A)  $0.5\text{ mA}\cdot\text{cm}^{-2}$  and (B)  $1\text{ mA}\cdot\text{cm}^{-2}$  at a limited capacity of  $0.5\text{ mAh}\cdot\text{cm}^{-2}$  (C) Galvanostatic cycling results of Li-air cell at the current density and capacity of  $1\text{ mA}\cdot\text{cm}^{-2}$  and  $1\text{ mAh}\cdot\text{cm}^{-2}$ , respectively.**

To further confirm and quantify the discharge products, we carried out in-situ differential electrochemical mass spectroscopy (DEMS) and analyzed the evolved gases during the charging process. It showed nearly one-electron per  $\text{O}_2$  reaction and can be associated with the decomposition of  $\text{LiO}_2$  during charge. There was no evidence for the side reactions involving gaseous products, as oxygen was the only detected species, and neither  $\text{CO}_2$  nor  $\text{H}_2\text{O}$  were detected. Finally, we carried out hydrolysis experiments to help quantify the amount of  $\text{LiO}_2$  and  $\text{Li}_2\text{O}_2$  produced by the  $\text{SnIrS}_{3.6}$  catalyst. This included titration using titanium oxysulfate solution  $\text{Ti(IV)OSO}_4$  to measure  $\text{Li}_2\text{O}_2$  and pH measurement to quantify the amount of  $\text{LiO}_2$ . Titration results indicated a small amount of  $\text{Li}_2\text{O}_2$  product for current densities up to  $0.5\text{ mA}\cdot\text{cm}^{-2}$ . Along with DEMS results, we conclude here that  $\text{LiO}_2$  is the predominant discharge product.

#### Surface structures of the new di-iridium sulfur-based catalyst

Computational studies of the structure of the bulk and surfaces of the new di-iridium sulfur-based catalyst were carried out for modeling of the reaction mechanisms on the surfaces in a Li- $\text{O}_2$  battery. Spin-polarized density functional (DFT) calculations were carried out to obtain the surface structures of  $\text{IrSnS}_{3.6}$ . The unit cell structure includes 9 Ir atoms, 9 Sn atoms, and 36 S atoms. We also simulated the XRD spectra of  $\text{IrSnS}_{3.6}$  bulk and the main peaks from the simulations are consistent with the experimental characterization. The density of states of  $\text{IrSnS}_{3.6}$  were obtained and continuous states near the Fermi level suggest  $\text{IrSnS}_{3.6}$  is conductive in nature and can act as an electrocatalyst for oxygen reduction and evolution reactions.

In order to find the most stable surface structures for  $\text{IrSnS}_{3.6}$ , we ran surface energy calculations for the (100), (010), (001), (110), (101), (011), and (111) facets with three terminations for each of them, i.e. Ir, Sn and S terminations. The surface energy of each terminated surface was calculated by referencing to the energy of bulk. The calculations were used to get trends and we did not consider asymmetry in the vertical direction of the slab. The calculated surface energies are plotted in Figure XV.2.3A, which suggests that the Sn terminated (100) surface, as shown in Figure XV.2.3B, has the lowest surface energy, which will be treated as the most stable surface of the investigated surfaces. The Ir terminated (100) surface shown in Figure XV.2.3C is the second most stable one with only an energy difference of  $0.1\text{ eV}$  compared to the most stable Sn terminated (100) surface. Thus, both Sn and Ir terminated (100) surfaces will be tested to investigate the reaction mechanisms for  $\text{LiO}_2$  and  $\text{Li}_2\text{O}_2$  formation. Due to the asymmetry of the Sn or Ir terminated (100) surfaces, we calculated four surfaces for the discharge reactions on the cathode, including Sn terminated and Ir terminated (100) surfaces and the bottom surfaces (Figure XV.2.3D and Figure XV.2.3E).

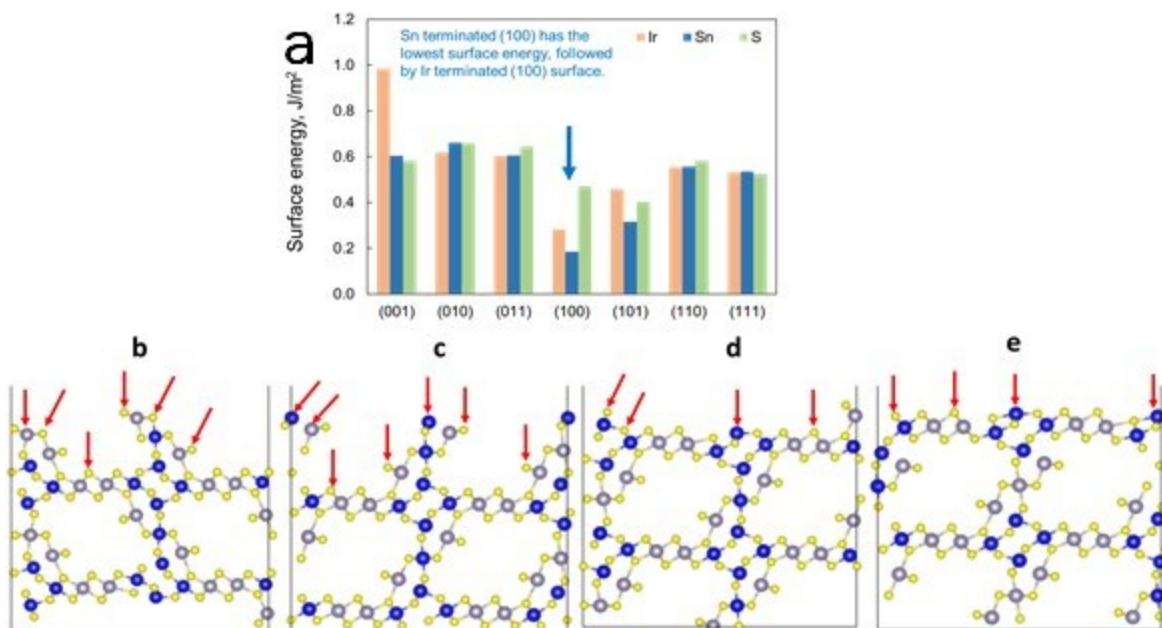


**Figure XV.2.3 (A)** The surface energies of different facets with different terminations. The blue arrow points to the most stable Sn terminated (100) surface. The side views of (B) Sn terminated, (C) Ir terminated, (D) bottom of Sn terminated, (E) bottom of Ir terminated (100) surfaces. The Ir, Sn, and S atoms are in blue, light purple, and yellow, respectively. The black lines represent the periodic boundaries. The red arrows point to possible O<sub>2</sub> adsorption sites to be investigated.

We also constructed the interface of LiO<sub>2</sub> and IrSnS<sub>3.6</sub> to investigate the lattice mismatch and interfacial surface energy between IrSnS<sub>3.6</sub> and LiO<sub>2</sub>. We utilized an orthorhombic LiO<sub>2</sub> bulk structure within Pnnm symmetry. The lattice constants converged to 2.96 Å, 3.94 Å, and 4.92 Å. A (1x5) LiO<sub>2</sub>(101) supercell and a (1x1) IrSnS<sub>3.6</sub>(100) supercell are used to build the LiO<sub>2</sub>-IrSnS<sub>3.6</sub> interface. The LiO<sub>2</sub>(101) surface was chosen because of the low surface energy and its orthogonal lattices, while IrSnS<sub>3.6</sub>(100) is the most stable surface according to surface energy calculations in Figure XV.2.3A. The lattice mismatch results indicate that the templating mechanism likely will not work for LiO<sub>2</sub> growth. As a result we explored another new mechanism for lithium superoxide growth as explained below.

#### DFT studies of reaction mechanism

We used density functional theory (DFT) to study the reaction mechanism occurring on the surfaces of the new IrSnS<sub>3.6</sub> catalyst used in the Li-O<sub>2</sub> batteries. The calculations reveal a new mechanism for formation of LiO<sub>2</sub> that involves a di-iridium sulfur bridge site where O<sub>2</sub> is strongly bound for oxygen reduction and results in strongly bound LiO<sub>2</sub> preventing disproportionation from being energetically favorable.

We investigated by DFT the reaction pathways for LiO<sub>2</sub> formation through one (Li<sup>+</sup> + e<sup>-</sup>) transfer and Li<sub>2</sub>O<sub>2</sub> production via either LiO<sub>2</sub> disproportionation or the second (Li<sup>+</sup> + e<sup>-</sup>) transfer to LiO<sub>2</sub> on four surfaces of IrSnS<sub>3.6</sub>. The reaction free energies were calculated to determine whether LiO<sub>2</sub> or Li<sub>2</sub>O<sub>2</sub> formation will be favored. The adsorption energies of O<sub>2</sub>, LiO<sub>2</sub>, and Li<sub>2</sub>O<sub>2</sub> were calculated on both Sn and Ir terminated IrSnS<sub>3.6</sub>(100) surfaces to get the free energy of each step. On an Ir-terminated IrSnS<sub>3.6</sub>(100) surface, O<sub>2</sub> binds on a di-iridium sulfur bridge (DISB) site with a free energy of -1.85 eV (see Figure XV.2.4A). Due to the strong adsorption the O<sub>2</sub> bond length increases from 1.23 Angstroms in the gas phase molecule to 1.38 Angstroms in the adsorbed molecule. The most stable adsorption geometry of LiO<sub>2</sub> indicate that the DISB sites are very favorable adsorption sites for this species as well (see Figure XV.2.4B). A close-up structure of O<sub>2</sub> on the di-iridium sulfur bridge site is shown in Figure XV.2.4D. A close-up structure of LiO<sub>2</sub> on the site is shown in Figure XV.2.4E from a different perspective. The formation of LiO<sub>2</sub> is very exothermic with a reaction-free

energy of -3.45 eV from adsorbed  $O_2$  on an Ir-terminated (100) surface. Due to the strong  $LiO_2$  adsorption at the DISB site,  $Li_2O_2$  formation (Figure XV.2.4C) is not favorable either by  $LiO_2$  disproportionation, which is uphill by 3.51 eV, or by a subsequent  $(Li^+ + e^-)$  transfer reaction to form  $Li_2O_2$ , which is slightly uphill as shown in the energy profile in Figure XV.2.4F. A schematic illustrating the involvement of the di-iridium sulfur bridge site in the  $LiO_2$  reaction is shown in Figure XV.2.4G.

The surface reaction calculations on  $IrSnS_{3.6}(100)$  surfaces demonstrate that the formation of  $Li_2O_2$  via  $LiO_2$  disproportionation is not favorable on three of the four surfaces, and thus the reaction is likely to stop at  $LiO_2$  on those surfaces. The fourth surface is likely to be passivated as  $O_2$  dissociates. The disproportionation to  $Li_2O_2$  is unfavorable because of the strong binding of  $LiO_2$  on the di-iridium sulfur bridge (DISB) sites of  $IrSnS_{3.6}$ . Since the surface sites will likely all get covered with  $LiO_2$ , the continued growth of  $LiO_2$  in the absence of open DISB sites probably occurs because of the formation of an  $LiO_2$  structure that promotes continued  $LiO_2$  growth. We have investigated the reason for the reactivity of the DISB site that suppresses  $LiO_2$  disproportionation. Ir metal is known to react strongly with  $O_2$  and cause dissociation. However, the d-band center of Ir in  $IrSnS_{3.6}$  is -1.67 eV, which is higher than metallic Ir (-2.11 eV), so that non-dissociative  $O_2$  adsorption does not occur on the DISB sites. The effectiveness of the DISB sites for  $LiO_2$  growth over  $Li_2O_2$  growth probably can be attributed to the Sabatier principle with appropriate  $O_2$  binding strength on the  $IrSnS_{3.6}$  surface instead of too strong  $O_2$  binding, which would result in dissociative adsorption, and too weak  $O_2$  (and  $LiO_2$ ) binding, which would result in the disproportionation of  $LiO_2$  to  $Li_2O_2$ .

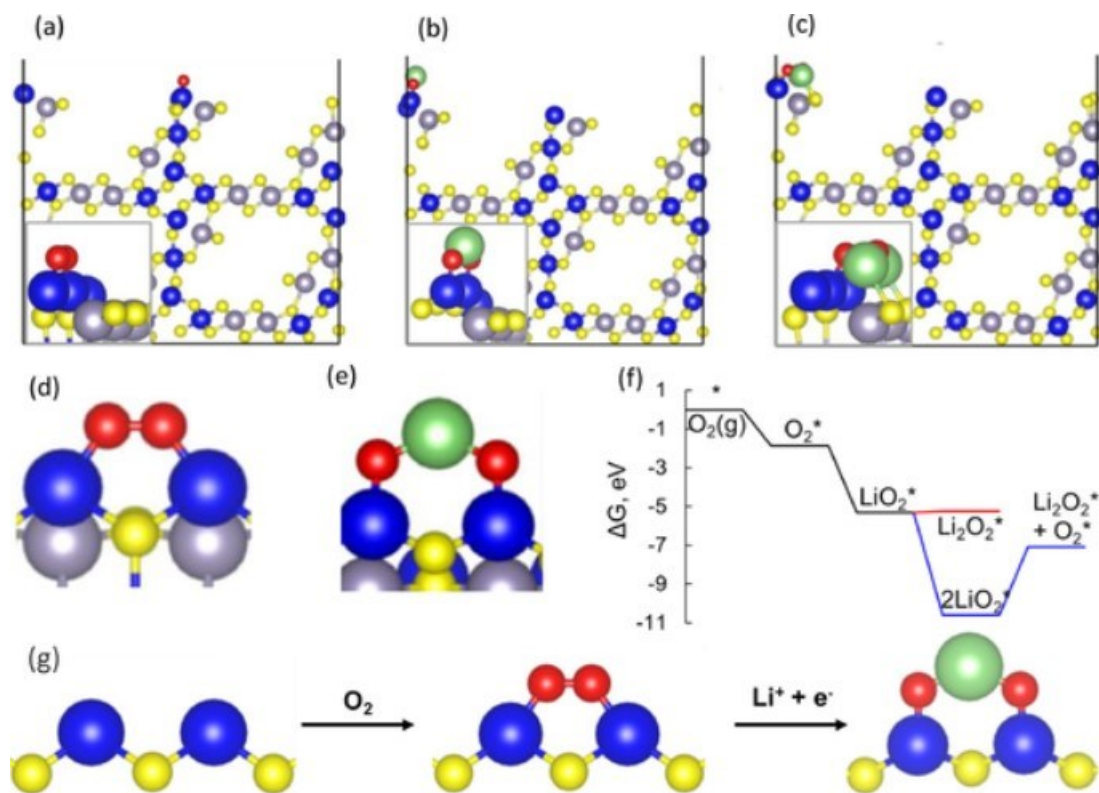


Figure XV.2.4 The most favorable adsorption structure of (A)  $O_2$ , (B)  $LiO_2$ , and (C)  $Li_2O_2$  on the Ir terminated  $IrSnS_{3.6}(100)$  surface. Close-up structure of  $O_2$  in (A) on the di-iridium sulfur bridge site is shown in (D). Close-up structure of  $LiO_2$  in (B) on this same is shown in (E) from a different perspective. (f) Reaction free energies plot for  $LiO_2$  formation and  $Li_2O_2$  formation on the Ir terminated  $IrSnS_{3.6}(100)$  surface. (G) Schematic illustrating the involvement of the di-iridium sulfur bridge site in the  $LiO_2$  reaction. The Ir, Sn, S, O, and Li atoms are in blue, light purple, yellow, red, and green, respectively. Black lines in (A)–(C) are the periodic boundaries. The blue line in (f) represents the  $LiO_2$  disproportionation reaction pathway, while the red line shows a  $(Li^+ + e^-)$  transfer to  $LiO_2$  to form  $Li_2O_2$ .

## Conclusions

We synthesized a new class of catalysts based on bi- and tri-metallic systems with dichalcogenides for use as catalyst in Li-O<sub>2</sub> batteries including porous dichalcogenides with bridging transition metal active sites. Such alloys should have high entropy and be more likely to withstand higher rates desired in a Li-O<sub>2</sub> battery. The studies reported here are on powders of SnIrS<sub>3.6</sub> crystals synthesized by the chemical vapor transport. A liquid-phase exfoliation method was used to exfoliate SnIrS<sub>3.6</sub> into nanoflakes. The use of this new catalyst results in a Li-Air battery system that operates under high current rates (up to 1 mAcm<sup>-2</sup>) with LiO<sub>2</sub> as the primary discharge product instead of the commonly reported Li<sub>2</sub>O<sub>2</sub>. This LiO<sub>2</sub> based battery at high rates is through a combination of an as-synthesized new one-dimensional (1D) transition metal trichalcogenide mid-entropy alloy of SnIrS<sub>3.6</sub> as a cathode catalyst and an electrolyte blend with a SnI<sub>2</sub> bi-functional additive. The SnIrS<sub>3.6</sub> has a microporous structure composed of six- and five-coordinated metal atoms, forming octahedral and triangular bipyramids which has not been observed in other layered chalcogenide materials. DFT calculations were used to determine the lowest energy surfaces for this material, which were then used to study possible reaction mechanisms. The calculations reveal that the SnIrS<sub>3.6</sub> structure can result in LiO<sub>2</sub> formation through di-iridium sulfur bridge active sites that results in strong binding of O<sub>2</sub> and LiO<sub>2</sub> preventing disproportionation to Li<sub>2</sub>O<sub>2</sub>.

## Key Publications

1. “Lithium superoxide-based high rate Li-Air batteries enabled by Di-iridium sulfur bridge active sites” Chengji Zhang, Shuxi Wang, Taimin Yang, Nannan Shan, Sachin Kumar Singh, Ahmad Jaradat, Musawenkosi K Ncube, Paul Redfern, Arunkumar Subramanian, Zhehao Huang, Anh T Ngo, Larry A Curtiss, Amin Salehi-kKhojin, *Energy Storage Materials*, 60, 102844 (2023) [doi.org/10.1016/j.ensm.2023.102844](https://doi.org/10.1016/j.ensm.2023.102844)
2. A high-rate lithium-air battery enabled by a MnO<sub>2</sub> based colloidal electrolyte, Sina Rastegar, Zahra Hemmat, Sachin Kumar Singh, Naveen Dandu, Chengji Zhang, Alireza Ahmadiparidari, Tomas Rojas, Leily Majidi, Shuxi Wang, Ahmad Jaradat, Rajeev Assary, Paul Redfern, Sanja Tepavcevic, Arunkumar Subramanian, Anh T. Ngo, Larry A. Curtiss, Amin Salehi-Khojin, *ACS Nano* 16, 11, 18187–18199 (2022) <https://doi.org/10.1021/acsnano.2c05305>

## Acknowledgements

Other participants who have contributed to this project include Nannan Shan (ANL/Purdue), Arunkumar Subramanian (UIC), Paul Redfern (ANL), Chengji Zhang (UIC), Musawenkosi K Ncube (UIC/ANL)



## XV.3 Development of a High-Rate Lithium-Air Battery Using a Gaseous CO<sub>2</sub> Reactant (UIC)

### Amin Salehi, Principal Investigator

University of Illinois at Chicago  
 Department of Mechanical and Industrial Engineering  
 Chicago, IL 60607  
 Email: [salehikh@uic.edu](mailto:salehikh@uic.edu)

### Anh T. Ngo, Co-Principal Investigator

University of Illinois at Chicago  
 Department of Chemical Engineering  
 Chicago, IL 60607  
 Email: [ahnngo@uic.edu](mailto:ahnngo@uic.edu)

### Vikas Berry, Co-Principal Investigator

University of Illinois at Chicago  
 Department of Chemical Engineering  
 Chicago, IL 60607  
 Email: [vikasb@uic.edu](mailto:vikasb@uic.edu)

### Haiyan Croft, DOE Technology Development Manager

U.S. Department of Energy  
 E-mail: [Haiyan.Croft@ee.doe.gov](mailto:Haiyan.Croft@ee.doe.gov)

Start Date: October 1, 2021  
 Project Funding: \$1,500,000

End Date: December 31, 2022  
 DOE share: \$1,500,000

Non-DOE share: \$0

### Project Introduction

Li-air batteries are considered as a potential alternative to Li-ion batteries for transportation applications due to their high theoretical specific energy. Most work in this area focuses on use of O<sub>2</sub> as the reactant. However, newer concepts for using gaseous reactants (such as CO<sub>2</sub>, which has a theoretical specific energy density of 1,876 Wh/kg) provide opportunities for further exploration. This project will produce a thorough understanding of key chemical and electronic parameters that govern the operation of Li-CO<sub>2</sub> batteries in realistic conditions. Achieving the project objectives will generate a library of fundamental properties of TMD- and IL-based electrolytes with the most promise for Li-CO<sub>2</sub> battery applications. The methodologies employed, and the insight generated, will also be valuable beyond advancing the field of Li-CO<sub>2</sub> batteries.

### Objectives

The main objective of this project is to develop a novel strategy to enable operation of Li-CO<sub>2</sub> batteries at high-capacity high-rate with a long-cycle-life. The experiments will be performed in both Swagelok and pouch cells. In the former case, the team will use: (1) a novel co-catalyst system comprised of inexpensive and earth-abundant transition metal dichalcogenide (TMD) materials that work in synergy with ionic liquid (IL) – based electrolytes to enhance efficiency of reactions during discharge and charge processes, (2) a solution-based catalyst (redox mediator, or RM) to reduce charge overpotential and increase energy efficiency of the battery, (3) high-porosity cathode electrodes to increase electrode surface area, gas permeability, stability, electrical conductivity, and lifetime of battery operation, and (4) solid-electrolyte interphase layer to protect the anode against oxidation without affecting the ionic transport of Li<sup>+</sup> species in the system. At the pouch-cell level, the team will design and construct a stackable pouch cell to deliver a capacity of > 200 mAh.

## Approach

The above targets will be achieved through an integrated approach based on materials synthesis, testing, characterization, analysis, and computation. The team will synthesize catalysts and test them in cells along with developing new electrolytes and additives. These cathode materials with new electrolyte blends and additives will work in synergy to reduce charge potentials and increase battery stability. Density functional theory (DFT) and *ab initio* molecular dynamics simulations will be performed to understand battery operation and make predictions of new materials for the Li-CO<sub>2</sub> battery. The out-year goals are to find novel two-dimensional catalysts and IL-based electrolytes that give high capacities and long cycle life in a CO<sub>2</sub> atmosphere. The following were the milestones:

- Testing and analysis of four synthesized alloy catalysts in a Swagelok cell with CO<sub>2</sub> as reactant. (Completed)
- Stability of TMD alloys in presence of electrolyte. (Completed).
- Evaluation of four solvent blends for use with catalysts. (Completed).
- Evaluation of four RMs for use with catalysts. (Completed)
- Characterization of a Li-CO<sub>2</sub> battery using a selected TMD alloys by experiment and computations (Completed).
- Testing and analysis of other synthesized alloy catalysts in a Swagelok cell with CO<sub>2</sub> as reactant (Completed).
- Optimization of anode SEI layer (Completed).
- Stability analysis of redox mediators for longer lifetimes (Completed).

## Results

In the first quarter, we reported the findings on a new catalytic system based on 2D based medium-entropy alloys as cathode catalysts comprised of S and Te chalcogenides that work in synergy with an electrolyte blend of ionic liquid (IL) of 1-Ethyl-3-methylimidazolium tetrafluoroborate (EMIM-BF<sub>4</sub>) and dimethyl sulfoxide (DMSO) with the volumetric ratio of 1:9, ZnI<sub>2</sub> redox mediator, lithium bis(trifluoromethanesulfonyl)imide (LiTFSI) salt. It was uncovered that: (i) the nature of charge transfer for both CO<sub>2</sub>RR and CO<sub>2</sub>ER is similar. Usually, the kinetics of reaction during CO<sub>2</sub>ER is a sluggish process and charge transfer in CO<sub>2</sub>ER is much slower than CO<sub>2</sub>RR. This is not the case in this new system; (ii) the role of chalcogen elements on the electronic and catalytic properties of the catalyst structures is significant where the catalyst with Te chalcogen shows much improved catalytic activities compared to that with S chalcogen; (iii) the role of ionic liquid electrolyte was found to be deterministic in the basic reactions occurring during discharge and charge resulting in much improved battery cycling. These three features are key to operate the battery at high rates.

Linear sweep voltammetry (LSV) experiments were performed on both catalysts within potential range of 2.4-4.5 V to determine the electrochemical activity of catalysts and in particular the role of chalcogenides (S and Te) on CO<sub>2</sub>RR and CO<sub>2</sub>ER. Figure XV.3.1A illustrates the CO<sub>2</sub>RR results with a current density of 23.5 mA/cm<sup>2</sup> for Te based catalyst compared to 15.4 mA/cm<sup>2</sup> for S based catalyst at the applied potential of 2.4 V. Figure XV.3.1B shows CO<sub>2</sub>ER results which indicate the CO<sub>2</sub>ER current density of 23.7 mA/cm<sup>2</sup> for Te based catalyst compared to 13.1 mA/cm<sup>2</sup> for S based catalyst at 4.5 V. These results are much higher than those obtained for Pt and Au nanoparticles (NPs) under identical experimental conditions. Moreover, the results indicate that Te based structure shows 1.5- and 1.8-times higher activities for CO<sub>2</sub>RR and CO<sub>2</sub>ER, respectively. Figure XV.3.1C-D depicts the charge transfer resistance ( $R_{ct}$ ) of the catalysts during CO<sub>2</sub>RR and CO<sub>2</sub>ER at two different overpotentials measured by electrochemical impedance spectroscopy (EIS). Results in Figure XV.3.1C indicate small  $R_{ct}$  for Te based catalyst with values of 48.93 ohms and 50.53 ohms at overpotentials of 500 mV and 1000 mV, respectively, compared to 108.53 ohms and 144.84 ohms for S based catalyst at same overpotentials during CO<sub>2</sub>RR. EIS results during CO<sub>2</sub>ER (Figure XV.3.1D) shows the  $R_{ct}$  values of 50.21 Ohms and 58.43 Ohms at the overpotentials of 500 mV to 1000 mV for Te based catalysts compared to 129 ohms to 164 ohms for S based catalyst.

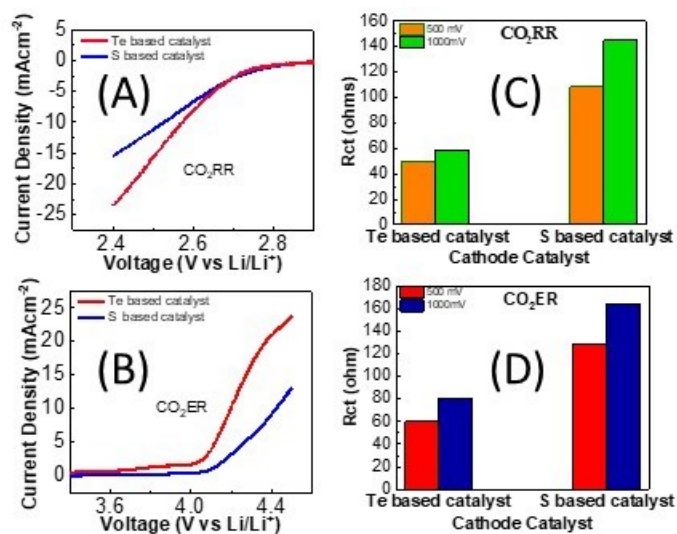


**Figure XV.3.1 (A-B) Linear sweep voltammetry results of Te and S based catalysts during: (A) CO<sub>2</sub>RR and (B) CO<sub>2</sub>ER. (C-D) EIS measurements for both catalysts at two different overpotentials during: (C) CO<sub>2</sub>RR and (D) CO<sub>2</sub>ER.**

A unique feature of these catalysts is that the current density and  $R_{ct}$  values for both CO<sub>2</sub>RR and CO<sub>2</sub>ER are similar as shown in Figure XV.3.1A-D. Usually, these numbers are much smaller in CO<sub>2</sub>ER as we observed for Pt NPs and Au NPs. The sluggish kinetics during evolution reaction was also observed in Li-O<sub>2</sub> chemistry which is attributed to the diabatic charge transfer process. However, results in Figure XV.3.1A-D suggest that the nature of charge transfer during CO<sub>2</sub>RR and CO<sub>2</sub>ER in both catalysts is similar, resulting in much improved electrochemical activity during CO<sub>2</sub>ER.

To study the contribution of ionic liquid on the battery performance, we first carried out LSV experiments with different IL to DMSO ratios (1:9, 4:6 and 9:1) using Te based catalyst during CO<sub>2</sub>RR/CO<sub>2</sub>ER and results are shown in Figure XV.3.2A-B. The current density with 1:9 IL:DMSO is 23.2 mA/cm<sup>2</sup> at 2.4 V during CO<sub>2</sub>RR which is increased to 30.3 mA/cm<sup>2</sup> with 4:6 ratio and then decreased to 8.4 mA/cm<sup>2</sup> with 9:1 ratio (Figure XV.3.2A). Similarly, at 4.5 V during CO<sub>2</sub>ER, the current density is increased from 23.7 mA/cm<sup>2</sup> with 1:9 IL:DMSO ratio to 33.2 mA/cm<sup>2</sup> with 4:6 ratio then decreased to 12 mA/cm<sup>2</sup> with 9:1 ratio (Figure XV.3.2B). Figure XV.3.2C-D depicts the  $R_{ct}$  results at two different overpotentials (500 mV and 1000 mV) and three IL:DMSO ratios. For instance, Figure XV.3.2C reveals that the IL:DMSO ratio of 6:4 gives the smallest  $R_{ct}$  of 48.93 ohms at the overpotential of 500 mV compared to 57.32 ohms at 9:1 (IL: DMSO) ratio and 140.2 ohms at the ratio of 1:9. EIS results during CO<sub>2</sub>ER (Figure XV.3.2D) also shows the  $R_{ct}$  values of 50.21 Ohms for 6:4 ratio compared to 60 ohms and 160 ohms for ratios of 1:9 and 9:1, respectively. These set of results suggest the ratio of 4:6 IL:DMSO produces the best LSV and  $R_{ct}$  results for both reaction compared to ratios 1:9 and 9:1. It is also suggest that the nature of charge transfer is similar for both reactions occurring during discharge and charge process.

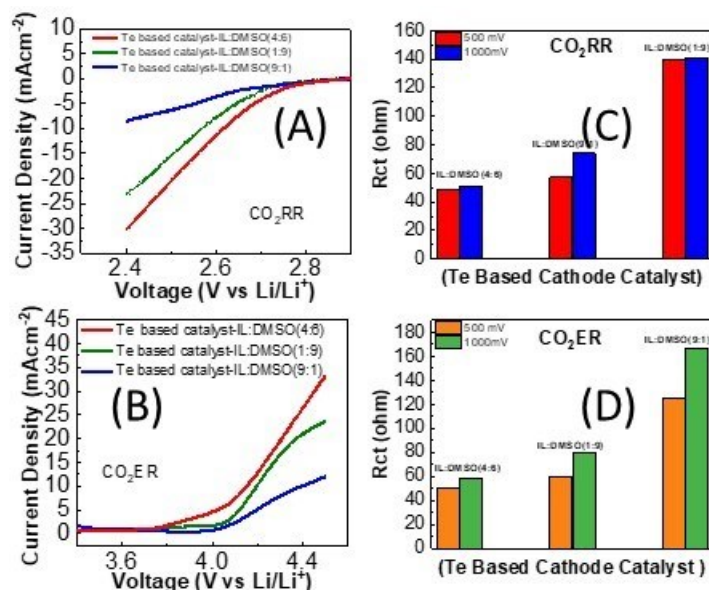


**Figure XV.3.2 (A-B)** Linear sweep voltammetry results of Te and S based catalysts at three different IL:DMSO ratios during: (A) CO<sub>2</sub>RR and (B) CO<sub>2</sub>ER. (C-D) EIS measurements for three different IL/DMSO ratios for both catalysts at two different overpotentials during: (C) CO<sub>2</sub>RR and (D) CO<sub>2</sub>ER.

Figure XV.3.3 shows cycling stability results of batteries at different IL:DMSO ratios. Consistent with the results of LSV and R<sub>ct</sub> experiments, the highest cyclability (220 cycles) was obtained at IL: DMSO ratio of 4:6 followed by 150 cycles at the ratio of 1:9 and a few cycles at 9:1 ratio. An early failure of the battery with IL:DMSO ratio of 9:1 is attributed to low salt solubility resulting in decreased electrolyte conductivity as well as high viscosity of the electrolyte. Higher cyclability at 4:6 ratio of IL:DMSO is attributed to high CO<sub>2</sub> solubility in the electrolyte which is discussed below.

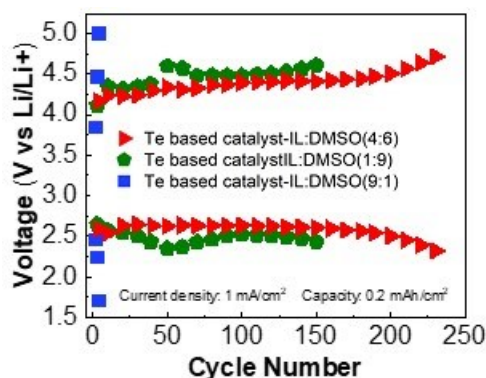


**Figure XV.3.3** Cycling results for Te based catalyst at different DMSO:IL ratios.

In the second quarter, density functional calculations were carried out on Sb<sub>0.67</sub>Bi<sub>1.33</sub>Te<sub>3</sub> and Sb<sub>0.67</sub>Bi<sub>1.33</sub>S<sub>3</sub> to help understand the experimental results for their use as catalysts in the Li-CO<sub>2</sub> batteries. Bulk Sb<sub>0.67</sub>Bi<sub>1.33</sub>Te<sub>3</sub> and Sb<sub>0.67</sub>Bi<sub>1.33</sub>S<sub>3</sub> structures were built based on the structures of Bi<sub>2</sub>Te<sub>3</sub>, Bi<sub>2</sub>S<sub>3</sub>, Sb<sub>2</sub>Te<sub>3</sub> and Sb<sub>2</sub>S<sub>3</sub> molecules from the Materials Project. Different possible structures were optimized and the most favorable (i.e. with the lowest optimization energy) ones found were based on Sb<sub>2</sub>Te<sub>3</sub> and Bi<sub>2</sub>S<sub>3</sub>. Density of state calculations were then carried out to determine the band gaps for these bulk structures. The density of states is shown in Figure XV.3.4A and B. The band gaps are approximately 0.32 eV for Sb<sub>0.67</sub>Bi<sub>1.33</sub>Te<sub>3</sub> and 1.20 eV for Sb<sub>0.67</sub>Bi<sub>1.33</sub>S<sub>3</sub>. These values lie between the theoretical band gaps for the base structures Sb<sub>2</sub>Te<sub>3</sub> and Bi<sub>2</sub>S<sub>3</sub>. Comparing the band gaps of the two bulk structures, we conclude Sb<sub>0.67</sub>Bi<sub>1.33</sub>Te<sub>3</sub> is more likely to exhibit semiconductor

properties than  $\text{Sb}_{0.67}\text{Bi}_{1.33}\text{S}_3$ , consistent with its performance as a catalyst for the Li-CO<sub>2</sub> battery found in our studies.

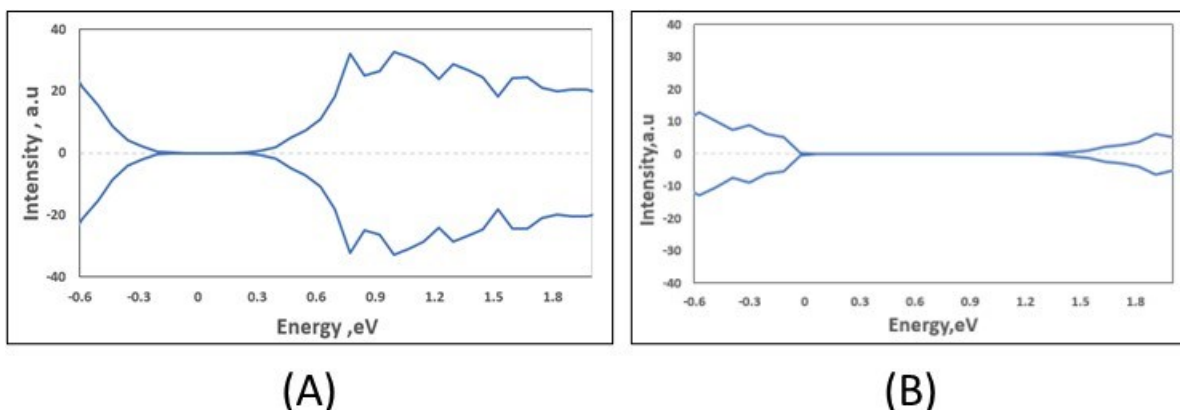


Figure XV.3.4 Band gaps determined from density of state calculations (A)  $\text{SbBiTe}_3$  (B)  $\text{SbBiS}_3$

DFT calculations were also used to investigate the surface energies of  $\text{Sb}_{0.67}\text{Bi}_{1.33}\text{Te}_3$  for use in selecting surfaces for studying the  $\text{Li}_2\text{CO}_3/\text{C}$  formation mechanism. The energies of the 001, 010, 015, 100, 101, 102, 110 and 111 facets with Bi, Sb and Te terminations were calculated. The surface energies were calculated using  $\sigma = \frac{1}{2A}(E_{\text{slab}} - n_{\text{slab}}E_{\text{bulk}})$  where  $A$  is the area of the surface,  $E_{\text{slab}}$  is the energy of the slab,  $n_{\text{slab}}$  is the number of bulk units in the surface slab and  $E_{\text{bulk}}$  is the energy of one unit in the bulk. The calculated surface energies are given in Figure XV.3.5. The Te-terminated 001, 015, and 110 surfaces had the lowest surface energies of 0.00272 eV/A<sup>2</sup>, 0.01156 eV/A<sup>2</sup> and 0.01833 eV/A<sup>2</sup>, respectively.

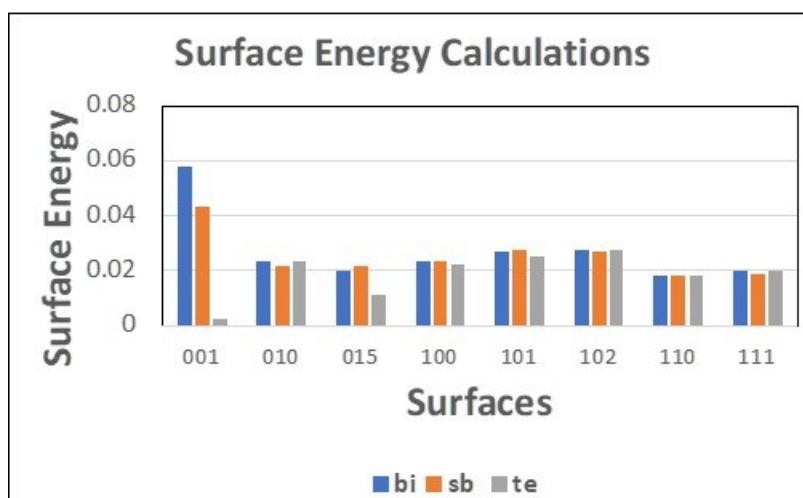


Figure XV.3.5 24 surface energies with different terminations (including 001, 010, 015, 100, 101, 102, 110, 111 facets).

We explored different possible reaction mechanisms for  $\text{Li}_2\text{CO}_3/\text{C}$  formation using the various lowest energy surfaces. The Gibbs free energy ( $G$ ) for the different steps were calculated using  $G = E + \text{ZPE} + \int_0^T C_p dT - T^*S$  where ZPE (zero-point energy),  $S$  (entropy at temperature  $T$ ) and  $C_p$  (heat capacity) are the corrections to the electronic energy ( $E$ ). The most favorable reaction pathway located is on a (110) Sb-terminated surface of  $\text{Sb}_{0.67}\text{Bi}_{1.33}\text{Te}_3$ . The structures in the reaction pathway are shown in Figure XV.3.6. The Te is the most stable adsorption site for the  $\text{LiCO}_2$  and  $\text{Li}_2\text{CO}_2$  intermediates as shown in Figure 3. The binding is between Li and Te. The  $\text{Li}_2\text{CO}_2$  and  $\text{CO}_2$  further react to form  $\text{Li}_2\text{CO}_3$  and  $\text{CO}$ , which is a favorable downhill step with a free energy of -1.7 eV. The formation of carbon is explained by the reaction of  $\text{CO}_2$  and  $\text{CO}$ , an endergonic step

(2.8 eV) that also produces  $\text{CO}_3$  on the surface. The C was observed to bind on the surface with a Te-C bond while oxygen seems to have a preference for Bi. Therefore, the optimized adsorption geometries for CO and  $\text{CO}_3$  involve a Bi-O bond. A potential was applied to level up the electrochemical step i.e., the formation of  $\text{LiCO}_2$  from  $(\text{Li}^+ + e) + \text{CO}_2$ . This occurs at a potential below 2.3 V versus  $\text{Li}/\text{Li}^+$ , which is similar to the reported experimental discharge potential.

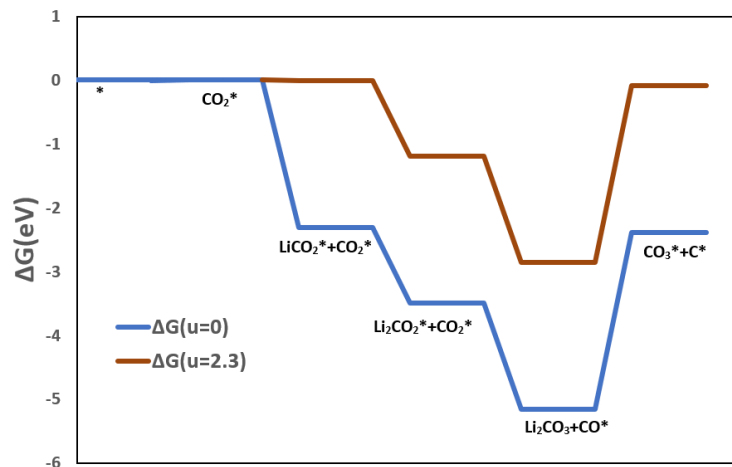


Figure XV.3.6 A plot of the elementary reactions for the discharge mechanism of  $\text{Li}_2\text{CO}_3$  and C.

In the third quarter, we performed additional control experiments and detailed characterization of cathode and anode materials. First, in order to characterize the discharge products, a wide range of characterization techniques including Transmission Electron Microscopy (TEM), Electron Energy Loss Spectroscopy (EELS), SEM, Differential Electrochemical Mass Spectroscopy (DEMS) and Raman spectroscopy were utilized (Figure XV.3.7). Figure XV.3.7A shows that  $\text{Sb}_{0.67}\text{Bi}_{1.33}\text{Te}_3$  flake is surrounded with the discharged products of  $\text{Li}_2\text{CO}_3$  and amorphous carbon (a-C), marked by yellow dashed lines. A high-resolution image of  $\text{Li}_2\text{CO}_3$  as shown in Figure XV.3.7B, displays a crystalline structure with lattice spacing of 4.2 Å and 2.3 Å. The lattice spacing measured here matches the values reported for monoclinic  $\text{Li}_2\text{CO}_3$  in the Materials Project (mp-3054). A Fast Fourier Transform (FFT) of the  $\text{Li}_2\text{CO}_3$  is shown in Figure XV.3.7B (inset) and the FFT pattern obtained is indexed as monoclinic  $\text{Li}_2\text{CO}_3$  as well. The EELS spectra of the discharged products contain sharp Li K-, C K- and O K- edges confirming the presence of these elements. In fact, the EELS dataset is found to match well with the previously reported dataset for  $\text{Li}_2\text{CO}_3$ . The EELS spectra taken from the carbon (C) region is shown in Figure XV.3.7C which is consistent with the EELS dataset reported for amorphous carbon. Figure XV.3.7D shows SEM results of the cathode after discharge illustrating the presence of discharge products. To elucidate the product formation mechanism, Figure XV.3.7E presents the DEMS results revealing that the  $e^-/\text{CO}_2$  for charge process equals to 4.04 which is consistent with formation  $\text{Li}_2\text{CO}_3$  from a four-electron reaction. To verify the catalyst structural integrity while cycling, we performed Raman spectroscopy on cathode before and after 100 cycles. Results shown in Figure XV.3.7F illustrate the same peaks before and after cycling indicating the catalyst could sustain high current rate at long cycling. These peaks are located at  $66\text{ cm}^{-1}$ ,  $108\text{ cm}^{-1}$  and  $155\text{ cm}^{-1}$ , and can be assigned to the  $A_{1g}^1$ ,  $E_g^2$ , and  $A_{1g}^2$  modes, respectively.

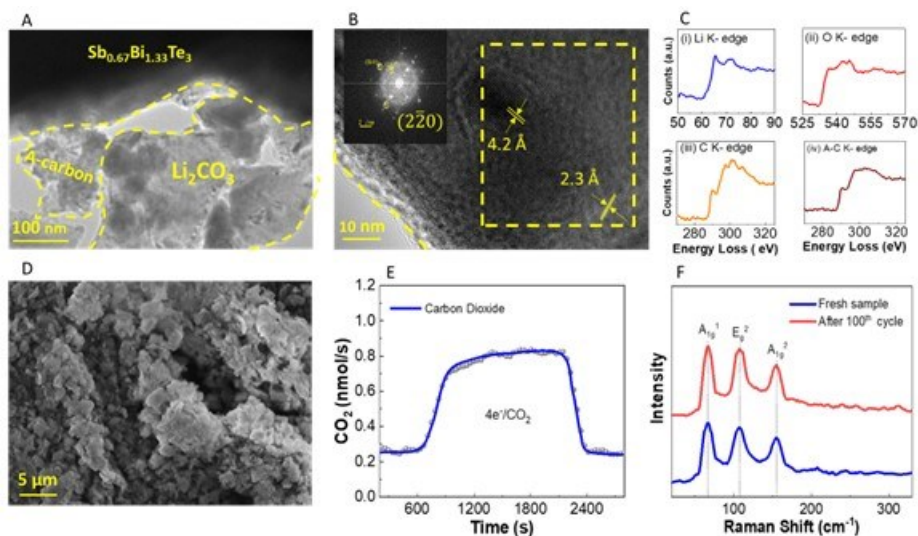


Figure XV.3.7 (A-B) Low- and high-resolution TEM images of discharged cathode showing  $\text{Li}_2\text{CO}_3$  and C deposited on a  $\text{Sb}_{0.67}\text{Bi}_{1.33}\text{Te}_3$  cathode. (C) EELS spectra of  $\text{Li}_2\text{CO}_3$  and C on the cathode surface after its 5<sup>th</sup> discharge cycle; (i) Li K-edge, (ii) O K-edge, (iii) C K-edge, and (iv) A-C K-edge. (D) SEM image of cathode after 5<sup>th</sup> discharge cycle. (E)  $\text{CO}_2$  evolution results of a cell charged at current density of  $1 \text{ mA/cm}^2$  using DEMS. (F) Stability of the  $\text{Sb}_{0.67}\text{Bi}_{1.33}\text{Te}_3$  catalyst after 100 cycles.

The structure of the electrolyte/catalyst interface was investigated using Ab Initio Molecular Dynamics (AIMD). The (110) Se terminated surface of  $\text{Sb}_{0.67}\text{Bi}_{1.33}\text{Te}_3$  was used for these calculations. The results are shown in Figure XV.3.8. Increasing the ionic liquid content to 40% resulted in  $\text{CO}_2$  being close to the catalyst surface (Figure XV.3.8) and at 10% ionic liquid content the  $\text{CO}_2$  is located away from the surface (Figure XV.3.8). These results help to explain the improved performance of the Li- $\text{CO}_2$  battery with the larger volume ratio of ionic liquid, i.e. its presence near the surface helps to attract more  $\text{CO}_2$  molecules to the surface where it can participate in the electrochemical reaction.

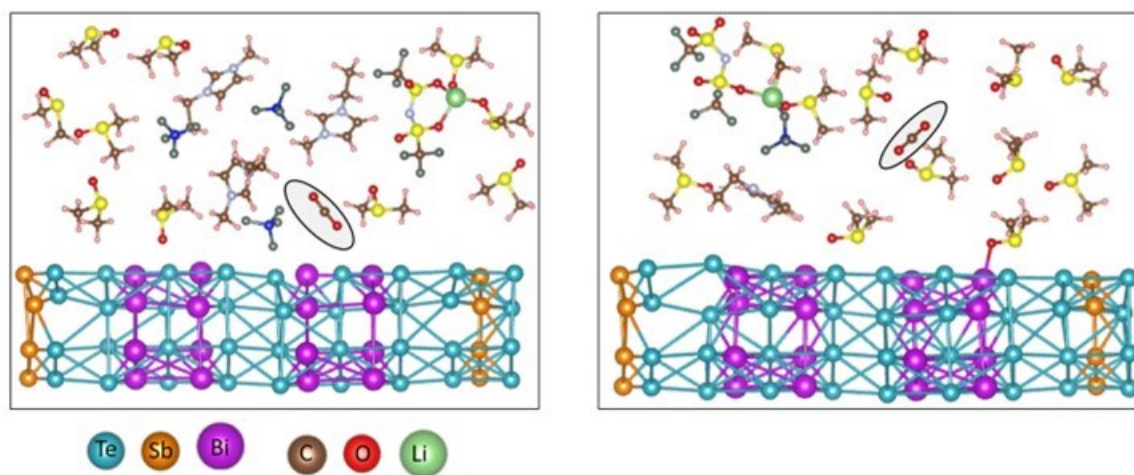
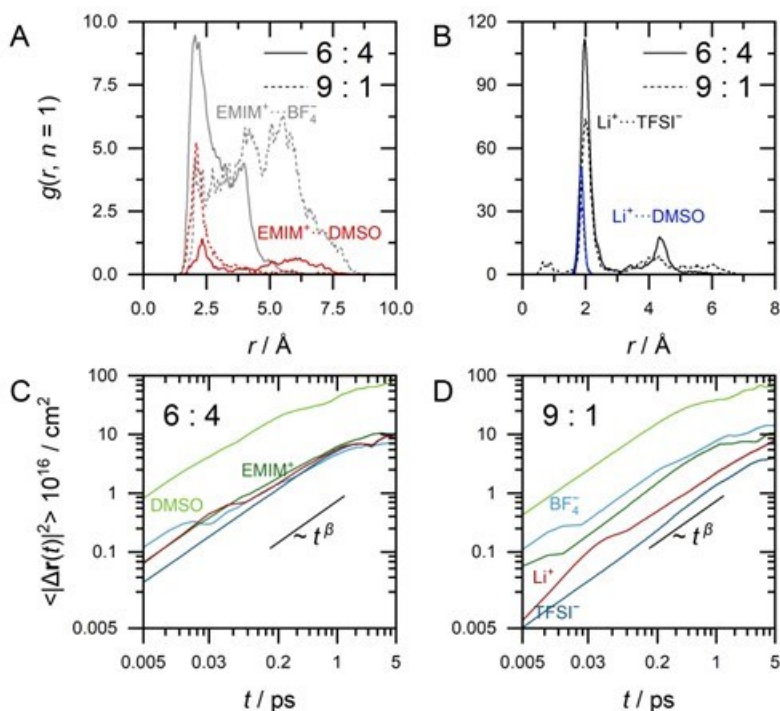


Figure XV.3.8 AIMD results for  $\text{CO}_2$  in  $\text{EMIM-BF}_4/\text{DMSO}/1\text{M LiTFSI}$  electrolyte with: (left) 6:4 and (right) 9:1 volume ratios of  $\text{DMSO}/\text{EMIM-BF}_4$ .



**Figure XV.3.9 (A-B)** Nearest neighbor radial distribution describing interionic interactions between H<sup>2</sup> site of EMIM<sup>+</sup> (A) and Li<sup>+</sup> (B) and the most electronegative atoms of BF<sub>4</sub><sup>-</sup> and TFSI<sup>-</sup> and ion-molecular interactions involving O atom of DMSO. (C-D) Mean-square displacement of the center-of-mass of electrolyte constituents in 6:4 (C) and 9:1 (D) DMSO/EMIM-BF<sub>4</sub> mixture compositions.

The structure of the electrolyte from the AIMD calculations was also analyzed in terms of the intermolecular, interionic, and ion-molecular nearest neighboring radial distributions of the representative atomic sites of the interacting structural units (Figure XV.3.9). According to the obtained results, we can observe relatively strong interionic interactions involving the H<sup>2</sup> site of EMIM<sup>+</sup> and the F atom of BF<sub>4</sub><sup>-</sup>, which are particularly prominent for the 6:4 DMSO/EMIM-BF<sub>4</sub> composition (Figure XV.3.9A). As previously shown in the literature, in imidazolium based ILs the nature of such interactions is electrostatic and usually associated with the formation of hydrogen bonds. Thus, the EMIM<sup>+</sup>···TFSI<sup>-</sup> interactions were found to be significantly weaker, apparently due to stronger interactions with Li<sup>+</sup> (Figure XV.3.9B). On the other hand, in the 6:4 DMSO/EMIM-BF<sub>4</sub> composition, the Li<sup>+</sup>···BF<sub>4</sub><sup>-</sup> interactions are disrupted in favor of EMIM<sup>+</sup>. The strength of intermolecular DMSO···DMSO interactions remain relatively stable in both electrolyte compositions, however their role in cation solvation is different with respect to LiTFSI and EMIM-BF<sub>4</sub>, respectively. More precisely, decreasing the IL content leads to desolvation of EMIM<sup>+</sup> due to the weakening of ion-molecular hydrogen bonding, whereas the situation is opposite for Li<sup>+</sup>. Dynamically, such structural reorganization may be expressed by the behavior of mean-square displacements of the center-of-mass of the considered species (Figure XV.3.9C-D). Therefore, a higher IL content leads to an essential reduction of DMSO and LiTFSI mobility in favor of EMIM-BF<sub>4</sub>. The diffusivity of Li<sup>+</sup> in both electrolyte compositions is found to be higher compared to TFSI, while the mobility of BF<sub>4</sub><sup>-</sup> increases in a 9:1 DMSO/EMIM-BF<sub>4</sub> composition.

In the fourth quarter, a new Cu-based catalyst was synthesized by Chemical Vapor Transport (CVT) technique. The catalyst was exfoliated using probe sonication and then coated on carbon cloth cathode. A Switchlok cell was used for the battery cycling experiments, as it allows the better control of gaseous reactant. More specifically, the assembly of the cells was performed inside a glovebox, which was then followed by the direct purging with pure CO<sub>2</sub> gas, thus ensuring the absence of any air/O<sub>2</sub> traces in the cells. As preliminary experiments, various electrolyte blends were tested using different ionic liquids such as EMIM-NO<sub>3</sub>, EMIM-BF<sub>4</sub> and OMIM-PF<sub>6</sub>. The results showed that EMIM-BF<sub>4</sub> gives a marginally better cycling stability, so it was chosen for the subsequent experiments. Also, tests with different SnI<sub>2</sub> redox mediator (RM) concentrations were performed, revealing that the optimum RM concentration is at 0.008M.



In order to determine the electrochemical behavior of the catalyst, Cyclic Voltammetry (CV) and Linear Sweep Voltammetry (LSV) experiments were performed. The CV plot in Figure XV.3.10A shows the catalyst redox peaks at 2.38 V and 3.52 V, respectively, indicating the reversible reduction and oxidation reactions. The Electrochemical Impedance Spectroscopy (EIS) measurements in Figure XV.3.10B depict the charge transfer resistance ( $R_{ct}$ ) of the catalyst at two different overpotentials. To investigate the performance of the new catalyst, galvanostatic cycling experiments were carried out in a Switchlok type cell under pure  $\text{CO}_2$ . As seen in Figure XV.3.10C, the battery was able to operate for 1300 cycles at current density of  $0.2 \text{ mA/cm}^2$  and capacity of  $0.1 \text{ mAh/cm}^2$ . Furthermore, it could operate up to 500 cycles for current densities of  $0.2 \text{ mA/cm}^2$  and  $0.4 \text{ mA/cm}^2$  at the capacity of  $0.2 \text{ mAh/cm}^2$  (Figure XV.3.10D-E). In all occasions, the charge potential never exceeded the value of  $4.0 \text{ V}$ , which matches the objective of this year. It is worth noting that comparatively, at current density of  $0.2 \text{ mA/cm}^2$  and capacity of  $0.2 \text{ mAh/cm}^2$ , the battery without  $\text{SnI}_2$  could only last for  $\sim 200$  cycles. However, the charge and discharge potentials were similar to those of the battery with  $\text{SnI}_2$ . This indicates that  $\text{SnI}_2$  does not have the traditional role of redox mediator in reducing the charge potential, but rather participates in the formation of solid-electrolyte interface (SEI) layer that protects the Li anode and extends the life of the battery. Figure XV.3.10F shows the consistency of the battery when applying different current densities (from  $0.1 \text{ mA/cm}^2$  to  $0.4 \text{ mA/cm}^2$  and then back to the initial value) at the capacity of  $0.4 \text{ mAh/cm}^2$ . No significant voltage deviation was observed when the battery ran for up to 26 hours, which demonstrates the robustness of the cathode and electrolyte pair during the process.

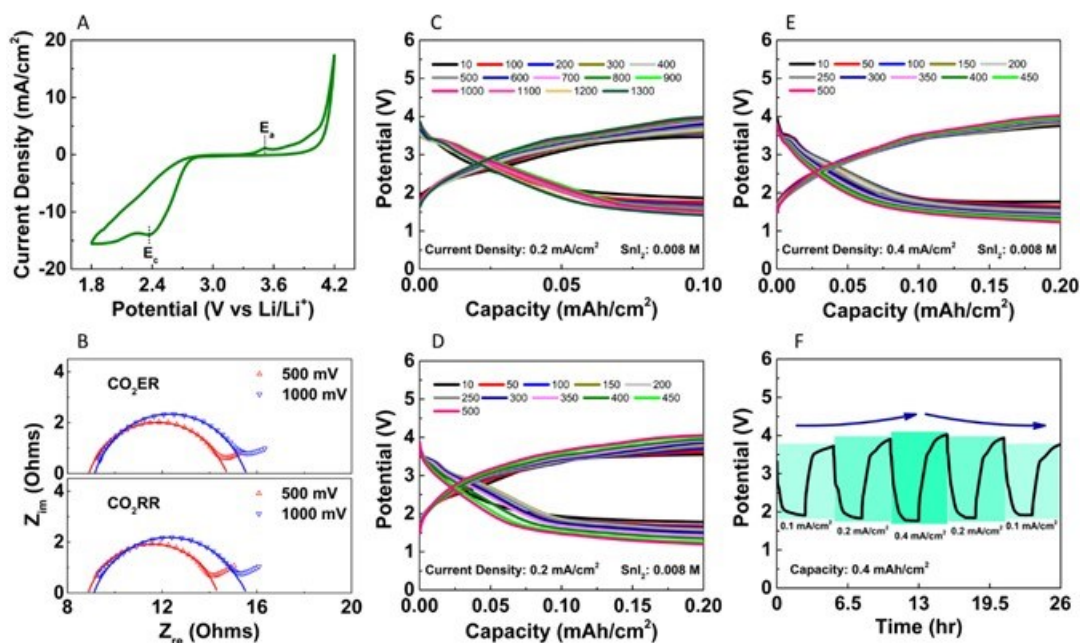
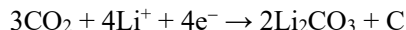


Figure XV.3.10 (A-B) CV and LSV results. (C-E) Galvanostatic cycling at different current densities and capacities. (F) Stability of the catalyst through a continuous series of varying current densities.

To identify the discharge products, a wide range of characterization techniques was utilized including XRD and Raman spectroscopy. The XRD patterns performed at different cycles (Figure XV.3.11A) reveal the formation of  $\text{Li}_2\text{CO}_3$  (PDF #22-1141) during discharge and its decomposition during charge. Additionally, Raman spectroscopy was performed using nickel foam cathodes to eliminate the background presence of carbon (Figure XV.3.11B). The results after discharge reveal peaks located at  $1088 \text{ cm}^{-1}$  corresponding to  $\text{Li}_2\text{CO}_3$ , as well as at  $1335 \text{ cm}^{-1}$  and  $1560 \text{ cm}^{-1}$  corresponding to D and G carbon, respectively. After charge, no relevant peaks are found verifying the decomposition of the discharge products and the reversibility of the process. To rule out parasitic electrochemical reactions effect induced by the electrolyte, discharge product characterization was also performed under Ar atmosphere. As shown in Figure XV.3.11C, there are no  $\text{Li}_2\text{CO}_3$  related peaks detected after discharge. To further elucidate the reaction mechanism, Differential Electrochemical Mass Spectroscopy (DEMS) was employed. The results in Figure XV.3.11D reveal that only

CO<sub>2</sub> is detected as gaseous product during charge process (no CO or O<sub>2</sub>), which is consistent with formation Li<sub>2</sub>CO<sub>3</sub> through the mechanism:



The electrolyte stability throughout the battery cycling was also evaluated using Nuclear Magnetic Resonance spectroscopy (NMR). As seen in Figure XV.3.11E, the electrolyte peaks remain unchanged even after 500 cycles, which definitely has a major contribution to the long-term efficiency of the battery. The electrochemical redox stability of the electrolyte was also determined by LSV experiment (Figure XV.3.11F), where it is evident that there are no peaks related to the reaction of electrolyte within the region of 1 V - 4.5 V. The two peaks located at 3.8 V and 4.25 V are attributed to the SnI<sub>2</sub> and specifically the I<sup>-</sup>/I<sub>3</sub><sup>-</sup> (reversible) and I<sub>3</sub><sup>-</sup>/I<sub>2</sub> (irreversible) transitions, respectively. In fact, only the I<sup>-</sup>/I<sub>3</sub><sup>-</sup> transition is observed inside the working voltage range of this work (below 4 V), which is important for the reversibility of the reactions that occur within the anode-electrolyte-cathode assembly. These results further verify that there are no parasitic electrochemical reactions and thus the catalytic activity can be solely attributed to the reaction of CO<sub>2</sub>.

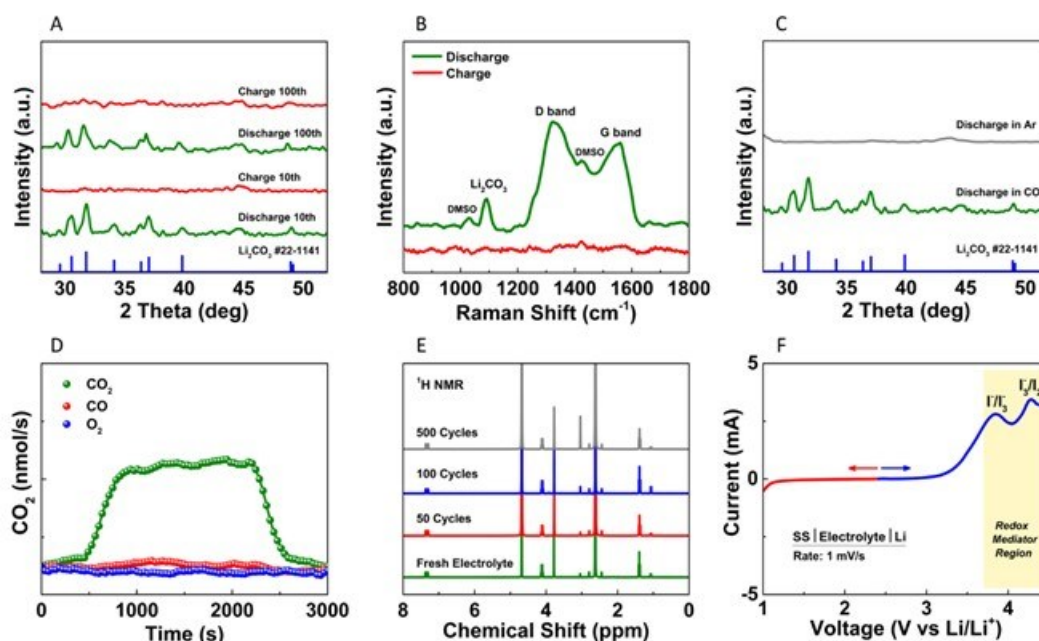


Figure XV.3.11 (A-B) XRD and Raman characterization of the charge and discharge products. (C) Discharge product characterization under Ar atmosphere. (D) DEMS analysis of the gaseous products during charge. (E-F) Electrolyte stability using NMR and LSV methods.

The solid-electrolyte interface (SEI) layer formed on the anode surface at different cycles was analyzed with X-Ray Photoelectron Spectroscopy (XPS) and the results are shown in Figure XV.3.12A-C. In the Sn spectrum, two major peaks were observed at 486.4 eV (Sn 3d<sub>5/2</sub>) and 494.8 eV (Sn 3d<sub>3/2</sub>), attributed to Sn-O bond. The peak observed in O spectrum at 531.7 eV, also implies the existence of Sn-O bond. Finally, no peaks were detected in the I spectrum which indicates the protection of the anode due to the Sn layer. To further verify the SEI layer formation, EIS measurements were performed at different cycles (0, 5, 10, 20, 50). As evident in Figure XV.3.12D, the R<sub>ct</sub> values of the battery increase during cycling reaching ~121 Ohms after 50 cycles, which indicates the gradual formation of the protective SEI layer on the anode.

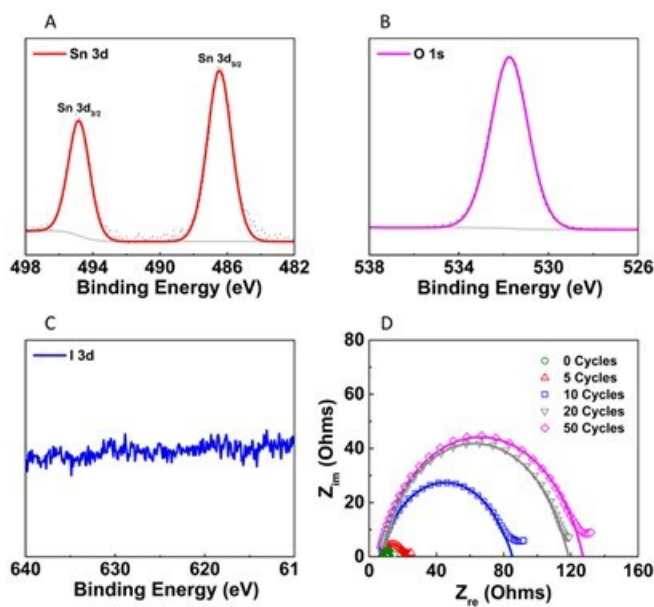


Figure XV.3.12 (A-C) XPS characterization of the SEI layer. (D) Charge transfer resistance at different cycles measured with EIS.

The structure and morphology of the catalyst is also being studied. Due to its complicated characteristics, thorough TEM investigation under different angles as well as XRD simulations are required. These results will be then used by the computational group for the DFT calculations in order to clarify the reaction pathways and mechanisms.

## Conclusions

A new medium-entropy cathode catalyst,  $(\text{NbTa})_{0.5}\text{BiS}_3$ , is found to enable reversible Li/CO<sub>2</sub> electrochemistry to operate at high rates. This medium-entropy cathode catalyst is combined with an ionic liquid-based electrolyte blend to give a Li-CO<sub>2</sub> battery that operates at a high current density of 0.5 mA/cm<sup>2</sup> and capacity of 0.5 mAh/cm<sup>2</sup> for up to 125 cycles. This far exceeds Li-CO<sub>2</sub> batteries previously reported in the literature. Density functional calculations of 21 surfaces of  $(\text{NbTa})_{0.5}\text{BiS}_3$  revealed that many of them are exceptionally stable surfaces and is likely the reason for the capability the Li-CO<sub>2</sub> battery based on it to operate at such high rates. The stability is also confirmed by experimental characterization. In addition, the calculations indicate that a Nb terminated surface promotes Li-CO<sub>2</sub> electrochemistry resulting in Li<sub>2</sub>CO<sub>3</sub> and carbon formation, consistent with the products found in the cell. These results open new direction to design and develop high performance Li-CO<sub>2</sub> batteries.

## Key Publications

1. A. Jaradat, C. Zhang, S. Shashikant Sutar, N. Shan, S. Wang, S. K. Singh, T. Yang, K. Kumar, K. Sharma, S. Namvar, A. Ahmadiparidari, T. Rojas, V. Berry, J. Cabana, Z. Huang, A. Subramanian, A.T. Ngo, L. A. Curtiss, A. Salehi-khojin, A High-Rate Li-CO<sub>2</sub> Battery Enabled by 2D Medium-Entropy Catalyst, *Advanced Functional Materials*, 2300814, 2023.

## Acknowledgements

This project collaborated with L. A. Curtiss (Argonne National Laboratory), F. Khalili-Araghi (University of Illinois, Chicago, or UIC), A. Subramanian (UIC), and Z. Huang (Stockholm University).

## XVI Beyond Li-ion R&D: Sodium-Ion Batteries

The rechargeable sodium-ion battery uses sodium ions ( $\text{Na}^+$ ) as its charge carriers, but its working principle and cell construction are analogous to those for lithium-ion batteries – the main difference is the use of sodium instead of lithium. Such batteries are of interest because unlike lithium-ion, they may be less dependent on critical materials in short supply (or materials limited to certain parts of the earth, or materials having an adverse environmental impact). A significant advantage of using sodium-ion batteries would be the abundant availability of sodium. However, they face some challenges to their large-scale commercialization in electric drive applications, including their relatively low energy density and limited cycle life.

The rest of this chapter contains detailed reports on the status of the following individual projects.

- An Exploratory Study of Novel Sodium-Ion Battery Systems (BNL)
- Development of Advanced High-energy and Long-life Sodium-ion Battery (ANL)
- Tailoring High Capacity, Reversible Anodes for Sodium-Ion Batteries (LBNL)
- Electrolytes and Interfaces for Stable High-Energy Sodium-ion Batteries (PNNL)

## XVI.1 An Exploratory Study of Novel Sodium-Ion Battery Systems (BNL)

### **Xiao-Qing Yang, Principal Investigator**

Chemistry division, Brookhaven National laboratory  
Bldg. 555, Brookhaven National Lab.  
Upton, NY 11973  
E-mail: [xyang@bnl.gov](mailto:xyang@bnl.gov)

### **Enyuan Hu, Co-Principal Investigator**

Chemistry division, Brookhaven National laboratory  
Bldg. 555, Brookhaven National Lab.  
Upton, NY 11973  
E-mail: [enhu@bnl.gov](mailto:enhu@bnl.gov)

### **Tien Duong, DOE Technology Development Manager**

U.S. Department of Energy  
E-mail: [Tien.Duong@ee.doe.gov](mailto:Tien.Duong@ee.doe.gov)

Start Date: October 1, 2022

End Date: September 30, 2023

Project Funding (FY23): \$200,000

DOE share: \$200,000

Non-DOE share: \$0

### **Project Introduction**

The next generation of rechargeable battery systems with higher energy and power density, lower cost, better safety characteristics, and longer calendar and cycle life need to be developed to meet the challenges to power electrified vehicles in the future. Na-ion battery systems have attracted more and more attention due to the more abundant and less expensive nature of Na resources. However, building a sodium battery requires redesigning battery technology to accommodate the chemical reactivity and larger size of sodium cations. Since Na-ion battery research is an emerging technology, new materials to enable Na electrochemistry and the discovery of new redox couples and the related diagnostic studies of these new materials and redox couples are quite important. This project uses the synchrotron based in situ x-ray diagnostic tools developed at BNL to evaluate the new materials and redox couples, to explore in-depth fundamental understanding of the reaction mechanisms aiming to improve the performance of these materials and provide guidance for new material developments. This project also focuses on developing advanced diagnostic characterization techniques for these studies. The synchrotron based in situ X-ray techniques (x-ray diffraction, x-ray pair distribution function, or PDF, and x-ray absorption XAS) are combined with other imaging and spectroscopic tools such as transmission electron microscopy (TEM), scanning transmission electron microscopy (STEM), mass spectroscopy (MS), transmission x-ray microscopy (TXM), as well as neutron diffraction (ND) and neutron PDF (NPDF). In FY2023, this BNL team performed several successful experimental studies at various beamlines of National Synchrotron Light Source II (NSLSII) such as x-ray Powder diffraction (XPD), and ISS beamlines. In FY2023, in collaboration with scientists at Oak Ridge National Lab., this project focused on the studies of structure and redox mechanism of a new cathode material  $\text{Na}_{0.75}\text{Li}_{0.08}\text{Cu}_{0.25}\text{Mn}_{0.66}\text{O}_2$  for Na-ion batteries with increased capacity by lithium substitution enhanced oxygen redox. In FY2023, through collaboration with scientists at Harvard University, this team carried out hard and soft x-ray XAS studies on a new Mg doped cathode materials  $\text{P2-Na}_{2/3}\text{Mg}_{0.205}\text{Ni}_{0.1}\text{Fe}_{0.05}\text{Mn}_{0.645}\text{O}_2$  for Na-ion batteries. Through collaboration with scientists at University of Science and Technology of China, X-ray near-edge structure (XANES) and extended X-ray absorption fine structure (EXAFS) were used to study the single atom transition metal catalysts with N, S coordination environments. The results of this work were published on *Energy Storage Materials*.

## Objectives

The primary objective of this project is to develop new advanced in situ material characterization techniques and to apply these techniques to support the development of new cathode, anode, and electrolyte materials with high energy and power density, low cost, good abuse tolerance, and long calendar and cycle life for the next generation of Sodium-ion batteries (SIBs) to power plug-in hybrid electric vehicles (PHEV) and electric vehicles (EV). The diagnostic studies have been focused on issues relating to capacity retention, thermal stability; cycle life and rate capability of advanced Na-ion and beyond Li-ion batteries.

## Approach

This project has used the synchrotron based in situ and ex situ x-ray diagnostic tools developed at BNL to evaluate the new materials and redox couples to enable a fundamental understanding of the mechanisms governing the performance of these materials and provide guidance for new material and new technology development regarding Na-ion battery systems. These techniques include:

- Using XRD techniques at beamlines of NSLSII to study the structural changes of new cathode materials for Na-ion batteries.
- Using hard and soft x-ray absorption (hard XAS and sXAS) to study redox mechanism of new cathode materials for Na-ion batteries.
- Using resonant inelastic x-ray scattering mapping (mRIXS) technique (through collaboration with scientists at Lawrence Berkeley National Lab. to study the oxygen redox process of new cathode materials for Na-ion batteries.

## Results

In FY2023, in collaboration with scientists at the Oakridge National Laboratory, we optimized the synthesis conditions and obtained P3-structured  $\text{Na}_{0.75}\text{Li}_{0.08}\text{Cu}_{0.25}\text{Mn}_{0.66}\text{O}_2$  with high purity. In FY22, we worked on P3- $\text{Na}_{2/3}\text{Cu}_{1/3}\text{Mn}_{2/3}\text{O}_2$  and concluded that it is possible to increase the capacity of this material by activating the oxygen redox. This may be fulfilled by substituting part of Cu with Li and therefore introducing the Na-O-Li structural motif which has been suggested to have influence on oxygen activity by theoretical studies. The synchrotron XRD pattern of  $\text{Na}_{0.75}\text{Li}_{0.08}\text{Cu}_{0.25}\text{Mn}_{0.66}\text{O}_2$  is shown in Figure XVI.1.1. Rietveld refinement using a model structure having P2<sub>1</sub>/c space group symmetry leads to excellent fitting. The structure has orderings both within the Li/TM (transition metal Cu, Mn) layer and the Na layer. The XRD data has obvious anisotropic broadening, indicating there are possible stacking faults in the pristine material. We first used the conventional 1 M NaPF<sub>6</sub> in ethylene carbonate/propylene carbonate as the electrolyte but the  $\text{Na}_{0.75}\text{Li}_{0.08}\text{Cu}_{0.25}\text{Mn}_{0.66}\text{O}_2||\text{Na}$  cell cannot be cycled. Then we changed the salt from NaPF<sub>6</sub> to NaClO<sub>4</sub> and added fluoroethylene carbonate into the electrolyte, that enables cycling of the cell, and the electrochemical data is shown in Figure XVI.1.1b. The electrochemical data of the non-substituted material-  $\text{Na}_{0.66}\text{Cu}_{0.33}\text{Mn}_{0.66}\text{O}_2$  is shown in Figure XVI.1.1c for comparison. They clearly show that after introducing lithium substitution, the capacity is significantly increased. The first cycle discharge capacity increased from 80 mAh/g in  $\text{Na}_{0.66}\text{Cu}_{0.33}\text{Mn}_{0.66}\text{O}_2$  to 130 mAh/g in  $\text{Na}_{0.75}\text{Li}_{0.08}\text{Cu}_{0.25}\text{Mn}_{0.66}\text{O}_2$ . The first charge process in  $\text{Na}_{0.75}\text{Li}_{0.08}\text{Cu}_{0.25}\text{Mn}_{0.66}\text{O}_2$  features a long plateau at around 4.2 V, which is likely associated with the activation of oxygen redox. In comparison, such plateau is absent in  $\text{Na}_{0.66}\text{Cu}_{0.33}\text{Mn}_{0.66}\text{O}_2$  even though it is charged to the same voltage.  $\text{Na}_{0.75}\text{Li}_{0.08}\text{Cu}_{0.25}\text{Mn}_{0.66}\text{O}_2$  delivers considerable amount of capacity in the <3V region during discharge while  $\text{Na}_{0.66}\text{Cu}_{0.33}\text{Mn}_{0.66}\text{O}_2$  has little capacity in the same region. Such discharge capacity is likely to arise from the oxygen redox during discharge. The oxygen redox voltage difference between charge and discharge is likely caused by hysteresis. It is also noted that while lithium substitution successfully increases the capacity, the capacity fades more rapidly than the non-substituted material.

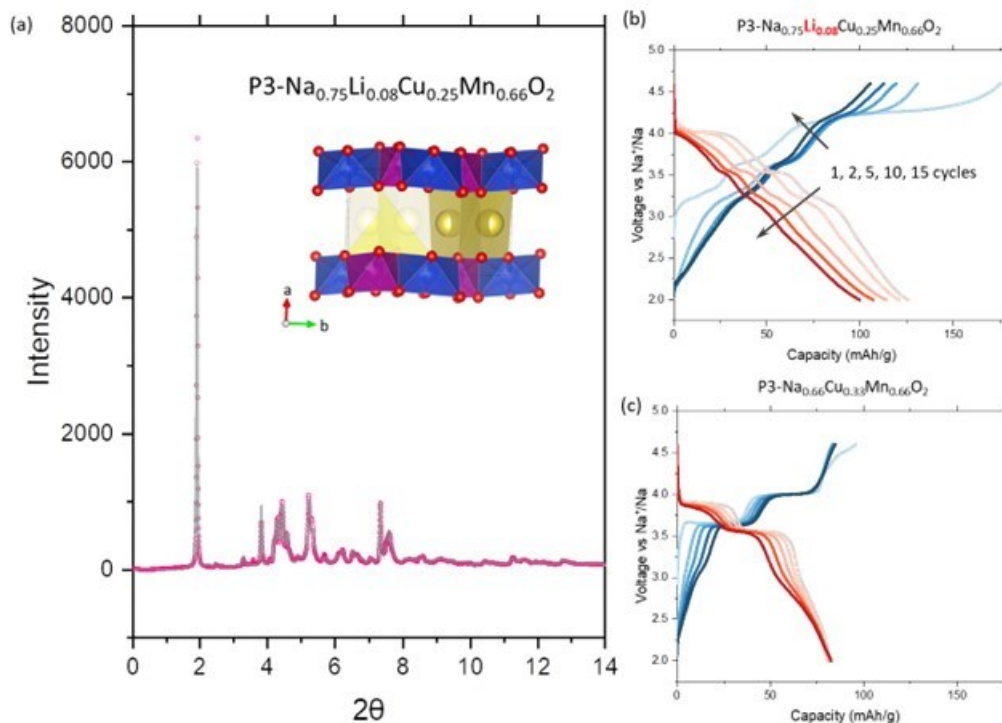


**Figure XVI.1.1 XRD data and Rietveld refinement of P3 Na<sub>0.75</sub>Li<sub>0.08</sub>Cu<sub>0.25</sub>Mn<sub>0.66</sub>O<sub>2</sub> with the inset graph showing the solved crystal structure. (b) Selected charge-discharge profiles of Na<sub>0.75</sub>Li<sub>0.08</sub>Cu<sub>0.25</sub>Mn<sub>0.66</sub>O<sub>2</sub> from the first 15 cycles. (c) Selected charge-discharge profiles of Na<sub>0.66</sub>Cu<sub>0.33</sub>Mn<sub>0.66</sub>O<sub>2</sub> from the first 15 cycles.**

In FY2023, BNL team successfully completed the *in operando* x-ray absorption spectroscopy (XAS) experiments for the P3 type Na<sub>0.75</sub>Li<sub>0.08</sub>Cu<sub>0.25</sub>Mn<sub>0.66</sub>O<sub>2</sub> cathode material. Figure XVI.1.2a and Figure XVI.1.2b are the X-ray absorption near edge structure (XANES) data for Mn K-edge and Cu K-edge, respectively. It is clear that Mn and Cu XANES spectra have edge shift during the charge-discharge, indicating both elements are redox active and contribute to the overall capacity of Na<sub>0.75</sub>Li<sub>0.08</sub>Cu<sub>0.25</sub>Mn<sub>0.66</sub>O<sub>2</sub> cathode. During charge, the edge of Mn XANES spectrum shifts to higher energy, suggesting that Mn is oxidized during the process. Most of the Mn edge shift takes place between 2.0V and 3.5V, indicating that Mn is likely the element making dominant contribution to the charge capacity in this voltage region. After 3.5V, little edge shift is observed for the Mn spectra which means other elements such as Cu or/and O may take up the role of charge compensation in the high voltage region. During discharge, the Mn edge shifts back to lower energy, suggesting its reduction. Most of the Mn edge shift takes place between 3.0V and 2.4V, suggesting the activity of Mn in this voltage region. Following similar analysis, it can be concluded that during charge, Cu mainly contributes to the capacity in the voltage region between 3.5V and 4.0V. During discharge, Cu contributes to the capacity in the voltage region between 4.0V and 3.0V. Combining the results about Mn and Cu redox activity during charge-discharge, it can be found that neither Mn nor Cu is contributing to the voltage region above 4.0V during charge and the voltage region below 2.4V during discharge. It is very likely that O is the element responsible for the charge compensation mechanism in these voltage regions. It should be noted that both Mn and Cu redox activities show great reversibility as indicated by the great overlap between the end-of-discharge spectrum and the beginning-of-charge one. However, the overall discharge capacity is about 10mAh/g less than the overall charge capacity. Considering the reversibility of Mn and Co redox couples, the overall irreversibility is likely caused by the oxygen redox which may suffer from issues such as oxygen release. In addition to the irreversibility, another issue with oxygen redox is probably hysteresis, which is voltage difference between oxygen redox during charge and that during the discharge. Based on the previous discussion, the oxygen redox may be active above 4.0V during charge but below 2.4V during discharge, causing a voltage difference that is as large as 1.6V. A summary of these results is illustrated in Figure XVI.1.2c.

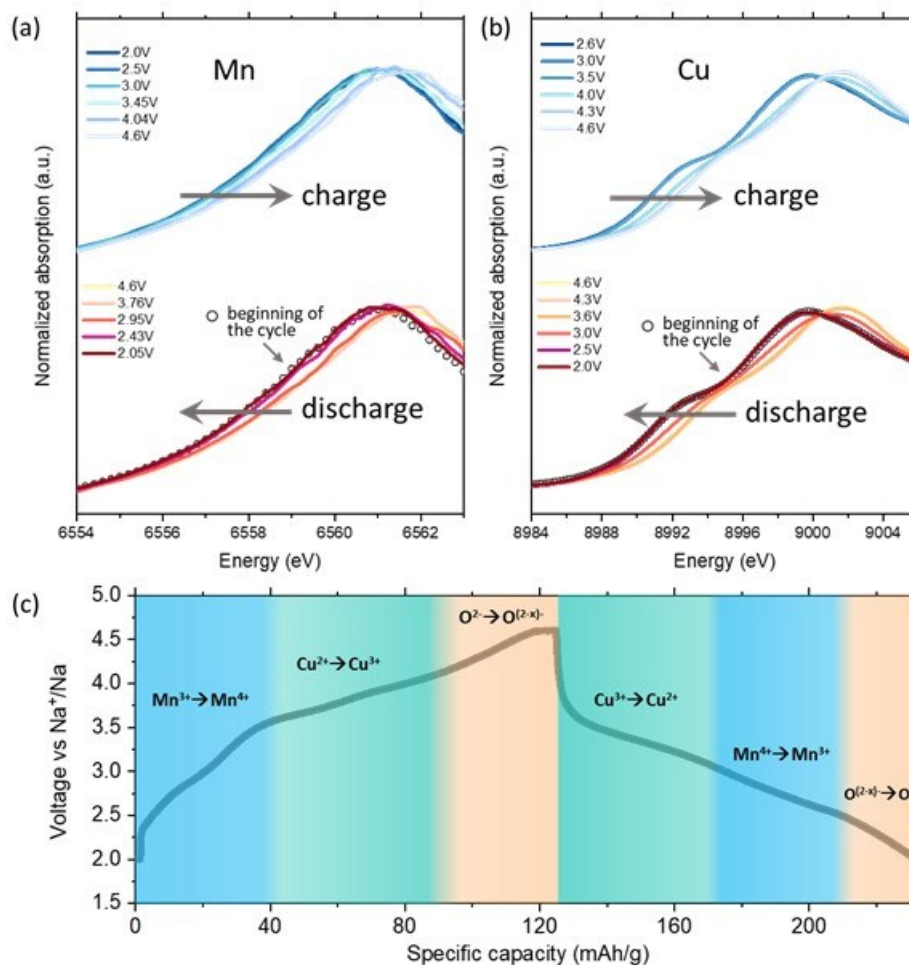


**Figure XVI.1.2** Selected (a) Mn K-edge XANES spectra and (b) Cu K-edge XANES spectra from the *in operando* XAS experiments for P3 type  $\text{Na}_{0.75}\text{Li}_{0.08}\text{Cu}_{0.25}\text{Mn}_{0.66}\text{O}_2$ . (c) Summarized charge compensation mechanism of P3 type  $\text{Na}_{0.75}\text{Li}_{0.08}\text{Cu}_{0.25}\text{Mn}_{0.66}\text{O}_2$  based on the XAS study.

In FY2023, BNL team completed *in situ* x-ray diffraction (XRD) and *ex situ* soft x-ray absorption spectroscopy (sXAS) for P3- $\text{Na}_{0.75}\text{Li}_{0.08}\text{Cu}_{0.25}\text{Mn}_{0.66}\text{O}_2$  to understand its structural evolution, redox mechanism and surface chemistry during electrochemical cycling. *In situ* XRD was done at the beamline 28-ID-2 of National Synchrotron Light Source II (NSLS II) at BNL. *In situ* cell with P3- $\text{Na}_{0.75}\text{Li}_{0.08}\text{Cu}_{0.25}\text{Mn}_{0.66}\text{O}_2$  as the cathode and sodium metal as the anode was cycled at a rate of C/5 in the voltage range of 2.0V-4.6V (Figure XVI.1.3). The *in situ* XRD patterns are shown in Figure XVI.1.3a and the electrochemistry data of the *in situ* cell is shown in Figure XVI.1.3b. The colored dots in Figure XVI.1.3b indicate the points where the *in situ* XRD were measured. The XRD data indicate a generally reversible phase transformation in the first cycle. The evolution of (100) peak shows the change of *a* axis. Due to the unique crystallographic setting of P3- $\text{Na}_{0.75}\text{Li}_{0.08}\text{Cu}_{0.25}\text{Mn}_{0.66}\text{O}_2$ , the *a* axis corresponds to the stacking direction of the structure. During charge, (100) peak first shifts to lower angles, indicating an expansion of *a* axis and an increase in the  $\text{NaO}_6$  slab distance. At the late stage of charge, (100) peak shifts back to higher angles, indicating a shrinkage of *a* axis and a decrease in the  $\text{NaO}_6$  slab distance. During the discharge, the shrinkage of *a* axis and the decrease in the  $\text{NaO}_6$  slab distance continues at the initial stage before the expansion of *a* axis and the increase in the  $\text{NaO}_6$  slab distance takes over. At the end of discharge, the position of (100) is about the same as that for the pristine



material, indicating good structural reversibility. The pattern of structural change can also be seen from the evolution of (200), (30 $\bar{2}$ ), (23 $\bar{3}$ ) peaks shown Figure XVI.1.3a.

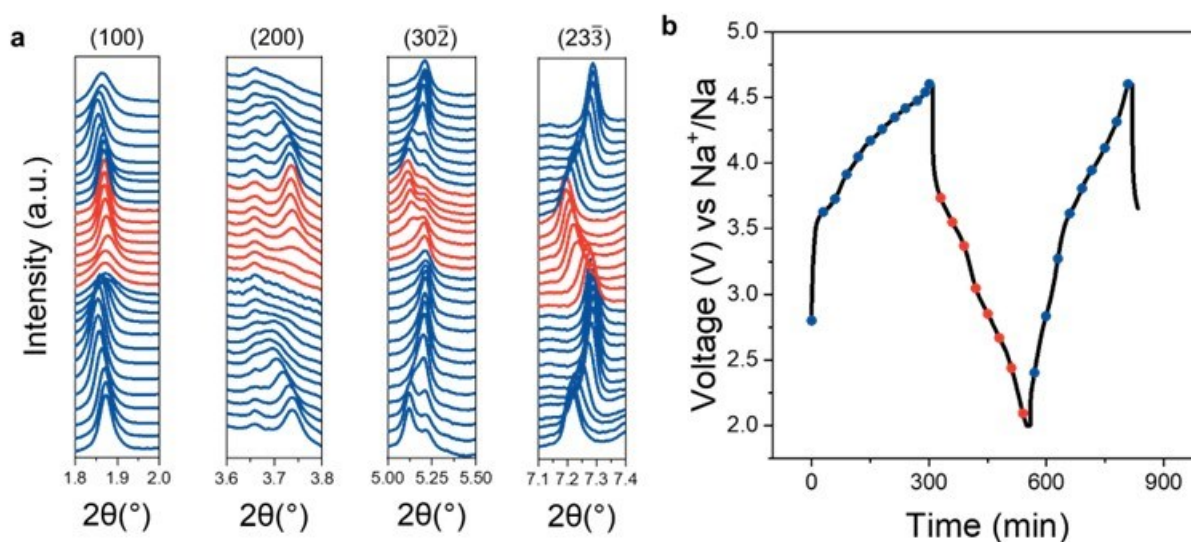


**Figure XVI.1.3 (a)** In situ XRD patterns of P3-Na<sub>0.75</sub>Li<sub>0.08</sub>Cu<sub>0.25</sub>Mn<sub>0.66</sub>O<sub>2</sub> at C/5 rate. **(b)** Charge-discharge curve of in situ battery cycling and the states of charge where the XRD patterns were taken in (a).

*Ex situ* soft x-ray absorption spectroscopy (sXAS) was measured for P3-Na<sub>0.75</sub>Li<sub>0.08</sub>Cu<sub>0.25</sub>Mn<sub>0.66</sub>O<sub>2</sub> electrode cycled to different states of charge at the beamline 23-ID-2 of NSLS II at BNL. The measurement was conducted in both the total electron yield (TEY) mode, which probes the very surface region of the material, as well as the partial fluorescence yield (PFY) mode, which probes the bulk. Oxygen K-edge TEY (Figure XVI.1.4a) indicates that there are carbonate species on the surface of the pristine material, which may be formed during the material synthesis or sample storage. Interestingly, the carbonates decompose during charge but reform during discharge. The reformation is likely due to the decomposition of electrolyte which contains a lot of carbonate solvents such as propylene carbonate (PC) and fluoro ethylene carbonate (FEC). In oxygen K-edge PFY data (Figure XVI.1.4b), the appearance of the new peak at around 528.2 eV for the highly charged sample is likely due to the oxygen redox reaction. For Mn, only TEY data was obtained and the PFY data was not usable due to the self-absorption issue, a common challenge facing Mn-containing oxides. The Mn L-edge TEY data (Figure XVI.1.4c) shows Mn is mostly tetravalent on the surface of the pristine material. Mn experiences reduction during charge, likely due to the surface reconstruction process typically seen for lithium and sodium oxide cathode materials. As the previous *in situ* hard XAS suggests (Shown in Figure XVI.1.2), Mn participates in the redox reaction at the late stage of discharge. The Mn sXAS data for the discharged to 2.0V confirms this point as the data shows significant amount of Mn<sup>2+</sup>/Mn<sup>3+</sup> is formed on the surface. For the Cu L-edge sXAS, the valence of Cu on the surface (Figure XVI.1.4d) is mostly invariant during the charge-discharge, suggesting little if any participation of Cu in the surface chemistry. For the bulk (PFY data, Figure XVI.1.4e), Cu<sup>2+</sup> in the pristine material is oxidized to Cu<sup>3+</sup> when the material is charged to 4.1 V. Further charging the cell to 4.6 V may induce oxygen oxidation and generate a complicated electronic state for Cu in which there are strong correlation between the electronic structure of Cu and that of O.

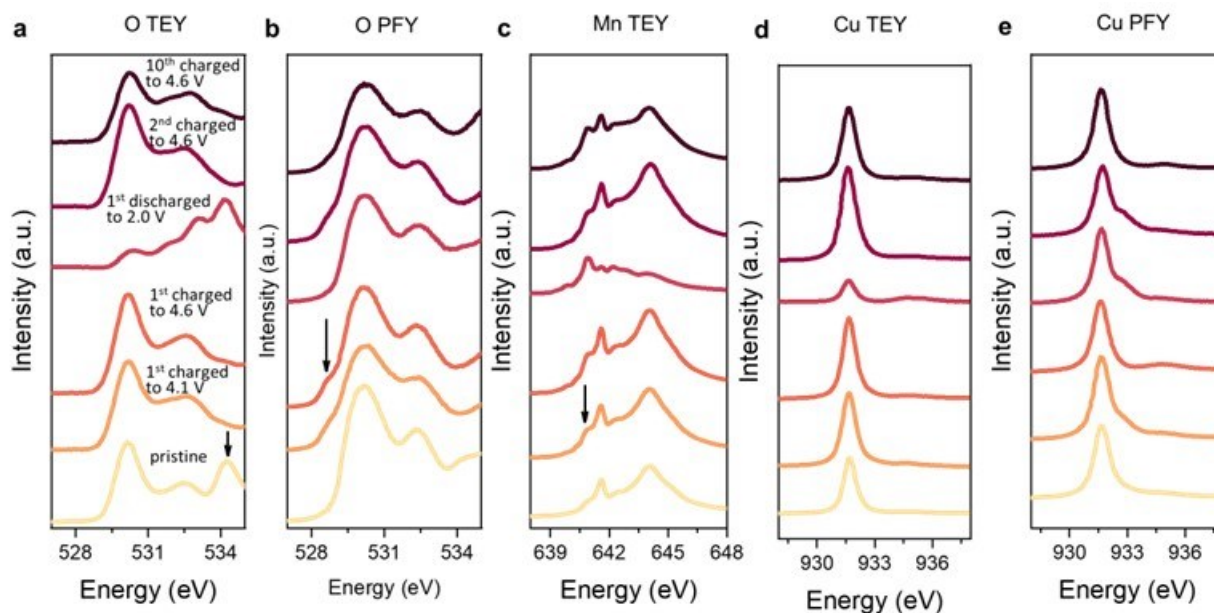


**Figure XVI.1.4** (a) Oxygen K-edge TEY. The arrow indicates the peak from  $\text{Na}_2\text{CO}_3$ . (b) Oxygen K-edge PFY. The arrow indicates the peak from oxidized lattice oxygen. (c) Mn L-edge TEY (d) Cu L-edge TEY. The arrow indicates the peak from reduce Mn. (e) Cu L-edge PFY data of  $\text{P3-Na}_{0.75}\text{Li}_{0.08}\text{Cu}_{0.25}\text{Mn}_{0.66}\text{O}_2$  at different states

Hard XAS is the conventional tool for studying redox mechanism and the Cu K-edge XAS data is shown in Figure XVI.1.5a. It indicates that the spectrum of the 4.1 V sample is almost the same as that of the 4.6 V sample. This suggests that the high voltage redox is complicated and may not be based on the Cu cations. An alternative tool, the soft XAS was employed for the characterization. For soft XAS, the data in total electron yield (TEY) mode is surface-sensitive and therefore not capable of revealing the redox mechanism in the bulk. In contrast, the soft XAS in total fluorescence yield (TFY) mode can probe the bulk region and therefore is a more suitable tool than TEY in studying the redox mechanism. In TFY data, a clear difference is noticed between the spectrum of the 4.1 V sample and that of the 4.6 V sample. Compared with the spectrum of the 4.1 V sample, Figure XVI.1.5b shows a clear enhancement in fluorescence yield at around 531 eV in the spectrum of the 4.6 V sample. In TFY mode, only the number of emitted photons is counted but the kinetic energies of those photons are not recorded. As a result, the obtained information is limited and may not be able to decipher complicated redox mechanism for the sample studied here. A more advanced technique, resonant inelastic x-ray scattering mapping (mRIXS), which registers the kinetic energy of each emitted photon, provides much richer information and has been proved to be an effective tool in studying complicated redox mechanism in battery materials, was used for this study. Through collaborating with scientists at Lawrence Berkeley National Laboratory, the mRIXS experiment was carried out at Advanced Light Source (ALS) and the results are shown in Figure XVI.1.5c. The vertical axis corresponds to the excitation energy, which has the same meaning and the same range as that used for soft XAS studies. The horizontal axis corresponds to the kinetic energy of emitted photons. The color contour indicates the number of photons at each coordinate on the 2D mapping (with specific excitation energy and specific emission energy). Brown is the strongest, followed by yellow, green, and blue. Clearly, when the excitation energy is around 531 eV, a sharp emission feature at 523.5 eV is distinguished at an excitation energy of 531 eV in mRIXS. Based on previous theoretical calculations in the literature report, the enhanced emission in this energy region originates from decay channels that are caused by the oxidation of oxygen anions. This feature can also be clearly seen in Figure XVI.1.5d which integrates the energy-dependent photon emission spectra at excitation energy around 531 eV. This is the reason why there is an enhancement in the TFY spectrum of the 4.6 V sample. Based on the studies of these studies, we can conclude that the redox mechanism in  $\text{P3-Na}_{0.75}\text{Li}_{0.08}\text{Cu}_{0.25}\text{Mn}_{0.66}\text{O}_2$  is based on both copper and oxygen. Below 4.1 V, the dominated process is the copper redox corresponding to  $\text{Cu}^{2+}$  to  $\text{Cu}^{3+}$ , with the possibility of forming Zhang-Rice Singlet. Above 4.1 V, it is the oxygen redox corresponding to  $\text{O}^{2-}$  to  $\text{O}^-$ . Such activation of oxygen redox increases the discharge capacity by around 35 mAh/g above 4.0 V and the overall capacity to

around 130 mAh/g in the voltage window of 4.1 V to 2 V. Even though there are multiple issues to be addressed for oxygen-redox-active cathode similar to the lithium-ion battery cathodes, the benefits of increasing capacity and voltage may still make oxygen redox an interesting topic to investigate further.

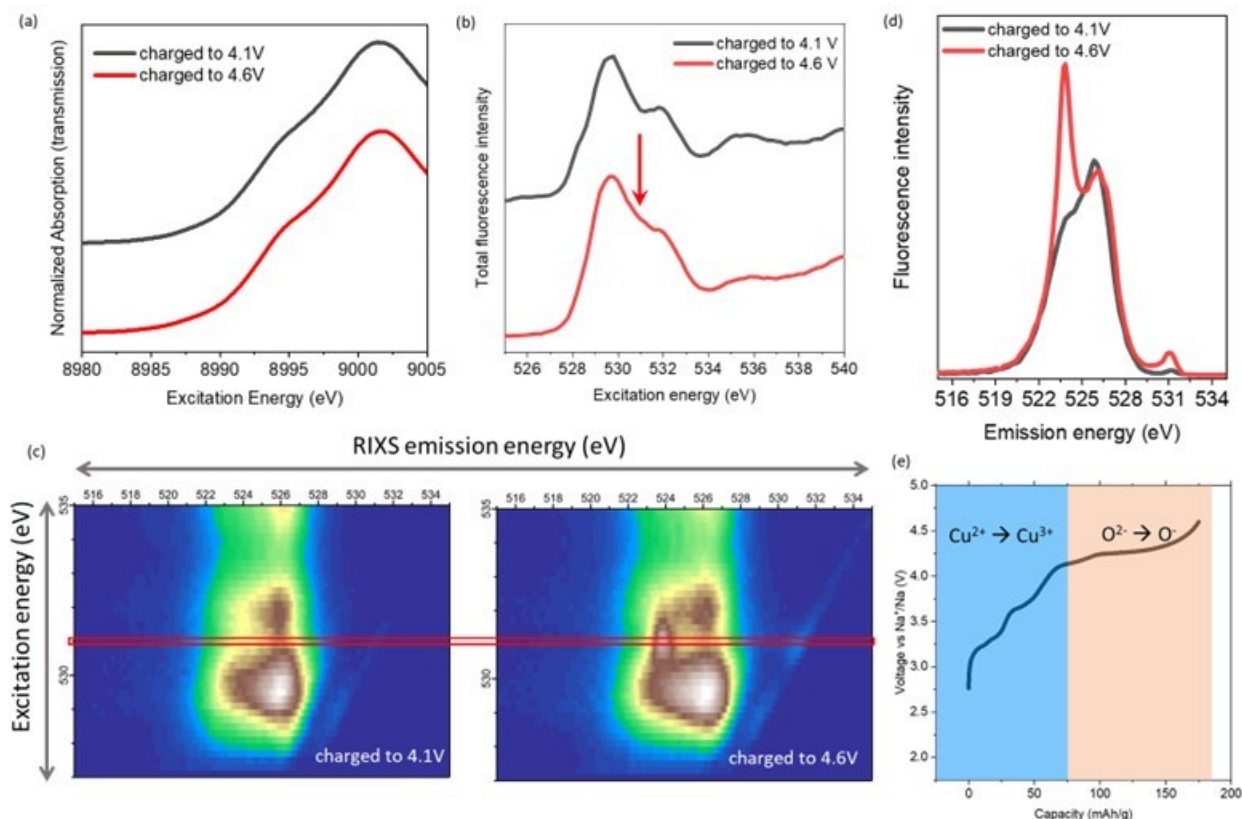


Figure XVI.1.5 (a) hard XAS of charged P3- $\text{Na}_{0.75}\text{Li}_{0.08}\text{Cu}_{0.25}\text{Mn}_{0.66}\text{O}_2$  electrode. (b) soft XAS in TFY mode of charged P3- $\text{Na}_{0.75}\text{Li}_{0.08}\text{Cu}_{0.25}\text{Mn}_{0.66}\text{O}_2$  electrode. The arrow indicates the region with enhanced fluorescence yield. (c) mRIXS of charged P3- $\text{Na}_{0.75}\text{Li}_{0.08}\text{Cu}_{0.25}\text{Mn}_{0.66}\text{O}_2$  electrodes. (d) Integrated energy-dependent photon emission spectra of charged P3- $\text{Na}_{0.75}\text{Li}_{0.08}\text{Cu}_{0.25}\text{Mn}_{0.66}\text{O}_2$  electrodes. The excitation energies used for emission spectra are 530.9, 531.1 and 531.3 eV. (e) summarized redox couple mechanism of P3- $\text{Na}_{0.75}\text{Li}_{0.08}\text{Cu}_{0.25}\text{Mn}_{0.66}\text{O}_2$  during charging.

## Conclusions

This project, “Exploratory Studies of Novel Sodium-Ion Battery Systems (BNL)”, has been successfully completed in FY2023. All milestones have been completed. The publication records are very good. Extensive collaboration with other national Labs, US universities and international research institutions were well established.

## Key Publications

### Publications

1. Yichao Wang, Zulipiya Shadike, William Fitzhugh, Fan Wu, Sang-Jun Lee, Jun-Sik Lee, Xi Chen, Yuanzheng Long, Enyuan Hu, Xin Li\*, “Tuning discharge voltage by Schottky electron barrier in P2- $\text{Na}_{2/3}\text{Mg}_{0.205}\text{Ni}_{0.1}\text{Fe}_{0.05}\text{Mn}_{0.645}\text{O}_2$ ”, *Energy Storage Materials*, 2023, 55, 587-596. Doi: 10.1016/j.ensm.2022.12.027. Publication date: December 17<sup>th</sup>, 2022.
2. Ruilin Bai, Qiaosong Lin, Xinyu Li, Fangxin Ling, Huijuan Wang, Sha Tan, Lingxiang Hu, Mingze Ma, Yu Shao, Xiaojun Wu, Xianhong Rui, Enyuan Hu\*, Yu Yao\*, Yan Yu\*. Toward Complete Transformation of Sodium Polysulfides by Regulating the Second-Shell Coordinating Environment of

Atomically Dispersed Fe. *Angew. Chem., Int. Ed.* 2023 Doi: 10.1002/ange.202218165. Published on March 14, 2023

3. Wu, Zhonghan, Youxuan Ni, Sha Tan, Enyuan Hu, Lunhua He, Jiuding Liu, Machuan Hou, Peixin Jiao, Kai Zhang\*, Fangyi Cheng\*, Jun Chen "Realizing High Capacity and Zero Strain in Layered Oxide Cathodes via Lithium Dual-Site Substitution for Sodium-Ion Batteries." *Journal of the American Chemical Society* 2023, 145, 9596-9606.

### **Acknowledgements**

This project was supported by the Assistant Secretary for Energy Efficiency and Renewable Energy, Vehicle Technology Office of the U.S. DOE through the Advanced Battery Materials Research (BMR) Program under contract No. DE-SC0012704.

## XVI.2 Development of Advanced High-energy and Long-life Sodium-ion Battery (ANL)

### **Khalil Amine, Principal Investigator**

Argonne National Laboratory  
9700 South Cass Avenue  
Lemont, IL 60439  
E-mail: [amine@anl.gov](mailto:amine@anl.gov)

### **Christopher S. Johnson, Co-Principal Investigator**

Argonne National Laboratory  
9700 South Cass Avenue  
Lemont, IL 60439  
E-mail: [cjohnson@anl.gov](mailto:cjohnson@anl.gov)

### **Tien Duong, DOE Technology Development Manager**

U.S. Department of Energy  
E-mail: [Tien.Duong@ee.doe.gov](mailto:Tien.Duong@ee.doe.gov)

Start Date: January 1, 2019

End Date: September 30, 2023

Project Funding (FY23): \$585,000

DOE share: \$585,000

Non-DOE share: \$0

### **Project Introduction**

Considering the natural abundance and low cost of sodium resources, sodium-ion batteries (SIBs) have received much attention for large-scale electrochemical energy storage.[1] However, the larger ionic radius of Na<sup>+</sup> (1.02 Å) than Li<sup>+</sup> (0.67 Å) brings more challenges on the development of good Na-host materials with optimal electrochemical properties. On one hand, although most SIBs cathode materials are either imitating or duplicating from lithium analogues, there are significant differences in the intercalation chemistries between sodiation and lithiation. The layered oxides cathodes deliver very high energy density, but undergo more complex phase transition during charge/discharge, resulting in severe capacity fade during prolonged cycling. [2] On the other hand, the absence of suitable anode materials has obstructed progress in the development of SIBs. Two of the most promising anode materials, graphite and silicon have limited sodium storage capability. Hard carbon can demonstrate reversible sodiation/de-sodiation, but the capacity is lower than 300 mAh g<sup>-1</sup>, significantly limiting the energy density of SIBs. [3,4] Alloying anode materials such as phosphorus can deliver high capacity, but suffer from huge volume changes and severe parasitic reactions with the electrolytes, resulting in rapid capacity degradation during long-term cycling. [5]

*Via* advanced diagnostic tools including synchrotron X-ray probes and computational modeling, the team led by Dr. Khalil Amine and Dr. Christopher S. Johnson at Argonne National Laboratory (ANL) is focusing on the development of rational cathode materials, anode materials and electrolytes to develop long life and high energy SIBs with low cost and high safety.

### **Objectives**

The project objective is to develop high-energy SIBs with long life, low cost and high safety. The energy density target is 200 Wh kg<sup>-1</sup> and/or 500 Wh L<sup>-1</sup>, wherein the anode capacity and cathode capacity targets are 600 mAh g<sup>-1</sup> and 200 mAh g<sup>-1</sup>, respectively.

### **Approach**

In a team approach, the Na-ion battery group will create a versatile Na-ion battery chemistry with beneficial advantages such as low cost, safety, recycling, and sustainability of materials used. The team will work in a synergistic way so that the final design is the culmination of advances in phosphorus-carbon composites mated

with optimized lead or other highly dense metalloids, such as tin and/or antimony and derivatives thereof, for the recyclable anode. Synthesis and optimization of such blended composite anodes will be conducted in parallel to diagnostic characterization of structures, phase formation, and cycling stability. Cathode work will involve (1) gradient cathodes consisting of Fe-Mn compositions, and (2) intergrowths of layer stacking sequenced oxides. If resources allow, the team also will attempt to stabilize cathode surfaces using oxidative chemical vapor deposition or atomic layer deposition methods, particularly for the benefit of staving off dissolution of manganese and iron/electrolyte reactivity.

## Results

### *Design of full concentration gradient O3-type $\text{NaNi}_{0.8}\text{Co}_{0.1}\text{Mn}_{0.1}\text{O}_2$ cathode towards long cycling stability*

O3-type layered oxide materials are considered to be a class of highly promising cathode for sodium-ion batteries due to their high Na stoichiometry (close to 1). Unfortunately, rapid capacity fading caused by serious structural transformation and interfacial degradation upon charge/discharge limits their practical application, in particular during high voltage cycling. Full concentration gradient layered oxide cathode, where the concentration of reactive elements (e.g., Ni) decreases linearly whereas the concentration of less reactive elements (e.g., Mn) increases linearly from the center to the outer layer of each particle, has been used in lithium-ion batteries to successfully suppress the capacity fade during long-term cycling. In FY23, we validated this FCG idea in sodium-ion batteries by using  $\text{NaNi}_{0.8}\text{Co}_{0.1}\text{Mn}_{0.1}\text{O}_2$  as an example. Please note that we only use this material for a demonstration of the concept. Future efforts will be focused on development of Ni/Co-free FCG layered cathodes.

The FCG layered O3  $\text{NaNi}_{0.8}\text{Co}_{0.1}\text{Mn}_{0.1}\text{O}_2$  (O3-FCG811) cathode was synthesized by solid state reactions between NaOH and  $\text{Ni}_{0.8}\text{Co}_{0.1}\text{Mn}_{0.1}(\text{OH})_2$ . The hydroxide precursor  $\text{Ni}_{0.8}\text{Co}_{0.1}\text{Mn}_{0.1}(\text{OH})_2$  was synthesized through careful control of coprecipitation process. Figure XVI.2.1a shows the cross-section scanning electron microscopy (SEM) images and the corresponding Energy-dispersive X-ray analysis (EDX) mapping of the as-prepared O3-FCG811 cathode. As shown, the cathode exhibits a spherical particle shape with the concentration of Ni rich at core while Co/Mn rich on the surface. Such design is intended to provide high specific capacity from redox reaction of Ni while suppressing the surface reactivity with the electrolytes via using Mn. Figure XVI.2.1b shows the corresponding XRD pattern of O3-FCG811 cathode, which exhibits a typical layered  $\text{NaFeO}_2$  structure without noticeable impurity. Figure XVI.2.1c shows the cycling performance of O3-FCG811 cathode during charge/discharge within 1.5-3.9 V (vs.  $\text{Na}/\text{Na}^+$ ) at a current density of  $75 \text{ mA g}^{-1}$  ( $\sim 0.5 \text{ C}$ ). The cathode delivered a high initial discharge specific capacity of  $\sim 150 \text{ mAh g}^{-1}$ , and can still maintain a reversible capacity of  $\sim 120 \text{ mAh g}^{-1}$  after 300 cycles, resulting in a good capacity retention of 80%. Our results indicate that concentration gradient could pave a new way to stabilize high-capacity and earth abundant layered oxide cathodes for sodium-ion batteries, for example Fe-rich core with Mn-rich shell.

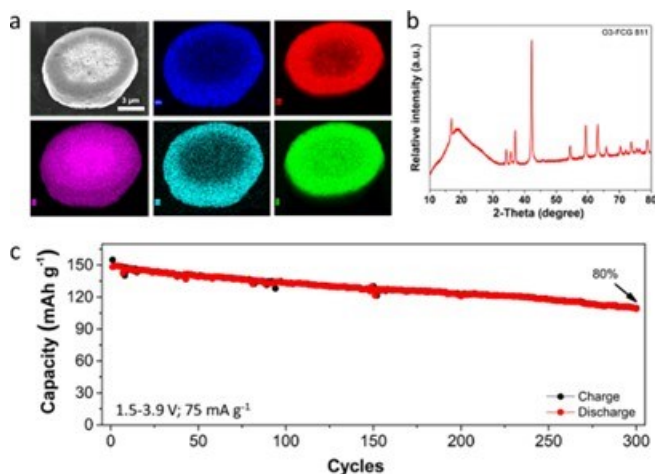


**Figure XVI.2.1 (a) SEM and the corresponding EDX mapping; (b) XRD pattern; and (c) cycling performance of the developed O3 FCG  $\text{NaNi}_{0.8}\text{Co}_{0.1}\text{Mn}_{0.1}\text{O}_2$  cathode.**

#### **Developing P2-type Ni/Co-free $\text{Na}_{2/3}\text{Fe}_{0.5}\text{Mn}_{0.5}\text{O}_2$ cathode through bulk cation doping**

On the other hand, to address the critical raw material supply chain challenge and improve the sustainability of sodium-ion battery, we have further developed an earth-abundant layered cathode materials. P2-type layered oxides based on earth-abundant Mn and Fe elements have garnered much attention for their potential in low-cost and high performance. However, the P2-type cathodes such as  $\text{Na}_{0.67}[\text{Mn}_{0.5}\text{Fe}_{0.5}]\text{O}_2$  still suffer from capacity fading during cycling, which is mainly caused by the undesired P2-O2 phase transition and lattice oxygen release in high-voltage region. Additionally, the P2–P2' phase transformation that occurs at low voltage region also damages the long term cycle performance of the material. Element doping strategy has been used as an effective and simple method for stabilizing the crystal structure, enhancing ion or electron diffusion, and stabilizing the phase transformation.

Firstly, the effect of Al, which is a widely used doping element stabilizing the structure of layered lithium transition metal oxides, has been investigated in P2- $\text{Na}_{0.67}[\text{Fe}_{0.5}\text{Mn}_{0.5}]_{1-x}\text{Al}_x\text{O}_2$  (where  $0 \leq x \leq 0.08$ ). The samples synthesized through solid-state reactions by homogeneously mixing precursors followed by heat treatment. XRD analysis confirmed the P2-type layered structure without any detectable impurities (data not shown). The *c*-axis parameters decrease with increasing Al concentration.  $\text{Al}^{3+}$  (0.535 Å) is smaller than  $\text{Fe}^{3+}$  (0.654 Å), and the Al–O bond has greater bonding energy (512 kJ mol<sup>-1</sup>) compared to Fe–O (409 kJ mol<sup>-1</sup>) and Mn–O (402 kJ mol<sup>-1</sup>). Therefore, it is anticipated that Al substitution for Fe and Mn results in tighter TM–O bonds and reduced electrostatic interaction between Na and O, which facilitate migration of Na ions in the sodium layer. The initial charge-discharge voltage profiles of P2- $\text{Na}_{0.67}[\text{Fe}_{0.5}\text{Mn}_{0.5}]\text{O}_2$  (denoted as NFM) and P2- $\text{Na}_{0.67}[\text{Fe}_{0.47}\text{Mn}_{0.47}\text{Al}_{0.06}]\text{O}_2$  (NFMA) cathodes (Figure XVI.2.2a) show that substitution of Mn and Fe with Al, which is electrochemically inactive, does not negatively affect the specific capacity of NFM, and in fact, slightly increases the value. In Figure XVI.2.2b and Figure XVI.2.2c, area-specific impedance (ASI) analysis conducted by a hybrid pulse power characterization (HPPC) method shows that cycle-to-cycle ASI build-up is suppressed by Al doping, suggesting mitigated surface or bulk degradations. The NFMA cathode also exhibits slightly improved cycle stability (Figure XVI.2.2d), coulombic efficiency (Figure XVI.2.2e), and rate capability (Figure XVI.2.2f).

To discern the impact of Al doping across the charge-discharge voltage regions, cells were cycled between different voltage ranges of 1.5 – 4.0 V (low voltage region) and 2.5 – 4.5 V (high voltage region). It was found that Al doping improves cycling stability in the low voltage range; however, no performance enhancement is observed for the high voltage range cycling. Ex situ XRD analysis was conducted to examine the structural changes induced by extreme charging (4.5 V) and deep discharging (1.5 V) conditions. In Figure XVI.2.3a-c, the disappearance of the (002) main peak at 15° and the emergence of a diffuse peak at approximately 17.5°

observed in both NFM and NFMA upon charging to 4.5 V indicate a transition of the pristine P2-phase to a defect-rich O2-type layered structure. This P2-to-O2 phase transition results in contraction of the interlayer spacing but marginal irreversibility of this phase transition leads to capacity decay. Upon discharging the electrodes to 2.5 V, the original O2 phase is restored. A subsequent deep discharge to 1.5 V induces a transition from P2 to a Jahn-Teller distorted P'2 phase, that is dominated by the presence of Mn(III). The comparatively minor shift in the P2'-(002) peak for the NFMA electrode suggests mitigated structural distortion by Al doping. In summation, our data reveals that while Al doping effectively curtails Jahn-Teller induced structural disruptions during deep discharge cycles, it has limited efficacy in rectifying the high voltage stability complications associated with P2-type layered cathodes.

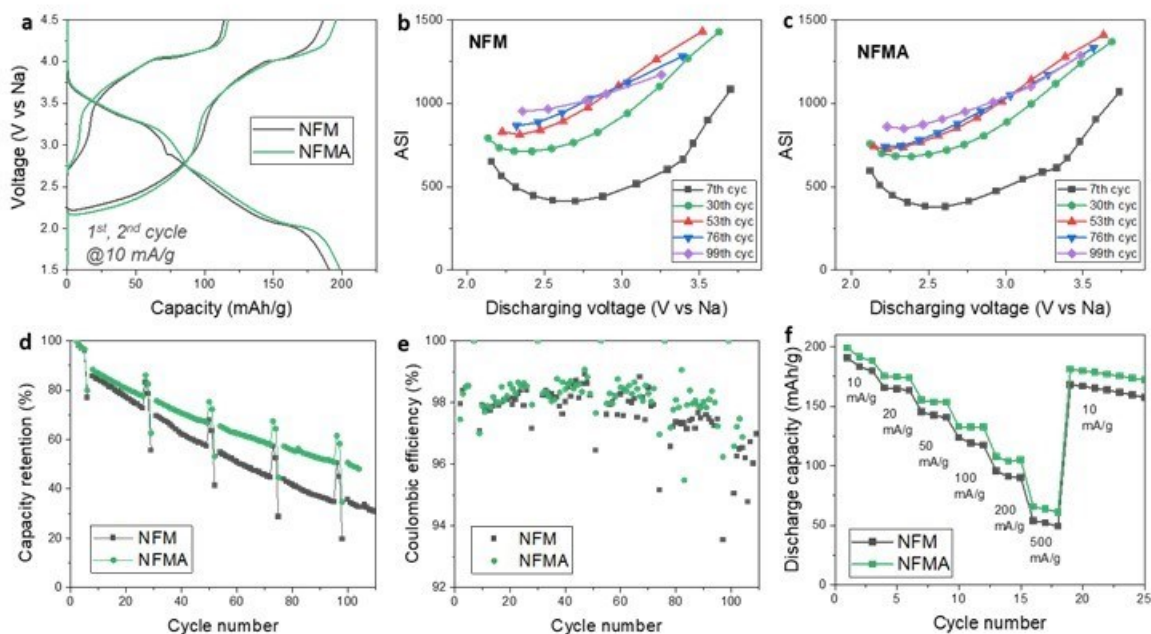
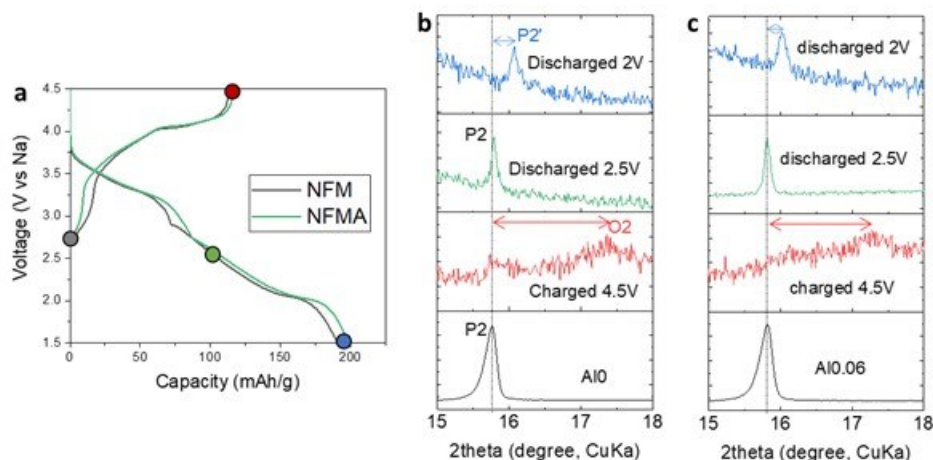


Figure XVI.2 (a) Charge-discharge voltage profiles, (b, c) area specific impedance (ASI) analysis, (d) capacity retention, and (e) coulombic efficiency of NFM and NFMA cathodes cycled between 1.5 – 4.5 V vs. Na. (f) Rate performance at current density from 10 mA/g to 500 mA/g.





**Figure XVI.2.3** Ex-situ XRD analysis collected at various charged and discharged states marked in (a) for the (b) NFM and (c) NFMA electrodes.

In our next attempt to further improve the high voltage cycling stability, the Mg and Ti co-doping strategy was explored. The P2  $\text{Na}_{0.67}\text{Fe}_{0.5}\text{Mn}_{0.5}\text{O}_2$  with Mg/Ti co-doping is denoted as NFMMT. Figure XVI.2.4a and Figure XVI.2.4b compare the XRD patterns of NFM and NFMMT, respectively. As shown, both materials exhibit a typical P2-type structure (space group P63/mmc (194)). In this structure, the “ABAB” stacking sequence of oxygen packing constitutes the main frame, transition metal (TM) ions are located in the center of  $\text{TMO}_6$  octahedrons, and  $\text{Na}^+$  ions occupy the prismatic sites between TM layers. The Rietveld refinement results further indicate the P2 structure for both materials with no impurity phase. The obtained lattice parameters of NFM and NFMMT are  $a=2.922(3) \text{ \AA}$ ,  $c=11.242(5) \text{ \AA}$  and  $a=2.917(2) \text{ \AA}$ ,  $c=11.239(8) \text{ \AA}$ , respectively. The slight shrinkage of lattice parameters in NFMMT originated from the smaller ionic radius of  $\text{Mg}^{2+}$  and  $\text{Ti}^{4+}$  than those of Mn and Fe ions. The morphology of NFMMT was examined by scanning electron microscopy (Figure XVI.2.4c), showing the typical particle size of 1-2  $\mu\text{m}$ , and homogeneous distribution of Na, Fe, Mn, Mg and Ti within the single-crystalline particles (Figure XVI.2.4d).

Figure XVI.2.5a and Figure XVI.2.5b shows the charge/discharge curves of NFM and NFMMT cycled between 1.5-4.5 V vs. Na, respectively. The NFM cathode could deliver an initial high specific capacity of  $216 \text{ mAh g}^{-1}$  with an average working voltage of 2.6 V. However, upon cycling, NFM exhibits a continuous loss in both capacity and working voltage. By sharp contrast, after Mg/Ti co-doping, the initial specific capacity of NFMMT cathode was slightly decreased to  $209 \text{ mAh g}^{-1}$ , while the voltage/capacity stability were significantly improved. After 50 cycles of charge/discharge at  $20 \text{ mA g}^{-1}$ , NFMMT cathode could still maintain a reversible capacity of  $> 160 \text{ mAh g}^{-1}$ , much higher than that of NFM ( $< 100 \text{ mAh g}^{-1}$ ). The cycling performance of NFM and NFMMT cathode were further tested at a higher current density of  $200 \text{ mA g}^{-1}$ . As shown in Figure XVI.2.5c, after the activation for the initial 3 cycles, the reversible capacity of NFM degrades rapidly upon cycling owing to the unfavorable phase transition and Jahn-Teller effect of  $\text{Mn}^{3+}$  ions, leading to a capacity retention of only  $31.2 \pm 1.4\%$  after 150 cycles at  $200 \text{ mA g}^{-1}$ . In sharp contrast, without any structural modification, NFMMT exhibits a promising capacity retention of  $72.6 \pm 0.8\%$  at  $200 \text{ mA g}^{-1}$  between 1.5-4.5 V after 300 cycles. The results indicate that dopant engineering could significantly alleviate the structural degradation of sodium layered cathodes at high voltage. We will explore multi-cation doping in the next year to achieve even better fast charging and long-term cycling stability.

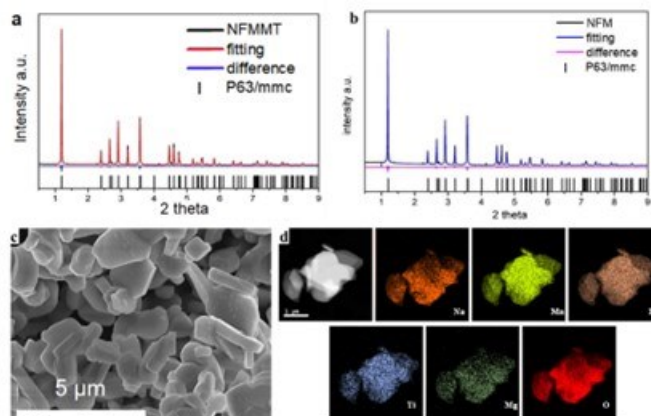


Figure XVI.2.4 XRD patterns of (a) NFM and (b) NFMMT. SEM images of (c) NFM and (d) NFMMT.

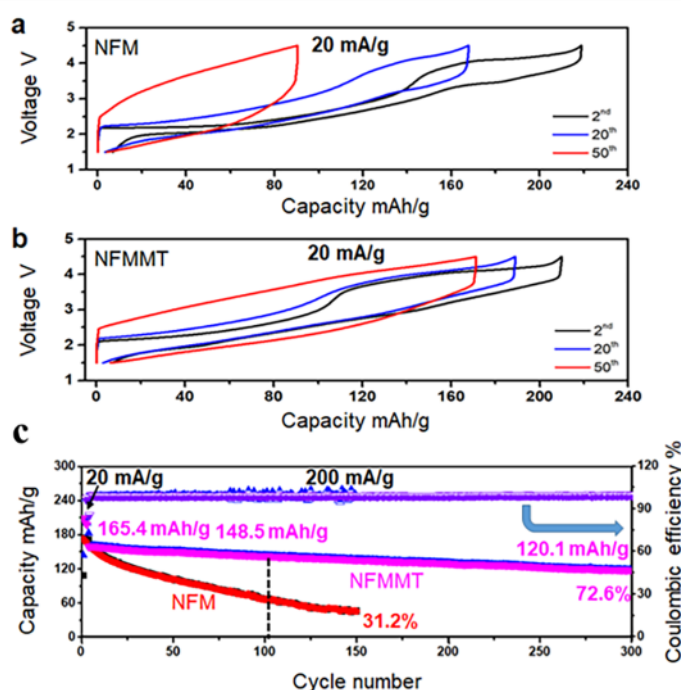


Figure XVI.2.5 Electrochemical performance of NFM and NFMMT. (a, b) Charge and discharge profiles of NFM (a) and NFMMT (b) at  $20 \text{ mA g}^{-1}$  in the voltage range of 1.5–4.5 V. (c) Long-cycle performance of NFM and NFMMT at  $200 \text{ mA g}^{-1}$  between 1.5 and 4.5 V.

### Surface coating

The previous section has highlighted the critical role of bulk cation substitution in mitigating structural degradation during the charge-discharge cycles of the P2-type layered cathodes at both high and low voltages. Concurrently, there has been considerable investigation into surface coatings as a protective layer for cathode surfaces. Despite the proven benefits of surface coatings on NMC-based lithium-ion battery cathodes, their application to the sodium-ion battery cathodes based on earth-abundant elements introduces spectrum of complexity, marked by a series of unresolved questions and uncertainties. In our efforts to reproduce the previously reported results, where enhanced capacity and cycle performance were observed with  $\text{Al}_2\text{O}_3$  surface coating on P2-type layered cathodes, we discovered that the effectiveness of the coating layer is highly influenced by the coating process and the quality of the baseline cathode materials.  $\text{Al}_2\text{O}_3$  atomic layer deposition (ALD) process relies on trimethylaluminum (TMA) reaction with water dosing at the material surface. Sodium

transition metal oxides are sensitive to moisture and air, and thus the coating process can introduce significant modifications to the cathode surface if not meticulously controlled. The amount of surface residual sodium species can also impact the quality and effectiveness of the final coating product. Consequently, precise control over the coating process and a detailed analysis of the surface coating chemistry are essential to unravel the true role of the surface coating layers on the performance of sodium cathode materials.

Figure XVI.2.6 presents the example of  $\text{AlF}_3$  coating applied on  $\text{P2-Na}_{2/3}\text{Ni}_{1/3}\text{Mn}_{2/3}\text{O}_2$  (NNM) cathode particles via ALD method. Unlike the conventional  $\text{Al}_2\text{O}_3$  ALD process where water is one of the reactants, the ALD process for  $\text{AlF}_3$  does not require water for the process and surface of the sodium transition metal cathode remains inert during the entire coating process. The ALD- $\text{AlF}_3$  coated NNM samples exhibit a marginal reduction in initial discharge capacity. Nonetheless, the coating markedly improves the capacity retention as depicted in Figure XVI.2.6d. The uncoated NNM samples show the steep capacity decline during the initial ~10 cycles, which then tapers off after about 15 cycles. By contrast, the ALD- $\text{AlF}_3$  coated cathodes exhibit a consistent and gradual capacity drop over the entire testing period. It is presumed that the initial rapid capacity decay of the uncoated cathode is due to the severe surface damage, which is effectively mitigated by surface modification through the ALD- $\text{AlF}_3$  coating. Nonetheless, the surface coating layer does not seem to fully prevent the bulk structural transitions and associated degradation of the cathodes. These initial findings underscore the critical need for precise control and thorough analysis of the coating's chemistry to fully understand its influence on the performance of sodium-ion cathode materials.

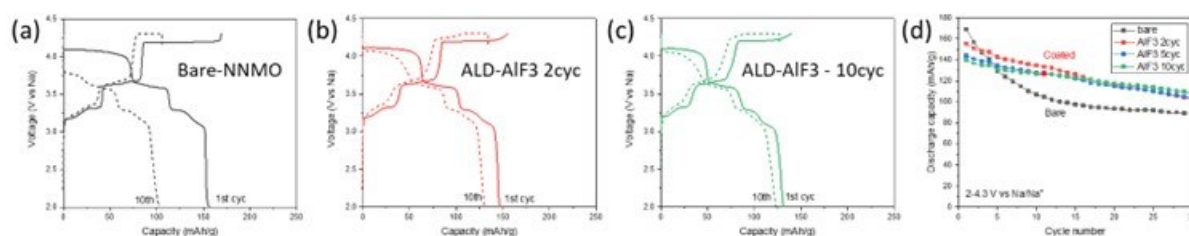


**Figure XVI.2.6** (a-c) Voltage profiles and (d) capacity retention of the bare and ALD- $\text{AlF}_3$  coated NNM cathodes; voltage ranges of 2.0 – 4.3 V vs. Na; current density of 15 mAh/g for (a-c) and 100 mAh/g for (d).

*Exploring high-capacity phosphorus anode for sodium-ion batteries towards fast charging and high areal capacity*

On the anode side, we have explored the cell performance of ANL's patented Sb-doped red phosphorus ( $\text{Sb}_7\text{-RP}_{63}/\text{C}_{30}$ , the number corresponds to weight percentage) anode materials (US Patent 11,394,022) using localized highly concentrated electrolytes (LHCE: 1.2 M NaFSI in dimethoxyethane (DME) with (bis(2,2,2-trifluoroethyl) ether (BTFE) as the co-solvent) that developed by Dr. Xiaolin Li at PNNL. Figure XVI.2.7 shows the electrochemical performance of  $\text{Sb}_7\text{-RP}_{63}/\text{C}_{30}$  anode in the LHCE electrolyte. As shown, the  $\text{Sb}_7\text{-RP}_{63}/\text{C}_{30}$  anode could deliver a highly reversible capacity of  $\sim 2500 \text{ mAh g}^{-1}$  with high initial coulombic efficiency of 85.7% and stable cycle life for up to 70 cycles. Furthermore, it has demonstrated excellent fast charging capability, which can maintain a high specific capacity of  $> 2000 \text{ mAh g}^{-1}$  at 3C ( $1\text{C}=2596 \text{ mA g}^{-1}$ ).

To understand the solid-electrolyte interphase (SEI) of  $\text{Sb}_7\text{-RP}_{63}/\text{C}_{30}$  anode in the LHCE electrolyte, we conducted X-ray photoelectron spectroscopy (XPS) analysis before and after charge/discharge. Figure XVI.2.8a shows the corresponding P 2p XPS spectra. The pristine electrode shows two major peaks at 129.0 and 130.0 eV, which can be assigned to the P 2p<sub>3/2</sub> and P 2p<sub>1/2</sub> doublet of the element P. In addition, a weak P–O peak at 133.2 eV can be observed, which is due to the partial oxidation of  $\text{Sb}_7\text{-RP}_{63}/\text{C}_{30}$  during laminate fabrication under ambient atmosphere. When the cell was discharged to 0.02 V, two new peaks appeared at 136.9 and 126.8 eV. The peak at 126.8 eV is attributed to the formation of  $\text{Na}_3\text{P}$ , which leads to a significant decrease of the P 2p peaks at 130 and 129 eV. After charging back to 2.0 V, the P 2p peaks of  $\text{Sb}_7\text{-RP}_{63}/\text{C}_{30}$  were recovered along with the disappearance of the  $\text{Na}_3\text{P}$  peak due to the de-sodiation of  $\text{Na}_3\text{P}$  to P during charge. The identification

of the Na<sub>3</sub>P and P 2p peaks during charge/discharge in the XPS clearly demonstrates that the SEI layer on the Sb<sub>7</sub>-RP<sub>63</sub>/C<sub>30</sub> anode is very thin (<10 nm due to the penetration depth limit of XPS). Moreover, The depth profile XPS C 1s result in Figure XVI.2.8b clearly confirmed that the thickness of solvent decomposition is < 5 nm, as can be seen from the disappearance of O–C–O and C–O peaks and increase of –COOH (~290 eV, belong to the binder), C–C (C–H), and sp<sup>2</sup> carbon peaks after etching. The depth profile XPS F 1s result (Figure XVI.2.8c) indicated that the formed SEI is F-enriched, which can accommodate the plastic deformation of the sodiated alloy during cycling.

We further tested the electrochemical performance of Sb<sub>7</sub>-RP<sub>63</sub>/C<sub>30</sub> anode under a higher areal loading of 2.12 mg cm<sup>-2</sup>, which can deliver a high areal capacity loading of > 4 mAh cm<sup>-2</sup> and a high initial Coulombic efficiency of ~ 85% at C/3 in both carbonate-based and LHCE electrolytes (Figure XVI.2.9a). However, the half-cells using Na metal anode exhibited a rapid failure (Figure XVI.2.9b), which is attributed to the poor stripping/plating of Na metal in the carbonate and LHCE electrolytes at high areal capacities. As shown in Figure XVI.2.9c and Figure XVI.2.9d, the Na/Na symmetric cells exhibited significantly increased voltage polarization within < 100 h in both electrolytes under a high areal capacity of 4 mAh cm<sup>-2</sup> at a current density of 1 mA cm<sup>-2</sup>, though LHCE electrolytes exhibit slightly improved performance than carbonate electrolytes. Future studies will be focused on full cell study using the developed O3 cathode and phosphorus-based anode. The effect of electrolytes will also be explored in FY24.

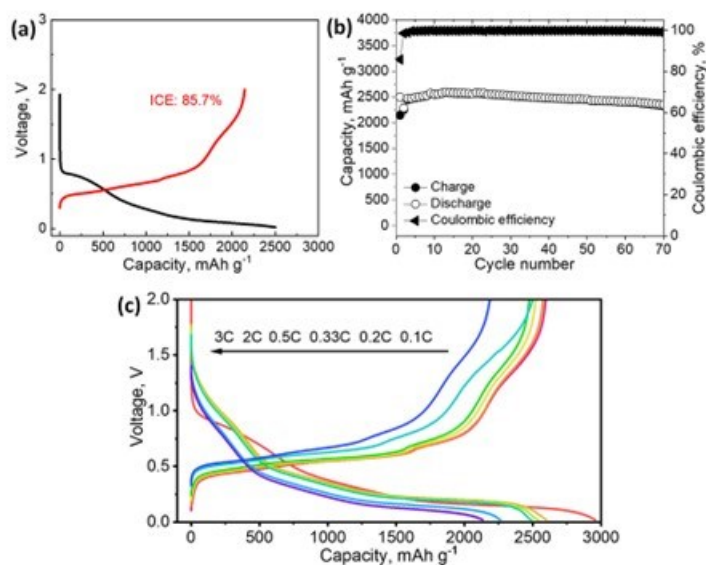


Figure XVI.2.7 (a) The 1<sup>st</sup> voltage curve, cycling performance and rate capability of Sb<sub>7</sub>-RP<sub>63</sub>/C<sub>30</sub> anode during charge/discharge in LHCE electrolytes.

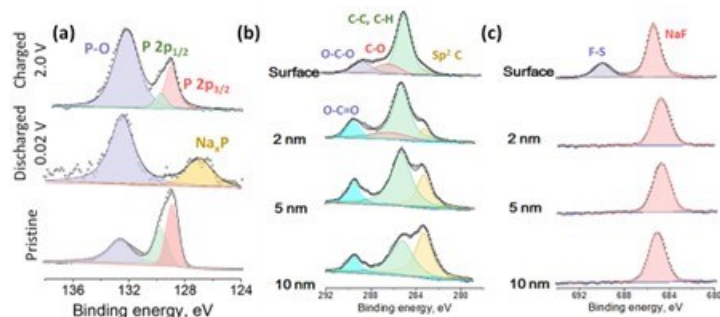


Figure XVI.2.8 (a) P 2p XPS spectra of the Sb<sub>7</sub>-RP<sub>63</sub>/C<sub>30</sub> anode during charge/discharge in the LHCE electrolytes. Depth profile XPS (b) C 1s and (c) F 1s of discharged Sb<sub>7</sub>-RP<sub>63</sub>/C<sub>30</sub> anode in the LHCE electrolytes.

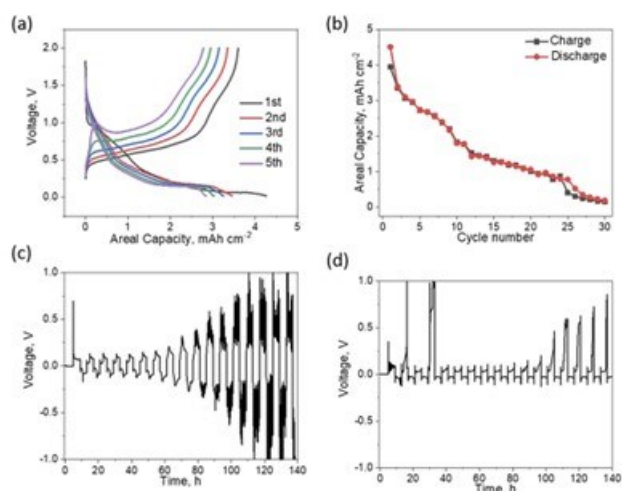


Figure XVI.2.9 (a) Charge/discharge curves in the carbonate electrolytes and (b) cycling performance in the LHCE electrolytes of Sb<sub>7</sub>-RP<sub>63</sub>/C<sub>30</sub> anode with an areal Sb<sub>7</sub>-RP<sub>63</sub> loading of 2.12 mg cm<sup>-2</sup> at C/3; Stripping/plating of Na metal in the (c) carbonate and (d) LHCE electrolytes using Na/Na symmetric cell with a high areal capacity loading of 4.0 mAh cm<sup>-2</sup> at a current density of 1.0 mA cm<sup>-2</sup>.

## Conclusions

In summary, we have developed several types of sodium layered oxide cathodes through concentration gradient design, bulk cation dopant engineering, and surface coating to suppress the undesired phase transformation during charge/discharge, which significantly improved their cycling stability. We also explored the electrochemical performance of phosphorus-based anode towards high charge/discharge rate and high areal capacity loading. Advanced characterization such as synchrotron X-ray techniques will be used to elucidate the underlying mechanism. Single-layer sodium-ion pouch cells using our cathode and anode technology will be explored in the next year.

## Key Publications

### Patent

- “Lead-lead oxide-carbon nanocomposite for energy storage cells and method of preparation,” C. S. Johnson, E. Lee, J. Han, J. Park, US11611069, Granted in March 2023.

### Publications

- Daali, X. Zhou, C. Zhao, I. Hwang, Z. Yang, Y. Liu, R. Amine, C. J. Sun, O. Wilkistar, G. L. Xu\*, K. Amine\*, "In situ microscopy and spectroscopy characterization of microsized Sn anode for sodium-ion batteries," *Nano Energy* 2023, 115, 108753.
- J. Huang, E. Kim, S. Li, L. Cheng, G. L. Xu\*, K. Amine, C. Wang\*, C. Luo\*, "A Self-Healing Chemistry Enabled Organic Cathode for Sustainable and Stable Sodium Ion Batteries," *Small structures* 2023, 2300211.
- J. Park, K. Ku\*, J. Gim, S.-B. Son, H. Jeong, L. Cheng, H. Iddir, D. Hou, H. Xiong, Y. Liu, and E. Lee\*, C. S. Johnson, "Multi-functional effect of Fe substitution in Na layered cathode materials for enhanced storage stability," *ACS Appl. Mater. Interfaces* 2023, 15, 38454.
- J. Park, J. Han, J. Gim, J. Garcia, H. Iddir, S. Ahmed, G. Xu, K. Amine, C. Johnson, Y. Jung, Y. Kim, S.M. Bak, E. Lee, "Evidence of Zintl Intermediate Phase and Its Impacts on Li and Na Storage Performance of Pb-Based Alloying Anodes", *Chem. Mater.* 2023, 35, 11, 4171-4180.

### Presentations

- Eungje Lee, "Advanced Materials for Next-Generation Li- and Na-Batteries," Korea-US Advanced Industry and Technology Cooperation Forum, Seoul, South Korea, September 21, 2023. (Invited)
- Eungje Lee, "Development of Sustainable Materials for Sodium-Ion Batteries at Argonne National Laboratory," Faraday Institute NEXGENA Seminar, Virtual, February, 1, 2023. (Invited)
- Wenhua Zuo, Guiliang Xu and Khalil Amine. The Air Stability of Sodium Layered Oxide Cathodes. Poster presented at the 242<sup>nd</sup> Electrochemical Society Meeting, , October 9, 2022-October 13, 2022.
- Daali, Amine, Rachid Amine, Guiliang Xu, Wilkistar Otieno and Khalil Amine. Composition and structural control of Phosphorus-based anode for high-energy lithium-ion batteries." Poster presented at the 13th International Conference on Advanced Lithium Batteries for Automobile Applications and Young Researcher's Day, Ben Guerir MA, October 1, 2022-October 21, 2022.
- Guiliang Xu, Xiang Liu, Chen Zhao and Khalil Amine. "Origin and regulation of oxygen redox instability in high-voltage battery cathodes." Poster presented at the 13th International Conference on Advanced Lithium Batteries for Automobile Applications and Young Researcher's Day, Ben Guerir MA, October 1, 2022-October 21, 2022.

### References

1. N. Yabuuchi, et al., *Chemical Reviews* 114 (2014):11636-11682.
2. M. Han, et al., *Energy & Environmental Science* 8 (2015):81-102.
3. Y. Wen, et al., *Nature Communications* 5 (2014): 4033.
4. S. Huang, et al., *Adv. Mater.* 30 (2018):1706637.
5. H. Kang, et al., *Journal of Materials Chemistry A* 3 (2015):17899-17913.
6. C. Johnson, et al., *Electrochem. Commun.* 18 (2012):66-69.
7. N. Yabuuchi, et al., *J. Electrochem. Soc.* 160 (2013):A3131-A3137.
8. D. Yuan, et al., *ACS Appl. Mater. Interfaces* 7 (2015):8585-8591.
9. Y.-K. Sun, et al., *J. Power Sources* 324 (2016): 106-112.
10. Z.-F. Ma, et al., *J. Alloys Compounds* 724 (2017): 465-473.

### Acknowledgements

Support from Tien Duong of the U.S. DOE's Office of Vehicle Technologies Program is gratefully acknowledged. We would like to thank Dr. Guiliang Xu and Dr. Eungje Lee at ANL for their major contribution to this project.

## XVI.3 Tailoring High Capacity, Reversible Anodes for Sodium-Ion Batteries (LBNL)

### Marca M. Doeff, Principal Investigator

Lawrence Berkeley National Laboratory  
1 Cyclotron Road  
Berkeley, CA 94720  
E-mail: [mmdoeff@lbl.gov](mailto:mmdoeff@lbl.gov)

### Tien.Duong, DOE Technology Development Manager

U.S. Department of Energy  
E-mail: [Tien.Duong@ee.doe.gov](mailto:Tien.Duong@ee.doe.gov)

Start Date: October 1, 2022

End Date: September 30, 2023

Project Funding (FY23): \$300,000

DOE share: \$300,000

Non-DOE share: \$0

### Project Introduction

Stepped layered titanates are promising materials for use as anodes in sodium-ion batteries, due to their earth-abundance, low cost, reasonably high density, and low sodium insertion potentials ( $\sim 0.3$ – $0.6$  V vs.  $\text{Na}^+/\text{Na}$ , on average). We have identified several materials that deliver capacities in excess of 200 mAh/g and cycle reversibly in sodium half-cell configurations [1-3]. In particular, the physical and electrochemical properties of lepidocrocite-type titanates having the general formula  $\text{A}_x\text{Ti}_{2-y}\text{M}_y\text{O}_4$  ( $\text{A}=\text{K}^+$ ,  $\text{Cs}^+$ ,  $\text{Rb}^+$  and  $\text{M}=\text{metal}$  or vacancy located in the transition metal layer), can be readily tuned by exchanging the large cations, A, with  $\text{Na}^+$ , and by varying the identity of M, as well as the overall composition (x and y). For example, additional diffusional pathways for  $\text{Na}^+$  are present when M is a mobile cation such as  $\text{Li}^+$  compared to the less mobile  $\text{Mg}^{2+}$  cation, resulting in higher practical capacities [4]. Based on a similar principle, capacities in excess of 220 mAh/g can be obtained when vacancies are incorporated in the transition metal layer [3]. In addition to composition, however, it is clear that the electrochemical properties of these materials are very sensitive to preparation conditions such as dehydration temperature, as well as details of the cell assembly, such as the type of electrolytic solution used [3, 5]. Furthermore, an analysis of cyclic voltammetry data on cells made with vacancy-containing lepidocrocite titanates indicated that the redox mechanism is complex, including both surface and diffusional components. In particular, small features (plateaus) above 1 V vs  $\text{Na}^+/\text{Na}$  appear to have pseudo-capacitive character. Further evidence for this is that less titanium is reduced than expected, assuming a purely diffusional redox process, as observed by Ti K-edge X-ray absorption experiments on pristine, discharged, and partially discharged electrodes. Capacity loss during cycling is primarily due to the high voltage processes. Heat treatment of the vacancy containing lepidocrocite type titanate results in temperature-dependent structural and surface changes, which influence the electrochemical properties [6]. Cycling is markedly improved for a material treated at 500°C, although a break-in process is needed (either by an initial discharge to 0.05 V in a sodium half-cell or repeated cycling to 0.1 V). There is less loss upon cycling above 1 V vs.  $\text{Na}^+/\text{Na}$  and less capacity overall in this region, compared to a material heated to 60°C. The 500°C material also amorphizes during cycling but retains 80% of its original capacity after 740 cycles. Another promising material is sodium nonatitanate ( $\text{NaTi}_3\text{O}_6(\text{OH})\cdot 2\text{H}_2\text{O}$ ) or NNT, which is made hydrothermally, and can be dehydrated at temperatures at 600°C or higher. When properly optimized, it can deliver capacities of 200 mAh/g [5]. Of the two types of materials (lepidocrocite-structured titanate and NNT), NNT is probably more practical to use, as it does not require an ion-exchange step, and is less hygroscopic.

### Objectives

The planned work is conceived to overcome the main obstacle to the practical realization of sodium-ion batteries; the lack of a suitable anode material. Experiments are designed to improve the practical reversible capacities and overcome the high first cycle coulombic inefficiencies of promising low voltage sodium titanates, as well as to assess the stabilities of the sodiated (partially and fully discharged) products of the

electrochemical reactions. Some effort is devoted to consideration of electrolytes and understanding of the electrolyte/anode interface, which must go hand-in-hand with anode development. The ultimate goal is to produce a high capacity (200-250 mAh/g), stable, and reversible low voltage anode material suitable for use in a sodium-ion battery configuration. An ideal electrode would be able to deliver 225 mAh/g at C/3 rate, with good capacity retention (80% or better) in a full cell configuration for at least 100 cycles.

### Approach

Candidate stepped layered titanates are synthesized by appropriate routes (hydrothermal, solid-state methods, etc.) and ion-exchanged by soft chemical techniques if deemed necessary. Materials are then characterized physically using both laboratory techniques and synchrotron techniques, including X-ray diffraction (XRD), Fourier transform infrared spectroscopy (FTIR), Raman spectroscopy, scanning electron microscopy (SEM), transmission electron microscopy (TEM), X-ray absorption spectroscopy (XAS), X-ray photoelectron spectroscopy (XPS), etc. Structure-function relationships are built to correlate the effect of changing structure and surface characteristics on electrochemical properties. Sodium half-cells are built and cycled under a variety of conditions to understand the electrochemistry and the limitations of the materials. Techniques commonly used include galvanostatic cycling, potentiostatic or galvanostatic intermittent titration technique (PITT or GITT) and cyclic voltammetry (CV). Some attention is paid to the effect of changing electrolytic solution on properties such as first cycle coulombic efficiency. Ex situ and in situ experiments such as XPS on partially or fully discharged or cycled electrodes are used to gain understanding about redox mechanisms. The thermal behavior of candidate materials is also examined by subjecting materials to various heating regimes and examining structural changes by carrying out in situ XRD and spectroscopic analysis. Some work is also directed towards full cell cycling.

### Results

Our prior results indicated that the vacancy-containing lepidocrocite-structured compound  $\text{Na}_{0.74}\text{Ti}_{1.815}\square_{0.815}\text{O}_4$  (NTO) could deliver in excess of 225 mAh/g in a sodium half-cell configuration, with an average potential of 0.5V vs.  $\text{Na}^+/\text{Na}$ , making it a promising anode material. Capacity above 1V is mainly pseudocapacitive in the material dried at 60°C, as shown by power law analysis of cyclic voltammetry results, and is the main culprit implicated in fading upon cycling. Most likely the pseudocapacitive character is due to defect sites on the surface induced by the ion-exchange process used to prepare the material. The defects can be annealed away by heat-treatment, resulting in better cycling; however, the high temperature treatment also results in structure change making it difficult to determine which factor (structure or surface) is most responsible for the improved cycling properties. It is also possible to modify the surface of the material heated to 60°C by dry ball-milling it with acetylene black, which does not change the bulk structure. It can be seen in Figure XVI.3.1c that the voltage profile changes for the carbon-coated material; most notably, the high voltage plateaus are absent. The initial capacity is also lower, but the cycling is markedly improved (Figure XVI.3.1d). Some capacity is regained when carbon nanotubes are added.



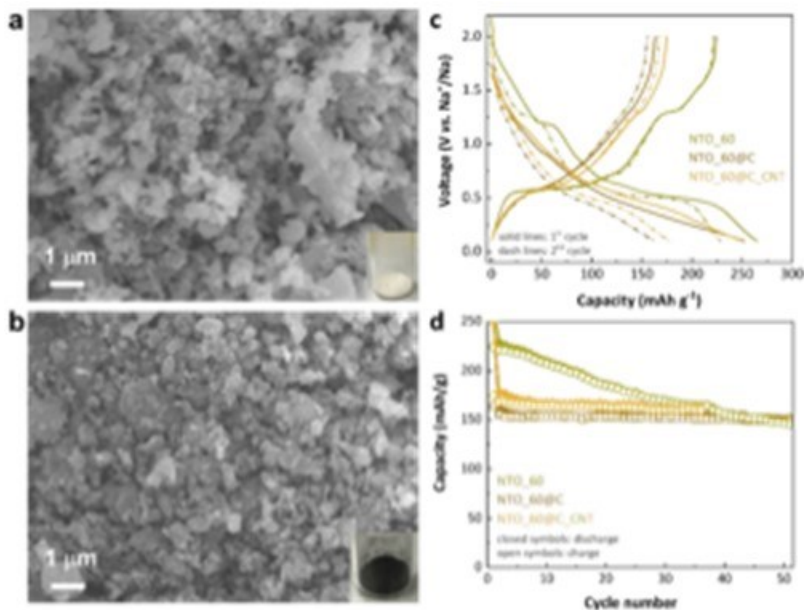


Figure XVI.3.1 a) SEM image of NTO powder after heating to 60°C. Inset shows optical image of white powder, b) SEM image of NTO powder after dry ball milling with acetylene black. Inset shows optical image of powder, now colored black, c) 1<sup>st</sup> and 2<sup>nd</sup> cycles of sodium half cells containing NTO powder heated to 60°C, carbon-coated NTO, and carbon coated NTO with carbon nanotubes added, d) capacity as a function of cycle number for the three types of cells. All the cells were cycled at 8 mA g<sup>-1</sup> using an electrolyte of 0.5 M sodium tetraphenylborate (NaBPh<sub>4</sub>) in diethylene glycol dimethyl ether (DEGDME).

Carbon coating also improves the performance of the NTO heated to 500°C. In this case, these were prepared by wet-coating the particles with polyacrylonitrile (PAN) prior to heating, adjusting the PAN/NTO mass ratio so that carbon contents ranged from 3.3-30 wt. %. Figure XVI.3.2a and c compare the capacity retention profiles and coulombic efficiencies of sodium half-cells made with 500 °C-heated NTO electrodes with carbon coatings of 3.3 wt.%, 5 wt.%, and 10 wt.%. While NTO electrode coated with 3.3 wt.% carbon still shows some capacity fading over the initial 30 cycles, the electrodes with higher carbon amounts of 5 wt.% and 10 wt.% exhibit stable cycling with slight capacity increases after 15 cycles. The 5 wt.%-carbon-coated NTO electrode delivers the highest capacities. These results suggest that carbon coating actually has a two-fold aspect: on the one hand, sufficient amount of surface carbon coating improves the capacity retention; on the other hand, too much carbon coating at the surface makes NTO less accessible for sodium insertion and adversely affects the capacity. Figure XVI.3.2b compares results of NTO, NTO with 20 wt. % carbon additive and 5% carbon coated NTO with and without 20 wt. % carbon additive. Here it can be seen that the carbon coating results in improved overall capacity and capacity retention compared to bare NTO, even with 20% carbon additive.

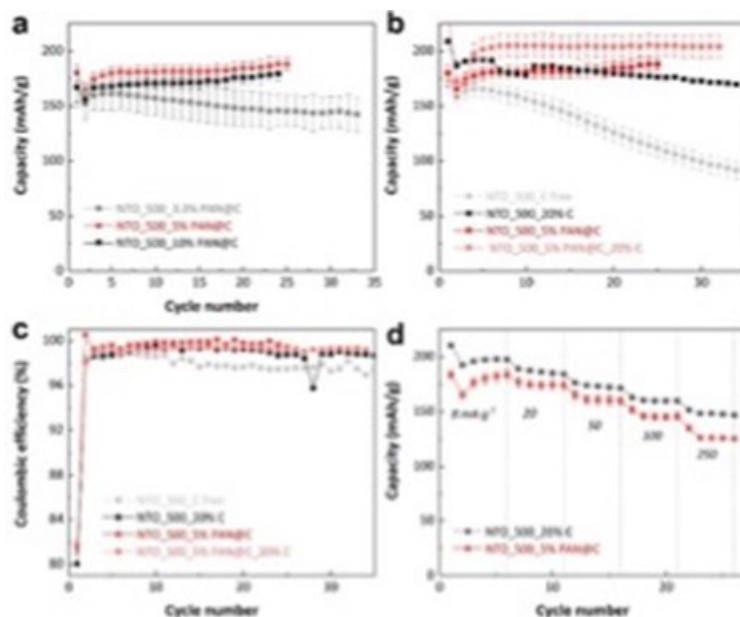


Figure XVI.3.2 (a, b) capacity retention and (c) first-cycle Coulombic efficiency of sodium half-cells containing 500°C-heated NTO with and without 20 wt.% carbon additive and carbon-coated 500 °C-heated NTO without and with 20 wt.% carbon additives (d) rate capability of selected cells. All the cells were cycled at 8 mA g<sup>-1</sup> between 0.05 and 2.0 V. The capacity was normalized only based on the mass of 500 °C-heated NTO. All the cells were cycled at 8 mA g<sup>-1</sup> using an electrolyte of 0.5 M sodium tetraphenylborate (NaBPh<sub>4</sub>) in diethylene glycol dimethyl ether (DEGDME).

The best-performing 5 wt.%-carbon-coated NTO anodes were paired with with Na<sub>3</sub>V<sub>2</sub>(PO<sub>4</sub>)<sub>3</sub> (NVP) cathodes to assemble sodium-ion full cells using electrolyte of 1 M sodium bis(trifluoromethanesulfonyl)imide (NaTFSI)-ethylene carbonate (EC)/diethyl carbonate (DEC). When cycled in a voltage window of 3.4 - 0.8 V vs. Na<sup>+</sup>/Na at a current rate of C/10 (calculated based on NVP), the cell delivers an initial charge capacity of 130 mAh g<sup>-1</sup> and a discharge capacity of 57 mAh g<sup>-1</sup> (capacity normalized based on NVP, Figure XVI.3.3a). The discharge capacity is lower than the 112 mAh g<sup>-1</sup> obtained from an NVP/Na half-cell. Na<sup>+</sup> consumption during the solid-electrolyte-interface (SEI) formation at the NTO anode side is partly responsible for the irreversible loss. Cycling the negative electrode in a half-cell configuration before incorporating it in the full cell would improve results, as we have shown in previous attempts with different titanate materials.

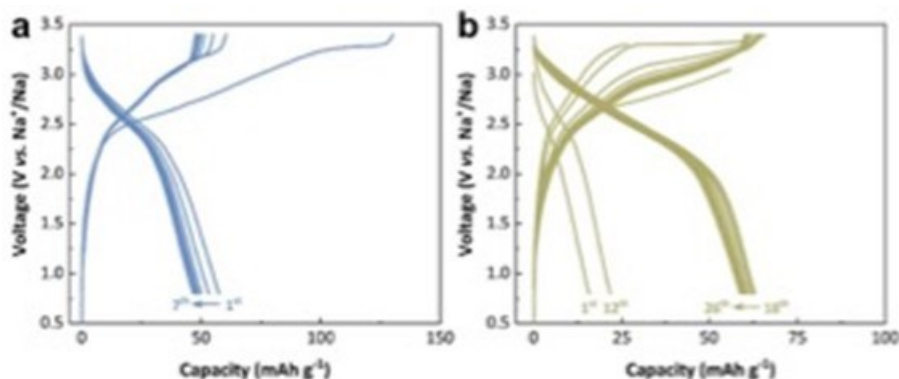
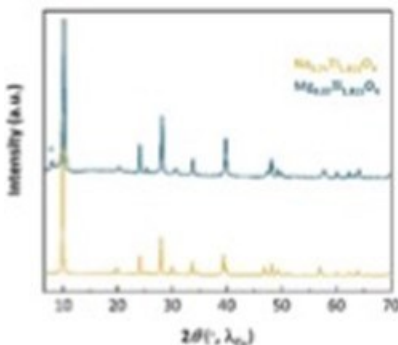


Figure XVI.3.3 (a, b) The cycling profiles of sodium vanadium phosphate (NVP)/500 °C-heated NTO full-cells cycled in 1 M sodium bis(trifluoromethanesulfonyl)imide (NaTFSI)-ethylene carbonate (EC)/diethyl carbonate (DEC) electrolyte. All the cells were cycled at a current rate of C/10 calculated based on NVP and capacity is normalized based on NVP. The N/P ratio is ~1.1 - 1.5.

Some work was directed towards understanding the role that interlayer cations play in determining electrochemical properties. The NTO materials discussed above were all made by ion-exchanging a Cs-containing precursor with sodium and then heating to the indicated temperatures. However, the material can also be exchanged with other monovalent or divalent ions to form new materials with different properties. The replacement of  $\text{Cs}^+$  directly with  $\text{Mg}^{2+}$  should result in more sites for sodium insertion, since each  $\text{Mg}^{2+}$  ion replaces two monovalent cations residing in the interlayer space. The fully exchanged product has a nominal composition of  $\text{Mg}_{0.37}\text{Ti}_{1.815}\text{O}_4$  (compared to NTO,  $\text{Na}_{0.74}\text{Ti}_{1.815}\text{O}_4$ ). The resulting  $\text{Mg}^{2+}$  ion-exchanged phase retains the same body-centered orthorhombic symmetry as the  $\text{Na}^+$  ion-exchanged phase, but a highly swollen phase (probably a bilayer hydrate, marked with an asterisk in Figure XVI.3.4). The swollen phase disappears after drying at  $100^\circ\text{C}$  overnight under vacuum.



**Figure XVI.3.4** Synchrotron XRD patterns of NTO (bottom, in gold) and  $\text{Mg}_{0.37}\text{Ti}_{1.815}\text{O}_4$  (top, in blue). An asterisk marks the swollen phase of the latter. This peak disappears after the material is dried.

Figure XVI.3.5 compares electrochemical data for the Mg-exchanged phase in sodium half-cells to that of NTO dried at  $60^\circ\text{C}$ . The capacity of the Mg-exchanged phase is slightly lower, in spite of the presence of more empty sites in the pristine material. It is likely that Mg blocks diffusion of sodium because it is so immobile, resulting in reduced practical capacity. DFT calculations on lepidocrocite titanates containing Mg in the titanate layer (e.g.,  $\text{Na}_{0.75}\text{Ti}_{1.625}\text{Mg}_{0.375}\text{O}_4$ ) showed that Mg blocks sodium diffusion in the *b*-direction (through the titanate layer into the sodium layer) resulting in lower capacities compared to  $\text{Na}_{0.8}\text{Ti}_{1.73}\text{Li}_{0.27}\text{O}_4$ , where the mobile Li cation can drop into the sodium layer and provide an additional diffusion pathway [4]. In spite of this, the Mg-substituted material seems to have better capacity retention upon cycling, and a lower average insertion potential, advantageous for anode materials.

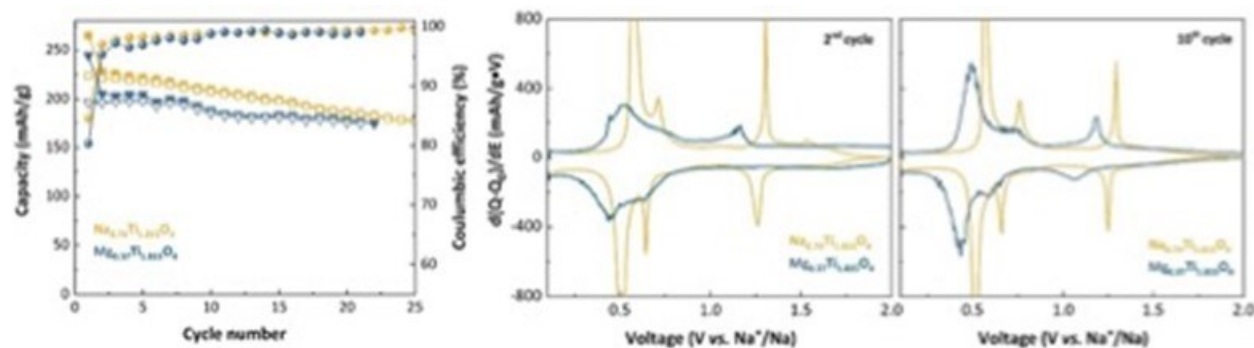


**Figure XVI.3.5** (left) Discharge/charge capacity retentions (discharge-open squares and triangles, charge closed symbols) and coulombic efficiencies (filled circles) of cells containing  $\text{Mg}_{0.37}\text{Ti}_{1.815}\text{O}_4$  (in blue) and  $\text{Na}_{0.74}\text{Ti}_{1.815}\text{O}_4$  (in gold) electrodes. (Middle and right)  $2^{\text{nd}}$  and  $10^{\text{th}}$  cycle  $dQ/dV$  plots of these cells. All the cells were cycled in 0.5 M NaPh<sub>4</sub>B/DEGDME electrolyte at a current rate of 8 mA  $\text{g}^{-1}$ .

Hard and soft X-ray absorption spectroscopy were utilized to obtain insights on the redox properties of  $\text{Mg}_{0.37}\text{Ti}_{1.815}\text{O}_4$  when used as a sodium-ion anode material (Figure XVI.3.6a, b, and c). While hard XAS probes the transition metal K-edge in the bulk of the material, soft XAS probes the L-edge in the sub-surface regions of the material, with the depth dependent on the detection mode. The fluorescence yield (FY) mode penetrates approximately 100 nm into the sample. The Ti oxidation state is  $4+$  in the pristine material. On discharging to 0.1 V vs.  $\text{Na}^+/\text{Na}$ , a slight shift to lower energy indicating partial reduction of  $\text{Ti}^{4+}$  to  $\text{Ti}^{3+}$ . However, after the first cycle, the edge energy did not fully recover to the pristine state, indicating that not all of the titanium is re-oxidized to the tetravalent state. This apparent irreversibility is also observed in the Ti L-edge spectra.

*Ex-situ* synchrotron X-ray diffraction experiments were conducted to study the structural changes of the  $\text{Mg}_{0.37}\text{Ti}_{1.815}\text{O}_4$  electrode during (de)sodiation (Figure XVI.3.6d). The insertion of large sodium ions should result in an increase in the interlayer spacing. However, in the XRD pattern of the fully discharged electrode, the (020) reflection (ca.  $2\theta=10$  degree) moved slightly to the right suggesting a slight contraction in the  $b$  direction. This probably implies that some interlayer water was expelled upon insertion of  $\text{Na}^+$ . In addition, all the reflections were broadened and less intense than those of the pristine electrode suggesting some structural disordering. Upon recharging to 2.0 V vs.  $\text{Na}^+/\text{Na}$ , the (020) reflection moves back almost to its original position and all the reflections become narrower and more intense, suggesting good structural integrity of  $\text{Mg}_{0.37}\text{Ti}_{1.815}\text{O}_4$ .

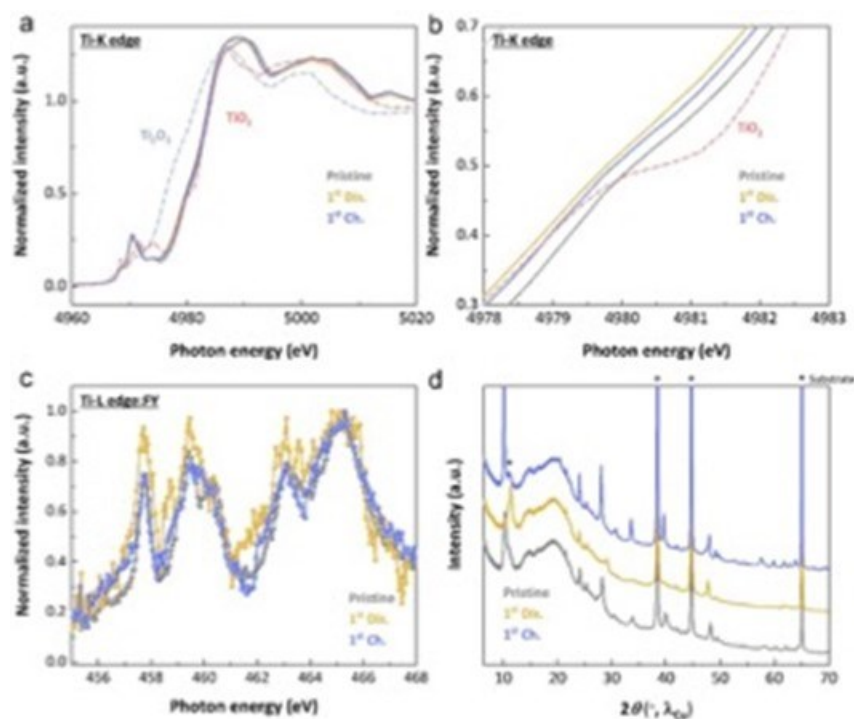


**Figure XVI.3.6** (a, b) Ti K-edge spectra in the XANES region for  $\text{Mg}_{0.74}\text{Ti}_{1.815}\text{O}_4$  electrodes at the end of the 1<sup>st</sup> discharge and charge, and an expanded view, (c) Ti L-edge spectra in the fluorescence yield (FY) mode, and (d) *ex-situ* synchrotron XRD patterns of  $\text{Mg}_{0.74}\text{Ti}_{1.815}\text{O}_4$  electrodes at end of the 1<sup>st</sup> discharge and charge.

Finally, some additional work on NNT was carried out late this year. NNT has some advantages over the lepidocrocite titanates; processing is less complicated and it has a lower average insertion potential, which is desirable for anode materials. NNT is made hydrothermally and can be dehydrated by heating; unlike the lepidocrocite titanates, it is not hygroscopic once it has been dried. It has remarkable thermal stability; the structure is largely maintained upon drying in air to approximately 600°C. We recently found that it is even more stable (up to 700°C) if processed under Ar, and delivers in excess of 200 mAh/g in a sodium half-cell configuration on the second cycle (Figure XVI.3.7). The voltage profiles and  $dQ/dV$  plots differ slightly for NNT heated to 500°C or 700°C, although for both materials, the main redox activity for sodium insertion is at about 0.3V vs.  $\text{Na}^+/\text{Na}$ . There are small plateaus at higher potentials (above about 0.75V in sodium half-cells)

similar to what is seen in some of the NTO samples, and slight differences in the electrochemical properties depending on heating temperature. While the high voltage features in NTO processed at 60°C show some pseudocapacitive character, they are annealed away when the NTO is heated to higher temperatures or when the NTO is milled with acetylene black as explained above. Given the high processing temperatures for NNT, it seems unlikely that the high voltage features are surface-related, although that remains to be proven conclusively.

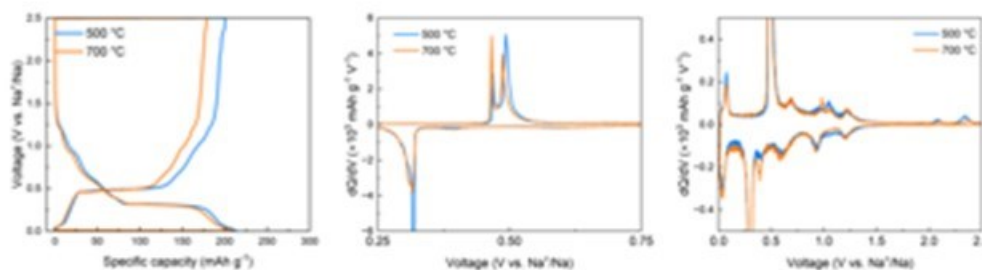


Figure XVI.3.7 (left) Second cycles of two sodium half-cells containing NNT heated to either 500°C or 700°C in argon, showing slight differences, (middle)  $dQ/dV$  plot of the same data, and (right) expanded  $dQ/dV$  plot showing details. Both cells were cycled in 0.5 M NaPh<sub>4</sub>B/DEGDME electrolyte at a current rate of 10 mA g<sup>-1</sup>.

### Conclusions

The electrochemical properties (voltage profiles, initial capacities, capacity retention) of NTO lepidocrocite titanates vary depending on a number of factors, including the presence or absence of vacancies, surface properties, and the identity of the interlayer cations. These can be manipulated by processing materials at different temperatures, ion-exchange with different cations, and by carbon coating using a variety of techniques. The best-performing NTO (reported in reference 6) has been cycled over 700 times retaining a capacity of over 80% of that obtained on the second cycle. An alternative titanate anode material is NNT, which is easier to process and less hygroscopic and may be more practical to use in full cells for these reasons. It shows remarkable thermal stability and can deliver in excess of 200 mAh/g with a sodium insertion potential mostly centered at 0.3V vs. Na<sup>+</sup>/Na, making it extremely attractive as an anode for sodium-ion batteries.

### References

1. Shirpour, M., Cabana, J., and Doeff, M., “New Materials based on a Layered Sodium Titanate for Dual Electrochemical Na and Li Intercalation Systems” *Energy & Environ. Sci.*, 6, (2013): 2538-2547.
2. Shirpour, Mona, Cabana, Jordi, and Doeff, Marca “Lepidocrocite-type Layered Titanate Structures: New Lithium and Sodium Ion Intercalation Anode Materials”, *Chem. Mater.* 26, (2014): 2502-2512.
3. Yin, W., Alvarado, J., Barim, G., Scott, M.C., Peng, X. and Doeff, M., “A Layered Nonstoichiometric Lepidocrocite-type Sodium Titanate Anode Material for Sodium-Ion Batteries” *MRS Energy & Sustainability* (2021): DOI: 10.1557/s43581-021-00008-6.
4. Markus, Isaac, Engelke, Simon, Shirpour, Mona, Asta, Mark, and Doeff, Marca “Experimental and Computational Investigation of Lepidocrocite Anodes for Sodium-Ion Batteries” *Chem. Mater.* 28, (2016): 4284-4291.
5. Alvarado, J., Barim, G., Quilty C.D., Yi, E., Takeuchi K. J., Takeuchi, E.S., Marschilok, A. C., and Doeff, M. M., “Optimization of Nonatitanate Electrodes for Sodium-ion Batteries”, *J. Mater. Chem. A* 8 (2020): DOI:10.1039/D0TA07561B.
1. Yin, W., Barim, G., Peng, X., Kedzie, E.A., Scott, M. C., McCloskey B., and Doeff M. M., “Tailoring the Structure and Electrochemical Performance of Sodium Titanate Anodes by Post-synthesis Heating”, *J. Mater. Chem. A* (2022) <https://doi.org/10.1039/D2TA07403F>.

## XVI.4 Electrolytes and Interfaces for Stable High-Energy Sodium-ion Batteries (PNNL)

### Phung M. Le, Principal Investigator

Pacific Northwest National Laboratory  
902 Battelle Boulevard  
Richland, WA 99354  
E-mail: [phung.le@pnnl.gov](mailto:phung.le@pnnl.gov)

### Tien Duong, DOE Technology Development Manager

U.S. Department of Energy  
E-mail: [Tien.Duong@ee.doe.gov](mailto:Tien.Duong@ee.doe.gov)

Start Date: October 1, 2022

End Date: September 30, 2023

Project Funding (FY23): \$500,000

DOE share: \$500,000

Non-DOE share: \$0

### Project Introduction

Sodium-ion batteries (SIBs) have recently become an alternative energy source for replacing lithium-ion batteries (LIBs) in electric vehicles and grid applications because of their cost-effective and the wide distribution of sodium on the earth's crust. To achieve the equivalent energy density as Li-ion analogue, state-of-art of NIBs has been also focusing on the high voltage cathode materials like layered oxides ( $\text{NaCo}_x\text{Ni}_y\text{Mn}_{1-x-y}\text{O}_2$ ,  $\text{NaNi}_x\text{Fe}_y\text{Mn}_{1-x-y}\text{O}_2$ ); polyanion-base cathodes ( $\text{Na}_3\text{V}_2(\text{PO}_4)_2$ ,  $\text{Na}_4\text{VFe}(\text{PO}_4)_3$ , etc.) and Prussian blue analogues (PBA). The recent full-battery configuration demonstrated by Faradion (UK) show the competitive energy level as the lithium-ion using  $\text{LiFePO}_4$  cathode. In parallel, new high voltage cathode materials with abundant elements materials have been developed to continuously increase the energy density level of the battery cell. However, the stability of these cathodes at high voltage conditions is strongly limited by the electrochemical window of electrolytes. Although the capacity of these cathode increases with increasing voltage, its cycle life decreases at such high voltage. The aging of NIBs at such high voltage is a complex phenomenon, which is mainly originated by the unstable solid electrolyte interphase (SEI) formed on anode and cathode electrolyte interphase (CEI) landed on the cathode of NIBs. As earlier reported, SEI in NIBs is severe dissolution over cycling, leading to poor cycling performance and the dramatical gas release due to subsequent parasitic reaction between the electrode and the electrolyte. In addition, the flammability of conventional electrolyte is also a big safety concern. Therefore, developing stable and safe electrolytes to enable applications of high voltage cathode is critical to reach the high energy density batteries. In developing the electrolytes, a fundamental understanding on the nature of the dynamic interface between electrode and electrolyte should be deeply explored, which helps to unravel the challenge of sluggish redox kinetics inside the batteries.

### Objectives

1. Develop nonflammable and safe electrolytes based on fluorinated solvent, new sodium salt and polymer matrix to be compatible with different commercial cathode materials (Prussian blue/white or  $\text{NaNi}_{0.4}\text{Fe}_{0.4}\text{Mn}_{0.2}\text{O}_2$ )
2. Investigate the thermal, physical chemical properties and redox stability of some developed electrolytes.
3. Study on different factors (electrolyte, current collector, temperature) affecting the efficiency of Na stripping/plating process and cycling performance of anode-free sodium batteries (AFSB)
4. Explore the fundamental mechanism behind the stability of electrolytes and electrodes, especially on their interphases by advanced techniques XPS, TEM, EIS, etc.

### Approach

- Optimize the electrolyte components (salt/solvent/additive) to develop innovative electrolytes for improving the electrochemical and physical properties. Phosphate and fluorinated phosphate-based

electrolytes will be investigated to improve the cycling performance of high voltage and high energy NIB. Ether-based electrolyte will be also optimized to stabilize the sodium metal anode and demonstrate anode-less sodium batteries.

- Perform in-situ and ex-situ spectroscopy methods to unravel the origin of the SEI/CEI layer at the dynamic interface, providing a guidance for the electrolyte and interface design and enabling high capacity and long life of Na-ion batteries.

## Results

### *Develop nonflammable and safe electrolytes based on fluorinated solvent, new sodium salt, and polymer matrix for cathode materials (Prussian blue/ white)*

Prussian Blue (PB) material purchased from Altris (Sweden) is selected to investigate as promising cathode for sodium-ion batteries material for due to its low cost, facile synthesis, and outstanding electrochemical performance. The high-loading-capacity PB cathode is essentially required for a high energy density SIB to reach the level of practical application comparable to Li-ion batteries. However, the poor conductivity and a significant volume change during the subsequent charge/discharge process might harm the electrochemical properties of the PB electrode and its interface. Therefore, several efforts should be made to solve these issues, such as the electrode formation process and electrolyte formulations. Herein, we investigated the formulation of PB electrodes at 85 and 90 %wt. active mass (in the total cathode slurry) and electrode formation with and without calendaring. Then, the PB electrodes were subsequently examined with different as-prepared electrolytes by using a half-cell configuration. Also, the new high-concentrated electrolyte using PEO matrix was developed and tested the compatibility with PB electrodes.

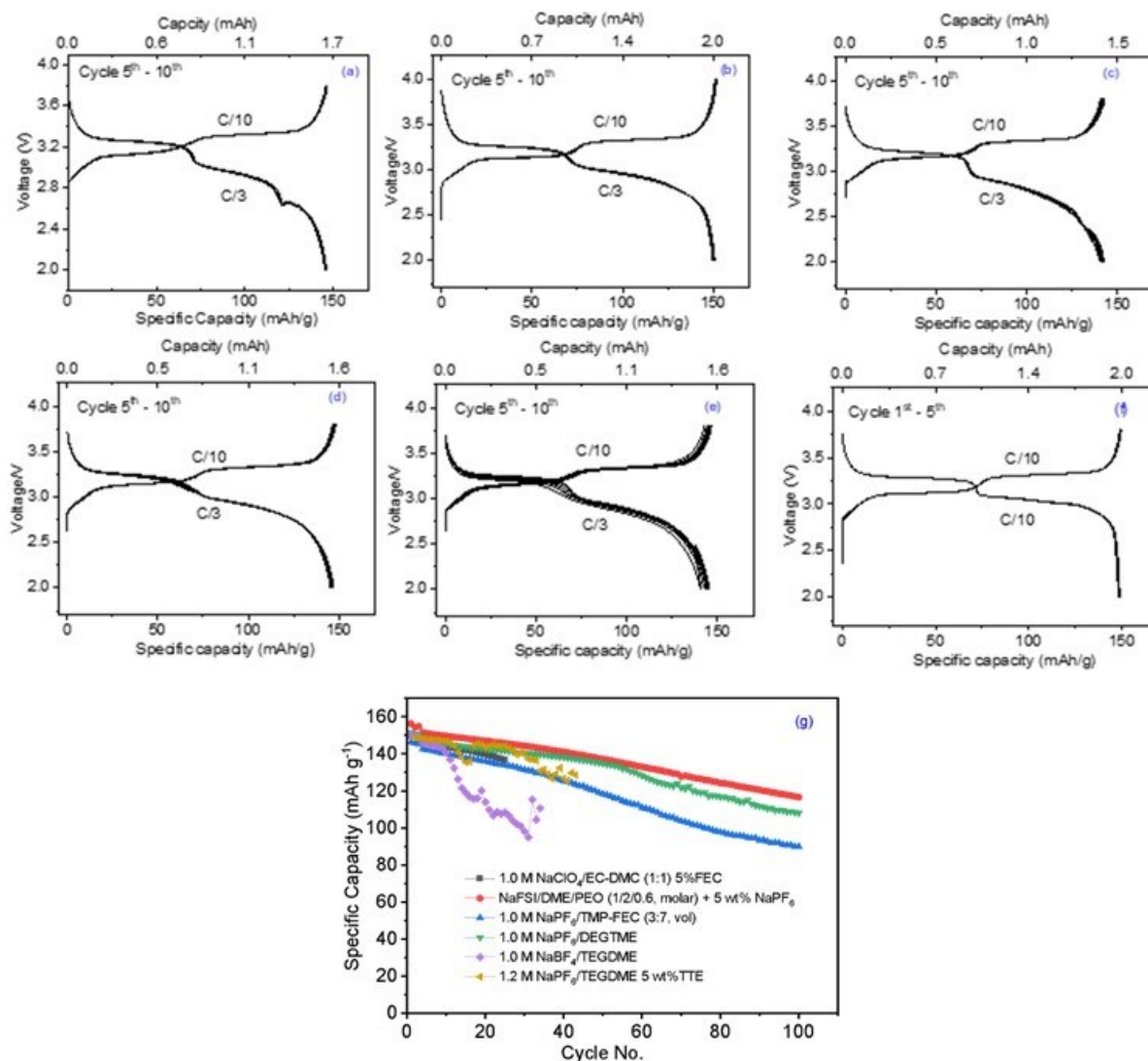


**Figure XVI.4.1** Charge – discharge profile of PB cathodes in half-cell with sodium metal, 85 % active material loading capacity: 1.5 – 2.0 mAh/cm<sup>2</sup>; (a) baseline 1M NaClO<sub>4</sub>/EC-DMC (1:1 in vol) + 5 %wt. FEC; (b) NaFSI/DME/PEO (1/2/0.6 molar ratio) + 5 %wt. NaPF<sub>6</sub>; (c) 1.0 M NaPF<sub>6</sub>/TMP-FEC (3:7 in vol.); (d) 1.0 M NaPF<sub>6</sub>/DEGDME; (e) 1.0 M NaBF<sub>4</sub>/TEGDME; (f) 1.2 M NaPF<sub>6</sub> in TEGDME 5%wt. TTE; (g) Cycling performance of PB cathodes in different electrolytes.

In general, PB cathode typically exhibited two voltage plateaus at 3.35 – 3.25 V and 2.90 – 3.10 V, with the shoulder point at 3.2 V. Among the electrolytes, DEGDME and PEO/DME-based offer the highest discharge capacity and highly symmetrical voltage profile compared to the others. (Figure XVI.4.1b and Figure XVI.4.1f). In addition, the cycling performance of all prepared electrolytes showed that NaFSI/DME/PEO electrolytes exhibited the highest initial discharge capacity (158 mAh g<sup>-1</sup>) and capacity retention (~ 80% after 100 cycles) in comparison to others.



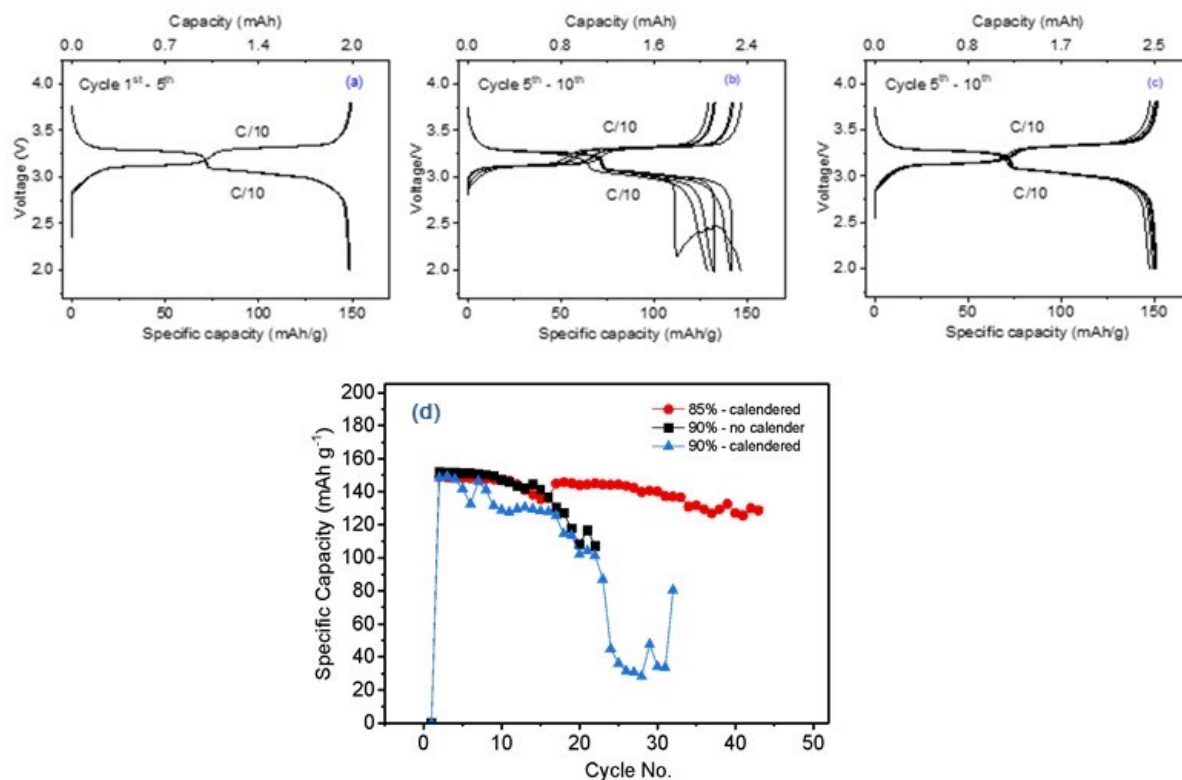


**Figure XVI.4.2 Charge–discharge profile of PB cathodes in half-cell with sodium metal at different percentages of active mass: (a) 85 % active material, calendaring electrode; (b) 90 % active material, calendaring electrode; (c) 90 % active material, non-calendaring electrode, the electrolyte of 1.2 M NaPF<sub>6</sub> in TEGDME 5%wt. TTE; (g) Cycling performance of different PB cathodes, loading capacity: 1.5 – 2.0 mAh/cm<sup>2</sup>.**

The variation of PB active material percentage in the slurry was also studied (Figure XVI.4.2). It could be observed that 90 % PB active induced a dramatic capacity drop than 85 % active material due to the higher oxidation rate of electrolyte on the electrode surface. In addition, the calendaring and non-calendaring electrodes at 90 %wt. PB exhibited the fast capacity decline, only after 20 cycles. Indeed, the high content of active material up to 90 %wt. needs to have a very stable electrolyte to stabilize the long-cycling performance.

***Investigate the thermal, physical, and chemical properties and the redox stability of developed electrolytes.***

Some electrolytes that could be compatible with Prussian blue cathode (Altris Inc., Sweden) were recently studied. The conventional carbonates (ethylene carbonate (EC), dimethyl carbonate (DMC) and fluoro-ethylene carbonate (FEC), ether (tetraglyme), and fluorinated solvent are selected to formulate the sodium-ion electrolyte with different salts: NaClO<sub>4</sub>, NaPF<sub>6</sub>, and NaFSI. These electrolytes have been investigated regarding flammability, ionic conductivity, and redox stability. In Figure XVI.4.3, the flammability test was conducted on three different electrolytes, and the self-extinguish time was recorded once the ignition source was removed.

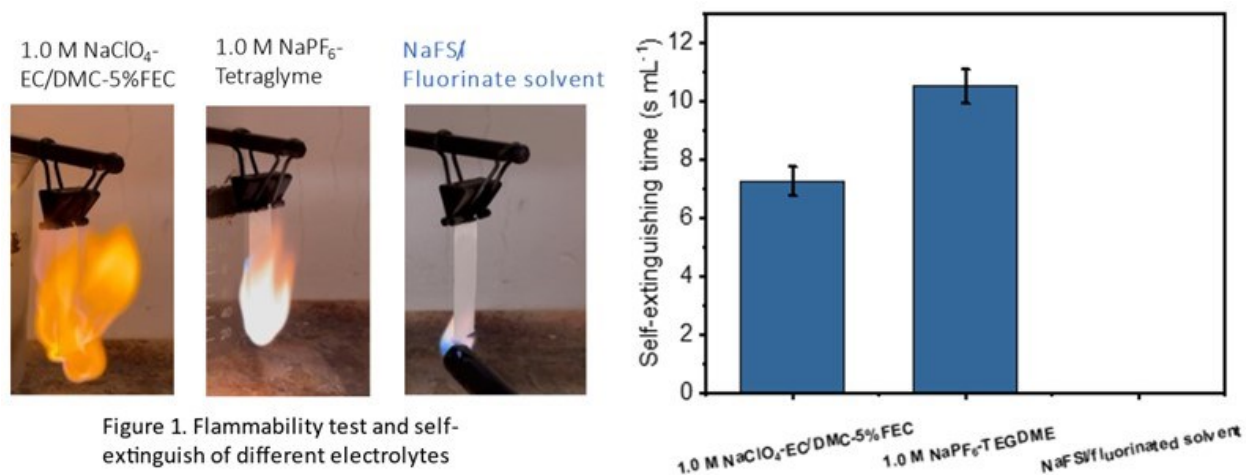


Figure 1. Flammability test and self-extinguish of different electrolytes

Figure XVI.4.3 Flammability test and self-extinguish of different electrolytes.

As seen in Figure XVI.4.3, fluorinated solvent is mostly inflammable with the negligible SET value while ether-based electrolyte has the highest SET value. Indeed, fluorinated solvent is very resistive to the flame and a good solvent to replace the flammable ones like ether or carbonate for the practical applications to enhance the battery safety. Next, the ionic conductivity along with the oxidation stability were also evaluated for these electrolytes (Figure XVI.4.4 & Figure XVI.4.5).

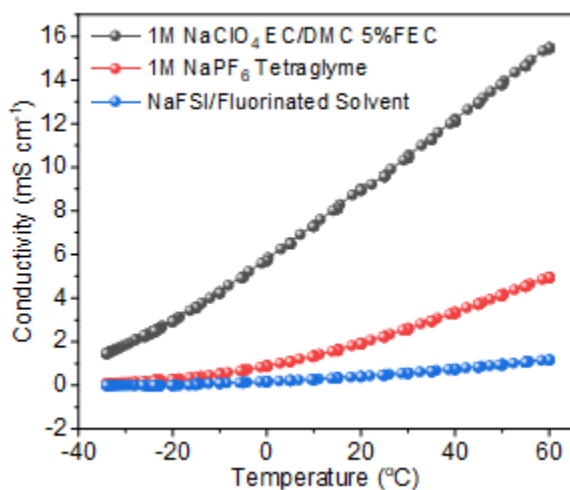


Figure XVI.4.4 Ionic conductivity of three electrolytes

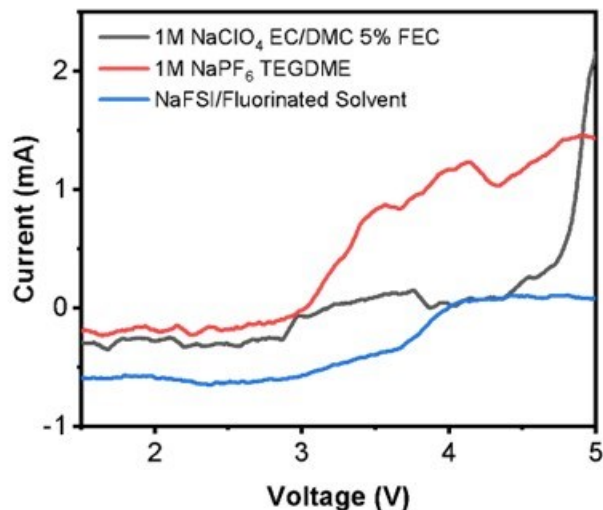


Figure XVI.4.5 Redox stability of three electrolytes

Regarding the ionic conductivity, fluorinated solvent exhibits the lowest value compared to other electrolytes. At room temperature, fluorinated-based electrolyte displays a value of  $0.45 \text{ mS cm}^{-1}$  towards  $2.26 \text{ mS cm}^{-1}$  and  $9.58 \text{ mS cm}^{-1}$  of TEGDME and EC/DMC based electrolytes, respectively. The low ionic conductivity of fluorinated electrolytes may be due to the higher viscosity of fluorinated solvent in comparison with the ether or carbonate. However, the fluorinated electrolyte offers higher oxidation stability, which is over 4 V vs  $\text{Na}^+/\text{Na}$  why the ether-based starts to be oxidized at early 3.0 V, and a very sharp increase of the oxidation current was observed for the carbonate-based electrolyte at around 4.25 V vs  $\text{Na}^+/\text{Na}$ . Therefore, it could provide a robust CEI layer for preventing further side reactions between electrolyte – electrodes at high voltage or high-loading-capacity electrodes.

***Study on different factors (electrolyte composition, current collectors, cycling protocol, temperature) affecting the efficiency of Na stripping/plating process and cycling performance of AFSB.***

To stabilize the sodium anode in anode-free configuration, different approaches have been using to achieve the highly reversibility of sodium stripping/plating process. Firstly, different current collectors are selected and studied for the reversibility of sodium cycling. In parallel, the variation of electrolytes composition is also investigated to be compatible with the selected current collectors. Table XVI.4.1 summarizes the Coulombic efficiency (CE) of sodium stripping/plating process of different current collectors along with the change of the electrolyte's composition. C@Al anode shows very good reversible cycling through high CE values, typically, in the LPH electrolytes. However, in some electrolytes, CE values are much higher than 100 %, which might indicate the side-reaction at the end of charge state between the current collector and electrolyte.

**Table XVI.4.1 Reversibility of Sodium Stripping/plating Process Evaluated Through CE Values In Varying The Current Collector And Electrolyte Composition.**

Electrolyte composition	Variation of current collectors			
	Na    Cu	Na    C@Cu	Na    Al	C@Al    Na
1M NaPF <sub>6</sub> /TEGDME	99.7	-	-	97.3
1M NaPF <sub>6</sub> /DEGDME	99.7	-	-	-
1M NaOTf/TEGDME	99.5	99.0	98.2	99.6
1M NaOTf/DEGDME	99.8	98.5	98.5	99.6
1M NaBF <sub>4</sub> /TEGDME	99.5	98.3	97.7	99.2
1M NaBF <sub>4</sub> /DEGDME	95.6	-	-	-
LHCE (1:1:2)	98.1	94.8	-	94.9
LPH-01	99.6	101.4	113.3	~99.9
LPH-02	99.6	99.7	97.5	~99.9
LPH-03	98.8	104.4	98.6	~99.9
LPH-04	97.2	102.6	103.0	~99.9
LPH-05	98.5	99.1	97.8	99.2

(\*Stripping/plating condition: plating 4 mAh cm<sup>-2</sup> and fully stripping to 1 V

- Depositing the Na reservoir ( $Q_T = 4 \text{ mA h cm}^{-2}$ ) at  $0.4 \text{ mA cm}^{-2}$  and cycling ( $Q_C = 1 \text{ mA h cm}^{-2}$ ) for 10 cycles at  $0.5 \text{ mA cm}^{-2}$
- Final stripping is performed at  $0.5 \text{ mA cm}^{-2}$  to 1 V)
  - NaOTf: sodium triflate
  - LCHE: Localized high concentrated electrolyte
  - LPH-01: conventional concentration ~ 1.0 M while the others are > 1.0 M salt.

Apart of the selection of good current collector and the best compatible electrolyte, the cycling protocol should be also optimized to achieve the stable performance. Herein, the pre-cycling cathode or conditioning the current collector may be required to reach the highest CE of free-anode cell configuration. In addition to that, the formation cycle is particularly considered to achieve the stable interface and long-cycle life. Figure XVI.4.6 shows the anode-free cells with/without pre-sodiated Na<sub>3</sub>V<sub>2</sub>(PO<sub>4</sub>)<sub>3</sub> cathode combined with C@Al anode. The activated cathode in several cycles reach the CE of charge/discharge up to 99.8 instead of 99.0 % at the initial cycle (without pre-sodiated). Therefore, it would be beneficial for achieving stable and long-lasting performance of anode-free cell as the Na-loss inventory is minimized and CEI layer is already formed and stabilized. Indeed, the capacity retention of pre-cycled NVP cathode-based cell is much higher than the other. Typically, this cell remained ~ 46% of the initial capacity compared to ~ 30% of the other one.

In Figure XVI.4.7 the formation cycle is thoroughly investigated with/without the resting time at the cut-off voltage 3.8 V in 10 minutes. It seems that the resting step at high voltage is required to stabilize the formation of interfacial layers and help for the interfacial reaction occurring completely (Na<sup>+</sup>-ion removed from cathode and deposited on the current collector). After 40 cycles, the discharge capacity of the cell with a resting stage is about 30 mAh/g while the cell without this stage showed only a half of this value (~ 15 mAh/g)

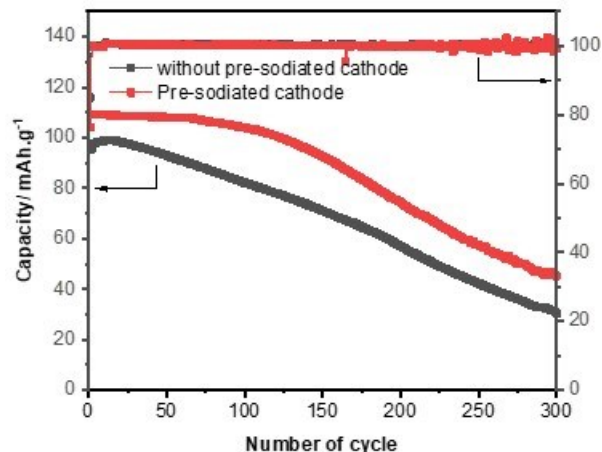


Figure XVI.4.6 Cycling performance of C@Al | NVP cell at the voltage of 2.5 – 3.8 V using pristine NVP or pre-cycled NVP cathode in LPH03 electrolyte (condition: formation 1 cycle at C/10, 9 cycles at C/20 and long cycling at C/3)

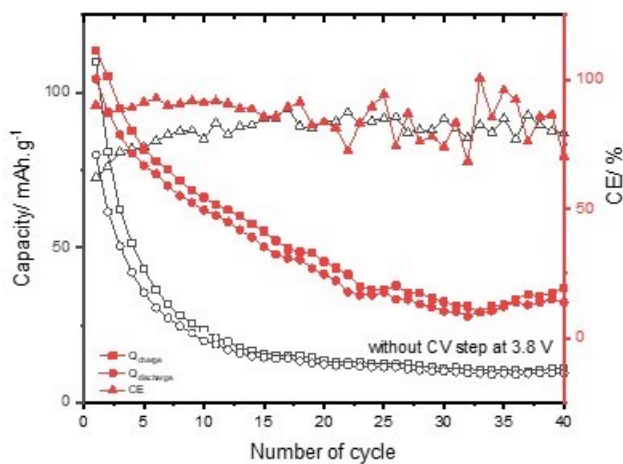
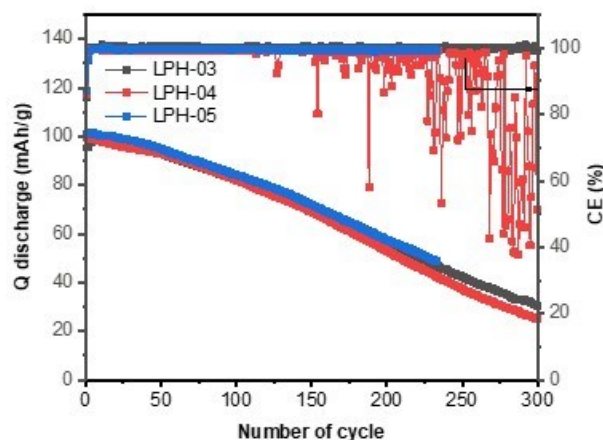


Figure XVI.4.7 Cycling performance of Cu | NVP cell at the voltage of 2.5 – 3.7 V with and without constant voltage step at 3.7 V in LCHE electrolyte (condition: formation 1 cycle at C/10, 9 cycles at C/20 and long cycling at C/3)



**Figure XVI.4.8** Cycling performance of C@Al||NVP cell at the voltage of 2.5 – 3.8 V using pristine NVP and electrolytes LPH03-LPH-05 (condition: formation 1 cycle at C/10, 9 cycles at C/20 and long cycling at C/3, resting time at 3.8 V in 10 minutes)

In varying the electrolyte concentration (LPH-03 to LPH-05), free-anode cell C@Al||NVP without pre-cycling NVP show a similar trend of capacity decline. It means that the impact of salt concentration on the stability of performance is less significant than the factor of pre-sodiated cathode before matching the cell. All the cells displayed about 80 % drop of capacity after 300 cycles at C/3 rate (Figure XVI.4.8). Therefore, the pre-sodiated cathode could be a critical factor to achieve a stable cycling performance of sodium free-anode cell.

***Characterize CEI/SEI interphase properties in optimized electrolytes to probe the underlying mechanism of cycling stability of NIBs and ASFB***

The formation of interfacial layers in the anode-free sodium batteries (AFSBs) was deeply explored to probe the underlying mechanism of cell stability. As earlier reported, the stabilization of AFSBs cycling depends significantly on the protocol of cycling and the pre-treatment of current collector anodes as well as cathode. To understand the effect of different factors such as: current collector type, pre-treatment and cycling protocol, in-situ/ex-situ TEM, cryo PFIB SEM have been applied for the AFSB cells.

Figure XVI.4.9 showed the images of initial deposition of sodium in ether-based electrolyte LPH-03 (electrolyte code) on different current collectors: Cu, C@Cu, C@Al characterized by cryo-PIFB-SEM. It seems like the plated sodium metal on the Cu current collector is dense and agglomerated to form large grains within the irregular shapes. In a sharp contrast, the deposited sodium is porous with a long whisker-like microstructure connected on the C@Cu forming some holes while the larger whiskers tend to form the homogenous Na dense and large nodules deposited on the C@Al. These different morphologies can be explained by the distribution of electronic charge and the nature of current collector which directly influence on the growth of the formation and nucleation process of sodium dendrite. The deposited sodium with irregular shapes or a whisker-like microstructure can result in a large pin hole when stripping leading to the fragile electrical connection and “dead” sodium easily formed. Therefore, it could be expected that the growth of sodium dendrite is slower on C@Al than on the other current collectors.

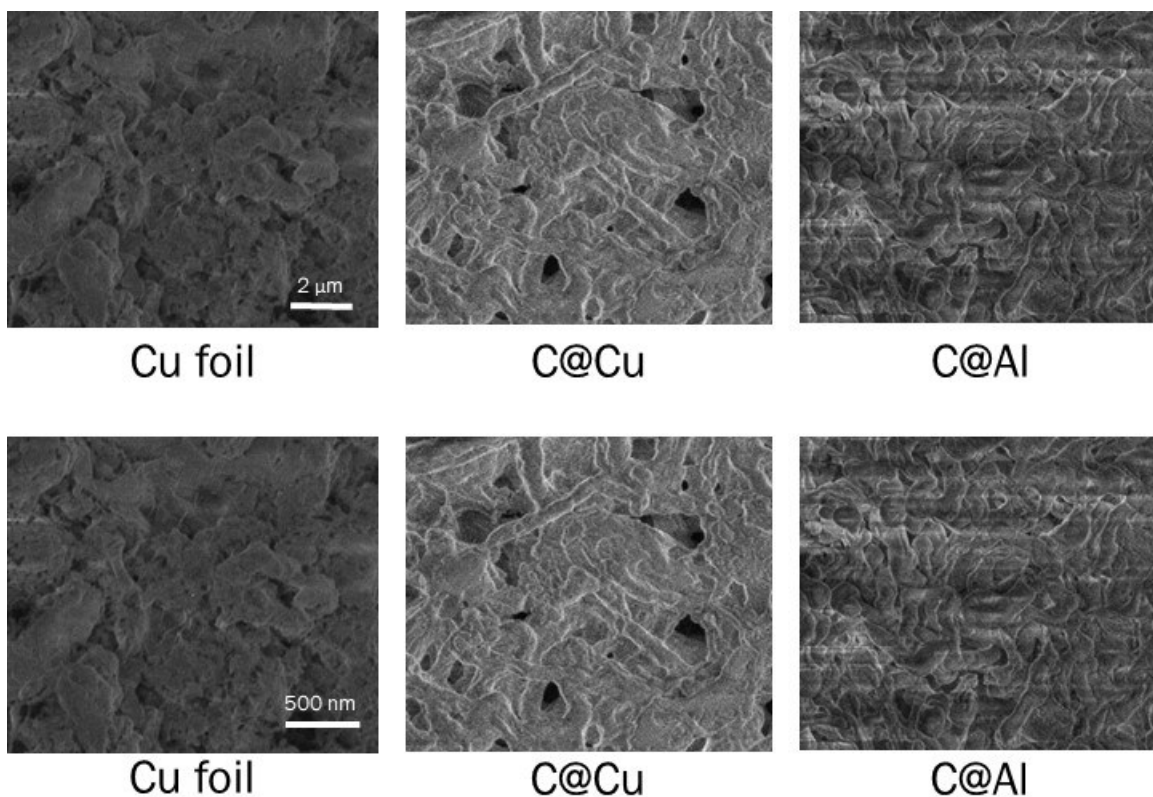


**Figure XVI.4.9 Cryo-PFIB-SEM of sodium morphology after an initial plating at  $1.0 \text{ mA/cm}^2$  on different current collectors: Cu; C@Cu and C@Al (from left to right) at the magnification of  $2 \mu\text{m}$  and  $50 \text{ nm}$  in ether-based electrolyte LPH-03 ( $\text{NaPF}_6$  salt concentration  $>1 \text{ M}$ ).**

In-situ TEM was also conducted to understand the sodium growth and nucleation in plating/stripping process at  $2.5 \text{ V}$  without the presence of the electrolyte to reveal the effect of current collector itself. As shown on the Figure XVI.4.10, the behavior of sodium growth is very distinguished like the direction of sodium formation and the morphology. In case of C@Cu or C@Al, the sodium is growing directly on the carbon layer and merged into it. Figure XVI.4.11 indicates the sodium growth rate on the normalized surface area in the plating process. It seems like the sodium growth on C@Cu is much faster than the other substrates after certain time while the first sodium chunk was observed at  $5 \text{ s}$  for Cu substrate (Figure XVII.4.10). In sharp contrast, on C@Al, the sodium grows very slowly during the plating process with the lowest rate (compared to other substrates), which can be expected the lowest dendrite formation. This result is very consistent with the cryo-PFIB-SEM in Figure XVI.4.9 and the collected electrochemical data that the sodium free-cell C@Al||NVP achieved longer cycle life than the other AFSBs.

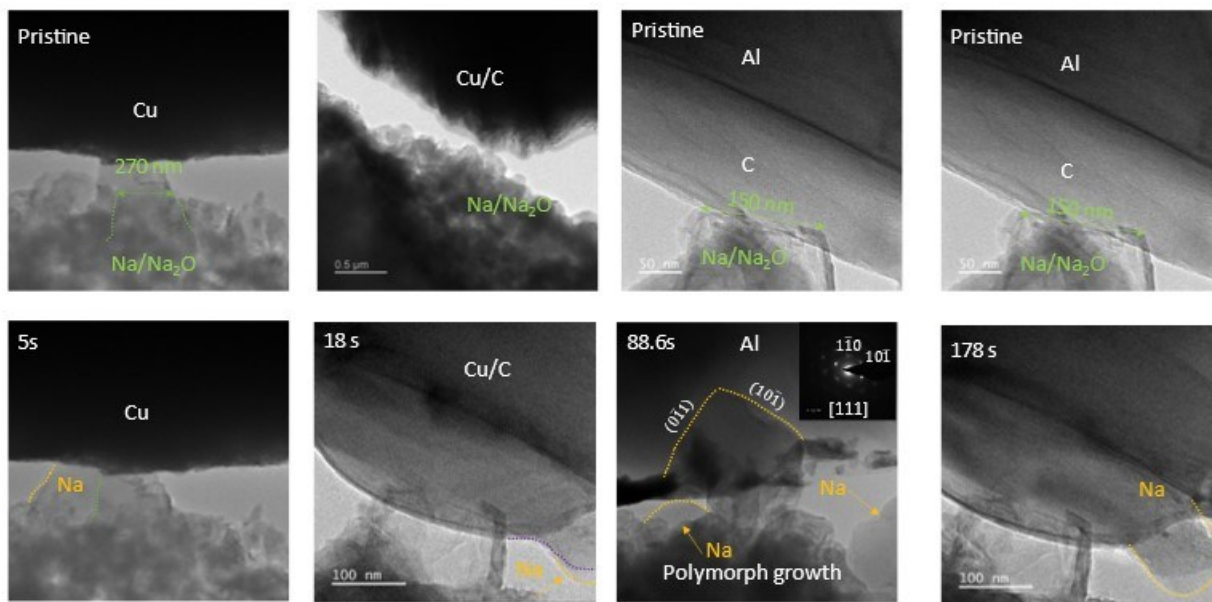


Figure XVI.4.10 In-situ TEM to observe the sodium growth on different current collectors: Cu, C@Cu, Al, C@Al at very low current and at 2.5 V. The apparition of sodium chunk can be seen by the orange dotted line at time different depending on the kind of substrates.

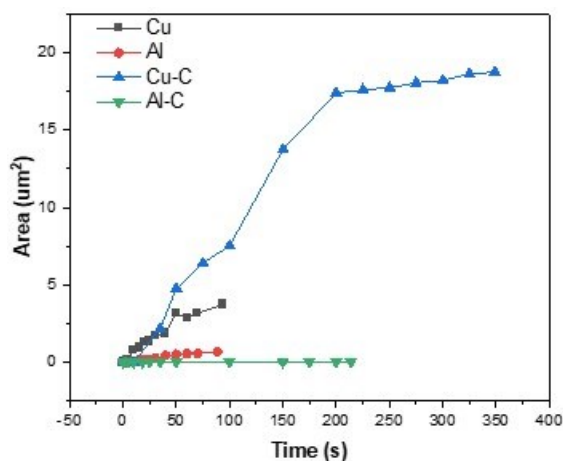


Figure XVI.4.11 The growth rate of sodium represented by the time area curve with contact area normalization based the data of Figure XVII.4.10.

To understand the role of pre-treatment NVP cathode in AFSBs, ex-situ TEM was conducted to determine cathode electrolyte interphase (CEI) layer of NVP in half-cell Na||NVP (after 10 cycles pretreated) and in AFSB (using pretreated NVP). Specifically, the CEI formed at the thickness of 9 nm consists of Na, O, P and F indicating the organic/inorganic based components. In AFSB, after 1 cycle formation, CEI decreased to 6 nm which is thin and homogenous (Figure XVI.4.12). Thus, it can be expected to ensure the effective protection of cathode and long cycling performance.



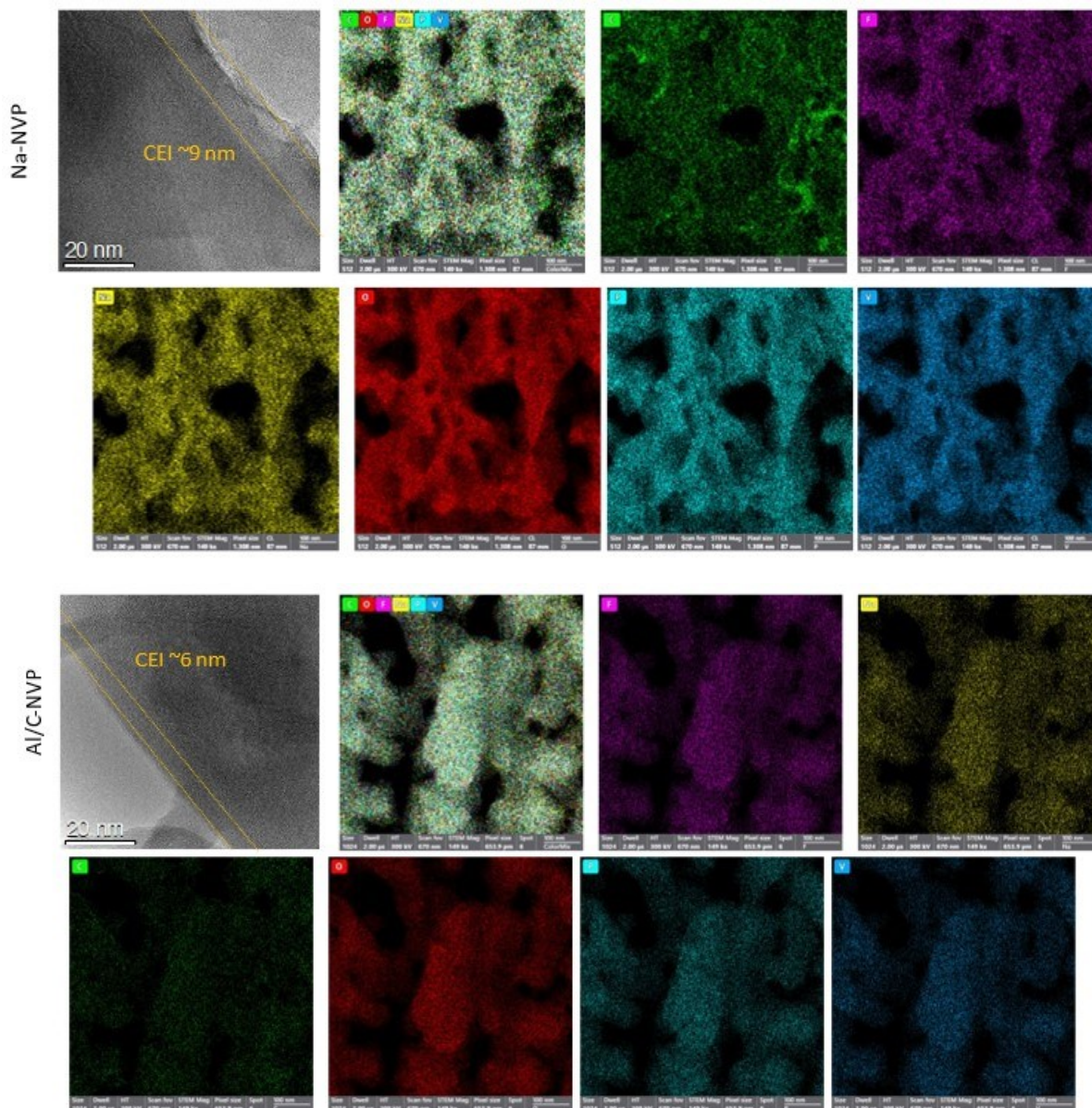


Figure XVI.4.12 Ex-situ TEM and energy dispersive spectroscopy (EDS) mapping of pre-cycled  $\text{Na}_3\text{V}_2(\text{PO}_4)_3$  (NVP) cathode in Na||NVP half-cell at C/5 and the NVP cathode in AFSBs C@Al||NVP after one cycle.

### Conclusions

- Designed safe and non-flammable electrolyte using fluorinated solvent and polymer matrix which is compatible with the high-loading electrode using Prussian Blue cathode materials.
- Understanding different factors (electrolyte composition, current collector, cycling protocol, etc.) affected the stability of AFSB and selecting the optimized factors to achieve the long-cycle performance of AFSB.
- In-situ HRTEM and cryo-PFIB-SEM showed the behavior and morphologies of sodium plating and growth differentiated on different current collectors. The growth rate of sodium on the substrate can help to predict the dendrite formation as well as the cycle life of AFSB.

**Key Publications**

- Thanh-Nhan Tran and Phung ML Le, “High-Loading-Capacity Prussian Blue as Promising Cathode Material for Sodium-ion Batteries”, IBA2023 Meeting, March 05-10, Austin, Texas, Poster presentation.
- Yan Jin, Phung M Le, Ji-Guang Zhang, “Novel electrolyte for high-voltage sodium-ion batteries”, American Society of Mechanical Engineers (ASME), Columbia Basin Section Richland, February 7, WA, Invited talk.
- Phung ML Le, Yan Jin, Thanh Vo, Nhan T. Tran and Ji-Guang Zhang, “Achieving stable interfacial reactions in sodium batteries through electrolyte engineering”, 243rd ECS Meeting, May 27 – June 02, Boston, Invited talk.
- Phung ML Le, Nhan T. Tran, Kha M. Le, Yan Jin, Yaobin Xu, Biwei Xiao, Mark Engelhard, Chongming Wang, Ji-Guang Zhang, “Design of functional phosphate-based electrolyte for stabilizing the performance of sodium-ion batteries”, ABAA-14, October 30 – November 1, Ho Chi Minh city, Poster presentation.

**References**

1. Tingzhou Yang, Dan Luo Yizhou Liu, Aiping Yu, and Zhongwei Chen, Anode-free sodium metal batteries as rising stars for lithium-ion alternatives, *iScience* 26, 105982, 2023.
2. Liyu Zhu, Yucheng Li, Jingyang Zhao, Jing Liu, Luying Wang, Jiandu Lei, Recent advanced development of stabilizing sodium metal anodes, *Green Energy & Environment* 8, 1279 – 1307, 2023.
3. L. Hartmann, J. Deshmukh, L. Zhang, and M. Metzger, “Reversing the Chemical and Structural Changes of Prussian White After Exposure to Humidity to Enable Aqueous Electrode Processing for Sodium-ion Batteries”, *J. Electrochem. Soc.* 170, 030540, 2023.

**Acknowledgements**

Key contributors include Dr. Nhan Tran and Kha Le.

Key collaborators include Dr. Chongming Wang and Mark Engelhard.

## XVII Beyond Li-ion R&D: Battery500

The Battery500 Consortium (B500) has the goal to increase the energy density of advanced lithium (Li) batteries to beyond what can be achieved in today's Li-ion batteries. Specifically, the B500 aims to increase the specific energy (up to 500 Wh/kg) relative to today's battery technology, achieve 1,000 charge/discharge cycles, and reduce the cost of cells to significantly less than \$100 kWh<sup>-1</sup>, an important U.S. Department of Energy (DOE) goal for carbon-neutral energy and electrification. The consortium objectives are to: (i) overcome the fundamental scientific barriers to extract the maximum capacity from electrode materials for next-generation Li batteries on the pouch cell level; (ii) leverage and integrate the latest advances in electrode materials and battery chemistries; (iii) optimize cell design and properties of the best electrode materials on the cell level; and (iv) validate cell performance and scale up to industry-relevant levels.

The consortium focuses on two most promising battery chemistries, Li-metal anode with high-voltage/high-capacity metal oxide cathodes like LiNi<sub>x</sub>Mn<sub>y</sub>Co<sub>1-x-y</sub>O<sub>2</sub> (NMC) and Li metal with sulfur (S) cathodes, to achieve the 500 Wh kg<sup>-1</sup> goal. The consortium addresses the fundamental challenges of Li dendrite formation, undesired interfacial reactions, structural degradation, poor ionic and electronic transport, and poor accessibility of active materials, as well as shuttling reaction products in high-energy batteries at the cell level. B500 will develop an integrated approach to rapidly incorporate the latest advances in materials discoveries and breakthroughs into advanced cell-level designs and fabrication, and to optimize and validate the cell properties under realistic conditions. The consortium involves three keystone projects and a cross-cutting project: (1) materials and interfaces; (2) electrode architectures; (3) cell fabrication and validation; and (4) cross-cutting research. Each keystone project and the cross-cutting task address specific scientific challenges required to deliver next-generation, high-energy, Li battery technologies to industry, including high-energy Li||NM cells, high-energy Li||S cells, and low-cost S cells.

This rest of this chapter contains a description of the current phase (Phase 2) of the efforts by the multitude of team members of the Battery500 Consortium.

## XVII.1 Battery 500 phase 2: B500 Innovation Center (PNNL)

### Jun Liu, Principal Investigator

Pacific Northwest National Laboratory  
902 Battelle Boulevard  
Richland, WA 99354  
E-mail: [jun.liu@pnnl.gov](mailto:jun.liu@pnnl.gov)

### Yi Cui, Co-Principal Investigator

Stanford University/SLAC  
450 Serra Mall  
Stanford, CA 94305  
E-mail: [yicui@stanford.edu](mailto:yicui@stanford.edu)

### Tien Duong, DOE Technology Development Manager

U.S. Department of Energy  
E-mail: [Tien.Duong@ee.doe.gov](mailto:Tien.Duong@ee.doe.gov)

Start Date: October 1, 2022  
Project Funding: \$15,000,000

End Date: September 30, 2023  
DOE share: \$15,000,000

Non-DOE share: \$0

### Project Introduction

The overall goal of the Battery500 Consortium phase 2 (B500) is to increase the energy density of advanced lithium (Li) batteries to beyond what can be achieved in today's Li-ion batteries. Specifically, the B500 aims to increase the specific energy (up to 500 Wh kg<sup>-1</sup>) relative to today's battery technology, achieve 1,000 charge/discharge cycles, and reduce the cost of cells to significantly less than \$100 kWh<sup>-1</sup>, an important U.S. Department of Energy (DOE) goal for carbon-neutral energy and electrification. The consortium objectives are to: (i) overcome the fundamental scientific barriers to extract the maximum capacity from electrode materials for next-generation Li batteries on the pouch cell level; (ii) leverage and integrate the latest advances in electrode materials and battery chemistries; (iii) optimize cell design and properties of the best electrode materials on the cell level; and (iv) validate cell performance and scale up to industry-relevant levels.

The consortium focuses on two most promising battery chemistries, Li-metal anode with high-voltage/high-capacity metal oxide cathodes like LiNi<sub>x</sub>Mn<sub>y</sub>Co<sub>1-x-y</sub>O<sub>2</sub> (NMC) and Li metal with sulfur (S) cathodes, to achieve the 500 Wh kg<sup>-1</sup> goal. The consortium addresses the fundamental challenges of Li dendrite formation, undesired interfacial reactions, structural degradation, poor ionic and electronic transport, and poor accessibility of active materials, as well as shuttling reaction products in high-energy Li-sulfur (Li-S) batteries at the cell level. B500 will develop an integrated approach to rapidly incorporate the latest advances in materials discoveries and breakthroughs into advanced cell-level designs and fabrication, and to optimize and validate the cell properties under realistic conditions. The consortium involves four keystone projects including a cross-cutting project: (1) materials and interfaces; (2) electrode architectures; (3) cell fabrication and validation; and (4) cross-cutting research. Each keystone project and the cross-cutting task address specific scientific challenges required to deliver next-generation, high-energy, Li battery technologies to industry, including high-energy Li||NMC cells, high-energy Li||S cells, and low-cost Li-S cells.

### Objectives

The overall goal of the consortium is to increase the energy density of advanced lithium batteries to beyond what can be achieved in today's state-of-the-art Li-ion batteries. The Battery500 Consortium aims to increase the specific energy (up to 500 Wh kg<sup>-1</sup>) and achieve 1,000 charge/discharge cycles, with cost reduction of the cells to significantly less than \$100 per kWh<sup>-1</sup>. This goal directly addresses the U. S. Department of Energy priority to achieve a carbon-free electricity sector by 2035 and to decarbonize the transportation sector by

developing and manufacturing the next-generation, high-energy, low-cost batteries to enable a wide deployment of electric vehicles (EVs) in the marketplace.

### Approach

This project focuses on the two most promising battery chemistries: Li-metal anode with high-voltage/high-capacity metal oxide cathodes like  $\text{LiNi}_x\text{Mn}_y\text{Co}_{1-x-y}\text{O}_2$  (NMC), and lithium metal with sulfur cathodes. The project focus is to design novel electrode and cell architectures to meet the 500 Wh/kg goal. The consortium will work closely with battery/material manufacturers, suppliers, and end users / original equipment manufacturers in the United States to ensure the technologies being developed by this project are well aligned with industry needs, poised for transitioning to real production, and helpful in securing the supply chain in the United States.

### Results

#### 1. *Keystone project 1: Materials and interfaces.*

Keystone Project 1 addresses the general approaches to attain the goal of robust 500 Wh/kg cells through materials development for cathode, anode, and electrolytes.

#### *Comparison of reactivities of different commercial NMC 811 cathodes.*

NMC is the baseline material for the Battery500 consortium. In FY2023, the Binghamton team evaluated the reactivities of different commercial NMC 811 cathodes through (1) electrochemical tests and (2) thermal studies.

As shown in Figure XVII.1.1a, the commercial NMC 811 cathodes obtained from different vendors have different particle sizes and morphologies (EcoPro vs. Targray); even for the same vendor (Targray), the different batches of products they provide can have different modifications. These differences impact the reactivity of the NMC 811.

EcoPro NMC 811 has smaller primary particles and denser secondary particles (Figure XVII.1.1a), which contributed to better cycling performance (Figure XVII.1.1c) and thermal stability (Figure XVII.1.1e) than the unmodified Targray NMC 811. However, surface modification with boron (B) containing compound thoroughly enhanced the performance of Targray NMC 811 (Figure XVII.1.1b-e): smaller 1<sup>st</sup> capacity loss, better capacity retention, more stable Coulombic efficiency, and higher thermal stability, indicating the importance of surface modifications, which not only improves the interfacial kinetics but also suppresses the surface reactivity of the particles. The latest NMC 811 from Targray (Targray + B + Zr), which contains smaller secondary particles and B + Zr modification, gave even better electrochemical performance (Figure XVII.1.1b-d). Studies here show the critical role of particle size, morphology, distribution, and surface or bulk modification, in suppressing undesired side reactions and structural degradation. Minimizing the latter two improves the capacity and capacity retention of the operating cells.

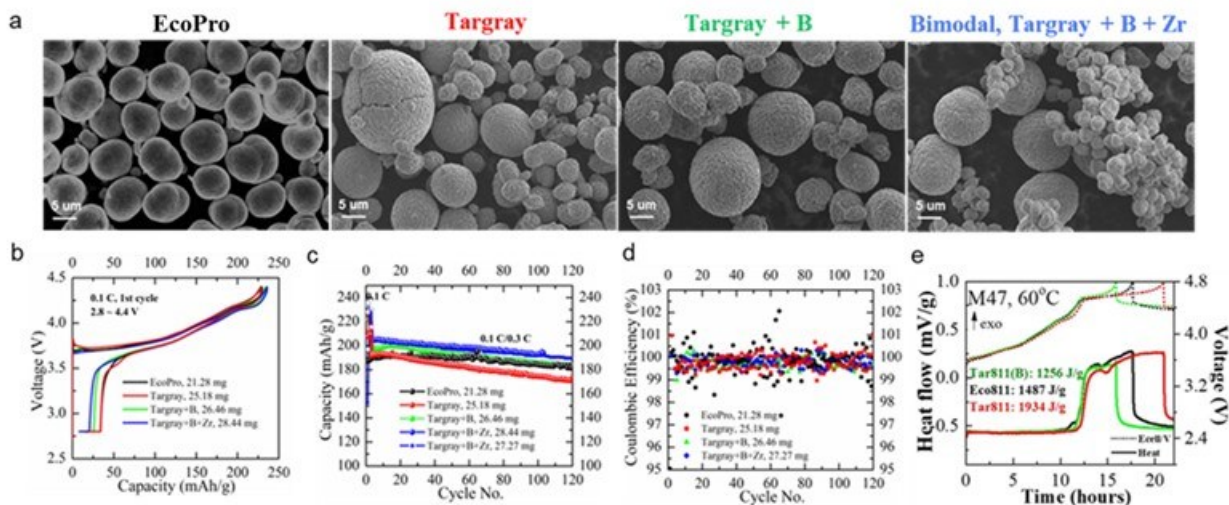


**Figure XVII.1.1** (a) SEM images of different commercial NMC 811 cathodes. (b) 1<sup>st</sup> cycles, (c) Cycling performances, and (d) Coulombic efficiencies of different commercial NMC 811 cathodes cycled between 2.8 ~ 4.4 V with the charge current of C/10 and discharge current of C/3 vs. Li metal anode tested inside coin cells with 50  $\mu$ L LP30 electrolyte. (e) Heat evolved for three different NMC 811s (EcoPro vs. Targray vs. Targray + B) with the M47 electrolyte using the aluminum protected Hohsen coin cells during the charging to 4.8 V at 60  $^{\circ}$ C.

### Electrolytes.

The University of Texas (UT Austin) team investigated the mechanisms of the significantly improved cycling stability of high-Ni cathode (Cobalt-free  $\text{LiNiO}_2$ ) with the localized saturated electrolyte (LSE) that has been developed as the high-voltage electrolyte in this team. Figure XVII.1.2a compares the anodic linear sweep voltammetry (LSV) measurement results from 3.0 to 5.0 V at a scan rate of 0.05  $\text{mV s}^{-1}$  for the LSE and the baseline LP57 electrolyte. The leakage current at 5.0 V is reduced from 2.0 (LP57) to 0.3  $\mu\text{A cm}^{-2}$  (LSE). The improved high voltage stability in the LSE can be attributed to its unique  $\text{Li}^+$  solvation structure that is dominated by contact ion pairs and cation-anion aggregates due to the limited number of solvent molecules. Such a solvation structure can lower the HOMO level of the solvent molecules, and thus improve the oxidative stability of the electrolyte. Figure XVII.1.2b compares the cycling stability of  $\text{LiNiO}_2$  electrodes in the two electrolytes cycled in the voltage range of 2.8 – 4.4 V. The cell with LSE displays a slightly increased initial discharge capacity (223  $\text{mA h g}^{-1}$ ) compared to that with LP57 (217  $\text{mA h g}^{-1}$ ). The capacity retention after 400 cycles is greatly increased from 28% (LP57) to 85% (LSE). Figure XVII.1.2c compares the charge curves at C/2, C/10, and C/100 for the two types of cells after 400 cycles. Most of the capacity is recovered by testing at low C-rates for the cell that was cycled in the LP57 electrolyte. Figure XVII.1.2d further quantifies the charge capacities at low C-rates compared to the highest charge capacity during the three formation cycles. For the cell that was cycled in the LP57 electrolyte, the charge capacity at C/2 rate only retained 23% of its initial capacity but 75% of its initial capacity at C/100 rate. The voltage plateau at 4.2 V also appears at an extremely low C rate (C/100), indicating that the kinetic barrier in the  $\text{LiNiO}_2$  cathode is the major contributor to its severe capacity degradation. In comparison, for the cell tested in LSE, the capacity retention increased from 73% at C/2 rate to 92% at C/100 rate, both of them are significantly higher than the 23% and 75% retention for LP57 cell. Structural degradation of the  $\text{LiNiO}_2$  surface, along with the reduction of  $\text{Ni}^{4+}$  and oxygen loss, can lead to the formation of spinel-like structures and rock-salt phases during cycling, which is believed to be harmful to the overall performance of the electrode. Advanced high-angle annular dark-field scanning transmission electron microscopy (HAADF-STEM) was thus applied to investigate the surface structure of cycled  $\text{LiNiO}_2$  using those two electrolytes. Five different types of degraded phases were observed in the two cycled  $\text{LiNiO}_2$ : spinel  $\text{LiNi}_2\text{O}_4$ , spinel  $\text{Li}_{1-x}\text{Ni}_{2+x}\text{O}_4$ , spinel  $\text{Ni}_3\text{O}_4$ , rock-salt  $\text{Li}_x\text{Ni}_{1-x}\text{O}$ , and rock-salt  $\text{NiO}$ . The distribution of these five phases on the surface of the two cycled  $\text{LiNiO}_2$  particles is shown in Figure XVII.1.2e, f. Figure XVII.1.2g further compares the amount of the five degraded phases on the surface of the

two cycled  $\text{LiNiO}_2$  samples. The results indicate that the LP57 electrolyte promotes the formation of  $\text{NiO}$  and  $\text{Ni}_3\text{O}_4$  on the surface of  $\text{LiNiO}_2$ , while the LSE helps in forming  $\text{LiNi}_2\text{O}_4$  on the surface of the electrode. Compared to  $\text{NiO}$  and  $\text{Ni}_3\text{O}_4$ ,  $\text{LiNi}_2\text{O}_4$  with direct Ni-Ni interaction along the shared octahedral edges and no nickel in the tetrahedral sites of the 3-dimensional spinel lattice has much higher  $\text{Li}^+$ -ion and electronic conductivity. More importantly, Figure XVII.1.2e, f shows that the conductive  $\text{LiNi}_2\text{O}_4$  phase is distributed on the top surface of the cycled  $\text{LiNiO}_2$  particle using the LSE (Figure XVII.1.2f), while it is buried under the insulating  $\text{NiO}$  and  $\text{Ni}_3\text{O}_4$  phases on the surface of the electrode with the LP57 electrolyte (Figure XVII.1.2e). The quantity and distribution of these degraded phases on the surface of the two samples explain why the kinetics is better maintained in the cycled  $\text{LiNiO}_2$  cell using the LSE (Figure XVII.1.2c, d). Intergranular cracking in secondary particles has been considered a major cause of long-term capacity fade in high-Ni cathodes. Cross-section scanning electron microscopy (SEM) images were taken to study the effect of LP57 electrolyte and LSE on the intergranular cracking of cycled  $\text{LiNiO}_2$  electrodes. Figure XVII.1.2h, i shows the images of fully discharged  $\text{LiNiO}_2$  electrodes after 400 cycles using these two electrolytes. Large cracks (red arrows) appear in almost all the imaged  $\text{LiNiO}_2$  secondary particles when tested in the LP57 electrolyte (Figure XVII.1.2h), while the cracks were limited to the edge regions of the particles with a short length when tested in the LSE (Figure XVII.1.2g). The representative cracking of these images was also confirmed by the SEM images at other locations (not shown here). Therefore, the LSE suppresses intergranular cracking in the  $\text{LiNiO}_2$  electrode during long-term cycling, correlated to the lower surface degradation shown in the STEM (Figure XVII.1.2e, f). It is worth noting that the  $\text{LiNiO}_2$  electrode tested in the LSE went through more repeated H2 - H3 phase transition at the high voltage region than the electrode tested in the LP57 electrolyte during the continuous cycling. The reduced intergranular cracking in the  $\text{LiNiO}_2$  electrode with the LSE indicates that there are other dominant factors to the cracking process besides the repeated H2 - H3 phase transition. These factors could be the improved surface stability and reaction homogeneity of the  $\text{LiNiO}_2$  electrodes tested in the LSE. A similar phenomenon has been found in recent literature which reported that advanced electrolytes reduce intergranular cracking in high-Ni cathodes during cycling. Therefore, the intergranular cracking in high-Ni layered oxide cathodes is affected by multiple competitive factors, and we believe that improving the surface stability is an effective way to inhibit the process during extended cycling.

The Pennsylvania State University (PSU) team continued to investigate the electrochemical performance of  $\text{Li}|\text{NMC811}$  full cell under the conventional electrolyte E1, fluorinated saturated electrolyte (FSE), and fluorinated saturated electrolyte with additives (the AFSE, which is based on FSE with 0.1 wt.% additive). The AFSE electrolyte is a new electrolyte formulation with solvents, salts, and additives optimized to achieve the target Coulombic efficiency (CE) of 99.5% and was introduced in the last quarter. Figure XVII.1.3a indicated that the FSE and AFSE significantly improved the cycling stability of NMC 811 with a cutoff voltage of 4.3 V. All the cycling data were collected with CR- 2016 type coin cells with a high loading cathode of  $4 \text{ mAh cm}^{-2}$  (i.e.,  $3.14 \text{ mAh/electrode}$ ) a  $50 \mu\text{m}$  thin lithium metal anode, and a lean electrolyte usage of  $5 \mu\text{L mAh}^{-1}$ . It suggested that the NMC811 cell with the FSE showed an initial discharge capacity of 2.78 mAh at 0.5C and retains 80% of its initial capacity after 265 cycles. AFSE enabled significantly improved cycling stability, delivering an 80% capacity retention of 2.66 mAh after 280 cycles. And the average Coulombic efficiency (CE) was nearly 99.9% for the cells tested with FSE and AFSE. By comparison, using the baseline electrolyte of E1, the cell decayed quickly and reached 70% of its original capacity of 2.79 mAh after only 50 cycles. The average CE was only 99.0 % in the first 50 cycles (Figure XVII.1.3a). A full cell with ultra-high loading cathode of  $5 \text{ mAh g}^{-1}$  (i.e.,  $4 \text{ mAh/electrode}$ ) with leaner electrolyte condition of only  $4 \mu\text{L mAh}^{-1}$  was conducted to further evaluate the advanced electrolyte under more practical conditions (Figure XVII.1.3b). The cell showed initial capacity of  $\sim 4 \text{ mAh}$  and a capacity retention of 80% after 120 cycles. The rate performance test (Figure XVII.1.3c) shows the cell using the AFSE showed higher capacity that the cell with E1 electrolyte and recovered to original capacity at 0.1C after a fast discharge at 3C. The improved rate performance could be attributed to the reduced interfacial charge-transfer resistance that is generally observed in localized high concentration electrolyte (LHCE). Thus, it was crucial to add a fluorinated diluent to promote the  $\text{Li}^+$  kinetics in the electrolyte. A Li metal pouch cell was then assembled and tested toward achieving high energy density, with a high areal capacity ( $4.0 \text{ mAh cm}^{-2}$ ) NMC811 cathode, a  $50 \mu\text{m}$  thin Li metal anode, and a lean electrolyte ( $3.0 \text{ g Ah}^{-1}$ ) (Figure XVII.1.3d).

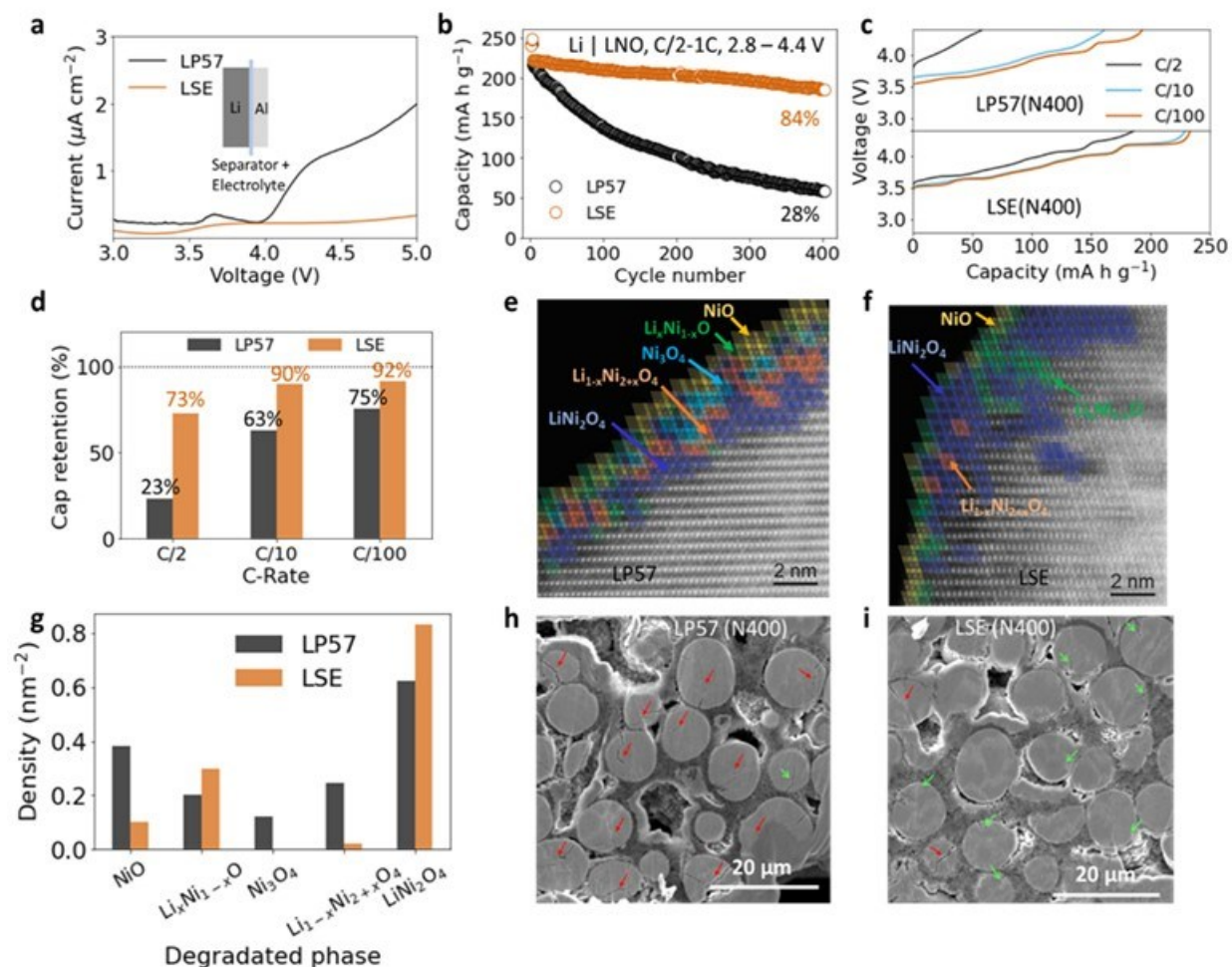


Figure XVII.1.2 (a) Linear sweep voltammetry of Li|Al cells with LP57 electrolyte and LSE; the inset shows the components within the test cell. (b) Cycling performances of Li|LiNiO<sub>2</sub> cells at room temperature with the listed cycling parameters. (c) Charge curves at different C-rates after 400 cycles and (d) the corresponding capacity retention compared to the maximum charge capacity during the formation cycle. (e, f) HAADF-STEM images of cycled LiNiO<sub>2</sub> electrode with the (e) LP57 electrolyte and (f) LSE. Surface degraded phases are identified and labeled. The diamonds represent the different atomic arrangements in each material based on the intensity profiles for those areas. Anything not indicated with a diamond has the standard layered oxide structure of Li<sub>1-x</sub>NiO<sub>2</sub>. (g) Semi-quantitative densities of the various atomic arrangements found in each sample. (h, i) Cross-section SEM images of cycled LiNiO<sub>2</sub> cathodes with the (h) LP57 electrolyte and the (i) LSE. Green arrows and red arrows are used, respectively, to highlight small cracks (smaller than the radius of the particle) and large cracks (larger than the radius of the particle) within each secondary particle.



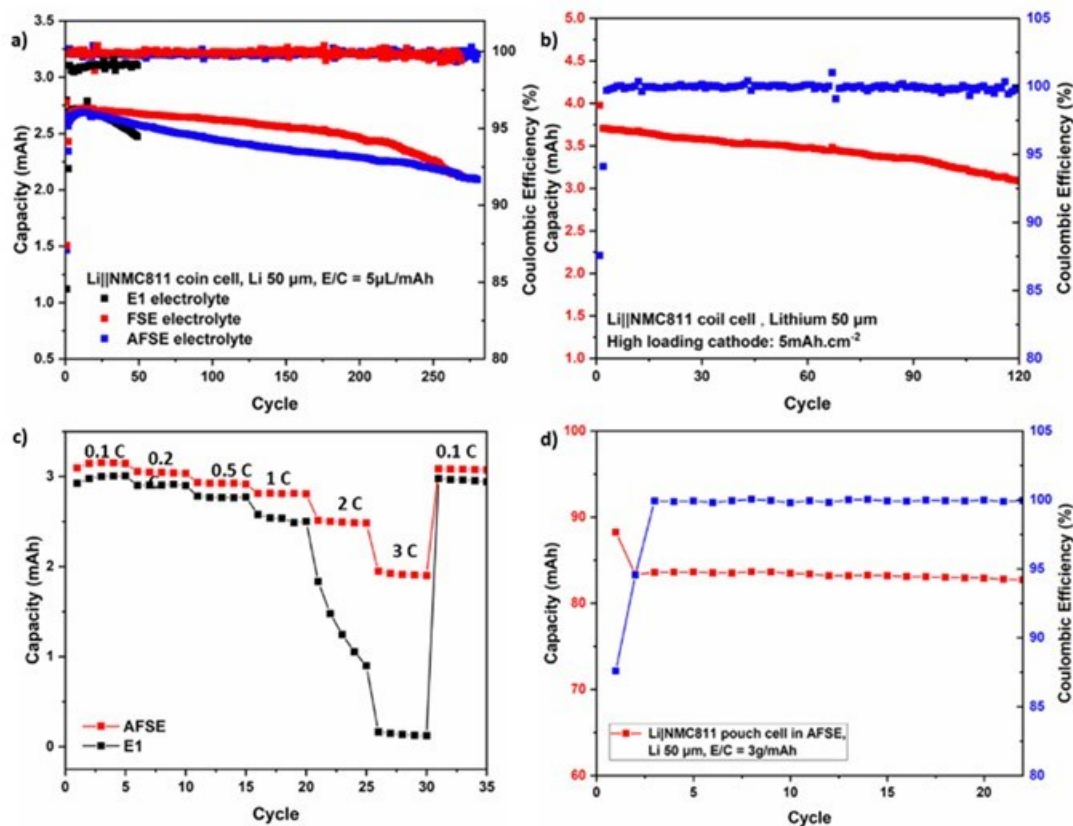
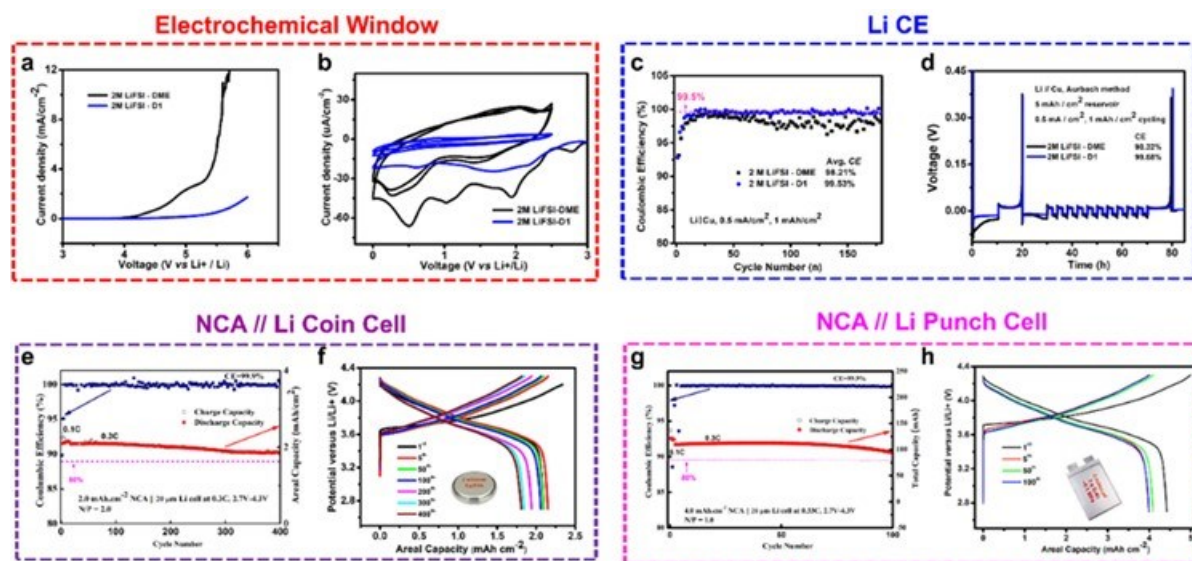


Figure XVII.1.3 (a) Electrochemical performance of the Li||NMC811 full cell tested in different electrolytes; (b) Electrochemical performance of the Li||NMC811 full cell in AFSE at high loading cathode; (c) Rate capacity of the NMC811||Li coin cells tested in different electrolytes; (d) NMC811||Li pouch cell.

To study the SEI compositional difference between the three electrolytes, XPS was performed on the cycled Li metal anode after 10 cycles. For samples using FSE or AFSE electrolytes, the percentages of  $\text{Li}_x\text{P}_y\text{O}_z\text{F}$  and  $\text{Li}-\text{CO}_2^-$  were markedly lower, whereas the percentage of LiF and  $\text{RO}-\text{CO}_2\text{R}$  were significantly higher than those formed in the conventional electrolyte. As known, LiF has been considered an excellent SEI component to suppress Li dendrite growth and promote uniform Li deposition owing to its high interfacial energy on Li metal and low surface barriers for Li-ion transport. The high content of LiF from AFSE electrolytes may be the main reason in the formation of stable SEI to deliver improved performance stability of lithium metal batteries (LMBs) over long-term cycling.

The University of Maryland at College Park (UMD) team focused their studies on the electrolyte designing approach to obtain robust ceramic LiF-rich SEI to suppress Li dendrite growth and enable long cycle life for LMBs. In the presentation for Battery500 biweekly meeting last quarter, the UMD team reported a new ether-based electrolyte of 2.0 M LiFSI-D1 that could achieve a high Li CE of 99.7%. Figure XVII.1.4 summarizes the electrochemical performance of ether-based 2.0 M LiFSI-D1 electrolyte. Through molecule design, the anodic stability of ether electrolytes was extended to > 5.0V (Figure XVII.1.4a) with no sacrifice on anode stability. As shown in Figure XVII.1.4b, compared to the same concentration DME electrolyte, the 2.0 M LiFSI-D1 electrolyte can effectively passivate the Cu surface, demonstrating a LiF-rich SEI formation and low reduction potential in this new electrolyte through molecular design approach. High Li CE of 99.53% and 99.68% was achieved at a capacity of 1.0 mAh cm<sup>-2</sup> and current of 0.5 mA cm<sup>-2</sup> in both full plating/stripping (Figure XVII.1.4c) and Li reservoir conditions (Figure XVII.1.4d), respectively. The consistency with both Battery500 Li-Cu cycle protocols further confirms the superior reversibility of 2.0 M LiFSI-D1 electrolyte for smooth Li plating/stripping. After demonstrating the Li reversibility, a controlled lithium metal deposited on

copper foil as anode ( $20\ \mu\text{m}$ ,  $\sim 4\ \text{mAh cm}^{-2}$ ) was paired with a high energy cathode  $\text{LiNi}_{0.8}\text{Co}_{0.15}\text{Al}_{0.05}\text{O}_2$  (NCA) for full cell test. Figure XVII.1.4e, f demonstrated  $>400$  long cycles of the coin cell at  $0.3\text{C}$  with a high cycle CE of  $>99.9\%$  and high capacity retention. The  $2.0\ \text{M LiFSI-D1}$  electrolyte is further tested under harsh conditions in a large pouch cell with an increased areal capacity to  $4.0\ \text{mAh cm}^{-2}$ . Figure XVII.1.4g, h) The  $100\ \text{mAh}$  lab-made pouch cell also guarantees a smooth cycle over  $100$  cycles with CE of  $>99.9\%$ , verifying the high compatibility of their designed electrolyte to high voltage NCA/Li full batteries. The discharge voltages of NCA at  $5^{\text{th}}$ ,  $50^{\text{th}}$ , and  $100^{\text{th}}$  cycles overlap well with each other, suggesting no significant structural change of the material nor continuous build-up of the cathode electrolyte interface (Figure XVII.1.4h). The initial capacity loss in the full cell (Figure XVII.1.4h, black line) was probably caused by  $\text{Li}^+$  consumption for SEI formation. The capacity loss is most rapid for the first three formation cycles and gradually slows down in the subsequent cycles at  $0.3\text{C}$ .



**Figure XVII.1.4** Electrochemical Performance of  $2.0\ \text{M LiFSI-D1}$  electrolyte. (a,b) Electrochemical window compared with  $2.0\ \text{M LiFSI-DME}$  electrolyte tested with  $\text{Al}||\text{Li}$  cell (a), and  $\text{Cu}||\text{Li}$  cell, the scan rate is  $0.5\ \text{mV/s}$ ; (c,d) Li stripping and plating CE under full plating/stripping conditions (c) and with  $5\ \text{mAh Li}$  reservoir (d), the cycle current is  $0.5\ \text{mA cm}^{-2}$  and capacity loading is  $1\ \text{mAh cm}^{-2}$ ; (e,f) full cell NCA||Li performance with N/P ratio of 2, areal capacity of  $2.0\ \text{mAh cm}^{-2}$ . (g,h)  $100\ \text{mAh}$  homemade pouch cell performance with NCA areal loading of  $4.0\ \text{mAh cm}^{-2}$

#### **Current-dependent lithium plating morphology in the presence of residual solid electrolyte interphase.**

The Stanford University (Stanford) team previously observed a strong dependence of  $\text{Li}||\text{NMC811}$  ( $4.5\ \text{mAh cm}^{-2}$ ) cycle life on charging current densities in three types of weakly solvating fluoroether electrolytes of  $1\ \text{M LiFSI}$  in FDMB,  $1.54\ \text{M LiFSI}$  in 1:3.6 (v/v) DME:TTE, and  $1\ \text{M LiFSI}$  in 1:3 (v/v) DEE:FDEB, where soft shorting was observed above  $2\text{--}5.2\ \text{mA cm}^{-2}$ . They further investigated the morphology dependence of Li and residual solid electrolyte interphase (rSEI) on plating current density. Thin Li ( $50\ \mu\text{m}$  thick) half cells were constructed with a piece of thick Li as the counter electrode in DEE-FDEB electrolyte. All cells were activated at  $0.4\ \text{mA cm}^{-2}$  and  $4\ \text{mAh cm}^{-2}$  for 2 cycles, followed by 10 cycles at  $0.4$  or  $4\ \text{mA cm}^{-2}$  plating current densities to form rSEI (low-current or high-current formation). In the final step,  $0.2$ ,  $0.5$ , or  $1\ \text{mAh cm}^{-2}$  capacity Li was plated at  $4\ \text{mA cm}^{-2}$  (high-current plating) or  $0.4\ \text{mA cm}^{-2}$  (low-current plating). These final plating capacities were less than 25% of the cycling capacity, which enabled the observation of initial Li growth by scanning electron microscope (SEM). The results of such morphology dependence on current profiles are shown in Figure XVII.1.5.

Under the low-current formation and low-current plating condition, large Li grains were observed which are separated by rSEI (Figure XVII.1.5a-c). Elemental mapping by energy dispersive X-ray spectroscopy (EDS) confirmed the different regions of Li and rSEI, which are marked by yellow and green arrows respectively in Figure XVII.1.5b. The Li plating morphology observed here validated their previous hypothesis that in some weakly solvating fluoroether electrolytes the plated Li first grew through the porous rSEI layer before forming the typical pancake-like morphology on top of the rSEI. Under the slow-charging condition here, a minimum of 25% of cycled Li (1 out of 4 mAh cm<sup>-2</sup>) was surrounded by rSEI as evidenced by the lack of Li plating above rSEI in Figure XVII.1.5c. Under the high-current formation and high-current plating condition, a very different surface morphology was observed (d-f). The regions of Li and rSEI were confirmed by EDS. A compact rSEI structure was formed (Figure XVII.1.5d). At 0.2 mAh cm<sup>-2</sup> deposition capacity, scarce and inhomogeneous Li nucleation was observed on top of rSEI (Figure XVII.1.5d). As deposition capacity increased, the Li grain size continued to increase (Figure XVII.1.5d-f) but remained smaller than those in Figure XVII.1.5a-c. Importantly, unlike the morphology observed under the slow-charging condition, the plated Li was not surrounded by rSEI after merely 0.2 mAh cm<sup>-2</sup> capacity under the fast-charging condition. Since SEI should be electrically insulating, there must be a small amount of Li growth within the rSEI (<0.2 mAh cm<sup>-2</sup> or <5% of cycling capacity) connecting the uncycled Li underneath rSEI and the plated Li above rSEI. Such scarce and dispersed points for Li deposition led to significant inhomogeneity and hotspots for Li growth. As a control experiment, they formed rSEI at 4 mA cm<sup>-2</sup> followed by plating Li at 0.4 mA cm<sup>-2</sup> (high-current formation, low-current plating) (Figure XVII.1.5g-i) to investigate the relative contributions from current density and rSEI structure to Li morphology. Compared to Figure XVII.1.5d-f (high-current formation, high-current plating), the amount of Li plated within rSEI was higher in Figure XVII.1.5g-i as evidenced by the lower coverage of Li on top of rSEI. In addition, the Li grain size was larger in Figure XVII.1.5g-i. These differences validated that the upward anisotropic growth of Li is favored under higher current densities even in the presence of the same rSEI. Compared to the Li morphology in Figure XVII.1.5a-c (low-current formation, low-current plating), the plated Li was less homogeneous and grew well above rSEI in Figure XVII.1.5g-i. Therefore, the rSEI structure formed under high current densities can indeed guide undesirable Li deposition morphology even after switching to lower plating current densities. This leads to the inhomogeneous electrochemically active surface for further Li deposition above rSEI.

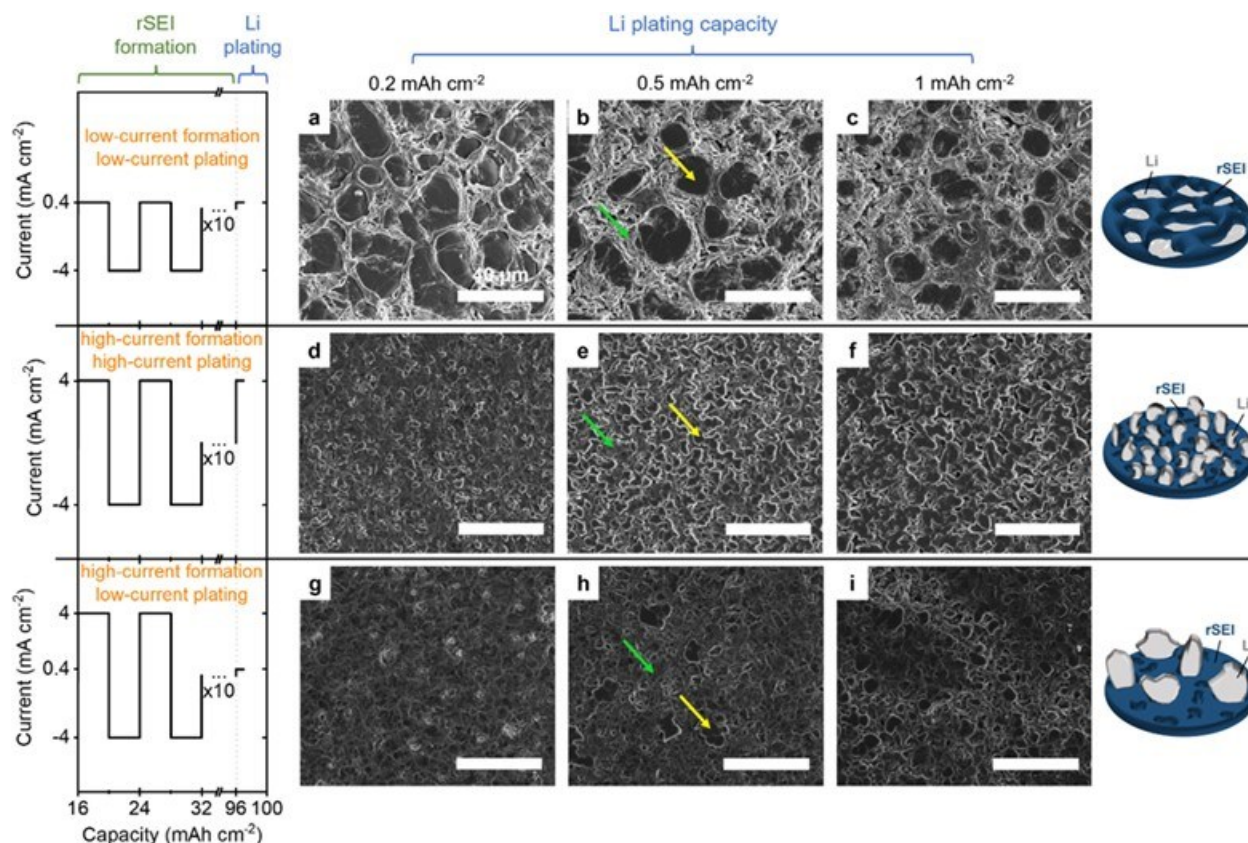


**Figure XVII.1.5** SEM images of Li plating morphology on 50  $\mu\text{m}$  Li electrode at various current densities and areal capacities in DEE-FDEB electrolyte. The rSEI was formed by 10 cycles at either 4  $\text{mA cm}^{-2}$  plating and stripping (high-current formation) or 0.4  $\text{mA cm}^{-2}$  plating and 4  $\text{mA cm}^{-2}$  stripping (low-current formation) for 4  $\text{mAh cm}^{-2}$ . In the final step, 0.2, 0.5 or 1  $\text{mAh cm}^{-2}$  capacity was plated at 4  $\text{mA cm}^{-2}$  (high-current plating) or 0.4  $\text{mA cm}^{-2}$  (low-current plating). The applied current profiles for rSEI formation and final Li plating are shown on the left. The capacities of final Li plating are labeled by columns on the top. Yellow and green arrows indicate Li and rSEI respectively. The scale bars are 40  $\mu\text{m}$ . The schematics on the right illustrate the top surface morphology of Li and rSEI.

The Pacific Northwest National Lab (PNNL) team continuously improves performance of Li||NMC811 (4  $\text{mAh cm}^{-2}$ ) cells by using a new diluent (DB) in their localized high concentration electrolyte (LHCE). The LHCE electrolytes using new diluent DB and different solvent to diluent ratios were named as LHCE-1 (LiFSI:DME:DB=1:1.25:2), LHCE-2 (LiFSI:DME:DB=1:1.15:3), and LHCE-3 (LiFSI:DME:DB = 1:1.1:3). First, the average Li coulombic efficiency (CE) of these electrolytes was measured in Li||Cu cells by using the Battery500 protocol. As shown in Figure XVII.1.6a, all these three electrolytes demonstrate a high average Li CE of 99.4 – 99.6%, indicating the high reversibility of Li deposition and stripping on the Li anode. To evaluate the oxidation stability of the electrolytes, the Li||LiMn<sub>2</sub>O<sub>4</sub> (LMO) cell was used. The potential was scanned from open circuit voltage ( $\sim 2.9$  V) to 5.0 V with a scan rate of 0.05  $\text{mV s}^{-1}$  in the LSV test. Figure XVII.1.6b shows the delithiation process of LMO in the potential range of 3.9 – 4.4 V, and the slight increase in current after 4.5 V could be associated with the oxidation process of the electrolytes on the LMO electrode. These results suggest that all as-prepared electrolytes with the new diluent could be stable up to 4.5 V and compatible with the Li metal anode. The electrolytes were further evaluated in the Li||NMC811 coin cell system (Al-Clad CR2032, MTI) in a voltage range of 2.8 – 4.4 V. The cells were performed two cycles at C/10 to stabilize SEI formation, and then cycled at C/10 charge and C/3 discharge using different LHCEs. All the cells show similar voltage profiles during the formation cycle and high discharge capacities of 194, 191, and 191  $\text{mAh g}^{-1}$  for LHCE-1, LHCE-2, and LHCE-3, were obtained respectively, as shown in Figure XVII.1.6c. Figure XVII.1.6d shows the cycling performance of the three electrolytes, which exhibit a capacity retention of

> 90% after 195 cycles, and all cells are still running when this report is being written. Notably, the LHCE-1 reveals a higher capacity at the initial cycles but slightly lower capacity at the later cycles, suggesting that the solvent to diluent ratios could affect the cycling stability of the LHCE in Li||NMC811 cells.

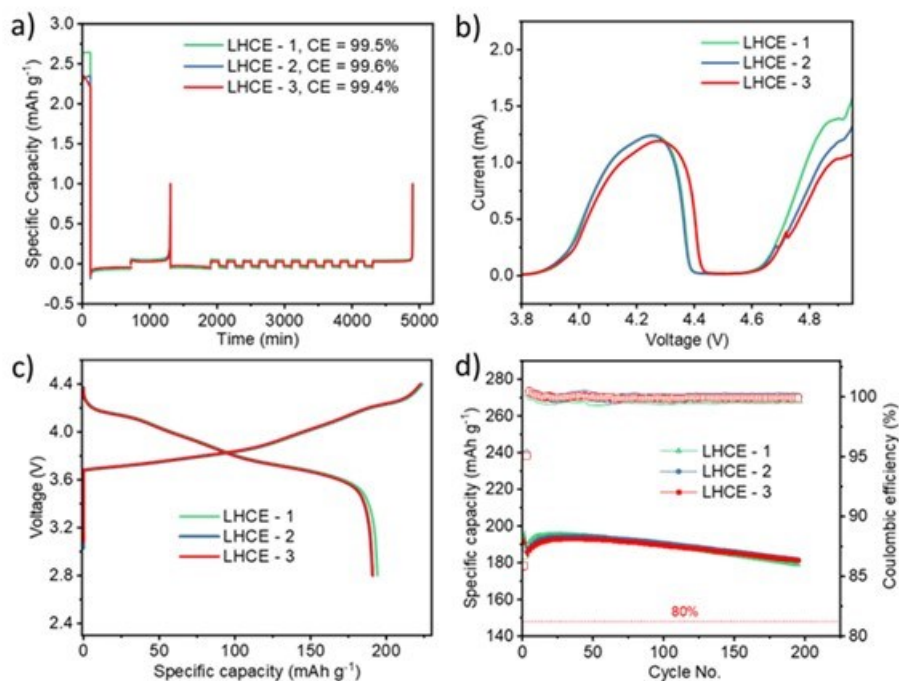


**Figure XVII.1.6** Electrochemical performance of Li||NMC811 cells with different LHCE electrolytes. (a) Li plating/stripping curves in Li||Cu cells, (b) LSV curves with scan rate  $0.05 \text{ mV s}^{-1}$  from OCV ( $\sim 2.9 \text{ V}$ ) to  $5.0 \text{ V}$ , (c) first cycle charge/discharge profiles at C/10, (d) cycling performance of the cells with charging at C/10 and discharging at C/3. Li metal ( $50 \mu\text{m}$  thick) on Cu foil and  $75 \mu\text{L}$  electrolyte were used for coin cells.

The UT Austin team investigated the mechanism of organopolysulfide-based additives to stabilize Li metal anode for use in Li-S batteries. The Li-metal stripping/plating performance in a Li||Ni cell with  $1 \text{ M LiTFSI}$  and  $0.2 \text{ M LiNO}_3$  in dimethoxyethane (DME) and dioxolane (DOL) electrolyte using either lithium polysulfide ( $\text{Li}_2\text{S}_8$ , LiPS) as an additive or diallyl polysulfide (DAPS) as an additive was studied. It is evident that the Li-metal anode cycles with a Coulombic efficiency of 99.16% in the DAPS-containing electrolyte, which is higher than that of the LiPS-containing electrolyte that cycles with only 96.15% Coulombic efficiency. Consequently, the Li-metal morphology is smoother and denser in the presence of DAPS. To investigate the origin of the stabilizing effect of a thiolate-rich SEI, the density functional theory calculations were performed.

#### **Theoretical and computational analysis on interfacial evolution.**

The Texas A&M University (TAMU) team conducted the theoretical and computational analysis which provides new insights into the cathode/electrolyte interface (CEI) interactions on interfacial evolution. Electrolyte oxidative deprotonation reactions result in proton insertion in surface layers, and Ni reduction from +3 to +2 with subsequent Ni-O bond weakening.  $\text{Ni}^{2+}$  cations migrate to Li vacancies initiating structural degradation. It is shown that proton insertion yields water and HF via salt hydrolysis, and Ni cation dissolution. Current studies address the effect of Ni ion migration to the anode on the SEI formation on Li metal. The TAMU team also addressed the thermal-driven degradation pathways of the solid electrolyte interphase on lithium metal electrodes via first-principles methods in collaboration with experimentalists from the Binghamton University team. First, the SEI growth is modeled using a hybrid ab initio and reactive molecular dynamics (HAIR and MD) simulation scheme that allows the formation of extended organic and inorganic phases within the SEI along with the dissolution of remanent lithium metal into  $\text{Li}^+$  ions. The

simulation scheme produces an SEI structure that reproduces its main structural features. Next, they follow the SEI thermal evolution through ab initio molecular dynamics simulations following a linear heating ramp. Preliminary results from the TAMU simulations indicate that the destruction of the organic SEI precedes lithium leaching, and the inorganic SEI sustains the induced thermal stresses enforced within their achievable simulation window. Collaboration with the Binghamton research group is fundamental for fine-tuning the SEI composition. XPS and DSC data measured on SEI layers grown on lithium metal at open circuit voltage conditions allow them to modulate the electrolyte-to-anode ratio in their simulation cells to reproduce the SEI's structural and compositional features while leaving some unreacted lithium metal, which is essential to follow the SEI/lithium metal interface response in high-temperature regimes.

#### **Determine the role of niobium (Nb) stabilization for ether-based electrolytes.**

The BU team studied the role of Nb in ether-based electrolytes through (1) cycling stability, (2) structure stability, and (3) thermal stability. Starting from the same co-precipitated NMC hydroxide precursor, Co, Al and Nb modified 90% Ni NMC were synthesized with the same precursors' ratio of Li:Ni:Mn:Co:X (X = Nb, Co, Al) = 1.03:0.9:0.05:0.033:0.017 at 775 °C in O<sub>2</sub> for 20 h. Although very similar morphologies were obtained among the NMC materials, distinct cycling stabilities were manifested (Figure XVII.1.7a): Nb modification gives the best cycling performance. The charge and discharge curves at different cycle numbers (10, 50, 100 and 150) in Figure XVII.1.7b-d, clearly show that Nb modification can significantly improve the electrochemical reversibility, contributing to the perfectly overlapped charge/discharge curves for different cycle numbers.

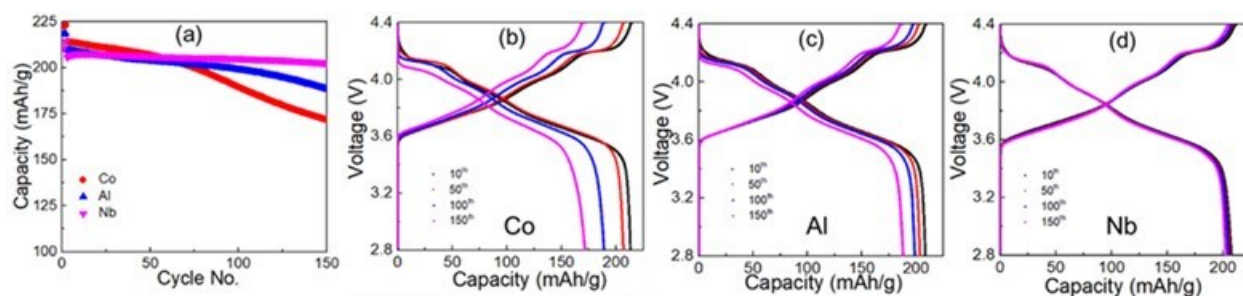


**Figure XVII.1.7 (a) Cycling performance of Co, Al and Nb modified 90% Ni NMC tested with the M47 electrolyte (PNNL) using the aluminum protected Hoshen coin cells in the voltage range of 2.8 to 4.4 V with C/10 charge and C/3 discharge current at 30 °C. The charge and discharge curves of (b) Co, (c) Al and (d) Nb modified samples at cycle 10, 50, 100 and 150.**

This perfect reaction reversibility was also represented by the  $dQ/dV$  vs. V studies: Nb modified sample showed almost overlapped redox peaks with cycling, while apparent shifts were observed for other samples, indicating that Nb modification can help to eliminate structural transformation of high nickel NMC, which significantly improve the structural stability in ether-based electrolytes.

Furthermore, thermal studies demonstrated that Nb modification gives the lowest heat flow and highest peak temperature (greatest stability to oxygen evolution) when heating the charged electrode with ether-based electrolytes, showing great benefits of Nb modification on thermal stability. All indications are that a high-valent Nb substituent stabilizes the NMC lattice allowing enhanced capacity retention.

#### **Air stability of high-Ni layered oxide cathodes.**

The UT Austin team investigated the formation and accumulation of surface residual Li containing species, including Li<sub>2</sub>CO<sub>3</sub> and LiOH, (a term of “residual Li” will be used to describe them in this report) on a group of LiNiO<sub>2</sub> (LNO)-based high-Ni cathodes, which include LiNi<sub>0.95</sub>Co<sub>0.05</sub>O<sub>2</sub> (NC), LiNi<sub>0.95</sub>Mn<sub>0.05</sub>O<sub>2</sub> (NM), and LiNi<sub>0.95</sub>Al<sub>0.05</sub>O<sub>2</sub> (NA) with a same 5 mol% doping of Co, Mn, and Al, respectively, comparing with undoped LNO itself. The surface residual Li content was determined by an acid-base titration method in solutions subjected to cathode powder washing.

Figure XVII.1.8a compares the surface residual Li content for fresh cathodes and cathodes aged in ambient air for one, two, and three months. As seen, the fresh LNO shows the highest content of residual Li of  $\sim 3,500$  ppm, followed by NC ( $\sim 3,100$  ppm), NA ( $\sim 3,100$  ppm), and NM ( $\sim 2,300$  ppm). Such a trend remains nearly unchanged during the entire aging period. After three months, the residual Li content on LNO increased by  $\sim 37\%$  to  $\sim 4,800$  ppm, followed by NA ( $\sim 4,600$  ppm), NC (4,400 ppm), and NM (3,500 ppm). Overall, it is shown that Mn-doping is more beneficial in suppressing residual Li formation and buildup than Co-doping and Al-doping. Reducing the residual lithium will suppress clogging during electrode preparation and capacity fade during cycling.

Figure XVII.1.8b compares the cycling stability of fresh and aged LNO, NC, NM, and NA cathode electrodes. The cells with fresh LNO, NC, NM, and NA deliver capacities of 246, 242, 236, and 238 mA h g<sup>-1</sup>, respectively (at a rate of C/10). In sharp contrast, after three-month aging in the air, all the cathodes suffer from a dramatic decline in the deliverable capacity. Specifically, aged LNO, NC, NM, and NA retain only 85%, 89%, 69%, and 82% of deliverable capacity, respectively, compared to the corresponding fresh cathodes. Interestingly, although NM has been demonstrated to be most effective in mitigating residual Li buildup, it shows the largest capacity penalty after aging. Such a counterintuitive phenomenon suggests that surface reconstruction pathways of LiNiO<sub>2</sub>-based cathodes during air storage can be affected by the type of dopant. UT Austin is actively collaborating with other institutions to elucidate this.

Figure XVII.1.8c further compares the rate performance of the fresh and aged cathodes. The rate capability of aged cathodes shares the same trend as the fresh cathodes, which is NC > NA > LNO > NM. The maintenance of Ni as Ni<sup>3+</sup> in NC, NA, and LNO offers better electronic conductivity with less cation mixing of Li and transition metal sites, resulting in higher rate capability. The reduction of some Ni<sup>3+</sup> to Ni<sup>2+</sup> by Mn<sup>4+</sup> in NM increases cation mixing and reduces electronic conductivity, resulting in lower rate capability.

All-solid-state batteries with LiNiO<sub>2</sub> cathodes. The UT Austin team also investigated the electrochemical properties of polycrystalline and single-crystalline LiNiO<sub>2</sub> (LNO) cathodes with sulfide and halide solid electrolytes (SEs) in all-solid-state batteries (ASSBs). The single crystalline LNO cathodes were synthesized with the morphologies and particle sizes of polycrystalline LNO (PC-LNO), nano single-crystalline LNO (nSC-LNO), and micron single-crystalline LNO ( $\mu$ SC-LNO). All LNO cathodes with halide SEs show improved capacities and CEs compared to the sulfide counterparts. The  $\mu$ SC-LNO shows a high capacity of 205 mA h g<sup>-1</sup> and a high CE of 83.4%. In addition, all LNO cathodes with the halide SEs show stable cycling performance at C/10 rate. It is believed that the SC-LNO is promising for realizing high energy density for all-solid-state batteries.

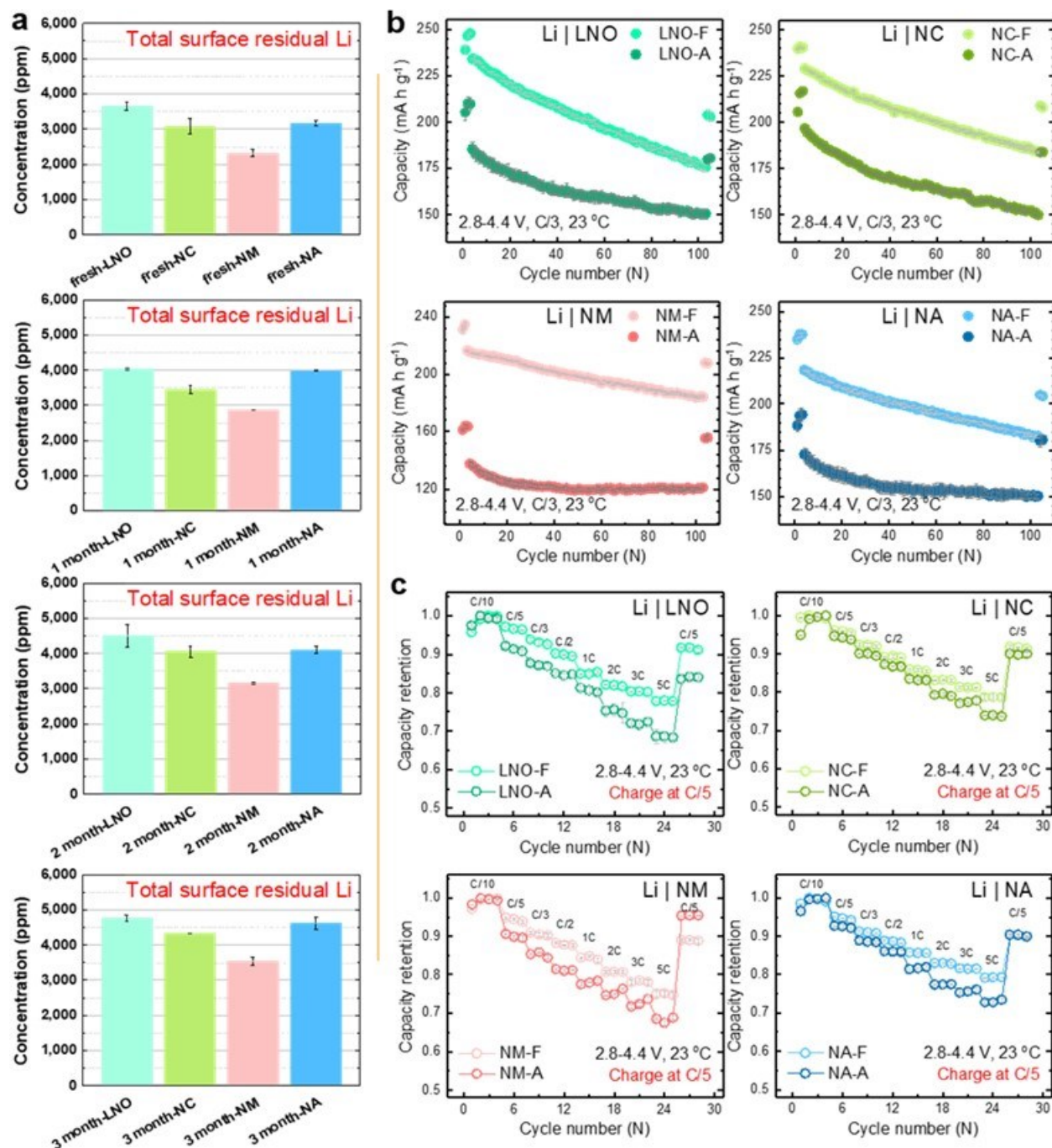


Figure XVII.1.8 (a) Surface residual Li contents of pristine and aged (stored in ambient air for 1–3 months) LNO, NC, NM, and NA cathodes, showing the accumulation of residual Li species as a function of storage period and dopant. (b) Cycling performance of fresh and aged (3 months) LNO, NC, NM, and NA cathodes. The cells were cycled between 2.8 and 4.4 V at a C/3 rate for 100 cycles after three formation cycles at a C/10 rate. After 100 cycles, the cells were cycled for another two cycles at a C/10 rate for capacity check. (c) Rate performance test of the fresh and aged (3 months) LNO, NC, NM, and NA cathodes. The fresh cathodes are termed as LNO-F, NC-F, NM-F, NA-F, while the aged cathodes are termed as LNO-A, NC-A, NM-A, and NA-A.

The PSU team introduced a novel carbonate-based electrolyte developed to investigate the cycling stability of Li metal batteries. This electrolyte demonstrated an improved cycling stability with capacity retention of 97.0% after 50 cycles. The PSU team also developed new electrolytes for Lithium-sulfur batteries with



different additives. Using the General Motors (GM) cathodes with high loading of  $4\text{--}5\text{ mg}\cdot\text{cm}^{-2}$ , the coin cells were discharged/charged at  $0.05\text{ C}$  for the first two formation cycles and then cycled at  $0.1\text{ C}$  for the following cycles. As shown in Figure XVII.1.9a, the electrolyte with  $0.1\text{ wt}\%$  A3 additive had the best performance compared to the other electrolytes and outperformed the baseline electrolytes with  $1.0\text{ M LiTFSI}$  in DOL/DME ( $1:1\text{ v/v}$ ) +  $0.2\text{ M LiNO}_3$ . The A3 additive reduced the activation energy of  $\text{Li}_2\text{S}$  dissolution process as shown in the inset in Figure XVII.1.9b, resulting in a much more reversible charge/discharge capacity than the other electrolytes.

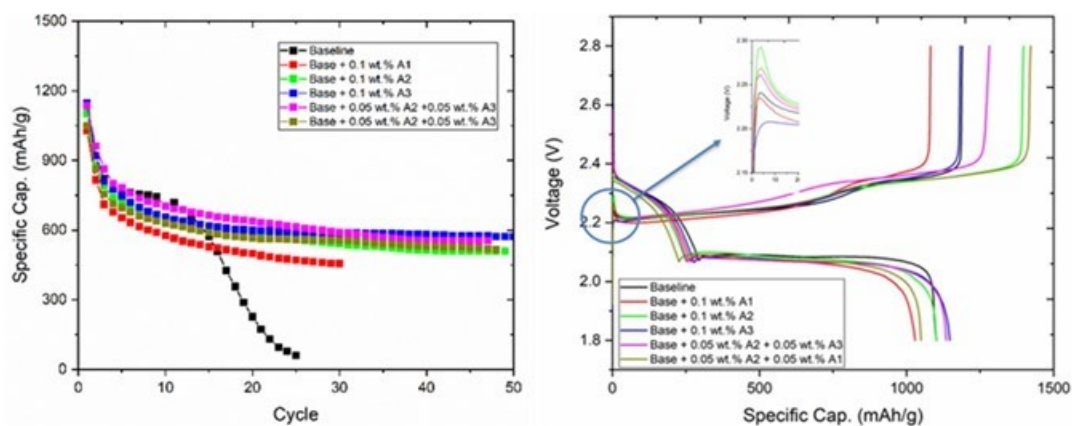
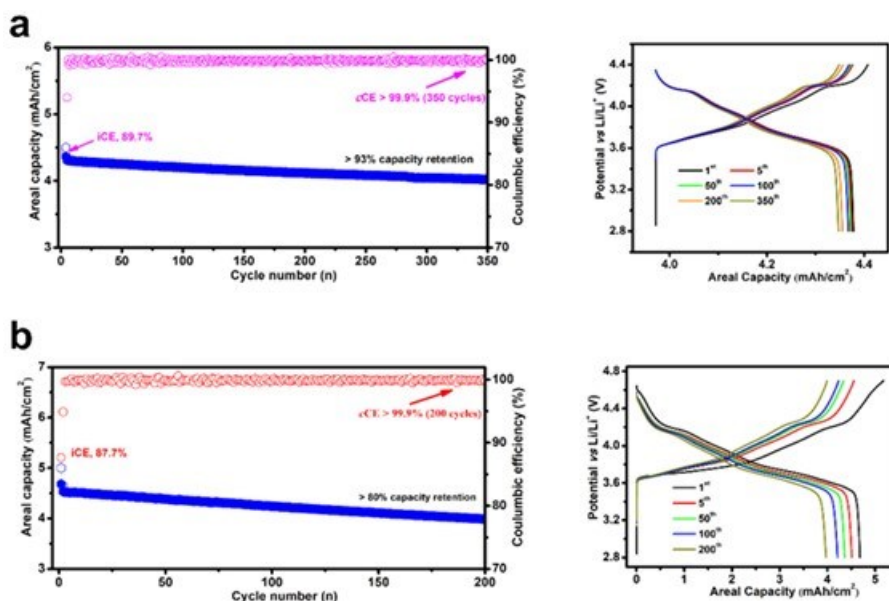


Figure XVII.1.9 (a) Electrochemical performances; (b) Voltage profiles of Lithium sulfur batteries with different electrolytes.

The UMD team developed a new ester-based electrolyte (M1 electrolyte) with high voltage stability to fulfill the Bat500 project goal of a long cycle life for NMC811||Li cells. M1 is used to represent the electrolyte containing LiFSI salt and the designed new solvent. This M1 electrolyte has high-voltage cathode stability as well as high Li anode compatibility. The  $4.5\text{ mAh}\cdot\text{cm}^{-2}$  NMC811|| $20\mu\text{m}$ -Li foil full cell was first tested in a coin cell configuration. The cell was charged to  $4.4\text{ V}$  and discharged to  $2.8\text{ V}$  according to the Bat500 protocol (Figure XVII.1.10a). One formation cycle at  $0.1\text{ C}$  was given before the  $0.3\text{ C}$  long cycle. The discharge voltages of NMC811 at  $5^{\text{th}}$ ,  $50^{\text{th}}$ ,  $100^{\text{th}}$ ,  $200^{\text{th}}$ , and  $350^{\text{th}}$  cycles overlap well with each other, indicating stable interphases formed on both Li anode (SEI) and NMC811 cathode (CEI). The cell runs for  $>350$  cycles with a high-capacity retention of  $>93\%$ . Because of the high voltage compatibility of M1 electrolytes, it was able to charge the NMC811||Li cell to an ultra-high voltage of  $4.7\text{ V}$  versus  $\text{Li}^+/\text{Li}$ , delivered more energy from the NMC811 cathode (Figure XVII.1.10b). The high-voltage cell was able to run for over 200 cycles with a capacity retention of  $>80\%$  and a high cycle CE of  $>99.9\%$ .



**Figure XVII.1.10** Electrochemical performance of NMC811|Li cells in M1 electrolyte. (a) Cycle performance of (4.5 mAh cm<sup>-2</sup>) NMC811|Li (20 μm) cell in the voltage range of 2.8 V to 4.4 V at 0.3C, the voltage profile is shown on the right; (b) Cycle performance of (4.5 mAh cm<sup>-2</sup>) NMC811|Li (20 μm) cell in the voltage range of 2.8 V to 4.7 V at 0.3C, the voltage profile is shown on the right.

The Stanford team evaluated commercially available FDMB (2,2,3,3-tetrafluoro-1,4-dimethoxybutane, CAS: 2738080-99-2) as the organic solvent in LiFSI-based liquid electrolyte for Li-metal batteries, comparing its performance with the FDMB electrolyte developed by the Stanford team (*Nat. Energy* 2020). The major suppliers of FDMB are 1. SynQuest Labs with 98% purity; 2. TCI America with 98% purity; and 3. Fluorxy Labs with 99% purity. Stanford team tested the FDMB from TCI America. Considering its lower purity compared to the other two sources, if its CE quality is comparable to the Stanford FDMB, it would suggest that other higher purity sources will have similar or better CE. The average CE using as-received FDMB was found to be 99.42% (one repetition), which was close to the reported values of Stanford electrolyte (99.52%, to 99.4%). The average CE using molecular sieve dried FDMB was found to be 99.37±0.07% (2 repetitions), close to the CE result obtained for the as-received sample. However, the drying procedure reduced the cell overpotentials, both in the Li plating and stripping steps. For example, the plating overpotential in the first cycle dropped from 75 mV to 58 mV. This suggests that molecular sieve drying removed water from the FDMB electrolyte, which has minimal effect on CE but is beneficial for reducing overpotential during charge-discharge cycling. The composition of the FDMB (98%, TCI) was further analyzed using liquid <sup>1</sup>H and <sup>19</sup>F NMR by comparison with possible synthetic intermediates (2,2,3,3-tetrafluoro-4-methoxybutan-1-ol, MFB; 2,2,3,3-tetrafluorobutane-1,4-diol, FB), as shown in Figure XVII.1.11. A quick comparison shows that a small amount (<1%) of MFB and a trace amount of unidentified aliphatic compound are likely present as impurities. The hydroxyl group in MFB can react with Li metal and cause a reduction of CE and an increase of overpotential. The water content was unable to be determined in NMR because of the water already present in the deuterated solvents. The combination of NMR with chromatographical techniques such as GC-MS can potentially help further identify the impurities.

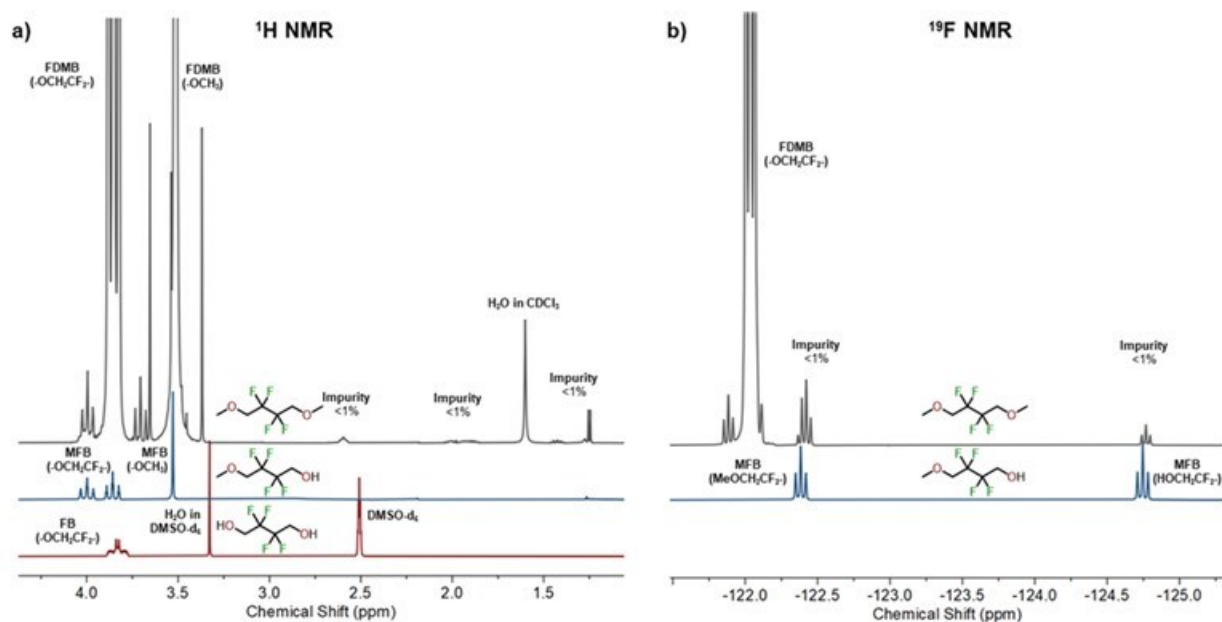


**Figure XVII.1.11 Stacked (a) $^1\text{H}$  and (b) $^{19}\text{F}$  NMR spectra of FDMB (in  $\text{CDCl}_3$ ) and its possible synthetic intermediates MFB (in  $\text{CDCl}_3$ ) and FB (in  $\text{DMSO-d}_6$ ). The spectra of FDMB have been zoomed in vertically for easy comparison with the other compounds.**

The PNNL team has developed new electrolytes for  $\text{Li||S}$  ( $4 \text{ mAh cm}^{-2}$ ) cells by utilizing a dual- or tri-solvent system aimed at designing a series of moderately solvating electrolytes to control the amount of dissolution of polysulfide species in the electrolyte and improve the overall cell cycle life and stability with the S/C composite cathode and Li metal anode. The new electrolytes were developed with a range of concentrations of  $0.6 \text{ M} - 1.2 \text{ M}$  LiTFSI in the new solvent system with  $2\% \text{ LiNO}_3$ , which are referred to as DMFN and were compared to the baseline electrolyte of  $1 \text{ M}$  LiTFSI in  $\text{DOL:DME}$  ( $1:1 \text{ v:v}$ ) +  $2\% \text{ LiNO}_3$ . First, the average Li Coulombic efficiency (CE) of these electrolytes was measured in  $\text{Li||Cu}$  cells using the Battery500 protocol. As shown in Figure XVII.1.12a, all the DMFN electrolytes demonstrated a higher average Li CE of  $99.35\% - 99.66\%$  compared to the Li CE of the baseline electrolyte at  $99.19\%$ , indicating a higher reversibility of Li stripping and plating on the Li metal anode. The ionic conductivity of these electrolytes was measured and the conductivity values of the DMFN electrolytes were roughly half of the baseline, ranging from  $6.02 - 6.77 \text{ mS cm}^{-1}$ , slightly increasing with increased concentration of LiTFSI (Figure XVII.1.12b). The rate capability test (Figure XVII.1.12c) shows the DMFN electrolytes can maintain comparable discharge capacity and cycling stability with the baseline electrolyte up to a  $1\text{C}$  charge rate with a constant  $C/10$  discharge rate. The electrolytes were further evaluated in long-term cycling tests in  $\text{Li||S}$  coin cells. The cells were performed two formation cycles at  $C/20$  in  $1.8 - 2.8 \text{ V}$ , and then cycled at  $C/10$  or  $C/5$  in  $1.7 - 2.8 \text{ V}$  in the baseline and DMFN electrolytes with an E/S ratio of  $8 \mu\text{L/mg-S}$ . The voltage profiles of the first cycle charge/discharge at  $C/20$  show that the DMFN electrolytes have a smaller initial voltage slope between  $2.1 - 2.4 \text{ V}$  indicating a reduced degree of soluble  $\text{Li}_2\text{S}_{6-8}$  species that may dissolve into the electrolyte during the  $\text{Li}^+$  migration onto the C/S electrode. The voltage slope decreases with the increasing concentration of the DMFN electrolyte, as shown in Figure XVII.1.12d. Figure XVII.1.12e shows the cycling performance of the electrolytes at a  $C/10$  charge and discharge rate. All four DMFN electrolytes show enhanced cycling stability and CEs of  $97\% - 99\%$ , compared to the baseline electrolyte, over nearly 100 cycles. The cycling performance for all DMFN electrolytes is improved when cycled at a  $C/5$  charge and discharge rate, showing improved cycling stability and CE over 100 cycles, as shown in Figure XVII.1.12f. Notably, the  $0.8 \text{ M}$  DMFN electrolyte reveals a higher capacity than other concentrations of DMFN electrolytes when cycled at both  $C/10$  and  $C/5$  rates.

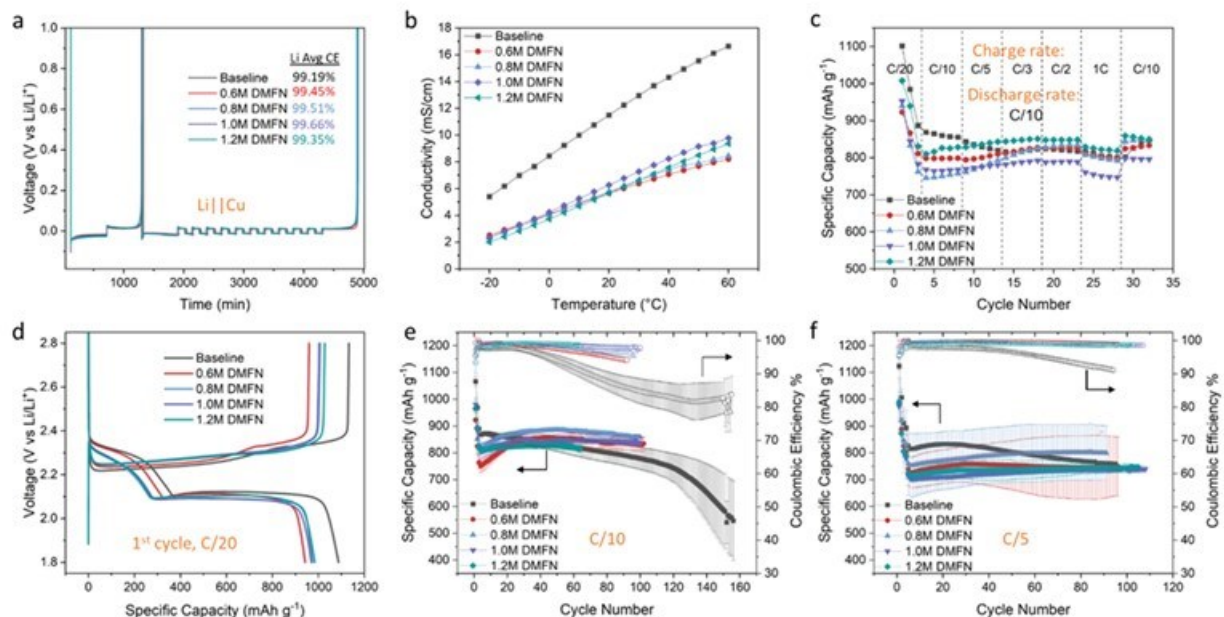


**Figure XVII.1.12** Electrochemical performance of Li||S cells with Baseline and DMFN series of electrolytes. (a) Li plating/stripping curves in Li||Cu cells, (b) Ionic conductivity plots from  $-20^{\circ}\text{C}$  to  $60^{\circ}\text{C}$ , (c) Charge rate capability test of Li||S full cell tested in different electrolytes (d) First cycle charge/discharge voltage profiles at C/20 (1.8 – 2.8 V), cycling performance of full cell at (e) C/10 and (f) C/5 charge and discharge rates (1.7 – 2.8 V). Li metal (250  $\mu\text{m}$  thick) and an E/S ratio of 8  $\mu\text{L}/\text{mg-S}$  were used in the Li||S full cells.

**Compare the cycling performance of high Ni NMC with Co, Al, and Nb modification at elevated temperature using electrolytes developed by K1 team of Battery500 consortium.**

The Binghamton team studied the cycling performance of Nb-modified NMC9055 at elevated temperature ( $45^{\circ}\text{C}$ ) compared with Co and Al modification and studied their cycling performance in pouch cells using PNNL M47 electrolyte and UMD electrolyte respectively. It was shown that for Co, Al and Nb modified 90% Ni NMC, Nb modification gives the best cycling performance at  $30^{\circ}\text{C}$  and the lowest heat release when heating the charged electrode with ether-based electrolyte. Studies of these materials were also carried out at an elevated temperature,  $45^{\circ}\text{C}$  (Figure XVII.1.13). With increased temperature, the initial capacities were increased to about 220 mAh/g for all the cells with different cathode modifications. Superior to the Co and Al modifications, Nb modification showed the best cycling stability (Figure XVII.1.13a) and excellently overlapped  $dQ/dV$  vs. V curves for different cycle numbers (Figure XVII.1.13d), which are almost the same as the results tested at  $30^{\circ}\text{C}$ . This excellent cycling performance at elevated temperatures further demonstrated that Nb modification is a very effective strategy to significantly improve structural stability and performance even at elevated temperatures.

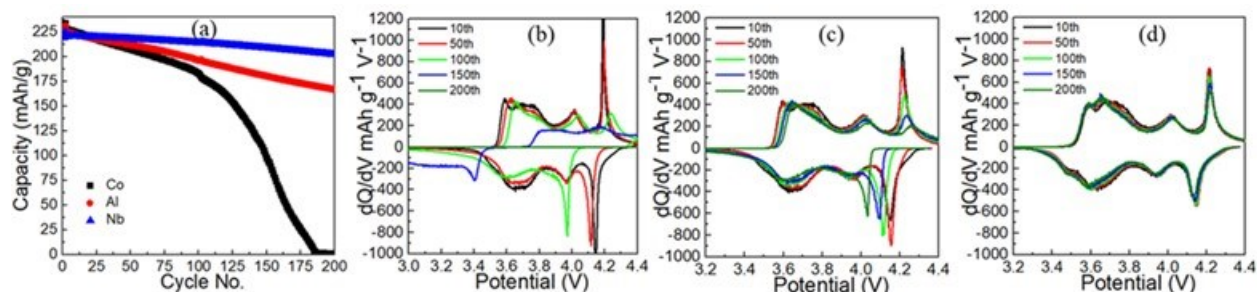


**Figure XVII.1.13** (a) Cycling performance of Co, Al and Nb modified 90% Ni NMC tested with the M47 electrolyte (PNNL) using the aluminum protected Hohen coin cells in the voltage range of 2.8 to 4.4 V with C/10 charge and C/3 discharge current at 45 °C. dQ/dV vs. V curves at cycle 10, 50, 100, 150 and 200 of (b) Co, (c) Al and (d) Nb modified 90% Ni NMC tested with the M47 electrolyte (PNNL) using the aluminum protected Hohen coin cells in the voltage range of 2.8 to 4.4 V with C/10 charge and C/3 discharge current at 45 °C.

Furthermore, the cycling performance of Nb modified samples were also studied in single layer pouch cells using PNNL M47 electrolyte and UMD electrolyte respectively. For M47 electrolyte, above 80% capacity can be maintained for up to 225 cycles. A little better cycling performance was observed for the UMD electrolyte with a slightly higher charging cut-off voltage (4.5 V for UMD electrolyte vs. 4.4 V for M47)

#### **Effect of Various Common Dopants on the Thermal stability of LiNiO<sub>2</sub>**

The UT Austin team systematically investigated the effect of 5 atom % of four common dopants (Co, Mn, Al, and Mg) on the thermal stability of LiNiO<sub>2</sub> (LNO) using differential scanning calorimetry (DSC). The compositions of the materials investigated are LiNi<sub>0.95</sub>Co<sub>0.05</sub>O<sub>2</sub> (NC), LiNi<sub>0.95</sub>Mn<sub>0.05</sub>O<sub>2</sub> (NM), LiNi<sub>0.95</sub>Al<sub>0.05</sub>O<sub>2</sub> (NA), and LiNi<sub>0.95</sub>Mg<sub>0.05</sub>O<sub>2</sub> (NMg). To rigorously elucidate the thermal stability as a function of state-of-charge (SOC), the DSC data were collected for nine SOC states with each cathode, and three times for each SOC state to ensure reproducibility and consistency. As shown in Figure XVII.1.14a, at high SOC states (230 and 240 mA h g<sup>-1</sup>), although all the cathodes display sharp and strong DSC peaks, the peak temperatures for NA (203 °C) and NMg (201 °C) are higher than those for LNO (189 °C), NC (189 °C), and NM (189 °C). As the SOC state gradually decreases below a critical value, the DSC peaks become abruptly weaker and broader. The critical SOC state is influenced by the dopant, as seen in Figure XVII.1.14a,b, and it decreases in the order NMg (224 mA h g<sup>-1</sup>) = NA (224 mA h g<sup>-1</sup>) > NM (210 mA h g<sup>-1</sup>) = LNO (210 mA h g<sup>-1</sup>) > NC 190 mA h g<sup>-1</sup>). The data illustrates that both Al- and Mg-doping can improve the thermal stability of high-Ni cathodes at high SOC states. In contrast, Co-doping in LNO can cause problems for safe operation even at a relatively low SOC. This trend can be understood as the Co<sup>3+/4+</sup>:t<sub>2g</sub> band overlaps with the top of the O<sup>2-</sup>:2p band, increasing the metal-oxygen covalence, while both the inert Al and Mg without any d electrons make the metal-oxygen bond stronger. Figure XVII.1.14c further quantitatively compares the DSC heat release and peak temperature for all the cathodes at various delithiation states. First, NA shows the lowest heat release and highest peak temperature at all delithiation states, illustrating that Al-doping is very beneficial for thermal stability. Second, Mg-doped NMg also evidently elevates the DSC peak temperature, especially at high delithiation states. Third, although NM shows the DSC profiles similar to NC and LNO at high delithiation states, the DSC peak temperature of NM increases more quickly at low delithiation states. Fourth, compared to LNO, NC shows higher heat release at high delithiation states and a lower critical delithiation state below which the DSC peak becomes significantly weaker. Therefore, it can be concluded that the thermal stability of the cathodes decreases in the order NA > NMg > NM > LNO > NC.

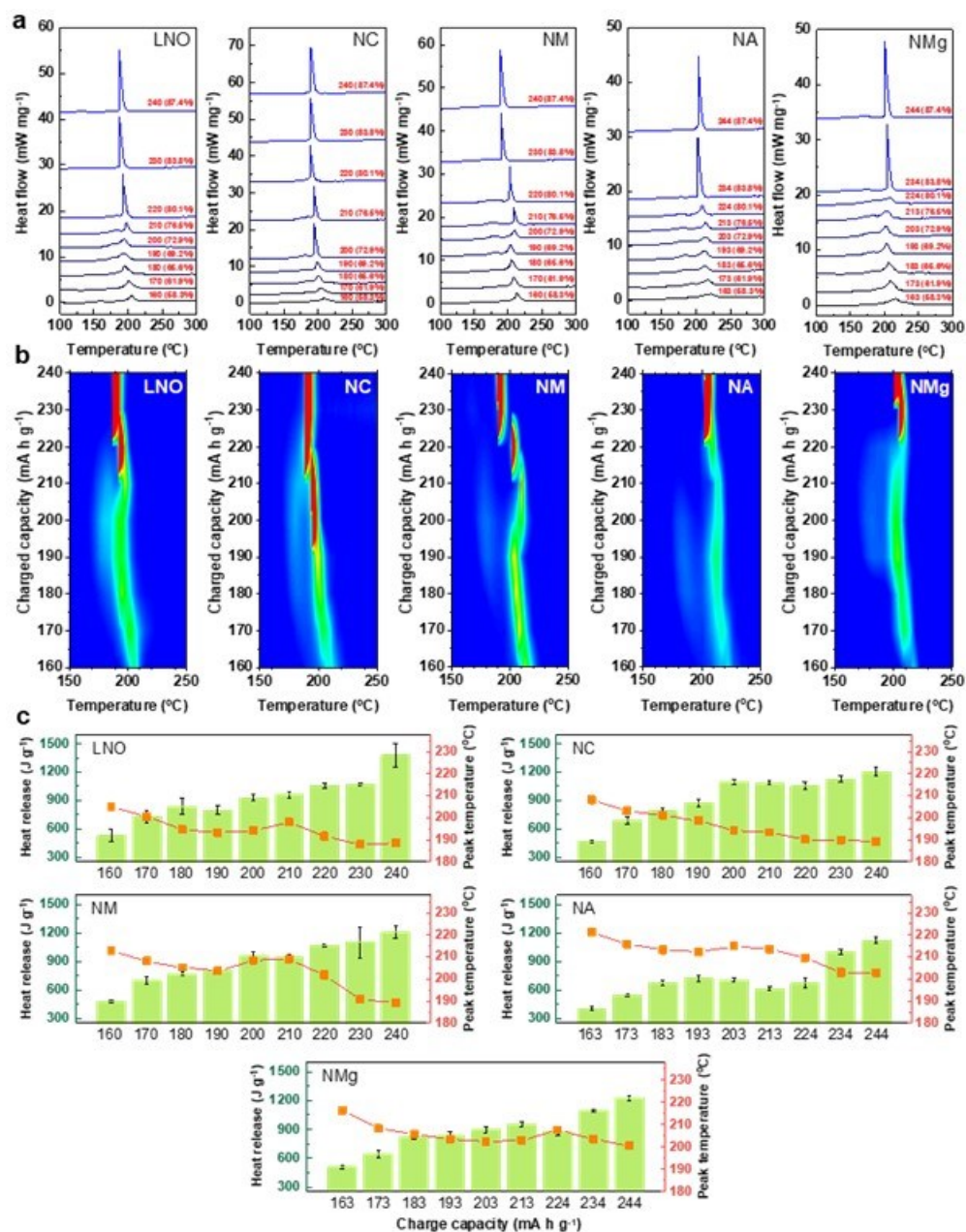
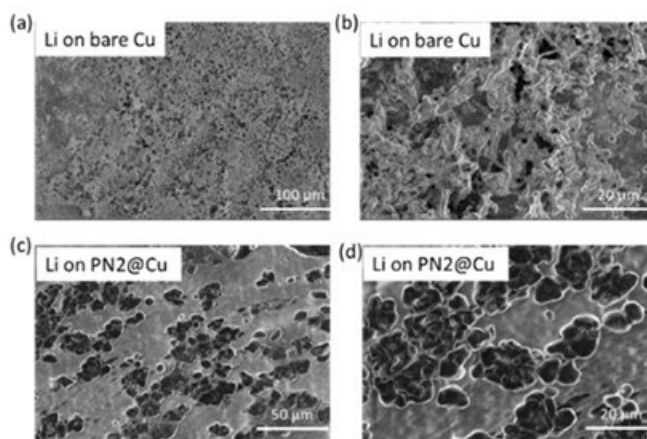


Figure XVII.1.14 (a) Evolution of the DSC peaks with LNO, NC, NM, NA, and NMg cathodes as a function of SOC state. (b) 2D contour plots of the evolution of DSC peaks. (c) Evolution of the DSC peak temperature and heat release from the cathodes as a function of SOC state. Cathodes with different SOC states were obtained by charging the cathode to different capacities.

To achieve the dendrite-free Li metal battery, a novel functional polymer PN2 was designed and synthesized by the PSU team as an artificial protection layer for the Li metal anode. The functional polymer was designed to have a strong complex effect with Li ions and an ability to concentrate the Li ions on the Li metal anode surface, thus, capable to change the nucleation and suppress the growth of Li dendrites in the plating process. Firstly, the morphologies of nucleated Li particles on Cu substrate were investigated by using scanning electron microscopy (SEM). A small amount of Li (0.1 mAh cm<sup>-2</sup>) was plated onto the bare Cu substrate and the polymer PN2 coated Cu substrate respectively. As shown in Figure XVII.1.15 the deposited Li did not cover the entire Cu surface. Figure XVII.1.15a-b show the morphologies of Li seeds formed on a bare Cu foil

with  $6.0 \text{ mA cm}^{-2}$  current density at  $25 \text{ }^\circ\text{C}$ . Obvious needle-shaped Li seeds can be observed. It implies that the Li dendrite was formed quite easily at a very early nucleation stage during plating on bare Cu foil, which would trigger more severe Li dendrite growth in the subsequent deposition process. In contrast, when the Cu foil was coated by a thin layer of functional polymer PN2, the nucleated Li particles show quite different morphology. As shown in Figure XVII.1.15c-d, a lots of island-shaped Li particles can be seen on the surface of the PN2@Cu foil and the size of Li particles are bigger than those on the bare Cu foil with smaller specific areas for the Li particles deposited on the PN2@Cu, indicating less area of Li particles exposed to the electrolyte. Therefore, the undesired side reactions with electrolyte are reduced and the cycle life of the cell is improved.



**Figure XVII.1.15 SEM images of Li deposition on the (a and b) bare Cu foil and (c and d) polymer PN2 coated on Cu foil at a high current density of  $6.0 \text{ mA cm}^{-2}$  and  $25 \text{ }^\circ\text{C}$ . The time for deposition is 1 min, so the Li deposition amounts are  $0.1 \text{ mAh cm}^{-2}$ . The electrolyte used in the Li-Cu cells: 1 M LiPF<sub>6</sub> in EC/DEC (wt% 1:1) + 15wt.% FEC + 1wt.% LiDFOB.**

#### ***Development of a new electrolyte with high rate and high voltage stability.***

The UMD team optimized the electrolytes formula that will be compatible with both Li metal anode and high-capacity cathodes (NMC811). They designed two electrolytes with a high Li CE of  $> 99.5\%$ . The ether-based electrolytes (2.0 M LiFSI-D1) enable  $>400$  stable cycles in the Li||LiNi<sub>0.8</sub>Co<sub>0.15</sub>Al<sub>0.05</sub>O<sub>2</sub> (NCA) cell (N/P = 2.0) with a high cycle CE of  $>99.9\%$  and high-capacity retention of  $> 85\%$  after 400 cycles. They found that the FSI-promoted reduction leads to a ceramic SEI that is mainly made of LiF-rich inorganics that allows the smooth and chunky Li deposition, which is accountable for the excellent cycling performance of NCA||Li full cell. Based on this inspiring result, they developed an ester-based (LiFSI/M1) electrolyte with high-voltage stability to fulfill the Bat500 project goal of a long cycle life for high-energy Li||NMC811 cells. The LiFSI/M1 electrolytes demonstrated high anodic stability of  $>5.3\text{V}$  in Li||Al half-cell and kept a high Li reversibility with excellent CE of  $>99.7\%$ . The  $20\mu\text{m-Li||NMC811}$  ( $4.5 \text{ mAh cm}^{-2}$ ) coin cell showed superior cyclability with  $>93\%$  capacity retention for  $>350$  cycles under Bat500 cycle protocol (cycled between 2.8 to 4.4 V). Even at high voltage of 4.7 V charging, Li||NMC811 cell also demonstrated a capacity retention of  $> 80\%$  in 200 cycles. The UMD team further investigated LiFSI/M1 electrolytes for practical pouch type Li||NMC811 cell. As shown in Figure XVII.1.16, the 90 mAh homemade single-layer pouch cell with LiFSI/M1 electrolytes showed superior long-term cyclability under practical conditions of low external pressure (0.1 MPa), lean electrolytes ( $4 \text{ gE Ah}^{-1}$ ), and high charge/discharge rate of 0.3C. A high capacity retention of  $>83\%$  was obtained after 300 cycles, demonstrating the excellent compatibility of the LiFSI/M1 electrolytes with both the Li metal anode and high-energy NMC811 cathode.

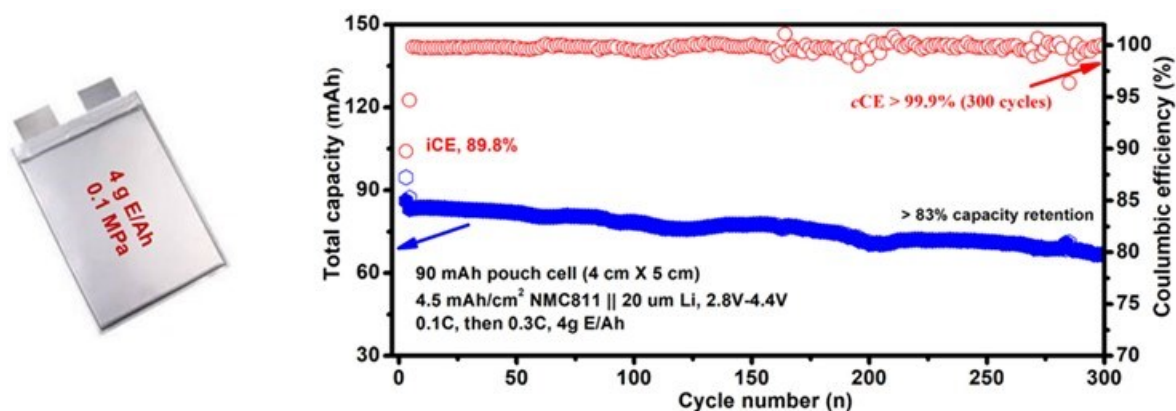


Figure XVII.1.16 The long cycle performance of 90 mAh Li||NMC811 pouch cell in LiFSI/M1 electrolytes. The 4 cm x 5 cm homemade pouch cell is fabricated and assembled in a glovebox with the NMC811 cathode areal loading of 4.5 mAh cm<sup>-2</sup> and lithium thickness of 20 μm. The electrolytes are controlled to 4 g Ah<sup>-1</sup>. The cell is cycled between 2.8V and 4.4V with the first formation cycle at 0.1C, then a long cycle at 0.3C for both charge and discharge. The carton on the left side shows the actual pouch cell.

#### Tuning the fluorination degree of solvent to enhance its electrochemical stability.

Stanford University team tuned the fluorination degree by attaching a monofluorine substituent on one ethoxy group of 1,2-diethoxyethane (DEE) and varying the fluorination degree on the other one, providing three new fluorinated DEE solvent molecules (i.e., F1F0, F1F1 and F1F2) with a relatively low fluorination degree (see top part of Figure XVII.1.17). Three single-solvent electrolytes were prepared by adding 1.2 mmol of lithium bis(fluoromethanesulfonyl)imide (LiFSI) into 1 mL of each of the solvent molecules. Results of <sup>7</sup>Li NMR show that increasing the fluorination degree of ether solvent reduces its solvation ability. However, the impact on chemical shifts are not as pronounced as those of highly fluorinated FxDEE electrolytes reported before, indicating improved salt solvation (or cation-anion dissociation) in these new FIFx-based electrolytes. All three electrolytes exhibited relatively higher ionic conductivities compared with previous FxDEE counterparts (0.05–0.17 mS/cm), and they follow the trend F1F0 > F1F1 > F1F2, in alignment with the solvation strength. Interestingly, F1F0 showed ionic conductivity that is even higher than the nonfluorinated DEE electrolyte. It is attributed to the fact that the F substituent increases the polarity of molecule and provides an additional binding to the Li<sup>+</sup>, resulting in less compact cation-anion cluster, as indicated by <sup>19</sup>F NMR spectra. All three electrolytes exhibit a relatively small current (< 5 μA) at up to 5 V in linear sweep voltammetry of Li||Al half cells at the scanning rate of 1 mV/s. These observed low leakage current are comparable to previously reported FxDEE electrolytes. Li||NMC811 full battery using these three electrolytes were tested under the same conditions as reported for FxDEE electrolytes, i.e., pairing 50-μm-thick Li foil (10.3 mAh/cm<sup>2</sup>) with high-loading NMC811 cathode (4.8 mAh/cm<sup>2</sup>) to yield a negative-to-positive electrode ratio (N/P) of ~2.1; using electrolyte-to-cathode ratio (E/C) of ~8 g/Ah; and cycling at C/5 charging and C/3 discharging rates, for the purpose of comparing with previous studies and evaluating the effects of fluorination degree. As shown in Figure XVII.1.17a, a clear trend of cycling life was observed: F1F0 < F1F1 < F1F2. The capacity of F1F0 decayed quickly to near zero within 30 cycles, and its CE dropped significantly despite the presence of excess Li reservoir, indicating the instability of F1F0 against both anode and cathode. The capacity decay pattern is different than that for the DEE electrolyte (non-fluorinated electrolyte), where the capacity is steady without significant reduction in the beginning 18 cycles and then drop quickly to 80% capacity in the following 37 cycles. For F1F0, the continuous capacity decay suggests the negative impact of mono-fluorination on DEE. For F1F1, the capacity remained almost unchanged in the first 20 cycles but then quickly reduced in the following cycles. In stark contrast, F1F2 exhibited stable cycling without substantial capacity decay for ~80 cycles. The Stanford team further studied the charge/discharge curves at different cycles. Figure XVII.1.17b shows the charge/discharge curves of F1F0 at 1st, 10th and 20th cycles, where the overpotential at the start of charge/discharge remains nearly unchanged while the capacity fades quickly over cycling, indicating the retained bulk and interfacial resistance, as well as the electrode degradation. Specifically, the 10th discharge



process only gave ~2.6 mAh, which corresponds to ~84% of the 10th charging capacity (~3.1 mAh). Because the high initial Li reservoir (N/P ~ 2.1) would guarantee the 3.1 mAh capacity when discharge at the 10th cycle, the observed capacity loss would highly suggest cathode degradation during the 10 charge-discharge cycles. This instability can be ascribed to the intrinsic low oxidative stability of F1F0 (as will be discussed later), and the resulting side reactions deteriorate the cathode integrity. In contrast, F1F1 showed slightly less capacity loss over cycling, but a substantial polarization (decrease in the discharge voltage and/or increase in the charge voltage) implies the raised bulk and interfacial resistance. In the case of F1F2, the capacity loss is even less and the polarization over cycles is not as pronounced. Therefore, compared with F1F0, the improved oxidative stability of F1F1 benefits the cathode performance but induces polarization while F1F2 overcomes both drawbacks.

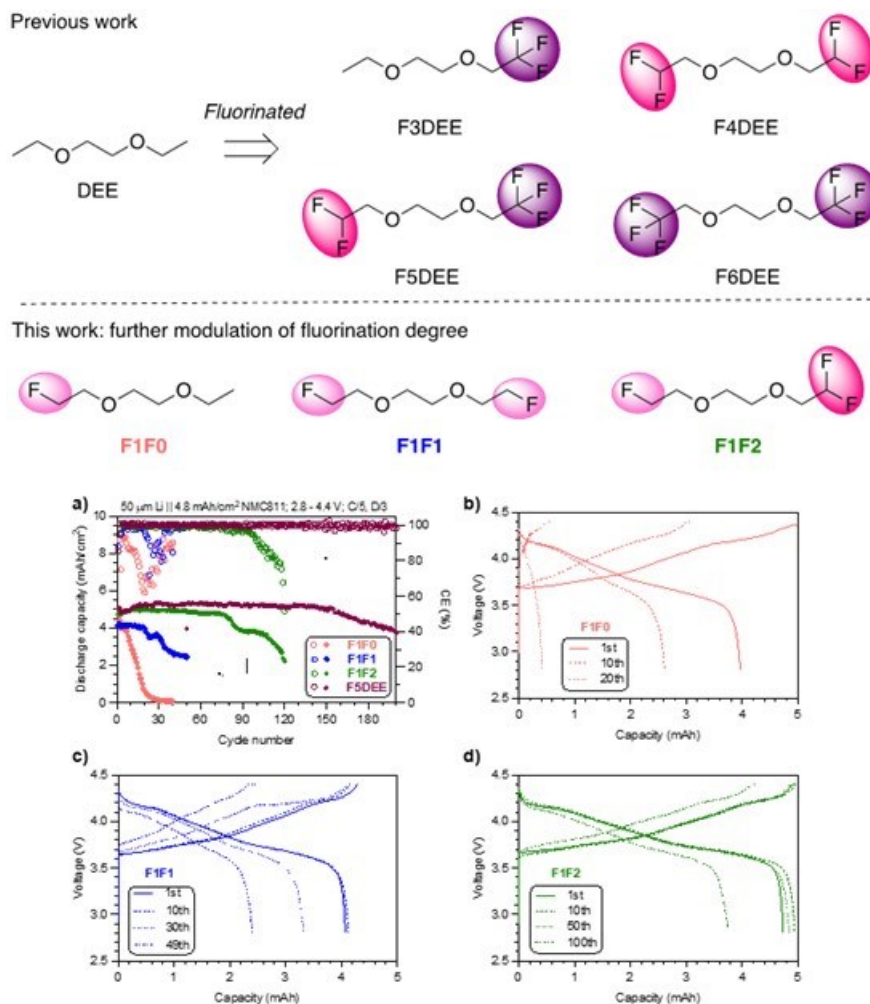


**Figure XVII.1.17** Top part: Chemical structures of fluorinated 1,2-diethoxyethane solvent molecules. a) Capacity and CE retention of F1F0, F1F1 and F1F2 electrolytes over cycling number. The data of F5DEE was adapted from previous results. The charge/discharge curves of b) F1F0, c) F1F1 and d) F1F2 at various cycles.

The PNNL team continues to develop a new type of diluent for localized high concentration electrolyte (LHCE). As shown in Table XVII.1.1. The new diluent (ND) has the HOMO value of -9.7 eV, which is much smaller compared to the value of previously studied diluents of bis(2,2,2-trifluoroethyl) ether (BTFE), 1,1,2,2-tetrafluoroethyl-2,2,3,3-tetrafluoropropyl ether (TTE) and tris(2,2,2-trifluoroethyl) orthoformate (TFEO), indicating a higher oxidative stability of ND than the previous diluents. In the meantime, the ND has slightly lower LUMO value that makes it easier to be reduced at the Li anode side.

**Table XVII.1.1 The Highest Occupied Molecular Orbital (HOMO) and the Lowest Unoccupied Molecular Orbital (LUMO) Energy for the Diluents.**

Diluent	BTFE	TTE	TFEO	ND
D-HOMO / eV	-8.76	-9.31	-8.84	-9.7
D-LUMO / eV	-0.5	-0.5	-0.4	-0.55

As shown in the projected density of states (PDOS) plots of the LHCEs using TTE and ND as diluent (Figure XVII.1.18a and Figure XVII.1.18b), the conduction band minimum (CBM) in the LHCE-TTE is on the FSI<sup>-</sup> anion, implying that the FSI<sup>-</sup> anions are predominantly reduced, while the CBMs in the LHCE-ND are on both FSI<sup>-</sup> and ND, implying both FSI<sup>-</sup> and ND can be reduced on the Li anode. The joint decomposition of FSI<sup>-</sup> and ND could lead to a synergistic effect in the SEI formation and has strong effects on Li deposition. SEM images in Figure XVII.1.18c and Figure XVII.1.18d show the cross-sectional views of the two samples retrieved from the Li||Cu cells with 4 mAh cm<sup>-2</sup> Li deposited on the Cu electrode at a current density of 0.5 mA cm<sup>-2</sup>. As shown in Figure XVII.1.18c, Li thickness deposited in the baseline LHCE using TTE is of 32 μm, while those deposited in the LHCE using ND is only 23 μm. A more compact Li film deposited in LHCE-ND leads to a smaller surface area and less side reactions between Li and electrolyte.

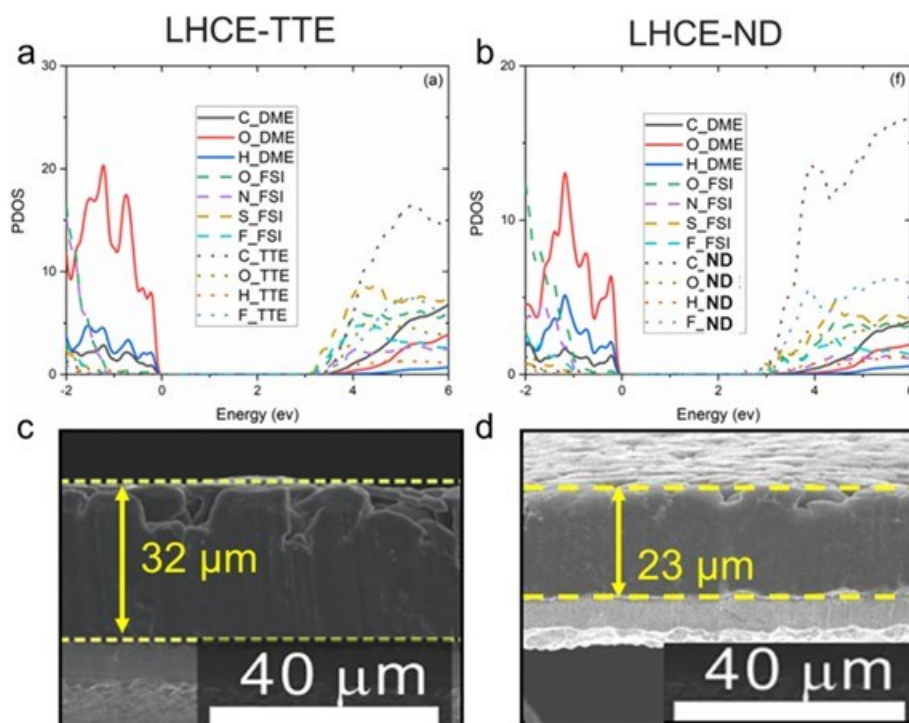


**Figure XVII.1.18** (a), (b) Projected density of states (PDOS) of LHCEs with diluent of (a) TTE, (b) ND. (c), (d) Thickness of the 4 mAh cm<sup>-2</sup> Li deposited on Cu electrode using LHCEs with diluent of (c) TTE, (d) ND

#### **Comparing stability of NMC coatings prepared using NMP vs UV curing.**

The Binghamton University (Binghamton) team compared the technology of coating lithium nickel manganese cobalt oxide (NMC) cathode by N-Methyl-2-pyrrolidone (NMP) solvent and NMP-free ultraviolet (UV) curing. UV curing technology is very attractive for electrodes manufacturing because this innovative approach can dramatically increase the processing speed and eliminate the harmful NMP, and the associated drying & recovery systems, which reduce cost, environmental concerns, and energy consumption significantly. A DOE

funded effort with Miltec, ANL and ORNL to develop and demonstrate high-speed electrode coating with UV curing technology indicated that the manufacturing cost of an electrode could be reduced 80-85% and the total cost of the electrode including the material costs could be reduced 25% by using UV. They demonstrated 90/5/5 cathode coatings could be UV cured at 100 meters/min with good capacity retention and gave the equivalent performance as conventional electrodes with PVDF binder. However, a major limitation was identified: namely the maximum practical coating thickness is 50  $\mu\text{m}$  or 10  $\text{mg}/\text{cm}^2$  loading at any speed, because of the limited penetration power of UV. This would thus require multi-layer coatings to achieve higher thickness/loading. Although shown to be viable, this would complicate processing and cost. It is thus concluded that UV coating is not a practical approach for the thick electrodes needed to obtain the 500 Wh/kg goals for the Battery500 consortium. The Binghamton team therefore does not plan to experimentally pursue this approach further.

### ***Developing localized high-concentration electrolytes for high-Ni cathodes.***

The UT Austin team systematically investigated four novel cost-effective diluents in localized high-concentration electrolytes (LHCEs) and compared their performances in cells with  $\text{LiNiO}_2$  (LNO) cathode and Li-metal anode (LMA). As shown in Figure XVII.1.19a, diluents investigated here are five fluorinated ethers, including 1,1,2,2-tetrafluoroethyl 2,2,3,3-tetrafluoropropyl ether (TTE), 1H,1H,5H-octafluoropentyl 1,1,2,2-tetrafluoroethyl ether (OTE), 2,2,2-trifluoroethyl 1,1,2,2-tetrafluoroethyl ether (TTEE), 1,1,1,3,3,3-hexafluoro-2-(fluoromethoxy) propane (HFP), and ethyl 1,1,2,2-tetrafluoroethyl ether (ETE). The LHCEs were prepared by diluting the high-concentration electrolyte (lithium bis(fluorosulfonyl)imide (LiFSI) : 1,2-dimethoxyethane (DME) = 1 : 1.2 in molar) to 1.5 M with these diluents, which are denoted hereafter as LHCE-TTE, LHCE-OTE, LHCE-TTEE, LHCE-HFP, and LHCE-ETE, respectively. Figure XVII.1.19a b shows the impact of solvation between LiFSI and DME, as evidenced by the C–O–C stretching mode of DME in Fourier-transform infrared spectroscopy (FT-IR). After the addition of salt, the C–O–C peak shifts from free DME (1,125  $\text{cm}^{-1}$ ) to solvating DME (1,075  $\text{cm}^{-1}$ ). With an increase in salt concentration, a greater number of DME molecules engage in solvation with the salt, leading to an increase in the intensity of the solvating DME peak. Notably, the solvating C–O–C peak remains after the addition of diluents. Figure XVII.1.19a c shows the high voltage stabilities of the electrolytes by linear sweep voltammetry. The LHCEs demonstrate a decent high-voltage stability up to 4.6 V, which is a substantial improvement over the traditional ether-based electrolytes. Figure XVII.1.19a d shows that LHCE-OTE displays the highest Coulombic efficiency (CE) of 99.81%. All the other LHCEs also exhibit exceptional CEs of > 99.38%, which are much higher than that with LP57 (91.37%). The results indicate that the Li stripping/plating process exhibits good reversibility, which can be attributed to the high stability of the interphases. Interestingly, although LHCE-OTE shows the highest CE, it also exhibits the highest overpotential during the test. Figure XVII.1.19a e shows the cycling performance of the electrolytes in Li || LNO half-cells. The cell with LP57 suffers from severe capacity degradation, dropping from 207  $\text{mA h g}^{-1}$  to 134  $\text{mA h g}^{-1}$  after 200 cycles, corresponding to a capacity retention of only 64.6%. In contrast, all the cells cycled in the various LHCEs exhibit superior cycling performances. The discharge capacity of the cells at the 250<sup>th</sup> cycle follows the order of LHCE-TTEE (190  $\text{mA h g}^{-1}$ ) > LHCE-ETE (182  $\text{mA h g}^{-1}$ ) > LHCE-HFP (180  $\text{mA h g}^{-1}$ ) > LHCE-TTE (175  $\text{mA h g}^{-1}$ ) > LHCE-OTE (170  $\text{mA h g}^{-1}$ ). The capacity retention of the cells after 250 cycles is quite similar for the LHCEs: LHCE-HFP (88.0%) > LHCE-TTEE (87.1%) = LHCE-ETE (87.1%) > LHCE-TTE (87.0%) > LHCE-OTE (85.1%). Figure XVII.1.19a f shows that all the LHCE cells exhibit significantly smaller impedance growth when compared to the LP57 cell. In addition, Figure XVIII.1-1-19h depicts the discharge capacities of the anode-free cells. The discharge capacity of the cell with LP57 drops rapidly below 60  $\text{mA h g}^{-1}$  after 50 cycles. In contrast, the anode-free cells with LHCEs still maintain a decent capacity of >125  $\text{mA h g}^{-1}$ . Moreover, LHCEs also demonstrate a higher CE (> 98%) during cycling than LP57 (97.5%), indicating a higher Li utilization efficiency enabling a more stable SEI. The rate capabilities of the electrolytes were tested in Li || LNO cells (Figure XVII.1.19a g). LHCE-OTE shows the worst rate performance, with a 5C discharge capacity of only 81  $\text{mA h g}^{-1}$ . However, the discharge capacity recovers back to 246  $\text{mA h g}^{-1}$  when the discharge rate returns to 0.1C. On the other hand, cells with LHCE-ETE, LHCE-TTEE, and LHCE-HFP exhibit excellent rate performance, with a discharge capacity exceeding 193  $\text{mA h g}^{-1}$  even at a 5C rate. Overall, TTEE, HFP, and ETE are better diluents for LHCE than TTE and OTE, which may be attributed to the better kinetics enabled by their low viscosity.

Post-mortem X-ray photoelectron spectroscopy (XPS) analysis of the cycled Li-metal anodes and LNO cathodes was carried out to investigate the composition and structure of the solid-electrolyte interphase (SEI) and cathode-electrolyte interphase (CEI). The SEI layer formed in LP57 electrolyte is more organic-rich than those formed in LHCEs. Especially after sputtering, the carbon content decreases to  $\sim 20\%$  for the LHCEs, but only by  $\sim 5\%$  for LP57; in contrast, the fluorine content increases by  $\sim 6\%$  for the LHCEs, but only  $\sim 2\%$  for LP57. This indicates that LHCEs can help build an inorganic-rich SEI inner layer and an organic outer layer. Moreover, LHCE-OTE has a significantly higher fluorine concentration, suggesting that fluorine comes from the decomposition of both the FSI anion and the OTE solvent molecule. The other LHCEs have similar atomic concentrations with comparable fluorine and sulfur contents, implying that most of the fluorine in the SEI is salt-derived and the contribution from diluent decomposition is relatively small. Unlike the SEI, the CEI has a more organic inner layer and a more inorganic outer layer. The CEI also contains more organic species ( $\sim 60\%$ ) than the SEI ( $\sim 50\%$ ), with significantly higher fluorine contents ( $\sim 20\%$ ) than sulfur ( $\sim 2\%$ ) and nitrogen ( $\sim 1\%$ ), indicating that most of the fluorine in the CEI is from the PVDF binder and the diluents rather than from the FSI anions. Moreover, LHCE-OTE and LHCE-ETE have higher sulfur contents in the outer layer of CEI, indicating a higher percentage of LiFSI salt decomposition compared to that with LHCE-TTE, LHCE-TTEE, and LHCE-HFP

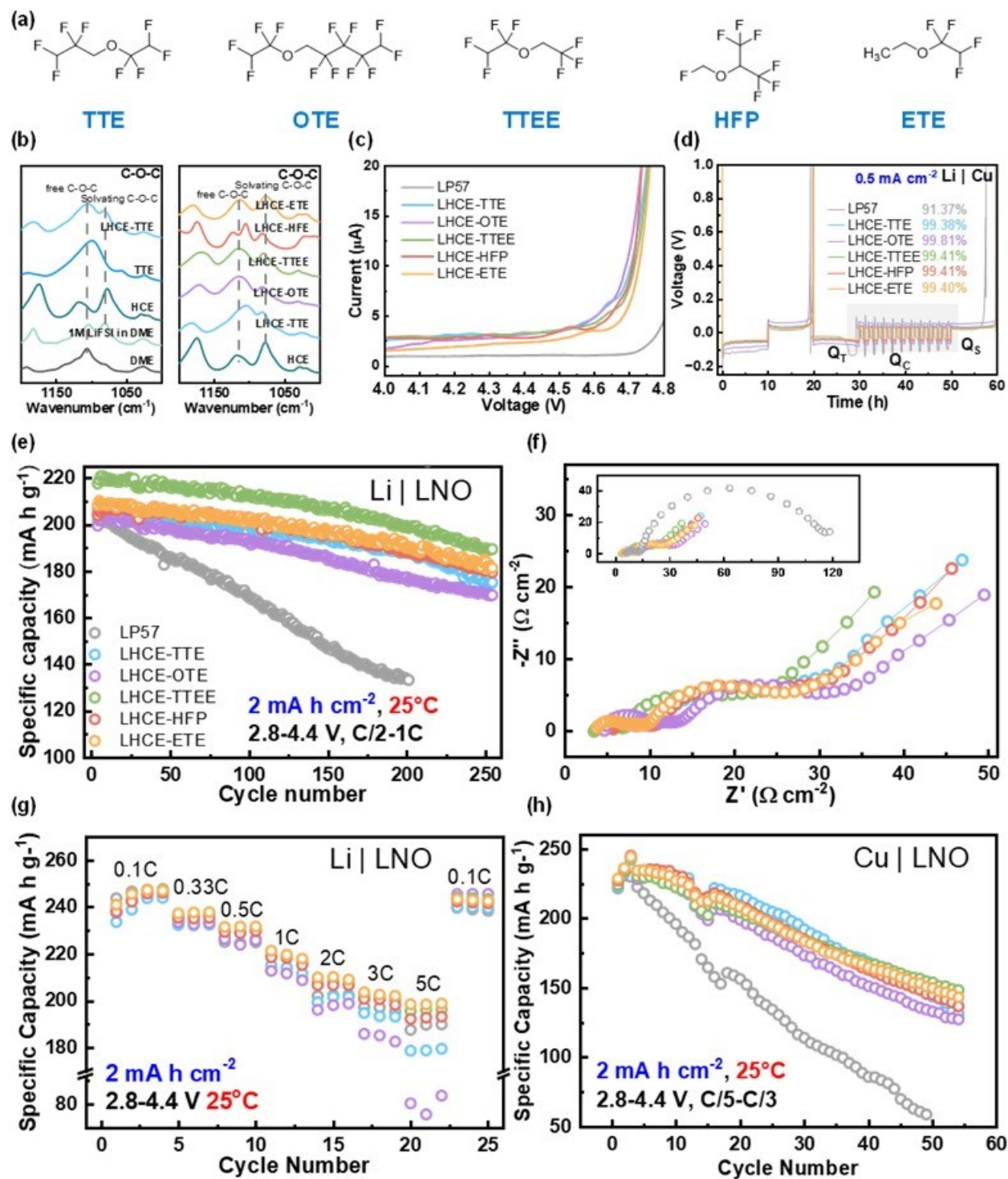
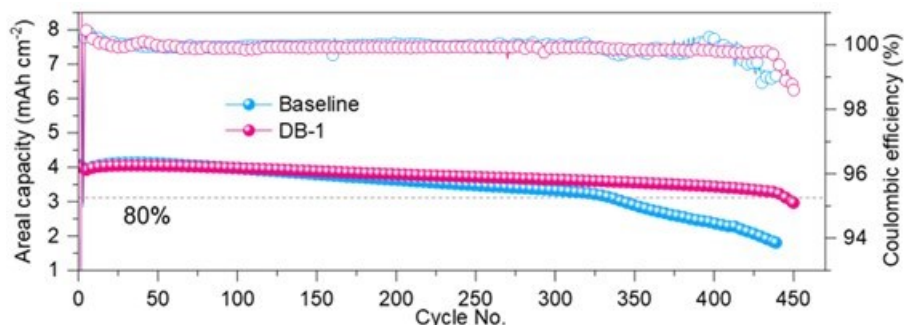


Figure XVII.1.19 (a) Molecular structures of the diluents. (b) C-O-C stretching modes of DME in the FT-IR of the solvents and electrolytes. (c) LSV of the electrolytes in Li || Carbon cells. (d) Voltage profiles of the Li || Cu cell employed for CE testing. Q<sub>T</sub> is the capacity of Li deposited as a Li reservoir. Q<sub>C</sub> is the capacity of Li plated and stripped during the cycling process. Q<sub>S</sub> is the capacity of Li that can be stripped after the cycling process. (e) Discharge specific capacities of Li || LNO cells. (f) EIS data of the Li || LNO cells after 200 cycles tested at 3.8 V. (g) Rate performances of Li || LNO cells. (h) Cycling performances of anode-free Cu || LNO cells.

The PNNL team continuously improves the performance of Li||NMC batteries using LHCEs consisting of LiFSI salt, DME solvent, and a new diluent (coded as DB). The electrolytes were examined in the coin-cell configuration with Li metal (50  $\mu\text{m}$  thick), NMC811 (96%,  $\sim 4.1 \text{ mAh cm}^{-2}$ ), and polyethylene separator. For comparison, M47 (LiFSI:DME:TTE in a molar ratio of 1:1.2:3) was used as the baseline electrolyte. The cells were charged/discharged at 0.1C for 2 formation cycles and then charged/discharged at 0.1C/0.33C for cycling in the potential range of 2.8 – 4.4 V. As shown in Figure XVII.1.20, the cell with DB-1 electrolyte (LiFSI-1.2DME-3DB by mol) exhibited a high-capacity retention of 80% after 445 cycles. In contrast, the cell with M47 electrolyte will drop below 80% in 334 cycles.



**Figure XVII.1.20** Long-term cycling performance of Li||NMC811 full cells with baseline (M47) and DB-based electrolytes.

The morphologies of deposited Li metal anodes were characterized by scanning electron microscopy (SEM) and XPS. The cross-sectional SEM images of the initial Li films of  $4.0 \text{ mAh cm}^{-2}$  deposited on Cu substrates at  $0.5 \text{ mA cm}^{-2}$  in the M47 and DB-1 electrolytes were obtained. DB-1 leads to an apparently thinner and denser Li deposition than the baseline electrolyte (31  $\mu\text{m}$  vs. 35  $\mu\text{m}$ ). On the other hand, morphology of Li metal anode (initial thickness is 50- $\mu\text{m}$ ) in Li||NMC811 cells with M47 and DB-1 electrolytes are quite different. The Li anode cycled in M47 electrolyte has a thick and porous cycled layer, and most of Li metal was consumed after 439 cycles. In contrast, the Li anode cycled in DB-1 electrolyte still remains an  $\sim 37 \mu\text{m}$  of uncycled Li metal layer, and a thinner and denser cycled layer was found at the. Better cycling stability and more Li reserve found in the cells with DB-based electrolyte could be attributed to the formation of more inorganic components (such as  $\text{Li}_2\text{O}$ ,  $\text{LiF}$ ,  $\text{Li-N}$ , and  $\text{Li}_2\text{S}$ ) in the SEI layer which are very effective in improving the cycling stability of Li metal batteries.

#### ***Tuning molecular structure of ether solvent to boost electrochemical performance.***

The Stanford team continued to work on tuning the molecular structure of ether-based electrolytes to further boost their performance in Li metal batteries. Following the fluorinated 1,2-diethoxyethane (FDEE) series, a novel electrolyte is developed by changing the backbone structure to 1,2-diethoxymethane (DEM) and reducing the degree of fluorination. The resulting solvent (F2DEM) features an acetal backbone with one fluorine on each end of DEM structure (Figure XVII.1.21). The acetal backbone is incorporated to weaken the chelation effect commonly observed with the DEE system. This would allow for weaker coordination of the solvent to the Li cation, resulting in less solvent-populated solvation structure, ultimately leading to more stable salt-derived SEI. To ensure cathode stability, fluorine atoms are also incorporated on both ends of DEM. Through backbone engineering and fluorination, F2DEM demonstrates excellent stability against the anode, as well as improved oxidative stability and conductivity.

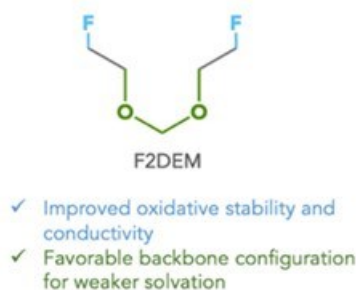


**Figure XVII.1.21 Molecular design of F2DEM.**

The Stanford team then investigated F2DEM's performance in Li||Cu half cells to assess its stability with the Li anode. The average Li CE was determined by the Aurbach method and found to be  $99.53 \pm 0.03\%$  for F2DEM, outperforming F5DEE ( $99.46 \pm 0.01\%$ ) and DEM ( $99.19 \pm 0.07\%$ ) in previous tests. Furthermore, the team corroborated these observations through long-term cycling of Li||Cu half cells. Long-term cycling revealed rapid activation for F2DEM (fewer cycles required to reach 99% CE), indicating minimal capacity loss during the initial cycles, making it highly suitable for anode-free cells with limited Li supply. The average CE of F2DEM in cycles 5-50 ( $99.44\%$ ) remained higher than that of F5DEE and DEM (both at  $99.29\%$ ). Harsher testing conditions ( $1 \text{ mA cm}^{-2}$  plating,  $0.4 \text{ mA cm}^{-2}$  stripping,  $2 \text{ mAh cm}^{-2}$  capacity) further corroborate F2DEM's superior cycling stability with a higher CE over 250 cycles compared to F5DEE and DEM. Considering the modified solvation environment and addition of electro-withdrawing fluorine atoms in F2DEM molecules, an improved oxidative stability of F2DEM is expected when compared to DEM. To confirm this enhancement, linear sweep voltammetry (LSV) on the three distinct electrolytes was conducted. As depicted in Figure XVII.1.22 d, we observed a leakage current with an onset voltage of approximately 4 V for F2DEM, surpassing the 3 V observed with DEM. In the case of F5DEE, featuring a higher degree of fluorination, it unsurprisingly exhibited an even higher onset voltage of around 4.5 V. This pattern aligns well with the hypothesis that an increased degree of fluorination enhances oxidative stability.

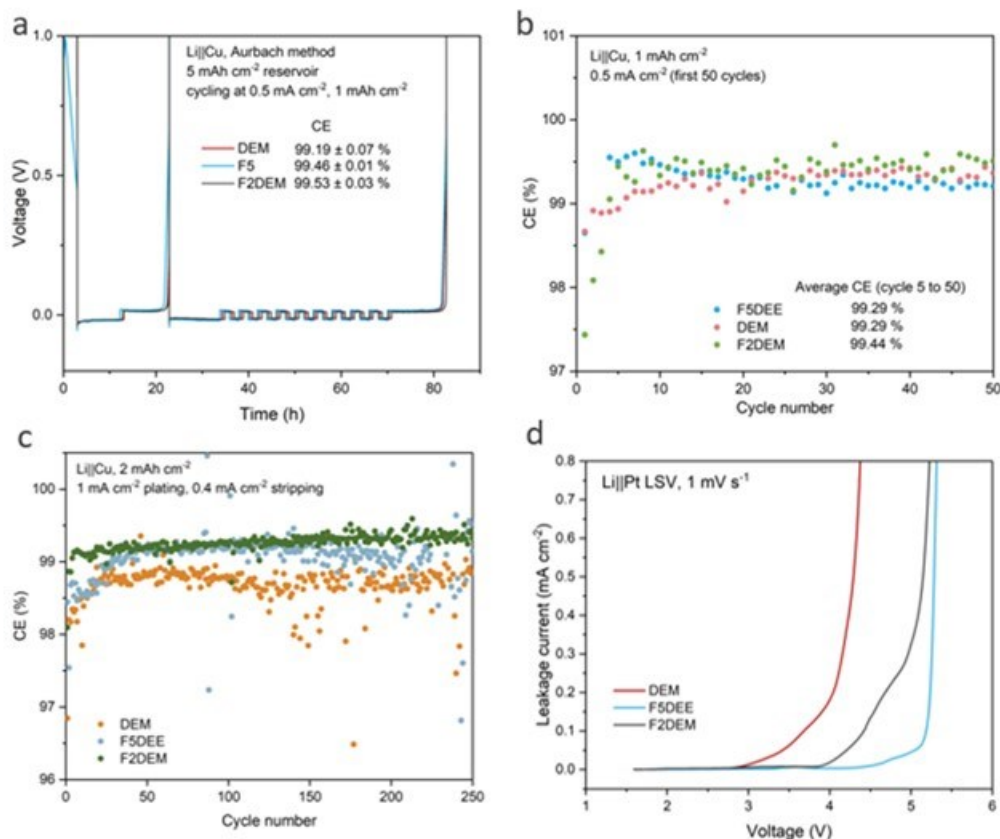


**Figure XVII.1.22** (a) The CE measurements of the three electrolytes based on the modified Aurbach method. (b) Li||Cu CE of all three electrolytes. The cells were cycled at 0.5 mA cm<sup>-2</sup> for 1 mAh cm<sup>-2</sup> and stripped to 1 V at 0.5 mA cm<sup>-2</sup>. (c) Li||Cu CE over 250 cycles under a fast plating (1 mA cm<sup>-2</sup>) and slow stripping (0.4 mA cm<sup>-2</sup>) condition. (d) LSV in Li||Pt cells. The leakage currents of the three electrolytes were measured by sweeping up to 7 V at 1 mV s<sup>-1</sup>.

The performance of 2 M F2DEM was further assessed in Cu||LFP anode-free pouch cells, with a voltage range from 2.5 V to 3.65 V. Various charging and discharging rates were implemented to fully assess the pouch cell performance of F2DEM (1C = 200 mA or 2 mA cm<sup>-2</sup>). Under all conditions, 2 M F2DEM showed a higher capacity utilization and a slower capacity loss compared to the reference electrolytes (Figure XVII.1.23). Especially under C/2 charge and a slower C/5 discharge rate, significant improvement in discharge capacity and CE was observed in F2DEM. This is the more demanding condition since it has been reported that slower discharge than charge can lead to higher surface area Li morphology. However, this is also the condition that can best resemble the real-life battery charging and discharging condition. The improvement seen in F2DEM under a slower discharge rate potentially indicates that F2DEM can facilitate the formation of a more stable SEI.



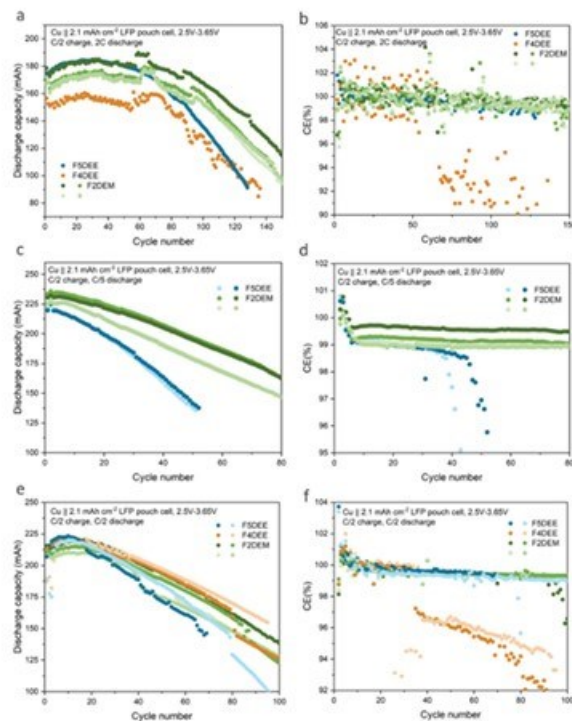


**Figure XVII.1.23 Performance of Cu||LFP pouch cell cycling between 2.5 V and 3.65 V. (a, b) C/2 charge and 2C discharge capacity (1C = 200 mA or 2 mA cm<sup>-2</sup>) and CE profile over 80 cycles. (c, d) C/2 charge and C/5 discharge capacity and CE profile over 150 cycles. (e, f) C/2 charge and C/2 discharge capacity and CE profile over 100 cycles.**

In summary, F2DEM, a monofluorinated ether electrolyte, enhances the CE and cycling stability in Li metal batteries. This is due to the acetal backbone's excellent compatibility with the Li anode, as well as enhanced oxidative stability with monofluorine substitution. Future studies on further enhancing the cathodic stability of F2DEM would be essential, especially for application in high voltage NMC811 full cells.

#### **Developing new electrolytes for high-voltage cathodes.**

To improve the high-voltage stability and make the electrolytes compatible with the NMC811 cathode, the UMD team further developed the LiFSI/M1 electrolytes, where all ether groups were removed by chemical modification. The optimized LiFSI/M1 electrolytes were demonstrated with high anodic stability of >5.3 V in Li||Al half cells and kept a high Li reversibility with superior Li CE of >99.7%. Both 4.5 mAh cm<sup>-2</sup> 20μm-Li||NMC811 coin cell and 90 mAh homemade single-layer pouch cell showed stable cyclability with >83% capacity retention for over 300 cycles under the Batt500 cycle protocol. Furthermore, the team also demonstrated the success cycle of Li||NMC811 cell at an ultrahigh voltage of 4.7 V for >200 cycles with a high capacity retention of >80%. The continuous investigations on LiFSI/M1 electrolytes for practical Li||NMC811 cell are updated below.

The high stability of LiFSI/M1 electrolytes on both the Li metal anode and NMC811 cathode enables to cycle high-energy electrodes with areal loadings beyond the practical requirement of ~5 mAh cm<sup>-2</sup>. As shown in Figure XVII.1.24, the 10 mAh cm<sup>-2</sup> NMC811 was paired with 50 μm Li to assemble the full cell and to evaluate the electrolyte stability. With controlled electrolyte injection of ~5 g (Ah)<sup>-1</sup>, the high areal loading coin cell was able to cycle at a high rate of 0.3C for 200 cycles with >99.9% CE (Figure XVII.1.24a), which delivers our scheduled milestone for this quarter. A high capacity of >90% was retained after 200 cycles, demonstrating the excellent compatibility of LiFSI/M1 electrolytes with both the Li anode and the high-loading NMC811 cathode. The overpotential barely changed along the cycling, indicating robust and high Li<sup>+</sup> conductive interphase films were formed on both electrodes (Figure XVII.1.24b).

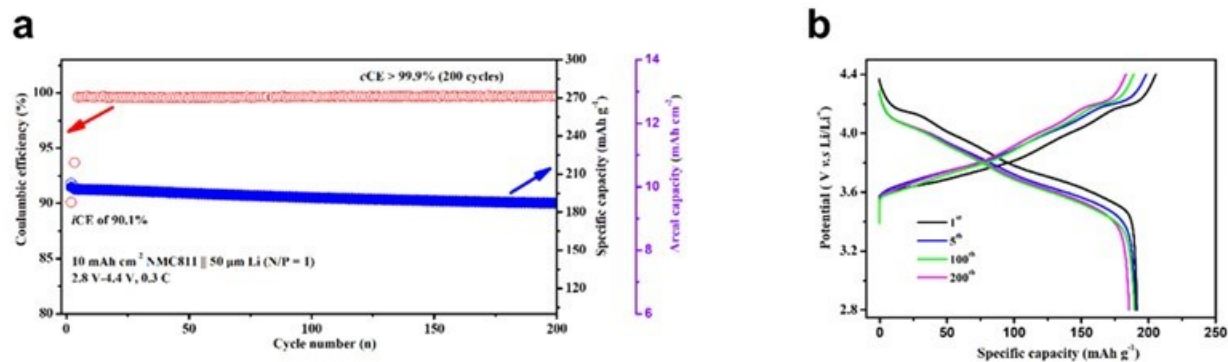


Figure XVII.1.24 (a) The long cycle performance of the  $10 \text{ mAh cm}^{-2}$  NMC811 || Li (N/P = 1) coin cell in LiFSI/M1 electrolytes. The electrolytes are controlled to  $\sim 5 \text{ g Ah}^{-1}$ . The cell is cycled between 2.8V and 4.4V with the first formation cycle at 0.1C, then a long cycle at 0.3C for both charge and discharge. The areal capacity was shown on the right axis beside the specific capacity. (b) Selected charge/discharge voltage profiles at 1<sup>st</sup>, 5<sup>th</sup>, 100<sup>th</sup>, and 200<sup>th</sup> cycle.

The oxidation stability of the electrolytes was demonstrated in the Li||NCM811 full cell as shown in Figure XVII.1.25. The electrolyte realized stable cycling at 4.7 V cut-off voltage with 99.72 % CE and 80.2 % capacity retention after 100 cycles. It suggests the outstanding oxidation stability of the electrolyte and a robust CEI formation. The Li metal battery full cells with practical cell configurations and cycling rates were further studied. High loading of NCM811 cathode ( $5.5 \text{ mAh cm}^{-2}$ ) was tested under lean electrolyte ( $\text{E/C} = 2.5 \text{ g (Ah)}^{-1}$ ) and Li metal amount (N/P=0 or 0.72), and high current density ( $1.5 \text{ mA cm}^{-2}$ , 0.3 C charge;  $2.5 \text{ mA cm}^{-2}$ , 0.5 C discharge). The anode-free full cell retained 78.4 % capacity after 50 cycles. Its average CE of 99.4 % is consistent with the Li||Cu half-cell data. The Li||NCM811 full cell with thin Li demonstrates prolonged cycling stability with an average CE close to 99.8 %. Currently further investigations using this concept are in progress. Mechanism understandings including electrolyte solvation structure, interfacial behaviors, and in-depth electrochemical characterizations will be investigated.

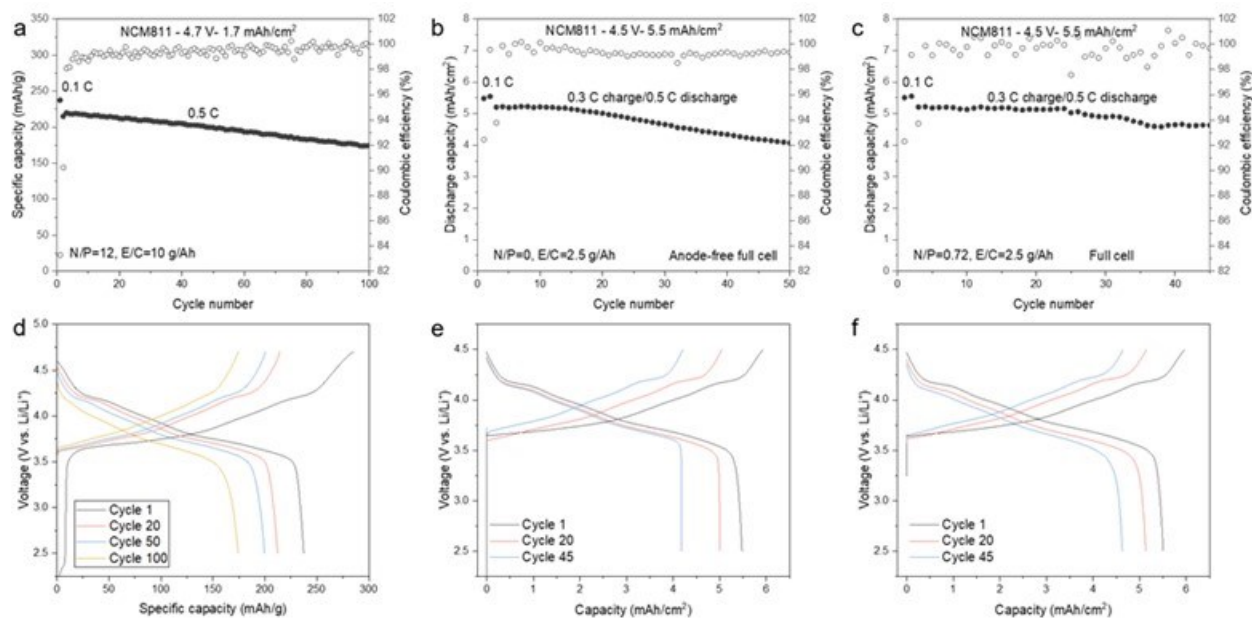


Figure XVII.1.25 The Li || NCM811 full cell study of the representative electrolyte. (a). The full cell with medium loading cycling between 2.5 V and 4.7 V and the voltage profiles (d). The anode-free (b, e) and Li || NCM811 (c, f) full cell with practical cell configuration cycling between 2.5 and 4.5 V.

### Developing new carbonate-based electrolyte for NMC.

The PSU team continued the evaluation of the newly formulated carbonate-based electrolyte in Li||NMC811 full cells. The areal capacity of NMC811 cathode was 4.3 mAh/cm<sup>2</sup> and the thickness of Li metal anode was 50 μm. After two formation cycles at 0.1C for charge/discharge, the tested cells were charged at C/3 and discharged at C/3 between 2.8 and 4.4 V. As shown in Figure XVII.1.26, Li||NMC811 full cell with the new carbonate-based electrolyte delivers an improved cycling stability with an 80% capacity retention after 218 cycles. In contrast, the cell with the baseline electrolyte of 1 M LiPF<sub>6</sub> in EC/DEC (v/v = 1:1) with 15 wt % FEC and 1 wt % LiDFOB results in a fast decay and an 80% retention after 180 cycles only. These results confirm that the new carbonate-based electrolyte is effective in maintaining stable electrochemical performance, even at high charge voltages (4.4 V), compared to the standard carbonate electrolyte.

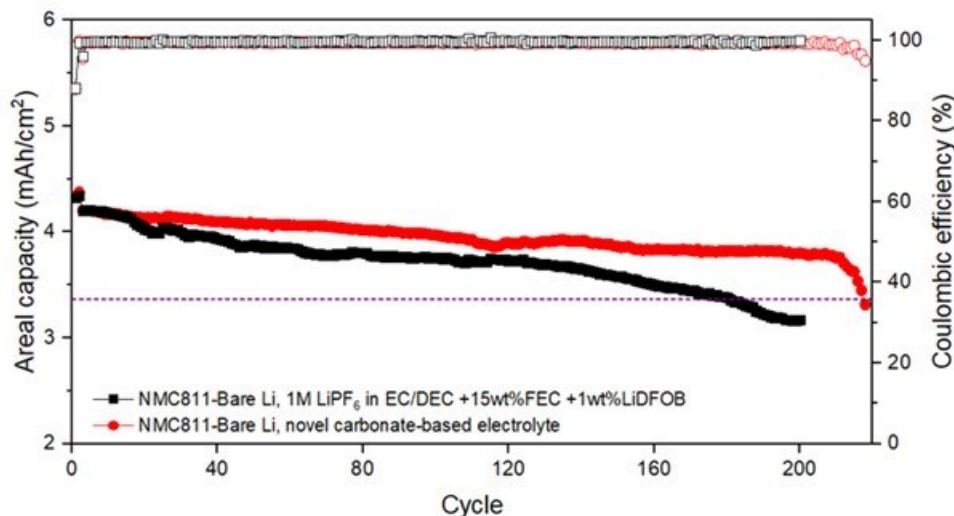
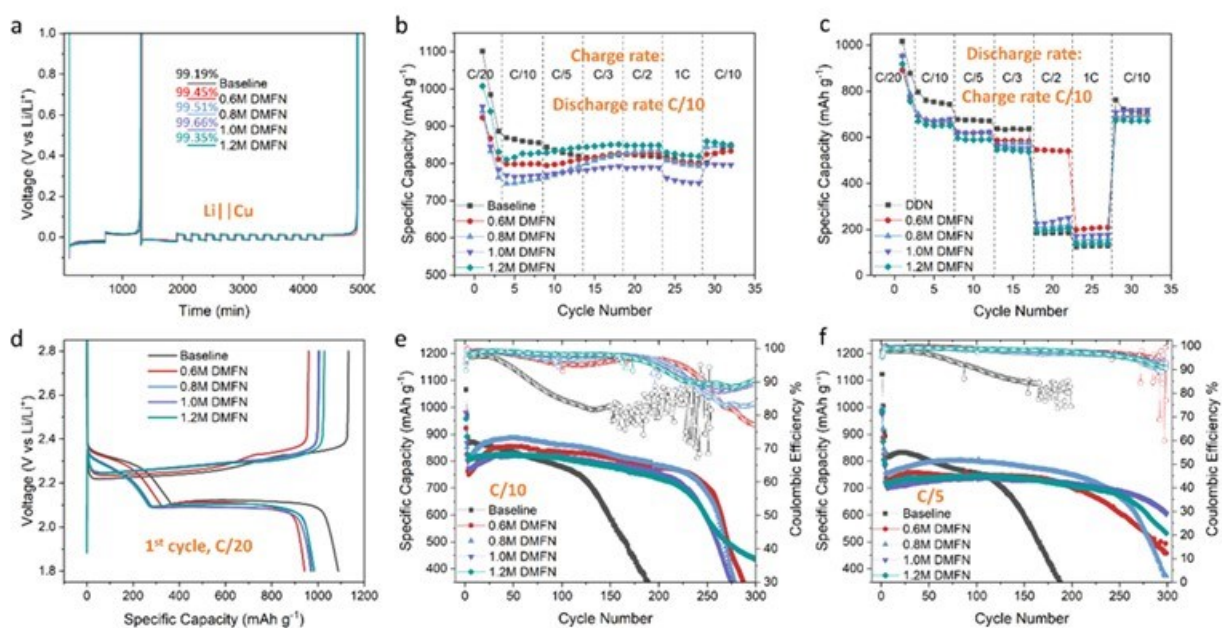


Figure XVII.1.26 Electrochemical performance of Li || NMC811 coin cell in 1 M LiPF<sub>6</sub> in EC/DEC (v/v = 1:1) with 15 wt % FEC and 1 wt % LiDFOB, or the novel carbonate-based electrolyte, between 2.8 V to 4.4 V when charging at C/3 and discharging at C/3. A constant-current-constant-voltage protocol was used for cycling: the cell was charged to 4.4 V and then held at that voltage until the current dropped below C/20. 2 formation cycles at 0.1C for charge/discharge between 2.8 V to 4.4 V. 1 C = 4.3 mA/cm<sup>2</sup>.

### Electrolyte development for Li metal batteries with elemental S cathodes

The PNNL team developed new electrolytes for Li||S (4 mAh cm<sup>-2</sup>) cells by utilizing a dual- or tri-solvent system to form a series of moderately solvating electrolytes in an effort to control the amount of dissolution of polysulfide species in the electrolyte and improve the overall cell cycle life and stability with the S/C composite cathode and Li metal anode. The new electrolytes were developed with a range of concentrations of 0.6 M – 1.2 M LiTFSI in the new solvent system with 2% LiNO<sub>3</sub>, which are referred to as DMFN. Figure XVII.1.27 compares the electrochemical performances of Li||S batteries using different concentrations of LiTFSI salt in DMFN. As a comparison, the performance of the cells with the baseline electrolyte (1 M LiTFSI in DOL: DME (1:1 v:v) + 2% LiNO<sub>3</sub>) is also included in Figure XVII.1.27. First, the average Li CE of these electrolytes was measured in Li||Cu cells using the Battery500 protocol. As shown in Figure XVII.1.27a, Li||Cu cells with all the DMFN electrolytes demonstrated a higher average Li CE of 99.35-99.66% compared to the Li CE of the baseline electrolyte at 99.19%, indicating a higher reversibility of Li stripping and plating on the Li metal anode. The charge rate capability test of Li||S cells (see Figure XVII.1.27b) shows the DMFN electrolytes can maintain comparable discharge capacity and cycling stability with the baseline electrolyte up to a 1C charge rate with a constant C/10 discharge rate. The discharge rate capability test (see Figure XVII.1.27c) shows the DMFN electrolytes can maintain slightly lower discharge capacity and cycling stability with the baseline electrolyte up to a C/3 discharge rate with a constant C/10 charge rate. However, the 0.6 M DMFN electrolyte was able to maintain cyclability up to a discharge rate of C/2 while the baseline and other DMFN electrolytes had a large cell polarization leading to premature voltage cutoff and low capacity at higher

current density. These electrolytes were further evaluated in long-term cycling test in Li||S coin cells. The cells were performed two formation cycles at C/20 in 1.8 – 2.8 V, and then cycled at C/10 or C/5 in 1.7 – 2.8 V in the baseline and DMFN electrolytes with an E/S ratio of 8  $\mu\text{L}/\text{mg-S}$ . The voltage profiles of the first cycle charge/discharge at C/20 show that the DMFN electrolytes have a smaller initial voltage slope between 2.1 – 2.4 V that indicates a reduced degree of soluble  $\text{Li}_2\text{S}_{6-8}$  species that may dissolve into the electrolyte during the  $\text{Li}^+$  migration onto the C/S electrode. The voltage slope decreases with the increasing concentration of the DMFN electrolyte, as shown in Figure XVII.1.27d. Figure XVII.1.27e shows the cycling performance of the electrolytes at a C/10 charge and discharge rate. Compared to the cells with baseline electrolyte, the cells with four DMFN electrolytes all show enhanced cycling stability and CEs of 97-99% over 300 cycles. This is especially evident in the cell with 0.8M DMFN which demonstrates the highest capacity and stable cycle life over 250 cycles. The cycling performances of Li||S cells with all DMFN electrolytes have been improved when cycled at a C/5 charge and discharge rate, showing better cycling stability and CE over 100 cycles (see Figure XVII.1.27f). Notably, the cell with 0.8 M DMFN electrolyte again shows a higher capacity than the cells with other concentrations of DMFN electrolytes when cycled at C/5, but the cells with 1 M DMFN electrolyte maintains the highest capacity retention after the 300 cycles.



**Figure XVII.1.27** Electrochemical performance of Li||S cells with Baseline and DMFN series of electrolytes.

(a) Li plating/stripping curves in Li||Cu cells. (b) Charge rate capability test of Li||S full cell tested in different electrolytes. (c) Discharge rate capability test of Li||S full cell tested in different electrolytes. (d) First cycle charge/discharge voltage profiles at C/20 (1.8 – 2.8 V). (e, f) Cycling performance of full cell at (e) C/10 and (f) C/5 charge and discharge rates (1.7 – 2.8 V). Li metal (250  $\mu\text{m}$  thick) and an E/S ratio of 8  $\mu\text{L}/\text{mg-S}$  were used in the Li||S full cells.

The PSU team also developed new electrolytes for Li||S batteries with new co-solvent and additives. The GM cathodes with high loading 4-5  $\text{mg}\cdot\text{cm}^{-2}$  were used to test the cycling properties. The coin cells with 8  $\text{mL}/\text{mgS}$  for each were discharged/charged at 0.05 C for the first two formation cycles and then cycled at 0.1 C for following cycles. The electrolyte with 1 M LiTFSI in DOL/DME/Co-solvent A + 2 wt.%  $\text{LiNO}_3$  + 0.5 wt. % additive B (denoted as LS76) had the outperformed behavior and stable cycling compared to baseline electrolyte with 1 M LiTFSI in DOL/DME (1:1 v/v) + 0.2 wt. %  $\text{LiNO}_3$ . After cycling, some characterizations were carried out to figure the effects of the new co-solvent and additive. As shown in Figure XVII.1.28, the LS76 electrolyte also provided less S accumulated on Li anodes after 1<sup>st</sup> cycle which indicated that  $\text{Li}_2\text{S}$  formation on the anode was dissolved back during charge more efficient than the baseline. The phenomenon is

very similar for the S cathodes using LS76, the cathodes had less  $\text{Li}_2\text{S}$  accumulation than the cathode using baseline. In addition, the S cathodes using LS76 preserved its original morphology after 1<sup>st</sup> cycle.

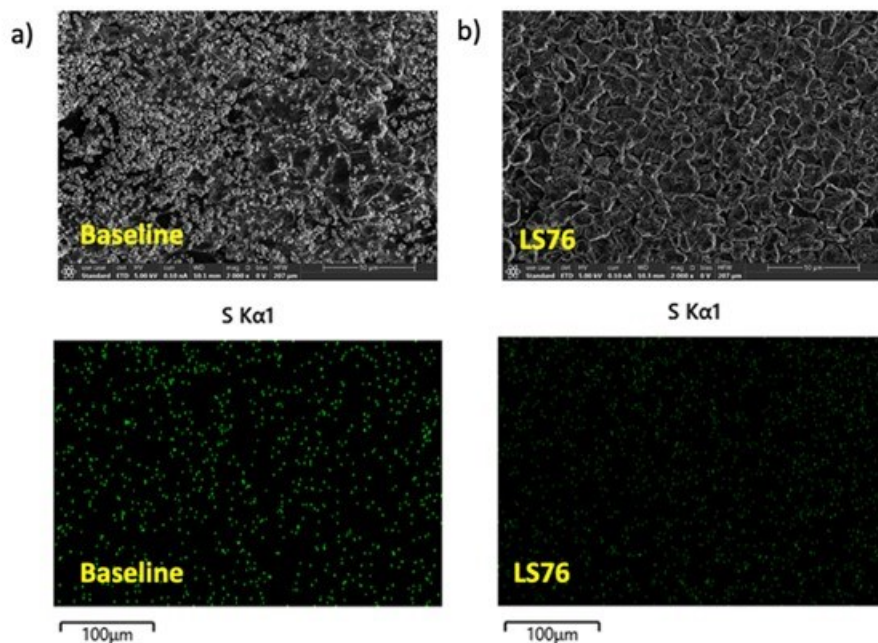


Figure XVII.1.28 SEM-EDS of Li anodes in a) Baseline electrolyte and b) LS76.

Figure XVII.1.29 shows the XPS results of the Li anodes and S cathodes after 1<sup>st</sup> cycle using baseline and LS76 electrolytes. Li anode with LS76 had less decomposed products from the electrolyte than the one with baseline electrolyte. Also, S cathode with LS76 still remained some elemental S after cycling and  $\text{Li}_2\text{S}$  did not cover the surface of the cathode as much as on the cathode with baseline. It is indicated that the new additive in the Li-S electrolyte could change the kinetics of polysulfide reactions and promote  $\text{Li}_2\text{S}$  dissolution, which eliminates the sulfur loss after cycling.

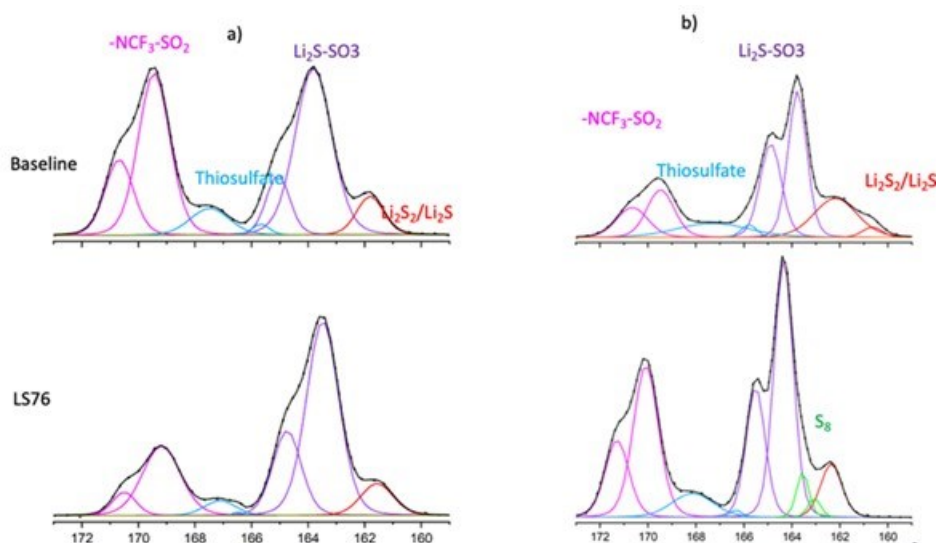
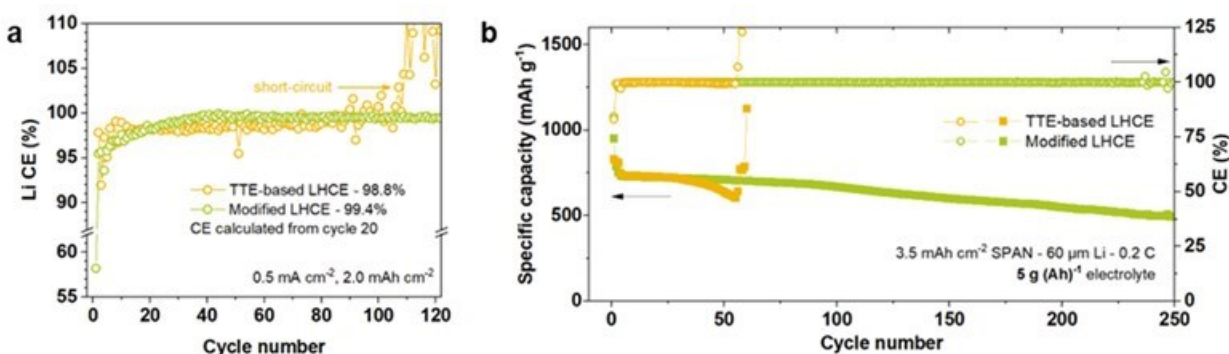


Figure XVII.1.29 XPS of a) Li anodes and b) sulfur cathodes in the baseline and LS76 after 1<sup>st</sup> cycle.

### Development of electrolytes for SPAN cathodes

The UMD team continued the study of a modified LHCE which is compatible with both Li metal anode and SPAN cathode (Figure XVII.1.30). Due to the improved electrochemical stability, this electrolyte is less consumed during the long cycle of Li||SPAN full-cells, resulting in better cyclability under a lean electrolyte condition of  $5 \text{ g (Ah)}^{-1}$ , compared to the TTE-based LHCE (Figure XVII.1.30) (Note: the solvating solvent is not DME).



**Figure XVII.1.30** Electrochemical performance of modified LHCE compared to TTE-based LHCE in (a) Li||Cu half-cells and (b) Li||SPAN full-cells at lean electrolyte condition of  $5 \text{ g (Ah)}^{-1}$ .

The UMD team performed post-mortem analyses to clarify the source of improvements. SEM images (Figure XVII.1.31a) revealed that the Li deposited in TTE-based LHCE was nodule-like but rather non-uniform with a scattering of Li dendrites. Meanwhile, Li deposited in the modified LHCE electrolyte exhibits flat and dense morphology with relatively large ( $\sim 10 \mu\text{m}$ ) and faceted particles. This difference can be attributed to the fact that the SEI formed in the modified LHCE was richer in robust inorganic compounds, such as LiF and  $\text{Li}_3\text{N}$  (Figure XVII.1.31b), suggesting a more favorable decomposition of the FSI anion. Similarly, the CEI formed in the modified LHCE is also more inorganic-rich than that formed in TTE-based LHCE, as evidenced by the negligible non-binder-derived carbon content and the high ratio between stable fluorine (LiF) versus organic/metastable fluorine (C-F/S-F). The superior interphase results in better electrochemical stability of the modified LHCE compared to the TTE-based counterpart, which in turn, leads to more electrolyte retention, as confirmed by quantitative  $^1\text{H-NMR}$  analysis (Figure XVII.1.31c), and better cyclability with fewer electrolytes.

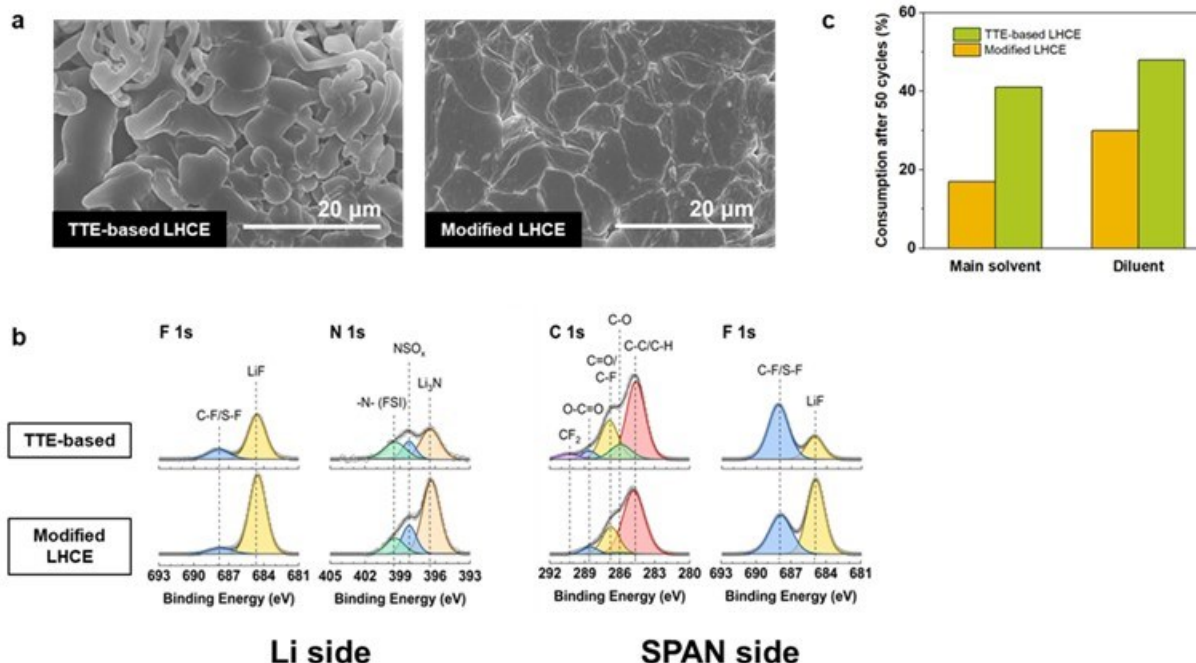


Figure XVII.1.31 Post-mortem analysis performed on Li-SPAN full-cells following 50 cycles in TTE-based versus modified LHCE: (a) SEM images of Li anodes; (b) XPS results showing interphase chemistry on both Li anode and SPAN cathode; (c) Electrolyte consumption calculated from <sup>1</sup>H-NMR analysis.

## 2. Keystone project 2: Electrode architectures

The goal of Keystone project 2 is to design, model, fabricate and characterize the effect of electrode architecture on electrode and cell performance in support of reaching the project of 500 Wh kg<sup>-1</sup> cell specific energy. Such studies include both high-capacity cathode materials such as high Ni content NMC and sulfurized polymer cathode, as well as lithium metal anodes.

### Oxide Cathode Thickness Optimization.

The University of Washington (UW) team continued work on examining the diffusion limits of thick cathode materials to determine optimal cathode thickness for high energy density and high capacity. Previously reported data from UW indicated that for high-Ni NMC cathodes with thicknesses of 50–200 μm, there does not appear to be a thickness dependence on the diffusion limit, counters to models in literature. This lack of dependence was noted in literature only for lithium iron phosphate (LFP) cathodes. The same testing of capacity vs current density for high-Ni NMC cells was used in cells using Li-foil anodes and LFP cathodes of thickness from 32–85 μm (Figure XVII.1.32) as a parallel study. They observed the same lack of dependence of thickness on specific capacity in the LFP as the high-Ni NMC reported previously by UW. Such lack of thickness dependence for both high-Ni NMC and LFP is hypothesized that the upper limit of thickness has not been reached to observe diffusion-limited effects, particularly in the high-Ni NMC cathodes. Work will continue in fabricating and testing thicker cathode, both of NMC and LFP, to attempt to reach that limit. Additional tests are being developed to probe into the fundamental mechanism of diffusion in these thick electrodes.

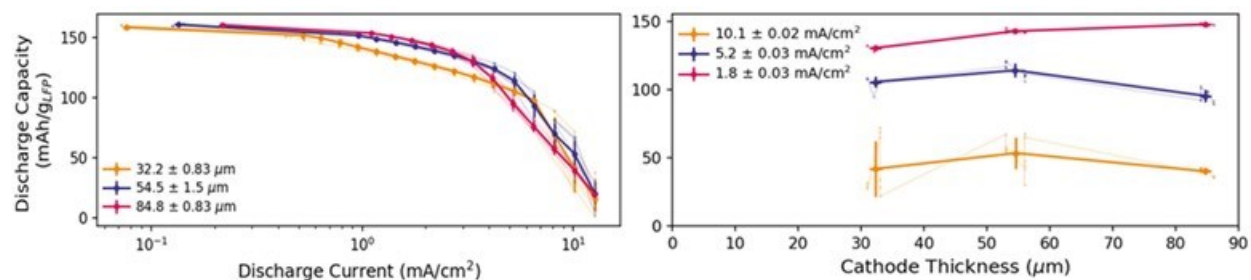


Figure XVII.1.32 Data of LFP cathodes of various thicknesses show no significant impact of thickness on specific capacity, as was observed for high-Ni NMC cathodes.

### SPAN Composite Cathode.

The University of California at San Diego (UCSD) team developed SPAN that reached a capacity of over 720 mAh g<sup>-1</sup>, which is higher than its theoretical capacity (650 mAh g<sup>-1</sup>) based on a C<sub>3</sub>NS stoichiometry. This phenomenon indicates that the nitrogen in the SPAN fused-pyridine matrix might host extra sulfur by forming a N-S bond. Based on this hypothesis, short chain sulfur species could be integrated with SPAN, thus further enhancing the sulfur loading and capacity of SPAN. The theoretical capacity could reach over 940 mAh g<sup>-1</sup> assuming a composition of C<sub>3</sub>NS<sub>2</sub>. This proposed mechanism can guide new synthesis designs for higher capacity SPAN. Based on this proposed mechanism, the UCSD team synthesized a SPAN composite, named CS SPAN. This material has a sulfur loading of over 60%, much higher than that of SPAN (39wt%). In a localized high concentration electrolyte (2 M Lithium bis(fluorosulfonyl)imide (LiFSI) in 1,2-Dimethoxyethane/Bis(2,2,2-trifluoroethyl) ether (DME/BTFE) (1:4 by weight) (LDME)), the CS SPAN shows a much higher capacity than SPAN. As shown in Figure XVII.1.33a and Figure XVII.1.33b, after the 1<sup>st</sup> formation cycle, CS SPAN delivered a capacity of over 900mAh g<sup>-1</sup> at a 0.2C rate even after 50 cycles. This represents a capacity improvement of about 200 mAh g<sup>-1</sup>. It is noted that the discharge profile of CS SPAN after the formation cycle does not show the features of undesired soluble polysulfides, essential for its cycling stability.

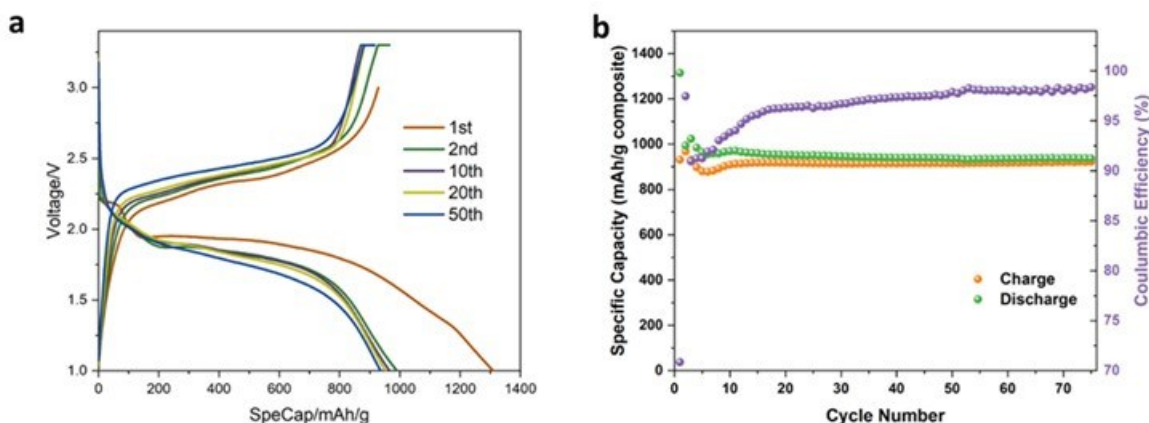


Figure XVII.1.33 High-capacity SPAN composite (CS SPAN). (a) battery curve and (b) cycling performance for CS SPAN composite with LDME electrolyte at 0.2C.

### Surface Chemical Modification of 2D and 3D Substrates for Li Anodes.

Ping Liu's group of UCSD completed a study of growing single-crystalline Li seeds on a 2D Fe/LiF substrate for fast-charging lithium metal batteries. Depositing lithium onto a Cu substrate modified with a thin film of Fe/LiF resulted in the formation of faceted, single crystalline seeds (Figure XVII.1.34(a)). This takes place despite the fact that Fe/LiF is a lithiophobic composite material. It is hypothesized that the uniformly distributed Fe nanoparticles serve as nucleation sites while LiF enables rapid Li transport. This hexagonal seed



layer facilitates subsequent lithium growth without dendrites formation even at high current densities. As shown in Figure XVII.1.34(b), lithium deposited on the Fe/LiF nanocomposite substrates are consistently denser than on Cu at current densities from  $0.5 \text{ mA cm}^{-2}$  to  $3 \text{ mA cm}^{-2}$ . In fact, the advantages of the Fe/LiF substrate become more obvious at higher current densities. The cryo-FIB-SEM images in Figure XVII.1.34(c) also show that the Li deposited on Fe/LiF has much less porosity than the Li deposited on Cu. These results suggest that the crystalline seeds formed can induce subsequent dendrite-free and dense lithium deposition even at fast charging rates. The advantage of the new substrate also translates to performance advantages in full cells. The capacity retention of cells using a  $3 \text{ mAh cm}^{-2}$   $\text{LiNi}_{0.8}\text{Mn}_{0.1}\text{Co}_{0.1}\text{O}_2$  (NMC811) cathode, 1-fold excess of lithium anode, and  $3 \text{ g Ah}^{-1}$  electrolyte. The cell with a lithium anode based on the Fe/LiF substrate is cycled at 1C rate for more than 130 cycles with 80% capacity retention, a 550% improvement over the baseline cells (80% retention at 25 cycles only). Their findings advance the understanding of lithium nucleation and pave the way for realizing high-energy, fast-charging Li metal batteries.

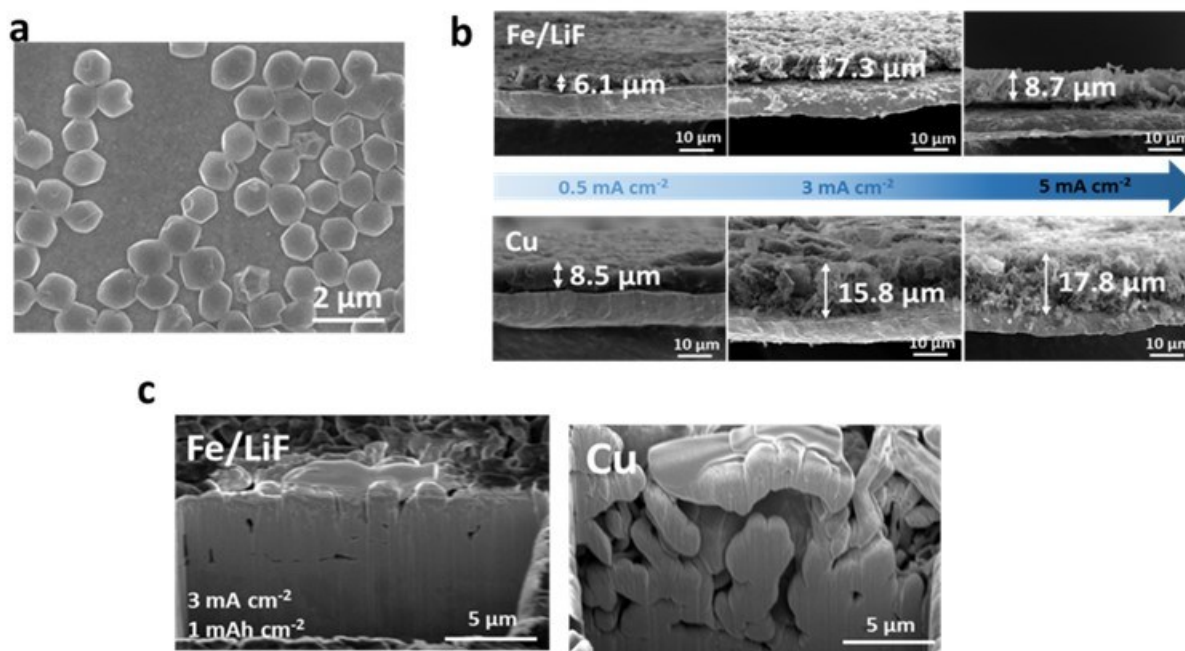


**Figure XVII.1.34** Morphology of deposited Li layer on different substrate. (a) SEM images of top-view Li crystalline seed deposited on the Fe/LiF substrate; (b)  $1 \text{ mAh cm}^{-2}$  Li plated on the Fe/LiF nanocomposite and Cu substrate, under  $0.5$ ,  $3$ ,  $5 \text{ mA cm}^{-2}$ . (c) Cryo-FIB-SEM images of  $1 \text{ mAh cm}^{-2}$  Li deposited on the Fe/LiF nanocomposite and Cu substrate under  $3 \text{ mA cm}^{-2}$ .

#### **Computational identification of Functional electrocatalysts enabling conversion of $\text{Li}_2\text{S}_2$ to $\text{Li}_2\text{S}$**

The University of Pittsburgh (U-Pitt) team continued to conduct theoretical modeling to probe the conversion of  $\text{Li}_2\text{S}_2$ , the intermediate polysulfide phase, to  $\text{Li}_2\text{S}$ , the final phase. As already discussed in the previous reports, achieving the complete conversion of  $\text{Li}_2\text{S}_2$  to  $\text{Li}_2\text{S}$  is of prime importance for the discharge process since the very sluggish kinetics of this reaction prevents the full utilization of sulfur in the sulfur cathode. The typical end products of the discharge process are  $\text{Li}_2\text{S}$  and  $\text{Li}_2\text{S}_2$  mixtures giving significantly lower capacity of almost 50% and consequently, the energy density as well commensurate with the lower S utilization opposed to pure  $\text{Li}_2\text{S}$  due to the high activation barrier associated with the complete conversion of  $\text{Li}_2\text{S}_2$  to the desired, final state of  $\text{Li}_2\text{S}$ . Thus, calculation of this kinetic reaction barrier and identification of the appropriate electrocatalysts substantially decreasing or even leading to complete elimination of this activation barrier will result in efficient utilization of S. Thus, the main aim of the present computational study is to identify functional electrocatalysts which can decrease the activation barriers and promote rapid conversion of  $\text{Li}_2\text{S}_2$  to  $\text{Li}_2\text{S}$  during discharge and the corresponding backward reaction from  $\text{Li}_2\text{S}$  to  $\text{Li}_2\text{S}_2$  during the charge process.

To obtain the thermodynamic properties, the density functional theory (DFT) approaches implemented in the Vienna Ab-initio Simulation Package (VASP) have been used, while a climbing image nudged elastic band (CNEB) method was utilized for the determination of the activation energies and other pertinent kinetic parameters of the elementary reactions on the different prospective functional electrocatalytic surfaces. The model of the functional electrocatalyst considered consists of a surface slab with the most stable crystallographic orientation containing the attached  $\text{Li}_2\text{S}_2$  or  $\text{Li}_2\text{S}$  molecules. The slab with a thickness of approximately 5-7 Å is separated from its image perpendicular to the surface direction by  $\sim 20$  Å to avoid their mutual interaction. The bottom two-three layers of the slab are then fixed with lattice parameters corresponding to the bulk state, while the remaining top layers along with the attached polysulfide molecule is allowed to completely relax. All the species are adsorbed on the functional electrocatalyst surface including the Li and S atoms. The activation barriers for the elementary reactions were estimated using the CNEB method, where 5 different intermediate points were chosen for calculations of the potential energy profile between the initial and final position of the Li-ion for the reaction 1 and S atom for the reaction 2 at the functional electrocatalytic surface (totally 7 points). All computations have been executed within the projector-augmented wave (PAW) method and the generalized gradient approximation (GGA) as the exchange-correlation energy functionals in a form described by Perdew and Wang implemented in the VASP software. To maintain the desired high precision for all the total energy and electronic structure calculations, a plane wave cutoff energy of 520 eV has been chosen. The relaxation procedure has been used to optimize the internal positions as well as the lattice parameters of the supercell. Additionally, the Monkhorst-Pack scheme has been used to sample the Brillouin zone and create the k-point grid for all the functional electrocatalytic surface slabs used in the current study. The selection of the appropriate numbers of k-points in the irreducible parts of the Brillouin zone were made on the grounds of the convergence of the total energy to 0.1 meV/atom. In the previous report, the U-Pitt team demonstrated the potential energy profiles for Reaction 2 calculated for functional electrocatalysts comprising Functional Catalysts III, Type III family and Functional Catalysts IV, Type IV family. In this report, the potential energy profiles for Reaction 2 calculated for functional electrocatalysts comprising Functional Catalysts V, Type V and Functional Catalysts VI, Type VI are shown in Figure XVII.1.35a and b, respectively. It can be observed that for all the probed materials of both functional electrocatalysts of types V and VI, Reaction 2 in the discharge direction is exothermic, as expected, with the final product ( $\text{Li}_2\text{S}+\text{S}$ ) being more energetically favorable compared to  $\text{Li}_2\text{S}_2$ . However, in contrast to the spontaneous Reaction 1 discussed in previously, this reaction is not spontaneous with substantial activation barriers needed for the different electrocatalytic materials considered. The type V electrocatalysts are split into two subgroups with distinctly different average activation barriers: Cat25, Cat26, Cat27 with the average barrier value of  $\sim 0.48\text{eV}$  and Cat28, Cat29, Cat30 with the average barrier value of  $\sim 1.2\text{eV}$ . Type V is a multicomponent composition group of materials and demonstrates larger variation in the activation barriers values than those for Types I-IV studied and reported in the earlier quarters of the project. In the Type V functional electrocatalyst as shown in Figure 1a, the lowest activation barrier is demonstrated by the multicomponent composition Cat26 with corresponding value of 0.45 eV, while the lowest barriers value in the Type VI as shown in Figure XVII.1.35b belongs to another multicomponent composition Cat32 with the corresponding value of 0.26 eV. As of now, this is the lowest activation barrier determined by the U-Pitt team amongst the different types of functional electrocatalyst materials considered in the present project since the project was initiated. However, there is still the need to further decrease the activation barriers for Reaction 2 which will then likely yield much higher specific capacity values for sulfur in the S-cathode.

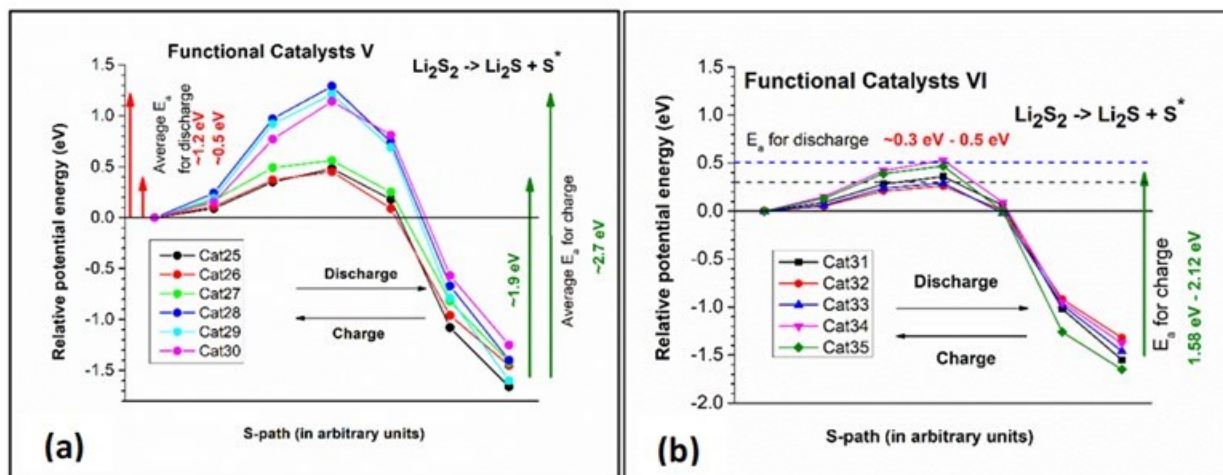
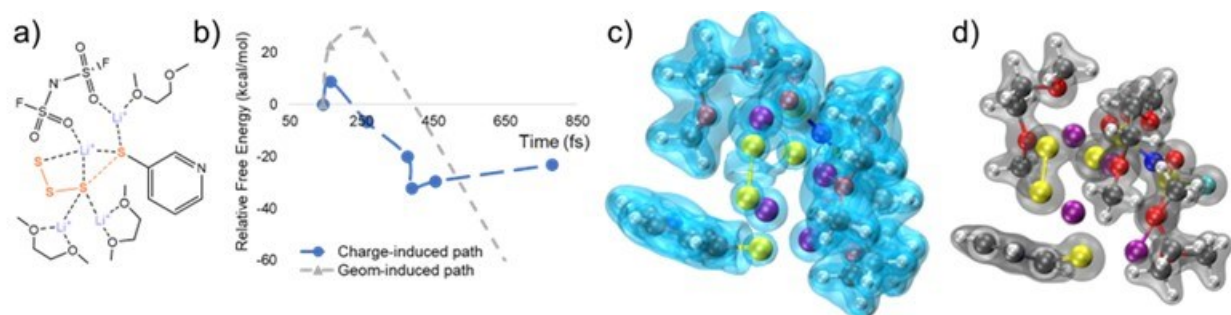


Figure XVII.1.35 Potential energy profiles for Reaction 2 ( $\text{Li}_2\text{S}_2 \rightarrow \text{Li}_2\text{S} + \text{S}^*$ ) for the two different types of functional electrocatalysts considered.

The TAMU team completed a theoretical-computational study this quarter that provides an overview of the lithiation reactions and solvation effects in different SPAN structures by comparing the lithiation energetics at different sites of SPAN. Two types of electrolytes were analyzed: a diluted solution of LiFSI, based on DMC or DME as solvents, and a localized high concentration electrolyte with two different fluorinated diluents. To further assess the interactions between electrolyte species and reaction intermediates during electrochemical lithiation, artificial intelligence enhanced molecular dynamic (AIMD) simulations incorporating detailed electronic structure analysis of the key structures in major chemical events were employed. The thermodynamics of the SPAN structures were evaluated, using 4 pyridine units to serve as PAN backbone in DFT optimizations. After obtaining the vulcanization reaction energetics in forming different polysulfide (PS) chain categories, the lithiation free energy profiles of each feasible structure were also evaluated. It was found that when clustered with polysulfide chains, the electronic structures and binding energetics of solvated Li cations are profoundly altered. The AIMD simulations provided details about the solvent, anion, and diluents stability during discharge. In both the DMC- and DME-solvated systems, lithium-mediated solvent-SPAN interactions play significant roles in the S-S and C-S cleavage reactions. In DME-based electrolyte system, the electrolyte salt LiFSI is also involved in the sulfur chain cleavage pathways (Figure XVII.1.36a). In the DMC-solvated system, solvent stabilization is less significant than DME, resulting in less dissolution of  $\text{S}_x$  chains. When 4 external Li atoms enter the simulation slab, sulfur chain migration takes place. An  $\text{S}_4$ -chain experiences cleavage, rearranges to bond with a neighboring  $\text{S}_3$ -chain, leaving an individual S atom not bonded to any of neighbor S atoms. Being consistent with the molecular geometries, Li-S is more of electrostatic interaction properties than covalently shared electronic orbitals.



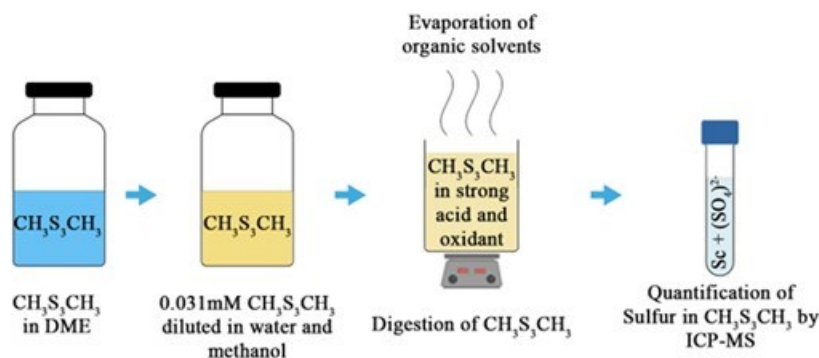
**Figure XVII.1.36** (a) Solvation structure, (b) free energy profile, (c) electronic Laplacian revealing the type of bonding, and (d) electron density isosurfaces. The key geometries obtained from AIMD frames revealed two types of pathways as shown in (b). The grey curve stands for the geometry-induced pathway which includes charge variation throughout the reaction, and the blue one indicates the pathway where electron uptake happens prior to the S-S cleavage. This event series takes place when Li:S = 1:2

#### **Quantification of Lithium (Li) and Sulfur (S) inventory loss in Li-S Batteries.**

Previously, the Meng's group at UCSD reported High-Performance Liquid Chromatography–Ultra-Violet Spectroscopy (HPLC-UV) calibration data for quantifying dissolved elemental sulfur and two shorter-chain methylated polysulfides:  $\text{CH}_3\text{S}_2\text{CH}_3$  and  $\text{CH}_3\text{S}_3\text{CH}_3$ . The team also identified and confirmed the position of longer chain methylated polysulfides  $\text{CH}_3\text{S}_x\text{CH}_3$  ( $x \in \{4,8\}$ ) by HPLC-UV and High-Performance Liquid Chromatography–Atmospheric Pressure Chemical Ionization Mass Spectroscopy (HPLC-APCI-MS)-negative mode. To quantify those species, the team plan to collect them in quantifiable amounts by doing semi-preparative HPLC and then quantify the Sulfur amount in each collected fraction by Inductively Coupled Plasma-Mass Spectroscopy (ICP-MS). There were some challenges related to ICP sample digestion protocols that the team has overcome. The final goal is to track the contribution of the loss of each component (lithium metal, elemental sulfur, and dissolved polysulfides) to the total full cell capacity losses. First, a commercially available standard methylated polysulfide sample of  $\text{CH}_3\text{S}_3\text{CH}_3$  was used to test and screen the digestion protocols (Figure XVII.1.37a). By dissolving 5  $\mu\text{L}$   $\text{CH}_3\text{S}_3\text{CH}_3$  to 5 mL DME solvent, 9.517 mM solution was made, which was further diluted up to 0.031 mM by adding water and methanol (1:1 v/v), which is approximately (same order of magnitude) equivalent concentration of  $\text{CH}_3\text{S}_3\text{CH}_3$  in the HPLC column. The sample was prepared to create conditions identical to the fractions collected by semi-preparative HPLC. If digested properly, sulfur oxidizes to  $\text{SO}_4^{2-}$  and is later ionized to  $[\text{SO}]$  (quantifiable species) by ICP-MS- $\text{O}_2$  reaction mode. 457 ppb of oxidized sulfur ion in the form of  $[\text{SO}]$  in a 12 mL sample was expected. Scandium (Sc) internal standard was used and recovered in the ICP test to avoid interferences caused by organic solvents such as methanol. Scandium recovery of 80% - 120% is considered acceptable and used to adjust the rest of the ions. Sulfur recovery was calculated based on observed and expected values of  $[\text{SO}]$  for a given concentration. Notably, simple digestion of the sample in a conventional 10% nitric acid matrix could not avoid methanol interference, and it had very low sulfur and scandium recovery. Increasing the concentration of strong acid and adding hydrogen peroxide (a strong oxidant) helped oxidize sulfur, improving the sulfur recovery to 97%. However, a relatively low scandium recovery of 60.7% indicated that methanol was still residual in the sample. Thus, a heating step of 180  $^\circ\text{C}$  for 3 hours was added to overcome this issue. The heating was done separately in a closed pressure vessel and an open vial. Both gave acceptable sulfur recovery of 99%-101%, but only the open system reduced the methanol amount providing a high scandium recovery of 120.5% compared to 62.5% scandium recovery in the closed system. After identifying the appropriate protocol above for digesting standard samples, digestion for actual fractions collected by semi-preparative HPLC was performed. A schematic of the detailed processes involved is described in Figure XVII.1.37b. The team prepared a methylated polysulfide solution, separated the species by semi-preparative HPLC-UV, and collected and digested the fractions for each polysulfide. The protocol developed for the standard sample did not work for digesting the fractions collected in semi-preparative HPLC. It was later identified that a high amount of methanol in the fractions was troublesome. If the samples were heated at very high temperatures (250  $^\circ\text{C}$ ), the evaporation rate was high, which could have led to the potential loss of sulfur species. On the

other hand, by reducing the heating time, the oxidation of polysulfides was limited. So, a step of resting the samples was added, which helped to improve the sulfur recovery substantially. Besides, a wrong sequence of digestion procedure caused methanol to reside in some samples. The final protocol was developed by correcting the order of digestion steps, which helps in oxidation by resting the samples and then removing leftover organics by heating. The team plans to follow this optimized protocol in their future studies of quantifying longer-chain polysulfides.

(a) Digestion of the standard sample of  $\text{CH}_3\text{S}_3\text{CH}_3$



(b) Digestion of the fractions of methylated polysulfide species collected by semi-preparative HPLC-UV

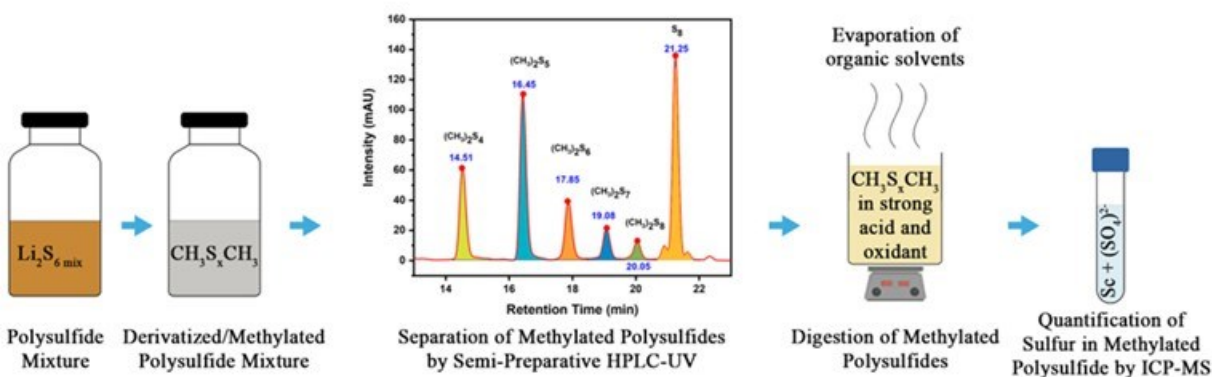
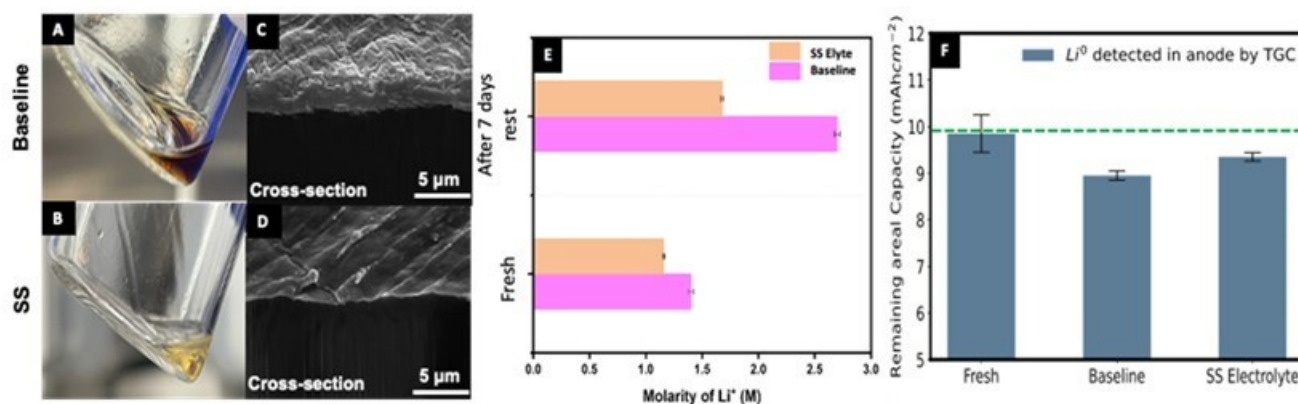


Figure XVII.1.37 (a) The schematic of the processes involved in the methodology to quantify the standard sample of  $\text{CH}_3\text{S}_3\text{CH}_3$  by ICP-MS, and (b) the longer chain polysulfides by combining semi-preparative HPLC-UV with ICP-MS

**Quantifying Lithium inventory in Lithium-Sulfur Batteries during calendaring.**

One of the issues in lithium-sulfur battery commercialization is self-discharge and capacity loss (irreversible and reversible) during storage. The self-discharge of Li-S batteries after the electrochemical operation is mostly due to diffusion and reactions of polysulfides at the anode surface. The UCSD team is taking the approach of quantifying lithium inventory in the Li-S pouch cell. Quantifying the Li inventory in anode, cathode, and electrolyte will reveal the reversible and irreversible capacity loss during storage. Additionally, the team is engaged in comparing self-discharge behavior in two different kinds of electrolyte, i.e., moderately solvating (Baseline) electrolyte (1 M LiTFSI in DME: DOL=1:1 (v/v) with 2 wt.% LiNO<sub>3</sub>) and sparingly solvating (SS) electrolyte (provided by NexTech Batteries). Figure XVII.1.38 a and b show significant electrolyte color changes after 7 days of storage. The baseline electrolyte appears dark yellow, compared to pale yellow in the SS electrolyte, indicating more polysulfide dissolution occurred in the Baseline electrolyte. The effect on morphology was observed by milling lithium foil using Cryo-FIB/SEM. The baseline electrolyte shows higher surface roughness than the SS electrolyte, as shown in Figure XVII.1.38 c and d. Additionally, lithium foil in pouch cells with baseline electrolyte shows a passivation layer of 2-3  $\mu\text{m}$ , compared to less than

1  $\mu\text{m}$  in SS electrolyte. Though no electrochemical operation was performed,  $\text{S}_{8(s)}$  is converted and equilibrated with  $\text{S}_{8(l)}$  while resting. It migrates towards lithium metal foil and reduces  $\text{S}_{8(l)}$  to polysulfides. This phenomenon is more evident when polysulfides are more soluble in baseline electrolytes than SS electrolyte. The ICP-MS results for  $\text{Li}^+$  quantification in the electrolyte can be visualized in Figure XVII.1.38 e. Fresh baseline and SS electrolyte samples have  $\text{Li}^+$  molarity of  $1.4 \pm 0.01 \text{ M}$  and  $1.18 \pm 0.05 \text{ M}$  respectively. After 7 days of resting,  $\text{Li}^+$  molarity increases by  $2.8 \pm 0.04 \text{ M}$  in the baseline electrolyte, compared to  $1.8 \pm 0.08 \text{ M}$  in the SS electrolyte. The results indicate that more Li dissolution occurred in the baseline electrolyte compared to the SS electrolyte. TGC is applied to quantify the Li inventory (after resting) in the anode, and the results are shown in Figure XVII.1.38 f. The lithium inventory (after resting) in the anode measured in the baseline electrolyte was  $8.95 \pm 0.1 \text{ mAh cm}^{-2}$ , whereas in the SS electrolyte, it was  $9.35 \pm 0.3 \text{ mAh cm}^{-2}$ . The pristine lithium foil has  $9.85 \pm 0.4 \text{ mAh cm}^{-2}$ . The loss of lithium inventory from the anode is noticeable. Some Li dissolves in the electrolyte, while another portion is lost in passivation layers formation on electrode surfaces. Based on TGC and ICP-MS results, after 7 days of storage, low Li inventory loss in the SS electrolyte was observed compared to the baseline electrolyte, likely due to the low polysulfide dissolution. The same quantification will be performed after 24 hours and 30 days of rest to understand the Li inventory evolution during storage.



**Figure XVII.1.38** After 7 days resting period: Electrolyte collected in (a) baseline and (b) SS electrolyte; Cross-section images of Lithium in (c) baseline electrolyte and in (d) SS electrolyte; (e)  $\text{Li}^+$  detected by ICP-MS in different electrolytes; (f)  $\text{Li}^0$  detected in anode by TGC. Green dotted line indicates  $\text{Li}^0$  amount in pristine foil.

#### Analyze the structure of SPAN with post-thermal treatment.

The Liu's group at UCSD focused on analyzing the effects and mechanism of post-thermal treatment on the SPAN structure and irreversible capacity loss in the Li-SPAN battery. In previous quarters, this group developed a synthesis procedure to suppress the 1st cycle irreversible capacity loss of SPAN, and over 50% of it was eliminated with extended annealing at a decent temperature. Electrochemical testing showed that both post-treated and reference SPAN samples had nearly identical reversible capacity, but post-thermal treatment reduced the 1st cycle irreversible capacity loss to  $\sim 100 \text{ mAh g}^{-1}$ , compared to  $225 \text{ mAh g}^{-1}$  for the reference SPAN (Figure XVII.1.39a). To understand how post-thermal treatment can impact the irreversible capacity of SPAN, the Liu's group applied thermal gravimetric analysis-mass spectrometry (TGA-MS) to analyze the gas evolution before and after post-thermal treatment. In Figure XVII.1.39b, TGA-MS results show that the pristine SPAN starts to release  $\text{H}_2\text{S}$  gas at  $250^\circ\text{C}$ , which is not experienced by the post-treated SPAN. This result agrees with the team's previous study in FY2023Q1 report that an intra-polymer elimination of  $\text{H}_2\text{S}$  takes place during the post-thermal treatment process. There is also some sulfur loss in the pristine SPAN at above  $210^\circ\text{C}$ , which could be attributed to the loss of long chain sulfur. Based on these results, a proposed mechanism for the intra-polymer elimination of  $\text{H}_2\text{S}$  and sulfur through post-thermal treatment is presented in Figure XVII.1.39 c. Since the irreversible components in the battery had been eliminated during the post-thermal treatment, the irreversible capacity loss in SPAN was retarded. This group aims to optimize the

molecular modification of SPAN in the future to not only reduce its irreversible capacity loss but also increase its reversible capacity.

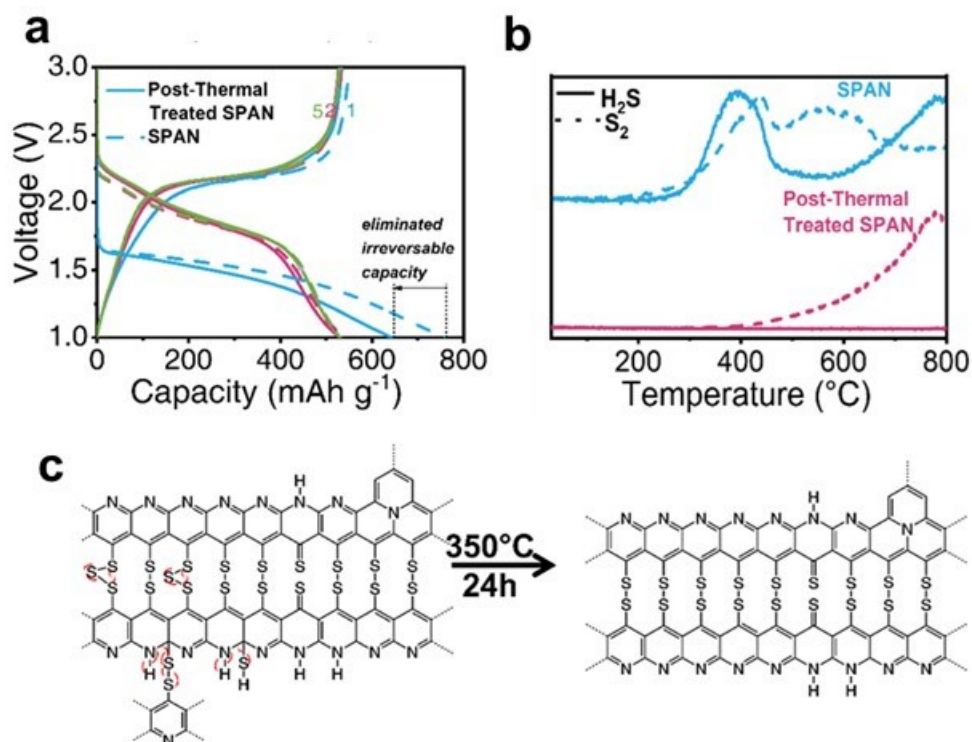


Figure XVII.1.39 (a) the discharge/charge profiles for SPAN before and after post-thermal treatment at 0.2C ( $1C=600 \text{ mAh g}_{\text{SPAN}}^{-1}$ ); (b) TGA-Mass Spectrometry (TGA-MS) results for mass traces at  $m/z=34$  ( $\text{H}_2\text{S}$ ) and  $64$  ( $\text{S}_2$ ); (c) the proposed structural change for SPAN before and after post-thermal treatment.

#### Phosphide-based electrocatalyst for anode-free cells with $\text{Li}_2\text{S}$ cathodes.

Manthiram's group at UT Austin explored the benefits of mono-metallic (MoP, Ni<sub>2</sub>P) vs. bi-metallic (NiMoP) phosphide-based electrocatalysts to enhance the electrochemical utilization of sulfur with  $\text{Li}_2\text{S}$  cathodes. To compare the catalytic activity of different phosphides, cyclic voltammetry (CV) was conducted in symmetric cells with electrocatalysts-based compounds as both working and counter electrodes and  $0.1 \text{ mol L}^{-1}$  polysulfide ( $\text{Li}_2\text{S}_6$ ) as the electrolyte additive. As shown in Figure XVII.1.40a, the CV curves of NiMoP-based electrodes display higher peak current densities compared to MoP and Ni<sub>2</sub>P, suggesting a facile reaction kinetics for the conversion of polysulfide species. Due to the improved charge-transfer kinetics, the NiMoP catalysts show a high-rate capacity of  $530 \text{ mA h g}^{-1} \text{ Li}_2\text{S}$  at 1C rate, when the electrocatalyst is mechanically ball-milled with  $\text{Li}_2\text{S}$  and carbon (Figure XVII.1.40b). Moreover, the capacities of  $\text{Li}_2\text{S} @ \text{NiMoP} @ \text{C}$  are consistently higher than those of MoP and Ni<sub>2</sub>P throughout the whole rate cycles. To investigate the origin of the superior catalytic performance of bi-metallic phosphides relative to mono-metallic phosphides, a visual adsorption test followed by ultraviolet-visible spectroscopy (UV-vis) analysis was conducted. As shown in Figure XVII.1.40c, the  $\text{Li}_2\text{S}_6$  solutions with NiMoP exhibit a much lighter color compared to that with the other catalysts after standing for 2 h. This indicates a relatively stronger polysulfide adsorption capability of NiMoP, as confirmed by UV-vis data. According to the Sabatier principle, too strong interfacial interaction between the catalysts and reactants may impede the redox transformation by blocking the active sites for the consequent reactions. However, the semi-metallic nature of NiMoP might provide sufficient diffusion properties that can efficiently disperse the redox products throughout the surface without blocking the active nickel or molybdenum sites, leading to the high polysulfide conversion ability of bi-metallic phosphides. Based on the superior catalytic activity of bi-metallic NiMoP catalysts, a one-step carbothermal reduction of

lithium sulfate, metal phosphates, and carbon precursors was conducted to integrate  $\text{Li}_2\text{S}$ ,  $\text{NiMoP}$ , and carbon well. The reduction of sulfate and phosphates yields  $\text{Li}_2\text{S} @ \text{Ni}_x\text{Mo}_y\text{P}_z @ \text{C}$  composites, as shown by the X-ray diffraction pattern (Figure XVII.1.40d). The molecular level mixing of precursors ensures intimate contact between the  $\text{Li}_2\text{S}$  and nano-sized electrocatalysts, which are covered with uniform fiber-like carbon coating on the surface (Figure XVII.1.40e). The well-integrated  $\text{Li}_2\text{S} @ \text{Ni}_x\text{Mo}_y\text{P}_z @ \text{C}$  composites enable a stable cycling performance of  $420 \text{ mA h g}^{-1} \text{ Li}_2\text{S}$  after 300 cycles in an anode-free configuration, as shown in Figure XVII.1.40f.

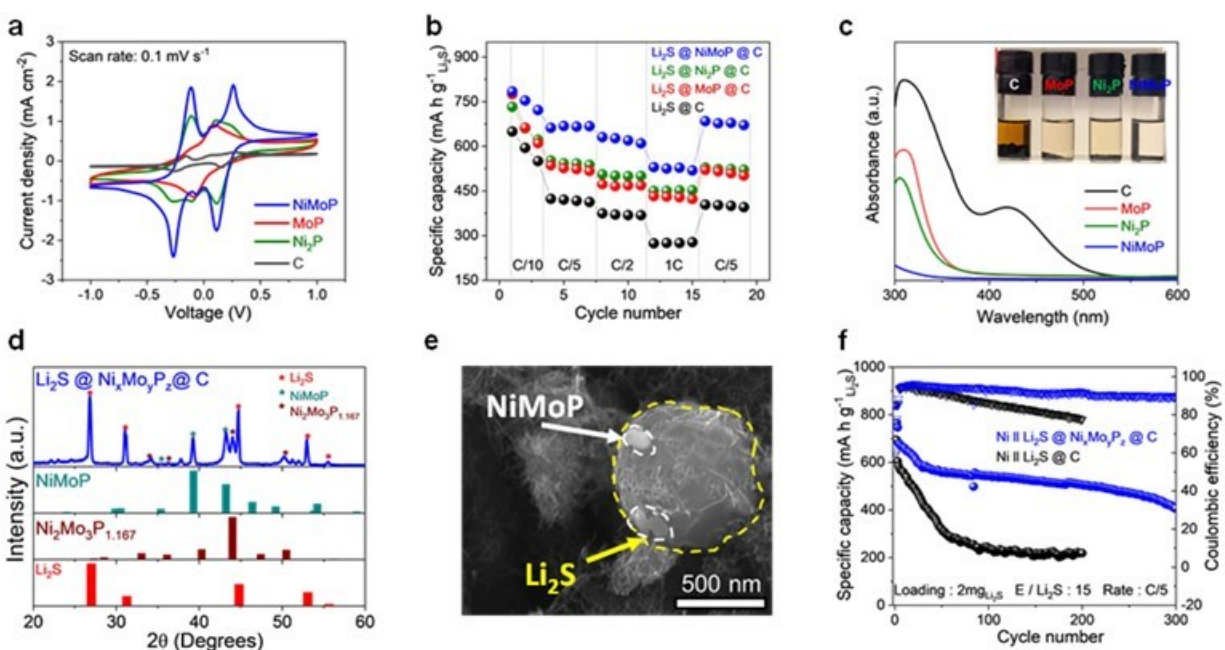


Figure XVII.1.40 (a) CV profiles of NiMoP, MoP, Ni<sub>2</sub>P, and carbon symmetric cells at a scan rate of  $0.1 \text{ mV s}^{-1}$ . (b) Rate performance of  $\text{Li}_2\text{S}$  mechanically mixed with NiMoP, MoP, Ni<sub>2</sub>P, and carbon at the rates ranging from C/10 to 1 C. (c) UV-vis spectra recorded after immersing NiMoP, MoP, Ni<sub>2</sub>P, and C in  $\text{Li}_2\text{S}_6$  solution for 2 h. Inset: digital images for  $\text{Li}_2\text{S}_6$  adsorption. (d) XRD patterns and (e) SEM image of the synthesized  $\text{Li}_2\text{S} @ \text{Ni}_x\text{Mo}_y\text{P}_z @ \text{C}$  composite with a one-step carbothermal reduction. (f) Long-term cycling performance of anode-free Ni ||  $\text{Li}_2\text{S} @ \text{Ni}_x\text{Mo}_y\text{P}_z @ \text{C}$  and Ni ||  $\text{Li}_2\text{S} @ \text{C}$  cells

#### Computational identification of Functional electrocatalysts enabling conversion of $\text{Li}_2\text{S}_2$ to $\text{Li}_2\text{S}$

The Kumta's team at the University of Pittsburgh (U-Pitt) continued to conduct theoretical modeling to probe the conversion of  $\text{Li}_2\text{S}_2$ , the intermediate polysulfide (PS) phase, to  $\text{Li}_2\text{S}$ , the final phase. The density functional theory (DFT) approaches implemented in the Vienna Ab-initio Simulation Package (VASP) were used to obtain all thermodynamic and kinetic properties of Reaction 2. The model considered for the computational identification of the functional electrocatalyst as described in earlier reports consists of a surface slab with the most stable crystallographic orientation containing the attached  $\text{Li}_2\text{S}_2$  or  $\text{Li}_2\text{S}$  molecules. The slab with a thickness of approximately 5-7 Å is separated from its image perpendicular to the surface direction by  $\sim 20 \text{ Å}$  to avoid their mutual interaction. The bottom two-three layers of the slab are then fixed with lattice parameters corresponding to the bulk state, while the remaining top layers along with the attached polysulfide molecule are allowed to completely relax. All the species are correspondingly adsorbed on the functional electrocatalyst surface including the Li and S atoms. As outlined in the earlier reports, the activation barriers for the elementary reactions were estimated using the climbing nudged elastic band (CNEB) method, wherein 5 different intermediate points were chosen for calculating the potential energy profile between the initial and final position of the Li-ion for the reaction 1 and S atom for the reaction 2 at the functional electrocatalytic



surface (in total 7 points). All the computations have been executed within the projector-augmented wave (PAW) method and the generalized gradient approximation (GGA) for the exchange-correlation energy functional in a form described by Perdew and Wang implemented in the VASP software. To maintain the desired high precision for all the total energy and electronic structure calculations, the plane wave cutoff energy of 520 eV has been chosen. The relaxation procedure has been used to optimize the internal positions as well as the lattice parameters of atoms within the supercell. Additionally, the Monkhorst-Pack scheme has been used to sample the Brillouin zone and create the k-point grid for all the functional electrocatalytic surface slabs used in the current study. The selection of the appropriate numbers of k-points in the irreducible parts of the Brillouin zone were made considering the convergence of the total energy to 0.1 meV/atom. In the previous report of FY2023Q1, the U-Pitt Kumta team demonstrated the potential energy profiles for Reaction 2 calculated for the functional electrocatalysts comprising various multicomponent electrocatalysts of which the best functional electrocatalysts was Cat38 with a calculated corresponding activation barrier of 0.26 eV as shown in Figure XVII.1.41a for illustrative purposes only for Group VII system of functional electrocatalysts. The U-Pitt team are presenting the results of the continued computational screening studies conducted for identifying the prospective functional electrocatalytic materials, and correspondingly extended their research study further to explore other types of multicomponent functional electrocatalyst materials containing different metallic and non-metallic elements. The potential energy profiles for Reaction 2 calculated for these multicomponent functional electrocatalysts during the current quarter of the project are shown in Figure XVII.1.41 b-d. From Figure XVII.1.41, it can be perceived that for all the probed functional electrocatalyst materials considered, Reaction 2 in the discharge direction is exothermic, as expected, with the final reaction product ( $\text{Li}_2\text{S}+\text{S}$ ) being more energetically favorable compared to  $\text{Li}_2\text{S}_2$ . However, in contrast to the spontaneous Reaction 1 discussed in FY2022 report, this reaction is not spontaneous, but has substantial activation barriers that need to be considered for the different functional electrocatalytic materials. The multicomponent functional electrocatalysts considered from the Group IX system of functional electrocatalysts studied as shown in Figure XVII.1.41b demonstrate similar activation barriers to the functional electrocatalyst materials from Group VII system shown in Figure XVII.1.41a. For example, the functional electrocatalyst, Cat50 is the best functional electrocatalyst material within this group with an activation barrier of 0.28 eV, which is very close to Cat 38, the functional electrocatalyst material identified from the previous group of functional electrocatalysts, namely, the Group VII system of functional electrocatalysts with a barrier of 0.26 eV. Furthermore, Cat46 with an activation barrier of 0.38 eV is the best functional electrocatalyst of all the materials considered in the Group VIII system of functional electrocatalysts shown in Figure XVII.1.41c, although exhibiting a higher activation barrier than the previously identified Cat38 functional electrocatalyst from the Group VII system possessing an activation barrier of 0.26 eV. Finally, functional electrocatalyst materials in the Group X systems were also considered in this quarter and the results of the calculated activation barriers are shown in Figure XVII.1.41d. Of the various functional electrocatalyst materials combinations studied, Cat55 is the best functional electrocatalyst material amongst the 5 functional electrocatalyst materials considered exhibiting an activation barrier of 0.45 eV, which is albeit, still higher than the previously considered Cat38 and Cat50 functional electrocatalysts from Group VII and Group IX systems, respectively, correspondingly possessing activation barriers of 0.26 eV and 0.28 eV, respectively. These two functional electrocatalysts are thus, currently the best functional electrocatalyst materials identified from the theoretical computational modeling studies promoting the reversible rapid conversion of polysulfide to  $\text{Li}_2\text{S}$  and back to elemental Li metal and S determined by the U-Pitt Kumta team.

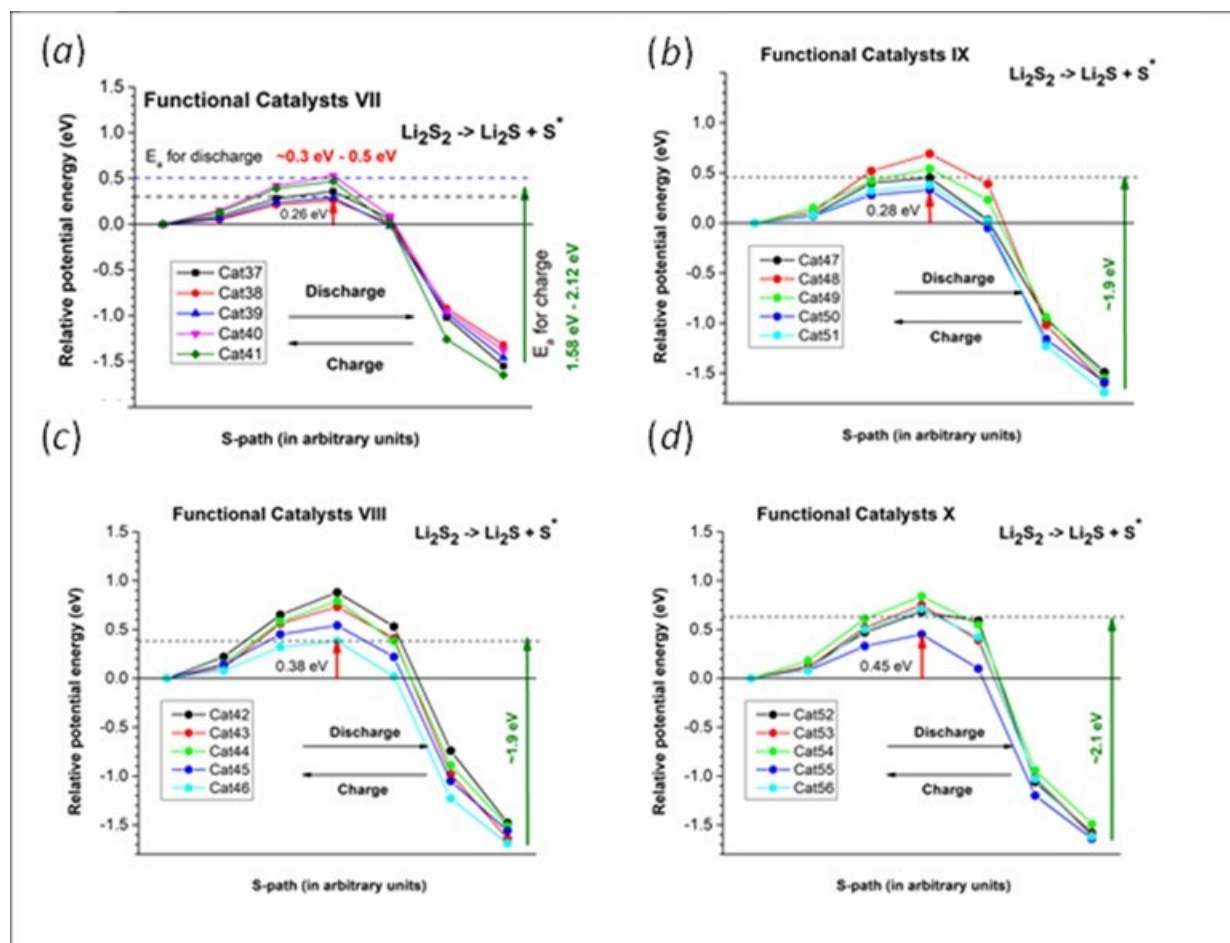
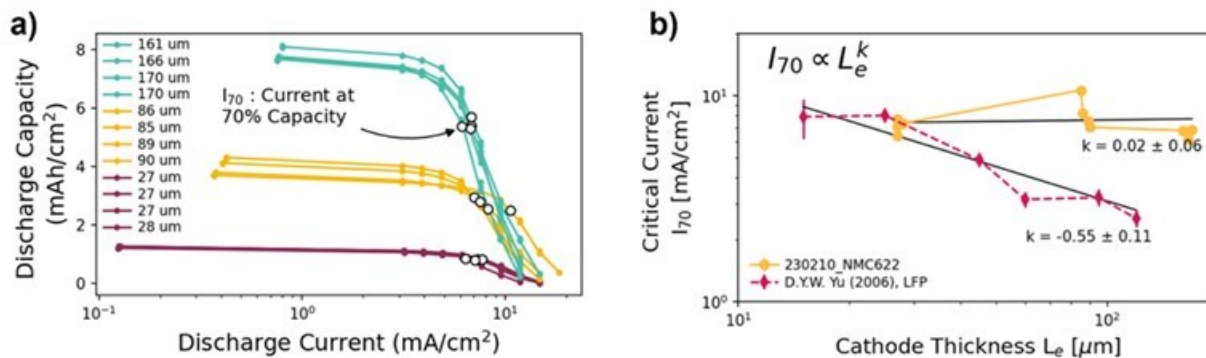


Figure XVII.1.41 Potential energy profiles for Reaction 2 ( $\text{Li}_2\text{S}_2 \rightarrow \text{Li}_2\text{S} + \text{S}^*$ ) for various multicomponent functional electrocatalysts systems considered in this study

### Cathode Thickness Optimization.

The UW team continued their studies on examining the diffusion limits of thick cathode materials to determine optimal cathode thickness for high energy density and high capacity. A new analysis was pursued, in which, when the discharge capacity reached 70% of the total discharge capacity at  $C/10$ , the current value was extracted and then plotted against the cathode thickness (Figure XVII.1.42). These data were then fitted with a power law function to extract the exponent, here  $k$ . Based on relationships found in literature, it is suggested that a  $k$  value of 1 corresponds to discharge capacities determined by unutilized active particles and that a  $k$  value of -1 corresponds to capacities limited by unutilized depth of the cathode. A range of published data with a variety of cathode materials was analyzed and  $k$  calculated. Of most note, the  $k$  values determined for NMC cathodes hover around 0, which suggests that there are more complicated causes of the sharp capacity drop observed at increased discharge currents. Work is ongoing to probe these causes and determine what impact they have on the choice of cathode thickness for high energy density lithium metal pouch cells.



**Figure XVII.1.42** The discharge current at which the discharge capacity reached 70% of the discharge capacity at C/10 was identified (a), plotted vs cathode thickness (b), and fitted with a power law relationship. The determined exponent  $k$  is indicative of the limiting factor of the discharge capacity

The UCSD team has been working on improvements of the cycling stability of a new sulfurized polyacrylonitrile (SPAN) material. Previously, the UCSD team successfully synthesized a sulfur-enriched SPAN composite, CS SPAN. CS SPAN is a composite that contains an excess of short chain sulfur and SPAN polymer. When tested in a localized high concentration electrolyte (LHCE), specifically 2M LiFSI in DME-BTTFE solvent (LDME), CS SPAN delivered promising capacities. At the electrode level, CS SPAN showed an impressive capacity of over 650 mAh g<sup>-1</sup>, a significant improvement over standard SPAN, which typically delivers 570 mAh g<sup>-1</sup>. However, the cycling stability of this material needs improvement. The focus of UCSD evaluated the effects of conductive additive on the cycling stability. As depicted in Figure XVII.1.43a, the CS SPAN electrode without additional additives can provide over 650 mAh g<sup>-1</sup> specific capacity. After 200 cycles, however, there is a discernible capacity decay. In contrast, Figure XVII.1.43b shows that the addition of 3% Super-P into the cathode can effectively prevent this capacity decay. After the initial formation cycles, the CS SPAN electrode can cycle over 250 times without any notable capacity decay. Figure XVII.1.43c and Figure XVII.1.43d show that, in the absence of carbon additives, the overpotential increases significantly and the capacity contribution from constant voltage charge at the end of charging process rises from the 25th to the 250th cycle. This indicates that the cathode active particles lose contact with one another due to insufficient conductivity and volume expansion. However, by introducing a small amount (3%) of Super-P, these issues were mitigated quite effectively.

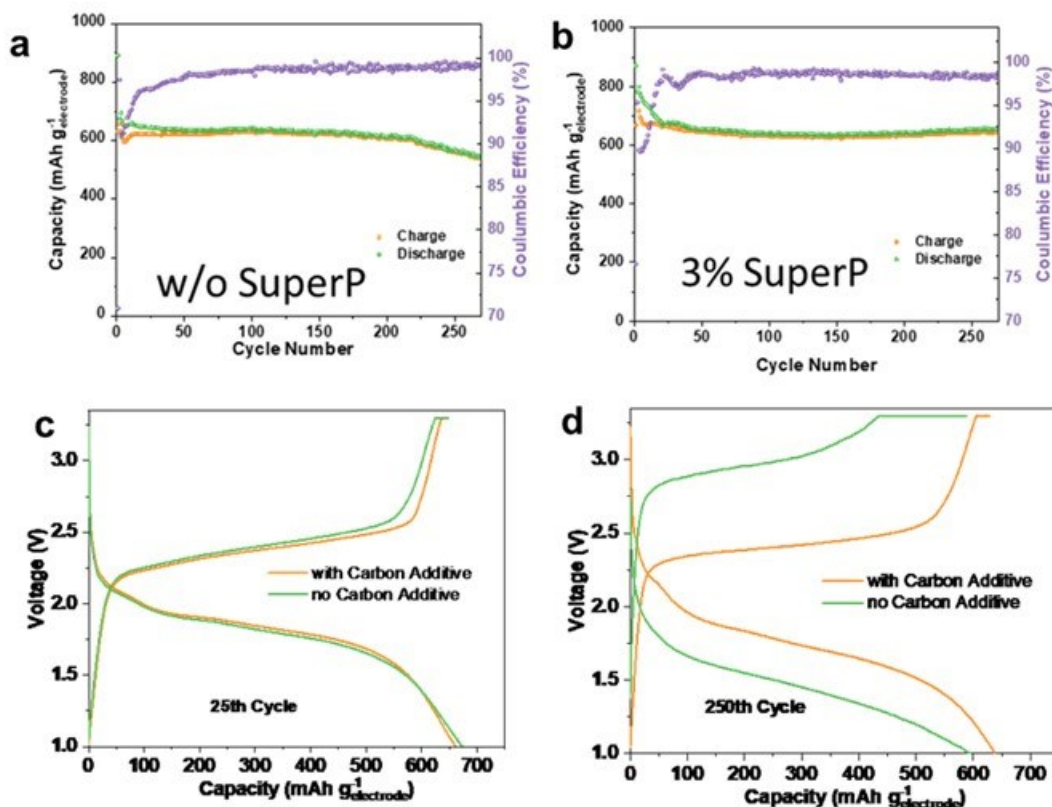


Figure XVII.1.43 Electrochemical performance of CS SPAN with/without conductive additives. Cycling performance of CS SPAN (a) without super-p; (b) with 3% super-p; charge/discharge curves for CS SPAN with/without carbon additive at (c) 25<sup>th</sup> cycle; and (d) 250<sup>th</sup> cycle. Electrolyte: 2M LiFSI in DME-BTFE solvent, LDME. Rate C/5 (1C = 600 mAh g<sup>-1</sup>, CCCV to 0.05C at 3.3V)

#### Phosphide-based electrocatalysts for lithium-limited lithium-sulfur cells.

The UT Austin team integrated different types of metal phosphide-based electrocatalysts with high electrical conductivity into the Li-S system. Titanium phosphides (TiP and TiP<sub>2</sub>) were synthesized via a facile one-step mechanochemical synthesis procedure that does not generate PH<sub>3</sub> gas. Specifically, TiP<sub>2</sub> was demonstrated to be an effective dual-function material, capable of enhancing the sulfur redox kinetics at the cathode as well as stabilizing the lithium metal at the anode. As depicted in Figure XVII.1.44a, the Li-TiP<sub>2</sub>/carbon nano tube (CNT) | Li-TiP<sub>2</sub>/CNT symmetric cell with 0.2 M Li<sub>2</sub>S<sub>6</sub> added to the electrolyte can stabilize the lithium-metal cycling faster and better compared to the Li-CNT | Li-CNT or Li | Li symmetric cells without TiP<sub>2</sub>. With TiP<sub>2</sub>, the stripping and plating overpotential was quickly stabilized at 10 mV and remained stable for more than 600 h. In contrast, for the Li | Li cells, a stable interface could not be formed until after 250 h when the overpotential stabilized at 25 mV. To demonstrate the dual-functional nature of TiP<sub>2</sub>, full cells were assembled where TiP<sub>2</sub> was implemented into both the cathode and anode, as shown in Figure XVII.1.44b. By substituting Li metal with a Li-TiP<sub>2</sub>/CNT composite as the anode, the capacity retention is improved to 91.6% from 51.8% after 50 cycles when using a lower N/P ratio of 7. By further integrating TiP<sub>2</sub> into the cathode in a Li-TiP<sub>2</sub>/CNT || Li<sub>2</sub>S<sub>6</sub>@TiP<sub>2</sub>/C cell, the initial capacity increases from 787 to 980 mAh g<sup>-1</sup> with a reduction in charge-discharge polarization, as shown in Figure XVII.1.44c. Moreover, bi-metallic phosphides (NiMoP) are found to offer higher catalytic performance compared to mono-metallic phosphides (MoP, Ni<sub>2</sub>P). For example, the cells with the bimetallic NiMoP catalyst incorporated into Li<sub>2</sub>S cathodes display a higher initial capacity (827 mAh g<sup>-1</sup>) compared to those with Ni<sub>2</sub>P (767 mAh g<sup>-1</sup>) or MoP (726 mAh g<sup>-1</sup>) catalysts, as depicted in Figure XVII.1.44d. The bi-metallic catalyst also demonstrates superior capacity retention during cycling compared to the mono-metallic counterparts, with NiMoP exhibiting a retention of 75 % compared to 70 % for

Ni<sub>2</sub>P and 67 % for MoP over 100 cycles. X-ray photoelectron spectroscopy (XPS) characterization was performed on the NiMoP particles after immersing in a Li<sub>2</sub>S<sub>6</sub> solution to explore the underlying factors contributing to their superior catalytic performance. Figure XVII.1.44e and Figure XVII.1.44f reveals a notable decrease in the binding energies of Ni-P and Mo-P bonds by 0.63 and 0.62 eV, respectively, indicating the remarkable electron acceptor character of Ni and Mo atoms. The significant electron transfer from Li<sub>2</sub>S<sub>6</sub> to Ni and Mo atoms validates the strong high-order polysulfide adsorption capability of NiMoP catalysts. Scanning electron microscopy (SEM) was employed to compare the nucleation trend of low-order polysulfides (Li<sub>2</sub>S/Li<sub>2</sub>S<sub>2</sub>). Figure XVII.1.44g illustrates that the NiMoP catalysts exhibit a uniform nucleation morphology with a nano-sized particle distribution. In contrast, both the Ni<sub>2</sub>P and MoP catalysts display an agglomerated nucleation trend with a distribution of micron-sized Li<sub>2</sub>S/Li<sub>2</sub>S<sub>2</sub>. The characterization results indicate that the bi-metallic NiMoP catalyst exhibits enhanced high-order polysulfide adsorption capabilities and improved low-order polysulfide nucleation behavior compared to the mono-metallic Ni<sub>2</sub>P and MoP catalysts, resulting in superior cell performance. Encouraged by the superior catalytic activity of bi-metallic NiMoP catalysts, a one-step carbothermal reduction of lithium sulfate, metal phosphates, and carbon precursors was conducted to integrate Ni<sub>x</sub>Mo<sub>y</sub>P<sub>z</sub> and carbon into Li<sub>2</sub>S (Figure XVII.1.44h). The well-integrated Li<sub>2</sub>S @ Ni<sub>x</sub>Mo<sub>y</sub>P<sub>z</sub> @ C composites enable a stable cycling performance in anode-free pouch cells, as shown in Figure XVII.1.44i. This one-step catalyst integration technique maximizes the contact between the catalyst and active material, thereby enhancing the electrochemical utilization of Li<sub>2</sub>S and the overall performance.

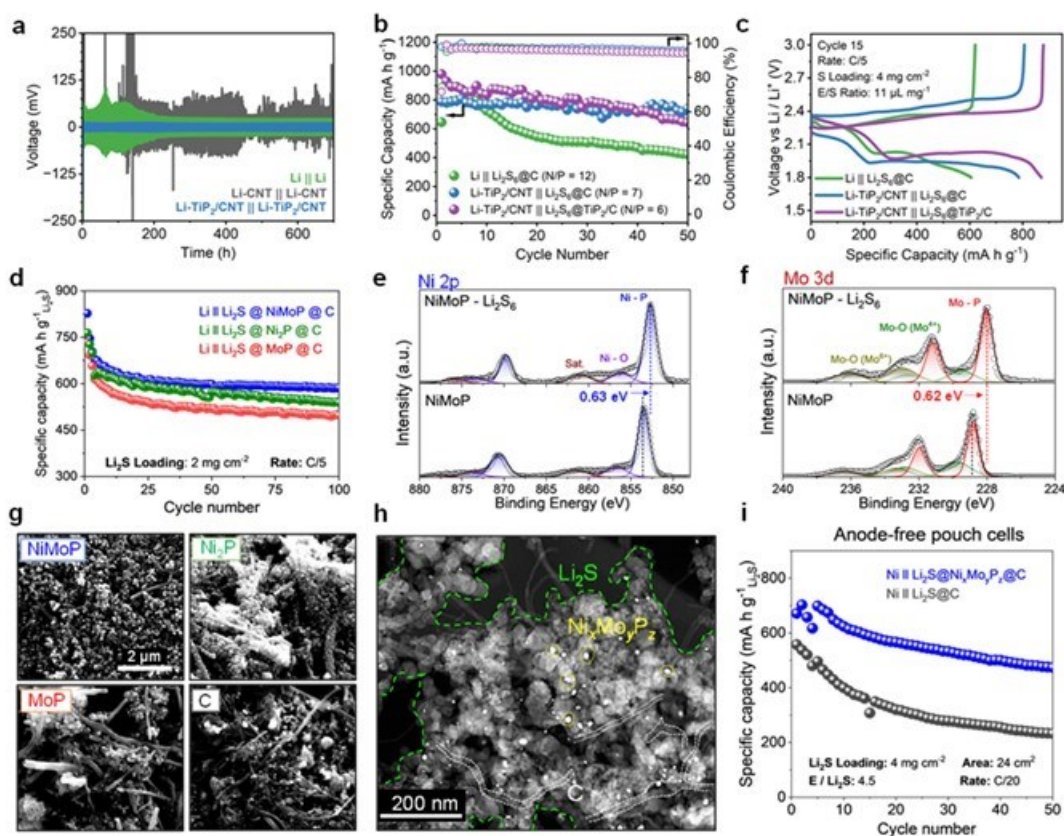


Figure XVII.1.44 (a) Symmetric cells cycled in an electrolyte with 0.2 M Li<sub>2</sub>S<sub>6</sub> added. (b) Comparison of high-sulfur loading (4 mg cm<sup>-2</sup>) cycling performances of cells with and without the TiP<sub>2</sub> catalyst. (c) Galvanostatic charge-discharge voltage profiles over the 15th cycle for cells with and without TiP<sub>2</sub> catalyst. (d) Long-term cycling performances of cells with different catalysts integrated into Li<sub>2</sub>S cathodes: NiMoP (Blue), Ni<sub>2</sub>P (Green), MoP (Red). High-resolution XPS data of NiMoP particles before and after adsorbing Li<sub>2</sub>S<sub>6</sub>: (e) Ni 2p and (f) Mo 3d. (g) SEM image of Li<sub>2</sub>S nucleation morphology on NiMoP, Ni<sub>2</sub>P, MoP, and C. (h) TEM image of Li<sub>2</sub>S @ Ni<sub>x</sub>Mo<sub>y</sub>P<sub>z</sub> @ C. (i) Cycling performances of anode-free pouch cells at C/20 rate.

Theoretical Modelling and Identification of  $\text{Li}_2\text{S}_2$  to  $\text{Li}_2\text{S}$  Conversion in Sulfur Cathode. The University of Pittsburgh (U-Pitt) team carried out theoretical modeling to improve the conversion of  $\text{Li}_2\text{S}_2$  to  $\text{Li}_2\text{S}$ , an essential process for enhancing the specific capacity of S-cathodes in batteries. They utilized the Vienna Ab-initio Simulation Package (VASP) to simulate the kinetic and thermodynamic properties of this conversion, with the primary focus on overcoming the kinetic barriers involved. The study applied the climbing nudged elastic band method to determine activation barriers, with computations executed using the projector-augmented wave method. The team successfully identified several functional electrocatalysts that displayed promising potential to promote the desired conversion. Previous studies pointed to Cat38 as an optimal catalyst, demonstrating a relatively low kinetic activation barrier of 0.26 eV (Figure XVII.1.45a). This finding instigated further exploration into potential electrocatalysts, resulting in the identification of Cat62 and Cat65 from Group XI and XII (Figure XVII.1.45b and Figure XVII.1.45c), each exhibiting comparable kinetic barrier values of 0.39 eV and 0.35 eV respectively. Group XIII (Figure XVII.1.45d), an amalgamation of primary anionic elements from Groups II, XI, III, and XII, yielded even lower kinetic barriers, averaging around 0.3 eV. The best performing electrocatalyst from this group, Cat72, demonstrated an effective activation barrier of 0.25 eV, matching the performance of the previously identified Cat38 and Cat50. In conclusion, through extensive computational modeling, U-Pitt has identified promising electrocatalysts Cat72, Cat38, and Cat50 to enhance the conversion of  $\text{Li}_2\text{S}_2$  to  $\text{Li}_2\text{S}$ .

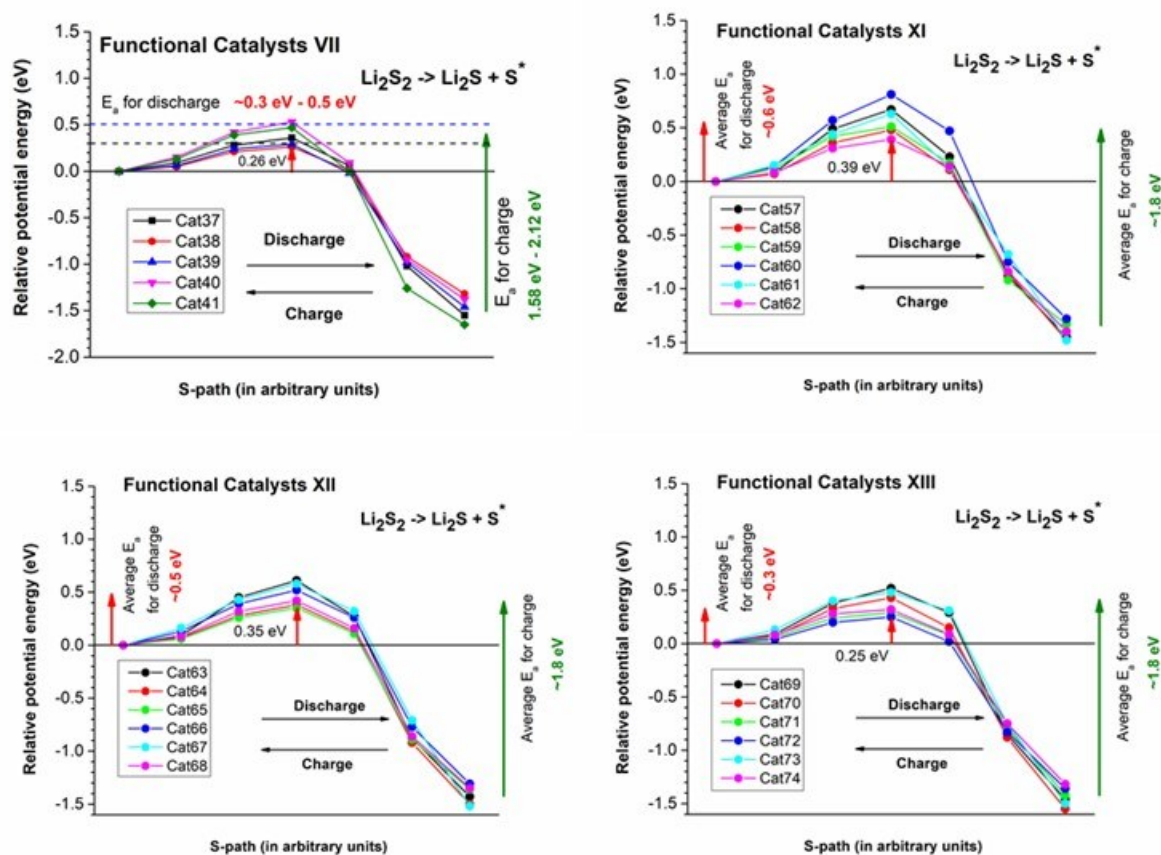


Figure XVII.1.45 (Potential energy profiles for Reaction 2 ( $\text{Li}_2\text{S}_2 \rightarrow \text{Li}_2\text{S} + \text{S}^*$ ) for the various multicomponent functional electrocatalysts systems considered in this research study.

#### Optimal Cathode Thickness: Rate Performance of Thick Cathodes.

The UW team studied the rate performance of the thick NMC cathodes. Increasing the thickness of electrode allows for increased energy density at the cell level due to the reduced weight percentage of inactive separator

and current collector materials. However, the thickness of a cathode film negatively impacts the rate performance of the device. Therefore, both the rate requirements and the energy density of the device need to be considered to optimize the cathode thickness. For a cathode of any thickness, initial increases to the C-rate lead to a gradual drop in discharge capacity due to the solid-state diffusion limit of the NMC particles. In excessively thick cathodes, an increasing discharge current eventually leads to a depletion of lithium ions ( $\text{Li}^+$ ) in the electrolyte close to the current collector. When the C-rate increases above this point,  $\text{Li}^+$  depletion leads to a rapidly increasing overpotential causing a drastic reduction in discharge capacity. This is indicative of a Diffusion-limited Discharge, as shown in Figure XVII.1.46a. Thin cathodes, however, experience IR-limited Discharge before any diffusion limit is reached due to  $\text{Li}^+$  depletion in the electrolyte (Figure XVII.1.46b and c). At lower C-rates it is possible to utilize much thicker cathodes without running into either of these limits. At C/3 for example it is possible to fully utilize a cathode as thick as  $\sim 370\mu\text{m}$ . The thicker cathode can help in realizing higher cell level energy density or allowing the use of a lower cutoff voltage for longer cycle life without sacrificing energy density.

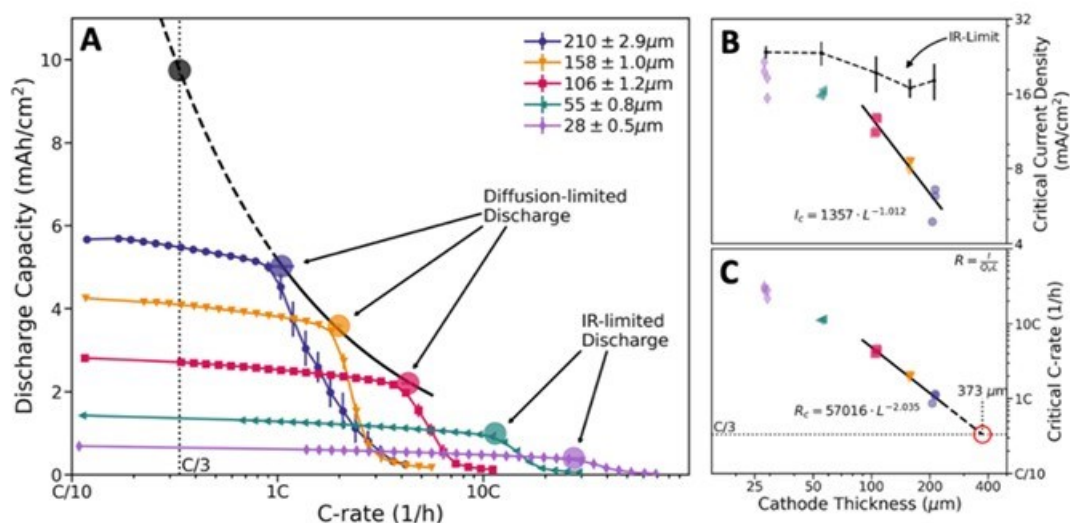
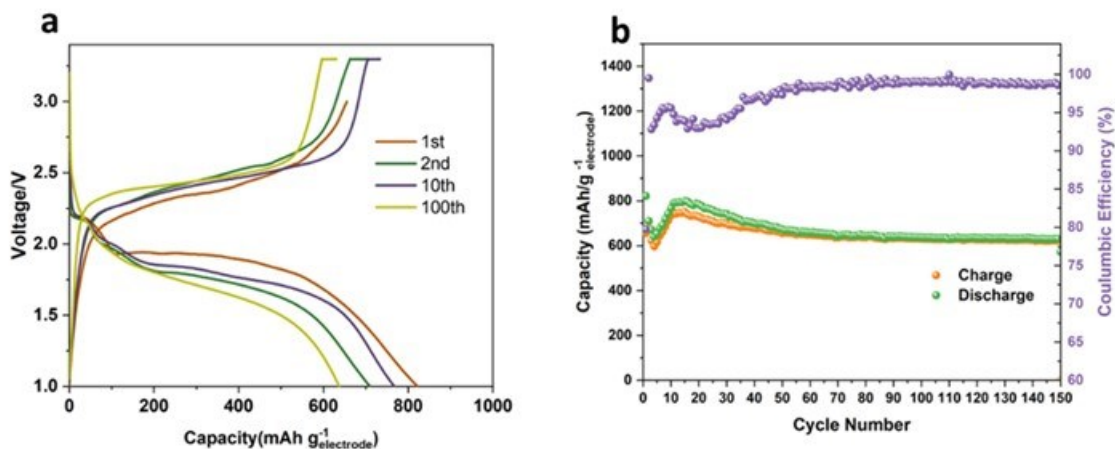


Figure XVII.1.46 Plot of measured discharge capacity for various cathode thicknesses as a function of increasing C-Rate. Plot of the b) critical current density, and c) critical C-rate for each cathode thickness.

#### Improve CS SPAN Cathode Cycling Stability

The UCSD team continued to focus on enhancing the cycling stability of a high-S content SPAN material, often denoted as CS SPAN. This effort is essential to improve the efficacy of CS SPAN batteries. They have successfully synthesized a sulfur-rich SPAN material, termed CS SPAN. Evaluations at the electrode level revealed that the CS SPAN displays a promising capacity exceeding  $650\text{mAh g}^{-1}$  electrode. This value surpasses the typical SPAN capacity of  $550\text{mAh g}^{-1}$  electrode. However, certain limitations were observed with the CS SPAN material, notably their cycling stability and performance at a higher than  $1\text{mg cm}^{-2}$  loading. Addressing these challenges, they focused on improving the cycling stability and areal loading of CS SPAN. This is achieved by integrating a conductive additive composed of CNT and a PAA-based binder. Figure XVII.1.47a and Figure XVII.1.4b illustrate the battery's cycling stability. With over  $3\text{mg cm}^{-2}$  in areal loading, the electrode shows  $>150$  cycles of stable cycling. Impressively, during the initial cycles, the electrode reaches a capacity of close to  $800\text{mAh g}^{-1}$  electrode, a performance that rivals the best sulfur-based electrodes (including those made of elemental sulfur).



**Figure XVII.1.47** CS SPAN with optimized additive. (a) Charge/discharge curves; (b) Cycling performance. Cathode: 90% CS SPAN, 2% super-p, 6% PAA, and 2% CNT. Active material areal loading is  $> 3 \text{ mg cm}^{-2}$ . Electrolyte: 2M LiFSI in DME-BTFE solvent, LDME. Rate C/2 (1C =  $600 \text{ mAh g}^{-1}$ , CCCV to 0.05C at 3.3V)

To discern the working mechanisms of CS SPAN, we employed X-Ray photoelectron spectroscopy (XPS). Figure XVII.1.48a indicates that in the early cycles, the long-chain sulfur ( $> 164 \text{ eV}$ ) transitions into its short-chain counterpart (below  $163 \text{ eV}$ ). This shift suggests that the presence of SPAN facilitates the cleavage of long-chain sulfur, thereby limiting any potential shuttling effect. Additionally, as revealed in Figure XVII.1.48b, depth-profile XPS shows that the proportion of long-chain sulfur to short-chain sulfur remains consistent across various interfaces and depth, such as cathode/electrolyte and cathode/current collector. This consistency signifies that the SPAN-mediated cleavage of long-chain sulfur is uniform throughout the entire cathode.

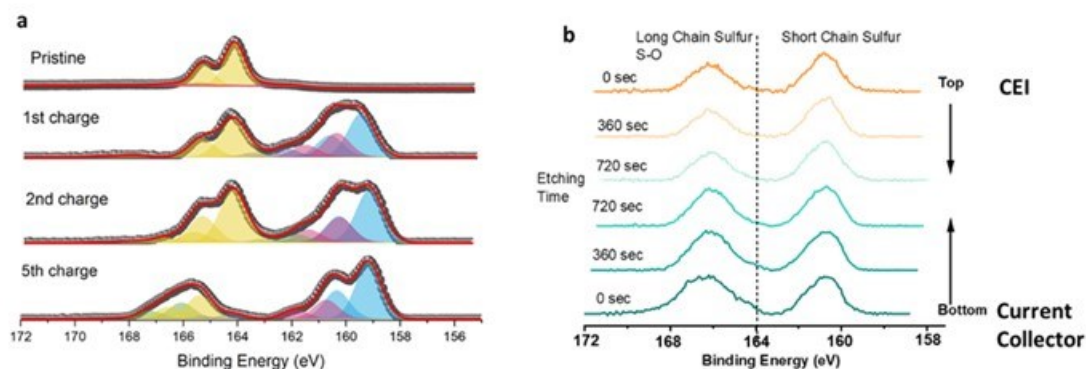


**Figure XVII.1.48** XPS S 2p spectra for CS SPAN cathodes. (a) S 2p spectra of different cycles; (b) the charged CS SPAN depth-profile S 2p spectra, which results collected from the cathode/electrolyte and cathode/current collector interfaces.

### **High-loading Lithium-sulfur Batteries with Solvent-free Dry-electrode Processing**

In this quarter, the University of Texas Austin (UT Austin) team investigated an industrially viable, solvent-free dry-processing method to produce high sulfur loading cathodes, utilizing polytetrafluoroethylene (PTFE) binder fibrillation. The traditional electrode manufacturing process involves mixing active materials and conductive agents with a polymeric binder in solvents, followed by casting the slurry onto the current collector. However, the slurry-processing method has inherent limitations when achieving high sulfur loading cathodes due to several factors, such as (i) binder migration and (ii) capillary stress generated during the



solvent-drying process, which weakens the mechanical integrity and electrochemical performance of the electrode. Unlike the slurry-processing method, the solvent-free dry-processing method utilizes only solid powders and binders to create free-standing electrode films. By eliminating the solvent evaporation step, the dry-processing method avoids the above-mentioned issues and allows for the production of extremely thick electrodes without cracking. Figure XVII.1.49a demonstrates the dry electrode fabrication procedure. A mixture of sulfur/ketjen black composite (S/KB), multi-wall carbon nanotubes (MWCNT), Super P, and PTFE powders were low-energy ball-milled for 8 h in a mass ratio of 80 : 9.5 : 9.5 : 1. The powder mixture was processed into electrode sheets by shearing forces under heated conditions at 80 °C, and then laminated onto an aluminum current collector to be used as the cathode. The surface of the dry-processed electrodes and slurry-processed electrodes with high sulfur loadings of 8 mg cm<sup>-2</sup> are compared by scanning electron microscopy (SEM) in Figure XVII.1.49b and Figure XVII.1.49c. Figure XVII.1.49b reveals that the dry-processed electrode maintains a uniform and flat surface across the entire cathode. The fibrillated PTFE exhibits effective adhesion to the S/KB composite and carbon, ensuring a well-integrated architecture without any major defects or cracks. Contrarily, the slurry-processed electrode displays pronounced irregularities and a convoluted surface topology, as shown in Figure XVII.1.49c. It seems that the considerable capillary stress generated during solvent evaporation leads to the formation of severe cracks on the surface, resulting in such non-homogeneous electrodes. Some portions of the active materials and carbon are loosely attached, making them prone to detachment even with slight agitation. Cross-sectional SEM images are also compared between the dry-processed electrode and the slurry-processed electrode in Figure XVII.1.49d and Figure XVII.1.49e. Figure XVII.1.49d shows an impressive consistent thickness (~ 97 μm) of the dry-processed electrode, whereas the slurry-processed electrode displays a considerable inconsistency in electrode thickness, as seen in Figure XVII.1.49e. The SEM images reveal that the dry-processed electrodes form a much more uniform and denser electrode compared to the slurry-processed electrode.

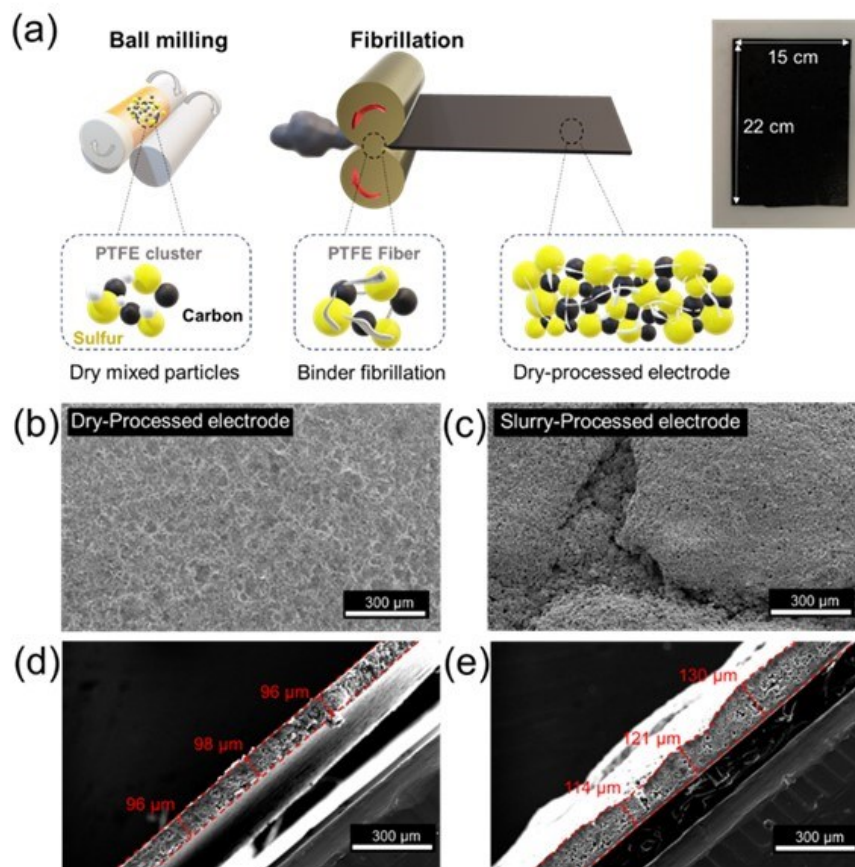


**Figure XVII.1.49** (a) Schematic of dry electrode fabrication procedure. Surface SEM images of the (b) dry-processed electrode and (c) slurry-processed electrode. Cross-sectional SEM images of (d) dry-processed electrode and (e) slurry-processed electrode. The sulfur loading is  $8 \text{ mg cm}^{-2}$ .

Figure XVII.1.50a shows the cycling performances of the high sulfur loading slurry-processed and dry-processed electrodes. The slurry-processed electrodes with sulfur loadings of  $7$  and  $8 \text{ mg cm}^{-2}$  exhibit rapid capacity decay, resulting in poor cycling stability with only 37 % and 7 % capacity retention, respectively, after 80 cycles. In sharp contrast, the dry-processed electrode with a high sulfur loading of  $8 \text{ mg cm}^{-2}$  shows a remarkably different cycling trend. Despite its relatively lower initial capacity ( $651 \text{ mA h g}^{-1}$ ) compared to the slurry-processed electrodes ( $1,098 \text{ mA h g}^{-1}$ ), the cell demonstrates a stable cycling performance over 80 cycles with 79 % overall capacity retention. To investigate the superior cycling stability of the dry-processed electrode compared to the slurry-processed electrode, the cycled cathode surfaces were imaged with SEM. Figure XVII.1.50b shows that the dry-processed electrode maintains good mechanical integrity without major cracks, whereas the slurry-processed electrode exhibits pronounced cracks and deep crevices (Figure XVII.1.50c).

Based on the cell cycling data, two questions can be raised: (1) Why does the dry-processed electrode exhibit a lower initial capacity compared to the slurry-processed electrode? (2) Could the disparity in cycling stability observed between the dry-processed and slurry-processed electrodes be primarily attributed to electrode fracturing? The elevated initial capacity of the slurry-processed electrode implies the production of an increased quantity of polysulfides, potentially accelerating the degradation of both the cathode and the anode. Therefore, verification is needed to determine whether the extent of electrode cracking, based on different electrode processing methods, is indeed the primary cause for the varying capacity decay trends. As widely known, sulfur cathodes need to maintain a certain level of porosity to provide space for filling them with electrolyte, establishing interconnected Li-ion transfer pathways between particles, and aiding the redox

reaction of sulfur. Furthermore, the reaction mechanism of Li-S batteries involves the dissolution and deposition of polysulfides, which heavily depends on the degree of electrolyte penetration into the electrode to wet the active material and carbon. When electrode porosity decreases significantly, the electrolyte might not reach the active material properly, causing insufficient Li-ion supply and poor polysulfide dissolution and nucleation. As previously mentioned, dry-processed electrodes exhibit a dense and less porous structure compared to slurry-processed electrodes. The limited active surface area could hinder the continued reaction of polysulfides in the electrolyte, resulting in a reduced overall capacity of the dry-processed electrode. To investigate whether electrode porosity is the main factor influencing the initial capacity, the cell performance was evaluated under the same electrode volume condition by equalizing the overall thickness of the dry-processed and slurry-processed electrodes to  $97\ \mu\text{m}$  at a sulfur loading of  $8\ \text{mg cm}^{-2}$ . The dry-processed electrodes were used as is, while the slurry-processed electrodes underwent a calendaring process to reduce their thickness. To assess the calendaring effect on the electrode, the resistances of the cells were measured with electrochemical impedance spectroscopy (EIS), as shown in Figure XVII.1.50d. The calendaring process of slurry-processed electrode appears to enhance electrode conductivity by improving inter-particle contact and ensuring optimal electronic contact between the active material and the current collector. For dry-processed electrode, since the electrode is initially constructed from stacked powdered materials without solvents, significantly fewer void spaces lead to the lowest cell charge-transfer resistance. Furthermore, the dry-processed electrode employed a mere 1 wt. % of PTFE binder content, consequently increasing the carbon content within the electrode and yielding superior conductivity compared to the slurry-processed electrodes. The performance of the cells is compared between the slurry-processed and dry-processed electrodes with the same electrode thickness in Figure XVII.1.50e. The initial capacities became similar after matching the thickness of both electrodes ( $711\ \text{mA h g}^{-1}$  for the dry-processed electrode and  $693\ \text{mA h g}^{-1}$  for the slurry-processed & calendared electrode). The convergence of the initial capacities between the two electrodes, achieved by calendaring the slurry-processed electrode to reduce overall electrode porosity under the same electrode thickness condition, suggests that electrode porosity plays a dominant role in influencing the cell initial capacity. Thus, the lower initial capacity of the dry-processed electrode appears to stem from the self-calendaring effect during the PTFE fibrillation process, which leads to a less porous electrode architecture. The cell performance data presented in Figure XVII.1.50e also provides insights into the second question raised above: is the difference in cycling stability between the dry-processed electrode and the slurry-processed electrode related to electrode cracking? The similar initial capacities of both electrodes suggest comparable amounts of active polysulfide generation in the Li-S system. While the dry-processed electrode exhibits stable capacity retention over 50 cycles, the slurry-processed & calendared electrodes demonstrate rapid capacity decay starting from the 10th cycle. Considering that all cell components are the same and the amount of active polysulfide generated is similar, the only distinguishable factor is the different types of electrodes applied. Thus, such a difference in cycling performance can be attributed to the different architecture of the cathodes. Under high sulfur loading conditions, the inadequate mechanical stability of the slurry-processed electrode results in cathode pulverization, leading to a loss of electronic contact in the active material, whereas the dry-processed electrode retains its contact with a well-integrated electrode architecture. Based on the cell cycling performance at the same electrode thickness, it seems that the occurrence of electrode cracking, depending on the processing method, has a direct impact on cell cyclability.

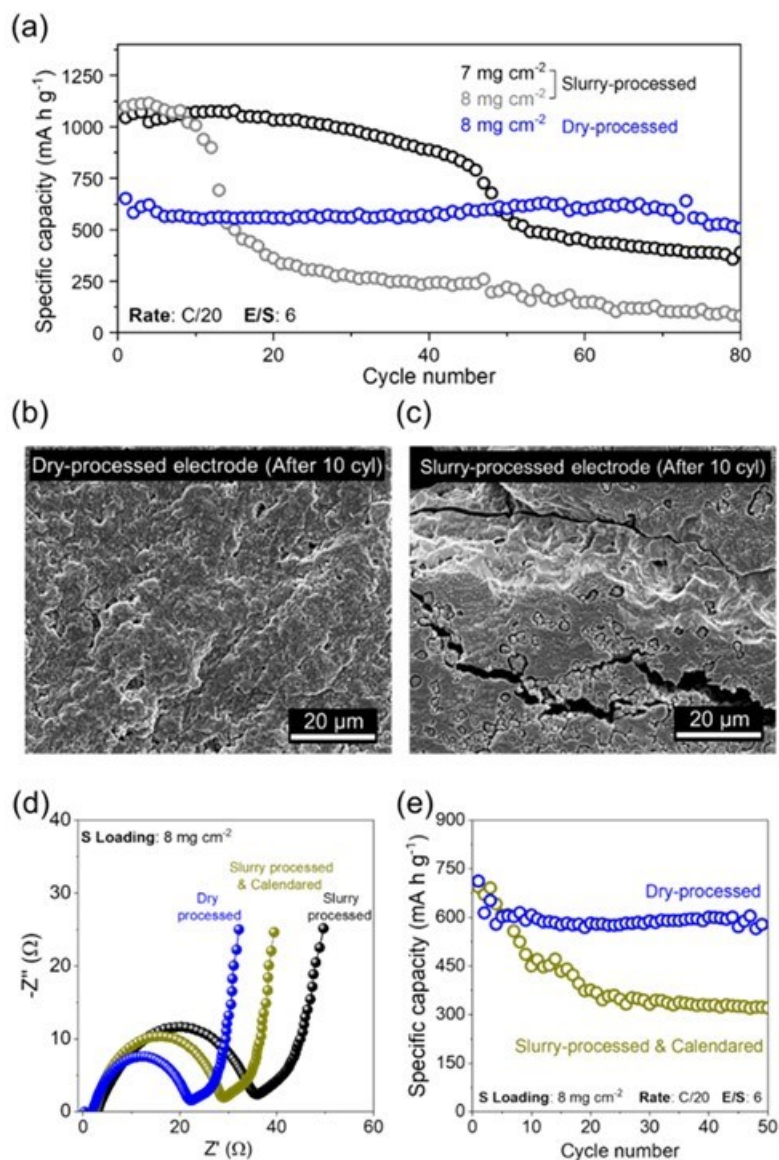


Figure XVII.1.50 (a) Cycling performances of slurry-processed and dry-processed electrodes. SEM images of (b) dry-processed and (c) slurry-processed electrodes after 10 cycles. The sulfur loading is  $8 \text{ mg cm}^{-2}$ . (d) Nyquist plots of dry-processed, slurry-processed & calendared, and slurry-processed electrodes. (e) Cycling performances of dry-processed and slurry-processed & calendared electrodes.

#### Theoretical Modeling and Identification of Functional Electrocatalysts Promoting $\text{Li}_2\text{S}_2$ to $\text{Li}_2\text{S}$ Conversion in Sulfur Cathode

The University of Pittsburgh (U-Pitt) team is focused on computational studies. The team utilized theoretical modeling to improve the conversion of  $\text{Li}_2\text{S}_2$  to  $\text{Li}_2\text{S}$ , an essential process for enhancing the specific capacity of experimentally designed S-cathodes in Li-S batteries. They utilized the Vienna Ab-initio Simulation Package (VASP) to simulate the kinetic and thermodynamic properties of this conversion reaction, with the primary focus directed at overcoming the kinetic barriers involved. The study was continued by applying the climbing nudged elastic band method to determine activation barriers, with computations executed using the projector-augmented wave method. The team successfully identified several functional electrocatalysts that displayed promising potential to promote the desired conversion reaction.

Previous results indicated that Cat38 is an optimal functional electrocatalyst, demonstrating a relatively low kinetic activation barrier of 0.26 eV (Figure XVII.1.51a). This finding instigated further exploration into identifying other potential functional electrocatalysts, resulting in the identification of Cat72 from Group XIII (Figure XVII.1.51b), exhibiting even lower kinetic barrier values of 0.25 eV. Group XIV and XV (Figure XVII.1.51c and Figure XVII.1.51d), which represent an amalgamation of primary anionic elements from Groups II, XI, III, and XII along with binary metals from Groups VII and XIII, yielded even lower kinetic barriers. The best performing functional electrocatalyst from this group, Cat77 and Cat82 demonstrated an effective kinetic activation barriers of 0.23eV and 0.25 eV, respectively, averaging around 0.28eV representing an improvement over the performance of the previously identified Cat38 with a low kinetic activation barrier of 0.26eV from the lower group of functional electrocatalyst systems shown in Figure XVII.1.51a and Cat72 shown in Figure XVII.1.51b with an activation barrier of 0.25eV. It can also be noted that Cat38 is the lowest from the group of functional electrocatalysts showing an average kinetic barrier of  $\sim 0.3$ eV while the other functional electrocatalysts in the same group have an average kinetic barrier of  $\sim 0.5$ eV. On the other hand, Cat72 is the lowest from the group of functional electrocatalysts shown in Figure XVII.1.51b also exhibiting an average kinetic barrier of  $\sim 0.3$ eV. In conclusion, through extensive computational modeling, the U-Pitt team has identified several promising functional electrocatalysts, namely, Cat38, Cat72, Cat77 and Cat82 that enhance the conversion of  $\text{Li}_2\text{S}_2$  to  $\text{Li}_2\text{S}$ . Despite these achievements, ongoing research is aimed at discovering improved functional electrocatalysts that will exhibit even lower kinetic barriers to improve the S-cathode specific capacity.

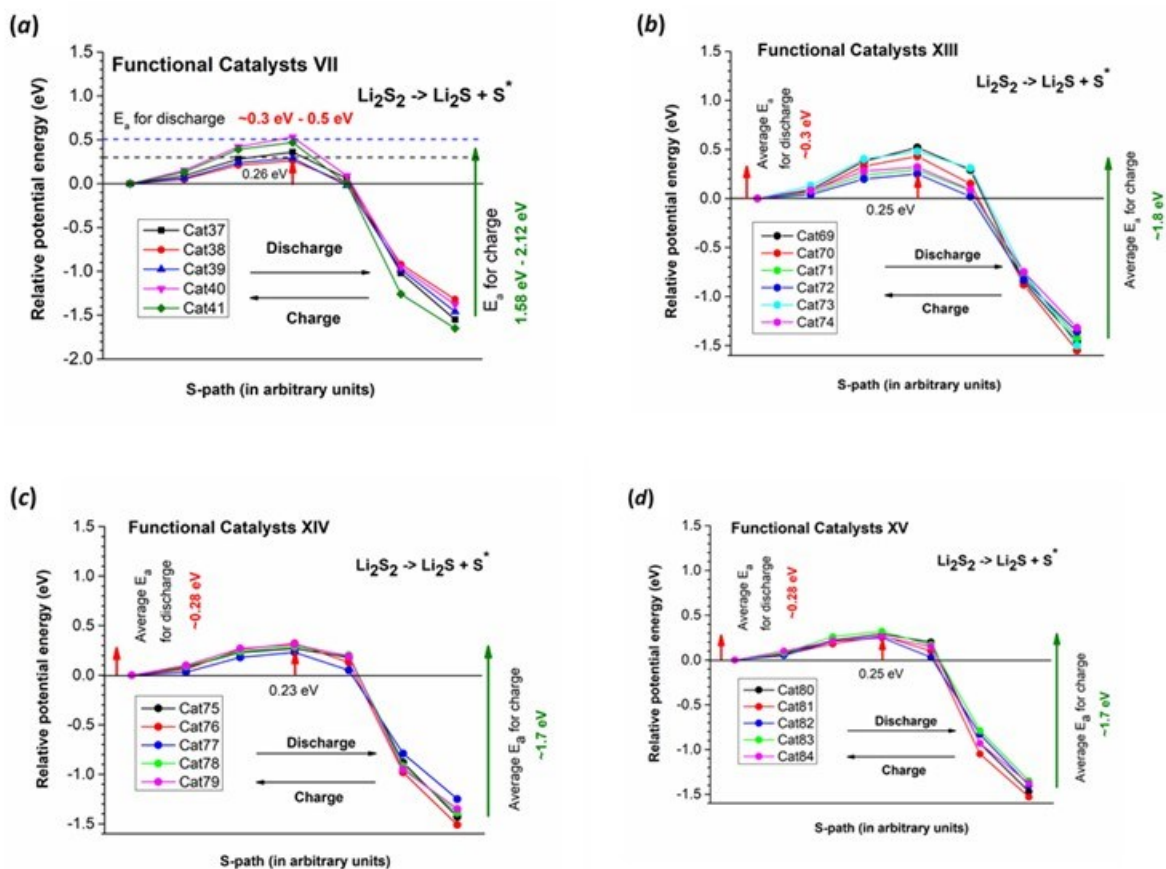
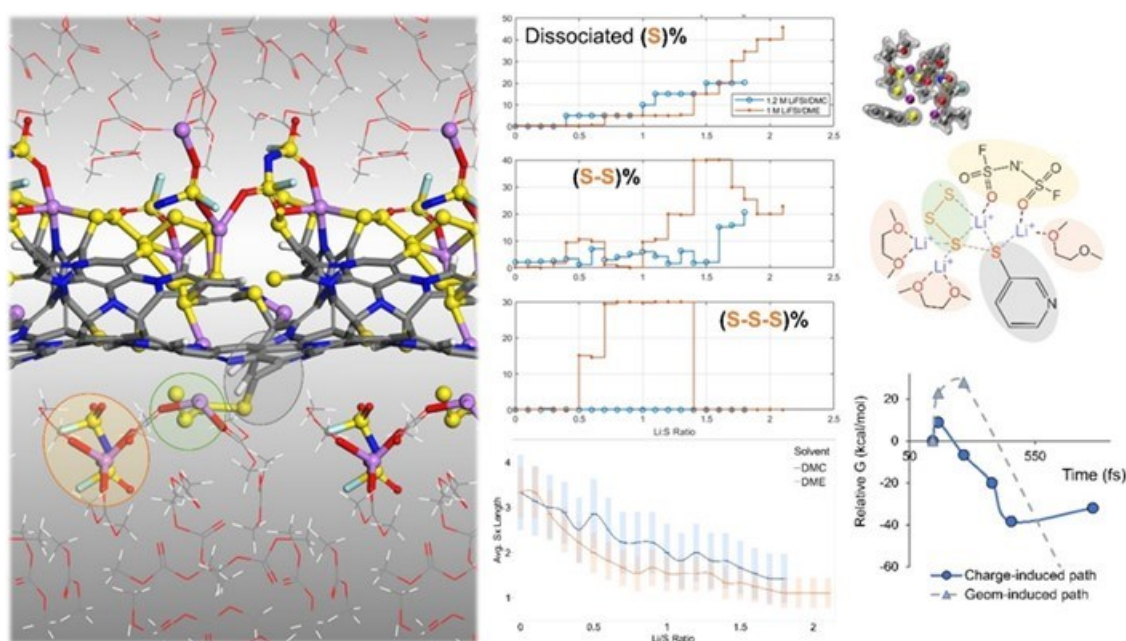


Figure XVII.1.51 Potential energy profiles of  $\text{Li}_2\text{S}_2 \rightarrow \text{Li}_2\text{S} + \text{S}^*$  reaction for the various multicompound functional electrocatalysts systems considered in this research study

### Computational Analysis of the Effects of Electrolyte on the Lithiation of SPAN

The Texas A&M University (TAMU) team employed ab initio molecular dynamics simulations to understand the electrolyte's role in the interfacial lithiation of SPAN material. We compared the solvation effects of DMC and DME electrolyte systems. DME poses strong solvation and stabilization to polysulfide, which results in a higher likelihood for SPAN to experience S-S cleavage and yield disulfides and trisulfides to enter the electrolyte phase. On the other hand, DMC's weaker solvation effects create a favorable environment for generating short PS fragments, and that is reflected in the average PS chain length evolution as well. In addition, we also found that the electrolyte salt, LiFSI, is not simply the charge carrier and source materials of SEI. It also mediates the electrochemistry of SPAN reduction by forming semi-covalent Li-O bonds, and the Li is also electrostatically bonded with sulfides which are leaving the SPAN structure (Figure XVII.1.52). As the free energy profile shows, such a LiFSI-mediated S-S cleavage reaction is driven by electron transfer with an energy barrier below 3 kcal/mol.



**Figure XVII.1.52** Left: Snapshot from AIMD simulations illustrating interfacial effects of SPAN with electrolyte molecules. Center: Graphs show percent of sulfur fragments dissolved in the electrolyte phase during discharge for DMC (blue) and DME (orange) solutions. Right: Electron density map depict molecular interactions among SPAN, LiFSI and solvent molecules. Dotted lines indicate bond cleavage. At the bottom, the free energy evolution is shown during two simulations: one where charge transport drives reactivity (blue solid line), and another where the system reactivity follows molecular restructuring (dashed line). Color code for atoms: Li purple; O: red; S: yellow; N: blue; C: gray; H: white; F light blue

### Comparison of Effect of Current Collector Architecture and Electrolyte Chemistry in Lithium Metal Cells.

The University of Washington (UW) team continued investigating 3D-structured current collectors for Li-metal anodes in Li-metal cells, specifically considering whether current collector structure or electrolyte chemistry dominates effects on CE. Half cells of lithium versus either copper foil or copper foam (MTI Corp, 180  $\mu\text{m}$ ) were assembled with four different electrolytes: a localized high concentration electrolyte (labeled as LHCE) consisting of a 1:1.2:3 molar ratio of lithium bis(fluorosulfonyl)imide (LiFSI), 1,2-dimethoxyethane, and 1,1,2,2-tetrafluoroethyl 2,2,3,3-tetrafluoropropyl ether; an ether-based electrolyte (labeled as LiTFSI) of 1M lithium bis(trifluoromethanesulfonyl)imide in a 1:1 ratio of 1,2-dimethoxyethane and 1,3-dioxolane; an electrolyte of 1.2M LiFSI in F4DEE (in the family of fluorinated-1,2-diethoxyethane molecules) (labeled as F4); and an electrolyte of 1.2M LiFSI in F5DEE (in the family of fluorinated-1,2-diethoxyethane molecules)

(labeled as F5). Cells were cycled using a modified Aurbach protocol consisting of eight formation cycles of plating at  $0.4 \text{ mA/cm}^2$  up to  $4 \text{ mAh/cm}^2$  and stripping at  $0.4 \text{ mA/cm}^2$  to  $1\text{V}$ , plating of a reservoir of  $4 \text{ mAh/cm}^2$  of lithium at  $0.4 \text{ mA/cm}^2$ , followed by 150 shallow plating/stripping cycles at  $0.4 \text{ mA/cm}^2$  up to  $0.5 \text{ mAh/cm}^2$ , with a final strip to  $1\text{V}$  at  $0.4 \text{ mA/cm}^2$ . CE was determined from the capacity of the initial reservoir, the number and capacity of the shallow cycles, and the capacity of the final strip.

Figure XVII.1.53 compares the average CE of cells with each combination of current collector and electrolyte. No current collector architecture consistently shows improved CE across all electrolytes, nor does any electrolyte show markedly greater CE for both current collectors. From these data, the team theorizes that electrolyte has a greater impact on CE than current collector architecture.

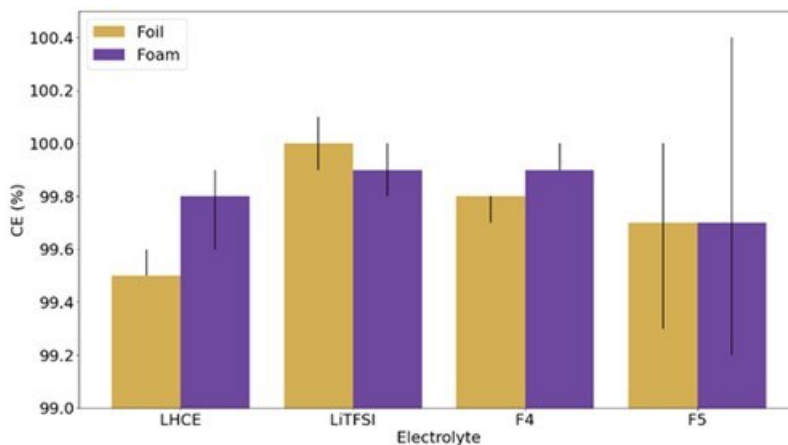


**Figure XVII.1.53 Comparison of CE values of lithium half cells with one of four electrolyte (LHCE, LiTFSI, F4, or F5) and one of two current collector architectures (foil in fold or foam in purple). Bars indicate the average CE of 3 cells tested for each condition while the error bars mark the extreme values of the cells measured. No trend is observed in CE for either structure across electrolyte.**

Electrochemical impedance spectroscopy (EIS) was performed to examine what electrical and electrochemical properties change during cycling for the different substrates and electrolytes. Figure XVII.1.54 displays the EIS spectra for sample cells of either a copper foil or copper foam substrate with either the LHCE or LiTFSI electrolytes at four different stages of cycling. The EIS spectrum was taken after the eight initial formation cycles and plating of lithium reservoir (8FC+Res), and then after 20 shallow plating and stripping cycles (20SC), 100 shallow cycles (100SC), and 150 shallow cycles (150SC). Generally, overall cell resistance (the real resistance at which the spectra first appear) and resistance and capacitance of the SEI layer (the first semi-circle seen) changed to a greater degree between electrolytes than between substrates with the same electrolyte, though not to the order of a full degree of magnitude. Additionally, all cells apart from the foil substrate with LHCE electrolyte displayed only two distinct frequency regimes at which processes occurred, high frequency relating to SEI resistance and low frequency relating to diffusion. The foil and LHCE electrolyte cell registered a charge-transfer resistance in the mid-frequency regime in later cycling, namely at 100 shallow cycles and beyond. Equivalent circuit modeling and analysis is on-going to quantify these differences and theorize their effect on CE.

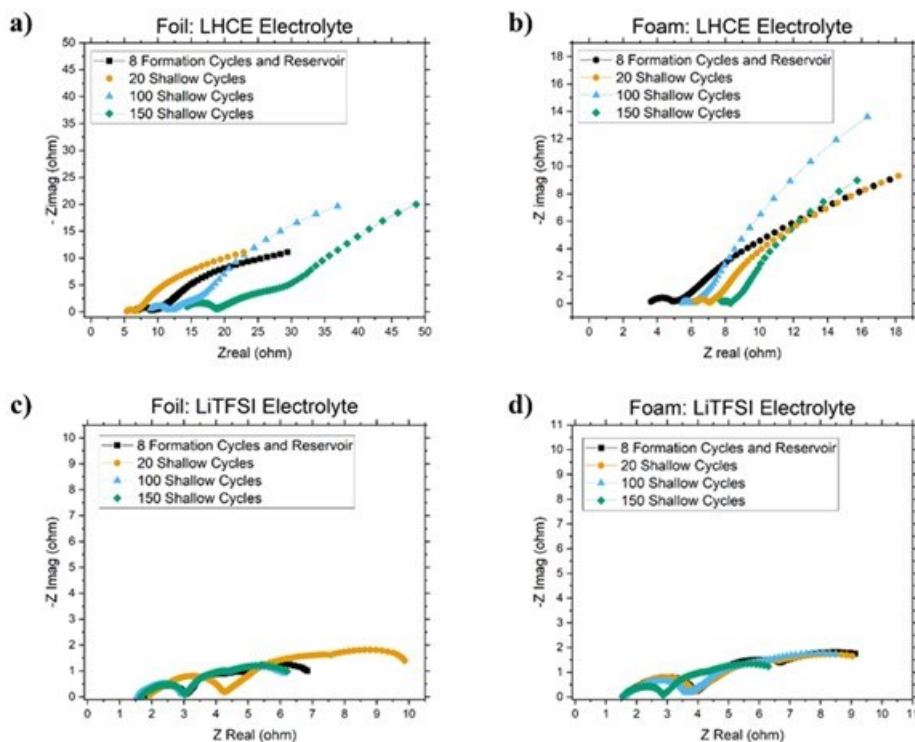


Figure XVII.1.54 Electrochemical impedance spectra collected at four points of the cycling protocol for cells with a) copper foil substrate and LHCE electrolyte; b) copper foam substrate and LHCE electrolyte; c) copper foil substrate and LiTFSI electrolyte; and d) copper foam substrate and LiTFSI electrolyte.

### 3. Keystone project 3: Cell fabrication, testing and diagnosis

The goal of Keystone Project 3 is to focus on pouch cell design, integration, fabrication, and testing using new materials and cell components provided across different teams in the consortium. The project team will focus on addressing the science and engineering challenges at pouch cell levels, while the other two keystone projects will support this effort by scaling up new materials and identifying feasible solutions for electrode coating using nano or nanostructure materials at scales that can be adopted for fabricating practical cells.

Optimization of Li-S batteries. Monitoring specific capacity trends by porosity modulation. The GM team conducted a series of experiments regarding electrode processing and cell assembly to further improve Li-S cells. Incongruencies in cathode testing data across GM team and their collaborators, the need to pinpoint specific ways in which cathode performance can be improved, and oppositely, how performance could be compromised has been demonstrated. GM checked minor porosity reduction from the fresh uncalendered samples. The sulfur electrodes with the porosities varying from 65%, 64%, 62%, to 60% were further evaluated in coin cell format. As the voltage profiles shown in

Figure XVII.1.55 of selected cycles, all calendered samples show higher specific capacity than the uncalendered sample. The main discharge plateau of all samples keeps at similar voltage, which suggests no significant differences in overpotential. This observation is also consistent with their phase I study, in which appropriate compression of the electrode would help with the conductivity. For the initial charging process, the samples with 62% and 60% porosity even showed fully overlapped voltage profile. In the 15th cycle, the capacity difference among all samples becomes more obvious. The samples with the porosities of 62 and 60% showed better capacity retention than the uncalendered sample. This observation suggested reduction of electrode porosity, to a certain level, would be helpful for the cyclability. This behavior may be related to



several factors including carbon framework and/or active material integrity, electronic conductivity, polysulfide confinement, etc. Further characterization and testing are underway to reveal more details.

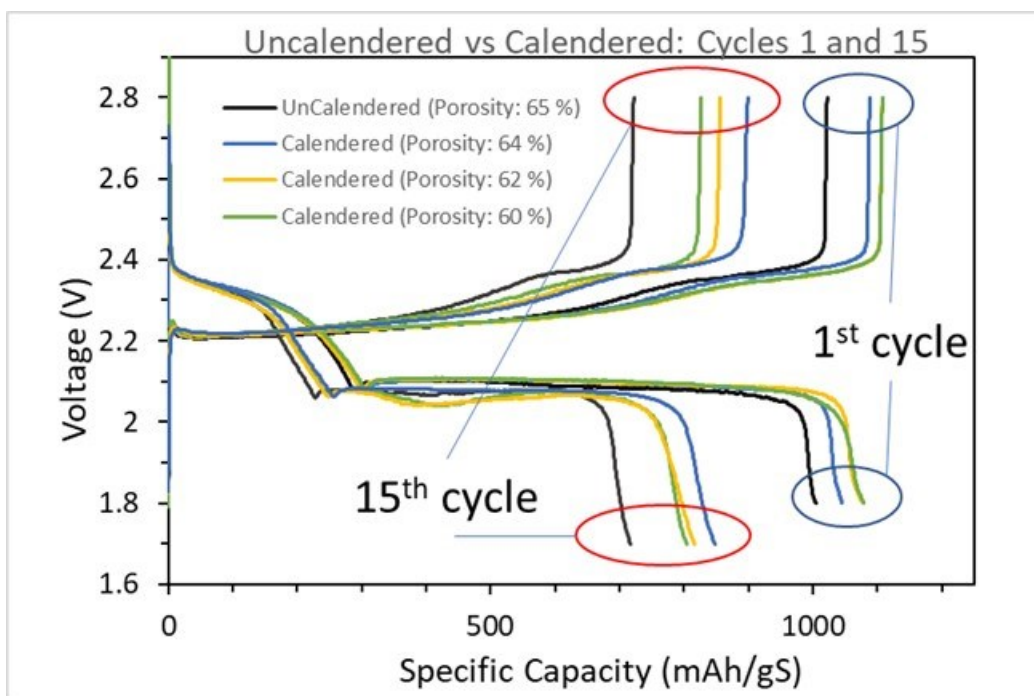


Figure XVII.1.55 Electrochemical performance of a single cathode batch (loading: 4.05 mgS/cm<sup>2</sup>) calendered from 65% to 64, 62, and 60 %, with 8µL/mg electrolyte amount control. 1st cycle is cycled at 0.05 C rate, rest of the cycles, cycled at 0.1 C

#### **Effects of low internal pressure vs. high internal pressure for coin cell assembly.**

Besides the electrode porosity, GM team also checked the influence of the internal pressure, which was induced by different spacer thickness in the coin cell. The pressure influence on lithium metal batteries was already well studied by many research institutes. For Li-S chemistry, some B500 program teams (for example, INL team) have also initiated some studies using pouch cells. In this study, the GM team picked 2 spacer thickness selections to make the coin cells to check the difference of the performance caused by internal pressure. The “high pressure” cell in Figure XVII.1.56 uses a 1.0 mm spacer with 600 µm lithium chip, which is standard in most current and past cell constructions. In comparison, 0.5 mm spacer was used to present low pressure condition with the same lithium anode. The voltage profile of the first 3 cycles of both configurations were shown in Figure XVII.1.56. It is very clear that the “low pressure” cell only delivered around 900 mAh/gS specific capacity. The main discharge plateau was much lower than that of “high pressure” case, which suggests much larger resistance. In the 2<sup>nd</sup> cycle, the “high pressure” cell showed normal voltage profile, while the “low pressure” cell showed distorted voltage profile with a “valley” in the main discharge plateau, which is similar to the behavior of the cell with deficient electrolyte. The specific capacity quickly decayed to lower than 400 mAh/gS for the “low pressure” cell in the 3<sup>rd</sup> cycle, while the specific capacity of the “high pressure” cell still maintained above 800 mAh/gS.

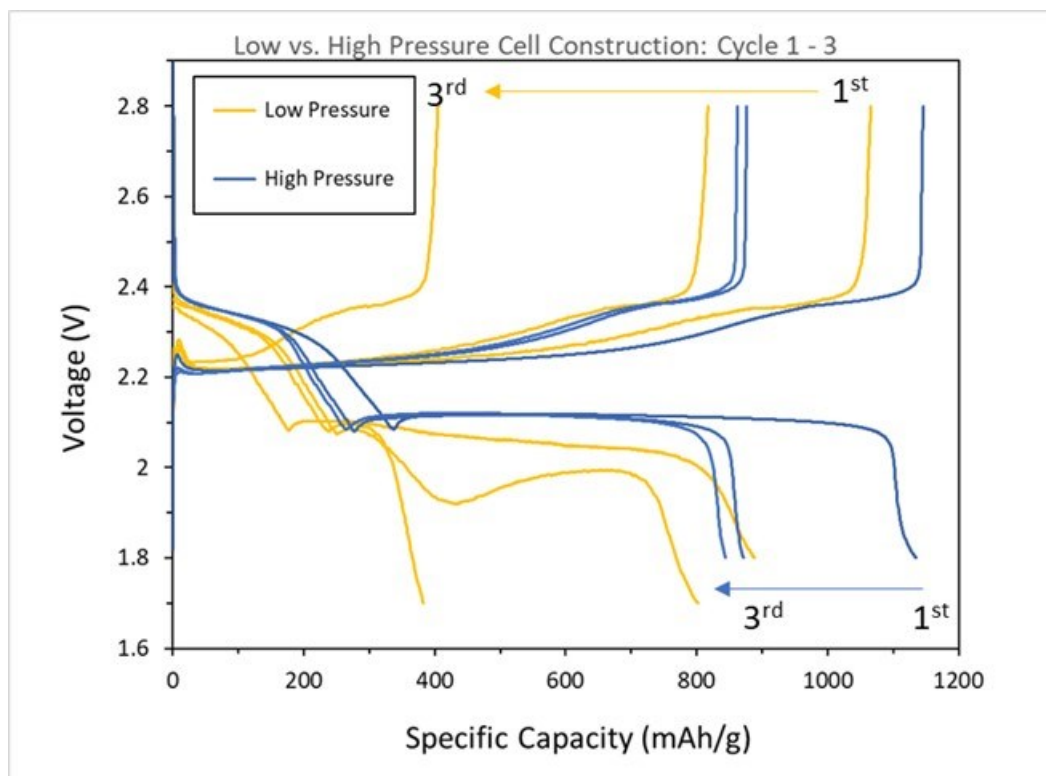
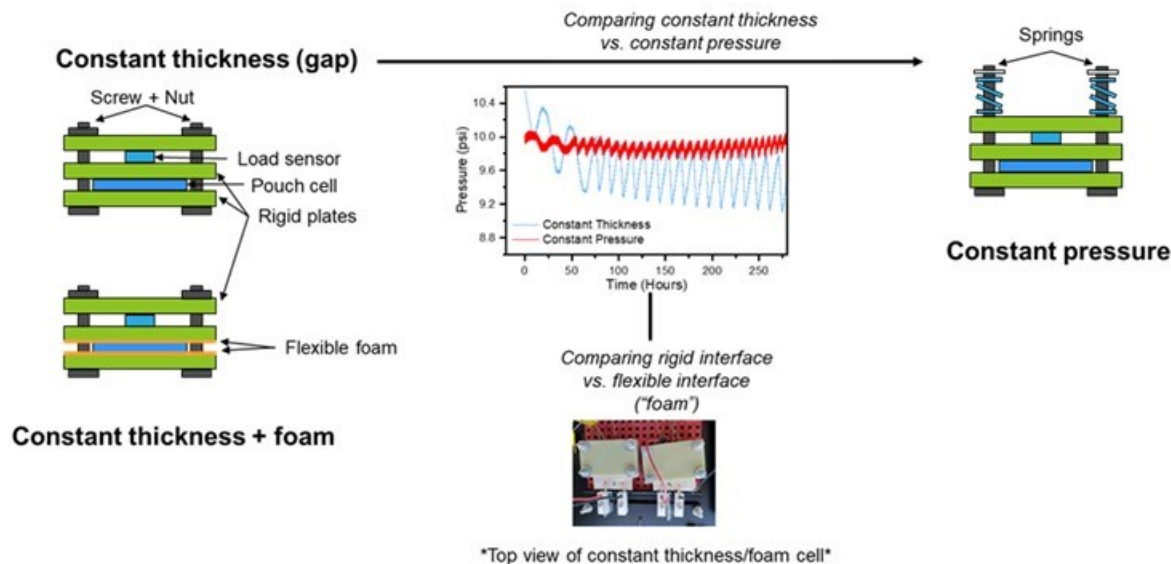


Figure XVII.1.56 Electrochemical performance of coin cell assembly with low and high pressure (loading: 3.82 mgS/cm<sup>2</sup>). Low and high pressure cells differ only by the use of a 0.5 mm spacer and a 1.0 mm spacer, respectively

#### Operation optimization of Li-NMC811 single layer pouch cells (SLPCs).

The INL team focuses on the operation optimization of Li-NMC811 SLPCs to improve their performances. As was reported by INL and other team members in Battery500, applying an appropriately high external pressure on the Li-metal pouch cells can benefit the cycling performances by suppressing dendrite growth at the anode side. In most cases, the pouch cells were sandwiched between two rigid plates and the gap distance between two rigid plates kept constant during cycling. Such a pressure fixture design is called “constant thickness” design. In order to further improve the cell performance, INL team proposed another two pressure fixture designs: “constant pressure” design and “constant thickness + foam” design. In the former design, springs were added on the top of one of rigid plates to maintain almost constant pressure during cell cycling. In the latter design, soft foams were added at both sides of the pouch cells. The three kinds of pressure fixture designs are schematically shown in Figure XVII.1.57.



**Figure XVII.1.57** Three pressure fixture designs used in pouch cells to apply external pressures. The electrochemical performances of Li-NMC811 SLPCs were studied based on the three pressure fixture designs. In Li-NMC811 SLPCs, 50  $\mu\text{m}$ -thickness Li metal foil, NMC811 electrode with the areal capacity of 4.2 mAh/cm<sup>2</sup>, LiFSI-DME-TTE (molar ratio: 1:1.2:3) were used as the anode, cathode, and electrolyte, respectively.

These cells were all cycled at  $C/10$  during charge and  $C/3$  during discharge under the lean-electrolyte conditions (3.0 Ah/g electrolyte added). For all the three fixture designs, the initial external pressures were set to be 10 psi. It can be seen from Figure XVII.1.58a, the “constant thickness + foam” design can help with longer lifespan. The addition of foams was expected to realize more uniform pressure distribution across pouch cells. The “constant pressure” design enables the cells to deliver the lowest initial specific capacity and shortest lifespan. The overpotentials of charge/discharge based on the three pressure fixture designs were calculated and displayed in Figure XVII.1.58b. We can see that the cell with the “constant pressure” design shows much faster growing charge/discharge overpotentials over cycling than the other two cells, suggesting larger cell resistances and shorter lifetime. The growth of charge/discharge overpotential for the cell with the “constant thickness + foam” design is slowest, implying longer lifetime. These results agree well with electrochemical performances of the cells shown in Figure XVII.1.58a. The characterizations of SLPCs based on the three pressure fixture designs are underway and the underlying mechanisms are being investigated and will be reported later.

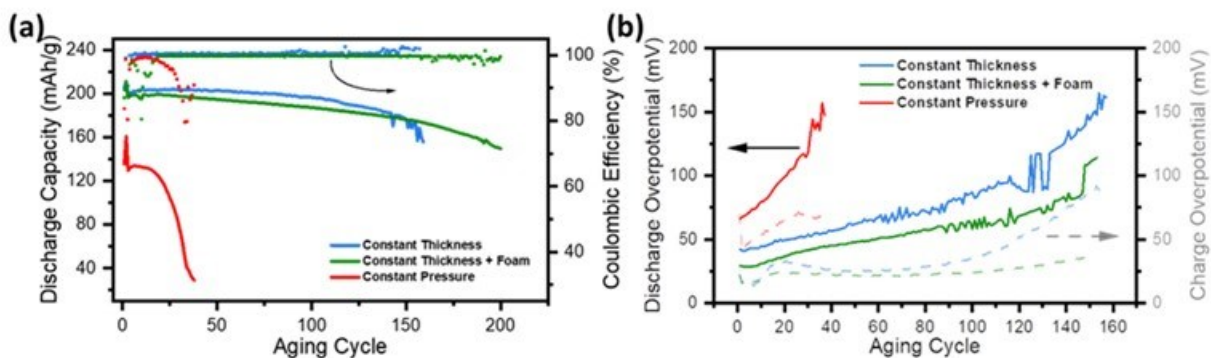


Figure XVII.1.58 The cycling performances (a) and charge/discharge overpotentials over cycling (b) of the Li-NMC811 SLPCs based on three pressure fixture designs.

### Safety properties of Li Metal Batteries.

Li metal anodes are essential for developing next-generation high-energy-density batteries. Numerous concerns on the potential safety hazards of the Li metal have been brought up before its massive application in commercialized battery packs. However, few investigations have been performed to systematically evaluate the reactivity of Li metal anode in full cell level. Here, Meng's group of the UCSD team reports their results aimed to quantitatively investigate the Li metal reactivity and compared that with Lithiated graphite (Li-Gr) and lithiated silicon (Li-Si) samples. Three anodes including Gr, Si and bare Cu (no excess Li) were charged with the controlled lithiation/plating amount of 3 mAh/cm<sup>2</sup> for Gr or 5 mAh/cm<sup>2</sup> for Si and bare Cu in the half cell. Instead of 5 mAh/cm<sup>2</sup>, 3 mAh/cm<sup>2</sup> capacity is chosen for the Gr because it is the most widely available capacity among commercialized Li-ion cells. The prepared anodes were sealed in a DSC pan with controlled amount of electrolyte (electrolyte/capacity ratio ~ 3mg/mAh), and then transferred into the DSC-FTIR station for thermal analysis. All DSC tests were done at least twice to make sure that the obtained results are reproducible. Figure XVII.1.59 shows the DSC curves of Li-Gr, Li-Si, plated-Li in the carbonate-based electrolyte (Carbonate, 1.2 M Lithium hexafluorophosphate (LiPF<sub>6</sub>) dissolved in ethylene carbonate (EC): diethyl carbonate (DEC) (1:1 by weight) with 10% fluoroethylene carbonate (FEC)). In addition, plated-Li in Localized High Concentration Electrolyte (LHCE, Lithium bis(fluorosulfonyl)imide (LiFSI), 1,2-dimethoxyethane (DME) and 1,1,2,2-Tetrafluoroethyl-2,2,3,3-Tetrafluoropropyl Ether (TTE) with molar ratio 1:1.2:3) was also prepared. In both Li-Gr and Li-Si, most heat-absorbing peaks are associated with the evaporation of electrolyte solvents such as DEC and EC (Figure XVII.1.59a and Figure XVII.1.59b). No significant heat-releasing peaks exist in the Li-Gr and Li-Si samples when heated up to 400°C. However, when the plated-Li in the Carbonate electrolyte was heated during the DSC measurement, two heat-releasing peaks overlap with the evaporations of DEC and EC solvents, respectively (Figure XVII.1.59c). When Li plated cell was heated at around 180°C, a sharp heat-absorbing peak appeared. The exothermic reactions might be caused by the melted Li quickly reacting with the remaining EC solvent and LiPF<sub>6</sub> salt. Figure XVII.1.59d shows the DSC curves of the plated-Li in LHCE electrolyte. The DME and TTE solvents are mostly evaporated before 100°C because of the low evaporation points, rather than reacting with the Li. A sharp Li melting peak is also shown around 180°C in Figure XVII.1.59d, which indicates that the Li was mostly melted rather than oxidized during the heating process. A small oxidation peak can be observed after the complete melting of Li, which is associated with the decomposition of electrolyte salts. In the future, the Li anodes reactivity after long cycling will be further analyzed.

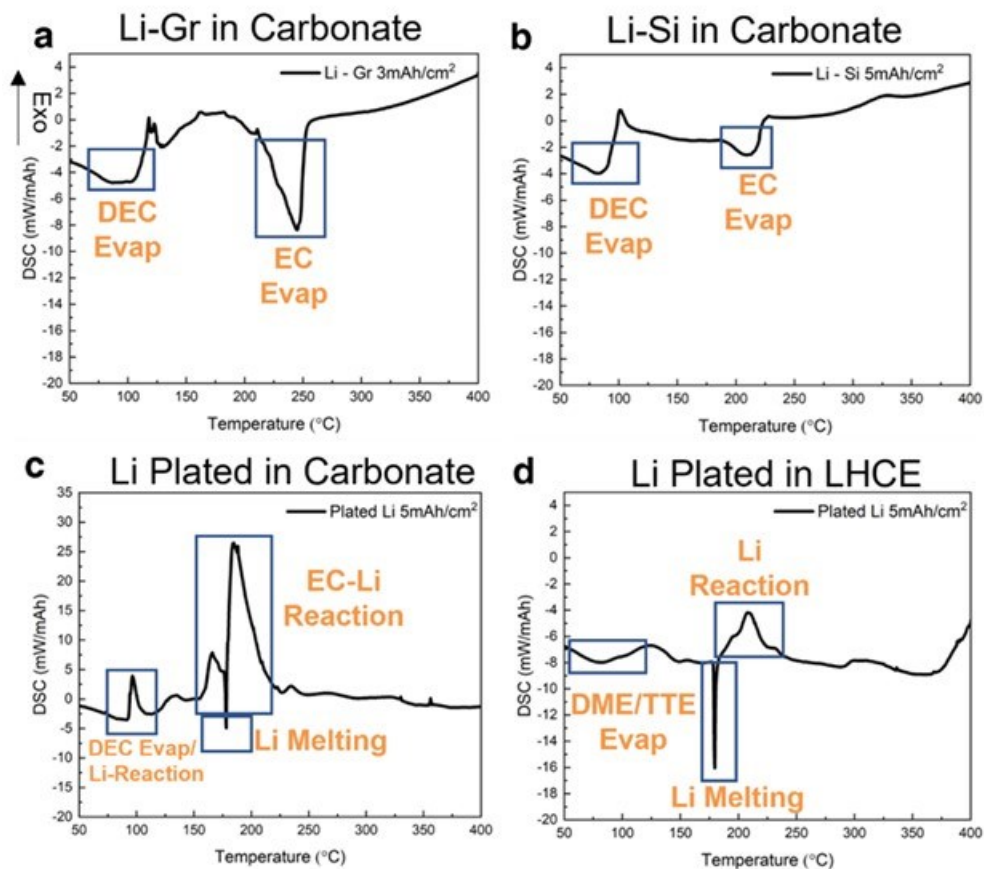


Figure XVII.1.59 The DSC curves of (a) Li-Gr, (b) Li-Si, (c) Li metal plated in Carbonate and (d) Li metal plated in LHCE. Graphite and Si anodes are lithiated to the desired capacity in half cell setup with the rate of C/20. Li metal is plated in Li|Cu coin cell to the desired capacity at a current density of 0.5mA/cm<sup>2</sup>.

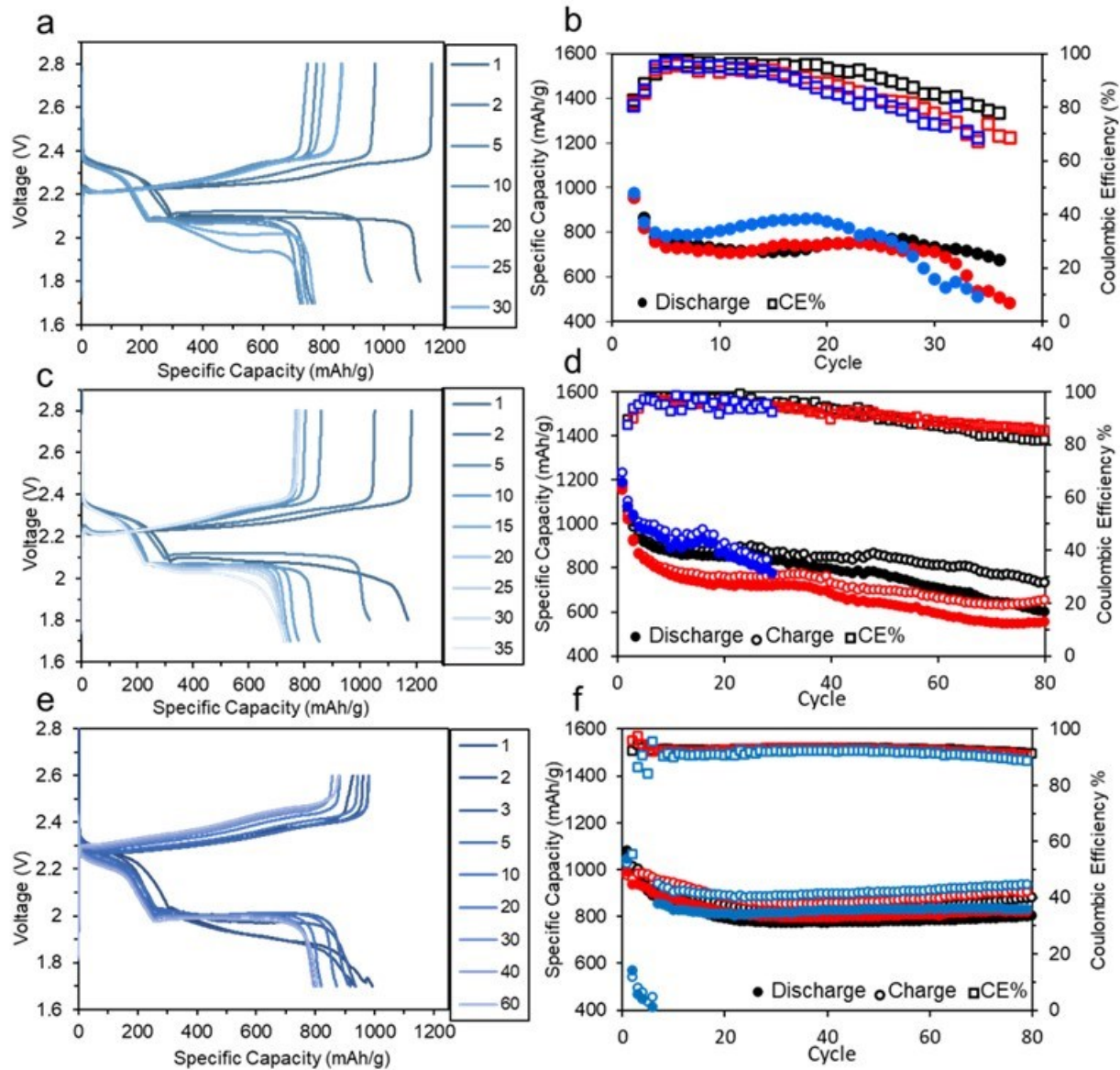
#### Optimization of C/S composite baseline electrode.

To improve the mechanical integrity and electrochemical performance of the C/S electrodes, various formulations were investigated by the GM team. Table XVII.1.2 summarizes the study on different combinations of conductive additives and binders used with 'Gen 1 modified' C/S composite material. GM team examined three conductive additives and the formulations with A3, a mixture of multi-wall carbon nano tubes (MWCNTs) and demonstrated promising electrode mechanical integrity and performance. Subsequently, the performance of various binders was investigated using A3 conductive additive.

**Table XVII.1.2 Combination of Conductive Additives and Binders Examined to Develop Gen 1 Modified Sulfur Cathodes.**

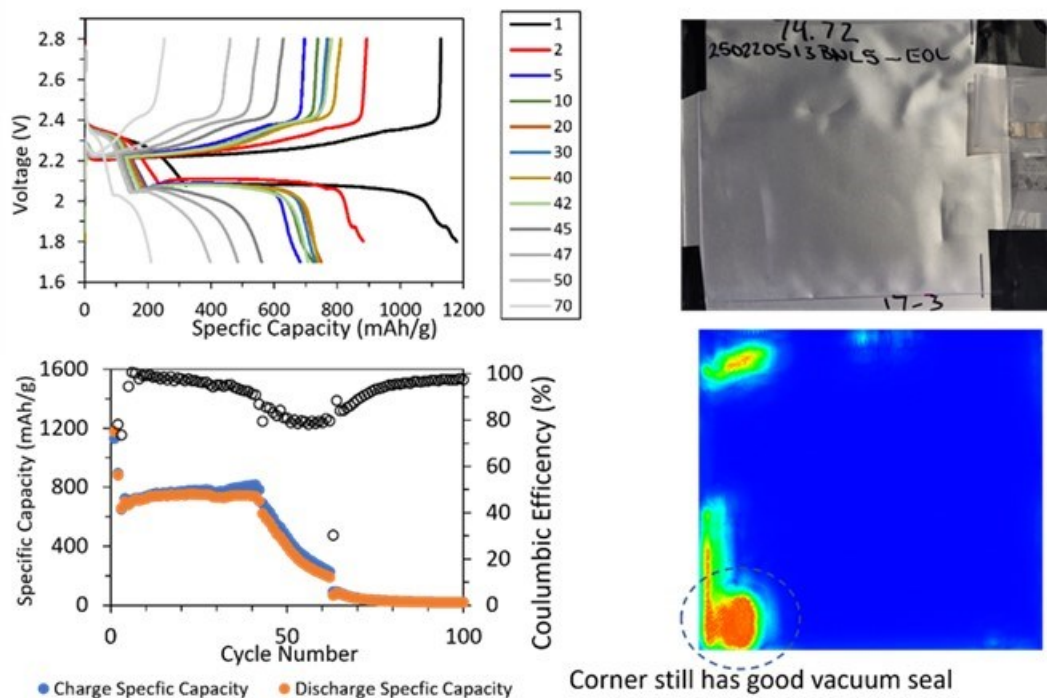
Conductive Additive	Binder			
	B1(CMC)	B2 (CMC/SBR)	B3 (PAA-co-acrylamide)	B4 (CMC-Li)
A1(KB+SWCNT suspension)				
A2 (MWCNT pure)				
A3 (MWCNT blend)				Ongoing

Figure XVII.1.60 shows the electrochemical performance of Li-S coin cells developed with selected electrode formulations. Electrochemical performance of electrodes with CMC binder is shown in Figure XVII.1.60 (a) and (b). The capacity of cells reached 750 mAh/g at 30 cycles; however, a poor capacity retention and cycling stability was observed. The binding ability and mechanical strength of electrodes improved by using CMC/SBR, and more uniform coatings were achieved. This also enhanced the electrochemical performance of electrodes as shown in Figure XVII.1.60 (c) and (d), where there is less overcharge present and cells maintained an average capacity of 800 mAh/g up to 40 cycles. Although the cells continue cycling beyond 40 cycles, decay in capacity and overcharging due to PS shuttling becomes more significant. Considering other binders with high adhesive properties and mechanical properties to retain electrode integrity, Poly(acrylic acid) (PAA) has been recommended by PNNL and other researchers. Here, we evaluated electrodes prepared by using PAA-co-acrylamide as binder. The electrochemical performance shown in Figure XVII.1.60 (e) and (f) clearly demonstrate a superior electrode performance where an average capacity of 800 mAh/g is maintained at 80 cycles with coulombic efficiency of 90%. We observed that charge-discharge profile of cells using PAA-co-acrylamide exhibits a larger polarization compared to cells using carboxymethyl cellulose (CMC) and CMC/styrene-butadiene rubber (SBR) binder. This could be associated with the properties of the binder which could impact the wettability of the active materials. On the other hand, the improved electrochemical performance suggests that PAA-co-acrylamide may interact with PS or play a role in confining PS within electrode structure. Further characterization will be carried out to understand the impact of binders with different physicochemical properties on the performance of Li-S cells.



**Figure XVII.1.60** Electrochemical performance of Li-S coin cells with electrode formulations using different binders: (a,b) CMC, (c,d) CMC/SBR, and (e,f) PAA-co-acrylamide. Average areal loadings of corresponding electrodes are: 3.9, 3.5, and 3.5 mg-S/cm<sup>2</sup>. The standard DOL/DME electrolyte at electrolyte-to-sulfur ratio (E/S ratio) of 8:1 ( $\mu\text{l}/\text{mg}$ ) was used. 1st and 2nd cycles are cycled at 0.05 C rate, rest of the cycles, cycled at 0.1 C

Ultrasonic mapping characterization of Li-S pouch cells. The GM team used ultrasonic characterization as a non-destructive tool to obtain more understanding on degradation and failure mechanism of Li-S pouch cells. Ultrasonic mapping was conducted on single-layer pouch (SLP) cells at EOL and after 4 months shelf-life. Figure XVII.1.61 shows the electrochemical performance of a pouch cell without external pressure during cycling. As shown by cycling performance, the SLP delivered a capacity of 750 mAh/g up to 50 cycles and reached EOL after 60 cycles. The ultrasonic mapping of the pouch cell performed after EOL clearly shows a complete electrolyte consumption consistent with the cycle performance.



**Figure XVII.1.61** Electrochemical performance Li-S SLP cell and ultrasonic mapping characterization at the EOL. Electrode areal loading is  $4.4 \text{ mg-S/cm}^2$ . The standard DOL/DME electrolyte at electrolyte-to-sulfur ratio (E/S ratio) of 8:1 ( $\mu\text{l/mg}$ ) was used. 1st and 2nd cycles were cycled at 0.05 C rate, rest of the cycles were cycled at 0.1 C. In the ultrasonic mapping of the cell at the EOL in the lower right panel, the blue color area indicates the less electrolyte while red color indicates more electrolyte.

To understand the effect of shelf-life on electrolyte distribution and overall cell performance, a SLP was filled with electrolyte and stored for 4 months. The ultrasonic mapping was conducted periodically after cycling the pouch cell without external pressure. As shown in Figure XVII.1.62, before cycling, an even distribution of electrolyte can be seen throughout the SLP cell. After 4 cycles, areas with less amount of electrolyte becomes visible (shown in blue) which extends to most parts of the electrode area with further cycling. After cycling, the cell showed slight bulging suggesting that electrolyte has been consumed and gases were generated with electrochemical cycling, further supporting the results obtained by ultrasonic mapping. The results also show a close correlation between electrolyte distribution and cell performance.



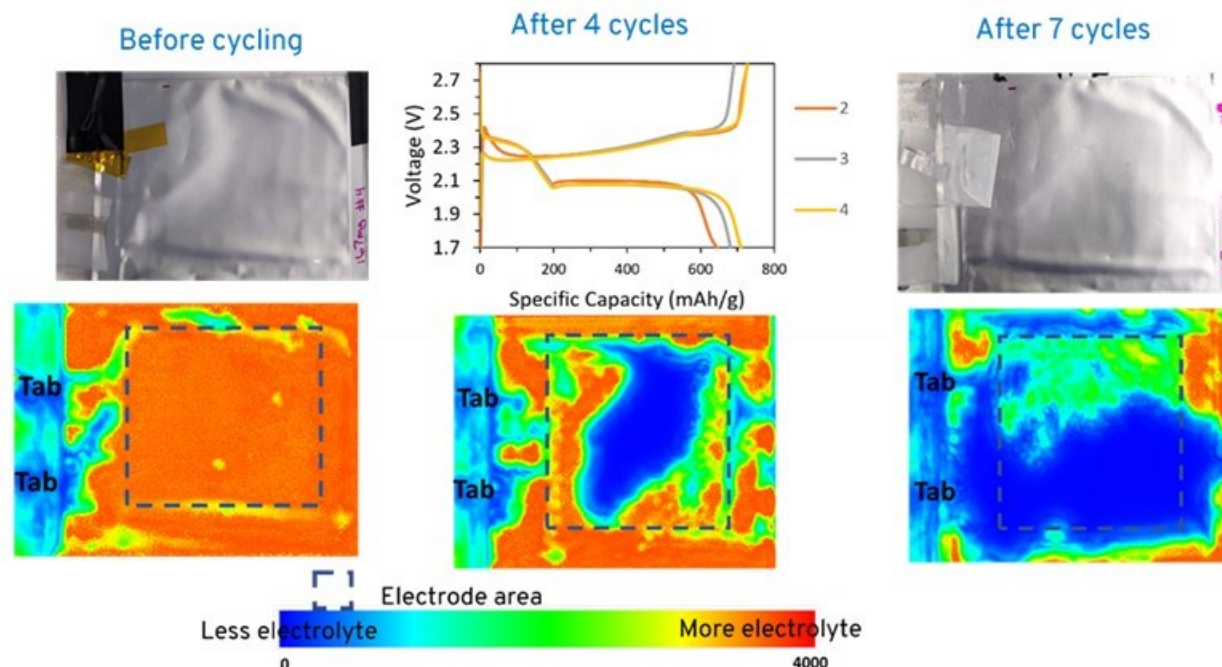


**Figure XVII.1.62** Electrochemical performance Li-S SLP cell and ultrasonic mapping characterization after 4 month shelf-life. Electrode areal loading is 4.8 mg-S/cm<sup>2</sup>. The standard DOL/DME electrolyte at electrolyte-to-sulfur ratio (E/S ratio) of 8:1 ( $\mu\text{l}/\text{mg}$ ) was used. 1st and 2nd cycles were cycled at 0.05 C rate, rest of the cycles were cycled at 0.1 C.

#### **Operation optimization of Li-NMC811 single layer pouch cells (SLPCs).**

The INL team focused on the operation optimization of Li-NMC811 SLPCs to improve cell performance. As reported by INL previously, applying an appropriately high external pressure on the Li-metal pouch cells can improve cycling performance by suppressing dendrite growth at the anode. INL investigated three pressure fixture designs: “constant thickness (gap),” “constant thickness + foams” and “constant pressure.” In addition to electrochemical performance of Li-NMC811 single-layer pouch cell under an initial pressure of 10 psi, we characterized the anodes and cathodes at the beginning of life (BOL) and end of life (EOL) used in the three pressure fixture designs. Effect on Li metal anode. As shown in Figure XVII.1.63, we characterized anodes in six separate locations with SEM. The results showed that the “constant thickness + foams” design resulted in denser Li deposition. “Constant pressure” led to more porous Li deposition. Inherent impurities or tips on the surface of Li metal anode may promote selective growth of metallic Li in certain locations. The addition of foams could help the pressure distribution across the whole electrode area more uniformly, inhibiting dendrite growth at elevated surface. In the “constant pressure” design, the selective growth of Li metal in certain locations would change the gap distance of the pressure fixture to maintain constant pressure, resulting in increased cell resistance and reduced capacity. Thus, dendrite growth was not suppressed but promoted. These results coincide with the observations in the cell performance.

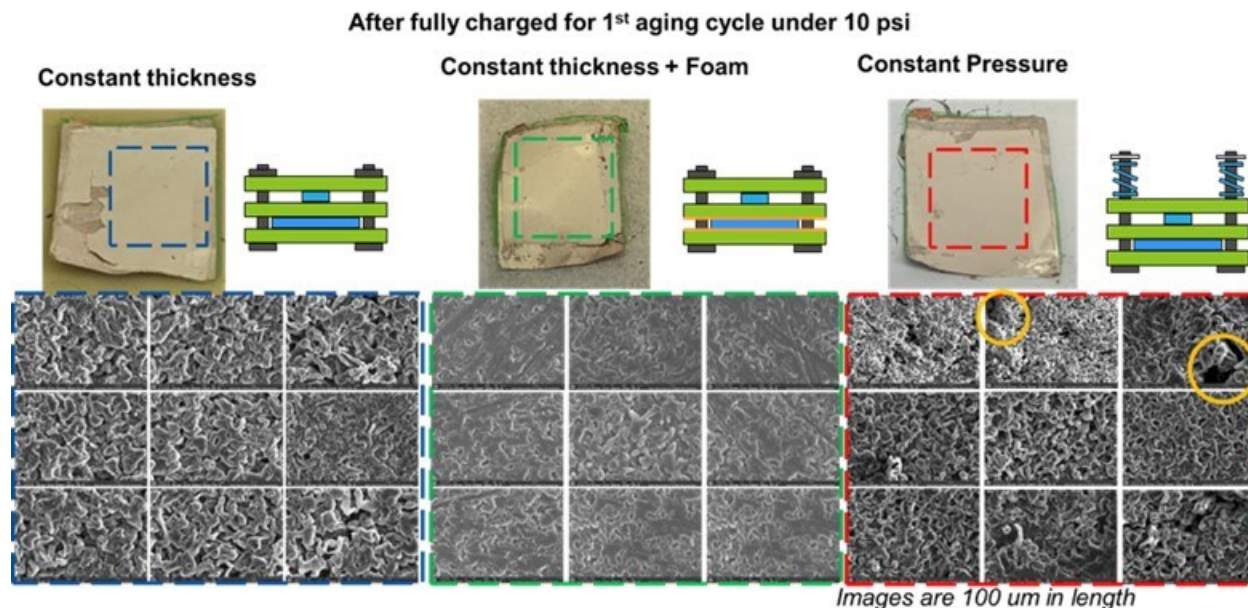
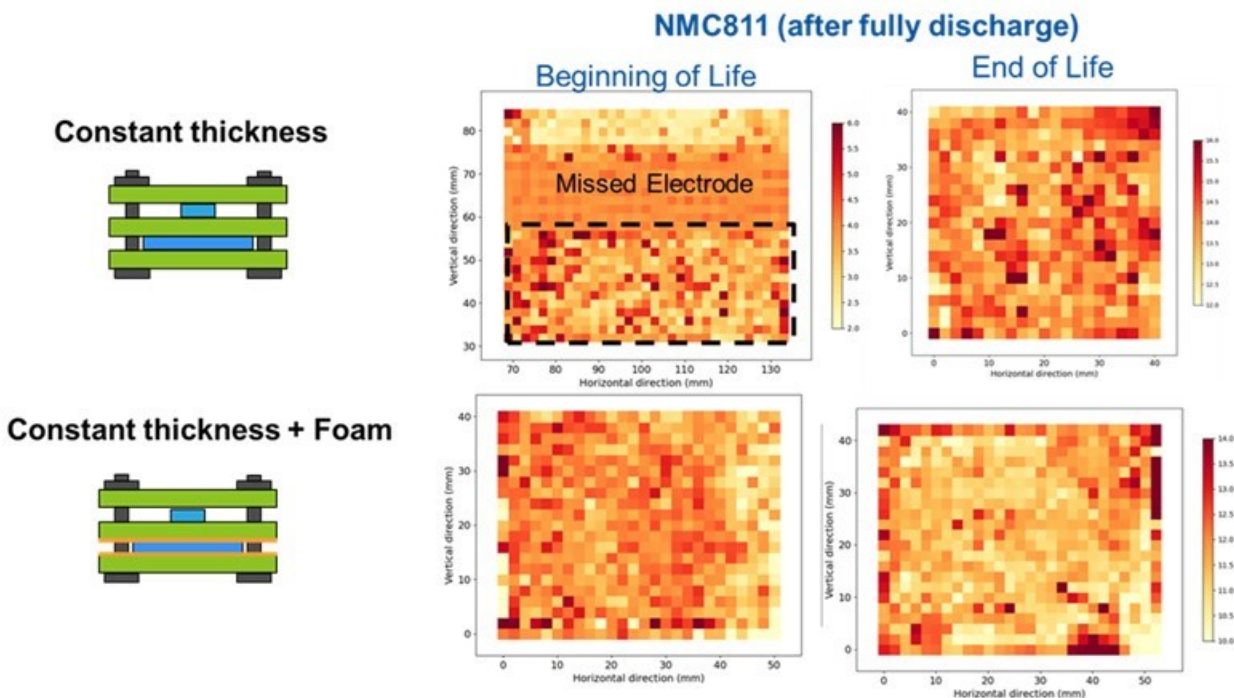


Figure XVII.1.63 The morphologies of Li metal anode of Li-NMC811 single-layer pouch cell after fully charged under 10 psi in the three pressure fixture designs: “constant thickness,” “constant thickness + forms,” and “constant pressure.”

#### ***Effect on NMC811 cathode.***

The cathodes at beginning of life (BOL) and end of life (EOL) were characterized by *ex-situ* synchrotron XRD mapping. Figure XVII.1.64 showed that in the “constant thickness” design, hot or cold spots were found across the cathode surface in BOL and EOL cells, suggesting nonuniform NMC811 cathode material utilization. The addition of the foams improves the cathode material utilization from BOL to EOL with less hot or cold spots. Therefore, the pressure fixture design can also affect the cathode performance. If the initial pressure increased to 30 psi in the three pressure fixture designs, the electrochemical performances of the pouch cells are different from those at 10 psi.



**Figure XVII.1.64 Ex-situ synchrotron XRD mapping of NMC811 cathodes from Li-NMC811 single-layer pouch cells under 10 psi at BOL and EOL in the “constant thickness and “constant thickness + foams” designs**

**Improved performances of C/S composite baseline electrode.**

The GM team verified the performance of baseline electrodes in coin cells to demonstrate the reproducibility of the results and its correlation to the quality of the fabricated cathodes. Figure XVII.1.65 shows examples of cycle life comparison between coin cells fabricated using different batches of electrodes. A representative data is shown in Figure XVII.1.65 (a) and (b) for electrode performances of two different batches of electrodes prepared with same formulation. Figure XVII.1.65 (a) demonstrates an average specific discharge capacity for electrode samples from four sections of coated electrode. The significant variation in specific capacity observed in Figure XVII.1.65 (a) is indicative of a poor-quality cathode. This could be impacted by different factors including uneven S distribution in carbon host material, inadequate slurry mixing procedure, and uneven distribution of active material throughout the coated electrode. In contrast, Figure XVII.1.65 (b) shows that with the same formulation but improved fabrication procedure, a stable average capacity of 800 mAh/g can be achieved at 60 cycles. As shown in Figure XVII.1.65 (c), using a different binder, PAA-co-acrylamide, improved performance of C/S electrodes were obtained resulting in enhanced cycle stability with an average capacity of 800 mAh/g at 100 cycles. While we continue to implement more quality control steps for electrode processing, these electrodes can serve as a baseline for further studies.

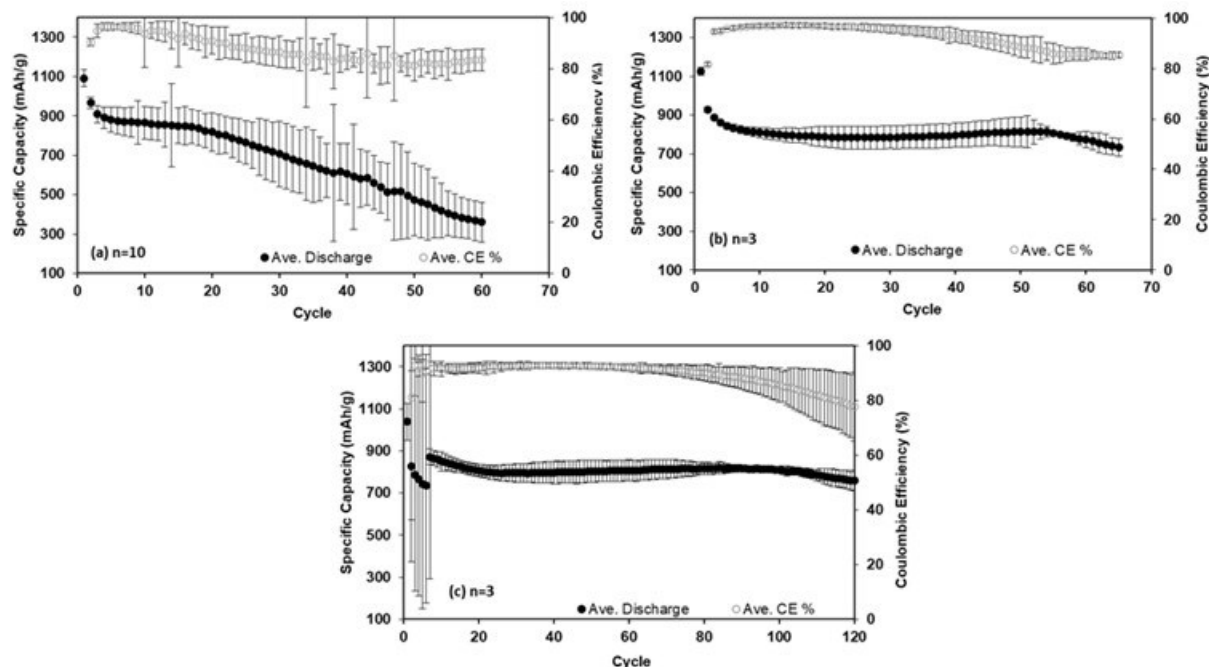


**Figure XVII.1.65** Cycling performances of Li-S coin cells with electrode formulations using different binders: (a,b) CMC/SBR, and (c) PAA-co-acrylamide. Average areal loading of corresponding electrodes between 3.5-3.8 mg-S/cm<sup>2</sup>. The standard DOL/DME electrolyte at electrolyte-to-sulfur ratio (E/S ratio) of 8:1 ( $\mu\text{l}/\text{mg}$ ) was used. All the cells were cycled at 0.05 C rate for the first two cycles and at 0.1 C for the rest of the cycles.

#### **Improved performance of Li-S cells with gel polymer electrolytes.**

Replacing liquid electrolytes with polymer electrolytes is one of the promising approaches to suppress the dissolution of polysulfides in Li-S battery. However, a pure solid-state electrolyte could impose challenges such as low ionic conductivity leading to slow kinetics of polysulfide conversion reactions. Therefore, the GM team developed gel polymer electrolytes using two methods: *ex-situ* and *in-situ*. In the *ex-situ* method, a thin polymer electrolyte was *ex-situ* coated on Li metal anode first, and then the coated Li using this gel electrolyte was tested in a Li-S coin cell using DOL/DME standard electrolyte. Figure XVII.1.66 (a) and (b) demonstrate the voltage profile and cycle life of the corresponding cells which delivered a specific discharge capacity of 850 mAh/g similar to cells using standard liquid electrolyte. These cells are continuously being cycled. Their performance beyond 30 cycles will be compared to the standard liquid electrolytes reported in the future.

In the *in-situ* method, the standard DOL/DME electrolyte was converted *in-situ* into a semi-solid electrolyte by introducing a polymer network. Then this semi-solid electrolyte was used for Li-S coin cells. As shown in Figure XVII.1.66 (c) and (d), these cells maintain a discharge capacity of 700 mAh/g with a high coulombic efficiency of 96% at 70 cycles. Both gel polymer and semi-solid electrolytes show encouraging performance as no significant cell polarization is introduced. Further characterization is ongoing to understand the structural stability of gel and semi-solid electrolyte and its impact on polysulfide dissolution.

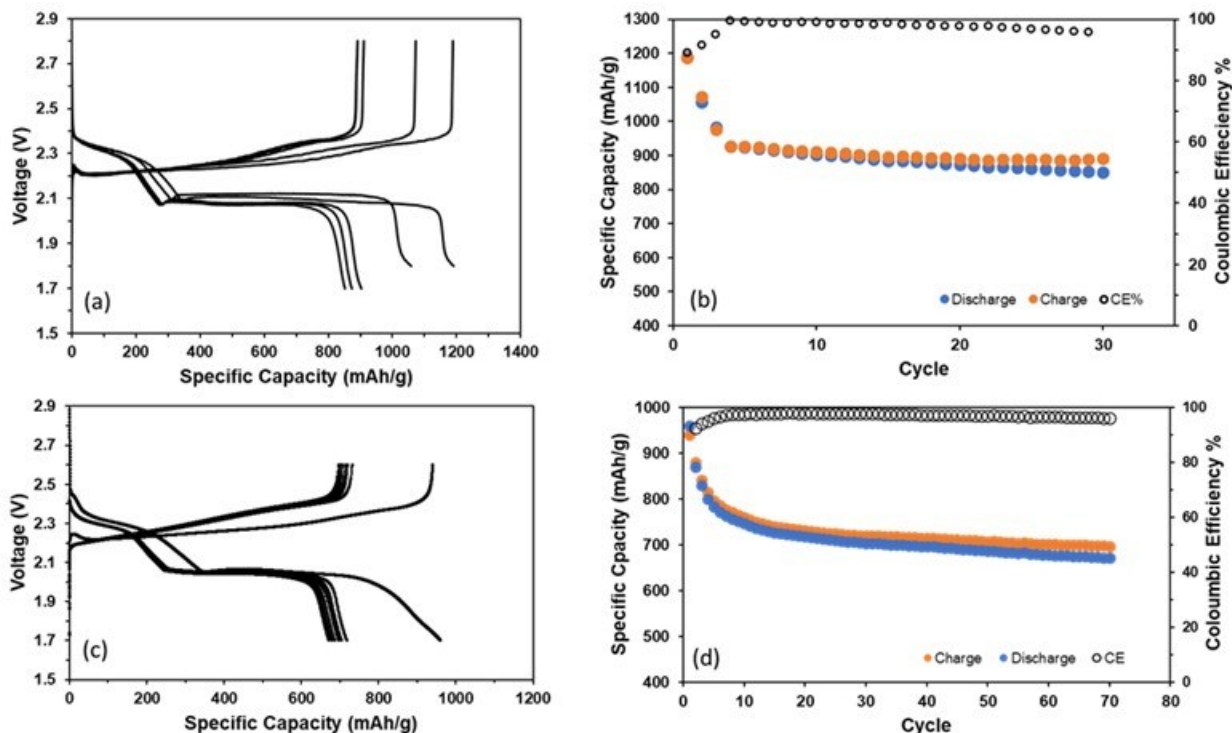


Figure XVII.1.66 Voltage profile and cycling performances of Li-S coin cells with (a,b) *ex-situ* gel polymer electrolyte and CMC/SBR sulfur electrode formulation and (c,d) *in-situ* semi-solid electrolyte and PAA-co-acrylamide sulfur electrode formulation. The average areal loading of electrodes for (a,b) and (c,d) are 3.5 mg-S/cm<sup>2</sup> and 4.2 mg-S/cm<sup>2</sup>, respectively. The standard DOL/DME electrolyte at electrolyte-to-sulfur ratio (E/S ratio) of 8:1 (μl/mg) was used. All the cells were cycled at 0.05 C rate for the first two cycles and at 0.1 C for the rest of the cycles

#### Baseline testing for Li-NMC811 and Li-SPAN single-layer pouch cells (SLPCs).

The INL team is responsible for evaluating new materials developed by B500 consortium at SLPC level and for discovering and addressing new issues beyond those observed in coin cells. The suggestions will be provided to other team members to further modify materials and improve multi-layer pouch cell performance. In order to achieve these goals, it is essential to develop baseline testing protocols and obtain reliable baseline testing results. INL has finished baseline testing for both Li-NMC811 and Li-SPAN SLPCs, which are shown in Figure XVII.1.67. The cell components and testing conditions are also shown in Figure XVII.1.67. For testing conditions, charge/discharge rates and cut-off voltages in SLPCs were the same as those used for coin cell baseline testing. The external pressures applied onto SLPCs were optimized by the INL team to ensure longer lifespan. In addition, the filling procedure of electrolyte is established, enabling minimum electrolyte loss during vacuum sealing of pouches, an important consideration in setting up the SLPC under “lean electrolyte” conditions.

The newly developed Battery500 electrolytes for Li-NMC811 SLPCs and Li-SPAN SLPCs as well as the high-Ni cathodes are being evaluated at INL, following SLPC baseline testing protocols. Those results will be reported later.

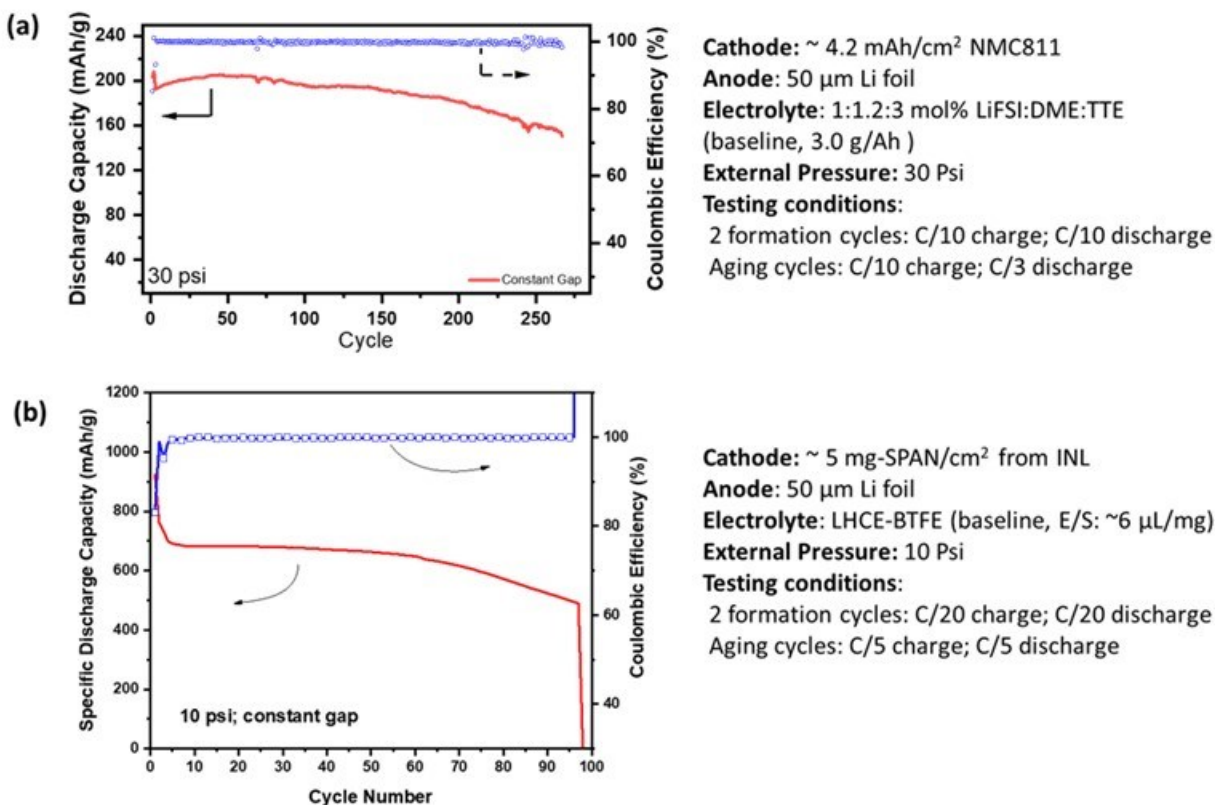


Figure XVII.1.67 SLPC baseline testing protocols and results of (a) Li-NMC811 and (b) Li-SPAN

#### Cathode factors and process variables study

In the development of lithium-sulfur (Li-S) pouch cells, The PNNL team works with other consortium teams and focuses on the cathode materials development, electrode optimization and processing, and performance evaluation in both coin and pouch cells. In this quarter, to address the complex challenges associated with sulfur electrode processing, PNNL team developed a methodology using design of experiments (DoE) to systematically explore the interactions and trade-offs among the intertwined cathode factors (active material, binder, conductor) and process variables. This study examines the impact of input factors on electrode properties and electrochemical performance and identifies and estimates interaction effects between the factors. Further, these estimates were extended using the empirical model developed to predict factor combinations that would lead to improved performance. Through the DoE methodology, we can accelerate development and optimization based on a down-selected set of screening experiments, and ultimately achieved improved cell performance under both high-loading and lean electrolyte conditions. Taking electrode formulation study as an example, twelve different sulfur electrodes were fabricated and processed. Of the 64 possible combinations for the 4 electrode factors (percentage of PAA binder, PEGDME additive, CNF conductor, and LiOH additive) and the 2 processing factors (cathode thickness reduction via calendaring and E/S ratio of electrolyte), 24 coin cells were assembled. Note, sulfur mass loading is  $>4 \text{ mg/cm}^2$  for all the cells used in the study. Figure XVII.1.68 shows the specific capacity and median voltage versus cycle number for each coin cell for the first 15 cycles. While the long-term cycling performance is important for identifying promising combinations of cathode, anode and electrolyte, the goal of this screening experiment is rather to focus on the optimal cathode and processing. For this reason, cell performance of the first 15 cycles were compared to identify positive and negative effects from factors and interactions, and sufficient to observe meaningful differences between the cathodes. For ease of comparison, graphs are divided by sub-plot factors (1) densely calendared with flooded electrolyte ( $E/S = 10 \text{ mL g}^{-1} \text{ S}$ ), (2) densely calendared and lean electrolyte ( $E/S = 4 \text{ mL g}^{-1} \text{ S}$ ), (3) porous calendaring and flooded electrolyte, and (4) porous calendaring and

lean electrolyte. From the electrochemical data, preliminary comparisons and conclusions can be drawn. When electrolyte is flooded, after the two formation cycles, no cells exhibit higher than  $900 \text{ mAh g}^{-1}$  in discharge capacity. This is primarily due to the increased dissolution of soluble lithium polysulfide species (LiPS) in the presence of excess amount of electrolyte which affects reversibility of sulfur species available for repeated electrochemical reactions. With lean electrolyte conditions, the discharge capacity observed for the coin cells has the highest range, including the best performing cells and the worst performing cells. For both lean and flooded electrolyte conditions, the given degree of calendaring (5-20% reduction) did not have a significant impact on specific discharge capacity. Average voltage was more variable under lean electrolyte conditions, while it was more consistent across all cells when electrolyte was flooded. Average voltage informs the electrochemical reactions occurring within the cell and has significant impact on the power of the cell.

Through the DoE approach, significant interaction terms can be identified. For example, the interactions between CNF and LiOH have apparent effects on 1) specific discharge capacity, 2) charge transfer resistance, and 3) electrode resistivity (detailed data was not shown here). Specifically, when the amount of LiOH is low, there is a minimal difference in the effect of CNF on the specific capacity. However, when LiOH is high, the effect of CNF is quite different, larger amounts leading to improved performance. A similar effect is shown in the electrode resistivity, where high LiOH and high CNF lead to the lowest overall resistivity, while high LiOH and low CNF lead to the highest resistivity. Effects on charge transfer resistance are unclear due to the wide and overlapping range of values in each subset. These results may be partially explained by other system variables that exhibit dependency on LiOH and contribute to electrode resistance. For example, increasing LiOH simultaneously decreased the NKB/S loading of the cathodes and increased porosity. This could be a result of the increased slurry viscosity caused by the LiOH:PAA interaction which extends polymer chains, requiring more solvent to solvate PAA. This in turn contributes to greater solvent volume in the same cross-sectional gap enforced by the doctor blade during coating, reducing the amount of other slurry components spread over the same surface area and increasing porosity when dried. Both effects increase electrode resistivity. In addition, a slight interaction was uncovered between LiOH and CNF that also added to higher mass loadings when both components were set to their high values. One explanation is that when CNF and LiOH were both high, the effects of increased porosity and reduced active material due to high LiOH are outweighed by the CNF, so the overall resistance remains low. When the amount of CNF is reduced, the combined insulating effect of high porosity and lower S-loading due to the high LiOH overcomes the conductivity of CNF and the overall resistance is high. A more detailed experimental study is in progress and the extracted results will be used as inputs for a prediction model.

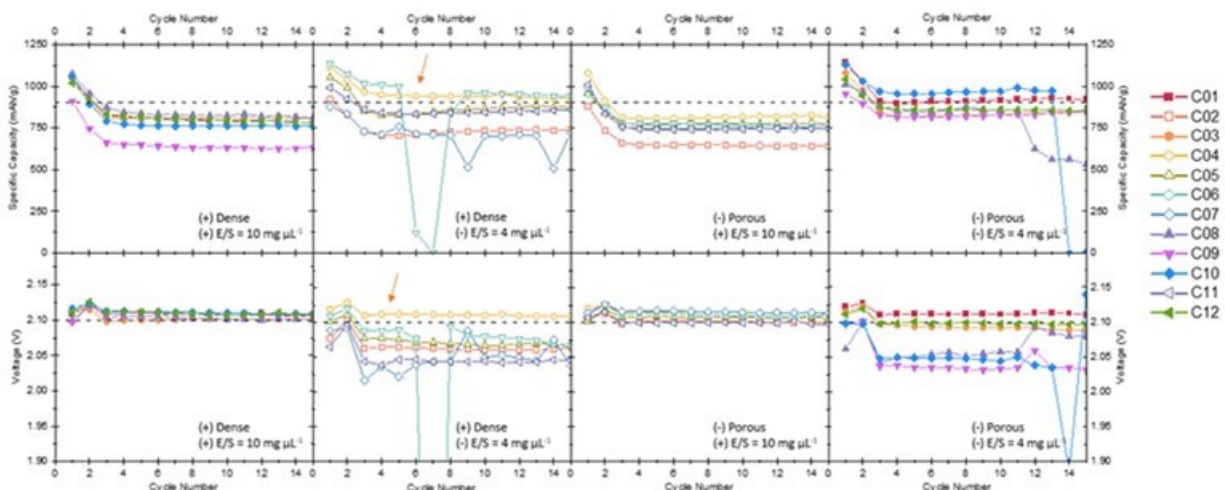


Figure XVII.1.68 Coin cell results for cathodes C01-C12 showing (a-d) specific discharge capacity versus cycle number and (e-h) median discharge voltage versus cycle number for the first 15 cycles. For every cell, there were two formation cycles at 0.05C charge and discharge followed by cycling at 0.1C for charge and discharge. Electrochemical results are divided four ways: (a,b-e,f) densely cathodes with a reduction in dry cathode thickness of 20%, (c,d-g,h) porous cathodes with a reduction in dry cathode thickness of 5%, (a, c, e, g) E/S = 10  $\mu\text{L mg}^{-1}\text{S}$ , and (b, d, f, h) E/S = 4  $\mu\text{L mg}^{-1}\text{S}$ . Hollow and solid markers were used to distinguish between cathode blocks more easily.

#### Binder alternative with electrode formulation study

In this quarter, the GM team focused on optimizing the sulfur electrode formulation with binder alternative investigation. As shown in the previous report, electrode formulation using PAA-co-acrylamide binder has shown high cycle stability over 100 cycles and maintaining a capacity of 800 mAh/g. While using this binder outperformed the performance of cells with CMC-SBR in coin cells, large charge-discharge polarization was observed in single layer (0.1 Ah) pouch cell. One approach currently under investigation is the cathode processing protocol to achieve homogeneous slurry and another approach is recommendation received by PNNL to use Li-PAA or PAA binder and explore feasibility for roll-to-roll electrode fabrication. Figure XVII.1.69 shows electrochemical performance of C/S electrodes with Li-PAA as binder. Both charge/discharge profiles and cycle life show a stable capacity of 900 mAh/g over 80 cycles with CE of 90%. Similar to electrode formulation with PAA-co-polymer the capacity increases and becomes stable after 10-20 cycles which could be due to increase in wettability of active material during cycling. Next step, we will develop roll-to-roll electrodes using PAA and Li-PAA binder to evaluate the performance of pouch cells.

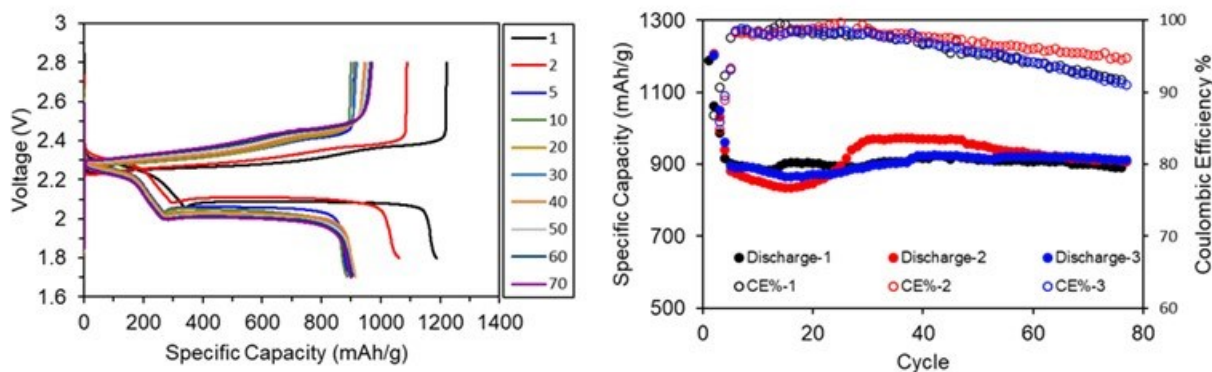
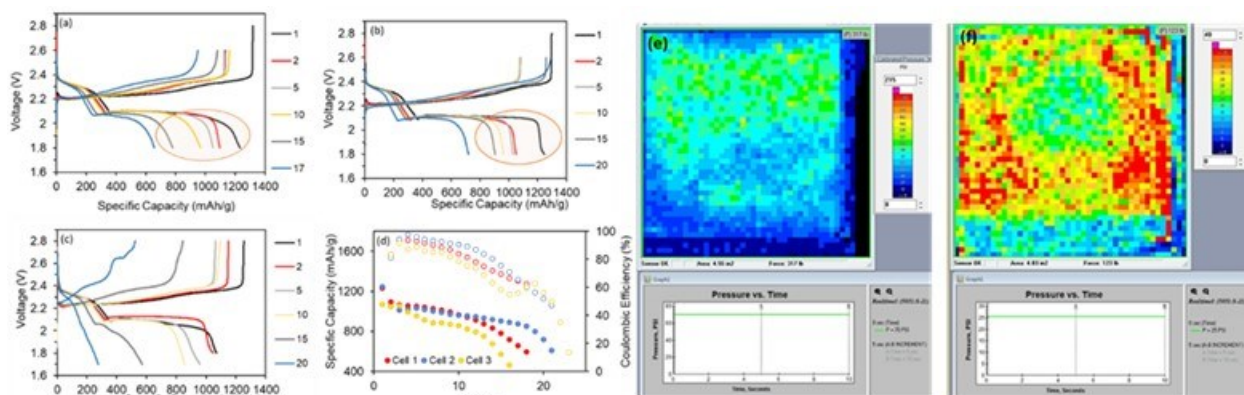


Figure XVII.1.69 Voltage profiles and cycle life performance of Li-S coin cells with Li-PAA binder formulation. Average areal loading of 3.5 mg-S/cm<sup>2</sup>. The standard DOL/DME electrolyte at electrolyte-to-sulfur ratio (E/S ratio) of 8:1 ( $\mu\text{L}/\text{mg}$ ) was used. 1st and 2nd cycles are cycled at 0.05 C rate, rest of the cycles, cycled at 0.1 C



### Performance of multi-layer pouch cells

The GM team fabricated and tested several multi-layer pouch cells (0.7 Ah and 1 Ah). Baseline C/S electrodes with CMC-SBR as binder formulation were developed using roll-to-roll process for use in pouch cells. The average cathode loading was 3.5 mg-S/cm<sup>2</sup>. In Figure XVII.1.70, charge/discharge voltage profiles and cycling performance of 0.7 Ah pouch cells are presented. The initial pressure was set at 10 PSI using metal plate fixtures which was also monitored at the end of cycling. Figure XVII.1.70 (a) and 16 (b) compare the performance of pouch cells using standard electrolyte 1M LiTFSI and 2 wt% LiNO<sub>3</sub> (DOL:DME) and 0.6M LiTFSI and 2.4 wt% LiNO<sub>3</sub> (DOL:DME), respectively. Both pouch cells showed a similar discharge capacity of about 1200 mAh/g in the first cycles. In Figure XVII.1.70 (a) the discharge voltage profile represents a more sluggish polysulfide conversion which may be due to the higher concentration of LiTFSI in the electrolyte. This behavior was consistent with our single-layer pouch results. Figure XVII.1.70 (c) represents a pouch cell which delivered similar capacity but showed rapid decay over cycling. This is also shown in Figure XVII.1.70 (d) where all cells maintain capacity up to 10 cycles however the decay is more significant for 3<sup>rd</sup> cell. Figure XVII.1.70 (e) and Figure XVII.1.70 (f) depict the pressure mapping of pouch cells once the capacity started decaying. Both cell 1 and 2 (e) showed pressure increase to 70 psi while cell 3 (f) only showed pressure increase to 25 psi. However, the non-uniform pressure distribution shown for cell 3 clearly indicates a possible cause for the rapid capacity decay. These results suggest that gas generation in Li-S pouch cells have severe impact on the cycling stability which needs to be addressed.



**Figure XVII.1.70 Voltage profiles and cycle life performance of Li-S pouch cells (0.7 Ah) with electrode formulations using CMC/SBR. Average areal loading of electrodes is 3.5 mg-S/cm<sup>2</sup>. The standard DOL/DME electrolyte at electrolyte-to-sulfur ratio (E/S ratio) of 5:1 (μl/mg) was used. 1st and 2nd cycles are cycled at 0.05 C rate, rest of the cycles, cycled at 0.1 C. (a) cell 1, (b) cell 2, and (c) cell3. Pressure mapping of pouch cells 1 and 2 (e) and cell 3 (f) at the end of cycling.**

To validate the impact of gas generation on cycling performance, currently we modified the pouch design to allow for degassing. Shown in Figure XVII.1.71 are 1Ah pouch cells fabricated using electrodes with loadings of 3.6 mg-S/cm<sup>2</sup> (a and b) and 2.5 mg-S/cm<sup>2</sup> (c and d), respectively. As expected, the pouch cell with lower electrode loading achieves a capacity of above 1000 mAh/g which is maintained over 10 cycles while with higher loading more overcharge (i.e., polysulfide shuttling) was observed. The pressure of both pouches is currently monitored overtime and will be correlated to the cell performance. It should be noted that the gas generation in Li-S pouch cells needs detailed studies to identify the reaction products and therefore modify electrolytes accordingly.

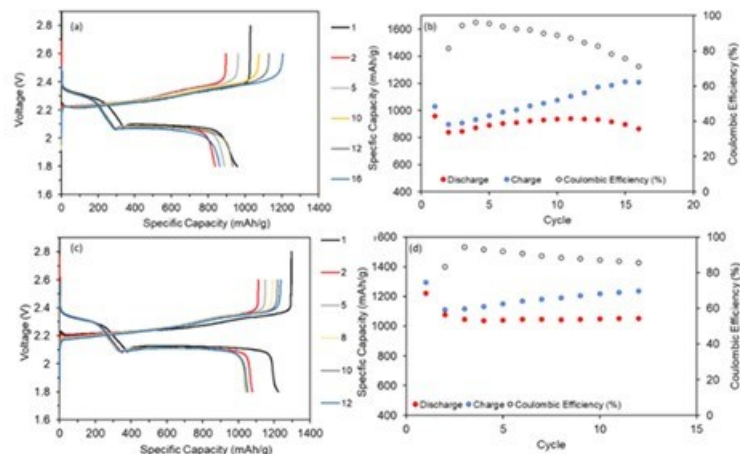


**Figure XVII.1.71** Voltage profiles and cycle life performance of Li-S pouch cells (1 Ah) with electrode formulations using CMC/SBR. Average areal loading of electrodes is 3.6 mg-S/cm<sup>2</sup> (a and b) and 2.5 mg-S/cm<sup>2</sup> (c and d). The standard DOL/DME electrolyte at electrolyte-to-sulfur ratio (E/S ratio) of 5:1 (μl/mg) was used. 1st and 2nd cycles are cycled at 0.05 C rate, rest of the cycles, cycled at 0.1 C.

#### Calendar condition impact on cell failure modes

The INL team has looked at the impact on calendar life and failure modes under different conditions using single layer pouch cells (SLPCs). Currently, the study includes a suite of conditions at different states-of-charge (SOC), temperatures, pressures and voltage hold conditions using Li||Li[Ni<sub>0.8</sub>Mn<sub>0.1</sub>Co<sub>0.1</sub>]O<sub>2</sub> and localized high-concentration electrolyte (LHCE). Specific conditions include varying SOC (70 % and 100 %), temperatures (25 °C and 45 °C), pressures (10 psi and 50 psi), and operational modes (open-circuit voltage, OCV and constant voltage, CV). For the most moderate and most likely to occur in application setting (i.e., OCV, 70 % SOC, 25 °C, and 10 psi) over 18 months less than 1% capacity fade has been observed (Figure XVII.1.72). For this condition, the calendar life is conservatively projected at 31 months based on the quantity of Li remaining on the negative electrode as determined in a post-test analysis. Additional conditions including the use of high temperature (45 °C), 100 % SOC, and at CV have shown the promise which can be used as testing routes to accelerate aging and guidance for future charge protocol development. As with cycle aging applied pressure helps mitigate dendritic growth and increases the calendar life of the LMB.

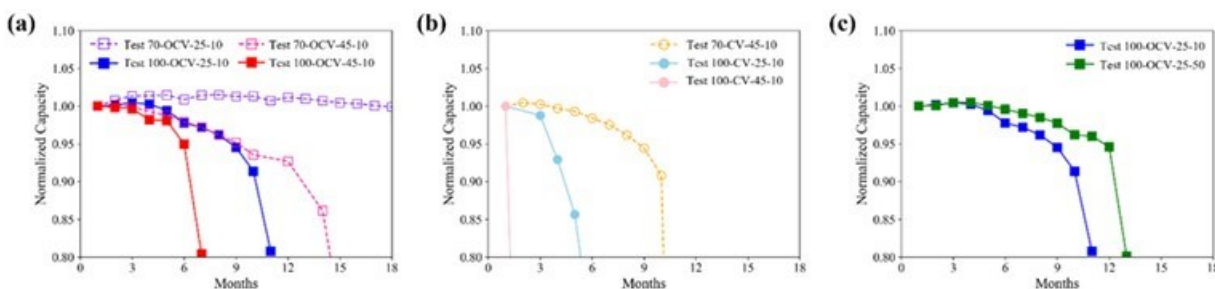


**Figure XVII.1.72** Performance of Li||NMC811 pouch cells experiencing different calendar aging condition including variations in SOC and temperature (a) OCV and 10 psi, (b) CV and 10 psi, and (c) pressure 50 vs 10 psi. Capacity fade is based on a C/3 discharge followed by C/10 charge during reference performance tests which occurred every 28 days

In addition to tracking the electrochemical performance of cells, INL also partnered with BNL to characterize the state of the cathode using X-ray diffraction (XRD). Using previously developed high energy XRD lateral

mapping the team was able to identify the sample which was held at constant voltage during calendar periods with distinct inhomogeneity in cathode utilization as shown in Figure XVII.1.73. These areas of non-uniformity in cathode SOC align with similar markings on the Li metal surface and are attributed to gas generation during the aging of the cell.

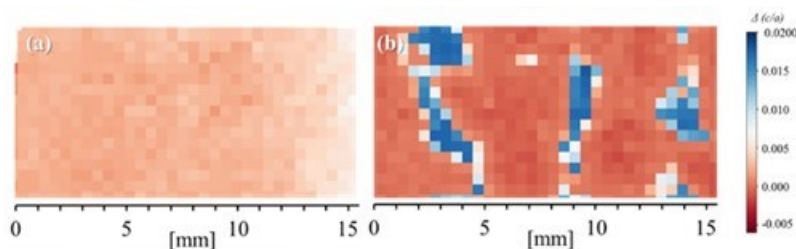


**Figure XVII.1.73 High energy lateral XRD maps showing differences in cathode utilization for (a) Test 100-OCV-25-10, which was aged at open circuit, exhibiting expected homogeneity and from (b) Test 100-CV-25-10 exhibiting marked inhomogeneity due to aging while held at constant voltage. The increased inhomogeneity in Test 100-CV-25-10 is attributed to gas generation which blocks access to part of the electrode creating non-uniform utilization of the NMC.**

#### **4. Keystone project 4: Cross-Cutting Research**

The goal of the Cross-cutting team is to develop & deploy advanced characterization tools in support of the three Keystone efforts, with a focus on probing specific materials and interfaces for Keystone 1, probing individual electrodes for Keystone 2, and probing the whole cell for Keystone 3.

##### **Quantifying transition metal deposition on lithium anode at electrode scale.**

The BNL team characterized the electrochemistry and the transition metal dissolution behavior of cells prepared with novel electrolytes developed by Battery500 collaborators at Stanford University (Stanford) and the Stanford Linear Accelerator Center (SLAC). Three fluorinated ether electrolyte systems were tested: 1.2 M LiFSI in F5DEE (F5), 1.2 M LiFSI in F4DEE with DFOB additive (F4-DFOB), and 1.2 M LiFSI in FDMB. The molecular structures of F5, F4, FDMB, and DFOB are shown in Figure XVII.1.74a. The cyclability of NMC811||Li cells using these electrolytes is shown in Figure XVII.1.74b and Figure XVII.1.74c. The Battery500 coin cell test protocol was rigorously followed. Both FDMB and F5 deliver stable cycling in the voltage range of 2.8-4.4V while the cell using F4-DFOB electrolyte shows capacity fade after only 40 cycles. When increasing the charge voltage to 4.6V, both FDMB and F5 electrolytes can still sustain long cycles while F4-DFOB electrolyte fails to do so. Such results are consistent with the data shown by the Stanford team and other Battery500 Consortium members.

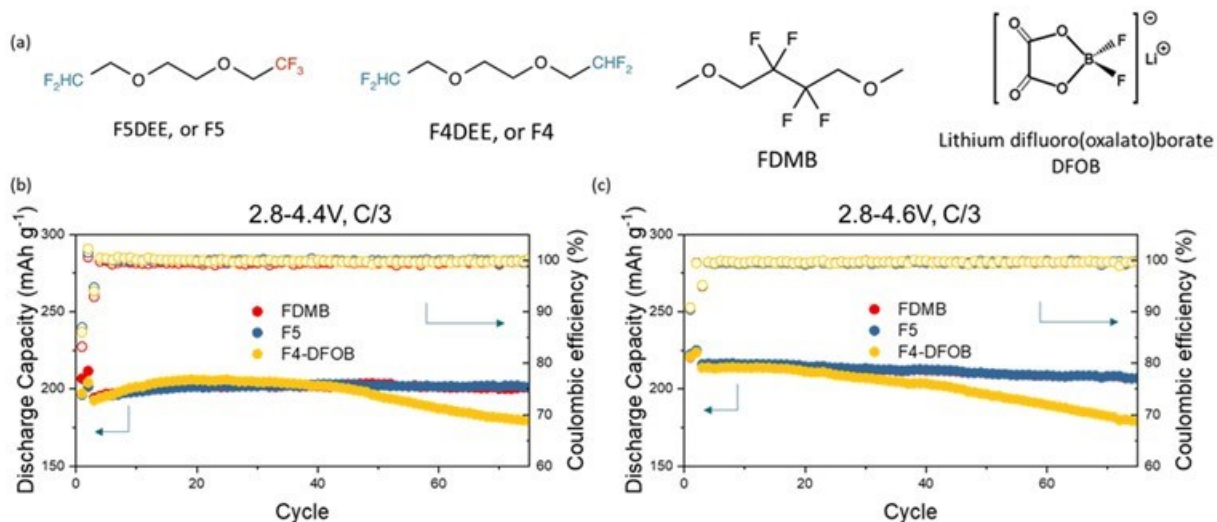


**Figure XVII.1.74** (a) Molecule structures of the solvents and additives used in the Stanford electrolytes. (b) Cycling data of coin cells using Stanford electrolytes in different voltage windows. The Battery500 coin cell test protocol is followed.

To understand the transition metal (TM) dissolution behavior (and especially how this influences the lithium metal anode), the amount of transition metal deposited on lithium metal anode at electrode scale was quantified by the BNL team using synchrotron-based X-ray fluorescence mapping. The mapping results indicate there is significant heterogeneity in TM deposition on lithium metal anode, emphasizing the importance of characterization at the whole electrode scale, not just a small spot of the electrode. Such heterogeneity may result from nonuniformities in the local current density due to variations in the applied pressure or in the local composition and thickness of the interphase. The deposited TM amount is quantified and analyzed in detail as shown in Figure XVII.1.75. In general, the deposited TM amount is on the scale of  $\mu\text{g}/\text{cm}^2$ . Considering the area of the electrode and the mass loading on the cathode side, this means the bulk cathode loses less than 0.1% of its TM after 100 cycles. Therefore, the negative effect of TM dissolution and deposition is more likely associated with surface and interphase damage, rather than TM inventory loss. The left panel in Figure XVII.1.75 shows the absolute amount of TM deposition, indicating that nickel deposition is most serious, followed by manganese and cobalt. This is contrary to the popular belief that manganese deposition is most serious among all the TMs. Figure XVII.1.75 also shows the deposited TM amount increases considerably when the charge voltage is increased. Generally, the F5 electrolyte seems to be most effective in suppressing TM dissolution and deposition, in accordance with its superior cycling performance. However, its capability of suppressing TM dissolution at high voltages (*e.g.*, 4.6 V) needs to be improved. Considering nickel, manganese and cobalt are present in different fractions in NMC811, the deposited TM amount should be normalized by stoichiometry, leading to results shown in the right of Figure XVII.1.75. Interestingly, the normalized deposition is highest for manganese, followed by nickel and cobalt. This may suggest that after extended cycling, the relative ratio of TM on cathode surface is no longer the same as that in the pristine material. It is possible that the surface becomes cobalt-enriched since cobalt is the least dissolved and deposited TM.

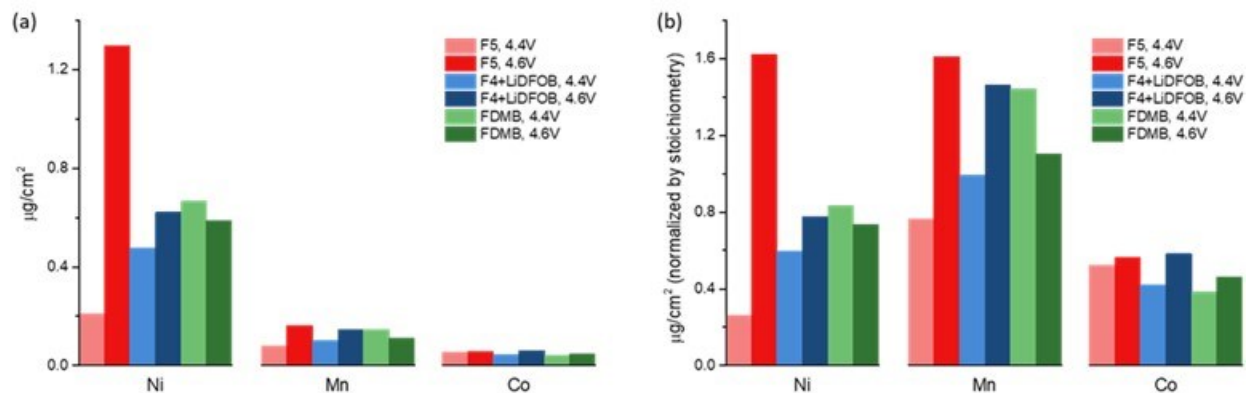


Figure XVII.1.75 (a) The absolute amount of TM deposition quantified from X-ray fluorescence mapping. (b) The normalized amount (normalized by TM stoichiometry in NMC811) of TM deposition quantified from X-ray fluorescence mapping.

#### ***Mechanical properties of SEI on Li metal.***

The SLAC team carried out mechanical measurements on the SEI. This set of measurements, leveraging the in-situ capabilities of a glovebox atomic force microscope, develops understandings of how SEI grown on lithium metal surfaces plays a role in regulating lithium metal deposition and morphology, and ultimately cell performances. Building on work done by other teams within the Battery500 consortium, they have probed local mechanics of the SEI grown in both conventional carbonate electrolytes (1:1 of EC:DEC with 1M LiPF<sub>6</sub>) as well as SEI grown on localized high concentrated electrolyte (LHCE). In addition to Young's modulus (Figure XVII.1.76), they have also performed viscoelastic measurements by locally indenting the SEI under constant loading and then observing the resulting SEI creep. Surprisingly, the plasticity of the SEI, measured by the amount of creep observed in one second of loading, proves to be a better predictor of cell performance than the more commonly reported modulus measurements. Because viscosity of the SEI is likely driven by the composition of the organic SEI phases, which are challenging to characterize with other nanoscale characterization techniques, they believe that this approach represents a novel and promising approach to electrolyte screening for future electrolyte engineering. To further characterize and understand the influence of the SEI nanomechanics on cell performance, they intend to perform further mechanical studies on more electrolytes as well as repeating the previous measurements in-situ to capture the role of SEI chemistry and mechanics on battery performance.

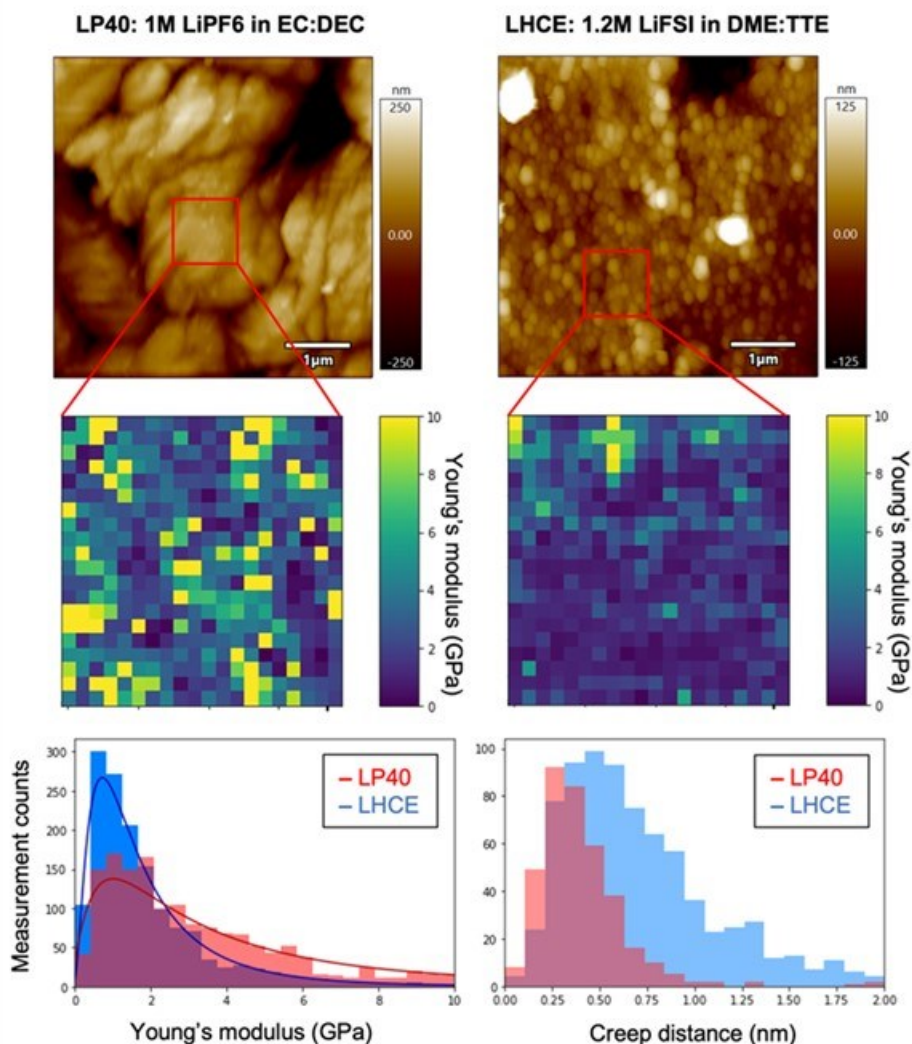
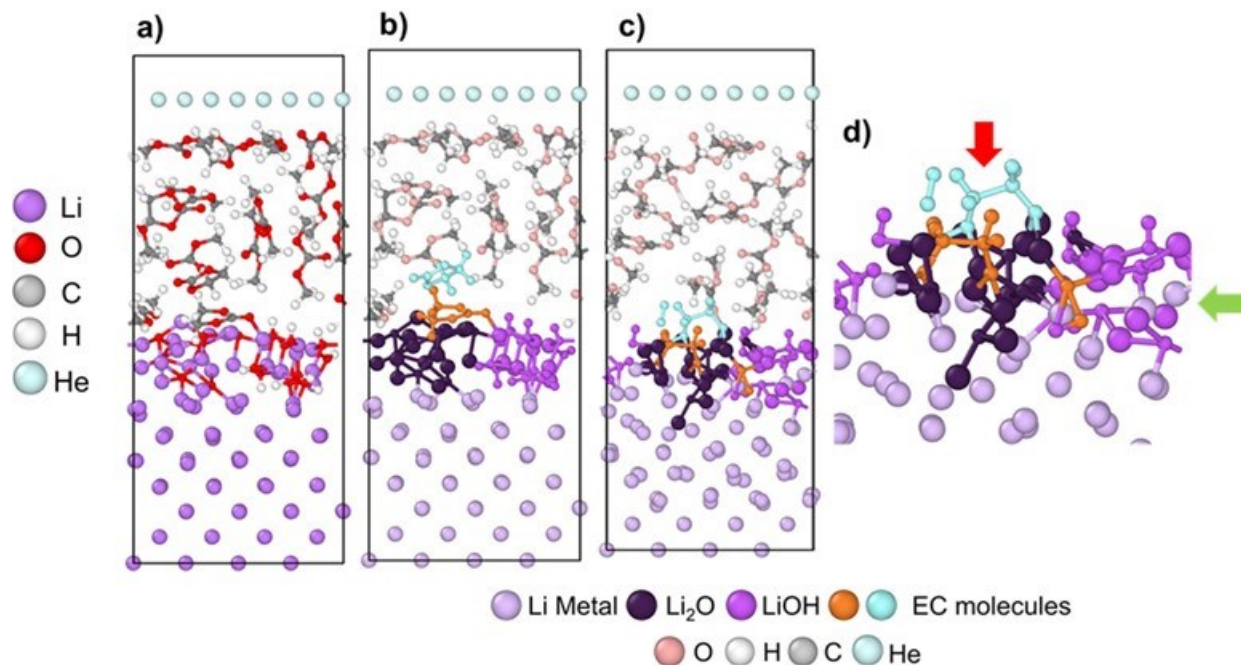


Figure XVII.1.76 Nanoscale Young's modulus measurement performed on SEI formed on Li metal in 1M LiPF<sub>6</sub> in EC:DEC (left) and in 1.2M LiFSI in DME:TTE electrolyte (right).

#### ***Growth of SEI at the surface of Li meta.***

A new fundamental understanding of ion transport and deposition in complex interphases was obtained at TAMU using first-principles simulations. Depending on the state of charge of the surface, clear differences are observed in the behavior and energy profile for ion transport at the interface. In the electron-rich environment provided by charged surfaces, the final charge transfer that leads to the ion reduction and deposition comes both from the partially charged solvation shell that assisted ion transport in the diffuse interfacial layer and from the Li metal surface. When the Li surface is partially covered by a Li<sub>2</sub>O SEI, it is found that the ion motion occurs through the border of the SEI structure where the cation moves through coordination with oxygen anions and displacement of the Li cations in the oxide surface (Figure XVII.1.77). On the other hand, for LiOH SEIs, the Li-ion enters the SEI structure and substitutes one of the SEI Li atoms, with another Li being released from the SEI to the electrolyte. Although the free energy profiles for the ion coming from the electrolyte into the Li surface looks similar to that of the ion traveling in the opposite direction, there is asymmetry in the magnitude of the barriers for solvation and desolvation, with the desolvation barrier for the ion to integrate with the SEI being higher than the solvation of the ion to enter the electrolyte phase. The LiOH structure offers better passivation properties than the Li<sub>2</sub>O; this is evident from the reactivity of solvent

properties on both surfaces. Inhomogeneous Li deposits on pristine surfaces were found to be unstable, triggering a surface self-healing mechanism. However, uneven Li deposits were found to be stable if located near SEI nuclei. Depending on the chemistry, the SEI blockage might become the focus for further electrolyte reduction (observed in  $\text{Li}_2\text{O}$ ) and ion motion is promoted through its border. This study also demonstrates that versatile computational chemistry tools allow elucidation of transport mechanisms in complex interphases, including SEI mixtures with various degrees of crystallinity. The results of this study were published in *ACS Appl. Mater. Interfaces* 2022, 14, 56758–56766, (2022).



**Figure XVII.1.77** AIMD simulation showing interfacial structural evolution for a Li metal surface covered with SEI formed with  $\text{Li}_2\text{O}$  and  $\text{LiOH}$ , in contact with a 1:2 EC:DMC electrolyte. a) Initial structure, b) initial structure color coded showing  $\text{Li}_2\text{O}$  and  $\text{LiOH}$  regions on the Li metal surface, c) final structure after  $\sim 11$  ps (AIMD at 300 K) showing EC molecules reacting preferentially on the  $\text{Li}_2\text{O}$  surface, and d) close-up of structure shown in c. The red arrow highlights reduced EC molecules and the green arrow shows the motion of the Li metal atoms towards the SEI surface.

#### ***Determining the relationship of equilibrium potential versus Li content in NMC 811 cathode for battery cell performance assessment and diagnostics.***

The INL team has recently developed a method to determine the equilibrium potential ( $V_{\text{eq}}$ ) of NMC 811 cathode as a function of the Li content in the NMC cathode active material (CAM) stoichiometry (i.e.,  $x$  in  $\text{Li}_x\text{Ni}_{0.8}\text{Mn}_{0.1}\text{Co}_{0.1}\text{O}_2$  or NMC 811). This  $V_{\text{eq}}$  vs.  $x$  relationship can provide a reliable and consistent basis for assessing the utilization of CAM in the high-energy battery designs to achieve cell development goals. The  $V_{\text{eq}}$  vs.  $x$  relationship is often determined by the galvanostatic intermittent titration technique (GITT). The experiment is typically conducted by passing a certain amount of charge to the CAM composition in a stepwise manner incrementally and measuring the steady equilibrium potential of the electrode ( $V_{\text{eq}}$ ) over a sufficient rest period in each step of the charge increase. Thus, the  $V_{\text{eq}}$  as a function of the charge increment is the same as the  $V_{\text{eq}}$  vs.  $x$  relationship with a presumption that the charge-composition correspondence is unity. The caveat is “if the CAM composition is fully utilized to assure that the presumption of a unified charge-composition correspondence is validated. Recently, through collaboration with Binghamton University, INL carefully examined the GITT data obtained from coin cells made of pristine EcoPro NMC 811 electrodes (named as E-C cells to stand for EcoPro-coin cells). Independently, INL conducted evaluations using cells made of Targray NMC 811 electrodes (named as T-C cells to denote Targray-coin cells). To evaluate cell

performance, they typically conduct reference performance tests (RPTs) with a specific protocol to ensure consistency in the assessment using the same condition for analysis. During the initial reference performance test (RPT 0) using C/20 rate in a charge-discharge process, they obtained a reliable pseudo-open-circuit-voltage (pseudo-OCV) versus state-of-charge (SOC) curve, where the SOC is the normalized specific capacity. To obtain this pseudo-OCV vs. SOC curve, the process usually entails a normalization of the voltage profiles using the specific capacity measured in each of the charge-discharge process to obtain a normalized specific capacity in percentage or capacity ratio and use it as the SOC. Subsequently, a process of averaging the voltage profiles according to the SOC is performed to obtain the pseudo-OCV. At C/20 rate, the polarization effect is assumed small, and averaging the voltage profiles is further assumed capable of annihilating the polarization effect and yielding a dependable pseudo-OCV in correspondence with SOC. The caveat is “if the SOC represents the Li content  $x$ ?”. The conundrum, either the GITT data (for Cell ID: E-C #3\_4.4 as an example) or the pseudo-OCV profile (for Cell ID: T-C\_4.4) in correspondence with specific capacity, as shown in Figure XVII.1.78a, is a riddle that has not been answered to date. The differences from the experimental measurements are hard to pinpoint where the origin(s) of the differences came from. If we use the normalized specific capacity as SOC to present the data, as shown in Figure XVII.1.78b, the similarity and consistency among the three profiles are improved but the disparities in voltage correspondence with SOC among the three remain difficult to explain, since that the polarization potential has been removed in the analysis. It could be suspected that the state of the cell during the measurement had not reached equilibrium, thus a certain degree of inhomogeneity may exist. However, the voltage and capacity of the cell should represent the volume-averaged results, so such an inhomogeneity should not be revealed on the global scale in this case. To resolve this conundrum, a proper analytic method would be highly desired.

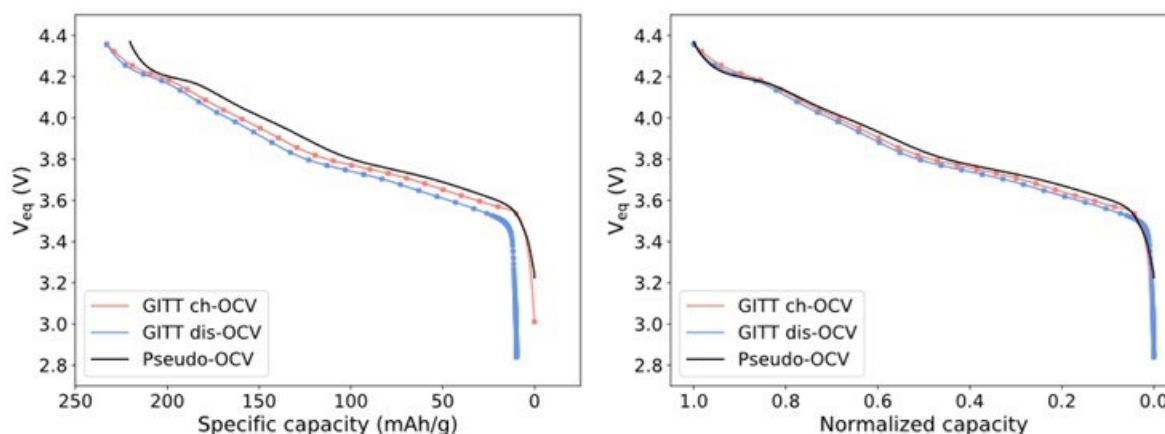


**Figure XVII.1.78** (a) Voltage profiles obtained from a GITT experiment using an EcoPro NMC 811 cathode by the Univ. Binghamton team (Cell ID: E-C #3\_4.4) and the pseudo-OCV profile obtained from a RPT 0 test using a Targray NMC 811 cathode by INL (Cell ID: T-C\_4.4). (b) Voltage profiles presented in normalized capacity as SOC.

In collaboration with Stanford team, the BNL team characterized the SEI formed in Stanford electrolyte and studied its evolution during cycling and its breathing during charge-discharge. Figure XVII.1.79a shows the cyclability of NMC811||Li full cell using coin cell configuration and following the PNNL test protocol. The stable cycling is consistent with the results previously reported by the Stanford team and other Battery500 Consortium members. SEI samples are collected from lithium metal anode surface at various cycles and characterized by high energy synchrotron X-ray for XRD and pair distribution function (PDF) results. The XRD data in Figure XVII.1.79b suggests XRD patterns of the SEI samples change as the battery goes through cycles, indicating an evolution of the SEI composition. The changes are mainly in the blue, green and yellow regions which are zoomed in for more details in Figure XVII.1.79c. The blue region indicates LiOH, which is present in native surface film on Li foil anode as suggested by our previous studies, as well as many other



reports, is gradually consumed during cycling and converts to LiH and Li<sub>2</sub>O in the SEI. The extremely broad peak at around 2.5° is from the amorphous phase and its steady growth during cycling suggests that amorphous phase is continuously produced. The green region indicates that Li<sub>2</sub>O is also continuously produced during cycling. In initial cycles, the production of Li<sub>2</sub>O is at least partially contributed by the conversion of LiOH. After LiOH is exhausted, the production of Li<sub>2</sub>O continues, suggesting its formation is then exclusively from electrolyte decomposition. It is noted that the width of Li<sub>2</sub>O peak is becoming sharper in longer cycles, suggesting Li<sub>2</sub>O is experiencing microstructural evolution, and the grain size is likely to increase during cycling. The yellow region suggests that LiF peaks have an evolution pattern that is similar to Li<sub>2</sub>O peaks, meaning that it also experiences continuous production and grain size increase during cycling.

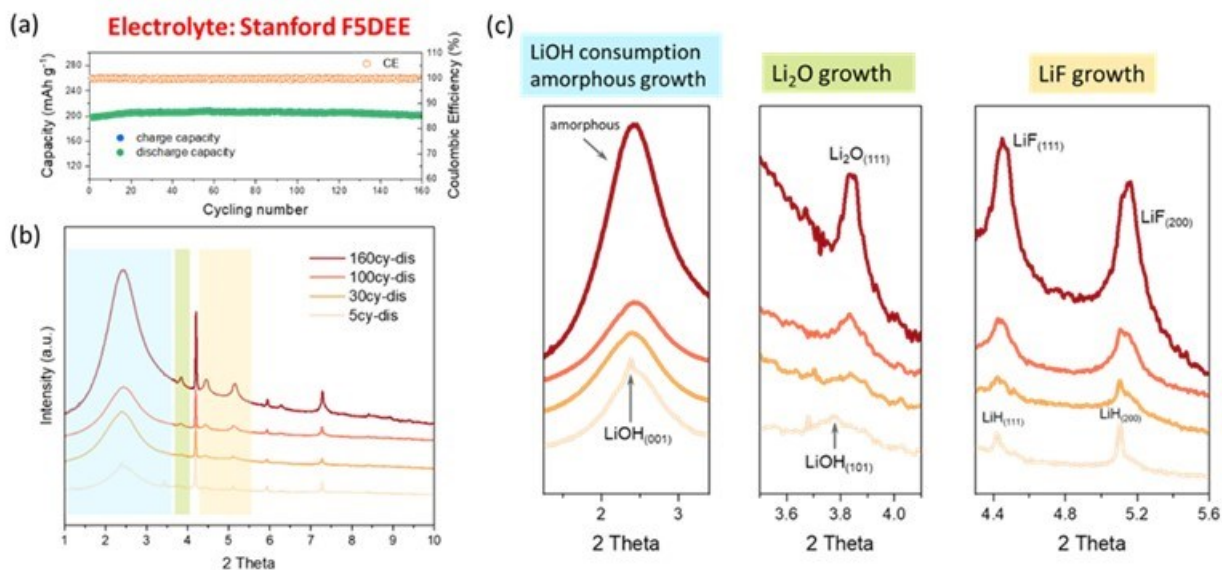


**Figure XVII.1.79** (a) Coulombic efficiency and capacity retention of NMC811 || Li cells using Stanford F5DEE electrolyte. (b) Synchrotron XRD data of SEI samples from different cycles. The wavelength used is 0.1818 Å. (c) The zoomed in regions in (b).

The PDF data in Figure XVII.1.80 provides detailed information about the evolution of amorphous phases in the SEI. In Figure XVII.1.80a, the peak in blue region can only be from amorphous phases which are dominated by short bonds such as C-C/O/F and S-N/O/F. In contrast, the peak in the yellow region can only be from crystalline phases which are dominated by long bonds such as Li-O/F. Therefore, Figure XVII.1.80a indicates amorphous phases are always the dominant components in lithium metal SEI. More detailed analysis of PDF peaks in Figure XVII.1.80b reveal the evolution of amorphous phases. The first panel in Figure XVII.1.80b shows peaks from direct bonds. Upon cycling, the peak position shifts to lower  $r$  region, indicating there are more short bonds in the amorphous phases in long cycled samples. As the amorphous phases from solvent and salt decomposition are dominated by carbon based shorter bonds (~1.4 Å) and sulfur based longer bond (~1.5 Å) respectively, the peak shift in Figure XVII.1.80b indicates that as the battery cycles, solvent decomposition gradually plays more important role in SEI amorphous component. This is further confirmed by analyzing PDF peaks in higher  $r$  regions that contain the second correlation (Figure XVII.1.80 b, middle panel) and the third correlation (Figure XVII.1.80b, right panel). Feature A can only be from solvent molecules which have two fluorine atoms bridged by a carbon atom. Feature B is also only from solvent molecules which have two oxygen atoms bridged by an ethyl group. These features are mostly absent in the PDF data of initial cycled SEI but become strong in the data of long cycled SEI, suggesting the long-cycled SEI has considerable amount of solvent decomposition products.

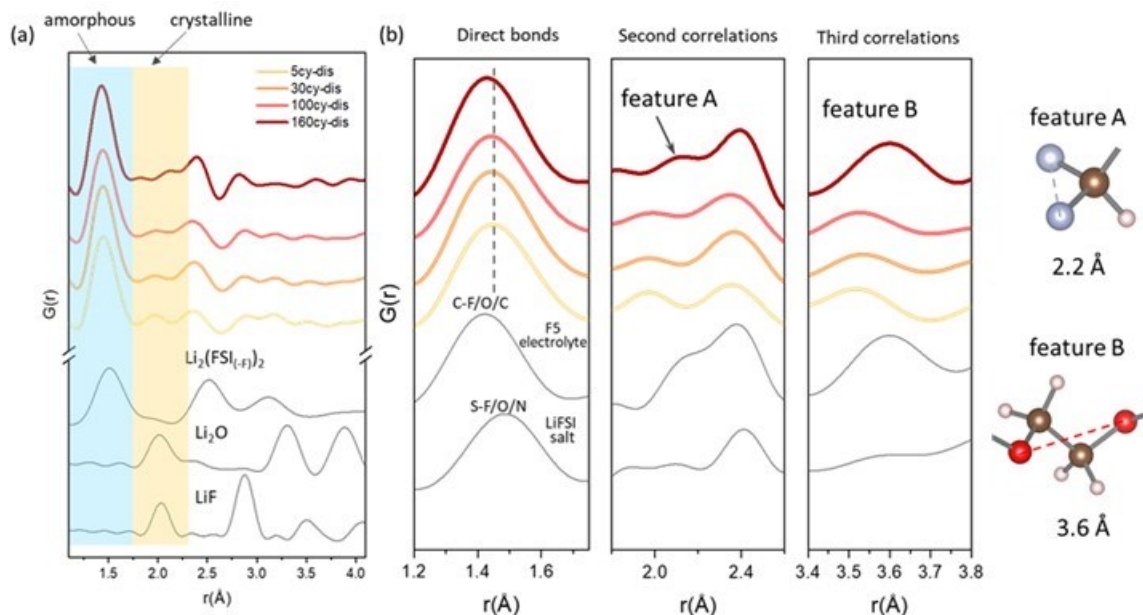


**Figure XVII.1.80** a) PDF data of SEI samples from various cycles. The reference data at the bottom are calculated from model compounds. (b) Selected zoomed-in regions in (a). The reference data at the bottom are measured.

In addition to studying the evolution of SEI at different cycles, the SEI components are also analyzed for both the charged and the discharged states to understand possible differences. As Figure XVII.1.81a suggests, the XRD patterns for the charged state and the discharged state have large differences, mostly in the peak that is from the amorphous phase. These results show clearly that more amorphous phases are in the charged state SEI than in the discharged state SEI, indicated by the peak intensity variation. To understand such difference, sulfur X-ray absorption spectroscopy was measured for the SEI samples both at charged and discharged states as shown in Figure XVII.1.81b. It indicates that for the SEI at charged state, there are several sulfur-based species including sulfones and their reduced forms such as sulfoxides and sulfides. However, for the SEI at discharged state, mostly only sulfone species are found. Combining the information from Figure XVII.1.81a and Figure XVII.1.81b, a possible scenario can be proposed for understanding the SEI variation from charged to discharged states. The illustration is shown in Figure XVII.1.81c. The sulfone species that are formed from anion decomposition may be gradually reduced during the charge process of the battery (the anode side is receiving electrons from the circuit and therefore highly reducing), forming species like sulfoxides and sulfides. The polarities of these reduced products are much lower than that of the sulfone species, making sulfoxides and sulfides more prone to dissolution in the fluorinated ether electrolyte. As a result, when the battery is discharged, the previously formed reduced species are gradually dissolved by the electrolyte, causing a decrease in the SEI amorphous components as observed in Figure XVII.1.81a.

These results advance our understanding of the SEI formed in Stanford electrolyte and will help us to provide guidance that may help to improve the electrolyte further for even longer cycles of NMC811||Li batteries.

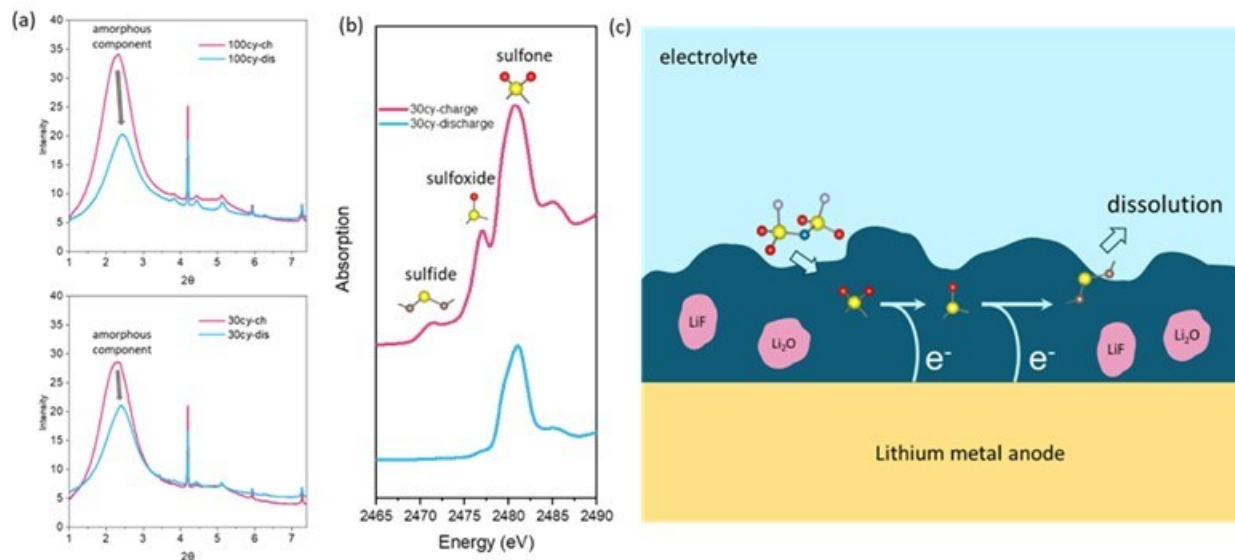


**Figure XVII.1.81** (a) The XRD patterns of SEI samples collected from both charged and discharge states. The top panel is for the 100<sup>th</sup> cycle and the bottom for the 30<sup>th</sup> cycle. (b) Sulfur K-edge X-ray absorption spectroscopy of SEI samples at charged and discharged states (both from 30<sup>th</sup> cycle). (c) Schematic illustration of the SEI reduction and dissolution process during charge-discharge.

#### **SEI mechanical properties.**

The mechanical property of the SEI has a significant effect on the morphology of plated lithium metal during cycling. To understand this coupling, the Stanford team (Chueh & Bao) employed atomic force microscopy to quantify the nanoscale mechanical property of SEI on lithium metal. Specifically, we compared indentation curves for SEI grown in both LP40 baseline electrolyte and in the LHCE electrolyte. To minimize the substrate effect (i.e., lithium metal), we take the force curve from the first 3 nm of the indentation (Figure XVII.1.82). The SEI in LHCE has a lower Young's modulus, despite exhibiting substantially better coulombic efficiency. This surprising result is under further investigation. The SEI in LHCE is also plastic, which could be the key parameter influencing the lithium metal morphology.

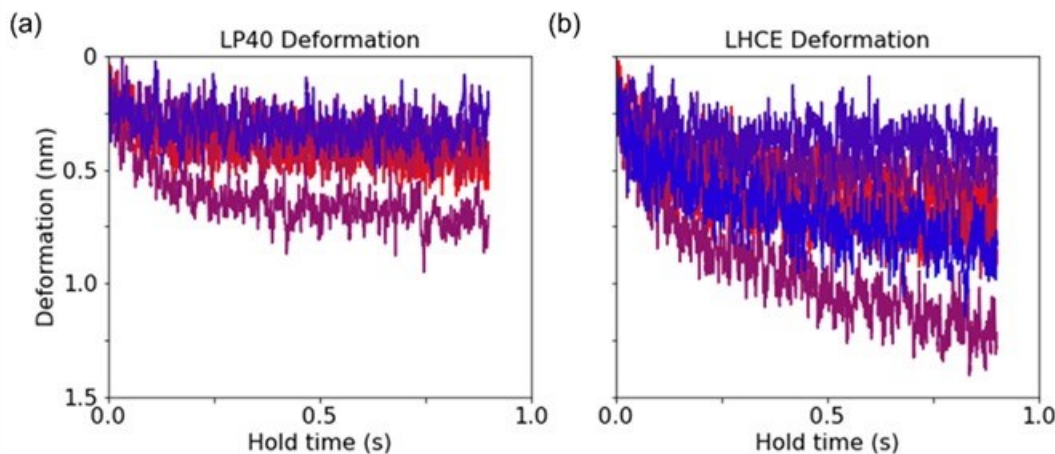


**Figure XVII.1.82** Comparison of indentation deformation curves via atomic force microscope for SEI on lithium metal for LP40 baseline electrolyte and LHCE electrolyte

**Safety Properties of Li Metal Batteries.**

Meng's group at UCSD found that electrolyte plays a major role in controlling the thermal stability of Li in liquid electrolyte. The UCSD team further explored the effect of the cycle number on the thermal stability of the Li anodes. The reactivity of the three types of anodes was also studied after 10 cycles. Figure XVII.1.83 a-c shows the DSC curve and the morphology of the lithiated Graphite anode after 10 cycles. Similar to those reported in FY2023Q1 for the 1st cycle charged Graphite samples, most of the DSC peaks in Figure XVII.1.83 for samples after 10 cycles are associated with the evaporation of the electrolyte solvents, with the exception of two exothermic peaks near the temperature ranges of such solvent evaporation. As shown in Figure XVII.1.83 b and c, there seems to be some SEI accumulation on the Graphite surface as the layered surface morphology of graphite disappeared after 10 cycles. The above mentioned two small heat releasing peaks (at around 100°C and 230°C) might be associated with the oxidation of the Li-Gr electrode during the solvent evaporation process. A similar trend is found in the 10-cycled Si anode (Figure XVII.1.83 d-f), where two exothermic peaks (at around 100°C and 230°C) are also found during the same temperature range. The SEI accumulation is also obvious on the Si surface (Figure XVII.1.83 e-f). The accumulation of SEI and trapped Li in the Gr and Si electrodes after 10 cycles might contribute to the two small heat releasing peaks observed in the DSC. Overall, the reactivity of lithiated Si and Graphite is relatively low, as no large exothermic peaks are observed during the heating process. Figure XVII.1.83 g shows the DSC curve of the plated-Li in LHCE electrolyte after 10 plate-strip cycles. As the inserted images and SEM images are shown (Figure XVII.1.83 h-i), because of the superior performance of the LHCE, the deposited Li is still shiny, and the Li particles are bulky after 10 cycles. In addition to that, most of the electrolyte solvents are evaporated before the Li melting point. As a result, the thermal response of the Li in LHCE is still relatively low, with only 39.8J/mAh of heat released during the heating process, which is in the same magnitude as the Li-Gr and Li-Si cases. However, for the plated-Li in Carbonate electrolyte, there is a large amount of mossy Li accumulated on the electrode surface (Figure XVII.1.83 k-l and insert of Figure XVII.1.83 j). Because of the low cycling Coulombic efficiency (CE) of the Carbonate electrolyte, there is a significant amount of nano-size inactive Li accumulated on the electrode, which can be seen as the mossy Li (Figure XVII.1.83 l). The accumulation of these nano-size inactive Li eventually caused an explosion of the DSC Pan during the heating process. Based on the results so far, it can be seen that both the electrolyte used, and the morphology of Li play significant roles in controlling the reactivity of Li.

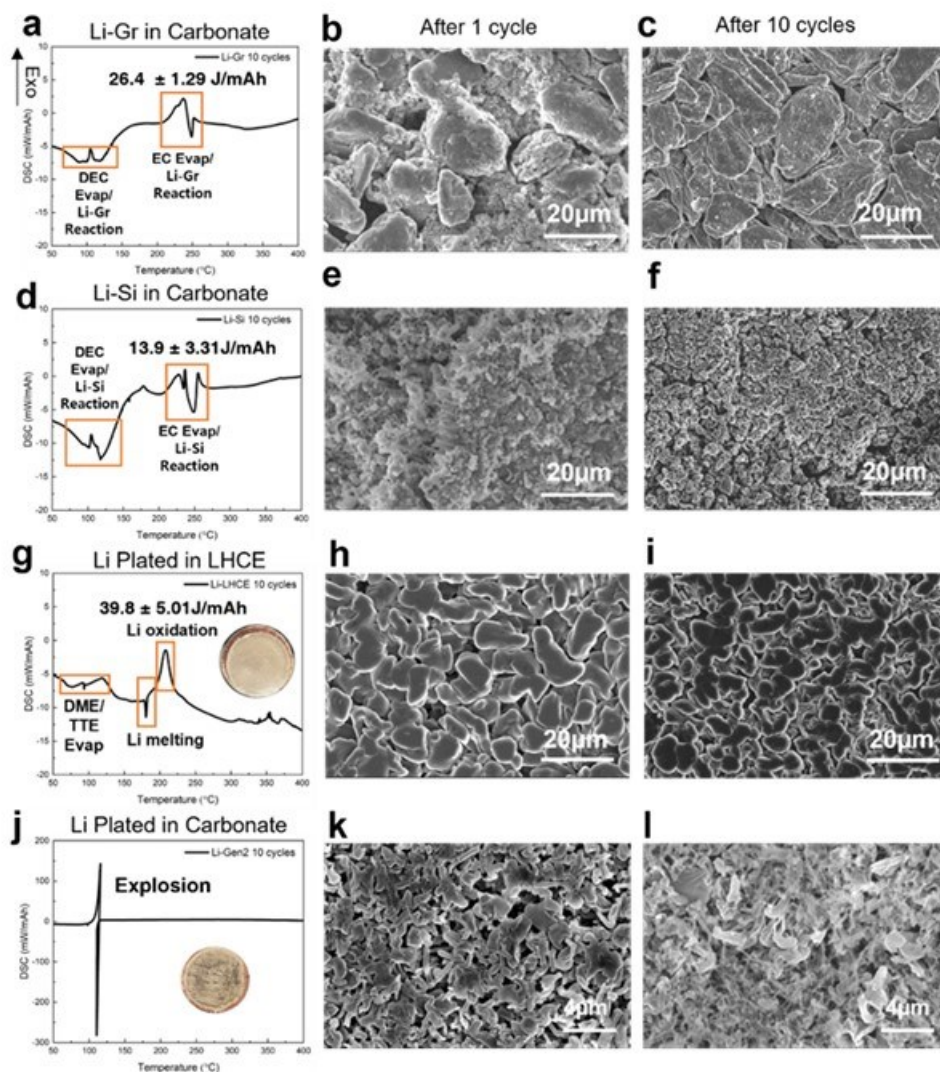


**Figure XVII.1.83** The DSC curves of (a) Li-Gr, (d) Li-Si, (g) Li plated in LHCE, and (j) Li plated in Carbonate after 10 cycles. The SEM images of anode morphology after 1 cycle and after 10 cycles: (b-c) graphite, (e-f) Si, (h-i) Li plated in LHCE, and (k-l) Li plated in Carbonated electrolyte. Inserts: the digital images of Li plated on the Cu after 10 cycles. The amount of heat released from the oxidation peak of each DSC curve is labeled in the corresponding figures. Graphite and Si anodes are cycled in half-cell configuration at a rate of C/20, and Li metal anodes are cycled in Li|Cu cells at a rate of 0.5mA/cm<sup>2</sup>

The TAMU team developed a new first-principles computational method to investigate the origin of battery runaway reactions. In this theoretical/computational approach, a component of the battery (anode, cathode, electrolyte, SEI, CEI) is subject to a heat rate and the corresponding free energy of the sample is computed as a function of temperature  $T$ . In this way, thermal decomposition reactions are monitored as a function of time. The new method emulates the DSC experiments where a sample is exposed at a given heat rate and the heat flow is measured. As the temperature increases, the DSC experiment shows maxima and minima in the measured heat flow that correspond to minima and maxima respectively in the computed free energy curve. By comparing results from different cell components, it is possible to infer the mechanism that may trigger a runaway reaction. This method was applied to SEIs formed at electrolyte/Li-metal interfaces for B500 electrolytes. The new method illustrated in Figure XVII.1.84 consists of two steps: first, the SEI corresponding to a given electrolyte formulation is computed with the hybrid AIMD/CMD method introduced in previous reports (and also plotted in Figure XVII.1.84 a). Once the SEI morphology and composition is

found, the system is heated at a given heat rate (in this case 30 K/ps), and the free energy is recorded as a function of temperature (Figure XVII.1.84 b). The sharp decrease and minimum in the free energy at temperatures in the order of 400K correspond to the first (very exothermic) thermal decomposition of SEI organic components; it is followed by other reactions that lead to changes in the heat flow. As T increases, the system becomes highly unstable as shown by the sharp increase in the free energy. For the LP30 electrolyte, 1M LiPF<sub>6</sub> in EC:DMC (1:1 by vol) in Figure XVII.1.84, the SEI reveals the presence of Li<sub>x</sub>O and Li<sub>x</sub>F nuclei that tend to form extended amorphous regions of oxides and fluorides. Hybrid inorganic-organic nuclei (e.g. Li<sub>x</sub>O-CH<sub>3</sub>) are also detected in this SEI.

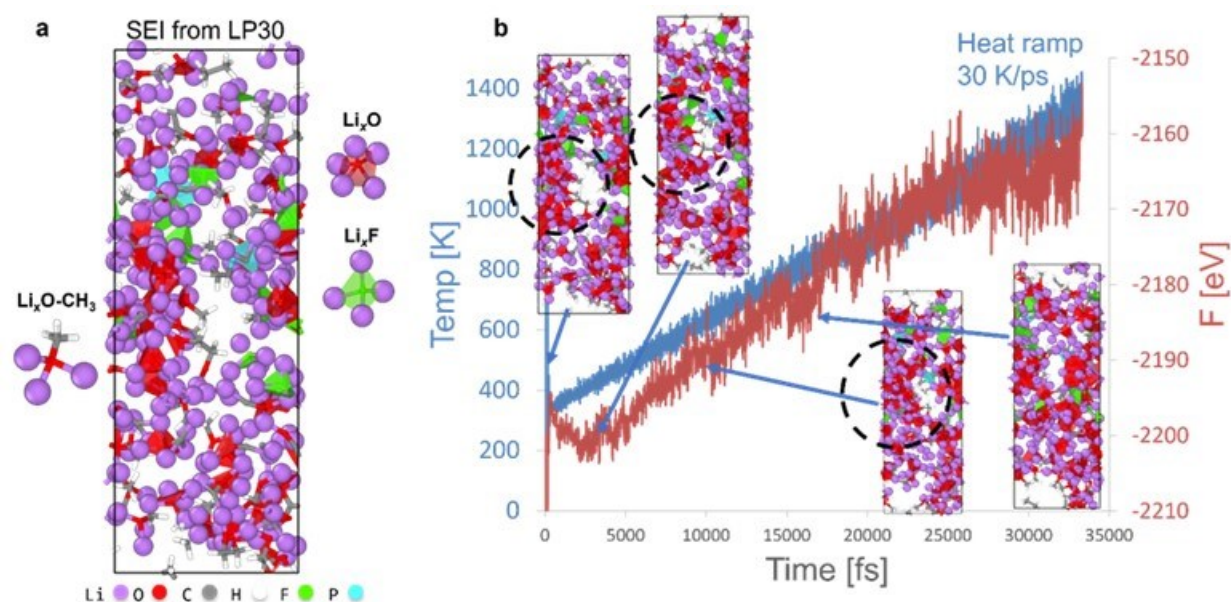


**Figure XVII.1.84** (a) SEI computed for LP30 electrolyte. It is an amorphous structure composed by nuclei of Li<sub>x</sub>O, Li<sub>x</sub>F, and hybrid structures as Li<sub>x</sub>O-CH<sub>3</sub>. Organic fragments are attached to the inorganic nuclei surface. (b) SEI thermal decomposition induced by a temperature ramp of 30 K/ps (blue line). At each temperature, the free energy F of the sample is evaluated (red curve). The first minimum in F corresponds to the thermal decomposition at about 400K of the organic fragments located in the open spaces of the porous SEI. The second minimum in F (~550 K) reveals decomposition of the organic fragments on the surface of the inorganic nuclei. At higher temperatures other minima reveal melting of the surface inorganic nanoparticles, and the overall system becomes highly unstable.

#### **High-Performance Liquid Chromatography–Ultra-Violet Spectroscopy (HPLC-UV).**

Meng's group at UCSD reported High-Performance Liquid Chromatography–Ultra-Violet Spectroscopy (HPLC-UV) calibration data for quantifying dissolved elemental sulfur and two shorter-chain methylated polysulfides: CH<sub>3</sub>S<sub>2</sub>CH<sub>3</sub> and CH<sub>3</sub>S<sub>3</sub>CH<sub>3</sub>. The team identified and confirmed the position of other longer-chain methylated polysulfides CH<sub>3</sub>S<sub>x</sub>CH<sub>3</sub> (x =4, 5, 6, 7, 8) by HPLC-UV and High-Performance Liquid Chromatography–Atmospheric Pressure Chemical Ionization Mass Spectroscopy (HPLC-APCI-MS)-negative mode. They proposed a methodology involving semi-preparative HPLC-UV and Induced Coupled Plasma-Mass Spectroscopy (ICP-MS) to quantify those species. The correlations of the area under the HPLC-UV curve for each species was obtained by ICP-MS. The final goal is to track the contribution of each component (lithium metal, elemental sulfur, and dissolved polysulfides) loss to the total full cell capacity losses. Firstly, the UCSD team prepared derivatized polysulfide mixtures of five different concentrations based on protocols reported before. This gave five different concentrations of each methylated polysulfide species and related semi-preparative HPLC-UV areas under the curves as seen in the chromatograms (Figure XVII.1.85). Well-separated peaks of each species make the fraction collection process simple, subsequently the collected species can be digested with the optimized ICP protocols reported in the last report, which were heating the fractions of each species of each concentration separately for 3 hours at 180°C after digesting them for three days in

concentrated acid and oxidizer solution. Then injected 100  $\mu\text{L}$  of each derivatized polysulfide mixture and collected each fraction which were then diluted to make a final sample of 10 mL. Thus, when ppb amounts of [SO] are obtained for ICP samples, a simple dilution factor of 100 is considered to calculate the species concentration in the original solution ( $\text{mg}\cdot\text{L}^{-1}$ ). This includes calculating species moles based on the sulfur moles obtained after digesting each species of  $(\text{CH}_3\text{S}_x\text{CH}_3)$ . Note that only the polysulfide species that are confirmed by HPLC-APCI-MS will be quantified.

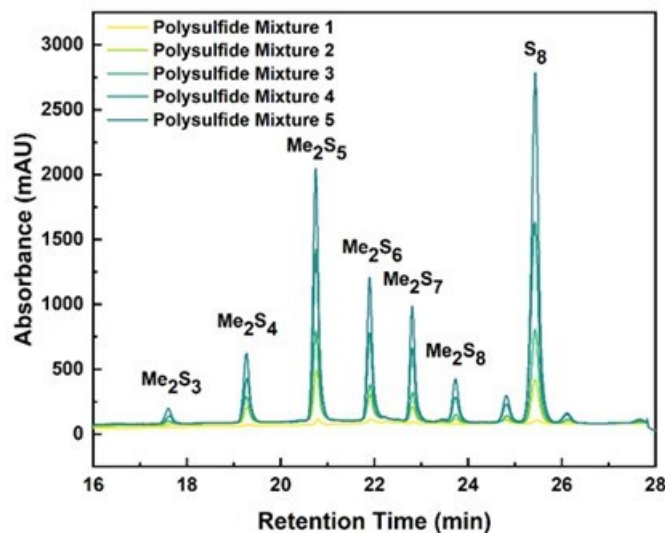


Figure XVII.1.85 The schematic of the semi-preparative HPLC-UV chromatograms of five different concentrations of derivatized polysulfide mixtures

#### **Quantifying Lithium inventory in Lithium-Sulfur Batteries during calendaring.**

The self-discharge of Li-S batteries is mostly due to diffusion and reactions of Sulfur and polysulfides (PS) at the anode-electrolyte interface. This study used 5 electrode layer pouch cells with lean electrolyte (E:S = 5) and thin Lithium foil (N:P = 2). Meng's Lab at UCSD compared two types of electrolytes for this study (i) Moderately PS solvating electrolyte (1 M LiTFSI in DME:DOL=1:1 (v/v) with 2 wt.%  $\text{LiNO}_3$ ) (ii) Weakly PS solvating electrolyte (provided by NexTech Batteries). In FY2023Q2, Lithium inventory in Li sulfur cells after 7 days resting was quantitatively measured by TGC methodology when no electrochemical operation was taken as shown in Figure XVII.1.86a. Sulfur dissolution in electrolytes is the triggering point for lithium inventory loss. Compared to the weakly solvating electrolyte, the moderately solvating electrolyte has more PS solubility, which is generated by the reduction of Sulfur on the lithium metal anode, even though no external current is applied. A similar study was conducted for 24 hours and 30 days of resting. According to Figure XVII.1.86b, the amount of lithium in the Moderately solvating electrolyte decreases faster than the Weakly solvating electrolyte. Initially, the pristine lithium foil had a measured inventory of  $9.85 \pm 0.18 \text{ mAh}\cdot\text{cm}^{-2}$ . After 24 hours, the lithium inventory detected by TGC was  $9.15 \pm 0.2 \text{ mAh}\cdot\text{cm}^{-2}$  in the Moderately solvating electrolyte, while in the Weakly solvating electrolyte, it was  $9.70 \pm 0.12 \text{ mAh}\cdot\text{cm}^{-2}$ . Similarly, after 7 days and 30 days of rest, the remaining active  $\text{Li}^0$  inventory in the Moderately solvating electrolyte was  $8.95 \pm 0.1 \text{ mAh}\cdot\text{cm}^{-2}$  and  $8.45 \pm 0.2 \text{ mAh}\cdot\text{cm}^{-2}$ , respectively. In the weakly solvating electrolyte, the measured values were  $9.47 \pm 0.2 \text{ mAh}\cdot\text{cm}^{-2}$  and  $9.25 \pm 0.14 \text{ mAh}\cdot\text{cm}^{-2}$  after 7 days and 30 days of resting, respectively. The difference in  $\text{Li}^0$  inventory widens as the resting period duration increases. In the Moderately solvating electrolyte, a portion of the  $\text{Li}^0$  inventory dissolves in the electrolyte as long-chain lithium polysulfides, while the rest is transformed into short-chain polysulfides with poor electrochemical activity, such as  $\text{Li}_2\text{S}$ .

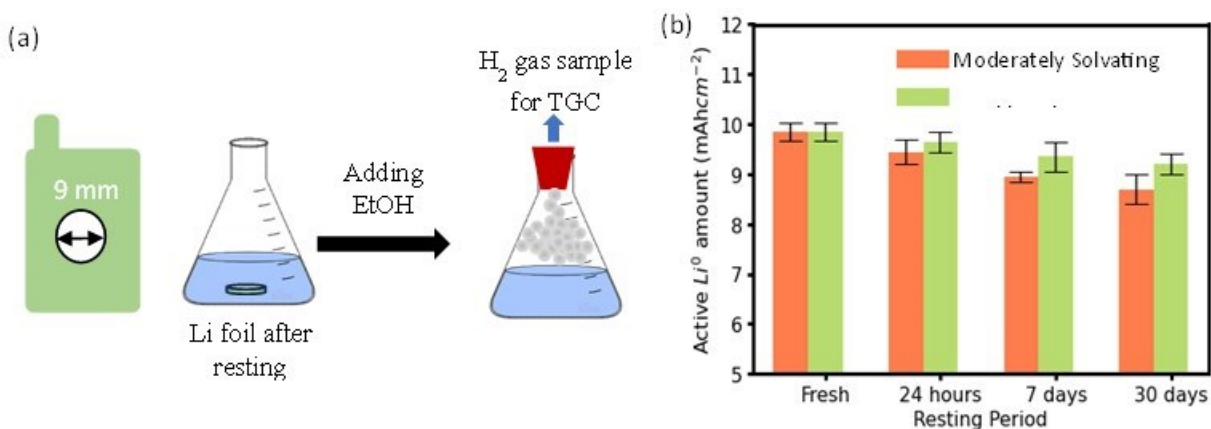


Figure XVII.1.86 (a) Quantification of Lithium after, when no electrochemical operation is performed (b) Lithium inventory after resting

After resting for different periods without electrochemical operation, lithium top morphology becomes rougher in Moderately solvating electrolytes, compared to the Weakly solvating electrolyte, witnessed in Figure XVII.1.87. Since lithium metal is highly air-sensitive, the lithium metal samples were prepared in an Ar-filled glovebox. To protect lithium from ambient conditions, the top and cross-section SEM images were taken under cryo temperature (approx.  $-180^{\circ}\text{C}$ ). This also reduces sample damage due to gallium ion beam. Here, Figure XVII.1.87a and Figure XVII.1.87e represent the fresh lithium metal foil. It is observed that in moderately solvating electrolyte, lithium corrosion starts within 24 hours, more severe compared to weakly solvating electrolyte. The high roughness due to lithium corrosion is more evident in moderately solvating electrolyte after 7 days (Figure XVII.1.87c) and 30 days (Figure XVII.1.87g), compared to weakly solvating electrolyte after 7 days (Figure XVII.1.87d) and 30 days (Figure XVII.1.87h).

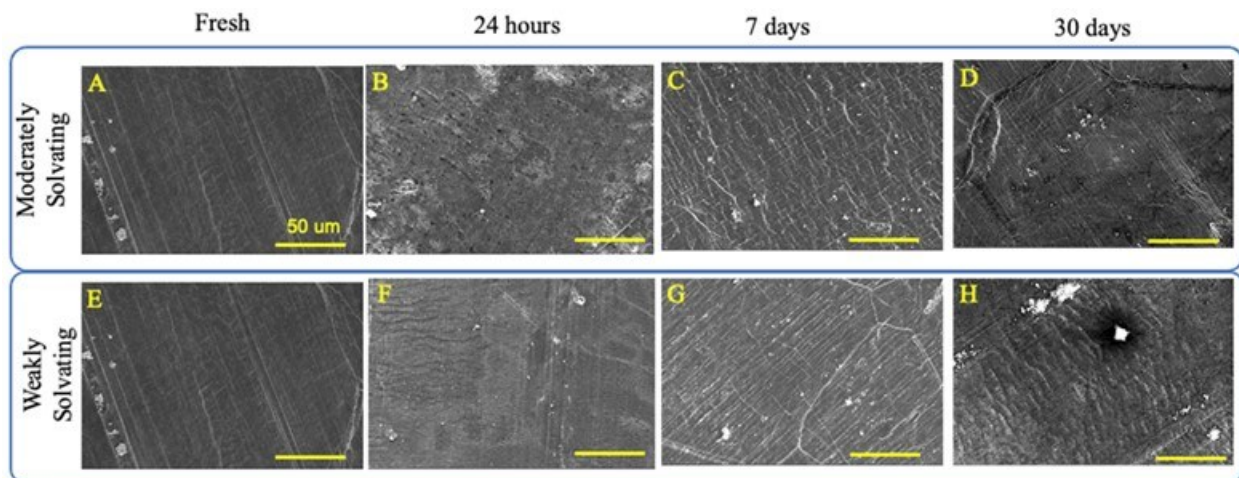
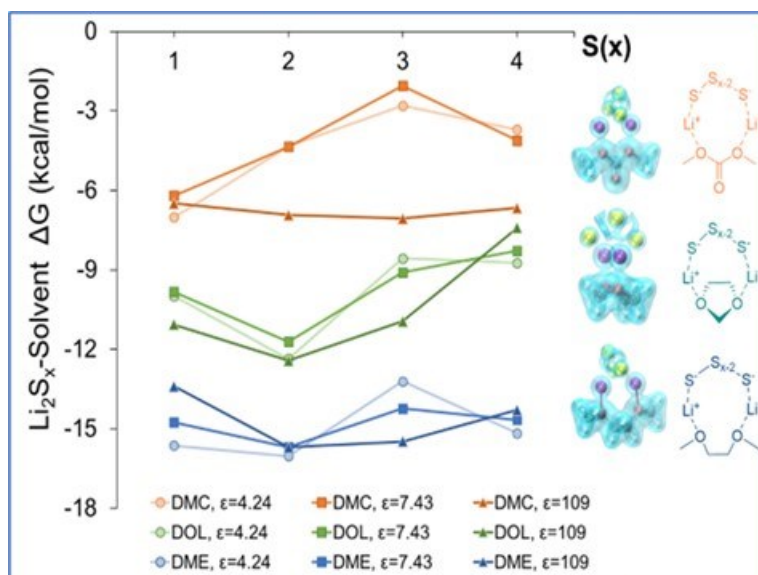


Figure XVII.1.87 Lithium metal morphology after resting in moderately (a, b, c, d) and Weakly solvating electrolyte (e, f, g, h). Here, images are from fresh lithium (a, e), 24 hours rest (b, f), 7 days rest (c, g); and 30 days (d, h)

Electrolyte effects on SPAN cathodes. The TAMU team studied electrolyte effects on discharge reactions in SPAN. The theoretical-computational study provides an overview of the lithiation reactions and solvation effects in SPAN structures. Analyses include a diluted solution of LiFSI, based on DMC or DME as solvents.



AIMD simulations were used to follow major chemical events between electrolyte species and reaction intermediates during electrochemical lithiation. The thermodynamics of the SPAN structures was evaluated using four pyridine units to serve as PAN backbone in DFT optimizations. Figure XVII.1.88 shows that in the DMC-solvated system, solvent stabilization revealed by the free energies (vertical axis) is much less significant than in DOL and DME, resulting in less dissolution of  $S_x$  chains. The clear boundaries between Li and S atoms in electronic Laplacian isosurfaces (Figure XVII.1.88, right) indicate ionicity of the bonding between  $Li^+$  and  $S_x^{2-}$ . In contrast, despite poor electronic density overlap between Li and  $O_{(solvent)}$  in all clusters, the positive Laplacian values in their bridging spaces suggest the  $Li^+-O_{(solvent)}$  bonding is semi-covalent. In  $Li^+$ -mediated solvent-SPAN interactions, the PSs bonded on PAN backbone display the consistent  $Li^+-S$  or  $Li^+-O_{(solvent)}$  bonding nature as discussed. Therefore, it is reasonable to treat  $[Li^+-solvent]$  as an ionic cluster which dissolve PSs via electrostatic forces.



**Figure XVII.1.88**  $Li^+$ -coordinated polysulfide-solvent interactions have strong dependence on solvation environments. Left: Free energy of  $Li_2S_x$  interaction with DMC, DOL, and DME. Right: Electronic Laplacian isosurfaces (iso-value = 0.09) of the corresponding structures (only showing  $x = 3$  cases) illustrate the solvent effect on the type of bonding

#### **Crosstalk effects between cathode and anode in lithium metal batteries.**

By collaborating with the PNNL team, the BNL team studied the cathode-to-anode crosstalk effect and its impact on the formation of the anode interphase, or the conventionally called solid-electrolyte-interphase (SEI). The desired SEI component  $LiF$  is usually formed when using high concentration electrolyte (HCE) or localized high concentration electrolyte (LHCE) which use a large number of expensive salts. Here the team explores the possibility of  $LiF$  formation in low concentration electrolyte which can be more cost-effective than HCE and LHCE.

The  $Li||Cu$  and  $Cu||NMC$  ( $LiNi_{0.8}Mn_{0.1}Co_{0.1}O_2$ ) cells were prepared and cycled with 1M lithium bis(fluorosulfonyl)imide ( $LiFSI$ ) in 1,2-dimethoxyethane (DME). The electrochemical results are shown in Figure XVII.1.89a and Figure XVII.1.89b, respectively. Because of the relative stability of DME against  $Li^0$ ,  $Li||Cu$  cell has a Coulombic efficiency of  $\sim 90\%$  and runs for at least 50 cycles. In comparison, the  $NMC||Cu$  cell experienced rapid capacity decay, due to the limited Li source and the instability of DME at high voltage. Figure XVII.1.89c and Figure XVII.1.89d compare the X-ray diffraction (XRD) results of the SEIs formed in both situations. The crystalline components of the SEI in  $Li||Cu$  are mostly  $LiH$  and  $LiOH$ , with little if any  $LiF$  present. This is consistent with the current understanding of the SEI in low concentration electrolyte which

is mainly from solvent decomposition. Surprisingly, a large amount of LiF was observed in the SEI formed in NMC||Cu cell even though the same low concentration electrolyte was used. Our previous work has indicated that the LiF phase in SEI has distinct microstructural properties from the standard bulk LiF, so the notation LiF<sub>(SEI)</sub> is used to differentiate it from bulk LiF. Since FSI<sup>-</sup> anion is the only fluorine source, the abundance of LiF<sub>(SEI)</sub> indicates that anion decomposition makes major contributions to the SEI formation. Comparing with results from the Li||Cu cell, it is very likely that anion decomposition in NMC||Cu cell is caused by the presence of NMC cathode.

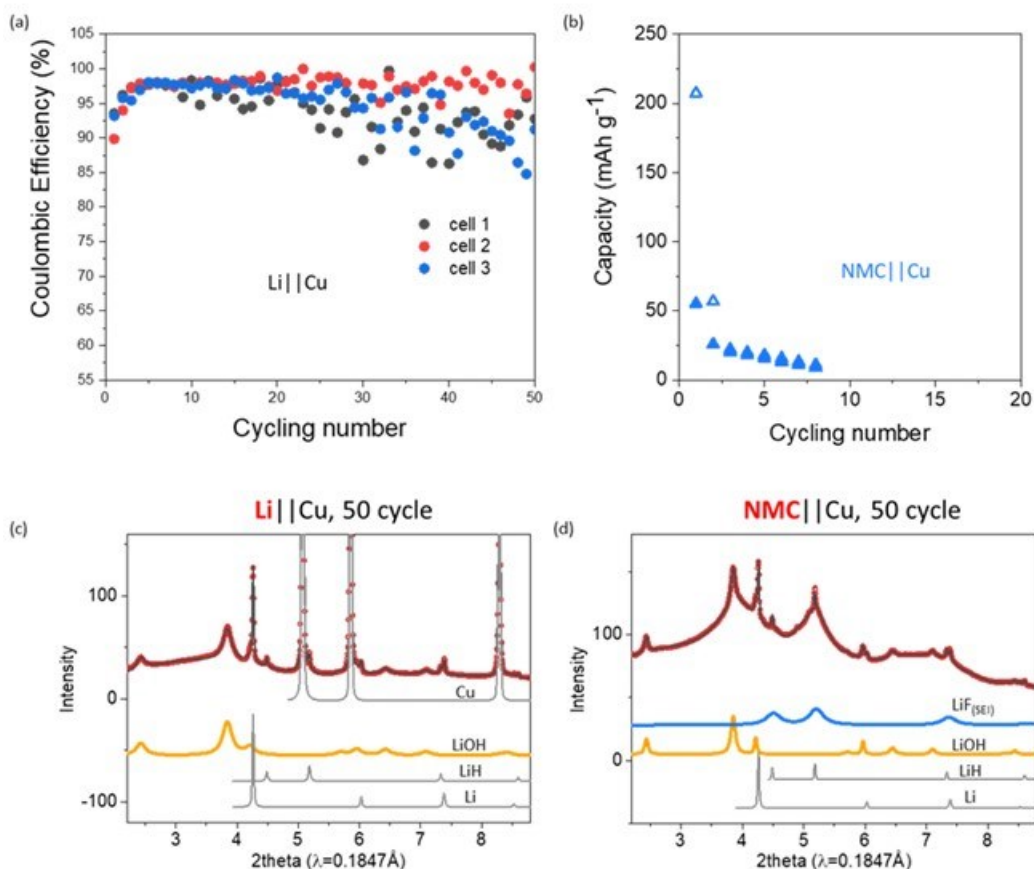


**Figure XVII.1.89** Electrochemical cycling results of (a) Li||Cu and (b) NMC||Cu cells. XRD Rietveld refinement results of SEI collected on Cu foil of (c) Li||Cu and (d) NMC||Cu cells after 50 cycles.

A possible scenario is proposed to explain the observed results (Figure XVII.1.90a and Figure XVII.1.90b): The FSI<sup>-</sup> decomposition might be initiated by the NMC cathode which operates at high voltage and contains chemically catalytic elements such as Ni, Mn and Co. This is supported by the previous literature report on the oxidation instability of LiFSI salt. The catalytic effect of transition metal is evidenced by comparing the XPS results for SEIs in Li||NMC811 and Li||Carbon cells (Figure XVII.1.90c). It suggests that in addition to the application of high voltage, the presence of NMC cathode is required to induce the anion decomposition. The XPS result for cathode-electrolyte-interphase (CEI) in Figure XVII.1.90 suggests it is likely that anion first decomposes on the cathode side, forming SO<sub>2</sub>F<sub>y</sub><sup>-</sup> species which are highly soluble in DME-based electrolyte, before migrating to the anode side and further decomposes into LiF<sub>(SEI)</sub> and other anion-derived species. Such a possibility is also supported by the fact that unlike the anode side, where the anion must overcome the Coulombic repulsion to get reduced, the cathode is a natural attraction for negatively charged anions.

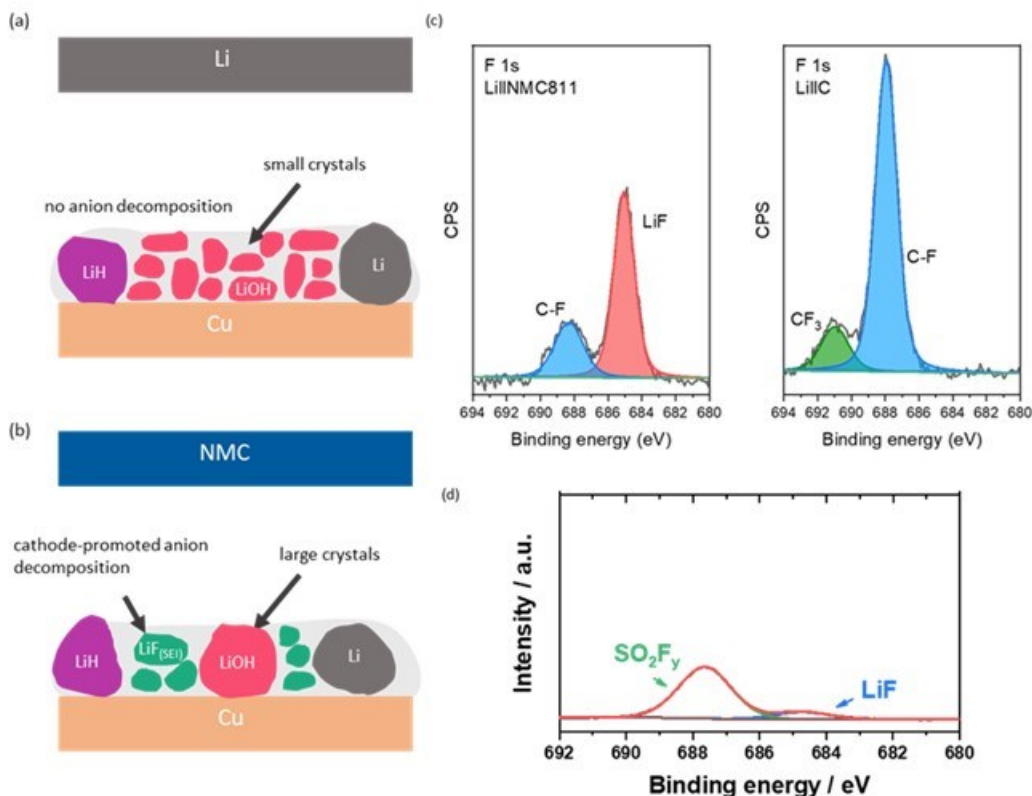
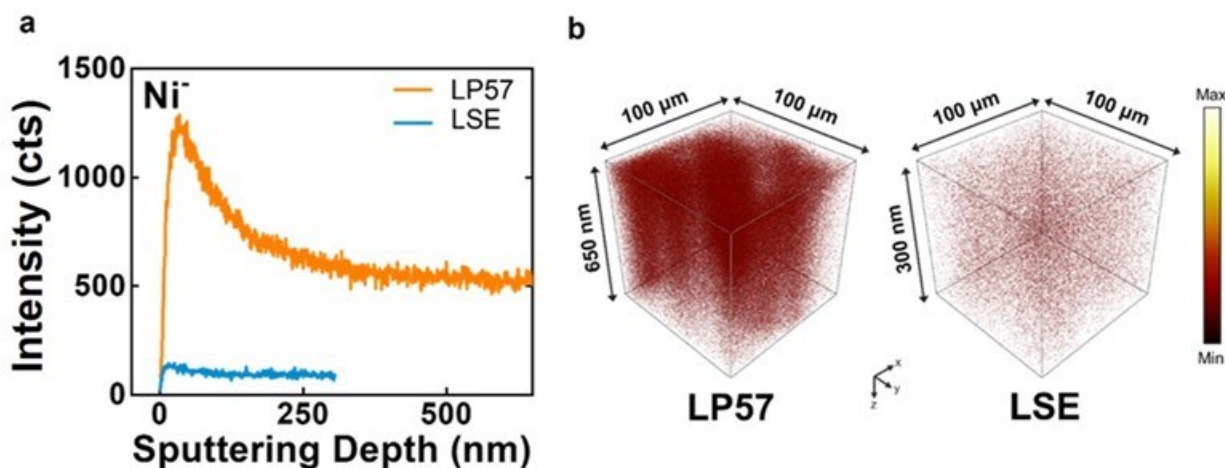


Figure XVII.1.90 (a-b) Schematic pictures of the SEI compositions and structures based on XRD results. (c) F1s XPS spectra on the surface of Li metal anodes after three cycles of cyclic voltammetry using Li || NMC811 and Li || Carbon cells in the voltage range of 2.8-4.2 V. (d) F1s spectra of the cycled NMC811 in Li || NMC811 cycles.

Similar crosstalk effect is also observed in Li||NMC cell. The SEI XRD results suggest the abundance of LiF<sub>(SEI)</sub> due to the presence of NMC cathode. Since LiF<sub>(SEI)</sub> has been generally regarded as a beneficial interphase component for electrochemical performance, the crosstalk effect could be potentially useful for lithium metal batteries. To test this idea, crosstalk is purposely enhanced by increasing the charging cut-off voltage during the formation cycle. After the formation cycle, the exact same cycling protocol is used for both the baseline cell and the 'crosstalk-enhanced' cell. The results show that the 'crosstalk-enhanced' cell indeed has better capacity retention than the baseline cell, demonstrating the possibility of leveraging the crosstalk effect for benefits in cycle life.

UT Austin team conducted an advanced high-resolution 3-D chemical analysis with time-of-flight secondary-ion mass spectrometry (TOF-SIMS) to understand the effects of transition-metal crossover in cells cycled with two different electrolytes. Li | LiNi<sub>0.7</sub>Mn<sub>0.25</sub>Al<sub>0.05</sub>O<sub>2</sub> half-cells that were cycled to 4.6 V vs. Li/Li<sup>+</sup> for 500 cycles with the conventional LP57 electrolyte or localized saturated electrolyte (LSE) were studied to understand the effect of high voltage cycling. LP57 consists of 1 M LiPF<sub>6</sub> dissolved in a binary solvent system of ethylene carbonate (EC) and ethyl methyl carbonate (EMC) with 2 wt % of vinylene carbonate. The LSE was prepared with a binary solvent system of EC : EMC (3 : 7) by weight that is first saturated with 3 M LiPF<sub>6</sub> salt, followed by adding the diluent 1,1,2,2-tetrafluoroethyl-2,2,3,3-tetrafluoropropyl ether (TTE) to lower the overall concentration of LiPF<sub>6</sub> from 3 to 1 M and retain the solvated salt-solvent clusters in solution. Then, a 3 vol % fluoroethylene carbonate (FEC) was added to the LSE as an additive. Figure XVII.1.91 shows the TOF-SIMS results obtained on the lithium-metal anodes after 500 cycles. It is clear that there is a pronounced effect of the electrolyte on the amount of transition-metal dissolution that has occurred within the system. In particular, the absolute amount of transition metals found on the anodes cycled in LP57 exhibit one

order of magnitude higher signal ( $\sim 1,250$  counts) than that found with the LSE ( $\sim 125$  counts) (Figure XVII.1.91a). Furthermore, the 3-D spatial renders of the Ni<sup>-</sup> species on Li-metal indicates that the transition metals are heterogeneously distributed in the case of LP57 cell compared to the more homogeneously distributed in LSE cell (Figure XVII.1.91a). Additional work is currently ongoing to uncover how this heterogeneity affects electrochemical performance and elucidate the mechanisms behind how the LSE reduces transition-metal dissolution and crossover.



**Figure XVII.1.91** Comparison of the amount of Ni<sup>-</sup> present in the SEIs of the anodes cycled in LP57 and LSE. (a) Absolute intensities versus sputtering depth (nm) for the Ni<sup>-</sup> secondary ion fragments. (b) 3-D rendered volumes displaying the distribution of Ni<sup>-</sup> throughout the bulk of the SEI. The color of the pixels in the 3-D renders correspond to the intensity that is denoted with the color bar. Data were collected on lithium-metal anodes obtained from Li | LiN<sub>0.7</sub>Mn<sub>0.25</sub>Al<sub>0.05</sub>O<sub>2</sub> cells cycled for 500 cycles at 2.8 – 4.6 V vs. Li/Li<sup>+</sup>.

***Elucidate the effect of SEI mechanical properties on Lithium metal battery performance.***

The Chueh's group at Stanford found that increasing the fluorination of the electrolyte, both by increasing salt concentration and exchanging non-fluorinated solvents for partially fluorinated diluents, simultaneously changes the solvation structure, the electrochemical kinetics, and the composition of the solid electrolyte interphase (SEI). One commonly cited explanation is that the increased fluorine content in the electrolyte leads to improved cycling by producing a stiffer, more inorganic SEI. To elucidate the role of SEI mechanical properties played in lithium metal battery performance, the team used atomic force microscopy to measure in-situ the Young's modulus and the creep depth of the solid electrolyte interphase on lithium metal for four different electrolytes. The experiment was performed by plating lithium metal in coin cells at  $0.25 \text{ mA} \cdot \text{cm}^{-2}$  for a total capacity of  $4 \text{ mA} \cdot \text{cm}^{-2}$ , then aging the lithium metal in the coin cell for one hour before disassembling and inserting into a custom in-situ AFM cell where the mechanical properties could be measured by indentation with an AFM tip. Young's modulus was extracted by indenting the SEI with an AFM tip and fitting the resulting indentation-force curve, while creep depth was observed by applying a 100ms hold at the peak force of 100 nN and observing the change in indentation. By taking over 1,000 force curves per electrolyte across  $>5$  regions as shown in Figure XVII.1.92, the team were able to provide statistically significant comparisons between electrolyte systems. Electrolytes were selected to enable the comparison of traditional electrolytes (LP40), ether electrolytes, highly concentrated electrolytes (HCE) and locally highly concentrated electrolytes (LHCE). As shown above, the largest difference occurred between the LHCE and ether electrolytes, despite similar solvation structures LHCE and HCE derived SEIs had very different mechanical properties. Similarly, despite a trend between modulus and performance across all ether-based electrolytes, the lowest performing electrolyte (LP40) had higher modulus than the 1M ether, and comparable performance to the high performing HCE electrolyte. The data shown demonstrates a lack of correlation between modulus and coulombic efficiency and weak correlation between creep and coulombic efficiency, suggesting that mechanical properties are not the key driver of lithium metal coulombic efficiency.

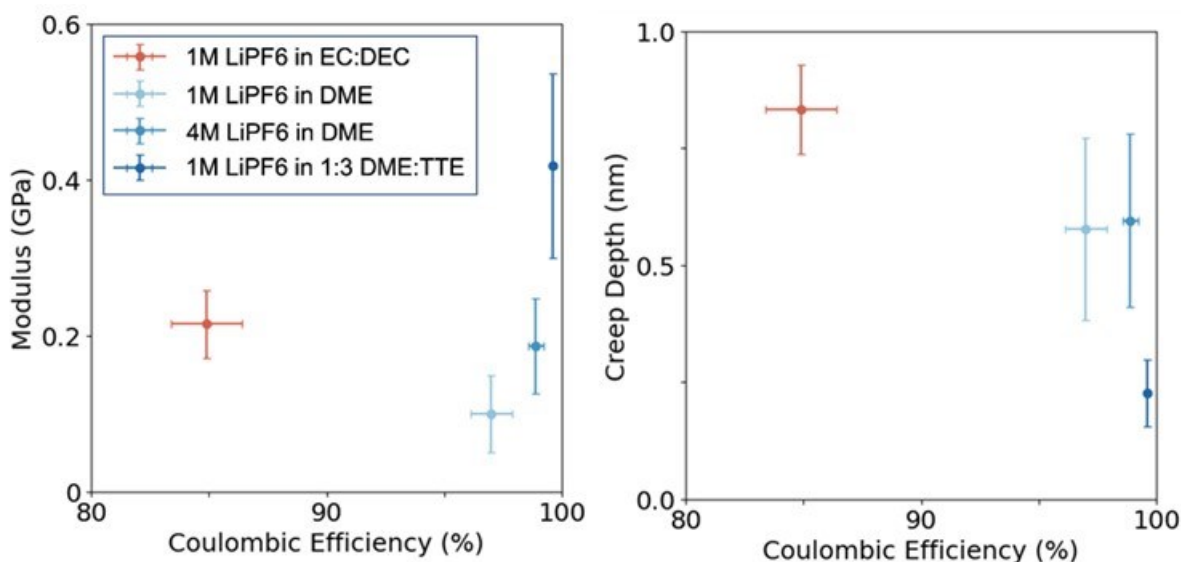


Figure XVII.1.92 Nanomechanical properties of SEI on lithium metal formed on several electrolytes.

#### **Mapping the heterogeneous SOC of NMC cathodes.**

The Weker group at SLAC performed in situ X-ray measurements using beamline 7-2 to collect data from two pouch cells cycled for long term. Both cells were mapped using micro-X-ray fluorescence ( $\mu$ -XRF) at Ni-edge energy.  $\mu$ -XRF is a non-destructive technique capable of simultaneously measuring the thickness and composition of the cathode, as well as observing the uniformity of both aspects. Figure XVII.1.93 shows the obtained maps corresponding to Ni, Co, and Mn of both cells. Using a focusing optics of 100  $\mu$ m in beamline 7-2, it was possible to obtain detailed information on the distribution of the three transition metals throughout the cell and to map the complete NMC811 electrode inside the Al pouch cell. The variation of the measured fluorescence intensity in a cell can be correlated with differences in material thickness. In the case of the cell in Figure XVII.1.93a, the Ni, Co and Mn signals have relatively uniform intensity throughout the NMC811 cathode but show areas around the edges of the electrode where the intensity decreases, indicating that the thickness in those areas is less. This could suggest that the electrodes are not evenly coated over the current collector during the electrode fabrication process. Conversely, for the cell shown in Figure XVII.1.93b, the thickness is not as uniform, presenting small islands of higher intensity, indicating that these areas are thicker. Nevertheless, it is important to note that the nature of the technique and the in situ measurement, where the electrode is inside the Al pouch, can generate shadowing effects on the detector, resulting in heterogeneous observed intensity at the electrode. Thus, the team will use lab-based microcomputed tomography ( $\mu$ -CT) to image the electrode thickness directly.

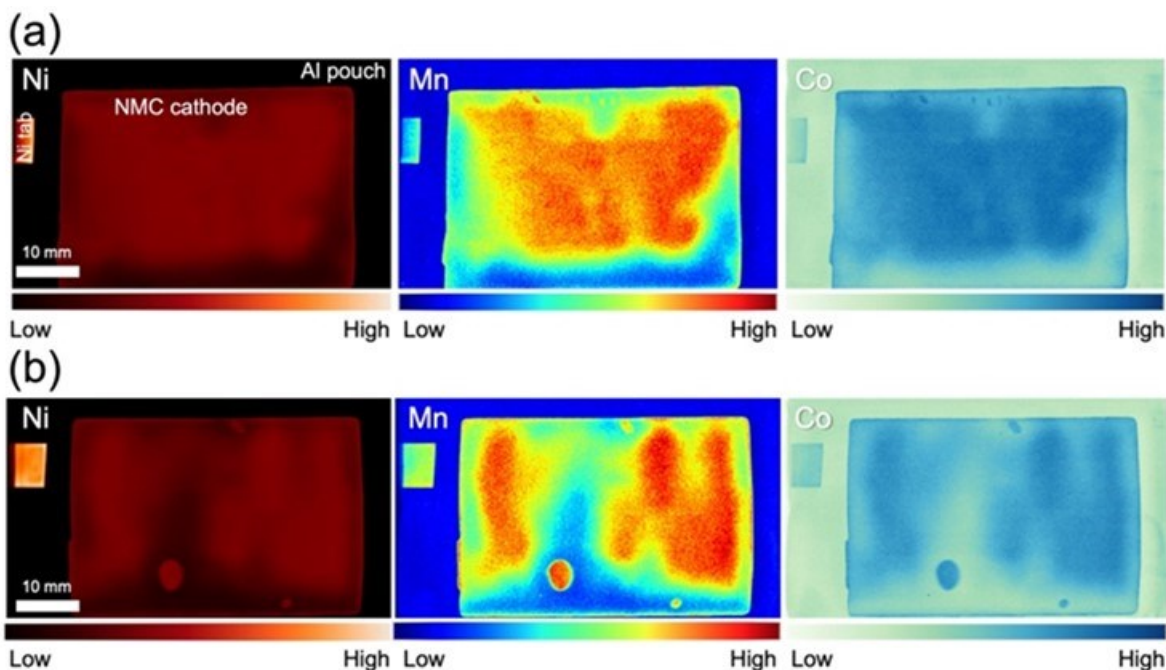


Figure XVII.1.93 (a)  $\mu$ -XRF maps corresponding to Ni, Co, and Mn at the first electrode cycled 600 times at 4.15 V. (b)  $\mu$ -XRF maps corresponding to Ni, Co, and Mn at the second electrode cycled 600 times at 4.1 V with the 100  $\mu$ m focusing optics.

Using the obtained elemental maps, several points of interest were selected in the pouch cell with NMC cathodes, where X-ray near-edge absorption micro-spectroscopy ( $\mu$ -XANES, specifically Mn and Ni-edge energies) was used to study the effects of aging on cell capacity degradation.  $\mu$ -XANES provides information on the oxidation states of different transition metals, which allows distinguishing differences in the state of charge (SOC) in regions of interest within the cathode. Eight points of interest with different contrasts were selected for one of the cells to obtain  $\mu$ -XANES spectra. However, the spectra taken at Ni energy show no variation, neither in the pre-edge nor in the edge region, i.e., it is not possible to distinguish a difference in the oxidation states depending on the cathode region. A similar behavior was observed when taking  $\mu$ -XANES with Mn-edge energy. Due to the lower Mn content in the cathode (10%), nonetheless, the signal obtained is noisier than those obtained for Ni.

#### **Comparison of a matrix comprising cells with diverse formulations and configurations.**

The INL team developed a rationalized approach as a cross-platform tool capable of comparing results from cells of dissimilar formulations or of the same formulation but in different test conditions. In this tool, we used the theoretical capacity of a transition metal oxide to convert measured capacity into a Li inventory analysis. Li inventory in electrodes were tracked reliably to reveal how battery formulations and test methods affect results in performance. Contrary to capacity, Li inventory tracking shows stoichiometric variations in electrodes. Verifiable results and differences reduced interferences from cell formulation and experimental manipulation. The approach revealed cathode active material (CAM) utilization and cell performance in depth that the conventional capacity analyses could not offer.

#### **Identification of $\text{CsNO}_3$ as electrolyte additive and its protection mechanism**

The BNL team identified  $\text{CsNO}_3$  as an effective additive for lithium metal battery electrolyte and studied the mechanism of how it protects the lithium metal anode. Coulombic efficiency (CE) of Li plating and stripping (Figure XVII.1.94a) was obtained in Li||Cu cells following the method proposed by the PNNL team for the baseline electrolyte (1.5 M LiFSI in DME) and electrolyte with  $\text{CsNO}_3$  additive. The electrolyte with  $\text{CsNO}_3$  additive has a higher CE (99.46%) than the baseline electrolyte (99.11%) in the Li||Cu cell as shown in Figure

XVII.1.94a. This indicates an enhanced stability of the Li metal anode in the CsNO<sub>3</sub>-containing electrolyte. Li metal cells were constructed with a Li metal anode and an NMC811 cathode to evaluate the performance of baseline electrolyte and electrolyte with CsNO<sub>3</sub> additive. As shown in Figure XVII.1.94b, using the baseline electrolyte, cells can maintain stable cycling for up to 70 cycles under mild conditions (250 μm thick Li, 9mg/cm<sup>2</sup> cathode). However, a rapid capacity drop is observed afterwards. In contrast, the electrolyte containing the CsNO<sub>3</sub> additive significantly improved the cyclability of the cell. Over 70% capacity retention was maintained even after 300 cycles (Figure XVII.1.94b). As CsNO<sub>3</sub> is used only in small amounts, CsNO<sub>3</sub>-containing electrolyte is expected to inherit the high ionic conductivity of DME-based electrolyte. This is shown in Figure XVII.1.94c. Both the baseline electrolyte and the CsNO<sub>3</sub>-containing electrolyte exhibit ionic conductivities that are twice as high as the commercial electrolyte based on LiPF<sub>6</sub> and carbonates. Based on the lithium metal protection capability and the high ionic conductivity of CsNO<sub>3</sub>-containing DME based electrolyte, it may potentially offer great opportunity for cycling the lithium metal cell using fast charge-discharge rate. Figure XVII.1.94d shows the high rate cycling performance of lithium metal cells using high loading NMC811 and low N/P ratio. The cells first went through two formation cycles at C/10 rate and 5 cycles at C/5 rate and then were cycled at 1C rate corresponding to 4mA/cm<sup>2</sup>. Even under harsh conditions (50 μm thick Li foil, 21 mg/cm<sup>2</sup> NMC811 cathode, N/P ratio = 2), the cell using electrolytes with the CsNO<sub>3</sub> additive maintains more than 80% of the initial capacity after 200 cycles (Figure XVII.1.94d and Figure XVII.1.94e). In comparison, the cell using the baseline electrolyte experienced a quick loss of capacity within 20 cycles.

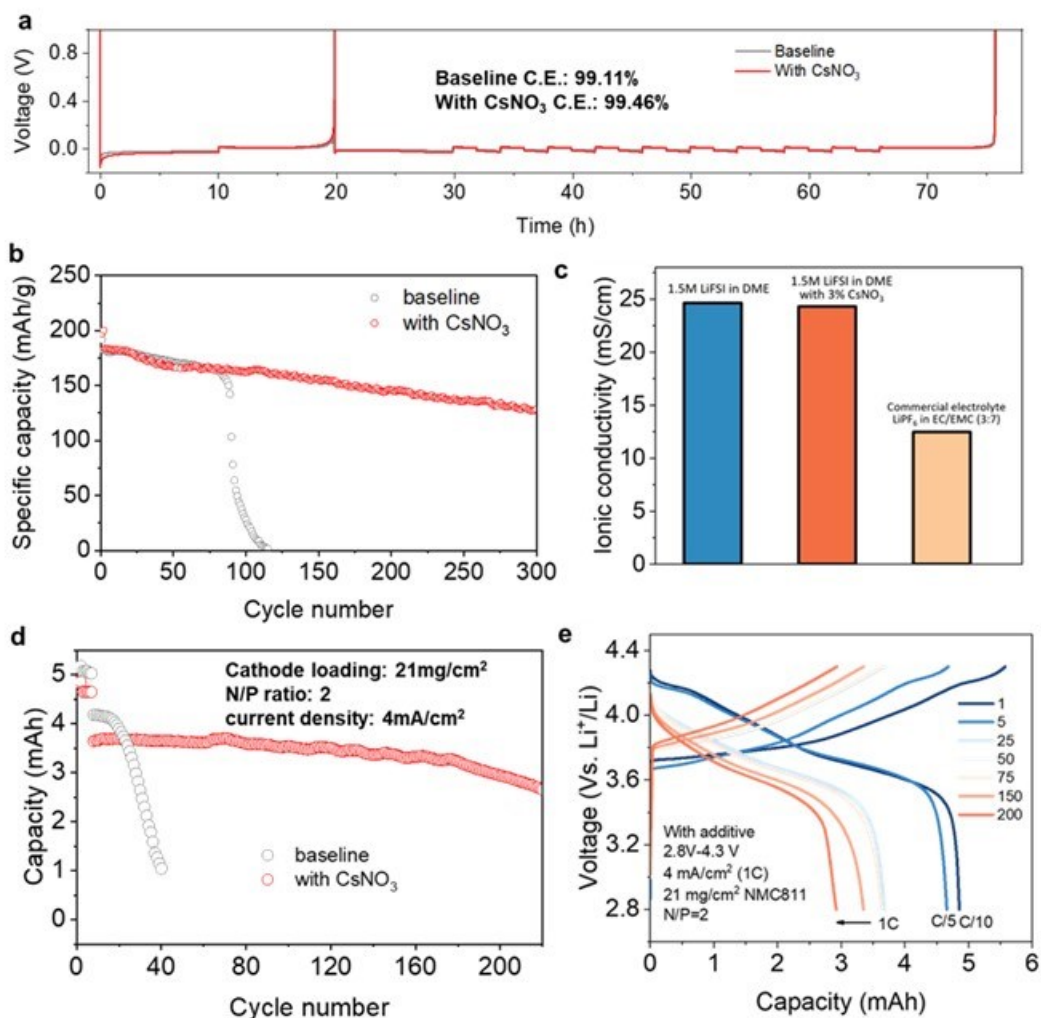
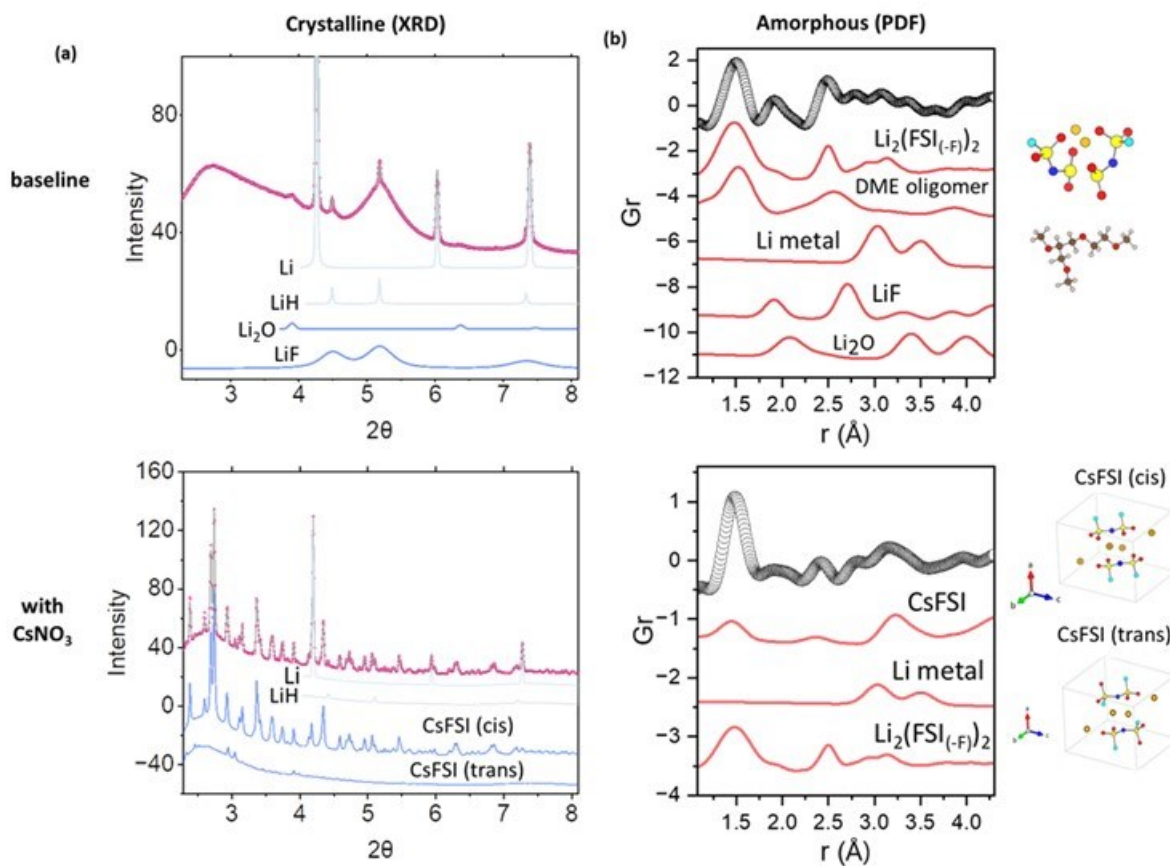


Figure XVII.1.94 Electrochemical cycling performance of Li metal batteries in baseline electrolyte and with CsNO<sub>3</sub> additive. (a) Coulombic efficiency measurement in a Li|Li<sup>+</sup>|Cu cell. (b) Cycling stability of Li metal cell with NMC811 cathode and Li metal anode with baseline electrolyte and electrolyte containing 3 wt% CsNO<sub>3</sub> additive. NMC811 loading is 9 mg/cm<sup>2</sup> and Li metal anode used is 250 μm thick. Cycling is performed at C/2 rate. (c) Ionic conductivity of baseline electrolyte, CsNO<sub>3</sub>-containing electrolyte and commercial electrolyte using 1M LiPF<sub>6</sub> in EC/EMC (volume ratio 3:7). (d) Cycling stability of Li metal cell using NMC811 cathode with 21 mg/cm<sup>2</sup> loading and 50 μm thick Li metal anode in the electrolyte containing 3 wt% CsNO<sub>3</sub> additive. The cells go through two formation cycles at a rate of C/10 and five cycles at C/5 rate before being cycled at 1C rate and 2C for later cycles. (e) Selected charge-discharge profiles of Li|NMC811 cell cycled at under conditions specified in (d) using CsNO<sub>3</sub>-containing electrolyte.

The BNL team went further to study the interphase formation mechanism of both the baseline electrolyte and the CsNO<sub>3</sub>-containing electrolyte. XRD and PDF techniques, which offer insights into both the crystalline and amorphous aspects of the interphase, were employed. The XRD pattern of the anode interphase resulting from the baseline electrolyte is shown in the upper panel of Figure XVII.1.95a. Thanks to the high quality of synchrotron XRD, Rietveld refinement can be carried out reliably. It has typical anode interphase components such as LiH, Li<sub>2</sub>O, and nanocrystalline LiF that result from electrolyte decomposition. In sharp contrast, the anode interphase resulting from the electrolyte with CsNO<sub>3</sub> additive is completely different as shown in the lower panel in Figure XVII.1.95a. Instead of Li<sub>2</sub>O and LiF, cesium bis(fluorosulfonyl) imide (CsFSI) is the dominant inorganic species in the anode interphase. Detailed Rietveld refinement indicates that there are two kinds of CsFSI present, one being cis-CsFSI (major) and the other being trans-CsFSI (minor). They have



similar crystal packing modes but differ in the arrangement of atoms in the FSI anion. The formation of CsFSI may not consume electrons from the circuit compared with the formation of  $\text{Li}_2\text{O}$  and  $\text{LiF}$ , both of which do consume electrons. As a result, CsFSI formation may be favorable for improving Coulombic efficiency. While XRD data reveals the crystalline components in the anode interphase, PDF data provides information on the amorphous phases (Figure XVII.1.95b). For the baseline electrolyte, the first PDF peak is attributed to the presence of S=O, S-F, or S-N bonds (around 1.5 Å) that belong to species resulting from FSI anion decomposition. The calculated structure and PDF pattern of a model compound  $\text{Li}_2(\text{FSI}(-\text{F}))_2$  (-F means one fluorine atom is lost from the FSI anion) are shown for illustration. The first PDF peak is asymmetric and has some intensity in the lower  $r$  region, suggesting the presence of some shorter bonds which are likely carbon-based bonds such as C-O, C=O, and C-C. These bonds belong to species such as DME oligomer that result from solvent decomposition. The calculated structure and PDF data of DME oligomer are also shown in the figure. Other PDF peaks can be well accounted for by the presence of interphase components such as lithium metal,  $\text{LiH}$ ,  $\text{Li}_2\text{O}$ , and  $\text{LiF}$ . The peak at 2.0 Å can only be assigned to those related to the inorganic species such as  $\text{LiH}$ ,  $\text{Li}_2\text{O}$ , and  $\text{LiF}$ . Its relative strong intensity suggests that there are abundant inorganic species in the anode interphase formed by the baseline electrolyte decomposition. Following the same analysis method, the lower panel of Figure XVII.1.95b suggests that the amorphous phase resulting from FSI anion decomposition has dominant percentage in the anode interphase formed by electrolyte containing  $\text{CsNO}_3$  additive. The predominant inorganic species in the anode interphase is CsFSI, with minimal to no presence of  $\text{Li}_2\text{O}$  or  $\text{LiF}$ . The significant difference in anode interphase components may be caused by the solvation structure, which is influenced by the presence of  $\text{Cs}^+$  cation. In the baseline electrolyte, due to the relatively small size of the  $\text{Li}^+$  cation and the strong solvation interaction between DME solvent and the  $\text{Li}^+$  cation, FSI anions have small chance of entering the solvation sheath and participating in the interphase formation. When the  $\text{Cs}^+$  cation is present, its large size ( $\text{Li}^+$  radius: 0.59 Å;  $\text{Cs}^+$ : 1.67 Å) greatly weakens the solvation interaction between DME solvent and  $\text{Cs}^+$  cation. As a result, more anions can enter the solvation sheath and contribute to the interphase formation. Such formed interphase contains both FSI anion derived amorphous components and CsFSI inorganic species, which is robust and capable of extending long cycle life.



**Figure XVII.1.95** Crystalline and amorphous components in lithium metal anode interphase. (a) Crystalline components of the anode interphase revealed by synchrotron XRD and Rietveld refinement. The red is the fit and the blue is the XRD pattern for individual phases calculated from Rietveld refinement. (b) Amorphous components of the anode interphase revealed by PDF studies. The scattered plot is the measured PDF data, and the red is the PDF pattern calculated from the possible individual components of the SEI. SEI species were characterized after 50 cycles in the baseline electrolyte and after 200 cycles in the electrolyte containing the CsNO<sub>3</sub> additive. The cycling was performed at C/2 rate. The color code for the atoms is the same in all subfigures: red: oxygen; blue: nitrogen; cyan: fluorine; brown: carbon; white: hydrogen; gold: lithium; dark yellow: cesium, light yellow: sulfur.

#### **Role of Transition-metal Crossover on SEI formation in lithium-metal cells**

The UT Austin team conducted an investigation to understand the influence of transition-metal crossover on the distribution of solid-electrolyte interphasial (SEI) products through advanced, high-resolution 3-D chemical analysis with time-of-flight secondary-ion mass spectrometry (TOF-SIMS). Transition-metal crossover is well-known to induce greater SEI decomposition on graphite, but limited studies have focused on its effects on lithium metal. In particular, maintaining a uniform coverage of the SEI on Li-metal anode is important. It is postulated that the crossed over transition metals from the cathode will affect SEI formation and lithium deposition, which are two processes that are critical to lithium-metal battery performance. TOF-SIMS is one of the most powerful techniques to understand the distribution of the SEI components, as it enables the identification, localization, and relative quantification of products within the anode SEI at a high 3-D spatial resolution. The systems investigated in this work are Li-metal anodes from Li | LP57 or HVE | LiNi<sub>0.7</sub>Mn<sub>0.25</sub>Al<sub>0.05</sub>O<sub>2</sub> (NMA-70) half cells, which have been cycled to an upper cut-off voltage of 4.6 V vs Li/Li<sup>+</sup> for 500 cycles to induce significant transition-metal dissolution. LP57 is composed of 1 M LiPF<sub>6</sub> dissolved in a binary solvent system of ethylene carbonate (EC) and ethyl methyl carbonate (EMC) with 2 wt. % of vinylene carbonate added as an additive. The high-voltage electrolyte (HVE) was prepared with a binary solvent system of EC : EMC (3 : 7) by weight that is first saturated with 3 M LiPF<sub>6</sub> salt, followed by adding

the diluent 1,1,2,2-tetrafluoroethyl-2,2,3,3-tetrafluoropropyl ether (TTE) to lower the overall concentration of  $\text{LiPF}_6$  from 3 to 1 M and retain the solvated salt-solvent clusters in solution. 3 vol % fluoroethylene carbonate was added to this electrolyte as an additive. A series of secondary-ion fragments of interest were selected, representing the most commonly found degradation products formed in the SEI. In this analysis, organic electrolyte decomposition products are represented by  $\text{C}_2\text{HO}^-$ , inorganic salt decomposition products by  $\text{LiF}_2^-$  and  $\text{PO}_2^-$ , redeposited/bulk Li with  $\text{Li}_2^-$ , and deposited transition-metals by  $\text{Ni}^-$ . We first highlight the influence of deposited transition metals on the localization of SEI components in the LP57 electrolyte, relatively quantify transition-metal dissolution in the LP57 and HVE electrolyte, and then provide quantitative measures of spatial heterogeneity between SEI components in the LP57 and HVE systems.

Figure XVII.1.96a and b show a series of views of the measured  $\text{Ni}^-$ ,  $\text{PO}_2^-$ ,  $\text{C}_2\text{HO}^-$ ,  $\text{Li}_2^-$ , and  $\text{LiF}_2^-$  fragments from the SEI of the Li-metal anode. Brighter regions represent locations with higher secondary-ion yield (SI yield). The value of the SI yield is directly proportional to the concentration of the species detected within the SEI.

Figure XVII.1.96a presents the through-plane X-Y views of the 3-D renders for the  $\text{Ni}^-$ ,  $\text{PO}_2^-$ ,  $\text{C}_2\text{HO}^-$ , and  $\text{LiF}_2^-$  fragments. Qualitatively, it is clear that the spatial distributions of common electrolyte degradation products closely follow the spatial distribution of  $\text{Ni}^-$ . This is confirmed within a large,  $100\ \mu\text{m} \times 100\ \mu\text{m}$  analysis region, as well as for a series of X-Y planes extending deeper into the SEI. Figure XVII.1.96b presents the total-yield maps of the  $\text{Ni}^-$  to  $\text{Li}_2^-$  secondary-ion fragments to investigate the effects of these transition-metals on lithium deposition. The total-yield maps are 2-D projections that are calculated from a through-plane sum of all X-Y views of the 3-D renders. Comparing between these maps, it is revealed that there is a greater amount of lithium metal at locations with the lowest concentrations of transition metals. In essence, the presence of these transition metals on the anode are revealed to induce heterogenous SEI formation, as well as lithium deposition. Figure XVII.1.96c, and d show the relative quantification of deposited Ni for two different electrolytes, LP57 and HVE, to investigate the influence of the electrolyte on the degree of transition-metal crossover. It is highlighted in Figure XVII.1.96c that there is a pronounced effect of the electrolyte on the amount of deposited Ni found on the cycled anodes. Figure XVII.1.96d provides the results from integrating the SI yield profiles for various secondary-ion fragments. The typical shape of the SI yield profiles is an asymmetric bell curve. The integration of each secondary-ion fragment was conducted between the crossing depths at 0.6 of its maximum from the SI yield profile. A magnitude higher concentration of Ni was found to have been deposited onto the anodes cycled in LP57 than in HVE. Furthermore, greater amounts of organic/inorganic decomposition products are also detected for the LP57 electrolyte than for the HVE. The exacerbated degree of electrolyte decomposition is primarily attributed to differences in the deposited Ni, as dissolved and deposited transition metals are well-known to serve as catalytic centers for electrolyte decomposition.

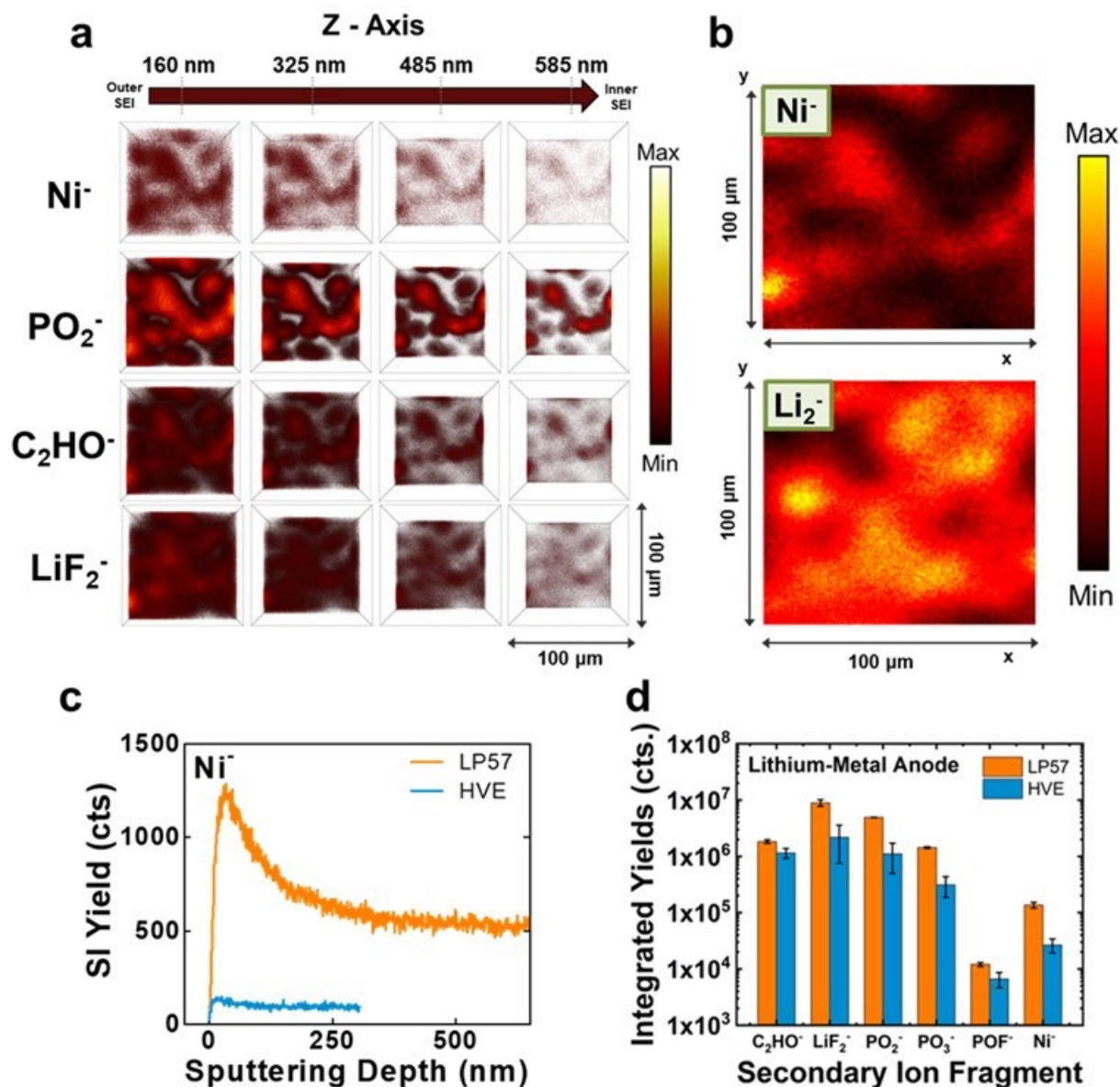


Figure XVII.1.96 Spatial distributions of Ni<sup>-</sup> to other electrolyte decomposition fragments detected in the anode SEI formed in LP57 and relative quantifications of the various secondary-ion fragments detected within the SEI of cycled lithium-metal anodes. (a) A series of X-Y views at various sputtering depths of the sputtered volume in the depth profiles of the Ni<sup>-</sup>, PO<sub>2</sub><sup>-</sup>, C<sub>2</sub>HO<sup>-</sup>, and LiF<sub>2</sub><sup>-</sup> secondary ion fragments from the SEI formed with LP57. (b) Total yield maps of the Ni<sup>-</sup> to Li<sub>2</sub><sup>-</sup> secondary-ion fragments from the SEI formed with LP57. (c) Absolute secondary-ion yields versus sputtering depth (nm) for the Ni<sup>-</sup> secondary ion fragment measured for LP57 and HVE. (d) Net integrated yields for all fragments of interest that were integrated between the crossing depths at 0.6 of its maximum from the SI yield profile for LP57 and HVE. The analyzed volume for LP57 corresponds to a 100 μm x 100 μm analysis area by 650 nm in depth. The analyzed volume for HVE corresponds to a 100 μm x 100 μm analysis area by 300 nm in depth. The color of the pixels in the TOF-SIMS renders correspond to yields that are denoted with the color bar. Data were collected on lithium-metal anodes from NMA-70 half-cells with LP57 (Figures 1a-d) or HVE (Figures 1c,d) electrolyte that were cycled for 500 cycles at a voltage window of 2.8 – 4.6 V vs Li/Li<sup>+</sup>.

Figure XVII.1.97 presents the results from an analysis to quantify heterogeneity between the spatial distributions of different secondary-ion fragments. To quantify the degree of heterogeneity between the

chemical maps of different species of interest, we look at the net squared deviation (NSD) between these maps. The maps were smoothed with a 2-point interpolation applied to the profiles in the X and Y directions prior to calculation of the squared deviation maps. The squared deviation map between two chemical maps is simply the squared difference between the two maps range-normalized. A normalization with the range was necessary to account for differences in the baseline values between different fragments of interest. These squared deviation maps are calculated between each two fragments of interest ( $F_1$  and  $F_2$ , where  $F_1 = (C_2HO^-, LiF_2^-, Li_2^-, PO_2^-, or Ni^-)$ , with  $i = 1, 2$ ). The NSD is then calculated from the total sum of the squared deviations at all points.

Figure XVII.1.97 a, b shows the net squared deviation matrix for the five fragments of interest ( $C_2HO^-$ ,  $LiF_2^-$ ,  $Li_2^-$ ,  $PO_2^-$ , or  $Ni^-$ ), that is color-coded based on the magnitude of the NSD. A larger NSD (yellow) indicates a lower similarity between the maps of two fragments. As expected, the values in Figure 2a for the NSD calculated for LP57 between the  $Ni^-$ ,  $PO_2^-$ ,  $LiF_2^-$ , and  $C_2HO^-$  spatial maps are low (black), supporting the strong positive correlation between the distributions of transition metals and SEI decomposition products. On the other hand, the NSD of the  $Li_2^-$  map to the other fragments  $Ni^-$ ,  $PO_2^-$ ,  $LiF_2^-$ , and  $C_2HO^-$  are high (yellow), confirming that lithium metal is preferentially deposited separately with respect to the other SEI species at Li-anode surface. Interestingly, a similar trend is observed for the HVE in Figure 2b, but the values of the NSD between the  $Li_2^-$  map and the other fragments  $Ni^-$ ,  $PO_2^-$ ,  $LiF_2^-$ , and  $C_2HO^-$  for the HVE are noticeably lower than those for LP57. Additionally, the HVE exhibits higher values of the NSD between the  $Ni^-$ ,  $PO_2^-$ ,  $LiF_2^-$ , and  $C_2HO^-$  spatial maps, which reveals mild differences between their individual distributions on the surface of lithium-metal anode. Subsequently, it is believed that the concentration of deposited transition metals for the anodes cycled in HVE may not be high enough to induce a strong localization of individual SEI components, which allows them to be dispersed across different regions of the anode (Figure XVII.1.97 c, d). Overall, the higher amount of Ni dissolution and crossover from cathode to anode in the LP57 electrolyte compared to that in the advanced HVE leads to a more severe localization of SEI formation and lithium deposition onto lithium-metal anode in LP57.

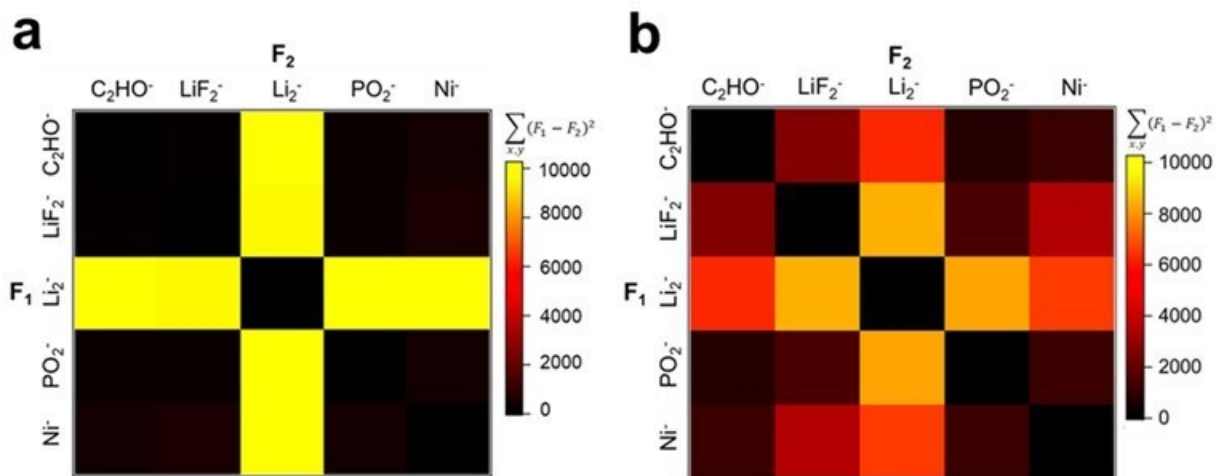
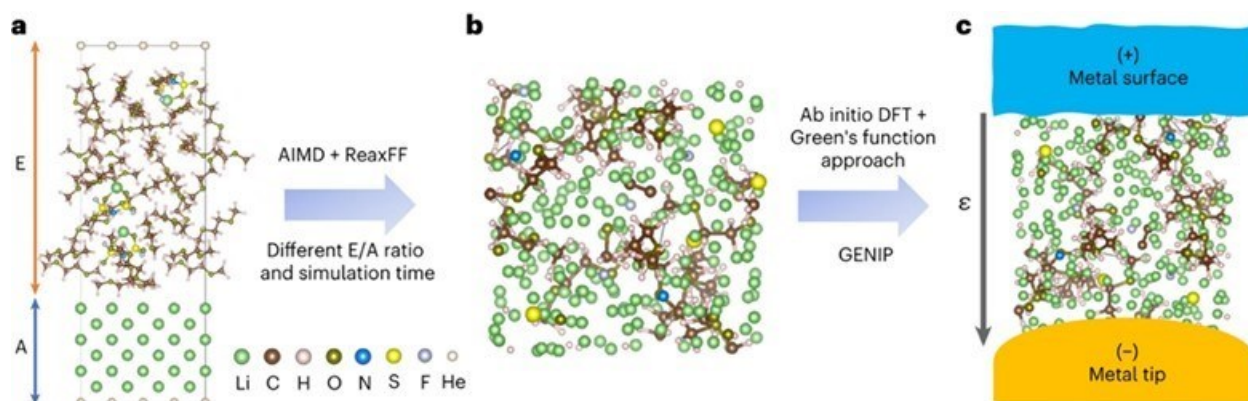


Figure XVII.1.97 Square deviation matrices presenting the net squared deviations between two secondary-ion fragment maps ( $F_1$  and  $F_2$ ) for (a) LP57 and (b) HVE. The boxes are color-coded based on the magnitude of the net squared deviation. Larger values (yellow) indicate a lower similarity between the spatial distributions of two secondary-ion fragments. Data were collected on lithium-metal anodes from NMA-70 half-cells with LP57 or HVE electrolyte that were cycled for 500 cycles at a voltage window of 2.8 – 4.6 V vs Li/Li<sup>+</sup>.

#### **Theoretical characterization of SEI composition, morphology, and electrical properties.**

The TAMU team through collaboration with PNNL, analyzed the electrical behavior of the SEI formed on the Li metal anode using four different electrolytes. The PNNL group carried out current-voltage measurements of each of the SEI samples that were also fully characterized with various techniques regarding chemical

composition, morphology, and Li plating/stripping morphologies. The TAMU team used first-principles simulations to study the initial formation and growth of the SEI for the chosen four different electrolyte formulations. The calculated SEI structures were used as input to evaluate the conductance behavior of each sample using *ab initio* methods. Figure XVII.1.98 shows a schematic description of the theoretical approach. The predicted conductance and differential conductance as a function of bias voltage were in excellent agreement with the PNNL experimental measurements. As a result, we were able to provide new insights into the role of electrolyte chemistry on the SEI structure, composition, thickness, and electrical behavior which were all correlated to cell performance. The results were published in Nature Energy.



**Figure XVII.1.98** Computational setting for the analysis and evaluation of electrical conductance in the SEI. (a) Simulation cell with different E/A ratio. (b) Final states of the SEI formed by reaction between electrolyte and Li metal with different E/A ratio and simulation time via AIMD and ReaxFF method. (c) Schematic of I–V curve calculation set-up of simulated SEI via ab initio DFT with a Green's function approach.  $\epsilon$ , voltage

New theoretical tools for understanding SEI evolution and electrochemical cycling.

The TAMU team developed a new methodology to characterize the simultaneous events occurring during SEI formation and growth and simultaneous plating or stripping during cell cycling. The novel method is based on a kinetic Monte Carlo (kMC) scheme. All possible reactions, diffusion, or other events are incorporated and at each step the kinetically favorable reaction or physical event takes place, triggering a dynamic motion and describing the surface evolution. In the illustration of Figure XVII.1.99, we show simultaneous plating, stripping, and electrolyte decomposition reactions are included in the “reactions catalog”. In conjunction with the ab initio analysis, the kMC method is a useful tool for evaluation of new electrolytes, effects on Li morphologies, and many other scenarios that enhance our understanding at the cell level. An article is prepared for publication.

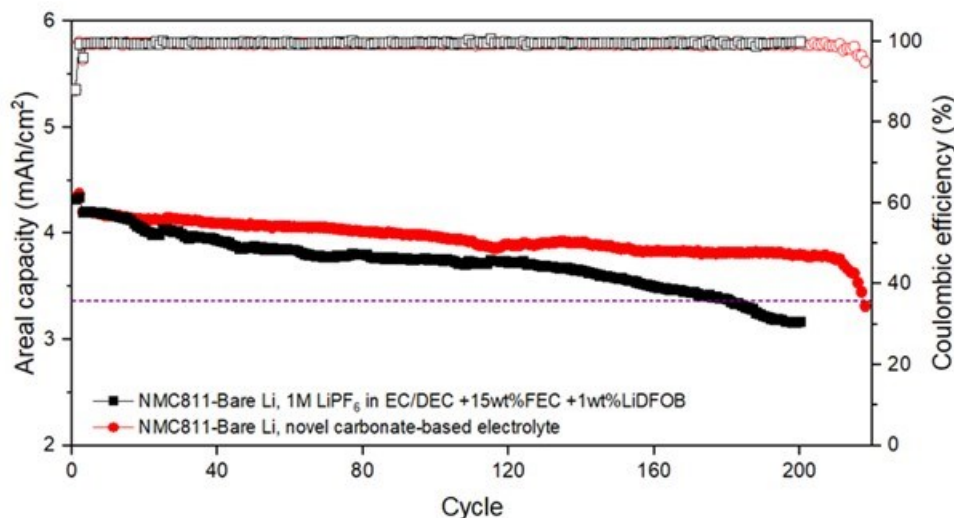


Figure XVII.1.99 Illustration of reactions over Li metal during cycling as captured by the kMC approach.

The Weker group at SLAC, in collaboration with UT Austin, performed *ex situ* X-ray measurements using beamline 6-2 to collect data from Ni-based cathodes ( $\text{LiNiO}_2$ ,  $\text{LiNi}_{0.95}\text{Co}_{0.05}\text{O}_2$ ,  $\text{LiNi}_{0.95}\text{Mn}_{0.05}\text{O}_2$ ,  $\text{LiNi}_{0.95}\text{Al}_{0.05}\text{O}_2$ ) cycled at UT Austin at three different states of charge (SOCs). The goal is to understand the complex interaction of key elements such as cobalt, manganese, and aluminum for use in the rational design of Ni-rich cathodes and to observe the influence of these dopants on the electrochemical performance of the  $\text{LiNiO}_2$  cathodes. All the samples were measured using X-ray transmission microscopy (TXM) to observe the morphology and X-ray near-edge absorption structure (XANES) to obtain chemical information at the Ni K-edge energy. The characterized cathodes were vacuum dried ( $120^\circ\text{C}$ ), calendered, and punched into 12 mm round disks. Electrodes were then assembled in 2032 coin cells and charged at a  $C/10$  rate to 73% and 87% SOC. A pristine cathode was characterized as a reference point. Figure XVII.1.100 shows the transmission images taken at the Ni energy K-edge of the  $\text{LiNiO}_2$  cathodes. The TXM images show spherical morphology particles of  $\text{LiNiO}_2$  with an average particle size of  $\sim 12\ \mu\text{m}$ . The spherical shape remains after the removal of the Li ions. However, some cracks are observed (blue arrows) in the cycled particles, which are likely the result of the charging process.

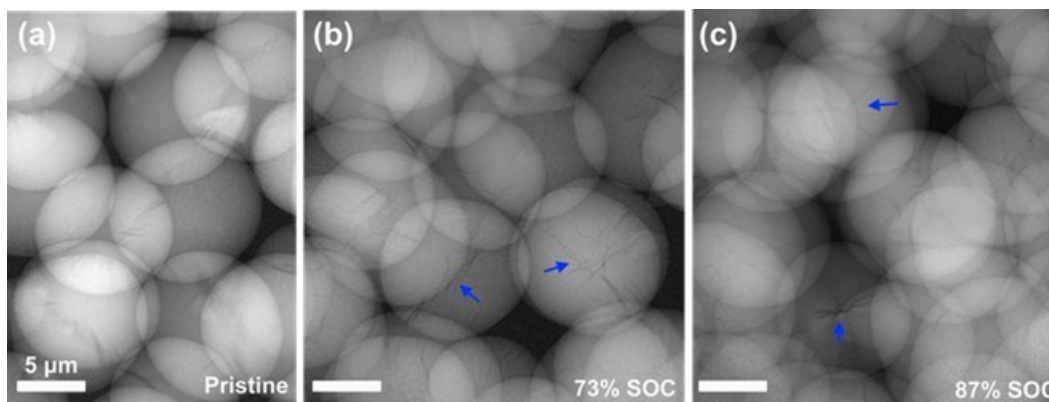


Figure XVII.1.100 TXM images above Ni K-edge (8350 eV) of the  $\text{LiNiO}_2$  cathodes at (a) pristine state, (b) 73% SOC, and (c) 87% SOC. The blue arrows point to some cracks in the  $\text{LiNiO}_2$  particles.

The chemical composition and local valence states of elements can be determined by combining TXM with X-ray spectroscopy. By probing the absorption edge of a specific element (Ni K-edge for this analysis) with the

appropriate X-ray energy. It is possible to visualize the distribution of different chemical species or to monitor elements as they are reduced or oxidized. Beamline 6-2 at SSRL combines spectroscopy and microscopy to obtain data with both energy and spatial dimensions, providing excellent capabilities to observe and study the chemical and morphological information of the Ni-based cathodes.

Figure XVII.1.101 shows the variation of the energy edge position for the  $\text{LiNiO}_2$  cathode in its pristine state

Figure XVII.1.101a, at 73% SOC

Figure XVII.1.101b, and at 87% SOC

Figure XVII.1.101c. The edge energy positions, as indicated by color, do not vary much within the electrode, but there is variation between the pristine and the charged cathodes. We believe the local state of charge variation within the cathodes equilibrates while at rest. Thus, our follow up study will explore the state of charge variation during cycling. The *operando* analyses will provide a more detailed understanding of the interaction and influence of dopants in  $\text{LiNiO}_2$ .

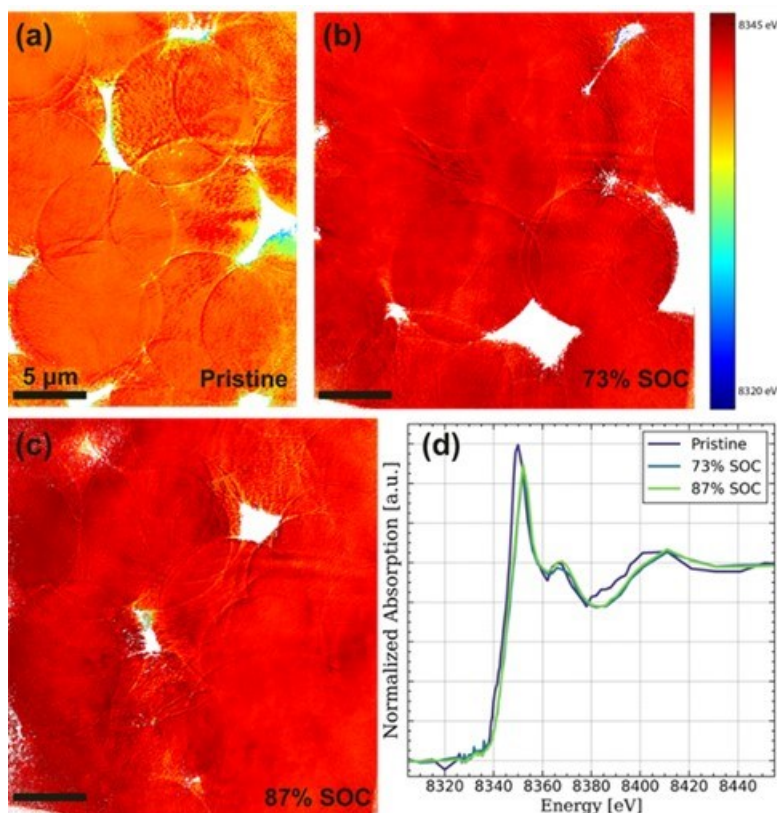


Figure XVII.1.101 Variation of the energy edge position map for the  $\text{LiNiO}_2$  cathode in (a) its pristine state, (b) at 73% SOC, and (c) at 87% SOC. (d) Shows the summed XANES spectra corresponding to (a), (b) and (c).

#### *In-situ measurements of the SEI nanomechanics*

To better understand the mechanical properties of the SEI and what role it plays in cell cycling, the Chueh and Bao groups at Stanford/SLAC collected *in-situ* measurements of the SEI nanomechanics (Figure XVII.1.102a) for four different electrolytes of interest to lithium metal batteries. In addition to the traditionally reported property of Young's modulus, this study collected quantitative measurements of SEI viscoelasticity using an indentation protocol incorporating both indentation and constant force hold segments. To enable the robust comparison of SEI mechanical properties across different electrolytes, samples were prepared by electrodepositing lithium onto copper in four different electrolytes. The four electrolytes consisted of a



conventional carbonate electrolyte (CCE) composed of 1M LiPF<sub>6</sub> in a 1:1 ethylene carbonate and diethyl carbonate solvent; a low concentration electrolyte (LCE) with 1M LiFSI salt in dimethoxyethane, also known as DME; a high concentration electrolyte (HCE) with 4M LiFSI salt also in DME; and a locally highly concentrated electrolyte (LHCE) with 1M LiFSI salt in a 1:3 ratio of DME to TTE, a partially fluorinated ether solvent. The first comparison of interest is the influence of salt choice on modulus by comparing SEI in CCE to SEI in other electrolytes. Second, the impact of solvation structure was investigated by comparing LCE where lithium is primarily solvated by DME molecules to HCE and LHCE where the solvent structure incorporates both salts and solvents. Finally, by including electrolytes across a broad range of cycling performance, these experiments enable investigation into the relationships between the mechanical properties of the SEI and the viability of the corresponding electrolyte for commercial lithium metal batteries. To maximize robustness of comparison between the various electrolytes, samples were prepared by plating lithium metal at low current densities to produce samples with locally smooth and flat morphologies, as shown by the SEM images in Figure XVII.1.102b. Between the low plating current of 0.25mA/cm<sup>2</sup> and the pressure applied by the coin cell, all electrolytes, including the CCE, produced morphologies that were locally flat, as shown in Figure XVII.1.102c, consistent with the SEM images as well as prior literature. Within the locally flat regions of these images, as shown in Figure XVII.1.102d, mechanical measurements were then performed by indenting the AFM tip into the SEI that covers the lithium metal surface and recording the force response and the indentation depth, as shown in Figure XVII.1.102d. Surface roughness, extracted from locally planar regions is listed below each high-resolution image. The roughness values, between 2 and 10nm likely contribute to some of the spread in the data but are generally lower than the indentation depth, allowing for interpretable mechanical measurements.

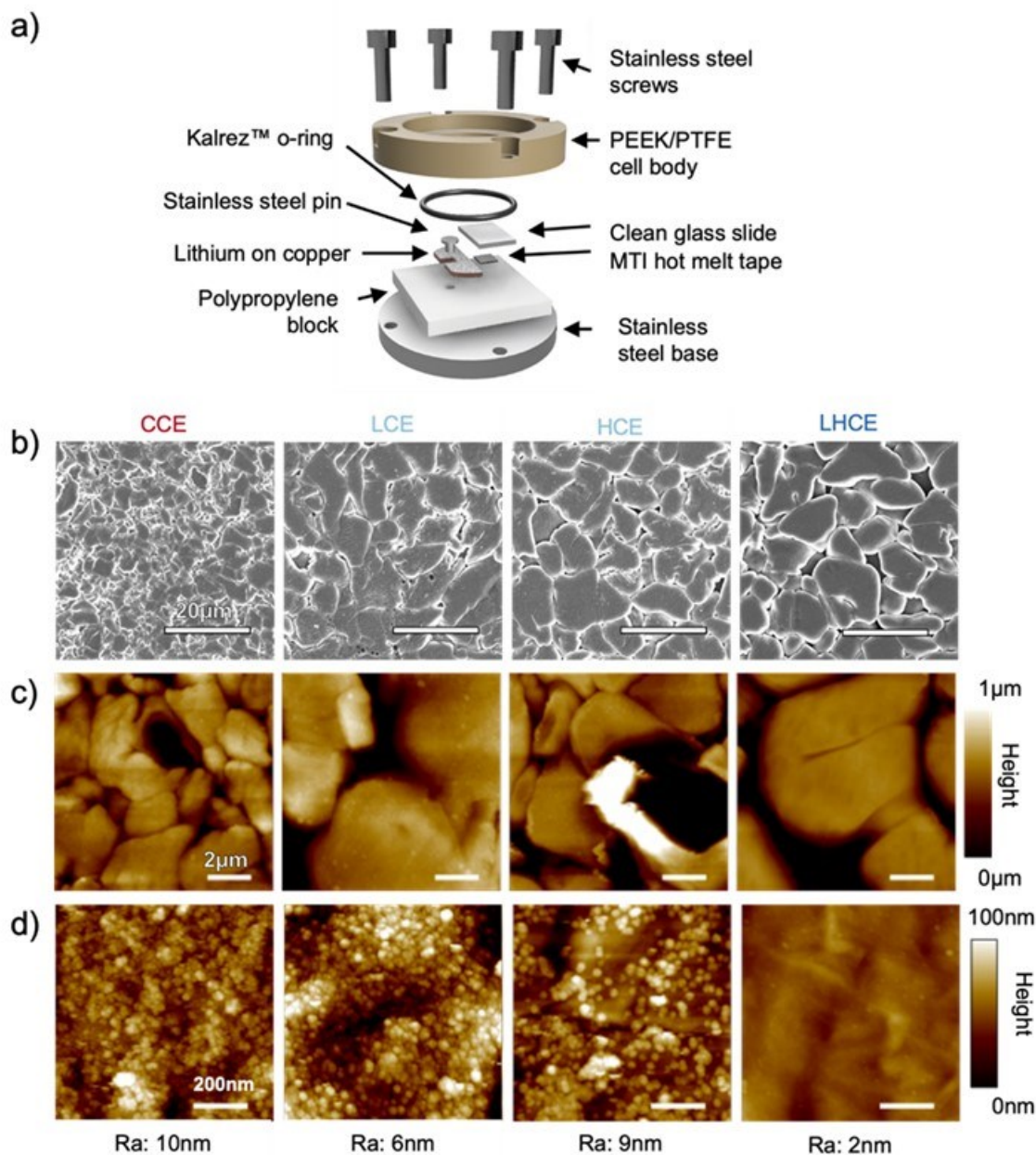


Figure XVII.1.102 (a) Schematic of *in-situ* cell use for AFM experiments with labeled parts. (b) SEM images of lithium metal deposited on a copper substrate under same conditions as used in AFM experiments (c) *In-situ* tapping mode images of lithium metal deposited in coin cells and transferred to *in-situ* cell (d). Higher resolution tapping mode images showing the SEI morphology and associated roughness measurements.

In addition to the traditional approach and withdrawal segments plotted in color, the measurement also incorporated a hold with quasi-static force plotted in black. To better visualize how these two measurements form a traditional stress-strain curve the measurements are plotted parametrically in Figure XVII.1.103b and Figure XVII.1.103c, showing the approach segment, from which the elastic properties are calculated, as well as the hold and withdrawal segments which contain information about the inelastic properties of the SEI. The force curve also shows visible hysteresis due to inelastic contributions to the mechanical properties which is also evidenced by the small amount of creep during the constant force hold.

To enable easy comparison of the pooled measurements from different electrolytes, the mean of the individual measurements is plotted superimposed for each electrolyte (Figure XVII.1.103d). Comparing the measured moduli in this study to the solvation structures proposed in literature supports the hypothesis that solvation structure plays a substantial role on SEI modulus. SEI formed in the CCE electrolyte, where lithium is primarily solvated by carbonate solvent molecules shows a different modulus from SEI derived from LCE where lithium is solvated by DME molecules which is in turn different from HCE and LHCE which have similar solvation structures of DME and FSI anion aggregates. However, despite the correlation between SEI modulus solvation structure, the relationship between modulus and performance is much less clear. As observed in prior literature, lithium metal deposited in CCE has a wiry and uneven morphology even when compared to the LCE, despite measurements here showing a higher modulus. Because lithium morphology plays a substantial role in cyclability this also results in a substantially lower coulombic efficiency in the CCE than the LCE, once again despite the higher modulus of the SEI in CCE. This deviation from the previously reported trend is less surprising given the relatively low SEI moduli reported here, since mechanical suppression of lithium metal plating by a layer that is both thin and soft is unlikely to occur. Note that this is not to say that other mechanical properties of the SEI do not play a role in cycling performance – both fracture toughness and strain tolerance are hypothesized to play a role in maintaining SEI integrity during cycling, neither of which necessarily correlate with modulus.

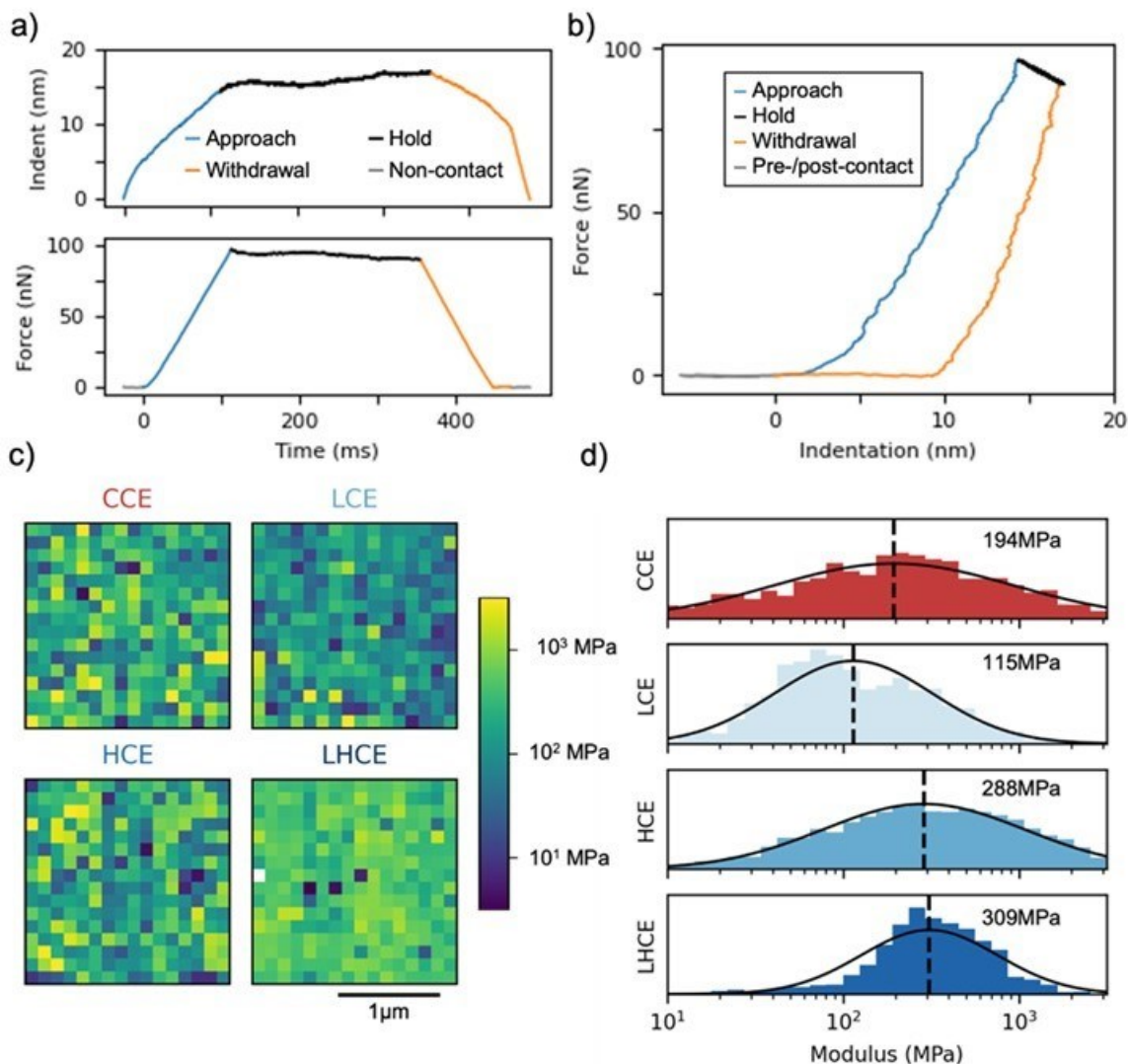


Figure XVII.1.103 Example force vs. time and indentation vs. time curves, including the hold segment (a). The same force curves plotted as a traditional force-indentation force curve (b). 2D image of modulus measurements of representative  $2 \times 2 \mu\text{m}$  sample regions (c). Histograms of all modulus measurements on a log scale, with associated geometric mean (d).

#### Quantification of Lithium (Li) and Sulfur (S) inventory loss in Li-S Batteries

Previously, the UCSD team reported calibration data for quantifying dissolved elemental Sulfur and methylated polysulfides  $\text{CH}_3\text{S}_x\text{CH}_3$  ( $x \in \{2,8\}$ ) through a proposed methodology involving semi-preparative High-Performance Liquid Chromatography -Ultra Violet Spectroscopy (HPLC-UV) and Induced Coupled Plasma-Mass Spectroscopy (ICP-MS). Preliminary data on conventional C/S systems after 1<sup>st</sup> discharge, 1<sup>st</sup> charge, and after two formation cycles are discussed. For this analysis, the UCSD team have used C/S cathodes with  $3.5 - 4 \text{ mg cm}^{-2}$  sulfur loading from General Motors. The coin cell is assembled with lean electrolyte (E: S=8) and thin Lithium foil (100  $\mu\text{m}$ ). The electrolyte used in this report is 1 M LiTFSI in DOL: DME (1:1 v/v) with 2 wt.%  $\text{LiNO}_3$  (baseline). The Battery500 formation cycles protocol was followed. Near real-time derivatization is performed by washing the Li chip with derivatization solution (Methyl triflate) and then putting all other cell components into it. After washing, the Li foil is taken to quantify the remaining Li metal using Titration Gas Chromatography (TGC), and the cathode from the coin cell is taken into another volumetric flask to quantify the Sulfur left on the cathode using HPLC-UV. HPLC-UV is performed for the derivatized mixture to quantify methylated species and dissolved Sulfur. In the Li-S battery, the expected

behavior, according to theoretical charge transfer, is that all elemental sulfur should convert to  $\text{Li}_2\text{S}$  upon cell discharge and revert to elemental sulfur upon charging. But, as discussed in the literature, all polysulfides consistently persist in the system. HPLC-UV curves of derivatized species, illustrated in Figure XVII.1.104a and Figure XVII.1.104b, clearly show that there is little to no Sulfur left in the electrolyte when the cell is fully discharged. Qualitatively, we can also see that polysulfide amounts increase when the cell is charged back. This is because the equilibrium shifts towards Sulfur. We could get all the sulfur back in different forms after 1 cycle. As expected at the charged state, the sulfur peak is present after two formation cycles. Still, all other polysulfides are also present, which represents that not all polysulfides are converted to elemental sulfur. To achieve the milestones for this quarter, we performed similar analysis after 50 and 100 cycles as well. After 50 and 100 cycles, almost 70% of Sulfur was lost in  $\text{Li}_2\text{S}$ ,  $\text{Li}_2\text{S}_2$ , SEI, and CEI. We could only account for around 46.1% of Sulfur in polysulfide form as direct quantification after 1 cycle. About 53.9% of Sulfur was considered  $\text{Li}_2\text{S}$ ,  $\text{Li}_2\text{S}_2$ , SEI and CEI.

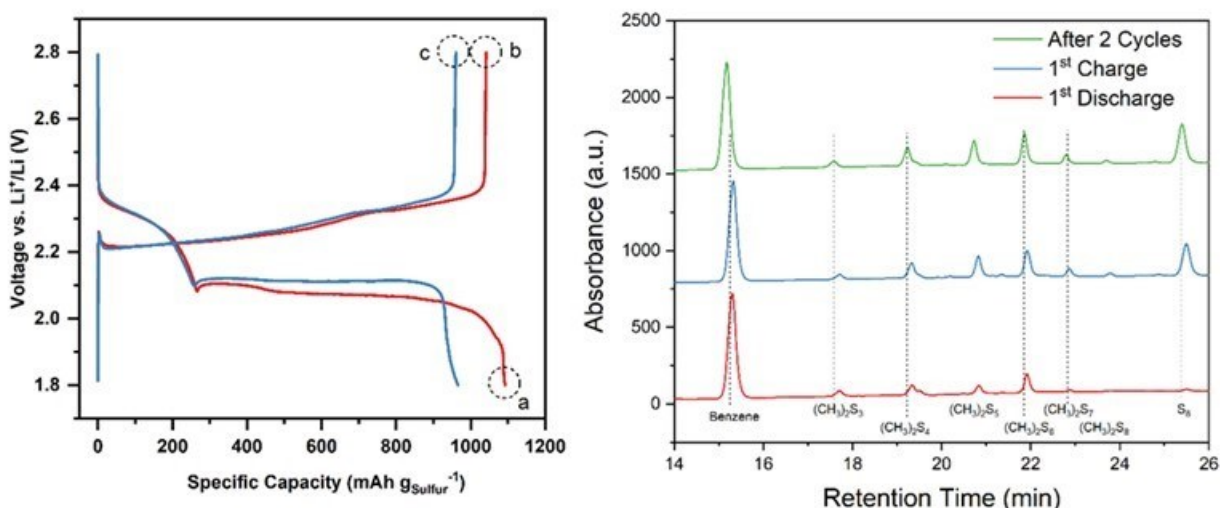


Figure XVII.1.104 (a) Charge discharge curves of first (Red) and second (Blue) cycle and points a, b, and c at which the cells were stopped and (b) HPLC-UV data of derivatized polysulfide solution after 1<sup>st</sup> discharge (Red), 1<sup>st</sup> charge (Blue) and two formation cycles (Green).

The UCSD team also looked at whether the SPAN cathode produces any polysulfides by quantifying polysulfides by HPLC-UV. We observed (Figure XVII.1.105) that the SPAN cathode did not show any polysulfide peaks and hence it's evident that the working mechanism of conventional C-S chemistry and SPAN is very different, and SPAN does not depend on the formation of polysulfides.

In summary, the methodology helps qualitatively understand the system and its limitations. Our further plan is to quantitatively evaluate polysulfides in real Li-S cells using electrolyte systems and cathodes.

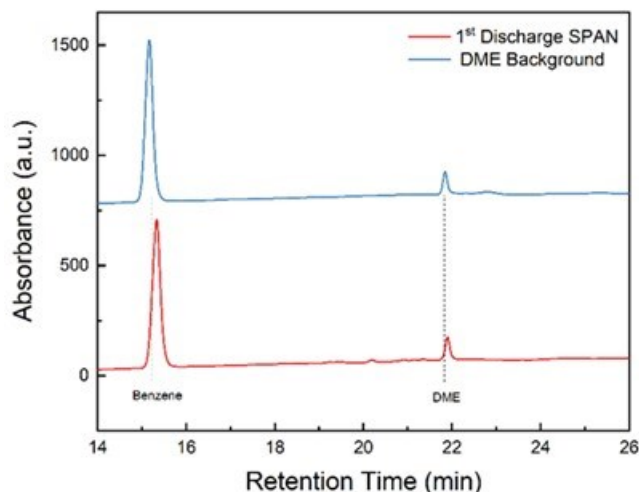
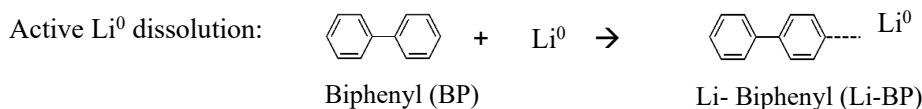


Figure XVII.1.105 HPLC-UV data of derivatized polysulfide solution after 1<sup>st</sup> discharge in SPAN (Blue) and DME solvent background (Red)

#### Quantifying Lithium inventory in Lithium-Sulfur Batteries during calendar aging

The self-discharge of Li-S batteries is mostly due to diffusion and reactions of sulfur and polysulfides (PS) at the anode-electrolyte interface. For this study, the UCSD team used a 5-electrode layer pouch cell with lean electrolyte (E:S = 5) and thin Lithium foil (N:P = 2). We have compared two types of electrolytes for this study (i) Moderately PS solvating electrolyte and (ii) Weakly PS solvating electrolyte. Last quarter, Lithium inventory in Li sulfur cells after 24 hours, 7 days, and 30 days resting when no electrochemical operation is performed, was quantitatively measured by TGC methodology. We learned that the amount of lithium in the Moderately solvating electrolyte is decreasing at a faster rate compared to the Weakly solvating electrolyte. The difference in Li<sup>0</sup> inventory widens as the resting period duration increases. In the Moderately solvating electrolyte, a portion of the Li<sup>0</sup> inventory dissolves in the electrolyte as long-chain lithium polysulfides, while the rest is transformed into electrochemically poor active short-chain polysulfides, such as Li<sub>2</sub>S. In this quarter report, we would like to extend a similar study in pouch cells that have gone through electrochemical operations. After cycling, we are expecting to observe inactive Li<sup>0</sup> as well as active Li<sup>0</sup>. Consequently, there arises a necessity for developing quantification methodology to distinguish active and inactive Li<sup>0</sup> in the Li-S System. Previously, we have reported a novel chemical analytical methodology to quantitatively distinguish the active Li<sup>0</sup> from inactive Li<sup>0</sup> in cycled lithium metal batteries. Biphenyl/THF solution is employed to dissolve the active Li<sup>0</sup> through complexation but to preserve the completeness of SEI that encapsulates the inactive Li<sup>0</sup> (Deng, W., Yin, X., Bao, W. *et al.*, Nature Energy 7, 1031–1041 (2022)). The above methodology is developed based on carbonate-based electrolyte. We have used water as the titrating agent. The reaction is as follows:



Therefore, before applying the methodology, the first and most important step is to verify if the SEI components of the Li-S cell are stable with the solvent. The potential SEI components in the Li-S cell consist of Li<sub>2</sub>S, Li<sub>2</sub>O, LiF, Li<sub>2</sub>CO<sub>3</sub>, Li<sub>2</sub>SO<sub>4</sub>, and LiOH based on previously reported XPS results. To verify that approx. 0.5 g of potential SEI species is added in 6 ml of 6wt.% BP/THF solution. As some of the SEI components are micron-sized and suspended in the solution, we used a 0.22 μm syringe filter to avoid SEI components in ICP-MS sample preparation. As shown in Figure XVII.1.106 and Table XVII.1.3; the vials of

LiOH, Li<sub>2</sub>CO<sub>3</sub>, Li<sub>2</sub>SO<sub>4</sub>, and Li<sub>2</sub>O show sedimented SEI species, whereas the vials of Li<sub>2</sub>S, and LiF show suspended particles. However, the solution appears transparent once the solution is filtered using a 0.22  $\mu$ m filter as shown in Figure XVII.1.106. The verification of the solubility of SEI species, both unfiltered and filtered, is performed using ICP-MS. The solubility of SEI components is less than 0.25 mM. All SEI species show lower or negligible solubility in BP/THF solution. This indicates that the methodology can be applied in Lithium-sulfur batteries for inactive Li<sup>0</sup> and active Li<sup>0</sup> quantification.

**Table XVII.1.3 The Highest Occupied Molecular Orbital (HOMO) and the Lowest Unoccupied Molecular Orbital (LUMO) Energy for the Diluents.**

SEI Components	Mass of the salt (g)	Dissolved in BP/THF solution (ml)	No filter		With a 0.22 $\mu$ m filter	
			Detected amount by ICP-MS (ppb)	Solubility (mM)	Detected amount by ICP-MS (ppb)	Solubility (mM)
LiOH	0.507	6	0.542	1.41	N/A	N/A
Li <sub>2</sub> CO <sub>3</sub>	0.5019	6	0.0065	0.005	N/A	N/A
LiF	0.5018	6	38.07	91.72	0.007	0.0168
Li <sub>2</sub> S	0.5008	6	10.495	14.27	N/A	N/A
Li <sub>2</sub> SO <sub>4</sub>	0.5009	6	2.445	1.51	0.0335	0.232
Li <sub>2</sub> O	0.5063	6	88.835	5.57	0.0145	0.03



Figure XVII.1.106 Potential Li-S Batteries' SEI components (a) LiOH (b)  $\text{Li}_2\text{CO}_3$  (c) LiF (d)  $\text{Li}_2\text{S}$  (e)  $\text{Li}_2\text{SO}_4$  (f)  $\text{Li}_2\text{O}$ . before filtering (left) and after filtering (right)

### Conclusions

This project was successfully completed in FY2023. All milestones have been completed. The publication records are very good: 1 US patent applications were filed by the Battery500 team member institutions. 50 peer reviewed papers were published, and more than 71 invited presentations were delivered in FY2023. Extensive collaboration within the consortium, between the consortiums and seedling teams, as well as with other national Labs and US universities has been well established and achieved very fruitful results.

### Key Publications

#### Patents

Patent Title: Dendrite-free anodes and current collectors for Li metal batteries and Li-ion batteries.  
 Inventors: Prashant N. Kumta, Mayur Gaikwad, Ramalinga Kuruba, and Oleg I Velikokhatnyi,  
 University of Pittsburg  
 Filed date: August 22, 2023

#### Publications

1. X. Zhang†, P. Gao†, Z. Wu, M.H. Engelhard, X. Cao, H. Jia, Y. Xu, H. Liu, C. Wang, J. Liu, J.-G. Zhang, P. Liu\*, W. Xu\*, "Pinned Electrode/Electrolyte Interphase and Its Formation Origin for Sulfurized Polyacrylonitrile Cathode in Stable Lithium Batteries", *ACS Applied Materials & Interfaces*, 2022, 14(46), 52046-52057. DOI:10.1021/acsmami.2c16890. Publication date (web): November 15, 2022.
2. Boyle, D. T.; Kim, S. C.; Oyakhire, S. T.; Vilá, R. A.; Huang, Z.; Sayavong, P.; Qin, J.; Bao, Z.; Cui, Y. "Correlating Kinetics to Cyclability Reveals Thermodynamic Origin of Lithium Anode Morphology in Liquid Electrolytes". *J. Am. Chem. Soc.* <https://doi.org/10.1021/jacs.2c08182>. Publication date (web): November 1, 2022.
3. Gong, H.; Chen, Y.; Chen, S.; Xu, C.; Yang, Y.; Ye, Y.; Huang, Z.; Ning, R.; Cui, Y.; Bao, Z. "Fast-Charging of Hybrid Lithium-Ion/Lithium-Metal Anodes by Nanostructured Hard Carbon Host". *ACS Energy Lett.*, 4417–4426. <https://doi.org/10.1021/acsenrgylett.2c02130>. Publication date (web): November 14, 2022.



4. Zhuojun Huang, Jian-Cheng Lai, Xian Kong, Ivan Rajkovic, Xin Xiao, Hasan Celik, Hongping Yan, Huaxin Gong, Paul E. Rudnicki, Yangju Lin, Yusheng Ye, Yanbin Li, Yuelang Chen, Xin Gao, Yuanwen Jiang, Snehashis Choudhury, Jian Qin, Jeffrey B.-H. Tok, Yi Cui, Zhenan Bao, “A Solvent-Anchored Non-Flammable Electrolyte”. *Matter.*, 1–15. <https://doi.org/10.1016/j.matt.2022.11.003>. Publication date (web): November 30, 2022.
5. David T. Boyle, Yuzhang Li, Allen Pei, Rafael A. Vilá, Zewen Zhang, Philaphon Sayavong, Mun Sek Kim, William Huang, Hongxia Wang, Yunzhi Liu, Rong Xu, Robert Sinclair, Jian Qin, Zhenan Bao, and Yi Cui, “Resolving Current-Dependent Regimes of Electroplating Mechanisms for Fast Charging Lithium Metal Anodes”. *Nano Lett.*, 22 (20), 8224–8232. <https://doi.org/10.1021/acs.nanolett.2c02792>. Publication date (web): October 10, 2022.
6. Yuxun Ren, Arumugam Manthiram, “A Dual - Phase Electrolyte for High - Energy Lithium-Sulfur Batteries,” *Advanced Energy Materials* 2022. DOI: <https://doi.org/10.1002/aenm.202202566>. Publication date (web): October 7, 2022.
7. Laisuo Su, Shwetha S. Kumar, Arumugam Manthiram, B. Reeja-Jayan, “A Review on Application of Poly(3,4-Ethylenedioxythiophene) (PEDOT) in Rechargeable Batteries,” *Organic Materials* 2022. DOI: <https://doi.org/10.1055/a-1990-3149>. Publication date (web): November 30, 2022.
8. Ruijun Pan, Eunmi Jo, Zehao Cui, Arumugam Manthiram, “Degradation Pathways of Cobalt - Free LiNiO<sub>2</sub> Cathode in Lithium Batteries,” *Advanced Functional Materials* 2022. DOI: <https://doi.org/10.1002/adfm.202211461>. Publication date (web): December 21, 2022.
9. Stefany Angarita-Gomez and Perla B. Balbuena, “Lithium-ion Transport through Complex Interphases in Lithium Metal Batteries,” *ACS Appl. Mater. & Interfaces.*, 14, 56758-56766, (2022) <https://doi.org/10.1021/acsami.2c16598>. Publication date: December 15, 2022.
10. Saul Perez Beltran and Perla B. Balbuena, “SEI Formation Mechanisms and Li<sup>+</sup> Dissolution in Lithium Metal Anodes: Impact of the Electrolyte Composition and the Electrolyte-to-Anode Ratio,” *J. Power Sources*, 551, 232203 (2022) <https://doi.org/10.1016/j.jpowsour.2022.232203>. Publication date: October 8, 2022.
11. Bingyu Lu, Weikang Li, Diyi Cheng, Miguel Ceja, Wurigumula Bao, Chengcheng Fang, Ying Shirley Meng, “Suppressing Chemical Corrosions of Lithium Metal Anodes”, *Adv. Energy Mater.* 2022, 2202012. Publication date (web): October 28, 2022
12. B. Liaw, G. Pawar, Y. S. Meng, C. Fang, B. Lu, “Perspective—Lithium metal nucleation and growth on conductive substrates: A multi-scale understanding from atomistic, nano-, meso-, to micro-scales.” In Special Issue on Nucleation and Growth: Measurements, Processes, and Materials, *J. Electrochem. Soc.* 169 (2022) 112505. <https://doi.org/10.1149/1945-7111/ac9a08>. Publication date (web): November 7, 2022.
13. Sha Tan, Ju-Myung Kim, Adam Corrao, Sanjit Ghose, Hui Zhong, Ning Rui, Xuelong Wang, Sanjaya Senanayake, Bryant J. Polzin, Peter Khalifah, Jie Xiao, Jun Liu, Kang Xu, Xiao-Qing Yang, Xia Cao\* & Enyuan Hu\*, “Unravelling the convoluted and dynamic interphasial mechanisms on Li metal anodes”, *Nature Nanotechnology*, DOI:10.1038/s41565-022-01273-3. Publication date (web): December 05, 2022
14. Mun Sek Kim, Zewen Zhang, Jingyang Wang, Solomon T. Oyakhire, Sang Cheol Kim, Zhiao Yu, Yuelang Chen, David T. Boyle, Yusheng Ye, Zhuojun Huang, Wenbo Zhang, Rong Xu, Philaphon Sayavong, Stacey F. Bent, Jian Qin, Zhenan Bao, and Yi Cui\*, “Revealing the Multifunctions of Li<sub>3</sub>N in the Suspension Electrolyte for Lithium Metal Batteries”. *ACS Nano* 2023, 17 (3), 3168–3180. DOI: 10.1021/acs.nano.2c12470. Publication date (Web): January 26, 2023.
15. Sang Cheol Kim, Solomon T. Oyakhire, Constantine Athanitis, Jingyang Wang, Zewen Zhang, Wenbo Zhang, David T. Boyle, Mun Sek Kim, Zhiao Yu, Xin Gao, Tomi Sogade, Esther Wu, Jian Qin, Zhenan Bao, Stacey F. Bent, and Yi Cui\*, “Data-Driven Electrolyte Design for Lithium Metal Anodes”. *Proceedings of the National Academy of Sciences* 2023, 120 (10), e2214357120. DOI: 10.1073/pnas.2214357120. Publication date (Web): February 27, 2023.
16. Isik Su Buyuker, Ben Pei, Hui Zhou, Xia Cao, Zhiao Yu, Sufu Liu, Weiran Zhang, Wu Xu, Ji-Guang Zhang, Zhenan Bao, Yi Cui, Chunsheng Wang, and M. Stanley Whittingham, “Voltage and

- Temperature Limits of Advanced Electrolytes for Lithium-Metal Batteries”, *ACS Energy Letters*, 2023, 8: 1735–1743. DOI: 10.1021/acscenergylett.3c00235. Publication date: March 7, 2023.
17. Jun Liu, Jie Xiao, Jihui Yang, Wei Wang, Yuyan Shao, Ping Liu, and M. Stanley Whittingham, “The TWh challenge: Next generation batteries for energy storage and electric vehicles”, *Next Energy*, 2023, on-line. DOI: 10.1016/j.nxener.2023.100015. Publication date: March 6, 2023.
  18. Jijian Xu, Travis P. Pollard, Chongyin Yang, Naveen K. Dandu, Sha Tan, Jigang Zhou, Jian Wang, Xinzi He, Xiyue Zhang, Ai-Min Li, Enyuan Hu, Xiao-Qing Yang, Anh Ngo, Oleg Borodin, Chunsheng Wang\*, “Lithium halide cathodes for Li metal batteries”, *Joule*, Volume 7, Issue 1, Pages 13-14. DOI: 10.1016/j.joule.2022.11.002 Publication date: January 18, 2023,
  19. Laisuo Su, Karalee Jarvis, Harry Charalambous, Andrei Dolocan, Arumugam Manthiram, “Stabilizing High-Nickel Cathodes with High-Voltage Electrolytes,” *Advanced Functional Materials* 2023. DOI: <https://doi.org/10.1002/adfm.202213675>. Publication date (web): January 15, 2023.
  20. Zehao Cui, Zezhou Guo, Arumugam Manthiram, “Assessing the Intrinsic Roles of Key Dopant Elements in High-Nickel Layered Oxide Cathodes in Lithium-Based Batteries,” *Advanced Energy Materials* 2023. DOI: <https://doi.org/10.1002/aenm.202203853>. Publication date (web): February 13, 2023.
  21. Richard Sim, Jayse Langdon, Arumugam Manthiram, “Design of an Online Electrochemical Mass Spectrometry System to Study Gas Evolution from Cells with Lean and Volatile Electrolytes,” *Small Method* 2023. DOI: <https://doi.org/10.1002/smt.202201438>. Publication date (web): March 12, 2023.
  22. J. Brandon Adamo, Laisuo Su, Arumugam Manthiram, “Operation of Layered LiCoO<sub>2</sub> to Higher Voltages with a Localized Saturated Electrolyte,” *ACS Applied Materials & Interfaces* 2023. DOI: <https://doi.org/10.1021/acscami.2c22786>. Publication date (web): March 15, 2023.
  23. Amruth Bhargav and Arumugam Manthiram, “Li-S batteries, What's Next?” *Next Energy*, 2023. DOI: <https://doi.org/10.1016/j.nxener.2023.100012>. Publication date: March 8, 2023.
  24. Zhaohui Wu, Chunyang Wang, Zeyu Hui, Haodong Liu, Shen Wang, Sicen Yu, Xing Xing, John Holoubek, Qiushi Miao, Huolin L. Xin\*, and Ping Liu\*, “Growing single-crystalline seeds on lithiophobic substrates to enable fast-charging lithium-metal batteries”, *Nature Energy*, DOI: [doi.org/10.1038/s41560-023-01202-1](https://doi.org/10.1038/s41560-023-01202-1), Publication date: February 09, 2023.
  25. Xia Cao, Yaobin Xu, Lianfeng Zou, Jie Bao, Yunxiang Chen, Bethany E. Matthews, Jiangtao Hu, Xinzi He, Mark H. Engelhard, Chaojiang Niu, Bruce W. Arey, Chunsheng Wang, Jie Xiao, Jun Liu, Chongmin Wang, Wu Xu, and Ji-Guang Zhang, “Stability of solid electrolyte interphases and calendar life of lithium metal batteries”, *Energy Environ Sci*, DOI: 10.1039/D2EE03557J, Publication date: February 24, 2023.
  26. Fengxia Xin, Anshika Goel, Hui Zhou, and M. Stanley Whittingham. “Enabling Long Cycling with Excellent Structure Stability for High-Nickel Layered Cathodes in Lithium Metal Batteries”, *ACS Materials Letters*, 2023, 5: 1969–1973. DOI:10.1021/acsmaterialslett.3c00301 Publication date: June 15, 2023.
  27. Amruth Bhargav, Hooman Yaghoobnejad Asl, and Arumugam Manthiram, “Mechanistic Understanding of Lithium-anode Protection by Organosulfide-based Solid-electrolyte Interphases and its Implications,” *Journal of Materials Chemistry A*, 2023. DOI: <https://doi.org/10.1039/D3TA00417A>. Publication date: April 20, 2023.
  28. Richard Sim, Laisuo Su, and Arumugam Manthiram, “A High Energy - Density, Cobalt - Free, Low - Nickel LiNi<sub>0.7</sub>Mn<sub>0.25</sub>Al<sub>0.05</sub>O<sub>2</sub> Cathode with a High - Voltage Electrolyte for Lithium - Metal Batteries,” *Advanced Energy Materials*, 2023. DOI: <https://doi.org/10.1002/aenm.202300096>. Publication date (web): April 24, 2023.
  29. Dongsoo Lee and Arumugam Manthiram, “Stable Cycling with Intimate Contacts Enabled by Crystallinity-Controlled PTFE-Based Solvent-Free Cathodes in All-Solid-State Batteries” *Small Methods*, 2023. DOI: <https://doi.org/10.1002/smt.202201680>. Publication date: April 25, 2023.
  30. Michael Yi, Laisuo Su, and Arumugam Manthiram, “Tuning and Understanding the Solvent Ratios of Localized Saturated Electrolytes for Lithium-metal Batteries,” *Journal of Materials Chemistry A*, 2023. DOI: <https://doi.org/10.1039/D3TA01061A>. Publication date: May 10, 2023.
-

31. Zehao Cui and Arumugam Manthiram, “Thermal Stability and Outgassing Behaviors of High - nickel Cathodes in Lithium - ion Batteries” *Angewandte Chemie International Edition*, 2023. DOI: <https://doi.org/10.1002/anie.202307243>. Publication date: June 9, 2023.
32. Zhuojun Huang, Jian-Cheng Lai, Sheng-Lun Liao, Zhiao Yu, Yuelang Chen, Weilai Yu, Huaxin Gong, Xin Gao, Yufei Yang, Jian Qin, Yi Cui, Zhenan Bao, A salt-philic, solvent-phobic interfacial coating design for lithium metal electrodes, *Nature Energy* 2023, 8, 577-585. DOI: 10.1038/s41560-023-01252-5. Publication date: April 24, 2023
33. Chibueze V Amanchukwu, Anna B Gunnarsdóttir, Snehashis Choudhury, Tamsin L Newlove, Pieter CMM Magusin, Zhenan Bao, Clare P Grey, Understanding Lithium-ion Dynamics in Single-ion and Salt-in-polymer Perfluoropolyethers and Polyethyleneglycol Electrolytes using Solid-state NMR, *Macromolecules* 2023, 56, 10, 3650–3659. DOI: 10.1021/acs.macromol.2c02160. Publication Date: April 28, 2023.
34. Philaphon Sayavong, Wenbo Zhang, Solomon T Oyakhire, David T Boyle, Yuelang Chen, Sang Cheol Kim, Rafael A Vilá, Sarah E Holmes, Mun Sek Kim, Stacey F Bent, Zhenan Bao, Yi Cui, Dissolution of the Solid Electrolyte Interphase and Its Effects on Lithium Metal Anode Cyclability, *Journal of the American Chemical Society*, 145, 22, 12342–12350 (2023). DOI: 10.1021/jacs.3c03195. Publication Date: May 23, 2023
35. Sha Tan, Muhammad Mominur Rahman, Zhaohui Wu, Haodong Liu, Shen Wang, Sanjit Ghose, Hui Zhong, Iradwikanari Waluyo, Adrian Hunt, Ping Liu, Xiao-Qing Yang, and Enyuan Hu\*, “Structural and Interphasial Stabilities of Sulfurized Polyacrylonitrile (SPAN) Cathode”, *ACS Energy Letters*, DOI: 10.1021/acsenerylett.3c00281, Publication date: May 08, 2023.
36. Bingyu Lu, Diyi Cheng, Bhagath Sreenarayanan, Weikang Li, Bhargav Bhamwala, Wurigumula Bao\*, and Ying Shirley Meng\*. "Key Parameters in Determining the Reactivity of Lithium Metal Battery." *ACS Energy Letters*, 2023, 8, 7, 3230–3238, DOI: 10.1021/acsenerylett.3c01001. Publication Date: July 5, 2023.
37. Isiksu Buyuker, “An Assay on Next Generation of Battery Materials – High Energy Cathodes, Beyond-Li-Ion Anodes and Safety of Advanced Electrolytes”, PhD thesis, Binghamton University, July 7th, 2023.
38. Ben Pei, “Improving The Stability of Lithium Metal Batteries at Multiple Levels”, PhD thesis, Binghamton University, August 7th 2023.
39. L. Su, S. Zhang, A. J. H. McGaughey, B. Reeja-Jayan, and A. Manthiram, “Battery Charge Curve Prediction via Feature Extraction and Supervised Machine Learning,” *Advanced Science*, 2023. DOI: <http://doi.org/10.1002/advs.202301737>. Publication date (web): July 02, 2023.
40. R. Torres, A. Bhargav, and A. Manthiram, “Poly(vinylferrocene) as an Ionomer and Sulfur-confining Additive for Lithium-sulfur Batteries,” *ACS Applied Materials & Interfaces*, 2023. DOI: <https://pubs.acs.org/doi/10.1021/acsemi.3c05567>. Publication date (web): August 10, 2023.
41. Z. Guo, Z. Cui, R. Sim, and A. Manthiram, “Localized high-concentration electrolytes with low-cost diluents compatible with both cobalt-free LiNiO<sub>2</sub> cathode and lithium-metal anode,” *Small*, 2023. DOI: <https://doi.org/10.1002/sml.202305055>. Publication date (web): August 11, 2023.
42. A. Mesnier and A. Manthiram, “Influence of Single-crystalline Morphology on the Electrochemical Behavior of High-nickel Layered Oxide Cathodes,” *Journal of the Electrochemical Society*, 2023. DOI: <https://iopscience.iop.org/article/10.1149/1945-7111/aceca6>. Publication date (web): August 11, 2023.
43. D. Lee, Z. Cui, J. B. Goodenough, and A. Manthiram, “Interphase Stabilization of LiNi<sub>0.5</sub>Mn<sub>1.5</sub>O<sub>4</sub> Cathode for 5 V–Class All-solid-state Batteries,” *Small*, 2023. DOI: <https://onlinelibrary.wiley.com/doi/full/10.1002/sml.202306053>. Publication date (web): September 1, 2023.
44. K. Liao, A. Bhargav, and A. Manthiram, “Scalable Metal Phosphides as a Dual-function Catalyst and Lithium-metal Stabilizer for Lithium-sulfur Batteries,” *ACS Applied Energy Materials*, 2023. DOI: <https://pubs.acs.org/doi/10.1021/acsaem.3c01606>. Publication date (web): September 11, 2023.

45. Xin Gao, Zhiao Yu, Jingyang Wang, Xueli Zheng, Yusheng Ye, Huaxin Gong, Xin Xiao, Yufei Yang, Yuelang Chen, Sharon E Bone, Louisa C Greenburg, Pu Zhang, Hance Su, Jordan Affeld, Zhenan Bao, Yi Cui, Electrolytes with moderate lithium polysulfide solubility for high-performance long-calendar-life lithium–sulfur batteries, *Proceedings of the National Academy of Sciences* 2023, 120, 31, e2301260120. DOI: 10.1073/pnas.2301260120. Publication date (web): July 24, 2023
46. Snehashis Choudhury, Zhuojun Huang, Chibueze V Amanchukwu, Paul E Rudnicki, Yuelang Chen, David Thomas Boyle, Jian Qin, Yi Cui, Zhenan Bao, Ion Conducting Polymer Interfaces for Lithium Metal Anodes: Impact on the Electrodeposition Kinetics, *Advanced Energy Materials* 2023, 13, 35, 2301899. DOI: 10.1002/aenm.202301899. Publication date (web): July 28, 2023
47. Yangju Lin, Zhiao Yu, Weilai Yu, Sheng-Lun Liao, Zhuojun Huang, Yuelang Chen, Elizabeth Zhang, Jian Qin, Yi Cui, Zhenan Bao, “Impact of Fluorination Degree of Ether-Based Electrolyte Solvent on Li-metal Battery Performance”, *ChemRxiv* (2023). DOI: 10.26434/chemrxiv-2023-ppgxx. Publication date (web): July 31, 2023.
48. Sicen Yu, Shen Wang, Qiushi Miao, Zeyu Hui, Gayea Hyun, John Holoubek, Xiaolu Yu, Junwei Gao, Ping Liu, “Composite Lithium Metal Structure to Mitigate Pulverization and Enable Long-Life Batteries”, *Advanced Energy Materials*, DOI:10.1002/aenm.202302400, Publication date (web): September 13, 2023.
49. Yaobin Xu, Hao Jia, Peiyuan Gao, Diego E. Galvez-Aranda, Saul Perez Beltran, Xia Cao, Phung M. L. Le, Jianfang Liu, Mark H Engelhard, Shuang Li, Gang Ren, Jorge M. Seminario, Perla B. Balbuena, Ji-Guang Zhang, Wu Xu, Chongmin Wang, “Direct in-situ measurement of electrical properties of solid electrolyte interphase on lithium metal anode,” *Nature Energy*, DOI: 10.1038/s41560-023-01361-1; Publication date (web): September 28, 2023.
50. Muhammad Mominur Rahman, Enyuan Hu, “Electron Delocalization Enables Sulfone-based Single-solvent Electrolyte for Lithium Metal Batteries”, *Angew. Chem. Int. Ed.* 2023, DOI: 10.1002/anie.202311051, Publication date: September 13, 2023.

#### *Presentations (Invited)*

1. X. Cao, W. Xu, J. Kim, and J.-G. Zhang. "Development of Li Metal Batteries with Improved Safety". Presented by X. Cao at 242nd ECS Meeting, Atlanta, Georgia, on 10/09/2022.
2. W. Xu, J.-G. Zhang, X. Cao, and X. Ren. "Enabling Lithium Metal Anode by Advancing Electrolytes and Lithium Protection". Presented by W. Xu at 2022 ACS Western Regional Meeting, Las Vegas, Nevada, on 10/20/2022.
3. A. Manthiram, “Pushing the Limits of Layered Oxide Cathodes,” 2022 International Battery Association Meeting (IBA22), Bled, Slovenia, October 2 – 7, 2022 (invited plenary talk).
4. A. Manthiram, “Sustainable Battery chemistries for a Cleaner Planet,” IEEE Electrical Energy Storage Applications and Technologies (EESAT) 2022, Austin, TX, November 7 – 9, 2022 (invited plenary talk).
5. A. Manthiram, “Sustainable Battery Technologies for a cleaner Environment,” 11th Sustainable Nanotechnology Organization Conference, Austin, TX, November 11 – 13, 2022 (invited plenary talk).
6. Ping Liu. “Pushing lithium-metal batteries to the limit: fast charging, low temperature, and safety”, The Electrochemical Society 2022 Fall Meeting, Atlanta, GA, October 2022.
7. Ping Liu. “Developing high performance and safe lithium batteries”, Korean Institute of Science and Technology, Seoul, Korea, December 2022.
8. Ping Liu, invited talk, “Approaches to long-life Li-S batteries”, Advanced Automotive Battery Association-13, Marakesh, Morocco, October 2022.
9. Ping Liu, invited talk, “Approaches to long-life Li-S batteries”, Korea Brainlink Conference, Incheon, Korea, November 2022.
10. Perla B. Balbuena, "Role of polymers at interfaces in advanced batteries," Seminar to Polymer Technology Center, Texas A&M University, October 7, 2022.

11. Perla B. Balbuena, "On the importance of assessing interfacial instabilities in materials design," Department of Chemical Engineering, Georgia Tech, November 9, 2022.
12. Perla B. Balbuena, "SEI Formation at the Li Metal/Electrolyte Interface: Structure, Morphology, Composition, and Properties," Department of Electrical Engineering, University of Houston, December 2, 2022.
13. Prashant N. Kumta, "From Lithiated Transition Metal Oxides to Silicon to Lithium-Sulfur: Evolution of Electrochemically Active Materials", paper presented in the Symposium entitled, "Research and Development of Primary and Secondary Batteries" at the 242nd Electrochemical Society Meeting held in Atlanta, October 9-13. (invited).
14. Y. Shirley Meng, invited talk, "The Key Challenges for Rechargeable Lithium Metal Batteries", 13th Advanced Lithium Batteries for Automobile Applications ABAA Meeting, Morocco, Oct. 19th, 2022
15. B. Li, invited talk, "Understanding and Improvement of High-Energy Density Li Metal Batteries", ACS WRM 2022, Las Vegas, Oct. 20, 2022.
16. B. Liaw and M. Li, "A new perspective on layered transition metal oxides as cathode active materials." The 242nd Electrochemical Society meeting, Atlanta, GA, October 9-13, 2022.
17. B. Liaw and M. Li, "A unified perspective and analytical approach of layered cathode active materials." International Battery Association 2022 meeting, Bled, Slovenia, October 2-7, 2022.
18. P. Khalifah, "Clockwork inside cathodes – unparalleled insights into defects and inhomogeneities", Muhlenberg College, Nov. 4, 2022
19. Weilai Yu, Yi Cui, and Zhenan Bao, "Understanding the Solid-Electrolyte Interphase (SEI) of Li-metal Anode by XPS", 2023 The Center for Advanced Materials Characterization in Oregon (CAMCOR) workshop on Advanced Battery Characterization, Eugene OR, March 8-9, 2023.
20. M. Stanley Whittingham, "Innovation, Manufacturing, Workforce Development: Why Batteries? Why New York? Why Now?", Sierra Club Susquehanna Section, January 17th, 2023.
21. M. Stanley Whittingham, "50 Years Old: What are the Ultimate Limits of Lithium Batteries and How do we get there", Arizona State University, Tempe AZ, February 20th, 2023.
22. M. Stanley Whittingham, "Opportunities and Challenges of Nanomaterials for Energy Storage", Gordon Research Conference, Ventura CA, February 26th, 2023.
23. M. Stanley Whittingham, "Pushing Lithium Batteries to their Limits, and What's Next ", IBA Conference, Austin TX, March 6th, 2023.
24. W. Xu, X. Zhang, and P. Gao. "Study on Sulfurized Polyacrylonitrile Cathode in Lithium Metal Batteries." Presented by W. Xu at ACS Spring 2023, on March 27, 2023, Indianapolis, Indiana.
25. W. Xu. "Electrolytes for Lithium Batteries." Presented at Virtual Seminar at Chemours, on February 01, 2023, Newark, Delaware.
26. Xia Cao, Yaobin Xu, Chongmin Wang, Wu Xu, and Ji-Guang Zhang\*, "Stability of Solid Electrolyte Interphase and Calendar Life of Li Metal Batteries." An invited talk presented by Ji-Guang Zhang in the International Battery Materials Association Meeting 2023 (IBA2023) held in Austin, Texas. USA, March 5-10, 2023.
27. Enyuan Hu, "Cathode-electrolyte-interphase, anode-electrolyte-interphase, and their interactions in lithium metal batteries" (Invited award presentation), International Battery Materials Association Meeting 2023 (IBA2023), Austin, Texas, USA, March 9th, 2023.
28. Perla B. Balbuena, "Interfacial Phenomena in Battery Materials: Insights from Theory and Computation," Invited Talk to the International Battery Materials Association Meeting (IBA2023), Austin, TX, March 8, 2023.
29. A. Manthiram, "Sustainable Next-generation Battery Chemistries," Conference on Advances in Renewable Energy (CARE 2023), Prayagraj, India, February 2 – 4, 2023 (invited plenary talk).
30. A. Manthiram, "Sustainable Battery Technologies for a cleaner Environment," International Conference on Consortium of Universal Research Erudition (iCURE), Madurai, India, February 3 – 6, 2023 (invited plenary talk).
31. A. Manthiram, "Lithium-metal Anode Stabilization with Advanced Electrolytes," International Battery Seminar, Orlando, FL, March 20 – 23, 2023 (invited featured talk).

32. Prashant N. Kumta, “Evolution of Electrochemically Active Materials for High-Energy Density Li-S Batteries”, Invited talk presented at the Division of Energy and Fuels: Next Generation Conversion/alloying Chemistries for High-Capacity Batteries Symposium for the American Chemical Society Meeting held in Indianapolis, Indiana, March 26-30, 2023.
33. Prashant N. Kumta, “Emergent Electrochemically Active Dendrite Free Materials for High-Energy Density Li-S Batteries”, Invited talk presented at the 47th International Conference & Exposition on Advanced Ceramics & Composites Symposium 6: Advanced Materials and Technologies for Rechargeable Energy Storage, January 22-27, 2023, Hilton Daytona Beach Resort and Ocean Center, Daytona Beach, Florida, USA.
34. Ying Shirley Meng, “Next-Generation Batteries – An Update on Li Metal Battery and All-Solid-State Battery,” 40th International Battery Seminar & Exhibition, Florida, USA; March 20 -23, 2023, invited plenary Talk.
35. M. Stanley Whittingham, “The Lithium Battery: From a Dream to Domination”, SLAC Energy Center Conference, Stanford, CA, April 12th, 2023.
36. M. Stanley Whittingham, John E. Dorn Lecture “The Lithium Ion Battery, from a Dream to Domination of Energy Storage – Future Materials Challenges”, Northwestern University, IL, May 2nd, 2023.
37. M. Stanley Whittingham, “The Lithium Ion Battery, from a Dream to Domination of Energy Storage”, New Jersey Institute of Technology, Newark, NJ, May 4th, 2023.
38. M. Stanley Whittingham, “50 Years Old: What are the Ultimate Limits of Lithium Batteries and How Do We Get There”, ICMAT Opening Lecture, Singapore, June 26th, 2023.
39. M. Stanley Whittingham, “Energy Storage will reduce Global Warming”, ICMAT, Singapore, June 30th, 2023.
40. A. Manthiram, “Oxide Revolution in Energy Storage,” 243rd Electrochemical Society Meeting, Boston, MA, May 28 – June 2, 2023 (John Goodenough Award Talk).
41. A. Manthiram, “Degradation Pathways of High-nickel Layered Oxide Cathodes in Lithium-based Batteries,” 11th International Conference on Materials for Advanced Technologies, Singapore, June 26 – 30, 2023 (invited talk).
42. Xia Cao, Yaobin Xu, Chongmin Wang Wu Xu and Ji-Guang Zhang. “Important Factors Affecting Calendar Life of Lithium Metal Batteries”, Presented by Xia Cao at 243rd ECS Meeting, Boston Massachusetts, May 31, 2023.
43. Perla B. Balbuena, “Interfacial Phenomena at Electrochemical Interfaces,” Exxon Mobil Lecture, Invited, University of Massachusetts, Amherst, MA, April 4, 2023.
44. Perla B. Balbuena, “Thermodynamics and Kinetics of Ion Solvation/Desolvation at Electrochemical Interfaces,” Invited Speaker, 16th International Conference on Properties and Phase Equilibria for Product and Process Design, Tarragona, Spain, May 23, 2023
45. Perla B. Balbuena, “Electrode/Electrolyte Interfacial Phenomena: Impact on Battery Performance,” Keynote Speaker, ECS Symposium F02 Multiscale Modeling, Simulation, and Design in Honor of Ralph White, May 30, 2023.
46. Perla B. Balbuena, “Understanding solid electrolyte interphase (SEI) reactions in Lithium metal and Lithium-Sulfur batteries,” BAT 553, poster presentation, 2023 DOE Vehicle Technologies Office Annual Merit Review, June 12-15, 2023.
47. Ying Shirley Meng, “Understanding the Interphasial Phenomena in All Solid State Batteries”, Invited Speaker, 243rd ECS Meeting, Boston, USA; May 28 – June 2, 2023 Ying Shirley Meng, “ From atom to system advanced characterization for lithium metal batteries”, Keynote Speaker, Kraftwerk Batterie – Advanced Battery Power, Aachen, Germany; April 27-28, 2023.
48. J. Xiao, “Accelerating Next-Generation Battery Technology Development and Manufacturing”, Seminar at Albemarle, Kings Mountain, NC, April 20th, 2023.
49. Prashant N. Kumta, “Evolution of Electrochemically Active Materials – Meeting the High-energy Density Challenge”, paper presented at the 4th International Conference on Materials Science &

- Engineering Meeting held at the Double Tree by Hilton, Houston Intercontinental Airport, Houston, Texas, April 24-26, 2023.
50. M. Stanley Whittingham, “Pushing the Limits of High Nickel NMC”, Nickel Institute Battery Day, July 2nd, 2023, on-line.
  51. M. Stanley Whittingham, “50 Years Old: Lithium Batteries now play Key Role in Renewable Energy and Climate Change”, Syngentia at Jealott’s Hill, England, July 24th, 2023.
  52. M. Stanley Whittingham, “Federal Initiatives and State Mandates accelerating use and domestic manufacturing of Lithium Batteries (Grid and EVs)”, UK BIC, Warwick, England, July 25th, 2023.
  53. M. Stanley Whittingham, “Lithium-Ion Batteries: From a Dream to Domination of Energy Storage - Future Opportunities and Challenges”, U. Warwick, England, July 27th, 2023.
  54. M. Stanley Whittingham, “50 Years Old: What are the Ultimate Limits of Lithium Batteries and How can they lead to a Cleaner Fossil-Fuel Free Society”, 23rd Putcha Venkateswarlu Memorial Lecture, Alabama A&M. September 15th, 2023.
  55. M. Stanley Whittingham, “50 Years Old: Now pushing Lithium Batteries to their Ultimate Limits leading to a Cleaner Fossil-Fuel Free Society”, Galvani Medal Award, Italian Chemical Society, Cefilu, Italy, September 20th, 2023.
  56. M. Stanley Whittingham, “50 Years Old: Pushing Lithium Batteries to their Ultimate Limits leading to a Cleaner Fossil-Fuel Free Society based on American Technology”, Clean Energy Forum, La Jolla, CA September 25th 2023.
  57. M. Stanley Whittingham, “50 Years Old: Pushing Lithium Batteries to their Ultimate Limits – Is Solid-State the Answer?”, NSF-IUCRC-CEPS, Syracuse University, September 28th, 2023.
  58. A. Manthiram, “Lithium-sulfur Batteries with Stabilized Electrodes and Interfaces,” 10th Workshop on Lithium-sulfur Batteries, Dresden, Germany, July 3 – 4, 2023 (invited plenary talk).
  59. A. Manthiram, “A Materials Perspective on the Safety of Lithium-ion Batteries,” Battery Safety Summit, Mexico City, Mexico, August 8 – 9, 2023 (invited keynote talk).
  60. A. Manthiram, “Sustainable Next-generation Battery Chemistries,” International Conference on Advances in Functional Materials, University of California Los Angeles, CA, August 10 – 12, 2023 (invited keynote talk).
  61. A. Manthiram, “Cobalt-free Oxide Cathodes for High Energy Density Lithium Batteries,” 24th Annual Conference on Materials Science – YUCOMAT 2023, Materials Research Society of Serbia, Herceg Novi, Montenegro, Serbia, September 4 – 8, 2023 (invited plenary talk).
  62. A. Manthiram, “Intricacies of High-energy Cathodes for Lithium-ion Batteries,” Electrochemical Society Webinar, Austin, TX, September 20, 2023 (invited talk).
  63. A. Manthiram, “Sustainable Next-generation Battery Technologies, University of North Texas, Denton, TX, September 29, 2023
  64. Wurigumula Bao, “Understanding Li Metal Anode in Liquid Electrolyte Metal Battery Systems” - UL Research Institutes 2023 Annual Research Symposium, Northwestern University; July 31-August 2, 2023
  65. Yuelang Chen, Yi Cui, Zhenan Bao, “Fast-charging limitations of advanced electrolytes for lithium metal batteries”, Stanford Energy Student Lectures, Stanford, CA, Aug 21, 2023
  66. Ping Liu, “Lithium metal anodes: stripping, nucleation, and growth”, Korean Research Institute of Chemical Technology, Dajeon, Korea, September 19, 2023
  67. Ping Liu, “Engineered lithium anodes: controlling nucleation and mitigating pitting”, Hanyang University, Seoul, Korea, September 20, 2023
  68. Ping Liu, “Development of Long-Life Li-S Batteries”, Korea-US Advanced Industry and Technology Cooperation Forum 2023, Seoul, Korea, September 21, 2023.
  69. Perla B. Balbuena, Invited lecture, “Ionic transport at interfaces from first principles atomistic simulations,” Karlsruhe Institute of Technology, August 4, 2023.
  70. Jorge M. Seminario, Invited Lecture, “Density Functional Theory—Ab Initio Molecular Dynamics (DFT-AIMD) Simulations of Lithium-Metal Rechargeable Batteries,” Karlsruhe Institute of Technology, August 4, 2023.

71. Jorge M. Seminario, "Electrification of vehicular transport: The transition from fossil fuels to rechargeable electric batteries", Keynote Lecture at the 8th World Forum of Energy Regulators (8th WFER), Lima, Peru, August 24, 2023



(This page intentionally left blank)

U.S. DEPARTMENT OF  
**ENERGY**

*Office of*  
**ENERGY EFFICIENCY &  
RENEWABLE ENERGY**

For more information, visit:  
[energy.gov/vehicles](https://energy.gov/vehicles)

DOE/EE-2876 • August 2024